

FORTY-SECOND ANNUAL REPORT
OF THE
NATIONAL ADVISORY COMMITTEE
FOR AERONAUTICS

1956

ADMINISTRATIVE REPORT
INCLUDING TECHNICAL REPORTS
NOS. 1254 to 1295



UNITED STATES
GOVERNMENT PRINTING OFFICE
WASHINGTON : 1957

CONTENTS

	Page
Letter of Transmittal	v
Letter of Submittal	vii
Forty-second Annual Report	ix
Part I. Technical Activities	1
The NACA—What It Is and How It Operates	1
Boundary-Layer Control	2
High-Speed Flight Research	5
Aerodynamics	10
Power Plants for Aircraft	38
Aircraft Construction	53
Operating Problems	62
Research Publications	69
Part II. Committee Organization and Membership	80
Part III. Financial Report	89
Technical Reports	91

TECHNICAL REPORTS

No.	Page
1254. Friction, Wear, and Surface Damage of Metals as Affected by Solid Surface Films. By Edmond E. Bisson, Robert L. Johnson, Max A. Swikert and Douglas Godfrey, NACA.....	91
1255. An Analysis of the Stability and Ultimate Compressive Strength of Short Sheet-Stringer Panels with Special Reference to the Influence of the Riveted Connection Between Sheet and Stringer. By Joseph W. Semonian and James P. Peterson, NACA.....	113
1256. Axially Symmetric Shapes with Minimum Wave Drag. By Max. A. Heaslet and Franklyn B. Fuller, NACA.....	131
1257. On the Kernel Function of the Integral Equation Relating Lift and Downwash Distributions of Oscillating Wings in Supersonic Flow. By Charles E. Watkins and Julian H. Berman, NACA.....	147
1258. A Wind-Tunnel Test Technique for Measuring the Dynamic Rotary Stability Derivatives at Subsonic and Supersonic Speeds. By Benjamin H. Beam, NACA.....	165
1259. Some Possibilities of Using Gas Mixtures Other Than Air in Aerodynamic Research. By Dean R. Chapman, NACA.....	179
1260. Studies of the Speed Stability of a Tandem Helicopter in Forward Flight. By Robert J. Tapscott and Kenneth B. Amer, NACA.....	201
1261. The Near Noise Field of Static Jets and Some Model Studies of Devices for Noise Reduction. By Leslie W. Lassiter and Harvey H. Hubbard, NACA.....	213
1262. Theoretical and Experimental Investigation of the Effect of Tunnel Walls on the Forces on an Oscillating Airfoil in Two-Dimensional Subsonic Compressible Flow. By Harry L. Runyan, Donald S. Woclston, and A. Gerald Rainey, NACA.....	225
1263. Investigation of the Aerodynamic Characteristics of a Model Wing-Propeller Combination and of the Wing and Propeller Separately at Angles of Attack up to 90°. By Richard E. Kuhn and John W. Draper, NACA.....	247
1264. A Thermal Equation for Flame Quenching. By A. E. Potter, Jr., and A. L. Berlad, NACA.....	287
1265. A Theory for Stability and Buzz Pulsation Amplitude in Ram Jets and an Experimental Investigation Including Scale Effects. By Robert L. Trimpi, NACA.....	295
1266. Charts for Estimating Performance of High-Performance Helicopters. By Alfred Gessow and Robert J. Tapscott, NACA.....	319
1267. Plastic Deformation of Aluminum Single Crystals at Elevated Temperatures. By R. D. Johnson, A. P. Young, and A. D. Schwope, Battelle Memorial Institute.....	353
1268. Theoretical Calculations of the Pressures, Forces, and Moments at Supersonic Speeds Due to Various Lateral Motions Acting on Thin Isolated Vertical Tails. By Kenneth Margolis and Percy J. Bobbitt, NACA.....	385

No.	Page
1269. Theoretical Span Load Distributions and Rolling Moments for Sideslipping Wings of Arbitrary Plan Form in Incompressible Flow. By M. J. Queijo, NACA.....	429
1270. Review of Experimental Investigations of Liquid-Metal Heat Transfer. By Bernard Lubarsky and Samuel J. Kaufman, NACA.....	445
1271. On Boattail Bodies of Revolution Having Minimum Wave Drag. By Keith C. Harder and Conrad Rennemann, Jr., NACA.....	479
1272. A Reevaluation of Data on Atmospheric Turbulence and Airplane Gust Loads for Application in Spectral Calculations. By Harry Press, May T. Meadows, and Ivan Hadlock, NACA.....	489
1273. A Study of the Zero-Lift Drag-Rise Characteristics of Wing-Body Combinations Near the Speed of Sound. By Richard T. Whitcomb, NACA.....	519
1274. Second-Order Subsonic Airfoil Theory Including Edge Effects. By Milton D. Van Dyke, NACA.....	541
1275. The Proper Combination of Lift Loadings for Least Drag on a Supersonic Wing. By Frederick C. Grant, NACA.....	565
1276. Wind-Tunnel and Flight Investigations of the Use of Leading-Edge Area Suction for the Purpose of Increasing the Maximum Lift Coefficient of a 35° Swept-Wing Airplane. By Curt A. Holzhauser and Richard S. Bray, NACA.....	575
1277. Interaction of a Free Flame Front With a Turbulence Field. By Maurice Tucker, NACA.....	599
1278. Effect of Interaction on Landing-Gear Behavior and Dynamic Loads in a Flexible Airplane Structure. By Francis E. Cook and Benjamin Milwitzky, NACA.....	619
1279. Theoretical Analysis of Incompressible Flow Through a Radial-Inlet Centrifugal Impeller at Various Weight Flows. By James J. Kramer, Vasily D. Prian, and Chung-Hua Wu, NACA.....	649
1280. Theoretical Investigation of Flutter of Two-Dimensional Flat Panels With One Surface Exposed to Supersonic Potential Flow. By Herbert C. Nelson and Herbert J. Cunningham, NACA.....	665
1281. Flight Determination of Drag of Normal-Shock Nose Inlets with Various Cowling Profiles at Mach Numbers from 0.9 to 1.5. By R. I. Sears, C. F. Merlet, and L. W. Putland, NACA.....	689
1282. A Special Method for Finding Body Distortions that Reduce the Wave Drag of Wing and Body Combinations at Supersonic Speeds. By Harvard Lomax and Max. A. Heaslet, NACA.....	709
1283. Extrapolation Techniques Applied to Matrix Methods in Neutron Diffusion Problems. By Robert R. McCreedy, NACA.....	747
1284. Theory of Wing-Body Drag at Supersonic Speeds. By Robert T. Jones, NACA.....	757
1285. Summary of Derived Gust Velocities Obtained from Measurements Within Thunderstorms. By H. B. Tolefson, NACA.....	765
1286. Propagation of a Free Flame in a Turbulent Gas Stream. By William R. Mickelsen and Norman E. Ernstein, NACA.....	773

III

Preceding Page Blank

IV

TECHNICAL REPORTS

No.	Page	No.	Page
1287. Spark Ignition of Flowing Gases. By Clyde C. Swett, Jr., NACA.....	799	1292. Intensity, Scale, and Spectra of Turbulence in Mixing Region of Free Subsonic Jet. By James C. Laurence, NACA.....	891
1288. Cooperative Investigation of Relationship Between Static and Fatigue Properties of Wrought N-155 Alloy at Elevated Temperatures. By NACA Subcommittee on Power-Plant Materials.....	817	1293. Similar Solutions for the Compressible Laminar Boundary Layer with Heat Transfer and Pressure Gradient. By Clarence B. Cohen and Eli Reshotko, NACA.....	919
1289. Contributions on the Mechanics of Boundary-Layer Transition. By G. B. Schubauer and P. S. Klebanoff, National Bureau of Standards.....	853	1294. The Compressible Laminar Boundary Layer with Heat Transfer and Arbitrary Pressure Gradient. By Clarence B. Cohen and Eli Reshotko, NACA.....	957
1290. Development of Craze and Impact Resistance in Glazing Plastics by Multiaxial Stretching. By G. M. Kline, I. Wolock, B. M. Axilrod, M. A. Sherman, D. A. George, and V. Cohen, National Bureau of Standards.....	865	1295. An Analysis of Once-Per-Revolution Oscillating Aerodynamic Thrust Loads on Single-Rotation Propellers on Tractor Airplanes at Zero Yaw. By Vernon L. Rogallo, Paul F. Yaggy, and John L. McCloud III, NACA.....	973
1291. Lift Hysteresis at Stall as an Unsteady Boundary-Layer Phenomenon. By Franklin K. Moore, NACA.....	881		

Letter of Transmittal

To the Congress of the United States:

In compliance with the provisions of the act of March 3, 1915, as amended, establishing the National Advisory Committee for Aeronautics, I transmit herewith the Forty-second Annual Report of the Committee covering the fiscal year 1956.

DWIGHT D. EISENHOWER.

THE WHITE HOUSE,
JANUARY 28, 1957.

v

Preceding Page Blank

Letter of Submittal

NATIONAL ADVISORY COMMITTEE FOR AERONAUTICS

WASHINGTON, D. C., *October 17, 1956.*

DEAR MR. PRESIDENT:

In compliance with the act of Congress approved March 3, 1915, as amended (U. S. C. title 50, sec. 151), I submit herewith the Forty-second Annual Report of the National Advisory Committee for Aeronautics for 1956.

Aeronautics is progressing at a remarkable rate. Scientific problems are multiplying in number, difficulty, and cost. Under military stimulation, development efforts are extending beyond our basic knowledge. Real progress can be accelerated, and on a more economical basis were scientific research accorded priority and conducted on an adequate basis in advance of development.

There is a growing demand for more scientists and engineers. Long range measures are being taken to stimulate the education of larger numbers. In the meantime, the law of supply and demand is forcing salaries up. Government research organizations, operating under rates of compensation fixed by law, cannot recruit or retain adequate numbers of scientists and engineers. NACA is losing outstanding and irreplaceable leaders in aeronautical science. This weakening trend must be reversed. The simplest and the best remedy is the enactment of legislation authorizing the Government to pay the going rates for scientists and engineers. Leadership in aeronautical science and American supremacy in the air are at stake. The necessary legislation is strongly recommended.

Respectfully submitted.

JEROME C. HUNSAKER,
Chairman.

THE PRESIDENT,
The White House, Washington, D. C.

VII

Preceding Page Blank

National Advisory Committee for Aeronautics

Headquarters, 1512 H Street NW., Washington 25, D. C.

Created by Act of Congress approved March 3, 1915, for the supervision and direction of the scientific study of the problems of flight (U. S. Code, title 50, sec. 151). Its membership was increased from 12 to 15 by act approved March 2, 1929, and to 17 by act approved May 25, 1948. The members are appointed by the President and serve as such without compensation.

JAMES H. DOOLITTLE, Sc. D., Shell Oil Company, *Chairman*

LEONARD CARMICHAEL, Ph. D., Secretary, Smithsonian Institution, *Vice Chairman*

JOSEPH P. ADAMS, LL. B., Vice Chairman, Civil Aeronautics Board.

ALLEN V. ASTIN, Ph. D., Director National Bureau of Standards.

PRESTON R. BASSETT, M. A., Vice President, Sperry Rand Corp.

DETLEV W. BRONK, Ph. D., President, Rockefeller Institute for Medical Research.

FREDERICK C. CRAWFORD, Sc. D., Chairman of the Board, Thompson Products, Inc.

WILLIAM V. DAVIS, JR., Vice Admiral, United States Navy, Deputy Chief of Naval Operations (Air).

CLIFFORD C. FURNAS, Ph. D., Assistant Secretary of Defense (Research and Development).

JEROME C. HUNSAKER, Sc. D., Massachusetts Institute of Technology.

CARL J. PFINGSTAG, Rear Admiral, United States Navy Assistant Chief for Field Activities, Bureau of Aeronautics.

DONALD L. PUTT, Lieutenant General, United States Air Force, Deputy Chief of Staff, Development.

ARTHUR E. RAYMOND, Sc. D., Vice President—Engineering, Douglas Aircraft Co., Inc.

FRANCIS W. REICHELDERFER, Sc. D., Chief, United States Weather Bureau.

EDWARD V. RICKENBACKER, Sc. D., Chairman of the Board, Eastern Air Lines, Inc.

LOUIS S. ROTHSCHILD, Ph. B., Under Secretary of Commerce for Transportation.

NATHAN F. TWINING, General, United States Air Force, Chief of Staff.

HUGH L. DRYDEN, Ph. D., *Director*

JOHN F. VICTORY, LL. D., *Executive Secretary*

JOHN W. CROWLEY, JR., B. S., *Associate Director for Research*

EDWARD H. CHAMBERLIN, *Executive Officer*

HENRY J. E. REID, D. Eng., Director, Langley Aeronautical Laboratory, Langley Field, Va.

SMITH J. DeFRANCE, D. Eng., Director, Ames Aeronautical Laboratory, Moffett Field, Calif.

EDWARD R. SHARP, Sc. D., Director, Lewis Flight Propulsion Laboratory, Cleveland, Ohio

WALTER C. WILLIAMS, B. S., Chief, High-Speed Flight Station, Edwards, Calif.

FORTY-SECOND ANNUAL REPORT

OF THE

NATIONAL ADVISORY COMMITTEE FOR AERONAUTICS

WASHINGTON, D. C., *October 17, 1956.*

To the Congress of the United States:

In accordance with Act of Congress, approved March 3, 1915, as amended (U. S. C. title 50, sec. 151), which established the National Advisory Committee for Aeronautics, the Committee submits its Forty-second Annual Report for the fiscal year 1956.

The airplane looms as the instrumentality that has changed previous concepts of military power and the course of history. In addition to the airplane, the missile has become a major factor in warfare. In the emergency created by the present international situation, the United States is expending unprecedented sums for the production of aircraft and missiles, on the effectiveness of which the security of the Nation may largely depend.

Numbers of aircraft and missiles alone are insufficient unless their performance is at least equal to those they may be called upon to oppose. This makes it essential to choose the most advanced designs for production, but allows little time to prove the new features incorporated. It falls to the aeronautical laboratories not only to provide the new ideas necessary to insure superior performance, but at the same time to prove in advance the soundness of the design as a whole. The Committee's work, therefore, falls into two principal categories; namely, research to furnish new ideas; and the application of those ideas to current military designs in cooperation with industry. The present emergency has naturally revised the priorities in connection with the long-range research program, to the end that those things which give most immediate promise are emphasized.

Only continued scientific research, on a scale adequate to meet growing needs, can give the Nation assurance that its aircraft and missiles will be kept at least the equal of those of any other nation. In order to develop them to their full potentialities, both in peace and in war, scientific research must be prosecuted with vigor and imagination.

In the last fifteen years, the speed of tactical aircraft has been increased from less than 400 to more than 1,000 mph. Through the use of special research airplanes, we have been able to penetrate the so-called sound barrier to the point where our research airplanes are flying faster than $2\frac{1}{2}$ times the velocity of sound. We see the day, not too distant, when man can fly to any point on the globe in but a few hours.

To satisfy military requirements we must learn how to project missiles at thousands of miles per hour, along ballistic trajectories to targets far across the seas. At the same time, we are striving for the knowledge that will make possible satellites probing into regions beyond the earth's atmosphere and obtaining valuable information.

For the ballistic missile, a temperature of many thousands of degrees—higher than that on the surface of the sun—will be generated in the air near the surface of the missile. Under such conditions, the air molecules dissociate or split apart into their constituent atoms, and electrons are knocked out of atoms to make the air ionized and electrically conducting.

We need to duplicate in the laboratory the strange and difficult conditions of future flight, so that practical solutions of these problems can be found. Recently it has become possible to make small, pilot models with which to prove the practicability of constructing the expensive new tools of research necessary for the extension of the present limits of our knowledge.

But laboratory equipment for the experimental study of aerodynamic heating and other complex flight problems is only one requirement. More teams of talented young men competent to work in the new scientific fields are urgently needed. This requires a realistic approach to the pay problem. The attractiveness of public service has been critically depreciated by private industry offering salaries and "fringe benefits" far greater than the NACA is allowed by law to pay. We do not quarrel with the salaries paid by industry. We must, however, not only provide additional fringe benefits, but also offer rates of compensation sufficient to recruit, and to hold, the scientists and engineers necessary to perform the fundamental research that governs progress.

Over the years the career scientists of the NACA have made large contributions to the advancement of aeronautics, yet the cost has been very small when compared with the value of the results. Costs are increasing. Further advances in the art and science at a greatly accelerated rate are essential to our national security. We are confident that the National Advisory Committee for Aeronautics can continue to show the way to important advances in aeronautics if the Congress will provide the required support.

Respectfully submitted.

JEROME C. HUNSAKER,
Chairman.

Part I—TECHNICAL ACTIVITIES

THE NACA—WHAT IT IS AND HOW IT OPERATES

During the 41 years since the Congress founded it as an independent Federal agency, the National Advisory Committee for Aeronautics has sought to assess the current stage of development of aircraft, both civil and military; to anticipate the research needs of aeronautics; to build the scientific staff and unique research facilities required for these research needs; and to acquire the needed new knowledge as rapidly as the national interest requires.

By discharging its primary responsibility—scientific laboratory research in aeronautics—the NACA serves the needs of all departments of the Government. The President appoints the 17 unpaid members of the Committee, who report directly to him. They establish policy and plan the research to be carried out by the 7,900 scientists, engineers, and other persons who make up the staff of the agency.

The NACA research programs have both the all-inclusive, long-range objective of acquiring new scientific knowledge essential to assure United States leadership in aeronautics and the immediate goal of solving, as quickly as possible, the most pressing problems. In this way, they effectively support the Nation's current aircraft and missile construction program.

Most of the problems to be studied are assigned to the NACA's research centers. The Langley Aeronautical Laboratory in Virginia works on structural, general aerodynamic, and hydrodynamic problems. The Ames Aeronautical Laboratory in California concentrates on high-speed aerodynamics. The Lewis Flight Propulsion Laboratory in Ohio is a center for power-plant studies. At the High-Speed Flight Station in California special fully instrumented research aircraft probe transonic and supersonic problems in flight. The Pilotless Aircraft Research Station at Wallops Island, Virginia, is a branch of the Langley Laboratory where rocket-powered free-flight models are used to attack aerodynamic problems in the transonic and supersonic speed ranges.

A major task of the NACA since its beginning in 1915 has been coordinating aeronautical research in the U. S. Through the members of the Committee and its 28 technical subcommittees, the NACA links the military and civil government agencies concerned with flight. The aviation industry, allied industries, and scientific institutions are also represented.

Assisting the Committee in determining and coordinating research programs are 4 major and 24 subordinate technical committees with a total membership

of nearly 500. Members are chosen because of technical ability, experience, and recognized leadership in a special field. They also serve without pay, in a personal and professional capacity. They furnish valuable assistance in considering problems related to their technological fields, review research in progress at NACA laboratories and in other establishments, recommend new research to be undertaken, and assist in coordinating research programs.

Members of the technical committees and subcommittees and of the Industry Consulting Committee are listed in Part II of this report, beginning on page 80.

Research coordination is also accomplished through frequent discussions by NACA scientists with the staffs of research organizations of the aircraft industry, educational and scientific institutions, and other aeronautical agencies. Through a west coast office the NACA maintains close liaison with aeronautical research and engineering staffs in that important aviation area.

The NACA sponsors and finances a coordinated research program at 33 nonprofit scientific and educational institutions, including the National Bureau of Standards. In this way scientists and engineers whose skills and talents might otherwise not be available contribute importantly to Federal aeronautical research.

During the fiscal year 1956, the following institutions participated in NACA contract research:

- National Bureau of Standards
- University of Alabama
- Battelle Memorial Institute
- Polytechnic Institute of Brooklyn
- Brown University
- California Institute of Technology
- University of California
- Carnegie Institute of Technology
- Case Institute of Technology
- University of Cincinnati
- Columbia University
- Cornell University
- Franklin Institute
- Forest Products Laboratory
- Georgia Institute of Technology
- Johns Hopkins University
- University of Kentucky
- Lightning & Transients Research Institute
- Massachusetts Institute of Technology
- University of Michigan

University of Minnesota
 New York University
 University of North Carolina
 University of Oklahoma
 Purdue University
 Syracuse University
 University of Washington
 University of Wisconsin
 Southwest Research Institute
 Stanford Research Institute
 Stanford University
 Stevens Institute of Technology
 Yale University

Proposals from such institutions are carefully weighed to assure best use of the limited funds available to the NACA for sponsoring research outside its own facilities. Published research reports of the useful results of this part of the NACA program are distributed as widely as other NACA publications.

During the fiscal year, most of the NACA technical subcommittees reviewed research proposals from outside organizations or gave attention to research reports

of completed contracts. There were 43 sponsored-research reports released during fiscal 1956.

Most of NACA's research information is distributed by means of its publications. Technical Notes and Reports are not classified for military security reasons and are available to the public in general. Translations of important foreign research reports appear as Technical Memorandums. The NACA also prepares research reports containing classified information. For reasons of national security, these receive carefully controlled circulation. When such information can be declassified, the research reports may be given wider distribution. Current NACA publications are announced in the NACA Research Abstracts.

Every year the NACA holds a number of technical conferences with representatives of the aviation industry, the universities, and the military services present. Attendance at these conferences is restricted because classified material is presented and the subject matter discussed at each conference is focused on a specific field of interest.

BOUNDARY-LAYER CONTROL

"It is established by reliable experiments that fluids like water and air never slide on the surface of the body; what happens is the final fluid layer immediately in contact with the body is attached to it (is at rest relative to it), and all the friction of fluids with solid bodies is therefore an internal friction of the fluid. Theory and experiment agree in indicating that the transition from the velocity of the body to that of the stream in such a case takes place in a thin layer of the fluid, which is so much the thinner, the less the viscosity. In this layer, which we call the boundary layer, the forces due to viscosity are of the same order of magnitude as the forces due to inertia. . . ."

Publication 35 years ago of the NACA document containing the above definition of the boundary layer (Report 116, "Applications of Modern Hydrodynamics to Aeronautics," by Ludwig Prandtl, 1921) together with issuance of Glauert's volume, "Aerofoil and Airscrew Theory," in 1926 has been credited by Sir William S. Farren with having "revolutionized our understanding and powers of analyzing the main phenomena which determine the lift and drag of aircraft, the thrust and torque of propellers, and the interference of wind tunnel constraints. It is hardly too much to say that a mass of indigestible 'facts' was rendered of historical interest by a few pages of inspired theoretical work." Even earlier (in 1904 in a paper read to the Third Congress of Mathematicians at Heidelberg) Prandtl had laid down the bases of the boundary-layer theory.

For more than a half century, then, the very complicated mechanics of the boundary layer have been studied. Especially at high lift, high pressure gradi-

ents exist on the upper surface of a wing, that is, regions where the upper surface pressures increase rapidly in a positive sense toward the wing trailing edge. Such a gradient will exist just aft of the wing leading edge and at the forward edge of a deflected flap.

As boundary-layer air traverses these pressure gradients, the pattern of velocity distribution within the boundary layer changes from one in which velocity increases rapidly from zero at the surface to a free-stream value just above the surface to a pattern in which for a short distance above the surface velocity is zero, and thence to a pattern in which flow reverses in a region just above the surface and goes toward the wing leading edge. This condition arises when the air next to the surface has not enough dynamic energy to move in the direction of the wing trailing edge against the increasing pressure of the stagnant layer.

With the occurrence of reverse flow, the whole flow mass breaks away, or separates, from the upper surface and lift is sharply reduced. The pressure gradient at the leading edge increases with increase in angle of attack; when the pressure gradient becomes so steep that the boundary layer separates from the airfoil surface, further increase in angle of attack produces no increase in lift, and frequently produces a significant loss.

Aerodynamicists recognized early that gains of increased lift and reduced drag could be made by preventing or delaying this separation of the air flowing, over the upper surface of the wing. Suggested ways to provide a measure of boundary-layer control included slots and flaps actuated by the pressure difference

between the upper and lower surface of the wing, served as "natural" pumps by providing a flow of air that delayed separation.

What is believed to have been the first use of such a device came soon after World War I. Gustav Lachmann in Germany and Sir Frederick Handley-Page in England, working independently at first and then together, developed leading edge slots. These opened when the wing was inclined to a high angle of attack, thus preventing flow separation near the leading edge. Another device, developed for delaying separation and installed on airplanes in later years, is the slotted flap near the trailing edge of the wing.

In the late thirties, the NACA developed airfoils which provided laminar (non separated) flow to a degree far greater than that previously obtainable.

This work of changing the shape of the airfoil, performed at the Langley Aeronautical Laboratory, made it possible to delay the transition from smooth, laminar flow to turbulent or eddying flow to such an extent that the skin friction, or basic air resistance, of a wing could be reduced by almost two-thirds. When first adapted for use, on the North American P-51 Mustang, the so-called laminar-wing principle enabled design of a high-speed fighter with superior long-range capabilities.

Another way of postponing the transition to turbulent air flow through boundary-layer control is that of using mechanical pumps to suck in air and thereby limit the growth of the boundary layer. By 1940, study of this aspect of the boundary-layer-control problem had begun at the Langley Laboratory, and by the early years of World War II the work had progressed to full-scale flight testing.

In 1927, to cite an example of early research on the use of mechanical methods to provide boundary-layer control for high lift, a Navy trainer, a Curtiss TS-1, was modified at the Langley Laboratory for flight study of the system of boundary-layer control by blowing which Richard Katzmayer of Vienna had suggested. Two spanwise slots were installed on the upper surface of the upper wing to blow away the boundary-layer air. Blowing air was supplied by a conventional supercharger.

In the following 20 years, wind-tunnel investigations repeatedly demonstrated that large aerodynamic gains could be obtained from use of boundary-layer control. NACA Report 385, published in 1931, presented results showing that the maximum lift coefficient could be increased as much as 96 percent. Although large aerodynamic benefits were thus demonstrated, there was little enthusiasm for adapting such boundary-layer control schemes to airplanes of those days. Not only was the weight of the required pumping equipment considered prohibitively high, but, for airplanes of low wing loading, the use of large span flaps usually provided lift coefficients sufficiently high to permit acceptably low landing speeds.

In the middle forties, the design changes required to enable airplanes to reach supersonic speeds (as well as very low flight speeds) made development of useful, mechanical boundary-layer-control systems which could produce high lift a matter of greatly increased interest. Too, the tremendous increase in power available in the newly developed turbojet engines offered attractive possibilities for the needed supplies of suction or blowing air.

Among factors limiting the high-lift capabilities of modern high-speed airplanes have been the following: (1) Reduced wing aspect ratio and increased wing sweep, which reduce wing lift at a given angle of attack and also reduce the lift increment produced by flap deflection; (2) wing-thickness reduction which lowers the stalling angle of attack, and thus limits maximum lift, and (3) reduction in wing stiffness, requiring that ailerons be moved inboard to avoid aileron reversal at high speeds, leaving little or no wing area to convert to flaps.

Boundary-layer control is applied to trailing-edge flaps to achieve all the lift that theory indicates is available. If the increase in lift with increasing flap deflection for any given wing with conventional flaps is compared with that under the ideal conditions of theory, it is found that even for flap deflections as low as 20° the lift increment falls short of the theoretical value. At flap deflections as high as 60° , the lift increment may be only half that suggested by theory. If the flaps could be made to act as theory predicts, a substantial increase in lift could be realized on any flapped wing, without changes in other design features.

Proper application of boundary-layer control to the flaps will result in approaching the theoretical values of lift up to flap deflections of 60° to 70° . This has been demonstrated on a wide variety of wings ranging from those typical of fighters (thin, low aspect ratio, and high sweep) or bombers and jet transports (moderate thickness, high aspect ratio, and moderate sweep) to those of slow-speed airplanes (thick, high aspect ratio, and no sweep).

Design details differ, of course, but the prime objective was realized in each of these cases. An interesting corollary of these results is that with the flap effectiveness maintained to high flap deflections, the function of flaps and ailerons can be combined in a single unit without a major sacrifice in the effectiveness of either.

Research has demonstrated that boundary-layer control applied to a wing leading edge or to a wing leading-edge flap can greatly extend the useful angle-of-attack range. Boundary-layer control of the wing leading edge has also been successfully applied to a variety of airplane types.

Again, design details must differ because of differences in airplane design. For example, the application of boundary-layer control to the wing leading edge can have powerful and differing effects on the longitudinal

stability of the airplane, depending on the location of the horizontal tail.

It is believed, however, that sufficient research has been completed on the application of boundary-layer control to a wing leading edge to enable the designer to use it with no more detailed "tailoring" for his specific design than would be required for a leading edge without boundary-layer control.

One point worthy of comment has been noted often in the course of boundary-layer-control studies. This is the need for more effort to be devoted to the problem of stall occurring at the wing leading edge as a result of trailing-edge flap effectiveness being increased. It was found that with boundary-layer control applied to trailing edge flaps of wings incorporating conventional slats at the leading edge the greater lift due to boundary-layer control results in the slats being unable to delay leading-edge stall to the desired angles of attack. In other words, although the flap lift increment of the basic design was increased a significant amount, the maximum total lift was limited by leading-edge stall. It may well be that the stall may be delayed sufficiently at the wing leading edge only through mechanical boundary-layer control.

It is important to note, then, that the apparently simple expedient of applying boundary-layer control to the trailing-edge flaps of an existing airplane may result in disappointing lift characteristics. Like many other facets of airplane design, satisfactory application of boundary-layer control cannot be realized by focusing attention on one phase only. The effects of boundary-layer control must be considered in the whole design.

In achieving boundary-layer control by removing the low-energy air, a theory was developed which predicted that if suction over one long slot, rather than through a number of separate slots could be realized, the total volume of air required would be reduced very greatly. Experiments showed that this result could be largely realized where use of sintered metals permitted approximately continuous suction. Although the flow volume needed to achieve boundary-layer control was not reduced to the level predicted by theory, it was brought down to a practical value when considered in terms of duct size and pumping equipment.

The range of experiments, using suction through sintered metal, covered applications to wing leading edges and leading-edge flaps and to wing leading-edge flaps on 10 different wings typical of turbojet fighters and bombers and propeller-driven transports. For example, on a North American F-86 airplane, area-suction boundary-layer control increased flap lift 50 percent at a flap deflection of 55° .

In this instance the required boundary-layer control was obtained with a 12-horsepower motor drawing 20 cubic feet of air per second through a 20-square-inch duct. Similarly, practical installations appear possible

in other instances of area suction that have been examined.

Major research effort on blowing boundary-layer control has been directed toward reducing the mass flows required at high pressure ratios to a point where the use of flowing boundary-layer control would not compromise the engine or airplane operation. For example, the amount of bleed air required at the pressure ratios available during take-off must be low enough that the accompanying engine thrust loss does not cancel potential improvement in take-off characteristics resulting from the higher lift due to boundary-layer control. Also, the bleed air required at the pressure ratios available during approach and landing must be low enough that the engine is not operated at high values of rpm and thrust simply to provide an air supply for the boundary-layer control.

The effectiveness of blowing-air boundary-layer control depends upon the thrust of the issuing jet. In other words, the same effectiveness can be obtained by discharging small quantities of air at very high velocities as with large quantities of air at relatively low velocities. This fact makes easier the matching of boundary-layer-control requirements with jet-engine characteristics.

The experiments and analyses made to date show that in every case studied, careful design based on the research data will enable these conditions to be met while realizing full benefits of the boundary-layer control. For instance, on a swept-wing airplane design typical of proposed light transports for bombers and powered by two Pratt & Whitney J-57 turbojet engines, full boundary-layer control on the trailing-edge flaps could be realized by use of 6 pounds of air per second at a pressure ratio of 5. This air quantity can be provided by one J-57 engine at idle conditions, without affecting its operation significantly. At higher engine thrust conditions, of course, the engine can supply considerably more pressure and air than is required.

Flight research on boundary-layer control has been carried on at the Ames and Langley Laboratories. Principal goals of this full-scale research, now concentrated at Ames, are three-fold: (1) to verify results which were demonstrated in the wind tunnels, (2) to gain firsthand experience with the practical problems of using boundary-layer control, and (3) to obtain both qualitative and quantitative measurements of pilots' reactions to the use of boundary-layer control.

At the Ames Laboratory, North American F-86 and FJ-3 airplanes have been modified and flown with area suction boundary-layer control applied to the wing leading edge and to the trailing-edge flaps and with blowing boundary-layer control applied to the trailing-edge flaps. In no case was it practicable to modify the structure to permit installation of a complete (both leading-edge and trailing-edge) system. In all cases, because the boundary-layer-control installation was not part of the basic, original design, the improvement

in the overall performance characteristics fell short of what otherwise would have resulted.

Nevertheless, very useful results have been obtained and the program is being extended at Ames to include application of blowing boundary-layer control to both leading-edge and trailing-edge flaps on a North American F-100. In addition, NACA pilots have flown, and to varying degrees evaluated, most of the few airplanes modified by the aircraft industry to include boundary-layer control.

The study of pilot reaction to the use of boundary-layer control for high lift is being expanded into a more general study of the factors involved in choice of landing and take-off techniques. It has been noted that every pilot has taken advantage of some or all of the gain in lift brought about by the use of boundary-layer control, resulting in reduced landing speeds. Without exception, pilots have commented on the increased smoothness of flight and increased controllability resulting from boundary-layer control. The chosen approach speed of a North American F-86 in a GCA approach was dropped from 140 to 115 knots, and the pilot commented that even at the lower speed the airplane was easier to hold to the desired flight path.

Perhaps the most interesting, though as yet tentative, conclusion drawn from the flight-test results is that boundary-layer control is tending to remove lift as a limiting factor in choosing a minimum flight speed. In its place the pilots are stating that "altitude control" or "ability to check sink" is becoming the limiting speed factor. Exploratory studies indicate that the pilots are using engine thrust for this control and that their minimum speed choice is significantly affected by

the minimum rpm at which adequate engine response can be obtained.

Lack of space in this report prevents consideration of a number of other interesting aspects of boundary-layer-control research by NACA scientists. Among them are the investigation of the whole area of boundary-layer control from inlet to exhaust of the power-plant system and the renewed efforts being made to learn how to employ boundary-layer control for drag reduction at very high speeds.

Today, the necessary basic research on the problems of boundary-layer control for high-lift conditions have been essentially completed. Now, it is possible to estimate with a fair degree of accuracy the gains to be realized in lift, the necessary cost in power required, and the design details associated with the use of boundary-layer control for a specific airplane. Information now in hand strengthens the belief that further effort to utilize boundary-layer control in future designs will be repaid by substantial performance improvement.

As wing loadings are increased to values beyond 100 pounds per square foot, entirely new concepts may be required to provide desired landing and take-off performance. Under study at the Langley Laboratory is the jet-flap principle, where a large percentage, or even all, of the primary power-plant jet exhaust thrust is used to augment lift. Exploitation of this idea may make it possible for the high-performance airplanes of the future, both civil and military, to take off and land at airports of present day proportions. Substantial application of the concept in the design of vertical- and short-takeoff-and-landing aircraft also appears likely.

HIGH-SPEED FLIGHT RESEARCH

From its conception in 1944 as a device for obtaining essential information about the problems of transonic and supersonic flight (information at the time mostly unobtainable in wind tunnels) the specially-designed, specially-instrumented airplane has become one of the most valuable tools of aeronautical research. So rapid and so spectacular have been the performance gains that it may be difficult to recall that, only 12 years ago, even the most advanced airplanes were limited by "compressibility" to Mach numbers below 0.85.

The first and most obvious benefit from the trail-blazing speeds and altitudes made by research airplanes was the confidence engendered by the demonstration in 1947 that flight through the fully unknown transonic range was possible. Almost overnight, supersonic flight by tactical aircraft became possible by straightforward means.

More important to the rapid performance improvement of our tactical airplanes has been the mass of detailed information resulting from intensive use of the research airplanes. To date, nearly 400 technical

reports have been prepared by the NACA, covering flight-test results together with related wind tunnel investigations and theoretical studies. So rapidly has the information been assimilated into design practice that today one of the most challenging aspects of the continuing research-airplane program is the task of acquiring additional data fast enough to stay ahead of the new, high-performance airplanes now being designed and built.

Conduct of the research-airplane program has been a wholly cooperative venture, with the resources of the Air Force and the Navy, the participating airframe and engine manufacturers, and the NACA being used as needed. The military services have provided funds and generally have performed the mission of exploring and exploiting the maximum performance capabilities of the airplanes. The manufacturers, of course, have designed and built the airplanes and engines and in most instances, their pilots have carried out demonstration flights to satisfy contractual requirements. The NACA has furnished the latest research information for

application in design of the airplanes, has made necessary wind-tunnel investigations using models of the airplanes, has provided data-gathering instrumentation for the planes, and has conducted the research flight programs.

What follows is a summary of this fruitful program, with special emphasis on the part the NACA has played.

Although the bulk of the NACA's research effort in the years of World War II was concentrated upon obtaining the quick-fix answers needed for performance improvement of airplanes already in production, it was obvious as early as 1943 that the very large amounts of thrust inherent in the turbojet and rocket engines coming into use offered the means of attaining supersonic flight. It was realized, however, that diligent and vigorous research effort using new tools and new techniques was essential—new aerodynamic knowledge had to be acquired before the supersonic speed potential could be exploited.

Existing knowledge of transonic air flow was pitifully small, and earlier efforts to develop a body of useful transonic theory generally had been unsuccessful. It was necessary to use experiment, but the principal tool of aerodynamic research, the wind tunnel, was subject to "choking" near the speed of sound and new techniques had to be devised. As victory loomed in Europe and the Far East, the NACA's effort in this direction was increased and broadened to include all approaches which offered promise.

Among the techniques employed were: (1) Specially instrumented aerodynamic bodies dropped from airplanes at high altitude; (2) small models placed on the wings of airplanes to capitalize upon the accelerated air flow above a curved surface, and (3) rocket-propelled models fired from the ground. With later advances in radar and radio-telemetering equipment, the rocket-propelled model has proved most valuable in research.

One of the earliest ideas for exploring the transonic speed range was suggested in 1943. Specially designed airplanes could be used to probe the transonic speed range. They could be propelled by the most powerful engines available; they could be loaded with data-recording instruments. Danger could be minimized if the research were performed at great altitude and in level flight; the loads imposed upon the structure would thus be kept low, and, if trouble developed, the pilot could throttle back to lower speed. For this conception of the research airplane, John Stack of the Langley Aeronautical Laboratory shared the 1947 Collier Trophy with the late Lawrence D. Bell, president of Bell Aircraft Corp. which built the X-1, and with then Capt. Charles E. Yeager, USAF, the first man to fly supersonically.

In 1944 contracts were let for construction of the first two research airplanes. Bell Aircraft Corp. began design of the X-1 (originally known as Project MX653 and later as XS-1) under Air Force sponsorship, and the Douglas Aircraft Co. about the same time undertook

construction of the D-558, sponsored by the Navy. The first of these was to be powered by a rocket motor; the second, by a turbojet engine.

First to reach the flight-test stage was the X-1, of which two originally were constructed. The fuselage lines were adapted from the basic shape of a 0.50 calibre bullet. Straight wings, with thick, tapered aluminum skin, were provided to insure enough structural strength to withstand the loads expected at the altitudes and speeds programmed. The strength factor was specified at 18g, instead of the 12g then required for fighters. One set of wings had a thickness of 10 percent, much less than anything then flying; the second set was only 8 percent thick.

The power plant of the X-1 was a four-barrel rocket engine developed by Reaction Motors, Inc., under Navy contract. The engine used a simple but effective system of regenerative cooling (one of the liquid propellants was passed over the outer surface of the combustion chamber before being injected into the combustor) conceived in the midthirties by James H. Wyld, one of the founders in 1941 of Reaction Motors, Inc. Each rocket barrel produced 1,500 pounds of thrust, for a total engine thrust of 6,000 pounds.

Originally the R. M. I. rocket engine was to have incorporated a turbine pump to force the liquid-oxygen and alcohol-water fuel into the combustion chamber at a high rate. When development of a pump capable of operating at the required low temperatures impeded construction of the rocket engine, it was decided to use nitrogen under pressure to handle the fuel flow despite the resulting reduction in fuel carried.

In the fall of 1945, before the rocket engine was ready, the airframe of the X-1 was completed. To save time, Bell engineers proposed carrying the airplane aloft in a "mother ship," then releasing it to fly without power. In this way the general airworthiness of the X-1 could be determined before the rocket motor was completed. These tests were conducted early in 1946 at Pinecastle Air Force Base, Florida, and a group from the Langley Laboratory was sent to maintain and operate the 500 pounds of instrumentation carried by the X-1 and to provide technical guidance. The "mother ship" technique has been used since with others of the research-airplane series.

Following the successful glide tests it was decided that, in the interest of maximum safety for the pilot, powered flights should be made in the vicinity of the largest available landing area. The choice was the Air Force installation on the edge of Rogers Dry Lake in the Mojave Desert of California, known then as Muroc and now as Edwards Air Force Base.

After installation of the R. M. I. engine at Bell Aircraft's Niagara Falls plant, the first of two X-1 research airplanes was taken to Edwards early in October 1946. The previous month, 13 engineers, instrument technicians, and technical observers, all from Langley, were

designated the NACA Muroc Flight Test Unit. On September 30 they began work at the desert base. The first successful rocket-powered flight was made December 9 by Chalmers H. ("Slick") Goodlin, company test pilot. By June 1947 performance up to a Mach number of 0.8 was fully demonstrated by Bell Aircraft pilots in a series of 21 powered flights.

On June 30, at a meeting at Wright-Patterson Air Force Base the Air Force and NACA agreed to divide responsibilities. Each agency was to use one of the X-1 airplanes in complementary flight programs. The Air Force objective was to exploit the airplane's maximum performance in as few flights as were reasonable, consistent with safety. The NACA program was necessarily more extensive: to acquire the desired detailed information. The NACA group, now permanently assigned at Edwards, was to furnish engineering and instrumentation assistance to the Air Force group, while the air launching of the NACA airplane was to be handled by the Air Force.

The Air Force received its X-1 in August 1947; mechanical difficulties delayed flights of the other model by the NACA until after the first of the year. Details of the historic first supersonic flight on October 14, 1947, by then Capt. Charles E. Yeager, USAF, are so well known as to need no recounting here. On March 4, 1948, NACA pilot Herbert Hoover became the first civilian to fly faster than sound.

Before turning attention to the research airplanes which came later, the following quotation from Maj. Gen. Albert Boyd, USAF, himself one of the first to fly supersonically, is given as a summation of the effectiveness of the cooperative program:

"The combination of talents served two purposes. First, the accelerated USAF program permitted a rapid exploration of the capabilities of the X-1 to the highest speed attained; and, secondly, the detailed NACA program provided the comprehensive data needed to develop complete envelopes of aircraft performance which might reveal unsatisfactory flight characteristics at some intermediate point. When considered separately, each program was a notable contribution to flight research, however, when combined, the results stand as a monumental tribute to both the USAF and NACA since the sonic barrier monster was not only completely licked, but a blow-by-blow account of its defeat was recorded for future use.

"The end results of high-speed flight-research programs conducted jointly made available to aircraft designers, for the first time in the history of flight testing, sorely needed information which served a dual purpose. The rapid but sketchy USAF portion of the program supplied answers which went toward determining the military applicability of a research aircraft, whereas the lengthy but detailed NACA program confirmed or refuted wind-tunnel data and at the same time provided information which would

permit aircraft designers to avoid dangerous flight characteristics in future military and civilian aircraft of a more advanced design."

The Douglas D-558 research airplane project, sponsored by the Navy, quickly became a two-fold effort. The phase-one airplane, christened Skystreak, was similar to the X-1 in general layout. It was powered by a General Electric TG-180 turbojet instead of a rocket engine, and, because its potential was limited to transonic speed, the strength requirement was dropped from 18g to 12g.

Flown for the first time in mid-March, 1947, the Skystreak was used in manufacturer's performance demonstrations for about 5 months. On August 20 of that year the Navy Skystreak project officer, then Comdr. Turner Caldwell, flew the airplane to a new world's speed record, 640.7 mph. Five days later, then Maj. Marion Carl, USMC, added another 10 mph.

Three Skystreaks were built. One was destroyed on take-off in May 1948. The two other D-558-I airplanes were used intensively by the NACA in study of flight problems at speeds up to a Mach number of 0.9. As the program developed, the X-1 and D-588-I were used in combination. The turbojet-powered Skystreak, having longer flight duration, was used for the heavy work up to low transonic speeds, while the X-1 flights were at higher speeds.

Instrumentation for these flights made possible precise measurement of performance (lift and drag), stability and control, and aerodynamic loads. For the loads work, instrumentation covered measurements both by strain gauges and detailed pressure-distribution pickups. This basic pattern, supplemented by special recording devices to obtain other data, has been used with the later research aircraft.

NACA's first facilities at the Dry Lake base were entirely makeshift, consisting of wire cages in one Air Force hangar. In fact, Air Force facilities at the Base were generally inadequate. In 1948, the NACA took over a small hangar and built lean-to structures alongside for shops and offices. By the end of 1948, the complement of the NACA's Muroc Flight Test Unit had been increased to 60; the following year the group name was changed to High Speed Flight Research Station.

By early 1949 the Douglas Skyrocket, the second phase of the D-558 program, was nearing completion of contractor performance demonstrations, using only turbojet power. The airplane differed from the Phase I in two important details. It had both a Westinghouse J-34 turbojet engine and a R. M. I. rocket motor, and its wings were swept. At first the wing sweep was specified at 45°, but because so little about its effect was then known (except that it reduced lift capabilities of the wing) sweep was reduced first to 40° and finally to 35°. Automatic leading-edge slots

and wing fences were provided to overcome some disadvantages of sweepback.

Later in 1949, the Skyrocket first flew with both jet and rocket power. It soon became clear that the rocket engine would be necessary, in addition to the turbojet, for ground take-off in the heavily loaded condition. Such a requirement meant there would be little rocket fuel available for high-speed flight at altitude. Consequently, the NACA recommended modification of the D-558-II for air-launching. While this work was being done, one of the Skyrockets was further modified by removing the jet engine and its fuel tanks, to provide additional rocket fuel for longer high-speed flight.

The Douglas Company in 1950 began air-launched flights, and early the next year began maximum performance flights for the Navy, using the all-rocket D-558-II. William Bridgeman, the pilot, that year exceeded 1,200 mph (Mach number of 1.87). In the summer of 1951, Col. Carl, USMC, reached 82,000 ft. altitude. It was not until November 20, 1953, however, that the maximum velocity of the D-558-II was attained. On that day, NACA pilot Scott Crossfield became the first man to reach a Mach number of 2, or 1,328 mph.

The problem of longitudinal stability (pitch-up), as experienced by airplanes with swept-back, low-aspect-ratio wings, was first met in flight with the D-558-II airplanes. The onset of pitch-up (where the airplane noses up abruptly) was not unexpected; wind-tunnel investigations had suggested this might happen. It was not until the problem could be studied in flight that its severity could be fully evaluated. In the Skyrocket, many types of wing devices were used in efforts to lessen the pitch-up severity.

The Skyrocket further was used effectively in the study of the violent lateral oscillations which may occur at high speed when the airplane is in low-angle-of-attack attitude. When Bridgeman made his flight at a Mach number of 1.87, he experienced lateral oscillations of as much as 75°. After a detailed study of the stability problems in flight, the NACA was able to dampen the lateral oscillations sufficiently to permit maximum flight to Mach number of 2.01.

One of the major problems faced by designers of supersonic fighters which can be studied in the wind tunnel as well as in flight is the decrease in directional stability that occurs as speed increases. What happens is that conventional lifting surfaces, such as the vertical tail, tend to lose their lift effectiveness with increase in Mach number. The positive directional stability of an airplane may decrease to the point where it is unacceptable. By increasing the wind-tunnel speed to and above this point, the advent and seriousness of the phenomenon as it affects a particular design can be studied in detail.

This problem was experienced first in the Skyrocket program. It has been studied with succeeding airplanes available to the NACA Station.

During 1949 and the first months of 1950, the Northrop X-4, a tailless, swept-wing airplane powered by two Westinghouse J-30 turbojet engines was undergoing contractor trials. Sponsored by the Air Force, the airplane was assigned to the NACA in mid-1950. For several years thereafter, the X-4 was flown many times to investigate problems peculiar to a tailless design. Stability difficulties encountered at higher speeds made impossible attainment of speed beyond a Mach number of 0.95. In the X-4 program, much of value was learned about the stability and control characteristics of this type of airplane. Perhaps of even greater importance was the ability to acquire trend information (hints of things to come) about dynamic stability involving the coupling of the aerodynamic and mass characteristics of an airplane.

By the beginning of 1952, when the variable-sweep wing Bell X-5 became available to the NACA, the staff of its High-Speed Flight Research Station numbered nearly 200. The X-5 was designed to permit flight investigation of difficulties resulting from the fact that although wing sweep was obviously of great utility in alleviating or delaying the large drag rise occurring near the speed of sound, its use entailed numerous problems associated with landing at low speeds. An airplane able to land and take off with its wings essentially straight, and then sweep them back 20° to 60° in flight, offered obvious advantages. The most modern airplanes being flown at the time had little more than 35° sweepback. It was felt necessary to acquire flight experience with airplanes having highly swept wings, up to 60°, and the X-5 offered the best means of accomplishing this.

Before the end of the year the X-5, powered by an Allison J-35 engine, was flying supersonically. Among other studies, it was used to investigate the change in gust response with large differences in sweep. When flown with 59° of sweep, the airplane showed considerably less response to gusts than when flown with 20° of sweep. In fact, although lateral stability deteriorated as expected with the extreme angle of sweep, pilots could fly it with 59° of sweep under atmospheric conditions that were impossible with 20°. The airplane was simple to maintain and easy to fly. The X-5 program never was spectacular but the airplane proved itself a most useful research vehicle.

In 1952 the research airplane program was broadened to include flight studies with the XF-92A. Convair built this model to acquire experience with the delta-wing configuration prior to design of the F-102. The XF-92A originally was powered by an Allison J-33 turbojet; modified to use an afterburner, it was capable of transonic performance. The NACA cooperated with the Air Force in evaluating the airplane, which

work yielded some of the first full-scale information about drag of delta-wing designs. Detailed measurements were made of pressure distributions over the aircraft surfaces.

Perhaps most important among test results was the evaluation of pitch-up characteristics of the delta-wing, which proved unlike those of the other research airplanes. In flight at Edwards and in NACA wind tunnels, the XF-92A program concentrated on problems of pitch-up and lateral stability, resulting in an arrangement of wing fences which gave satisfactory flight characteristics later on the F-102.

A "by-product" of the research-airplane program was the cooperative effort in 1952 by the Air Force, Northrop, and the NACA to determine the cause of a series of structural failures in the F-89. It was believed the wings might be under strength because loadings encountered in flight were higher than stress-analysis estimates. The NACA Station had large experience in the art and science of flight measurement of aerodynamic loads by strain gauges. NACA scientists were assigned temporarily to the Edwards Northrop facility to direct installation and calibration of strain gauges, and reduction and analysis of data to determine the validity of beliefs. Once this work was done and remedies were applied, the F-89 structural failures ended.

From 1950 to 1953 the NACA Station continued to grow, but slowly, reaching 222 employees in early 1953. Additional temporary structures were erected and other temporary buildings were obtained from the Air Force. The result was an operation spread over a greater part of the east end of Edwards AFB. Meantime, beginning in 1951, the USAF master plan for enlargement of the Base was approved, and construction of large, permanent structures began. At about the same time, it became apparent the NACA flight research operation at Edwards would be continued indefinitely. A permanent facility was requested and approved by the Congress, with appropriations voted for the fiscal year 1952. The Air Force leased 175 acres of land to NACA, and in 1953 NACA began construction of a large, single building to include hanger space, instrumentation facilities, shops and offices.

In 1953, the High-Speed Flight Research Station obtained a Boeing B-47 for study of the problems peculiar to an airplane with a high degree of structural flexibility. It was desired especially to investigate aeroelastic effects on the loading encountered by this airplane in flight and its stability and control characteristics. The test program was conducted in cooperation with the Langley and Ames Aeronautical Laboratories. This long-term program, now completed, has provided valuable information about the effects of the flexing of the wing, fuselage, and tail group upon the characteristics of an airplane. At present the B-47 is being used in a program to measure

accurately the noise created by a large turbojet-powered airplane and the several sources of noise. It is hoped the research results will aid efforts to quiet the jet transports which will soon be put into commercial service in the United States.

Flight tests of the Douglas X-3, powered by two Westinghouse J-34 turbojet engines, began in 1953. The Air Force sponsored airplane was delivered the following year to the NACA. This research craft, because of development difficulties with more advanced engines, never reached the desired performance goals.

Nevertheless, its layout (a very thin, straight wing mounted on a long fuselage in which most of the weight was concentrated along the centerline) generally represented the design thinking about high-performance tactical aircraft of the future. As such, the X-3 was of considerable interest, especially in the field of airplane dynamics, and much valuable information was obtained in flights reaching into the low supersonic range.

It was in the X-3 that the frightening phenomenon, now known generally as inertia coupling, was first experienced. Inertia coupling, characterized by large divergent motions of the airplane in rapid aileron rolls, was determined to result from high rates of rolling and from the concentration of the weight of the airplane within the fuselage and on a great length.

Work to analyze and understand the problem was just getting well under way in mid-1954, when an NACA aeronautical research pilot experienced the inertia coupling in a North American F-100 Super Sabre. During preliminary tests the airplane exhibited strange behavior in rapid aileron rolling maneuvers, resulting in large divergencies in yaw and pitch that could be both destructive to the airplane and, to say the least, extremely disconcerting to the pilot.

The F-100 was just going into Air Force service, where the phenomenon likewise was encountered. Several airplanes were lost and the F-100 was grounded until a solution to the problem could be found. Following intensive cooperative action by the Air Force, North American Aviation, Inc., and the NACA, a joint flight test program was undertaken. Fortunately, both improved understanding of the phenomenon and a practical solution were soon determined. By enlarging the vertical tail of the airplane and performing other seemingly minor modifications, the airplane was "cured" of its troubles and soon returned to full service.

In 1954, when the new quarters for the NACA at Edwards were completed and occupied, the name of the unit was changed to High Speed Flight Station. At the same time it was raised to independent status, directly under NACA Headquarters instead of reporting to the Langley Laboratory. Additions to the staff since have increased its total complement to 300.

Research on problems of delta-wing airplanes continued with the acquisition in the fall of 1954 of the

Convair YF-102. Flight measurements of lift and drag with this aircraft were especially useful in corroborating wind-tunnel data on Richard T. Whitcomb's area rule. These data indicated that the Whitcomb principle would be valuable when applied to the Convair airplane. A study also was made of the inertia-coupling characteristics and, on the basis of information about the delta wing, together with data from the F-100 and X-3 designs, the manufacturer was enabled to free the production F-102A of inertia-coupling troubles. More recently, the High Speed Flight Station has received an F-102A. This model permits extension of flight research with delta-wing airplanes into the supersonic range.

Looking back for a moment, the X-1A, carrying a larger store of rocket fuel than the original X-1, underwent contractor trials in 1952-53. This program was climaxed December 12, 1953 when Maj. Yeager reached a Mach number of 2.5, approximately 1,650 mph. Military pilots later flew it to altitudes as high as 90,000 feet.

In 1954, both the X-1A and the X-1B (specially instrumented for full scale aerodynamic-heating research in flight) were delivered to the NACA. The first of these was lost in 1955 when, in the course of air launching from the B-29 mother ship, an explosion caused serious structural damage to the X-1A. Unable to jettison fuel, the crew found it necessary to release the research plane and let it fall to earth. Fortunately there was no injury to personnel—due in no small part to the heroism of the flight crews.

Among the newer airplanes now being used at the Station is the Lockheed XF-104A, which is capable of speeds near a Mach number of 2.0. This airplane will offer the opportunity to study inlet problems or problems of air-breathing engines, as well as problems associated with sustained high supersonic speeds, including aerodynamic heating, supersonic speed stability, and related subjects.

Another of the X-1 series, the "E" model, was modified from one of the original X-1's. It incorporates a 4-percent-thick wing and a new propellant and tankage system. The X-1E is being used to study problems of very thin wings (proportionally about as thin as a razor blade) at high supersonic speeds and altitudes.

In 1956, following more than a decade of development effort, the Bell X-2 became operational. Made of stainless steel and Monel metal, it was designed for study of aerodynamic heating at speeds near, if not above, a Mach number of 3.0. Because of fabrication difficulties inevitable with new materials and techniques, and even more, because of problems of developing satisfactory throttling apparatus for the Curtiss-Wright rocket engine, the airplane was delivered several years late.

Late in the spring, Col. Frank Everest, USAF, flew the X-2 to a new speed record and soon after, Maj. Iven Kincheloe climbed to a higher altitude than ever previously reached by man. In one of the last flights scheduled in the Air Force performance program, Capt. Milburn G. Apt was killed.

The tragic loss of the Bell X-2 inevitably will slow the rate of full-scale research on aerodynamic-heating problems, but both the X-1B and X-1E are being used profitably in this program. The first of these airplanes, instrumented with some 500 thermocouples to permit detailed evaluation of the heating problem, can be flown at speeds above a Mach number of 2.0. The thin-wing X-1E, with its increased fuel supply, can fly above a Mach number of 2.0 for a somewhat longer time.

How serious the aerodynamic-heating problem already has become may be seen from the fact that at sustained speed in the Mach number 2.0 range a temperature rise of as much as 300° F may be experienced. Further, the temperature due to aerodynamic heating rises as the square of the velocity: at a Mach number of 3.0 the temperature rise during sustained flight would be about 660° F.

Also planned for use in study of such problems as aerodynamic heating and stability and control at high altitude, and now under construction, is the X-15. North American Aviation, Inc., is the contractor, and the Air Force the sponsoring service. As with previous research airplanes, the NACA is an active partner, participating fully in the grave decisions implicit in design and construction of an airplane of new concept that is intended to fly still faster and higher than man has attempted. Because of the loss of the X-2, the need for earliest possible completion of this project has become imperative.

AERODYNAMIC RESEARCH

Man's efforts to fly faster and higher have never before been so intense, and success is dependent upon gaining a greater knowledge and understanding of the fundamental problems of fluid mechanics of supersonic and hypersonic flows along with other factors affecting aircraft performance, stability, and control. Hence a major portion of NACA research has been

devoted to experimental and theoretical aerodynamic investigations. In addition to many studies of generalized aircraft configurations, programs have been undertaken at the request of the military services to assist in the development of specific military airplanes or missiles. Such studies uncover problems which lead to general research programs. In the past year, for

example, considerable effort has been expended on the methods of eliminating the decrease in directional stability associated with increasing Mach number and angle of attack, which is a serious problem in the design of high-speed airplanes.

Aerodynamic problems of the long-range ballistic missile, such as aerodynamic heating, dynamic stability, and the determination of optimum shapes for reentering the earth's atmosphere, have also become increasingly important.

The results obtained from flight programs on research airplanes undertaken at the NACA High-Speed Flight Station are of considerable value for future airplane designs. Flight programs conducted on current service airplanes by the various laboratory flight groups are also of special value to the services and their contractors. The results often lead to the development of more advanced airplanes and, in particular, aid in obtaining satisfactory flying qualities.

Continued assistance has been given the NACA in planning and conducting its aerodynamic research programs by the Committee on Aerodynamics and its technical Subcommittees on Fluid Mechanics, High-Speed Aerodynamics, Internal Flow, Propellers for Aircraft, Seaplanes, and Helicopters. In order to handle the large field formerly covered by the Subcommittee on Stability and Control more effectively, two new subcommittees were formed during the year: The Subcommittee on Aerodynamic Stability and Control and the Subcommittee on Automatic Stabilization and Control.

As in previous years, dissemination of important new aerodynamic research results by means of a special NACA conference was found to be effective. The conference, attended by representatives of the military services and many of their contractors, was concerned with the aerodynamic problems of high-speed aircraft.

Some of the recent unclassified studies conducted by the NACA in the field of aerodynamics are described in the following paragraphs.

FLUID MECHANICS

Boundary-Layer Research

The importance of obtaining extensive regions of laminar flow on all surfaces during high-speed flight stems from the benefits of reduced heat transfer, equilibrium temperatures, and skin friction. The Reynolds number for transition at a Mach number of 6.9 was found in the Langley 11-inch hypersonic tunnel. The test model was a hollow cylinder and measurements were made on its outside surface with heat transfer from the boundary layer to the wall. The boundary-layer nature was determined from impact-pressure surveys. As reported in Technical Note 3546, the data obtained at a Reynolds number of

0.34×10^6 per inch in a portion of the nozzle which had a small Mach number variation show that the transition Reynolds number occurred between 4×10^6 and 6×10^6 . When the cylinder protruded into a region of the nozzle where a considerable negative pressure gradient existed, the Reynolds number for transition approached 8×10^6 for one set of data. At a Reynolds number of 0.26×10^6 per inch, the Reynolds number for transition varied from about 4×10^6 to 4.5×10^6 . From a correlation of results obtained at lower supersonic Mach numbers (Mach numbers from 2.0 to 4.5), leading-edge thickness and free-stream Reynolds number per inch appear important in determining flat-plate transition. Results from various research facilities would not appear to be comparable unless these factors are taken into account. At a given Mach number the Reynolds number based on leading-edge thickness appears to be a significant parameter and should be considered in comparisons of flat-plate or hollow-cylinder boundary layer-transition data obtained from various research facilities.

A number of the factors that presumably affect boundary-layer transition have been investigated at the Lewis Laboratory. The effects on transition of heating and cooling the surfaces of cone-cylinder and parabolic-nose-cylinder models are reported in Technical Note 3562. Cooling the cone-cylinder model to a ratio of wall to free-stream static temperature of approximately 1.4 increased the transition Reynolds number from about 2.0×10^6 to 10.6×10^6 at equilibrium. For temperature ratios less than 1.4, the boundary-layer flow was laminar over the entire model.

For the parabolic-nosed body, the boundary-layer-transition Reynolds number was about twice that of the cone-cylinder model over the temperature range investigated.

Another factor considered was the effect of leading-edge geometry on transition position, recovery-factor distribution, boundary-layer profile, and the roughness required to induce transition. Results of the investigation conducted at Mach 3.1 with a hollow cylinder aligned with the air stream are reported in Technical Note 3659. A large downstream displacement of the transition point and an increase in recovery factor were noted when a sharp leading edge was blunted very slightly. These effects may be attributed to the formation of an inviscid shear layer near the surface which was caused by the curvature of the leading-edge shock. The boundary layer thus develops in a region of lower Mach number which exists within this shock-produced shear layer. The delay in transition is predominantly an effect of a Reynolds number reduction within the reduced velocity region of the inviscid shear layer. A still larger downstream displacement of the transition point was observed for an externally beveled leading edge.

Much work has been done to determine the transition point on bodies of revolution and unswept surfaces at zero angle of attack. For supersonic configurations, however swept wings operating at angles of attack are common, and questions about the effects of sweep and angle of attack on boundary-layer transition arise. Very little theoretical or experimental work has been done on these problems at supersonic speeds.

An experimental investigation was therefore conducted at the Langley Laboratory to determine the effects of leading-edge sweep, angle of attack, and leading-edge thickness on boundary-layer transition of flat-plate wings at a Mach number of 4.04. The data presented in Technical Note 3473 show that transition always occurred along a front parallel to the leading edge of the wing. Increasing the leading-edge sweep angle or increasing the angle of attack between the undisturbed air stream and the wing surface caused the transition line to move closer to the wing leading edge and generally decreased the Reynolds number at which transition occurred. An increase in leading-edge thickness from 0.25 mil to 6 mils caused large increases in the local Reynolds numbers at which transition occurs for a flat-plate wing with an unswept leading edge. On wings with 45° and 60° leading-edge sweep, however, an increase in the leading-edge thickness had no apparent effect on the local normal transition Reynolds number. For small angles of leading-edge sweep, the favorable pressure gradient due to the curved profile of the NACA 65A004 airfoil section produced longer lengths of laminar flow than were obtained on the flat-plate section. For larger sweep angles, the destabilizing effect of the curved streamline outside the boundary layer caused transition to occur earlier than on the flat plate.

Until recently, studies of unsteady laminar boundary layers were limited to either the early stages of the motion (i. e., the transient state) or oscillatory motions without a mean flow. The fluid, furthermore, was assumed to be incompressible. It was felt that the boundary-layer growth occurred in so short a period of time that, for engineering purposes, the flow could be assumed to be steady. However, in many present-day applications, consideration must be given to the unsteady flow effects for long time periods and to high-speed flows in which compressibility becomes important. For example, the skin friction and heat transfer of a rocket missile varies over its entire flight because of the unsteady flow caused by the varying flight speed throughout its trajectory. Blades rotating in non-uniform air streams, unsteady nozzle flow, and oscillating wings are some of the other important cases.

The results of a study at the Lewis Laboratory concerned with such unsteady flow are given in Technical Note 3569. In this paper, consideration is given to the laminar compressible boundary layer and heat transfer over a semi-infinite flat plate. The plate was main-

tained at a uniform (both temporally and spatially) temperature and moved with a continuous but otherwise arbitrary time-dependent velocity. The solutions were obtained as a series about the quasi-steady state.

The lack of knowledge about the proper definition of an "origin," that is, of an absolute streamwise Reynolds number scale of a turbulent boundary layer, makes it difficult to find a satisfactory way of comparing skin-friction coefficients of low- and high-speed turbulent boundary layers.

This problem, which is of major importance at some Reynolds numbers, is discussed in Technical Note 3486. The report describes the design and construction of a floating-element skin-friction balance. This instrument, which is similar to Dhawan's balance, measured the local skin friction in the turbulent boundary layer of a smooth flat plate at high-subsonic Mach numbers and supersonic Mach numbers up to 1.75. The measured skin-friction coefficients are consistent with the results of other investigations at subsonic and supersonic speeds. The principal difficulties in comparing skin-friction coefficients at various Mach numbers are discussed. The study was conducted by the Guggenheim Aeronautical Laboratory of the California Institute of Technology under the sponsorship of the NACA.

In recent years the phenomena associated with shock-induced separation of the boundary layer have received increased attention because of the important influence that separation may have upon the overall aerodynamic characteristics of complete aircraft configurations by affecting the performance of individual components. A study has been made at the Langley Laboratory of some recent contributions to the problem of shock-induced boundary-layer separation. Analytical and experimental results of this study are presented in Technical Note 3601. The probable ranges within which the pressure rise and flow deflections associated with separation may be expected to lie are shown. Consideration is given to the effects of Mach number, adverse pressure gradients, and Reynolds number for laminar boundary layers, and to the effects of Mach number, Reynolds number, and ratio of specific heat, for turbulent boundary layers.

The results of a study at the Lewis Laboratory of the boundary layer behind a shock wave advancing into a stationary fluid are presented in Technical Note 3712. In this study, the laminar-boundary-layer problem, except for the weak wave case (which can be solved analytically), was solved by numerical integration. Integral (Kármán-Pohlhausen type) solutions were obtained to provide a guide for determining expressions which accurately represent the numerical data. Analytical expressions for various boundary-layer parameters are presented and these agree with the numerical integrations to within 1 percent. The turbulent-boundary-layer problem was solved by using integral

methods similar to those employed for the solution of turbulent compressible flow over a semi-infinite flat plate. The fluid velocity, relative to the wall, was assumed to have a seventh-power profile. A form of the Blasius equation which accounted for compressibility and related turbulent skin friction and boundary-layer thickness was utilized.

In flows which are suddenly accelerated in a shock tube, departures of the real fluid from results predicted by both the nonviscous-unsteady-flow theory and the viscous steady-flow theory occur. The effect of skin friction has been studied at the Langley Laboratory by artificially increasing the friction by using surface roughness, which created very thick boundary layers. Measurements of the unsteady-flow turbulent-boundary-layer characteristics were made using a new technique involving study of the shape of the bow wave from a bullet fired through the flow. The boundary-layer-thickness measurements agreed well with both steady-flow experiments and theory. The measured unsteady-flow velocity profiles were considerably less full than the steady-flow theoretical profiles but agreed with some of the steady-flow data. Shock-attenuation measurements were also made and agreed with the results of simple theory at small values of boundary-layer-displacement thickness but were much lower than theoretical results at large values. Results of this study are presented in Technical Note 3627.

Heat Transfer

Aerodynamic heating in supersonic flight has long been recognized as a major problem in the design of supersonic aircraft, and experimental heat-transfer data for high Mach numbers and Reynolds numbers are in great demand. Except for some work done on the V-2 rocket, most of the convective heat-transfer work has been done in wind tunnels under steady-state conditions. In Technical Note 3623 results are presented for the transient conditions encountered along the trajectory of two parabolic bodies of revolution as obtained in free flight at the Langley Pilotless Aircraft Research Division. The tests covered Mach numbers from 1.02 to 2.48 and Reynolds numbers from 3×10^6 to 164×10^6 . The experimental heat-transfer coefficient values obtained are about 15 percent higher than those measured in other tests on a V-2 research missile and approximate the values given by subsonic flat-plate theory with a Reynolds number analogy factor of 0.6.

In order to extend the Mach number range of previous studies of heat transfer over hemisphere cylinders, an investigation was conducted in the Langley 11-inch hypersonic tunnel at a Mach number of 6.8 and Reynolds numbers from approximately 1.09×10^5 to 1.03×10^6 based on diameter and free-stream conditions. In this investigation the boundary layer was laminar and had average T_t/T_∞ values of about 7 at the nose and about 6 on the cylinder (T_t is the local free-stream

temperature just outside the boundary layer and T_∞ is the free-stream temperature ahead of the normal shock). The investigation utilized data from transient nonisothermal temperature distributions since, at the high-temperature levels involved, an isothermal surface is difficult to obtain. The data presented in Technical Note 3706 have been correlated with theoretical analyses and the results of other experiments obtained at lower Mach numbers. The experimental heat-transfer coefficients from this investigation were slightly less over the whole body than those predicted by the theory of Stine and Wanlass for an isothermal surface. A modification of Sibulkin's stagnation-point solution gave the trend of the local Stanton number with local Reynolds number for angles up to 45° from the stagnation point. The calculated values, however, were approximately 12 percent higher than the experimental values.

Pitot profiles taken in this study at a Mach number of 6.8 verify that the local Mach number or velocity outside the boundary layer, required in the use of theory, may be computed from the surface pressures by using isentropic flow relations and conditions behind a normal shock. The experimental pressure distribution at a Mach number of 6.8 is closely predicted by the modified Newtonian theory. The velocity gradients calculated by using the modified Newtonian theory at the stagnation point vary with Mach number and are in good agreement with those obtained from measured pressures for Mach numbers from 1.2 to 6.8.

At the stagnation point a second modification of the theory of Sibulkin using the diameter and condition behind the normal shock was in good agreement with experiment when the velocity gradient at the stagnation point appropriate to the free-stream Mach number was used.

Engineering information relative to the heat-transfer coefficient and temperature recovery factor is required over a wide range of Mach numbers and Reynolds numbers. Such information is especially important in the computation of aerodynamic heating. A project is under way at the Langley Laboratory to obtain such information for the zero-pressure-gradient, two-dimensional case with turbulent flow for values of Reynolds number from about 1×10^6 to 1×10^8 . Previously, data have been published at Mach numbers of 1.62, 2.06, and 3.03. In the past year the range has been extended with results for a Mach number of 0.87 published in Technical Note 3599. The heat-transfer coefficients and recovery factors determined in this study are in fairly good agreement with the theoretical predictions of Van Driest throughout the investigated range of Mach numbers and Reynolds numbers.

An interesting natural convection problem is that concerning the thermally unstable configuration obtained when a fluid is heated from below. The effects of frictional heating and heat sources on this phenome-

non, as determined from a study at the Lewis Laboratory, are reported in Technical Note 3458. In this study, the effects of heat sources and frictional heating on the laminar fully developed channel flow subject to a body force between two parallel plates oriented in the direction of the body force are analyzed. Solutions are obtained for combined forced- and natural-convection flows for the cases in which the wall temperature variations are linear and (1) the wall temperatures are specified, (2) the walls are insulated, and (3) the net mass flow in the channel is zero. These solutions depend on the Rayleigh number which was previously found to be the factor determining the stability and type of flow for horizontal and vertical layers of fluids heated from below but without heat sources or frictional heating. Similar stability characteristics were displayed in this study, and the heat sources affect the flows only in a quantitative manner.

The cooling of aerodynamically heated surfaces has gained attention in connection with rocket walls, turbine blades, and high-speed flow over aircraft surfaces. A promising means of cooling such surfaces appears to be transpiration or sweat cooling, a method in which the surface is made porous and a comparatively small quantity of cool fluid per unit time is injected through the pores into the main stream. Separation may be of particular interest in connection with flow over a transpiration-cooled surface because a normal mass flow strongly tends to promote separation by moving the separation point upstream. On the other hand, cooling of the wall tends, by itself, to delay separation by moving the separation point downstream.

In order to determine the actual net effect of simultaneous normal mass flow and cooling of the wall on conditions of separation over a sweat-cooled surface, a theoretical analysis of laminar separation in compressible flow over a transpiration-cooled surface maintained at a uniform wall temperature has been made at the Polytechnic Institute of Brooklyn under NACA sponsorship. In Technical Note 3559 a simple method of calculating the separation point over such surfaces for a given adverse pressure gradient, Mach number, wall temperature, and uniform coolant temperature is developed. This method is expected to be sufficiently accurate for most purposes. To show the effects of these parameters on the separation point a numerical example is worked out in detail. The normal mass flow was found to have a predominate effect on the separation-point location, since separation over a transpiration-cooled wall occurs upstream of the separation point location of a heat-insulated wall without normal mass flow at the same adverse pressure gradient and Mach number.

Gas Dynamics

The calculation of flows about objects, primarily missiles, traveling at high supersonic speeds is a matter

of great practical interest. These calculations are difficult because at high supersonic speeds the disturbance velocities are not necessarily small compared with the velocity of sound, nor are entropy gradients necessarily negligible in the disturbed flow field about a body, even though it may be of normal slenderness. Thus, for example, the simple linear theory, which is valuable in studying flows at low supersonic speeds, loses much of its utility in the study of high-supersonic-speed flows.

A procedure has been developed at the Ames Laboratory for calculating three-dimensional steady and non-steady supersonic flows using the method of characteristics. An approximate method was deduced and shown to be of practical value for pointed bodies of revolution at high supersonic speeds. In the application of the approximate method, flow at the vertex is analyzed using a generalized Prandtl-Meyer expansion theory. Surface pressures and bow shock waves for inclined ogives determined by using the approximate method were compared with experimental results obtained at Mach numbers from 3 to 6.3. Theoretical predictions and experimental results are in good agreement for values of the hypersonic similarity parameter greater than about 1. It was also found that the concept of two-dimensionality in inviscid hypersonic flows has a counterpart in hypersonic boundary-layer flows. From this result, a unified two-dimensional approach to three-dimensional hypersonic flows was developed. The results of this investigation are presented in Report 1249.

The application of this theory to bodies traveling at large Mach numbers is often limited, however, by the restriction that the maximum slope of the body must be less than the slope of a free-stream Mach line. The applicability of the generalized shock-expansion method and that of the second-order potential theory do not always overlap, and there remain flows at certain combinations of Mach number and body shape which cannot be treated by either theory. Normally, these intermediate flows are encountered when the hypersonic similarity parameter based on nose fineness ratio is in the neighborhood of 1.

Since this is a range of practical interest, a new second-order shock-expansion method has been developed at the Ames Laboratory. This method applies to flows about bodies of revolution characterized by values of the hypersonic similarity parameter near 1 (i. e., the ratio of free-stream Mach number to body fineness ratio). The method has been applied to the calculation of pressure distribution, normal-force curve slope, and center-of-pressure position on bodies of revolution at zero lift. An experimental investigation was conducted in the Ames 10- by 14-inch supersonic wind tunnel to assess the accuracy of the method. Cone-cylinder and ogive-cylinder bodies with fineness ratios from 3 to 17 were tested at Mach numbers from 3.0 to 6.3 to determine normal-force-curve slope and center-

of-pressure position at zero lift. The theoretical method predicts these aerodynamic characteristics within the accuracy of the experimental results throughout the range of test variables investigated. The results of this investigation are reported in Technical Note 3527.

A method based upon the theory of characteristics has been developed at the Langley Laboratory to compute the contour of a body of revolution for a prescribed pressure distribution at isupersonic speeds. The design of such a body would be useful in the investigation of many aerodynamic problems such as those associated with body-wing interaction, inlets, boundary-layer transition, separation, and shock-wave interaction. The evaluation of the flow properties at any point along the surface of the body is determined by an iteration process. This method, described in Technical Note 3555, was used to compute the contour of a body with a constant pressure gradient. This pressure distribution was chosen because the theoretical approach to the transition problem indicated that a constant pressure gradient would be desirable for certain experimental studies. A model was constructed and tested at Mach numbers of 3.05 and 3.13. Excellent agreement with the computed distribution was obtained.

Even when the compressible-flow equations can be solved precisely in a particular case, the numerical computation is usually laborious. If it becomes necessary to extend the calculations to related and perhaps more complicated cases, it is often desirable, or necessary to resort to approximate solutions. In Technical Note 3485, it is shown that the streamlines near an unyawed circular cone with an attached shock wave are, to a first approximation, portions of hyperbolas. This result is used as a basis for the development of an approximate solution for the cone in which the shock-wave orientation and the flow field behind the shock wave are given explicitly in terms of the free-stream Mach number, the vertex angle of the body cone, and the ratio of specific heats of the gas. The possible application of a part of this solution to the analysis of real-gas effects on the high-speed flow over a cone is discussed.

One of the transonic flow problems of interest is that of a double-wedge airfoil in slightly supersonic flow. Previous experimental work has provided a detailed description of the flow characteristics for nonlifting wedges. The data for lifting wedges, however, are far less complete. Measurements were, therefore, made at the Langley Gas Dynamics Laboratory of the flow around two wedges at Mach numbers of 1.30 and 1.41 by means of a Mach-Zehnder interferometer for various angles of attack up to 5° . The results presented in Technical Note 3626 show that pressure distributions for different Mach numbers on wedges of different thickness are similar at the same values of transonic similarity parameter and reduced angle of attack for angles of attack as large as the thickness ratio, that the lift-curve

slope is nearly independent of the angle of attack for angles of attack from -2° to 2° , and that, for the airfoils tested at Mach numbers greater than the attachment value, the center-of-pressure location is nearly independent of the angle of attack.

The problem of determining the shape of slender boat-tail bodies of revolution for minimum wave drag has been reexamined. In Technical Note 3478 it is shown that minimum solutions for Ward's slender-body drag equation can exist only for the restricted class of bodies for which the rate of change of cross-sectional area at the base is zero. In order to eliminate this restriction, certain higher order terms must be retained in the drag equation and isoperimetric relations. The minimum problem for the isoperimetric conditions of given length, volume, and base area is treated as an example. According to Ward's drag equation, the resulting body shapes have slightly less drag than those determined by previous investigators.

If especially advantageous arrangements for supersonic aircraft are not to be overlooked it becomes necessary to study completely general or arbitrary arrangements of airfoils and bodies in three-dimensional space. In Technical Note 3530 the problem of minimizing the wave drag for a given total volume and a given total lift is discussed. The volume and lift may be carried by any number of slender bodies or thin airfoils, but to make the problem definite, they are confined to the interior of a given fixed region which may outline the maximum permissible dimensions of the aircraft.

In a related study, reported in Technical Note 3667, several variations involving optimum wing and body combinations having minimum wave drags are analyzed for different geometrical restraints. Particular attention is paid to the effect on the wave drag of shortening the fuselage and, for slender axially symmetric bodies, the effect of fixing the fuselage diameter at several points or even of fixing portions of its shape.

A great deal of effort is presently being expended in correlating the zero-lift drag rise of wing-body combinations on the basis of their streamwise distribution of cross-section area. This work is based on the discovery of the concept, known as the transonic area rule, that "near the speed of sound, the zero-lift drag rise of thin low-aspect-ratio wing-body combinations is primarily dependent on the axial distribution of cross-sectional area normal to the airstream." Since an accurate prediction of drag is vital to the designer and since the use of such a simple rule is appealing, it is very important to investigate the applicability of the rule to the widest variety of shapes of aerodynamic interest. Some insight into the applicable range of the transonic area rule has been gained in a study at the Ames Laboratory comparing it with the appropriate similarity rule of transonic-flow theory and its results with available experimental data for a large family of rectangular wings having NACA 63AXXX profiles. In spite of the small

number of geometric variables available for such a family, the range is sufficient to include cases both compatible and incompatible with the area rule. A résumé of the study is given in Technical Note 3673.

The precise experimental determination of the structure and thickness of the normal shock wave is of fundamental interest in the study of gas dynamics because it does much to define the usefulness of the Navier-Stokes equations, or of alternative equations, for predicting the behavior of a nonuniform gas. In addition, observations of the nature of the shock wave shed considerable light on the magnitude and character of so-called "relaxation effects" associated with the finite time required to obtain equipartition of energy among the translational and internal motions of a polyatomic molecule.

To provide additional information, the profiles and thicknesses of normal shock waves of moderate strength have been determined experimentally at the University of California under the sponsorship of the NACA in terms of the variation of the equilibrium temperature of an insulated transverse cylinder in free-molecule flow. Steady-state shock waves were produced in the jet of a low-density wind tunnel at initial Mach numbers of 1.72 and 1.82 in helium and 1.78, 1.85, 1.90, 1.98, 3.70, and 3.91 in air. The shock thickness, determined from the maximum slope of the cylinder temperature profile, varied from $3\frac{1}{2}$ to 5 times the length of the Maxwell mean free path in the supersonic stream. A comparison between the experimental shock profiles and various theoretical predictions leads to the tentative conclusions that: (1) The Navier-Stokes equations are adequate for the description of the shock transition for initial Mach numbers up to 2, and (2) the effects of rotational relaxation times in air can be accounted for by the introduction of a "second" or "bulk" viscosity coefficient equal to about two-thirds of the ordinary shear viscosity.

The results of a study conducted at Iowa State College under the sponsorship of the NACA in which the relaxation times for the excitation of molecular vibrations in a number of heavy gases were measured with an acoustic interferometer are reported in Technical Note 3558. All the gases studied were found to have a single relaxation time, indicating that intermodal coupling in these gases is strong. Only binary collisions were found to be important in the excitation of vibrations. The probability, in a given collision, of exciting or deexciting molecular vibrations in the halogen-substituted methanes appears to depend upon the relative energy of approach of the colliding molecules rather than upon the relative velocity. The excitation of vibrations in polyatomic gases may involve the formation of a complex molecule with a very short life.

The shock waves produced during flight at higher hypersonic speeds result in air temperatures high enough to cause at least a partial dissociation of the

air molecules. This dissociation has some effect on the rate of aerodynamic heating. Since dissociation occurs at a finite rate, a thorough understanding of aerodynamic heating requires information on the rate of dissociation. In Technical Note 3634, the collision-theory equation for rate of dissociation has been applied to the flow behind normal shock waves at Mach numbers of 10, 12, and 14 to find the distance required for a moderately large fraction of the oxygen to dissociate. This distance was found to vary widely with Mach number and density from a fraction of a millimeter to hundreds of meters.

Research Equipment and Techniques

Proper design of wings, flaps, inlets, or wind tunnels in which area suction is to be used requires accurate and comprehensive information on the permeability characteristics of the porous materials involved. In most instances, the available information on each porous material was obtained with a single fixed relation between Mach number and Reynolds number, which is not sufficient for predicting permeability characteristics for a range of operating conditions. Experiments performed in the Langley 19-foot pressure tunnel on rolled wire cloth and sintered bronze showed that the permeability characteristics were affected by absolute pressure, flow choking, and material thickness. This information has been presented in Technical Note 3596 together with simple calculation and correlation procedures for determining permeability characteristics with reasonable accuracy when experimental data are limited.

A general investigation is being conducted to determine the relative smoothness of the flows in the various supersonic facilities of the National Advisory Committee for Aeronautics. As part of this investigation, tests have been conducted in the Langley 4- by 4-foot supersonic wind tunnel to determine the transition Reynolds number for a 10° cone at Mach numbers of 1.41, 1.61, and 2.01. The results of these tests, given in Technical Note 3648, indicate that, on the average, the transition Reynolds numbers for a smooth cone increased with tunnel stagnation pressure from about 7×10^6 at a test Reynolds number of 4×10^6 per foot to approximately 8×10^6 at a test Reynolds number of 9×10^6 per foot for all test Mach numbers. There was no effect of Mach number on transition Reynolds number in the range investigated. The results also indicated that the transition point was unsteady and tended to oscillate approximately ± 10 percent about the mean value of transition Reynolds number. The values of transition Reynolds number obtained were higher than those for any other tunnel for which similar data were available, which is indicative of a low tunnel turbulence level and freedom from extraneous flow disturbances. In addition, it was found that a single-element two-dimensional surface roughness of one layer of $\frac{1}{2}$ -inch-

wide and 0.003-inch-thick cellulose tape caused a larger decrease in transition Reynolds number than was experienced in low-speed or in other supersonic wind-tunnel investigations.

A continuing search is being carried out for techniques for producing high-stagnation-temperature hypersonic airstreams. One method involves use of the heat release given by chemical reactions. Here, the requirement is that not only the chemical used must liberate sufficient heat but also that the products of the reaction must have as nearly as possible the same flow properties as air for tunnel flow. Nitrous oxide was found to be promising for this use. Theory indicates that the thermal decomposition of nitrous oxide at constant volume can produce a temperature of 4,050° F and that the end products consist of two parts of nitrogen to one part of oxygen, which is reasonably close to the composition of air.

Preliminary laboratory tests made to verify theory for both a constant-volume and a constant-pressure decomposition show, as reported in Technical Note 3624, that a more complete decomposition was obtained at high-pressure conditions. Pressure up to 1,930 atmospheres was obtained for the constant-volume process, whereas the constant-pressure process was operated at 70 atmospheres, and theoretically predicted temperatures were approached. Decompositions up to 98 percent complete for the constant-volume process and 90 percent complete for the constant-pressure process were obtained. Results of comparison tests made in a small-scale wind tunnel at Mach numbers up to about 7 on air and on the products of nitrous oxide decomposed at constant pressure showed no significant difference.

In order to simplify the problem of model support for the measurement of forces at large angles of attack at high Reynolds numbers and supersonic speeds, nozzles exhausting directly to the atmosphere are used at the Langley gas dynamics laboratory. At the higher Mach numbers the separation of the boundary layer from the nozzle contours resulted in excessive stagnation pressures being required for establishing supersonic flow in the test section. An investigation, reported in Technical Note 3545, was made at Mach numbers of 2.7, 3.0, 3.5, 4.0, and 4.5 to determine the effect of short, fixed, wedge diffusers on the starting characteristics of these jets. Wedge diffusers that were extensions of the nozzle contours reduced the pressure ratios required for starting to less than one-half the values obtained without a diffuser. Central-body diffusers were not so effective as wedge extensions of the nozzle contours. With the wedge extensions of the nozzle contours, the jets could be started at each test Mach number for values of diffuser minimum area considerably below the values predicted by one-dimensional theory. The central-body diffusers required diffuser minimum area at least as large as theoretical values.

A series of wind-tunnel investigations has been conducted to determine the effect of inclination of the airstream on the measured pressures of a number of total-pressure tubes through a wide angle-of-attack range at subsonic, transonic, and supersonic speeds.

These investigations were conducted to obtain information which would lead to the design of rigid-type tubes capable of measuring total pressures correctly at high angles of attack and at high speeds. The need for this information has arisen because of the development of airplanes capable of maneuvering to high angles of attack at supersonic speeds and because conventional tubes, both rigid and swiveling, are unsatisfactory under these conditions. Conventional rigid tubes, that is, those with hemispherical or ogival nose shapes, are unsatisfactory because the measured pressure begins to deviate from the free-stream value at moderate angles of attack. Swiveling tubes, on the other hand, are considered undesirable because of possible structural failure at high speeds. Technical Note 3641 summarizes these results and presents the data in a form permitting a more detailed comparison of the effects of pertinent design variables.

The various tubes studied differed in regard to external shape, internal shape, and type of total-pressure entry. For simple nonshielded tubes, the best combination of these design variables produced a usable angle-of-attack range of $\pm 28^\circ$ at a Mach number of 0.26. For the more complicated shielded tubes, the best design produced a usable angle-of-attack range of $\pm 63^\circ$ at a Mach number of 0.26. The throats of the shielded tubes were vented through the walls of the shields, a design feature permitting end-mounting of the tube on a horizontal boom. There was considerable effect of Mach number on both unshielded and shielded tubes. For most of the unshielded tubes, the usable range increased the Mach number, whereas that of the shielded tubes decreased with Mach number.

In the description of random fields, the correlation function is an important tool. An instrument of fairly simple design for measuring time correlation functions of two stationary random electrical signals is discussed in Technical Note 3682. It is intended primarily for use in problems connected with aerodynamically produced acoustic fields but has properties suitable for application to a rather wide range of aerodynamic problems involving turbulent-flow fields. It has been designed and constructed with a view to economy and simplicity of operation and makes extensive use of the general statistical properties of the problems for which it is intended. A few experimentally determined autocorrelation functions are given in the Technical Note to indicate the degree of accuracy achieved. The Fourier transform of the autocorrelation function of a random input is compared with the power spectrum of the same function. The study was conducted at the Guggenheim Aeronautical Laboratory of the California

Institute of Technology under the sponsorship of the NACA.

HIGH-SPEED AERODYNAMICS

Airfoils and Wings

Designers of aircraft and aircraft propellers have repeatedly expressed the need for airfoil-section data in the transonic speed range. Almost all airfoil-section data in the subsonic speed range have been obtained from closed-throat tunnels which limited the tests to Mach numbers less than about 0.9. One method of extending speed range of two-dimensional experimental tests is by utilization of the open-jet principle to eliminate the choking limitations of closed-throat tunnels. Tests of a group of related NACA airfoil sections varying in maximum-thickness location, design lift coefficient, and thickness distribution have been conducted in a two-dimensional, open-throat-type wind tunnel at Mach numbers from 0.3 to about 1.0 and Reynolds numbers from 0.7×10^6 to 1.6×10^6 . The results of the tests, reported in Technical Note 3607, indicate that near sonic speeds the maximum normal-force—drag ratio approaches the low values theoretically determined for a biconvex airfoil in supersonic flow. Contrary to low-speed results, the maximum normal-force—drag ratio increased as either the thickness ratio or the camber was decreased. At all Mach numbers the normal-force coefficient for maximum normal-force—drag ratio generally increased with increases in thickness ratio and camber, and also with forward movement of the position of maximum thickness. The trends of the data in the highest test Mach number range indicated that the normal-force-curve slopes of all airfoils tested are approximately equal at a Mach number of 1.0, the value being about the same as at low speeds.

As part of the NACA program to determine the zero-lift drag characteristics of various wings at supersonic, transonic, and high-subsonic speeds, the Langley Pilotless Aircraft Research Station has conducted tests of a series of 60° delta wings. These wings had varying airfoil sections and were mounted on rocket-propelled test bodies.

The sections investigated were three double-wedge airfoils of 6-percent-thickness ratio with the position of maximum thickness at 20, 50, and 80 percent of the chord, an NACA 65-006 airfoil section, and a double-wedge 3-percent-thick wing with maximum thickness at 50 percent chord. The results, determined at Mach numbers from 0.7 to 1.6 and presented in Technical Note 3650, show that the forward locations of wing maximum thickness were better from a drag standpoint and that the thinnest section gave the lowest drag. Theoretical wing drag compared well with experimental. In related tests on 6-percent-thick, 2.7-aspect-ratio rectangular wings, varying the section from a circular arc

to a symmetrical diamond section, as reported in Technical Note 3548, decreased the drag at supersonic speeds and increased it at high subsonic speeds.

The aerodynamic properties of wedges of infinite span at Mach numbers near shock attachment have now been well explored. Information on wedges of finite span is less extensive. Since three-dimensional problems are beyond the reach of presently used transonic theory, knowledge here must come from experiment. A wind-tunnel study has therefore been made in the Ames 6- by 6-foot supersonic tunnel of the transonic flow over two rectangular wings of double-wedge section and aspect ratios of 2 and 4. The data cover the Mach number range from 1.166 to 1.377, which brackets the theoretical value at which the shock wave attaches to the leading edge of these wings at zero angle of attack. The effects of finite aspect ratio on the section characteristics of a double wedge were determined by comparing the present results with previous data for an infinite aspect-ratio wedge and also with two-dimensional theory for this shape.

The pressure-drag coefficient at zero lift is found to decrease with decrease in aspect ratio for all values of the test Mach number. Also, decreasing the aspect ratio reduces the lift-curve slope. The drag due to angle of attack is affected by variation of chord forces as well as normal force.

Theoretical considerations also lead to certain conclusions regarding wave detachment. In particular, detachment of a shock wave from a wedge of finite span occurred at the same free-stream Mach number as that from a wedge of infinite span. Results of this investigation are presented in Technical Note 3522.

Recent systematic experimental investigations of the effects of wing aspect ratio, thickness, and camber for wings of rectangular plan form at transonic speeds have provided data ideally suited for correlation by means of the transonic similarity parameters. Report 1253 indicates that the experimental data obtained on a series of 40 wings in the Ames 14-foot wind tunnel could be, for the most part, successfully correlated throughout the subsonic, transonic, and moderate supersonic regimes. By proper choice of parameters, the force and moment data could be presented in a concise manner effectively displaying the transonic characteristics of wings of both large and small aspect ratios. In many instances, it was found possible to predict from the correlation studies an expected range of validity for slender-body concepts. It appears that slender-body theory is adequate at sonic speed for rectangular wings of symmetrical profile if the product of the aspect ratio and the $\frac{1}{2}$ power of the thickness ratio is less than unity. A study of simple flow compression or expansion at near sonic speeds is also included. Transonic approximations for the classical shock polar and for Prandtl-Meyer flow are derived

and a limit for linearized two-dimensional flow theory at slightly supersonic speeds is given.

The problem of minimizing the supersonic drag for a given lift on a fixed plan form has been approached in several different ways. In Technical Note 3533, Lagrange's method of undetermined multipliers, is applied to the problem. The method indicates that a constant interference drag exists between the optimum loading and any other loading at the same lift coefficient. This is an integral form of a criterion established by Dr. Robert T. Jones. The best combination of four simple lift loadings on a delta wing with subsonic leading edges is calculated as a numerical example. The calculations show that the best combination of the four nonsingular loadings has about the same drag as a flat plate with full leading-edge thrust.

Recent experiments indicate that airfoil sections having sharp leading and trailing edges, heretofore considered good at supersonic speeds, may be inferior to blunt-trailing-edge airfoils when compared on the basis of drag-stiffness ratio and when used as control surfaces. The results of a Langley free-flight rocket-propelled model investigation of the effect of trailing-edge thickness on the zero-lift drag for an unswept wing mounted on an ogive-cylinder body for Mach numbers from 0.7 to 1.6 are presented in Technical Note 3550. The basic wing had an aspect ratio of 3.11, a taper ratio of 0.423, and 4-percent-thick circular-arc sections. The trailing-edge thicknesses investigated were 0, $\frac{1}{8}$, $\frac{3}{8}$, and $\frac{5}{8}$ of the maximum thickness. It was found that wing drag increased with trailing-edge thickness, whereas the trailing-edge base pressures appeared independent of the thicknesses used. The calculated wing drag compared favorably with the experimental.

Results of tests, reported in Technical Note 3548, of a rectangular wing of aspect ratio 2.7 with 6-percent-thick diamond sections through the aforementioned range show that the blunt trailing edge gives the higher drag because of trailing-edge suction throughout the test range.

The effects of drooped leading edges on the flow over delta wings are described in Technical Note 3614. Vapor-screen, pressure-distribution, and ink-flow tests were conducted at the Langley Gas Dynamics Laboratory on a series of semispan delta wings. The delta wings had semiapex angles of 15° , 22.5° , and 31.75° and 10 and 20 percent of the semispans drooped 15° in streamwise sections. The tests were made at a Mach number of 1.9 and indicate that flow separation occurred on all the wings in the series tested. The separated regions on the wings with 10 and 20 percent of the semispans drooped were similar to one another. Integrated pressure distributions show that, for equal angles of attack, the loadings on the wings with 20 percent of the semispans drooped were less than those on the wings with 10 percent of the semispans drooped. In

a general comparison with undrooped delta wings, the drooped-leading-edge wings show no particular advantage from a standpoint of preventing separation. The drooped-leading-edge wings had a disadvantage in loading, the loading in some cases being considerably less than that on the corresponding undrooped wings.

A knowledge of the effects of sweep and Mach number on wing aerodynamic characteristics near maximum lift is becoming more important as the speeds and altitudes flown by modern aircraft continue to increase. High-speed, high-altitude aircraft fly at rather high lift coefficients and in maneuvers may reach or exceed the angle of attack for maximum lift of the aircraft. Since sweptback wings are being used to delay and to minimize the effects of compressibility on some aircraft, it is important that the effects of sweep on the maximum lift coefficient are known. Considerable data are available for both swept and unswept wings up to maximum lift at low Mach numbers, but only a limited amount is available above a Mach number of approximately 0.60.

An investigation at transonic speeds was therefore made in the Langley high-speed 7- by 10-foot tunnel to determine the effect of wing sweep on the maximum-lift characteristics of a series of wings having aspect ratio of 4, taper ratio of 0.6, and NACA 65A006 airfoil sections. The Mach number varied from 0.61 to 1.20. It was found, as reported in Technical Note 3468, that the maximum lift coefficients increased with increased sweep at the lower Mach numbers but decreased with increased sweep at the higher Mach numbers. This resulted in less variation of the maximum lift coefficient with Mach number as the sweep was increased.

Several other studies concerned with the effects of wing plan form have been reported recently. For example, an investigation reported in Technical Note 3671 was conducted on the transonic bump of the Ames 16-foot high-speed wind tunnel to determine the effect of clipping the tips of a triangular wing. Four basic triangular-wing plan forms having aspect ratios of 2.0, 2.5, 3.0, and 4.0 were tested. The tips of these wings were progressively clipped to provide taper ratios of 0.1, 0.2, 0.3, 0.4, and, in some cases, 0.5. The NACA 63A004 profile was used with thickness-to-chord ratios of 0.02, 0.04, and 0.06. Lift, drag, and pitching-moment data were obtained for Mach numbers from 0.60 to 1.10, corresponding to test Reynolds numbers, from 1.85×10^6 to 2.90×10^6 . For aspect ratios of 2.0 or greater the wings with pointed tips had lift-curve slopes that were consistently lower than those for the wings with clipped tips. Values of drag-rise factor were higher in each case for the wings with taper ratios of 0 than for any other values of taper ratio. Generally, the most significant decreases in drag-rise factor were realized when the taper ratio was increased from 0 to 0.1. The cambered wings had consistently lower values of drag-rise factor than the

uncambered wings. In general, the values of the pitching-moment curve slope became less negative with increasing taper ratio. All wings tested exhibited a characteristic rearward shift of the center of pressure in going from subsonic to supersonic speeds. In general, decreasing the taper ratio decreased this rearward shift of the center of pressure.

In another study the effect of taper ratio on the zero-lift drag of a sweptback wing has been determined using rocket-powered models. Theoretical calculations were made for Mach numbers from 1.2 to 1.8 and were found to be in good agreement with the experimental data. The results are presented in Technical Note 3697.

Bodies

The Langley Pilotless Aircraft Research Division has conducted an investigation to determine the drag of practical fuselage shapes at transonic and supersonic speeds. One phase of this program is an investigation of how changes in nose shape affect the drag of an airplane or missile configuration. Linearized theory and some experimental data have indicated that, for minimum drag at supersonic speeds, the fuselage nose profile must be of high fineness ratio and tapered to almost a point at the vertex. It is of particular interest to determine how far practical designs can deviate from such profiles without severe reductions in speed and range.

In Technical Note 3549, drag data obtained during this study are presented for fin-stabilized bodies of revolution whose noses, originally pointed with fineness ratios about of $3\frac{1}{2}$, have been rounded off with radii equal to $\frac{1}{4}$ the maximum body radii. By comparing the measured values of drag coefficient based on frontal area for the blunt- and pointed-nose models, it is found that, within the accuracy and range of the present tests, rounding off the sharp noses produced no increase in the total drag of either configuration.

Considerable interest exists at the present time in the drag characteristics at supersonic speeds of nonlifting bodies of revolution designed for minimum wave drag. One such family of boattail bodies has been investigated previously to assess the effect of Reynolds number and Mach number upon the wave-drag characteristics.

In order to find body profiles which have minimum total drag, the base-pressure drag (if no jet exists at the body base) and the skin-friction drag must also be considered. The results of experimental measurements made in the Langley 9-inch supersonic tunnel, presented in Technical Note 3708, show that the base drag and, in general, the total drag, increase with increasing values of the ratio of base area to the maximum cross-sectional area B/S_{\max} . The results also show that the laminar skin-friction drag is in agreement with the theoretical predictions used, and, within

the Mach number range of the tests (1.62, 1.93, and 2.41), the simple Blasius incompressible theory gives a satisfactory prediction. Except for the values of B/S_{\max} near 1, the transition Reynolds number increases with increasing Mach number and, as this ratio approaches 1, the variation reverses. These variations in Reynolds number of transition with Mach number appear to be associated with changes in the pressure gradient over the rear of the bodies.

The shapes of nonlifting bodies of revolution having minimum pressure drag at supersonic speeds have also been the subject of numerous theoretical investigations. In Technical Note 3666, Newtonian impact theory is used in combination with the calculus of variations to determine body shapes for minimum pressure drag, neglecting base drag, at high supersonic airspeeds. Shapes are determined for various combinations of given length, base diameter, surface area, and volume. In addition, an estimate is made of centrifugal forces and their effects on the minimum-drag shapes were considered. In order to check the analysis, an experimental investigation was conducted in the Ames 10-by 14-inch supersonic wind tunnel on a family of bodies, including two of the minimum-drag shapes. The test results were found to substantiate the theoretical analysis.

A body moving at supersonic speeds has a wave drag which can be calculated either from integrations based upon the pressure at the surface of the body or by means of a momentum balance over a control surface surrounding the body. The control-surface approach shows more clearly that the wave drag is related to the transport of momentum in the Mach waves created by the body. This approach also suggests the scheme of reducing or destroying the wave drag through the use of a shroud as first shown by Ferrari. With such a shroud, the waves are caught and reflected to the body surfaces where they may be absorbed without further reflection. From the standpoint of the pressure exerted on the body itself, it follows that the reflected waves may strike the rear portion of the body in such a way as to provide a buoyancy to overcome the resistance of the body alone.

In Technical Note 3718, formulas for the wave drag of shrouded symmetrical airfoils and shrouded bodies of revolution of arbitrary shape are derived. The airfoil is shrouded by flat plates and the body of revolution is shrouded by a cylindrical shell. Although many configurations are possible, this analysis considers the particular arrangement where the shroud extends at least far enough forward to catch the Mach wave emanating from the body nose and far enough rearward to cast Mach waves on the base of the body. As a special application of the results obtained, a class of body shapes, similar to those given by Busemann and Ferri, was found for which the wave drag is theoretically zero.

Wing-Body Combinations

As part of a transonic-speed research program recommended by the NACA special subcommittee on research problems of transonic aircraft design, a systematic investigation of the effects of wing thickness and plan form on the aerodynamic characteristics in the transonic range has been conducted in the Langley highspeed 7- by 10-foot tunnel by the transonic-bump method.

A summary of the results of this investigation, presented in Technical Note 3469, indicates that, for subsonic Mach numbers below the force break, theoretical lift-curve-slope calculations were in fair agreement with the experimental results. In the supersonic range, however, the theoretical values were considerably higher than the experimental values. Increasing the thickness ratio caused rather large losses of lift in the transonic speed range, and increasing the sweep angle decreased these losses. Decreasing the thickness ratio and increasing the sweep angle increased the drag-rise Mach number and reduced the pressure drag. In general, the drag due to lift was increased by decreases in thickness ratio, increases in sweep angle, and decreases in aspect ratio.

The effect of sweep on delaying the onset of compressibility drag has generally been somewhat less beneficial than that indicated by simple sweep theory. This is caused, for the most part, by an adverse pressure distribution at the root of swept wings. A body-contouring method for alleviating this adverse interference at the root of a high-aspect-ratio swept-back wing has been studied in the Ames 14-foot wind tunnel. In this method the design objective is to alter the body shape so that the pressure distribution at zero lift, for a given subsonic design Mach number, will be the same at the wing-body junction as that on an infinite yawed wing at the same Mach number. This method of body contouring is primarily concerned with eliminating the interference at the root of a swept wing and should not be confused with the area rule which alters the axial distribution of cross-sectional area so as to minimize the wave drag at near sonic or supersonic speeds. Results of the study, presented in Technical Note 3672 show that beneficial results were obtained at free-stream Mach numbers above the critical, although modifying the body shape did not significantly affect the aerodynamic characteristics at subcritical speeds. Improved aerodynamic characteristics were evidenced by large reductions of drag, an increase in lift-curve slope, and a reduced change of pitching-moment-curve slope with increasing Mach number.

In Report 1252 a theoretical method developed at the Ames Laboratory is presented for calculating the supersonic flow field about wing-body combinations of bodies deviating only slightly in shape from a circular cylinder. If the combinations possess horizontal planes

of symmetry, no restrictions are required on wing plan form for the zero-angle-of-attack condition; if the combination is lifting, the method requires that the flow over the wing leading edges be supersonic. The method was applied to the calculation of the pressure field acting between a circular cylindrical body and a rectangular wing. An experiment was performed especially for the purpose of checking the calculated examples. For very small angles of attack the method predicted the pressure distribution with good accuracy. For higher angles, nonlinear effects of viscosity and compressibility were encountered.

In problems involving interference drag, the detailed pressure distributions are usually not calculated. In Technical Note 3674, slender-body theory is used to calculate the pressure distribution for some nonlifting wing-body combinations in subsonic and supersonic flow. It was found that when the body is indented so that a constant total area of the cross sections normal to the stream is maintained, the pressures over the wing remain small throughout the transonic range and the isobars tend to remain smooth and nearly parallel to the sweep angle of the wing.

The flow fields and shock formations about a wing-body combination and its equivalent body of revolution as determined by the transonic area rule must correspond if there is to be a correspondence between the drags of the two bodies. Some limited information on the flow fields indicated that such a correspondence existed. In the absence of information whereby a comparison of the complete flow fields past a wing-body combination and its equivalent body could be made, tests utilizing the schlieren method of flow photography have been conducted in the Langley 4- by 19-inch tunnel. In Technical Note 3703, the flow fields past an unswept- and a swept-wing-body combination are compared with the flow fields past their equivalent bodies of revolution at Mach numbers around 1.0. The results of the tests indicate that the flow past the equivalent body of revolution duplicates, or closely approximates, that past the wing-body combinations. The results indicate, furthermore, that, as the bump representing the wing area on the equivalent body departs radically from a slender bump or small disturbance, the similarity of flow between the wing-body combination and its equivalent body decreases.

AERODYNAMIC STABILITY AND CONTROL

Static Stability

Considerable information is available on the influence of the wing, fuselage, and tail geometry on the static stability characteristics of high-aspect-ratio unswept-wing configurations. However, there is little information of a systematic nature on the effects of wing aspect ratio for complete models. An experimental investigation has therefore been made at low speed in the Langley

stability tunnel to determine the effects of the various components and combinations of components on the static longitudinal and static lateral stability characteristics of models having unswept wings with aspect ratios of 2, 4, or 6. The results of this investigation, presented in Technical Note 3649, show that, at angles of attack near maximum lift, there was a pronounced increase in longitudinal stability for all wing-body combinations. At low and moderate angles of attack, decreasing the wing aspect ratio decreased the tail contribution to longitudinal stability. For the complete model, changes in wing aspect ratio generally had little effect on the tail contribution to directional stability throughout the angle-of-attack range investigated. The most noticeable effect of wing aspect ratio on the lateral stability characteristics occurred for configurations involving wing-fuselage combinations having an aspect ratio of 2. These configurations showed abrupt variations in the sideslip derivatives occurring at small angles of sideslip for angles of attack of about 20° and 26° , respectively.

A large decrease existed in the vertical-horizontal tail contribution to directional stability at moderate and high angles of attack. This was caused by the effect of wing-fuselage interference at the tail which was counteracted by a stable shift in the directional stability of all wing-fuselage combinations investigated. As a result of these combined effects, all complete-model configurations were directionally stable throughout the angle-of-attack range investigated.

The stability derivatives of such midwing research models which have simple bodies of revolution can, in general, be estimated with good accuracy in the low angle-of-attack range by various theoretical and empirical methods. Unpredictable interference effects caused by the addition of ducts, canopies, or other protuberances, makes the estimation of the stability derivatives more difficult and often impossible.

These models were modified to find the effects of size and position of closed wing-root air ducts on the static longitudinal and static lateral stability characteristics. In addition, the effects of top and bottom fuselage ducts on these characteristics were found for model configurations employing the wing having an aspect ratio of 2.

These results, reported in Technical Note 3481, show that, in the low angle-of-attack range, the addition of and increase in size of the wing-root ducts on model configurations employing the unswept wing with an aspect ratio of 2 resulted in a large forward movement of the aerodynamic center. This forward movement resulted regardless of whether the horizontal tail was located at the base or at the tip of the vertical tail. Increasing the wing aspect ratio from 2 to 6 made this effect more pronounced. A slight rearward movement in the aerodynamic center resulted from the addition of and increase in size of the top and bottom fuselage ducts. Regardless of the aspect ratio of the wing, the addition

of and increase in size of the wing-root ducts caused an increase in directional stability for the complete models at low angles of attack. The addition of and increase in size of top and bottom fuselage ducts on the complete model with the aspect-ratio-2 wing, however, resulted in a large decrease in directional stability which was about constant throughout the angle-of-attack range investigated.

In another study the effect of fuselage cross-sectional shape was determined for models having 0° or 45° sweptback wing. The results, presented in Technical Note 3551, show that the direct contribution of the fuselage cross section affects the longitudinal and directional stability characteristics at low angles of attack. At high angles of attack, in addition to the direct contributions of the fuselage, wing-fuselage interference (sidewash) with the tail decreases the directional stability. The configuration with the shallow fuselage suffered the least from this detrimental effect. In general, the configuration with a deep fuselage had the poorest directional characteristics of the models investigated.

One longitudinal stability problem of particular concern with respect to swept-wing airplanes is the "pitch up" which manifests itself essentially in a reversal of the variation of elevator control position and force with normal acceleration. This pitch-up behavior, as far as the pilot is concerned, limits the useful maneuvering range of the aircraft. Tests are continuing, therefore, so that this condition can be better understood and eliminated. In one Ames Laboratory study, flight tests were conducted on a 35° swept-wing aircraft to determine the origin of the pitch up. The results, presented in Report 1237, show that the pitch up encountered in a turn at constant Mach number was caused by an unstable break in the wing pitching moment with a corresponding increase in lift. The pitch up encountered at about 0.95 Mach number in a dive-recovery maneuver was due chiefly to a reduction in the wing-fuselage stability with decreasing Mach number. The unstable break in the wing pitching moment has been linked in part to separated flow over the wings. This can also result in buffeting and wing dropping.

Among the modifications studied at the Ames Laboratory to reduce the effects of flow separation, vortex generators, a development by H. D. Taylor of the United Aircraft Corporation, are shown in Technical Note 3523 to be effective. These devices are small airfoils placed perpendicular to the surface in a flow field in such a manner as to create vortices with axes aligned in the flow direction. Properly designed vortex generators thus provide intermixing of the retarded boundary-layer flow with the higher energy flow further from the surface and, hence, tend to delay separation. Vortex generators of proper design were effective in delaying the lift coefficient at which the

pitch up occurs as well as in reducing the severity of wing dropping.

Considerable research effort has also been devoted to improving undesirable pitching-moment characteristics of swept wings by use of slats, fences, and other devices. In one flight investigation made at the Ames Laboratory with a 35° swept-wing airplane, the effects of a partial-span, 15-percent-chord leading-edge extension were evaluated. The extension was found to be highly effective in eliminating the stick-fixed instability (pitch up) for Mach numbers below 0.84, though no benefit was observed at Mach numbers between 0.84 and 0.88. For Mach numbers above 0.88, the lift coefficient at which the pitch up commenced was increased somewhat but the severity was not significantly changed. Pilot opinion indicated improvement in the modified airplane flight characteristics at Mach numbers at which the pitch up was eliminated.

In another flight investigation, undertaken at the Ames Laboratory, the effect on the outboard wing sections of reducing the trailing-edge angle by using blunt trailing-edge ailerons was determined. Wind-tunnel tests had indicated that reduced trailing-edge angles would be beneficial. The results show significant improvement in the pitch-up characteristics at Mach numbers around 0.90.

Another strong influence on the longitudinal stability of an airplane is the downwash. Until recently, little information of a systematic nature was available relative to the effects of wing geometry on the downwash characteristics at transonic speeds. As part of a transonic research program, however, the effects of changes in wing plan form and thickness were investigated through a Mach number range of approximately 0.6 to 1.1 by utilizing the Langley high-speed 7- by 10-foot tunnel transonic bump. Downwash information was obtained by the use of floating vanes mounted at various positions behind eleven wings of various plan forms and profiles. Theoretical estimates of the downwash were made for all of the wings at subsonic and low supersonic speeds by use of compressible vortex theory and 20-step wing spanwise loadings. Reasonable agreement between theory and experiment was obtained except for the chord-plane location at subsonic speeds. It was found that the agreement for this condition could be improved by assuming a completely rolled-up vortex sheet. Results are presented in Technical Note 3628.

The effects of wing sidewash on the vertical tail can also be of considerable importance. In Technical Note 3609, results are presented of a theoretical analysis, conducted in the theoretical aerodynamics section of the Langley Stability Research Division to determine by means of linearized lifting-surface and lifting-line theories the sidewash field behind rolling triangular wings with subsonic leading edges for supersonic flight speeds. The analysis also includes the development

of an expression for the sidewash based on horseshoe-vortex approximate-lifting-line theory. The approximate procedure, which is useful in computing the sidewash for wings of arbitrary plan form and span loading is in good agreement, in general, when compared with the more exact calculations for the triangular wing. Variations of the sidewash with longitudinal distance in the vertical plane of symmetry are presented in graphical form; illustrative calculations of the resultant induced force acting on various vertical tails are also included.

It has been recognized for some time that interference among the various airplane components can be very important in determining the aerodynamic characteristics of slender configurations. The use of slender-body theory for treating entire wing-body combinations is not new, and for cases falling into this category considerable simplification has resulted. The calculation of interference effects due to wing wakes (wing-tail or wing-afterbody interference), on the other hand, is not so clear cut. Unlike the wing-body problem, this calculation becomes more difficult as the effects become more important, since the rolling up and displacement of the wing vortex sheets cannot be ignored for long slender configurations.

In Technical Note 3525, formulas are developed for the forces and moments caused by vortex interference on slender wing-body-tail combinations of general cross section in terms of the positions and strengths of the shed vortices. The analysis is applicable to steady motion and to motions which can be considered as a succession of steady states (i. e., quasi-steady motions). In order to illustrate the application of the analysis, the interference lift of a plane wing-body-tail combination in steady straight flight was determined by utilizing vortex positions obtained by numerical methods. It was found that the impulse of each shed vortex and its image vortex in a transformed circle plane enter into all the interference forces and moments on the airplane. A simple theorem is given for the interference forces in steady straight flight; these forces are found to depend on this impulse evaluated only at the wing trailing edge and at the base of the configuration.

In another theoretical study, the pressures, loadings, forces, and vortex wake associated with low-aspect-ratio cruciform wing arrangements were determined. For 45° bank, the wake of a cruciform wing is treated numerically with 40 vortices and analytically with 4 vortices. Comparisons are made with water-tank measurements. Formulas are also given for the calculation of loads on a cruciform tail operating in the wake of a wing. These results are reported in Technical Note 3528.

A method (described in Technical Note 3670) has also been developed by the Ames Laboratory for calculating vortex paths. The method is applicable to any

situation where the initial positions and strengths of the vortices are known. The method was then applied to computation of vortex positions behind a slender equal-span cruciform wing at several different bank angles and from these computed positions the interference forces on a tail were calculated. Comparison with the known analytical solution for 45° bank angle shows good agreement.

In exploring the possibilities for the attainment of long range in airplanes designed to fly at high subsonic speeds, consideration has been given to the aerodynamic problems associated with the use of turbine-driven propellers operating ahead of a sweptback wing of high aspect ratio. The effects of operating propellers on the stability and control of multiengine aircraft having unswept wings have been quite thoroughly investigated in past years. The newer configurations, however, involve several elements which make the results of the earlier work either inapplicable or inadequate. Of paramount importance is the large increase in propeller disk loading (with the associated increase in slipstream intensity) which, in combination with wing sweepback, might be expected to create longitudinal stability difficulties.

A related investigation was carried out in the Ames 12-foot pressure wind tunnel to evaluate the effects of operating propellers on the longitudinal aerodynamic characteristics of a representative four-engine airplane configuration with a 40° sweptback wing. The wind-tunnel model was designed to simulate an airplane capable of long-range operation at a cruising speed of 550 miles per hour at an altitude of 40,000 feet with very high wing loadings. The thrust of the single-rotation propellers was sufficient to simulate up to 10,000 horsepower per engine at sea level, assuming the model to be 1/12 scale. The tests were conducted at Mach numbers from 0.08 to 0.92 and included measurements of lift, longitudinal force, pitching moment, propeller thrust, and propeller power for a number of model configurations. These results, published in Technical Note 3789, show that for the configuration investigated, the use of propellers presents no serious longitudinal-stability problems at high speeds nor is the drag or the Mach number for drag divergence adversely affected by propeller operation. At low-speed conditions corresponding to take-off and landing, however, destabilizing effects of operating propellers may be very large, requiring, therefore, careful attention in aerodynamic design. The measurements were in sufficient detail to permit determination of the origin, nature, and intensity of the various components of the total measured effects of the operating propellers. Such an analysis has been published in Technical Note 3790, along with recommendations for reducing or avoiding adverse effects of propellers on similar configurations.

With the trend of modern high-speed aircraft,

particularly missiles, toward the use of tail configurations incorporating surfaces of low aspect ratio, a number of theoretical papers have been published on the determination of the stability characteristics of this type of configuration. Although most of these papers are concerned primarily with supersonic flow, some, which are based on slender-body theory (i. e., covering thin wings of extremely low aspect ratio and slender bodies), are applicable also at subsonic speeds. The theoretical stability characteristics for some tail configurations have been verified experimentally; however, only meager or no experimental data exist for a range of V-, Y-, and cruciform-tail configurations, particularly at low speeds. A low-speed experimental investigation was therefore made in the Langley stability tunnel to determine the static lateral and static rolling stability derivatives of a series of cruciform, inverted T-, V-, and Y-configurations composed of low-aspect-ratio triangular surfaces. The derivatives are presented as functions of the geometric characteristics of the models in Technical Note 3532, and for two configurations (a planar wing and an inverted T), as functions of angle of attack. Where possible, comparisons have been made between experiment and existing theory; in general, it was found that better agreement between theory and experiment was obtained for the sideslip derivatives than for the rolling derivatives.

Dynamic Stability

As part of a general research program concerned with the lateral dynamic stability and handling characteristics of high-speed, high-altitude airplanes, the Ames Aeronautical Laboratory has tested a 35° swept-wing fighter airplane through a wide range of flight speeds and altitudes. In Technical Note 3521 are presented results of tests of the lateral oscillatory characteristics made during a series of four flights. Comparisons are included of the computed variation of period and damping of the lateral oscillation with the measured values. These comparisons indicate the accuracy with which the oscillatory behavior of an airplane can be predicted under various flight conditions using available or estimated mass parameters and stability derivatives and neglecting such effects as aeroelasticity and unsteady lift.

The airplane was found to be laterally stable, statically and dynamically, throughout the speed range tested. The variation with Mach number of the period of the lateral oscillation was satisfactorily predicted from available and estimated aerodynamic and mass parameters. The time required to damp to half amplitude, as measured from flight, varied with Mach number in essentially the same manner as predicted from computations. The measured damping was somewhat better than that obtained from computations at an altitude of 35,000 feet, particularly

at a Mach number of 0.92. An increase in time to damp to half amplitude was noted between Mach numbers of 0.95 and 1.04.

Several modern high-speed airplanes incorporate structural components that are more flexible than those previously used. There has been concern that the increased flexibility might appreciably modify the dynamic stability characteristics as predicted by rigid-airplane theory. Particular concern was felt for the possibility of interaction between structural and stability vibratory modes because the natural frequencies of the major structural components are approaching the natural frequencies of the short-period stability mode.

The problem of the effect of wing flexibility on the dynamic longitudinal stability of large airplanes has already been treated analytically in the subcritical speed range by a simplified semirigid method. In Technical Note 3543, the effects of fuselage flexibility are studied by the same method for the same class of airplanes.

Results of the study indicate that no serious problems are introduced insofar as the dynamic longitudinal stability of high-speed bomber airplanes in the subcritical speed range is concerned. The results further indicate that, if desired, future designs may incorporate somewhat more flexible fuselages than the typical current design studied and still have dynamic longitudinal characteristics approximately equal to those predicted by quasi-static theory and roughly equivalent to those predicted by rigid-body theory. The aerodynamic restoring forces which act on the airplane are sufficient to increase the frequency of the fuselage oscillatory mode in flight so that the latter frequency is always higher than either the fuselage-ground structural frequency or the airplane-stability natural frequency. Thus, the occurrence of a resonant condition is avoided. The changes in static characteristics caused by increased fuselage flexibility appear as decreased straight-flight and increased maneuvering-flight stability margins and increased elevator control deflections required for balance. The need for a means of longitudinal balance in steady maneuvering flight, other than elevator or horizontal-tail deflection, is indicated if flight is desired at low altitude and high speed with large airplanes that have fuselage natural frequencies much below those representative of current design practice.

In the design of automatic-control equipment for high-performance aircraft, the dynamic response characteristics of the aircraft must be considered. Often these dynamic characteristics can be predicted by using stability derivatives obtained from wind-tunnel tests. In many cases, however, particularly in the transonic speed range, flight-test procedures are desirable to document the dynamic behavior of the

airplane. Flight tests also serve the additional purpose of enabling comparisons to be made with predicted results, thus aiding in the development of more refined prediction methods.

A related flight investigation has been conducted by the Ames Laboratory in which the longitudinal and lateral-directional dynamic-response characteristics of a 35° swept-wing fighter-type airplane were evaluated from Mach numbers of 0.50 to 1.04. The results of the study are given in Report 1250. Responses to transient rather than sinusoidal control inputs were chosen for analysis because of convenience in making flight measurements. These transient data were converted into frequency-response form by means of the Fourier integral and compared with predicted responses calculated from the basic equations of motion. The equations, or transfer functions, that best describe the various measured responses were evaluated by a curve-fitting process involving the use of templates and an analog computer. By this method it was generally possible to find equations, of simple form, that closely matched the experimental frequency responses between 1 and 10 radians per second and at the same time adequately described the recorded time histories. Experimentally determined transfer functions were used for the evaluation of the stability derivatives that have the greatest effect on the dynamic response of the airplane. The values of these derivatives, in most cases, agreed favorably with predictions over the Mach number range of the tests.

Recent work on wing configurations designed to redirect propeller slipstreams downward has demonstrated that this principle can be used to provide direct lift for vertical take-off and landing. With transport aircraft, using this principle, it is possible to keep the fuselage approximately horizontal at all times.

The program of the Langley 7- by 10-foot tunnels which is concerned with the study of the promising double-slotted-flap configurations, has been extended to determine the effect of ground proximity and to develop a leading-edge longitudinal-control device. In Technical Note 3629 it is shown that, with the propeller-thrust axis on the wing-chord plane, both the slipstream deflection and the ratio of resultant force to thrust are reduced as the ground is approached. It is also shown that lowering the thrust axis below the wing-chord plane tends to alleviate these adverse ground effects while at the same time reducing the large diving moments associated with the slotted-flap configuration. Technical Note 3692 presents results which indicate that, for configurations utilizing deflected slipstreams, a leading-edge slat, preferably above the wing-chord plane, can provide increments of pitching moment of the order of those required for control and change in trim with center-of-gravity travel for a vertically rising airplane in hovering flight. In the ground-effect region,

however, the slat is generally ineffective as a longitudinal-control device.

In another Langley investigation, the stability and control characteristics of a low-wing four-engine transport vertical-take-off airplane have been determined with a remotely controlled free-flight model. In order to provide direct lift for hovering flight with the fuselage horizontal, the wing and propellers were rotated 90° with respect to the fuselage. Despite the fact that the pitching and rolling motions of the model were unstable oscillations, the model could be flown smoothly and easily without the use of any automatic stabilization devices because the periods of the oscillations were fairly long and the controls were powerful. The pitching oscillation could be completely stabilized by the use of artificial damping in pitch; thus the model could be flown in pitch for long periods of time without the use of the manual pitch control. Although there was no stability of yaw position, the model was easy to control in yaw because the motions were slow and the yaw control was powerful. There were no noticeable interactions between the rolling and yawing motions or between the roll and yaw controls. Vertical take-offs and landings could be performed fairly easily, although some forward or backward motion of the model was often present. Results of the study are given in Technical Note 3630.

Damping Derivatives

One of the more important factors entering in aircraft stability and control calculations is the aerodynamic resistance to roll or damping in roll. The damping in roll is generally expressed in terms of the nondimensional parameter C_{lp} which is the rate of change of rolling-moment coefficient with change of wing-tip helix angle, $pb/2V$. To check the validity of theoretical results, data were obtained by means of a forced-roll technique which consisted of rolling various wings in the Langley 9-inch supersonic tunnel at various constant rolling velocities and then measuring the aerodynamic resistance. Some of the results for the rectangular and triangular plan forms, obtained at Mach numbers of 1.62 and 1.92, are reported in Technical Notes 3740 and 3745. Comparisons of the experimental results with predictions based on linearized theory indicate that the damping in roll was predicted accurately for rectangular wings and for all other wings at Mach numbers for which the leading edge was decidedly supersonic (leading edge swept well ahead of the Mach trace emanating from the apex). When the leading edge was substantially subsonic (leading edge swept well behind the Mach trace), theory satisfactorily predicted the damping for triangular wings but appeared to overestimate (in some cases considerably) the values obtained for the sweptback, tapered wings. In the transition range, where the leading edge was near sonic,

the theory, as expected, overestimated the damping in roll for all applicable plan forms.

As part of a continuing investigation of the effects of unsteady motion on the lateral stability derivatives of airplane models, tests were made in the Langley stability tunnel at low speeds to determine the effects of frequency and amplitude on the yawing moment due to rolling and the damping in roll for an unswept-wing airplane model. These tests, which were preliminary in nature, involved the forced oscillation in roll of the model about its longitudinal wind axis through a range of frequencies and amplitudes of motion. The results obtained were primarily for an angle of attack of 0° . Steady-state derivatives were measured by means of tests made with the model stationary in rolling flow and with the model rolling steadily at several rotary velocities in straight flow. These steady results are regarded as zero-frequency oscillation data and form the basis for a comparison of the unsteady-state and the steady-state rolling derivatives. Theoretical values for the steady-state rolling derivatives were also used for comparison with the experimental data.

The results of the investigation, presented in Technical Note 3554, show that, in the range covered, variations in the frequency and the amplitude of oscillation at 0° angle of attack had no important effect on either the yawing moment due to rolling or the damping in roll of the complete model. The fuselage-tail combination experienced a reduction in the yawing moment due to rolling as either the frequency or amplitude was increased. The values of the rolling derivatives obtained by oscillation methods were consistent with the values measured by means of rolling-flow tests at an angle of attack of 0° . At a high angle of attack, the model with the wing had a different oscillatory yawing moment due to rolling when compared with that determined under steady-state conditions.

Control

Some effects of wing geometric characteristics, aeroelasticity, and Mach number (from 0.6 to 1.8) on the rolling effectiveness of various types of ailerons have been obtained from a general investigation of lateral controls by the Langley Pilotless Aircraft Research Division with the use of free-flight rocket-propelled models. For plain, sealed, 0.2-chord, full-span, flap-type ailerons, the control effectiveness at supersonic speeds was found to be markedly less than at subsonic speeds for all the configurations tested; however, increasing the wing sweepback decreased the abruptness of the change in rolling effectiveness between subsonic and supersonic speeds and reduced the general level of rolling effectiveness throughout the speed range. Furthermore, the effectiveness increases with decreasing aspect ratio. Tapering the wing was found to have a beneficial effect on control effectiveness for unswept

wings but somewhat detrimental effect in the transonic region for wings swept back 45° . It was also shown that increased control effectiveness in the transonic region resulted from reducing the section thickness from 0.09 to 0.06 for an unswept wing but had little or no effect upon a 45° swept wing.

It was also found that small changes in the shape of the forward part of the airfoil do not appreciably change the control effectiveness, but trailing-edge angle has a powerful effect upon the control effectiveness; that is, positive control was obtained over the Mach number range when the airfoil-section trailing-edge angle was of the order of 10° or less; control reversal was encountered when the trailing-edge angle was of the order of 16° to 20° . A convenient way to achieve the beneficial effects of a small trailing-edge angle is to use slab-sided ailerons with thickened trailing edges. Camber was found to have little or no effect upon the rolling effectiveness of an outboard partial-span aileron on an inverse tapered swept wing.

Results of tests of a thin unswept wing with outboard partial-span ailerons show a very rapid decrease in control effectiveness with increasing Mach number above about 0.9. At supersonic speeds, the rolling effectiveness was only a small fraction of that obtained for a Mach number of 0.9. Tests with steel and aluminum-alloy wings indicate that the losses in control effectiveness due to aeroelasticity were negligible for this configuration. Other tests of a swept-tapered-wing research airplane with outboard partial-span ailerons show severe losses in control effectiveness (including control reversal) because of wing flexibility when scale wing stiffness was considered. Increasing the sweepback angle of the wings increased the Mach number for control reversal.

Results of tests of delta wings with ailerons show that the rolling effectiveness of constant-chord full-span flap-type ailerons on 45° and 60° swept delta wings and a delta-wing tip aileron on a 45° swept wing were about the same at Mach numbers less than 0.9. All controls exhibited a loss in effectiveness at supersonic speeds, but the rolling effectiveness of the delta-wing tip ailerons was about twice that of the constant-chord ailerons.

The control forces on aircraft operating at supersonic speeds are so high that very substantial power-boost systems are usually required to handle the hinge moments. In an attempt to find a solution to the problem of reducing the size and work requirements of boost systems for such aircraft, theoretical analyses have been made of the hinge moments due to deflection of unbalanced trailing-edge flap-type controls. These controls had plan forms varying throughout the range in which the control leading and trailing edges are supersonic and the control tips are streamwise. Ratios of lift and rolling moment to hinge moment and ratios of lift and rolling moment

to deflection work at fixed values of lift and rolling effectiveness were used as bases for the analyses, reported in Technical Note 3471.

Results of the analyses for longitudinal controls show that high-aspect-ratio untapered controls possess maximum ratios of lift to hinge moment. When low-aspect-ratio controls must be used, however, controls with triangular plan forms and highly swept hinge lines are shown to have higher values of the ratio of lift to hinge moment than untapered controls. Ratios of lift to deflection work for untapered controls are in most cases shown to be higher than those for controls with tapered plan forms.

On wings with sweptforward and unswept trailing edges, inversely tapered controls with triangular plan forms of moderate or low aspect ratio are shown to have maximum ratios of rolling moment to hinge moment. On wings with sweptback trailing edges, maximum values of this ratio are shown for either untapered or normally tapered controls. For any given control shape, the analysis illustrates the importance of using small controls with high deflections to obtain large values of rolling moment to hinge moment ratio.

Maximum ratios of rolling moment to deflection work on wings with sweptforward trailing edges are in most cases obtained with inversely tapered controls with triangular plan forms. On wings with unswept and sweptback trailing edges, the deflection work required is near minimum for untapered controls with spans of about two-thirds the wing semispan. Results indicate that large controls will in most cases have higher ratios of rolling moment to deflection work than smaller controls.

Another approach to this problem is to link the trailing-edge control to a leading-edge flap to cancel hinge moments. A theoretical study of such linked controls operating at supersonic speeds has been made in the Langley 19-foot pressure tunnel. The results reported in Technical Note 3617 indicate that substantial reductions in hinge moment can be realized, particularly for sweptback wings.

Another related investigation was made in the Langley high-speed 7- by 10-foot tunnel to determine the feasibility of using a servovane control at high subsonic and low transonic speeds. This servovane control, located ahead of and geared to a flap-type control, could presumably be deflected with relatively low control forces compared with flap-type controls. The control was tested on an untapered semispan wing of aspect ratio 3 with 35° of sweepback. Throughout the speed range tested (Mach numbers from 0.6 to 1.0), increments of lift, pitching moment, and rolling moment were produced in the correct direction over most of the angle-of-attack range tested. At an angle of attack of 0° the servovane control gave a higher incremental lift coefficient and had a more forward location of center of

pressure of lift than a comparable flap-type control. Results of the study are given in Technical Note 3689.

The emphasis on simplifying or eliminating power-boost systems required to move the controls of high-speed aircraft has led to consideration of using some part or all of the jet-engine air to provide control. In order to keep the quantity of air used to a minimum, a control system has been devised that obtains its effectiveness both from the reaction of the jet of air being ejected out of the wing and from the change in circulation about the wing resulting from the jet acting as a spoiler. The fact that a jet of air provides changes in lift similar to a plain spoiler has been known for some time, but the results have been limited to two-dimensional, very thick, airfoils. One advantage of this type of control is that an emergency control can be obtained by using air at stagnation pressure if the jet engine fails.

A related low-speed wind-tunnel investigation was made in the Langley 300 mph 7- by 10-foot tunnel of such a jet control as an aileron, a 35° sweptback wing having an aspect ratio of 4.76. The investigation was of an exploratory nature and was limited to the case where the jet was supplied with air at stagnation pressure. The results indicate that the air at stagnation pressure will provide adequate control for emergency flight for a system in which normal control is obtained by using a jet of air at high pressure or in which a spoiler is used in conjunction with the jet at stagnation pressure.

The spoiler used as a lateral-control device has been the subject of considerable investigation at low and high speeds, and on both swept and unswept wings. Recent investigations of spoilers used as lateral-control devices have shown that on thin wings with small leading-edge radii the unvented spoiler loses effectiveness rapidly as the angle of attack is increased above about 8°. It has been found that this loss in effectiveness at the higher angles of attack can be reduced at low speeds by using a slot in the wing behind the spoiler that allows the air to flow through the wing from the lower to the upper surface when the spoiler is deflected.

To determine whether a slot plus a deflector is as effective at high subsonic speeds as it was at low speeds, an investigation was conducted in the Langley high-speed 7- by 10-foot tunnel for a Mach number range from 0.40 to 0.91 of a 50-percent-semispan, inboard, spoiler-slot-deflector configuration on an aspect-ratio-4 wing with the quarter-chord line swept back 32.6°. The spoiler-slot deflector was located between the 55- and 70-percent-chord line. The results of the investigation indicate that the loss in rolling-moment effectiveness of an unvented spoiler at high wing angles of attack is materially reduced by the incorporation of a slot and deflector at Mach numbers up to 0.91. The optimum ratio of deflector to spoiler projection for best results varied with angle of attack, but a ratio of three-fourths

to one gave appreciable rolling-moment effectiveness through the angle-of-attack range from 0° to 20°.

High Lift and Stall

Final results of an extensive investigation into the possibilities of obtaining reliable lateral control at the lowest flight speeds of light airplanes are reported in Technical Notes 3676 and 3677. Previous results were reported in Technical Note 2948. This investigation was conducted at the Texas Agricultural and Mechanical College under the sponsorship of the NACA. It was found that, for all of the aircraft tested, adequate lateral control is available up to some critical angle of attack that is always within 2° of the angle of attack for maximum lift. The elevator deflection required to trim at this condition has been found, with power off and power on, for each of the aircraft tested, as well as the elevator deflection required to make a three-point landing. Flight tests were also made with one airplane having two different horizontal tail configurations in an attempt to provide an arrangement that would give near-optimum conditions with regard to the effect of power change on longitudinal trim near the stall. This attempt was successful with one of the configurations tested, so that under all of the conditions of power setting and center-of-gravity position tested the available elevator deflection was sufficient only to maintain the angle of attack at a point where lateral control remained adequate. The increase in minimum speed was negligible.

Analytical means are provided by which designers may estimate the elevator deflection required to trim in steady longitudinal flight; the effects on longitudinal trim of changes in some of the more important design parameters are demonstrated in a quantitative manner. It is concluded that the procedures suggested can result in a design in which the maximum up-elevator deflection may be maintained within the highest value that will result in satisfactory damping in roll and reliable lateral control under all flight conditions, while, at the same time, adequate longitudinal control is available.

In view of the successful application of vortex generators for reducing or eliminating flow separation under certain conditions, a limited flight investigation was made to determine whether vortex generators might reduce the separation on a trailing-edge flap sufficiently to improve the flap effectiveness. The results, presented in Technical Note 3536, show that none of the three vortex-generator configurations tested provided any increase in flap effectiveness for flap deflections of 45°. With a flap deflection of 20°, one of the configurations gave an increase in lift at a given angle of attack equivalent to about an 8° increase in flap deflection. However, the drag was also increased by about the amount that would be caused by the equivalent increase in flap deflection. The vortex-generator arrangements

tested, therefore, provided no net improvement in flap effectiveness from the standpoint of high-lift capabilities, although they appeared to offer some possibilities, through their effect at moderate flap angles, of improvement of flap-type control characteristics.

Spinning

In order to obtain a broader understanding of the factors which affect spin and recovery motions, a technique has been devised for determining time histories of the attitudes and velocities of free-spinning-tunnel models from film taken by two motion-picture cameras operating simultaneously. The method devised and the results of an initial application of the method in which time histories of attitudes and velocities have been determined for one medium-attitude, moderately oscillatory, developed spin and the recovery therefrom for a model representative of a contemporary fighter airplane, are described in Technical Note 3611.

The time-history curves indicate that the oscillatory motion of the spin was not completely regular, inasmuch as the period and amplitude of any one cycle of the time histories were not exactly the same as those for the preceding and following cycles. After rudder reversal from "with" to "against" the spin, some increases occurred in the amplitude of the oscillations, particularly in the lateral attitude angles of sideslip and wing tilt. The recovery was completed about $1\frac{1}{2}$ turns after the rudder was reversed. One factor which appeared to have an important part in the recovery from the spin in this investigation was a relatively high inward sideslip reached during the oscillations following rudder reversal. Analysis indicates that the high inward sideslip apparently caused a relatively large negative aerodynamic rolling moment which caused a large decrease in rolling velocity. As a result, there was a corresponding large decrease in the gyrodynamic pitching moment which had been holding the model in a nose-up spinning attitude.

The results of an investigation made in the Langley 20-foot free-spinning tunnel to study the gyroscopic effects of jet-engine rotating parts (or of rotating propellers) on erect spin and spin-recovery characteristics are presented in Technical Note 3480. The angular momentum of the rotating parts was simulated on the model by a rotating flywheel powered by a model airplane engine. The rotating flywheel (rotating clockwise as viewed from the cockpit) generally caused the model to spin at a decreased angle of attack and an increased rate of rotation in right spins, and at an increased angle of attack and a decreased rate of rotation in left spins. The recovery characteristics generally changed from satisfactory to unsatisfactory for right spins. For left spins, however, the satisfactory recovery characteristics obtainable with the flywheel not rotating were not appreciably altered when the fly-

wheel was rotating. Results indicate that the effect of rotating the flywheel could be influenced by loading.

Research Equipment and Techniques

A simplified method for obtaining free-flight measurements of longitudinal aerodynamic characteristics of airplanes and missiles has been developed by the Langley Pilotless Aircraft Research Division for use with rocket-powered models. The basic principle of this method is that the horizontal tail of a configuration is mass balanced and hinged rearward of its aerodynamic center as an all-movable tail. A continuous pitching oscillation of approximately constant amplitude is sustained throughout the Mach number range as the tail automatically flips between stop settings when the tail lift changes direction. This technique has been applied experimentally to a rocket-powered model of an arrow-wing airplane configuration having a T-tail arrangement. Data were obtained for this configuration on the drag due to lift, lift-curve slope, tail effectiveness, and effective downwash at the tail. Both preflight calculations and flight-test data showed that downwash from the wing increases the angle of attack at which the tail will flip. The steady-state angle-of-attack response to a unit tail deflection, therefore, should be slightly greater than the required angle of attack to flip the tail in order to insure that a continuous pitching oscillation will develop.

Free-flying dynamic scale models, frequently used for securing aerodynamic research data, generally use movable aerodynamic surfaces in order to furnish disturbing or restoring forces and moments for purposes of investigating the response of the model. Often, these aerodynamic surfaces are in unsteady or unknown flow fields; consequently, the magnitudes of forces or moments being applied are not accurately known. The use of small rockets to produce the required disturbing forces or moments minimizes these difficulties. Rocket motors have been used with good results to disturb the flight of rocket-powered research models in pitch and yaw. Recently, a requirement for the disturbance of a free-spinning model in the Langley 20-foot free-spinning tunnel resulted in the development of a miniature rocket producing 3 ounces of thrust for 2 seconds. The engineering methods necessary to produce the desired characteristics and the steps of research and design necessary to fabricate such a rocket are presented in Technical Note 3620.

AUTOMATIC STABILIZATION AND CONTROL

The problem of determining the differential equations governing the behavior of a dynamical system, given a time history of the response of the system to some input, has been of interest to aerodynamicists for some years. A general theory for the analysis of

dynamical systems has been developed at the Ames Laboratory ("equations-of-motion" method). This theory was presented at the Conference on Nonlinear Control Systems conducted jointly by the American Society of Mechanical Engineers and the American Institute of Electrical Engineers. It was noted that, when looked at from a new point of view, all such methods can be generalized so as to apply to linear and nonlinear systems alike. Use of this theory also has shown how new methods can be developed to satisfy the requirements of particular problems. One method developed has certain advantages over methods heretofore used. Its superiority is based on two facts: (1) The heavy dependence on the initial conditions which occur when using most of the previously known equations-of-motion methods is eliminated, and (2) there is no need for infinitely long records of the motions of the system following a disturbance. Finally, the time of application of the new method is no greater than that for existing methods and it is well suited to machine computation.

One of the factors that affects the precision of such flight operations as landing and air gunnery is the response of the airplane to gust disturbances. Therefore, it is highly desirable to study the motions of airplanes and airplane-autopilot combinations which result from gusts and to establish which combinations are best suited to minimize the motions. A related theoretical study has been made at the Langley Laboratory to determine the lateral response of a fighter airplane to atmospheric turbulence as approximated by side gusts and rolling gusts. The frequency response and power spectral density of the motions of the airplane with controls fixed and in combination with three different basic types of attitude autopilots are presented in Technical Note 3603. It was found that the airplane alone exhibited a large resonance to gust inputs associated with the Dutch roll mode. The addition of a yaw damper eliminated the resonance. The autopilot designed to provide regulation in yaw and roll greatly reduced the response to gusts. The autopilots designed to provide good course response to automatic lateral-steering command signals resulted in a large undesirable roll and yaw response to side gusts.

It was felt that this difficulty might not be basic and that the gust-response characteristics might be improved without deteriorating the command characteristics. A simplified theoretical study of methods to correct the undesirable gust response was therefore undertaken. The results of this study are presented in Technical Note 3635 which describes a simple modification to the yaw channel of an autopilot which reduces the roll response to side gusts while causing no change in course response. The study indicates that response to side gusts will be greatly reduced.

A theoretical study using an electronic analog

computer has also been made of the response to step gusts of an airplane equipped with a system which operates to reduce accelerations in rough air. In this system, modified wing flaps and the elevator are actuated by an automatic control system in response to the indications of an angle-of-attack vane. The effect of interconnection of the flap-operating mechanism with the pilot's control system is also included. The analysis, given in Technical Note 3597, shows that modified trailing-edge wing flaps and a coupled elevator operated by a vane-controlled servo system are effective in reducing normal acceleration and pitching velocity due to step gusts when the flap-elevator system is adjusted to maintain a steady-state constant lift and zero pitching moment about the wing aerodynamic center.

It was also found that desirable dynamic stability and control characteristics of this arrangement could be obtained without greatly altering the normal-acceleration alleviation characteristics of the system by providing a small but reasonable static margin for the airplane. Interconnection of the flap-operating mechanism and the pilot's elevator control appears to allow satisfactory longitudinal control of the airplane. In addition, it was found that the interconnected system resulted in a more rapid change in normal acceleration than was obtained by elevator control alone.

Based on the results of the theoretical investigation just discussed a light transport airplane was modified at the Langley Laboratory to incorporate the controls necessary for gust alleviation. Fundamentally, the system used full-span wing flaps to maintain constant lift in flight through rough air. A portion of the elevator control was geared to the flaps to adjust the pitching moment due to flap deflection. An angle-of-attack vane located on a boom at the nose of the airplane was used to sense the variations in gust velocity. Signals from the vane were supplied to an automatic control system which operated the flap controls in proportion to the change in angle of attack. The automatic control system was designed to attenuate sharply the gust inputs at frequencies in the neighborhood of the airplane structural frequencies in order to prevent excitation of flutter.

The initial results, reported in Technical Note 3612, indicate that the system is at least capable of reducing the normal accelerations due to gusts by about 50 percent at a frequency of 0.6 cycle per second, the natural frequency of the airplane, and by about 40 percent at a frequency of 2 cycles per second. The controllability of the airplane with the gust-alleviation system in operation is adequate and it is felt that this type of control may result in improved handling qualities of the airplane.

As a result of the present interest in the spiral-stability problem associated with most personal-owner air-

planes, the Flight Research Division of the Langley Laboratory has undertaken a program to investigate the effectiveness of a spiral-stability augmenting device. The specific problem facing the pilot of a personal-owner airplane is to maintain his airplane in wings-level flight during times when he has no natural-horizon reference and to keep the airplane from diverging spirally while he may be preoccupied with navigational problems. It has been demonstrated that the pilot's sense of orientation is unreliable in the absence of a visual reference, as may be the case when inadvertently or unavoidably encountering instrument weather. Also, many personal airplanes are equipped with only the basic instruments for instrument flight (turn indicator, ball-bank indicator, altimeter, and airspeed meter). Considerable proficiency in instrument flying is required to interpret the indications of these instruments properly and, in many cases, personal-airplane pilots are not sufficiently skilled in instrument flying to undertake it with safety. Although most present-day personal-owner airplanes, particularly those with high-wing designs, possess a slight degree of inherent spiral stability in cruising flight, they show unstable spiral tendencies under operational conditions. The main reasons for this apparent spiral instability are a lack of means for trimming the airplane laterally or directionally, a variation of lateral and directional trim with airspeed, and control-system friction which prevents the control surfaces from returning to trim position after a control deflection, even if there had been a means for initially trimming the airplane.

The device studied utilizes a rate-gyro sensing element to switch the control effort of an on-off type of control. This control deflects the ailerons at a constant rate relative to a spring preloaded aileron neutral position. An analytical study using phase-plane and analog-computer methods was carried out to determine a desirable control-effort switching function for the on-off or nonlinear control used in this device. Results of the analytical study indicate that the nonlinear control is effective in compensating for directional trim changes of the airplane due to changing flight conditions and also in rapidly returning the airplane to level flight from an initial roll displacement. Results of the flight-test program reported in Technical Note 3637 essentially verified the analytical results; that is, the device is capable of maintaining the airplane in equilibrium over its operational speed range under directional out-of-trim conditions that would cause rapid divergence of the normal airplane. The device also prevents excessive heading wander and airplane gyrations in turbulent air without pilot control. A means for holding the airplane in a stabilized turn to facilitate mild maneuvering through use of the automatic control is provided.

As part of a general research program for testing various means of automatic stabilization, the Pilotless

Aircraft Research Division of the Langley Aeronautical Laboratory has been conducting an investigation of various autopilot systems, including both linear and nonlinear systems. Nonlinear control systems have been considered as an effective, and possibly a simple way, of obtaining desired missile responses automatically. One such system, using a mechanical linkage with a dead or inoperative region as a means of providing an effective rate signal in an autopilot, has been studied in laboratory tests and through calculations of resulting missile motions in roll. Thus, a mechanical device is used to improve system performance in a manner similar to that which would be obtained by using a rate gyroscope. Laboratory tests of an actual servo using this device in connection with an electro-mechanical simulator of the rolling motion of a missile show the conditions under which a higher degree of stability is obtained with this nonlinear arrangement than with that of a comparable linear system. Results of this study are given in Technical Note 3602.

The Ames Aeronautical Laboratory has conducted extensive research on the various factors which influence a pilot's ability to track a target with fighter-type airplanes. Normally, simulated aerial attacks have been made against target airplanes and tracking errors have been evaluated from motion pictures of the target. In order to eliminate the trouble and expense of a second airplane, it appeared desirable to replace the target airplane by a simulated target projected on the wind-screen. Selected attack situations and target maneuvers could thus be repeated quickly and accurately, and tracking errors could be continuously recorded for rapid analysis. To investigate this method, which is described in a paper presented at the Institute of Aeronautical Sciences, a prototype optical target simulator was constructed and evaluated in flight.¹ Initial experience with this equipment led to application of its principles to other flight-research devices and problems. The related equipment which has been developed includes a target simulator for tracking research on a scope-presentation fire-control system; an airborne drone aircraft simulator for use in studies of simple remote-control systems, and a windscreen-instrument display for the pilot's use in performing prescribed maneuvers.

Pilot opinions indicated that an optical target simulator (installed in an F-80 airplane) provided good qualitative matching of actual tracking problems. Tracking errors against actual and simulated targets were equal in steady, straight tail chases and slightly greater against the simulated target in steady turning flight. The most apparent difference was the large error against the simulated target during abrupt turn entries, due possibly to a lack of bank-angle information to the tracking pilot.

¹ See Kauffman paper listed on p. 77.

The target simulator used with the scope-presentation fire-control system included a tracking radar for obtaining target-motion data, and an oscilloscope for displaying computed steering errors to the pilot for corrective action. It was the pilot's opinion that the scope-presentation target simulator gave a good representation of the steering problem encountered in final attack runs against actual targets.

In the airborne drone simulator, pilots' maneuvering commands to the drone are applied by use of a switch on the control stick. These signals are then fed to an airborne drone dynamic analog computer which approximates the behavior of the line of sight to the actual drone. The output of the analog then controls a dot appearing on the windscreen, indicating the simulated drone motions.

Principles and features similar to those used in these studies appear to have application to a wide variety of weapon-systems development, training, and instrument-flight problems.

INTERNAL FLOW

Inlets

Although external compression inlets have produced relatively efficient supersonic compression of the induction air, the wave drag of the external cowl has been high and as much as 10 to 20 percent of the total airplane drag at Mach numbers above 2. An experimental investigation was conducted at the Ames Laboratory therefore to study the feasibility of using inlets having internal contraction at supersonic speeds and in which the external angle of the lip would be small, thereby resulting in little or no drag penalty. The internal compression inlet studied was circular in cross section and had a translating center body which could be moved forward in order to increase the throat area of the inlet, thereby permitting supersonic flow to start in the converging portion of the inlet. The center body then could be moved rearward in order to reduce the throat area to nearly the isentropic value for a convergent-divergent nozzle. The results have shown that with such an inlet the external drag was essentially zero and the total pressure measured at the simulated compressor face was as good as that measured with single-cone, external compression inlets at Mach numbers from 2.1 to 3, the limit of the investigation.

The use of a deflector ahead of the inlet at angle of attack resulted in maintaining satisfactory pressure-recovery characteristics up to angles of attack of approximately 12° . Boundary-layer control on the center-body annulus through porous surfaces in the vicinity of the throat of the internal contraction inlet improved the pressure-recovery characteristics of the inlets by as much as 10 percent. In addition to satisfactory total pressure-recovery characteristics, the total pressure variation at the simulated compressor station

was small and within 12 percent of the average value for the Mach number range from 2.1 to 2.5.

The design of the internal-flow system of a turbojet-powered aircraft for optimum operation at transonic or supersonic speeds usually compromises operation of the system during take-off and low-speed operation. In order to study this problem, two annular conical-shock inlets and several open-nose inlets of varying proportions and lip profiles have been investigated in the Langley 8-foot transonic tunnel under static operating conditions. Measurements were made of pressure recovery, lip pressure distribution, total-pressure distribution, and mass flow. Results indicate that the pressure recovery and the choking mass-flow rate were greatly improved by replacing the sharp lip on the open-nose inlet with more rounded lips. The open-nose inlets provided greater pressure recoveries than did the annular conical-shock inlets.

Charts and tables for the design of axisymmetric and two-dimensional inlets and exits have been prepared at the Lewis Laboratory and are presented in Technical Note 3589 for supersonic Mach numbers up to 4.0. The report also indicates a compression limit for isentropic inlets that restricts obtainable pressure recoveries to values considerably less than unity.

The internal space requirements for instrumentation and armament frequently dictate that the engine air inlet be located on the sides of the fuselage as a single- or twin-scoop configuration. An investigation has been conducted in the Langley 8-foot transonic tunnel of a twin divergent-walled submerged inlet. The pressure recoveries of the inlet at zero angle of attack varied from 98 percent at a free-stream Mach number, M_o , of 0.60 to 93 percent at $M_o=1.1$. Extensive total-pressure losses, together with severe flow oscillations, were observed at angles of attack greater than 7.3° for all Mach numbers.

Preliminary flight tests at the Ames Laboratory on a jet airplane equipped with submerged-type side inlets indicated performance considerably below the design estimates. Further flight tests were made on a similar airplane which featured a scoop-type inlet and a fuselage with a smaller aft end. In order to determine to what extent the inlet change contributed to the performance increase, the two different inlets were flight tested using the same after-fuselage configuration. The comparison was made on three bases: (1) The induction-system efficiency (ram recovery ratio at the inlet and at the compressor face, and engine power output), (2) the overall airplane drag coefficient, and (3) a computed factor of relative effectiveness.

The results indicate that the submerged inlet had a higher pressure recovery but also had a higher drag than the scoop inlet. Compared on the basis of a factor of relative effectiveness, the two inlet installations were found to be of about equal merit. Sealing the boundary-layer bleeds on the scoop inlet raised

the low recovery (below a Mach number of 0.85), whereas sealing the bleeds on the submerged inlet decreased the airplane drag coefficient.

One of the problems associated with the design of an efficient twin-scoop air-induction system on the side of the fuselage is the manner of handling the boundary-layer air ahead of the inlet. Two methods of boundary-layer control in a twin-scoop induction system were recently investigated at the Ames Laboratory: one allowed the low-energy air to pass under a compression ramp placed one boundary-layer height away from the fuselage; and in the other a portion of the low-energy air was drawn off through a permeable compression ramp placed contiguous to the fuselage surface. The results indicated that in both cases the boundary-layer control had a favorable effect on the total-pressure recovery and inlet airflow steadiness. A comparison of the two types of boundary-layer-control systems investigated showed that, in general, the system in which the boundary-layer air was allowed to pass under the compression ramp had a higher net propulsive thrust and a larger stable range of operation than the system in which the boundary-layer air was drawn off through the permeable compression ramp.

In the design of auxiliary air inlets or boundary-layer-removal systems, estimates of the entering boundary-layer mass flow and momentum must be made. Charts have been prepared at the Lewis Laboratory for evaluating these quantities for various turbulent boundary-layer profiles and are presented in Technical Note 3583.

Inlets designed for supersonic jet engines are generally unstable at certain operating conditions. It is desirable to determine criteria which define the stable operating range of such inlets. This problem has been studied at the Lewis Laboratory and is presented in Technical Note 3506, wherein the jet engine is likened to a Helmholtz resonator having a through flow. It is assumed therein that at each instant, conditions in the combustion chamber are uniform. The latter assumption is relaxed in Technical Note 3574, which applies acoustic impedance techniques in a study of inlet stability.

Supersonic inlets of ram-jet-engine installations are also susceptible to unstable oscillations when the engine is not operating at either design Mach number or air-fuel ratio. Since this unstable inlet operation, known as buzz, has a strong detrimental effect on ram-jet performance, it is essential that this phenomenon be thoroughly understood so that the problem may be eliminated. Technical Note 3695, prepared at the Langley Laboratory, reports on a study, in which a modified nonstationary one-dimensional wave theory is employed, of the various waves which comprise the buzzing cycle. This analysis predicts the complex pressure-time variation in the ram jet, found

experimentally, and also shows how the oscillation begins and is perpetuated.

Diffusers

Tests have been conducted with a series of diffuser shapes defined by empirical equations having constants which are related to the initial boundary-layer thickness. The shapes were designed to provide high pressure recovery at near-sonic inlet Mach numbers. The tests were conducted at the Ames Laboratory through the mass-flow range with a variety of attached and separated initial boundary layers and also with two offset ducts, with a variety of surface conditions in the shortest duct.

The experimental results, reported in Technical Note 3668, provide substantiation for the design trends upon which the empirical equations were based. In addition, it was found that, for the axially symmetric ducts tested, the effect of initial boundary-layer thickness on pressure recovery was as important as that of duct shape. The best performance was obtained with a short duct with a thin initial boundary layer. With separated boundary layers, extended entry lengths provided markedly improved pressure recovery and flow steadiness relative to a similar duct with no entry extension. The offset ducts suffered losses in all performance parameters relative to a similar axially symmetric duct. Near maximum mass flow, the surface conditions investigated had only small adverse effects on pressure recovery. A loss of several percent in total-pressure recovery occurred with air leakage into the duct near the throat.

In many installations a short diffuser would be extremely desirable, but its use has been prevented by the total-pressure and static-pressure losses incurred by airflow separation resulting from the large included angles of a short diffuser. To determine whether this separation could be eliminated by using area suction, an exploratory investigation was performed with a 30° and a 50° porous, conical diffuser having area ratios of 2. The tests, at the Ames Laboratory, made at a mean inlet Mach number of 0.2, indicated that area suction eliminated airflow separation in the 30° and 50° diffusers with suction mass flows of 3 and 4-percent of the inlet mass flows, respectively. By eliminating airflow separation, the total-pressure and static-pressure losses of the 30° and 50° diffusers were less than those of a 10° diffuser without boundary-layer control.

Studies of various means of boundary-layer control for the purpose of increasing the efficiency of short diffusers have continued at the Langley Laboratory also. The results obtained in two investigations of the application of vortex generators, boundary-layer suction, and high-energy-air injection into the boundary layer to short, annular diffusers show that vortex generators are ineffective for extremely short diffusers. It also was found that a net gain in overall efficiency cannot be

obtained by suction or injection boundary-layer controls unless the auxiliary pumping power is held to a minimum by eliminating all flow separation upstream of the control point and by specially shaping the wall contours downstream of this point to suit the flow conditions prevailing with the control operating. The increase in static-pressure rise obtained through the use of boundary-layer controls was of the order of 40 percent.

Ducts and Outlets

In continuation of the studies of the Langley Laboratory of means for increasing the efficiency of internal-flow systems, an investigation was conducted to determine the maximum flow capacity and the pressure drop of 90° bends in ducts of circular cross section. It was found, in Technical Note 3696, that a mean radius of turn of 2.5 duct diameters was approximately optimum with regard to both characteristics. A duct bend with this radius of turn provided a maximum flow equal to 95 percent of the theoretical choking flow and experienced an increase in total-pressure-loss coefficient of only 31 percent as its entrance Mach number was varied from low values to the choking value. The effects of changes in inlet boundary-layer thickness were found to be unimportant.

The high auxiliary-air requirements of high-speed aircraft continue to emphasize the importance of the handling of this air. In order to obtain additional design information applicable to this problem, a transonic investigation of the performance of rectangular thin-plate and ducted outlets located in a surface parallel to the flow has been made by the Langley internal aerodynamics laboratory. As reported in Technical Note 3466, it was found that the thin-plate outlets provided higher discharge coefficients at low discharge pressure differentials and that their performance increased substantially as their aspect ratio was decreased below unity. All of the flush ducted outlets had approximately the same discharge coefficients regardless of inclination or curvature of the duct axis and provided more flow than the thin-plate outlets at high supply pressures. The discharge coefficients of these outlets were increased by recessing their downstream surfaces. Surface dynamometer measurement showed that the thrusts produced by outlets of these types corresponded approximately to the streamwise components of the calculated theoretical thrusts.

Thrust Reversers

Many uses for thrust reversers on jet aircraft have been proposed. They include braking the landing roll, reversing or spoiling thrust during the landing approach so that maximum engine speed may be maintained, and braking during diving maneuvers to limit flight speed. To be used effectively, the reverser must give the desired amount of reverse thrust without affecting

engine operation. Also, the design must lend itself to stowage with a minimum amount of boattail or base drag.

As part of an overall investigation of thrust reversers and their associated problems, studies were conducted with cold flow on thrust-reverser models. This work was done on a small-scale unheated-air-duct setup equipped with a 4-inch-diameter exhaust nozzle at the Lewis Laboratory.

The performance of a hemispherical thrust reverser over a range of geometric variables and some of the factors that affect reverse-thrust performance were investigated. The effects of most of the design variables of the reverser were obtained at an exhaust-nozzle total- to ambient-pressure ratio of 2.0. The basic data over a wide range of conditions were also obtained, however, so that other comparisons could be made.

The performance of cylindrical-type thrust reversers and the effects of several modifications on their performance were also investigated at an exhaust-nozzle pressure ratio of 2.0. These modifications included changes in frontal area, width-to-height ratio, depth, lip angle, end-plate depth, and end-plate shape. The performance of swept-type cylindrical thrust reversers, the relation of reverse-thrust ratio to reversed-flow attachment, and thrust-modulation characteristics were included in the study.

Preliminary data have been obtained on the performance of several cascade-type thrust reversers located upstream of the exhaust nozzle at exhaust-nozzle pressure ratios up to 2.4. Such reversers are referred to as the tail-pipe-cascade type. A total of 15 different tail-pipe-cascade configurations was investigated. These included two blade shapes, several cascade length-to-span ratios, and various innerbody lengths. For some of the configurations, modulation performance and surveys of total pressure and flow angle were obtained at the cascade discharge.

Technical Note 3664 presents several types of thrust reversers investigated under the overall NACA program, summarizes the important performance characteristics, and presents proposed operation methods. Three types of reversers were investigated: target, tail-pipe cascade, and ring cascade. The effects of design variables on performance, reversed-flow fields, and thrust-modulation characteristics were determined for each type.

PROPELLERS FOR AIRCRAFT

Aerodynamic Problems

Continued interest in propellers as propulsive devices capable of efficiently utilizing the high power available from modern gas-turbine engines has emphasized the need for data defining their characteristics in their various flight regimes. In addition to their performance at high speeds, there is equal need to know their

behavior in the negative-thrust range, where extremely large forces can result in the event of engine failure and in the high-thrust conditions occurring during the low-speed take-off run. The dual-rotation propeller is of particular interest since it offers the advantage of smaller diameter, higher efficiency, absence of reaction torque, and less noise as compared with the single-rotation propeller capable of absorbing the same power. To provide data useful in the design and development of these propellers, an investigation has been made in the Ames 12-foot pressure wind tunnel of NACA 4-(5)(05)-037, six- and eight-blade, dual-rotation propellers. These propellers were operated at positive and negative thrusts, at blade angles from -20° to 70° , and at Mach numbers up to 0.90, including operation at low-speed, near-static conditions. At high speed, $M=0.72$, these propellers had an efficiency of 0.80 for a blade angle of 65° , and at low-speed near-static conditions they produced about 3 pounds of thrust per horsepower at their design power loading.

The flow of air through the plane of a propeller is greatly influenced by the type of spinner used. Generally, propellers are designed for operation in a flow having uniform axial velocity over the propeller disk. Frequently this ideal flow is not realized because of spinner disturbance to the flow field. A flight investigation was made on three full-scale propeller spinners using the XF-88B propeller research airplane to obtain information on the spinner pressure distributions and on the radial extent of flow-field distortion by the spinner. One was a conventional conical spinner and the others, differing in size, had spherical midsections. Measurements reported in Technical Note 3535 show that distortion of the flow in the propeller plane amounting to 10 percent of the free-stream velocity extended outward from the spinner surface from 30 to 100 percent of the spinner radius. On the large spherical and conical spinner, the extent was greater than with the small spherical spinner; this indicates that there are some shapes for which the extent of flow disturbance can be minimized. Also, it is apparent from measurements with the conical spinner that the velocity of flow may be considerably reduced in the vicinity of the spinner. It is also pointed out that unfavorable flow separation could result with spherical spinners.

As part of a general investigation of the static characteristics of propellers, empirical methods for estimating static thrust, based on propeller charts, have been compared with a newer strip-theory method. The comparisons of experimental data with thrust and power coefficients calculated by strip theory show good agreement where adequate airfoil data are available, and the strip theory yields better results than the empirical method.

In the increasingly important field of vertical and short takeoff and landing, high thrust at low speeds

and cancellation of torque reaction make dual-rotation propellers an attractive means of propulsion. In order to fulfill a need for information concerning dual-rotation-propeller static-thrust characteristics, an investigation of six- and eight-blade dual-rotation propellers operating at zero advance was conducted at the propeller static test stand of the Langley 16-foot transonic tunnel. These propellers were made up of blades having the NACA 8.75-(5)(05)-037 design number. Static thrust and torque characteristics were investigated. Some types of vertical-take-off aircraft depend, for longitudinal and directional control, at zero or low forward speeds, upon the action of the slipstream on control surfaces. Velocity distributions, therefore, were also measured in the wake of the six- and eight-blade dual-rotation propellers. A major part of the investigation of dual-rotation propellers pertained to a study of vibratory stresses excited by mutual interference of the propeller blades of the front and rear components. The principal finding is that blade passage in a dual-rotation propeller is a fairly strong source of aerodynamic vibratory excitation. High stresses, however, were not encountered under any of the test conditions, and only moderate stress rise was encountered at resonant conditions, primarily in the torsional mode.

In connection with research leading to improved aerodynamic qualities in vertical-take-off aircraft, an investigation (reported in Technical Note 3547) was made to determine the effects of airspeed and angle of attack on the lift, drag, and pitching moment of a shrouded-propeller model. The model had a shroud length of about two-thirds the propeller diameter and was tested over an angle-of-attack range from 0° to 90° . Tests were made of the complete model with the propeller operating and also of the shroud and motor combination with the propeller removed. Static-thrust efficiency was found to increase with increasing radius of the shroud inlet lip.

Propeller Stall Flutter

In the design of a supersonic-type propeller, primary consideration has been given to reducing blade-section thickness ratios to as low a value as stress considerations will permit. However, the propeller blade with very thin sections has low torsional rigidity and is susceptible to stall flutter; consequently, the power capacity of such propellers during take-off may be limited by flutter rather than by aerodynamic characteristics. In an effort to improve the flutter characteristics of propellers and yet maintain thin blade sections, the effect of blade-section camber on the stall-flutter characteristics of three NACA propellers was investigated. An increase in blade-section camber was found to produce an important reduction in blade stresses due to flutter at blade-angle settings up to 28° .

HELICOPTERS

Rotor Aerodynamics

The need for research work on helicopters arises both from the desire of the user for a better, more reliable, or less expensive helicopter to do an existing job and from the desire to develop designs which will permit successful application to new missions. For both purposes, improved rotor aerodynamic theory and coordinated experimental research are required. In recent years, modern high-speed automatic computing machines have become generally available to research institutions and to industry. This availability, in turn, has made possible the application of these machines to the problem of computing the aerodynamic characteristics of lifting rotors by numerical methods. By means of such methods, factors that are normally omitted from conventional analytical rotor treatments, such as stall and compressibility effects and combinations of such design parameters as hinge offset, blade twist and taper, and root cutout, can be accounted for. Greater accuracy is thus obtained for designs of conventional types, while design studies for radically different helicopters (particularly designs aimed at higher forward speeds) become practical. The necessary equations and procedures for carrying out the numerical computations involved are presented in Technical Note 3747. Rotor characteristics considered included thrust, profile drag, total power, flapping, rolling and pitching moments, direction of the resultant-force vector, and the harmonic contributions of the shear-force input to the hub.

A knowledge of the steady-state flapping behavior of lifting rotors is necessary in the design of helicopter hubs and control systems, in estimating rotor-fuselage clearances, and as a prerequisite to the numerical evaluation of the aerodynamic characteristics of rotors. Equations for calculating rotor-blade flapping have been available from various theories. In order to reduce computation to a minimum, theoretical flapping values can be obtained directly from charts which were constructed and are presented in Technical Note 3616. The charts are applicable over a wide range of helicopter operating conditions and for blade twists of 0° , -8° , and -16° .

The recent emphasis on helicopter-rotor vibration and the consideration of compound helicopters and convertiplanes require a more complete evaluation of the induced velocity field near a lifting rotor and of the rotor downwash in the regions of wings and tail planes. The preliminary report of this experimental investigation has been supplemented in Technical Note 3691 by a complete presentation of results and a comparison with theoretically predicted flow fields.

The normal component of induced velocity of a lifting rotor can be calculated with good accuracy as far rearward as three-quarters of a diameter behind

the front edge of the rotor, provided a realistic non-uniform (essentially triangular) disk loading is assumed. Because of the rapid rolling up of the trailing vortex system, the induced-velocity calculations at the rear quarter of the disk do not accurately predict the measured results. In the far field behind the rotor the induced flow can be more accurately predicted by considering a uniformly loaded rotor in the same manner as a rectangular wing. Charts of the normal component of induced velocity in the longitudinal plane of symmetry in the near and far fields of the rotor determined analytically for different nonuniform, circularly symmetrical disk loadings are presented in Technical Note 3690.

One of the more difficult problems facing the helicopter designer is the calculation of the rotor-blade aerodynamic loading. The problem is difficult because of the complexity of the rotor flow and the uncertainties of the assumed distribution of induced velocity across the rotor disk. An extensive investigation to determine experimentally the helicopter rotor-blade loads for both the hovering and forward-flight conditions has been conducted in the Langley full-scale tunnel. The static-thrust information on a single rotor is presented in Technical Note 3688. A rapid dropoff in load per foot of span is shown near the blade tip. A comparison of the blade-section loadings with theory shows that a tip-loss factor which varies with thrust coefficient gives more accurate results than the commonly employed constant tip-loss factor.

The effects of compressibility arising from high tip-speed operation on the flapping, thrust, and power of a helicopter rotor over a wide range of forward flight conditions were investigated by the use of numerical methods and are reported in Technical Note 3798. With the particular airfoil characteristics used, the results indicated minor increases in rotor flapping and thrust when rotor tip speed was increased from 350 to 750 feet per second. The largest effect noted was an increase in profile-drag power in the advancing side of the disk that was proportional to the amount by which the blade-tip Mach number exceeded the drag-divergence Mach number. These effects of compressibility appeared to be independent of blade twist but are, of course, a function of the airfoil characteristics employed in the analysis.

Propulsion

The large load-lifter type of helicopters are particularly well suited to benefit from use of rotor-blade tip-mounted jet-propulsion power plants. A pulse-jet unit having high ratios of thrust to frontal area had previously been studied on the Langley helicopter test tower. In order to determine centrifugal-field effects on the propulsive characteristics, the same pulse-jet unit was tested over a range of yaw angles and forward speeds in the Langley 16-foot transonic tunnel. A

comparison of the nonwhirling and whirling results, presented in Technical Note 3625, indicates that the pulse jet is subject to reduced performance. This reduction results from centrifugal distortion of the fuel-spray pattern for centrifugal accelerations greater than 200g (a value high enough to indicate that no difficulty of this nature should be encountered with the largest load lifters but indicating an area requiring careful consideration for smaller pulse-jet designs).

A performance analysis of fixed- and free-turbine helicopter engines has resulted in performance charts and comparisons of the off-design specific fuel consumption, altitude performance, power-speed characteristics, and response times. The results presented in Technical Note 3654 indicate that power modulation of the fixed-turbine engine was more rapid than the free-turbine engine at constant shaft speed, although simultaneous changes in speed and power were executed by both engines in about the same time. At constant temperatures, the free-turbine power varies only slightly with shaft speed, whereas the fixed-turbine power decreases significantly with shaft speed.

Solutions of the problems of excessive vibration, structural fatigue, roughness of control, and rotor interference would become more evident if the nature of the rotor disturbances was known. With a reasonable knowledge of inflow variations, it may at least be possible to design away from these adverse characteristics. The available current experimental inflow data are not adequate to permit a thorough evaluation of existing theories. With the exception of the hovering condition, therefore, only a limited amount of material has been published about the correlation between inflow theory and experiment. Since no force and moment data for offset-flapping-hinge rotors were available, a study was undertaken by the Massachusetts Institute of Technology, under the sponsorship of the NACA.

Inflow distributions, azimuth and spanwise, were determined analytically from measured pressure distributions and blade-motion data on a model helicopter rotor blade under hovering and simulated forward-flight conditions. Pressures and corresponding blade flapping were recorded for various rotor conditions at tip-speed ratios of 0.10 to 1.00. Covered in this study are one-bladed-rotor operation effects, deliberate blade stall, data on the effects of cyclic pitch, and tests on a rotor with a 13-percent-offset flapping hinge. Since the offset-flapping-hinge rotor was used primarily as a means of alleviating stall in order to obtain inflow data at high tip-speed ratios, μ , in the vicinity of 1.0, no cyclic pitch was used to balance out the hub moments resulting from the incorporation of offset hinges. It is these moments which are the primary source of stall alleviation. The inflow plots presented in Technical Note 3492 indicate variations very different from the uniform distributions which are sometimes associated with a rotor disk. An extensive investigation of the $\mu=0.30$,

zero-offset rotor condition showed that larger inflow variations than those predicted by theory can exist. In addition, however, upflow over the forward portion of the disk and relatively large induced velocity at the trailing edge are verified. The inflow patterns for the zero-offset and 13-percent-offset rotors under the same conditions of operation, except for the presence of hub moments in the offset-hinge case, are found to be very different in general character.

SEAPLANES

Hydrodynamic Elements

Experimental and theoretical research on planing surfaces has been extended to include pressure-distribution surveys for a series of related prismatic planing surfaces having angles of dead rise from 0° to 40°, with and without chine flare. These pressure distributions are presented in Technical Note 3477 for a wide range of wetted length and trim.

The results substantiate the use of the normal-load coefficient as the key parameter in predicting flat-plate center-line pressures. The results further show that flat-plate pressure distributions can be adequately predicted from existing theories. The reduction in pressure accompanying an increase in angle of dead rise is about as expected on the basis of previous force measurements. The addition of horizontal chine flare increases the pressure near the chines and extends the region of positive pressures further forward of the stagnation point in the vicinity of the chines. Existing theories are in poor agreement with the experimental pressure distributions obtained for surfaces having dead rise. The lift and centers of pressure, predicted on the basis of the pressure distributions, are in good agreement with recent experimental and theoretical NACA research on planing surfaces.

Interest has been developing in the operation of water-based aircraft off ramps or beaches where the water depth approaches zero. In view of this, an experimental investigation was made to determine the effect of shallow water on the hydrodynamic characteristics of a flat-bottom planing surface. These data are reported in Technical Note 3642 and show that the lift, drag, and trimming moment about the trailing edge of the model increased as the clearance between the model and the tank bottom decreased. The most apparent increases occurred at clearances below one beam. With combinations of high-wetted length and high trim, however, the values began to increase at somewhat greater clearances. The lift-drag ratio increased with decreasing clearance for wetted length-beam ratios greater than 0.8 and trims less than 16°. The roach in the wake of the model increased in height and moved aft of the model as the clearance decreased.

In the past, seaplane-spray investigations were primarily concerned with the definition and reduction of spray impinging on the seaplane. Recent develop-

ments have somewhat altered the spray considerations since modern seaplane designs have closely coupled aerodynamic and hydrodynamic components which are constructed strong enough that considerable forces may be developed on the surfaces by impinging spray. A study of the scale relations for converting model spray-force data to full size is reported in Technical Note 3615. The results show that spray lift forces can be scaled by the conventional Foude relations but that a Reynolds number effect on spray drag is indicated. An empirical method is suggested for correcting the spray frictional-drag coefficients on a Reynolds number basis.

Results of a preliminary investigation of self-excited vibrations of a single planing surface are reported in Technical Note 3698. Research on vibrations of planing surfaces is of considerable significance in the application of hydro-skis to water-based aircraft, since such vibrations have been known to cause structural damage to the aircraft. This research has indicated that self-excited vibrations occur with high aspect ratio (on the order of 10) of the wetted portion of the planing surface and appear to be essentially an oscillation in trim or rise, or a combination of these motions. The oscillations can be decreased in severity or eliminated by using planing surfaces which limit the wetted aspect ratio. Dead rise, transverse curvature, and a pointed trailing edge are all effective.

In order to provide for flush retraction of hydro-skis on high-speed water-based aircraft, it is sometimes desirable to form these components from portions of the airplane which can be extended for landing and take-off. Since the bottom of these skis will then conform to the shape of the fuselage which is generally rounded or to that of the wing which is more or less flat, the skis also will generally have rounded or flat cross sections. Because of this,

an investigation was initiated to determine the characteristics of planing surfaces of several plan forms and transversely curved bottoms. One surface was of rectangular plan form with a flat bottom; the second had a rectangular plan form with transversely curved bottom; and a third surface had a flat bottom but was triangular in plan form. The trims investigated ranged from 4° to 20°. The data were reduced in the form of load, resistance, trimming moment, and draft plotted against wetted area.

Research Equipment and Techniques

The rapid increase in the landing speeds of current airplanes has caused a corresponding increase in the water speeds at which seaplanes operate. As a result, the gap between the speeds available in the existing hydrodynamic testing facilities and full-scale speeds has widened to an extent sufficient to make it advisable to ascertain whether these differences in speed are causing any significant differences in force coefficients. In an attempt to close this gap, an investigation has been made of the feasibility of obtaining hydrodynamic data at full-scale speeds by utilizing a rectangular 3- by 3¼-inch free-water jet actuated by compressed air. A comparison of planing data obtained in the water jet with similar data obtained in conventional towing tanks indicates that it is feasible to use a free-water jet as a hydrodynamic test facility for obtaining planing data at very high speeds. The main problem appears to be in establishing an adequate method of correcting the jet data for the limited boundaries. Consideration has been given to a simple empirical method of correcting planing data for the jet boundaries. This method gave reasonable results for the limited data available.

POWER PLANTS FOR AIRCRAFT

The ever increasing range, speed, and altitude requirements specified for supersonic airplanes and missiles has necessitated consideration of new types of power plants as well as the refinement of the more familiar types of turbojet, ram-jet, and rocket engines. As in the past the goal of NACA research in this field has been information leading to the development of light-weight, highly efficient propulsion systems, utilizing both chemical and nuclear fuels.

Increased emphasis has been placed on new fuels and rockets problems and on the effects of high temperature environment on engine performance and reliability. Of particular interest at high altitude is the performance of the combustion chamber. Much research has been done in order to understand the differences between theory and experiment for the effects of turbulence on flame ignition, propagation, and heat release.

In order to summarize the present "state-of-the-art" of airbreathing powerplants research, a technical con-

ference was held at the Lewis Laboratory in December 1955.

A description of the Committee's recent unclassified research in the field of aircraft propulsion is given on the following pages.

AIRCRAFT FUELS

Fuels Performance Evaluation

Because the ram-jet engine requires no significant moving parts for its operation, a greater variety of potential fuels is available for the ram-jet engine than for the turbojet and reciprocating engines. Specifically, the ram-jet engine is capable of utilizing fuels that may produce considerable solid materials in the process of combustion. A number of conventional and unconventional ram-jet fuels have been suggested for research because of the need for ram-jet fuels that may permit the realization of flight range and thrust beyond the

limits attainable with conventional hydrocarbon fuels. The adiabatic combustion flame temperature, combustion equilibrium-gas composition, air specific impulse, and fuel-weight specific impulse were investigated for each of several fuels. These fuels included octene-1, aluminum, aluminum-octene-1 slurries, magnesium, magnesium-octene-1 slurries, diborane, pentaborane, boron, boron-octene-1 slurries, hydrogen, α -methylnaphthalene, and graphite.

The desire for higher flight speeds has increased the demand for greater power per pound of fuel, and per unit volume of fuel. Emphasis has therefore been placed on the development of ram-jet engines and on turbojet engines equipped with afterburners suitable for operation on special fuels.

An analytical investigation was conducted to determine the theoretical air-specific-impulse performance of several fuels over a range of equivalence ratios, inlet-air temperatures, and combustion pressures. The fuels included octene-1, 50-percent-magnesium slurry, boron, pentaborane, diborane, hydrogen, carbon, and aluminum. Inlet-air temperatures between 100° and 900° F are considered at a combustion pressure of 2 atmospheres; a combustion pressure of 0.2 atmosphere is also considered at an inlet-air temperature of 100° F. Also discussed are the determination of air-specific-impulse efficiency and combustion efficiency for experimental data by the use of theoretical results and the estimation of the relative amounts of various fuels required to maintain a fixed engine thrust level.

For some time fuel cost has been accepted as a major consideration in the conversion of commercial airline operations from piston-engine aircraft to gas-turbine-engine aircraft. The most frequently proposed fuel for use in gas-turbine transports is kerosene; however, there has been interest in the possibility of further fuel-cost reductions by use of low-cost distillate and the residual fuel oils. These fuel oils are considerably cheaper than aviation gasoline, and the residual types are substantially less costly than kerosene. Despite the cost attractiveness the physical properties and combustion characteristics of such fuels offer many problems that must be solved before they can be successfully utilized in commercial aircraft. The properties of distillate and residual fuel oils and the influence of these properties on engine performance and handling procedures have been studied.

Combustion-chamber carbon deposition is a significant factor influencing the choice of fuels for the turbojet engine. A number of carbon-deposition tests were conducted in a single-tube combustor and in full-scale engines to provide some information concerning the relation between single-combustor and full-scale-engine carbon deposition. These data together with limited flight operational data provide some indication of the tolerable limits of deposition and of the neces-

sary control test limits that would ensure adequate fuel quality.

Thermal Properties of Aircraft Fuels

Sodium, beryllium, and magnesium alkyls thermally decompose under vacuum at 100° to 200° F. The main products are a metal hydride or an alkyl metal hydride and an olefin of the same number of carbon atoms as the original alkyl group. Recently, it has been observed that a boron alkyl, tri-*n*-butylborane, decomposed upon heating under vacuum; the products were dibutyldiborane and butene.² The similarity both in the nature of the products and the experimental conditions suggests that the same mechanism is involved in all these metal alkyl decompositions.

In some present-day turbojet engines, the engine lubricant is cooled in a heat exchanger by means of the fuel as it flows to the combustor. As a result, the fuel may be heated to temperatures high enough to cause the formation of insoluble, gum-like substances. These insoluble materials, if not removed or adequately dispersed, may foul the heat exchanger so that the lubricant is not adequately cooled or clog the filter screens or the injector orifices so that the fuel flow is reduced to the point of engine failure. The thermal stability of jet fuels is affected not only by the temperature, but also by the residence time of the fuel in the heated zone. Since fuel-flow rates decrease with increasing altitude, the problem becomes more severe at high altitudes where both higher fuel temperatures and longer residence times are encountered. The effect of dissolved oxygen on the filter-clogging characteristics of three JP-4 and two JP-5 fuels was studied at 300° to 400° F. in a bench-scale rig employing filter paper as the filter medium.

Synthesis and Analysis

Only recently have accurate thermochemical data on boron-containing molecules become available. The data have been used to calculate the electronegativity of boron and the boron-to-boron bond energy which were used to compute the average bond energies $\bar{D}_{gm}(B-Z)$ from the Pauling electronegativity equation. The calculated values of $\bar{D}_{gm}(B-Z)$ were compared with experimental values, and the differences between the values have been interpreted in terms of partial double-bond character and resonance in BZ_3 compounds.

Recent measurements of the lattice constants of the alkali metal borohydrides make possible a theoretical calculation of the lattice energies of $NaBH_4$, KBH_4 , $RbBH_4$, and $CsBH_4$. The entropies and free energies of the reactions of $BH_3(g)$ and $B_2H_6(g)$ with $H^-(g)$ to form $BH_4^-(g)$ can also be calculated. These various thermodynamic properties were obtained in an investigation.³

² See paper by Rosenblum listed on p. 78.

³ See paper by Altschuller listed on p. 76.

COMBUSTION

Fundamentals of Combustion

Although conditions which may lead to the spontaneous ignition of fuels have been a subject of investigation for many years, the results of various researchers are in most instances not directly comparable, since the experimental conditions at the point of ignition may vary. An attempt was made to clarify in particular the effects of such parameters as fuel and oxygen concentration, pressure, temperature, and inert diluents on ignition delay. Furthermore, such data may help to elucidate the chemistry of the ignition reactions. Reactants were mixed at the desired temperature in a time much shorter than the ignition lag. The results on propane flames were obtained over a wide range of fuel percentages at atmospheric pressure and temperatures from 520° C to 740° C.

The spontaneous ignition temperatures of eight structurally different hydrocarbons were determined and correlated with the behavior of the same hydrocarbons toward vapor-phase oxidation (Technical Note 3579).

Much work has been done on the relative ease of oxidation of hydrocarbons, but the similarity in susceptibility to oxidation of the different bonds within the hydrocarbon molecule makes it difficult to isolate the separate steps in the reaction. The introduction of a metal atom into a molecule may add certain bonds which are more easily attacked by oxygen than the remainder of the molecule, and, hence, it may be possible to follow more readily the initial attack on the molecule by oxygen. Because of its similarity to carbon, silicon is a reasonable metal atom to use in such a study. Consequently, several alkylsilanes were prepared, and a study of the oxidation properties of these fuels was conducted.

In spite of the expanded efforts on combustion research in recent years, there is relatively little information on the detailed mechanism of the combustion of metals. The gross physical mechanism of the combustion of relatively small quantities of magnesium metal was studied in order to determine whether a vapor phase or surface mechanism is involved; further, to examine the effect of the composition of the oxidizing atmosphere, both as a matter of general interest and to determine if such studies might be informative as to the details of the physical and/or chemical processes involved.

A previous investigation resulted in a theory of spark ignition in nonturbulent and turbulent flowing gases using long-duration discharges. This theory is based on thermal processes and relates the spark discharge energy with gas density and velocity, electrode spacing, spark duration, intensity of turbulence, and constants of the fuel. A recent study was conducted to show the effect of fuel-air ratio and initial temperature on spark-

ignition energy and to apply these results to this developed theory of ignition. Data were obtained at a pressure of 5.0 inches of mercury absolute, gas velocity of 50 feet per second, low-turbulent flow condition, and with long-duration spark discharges.

Flame quenching may be studied by simple experiments. A flame is introduced into one end of a tube filled with a combustible mixture. The flame will either burn through the length of the tube or will be extinguished (quenched) by the tube. Experiments show that the ability of a flame to get through the tube depends on the following factors: (1) pressure; (2) temperature; (3) kind of fuel, oxidant, and inert diluent; (4) relative concentrations of fuel, oxidant, and inert diluent; and (5) cross-sectional shape and size of the tube. Recently, a diffusional quenching equation was proposed. This equation correlates the effect on quenching of such diverse factors as fuel type, tube geometry, fuel and oxygen concentrations, and temperature. A thermal analog of this equation has been developed and shown to correlate the same quenching data satisfactorily. The two equations predict effects of different extent when helium is replaced by argon in an inflammable mixture. Thus, comparisons with experiment should indicate which of the two approaches is more useful. Consequently, a study was made of the effect produced by replacement of helium by argon on the quenching of propane-oxygen-inert flames.⁴

Recent flame-quenching research has indicated that there should be a set of simple relations among the various channel geometries which are capable of just quenching a given flame at a given pressure. In an investigation recently conducted and reported, the following points were discussed: (1) The derivation of a set of equations which predict the relations among the dimensions of a number of simple geometries capable of just quenching a given flame at a given pressure and (2) the evaluation of several of these relations by determining experimentally the wall quenching of downward-propagating propane-air flames as a function of fuel-air ratio and pressure for rectangular slots, cylinders, and cylindrical annuli.⁵

With the growing interest in high-speed combustion systems in which the attainment of greater heat-release rates per unit volume is demanded, it becomes more important to know how faster-burning fuel-air mixtures can be obtained. It has long been known that one way to increase the burning rate of a gaseous mixture is to preheat it. The question arises as to how far this process of increasing the flame velocity by increasing the initial temperature can be carried. Therefore, a study was made to (1) determine experimentally whether the flame velocity is affected by contact time between fuel and air at temperatures previously studied, (2) extend propane-air flame velocity data to higher

⁴ See paper by Potter and Berlad listed on p. 78.

⁵ See paper by Berlad and Potter listed on p. 76.

temperatures, (3) increase contact times and temperatures until appreciable effects of slow oxidation on flame velocity were observed, and (4) obtain information on the major products of the slow oxidation in near-stoichiometric propane-air mixtures as determined under steady-state flow conditions.

Space-heating-rate measurements can yield information useful in characterizing turbulent combustion. Technical Note 3277 indicates that for Bunsen burner flames stabilized over a field of pipe-induced turbulence, the space-heating rate was decreased with increasing linear flow and burner diameter and was independent of pilot conditions. Turbulent burning velocities over the same flow range were correlated by linear velocity at constant burner diameter, but the variation with burner diameter could not be expressed by a simple correlation.

For laminar flames, the determination of burning velocity is fairly direct because the reaction zone is thin and stream tubes may be identified. Turbulent flames, however, are not so easily characterized in this way. Even when a turbulent flame is stabilized, the volume occupied by the fluctuating reaction zone is large compared with the volume of a laminar flame zone. A characterization parameter, the space rate, for turbulent flames has been defined.⁶ Measurements show that the space rate is directly proportional to the laminar burning velocity and indirectly proportional to the burner diameter. The space rate multiplied by the heat of combustion gives directly the heat-release rate per unit volume of space needed for the combustion.

The effect of turbulence on the propagation of a free flame has recently been investigated and reported. In this study free flames were spark ignited in a flowing turbulent stream of combustible gas. The propagation rate of the free-flame globule was observed photographically and with ionization gaps which defined the cone swept out by the globule as it was carried along by the stream.

Jet engine requirements have increased the need for understanding the mechanism governing the high volumetric heat-release rates of a fuel-air mixture. The burning velocities of premixed open propane turbulent flames and the effect of turbulence and turbulent-flow parameters on a variety of these flames was studied (Technical Note 3575).

The turbulent mixing of mass and heat is of major importance to the performance of jet-engine combustors. For example, mixing is largely responsible for the preparation of desired fuel-air mixtures and also affects the overall combustion process. In Technical Note 3570 an experimental comparison is presented between the Lagrangian and Eulerian correlation coefficients in the homogeneous isotropic central core of a turbulent pipe flow. The Lagrangian correlation coefficient was characterized by measurements of the turbulent diffu-

sion of helium from a point source. The general objective of this investigation was to determine relations between turbulent-mixing theory and experiment that would provide sufficient information for the direct solution of practical mixing problems.

Low-volatility fuels, such as JP-5, are desirable for use in high-altitude jet engines from the standpoint of low fuel-tank losses. Also they present less fire hazard, under some conditions, than currently used JP-4 fuel. The very low evaporation rate of such fuels, however, may yield poor combustor performance. Therefore, knowledge of the factors that affect the evaporation rate of JP-5 fuel is useful to the combustor designer. A continuous sampling-probe technique was used to determine the percentage of JP-5 fuel spray evaporated under conditions common in ram-jet engines.

Experimental and calculated mass and temperature histories of fuel drops vaporizing with a constant velocity relative to the air were determined and reported in Technical Note 3490. Under some conditions the unsteady state or time required for the drops to reach the wet-bulb temperature is an appreciable portion of the total vaporization time.

The burning of clouds of particles, such as those existing in fuel sprays, has received relatively little attention because of the difficulty of the problems. With respect to theory, there are such complicating factors as interaction between drops, extinction of flame surrounding drops at high relative drop-air velocities, and complex turbulent systems such as those existing in the combustion chamber. There may be conditions under which diffusion is no longer the controlling element, and the rate of chemical reaction becomes dominant. A discussion of those factors normally associated with diffusion flames is presented. In addition, the efficiency of combustion of liquid fuels in turbojet combustors as affected by fuel volatility, spray characteristics, and the burning rate of single drops is treated.

The use of liquid fuels in combustion systems involves the processes of atomization, evaporation, mixing, and burning. In some systems, atomization, evaporation, and mixing of fuel and air may be accomplished sufficiently remote from the flame that the principles of gaseous combustion are applicable. Usually, however, the small available combustion volumes and residence times preclude the separation of these individual steps, and burning occurs in the presence of liquid fuel which acts as a local source of combustible. Although the usual liquid-fuel combustion system involves a simultaneous occurrence of all these steps, much of the published research deals with only the individual steps in the use of liquid fuels. This is necessary because of the great complexity which results when the problems of atomization and evaporation are added to the already difficult problem of combustion. The status of

⁶ See paper by Simon and Wagner listed on p. 79

research pertinent to the combustion of sprays is presented with the intention of indicating fruitful areas for further research.

A number of theories have been proposed to explain the mechanism by which smoke is formed in diffusion flames, but at present no definite and completely consistent theory seems to be available. With the belief that still more experimental work might be helpful in understanding the overall mechanism, several experimental projects were undertaken. Smoke formation was investigated from the standpoint of the effect of pressure, fuel type, external airflow, rate, oxygen enrichment, argon substitution in external air, and fuel temperature. The experimental results were interpreted to indicate a possible step involved in the early stages leading to smoke formation. The understanding gained from these experiments, together with information from the literature, has been used to postulate a possible and relatively complete mechanism of smoke formation.

A comparison of the reaction kinetic processes of several aliphatic hydrocarbons with those of heptane and isooctane is presented in Technical Note 3384. This study included work on the behavior of olefines and exploratory work on the effect of surface-volume ratio on the extent of early stage oxidation of the hydrocarbon.

In aircraft operations there is a need for potent fire-extinguishing agents. In addition to potency, the agents must have properties that make them suitable for use in aircraft environments. For example, the corrosiveness, freezing point, toxicity, and electrical conductivity must be considered. The chemical mechanism chosen for study is that of chain-breaking reactions between agent and active particles (hydrogen and oxygen atoms and hydroxyl radicals). The action of halogenated agents in preventing flame propagation in fuel-air mixtures in laboratory tests is discussed in Technical Note 3565.

Aerodynamic mixing is an important factor in fuel-air preparation, combustion, and exhaust-gas mixing in jet-engine combustors. Because of its importance, it is of interest to investigate aerodynamic mixing under flow conditions commonly found in combustors. Although jet-engine combustors often have extremely intense sound fields, little attention has been given to the effect of sound-wave disturbances on aerodynamic mixing. Technical Note 3760 describes a theoretical and experimental investigation of the aerodynamic mixing of heat by standing sound wave downstream of a continuous line source.

In many technical problems involving heat transfer, the thermal conductivities of gas mixtures are required, often under conditions in combustion systems where measurement is difficult or impossible. An empirical technique for estimating conductivities of mixtures of

nonpolar gases is presented.⁷ Thermal conductivities of a mixture may be estimated quickly; only the composition of the mixture and conductivities of component gases are required. Accuracy is comparable to that of the more complicated methods which have been previously proposed.

A knowledge of the combustion temperature or of the quantity of fuel required to obtain a specified combustion temperature is necessary in the performance analyses of turbojet and ram-jet engines. With dissociation, the ideal combustion temperature is dependent on combustion-pressure level. Nomographic charts, from which the ideal temperature rise or the ideal quantity of fuel required for a specified combustion temperature may be obtained for a comprehensive range of operating conditions of turbojet- and ram-jet engines, have been prepared. These charts are applicable only to a fuel having a hydrogen-carbon mass ratio of 0.168, which closely approximates the fuel presently used in most turbojet and ram-jet engines. The charts are based on a constant-pressure adiabatic combustion process covering a range of fuel-air ratios from 0 to 1.2 fraction of stoichiometric, a range of combustion pressures from 1/16 to 64 atmospheres, and a range of inlet-air temperatures from 400° to 1600° R.

Combustion-Chamber Research

In the calculation of total-pressure loss and liner airflow distribution for turbojet and can-type ram-jet combustors, it is essential to know the discharge coefficients of combustor-liner wall openings. A study was made to determine the effects of various geometric and flow factors on the discharge coefficients for circular holes having flow parallel to the plane of the hole (Technical Note 3663). The geometric and flow factors considered were hole diameter, wall thickness at the hole, parallel-flow duct height, boundary-layer thickness, parallel-flow velocity, static-pressure level, and pressure ratio across the test hole.

Because the effectiveness of the turbojet engine increases with flight speed and altitude, the service requirements of turbojet engines demand operation at even higher and higher altitudes and flights speeds. The problem of maintaining high combustion efficiency is one of the most important problems of altitude operation. The research approach to the problem has involved both systematic investigations of the effect of individual variables on combustor performance and attempts to relate fundamental combustion parameters such as fuel-spray characteristics, ignition limits, and flame speeds to the observed combustor performance.⁸

While performance studies of various gas-turbine combustors have yielded a large amount of combustor performance data, no method has been presented for

⁷ See paper by Brokaw listed on p. 76.

⁸ See paper by Olson, Childs, and Jonash listed on p. 78.

correlating these data in terms of fundamental parameters. An empirical correlation of the combustion efficiency data previously obtained in experimental investigations with fourteen aircraft gas-turbine combustors has been developed. A theoretical analysis based on the kinetics of a bimolecular chemical reaction is also presented which, with additional assumptions regarding the mechanism of the combustion process, yields the correlation parameter previously obtained by empirical means.

The low pressure and low temperature encountered at altitude result in reduced combustion efficiency. An explanation of this effect in terms of basic processes is one of the goals of fundamental combustion research. Therefore, an investigation was made to determine the importance of molecular-scale processes in the overall turbojet combustion process. Attempts were made to correlate combustion efficiency with selected fundamental combustion properties and with a simplified reaction-kinetics equation.

In order to determine the relative importance of the basic processes involved in the overall turbojet combustion mechanism, a study was conducted of the effect of oxygen concentration of the inlet oxygen-nitrogen mixture on the combustion efficiency of a J33 single combustor operating with gaseous propane fuel.

Experimental investigations with both turbojet and ramjet combustors have shown that combustion efficiency is adversely affected by the high velocities at which these combustors are required to operate and by the low pressures and low inlet temperatures encountered at high altitudes. A theory of the jet-engine combustion process is therefore needed in order to explain these effects and to indicate the design approaches that are most promising for alleviating these adverse effects. A preliminary theoretical treatment of the combustion process as it occurs in turbojet combustors has been completed.

The trend in afterburner and ramjet-combustor development for increased thrust has resulted in combustors that operate at higher pressures, higher combustion temperatures, and higher velocities. With the development of these high-output combustors, the phenomenon known as screech has been widely encountered. Screech derives its name from the high-pitched audible sound produced. Other manifestations of screech are high-frequency pressure oscillation in the combustor and an increased rate of heat transfer, which have resulted in rapid deterioration or failure of combustor shell, flameholder, and other combustor parts. Screech instrumentation has therefore been developed and the mechanism of screech studied in a 6-inch-diameter simulated afterburner (Technical Note 3567).

Violent lateral oscillations which often occur in the combustion chambers of rocket and jet engines are analyzed.⁹

The formation of carbon in turbojet combustors presents a number of major engine operational problems. Carbon deposition on walls, fuel-injector nozzles, and ignitors affects combustion efficiency, altitude operational limit, and ignition characteristics of the combustor. Also, the distorted airflow and fuel-flow patterns which result from carbon deposits frequently cause warping and burning of the combustor liners. Carbon dispersed in the gas stream as smoke would also be objectionable in military operations where smoke trails remaining in the wake of jet-powered aircraft may be easily detected. An investigation was therefore conducted to determine the effect of systematic variations in inlet-air and fuel parameters on the smoking characteristics of a single tubular turbojet-engine combustor.

Research has been conducted on design and operating factors which may affect ignition limits of combustors and improve the altitude starting characteristics of turbojet engines. Prior studies have evaluated the influence of fuel volatility, spark-plug location, and spark energy on ignition characteristics in both full-scale turbojet engines and single-combustor installations. In addition to these factors, still another variable, spark-repetition rate, must be considered in the study of ignition limits. Data have been obtained for two fuels of different volatility, two spark-energy levels, and three airflow rates in the range of altitude engine-windmilling conditions.

An understanding of the basic processes controlling combustion in a ram-jet engine is one of the ultimate goals of research. Research into the combustion mechanism was continued by determining the variation of combustion efficiency with several pure fuels and fuel blends in a simple ram-jet-type combustor. Combustion-efficiency data were obtained for a 5-inch ram-jet-type combustor employing a simple V-gutter flameholder over a range of inlet static pressures and velocities.

Combustion in a ram-jet engine, or other engines requiring a similar high-speed combustion, may be considered to be a stepwise process. An attempt to evaluate the importance of any one of the steps in controlling the rate of the overall process is obviously difficult in a system in which all the steps vary simultaneously. It is possible to investigate the combustion process separately from the fuel preparation by the use of homogeneous fuel-air mixtures. Such an experimentally idealized system does not necessarily represent a practical ram-jet-type combustor, but will contribute to a better understanding of high-speed combustion processes for such an application. Combustion-efficiency data have been obtained from a 5-inch-diameter combustor employing a straight V-gutter flameholder and a simple cone flameholder. The data obtained cover a range of inlet static pressures, temperatures, and velocities for four fuels.

⁹ See paper by Maslen and Moore listed on p. 78.

The maintenance of stable and efficient combustion with low-drag combustors at high heat-release rates is an important objective. The phenomenon of surface combustion and its coincident high reaction rates is well known; however, the process normally involves high pressure losses, which prohibit the conventional use of surface combustion in a ram-jet combustor. The beneficial effects on stability limits and combustion efficiency produced by the application of surfaces immersed in the combustion zone to a ram-jet type burner have been determined. Investigations were made with one, two, three, and four rows of wedges at simulated sea-level and at altitude subsonic ram-jet flight conditions.

A study was made of combustor design factors leading to a sufficiently high heat release and low internal drag to power a high-thrust, low-drag ram-jet engine. Two design principles investigated were the use of flameholders that employed incandescent surfaces heated by immersion in flame and the elimination of the separate fuel-air mixing length by injecting the fuel directly at the upstream end of the flameholder. The scope of this investigation included a series of flameholders designed to provide a high combustion efficiency in a 4- by 8-inch ram-jet combustor 24 inches long at an inlet-air velocity of 200 feet per second, inlet-air pressure of 60 inches of mercury absolute, inlet-air temperature of 200° F, and near stoichiometric fuel-air ratio.

Several investigations have been made on the operational characteristics of the V-gutter flameholder. These studies demonstrate that fuel distribution exerts an important influence on combustor performance. At lean overall fuel-air ratios, the fuel distribution has a greater effect than that of flameholder geometry upon combustor performance. The primary objective of this work was therefore to determine the effect of combustion on the diffusion coefficient in the fuel preparation zone and to design, with the aid of this information, a combustor that will provide the fuel-air distribution necessary for efficient combustion at lean fuel-air ratios.

Jet-engine combustion-chamber design must conform to many requirements specified by carbon deposition, liner temperature, size, combustion stability, temperature profile, pressure drop, and combustion efficiency. Many of these requirements may be evaluated by inspection and simple measurements, but evaluation of temperature profile, pressure drop, and combustion efficiency entails more elaborate research instrumentation. An automatic polar-coordinate traversing system for determining jet-engine combustor performance was devised (Technical Note 3566). A combined temperature and pressure probe is swept circumferentially through a quarter-annular exhaust duct at selected radial positions. Data are recorded as a function of probe position. This method furnishes complete

temperature, pressure, and flow profiles with a single probe.

LUBRICATION AND WEAR

Fundamentals of Friction and Wear

The lubricated parts of turbine engines and aircraft components are required to operate at continually increasing temperature levels. This trend is unavoidable where higher performance engines and greater flight speeds are the ultimate objectives. Adequate bearings, seals and lubricants must be available for operation at these high temperature levels.

To fill the lubricant need, silicone-diester blends were formulated on the basis of fundamental studies on lubrication with silicones. Because it had excellent viscometric properties and relatively good thermal stability, one blend (SD-17) was considered as a possible turboprop-engine lubricant. It was found to be a very good gear lubricant. The blend performed satisfactorily in more than 17 hours of operation at moderate power levels during a functional check in a T-38 turboprop engine. However, subsequent studies showed the blend to be subject to foaming at bulk oil temperatures (300° F) necessary for high-performance turbojet engines. Under foaming conditions and at high temperatures, excessive oxidative and thermal degradation occurred.

Halogen-substituted methane and ethane gases continue to be of interest as high-temperature boundary lubricants. Because the functioning of these gases depends on chemical reaction between chlorine atoms of the decomposed gas and the surfaces being lubricated, the bearing materials are very important.¹⁰ With steel surfaces, the best results were obtained when both slider surfaces were of nearly the same hardness. Modified H-Monel and beryllium copper were successfully lubricated by difluoro-dichloromethane; in both cases the mating material was hardened tool steel. Other common bearing materials such as silver were not lubricated by the gas. Boundary lubrication by gases appears feasible for temperatures up to 1,000° F.; few known liquids have any promise for lubrication of bearing surfaces operating at temperatures above 700° F.

Because solid lubricants are among the most promising high-temperature lubricants, an experimental friction study was made using graphite and mixtures of graphite with lead oxide, cadmium oxide, sodium sulfate, or cadmium sulfate as solid lubricants. Runs were made at temperatures to 1,000° F. with various steel and Inconel combinations (Technical Note 3657).

Graphite powder lubricated metal surfaces at temperatures sufficiently high to promote oxidation of the

¹⁰ See paper by Murray, Johnson, and Swikert listed on p. 78.

metal surfaces. At intermediate temperatures, graphite powder alone failed to function as a lubricant. Graphite would not lubricate cast Inconel on Inconel X at temperatures between approximately 150° and 800° F. Similarly, with steel, which oxidized more readily than Inconel, the temperature below which graphite would not lubricate was 475° F. as compared with 800° F. for Inconel. Mixtures of some metallic compounds and graphite were effective lubricants from room temperature to 1,000° F. In some room-temperature experiments, CdI_2 and CdCl_2 were effective solid lubricants for titanium.¹¹

The usefulness of liquid lubricants has been seriously impaired by oxidation at engine operating temperatures. One method of minimizing this problem is to obtain more effective sealing of the lubrication system and thereby limit the amount of air to which the lubricant is exposed. Sliding-contact seals are necessary for closed lubrication systems. Wear and friction studies were therefore made to show the effects on performance of temperature, type of mating material, and minor composition changes in typical carbon-seal materials (Technical Note 3595). Wear of carbon-seal materials increased rapidly with temperatures between 400° and 700° F. The effect of temperature on wear was reduced by using chromium-plated steel as the mating surface rather than stainless or tool steel. In general, the type of carbon and impregnation of the carbon-seal material had little effect on wear compared with the effect of the mating material.

Bearing Research

The effect of air and nitrogen atmospheres on the temperature limitations of liquid and solid lubricants was studied using small ball bearings.¹² All lubricants tested in both nitrogen and air atmospheres were effective to higher temperatures in a nitrogen atmosphere, and the solid lubricants (molybdenum disulfide and graphite) were best. Both graphite in air and molybdenum disulfide in nitrogen were effective to 1,000° F. These studies, which showed that the limiting temperatures of liquid lubricants could be extended by preventing oxygen from the atmosphere from contacting the lubricant, led to further tests to determine the role of oxygen. The results of an investigation to determine the effect of oxygen concentration in the atmosphere on oil lubrication of small ball bearings at high temperatures are reported.¹³ The results showed that a 20-millimeter-bore ball bearing will run at temperatures to 850° F. with oil lubrication if the oil flow exceeds a critical amount.

Early detection of bearing failures in bearing research is important because detection of incipient failure early enough can often avoid a total failure, and additional

information on the cause of failure can be obtained. In contrast to the slow response of temperature, the second derivative of temperature with respect to time (the acceleration) reaches a high positive value before significant temperature changes are noticed. Accordingly, an instrument for measuring the magnitude and sign of temperature acceleration was developed and found to be effective in detecting incipient bearing failures in 75-millimeter-bore roller bearings.¹⁴ Incipient failures were reproduced by shutting off the oil flow, and in each test it was found that temperature acceleration gave a faster warning than temperature, motor torque, or noise level. Total failures were thus avoided when using temperature acceleration as a warning device.

An experimental investigation of eccentricity ratio, friction and oil flow of long and short journal bearings was conducted at Cornell University under NACA sponsorship and is reported in Technical Note 3491. The data provide charts of plain bearing performance which cover the range of length-diameter ratio of $\frac{1}{4}$ to 2.

COMPRESSORS AND TURBINES

Compressor Research

As part of the investigation of the fundamental nature of compressor stall, a theory of stall propagation was developed and reported in Technical Note 3580. Experimental results obtained from a stationary circular cascade and a single-stage axial-flow compressor indicate that the theory predicts propagation velocities within 25 percent over a wide range of wave lengths.

To obtain a better understanding of the stall phenomenon by providing detailed information regarding the stall mechanism, pressure, temperature, and flow fluctuations, an investigation of the rotating-stall characteristics of a compressor with a 0.9 hub-tip radius ratio was undertaken. A study of a rotor having a 0.9 hub-tip ratio (no guide vanes or stators) showed stall patterns consisting of two, three, and one total-span stall zones developing in that order upon reduction of flow coefficient. The one-stall-zone pattern caused the most severe pressure, temperature, and flow fluctuations (Technical Note 3518). The rotating-stall characteristics of the 0.9 hub-tip-ratio stage were extended to include several guide-vane rotors and guide-vane rotor-stator configurations. Guide vanes having turning angles of -22.5° , 0° , 22.5° , and 40° were used. Results indicate that the initial rotating-stall point, number of stall zones formed, and stall propagation rate of a configuration depend not only upon blade-row inlet angle and pressure-rise characteristic but also upon the overall characteristics of the multiblade row unit as well. The addition of stators to a particular guide-vane-rotor configuration generally increased the flow coefficient where rotating stall was initially encountered

¹¹ See paper by Peterson and Johnson listed on p. 78.

¹² See paper by Nemeth and Anderson listed on p. 78.

¹³ See paper by Nemeth and Anderson listed on p. 78.

¹⁴ See paper by Schmidt and Anderson listed on p. 78.

and lowered the stall propagation rate. The number of stall zones formed in the annulus did not appear to depend upon guide-vane turning or the presence of stators (Technical Note 3711).

Incompressible two-dimensional flow was analyzed specifically to establish simplified equations and considerations that may prove useful in the estimation of profile losses and in the correlation of experimental data in the low-speed two-dimensional cascades. The relative importance of the various factors entering the loss relations was evaluated and relations were obtained for the mixing-loss ratio and for the effect of trailing-edge thickness (Technical Note 3662).

Information was obtained (Technical Note 3568) on the average pressure indicated by a total-pressure probe subjected to a stagnation pressure that alternates periodically between two constant values. The errors were reduced when the probe design was such as to ensure laminar-flow pulsations in the probe at all times. The averaging error was minimized when the inside diameter of the probe entrance tube was made as small as possible and its length as great as possible consistent with an acceptable time lag.

Turbine Aerodynamics

The smoke-visualization studies of the secondary-flow in turbine-blade passages have been continued by investigating secondary flow in the rotor-blade tip region of a low-speed turbine. The present investigation (Technical Note 3519) was conducted to obtain a visualization of the tip-flow phenomena and to determine which factors of blade geometry and tip condition influence the types of secondary-flow behavior encountered at the blade tip. Results of the investigation include qualitative information on tip-clearance flow, crossflow, and scraping flow and should aid in extending the study to higher air speeds.

An analysis was derived (Technical Note 3651) for three-dimensional boundary-layer flow over a flat surface with a leading edge under main-flow streamlines which are representable by polynomial expressions. The boundary layers are laminar and incompressible, and the profiles of their velocity components have similarity with respect to their rectangular coordinates. Solutions were obtained for main-flow streamlines representable by polynomials up to the eleventh order. Flow-visualization experimental checks of the theory are provided for several flow configurations and for comparisons of the behavior of thick and thin boundary layers.

One of the principal objectives of turbine research is a better understanding of the fundamental nature of the flow and the loss sources encountered in turbomachine blade rows. The effect of compressibility on the loss characteristics downstream of two-dimensional turbomachine blade rows is therefore analyzed in Technical Note 3515. Equations are derived for obtaining the

compressible-flow boundary-layer characteristics for a simple power-velocity distribution. Loss coefficients at the blade trailing edge are then obtained in terms of these characteristics. Finally, overall loss coefficients, including the effect of mixing downstream of the blade row, are obtained in terms of these characteristics.

Turbine Cooling

Gas-to-gas heat exchangers find many uses in modern aircraft and missiles. Usually, a large number of calculations must be carried out for the design of such a heat exchanger. It is, therefore, of advantage to have a simple method available by which the dimensions of the heat-exchanger core can be rapidly calculated. Such a calculation procedure is described in Technical Note 3655. The dimensions of the core of a gas-to-gas cross-flow heat exchanger with prescribed heat-transfer surface can be determined rapidly.

The problem of selecting heat-exchanger configurations for optimum performance was investigated. The fluid on one side of the exchanger was assumed to have negligible heat-transfer resistance, and the amount of heat exchanged per unit time and the mass flow and inlet state of each fluid were prescribed. Any one of the parameters, power expended, weight, volume, or frontal area, can be optimized with respect to any one of the three remaining parameters when the heat exchanger is arranged normal to the approaching primary fluid. When the heat exchanger is inclined at an angle to the upstream direction, any one of the parameters, power, weight, or volume, can be optimized with respect to any one of the two remaining parameters. With this arrangement, the projected frontal area of the inclined heat exchanger will be equal to that of the heat exchanger requiring the minimum duct cross-sectional area when arranged normal to the primary fluid flow (Technical Note 3713).

Experimental investigations of free-convection effects on heat transfer for fluids flowing vertically through tubes with small and large length-to-diameter ratios were made by NACA and the Massachusetts Institute of Technology, respectively. However, the data from the two investigations were not analyzed on the same basis. In Technical Note 3584, therefore, experimental heat-transfer data for the turbulent flow of fluids through stationary vertical tubes with both small and large length-to-diameter ratios (to 40) are compared. The limits of the different regions, originally established for a tube with small length-to-diameter ratio, apply on the basis of existing data to a tube with large length-to-diameter ratio.

The literature contains many investigations on wedge-type flow, including results for fluids with different Prandtl numbers flowing through porous flat plates. A summary of exact solutions of the laminar boundary-layer equations for wedge-type flow, useful in estimating heat transfer to such arbitrarily shaped bodies as

turbine blades, is presented in Technical Note 3588. The principal results are restricted to a Prandtl number of 0.7 at the wall and are presented for large temperature changes through the boundary layer adjacent to a constant-temperature wall and for small temperature changes through the boundary layer adjacent to a wall of either a constant or a variable temperature.

Blade Vibration and Flutter

The problem of the failure of compressor blades in the stall region has become more acute in recent years with the greater use of high-compression-ratio engines. A study of the vibrations occurring in the stall region is described in Technical Note 3581. A compressor-type annular cascade of airfoils was used to determine the effects of varying the angle of attack, blade chord and spacing, number of blades, and air velocity on the vibrations.

The phenomenon of rotating stall or stall flutter in axial compressors is discussed in Technical Note 3571 by means of an unsteady boundary-layer analysis.

Heat Transfer

Knowledge of the flow characteristics of various liquids in passages having both circular and noncircular cross sections is important in the removal of heat from nuclear reactors. An experimental investigation of the flow patterns in a narrow vertical enclosure was therefore made. A shadowgraph was used in the investigation to study the free-convection flow of water in the narrow enclosure, which was cooled at the top through a copper surface and open at the bottom to a heated reservoir. This visual inspection of flow patterns yielded information on the steadiness of flow patterns with time, the size and uniformity of the various upflow and downflow regions, and the direction of flow velocities with particular attention to nonvertical components. The dominating characteristics of the flow patterns were instability and change.

It is often desirable to use short passages in heat exchangers in order to take advantage of the high heat-transfer coefficients in the entrance region. The effect of various factors on the turbulent heat transfer and friction in the entrance regions of smooth passages was investigated analytically.¹⁵ The influence of Reynolds number, Prandtl number, initial velocity distribution, wall boundary condition, passage shape, and of variable fluid properties was predicted. The results indicated that approximately fully developed heat transfer and friction are, in general, attained in an entrance length of less than 10 diameters. Substantial agreement between analysis and experiment was obtained for heat transfer to air in the entrance regions of tubes and parallel plates.

ENGINE PERFORMANCE AND OPERATION

Turbine Engines for Helicopters

The gas-turbine engine shows considerable promise as a solution to the propulsion requirements of the high-performance helicopter. These requirements are (1) high ratio of rotor power available to engine weight, (2) speed-power characteristics that permit a relatively free choice of rotor tip speeds, (3) satisfactory fuel economy over a wide range of speed and power settings, and (4) dynamic response characteristics that are suitable to transitional flight operations. In a number of prior investigations these requirements were shown to be more nearly satisfied by the free-turbine engine than by the fixed-turbine engine.

An analysis of fixed- and free-turbine engines applicable to helicopter propulsion was made. Calculated performance characteristics of the two engines are presented in Technical Note 3654 in terms of the appropriate equivalent parameters. Performance comparisons are drawn for off-design-point and altitude conditions of engine operation. The behavior of the engines during rapid power and speed modulation and their dynamic response characteristics when coupled to a helicopter rotor are also examined.

The flow with heat addition in which a body force acts transverse to the flow is treated in Technical Note 3594. The results may be applied to flow with heat addition in pipe bends, through helicopter rotor-tip combustors, and through ram jets in abrupt maneuvers.

Foreign-Object Damage

Severe damage to jet engines may result from the impact of foreign objects on compressor and turbine blades. An investigation was therefore undertaken to determine the effect of typical impact damage on the fatigue strength of jet-engine compressor blades. First-stage compressor-rotor blades from a production engine which had suffered foreign-object damage were fatigue tested at the endurance limit of the blade material. The number of cycles to failure was correlated with the depth, location, frequency, and type of damage. The most serious damage to the blades, as measured by the reduction in fatigue strength, resulted from nicks at the leading and trailing edges in the vicinity of the maximum-vibratory-stress section of the airfoil. The strength of dented blades could be restored by reworking, but seriously nicked blades could not be reliably restored (Technical Note 3275).

Ground and Flight Investigations of Ram-Jet Engines

An investigation was conducted in a blowdown jet of a 6.5-inch-diameter ram-jet engine at Mach numbers of 1.81 and 2.00. The engine was demonstrated to have wide combustion limits, reliable ignition character-

¹⁵ See paper by Deissler listed on p. 77.

istics, and good combustion efficiency when operated on ethylene (C_2H_4) fuel. The same type of engine was used to perform flight tests. The flight investigation covered Mach numbers from 1.9 to 3.0 and altitudes from 1,800 to 40,900 feet. Good agreement with the static test performance was obtained. The engines operated reliably until the fuel was expended. During the flight tests, the engines accelerated the test vehicle at a maximum acceleration of 3.6g.

Miniature Ram-Jet Engine

In order to facilitate the determination of jet effects in wind-tunnel model tests at supersonic speed, a small (1.1-inch-diameter) ram-jet was designed and its performance was investigated. The engine, which burned a gaseous fuel, was operated over at Mach numbers from 1.42 to 2.28 and at Reynolds numbers which were equivalent to an 18-inch-diameter ram-jet flying at an altitude of 74,000 feet. Reliable operation was obtained over a wide range of thrust coefficients and fuel-air ratios. Spark ignition was demonstrated to be rapid and reliable.

Thrust Reversal

Many uses for thrust reversers on jet aircraft have been proposed. They include braking the landing roll, reversing or spoiling thrust during the landing approach so that maximum engine speed may be maintained, and braking during diving maneuvers to limit flight speed. To be used effectively, the reverser must give the desired amount of reverse thrust without affecting engine operation. Also, the design must lend itself to stowage with a minimum amount of boattail or base drag.

As part of an overall investigation of thrust reversers and their associated problems, studies were conducted with cold flow on thrust reverser models. This work was done on a small-scale unheated-air-duct setup equipped with a 4-inch-diameter exhaust nozzle.

The performance of a hemispherical thrust reverser over a range of geometric variables and some of the factors that affect reverse-thrust performance have been obtained. The effects of several simplifications to the hemispherical design are also shown. The effects of most of the design variables of the reverser were obtained at an exhaust-nozzle total- to ambient-pressure ratio of 2.0. The basic data over a wide range of conditions are also included, however, so that other comparisons may be made.

The performance of cylindrical-type thrust reversers and the effects of several modifications on their performance were investigated at an exhaust-nozzle pressure ratio of 2.0. These modifications include changes in frontal area, width-to-height ratio, depth, lip angle, end-plate depth, and end-plate shape. The performance of swept-type cylindrical thrust reversers, the relation of reverse-thrust ratio to reversed-flow

attachment, and thrust-modulation characteristics were also investigated.

Preliminary data were obtained on the performance of several cascade-type thrust reversers located upstream of the exhaust nozzle up to an exhaust-nozzle pressure ratio of 2.4. Such reversers are herein referred to as the tail-pipe-cascade type. A total of 15 different tail-pipe-cascade configurations were investigated. These included two blade shapes, several cascade length-to-span ratios, and various innerbody lengths. Basic airflow characteristics and reverse-thrust ratio are plotted against exhaust-nozzle pressure ratio for all 15 configurations at full reversal. For some of the configurations, modulation performance and surveys of total pressure and flow angle were obtained at the cascade discharge.

Technical Note 3664 presents the types of thrust reversers investigated under the overall NACA program, summarizes the important performance characteristics, and presents proposed operation methods. Three types of reversers were investigated, target, tail-pipe cascade, and ring cascade. The effects of design variables on performance, reversed-flow fields, and thrust-modulation characteristics were determined for each type.

The performance of a hemispherical target, which is a basic thrust-reverser type, was evaluated in full-scale tests (Technical Note 3665). A turbojet engine equipped with such a device was pylon-mounted under the wing of a cargo airplane, the installation simulating that on a jet bomber or transport. The thrust reverser was operated at both stationary and taxi conditions, but the airplane was not flown. In addition to obtaining the performance of the thrust reverser, the heat-rise patterns and rates resulting from impingement of the reversed hot gases on a simulated lower wing surface were also measured. Because, during stationary operation, some of the hot reversed gases penetrated as far forward as the engine inlet and were reingested, taxi tests were conducted to estimate the ground speeds required to disperse the reversed gas flow and prevent reentry into the engine inlet.

Ducts

Size and weight penalties of air-induction systems would be decreased by the development of efficient short subsonic diffusers. Preliminary tests on a series of such diffusers employing various flow control devices have been completed.

Engine Controls

In order to facilitate consideration of control systems for two-spool turbojet engines, a brief analysis of the linear response characteristics of this type of engine is presented in Technical Note 3274. The analysis is concerned with the linear responses of the two spools to changes in turbine-inlet temperature at constant

exhaust-nozzle area and to changes in exhaust-nozzle area at constant turbine-inlet temperature.

General equations of response are developed from linearization of functional relations. The general equations are then evaluated at design speed by means of representative engine thermodynamic relations. The resultant equations are corroborated with experimental data.

POWER-PLANT MATERIALS

High-Temperature Materials

Improved performance of turbojet engines and the realization of nuclear-powered weapons is to a large degree dependent on the development of materials capable of withstanding severe conditions of corrosion, temperature, and stress. Research is continuing in an effort to improve existing materials and to develop new materials to fulfill these conditions.

Many intermetallic compounds have for some time been of interest for high-temperature application. However, there is very little generalized knowledge by which the potentialities of materials in this category can be evaluated. To build up a background of information from which theories can be formulated, as well as to provide specific data on an intermetallic of interest, Ni_3Al was studied. This material is of particular interest because of its high melting point and stability at high temperatures. An investigation (Technical Note 3660) of the effects of homogenization and of composition on the tensile properties of as-cast Ni_3Al intermetallic phase alloys showed that the tensile strengths of these alloys at both room and elevated temperature are very sensitive to composition, structure, and grain size.

For high-temperature applications, many brittle alloys, cermets, and ceramics are of interest. In order to utilize these materials in advanced turbojet engines, improved methods of fastening, designed to reduce bending stresses and to minimize stress concentrations, are required. An improved cermet bladed design, utilizing a curved root, was developed. This design eliminates the need for a blade platform and results in significantly reduced stresses.

Recent efforts to develop alloys of superior elevated-temperature creep resistance have heightened interest in the function of grain boundaries in creep, both because coarse grained materials are found to exhibit greater creep resistance at high temperature and because high-temperature creep is usually intergranular. The gliding of one metal crystal with respect to another parallel to their mutual grain boundary has been studied in pure aluminum bicrystals (99.95% Al, balance copper, iron, chromium, silicon, and magnesium) during isothermal creep at temperatures ranging from 200° to 650° C under static stresses from 10 to 1,600 psi (Technical Note 3556). The mechanism of grain boundary gliding was found to be a coordinated alterna-

tion of slip and recovery in a chain of subgrains along the grain boundary which was highly sensitive to crystal orientation. It was postulated that the addition of alloying elements should affect the process most markedly in those respects relating to the occurrence of recovery. Consequently, studies of the effects of Cu (0.1 to 3 percent) on Al were made (Technical Note 3678). It was found that the minimums in stress and temperature, below which grain boundary motion does not occur, increase regularly with the copper content, as would be expected if recovery is necessary for movement. Otherwise, the effects, if any, of the copper solute upon grain boundary displacement and its rate were too small for identification by the experimental technique employed.

The mechanism responsible for the bonding of ceramics to metals has been under study for several years. Earlier work was concerned with the manner in which adherence develops when cobalt ions are present in the coating, using radioactive cobalt 60 as a tracer technique. A similar study of the effect of nickel dipping on adherence has been conducted using radioactive nickel 63, produced by pile irradiation of highly purified cobalt-free nickel (Technical Note 3577). It may be concluded that the nickel from the nickel dip remains as metal at the enamel-metal interface as it does not oxidize during the firing treatment. Further, the presence of nickel from the nickel dip had little or no effect on the deposition of cobalt metal during firing. A further study of the influence of copper ions on adherence of vitreous coatings to stainless steel has been completed (Technical Note 3679). In general, the presence of copper ions in the coating produced a significant increase in adherence. However, this effect decreased with increased firing time and temperature.

Stresses Research

The thermal-shock problem is of vital importance in jet engines, nuclear powerplants, rockets, and high-speed missiles subjected to aerodynamic heating. Since structural damage may be caused by rapid temperature changes, there is a need for a better understanding of the factors affecting the thermal-shock resistance of materials. Two theories predicting the thermal-shock resistance of brittle materials are described and compared with experimental results.¹⁶ Equipment for testing specimens over a wide range of heat-transfer coefficient is described and four independent methods of determining the thermal-shock parameter are shown. A simple approximate method for computing transient thermal stresses in hollow cylinders, plates, and hollow spheres is reported.¹⁷ These bodies were used to approximate the more complex configurations found in practice. The method

¹⁶ See paper by Manson and Smith listed on p. 78.

¹⁷ See paper by Mendelson and Manson listed on p. 78.

makes use of polynomial approximations to the temperature distribution. Using these approximations reduces the partial differential equations of the problem to first-order ordinary differential equations, making possible practical solution of the problems in relatively little time.

In tension or creep testing, misalignment between the specimen axis and the loading axis can influence the results by causing a bending stress to be superimposed on the applied tensile stress. This bending stress is particularly important when materials of limited ductility such as some of the very high-strength creep-resisting alloys and cermets are used. Conventional testing equipment permits considerable misalignment, which varies in an uncontrollable manner from test to test. This variation introduces scatter into the test results. A new axial-loading creep machine was developed that reduces the misalignment to a minimum and represents a large improvement over conventional equipment.¹⁸

Physics of Solids

In order to continue the advanced development of materials for aircraft applications, a basic knowledge of the solid state must be acquired. Physics-of-solids research is designed to gain a greater understanding of solids on an atomic and microstructural level in those areas related to the mechanical, corrosion, and temperature properties of materials.

Because of the presence of oxygen atoms in rocket-engine and reactor atmospheres, it is important to consider the effect of oxygen atoms on the oxidation rate of metals. An investigation has been made of this effect on platinum. The rate of surface oxidation was found to be markedly increased by the presence of oxygen atoms. Surface oxidation was examined at 1000° C and a pressure of 0.50 millimeter of mercury under such conditions that ionic sputtering was insignificant. The reaction was found to obey a linear law, and oxygen atoms were shown to be at least 400 times more reactive than oxygen molecules.¹⁹ In studies of the oxidation of metals at high temperatures, an accurate method of measuring the extent of oxidation is necessary. The conductometric method has been successfully applied to the oxidation of iron at approximately 600° C. Iron ribbons of known thickness were used in the tests and the conductance of the central portion of the specimens was measured by the potentiometer method. A constant current of 50 milliamperes, small enough to prevent heating even in vacuum, was used. The conductometric method gave a true measure of the extent of oxidation, which is in agreement with the gravimetric method. An analytical method of measuring the amount of unoxidized iron remaining in the specimens is briefly described.

It has been known for many years that surface cracks play a large part in decreasing the strength of materials below the theoretical maximum value. The presence of such cracks was previously inferred by indirect methods. It is shown that the crystallization behavior of metallic films deposited on alkali-halide, single-crystal surfaces allows a direct method of observing the formation of cracks on surfaces.²⁰ This method was used to measure the rate of crack formation at various temperatures.

The nature of solid surfaces is important in determining the physical properties, such as strength, of solids. An investigation was conducted to clarify the effects of radiation on the surface of brittle materials. Electron-diffraction studies have shown that after sufficient irradiation the surfaces of sodium chloride crystals break up into small crystallites, which exhibit preferred orientations. The irradiation time required to produce surface damage is much greater for water-polished crystals than for untreated ones. The results are discussed on the hypothesis that the large increase in vacancy concentration accompanying F-center formation may aid in relieving strains and result in re-orientation of blocks of ions.²¹

The effect of vacancy and F-center concentration, as produced by X-irradiation, on the room-temperature creep properties of NaCl single crystals has been studied. Under a load of 1.200 grams per square millimeter, logarithmic creep behavior was noted for both annealed and quenched crystals before or after irradiation. Irradiation with 50-kilovolt X-rays was found to have a marked effect on both initial deformation and subsequent creep, causing an initial softening followed by hardening as irradiation is continued. The behavior after irradiation can be explained on the basis of the changes in vacancy concentration and distribution that accompany F-center formation. Experiments in which the vacancy concentration was changed by quenching from various temperatures indicate that the creep rate may depend in a simple way on the number of vacancies.²²

Further work on color-center precursors is reported. It was previously found that NaCl crystals which had undergone electrolysis, but which remained colorless, were much more sensitive to irradiation with X-rays. Recent work shows that these same properties exist in NaCl crystals when they are colored additively and then bleached by electrolysis.

An insight into the nature of the state of cold-worked alloys is provided. Measurements were made of the resistivity and thermoelectric power of samples of AuCu in various nonequilibrium states. One set of samples was disordered by quenching from 750° C, and annealing curves were obtained at various tempera-

¹⁸ See paper by Jones and Brown listed on p. 77.

¹⁹ See papers by Fryburg listed on p. 77.

²⁰ See paper by Metz and Lad listed on p. 78.

²¹ See paper by Leider listed on p. 78.

²² See paper by Lad and Metz listed on p. 77.

tures. A second set was first ordered and then cold-worked essentially to complete disorder, and annealing curves were taken at several temperatures. It follows from the detailed results that to specify the state of an alloy, it is necessary to give, in addition to resistivity and thermoelectric power, at least one other quantity such as the coefficient of magnetoresistivity.

Near the melting point, solids may be disordered sufficiently so that they could be described by the methods-of-liquid theory. One of the difficulties in liquid theory is the computation of the potential energy of a molecule in the liquid. A method of computing this energy has been devised which is based on a knowledge of the radial-distribution function and the intermolecular-potential-energy function. Calculations for argon indicate that the method gives satisfactory results. The unique properties of the MgCd alloy system afford a convenient "testing ground" for the various theories of ordering in binary alloys. An experimental investigation of the specific heat of this system as a function of temperature was carried out with an adiabatic vacuum calorimeter.

In studying the fundamental properties of some semiconducting materials, it was found that the electromotive force developed parallel to the gradient of light absorption in germanium crystal is reduced by the application of a transverse magnetic field.

The logarithmic expression for the temperature dependence of viscosity satisfactorily describes the behavior of a large number of normal liquids but fails when applied to associated liquids. A method is given for deriving the temperature dependence of viscosity by considering the molecule to consist of two force centers, an ordinary van der Waals force center, and a dipole center. The resulting equation is successfully applied to a number of associated liquids. The relation between this equation and vapor pressure is also deduced, and results are given for water.

In designing nuclear reactors, calculation of neutron flux distributions and the critical mass is essential. The fuel elements consist of thin strips of uranium adjacent to moderator material or of solutions of enriched uranium salt in a liquid moderator. The analysis is usually simplified by assuming the fuel and moderator to be homogeneously mixed. In practical assemblies, the core may consist of repetitive "cells" in a fuel-moderator assembly. These are much less than the order of a mean free path, so that solutions of a higher order than diffusion theory are required to evaluate departures from homogeneous conditions. The steady-state diffusion-theory solutions and the next higher order approximation of several self-shielding problems have been obtained for multiregion cells of rectangular and cylindrical geometry (Technical Note 3661). The neutrons were assumed to be monoenergetic, and their distribution function was assumed to be dependent only upon one spatial coordinate. A spherically symmetrical

scattering in the center of the mass system was also assumed. The solutions of the diffusion theory and the transport-theory flux equations were obtained by a differential analyzer. Additional results were obtained by approximating the effects of molecular binding in the water molecule. The thermal neutron flux distributions were used to compute the ratio of total absorption in uranium to the total absorption in the cell.

Additional studies of the multiple scattering of slow (less than 100 kiloelectronvolts) alpha-particles were made. These studies had previously been neglected because of the difficulty of introducing the particles into apparatus with known energies. This difficulty was overcome by first passing the alpha-particles through a velocity selector and then through a thin nylon window into the cloud chamber. For charged particles of medium energies, the experimental data and the theory are in reasonable agreement. For low-energy nuclear particles, however, there is no adequate theory and there are very few data.²³

ROCKET ENGINES

Propellants

A continuing interest in hydrocarbon fuels and liquid oxygen as rocket propellants is assured by favorable logistics and relatively high specific impulse. Theoretical rocket performance for frozen composition during expansion was calculated for the propellant combination of JP-4 fuel and liquid oxygen at two chamber pressures and several pressure ratios and oxidant-fuel ratios.

A knowledge of flame propagation limits is necessary for designing combustors and specifying pressures, compositions, and temperatures in which a given gaseous fuel-oxidant combination will burn. With respect to theory, flame propagation limits are important because they can be correlated with other combustion parameters and thus aid in the fundamental understanding of combustion. Flame-propagation limits of propane and *n*-propane in oxides of nitrogen were obtained (Technical Note 3520) at subatmospheric pressures in a 2-inch-diameter by 48-inch-length tube.

Experiments in which the rocket propellant, crude N-ethylaniline (monoethylaniline) and mixed acid (nitric plus sulfuric), failed to ignite satisfactorily at low temperature indicated the necessity of a knowledge of the self-ignition properties of certain rocket propellants at low temperatures as well as at moderate temperatures inasmuch as rockets may be required to start at high altitudes or under arctic conditions. An investigation was therefore conducted to determine possible rocket fuels that ignite spontaneously at low temperatures with mixed acid (nitric plus sulfuric) in a more reliable manner than crude N-ethylaniline. Experiments were also conducted at sea level and at a pressure altitude of approximately 55,000 feet at various temperatures in

²³ See paper by Allen, Webeler, and Barile listed on p. 76.

order to determine the starting characteristics of a commercial 220-pound-thrust rocket engine using crude monoethylaniline and other fuels with mixed acid.

The freezing points and low-temperature fuel-igniting properties of fuming nitric acids are of current interest because of a demand to extend the use of these oxidants to rockets operating at low temperature. The inter-related effects of water, from 0 to 10 percent by weight, and nitrogen tetroxide, from 0 to 25 percent by weight, in fuming nitric acid were studied with respect to the freezing points of the acid and the ignition delays with several fuels. Several possible chemical causes for the opposing effects of water and nitrogen tetroxide on ignition have been proposed.

Ignition delays of several propellant combinations obtained with a modified open-cup apparatus and a small-scale rocket engine of approximately 50 pounds thrust were compared to study any correlations that might exist between the two methods of ignition-delay determination. The results were used in determining the relative utility of each apparatus.

The literature pertaining to the preparation, physical properties, corrosiveness, thermal stability, constitution, and analysis of various nitric acids has been reviewed primarily with respect to their use as rocket oxidants. Conflicting data are evaluated and recommendations for additional experimental work are indicated.

Numerous studies have been made of the vapor pressure of essentially pure nitric acid and of the binary system, nitric acid-water. Data for the ternary system, nitric acid-water-nitrogen dioxide, are for the most part lacking. Work was therefore undertaken to provide more complete vapor-pressure data for the ternary system at physical equilibrium. Mixtures containing 71 to 97 weight-percent nitric acid, 0 to 20 percent nitrogen dioxide, and 0 to 15 percent water were used.²⁴

Because the storage of fuming nitric acids presents a serious operating problem, means for improving the storage properties of this acid were sought. The storage properties of fuming nitric acids, with and without additives, were studied at a temperature of 170° F in closed containers of approximately 100-milliliter capacity; the containers had aluminum bodies and stainless-steel caps.

Among the storage properties of fuming nitric acid, corrosion and decomposition are of foremost concern. Additional information concerning the effectiveness of fluorides as corrosion inhibitors in fuming nitric acid was therefore obtained. It was found that for acids containing no fluorides, the weight loss of aluminum was approximately one-fifth that of stainless steel. Addition of 1-percent fluoride ion to the acid reduced the

weight loss of both metals to practically zero even after 26 days of exposure to the acid at 170° F. Additional information concerning the effect of fluorides on corrosion was obtained by measuring the electrode potentials of the metals against a platinum reference electrode.

Rocket Combustion

Ignition-delay determinations of several fuels with nitric-acid oxidants were made at simulated altitude conditions from sea level to 100,000 feet utilizing a small-scale rocket engine of approximately 50 pounds thrust. Included in the fuels were aniline, hydrazine hydrate, furfuryl alcohol, furfuryl mercaptan, turpentine, and mixtures of triethylamine with mixed xylydines and diallylaniline. Red-fuming, white-fuming, and anhydrous nitric acids were used with and without additives.

The rocket phenomenon known as screaming often causes chamber, injector, or nozzle burnout failures and has been observed to increase the specific impulse. Rocket-engine screaming is a type of combustion-driven oscillation, with frequencies from 1,000 to 10,000 cycles per second, and is characterized by an audible wailing exhaust sound, by a bluish almost-invisible exhaust jet in which the shock positions oscillate (making the shock pattern appear fuzzy to the eye) and by increased heat transfer to the chamber surfaces. The high-frequency oscillations have been attributed to a combustion-reinforced pressure wave passing through the chamber and reflecting from the chamber surfaces to trigger the succeeding combustion surge. The frequency would therefore be governed by the velocity of wave propagation and the geometry of the chamber. A simplified analysis, based on the concept of acoustical resonance, has been developed to correlate scream frequencies with chamber geometry in terms of experimentally measurable quantities. The derived parameter is substantially independent of propellant combination or operating conditions.

The application of radiation-measurement techniques to the determination of gas temperatures in the flame resulting from liquid propellant reactions has recently been investigated. Such techniques are desirable in rocket combustion and injector design studies because they permit the study of conditions in a flame zone without disturbing the flow and without the necessity of maintaining a probe in the chamber. Radiation-temperature measurements were made throughout the flame developed within an open-tube combustor using liquid oxygen and a heptane-turpentine mixture as the reactants.²⁵ The temperature measurement utilizes carbon radiation from the flame.

²⁴ See paper by McKeown and Belles listed on p. 78.

²⁵ See paper by Auble and Heidmann listed on p. 76.

AIRCRAFT CONSTRUCTION

Problems associated with the structural integrity of aircraft in the subsonic and lower supersonic range are many and complex. Aerodynamic heating resulting from greater speeds continues to add a host of new problems and to complicate those of a long standing nature further. The need for increased research in the field of aircraft construction is evident.

The NACA, during the past year, has continued its efforts on the important problems associated with structural strength, efficiency, loading, flutter, fatigue, and materials under normal temperatures. It has also developed research tools and techniques for investigating aircraft under the elevated-temperature conditions encountered in high-speed flight. Further, it has succeeded in defining and exposing new thermal problems which future high-speed aircraft will encounter and has found solutions to certain of these problems.

Most of this research has been performed at the NACA laboratories with additional assistance provided by educational and other nonprofit institutions under contract to the NACA. A description of the Committee's recent unclassified research in the field of aircraft construction is given in the following pages and is divided into four sections: (1) Aircraft Structures; (2) Aircraft Loads; (3) Vibration and Flutter; and (4) Aircraft Structural Materials.

AIRCRAFT STRUCTURES

Static Properties

The use of integrally stiffened skins on aircraft is increasing because of the possibilities of saving weight and eliminating rivets and bolts. Compared with riveted-on stiffeners, integral stiffeners participate more fully with the skin in resisting external loads but, because of this action, may lead to an undesirable coupling of plate distortions for certain proportions and loading conditions. The nature of this problem is discussed in Technical Note 3646 where the modifications to the equations for stress distribution and deflection are made to account for the effects of coupling. Conditions under which the effects of coupling are significant are given in this paper.

Because engineering beam theory fails for deflection analysis of thin low-aspect-ratio wings, the development of efficient methods of analysis has become a problem. A matrix method based on energy principles for obtaining influence coefficients is presented in Technical Note 3640. The required matrices may be set directly from the data of the wing design. The necessary calculations have been arranged to take full advantage of automatic computing machines.

The thick-skin multiweb box beam is representative of wings of high-speed aircraft. Experimental data and strength analysis of this component are presented

in Technical Note 3633. The combinations of design parameters which lead to minimum structural weight for various values of a loading index are given. The results are presented in such a manner that the lightest weight structure which satisfies wing-stiffness requirements can be found.

Classical theories of the structural strength and stability of plates assume that the plate deflections experienced are small in comparison with the plate thickness. In order to evaluate the inaccuracies resulting when this assumption is not fulfilled, Columbia University has developed a nonlinear plate theory of motion and solved the equations for certain dynamic cases. Underlying assumptions of various plate equations have also been studied. The results of this study are presented in Technical Note 3578.

Comparisons between the results of a theory for calculating stresses around cutouts in stiffened cylinders and the results of experiment are presented in Technical Note 3544. The data and the theory were previously published and coefficients for use with the theory have been calculated and published in Technical Note 3460. The theory takes into account the bending flexibility of the ring stiffeners. The comparisons show that good agreement is obtained if this factor is correctly accounted for.

New York University has conducted, under NACA sponsorship, a critical review of the literature published since 1940 on buckling and failure of plate elements. The results of this review, including a compilation of existing theories and experimental data, are presented in Technical Note 3781. A similar review has also been made at New York University of the existing literature on buckling of composite elements. The results of this review are presented in Technical Note 3782. During these reviews, general equations for the plastic buckling of cylinders were derived. These equations were then used to obtain solutions for the compressive and torsional buckling of long cylinders in the plastic region. These results, as well as comparisons between computed and test data, are presented in Technical Note 3726.

An analysis of the stresses in the plastic range around a circular hole in a plate was made both to explore means for solving stress problems in the plastic range and to obtain the solution of this basic problem. The results are presented in Technical Note 3542. Calculations were made for four different materials and the resulting stress-concentration factors are compared with those derived from a previously developed approximate formula.

Dynamic Properties

The major role that flutter plays in the design of high-performance aircraft requires that methods for

computing accurate vibration modes and frequencies be obtained. In Technical Note 3636, the investigation of the usefulness of the substitute-stringer method for including the effects of shear lag in the calculation of the transverse modes and frequencies of box beams is continued. Box beams, the covers of which consist of normal-stress-carrying stringers on sheets carrying not only shear but also normal stress, are analyzed exactly. Frequencies of beams with various numbers of stringers, obtained by means of this exact analysis, serve to determine the possible accuracy of the frequencies obtained by the substitute-stringer approach. A combined experimental and theoretical investigation of the modes and frequencies of a large-scale built-up box beam is reported in Technical Note 3618. For bending vibrations, frequencies obtained from an analysis of a substitute-stringer structure which includes the influence of transverse shear deformation and shear lag were found to agree very well with those obtained experimentally. In the case of torsional vibrations, the frequencies obtained from either an elementary or a four-flange beam analysis which includes the effects of restraint of warping were found to be in satisfactory agreement with the experimental frequencies.

The vibration characteristics of hollow thin-walled rectangular beams have been investigated to obtain insight into the factors affecting the modes and frequencies of wings. The experimental results from this study are presented in Technical Note 3463 and indicate that the effect of shear deformation of the cross section on the torsional frequencies can be large. Further evaluation of this effect has been made and is presented in Technical Note 3464.

Thermal Properties

Rapid changes in temperature of the surface of an aircraft can induce thermal loads in the primary structure which may have serious aerodynamic and structural consequences. The nature of this problem was investigated by subjecting box beams which simulate high-speed-wing structure to a high-intensity heat source. These tests are reported in Technical Note 3474. It was found that the internal structure of the beams provided enough restraint against expansion of the heated skin surfaces to cause severe buckling of the skin. Buckling of the shear webs occurred during the cooling phase of the test when the temperature of the internal structure exceeded that of the skin. Measured strains were used to determine distortions and stresses which were found to agree with a thermal stress analysis of the test conditions.

One of the most important structural problems resulting from aerodynamic heating is the deterioration of material properties at elevated temperatures. This deterioration of material properties produces loss of strength and creep of structures and can lead to weight

increases that adversely affect the performance of high-speed aircraft. A study has been made of the strength and creep behavior of aircraft structural elements at elevated temperatures to obtain methods for predicting structural behavior from material characteristics. One of these studies, reported in Technical Note 3552, was concerned with the elevated-temperature compressive strength and creep lifetime of simply supported plates. A similar study on the compressive strength and creep lifetime of skin-stringer panels is reported in Technical Note 3647. Both studies indicate that elevated-temperature strength of structural elements can be predicted from methods available for determining room-temperature strength provided that the appropriate stress-strain curve for elevated-temperature material is used. Previously reported studies of the elevated-temperature buckling strength of structural components have indicated similar results. The present studies also show that creep lifetime of structural elements may be determined from methods used to determine structural strength if the compressive creep properties of the material are substituted for the material stress-strain curve. The results make it possible to estimate the effect of creep on the weight of structures that are designed to operate at elevated temperatures.

The transient thermal stresses produced by aerodynamic heating of supersonic aircraft depend upon the temperature distribution within the structure, which, in turn, can be markedly influenced by the thermal conductivity of any joints present. In order to investigate the effects of joint conductivity on the thermal stresses in aerodynamically heated skin-stiffener combinations under various aerodynamic conditions, a theoretical study was made. In this study an aerodynamic heat-transfer parameter (called the Biot number), a joint-conductivity parameter, and geometrical proportions were varied. The results, presented in Technical Note 3699, indicate that increasing the joint conductivity beyond a certain value results in almost no change in the maximum skin or stiffener stresses; but, as the joint conductivity approaches zero, the maximum skin and stiffener stresses increase appreciably. Increasing the Biot number, an index of the rate of transfer of external heat to internal heat, can also cause a considerable increase in the maximum skin and stiffener stresses. However, when the Biot number is large (high rate of external heating), the value of the joint conductivity is relatively unimportant since the structure is heated so fast that there is no time for heat to be conducted into the interior of the structure; the joint conductivity thus affects the thermal stresses most significantly when the external heating rate is low. Changing the geometric characteristics produces results which are essentially independent of the joint conductivity and the Biot number.

In the design of aircraft structures, where aerody-

dynamic heating is encountered, knowledge of the temperature distribution within the structure is of considerable importance. Because interior elements of the structure are heated by conduction through joints, the influence of various joint properties on thermal conductance has been investigated previously and reported by Syracuse University. Before extending this investigation, Syracuse University explored the influence of joint conductance on the transient temperature distribution in composite aircraft joints. Fabricated specimens representative of typical skin-stringer cross sections, as well as geometrically similar specimens without joints, were tested under aerodynamic heating conditions and the results from the two sets of joints were compared. The results, which are presented in Technical Note 3824, indicate that, in the practical case, joint conductance must be taken into account if temperature distributions throughout composite structures are to be predicted accurately.

Aircraft structures for high-speed flight must be designed so that excessive creep deformation and creep rupture does not occur during the design lifetime of the structure. An understanding of the creep behavior of structures is therefore necessary in order to eliminate such failures. A previously reported investigation by the National Bureau of Standards indicated that creep deformations within joints may be responsible for a considerable portion of the overall deformation of structures. However, no correlation was obtained between the creep of a riveted joint and the creep of its component materials. This study has now been extended and creep-test results of a number of additional joints are reported in Technical Note 3842. Methods are presented by which the time to rupture, the mode of rupture, and the deformation of structural joints in creep may be predicted. These methods are based upon the creep properties of the materials of the joint in tension, shear and bearing.

Aircraft structural elements subjected to long periods of heating and compressive loadings can buckle even though the applied load is less than the critical load of the element at the elevated temperature. This phenomenon is called creep buckling. Research equipment and techniques have been developed at the Polytechnic Institute of Brooklyn and are presented in Technical Note 3493. Additional creep-buckling tests of 2024T-4 aluminum alloy columns besides those published in this report have been conducted and the results correlated with theory.

The aircraft designer at the present time must deal with a multiplicity of materials and material properties which vary with temperature. It is essential, therefore, that speedy and accurate methods for predicting the influence of changes in material properties on structural strength be available. Such methods are given in Technical Note 3553 and Technical Note 3600 for various types of structural components which fail by compressive

crippling. The methods utilize the concept of crippling-strength moduli which are readily calculated from the compressive properties of the material in the structure. Accuracy of the methods is illustrated with experimental data obtained in various materials and under different temperature conditions.

The transient temperature distributions produced by aerodynamic heating of thin solid wings induce thermal stresses that may effectively reduce the stiffness of the wing. This is a new problem that can be a significant factor in the aero-elastic behavior of aircraft structures. Such reductions in stiffness have been investigated experimentally by rapidly heating the edges of a cantilever plate. The midplane thermal stresses imposed by the nonuniform temperature distribution caused the plate to buckle torsionally, increased the deformations of the plate under a constant applied torque, and reduced the frequency of the first two natural modes of vibration. Small-deflection plate theory, employing energy methods, predicted the general effects of the thermal stresses but became inadequate when plate deflections were large. Additional studies have been initiated to investigate these effects.

AIRCRAFT LOADS

Basic Load Distribution

Extensive flight investigations have been made with the X-5 variable-wing-sweep research airplane at Mach numbers up to 1.0 to determine the effects on the wing and horizontal tail loads of varying the angle of wing sweep without modifying the other characteristics of the airplane. Up to a Mach number of 0.85, the balancing horizontal-tail loads measured in flight show a consistent variation as the wing sweep angle is increased from 20° to 59° with the greatest down tail load occurring at sweep angles of about 36°. The wing loads were found to have a nonlinear variation with airplane angle of attack and to reflect the changes that occurred in the wing characteristics. In another flight investigation, pressure measurements over the midspan station of the 8-percent-thick wing on the X-1 airplane in the transonic speed range showed a rearward movement of the chordwise load center with increasing Mach number with a particularly rapid and large movement in the Mach number range of 0.82 to 0.88. In the Mach number range 0.95 to 1.25 at high normal force coefficients, upper surface pressure distributions approached a rectangular slope.

In Technical Note 3476, spanwise lift distributions have been calculated for 61 swept wings with various aspect and taper ratios and a variety of angle-of-attack distributions including flap and aileron deflections. The information presented can be used both in the analysis of untwisted wings or wings with known twist distributions and in aeroelastic calculations involving

initially unknown twist distributions. The information presented in Technical Note 3476 supplements similar information previously given in Technical Note 3014 for unswept wings so that the two papers cover all practical plan forms.

A method for computing the span loads and the resulting rolling moments for sideslipping wings of arbitrary plan form in incompressible flow is presented in Technical Note 3605. The basic method requires mechanical differentiation and integration to obtain the rolling moment for a wing of arbitrary plan form in sideslip when the span load at zero sideslip is known. The mechanical differentiation and integration can be avoided, however, by use of a step-load method which is also derived. A comparison of the calculated span loads and rolling-moment parameters with available experimental data shows good agreement.

The development of new-type control devices requires that structural design data be provided. The effects, therefore, on the chordwise pressures and section forces and moment coefficients near midspan of deflecting various plain spoilers and a flap-type control with and without an attached tab on a swept wing have been investigated at Mach numbers from 0.60 to 0.93.

In order to design aircraft one must have a knowledge of body effects on the wing spanwise load distribution at all speeds. Although methods exist for predicting such body effects on sweptback wings at low speeds, practically no direct experimental verifications have been available. In a recent investigation, detailed wing pressure-distribution data that permit the desired comparison were obtained. The data, reported in Technical Note 3730, indicated that, although previous methods did not satisfactorily predict body effects on the unflapped uncambered wing, a swept-wing method employing 19 spanwise lifting elements and control points gave good agreement except when the wing had deflected trailing-edge flaps or was cambered and twisted.

Normal-force and normal-pressure distributions for an ogive-cylinder body of revolution of fineness ratio 10 are reported in Technical Note 3716 for a free-stream Mach number of 1.98 and an angle-of-attack range from 0° to 20° . Comparisons of experimental and theoretical normal-force and normal-pressure distributions indicate that available theoretical methods can be used to predict experimental results with good accuracy for angles of attack to about only 5° . At greater angles of attack, the normal-force distributions differ significantly from those calculated in accordance with theories which include methods of estimating the effects of viscosity on the forces and moments for inclined bodies. Analysis of the data shows that these differences are, in general, attributable to inadequate estimates of the magnitude and distribution of the cross forces resulting from flow separation. A correlation curve for the longitudinal distribution of the

cross-flow drag coefficient for laminar boundary-layer flow has been developed and is based upon the assumption that the distribution depends primarily upon the body shape. It is believed that use of this curve for the viscous cross-force contribution in conjunction with first-order linear theory for the potential cross force provides a satisfactory method for estimating normal-force and pitching-moment characteristics for similarly shaped bodies with laminar-boundary-layer flow.

In Technical Note 3479, horizontal-tail loads measured in gradual and abrupt longitudinal maneuvers on two configurations of a four-engine jet bomber are presented. The least-squares procedures were used to determine aerodynamic loads from strain-gage measurements of structural loads. The results are analyzed to determine the flight values of the aerodynamic coefficients which are important in calculations of horizontal-tail loads for comparison with wind-tunnel results. The effects of fuselage flexibility on the loads are determined and some calculations of critical horizontal-tail loads beyond the range of the tests are compared with the design loads.

Some indication of the importance of the directional-stability characteristics of present-day high-speed airplanes with increasing angle of attack and Mach number has become apparent from recent wind-tunnel tests. An analysis of wind-tunnel data has shown that the vorticity shed from the nose of the fuselage and directed by the wing to strategic locations in the vicinity of the vertical tail markedly affects the load on the vertical tail in sideslip at high angles of attack and supersonic Mach numbers. For such conditions, the directional stability of the airplane may become negative.

Gust Loads

The collection of data with NACA VG and VGH recorders to determine the magnitude and frequency of occurrence of the gusts and gust loads and the operating air speeds and altitudes of commercial transport airplanes has been continued. The VGH data covering about 3,000 hours of operation from two types of four-engine transport airplanes currently in use on transcontinental and eastern United States routes are presented in Technical Notes 3475 and 3483. The analysis of these data indicates that the more severe gust loads occurred for operations over the eastern portion of the United States, a result attributable to the higher operating speeds in rough air for these operations. A related study of approximately 70,000 hours of VG data from six different operations of twin-engine transport airplanes over the past eight or nine years, presented in Technical Note 3621, indicates that the loads and gusts were comparable with those experienced in previous operations of the same type of airplane.

The information available on the spectrum of atmospheric turbulence is briefly reviewed in Technical Note

3540 and a method is presented for converting available gust statistics normally given in terms of counts of gust peaks into a form appropriate for use in spectral calculations. The fundamental quantity for this purpose appears to be the probability distribution of the root-mean-square gust velocity. Estimates of the variation of this distribution with altitude and weather condition are also derived from available gust statistics. A critical problem in connection with the design and operation of missiles and airplanes capable of high-speed vertical flight arises from the loads and motions experienced when intense layers of wind shear are encountered. As a consequence, data on the magnitude and frequency of occurrence of the shear layers at different altitudes and seasons were determined from U. S. Weather Bureau rawinsonde data and are reported in Technical Note 3732. These data indicate that maximum shear intensities of about 120 feet per second per 1,000 feet occur at altitudes of about 50,000 feet during the spring and winter seasons but occur in relatively thin layers having thicknesses not greater than about 3,000 feet.

A method for obtaining a power spectrum of vertical gust velocity over a wide range of wave length has been devised and test results are published in Technical Note 3702. A spectrum of vertical gust velocity was measured at low altitude in clear-air turbulence having a root-mean-square intensity of 5 feet per second for wave lengths from 10 feet to 60,000 feet. At the higher frequencies (short wave lengths), the power spectral density varied at a rate which was approximately predicted by theory. The spectrum which was obtained tended to flatten out for the longest test wave lengths. The break frequency which provides an indication of the scale of the turbulence occurred at a wave length of approximately 6,000 feet.

Calculated unsteady-lift functions and spanwise lift distributions for delta, rectangular, and elliptical wings undergoing a sudden change in sinking speed are presented in Technical Note 3639. These data indicate that the normalized unsteady-lift functions are substantially independent of the plan form for elliptical, rectangular, or moderately tapered wings, but for delta wings the increase of lift toward the steady-state value is much more rapid. The results in this report corroborate the results of other investigations which show that the rate of growth of lift tends to increase with a decrease in aspect ratio and that spanwise distributions of the indicial lift seem to be independent of time for rectangular and elliptical wings. In Technical Note 3748, reciprocal relations for unsteady flow are used to calculate total-lift responses of wings to sinusoidal gusts and to sinusoidal vertical oscillations. A variety of plan forms are considered for incompressible, subsonic compressible, sonic, and supersonic flow. A theory is presented in Technical Note 3805 for calculating the variation with frequency of the lateral-force and yawing-moment coefficients due to sinusoidal side gusts

passing over the profile of a simple fuselage combined with a vertical fin. Since slender-body theory is used, the results are applicable to both subsonic and supersonic airspeeds, provided the local flow angles between the profile and the airstream are small.

An investigation to determine the gust-alleviation capabilities of fixed spoilers and deflectors on a transport-airplane model incorporating a straight wing is reported in Technical Note 3705. The results indicate about equal effectiveness (from 20 to 40 percent) of spoilers or deflectors in reducing normal accelerations in rough air through reductions in lift-curve slope. Both devices were also equally effective in decreasing the airspeed through increased drag. In Technical Note 3746, the wing and horizontal-tail loads and spar strains measured on a twin-engine light transport airplane, modified by a gust-alleviating device for passenger comfort, were presented. The results presented are an initial analysis of samples of measurements obtained in clear-air turbulence with the alleviation system both off and on. Although the alleviation system was not optimum, the root-mean-square normal acceleration at the airplane center of gravity was reduced by 43 percent and the wing bending strains were reduced, but wing-shear strains and horizontal-tail shear and bending strains were increased.

Landing Loads

In Technical Note 3541, a method is presented for statistically deriving contact vertical velocities of airplanes from measurements of maximum incremental center-of-gravity acceleration at contact. Probability curves of derived velocities for a test airplane when compared with curves of measured velocities show a difference of less than 0.2 foot per second throughout the velocity range covered in the investigation. A statistical comparison of the landing-impact velocities of the first and second wheel to touch ground from about 350 transport landings is reported in Technical Note 3610. The comparison indicates that the mean vertical velocity at the instant of contact was about the same for either wheel but that the probability of a high value of vertical velocity was somewhat greater for the second wheel to touch than for the first. The effect of the rolling velocity of the airplanes at the instant of initial contact was to increase the vertical velocity of impact of the wheel toward which the airplane was rolling regardless of whether it was the first or second wheel to touch. There appeared to be no definite influence of the ratio of landing-gear tread to radius of gyration of the airplanes on the relative vertical velocities of the first and second wheels to touch, as would be expected from theoretical considerations.

Technical Note 3604 reports results of tests made to determine the lateral or cornering force, drag force, torsional moment or self-aligning torque, pneumatic caster, vertical tire deflection, lateral tire deflection, wheel

torsion or yaw angle, rolling radius, relaxation length, tire footprint area, and variation of unloaded tire radius with inflation pressure for two 26- by 6.6-inch, type VII, 12-ply-rating tires. Data were recorded for conditions of rectilinear-yawed rolling over a range of inflation pressures and yaw angles at the rated vertical load and at twice the rated vertical load. Vibration tests were made to determine the dynamic lateral elastic characteristics of the tires. During rectilinear-yawed rolling, the normal force generally increased with increasing yaw angle within the test range, the variation of normal force with yaw angle differed for the two vertical loads tested, the pneumatic caster was a maximum at small yaw angles and tended to decrease with increasing yaw angle, and the sliding drag coefficient of friction tended to decrease with increasing bearing pressure.

A comprehensive correlation, evaluation, and extension of linearized theories for tire motion and wheel shimmy has been made and is reported in Technical Note 3632. It is demonstrated that most of the previously published theories represent varying degrees of approximation to a summary theory developed therein which is a minor modification of the basic theory of Von Schlippe and Dietrich. In most cases where strong differences exist between the previously published theories and the summary theory, the previously published theories are shown to possess certain deficiencies. Comparison of the existing experimental data with the predictions of the summary theory provides a fair substantiation. Some discrepancies exist however, which may be due to tire hysteresis effects or other unknown influences.

Theory indicates a sharp increase in the hydrodynamic load as the dead-rise angle approaches zero. There have been, however, few experimental data available for verifying the loads predicted by theory for angles of dead rise below 20°. Results of a brief investigation of the loads in smooth water for 10° angle of dead rise are reported in Technical Note 3608 and are compared with theory for immersed hydrodynamic impact of nonchine bodies. The trend of the experimental variation of load-factor coefficient, draft coefficient, time coefficient and velocity ratio is in good agreement with the theoretical variation.

Technical Note 3619 presents data showing the effect of horizontal restraint of carriage mass in experimental testing facilities upon the general theoretical equations of motion for the prismatic body during a hydrodynamic impact. The data indicate that the carriage mass has little effect for the low trims, since at this condition the resisting water force has only a small component in the horizontal direction, but for the higher trims the effect is appreciable. For the more usual seaplane-design conditions, that is, approach parameters larger than 1.0 and trims up to 15°, the

maximum correction for any of the coefficients is 10 percent or less.

Research Techniques

It is frequently desirable to predict the loads that would be experienced with more hazardous control motions or flight conditions than those for which test data exist. Accordingly, considerable effort has been expended in developing and comparing various methods by which such predictions can be made. Fourier and Laplace transforms and the type of analyses used in studies of servomechanisms have been used extensively in this development. It appears from the work accomplished that the concept and use of a unit impulse as a research technique has considerable merit. Simple and rapid methods for determining the time response to a unit impulse from frequency-response data and for evaluating the Fourier transform as a function of time have been derived and are presented in Technical Note 3598. These methods are applicable to linear functions for which Fourier transforms exist, which is usually the case in the treatment of airplane maneuvers. In Technical Note 3701, the method developed in Technical Note 3598 is compared with several other methods of obtaining the time response of linear systems to either a unit impulse or to an arbitrary input from frequency-response data. The comparisons indicate that most methods gave good accuracy when applied to a second-order system; the main difference is in the computing time. In general, the method of Technical Note 3598 was advantageous in all respects, since it was more accurate and required less time.

VIBRATION AND FLUTTER

Flutter

The sonic and supersonic speeds of modern aircraft plus their use of relatively flexible thin wings and stabilizers have caused flutter to assume a more important role in aircraft design. In addition to research on the flutter characteristics of typical aircraft configurations, research is also being carried out to understand better the aerodynamic, structural, and inertial considerations inherent in flutter.

On the basis of an analysis of a large quantity of flutter data taken from subsonic, transonic, and supersonic wind tunnels and from rocket- and bomb-drop tests for a wide variety of wing plan forms, a criterion was derived which permits a rapid estimate of the probability of flutter for lifting surfaces. This criterion groups the significant parameters into simple geometric dimensions and structural properties. Another simple criterion was developed for stall flutter.

A number of swept wings having systematic variations in plan form and structural characteristics have been flutter tested in transonic and supersonic wind tunnels to establish the effect of various parameters

on flutter and to serve as a basis for evaluating analytical procedures. Because of the large number of parameters involved, this is a large test program and is still underway.

An alternative to the testing of a systematic series of wind-tunnel models in order to establish the influence on flutter of elastic and inertial structural characteristics is to employ an analog computer whose electrical elements and behavior approximate the elements and dynamic behavior of the structure. Such an analog study has been carried out at the California Institute of Technology and is discussed in Technical Note 3780. Four wings representative of those of current aircraft were considered and the effects of changes in bending and torsional stiffnesses, mass distribution and angle of sweep on the flutter characteristics were determined. A sufficient number of cases were treated to establish the trend over a sizeable range for each parameter.

As reported in the Forty-First Annual Report, 1955, a theoretical study of the flutter of two-dimensional panels was reported in Technical Note 3465. More recently, flutter of panels mounted on the wall of a supersonic wind tunnel was obtained at a Mach number of 1.3. It was found that, at the flow conditions of these tests, increasing the tensile forces in the panel was effective in eliminating flutter, as was shortening the panels or increasing their bending stiffness. No apparent systematic trends in the flutter modes or frequencies could be observed, and it is significant that the panel flutter sometimes involved higher modes and frequencies. The presence of a pressure differential between the two surfaces of a panel was observed to have a stabilizing effect. Initially buckled panels were more susceptible to flutter than panels without buckling. Buckled panels with all four edges clamped were less liable to flutter than buckled panels clamped only on the front and rear edges.

In Technical Note 3638, a preliminary theoretical investigation of the panel flutter and divergence of infinitely long, unstiffened and ring-stiffened, thin-walled, circular cylinders is described. Linearized unsteady potential-flow theory was utilized in conjunction with Donnell's cylinder theory to obtain equilibrium equations for panel flutter. Where necessary, a simplified version of Flügge's cylinder theory was used to obtain greater accuracy. By applying Nyquist diagram techniques, analytical criteria for the location of stability boundaries were derived. This report also includes a limited number of computed results.

One of the most troublesome types of flutter is that involving oscillations of a control surface at transonic speeds, commonly referred to as buzz. In Technical Note 3687, results of wind-tunnel tests of three wing models are presented and it is shown that a large range of change in density of the test medium had little effect on the initial magnitude and initial Mach number of

buzz. The buzz frequency decreased somewhat with decrease in density. The Mach number corresponding to the onset of buzz decreased as the wing angle of attack was increased. Mass balance and changes in spring stiffness changed only the oscillation frequency. The test results indicated that placing the aileron at the wing tip delayed the onset of buzz to higher Mach numbers. A comparison of the experimental results with two published empirical analyses showed only qualitative agreement.

Designers of thin aircraft wings must consider the possibility of wing torsion flutter at high angles of attack, which is referred to as stall flutter. The results of an exploratory, analytical, and experimental study of some of the factors which might be of importance in the stall-flutter characteristics of thin wings are presented in Technical Note 3622. The factors considered were Mach number, Reynolds number, density, aspect ratio, sweepback, structural damping, location of the torsion node line, and presence of concentrated tip weights. The importance of aerodynamic torsional damping on the stall flutter of thin wings was demonstrated by comparison of the regions of negative torsional damping measured on a spring-mounted model with the regions of flutter. The results of a series of experiments on a thin wing tested at various spans indicated that compressibility alters the stall-flutter characteristics and that these effects depend upon aspect ratio. A brief study of the inertia effects of concentrated weights at the tip indicated that such effects can be important. An approximate analysis is presented for such configurations.

Aerodynamics of Flutter

It has been demonstrated that generalized forces for a harmonically oscillating wing in pure supersonic flow may be expressed in terms of certain integrals commonly referred to as f_λ functions. These functions have been tabulated on a large computer for a wide range of parameters important to flutter and the tabulated results are presented in Technical Note 3606.

A fundamental study of the aerodynamic forces on an oscillating wing is presented in Technical Note 3643. This report presents the magnitude and phase angle of the components of normal force and pitching moment acting on an airfoil oscillating in pitch about the mid-chord at both high and low mean angles of attack and for Mach numbers of 0.35 and 0.70. The magnitudes of normal-force and pitching-moment coefficients were much higher at high mean angles of attack than at low angles of attack for some conditions. Large regions of angle of attack and reduced frequency were found wherein one-degree-of-freedom torsion flutter is possible. It was shown that the effect of increasing the Mach number from 0.35 to 0.70 was to decrease the initial angle of attack at which unstable damping occurred. In addition, the aerodynamic damping in essentially the

first bending mode was measured for two finite-span, 3- and 10-percent-thick wings for a range of mean angles of attack and reduced frequencies. No regions of negative damping were found for this motion, and it was found that the damping measured at high angles of attack was generally larger than that at low angles of attack.

An experimental study of the lift and moment about the quarter chord of an oscillating wing at high subsonic Mach numbers is presented in Technical Note 3686. A comparison of the experimental magnitude of the lift vector with the theory as given by Dietze showed good agreement. Comparisons with theory of the moments and the out-of-phase component of lift indicated that some refinements in the testing technique are necessary for the experimental determination of these quantities in the transonic speed range.

An experimental wind-tunnel investigation was carried out of the forces, moments, and phase angles on a two-dimensional wing equipped with an oscillating circular-arc spoiler. Schlieren photographs were obtained which showed the flow over and behind the spoiler while it was oscillating. The forces and moments on the wing were obtained from instantaneous pressure-distribution measurements. The results indicated that the effects of Reynolds number on the normal-force and moment coefficients and their phase angles were very small and somewhat erratic. An increase in Mach number increased the normal-force coefficient and had no consistent effect on the moment coefficient, while the phase lag of both the normal force and moment decreased. There was little effect of reduced frequency on the normal-force coefficient; however, increasing the reduced frequency produced an essentially linear increase in the phase lag of the normal force.

Buffeting

Several studies have been made of the available transonic Mach number data on wing dropping, low-lift buffeting, buffet boundaries, and changes in the angle of zero lift for symmetrical airfoils and various airplane configurations. These phenomena are indicated to be allied and are probably the result of shock-induced separated flow. It was found that unswept wings which have airfoil sections 9 percent thick or thicker are susceptible to wing dropping at transonic speeds. Wing dropping may occur even for thin wings, however, if the airfoil contour is not fair. Sweepback only partially relieves the wing dropping and buffeting problem for thick wings. The studies have also indicated that there are combinations of airfoil-thickness ratio, aspect ratio, and sweep angle which may allow flight through the transonic speed range without either wing dropping or buffeting at low lift. Decreases in aspect ratio and thickness ratio and increases in sweepback all tend to alleviate high-speed buffeting. Low-

lift buffeting, however, may be induced by the interference effects of thin intersecting surfaces such as a tail arrangement in which the horizontal tail is mounted above the fuselage on the vertical tail. Such a tail arrangement may also be partially responsible for large transonic trim changes and may exhibit an increase in drag over that for a comparable tail arrangement where the horizontal tail is mounted on the fuselage.

An analysis of some statistical properties of the buffet loads measured on the unswept wing and tail of a fighter airplane has indicated that buffeting can be considered as a random process. Buffet loads measured on the wing and tail in both the stall and shock regimes indicated that the wing loads in buffeting can be treated as the response of a simple elastic system to a random input. The wing buffet loads were normally distributed and the probability that a peak load would exceed a given level was in agreement with theoretical results. There was evidence that the tail buffet loads were not normally distributed as the wing loads but appeared to represent a more complicated process. The spectrum of the wing-root shear indicated that the buffet loads were primarily associated with response in first symmetrical bending. The spectrum for the tail-root shear indicated that the tail buffet loads were associated with the fuselage-torsion or tail-rocking mode. This study was reported in Technical Note 3733.

AIRCRAFT STRUCTURAL MATERIALS

Structural Materials at High Temperatures

Aerodynamic heating continues to be the source of the most perplexing and urgent problems in the field of aircraft structural materials. This is true in extreme cases such as long-range ballistic missiles where the severity of the requirements will clearly necessitate the development of new kinds of structural materials and new kinds of test facilities. In addition, it is true for less severe applications such as manned airplanes, where the effects of high temperatures on the common engineering properties of existing materials are so inadequately known that the designer lacks the handbook data he needs to arrive at an efficient, yet safe, design. In effect, heat has introduced a new dimension in all material problems; strain-rate effects, changes in modulus, creep, stress rupture, thermal stress, thermal conductivity, and many other temperature-linked characteristics, which heretofore could be ignored, will have to be taken into consideration in the future. Some of these problems are under attack on several fronts.

The tensile properties of a number of structural materials under rapid-heating conditions were determined by means of a new type of test (a so-called rapid-heating test) in which the material is first loaded and then heated at various heating rates until yield and failure occur. Sheet materials used in this investigation included 7075-T6 and 2024-T3 aluminum alloys (Tech-

nical Note 3462, reported in the Forty-first, 1955, Annual Report), Inconel and RS-120 titanium alloy (Technical Note 3731), HK31XA-H24 magnesium alloy (Technical Note 3742), and AZ31A-O magnesium alloy (Technical Note 3752). In these tests, heating rates have been varied from 0.2° to 100°F per second. At the higher heating rates, the materials were found to be stronger, in general, than under constant-temperature conditions when loaded at a strain rate of 0.002 per minute. In most cases, yield stress, rupture stress, and temperature have been found to be correlated by means of a temperature-rate parameter. Some of the materials, such as the new high-temperature magnesium alloy HK31XA-H24, exhibited a marked increase in strength at high heating rates in the high-temperature region. Other materials, such as 2024-T3 aluminum alloy and RS-120 titanium alloy, behaved in a very complicated manner under rapid heating.

In an investigation, conducted at the University of Alabama under NACA sponsorship, the fatigue strengths at 10 million cycles of two of the more promising titanium alloys, 3Mn Complex and 3Al-5Cr, were determined at 200°, 400°, 600°, 800°, and 1,000°F. Data of this sort are needed for the evaluation of these new alloys of titanium before the role they can play in the solution of some phases of the high-temperature problem can be predicted.

The use of thermal insulation on the surface of structural materials is one of several possible methods of defeating the adverse effects of aerodynamically generated heat. However, there are many fundamental and technological difficulties, such as the realization of adequate strength of the coating-to-metal bond, which stand in the way of achieving practicable coatings. Results of an investigation conducted at the National Bureau of Standards and reported in Technical Note 3679 show that copper ions in the coating have the effect of producing a significant increase in the adhesion between the coating and the surface of stainless steel.

Laminates of nonmetallic materials possess characteristics which uniquely suit them for use in certain components of aircraft. The rate of deterioration of their mechanical properties with temperature, however, is a deterrent to their use in very fast aircraft. Future progress demands that improved materials be developed and further test data be obtained to enable the designer to gage the range of applicability of existing laminates. In an investigation conducted at the University of Illinois and reported in Technical Note 3414 the static-tension, static-compression, tension-creep, and time-to-fracture characteristics of melamine-resin glass-fabric laminates and silicone-resin glass-fabric laminates at temperatures up to 600°F were determined. In the analysis of the creep data an equation based on the activation-energy theory, which describes the effects of stress, time, and temperature is reported.

Fatigue

Failure by fatigue has always been and still is a potential hazard in aircraft structures and is therefore an important subject for research. Although steady and significant progress has been made in understanding the phenomena of fatigue and in designing structures that will incorporate characteristics that both lessen the likelihood of fatigue cracks and preserve the integrity of the structure when a crack does develop, there are still many aspects of the fatigue problem that require solution. Among these is the stress-concentration effect of geometrical discontinuities on fatigue properties of aircraft structural materials. Technical Note 3631 presents the results of axial-load fatigue tests on 2024-T3 and 7075-T6 aluminum-alloy sheet specimens with central holes. Specimens with various combinations of hole diameters and widths were tested to provide data suitable for study of the geometrical size effect.

In Technical Note 3293, which reports an investigation conducted at the National Bureau of Standards, the results of cumulative-damage tests of 7075S-T6 and 2024S-T3 aluminum-alloy sheets under various loading conditions are given. The cumulative damage ratio, which should be unity if the theory were absolutely correct, was found to vary from 0.568 to 1.440; however, 40 percent of the cumulative damage ratios were within 10 percent of unity.

At the University of California, a study (Technical Note 3495) was made of fatigue under combined repeated stresses with superimposed static stress. A comprehensive critical review of the literature where such tests were reported was made. In addition, tests were performed to determine the effects of static compression on alternating torsion, which was the only combination that had received no previous attention. The results were compared with the predictions of theory. It was shown that the Orowan theory of the effects of combined stress and cyclic stress on fatigue can be modified to predict the observed test results.

In an investigation conducted at the Battelle Memorial Institute, effects of notch severity on the initiation and propagation of fatigue cracks in ¼- and 2-inch-diameter notched bars were determined in rotating bending fatigue tests. These bars consisted of 2024S-T4 aluminum alloy with stress concentration factors of 5.2 and 13.9. The results reported in Technical Note 3685 indicate that cracks initiate in severely notched bars earlier than in unnotched or mildly notched bars. Discernible cracks occurred at 1,000 cycles at stress levels that would result in failure at 200,000 to 1,700,000 cycles. Differences in results of the tests of the ¼- and 2-inch-diameter bars indicated a size effect, which was attributed to residual stresses in the larger bars.

Fatigue stressing and the accumulation of damage have effects on the internal friction of metals and alloys.

Internal friction measurements are therefore useful in the study of the fundamentals of fatigue. In an investigation conducted at the California Institute of Technology and reported in Technical Note 3755, a correlation of internal friction and torsional fatigue was made at various temperatures. The results indicated the existence of a critical temperature at which fatigue life reached a minimum, and the effect of this temperature on internal friction was found to be substantial. In addition, the recovery of internal friction during periods of rest after fatigue stressing was observed. This recovery was found to be dependent on both stress level and temperature. Attempts were made to rationalize the relationship between the changes in the characteristics of internal friction and the inadequately understood phenomena of damage, recovery, and coaxing in fatigue.

Plastic Behavior of Metals

An understanding of the plasticity of metals is essential to the understanding of strength, ductility, resistance to brittle fracture, workability, and other properties of metals which account for their usefulness as aircraft structural materials. The NACA is conducting research in various areas of this field.

Technical Note 3681 reports results of an investigation conducted at the Battelle Memorial Institute on the plastic behavior of binary aluminum alloys by internal-friction methods. Effects of strain rate, amount of strain, heat treatment, temperature, and cyclic frequency on internal friction were determined, and the results were analyzed and rationalized in the framework of the dislocation theory of plasticity.

During plastic deformation of materials, distortions occur which are not predictable by the usual assumption of isotropy. Errors in strain of 50 percent and more resulting from anisotropy in the plastic range would

not be uncommon for some of the materials used in aircraft construction. A series of tests, described in Technical Note 3736, are utilized to establish semi-empirical relationships between Poisson's ratio and the properties of the materials as shown by their stress-strain curves. The tests also show that there is no permanent change in volume of the metals tested after stressing into the plastic range.

In an investigation conducted at Battelle Memorial Institute and reported in Technical Note 3728, the structure of slip lines developed in single crystals of aluminum at various stages during tensile deformation were examined in an electron microscope. On the basis of experimental results from this work and others from the literature, a mechanism for slip-band formation based on dislocation theory was formulated. The possible effects of short-range ordering on deformation modes are discussed.

Non-Metallic Materials

Cotton fabric-phenolic laminates are useful structural materials for aircraft, but the knowledge of the effects of processing and manufacturing variables on their properties is inadequate. In an investigation conducted at the National Bureau of Standards and reported in Technical Note 2825, tests were conducted to determine strength properties of (1) several untreated commercial cotton fabric-phenolic sheet laminates, (2) the same materials after exposure to typical postforming heating cycles, (3) industrially postformed shapes made from one of these materials, (4) industrially-made and laboratory-molded shapes, and (5) flat panels postformed from the laboratory-molded shapes. It was shown that molding of phenolic laminates may or may not affect the strength, depending on the fabrication techniques used.

OPERATING PROBLEMS

During the past year, the NACA has continued to conduct research on various problems that are associated with the operation of today's modern high-speed aircraft. It is recognized that as the performance of the nation's aircraft is increased new problems are encountered and some old problems become more important in the day-to-day operation of these aircraft. Some of the most important current problems include the effect of aircraft noise on aircraft and people; atmospheric effects such as icing, turbulence, lightning, temperature, and density; and flight safety, which includes crash fire, survival, aircraft braking, visibility, engine reliability, foreign-object damage, and other problems. Working with the NACA Committee on Operating Problems are the Subcommittee on Aircraft Noise, the Subcommittee on Meteorology Problems, the Subcommittee on Icing Problems, and the Subcommittee on Flight Safety.

The effects of the intense noise from modern aircraft and missiles present one of the most serious problems which faces the civil and military aircraft operators today. This problem offers a great challenge to our technical ability to find a satisfactory solution. The NACA with the advice and active help of the Subcommittee on Aircraft Noise has expanded its research on noise with particular emphasis on understanding the mechanisms of noise production and noise suppression. The scope of the last several meetings of this Subcommittee has been expanded to be, in effect, limited conferences on aircraft noise and have had international participation. These meetings were arranged to provide a free and comprehensive discussion of the noise problems and research efforts of various groups active in this field. The results of such meetings have been profitable: A cooperative effort to utilize the intellectual resources and research facilities of all concerned with

aircraft noise is essential to the solution of the noise problem.

As part of the constant NACA effort to summarize, discuss, and present recent NACA research results so that industry can best use these results for practical aircraft applications, technical conferences are held when appropriate for representatives of pertinent segments of the aircraft industry. On April 17, 1956, the NACA Conference on Airplane Crash-Impact Loads, Crash Injuries, and Principles of Seat Design for Crash Worthiness was held at the Lewis Flight Propulsion Laboratory. The NACA summarized the results of several years' work in the field of crash survival and proposed design criteria which, if applied, could improve aircraft seat design for crash survival. Civil and Military aircraft operators, manufacturers, and seat manufacturers now have the material presented at this conference as a guide for seat design. This material for the first time includes experimental data from actual dynamic-crash-load studies utilizing actual full-scale cargo, transport, and fighter-type aircraft.

A Summary of results of most of the recent unclassified investigations on operating problems is presented in the following paragraphs.

AIRCRAFT NOISE

The noises produced by current aircraft and missile power plants have increased to such intense levels that they affect the integrity of aircraft and missile structures, equipment, and control systems as well as present serious bioacoustic, efficiency, and annoyance problems for persons exposed to the noises. The effect of noises and related vibrations must now be considered as one of the principal elements of aircraft or missile design, and a specific NACA research program is directed toward obtaining full understanding and control of the production and effects of high-intensity noises.

While the noises produced by jet exhausts remain of primary concern to the NACA, research is also being conducted on boundary-layer and propeller noise, on the effects of noise on structures, and on propagation of noise through the atmosphere.

Jet Noise

NACA research has established that jet noise is produced by the turbulent mixing of the jet exhaust with the surrounding air; consequently, detailed investigations of the mixing phenomena are under way. One phase of this study consisted of measuring the turbulence in a subsonic jet by use of a hot-wire anemometer. The results are described in Technical Note 3561.

The studies begun last year of devices for altering the jet exhaust flow and thereby reducing jet noise are continuing. Tests on toothed and ejector nozzles are

described in Technical Notes 3516 and 3573. Tests of the use of square, rectangular, and elliptical nozzles for subsonic jets, as reported in Technical Note 3590, showed that simple changes in jet-nozzle shape had very little effect on noise generation. It is shown in that report, however, that if the exiting flow is supersonic, a convergent-divergent nozzle operating near its design point will produce less noise than an ordinary convergent nozzle.

With the data presented in Technical Note 3591 for an investigation of the scaling parameters between various jet engines and model jets, it is possible to estimate the far noise field of a jet engine from its flow characteristics. Detailed data are also presented in that report for the noise field around a modern jet engine operating under static conditions with and without afterburner.

A method for limiting the noise received on the ground during takeoff of a jet aircraft is to control the operational techniques. A study of the effects of various climbing procedures, reported in Technical Note 3582, showed that lowest effective noise levels over the largest ground area will be obtained when the aircraft is climbing on the steepest flight path consistent with minimum safe airspeed.

Boundary Layer Noise

In addition to the noise problems caused by a jet exhaust, serious problems result from the noise produced by the boundary layer flow over the surface of the fuselage and wings. Preliminary flight tests have been made to determine the surface pressure fluctuations caused by a turbulent boundary layer. The relation of boundary-layer noise to Reynolds number, velocity, and altitude has been studied and further work is being done on flight at high subsonic velocities.

A study by the California Institute of Technology of subsonic and supersonic flow of air past rectangular cavities cut into a flat surface indicated that the cavities would emit a strong acoustic radiation. From that work as reported in Technical Note 3487 and the above NACA flight tests it appears that noise considerations may be a primary factor in establishing the limits for such items as surface finish and size and shape of surface cutouts or protuberances for high-speed aircraft.

As a part of its work on aerodynamic noises under NACA sponsorship, the California Institute of Technology developed an instrument of fairly simple design for measuring time correlation functions of two stationary random-input signals. The device and its use in determining auto-correlation functions are discussed in Technical Note 3682.

Propeller Noise

Instrumentation suitable for making flight measurements of the free-space sound pressures in the immedi-

ate vicinity of a propeller in forward flight has been developed and successfully used on a fighter airplane up to a Mach number of 0.72. The sensing element is a capacity microphone housed in a streamlined probe and used in conjunction with an oscillator to convert the pressure pulses into a frequency-modulated signal which is telemetered to the ground. At the ground receiving station, the telemetered signal is detected and recorded on magnetic tape. Subsequently, the recorded signal is converted to a varying voltage which is fed into a heterodyne frequency analyzer. This instrumentation is reported in Technical Note 3534.

Effects of Noise on Structures

NACA research is continuing on the problems of designing and constructing structures that will be suitable for use in the intense-noise-pressure fields near propellers and jets. The response of various structural systems to acoustic inputs, the stresses encountered in the systems, the fatigue characteristics of the systems, and the effects of insulation and damping on the structure are all under study. Stress data has been obtained for panels exposed to discrete and random noise levels of over 160 decibels. The fatigue life of panels was noted to decrease markedly for further nominal increases in the noise intensity level.^{26 27}

Attenuation of Noise

The NACA has continued its sponsorship of research at the Massachusetts Institute of Technology to determine the effects of terrain and atmospheric conditions on the attenuation of noise. A theoretical and experimental investigation of the sound field about a point source over a plane boundary in the presence of a vertical temperature gradient is reported in Technical Note 3494. Methods are presented for analyzing the effects of temperature gradients on the attenuation of sound in the shadow zone of a sound field. A further study has produced a semiempirical method for the calculation of a sound field about a source over ground. This study considered the effects of vertical temperature as well as wind gradients and the scattering of sound by turbulence into the shadow zone (Technical Note 3779).

A theoretical study of the sound field from a random noise source above ground as measured by a receiver with finite band width is presented in Technical Note 3557. It is shown that the far sound field still contains two major regions so far as attenuation over ground is concerned. In the first region, the sound pressure level decreases approximately 6 decibels per doubling of distance. In the second region, however, beyond a certain distance from the source, the level decreases monotonically 12 decibels per doubling of distance.

FLIGHT SAFETY

During this second year of its existence the NACA Subcommittee on Flight Safety has not only monitored research into problems directly related to safety, such as fire, ditching, engine reliability, crash loads, and crash survival, but also studied results of research in other specialized fields so that they could be channeled directly to aircraft designers and operators through their safety organizations for immediate consideration. The following information shows the results of varied research projects that are significant for particular phases of aircraft operation which are considered to be most important from a safety standpoint.

Landing Problems

Operating statistics indicate that the landing phase of flight is most important from the standpoint of safety. There is much to be learned about the many facets of the landing problem. The NACA is actively studying many parts of the problem and has during the past year reported the results obtained with respect to landing loads, landing statistics, runway roughness and aircraft braking. In addition, the NACA has given wide distribution to the results obtained by other organizations investigating specific phases of the problem, namely nose-wheel shimmy (Technical Memorandum 1391) and friction of aircraft tires (Technical Note 3294). In the first of these two reports, general concepts regarding the effects of the condition of the tire, the type of rolling motion, and the loading are discussed. In Technical Note 3294, the results of a systematic study to determine the effects of temperature and normal pressure on frictional resistance between tire-tread material and concrete are given. Although these data are only a small part of the overall problem, they do offer some insight into the problem of tire-to-runway friction coefficient problem which is being attacked through both experimental flight and laboratory studies at the NACA Langley Laboratory.

In recent years, propeller reversing has been employed very effectively to assist in braking the aircraft during the landing roll on modern propeller-driven aircraft. A similar reverse-thrust device for the modern jet aircraft would be equally useful and can be accomplished by the reversing of the direction of the propulsive jet during landing. The NACA has completed an experimental investigation in which three types of thrust reversers were studied. Models of a target type, a tailpipe cascade type, and a ring cascade type were tested and the effects of design variables on performance and reversed-flow boundaries were determined. This work was reported in Technical Note 3664 and the results indicate that reverse-thrust ratios of from 40 to 80 percent could be obtained and

²⁶ See Regier paper listed on p. 78.

²⁷ See Lassiter, Hess, and Hubbard paper listed on p. 78.

that all three types had satisfactory thrust-modulation characteristics. Performance and operational studies of a full-scale jet engine thrust reverser (Technical Note 3665) of the target type utilized on a turbojet engine were also conducted. This device was pylon mounted under the wing of a cargo airplane to simulate a jet transport. The thrust reverser was operated for both stationary and taxi conditions, but the airplane was not flown. In addition to obtaining the performance of the thrust reverser, heat-rise patterns and rates resulting from impingement of the reversed hot gases on a simulated lower wing were also measured during periods of thrust reversal. Reingestion of the reversed hot gases into the engine inlet constituted an additional operating problem in that the temperature levels were raised throughout the engine and the reversed-thrust ratio was reduced. Taxi tests indicated that at ground speeds of 62 knots, the free-stream velocity was sufficient to prevent the reversed gas flow from entering the engine inlet.

Fire

The NACA has continued its research with turbojet and turboprop types of engines into the problems of crash-fire inerting and, in addition, has been studying the problems of flight fires in jet aircraft. Effective fire-fighting methods are still an important aspect of the problem. At the heart of the problem is the need for potent fire-extinguishing agents which have properties that make them suitable for use on aircraft. In Technical Note 3565, the results of a study which explains the quenching action of halogenated agents in the fire-extinguishing process are given. It is concluded that the presence of halogen in an agent need not reduce its fire-fighting ability provided that there is enough halogen to make the agent noninflammable. The assumption that halogenated agents act merely by chain-breaking reactions with active particles is consistent with the experimental facts available and will help guide the selection of other halogenated agents for further tests of their fire-fighting properties.

Technical Note 3560 presents the results of an investigation conducted at the University of Cincinnati under the sponsorship of the NACA on the spontaneous ignition of lubricants of reduced inflammability. In the initial phase of the investigation, the spontaneous-ignition characteristics of approximately 50 organic compounds were investigated and observations were made on the effects of structure on ignition. In studying compounds of interest as lubricants, it was found that hydrogenated polyisobutylene showed remarkable resistance to spontaneous ignition. Results indicate that those esters possessing high auto-ignition temperatures have low molecular weights, while those having low molecular weights in the lubricant range show poor resistance to spontaneous ignition.

Gust Alleviation

Whenever rough air is encountered in flight, the recommended practice is to reduce the speed of the airplane to the design speed for maximum gust intensity. When encountering rough air, the pilot does not always have time or advanced warning so that he can reduce the airspeed to the design speed. In these cases, the distance and maneuvering required to reduce speed may have an important bearing on the loads imposed on the airframe. Technical Note 3613 presents the results of an investigation of the problem of reducing the speed of a jet transport in flight. It was found that the required distance was much greater for a jet transport than for a typical piston-engine transport at the same altitude. The distance was also found to increase with altitude up to the altitude for maximum true airspeed. The increased distance for the jet transport was primarily the result of increased kinetic energy and to a lesser extent that of lower drag coefficients. These results are believed to be qualitatively correct for high-speed transport aircraft. The use of aerodynamic brakes, thrust reversal, or a climbing maneuver has been shown to be effective in reducing the distance required to reach the rough-air speed.

The ability of the human pilot to fly a precision course in rough air has been questioned and compared with the ability of an airplane autopilot combination to do the same task. Although the NACA has not studied this question directly, it has conducted theoretical studies involving various types of autopilots in an attempt to learn the characteristics of airplane response to gusts. The results of two such investigations have been published in Technical Notes 3635 and 3603. The results given in the former report indicate that the response to side gusts can be noticeably reduced. In the latter report, when the airplane was flown by various autopilots, the increased yaw damping greatly reduced the resonance associated with Dutch-roll of the airplane. The addition of an autopilot supplied directional stability and roll stability and greatly reduced the yaw and roll responses to gusts. Autopilots that held side forces to low values and provided good course response to command signals allowed large roll response to side gusts.

The NACA has been studying various means of increasing the smoothness of flight through rough air, both theoretically and experimentally. One of the most promising methods utilizes an autocontrol system in which the flaps and elevators are operated in accordance with indications of changes in angle of attack to maintain constant lift and zero pitching moment of the airplane. A detailed analysis of this system and its various refinements is presented in Technical Note 3597, including a study of the transient response of the airplane for both gust disturbances and longi-

tudinal control inputs. The aerodynamic characteristics necessary for optimum gust alleviation are derived and the response of this system is compared with that of the basic airplane. In order to study these analytical results in flight, an experimental investigation was conducted with a light transport airplane whose controls were modified to the extent necessary to provide gust alleviation. The results indicate that the gust alleviation system is at least capable of alleviating the normal acceleration due to gusts by 50 percent at a frequency of 0.6 cycle per second, the natural frequency of the airplane, and by 40 percent at a frequency of 2 cycles per second. The airplane can be controlled adequately when this gust alleviation system is operating.

Other devices that have been proposed for reducing the acceleration effects of rough air are spoilers, deflectors, and spoiler-deflector combinations. These devices have been investigated for both swept- and unswept-wing models. The results have been reported in Technical Note 3705 and it would appear from gust-tunnel and wind-tunnel tests that a forward-located fixed deflector would be a practical and effective alleviator of gust loads on an airplane having unswept wings. Preliminary results on a model having a 35°-swept-back wing have indicated that deflectors, in order to have the same effectiveness as reported for the unswept wing model, would have to be located more to the rearward on the swept wing and would possibly require larger projections if they are to have the same effectiveness they had on the unswept-wing airplane.

Optimum Flight Paths

The climb of turbojet aircraft, and the effects of tangential accelerations, have been analytically determined for minimum time of climb, climb with minimum fuel consumption, and steepest climb. For each flight condition, the optimum Mach number was obtained from the solution of a sixth-order equation whose coefficients are functions of two fundamental parameters: the ratio of minimum drag in level flight to the thrust and the Mach number which represents the flight at constant altitude and maximum lift-drag ratio. Diagrams have been prepared for the quick calculation of the optimum Mach numbers and the effect of acceleration on the rate of climb in tropospheric and stratospheric flight.

Airspeed Measuring Systems

Accurate determination of Mach number is fundamental to any detailed flight research and is of particular importance in the transonic speed range where many of the aerodynamic parameters vary markedly with Mach number. In order to conduct extensive research in this speed range, it was necessary that a suitable airspeed system be devised. Accordingly, calibrations of four airspeed systems installed in a turbojet fighter

were determined in flight at Mach numbers up to 1.04 by the NACA radar-phototheodolite method (Technical Note 3526). The results indicate that, of the systems investigated (a nose boom, two different wing-tip booms, and a fuselage-mounted service system), the nose-boom installation is the most suitable for research use at transonic and low supersonic speeds. The static-pressure error of the nose-boom system is small and constant above a Mach number of 1.03 after passage of the fuselage bow shock wave over the airspeed head.

The need for design information to provide rigid tubes to measure total head pressures correctly at high angles of attack and at high speeds has arisen because of the development of airplanes having good maneuverability at supersonic speeds. Conventional tubes, both rigid and swiveling, are unsatisfactory under these conditions. In Technical Note 3641, the results of wind-tunnel tests of 54 total-pressure tubes have been summarized and data are presented on the effects of inclination of the airstream on measured pressures at subsonic, transonic, and supersonic speeds. These data are in a form which permits a more detailed comparison of the effects of pertinent design values.

Spin Hazards and Recovery

The pilot's loss of orientation during spins, especially during unintentional spins, is a rising problem and has apparently led to a number of recent accidents and near-accidents with both trainer and fighter aircraft during acrobatic maneuvers and after recovery from erect spins. In Technical Note 3531, the nature of inverted spins, the optimum control technique for recovery, and some of the apparent reasons for a pilot's loss of orientation are discussed. It is pointed out that a pilot in an inverted spin should attempt to orient himself with respect to direction of turn by referring to the airplane rate-of-turn indicator in order to determine properly the direction of the yawing component of the total spin rotation. Optimum recovery from the inverted spin should then be obtainable by rapidly reversing the rudder from full with this yawing rotation to full against it while the control stick is held full forward and laterally neutral and, shortly thereafter, the stick should be moved from full forward to full back while it is maintained laterally neutral.

The general policy for recovery from either intentional or accidental spins has been to cut off power as soon as possible after the spin is initiated, because of possible adverse effects. In some instances however, pilots have flown out of an otherwise uncontrollable spin by application of full power in a propeller-driven airplane. Such results from power-on spins may have been due to increased effectiveness of the controls in the slipstream. For a jet engine, however, the situation is different, and unpublished data indicate that thrust alone might be

of little assistance. For both propeller-driven and jet-propelled airplanes, spin and spin-recovery characteristics may differ for power-on and power-off conditions, as well as for power-on spins to the right and to the left. These differences may at times have caused serious difficulty in recovering from spins in one direction, whereas recoveries from spins in the other direction could be readily achieved. The differences in spins and recoveries may have been due, in part, to the gyroscopic moments produced by rotating propellers or rotating parts of jet engines. For a jet-propelled airplane, the rotating parts of the engine may continue to rotate at nearly full speed for a long time after power is cut off. A preliminary investigation has been made and reported in Technical Note 3480 to determine the gyroscopic effects of jet-engine rotating parts on the erect spin and recovery characteristics of a model of a military attack airplane. Results indicate that rotating parts affected the spin characteristics differently depending on the type of mass load distribution and the direction of spin.

Control Device for Personal-Owner-Type Airplanes

Although most present-day personal-owner-type airplanes possess a slight degree of inherent spiral stability in cruising flight, they show unstable spiral tendencies under operational conditions. The main reasons for this apparent spiral instability are a lack of means for trimming the airplane laterally and directionally. A variation of lateral and directional trim with airspeed and control-system friction prevents the control surfaces from returning to trim position after control deflection. The specific problems facing the pilot of a personal-owner-type airplane are that of maintaining the airplane in wings-level position during times when there is no natural horizon reference and that of keeping the airplane from diverging spirally while he may be preoccupied with navigational problems. It has been demonstrated that the pilot's sense of orientation is unreliable in the absence of a visual reference, as may be the case when inadvertently or unavoidably encountering instrument weather. Technical Note 3637 describes the results of a flight investigation to determine the effectiveness of an automatic aileron trim control device installed in a personal-owner-type airplane. The results indicate that the device is capable of maintaining the airplane in equilibrium over its operational speed range under directional out-of-trim conditions that would cause rapid divergence of the basic airplane. The device also prevents excessive heading wander and airplane gyration in turbulent air without pilot control. A means is provided for holding the airplane in a stabilized turn to facilitate mild maneuvering through the use of the automatic control.

Precision of Instrument Flight in Helicopters

Early studies of helicopter instrument flight indicated

the need for improved handling qualities, particularly for low-speed flight and for precision maneuvers such as instrument approaches, sonar dipping, or hoist operations. Although a number of stability parameters affect the handling characteristics, damping about the principal axes appeared to be a worthwhile subject for initial study. Technical Note 3537 presents the results of a study of the effects of increased damping in roll, pitch, and yaw on the instrument flight-handling qualities of a single-rotor helicopter. Electronic components were used to vary the damping of the helicopter, and these variations were evaluated by performing precision maneuvers while flying on instruments. The studies indicated that, for a representative single-rotor helicopter, increased damping can improve the accuracy of the maneuvers and reduce the effort required of the pilot, particularly at low forward speeds. For the speed range considered (25 to 65 knots), increased damping in roll was found to be particularly effective, much more effective than corresponding changes in yaw and pitch.

AERONAUTICAL METEOROLOGY

Atmospheric Turbulence

Previously evaluated effective gust velocities, U_e , from the data available for both convective and frontal types of thunderstorms have been converted to the recently defined derived gust velocities, U_{de} , which take into account the variations with altitude of the airplane response to gusts. The results, given in Technical Note 3538, indicate that the intensities of the derived gust velocities are essentially constant for altitudes up to approximately 20,000 feet in thunderstorms and that an approximate 10-percent reduction in the intensity occurs as altitude is increased to 30,000 feet.

The NACA provided the Cambridge Research Center of the Air Force with a VGH recorder for measuring turbulence in a flight investigation of the jet stream and the Sierra Mountain Wave. Evaluation of the data showed that the turbulence encountered during the flights was generally light.

A review was made of available information concerning continuous operation of airplanes through rough air at low altitudes and high speeds. From the standpoints of crew efficiency and flight precision, it appears that reductions in the loads and motions due to turbulent air to about one-third of those for present operational airplanes may be required for low-altitude flight. A study of design features indicated that the major factors that effect such reductions are increased wing loadings and reduced lift-curve slopes. Reductions in lift-curve slopes accompany low-aspect-ratio, swept-back, and flexible wings. Changes in stability for airplanes with satisfactory stability characteristics were not significant when the loads were changed in rough

air. For configurations with low damping, which causes amplification of the loads in continuous turbulence, the use of augmented damping can result in significant reductions in loads.

Characteristics of Icing Cloud

A statistical survey and a preliminary analysis were made of icing data collected from scheduled flights over the United States and Canada from November 1951 to June 1952 by airline aircraft equipped with NACA pressure-type icing-rate meters. Over 600 icing encounters were logged by three airlines operating in the United States, one operating in Canada, and one operating up the Pacific Coast to Alaska. The data provide relative frequencies of icing cloud variables such as horizontal extent of icing, vertical thickness of icing clouds, air temperature, icing rate, liquid-water content, and total ice accumulation.

Liquid-water contents were higher than those from earlier research flights in layer-type clouds but slightly lower than previous ones from cumulus clouds. Broken-cloud conditions, indicated by intermittent icing, accounted for nearly one-half of all the icing encounters. About 90 percent of the encounters did not exceed a distance of 120 miles, and continuous icing did not exceed 50 miles for 90 percent of the unbroken conditions. Icing-cloud thicknesses measured during climbs and descents were less than 4,500 feet for 90 percent of the vertical cloud traverses.

ICING PROBLEMS

Droplet Impingement

Experimental studies have been made in the NACA icing tunnel to determine the effect of a flapped truncated airfoil on surface velocity distribution and droplet-impingement rates and limits. A 6-foot-chord NACA 65₁-212 airfoil was cut successively at the 50- and 30-percent-chord stations to produce the truncated airfoil sections, which were equipped with trailing-edge flaps to alter the flow field. The results indicated that the correct use of such airfoils may permit impingement and icing studies to be conducted with full-scale leading-edge sections in existing small icing tunnels.

The paths of icing cloud droplets into two engine inlets have been calculated (Technical Note 3593) for 0° angle of attack and for a wide range of meteorological and flight conditions. In both types of inlets, the inlet air velocity of one being 0.7 that of the other, a prolate ellipsoid of revolution (10 percent thick) represents either part or all of the forebody at the center of an annular inlet to an engine. The configurations can also represent the fuselage of an airplane with side ram-scoop inlets. Results indicated that the amount of water ingested is not sensitive to small changes in shape of the outer wall, that impingement on the cowl (i. e.,

amount and distribution) is quite sensitive to the physical shape and surface condition of the wall, and that the use of screens and boundary-layer-removal scoops at the entrance requires careful design because of the shadow zone (zero water concentration) and regions of high concentration. In addition, a general concept showed that lowering the inlet velocity ratio lowers the ingestion efficiency.

The impingement characteristics of several other bodies have been obtained from droplet-trajectory calculations. For an NACA 65A004 airfoil at 0° angle of attack, the amount of water in droplet from impinging on the airfoil, the area of droplet impingement, and the rate of droplet impingement per unit area of the airfoil surface were calculated as given in Technical Note 3586. The results were compared with those previously reported for the same airfoil at angles of attack of 4° and 8°.

For a sphere in an ideal fluid flow, droplet impingement data and equations for determining the collection efficiency, the area, and the distribution of impingement have been presented in terms of dimensionless parameters (Technical Note 3587). The range of flight and atmospheric conditions covered in the calculations was extended considerably beyond the range covered by previously reported calculations for a sphere.

A study has also been made of water-droplet impingement on a rectangular half body in a two-dimensional incompressible flow field (Technical Note 3658). Data on collection efficiency and distribution of water-droplet impingement were obtained by means of a mechanical differential analyzer.

Icing Protection

A better understanding of the performance and penalties of pneumatic de-icers can aid in selecting ice-protection systems for aircraft. Accordingly, an evaluation in icing conditions was made of two types of pneumatic de-icers, one having spanwise inflatable tubes and the other having chordwise inflatable tubes (Technical Note 3564). Measurements were made to determine lift, drag, and pitching-moment changes caused by inflation of the de-icer boots and by ice formations on the boots. In order to help determine the aerodynamic effects of size and location of ridge-type ice formations on an airfoil, spanwise spoilers mounted on the airfoil at various chordwise locations were also studied.

A preliminary experimental study was conducted to determine the feasibility of preventing rain from impinging on aircraft windshields by use of a high-velocity jet-air blast. By this means, raindrops are broken up into a multitude of small droplets by the jet-air blast and deflected around the windshield. The deflection appears feasible for flight speeds up to 150 miles per hour for low-angle (35° or less) windshields. However, visibility through the mist generated by raindrop breakup is a problem requiring solution.

RESEARCH PUBLICATIONS

REPORTS

1210. Analysis of Turbulent Heat Transfer, Mass Transfer, and Friction in Smooth Tubes at High Prandtl and Schmidt Numbers. By Robert G. Deissler.
1211. Experimental Investigation of Free-Convection Heat Transfer in Vertical Tube at Large Grashof Numbers. By E. R. G. Eckert and A. J. Diaguila.
1212. Analog Study of Interacting and Noninteracting Multiple-Loop Control Systems for Turbojet Engines. By George J. Pack and W. E. Phillips, Jr.
1213. Minimum-Drag Ducted and Pointed Bodies of Revolution Based on Linearized Supersonic Theory. By Hermon M. Parker.
1214. Statistical Measurements of Contact Conditions of 478 Transport-Airplane Landings During Routine Daytime Operations. By Norman S. Silsby.
1215. Impingement of Cloud Droplets on a Cylinder and Procedure for Measuring Liquid-Water Content and Droplet Sizes in Supercooled Clouds by Rotating Multicylinder Method. By R. J. Brun, W. Lewis, P. J. Perkins, and J. S. Serafini.
1216. Charts for Estimating Tail-Rotor Contribution to Helicopter Directional Stability and Control in Low-Speed Flight. By Kenneth B. Amer and Alfred Gessow.
1217. Theoretical Prediction of Pressure Distributions on Non-lifting Airfoils at High Subsonic Speeds. By John R. Spreiter and Alberta Alksne.
1218. Effect of Ground Interference on the Aerodynamic and Flow Characteristics of a 42° Sweptback Wing at Reynolds Numbers up to 6.8×10^6 . By G. Chester Furlong and Thomas V. Bollech.
1219. Measurement and Analysis of Wing and Tail Buffeting Loads on a Fighter Airplane. By Wilber B. Huston and T. H. Skopinski.
1220. Calculations of Laminar Heat Transfer Around Cylinders of Arbitrary Cross Section and Transpiration-Cooled Walls With Application to Turbine Blade Cooling. By E. R. G. Eckert and J. N. B. Livingood.
1221. Theoretical Study of the Tunnel-Boundary Lift Interference Due to Slotted Walls in the Presence of the Trailing-Vortex System of a Lifting Model. By Clarence W. Matthews.
1222. A Free-Flight Wind Tunnel for Aerodynamic Testing at Hypersonic Speeds. By Alvin Seiff.
1223. Theoretical and Experimental Investigation of Heat Transfer by Laminar Natural Convection Between Parallel Plates. By A. F. Lietzke.
1224. Effects of Wing Position and Fuselage Size on the Low-Speed Static and Rolling Stability Characteristics of a Delta-Wing Model. By Alex Goodman and David F. Thomas, Jr.
1225. Determination of Lateral-Stability Derivatives and Transfer-Function Coefficients from Frequency-Response Data for Lateral Motions. By James J. Donegan, Samuel W. Robinson, Jr., and Ordway B. Gates, Jr.
1226. A Method for the Design of Sweptback Wings Warped to Produce Specified Flight Characteristics at Supersonic Speeds. By Warren A. Tucker.
1227. An Investigation of the Maximum Lift of Wings at Supersonic Speeds. By James J. Gallagher and James N. Mueller.
1228. Calculated Spanwise Lift Distributions, Influence Functions, and Influence Coefficients for Unswept Wings in Subsonic Flow. By Franklin W. Diederich and Martin Zlotnick.
1229. Exact Solutions of Laminar-Boundary-Layer Equations with Constant Property Values for Porous Wall with Variable Temperature. By Patrick L. Donoughe and John N. B. Livingood.
1230. Generalized Indicial Forces on Deforming Rectangular Wings in Supersonic Flight. By Harvard Lomax, Franklyn B. Fuller, and Loma Sluder.
1231. NACA Transonic Wind-Tunnel Test Sections. By Ray H. Wright and Vernon G. Ward.
1232. A Theoretical and Experimental Investigation of the Lift and Drag Characteristics of Hydrofoils at Subcritical and Supercritical Speeds. By Kenneth L. Wadlin, Charles L. Shuford, Jr., and John R. McGehee.
1233. Shock-Turbulence Interaction and the Generation of Noise. By H. S. Ribner.
1234. On the Kernel Function of the Integral Equation Relating the Lift and Downwash Distributions of Oscillating Finite Wings in Subsonic Flow. By Charles E. Watkins, Harry L. Runyan, and Donald S. Woolston.
1235. Standard Atmosphere—Tables and Data for Altitudes to 65,800 feet. By International Civil Aviation Organization and Langley Aeronautical Laboratory.
1236. Arrangement of Fusiform Bodies to Reduce the Wave Drag at Supersonic Speeds. By Morris D. Friedman and Doris Cohen.
1237. A Flight Evaluation of the Longitudinal Stability Characteristics Associated with the Pitch-Up of a Swept-Wing Airplane in Maneuvering Flight at Transonic Speeds. By Seth B. Anderson and Richard S. Bray.
1238. Investigation at Supersonic Speeds of 22 Triangular Wings Representing Two Airfoil Sections for Each of 11 Apex Angles. By Eugene S. Love.
1239. Error in Airspeed Measurement Due to the Static-Pressure Field Ahead of an Airplane at Transonic Speeds. By Thomas C. O'Bryan, Edward C. B. Danforth, and J. Ford Johnston.
1240. An Investigation of the Effects of Heat Transfer on Boundary-Layer Transition on a Parabolic Body of Revolution (NACA RM-10) at a Mach Number of 1.61. By K. R. Czarnecki and Archibald R. Sinclair.
1241. Theoretical and Analog Studies of the Effects of Non-linear Stability Derivatives on the Longitudinal Motions of an Aircraft in Response to Step Control Deflections and to the Influence of Proportional Automatic Control. By Howard J. Curfman, Jr.
1242. Transonic Flow Past Cone Cylinders. By George E. Solomon.
1243. High-Resolution Autoradiography. By George C. Towe, Henry J. Gomberg, and J. W. Freeman.
1244. Free-Stream Boundaries of Turbulent Flows. By Stanley Corrsin and Alan L. Kistler.
1245. Analysis and Calculation by Integral Methods of Laminar Compressible Boundary Layer With Heat Transfer and

- With and Without Pressure Gradient. By Morris Morduchow.
1246. The Hydrodynamic Characteristics of Modified Rectangular Flat Plates Having Aspect Ratios of 1.00, 0.25, and 0.125 and Operating Near a Free Water Surface. By Kenneth L. Wadlin, John A. Ramsen, and Victor L. Vaughan, Jr.
1247. Characteristics of Turbulence in a Boundary Layer With Zero Pressure Gradient. By P. S. Klebanoff.
1248. An Experimental Study of Applied Ground Loads in Landing. By Benjamin Milwitzky, Dean C. Lindquist, and Dexter M. Potter.
1249. A Unified Two-Dimensional Approach to the Calculation of Three-Dimensional Hypersonic Flows, With Application to Bodies of Revolution. By A. J. Eggers, Jr., and Raymond C. Savin.
1250. The Dynamic-Response Characteristics of a 35° Swept-Wing Airplane as Determined From Flight Measurements. By William C. Triplett, Stuart C. Brown, and G. Allen Smith.
1251. Stress Analysis of Circular Semimonocoque Cylinders With Cutouts. By Harvey G. McComb, Jr.
1252. Quasi-Cylindrical Theory of Wing-Body Interference at Supersonic Speeds and Comparison With Experiment. By Jack N. Nielsen.
1253. A Correlation by Means of Transonic Similarity Rules of Experimentally Determined Characteristics of a Series of Symmetrical and Cambered Wings of Rectangular Plan Form. By John B. McDevitt.
3415. A Universal Column Formula for Load at Which Yielding Starts. By L. H. Donnell and V. C. Tsien.
3419. NACA Model Investigations of Seaplanes in Waves. By John B. Parkinson.
3421. Aerodynamics of a Rectangular Wing of Infinite Aspect Ratio at High Angles of Attack and Supersonic Speeds. By John C. Martin and Frank S. Malvestuto, Jr.
3422. Noise Survey of a 10-Foot Four-Blade Turbine-Driven Propeller Under Static Conditions. By Max C. Kurbjun.
3455. Recovery and Time-Response Characteristics of Six Thermocouple Probes in Subsonic and Supersonic Flow. By Truman M. Stickney.
3456. Propagation of a Free Flame in a Turbulent Gas Stream. By William R. Mickelsen and Norman E. Ernstein.
3458. Unstable Convection in Vertical Channels With Heating From Below, Including Effects of Heat Sources and Frictional Heating. By Simon Ostrach.
3460. Tables of Coefficients for the Analysis of Stresses About Cutouts in Circular Semimonocoque Cylinders With Flexible Rings. By Harvey G. McComb, Jr., and Emmet F. Low, Jr.
3462. Tensile Properties of 7075-T6 and 2024-T3 Aluminum-Alloy Sheet Heated at Uniform Temperature Rates Under Constant Load. By George J. Heimerl and John E. Inge.
3463. Investigation of the Vibrations of a Hollow Thin-Walled Rectangular Beam. By Eldon E. Kordes and Edwin T. Kruszewski.
3464. Influence of Shear Deformation of the Cross Section on Torsional Frequencies of Box Beams. By Edwin T. Kruszewski and William W. Davenport.
3465. Theoretical Investigation of Flutter of Two-Dimensional Flat Panels With One Surface Exposed to Supersonic Potential Flow. By Herbert C. Nelson and Herbert J. Cunningham.
3466. An Investigation of the Discharge and Drag Characteristics of Auxiliary-Air Outlets Discharging Into a Transonic Stream. By Paul E. Dewey and Allen R. Vick.
3467. Effect of Interaction on Landing-Gear Behavior and Dynamic Loads in a Flexible Airplane Structure. By Francis E. Cook and Benjamin Milwitzky.
3468. Effects of Sweep on the Maximum-Lift Characteristics of Four Aspect-Ratio-4 Wings at Transonic Speeds. By Thomas R. Turner.
3469. Summary of Results Obtained by Transonic-Bump Method on Effects of Plan Form and Thickness on Lift and Drag Characteristics of Wings at Transonic Speeds. By Edward C. Polhamus.
3470. Gust-Tunnel Investigation of the Effect of a Sharp-Edge Gust on the Flapwise Blade Bending Moments of a Model Helicopter Rotor. By Domenic J. Maglieri and Thomas D. Reisert.
3471. Theoretical Analyses to Determine Unbalanced Trailing-Edge Controls Having Minimum Hinge Moments Due to Deflection at Supersonic Speeds. By Kenneth L. Goin.
3472. Flow Studies on Flat-Plate Delta Wings at Supersonic Speed. By William H. Michael, Jr.
3473. Effects of Sweep and Angle of Attack on Boundary-Layer Transition on Wings at Mach Number 4.04. By Robert W. Dunning and Edward F. Ulmann.
3474. Rapid Radiant-Heating Tests of Multiweb Beams. By Joseph N. Kotanchik, Aldie E. Johnson, Jr., and Robert D. Ross.
3475. An Analysis of Acceleration, Airspeed, and Gust-Velocity Data From One Type of Four-Engine Transport Air-

TECHNICAL NOTES ¹

3218. Flight Determination of the Drag and Pressure Recovery of an NACA 1-40-250 Nose Inlet at Mach Numbers From 0.9 to 1.8. By R. I. Sears and C. F. Merlet.
3271. Thermodynamic Properties of Gaseous Nitrogen. By Harold W. Woolley.
3272. Generalized Tables of Corrections to Thermodynamic Properties for Nonpolar Gases. By Harold W. Woolley and William S. Benedict.
3274. Some Linear Dynamics of Two-Spool Turbo Jet Engines. By David Novik.
3275. Investigation of the Effect of Impact Damage on Fatigue Strength of Jet-Engine Compressor Rotor Blades. By Albert Kaufman and André J. Meyer, Jr.
3277. Space Heating Rates for Some Premixed Turbulent Propane-Air Flames. By Burton D. Fine and Paul Wagner.
3293. Cumulative Fatigue Damage of Axially Loaded Alclad 75S-T6 and Alclad 24S-T3 Aluminum-Alloy Sheet. By Ira Smith, Darnley M. Howard, and Frank C. Smith.
3294. Friction Study of Aircraft Tire Material on Concrete. By W. G. Hamble.
3298. A Low-Density Wind-Tunnel Study of Shock-Wave Structure and Relaxation Phenomena in Gases. By F. S. Sherman.
3384. Effect of Hydrocarbon Structure on Reaction Processes Leading to Spontaneous Ignition. By Donald E. Swarts and Charles E. Frank.
3413. Investigation of the Use of a Rubber Analog in the Study of Stress Distribution in Riveted and Cemented Joints. By Louis R. Demarkles.
3414. Influence of Temperature on Creep, Stress-Rupture, and Static Properties of Melamine-Resin and Silicone-Resin Glass-Fabric Laminates. By William N. Findley, Harlan W. Peithman, and Will J. Worley.

¹ The missing numbers in the series of Technical Notes were released before or after the period covered by this report.

- plane Operated Over Two Domestic Routes. By Martin R. Copp and Thomas L. Coleman.
3476. Calculated Spanwise Lift Distributions and Aerodynamic Influence Coefficients for Swept Wings in Subsonic Flow. By Franklin W. Diederich and Martin Zlotnick.
3477. Hydrodynamic Pressure Distributions Obtained During a Planing Investigation of Five Related Prismatic Surfaces. By Walter J. Kapryan and George M. Boyd, Jr.
3478. On Boattail Bodies of Revolution Having Minimum Wave Drag. By Keith C. Harder and Conrad Rennemann, Jr.
3479. Analysis of the Horizontal-Tail Loads Measured in Flight on a Multiengine Jet Bomber. By William S. Aiken, Jr. and Bernard Wiener.
3480. Free-Spinning-Tunnel Investigation of Gyroscopic Effects of Jet-Engine Rotating Parts (Or of Rotating Propellers) on Spin and Spin Recovery. By James S. Bowman, Jr.
3481. Wind-Tunnel Investigation at Low Speed of Effect of Size and Position of Closed Air Ducts on Static Longitudinal and Static Lateral Stability Characteristics of Unswept-Midwing Models Having Wings of Aspect Ratio 2, 4, and 6. By Byron M. Jaquet and James L. Williams.
3482. Supplementary Charts for Estimating Performance of High-Performance Helicopters. By Robert J. Tapscott and Alfred Gessow.
3483. An Analysis of Acceleration, Airspeed, and Gust-Velocity Data From a Four-Engine Transport Airplane in Operations on an Eastern United States Route. By Thomas L. Coleman and Mary W. Fetner.
3484. On Spectral Analysis of Runway Roughness and Loads Developed During Taxiing. By John C. Houbolt, James H. Walls and Robert F. Smiley.
3485. An Approximate Solution for Axially Symmetric Flow Over a Cone With an Attached Shock Wave. By Richard A. Hord.
3486. Measurements of Turbulent Skin Friction on a Flat Plate at Transonic Speeds. By Raimo Jaakko Hakkinen.
3487. Acoustic Radiation From Two-Dimensional Rectangular Cutouts in Aerodynamic Surfaces. By K. Krishnamurty.
3488. Some Measurements of Flow in a Rectangular Cutout. By Anatol Roshko.
3489. Contributions on the Mechanics of Boundary-Layer Transition. By G. B. Schubauer and P. S. Klebanoff.
3490. Experimental and Calculated Temperature and Mass Histories of Vaporizing Fuel Drops. By M. M. El Wakil, R. J. Priem, H. J. Brikowski, P. S. Myers, and O. A. Uyehara.
3491. Experimental Investigation of Eccentricity Ratio, Friction, and Oil Flow of Long and Short Journal Bearings With Load-Number Charts. By George B. DuBois, Fred W. Ocvirk, and R. L. Wehe.
3492. Determination of Inflow Distributions From Experimental Aerodynamic Loading and Blade-Motion Data on a Model Helicopter Rotor in Hovering and Forward Flight. By Gaetano Falabella, Jr., and John R. Meyer, Jr.
3493. Development of Equipment and of Experimental Techniques for Column Creep Tests. By Sharad A. Patel, Martin Bloom, Burton Erickson, Alexander Chwick, and Nicholas John Hoff.
3494. Sound Propagation Into the Shadow Zone in a Temperature-Stratified Atmosphere Above a Plane Boundary. By David C. Pridmore-Brown and Uno Ingard.
3495. Failure of Materials Under Combined Repeated Stresses With Superimposed Static Stresses. By George Sines.
3497. Summary of Results of a Wind-Tunnel Investigation of Nine Related Horizontal Tails. By Jules B. Dods, Jr. and Bruce E. Tinling.
3500. Correction of Additional Span Loadings Computed by the Weissinger Seven-Point Method for Moderately Tapered Wings of High Aspect Ratio. By John DeYoung and Walter H. Barling, Jr.
3503. Reduction of Profile Drag at Supersonic Velocities by the Use of Airfoil Sections Having a Blunt Trailing Edge. By Dean R. Chapman.
3505. An Experimental Investigation of Regions of Separated Laminar Flow. By Donald E. Gault.
3506. Criteria for Prediction and Control of Ram-Jet Flow Pulsations. By William H. Sterbentz and John C. Evvard.
3507. Practical Considerations in Specific Applications of Gas-Flow Interferometry. By Walton L. Howes and Donald R. Buchele.
3508. Laminar Free Convection on a Vertical Plate With Prescribed Nonuniform Wall Heat Flux or Prescribed Nonuniform Wall Temperature. By E. M. Sparrow.
3509. A Study of Boundary-Layer Transition and Surface Temperature Distributions at Mach 3.12. By Paul F. Brinich.
3510. An Automatic Viscometer for Non-Newtonian Materials. By Ruth N. Weltmann and Perry W. Kuhns.
3511. Extrapolation Techniques Applied to Matrix Methods in Neutron Diffusion Problems. By Robert R. McCready.
3512. Effect of Some Selected Heat Treatments on the Operating Life of Cast HS-21 Turbine Blades. By Francis J. Clauss, Floyd B. Garrett and John W. Weeton.
3513. Heat Transfer at the Forward Stagnation Point of Blunt Bodies. By Eli Reshotko and Clarence B. Cohen.
3514. Response of Homogeneous and Two-Material Laminated Cylinders to Sinusoidal Environmental Temperature Change, With Applications to Hot-Wire Anemometry and Thermocouple Pyrometry. By Herman H. Lowell and Norman A. Patton.
3515. Analysis of Two-Dimensional Compressible-Flow Loss Characteristics Downstream of Turbomachine Blade Rows in Terms of Basic Boundary-Layer Characteristics. By Warner L. Stewart.
3516. Summary Evaluation of Toothed-Nozzle Attachments as a Jet-Noise-Suppression Device. By Warren J. North.
3517. Approximate Method for Determining Equilibrium Operation of Compressor Component of Turbojet Engine. By Merle C. Huppert.
3518. Rotating-Stall Characteristics of a Rotor With High Hub-Tip Radius Ratio. By Eleanor L. Costilow and Merle C. Huppert.
3519. Visualization Study of Secondary Flows in Turbine Rotor Tip Regions. By Hubert W. Allen and Milton G. Kofskey.
3520. Flame Propagation Limits of Propane and n -Pentane in Oxides of Nitrogen. By Riley O. Miller.
3521. A Comparison of the Measured and Predicted Lateral Oscillatory Characteristics of a 35° Swept-Wing Fighter Airplane. By Walter E. McNeill and George E. Cooper.
3522. Measurements of the Effects of Finite Span on the Pressure Distribution Over Double-Wedge Wings at Mach Numbers Near Shock Attachment. By Walter G. Vincenti.
3523. The Effectiveness of Wing Vortex Generators in Improving the Maneuvering Characteristics of a Swept-Wing Airplane at Transonic Speeds. By Normam M. McFadden, George A. Rathert, Jr., and Richard S. Bray.

3524. The Effect of Reynolds Number on the Stalling Characteristics and Pressure Distributions of Four Moderately Thin Airfoil Sections. By George B. McCullough.
3525. Vortex Interference on Slender Airplanes. By Alvin H. Sacks.
3526. Flight Calibration of Four Airspeed Systems on a Swept-Wing Airplane at Mach Numbers up to 1.04 by the NACA Radar-Phototheodolite Method. By Jim Rogers Thompson, Richard S. Bray, and George E. Cooper.
3527. A Second-Order Shock-Expansion Method Applicable to Bodies of Revolution Near Zero Lift. By Clarence A. Syvertson and David H. Dennis.
3528. A Theoretical Study of the Aerodynamics of Slender Cruciform-Wing Arrangements and Their Wakes. By John R. Spreiter and Alvin H. Sacks.
3529. The Transonic Characteristics of 36 Symmetrical Wings of Varying Taper, Aspect Ratio, and Thickness as Determined by the Transonic-Bump Technique. By Warren H. Nelson, Edwin C. Allen, and Walter J. Krumm.
3530. Minimum Wave Drag for Arbitrary Arrangements of Wings and Bodies. By Robert T. Jones.
3531. Pilot's Loss of Orientation in Inverted Spins. By Stanley H. Scher.
3532. Low-Speed Static Lateral and Rolling Stability Characteristics of a Series of Configurations Composed of Intersecting Triangular Plan-Form Surfaces. By David F. Thomas, Jr.
3533. The Proper Combination of Lift Loading for Least Drag on a Supersonic Wing. By Frederick C. Grant.
3534. Instrumentation for Measurement of Free-Space Sound Pressure in the Immediate Vicinity of a Propeller in Flight. By William D. Mace, Francis J. Haney, and Edmund A. Brummer.
3535. Flight Investigation of the Surface-Pressure Distribution and the Flow Field Around a Conical and Two Spherical Nonrotating Full-Scale Propeller Spinners. By Jerome B. Hammack, Milton L. Windler, and Elwood F. Scheithauer.
3536. A Limited Flight Investigation of the Effect of Three Vortex-Generator Configurations on the Effectiveness of a Plain Flap on an Unswept Wing. By Garland J. Morris and Lindsay John Lina.
3537. Helicopter Instrument Flight and Precision Maneuvers as Affected by Changes in Damping in Roll, Pitch, and Yaw. By James B. Whitten, John P. Reeder and Almer D. Crim.
3538. Summary of Derived Gust Velocities Obtained From Measurements Within Thunderstorms. By Harold B. Tolefson.
3539. Some Effects of System Nonlinearities in the Problem of Aircraft Flutter. By Donald S. Woolston, Harry L. Runyan, and Thomas A. Byrdsong.
3540. A Reevaluation of Gust-Load Statistics for Applications in Spectral Calculations. By Harry Press and May T. Meadows.
3541. A Method for Obtaining Statistical Data on Airplane Vertical Velocity at Ground Contact From Measurements of Center-of-Gravity Acceleration. By Robert C. Dreher.
3542. Analysis of Stresses in the Plastic Range Around a Circular Hole in a Plate Subjected to Uniaxial Tension. By Bernard Budiansky and Robert J. Vidensek.
3543. Some Effects of Fuselage Flexibility on Longitudinal Stability and Control. By Bernard B. Klawans and Harold I. Johnson.
3544. Comparison Between Theoretical and Experimental Stresses in Circular Semimonocoque Cylinders With Rectangular Cutouts. By Harvey G. McComb, Jr., and Emmet F. Low, Jr.
3545. Investigation of the Effect of Short Fixed Diffusers on Starting Blowdown Jets in the Mach Number Range From 2.7 to 4.5. By John A. Moore.
3546. Exploratory Investigation of Boundary-Layer Transition on a Hollow Cylinder at a Mach Number of 6.9. By Mitchel H. Bertram.
3547. Aerodynamic Characteristics of a Small-Scale Shrouded Propeller at Angles of Attack From 0° to 90°. By Lysle P. Parlett.
3548. Flight Investigation at Mach Numbers From 0.6 to 1.7 to Determine Drag and Base Pressures on a Blunt-Trailing-Edge Airfoil and Drag of Diamond and Circular-Arc Airfoils at Zero Lift. By John D. Morrow and Ellis Katz.
3549. Flight Investigation at Mach Numbers From 0.8 to 1.5 to Determine the Effects of Nose Bluntness on the Total Drag of Two Fin-Stabilized Bodies of Revolution. By Roger G. Hart.
3550. Measurements of the Effect of Trailing-Edge Thickness on the Zero-Lift Drag of Thin Low-Aspect-Ratio Wings. By John D. Morrow.
3551. Experimental Investigation at Low Speed of Effects of Fuselage Cross Section on Static Longitudinal and Lateral Stability Characteristics of Models Having 0° and 45° Sweptback Surfaces. By William Letko and James L. Williams.
3552. Investigation of the Compressive Strength and Creep Lifetime of 2024-T3 Aluminum-Alloy Plates at Elevated Temperatures. By Eldon E. Mathauser and William D. Deveikis.
3553. Compressive Crippling of Structural Sections. By Melvin S. Anderson.
3554. A Preliminary Investigation of the Effects of Frequency and Amplitude on the Rolling Derivatives of an Unswept-Wing Model Oscillating in Roll. By Lewis R. Fisher, Jacob H. Lichtenstein, and Katherine D. Williams.
3555. A Method for Calculating the Contour of Bodies of Revolution With a Prescribed Pressure Gradient at Supersonic Speed With Experimental Verification. By Paige B. Burbank.
3556. Grain-Boundary Behavior in Creep of Aluminum Bicrystals. By F. N. Rhines, W. E. Bond, and M. A. Kissel.
3557. A Theoretical Analysis of the Field of a Random Noise Source Above an Infinite Plane. By Peter A. Franken.
3558. Heat Capacity Lag of Gaseous Mixtures. By Thomas D. Rossing, Robert C. Amme, and Sam Legvold.
3559. Laminar Separation Over a Transpiration-Cooled Surface in Compressible Flow. By Morris Morduchow.
3560. Spontaneous Ignition Studies Relating to Lubricants of Reduced Flammability. By Kenneth T. Mecklenborg.
3561. Intensity, Scale, and Spectra of Turbulence in Mixing Region of Free Subsonic Jet. By James C. Laurence.
3562. Variation of Boundary-Layer Transition With Heat Transfer on Two Bodies of Revolution at a Mach Number of 3.12. By John R. Jack and N. S. Diaconis.
3563. Heat Loss From Yawed Hot Wires at Subsonic Mach Numbers. By Virgil A. Sandborn and James C. Laurence.
3564. Effect of Pneumatic De-Icers and Ice Formations on Aerodynamic Characteristics of an Airfoil. By Dean T. Bowden.

3565. Chemical Action of Halogenated Agents in Fire Extinguishing. By Frank E. Belles.
3566. A Polar-Coordinate Survey Method for Determining Jet-Engine Combustion-Chamber Performance. By Robert Friedman and Edward R. Carlson.
3567. Study of Screeching Combustion in a 6-Inch Simulated Afterburner. By Perry L. Blackshear, Warren D. Rayle, and Leonard K. Tower.
3568. Averaging of Periodic Pressure Pulsations by a Total-Pressure Probe. By R. C. Johnson.
3569. Compressible Laminar Boundary Layer and Heat Transfer for Unsteady Motions of a Flat Plate. By Simon Ostrach.
3570. An Experimental Comparison of the Lagrangian and Eulerian Correlation Coefficients in Homogeneous Isotropic Turbulence. By William R. Mickelsen.
3571. Lift Hysteresis at Stall as an Unsteady Boundary-Layer Phenomenon. By Franklin K. Moore.
3572. Amplitude of Supersonic Diffuser Flow Pulsations. By William H. Sterbentz and Joseph Davids.
3573. Effect of Exhaust-Nozzle Ejectors on Turbojet Noise Generation. By Warren J. North and Willard D. Coles.
3574. Acoustic Analysis of Ram-Jet Buzz. By Harold Mirels.
3575. Burning Velocities of Various Premixed Turbulent Propane Flames on Open Burners. By Paul Wagner.
3577. The Nickel Dip: A Radioisotope Study of Metallic Deposits in Porcelain Enameling. By Joseph C. Richmond, Harry B. Kirkpatrick, and William N. Harrison.
3578. Influence of Large Amplitudes on Flexural Motions of Elastic Plates. By George Herrmann.
3579. Vapor-Phase Oxidation and Spontaneous Ignition-Correlation and Effect of Variables. By Donald E. Swarts and Milton Orchin.
3580. Stall Propagation in Axial-Flow Compressors. By Alan H. Stenning, Anthony R. Kriebel, and Stephen R. Montgomery.
3581. Experimental Investigation of Blade Flutter in an Annular Cascade. By J. R. Rowe and A. Mendelson.
3582. Effect of Climb Technique on Jet-Transport Noise. By Warren J. North.
3583. Charts of Boundary-Layer Mass Flow and Momentum for Inlet Performance Analysis Mach Number Range, 0.2 to 5.0. By Paul C. Simon and Kenneth L. Kowalski.
3584. Free-Convection Effects on Heat Transfer for Turbulent Flow Through a Vertical Tube. By E. R. G. Eckert, Anthony J. DiGiulio, and John N. B. Livingood.
3586. Impingement of Water Droplets on NACA 65A004 Airfoil at 0° Angle of Attack. By Rinaldo J. Brun and Dorothea E. Vogt.
3587. Impingement of Water Droplets on a Sphere. By Robert G. Dorsch, Paul G. Saper, and Charles F. Kadow.
3588. Summary of Laminar-Boundary-Layer Solutions for Wedge-Type Flow Over Convection- and Transpiration-Cooled Surfaces. By John N. B. Livingood and Patrick L. Donoughe.
3589. Design Criteria for Axisymmetric and Two-Dimensional Supersonic Inlets and Exits. By James F. Connors and Rudolph C. Meyer.
3590. Investigation of Far Noise Field of Jets. I—Effect of Nozzle Shape. By Edmund E. Callaghan and Willard D. Coles.
3591. Investigation of Far Noise Field of Jets. II—Comparison of Air Jets and Jet Engines. By Willard D. Coles and Edmund E. Callaghan.
3592. An Oil-Stream Photomicrographic Aeroscope for Obtaining Cloud Liquid-Water Content and Droplet Size Distributions in Flight. By Paul T. Hacker.
3593. Cloud-Droplet Ingestion in Engine Inlets With Inlet Velocity Ratios of 1.0 and 0.7. By Rinaldo J. Brun.
3594. Effect of Transverse Body Force on Channel Flow With Small Heat Addition. By Simon Ostrach and Franklin K. Moore.
3595. Wear of Typical Carbon-Base Sliding Seal Materials at Temperatures to 700° F. By Robert L. Johnson, Max A. Swikert, and John M. Bailey.
3596. On the Permeability of Porous Materials. By E. Carson Yates, Jr.
3597. Analysis of a Vane-Controlled Gust-Alleviation System. By Robert W. Boucher and Christopher C. Kraft, Jr.
3598. Method and Tables for Determining the Time Response to a Unit Impulse From Frequency-Response Data and for Determining the Fourier Transform of a Function of Time. By Carl R. Huss and James J. Donegan.
3599. Turbulent Heat-Transfer Measurements at a Mach Number of 0.87. By Maurice J. Brevoort and Bernard Rashis.
3600. Correlation of Crippling Strength of Plate Structures With Material Properties. By Roger A. Anderson and Melvin S. Anderson.
3601. Pressure Rise Associated With Shock-Induced Boundary-Layer Separation. By Eugene S. Love.
3602. Laboratory Investigation of an Autopilot Utilizing a Mechanical Linkage With a Dead Spot to Obtain an Effective Rate Signal. By Ernest C. Seaberg.
3603. Theoretical Study of the Lateral Frequency Response to Gusts of a Fighter Airplane, Both With Controls Fixed and With Several Types of Autopilots. By James J. Adams and Charles W. Mathews.
3604. Low-Speed Yawed-Rolling Characteristics and Other Elastic Properties of a Pair of 26-Inch-Diameter, 12-Ply-Rating, Type VII Aircraft Tires. By Walter B. Horne, Robert F. Smiley, and Bertrand H. Stephenson.
3605. Theoretical Span Load Distributions and Rolling Moments for Sideslipping Wings of Arbitrary Plan Form in Incompressible Flow. By M. J. Queijo.
3606. Tabulation of the $f\lambda$ Functions Which Occur in the Aerodynamic Theory of Oscillating Wings in Supersonic Flow. By Vera Huckel.
3607. Effect of Thickness, Camber, and Thickness Distribution on Airfoil Characteristics at Mach Numbers up to 1.0. By Bernard N. Daley and Richard S. Dick.
3608. Hydrodynamic Impact Loads in Smooth Water for a Prismatic Float Having an Angle of Dead Rise of 10°. By Philip M. Edge, Jr.
3609. Linearized Lifting-Surface and Lifting-Line Evaluations of Sidewash Behind Rolling Triangular Wings at Supersonic Speeds. By Percy J. Bobbitt.
3610. Comparison of Landing-Impact Velocities of First and Second Wheel to Contact From Statistical Measurements of Transport Airplane Landings. By Eziaslav N. Harrin.
3611. Analysis of a Spin and Recovery From Time Histories of Attitudes and Velocities as Determined for a Dynamic Model of a Contemporary Fighter Airplane in the Free-Spinning Tunnel. By Stanley H. Scher.
3612. Initial Results of a Flight Investigation of a Gust-Alleviation System. By Christopher C. Kraft, Jr.
3613. The Problem of Reducing the Speed of a Jet Transport in Flight. By Don. D. Davis, Jr.
3614. Flow Studies on Drooped-Leading-Edge Delta Wings at Supersonic Speed. By William H. Michael, Jr.
3615. An Experimental Investigation of the Scale Relations for the Impinging Water Spray Generated by a Planing Surface. By Ellis E. McBride.

3616. Charts for Estimating Rotor-Blade Flapping Motion of High-Performance Helicopters. By Robert J. Tapscott and Alfred Gessow.
3617. Theoretical Analysis of Linked Leading-Edge and Trailing-Edge Flap-Type Controls at Supersonic Speeds. By E. Carson Yates, Jr.
3618. Experimental Investigation of the Vibrations of a Built-Up Rectangular Box Beam. By Eldon E. Kordes and Edwin T. Kruszewski.
3619. Effect of Carriage Mass Upon the Loads and Motions of a Prismatic Body During Hydrodynamic Impact. By Melvin F. Markey.
3620. The Design of a Miniature Solid-Propellant Rocket. By Robert H. Heitkotter.
3621. Gust-Load and Airspeed Data From One Type of Two-Engine Airplane on Six Civil Airline Routes From 1947 to 1955. By Walter G. Walker.
3622. Preliminary Study of Some Factors Which Affect the Stall-Flutter Characteristics of Thin Wings. By A. Gerald Rainey.
3623. Correlation of Supersonic Convective Heat-Transfer Coefficients From Measurements of the Skin Temperature of a Parabolic Body of Revolution (NACA RM-10). By Leo T. Chauvin and Carlos A. deMoraes.
3624. Investigation of the Use of the Thermal Decomposition of Nitrous Oxide to Produce Hypersonic Flow of a Gas Closely Resembling Air. By Alexander P. Sabol and John S. Evans.
3625. Investigation of the Propulsive Characteristics of a Helicopter-Type Pulse-Jet Engine Over a Range of Mach Numbers and Angle of Yaw. By Paul J. Carpenter, James P. Shivers, and Edwin E. Lee, Jr.
3626. Experimental Investigation of the Flow Around Lifting Symmetrical Double-Wedge Airfoils at Mach Numbers of 1.30 and 1.41. By Paul B. Gooderum and George P. Wood.
3627. Boundary-Layer Growth and Shock Attenuation in a Shock Tube With Roughness. By Paul W. Huber and Donald R. McFarland.
3628. An Analysis of Estimated and Experimental Transonic Downwash Characteristics as Affected by Plan Form and Thickness for Wing and Wing-Fuselage Configurations. By Joseph Weil, George S. Campbell and Margaret S. Diederich.
3629. Investigation of the Effects of Ground Proximity and Propeller Position on the Effectiveness of a Wing With Large-Chord Slotted Flaps in Redirecting Propeller Slipstreams Downward for Vertical Take-Off. By Richard E. Kuhn.
3630. Hovering-Flight Tests of a Model of a Transport Vertical-Take-off Airplane With Tilting Wing and Propellers. By Powell M. Lovell, Jr., and Lysle P. Parlett.
3631. Results of Axial-Load Fatigue Tests on Electro-Polished 2024-T3 and 7075-T6 Aluminum-Alloy-Sheet Specimens With Central Holes. By Charles B. Landers and Herbert F. Hardrath.
3632. Correlation, Evaluation, and Extension of Linearized Theories for Tire Motion and Wheel Shimmy. By Robert F. Smiley.
3633. Analysis of the Ultimate Strength and Optimum Proportions of Multiweb Wing Structures. By B. Walter Rosen.
3634. Calculations of the Rate of Thermal Dissociation of Air Behind Normal Shock Waves at Mach Numbers of 10, 12, and 14. By George P. Wood.
3635. Analytical Study of Modifications to the Autopilot of a Fighter Airplane in Order to Reduce the Response to Side Gusts. By Charles W. Mathews and James J. Adams.
3636. The Accuracy of the Substitute-Stringer Approach for Determining the Bending Frequencies of Multistringers Box Beams. By William W. Davenport.
3637. Flight Investigation of the Effectiveness of an Automatic Aileron Trim Control Device for Personal Airplanes. By William H. Phillips, Helmut A. Kuehnelt and James B. Whitten.
3638. On Panel Flutter and Divergence of Infinitely Long Unstiffened and Ring-Stiffened Thin-Walled Circular Cylinders. By Robert W. Leonard and John M. Hedgepeth.
3639. Approximate Indicial Lift Functions for Several Wings of Finite Span in Incompressible Flow as Obtained From Oscillatory Lift Coefficients. By Joseph A. Drischler.
3640. A Method for Deflection Analysis of Thin Low-Aspect-Ratio Wings. By Manuel Stein and J. Lyell Sanders, Jr.
3641. Wind-Tunnel Investigation of a Number of Total-Pressure Tubes at High Angles of Attack. Subsonic, Transonic, and Supersonic Speeds. By William Gracey.
3642. Effect of Shallow Water on the Hydrodynamic Characteristics of a Flat-Bottom Planing Surface. By Kenneth W. Christopher.
3643. Measurement of Aerodynamic Forces for Various Mean Angles of Attack on an Airfoil Oscillating in Pitch and on Two Finite-Span Wings Oscillating in Bending With Emphasis on Damping in the Stall. By A. Gerald Rainey.
3645. Wind-Tunnel Investigation of Effects of Fuselage Cross-Sectional Shape, Fuselage Bend, and Vertical-Tail Size on Directional Characteristics of Nonoverlap-Type Helicopter Fuselage Models Without Rotors. By James L. Williams.
3646. A Theory for the Elastic Deflections of Plates Integrally Stiffened on One Side. By Robert F. Crawford.
3647. Investigation of the Compressive Strength and Creep Lifetime of 2024-T Aluminum-Alloy Skin-Stringer Panels at Elevated Temperatures. By Eldon E. Mathauser and William D. Deveikis.
3648. Investigation of Boundary-Layer Transition on 10° Cone in Langley 4-by-4-Foot Supersonic Pressure Tunnel at Mach Numbers of 1.41, 1.61, and 2.01. By Archibald R. Sinclair and K. R. Czarnecki.
3649. Static Longitudinal and Lateral Stability Characteristics at Low Speed of Unswept-Midwing Models Having Wings With an Aspect Ratio of 2, 4, or 6. By Walter D. Wolhart and David F. Thomas, Jr.
3650. Results of a Flight Investigation to Determine the Zero-Lift Drag Characteristics of a 60° Delta Wing With NACA 65-006 Airfoil Section and Various Double-Wedge Sections at Mach Numbers From 0.7 to 1.6. By Clement J. Welsh.
3651. Cross Flows in Laminar Incompressible Boundary Layers. By Arthur G. Hansen and Howard Z. Herzig.
3652. Experimental Investigation of Air-Flow Uniformity and Pressure Level on Wire Cloth for Transpiration-Cooling Applications. By Patrick L. Donoughe and Roy A. McKinnon.
3653. Some Effects of Bluntness on Boundary-Layer Transition and Heat Transfer at Supersonic Speeds. By W. E. Moeckel.
3654. Performance Analysis of Fixed- and Free-Turbine Helicopter Engines. By Richard P. Krebs and William S. Miller, Jr.
3655. Method of Calculating Core Dimensions of Crossflow Heat Exchanger With Prescribed Gas Flows and Inlet and

- Exit States. By E. R. G. Eckert and Anthony J. Diaguila.
3657. Friction Studies of Graphite and Mixtures of Graphite With Several Metallic Oxides and Salts at Temperatures to 1000° F. By Marshall B. Peterson and Robert L. Johnson.
3658. Impingement of Water Droplets on a Rectangular Half Body in a Two-Dimensional Incompressible Flow Field. By William Lewis and Rinaldo J. Brun.
3659. Effect of Leading-Edge Geometry on Boundary-Layer Transition at Mach 3.1. By Paul F. Brinich.
3660. Investigation of the Ni₃Al Phase of Nickel-Aluminum Alloys. By Edward M. Grala.
3661. Self Shielding in Rectangular and Cylindrical Geometries. By Harold Schneider, Paul G. Saper, and Charles F. Kadow.
3662. Theoretical Loss Relations for Low-Speed Two-Dimensional-Cascade Flow. By Seymour Lieblein and William H. Roudebush.
3663. Discharge Coefficients for Combustor-Liner Air-Entry Holes. I—Circular Holes With Parallel Flow. By Ralph T. Dittrich and Charles C. Graves.
3664. Summary of Scale-Model Thrust-Reverser Investigation. By John H. Povolny, Fred W. Steffen, and Jack G. McArdle.
3665. Performance and Operational Studies of a Full-Scale Jet-Engine Thrust Reverser. By Robert C. Kohl.
3666. Bodies of Revolution Having Minimum Drag at High Supersonic Airspeeds. By A. J. Eggers, Jr., Meyer M. Resnikoff, and David H. Dennis.
3667. Wing-Body Combinations With Certain Geometric Restraints Having Low Zero-Lift Wave Drag at Low Supersonic Mach Numbers. By Harvard Lomax.
3668. Preliminary Investigation of a Family of Diffusers Designed for Near Sonic Inlet Velocities. By Richard Scherrer and Warren E. Anderson.
3669. Perforated Sheets as a Porous Material for Distributed Suction and Injection. By Robert E. Dannenberg, Bruno J. Gambucci, and James A. Weiberg.
3670. Determination of Vortex Paths by Series Expansion Technique With Application to Cruciform Wings. By Alberta Y. Alksne.
3671. Wind-Tunnel Investigation of the Effect of Clipping the Tips of Triangular Wings of Different Thickness, Camber, and Aspect Ratio—Transonic Bump Method. By Horace F. Emerson.
3672. Investigation at High Subsonic Speeds of a Body-Contouring Method for Alleviating the Adverse Interference at the Root of a Sweptback Wing. By John B. McDevitt and William M. Haire.
3673. On the Range of Applicability of the Transonic Area Rule. By John R. Spreiter.
3674. Theoretical Pressure Distributions for Some Slender Wing-Body Combinations at Zero Lift. By Paul F. Byrd.
3676. Investigation of Lateral Control Near the Stall. Flight Tests With High-Wing and Low-Wing Monoplanes of Various Configurations. By Fred E. Weick and H. Norman Abramson.
3677. Investigation of Lateral Control Near the Stall. Analysis for Required Longitudinal Trim Characteristics and Discussion of Design Variables. By Fred E. Weick and H. Norman Abramson.
3678. Influence of Alloying Upon Grain-Boundary Creep. By F. N. Rhines, W. E. Bond, and M. A. Kissel.
3679. Influence of Copper Ions on Adherence of Viterous Coatings to Stainless Steel. By D. G. Moore and A. G. Eubanks.
3681. Investigation of Plastic Behavior of Binary Aluminum Alloys by Internal-Friction Methods. By R. E. Maringer, L. L. Marsh, and G. K. Manning.
3682. Time Correlator for Problems in Aerodynamics. By George Tolmie Skinner.
3685. Fatigue Crack Propagation in Severely Notched Bars. By W. S. Hyler, E. D. Abraham, and H. J. Grover.
3686. Experimental Measurements of Forces and Moments on a Two-Dimensional Oscillating Wing at Subsonic Speeds. By Sherman A. Clevenson and Edward Widmayer, Jr.
3687. Some Wind-Tunnel Experiments on Single-Degree-of-Freedom Flutter of Ailerons in the High Subsonic Speed Range. By Sherman A. Clevenson.
3689. Investigation by the Transonic-Bump Method of a 35° Sweptback Semispan Model Equipped With a Flap Operated by a Series of Servovanes Located Ahead of and Geared to the Flap. By William H. Phillips and Robert F. Thompson.
3690. Normal Component of Induced Velocity in the Vicinity of a Lifting Rotor With a Nonuniform Disk Loading. By Harry H. Heyson and S. Katzoff.
3691. Analysis and Comparison With Theory of Flow-Field Measurements Near a Lifting Rotor in the Langley Full-Scale Tunnel. By Harry H. Heyson.
3692. Investigation at Zero Forward Speed of a Leading-Edge Slat as a Longitudinal Control Device for Vertically Rising Airplanes that Utilize the Redirected-Slipstream Principle. By Richard E. Kuhn.
3693. Preliminary Investigation of the Effectiveness of a Sliding Flap in Deflecting a Propeller Slipstream Downward for Vertical Take-Off. By Richard E. Kuhn and Kenneth P. Spreemann.
3696. A Study of the High-Speed Performance Characteristics of 90° Bends in Circular Ducts. By James T. Higginbotham, Charles C. Wood, and E. Floyd Valentine.
3697. Flight Tests at Supersonic Speeds to Determine the Effect of Taper on the Zero-Lift Drag of Sweptback Low-Aspect-Ratio Wings. By Murray Pittel.
3698. Preliminary Investigation of Self-Excited Vibrations of Single Planing Surfaces. By Elmo J. Mottard.
3699. Some Effects of Joint Conductivity on the Temperatures and Thermal Stresses in Aerodynamically Heated Skin-Stiffener Combinations. By George E. Griffith and Georgene H. Miltonberger.
3702. Measurements of Atmospheric Turbulence Over a Wide Range of Wavelength for One Meteorological Condition. By Harold L. Crane and Robert G. Chilton.
3703. The Flow Past and Unswept- and a Swept-Wing-Body Combination and Their Equivalent Bodies of Revolution at Mach Numbers Near 1.0. By Walter F. Lindsey.
3705. An Investigation of Forward-Located Fixed Spoilers and Deflectors as Gust Alleviators on an Unswept-Wing Model. By Delwin R. Croom, C. C. Shufflebarger, and Jarrett K. Huffman.
3708. Investigation at Supersonic Speeds of the Variation With Reynolds Number and Mach Number of the Total, Base, and Skin-Friction Drag of Seven Boattail Bodies of Revolution Designed for Minimum Wave Drag. By August F. Bromm, Jr., and Julia M. Goodwin.
3711. Some Effects of Guide-Vane Turning and Stators on the Rotating Stall Characteristics of a High Hub-Tip Ratio Single-Stage Compressor. By Eleanor L. Costilow and Merle C. Huppert.
3712. Boundary Layer Behind Shock or Thin Expansion Wave Moving Into Stationary Fluid. By Harold Mirels.
3713. Selection of Optimum Configurations for Heat Exchanger With One Dominating Film Resistance. By E. R. G. Eckert and T. F. Irvine, Jr.

3714. A Sonic-Flow Orifice Probe for the Inflight Measurement of Temperature Profiles of a Jet Engine Exhaust With Afterburning. By C. Dewey Havill and L. Stewart Rolls.
3715. Comparison of the Experimental and Theoretical Distributions of Lift on a Slender Inclined Body of Revolution at $M=2$. By Edward W. Perkins and Donald M. Kuehn.
3716. Comparison of Experimental and Theoretical Normal-Force Distributions (Including Reynolds Number Effects) on an Ogive-Cylinder Body at Mach Number 1.98. By Edward W. Perkins and Leland H. Jorgensen.
3718. Theoretical Wave Drag of Shrouded Airfoils and Bodies. By Paul F. Byrd.
3720. Comparison Between Experimental and Predicted Downwash at a Mach Number of 0.25 Behind a Wing-Body Combination Having a Triangular Wing of Aspect Ratio 2.0. By Norman E. Sorensen and Edward J. Hopkins.
1397. Interim Report on Fatigue Characteristics of a Typical Metal Wing. By J. L. Kepert and A. O. Payne. From Aeronautical Research Laboratories Melbourne, Australia.
1398. Formation of a Vortex at the Edge of a Plate. By Leo Anton. From Göttinger Dissertation, Ingenieur-Archiv, vol. X, 1939.
1399. Acoustics of a Nonhomogeneous Moving Medium. By D. I. Blokhintsev. From Ogiz, Gosudarstvennoe Izdatel'stvo, Tekhniko-Teoreticheskoi Literatury, Moskva, 1946, Leningrad.
1400. Boundary Layer. By L. G. Loitsianskii. From Mechanics in the U.S.S.R. over Thirty Years, 1917-1947.
1401. Directional Stability of Towed Airplanes. By W. Söhne. From Deutsches Ingenieur-Archiv, vol. 21, no. 4, 1953.
1403. On the Instability of Methods for the Integration of Ordinary Differential Equations. By Heinz Rutishauser. From ZAMP, Kurze Mitteilungen, vol. III, 1952.
1415. Laminar Flow About a Rotating Body of Revolution in an Axial Airstream. By H. Schlichting. From Ingenieur-Archiv, vol. XXI, no. 4, 1953.

TECHNICAL MEMORANDUMS ¹

1330. Theory of Dynamic Creep. By A. A. Predvoditelev and B. A. Smirnov. From Vestnik Moskovskogo Univ., Phys., vol. 8, no. 8, 1953.
1369. Flat Plate Cascades at Supersonic Speed. By Rashad M. El Badrawy. From Mitteilungen aus dem Institut für Aerodynamik an der E. T. H., no. 19, 1952.
1377. The Theories of Turbulence. By L. Agostini and J. Bass. From Publications Scientifiques et Techniques du Ministère de L'Air, No. 237, 1950.
1384. Metallography of Aluminum and Its Alloys Use of Electrolytic Polishing. By P. A. Jacquet. From Office National d'Etudes et de Recherches Aéronautiques, Publication No. 51, 1952.
1385. On the Gas Dynamics of a Rotating Impeller. By A. Busemann. From Zeitschrift für angewandte Mathematik und Mechanik, vol. 18, issue 1, Feb. 1938.
1386. Remark on the Theory of Lifting Surfaces. By Aldo Muggia. From Atti della Accademia delle Scienze di Torino, vol. 87, 1952-1953.
1388. General Solutions of Optimum Problems in Nonstationary Flight. By Angelo Miele. From L'Aerotecnica, n. 3, vol. XXXII, 1952.
1389. Optimum Flight Paths of Turbojet Aircraft. By Angelo Miele. From L'Aerotecnica, n. 4, vol. XXXII, 1952.
1390. On the Mechanism of Buckling of a Circular Cylindrical Shell Under Axial Compression. By Y. Yoshimura.
1391. Reduction of the Shimmy Tendency of Tail and Nose-Wheel Landing Gears by Installation of Specially Designed Tires. By H. Schrode. From Bericht der Deutschen Versuchsanstalt für Luftfahrt E. V., Berlin-Adlershof. Technische Berichte, Bd. 10, 1943.
1392. On the Buckling of Bars and Plates in the Plastic Range. Part. II. By J. P. Benthem. From Nationaal Luchtvaartlaboratorium, Amsterdam, Rapport S. 423, Jan. 1954.
1393. Flow of Gas Through Turbine Lattices. By M. E. Deich. From (Tekhnicheskaya gazodinamika) ch. 7, 1953.
1394. A Flat Wing With Sharp Edges in a Supersonic Stream. By A. E. Donovan. From Izvestia-Akademia, NAUK, USSR, 1939.
1396. From Linear Mechanics to Nonlinear Mechanics. By Julien Loeb. From Annales des Télécommunications, vol. 5, no. 2, Feb. 1950.

OTHER TECHNICAL PAPERS BY STAFF MEMBERS

- Allen, Gabriel. Webeler, Rayjor W., and Barile, Sam: Multiple Scattering of Low-Energy Alpha Particles in Gas. Phys. Rev., vol. 99, no. 2, July 15, 1955, pp. 556-558.
- Allen, H. Julian: Development of Two Hypersonic Test Facilities at the National Advisory Committee for Aeronautics Ames Aeronautical Laboratory. Presented at the Sixth Meeting of the Wind Tunnel and Model Testing Panel (Paris, Nov. 2-6, 1954), Advisory Group for Aeronautical Research and Development AG 17/7, pp. 333-372.
- Allen, H. Julian: Transonic Wind Tunnel Development at the National Advisory Committee for Aeronautics. Presented at the Sixth Meeting of the Wind Tunnel and Model Testing Panel (Paris, Nov. 2-6, 1954), Advisory Group for Aeronautical Research and Development AG 17/7, pp. 198-217.
- Altschuller, Aubrey P.: Lattice Energies and Related Thermodynamic Properties of the Alkali Metal Borohydrides and of the Borohydride Ion. Jour. Am. Chem. Soc., vol. 77, no. 21, Nov. 5, 1955, pp. 5455-5457.
- Anderson, Roger A.: Weight Efficiency Analysis of Thin Wing Construction. Paper 56-AV-13, A. S. M. E., 1956.
- Aron, Jack, and Groetzinger, Gerhart: Longitudinal Photo-magnetoelectric Effect in Germanium. Phys. Rev., vol. 100, no. 4, Nov. 15, 1955, pp. 1128-1129.
- Auble, Carmon M., and Heidmann, Marcus F.: The Application of Radiation Measurement Techniques to the Determination of Gas Temperatures in Liquid Propellant Flames. Jet Propulsion, vol. 25, no. 9, pt. 1, Sept. 1955, pp. 449-453, 467.
- Benser, William A., and Finger, Harold B.: Compressor-Stall Problems in Gas-Turbine Type Aircraft Engines. Preprint 751, SAE, 1956.
- Berlad, Abraham L., and Potter, Andrew E.: Prediction of the Quenching Effect of Various Surface Geometries. Fifth Symposium (International) on Combustion (Combustion in Engines and Combustion Kinetics), University of Pittsburgh, Aug. 30-Sept. 3, 1954. Reinhold Pub. Corp., N. Y., 1955, pp. 728-735.
- Brokaw, Richard S.: Estimating Thermal Conductivities for Nonpolar Gas Mixtures. Ind. and Eng. Chem., vol. 47, no. 11, Nov. 1955, pp. 2398-2400.
- Brokaw, Richard S.: Thermal Ignition, With Particular Reference to High Temperatures. Selected Combustion Problems II—Combustion Colloquium, Advisory Group for Aeronautical Research and Development (Liege, Belgium, Dec.

¹ The missing numbers in the series of Technical Memorandums were released before or after the period covered by this report.

- 5-9, 1955), Butterworths Sci. Pubs. (London), 1956, pp. 115-138.
- Brooks, George W.: Analytical Determination of the Natural Couple Frequencies of Tandem Helicopters. Preprint 620, Inst. Aero. Sci., 1956.
- Buckner, Howard A., Jr., and Rebeske, John J., Jr.: Application of High-Speed Strain-Gage Torquemeter to Turbomachinery Research. Trans. A. S. M. E., vol. 77, no. 5, July 1955, pp. 597-603.
- Budiansky, Bernard, and Mayers, Jean: Influence of Aerodynamic Heating on the Effective Torsional Stiffness of Thin Wings. Preprint 579, Inst. Aero. Sci., 1956.
- Busemann, Adolf: The Relation Between Minimizing Drag and Noise at Supersonic Speeds. Proceedings of the Conference on High-Speed Aeronautics (Brooklyn, Jan. 20-22, 1955), Polytechnic Inst. of Brooklyn, 1955, pp. 133-144.
- Cooper, H., Schwed, Philip, and Webeler, Raynor W.: Thermo-electric Power of AuCu in Nonequilibrium States. Jour. Appl. Phys., vol. 27, no. 5, May 1956, pp. 516-518.
- Cortright, Edgar M., Jr.: Some Aerodynamic Considerations of Nozzle-Afterbody Combinations. Preprint 614, Inst. Aero. Sci., 1956.
- Crocco, Luigi, and Cohen, Clarence B.: Compressible Laminar Boundary Layer With Heat Transfer and Pressure Gradient. 50 Jahre Grenzschichtforschung, Eine Festschrift in Originalbeitragen, H. Görtler and W. Tollmien, eds., Friedr. Vieweg & Sohn (Braunschweig, Germany), 1955, pp. 280-293.
- Deissler, Robert G., and Loeffler, Albert L., Jr.: Turbulent Flow and Heat Transfer on a Flat Plate at High Mach Number With Variable Fluid Properties. Paper 55-A-133, A. S. M. E., 1955.
- Deissler, Robert G.: Turbulent Heat Transfer and Friction in the Entrance Regions of Smooth Passages. Trans. A. S. M. E., vol. 77, no. 8, Nov. 1955, pp. 1221-1233.
- Dimeff, John, Carson, James A., and Charters, Alex C., Jr.: Piston-Type Strain Gauge for Measuring Pressures in Interior Ballistics Research. Rev. Sci. Instr., vol. 26, no. 9, Sept. 1955, pp. 879-883.
- Dryden, Hugh L., and Duberg, John E.: Aeroelastic Effects of Aerodynamic Heating. Presented at the Fifth General Assembly (Ottawa, June 10-17, 1955), Advisory Group for Aeronautical Research and Development AG20/P10, pp. 102-107.
- Dryden, Hugh L.: Ballistics Research—The Scientific Bases of Airplane, Projectile, and Missile Development. Ordnance, vol. 40, no. 215, Mar./Apr. 1956, pp. 893-897.
- Dryden, Hugh L.: The International Geophysical Year. Nat. Geographic, vol. 109, no. 2, Feb. 1956, pp. 285-298.
- Dryden, Hugh L.: Problems in Ultra-High-Speed Flight. Inst. Radio Engrs.—Trans. on Telemetry and Remote Control, vol. TRU-1, no. 3, Aug. 1955, pp. 2-4.
- Dryden, Hugh L.: Recent Investigations on the Problem of Transition. Zeit. für Flugwissenschaften, vol. 4, no. 3/4, Mar./Apr. 1956, pp. 89-95.
- Dryden, Hugh L.: Transition From Laminar to Turbulent Flow at Subsonic and Supersonic Speeds. Proceedings of the Conference on High-Speed Aeronautics (Brooklyn, Jan. 20-22, 1955), Polytechnic Inst. of Brooklyn, 1955, pp. 41-74.
- Duberg, John E.: High Temperature Structural Research at the National Advisory Committee for Aeronautics. Proceedings of the Conference on High-Speed Aeronautics (Brooklyn, Jan. 20-22, 1955), Polytechnic Inst. of Brooklyn, 1955, pp. 213-232.
- Duberg, John E.: Some NACA Research on the Effect of Transient Heating on Aircraft Structures. Paper 56-AV-16, A. S. M. E., 1956.
- Fryburg, George C.: The Conductometric Method Applied to the High Temperature Oxidation of Iron. Corrosion, vol. 12, no. 2, Feb. 1956, pp. 40-42.
- Fryburg, George C.: Enhanced Oxidation of Platinum in Activated Oxygen. Jour. Chem. Phys., vol. 24, no. 2, Feb. 1956, pp. 175-180.
- Gerstein, Melvin, and Coffin, Kenneth P.: Combustion of Solid Fuels. High Speed Aerodynamics and Jet Propulsion, Vol. II—Combustion Processes, Princeton University Press (Princeton), 1956, pp. 444-469.
- Gessow, Alfred: The Future Role of the Helicopter (Editorial). Jour. Am. Helicopter Soc., vol. 1, no. 2, April 1956, pp. 1-2.
- Godfrey, Douglas: A Study of Fretting Wear in Mineral Oil. Lubrication Eng., vol. 12, no. 1, Jan./Feb. 1956, pp. 37-42.
- Golosman, Bernard S.: Analysis of a Regenerative Amplifier With Distributed Amplification (Extract From a Thesis Submitted for M. S. Degree at Cal. U.). Proc. Inst. Radio Engineers, vol. 44, no. 4, April 1956, pp. 533-534.
- Gustafson, Frederic B.: A History of NACA Research on Rotating-Wing Aircraft. Jour. Am. Helicopter Soc., vol. 1, no. 1, Jan. 1956, pp. 16-26.
- Hamrick, Joseph T.: Some Aerodynamic Investigations in Centrifugal Impellers. Trans. A. S. M. E., vol. 78, no. 3, Apr. 1956, pp. 591-602.
- Heaslet, Maxwell A.: Reducing Supersonic Wave Drag. Aviation Age, vol. 25, no. 6, June 1956, pp. A:6-A:9.
- Heldenfels, Richard R.: Some Elevated Temperature Structural Problems of High-Speed Aircraft. Preprint 599, SAE, 1956.
- Herzig, Howard Z., and Hansen, Arthur G.: Experimental and Analytical Investigation of Secondary Flows in Ducts. Preprint 593, Inst. Aero. Sci., 1956.
- Hibbard, Robert R., and Barnett, Henry C.: Fuels for Turbojet Powered Aircraft. Selected Combustion Problems II—Combustion Colloquium, Advisory Group for Aeronautical Research and Development (Liege, Belgium, Dec. 5-9, 1955), Butterworths Sci. Pubs. (London), 1956, pp. 30-53.
- Huntsberger, Ralph F., and Parsons, John P.: The Design of Large High-Speed Wind Tunnels. Presented at the Fifth Meeting of the Wind Tunnel and Model Testing Panel (The Hague, Netherlands, May 3-7, 1954), Advisory Group for Aeronautical Research and Development AG15/P6, pp. 127-152.
- Jones, Melvin H., and Brown, William F., Jr.: An Axial Loading Creep Machine. A. S. T. M. Bull. no. 211, Jan. 1956, pp. 53-60.
- Jones, Melvin H., Brown, William F., Jr., and Newman, David P.: Creep Damage in a Cr-Mo-V Steel as Measured by Retained Stress Rupture Properties. Paper 55-A-175, A. S. M. E., 1955.
- Jones, Robert T.: Possibilities of Efficient High-Speed Transport Airplanes. Proceedings of the Conference on High-Speed Aeronautics (Brooklyn, Jan. 20-22, 1955), Polytechnic Inst. of Brooklyn, 1955, pp. 145-156.
- Kauffman, William M.: Flight Application of Target-Simulator Principles. Preprint 649, Inst. Aero. Sci., 1956.
- Kauffman, William M., and Drinkwater, Fred J., III: Variable-Stability Airplanes in Lateral-Stability Research. Aero. Eng. Rev., vol. 14, no. 8, Aug. 1955, pp. 29-35.
- Kuhn, Paul: Effect of Geometric Size on Notch Fatigue. International Union of Theoretical and Applied Mechanics (IUTAM) Colloquium on Fatigue (Stockholm, Sweden, May 25-27, 1955), Proc., Springer (Berlin-Göttingen-Heidelberg, Germany), 1956, pp. 131-140.
- Kuhn, Paul: Stresses in Aircraft Structures. McGraw-Hill Publications in Aeronautical Science, McGraw-Hill Book Co., Inc., (N. Y.), 1956.
- Lad, Robert A., and Metz, Florence I.: An Experimental Investigation of the Effect of Vacancy and F-Centre Concentrations on the Transient Creep of Sodium Chloride Single Crystals. Jour. Mech. of Phys. of Solids, vol. 4, no. 1, Oct. 1955, pp. 28-37.

- Ladanyi, Dezso J., and Miller, Riley O.: Two Methods for Measuring Ignition Delays of Self-Igniting Rocket Propellant Combinations. *Jet Propulsion*, vol. 26, no. 3, Mar. 1956, pp. 157-163.
- Lassiter, Leslie W., Hess, Robert W., and Hubbard, Harvey H.: An Experimental Study of the Response of Simple Panels to Intense Acoustic Loading. Preprint 632, *Inst. Aero. Sci.*, 1956.
- Leider, R. Herman: Effect of X-Irradiation on Surface Structure of Sodium Chloride Crystals. *Phys. Rev.*, vol. 101, no. 1, Jan. 1, 1956, pp. 56-58.
- Lomax, Harvard, and Heaslet, Max A.: Recent Developments in the Theory of Wing-Body Wave Drag. Preprint 617, *Inst. Aero. Sci.*, 1956.
- McKeown, Anderson B., and Belles, Frank E.: Nitric Acid-Nitrogen Dioxide-Water System. Vapor Pressures and Related Properties. *Ind. and Eng. Chem.*, vol. 47, no. 12, Dec. 1955, pp. 2540-2543.
- McKinney, Marion O., Kuhn, Richard E., and Hammack, Jerome B.: Problems in the Design of Propeller-Driven Vertical Take-Off Transport Airplanes. *Aero. Eng. Rev.*, vol. 15, no. 4, Apr. 1956, pp. 68-75, 84.
- McLellan, Charles H.: An Investigation of the Melting of Bodies Due to Aerodynamic Heating. *Trans. A. S. M. E.*, vol. 77, no. 5, July 1955, pp. 727-733.
- McNulty, James F.: Thrust Loading on Piles. *Am. Soc. Civil Engineers Proc.*, vol. 82 (SM 2, no. 940), Apr. 1956, pp. 1-25.
- Manson, Samuel S., and Smith, Robert W.: Quantitative Evaluation of Thermal-Shock Resistance. *Trans. A. S. M. E.*, vol. 78, no. 3, Apr. 1956, pp. 533-544.
- Martin, Frank E., and Raring, Richard H.: High Speed Quenching Dilatometer. *Jour. Metals*, vol. 8, no. 2, Sec. 2, Feb. 1956, pp. 191-195.
- Maslen, Stephen H., and Moore, Franklin K.: On Strong Transverse Waves Without Shocks in a Circular Cylinder. *Jour. Aero. Sci.*, vol. 23, no. 6, June 1956, pp. 583-593.
- Mendelson, Alexander, and Manson, Samuel S.: Approximate Solution to Thermal-Shock Problems in Plates, Hollow Spheres, and Cylinders With Heat Transfer at Two Surfaces. *Trans. A. S. M. E.*, vol. 78, no. 3, Apr. 1956, pp. 545-553.
- Metz, Florence I., and Lad, Robert A.: The Effect of Substrate on the Crystallization of Metallic Films. *Jour. Phys. Chem.*, vol. 60, no. 3, Mar. 1956, pp. 277-280.
- Miller, William S., Jr., Krebs, Richard P., and Blaschke, T. C.: Shaft Gas Turbines for Helicopters. Preprint 515, SAE, 1955.
- Moore, Franklin K.: Three-Dimensional Boundary Layer Theory. *Advances in Applied Mechanics*, vol. IV, H. L. Dryden and Th. von Karman, eds., Acad. Press, Inc., (N. Y.), 1955, pp. 160-228.
- Moshos, George J.: Analog Interpolator for Automatic Control. *Jour. Assoc. Computing Machinery*, vol. 2, no. 2, Apr. 1955, pp. 83-91.
- Murray, Sylvester F., Johnson, Robert L., and Swikert, Max A.: Difluorodichloromethane as Boundary Lubricant for Steel and Other Metals. *Mech. Eng.*, vol. 78, no. 3, Mar. 1956, pp. 233-236.
- Neihouse, Anshal I.: Design and Operating Techniques of Vertical Spin Tunnels. Presented at the Sixth Meeting of the Wind Tunnel and Model Testing Panel (Paris, Nov. 2-6, 1954), Advisory Group for Aeronautical Research and Development AG 17/7, pp. 399-420.
- Nemeth, Zolton N., and Anderson, William J.: Effect of Air and Nitrogen Atmospheres on the Temperature Limitations of Liquid and Solid Lubricants in Ball Bearings. *Lubrication Eng.*, vol. 11, no. 4, July/Aug. 1955, pp. 267-273.
- Nemeth, Zolton N., and Anderson, William J.: Effect of Atmospheric Moisture and Oxygen Content on High-Temperature Lubrication of Ball Bearings With Graphite. *Lubrication Eng.*, vol. 12, no. 3, May/June 1956, p. 169.
- Nemeth, Zolton N., and Anderson, William J.: Effect of Oxygen Concentration in Atmosphere on Oil Lubrication of High-Temperature Ball Bearings. Paper 55-Lub-8, A. S. M. E., 1955.
- Nemeth, Zolton N., and Anderson, William J.: Temperature Limitations of Petroleum, Synthetic, and Other Lubricants in Rolling-Contact Bearings. *Trans. SAE*, vol. 63, 1955, pp. 556-566.
- Olson, Walter T., Childs, J. Howard, and Jonash, Edmund R.: The Combustion-Efficiency Problem of the Turbojet at High Altitude. *Trans. A. S. M. E.*, vol. 77, no. 5, July 1955, pp. 605-615.
- Ostrach, Simon: Convection Phenomena in Fluids Heated From Below. Paper 55-A-88, A. S. M. E., 1955.
- Ostrach, Simon: On the Flow, Heat Transfer, and Stability of Viscous Fluids Subject to Body Forces and Heated From Below in Vertical Channels. 50 Jahre Grenzschichtforschung, Eine Festschrift in Originalbeitragen, H. Görtler and W. Tollmien, eds., Friedr. Vieweg & Sohn (Braunschweig, Germany), 1955, pp. 226-235.
- O'Sullivan, William J., Jr.: Some Thermal and Mechanical Properties of Inconel at High Temperatures for Use in Aerodynamic Heating Research. *Proc. A. S. T. M.*, vol. 55, 1955, pp. 757-764.
- Peters, Roger W.: The NACA Combined Load Testing Machine. *Proc. Soc. Exp. Stress Analysis*, vol. 13, no. 1, 1955, pp. 181-198.
- Peterson, Marshall B., and Johnson, Robert L.: Factors Influencing Friction and Wear With Solid Lubricants. *Lubrication Eng.*, vol. 11, no. 5, Sept./Oct., 1955, pp. 325-331.
- Peterson, Marshall B., and Johnson, Robert L.: Solid Lubricants for Titanium. *Lubrication Eng.*, vol. 11, no. 5, Sept./Oct., 1955, pp. 297, 299.
- Pinkel, I. Irving: Crash-Fire Research With Jet Aircraft. *Aero. Eng. Rev.*, vol. 15, no. 1, Jan. 1956, pp. 53-57.
- Potter, Andrew E., and Berlad, Abraham L.: The Quenching of Flames of Propane-Oxygen-Argon and Propane-Oxygen-Helium Mixtures. *Jour. Phys. Chem.*, vol. 60, no. 1, Jan. 1956, pp. 97-101.
- Povolny, John H., and McArdle, Jack G.: NACA Investigation of Thrust Reversal Techniques. Preprint 591, SAE, 1955.
- Press, Harry: Time Series Problems in Aeronautics. *Jour. Am. Statistical Assoc.*, vol. 50, no. 272, Dec. 1955, pp. 1022-1039.
- Regier, Arthur A.: Noise, Vibration, and Aircraft Structures. Preprint 631, *Inst. Aero. Sci.*, 1956.
- Regier, Arthur A.: Why Do Airplanes Make Noise? *Trans. SAE*, vol. 63, 1955, pp. 275-283.
- Reshotko, Eli: Heat Transfer to a Yawed Infinite Cylinder in Compressible Flow. 1956 Heat Transfer and Fluid Mechanics Institute (Stanford Univ., June 21-23, 1956), Stanford Univ. Press (Stanford, Cal.), 1956, pp. 275-220.
- Rosenblum, Louis: The Thermal Decomposition of Tri-n-Butylborane. *Jour. Am. Chem. Soc.*, vol. 77, no. 19, Oct. 5, 1955, pp. 5016-5017.
- Sanders, Newell D., and Laurence, James C.: Fundamental Investigation of Noise Generation by Turbulent Jets. Preprint 744, SAE, 1956.
- Schmidt, W. C., and Anderson, William J.: Detecting Bearing Failures by Measuring Temperature Acceleration. *Lubrication Eng.*, vol. 11, no. 4, July/Aug. 1955, pp. 274-276.
- Sharp, Elmer M.: Experiences With Automatic Digital Data Processing. *Am. Documentation*, vol. 7, no. 1, Jan. 1956, pp. 22-28.

- Shortal, Joseph A.: Techniques of Model Testing in Free Flight. Presented at Fifth Meeting of the Wind Tunnel and Model Testing Panel (The Hague, Netherlands, May 3-7, 1954), Advisory Group for Aeronautical Research and Development AG15/P6, pp. 56-68.
- Silverstein, Abe: Concepts on Turbojet Engines for Transport Application. Preprint 721, SAE, 1956.
- Silverstein, Abe: The Future in Ramjets. *Aviation Age*, vol. 25, no. 6, June 1956, pp. B:6-B:9.
- Simon, Dorothy M., and Wagner, Paul: Characterization of Turbulent Combustion by Flame Space and Space Heating Rates. Propane-Oxygen-Nitrogen Flames. *Ind. and Eng. Chem.*, vol. 48, no. 1, Jan. 1956, pp. 129-133.
- Sommer, Simon C., and Short, Barbara J.: Free-Flight Measurements of Skin Friction of Turbulent Boundary Layers With High Rates of Heat Transfer at High Supersonic Speeds. *Jour. Aero. Sci.*, vol. 23, no. 6, June 1956, pp. 536-542.
- Sparrow, Ephraim M., and Gregg, John L.: Laminar Free Convection From a Vertical Plate With Uniform Surface Heat Flux. *Trans. A. S. M. E.*, vol. 78, no. 2, Feb. 1956, pp. 435-440.
- Tapscott, Robert J., and Gustafson, Frederic B.: Helicopter Blade Flapping. *Aero. Eng. Rev.*, vol. 14, no. 9, Sept. 1955, pp. 46-51.
- Van Dyke, Milton D.: The Slender Elliptic Cone as a Model for Non-Linear Supersonic Flow Theory. *Jour. Fluid Mechanics*, vol. 1, no. 1, May 1956, pp. 1-15.
- Warshawsky, Isidore: Multiple-Bridge Circuits for Measurement of Small Changes in Resistance. *Rev. Sci. Instr.*, vol. 26, no. 7, July 1955, pp. 711-715.
- Weltmann, Ruth N.: Friction Factors for Flow of Non-Newtonian Materials in Pipelines. *Ind. and Eng. Chem.*, vol. 48, no. 3, pt. 1, Mar. 1956, pp. 386-387.
- Whitcomb, Richard T.: NACA Details Area Rule Breakthrough. *Aviation Week*, vol. 63, no. 12, Sept. 19, 1955, pp. 28-31, 33, 35-36, 38, 41-42, 44, 46-47.
- Whitcomb, Richard T.: Zero-Lift-Drag Characteristics of Wing-Body Combinations at Transonic Speeds. *Aero. Eng. Rev.*, vol. 15, no. 6, June 1956, pp. 42-45.
- Wiener, Bernard, Groetzinger, Gerhart, and McCollum, Rathuel: Specification of Thermally and Mechanically Induced Non-equilibrium States in AuCu by Resistivity and Magnetoresistivity. *Jour. Appl. Phys.*, vol. 26, no. 7, July 1955, pp. 857-862.
- Williams, Walter C.: Flight Research at High Altitudes and High Speeds With Rocket-Propelled Research Airplanes. Preprint 601, SAE, 1955.
- Woolston, Donald S., Runyan, Harry L., and Andrews, Robert E.: An Investigation of Effects of Certain Types of Structural Nonlinearities on Wing and Control Surface Flutter. Preprint 633, *Inst. Aero. Sci.*, 1956.
- Yeates, John E., Jr.: A Discussion of Helicopter Vibration Studies Including Flight Test and Analysis Methods Used to Determine the Coupled Response of a Tandem Type. Preprint 625, *Inst. Aero. Sci.*, 1956.
- Zimmerman, Charles H.: Some General Considerations Concerning VTOL Aircraft. Preprint 737, SAE, 1956.
- Zimmerman, Charles H.: Some Stability Problems of Vertically Rising Aircraft. *Proc. of Second Annual Western Forum of American Helicopter Society* (Los Angeles, Sept. 21-22, 1955), *Am. Helicopter Soc., Inc. (N. Y.)*, 1955, pp. 6-32.

Part II—COMMITTEE ORGANIZATION AND MEMBERSHIP

The National Advisory Committee for Aeronautics was established by Act of Congress approved March 3, 1915 (U. S. Code, title 50, sec. 151). The Committee consists of seventeen members appointed by the President, and includes two representatives each of the Department of the Air Force, the Department of the Navy, and the Civil Aeronautics Authority; one representative each of the Smithsonian Institution, the United States Weather Bureau, and the National Bureau of Standards; and "one Department of Defense representative who is acquainted with the needs of aeronautical research and development." In addition seven members are appointed for five-year terms from persons "acquainted with the needs of aeronautical science, either civil or military, or skilled in aeronautical engineering or its allied sciences." The representatives of the Government organizations serve for indefinite periods, and all members serve as such without compensation.

The following changes in membership have taken place during the past year:

The Committee lost a valuable member by the death on January 4, 1956, of Mr. Ralph S. Damon, President of Trans World Air Lines, Inc., who had been serving as Chairman of the important NACA Committee on Operating Problems. In its tribute to Mr. Damon's memory, the NACA at its meeting on January 19, 1956, said: "His intelligence, enthusiasm, sound judgment, and high qualities of integrity and sincerity, together with his wealth of experience, enabled him to support most effectively the responsibilities of the Committee and to provide highly competent leadership."

To succeed Mr. Damon, President Eisenhower on April 14, 1956, appointed the well-known World War I ace and aviation executive, Captain Edward V. Rickenbacker, Chairman of the Board of Eastern Air Lines, Inc., to membership on the NACA.

On January 6, 1956, the President appointed Hon. Clifford C. Furnas, Assistant Secretary of Defense (Research and Development), a member of NACA. Dr. Furnas succeeded Hon. Donald A. Quarles, Secretary of the Air Force, who had previously served in Dr. Furnas' present post in the Department of Defense.

Vice Admiral William V. Davis, USN, Deputy Chief of Naval Operations (Air), was appointed a member of the NACA on August 2, 1956, succeeding Vice Admiral Thomas S. Combs, who had just been detached from the same Navy post and assigned to other duty.

In accordance with the regulations of the Committee as approved by the President, the chairman and vice

chairman and the chairman and vice chairman of the Executive Committee are elected annually.

Prior to the annual meeting of the NACA on October 17, 1956, Dr. Jerome C. Hunsaker, who had been chairman since August 1941, indicated his desire to retire from the chairmanship of the NACA and of the Executive Committee. At the meeting the NACA elected Dr. James H. Doolittle chairman of the NACA and of the Executive Committee. Dr. Leonard Carmichael was re-elected vice chairman of the NACA and Dr. Detlev W. Bronk vice chairman of the Executive Committee.

The Committee membership is as follows:

James H. Doolittle, Sc. D., Shell Oil Company, Chairman.
Leonard Carmichael, Ph. D., Secretary, Smithsonian Institution, Vice Chairman.
Joseph P. Adams, LL. B., Vice Chairman, Civil Aeronautics Board.
Allen V. Astin, Ph. D., Director, National Bureau of Standards.
Preston R. Bassett, M. A., Vice President, Sperry Rand Corporation.
Detlev W. Bronk, Ph. D., President, Rockefeller Institute for Medical Research.
Frederick C. Crawford, Sc. D., Chairman of the Board, Thompson Products, Inc.
William V. Davis, Jr., Vice Admiral, United States Navy, Deputy Chief of Naval Operations (Air).
Clifford C. Furnas, Ph. D., Assistant Secretary of Defense (Research and Development).
Jerome C. Hunsaker, Sc. D., Massachusetts Institute of Technology.
Carl J. Pfingstag, Rear Admiral, United States Navy, Assistant Chief for Field Activities, Bureau of Aeronautics.
Donald L. Putt, Lieutenant General, United States Air Force, Deputy Chief of Staff, Development.
Arthur E. Raymond, Sc. D., Vice President—Engineering, Douglas Aircraft Company, Inc.
Francis W. Reichelderfer, Sc. D., Chief, United States Weather Bureau.
Edward V. Rickenbacker, Sc. D., Chairman of the Board, Eastern Air Lines, Inc.
Louis S. Rothschild, Under Secretary of Commerce for Transportation.
Nathan F. Twining, General, United States Air Force, Chief of Staff.

Assisting the Committee in its coordination of aeronautical research and the formulation of its research programs are four main technical committees: Aerodynamics, Power Plants for Aircraft, Aircraft Construction, and Operating Problems. Each of these committees is assisted by four or more subcommittees. Effective January 1, 1956, two new subcommittees were established under the Committee on Aerodynamics in place of the Subcommittee on Stability and Control,

namely: Aerodynamic Stability and Control, and Automatic Stabilization and Control. This action was taken because of the increase in the importance of the problems of automatic stabilization and control in connection with both piloted aircraft and missiles.

The Committee is advised on matters of policy affecting the aircraft industry by an Industry Consulting Committee.

The membership of the committees and their subcommittees is as follows:

COMMITTEE ON AERODYNAMICS

Mr. Preston R. Bassett, Vice President, The Sperry Rand Corp., Chairman.
 Dr. Theodore P. Wright, Vice President for Research, Cornell University, Vice Chairman.
 Col. Daniel D. McKee, USAF, Wright Air Development Center.
 Rear Adm. W. A. Schoech, USN, Assistant Chief of the Bureau of Aeronautics for Research and Development, Department of the Navy.
 Mr. F. A. Loudon, Bureau of Aeronautics, Department of the Navy.
 Dr. H. H. Kurzweg, Associate Technical Director for Aeroballistic Research, Naval Ordnance Laboratory.
 Maj. Gen August Schomburg, USA, Assistant Chief of Ordnance for Research and Development, Department of the Army.
 Mr. D. M. Thompson, Office of the Chief of Transportation, Department of the Army.
 Mr. Harold D. Hoekstra, Civil Aeronautics Administration.
 Dr. Hugh L. Dryden (ex officio).
 Mr. Floyd L. Thompson, NACA Langley Aeronautical Laboratory.
 Mr. Russell G. Robinson, NACA Ames Aeronautical Laboratory.
 Capt. W. S. Diehl, USN (Ret.).
 Mr. L. L. Douglas, Vice President—Engineering, VERTOL Aircraft Corp.
 Rear Adm. R. S. Hatcher, USN (Ret.), Professor and Chairman, Department of Aeronautical Engineering, New York University.
 Mr. Clarence L. Johnson, Chief Engineer, Lockheed Aircraft Corp.
 Dr. A. Kartveli, Vice President—Engineering, Republic Aviation Corp.
 Mr. Schuyler Kleinhans, Assistant Chief Engineer, Santa Monica Division, Douglas Aircraft Co.
 Dr. Albert E. Lombard, Jr., Director of Research, McDonnell Aircraft Corp.
 Dr. Clark B. Millikan, Director, Daniel Guggenheim Aeronautical Laboratory, California Institute of Technology.
 Dr. William J. O'Donnell, Assistant Chief Engineer—Development and Experimental, Republic Aviation Corp.
 Mr. Kendall Perkins, Vice President—Engineering, McDonnell Aircraft Corp.
 Mr. H. A. Storms, Jr., Chief, Technical Engineering, North American Aviation, Inc.
 Mr. Charles Tilgner, Jr., Chief Aeronautical Engineer (Staff), Grumman Aircraft Engineering Corp.
 Mr. George S. Trimble, Jr., Vice President—Chief Engineer, The Martin Co.
 Mr. Robert J. Woods, Chief Design Engineer, Bell Aircraft Corp.

Mr. Milton B. Ames, Jr., Secretary

Subcommittee on Fluid Mechanics

Dr. William R. Sears, Cornell University, Chairman.
 Maj. Eugene W. Geniesse, USAF, Air Research and Development Command.
 Mr. E. Haynes, Air Research and Development Command.
 Mr. Phillip Eisenberg, Office of Naval Research, Department of the Navy.
 Mr. John D. Nicolaides, Bureau of Ordnance, Department of the Navy.
 Dr. Joseph Sternberg, Ballistic Research Laboratories, Aberdeen Proving Ground.
 Dr. G. B. Schubauer, Chief, Fluid Mechanics Section, National Bureau of Standards.
 Dr. Adolf Busemann, NACA Langley Aeronautical Laboratory.
 Mr. John Stack, NACA Langley Aeronautical Laboratory.
 Dr. D. R. Chapman, NACA Ames Aeronautical Laboratory.
 Mr. Robert T. Jones, NACA Ames Aeronautical Laboratory.
 Dr. John C. Evvard, NACA Lewis Flight Propulsion Laboratory.
 Prof. Walker Bleakney, Princeton University.
 Dr. J. V. Charyk, Aeronutronics Systems, Inc.
 Dr. Francis H. Clauser, The Johns Hopkins University.
 Dr. Wallace D. Hayes, Princeton University.
 Dr. Hans W. Liepmann, California Institute of Technology.
 Prof. C. C. Lin, Massachusetts Institute of Technology.
 Prof. Wilbur C. Nelson, Chairman, Aeronautical Engineering Department, University of Michigan.
 Prof. E. L. Resler, Jr., Cornell University.

Mr. Ernest O. Pearson, Jr., Secretary.

Subcommittee on High-Speed Aerodynamics

Dr. Clark B. Millikan, Director, Daniel Guggenheim Aeronautical Laboratory, California Institute of Technology, Chairman.
 Maj. Eugene W. Geniesse, Jr., USAF, Air Research and Development Command.
 Mr. Joseph Flatt, Wright Air Development Center.
 Mr. Oscar Seidman, Bureau of Aeronautics, Department of the Navy.
 Dr. H. H. Kurzweg, Associate Technical Director for Aeroballistic Research, Naval Ordnance Laboratory.
 Mr. C. L. Poor, 3d, Chief, Exterior Ballistics Laboratory, Ballistic Research Laboratories, Aberdeen Proving Ground.
 Mr. John Beebe, Office of the Chief of Transportation, Department of the Army.
 Mr. John Stack, NACA Langley Aeronautical Laboratory.
 Mr. H. Julian Allen, NACA Ames Aeronautical Laboratory.
 Mr. Abe Silverstein, NACA Lewis Flight Propulsion Laboratory.
 Mr. Walter C. Williams, NACA High-Speed Flight Station.
 Mr. John R. Clark, Assistant Chief Engineer, Chance Vought Aircraft, Inc.
 Mr. Philip A. Colman, Chief Preliminary Design Engineer, Lockheed Aircraft Corp.
 Mr. Alexander H. Flax, Vice President—Technical Operations, Cornell Aeronautical Laboratory, Inc.
 Mr. L. P. Greene, Chief Aerodynamicist, North American Aviation, Inc.
 Mr. Robert L. Gustafson, Chief of Aerodynamics, Grumman Aircraft Engineering Corp.
 Mr. C. J. Koch, The Martin Co.
 Mr. John G. Lee, Director of Research, United Aircraft Corp.
 Mr. David S. Lewis, Jr., McDonnell Aircraft Corp.
 Mr. Harlowe J. Longfelder, Chief—Preliminary Design, Seattle Division, Boeing Airplane Co.

Prof. John R. Markham, Professor of Aeronautical Engineering, Massachusetts Institute of Technology.

Mr. K. E. Van Every, Chief, Aerodynamics Section, El Segundo Division, Douglas Aircraft Co., Inc.

Mr. Albert J. Evans, Secretary

Subcommittee on Aerodynamic Stability and Control

Capt. W. S. Diehl, USN (Ret.), Chairman.

Mr. Melvin Shorr, Wright Air Development Center.

Mr. Jerome Teplitz, Bureau of Aeronautics, Department of the Navy.

Mr. L. L. Liccini, Bureau of Ordnance, Department of the Navy.

Maj. William H. Brabson, Jr., USA, Office of the Chief of Research and Development, Department of the Army.

Mr. John A. Carran, Civil Aeronautics Administration.

Mr. Thomas A. Harris, NACA Langley Aeronautical Laboratory.

Dr. J. N. Nielsen, NACA Ames Aeronautical Laboratory.

Mr. Hubert M. Drake, NACA High-Speed Flight Station.

Mr. M. J. Abzug, Douglas Aircraft Co., Inc.

Prof. Joseph Bicknell, Massachusetts Institute of Technology.

Mr. E. A. Bonney, Applied Physics Laboratory, The Johns Hopkins University.

Mr. J. E. Goode, Jr., Convair, Division of General Dynamics Corp.

Mr. George S. Graff, Chief of Aerodynamics, McDonnell Aircraft Corp.

Mr. William T. Hamilton, Chief Aerodynamics Engineer, Boeing Airplane Co.

Mr. Maxwell W. Hunter, Assistant Chief Project Engineer—Missiles, Douglas Aircraft Co., Inc.

Mr. R. B. Katkov, Northrop Aircraft, Inc.

Mr. Conrad A. Lau, Chance Vought Aircraft, Inc.

Mr. W. F. Milliken, Jr., Manager, Flight Research, Cornell Aeronautical Laboratory, Inc.

Mr. Frank J. Mulholland, Assistant Chief Development Engineer, Republic Aviation Corp.

Mr. Jack D. Brewer, Secretary

Subcommittee on Automatic Stabilization and Control

Mr. Warren E. Swanson, North American Aviation, Inc. Chairman.

Mr. George L. Yingling, Wright Air Development Center.

Mr. William Koven, Bureau of Aeronautics, Department of the Navy.

Mr. Marvin Schuldenfrei, Bureau of Aeronautics, Department of the Navy.

Mr. J. M. Lee, Bureau of Ordnance, Department of the Navy.

Mr. Paul R. Miles, Signal Corps Engineering Laboratories.

Mr. Charles W. Mathews, NACA Langley Aeronautical Laboratory.

Mr. Harry J. Goett, NACA Ames Aeronautical Laboratory.

Mr. M. J. Abzug, Douglas Aircraft Co., Inc.

Mr. Frank A. Gaynor, General Electric Co.

Dr. William J. Jacobi, The Ramo-Wooldridge Corp.

Mr. W. F. Milliken, Jr., Manager, Flight Research, Cornell Aeronautical Laboratory, Inc.

Mr. Louis A. Payne, Convair, Division of General Dynamics Corp.

Mr. Thomas L. Phillips, Raytheon Manufacturing Co.

Mr. Donald J. Povejsil, Westinghouse Electric Corp.

Dr. Allen E. Puckett, Head, Missile Aerodynamics Department, Hughes Aircraft Co.

Mr. O. H. Schuck, Minneapolis-Honeywell Regulator Co.

Dr. Robert C. Seamans, Jr., RCA Aviation Systems Laboratory.

Mr. Bernard Maggin, Secretary

Subcommittee on Internal Flow

Dr. William J. O'Donnell, Assistant Chief Engineer—Development and Experimental, Republic Aviation Corp., Chairman.

Mr. Frederick T. Rall, Jr., Wright Air Development Center.

Mr. Robert E. Roy, Wright Air Development Center.

Mr. R. T. Miller, Bureau of Aeronautics, Department of the Navy.

Dr. Thomas W. Williams, Office of Naval Research, Department of the Navy.

Mr. V. S. Kupelian, U. S. Naval Ordnance Experimental Unit at National Bureau of Standards.

Mr. John V. Becker, NACA Langley Aeronautical Laboratory.

Mr. Wallace F. Davis, NACA Ames Aeronautical Laboratory.

Mr. DeMarquis D. Wyatt, NACA Lewis Flight Propulsion Laboratory.

Mr. J. S. Alford, General Electric Co.

Mr. Bernard F. Beckelman, Boeing Airplane Co.

Mr. William J. Blatz, McDonnell Aircraft Corp.

Mr. John A. Drake, Director of Long-Range Planning and Research Programs, Marquardt Aircraft Co.

Mr. Harry Drell, Group Engineer—Power Plant Analysis, Lockheed Aircraft Corp.

Dr. Antonio Ferri, Polytechnic Institute of Brooklyn.

Mr. Donald J. Jordan, Pratt & Whitney Aircraft, United Aircraft Corp.

Mr. M. A. Sulkin, Chief Thermodynamicist, North American Aviation, Inc.

Mr. William M. Zarkowsky, Chief of Propulsion, Grumman Aircraft Engineering Corp.

Mr. Albert J. Evans, Secretary

Subcommittee on Propellers for Aircraft

Mr. D. H. Jacobson, Aeroproducts Operations, Allison Division, General Motors Corp., Chairman.

Capt. William G. Alexander, USAF, Air Research and Development Command.

Mr. Daniel A. Dickey, Wright Air Development Center.

Lt. Commander Hugh L. H. Collins, USN, Bureau of Aeronautics, Department of the Navy.

Mr. John Beebe, Office of the Chief of Transportation, Department of the Army.

Mr. John C. Morse, Civil Aeronautics Administration.

Mr. Eugene C. Draley, NACA Langley Aeronautical Laboratory.

Mr. Donald H. Wood, NACA Ames Aeronautical Laboratory.

Mr. George W. Brady, Director of Engineering, Propeller Division, Curtiss-Wright Corp.

Mr. Frank W. Caldwell.

Mr. R. Richard Heppe, Department Head, Aerodynamics, Lockheed Aircraft Corp.

Mr. R. S. Kelso, Cornell Aeronautical Laboratory, Inc.

Mr. Frank W. Kolk, American Airlines, Inc.

Mr. Thomas B. Rhines, Assistant Chief Engineer, Hamilton Standard Division, United Aircraft Corp.

Mr. Kenneth E. Ward, Convair, Division of General Dynamics Corp.

Mr. Ralph W. May, Secretary

Subcommittee on Seaplanes

Rear Adm. R. S. Hatcher, USN (Ret.), Professor and Chairman, Department of Aeronautical Engineering, New York University, Chairman.

Mr. Robert F. Robinson, Air Research and Development Command.

Mr. Eugene H. Handler, Bureau of Aeronautics, Department of the Navy.

Mr. F. W. S. Locke, Jr., Bureau of Aeronautics, Department of the Navy.
 Mr. Marshall P. Tulin, Office of Naval Research, Department of the Navy.
 Mr. M. St. Denis, David W. Taylor Model Basin.
 Comdr. H. C. Weart, USN, Naval Air Test Center, Patuxent.
 Mr. Joseph Matulaitis, Office of the Chief of Transportation, Department of the Army.
 Capt. Reinhold R. Johnson, USCG, Coast Guard Station, Brooklyn.
 Mr. Robert Rosenbaum, Civil Aeronautics Administration.
 Mr. John B. Parkinson, NACA Langley Aeronautical Laboratory.
 Mr. H. E. Brooke, Chief of Hydrodynamics, Convair, Division of General Dynamics Corp.
 Mr. Robert B. Cotton, Vice President, All American Engineering Co.
 Mr. C. L. Fenn, Chief Engineer, Edo Corp.
 Mr. Wilfred C. Hugli, Jr., Stevens Institute of Technology.
 Mr. Grover Loening.
 Mr. J. D. Pierson, The Martin Co.

Mr. Ralph W. May, Secretary

Subcommittee on Helicopters

Mr. L. L. Douglas, Vice President—Engineering, VERTOL Aircraft Corp., Chairman.
 Mr. Bernard Lindenbaum, Wright Air Development Center.
 Mr. Paul A. Simmons, Jr., Wright Air Development Center.
 Capt. James W. Klopp, USN, Bureau of Aeronautics, Department of the Navy.
 Mr. T. L. Wilson, Office of Naval Research, Department of the Navy.
 Lt. Col. M. J. Strok, USA, Office of the Chief of Research and Development, Department of the Army.
 Mr. J. Wallace McDonald, Office of the Chief of Transportation, Department of the Army.
 Comdr. James W. Williams, USCG, Headquarters, U. S. Coast Guard.
 Mr. Herbert H. Slaughter, Jr., Civil Aeronautics Administration.
 Honorable Joseph P. Adams (ex officio), Vice Chairman, Civil Aeronautics Board.
 Mr. Richard C. Dingeldein, NACA Langley Aeronautical Laboratory.
 Mr. F. B. Gustafson, NACA Langley Aeronautical Laboratory.
 Mr. Charles W. Harper, NACA Ames Aeronautical Laboratory.
 Mr. Friedrich L. V. Doblhoff, Chief Engineer, Helicopter Engineering Division, McDonnell Aircraft Corp.
 Mr. Jack E. Gallagher, Chief Engineer and Operations Manager, New York Airways, Inc.
 Mr. Bartram Kelley, Chief Helicopter Engineer, Bell Aircraft Corp.
 Mr. Ralph B. Lightfoot, Sikorsky Aircraft, United Aircraft Corp.
 Prof. R. H. Miller, Associate Professor of Aeronautical Engineering, Massachusetts Institute of Technology.
 Mr. Charles M. Seibel, Chief Engineer, Helicopter Division, Cessna Aircraft Co.
 Mr. N. M. Stefano, Chief—Rotary Wing, Fairchild Aircraft Division, Fairchild Engine and Airplane Corp.
 Mr. Robert Wagner, Chief Engineer, Hiller Helicopters

Mr. P. M. Lovell, Jr., Secretary

COMMITTEE ON POWER PLANTS FOR AIRCRAFT

Dr. Frederick C. Crawford, Chairman of the Board, Thompson Products, Inc., Chairman.

Dean C. R. Soderburg, Dean of Engineering, Massachusetts Institute of Technology, Vice Chairman.
 Col. Donald Heaton, USAF, Directorate of Research and Development.
 Col. John J. B. Calderbank, USAF, Wright Air Development Center.
 Capt. Thomas B. Haley, USN, Bureau of Aeronautics, Department of the Navy.
 Col. C. L. Register, USA, Ballistic Research Laboratories, Aberdeen Proving Ground.
 Lt. Col. Michael J. Strok, USA, Office of Chief of Research and Development, Department of the Army.
 Mr. Stephen H. Rolle, Chief, Power Plant Branch, Aircraft Engineering Division, Civil Aeronautics Administration.
 Dr. Hugh L. Dryden (ex officio).
 Mr. Abe Silverstein, NACA Lewis Flight Propulsion Laboratory.
 Mr. John G. Borger, Pan American Airways System.
 Mr. Allan Chilton, Chief Engineer, Aircraft Gas Turbine Division, Westinghouse Electric Corp.
 Mr. D. Cochran, General Manager, AGT Development Department, General Electric Co.
 Mr. J. T. Cooley, Vice President, California Research Corp.
 Mr. Dimitrius Gerdan, Director of Engineering, Allison Division, General Motors Corp.
 Mr. Wilton G. Lundquist, Vice President, Curtiss-Wright Corp.
 Mr. Thomas E. Myers, North American Aviation, Inc.
 Mr. Wright A. Parkins, General Manager, Pratt & Whitney Aircraft, United Aircraft Corp.
 Mr. Ivar L. Shogran, Douglas Aircraft Co., Inc.
 Mr. Rudolf H. Thielemann, Senior Metallurgist, Stanford Research Institute.

Mr. William H. Woodward, Secretary

Subcommittee on Aircraft Fuels

Mr. J. L. Cooley, Vice President, California Research Corp., Chairman.
 Maj. Eugene Finke, USAF, Directorate of Research and Development, U. S. Air Force.
 Mr. Marc P. Dunnam, Wright Air Development Center.
 Comdr. B. L. Towle, USN, Bureau of Aeronautics, Department of the Navy.
 Mr. Donald D. Weidhuner, Office of Chief of Transportation, Department of the Army.
 Mr. N. L. Klein, Office of the Chief of Ordnance, Department of the Army.
 Mr. Ralph S. White, Civil Aeronautics Administration.
 Mr. Henry C. Barnett, NACA Lewis Flight Propulsion Laboratory.
 Dr. D. P. Barnard, Standard Oil Co. of Indiana.
 Mr. A. J. Blackwood, Esso Research and Engineering Co.
 Mr. C. S. Brandt, Convair, Division of General Dynamics Corp.
 Mr. F. G. Dougherty, Allison Division, General Motors Corp.
 Mr. E. A. Droegemueller, Pratt & Whitney Aircraft, United Aircraft Corp.
 Mr. D. N. Harris, Shell Oil Co.
 Dr. J. Bennett Hill, Director, Research and Development Department, Sun Oil Co.
 Mr. W. M. Holaday, Deputy Assistant Secretary of Defense (Research and Development).
 Mr. J. N. Krebs, General Electric Co.
 Prof. Carl C. Monrad, Head, Department of Chemical Engineering, Carnegie Institute of Technology.
 Mr. James S. Reid, Phillips Petroleum Co.

Mr. Harold F. Hipsher, Secretary

Subcommittee on Combustion

Dr. Alfred G. Cattaneo, Shell Development Co., Chairman.
 Mr. Howard P. Barfield, Wright Air Development Center.
 Dr. Lloyd A. Wood, Wright Air Development Center.
 Mr. Nelson F. Rekos, Bureau of Aeronautics, Department of the Navy.
 Mr. Alfred G. Lundquist, Office of Naval Research, Department of the Navy.
 Dr. Frank E. Marble, Jet Propulsion Laboratory, California Institute of Technology (representing Department of the Army).
 Mr. F. R. Caldwell, National Bureau of Standards.
 Dr. Walter T. Olson, NACA Lewis Flight Propulsion Laboratory.
 Dr. W. H. Avery, Applied Physics Laboratory, The Johns Hopkins University.
 Mr. William J. Bennet, Marquardt Aircraft Co.
 Mr. William V. Hanzalek, Assistant to General Manager, Research Division, Curtiss-Wright Corp.
 Dr. Bernard Lewis, Combustion and Explosives Research, Inc.
 Dr. John P. Longwell, Esso Research and Engineering Co.
 Dr. S. S. Penner, California Institute of Technology.
 Mr. Paul A. Pitt, Chief Development Engineer, Solar Aircraft Co.
 Mr. W. D. Pouchot, Supervising Engineer, Combustion Section, Aviation Gas Turbine Division, Westinghouse Electric Corp.
 Prof. Glenn C. Williams, Massachusetts Institute of Technology.
 Dr. Kurt Wohl, Professor of Chemical Engineering, University of Delaware.

Mr. Benson E. Gammon, Secretary.

Subcommittee on Lubrication and Wear

Dr. Robert G. Larsen, Research Director, Martinez Refinery, Shell Oil Co., Chairman.
 Mr. C. M. Michaels, Wright Air Development Center.
 Mr. Bernard Rubin, Wright Air Development Center.
 Mr. Charles C. Singleterry, Bureau of Aeronautics, Department of the Navy.
 Mr. R. E. Streets, Office of the Chief of Ordnance, Department of the Army.
 Mr. Joseph Matulaitis, Office of the Chief of Transportation, Department of the Army.
 Mr. Edmond E. Bisson, NACA Lewis Flight Propulsion Laboratory.
 Dr. W. E. Campbell.
 Mr. A. B. Crampton, Standard Oil Company of New Jersey.
 Dr. Merrell R. Fenske, Director, Petroleum Refining Laboratory, School of Chemistry and Physics, The Pennsylvania State University.
 Mr. A. S. Irwin, Assistant Chief Engineer—Aircraft, Marlin-Rockwell Corp.
 Dr. E. G. Jackson, General Electric Co.
 Dr. M. Eugene Merchant, Cincinnati Milling Machine Co.
 Mr. V. W. Peterson, Allison Division, General Motors Corp.
 Mr. Earle A. Ryder.
 Prof. L. M. Tichvinsky, Professor of Mechanical Engineering, University of California.
 Mr. George P. Townsend, Jr., Chief Engineer, Sundstrand Aviation—Denver.
 Mr. Frank W. Wellons, Assistant Chief Engineer, SKF Industries, Inc.

Mr. Harold F. Hipsher, Secretary.

Subcommittee on Compressors and Turbines

Mr. John M. Wetzler, Allison Division, General Motors Corp., Chairman.
 Mr. Ernest C. Simpson, Wright Air Development Center.

Mr. John C. Schettino, Bureau of Aeronautics, Department of the Navy.
 Comdr. L. K. Bliss, USN, Office of Naval Research, Department of the Navy.
 Mr. Edward F. Blackburne, Detroit Arsenal.
 Mr. Donald D. Weidhuner, Office of the Chief of Transportation, Department of the Army.
 Mr. John R. Erwin, NACA Langley Aeronautical Laboratory.
 Mr. William A. Benser, NACA Lewis Flight Propulsion Laboratory.
 Mr. William G. Cornell, General Electric Co.
 Dr. Robert C. Dean, Jr., Assistant Professor of Mechanical Engineering, Massachusetts Institute of Technology.
 Mr. Walter Doll, Pratt & Whitney Aircraft, United Aircraft Corp.
 Prof. Howard W. Emmons, Harvard University.
 Mr. John E. Sanders, Curtiss-Wright Corp.
 Mr. V. V. Schloesser, Director—Development, Aviation Gas Turbine Division, Westinghouse Electric Corp.
 Mr. M. A. Sulkin, Chief Thermodynamicist, North American Aviation, Inc.
 Dr. George F. Wislicenus, Director, Garfield Thomas Water Tunnel, Ordnance Research Laboratory, The Pennsylvania State University.

Mr. Curtis L. Walker, Secretary.

Subcommittee on Engine Performance and Operation

Mr. Perry W. Pratt, Chief Engineer, Pratt & Whitney Aircraft, United Aircraft Corp., Chairman.
 Col. Paul F. Nay, USAF, Air Research and Development Command.
 Mr. Ewell C. Phillips, Wright Air Development Center.
 Mr. Richard J. Maurer, Bureau of Aeronautics, Department of the Navy.
 Mr. Edward F. Blackburne, Detroit Arsenal.
 Mr. Donald D. Weidhuner, Office of the Chief of Transportation, Department of the Army.
 Col. E. O. Meals, Deputy Director, Aircraft Reactor Branch, Division of Reactor Development, Atomic Energy Commission.
 Mr. Bruce T. Lundin, NACA Lewis Flight Propulsion Laboratory.
 Mr. Rudolph Bodemuller, Bendix Products Division, Bendix Aviation Corp.
 Mr. C. J. McDowall, Chief Engineer—Advanced Design and Development, Allison Division, General Motors Corp.
 Mr. Maynard L. Pennell, Chief Engineer, Transport Division, Boeing Airplane Co.
 Mr. Erol F. Pierce, Assistant Chief Engineer, Technical Services, Wright Aeronautical Division, Curtiss-Wright Corp.
 Mr. Arnold H. Redding, Section Manager, Preliminary Design Division, Aviation Gas Turbine Division, Westinghouse Electric Corp.
 Mr. Thomas B. Rhines, Assistant Chief Engineer, Hamilton Standard Division, United Aircraft Corp.
 Mr. Dale D. Streid, Aircraft Gas Turbine Division, General Electric Co.
 Mr. Elwood B. Taylor, Chief Power Plant Engineer, El Segundo Division, Douglas Aircraft Co., Inc.
 Mr. George S. Trimble, Jr., Vice President—Chief Engineer, The Martin Co.
 Mr. Don L. Walter, Vice President—Engineering, Marquardt Aircraft Co.
 Mr. R. H. Widmer, Assistant Chief Engineer, Convair, Division of General Dynamics Corp.
 Mr. Lee R. Woodworth, Propulsion Research Corp.

Mr. Richard S. Cesaro, Secretary.

Subcommittee on Power Plant Controls

Mr. Rudolph Bodemuller, Bendix Aviation Corp., Chairman.
 Mr. J. G. Barrett, Wright Air Development Center.
 Mr. A. S. Atkinson, Bureau of Aeronautics, Department of the Navy.
 Maj. William H. Brabson, Jr., USA, Office of Chief of Research and Development, Department of the Army.
 Mr. John C. Sanders, NACA Lewis Flight Propulsion Laboratory.
 Dr. John L. Barnes, University of California.
 Mr. A. B. Chudyk, Assistant Chief Engineer, Design and Development Department, Minneapolis-Honeywell Regulator Co.
 Dr. C. Stark Draper, Head, Department of Aeronautical Engineering, Massachusetts Institute of Technology.
 Mr. R. T. Dungan, Marquardt Aircraft Co.
 Mr. Harold E. Francis, Wright Aeronautical Division, Curtiss-Wright Corp.
 Dr. E. H. Gamble, General Electric Co.
 Mr. William H. Hand, North American Aviation, Inc.
 Mr. James R. Kessler, Supervisor of Aircraft Accessory Design, Aeroproducts Operations, Allison Division, General Motors Corp.
 Mr. Bruce N. Torell, Pratt & Whitney Aircraft, United Aircraft Corp.
 Mr. James W. Wheeler, Department Head for Engine Instruments, Sperry Gyroscope Co., Division of Sperry Rand Corp.

Mr. Curtis L. Walker, Secretary.

Subcommittee on Power Plant Materials

Mr. Rudolf H. Thielemann, Senior Metallurgist, Stanford Research Institute, Chairman.
 Mr. J. B. Johnson, Wright Air Development Center.
 Mr. Nathan E. Promisel, Bureau of Aeronautics, Department of the Navy.
 Mr. J. J. Harwood, Office of Naval Research, Department of the Navy.
 Mr. Normal L. Reed, Watertown Arsenal.
 Mr. S. S. Manson, NACA Lewis Flight Propulsion Laboratory.
 Mr. W. L. Badger, General Electric Co.
 Mr. Lee S. Busch, Mallory-Sharon Titanium Corp.
 Dr. F. N. Darmara, Vice President, Utica Drop Forge & Tool Corp.
 Mr. Charles T. Evans, Jr., Vice President—Technology and Development, Universal-Cyclops Steel Corp.
 Mr. Glenn A. Fritzlen, Technical Director, Development and Technical Services, Haynes Stellite Co.
 Prof. Nicholas J. Grant, Massachusetts Institute of Technology.
 Mr. Arthur W. F. Green, Technical Assistant to Executive Engineer, Allison Division, General Motors Corp.
 Mr. J. J. Heger, United States Steel Corp.
 Mr. William D. Manly, Associate Director, Metallurgy Division, Oak Ridge National Laboratory, Union Carbide & Carbon Corp.
 Mr. Andrew G. Slachta, Wright Aeronautical Division, Curtiss-Wright Corp.
 Dr. L. F. Yntema, Director of Research, Fansteel Metallurgical Corp.

Mr. William H. Woodward, Secretary.

Subcommittee on Rocket Engines

Mr. Thomas E. Myers, North American Aviation, Inc., Chairman.
 Lt. Col. Richard T. Hemsley, USAF, Air Research and Development Command.

Lt. Col. L. F. Ayres, USAF, Western Development Division, Air Research and Development Command.
 Lt. Comdr. R. J. Kauffman, USN, Bureau of Aeronautics, Department of the Navy.
 Mr. Frank I. Tanczos, Bureau of Ordnance, Department of the Navy.
 Mr. James R. Patton, Office of Naval Research, Department of the Navy.
 Dr. Eugene Miller, Redstone Arsenal.
 Mr. John L. Sloop, NACA Lewis Flight Propulsion Laboratory.
 Mr. Richard B. Canright, Douglas Aircraft Co., Inc.
 Dr. H. F. Dunholter, Chief of Thermodynamics, Convair, Division of General Dynamics Corp.
 Mr. R. Bruce Foster, Group Leader, Preliminary Design, Rocket Engine Department, Bell Aircraft Corp.
 Mr. William P. Munger, Engineering and Research Manager, Reaction Motors, Inc.
 Mr. C. C. Ross, Manager, Liquid Engine Division, Aerojet-General Corp.
 Dr. C. N. Satterfield, Professor of Chemical Engineering, Massachusetts Institute of Technology.
 Mr. Frederick E. Schultz, General Electric Co.
 Dr. H. S. Seifert, The Ramo-Wooldridge Corp.
 Dr. A. J. Stosiek, Union Carbide & Carbon Corp.
 Dr. Maurice J. Zucrow, Professor of Jet Propulsion, School of Mechanical Engineering, Purdue University.

Mr. Benson E. Gammon, Secretary.

COMMITTEE ON AIRCRAFT CONSTRUCTION

Dr. Arthur E. Raymond, Vice President—Engineering, Douglas Aircraft Co., Inc., Chairman.
 Mr. George Snyder, Chief Project Engineer, Pilotless Aircraft Division, Boeing Airplane Co., Vice Chairman.
 Mr. E. H. Schwartz, Wright Air Development Center.
 Capt. James W. Klopp, USN, Bureau of Aeronautics, Department of the Navy.
 Dr. Wernher von Braun, Army Ballistic Missile Agency.
 Mr. D. M. Thompson, Office of the Chief of Transportation, Department of the Army.
 Mr. Albert A. Vollmecke, Civil Aeronautics Administration.
 Dr. Hugh L. Dryden (ex officio).
 Mr. Robert R. Gilruth, NACA Langley Aeronautical Laboratory.
 Mr. John F. Parsons, NACA Ames Aeronautical Laboratory.
 Dr. William F. Ballhaus, Chief Engineer, Northrop Aircraft, Inc.
 Prof. Raymond L. Bisplinghoff, Professor of Aeronautical Engineering, Massachusetts Institute of Technology.
 Mr. G. C. Covington, Vice President—Airplane Engineering, McDonnell Aircraft Corp.
 Mr. Martin Goland, Vice President, Southwest Research Institute.
 Mr. D. R. Kirk, Convair, Division of General Dynamics Corp.
 Mr. Jerome F. McBrearty, Chief Structures Engineer, Lockheed Aircraft Corp.
 Mr. George D. Ray, Chief Preliminary Design Engineer, Bell Aircraft Corp.
 Dr. Leo Schapiro, Head, Metallurgical and Physical Testing Laboratory, Douglas Aircraft Co., Inc.
 Mr. Richard L. Schleicher, Chief Structures Engineer, North American Aviation, Inc.
 Prof. F. R. Shanley, University of California.
 Mr. Robert J. Woods, Chief Design Engineer, Bell Aircraft Corp.

Mr. Franklyn W. Phillips, Secretary.

Subcommittee on Aircraft Structures

Mr. George D. Ray, Chief Preliminary Design Engineer, Bell Aircraft Corp., Chairman.

Capt. W. T. McGinness, USAF, Air Research and Development Command.
 Mr. William B. Miller, Wright Air Development Center.
 Mr. Ralph L. Creel, Bureau of Aeronautics, Department of the Navy.
 Mr. Emil A. H. Hellebrand, Army Ballistic Missile Agency.
 Capt. Earl P. Ford, USA, Office of the Chief of Transportation, Department of the Army.
 Mr. Milton Jakosky, Civil Aeronautics Administration.
 Mr. Richard R. Heldenfels, NACA Langley Aeronautical Laboratory.
 Mr. O. W. Boden, Chief of Missile Design Section, North American Aviation, Inc.
 Mr. L. M. Hitchcock, Chief—Technical Staff, Seattle Division Boeing Airplane Co.
 Dr. Nicholas J. Hoff, Head, Department of Aeronautical Engineering and Applied Mechanics, Polytechnic Institute of Brooklyn.
 Mr. Antonio L. LoPresti, North American Aviation, Inc.
 Mr. George N. Mangurian, Chief Analytical Engineer, Northrop Aircraft, Inc.
 Mr. William R. Micks, The RAND Corp.
 Mr. Herman Pusin, Chief Engineer, Engineering Division, The Marin Co.
 Prof. Paul E. Sandorff, Massachusetts Institute of Technology.
 Prof. E. E. Sechler, Professor of Aeronautics, California Institute of Technology.
 Mr. E. H. Spaulding, Division Engineer, Structural Engineering, Lockheed Aircraft Corp.
 Mr. C. H. Stevenson, Douglas Aircraft Co., Inc.

Mr. Melvin G. Rosché, Secretary.

Subcommittee on Aircraft Loads

Mr. Jerome F. McBrearty, Chief Structures Engineer, Lockheed Aircraft Corp., Chairman.
 Lt. Col. L. S. Jablecki, USAF, Air Research and Development Command.
 Mr. Joseph H. Harrington, Wright Air Development Center.
 Mr. Clinton T. Newby, Bureau of Aeronautics, Department of the Navy.
 Mr. John Carlson, Office of the Chief of Transportation, Department of the Army.
 Mr. Burdell L. Springer, Civil Aeronautics Administration.
 Mr. Philip Donely, NACA Langley Aeronautical Laboratory.
 Mr. Manley J. Hood, NACA Ames Aeronautical Laboratory.
 Mr. D. E. Beeler, NACA High-Speed Flight Station.
 Mr. Ralph B. Davidson, Director of Engineering Services, Radioplane Co.
 Mr. J. A. Dillworth, III, Structural Requirements Division Engineer, Georgia Division, Lockheed Aircraft Corp.
 Mr. E. Z. Gray, Boeing Airplane Co.
 Mr. H. J. Hoge, North American Aviation, Inc.
 Mr. H. W. Huntley, North American Aviation, Inc.
 Mr. William W. Jenney, Douglas Aircraft Co., Inc.
 Mr. J. A. Johnson, Lockheed Aircraft Corp.
 Mr. Alfred I. Sibila, Chief of Engineering Personnel and Planning, Chance Vought Aircraft, Inc.
 Mr. Harry Tobey, Chief of Structures, Vertol Aircraft Corp.

Mr. R. Fabian Goranson, Secretary.

Subcommittee on Vibration and Flutter

Mr. Martin Goland, Vice President, Southwest Research Institute, Chairman.
 Mr. Fred L. Daum, Wright Air Development Center.
 Mr. W. J. Mykytow, Wright Air Development Center.

Mr. Douglas Michel, Bureau of Aeronautics, Department of the Navy.
 Mr. Philipp W. Zettler-Seidel, Army Ballistic Missile Agency.
 Mr. J. Wallace McDonald, Office of the Chief of Transportation, Department of the Army.
 Mr. Robert Rosenbaum, Civil Aeronautics Administration.
 Mr. I. E. Garrick, NACA Langley Aeronautical Laboratory.
 Mr. Albert Erickson, NACA Ames Aeronautical Laboratory.
 Mr. André J. Meyer, Jr., NACA Lewis Flight Propulsion Laboratory.
 Prof. Lee Arnold, Columbia University.
 Prof. Holt Ashley, Massachusetts Institute of Technology.
 Mr. Eugene F. Baird, Chief Flutter and Vibration Engineer, Grumman Aircraft Engineering Corp.
 Mr. Douglas G. Dill, Douglas Aircraft Co., Inc.
 Mr. Michael Dublin, Chief of Dynamics, Convair, Division of General Dynamics Corp.
 Mr. H. Clay Johnson, Jr., Supervisor, Structural Dynamics, The Martin Co.
 Mr. William R. Laidlaw, North American Aviation, Inc.
 Mr. E. L. Leppert, Jr., Research Specialist, Flutter and Vibration, Lockheed Aircraft Corp.
 Mr. M. J. Turner, Unit Chief—Structural Dynamics, Seattle Division, Boeing Airplane Co.

Mr. Harvey H. Brown, Secretary.

Subcommittee on Aircraft Structural Materials

Dr. Leo Schapiro, Head, Metallurgical and Physical Testing Laboratory, Douglas Aircraft Co., Inc., Chairman.
 Mr. J. B. Johnson, Wright Air Development Center.
 Mr. Nathan E. Promisel, Bureau of Aeronautics, Department of the Navy.
 Dr. W. H. Steurer, Redstone Arsenal.
 Mr. L. J. Borges, Office of the Chief of Transportation, Department of the Army.
 Dr. Gordon M. Kline, Chief, Organic and Fibrous Materials Division, National Bureau of Standards.
 Mr. James E. Dougherty, Jr., Chief, Materials and Processes Section, Civil Aeronautics Administration.
 Mr. Paul Kuhn, NACA Langley Aeronautical Laboratory.
 Mr. G. Mervin Ault, NACA Lewis Flight Propulsion Laboratory.
 Mr. Robert S. Ames, Goodyear Aircraft Corp.
 Mr. Harry A. Campbell, Bell Aircraft Corp.
 Mr. Edgar H. Dix, Jr., Assistant Director of Research, Aluminum Company of America.
 Prof. Pol Duwez, California Institute of Technology.
 Dr. Walter L. Finlay, Vice President and Manager of Research, Rem-Cru Titanium, Inc.
 Mr. L. R. Jackson, Assistant Director, Battelle Memorial Institute.
 Dr. J. C. McDonald, Assistant Technical Director, Magnesium Department, The Dow Chemical Co.
 Mr. Peter Payson, Assistant Director of Research, Crucible Steel Company of America.
 Dr. Dana W. Smith, Associate Director, Division of Metallurgical Research, Kaiser Aluminum and Chemical Corp.
 Dr. George V. Smith, Professor of Metallurgical Engineering, Cornell University.

Mr. R. H. Raring, Secretary.

COMMITTEE ON OPERATING PROBLEMS

Capt. Edward V. Rickenbacker, Chairman of the Board, Eastern Air Lines, Inc., Chairman.
 Mr. William Littlewood, Vice President—Equipment Research, American Airlines, Inc., Vice Chairman.

Col. Joseph Davis, Jr., USAF, Wright Air Development Center.
 Brig. Gen. Albert T. Wilson, Jr., USAF, Deputy Chief of Staff, Operations, Military Air Transport Service.
 Capt. S. R. Ours, USN, Bureau of Aeronautics, Department of the Navy.
 Lt. Col. John L. Rowan, USA, Office of the Deputy Chief of Staff for Military Operations, Department of the Army.
 Col. George P. Seneff, Jr., USA, Office of the Chief of Research and Development, Department of the Army.
 Mr. William B. Davis, Director, Office of Aviation Safety, Civil Aeronautics Administration.
 Mr. Donald M. Stuart, Director, Technical Development and Evaluation Center, Civil Aeronautics Administration.
 Dr. F. W. Reichelderfer (ex officio), Chief, U. S. Weather Bureau.
 Dr. Hugh L. Dryden (ex officio).
 Mr. Melvin N. Gough, NACA Langley Aeronautical Laboratory.
 Mr. Lawrence A. Clousing, NACA Ames Aeronautical Laboratory.
 Mr. Eugene J. Manganiello, NACA Lewis Flight Propulsion Laboratory.
 Mr. M. G. Beard, Assistant Vice President—Equipment Research, American Airlines, Inc.
 Mr. John G. Borger, Pan American World Airways System.
 Mr. Warren T. Dickinson, Assistant to Chief Engineer, Douglas Aircraft Co., Inc.
 Mr. Charles Froesch, Vice President—Engineering, Eastern Airlines, Inc.
 Mr. Raymond D. Kelly, Superintendent of Technical Development, United Air Lines, Inc.
 Mr. Jerome Lederer, Director, Flight Safety Foundation.
 Mr. W. C. Mentzer, General Manager—Engineering, United Air Lines, Inc.
 Mr. Robert W. Rummel, Vice President—Engineering, Trans World Airlines, Inc.
 Mr. Clarence N. Sayen, President, Air Line Pilots Association.
 Mr. Arthur E. Smith, Engineering Manager, Pratt & Whitney Aircraft, United Aircraft Corp.
 Mr. R. L. Thoren, Chief Flight Test Engineer, Lockheed Aircraft Corp.
 Mr. H. W. Withington, Staff Engineer—Systems, Boeing Airplane Co.

Dr. T. L. K. Smull, Secretary.

Subcommittee on Meteorological Problems

Dr. F. W. Reichelderfer, Chief, U. S. Weather Bureau, Chairman.
 Brig. Gen. Thomas S. Moorman, Jr., USAF, Commander, Air Weather Service.
 Mr. C. N. Touart, Chief, Atmospheric Analysis Laboratory, Geophysics Research Directorate, Air Force Cambridge Research Center.
 Capt. Paul R. Drouilhet, USN, Head, Naval Aerology Branch, Office of Chief of Naval Operations.
 Mrs. Frances L. Whedon, Office of the Chief Signal Officer, Department of the Army.
 Dr. Ross Gunn, Director, Physical Research Division, U. S. Weather Bureau.
 Dr. Harry Wexler, Chief, Scientific Services Division, U. S. Weather Bureau.
 Mr. Robert W. Craig, Civil Aeronautics Administration.
 Mr. George M. French, Civil Aeronautics Board.
 Mr. Harry Press, NACA Langley Aeronautical Laboratory.
 Mr. William Lewis, NACA Lewis Flight Propulsion Laboratory.
 Mr. Robert N. Buck, Trans World Airlines, Inc.
 Dr. Horace R. Byers, Professor of Meteorology, The University of Chicago.
 Mr. Martin B. Cahill, Engineering Pilot, Northwest Airlines, Inc.
 Mr. Joseph J. George, Eastern Air Lines, Inc.

Mr. Henry T. Harrison, Jr., Director—Meteorology, United Air Lines, Inc.
 Prof. H. G. Houghton, Massachusetts Institute of Technology.
 Mr. H. J. Reid, Manager, Flight Operations, Capital Airlines, Inc.
 Dean Athelstan F. Spilhaus, University of Minnesota.
 Dr. George F. Taylor, Chief, Upper Atmosphere Department, Missile Systems Division, Lockheed Aircraft Corp.
 Mr. Frank C. White, Air Transport Association of America.

Mr. Mason T. Charak, Secretary.

Subcommittee on Icing Problems

Mr. W. W. Reaser, Douglas Aircraft Co., Inc., Chairman.
 Lt. Col. George B. Eldridge, USAF, Air Research and Development Command.
 Mr. Carl L. Oakes, Jr., Wright Air Development Center.
 Dr. Robert M. Cunningham, Air Force Cambridge Research Center.
 Mr. R. T. Miller, Bureau of Aeronautics, Department of the Navy.
 Mr. Harcourt C. Sontag, Bureau of Aeronautics, Department of the Navy.
 Dr. Henri Bader, Chief Scientist, Snow, Ice, Permafrost Research Establishment.
 Maj. John W. Elliott, USA, Office of the Chief of Transportation, Department of the Army.
 Mr. Dwight B. Kline, U. S. Weather Bureau.
 Mr. Robert J. Auburn, Civil Aeronautics Administration.
 Mr. Uwe H. von Glahn, NACA Lewis Flight Propulsion Laboratory.
 Mr. J. S. Alford, Aircraft Gas Turbine Department, General Electric Co.
 Mr. Victor Hudson, Senior Thermodynamics Engineer, Convair, Division of General Dynamics Corp.
 Mr. G. Donald Linklater, Senior Meteorologist, Northwest Airlines, Inc.
 Mr. Bernard L. Messinger, Department Manager, Thermodynamics, Lockheed Aircraft Corp.
 Mr. Robert A. Paselk, North American Aviation, Inc.
 Mr. Duane M. Patterson, Director, Aeronautical Icing Research Laboratories, Smith, Hinchman & Grylls, Inc.
 Mr. D. A. Richardson, Assistant to Chief Design Engineer, Vertol Aircraft Corp.

Mr. Mason T. Charak, Secretary.

Subcommittee on Flight Safety

Mr. Charles Froesch, Vice President—Engineering, Eastern Air Lines, Inc., Chairman.
 Dr. Albert A. Hetherington, Jr., Air Research and Development Command.
 Lt. Col. John P. Stapp, USAF, Chief, Aeromedical Field Laboratory, Holloman Air Development Center.
 Mr. Sydney D. Berman, Office of the Inspector General, U. S. Air Force.
 Comdr. Forrester C. Auman, USN, Office of Deputy Chief of Naval Operations (Air).
 Col. James F. Wells, USA, Office of the Deputy Chief of Staff for Military Operations, Department of the Army.
 Mr. L. J. Borges, Office of the Chief of Transportation, Department of the Army.
 Mr. W. A. Klikoff, Deputy Chief, Aircraft Engineering Division, Civil Aeronautics Administration.
 Mr. John M. Chamberlain, Director, Bureau of Safety Regulation, Civil Aeronautics Board.
 Honorable Joseph P. Adams (ex officio), Vice Chairman, Civil Aeronautics Board.

Mr. Melvin N. Gough, NACA Langley Aeronautical Laboratory.
 Mr. I. Irving Pinkel, NACA Lewis Flight Propulsion Laboratory.
 Mr. Carl M. Christenson, United Air Lines, Inc.
 Mr. Allen W. Dallas, Director, Engineering Division, Air Transport Association of America.
 Dr. Paul M. Fitts, Jr., Ohio State University.
 Mr. Scott Flower, Pan American World Airways, Inc.
 Mr. A. Howard Hasbrook, Director, Aviation Crash Injury Research of Cornell University.
 Mr. Otto E. Kirchner, Sr., Senior Group Engineer, Preliminary Design Unit, Boeing Airplane Co.
 Mr. Jerome Lederer, Director, Flight Safety Foundation.
 Dr. Ross A. McFarland, Harvard School of Public Health.
 Mr. William I. Stieglitz, Design Safety Engineer, Republic Aviation Corp.
 Mr. H. H. Young, Flight Safety Engineer, Douglas Aircraft Co., Inc.

Mr. Boyd C. Myers, II, Secretary.

Subcommittee on Aircraft Noise

Mr. William Littlewood, Vice President—Equipment Research, American Airlines, Inc., Chairman.
 Dr. H. O. Parrack, Wright Air Development Center.
 Capt. R. L. Christy, (MC) USN, Bureau of Aeronautics, Department of the Navy.
 Capt. C. P. Phoebus, (MC) USN, Office of Naval Research, Department of the Navy.
 Mr. Joseph Matulaitis, Office of the Chief of Transportation, Department of the Army.
 Mr. Stephen H. Rolle, Chief, Power Plant Branch, Civil Aeronautics Administration.
 Dr. Richard K. Cook, Chief, Sound Section, National Bureau of Standards.
 Mr. Macon C. Ellis, Jr., NACA Langley Aeronautical Laboratory.
 Mr. Arthur A. Regier, NACA Langley Aeronautical Laboratory.
 Mr. Newell D. Sanders, NACA Lewis Flight Propulsion Laboratory.

Dr. Richard H. Bolt, Massachusetts Institute of Technology.
 Mr. Allen W. Dallas, Director, Engineering Division, Air Transport Association of America.
 Dr. Robert O. Fehr, Manager, Mechanical Engineering Laboratory, General Electric Co.
 Dr. Stacy R. Guild, Johns Hopkins Hospital.
 Dr. Cyril M. Harris, Director, Acoustics Laboratory, Columbia University.
 Dr. Hans W. Liepmann, California Institute of Technology.
 Mr. Karl Martinez, Boeing Airplane Co.
 Mr. M. M. Miller, Chief, Acoustics Section, Douglas Aircraft Co., Inc.
 Dr. Charles T. Molloy, Lockheed Aircraft Corp.
 Mr. John M. Tyler, Pratt & Whitney Aircraft, United Aircraft Corp.
 Dr. P. J. Westervelt, Assistant Professor, Department of Physics, Brown University.
 Mr. John M. Whitmore, Allison Division, General Motors Corp.

Mr. George P. Bates, Jr., Secretary

INDUSTRY CONSULTING COMMITTEE

Mr. William Littlewood, Vice President—Equipment Research, American Airlines, Inc., Chairman.
 Mr. L. R. Grumman, Chairman of the Board, Grumman Aircraft Engineering Corp., Vice Chairman.
 Mr. J. L. Atwood, President, North American Aviation, Inc.
 Mr. J. H. Carmichael, President, Capital Airlines, Inc.
 Dr. M. P. Ferguson, President, Bendix Aviation Corp.
 Mr. Harvey Gaylord, Vice President—Helicopters, Bell Aircraft Corp.
 Mr. L. S. Hobbs, Vice Chairman, United Aircraft Corp.
 Mr. C. W. LaPierre, Executive Vice President, General Electric Co.
 Mr. Mundy I. Peale, President, Republic Aviation Corp.
 Mr. Dwane L. Wallace, President and General Manager, Cessna Aircraft Co.

Dr. T. L. K. Smull, Secretary

Part III—FINANCIAL REPORT

Funds appropriated for the Committee for the fiscal years 1956 and 1957 and obligations against the fiscal year 1956 appropriations are as follows:

	Fiscal year 1956		Fiscal year 1957
	Allotments	Obligations	Allotments
SALARIES AND EXPENSES APPROPRIATION			
NACA Headquarters.....	\$1, 557, 745	\$1, 541, 237	\$1, 624, 050
Langley Aeronautical Laboratory.....	22, 141, 400	22, 051, 384	23, 778, 100
Ames Aeronautical Laboratory.....	10, 929, 250	10, 850, 663	12, 978, 600
Lewis Flight Propulsion Laboratory.....	20, 237, 805	20, 200, 066	21, 591, 244
High-Speed Flight Station.....	1, 929, 695	1, 913, 134	2, 090, 950
Pilotless Aircraft Station.....	928, 500	908, 622	1, 095, 335
Western Coordination Office.....	23, 935	19, 979	32, 105
Wright-Patterson Liaison Office.....	15, 604	15, 439	16, 116
Research contracts with educational institutions.....	750, 300	750, 291	770, 000
Research contracts with Government agencies.....	198, 000	198, 000	200, 000
Savings reserved for reappropriation.....	1, 422, 766	1, 500, 000	-----
Unobligated balance.....	-----	186, 185	-----
Total.....	¹ 60, 135, 000	60, 135, 000	² 64, 176, 500
CONSTRUCTION AND EQUIPMENT APPROPRIATION			
Langley Aeronautical Laboratory.....	3, 325, 000	31, 741	7, 826, 000
Ames Aeronautical Laboratory.....	1, 055, 000	418, 898	906, 000
Lewis Flight Propulsion Laboratory.....	8, 395, 000	1, 796, 349	5, 712, 000
Pilotless Aircraft Station.....	90, 000	1, 595	-----
Reserve transferred from prior years.....	— 300, 000	— 32, 013	— 444, 000
Unobligated balance.....	-----	³ 10, 348, 430	-----
Total.....	¹ 12, 565, 000	12, 565, 000	² 14, 000, 000

¹ Appropriated in the Independent Offices Appropriation Act, 1956, approved June 30, 1955.

² Appropriated in the Independent Offices Appropriation Act, 1957, approved

June 27, 1956, and the First Supplemental Appropriation Act, 1957, approved July 27, 1956. Includes \$1,500,000 reappropriation of fiscal year 1956 funds.

³ This balance remains available until expended.

REPORT 1254

CONTENTS

	Page
SUMMARY.....	93
INTRODUCTION.....	93
THEORY.....	93
APPARATUS AND PROCEDURE.....	94
Apparatus.....	94
Materials and Procedure.....	95
RESULTS AND DISCUSSION.....	95
Clean Steel on Clean Steel.....	95
Naturally Formed Surface Films.....	96
Iron oxide films.....	96
Miscellaneous films.....	98
Nickel oxide films.....	99
Lacquer or varnish films.....	99
Preformed Films.....	99
Iron oxide films.....	99
Chlorides and sulfides.....	100
Metallic soaps.....	101
Solid lubricants.....	101
Nickel oxide.....	102
Lacquers or varnishes.....	102
Platings.....	103
Other Methods of Lubrication by Solids.....	103
Bonding of solid lubricants.....	103
MoS ₂ as a solid lubricant.....	104
Other solids as lubricants.....	106
SUMMARY OF RESULTS.....	107
APPENDIXES	
A—ADHESION THEORY OF FRICTION.....	108
B—FILM PREPARATION.....	108
REFERENCES.....	110
TABLE I.—PHYSICAL AND CHEMICAL PROPERTIES OF SOLID LUBRICANTS.....	111

REPORT 1254

FRICTION, WEAR, AND SURFACE DAMAGE OF METALS AS AFFECTED BY SOLID SURFACE FILMS¹

By EDMOND E. BISSON, ROBERT L. JOHNSON, MAX A. SWIKERT, and DOUGLAS GODFREY

SUMMARY

As predicted by friction theory, experiments showed that friction and surface damage of metals can be reduced by solid surface films. The ability of materials to form surface films that prevent welding was a very important factor in wear of dry and boundary lubricated surfaces. Films of graphitic carbon on cast irons, NiO on nickel alloys, and FeO and Fe₃O₄ on ferrous materials were found to be beneficial. Abrasive films such as Fe₂O₃ or MoO₃ were definitely detrimental. It appears that the importance of oxide films to friction and wear processes has not been fully appreciated.

The chemical reaction films FeS and FeCl₂ were both effective in the prevention of surface welding. Because of its lower shear strength, FeCl₂ was more effective than FeS in reducing friction.

Solid lubricants such as molybdenum disulfide and graphite warrant careful consideration for use under severe conditions such as high temperatures. Surface films of those materials were found to have beneficial results in friction studies at high loads and high sliding velocities. Bonding mechanism studies showed that both MoS₂ and graphite can be bonded to many surfaces by use of a resin-forming liquid. Rolling contact bearing experiments showed that effective lubrication could be maintained at temperatures of 1000° F by injection of minute amounts (0.001 lb/min) of these solids. In the presence of oxygen, MoS₂ oxidizes to MoO₃ at a very low rate at 750° F, the process becoming rapid at temperatures above 1050° F.

INTRODUCTION

This paper is based on NACA research data obtained during a series of investigations in the field of lubrication, friction, and wear conducted from 1946 to 1954. Each investigation in the series had specific objectives, but all were directed toward determination of the role of surface films in friction and wear.

As is well known, the presence of a contaminating film between sliding surfaces can have a marked effect on friction, wear, and surface damage. (A contaminant is defined as any material other than those comprising the sliding surfaces.) Some contaminants are beneficial (lubricants), while others are detrimental (abrasives). Considerable evidence (refs. 1 to 8) indicates the importance of solid surface films to the compatibility of sliding surfaces. Physical and chemical surface changes have been associated with satisfactory and with unsatisfactory operation of metallic sliding

surfaces (ref. 2). As an example, "run-in" has long been known to be effective in improving the performance and the load-carrying capacity of surfaces. Among the factors that lead to satisfactory performance are the formation and maintenance of certain beneficent solid surface films.

Such solid films are commonly formed on sliding surfaces by use of extreme-pressure additives in lubricants; chemical films of low shear strength or of low melting point are formed by reaction between additives and the sliding surfaces under conditions of extreme pressure and temperature. Theories for the mechanism of extreme pressure lubrication are discussed in references 3 and 8.

A complete study of the mechanism of action of solid surface films and their effect on friction and surface damage to sliding surfaces encompasses a large number of factors. Some of the fundamental factors are discussed in the THEORY section of this report; factors that are important in the use of solid films have been studied experimentally, and the results obtained are presented herein.

The purpose of this report is to show the relation of surface films to the friction, wear, and surface damage of sliding metals. Study of the role of surface films requires consideration of how the film is formed. The film may be (1) formed naturally, (2) preformed, or (3) formed by other methods having practical value.

A modified version of this paper was submitted by E. E. Bisson to the University of Florida, College of Engineering, as a thesis in partial fulfillment of the requirements for the professional degree of Mechanical Engineer, May, 1954.

THEORY

Analysis of the effects of solid surface films should include a review of the generally accepted theory of dry friction. This theory predicates adhesion between contacting surfaces. (It is of interest to note that, as early as 1785, Coulomb (ref. 9) recognized that "cohesion" between solids was a factor, although he believed "cohesion" contributed a relatively small part of the total friction force.) The adhesion theory of friction (appendix A) was independently advanced by Merchant in this country (ref. 10) and by Bowden and Tabor in England (ref. 8) at about the same time (1940 to 1942).

The adhesion theory of friction predicates the contact of surfaces through asperities; this theory proposes that friction force is equal to the sum of two terms: a shear term and a ploughing or a roughness term. Since the contact of surfaces

¹ Supersedes NACA TN 3444, "Friction, Wear, and Surface Damage of Metals as Affected by Solid Surface Films," by Edmond E. Bisson, Robert L. Johnson, Max A. Swikert, and Douglas Godfrey, 1955.

is through surface asperities, it has been postulated (ref. 8) that plastic flow occurs at the points of contact until the real contact area A is great enough to support the load. The area A then equals W/p , where W is load and p is flow pressure (yield strength in compression). The initial surface contact stress under these conditions is not a low value, but is equal to the flow pressure. Pressure welding occurs at these highly stressed contact points, and the welded junctions must shear before relative motion can take place. The force required to shear them is one of the components of the friction force, generally called the "shear" term.

Appendix A shows the development of the equations expressing the adhesion theory by Bowden and Tabor and by Merchant. Under certain conditions (as when the surfaces are quite clean), the shear term may be the more important of the two, and the second term may be neglected. In appendix A, surface contact pressure is represented by Bowden and Tabor as the symbol p for flow pressure and by Merchant as the symbol H for pressure surface hardness. These two pressures are the same.

For cases in which the ploughing term is negligible, coefficient of friction μ (defined as ratio of friction force to applied load) is shown (appendix A) to be equal to the ratio of shear strength to flow pressure, that is, $\mu = s/p$. Reduction in friction coefficient for this case therefore depends on reduction in the value of ratio of shear strength to yield strength. The ratio can be reduced by: (1) decreasing shear strength, (2) increasing yield strength, or (3) a combination of (1) and (2). Obtaining both conditions in one material is practically impossible because those materials with low shear strength have low yield strength and vice versa. However, by the use of low-shear-strength films (with thicknesses as small as millionths of an inch) on hard base materials, both desirable conditions may be obtained (ref. 8, p. 112). Thus, low shear strength is obtained without appreciable decrease of the yield strength of the combination. The load will thus be sup-

ported through the film by the hard base material, while shearing occurs within the soft thin film. These low-shear-strength films can be of the following types: chemical reaction products (oxides, chlorides, sulfides), metals, fluid lubricants, and so forth.

Among the properties other than shear strength, flow pressure, and hardness that are important in the action of solid films are: crystalline structure and orientation, chemical composition, chemical activity, and adsorption.

An important function of surface films (frequently neglected in analyses of their action) is to act as a contaminant for the reduction of welding or adhesion between rubbing surfaces; contaminants reduce welding by reducing contact of clean metal to clean metal. The better the bond between film and surface, the greater the resistance to rupture of the film, and, consequently, the greater the protection from welding.

The discussion of this section shows that the basic requirement for reduction of friction, wear, and surface damage of sliding surfaces is the presence of a low-shear-strength contaminant. This contaminant serves two functions, either or both of which may be influential: (1) to reduce the amount of welding at the surface asperities, and (2) to decrease the shear force. In order to carry out the second function, the contaminant must be a material of lower shear strength than the softer of the two materials which are sliding one against the other (appendix A).

APPARATUS AND PROCEDURE

APPARATUS

In the investigations reported, five different pieces of apparatus were used. These are identified as A, B, C, D, and E; general descriptions of them are given in the following paragraphs, and detailed descriptions in the references noted. Data presented in this report are identified in the various figures according to the apparatus used.

Apparatus A; for kinetic friction (ref. 11).—Most of the

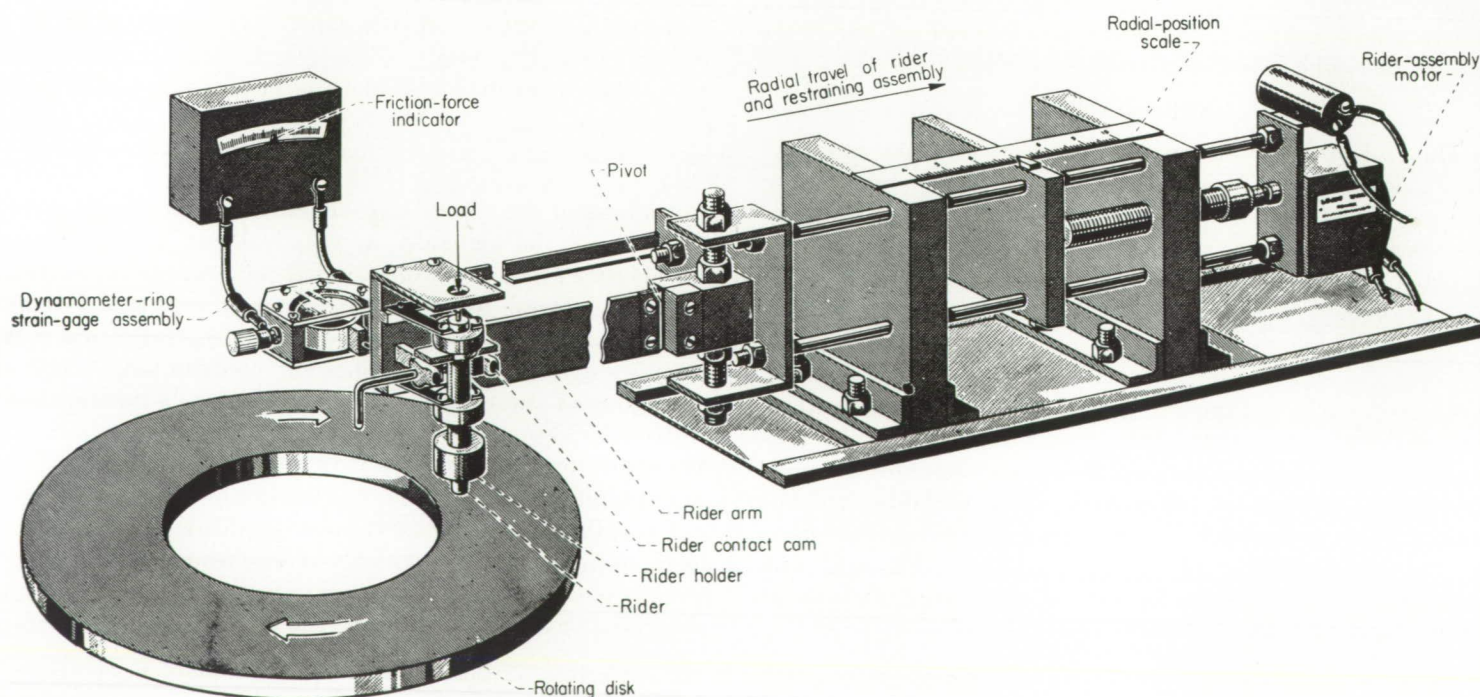


FIGURE 1.—Kinetic-friction apparatus; apparatus A (ref. 11).

experimental friction and wear studies were conducted with the kinetic friction apparatus shown in figure 1. The principal elements of the apparatus are the specimens, which are an elastically restrained spherical rider (either $\frac{1}{8}$ - or $\frac{1}{16}$ -in. radius) and a rotating disk 13 inches in diameter. The rider is loaded by a weight applied along its vertical axis. Friction force between the rider and the disk is measured by four strain gages mounted on a beryllium-copper dynamometer ring. The coefficient of friction is computed by dividing the measured friction force by the applied normal load: $\mu = F/W$. A radial-feed mechanism, when operating, causes the rider to traverse a spiral track on the rotating disk; the rider then slides on virgin surface of the disk. Where solid surface films were investigated, they were usually applied to the disk specimen before testing.

Apparatus B; for kinetic friction (ref. 12).—In some of the endurance runs to check the wear or life of bonded films, an apparatus similar in principle to apparatus A was used. It differs from apparatus A in that no radial traverse takes place; the rider thus slides in the same wear track on the disk specimen at all times. It is a modification of the apparatus described in detail in reference 12. The spherical rider specimens have a radius of $\frac{3}{16}$ inch and the disk specimens are $2\frac{1}{2}$ inches in diameter.

Apparatus C; for static friction (ref. 13).—The principal elements of the static-friction apparatus are a rider assembly, in which three $\frac{1}{4}$ -inch steel balls are rigidly clamped, and a stationary horizontal plate on which the rider assembly is supported by the balls. The applied load was distributed equally among the three balls, and the rider assembly was moved over the plate by application of a horizontal tugging force. Friction-force measurements were made with strain gages mounted on a beryllium-copper dynamometer ring between the tugging force and the rider assembly. Force was applied slowly, elastically extending the dynamometer ring until the force was great enough to overcome static friction and slip of the carriage occurred. Initial slip of the rider assembly was determined by observation through a telescope equipped with cross hairs. When motion was observed, an indicating mark was made on the time-force record of the potentiometer chart.

Apparatus D; for reciprocating sliding (ref. 2).—Some of the earlier studies of naturally forming surface films were made with a reciprocating slider mechanism. It applied normal load to two contacting surfaces, and slowly reciprocated one of the surfaces.

Apparatus E; for kinetic friction (ref. 14).—Experiments on solid lubricants, used in loose powder form, were conducted on an apparatus similar in principle to apparatus A. A ring with three equally spaced axial nodes was used as the rider specimen. The nodes were ground with a cylindrical face of 2-inch radius, parallel to the ring radius, so that in theory, line contact existed between each of the three sliding nodes and the disk. The rider specimens were of SAE 4620 steel, case hardened to Rockwell C-62. The disk specimens were of SAE 1020 steel.

MATERIALS AND PROCEDURE

Most of the studies have been made with both specimens of steel, with the films under study applied to the disk

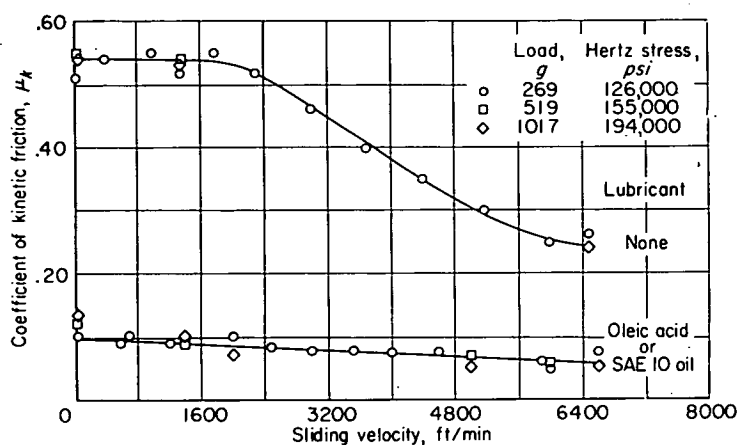


FIGURE 2.—Friction at high sliding velocities of steel on steel (ref. 11). Apparatus A; radius of spherical rider specimen, $\frac{1}{8}$ inch.

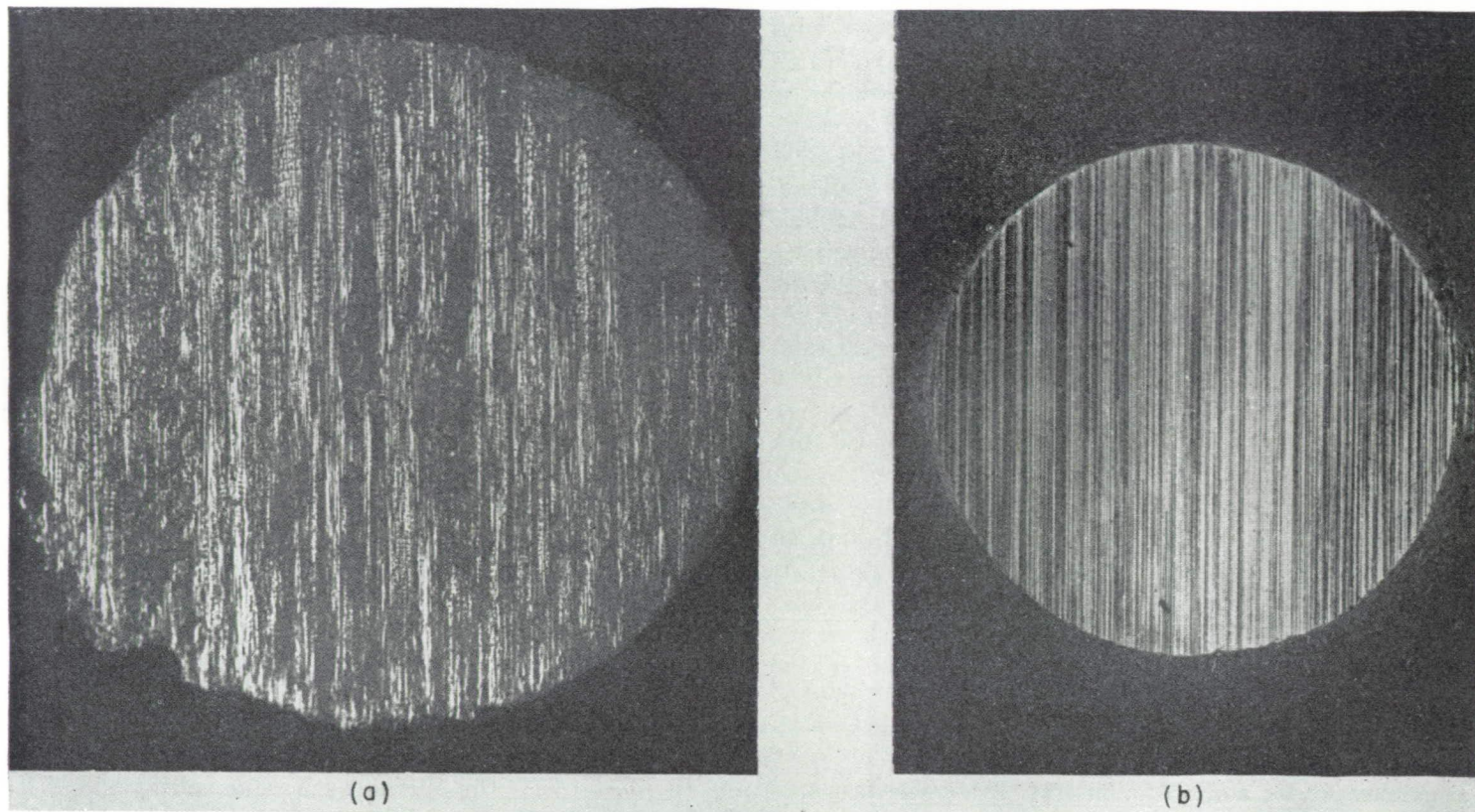
specimen. Some studies were made with a nonferrous alloy, such as one of the various nickel or copper alloys, as the spherically tipped ($\frac{1}{16}$ -in. radius) rider specimen. Solid films investigated included various oxides, sulfides, and chlorides of iron, as well as materials such as molybdenum disulfide and graphite. Formation of various preformed films is described in detail in appendix B.

In most cases, the specimens were a sphere and a flat surface so as to enable calculation of both initial contact area and initial contact stress by the Hertz equations. The friction data presented are typical of data obtained in many runs. The limits of experimental error in the friction values presented were not uniform among all experiments because of the difficulties in maintaining absolute control of film thickness. In all but isolated cases, however, the maximum experimental error in friction coefficient, based on reproducibility, was ± 0.03 . In most cases, it was considerably less than 0.03. For comparative purposes, a load of 269 grams was used in obtaining most of the data presented. This load produces an initial Hertz surface stress (126,000 psi) that is in the range of contact stresses commonly present in aircraft engine components that require lubrication. According to reference 15, this stress is within the range of normal stresses (69,000 to 282,000 psi) for turbine-engine rolling contact bearings. At the same time, surfaces in contact under relatively light load and having a large apparent area of contact can have high stresses at localized contact areas (the contacting asperities). Even with lightly loaded surfaces, local pressure at these small points of contact is equal to the flow pressure of the materials (ref. 8) and causes plastic flow at these points.

RESULTS AND DISCUSSION

CLEAN STEEL ON CLEAN STEEL

For steel-on-steel surfaces cleaned by outgassing at 1000°C in vacuum, friction coefficients in vacuum as high as 3.5 have been measured (ref. 16). These surfaces were considered to be free of ordinary contaminants and most of the oxides. For steel-on-steel surfaces cleaned in air by the method presented in appendix B, maximum friction coefficient in air is 0.54 (fig. 2). The surfaces operating with a friction coefficient of 0.54 were known to have a film of Fe_3O_4 approxi-



(a) Clean and dry. (b) Effective boundary lubrication.

FIGURE 3.—Surfaces of rider specimens after tests of figure 2.

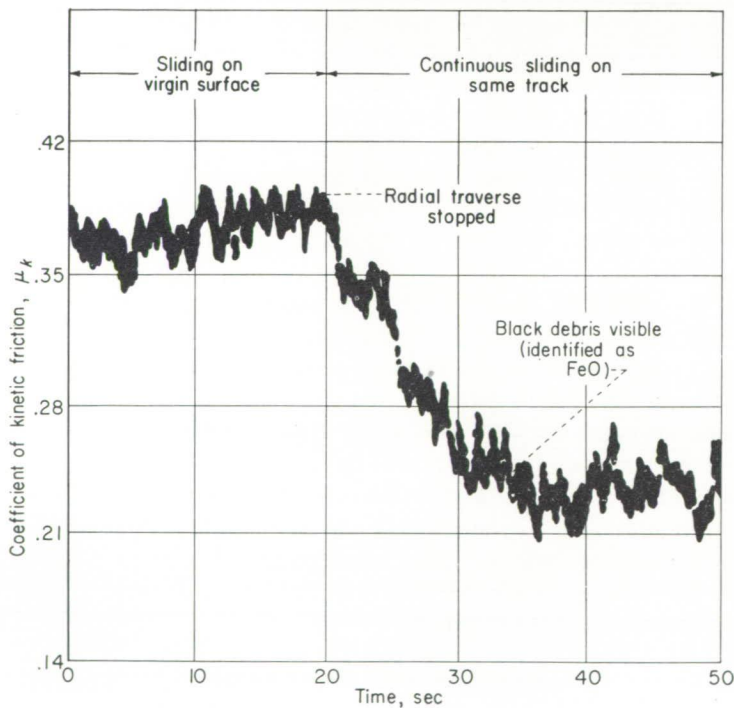


FIGURE 4.—Recording potentiometer tracing showing effect of high-velocity sliding over a continuous path (without radial traverse) on coefficient of kinetic friction. Black wear debris (ferrous oxide FeO) was visible at beginning of lower stable friction value (ref. 11). Apparatus A; unlubricated steel; load, 269 grams; sliding velocity, 4000 feet per minute; radius of spherical rider specimen, $\frac{1}{8}$ inch.

mately 25 Å thick (about 10^{-7} in.) (refs. 17 and 18). As sliding velocity is increased, friction coefficient is relatively constant at a value of 0.54 up to about 1600 feet per min-

ute; above this value, a downward trend can be observed. For steel-on-steel surfaces lubricated with either oleic acid or SAE 10 lubricant, friction coefficient was approximately 0.10 at minimum sliding velocity, decreasing to 0.06 at 6600 feet per minute (fig. 2). For these results (discussed in more detail in ref. 11) the classical laws of friction are confirmed: friction coefficient is essentially independent of load and, at the lower speeds, is independent of sliding velocity.

Surface appearance of the ball specimens from the dry and the lubricated runs of figure 2 is shown in figure 3. The photomicrographs show that surface failure by welding occurred with the dry specimen; no surface failure (welding) is evident for the lubricated specimens but ploughing is apparent. The welding for dry steel was extensive, resulting in appreciable "tearing-out" and metal transfer.

NATURALLY FORMED SURFACE FILMS

Iron oxide films.—In figure 2, the downward trend of friction coefficient for the dry steel specimens at the higher sliding velocities is not considered a violation of one of the classical friction laws (friction is independent of velocity); rather, it is considered the result of other variables entering into the mechanism. The downward trend is considered primarily a result of formation of beneficial iron oxide films of appreciable thickness; formation of oxide films would be accelerated at higher sliding velocities because of higher rate of heat generation at the sliding surfaces resulting from the greater release of frictional energy. In partial confirmation of this concept, when the steel slider was permitted to traverse the same wear track on the disk (fig. 4), FeO was identified (by X-ray diffraction) as the chief constituent in

the wear debris; there was a coincident reduction in friction coefficient from 0.38 to 0.24. It is reasonable to assume that the FeO film was being formed at all times; during the 30-second traverse of the same track on the disk, the film attained a thickness such that it became visible to the unaided eye. The gradual decrease in friction coefficient could be the result of the gradual increase in film thickness. Inasmuch as film thickness growth is limited by wear and rupture, friction coefficient would be expected to reach a stable value as film thickness stabilizes. No measurement of the film thickness could be made under the dynamic conditions; the appearance of the wear track was, however, somewhat similar to wear tracks produced on prepared oxide films approximately 1000 Å thick.

It is hypothesized that, under sliding conditions of variable severity for specimens of steel on steel, surface oxides form in the order FeO to Fe_3O_4 to Fe_2O_3 . Considerable confirming evidence (refs. 2, 4, 5, 16, 19, and 20) shows the importance of oxides in the reduction of friction, wear, and surface damage of sliding surfaces. On most run-in surfaces, oxides have been identified (refs. 2, 19, and 20). Figure 5, based on references 2 and 19 shows (qualitatively only) the estimated amounts of Fe_3O_4 and Fe_2O_3 present after various degrees of run-in. As shown, the amount of Fe_3O_4 increases to a maximum for the "fully run-in" condition; after further operation at higher load, less Fe_3O_4 is present. On the other hand, Fe_2O_3 shows a slight increase with degree of run-in to the "fully run-in" point, after which a marked increase in Fe_2O_3 is observed with failure of the surfaces. The surface films were identified by X-ray diffraction. In reference 19, it is shown that, at the minimum wear rate (which is usually associated with attainment of a "well run-in" condition), the amount of Fe_3O_4 is large; at the maximum wear rate (implying incipient surface failure), the amount of Fe_3O_4 is lower and the amount of Fe_2O_3 is larger than at the minimum wear rate. These data may also show why there has been considerable controversy in published literature about whether oxides of iron are good or bad from considerations of friction and wear. This controversy was an incentive for the NACA to obtain fundamental information on the specific oxides of iron: Fe_3O_4 and Fe_2O_3 .

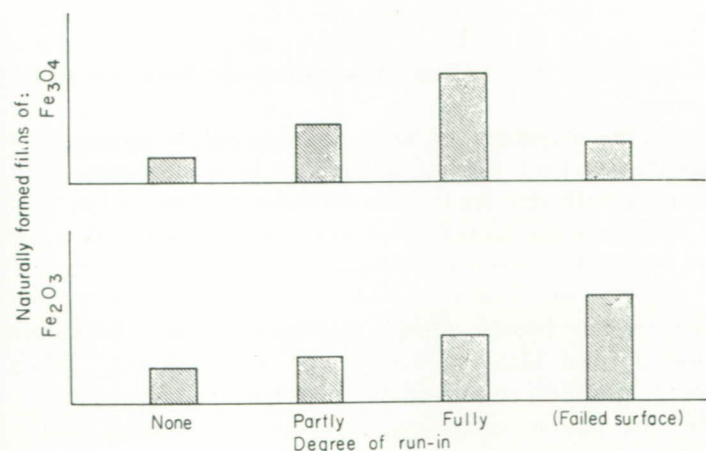


FIGURE 5.—Effect of run-in on formation of natural films of Fe_3O_4 and Fe_2O_3 . Data are qualitative and are estimated from X-ray diffraction results of reference 2 (apparatus D) and from reference 19.

In agreement with the implications of figure 5, Finch (ref. 20) states that iron oxide layers are detected on most run-in surfaces. He indicates (as does Campbell, ref. 6) that oxides play a part in the mechanism of friction by affecting the ratio of welded to unwelded area. He also indicates that injurious oxides can be formed by excessive loading. This point is confirmed in the data of figure 5, which show that the oxide film Fe_2O_3 appears on the surface under "surface failure" conditions.

Recent experiments on the influence of adsorbed films were conducted by Bowden and Young (ref. 16). Their experiments showed the very marked effect of oxygen in reducing friction for iron-iron combinations that had been thoroughly outgassed at 1000°C in vacuum (10^{-6} mm Hg). The surfaces used had a coefficient of friction of 0.4 before outgassing. Removal of contaminating films, including the oxides, increased coefficient of friction to 3.5, and led to complete seizure under certain conditions. Admission of oxygen to the vacuum chamber reduced friction coefficient from 3.5 to 1.2; with oxygen present, complete seizure no longer occurred.

Data of reference 21 show that exclusion of oxygen from clean specimens by use of a "blanketing" medium, such as highly purified cetane for steel-on-steel specimens, produces a high friction coefficient; these data are shown in figure 6. As sliding velocity increases above 2000 feet per minute, friction coefficient shows a downward trend for the dry specimens, but shows a very marked upward trend for similar specimens immersed in cetane, reaching a value greater than 1.0. The increase in friction is probably due to the absence of the beneficial oxide films; their formation would be prevented by the cetane, which excludes oxygen. Figure 6 shows that at low sliding velocities friction coefficient is lower for specimens with cetane than for dry specimens; the cetane may act as a contaminant between the surfaces. This beneficial effect might be expected to be greater at low than at high sliding velocities because of lower surface temperatures. Similar results on the action of benzene as a "blanketing" medium in metal cutting experiments are reported by Ernst and Merchant (ref. 22); they found that

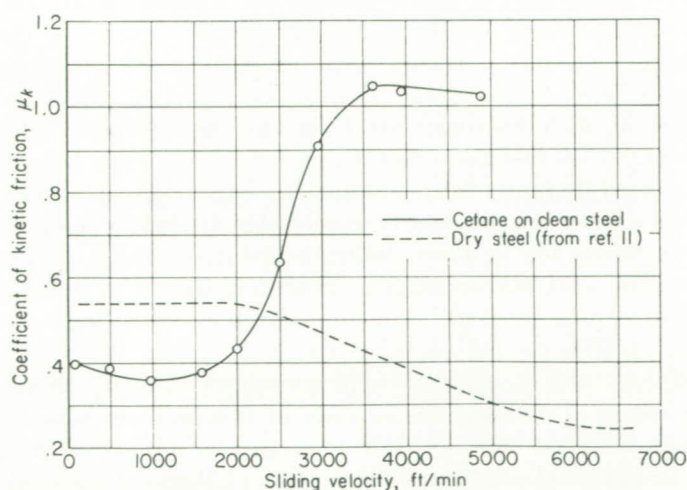


FIGURE 6.—Data showing effect of cetane as blanketing medium (to restrict availability of oxygen to specimen surfaces) on friction of steel against steel (ref. 21). Apparatus A; load, 269 grams; radius of spherical rider specimen, $\frac{1}{8}$ inch.

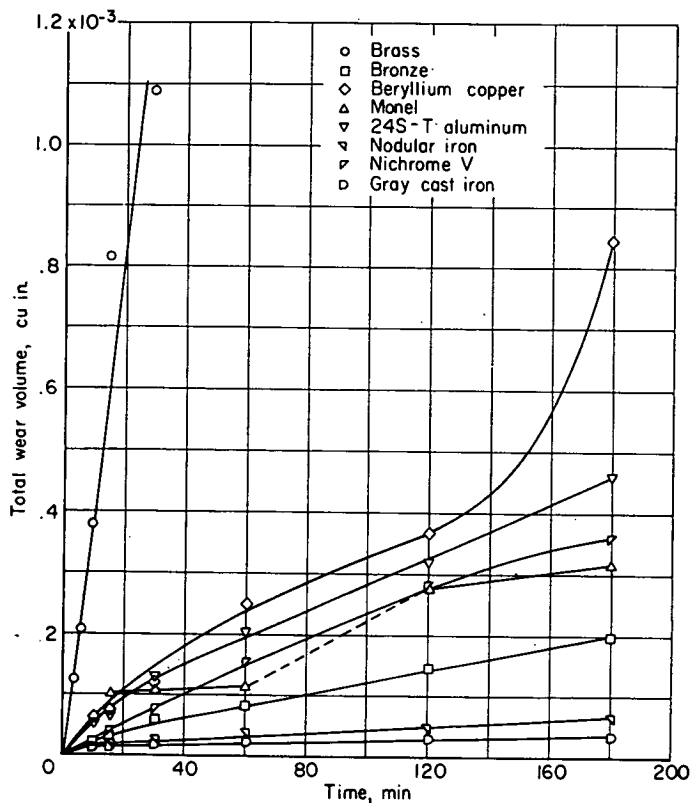


FIGURE 7.—Wear of several materials sliding against hardened SAE 52100 steel without lubricant (ref. 23). Apparatus A; sliding velocity, 5000 feet per minute; load, 50 grams; radius of spherical rider specimen, $\frac{3}{16}$ inch.

friction coefficient was increased in the presence of benzene and decreased in its absence.

Thus, there is considerable evidence indicating the fundamental and important effect of oxides on the friction and surface damage of sliding metals. Not all oxides, however, are beneficial; detrimental oxide films can be produced under certain conditions (refs. 2 and 20). Additional discussion of the effect of specific oxides is given in the section Preformed Films.

Miscellaneous films.—In some practical applications, surface films have a marked effect on friction, wear, and damage of sliding surfaces (refs. 23 to 25). Most of the bearings employed in turbine-type aircraft engines are rolling contact bearings (ref. 23). One of the principal sources of failure in such bearings has been the cage (separator or retainer). As discussed in reference 23, most cage failures are caused by faulty lubrication at the cage-locating surface. This location is particularly susceptible to failure because the surfaces are in pure sliding at relatively high sliding velocities; also, the configuration is such that it is difficult to maintain a lubricant film between the sliding surfaces. These conditions reduce lubrication to extreme boundary conditions, and excessive metallic adhesion frequently occurs. One means of reducing the severity of this problem is use of a cage material that has less tendency to adhere to steel (under marginal conditions of lubrication) than the materials in current use. The NACA approach was to study the friction and wear properties of various materials, both dry and lubricated; the results were analyzed to determine the film-forming properties of the several materials. The studies

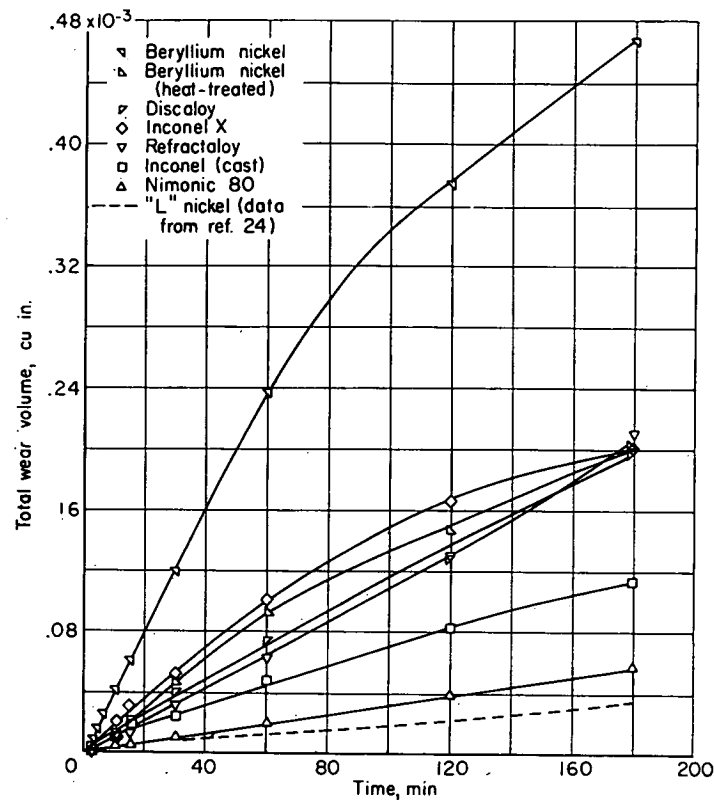


FIGURE 8.—Wear of several materials sliding against hardened SAE 52100 steel without lubricant (ref. 25). Apparatus A; sliding velocity, 5000 feet per minute; load, 50 grams; radius of spherical rider specimen, $\frac{3}{16}$ inch.

of reference 1 show that the mechanism of lubrication prevailing in bearing materials containing low-shear-strength components and in cast iron containing graphite involves the smearing of the low-shear-strength phase over a hard matrix.

Results of the NACA study of cage materials are described in detail in reference 23. The investigation covered the sliding against SAE 52100 of materials such as bronze (containing 7.5 percent lead), beryllium copper, Nichrome V, nodular iron, and gray cast iron. Figure 7 shows some of the wear data obtained at a sliding velocity of 5000 feet per minute and a load of 50 grams. (For these experiments, the rider specimen, $\frac{3}{16}$ -in. radius, was of the various materials and the disk specimen was of SAE 52100 steel hardened to Rockwell C-60. Size of the wear spot on the rider was measured, and wear volume was calculated from this measurement.)

From this investigation, ability of materials to form surface films that prevent welding appears to be a most important factor in both dry friction and boundary lubrication (ref. 23). The surface films formed were derived from within the structure of the various materials (e. g., graphitic carbon in the cast iron and lead in the bronze). Under both dry and lubricated conditions, monel, Nichrome V, and beryllium copper formed films believed to be nickel oxides. When present, the films improved the performance of these materials. In this investigation, the films apparently had a greater effect on reduction of surface damage and of wear than on reduction of friction. The friction coefficient with the best materials of this investigation, the cast irons, was relatively high (approximately 0.5).

Nickel oxide films.—References 24 and 25 report an investigation of the wear and sliding friction properties of nickel alloys operated against various steels. Several monel metal alloys and other nickel alloys that have good high-temperature physical properties (such as Inconel and Nimonic 80) were investigated. As in the studies of reference 23, it was found that desirable performance characteristics and absence of extreme mass welding of all the materials studied could be associated with the development on the sliding surfaces of a naturally formed film. The film was identified as nickel oxide NiO by X-ray diffraction. Wear data for some of these alloys at a sliding velocity of 5000 feet per minute and a load of 50 grams are shown in figure 8 (note that the wear scale for figs. 7 and 8 are different). On the basis of wear and friction properties, cast Inconel performed very well in these experiments and compares favorably with nodular iron (which proved better than bronze, ref. 23). Nimonic 80 also showed promise as a possible cage material. Both of these nickel alloys have considerably better high-temperature properties than does nodular iron.

Other studies showing the important effect on wear of nickel oxide are described in the section Preformed Films.

Wear and friction experiments were conducted with some of the cage materials, listed in figures 7 and 8, sliding against disks of tool steels (molybdenum and tungsten types). The wear and friction results showed trends similar to those for tests against 52100 disks (figs. 7 and 8).

Lacquer or varnish films.—With reciprocating engines, good wear performance of piston ring—cylinder barrel combinations has been associated with formation of a very thin lacquer or varnish film on the surfaces. It has also been shown (ref. 26) that, for a journal bearing employing a lubricant of relatively poor lubricating ability or "film strength" (a silicone), formation of a lacquer film provides a margin of safety and increases the load-carrying capacity of the bearing.

The aircraft turbine engine is generally characterized by high operating temperatures; these high temperatures accelerate the process of oxidation, polymerization, and decomposition of the lubricant. These processes of degradation of lubricant result in formation of lacquer films on hot surfaces such as bearings. Because these films are naturally occurring, a fundamental evaluation of the role of such films in friction and surface damage would be worth while. Their influence on surface damage is particularly important in the case of the aircraft gas-turbine engine, which has a bearing or bearings operating dry for a short time after start of the engine. This condition is the result of the "high-temperature soak-back" of the turbine bearing after shutdown of the engine (refs. 27 and 28). Since the flow of coolant (lubricant) stops with shutdown, the bearing temperature increases because of the large reservoir of heat in adjacent large metal masses (such as the turbine wheel, immediately adjacent to the turbine bearing). Both Hunt (ref. 27) and Gurney (discussion, ref. 28) show that bearing temperatures on the order of 500°F prevail under the soak-back condition. When the engine is restarted after a period of shutdown, the bearings operate without lubricant

for a short time until lubricant flow is established. During this initial period, the bearing parts (including the cage) are operating under conditions of dry friction. Because the cage has been a principal source of bearing failures and these cage failures have been established as lubrication failures (ref. 28), a study was made of the friction and surface-damage characteristics of films formed on steel surfaces by decomposition of several types of lubricant. These results are reported in the following section under **Lacquers or varnishes**.

PREFORMED FILMS

Studies were made of a number of preformed solid surface films of the type formed: (1) naturally (as in the case of oxides), (2) by chemical reaction of surfaces with chemically active additives (extreme pressure lubricant additives), or (3) from solid lubricants (such as molybdenum disulfide and graphite) that function as supplemental lubricants (ref. 29). Formation of the various preformed films is described in detail in appendix B.

Iron oxide films.—Because of the importance of iron oxides, data were obtained on films (1200 Å thick) of the specific oxides Fe_3O_4 and Fe_2O_3 . These data, shown in figure 9, are from reference 30. The friction coefficients, as well as visual examination of the surfaces, show that Fe_3O_4 can be quite beneficial in decreasing friction and in preventing surface damage. In comparison, Fe_2O_3 showed high friction and excessive welding and surface damage. Figure 10 shows a comparison of the rider specimens after investigation; surface protection was much better with the Fe_3O_4 , which largely prevented surface welding and metal transfer.

Confirming evidence of the importance of the specific iron oxide is available in references 31 and 32. Fretting (fretting corrosion) is a concentrated and severe form of wear. With specimens of steel against glass (ref. 31), the first wear particles produced during fretting were extremely small and apparently virgin material. These particles oxidized when exposed to air. Visual observations (ref. 31) showed color changes that suggested successive oxidation of

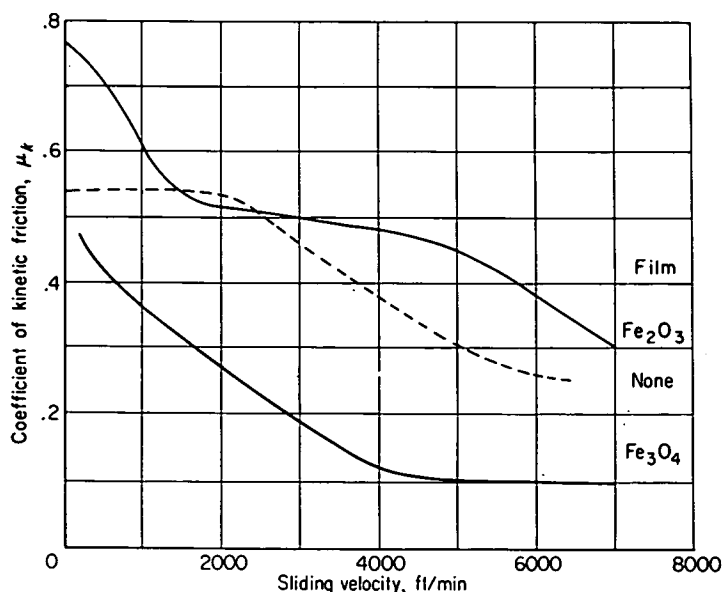
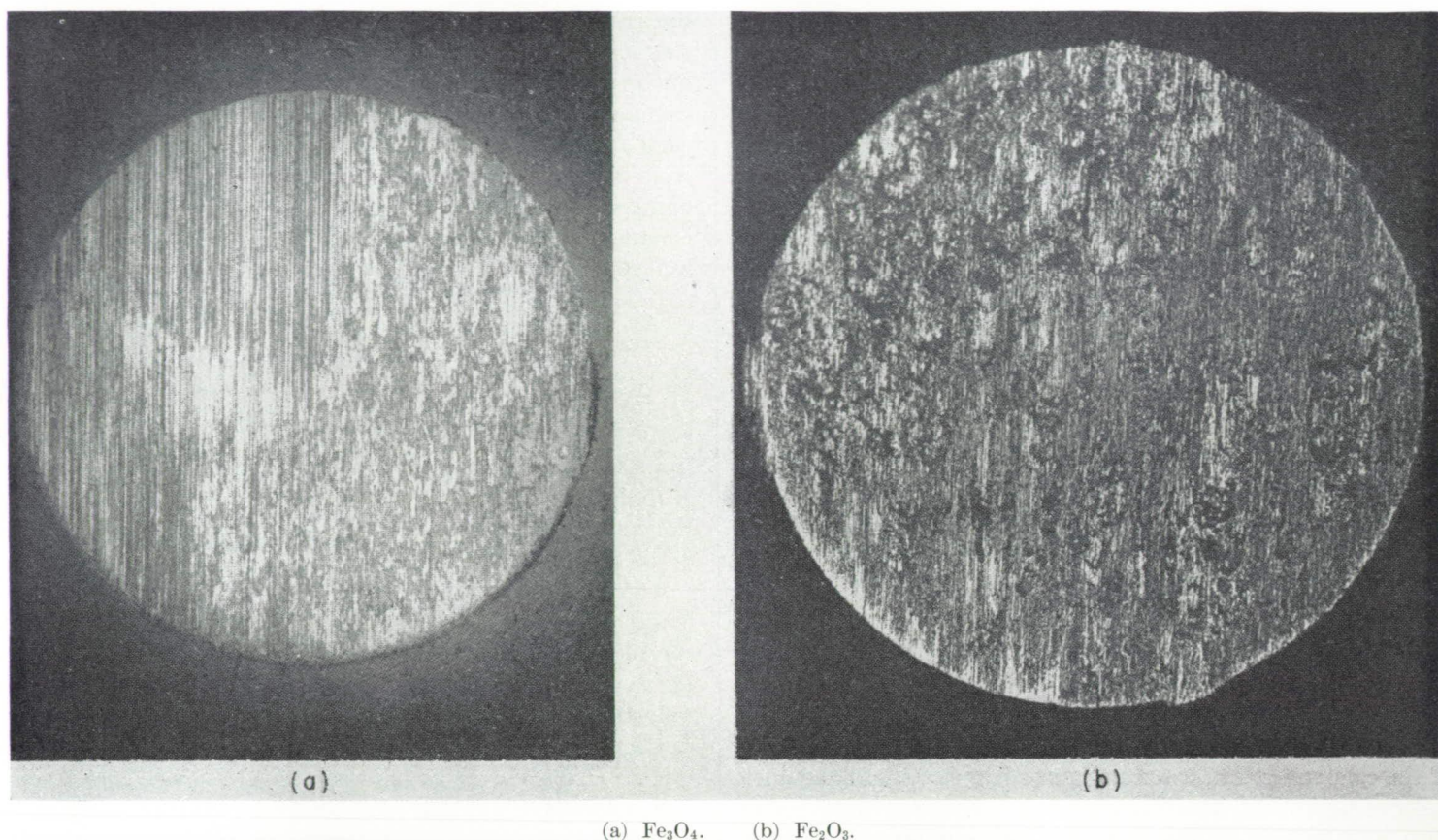


FIGURE 9.—Friction at high sliding velocities of dry unlubricated steel against steel with no film and with preformed films of Fe_3O_4 and Fe_2O_3 approximately 1200 Å thick (ref. 30). Apparatus A; radius of spherical specimen, $\frac{1}{8}$ inch.



(a) Fe_3O_4 . (b) Fe_2O_3 .
 FIGURE 10.—Surfaces of rider specimens after tests of figure 9.

Fe to FeO, to Fe_3O_4 , and finally to Fe_2O_3 , which is hard and highly abrasive. Friction coefficient of powdered Fe_2O_3 compacts reciprocated against each other was relatively constant (after a few hundred cycles) at a value of approximately 0.5 (ref. 32). The friction coefficient of steel on steel (0.6) was not too different from that with the Fe_2O_3 compacts. With powdered Fe_3O_4 compacts reciprocating against each other, friction coefficient was at first low (0.3), but gradually increased until, at 600 cycles, the value was 0.5, the same as that for the Fe_2O_3 compacts. Examination and chemical analysis of the debris on the surface of the Fe_3O_4 compacts showed that Fe_2O_3 was present. Thus the fretting in all three cases, (1) steel on steel; (2) Fe_2O_3 on Fe_2O_3 ; and (3) Fe_3O_4 on Fe_3O_4 , was, after a number of cycles, essentially that of Fe_2O_3 against Fe_2O_3 as suggested by the measured values of friction coefficient.

These data, as well as the data on naturally occurring iron oxide films previously discussed, emphasize the importance of iron oxide films to friction, wear, and surface damage. Effective lubrication under conditions of extreme boundary lubrication (where metal-to-metal contact takes place) is very often a function of the *nature* of the oxide films present. When surfaces are lubricated with fatty acids, oxide films may also contribute to the formation of metallic soap films at the surface. This point is developed in the section **Metallic soaps**.

Chlorides and sulfides.—The mechanism of the action of extreme pressure lubricants is considered to be one of chemical reaction between active additives and the metal surfaces. Compounds of chlorine, sulfur, or phosphorous are formed, depending upon the type of additive used.

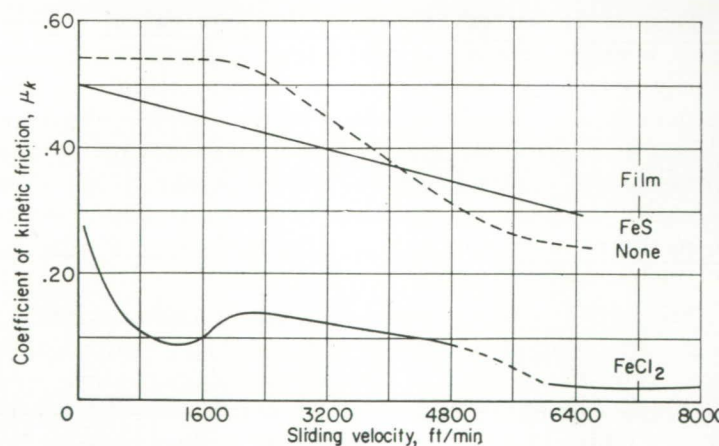


FIGURE 11.—Friction at high sliding velocities of steel against steel with no film and with preformed films of FeCl_2 and FeS approximately 1000 Å thick (ref. 30). Apparatus A; radius of spherical rider specimen, $\frac{1}{8}$ inch.

Results of an investigation (ref. 30) on preformed chloride and sulfide films approximately 1000 Å thick are shown in figure 11. Visual examination of the surfaces showed that both FeS and FeCl_2 are effective in preventing excessive surface damage; FeCl_2 is much more effective than FeS in reducing friction. The difference in friction coefficient corresponds to the difference in shear strengths of the two compounds. If the reaction products from extreme-pressure lubricant additives of the chlorine and sulfur types are primarily FeCl_2 and FeS , respectively, the effectiveness of the additive containing chlorine should be appreciably superior. The superiority of chloride films over sulfide films

is confirmed by Bowden and Tabor (ref. 8), who found similar differences in friction coefficient.

Effectiveness of sulfide films in reducing friction has been shown to be very much a function of film thickness (refs. 6 and 13). Campbell shows that, on copper, friction coefficient decreases as sulfide film thickness increases up to about 1000 Å. Results obtained by Greenhill (ref. 33) indicate that sulfide films on steel, copper, or silver showed maximum reduction in friction when the thickness exceeded about 1500 Å. Under the conditions of experiments with sulfide films of FeS on steel reported in reference 13, a thickness of approximately 6000 Å is required for minimum friction coefficient, although surface welding was effectively prevented by films 4500 Å thick. These data are shown in figure 12. Since the data of figure 11 are for an FeS film of approximately 1000 Å where welding was effectively prevented, the value of 4500 Å for the studies of reference 13 appears to be peculiar to the conditions under which it was observed.

Metallic soaps.—There is rather general acceptance at the present time of the theory that boundary lubrication by materials such as fatty acids is effected primarily by chemisorption rather than physical adsorption. Lubrication is most effective, therefore, when there is some reaction of the fatty acids with the metals to form a metallic soap (refs. 8 and 34). Reference 8 shows that lubrication with fatty acids can be maintained at temperatures considerably above the melting temperature or desorption temperature of the fatty acids; in fact, the temperature at which lubrication failure takes place correlates remarkably well with the melting temperature of the metallic soap that is believed to be formed in the chemisorption of the fatty acids on the surface. It has been shown (ref. 8) that the formation of a metallic soap is very markedly affected by the presence or absence of oxide films. In experiments on steel, the results of reference 35 show that the *type* of oxide film is also extremely important. With a film of Fe_2O_3 on the surface, stearic acid in cetane was effective as a lubricant at sliding velocities only up to 3000 feet per minute; with a film of Fe_3O_4 on the surface, the same concentration of stearic acid in cetane was effective at sliding velocities higher than 7000 feet per minute.

Solid lubricants.—Because solid lubricants are frequently used as supplemental lubricants, they must be effective under conditions under which liquid lubricants become ineffective (ref. 29). In order to be effective, a solid lubricant must be

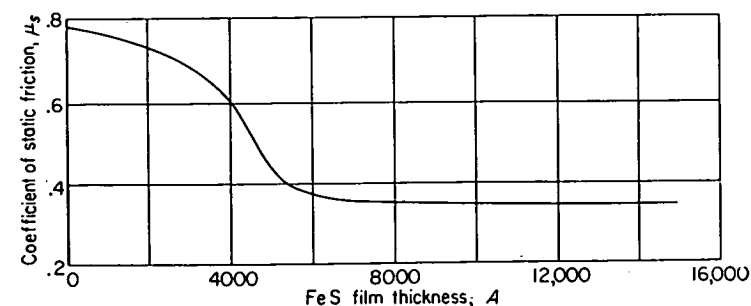


FIGURE 12.—Effect of thickness of film of FeS on static coefficient of friction of steel against steel (ref. 13). Apparatus C; load, 2400 grams; radius of spherical rider specimen, $\frac{1}{8}$ inch.

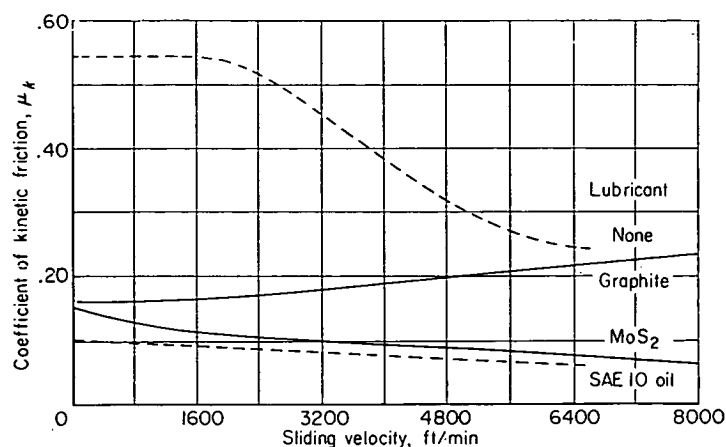


FIGURE 13.—Friction at high sliding velocities of steel against steel with preformed films of MoS_2 and graphite (ref. 30). Apparatus A; radius of spherical rider specimen, $\frac{1}{8}$ inch.

maintained in place at the contact surface (ref. 36); that is, it must be strongly adherent to the surface and the film must be continuous. As indicated in reference 36, a "self-repairing" film is the most effective means of maintaining a film at the surface. Other types of film are, however, effective for limited periods of time.

In addition to the requirement that the lubricant film be strongly adherent to the surface, solids for use in the film must meet other requirements. Materials for this application should have the following physical and chemical properties: (1) high melting point, because of the high temperatures involved, (2) low hardness, because low hardness in a material is associated with low shear strength and consequently low friction (see appendix A), (3) laminar structure (some layer-lattice materials have been quite effective as solid lubricants), (4) limited solubility, (5) limited chemical reactivity, and (6) surface adherence. The five materials included in table I should be relatively effective in reducing friction and wear. On the basis of their properties, MoS_2 and graphite were indicated to be the materials of most interest.

Campbell (ref. 6) discussed the desired properties of solid lubricants and included, in addition to the mentioned points, the following: (1) The film should have good elastic properties; and (2) for a specific application, certain other properties may be required of the solids: high electrical conductivity, high thermal conductivity, corrosion inhibition, low density, small particle size, and freedom from abrasive contaminants. The requirement of freedom from abrasive contaminants is extremely important and is discussed later.

As shown in table I, both graphite and MoS_2 have excellent properties from the standpoint of possessing high melting point, laminar structure, low hardness (which corresponds to low shear strength), and relative chemical inertness. Since both of these materials have a laminar structure, shear within the material (in the plane of the laminae) should readily occur. Experimental friction results with MoS_2 and graphite are shown in figure 13; these data are discussed in detail in reference 30. At room temperature and low speed, there is little choice between the two materials. At the higher speeds, the friction coefficient of MoS_2 is lower. Visual observation of the rider specimens indicated that some

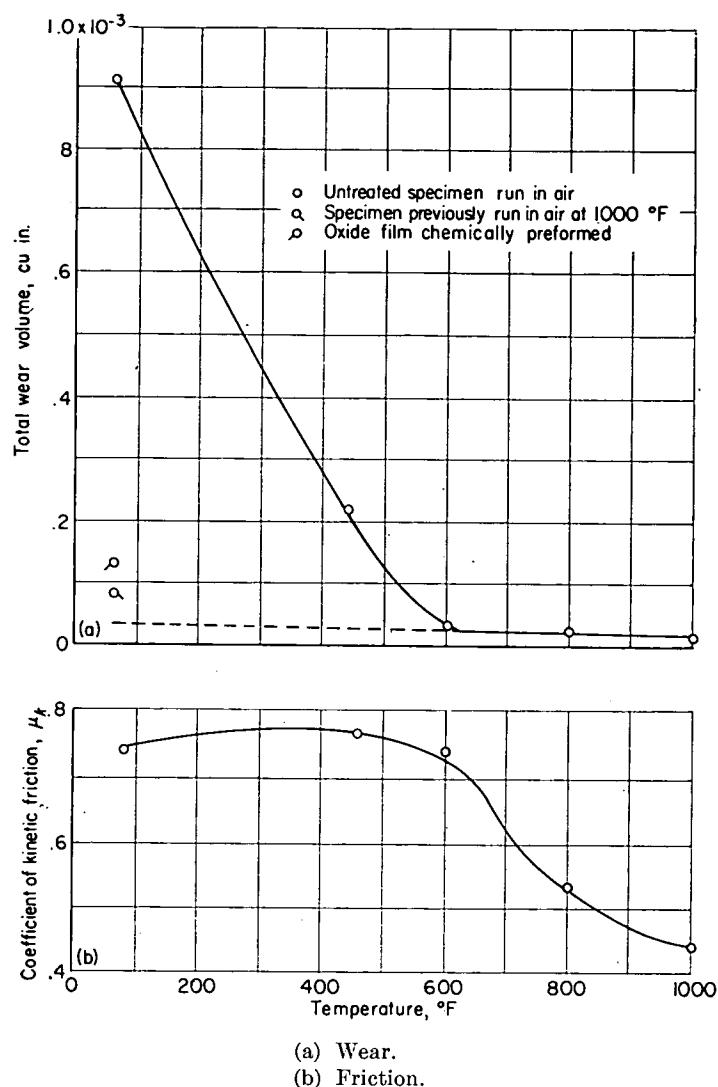


FIGURE 14.—Wear and friction of cast Inconel (rider) sliding against M-10 tool steel (disk) unlubricated. Apparatus B; sliding velocity 120 feet per minute; load, 1200 grams; radius of spherical rider specimen, $\frac{3}{16}$ inch.

welding had occurred with the graphite film and none with the MoS_2 film. Occurrence of welding with the graphite film may have been affected by manner of film formation or by humidity. An important difference between the graphite and the MoS_2 films is the manner in which the two films were formed; the graphite film was a rubbed film and may not have adhered well or been completely continuous on the surface. The MoS_2 film was a continuous film, bonded to the surface by the corn syrup method described in appendix B. The second factor involves the presence or absence of adsorbed water films. Considerable research (conducted by Savage, Ramadanoff, Campbell, and others, and reviewed by Campbell, ref. 6) has shown that the presence of adsorbed water or oxygen films promotes ease of slip between adjacent crystal planes of graphite. Thus, in low humidities or in a vacuum, wear and friction with graphite are very high. Campbell also states that, if the graphite is properly run-in under normal conditions so that sufficient water is adsorbed, a high degree of orientation is produced with the slip layers parallel to the supporting surface. After such run-in, wear is very low

even in relative humidities as low as 0.4 percent. With the NACA rubbed films, no run-in was attempted; thus, sliding under severe conditions (such as the higher sliding velocities of fig. 13) generated considerable frictional heat at the contacting surfaces. This heat may have desorbed any water films at the surface, and consequently reduced the lubricating effectiveness of the graphite.

Nickel oxide.—It was observed (refs. 24 and 25) that good performance characteristics (low wear and prevention of surface damage) of nickel alloys were obtained when a surface film of NiO was present; when no surface film was present, poor performance was obtained.

Research at this laboratory has shown that, with increase in temperature, wear of Inconel decreases. This result would be expected, since an oxide film could form more readily at the higher temperatures. The reduction in both wear and friction with increase in temperature is shown in figure 14. The data show that wear at temperatures between 600° and 1000° F is approximately one-twentieth that at 75° F. The effect of the film on wear was checked with two types of experiment: In the first, specimens with preformed NiO films were tested; in the second, an attempt was made to prevent the natural formation and repair of the oxide film by limiting the availability of oxygen to the specimens.

Films were preformed by two methods. One film was preformed on a cast Inconel specimen by making a wear run in air at 1000° F; a room-temperature wear run was then made with this same specimen. As indicated in figure 14 (a), the wear rate was approximately one-tenth of that obtained with an untreated specimen at room temperature. A film was preformed on a second cast Inconel specimen by heating it in molten caustic (NaOH). The specimen was then run at room temperature, and the data (fig. 14 (a)) show that wear was again approximately one-tenth of that obtained under similar conditions with an untreated specimen of the same material. The experiment involving oxygen availability was made with cast Inconel at 1000° F in an atmosphere of argon. Although some oxide was undoubtedly present (because air was present as a contaminant), wear was higher by a factor of 4. These results point to the beneficial effect of the nickel oxide film on both wear and prevention of surface damage.

Lacquers or varnishes.—The study on lacquers and varnishes (referred to in the section Naturally Formed Surface Films) was made on friction specimens to which had been applied lacquer or varnish films from decomposition of several

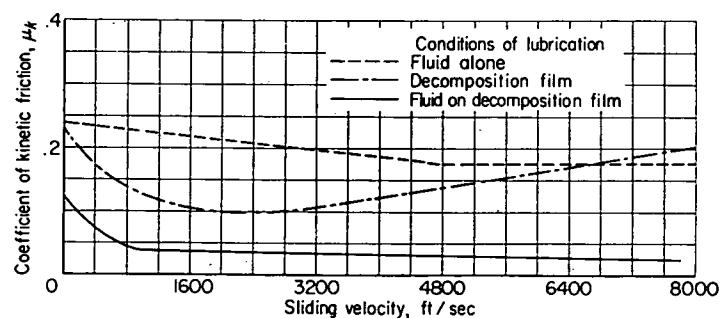


FIGURE 15.—Effect of sliding velocity on kinetic friction of steel against steel lubricated with silicone fluid and decomposition films formed from a silicone (ref. 37). Apparatus A; load, 269 grams; initial Hertz surface stress, 126,000 psi; radius of spherical rider specimen, $\frac{1}{8}$ inch.

types of lubricant. These lubricant types included ordinary petroleum and synthetic lubricants of the diester, glycol, and silicone types. Results of this investigation are reported in detail in reference 37.

In general, the data of reference 37 show that the decomposition products reduced friction and surface damage of slider surfaces when compared with dry, clean steel surfaces. The effect of surface films in reducing friction and protecting the surfaces is strikingly demonstrated in figure 15, which shows friction coefficient under three conditions: (1) with silicone (a poor lubricant) alone, (2) with a silicone decomposition film, and (3) with silicone fluid over the decomposition film. The marked reduction in friction with decomposition films is apparent. Furthermore, with the fluid alone, surface damage was severe; appearance of the rider was similar to that shown in figure 3 (a). With the decomposition film alone and with the fluid over its decomposition film, damage to the surfaces was very slight; rider appearance was similar to that of figure 3 (b).

Platings.—Bowden and Tabor (ref. 8) have shown that plated films of soft metals can produce extremely low friction coefficients, provided the underlying metals do not contact each other through the film. This finding implies a limiting film thickness below which protection to the surfaces is inadequate. Bowden and Tabor found that the limiting thickness was of the order of 10^{-5} centimeter for indium films. Other metals such as lead, silver, cadmium, and copper have been used as friction-reducing platings. The data of reference 8 (pp. 113-114 and 95-97) confirm the theory (appendix A) that the lower the shear strength of the film material, the lower will be the value of friction. Their results showed that "... friction of copper > lead > indium and that the values of friction ... are roughly proportional to the shear strengths of these metals." From friction results obtained with a steel slider sliding on surfaces of steel, copper, lead, and indium, Bowden and Tabor calculated shear strengths of these materials. These values are given in the following table (ref. 8, p. 97); measured shear strengths of the pure metals are included for comparison:

Metal	Shear strength, g/mm ²	
	Calculated from friction measurements	From direct measurement
Steel	140,000	90,000
Copper	25,000	16,000
Lead	1,600	750
Indium	325	220

In a practical application involving the cages of rolling contact bearings for aircraft gas-turbine engines, silver has been used (ref. 38) as a plating material. Its use prevented excessive metal transfer and "pickup" of the bronze cage material to the steel bearing material during operation after high-temperature soak-back.

OTHER METHODS OF LUBRICATION BY SOLIDS

In practice, solids may be used to lubricate by two methods: (1) inclusion of the solid as a minor constituent of the materials to be lubricated; this method provides lubrication by formation of a film on the surface from within the

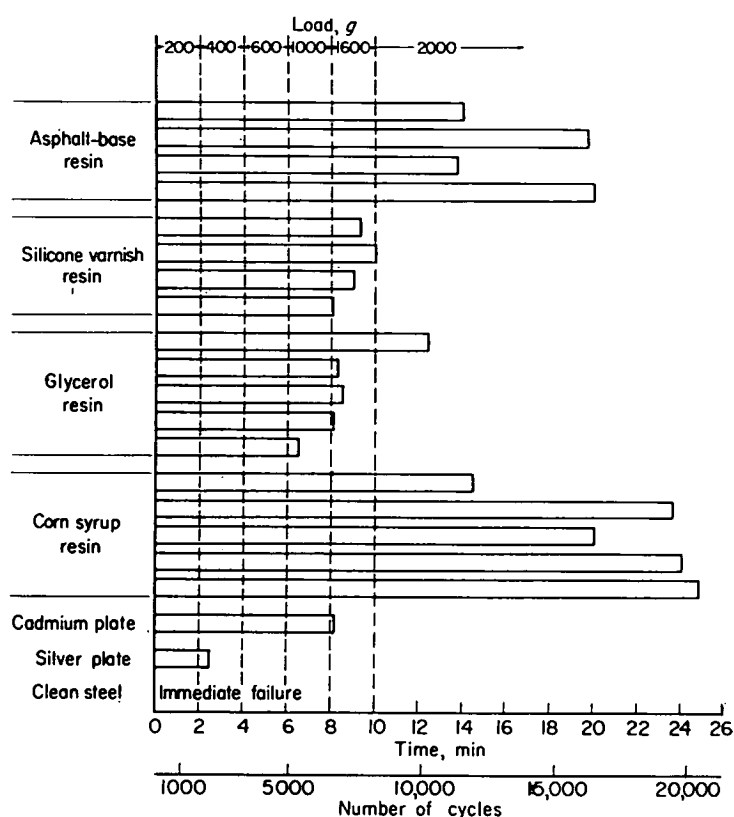


FIGURE 16.—Endurance tests showing total number of cycles to failure for several runs of solid-film lubricants of MoS_2 using four different resin-forming liquids. Cadmium-plated, silver-plated, and clean unlubricated specimens included for comparison. Film thicknesses, 0.0002 to 0.0005 inch. Failure was determined by high friction force and chattering of specimens (ref. 40). Apparatus B; radius of spherical specimens, $\frac{1}{8}$ inch.

structure of the material, and (2) preformation of a surface film and constant repair of this film. In method (1), the bearing material can be made by powder metallurgy with a solid minor constituent that is an excellent lubricant. With method (2), the surfaces may have a preformed lubricant film, and some external means may be provided to replenish the material so as to maintain a continuous film.

Bonding of solid lubricants.—References 39 and 40 cover investigations made to determine the mechanism of bonding of MoS_2 and other solid lubricants to various materials and to determine the friction and wear characteristics of such bonded films. It is shown in reference 39 that, when a solid powder suspended in a resin-forming liquid vehicle is applied to a hot surface, the liquid decomposes or polymerizes to resins that bind the particles of powder together and to the surface. Powders can be bonded in this way to materials such as steel, aluminum, brass, stainless steel, or glass. The resin-forming liquids that were investigated are: asphalt-base varnish, silicones, glycerin, ethylene glycol, polyglycol ether, and corn syrup. Solid lubricants bonded by this method were MoS_2 , graphite, and Fe_3O_4 . Electron diffraction studies (ref. 39) of a MoS_2 film bonded to steel showed no evidence of chemical reaction between the MoS_2 and the steel. As a part of the bonding investigation, rubbed films were also studied. Rubbing of MoS_2 and graphite was shown (refs. 39 and 30) to produce orientation of the materials.

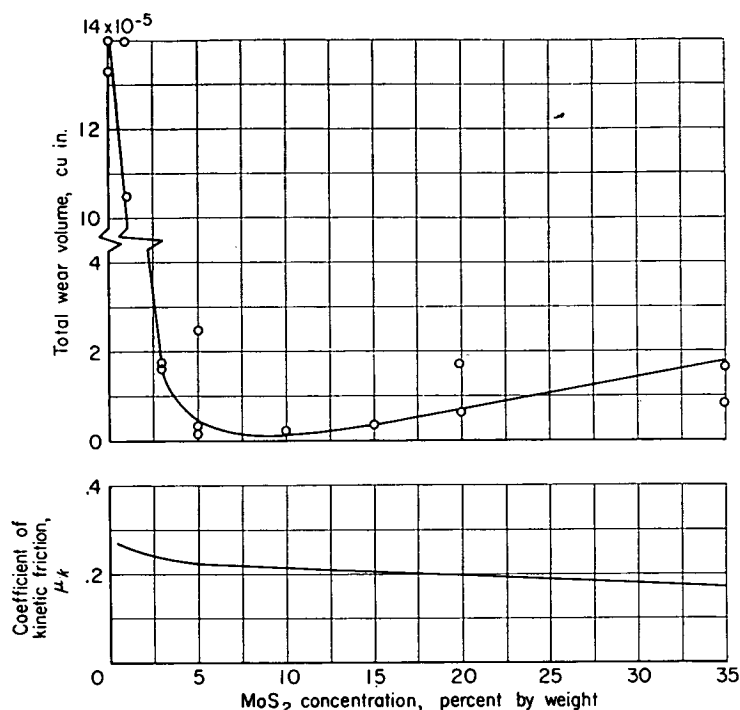


FIGURE 17.—Wear and friction of hot-pressed bearing material containing MoS₂. Rider specimens (on which wear was measured) were composed of 5 percent copper (by weight), 95 to 60 percent silver, and 0 to 35 percent MoS₂. Disk specimens were 1020 steel (ref. 41). Apparatus A; sliding velocity, 5000 feet per minute; load, 519 grams; time, 60 minutes; radius of spherical specimen, $\frac{3}{16}$ inch.

The studies of reference 39 showed that resin-forming fluids on steel surfaces chemically reduce Fe₂O₃ to Fe₃O₄. This conclusion was reached from electron-diffraction studies of a MoS₂ film bonded with corn syrup as well as from chemical analyses of various mixtures of MoS₂, corn syrup, iron, and Fe₂O₃. Presence in the bonded MoS₂ film of Fe₃O₄ rather than Fe₂O₃ (the oxide originally present on the surface before the MoS₂ film was bonded) should be advantageous because of the better friction and surface protecting properties of Fe₃O₄ (fig. 9 and ref. 30).

MoS₂ as a solid lubricant.—The studies of reference 40 showed that solid lubricants can be applied by a practical bonding method. The reported friction and endurance data, obtained under the severe conditions of completely dry operation and high surface stresses, showed that solid-film lubricants (from 0.0002 to 0.0005 in. thick) of MoS₂ bonded with various resins (including corn syrup) possessed good lubricating qualities (fig. 16). For comparison purposes, figure 16 presents results for clean steel specimens and for specimens with a 0.0005-inch plating of cadmium or of silver.

An investigation was made (ref. 41) to study the lubricating effectiveness of MoS₂ included as a minor constituent in materials made by powder-metallurgy techniques; such bearing materials might be capable of operating successfully even under extreme boundary-lubrication conditions (possibly even completely dry). For these experiments, the rider specimens were powder-metallurgy compacts of: copper, 5 percent (by weight); silver, 95 to 60 percent; and MoS₂, 0 to 35 percent. Values of friction and wear of these materials are shown in figure 17. Wear was determined

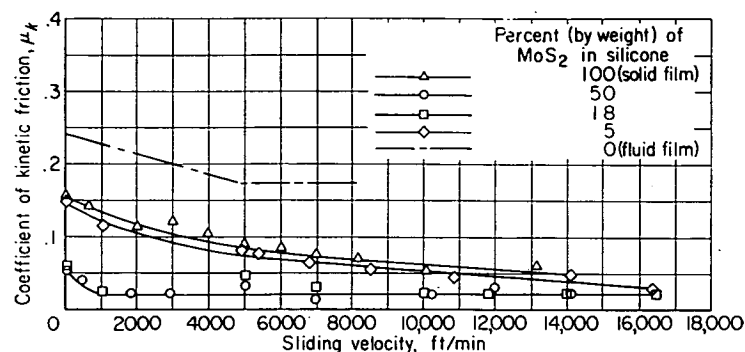


FIGURE 18.—Effect of sliding velocity on coefficient of friction for various mixtures of MoS₂ and a silicone fluid (a poor boundary lubricant) (ref. 43). Apparatus A; load, 269 grams; radius of spherical rider, $\frac{1}{8}$ inch. Solid film of MoS₂ formed by corn syrup method described in appendix B.

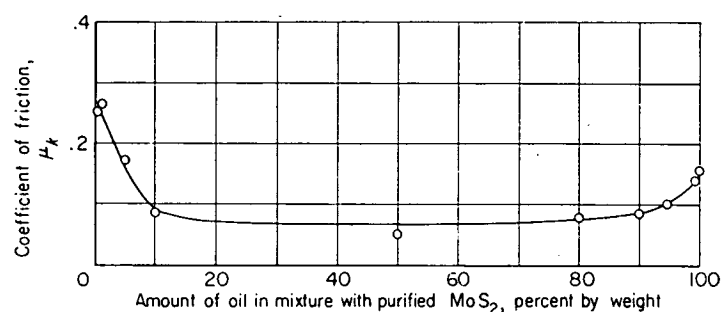


FIGURE 19.—Effect of mixtures of oil (white, medicinal) and MoS₂ on friction coefficient (ref. 44). Apparatus E; load, 40 pounds; sliding velocity, 6 feet per minute; radius of cylindrical rider specimen, 2 inches; steel on steel.

from the measured wear spot on the rider specimens. These data show that friction coefficient decreased progressively with increase in concentration of MoS₂. With wear, however, there was a definite optimum in MoS₂ concentration. High wear at low concentrations probably resulted from lack of effective lubrication; high wear at high concentrations probably resulted from lack of physical strength of the material. Since the specimens were operated without external lubrication, such materials show some promise for severe conditions of load, speed, and lack of lubrication. In these experiments, welding (as observed visually) was absent for all compacts that contained more than 5 percent MoS₂. The materials apparently formed an effective lubricating film on the surface by a transfer of solid lubricant from within the structure of the materials.

An investigation of lubrication by preformation of a surface film and constant repair of this film is reported in reference 42. The solid lubricant was supplied to the specimens with an "air-mist" system; the same effect could undoubtedly have been produced if the solid were supplied in a volatile liquid carrier. Preliminary investigations had shown that, with introduction of powdered MoS₂ in a rolling contact bearing, a continuous film of MoS₂ was formed on the contacting surfaces by the rolling action of the bearing components. It is possible (ref. 42) to operate conventional rolling contact bearings so lubricated either at high temperatures (approaching 1000° F) or at high speed (to *DN* values of 900,000, equivalent to a rotative speed of approximately 12,000 rpm for a 75-mm-bore bearing).

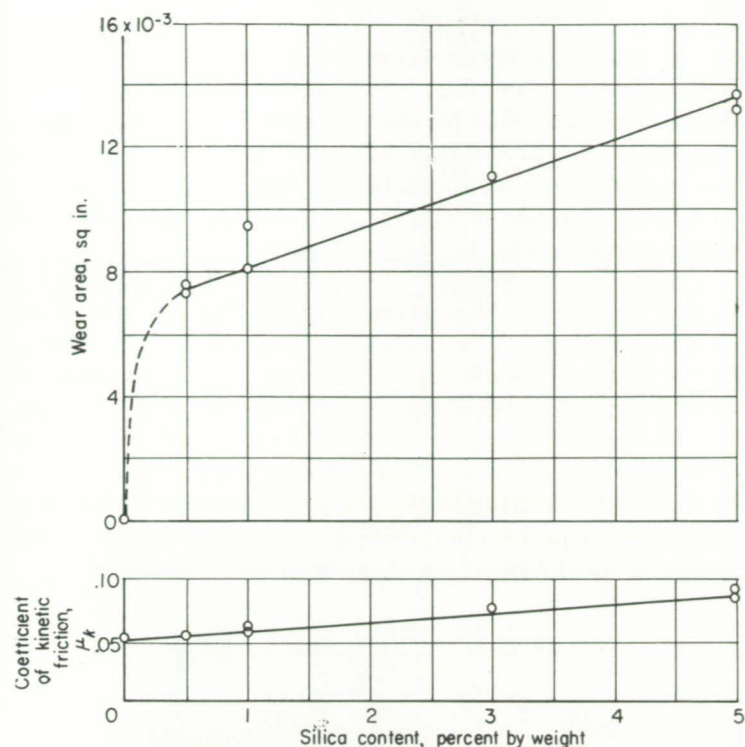


FIGURE 20.—Effect of silica additions to MoS_2 on wear and friction of steel specimens (ref. 44). Apparatus E; load, 40 pounds, sliding velocity, 6 feet per minute; duration, 6 hours; radius of cylindrical rider specimen, 2 inches; steel on steel.

Mixtures or suspensions of solids in liquid carriers may not at first consideration seem to fall in the class of solid surface-film lubricants as discussed in this report. Material so suspended may, however, provide lubrication by forming a solid film at the sliding surfaces. The studies presented in appendix E of reference 43 showed that low friction and complete protection of the surfaces from welding (as observed visually) could be obtained with mixtures of MoS_2 in a silicone fluid. These results were obtained with concentrations of 18 and 50 percent MoS_2 (fig. 18). The silicone fluid by itself was an extremely poor boundary lubricant for the steel-on-steel specimens of these experiments. Surface welding was prevented for MoS_2 concentrations as low as 5 percent. It should be recognized, however, that these particular mixtures were subject to settling, since they were not colloidal suspensions; such settling could be detrimental in a practical mechanism.

Mixtures of MoS_2 and a lubricant (white oil) produced friction coefficients (ref. 44) lower than those obtained with

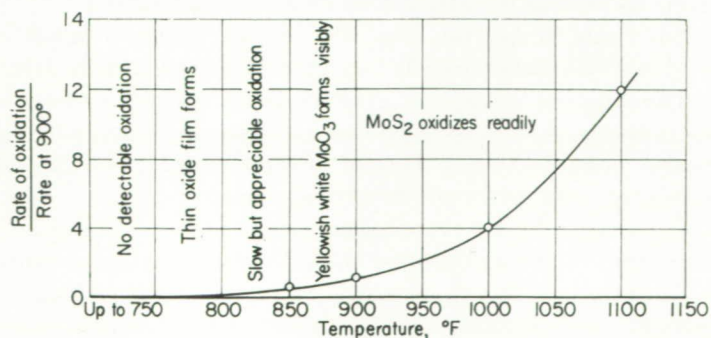


FIGURE 21.—Oxidation characteristics of MoS_2 in air. (Data from ref. 46.)

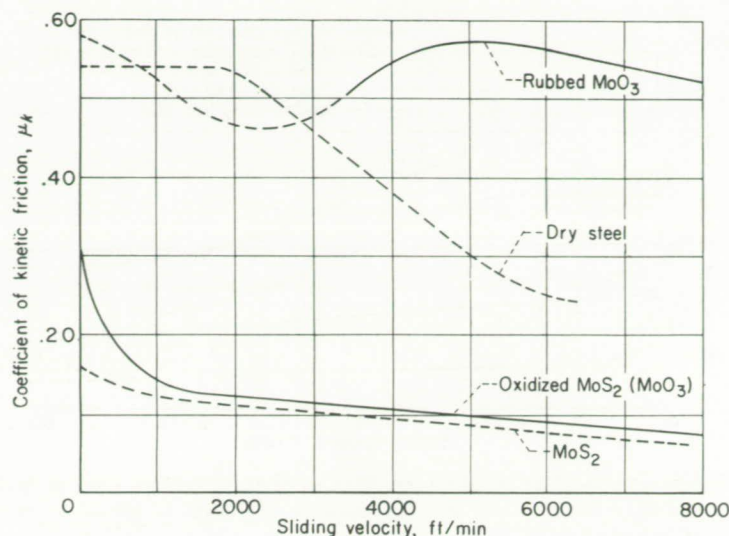


FIGURE 22.—Friction at high sliding velocities of steel against steel with preformed films of rubbed MoO_3 and oxidized MoS_2 (ref. 46). Apparatus A; radius of spherical rider specimen, $\frac{1}{8}$ inch.

either the MoS_2 alone or the oil alone (fig. 19). The lowest concentration of MoS_2 required for minimum friction coefficient is approximately 10 percent.

As previously discussed, contaminants may be important in the use of solid lubricants. An investigation of these effects, using MoS_2 as the solid lubricant, is described in references 44 and 14. The studies of reference 44 revealed that naturally present contaminants, such as silica, might increase wear considerably, even though friction coefficient was increased only slightly (fig. 20). Moisture has a very detrimental effect on lubrication with MoS_2 ; both friction and wear increase as moisture content increases (ref. 14). Moisture in MoS_2 also forms acids that may be corrosive. Purity of the MoS_2 is therefore of considerable importance.

Campbell (ref. 6) states: "When chemical conversion coatings are used in combination with other solid lubricants, a surface is produced which outwears by a large factor either lubricant alone." His data show that marked increases in life (as measured by cycles to failure) could be obtained with a graphite film over a phosphated surface; the phosphate treatment was presumed to improve adherence of the lubricant film. Barwell and Milne (ref. 45) showed similar improvements (reduction in scuffing wear and increase in seizure load) by the use of MoS_2 in association with phosphated surfaces.

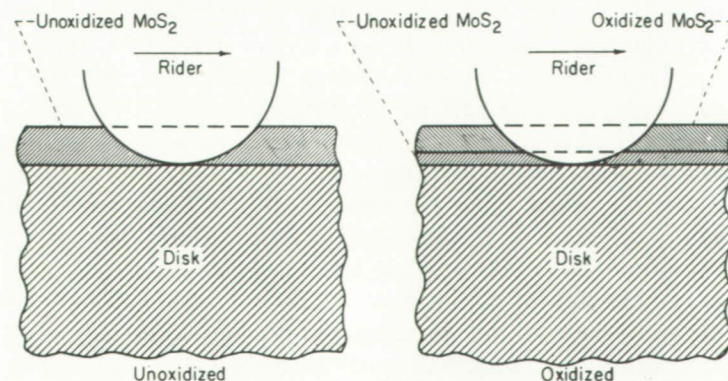


FIGURE 23.—Schematic representation of rider-disk combination, with unoxidized and with oxidized MoS_2 films.

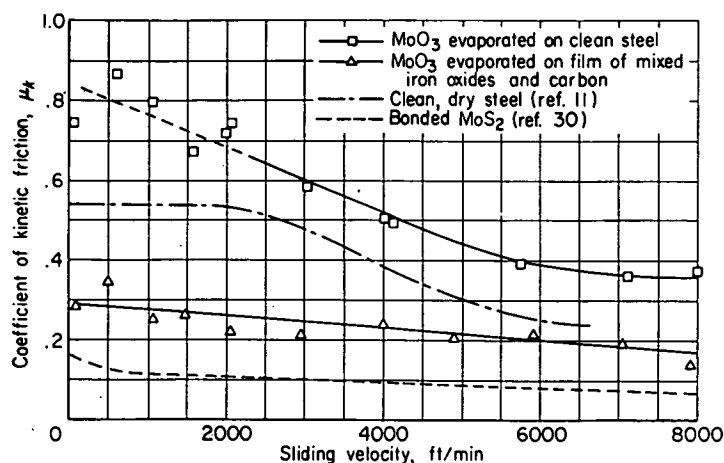


FIGURE 24.—Effect of MoO₃ on friction of steel against steel at high sliding velocities (ref. 46). Apparatus A; radius of spherical rider specimen, $\frac{1}{8}$ inch.

Since MoS₂ appeared promising in the investigations at room temperature, it was considered as a high-temperature lubricant. An X-ray diffraction investigation of its chemical stability at high temperatures was accordingly made (ref. 46). This investigation showed that in vacuum there is no phase change of the MoS₂ at temperatures below 1000° F. In the presence of the oxygen, however, MoS₂ was found to oxidize to molybdenum trioxide MoO₃ at a very low rate at 750° F; the rate of oxidation increases steadily with increase in temperature as shown in figure 21. Since MoO₃ is abrasive, the friction characteristics of both an oxidized film of MoS₂ and a rubbed film of pure MoO₃ were studied. The results are shown in figure 22. The data show that MoO₃ is a very poor lubricant and its use resulted in high friction and excessive welding. The "oxidized" MoS₂ film, however, showed results remarkably similar to those for the unoxidized MoS₂ film.

An explanation of the mechanism of action of the MoS₂ in the "oxidized" condition must consider the actual surface films in both the oxidized and the unoxidized conditions. Sketches of the two surface films, based on an hypothesis that explains the mechanism, are shown in figure 23. While conditions in these experiments were intended to give as near complete oxidation as possible, undoubtedly some fraction of the MoS₂ remains unoxidized; even though this fraction is extremely small, it acts as an effective solid lubricant at the surface. The film immediately adjacent to the surface appears to be that part which produces the beneficial results.

Studies were made (ref. 46) of a film of pure MoO₃ applied to a clean steel disk by an evaporation technique; the MoO₃ was condensed from the vapor state on a steel disk until a film approximately 0.003 inch thick was present. Friction coefficients obtained with this film (upper curve of fig. 24) were higher than those for clean steel on clean steel at all sliding velocities. Studies were also made (ref. 46) of an evaporated MoO₃ film applied to a steel disk on which there was a thin film of mixed iron oxides and carbon; this base film was produced by painting the surface of the hot disk with corn syrup. As previously discussed, the corn syrup reduces Fe₂O₃ to Fe₃O₄ at high temperatures (ref. 39). Friction with the evaporated MoO₃ film applied over the

mixed iron oxides and carbon is shown in figure 24; the data show that friction coefficient with this film is higher than that for a bonded MoS₂ film, but lower than that with either MoO₃ on clean steel or for clean, dry steel. This result again illustrates the importance of iron oxides to the friction mechanism; the reduction in friction (as compared with either MoO₃ on clean steel or with clean steel) is probably the result of surface protection by the Fe₃O₄ film.

The studies of reference 31 suggest that fretting damage is caused basically by high adhesive forces; the adhesion theory of friction predicts that a solid surface film of low shear strength should be effective in the mitigation, or inhibition, of fretting. Because of the effectiveness of MoS₂ as a solid-film lubricant, it was checked (ref. 47) for its effectiveness as an inhibitor of fretting. Data obtained that show MoS₂ to be an effective fretting inhibitor are presented in the following table; for comparison purposes, data for clean specimens and for specimens lubricated with mineral oil are included:

Specimens	Surface film	Cycles to start of fretting
Steel ball on glass flat	None.....	1-30
	Mineral oil.....	1,500
	MoS ₂ dusted.....	72,000
	MoS ₂ bonded.....	28,000,000
Steel flat on steel flat	None.....	100
	MoS ₂ bonded.....	10,000,000

These results show that a surface film (even mineral oil) delays the start of fretting; this effect is believed to result from reduction of the adhesive forces responsible for fretting. Of the various methods of applying MoS₂, bonding of the film was clearly superior, probably because of the strong adherence of the bonded film to the surface.

Other solids as lubricants.—As previously stated, graphite is a solid that has many of the properties desired of a solid lubricant for use at high temperatures. In consequence, graphite was included in a previously unreported investigation in which lubrication of bearings at high temperature was studied; method of application of the graphite was essentially the "air-mist" system of reference 42. The investigation showed that lubrication of a 20-millimeter-bore ball bearing operating at 2500 rpm with graphite was successful at temperatures to 1000° F. Good results were obtained with both dried and undried graphite. In contrast to the harmful (abrasive and corrosive) products from oxidation of MoS₂, the oxidation products from graphite are "harmless" (ref. 6). As indicated in reference 6, "graphite starts to oxidize to carbon dioxide at 350° C (662° F)."

Boyd and Robertson (ref. 48) investigated a number of solid lubricants at extremely high pressure (to 400,000 lb/sq in.) and found that MoS₂ and graphite were among the best of the various lubricants included in their investigation. It is also possible that oxides of several metals used in the powdered form might effectively lubricate.

There have been several practical instances at the Lewis laboratory that have proved the effectiveness of solid lubricants where extremely severe operating conditions are involved. For example, a large number of air-handling valves are required to operate in a corrosive atmosphere at ambient temperatures up to 600° F. An attempt to operate the

valves with a bearing combination of a relatively hard stainless steel journal and a hard stellite bearing resulted in bearing seizure. A bearing was designed that had an interrupted surface with the surface interruptions filled with a solid lubricant. Dry bearings of this type have operated satisfactorily over a period of time at temperatures up to 600° F.

SUMMARY OF RESULTS

Under extreme boundary-lubrication conditions, where metal-to-metal contact takes place, the generally accepted friction theory (according either to Bowden and Tabor or to Merchant) predicts that friction and tendency to surface failure (by welding) of rubbing metals can be reduced relatively simply; this reduction can be accomplished by a reduction of the ratio s/p where s is shear strength of the softer of the two contacting materials and p is flow (yield) pressure of the softer of the two contacting materials. The most practical means of reducing the ratio s/p is to reduce the value of s . The use of thin low-shear-strength films on hard base materials results in a reduction of s with negligible reduction of p . Thus any low-shear-strength material (for example, some oxides, sulfides, plated films, liquid lubricants, etc.) that acts as a contaminant between sliding surfaces should be effective in reducing friction and surface failure. Experimental investigations by the NACA produced the following results, which are consistent with this view:

Experiments with iron oxides showed that FeO and Fe_3O_4 are generally beneficial, while Fe_2O_3 is harmful. With steel specimens in sliding, exclusion of oxygen by use of a blanket-ing medium prevented the formation of the beneficial oxides and permitted extensive surface welding. In fact, the results of these and other investigations indicate that, with many metals and particularly ferrous alloys, effective lubrication is very often dependent on the presence of an oxide film that can serve either as a solid lubricant film itself or as a means of obtaining a metallic soap film (by reaction with fatty acids) which serves as the solid lubricant. The importance of oxides to the friction and wear processes has not always been fully appreciated.

Chemical reaction films such as FeS and FeCl_2 were effective in preventing surface welding; FeCl_2 was much more effective than FeS in reducing friction (for example, at 3000 ft/min sliding velocity, friction coefficient μ was approximately 0.13 for FeCl_2 and 0.40 for FeS). This difference in friction corresponds to the difference in shear strengths of the two compounds.

Wear studies showed that prevention of surface damage and maintenance of low wear could be associated with the formation of naturally occurring surface films on one or both of the sliding specimens; for cast irons, the surface film consisted of graphitic carbon and for various nickel alloys, the film consisted of the nickel oxide NiO . In one investigation with cast Inconel sliding against hardened M-10 tool steel at temperatures ranging from 75° to 1000° F, a very marked downward trend of wear with increase of temperature was observed. It is speculated that this downward trend was the result of formation of beneficial nickel oxide(s) at the higher temperature. In this same investigation, wear was reduced by a factor of 10 through pretreatment of the Inconel

specimen to form a nickel oxide surface film. It was possible to increase wear by limiting formation of the oxide film. This result was obtained by conducting tests at 1000° F in which the availability of oxygen was restricted by displacing the air surrounding the specimens with argon; under these conditions, wear increased.

Investigations of solid surface films of the lacquer or varnish type (preformed from decomposition of several petroleum and synthetic lubricants) showed that such films reduced friction and surface damage considerably, compared with dry clean steel surfaces. Furthermore, when a fluid silicone film is present over its lacquer or varnish film, the reduction in both friction and surface damage is quite marked as compared with the silicone film alone.

Various solids were considered for use as solid-film lubricants; of those considered, MoS_2 and graphite seemed best for use under severe operating conditions such as high temperatures, high loads, or any of the various operating conditions leading to extreme boundary lubrications. Investigations of these solids under high contact pressures, high temperatures, or high sliding velocities indicated that, in general, beneficial results were obtained with each material in the lubrication of steel on steel. These materials were therefore studied extensively with respect to: (1) methods of bonding to surfaces, (2) lubrication of rolling contact bearings, and (3) for MoS_2 , stability at high temperatures.

Studies of the mechanism of bonding showed that both MoS_2 and graphite could be bonded to most surfaces by the use of a resin-forming liquid vehicle. The films so bonded were quite effective in preventing damage and reducing friction over limited periods of time. The MoS_2 and graphite were used to lubricate rolling contact bearings at high temperature and provided effective lubrication up to 1000° F. This application required a solid lubricant film to be formed and maintained (repaired) by continual injection of small amounts (approximately 0.001 lb/min) of the solid lubricant.

X-ray diffraction studies of MoS_2 showed no phase changes below 1000° F in the absence of oxygen. Electron and X-ray diffraction experiments show that in the presence of oxygen MoS_2 oxidizes to molybdenum trioxide MoO_3 . The rate of oxidation increases steadily with increase in temperature: it is low below 750° F and becomes high at temperatures above 1050° F. Presence of a very small amount of unoxidized MoS_2 in oxidized bonded MoS_2 films will, however, maintain low friction and provide good protection from surface damage.

The general results of these investigations show that the presence of certain low-shear-strength solid surface films can markedly reduce friction, wear, and surface damage of rubbing metals operating under conditions of extreme boundary lubrication (where metal-to-metal contact takes place).

APPENDIX A

ADHESION THEORY OF FRICTION

Bowden and Tabor (ref. 8)

Friction, $F = S + P = \text{Shear} + \text{Ploughing}$

$$F = As + A'p$$

$$A = \frac{\text{Load}}{\text{Flow pressure}} = \frac{W}{p}$$

$$\mu = \frac{\text{Friction}}{\text{Load}} = \frac{F}{W} = \frac{As}{W} = \frac{A'p}{W}$$

$$\mu = \frac{s}{p} + \frac{A'p}{W}$$

When the ploughing term is negligible,

$$\mu = \frac{s}{p} = \frac{\text{Shear strength}}{\text{Flow pressure}}$$

Merchant (ref. 10)

$$\mu = \frac{s}{H} + \tan \theta = \text{Shear} + \text{Roughness}$$

When the roughness term is negligible,

$$\mu = \frac{s}{H} = \frac{\text{Shear strength}}{\text{Pressure surface hardness}}$$

where

 F friction force S shear force P ploughing force A shear area s shear strength A' ploughing area p flow pressure (in certain cases equivalent to yield strength in compression) W load θ average angle that planes of slip make with general plane of surface H pressure surface hardness (in certain cases equivalent to yield strength in compression)

APPENDIX B

FILM PREPARATION

The preparation of various preformed films is described in considerable detail in references 13, 30, 37, 40, and 46; a condensed version of the procedure for each specific film is included in this appendix.

The finishing and cleaning procedure summarized here is described in detail in reference 11. Each disk was subjected to a similar milling, grinding, and lapping procedure, which was followed by a cleaning procedure essentially as follows:

- (1) Degrease in low-aromatic cleaning naphtha
- (2) Abrade with 3/0 emery paper
- (3) Wash with mixture of 50 percent benzene and 50 percent acetone
- (4) Scrub with levigated alumina
- (5) Rinse with water
- (6) Rinse with 190 proof ethyl alcohol
- (7) Dry in clean, warm air

FORMATION OF Fe_3O_4 FILM (REF. 30)

A film of Fe_3O_4 was formed by heating steel in a restricted oxygen supply; the disk was heated to 375°C (707°F) in a metal bell jar in which the air pressure was 0.1 millimeter of mercury. After 30 minutes in the vacuum furnace, interference colors were obtained which indicated a thickness in the order of 1200 Å. The steel was cooled to room temperature in the furnace under the same low pressure.

FORMATION OF Fe_2O_3 FILM (REF. 30)

A film of the oxide Fe_2O_3 , which contains the greatest amount of oxygen of the iron oxide films investigated, was prepared by heating a steel disk to 350°C (662°F) in clean, dry air at atmospheric pressure. The disk was removed

from the source of heat when the interference colors on the surface indicated thickness about 1200 Å.

FORMATION OF FeCl_2 FILM (REF. 30)

A film of FeCl_2 was formed by exposing a warmed, clean steel disk to the hot vapors composed of an azeotropic solution of hydrochloric acid and water. The warm disk was placed in a hot gas chamber at 100°C (212°F), which was then partly evacuated. When a valve was opened at the inlet to the chamber, a vapor composed of 20 percent water and 80 percent hydrochloric acid could envelop the disk. A 2-minute exposure was sufficient to form a thin, white, uniform coating believed (on basis of interference colors) to be approximately 1000 Å thick.

FORMATION OF FeS FILM

Kinetic friction experiments of figure 11 (ref. 30).—A film of FeS was formed by exposing a heated disk to hydrogen sulfide H_2S gas. The clean steel disk was placed in a vacuum furnace at room temperature and the air pressure reduced to 0.25 millimeter of mercury. Hydrogen sulfide was admitted and the pressure again reduced. This process was repeated until the chamber was purged of air. The disk was then heated to 350°C (662°F) and an additional amount of H_2S was admitted. The film formed rapidly and the furnace was allowed to cool while the low pressure was maintained. The film thickness was believed (on basis of interference colors) to be approximately 1000 Å.

Static friction experiments of figure 12 (ref. 13).—Films of FeS were formed on the rider specimens (balls) by heating in an atmosphere of H_2S . Thickness of the films was calcu-

lated from weight gain and was checked by means of the modified chemical spot test, as discussed in reference 13. All weight gain was assumed to be caused by the addition of sulfur, which was stoichiometrically combined with iron to form iron sulfide.

FORMATION OF MoS_2 FILM

Corn syrup resin for film of figure 13 (ref. 30).—Molybdenum disulfide MoS_2 powder was mixed into a smooth paste with an organic binder (commercial corn syrup). The mixture was painted on a steel disk, the temperature of which was 350°C (662°F). After the disk cooled, loosely adhering MoS_2 was scraped off with a straight edge until the film was thin (approximately 0.005 in.), tenacious, gray-black, and very smooth. The disk was finished by light abrasion with 3/0 emery paper, followed by washing in 190 proof ethyl alcohol.

Corn syrup resin for film of figure 16 (ref. 40).—Equal parts by weight of MoS_2 and corn syrup were mixed to a paste. The disk was preheated to 250° to 300°C (482° to 572°F) and the paste applied to the disk. After the disk had cooled and the excess was scraped off, the surface was rubbed with fine steel wool and burnished with soft clean cloth to form a film of thickness from 0.0002 to 0.0005 inch.

Asphalt-base resin (ref. 40).—A mixture of 1 part (by weight) MoS_2 and 2 parts (by weight) asphalt-base varnish thinned 60 percent (by volume) with naphtha was brushed on a clean steel disk; the film was then air dried at room temperature until tack free. This film will become sufficiently hard (equivalent to hardness obtained when cured for 3 hr at 150°C) if enough time at room temperature is allowed. The disk was then rubbed with steel wool and burnished with a soft clean cloth to form a film of thickness from 0.0002 to 0.0005 inch.

Silicone varnish resin (ref. 40).—A mixture of 1 part (by weight) MoS_2 and 2 parts (by weight) silicone varnish thinned 20 percent (by volume) with xylene was brushed on a clean steel disk and dried under infrared rays until firm. The film was cured by heating at 200° to 250°C (392° to 482°F) for 3 hours. The disk was then scrubbed with steel wool and burnished with soft clean cloth to form a film thickness from 0.0002 to 0.0005 inch.

Glycerol resin (ref. 40).—A mixture of 1 part (by weight) MoS_2 and 2 parts (by weight) glycerin preboiled (to about one-fifth its original volume) was rubbed on a clean steel disk. The film was then dried either by (a) heating to 250° to 300°C (482° to 572°F) and repeating application of mixture with rubbing until film covered surface completely and continued heating until dry, or (b) drying under infrared until film was firm, then cured by heating for 3 hours at 250°C (482°F). The disk was then scrubbed with fine steel wool and burnished with soft clean cloth to form a film of thickness from 0.0002 to 0.0005 inch.

FORMATION OF OXIDIZED MoS_2 FOR FILM OF FIGURE 22 (REF. 46)

A disk, on which had been formed a film of MoS_2 in accordance with the method of reference 30, was placed in a

muffle furnace and heated $\frac{1}{2}$ hour at 1000°F . This treatment produced a top layer primarily of MoO_3 , with an underlying thin layer of mixed MoS_2 , iron oxides, and carbon.

FORMATION OF MoO_3

Rubbed MoO_3 for films of figure 22 (ref. 46).—Coarse, crystalline MoO_3 was rubbed on the flat disk to produce the rubbed MoO_3 film. This rubbing essentially resulted in filling the microscopic valleys of the steel surfaces.

Evaporated MoO_3 for film of figure 24 (ref. 46).—The MoO_3 was evaporated onto the surface of two disks. One of these disks was clean; the second had a film of mixed iron oxides and carbon on the surface. The mixture of iron oxides and carbon was obtained by painting the surface of a hot steel disk with corn syrup only. Evaporation of MoO_3 was done by heating molybdic acid H_2MoO_4 in a crucible; during heating, the acid dehydrated and became MoO_3 , which melted, evaporated, then condensed on the cool disk surface immediately above the crucible. The films were approximately 0.003 inch thick. Details of the film preparation are given in reference 46.

FORMATION OF GRAPHITE FILM (REF. 30)

Graphite was deposited on the surface of the steel disk by compressing flaky graphite into a cake, which was then pressed against the rotating disk. The resulting film, while not completely continuous, was estimated to be less than 0.0005 inch thick.

FORMATION OF NICKEL OXIDE

Nickel oxide films were preformed by two methods. In the first, the film was preformed on a cast Inconel specimen by running a sliding friction experiment in air at 1000°F ; previous sliding friction experiments with nickel alloys had shown that NiO was formed on the surface (refs. 24 and 25). In the second method, the film was preformed by heating a cast Inconel specimen in molten caustic NaOH . Exact thickness of these nickel oxide films is unknown.

FORMATION OF LACQUERS OR VARNISHES (REF. 37)

The lacquer or varnish films were formed by heating the disk specimen in air. Before heating, a thin film of fluid lubricant was uniformly deposited on the disk surface; in most cases, the quantity of fluid was approximately 1 cubic centimeter and the fluid was uniformly applied as a fine mist. Decomposition of the fluid lubricant was accomplished by heating the disks to temperatures slightly higher than those at which the first visible vaporization of the lubricant occurred. The temperatures were maintained as long as 14 hours.

PLATINGS

Cadmium plating.—The cadmium plate was applied using a lead anode in complex cyanide of cadmium bath. The thickness of the plate was 0.0005 inch.

Silver plating.—The silver plate was applied using a silver anode in a silver cyanide bath with aerosol as a brightener. The thickness of the plate was 0.0005 inch.

REFERENCES

1. Bowden, F. P., and Tabor, D.: The Lubrication by Thin Metallic Films and the Action of Bearing Metals. *Jour. Appl. Phys.*, vol. 14, no. 3, Mar. 1943, pp. 141-151.
2. Good, J. N., and Godfrey, Douglas: Changes Found on Run-In and Scuffed Surfaces of Steel, Chrome Plate, and Cast Iron. NACA TN 1432, 1947.
3. Prutton, C. F., Turnbull, David, and Dlouhy, George: Mechanism of Action of Organic Chlorine and Sulfur Compounds in Extreme-Pressure Lubrication. *Jour. Inst. Petr. (London)*, vol. 32, no. 266, Feb. 1946, pp. 90-118.
4. Hughes, T. P., and Whittingham, G.: The Influence of Surface Films on the Dry and Lubricated Sliding of Metals. *Trans. Faraday Soc.*, vol. XXXVIII, no. 249, pt. 1, Jan. 1942, pp. 9-27.
5. Webb, Wells A.: The Influence of Iron Oxide on Wear of Rubbing Surfaces. *Science*, vol. 99, no. 2575, May 5, 1944, pp. 369-371.
6. Campbell, W. E.: Solid Lubricants. *Lubrication Eng.*, vol. 46, no. 4, Aug. 1953, pp. 195-200.
7. Tingle, E. D.: The Importance of Surface Oxide Films in the Friction and Lubrication of Metals. *Trans. Faraday Soc.*, vol. 46, no. 326, pt. 2, Feb. 1950, pp. 93-102.
8. Bowden, F. P., and Tabor, D.: The Friction and Lubrication of Solids. Clarendon Press (Oxford), 1950.
9. Coulomb, M.: *Theorie des machines simple. Memoires de mathematique et de physique.* 1785, vol. 10, pp. 161-334.
10. Merchant, M. E.: The Mechanism of Static Friction. *Jour. Appl. Phys.*, vol. 11, no. 3, Mar. 1940, p. 230.
11. Johnson, Robert L., Swikert, Max A., and Bisson, Edmond E.: Friction at High Sliding Velocities. NACA TN 1442, 1947.
12. Murray, S. F., and Johnson, Robert L.: Effects of Solvents in Improving Boundary Lubrication of Steel by Silicones. NACA TN 2788, 1952.
13. Levine, Erva C., and Peterson, Marshall B.: Formation of Sulfide Films on Steel and Effect of Such Films on Static Friction. NACA TN 2460, 1951.
14. Peterson, Marshall B., and Johnson, Robert L.: Friction and Wear Investigation of Molybdenum Disulfide. I—Effect of Moisture. NACA TN 3055, 1953.
15. Macks, E. Fred: Preliminary Investigation of Needle Bearings of 1½-Inch Pitch Diameter at Speeds to 17,000 RPM. NACA TN 1920, 1949.
16. Bowden, F. P., and Young, J. D.: Friction of Clean Metals and the Influence of Adsorbed Films. *Proc. Roy. Soc. (London)*, ser. A, vol. 208, Sept. 7, 1951, pp. 311-325.
17. Harris, Jay C.: Films and Surface Cleanliness. *Metal Finishing*, vol. 44, nos. 8-9, Aug. and Sept. 1946, pp. 328-333, 386-388.
18. Nelson, H. R.: The Primary Oxide Film on Iron. *Jour. Chem. Phys.*, vol. 5, no. 4, Apr. 1937, pp. 252-259.
19. Pomey, J.: Friction and Wear; Translation of "Le Frottement et L'Usure." Rapport Technique no. 36, Office Nationale D'Etudes et de Recherches Aéronautiques, 1948. Travaux du Groupement Français pour le Développement des Recherches Aéronautiques (G. R. A.). (Available in English translation as NACA TM 1318.)
20. Finch, G. T.: The Structure of Sliding Surfaces. *Engineering (London)*, vol. CLIX, no. 4131, Mar. 16, 1945, p. 215.
21. Johnson, Robert L., Swikert, Max A., and Bisson, Edmond E.: Friction at High Sliding Velocities of Surfaces Lubricated with Sulfur as an Additive. NACA TN 1720, 1948.
22. Ernst, Hans, and Merchant, M. Eugene: Chip Formation, Friction and Finish. The Cincinnati Milling Machine Co., Aug. 24, 1940.
23. Johnson, Robert L., Swikert, Max A., and Bisson, Edmond E.: Investigation of Wear and Friction Properties under Sliding Conditions of Some Materials Suitable for Cages of Rolling-Contact Bearings. NACA Rep. 1062, 1952. (Supersedes NACA TN 2384.)
24. Johnson, Robert L., Swikert, Max A., and Bisson, Edmond E.: Wear and Sliding Friction Properties of Nickel Alloys Suited for Cages of High-Temperature Rolling-Contact Bearings. I—Alloys Retaining Mechanical Properties to 600° F. NACA TN 2758, 1952.
25. Johnson, Robert L., Swikert, Max A., and Bisson, Edmond E.: Wear and Sliding Friction Properties of Nickel Alloys Suited for Cages of High-Temperature Rolling-Contact Bearings. II—Alloys Retaining Mechanical Properties above 600° F. NACA TN 2759, 1952.
26. Brophy, J. E., Militz, R. O., and Zisman, W. A.: Dimethyl-Silicone-Polymer Fluids and Their Performance Characteristics in Unilaterally Loaded Journal Bearings. *Trans. A.S.M.E.*, vol. 68, no. 4, May 1946, pp. 355-360.
27. Hunt, Kenneth C.: Petroleum Requirements of British Gas Turbines. II—Lubricants. *SAE Jour.*, vol. 59, no. 11, Nov. 1951, pp. 20-21.
28. Wilcock, Donald F., and Jones, Frederick C.: Improved High-Speed Roller Bearings. *Lubrication Eng.*, vol. 5, no. 4, Aug. 1949, p. 184; discussion by Daniel Gurney.
29. Bisson, E. E., and Johnson, R. L.: NACA Friction Studies of Lubrication at High Sliding Velocities. *Lubrication Eng.*, vol. 6, no. 1, Feb. 1950, pp. 16-20.
30. Johnson, Robert L., Godfrey, Douglas, and Bisson, Edmond E.: Friction of Solid Films on Steel at High Sliding Velocities. NACA TN 1578, 1948.
31. Godfrey, Douglas: Investigation of Fretting by Microscopic Observation. NACA Rep. 1009, 1951. (Supersedes NACA TN 2039.)
32. Bailey, John M., and Godfrey, Douglas: Coefficient of Friction and Damage to Contact Area During the Early Stages of Fretting. II—Steel, Iron, Iron Oxide, and Glass Combinations. NACA TN 3144, 1954.
33. Greenhill, E. B.: The Lubrication of Metals by Compounds Containing Sulfur. *Jour. Inst. Petr. (London)*, vol. 34, no. 297, Sept. 1948, pp. 659-669.
34. Zisman, W. A.: Present Problems and Future Trends in Lubrication. NRL Rep. 4080, Chem. Div., Naval Res. Lab., Washington (D. C.), Nov. 26, 1952.
35. Johnson, Robert L., Peterson, Marshall B., and Swikert, Max A.: Friction at High Sliding Velocities of Oxide Films on Steel Surfaces Boundary-Lubricated with Stearic-Acid Solutions. NACA TN 2366, 1951.
36. Bisson, Edmond E.: The Influence of Solid Surface Films on the Friction and Surface Damage of Steel at High Sliding Velocities. *Lubrication Eng.*, vol. 9, no. 2, Apr. 1953, pp. 75-77.
37. Johnson, Robert L., Godfrey, Douglas, and Bisson, Edmond E.: Friction of Surface Films Formed by Decomposition of Common Lubricants of Several Types. NACA TN 2076, 1950.
38. Wilcock, Donald F., and Jones, Frederick C.: Improved High-Speed Roller Bearings. *Lubrication Eng.*, vol. 5, no. 3, June 1949, pp. 129-133.
39. Godfrey, Douglas, and Bisson, Edmond E.: Bonding of Molybdenum Disulfide to Various Materials to Form a Solid Lubricating Film. I—The Bonding Mechanism. NACA TN 2628, 1952.
40. Godfrey, Douglas, and Bisson, Edmond E.: Bonding of Molybdenum Disulfide to Various Materials to Form a Solid Lubricating Film. II—Friction and Endurance Characteristics of Films Bonded by Practical Methods. NACA TN 2802, 1952.

41. Johnson, Robert L., Swikert, Max A., and Bisson, Edmond E.: Friction and Wear of Hot-Pressed Bearing Materials Containing Molybdenum Disulfide. NACA TN 2027, 1950.
42. Macks, E. F., Nemeth, Z. N., and Anderson, W. J.: Preliminary Investigation of Molybdenum Disulfide—Air-Mist Lubrication for Roller Bearings Operating to DN Values of 1×10^6 and Ball Bearings Operating to Temperatures of 1000° F. NACA RM E51G31, 1951.
43. NACA Subcommittee on Lubrication and Wear: Review of Current and Anticipated Lubricant Problems in Turbojet Engines. NACA RM 51D20, 1951.
44. Peterson, Marshall B., and Johnson, Robert L.: Friction and Wear Investigation of Molybdenum Disulfide. II—Effects of Contaminants and Method of Application. NACA TN 3111, 1954.
45. Barwell, F. T., and Milne, A. A.: Use of Molybdenum Disulfide in Association with Phosphated Surfaces. Scientific Lub., vol. 3, no. 9, Sept. 1951, pp. 9–14.
46. Godfrey, Douglas, and Nelson, Erva C.: Oxidation Characteristics of Molybdenum Disulfide and Effect of Such Oxidation on Its Role as a Solid-Film Lubricant. NACA TN 1882, 1949.
47. Godfrey, Douglas, and Bisson, Edmond E.: Effectiveness of Molybdenum Disulfide as a Fretting-Corrosion Inhibitor. NACA TN 2180, 1950.
48. Boyd, John, and Robertson, B. P.: The Friction Properties of Various Lubricants at High Pressures. Trans. A.S.M.E., vol. 67, no. 1, Jan. 1945, pp. 51–56; discussion, pp. 56–59.

TABLE I.—PHYSICAL AND CHEMICAL PROPERTIES OF SOLID LUBRICANTS

Material	Melting point, °C	Hardness, mho	Crystalline properties			Solubility		Chemical reactivity
			Structure	Form	Orientation	In water	Other solvents	
Molybdenum disulfide MoS_2	1185	1.0–2.5	Hexagonal	Laminar	Random	Insoluble	H_2SO_4 , aq. reg.	Medium
Tungsten disulfide WS_2	1250	Friable	Hexagonal	Laminar	None	Insoluble	$\text{HNO}_3 + \text{HF}$	Medium
Graphite C	3527	1.0–2.0	Hexagonal	Laminar	Highly preferred	Insoluble	None	Low
Lead iodide PbI_2	402		Hexagonal	Laminar	None	Slightly	KI	Medium
Silver sulfate Ag_2SO_4	652		Orthorhombic		None	Slightly	HNO_3 , H_2SO_4	Medium

REPORT 1255

AN ANALYSIS OF THE STABILITY AND ULTIMATE COMPRESSIVE STRENGTH OF SHORT SHEET-STRINGER PANELS WITH SPECIAL REFERENCE TO THE INFLUENCE OF THE RIVETED CONNECTION BETWEEN SHEET AND STRINGER¹

By JOSEPH W. SEMONIAN and JAMES P. PETERSON

SUMMARY

A method of strength analysis of short sheet-stringer panels subjected to compression is presented which takes into account the effect that the riveted attachments between the plate and the stiffeners have on the strength of panels. An analysis of experimental data shows that panel strength is highly influenced by rivet pitch, diameter, and location and that the degree of influence for a given riveting depends on the panel configuration and panel material.

INTRODUCTION

Rivets have been used extensively for attaching the cover skin to the stringers and webs of aircraft wings. These rivets have been designed, to a large extent, by rule-of-thumb methods; yet, extensive experimental work of which reference 1 is representative has shown that the compressive strength of stiffened panels is greatly influenced by variations in diameter and pitch of the rivets. References 2 to 4, in which the mode of instability of plates in compression known as wrinkling or forced crippling has been analyzed, show that the panel strength is influenced also by the location (rivet offset) as well as the pitch and diameter of the rivets. This mode of instability results from the existence of a flexible attachment between the plate and its supporting members and has occurred more frequently as the compression skins have become heavier and the supporting members lighter.

The purpose of the present report is to evaluate the strength of short compression panels and in particular to determine the influence of the riveting used to fasten the stringers to the plate on the strength of the panel. Figure 1 shows the variation in panel strength with rivet pitch and names the various modes of failure involved. Only rivet pitch is considered to be varied in figure 1 but variations in strength could be obtained also by varying the rivet diameter or the rivet offset. When the rivet pitch is small, the panel of figure 1 fails in the local mode; for larger pitches, it may fail in either the wrinkling or the interrivet mode. Failures in the interrivet mode are not usually permitted in contemporary design; whereas, failures in the wrinkling mode are common. The problem of evaluating the effects of riveting on the strength of panels becomes, therefore, primarily a study of the wrinkling mode of failure. The local-mode section

of the curve of figure 1 is shown as a horizontal line. It is recognized that there may be some gain in strength with a favorable change in riveting after the riveting (pitch in fig. 1) is such that the local mode is obtained. The available test data indicate that the gain in strength is small and it is neglected in the analysis presented herein.

A study of the wrinkling mode is made with the use of the procedures established in references 3 and 4 in connection with the calculation of the strength of multiweb beams in bending. These procedures make use of a new structural parameter termed the "effective rivet offset" which plays an important role in determining the strength of riveted structures such as compression panels and multiweb beams and makes possible relatively simple structural analysis. The effective rivet offset is evaluated by using a relatively rigorous analysis of the initial instability of compression panels supplemented by experimental data and is applicable to the analysis of multiweb beams as well as panels. A semi-empirical maximum-strength analysis of panels which utilizes the effective-rivet-offset concept is made and compared with a large number of test results to show the accuracy and generality of the analysis. The analysis is exemplified in the appendix.

SYMBOLS

b_A	width of attachment flange of stiffener (see fig. 2), in.
b_F	width of outstanding flange of stiffener (see fig. 2), in.
b_H	width of top of hat for hat-section stiffeners, in.
b_O	geometric rivet offset (see fig. 2), in.
b_S	stiffener spacing (see fig. 2), in.
b_W	depth of web of stiffener (see fig. 2), in.
d	rivet diameter, in.
f	effective rivet offset (see fig. 5), in.
k_{cr}	buckling-stress coefficient
k_M	failing-stress coefficient
p	rivet pitch, in.
p_a	allowable rivet pitch, in.
r_A	radius of bend between attachment flange and web of stiffener (see fig. 2), in.
t_S	plate thickness (see fig. 2), in.
t_W	stiffener thickness (see fig. 2), in.

¹ Supersedes NACA Technical Note 3431 by Joseph W. Semonian and James P. Peterson, 1955.

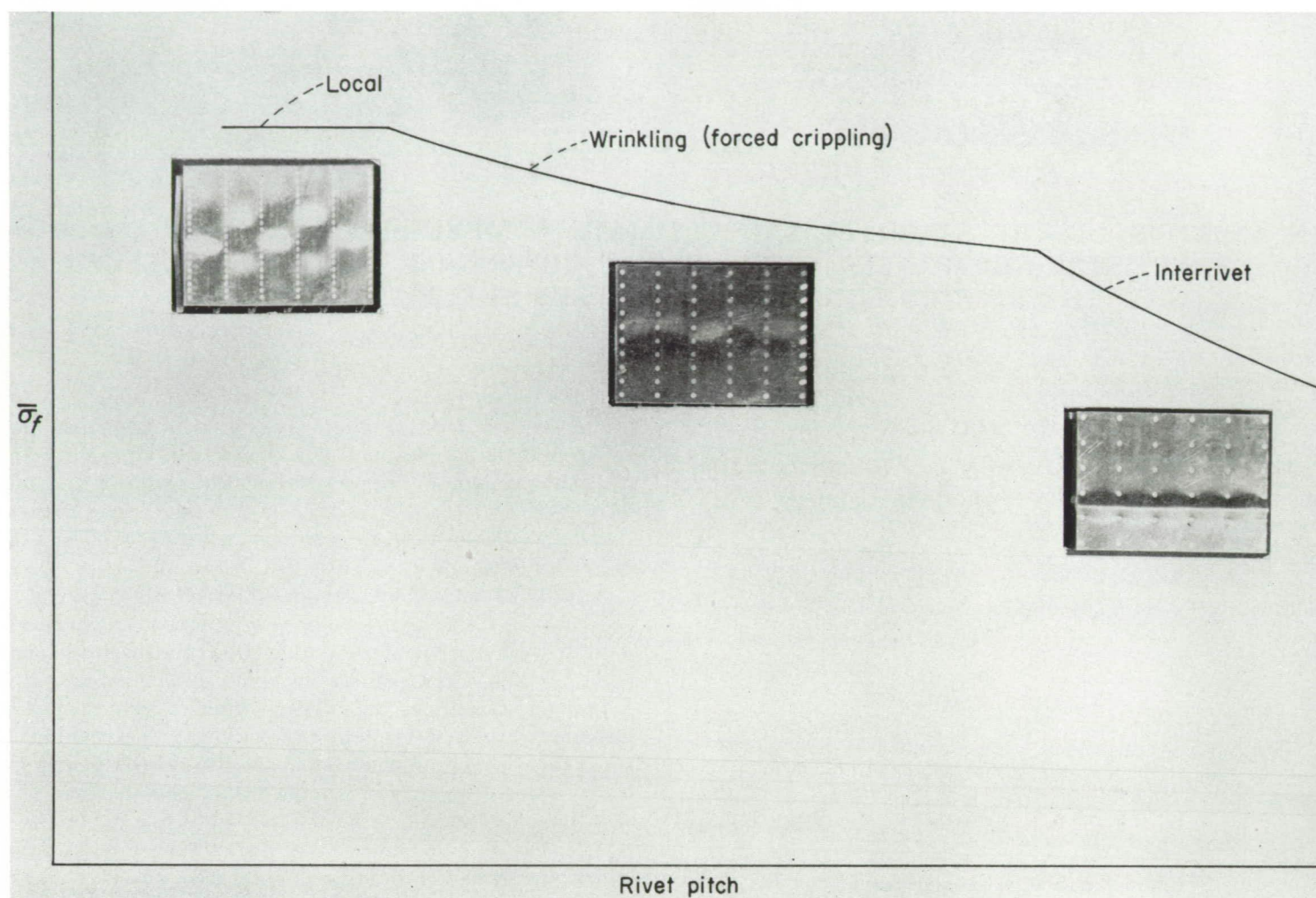


FIGURE 1.—The influence of rivet pitch on the strength of a short sheet-stringer panel showing the three predominant modes of failure.

A_z	cross-sectional area of Z-section stiffener, in. ²
D_s	plate flexural stiffness per unit width, $E_s t_s^3/12(1-\mu^2)$, in.-kips
D_w	flexural stiffness per unit width of web, $E_w t_w^3/12(1-\mu^2)$, in.-kips
E	Young's modulus, ksi
E_{sec}	secant modulus, ksi
E_{tan}	tangent modulus, ksi
E_s	Young's modulus of plate material, ksi
E_w	Young's modulus of stiffener material, ksi
R	rivet tensile strength, kips
R_R	required rivet tensile strength, kips
α	rotational stiffness per unit length (see fig. 5), kips

$$\beta = \frac{b_w/t_w}{b_s/t_s}$$

δ	lateral deflection of plate, in.
η	plasticity factor

$$\theta = \frac{\pi}{\lambda/b_s} \sqrt{\frac{\lambda}{b_s} \sqrt{k_{cr}} + 1}$$

λ	buckle length, in.
μ	Poisson's ratio
σ_{cr}	buckling stress, ksi
$\bar{\sigma}_f$	average stress in panel at failure, ksi

$\bar{\sigma}_{f_{crip}}$	average stress in panel at failure in local mode, ksi
σ_M	failing stress of plate, ksi
$\sigma_{Z_{crip}}$	crippling strength of Z-section stiffener, ksi
$\phi = \frac{\pi}{\lambda/b_s} \sqrt{\frac{\lambda}{b_s} \sqrt{k_{cr}} - 1}$	
ψ	deflectional stiffness per unit length, ksi

The designation for the various aluminum alloys has recently been changed. The old designation and the corresponding new designation for the aluminum alloys mentioned in this report are as follows:

Old designation	New designation
24S-T3	2024-T3
75S-T6	7075-T6
A17S-T3	2117-T3
2S-F	1100-F

STRUCTURAL ANALYSIS

A panel typical of those analyzed is shown in figure 2. The panel is considered to be short enough so that the column bending mode can be neglected yet long enough so that various local modes can form freely without end effects. The

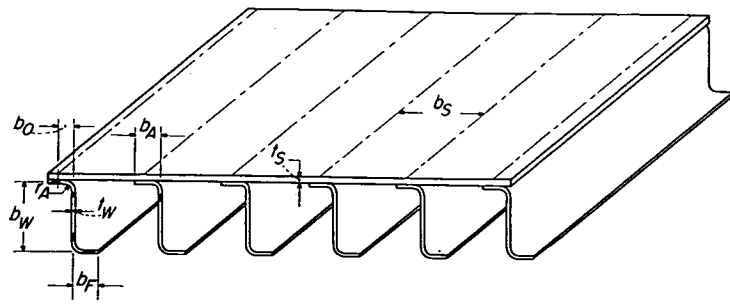


FIGURE 2.—A sheet-stringer panel.

panel is considered to be wide with many equally spaced stringers but the results of the analysis can be applied to panels with as few as four stringers without appreciable error.

The analysis is presented in four sections. The first section develops an initial-instability analysis which together with available experimental data is used in the second section to establish the effective rivet offset as a function of appropriate panel parameters. The values of effective rivet offset thus established are used in the third section to formulate a semi-empirical maximum-strength analysis. Finally, the fourth section is devoted to developing criteria which limit the pitch and diameter of rivets required to achieve the predicted strength of panels.

INITIAL INSTABILITY OF PANELS

The panel shown in figure 2 usually will buckle into either the local mode which has been analyzed in reference 5 or the wrinkling mode which will be analyzed herein. Another mode termed the "torsional cum local" mode was analyzed in reference 6. This mode may become the predominant mode when the width of the outstanding flange of the stiffener becomes small (say $b_f < 0.4b_w$) so the flange does not have enough stiffness to prevent the line of intersection between the flange and the web of the stiffener from translating when the panel buckles.

The wrinkling mode of instability can be analyzed by considering the plate to be supported by elastic springs with a deflectional stiffness per unit length of panel ψ as indicated in figure 3. A cross section of the plate through an up-

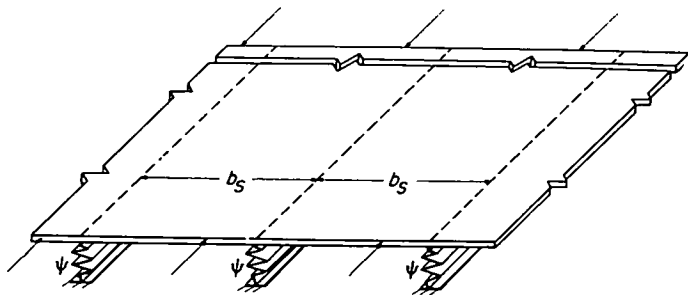


FIGURE 3.—Idealized structure used in analysis of sheet-stringer panel.



FIGURE 4.—Cross section of idealized structure at the crest of a buckle.

buckle is shown in figure 4. The stability criterion for the plate is given in reference 3 as

$$\frac{\psi b_s^3}{\pi^4 D_s} = \frac{\frac{4\sqrt{k_{cr}}}{\pi^2} \frac{\lambda}{b_s}}{\frac{\sin \phi}{\phi} \frac{\sinh \theta}{\theta}} \quad (1)$$

$$1 - \cos \phi \quad 1 - \cosh \theta$$

This expression has been solved and values of k_{cr} are plotted against values of λ/b_s for various values of the parameter $\psi b_s^3/\pi^4 D_s$ in figure 7 of reference 3.

The deflectional stiffness provided by a stringer of the same material as the plate is given by reference 4 as

$$\frac{\psi b_s^3}{\pi^4 D_s} = \frac{\frac{12}{\pi^4} \left(\frac{f}{b_w} \frac{\alpha}{D_w} + 1 \right)}{\left(\frac{f}{b_w} \beta \right)^3 \left(\frac{f}{b_w} \frac{\alpha}{D_w} + 4 \right)} \quad (2)$$

where the rotational stiffness α is a function of the web stress and the buckle length and can be taken from reference 7 which uses the symbol $4S^{II}$ to define this stiffness. The assumptions implied in the use of the above formulas have been given in reference 4 but are reviewed here for completeness of the present report.

Besides the restrictions on length and width of panel as discussed earlier, the implied assumptions are: (1) Deflections are small, (2) the structure is elastic, and (3) the stringer stiffness can be obtained from the idealization shown in figure 5. This idealization is based on the assumptions: (a) The effective rivet offset can be defined as the distance from the web of the stringer to a longitudinal line along which the rivets effectively clamp the attachment flange to the plate, (b) the longitudinal bending stiffness of the attachment flange can be neglected, and (c) the web can be assumed to be simply supported at the bottom. This last assumption will be good for webs of normal proportion as long as the width of the outstanding leg of the Z is about $0.4b_w$. At much larger values, it can become the unstable element and thereby initiate buckling; at much smaller values, it will not have enough depthwise stiffness to provide simple support to the web. For webs with small width thickness ratios a flange width greater than $0.4b_w$ is required to support the web against translation. For such cases the criterion of reference 8 should be used to design the outstanding flange.

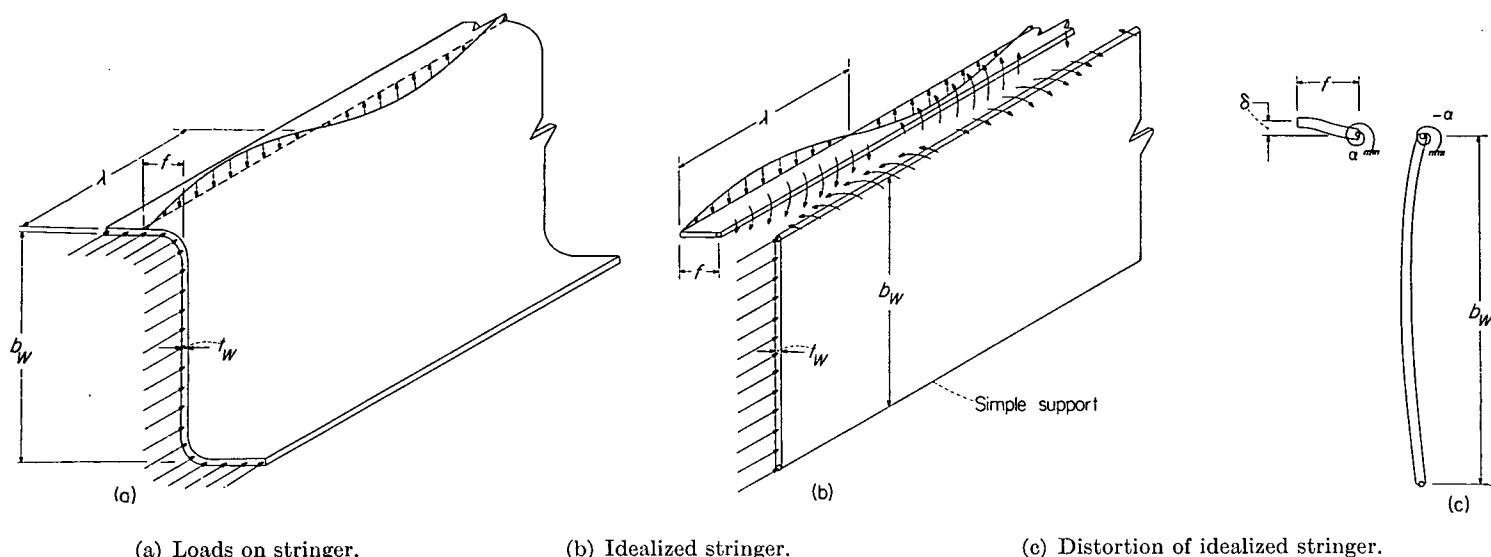


FIGURE 5.—Loads and deformations used in the calculation of the deflectional stiffness of short Z-section stringers.

Equations (1) and (2) have been solved and the results are given in figure 6. The buckling coefficient k_{cr} is plotted against the parameter β for various values of the parameter f/b_w . The buckling coefficient is related to the buckling stress by the relation

$$\frac{\sigma_{cr}}{\eta} = \frac{k_{cr}\pi^2 E}{12(1-\mu^2)} \left(\frac{t_s}{b_s} \right)^2 \quad (3)$$

A value of the plasticity factor η that has been found to give good correlation between test and calculation is

$$\eta = \frac{E_{sec}}{E} \left(\frac{1}{2} + \frac{1}{2} \sqrt{\frac{1}{4} + \frac{3}{4} \frac{E_{tan}}{E_{sec}}} \right) \quad (4)$$

This value of η is the value given by Stowell (ref. 9) for long simply supported flat plates in compression.

Local-buckling curves from reference 5 for $b_f/b_w=0.4$ and $t_w/t_s=0.63$ and 1.00 have been plotted in figure 6 for comparison with the wrinkling curves.

It will be noted that the buckling coefficient k_{cr} for the wrinkling mode is determined by the two parameters f/b_w and β even though these parameters are not sufficient to determine the panel configuration. The local-buckling curves, for instance, require the additional parameter t_w/t_s to fix their location on the plot of k_{cr} against β . This phenomenon was pointed out in reference 4 in connection with the calculation of wrinkling coefficients for multiweb beams.

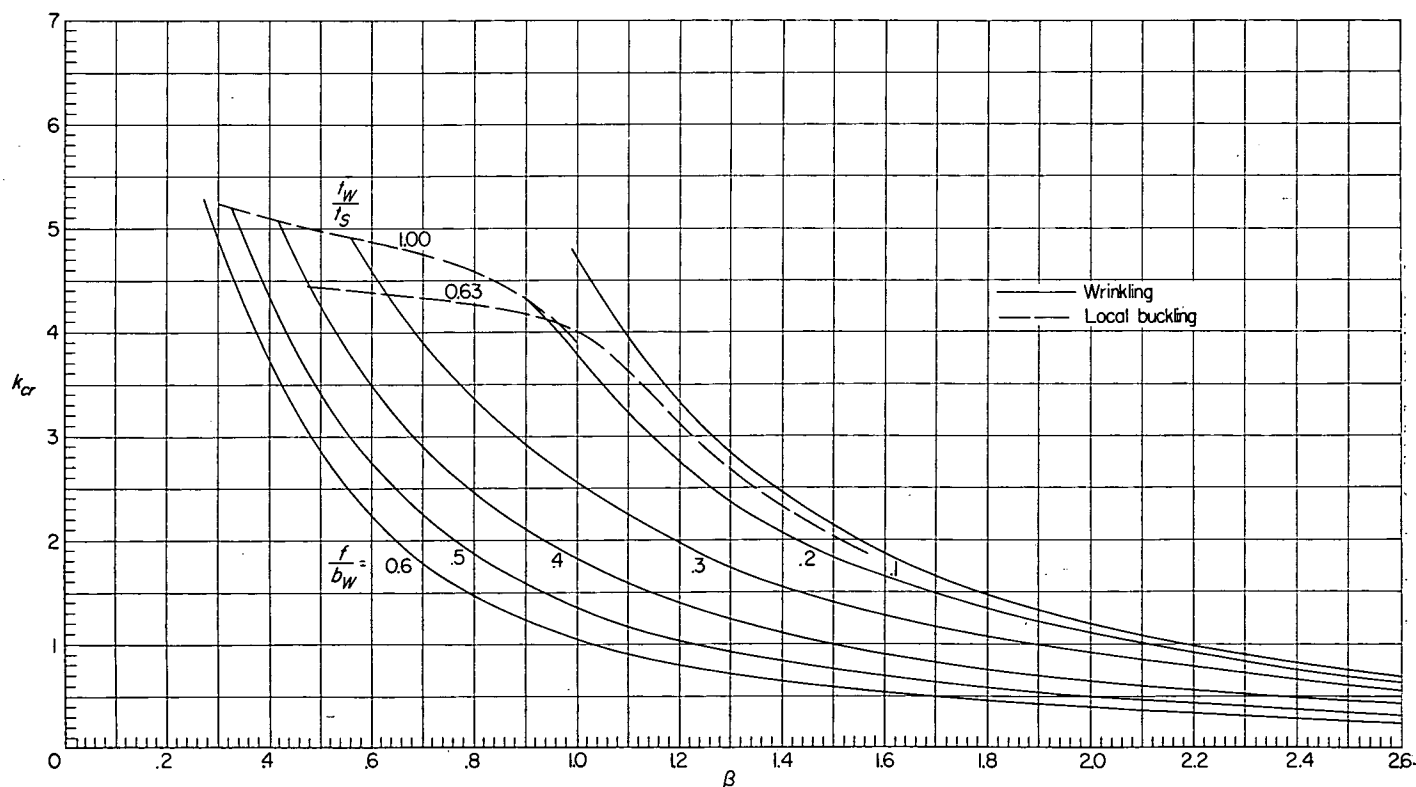


FIGURE 6.—The initial instability of Z-stiffened panels subjected to axial compressive loads. $\frac{\sigma_{cr}}{\eta} = \frac{k_{cr}\pi^2 E}{12(1-\mu^2)} \left(\frac{t_s}{b_s} \right)^2$.

and can be verified experimentally for panels by using data from reference 10. For example, figure 7 shows the failing stress for panels on which all structural parameters were held constant except t_w/t_s and it can be seen that the failing stress is independent of t_w/t_s within the accuracy of the tests. The fact that the data are maximum-strength data rather than buckling data does not appreciably affect the argument because the panels are of such proportions that the failing load is at most a few percent greater than the buckling load and is therefore closely related to the buckling load. The particular values of rivet pitch used in figure 7 were chosen because, after a preliminary study of the data, they

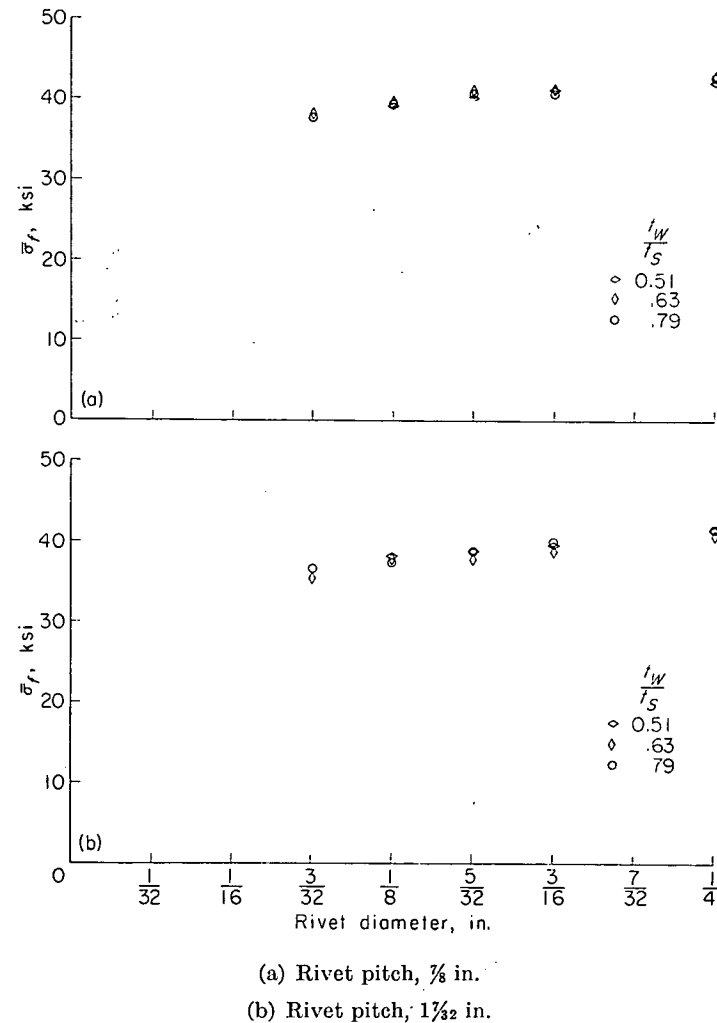


FIGURE 7.—Comparison of average stress at maximum load for panels of reference 10 for three values of t_w/t_s . $b_w/t_w=20$; $b_s/t_s=25$; $b_o/t_w=5.6$; $t_w=0.064$ in.

were felt to be large enough so that the panels did not fail in the local mode and small enough so that the panels did not fail in the interrivet mode. (See fig. 1.) Other values of rivet pitch and t_w/t_s given in reference 10 further substantiate the insensitiveness of the wrinkling stress to changes in t_w/t_s .

EXPERIMENTAL DETERMINATION OF f

The analysis developed in the preceding section gives the wrinkling stress of a panel provided the dimension f is known. Conversely, if the wrinkling stress of a panel is known, the

value of f can be determined. The existing panel data, however, are not very suitable for determining the dimension f for three main reasons: (1) The rivet offset b_o was usually not varied or even controlled because its influence on panel strength has only recently been understood; (2) the buckling stress was often never published or perhaps even measured because the interest was mainly directed toward finding the maximum strength of panels; and (3) the cases in which the panels did wrinkle and the buckling load was recorded often involved failure at such high stresses that the effects of plasticity must be known to a high degree of accuracy in order to determine f . In order to alleviate this situation, a series of 7075-T6 (previously designated as 75S-T6) aluminum-alloy panels, on which the rivet pitch, diameter, and offset as well as the radius of bend between the attachment flange and the web of the stiffener were systematically varied, were built and tested. The results of these tests are reported in table I. These data, and all other available data which were believed to be applicable, were plotted and cross-plotted until a best fit to the data was obtained. The result is shown in figure 8 where the distance f is given in terms of the rivet offset b_o and the pitch and diameter of the rivets. It will be noted that the radius of bend between the attachment flange and the web of the stringer as well as the type of rivets does not appear on this plot. Furthermore, the other dimensions appear only in very simple form. In spite of this simplicity, it is believed that figure 8 has rather general applicability. For instance, figure 8 can evidently be applied to panels with various types of rivets although most of the data used to establish the figure were obtained from tests on panels on which NACA countersunk rivets were used. The countersunk head of this type of rivet is formed from the rivet shank by driving the rivet and the excess material is then milled off flush. Figure 2 of reference 11 gives a comparison of failing loads for panels assembled with NACA rivets and similar panels assembled with flat-head rivets with the manufacturer's head on the plate side. The comparison shows little or no effect of type of rivet on the strength of panels which obviously failed by wrinkling. A few available tests from panels and multiweb beams which were assembled with universal-head or flat-head rivets on the stiffener side and a shop-driven head on the plate side further indicate that the error in using figure 8 for other types of rivets is small.

The data used to establish the chart of figure 8 were obtained from tests on panels assembled with rivets whose diameter was at least as great as 90 percent of the plate thickness ($d/t_s > 0.90$) and the chart should not be used for much smaller values of rivet diameter without confirmation.

Figure 8 is applicable to multiweb beams as well as panels and can be used in the application of the formulas and design charts of reference 4 to the analysis of the bending strength of multiweb beams.

FAILURE OF PANELS

The failure of short compression panels usually results from a growth of either local or wrinkling type of buckles. Less frequently, failure may result from rivet failure or growth of an interrivet type of buckle. The first two types of failures will be discussed in this section and the last two types

TABLE I
TEST DATA AND PROPORTIONS OF 7075-T6 ALUMINUM-ALLOY PANELS

$$\left[\frac{b_F}{b_W} = 0.40 \right]$$

t_w , in.	t_w/t_s	L/p	b_s/t_s	b_w/t_w	b_o/t_w	τ_A/t_w (a)	d , in. (b)	p/d	σ_{cr} , ksi	$\bar{\sigma}_f$, ksi
0.0660	0.640	20	24.6	18.7	5.2	3.0	$\frac{1}{16}$	14.0	45.2	45.2
0.0663	.636	20	24.5	18.5	5.0	3.0	$\frac{3}{32}$	9.3	49.5	52.0
0.0668	.650	20	24.8	19.2	6.2	3.0	$\frac{3}{32}$	9.3	48.0	48.5
0.0663	.630	20	24.3	19.4	7.2	3.0	$\frac{3}{32}$	9.3	41.0	44.3
0.0658	.640	20	24.8	19.6	8.6	3.0	$\frac{3}{32}$	9.3	38.8	41.2
0.0666	.645	20	24.7	18.2	5.0	3.0	$\frac{1}{8}$	7.0	54.0	55.0
0.0660	.628	20	24.2	19.2	6.1	3.0	$\frac{1}{8}$	7.0	51.3	53.0
0.0666	.635	20	24.2	19.2	7.1	3.0	$\frac{1}{8}$	7.0	45.4	48.1
0.0662	.633	20	24.4	19.4	8.3	3.0	$\frac{1}{8}$	7.0	42.1	45.3
0.0664	.641	20	24.6	18.3	5.1	3.0	$\frac{5}{32}$	5.6	55.4	56.2
0.0664	.630	20	24.2	19.4	6.2	3.0	$\frac{5}{32}$	5.6	53.2	54.6
0.0660	.638	20	24.6	19.5	7.4	3.0	$\frac{5}{32}$	5.6	49.2	51.0
0.0664	.633	20	24.3	19.2	8.2	3.0	$\frac{5}{32}$	5.6	45.8	47.6
0.0663	.634	20	24.4	19.0	5.4	3.0	$\frac{3}{16}$	4.7	58.7	59.2
0.0666	.636	20	24.4	19.2	6.1	3.0	$\frac{3}{16}$	4.7	55.2	57.0
0.0666	.636	20	24.4	19.3	7.2	3.0	$\frac{3}{16}$	4.7	50.3	52.8
0.0662	.631	20	24.4	19.4	8.2	3.0	$\frac{3}{16}$	4.7	46.8	50.2
0.0647	.620	20	24.5	18.2	3.8	1.0	$\frac{5}{32}$	5.6	60.7	62.8
0.0663	.640	20	24.5	19.3	6.6	4.0	$\frac{5}{32}$	5.6	53.1	54.6
0.0665	.639	20	24.5	19.3	7.2	5.0	$\frac{5}{32}$	5.6	49.6	52.0
0.0657	.635	20	24.7	19.6	8.5	6.0	$\frac{5}{32}$	5.6	49.7	51.3
0.0663	.641	20	24.6	19.0	8.1	6.0	$\frac{5}{32}$	5.6	50.5	52.5
0.0641	.610	20	24.2	18.5	4.5	1.0	$\frac{5}{32}$	5.6	59.7	62.0
0.0650	.625	20	24.6	18.3	5.5	1.0	$\frac{5}{32}$	5.6	55.0	56.3
0.0643	.610	20	24.2	18.5	6.5	1.0	$\frac{5}{32}$	5.6	52.5	54.2
0.0643	.615	20	24.4	18.4	7.6	1.0	$\frac{5}{32}$	5.6	48.4	49.8
0.0627	.605	30	39.5	19.0	4.1	1.0	$\frac{5}{32}$	5.6	27.6	46.4
0.0658	.639	30	39.6	19.6	5.3	3.0	$\frac{5}{32}$	5.6	26.5	44.9
0.0659	.633	30	39.2	19.5	6.4	4.0	$\frac{5}{32}$	5.6	24.2	42.7
0.0648	.627	30	39.5	19.8	7.3	5.0	$\frac{5}{32}$	5.6	24.6	43.7
0.0658	.630	30	39.0	19.3	8.3	6.0	$\frac{5}{32}$	5.6	26.2	41.2
0.0660	.636	30	39.3	19.4	8.2	6.0	$\frac{5}{32}$	5.6	25.5	39.2

*Stringers with $\tau_A/t_w=1.0$ were extruded. All others were formed.

^bAll rivets were 2117-T3 flat-head rivets with NACA countersink on the plate side. The depth of countersink for the $\frac{1}{16}$ -, $\frac{3}{32}$ -, $\frac{1}{8}$ -, $\frac{5}{32}$ -, and $\frac{3}{16}$ -inch-diameter rivets was 0.040, 0.050, 0.060, 0.070, and 0.080, respectively.

will be considered in the next section where rivet criteria are developed that can be used to prevent such failures.

Failure in the wrinkling mode.—Panels which buckle initially in the wrinkling mode usually fail in a similar mode. The plate configuration at failure, however, is simpler than the initial buckling configuration because, as the initial buckles grow with an increase in applied load, the plate buckle shape becomes more and more cylindrical until at failure it may be assumed to be cylindrical and the plate may be treated as a column on an elastic foundation. The plate in the column mode appears much like the well-known interrivet mode except the length of buckle is greater than the rivet pitch. The stringer, however, has a very different configuration. In the interrivet mode the stringer cross section may remain essentially undistorted while the plate and stringer separate. In the wrinkling mode of failure the attachment flange of the stringer follows the plate contour and causes the other plate elements of the stringer to distort also. The similarity between the appearances of the wrinkling mode and the interrivet mode has caused investigators to make strength calculations with interrivet-type formulas on panels which failed in the wrinkling mode. (See, for instance, ref. 12.) The panels of this reference evidently failed in the wrinkling mode and the strength of the panels can be calculated by the methods developed herein.

The stability criterion for the plate in the wrinkling mode of failure is given as (see ref. 13)

$$k_M = \frac{1}{\left(\frac{\lambda}{b_s}\right)^2} + \frac{\psi b_s^3}{\pi^4 D_s} \left(\frac{\lambda}{b_s}\right)^2 \quad (5)$$

The support stiffness was determined by trial to give the best correlation between panel strength and calculated strength. It was found that the support stiffness could be taken as

$$\frac{\psi b_s^3}{\pi^4 D_s} = \frac{\frac{12}{\pi^4} \left(3 \frac{f}{b_w} + 1\right)}{\left(\frac{f}{b_w} \beta\right)^3 \left(3 \frac{f}{b_w} + 4\right)} \quad (6)$$

This equation is identical to equation (2) except the rotational stiffness $\alpha \frac{b_w}{D_w}$ has been replaced by a constant value of 3. In the trial calculations used to determine the support stiffness, other values of $\alpha \frac{b_w}{D_w}$ were tried, including the apparent value as given by equation (2), but the value $\alpha \frac{b_w}{D_w} = 3$ was considered to give the best agreement between calculated strength and panel strength over a wide range of panel proportions. It gave particularly superior correlation compared with the apparent value when the webs of the stiffeners were relatively unstable because the apparent value (eq. (2)) gave the restraint at the onset of buckling of the webs and not the

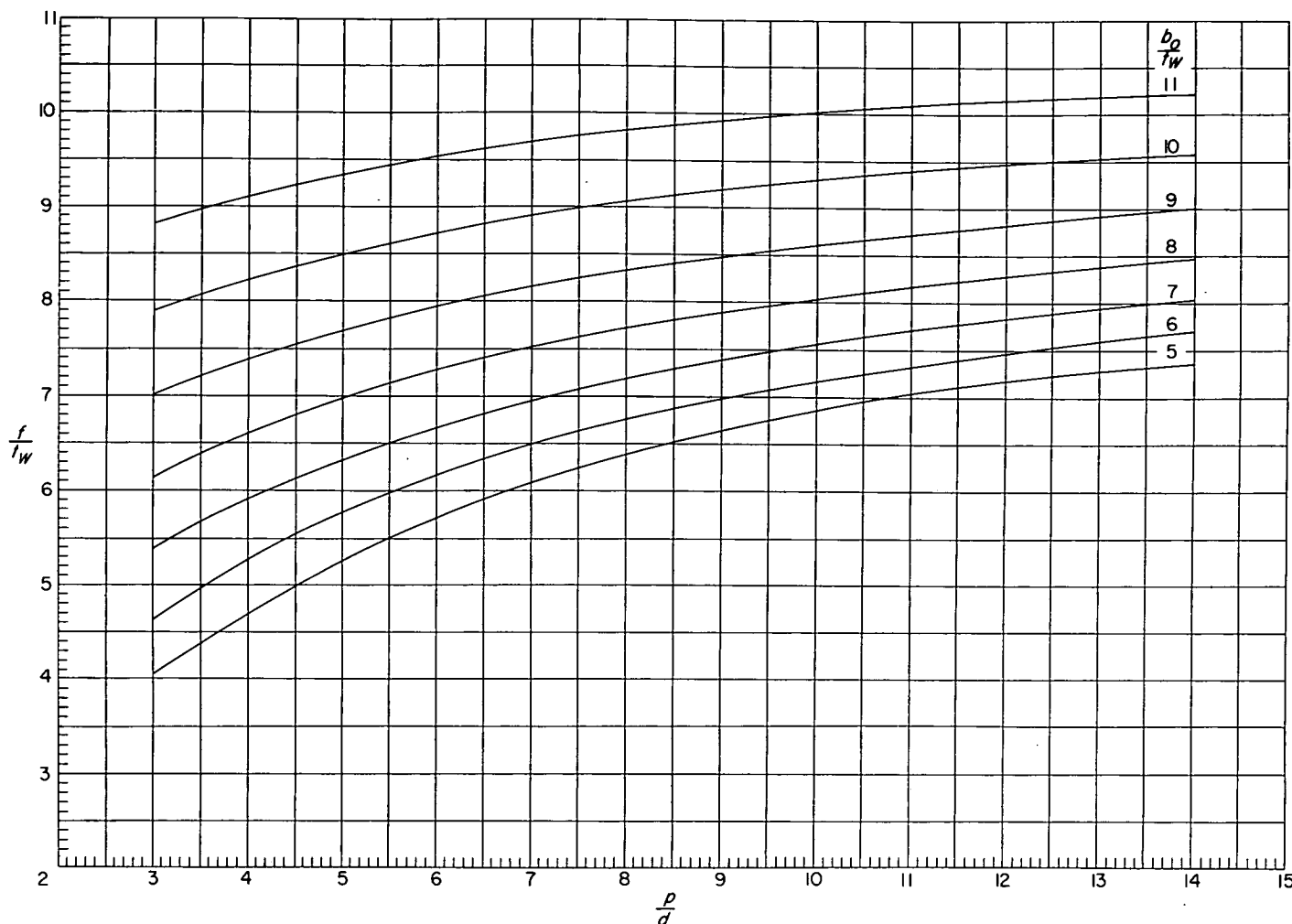


FIGURE 8.—Experimentally determined values of effective rivet offset for Z and channel stringers and full-depth channel webs.

restraint offered the skin at panel failure. The value $\alpha \frac{b_w}{D_w} = 3$ was also used in reference 4 to calculate the strength of multiweb beams in bending.

With the simplification implied by equation (6), that the support stiffness is independent of the buckle length, equation (5) can be simplified to read

$$k_M = 2 \sqrt{\frac{\psi b_s^3}{\pi^4 D_s}} \quad (7)$$

after k_M is minimized with respect to buckle length.

Equations (6) and (7) have been solved and the results are presented in figure 9 which gives the maximum stress that the plate can carry in the wrinkling mode. At this stress, the lateral deflections of the plate, and therefore the lateral forces on the stringers, become large and destroy the capacity of the stringers to carry additional load except for unusual panel proportions.

Experience in testing panels and multiweb beams indicates that a plate in the wrinkling mode suffers a relatively moderate redistribution of stress after initial buckling. The load-shortening curve for a plate in the wrinkling mode, therefore, nearly coincides with the stress-strain curve of the plate material until just prior to plate failure. The stringer on a panel which has buckled in the wrinkling mode appears

very much like a stringer on a panel which has buckled in the local mode and evidently suffers much the same redistribution of stress and loss of axial stiffness. In order to calculate the strength of a panel, it is necessary to know the load carried by the stringers at panel failure. (The plate load is given by fig. 9.) The load carried by the stringers depends on the proportions of the panel. If the stringers are relatively sturdy ($\beta < 1$), they will be stressed the same as the plate. If the stringers are unstable ($\beta > 1$), the stringers will not be loaded as heavily as the plate. An approximation which gives predictions which are slightly high when the stringers are unstable but which gives satisfactory results over the entire practical range of panel proportions is that the stringers take the same stress as the plate as long as that stress is not greater than the stringer crippling stress, in which case the stringers take their crippling stress. In addition, the calculated load carried by the panel must always be greater than the crippling load of the stringers tested without being fastened to the plate. This criterion takes care of the case when the area of the stringers is large compared with the area of the plate and the attachment between the plate and the stringer is so flexible that wrinkling occurs at a load less than the crippling load of the stringers. For this case, the lateral forces on the stringers are comparatively small and do not affect the strength of the stringers. Furthermore, at the shortening necessary for the

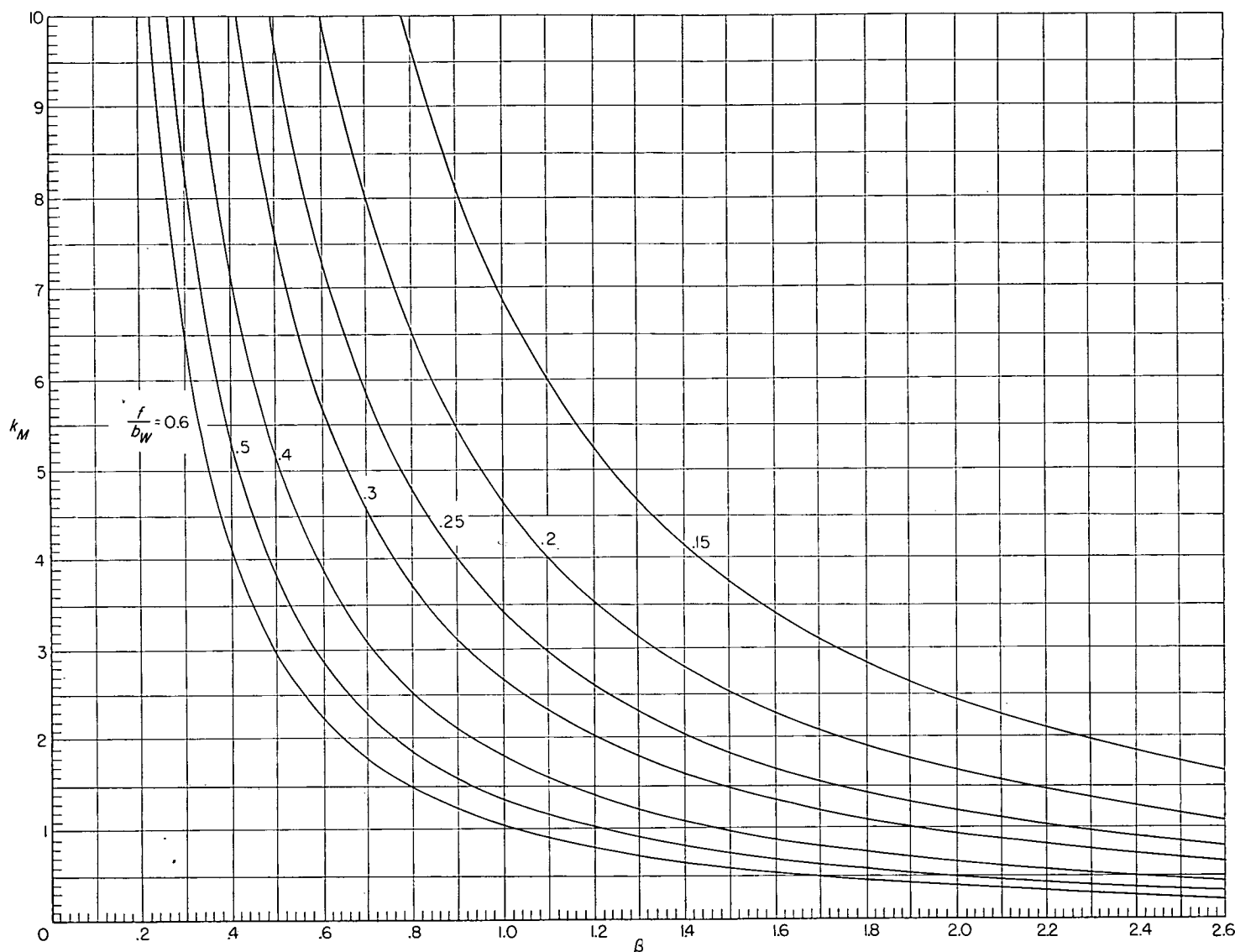


FIGURE 9.—Maximum stress coefficients for sheet-stringer panels that fail by wrinkling. $\frac{\sigma_M}{\eta} = \frac{k_M \pi^2 E}{12(1-\mu^2)} \left(\frac{t_s}{b_s}\right)^2$.

stringers to achieve their crippling stress, the load being carried by the plate has fallen to a negligible quantity and it may be assumed that the entire load is being carried by the stringers.

The value of the plasticity factor η to be used with figure 9 is given by equation (4). The use of a plasticity factor which is a function only of the stress-strain curve of the plate material and is applied to the average stress in the plate at failure may seem to be rather arbitrary for panels on which the proportions are such that the panels buckle at loads that are considerably less than the loads that the panels ultimately carry. Panels which buckle in the local mode, for instance, experience a severe redistribution of stress as the panel is loaded beyond the buckling load. The factor may not be too arbitrary for panels which fail in the wrinkling mode, however, because a plate in the wrinkling mode of failure is under relatively uniform stress across the width of the plate; that is, the stress is not peaked at the stringers as for a plate which has buckled in the local mode. The correlation between test and calculation obtained by using the plasticity factor given by equation (4) will be given

later and indicates that the factor is satisfactory even for panels with a large post-buckling strength.

When figure 9 is used to calculate the strength of a panel, the strength in the local mode as well as the strength in the wrinkling mode should be calculated and the load the panel can be expected to carry will be the lower of the two loads. The strength of panels in the local mode will be discussed in the next section.

Failure in the local mode.—Panels which buckle initially in the local mode may fail as a result of the growth of the local buckles. (See fig. 1.) A few panels have been observed to buckle in the local mode and to switch from local buckling to wrinkling at a higher stress level and eventually fail in the wrinkling mode. The data from such panels evidently would plot near the value of rivet pitch in figure 1 where the local mode ends and the wrinkling mode starts.

A study of the available data on compression panels on which the pitch and diameter of the attachment rivets were varied indicates that the gain in strength corresponding to a decrease in pitch or an increase in diameter of the rivets after the local buckling range has been reached is small

Consequently, for riveted panels there is a panel strength which is relatively independent of changes in riveting that corresponds to failure of the panel in the local mode. This characteristic has been recognized for a long time (see, for instance, ref. 11) and is responsible for the numerous investigations in the past on "strongly riveted panels" (the investigation of ref. 5, for instance). When these investigations were applied to the design of panels, however, the riveting required to make the panel behave as a strongly riveted panel was not known and rather severe rivet criteria had to be used. (See criterion of ref. 14.) The present analysis alleviates this difficulty by relating the strength of panels to the pitch, diameter, and offset of the attachment rivets.

Reference 5 shows that the ultimate strength of panels which buckle locally at high stresses is closely related to the buckling load and can be calculated by the buckling charts of that reference. The particular curves for a value of $\frac{b_F}{b_w}$

of 0.4 and values of $\frac{t_w}{t_s}$ of 0.63 and 1.00 are reproduced in figure 6. Reference 15 gives a method of predicting the strength of a panel in the local mode provided the strength of a nominally identical panel of another material is known. With the help of these references and the test data of references 1, 10, and 16 to 20, the strength of some panels which fail in the local mode was estimated and is given in figure 10. In the construction of figure 10, the method of reference 5 determined the indicated strength of the panels when the failing stress is high (usually panels with values of β of about unity and with small values of b_s/t_s and b_w/t_w). These particular panels require the most severe riveting criteria in order to force the panel to fail in the local mode and consequently their strengths are the most difficult to obtain experimentally. The available experimental data, supplemented by the procedure of reference 15, sufficed to determine the strengths of the other panels considered.

RIVET CRITERIA

The maximum-strength analysis of compression panels given in the preceding section requires certain limitations on the pitch and strength of rivets in order that the panel will carry the predicted load. The rivets must be spaced closely enough and have adequate strength to make the stringer flange follow the plate contour. If the spacing is too large, the panel may fail by interrivet buckling. If the strength is insufficient, the panel may fail prematurely because of rivet failure.

Rivet pitch.—An expression for buckle length which is consistent with the maximum-strength formulas (6) and (7) is

$$\frac{\lambda}{b_s} = \sqrt{\frac{2}{k_M}} \quad (8)$$

The allowable rivet pitch which must not be exceeded in order that the stringer flange follow the plate contour can logically be related to the buckle length as given by equation (8). It was found by trial that, if the rivet pitch was less than 90 percent of the calculated buckle length, wrinkling would occur rather than interrivet buckling. Hence, the rivet pitch must satisfy the criterion

$$\frac{p}{b_s} < 0.90 \sqrt{\frac{2}{k_M}} \quad (9)$$

Rivet strength.—The lateral force required to hold the compressed plate in its deflected position is proportional to the support stiffness and the lateral deflection of the plate. The force on a rivet near the crest of a buckle may be expressed approximately as

$$R \approx \psi \delta p \quad (10)$$

where δ is the lateral deflection of the plate at the crest of a buckle. The value of ψ may be taken from equation (A19) of reference 4. An appropriate value for the rotational stiffness $\frac{\alpha f}{D_f}$ in this equation is $\frac{\alpha f}{D_f} = 3 \frac{f}{b_w}$. In order to express formula (10) as a rivet-strength criterion, the value of lateral deflection must be known or assumed. Figure 3 of reference 21 indicates that, for an idealized H-section column, maximum load is reached before the lateral deflection is one-fifth of the column (or plate) thickness provided the buckling stress is at least half of the compressive yield stress of the column material. (For panels which buckle early a value larger than one-fifth should be used.) If this value is used in formula (10), the required tensile strength for a rivet becomes

$$R_R > \frac{E_w}{1-\mu^2} \frac{1}{\left(\frac{f}{t_w}\right)^3} \left(\frac{3 \frac{f}{t_w} + \frac{b_w}{t_w}}{3 \frac{f}{t_w} + 4 \frac{b_w}{t_w}} \right) \frac{t_s}{5} p \quad (11)$$

The tensile strength of a rivet is defined as the load required to cause any failure; it may be the load required to break the shank but more often it is the load required to pull the countersunk head through the plate or, when the stiffener gage is small, to pull the rivet head through the stiffener.

Reference 22 gives the strength of protruding-head rivets. Reference 23 gives strength data on NACA countersunk and conventional countersunk rivets. Additional rivet-strength data can be found in references 24 and 14.

Expression (11) gives the tensile strength of the attachment rivets that is required in order that the predicted strength of the panel in the wrinkling mode can be achieved. Obviously, when the panel fails in the local mode, expression (11) does not apply. The available data indicate that for this case the rivet strength need not be any greater than that required when failure is in the wrinkling mode and the stress levels at failure in the two modes are equal.

EXPERIMENTAL VERIFICATION

The data presented in this section have already been used to establish the empirical factors in the analysis presented earlier and will now be compared with the analysis to assess its validity. The data were taken, in large part, from published NACA panel data obtained from panels which were five bays wide (6 stringers) and had a slenderness ratio L/ρ of 20. The ends of the panels were ground flat and parallel in a special grinder prior to testing and the panels were tested flat-ended in a hydraulic testing machine. A large amount of wrinkling data is available on panels made from 2024-T3

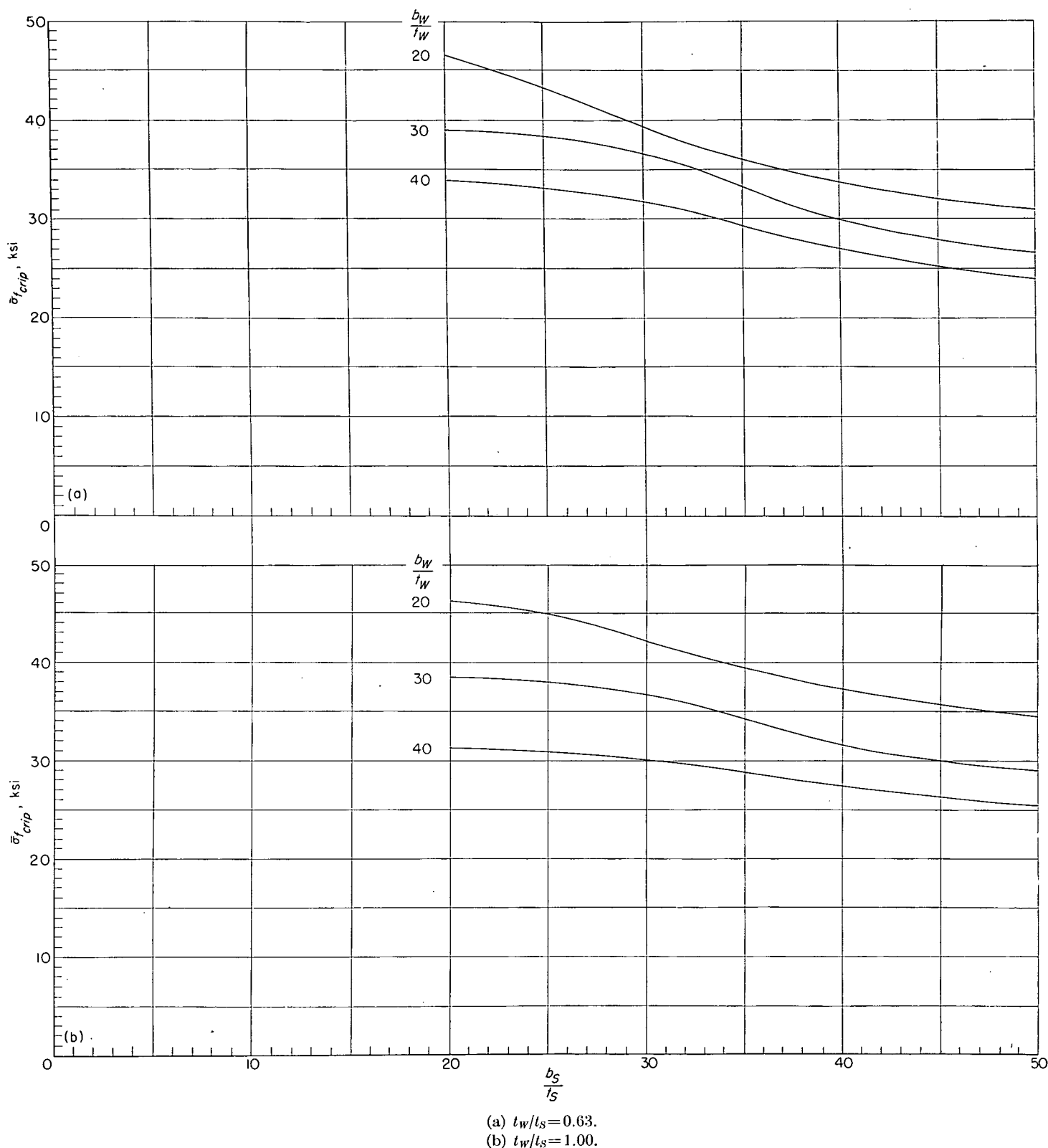


FIGURE 10.—The strength of 2024-T3 aluminum-alloy Z-stiffened panels in the local mode. $b_F/b_W = 0.40$.

(previously designated 24S-T3) aluminum alloy. The number of tests on panels which failed in the wrinkling mode and which were made from 7075-T6 aluminum alloy is much smaller for two reasons: (1) The investigation on the effect of riveting on panel strength was made on 2024-T3 aluminum-alloy panels first and later on 7075-T6 aluminum-alloy panels. The knowledge gained from the early experiments could be applied to the later tests and thereby reduce the

number of tests required. (2) The tests on 7075-T6 aluminum-alloy panels were made on panels with extruded stringers with small fillets so the rivet line could be moved in close to the web of the stiffener and thereby prevent the wrinkling type of failure. In order to relieve the shortage of data on 7075-T6 aluminum-alloy panels, a series of panel tests were made in the present investigation and are reported herein.

Data on panels with riveting which do not satisfy the criteria of expressions (9) and (11) and the additional criterion that the ratio p/d must be less than 15 will not be given in the presentation which follows. The latter criterion is included because available data on panels for which the failure was definitely wrinkling were considered to be inadequate to establish design curves for these high values of p/d . The restriction on panel design imposed by this criterion, however, is not considered to be severe because contemporary design rarely allows such large rivet pitches.

2024-T3 ALUMINUM-ALLOY PANELS

The data of references 10, 16, and 17 are shown in figures 11, 12, and 13, respectively, where the average stress in the panel at failure $\bar{\sigma}_f$ is plotted against the rivet parameter p/d . The data of reference 16 for panels with a b_s/t_s greater than 50 are not given because it is relatively easy to rivet such panels so that the panel will fail in the local mode. NACA counter-sunk rivets were used to assemble the panels. Other pertinent dimensions are given in the figures. The data plot against the parameter p/d with a small amount of scatter. This characteristic is responsible for the use of the $\frac{p}{d}$ -parameter on the f -chart of figure 8.

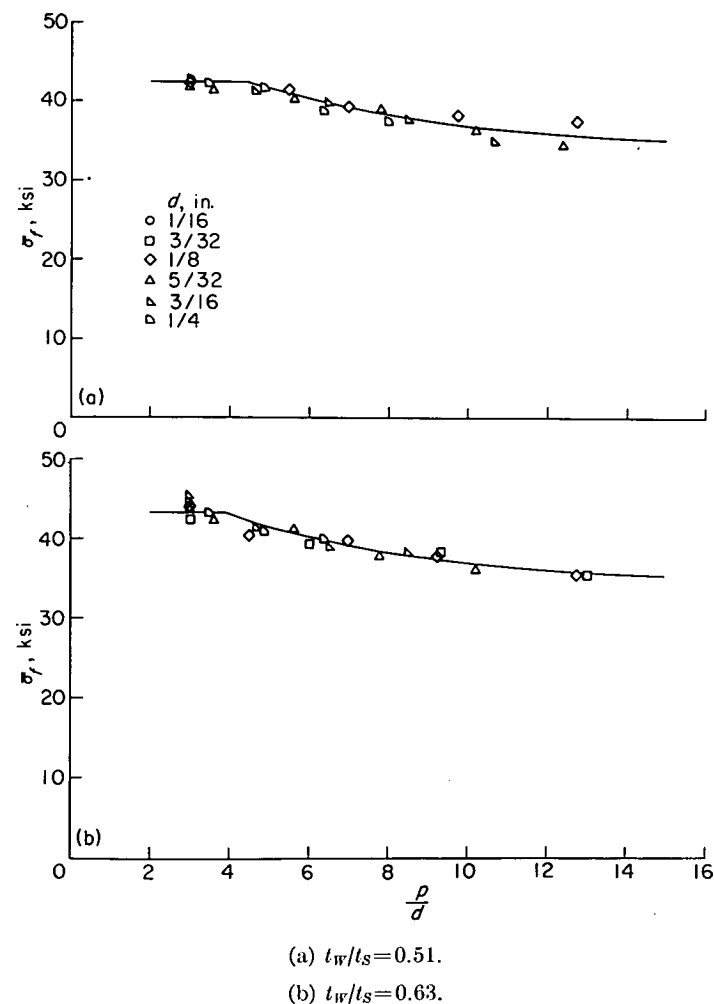


FIGURE 11.—Comparison of calculated and experimental failing stresses of 2024-T3 Z-stiffened panels of reference 10 for five values of t_w/t_s . $b_w/t_w = 20$; $b_s/t_s = 25$; $b_o/t_w = 5.6$; $t_w = 0.064$ in.

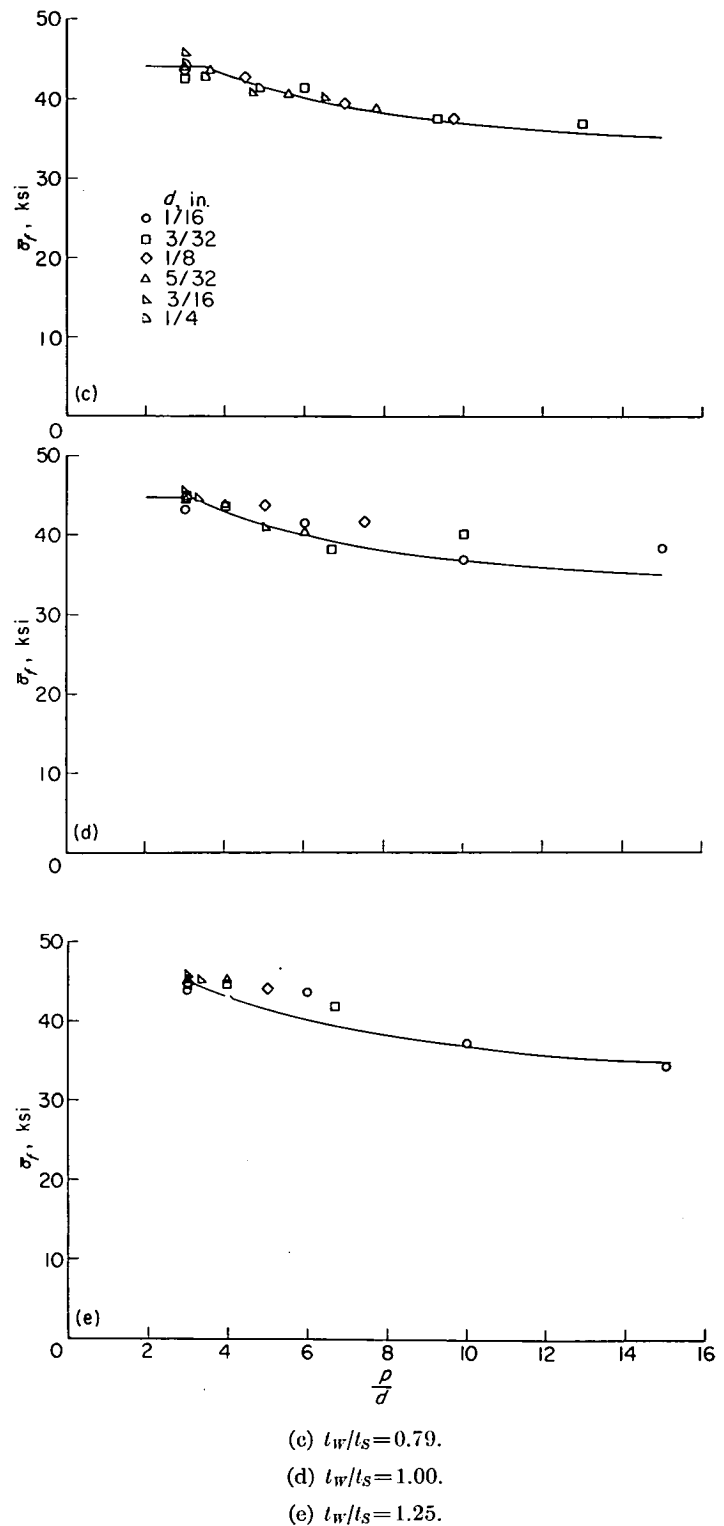


FIGURE 11.—Concluded.

The curves in figures 11 to 13 represent predicted panel strengths. The wrinkling section of the curves was obtained with the use of figures 8 and 9. For the panels represented by the data in figure 13, where the stringers are relatively unstable, the crippling strength of the stringers was required to obtain the panel strength in the wrinkling mode. The stringer crippling strength was taken from reference 25; the data were extrapolated when it was necessary. The curves predict the trend as well as the magnitude of the data within the accuracy of the panel tests; experience in testing panels

indicates that strength tests on two nominally identical panels usually give strengths which differ by less than 5 percent from the average strength although differences as great as 10 percent have been obtained. The wrinkling curves miss the middle of the scatter band of the data in some instances by about 5 percent. It is believed that such discrepancies are largely a result of neglecting the difference in material properties and panel parameters (particularly b_o/t_w) between one group of panels and another. The panels represented by the data of figures 12 and 13 were built in groups similar to the grouping used in the presentation of the data and are therefore particularly susceptible to errors common to a group of data. These differences were neglected in the presentation of the data because of the resulting simplicity and because only nominal values of the rivet offset b_o were known.

The local-mode section of the curves in figures 11 to 13 was obtained from figure 10 for the panel proportions cov-

ered by the figure. The local strength of the panels with a b_w/t_w of 25 and 50 which are not covered by figure 10 were obtained by interpolation and extrapolation of the data from figure 10 by using the present data as a guide. A study of figures 11 to 13 indicates that the strength of a panel in the local mode becomes increasingly difficult to attain as t_w/t_s is increased or as b_s/t_s is decreased. Accordingly, the closest riveting used in the investigation ($p/d=3.0$) was just adequate to attain the strength in the local mode of the panels of figure 11 with a thickness ratio $t_w/t_s=1.00$ and was inadequate to attain the local strength of the panels with $t_w/t_s=1.25$. For panels with much smaller values of b_s/t_s than were used in figure 11, it would be impossible to rivet the panels so that the local strength is obtained without the use of smaller values of the rivet offset b_o .

Some test data from reference 26 on panels with hat-section stiffeners are given in figure 14. The average stress in the panel at failure $\bar{\sigma}_f$ is plotted against b_s/t_s where $2b_s$ is the distance between similar locations on two adjacent hat stiffeners. Only data for the thickness ratio $t_w/t_s=0.35$

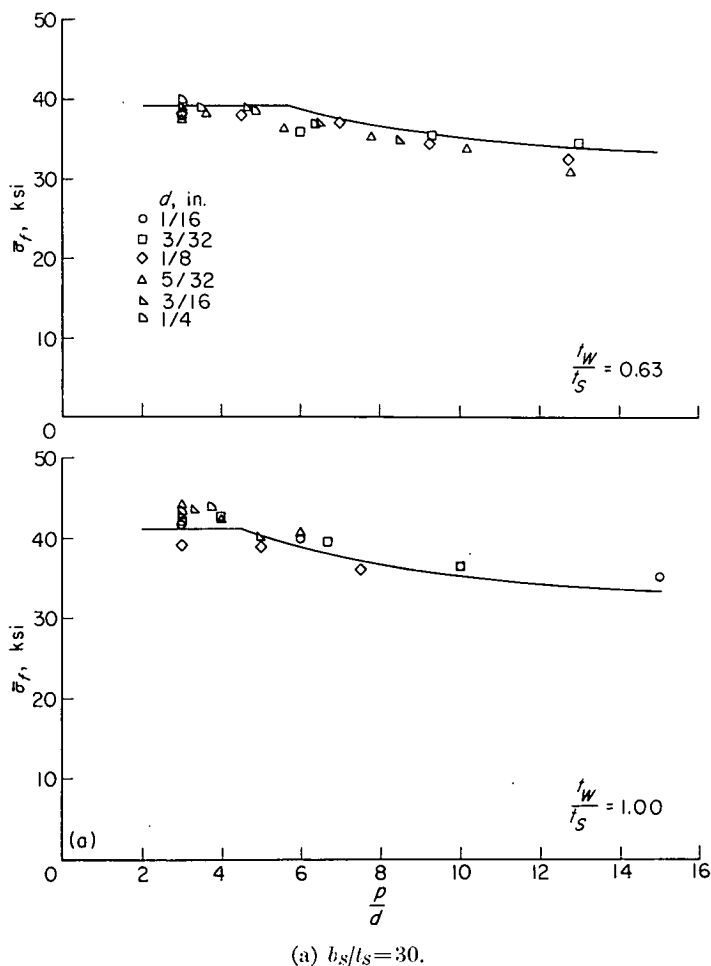


FIGURE 12.—Comparison of calculated and experimental failing stresses of 2024-T3 Z-stiffened panels of reference 16 for four values of b_s/t_s at two values of t_w/t_s . $b_w/t_w=20$; $b_o/t_w=5.6$; $t_w=0.064$ in.

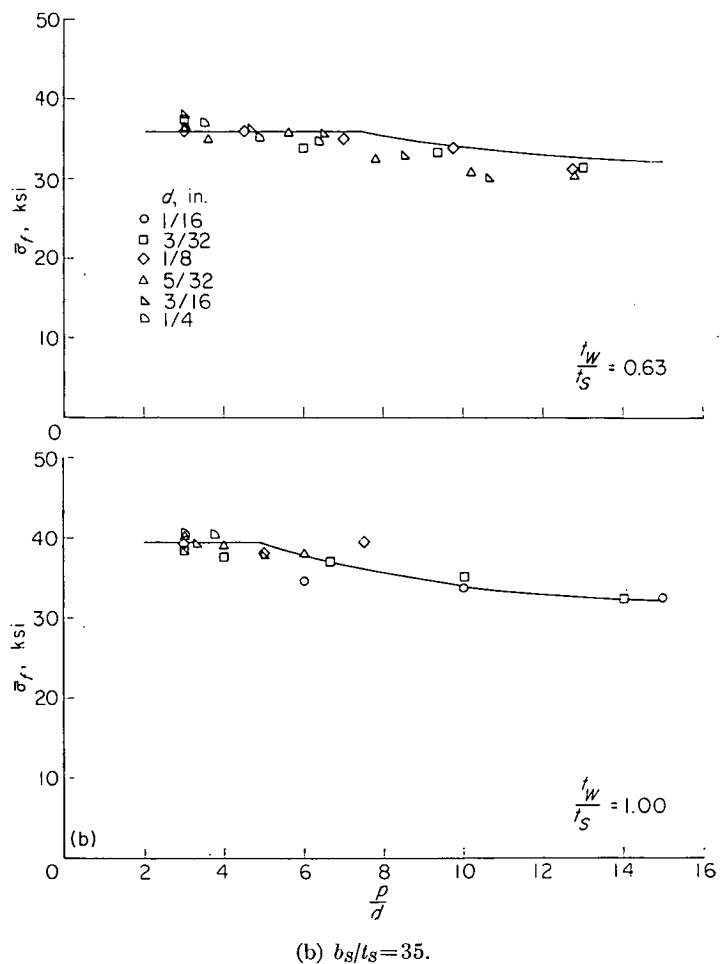
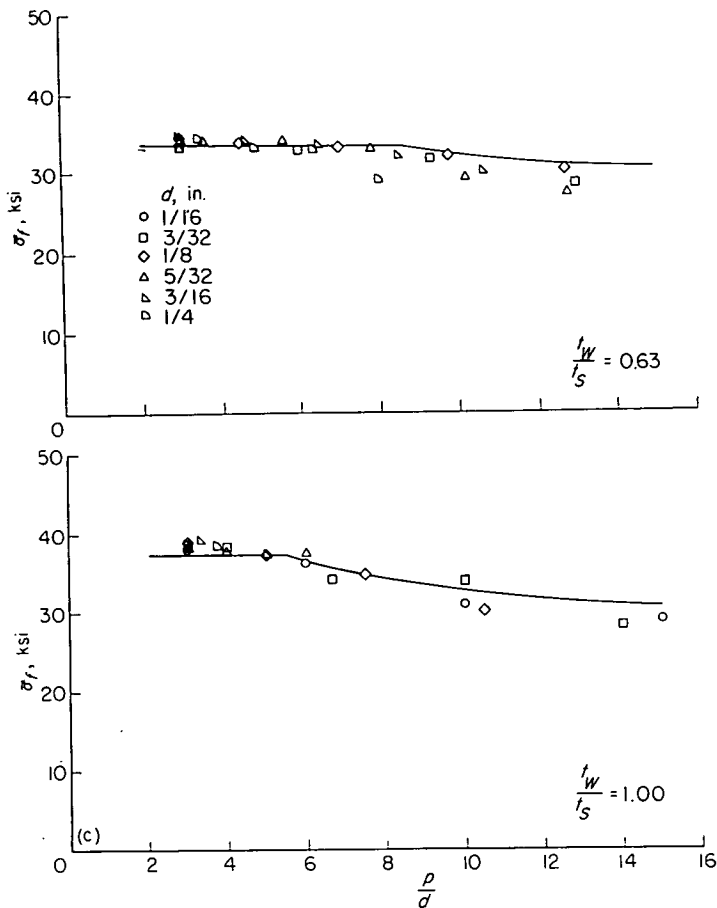
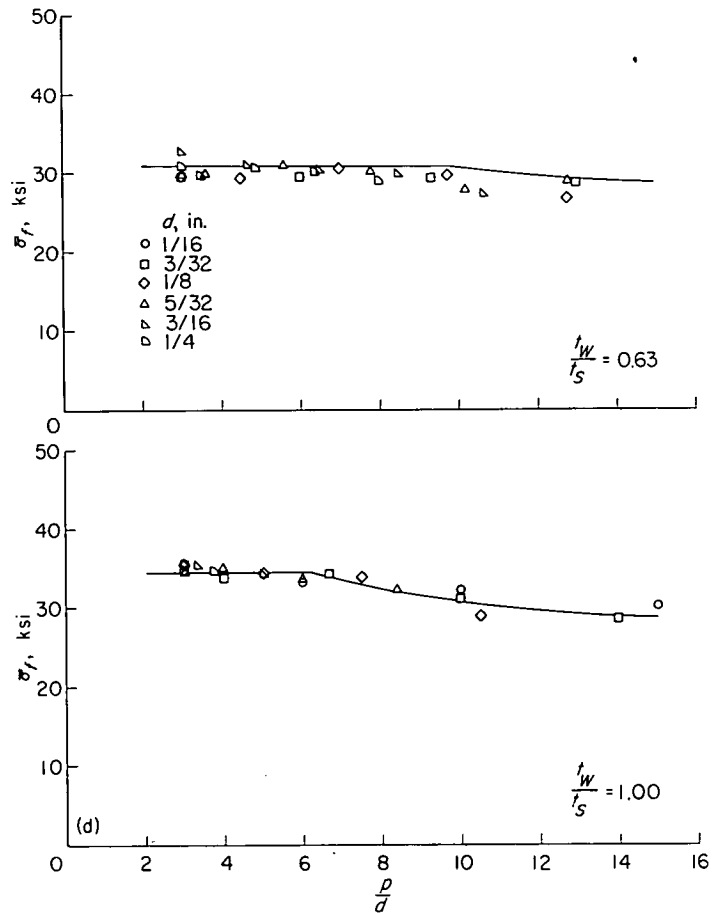


FIGURE 12.—Continued.



(c) $b_s/t_s = 40$.
FIGURE 12.—Continued.



(d) $b_s/t_s = 50$.
FIGURE 12.—Concluded.

are shown because they are considered to be sufficient to establish the concept that for panels with unequal stiffener spacings an average spacing can be used for predicting the maximum load of the panel in the wrinkling mode of failure. The particular thickness ratio $t_w/t_s = 0.39$ was chosen rather than some other because the panels with other thickness ratios had stiffer attachments between the hat-section stiffeners and the plate so that most of these panels failed in the local mode rather than in the wrinkling mode. The data for panels with elements having a width-thickness ratio b/t greater than 50 have not been shown.

The calculated curves in figure 14 are based on an average measured value of b_o/t_w rather than the nominal value.

7075-T6 ALUMINUM-ALLOY PANELS

The data of table I are shown in figure 15 where the average stress in the panel at failure is plotted against the parameter f/t_w . The predicted panel strengths are indicated by the curves and agree with the test data within the accuracy of

the data. The shaded test points represent panels which had stringers with a value of r_A/t_w of 6.0. Since the stringers had a value of b_w/t_w of 20, these stringers had a value of r_A/b_w of 0.30. These points all appear high on the figure and indicate that the attachment between the stringer and the plate was actually stiffer than figure 8 indicates. It is not known whether the test loads were high because r_A/t_w was large or whether it was because r_A/b_w was large or both. Inasmuch as the chart gives conservative predictions in this range, the uncertainty is not serious.

DISCUSSION OF RESULTS

A method has been developed whereby the strength of panels is related to the design of the attachment between the plate and the stiffener. The method makes use of an experimentally determined effective rivet offset f which is an important dimension in the determination of the strength of panels. The importance of this dimension as well as

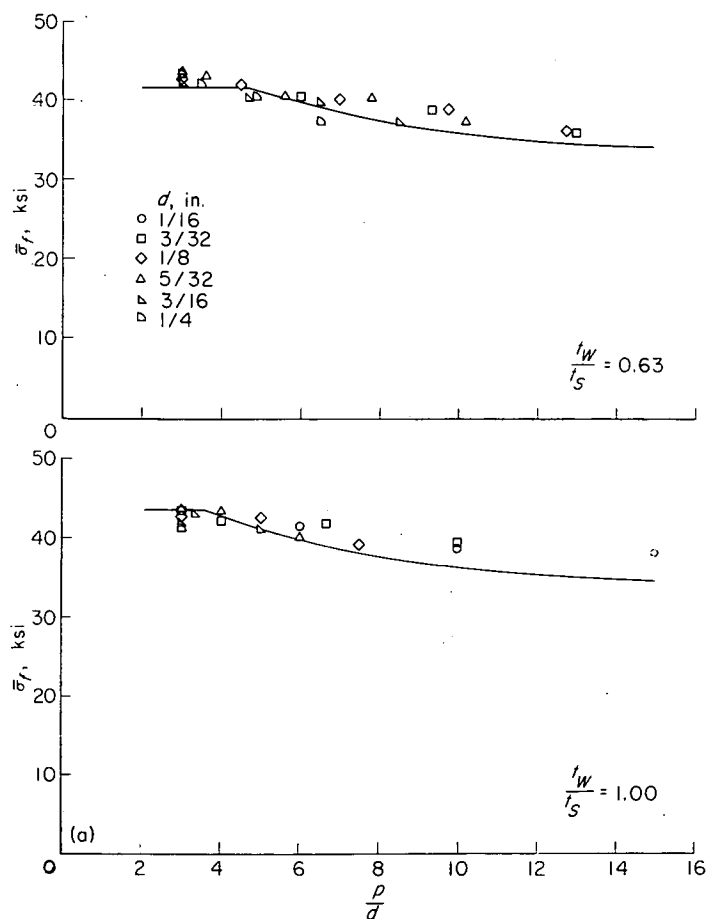
other panel dimensions on the strength of panels can be readily seen from the equation

$$\frac{\sigma_M}{\eta} = \frac{E}{1-\mu^2} \sqrt{\frac{1}{3} \frac{1}{b_s} \frac{1}{t_s} \frac{1}{\left(\frac{f}{t_w}\right)^3} \frac{3 \frac{f}{t_w} + \frac{b_w}{t_w}}{3 \frac{f}{t_w} + 4 \frac{b_w}{t_w}}} \quad (12)$$

This equation gives the strength of a plate in the wrinkling mode and is equivalent to the chart of figure 9. It is seen that the failing stress of the plate is approximately inversely proportional to $f^{3/2}$. Equation (12) has been used to estimate the strength of compression panels covering a wide range of the structural parameters t_w/t_s , b_s/t_s , and b_w/t_w and was found to give satisfactory correlation with test results.

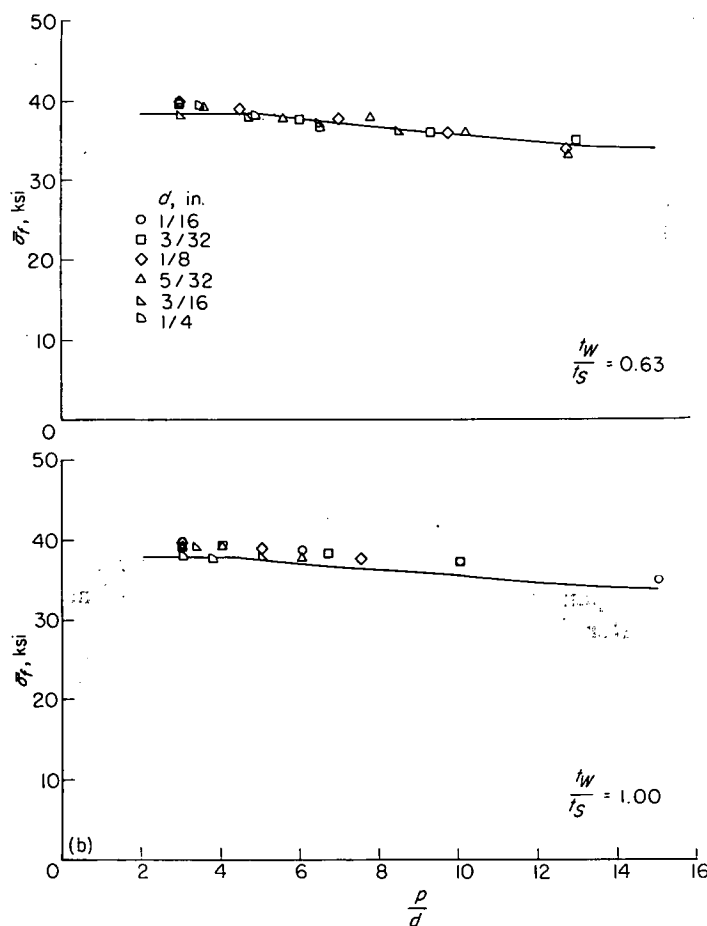
The f -chart of figure 8 was constructed from data of tests on 2024-T3 and 7075-T6 aluminum-alloy panels and multiweb beams which were assembled with 2117-T3 (previously designated A17S-T3) aluminum-alloy rivets. Since the rivet stiffness is a contributing factor in the determination of

the effective rivet offset f , changes in rivet material can be expected to make corresponding changes in f which would show up in a panel test as a change in panel strength. Reference 14, however, indicates that very little increase in panel strength can be expected from the use of rivet materials with a higher modulus of elasticity and strength than those of 2117-T3 aluminum alloy but reports on panels with one rivet material (FS-1 magnesium) which had a smaller modulus of elasticity and strength and which failed at loads that were consistently less than those of the panels with 2117-T3 aluminum-alloy rivets. Similarly, reference 14 reports on panels with blind-type Cherry rivets (AN 463) which failed at loads less than those of the panels with 2117-T3 aluminum-alloy rivets. Figure 8 should be used with caution, therefore, for rivet materials whose modulus of elasticity and strength are less than those of 2117-T3 aluminum alloy when used with aluminum-alloy sheet. The panels of reference 14 that were assembled with 1100-F (previously designated 2S-F) aluminum-alloy rivets do not satisfy the strength criterion of expression (11) and their low strengths are attributed to the low tensile strength of the rivets.



(a) $b_w/t_w = 25$.

FIGURE 13.—Comparison of calculated and experimental failing stresses of 2024-T3 Z-stiffened panels of reference 17 for four values of b_w/t_w and two values of t_w/t_s . $b_s/t_s = 25$; $b_o/t_w = 5.6$; $t_w = 0.064$ in.



(b) $b_w/t_w = 30$.

FIGURE 13.—Continued.

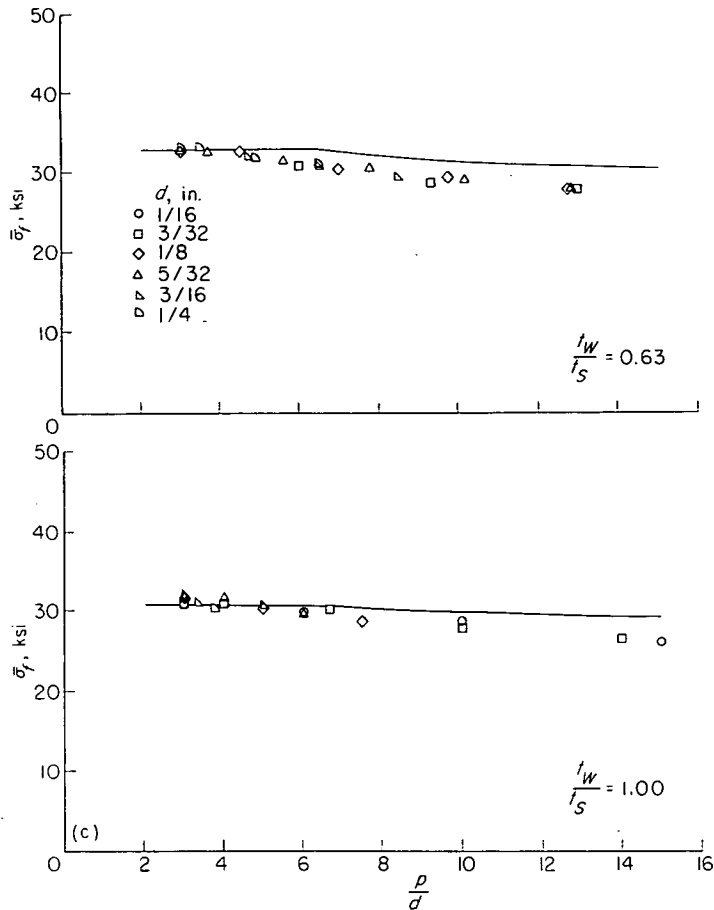
(c) $b_w/t_w = 40$.

FIGURE 13.—Continued.

Frequently panels are assembled by using extruded stringers which have a right-angle exterior corner between the web and the attachment flange. The use of such stringers usually eliminates the wrinkling mode except for very unusual proportions for two main reasons: (1) The small fillet between the web and the flange of the stringer allows the rivet to be moved in close to the web so that the rivet offset b_o is reduced and as a consequence f is also reduced and (2) the deflectional stiffness of such a stringer is greater than that of a bent-up stringer of similar proportions with the same rivet offset because of the large stiffness when the plate buckles toward the stringer. For this case, the stiffness may be more nearly that of the web rather than that of the cantilevered flange because the plate can bear directly on the web. The effective stiffness which determines the rivet offset f is some combination of this stiffness and the stiffness for the case when the plate buckles away from the stringer as shown in reference 4. The number of available tests are insufficient to establish a chart such as figure 8 for extruded stringers. These tests (from refs. 14, 19, and 20) indicate that figure 8 can be used to obtain a conservative estimate of the effective rivet offset. Expressions (9) and (11) for

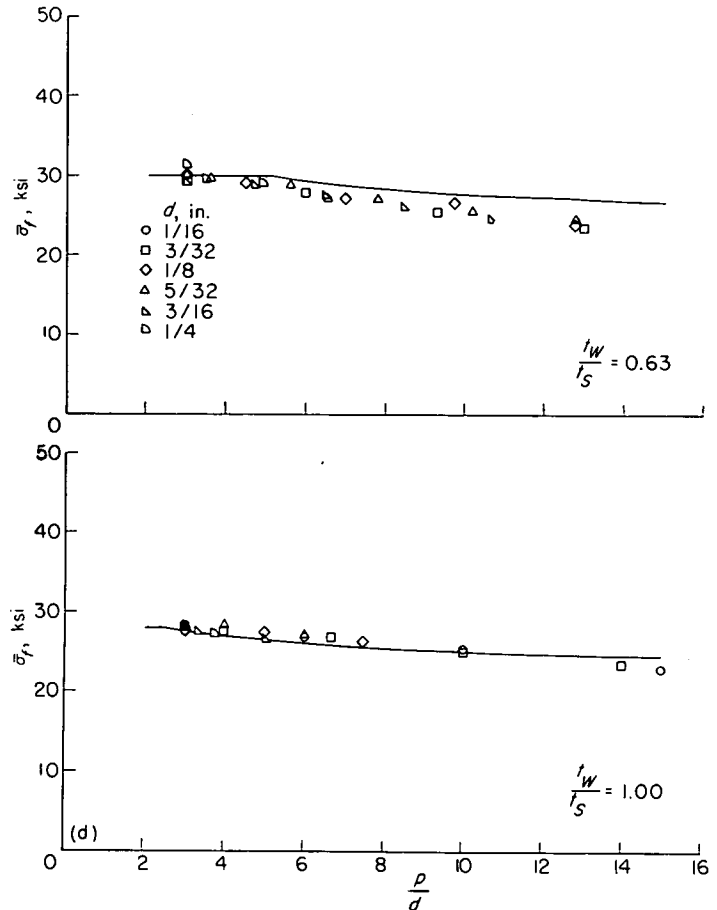
(d) $b_w/t_w = 50$.

FIGURE 13.—Concluded.

the required pitch and strength of rivets can also be used.

Previous investigations of the effect of riveting on the strength of panels of which reference 14 is the most recent have developed a rivet criterion whereby the strength of a panel with a given riveting (given pitch and diameter) is related to the strength of a similar but strongly riveted panel (panel which reaches its potential strength) by a master curve. The master curve is based on the lower limit of test data from panels of various configurations that were constructed of 2024-T3 and 7075-T6 aluminum alloy and were assembled with rivets of various materials. The present investigation has made a more detailed study of the data for panels with the smaller rivet pitches—the data on panels with p/d greater than 15 as well as the data on panels which developed interrivet buckling have not been analyzed. With this restrictive scope and the help of recently developed procedures of stress analysis, it was possible to make more accurate correlation of the strength of these panels with the riveting used to assemble the panels. For instance, the present investigation utilizes the concept that, after a certain critical value of f/t_w has been reached by decreasing the rivet pitch and/or offset and/or increasing rivet diameter, little

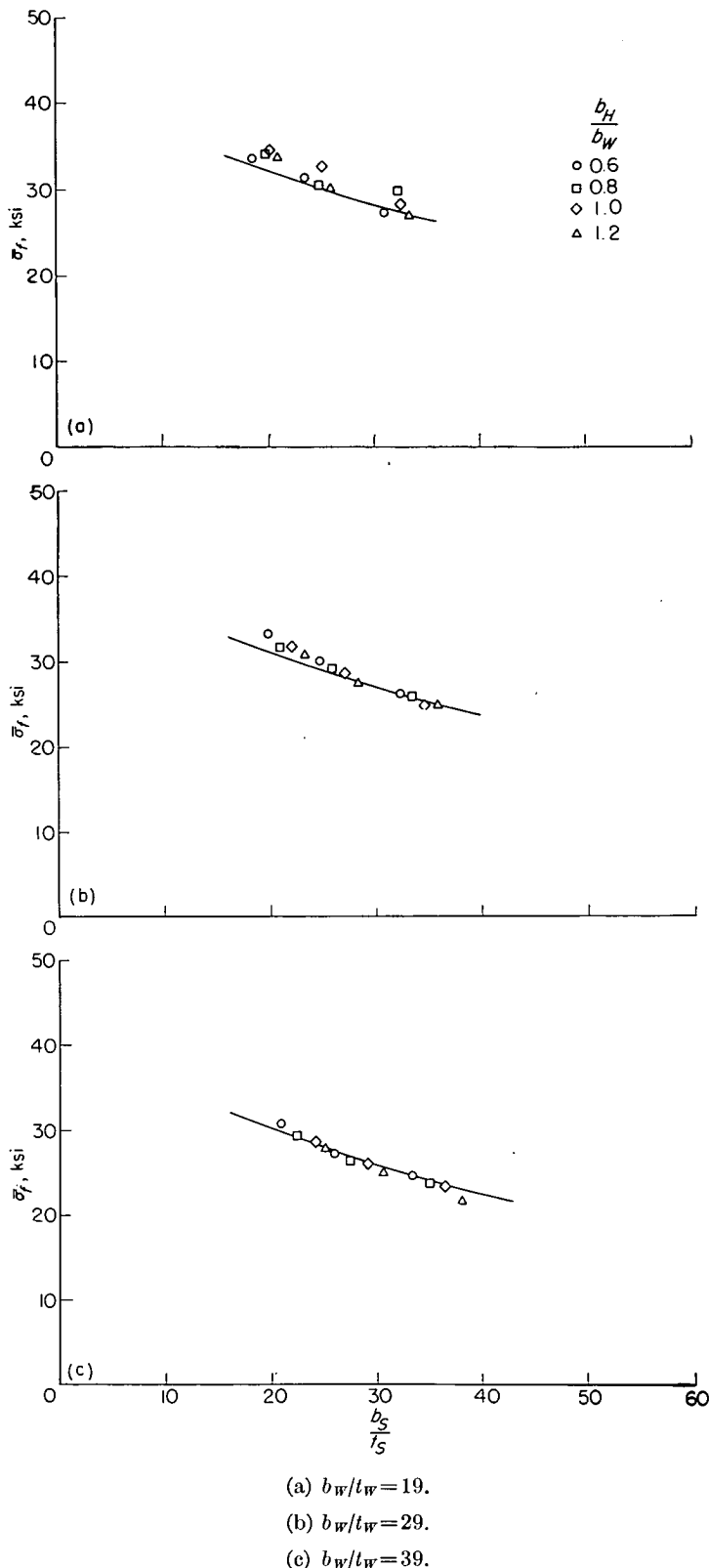


FIGURE 14.—Comparison of calculated and experimental failing stresses of 2024-T3 hat-stiffened panels of reference 26 for three values of b_w/t_w and four values of b_H/b_W . $t_w/t_s = 0.39$; $p/d = 16/3$; $b_o/t_w = 11.0$; $t_w = 0.040$ in.

or no additional gain in panel strength can be expected by further changes in rivet pitch, diameter, and offset. This critical value of f/t_w is different for different panel configurations. It is more difficult to achieve when the thickness ratio t_w/t_s is large or when the parameter b_s/t_s is small and in

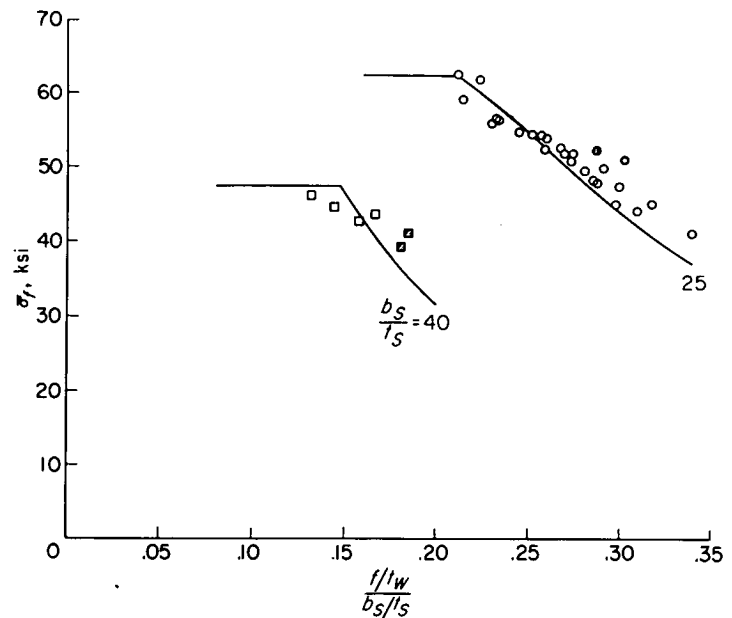


FIGURE 15.—Comparison of calculated and experimental failing stresses of 7075-T6 Z-stiffened panels of table I. The shaded points represent panels which had stringers with $r_A/t_w = 6.0$.

extreme cases may be impossible to achieve in riveted panels. The present investigation also makes use of the fact that variations in panel strength for a given change in riveting can be much greater for 7075-T6 aluminum-alloy panels than for 2024-T3 aluminum-alloy panels because plasticity may play a much smaller part in determining the strength of the 7075-T6 aluminum-alloy panels.

CONCLUSIONS

A method of strength analysis of short compression panels has been presented which relates the panel strength to the pitch, diameter, and location of the rivets used to assemble the panel. A large number of panels have been analyzed with this method. These panels covered a wide range of panel configurations. They had elements with aspect ratios b/t which ranged from 20 to 50 and were assembled with rivets which had pitch-diameter ratios p/d of from 3 to 15. Both 2024-T3 and 7075-T6 aluminum-alloy panels were considered. The following conclusions can be made from these studies:

1. Panel strength is highly influenced by variations in rivet pitch, diameter, and location.
2. Favorable variations in the pitch, diameter, and location of rivets for a given panel results in increased panel strength until the riveting is adequate to force failure in the local mode; further variations in riveting will produce negligible increases in panel strength.
3. The minimum riveting specifications that will force the panel to fail in the local mode depend on the panel configuration and on the panel material.

LANGLEY AERONAUTICAL LABORATORY,
NATIONAL ADVISORY COMMITTEE FOR AERONAUTICS,
LANGLEY FIELD, VA., January 17, 1955.

APPENDIX

NUMERICAL EXAMPLE

The use of the design charts and design procedures set forth in the body of the report are exemplified by analyzing a short, 2024-T3 aluminum-alloy, Z-stiffened, compression panel which is similar to the one shown in figure 2 and has the following dimensions and structural parameters:

$$\begin{aligned} t_w &= 0.064 \text{ in.} & b_w/t_w &= 40.0 \\ t_s &= 0.102 \text{ in.} & b_F/b_w &= 0.40 \\ t_w/t_s &= 0.63 & b_A/t_w &= 8.0 \\ b_s/t_s &= 30.0 & b_o/t_w &= 5.0 \end{aligned}$$

The panel is assembled with 3/32-inch, brazier-head (AN 456), 2117-T3 aluminum-alloy rivets spaced at 1 inch. The rivets have the manufacturer's head on the plate side and a shop-driven head on the stiffener side. Young's modulus of elasticity E is assumed to be 10,600 ksi and Poisson's ratio μ is taken as 0.32.

Additional parameters and information that can be obtained after the panel proportions are given and which will be useful in the analysis which follows are the parameters β and p/d , the area of a stringer A_z , and corresponding area of plate b_{st_s} , the local crippling stress of a stringer $\sigma_{z_{crip}}$, and the strength of the panel in the local mode $\bar{\sigma}_{f_{crip}}$. These parameters are as follows:

$$\beta = \frac{b_w/t_w}{b_s/t_s} = \frac{40.0}{30.0} = 1.33$$

$$p/d = \frac{1.00}{3/32} = 10.7$$

$$\begin{aligned} A_z &= t_w^2 \left(\frac{b_w}{t_w} + \frac{b_A}{t_w} + \frac{b_F}{b_w} \frac{b_w}{t_w} \right) = (0.064)^2 [40.0 + 8.0 + 0.40 (40.0)] \\ &= 0.262 \text{ in.}^2 \end{aligned}$$

$$b_{st_s} = \frac{b_s}{t_s} t_s^2 = 30.0 (0.102)^2 = 0.312 \text{ in.}^2$$

$$\sigma_{z_{crip}} = 27.5 \text{ ksi (ref. 25)}$$

$$\bar{\sigma}_{f_{crip}} = 31.6 \text{ ksi (fig. 10)}$$

When p/d and b_o/t_w are given, f/t_w can be read from figure 8 as

$$f/t_w = 6.98$$

The value of f/b_w is computed as follows:

$$\frac{f}{b_w} = \frac{f/t_w}{b_w/t_w} = \frac{6.98}{40.0} = 0.175$$

From figure 6,

$$k_{cr} = 2.38 \text{ (wrinkling)}$$

$$k_{cr} = 2.45 \text{ (local buckling, extrapolated)}$$

The panel should wrinkle at (see formula (3))

$$\sigma_{cr}/\eta = 25.5 \text{ ksi}$$

and since the plasticity factor for 2024-T3 aluminum alloy is unity at this stress

$$\sigma_{cr} = 25.5 \text{ ksi}$$

From figure 9

$$k_M = 3.64$$

and σ_M/η is computed as

$$\sigma_M/\eta = 39.2$$

With the use of a curve for σ against σ/η for 2024-T3 aluminum alloy with a compressive yield stress (0.2-percent offset stress) of 43.6 ksi, the plate failing stress is found to be

$$\sigma_M = 34.1 \text{ ksi}$$

Since σ_M is greater than the local crippling stress of the stringer found earlier, the load that the panel will carry in the wrinkling mode is determined by adding the loads carried by the stringers and the plate. The average stress in the panel is the panel load divided by the panel area; that is,

$$\bar{\sigma}_f = \frac{\sigma_M b_{st_s} + \sigma_{z_{crip}} A_z}{b_{st_s} + A_z} = \frac{34.1(0.312) + 27.5(0.262)}{0.312 + 0.262} = 31.1 \text{ ksi}$$

The stress $\bar{\sigma}_f$ is less than $\bar{\sigma}_{f_{crip}}$ found earlier so the panel should fail by wrinkling provided the criteria on rivet pitch and strength are met. By expression (9), the maximum allowable rivet pitch p_a is given as

$$p_a = 0.90 \sqrt{\frac{2}{3.64}} (30.0)(0.102) = 2.04 \text{ in.}$$

The actual rivet pitch of 1.00 inch is therefore small enough to prevent interrivet buckling. The allowable rivet strength is (expression (11))

$$R_R = \frac{10600}{[1 - (0.32)^2]} \frac{1}{(6.98)^3} \left[\frac{3(6.98) + 40}{3(6.98) + 160} \right] \frac{0.102}{5} (1.00) = 0.239 \text{ kips}$$

The load required to break the shank of a 3/32-inch rivet based upon an allowable stress of 57.0 ksi is 0.394 kips. Reference 22 shows that the rivet in question will shear its

head at 68 percent of the load required to break the shank; therefore,

$$R = 0.68(0.394) = 0.268 \text{ kips}$$

which is adequate rivet strength. The predicted buckling and failing stresses are those given previously.

REFERENCES

1. Dow, Norris F., and Hickman, William A.: Effect of Variation in Rivet Diameter and Pitch on the Average Stress at Maximum Load for 24S-T3 and 75S-T6 Aluminum-Alloy, Flat, Z-Stiffened Panels That Fail by Local Instability. NACA TN 2139, 1950.
2. Bijlaard, P. P., and Johnston, G. S.: Compressive Buckling of Plates Due to Forced Crippling of Stiffeners. Preprint No. 408, S.M.F. Fund Paper, Inst. Aero. Sci., Jan. 1953.
3. Anderson, Roger A., and Semonian, Joseph W.: Charts Relating the Compressive Buckling Stress of Longitudinally Supported Plates to the Effective Deflectional and Rotational Stiffness of the Supports. NACA Rep. 1202, 1954. (Supersedes NACA TN 2987.)
4. Semonian, Joseph W., and Anderson, Roger A.: An Analysis of the Stability and Ultimate Bending Strength of Multiweb Beams With Formed-Channel Webs. NACA TN 3232, 1954.
5. Gallaher, George L., and Boughan, Rolla B.: A Method of Calculating the Compressive Strength of Z-Stiffened Panels That Develop Local Instability. NACA TN 1482, 1947.
6. Argyris, J. H., and Dunne, P. C.: Part 2. Structural Analysis. Structural Principles and Data, Handbook of Aeronautics, No. 1, Pitman Pub. Corp. (New York), 1952.
7. Kroll, W. D.: Tables of Stiffness and Carry-Over Factor for Flat Rectangular Plates Under Compression. NACA WR L-398, 1943. (Formerly NACA ARR 3K27.)
8. Anderson, Melvin S.: Compressive Crippling of Structural Sections. NACA TN 3553, 1956.
9. Stowell, Elbridge Z.: A Unified Theory of Plastic Buckling of Columns and Plates. NACA Rep. 898, 1948. (Supersedes NACA TN 1556.)
10. Dow, Norris F., and Hickman, William A.: Effect of Variation in Diameter and Pitch of Rivets on Compressive Strength of Panels With Z-Section Stiffeners. I—Panels With Close Stiffener Spacing That Fail by Local Buckling. NACA WR L-44, 1945. (Formerly NACA RB L5G03.)
11. Dow, Norris F., and Hickman, William A.: Preliminary Investigation of the Relation of the Compressive Strength of Sheet-Stiffener Panels to the Diameter of Rivet Used for Attaching Stiffeners to Sheet. NACA WR L-61, 1944. (Formerly NACA RB L4I13.)
12. Holt, Marshall: Results of Edge-Compression Tests on Stiffened Flat-Sheet Panels of Alclad and Nonclad 14S-T6, 24S-T3, and 75S-T6 Aluminum Alloys. NACA TN 3023, 1954.
13. Timoshenko, S.: Theory of Elastic Stability. McGraw-Hill Book Co., Inc., 1936.
14. Dow, Norris F., Hickman, William A., and Rosen, B. Walter: Effect of Variation in Rivet Strength on the Average Stress at Maximum Load for Aluminum-Alloy, Flat, Z-Stiffened Compression Panels That Fail by Local Buckling. NACA TN 2963, 1953.
15. Dow, Norris F., and Anderson, Roger A.: Prediction of Ultimate Strength of Skin-Stringer Panels From Load-Shortening Curves. Preprint No. 431, S.M.F. Fund Preprint, Inst. Aero. Sci., Jan. 1954.
16. Dow, Norris F., and Hickman, William A.: Effect of Variation in Diameter and Pitch of Rivets on Compressive Strength of Panels With Z-Section Stiffeners—Panels of Various Stiffener Spacing That Fail by Local Buckling. NACA TN 1467, 1947.
17. Dow, Norris F., and Hickman, William A.: Effect of Variation in Diameter and Pitch of Rivets on Compressive Strength of Panels With Z-Section Stiffeners—Panels That Fail by Local Buckling and Have Various Values of Width-to-Thickness Ratio for the Webs of the Stiffeners. NACA TN 1737, 1948.
18. Schuette, Evan H.: Charts for the Minimum-Weight Design of 24S-T Aluminum-Alloy Flat Compression Panels With Longitudinal Z-Section Stiffeners. NACA Rep. 827, 1945. (Supersedes NACA WR L-197.)
19. Hickman, William A., and Dow, Norris F.: Data on the Compressive Strength of 75S-T6 Aluminum-Alloy Flat Panels Having Small, Thin, Widely Spaced, Longitudinal Extruded Z-Section Stiffeners. NACA TN 1978, 1949.
20. Hickman, William A., and Dow, Norris F.: Data on the Compressive Strength of 75S-T6 Aluminum-Alloy Flat Panels With Longitudinal Extruded Z-Section Stiffeners. NACA TN 1829, 1949.
21. Wilder, Thomas W., III, Brooks, William A., Jr., and Mathausen, Eldon E.: The Effect of Initial Curvature on the Strength of an Inelastic Column. NACA TN 2872, 1953.
22. Schuette, Evan H., Bartone, Leonard M., and Mandel, Mervin W.: Tensile Tests of Round-Head, Flat-Head, and Brazier-Head Rivets. NACA TN 930, 1944.
23. Mandel, Mervin W., and Bartone, Leonard M.: Tensile Tests of NACA and Conventional Machine-Countersunk Flush Rivets. NACA WR L-176, 1944. (Formerly NACA ARR L4F06.)
24. Schuette, Evan H., and Niles, Donald E.: Data on Optimum Length, Shear Strength, and Tensile Strength of Age-Hardened 17S-T Machine-Countersunk Rivets in 75S-T Sheet. NACA TN 1205, 1947.
25. Lundquist, Eugene E., Schuette, Evan H., Heimerl, George J., and Roy, J. Albert: Column and Plate Compressive Strengths of Aircraft Structural Materials—24S-T Aluminum-Alloy Sheet. NACA WR L-190, 1945. (Formerly NACA ARR L5F01.)
26. Hickman, William A., and Dow, Norris F.: Compressive Strength of 24S-T Aluminum-Alloy Flat Panels With Longitudinal Formed Hat-Section Stiffeners Having Four Ratios of Stiffener Thickness to Skin Thickness. NACA TN 1553, 1948.

REPORT 1256

AXIALLY SYMMETRIC SHAPES WITH MINIMUM WAVE DRAG¹

BY MAX. A. HEASLET and FRANKLYN B. FULLER

SUMMARY

The external wave drag of bodies of revolution moving at supersonic speeds can be expressed either in terms of the geometry of the body, or in terms of the body-simulating axial source as distribution. For purposes of deriving optimum bodies under various given conditions, it is found that the second of the methods mentioned is the more tractable. By use of a quasi-cylindrical theory, that is, the boundary conditions are applied on the surface of a cylinder rather than on the body itself, the variational problems of the optimum bodies having prescribed volume or caliber are solved. The streamwise variations of cross-sectional area and drags of the bodies are exhibited, and some numerical results are given. The solutions are found to depend upon a single parameter involving Mach number and the radius-length ratio of the given cylinder. Variation of this parameter from zero to infinity gives the spectrum of optimum bodies, for the prescribed condition, from the slender-body result to the two-dimensional. The numerical results show that for increasing values of the parameter, the optimum shapes quickly approach the two-dimensional.

A reciprocity relation for axial flow is derived, and it is used in formulating the variational problems in terms of the drag formula involving geometry. Formulation of the minimum problems in terms of combined flow fields is found to lead to extremely simple relations that are satisfied by the flow field induced by optimum bodies. The combined flow concepts are also useful, for example, in checking results found by other means.

INTRODUCTION

The design of minimum-drag configurations is one of the fundamental problems of aerodynamics. For many engineering purposes it is, furthermore, possible to make useful predictions and design calculations for steady flight by considering additively the drag attributable to the viscous nature of the air and the drag that occurs in an inviscid medium. Since efficient flight is closely associated with the use of aerodynamic shapes producing relatively small disturbances in the air, the analysis upon which the inviscid-fluid theory is based can, in many cases of practical interest, be further limited to first-order approximations involving small perturbations. For supersonic flight speeds such an analysis is linear, the perturbation velocity potential of the flow field satisfies the wave equation, and the pressure drag of nonlifting configurations results from the accumulation of energy in the waves induced by the body during its motion.

The purpose of the present paper is to show how most

favorable body shapes, under various given conditions, can be derived by using formulae for drag prediction that are based upon the linearized theory. The type of body to be treated is a nacelle- or duct-like configuration (nonlifting and having axial symmetry) which induces perturbations that are specified on the surface of a circular cylinder. The analysis might be termed quasi-cylindrical, since boundary conditions are applied on the surface of a cylinder rather than on the body itself. Only the external flow is considered.

There are two rather different methods available for the calculation of drag of such bodies. The first, given by Ward in reference 1, expresses the drag in terms of the geometry of the body and of a weighting function first encountered by Lighthill (ref. 2) in connection with the drag of fusiform bodies. The second result, published recently by Parker (ref. 3), is a formula in which the drag is expressed in terms of the strength of an axial source distribution that simulates the body shape. Generally speaking, the formula giving drag directly in terms of geometrical characteristics would be preferable, since the usual auxiliary conditions in variation problems, such as given volume, given caliber, etc., are also expressed in geometrical terms. Unfortunately, however, the variational problem in this case leads to an integral equation whose kernel is the Lighthill function mentioned previously, and the properties of this function are not at present well enough known to enable one to solve the integral equation by other than numerical methods. On the other hand, the expression for drag in terms of sources leads to a tractable integral equation, although the relations between source strength and geometry are somewhat complex.

Problems of the sort to be treated here have been attacked by Ferrari (refs. 4 and 5) and by Parker (ref. 3). The first-named author has approached the problem of minimum drag with assorted isoperimetric conditions by both the above-mentioned methods, but the main effort was made in connection with the source-strength method applied in conjunction with a control surface consisting of a frustum of a cone. A large number of cases have been worked out, mostly by numerical methods. The other work, reference 3, gives a solution to the problem of the minimum-drag body with given caliber, making use of boundary conditions on the Stokes' stream function, rather than the potential function.

In this paper we shall approach the problem by the use of both methods outlined above. In an introductory section, the operational approach to the wave equation is extended to bodies having peripheral as well as longitudinal variations

¹Supersedes NACA TN 3389 by Max. A. Heaslet and Franklyn B. Fuller, 1955.

Since this latter equation must be satisfied by all possible variations of the displacement function $g(x, \theta)$, it follows that the desired condition is

$$P'(x, R, \theta) + \mu = 0 \quad (47)$$

Stated in words, the condition for minimum wave drag of a quasi-cylindrical body of given volume is that the longitudinal gradient of pressure on the body in the combined forward and reverse flow field is a constant. Furthermore, from equation (44), minimum drag is then given by

$$D_{min} = \frac{\mu}{2} (V - \pi R^2 l) = \frac{\mu}{2} V_e \quad (48)$$

where μ can now be identified with the negative pressure gradient in the combined field and $(V - \pi R^2 l) = V_e$ is the volume exposed to the fluid around the cylindrical control surface $r = R$.

The actual cross-section-area variation of a minimum-drag constant-volume body and its pressure distribution are shown in figure 5 for the case in which axial symmetry

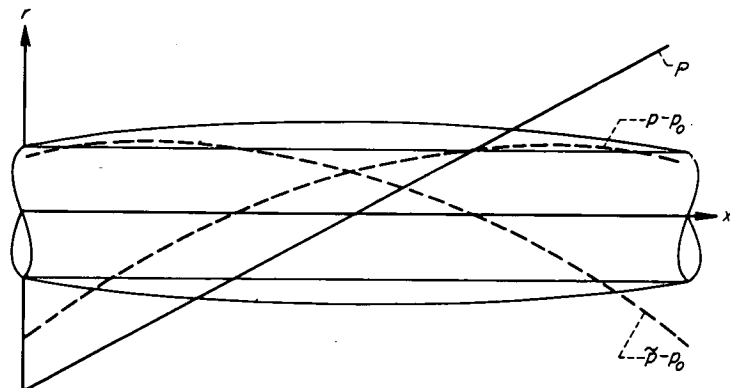


FIGURE 5.—Minimum drag body with pressure distributions in combined flow.

is imposed. Pressure coefficient in the combined flow field of an axially symmetric body has been given in equation (42). The geometric criterion just established then leads to the integral equation

$$2S'(x) - \int_0^l S'(x_1) W\left(\frac{|x-x_1|}{\beta R}\right) \frac{dx_1}{\beta R} = -\mu x + b \quad (49)$$

and the solution of this equation will determine the body geometry. In the following section an analogous integral equation will be derived but with the source-strength distribution chosen as the fundamental dependent variable.

The combined-flow-field technique can also be used to study the problem of minimizing wave drag for specified body caliber or, more generally, when the body has a fixed cross section at a specified longitudinal position. The resulting condition for minimum drag is that the pressure distribution on the body in the combined flow field is a constant forward and aft of the specified position. These conditions are all analogous to those obtained for planar problems by R. T. Jones (ref. 13).

DRAG MINIMIZATION

In this division, optimum bodies having certain prescribed geometric properties will be determined by standard variational methods. The analysis will, as mentioned previously, deal with the strength of an axial source distribution as the minimizing function, rather than the geometric quantity,

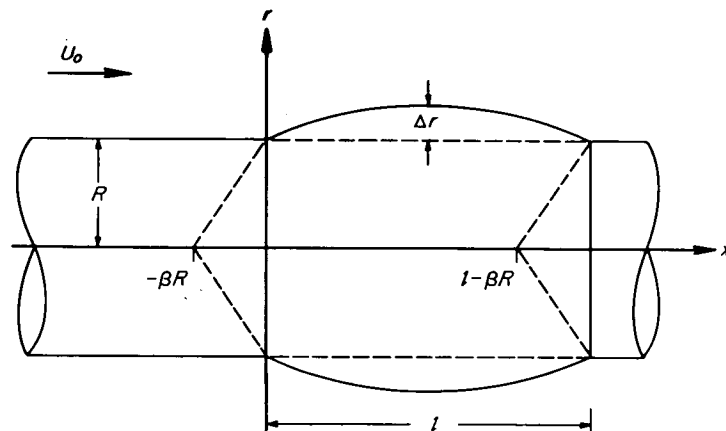


FIGURE 6.—Body and associated nomenclature used in drag minimization.

cross-sectional area. Thus, we shall be concerned with formula (32), giving drag in terms of the source distribution.

QUASI-CYLINDRICAL BODY OF REVOLUTION OF GIVEN VOLUME

Isoperimetric conditions.—The configuration to be considered, together with associated nomenclature, is shown in figure 6. The geometric properties of the body can be expressed in terms of the source distribution function $A_o(x)$ by using equation (20), namely,

$$S'(x) = \frac{2\pi R}{U_o} \varphi_r \Big|_{r=R} \quad (50)$$

Then, from equation (30)

$$S'(x) = \frac{1}{U_o} \int_{-\beta R}^{x-\beta R} \frac{A_o'(x_1)(x-x_1)}{\sqrt{(x-x_1)^2 - \beta^2 R^2}} dx_1 \quad (51)$$

If equation (51) is integrated x -wise it is seen that

$$S(x) - S(o) = \frac{1}{U_o} \int_0^x dz \int_{-\beta R}^{z-\beta R} \frac{(z-x_1)A_o'(x_1)dx_1}{\sqrt{(z-x_1)^2 - \beta^2 R^2}} \quad (52a)$$

By changing the order of integration and performing the integration with respect to z one finds

$$S(x) - S(o) = \frac{1}{U_o} \int_{-\beta R}^{x-\beta R} \frac{(x-x_1)A_o'(x_1)}{\sqrt{(x-x_1)^2 - \beta^2 R^2}} dx_1 \quad (52b)$$

or, integrating by parts,

$$S(x) - S(o) = \frac{1}{U_o} \int_{-\beta R}^{x-\beta R} A_o'(x_1) \sqrt{(x-x_1)^2 - \beta^2 R^2} dx_1 \quad (52c)$$

source and multipole singularities. This general solution can be found by use of the Laplace transformation. By definition, the Laplace transform² (see ref. 6) of a function $F(x, r, \theta)$ is $\bar{F}(s; r, \theta)$ where

$$\bar{F}(s; r, \theta) = \int_0^\infty e^{-sz} F(x, r, \theta) dx \quad (4)$$

If one employs this transformation and applies initial conditions consistent with supersonic flow theory (ref. 7), equation (3) becomes

$$\beta^2 s^2 \bar{\varphi} - \bar{\varphi}_{rr} - (1/r) \bar{\varphi}_r - (1/r)^2 \bar{\varphi}_{\theta\theta} = 0 \quad (5)$$

The transform of the perturbation velocity potential is assumed separable in the form

$$\bar{\varphi}(s; r, \theta) = \zeta(r, s) \cos m\theta$$

and it follows directly that $\zeta(r, s)$ must satisfy the ordinary differential equation

$$\frac{d^2 \zeta}{d(\beta r s)^2} + \frac{1}{\beta r s} \frac{d\zeta}{d(\beta r s)} - \left[1 + \frac{m^2}{(\beta r s)^2} \right] \zeta = 0$$

Thus, the solution can be written

$$\bar{\varphi}(s; r, \theta) = -\frac{1}{2\pi} \sum_0^\infty \cos m\theta [\bar{A}_m(s) K_m(\beta r s) + \bar{B}_m(s) I_m(\beta r s)]$$

where K_m and I_m are modified Bessel functions in the notation of reference 8. The asymptotic expansions for the Bessel functions show that I_m yields incoming waves suitable for the analysis of flow inside a tube or cylindrical control surface; K_m yields outgoing waves that are suited to the calculation of the field external to a tube. It follows that one has, in the latter case,

$$\bar{\varphi}(s; r, \theta) = -\frac{1}{2\pi} \sum_0^\infty \bar{A}_m(s) K_m(\beta r s) \cos m\theta \quad (6)$$

The inversion of equation (6) can be achieved in two ways. First, from reference 9, page 277, and the convolution integral, one gets

$$\varphi(x, r, \theta) = -\frac{1}{2\pi} \left[\int_0^{x-\beta r} \frac{A_0(x_1) dx_1}{\sqrt{(x-x_1)^2 - \beta^2 r^2}} + \sum_1^\infty \cos m\theta \int_0^{x-\beta r} \frac{A_m(x_1) \cosh \left(m \cosh^{-1} \frac{x-x_1}{\beta r} \right) dx_1}{\sqrt{(x-x_1)^2 - \beta^2 r^2}} \right] \quad (7)$$

Second (see, e. g., ref. 8, p. 79), one has

$$K_m(\beta r s) = (-1)^m \frac{r^m}{\beta^m s^m} \left(\frac{d}{r dr} \right)^m K_0(\beta r s)$$

Thus equation (6) can be rewritten as

$$\bar{\varphi}(s; r, \theta) = -\frac{1}{2\pi} \left[A_0(s) K_0(\beta r s) + \sum_1^\infty \left(-\frac{r}{\beta} \right)^m \cos m\theta \left(\frac{d}{r dr} \right)^m \frac{\bar{A}_m(s)}{s^m} K_0(\beta r s) \right]$$

and the inversion is

$$\varphi(x, r, \theta) = -\frac{1}{2\pi} \left[\int_0^{x-\beta r} \frac{A_0(x_1) dx_1}{\sqrt{(x-x_1)^2 - \beta^2 r^2}} + \sum_1^\infty \left(-\frac{r}{\beta} \right)^m \cos m\theta \left(\frac{d}{r dr} \right)^m \int_0^{x-\beta r} \frac{C_m(x_1) dx_1}{\sqrt{(x-x_1)^2 - \beta^2 r^2}} \right] \quad (8)$$

where the function $C_m(x)$ is given by (from operational calculus rules)

$$\begin{aligned} C_m(x) &= \int_0^x dx_m \cdots \int_0^{x_3} dx_2 \int_0^{x_2} A_m(x_1) dx_1 \\ &= \frac{1}{(m-1)!} \int_0^x (x-x_1)^{m-1} A_m(x_1) dx_1 \end{aligned} \quad (9)$$

Equation (8) expresses the solution in the usual form, given, for example, in reference 10, page 527. For some purposes, numerical calculations for example, equation (7) has advantages over equation (8). The two solutions express the perturbation velocity potential in terms of distributions of singularities along the central axis, the first term representing a distribution of supersonic sources of strength $A_0(x) dx$, and the subsequent terms representing multipoles of order m .

It is of interest to calculate the limiting forms of equations (7) and (8) for large and small values of r . For large r , equation (6) becomes

$$\bar{\varphi}(s; r, \theta) \sim -\frac{1}{2\pi} \sum_0^\infty \bar{A}_m(s) \sqrt{\frac{\pi}{2\beta r s}} e^{-\beta r s} \cos m\theta \quad (10)$$

where the asymptotic form

$$K_m(z) \sim \sqrt{\frac{\pi}{2z}} e^{-z}$$

has been used. The perturbation velocity potential is then

$$\varphi(x, r, \theta) \sim -\frac{1}{2\pi \sqrt{2\beta r}} \sum_0^\infty \cos m\theta \int_0^{x-\beta r} A_m(\xi) \frac{d\xi}{\sqrt{x-\xi-\beta r}} \quad (11)$$

The ultimate attenuation of φ with lateral distance is therefore fixed by the factor $1/\sqrt{r}$. For small r , equation (6) becomes

$$\begin{aligned} \bar{\varphi}(s; r, \theta) \approx & -\frac{1}{2\pi} \left[-\bar{A}_0(s) \left(\ln \frac{\beta r s}{2} + \gamma \right) + \sum_1^\infty \frac{\bar{A}_m(s)}{2} (m-1)! \left(\frac{2}{\beta r s} \right)^m \cos m\theta \right] \end{aligned} \quad (12)$$

where $\gamma = 0.577$ is Euler's constant. The inversion of equation (12) is

$$\begin{aligned} \varphi(x, r, \theta) \approx & \frac{1}{2\pi} \left[A_0(x) \ln \frac{\beta r}{2} + \frac{\partial}{\partial x} \int_0^x A_0(x_1) \ln |x-x_1| dx_1 + \sum_1^\infty \left(\frac{2}{\beta r} \right)^m \frac{(m-1)!}{2} \cos m\theta C_m(x) \right] \end{aligned} \quad (13)$$

where $C_m(x)$ is defined in equation (9). This result was used by Ward (ref. 11) as a basis for the development of slender-body theory.

* It will be assumed through the present section that the origin lies upstream of all disturbance points in the flow field. Subsequently, the origin will be shifted so as to lie at the upstream face of the control surface or body.

As presented, the above general solutions (eqs. (7) and (8)) were not related to specific boundary conditions. The formal development of this relation is straightforward and leads to an explicit solution for boundary conditions given on the cylindrical control surface at $r=R=\text{const.}$ Let the given conditions be

$$\varphi_r|_{r=R}=U_o G(x, \theta)=U_o \sum_0^{\infty} g_m(x) \cos m\theta \quad (14)$$

From equations (6) and (14), one has

$$\begin{aligned} \bar{\varphi}_r(s; r, \theta)|_{r=R} &= -\frac{1}{2\pi} \sum_0^{\infty} \bar{A}_m(s) \left[\frac{d}{dr} K_m(\beta rs) \right]_{r=R} \cos m\theta \\ &= U_o \sum_0^{\infty} \bar{g}_m(s) \cos m\theta \end{aligned} \quad (15)$$

Since

$$\frac{d}{dr} K_m(\beta rs) = \beta s K_m'(\beta rs)$$

equation (15) yields

$$\bar{A}_m(s) = -\frac{2\pi U_o}{\beta} \frac{\bar{g}_m(s)}{s K_m'(\beta Rs)} \quad (16)$$

and the transformed velocity potential is, from equation (6),

$$\bar{\varphi}(s; r, \theta) = -\frac{U_o}{\beta} \sum_0^{\infty} \frac{\bar{g}_m(s)}{s} \frac{K_m(\beta rs)}{K_m'(\beta Rs)} \cos m\theta \quad (17)$$

In order to give the desired expression for $\varphi(x, r, \theta)$ it is necessary to calculate the inverse Laplace transform of the functions $K_m(\beta rs)/K_m'(\beta Rs)$. This task has been undertaken by Mersman (ref. 12).

EXTERNAL WAVE DRAG OF QUASI-CYLINDRICAL BODY OF REVOLUTION IN TERMS OF ITS GEOMETRY OR SOURCE DISTRIBUTION

Attention is now restricted to flow fields possessing axial symmetry with respect to the stream direction. Independence with respect to θ then reduces equations (7) and (8) to

$$\varphi(x, r) = -\frac{1}{2\pi} \int_0^{x-\beta r} \frac{A_o(x_1) dx_1}{\sqrt{(x-x_1)^2 - \beta^2 r^2}} \quad (18)$$

and the velocity potential is expressed as a rectilinear distribution of supersonic source potentials. Operationally, equation (18) takes the form

$$\bar{\varphi}(s; r) = -\frac{1}{2\pi} \bar{A}_o(s) K_o(\beta rs) \quad (19)$$

The axes may now be considered as shifted so that the source distribution starts at $x=-\beta R$ and induces perturbation velocities on the cylindrical surface $r=R$, $0 \leq x \leq l$. For $r \geq R$ one then has the disturbance field associated with a body of revolution that deviates only slightly from the cylinder $r=R$. The wave drag of such a body can then be expressed in two ways: first, as a function of the body geometry; second, as a function of the source-strength distribution. The first result has been given in reference 1. To the order of accuracy to which this control-surface theory applies, the slope of the resulting surface is

$$\left[\frac{dr}{dx} \approx \frac{S'(x)}{2\pi R} \approx \frac{1}{U_o} \varphi_r \right]_{r=R} \quad (20)$$

where $S'(x)$ is the streamwise derivative of local cross-sectional area of the body. This condition, together with equation (19), yields

$$\frac{\bar{A}_o(s)}{U_o} = \frac{\bar{S}'(s)}{\beta R s K_1(\beta Rs)} \quad (21)$$

where $\bar{S}'(s)$ means the Laplace transform of $S'(x)$, and

$$\frac{\bar{\varphi}(s; R)}{U_o} = -\frac{\bar{S}'(s)}{2\pi \beta R s} \frac{K_o(\beta Rs)}{K_1(\beta Rs)} \quad (22)$$

In order to calculate drag, pressure on the body is next evaluated. Denoting by p and p_o local and free-stream pressure and setting $q_o = \frac{1}{2} \rho_o U_o^2$, one has in linearized theory

$$\left[\frac{p-p_o}{q_o} \right]_{r=R} = -\frac{2u(x, R)}{U_o} \quad (23)$$

From equation (22)

$$\begin{aligned} \frac{\bar{u}(s; R)}{U_o} &= -\frac{1}{2\pi \beta R} \frac{\bar{S}'(s)}{s} \frac{K_o(\beta Rs)}{K_1(\beta Rs)} \\ &= -\frac{\bar{S}'(s)}{2\pi \beta R} \left[1 - \frac{K_1(\beta Rs) - K_o(\beta Rs)}{K_1(\beta Rs)} \right] \end{aligned} \quad (24)$$

The inverse transform of the second term involving the Bessel function leads to the function $W(x)$ introduced by Lighthill (ref. 2). By definition, its transform is

$$\bar{W}(s) = \frac{K_1(s) - K_o(s)}{K_1(s)} \quad (25)$$

Pressure distribution on the body can then be calculated from the expression

$$\frac{p-p_o}{q_o} = \frac{1}{\pi \beta R} \left[S'(x) - \int_0^x S'(x_1) W\left(\frac{x-x_1}{\beta R}\right) \frac{dx_1}{\beta R} \right] \quad (26)$$

The function $W(x)$ is shown in figure 1; tabular values for $-2 < x < 10$ are given in reference 1.

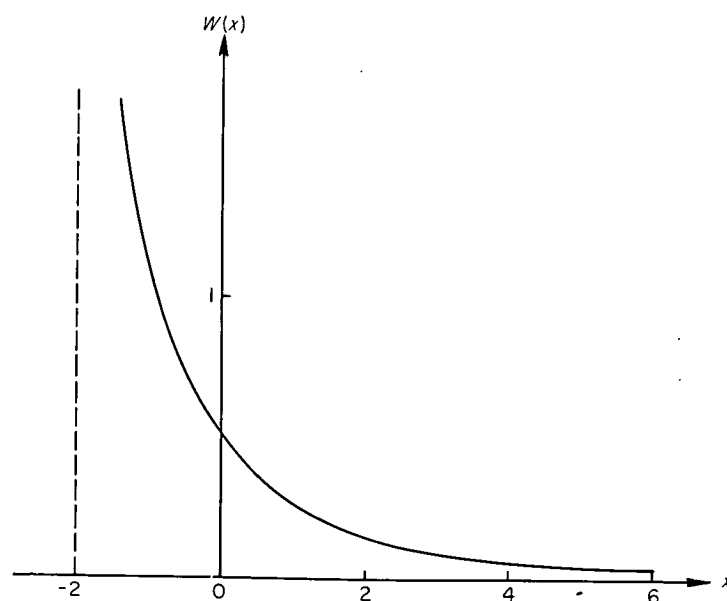


FIGURE 1.—The influence function $W(x)$.

The external wave drag C_{D_o} of the body is finally determined by direct integration

$$C_{D_o} = \frac{\text{drag}}{\pi R^2 q_0} = \frac{1}{\pi R^2} \int_0^l \frac{p-p_0}{q_0} S'(x) dx \quad (27)$$

and from equation (26) is

$$C_{D_o} = \frac{1}{2\beta\pi^2 R^3} \left\{ 2 \int_0^l [S'(x)]^2 dx - \frac{1}{\beta R} \int_0^l \int_0^l S'(x) S'(x_1) W\left(\frac{|x-x_1|}{\beta R}\right) dx dx_1 \right\} \quad (28)$$

In a later section entitled "Geometric Criteria for Minimum Drag," the role equation (28) plays in problems involving drag minimization will be discussed. For the present, it may be remarked that although the magnitude of the influence function $W(x)$ is known, its analytic properties are not well enough defined to permit easy manipulation. It will become more apparent later that for certain minimum-drag problems an advantage is provided when one deals directly with source distributions and establishes the relationship between geometry and source strengths as a separate part of the analysis.

Equation (18) expresses the potential of a source distribution of strength $A_o(x)$. On the cylindrical control surface $r=R$ and within the range $0 \leq x \leq l$ an effective body shape is induced and the drag of this body can be calculated as follows. The streamwise and lateral perturbation-velocity components are, respectively,

$$\varphi_x(x, r) = -\frac{1}{2\pi} \int_{-\beta R}^{x-\beta R} \frac{A_o'(x_1) dx_1}{\sqrt{(x-x_1)^2 - \beta^2 r^2}} \quad (29)$$

$$\varphi_r(x, r) = \frac{1}{2\pi r} \int_{-\beta R}^{x-\beta R} \frac{(x-x_1) A_o'(x_1) dx_1}{\sqrt{(x-x_1)^2 - \beta^2 r^2}} \quad (30)$$

where $A_o(x_1) = 0$ for $x_1 \leq -\beta R$. The effective body, within the range $0 \leq x \leq l$, is fixed by the boundary conditions of equation (20) and its external wave drag is

$$D = -2\pi \rho_0 R \int_0^l \varphi_x(x, R) \varphi_r(x, R) dx = \frac{\rho_0}{2\pi} \int_0^l dx \int_{-\beta R}^{x-\beta R} \frac{A_o'(x_1)(x-x_1) dx_1}{\sqrt{(x-x_1)^2 - \beta^2 R^2}} \int_{-\beta R}^{x-\beta R} \frac{A_o'(x_2) dx_2}{\sqrt{(x-x_2)^2 - \beta^2 R^2}} \quad (31)$$

The dummy variables x_1, x_2 can be interchanged; if one then combines the two expressions of equation (31) and inverts the order of integration,³ the integration with respect to x can be performed and there results

$$D = \frac{\rho_0}{4\pi} \int_{-\beta R}^{l-\beta R} A_o'(x_1) dx_1 \int_{-\beta R}^{l-\beta R} A_o'(x_2) \cosh^{-1} \left| \frac{(l-x_1)(l-x_2) - \beta^2 R^2}{\beta R(x_1-x_2)} \right| dx_2 \quad (32)$$

as given in reference 3.

It is of interest to remark that although equation (32) uses only a knowledge of the function $A_o(x)$ in the range $-\beta R \leq x \leq l-\beta R$, the drag that is calculated presupposes a

specific source distribution function in the range $l-\beta R < x$ if one wishes to identify the drag with a geometric shape. Thus, as in figure 2, if the body shape near $r=R$ is assumed to have some arbitrary variation for $0 \leq x \leq l$, and to straighten out into a purely cylindrical surface downstream of $x=l$, a source distribution is required downstream of $x=l-\beta R$ to produce the cylinder.

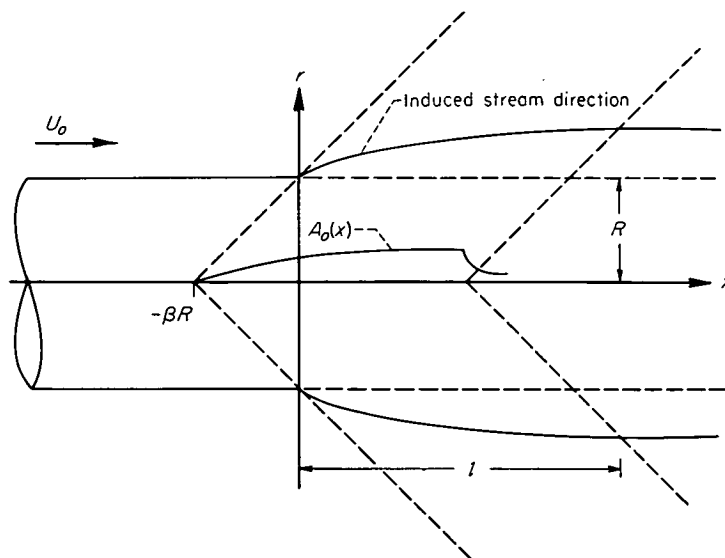


FIGURE 2.—Body induced on a control surface by an axial source distribution.

The fact that the stream velocity is supersonic means that upstream influences of $A_o(x)$ for $x > l-\beta R$ cannot be felt on the body and explains why the drag of a complete geometric shape can be determined from its source distribution without knowing the complete details of the distribution function.

As another example of the use of equation (32) consider, as in figure 3, a circular body extending from $x=-\beta R$ to $x=l$ with a cylindrical afterbody of radius R aft of $x=l$. If the source distribution of this body is known as, say, for example, in the case of a cone or slender body of revolution, the body drag can be determined by using the surface $r=R, 0 \leq x \leq l$ as a control surface and calculating momen-

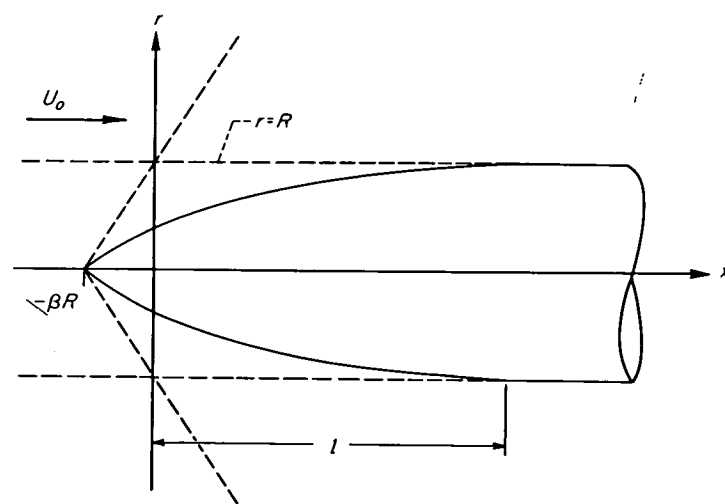


FIGURE 3.—Body nose induced by an axial source distribution.

³ The inversion of order is permissible only if $A_o(x)$ is suitably well behaved, a point that will arise later in the determination of the optimum body with given caliber.

tum transport through the control surface. Equation (32) is the exact expression for the body drag, and, again, requires no knowledge of source strength beyond $x=l-\beta R$.

COMBINED FLOW FIELDS

One method of attack that has proved to be extremely helpful in the analysis of problems in aerodynamic theory involves a symmetrization process in which flow fields in both forward and reverse flow are related. Attention, up to the present time, has been devoted principally to planar-type problems and in reference 13 Jones has used this approach to derive criteria that appear in the minimization of wave drag of, for example, nonlifting wings having specified thickness ratios or volumes. In this section, a brief discussion is given, using the methods of reference 14, of the way these concepts appear in cylindrical-control-surface analysis.

THE RECIPROCITY RELATION FOR AXIAL FLOW

Equation (1) can be written

$$L(\varphi) \equiv \beta^2 \varphi_{xx} - \varphi_{yy} - \varphi_{zz} = 0 \quad (33)$$

where $L(\varphi)$ is a self-adjoint linear operator. Let now $\psi(x, y, z)$ and $\Omega(x, y, z)$ be two solutions of equation (33) satisfying boundary conditions given on a circular cylinder. Reciprocal relations between ψ and Ω can be derived by applying Green's theorem over a prescribed geometric region. Consider, as shown in figure 4, the cylindrical control surface extending from $x=0$ to $x=l$ and draw the enveloping Mach cones at the front and rear of the surface.

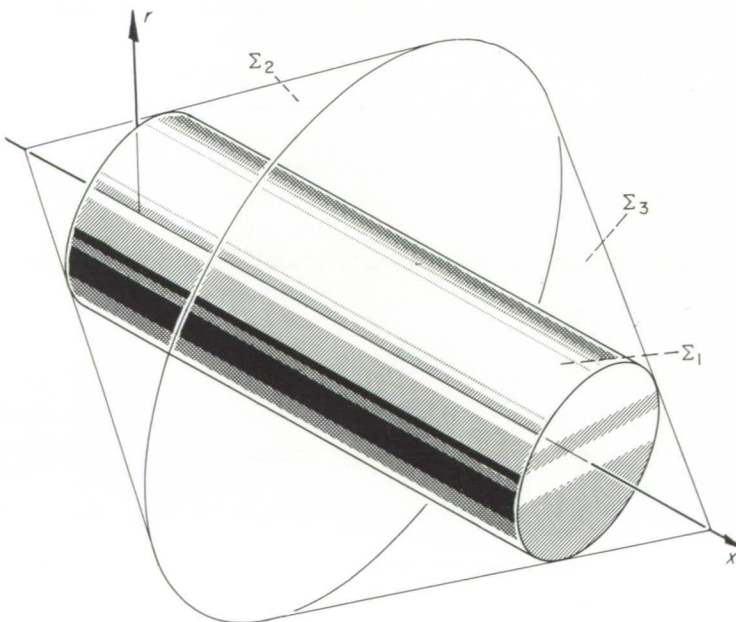


FIGURE 4.—Surfaces of integration for combined-flow analysis.

Denote the cylindrical surface by Σ_1 , the front Mach cone $x-\beta r=-\beta R$ by Σ_2 , and the rear cone $x+\beta r=l+\beta R$ by Σ_3 . These surfaces enclose a toroidal region, bounded internally by Σ_1 and externally by Σ_2 and Σ_3 . It follows from Green's theorem that the integral relation

$$\begin{aligned} \iint \psi \left(-\beta^2 n_1 \frac{\partial \Omega}{\partial x} + n_2 \frac{\partial \Omega}{\partial y} + n_3 \frac{\partial \Omega}{\partial z} \right) d\Sigma \\ = \iint \Omega \left(-\beta^2 n_1 \frac{\partial \psi}{\partial x} + n_2 \frac{\partial \psi}{\partial y} + n_3 \frac{\partial \psi}{\partial z} \right) d\Sigma \end{aligned} \quad (34)$$

applies where the surface integration extends over Σ_1 , Σ_2 , and Σ_3 , and n_1 , n_2 , n_3 are direction cosines, with respect to the x , y , z axes, of the surface normal directed inward into the region.

It is customary to re-express relations like equation (34) in terms of a newly defined directional derivative along a line termed the conormal. In this manner, the equation becomes

$$\iint \psi \Lambda \frac{\partial \Omega}{\partial \nu} d\Sigma = \iint \Omega \Lambda \frac{\partial \psi}{\partial \nu} d\Sigma \quad (35)$$

where

$$\frac{\partial \varphi}{\partial \nu} = \frac{\partial \varphi}{\partial x} \nu_1 + \frac{\partial \varphi}{\partial y} \nu_2 + \frac{\partial \varphi}{\partial z} \nu_3 \quad (36)$$

and the direction cosines ν_1 , ν_2 , ν_3 of the conormal are derived from

$$-n_1 \beta^2 = \Lambda \nu_1, \quad n_2 = \Lambda \nu_2, \quad n_3 = \Lambda \nu_3$$

By calculation of the respective normals n_1 , n_2 , n_3 and using the relation $\nu_1^2 + \nu_2^2 + \nu_3^2 = 1$, it is readily found from the equations defining the conormal that on the surface Σ_1 , the conormal is normal to the surface and $\Lambda=1$; on a Mach cone the conormal lies along the cone and $\Lambda=\beta$.

Let now ψ be set equal to $\varphi(x, r, \theta)$, the perturbation velocity potential associated with boundary conditions in the forward-flowing stream, and let Ω be $\tilde{u}(x, r, \theta)$, the x -component of perturbation velocity associated with boundary conditions in a stream flowing in the reverse direction. Under these conditions, equation (35) becomes

$$\begin{aligned} \int_0^{2\pi} R d\theta \int_0^l \tilde{u} \frac{\partial \varphi}{\partial r} dx + \beta \iint \tilde{u} \frac{\partial \varphi}{\partial \nu} d\Sigma_2 + \beta \iint \tilde{u} \frac{\partial \varphi}{\partial \nu} d\Sigma_3 \\ = \int_0^{2\pi} R d\theta \int_0^l \varphi \frac{\partial \tilde{u}}{\partial r} dx + \beta \iint \varphi \frac{\partial \tilde{u}}{\partial \nu} d\Sigma_2 + \beta \iint \varphi \frac{\partial \tilde{u}}{\partial \nu} d\Sigma_3 \end{aligned}$$

On the Mach cone Σ_2 , the perturbation potential may arbitrarily be set equal to zero and its conormal derivative also; the cone will also be zero; as a consequence, the second term on both sides of the equation vanish. Since the flow fields are irrotational, $\partial \tilde{u} / \partial r = \partial \tilde{v}_r / \partial x$ where v_r is radial velocity. After making this substitution and integrating the first term in the right member by parts, one gets

$$\begin{aligned} R \int_0^{2\pi} d\theta \int_0^l \tilde{u} v_r dx = R \int_0^{2\pi} \left[\varphi(l, R, \theta) \tilde{v}_r(l, R, \theta) - \int_0^l \tilde{v}_r u dx \right] d\theta \\ - \beta \int_0^{2\pi} d\theta \int_{x=l/2}^{x=l} r \left(\tilde{u} \frac{\partial \varphi}{\partial \nu} - \varphi \frac{\partial \tilde{u}}{\partial \nu} \right) d\nu \end{aligned}$$

The last integral becomes

$$- \beta \int_0^{2\pi} d\theta \int_{x=l/2}^{x=l} (\sqrt{r} \tilde{u})^2 \frac{d}{d\nu} \left(\frac{\varphi}{\tilde{u}} \right) d\nu$$

and for the given boundary conditions it is possible to show that along a conormal of Σ_3 the relation $\tilde{v}_r = \beta \tilde{u}$ holds and

$\sqrt{r} \tilde{u}$ is independent of ν . The integral then can be rewritten as

$$\beta \int_0^{2\pi} d\theta \int_{x=l/2}^{x=l} (\sqrt{r} \tilde{u})^2 \frac{d}{d\nu} \left(\frac{\varphi}{\tilde{u}} \right) d\nu = \beta R \int_0^{2\pi} \tilde{u}(l, R, \theta) \varphi(l, R, \theta) d\theta$$

and one has, finally, the desired reciprocal theorem

$$-R \int_0^{2\pi} d\theta \int_0^l \tilde{u}(x, R, \theta) v_r(x, R, \theta) dx = R \int_0^{2\pi} d\theta \int_0^l u(x, R, \theta) \tilde{v}_r(x, R, \theta) dx \quad (37)$$

It is not the purpose here to exploit the various applications of equation (37); rather, the role played by the reciprocal relation in drag calculations will be considered. In the forward and reverse flow fields, the pressure-velocity relations of linearized theory are

$$p - p_0 = -\rho_0 U_0 u, \quad \tilde{p} - p_0 = \rho_0 U_0 \tilde{u} \quad (38)$$

If, furthermore, thickness distributions of the form

$$r = f(x, \theta), \quad r = \tilde{f}(x, \theta)$$

are placed on the cylinder $r = R$, the boundary conditions are

$$\left[\frac{1}{U_0} \frac{\partial \varphi}{\partial r} \right]_{r=R} = \frac{\partial f}{\partial x}, \quad \left[\frac{1}{U_0} \frac{\partial \tilde{\varphi}}{\partial r} \right]_{r=R} = -\frac{\partial \tilde{f}}{\partial x}$$

Equation (37) can then be written

$$-\int_0^{2\pi} R d\theta \int_0^l (\tilde{p} - p_0) \frac{\partial f}{\partial x} dx = \int_0^{2\pi} R d\theta \int_0^l (p - p_0) \frac{\partial \tilde{f}}{\partial x} dx \quad (39)$$

An immediate consequence of this last result is that for a unique thickness distribution, that is, for $f(x, \theta) = \tilde{f}(x, \theta)$, the drag of a body in forward and reverse flow is the same. This follows from the fact that for quasi-cylindrical bodies the relations for drag are, respectively,

$$D = R \int_0^{2\pi} d\theta \int_0^l (p - p_0)_{r=R} \frac{\partial f}{\partial x} dx$$

$$\tilde{D} = -R \int_0^{2\pi} d\theta \int_0^l (\tilde{p} - p_0)_{r=R} \frac{\partial \tilde{f}}{\partial x} dx$$

For fixed geometry, therefore, drag is equal to half the sum of these two expressions

$$D = \frac{R}{2} \int_0^{2\pi} d\theta \int_0^l (p - \tilde{p})_{r=R} \frac{\partial f}{\partial x} dx$$

Defining pressure $P(x, r, \theta)$ in the combined flow fields by the following

$$P(x, r, \theta) = p - \tilde{p} = -\rho_0 U_0 (u + \tilde{u}) \quad (40)$$

one has

$$D = \frac{R}{2} \int_0^{2\pi} d\theta \int_0^l P(x, R, \theta) \frac{\partial f}{\partial x} dx \quad (41)$$

If the body has axial symmetry, equation (41) reduces to the form given in equation (28). To show this, one notes first that P and f are independent of θ and that equation (41) becomes

$$D = \frac{1}{2} \int_0^l P S'(x) dx$$

The proof follows from the relations

$$\left. \begin{aligned} S'(x) &= \tilde{S}'(x) \\ \frac{u(x, R)}{U_0} &= -\frac{1}{2\pi\beta R} \left[S'(x) - \int_0^x S'(x_1) W\left(\frac{x-x_1}{\beta R}\right) \frac{dx_1}{\beta R} \right] \\ \frac{\tilde{u}(x, R)}{U_0} &= -\frac{1}{2\pi\beta R} \left[S'(x) + \int_x^l S'(x_1) W\left(\frac{x_1-x}{\beta R}\right) \frac{dx_1}{\beta R} \right] \\ \frac{P(x, R)}{q_0} &= \frac{1}{\pi\beta R} \left[2S'(x) - \int_0^l S'(x_1) W\left(\frac{|x-x_1|}{\beta R}\right) \frac{dx_1}{\beta R} \right] \end{aligned} \right\} \quad (42)$$

GEOMETRIC CRITERIA FOR MINIMUM DRAG

Consider now the problem of minimizing the wave drag of a quasi-cylindrical body subject to the condition that the volume of the body is constant. The body surface may be defined by

$$r = f(x, \theta) = R + g(x, \theta) \quad (43)$$

The function $g(x, \theta)$ determines the magnitude of the surface displacement from the cylinder $r = R$; these displacements, as well as their gradients, are assumed small and we also assume

$$g(x, \theta) = 0 \text{ for } x \leq 0 \text{ and } l \geq x$$

If equation (41) is integrated by parts with respect to x , the wave drag of the body becomes

$$D = \frac{-R}{2} \int_0^{2\pi} d\theta \int_0^l P'(x, R, \theta) g(x, \theta) dx \quad (44)$$

where the prime indicates x -wise differentiation of P . The imposed geometric constraint on the variational problem is

$$\begin{aligned} \frac{1}{2} \int_0^{2\pi} d\theta \int_0^l f^2(x, \theta) dx &\approx \frac{1}{2} \int_0^{2\pi} d\theta \int_0^l [R^2 + 2Rg(x, \theta)] dx \\ &= \pi R^2 l + R \int_0^{2\pi} d\theta \int_0^l g(x, \theta) dx = V = \text{const.} \end{aligned} \quad (45)$$

where V is the total volume. The problem thus becomes one of minimizing the expression

$$D - \mu V = -R \left\{ \frac{1}{2} \int_0^{2\pi} d\theta \int_0^l P' g(x, \theta) dx + \mu \left[\pi R l + \int_0^{2\pi} d\theta \int_0^l g(x, \theta) dx \right] \right\} \quad (46)$$

where μ is the Lagrangian multiplier. Carrying out the variation, one has

$$\delta(D - \mu V) = -\frac{R}{2} \int_0^{2\pi} d\theta \int_0^l [P'(\delta g) + g(\delta P') + 2\mu \delta g] dx = 0$$

but from equation (37) or (39) it can be shown that the first two terms in the integrand yield equal integrals and the minimizing condition becomes

$$\int_0^{2\pi} d\theta \int_0^l [P'(x, R, \theta) + \mu] \delta g dx = 0$$

Since this latter equation must be satisfied by all possible variations of the displacement function $g(x, \theta)$, it follows that the desired condition is

$$P'(x, R, \theta) + \mu = 0 \quad (47)$$

Stated in words, the condition for minimum wave drag of a quasi-cylindrical body of given volume is that the longitudinal gradient of pressure on the body in the combined forward and reverse flow field is a constant. Furthermore, from equation (44), minimum drag is then given by

$$D_{min} = \frac{\mu}{2} (V - \pi R^2 l) = \frac{\mu}{2} V_e \quad (48)$$

where μ can now be identified with the negative pressure gradient in the combined field and $(V - \pi R^2 l) = V_e$ is the volume exposed to the fluid around the cylindrical control surface $r = R$.

The actual cross-section-area variation of a minimum-drag constant-volume body and its pressure distribution are shown in figure 5 for the case in which axial symmetry

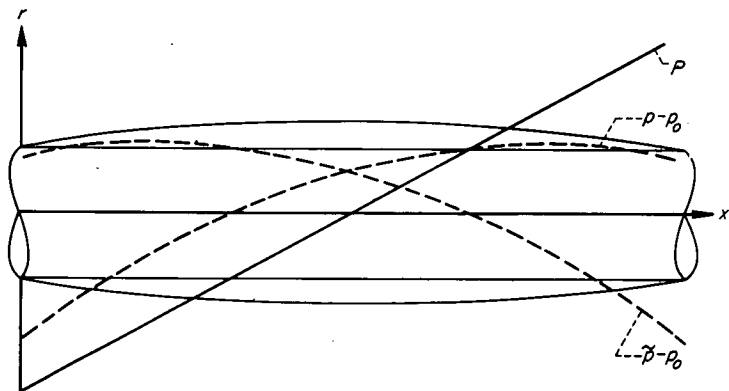


FIGURE 5.—Minimum drag body with pressure distributions in combined flow.

is imposed. Pressure coefficient in the combined flow field of an axially symmetric body has been given in equation (42). The geometric criterion just established then leads to the integral equation

$$2S'(x) - \int_0^l S'(x_1) W\left(\frac{|x-x_1|}{\beta R}\right) \frac{dx_1}{\beta R} = -\mu x + b \quad (49)$$

and the solution of this equation will determine the body geometry. In the following section an analogous integral equation will be derived but with the source-strength distribution chosen as the fundamental dependent variable.

The combined-flow-field technique can also be used to study the problem of minimizing wave drag for specified body caliber or, more generally, when the body has a fixed cross section at a specified longitudinal position. The resulting condition for minimum drag is that the pressure distribution on the body in the combined flow field is a constant forward and aft of the specified position. These conditions are all analogous to those obtained for planar problems by R. T. Jones (ref. 13).

DRAG MINIMIZATION

In this division, optimum bodies having certain prescribed geometric properties will be determined by standard variational methods. The analysis will, as mentioned previously, deal with the strength of an axial source distribution as the minimizing function, rather than the geometric quantity,

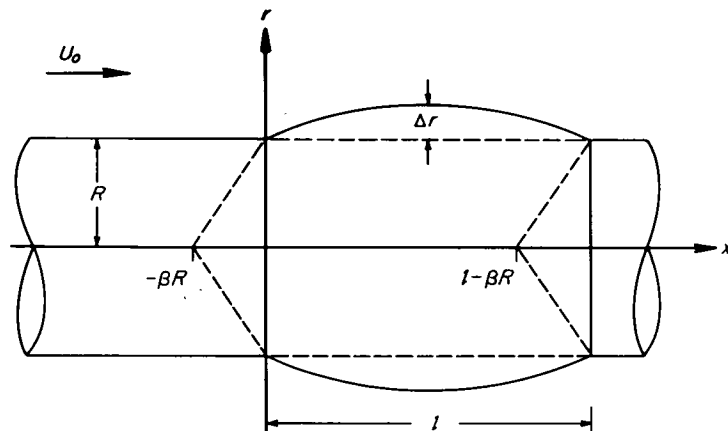


FIGURE 6.—Body and associated nomenclature used in drag minimization.

cross-sectional area. Thus, we shall be concerned with formula (32), giving drag in terms of the source distribution.

QUASI-CYLINDRICAL BODY OF REVOLUTION OF GIVEN VOLUME

Isoperimetric conditions.—The configuration to be considered, together with associated nomenclature, is shown in figure 6. The geometric properties of the body can be expressed in terms of the source distribution function $A_o(x)$ by using equation (20), namely,

$$S'(x) = \frac{2\pi R}{U_o} \varphi_r \Big|_{r=R} \quad (50)$$

Then, from equation (30)

$$S'(x) = \frac{1}{U_o} \int_{-\beta R}^{x-\beta R} \frac{A_o'(x_1)(x-x_1)}{\sqrt{(x-x_1)^2 - \beta^2 R^2}} dx_1 \quad (51)$$

If equation (51) is integrated x -wise it is seen that

$$S(x) - S(o) = \frac{1}{U_o} \int_0^x dz \int_{-\beta R}^{z-\beta R} \frac{(z-x_1)A_o'(x_1)dx_1}{\sqrt{(z-x_1)^2 - \beta^2 R^2}} \quad (52a)$$

By changing the order of integration and performing the integration with respect to z one finds

$$S(x) - S(o) = \frac{1}{U_o} \int_{-\beta R}^{x-\beta R} \frac{(x-x_1)A_o'(x_1)}{\sqrt{(x-x_1)^2 - \beta^2 R^2}} dx_1 \quad (52b)$$

or, integrating by parts,

$$S(x) - S(o) = \frac{1}{U_o} \int_{-\beta R}^{x-\beta R} A_o'(x_1) \sqrt{(x-x_1)^2 - \beta^2 R^2} dx_1 \quad (52c)$$

The magnitude of the additional volume wrapped around the cylinder is

$$V_e = \int_0^l [S(x) - S(0)] dx \quad (53a)$$

and, from equation (52b),

$$V_e = \frac{1}{U_o} \int_{-\beta R}^{l-\beta R} A_o(x_1) \sqrt{(l-x_1)^2 - \beta^2 R^2} dx_1 \quad (53b)$$

The variational problem.—The quantity to be minimized will be taken as $D - \mu_1 V_e$. From equation (32), the drag can be written, after an integration by parts,

$$D = \frac{\rho_o}{4\pi} \int_{-\beta R}^{l-\beta R} \frac{A_o(x_1) dx_1}{\sqrt{(l-x_1)^2 - \beta^2 R^2}} \int_{-\beta R}^{l-\beta R} \frac{A_o'(x_2) \sqrt{(l-x_2)^2 - \beta^2 R^2}}{x_1 - x_2} dx_2 \quad (54)$$

In addition to prescribing the volume added to the fundamental cylinder, we shall also require that the body return at the end to the same cross-sectional area as at the front. Thus, according to equation (52b),

$$0 = \int_{-\beta R}^{l-\beta R} \frac{(l-x_1) A_o(x_1) dx_1}{\sqrt{(l-x_1)^2 - \beta^2 R^2}} \quad (55)$$

$$A_o'(x) \sqrt{(l-x)^2 - \beta^2 R^2} = \frac{1}{\pi \sqrt{(l-\beta R-x)(x+\beta R)}} \left\{ \pi \int_{-\beta R}^{l-\beta R} \frac{A_o'(x_1) \sqrt{(l-x_1)^2 - \beta^2 R^2} dx_1 - \int_{-\beta R}^{l-\beta R} \frac{\lambda(l-x_1) + \frac{2\pi\mu_1}{\rho_o U_o} [(l-x_1)^2 - \beta^2 R^2]}{x-x_1} \sqrt{(l-\beta R-x_1)(x_1+\beta R)} dx_1 \right\}$$

The first integral on the right vanishes according to the closure condition (55) and, if the remaining integrations are performed, we find

$$A_o'(x) \sqrt{(l-x)^2 - \beta^2 R^2} = \frac{1}{\pi \sqrt{(l-\beta R-x)(x+\beta R)}} \left\{ \frac{l(l+4\beta R)}{16} \left(\frac{2\pi l}{\rho_o U_o} \mu_1 + 2\lambda \right) + \frac{l-\beta R-x}{8} \left[4\lambda(l-2x) + \frac{2\pi\mu_1}{\rho_o U_o} (3l^2 - 4\beta Rl - 8\beta^2 R^2 - 12lx + 8x^2) \right] \right\}$$

It will be noted that unless

$$\frac{2\pi l}{\rho_o U_o} \mu_1 + 2\lambda = 0$$

this solution for $A_o'(x)$ does not obey the closure requirement. Therefore we impose this last condition and finally obtain

$$A_o'(x) = \frac{\mu_1}{4\rho_o U_o} \frac{(l^2 - 4\beta Rl - 8\beta^2 R^2) - 8lx + 8x^2}{\sqrt{(l+\beta R-x)(x+\beta R)}} \quad (57)$$

The strength of the minimizing source distribution $A_o(x)$ is now obtained by integrating equation (57);

$$A_o(x) = \frac{\mu_1}{2\rho_o U_o} \left[(l-2x) \sqrt{(l+\beta R-x)(x+\beta R)} - 2\beta^2 R^2 \cos^{-1} \frac{l-2x}{l+\beta R} \right] \quad (58a)$$

is a condition to be met by the minimizing function $A_o(x_1)$, and by its variations.

The quantity $D - \mu_1 V_e$ can be formed from equations (53) and (54), and if the variation is performed, one finds the condition

$$\int_{-\beta R}^{l-\beta R} \frac{\delta A_o(x_1) dx_1}{\sqrt{(l-x_1)^2 - \beta^2 R^2}} \left\{ \int_{-\beta R}^{l-\beta R} \frac{A_o'(x_2) \sqrt{(l-x_2)^2 - \beta^2 R^2}}{x_1 - x_2} dx_2 - \frac{2\pi}{\rho_o U_o} \mu_1 [(l-x_1)^2 - \beta^2 R^2] \right\} = 0$$

If this last equation is compared with equation (55), it is seen that for admissible variations, the quantity within the brackets must be set equal to $\lambda(l-x_1)$, where λ is an arbitrary constant. Thus, the equation for determination of the optimizing source distribution under the conditions of given volume and closure is

$$\int_{-\beta R}^{l-\beta R} \frac{A_o'(x_1) \sqrt{(l-x_1)^2 - \beta^2 R^2}}{x-x_1} dx_1 = \lambda(l-x) + \frac{2\pi\mu_1}{\rho_o U_o} [(l-x)^2 - \beta^2 R^2] \quad (56)$$

Equation (56) is recognized as the familiar airfoil equation with $[A_o'(x_1) \sqrt{(l-x_1)^2 - \beta^2 R^2}]$ as the unknown. Thus we write the solution immediately as (see, e.g., ref. 15)

Properties of the optimal source distribution.—It is convenient to express the various quantities such as source strength, area distribution, etc., as dimensionless functions of the dimensionless variable $\eta = x/l$ and parameter $\sigma = \beta R/l$. Thus, indicating a dimensionless function by a star, we have from equation (58a)

$$A_o^*(\eta) = \frac{A_o(l\eta)}{lU_o} = \frac{l\mu_1}{4q_o} \left[(1-2\eta) \sqrt{(\eta+\sigma)(1-\eta+\sigma)} - 2\sigma^2 \cos^{-1} \frac{1-2\eta}{1+2\sigma} \right] \quad (58b)$$

It will be noted that if the radius of the control surface is taken very small, so that $\sigma \rightarrow 0$, formula (58b) becomes

$$A_o^*(\eta)|_{\sigma \rightarrow 0} = \frac{\mu_1 l}{4q_o} (1-2\eta) \sqrt{\eta(1-\eta)}$$

which is the well-known slender-body theory result for the source distribution corresponding to an optimum body of given volume (refs. 16 and 17.)

In order to determine the value of the Lagrange multiplier μ_1 , in terms of the prescribed volume V_e , it is convenient to find first the expression for the local cross-section area of the optimum body. Thus, using equation (52c) (with $S^*(\eta) = \frac{1}{l^2} S(l\eta)$),

$$S^*(\eta) - S^*(o) = \frac{\mu_1 l}{6q_o} \sqrt{(\eta+2\sigma)(1-\eta+2\sigma)} [\eta(1-\eta)E - \sigma(1-4\sigma)(K-E)] \quad (59)$$

where K and E are elliptic integrals of the first and second kinds, respectively, of modulus

$$k^2 = \frac{\eta(1-\eta)}{(\eta+2\sigma)(1-\eta+2\sigma)}$$

Using equation (59) in equation (53a), we find

$$V_e^* = \frac{\mu_1 l}{6q_o} \int_0^1 \sqrt{(\eta+2\sigma)(1-\eta+2\sigma)} [\eta(1-\eta)E - \sigma(1-4\sigma)(K-E)] d\eta$$

$$= \frac{\mu_1 l}{6q_o} B(\sigma) \quad (60a)$$

which expresses the constant μ_1 , in terms of the prescribed volume V_e^* ($= \frac{V_e}{l^3}$) and of a function B of the quantity $\sigma = \beta R/l$. A graph of this function $B(\sigma)$ versus σ is shown in

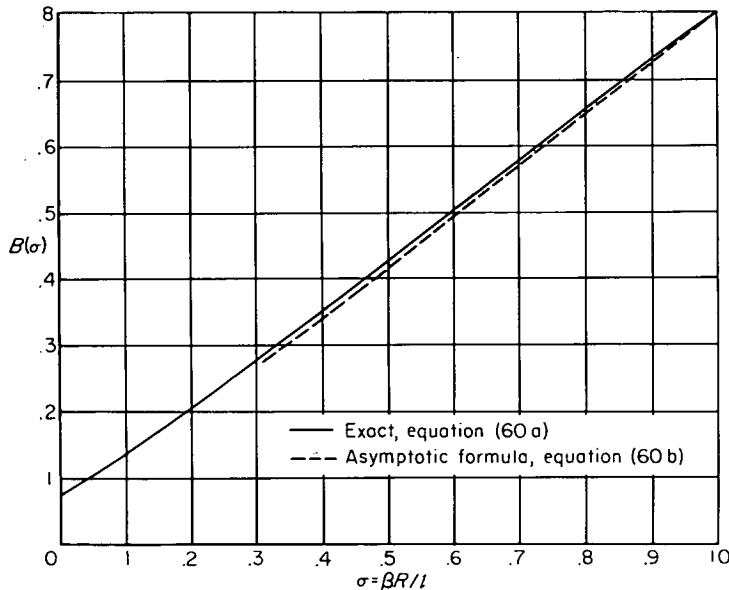


FIGURE 7.—The function $B(\sigma)$.

figure 7. Shown also in figure 7 is a dashed line that corresponds to the asymptotic form for $B(\sigma)$, which is

$$B(\sigma) \sim \frac{\pi}{16} (1+4\sigma) \sqrt{\frac{2\sigma}{1+2\sigma}} \quad (60b)$$

The closeness of the asymptotic values to the exact values even for relatively small values of σ is noteworthy.

The formulae (58b) and (59) for the source strength and cross-section area, respectively, can now be recast in terms of prescribed quantities

$$A_o^*(\eta) = \frac{3}{2} \frac{V_e^*}{B(\sigma)} \left[(1-2\eta) \sqrt{(\eta+\sigma)(1-\eta+\sigma)} - 2\sigma^2 \cos^{-1} \frac{1-2\eta}{1+2\sigma} \right] \quad (61)$$

$$\frac{S^*(\eta) - S^*(o)}{S^*(o)} = \frac{(V_e^*/V_o^*)}{B(\sigma)} \sqrt{(\eta+2\sigma)(1-\eta+2\sigma)} [\eta(1-\eta)E - \sigma(1-4\sigma)(K-E)] \quad (62a)$$

where V_o is the volume of the original cylinder section,

$$V_o = \pi R^2 l = l S(o) = l^3 V_o^*$$

Consider the expression (61) for the source function $A_o^*(\eta)$. In the parameter $\sigma = \beta R/l$, we may think of β as fixed and l as unity, so that variations in σ amount to variations in the size of the control surface of radius R . Thus, in figure 8, the

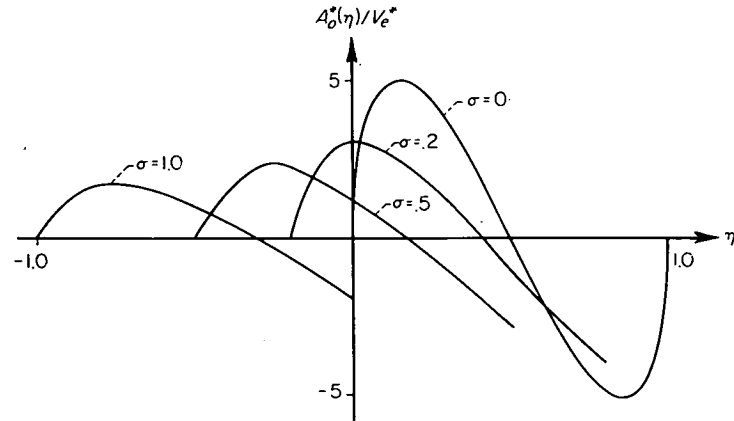


FIGURE 8.—Optimum source distributions for various values of the parameter σ .

case $\sigma = 0$ corresponds to the source distribution for the well-known Sears-Haack body (refs. 16 and 17). It will be noted in the cases where $\sigma > 0$ that the source functions become less steep and attain lesser maximum values because the volume remains the same while the control-surface cylinder is increasing, thus giving a smaller maximum radius of the added portion.

Next let us examine the expression (62a) for cross-sectional area. First, we notice that it can be written

$$S^*(\eta) - S^*(o) = \frac{V_e^*}{B(\sigma)} \sqrt{(\eta+2\sigma)(1-\eta+2\sigma)} [\eta(1-\eta)E - \sigma(1-4\sigma)(K-E)] \quad (62b)$$

in which form it reduces formally for $\sigma \rightarrow 0$ to

$$S^*(\eta) = \frac{128}{3\pi} V_e^* [\eta(1-\eta)]^{3/2} \quad (62c)$$

which is identical with the expression for cross-section area of a slender optimum body of prescribed volume (Sears-Haack body). Of course, V_e is, in this case, the total volume of the body. On the other hand, if we allow the radius of the control surface to increase indefinitely, equation (62b) gives (using the asymptotic form for $B(\sigma)$, eq. (60b))

$$S^*(\eta) - S^*(o) = 6V_e^* \eta(1-\eta)$$

In the case when R is very large, we take

$$S(x) - S(o) = 2\pi R \Delta r(x) \quad (63)$$

so we have, returning to the original variables,

$$\Delta r(x) = 6 \frac{V_e}{2\pi R l} \frac{x(l-x)}{l^2} \quad (64)$$

where $V_e/2\pi R l$ is a finite quantity, and, in fact, is the average height of the protuberance above the control cylinder. This

result is clear from physical reasoning, for one would expect that as the control cylinder increased in radius, the two-dimensional result for the optimum problem would become more nearly valid, and, indeed, equation (64) is the formula for a two-dimensional biconvex section, where Δr is distance from the mean line, l is chord length, and maximum thickness is $\left(\frac{3}{4} \frac{V_e}{\pi R l}\right)$.

It will be noted that the area distribution as given by equation (62b) has fore-and-aft symmetry, since the functional dependence upon η involves only the combination $\eta(1-\eta)$. The maximum cross-section of the optimum body then occurs at the midpoint $\eta = \frac{1}{2}$ and is given by (from eq. (62b))

$$S^*_{max} - S^*(o) = 2V_e^* \frac{1+4\sigma}{4B(\sigma)} \left[\frac{E}{4} - \sigma(1-4\sigma)(K-E) \right] = 2V_e^* T(\sigma) \quad (65)$$

where the modulus of the elliptic integrals is now $k = 1/(1+4\sigma)$. Figure 9 shows the function $T(\sigma)$ versus σ .

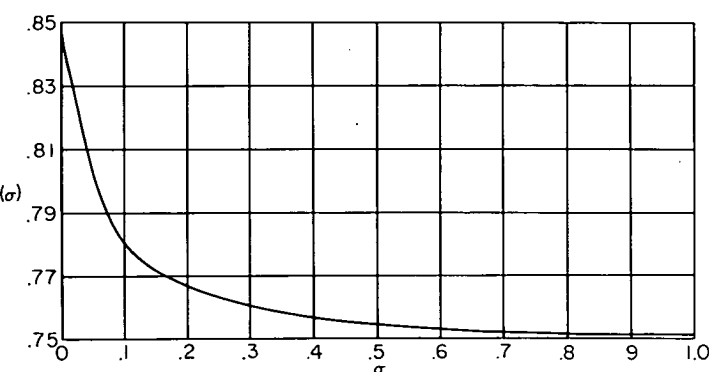


FIGURE 9.—The function $T(\sigma)$.

The drag of the optimum bodies can now be evaluated. From equations (54) and (56)

$$D = \frac{\rho_o}{4\pi} \int_{-\beta R}^{l-\beta R} \frac{A_o(\xi) d\xi}{\sqrt{(l-\xi)^2 - \beta^2 R^2}} \left\{ \lambda(l-\xi) + \frac{2\pi\mu_1}{\rho_o U_o} [(l-\xi)^2 - \beta^2 R^2] \right\}$$

The integral involving λ vanishes because of the closure condition. The remaining integration gives

$$D = \frac{\mu_1}{2U_o} \int_{-\beta R}^{l-\beta R} A_o(\xi) \sqrt{(l-\xi)^2 - \beta^2 R^2} d\xi = \frac{\mu_1 V_e}{2} \quad (66)$$

by equation (53b). Finally, using the evaluation of μ_1 of equation (60a), we have

$$\frac{D}{q_o} = 3 \frac{V_e^2}{l^4 B(\sigma)} \quad (67)$$

$$\frac{S^*(\eta) - S^*(o)}{\Delta S^*} = \frac{2}{\pi(1+4\sigma)} \frac{(1+2\sigma)(1+4\sigma)\Pi(\alpha^2, k) - (1-2\eta)(\eta+2\sigma)(1-\eta+2\sigma)E - (1+2\sigma)(1-\eta+2\sigma)K}{\sqrt{(\eta+2\sigma)(1-\eta+2\sigma)}} \quad (71)$$

where $\Pi(\alpha^2, k)$ is a complete elliptic integral of third kind of modulus $k^2 = \frac{\eta(1-\eta)}{(\eta+2\sigma)(1-\eta+2\sigma)}$ and parameter $\alpha^2 = \frac{-\eta}{1-\eta+2\sigma}$.

again K and E are complete elliptic integrals of the first and second kinds, respectively, of the same modulus k .

If we allow σ to approach zero, equation (71) becomes, in the limit,

Numerical results pertaining to the problem just solved will be given in a later section, and a summary of the important formulae is given in the appendix.

QUASI-CYLINDRICAL BODY OF REVOLUTION WITH GIVEN CALIBER

The variational problem.—For this problem, we prescribe the area at the base of the body, so the given condition is, from equation (52b)

$$\Delta S = S(l) - S(o) = \frac{1}{U_o} \int_{-\beta R}^{l-\beta R} \frac{(l-x_1) A_o(x_1) dx_1}{\sqrt{(l-x_1)^2 - \beta^2 R^2}} \quad (68)$$

The variation can be taken as before (now without invoking the closure condition) on the quantity $D + \lambda \Delta S$, and it leads to the integral equation

$$\int_{-\beta R}^{l-\beta R} \frac{A_o'(x_1) \sqrt{(l-x_1)^2 - \beta^2 R^2}}{x-x_1} dx_1 = -\frac{2\pi\lambda}{\rho_o U_o} (l-x) \quad (69)$$

The solution to equation (69) can be written immediately by analogy with that for equation (56). The presence of a linear singularity in $A_o'(x)$ must be disallowed, however, according to a condition mentioned in deriving the drag formula, equation (32). Thus, we have here to set

$$\lambda = -\frac{8q_o \Delta S}{\pi l(l+4\beta R)}$$

and the solution consistent with the given conditions is

$$A_o'(x) = \frac{4}{\pi} \frac{U_o(\Delta S)}{l(l+4\beta R)} \frac{l-2x}{\sqrt{(l+\beta R-x)(x+\beta R)}} \quad (70a)$$

Integrating this expression, we find for the strength of the optimizing source distribution

$$A_o(x) = \frac{8}{\pi} \frac{U_o(\Delta S)}{l(l+4\beta R)} \sqrt{(l+\beta R-x)(x+\beta R)} \quad (70b)$$

The source distribution of equation (70b) represents the first approximation to the result of reference 3 for nearly equal front and rear radii.

Properties of the solution.—As in the section on the body with prescribed volume, we now consider x made dimensionless by division by l , and again set $\sigma = \beta R/l$. The various quantities of interest in connection with the caliber problem then become

$$A_o^*(\eta) = \frac{8}{\pi} \frac{\Delta S^*}{1+4\sigma} \sqrt{(\eta+\sigma)(1-\eta+\sigma)} \quad (70c)$$

$$\frac{S^*(\eta)}{S^*(1)} = \frac{2}{\pi} [\sin^{-1} \sqrt{\eta} - (1-2\eta) \sqrt{\eta(1-\eta)}] \quad (72)$$

which is the shape function for the well-known Kármán ogive (ref. 18). At the other limit, when $\sigma \rightarrow \infty$, equation (71) gives (in the original variables)

$$\frac{S(x) - S(o)}{\Delta S} = \frac{x}{l}$$

or, using the approximation of equation (63),

$$\frac{\Delta r(x)}{\Delta r(l)} = \frac{x}{l} \quad (73)$$

which is again the expected two-dimensional result for specified caliber.

The drag can be found by substituting equation (69) in equation (54), and then using equation (52b). There results

$$\frac{D}{q_o} = \frac{4}{\pi(1+4\sigma)} \frac{(\Delta S)^2}{l^2} \quad (74)$$

A summary of formulae pertaining to this body will be found in the Appendix.

EXAMPLES OF OPTIMUM BODIES

The optimum body of given volume.—In order to examine in detail the dependence of the body geometry on the parameter σ , we may return to equation (62a). The quantity $[S^*(\eta) - S^*(o)]$ is actually the local cross-sectional area added to the basic cylinder by the action of the source distribution. In figure 10 are shown some cases of optimum bodies, having equal additional volume V_e^* , for several values of the parameter σ . Only half of each distribution is shown, since they are symmetric about the point $\eta=1/2$. The one labeled $\sigma=0$ is the Sears-Haack optimum body, and it will be noted that as σ increases, the curves depart rather quickly from this limiting case and approach the other limiting value of the biconvex distribution for $\sigma \rightarrow \infty$. In fact, a biconvex arc drawn through the end points of the $\sigma=1/2$ case is indistinguishable from the exact result in the scale used. In the inset of figure 10 is shown the variation of the drag of the optimum bodies as a function of σ . This drag is also based on equal volume, and shows a fairly rapid decrease with increasing values of σ , due to the decrease in the thickness of the exposed portion of the body. The dashed curve on the drag plot is the calculated drag $\left[\frac{D}{q_o(V_e/l^2)^2} = \frac{12}{\pi\sigma} \right]$ under the assumption that each meridian section of the body acts as an independent two-dimensional optimum airfoil. This admittedly crude approximation is of course very poor at low values of σ , but its accuracy becomes surprisingly good for σ greater than about 0.4, and the approximation becomes exact in the limit $\sigma \rightarrow \infty$.

The variation of local cross section with σ can be examined also on the basis of equal exposed area. Thus, using equation (65) in combination with equation (62b), we have

$$\frac{\Delta S^*(\eta)}{\Delta S^*_{max}} = \frac{1}{2T(\sigma)B(\sigma)} \sqrt{(\eta+2\sigma)(1-\eta+2\sigma)} \quad (75)$$

$$[\eta(1-\eta)E - \sigma(1-4\sigma)(K-E)]$$

Figure 11 shows plots of equation (75), and it is again noted that the departure from the slender-body approximation ($\sigma=0$) is rapid. The limiting variation of area for $\sigma \rightarrow \infty$ is also shown in figure 11, and it is seen again how closely the optimum body-shape functions approach this limiting result even for moderate values of σ . Also shown is the drag corresponding to these cases.

$$\frac{D}{q_o l^2 (\Delta S^*_{max})^2} = \frac{3}{4B(\sigma)[T(\sigma)]^2} \quad (76)$$

which shows a similar drop from the $\sigma=0$ value as σ is increased. Again, the effective fineness ratio of the body is increasing with σ , and, if frontal area exposed to the stream is held fixed, the maximum thickness of the excess thickness vanishes as $1/\sigma$ for large σ . The departure of the geometric variation from the slender-body case is most pronounced near the nose, $\eta=0$, where the slope is given by

$$\frac{dS^*(\eta)}{d\eta} = \frac{3\pi}{8} \frac{V_e^*}{B(\sigma)} (1+4\sigma) \sqrt{\frac{2\sigma}{1+2\sigma}} \quad (77)$$

which vanishes only as $\sqrt{\sigma}$ for $\sigma \rightarrow 0$.

The optimum body of given caliber.—In this case, the maximum cross-section occurs at $\eta=1$ so there is no longitudinal symmetry. Figure 12 shows, for several values of the parameter σ , the optimum, equal-caliber, incremental cross-section area given by equation (71). The inset shows the drag as a function of σ ; from equation (74)

$$\frac{D}{q_o \left(\frac{\Delta S}{l} \right)^2} = \frac{4}{\pi(1+4\sigma)}$$

Again in this case, the closeness of the optimum distribution as σ increases to the two-dimensional value ($\sigma \rightarrow \infty$) is noticeable. This point has also been made by Ferrari in reference 5 where problems similar to ours are treated by a different approach. If the expression for cross-section area (eq. (71)) is expanded in powers of $1/\sigma$, it is found that

$$\frac{\Delta S^*(\eta, \sigma)}{\Delta S^*(1, \sigma)} = \eta - \frac{\eta(1-\eta)(1-2\eta)}{32} \left(\frac{1}{\sigma} \right)^2 + \dots \quad (78)$$

which shows the smallness of the correction to the two-dimensional result for moderate values of σ .

RECIPROCITY RELATIONS

The optimum body of given volume.—The longitudinal and radial perturbation velocities can be determined by substituting the derivative of the source-distribution function (eq. (57)) into the formulae (29) and (30). We find, at any point (x, r) ($r \geq R$) in the field

$$\frac{\varphi_z(x, r)}{U_o} = -\frac{\mu_1}{8\pi q_o} \frac{1}{\sqrt{[x+\beta(r+R)][l-x+\beta(r+R)]}} \{ 4[x+\beta(r+R)][l-x+\beta(r+R)]E +$$

$$[l(l+4\beta R) - 4(l+2\beta R)(l-x+\beta r+\beta R)]K + 4(l+2\beta R)(l-2x)\Pi(\alpha^2, k) \} \quad (79)$$

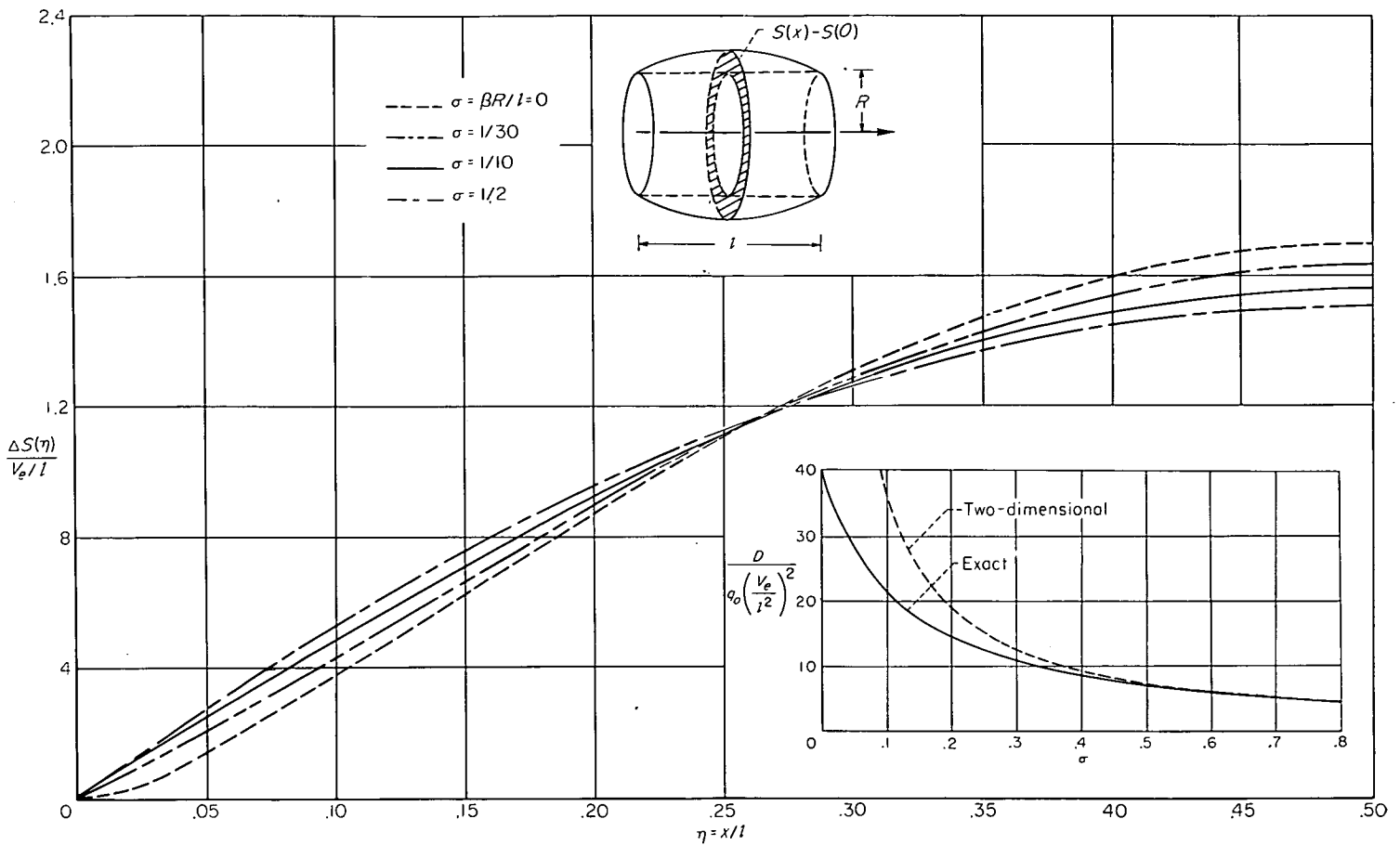


FIGURE 10.—Geometry and drag characteristics of optimum bodies of equal volume.

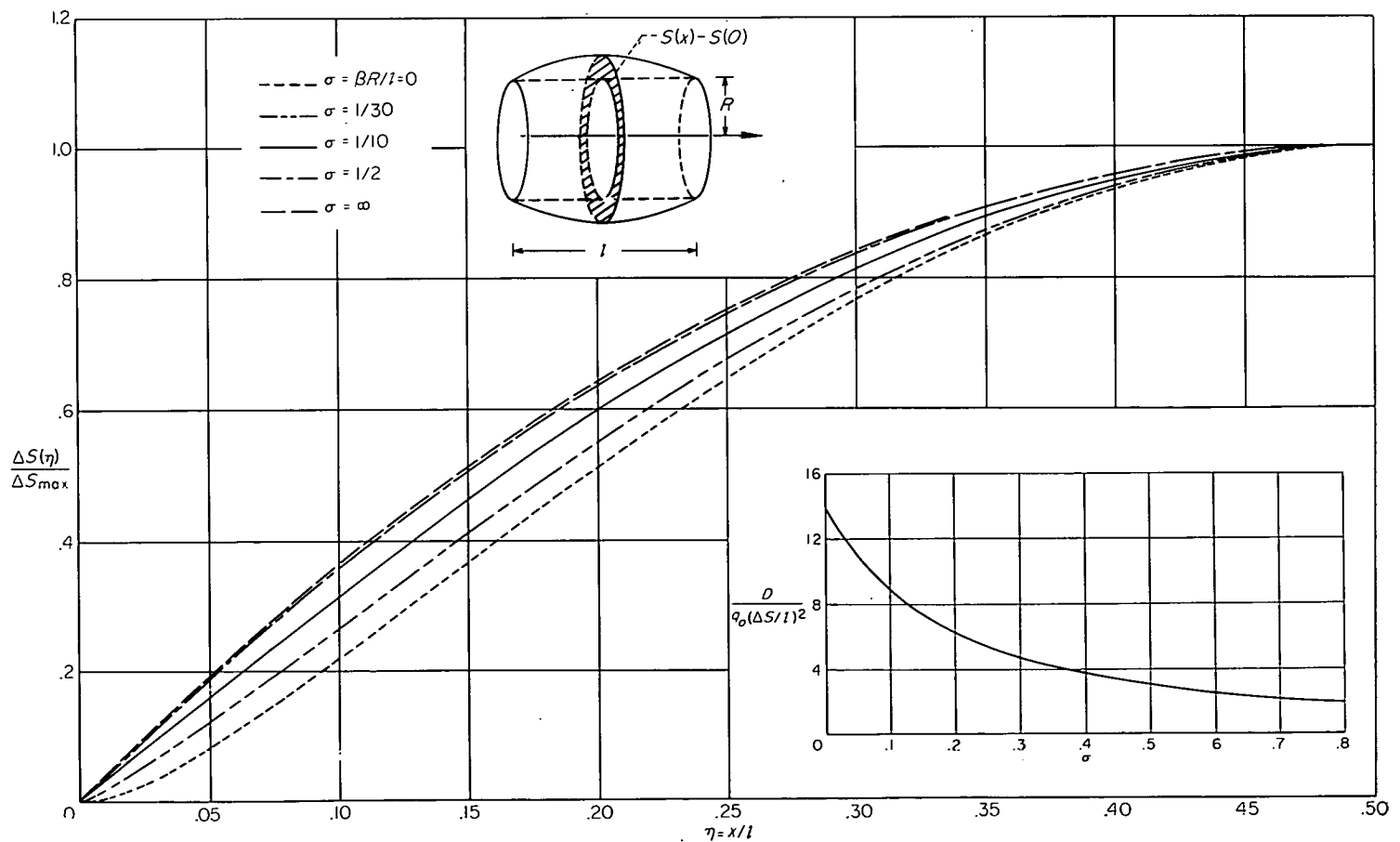


FIGURE 11.—Geometry and drag characteristics of optimum bodies of given volume (bodies having equal additional frontal area).

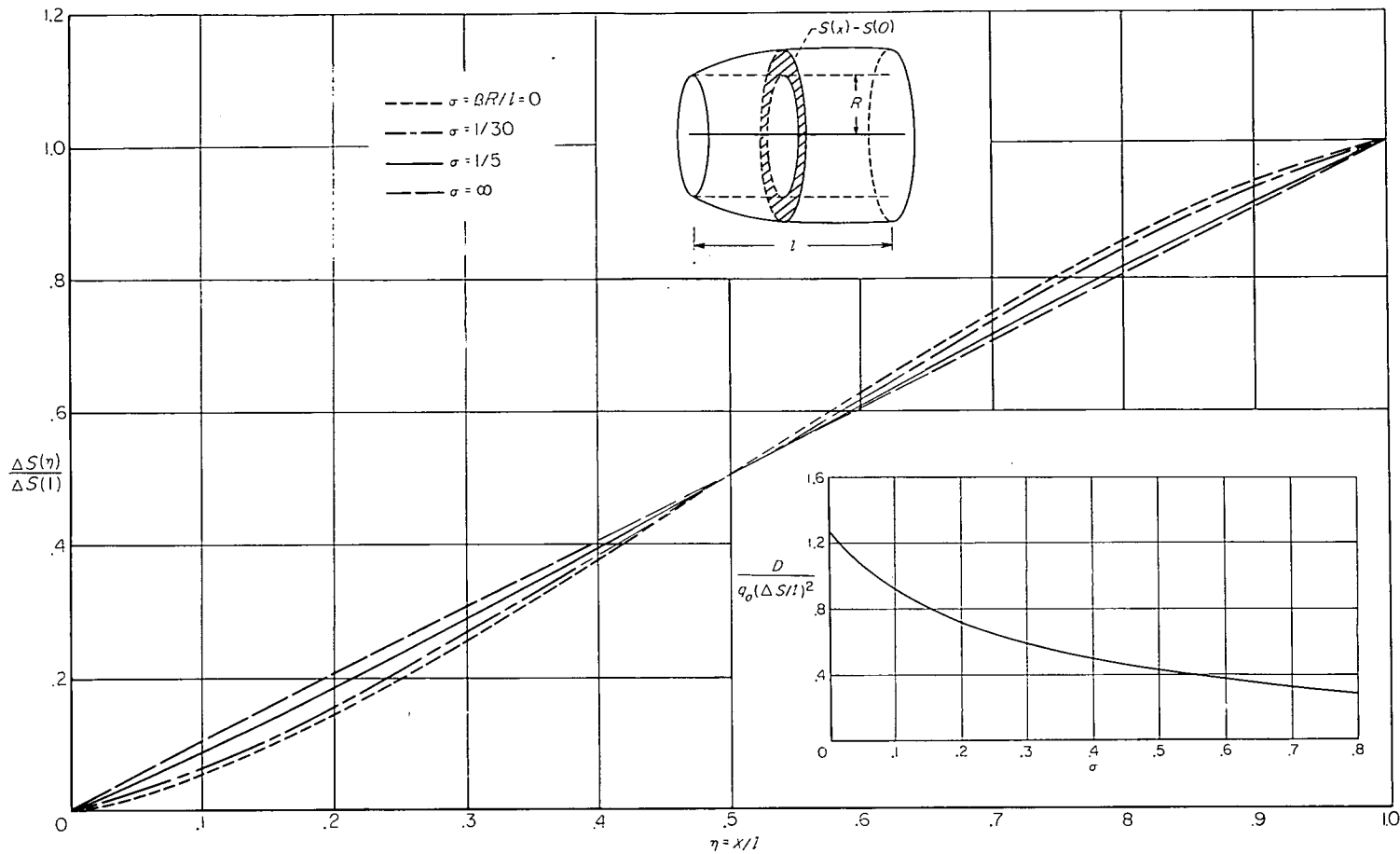


FIGURE 12.—Geometry and drag characteristics of optimum bodies of given caliber.

$$\frac{\varphi_r(x,r)}{U_o} = \frac{\mu_1}{8\pi q_o r} \frac{1}{\sqrt{[x+\beta(r+R)][l-x+\beta(r+R)]}} \{ (l-2x)[x+\beta(r+R)][l-x+\beta(r+R)]E - \beta r l [l-2x+2\beta(r-R)]K - 4\beta^2 R(r-R)[l-x+\beta(r+R)]K + 4\beta^2(r^2-R^2)(l+2\beta R)\Pi(\alpha^2, k) \} \quad (79b)$$

where now

$$k^2 = \frac{x(l-x)}{[x+\beta(r+R)][l-x+\beta(r+R)]}$$

$$\alpha^2 = -\frac{x-\beta(r-R)}{l-x+\beta(r+R)}$$

For the present axis system, the act of reversing the flow amounts to substituting $l-x$ for x , and, for the case of the symmetric body, the longitudinal perturbation velocity in the reversed flow is

$$\tilde{u}(x,r) = -u(l-x,r) = -\varphi_x(l-x,r)$$

Now, from equation (40), pressure in the combined field is given by

$$P = -\rho_o U_o(u + \tilde{u}) = -\rho_o U_o[\varphi_x(x,r) - \varphi_x(l-x,r)] \quad (80)$$

In order to verify this relation using equation (79a), the following result, which can be derived from formulae of reference 20, section 400, will be useful: Let

$$V_1(x) = \Pi(\alpha^2, k)$$

then

$$V_1(x) + V_1(l-x) = K + \frac{\pi}{2} \frac{\sqrt{[l-x+\beta(r+R)][x+\beta(r+R)]}}{l+2\beta R}$$

This, together with the fact that the modulus k is invariant to the substitution of $l-x$ for x , enables us to write immediately

$$P = \frac{\mu_1}{2} (l-2x) \quad (81)$$

Differentiating equation (81) we find

$$P' + \mu_1 = 0 \quad (82)$$

which agrees with the criterion for minimum drag with given volume established in equation (47). The Lagrange multiplier μ_1 is therefore identified as the pressure gradient in the combined flow field. It will be noted that equations (81) and (82) hold everywhere within the enveloping forward and rearward Mach cones of the quasi-cylindrical body (see fig. 4).

Now considering the radial component of perturbation velocity φ_r , we find, using the relations mentioned just previously

$$\frac{\varphi_r(x,r)}{U_o} + \frac{\varphi_r(l-x,r)}{U_o} = \frac{\beta^2(r^2-R^2)}{4q_o r} \mu_1 \quad (83)$$

so that the relation

$$\varphi_r(x,r) = -\varphi_r(l-x,r)$$

is satisfied on the quasi-cylinder itself, that is, when we set $r=R$.

The optimum body of given caliber.—For this case we find the following equations for the perturbation velocities:

$$\frac{\varphi_x(x,r)}{U_o} = -\frac{\lambda(l+2\beta R)}{2\pi q_o \sqrt{[x+\beta(r+R)][l-x+\beta(r+R)]}} [K-2\Pi(\alpha^2, k)] \quad (84a)$$

$$\frac{\varphi_r(x,r)}{U_o} = -\frac{\lambda}{2\pi q_o r \sqrt{[x+\beta(r+R)][l-x+\beta(r+R)]}} \{ [x+\beta(r+R)][l-x+\beta(r+R)]E - \beta r(l+2\beta R)K \} \quad (84b)$$

where the elliptic integrals have the same modulus and parameter as in the previous section.

In this case, the pressure in the combined flow field is

$$P = -\rho_o U_o [\varphi_x(x,r) + \varphi_x(l-x,r)] \quad (85)$$

which gives

$$P = -\lambda \quad (86)$$

so that in this instance, pressure itself is constant in the combined flow field.

From equation (84b), we see that

$$\varphi_r(x,r) = \varphi_r(l-x,r) \quad (87)$$

since the modulus of the elliptic integrals is invariant to the change $x \rightarrow l-x$.

Uses of reciprocity relations.—The reciprocity relations serve the dual function of checking the derived perturbation potential against minimization criteria based on other considerations (see eq. (47)) and of relating the Lagrangian multipliers to the pressure or pressure gradient in the combined flow field. Equations (81) and (86) also reveal that the expressions for pressure in the combined flow field hold, independently of r , throughout the entire region within the enveloping cones of the bodies. These results are generalizations of a similar effect noted in reference 19, where the combined pressure field associated with a Sears-Haack body was shown to have a constant gradient within the enveloping cones. In the latter reference, this property of the minimum-drag body was used to expedite the calculation of interference drag with a satellite body lying within the enveloping cones. Similar methods could obviously be applied to the present configurations.

AMES AERONAUTICAL LABORATORY

NATIONAL ADVISORY COMMITTEE FOR AERONAUTICS

MOFFETT FIELD, CALIF., Nov. 22, 1954

APPENDIX A

SUMMARY OF FORMULAE FOR THE OPTIMUM BODIES

The formulae derived in the text for the body shape function, pressure coefficient, and drag of optimum bodies having given volume or given caliber are repeated here for convenience. The type of configuration treated, and the nomenclature, are shown in figure 13.

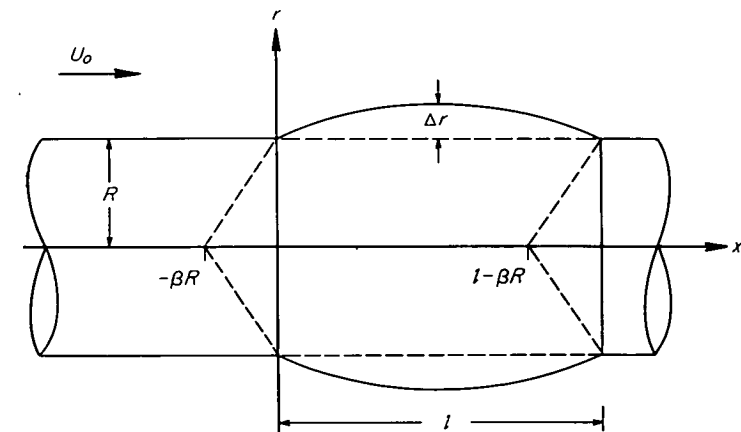


FIGURE 13.—Body and associated nomenclature used in drag minimization.

The pressure coefficient on the body is

$$C_p = \frac{p-p_o}{q_o} = -2 \frac{u}{U_o} = \frac{3}{2\pi} \frac{V_e}{l^4 B\left(\frac{\beta R}{l}\right)} \times \frac{4(x+2\beta R)(l-x+2\beta R)E - [l(l+4\beta R) - 4(l+2\beta R)(l-x+2\beta R)]K + 4(l+2\beta R)(l-2x)\Pi(\alpha^2, k)}{\sqrt{(x+2\beta R)(l-x+2\beta R)}} \quad (A2)$$

THE OPTIMUM BODY OF GIVEN VOLUME

The variation of ΔS for the optimum body with given volume is

$$\Delta S(x) = \frac{V_e}{l^4 B\left(\frac{\beta R}{l}\right)} \sqrt{(x+2\beta R)(l-x+2\beta R)} \{ x(l-x)E(k) - \beta R(l-4\beta R)[K(k) - E(k)] \} \quad (A1)$$

where

$$\Delta S(x) = \pi[(R+\Delta r)^2 - R^2]$$

V_e = volume of exposed portion

$B\left(\frac{\beta R}{l}\right) = B(\sigma)$ function defined in equation (60a) and shown in figure 7

$K(k)$ = complete elliptic integral of first kind of modulus k

$E(k)$ = complete elliptic integral of second kind of modulus k

$$k^2 = \frac{x(l-x)}{(x+2\beta R)(l-x+2\beta R)}$$

Examples of optimum bodies for a few values of the parameter $\beta R/l$ are shown in figures 10 and 11.

where $\Pi(\alpha^2, k)$ is a complete elliptic integral of third kind of modulus k and parameter α^2 (in the notation of ref. 20). The parameter α^2 is given by

$$\alpha^2 = -\frac{x}{l-x+2\beta R}$$

Figure 14 shows some plots of $C_p/(V_e/l^3)$ versus x/l for a few values of the parameter $\beta R/l$.

The wave drag of this optimum body is given by

$$\frac{D}{q_0} = 3 \frac{V_e^2}{l^4 B \left(\frac{\beta R}{l} \right)} \quad (A3)$$

The variation of drag with $\beta R/l$ is shown in figures 10 and 11.

THE OPTIMUM BODY OF GIVEN CALIBER

The variation of $\Delta S(x)$ for the optimum body of given caliber is

$$\Delta S(x) = \frac{2}{\pi} \frac{\Delta S(l)}{l(l+4\beta R)} \times \frac{l(l+2\beta R)(l+4\beta R)\Pi(\alpha^2, k) - (l-2x)(x+2\beta R)(l-x+2\beta R)E - l(l+2\beta R)(l-x+2\beta R)K}{\sqrt{(x+2\beta R)(l-x+2\beta R)}} \quad (A4)$$

where the symbols have been defined above. Examples of optimum bodies for a few values of the parameter $\beta R/l$ are shown in figure 12.

The pressure coefficient on the body is given by

$$C_p = \frac{8}{\pi^2} \frac{\Delta S(l)}{l} \frac{l+2\beta R}{l+4\beta R} \frac{2\Pi(\alpha^2, k) - K}{\sqrt{(x+2\beta R)(l-x+2\beta R)}} \quad (A5)$$

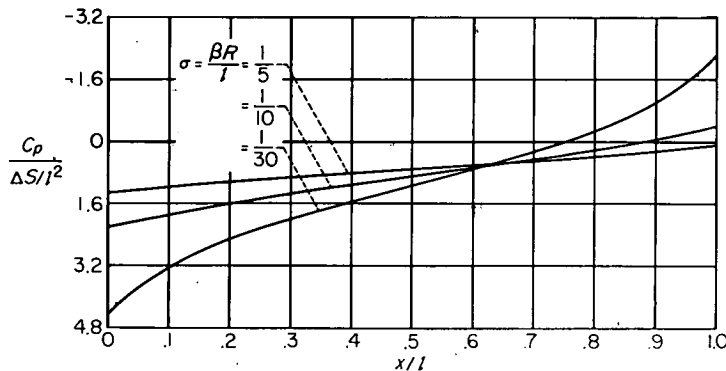


FIGURE 15.—Pressure distributions for various cases of the optimum body of given caliber.

Figure 15 shows some plots of $\frac{C_p}{\Delta S(l)/l^2}$ versus x/l for several values of the parameter $\beta R/l$.

The drag of this body is

$$\frac{D}{q_0} = \frac{4}{\pi(l+4\beta R)} \frac{[\Delta S(l)]^2}{l} \quad (A6)$$

and its variation with $\beta R/l$ is shown in figure 12.

REFERENCES

1. Ward, G. N.: The Approximate External and Internal Flow Past a Quasi-Cylindrical Tube Moving at Supersonic Speeds. *Quart. Jour. Mech. and Appl. Math.*, vol. I, pt. 2, June 1948, pp. 225-245.
2. Lighthill, M. J.: Supersonic Flow Past Bodies of Revolution. *R. & M. No. 2003* British A. R. C., 1945.
3. Parker, Hermon M.: Minimum Drag Ducted and Pointed Bodies of Revolution Based on Linearized Supersonic Theory. *NACA Rep. 1213*, 1955. (Formerly NACA TN 3189)
4. Ferrari, Carlo: Determination of the External Contour of a Body of Revolution with a Central Duct so as to Give Minimum Drag in Supersonic Flow, With Various Perimetral Conditions

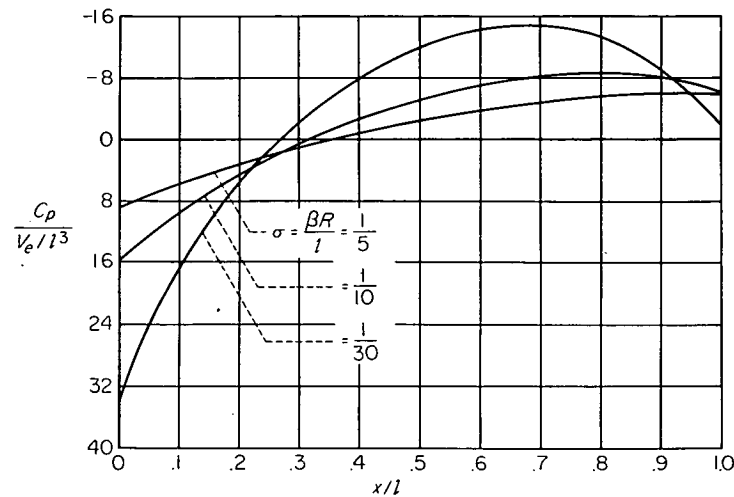


FIGURE 14.—Pressure distributions for various cases of the optimum body of given volume.

- Imposed Upon the Missile Geometry. Cornell Aero. Lab. Rep. AF-814-A-1, Mar. 1953.
5. Ferrari, Carlo: Determination of the External Contour of a Body of Revolution With a Central Duct so as to Give Minimum Drag in Supersonic Flow, With Various Perimetral Conditions Imposed Upon the Missile Geometry. Part III. Numerical Application. Cornell Aero. Lab. Rep. AF-8H-A-2, Nov. 1953.
6. Churchill, Ruel V.: *Modern Operational Mathematics in Engineering*. McGraw-Hill Book Co., Inc., N. Y., 1944.
7. Heaslet, Max. A., and Lomax, Harvard: Further Remarks Concerning Integral Transforms of the Wave Equation. *Jour. Aero. Sci.*, vol. 21, no. 2, Feb. 1954, p. 142.
8. Watson, G. N.: *A Treatise on the Theory of Bessel Functions*. Second ed. Cambridge Univ. Press, 1952.
9. Staff of Bateman Manuscript Project: *Tables of Integral Transforms*. Vol. I. McGraw-Hill Book Co., 1954.
10. Lamb, Horace: *Hydrodynamics*. Sixth ed., Dover Pub., 1945.
11. Ward, G. N.: Supersonic Flow Past Slender Pointed Bodies. *Quart. Jour. Mech. and Appl. Math.*, vol. II, pt. 1, 1949, pp. 75-97.
12. Mersman, W. A.: Numerical Calculation of Certain Inverse Laplace Transforms. Vol. 2 of *Proc. Intl. Cong. of Mathematicians*, Amsterdam, 1954.
13. Jones, Robert T.: The Minimum Drag of Thin Wings in Frictionless Flow. *Jour. Aero. Sci.*, vol. 18, no. 2, Feb. 1951, pp. 75-81.
14. Heaslet, Max. A., and Spreiter, John R.: Reciprocity Relations in Aerodynamics. *NACA Rep. 1119*, 1953. (Formerly NACA TN 2700)
15. Heaslet, Max. A., and Lomax, Harvard: Supersonic and Transonic Small Perturbation Theory. (Sec. D. of General Theory of High Speed Aerodynamics. Vol. VI of *High Speed Aerodynamics and Jet Propulsion*, W. R. Sears, ed., Princeton Univ. Press, 1954.)
16. Sears, William R.: On Projectiles of Minimum Wave Drag. *Quart. App. Math.*, vol. IV, no. 4, Jan. 1947, pp. 361-366.
17. Haack, W.: Geschossformen kleinsten Wellen-widerstandes. *Lilienthal-Gesellschaft für Luftfahrtforschung, Bericht 139*, Teil 1, October 9-10, 1941, pp. 14-28.
18. von Kármán, Th.: The Problem of Resistance in Compressible Fluids. *Proc. of the 5th Volta Congress (1935)*, Rome. Sept. 30-Oct. 6, 1935. (Also published as C. I. T., Guggenheim Aero. Lab. Pub. 75.)
19. Friedman, Morris D., and Cohen, Doris: Arrangement of Fusiform Bodies to Reduce the Wave Drag. *NACA TN 3345*, 1954 (Formerly NACA RM A51I20)
20. Byrd, Paul F., and Friedman, Morris D.: *Handbook of Elliptic Integrals for Engineers and Physicists*. Springer-Verlag (Berlin), 1954.

REPORT 1257

ON THE KERNEL FUNCTION OF THE INTEGRAL EQUATION RELATING LIFT AND DOWNWASH DISTRIBUTIONS OF OSCILLATING WINGS IN SUPERSONIC FLOW ¹

By CHARLES E. WATKINS and JULIAN H. BERMAN

SUMMARY

This report treats the kernel function of the integral equation that relates a known or prescribed downwash distribution to an unknown lift distribution for harmonically oscillating wings in supersonic flow. The treatment is essentially an extension to supersonic flow of the treatment given in NACA Report 1234 for subsonic flow. For the supersonic case the kernel function is derived by use of a suitable form of acoustic doublet potential which employs a cutoff or Heaviside unit function. The kernel functions are reduced to forms that can be accurately evaluated by considering the functions in two parts: a part in which the singularities are isolated and analytically expressed, and a nonsingular part which can be tabulated.

The kernel is treated for the two-dimensional case, and it is shown that the two-dimensional kernel leads to known lift distributions for both steady and oscillating two-dimensional wings. The kernel function for three-dimensional supersonic flow is reduced to the sonic case and is shown to agree with results obtained for the sonic case in NACA Report 1234, and the downwash functions associated with "horseshoe" vortices in supersonic flow are discussed and expressions are derived.

INTRODUCTION

In reference 1 the kernel function of an integral equation relating a known or prescribed downwash distribution to an unknown lift distribution for a harmonically oscillating finite wing of arbitrary plan form was treated for compressible subsonic flow. The purpose of the present report is to extend this treatment of the kernel function to supersonic flow.

The kernel functions under consideration arise when linearized-boundary-value problems for obtaining aerodynamic forces on oscillating wings are reduced to integral equations involving the distribution of pressure or wing loading as the unknown. In such integral equations the kernel functions play the important role of aerodynamic influence functions in that they give the normal induced velocity or downwash at any one point in the plane of the wing due to a unit pressure loading at any other point in the plane of the wing.

As the kernel functions arise in the analysis, they are mathematically defined by rather intricate improper integrals and possess singularities as high as second order. It is therefore desirable to isolate the singularities and determine

their explicit nature in order to make the integral equation more amenable to solution, in particular amenable to solution by approximate or numerical procedures.

Approximate lifting-surface theories for finite wings, such as the methods developed by Falkner and Multhopp (refs. 2 and 3) and others, have afforded considerable success in the calculation of aerodynamic coefficients for steady subsonic aerodynamics. Similar approximate methods have been successfully employed to obtain coefficients for two-dimensional oscillating wings in subsonic (compressible) flow (for example, refs. 4 and 5) and are now being extended to the finite oscillating wing in subsonic flow by Harry L. Runyan and Donald S. Woolston of the Langley Aeronautical Laboratory and by W. P. Jones (ref. 6). It is reasonable to expect that these methods can be further extended to apply to finite wings in supersonic flow.

In supersonic flow, solutions of the boundary-value problem for some particular plan forms and downwash conditions can be obtained in the form of infinite series in terms of a parameter involving the frequency of oscillation (see, for example, refs. 7 to 10) or in the form of rather complicated definite integrals (refs. 11 and 12). The infinite-series method furnishes a relatively simple means of obtaining the loading on oscillating wings for low values of the frequency parameter, but for large values of this parameter the series expansions converge so slowly that recourse must be had to other procedures for obtaining the wing loading. One feasible method is to study and develop approximate procedures for solving the integral equations that involve the unknown loading and its associated kernel function. The first step toward such a development is to isolate and determine the explicit nature of the singularities of the kernel function; this step is accomplished in the present report.

The report contains the derivation of the kernel function in the form of an improper integral and a reduction of this integral to proper form. The singularities of the kernel function are isolated and expressed analytically, and the nonsingular parts are reduced to a form readily amenable to numerical evaluation, as was done in reference 1 for subsonic flow. Some expanded forms of the kernel function are derived, and one of these is used to obtain a reduction to two-dimensional flow. In appendix A, the limiting case for sonic flow is derived and shown to agree with the results in reference 1. Appendix B is devoted to certain integrals of

¹ Supersedes NACA Technical Note 3438 by Charles E. Watkins and Julian H. Berman, 1955.

the kernel function. These integrals relate to "horseshoe" vortices in supersonic flow, as treated, for example, in the steady case by Schlichting in reference 13, and may be of interest in certain modes of application.

SYMBOLS

c	velocity of sound
$I_0, I_1(x)$	modified Bessel functions of first kind
$J_n(x)$	Bessel function of first kind
K_0, K_1	modified Bessel functions of second kind
$K(x_0, y_0)$	kernel function for three-dimensional flow
k	reduced-frequency parameter, ω/V
$K(x_0)$	kernel function for two-dimensional flow
$L(\xi, \eta), L(\xi)$	lift distributions
L_0, L_1	modified Struve function of first order
l	unit length
M	Mach number, V/c
p	perturbation pressure
$r = \sqrt{y_0^2 + z^2}$	
S	region of xy -plane occupied by wing
t	time
$U(x)$	unit function
V	forward velocity of wing
$w(x, y, t)$	downwash velocity, $e^{i\omega t}\bar{w}(x, y)$
$\bar{w}(x, y)$	complex amplitude function of prescribed vertical velocity
x, y, z	Cartesian coordinates attached to wing moving in negative x -direction
$x_0 = x - \xi$	
$y_0 = y - \eta$	
$\beta = \sqrt{M^2 - 1}$	
$\delta(x)$	Dirac delta function
ξ, η	Cartesian coordinates used to represent space location of doublets
ρ	fluid density
$\phi(x, y, z, t)$	velocity potential, $e^{i\omega t}\bar{\phi}(x, y, z)$
$\bar{\phi}(x, y, z)$	complex amplitude function of velocity potential
$\psi(x, y, z, t)$	acceleration potential, $e^{i\omega t}\bar{\psi}(x, y, z)$
$\bar{\psi}(x, y, z)$	complex amplitude function of acceleration potential
ω	circular frequency of oscillation
$\bar{\omega} = \omega/V\beta^2$	

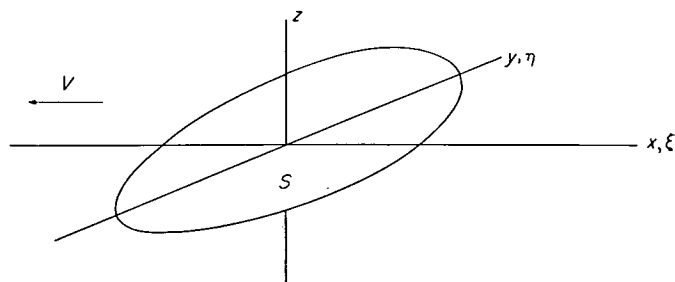
ANALYSIS

INTEGRAL EQUATION RELATING DOWNWASH AND LIFT DISTRIBUTION

The linearized-boundary-value problem for the determination of the aerodynamic forces on a wing can be immediately reduced to a problem of solving an integral equation that relates downwash and lift distribution. The purpose of this section is to introduce and briefly discuss this equation.

Since the integral equation has the same formal appearance for subsonic and supersonic flow and is derived in various publications (for example, refs. 1 and 14), the equation will not be rederived here but will be formally stated so as to

serve as a starting point in the analysis. In keeping with linear theory, the wing is considered as a plane, impenetrable surface S which lies nearly in the xy -plane as indicated in sketch (a).



Sketch (a)

The x, y, z coordinate system and the surface S are assumed to move in the negative x -direction at a uniform velocity V .

In terms of these coordinates, the integral equation may be formally written as

$$\bar{w}(x, y) = \frac{1}{4\pi\rho} \iint_S L(\xi, \eta) K(x - \xi, y - \eta) d\xi d\eta \quad (1)$$

where $\bar{w}(x, y)$ is the complex amplitude function of prescribed vertical velocity or downwash at points in S and is defined as follows:

$$w(x, y, t) = e^{i\omega t} \bar{w}(x, y)$$

where ω is the frequency of pulsation or oscillation. The kernel function $K(x_0, y_0)$ physically represents the contribution to the downwash at a point (x, y) in S due to the presence of a pulsating pressure doublet of unit strength located at some other point (ξ, η) in S . It is a function not only of x, y, ξ , and η but also of Mach number and frequency. The function $L(\xi, \eta)$ in equation (1) is the unknown lift distribution or local doublet strength. (Although it is usually convenient to factor out the density term $1/\rho$ as indicated in eq. (1), this was not done in ref. 1.)

Equation (1) pertains formally to either subsonic or supersonic flow; however, separate treatments of the two cases are required because of wide differences associated with flow characteristics. So far as the integral equation is concerned, the differences in the two cases lie mainly in the kernel functions. These differences are associated with the differences in character of doublets for the two cases. Although the main purpose of this analysis is to derive and treat the kernel function for the supersonic case, a necessary first step is to formulate a doublet suitable for such a treatment. In the following section, a desired form, which was arrived at by a convenient use of a cutoff, or Heaviside unit function, is presented in equation (5).

PULSATING DOUBLET MOVING AT SUPERSONIC SPEED

The governing differential equation for linearized unsteady flow at either subsonic or supersonic speeds, which the

doublet potentials must satisfy, is the well-known wave equation referred to a moving coordinate system:

$$\frac{\partial^2 \psi}{\partial x^2} + \frac{\partial^2 \psi}{\partial y^2} + \frac{\partial^2 \psi}{\partial z^2} - \frac{1}{c^2} \left(V \frac{\partial}{\partial x} + \frac{\partial}{\partial t} \right)^2 \psi = 0$$

Under the assumption that disturbances vary harmonically with respect to time, this equation becomes

$$\frac{\partial^2 \bar{\psi}}{\partial x^2} + \frac{\partial^2 \bar{\psi}}{\partial y^2} + \frac{\partial^2 \bar{\psi}}{\partial z^2} - \frac{1}{c^2} \left(V \frac{\partial}{\partial x} + i\omega \right)^2 \bar{\psi} = 0 \quad (2)$$

where $\bar{\psi}$ is a complex amplitude function defined by

$$\psi(x, y, z, t) = e^{i\omega t} \bar{\psi}(x, y, z) \quad (3)$$

It may appear that, since the same differential equation (eq. (2)) is involved, a logical way of obtaining the potential for a pulsating doublet moving at supersonic speed is by simple analogy or continuation from the potential for the doublet moving at subsonic speed. This procedure is applicable only in a broad sense because, as discussed in reference 15 with regard to sources in supersonic flow, the potential of a doublet moving at supersonic speed consists of the sum of two effects corresponding to a retarded-type potential and an advanced-type potential which relate to the two wave fronts encountered by a point at any time; whereas for subsonic speed only the retarded type of potential is admissible. (The advanced-type potential for subsonic or sonic speed does not satisfy the Sommerfeld radiation condition, which requires that disturbances be propagated away from their point of origin.) In the second place, the potential that may be obtained by analogy with the potential for subsonic speed must, as subsequently discussed, be rather severely restricted before it mathematically describes the physical realities of a disturbance moving at supersonic speed. In the following development, a desired form of the doublet potential is arrived at by consideration of these restrictions applied to both a retarded and an advanced type of potential that may be obtained by analogy with results for subsonic flow.

By analogy with results for subsonic speed (for example, eq. (A9) of ref. 1) or, more directly, from the discussion of source potentials in supersonic flow (ref. 15), the sum ψ_D of the retarded and advanced types of potentials required to form the doublet potential for supersonic speeds may be written with the doublet situated at the origin as

$$\begin{aligned} \psi_D &= \frac{\partial}{\partial z} \left[\frac{e^{i\omega \left(t - \frac{Mx}{c\beta^2} - \frac{\sqrt{x^2 - \beta^2 y^2 - \beta^2 z^2}}{c\beta^2} \right)}}{\sqrt{x^2 - \beta^2 y^2 - \beta^2 z^2}} + \frac{e^{i\omega \left(t - \frac{Mx}{c\beta^2} + \frac{\sqrt{x^2 - \beta^2 y^2 - \beta^2 z^2}}{c\beta^2} \right)}}{\sqrt{x^2 - \beta^2 y^2 - \beta^2 z^2}} \right] \\ &= 2 \frac{\partial}{\partial z} \frac{e^{i(\omega t - M^2 \bar{\omega} x)} \cos(M\bar{\omega} \sqrt{x^2 - \beta^2 y^2 - \beta^2 z^2})}{\sqrt{x^2 - \beta^2 y^2 - \beta^2 z^2}} \quad (4) \end{aligned}$$

where $M = V/c$, $\beta = \sqrt{M^2 - 1}$, and $\bar{\omega} = \omega/V\beta^2$. The restrictions that must be placed on this expression are: (a) only

real values of the radical term $\sqrt{x^2 - \beta^2 y^2 - \beta^2 z^2}$ are to be considered and (b) the values of the expression and its derivatives are to be considered zero when x is negative. These restrictions follow from the physical consideration that small disturbances propagate at sonic speed and in a supersonic stream do not progress forward of their point of origin.

A convenient way of writing the expression for ψ_D with these restrictions accounted for, as previously mentioned, is to employ a cutoff or unit function as a factor. Thus, if ψ_0 represents the restricted value of ψ_D , the amplitude function of ψ_0 may be written as

$$\bar{\psi}_0 = 2 \frac{\partial}{\partial z} e^{-iM^2 \bar{\omega} x} U(x - \beta \sqrt{y^2 + z^2}) \frac{\cos(M\bar{\omega} \sqrt{x^2 - \beta^2 y^2 - \beta^2 z^2})}{\sqrt{x^2 - \beta^2 y^2 - \beta^2 z^2}} \quad (5)$$

where

$$\left. \begin{aligned} U(x - \beta \sqrt{y^2 + z^2}) &= 1 & (x > \beta \sqrt{y^2 + z^2}) \\ U(x - \beta \sqrt{y^2 + z^2}) &= 0 & (x \leq \beta \sqrt{y^2 + z^2}) \end{aligned} \right\} \quad (6)$$

and only positive values of the radical $\sqrt{y^2 + z^2}$ are considered. A method whereby this form of potential can be determined in a more direct manner is discussed in detail in reference 16. The discussion in this reference is in connection with the Green functions associated with the dispersion of sound waves in an n -dimensional medium in which a pulsating source exists. When appropriate changes are made in notation, the expression for $\bar{\psi}_0$ given in equation (5) agrees essentially with results for the dispersion of waves in a three-dimensional space given in equation (55), chapter XVI of reference 16.

With regard to the unit function $U(x)$, in many applications where this function is employed it need not be defined as having any particular value when its argument is zero. In other applications, especially where the unit function is involved in a Fourier analysis, it must be defined as having a value of $\frac{1}{2}$ when its argument is zero. In the present case, it is conveniently defined, as may be noted in equation (6), as having zero value when its argument is zero.

Derivatives of the unit function give rise to an impulse function called the Dirac delta function. For example,

$$\frac{\partial}{\partial x} U(x) = \delta(x) = 0 \quad (x \neq 0)$$

$$\frac{\partial}{\partial x} U(x) = \delta(x) = \infty \quad (x = 0)$$

A useful integral property of this delta function is

$$\int_0^b f(x) \delta(x) dx = f(0)$$

The next step in the analysis is to make use of the doublet potential (eq. (5)) to derive the kernel function for supersonic speed.

DERIVATION AND REDUCTION OF KERNEL FUNCTION

In this section the kernel function is derived and presented.

The function is given in terms of an improper integral by equation (13) and in a reduced form with no improper integrals by equation (15). As it is frequently desirable to present results in terms of nondimensional length variables, the results given in equation (15) are presented in this manner in equation (16).

In order to derive the kernel function, the function $\bar{\psi}$ of equation (3) is considered as the complex amplitude of the acceleration potential. As such, ψ is directly proportional to a perturbation pressure field $p = e^{i\omega t} \bar{p}$, through the simple relation

$$\bar{p} = -\rho \bar{\psi} \quad (7)$$

and to a velocity potential

$$\phi = e^{i\omega t} \bar{\phi}$$

through the equation

$$V \frac{\partial \bar{\phi}}{\partial x} + i\omega \bar{\phi} = \bar{\psi} \quad (8)$$

By differentiation of equation (8) with respect to z and integration of the result with respect to x , the vertical velocity associated with the acceleration potential ψ is obtained. Thus, when ψ is considered as the potential of a pressure doublet, equation (8) affords a straightforward means for obtaining an equation for $K(x_0, y_0)$, namely:

$$K(x_0, y_0) = \frac{\partial}{\partial z} \bar{\phi}(x_0, y_0, z)_{z=0} \quad (9)$$

Details of the procedure are as follows:

The result of the differentiation of equation (8) with respect to z may be written as

$$V \frac{\partial}{\partial x} \frac{\partial \bar{\phi}}{\partial z} + i\omega \frac{\partial \bar{\phi}}{\partial z} = \frac{\partial \bar{\psi}}{\partial z} \quad (10)$$

When this equation is considered as an ordinary differential equation with dependent variable $\frac{\partial \bar{\phi}}{\partial z}$ and independent variable x , a complete solution is

$$\frac{\partial \bar{\phi}}{\partial z} = \frac{1}{V} e^{-\frac{i\omega x}{V}} \int_{-\infty}^x \frac{\partial}{\partial z} \bar{\psi}(\lambda, y, z) e^{\frac{i\omega \lambda}{V}} d\lambda \quad (11)$$

where the lower limit of integration is employed in place of a constant of integration and is chosen so as to satisfy the condition that $\bar{\phi}$ vanish far ahead of the origin $\lambda=0$. Thus, from equation (9) there is obtained

$$K(x_0, y_0) = \lim_{z \rightarrow 0} \frac{1}{V} e^{-\frac{i\omega x_0}{V}} \int_{-\infty}^{x_0} \frac{\partial}{\partial z} \bar{\psi}_0(\lambda, y_0, z) e^{\frac{i\omega \lambda}{V}} d\lambda \quad (12)$$

or, after substitution of the expression for $\bar{\psi}_0$ (eq. (5)) into equation (12), the results may be written as

$$K(x_0, y_0) = \frac{2}{V} \lim_{z \rightarrow 0} e^{-\frac{i\omega x_0}{V}} \int_{\beta r}^{x_0} e^{-i\omega \lambda} \frac{\partial^2}{\partial z^2} \left[\frac{U(\lambda - \beta r) \cos(M\bar{\omega} \sqrt{\lambda^2 - \beta^2 r^2})}{\sqrt{\lambda^2 - \beta^2 r^2}} \right] d\lambda \quad (13)$$

where $r = \sqrt{y_0^2 + z^2}$ and, since the integrand is zero for $\lambda < \beta r$, the lower limit of integration has been changed from $-\infty$ to βr .

It is apparent upon examination of equation (13) that, if the indicated differentiation under the integral sign is carried out, the integrand has singular and perhaps troublesome terms. The indicated differentiation with respect to z , however, can be replaced by equivalent operations and followed by integrations by parts that lead to a reduced form of the kernel function containing no improper integrals. These steps follow.

Reduced form of kernel function.—As may be directly verified, the indicated differentiation with respect to z in equation (13) is, in the limit $z \rightarrow 0$, identical with

$$\begin{aligned} & e^{-i\omega \lambda} \lim_{z \rightarrow 0} \frac{\partial^2}{\partial z^2} \left[\frac{U(\lambda - \beta r) \cos(M\bar{\omega} \sqrt{\lambda^2 - \beta^2 r^2})}{\sqrt{\lambda^2 - \beta^2 r^2}} \right] \\ &= -\frac{1}{y_0^2} \frac{\partial}{\partial \lambda} \left\{ U(\lambda - \beta|y_0|) e^{-i\omega \lambda} \left[\frac{\lambda \cos(M\bar{\omega} \sqrt{\lambda^2 - \beta^2 y_0^2})}{\sqrt{\lambda^2 - \beta^2 y_0^2}} + \right. \right. \\ & \quad \left. \left. \frac{i}{M} \sin(M\bar{\omega} \sqrt{\lambda^2 - \beta^2 y_0^2}) \right] \right\} - \frac{e^{-i\omega \lambda}}{y_0^2} \left[\frac{\beta^2 \bar{\omega}}{M} U(\lambda - \beta|y_0|) \right. \\ & \quad \left. \sin(M\bar{\omega} \sqrt{\lambda^2 - \beta^2 y_0^2}) - \frac{i}{M} \delta(\lambda - \beta|y_0|) \sin(M\bar{\omega} \sqrt{\lambda^2 - \beta^2 y_0^2}) - \right. \\ & \quad \left. \frac{\lambda - \beta|y_0|}{\sqrt{\lambda^2 - \beta^2 y_0^2}} \delta(\lambda - \beta|y_0|) \cos(M\bar{\omega} \sqrt{\lambda^2 - \beta^2 y_0^2}) \right] \end{aligned} \quad (14)$$

Since the coefficients of $\delta(\lambda - \beta|y_0|)$ in equation (14) vanish at $\lambda = \beta|y_0|$, it follows from the integral properties of $\delta(\lambda - \beta|y_0|)$ that, when equation (14) is substituted into equation (13), the integrals involving the delta function vanish and equation (13) becomes:

$$\begin{aligned} K(x_0, y_0) &= -\frac{2}{V y_0^2} e^{-\frac{i\omega x_0}{V}} \left[\frac{x_0 e^{-i\omega x_0} U(x_0 - \beta|y_0|)}{\sqrt{x_0^2 - \beta^2 y_0^2}} \cos(M\bar{\omega} \sqrt{x_0^2 - \beta^2 y_0^2}) + \right. \\ & \quad \left. \frac{i}{M} e^{-i\omega x_0} U(x_0 - \beta|y_0|) \sin(M\bar{\omega} \sqrt{x_0^2 - \beta^2 y_0^2}) + \right. \\ & \quad \left. \frac{\beta^2 \bar{\omega}}{M} \int_{\beta|y_0|}^{x_0} e^{-i\omega \lambda} U(\lambda - \beta|y_0|) \sin(M\bar{\omega} \sqrt{\lambda^2 - \beta^2 y_0^2}) d\lambda \right] \end{aligned} \quad (15)$$

Equation (15) provides an expression for the kernel function that involves no improper integrals. Except for the integral, the terms of the expression can be quite easily evaluated with the aid of trigonometric tables except at $y_0 = 0$, where the function is singular, and at $x_0 = \beta|y_0|$, where the function is indeterminate. The integral is well behaved and can be accurately evaluated by numerical or approximate procedures. The singularities and indeterminate values are isolated and discussed in a later section, but it is desirable first to express the function $K(x_0, y_0)$ in terms of nondimensional length variables. As a check on the correctness of equation (15), the expression for $K(x_0, y_0)$ is reduced to the limiting value for $M=1$ and compared in appendix A with the corresponding limiting value for the subsonic case.

The kernel function in terms of nondimensional length variables.—Although the preceding results contain dimensional length variables, it is usually desirable to have such results in terms of nondimensional length variables. By

employing the variables x_0 and y_0 in a new sense to mean that they have been referred to some chosen length l and by introducing the reduced-frequency parameter $k=\omega/V$, the length variables may be made nondimensional. (In flutter theory the reference length normally is selected as a semichord b .) The variables are used in this sense throughout the rest of this report. The kernel function (eq. (15)) can be written in terms of these nondimensional variables as

$$K(x_0, y_0) = -\frac{2}{V l^2 y_0^2} e^{-ikx_0} \left[\frac{x_0 e^{-\frac{ikx_0}{\beta^2}} U(x_0 - \beta|y_0|)}{\sqrt{x_0^2 - \beta^2 y_0^2}} \cos\left(\frac{Mk}{\beta^2} \sqrt{x_0^2 - \beta^2 y_0^2}\right) + \frac{i}{M} e^{-\frac{ikx_0}{\beta^2}} U(x_0 - \beta|y_0|) \sin\left(\frac{Mk}{\beta^2} \sqrt{x_0^2 - \beta^2 y_0^2}\right) + \frac{k}{M} \int_{\beta|y_0|}^{x_0} e^{-\frac{ik\lambda}{\beta^2}} U(\lambda - \beta|y_0|) \sin\left(\frac{Mk}{\beta^2} \sqrt{\lambda^2 - \beta^2 y_0^2}\right) d\lambda \right] \quad (16a)$$

An equivalent expression for $K(x_0, y_0)$ which will be useful in subsequent considerations is

$$K(x_0, y_0) = -\frac{2}{V l^2 y_0^2} \left\{ e^{-\frac{iM^2 k x_0}{\beta^2}} \left(\frac{\beta^2}{Mk} \frac{\partial}{\partial x_0} + \frac{i}{M} \right) \left[U(x_0 - \beta|y_0|) \sin\left(\frac{Mk}{\beta^2} \sqrt{x_0^2 - \beta^2 y_0^2}\right) \right] + \frac{k}{M} e^{-ikx_0} \int_{\beta|y_0|}^{x_0} e^{-\frac{ik\lambda}{\beta^2}} U(\lambda - \beta|y_0|) \sin\left(\frac{Mk}{\beta^2} \sqrt{\lambda^2 - \beta^2 y_0^2}\right) d\lambda \right\} \quad (16b)$$

Another equivalent expression for $K(x_0, y_0)$ that is more concise and, for many purposes, more attractive than equation (16a) is

$$K(x_0, y_0) = -\frac{2}{V l^2 y_0^2} e^{-ikx_0} U(x_0 - \beta|y_0|) \left[\frac{x_0 e^{-\frac{ikx_0}{\beta^2}}}{\sqrt{x_0^2 - \beta^2 y_0^2}} \cos\left(\frac{Mk}{\beta^2} \sqrt{x_0^2 - \beta^2 y_0^2}\right) + \frac{ik|y_0|}{2} \int_{\frac{1}{\beta^2|y_0|}(x_0 - M\sqrt{x_0^2 - \beta^2 y_0^2})}^{\frac{1}{\beta^2|y_0|}(x_0 + M\sqrt{x_0^2 - \beta^2 y_0^2})} \frac{\tau}{\sqrt{1 + \tau^2}} e^{-ik|y_0|\tau} d\tau \right] \quad (16c)$$

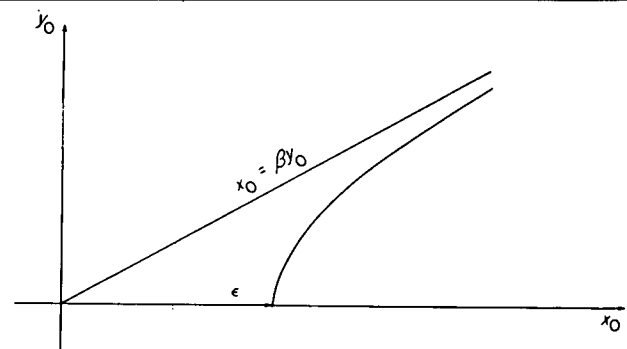
The reduction of equation (16a) to (16c) is given in appendix A. One noteworthy feature of equation (16c) is that the integral which remains to be evaluated has the same form as the integral occurring in the expression for the kernel function for subsonic speeds as presented in appendix D of reference 1.

ISOLATION AND DISCUSSION OF SINGULARITIES OF KERNEL FUNCTION

As previously mentioned and as may be noted in equations (15) and (16a), the kernel function becomes singular at $y_0=0$ and is of an indeterminate nature when $x_0=\beta|y_0|$. It is therefore desirable to make special treatment of the function in the neighborhood of these values of x_0 and y_0 in order to be able to express the function in a form which is more amenable for calculations. The indeterminate condition arises from the first term of equation (16a) because of the manner in which the unit function has been defined for this analysis. (The denominator of the first term vanishes at $x_0=\beta y_0$. The presence of the unit function in the numerator, however, renders this singularity indeterminate.)

In the next few sections the forms of the singularities are extracted (see eq. (24)) and the aforementioned indeterminate forms of the kernel function are explicitly determined (see eq. (20)). A form of the kernel function more suitable for calculation purposes, since the troublesome points are isolated, is presented in equation (26). A manner of integrating the kernel function across its singularities is given in equation (27). The singularities of the supersonic and subsonic cases are then compared.

Indeterminate form.—Consideration is first given to the indeterminate form, and it is convenient for this purpose to consider the value of $K(x_0, y_0)$ at points on the positive branch of a hyperbola. (See sketch (b)).



Sketch (b)

The equation of the hyperbola may be written as

$$\left. \begin{aligned} x_0 &= \epsilon \cosh \theta \\ \beta|y_0| &= \epsilon \sinh \theta \end{aligned} \right\} \quad (17)$$

In these equations $\epsilon=0$ corresponds to $x_0=\beta y_0$, since elimination of θ gives $x_0^2 - \beta^2 y_0^2 = \epsilon^2$.

After substitution of these expressions for x_0 and $\beta|y_0|$ into equation (16a), the results may be written as

$$K(\epsilon, \theta) = -\frac{2\beta^2 e^{-ik\epsilon \cosh \theta}}{V l^2 \epsilon^2 \sinh^2 \theta} \left[U(\epsilon e^{-\theta}) e^{-\frac{ik\epsilon \cosh \theta}{\beta^2}} \cosh \theta \cos \frac{Mk\epsilon}{\beta^2} + \frac{i}{M} U(\epsilon e^{-\theta}) e^{-\frac{ik\epsilon \cosh \theta}{\beta^2}} \sin \frac{Mk\epsilon}{\beta^2} + \frac{k}{M} \int_{\epsilon \sinh \theta}^{\epsilon \cosh \theta} e^{-\frac{ik\lambda}{\beta^2}} U(\lambda - \epsilon \sinh \theta) \sin\left(\frac{Mk}{\beta^2} \sqrt{\lambda^2 - \epsilon^2 \sinh^2 \theta}\right) d\lambda \right] \quad (18)$$

To obtain a limiting value of this equation for small values of ϵ , the trigonometric and exponential terms can be replaced by terms up to the second power of ϵ in a series expansion.

If the result of performing this expansion is denoted by K' , the equation

$$K'(\epsilon, \theta) = -\frac{2\beta^2 e^{-ik\epsilon \cosh \theta}}{V l^2} U(\epsilon e^{-\theta}) \left(\frac{\cosh \theta}{\epsilon^2 \sinh^2 \theta} - \frac{ik}{\beta^2 \epsilon} - \frac{k^2 \cosh \theta}{2\beta^4} - \frac{k^2}{2\beta^2} \log \frac{\cosh \theta + 1}{\sinh \theta} \right) \quad (19)$$

is obtained, which, in terms of the original coordinates x_0 and y_0 , is

$$K'(x_0, y_0) = -\frac{e^{-ikx_0}}{V l^2} U(x_0 - \beta|y_0|) \left[\frac{x_0}{\sqrt{x_0^2 - \beta^2 y_0^2}} \left(\frac{2}{y_0^2} - \frac{2ik}{x_0} - \frac{k^2}{\beta^2} \right) - k^2 \log \frac{x_0 + \sqrt{x_0^2 - \beta^2 y_0^2}}{\beta|y_0|} \right] \quad (20)$$

Although these equations were obtained in order to reveal the form of the indeterminate value of the kernel function, they are found to contain singularities at $y_0 = 0$. Prior to any further discussion of this result, it is desirable to consider the limiting form of $K(x_0, y_0)$ as y_0 approaches zero, to determine all the singularities at $y_0 = 0$.

Singularities at $y_0 = 0$.—For the purpose of obtaining a limiting value of the kernel function for vanishingly small values of y_0 , the integral appearing in equation (16a) may be written as the sum of two integrals, namely:

$$\begin{aligned} & \int_{\beta|y_0|}^{x_0} e^{-\frac{ik\lambda}{\beta^2}} U(\lambda - \beta|y_0|) \sin \left(\frac{Mk}{\beta^2} \sqrt{\lambda^2 - \beta^2 y_0^2} \right) d\lambda \\ &= \int_{\beta|y_0|}^{\infty} e^{-\frac{ik\lambda}{\beta^2}} U(\lambda - \beta|y_0|) \sin \left(\frac{Mk}{\beta^2} \sqrt{\lambda^2 - \beta^2 y_0^2} \right) d\lambda - \\ & \int_x^{\infty} e^{-\frac{ik\lambda}{\beta^2}} U(\lambda - \beta|y_0|) \sin \left(\frac{Mk}{\beta^2} \sqrt{\lambda^2 - \beta^2 y_0^2} \right) d\lambda \quad (21) \end{aligned}$$

The first of these integrals may be evaluated from the table of Laplace transforms of reference 17 and has the following value:

$$\int_{\beta|y_0|}^{\infty} e^{-\frac{ik\lambda}{\beta^2}} U(\lambda - \beta|y_0|) \sin \left(\frac{Mk}{\beta^2} \sqrt{\lambda^2 - \beta^2 y_0^2} \right) d\lambda = M|y_0| K_1(k|y_0|) \quad (22)$$

where K_1 is the modified Bessel function of the second kind, of first order. In the second integral, the integrand may be replaced by terms up to the second power of y_0 in a series expansion. Thus,

$$\begin{aligned} & \int_x^{\infty} e^{-\frac{ik\lambda}{\beta^2}} U(\lambda - \beta|y_0|) \sin \left(\frac{Mk}{\beta^2} \sqrt{\lambda^2 - \beta^2 y_0^2} \right) d\lambda \\ & \approx \int_{x_0}^{\infty} e^{-\frac{ik\lambda}{\beta^2}} U(\lambda - \beta|y_0|) \left(\sin \frac{Mk\lambda}{\beta^2} - \frac{Mk y_0^2}{2\lambda} \cos \frac{Mk\lambda}{\beta^2} \right) d\lambda \\ & = U(x_0 - \beta|y_0|) \left\{ \frac{1}{k} e^{-\frac{ikx_0}{\beta^2}} \left(M \cos \frac{Mkx_0}{\beta^2} + i \sin \frac{Mkx_0}{\beta^2} \right) + \right. \\ & \quad \left. \frac{Mk y_0^2}{4} \left[\text{Ci} \left(\frac{kx_0}{M+1} \right) + \text{Ci} \left(\frac{kx_0}{M-1} \right) + i \text{Si} \left(\frac{kx_0}{M+1} \right) - i \text{Si} \left(\frac{kx_0}{M-1} \right) \right] \right\} \quad (23) \end{aligned}$$

where Ci and Si denote the cosine integral function and sine integral function, respectively, which are defined as follows:

$$\text{Ci}(x) = -\int_x^{\infty} \frac{\cos t}{t} dt \quad \text{Si}(x) = \frac{\pi}{2} - \int_x^{\infty} \frac{\sin t}{t} dt$$

Substituting equations (22) and (23) into equation (16a) gives, as a limiting value of $K(x_0, y_0)$,

$$\begin{aligned} \lim_{y_0 \rightarrow 0} K(x_0, y_0) &= \lim_{y_0 \rightarrow 0} -\frac{2e^{-ikx_0}}{V l^2 y_0^2} \left\{ k|y_0| K_1(k|y_0|) - \frac{k^2 y_0^2}{4} \left[\text{Ci} \left(\frac{kx_0}{M+1} \right) + \text{Ci} \left(\frac{kx_0}{M-1} \right) + i \text{Si} \left(\frac{kx_0}{M+1} \right) - i \text{Si} \left(\frac{kx_0}{M-1} \right) \right] \right\} U(x_0 - \beta|y_0|) \\ &= \lim_{y_0 \rightarrow 0} -\frac{e^{-ikx_0}}{V l^2} U(x_0 - \beta|y_0|) \left\{ \frac{2}{y_0^2} + k^2 \left(\gamma - \frac{1}{2} \right) + k^2 \log \frac{k|y_0|}{2} - \frac{k^2}{2} \left[\text{Ci} \left(\frac{kx_0}{M+1} \right) + \text{Ci} \left(\frac{kx_0}{M-1} \right) + i \text{Si} \left(\frac{kx_0}{M+1} \right) - i \text{Si} \left(\frac{kx_0}{M-1} \right) \right] \right\} \quad (24) \end{aligned}$$

where the following series expression for $K_1(z)$ (see ref. 18) is employed:

$$K_1(z) = \left(\gamma + \log \frac{z}{2} \right) \left(\frac{z}{2} + \frac{z^3}{16} + \frac{z^5}{384} + \dots \right) + \frac{1}{z} - \left(\frac{z}{4} + \frac{5z^3}{64} + \frac{5z^5}{1152} + \dots \right) \quad (25)$$

where γ is Euler's constant ($\gamma = 0.5772157$). Examination of equation (24) shows that the only singular terms are the same as those which appear in equation (20), namely $-\frac{2e^{-ikx_0}}{y_0^2}$ and $-k^2 e^{-ikx_0} \log|y_0|$. Thus, for the purpose of isolating the singularities of the kernel function, only $K'(x_0, y_0)$, as defined in equation (20), need be considered. Nevertheless, the results given in equation (24) may be useful in some applications since they provide a ready means for evaluating the nonsingular part of $\lim_{y_0 \rightarrow 0} K(x_0, y_0)$.

Form of kernel function suitable for calculations.—As in the subsonic case, with knowledge of the critical values of the kernel function, an expression can be written in which the kernel function is separated into two parts, one of which contains no singularities or indeterminate values and the other of which contains all the singularities and critical values of the kernel function. This expression is

$$K(x_0, y_0) = [K(x_0, y_0) - K'(x_0, y_0)] + K'(x_0, y_0) \quad (26)$$

where $K(x_0, y_0)$ is defined in equations (15) or (16), and $K'(x_0, y_0)$ is defined in equation (20). The term $K(x_0, y_0) - K'(x_0, y_0)$ in equation (26) has no singular or indeterminate values. The term $K'(x_0, y_0)$ is singular at $y_0 = 0$ and indeterminate when $x_0 = \beta y_0$.

Integration of singularities of kernel function.—Since integration of the kernel function is often necessary, a few remarks on how to circumvent its inherent singularities are in order. Each term of $K'(x_0, y_0)$ in equation (20) possesses a simple indefinite integral with respect to the variable $\eta = y - y_0$. In performing integrations with respect to η that involve a passage across the line $\eta = y$, a principal value is to be taken. For example,

$$\oint_{-1}^1 \frac{U(x_0 - \beta|y_0|)x_0 d\eta}{(y - \eta)^2 \sqrt{x_0^2 - \beta^2(y - \eta)^2}} = \frac{1}{x_0} \left[\frac{U(x_0 - \beta|y - 1|) \sqrt{x_0^2 - \beta^2(y - 1)^2}}{y - 1} - \frac{U(x_0 - \beta|y + 1|) \sqrt{x_0^2 - \beta^2(y + 1)^2}}{y + 1} \right] \quad (27)$$

where the symbol \oint indicates that the singular integral is to be considered simply as a function of its limits. A justification for this consideration is that it leads to results that could, with considerable labor, be rigorously established by maintaining the variable z in the analysis until all operations are performed.

Comparison with singularities of subsonic case.—It may be of interest to compare the above results with corresponding results for the subsonic case, that is, for $x_0 > 0$ and $y_0 \approx 0$. Results for the subsonic case may be obtained from equation (31) of reference 1 as follows:

$$\lim_{y_0 \rightarrow 0} K'(x_0, y_0)_{M < 1} = \lim_{y_0 \rightarrow 0} \frac{1}{V l^2} e^{-ikx_0} \left\{ -\frac{\sqrt{x_0^2 + (1 - M^2)y_0^2} + x_0}{y_0^2 \sqrt{x_0^2 + (1 - M^2)y_0^2}} + \frac{ik}{\sqrt{x_0^2 + (1 - M^2)y_0^2}} - \frac{k^2}{2(1 - M^2)} \frac{x_0 - M\sqrt{x_0^2 + (1 - M^2)y_0^2}}{\sqrt{x_0^2 + (1 - M^2)y_0^2}} - \frac{k^2}{2} \log \frac{k[\sqrt{x_0^2 + (1 - M^2)y_0^2} - x_0]}{2(1 - M)} \right\} \\ = \frac{e^{-ikx_0}}{V l^2} \left[-\frac{2}{y_0^2} + \frac{ik}{x_0} - \frac{k^2}{2(1 + M)} - \frac{k^2}{2} \log \frac{k(1 + M)y_0^2}{4x_0} \right] \quad (28)$$

The singular terms of this expression for $x_0 > 0$ and $M < 1$ are

$$-\frac{2}{V l^2} e^{-ikx_0} \left(\frac{1}{y_0^2} + \frac{k^2}{z} \log |y_0| \right)$$

Comparison of this result with equation (20) shows that the singularities for subsonic and supersonic flow are of identical form.

SOME INFINITE-SERIES EXPANSIONS PERTINENT TO THE KERNEL FUNCTION

The kernel function can be expressed as a series by various expansion procedures. Some particular expansions, which should be useful in applications, are discussed in succeeding paragraphs. These are the power-series expansion in terms

of the reduced-frequency parameter (see eq. (29)) and an expansion in terms of Bessel functions. The latter expansion is used in a later section to obtain the kernel function for two-dimensional flow from that for three-dimensional flow.

Power-series expansion with respect to k .—As in the case of subsonic flow, the kernel function can be expanded into a power series with respect to k that, in the present case, is useful for small values of k/β^2 , a combination of reduced frequency and Mach number that is inherent in such an expansion of the supersonic kernel. The terms of the expansion may be simply obtained by expanding the terms of equation (16a) that are functions of k and collecting the results. The first few terms are

$$K(x_0, y_0) = -\frac{2e^{-ikx_0}}{V l^2 y_0^2} U(x_0 - \beta|y_0|) \left[\frac{x_0}{\sqrt{x_0^2 - \beta^2 y_0^2}} - \frac{ik}{\beta^2} \frac{\beta^2 y_0^2}{\sqrt{x_0^2 - \beta^2 y_0^2}} - \frac{1}{2} \left(\frac{k}{\beta^2} \right)^2 \left(\frac{\beta^2 y_0^2 x_0}{\sqrt{x_0^2 - \beta^2 y_0^2}} + \beta^4 y_0^2 \cosh^{-1} \frac{x_0}{\beta|y_0|} \right) + \frac{i}{6} \left(\frac{k}{\beta^2} \right)^3 \frac{(3M^2 - 1)\beta^2 y_0^2 x_0^2 + (2 - 3M^2)\beta^4 y_0^4}{\sqrt{x_0^2 - \beta^2 y_0^2}} + O \left(\frac{k}{\beta^2} \right)^4 \right] \quad (29)$$

Although this power-series expansion converges, to the appropriate value of $K(x_0, y_0)$ for all finite values of k/β^2 , a great number of terms are required unless k/β^2 is small. These first few terms of the expansion can be considered to represent the kernel function for values of k in the range of magnitudes generally encountered in dynamic-stability studies and, therefore, they are pertinent for obtaining time-dependent stability derivatives. A noteworthy feature of the expansion is that each term can be integrated, in the sense that it contains a simple indefinite integral, with respect to the variable $\eta = y - y_0$. When such integrations involve a passage across the line $\eta = y$, a principal value is to be taken in the sense described after equation (28).

Expansions in terms of Bessel functions.—The trigonometric terms appearing in the expression for $K(x_0, y_0)$ in equations (15), (16a), and (16b) can be expanded into infinite series involving Bessel functions of the first kind. Such expansions have good convergence properties, even for large values of the parameter k/β^2 , and each term possesses a simple indefinite integral with respect to η . Such Bessel function series are therefore useful for deriving an expansion for the indefinite integral of $K(x_0, y_0)$ with respect to η . The indefinite integral of $K(x_0, y_0)$ leads to the downwash associated with pulsating vortex lines ("horseshoe" vortices) and, as previously indicated, to the kernel function for two-dimensional flow. It might be useful to point out that the expansion of the cosine term into a series involving Bessel functions is also useful for studying distributions of pulsating sources.

For the purpose of expanding the trigonometric terms under discussion, consider the expressions

$$U(\lambda - a) \frac{\cos b\sqrt{\lambda^2 - a^2}}{\sqrt{\lambda^2 - a^2}} \quad (30)$$

and

$$U(\lambda - a) \sin(b\sqrt{\lambda^2 - a^2}) = -\frac{\partial}{\partial b} \left[U(\lambda - a) \frac{\cos(b\sqrt{\lambda^2 - a^2})}{\sqrt{\lambda^2 - a^2}} \right] \quad (31)$$

where a , b , and λ are positive.

By making use of a known Fourier transform relation, expression (30) can be equated to an infinite integral involving a Bessel function of the first kind (see, for example, p. 33 of ref. 17):

$$\left. \begin{aligned} \int_0^\infty J_0(\lambda\sqrt{\tau^2 + b^2}) \cos a\tau d\tau &= \frac{\cos(b\sqrt{\lambda^2 - a^2})}{\sqrt{\lambda^2 - a^2}} & (\lambda > a) \\ \int_0^\infty J_0(\lambda\sqrt{\tau^2 + b^2}) \cos a\tau d\tau &= 0 & (\lambda < a) \end{aligned} \right\} \quad (32)$$

By use of the addition formula for Bessel functions (see, for example, p. 358 of ref. 18), the Bessel function appearing in this equation can be written as an infinite sum of products of Bessel functions as follows:

$$J_0(\lambda\sqrt{\tau^2 + b^2}) = J_0(\tau\lambda)J_0(b\lambda) + 2 \sum_{n=1}^{\infty} (-1)^n J_{2n}(\tau\lambda)J_{2n}(b\lambda) \quad (33)$$

Thus,

$$\begin{aligned} \int_0^\infty J_0(\lambda\sqrt{\tau^2 + b^2}) \cos a\tau d\tau &= U(\lambda - a) \frac{\cos(b\sqrt{\lambda^2 - a^2})}{\sqrt{\lambda^2 - a^2}} \\ &= \int_0^\infty \left[J_0(\tau\lambda)J_0(b\lambda) + \right. \\ &\quad \left. 2 \sum_{n=1}^{\infty} (-1)^n J_{2n}(\tau\lambda)J_{2n}(b\lambda) \right] \cos a\tau d\tau \end{aligned} \quad (34)$$

In view of the relation (see ref. 17, p. 37)

$$\int_0^\infty J_{2n}(\tau\lambda) \cos a\tau d\tau = \frac{U(\lambda - a) \cos\left(2n \sin^{-1} \frac{a}{\lambda}\right)}{\sqrt{\lambda^2 - a^2}} \quad (35)$$

the indicated integration on the right-hand side of equation (34) can be carried out term by term so that

$$\begin{aligned} \frac{U(\lambda - a) \cos(b\sqrt{\lambda^2 - a^2})}{\sqrt{\lambda^2 - a^2}} \\ = \frac{U(\lambda - a)}{\sqrt{\lambda^2 - a^2}} \left[J_0(b\lambda) + 2 \sum_{n=1}^{\infty} (-1)^n J_{2n}(b\lambda) \cos\left(2n \sin^{-1} \frac{a}{\lambda}\right) \right] \end{aligned} \quad (36)$$

Substituting the expression on the right-hand side of equation (36) into equation (31) gives

$$\begin{aligned} U(\lambda - a) \sin(b\sqrt{\lambda^2 - a^2}) &= \frac{\lambda U(\lambda - a)}{\sqrt{\lambda^2 - a^2}} \left\{ J_1(b\lambda) - \sum_{n=1}^{\infty} (-1)^n \left[J_{2n-1}(b\lambda) - J_{2n+1}(b\lambda) \right] \cos\left(2n \sin^{-1} \frac{a}{\lambda}\right) \right\} \\ &= \frac{2\lambda U(\lambda - a)}{\sqrt{\lambda^2 - a^2}} \left\{ \cos\left(\sin^{-1} \frac{a}{\lambda}\right) \sum_{n=1}^{\infty} (-1)^{n-1} J_{2n-1}(b\lambda) \cos\left[(2n-1) \sin^{-1} \frac{a}{\lambda}\right] \right\} \end{aligned} \quad (37)$$

But, since

$$U(\lambda - a) \frac{\lambda}{\sqrt{\lambda^2 - a^2}} \cos\left(\sin^{-1} \frac{a}{\lambda}\right) \equiv U(\lambda - a) \quad (a \geq 0)$$

the expression for $U(\lambda - a) \sin(b\sqrt{\lambda^2 - a^2})$ may be written as

$$U(\lambda - a) \sin(b\sqrt{\lambda^2 - a^2}) = 2U(\lambda - a) \sum_{n=1}^{\infty} (-1)^{n-1} J_{2n-1}(b\lambda) \cos\left[(2n-1) \sin^{-1} \frac{a}{\lambda}\right] \quad (38)$$

By direct comparison, equations (36) and (38) can be used to write expanded forms of the trigonometric terms appearing in equations (15), (16a), and (16b). Expansions thus obtained will now be used to derive the kernel function for two-dimensional supersonic flow.

In contrast to three-dimensional flow, a physical interpretation of the kernel function for two-dimensional flow is that it represents the downwash at a given field point due to a pulsating bound vortex line of infinite length. This kernel function may be obtained by integrating the kernel function for three-dimensional flow from $-\infty$ to ∞ or, in view of the role of the unit function, from one Mach line to the other, with respect to the variable $\eta = y - y_0$. Pulsating "horseshoe" vortices may be obtained by integrating $K(x_0, y_0)$ over an arbitrarily finite range with respect to η .

DERIVATION OF KERNEL FUNCTION FOR TWO-DIMENSIONAL FLOW

In this section the kernel function for three-dimensional flow is reduced to the function for two-dimensional flow, and the final results of the reduction are given in equation (49). For the purpose of derivation, $K(x_0, y_0)$ will be considered as given in equation (16b). The two-dimensional kernel function can then be expressed as

$$\int_{-\infty}^{\infty} K(x_0, y_0) d\eta = -\frac{2}{Vl} \left\{ e^{-\frac{iM^2 k x_0}{\beta^2}} \oint_{-\infty}^{\infty} \frac{\frac{\beta^2}{Mk} \frac{\partial}{\partial x_0} + \frac{i}{M}}{y_0^2} \left[U(x_0 - \beta|y_0|) \sin \left(\frac{Mk}{\beta^2} \sqrt{x_0^2 - \beta^2 y_0^2} \right) \right] d\eta + \right. \\ \left. \frac{k}{M} e^{-ikx_0} \oint_{-\infty}^{\infty} \frac{d\eta}{y_0^2} \int_{\beta|y_0|}^{x_0} e^{-\frac{ik\lambda}{\beta^2}} U(\lambda - \beta|y_0|) \sin \left(\frac{Mk}{\beta^2} \sqrt{\lambda^2 - \beta^2 y_0^2} \right) d\lambda \right\} \\ = K(x_0) \quad (39)$$

$$K(x_0) = -\frac{2}{Vl} \left(e^{-\frac{iM^2 k x_0}{\beta^2}} I_1 + \frac{k}{M} e^{-ikx_0} I_2 \right) \quad (40)$$

where

$$I_1 = \oint_{-\infty}^{\infty} \frac{\left(\frac{\beta^2}{Mk} \frac{\partial}{\partial x_0} + \frac{i}{M} \right)}{(y - \eta)^2} \left[U(x_0 - \beta|y - \eta|) \sin \left(\frac{Mk}{\beta^2} \sqrt{x_0^2 - \beta^2 (y - \eta)^2} \right) \right] d\eta \quad (41a)$$

or

$$I_1 = \beta \left(\frac{\beta^2}{Mk} \frac{\partial}{\partial x_0} + \frac{i}{M} \right) \oint_{-x_0}^{x_0} \frac{U(x_0 - |\eta|)}{\eta^2} \sin \left(\frac{Mk}{\beta^2} \sqrt{x_0^2 - \eta^2} \right) d\eta \quad (41b)$$

and

$$I_2 = \beta \oint_{-x_0}^{x_0} \frac{1}{\eta^2} \left[\int_{|\eta|}^{x_0} e^{-\frac{ik\lambda}{\beta^2}} U(\lambda - |\eta|) \sin \left(\frac{Mk}{\beta^2} \sqrt{\lambda^2 - \eta^2} \right) d\lambda \right] d\eta \quad (42)$$

In equations (41) for I_1 and equation (42) for I_2 , infinite limits with respect to the integration of η are not necessary. In view of the role of the unit function in the integrands, limits of $\pm x_0$ include all values of η for which the integrands are different from zero. The symbol \oint indicates that the integrals are to be considered simply as functions of their limits or that the singularity at $\eta=0$ is to be ignored.

First consider equations (41) for I_1 and then perform an integration by parts. The expression for I_1 may then be written as

$$I_1 = \beta \left(\frac{\beta^2}{Mk} \frac{\partial}{\partial x_0} + \frac{i}{M} \right) \left[-\frac{1}{\eta} U(x_0 - |\eta|) \sin \left(\frac{Mk}{\beta^2} \sqrt{x_0^2 - \eta^2} \right) \right]_{-x_0}^{x_0} - \\ \frac{Mk}{\beta^2} \int_{-x_0}^{x_0} \frac{U(x_0 - |\eta|)}{\sqrt{x_0^2 - \eta^2}} \cos \left(\frac{Mk}{\beta^2} \sqrt{x_0^2 - \eta^2} \right) d\eta \\ = -2\beta \left(\frac{\partial}{\partial x_0} + \frac{ik}{\beta^2} \right) \int_0^{x_0} \frac{U(x_0 - |\eta|)}{\sqrt{x_0^2 - \eta^2}} \cos \left(\frac{Mk}{\beta^2} \sqrt{x_0^2 - \eta^2} \right) d\eta \quad (43)$$

By direct comparison with equation (36), equation (43) may be written in expanded form as

$$I_1 = -2\beta \left(\frac{\partial}{\partial x_0} + \frac{ik}{\beta^2} \right) \int_0^{x_0} \frac{U(x_0 - |\eta|)}{\sqrt{x_0^2 - \eta^2}} \left[J_0 \left(\frac{Mk}{\beta^2} x_0 \right) + \right. \\ \left. 2 \sum_{n=1}^{\infty} (-1)^n J_{2n} \left(\frac{Mk}{\beta^2} x_0 \right) \cos \left(2n \sin^{-1} \frac{\eta}{x_0} \right) \right] d\eta \quad (44)$$

In this equation, the terms involving J_{2n} do not contribute to the integral because

$$\int_0^{x_0} \frac{U(x_0 - |\eta|)}{\sqrt{x_0^2 - \eta^2}} \cos \left(2n \sin^{-1} \frac{\eta}{x_0} \right) d\eta \\ = \frac{1}{2n} \left[U(x_0 - |\eta|) \sin \left(2n \sin^{-1} \frac{\eta}{x_0} \right) \right]_0^{x_0} + \\ \int_0^{x_0} \frac{\eta}{|\eta|} \delta(x_0 - |\eta|) \sin \left(2n \sin^{-1} \frac{\eta}{x_0} \right) d\eta \equiv 0$$

Hence, since

$$\int_0^{x_0} \frac{U(x_0 - |\eta|)}{\sqrt{x_0^2 - \eta^2}} d\eta = U(x_0 - |\eta|) \sin^{-1} \frac{\eta}{x_0} \Big|_0^{x_0} + \int_0^{x_0} \frac{\eta}{|\eta|} \delta(x_0 - |\eta|) \sin^{-1} \frac{\eta}{x_0} d\eta = \frac{\pi}{2} U(x_0)$$

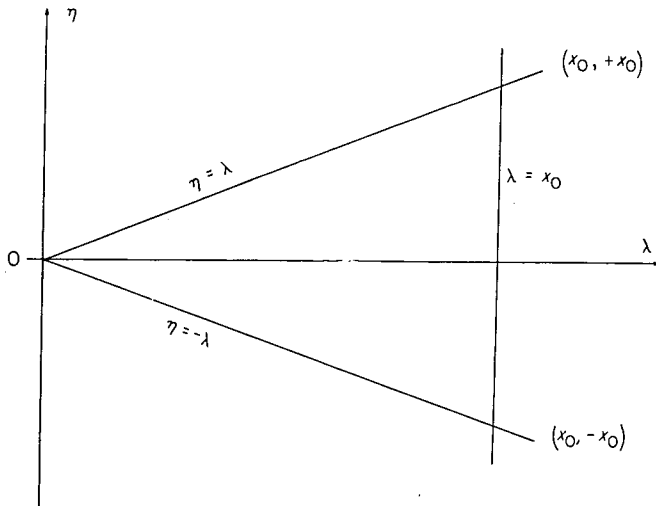
the expression for I_1 can be written as

$$\begin{aligned} I_1 &= -\pi\beta \left(\frac{\partial}{\partial x_0} + \frac{ik}{\beta^2} \right) U(x_0) J_0 \left(\frac{Mk}{\beta^2} x_0 \right) \\ &= -\pi\beta \left[\delta(x_0) + \frac{ik}{\beta^2} U(x_0) J_0 \left(\frac{Mk}{\beta^2} x_0 \right) - \frac{Mk}{\beta^2} U(x_0) J_1 \left(\frac{Mk}{\beta^2} x_0 \right) \right] \end{aligned} \quad (45)$$

Now consider equation (42) for I_2 , namely

$$I_2 = \beta \oint_{-x_0}^{x_0} \frac{1}{\eta^2} \left[\int_{|\eta|}^{x_0} e^{-\frac{ik\lambda}{\beta^2}} U(\lambda - |\eta|) \sin \left(\frac{Mk}{\beta^2} \sqrt{\lambda^2 - \eta^2} \right) d\lambda \right] d\eta$$

The double integral in this expression can be considered as a surface integral over a triangular region of the $\lambda\eta$ -plane cut out by the lines $\eta = \lambda$, $\eta = -\lambda$, and $\lambda = x_0$, as shown in sketch (c).



Sketch (c)

By a change in the order of integration, which is admissible since the singularity at $\eta = 0$ is to be ignored, the expression for I_2 may be written as

$$I_2 = \beta \int_0^{x_0} e^{-\frac{ik\lambda}{\beta^2}} d\lambda \oint_{-\lambda}^{\lambda} \frac{U(\lambda - |\eta|)}{\eta^2} \sin \left(\frac{Mk}{\beta^2} \sqrt{\lambda^2 - \eta^2} \right) d\eta \quad (46)$$

The inner integral in this equation is identical in form to the integral in equation (41). Hence, by observation of and comparison with the results obtained for I_1 in equations (43), (44), and (45), it is found that

$$\oint_{-\lambda}^{\lambda} \frac{U(\lambda - |\eta|)}{\eta^2} \sin \left(\frac{Mk}{\beta^2} \sqrt{\lambda^2 - \eta^2} \right) d\eta = -\frac{\pi Mk}{\beta^2} U(\lambda) J_0 \left(\frac{Mk}{\beta^2} \lambda \right) \quad (47)$$

The expression for I_2 can therefore be written

$$I_2 = -\frac{\pi Mk}{\beta} \int_0^{x_0} e^{-\frac{ik\lambda}{\beta^2}} U(\lambda) J_0 \left(\frac{Mk}{\beta^2} \lambda \right) d\lambda \quad (48)$$

Substituting this result and the results given in equation (45) for I_1 into equation (40) gives a desired form of the kernel function for two-dimensional supersonic flow:

$$\begin{aligned} K(x_0) &= \frac{2\pi\beta}{Vl} \left\{ e^{-\frac{iM^2 k x_0}{\beta^2}} \left[\delta(x_0) + \frac{ik}{\beta^2} U(x_0) J_0 \left(\frac{Mk}{\beta^2} x_0 \right) - \frac{Mk}{\beta^2} U(x_0) J_1 \left(\frac{Mk}{\beta^2} x_0 \right) \right] + \right. \\ &\quad \left. \frac{k^2}{\beta^2} e^{-ikx_0} \int_0^{x_0} e^{-\frac{ik\lambda}{\beta^2}} U(\lambda) J_0 \left(\frac{Mk}{\beta^2} \lambda \right) d\lambda \right\} \end{aligned} \quad (49)$$

Examination of equation (49) shows that the only singularity involved in the kernel function for two-dimensional supersonic flow is the δ -function. At zero frequency, all the terms of $K(x_0)$ except the δ -function vanish. The kernel function required to treat two-dimensional wings at steady angle-of-attack conditions is therefore proportional to this δ -function, and, as shown in the following section, leads in a very simple manner to the well-known Ackeret results.

The integral that remains to be evaluated in equation (49) is well behaved and similar to integrals, treated by Schwarz (ref. 19) and others, that arise in the velocity-potential approach for treating two-dimensional wings.

APPLICATION OF KERNEL FUNCTION TO LIFT DISTRIBUTIONS FOR TWO-DIMENSIONAL WINGS

The results obtained in the previous section for the two-dimensional kernel function are now employed to obtain the lift distribution on oscillating and steady two-dimensional wings moving at supersonic speed. (See eqs. (56) and (61).) Since the lift distributions so obtained agree with the Ackeret results for a steady wing and also with known results for the oscillating wing (ref. 15), they serve as a check on the correctness of the expressions for both the two-dimensional and three-dimensional kernel functions.

The integral equation that must be solved to obtain the lift distribution for two-dimensional wings in supersonic flow is particularly simple since it involves a single integral of the convolution type:

$$\bar{w}(x) = \frac{l}{4\pi\rho} \int_0^x L(\xi) K(x_0) d\xi = \frac{l}{4\pi\rho} \int_0^x L(\xi) K(x - \xi) d\xi \quad (50)$$

Integral equations of this type can be readily solved by Laplace transform procedures since the Laplace transform of a convolution integral is the product of the transforms of the functions that compose the integrand. In the present case, if s represents the Laplace transform operator defined by

$$L[f(x)] = \int_0^\infty e^{-sx} f(x) dx = f(s) \quad (51)$$

the transform of equation (50) may be written as

$$\bar{w}(s) = \frac{l}{4\pi\rho} L(s) K(s) \quad (52)$$

Solving this equation for $L(s)$ gives the Laplace transform

of the lift distribution:

$$L(s) = \frac{4\pi\rho}{l} \frac{\bar{w}(s)}{K(s)} \quad (53)$$

Inversion of the transform on the right-hand side of this equation gives the lift distribution.

For the case of a steady two-dimensional wing,

$$\begin{aligned} \bar{w}(x) &= V\alpha & \bar{w}(s) &= \frac{V\alpha}{s} \\ K(x) &= \frac{2\pi\beta}{Vl} \delta(x) & K(s) &= \frac{2\pi\beta}{Vl} \end{aligned}$$

Then

$$L(s) = \frac{2\rho V^2 \alpha}{\beta s} \quad (54)$$

The inverse transform of equation (54) gives for the lift distribution:

$$L(x) = \frac{2\rho V^2 \alpha}{\beta} U(x) \quad (55)$$

From this result, the total lift per unit of span is

$$l \int_0^{\text{Chord}} L(x) dx = \frac{2\rho V^2 \alpha \times \text{Chord}}{\beta} \quad (56)$$

This result agrees with the well-known Ackeret result.

Now consider the unsteady case for oscillatory translation,

$$\bar{w}(x) = i\omega l \bar{h} = iV k \bar{h} \quad (57)$$

where \bar{h} is the amplitude of displacement referred to l , and the Laplace transform of $\bar{w}(x)$ is

$$\bar{w}(s) = \frac{iV k \bar{h}}{s} \quad (58)$$

The Laplace transforms of the different terms of $K(x)$ (eq. (49)) can be simply derived or they may be obtained from Laplace transform tables (for example, ref. 16). After combining the transforms of the different terms, the results can be written as

$$K(s) = \frac{2\pi\beta}{Vl} \frac{\sqrt{\left(s + \frac{iM^2 k}{\beta^2}\right)^2 + \frac{M^2 k^2}{\beta^4}}}{s + ik} \quad (59)$$

Substituting equations (58) and (59) into equation (53) gives

for the transform of the lift distribution

$$L(s) = \frac{2i\rho V^2 k \bar{h}}{\beta} \frac{s + ik}{s \sqrt{\left(s + \frac{iM^2 k}{\beta^2}\right)^2 + \frac{M^2 k^2}{\beta^4}}} \quad (60)$$

The inverse of this transform gives for the lift distribution

$$\begin{aligned} L(x) = \frac{2i\rho V^2 k \bar{h}}{\beta} & \left[U(x) e^{-\frac{iM^2 k x}{\beta^2}} J_0\left(\frac{M k x}{\beta^2}\right) + \right. \\ & \left. ik \int_0^x U(\xi) e^{-\frac{iM^2 k \xi}{\beta^2}} J_0\left(\frac{M k \xi}{\beta^2}\right) d\xi \right] \quad (61) \end{aligned}$$

This result can easily be shown to check with the results of reference 15. Moreover, if $ik\bar{h}$ is set equal to α , and then k is allowed to approach zero, equation (61) reduces to the result for the steady case.

CONCLUDING REMARKS

The main purpose of this report was to derive and present in a form that could be numerically evaluated the kernel function of the integral equation relating downwash and lift distributions for oscillating wings in supersonic flow. This purpose has been achieved for three-dimensional flow, and the results have been converted to a form more suitable for calculation by isolating the singular or critical points. The kernel function for two-dimensional supersonic flow has been presented and the results show that the only singularity is a Dirac delta function, which appeared in such a manner that further reduction with regard to singularities is not required.

The results presented in this report for supersonic flow together with those previously obtained for subsonic flow provide a kernel function that is capable of being evaluated at any Mach number. As experience develops it is expected that use can be made of the kernel function to develop approximate procedures, that will be more or less uniform throughout the Mach number range, for calculating aerodynamic forces on oscillating (or steady) wings of arbitrary plan form and with arbitrary downwash conditions. The labor involved in such approximate or numerical procedures will indeed be prodigious and will require the use of modern high-speed computing equipment.

LANGLEY AERONAUTICAL LABORATORY,
NATIONAL ADVISORY COMMITTEE FOR AERONAUTICS,
LANGLEY FIELD, VA., February 15, 1955.

APPENDIX A

DERIVATION OF EQUATION (16c) AND REDUCTION OF THE KERNEL FUNCTION TO THE SONIC CASE

The purpose of this appendix is first to reduce equation (16a) to equation (16c) and then to reduce equation (16c) to the sonic case. The reduction to the sonic case, by comparison with results obtained from consideration of subsonic speeds for the sonic case in reference 1, provides a partial check on the correctness of results obtained for the supersonic case.

DERIVATION OF EQUATION (16c)

In order to reduce equation (16a) to equation (16c) consider the integral

$$\begin{aligned} \frac{k}{M} \int_{\beta|y_0|}^{x_0} e^{-\frac{ik}{\beta^2}\lambda} U(\lambda - \beta|y_0|) \sin\left(\frac{Mk}{\beta^2} \sqrt{\lambda^2 - \beta^2 y_0^2}\right) d\lambda \\ = \frac{k}{2iM} \int_{\beta|y_0|}^{x_0} e^{-\frac{ik}{\beta^2}\lambda} U(\lambda - \beta|y_0|) \left(e^{\frac{iMk}{\beta^2} \sqrt{\lambda^2 - \beta^2 y_0^2}} - e^{-\frac{iMk}{\beta^2} \sqrt{\lambda^2 - \beta^2 y_0^2}} \right) d\lambda \\ = \frac{k}{2iM} (I_1 - I_2) \end{aligned} \quad (A1)$$

where

$$I_1 = \int_{\beta|y_0|}^{x_0} U(\lambda - \beta|y_0|) e^{-\frac{ik}{\beta^2}(\lambda - M\sqrt{\lambda^2 - \beta^2 y_0^2})} d\lambda \quad (A2)$$

and

$$I_2 = \int_{\beta|y_0|}^{x_0} U(\lambda - \beta|y_0|) e^{-\frac{ik}{\beta^2}(\lambda + M\sqrt{\lambda^2 - \beta^2 y_0^2})} d\lambda \quad (A3)$$

In these expressions λ takes on only positive values, that is, $\beta|y_0| \leq \lambda \leq x_0$. Hence, consider for each integral the single-valued substitution

$$\lambda = |y_0|(+M\sqrt{1+\tau^2} - \tau) \quad (A4)$$

which, for $M \geq 1$, leads only to positive values of λ .

Solving this expression for τ gives

$$\tau = \frac{\lambda \pm M\sqrt{\lambda^2 - \beta^2 y_0^2}}{\beta^2 |y_0|} \quad (A5)$$

Thus, if the substitution

$$(\lambda - M\sqrt{\lambda^2 - \beta^2 y_0^2}) = \beta^2 |y_0| \tau \quad (A6)$$

is made in I_1 and the substitution

$$(\lambda + M\sqrt{\lambda^2 - \beta^2 y_0^2}) = \beta^2 |y_0| \tau \quad (A7)$$

is made in I_2 , there is obtained

$$I_1 = |y_0| \int_{\frac{1}{\beta}}^{\frac{1}{\beta^2 |y_0|}} (x_0 - M\sqrt{x_0^2 - \beta^2 y_0^2}) U\left(\tau - \frac{1}{\beta}\right) \left(\frac{M\tau}{\sqrt{1+\tau^2}} - 1\right) e^{-ik|y_0|\tau} d\tau \quad (A8)$$

and

$$\begin{aligned} I_2 = |y_0| \int_{\frac{1}{\beta}}^{\frac{1}{\beta^2 |y_0|}} (x_0 + M\sqrt{x_0^2 - \beta^2 y_0^2}) U\left(\tau - \frac{1}{\beta}\right) \left(\frac{M\tau}{\sqrt{1+\tau^2}} - 1\right) e^{-ik|y_0|\tau} d\tau \\ = |y_0| \int_{\frac{1}{\beta}}^{\frac{1}{\beta^2 |y_0|}} (x_0 - M\sqrt{x_0^2 - \beta^2 y_0^2}) U\left(\tau - \frac{1}{\beta}\right) \left(\frac{M\tau}{\sqrt{1+\tau^2}} - 1\right) e^{-ik|y_0|\tau} d\tau + \\ |y_0| U(x_0 - \beta|y_0|) \int_{\frac{1}{\beta^2 |y_0|}}^{\frac{1}{\beta}} (x_0 + M\sqrt{x_0^2 - \beta^2 y_0^2}) \left(\frac{M\tau}{\sqrt{1+\tau^2}} - 1\right) e^{-ik|y_0|\tau} d\tau \end{aligned} \quad (A9)$$

Combining these results gives for $\frac{k}{2iM} (I_1 - I_2)$

$$\begin{aligned} \frac{k}{2iM} (I_1 - I_2) = \\ - \frac{k|y_0| U(x_0 - \beta|y_0|)}{2iM} \int_{\frac{1}{\beta^2 |y_0|}}^{\frac{1}{\beta}} (x_0 + M\sqrt{x_0^2 - \beta^2 y_0^2}) \left(\frac{M\tau}{\sqrt{1+\tau^2}} - 1\right) e^{-ik|y_0|\tau} d\tau \end{aligned} \quad (A10)$$

or since

$$\int_{\frac{1}{\beta^2 |y_0|}}^{\frac{1}{\beta}} (x_0 + M\sqrt{x_0^2 - \beta^2 y_0^2}) e^{-ik|y_0|\tau} d\tau = - \frac{2e^{-\frac{ik}{\beta^2} x_0}}{k} \sin\left(\frac{Mk}{\beta^2} \sqrt{x_0^2 - \beta^2 y_0^2}\right) \quad (A11)$$

$$\begin{aligned} \frac{k}{2iM} (I_1 - I_2) = -|y_0| U(x_0 - \beta|y_0|) \left[\frac{ie^{-\frac{ik}{\beta^2} x_0}}{M} \sin\left(\frac{Mk}{\beta^2} \sqrt{x_0^2 - \beta^2 y_0^2}\right) + \right. \\ \left. \frac{k}{2i} \int_{\frac{1}{\beta^2 |y_0|}}^{\frac{1}{\beta}} (x_0 + M\sqrt{x_0^2 - \beta^2 y_0^2}) \frac{\tau}{\sqrt{1+\tau^2}} e^{-ik|y_0|\tau} d\tau \right] \end{aligned} \quad (A12)$$

Substituting this result into equation (16a) gives equation (16c) or

$$K(x_0, y_0) = - \frac{2}{v l^2 y_0^2} e^{-ikx_0} U(x_0 - \beta|y_0|) \left[\frac{x_0 e^{-\frac{ik}{\beta^2} x_0}}{\sqrt{x_0^2 - \beta^2 y_0^2}} \cos\left(\frac{Mk}{\beta^2} \sqrt{x_0^2 - \beta^2 y_0^2}\right) + \frac{ik|y_0|}{2} \int_{\frac{1}{\beta^2 |y_0|}}^{\frac{1}{\beta}} (x_0 + M\sqrt{x_0^2 - \beta^2 y_0^2}) \frac{\tau}{\sqrt{1+\tau^2}} e^{-ik|y_0|\tau} d\tau \right] \quad (16c)$$

REDUCTION OF EQUATION (16c) TO THE SONIC CASE

In order to reduce this result to the sonic case it is first necessary to discard terms arising from the advanced-type potentials employed in deriving the doublet potentials for supersonic flow. This may be accomplished by replacing $\cos\left(\frac{Mk}{\beta^2}\sqrt{x_0^2-\beta^2y_0^2}\right)$ with $\frac{1}{2}e^{\frac{iMk}{\beta^2}\sqrt{x_0^2-\beta^2y_0^2}}$. The limiting form of $K(x_0, y_0)$ as $M \rightarrow 1$ can then be written as

$$K(x_0, y_0)_{M=1} = \lim_{M \rightarrow 1} -\frac{1}{vl^2y_0^2} e^{-ikx_0} U(x_0 - \beta|y_0|) \left[\frac{x_0}{\sqrt{x_0^2 - \beta^2y_0^2}} e^{-\frac{ik}{\beta^2}(x_0 - M\sqrt{x_0^2 - \beta^2y_0^2})} + ik|y_0| \int \frac{\frac{1}{\beta^2|y_0|}(x_0 + M\sqrt{x_0^2 - \beta^2y_0^2})}{\frac{1}{\beta^2|y_0|}(x_0 - M\sqrt{x_0^2 - \beta^2y_0^2})} \frac{\tau}{\sqrt{1+\tau^2}} e^{-ik|y_0|\tau} d\tau \right] \quad (A13)$$

When the limit $M=1$ is approached from the supersonic side, the term M is conveniently replaced by

$$M = 1 + \frac{1}{2}\epsilon$$

where ϵ is infinitesimally small, so that

$$\beta^2 = (M-1)(M+1) = \frac{1}{2}\epsilon \left(2 + \frac{1}{2}\epsilon\right) \approx \epsilon \quad (A14)$$

With this approximation equation (A13) can be written as

$$\begin{aligned} K(x_0, y_0)_{M=1} &= \lim_{\epsilon \rightarrow 0} -\frac{e^{-ikx_0}}{vl^2y_0^2} U(x_0 - \sqrt{\epsilon}|y_0|) \left\{ \frac{x_0}{\sqrt{x_0^2 - \epsilon y_0^2}} e^{-\frac{ik}{\epsilon}[x_0 - (1+\frac{\epsilon}{2})\sqrt{x_0^2 - \epsilon y_0^2}]} + ik|y_0| \int \frac{\frac{1}{\epsilon|y_0|}[x_0 + (1+\frac{\epsilon}{2})\sqrt{x_0^2 - \epsilon y_0^2}]}{\frac{1}{\epsilon|y_0|}[x_0 - (1+\frac{\epsilon}{2})\sqrt{x_0^2 - \epsilon y_0^2}]} \frac{\tau}{\sqrt{1+\tau^2}} e^{-ik|y_0|\tau} d\tau \right\} \\ &= \lim_{\epsilon \rightarrow 0} -\frac{e^{-ikx_0}}{vl^2y_0^2} U(x_0) \left\{ e^{-\frac{ik}{\epsilon}[x_0 - (1+\frac{\epsilon}{2})(x_0 - \frac{\epsilon y_0^2}{2x_0})]} + ik|y_0| \int \frac{\frac{1}{\epsilon|y_0|}[x_0 + (1+\frac{\epsilon}{2})(x_0 - \frac{\epsilon y_0^2}{2x_0})]}{\frac{1}{\epsilon|y_0|}[x_0 - (1+\frac{\epsilon}{2})(x_0 - \frac{\epsilon y_0^2}{2x_0})]} \frac{\tau}{\sqrt{1+\tau^2}} e^{-ik|y_0|\tau} d\tau \right\} \end{aligned} \quad (A15)$$

or

$$K(x_0, y_0)_{M=1} = -\frac{e^{-ikx_0}}{vl^2y_0^2} U(x_0) \left\{ e^{\frac{ik}{2}(x_0 - \frac{y_0^2}{x_0})} + ik|y_0| \int \frac{\frac{1}{-2|y_0|}(x_0 - \frac{y_0^2}{x_0})}{\sqrt{1+\tau^2}} e^{-ik|y_0|\tau} d\tau \right\} \quad (A16)$$

In order to show that this result is equivalent to that given for the sonic case in reference 1, it is convenient to first express the integral term as the difference of two integrals

$$ik|y_0| \int \frac{\frac{1}{-2|y_0|}(x_0 - \frac{y_0^2}{x_0})}{\sqrt{1+\tau^2}} e^{-ik|y_0|\tau} d\tau = ik|y_0| \int_0^\infty \frac{\tau}{\sqrt{1+\tau^2}} e^{-ik|y_0|\tau} d\tau - ik|y_0| \int_0^{-\frac{1}{2|y_0|}(x_0 - \frac{y_0^2}{x_0})} \frac{\tau}{\sqrt{1+\tau^2}} e^{-ik|y_0|\tau} d\tau \quad (A17)$$

The first integral on the right of equation (A17) can be evaluated by comparison with the following results:

$$\begin{aligned} \int_0^\infty \frac{\tau}{\sqrt{1+\tau^2}} e^{-i a \tau} d\tau &= \int_0^\infty \frac{\tau}{\sqrt{1+\tau^2}} \cos a\tau d\tau - i \int_0^\infty \frac{\tau}{\sqrt{1+\tau^2}} \sin a\tau d\tau \\ &= \frac{\partial}{\partial a} \left(\int_0^\infty \frac{\sin a\tau}{\sqrt{1+\tau^2}} d\tau + i \int_0^\infty \frac{\cos a\tau}{\sqrt{1+\tau^2}} d\tau \right) \\ &= \frac{\partial}{\partial a} \left\{ \frac{\pi}{2} [I_0(a) - L_0(a)] + i K_0(a) \right\} \\ &= \frac{\pi}{2} [I_1(a) - L_1(a)] - 1 - i K_1(a) \end{aligned} \quad (A18)$$

where I_0 , I_1 , K_0 , K_1 are modified Bessel functions and L_0 and L_1 are modified Struve functions (see ref. 18, p. 172 and p. 332 for reductions of similar integrals). Thus

$$ik|y_0| \int_0^\infty \frac{\tau}{\sqrt{1+\tau^2}} e^{-ik|y_0|\tau} d\tau = k|y_0|K_1(k|y_0|) + \frac{\pi ik|y_0|}{2} [I_1(k|y_0|) - L_1(k|y_0|)] - ik|y_0| \quad (\text{A19})$$

In the second integral on the right of equation (A17) make the substitution

$$\tau = \frac{1}{2|y_0|} \left(\frac{y_0^2}{\lambda} - \lambda \right)$$

or

$$\lambda = |y_0| (\sqrt{1+\tau^2} - \tau)$$

This gives for the second integral

$$\begin{aligned} -ik|y_0| \int_0^\infty \frac{\tau}{\sqrt{1+\tau^2}} e^{-ik|y_0|\tau} d\tau &= ik \int_{|y_0|}^{x_0} \left(\frac{y_0^2 + \lambda^2}{2\lambda^2} - 1 \right) e^{\frac{ik}{2} \left(\lambda - \frac{y_0^2}{\lambda} \right)} d\lambda \\ &= e^{\frac{ik}{2} \left(\lambda - \frac{y_0^2}{\lambda} \right)} \Big|_{|y_0|}^{x_0} - ik \int_{|y_0|}^{x_0} e^{\frac{ik}{2} \left(\lambda - \frac{y_0^2}{\lambda} \right)} d\lambda \\ &= e^{\frac{ik}{2} \left(x_0 - \frac{y_0^2}{x_0} \right)} - 1 - ik \int_{|y_0|}^{x_0} e^{\frac{ik}{2} \left(\lambda - \frac{y_0^2}{\lambda} \right)} d\lambda \end{aligned} \quad (\text{A20})$$

Substituting this result and that given in equation (A19) for the integral in equation (A16) gives

$$K(x_0, y_0)_{M=1} = -\frac{e^{-ikx_0}}{v l^2 y_0^2} U(x_0) \left\{ 2e^{\frac{ik}{2} \left(x_0 - \frac{y_0^2}{x_0} \right)} - 1 - ik|y_0| + k|y_0|K_1(k|y_0|) + \frac{\pi ik|y_0|}{2} [I_1(k|y_0|) - L_1(k|y_0|)] - ik \int_{|y_0|}^{x_0} e^{\frac{ik}{2} \left(\lambda - \frac{y_0^2}{\lambda} \right)} d\lambda \right\} \quad (\text{A21})$$

A comparison of this result with the result given in equation (47a) of reference 1 shows that the two equations are equivalent.

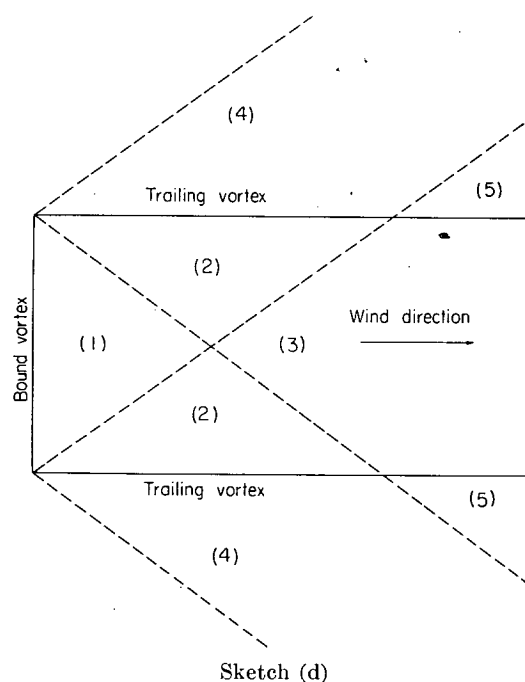
APPENDIX B

DERIVATION OF DOWNWASH FUNCTIONS ASSOCIATED WITH "HORSESHOE" VORTICES IN SUPERSONIC FLOW

The downwash associated with a vortex line can be obtained by an integration, between appropriate limits, of the kernel function $K(x_0, y_0)$ with respect to $\eta = y - y_0$. In order to perform such an integration analytically, recourse must be had to term-by-term integrations of an expanded form of $K(x_0, y_0)$. In this regard, use can be made of the expansions given in equations (36) and (38) of the analysis to obtain expanded forms of the downwash functions for vortex lines that have very good convergence properties, especially for the range of values of the parameter Mk/β^2 that would usually be of interest in applications. Expressions so obtained will be cumbersome and will require high-speed computing equipment to make them very useful.

In regard to "horseshoe" vortices in supersonic flow, there are five different significant regions in which a field point may be considered to be located (see sketch (d)).

Region (1) is between the Mach cones emanating from the end points of the bound-vortex line. The downwash at a point in this region is not affected by the trailing vortices but is created by the bound vortex alone. Therefore, the downwash is the same as would be produced by a bound vortex of infinite length and corresponds to the kernel function for two-dimensional flow discussed in the analysis. Region (2) is between the trailing-vortex lines and is within the Mach cone emanating from one end of the bound vortex but outside the Mach cone emanating from the other end. The downwash at a point in this region is created by the bound vortex and one of the trailing-vortex lines. The other trailing



vortex has no effect on the downwash. Region (3) is between the trailing-vortex lines and is within the Mach cones emanating from both ends of the bound vortex. Downwash in this region is created by the bound vortex and both trailing-vortex lines. Region (4) is outside the trailing-vortex lines and is within the Mach cone emanating from one end of

the bound vortex. The downwash is created by the bound vortex and only one of the trailing-vortex lines. Region (5) is outside the trailing-vortex line but within the Mach cones emanating from both ends of the bound vortex. The downwash is created by the bound vortex and both trailing-vortex lines.

For any of the five regions discussed in the preceding paragraph, the integral corresponding to the downwash function may be formally written, with use of equation (16b), as

$$\begin{aligned} \int_{\eta_1}^{\eta_2} K(x_0, y_0) d\eta &= -\frac{2}{Vl} \left[e^{-\frac{M^2 k x_0}{\beta^2}} \oint_{\eta_1}^{\eta_2} \frac{\frac{\beta^2}{Mk} \frac{\partial}{\partial x_0} + \frac{i}{M}}{y_0^2} U(x_0 - \beta|y_0|) \sin\left(\frac{Mk}{\beta^2} \sqrt{x_0^2 - \beta^2 y_0^2}\right) d\eta + \right. \\ &\quad \left. \frac{k}{M} e^{-ikx_0} \oint_{\eta_1}^{\eta_2} \frac{d\eta}{y_0^2} \int_{\beta|y_0|}^{x_0} e^{-\frac{ik\lambda}{\beta^2}} U(\lambda - \beta|y_0|) \sin\left(\frac{Mk}{\beta^2} \sqrt{\lambda^2 - \beta^2 y_0^2}\right) d\lambda \right] \\ &= \frac{2\beta}{Vl} \left(e^{-\frac{iM^2 k x_0}{\beta^2}} I_3 + \frac{k}{M} e^{-ikx_0} I_4 \right) \end{aligned} \quad (B1)$$

where use of the substitution $\beta y_0 = \zeta$ gives

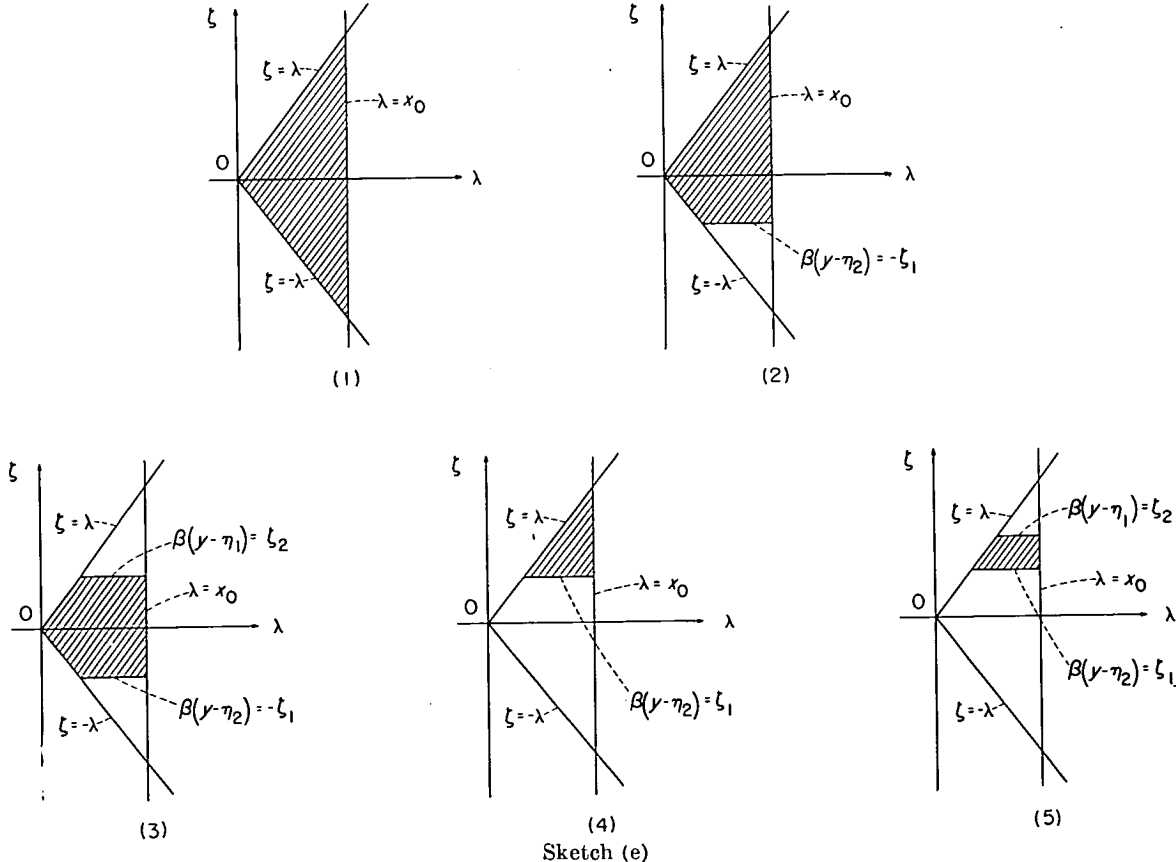
$$\begin{aligned} I_3 &= \frac{1}{\beta} \oint_{\eta_1}^{\eta_2} \frac{\frac{\beta^2}{Mk} \frac{\partial}{\partial x_0} + \frac{i}{M}}{y_0^2} U(x_0 - \beta|y_0|) \sin\left(\frac{Mk}{\beta^2} \sqrt{x_0^2 - \beta^2 y_0^2}\right) d\eta \\ &= \int_{\beta(y-\eta_2)}^{\beta(y-\eta_1)} \left(\frac{\beta^2}{Mk} \frac{\partial}{\partial x_0} + \frac{i}{M} \right) \frac{U(x_0 - \beta|\zeta|)}{\zeta^2} \sin\left(\frac{Mk}{\beta^2} \sqrt{x_0^2 - \zeta^2}\right) d\zeta \end{aligned} \quad (B2)$$

and

$$I_4 = \oint_{\beta(y-\eta_2)}^{\beta(y-\eta_1)} \frac{1}{\zeta^2} \left[\int_{|\zeta|}^{x_0} e^{-\frac{ik\lambda}{\beta^2}} U(\lambda - |\zeta|) \sin\left(\frac{Mk}{\beta^2} \sqrt{\lambda^2 - \zeta^2}\right) d\lambda \right] d\zeta \quad (B3)$$

In equations (B2) and (B3), a principal part—as described after equation (27) in the analysis—is to be taken when the integrations are carried across the line $\zeta=0$. The purpose now is to reduce these expressions to forms amenable to numerical evaluation. The first step in this procedure is a reduction of the expression for I_4 (eq. (B3)). The double integral in this expression can be considered as a surface integral in the $\lambda\zeta$ -plane where the order of integration is first with respect to λ and then with respect to ζ . The steps in the reduction are first to delineate the area of integration for each of the five different cases under consideration, and then to change the order of integration in the surface-integral representation of I_4 .

From the description of the different cases to be considered and by examination of the limits of integration in equations (B1), (B2), and (B3), the area of integration for the case of a field point in each of the aforementioned regions may be considered as shown by the hatched areas in the following sketches:



Expressions for I_4 for the five different regions or cases may then be expressed as simple integrals as follows:

Case (1):

$$I_4 = \int_0^{x_0} e^{-\frac{ik\lambda}{\beta^2}} F(\lambda, -\lambda) d\lambda \quad (B4)$$

Case (2):

$$I_4 = \int_0^{\xi_1} e^{-\frac{ik\lambda}{\beta^2}} F(\lambda, -\lambda) d\lambda + \int_{\xi_1}^{x_0} e^{-\frac{ik\lambda}{\beta^2}} F(\lambda, -\xi_1) d\lambda \quad (B5)$$

Case (3):

$$I_4 = \int_0^{\xi_1} e^{-\frac{ik\lambda}{\beta^2}} F(\lambda, -\lambda) d\lambda + \int_{\xi_1}^{\xi_2} e^{-\frac{ik\lambda}{\beta^2}} F(\lambda, -\xi_1) d\lambda + \int_{\xi_2}^{x_0} e^{-\frac{ik\lambda}{\beta^2}} F(\xi_2, -\xi_1) d\lambda \quad (B6)$$

Case (4):

$$I_4 = \int_{\xi_1}^{x_0} e^{-\frac{ik\lambda}{\beta^2}} F(\lambda, \xi_1) d\lambda \quad (B7)$$

Case (5):

$$I_4 = \int_{\xi_1}^{\xi_2} e^{-\frac{ik\lambda}{\beta^2}} F(\lambda, \xi_1) d\lambda + \int_{\xi_2}^{x_0} e^{-\frac{ik\lambda}{\beta^2}} F(\xi_2, \xi_1) d\lambda \quad (B8)$$

The expression

$$F(\lambda, -\lambda) = \int_{-\lambda}^{\lambda} \frac{U(\lambda - |\zeta|)}{\zeta^2} \sin \frac{Mk}{\beta^2} \sqrt{\lambda^2 - \zeta^2} d\zeta \quad (B9)$$

is evaluated in the text in connection with the derivative of the two-dimensional kernel function and is found to reduce (see eq. (47)) to

$$F(\lambda, -\lambda) = \frac{\pi Mk}{\beta^2} U(\lambda) J_0 \left(\frac{Mk}{\beta^2} \lambda \right) \quad (B10)$$

The F -function for other arguments can be obtained by substituting appropriate limits in an integration by parts of $F(\lambda, -\xi_1)$, namely (see the development following eq. (41) in the analysis):

$$\begin{aligned} F(\lambda, -\xi_1) &= \int_{-\xi_1}^{\lambda} \frac{U(\lambda - |\zeta|)}{\zeta^2} \sin \frac{Mk}{\beta^2} \sqrt{\lambda^2 - \zeta^2} d\zeta \\ &= -\frac{1}{\xi_1} U(\lambda - |\xi_1|) \sin \frac{Mk}{\beta^2} \sqrt{\lambda^2 - \xi_1^2} \Big|_{-\xi_1}^{\lambda} - \frac{Mk}{\beta^2} J_0 \left(\frac{Mk\lambda}{\beta^2} \right) U(\lambda - |\xi_1|) \sin^{-1} \frac{\xi_1}{\lambda} \Big|_{-\xi_1}^{\lambda} - \frac{Mk}{\beta^2} J_0 \left(\frac{Mk\lambda}{\beta^2} \right) \int_{-\xi_1}^{\lambda} \frac{\zeta}{|\zeta|} \delta(\lambda - |\zeta|) \sin^{-1} \frac{\zeta}{\lambda} d\zeta - \\ &\quad \frac{Mk}{\beta^2} \sum_{n=1}^{\infty} \frac{(-1)^n}{n} J_{2n} \left(\frac{Mk\lambda}{\beta^2} \right) \left[U(\lambda - |\xi_1|) \sin \left(2n \sin^{-1} \frac{\xi_1}{\lambda} \right) \Big|_{-\xi_1}^{\lambda} + \int_{-\xi_1}^{\lambda} \frac{\zeta}{|\zeta|} \delta(\lambda - |\zeta|) \sin \left(2n \sin^{-1} \frac{\zeta}{\lambda} \right) d\zeta \right] \end{aligned} \quad (B11)$$

After the first term on the right-hand side of equation (B11) has been expanded by comparison with the expansion given in equation (38) of the analysis and the limits of integration have been substituted, this expression may be written as

$$\begin{aligned} F(\lambda, -\xi_1) &= \frac{\pi Mk}{\beta^2} U(\lambda) J_0 \left(\frac{Mk\lambda}{\beta^2} \right) - U(\lambda - |\xi_1|) \left\{ \frac{Mk}{\beta^2} J_0 \left(\frac{Mk\lambda}{\beta^2} \right) \sin^{-1} \frac{\xi_1}{\lambda} + \sum_{n=1}^{\infty} \left[\frac{2(-1)^{n-1}}{\xi_1} J_{2n-1} \left(\frac{Mk\lambda}{\beta^2} \right) \cos \left[(2n-1) \sin^{-1} \frac{\xi_1}{\lambda} \right] + \right. \right. \\ &\quad \left. \left. \frac{Mk}{\beta^2} \frac{(-1)^n}{n} J_{2n} \left(\frac{Mk\lambda}{\beta^2} \right) \sin \left(2n \sin^{-1} \frac{\xi_1}{\lambda} \right) \right] \right\} \end{aligned} \quad (B12)$$

Substitution of ξ_2 for λ in the limits of equation (B11) gives

$$\begin{aligned} F(\xi_2, -\xi_1) &= -U(\lambda - |\xi_2|) \left\{ \frac{Mk}{\beta^2} J_0 \left(\frac{Mk\lambda}{\beta^2} \right) \sin^{-1} \frac{\xi_2}{\lambda} + \sum_{n=1}^{\infty} \left[\frac{2(-1)^{n-1}}{\xi_2} J_{2n-1} \left(\frac{Mk\lambda}{\beta^2} \right) \cos \left[(2n-1) \sin^{-1} \frac{\xi_2}{\lambda} \right] + \right. \right. \\ &\quad \left. \left. \frac{Mk}{\beta^2} \frac{(-1)^n}{n} J_{2n} \left(\frac{Mk\lambda}{\beta^2} \right) \sin \left(2n \sin^{-1} \frac{\xi_2}{\lambda} \right) \right] \right\} - U(\lambda - |\xi_1|) \left\{ \frac{Mk}{\beta^2} J_0 \left(\frac{Mk\lambda}{\beta^2} \right) \sin^{-1} \frac{\xi_1}{\lambda} + \right. \\ &\quad \left. \sum_{n=1}^{\infty} \left[\frac{2(-1)^{n-1}}{\xi_1} J_{2n-1} \left(\frac{Mk\lambda}{\beta^2} \right) \cos \left[(2n-1) \sin^{-1} \frac{\xi_1}{\lambda} \right] + \frac{Mk}{\beta^2} \frac{(-1)^n}{n} J_{2n} \left(\frac{Mk\lambda}{\beta^2} \right) \sin \left(2n \sin^{-1} \frac{\xi_1}{\lambda} \right) \right] \right\} \end{aligned} \quad (B13)$$

If $-\zeta_1$ is replaced by ζ_1 in the limits of equation (B11), then

$$F(\lambda, \zeta_1) = \frac{\pi M k}{\beta^2} U(\lambda) J_0 \left(\frac{M k \lambda}{\beta^2} \right) +$$

$$U(\lambda - |\zeta_1|) \left\{ \frac{M k}{\beta^2} J_0 \left(\frac{M k \lambda}{\beta^2} \right) \sin^{-1} \frac{\zeta_1}{\lambda} + \right.$$

$$\sum_{n=1}^{\infty} \left[\frac{2(-1)^{n-1}}{\zeta_1} J_{2n-1} \left(\frac{M k \lambda}{\beta^2} \right) \cos \left[(2n-1) \sin^{-1} \frac{\zeta_1}{\lambda} \right] + \right.$$

$$\left. \frac{M k (-1)^n}{\beta^2 n} J_{2n} \left(\frac{M k \lambda}{\beta^2} \right) \sin \left(2n \sin^{-1} \frac{\zeta_1}{\lambda} \right) \right] \} \quad (\text{B14})$$

Substitution of ζ_2 for λ and ζ_1 for $-\zeta_1$ in equation (B11) gives

$$F(\zeta_2, \zeta_1) = -U(\lambda - |\zeta_2|) \left\{ \frac{M k}{\beta^2} J_0 \left(\frac{M k \lambda}{\beta^2} \right) \sin^{-1} \frac{\zeta_2}{\lambda} + \right.$$

$$\sum_{n=1}^{\infty} \left[\frac{2(-1)^{n-1}}{\zeta_2} J_{2n-1} \left(\frac{M k \lambda}{\beta^2} \right) \cos \left[(2n-1) \sin^{-1} \frac{\zeta_2}{\lambda} \right] + \right.$$

$$\left. \frac{M k (-1)^n}{\beta^2 n} J_{2n} \left(\frac{M k \lambda}{\beta^2} \right) \sin \left(2n \sin^{-1} \frac{\zeta_2}{\lambda} \right) \right] \} +$$

$$U(\lambda - |\zeta_1|) \left\{ \frac{M k}{\beta^2} J_0 \left(\frac{M k \lambda}{\beta^2} \right) \sin^{-1} \frac{\zeta_1}{\lambda} + \right.$$

$$\sum_{n=1}^{\infty} \left[\frac{2(-1)^{n-1}}{\zeta_2} J_{2n-1} \left(\frac{M k \lambda}{\beta^2} \right) \cos \left[(2n-1) \sin^{-1} \frac{\zeta_2}{\lambda} \right] + \right.$$

$$\left. \frac{M k (-1)^n}{\beta^2 n} J_{2n} \left(\frac{M k \lambda}{\beta^2} \right) \sin \left(2n \sin^{-1} \frac{\zeta_1}{\lambda} \right) \right] \} \quad (\text{B15})$$

When equation (B10) and equations (B12) to (B15) are substituted into equations (B4) to (B8), respectively; they give the reduced forms of I_4 for the five cases under consideration.

After the reduction of I_4 , the corresponding reduction of I_3 is considered. As may be found by examination of the expression for I_3 (eq. (B2)) and the sketches showing the areas of integration for the different cases, reductions of I_3 corresponding to those of I_4 can be obtained from the F -functions (eqs. (B10) to (B15)). Results for the different cases may be expressed as follows:

Case (1):

$$I_3 = \lim_{\lambda \rightarrow x_0} \left(\frac{\beta^2}{M k} \frac{\partial}{\partial \lambda} + \frac{i}{M} \right) F(\lambda, -\lambda) \quad (\text{B16})$$

Case (2):

$$I_3 = \lim_{\lambda \rightarrow x_0} \left(\frac{\beta^2}{M k} \frac{\partial}{\partial \lambda} + \frac{i}{M} \right) F(\lambda, -\zeta_1) \quad (\text{B17})$$

Case (3):

$$I_3 = \lim_{\lambda \rightarrow x_0} \left(\frac{\beta^2}{M k} \frac{\partial}{\partial \lambda} + \frac{i}{M} \right) F(\zeta_2, -\zeta_1) \quad (\text{B18})$$

Case (4):

$$I_3 = \lim_{\lambda \rightarrow x_0} \left(\frac{\beta^2}{M k} \frac{\partial}{\partial \lambda} + \frac{i}{M} \right) F(\lambda, \zeta_1) \quad (\text{B19})$$

Case (5):

$$I_3 = \lim_{\lambda \rightarrow x_0} \left(\frac{\beta^2}{M k} \frac{\partial}{\partial \lambda} + \frac{i}{M} \right) F(\zeta_2, \zeta_1) \quad (\text{B20})$$

When the expressions for I_3 (eqs. (B16) to (B20)) and I_4 (eqs. (B4) to (B8)) that are associated with each particular case are substituted into equation (B1), expressions for the downwash at each of the five significant field-point locations may be obtained in terms of the F -functions (eqs. (B10) to (B15)) as follows:

Case (1):

$$\int_{\eta_1}^{\eta_2} K(x_0, y_0) d\eta = -\frac{2\beta}{l} \left[e^{-\frac{iM^2 k x_0}{\beta^2}} \lim_{\lambda \rightarrow x_0} \left(\frac{\beta^2}{M k} \frac{\partial}{\partial \lambda} + \frac{i}{M} \right) F(\lambda, -\lambda) + \right. \\ \left. \frac{k}{M} e^{-ikx_0} \int_0^{x_0} e^{-\frac{ik\lambda}{\beta^2}} F(\lambda, -\lambda) d\lambda \right] \quad (\text{B21})$$

Case (2):

$$\int_{\eta_1}^{\eta_2} K(x_0, y_0) d\eta = -\frac{2\beta}{l} \left\{ e^{-\frac{iM^2 k x_0}{\beta^2}} \lim_{\lambda \rightarrow x_0} \left(\frac{\beta^2}{M k} \frac{\partial}{\partial \lambda} + \frac{i}{M} \right) F(\lambda, -\zeta_1) + \right. \\ \left. \frac{k}{M} e^{-ikx_0} \left[\int_0^{\zeta_1} e^{-\frac{ik\lambda}{\beta^2}} F(\lambda, -\lambda) d\lambda + \int_{\zeta_1}^{x_0} e^{-\frac{ik\lambda}{\beta^2}} F(\lambda, -\zeta_1) d\lambda \right] \right\} \quad (\text{B22})$$

Case (3):

$$\int_{\eta_1}^{\eta_2} K(x_0, y_0) d\eta = -\frac{2\beta}{l} \left\{ e^{-\frac{iM^2 k x_0}{\beta^2}} \lim_{\lambda \rightarrow x_0} \left(\frac{\beta^2}{M k} \frac{\partial}{\partial \lambda} + \frac{i}{M} \right) F(\zeta_2, -\zeta_1) + \right. \\ \left. \frac{k}{M} e^{-ikx_0} \left[\int_0^{\zeta_1} e^{-\frac{ik\lambda}{\beta^2}} F(\lambda, -\lambda) d\lambda + \int_{\zeta_1}^{\zeta_2} e^{-\frac{ik\lambda}{\beta^2}} F(\lambda, -\zeta_1) d\lambda + \int_{\zeta_2}^{x_0} e^{-\frac{ik\lambda}{\beta^2}} F(\zeta_2, -\zeta_1) d\lambda \right] \right\} \quad (\text{B23})$$

Case (4):

$$\int_{\eta_1}^{\eta_2} K(x_0, y_0) d\eta = -\frac{2\beta}{l} \left\{ e^{-\frac{iM^2 k x_0}{\beta^2}} \lim_{\lambda \rightarrow x_0} \left(\frac{\beta^2}{M k} \frac{\partial}{\partial \lambda} + \frac{i}{M} \right) F(\lambda, \zeta_1) + \right. \\ \left. \frac{k}{M} e^{-ikx_0} \int_{\zeta_1}^{x_0} e^{-\frac{ik\lambda}{\beta^2}} F(\lambda, \zeta_1) d\lambda \right\} \quad (\text{B24})$$

Case (5):

$$\int_{\eta_1}^{\eta_2} K(x_0, y_0) d\eta = -\frac{2\beta}{l} \left\{ e^{-\frac{iM^2 k x_0}{\beta^2}} \lim_{\lambda \rightarrow x_0} \left(\frac{\beta^2}{M k} \frac{\partial}{\partial \lambda} + \frac{i}{M} \right) F(\zeta_2, \zeta_1) + \right. \\ \left. \frac{k}{M} e^{-ikx_0} \left[\int_{\zeta_1}^{\zeta_2} e^{-\frac{ik\lambda}{\beta^2}} F(\lambda, \zeta_1) d\lambda + \int_{\zeta_2}^{x_0} e^{-\frac{ik\lambda}{\beta^2}} F(\zeta_2, \zeta_1) d\lambda \right] \right\} \quad (\text{B25})$$

The results for case (1) (eq. (B21)) agree with results obtained for the two-dimensional kernel function given in equation (49) of the analysis.

REFERENCES

1. Watkins, Charles E., Runyan, Harry L., and Woolston, Donald S.: On the Kernel Function of the Integral Equation Relating the Lift and Downwash Distributions of Oscillating Finite Wings in Subsonic Flow. NACA Rep. 1234, 1955. (Supersedes NACA TN 3131.)
2. Falkner, V. M.: The Calculation of Aerodynamic Loading on Surfaces of Any Shape. R. & M. No. 1910, British A.R.C., Aug. 1943.
3. Multhopp, H.: Die Berechnung der Auftriebsverteilung von Tragflügeln. Luftfahrtforschung, Bd. 15, Lfg. 4, Apr. 6, 1938, pp. 153-169. (Available as R.T.P. Translation No. 2392, British M.A.P.)
4. Possio, Camillo: Aerodynamic Forces on an Oscillating Profile in a Compressible Fluid at Sub-Sonic Speed. Air Ministry Translation No. 830, British A.R.C., Nov. 24, 1938. (From Volume Commemorative del XXV Annuale del Laboratorio de Aeronautica del R. Politecnico di Torino. Turin 14-17, Oct. 1937, pp. 152-169.)
5. Schade, [Th.]: Numerische Lösung der Possioschen Integralgleichung der schwingenden Tragfläche in ebener Unterschallströmung. I.—Analytischer Teil. UM Nr. 3209, Deutsche Luftfahrtforschung (Berlin-Adlershof), 1944.
6. Jones, W. P.: The Calculation of Aerodynamic Derivative Coefficients for Wings of Any Plan Form in Non-Uniform Motion. R. & M. No. 2470, British A.R.C., 1946.
7. Watkins, Charles E.: Effect of Aspect Ratio on the Air Forces and Moments of Harmonically Oscillating Thin Rectangular Wings in Supersonic Potential Flow. NACA Rep. 1028, 1951.
8. Nelson, Herbert C., Rainey, Ruby A., and Watkins, Charles E.: Lift and Moment Coefficients Expanded to the Seventh Power of Frequency for Oscillating Rectangular Wings in Supersonic Flow and Applied to a Specific Flutter Problem. NACA TN 3076, 1954.
9. Watkins, Charles E., and Berman, Julian H.: Air Forces and Moments on Triangular and Related Wings With Subsonic Leading Edges Oscillating in Supersonic Potential Flow. NACA Rep. 1099, 1952.
10. Nelson, Herbert C.: Lift and Moment on Oscillating Triangular and Related Wings With Supersonic Edges. NACA TN 2494, 1951.
11. Stewartson, K.: On Linearized Potential Theory of Unsteady Supersonic Motion. Quarterly Jour. Mech. and Appl. Math., vol. III, pt. 2, June 1950, pp. 182-199.
12. Miles, John W.: The Oscillating Rectangular Airfoil at Supersonic Speeds. NAVORD Rep. 1170, NOTS 226, U. S. Naval Ordnance Test Station (Inyokern, Calif.), July 21, 1949.
13. Schlichting, H.: Airfoil Theory at Supersonic Speed. NACA TM 897, 1939.
14. Küssner, H. G.: General Airfoil Theory. NACA TM 979, 1941.
15. Garrick, I. E., and Rubinow, S. I.: Theoretical Study of Air Forces on an Oscillating or Steady Thin Wing in a Supersonic Main Stream. NACA Rep. 872, 1947. (Supersedes NACA TN 1383.)
16. Van der Pol, Balth., and Bremmer, H.: Operational Calculus Based on the Two-Sided Laplace Integral. Cambridge Univ. Press, 1950.
17. Magnus, Wilhelm, and Oberhettinger, Fritz: Formulas and Theorems for the Special Functions of Mathematical Physics. Chelsea Pub. Co. (New York), 1949.
18. Watson, G. N.: A Treatise on the Theory of Bessel Functions. Second ed., The Macmillan Co., 1944.
19. Schwarz, L.: Untersuchung einiger mit den Zylinderfunktionen nullter Ordnung verwandter Funktionen. Luftfahrtforschung, Bd. 20, Lfg. 12, Feb. 8, 1944, pp. 341-372.

REPORT 1258

A WIND-TUNNEL TEST TECHNIQUE FOR MEASURING THE DYNAMIC ROTARY STABILITY DERIVATIVES AT SUBSONIC AND SUPERSONIC SPEEDS¹

By BENJAMIN H. BEAM

SUMMARY

A method is described for measuring the dynamic stability derivatives of a model airplane in a wind tunnel. The characteristic features of this system are that single-degree-of-freedom oscillations were used to obtain combinations of rolling, yawing and pitching motions; that the oscillations were excited and controlled by velocity feedback which permitted operation under conditions unfavorable for more conventional types of oscillatory testing; and that data processing was greatly simplified by using analog computer elements in the strain-gage circuitry.

The system described is primarily for measurement of the damping derivatives C_{l_p} (damping in roll), $C_{m_q} + C_{m_{\dot{\alpha}}}$ (damping in pitch), $C_{n_r} - C_{n_{\dot{\beta}}}$ (damping in yaw), and the cross derivatives $C_{l_r} - C_{l_{\dot{\beta}}}$ (rolling moment due to yawing) and C_{n_p} (yawing moment due to rolling). The method of testing also permits measurement under oscillatory conditions of the static derivatives $C_{l_{\beta}}$ (rolling moment due to sideslip), $C_{n_{\beta}}$ (yawing moment due to sideslip), and $C_{m_{\alpha}}$ (pitching moment due to angle of attack). All these derivatives are of particular importance in estimating the short-period oscillatory motions of a rigid airplane.

A small number of experimental data are included to illustrate the general scope of results obtainable with this system.

INTRODUCTION

One important problem in the dynamic motions of airplanes is the nature and the stability of the oscillatory modes. In measuring the dynamic stability derivatives which apply to these motions there are certain advantages in employing oscillation methods in a wind tunnel, and the development of such methods has always been attractive to investigators. Most of the early measurements of damping in pitch were made from oscillation tests of a model in a wind tunnel. Damping in roll and damping in yaw have also been measured in this way but, in general, experimental difficulties have prevented the wide application of this method to the lateral motions. This is particularly true in the case of the cross derivatives, yawing moment due to rolling, and rolling moment due to yawing, although in one recently developed method (ref. 1) the yawing moment due to rolling has been successfully measured using a two-degree-of-freedom oscillatory technique.

Most of the studies of the lateral derivatives have been made on the basis of steady turning or rolling motions. Theoretical calculations of the derivatives are largely based on this assumption. The steady turning or rolling flow technique has been used in the systematic studies of the lateral derivatives in the Langley stability tunnel (e. g., refs. 2 and 3). Curved or rolling flight is approximated in the test section of this wind tunnel by causing the air to follow a curved or spiral path past a fixed model. At high speeds, the rolling derivatives have been measured by steadily rotating a sting-mounted model in a wind tunnel with a dynamometer and measuring the damping in roll, yawing moment due to rolling, and the side force due to rolling. These methods and other techniques have been described and referred to in various NACA publications on the stability derivatives for airplane and missile configurations.

The purpose of this report is to describe an oscillation technique for measuring the lateral and longitudinal dynamic stability derivatives in a wind tunnel. It was developed primarily for testing at high subsonic or supersonic speeds and for this reason three features are believed to be of special interest. One of these is the single-degree-of-freedom oscillatory system in which various components of pitch, roll, and yaw were obtained by varying the axis of oscillation. Second, the forcing system comprised a feedback loop in which velocity feedback was used to excite and control the amplitude of the model oscillation. A third feature is a system of strain-gage data processing in which electronic analog computer elements were used in measuring the amplitude and phase position of the oscillatory strain-gage deflections. The advice and assistance of the Ames instrument development branch was extremely valuable in developing this system of data processing.

The test apparatus is capable of measuring the moment derivatives which arise from angular motions of the airplane. This includes the rotary damping derivatives C_{l_p} , $C_{m_q} + C_{m_{\dot{\alpha}}}$, and $C_{n_r} - C_{n_{\dot{\beta}}}$; the cross derivatives C_{n_p} and $C_{l_r} - C_{l_{\dot{\beta}}}$; and the displacement derivatives $C_{l_{\beta}}$, $C_{n_{\beta}}$, and $C_{m_{\alpha}}$. These derivatives are of particular importance in estimating the short-period oscillatory motions of a rigid airplane.

Two systems of axes are used in this analysis. The stability system of axes with the positive directions of moments and angles referred to this system are illustrated in figure 1. The oscillation axes used for wind-tunnel measurements

¹ Supersedes NACA TN 3347 entitled "A Wind-Tunnel Test Technique for Measuring the Dynamic Rotary Stability Derivatives Including the Cross Derivatives at High Mach Numbers," by Benjamin H. Beam, 1955.

are illustrated in figure 2 and defined with respect to the stability axes by a set of direction cosines. Primes are used with aerodynamic moment and axis designations referred to the oscillation system of axes.

The various stability derivatives are defined as follows:

$$\begin{array}{ll}
 C_{l_p} = \frac{2}{\rho V^2 S b} \frac{\partial L}{\partial \frac{pb}{2V}} & C_{l_{\dot{\beta}}} = \frac{2}{\rho V^2 S b} \frac{\partial L}{\partial \frac{\dot{\beta} b}{2V}} \\
 C_{n_p} = \frac{2}{\rho V^2 S b} \frac{\partial N}{\partial \frac{pb}{2V}} & C_{n_{\dot{\beta}}} = \frac{2}{\rho V^2 S b} \frac{\partial N}{\partial \frac{\dot{\beta} b}{2V}} \\
 C_{l_r} = \frac{2}{\rho V^2 S b} \frac{\partial L}{\partial \frac{rb}{2V}} & C_{l'_\sigma} = \frac{2}{\rho V^2 S b} \frac{\partial L'}{\partial \sigma} \\
 C_{n_r} = \frac{2}{\rho V^2 S b} \frac{\partial N}{\partial \frac{rb}{2V}} & C_{m'_\sigma} = \frac{2}{\rho V^2 S b} \frac{\partial M'}{\partial \sigma} \\
 C_{m_q} = \frac{2}{\rho V^2 S \bar{c}} \frac{\partial M}{\partial \frac{q\bar{c}}{2V}} & C_{n'_\sigma} = \frac{2}{\rho V^2 S b} \frac{\partial N'}{\partial \sigma} \\
 C_{m_\alpha} = \frac{2}{\rho V^2 S \bar{c}} \frac{\partial M}{\partial \alpha} & C_{l'_\sigma} = \frac{2}{\rho V^2 S b} \frac{\partial L'}{\partial \frac{\dot{\sigma} b}{2V}} \\
 C_{m_{\dot{\alpha}}} = \frac{2}{\rho V^2 S \bar{c}} \frac{\partial M}{\partial \frac{\dot{\alpha} \bar{c}}{2V}} & C_{m'_\sigma} = \frac{2}{\rho V^2 S b} \frac{\partial M'}{\partial \frac{\dot{\sigma} b}{2V}} \\
 C_{l_{\dot{\beta}}} = \frac{2}{\rho V^2 S b} \frac{\partial L}{\partial \dot{\beta}} & C_{n'_\sigma} = \frac{2}{\rho V^2 S b} \frac{\partial N'}{\partial \frac{\dot{\sigma} b}{2V}} \\
 C_{n_{\dot{\beta}}} = \frac{2}{\rho V^2 S b} \frac{\partial N}{\partial \dot{\beta}} &
 \end{array}$$

The following symbols are used in the report:

A, B, \dots	direction cosines between primed and unprimed axes
H, J	axes
I	moment or product of inertia, depending on subscript, positive where negative moment results from positive acceleration, slug-ft ²
K	mechanical spring constant, positive where negative moment results from positive deflection, ft-lb/radian
L	aerodynamic rolling moment, ft-lb
M	aerodynamic pitching moment, ft-lb
N	aerodynamic yawing moment, ft-lb
P	mechanical damping-moment coefficient, positive where negative moment results from positive velocity, ft-lb sec/radian
R	resistance, ohms
S	wing area, sq ft
T	torque, ft-lb
V	air velocity, ft/sec
b	wing span, ft
\bar{c}	mean aerodynamic chord, ft
e	voltage, volts
f	frequency of sinusoidal oscillation, cps
g	transfer function, $\frac{\text{output}}{\text{input}}$
i	galvanometer current, amp

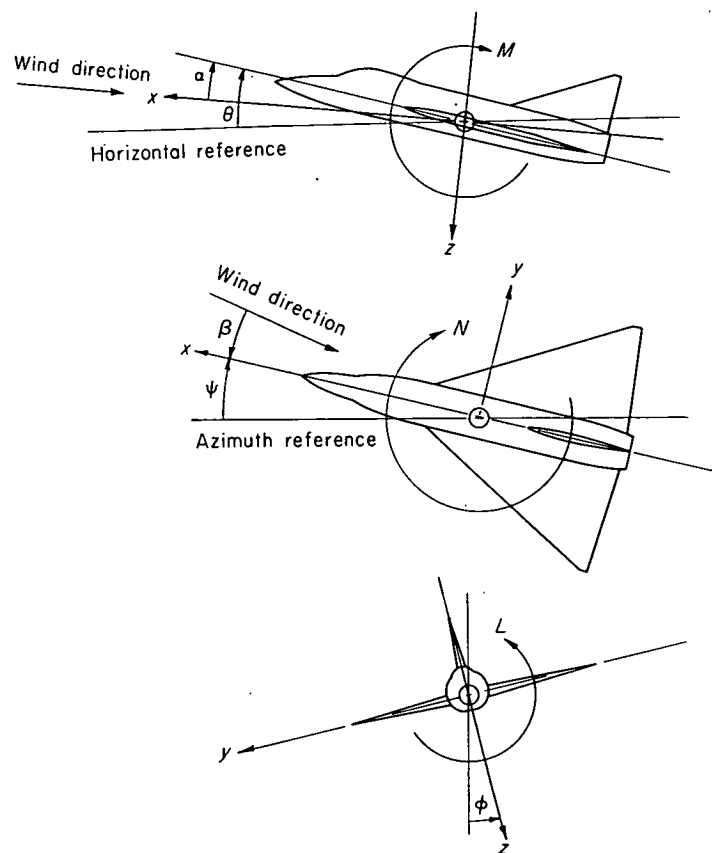


FIGURE 1.—The stability system of axes is an orthogonal system of axes having its origin at the center of gravity and in which the z axis is in the plane of symmetry and perpendicular to the relative wind, the x axis is in the plane of symmetry and perpendicular to the z axis, and the y axis is perpendicular to the plane of symmetry. Arrows indicate the positive directions of motions and moments.

k	strain-gage calibration constant, amp/volt/unit load
p	rolling velocity, radians/sec
q	pitching velocity, radians/sec
r	yawing velocity, radians/sec
t	time, sec
x, y, z	stability system of axes, defined in figure 1
x', y', z'	system of axes used for oscillation tests, defined with respect to the stability axes by the direction cosines
α	angle of attack, radians
α_m	mean or static angle of attack, deg
β	angle of sideslip, radians except where noted
θ	pitch angle, radians
ϕ	roll angle, radians
ψ	yaw angle, radians
σ	angle of rotation of model about x' axis, radians except where noted
ϵ	small angular displacement about y' or z' axis, radians
η, λ	direction angles, defined in figure 2, deg
μ, ν, ξ	phase angles of σ , T_x' , and ϵ_y' with respect to an arbitrary reference
ρ	air density, slugs/cu ft
ω	circular frequency of oscillation, $2\pi f$, radians/sec

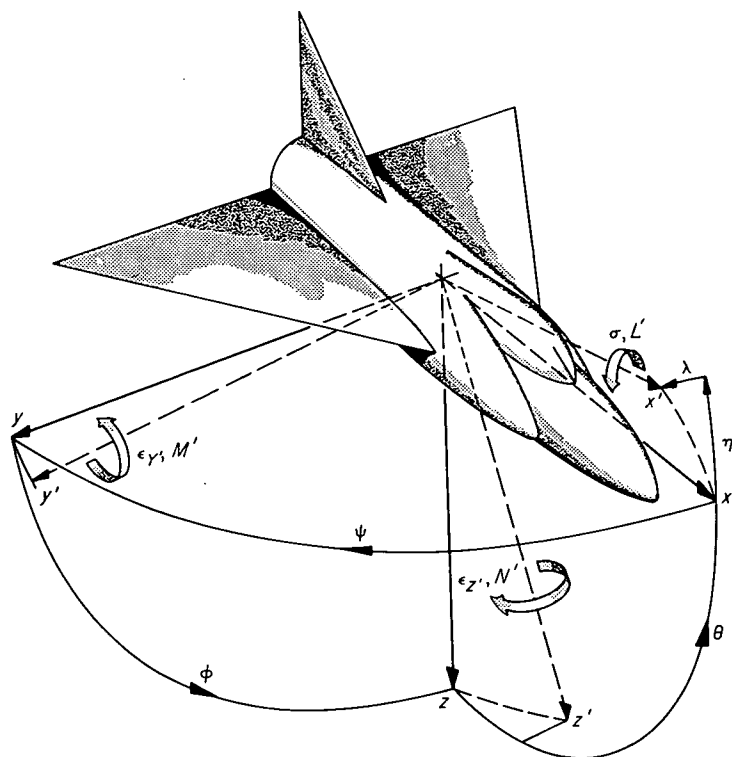


FIGURE 2.—The orientation of the oscillation axes, the x', y', z' system, is obtained by assuming an orthogonal system which is originally coincident with the stability system at zero angle of attack and with the same positive directions for forces, moments, and motions as being successively rotated about the y axis by an angle η and the x axis by an angle λ .

ω_o	wind-off circular frequency of oscillations, radians/sec
$(\dot{})$	$\frac{d()}{dt}$
$(\ddot{})$	$\frac{d^2()}{dt^2}$
$(\bar{})$	maximum value of a sinusoidally oscillating quantity ()
$\Delta()$	incremental value of a quantity ()

Subscripts define the particular axis or motion to which the general symbol applies.

THEORY

SINGLE-DEGREE-OF-FREEDOM OSCILLATORY SYSTEM

The general dynamic motion of a rigid airplane with no moving control surfaces requires six differential equations. Three of these define translation and three define rotation about the center of gravity. If the center of gravity of a model airplane is fixed in a wind tunnel, the equations involving translation can be eliminated and the motion is defined in terms of rotary motions and derivatives by three equations. The system can be further restrained so that rotation occurs about one arbitrary fixed axis only. In this case the motion is defined by one equation even though simultaneous rolling, pitching, and yawing motions may be involved.

Assume an orthogonal coordinate system, the $x'y'z'$ system (fig. 2), the origin of which is at the center of gravity of the model airplane and in which rotation of the model is always

about the x' axis. Equilibrium requires that the summation of the moments about the $x', y',$ and z' axes be equal to zero. The equation for small angular oscillations about a static equilibrium condition can be written in terms of a single variable

$$-I_{x'x'}\ddot{\sigma} - P_{x'}\dot{\sigma} - K_{x'}\sigma + \Delta L' + T_{x'} = 0 \quad (1)$$

The sign convention of figure 2 requires that if $I_{x'x'}$, $P_{x'}$, and $K_{x'}$ are considered positive quantities, their respective moments must be prefixed by a negative sign since they oppose the motion. The quantity $\Delta L'$ is the sum of all aerodynamic moments about the axis of oscillation arising from angular deflection, velocity, acceleration, etc., about the static equilibrium condition. The aerodynamic moments due to angular acceleration and higher-order terms are generally neglected in stability calculations, permitting the assumption that

$$\Delta L' = \frac{\partial L'}{\partial \sigma} \sigma + \frac{\partial L'}{\partial \dot{\sigma}} \dot{\sigma} \quad (2)$$

$$= \frac{1}{2} \rho V^2 S b \left(\frac{b}{2V} C_{l'_\sigma} \dot{\sigma} + C_{l'_\sigma} \sigma \right) \quad (3)$$

and equation (1) could be written

$$I_{x'x'}\ddot{\sigma} + \left(P_{x'} - \frac{1}{4} \rho V S b^2 C_{l'_\sigma} \right) \dot{\sigma} + \left(K_{x'} - \frac{1}{2} \rho V^2 S b C_{l'_\sigma} \right) \sigma = T_{x'} \quad (4)$$

It is apparent from the left-hand side of equation (4) that $C_{l'_\sigma}$ is an aerodynamic damping coefficient and that a negative value of $C_{l'_\sigma}$ would result in a positively damped oscillation. A negative value of the coefficient $C_{l'_\sigma}$ would result in a positive restoring moment about the axis of oscillation. The sign convention is thus parallel to that of the stability derivatives about the stability axes.

Equations expressing the equilibrium of moments about the y' and z' axes for small oscillations about the x' axis can also be written

$$-I_{x'y'}\ddot{\sigma} + \Delta M' - K_{y'}\epsilon_{y'} = 0 \quad (5)$$

$$-I_{x'z'}\ddot{\sigma} + \Delta N' - K_{z'}\epsilon_{z'} = 0 \quad (6)$$

Equations (5) and (6) can be written in this simple form only if $\epsilon_{y'}$ and $\epsilon_{z'}$ are sufficiently small compared with σ that their effects are negligible in equations (1), (5), and (6) except for the terms $K_{y'}\epsilon_{y'}$ and $K_{z'}\epsilon_{z'}$. This is accomplished by limiting $\epsilon_{y'}$ and $\epsilon_{z'}$ to very small values but making $K_{y'}$ and $K_{z'}$ very large. In other words, the model would be relatively easy to deflect about the x' axis but very stiff about the y' and z' axes. From a development similar to that of equations (3) and (4) it can be shown that

$$-I_{x'y'}\ddot{\sigma} + \frac{1}{2} \rho V^2 S b \left(\frac{b}{2V} C_{m'_\sigma} \dot{\sigma} + C_{m'_\sigma} \sigma \right) = K_{y'}\epsilon_{y'} \quad (7)$$

$$-I_{x'z'}\ddot{\sigma} + \frac{1}{2} \rho V^2 S b \left(\frac{b}{2V} C_{n'_\sigma} \dot{\sigma} + C_{n'_\sigma} \sigma \right) = K_{z'}\epsilon_{z'} \quad (8)$$

The values of the aerodynamic coefficients in equations (4), (7), and (8) will change with the orientation of the oscillation axes in the wind tunnel and the attitude of the model with respect to the air stream. These changes are related to

changes in magnitude and relative contribution of the stability derivatives, ordinarily measured about the stability axes defined in figure 1. The geometric relation between the oscillation system of axes (the $x'y'z'$ system) and the stability axes (the xyz system) is completely defined by the direction cosines between the two systems. These can be symbolized in the following matrix form

$$\begin{array}{c|ccc} & x' & y' & z' \\ \hline x & A & D & G \\ \hline y & B & E & H \\ \hline z & C & F & J \end{array} \quad (9)$$

where, for example, the cosine of the angle between the y and z' axes is H .

The numerical evaluation of these direction cosines is somewhat complicated since the stability axes do not remain fixed with respect to the oscillation axes as the angle of attack is changed, as is apparent from a study of figures 1 and 2. It will be shown later in the appendix that certain simplifications are possible in numerical calculations by a less direct approach through a set of model axes. Since, however, in the present discussion the direction cosines are considered only in symbolic form, it is not necessary to introduce this additional step.

Small angular motions about the axis of oscillation can be resolved into component motions of roll, pitch, and yaw about the stability axes. The relative magnitude of each component depends on the direction cosine between the x' axis and the roll, pitch, or yaw axes, and, with the approximations $\sin \sigma = \sigma$, $\cos \sigma = 1$

$$\left. \begin{array}{ll} \Delta\varphi = A\sigma & \dot{\varphi} = p = A\dot{\sigma} \\ \Delta\theta = B\sigma & \dot{\theta} = q = B\dot{\sigma} \\ \Delta\psi = C\sigma & \dot{\psi} = r = C\dot{\sigma} \end{array} \right\} \quad (10)$$

The moments about the stability axes can be expressed in terms of the aerodynamic stability derivatives

$$\Delta L = \frac{1}{2} \rho V^2 S b \left[\frac{b}{2V} (C_{l_p} \dot{\varphi} + C_{l_r} \dot{\psi} + C_{l_{\dot{\beta}}} \dot{\beta}) + C_{l_{\beta}} (\Delta\beta) \right] \quad (11)$$

$$\Delta M = \frac{1}{2} \rho V^2 S \bar{c} \left[\frac{\bar{c}}{2V} (C_{m_q} \dot{\theta} + C_{m_{\dot{\alpha}}} \dot{\alpha}) + C_{m_{\alpha}} (\Delta\alpha) \right] \quad (12)$$

$$\Delta N = \frac{1}{2} \rho V^2 S b \left[\frac{b}{2V} (C_{n_p} \dot{\varphi} + C_{n_r} \dot{\psi} + C_{n_{\dot{\beta}}} \dot{\beta}) + C_{n_{\beta}} (\Delta\beta) \right] \quad (13)$$

For straight flight, as in the wind tunnel, $\alpha = \theta$ and $\beta = -\psi$. The aerodynamic moments can then be referred back to the oscillation system of axes through the direction cosines.

$$\Delta L' = A(\Delta L) + B(\Delta M) + C(\Delta N) \quad (14)$$

$$\Delta M' = D(\Delta L) + E(\Delta M) + F(\Delta N) \quad (15)$$

$$\Delta N' = G(\Delta L) + H(\Delta M) + J(\Delta N) \quad (16)$$

Thus, the aerodynamic moments indicated in equations (1), (5), and (6) for oscillation about an arbitrary axis are defined in terms of moments about the stability axes by equations (14), (15), and (16). The aerodynamic coefficients which depend on the angular velocity of the model can be derived in terms of the stability derivatives as

$$C_{l'_{\dot{\sigma}}} = \frac{2}{\rho V^2 S b} \frac{\partial L'}{\partial \dot{\sigma}} = A^2 C_{l_p} + AC (C_{n_p} + C_{l_r} - C_{l_{\dot{\beta}}}) + B^2 \frac{\bar{c}^2}{b^2} (C_{m_q} + C_{m_{\dot{\alpha}}}) + C^2 (C_{n_r} - C_{n_{\dot{\beta}}}) \quad (17)$$

$$C_{m'_{\dot{\sigma}}} = ADC_{l_p} + CD (C_{l_r} - C_{l_{\dot{\beta}}}) + EB \frac{\bar{c}^2}{b^2} (C_{m_q} + C_{m_{\dot{\alpha}}}) + AFC_{n_p} + FC (C_{n_r} - C_{n_{\dot{\beta}}}) \quad (18)$$

$$C_{n'_{\dot{\sigma}}} = AGC_{l_p} + CG (C_{l_r} - C_{l_{\dot{\beta}}}) + HB \frac{\bar{c}^2}{b^2} (C_{m_q} + C_{m_{\dot{\alpha}}}) + AJC_{n_p} + CJ (C_{n_r} - C_{n_{\dot{\beta}}}) \quad (19)$$

Those coefficients which depend on displacement of the model become

$$C_{l'_{\sigma}} = \frac{2}{\rho V^2 S b} \frac{\partial L'}{\partial \sigma} = -ACC_{l_{\beta}} + B^2 \frac{\bar{c}}{b} C_{m_{\alpha}} - C^2 C_{n_{\beta}} \quad (20)$$

$$C_{m'_{\sigma}} = -DCC_{l_{\beta}} + EB \frac{\bar{c}}{b} C_{m_{\alpha}} - FCC_{n_{\beta}} \quad (21)$$

$$C_{n'_{\sigma}} = -GCC_{l_{\beta}} + HB \frac{\bar{c}}{b} C_{m_{\alpha}} - JCC_{n_{\beta}} \quad (22)$$

In equation (17) $C_{l'_{\dot{\sigma}}}$ is the aerodynamic damping coefficient measured about the axis of oscillation in the wind tunnel. If the x' axis coincides with the x axis, the oscillation would be pure roll. In this case $A^2 = 1$ and $AC = B^2 = C^2 = 0$ so the measured damping coefficient would be C_{l_p} , the damping-in-roll coefficient. Similarly, a pure pitching or yawing oscillation would result in the measurement of damping in pitch or damping in yaw.

In general, one stability derivative can be obtained from each separate physical measurement. In equations (17), (18), and (19) there are eight stability derivatives which depend on angular velocity; however, these derivatives form only five independent terms. The derivative C_{m_q} always appears with $C_{m_{\dot{\alpha}}}$ in the above since, for the pure rotary motions considered, \dot{q} is always equal to $\dot{\alpha}$. (See ref. 4.) Similarly, since $r = -\dot{\beta}$ in a test of this type, $C_{l_r} - C_{l_{\dot{\beta}}}$ appears as one term and $C_{n_r} - C_{n_{\dot{\beta}}}$ as another. The evaluation of these five terms (C_{l_p} , C_{n_p} , $C_{m_q} + C_{m_{\dot{\alpha}}}$, $C_{l_r} - C_{l_{\dot{\beta}}}$, and $C_{n_r} - C_{n_{\dot{\beta}}}$) requires five unique measurements.

Equations (17), (18), and (19) can be considered in a purely formal way as the basis for a system of equations containing the unknown stability derivatives. Assuming that five values of $C_{l'_{\dot{\sigma}}}$, $C_{m'_{\dot{\sigma}}}$, or $C_{n'_{\dot{\sigma}}}$ are available from wind-tunnel measurements, along with the appropriate direction cosines for the axes about which the measurements were

made, a system of five equations could be formed. These equations could then be solved simultaneously for the five stability derivatives, providing the equations are mathematically determinate.

The necessary values of $C_{l'_\sigma}$, $C_{m'_\sigma}$, or $C_{n'_\sigma}$ which lead to the velocity derivatives and $C_{l'_\sigma}$, $C_{m'_\sigma}$, or $C_{n'_\sigma}$ which lead to the static derivatives are obtained from physical measurements of the model oscillation through equations (4), (7), and (8). Measurements can be made of the frequency of oscillation ω , the input torque T_x , the oscillation amplitude σ , and the small angular deflections ϵ_y and ϵ_z . There is considerable latitude in the choice of axes of oscillation and the particular quantities to be measured within the general confines of mathematical determinateness of the stability derivatives. Note, however, that ϵ_y and ϵ_z are inherently more difficult to measure than σ . The small displacements and high stiffness required about the y' and z' axes to maintain the validity of equations (4), (7), and (8) impose a limitation on the accuracy of measurements about these axes. Friction, backlash, and interaction become of increasing importance as the displacement is reduced. Some measurements must be made in conjunction with large static pitching moments or aerodynamic disturbances of a random nature and these factors will affect the design of the apparatus and the accuracy of the system. These factors, and the methods used to relate the measurements of T_x , ω , σ , ϵ_y and ϵ_z to the derivatives $C_{l'_\sigma}$, $C_{n'_\sigma}$, etc., are discussed in subsequent sections. The direction cosines which relate the derivatives $C_{l'_\sigma}$, $C_{n'_\sigma}$, etc., to the various stability derivatives in equations (17) through (22) are given in the appendix.

FEEDBACK CONTROL

As indicated in the preceding section, measurement of the aerodynamic derivatives depends upon an analysis of a single-degree-of-freedom oscillation defined by equation (4) repeated here for convenience.

$$I_{xx}\ddot{\sigma} + \left(P_x - \frac{1}{4}\rho V S b^2 C_{l'_\sigma}\right)\dot{\sigma} + \left(K_x - \frac{1}{2}\rho V^2 S b C_{l'_\sigma}\right)\sigma = T_x \quad (4)$$

In the case of a free oscillation T_x would become zero and the oscillation would be a damped sinusoid. Use of this method is generally limited to test conditions which would not result in oscillatory instability as there is no control over the amplitude once the oscillation is initiated.

For the forced oscillation T_x in equation (4) is a sinusoidal function of time. One case of interest is where the frequency of the applied torque corresponds to the undamped natural frequency of the oscillatory system. At this frequency the inertia moments balance the restoring moments and the final amplitude after the decay of initial transients corresponds to a balance between the damping moments and the applied torque. The maximum angular velocity of oscillation can be obtained with a minimum of input torque at this frequency, as the entire input is used to overcome the damping. It is thus a desirable operating point both from the standpoint of power requirements and accuracy in measuring the damping.

One disadvantage with the forced-oscillation system operating at the resonant frequency is that, as with the free-oscillation system, testing cannot be conducted where oscillatory instability is encountered. At high Mach numbers and high angles of attack where minor changes in test conditions may produce changes in the aerodynamic derivatives, a steady-state oscillation is very difficult to maintain. In situations such as this, feedback control of the oscillation should be considered as it provides a means for automatically stabilizing the amplitude and the frequency of the oscillation for any variation of damping, either positive or negative, within the capacity of the forcing system.

The system of feedback control used in the present apparatus evolved from unsuccessful experiments with the forced-oscillation technique described above at high subsonic Mach numbers. After the development of the feedback system it was found that Bratt, Raymer, and Miles in England had used a similar technique in 1942 but the results of their experiments are not generally available. The principle of operation is similar to that of the amplitude-stabilized feedback oscillator.

The oscillatory system was formed by the moment of inertia of the model and the stiffness of the restoring springs. Torque was applied to this system in the present case through a linkage with an electromagnetic shaker. It is convenient to think of the shaker system as a transducer which converts an electrical signal input into a torque. A strain gage indicating the angular deflection of the model converted the oscillation amplitude into an electrical signal. Feedback was accomplished by using amplified voltage from the strain gage as a source of electrical signal to the shaker. Velocity feedback was used in this case and the strain-gage signal of oscillation amplitude was differentiated electronically before being introduced into the shaker.

Thus, for a system with velocity feedback

$$T_x = g\dot{\sigma} \quad (23)$$

and equation (4) could be written

$$I_{xx}\ddot{\sigma} + \left(P_x - \frac{1}{4}\rho V S b^2 C_{l'_\sigma} - g\right)\dot{\sigma} + \left(K_x - \frac{1}{2}\rho V^2 S b C_{l'_\sigma}\right)\sigma = 0 \quad (24)$$

If g and the aerodynamic derivatives are constants, equation (24) is linear. The case of interest is where

$$P_x - \frac{1}{4}\rho V S b^2 C_{l'_\sigma} - g = 0 \quad (25)$$

In this case,

$$\sigma = \bar{\sigma} e^{j\omega t} \quad (26)$$

The oscillations are sinusoidal and of constant amplitude. The oscillation frequency is the undamped natural frequency, given by

$$\omega = \sqrt{\frac{K_x - \frac{1}{2}\rho V^2 S b C_{l'_\sigma}}{I_{xx}}} \quad (27)$$

The peak amplitude of the oscillation, $\bar{\sigma}$, cannot be defined independently of initial conditions if the terms in equation

(24) are constant as assumed. Amplitude stabilization would require that the final oscillation amplitude be independent of the initial conditions in the same sense that a "limit cycle" is independent of the starting conditions in a nonlinear oscillatory system. The transfer function, g , of the feedback loop can be designed to vary with oscillation amplitude in such a way as to produce positive feedback at low amplitudes and negative feedback at high amplitudes with a limit cycle at some intermediate amplitude. This type of stabilization, however, would appear to conflict with the requirement that g and the other coefficients in equation (24) be constants for sinusoidal motion. These conflicting requirements can be satisfied within practical limits by allowing g to vary with oscillation amplitude, but at such a slow rate that it remains essentially constant through one cycle of operation.

A rudimentary circuit of a quasi-linear element which could be inserted in the feedback loop to stabilize the amplitude of oscillation is shown schematically in figure 3 (a) along with a sketch of its transfer function, figure 3 (b). The thermister is the nonlinear control element. It is characterized by a high negative temperature coefficient of resistance and as current, either alternating or direct, is passed through it the resultant heating causes its resistance to change. The thermal and heat-transfer characteristics of the thermister determine the time required to reach a new resistance following a change in current. There are many variations of the principle illustrated in figure 3 which would produce an equivalent result and which can be found in the

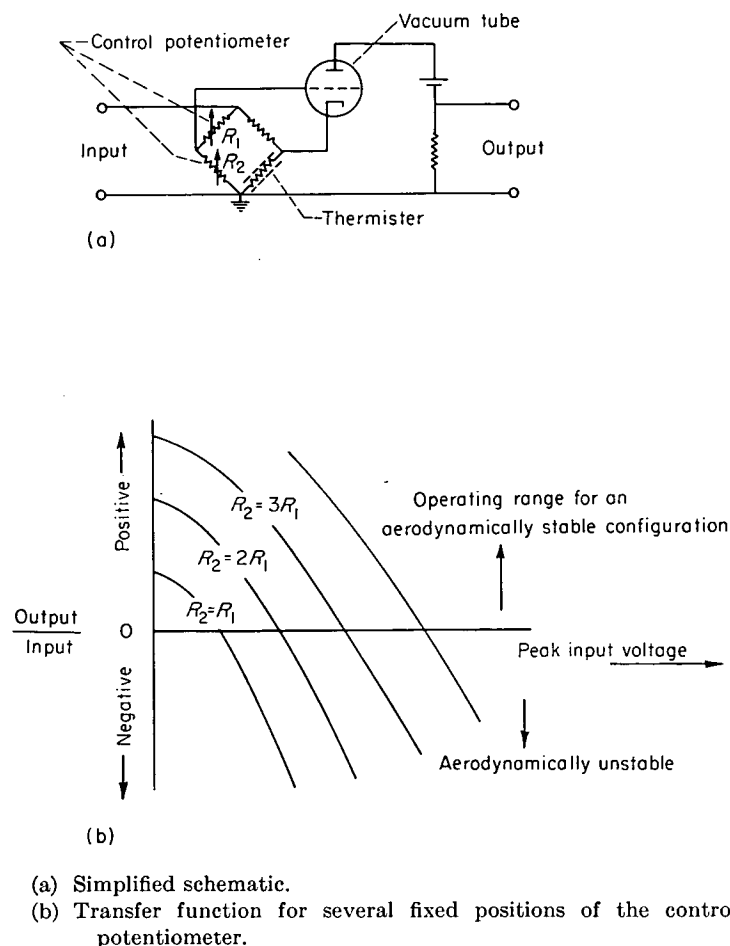


FIGURE 3.—Simplified characteristics of the amplitude-control circuit.

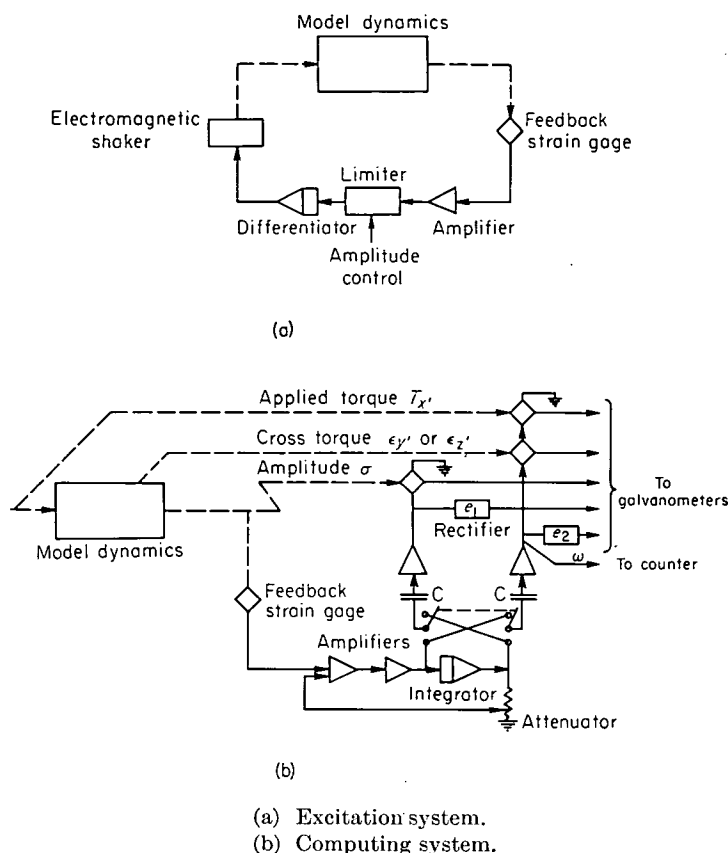


FIGURE 4.—Block diagram of the excitation and computing systems.

literature on amplitude stabilization of electronic oscillators.

A schematic diagram of the complete feedback control loop is shown in figure 4 (a). With this system the input torque, given by $g\sigma$, can be made equal and opposite to the damping moments acting on the model for any value of σ by an adjustment of the potentiometer in figure 3 (a). For amplitudes less than the desired amplitude the damping moment will be less than the applied torque and oscillations will build up from rest. For amplitudes greater than desired, the damping moments will be greater than the applied torque and oscillations will decrease. The only stable operating point is where

$$P_x - \frac{1}{4} \rho V S b^2 C_{l'_\sigma} - g = 0 \quad (28)$$

and this can be shown to apply whether the aerodynamic damping is positive or negative.

ANALOG COMPUTING SYSTEM

By use of the feedback control system described, the static derivatives C_{m_α} , C_{n_β} , and C_{l_β} can be determined from equation (27) and an accurate measurement of the change in oscillation frequency between the wind-on and wind-off test conditions. The equation for $C_{l'_\sigma}$ can be obtained from equation (27)

$$C_{l'_\sigma} = \frac{-2K_x}{\rho V^2 S b} \left[\left(\frac{\omega}{\omega_0} \right)^2 - 1 \right] \quad (29)$$

Three values of $C_{l'_\sigma}$ are required for different orientations of the axis of oscillation. Inserting these values into equation

20) with the appropriate direction cosines provides three equations for the unknowns $C_{m\alpha}$, $C_{n\beta}$, and $C_{l\beta}$.

Measurement of the velocity derivatives is more difficult. Early attempts to record the output of strain gages with an oscillograph and then to measure the amplitude and phase position of each trace proved to be an expensive and time-consuming task even with the aid of automatic digital computing equipment. The analog computing system discussed herein performs the same mathematical processes as the digital computing machine, but does so at the time the data are taken and results in a considerable saving in the time and expense devoted to data processing.

The measurements required in this case for a determination of the velocity derivatives were σ , T_x , and either ϵ_y or ϵ_z . Each of these time-varying quantities can be represented as a Fourier series in ωt by the general expression

$$F(t) = a_0 + a_1 \cos \omega t + b_1 \sin \omega t + \dots + a_n \cos n\omega t + b_n \sin n\omega t \quad (30)$$

where ω is the fundamental frequency of oscillation. Higher-order terms are always present to some degree because of buffeting of the model, wind-tunnel vibration, etc.; however, only the fundamental component in $F(t)$ is of interest. The amplitude and phase position of the fundamental can be determined from the Fourier coefficients, defined by

$$a_1 = \frac{1}{\pi} \int_{-\pi}^{\pi} F(t) \cos \omega t \, d(\omega t) \quad (31)$$

$$b_1 = \frac{1}{\pi} \int_{-\pi}^{\pi} F(t) \sin \omega t \, d(\omega t) \quad (32)$$

If strain-gage bridges are located in the oscillation apparatus in such a position as to indicate σ , T_x , and ϵ_y , the output of each gage would be proportional to the product of applied voltage and gage deflection. Introducing a voltage into each gage of $\bar{e} \cos \omega t$ results in a gage output current of

$$i = k\bar{e}F(t) \cos \omega t \quad (33)$$

As in equation (30), ω is the fundamental frequency of oscillation so that upon expanding, equation (33) becomes

$$i = k\bar{e} \left(a_0 \cos \omega t + \frac{a_1}{2} + \frac{a_1}{2} \cos 2\omega t + b_1 \sin \omega t \cos \omega t + \dots \right) \quad (34)$$

A well-damped deflection galvanometer having a time constant much greater than $\frac{2\pi}{\omega}$ will not respond to currents of fundamental frequency and above. Its deflection will be proportional to the average galvanometer current, given by

$$i_{av} = \frac{1}{2\pi} \int_0^{2\pi} i \, d(\omega t) \quad (35)$$

With equations (34) and (35), an expression for a_1 can be obtained in terms of the average galvanometer current

$$a_1 = \frac{2i_{av}}{k\bar{e}} \quad (36)$$

Wherein i_{av} and \bar{e} can be measured directly at the time of the test and k can be obtained from a static calibration of the strain gage. Similarly, b_1 can be measured using a sine wave of voltage in place of a cosine wave. The 90° phase separation between the sine and cosine voltages was obtained in this case using the input and output, respectively, of an electronic integrator. This integrator and other active components in the computing circuitry consist essentially of high gain d-c amplifiers in which the input and feedback impedances to each amplifier determine its specific function. Similar components were used in the feedback loop described previously.

A schematic diagram of the computing system used is shown in figure 4(b). The signal source for the sine and cosine voltages was the strain gage, indicating oscillation amplitude, that was used to excite the feedback loop. The reversing switch was used to apply the sine and cosine voltages alternately to each gage. These voltages were measured simultaneously with each reading by means of the rectifier circuits e_1 and e_2 and the galvanometers. The feedback loop through the attenuator was used to suppress any unusually large variations in direct current through the integrator, and the capacitors prevented this direct current from appearing at the output.

The in-phase and out-of-phase components, a_1 and b_1 , respectively, of T_x , ϵ_y , ϵ_z , and σ are used to determine the maximum amplitude and relative phase position of each. Only the component of T_x , ϵ_y , and ϵ_z in quadrature with the amplitude is required to calculate the mechanical damping and the velocity derivatives. For example, with the notation

$$\sigma = \bar{\sigma} \sin(\omega t + \mu)$$

$$T_x = \bar{T}_x \sin(\omega t + \nu)$$

$$\epsilon_y = \bar{\epsilon}_y \sin(\omega t + \xi)$$

the velocity coefficients for each oscillation condition can be calculated from equations (4) and (7) as

$$C_{l\sigma}' = \frac{4}{\rho V S b^2} \left[P_x - \frac{\bar{T}_x \sin(\nu - \mu)}{\omega \bar{\sigma}} \right] \quad (37)$$

$$C_{m\sigma}' = \frac{4}{\rho V S b^2} \frac{K_y \bar{\epsilon}_y}{\omega \bar{\sigma}} \sin(\xi - \mu) \quad (38)$$

Four values of $C_{l\sigma}'$ and one of $C_{m\sigma}'$ were required in this case which, with equations (17) and (18), yielded the five rotary derivatives C_{l_p} , C_{n_p} , $C_{m_q} + C_{m_\alpha}$, $C_{l_r} - C_{l_\beta}$, and $C_{n_r} - C_{n_\beta}$.

OPERATION

DESCRIPTION OF APPARATUS

The oscillation mechanism necessary for the dynamic tests was housed in a sting assembly which was matched to the dynamic model and the wind-tunnel model support in such a way that it was interchangeable with the stings normally used for static testing. It was thus possible to measure the static force and moment characteristics and the dynamic stability derivatives under identical test conditions.

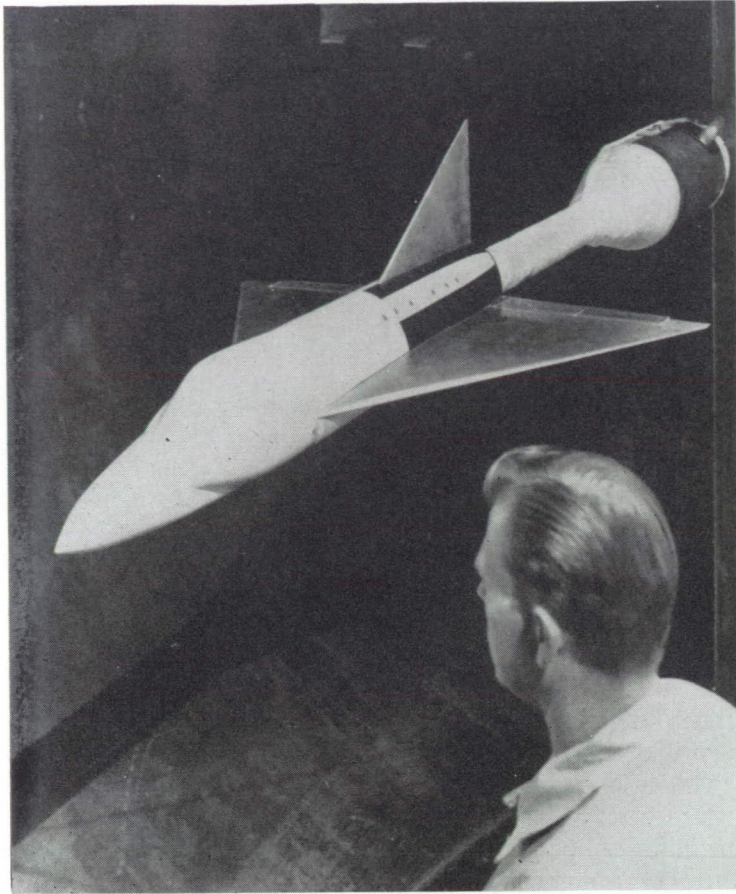


FIGURE 5.—Model airplane installed on oscillation mechanism in wind-tunnel test section.

A model airplane mounted on the oscillation equipment in the wind tunnel is shown in the photograph, figure 5. An electromagnetic shaker was housed in the enlarged portion of the sting downstream of the model airplane. Special model construction was required to obtain the necessary strength with a minimum of weight since a reduction in weight simplified many of the other design problems, particularly those relating to the supporting springs. Designed for a wing loading at high Mach numbers of approximately 400 pounds per square foot, the weight of the model in figure 5 is approximately 5 pounds per square foot of wing area.

A general view of the electronic equipment needed outside the test section is shown in the photograph, figure 6. The console on the right in the photograph is the power supply for the electromagnetic shaker housed in the model supporting sting. The panel rack on the left contains a counter for measuring frequency and the various electronic feedback and computing elements illustrated in the block diagrams, figure 4. The galvanometer and read-out system, not shown in figure 6, is the same as that normally used for static tests with a strain-gage balance.

Two oscillation mechanisms were built, one for pure pitching or yawing oscillations in which the oscillation axis was perpendicular to the longitudinal axis of the supporting sting, and one for combined rolling and pitching or rolling and yawing in which the axis of oscillation was inclined 45° to the longitudinal axis of the sting. The essential features

of these mechanisms are shown in figures 7, 8, and 9. The crossed flexure pivots position the model and provide the spring restraint for the oscillatory system. The axis at which the flexure pivots cross is the axis of oscillation. Several sets of flexure pivots of different thickness were provided which permitted testing at frequencies from approximately 3 to 10 cycles per second. Each of these mechanisms could be driven by a shaker with a reciprocating motion of the push rod.

The measurement of ϵ_y' and ϵ_z' required special consideration as these quantities are more difficult to measure than ω , T_x' , and σ because of the small deflections involved. An examination of equation (17) shows that all the stability derivatives which depend on angular velocity of the model influence the damping of the oscillation. The four groups of terms which appear in equation (17) can be resolved into measurements of ω , T_x' , and σ in a series of four tests in which all test conditions remain constant except for change in orientation of the axis of oscillation. In other words, $C_{m_q} + C_{m_{\dot{\alpha}}}$, C_{l_p} , and $C_{n_r} - C_{n_{\dot{\beta}}}$ can be resolved by measurements of damping, but only the sum of the cross derivatives $C_{n_p} + C_{l_r} - C_{l_{\dot{\beta}}}$ can be determined in this manner. At least one additional measurement of ϵ_y' or ϵ_z' , represented by equations (18) and (19), is required to resolve these two derivatives.

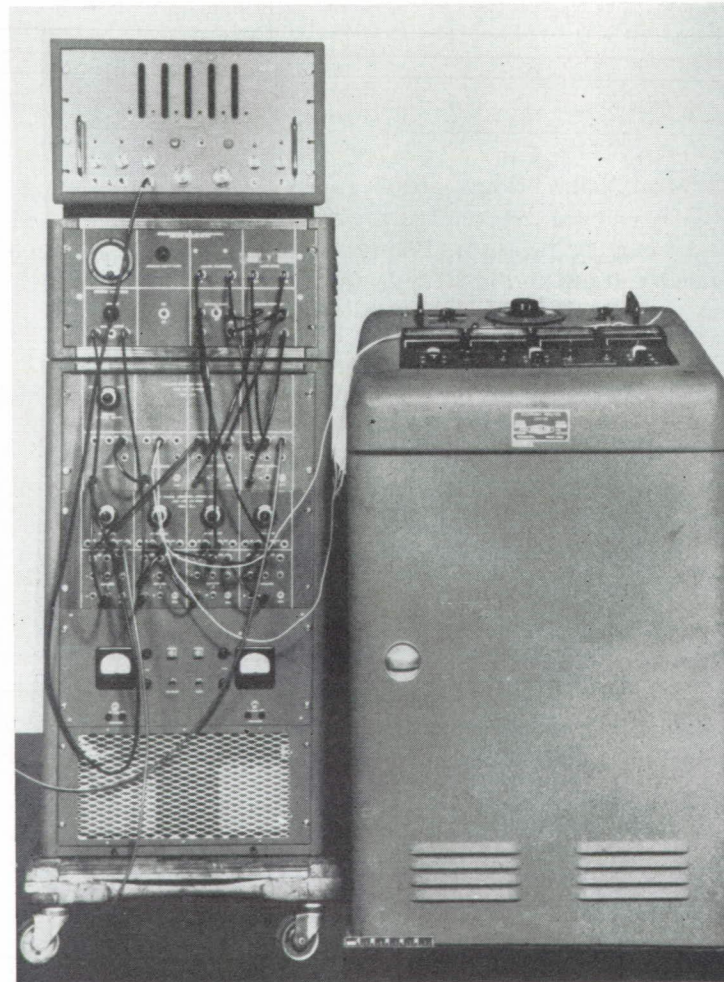


FIGURE 6.—General view of electronic feedback and computing equipment used for the oscillation tests.

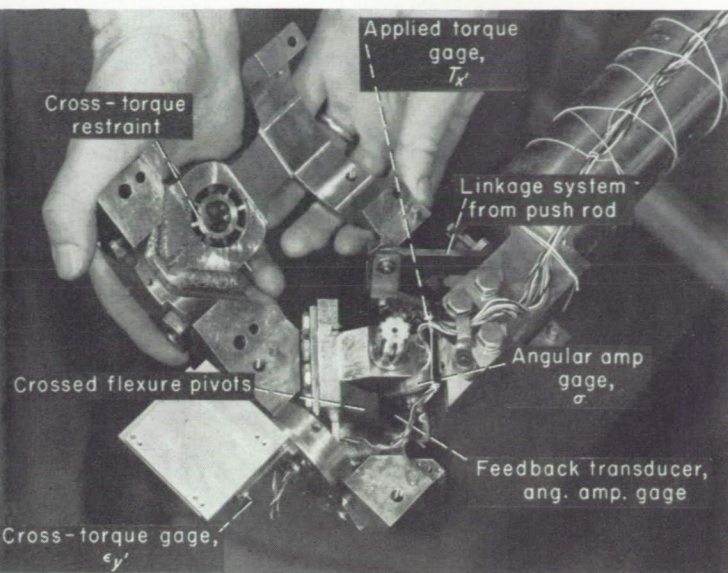


FIGURE 7.—Oscillation mechanism with oblique axes showing the cross-torque gage used in early tests.

Figure 7 represents an early version of the oscillation mechanism in which $\epsilon_{y'}$ was measured to obtain C_{n_p} in a rolling and pitching oscillation. Accuracy was expected to be a maximum here because moments due to other aerodynamic derivatives would have little effect on $\epsilon_{y'}$. This is apparent on substituting the direction cosines for a rolling and pitching oscillation from the appendix into equation (18). The strain gage indicating $\epsilon_{y'}$ was of the unbonded type since the angular deflection about the y' axis was ± 0.0005 radian or less. The deflection was held within the above limits by the radial flexures indicated as the cross-torque restraint in figure 7. This gage was used for testing only during rolling and pitching oscillations and was mechanically disconnected for other orientations.

This mechanical arrangement of the oscillation mechanism proved workable but experience gained over several months of wind-tunnel testing revealed some undesirable characteristics which could be corrected by redesign. One difficulty was due to an interaction between the cross torque and the applied torque. Analysis showed that deflections of the trunnion to which the crossed flexure pivots and the cross-torque restraint were attached could result in an indicated $\epsilon_{y'}$. It was established from a static calibration that approximately 6 percent of a moment about the x' axis was measured as a moment about the y' axis because of this interaction, and thus a correction to the measured values of $C_{m'_x}$ was necessary which amounted to approximately 6 percent of the measured values of $C_{l'_x}$.

One other difficulty with this system was due to unbalanced static aerodynamic moments, which do not appear in the dynamic equations because they remain constant, but which are also supported by the mechanism. The largest of these moments is normally the pitching moment, and the range of angles of attack for testing in the pitching mode is thus limited by the permissible angular deflection of the flexure pivots caused by the static pitching moment. It is seen that the cross derivative C_{n_p} is measured in a combined rolling and pitching mode in which the test range of angles

of attack is limited by these conditions; whereas the remaining lateral-directional derivatives are measured in a rolling and yawing mode or in a pure yawing mode and are thus not limited in angle-of-attack range by aerodynamic pitching moments.

A consideration of these features of the method for measuring C_{n_p} led to the design of an alternative arrangement in which the other cross derivative, $C_{l_r} - C_{l_{\dot{\beta}}}$, was measured. This was done by measuring the rolling moment in a yawing oscillation. This rolling moment includes a contribution from the sideslip derivative $C_{l_{\beta}}$ which at high speeds can be several times the magnitude of the moment due to $C_{l_r} - C_{l_{\dot{\beta}}}$. (The roll axis becomes the z' axis according to the convention of this report, and the moments are apparent from equations (8), (19), and (22) and the direction cosines for a yawing oscillation from the appendix.) Experience with the analog computing system, however, indicated that the accuracy of the system was adequate for separating the damping derivatives from the stiffness derivatives by their difference in phase, and that $C_{l_r} - C_{l_{\dot{\beta}}}$ could be measured in the presence of the larger moments due to $C_{l_{\dot{\beta}}}$.

An expanded view of the yawing oscillation mechanism which incorporates a cross-torque gage for measuring $C_{l_r} - C_{l_{\dot{\beta}}}$ is shown in figure 8. The z' , or cross-torque, axis lies along the longitudinal axis of the model. A strain-gage bridge for measuring $\epsilon_{z'}$ was formed consisting of two legs from each of the two unbonded strain gages shown in the photograph. Static tests showed that this gage arrangement eliminated interaction due to forces and moments about all other axes. Subsequent wind-tunnel tests showed that the lateral-directional derivatives could be measured through a wide range of angles of attack without the necessity of trimming the pitching moments. It was found that operation was fairly smooth even at high speeds and angles of attack near the stall. This improved performance was attributed to the fact that there were only slight changes in

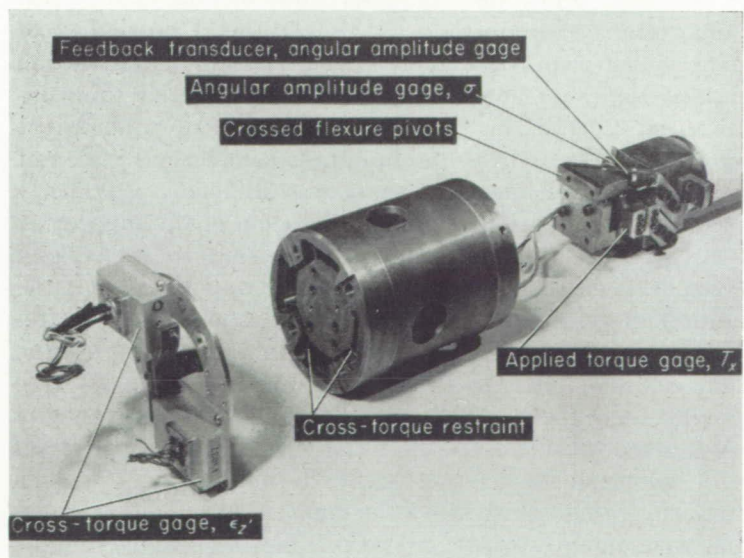


FIGURE 8.—Expanded view of a later version of the oscillation mechanism for yawing or pitching illustrating a more satisfactory method for measuring the cross torque.

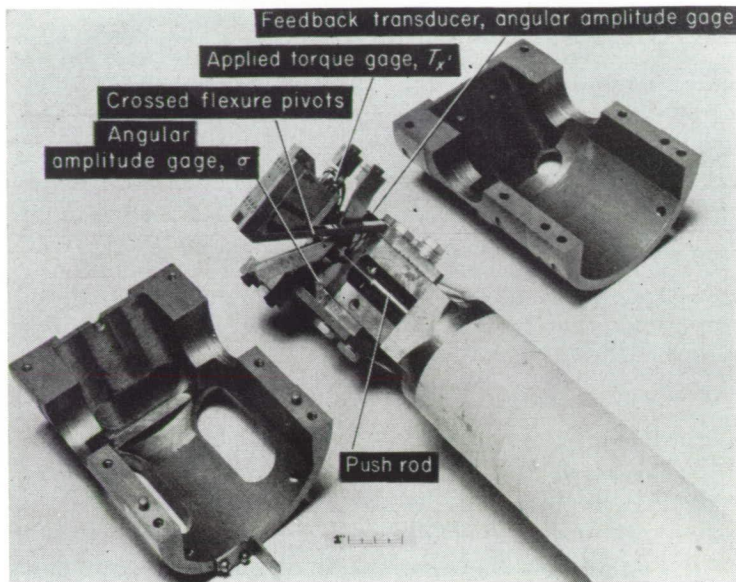


FIGURE 9.—Revised version of the mechanism illustrated in figure 7 in which the cross-torque gage has been eliminated.

effective angle of attack or lift on the wing during a yawing oscillation compared with the larger changes encountered during a pitching or rolling oscillation. This design thus proved to be superior to that shown in figure 7, and, as a result, the cross-torque gage and cross-torque restraint were eliminated from the roll and yaw oscillator as shown in figure 9.

The accuracy of the data obtained with this equipment is believed to be sufficient for most dynamic stability calculations. Errors directly assignable to the computing system are quite small, within 1 percent of the full-scale capacity and 1° of arc in the phase angle. Tare damping caused by friction and other internal effects in the model and mechanism was measured prior to each run, but this measurement was used primarily as an indication of trouble in the equipment since it was normally less than 2 percent of the full-scale capacity and was neglected in computing the derivatives. The vibration characteristics of the sting and supporting system introduced an additional possibility of error which required careful study. Calculated vibration characteristics of the support were used as a guide to evaluate the test conditions under which support vibration might affect the measured results, but these calculations were not found to be reliable because it was difficult to properly account for the various degrees of freedom of the supporting structure. In some cases it was necessary to attach guy wires between the sting and the tunnel wall to prevent the support system from vibrating at the model oscillation frequency and thus introducing errors in the measurements. In most tests, however, these objectionable frequencies were avoided and the results were the same whether the guy wires were attached to the sting or not. Through tests with independent variations in Mach number and Reynolds number, both of which affect the model oscillation frequency, and with the guy wires on and off, it was established that systematic errors due to model support vibration could be eliminated within the random error of the measurements.

The probable random error in a single measurement as a percent of the full-scale damping capacity was found to be less than $1\frac{1}{2}$ percent for both $C_{l'_\sigma}$ and $C_{n'_\sigma}$ from an analysis of repeated measurements on a typical model for Mach numbers from 0.25 up to 0.94 at zero angle of attack. The accuracy of measurement of a single derivative depends on its relation to the maximum value of $C_{l'_\sigma}$. Thus, for conventional airplane models the combined random and systematic uncertainty in a single damping derivative $C_{l'_p}$, $C_{n_r} - C_{n_\beta}$, or $C_{m_q} + C_{m_\alpha}$ would be of the order of 5 percent, with the cross derivatives, C_{n_p} and $C_{l_r} - C_{l_\beta}$, being subject to the same increment of certainty as $C_{l'_p}$ and $C_{n_r} - C_{n_\beta}$.

EXPERIMENTAL DATA

Figures 10, 11, and 12 have been prepared to illustrate the general scope of data obtainable with the oscillation apparatus described. These data were obtained at a low Mach number for the model configuration illustrated in figure 5. Similar data have been obtained at Mach numbers up to 0.95.

The effects of oscillation amplitude and reduced frequency at a selected angle of attack can be studied from measurements of the type shown in figure 10. It is sometimes desirable to measure only the effect of frequency or amplitude on certain combinations of derivatives, such as $C_{n_p} + C_{l_r} - C_{l_\beta}$ in figure 10, since this can be done with fewer measurements. These data confirm the assumption of linearity in the small oscillations of an airplane about an equilibrium

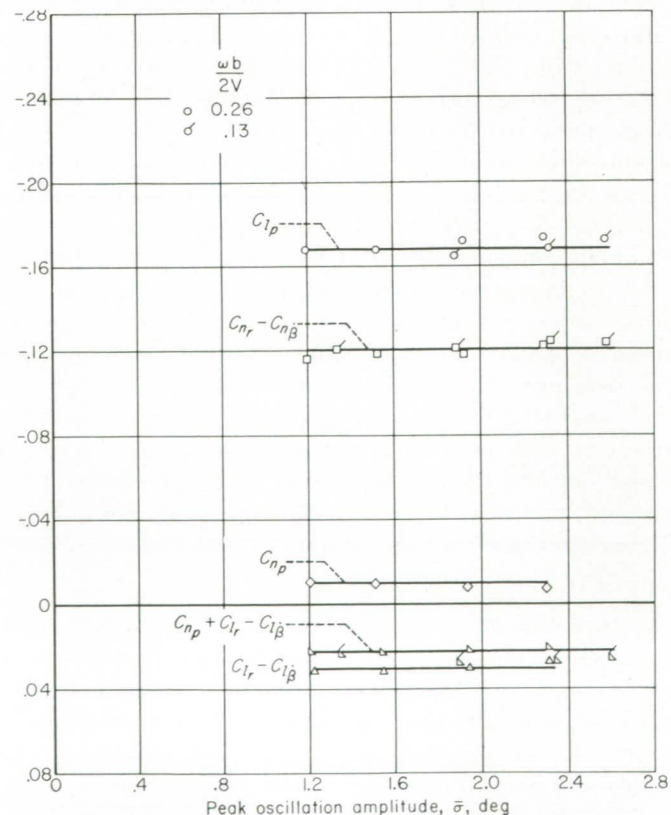


FIGURE 10.—The variation of some of the lateral stability derivatives with oscillation amplitude for two values of reduced frequency.

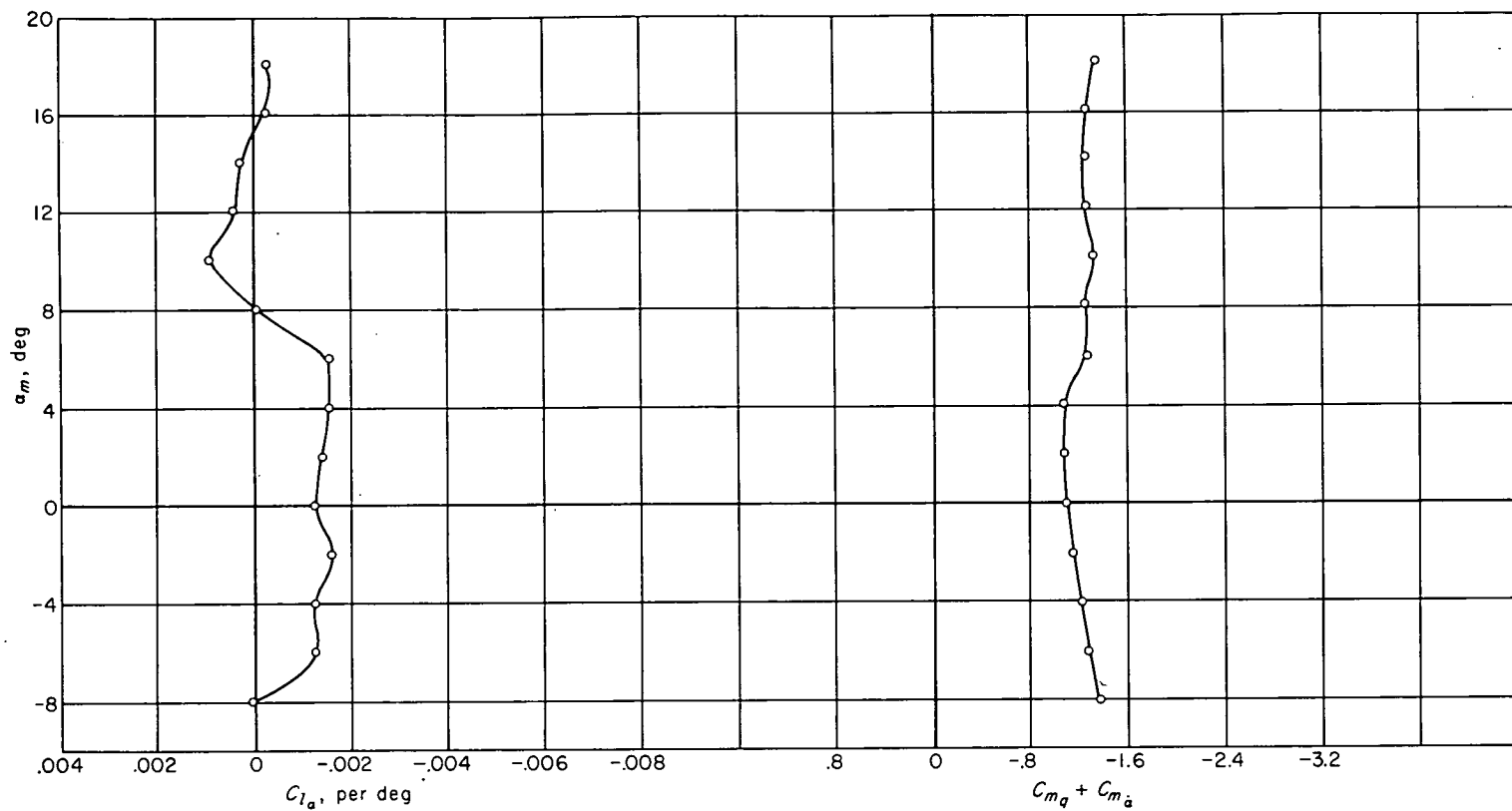


FIGURE 11. The variation of the longitudinal stability derivatives with angle of attack.

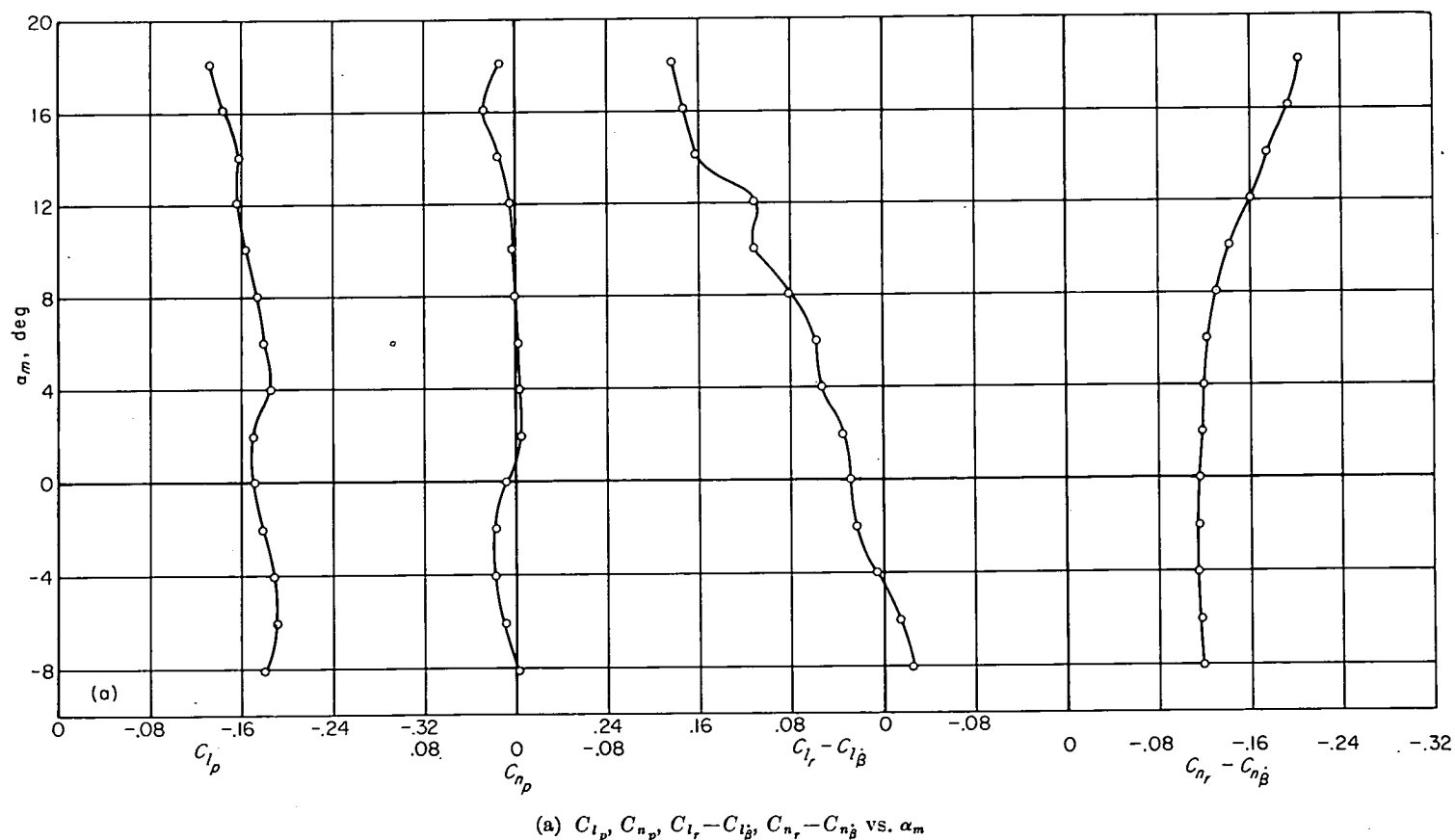


FIGURE 12.—The variation of the lateral stability derivatives with angle of attack.

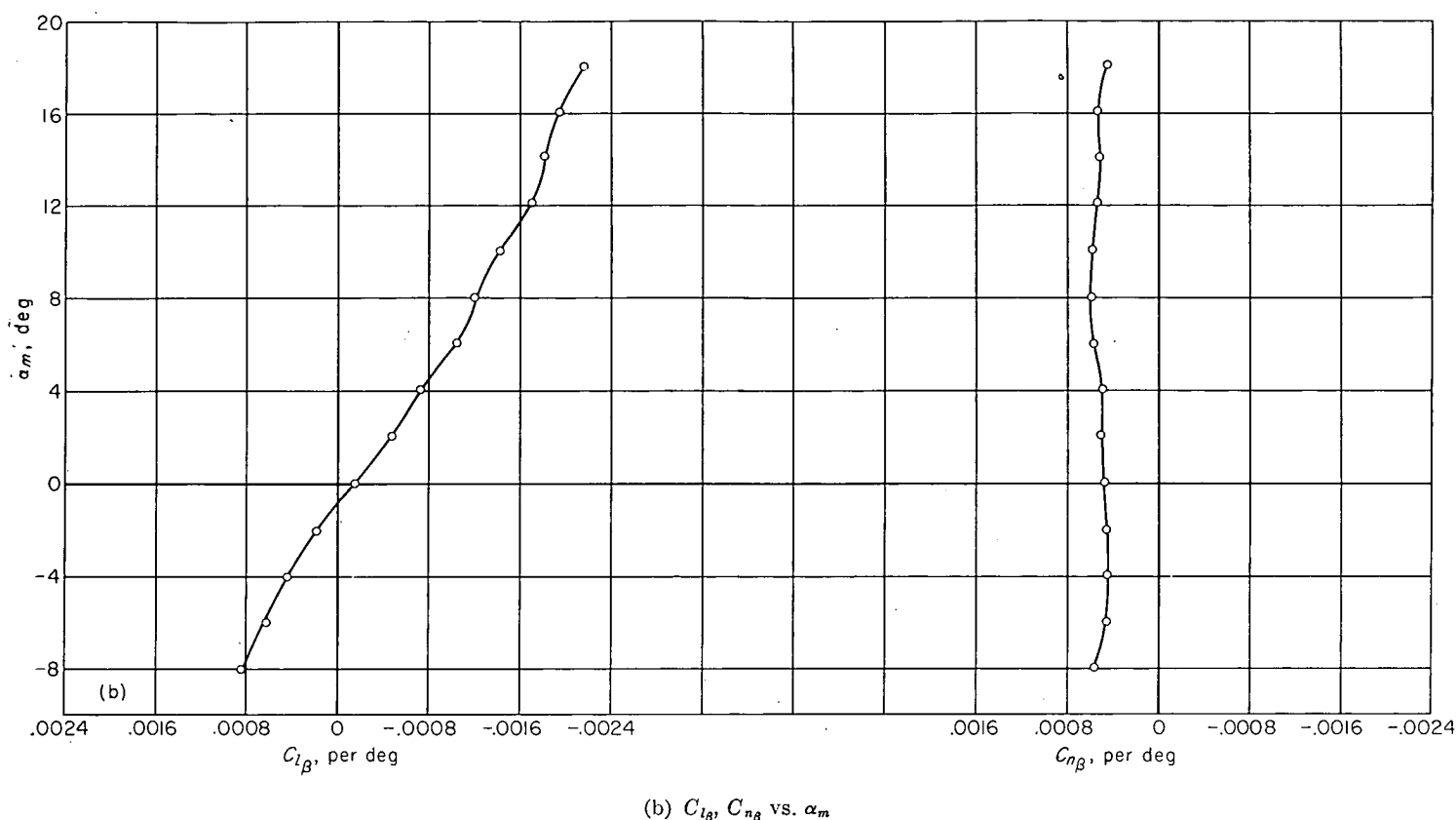


FIGURE 12.—Concluded.

librium position and indicate that the effects of frequency on the stability derivatives are negligible for the test conditions represented in figure 10.

Data of the type illustrated in figures 11 and 12 can be used to establish the variation of the stability derivatives with angle of attack for a mean oscillation amplitude and frequency as this is the form most useful in dynamic stability calculations. The data shown in figure 11, along with the lift-curve slope, are the aerodynamic parameters of primary importance in estimating the short-period dynamic longitudinal stability of an aircraft with the control surfaces fixed. The short-period motion in this case is essentially a pitching about the center of gravity combined with vertical translation. The desirability of experimentally separating $C_{m_{\alpha}}$ and C_{m_q} and evaluating other derivatives which may affect the longitudinal motion depends on the circumstances and on the precision required but, in general, the important features of the motion can be estimated without these additional aerodynamic parameters. In the stick-free case, a third degree of freedom is introduced by the elevator motion about its hinge which may markedly affect the response of the airplane and for which the aerodynamic contribution of the free control surface would have to be considered (ref. 5).

Data of the type illustrated in figure 12 can be used in calculating the dynamic lateral stability of an airplane. Analysis of the lateral oscillatory motion with the controls fixed is more complicated than in the longitudinal case because of the three degrees of freedom—rolling, yawing, and sideslipping. The aerodynamic parameters required,

in addition to those shown in figures 12 (a) and (b), are the side-force coefficients due to rolling velocity, yawing velocity, and sideslip (ref. 6). The side force due to sideslip can be measured or estimated from steady-flight considerations alone. Measured values of the side forces due to rolling velocity and yawing velocity would be desirable, but in many cases these forces are small or can be shown to have negligible effect on the motion (ref. 7). Here again, as in the case of the short-period longitudinal motion, free-control surfaces may radically alter the aircraft response (ref. 5).

Many of the suggested methods for calculating dynamic lateral stability (e. g., refs. 5, 6, and 7) do not consider the effects of sideslip velocity β because, for typical airplane configurations used in the past, these effects have been shown to be small (ref. 3). This may, however, not be the case for current and future airplane types. The effects of $C_{l_{\beta}}$ and $C_{n_{\beta}}$ on the lateral oscillatory motion can be approximated by introducing the terms $C_{l_r} - C_{l_{\beta}}$ and $C_{n_r} - C_{n_{\beta}}$ into the equations of motion (ref. 6) in place of C_{l_r} and C_{n_r} . This would indicate that, in the absence of independent measurements of $C_{l_{\beta}}$ and $C_{n_{\beta}}$, it would be desirable to obtain values of $C_{l_r} - C_{l_{\beta}}$ and $C_{n_r} - C_{n_{\beta}}$ from oscillation tests since this would approximately account for the possible effects of sideslip velocity in stability calculations.

AMES AERONAUTICAL LABORATORY,
NATIONAL ADVISORY COMMITTEE FOR AERONAUTICS,
MOFFETT FIELD, CALIF., Sept. 20, 1954.

APPENDIX

General methods are available for evaluating the direction cosines for an arbitrary rotation of one system of axes with respect to another. (See, e. g., ref. 8.) In the present case it would be most useful if the direction cosines were evaluated in terms of the angles η and λ illustrated in figure 2. The angle η represents the mechanical angle by which the axis of the crossed flexures is offset from the longitudinal axis of the sting and λ is determined by keying the oscillation apparatus to the sting in the proper rotational position. The direction cosines used in equations (17) through (22) then become

$$\left. \begin{aligned} A &= \cos \alpha_m \cos \eta - \sin \alpha_m \sin \eta \cos \lambda \\ B &= \sin \eta \sin \lambda \\ C &= -(\sin \alpha_m \cos \eta + \cos \alpha_m \sin \eta \cos \lambda) \\ D &= \sin \alpha_m \sin \lambda \\ E &= \cos \lambda \\ F &= \sin \lambda \cos \alpha_m \\ G &= \cos \alpha_m \sin \eta + \sin \alpha_m \cos \eta \cos \lambda \\ H &= -\sin \lambda \cos \eta \\ J &= -\sin \alpha_m \sin \eta + \cos \alpha_m \cos \eta \cos \lambda \end{aligned} \right\} \quad (39)$$

In the case of the velocity derivatives, a considerable simplification in the direction cosines can be obtained by referring them to a set of model axes which coincide with the stability axes at zero angle of attack. The velocity derivatives are then evaluated first about model axes for all angles of attack and then transformed to stability axes.

Inserting $\alpha_m = 0$ in the above expression for the direction cosines results in the following values for the tests discussed herein, where the double primes refer to model axes:

	Type of motion				
	Pitching	Yawing	Rolling plus pitching ¹	Rolling plus yawing	Rolling minus yawing
η	90°	90°	45°	45°	45°
λ	90°	0	90°	180°	0
A''	0	0	$\frac{1}{\sqrt{2}}$	$\frac{1}{\sqrt{2}}$	$\frac{1}{\sqrt{2}}$
B''	1	0	$\frac{1}{\sqrt{2}}$	0	0
C''	0	-1	0	$\frac{1}{\sqrt{2}}$	$-\frac{1}{\sqrt{2}}$
D''	----	----	0	----	----
E''	----	----	0	----	----
F''	----	----	1	----	----
G''	----	1	----	----	----
H''	----	0	----	----	----
J''	----	0	----	----	----

¹This mode used only in early tests (see fig. 7).

Use of these values for the direction cosines resulted in the determination of the velocity derivatives about model axes, using equation (17), (18), or (19), as explained in the section on Description of Apparatus. The transformation from model axes to stability axes was made with the following equations where the double-primed coefficients refer to model axes.

$$\left. \begin{aligned} C_{i_p} &= C_{i_p}'' \cos^2 \alpha_m + (C_{n_r}'' - C_{n_{\beta}}'') \sin^2 \alpha_m + \\ &\quad (C_{n_p}'' + C_{i_r}'' - C_{i_{\beta}}'') \sin \alpha_m \cos \alpha_m \\ C_{i_r} - C_{i_{\beta}} &= (C_{i_r}'' - C_{i_{\beta}}'') \cos^2 \alpha_m - C_{n_p}'' \sin^2 \alpha_m + \\ &\quad (C_{n_r}'' - C_{n_{\beta}}'' - C_{i_p}'') \sin \alpha_m \cos \alpha_m \\ C_{n_p} &= C_{n_p}'' \cos^2 \alpha_m - (C_{i_r}'' - C_{i_{\beta}}'') \sin^2 \alpha_m + \\ &\quad (C_{n_r}'' - C_{n_{\beta}}'' - C_{i_p}'') \sin \alpha_m \cos \alpha_m \\ C_{n_r} - C_{n_{\beta}} &= (C_{n_r}'' - C_{n_{\beta}}'') \cos^2 \alpha_m + C_{i_p}'' \sin^2 \alpha_m - \\ &\quad (C_{n_p}'' + C_{i_r}'' - C_{i_{\beta}}'') \sin \alpha_m \cos \alpha_m \\ C_{m_q} + C_{m_{\dot{\alpha}}} &= C_{m_q}'' + C_{m_{\dot{\alpha}}}'' \end{aligned} \right\} \quad (40)$$

The displacement derivatives $C_{m_{\alpha}}$, $C_{n_{\beta}}$, and $C_{i_{\beta}}$ were not evaluated by the above procedure as there was no computational advantage in this case. Equations (17) through (22) are developed about stability axes for which $\beta = -\psi$ and $\alpha = \theta$. The use of these same relations for the model axes system depends on the presence in equations (17) through (19) of the terms due to rolling velocity and the advantage in using the model axes system is that thereby certain terms are eliminated in the equations and simple solutions obtained for all angles of attack. On the other hand, the use of this relation for the displacement derivatives would require the introduction of corresponding terms due to roll deflection about model axes. It can be shown that when these terms are introduced, the resulting equations are as difficult from the computing standpoint as the direct evaluation of the displacement derivatives about stability axes; therefore, in evaluating the displacement derivatives $C_{m_{\alpha}}$, $C_{n_{\beta}}$, and $C_{i_{\beta}}$, equation (20) and the direction cosines for the stability system of axes, equation (39), were used.

It is important to note the difference between the model axes system used for equation (40) and the system of body axes used in many stability calculations. The orientation of the two systems of axes coincides but with the body axes system the sideslip angle β is defined as the angle between the relative wind and the plane of symmetry in the same manner as with the stability axes. With the approximations $\sin \sigma = \sigma$, $\cos \sigma = 1$, the sideslip angle referred to body axes would become

$$\begin{aligned} \beta &= -\psi'' \cos \alpha_m + \varphi'' \sin \alpha_m \\ &= (-C'' \cos \alpha_m + A'' \sin \alpha_m) \sigma \end{aligned}$$

This value for β could be inserted in equations (11), (13), and subsequent equations which would lead to modifications of equations (17) through (22) and these new equations would then represent the stability derivatives referred to body axes. Therefore, while there are many similarities in the two systems, the model axes system used in equation (40) is not a true system of body axes and should be considered only as a computational aid.

REFERENCES

1. Lessing, H. C., Fryer, T. B., and Mead, M. H.: A System for Measuring the Dynamic Lateral Stability Derivatives in High-Speed Wind Tunnels. NACA TN 3348, 1954.
2. MacLachlan, Robert, and Letko, William: Correlation of Two Experimental Methods of Determining the Rolling Characteristics of Unswept Wings. NACA TN 1309, 1947.
3. Bird, John D., Jaquet, Byron M., and Cowan, John W.: Effect of Fuselage and Tail Surfaces on Low-Speed Yawing Characteristics of a Swept-Wing Model as Determined in Curved-Flow Test Section of Langley Stability Tunnel. NACA TN 2483, 1951.
4. Jones, B. Melvill: Dynamics of the Airplane. Symmetric or Pitching Moments. Vol. V of Aerodynamic Theory, div. N, ch. I, sec. 40, W. F. Durand, ed., Julius Springer (Berlin), 1935, pp. 49-50.
5. Phillips, William H.: Appreciation and Prediction of Flying Qualities. NACA Rep. 927, 1949. (Supersedes NACA TN 1670.)
6. Campbell, John P., and McKinney, Marion O.: Summary of Methods for Calculating Dynamic Lateral Stability and Response and for Estimating Lateral Stability Derivatives. NACA Rep. 1098, 1952. (Supersedes NACA TN 2409.)
7. Sternfield, Leonard, and Gates, Ordway B., Jr.: A Simplified Method for the Determination and Analysis of the Neutral Lateral-Oscillatory-Stability Boundary. NACA Rep. 943, 1949. (Supersedes NACA TN 1727.)
8. Whittaker, Edmund Taylor: A Treatise on the Analytical Dynamics of Particles and Rigid Bodies, with an Introduction to the Problem of Three Bodies. Fourth ed., Dover Pub. (New York) 1944, p. 8.

REPORT 1259

SOME POSSIBILITIES OF USING GAS MIXTURES OTHER THAN AIR IN AERODYNAMIC RESEARCH ¹

By DEAN R. CHAPMAN

SUMMARY

A study is made of the advantages that can be realized in compressible-flow research by employing a substitute heavy gas in place of air. Most heavy gases considered in previous investigations are either toxic, chemically active, or (as in the case of the Freons) have a ratio of specific heats greatly different from air. The present report is based on the idea that by properly mixing a heavy monatomic gas with a suitable heavy polyatomic gas, it is possible to obtain a heavy gas mixture which has the correct ratio of specific heats and which is nontoxic, nonflammable, thermally stable, chemically inert, and comprised of commercially available components.

Calculations were made of wind-tunnel characteristics for 3 gas pairs comprising 21 different polyatomic gases properly mixed with each of three monatomic gases (argon, krypton, and xenon). For a given Mach number, Reynolds number, and tunnel pressure, a gas-mixture wind tunnel having the same specific-heat ratio as air would be appreciably smaller and would require much less power than a corresponding air wind tunnel. Analogous though different advantages can be realized in compressor research and in firing-range research.

The most significant applications, perhaps, arise through selecting and proportioning a gas mixture so as to have at ordinary wind-tunnel temperatures certain dimensionless characteristics which air at flight temperatures possesses but which air at ordinary wind-tunnel temperatures does not possess. Characteristics which involve the relaxation time (or bulk viscosity), the variation of viscosity with temperature, and the variation of specific heat with temperature fall within this category. Other applications arise in heat-transfer research since certain gas mixtures can be concocted to have any Prandtl number in the range at least between 0.2 and 0.8.

INTRODUCTION

The reasons for considering gases other than air as possible test media for compressible-flow research stem primarily from the relatively low speed of sound in certain gases. In general, the heavier the gas, the lower the speed of sound at a fixed temperature. Hence, experiments conducted at a given Mach number in a heavy gas will be conducted at lower velocity than the corresponding experiment in air. Some significant advantages of conducting wind-tunnel, firing-range, and compressor experiments at a reduced velocity have been noted previously in the work of Theo-

dorsen and Regier (ref. 1), Smelt (ref. 2), Kantrowitz (ref. 3), Huber (ref. 4), Buell (ref. 5), Donaldson (ref. 6), and von Doenhoff and Braslow (ref. 7). Some uses of gases other than air in shock tube research are discussed by Duff in reference 8. These investigations show that the substitution of a heavy gas for air offers the possibility of: (1) extending the range of existing research apparatus; (2) achieving greater economy of construction and operation of large high-speed wind tunnels; and (3) providing greater facility in obtaining data for special types of research. These advantages will be discussed briefly in the order listed.

The possibility of extending the range of existing apparatus was clearly demonstrated by the experiments of Theodorsen and Regier, which appear to be the first compressible-flow experiments in which supersonic aerodynamic data were obtained in a gas other than air. By rotating propellers in Freon 113 ($\text{CCl}_2\text{FCClF}_2$, having a speed of sound 0.39 times that of air, and a density 6.5 times as great) they were able to achieve tip Mach numbers of 2.7; whereas the highest tip Mach number achieved with the same apparatus using air was 1.0. Also, much higher Reynolds numbers were obtained. In a similar fashion, Buell employed the Freons, and Donaldson employed xenon as the test medium through which projectiles were fired in order to obtain Mach numbers much higher than could be obtained with the same apparatus by firing through air. An extended range of operation of a wind tunnel has been demonstrated by von Doenhoff and Braslow who report that the maximum attainable test-section Mach number of the Langley low-turbulence pressure tunnel was increased from 0.4 to 1.2 by replacing air with Freon 12.

A possibility of achieving greater economy by employing a substitute heavy gas in a wind tunnel arises because the test-section dimensions are smaller and the horsepower required is only a fraction of that required for an air wind tunnel operating at the same Mach number, Reynolds number, and pressure. Smelt has made a general study pointing out this possibility for various inert gases that have, unfortunately, a specific-heat ratio different from air. The importance of reduced power requirements, if accomplished without sacrifice in ratio of specific heats, needs no elaboration in view of the power of modern wind tunnels.

The third advantage mentioned, namely, facilitating certain types of aerodynamic research, arises in two separate

¹Supersedes NACA TN 3226 by Dean R. Chapman, 1954, to which various additions have been made in the present report.

ways. First, for a given Mach and Reynolds number, the use of a heavy gas with its low velocity of sound enables experiments to be conducted at lower velocity and lower pressure than if air were employed; this results, for example, in lower stresses in wind-tunnel models as well as in models launched from a gun. Similarly, the reduced velocity enables experiments on the release of objects from supersonic vehicles to be conducted at smaller scale while simulating the required value of the Froude number (U_∞^2/gl). Second, and more important, the use of certain gas mixtures other than air enables some of the dimensionless parameters pertinent to hypersonic flight through air to be simulated at the usual wind-tunnel temperatures which cannot be simulated by use of air at these wind-tunnel temperatures. Several of such possibilities are discussed later in this report.

As regards the various disadvantages involved by using substitute heavy gases in aerodynamic research, the main ones are: (1) The ratio of specific heats (γ) differs from that of air for the heavy gases proposed thus far; (2) the use of any gas other than air results in more severe practical problems of operating a research facility.² A general appraisal of the various advantages relative to disadvantages cannot be made since this would depend on each particular case. The purposes of this report are to study various heavy gas mixtures which appear satisfactory for aerodynamic testing and to evaluate the magnitude of the advantages such gases offer. Knowledge of these advantages will enable a comparison with the disadvantages to be made in a given case.

The present research was begun upon conception of the following simple idea:³ The proper ratio of specific heats ($\gamma=1.4$) can be achieved with a heavy gas by suitably mixing a heavy monatomic gas ($\gamma>1.4$) with a heavy polyatomic gas ($\gamma<1.4$). Exploitation of this simple idea turned out to be unexpectedly arduous because of difficulties involved in obtaining adequate chemical, physical, pharmacological, and thermodynamic data on the many polyatomic gases known to modern chemistry. Primarily as a result of recent developments in the field of fluorochemicals, it was possible to find among the known polyatomic gases over 30 which were indicated by available data to be sufficiently nontoxic, nonflammable, chemically inert, and thermally stable to justify consideration. Evaluation of the relative advantages of each polyatomic gas for aerodynamic testing requires calculating the thermodynamic properties from spectroscopic data, determining the proper proportions for mixing from thermodynamic properties, and then computing the density and viscosity that would result when mixed with each of three monatomic gases considered (argon, krypton, and xenon).

² A possible disadvantage sometimes expressed (e. g., ref. 9) is that the relaxation time for molecular vibrations in certain polyatomic gases would invalidate data obtained at supersonic velocities. However, for most gases considered here, this is believed not to be the case. Reasons for this are discussed later.

³ After completion of the main body of calculations, a short unpublished note by E. F. Relf, in England, became available in which the possibility of obtaining the proper ratio of specific heats through mixing gases also was pointed out. Relf made a rough estimation for a mixture of sulfur hexafluoride and xenon, which is one of the mixtures considered in the present research.

NOTATION

a	speed of sound
c	speed of light
c_p	specific heat per unit mass
C_p	specific heat per mole
CR	wind-tunnel compression ratio
g	acceleration of gravity
h	Planck's constant
H	molar enthalpy
HP	horsepower
k	Boltzman's constant
l	characteristic length of model
L	characteristic dimension of wind-tunnel test section
m	molecular weight (29 grams per mole for air)
M	Mach number
n	number of atoms per molecule
p	pressure
q	dynamic pressure, $\frac{1}{2}\rho u^2$
R	universal gas constant per mole (1.987 cal. mole ⁻¹ °K ⁻¹)
Re	Reynolds number
T	temperature
u	velocity
V	volume of gas
w	mass-flow rate, (ρu) times (cross-section area)
x	mole fraction, equal to ratio of partial pressure to mixture static pressure and equal to fraction by volume
τ	relaxation time
γ	ratio of specific heats
κ	bulk viscosity coefficient
ρ	mass density
μ	viscosity coefficient
ω	wave number (cm ⁻¹ , from spectroscopic data)

SUBSCRIPTS

∞	free-stream conditions in test section
c	critical conditions for gaseous phase of a compound
t	total conditions for gas brought isentropically to rest (wind-tunnel reservoir conditions)
$^\circ$	0° centigrade
1	monatomic gas
2	polyatomic gas

SUPERSCRIPTS

-	quantity divided by corresponding quantity for air
---	--

METHODS OF SELECTING GASES AND COMPUTING CHARACTERISTICS OF VARIOUS GAS MIXTURES

SELECTION OF GASES

The selection of monatomic gases for consideration is simple, since only four such gases are known—argon, krypton, xenon, and radon—that have a molecular weight greater than air. Radon, the heaviest of all, unfortunately must be excluded because of its radioactivity. The remaining three gases are completely inert. Some of their properties

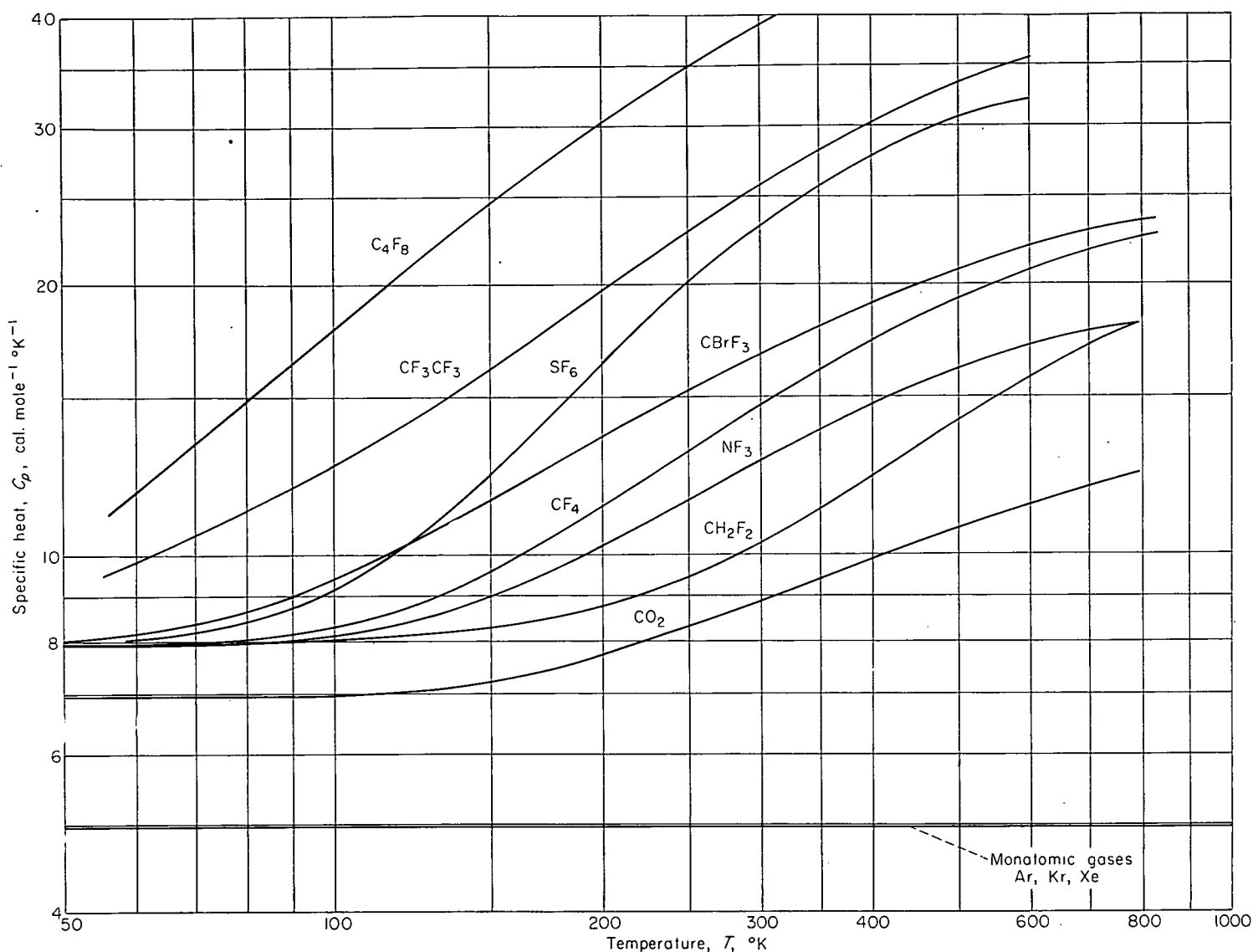


FIGURE 1.—Some typical examples of specific heat computed from spectroscopic data.

which experimental data could be found is given in the following table:

Gas	Viscosity at 0° C in micropoises	
	Calculated	Experimental
Ar.....	210	210
Kr.....	229	230
Xe.....	211	210
SF ₆	146	142
CCH ₂ F ₂	114	118
CHClF ₂	119	120
CO ₂	134	137
N ₂ O.....	132	135
Air.....	170	172

This agreement is satisfactory. Consequently, in the calculations of wind-tunnel power requirements, experimental values of μ are employed for the 9 gases listed above, but values computed from equation (12) are employed for the remaining gases for which experimental data are not available. Since molecules of the above 9 gases are either simple

or approximately spherical in structure, the accuracy of calculations from equation (12) is expected to be less for greatly different molecular structures, such as that of C₄F₁₀, but probably is sufficient for present purposes.

WIND-TUNNEL POWER AND SIZE

The general equation for compressor power required to maintain a steady rate of mass flow w of a perfect gas through a compression ratio CR starting with an initial temperature T_i is given by the equation

$$HP = J \frac{w c_p T_i}{\eta} [(CR)^{(\gamma-1)/\gamma} - 1] \quad (13)$$

where J is a numerical constant depending only on the units employed, η is the combined adiabatic and mechanical efficiency (assumed to be independent of the gas), and c_p is the specific heat per unit mass. It is noted that c_p in equation (13) is related to the molar specific heat C_p and the molar universal gas constant R through the equation

$$m c_p = C_p = \frac{\gamma}{\gamma - 1} R \quad (14)$$

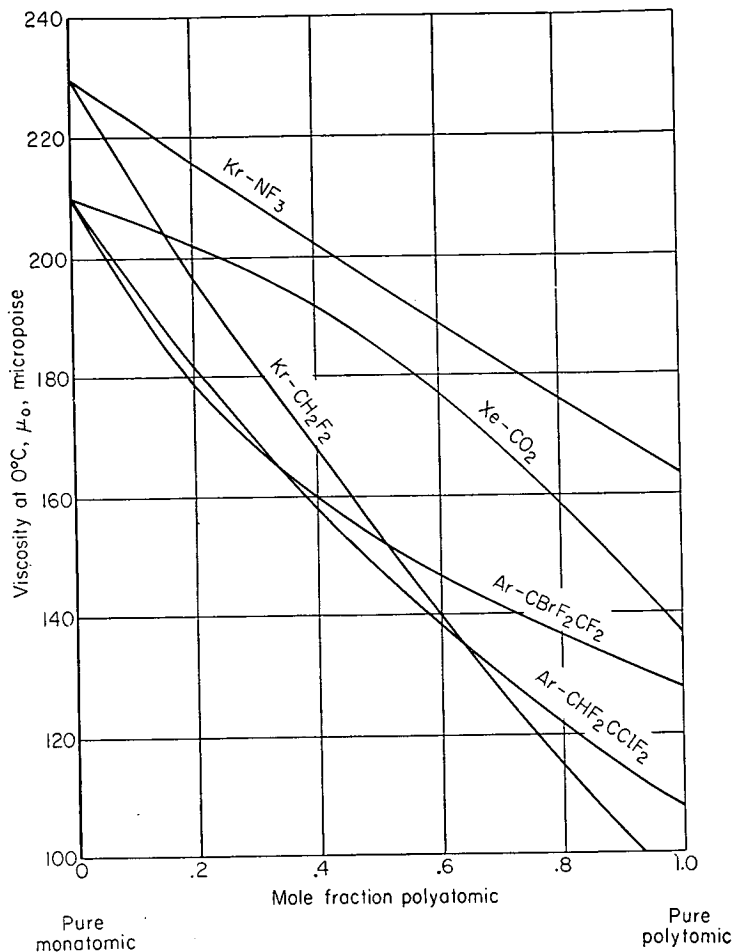


FIGURE 2.—Some typical examples of viscosity coefficient for gas mixtures.

By using a bar to denote a quantity divided by the corresponding quantity for air (e. g., $\bar{m} \equiv m/(m)_{\text{air}}$, $\bar{w} \equiv w/(w)_{\text{air}}$, $\bar{HP} \equiv HP/(HP)_{\text{air}}$, etc.), there results

$$\bar{HP} = \frac{\bar{w}}{\bar{m}} \bar{T}_i \bar{Y}(\gamma, CR) = \frac{\bar{p}_\infty \bar{u}_\infty \bar{L}^2}{\bar{m}} \bar{T}_i \bar{Y}(\gamma, CR) \quad (15)$$

where $Y(\gamma, CR) \equiv \frac{\gamma}{\gamma-1} [(CR)^{(\gamma-1)/\gamma} - 1]$, and L is a characteristic dimension of the test section. A more convenient equation is obtained by introducing the Reynolds number

$$\bar{HP} = \frac{\bar{Re} \bar{\mu} \bar{L}}{\bar{m}} \bar{T}_i \bar{Y}(\gamma, CR) \quad (16)$$

from which it is apparent that, as Smelt (ref. 2) has pointed out, power economy can be achieved by employing a gas with low viscosity and high molecular weight, or by testing at the lowest temperature possible, or by testing in the smallest facility (highest operating pressure) that will yield the given Reynolds number. The quantities \bar{Re} and \bar{L} are related to the relative operating tunnel pressure \bar{p}_i

$$\begin{aligned} \bar{Re} &= \frac{\bar{p}_\infty \bar{u}_\infty \bar{L}}{\bar{\mu}} = \left[\left(\frac{\rho_\infty}{\rho_i} \right) \frac{\bar{p}_i \bar{m}}{\bar{T}_i} \right] \left[\left(\frac{u_\infty}{a_i} \right) \sqrt{\frac{\gamma \bar{T}_i}{\bar{m}}} \right] \frac{\bar{L}}{\bar{\mu}} \\ &= \bar{p}_i \sqrt{\frac{\bar{m}}{\bar{T}_i}} \frac{\bar{L}}{\bar{\mu}} \left(\frac{\sqrt{\gamma \rho_\infty u_\infty}}{\rho_i a_i} \right) \end{aligned}$$

or, finally,

$$\bar{L} = \frac{\bar{Re} \bar{\mu} \sqrt{\bar{T}_i}}{\bar{p}_i \sqrt{\bar{m}} \bar{f}(\gamma, M_\infty)} \quad (17)$$

where

$$\bar{f}(\gamma, M_\infty) \equiv \left(\frac{\sqrt{\gamma \rho_\infty u_\infty}}{\rho_i a_i} \right)$$

Equation (17) shows that by increasing the molecular weight, or decreasing the viscosity, the size of wind tunnel required to obtain a given Reynolds number can be reduced. Hence, an alternate equation for relative wind-tunnel power is

$$\bar{HP} = \frac{(\bar{Re})^2 \mu^2 (\bar{T}_i)^{3/2}}{\bar{p}_i (\bar{m})^{3/2}} \frac{\bar{Y}(\gamma, CR)}{\bar{f}(\gamma, M_\infty)} \quad (18)$$

Equations (16), (17), and (18) are a generalization of similar equations developed by Smelt.

For subsequent computations, the above equations can be simplified. It will be assumed that CR depends only on M_∞ . (To achieve this in an air tunnel, the compressor speed would have to be reduced for a heavy gas.) For the case of transonic wind tunnels CR is the order of 1.3 or less, and direct numerical calculations show that $0.97 < \bar{Y}(\gamma, 1.3) < 1$ for any γ between 1.1 and 1.4. Hence, $\bar{Y} = 1$ is a good approximation for transonic wind tunnels irrespective of γ . For the case of supersonic wind tunnels, only gas mixtures having $\gamma \approx 1.4$ are considered, for which $\bar{Y}(1.4, CR) = 1$. Consequently, in all cases of concern here, $\bar{Y} = 1$ is an adequate approximation. A similar argument shows that the ratio $\bar{Y}(\gamma, CR)/\bar{f}(\gamma, M_\infty)$ is approximately unity for the range of γ and M_∞ considered here. Inasmuch as all calculations will be made on the basis that $\bar{T}_i = 1$, the above equations simplify to

$$\bar{HP} = \frac{\bar{Re} \bar{\mu} \bar{L}}{\bar{m}} \quad (16a)$$

$$\bar{L} = \frac{\bar{Re} \bar{\mu}}{\bar{p}_i \sqrt{\bar{m}}} \quad (17a)$$

$$\bar{HP} = \frac{(\bar{Re})^2 (\bar{\mu})^2}{\bar{p}_i (\bar{m})^{3/2}} \quad (18a)$$

Four illustrative cases will be considered: (1) given M_∞ , Re , and L ; (2) given M_∞ , L , and p_i ; (3) given M_∞ , L , and HP ; and (4) given M_∞ , Re , and p_i . Since for all cases $\bar{T}_i = \bar{M}_\infty = 1$, the reduction in velocity is always $\bar{u}_\infty = (\bar{m})^{-1/2}$.

Case (1): Given M_∞ , Re , and L .—This case corresponds to operating a given wind tunnel ($\bar{L} = 1$) with a gas other than air at the same values of M_∞ and Re as for air. The horsepower required for the gas mixture relative to that for air is $\bar{HP} = \bar{\mu}/\bar{m}$. However, from equation (17a), it is seen that $\bar{p}_i = \bar{\mu}/\sqrt{\bar{m}}$ for given values of Re and L . Hence, in order to achieve the same Re with a heavy gas as with air, the given tunnel would be operated at a lower pressure, resulting in model loads that are proportionately lower, since $\bar{q} = \bar{p}_i = \bar{\mu}/\sqrt{\bar{m}}$.

Case (2): Given M_∞ , L , and p_i .—This case corresponds to substituting a gas other than air in a given wind tunnel and operating at the same pressure and Mach number as for air. From equation (17a) it follows that $\bar{Re} = \sqrt{\bar{m}}/\bar{\mu}$. This indi-

icates that higher Reynolds numbers would be achieved with a heavy gas than with air, while (according to eq. (16a)) simultaneously drawing less power by the ratio $\overline{HP} = (\overline{m})^{-1/2}$. Since $\overline{p}_t = 1$, model stresses are unchanged for this case.

Case (3): Given M_∞ , L , and HP .—This case corresponds to replacing air in a given tunnel by a gas mixture and drawing the same power for a fixed Mach number. The Reynolds number, from equation (16a), would be increased by the factor $\overline{Re} = \overline{m}/\mu$. In order to draw the same power as with air, the pressure and, hence, model loads would have to be increased by the factor $\overline{p}_t = \sqrt{\overline{m}}$.

Case (4): Given M_∞ , Re , and p_t .—This case corresponds to conditions that might be prescribed in the initial design of a new wind tunnel whose size is to be determined by the required values of M_∞ and Re , by the selected value of p_t , and by the gas employed. From equation (18a) it is evident that in this case, the horsepower required for a heavy gas mixture is less than for air by the factor

$$\overline{HP} = \frac{(\overline{\mu})^2}{(\overline{m})^{3/2}} \quad (19)$$

This represents a greater power reduction than in the cases above because the gas-mixture wind tunnel, according to equation (17b), would be smaller than the corresponding air tunnel by the factor

$$\overline{L} = \overline{\mu}/\sqrt{\overline{m}} \quad (20)$$

The gas-mixture wind tunnel would produce the same aerodynamic data as the larger air tunnel with the same model stresses. Computations based on these latter two equations are presented later.

MACH NUMBER LIMIT FOR CONDENSATION

Although any of the polyatomic gases would be usable in apparatus where low temperatures are not involved, such as in a subsonic wind tunnel, a firing range, or a compressor research apparatus, only a limited number would be useful

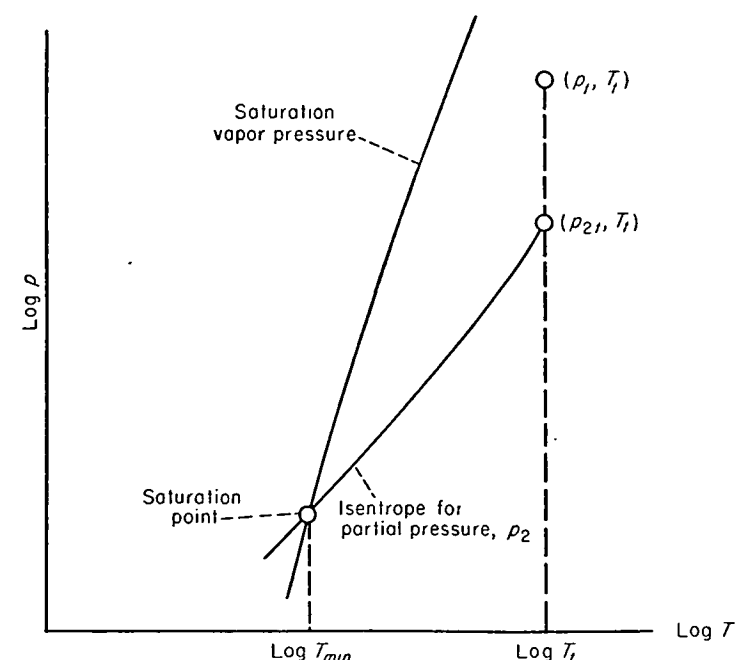


FIGURE 3.—Method of determining saturation limit.

in a supersonic wind tunnel where the static temperatures encountered are low and can result in condensation. An essential step in evaluating various polyatomic gases, therefore, is to determine the approximate useful Mach number range for each gas. The method of determining this was to draw the isentropic expansion curve for the partial pressure of each polyatomic gas on log-log paper together with the curve for saturation vapor pressure of that gas. As indicated in figure 3, the intersection point yields T_{min} , from which the maximum Mach number can be calculated from the relation

$$M^2 = \frac{2}{\gamma} \left(\frac{H_i}{RT} - \frac{H}{RT} \right)$$

where γ and H/T are determined from spectroscopic data by equations (4) through (10). Graphical solutions of this type were made for operating conditions of approximately 40° C (100° F) total temperature and several atmospheres total pressure. These solutions enabled the appropriate polyatomic gases to be selected for each of several design Mach numbers considered in the evaluation. It is emphasized that the graphical method included consideration of the variation of specific heat with temperature. As will be seen subsequently, such variation is of dominant importance in determining the limiting Mach number to which certain gases can be expanded without reaching saturation. Simplified criteria, such as boiling temperature, are quite inadequate for determining the saturation limit.

RESULTS AND DISCUSSION

WIND-TUNNEL POWER AND SIZE

Complete computations could not be made for 10 of the 31 polyatomic gases listed in table II, since the necessary spectroscopic data and critical constants were not available for these 10 gases. Calculations have been made, however, of the relative wind-tunnel power requirements for 63 gas pairs comprising mixtures of the 21 polyatomic gases for which data are available with each of the 3 monatomic gases. Mixture proportions were determined from equation (6) by substituting a value of 1.4 for γ_∞ . The calculations were made for three design Mach numbers, 1.3, 2.5, and 3.5. Results are tabulated in tables IV (a), IV (b), and IV (c), respectively. It should be noted that all 21 polyatomic gases are included in table IV (a), since all are free from condensation at $M_\infty = 1.3$. Only 7 gases for $M_\infty = 2.5$ (table IV (b)) and 2 gases for $M_\infty = 3.5$ (table IV (c)) have sufficiently low boiling points to avoid saturation for the assumed condition of 40° C total temperature. Operation at Mach numbers above about 3.5 would require total temperatures higher than the value of 40° C arbitrarily assumed.

The values of relative horsepower \overline{HP} given in table IV represent case (4) mentioned previously. This case corresponds to a comparison with an air wind tunnel for the same M_∞ , Re , and p_t . If desired, any of the other three cases mentioned, or any of the individual relative quantities such as \overline{u}_∞ or \overline{p}_∞ , can be readily calculated from the values of \overline{m} and $\overline{\mu}$ listed in the tables and from the appropriate equations developed earlier.

The tabulated results show that there is no single polyatomic gas which is best for all Mach numbers or for use with

all monatomic gases. For each monatomic gas, though, there are several polyatomic gases which appear roughly equal in their ability to require low wind-tunnel power. Of the gases that currently are commercially available and not classified questionable in table II, the most efficient ones for use with argon are: CH_2F_2 , CBrF_3 , and CCl_2F_2 for $M_\infty=1.3$; CBrF_3 and SF_6 for $M_\infty=2.5$; and CF_4 for $M_\infty=3.5$. In general, the horsepower and size of gas-mixture wind tunnels relative to equivalent air wind tunnels are very approximately as follows:

	Mixtures		
	Argon	Krypton	Xenon
Power relative to air, \overline{HP}	0.3	0.2	0.1
Test-section dimension relative to air, \overline{L}	0.7	0.6	0.5

These figures indicate significant advantages of gas mixtures as wind-tunnel test media.

It is interesting to note that the heaviest polyatomic gas— C_4F_{10} , having $\overline{m}_2=8.2$ —does not result in either the heaviest mixture or the best mixture. This is due to the high molar specific heat of C_4F_{10} which requires that only a small amount (6.5 percent) be mixed with a monatomic gas in order to obtain $\gamma=1.4$. However, for applications to low-speed subsonic research where the value of γ does not matter and, hence, a mixture is not needed, the heaviest gas is the best. For example, pure C_4F_{10} , having $\gamma=1.06$, would require only 1.8 percent of the power, and an apparatus one-fourth the size of that required by air for a given M_∞ , Re , and p_t . In this respect pure C_4F_{10} is several times more efficient than pure Freon 12. (See table III where corresponding values are given for all pure polyatomic gases considered.) It is evident that pure polyatomic gases having $\gamma \approx 1.1$ are more efficient in reducing wind-tunnel power requirements than are gas mixtures having $\gamma=1.4$.

A possibility that should not be overlooked is that a value of γ close to 1.4 may not be necessary for transonic wind tunnels or other transonic research apparatus. In view of the surprisingly small differences observed at transonic speeds by von Doenhoff and Braslow (ref. 7) between uncorrected results in Freon 12 ($\gamma=1.13$) and in air ($\gamma=1.4$), it would appear that a reduced value of γ , perhaps between 1.3 and 1.2, might yield transonic data directly applicable to air for practical purposes. If a considerably reduced value of γ is satisfactory in transonic wind tunnels (such is not anticipated in supersonic wind tunnels), then the possible advantages of gas mixtures for transonic speeds are greater than the above calculations for $\gamma=1.4$ would indicate. The following table for CBrF_3 -Ar mixtures at $M_\infty=1.3$ illustrates this:

γ	Case (4): given Re , p_t , and M_∞		Case (3): given \overline{HP} , M_∞ , and L
	\overline{HP}	\overline{L}	
1.4	0.37	0.74	2.0 (from table IV(a))
1.35	.30	.69	2.3
1.3	.22	.62	2.8
1.25	.16	.53	3.4
1.2	.10	.44	4.5
1.15	.06	.37	6.2 (pure CBrF_3)

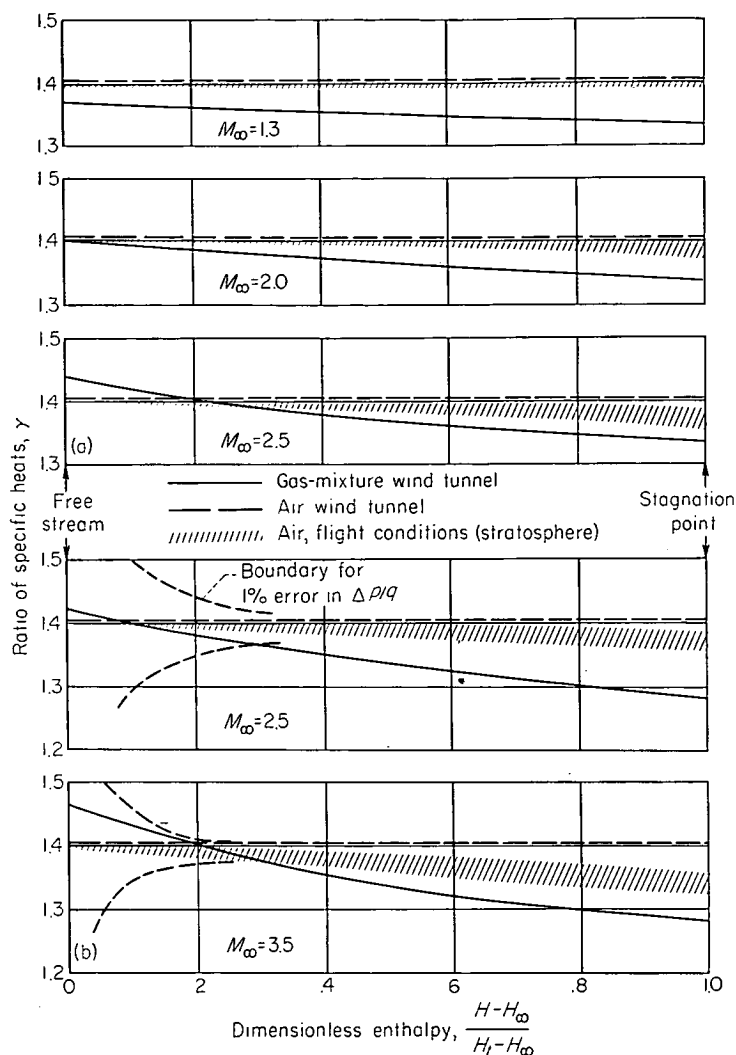
These figures, which are typical of many of the argon mixtures, show that by reducing γ to about 1.28, the power requirement for an argon gas mixture at transonic speeds would be about one-half that for the same type mixture proportioned to yield a γ of 1.4. This corresponds to one-fifth the power of an equivalent air wind tunnel operating at the same Reynolds number, total pressure, and Mach number (case (4)). Also, the Reynolds number of an existing transonic wind tunnel having a fixed horsepower (case (3)) would be about tripled if air were replaced by an argon gas mixture having $\gamma=1.28$, but only doubled by a mixture having $\gamma=1.4$. The advantages of reducing γ to the lowest practical value are apparent from the table. For xenon mixtures, however, there is less to gain by reducing γ below 1.4. It would be desirable to conduct some experiments varying the proportions of a gas mixture in order to determine to what limit γ can be reduced in a transonic flow and still yield data directly applicable to air for practical purposes.

DEVIATIONS FROM THERMAL AND CALORIC PERFECTION

Under wind-tunnel conditions air generally is considered as being both thermally perfect ($pm=\rho RT$) and calorically perfect ($\gamma=\text{constant}$). Most other gases can not be so considered. Calculations of the degree of deviation from thermal perfection for the various argon gas mixtures are presented in Appendix A. It will suffice here to state that such deviations are indicated to be unimportant for normal operating conditions of wind tunnels. The smallness of these deviations is due in part to the monatomic (argon) component, which by itself is almost thermally perfect, and, in part, to the fact that the polyatomic component is a fluorochemical. The unusually low intermolecular forces in fluorochemical gases result in small deviations from thermal perfection.

Deviations from caloric perfection, on the other hand, are not small and represent an important technical consideration. The specific heat of polyatomic gases varies widely, as figure 1 clearly indicates. Thus, a gas mixture proportioned to yield $\gamma=1.4$ for one Mach number will not yield the same value of γ at other Mach numbers. This may limit the Mach number range over which a single gas mixture could be used satisfactorily. Also, at a fixed Mach number, γ will vary with temperature. Under wind-tunnel conditions, γ for air is quite constant, but varies under flight conditions where higher temperatures are encountered.

To aid in evaluating the importance of caloric imperfections, the variation of γ with temperature has been computed for various gas mixtures and for air under both wind-tunnel and flight conditions. In these computations the spectroscopic frequencies listed in table III were employed to determine γ for the gas mixtures, whereas the tables of reference 62 were employed for air. Instead of showing the computed variation as a function of some temperature parameter, an enthalpy parameter $(H-H_\infty)/(H_t-H_\infty)$ is employed which always is zero for free-stream conditions and always is unity for reservoir conditions, regardless of the nature of the gas. Some of the results are shown in figure 4. Air under flight conditions at a given M_∞ is represented by a cross-sectioned band because ambient temperatures in the atmosphere vary considerably with altitude. Gases



(a) Gas mixture of 0.25 CBrF_3 with 0.75 monatomic.
 (b) Gas mixture of 0.4 CF_4 with 0.6 monatomic.

FIGURE 4.—Variation of specific-heat ratio between free-stream and stagnation conditions for various gas mixtures.

under wind-tunnel conditions are represented by a single curve since a fixed reservoir temperature (about $40^\circ\text{C} \approx 100^\circ\text{F}$) has been assumed. A single mixture of 25-percent CBrF_3 with 75-percent monatomic gas is considered in figure 4 (a). These proportions are about right for $M_\infty = 2.0$. At $M_\infty = 2.5$, γ_∞ is 1.44 and γ_t is 1.34. This variation does not seem excessive. At $M_\infty = 1.3$, γ is uniformly less than 1.4, varying between 1.37 and 1.34. In view of previous comments about the apparent insensitivity of transonic flows to much larger variations in γ , as well as the complete insensitivity of subsonic flows to variations in γ , it would appear that a single mixture could be used satisfactorily from low subsonic speeds to at least $M_\infty = 2.5$.

The situation is more complicated within the Mach number range between 2.5 and 3.5, as figure 4 (b) illustrates for the case of a single mixture of 40-percent CF_4 with 60-percent monatomic gas. It is to be noted that a variation of γ is not important at conditions close to free-stream conditions. For example, γ does not appear within the body of linearized subsonic or supersonic theory, but first appears in second-order terms. Hence, Busemann's second-order theory for two-dimensional flow has been used to estimate the range

within which γ must be maintained in order to introduce less than 1-percent error in $\Delta p/q$. The boundaries of this range, indicated by dotted lines in figure 4 (b), shrink together as $M_\infty \rightarrow 1$ and as $M_\infty \rightarrow \infty$. For the moderate Mach numbers under consideration, it is seen that only the region of abscissa between about 0.2 and 1.0 is important when assessing the variations in specific-heat ratio. Consequently, it is deduced that the gas mixture of figure 4 (b) approximates flight conditions at $M_\infty = 3.5$ about as well as does air in a wind tunnel. Such is not the case, though, at $M_\infty = 2.5$ (top portion of fig. 4 (b)), and it is not known whether moderate γ variations near the stagnation region of the magnitude shown are important.

If moderate variations in γ are important, then the flow in an air wind tunnel will also show important differences from the flow in flight through air at Mach numbers of about 4 or greater. Throughout this report the operating temperature of a wind tunnel is assumed to be, as is current practice, either room temperature or that temperature which is sufficient to avoid condensation. Figure 5 compares the values of γ in an air wind tunnel (long dashed curves) with the corresponding values of γ in flight (cross-sectioned region). The observed γ differences between air in flight and in wind tunnels are considerably greater than any of figure 4 (b) between flight and gas-mixture wind tunnels. It

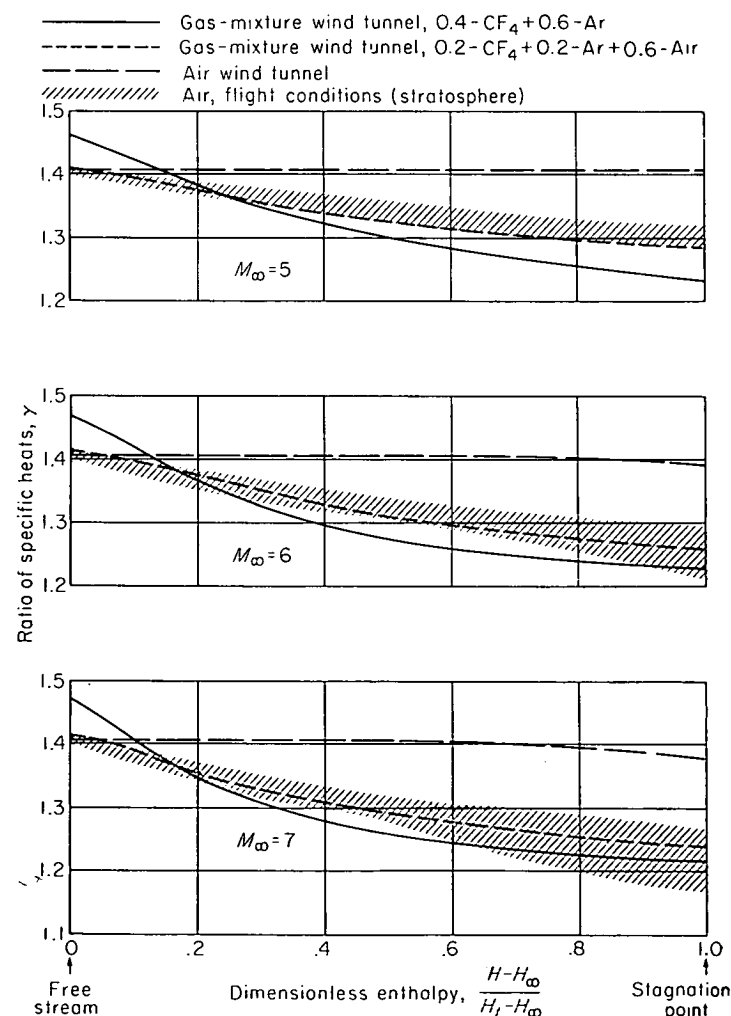


FIGURE 5.—Variation of specific-heat ratio between free-stream and stagnation conditions at hypersonic speeds.

is also evident from figure 5 that the temperature dependence of γ for polyatomic gases may actually represent a real virtue, particularly in hypersonic research. For polyatomic gases under wind-tunnel conditions, as well as for air under flight conditions, these caloric imperfections arise from a common physical phenomenon, namely, temperature dependent energy of vibration between atoms within a molecule. Under flight conditions at Mach numbers of about 6 or greater, additional energy can be transferred through dissociation, which is responsible for values of γ less than 1.28 in flight. Clearly, the ratio of specific heats is one dimensionless parameter pertinent to hypersonic flight through air—which is not simulated by air at wind-tunnel temperatures—but which is simulated by certain gas mixtures at wind-tunnel temperatures.

MACH NUMBER LIMIT FOR CONDENSATION

In order to achieve hypersonic Mach numbers in a wind tunnel without supersaturating the test medium, it is necessary, of course, to heat the medium. The approximate reservoir temperatures (estimated to nearest 25° K) corresponding to the particular gas mixtures considered in figure 4, are as follows:

Gas	Reservoir temperature °K to prevent saturation: $p_t = 100$ psia		
	$M_\infty = 5$	$M_\infty = 6$	$M_\infty = 7$
Air.....	350	450	550
0.4—CF ₄ +0.6—Ar.....	475	600	675
0.2—CF ₄ +0.2—Ar+0.6 air.....	500	625	750

As might be expected, the gas mixtures require higher operating temperatures than does air.

It is important to note that the trend of the results tabulated above can be reversed by not requiring that the γ variation of the gas mixtures in a wind tunnel duplicate that of flight through air. Certain pure polyatomic gases require less heating to achieve hypersonic flow without saturation than does air, as the following table illustrates:

Gas	T_b , °C	γ_∞	γ_t	Reservoir temperature °K to prevent saturation at $p_t = 100$ psia; $M_\infty = 7$
Air.....	-189	1.40	1.38	550
CF ₄	-128	1.33	1.12	450
SF ₆	-64	1.27	1.07	450
CF ₃ CF ₃	-78	1.19	1.07	375

For the three gases, air, CF₄, and CF₃CF₃, the above trend is opposite to what would be expected from consideration solely of the respective boiling points (-180° C for air, -128° C for CF₄, and -78° C for CF₃CF₃) because of the dominating effect of the reduced values of γ . Reducing γ will reduce the rate at which temperature varies with pressure in an expansion process, since $T \sim p^{(\gamma-1)/\gamma}$. This results in producing lower pressures, and hence higher Mach numbers, before the temperature is reduced to a point where saturation occurs. From a physical viewpoint, this phenomenon can be traced to the conversion of internal

vibrational energy of a molecule into directed kinetic energy during expansion of a polyatomic gas. To achieve a given ratio of directed to random energy (given Mach number), the polyatomic gas with large vibrational energy does not have to be expanded to as low a temperature as does a gas without vibrational energy.

DEVIATIONS FROM THERMAL EQUILIBRIUM (HEAT CAPACITY LAG)

When a polyatomic molecule passes through a region of rapid change in temperature, the energy stored in vibration between atoms within the molecules does not always adjust to its environment with sufficient rapidity to maintain thermodynamic equilibrium. This leads to a time lag in the heat capacity determined by the relaxation time τ . Measurements show that τ increases if either pressure or temperature decreases. An excessively long relaxation time could significantly affect a high-speed flow, especially in a wind tunnel where the pressures and temperatures encountered are low.

Detailed computations are presented in Appendix B which provide an estimate of relaxation-time effects for various gases. These estimates are based on a relation between relaxation time and bulk viscosity. The derivation of this relation, and a discussion of its range of validity are presented in Appendix C. Here, only end results are discussed. The relaxation time (τ_a) at atmosphere conditions is known for some of the fluorochemical gases, and generally is the order of 10^{-7} second. For others, τ_a is not known from direct measurements, but can be estimated from related measurements by using certain empirical relationships between relaxation time and molecular structure. Thus, τ_a for CBrF₃ is estimated to be in the range 10^{-8} to 10^{-7} second, and that for CF₃CF₃ to be in the range 10^{-9} to 10^{-8} second.

Relaxation time is not the only important quantity which must be considered. The basic parameters which measure effects of heat-capacity lag on a gas flow involve the product τC_i , where C_i is the heat capacity of internal vibrations within the molecules. From the estimates in Appendix B, heat-capacity lag appears of more importance in altering boundary-layer flow than in altering pressure distribution, and is of greatest importance at low Reynolds numbers. For air under wind-tunnel conditions, τ is so long that the small internal vibrational energy effectively is "frozen," thereby rendering relaxation effects negligible even at low Reynolds numbers. For most of the gas mixtures under wind-tunnel conditions, the estimated relaxation effects are negligible at Reynolds numbers of the order of 10^5 or greater. They can be significant, however, at low Reynolds numbers (the order of 10^4 or less). It should be remembered that for air under flight conditions, C_i is not negligible as it is in a wind tunnel. Thus, relaxation effects can be significant in flight, although the estimates of Appendix B suggest this may be the case only at high altitudes (low Reynolds numbers) and at high flight speeds. In broad terms, heat-capacity lag is estimated to be significant at Reynolds numbers below about 10^4 for moderate supersonic speeds, and below about 10^6 for hypersonic speeds. Although relaxation-time effects in flight would not be simulated in an air wind tunnel, it is possible to simulate them approximately in a gas-mixture

wind tunnel by employing two polyatomic gases in the mixture—one having τC_i greater than for flight through air, and the other having τC_i less than for flight through air. This possibility appears to be of interest in low-density, high Mach number research, and provides another example of an effect pertinent to hypersonic flight through air which cannot be studied in an air wind tunnel but can be studied in a gas-mixture wind tunnel.

It should be mentioned that the idea of employing more than one polyatomic gas in a mixture might be utilized profitably in other ways. For example, various pairs of some polyatomic gases when mixed in special proportions form an azeotropic mixture; that is, a mixture for which the boiling temperature is not intermediate between the boiling temperatures of the two constituent gases, as ordinarily is the case, but is lower than the boiling temperature of either constituent. A mixture of 32-percent C_3F_8 with 68-percent CH_2F_2 , for example, boils at $-58^\circ C$, whereas the respective individual gases boil at $-38^\circ C$ and $-52^\circ C$ (ref. 63). Thus, although neither C_3F_8 nor CH_2F_2 could individually be used at $M_\infty=2.5$ under normal wind-tunnel operating conditions without danger of condensation (and, hence, have not been included in table IV (b)), their azeotropic mixture would be usable under such conditions. Other gas pairs known to form azeotropic mixtures are CHF_3 with C_2F_6 , CF_2Cl_2 with CF_2CFCF_3 , $CHClF_2$ with CF_2CFCF_3 , and CF_2Cl_2 with CH_3CHF_2 (see refs. 48 and 63). A related point worth mentioning is that certain polyatomic gases which would not be usable singly because of flammability characteristics may be usable when mixed with other gases. An extreme example illustrating this point is the obviously flammable butane (C_4H_{10}) which, when mixed with CF_2Cl_2 in portions up to about 30 percent, is no longer flammable (ref. 64).

VISCOSITY VARIATION WITH TEMPERATURE AND PRANDTL NUMBER FOR VARIOUS GASES

Thus far, mention has been made of two effects associated with hypersonic flight through air which are not simulated in an air wind tunnel operating at conventional temperatures but which can be simulated in a gas mixture wind tunnel. These effects pertain to specific-heat variation with temperature and to relaxation-time phenomena (or bulk-viscosity phenomena). To this can be added a third effect; namely, that pertaining to variation of viscosity with temperature. It is to be remembered, though, that not all of the three effects are significant simultaneously in a given research problem; likewise, not all can be simulated simultaneously by a single gas mixture. One gas which—in a wind tunnel—approximates the temperature-viscosity relationship of flight conditions is pure helium, as illustrated in figure 6. A different gas which approximates the corresponding relationship of air in a wind tunnel is pure argon, as also illustrated in figure 6. The various curves representing wind-tunnel conditions in this figure correspond to reservoir temperatures which will avoid saturation at $M=5$. Helium and argon have the same value of γ , and very nearly the same value of Pr ; they differ in aerodynamic behavior only in their viscosity-temperature relationship. Separate measurements with these two gases, therefore, would single out any effect of viscosity-temperature relationship on a given

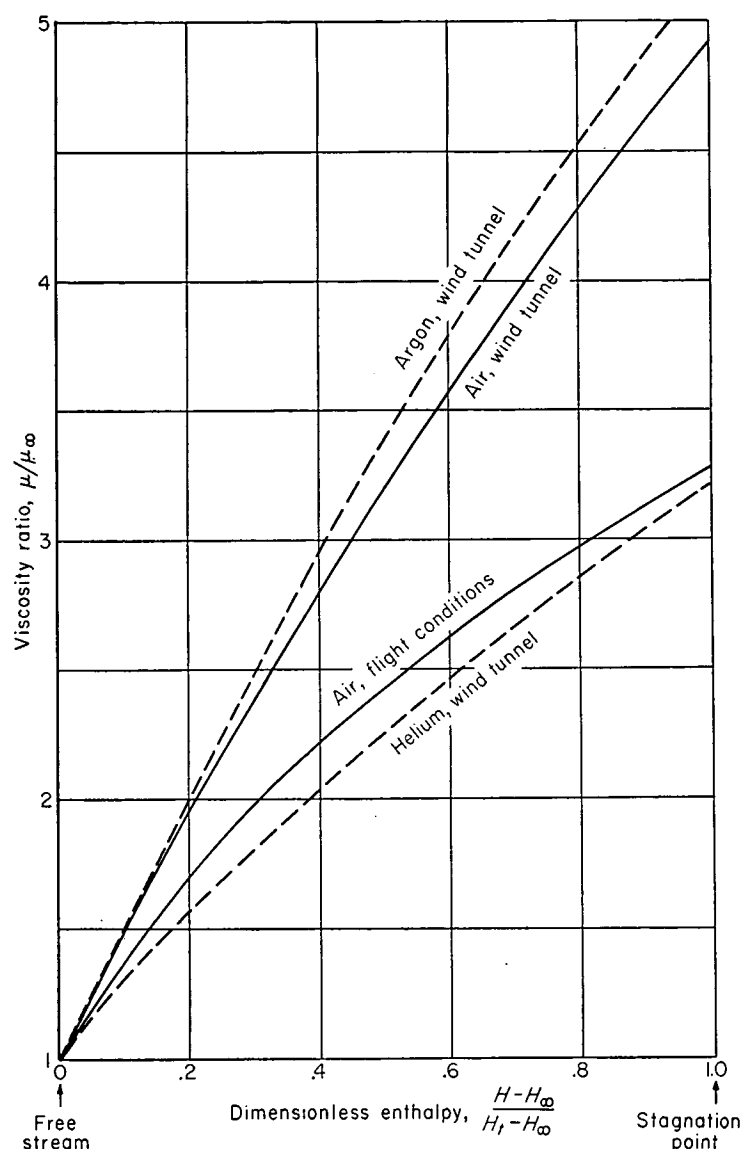


FIGURE 6.—Dimensionless viscosity variation for various gases at $M_\infty=5$.

phenomenon. This possibility would appear to be useful in boundary-layer research.

When gases are mixed in arbitrary proportions, the Prandtl number can vary markedly. A rather extreme example of this is afforded by He and SF_6 mixtures. At $0^\circ C$ the Prandtl number of He is the same as that of SF_6 , namely, 0.69. Mixture of these two gases, however, can result in values of Pr as low as 0.21, according to the calculated curve shown in figure 7. Similarly, Pr for argon is 0.67, but mixtures with helium can result in values as low as 0.41. These mixtures provide values of Pr less than that of air (0.7 at room temperature), but other mixtures can provide values greater than air. For example, mixtures of CCl_2F_2 and He (results not shown) cover the Pr range between 0.82 and 0.22. As a test of the calculation method, which indicates such large variations in Pr , some experiments are available for the case of He-A mixtures (ref. 65 for viscosity, ref. 66 for conductivity). Calculation and measurement agree well for this case as is evident from figure 7. The particular equations em-

ployed in the calculations⁵ are the rigorous mixture equations of kinetic theory developed by Hirschfelder, et al. (ref. 67). It is noted that the large reductions in Pr can be attributed primarily to the mixing of light with heavy molecules ($m_2/m_1=37$ for SF_6 -He, $m_2/m_1=10$ for A-He). If gases of more comparable molecular weight were mixed, say A and CF_4 ($m_2/m_1=2.2$), the corresponding reduction in Pr would not be large. Large variations in Pr afforded by special mixtures of gases would appear to be a significant tool for conducting supersonic heat-transfer research, since the Prandtl number is an important parameter in such phenomena.

CONCLUDING REMARKS

By employing in place of air a test medium consisting of a heavy monatomic gas mixed with a heavy polyatomic gas in proportions that yield the desired value of 1.4 for the ratio of specific heats, it appears possible in conducting aerodynamic research to realize certain significant advantages. The existence of some of these advantages has been demonstrated by previous investigations concerned with pure heavy, polyatomic gases, especially the Freons. Because pure polyatomic gases have a specific-heat ratio much lower than that of air, they cannot be employed to yield aerodynamic data directly applicable to air for flows involving extensive supersonic regions. Aerodynamic data obtained with the gas mixtures considered herein would directly apply to air.

Perhaps the most significant result of this study is the observation that a gas mixture can be concocted which behaves—under low-temperature wind-tunnel conditions—dynamically similar in several respects to air under high-temperature flight conditions, whereas air under low-temperature wind-tunnel conditions behaves dissimilarly. This situation arises because the flow of two gases can be made dynamically similar on a macroscopic scale, even though they differ in microscopic structure, provided all the pertinent, *dimensionless*, macroscopic parameters (such as involve, for example, relaxation-time phenomena, temperature variation of specific heat, and temperature variation of viscosity), are duplicated between the two gases. In achieving dynamic similarity, the *dimensional* quantities, such as temperature, are not duplicated.

Many of the fluorochemical gases studied in the present research are more inert than Freon 12. This extreme inertness is highly desirable, especially since some of these gases when mixed with the necessary small amount of oxygen can be breathed even in large quantities without observable effect by animals, and presumably also by man.

⁵ These calculations were made by Mr. Donald Doran. Intermolecular forces were represented, in the nomenclature of reference 67, by a Lennard-Jones potential for He- SF_6 and a modified Buckingham potential (with $\alpha=12.4$) for He-A. Force constants ϵ/K were 9.16° K for He, 239° K for SF_6 , and 123.2° K for A. Molecular dimensions were selected to yield the proper values of each transport property of the pure gas component.

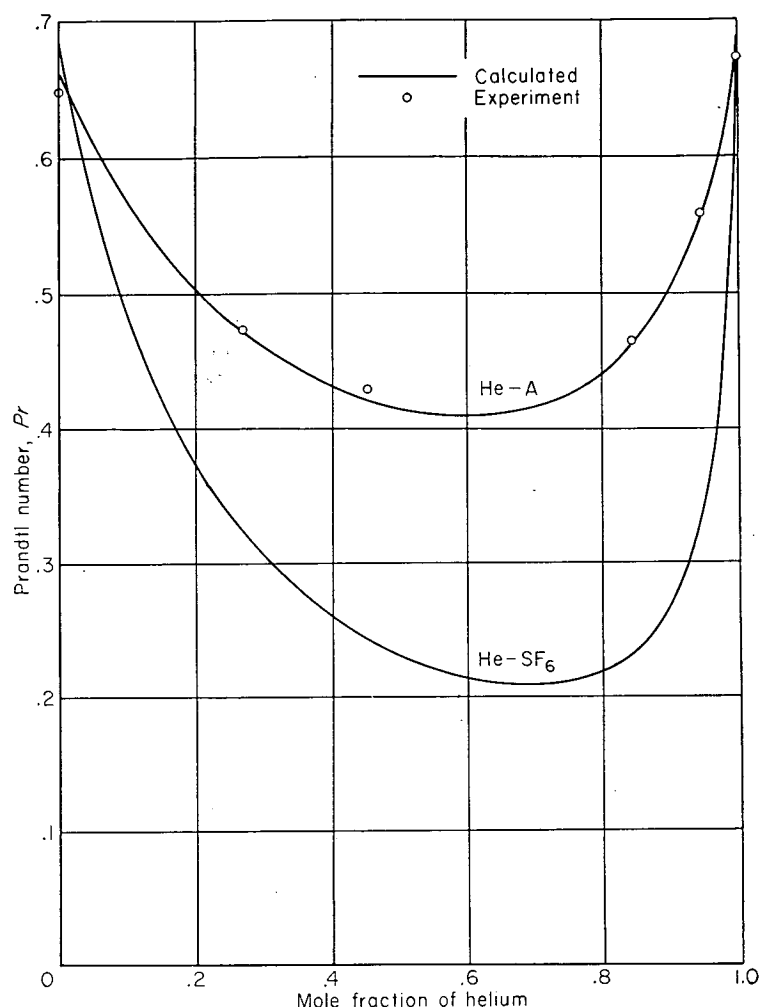


FIGURE 7.—Prandtl number variation for two gas mixtures containing helium; $T=0^\circ C$.

Likewise, because of their inertness they could be used without undesirable effect on machinery.

Since the magnitude of the advantages that can be realized through use of gas mixtures has been shown to be large, they may outweigh the evident operational disadvantages which result from use of any gas other than air. Whether or not the advantages surmount the disadvantages can only be ascertained by detailed study of individual cases. Clearly, though, the possible use of gas mixtures warrants consideration in the design of new research facilities. In view of the magnitude of the advantages, it appears that some experimental work with gas mixtures is in order.

AMES AERONAUTICAL LABORATORY
NATIONAL ADVISORY COMMITTEE FOR AERONAUTICS
MOFFETT FIELD, CALIF., Mar. 12, 1954

APPENDIX A

ESTIMATE OF DEVIATIONS FROM THERMAL PERFECTION

By definition, a thermally perfect gas obeys the equation of state $pm = \rho RT$ given previously as equation (2). Real gases closely follow this equation if the density is low, or if the temperature is near the Boyle temperature (about $2.6 T_c$), but deviate from it under other conditions. A more exact state equation is

$$\frac{pm}{\rho RT} = 1 + \frac{p}{RT} B(T) \quad (A1)$$

where $B(T)$ is the second virial coefficient having dimensions of volume. According to the law of corresponding states, $B(T)$ is proportional to the critical volume V_c .

From the results of reference 67, the second virial coefficient for a pure gas is approximately $0.75 V_c B^*(T^*)$, where $T^* \equiv 1.3T/T_c$ and where $B^*(T^*)$ is a fixed dimensionless function tabulated in reference 67. For a mixture of two gases the appropriate relations are:

$$B(T) = x_1^2 B_1(T) + 2x_1 x_2 B_{12}(T) + x_2^2 B_2(T) \quad (A2)$$

where

$$\left. \begin{aligned} B_1 &= 0.75 V_{c1} B^*(1.3T/T_{c1}) \\ B_2 &= 0.75 V_{c2} B^*(1.3T/T_{c2}) \\ B_{12} &= 0.75 \left(\frac{V_{c1}^{1/3} + V_{c2}^{1/3}}{2} \right)^3 B^*(1.3T/\sqrt{T_{c1} T_{c2}}) \end{aligned} \right\} \quad (A3)$$

By use of these equations, the term $pB(T)/RT$ of equation (A1)—which represents the fractional deviation from thermal perfection—has been calculated for the gas mixtures listed in table IV. Computations were made both for reservoir conditions (p_∞, T_∞) and test-section conditions (p_t, T_t) at Mach numbers of 1.3, 2.5, and 3.5. For $M_\infty = 1.3$ the values of $p_t B(T_t)/RT_t$ and $p_\infty B(T_\infty)/RT_\infty$ were about the same. The average value of $|pB(T)/RT|$ per atmosphere

of reservoir pressure varied from about 0.0014 (C_4F_8 , C_3F_8 , CF_3CF_3 , CF_4 , and NF_3 mixtures) to about 0.004 (CH_2F_2 mixture). Inasmuch as transonic research apparatus commonly are limited to reservoir pressures of several atmospheres (often because of critical model loads), the resulting deviations from thermal perfection would be within about 1 percent and can be neglected. For $M_\infty = 2.5$ and $M_\infty = 3.5$, the values of $|p_\infty B(T_\infty)/RT_\infty|$ are substantially lower than $|p_t B(T_t)/RT_t|$. Both are tabulated as follows:

Gas	$M_\infty = 2.5$		$M_\infty = 3.5$	
	$ p_\infty B(T_\infty) $	$ p_t B(T_t) $	$ p_\infty B(T_\infty) $	$ p_t B(T_t) $
	RT_∞	RT_t	RT_∞	RT_t
CBrF ₃	0.0017	0.0033	-----	-----
SF ₆0013	.0027	-----	-----
CF ₃ CF ₃0010	.0018	-----	-----
CClF ₃0016	.0030	-----	-----
CF ₄0012	.0019	0.0007	0.0023
NF ₃0012	.0019	.0007	.0022
CHF ₃0017	.0034	-----	-----
Air.....	.0005	.0002	.0002	.0002

It may be deduced that gas mixtures at test-section conditions (p_∞, T_∞) would deviate 1 percent from thermal perfection at reservoir pressures between about 6 and 10 atmospheres for $M_\infty = 2.5$, and at about 14 atmospheres for $M_\infty = 3.5$. Since practical operation pressures of wind tunnels are within these limits, the flow of these gas mixtures over a typical model can be regarded as closely approximating that of a thermally perfect gas. Deviations from thermal perfection at reservoir conditions (p_t, T_t) are two to three times as large as at test-section conditions. Hence, when computing test-section Mach number or dynamic pressure from measured values of p_t and T_t , the deviations near reservoir conditions may have to be considered for reservoir pressures of the order of 5 to 10 atmospheres or greater.

APPENDIX B

RELAXATION-TIME DATA AND ESTIMATE OF EFFECT FOR VARIOUS GAS MIXTURES

Results of measurements of relaxation time at atmospheric pressure (τ_a) for some of the polyatomic gases considered in this report are as follows:

Gas	Temperature, °K	τ_a micro-seconds	Reference
CCl ₂ F ₂	293	0.09	68, 4
CF ₄	373	.66	69
SF ₆	293	.59	70
CHF ₃	373	.42	69
CHClF ₂	293	.10	68
CH ₂ F ₂	373	.055	69
CO ₂	293	7.0	68
N ₂ O.....	293	1.1	68

Although measurements of τ_a could be found only for those gases listed, certain known characteristics of relaxation time enable a rough estimate to be made for some of the remaining gases; for example, molecules with freedom of internal rotation invariably have very short relaxation times, generally less than 10^{-8} second (see ref. 71, for example). Also the smaller the lowest fundamental vibration frequency, the shorter the relaxation time (see refs. 68 and 69). These general characteristics indicate that fluorocarbon molecules with internal rotation (e. g., CF₃CBrF₂, CF₃CClF₂, CF₃CF₃, CH₃CClF₂, CH₃CHF₂, C₃F₈, and C₄F₁₀, but not C₄F₈) would have relaxation times (τ_a) in the range 10^{-8} to 10^{-9} second, and that the methane-like gases CBrF₃ and CBrClF₂ would have a relaxation time in the range of 10^{-7} to 10^{-8} second. It is to be noted that relaxation times listed are for pure gases, and that the presence of certain impurities can reduce τ_a for those gases having relatively long relaxation times.

Inasmuch as the relaxation time depends on temperature and pressure, some method of estimating τ for the particular conditions encountered in wind tunnels must be employed. The analysis of Bethe and Teller (ref. 72) yields for the relaxation time τ_v of the lowest frequency (ν) mode

$$\tau_v = \frac{Z_{10}}{Z(1 - e^{-h\nu/kT})} \quad (B1)$$

where Z is the total number of collisions one molecule experiences per second, and Z_{10} is the average number of collisions required to deactivate the lowest mode from the first quantum state to the zero state. Subsequent calculations are based on the additional equations

$$Z = 1.3 \frac{p}{\mu} \quad (B2)$$

which is a result from the rigorous kinetic theory of gases (ref. 73),

$$\tau \approx \frac{C_i \tau_v}{C_v} \quad (B3)$$

which is a result of the assumption (ref. 74) that once the lowest frequency mode (specific heat C_v) is excited, energy is then rapidly transferred internally to all other modes (total internal specific heat C_i), and

$$Z_{10} \approx 25 \left(\frac{b}{T^{1/2}} \right)^{-3/2} e^{b/T^{1/2}} \quad (B4)$$

which is an approximate result of Bethe and Teller (ref. 72). In this last equation, b is a constant to be evaluated for each gas from measurements of τ_a at the temperatures listed in the above table. These equations were developed for pure polyatomic gases. They will be used also for gas mixtures since the basic theory (especially eq. (B4)) is highly approximate, and since the effectiveness of an argon molecule in exciting vibration generally is roughly the same as that of an inert polyatomic molecule. (See the summary table in ref. 75 and the specific data for CHClF₂-Ar mixtures in ref. 76.)

Relaxation times τ_∞ corresponding to free-stream conditions (T_∞, p_∞) in a wind tunnel have been calculated for assumed reservoir conditions of one atmosphere total pressure and 40° C total temperature. The results, together with the "relaxation distance" $d \equiv \tau_\infty u_\infty$ for the gas mixture were computed to two significant figures and are tabulated to one significant figure as follows:⁶

Polyatomic component	$M_\infty = 1.3, T_\infty = 230^\circ \text{K}, p_\infty = 0.36 \text{ atm}$		$M_\infty = 2.5, T_\infty = 140^\circ \text{K}, p_\infty = 0.059 \text{ atm}$		$M_\infty = 3.5, T_\infty = 105^\circ \text{K}, p_\infty = 0.013 \text{ atm}$	
	τ_∞, sec	$d, \text{in.}$	τ_∞, sec	$d, \text{in.}$	τ_∞, sec	$d, \text{in.}$
CCl ₂ F ₂	2×10^{-7}	0.002	-----	-----	-----	-----
CF ₄	2×10^{-6}	.02	2×10^{-5}	0.3	1×10^{-4}	3
SF ₆	1×10^{-6}	.01	9×10^{-6}	.15	-----	-----
CHF ₃	2×10^{-6}	.02	1×10^{-5}	.2	-----	-----
CHClF ₂	2×10^{-7}	.002	-----	-----	-----	-----
CH ₂ F ₂	9×10^{-5}	.001	5×10^{-7}	.008	-----	-----
CO ₂	3×10^{-5}	.4	-----	-----	-----	-----
N ₂ O.....	4×10^{-6}	.05	-----	-----	-----	-----

It is to be remembered that under wind-tunnel conditions, air has a much longer relaxation time than any of the gases tabulated above. At room temperature, for example, τ for air is the order of 10^{-3} second (ref. 77), which is 10^2 to 10^4 times as long as for the polyatomic gases. This does not mean, however, that relaxation effects are important for air in a wind tunnel because the amount of internal vibration heat capacity (C_i) that lags is very small. The effect of heat-capacity lag on flow conditions is influenced by both C_i and τ .

To determine the dimensionless parameters which form a pertinent measure of relaxation effects, use is made of the theoretical equivalence between relaxation phenomena and

⁶ Some of these values differ from corresponding values tabulated in the original publication of this research (TN 3226). Such differences are not large and are due to the use of a different definition of relaxation time (τ) in equation (B1). The relaxation time originally used is not consistent with the definition of Bethe and Teller, whereas that used above is (see Appendix C).

volume-viscosity (κ) phenomena. This equivalence is derived and discussed in Appendix C where the fundamental relation $\kappa = p\tau(\gamma-1)C_i/C_p$ is shown to be valid under conditions where the relaxation time is small compared to the characteristic time (l/u_∞ for aerodynamic problems). For purposes of estimation, then, the complete, first-order stress tensor, including the volume viscosity, is used as the basis of computation.

$$p_{ij} = (p_{ij})_{\text{Navier-Stokes}} + \kappa \frac{\partial u_\alpha}{\partial x_\alpha} \delta_{ij} \quad (\text{B5})$$

In this equation κ is the coefficient of volume viscosity, $\partial u_\alpha / \partial x_\alpha$ is (using summation convention) the divergence of the velocity vector, and δ_{ij} is unity if i is equal to j , but is zero otherwise. The above equation, together with the equation relating κ to τ , will be employed to estimate effects of heat-capacity lag both for inviscid flow and viscous flow.

For inviscid flow the Navier-Stokes portion of the stress tensor is simply the static pressure p . The pertinent similarity parameter involving relaxation time is $\kappa u_\infty / (pl) = \gamma(\gamma-1)(\tau u_\infty / l) C_i / C_p$. Since the equation of steady motion involves $\rho u_j \partial u_i / \partial x_j$ and $\partial p_{ij} / \partial x_j$, the ratio of the relaxation term to the other stress term is, in order of magnitude,

$$\frac{\frac{\partial}{\partial x} \left(\kappa \frac{\partial u_\alpha}{\partial x_\alpha} \right)}{\frac{\partial}{\partial x} (p)} \sim \frac{\kappa u_\infty}{pl} \quad (\text{B6})$$

which is seen to be the same as the similarity parameter.⁷ Hence, $\kappa u_\infty / pl$ is interpreted as a measure of the fractional effect of relaxation phenomena on pressure distribution. In a gas mixture, $C_i = x_i C_{i2}$. Computations of the resulting parameter $\kappa u_\infty / pl = \gamma(\gamma-1)(\tau u_\infty / l) C_i / (C_p)$ for wind-tunnel flow conditions over a 1-inch model yield the following results:⁸

Polyatomic component	$\gamma(\gamma-1) \frac{x_i C_{i2}}{C_p} \frac{\tau u_\infty}{l} = \frac{\kappa u_\infty}{pl}$ for $l=1$ in. and $p_t=1$ atm		
	$M_\infty=1.3$	$M_\infty=2.5$	$M_\infty=3.5$
CCl_2F_2	0.0002	-----	-----
CF_4002	0.01	0.04
SF_6002	.013	-----
CHF_3001	.006	-----
CHClF_2002	-----	-----
CH_2F_200005	.00008	-----
CO_202	-----	-----
N_2O003	-----	-----

For transonic wind tunnels it is seen that only CO_2 mixtures would exhibit appreciable relaxation effects on pressure distribution. On the other hand, for $M_\infty=3.5$, mixtures involving CF_4 would be affected roughly by 4 percent for the assumed conditions of $p_t=1$ atmosphere and $l=1$ inch. To maintain these effects below about 1 percent would require the product pl to be greater than 4 atmosphere-inches (e. g., a 1-inch model in a 4-atmosphere tunnel).

⁷ A more precise calculation of this ratio of stress terms can be made using the continuity equation to eliminate $\partial u_\alpha / \partial x_\alpha$. This procedure ultimately yields a value $(\kappa u_\infty / pl) [M^2 \partial(u / u_\infty) / \partial(x/l)]$, from which it can be deduced that, the simple parameter $(\kappa u_\infty / pl)$ will underestimate relaxation effects for bluff obstacles like the sphere, but will overestimate them for slender obstacles like an airfoil.

⁸ The contribution of rotational energy to κ is disregarded since this is small compared to the contribution of vibrational energy.

Such restrictions are believed not to represent significant limitations on the usefulness of gas mixtures, especially since the favorable effect of certain impurities in reducing τ has not been included in the analysis. It is concluded, then, that insofar as pressure distribution in inviscid flow is concerned, relaxation effects need not be considered for the usual wind-tunnel operation conditions at Mach numbers near 3.5 or below.

For viscous flow within a laminar boundary layer, the Navier-Stokes portion of the stress tensor customarily is approximated by $\mu \frac{\partial u}{\partial y}$. The ratio of the relaxation term to the ordinary term in the equation of motion is

$$\frac{\frac{\partial}{\partial x} \left(\kappa \frac{\partial u_k}{\partial x_k} \right)}{\frac{\partial}{\partial y} \left(\mu \frac{\partial u}{\partial y} \right)} \sim \frac{1}{\delta} \left(\kappa \frac{\partial u_\alpha}{\partial x_\alpha} \right) \sim \left(\frac{\delta}{l} \right) \frac{\kappa}{\mu} \frac{\partial u_\alpha}{\partial y}$$

Examination of the solution to boundary-layer equations for flow over a flat plate (e. g., ref. 78) indicates the average value of $(\partial u_k / \partial x_k) / (\partial u / \partial y)$ to be of the order of $(\gamma-1) M_\infty^2 / 10 \sqrt{Re}$, and δ/l to be of the order of $[6 + (\gamma-1) M_\infty^2] / \sqrt{Re}$. Hence,

$$\frac{\frac{\partial}{\partial x} \left(\kappa \frac{\partial u_\alpha}{\partial x_\alpha} \right)}{\frac{\partial}{\partial y} \left(\mu \frac{\partial u}{\partial y} \right)} \sim \frac{\kappa}{\mu} \left[\frac{(\gamma-1) M_\infty^2}{10 Re} \right] [6 + (\gamma-1) M_\infty^2] \quad (\text{B7})$$

This ratio, which is interpreted as a measure of the fractional effect of relaxation phenomena on boundary-layer flow, is important primarily at low Reynolds numbers and high Mach numbers, just as is the effect of relaxation phenomena on inviscid flow.

From the equation $\kappa u_\infty / pl = (\kappa / \mu) (\gamma M_\infty^2 / Re)$ and from the preceding table, the ratio κ / μ corresponding to free-stream conditions can be computed for the various gas mixtures. The results are as follows:

Polyatomic component	Calculated values of $(\kappa / \mu)_\infty$		
	$M_\infty=1.3$	$M_\infty=2.5$	$M_\infty=3.5$
CCl_2F_2	37	-----	-----
CF_4	350	410	370
SF_6	300	380	-----
CHF_3	230	170	-----
CHClF_2	37	-----	-----
CH_2F_2	8	2	-----
CO_2	3700	-----	-----
N_2O	530	-----	-----

At stagnation conditions κ / μ would be the same order as that tabulated for $M_\infty=1.3$; hence, broadly speaking, the various fluorochemical gas mixtures cover a range in values of κ / μ between about 2 and about 400. For the gases of most interest, namely, CF_4 and SF_6 , the corresponding value of κ / μ is seen to be about 400. Consequently, the value $\kappa / \mu = 400$ can be substituted into equation (B7) to obtain an estimate of relaxation-time effects on boundary-layer flow. The result is that the heat-capacity lag is found not to be significant except at low Reynolds numbers. In particular, at a Mach number of 3.5, it is indicated that only below or

near Reynolds numbers of about 2,000 would the effects of heat-capacity lag be significant. Even at a Mach number of 7 they would be significant only near or below Reynolds numbers of about 20,000.

Turning now to the case of air, a distinction must be made between wind-tunnel conditions and the conditions of flight. In a wind tunnel, the relaxation time for vibration is so long that the essential assumption inherent in the $\kappa-\tau$ relationship is not a valid assumption, since the vibration energy can lag far behind the translational energy. The energy in vibration for air at wind-tunnel temperatures, however, is negligible so that there are no appreciable effects of heat-capacity lag under such conditions. In flight, the situation is different, since the higher temperatures encountered reduce the relaxation time to values which are low enough to enable the vibrational energy almost to follow the translational energy. At a temperature of 1500° K, for example, the experiments of Blackman

(ref. 77) show the relaxation time for air to be the order of 10^{-5} second. At 3000° K it is the order of 10^{-6} second. These times are short enough to apply equation (C9) at the temperatures of flight. The result is that the ratio κ/μ is calculated to be the order 1,000 at 1500° K and the order of 50 at 3000° K. Even if the higher value ($\kappa/\mu=1000$) is used and substituted into equation (B7), the effects of heat-capacity lag in flight are found to be small, except under the combined conditions of a high Mach number and simultaneously a low Reynolds number. Under such conditions, the heat-capacity lag could be significant. In order to simulate in a low-density gas-mixture wind tunnel the heat-capacity lag that would exist in the boundary layer during flight, the ratio κ/μ would have to be simulated. It is possible to simulate approximately this ratio in a gas-mixture wind tunnel inasmuch as the range of values of κ/μ covered by the various polyatomic gases bracket the corresponding values for flight conditions in air.

APPENDIX C

RELATION BETWEEN BULK VISCOSITY AND RELAXATION TIME

The calculations of Appendix B are based on a relation between relaxation time τ and bulk viscosity coefficient κ . This relation can be derived from the general equations of motion for a viscous compressible gas by considering the definition of relaxation time and one of the fundamental properties of entropy. The method of derivation presented here is rather general and leads to a simple result which is compared later with results of other analyses of the problem.

The general equations of motion involve the viscous stress tensor

$$p_{ij} = \mu \left(\frac{\partial u_i}{\partial x_j} + \frac{\partial u_j}{\partial x_i} + \frac{2}{3} \delta_{ij} \frac{\partial u_\alpha}{\partial x_\alpha} \right) + \kappa \frac{\partial u_\alpha}{\partial x_\alpha} \delta_{ij} \\ = \left(p_{ij} \right)_{\text{Navier Stokes}} + \kappa \frac{\partial u_\alpha}{\partial x_\alpha} \delta_{ij} \quad (\text{C1})$$

and the energy dissipation function

$$\varphi = \frac{p_{ij}}{2} \left(\frac{\partial u_i}{\partial x_j} + \frac{\partial u_j}{\partial x_i} \right) \\ = \varphi_{\text{Navier Stokes}} + \kappa \left(\frac{\partial u_\alpha}{\partial x_\alpha} \right)^2 \\ = \varphi_{\text{Navier Stokes}} + \kappa \left(\frac{D\rho}{\rho Dt} \right)^2 \quad (\text{C2})$$

where the operator D represents the substantial differential, and the Navier-Stokes portion of φ involves only the ordinary coefficient of viscosity. The bulk viscosity κ —just like the ordinary viscosity μ —is regarded as a state property and, therefore, can be evaluated as a function of temperature and pressure from any pertinent experiment. For example, suppose an experiment with Couette-type flow were selected wherein the effects of bulk viscosity are negligible and the effects of ordinary viscosity are large (as would be the case at low speed under which condition $\partial u_\alpha / \partial x_\alpha = -D\rho / \rho Dt$ is negligible). The viscous stress tensor would reduce to $p_{xy} = \mu \partial u / \partial y$, so that measurement of the shear and the velocity gradient would enable the state property μ to be determined. On the other hand, suppose an experiment were selected wherein the effects of ordinary viscosity are negligible and the effects of bulk viscosity are large (as would be the case for the rapid compression in front of a small pitot tube or for the velocity dispersion of ultrasonic waves, under which conditions the time rate of change of density is the dominant term). In this case, the dissipation function (eq. (C2)) simplifies to the single term $\kappa (D\rho / \rho Dt)^2$, so that measurements of the energy dissipation (total pressure loss) and the rate of density variation would enable the state property κ to be determined.

By analysis of a flow wherein $D\rho / Dt$ is unusually large and, hence, wherein the bulk viscosity term dominates all other

terms in the stress tensor, a relationship can be established between κ and τ . For this type of flow, the energy equation can be written

$$\rho T \frac{DS}{Dt} = \varphi = \frac{\kappa}{\rho^2} \left(\frac{D\rho}{Dt} \right)^2 \quad (\text{C3})$$

where S is the *irreversible* entropy increase. The definition of relaxation time τ is

$$\frac{DE_i}{Dt} = \frac{E_i(T) - E_i}{\tau} \quad (\text{C4})$$

where T is the temperature corresponding to the translational degrees of freedom, $E_i(T)$ is the equilibrium value of internal energy corresponding to the temperature T , and E_i is the actual internal energy (corresponding to equilibrium at a different temperature T_i). From thermodynamic theory a third equation is obtained which completes the building blocks of the analysis; it provides an equation for the change of entropy when an amount of energy E_i flows from one source (translational energy at temperature T) to another source (vibration energy at temperature T_i).

$$DS = \frac{DE_i}{T_i} - \frac{DE_i}{T} \quad (\text{C5})$$

The above three basic equations can be combined to yield the desired relation between bulk viscosity and relaxation time.

It is emphasized that no assumption is made about the variation of specific heat with temperature, nor is any assumption made either about the magnitude of the internal energy or about the form which that internal energy takes. For example, the internal energy could be in rotation of the molecules, or in vibration between the atoms of molecules, or in electronic excitation. The essential assumption made is that the internal energy E_i does not lag far behind the equilibrium internal energy corresponding to the temperature T . In other words, it is assumed that the relaxation-time effects are small, so that a first-order theory is applicable. The various quantities are illustrated in figure 8. Since a first-order theory is being considered, the internal specific heat C_i can be regarded as constant over the small temperature range $T - T_i$, and the following approximation can be made:

$$DS = DE_i \frac{(T - T_i)}{T^2} = DE_i \frac{E_i(T) - E_i}{C_i T^2} \quad (\text{C6})$$

By combining this entropy equation with the equation defining relaxation time, there results

$$\frac{DS}{Dt} = \frac{[E_i(T) - E_i]^2}{\tau T^2 C_i} \quad (\text{C7})$$

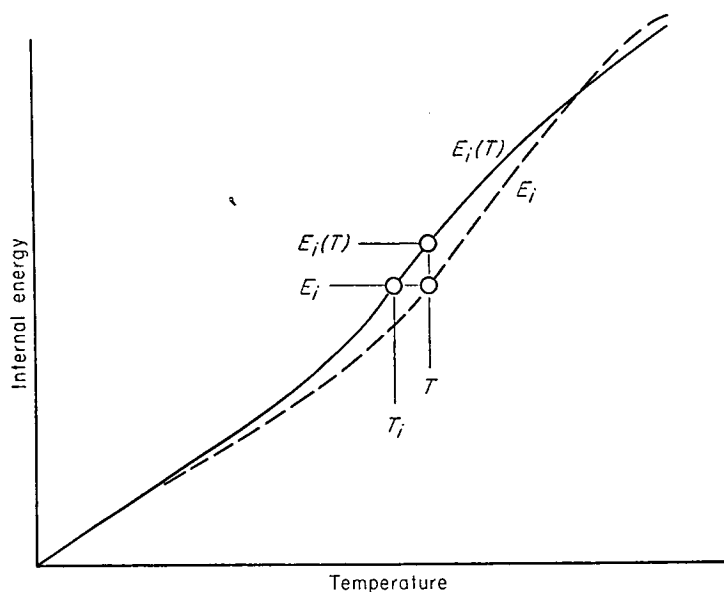


FIGURE 8.—Sketch of quantities related to internal energy lag.

Because the special experiment selected for consideration is an isentropic one except for first-order irreversible processes associated with κ , the following additional equations result from equation (C3):

$$\begin{aligned} \frac{\rho T}{\kappa} \frac{DS}{Dt} &= \frac{1}{\rho^2} \left(\frac{D\rho}{Dt} \right)^2 = \frac{1}{(\gamma-1)^2 T^2} \left(\frac{DT}{Dt} \right)^2 \\ &= \frac{1}{(\gamma-1)^2} C_i^2 T^2 \left(\frac{DE_i}{Dt} \right)^2 = \left[\frac{E_i(T) - E_i}{(\gamma-1) C_i T_\tau} \right]^2 \quad (C8) \end{aligned}$$

The final relation between bulk viscosity and relaxation time is obtained by combining equations (C8) and (C7) (and noting that $p = \rho RT = \rho(\gamma-1)C_v T$)

$$\kappa = p\tau(\gamma-1) \frac{C_i}{C_v} \quad (C9)$$

Inasmuch as C_i can represent either rotational energy or vibrational energy, several comparisons can be made with other analyses. In reference 79, Tisza compared the approximate equations for the dispersion of ultrasonic waves with corresponding equations from the Navier-Stokes relations and obtained exactly equation (C9). However, in comparing with the approximate equations from ultrasonic theory, Tisza assumed in effect that the amount of energy in internal motion E_i is small compared to the total energy, that is, he assumed that C_i is small compared to C_v . The above analysis shows that the relation obtained by Tisza actually applies to the case where the internal energy is a large portion of the total energy. Tisza assumed, of course, that the departures from equilibrium are small enough to be represented by a first-order theory (this assumption is made in all of the analyses discussed).

A different approach to the problem is taken by Kohler, reference 73, who employed the equations of kinetic theory involving the Maxwell-Boltzmann equation. Kohler considered two cases—first, that of rotational internal energy, and second, that of vibrational internal energy. The definition of relaxation time for rotation (τ_r) employed by

Kohler, however, is not the same as that employed above. The two are related by the equation

$$\frac{C_i + C_r}{C_i} \tau_r = \tau$$

where $C_i = 3R/2$ is the specific heat due to translational degrees of freedom. Letting f_r be the number of rotational degrees of freedom, then $C_r = f_r R/2$, and $R/(\gamma-1) = C_v = (3+f_r)R/2$, so that equation (C9) becomes

$$\kappa = \frac{2}{3} \frac{f_r}{3+f_r} p\tau_r$$

which is identical to an equation developed by Kohler. When Kohler considered vibrational energy, he used the same definition of relaxation time as that used herein, but he assumed that the internal energy in vibration (E_{vib}) is small even compared to the rotational internal energy. With this approximation Kohler could write $C_r + C_{vib} \approx C_r$, and thus obtained the equation

$$\kappa = (\gamma-1)p\tau \frac{C_{vib}}{C_v - C_{vib}}$$

Since $C_v - C_{vib} \approx C_v$ within the approximation made by Kohler, his result for vibrational internal energy is consistent with the basic equation (C9) of this appendix.

In reference 80 Meixner considers the problem from an entirely different viewpoint, namely, that of the theory of irreversible thermodynamics. Meixner assumes in effect, as did Kohler, that the internal energy is small compared to the translational energy. The equation Meixner obtained can be reduced to

$$\kappa = p\tau(\gamma-1) \frac{C_i}{C_v - C_i}$$

Just as in the case of Kohler's analysis, this result is seen to be consistent with that of equation (C9), provided it is remembered that the assumption of small internal energy enables $C_v - C_i$ to be approximated by C_v within the framework of Meixner's analysis.

In reference 81 Wang-Chang and Uhlenbeck considered the problem from the viewpoint of kinetic theory, only they did not assume as Kohler did that the internal energy was small. They did assume, however, that the internal energy did not vary significantly with temperature; that is, they assumed that the internal specific heat was constant, as this simplified their equations. Their final result can be written in the form

$$\kappa = p\tau(\gamma-1) \frac{C_i}{C_v}$$

which is identical to equation (C9) above. Thus, we see that the end result of the analysis of Wang-Chang and Uhlenbeck, just as the analysis of Kohler for rotational internal energy, actually applies to more general conditions than they assumed. Consequently, the derivation given above is seen to be rather general and to be confirmed by four separate analyses employing methods from several different fields of science.

REFERENCES

1. Theodorsen, Theodore, and Regier, Arthur: Experiments on Drag of Revolving Disks, Cylinders, and Streamline Rods at High Speeds. NACA Rep. 793, 1944.
2. Smelt, R.: Power Economy in High-Speed Wind Tunnels by Choice of Working Fluid and Temperature. RAE Rep. No. Aero 2081, British, 1945.
3. Kantrowitz, Arthur: The Supersonic Axial-Flow Compressor. NACA Rep. 974, 1946.
4. Huber, Paul W.: Use of Freon 12 As a Fluid for Aerodynamic Testing. NACA TN 1024, 1946.
5. Buell, C. E.: Spark Photography of Projectile Flight in Special Gases. Part I. The Freons. New Mexico School of Mines, Res. and Dev. Div. Tech. Rep. 453, 1948.
6. Donaldson, Coleman DuP., and Sabol, Alexander P.: Experiments on Aerodynamic Phenomena at Mach Numbers in the Range from 10 to 20. Proc. of First U. S. Nat. Cong. Appl. Mech., 1951, pp. 757-762.
7. von Doenhoff, A. E., and Braslow, A. L.: Studies of the Use of Freon-12 as a Wind-Tunnel Testing Medium. NACA TN 3000, 1953.
8. Duff, Russell E.: The Use of Real Gases in a Shock Tube. Univ. of Mich., Engr. Res. Inst. Proj. M720-4, Rep. 51-3, 1951.
9. Gunn, J. C.: Relaxation Time Effects in Gas Dynamics. British R. & M. No. 2338, British A. R. C., 1946.
10. Smout, Arthur: Discussion of paper "Titanium-A Survey" by P. L. Teed. Jour. of R. A. S., vol. 57, no. 508, Apr. 7, 1953, pp. 207-208.
11. Ruhemann, Martin.: The Separation of Gases. Second ed., ch. IX, Oxford Univ. Press, 1949.
12. Anon: Handbook of Chemistry and Physics. 33rd edition, 1951-1952. Chemical Rubber Publishing Company, Cleveland, Ohio.
13. Anon: Fluorocarbons Issue. Ind. Engr. Chem., Mar. 1947.
14. Simons, J. H., ed.: Fluorine Chemistry. Vol. 1. Academic Press Inc., N. Y., 1950.
15. Slessor, C., and Schram, S. R., eds.: Preparation, Properties, and Technology of Fluorine and Organic Fluoro Compounds. National Nuclear Energy Series, div. VII, vol. I, McGraw-Hill Book Co., New York, 1951.
16. Henne, Albert L.: Fluoroform. Jour. Am. Chem. Soc., no. 59, 1937, p. 1200.
17. Lester, D., and Greenberg, L. A.: The Toxicity of Sulfur Hexafluoride. Archives of Industrial Hygiene and Occupational Medicine, vol. 2, 1950, p. 348.
18. Lester, D., and Greenberg, L. A.: The Toxicity of Sulfur Pentafluoride. Archives of Industrial Hygiene and Occupational Medicine, vol. 2, 1950, p. 350.
19. Steunenberg, R. K., and Cady, G. H.: Pyrolysis of Fluorocarbons. Jour. Am. Chem. Soc., vol. 74, 1950, p. 4165.
20. Silvey, G. A., and Cady, G. H.: Trifluoromethylsulfur Pentafluoride. Jour. Am. Chem. Soc., vol. 72, 1950, p. 3624.
21. Chambers, William H., et al.: An Investigation of the Toxicity of Proposed Fire Extinguishing Fluids. Medical Div. Res. Rep. no. 23, CMLEM-52. Chem. Corps, Army Chem. Center, Maryland, 1950.
22. Wicklund, John S., Flieger, Howard W., and Masi, Joseph F.: Heat Capacity of Gaseous Hexafluoroethane. Nat. Bur. of Standards Jour. Res., vol. 51, no. 2, Aug. 1953, pp. 91-92.
23. Hendricks, James O.: Industrial Fluorochemicals. Ind. Engr. Chem., vol. 45, Jan. 1953, p. 99.
24. Nodiff, E. A., Grosse, A. V., and Hauptschein, M.: Physical Properties of n-Perfluoroalkyl Halides and Dihalides and a Comparison With Corresponding Alkyl Compounds. Jour. Org. Chem., vol. 18, 1953, p. 235.
25. Sidgwick, N. V.: The Chemical Elements and Their Compounds. Vols. I and II, Oxford Univ. Press, 1950.
26. Eiseman, B. J., Jr.: Pressure-Volume-Temperature Properties of the Freon Compounds. Refrig. Engr., vol. 60, Jan. 1952, pp. 496-503.
27. Miller, H. C., Verdelli, L. S., and Gall, J. F.: Some Physical Properties of Sulfur Hexafluoride. Ind. Engr. Chem., vol. 43, 1951, p. 1126.
28. Decker, C. E., Meister, A. G., and Cleveland, F. F.: Substituted Methanes. VI. Force Constants and Calculated Thermodynamic Properties for Some Trifluoromethanes. Jour. Chem. Phys., vol. 19, 1951, p. 784.
29. Lagemann, R. T., and Jones, E. A.: The Infrared Spectrum of Sulfur Hexafluoride. Jour. Chem. Phys., vol. 19, 1951, p. 534.
30. Plyler, E. K., and Benedict, W. S.: Infrared Spectra of Eighteen Halogen-Substituted Methanes. Nat. Bur. of Standards Jour. Res., vol. 47, Sept. 1951, pp. 202-220.
31. Cowan, R. D., Herzberg, G., and Sinha, S. P.: Rotation-Vibration Spectra of Diatomic and Simple Polyatomic Molecules with Long Absorbing Paths. IV. The Spectrum of Methyl Fluoroform (CH_3CF_3) from 19 to 0.7. Jour. Chem. Phys., vol. 18, 1950, p. 1538.
32. Nielsen, J. R., and Claassen, H. H.: Infra-Red and Raman Spectra of Fluorinated Ethanes. II. 1,1,1-Trifluoroethane. Jour. Chem. Phys., vol. 18, 1950, p. 1471.
33. Nielsen, J. R., Liang, C. Y., Smith, R. M., and Smith, D. C.: Infra-Red and Raman Spectra of Fluorinated Ethanes. V. The Series CF_3CF_3 , $\text{CF}_3\text{CF}_2\text{Cl}$, CF_3CFCl_2 , and CF_3CCl_3 . Jour. Chem. Phys., vol. 21, 1953, p. 383.
34. Nielsen, J. R., and Richards, C. M.: The Infra-Red Absorption Spectra of Hexafluoroethane Gas. Jour. Chem. Phys., vol. 16, 1948, p. 67.
35. McGee, P. R., Cleveland, F. F., Meister, A. G., Decker, C. E., and Miller, S. I.: Substituted Methanes. X. Infrared Spectral Data, Assignments, Potential Constants, and Calculated Thermodynamic Properties for CF_3Br and CF_3I . Jour. Chem. Phys., vol. 21, 1953, p. 242.
36. Smith, D. C., Saunders, R. A., Nielsen, J. R., and Ferguson, E. E.: Infrared and Raman Spectra of Fluorinated Ethanes. IV. The Series $\text{CH}_3\text{-CH}_3$, $\text{CH}_3\text{-CH}_2\text{F}$, $\text{CH}_3\text{-CHF}_2$, and $\text{CH}_3\text{-CF}_3$. Jour. Chem. Phys., vol. 30, no. 5, May 1952, pp. 847-859.
37. Smith, D. C., Brown, G. M., Nielsen, J. R., Smith, R. M., and Liang, C. Y.: Infrared and Raman Spectra of Fluorinated Ethanes. III. The Series CH_3CF_3 , $\text{CH}_3\text{CF}_2\text{Cl}$, CH_3CFCl_2 , and CH_3CCl_3 . Jour. Chem. Phys., vol. 20, 1952, p. 473.
38. Nuckolls, A. H.: The Comparative Life, Fire, and Explosion Hazards of Common Refrigerants. Underwriters Laboratories Reps. Misc. Hazard no. 2375, 1933; and, Nuckolls, Asa Hopkins: The Comparative Life, Fire, and Explosion Hazards of Difluoromonochloromethane ("Freon-22"). Underwriters Labs., Inc., Chicago, Misc. Hazard no. 3134, 1940.
39. White, Locke Jr., and Rice, O. K.: The Thermal Reaction of Hexafluoroethane with Quartz. Jour. Am. Chem. Soc., vol. 69, 1947, p. 267.
40. Kobe, K. A.: The Critical Properties of Elements and Compounds. Chem. Rev., vol. 52, 1953, p. 117.
41. Herzberg, Gerhard: Molecular Spectra and Molecular Structure. Vol. II. Infrared and Raman Spectra of Polyatomic Molecules. Van Nostrand, Inc., New York, 1945.
42. Yost, D. M., and Claassen, W. H.: The Thermochemical Constants of the Hexafluorides of Sulfur, Selenium and Tellurium. Jour. Am. Chem. Soc., vol. 55, 1933, p. 885.
43. Ruff, O.: Zur Kenntnis des Stickstoff-3-fluorids. Zeitschrift für anorganische und allgemeine chemie., vol. 197, 1933, p. 273.
44. Haszeldine, R. S., and Sharpe, R. G.: Fluorine and its Compounds. Methuen's Monographs on Chemical Subjects. John Wiley and Sons, New York, 1951.
45. Claassen, H. H.: Vibration Spectra and Normal Coordinate Treatment of Perfluorocyclobutane. Jour. Chem. Phys., vol. 18, 1950, p. 543.
46. Haszeldine, R. S.: Perfluoro-tert.-amines. Chem. Soc. Jour. I, 1951, p. 102.
47. Thompson, J., and Emeleus, H. J.: The Fluorination of Trimethylamine. Chem. Soc. Jour. 4, 1949, p. 3080.
48. Whipple, G. H.: Vapor-Liquid Equilibria of Some Fluorinated Hydrocarbon Systems. Ind. Engr. Chem., vol. 44, 1952, p. 1664.

49. Plyler, E. K., and Acquista, N.: Infrared Absorption Spectra of Five Halomethanes. Nat. Bur. of Standards Jour. Res., vol. 48, no. 1, Jan. 1952, pp. 92-97.
50. Yost, D. M.: The Raman Spectra of Volatile Fluorides. Applications of Raman Spectra to Chemical Problems. Proc. Indian Acad. Sci., vol. 8A, 1948, p. 33.
51. Masi, J. F.: Thermodynamic Properties of Gaseous Difluorodichloromethane. Jour. Amer. Chem. Soc., vol. 74, 1952, p. 4738.
52. Schumb, W. C.: Preparation and Properties of Sulfur Hexafluoride. Ind. Engr. Chem., vol. 39, no. 3, Mar. 1947, pp. 421-423.
53. Anon: Sulfur Hexafluoride. General Chem. Co. Tech. Service Bull. SF₆-A, 1952.
54. Wilson, M. K., and Polo, S. R.: The Infrared Spectra of NF₃ and PF₃. Jour. Chem. Phys., vol. 20, 1952, p. 1716.
55. Perkins, W. D., and Wilson, M. K.: The Infrared Spectrum of SO₂F₂. Jour. Chem. Phys., vol. 20, 1952, p. 1791.
56. Kirk, Raymond E., and Othmer F., eds.: Encyclopedia of Chemical Technology. Interscience Pub., Inc., N. Y., vol. 6, 1951, pp. 667-771.
57. Fowler, Ralph H., and Guggenheim, E. A.: Statistical Thermodynamics. Ch. III, Cambridge Univ. Press, 1952.
58. Hougen, Olaf A., and Watson, Kenneth M.: Chemical Process Principles. Vol. II of Thermodynamics. John Wiley and Sons, N. Y., 1947.
59. Wilke, C. R.: A Viscosity Equation for Gas Mixtures. Jour. Chem. Phys., vol. 18, 1950, p. 517.
60. Hirschfelder, Joseph O., Bird, R. Byron, and Spotz, Ellen L.: The Transport Properties of Gases and Gaseous Mixtures. II. Chemical Reviews., vol. 44, no. 1, 1949, pp. 205-231.
61. Sabatier, Germain: Viscosity des Gaz et Donnees Critiques. J. Chim. Phys., vol. 48, 1951, p. 113.
62. Staff of The Johns Hopkins University, Applied Physics Laboratory: Handbook of Supersonic Aerodynamics. Vol. V of Properties of Gases, sec. 15. Bur. of Ordnance, Navy Dept. NAV-ORD Rep. 1488, Aug. 1953.
63. Hadley, E. H., and Bigelow, L. A.: The Action of Elementary Fluorine Upon Organic Compounds. IX. The Vapor Phase Fluorination of Methane. Jour. Am. Chem. Soc. 62, 1940, p. 3302.
64. Midgley, T., Jr., and Henne, A. L.: Organic Fluorides as Refrigerants. Ind. Engr. Chem. 22, no. 5, 1931, p. 542.
65. Rietveld, A. O., Van Itterbeek, A., and Van Den Berg, G. J.: Measurements on the Viscosity of Mixtures of Helium and Argon. Physica vol. 19, June 1953, pp. 517-524.
66. Wachsmuth, Johannes: Über die Wärmeleitung in Gemischen zwischen Argon und Helium. Physikalische Zeitschrift vol. 9, 1908, pp. 235-240.
67. Hirschfelder, J. O., Curtiss, Charles F., and Bird, R. Byron: Molecular Theory of Gases and Liquids. John Wiley and Sons, Inc., 1954.
68. Griffith, Wayland: Vibrational Relaxation Times in Gases. Jour. Appl. Phys., vol. 21, no. 12, Dec. 1950, pp. 1319-1325.
69. Fogg, P. G. T., Hanks, P. A., and Lambert, J. D.: Ultrasonic Dispersion in Halo-Methane Vapors. Proc. Roy. Soc. (London). Series A, vol. 219, no. 1139, pp. 490-499, Oct. 7, 1953.
70. O'Connor, Brother C. Leonard: Thermal Relaxation of Vibrational States in Sulfur Hexafluoride. Jour. Acoust. Soc. Am., vol. 26, no. 3, May 1954, pp. 361-364.
71. Lambert, J. D., and Rowlinson, J. S.: Ultrasonic Dispersion in Organic Vapours. Proc. Roy. Soc. (London). Series A. no. 1078, Dec. 22, 1950, vol. 204, pp. 424-434.
72. Bethe, Hans Albrecht, and Teller, E.: Deviations from Thermal Equilibrium in Shock Waves. Aberdeen Proving Ground, Aberdeen, Md., Ballistic Research Laboratory. Rep. X-117, 1945.
73. Kohler, Max: Reibung in massig verdunnten Gasen als Folge Verzögerter einstellung der Energie. Zeit. f. Physik. 125, 715-732 (1949).
74. Schafer, Klaus: Die stossanregung intramolekularer schwingungen in gasen und gasmischungen. VII Theorie der schalldispersion bei vorhandensien mehrer normal-schwingungen. Zeit. f. Physikalische Chemie B 46, 212-228 (1940).
75. Walker, Richard: Heat Capacity Lag in Gases. NACA TN 2537, 1951.
76. Rossing, Thomas D., and Legvold, Sam: Heat Capacity Lag of Gas Mixtures. Iowa Engineering Experiment Station, Iowa State College, Ames, Iowa. Final Report, Contract NAW-6219, Aug. 17, 1952 to Aug. 17, 1953.
77. Blackman, Vernon H.: Vibrational Relaxation in O₂ and N₂. Tech. Rep. II-20, Princeton Univ., Dept. of Physics, May 1955.
78. Chapman, Dean R., and Rubesin, Morris W.: Temperature and Velocity Profiles in the Compressible Laminar Boundary Layer with Arbitrary Distribution of Surface Temperature. Jour. Aero. Sci., vol. 16, no. 9, Sept. 1949, pp. 547-565.
79. Tisza, L.: Supersonic Absorption and Stokes' Viscosity Relation. Phys. Rev., vol. 61, no. 7-8, Apr. 1-15, 1942, pp. 531-536.
80. Meixner, J.: Allgemeine Theorie der Schallabsorption in Gasen und Flussigkeiten unter Berücksichtigung der Transporterscheinungen. Acoustica, vol. 2, pp. 101-109, 1952.
81. Wang Chang, C. S., and Uhlenbeck, G. E.: Transport Properties in Polyatomic Gases. Rep. CM-681, Univ. of Mich. Engr. Res. Inst., July 10, 1951.

TABLE I.—PROPERTIES OF HEAVY MONATOMIC GASES AND AIR CONSTITUENTS

Symbol	Gas	m , gm. mole	Boiling temp., °C	Critical constants			Viscosity at 0° C μ , micropoise
				T_c , °K	p_c , atm.	V_c , cc/gm. mole	
Ar.....	argon.....	40	-186	151	48	75.3	210
Kr.....	krypton.....	84	-153	210	54	92.1	230
Xe.....	xenon.....	131	-107	290	58.2	114	210
N ₂	nitrogen.....	28	-196	126	33.5	90.0	166
O ₂	oxygen.....	32	-183	154	49.7	74.4	189
	air.....	29	-----	132	37.2	83	172

TABLE II.—GENERAL CHARACTERISTICS OF POLYATOMIC GASES

Formula	m_2 , gm. mole	Chemical name	Common or trade name	General classifi- cation (1)	Remarks	References		
						Spectro- scopic data	Toxicity data	Physical data
C ₄ F ₁₀ C ₃ F ₉ N.....	238 221	n-perfluorobutane..... perfluorotertiaryamine.....	S S?	Reported "as nontoxic as fluorocarbons." Chemistry resembles NF ₃ . Stable to at least 400° C.	14 56	14, 19, 15 14, 56, 44, 46, 23
C ₄ F ₈	200	perfluorocyclobutane.....	Freon C318.....	S	45	48, 15, 26
CF ₃ CBBrF ₂ CF ₃ SF ₅ SeF ₆	199 196 193	bromoethforane..... trifluoromethylsulfurpentafluoride..... selenium hexafluoride.....	S? S? S?	Toxicity unknown..... Toxicity, liquid density unknown..... Toxicity unknown..... 50	14, 56, 24 20 14, 25, 42
C ₃ F ₈ C ₂ F ₆ NF.....	188 171	perfluoropropane..... perfluorodimethylamine.....	S S?	Musty odor. Toxicity, liquid density un- known.	14	14, 56, 19 44, 47
CBBrClF ₂	165	bromochlorodifluoromethane.....	Freon 12B1.....	Q	Toxicity probably excessive. More toxic than CHClF ₂ .	49	21	26
CF ₃ CClF ₂ CF ₃ OCF ₃	155 154	chloroethforane..... perfluoroether.....	Freon 115.....	S S?	Reported "as nontoxic as fluorocarbons." Liquid density unknown. Stable to at least 400° C.	33 56	14, 26 14, 56, 44, 23
CBrF ₃	149	bromotrifluoromethane.....	Freon 13B1 Kulene 131.	S	Excellent fire extinguisher.....	35	21, 56	14, 26, 56
SF ₆	146	sulfurhexafluoride.....	S, I	Excellent high-voltage gaseous insulator. Ex- tremely inert chemically. Thermally stable to about 500° C.	29	17	14, 56, 25, 27, 52, 53
CF ₃ CF ₃ CClF ₂ CHF ₂	138 137	ethforane..... 1-chloro-2-hydroethforane.....	Freon 124a.....	S S?	Thermally stable to about 700° C..... Toxicity unknown.....	34	14, 56, 19, 39, 22 14, 26
CCl ₂ F ₂ CF ₃ NF ₂ CClF ₃	121 121 105	dichlorodifluoromethane..... perfluoromethylamine..... chlorotrifluoromethane.....	Freon 12..... Freon 13.....	S S? S Musty odor. Toxicity, liquid density unknown.....	30, 51 28, 30	18, 38, 63	14, 26, 63 14, 56, 44 14, 26
SO ₂ F ₂	102	sulfuryl fluoride.....	S?	Toxicity, liquid density unknown. Chemistry resembles SF ₆ .	55	14
CHF ₂ CHF ₂ CH ₃ CClF ₂	102 101	1-hydro-2-hydroethforane..... 1-chloro-1, 1-difluoroethane..... Genetron 101.....	S? Q	Toxicity, liquid density unknown..... Slightly flammable, toxicity marginal. (See remarks for Genetron 100.) 37 18	14 14, 26
FCONF ₂	99	carbonylnitrogen trifluoride.....	S?	Toxicity, liquid density unknown. Reported as very inert.	14
CF ₄	88	carbontetrafluoride.....	Freon 14.....	S	Extreme thermal stability and chemical inert- ness.	28, 30	21	14, 56, 19
CHClF ₂	87	chlorodifluoromethane.....	Freon 22.....	Q	Toxicity marginal (classified U. A. L. group 5A).	30	38	14
CH ₃ CF ₃ NF ₃	84 71	1,1,1-trifluoroethane..... nitrogen trifluoride.....	S? S?	Toxicity and flammability unknown..... Toxicity uncertain since early tests (Ruff, ref. 43) are questionable.	31, 32 54 43, 25	14 14, 43
CHF ₃	70	fluoroform.....	Freon 23.....	S, I	Thermally stable to at least 1100° C.....	28, 30	16	14
CH ₃ CHF ₂	66	1,1-difluoroethane.....	Genetron 100.....	Q	Slightly flammable, but forms nonflammable azeotropic mixture with Freon 12. Azeo- tropic mixture called "Carrene 7," has $m=$ 100, $T_b=-33^{\circ}$ C.	36	18, 25	14
CH ₂ F ₂	52	difluoromethane.....	Freon 32.....	S?	Flammability unknown.....	30	25	14
CO ₂	44	carbon dioxide.....	Q	Toxic for prolonged exposure at concentrations above about 3 per cent.	41	25	40, 13
N ₂ O.....	44	nitrous oxide.....	Q	Nonflammable but acts as oxidant at high tem- perature. Toxic at high concentrations.	41	25	40, 13

1S *satisfactory*, in that sufficient information is available to regard the gas as nontoxic, noncorrosive, nonflammable, thermally stable to at least about 200° C, and inert chemically.

S? *may be satisfactory*, but available information is insufficient to judge it so. (See remarks for each gas thus classified.)

Q *questionable* because of possessing at least one undesirable characteristic (see remarks) which, however, may not be totally disqualifying.

I *inert physiologically*, as determined by tests with small animals living in atmosphere of 20-percent oxygen, 80-percent gas in question, and showing no observable effects either during the duration of tests (usually several hours) or afterwards.

TABLE III.—PHYSICAL CHARACTERISTICS OF POLYATOMIC GASES

Formula	$\frac{m_2}{\text{mole}}$	Boiling temp., T_b , °C (1)	Critical constants (2)			Viscosity at 0° C μ , micropoise	$\frac{\bar{m}_2}{\mu}$	$\frac{(\bar{\mu}_2)^2}{(m_2)^{3/2}}$	Spectroscopic data fundamental wave numbers, ω , cm ⁻¹ (3)
			T_c , °K	p_c , atm.	V_c , cc/gm. mole				
C ₄ F ₁₀	238	-2	387	23	378	111	12.7	0.018	1431, 1385, 1340, 1285, 1239 (2), 1220, 1008 (2), 963, 745 (2), 699, 660 (2), 613, 569, 439, 350, 338 (2), 285, 273, 258, 250 (2), 192 (2), 173, 86
C ₃ F ₈ N.....	221	-11							
C ₄ F ₈	200	-6	390e		331e	111	10.7	.023	
C ₂ F ₅ CBBrF ₂	199	-22	386e	32e	263e	128	9.2	.031	
CF ₃ SF ₅	196	-20							
SeF ₆	193	-47 sub.	340e		219e	154	7.4	.047	787 (3), 708, 662 (2), 461 (3), 405 (3), 245 (3)
C ₃ F ₈	188	-38	344e	26e	298e	122	9.1	.030	
C ₂ F ₅ NF ₂	171	-37							
CBrClF ₂	165	-4	427	41.2	232	121	8.1	.036	
CF ₃ CClF ₂	155	-38	353	30.8	260	119	7.7	.039	
CF ₃ OCF ₃	154	-59							1207 (2), 1087, 762, 548 (2), 348, 297 (2)
CBrF ₃	149	-60	341		199	143	6.2	.059	
SF ₆	146	-64 sub.	319	36.8	201	142	6.1	.060	
CF ₃ CF ₃	138	-78	293	29.9	220	139	5.9	.063	
CClF ₂ CHF ₂	137	-10	400	36.7	251	108	7.5	.038	
CCl ₂ F ₂	121	-30	385	39.6	218	118	6.1	.055	1159, 1101, 906, 667, 473, 455, 437, 318, 261
CF ₃ NF ₂	121	-78							
CClF ₃	105	-80	302	39	180	136	4.6	.091	
SO ₂ F ₂	102	-55	340e						
CHF ₂ CHF ₂	102	-23							
CH ₃ CClF ₂	101	-9	411	40.7	232	97	6.2	.049	3035, 2965, 1447, 1395, 1231, 1202, 1127, 1103, 967, 904, 683, 544, 526, 435, 429, 334, 305, torsion
FCO ₂ NF ₂	99	-82							
CF ₄	88	-128	228	36.8	139	171	3.1	.19	
CHClF ₂	87	-41	370	48.5	165	120	4.3	.094	
CH ₃ CF ₃	84	-47							
NF ₃	71	-129	230e		125e	164	2.6	.24	1032, 647, 905 (2), 493 (2)
CHF ₃	70	-84	306	47	136	134	3.1	.16	
CH ₃ CHF ₂	66	-25	387	44.3	181	96	4.1	.091	
CH ₂ F ₂	52	-52	351		170	93	3.3	.12	
CO ₂	44	-79 sub.	304	72.9	96	137	1.9	.34	
N ₂ O.....	44	-88	310	71.7	98	135	1.9	.33	2237, 1288, 588 (2)

¹ sub. sublimes at atmospheric pressure.² e estimated from similar gases, or from liquid density and reduced orthobaric density of similar gases.³ number in parentheses denotes degree of degeneracy of wave number it follows.

TABLE IV.—CHARACTERISTICS OF GAS-MIXTURE WIND TUNNELS

Polyatomic gas			Mixture proportions		Mixture molecular weight relative to air			Mixture viscosity at 0° C relative to air			Size of gas-mixture wind tunnel relative to air wind tunnel for same M_∞ , Re , & T_t			Horsepower of gas-mixture wind tunnel relative to air tunnel for same M_∞ , Re , & p_t		
Formula	$\frac{m_2}{\text{mole}}$	$\frac{C_{p2}}{\text{cal. mole}^\circ\text{K}}$ (1)	x_2	x_1	argon \bar{m}	krypton \bar{m}	xenon \bar{m}	argon $\bar{\mu}$	krypton $\bar{\mu}$	xenon $\bar{\mu}$	argon \bar{L}	krypton \bar{L}	xenon \bar{L}	argon $\frac{HP}{HP}$	krypton $\frac{HP}{HP}$	xenon $\frac{HP}{HP}$
(a) Design Mach number 1.3; $T_\infty = 230^\circ\text{K}$																
C ₄ F ₁₀	238	35.8e	0.07	0.93	1.82	3.23	4.76	1.13	1.24	1.16	0.84	0.69	0.53	0.52	0.27	0.13
C ₃ F ₈	200	33.5	.07	.93	1.77	3.17	4.69	1.12	1.23	1.15	.84	.69	.53	.53	.27	.13
CF ₃ CBBrF ₂	199	24.4e	.10	.90	1.93	3.29	4.79	1.12	1.22	1.15	.80	.67	.53	.46	.25	.13
SeF ₆	193	22.5	.11	.89	1.98	3.31	4.79	1.17	1.25	1.17	.83	.69	.53	.49	.27	.13
C ₃ F ₈	188	29.5e	.08	.92	1.80	3.18	4.69	1.13	1.24	1.16	.84	.69	.53	.53	.27	.13
CBrClF ₂	165	15.8	.19	.81	2.18	3.41	4.76	1.03	1.13	1.08	.70	.61	.50	.34	.20	.11
CF ₃ CClF ₂	155	23.0	.11	.89	1.82	3.16	4.62	1.10	1.20	1.13	.81	.68	.53	.49	.26	.13
CBrF ₃	149	14.7	.21	.79	2.15	3.35	4.65	1.09	1.17	1.12	.74	.64	.52	.37	.22	.13
SF ₆	146	18.9	.14	.86	1.91	3.19	4.59	1.12	1.22	1.15	.81	.68	.53	.48	.26	.13
CF ₃ CF ₃	138	21.8	.12	.88	1.78	3.11	4.55	1.13	1.23	1.16	.85	.70	.54	.54	.28	.14
CCl ₂ F ₂	121	15.2	.20	.80	1.93	3.14	4.45	1.02	1.13	1.09	.74	.64	.52	.39	.23	.13
CClF ₃	105	13.8	.23	.77	1.89	3.05	4.35	1.06	1.16	1.12	.77	.67	.54	.44	.26	.14
CH ₃ CClF ₂	101	16.8	.17	.83	1.74	2.99	4.35	.99	1.12	1.08	.75	.65	.52	.43	.24	.13
CF ₄	88	12.5	.27	.73	1.82	2.93	4.14	1.15	1.23	1.17	.85	.72	.57	.53	.30	.16
CHClF ₂	87	12.0	.29	.71	1.84	2.92	4.10	.98	1.09	1.06	.73	.63	.53	.39	.24	.14
NF ₃	71	11.1	.33	.67	1.73	2.74	3.86	1.11	1.20	1.16	.85	.73	.59	.54	.32	.18
CHF ₃	70	10.7	.35	.65	1.74	2.72	3.79	1.01	1.11	1.08	.76	.67	.56	.44	.28	.16
CH ₃ CHF ₂	66	13.5	.24	.76	1.59	2.74	4.00	.95	1.09	1.06	.76	.66	.53	.45	.26	.14
CH ₂ F ₂	52	9.22	.47	.53	1.57	2.37	3.24	.78	.91	.93	.63	.59	.52	.31	.23	.15
CO ₂	44	8.11	.63	.37	1.47	2.03	2.63	.92	1.02	1.02	.76	.72	.63	.48	.36	.25
N ₂ O.....	44	8.45	.57	.43	1.46	2.11	2.81	.94	1.04	1.04	.78	.72	.62	.50	.35	.23
(b) Design Mach number 2.5; $T_\infty = 140^\circ\text{K}$																
CBrF ₃	149	11.0	.33	.67	2.62	3.62	4.73	1.03	1.10	1.06	.64	.58	.49	.25	.17	.11
SF ₆	146	11.5	.30	.70	2.49	3.54	4.69	1.04	1.12	1.07	.66	.59	.50	.28	.19	.11
CF ₃ CF ₃	138	15.3	.19	.81	2.03	3.25	4.57	1.09	1.17	1.12	.76	.65	.52	.41	.24	.13
CClF ₃	105	10.2	.39	.61	2.24	3.17	4.19	.98	1.07	1.05	.66	.60	.51	.29	.20	.13
CF ₄	88	9.31	.46	.54	2.14	2.95	3.90	1.10	1.16	1.13	.75	.68	.57	.39	.27	.17
NF ₃	71	8.74	.53	.47	1.94	2.65	3.43	1.05	1.13	1.10	.76	.69	.60	.41	.29	.19
CHF ₃	70	8.60	.55	.45	1.95	2.63	3.38	.92	1.00	1.00	.66	.62	.54	.31	.23	.16
(c) Design Mach number 3.5; $T_\infty = 105^\circ\text{K}$																
CF ₄	88	8.40	.58	.42	2.34	2.97	3.66	1.07	1.12	1.10	.70	.65	.58	.32	.25	.17
NF ₃	71	8.19	.62	.38	2.04	2.62	3.24	1.03	1.09	1.07	.72	.67	.60	.36	.28	.20

¹ e estimated from similar gases and from average bond frequencies of ref. 58.

REPORT 1260

STUDIES OF THE SPEED STABILITY OF A TANDEM HELICOPTER IN FORWARD FLIGHT¹

By ROBERT J. TAPSCOTT and KENNETH B. AMER

SUMMARY

Flight-test measurements, related analytical studies, and corresponding pilots' opinions of the speed stability of a tandem-rotor helicopter are presented. An undesirable instability, evidenced by rearward stick motion with increasing forward speed at constant power, is indicated to be caused by variations with speed of the front-rotor downwash at the rear rotor. An analytical expression for predicting changes in speed stability caused by changes in rotor geometry is derived and constants for use with the analytical expression are presented in chart form. Means for improving stability with speed are studied both analytically and experimentally.

The test results also give some information as to the flow conditions at the rear rotor.

INTRODUCTION

For the past several years the National Advisory Committee for Aeronautics has been studying the flying qualities of helicopters in order to set up flying-qualities criteria and to provide a basis for improvement. Information obtained during flying-qualities studies of a tandem helicopter in reference 1 indicated the tandem-rotor configuration to be susceptible to instability with speed in forward flight. That this instability with speed was a basic problem resulting from effects of front-rotor downwash on the rear rotor appeared likely. Hence, this aspect of the tandem configuration seemed worthy of study in order to provide a basis for improvement.

Basically, speed stability may be defined as the variation of pitching moment with speed. If an increase in forward speed of the helicopter, with control stick fixed, produces a nose-down moment, the speed will increase further due to the resulting nose-down attitude. Such an aircraft is unstable with speed. If a nose-up moment is associated with an increase in speed from trim with stick fixed, the resulting nose-up attitude tends to reduce the speed to the trim value. An aircraft exhibiting the latter characteristics is stable with speed. A more complete discussion of helicopter stability may be found in chapter 11 of reference 2.

Stability with speed is important primarily when a helicopter is being operated at or near the placard speed. At this condition, instability with speed increases the likelihood of inadvertently exceeding the placard speed with possible damage to the aircraft. At lower speeds, stability with speed is desirable as it simplifies maintaining desired speeds

and provides a logical variation of control position with speed. The military and civilian regulatory agencies are now generally requiring helicopters to exhibit speed stability. (See refs. 3 and 4.)

The investigation herein was undertaken to determine the minimum satisfactory speed stability for a tandem-rotor helicopter and to determine the factors that affect speed stability in order to provide a basis for improvement.

SYMBOLS

b	number of blades per rotor
r	radial distance to blade element, ft
R	blade radius, ft
c	blade-section chord, ft
c_e	equivalent blade chord (on thrust basis), $\frac{\int_0^R cr^2 dr}{\int_0^R r^2 dr}$, ft
σ	rotor solidity, $bc_e/\pi R$
Θ	instantaneous blade-section pitch angle; angle between line of zero lift of blade section and plane perpendicular to rotor shaft, radians
θ	collective pitch, average value around azimuth of Θ , radians
ρ	mass density of air, slugs/cu ft
ρ_0	mass density of air at sea level, slugs/cu ft
V	true airspeed of helicopter along flight path, fps
Ω	rotor angular velocity, radians/sec
α	rotor angle of attack; angle between flight path and plane perpendicular to axis of no feathering, positive when axis is inclined rearward, radians
μ	tip-speed ratio, $V \cos \alpha / \Omega R$, assumed equal to $V / \Omega R$
T	rotor thrust, component of rotor resultant force parallel to axis of no feathering, lb
C_T	rotor-thrust coefficient, $\frac{T}{\pi R^2 \rho (\Omega R)^2}$
L	rotor lift, lb
C_L	rotor-lift coefficient, $\frac{L}{\frac{1}{2} \rho \pi R^2 V^2}$
ϵ	angle of downwash at rear rotor due to front rotor (assumed equal to C_T / μ^2), radians
W	helicopter gross weight, lb
ΔL	difference in lift of front and rear rotors, positive when lift of rear rotor is greater, lb

¹ Supersedes recently declassified NACA Research Memorandum L53F15a by Robert J. Tapscott and Kenneth B. Amer, 1953.

ΔT	difference in thrust of front and rear rotors, positive when thrust of rear rotor is greater, lb
$\Delta\theta$	difference in collective-pitch angle of front and rear rotors, positive when pitch of rear rotor is greater, radians
ΔR	difference in blade radius of front and rear rotors, positive when blade radius of rear rotor is greater, ft
$\Delta(\Omega R)$	difference in blade tip speed of front and rear rotors, positive when tip speed of rear rotor is greater, fps
$\Delta\sigma$	difference in rotor solidity of front and rear rotors, positive when rotor solidity of rear rotor is greater
$\Delta\alpha$	total difference in angle of attack of front and rear rotors, positive when rear rotor is greater, radians
$\Delta\alpha_d$	difference in angle of attack of front and rear rotors due to swashplate dihedral, positive when angle of attack of rear rotor is greater, radians
δ	longitudinal position of control stick, positive when forward, in. from neutral
a'	longitudinal angle between rotor force vector and axis of no feathering, deg
x	distance from center of gravity to midpoint between line of action of thrust vectors or effective midpoint, positive when center of gravity is forward of effective midpoint, in.
x'	distance from effective midpoint to the midpoint between rotor shafts, positive when effective midpoint is forward, in.
x_0	distance from midpoint between rotor shafts to center of gravity, positive when center of gravity is forward, in.
h	vertical distance from center of gravity to the plane of the rotors, in.
B_1	longitudinal cyclic pitch with respect to shaft, positive when axis of no feathering is tilted forward with respect to the shaft, deg
Subscripts:	
fr	front rotor
av	average value

DESCRIPTION OF TEST HELICOPTER

The tandem helicopter used in the tests is shown in figure 1. It has a normal gross weight of approximately 7,000 pounds and has two rotors of equal size, each having a diameter of 41 feet. The rotors have equal rotational speed and solidity and are of equal distance above the center of gravity. There is no overlap of the swept areas of the rotors and the swashplates are parallel longitudinally to one another. The center-of-gravity range when measured along a line perpendicular to the shafts, which are parallel, is from 1 inch rearward to 18 inches forward of the midpoint between shafts. For the tests the center of gravity was 13 inches forward of this midpoint. The horizontal and twin vertical stabilizers have total areas of approximately 40 and 50 square



FIGURE 1.—Test helicopter.

feet, respectively. The helicopter has conventional pilot controls: stick, pedals, collective-pitch lever, and throttle. Longitudinal control is achieved by a longitudinal motion of the stick, which produces a combination of longitudinal cyclic pitch and differential collective pitch, the latter providing by far the larger magnitude of pitching moment. Lateral control is achieved by lateral motion of the stick which causes lateral cyclic pitch at both rotors; directional control is achieved by use of the pedals which causes differential lateral cyclic pitch. Longitudinal trim control is obtained through use of a control wheel which varies the differential collective pitch between rotors. For all of the tests the trim control was at an indicator setting of approximately 0.8° nose up.

For the latter part of the tests, in order to change the speed stability of the test helicopter, the rigging of the rotors was modified to incorporate what will henceforth be referred to as swashplate "dihedral." This consisted of adjusting the longitudinal control cables to give rearward cyclic and forward cyclic pitch on the front and rear rotors, respectively, while the control stick was locked in longitudinal neutral position, thus producing a fixed difference in the longitudinal cyclic pitch of the front and rear rotors at any stick position. Aerodynamically, this is equivalent to physically inclining the shafts toward one another. The total longitudinal swashplate travel was reduced to prevent exceeding a cyclic pitch of 6° , a limit set by linkage and clearance between the blade and droopstop, by use of a reducing bar on the longitudinal cyclic control cables. A calibration of the longitudinal cyclic pitch and differential collective pitch for the configuration with approximately 4.5° of longitudinal swashplate dihedral and trim setting of 0.8° nose up is shown in figure 2.

The test helicopter was equipped with synchronized standard NACA recording instruments that measured control position, airspeed along the flight path, and angle of attack at the nose of the helicopter of the plane perpendicular to the rotor shafts. The angle-of-attack and airspeed pick-up installation is shown in figure 3.

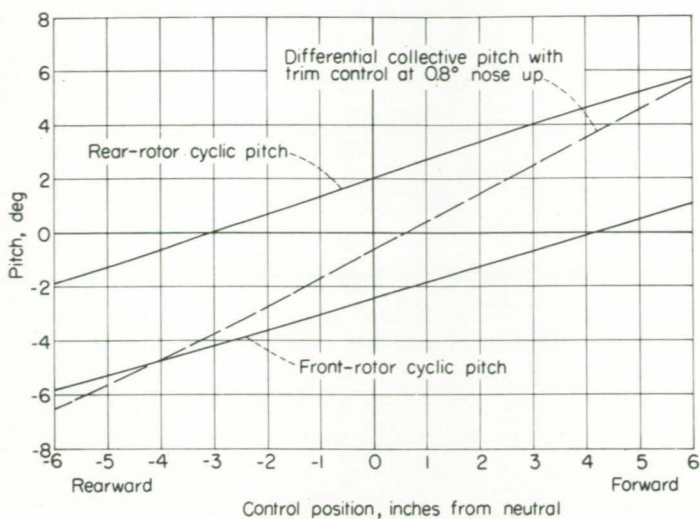


FIGURE 2.—Longitudinal control calibration of test helicopter with approximately 4.5° swashplate dihedral.

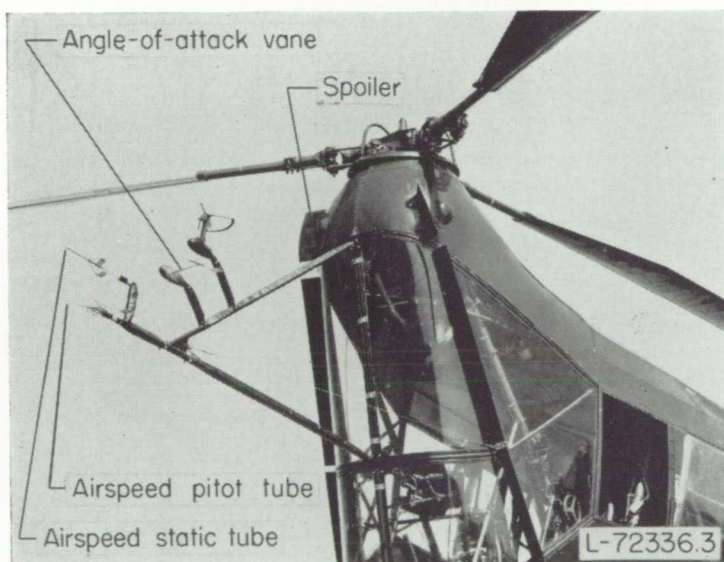


FIGURE 3.—Airspeed, angle-of-attack, and spoiler installation on test helicopter.

TESTING TECHNIQUE

In order to keep the pitching moments on the helicopter in flight trimmed during speed variation, any pitching moments resulting from speed changes must be counteracted by longitudinal motion of the control stick. Since speed stability is defined by the variation of pitching moment with speed, the variation of stick position in counteracting moments due to speed change is a measure of speed stability. Rearward stick motion would be needed to neutralize a nose-down moment while forward motion of the stick cancels a nose-up moment. Inasmuch as a nose-up moment associated with increased speed is stabilizing, forward stick motion with increasing speed signifies stability with speed.

Measurements were made in flight of the speed stability of the test helicopter in several configurations, the procedure being to trim the helicopter at a given speed and record stick

position and forward speed while varying the speed at constant power and collective pitch. It will be noted that the helicopter was not in level flight but descending or ascending as caused by increasing or decreasing speed at constant power.

The significance of this technique is that under the given conditions the stick motion is a measure of the speed stability exhibited by the helicopter in small disturbances from steady trimmed flight where power and collective pitch are constant. It is under these conditions that speed stability affects the pilots' opinions of flying qualities of the helicopter.

THEORETICAL ANALYSIS OF SPEED STABILITY

For purposes of subsequent comparison with experimental results and to form a basis for improvement of speed stability, the following theoretical analysis of speed stability is performed.

ASSUMPTIONS

The analysis in this report is based on the stability derivatives of reference 5 and therefore the assumptions of that reference are carried over. In addition, for the purposes of this analysis, the following simplifying assumptions are made:

(1) The pitching moments of the fuselage—horizontal-tail combination are zero. This assumption appears justified in view of the large magnitudes of the pitching moments caused by the rotors compared with the pitching moments caused by the fuselage-tail combination.

(2) The lift of the fuselage—horizontal-tail combination is zero.

(3) The front rotor is not affected by the rear rotor.

(4) The downwash angle at the rear rotor due to the lift of the front rotor is given by $C_{T_{fr}}/\mu^2 \approx C_{L_{fr}}/2$ where $C_{T_{fr}}$ and $C_{L_{fr}}$ are the thrust and lift coefficients, respectively, of the front rotor. Theoretically, this magnitude of downwash is not fully reached until at an infinite distance behind the front rotor; however, calculations of stability using the assumed value of downwash and theoretical calculations of downwash behind a rotor presented in reference 6 indicate it to be a reasonable assumption. The theory developed herein will be restricted to $\mu \geq 0.15$. Below this value of μ , the downwash formula becomes inaccurate.

(5) The stability with speed of the individual rotors and pitching moments due to changes in longitudinal cyclic pitch are neglected. Preliminary calculations show these quantities to be of only secondary importance.

DERIVATIONS OF EQUATIONS

In order that no pitching moments be produced as the speed of the helicopter is varied, the difference in the thrust of the front and rear rotors ΔT must remain at the trim value. The average thrust of rotors during steady flight is given by definition of the thrust coefficient as

$$T_{av} = \frac{W}{2} = \left(\frac{C_T}{\sigma} \right)_{av} \sigma_{av} \pi (R_{av})^2 \rho [(\Omega R_{av})^2] \quad (1)$$

Also, the thrust differential between rotors is

$$\Delta T = \Delta \left[\frac{C_T}{\sigma} \sigma \pi R^2 \rho (\Omega R)^2 \right]$$

Taking differentials,

$$\Delta T = \Delta \left(\frac{C_T}{\sigma} \right) [\sigma \pi R^2 \rho (\Omega R)^2]_{av} + \Delta \sigma \left[\frac{C_T}{\sigma} \pi R^2 \rho (\Omega R)^2 \right]_{av} + 2R_{av} \Delta R \left[\frac{C_T}{\sigma} \sigma \pi \rho (\Omega R)^2 \right]_{av} + 2(\Omega R)_{av} \Delta(\Omega R) \left[\frac{C_T}{\sigma} \sigma \pi R^2 \rho \right]_{av} \quad (2)$$

Dividing equation (2) by equation (1) gives

$$\frac{\Delta T}{W/2} = \frac{1}{\left(\frac{C_T}{\sigma} \right)_{av}} \Delta \frac{C_T}{\sigma} + \frac{\Delta \sigma}{\sigma_{av}} + \frac{2 \Delta R}{R_{av}} + \frac{2 \Delta(\Omega R)}{(\Omega R)_{av}} \quad (3)$$

However, $\Delta(C_T/\sigma)$ may be expressed as

$$\Delta \left(\frac{C_T}{\sigma} \right) = \left[\left(\frac{\partial \frac{C_T}{\sigma}}{\partial \alpha} \right)_{av} \Delta \alpha + \left(\frac{\partial \frac{C_T}{\sigma}}{\partial \theta} \right)_{av} \Delta \theta \right] \quad (4)$$

where $\left(\frac{\partial \frac{C_T}{\sigma}}{\partial \alpha} \right)_{av}$ and $\left(\frac{\partial \frac{C_T}{\sigma}}{\partial \theta} \right)_{av}$ are averages of the front and rear rotor derivatives.

Substituting equation (4) for $\Delta \left(\frac{C_T}{\sigma} \right)$ into equation (3), gives

$$\frac{\Delta T}{W/2} = \frac{1}{\left(\frac{C_T}{\sigma} \right)_{av}} \left[\left(\frac{\partial \frac{C_T}{\sigma}}{\partial \alpha} \right)_{av} \Delta \alpha + \left(\frac{\partial \frac{C_T}{\sigma}}{\partial \theta} \right)_{av} \Delta \theta \right] + \frac{\Delta \sigma}{\sigma_{av}} + \frac{2 \Delta R}{R_{av}} + \frac{2 \Delta(\Omega R)}{(\Omega R)_{av}} \quad (5)$$

When the above equation is solved for $\Delta \theta$ and differentiated with respect to μ , setting $\frac{\partial(\Delta T)}{\partial \mu} = 0$, the following expression is obtained:

$$\frac{d(\Delta \theta)}{d\mu} = - \frac{\left(\frac{C_T}{\sigma} \right)_{av}}{\left[\left(\frac{\partial C_T/\sigma}{\partial \theta} \right)_{av} \right]^2} \frac{d \left(\frac{\partial C_T/\sigma}{\partial \theta} \right)_{av}}{d\mu} \left\{ \frac{\Delta T}{W/2} - \left[\frac{\Delta \sigma}{\sigma_{av}} + \frac{2 \Delta R}{R_{av}} + \frac{2 \Delta(\Omega R)}{(\Omega R)_{av}} \right] \right\} - \frac{\left(\frac{\partial C_T/\sigma}{\partial \alpha} \right)_{av}}{\left(\frac{\partial C_T/\sigma}{\partial \theta} \right)_{av}} \frac{d(\Delta \alpha)}{d\mu} - \left\{ \frac{\frac{d \left(\frac{\partial C_T/\sigma}{\partial \alpha} \right)_{av}}{d\mu}}{\left(\frac{\partial C_T/\sigma}{\partial \theta} \right)_{av}} - \frac{\left(\frac{\partial C_T/\sigma}{\partial \alpha} \right)_{av}}{\left[\left(\frac{\partial C_T/\sigma}{\partial \theta} \right)_{av} \right]^2} \frac{d \left(\frac{\partial C_T/\sigma}{\partial \theta} \right)_{av}}{d\mu} \right\} \Delta \alpha \quad (6)$$

Under the assumption that the downwash angle at the rear rotor is

$$\epsilon = \left(\frac{C_T}{\mu^2} \right)_{rr} \quad (7)$$

the total difference in angle of attack between the front and rear rotors due to downwash and washplate dihedral becomes

$$\Delta \alpha = - \left(\frac{C_T}{\mu^2} \right)_{fr} + \Delta \alpha_d \quad (8)$$

Equation (6) was determined in terms of average values of C_T and μ . Therefore, $C_{T_{rr}}$ and μ_{rr} in equation (8) will be replaced in terms of average values in order that substitution into equation (6) can be made. The mathematics for determining $\Delta \alpha$ in terms of $C_{T_{av}}$ and μ_{av} are presented in appendix A and the resulting expression is

$$\Delta \alpha = - \left(\frac{C_T}{\mu^2} \right)_{av} \left(1 - \frac{\Delta T}{W} + \frac{\Delta R}{R_{av}} \right) + \Delta \alpha_d \quad (9)$$

which when differentiated with respect to μ gives

$$\frac{d(\Delta \alpha)}{d\mu} = 2 \left(\frac{C_T}{\mu^3} \right)_{av} \left(1 - \frac{\Delta T}{W} + \frac{\Delta R}{R_{av}} \right) \quad (10)$$

Substituting equations (9) and (10) into equation (6) and simplifying results in the following expression:

$$\frac{d(\Delta \theta)}{d\mu} = K_1 \left(\frac{C_T}{\sigma} \right)_{av} \left(\frac{\Delta T}{W} - \frac{\Delta R}{R_{av}} \right) + K_2 \left(\frac{C_T}{\sigma} \right)_{av} \left[\frac{\Delta \sigma}{\sigma_{av}} + 2 \frac{\Delta(\Omega R)}{(\Omega R)_{av}} \right] + K_3 \Delta \alpha_d + K_4 C_{T_{av}} \quad (11)$$

where

$$K_1 = -2 \frac{\frac{d \left(\frac{\partial C_T/\sigma}{\partial \theta} \right)_{av}}{d\mu}}{\left[\left(\frac{\partial C_T/\sigma}{\partial \theta} \right)_{av} \right]^2} + 2 \frac{\left(\frac{\partial C_T/\sigma}{\partial \alpha} \right)_{av} \sigma_{av}}{\left(\frac{\partial C_T/\sigma}{\partial \theta} \right)_{av} (\mu_{av})^3} - \left\{ \frac{\frac{d \left(\frac{\partial C_T/\sigma}{\partial \alpha} \right)_{av}}{d\mu}}{\left(\frac{\partial C_T/\sigma}{\partial \theta} \right)_{av}} - \frac{\left(\frac{\partial C_T/\sigma}{\partial \alpha} \right)_{av}}{\left[\left(\frac{\partial C_T/\sigma}{\partial \theta} \right)_{av} \right]^2} \frac{d \left(\frac{\partial C_T/\sigma}{\partial \theta} \right)_{av}}{d\mu} \right\} \frac{\sigma_{av}}{(\mu_{av})^2}$$

$$K_2 = \frac{\frac{d\left(\frac{\partial C_T/\sigma}{\partial \theta}\right)_{av}}{d\mu}}{\left[\left(\frac{\partial C_T/\sigma}{\partial \theta}\right)_{av}\right]^2}$$

$$K_3 = -\frac{\frac{d\left(\frac{\partial C_T/\sigma}{\partial \alpha}\right)_{av}}{d\mu}}{\left(\frac{\partial C_T/\sigma}{\partial \theta}\right)_{av}} + \frac{\left(\frac{\partial C_T/\sigma}{\partial \alpha}\right)_{av}}{\left[\left(\frac{\partial C_T/\sigma}{\partial \theta}\right)_{av}\right]^2} \frac{d\left(\frac{\partial C_T/\sigma}{\partial \theta}\right)_{av}}{d\mu}$$

$$K_4 = -\frac{\left(\frac{\partial C_T/\sigma}{\partial \alpha}\right)_{av}}{\left(\frac{\partial C_T/\sigma}{\partial \theta}\right)_{av}} \frac{2}{(\mu_{av})^3} +$$

$$\left\{ \frac{\frac{d\left(\frac{\partial C_T/\sigma}{\partial \alpha}\right)_{av}}{d\mu}}{\left(\frac{\partial C_T/\sigma}{\partial \theta}\right)_{av}} - \frac{\left(\frac{\partial C_T/\sigma}{\partial \alpha}\right)_{av}}{\left[\left(\frac{\partial C_T/\sigma}{\partial \theta}\right)_{av}\right]^2} \frac{d\left(\frac{\partial C_T/\sigma}{\partial \theta}\right)_{av}}{d\mu} \right\} \frac{1}{(\mu_{av})^2}$$

Note that in equation (11) changes in R are assumed to take place at constant σ and ΩR and that the derivatives are the average of front- and rear-rotor values.

Values for K_1 , K_2 , K_3 , and K_4 are plotted against μ in figure 4 for values of μ from 0.15 to 0.50 and for $\sigma=0.03$, 0.06, and 0.09. A direct calculation of the speed stability of a given configuration may be accomplished by using the K values of figure 4 and equation (11) when C_T , μ , and σ are known.

RESULTS AND DISCUSSION

SPEED STABILITY OF ORIGINAL CONFIGURATION

Measurements of speed stability.—Figure 5 (a) shows a plot of stick position against forward speed for the original configuration trimmed at approximately 70 knots in level flight which is approximately the cruising speed. The curve shows that rearward stick motion was necessary to maintain trim longitudinally as the speed increased throughout the speed range from 50 knots to 105 knots. The nose-up control moment was applied to counteract a nose-down moment due to the increased speed, since to maintain zero pitching acceleration the sum of the moments must be zero. Thus, figure 5 (a) indicates the test helicopter in its original configuration to be unstable with speed from 50 knots to 105 knots. The variation of slope with speed indicates some tendency for the instability to become smaller with increased speed particularly at the lower speeds. At 70 knots the stick slope is approximately -0.01 inch per knot.

Pilots' opinions.—The instability of the test helicopter was considered by the pilots to be undesirable in that it increased the likelihood of the placard speed being exceeded inadvertently. However, they considered this instability to be

less serious than the maneuver instability and lateral-directional instabilities reported in reference 1.

Source of instability.—The unstable variation of pitching moments with speed may be caused by the rotors or the fuselage. Chapter 11 of reference 2 indicates that the individual rotors are stable with speed and calculations indicate the contribution of the fuselage-tail combination to the moment variation with speed to be small with respect to that contributed by the rotors for the test helicopter. It is probable, therefore, that the greater part of speed instability is contributed by the rotor configuration and is caused by the variations of front-rotor downwash acting on the rear rotor.

In forward flight the rear rotor is operating in the downwash of the front rotor and is trimmed accordingly. As forward speed increases, the downwash angle is reduced because of the larger mass of air handled per second by the front rotor. The reduction of downwash angle with increased speed causes an increase in the rear-rotor angle of attack so that at constant control position a thrust increase is produced resulting in a nose-down or unstable pitching moment. The K_4 term in equation (11) accounts for this effect. Equation (10) shows that the rate of change of downwash with speed is reduced as the speed is increased. This reduction occurs more rapidly at the lower speeds. Experimental verification of this trend is noted in figure 5(a) wherein a reduction in the instability with speed of the test helicopter as the speed increased is noticeable particularly at the lower speeds.

Computation of speed stability at 70 knots.—The basic tandem configuration used in the tests had equal radius, equal tip speed, and equal solidity of the front and rear rotors and no swashplate dihedral. Under these conditions, equation (11) reduces to:

$$\frac{d(\Delta\theta)}{d\mu} = K_1 \left(\frac{C_T}{\sigma} \right)_{av} \frac{\Delta T}{W} + K_4 C_{T_{av}} \quad (12)$$

The second term in equation (12) is the important term and is the one that accounts for the effects of downwash variation. The first expression in equation (12) is retained because the center of gravity was approximately 13 inches forward of the midpoint; a difference therefore results in front and rear rotor thrusts at the trim condition. In addition to a physical shift of the center of gravity there is an effective shift introduced by the tilt of the rotor thrust vectors from the shaft axis. In the case under consideration, the increment ΔT due to the vector tilt was examined and found to have a negligible effect on speed stability. However, in some high-speed cases where the longitudinal tilt of the rotor force vector from the shaft may be large and where the effect of a thrust difference is more significant, a significant difference in the speed stability might result. A derivation of the method of accounting for the difference in thrust ΔT due to tilt of the thrust vectors is presented in appendix B.

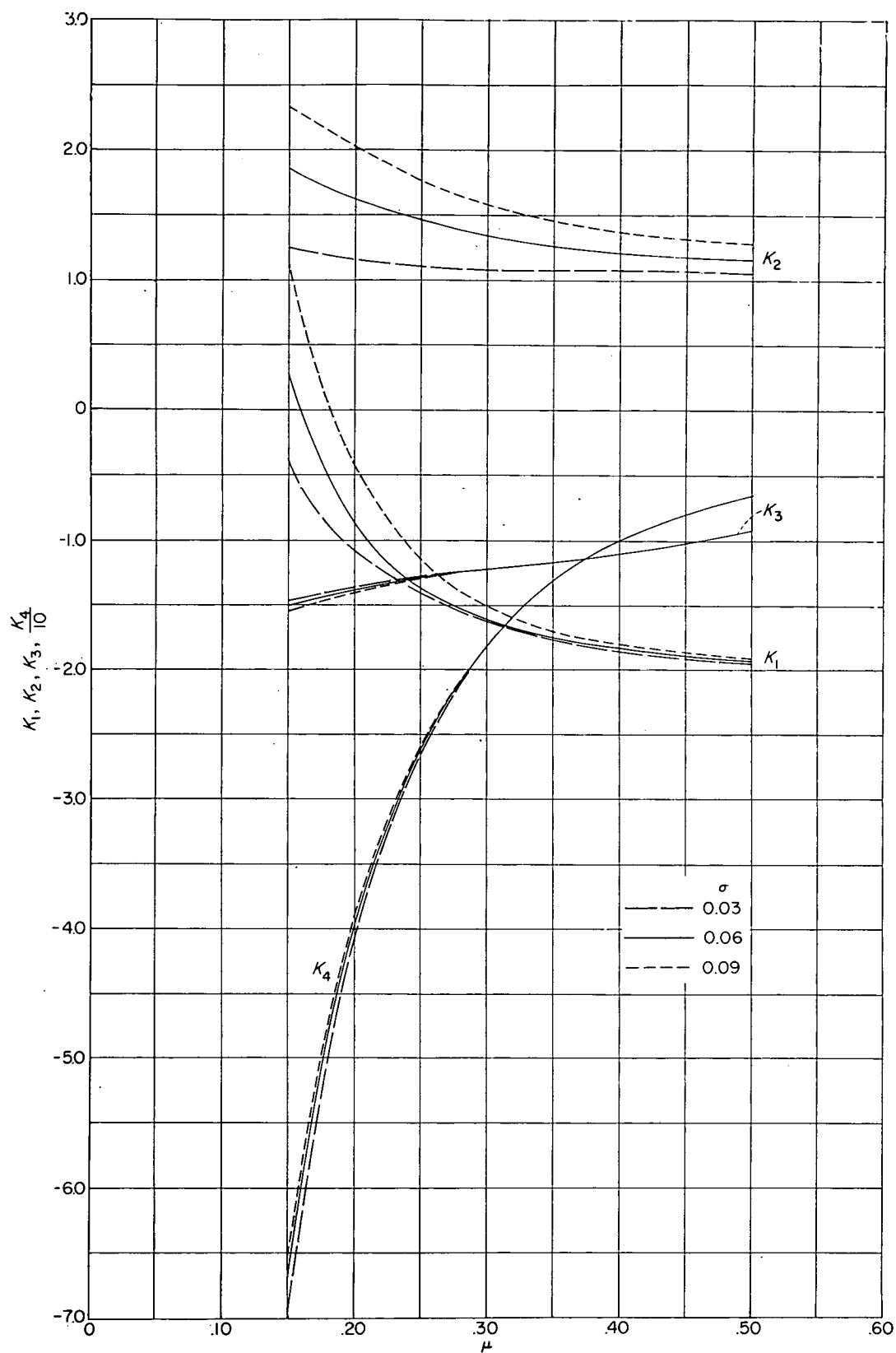


FIGURE 4.—Constants for use in speed-stability equation:

$$\frac{d(\Delta\theta)}{d\mu} = K_1 \left(\frac{C_T}{\sigma} \right)_{av} \left(\frac{\Delta T}{W} - \frac{\Delta R}{R_{av}} \right) + K_2 \left(\frac{C_T}{\sigma} \right)_{av} \left(\frac{\Delta\sigma}{\sigma_{av}} + 2 \frac{\Delta(\Omega R)}{(\Omega R)_{av}} \right) + K_3 \Delta\alpha_d + K_4 C_{T_{av}}$$

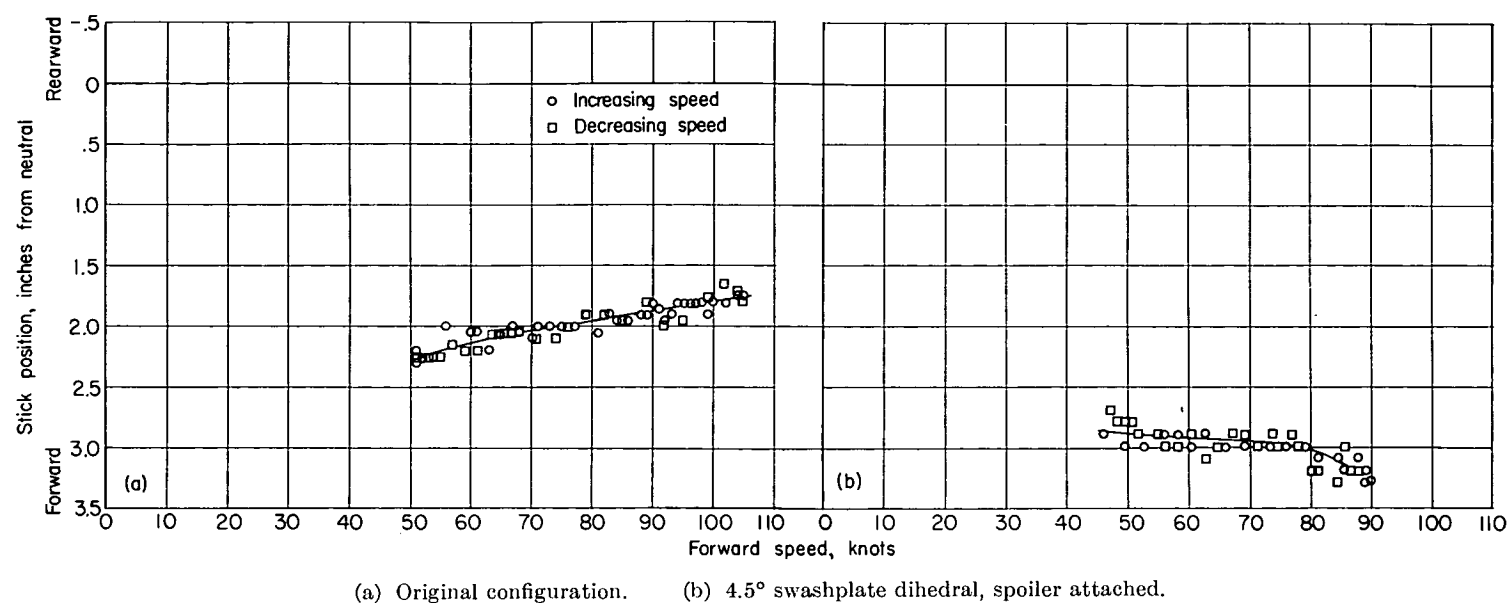


FIGURE 5.—Variation of longitudinal stick position with speed for test helicopter, trimmed at approximately 70 knots, in level flight.

For the test helicopter at 70 knots

$$\Delta T = -320 \text{ lb}$$

$$W = 6,750 \text{ lb}$$

$$\Delta T/W = -0.0474$$

$$\Omega R = 537 \text{ ft/sec}$$

$$\sigma_{av} = 0.052$$

$$C_{T_{av}} = 0.00424$$

$$\left(\frac{C_T}{\sigma}\right)_{av} = 0.0815$$

$$\rho/\rho_0 = 0.89$$

$$\mu = 0.22$$

From figure 4, $K_1 = -1.15$ and $K_4 = -33.5$. Substituting into equation (12)

$$\begin{aligned} \frac{d(\Delta\theta)}{d\mu} &= -1.15(0.0815)(-0.0474) - 33.5(0.00424) \\ &= 0.004 - 0.142 \end{aligned}$$

$$\frac{d(\Delta\theta)}{d\mu} = -0.138$$

Converting $\frac{d(\Delta\theta)}{d\mu}$ from radians per μ to degrees per knot gives

$$\frac{d(\Delta\theta)}{dV} = -0.025 \text{ degree per knot}$$

Knowing the ratio between differential collective pitch and stick motion, which as shown in figure 2 for the test helicopter is $1^\circ \Delta\theta$ per inch of stick travel, the stick travel per knot speed change can be computed. In this case,

$$\frac{d\delta}{dV} = -0.025 \text{ inch per knot}$$

Comparison of calculated and experimental values of speed stability.—The calculated value of speed stability for the test helicopter in its original configuration is -0.025 inch per knot whereas the measured value is -0.01 inch per knot. The orders of magnitude are in agreement and the difference, while large percentagewise, is probably within the accuracy of the data and the nature of the assumptions used in the theoretical analysis. Of the assumptions, the one neglecting the contribution of the fuselage-tail combination is considered most likely to be in error.

EFFECT OF SWASHPLATE DIHEDRAL ON SPEED STABILITY

Although, as indicated in the previous section, the assumptions used in the theory may cause some error in the estimation of the absolute value of speed stability, such errors should be due primarily to fuselage moments which remain constant with changes in rotor geometry. Hence the theory should be adequate to predict changes in speed stability brought about by changes in the rotor thrust contributions.

For the purposes of checking the theory and obtaining a condition of positive speed stability for pilots' opinions of flying qualities, swashplate dihedral was rigged into the control system of the test helicopter. It is understood that at least one manufacturer has experimented with swashplate dihedral with some success in improving the speed stability of the tandem configuration.

Improvement predicted by theory.—Inspection of equation (11) and figure 4 shows, inasmuch as K_3 is negative for $\mu = 0.15$ to 0.50 , that there will be a positive increment added to the speed stability when $\Delta\alpha_d$ is negative. Therefore, equation (11) suggests that a negative difference in angle of attack of rotors, that is, the swashplates tilted toward one another, improves the speed stability of the tandem configuration. The magnitude of the predicted improvement

is determined as follows:

For the test helicopter at cruise:

$$\begin{aligned} \mu & \text{-----} 0.22 \\ \sigma & \text{-----} 0.052 \end{aligned}$$

From figure 4, $K_3 = -1.33$ and, assuming $\Delta\alpha_d = -1^\circ$ or -0.0175 radian, equation (11) gives

$$\begin{aligned} \Delta \frac{d(\Delta\theta)}{d\mu} &= -1.33(-0.0175) \\ &= 0.023 \text{ radian per } \mu \text{ unit per degree dihedral} \end{aligned}$$

$$\Delta \frac{d(\Delta\theta)}{dV} = 0.004 \text{ degree per knot per degree dihedral}$$

Measured improvement.—Measurements in flight were made to confirm the effect of swashplate dihedral on the speed stability of the test helicopter. Data were obtained for the test helicopter with 2.7° and 4.5° of swashplate dihedral. Figure 5(b) is a plot of stick position against speed for the test helicopter with 4.5° of swashplate dihedral and shows the test helicopter now to have slightly positive speed stability. Comparison of figure 5(b) with figure 5(a) indicates a definite improvement in the speed stability with swashplate dihedral throughout the speed range from 50 knots to the maximum reached.

Comparison of experimental results with theory.—Spoilers were added to the fuselage for another investigation between the flights for obtaining the original data and the flights for obtaining the dihedral data. Intermediate flight tests indicated these spoilers to affect the speed stability adversely; thus, the incremental improvement in speed stability due to dihedral alone is best obtained by determining the improvement in going from 2.7° to 4.5° swashplate dihedral. The slope of the curve in figure 5 (b) at 70 knots and equivalent data for the 2.7° dihedral case are plotted in figure 6 along with the theoretical values. The experimental increment is computed to be 0.007 degree per knot per degree dihedral. Even though this value is somewhat higher than the value of 0.004 predicted by theory, the comparison is believed to be good enough to indicate the theory to be a useful tool for predicting changes in speed stability.

Pilots' opinions.—The pilots making the test flights considered the handling qualities of the test helicopter improved by the removal of the instability with speed.

CRITERIONS FOR SATISFACTORY SPEED-DISTURBANCE CHARACTERISTICS

While the pilots were certain that any instability with speed would be undesirable, they were not sure whether the speed-disturbance characteristics of the helicopter as modified with 4.5° of swashplate dihedral were satisfactory. As previously mentioned, the test helicopter with 4.5° swashplate dihedral was slightly stable with speed. When the controls of the helicopter were held fixed during flight in rough air, large disturbances in pitch attitude and hence in forward speed were produced from which the helicopter recovered slowly. Under contact conditions these large disturbances in speed were not bothersome in that they were easily prevented by control motion. Thus, for contact flight, slightly positive speed stability seems to be sufficient. However, the pilots felt that under blind-flying conditions,

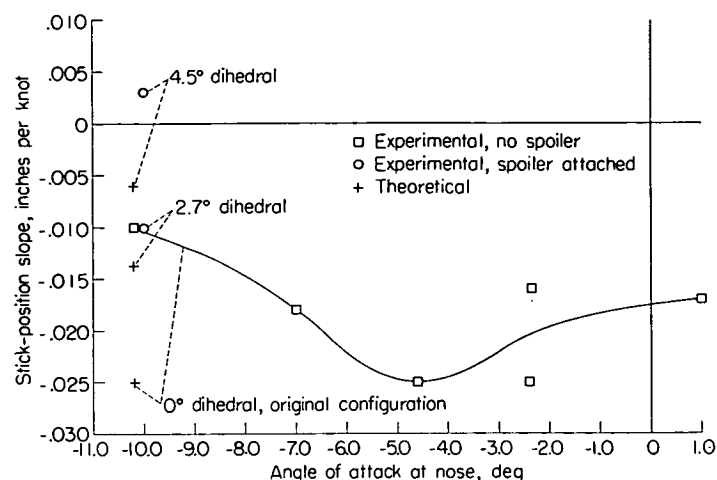


FIGURE 6.—Effect of swashplate dihedral and angle of attack at fuselage nose on speed stability at 70 knots.

these speed-disturbance characteristics might increase their difficulties excessively.

If, during blind flight, speed-disturbance characteristics such as those of the modified helicopter are actually found to be objectionable, it would appear desirable to modify such characteristics to reduce the amount of speed disturbance. From the pilots' point of view it might be desirable to limit the amount or percentage of speed disturbance after some period of time following a fixed longitudinal disturbance of the control stick. Modifications such as increases in stability with speed or in maneuver stability should tend to improve the helicopter's speed-disturbance characteristics.

In addition, it should be pointed out that an increase in speed stability will reduce the amount of forward longitudinal control available at the higher speeds for overcoming a nose up divergence in pitch. Thus, it appears that an effort to remove any maneuver instability of a tandem helicopter should precede any attempt to increase the speed stability.

EFFECT OF ANGLE OF ATTACK ON SPEED STABILITY

Figure 6 also shows how the slope of stick motion with speed at 70 knots for the original configuration varies with angle of attack at the nose. The angle of attack was varied by changing the rate of descent and was measured by the vane shown in figure 3. Figure 6 is obtained from data such as in figure 5 (a). For example, the slope of the curve in figure 5 (a) at 70 knots is found to be -0.01 inch per knot. The angle of attack at the nose at this condition was measured to be -10.2° . These values determine one point of the curve of figure 6. The additional points were obtained similarly from other runs at several power conditions.

Figure 6 shows that a variation of speed stability with rate of descent exists, indicating that as the rear rotor changes position with respect to the line of flight through the front rotor, a different trim value and hence a different rate of change with speed of front-rotor downwash is apparently encountered. The maximum value of downwash appears to occur when the rear rotor is on the line of flight of the front rotor. This tends to be in agreement with the vertical traverse measurements of downwash angle behind a rotor in a wind tunnel, presented in reference 7, which also indicates

such changes in downwash angle with perpendicular distance from the line of flight of a rotor to exist. The significance of this downwash variation with respect to angle-of-attack stability was discussed in reference 1.

EXPLANATION OF EFFECTS OF CONFIGURATION CHANGES ON SPEED STABILITY

In addition to the effects of downwash (K_4) and swashplate dihedral (K_3) equation (11) shows the manner in which differences in front- and rear-rotor solidity, tip speed, radius, and trim thrust affect the speed stability. (The difference in trim thrust is affected primarily by the center-of-gravity location with respect to the midpoint between rotors.) Inasmuch as the theory was found to give good results in predicting the effects of swashplate dihedral, the theory should also be adequate in general for predicting the effects of other configuration changes.

SWASHPLATE DIHEDRAL

The stabilizing effect of swashplate dihedral is caused by the rear rotor operating at a more negative angle of attack than the front rotor. Under such conditions, an increase in forward speed causes a greater increase in the downflow through the rear rotor than through the front rotor because of the greater axial component of forward velocity. The greater increase in downflow through the rear rotor causes a larger reduction in rear-rotor thrust than that experienced by the front rotor, hence contributing a nose-up or stabilizing moment.

In addition to the stabilizing effect, there is a smaller destabilizing effect caused by swashplate dihedral. Since the difference in rotor angles of attack is more negative than without swashplate dihedral, the trim value of the difference in collective pitch of the rotors must be more positive than without swashplate dihedral in order to maintain the trim values of thrust. This difference in trim values of collective pitch causes a larger increase of thrust with speed for the rear rotor and a smaller increase of thrust with speed for the front rotor. The destabilizing effect due to differences in the pitch angles of the front and rear rotors increases with speed, thus accounting for the overall reduction in effectiveness of swashplate dihedral at higher speeds as shown in figure 4 by the reduction in absolute magnitude of K_3 at high values of μ .

EFFECT OF TIP SPEED OR SOLIDITY DIFFERENTIAL

Since K_2 is shown by figure 4 to be positive at all values of μ from 0.15 to 0.50, equation (11) shows that positive differences in tip speed or solidity (rear rotor greater) have a stabilizing effect. (It should be noted, as previously pointed out, that in equation (11) changes in one parameter are assumed to cause no change in other parameters.) Figure 4 also shows that K_2 decreases as μ increases, indicating that tip-speed and solidity differences have a maximum effect at the lower speeds and decrease in effectiveness as the speed increases.

EFFECT OF CENTER-OF-GRAVITY LOCATION OR RADIUS DIFFERENTIAL

The effect on speed stability of center-of-gravity location or radius differential may be understood by considering

each parameter in the expression $K_1 (C_T/\sigma)_{av} \left(\frac{\Delta T}{W} - \frac{\Delta R}{R_{av}} \right)$ of equation (11). Figure 4 shows K_1 to be negative over most of the range of μ values covered. Since $(C_T/\sigma)_{av}$ is always positive, the above expression will generally show a positive increment of speed stability when ΔT is negative or when ΔR is positive. Inasmuch as ΔT is negative by definition when the front-rotor thrust is greater, location of the center of gravity forward of the midpoint between rotors will generally improve the speed stability.

Inasmuch as figure 4 shows that at the lower tip-speed ratios and higher solidities K_1 becomes small and may even become positive, forward center-of-gravity location or positive radius differential in such cases become less effective and may even have an adverse effect on speed stability. It is believed that the loss in effectiveness of these two parameters at low speeds is due to the fact that the front-rotor lift coefficient is increased. An increase in the effect of destabilizing downwash is therefore obtained, which overshadows the stabilizing tendency at low speeds. At high speeds the destabilizing effect due to downwash decreases and the stabilizing effect predominates.

MEANS FOR IMPROVING SPEED STABILITY

MAGNITUDE OF CONFIGURATION CHANGES REQUIRED TO ACHIEVE NEUTRAL STABILITY FOR THE TEST HELICOPTER

In order to compare the effectiveness of the various methods for improving speed stability, the calculated magnitudes of the changes in each parameter needed to make the test helicopter neutrally stable with speed are shown in table I. At $\mu=0.17$ the amount of thrust or radius differential needed, as shown by -2.3 and 2.3 , respectively, is impossible. The values of 0.6 and 0.3 for $\Delta\sigma/\sigma_{av}$ and $\Delta(\Omega R)/(\Omega R)_{av}$, respectively, indicate that relatively large though not impossible differences would be required. However, in the event that moderate amounts of these latter differentials were used to improve other characteristics, such as angle-of-attack stability, the effect on speed stability would be in the proper direction. Table I shows that at $\mu=0.17$, -3° of swashplate dihedral, a reasonable value, will cause the test helicopter to be neutrally stable with speed. Swashplate dihedral therefore seems to be the most practical means of improving the speed stability of the tandem-rotor helicopter at low speeds. The higher value of swashplate dihedral actually used on the test helicopter was needed because of the adverse effect of the spoiler installation.

At high speeds, as represented by values for $\mu=0.30$ in table I, the test helicopter could be made neutrally stable

TABLE I

MAGNITUDES OF CONFIGURATION CHANGES NEEDED TO GIVE NEUTRAL STABILITY ON TEST HELICOPTER

μ	Measured $\frac{d(\Delta\theta)}{d\mu}$ for test helicopter, radians/ μ	Difference in angle of attack due to swash- plate dihedral, $\Delta\alpha_d$, deg	$\frac{\Delta T}{W}$	$\frac{\Delta R}{R_{av}}$	$\frac{\Delta\sigma}{\sigma_{av}}$	$\frac{\Delta(\Omega R)}{(\Omega R)_{av}}$
0.17	-0.077	-3	-2.3	2.3	0.6	0.3
.30	-.027	-1.2	-.2	.2	.26	.13

with speed by using any of the methods individually. The values for $\Delta T/W$, $\Delta R/R_{av}$, $\Delta \sigma/\sigma_{av}$, and $\Delta(\Omega R)/(\Omega R)_{av}$ represent large although feasible differences in these parameters, while the value of -1.2° for swashplate dihedral is small. As at low speeds, swashplate dihedral is apparently the most effective single change. However, moderate amounts of other changes could be used simultaneously with good results. Although swashplate dihedral and solidity and tip-speed differential become less effective with increased speed, the lower amount of instability of the original configuration at the higher speed results in less configuration change needed for neutral stability than at the lower speed.

PRACTICAL CONSIDERATIONS REGARDING SWASHPLATE DIHEDRAL

The means for incorporating swashplate dihedral in the test helicopter, described in the section entitled "Description of Test Helicopter," was an expedient method and there are practical considerations to be given to its use. Because of the tilt of the swashplates at the neutral stick position, it was necessary to reduce the longitudinal cyclic-pitch range to avoid linkage interference. In addition, the droopstop clearance in flight of one or both rotors tends to be reduced. The pilots reported the reduction in longitudinal cyclic pitch produced no appreciable change in longitudinal control in flight. However, since cyclic pitch is the only longitudinal control available for taxiing, the reduction in longitudinal cyclic-pitch range might prove to be objectionable during attempts to taxi in high winds. For the test helicopter with the swashplate dihedral, no attempt was made to taxi in high winds.

For a helicopter in the design stages, a more suitable means of incorporating swashplate dihedral might be the inclination of the rotor shafts towards one another. By inclining the rotor shafts, the necessity for reducing the longitudinal cyclic-pitch range to avoid linkage interference and the possibility of blades hitting the droopstops are virtually eliminated. However, inclining the rotor shafts will not eliminate the problem of clearance between the rotors and fuselage.

Another practical consideration regarding swashplate dihedral—its effect on rotor stalling—is discussed in the next section.

In view of these adverse conditions which may arise from swashplate dihedral, some practical considerations must be given to its use.

EFFECT OF STALLING ON SPEED STABILITY

With the load equally distributed between the two rotors of the tandem-rotor configuration, the rear rotor, operating in the downwash of the front rotor, is in more of a climb condition and tends to stall first. When the rear rotor stalls, its lift decreases and with constant stick position a nose-up moment about the center of gravity is contributed. As the forward speed increases, the stalled area of the rotor disk becomes larger and with the stick position constant a nose-up moment is obtained due to the speed increase.

Thus, as rear-rotor stalling is encountered there is an increase in the speed stability. Although stalling of the rear rotor appears to be desirable for speed stability at high forward speeds, it is undesirable for angle-of-attack stability and performance. The effects of rear-rotor stalling on angle-of-attack stability and of stalling in general on performance are discussed, respectively, in reference 1 and chapter 10 of reference 2.

When swashplate dihedral is incorporated in the tandem-rotor configuration, the axis of no feathering of the rear rotor is inclined forward and the component of forward flight velocity along the axis of no feathering is increased. The increased downflow through the rear rotor causes it to be in more of a climb condition than normal thereby decreasing the forward speed at which it begins to stall. Calculations of angles of attack at the tip of the retreating blades for the configuration with 4.5° swashplate dihedral at a forward speed of 80 knots show that the rear rotor is beginning to stall while the front rotor is well below stalled conditions. These differences in stalling apparently account for the increase in speed stability of the modified configuration above approximately 80 knots as indicated by the change in the slope of the curve in figure 5 (b).

Other configuration changes that may be made for stability purposes, such as forward center of gravity and increased solidity or tip speed of the rear rotor, will tend to cause the front rotor to stall first.

It appears that the most desirable conditions regarding stalling from a performance standpoint would be the simultaneous stalling of both rotors. Under such conditions, with a fixed average value of C_T/σ , the forward speed at which stall begins would be a maximum. By considering, during the design stages, the amount of the various configuration changes needed for satisfactory stability and performance, a suitable combination of rotor geometry and center-of-gravity location might be attained whereby optimum stalling characteristics would result.

CONCLUSIONS

A study of the speed stability of a tandem-rotor helicopter in forward flight indicates the following conclusions:

1. The test helicopter is unstable with speed from 50 knots to 105 knots, which is the speed range covered in the tests, in that the stick position moved rearward with increasing forward speed at constant power. This result applies both with and without fuselage spoilers attached during the tests. The pilots consider this characteristic unsatisfactory.

2. An effort to remove any maneuver instability of the tandem helicopter should precede any attempt to improve the speed stability.

3. Instability with speed of the test helicopter is caused primarily by variations with speed of the front rotor downwash at the rear rotor and can be approximately predicted by theory.

4. Swashplate "longitudinal dihedral" (swashplates inclined towards each other) improves the stability with speed of the tandem-rotor helicopter. A value of 4.5° of swashplate dihedral made the test helicopter slightly stable (in spite of the adverse effect of fuselage spoilers) from 50 knots, the minimum speed tested, to the maximum speed tested. Some considerations must be given to the practical aspects of the use of swashplate dihedral.

5. The pilots considered the speed-disturbance characteristics of the test helicopter with only slightly positive speed stability to be satisfactory under contact conditions. The possible need for an additional criterion to limit the amount of speed disturbance during blind flight in rough air remains to be determined.

6. Improvement in speed stability due to swashplate dihedral can be predicted approximately by theory.

7. The speed stability of the tandem helicopter can be studied conveniently by a theoretical chart which is presented.

8. Instability with speed varies with rate of descent, probably as a result of the variation of downwash behind a rotor with perpendicular distance from the line of flight through the rotor.

LANGLEY AERONAUTICAL LABORATORY,
NATIONAL ADVISORY COMMITTEE FOR AERONAUTICS,
LANGLEY FIELD, VA., June 4, 1953.

APPENDIX A

DETERMINATION OF $\Delta\alpha$ IN TERMS OF AVERAGE VALUES OF C_T AND μ

The difference in angle of attack of the front and rear rotors is the sum of the downwash angle and the difference in angle due to the geometric swashplate dihedral and is expressed as follows:

$$\begin{aligned}\Delta\alpha &= -\frac{C_{T_{fr}}}{(\mu_{fr})^2} + \Delta\alpha_d \\ &= -\frac{C_{L_{fr}}}{2} + \Delta\alpha_d\end{aligned}\quad (A1)$$

where $C_{L_{fr}}$ is a front-rotor term. In order to express $\Delta\alpha$ in terms of average quantities, it is necessary to determine an expression for $C_{L_{fr}}$ in terms of $C_{L_{av}}$. By definition,

$$C_{L_{fr}} = \frac{L_{fr}}{\frac{1}{2} \rho V^2 \pi (R_{fr})^2} \quad (A2)$$

and

$$C_{L_{av}} = \frac{L_{av}}{\frac{1}{2} \rho V^2 \pi (R_{av})^2} \quad (A3)$$

Dividing equation (A2) by equation (A3) and solving for $C_{L_{fr}}$ gives:

$$C_{L_{fr}} = C_{L_{av}} \frac{L_{fr}}{L_{av}} \frac{(R_{av})^2}{(R_{fr})^2} \quad (A4)$$

Expressing L_{fr} and R_{fr} in terms of average values gives:

$$L_{fr} = L_{av} \left(1 - \frac{\Delta L}{W}\right) \quad (A5)$$

and

$$R_{fr} = R_{av} \left(1 - \frac{1}{2} \frac{\Delta R}{R_{av}}\right) \quad (A6)$$

Substituting equations (A5) and (A6) into equation (A4) and retaining only linear terms gives the following expression for $C_{L_{fr}}$ in terms of $C_{L_{av}}$:

$$C_{L_{fr}} = C_{L_{av}} \left(1 - \frac{\Delta L}{W}\right) \frac{1}{1 - \frac{\Delta R}{R_{av}}}$$

Expanding by the binomial theorem and once again retaining only linear terms

$$C_{L_{fr}} = C_{L_{av}} \left(1 - \frac{\Delta L}{W} + \frac{\Delta R}{R_{av}}\right) \quad (A7)$$

With the expression for $C_{L_{fr}}$ in terms of $C_{L_{av}}$ substituted into the original expression for $\Delta\alpha$, that expression becomes

$$\Delta\alpha = -\frac{C_{L_{av}}}{2} \left(1 - \frac{\Delta L}{W} + \frac{\Delta R}{R_{av}}\right) + \Delta\alpha_d$$

and assuming $L = T$

$$\Delta\alpha = -\left(\frac{C_T}{\mu^2}\right)_{av} \left(1 - \frac{\Delta T}{W} + \frac{\Delta R}{R_{av}}\right) + \Delta\alpha_d \quad (A8)$$

APPENDIX B

METHOD OF DETERMINING THE EFFECTIVE LOCATION OF THE CENTER OF GRAVITY

In order to determine accurately the load carried by each rotor, the center-of-gravity location with respect to the midpoint between the lines of action of the rotor resultant-force vectors, rather than the center-of-gravity location with respect to the midpoint between rotor shafts, must be considered. For the purposes of this analysis the rotor resultant-force vector is assumed to be equal in magnitude to the rotor thrust. A schematic diagram of the tandem-rotor system is shown in figure 7. From figure 7 the distance from the actual midpoint between rotors to the effective midpoint is

$$x' = h \tan(a' - B_1)_{av} \quad (B1)$$

Then the location of the center of gravity with respect to the effective midpoint is

$$x = x_0 - x'$$

Using this location of the center of gravity, the thrust carried by each rotor in steady flight can be determined accurately for known conditions of flight.

Sample calculations of effective center-of-gravity location.—For a sample case, assume

$$\begin{aligned} (C_T/\sigma)_{av} &= 0.10 \\ \mu &= 0.30 \\ h &= 100 \text{ inches} \\ \theta_{av} &= 8^\circ \\ B_{1av} &= 2.0^\circ \\ x_0 &= 12 \text{ inches} \end{aligned}$$

The preceding quantities pertaining to the rotors are average values and may be obtained from flight data or calculated. With the preceding quantities a'_{av} can be determined from figure 3 of reference 5. For the sample case

$$a'_{av} = 6.5^\circ$$

Substituting into equation (B1)

$$\begin{aligned} x' &= 100 \tan(6.5^\circ - 2.0^\circ) \\ &= 7.8 \text{ inches} \end{aligned}$$

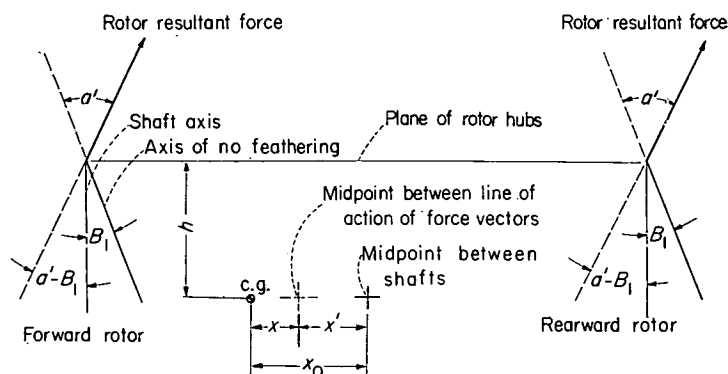


FIGURE 7.—Schematic side view of rotors of a tandem helicopter in forward flight.

The effective location of the center of gravity is $x = 12 - 7.8 = 4.2$ inches forward of the midpoint. In this sample case, note that the distance from the effective midpoint to the center of gravity is about one-third the distance from the geometric midpoint between shafts to the center of gravity. Failure to consider this difference might give misleading results.

REFERENCES

1. Amer, Kenneth B.: Some Flying-Qualities Studies of a Tandem Helicopter. NACA RM L51H20a, 1951.
2. Gessow, Alfred, and Myers, Garry C., Jr.: Aerodynamics of the Helicopter. The Macmillan Co., c. 1952.
3. Anon.: Military Specification; Helicopter Flying Qualities, Requirements for. Military Specification, MIL-H-8501, Nov. 5, 1952.
4. Anon.: Rotorcraft Airworthiness. Pt. 6 of Civil Air Regulations, Civil Aero. Board, U. S. Dept. Commerce, Jan. 15, 1951.
5. Amer, Kenneth B., and Gustafson, F. B.: Charts for Estimation of Longitudinal-Stability Derivatives for a Helicopter Rotor in Forward Flight. NACA TN 2309, 1951.
6. Castles, Walter, Jr., and De Leeuw, Jacob Henri: The Normal Component of the Induced Velocity in the Vicinity of a Lifting Rotor and Some Examples of Its Application. NACA Rep. 1184, 1954. (Supersedes NACA TN 2912.)
7. Fail, R. A., and Eyre, R. C. W.: Downwash Measurements Behind a 12-Ft Diameter Helicopter Rotor in the 24-Ft Wind Tunnel. R. & M. No. 2810, British A.R.C., Sept. 1949.

REPORT 1261

THE NEAR NOISE FIELD OF STATIC JETS AND SOME MODEL STUDIES OF DEVICES FOR NOISE REDUCTION¹

By LESLIE W. LASSITER and HARVEY H. HUBBARD

SUMMARY

Experimental studies of the pressure fluctuations near jet exhaust streams were made during unchoked operation of a turbojet engine and a 1-inch-diameter high-temperature model jet and during choked operation of various sizes of model jets with unheated air. The tests for unchoked operation indicate a random spectrum of rather narrow band width which varies in frequency content with axial position along the jet. Pressure surveys from the model tests along lines parallel to the 15° jet boundary indicate that the station of greatest pressure fluctuations is determined by the jet velocity and the radial distance, with a tendency of the maximum to shift downstream as either parameter is increased. From model tests the magnitude of the fluctuations appears to increase as about the second power of jet velocity at points just outside the jet boundary and as increasingly higher powers of jet velocity as distance from the boundary is increased. A laboratory method of noise reduction with model jets was found to produce large decreases in the magnitude of the lower-frequency components of the spectra and thereby also to reduce the total radiated energy.

Choked operation of model jets with unheated air indicates the appearance of a discrete-frequency component of very large magnitude. Shadowgraph records of the flow show that this condition is associated with the appearance of flow formations suggestive of partly formed toroidal vortices in the vicinity of the shocks. Elimination of these formations is found to eliminate the discrete component and thereby to reduce the overall noise level.

INTRODUCTION

It is well known that the turbojet is a generator of intense pressure fluctuations. In view of this fact, it is important that the designer and operator of turbojet-powered aircraft be able to predict the nature and severity of these fluctuations both in the vicinity of the engine (the near field) and at large distances from it (the far field).

The far-field aspect of the problem is of concern to a great number of people, including airport workers as well as the general public, and appreciable research, both theoretical and experimental, has been done on that phase of the problem. For example, reference 1 presents the results of an experimental evaluation from model jets of the effects of various

geometric and flow parameters and compares model and full-scale pressure fields, while a detailed survey of the pressure field of a full-scale configuration is given in reference 2. In reference 3 it has been shown that the problem is subject to qualitative analytical treatment for distances that are large relative to the radiated wavelengths.

Of the investigations reported to date, only that of reference 4 has dealt with the pressure fluctuations in the immediate vicinity of the jet (the near field), and it is in this region that some of the more serious problems arise. Service crews and test-stand personnel work regularly in the extremely high pressure levels of the near field. Occupants of the aircraft are, in a sense, in the near field also. Thus, from consideration of personal discomfort a smaller group is affected but to a much larger extent than the general public. Structural problems arise in the near field also. In several instances structural members of the aircraft have developed fatigue failures from the oscillatory loads imposed by pressure fluctuations from the engine. Generally, these failures have been in secondary members but, with more powerful engines, the possibility that the primary tail structure of some multi-engine configurations may be affected must be considered. Structural problems may also arise in the operation of ground mufflers which enclose the jet tailpipe with only small clearances between the cell walls and the jet stream. The purpose of the present investigation is therefore to make a systematic study of the near pressure field of both unchoked and choked jets. In discussion of unchoked operation, data from the survey of a full-scale engine are used primarily, although some data from high-temperature model jets are included to indicate probable trends and to clarify some of the full-scale results. Since an extensive range of overpressure is not generally available in static operation of turbojets, the characteristics of choked operation were explored with model jets only.

In order to avoid ambiguity of nomenclature, some explanation of the usage of the present report appears warranted. The terms "noise" and "sound pressure" are used interchangeably in discussion of the near-field pressure fluctuations. However, it is recognized that, because the measurements were made in the near field where sound pressure and particle velocity are not in phase, the data are in many cases not indicative of the radiated sound energy.

¹ Supersedes NACA Technical Note 3187 by Leslie W. Lassiter and Harvey H. Hubbard, 1954.

The choice of words is therefore primarily one of convenience.

SYMBOLS

\bar{p}	overall pressure fluctuations, lb/sq ft
x	distance along flow axis, in.
Δx	distance between shocks, in.
y	distance from longitudinal axis of jet, in.
z	distance from center of nozzle or orifice to observer, in.
d	radial distance from 15° boundary, in.
D	nozzle or orifice diameter, in.
D_a	diameter of auxiliary orifice
U	jet velocity, fps
T	jet-fluid temperature, °F
p	pressure, lb/sq in.
p_s/p_0	nozzle pressure ratio
f	frequency, cps or keps
λ	wavelength, in.
ψ	azimuth angle (zero or jet axis in front), deg
Subscripts:	
e	condition at jet exit
s	initial chamber condition (stagnation)
a	auxiliary
0	ambient-air conditions

APPARATUS AND METHODS

Tests were conducted with a full-scale turbojet engine and with various model nozzles and orifices of from 0.275 inch to 2.00 inches in diameter for the purpose of determining the characteristics of the near pressure field associated with their operation. The full-scale measurements were made during ground runs of a J-33-A-17a engine having a tailpipe diameter of 18½ inches and with a rated thrust of 3,825 pounds. The engine was installed in an operational fighter airplane, which was positioned on a paved taxi strip approximately 300 feet from any large reflecting surfaces other than the ground. The tailpipe center line was about 36 inches above ground level and parallel to it.

The model configurations were tested while fitted to the end of the settling chamber shown schematically in figure 1. The chamber had an inside diameter of 6.00 inches and a length of 6 feet and was supplied with air from a storage tank at a pressure of 100 lb/sq in. A large part of the chamber length was filled with a cylinder of porous, rubberized material for the purpose of minimizing extraneous noise generated inside the chamber and at the control valve.

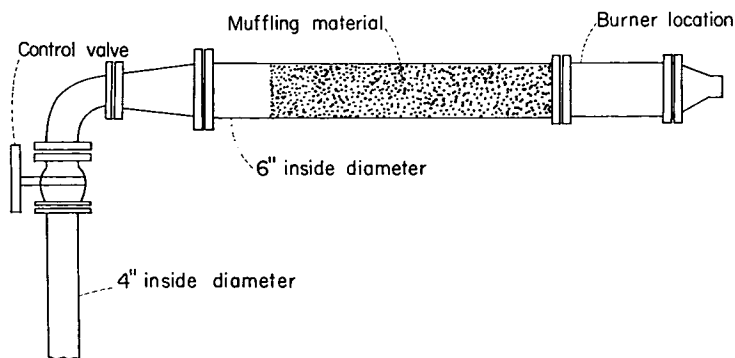


FIGURE 1.—Schematic layout of model test configuration.

This arrangement permitted measurements to be made at velocities as low as 100 fps without the appearance in the spectrum of extraneous components of any consequence.

During a part of the tests it was desired to operate the model at a temperature of the order of that in a turbojet. For this purpose, an acetylene burner of the ring type was installed in the settling chamber just downstream of the sound-absorbing material with an asbestos gasket inserted between the two chamber sections. With this arrangement temperatures up to 1,800° were readily obtained. Operation of the burner was generally limited to the unchoked-nozzle condition. All measurements during choked operation were made with unheated air; however, enough choked operation with heated air was employed to verify the existence of the phenomena observed with unheated air.

The instrumentation used is illustrated schematically in figure 2 (a). Pressure fluctuations were detected with two sound-pressure-measurement systems. The first of these and the one ordinarily used, has essentially a flat frequency response from 20 to 20,000 cps and cuts off at 15 and 38,000 cps. The second system, which was used only to monitor the first, has a response which is flat up to 100,000 cps. Output of the sound-measuring system was channeled to a cathode-ray oscillograph for waveform observation, an electronic voltmeter for overall pressure determination, and a Panoramic Sonic Analyzer for spectrum studies. The Panoramic is a variable-band-width instrument, the band width varying from 50 cps at 100 cps to 550 cps at 10,000 cps; thus it will not yield the true spectrum shape without correction, as will a constant-band-width analyzer. However, comparison of a few representative spectra from the Panoramic analyzer and from a constant-band-width analyzer indicated that for the qualitative purposes of this report the uncorrected Panoramic analysis is satisfactory.

Figure 2 (b) illustrates schematically the instrumentation used for motion studies of the shock formations during choked operation. The gas-discharge point-source light and the high-speed camera constitute a simple shadowgraph. Between these components is inserted a light baffle (oriented parallel to the jet axis) which allows only a fine line of light to reach the camera. The shock-wave segment being viewed then appears as a point of different intensity in that line and a time history of its axial motion is obtained as the film moves.

More detailed studies of the flow during choked operation were made with a conventional shadowgraph system, the design of which was essentially a duplication of that described in reference 5. The light system consisted of a 15,000-volt power supply used to charge a 0.125-microfarad condenser, a gate circuit for firing control, and an arc unit. The arc unit confined the discharge to a very small volume and produced an extremely intense light flash of short duration. The light source was effectively of only ¼-inch diameter and thus afforded excellent resolution in the photographs.

RESULTS AND DISCUSSION

Surveys of the near pressure field were made during unchoked operation of a turbojet engine and during both unchoked and choked operation of model jet configurations. Unless otherwise indicated all unchoked model data were

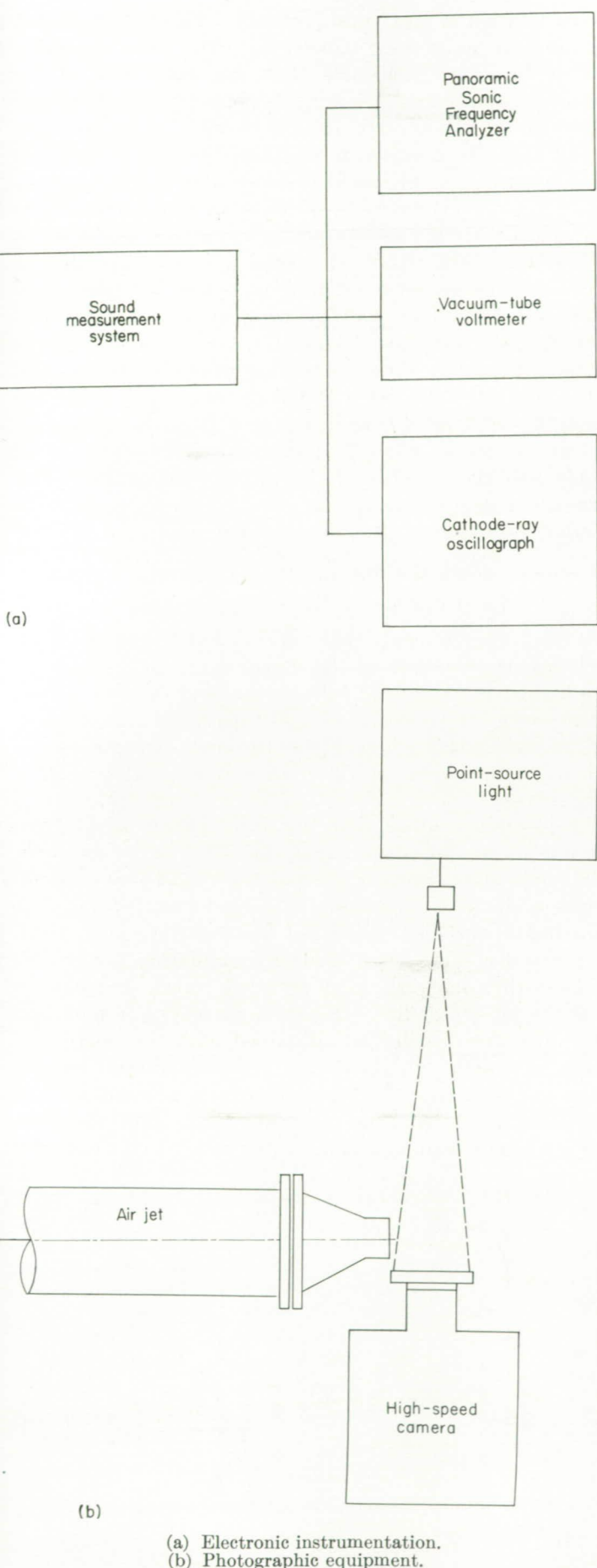


FIGURE 2.—Schematic diagram of instrumentation used in tests.

435875-57-15

obtained with heated air; whereas the entire choked survey was made with unheated air. The pressure measurements were made at various axial and radial positions near the jet boundary.

UNCHOKED OPERATION OF TURBOJET ENGINE

Frequency content.—The frequency spectrum of pressure fluctuations generated by subsonic flow from the turbojet is ordinarily continuous; that is, it contains all frequencies within a given band. In the proximity of the jet boundary the frequency band may become very narrow and its limits may vary with the point of observation along the boundary. A sample spectrum, obtained at a point 2 diameters from the boundary and 15 diameters downstream of the turbojet tailpipe, is shown in figure 3. This sample is a logarithmic plot of pressure fluctuation as a function of frequency, obtained by photographing the screen of the frequency analyzer during 15 consecutive trace sweeps. It illustrates the continuous nature of the frequency content and, by the vertical spread of successive traces, the randomness of amplitude also. Evident, too, is the fact that the more important pressure fluctuations occur within a rather narrow frequency band, which at this particular position is centered at about 0.1 kcps. At points nearer the nozzle the predominant components are of considerably higher frequency (600 to 1,000 cps at the nozzle) and the band tends to become broader.

Magnitude of pressure fluctuations.—The effects of axial and radial distance on the magnitude of the pressure fluctuations for the turbojet engine operating at rated thrust are given in figure 4. Figure 4 (a) illustrates the distribution of pressure in two arbitrary frequency bands along a line parallel to the 15° jet boundary and 2 nozzle diameters from the boundary. The two bands, 15 cps to 150 cps and 150 cps to 15,000 cps, were selected purely as a matter of convenience; however, the lower band may be of particular interest inasmuch as some important structural resonances occur in that range. In the higher frequency distribution, a maximum is indicated at a point 1 nozzle diameter downstream; however, the spectrum records

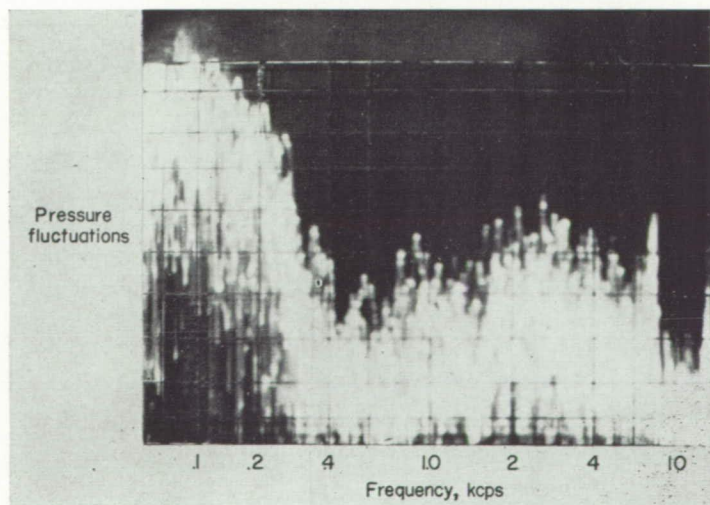


FIGURE 3.—Frequency spectrum of turbojet pressure fluctuations.

$$\frac{x}{D}=15; \frac{d}{D}=2.$$

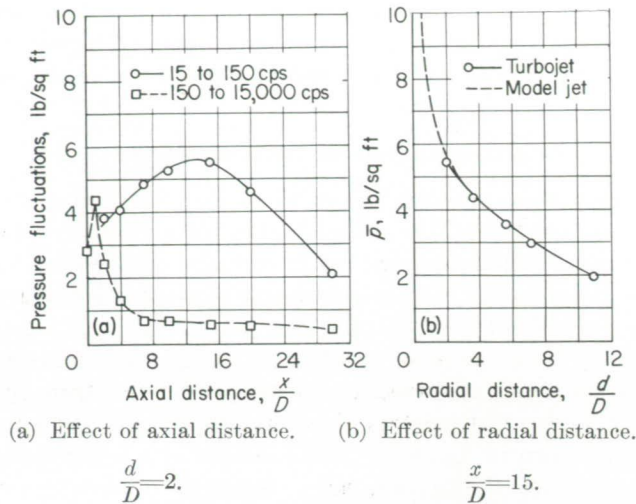


FIGURE 4.—Effects of distance on magnitude of pressure fluctuations of full-scale jet operating at rated thrust.

indicate that this maximum is largely due to a single high-pitched component of about 10,000 cps, which is presumably compressor or turbine whine. The more significant feature of the curve is that it clearly shows that the random pressure fluctuations in this frequency range are greatest near the nozzle and decrease rapidly with distance downstream.

On the other hand, the distribution of component pressure fluctuations in the frequency band from 15 to 150 cps indicates an increase with axial distance until a maximum pressure of about 5.5 lb/sq ft occurs at a point about 12 to 15 diameters downstream of the exit. Furthermore, the curve is comparatively flat, so that appreciable low-frequency content appears over a distance range of from approximately 2 to 20 diameters. In fact, comparison of the two curves of figure 4 (a) shows that at distances greater than about 2 diameters, the predominating pressure fluctuations are for frequencies lower than 150 cps.

From the practical standpoint, the effect of increasing radial distance on the magnitude of the fluctuations is of interest. Thus, the effects observed in a plane normal to the jet axis and located 15 diameters downstream (about at the maximum of the low-frequency curve) are shown in figure 4 (b) in the form of a radial pressure distribution. Since full-scale measurements were limited to a minimum distance of 2 diameters, some data from a 1-inch model jet having approximately the same temperature and velocity are included to indicate the probable trend at distances less than 2 diameters. The decrease of pressure with distance, as measured with the turbojet, is rather gradual. The model data, however, indicate that at distances less than 2 diameters from the boundary the curve becomes somewhat steeper. Even so, to obtain a 50-percent reduction in pressure requires an increase of radial distance from 0.5 to 3 diameters.

UNCHOKED OPERATION OF MODEL JETS

The scope of the full-scale measurements was somewhat limited by the test schedule of the airplane in which the engine was mounted; hence, it was deemed desirable to supplement the turbojet data with some results from a 1-inch model jet with heated air. The primary purpose of these model data, however, is to indicate general trends rather than to provide quantitative information.

Axial location of maximum pressure.—Figure 4 (a), which presents data taken along a line 2 diameters from the turbojet flow boundary, indicates that the magnitude of the pressure fluctuations is greatest at a point 12 to 15 diameters downstream of the nozzle. Results of model tests, however, indicate that the position of maximum pressure varies. It is dependent upon the radial distance at which the survey is made and upon the velocity of the jet. Figure 5 illustrates from model tests the nature of the variations produced by each of these parameters. In figure 5 (a) the distribution of pressure-fluctuation magnitude is plotted for four radial distances for a 1-inch jet operating at a temperature of 1,660° R and a velocity of 1,240 fps. As radial distance is increased, the point of maximum magnitude is seen to occur farther downstream. At a radial distance of 2 diameters (which is the same d/D as in figure 4 (a)), the maximum pressure occurs at 6 to 8 diameters downstream, or at roughly half the distance of the turbojet maximum. This difference is partly due to the velocity effect, which is illustrated in figure 5 (b). The curves apply to pressure distributions along the line $d/D = 2$ at a constant jet temperature of 1,660° R but at various velocities from 600 fps to 1,870 fps. They indicate that velocity has a decided effect, which results in a shift of the maximum from 3 diameters to 10 diameters within the velocity range of the test. Even so, the curve for a velocity of 1,870 fps has a maximum at only 10 diameters, whereas the turbojet of figure 4 (a) indicated a maximum at 12 to 15 diameters at a slightly lower velocity.

The possibility arose that this discrepancy might have been due to ground effects, since the full-scale jet was only 3 diameters above ground whereas the model was some 70 diameters above it. Therefore, the model was operated at approximate turbojet values of temperature and Mach number and a survey was made by simulating the ground surface with a large sheet of plywood placed 3 diameters below the jet center line. Figure 6 presents a comparison of the pressure distributions obtained with the board and without it. Although these data are not sufficient to give a clear-cut indication that ground effects account for the discrepancy in distribution, the evidence is that the pressures far downstream are increased by much larger amounts

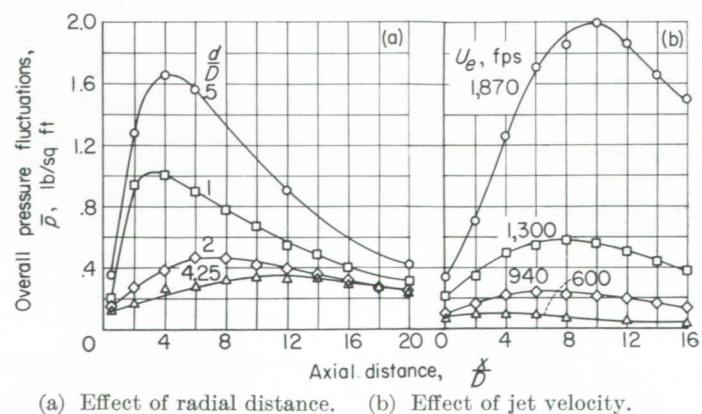


FIGURE 5.—Factors affecting the axial location of maximum pressure fluctuations from 1-inch model jet. $T_s = 1,660^\circ$ R.

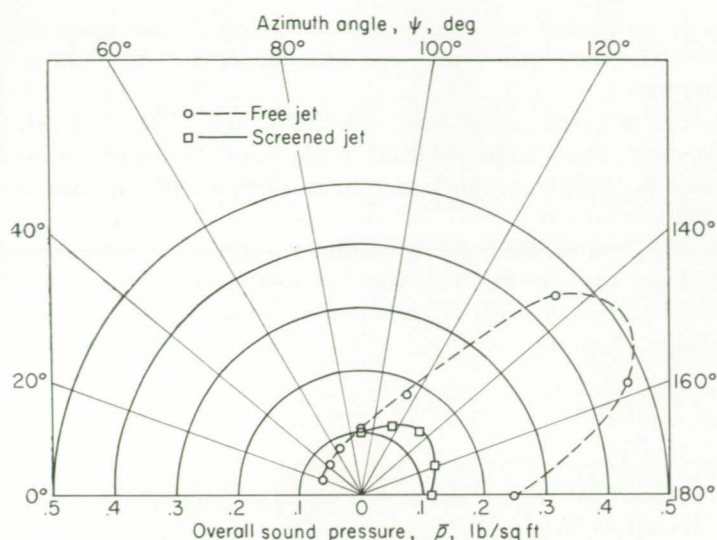


FIGURE 19.—Effect of a grid on the overall noise from a high-temperature model jet. $D=1$ inch; $\frac{z}{D}=150$; $T_s=1,400^\circ$ F.

SCREECH ELIMINATION IN CHOKED JETS

In references 4 and 6 several methods of obtaining reduction in the magnitude of pressure fluctuations from a choked jet were discussed. Among these were such devices as a toothed nozzle and a gauze-cylinder extension to the nozzle to allow shock-free expansion of the supersonic flow. Several exploratory methods of a similar nature were investigated during the present tests. One such method, not previously reported, proved very effective in reducing the magnitude of the screech component. This method involved the use of small auxiliary orifices to introduce turbulence into the main stream at a point just downstream of the main jet exit. (See sketch in fig. 20.) The configuration consisted of a 1-inch knife-edge orifice with four $\frac{1}{32}$ -inch holes drilled through the beveled face, whereby a small auxiliary supply

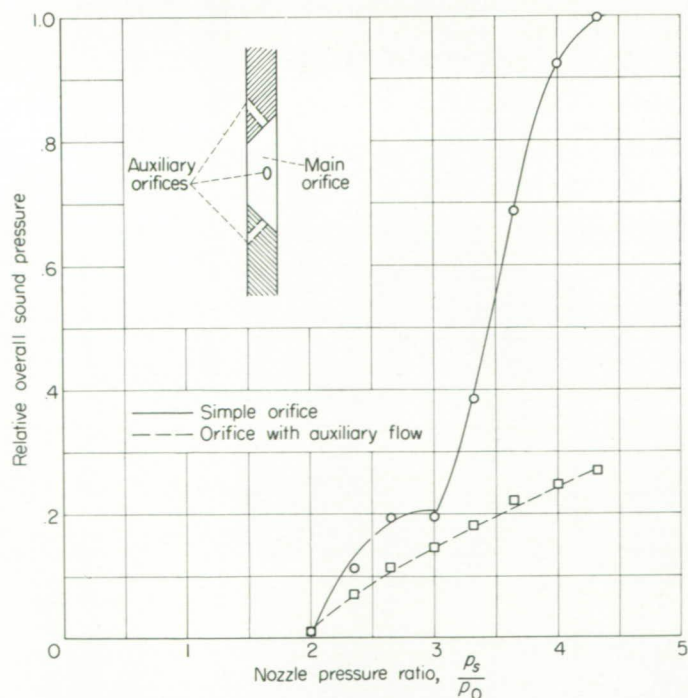
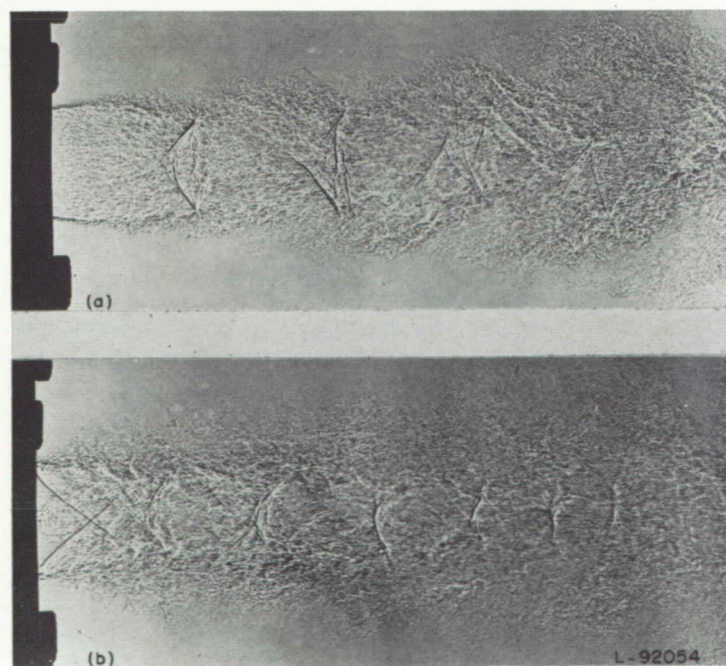


FIGURE 20.—Effect of auxiliary orifices on relative overall pressure-fluctuation magnitude. $D=1$ inch; $D_a=0.031$ inch.

of air from the settling chamber was allowed to enter the main flow at an angle of about 45° .

An illustration of the reduction in magnitude of the overall pressure fluctuations obtained by this method is shown in figure 20, which compares on a relative pressure basis the data obtained at a point just outside the jet boundary and approximately 3 diameters downstream. Any scheme which reduces the discrete frequency noise components will essentially eliminate the peaks in the axial pressure distribution curve of figure 15. The reductions obtained are a function of the relative contributions of the discrete component and the random components and, hence, are much greater at some field points than at others. This same result applies to locations in the far field where the amount of noise reduction is a function of the azimuth angle. The net result of eliminating the screech component appears to be a decrease of the total radiated acoustical energy. In one test configuration where screeching was severe, some noise reduction was obtained at all azimuth angles and this reduction resulted in a decrease of 3 decibels in the total radiated energy.

Shadowgraph records show that this decrease is coincident with elimination of the vortex flow patterns associated with screech. Figure 21 illustrates the change in the flow pattern when auxiliary orifices are used at the highest pressure ratio of the tests. The top record was obtained with the auxiliary orifices plugged. Screech was present and the vortex formations are evident. The lower record was obtained at the same pressure ratio with the auxiliary orifices in operation. The screech component was virtually eliminated and the flow disturbances are shown to be greatly reduced. Thus, the generation of screech is again indicated to be associated with formation of the vortex-like disturbances.



(a) No auxiliary orifices (screeching).
(b) With auxiliary orifices.

FIGURE 21.—Effect of auxiliary orifices on flow of choked jet. $\frac{p_s}{p_0}=3.67$;
 $D=1$ inch; $D_a=0.031$ inch.

CONCLUSIONS

Results have been presented from an investigation of the near sound-pressure field of a full-scale unchoked turbojet and of both choked and unchoked model jets.

The near-field investigation of pressure fluctuations from the full-scale turbojet engine indicates the following conclusions:

1. The fluctuations are random and the largest components occur within a fairly narrow band at frequencies less than 150 cps.

2. Along a line 2 nozzle diameters from the jet boundary, maximum pressure fluctuations occur at about 12 to 15 diameters downstream of the nozzle.

Results obtained with unchoked model jets indicate:

1. The position of maximum pressure magnitude along a line parallel to the jet boundary is a function of jet velocity and the radial distance of the survey.

2. Pressure magnitude is about 50 percent to 80 percent higher at a panel surface than in free space when the panel is oriented parallel to the jet boundary.

3. The overall magnitude of pressure fluctuations varies with jet velocity to about the second power near the jet, whether the velocity increase is effected at constant Mach number with variable temperature or at constant temperature with variable Mach number.

4. The exponent of the power function relating overall sound pressure and jet velocity increases systematically with radial distance from the nozzle.

5. The use of a wire screen in the jet flow at points a diameter or so downstream of the nozzle reduces the low-frequency components of the random noise spectrum by a considerable amount. Overall sound pressures at azimuth angles greater than 90° are thus lowered, primarily as a result of the large decreases in the lower-frequency components.

Results obtained with choked model jets indicate:

1. A high-intensity, discrete-frequency component occurs during a part of the choked operating range. This component

is associated with the presence of flow disturbances of toroidal-vortex form and with oscillation of the shock formations.

2. For a given nozzle size, the frequency of the screech component bears some relation to the shock spacing. Frequency is roughly proportional to the inverse of the nozzle diameter.

3. The use of four small auxiliary orifices to introduce turbulence into the main stream just downstream of the exit reduced the magnitude of the screech component by a considerable amount.

LANGLEY AERONAUTICAL LABORATORY,
NATIONAL ADVISORY COMMITTEE FOR AERONAUTICS,
LANGLEY FIELD, VA., February 19, 1954.

REFERENCES

1. Lassiter, Leslie W., and Hubbard, Harvey H.: Experimental Studies of Noise From Subsonic Jets in Still Air. NACA TN 2757, 1952.
2. Von Gierke, H. E., Parrack, H. O., Gannon, W. J., and Hansen, R. G.: The Noise Field of a Turbo-Jet Engine. Jour. Acous. Soc. Am., vol. 24, no. 2, Mar. 1952, pp. 169-174.
3. Lighthill, M. J.: On Sound Generated Aerodynamically. I. General Theory. Proc. Roy. Soc. (London), ser. A, vol. 211, no. 1107, Mar. 20, 1952, pp. 564-587.
4. Westley, R., and Lilley, G. M.: An Investigation of the Noise Field From a Small Jet and Methods for Its Reduction. Rep. No. 53, College of Aero., Cranfield (British), Jan. 1952.
5. Melton, Ben S., Prescott, Rochelle, and Gayhart, Everett L.: A Working Manual for Spark Shadowgraph Photography. Bumblebee Rep. No. 90 (Bur. Ord., U. S. Navy Contract No. NOrd 7386), The Johns Hopkins Univ., Appl. Phys. Lab., Dec. 1948.
6. Powell, Alan: A "Schlieren" Study of Small Scale Air Jets and Some Noise Measurements on Two-Inch Diameter Air Jets. Rep. No. NC 136, Univ. College, Southampton (British), Dec. 1951.
7. Powell, Alan: The Noise of Choked Jets. Jour. Acous. Soc. Am., vol. 25, no. 3, May 1953, pp. 385-389.

REPORT 1262

THEORETICAL AND EXPERIMENTAL INVESTIGATION OF THE EFFECT OF TUNNEL WALLS ON THE FORCES ON AN OSCILLATING AIRFOIL IN TWO-DIMENSIONAL SUBSONIC COMPRESSIBLE FLOW¹

By HARRY L. RUNYAN, DONALD S. WOOLSTON, and A. GERALD RAINERY

SUMMARY

This report presents a theoretical and experimental investigation of the effect of wind-tunnel walls on the air forces on an oscillating wing in two-dimensional subsonic compressible flow. A method of solving an integral equation which relates the downwash on a wing to the unknown loading is given, and some comparisons are made between the theoretical results and the experimental results. A resonance condition, which was predicted by theory in a previous report (NACA Rep. 1150), is shown experimentally to exist. In addition, application of the analysis is made to a number of examples in order to illustrate the influence of walls due to variations in frequency of oscillation, Mach number, and ratio of tunnel height to wing semichord.

INTRODUCTION

In the evaluation of results obtained by measurement of the forces on a wing in a wind tunnel, the question of the effect of the tunnel walls arises. In the case of steady flow the problem has been extensively investigated and, in general, relatively simple factors have been determined which can be used to modify measurements of the forces on a wing in a tunnel to correspond to free-air conditions. However, the corresponding problem of the effect of walls on an oscillating airfoil has received relatively little attention, particularly in the case of compressible flow. The present report concerns the wall effects in the oscillating case and treats the problem in two-dimensional subsonic compressible flow.

In incompressible flow, theoretical treatments of wall effects on oscillating wings have been made by several investigators and reported in references 1, 2, and 3. These investigators have shown generally that the tunnel-wall effects are a maximum for some small values of the reduced frequency and that the wall effects become negligible as the reduced frequency is increased. Extension of the theoretical treatment of the problem to include the effects of compressibility of the fluid has been reported in reference 4. In this

reference, it is shown that, in addition to the large effect noted at low values of the reduced frequency, under certain conditions, large effects of the walls may be encountered at higher values of the reduced frequency. These effects are due to an acoustic resonant phenomenon which occurs when a disturbance from the oscillating wing is reflected from the tunnel wall back to the wing with such a phase relationship that it reinforces a succeeding disturbance.

In reference 4, the problem was expressed as an integral equation which relates the known downwash distribution over the airfoil to the unknown lift distribution. One purpose of the present report is to discuss further the integral equation and to demonstrate a method of solving it. A second purpose is to present some results showing wall effects calculated by this procedure and, in some cases, to compare the calculated results with experimental results. This phase of the investigation is given in three parts: (1) A comparison between analytically and experimentally determined values for the lift and moment on a wing oscillating in pitch at several subsonic Mach numbers; (2) an analytical study of the effects of a variation in Mach number for a constant ratio of tunnel height to wing semichord; and (3) an analytical study of the effects of a variation in the ratio of tunnel height to wing semichord. Portions of this material have been reported previously in reference 5 and are included in the present report in order to provide a more extensive and unified presentation.

As a check, the integral equation for the downwash on a wing oscillating between walls in a compressible medium is reduced to the zero-frequency condition and is given in the appendix. The resulting expression is in agreement with steady-state results.

The calculation procedure and the results contained in this report are of significance for such problems as the experimental measurement of the forces on an oscillating airfoil, the determination of wing-flutter characteristics in wind tunnels, and also in certain possible types of flutter of airfoils in cascade.

¹ Supersedes NACA Technical Note 3416 by Harry L. Runyan, Donald S. Woolston, and A. Gerald Rainey, 1955.

SYMBOLS

a	velocity of sound, ft/sec
A_n	coefficients in series expression for lift distribution (eq. (16)), where $n=0, 1, 2, \dots$
b	wing semichord, ft
h	displacement of wing in vertical translation, ft
\bar{H}	height of tunnel, ft
H	height of tunnel referred to wing semichord
$H_0^{(2)}, H_1^{(2)}$	Hankel functions of the second kind
k	reduced-frequency parameter, $b\omega/U$
$K(M, z) + K(M, z, H)$	kernel of integral equation
$L(x_0), L(\theta_0)$	lift distribution, lb/ft/unit span
L_α	aerodynamic lift force per unit span due to pitch
L_h	aerodynamic lift force per unit span due to translation
M_α	aerodynamic moment per unit span due to pitch
M_h	aerodynamic moment per unit span due to translation
M	Mach number, U/a
$p = \frac{MkH}{2\pi\beta}$	
$R_n = \sqrt{(x-x_0)^2 + \beta^2(nH)^2}$	where $n=1, 2, 3, \dots$
U	stream velocity in chordwise direction, ft/sec
$w(x)$	vertical induced velocity (perpendicular to chord), ft/sec
x_α	axis of rotation measured from mid-chord, positive rearward, based on semichord
x, x_0, y, ξ	Cartesian coordinates
$z = k(x-x_0)$	
α	angular displacement of wing in pitch, radians
$\beta = \sqrt{1-M^2}$	
$\epsilon = \frac{ x-x_0 }{\beta H}$	
$\theta = -\cos^{-1}x$	
$\theta_0 = -\cos^{-1}x_0$	
$\mu = \frac{Mk}{\beta^2}$	
ρ	fluid density, slugs/cu ft
ϕ_{L_α}	phase angle between lift force and position of pitching wing, deg
ϕ_{L_h}	phase angle between lift force and position of translating wing, deg
ϕ_{M_α}	phase angle between moment and position of pitching wing, deg
ϕ_{M_h}	phase angle between moment and position of translating wing, deg
ω	circular frequency of oscillation, radians/sec
ω_{res}	circular frequency at resonance, radians/sec

Δp pressure difference between upper and lower surface, lb/sq ft
 Primed quantities refer to a wing in free air.

ANALYTICAL INVESTIGATION

This section is concerned with the development of a method for solving the integral equation, originally derived in reference 4, which relates the downwash to the loading on an oscillating wing. The basic integral equation and its kernel is given by equations (1) and (2). Reduction of the kernel is made in equations (3) to (10). Alternative series expressions for the kernel which are suitable for numerical computation are given by equations (11) to (15). The loading on the wing is given by equation (16), the downwash expression by equations (18) and (19), and finally the lift and moment expressions by equations (20).

THE INTEGRAL EQUATION AND ITS KERNEL FUNCTION

The integral equation.—The integral equation of reference 4 for the vertical velocity or downwash of an oscillating airfoil between plane walls may be written as

$$w(x) = \frac{\omega b}{\rho U^2} \int_{-1}^1 L(x_0) [K(M, z) + K(M, z, H)] dx_0 \quad (1)$$

where $w(x)$ is the known vertical velocity (or known motion of the wing) and $L(x_0)$ is the unknown lift distribution or the local strength of a distribution of oscillating pressure doublets. The functions within the brackets comprise the kernel function of the integral equation and appear formally as

$$K(M, z) = \frac{i}{4\beta k} \lim_{y \rightarrow 0} e^{-ik(x-x_0)} \int_{-\infty}^{x-x_0} e^{\frac{ik}{\beta^2} \xi} \frac{\partial^2}{\partial y^2} H_0^{(2)} \left(\frac{Mk}{\beta^2} \sqrt{\xi^2 + \beta^2 y^2} \right) d\xi \quad (2a)$$

$$K(M, z, H) = \frac{i}{4\beta k} \lim_{y \rightarrow 0} e^{-ik(x-x_0)} \int_{-\infty}^{x-x_0} 2 \sum_{n=1}^{\infty} (-1)^n e^{\frac{ik}{\beta^2} \xi} \frac{\partial^2}{\partial y^2} H_0^{(2)} \left[\frac{Mk}{\beta^2} \sqrt{\xi^2 + \beta^2 (y-nH)^2} \right] d\xi \quad (2b)$$

The first function $K(M, z)$ corresponds to the kernel for the free-air condition as given by Possio (ref. 6). The second function $K(M, z, H)$, containing the infinite summation, is the additional part of the kernel arising from the effect of the walls. Physically, a kernel function represents the contribution to the vertical velocity at a field point due to a pulsating pressure doublet of unit strength located at any other point in the field. For the particular case represented by equations (2), the kernel function gives the vertical velocity in the plane of a wing located in the center of the tunnel. The expression $K(M, z)$ gives the downwash of a doublet in the plane of the wing, whereas the expression $K(M, z, H)$ gives the downwash due to the system of images which mathematically represents the walls.

Reduction of the kernel function.—The integrals contained in the expressions for the kernel function in equations (2) are improper because they have an infinite limit and also because, at certain points, the integrands become singular. This section is concerned with the reduction of these integrals to a form more amenable to computation.

By making use of the fact that the Hankel functions in equations (2) satisfy the identity

$$\frac{\partial^2}{\partial y^2} H_0^{(2)} \left(\frac{Mk}{\beta^2} \sqrt{\xi^2 + \beta^2 y^2} \right) = -\beta^2 \frac{\partial^2}{\partial \xi^2} H_0^{(2)} \left(\frac{Mk}{\beta^2} \sqrt{\xi^2 + \beta^2 y^2} \right) - \frac{M^2 k^2}{\beta^2} H_0^{(2)} \left(\frac{Mk}{\beta^2} \sqrt{\xi^2 + \beta^2 y^2} \right) \quad (3)$$

there is obtained for the downwash

$$\begin{aligned} w(x) = & \frac{\omega b}{\rho U^2} \frac{-i}{4\beta k} \lim_{y \rightarrow 0} \int_{-1}^1 L(x_0) e^{-ik(x-x_0)} \left(\beta^2 \int_{-\infty}^{x-x_0} e^{\frac{ik}{\beta^2} \xi} \frac{\partial^2}{\partial \xi^2} H_0^{(2)} \left(\frac{Mk}{\beta^2} \sqrt{\xi^2 + \beta^2 y^2} \right) d\xi + \right. \\ & \frac{M^2 k^2}{\beta^2} \int_{-\infty}^{x-x_0} e^{\frac{ik}{\beta^2} \xi} H_0^{(2)} \left(\frac{Mk}{\beta^2} \sqrt{\xi^2 + \beta^2 y^2} \right) d\xi + \\ & \left. 2 \sum_{n=1}^{\infty} (-1)^n \left\{ \beta^2 \int_{-\infty}^{x-x_0} e^{\frac{ik}{\beta^2} \xi} \frac{\partial^2}{\partial \xi^2} H_0^{(2)} \left[\frac{Mk}{\beta^2} \sqrt{\xi^2 + \beta^2 (y-nH)^2} \right] d\xi + \right. \right. \\ & \left. \left. \frac{M^2 k^2}{\beta^2} \int_{-\infty}^{x-x_0} e^{\frac{ik}{\beta^2} \xi} H_0^{(2)} \left[\frac{Mk}{\beta^2} \sqrt{\xi^2 + \beta^2 (y-nH)^2} \right] d\xi \right\} \right) dx_0 \quad (4) \end{aligned}$$

The integrals of equation (4) that contain partial derivatives of Hankel functions can be integrated twice by parts to obtain

$$\begin{aligned} \int_{-\infty}^{x-x_0} e^{\frac{ik}{\beta^2} \xi} \frac{\partial^2}{\partial \xi^2} H_0^{(2)} \left[\frac{Mk}{\beta^2} \sqrt{\xi^2 + \beta^2 (y-nH)^2} \right] d\xi = & -\frac{Mk}{\beta^2} e^{\frac{ik}{\beta^2} (x-x_0)} \frac{x-x_0}{\sqrt{(x-x_0)^2 + \beta^2 (y-nH)^2}} H_1^{(2)} \left[\frac{Mk}{\beta^2} \sqrt{(x-x_0)^2 + \beta^2 (y-nH)^2} \right] - \\ & \frac{ik}{\beta^2} e^{\frac{ik}{\beta^2} (x-x_0)} H_0^{(2)} \left[\frac{Mk}{\beta^2} \sqrt{(x-x_0)^2 + \beta^2 (y-nH)^2} \right] - \frac{k^2}{\beta^4} \int_{-\infty}^{x-x_0} e^{\frac{ik}{\beta^2} \xi} H_0^{(2)} \left[\frac{Mk}{\beta^2} \sqrt{\xi^2 + \beta^2 (y-nH)^2} \right] d\xi \quad (5) \end{aligned}$$

The last integral of equation (5) may be written in two parts as

$$\begin{aligned} \sum_{n=1}^{\infty} (-1)^n \int_{-\infty}^{x-x_0} e^{\frac{ik}{\beta^2} \xi} H_0^{(2)} \left[\frac{Mk}{\beta^2} \sqrt{\xi^2 + \beta^2 (y-nH)^2} \right] d\xi \\ = \int_0^{\infty} e^{\frac{ik}{\beta^2} \xi} \sum_{n=1}^{\infty} (-1)^n H_0^{(2)} \left[\frac{Mk}{\beta^2} \sqrt{\xi^2 + \beta^2 (y-nH)^2} \right] d\xi + \\ \int_0^{x-x_0} e^{\frac{ik}{\beta^2} \xi} \sum_{n=1}^{\infty} (-1)^n H_0^{(2)} \left[\frac{Mk}{\beta^2} \sqrt{\xi^2 + \beta^2 (y-nH)^2} \right] d\xi \quad (6) \end{aligned}$$

The first integral on the right-hand side of equation (6) will be left temporarily in integral form and will be treated in the following section. (See evaluation of S_3 following eq. (13).)

The second integral on the right-hand side of equation (6) has not been integrated in closed form; however, in wind-tunnel problems it can be handled conveniently by approximate methods. (An alternative means of treating this integral, which avoids the approximation but is somewhat more tedious, will be indicated in the discussion following eq. 14(c).) A practical assumption which is often made in the analysis of the effect of wind-tunnel walls is that the tunnel height is considered large compared with the wing semichord. With this assumption the argument of the Hankel function in equation (6) can be written as (in the limit as $y \rightarrow 0$)

$$\frac{Mk}{\beta^2} \sqrt{\xi^2 + \beta^2 (nH)^2} = \frac{Mk}{\beta^2} \beta nH \sqrt{\left(\frac{\xi}{\beta nH} \right)^2 + 1} \approx \frac{Mk}{\beta} nH$$

provided that $\frac{\xi}{\beta nH} \ll 1$.

This approximation implies that the airfoil images, and, particularly the closest image $n=1$, are a sufficient distance from the airfoil so that the actual distance $\sqrt{\xi^2 + \beta^2 (nH)^2}$

may be replaced by the vertical distance βnH of the image above the airfoil. Of course, this approximation does not hold for Mach numbers close to or equal to unity. With this approximation, the second integral of equation (6) can be expressed as

$$\begin{aligned} \lim_{y \rightarrow 0} \int_0^{x-x_0} e^{\frac{ik}{\beta^2} \xi} \sum_{n=1}^{\infty} (-1)^n H_0^{(2)} \left[\frac{Mk}{\beta^2} \sqrt{\xi^2 + \beta^2 (y-nH)^2} \right] d\xi \\ = \sum_{n=1}^{\infty} (-1)^n H_0^{(2)} \left(\frac{MknH}{\beta} \right) \int_0^{x-x_0} e^{\frac{ik}{\beta^2} \xi} d\xi \\ = \sum_{n=1}^{\infty} (-1)^n H_0^{(2)} \left(\frac{MknH}{\beta} \right) \frac{\beta^2}{ik} \left[e^{\frac{ik}{\beta^2} (x-x_0)} - 1 \right] \quad (7) \end{aligned}$$

and these equations may be used to express equation (4) as

$$w(x) = \frac{\omega b}{\rho U^2} \int_{-1}^1 L(x_0) [K(M, z) + K(M, z, H)] dx_0 \quad (8)$$

where

$$\begin{aligned} K(M, z) = & \frac{1}{4\beta} e^{-iz} \left\{ e^{\frac{iz}{\beta^2}} \left[-H_0^{(2)}(\mu R_0) + \frac{iM(x-x_0)}{|x-x_0|} H_1^{(2)}(\mu R_0) \right] + \right. \\ & \left. i\beta^2 \left[\frac{2}{\pi\beta} \log_e \frac{1+\beta}{M} + \int_0^{\frac{v}{M}} e^{iu} H_0^{(2)}(M|u|) du \right] \right\} \quad (9) \end{aligned}$$

and

$$\begin{aligned} K(M, z, H) = & \frac{e^{-iz}}{2\beta} \left[-e^{\frac{iz}{\beta^2}} \sum_{n=1}^{\infty} (-1)^n H_0^{(2)}(\mu R_n) + \right. \\ & \left. \beta^2 \left(e^{\frac{iz}{\beta^2}} - 1 \right) \sum_{n=1}^{\infty} (-1)^n H_0^{(2)} \left(\frac{MknH}{\beta} \right) + \right. \\ & \left. ik \sum_{n=1}^{\infty} (-1)^n \int_0^{\infty} e^{-\frac{ik}{\beta^2} \xi} H_0^{(2)} \left[\frac{kM}{\beta^2} \sqrt{\xi^2 + \beta^2 (nH)^2} \right] d\xi + \right. \\ & \left. e^{\frac{iz}{\beta^2}} \sum_{n=1}^{\infty} (-1)^n \frac{iM(x-x_0)}{R_n} H_1^{(2)}(\mu R_n) \right] \quad (10) \end{aligned}$$

in which use has been made of

$$\mu = \frac{kM}{\beta^2} \quad u = \frac{k}{\beta^2} \xi \quad v = \frac{Mz}{\beta^2}$$

$$R_0 = |x - x_0| \quad R_n = \sqrt{(x - x_0)^2 + \beta^2(nH)^2}$$

Equation (8), together with the definition of equations (9) and (10), permits the determination of the effect of tunnel walls on a lift distribution $L(\theta_0)$ for a given downwash distribution $w(x)$. The integral equation for the case of no tunnel walls checks the results of Possio (ref. 6). For the case with walls and for the limiting steady-flow case of zero frequency, it is possible to obtain a mathematical check with some existing results; this check is shown in the appendix.

Alternative series expressions for kernel.—Although the form of the kernel $K(M, z, H)$, given by equation (10), could be used for calculation, alternative series which are more highly convergent may be used and are given in this section.

The kernel $K(M, z, H)$ is the sum of four infinite series which can be written as

$$K(M, z, H) = \frac{e^{-iz}}{2\beta} (C_1 S_1 + C_2 S_2 + C_3 S_3 + C_4 S_4) \quad (11)$$

where the S_n 's denote the indicated infinite summations of equation (10) and the C_n 's the respective multipliers.

Series S_1 and S_2 of equation (11) may be put in a more rapidly convergent form according to Infeld, Smith, and Chien (ref. 7). When the variables p and ϵ are introduced, where

$$p = \frac{MkH}{2\pi\beta}$$

and

$$\epsilon = \frac{|x - x_0|}{\beta H}$$

the series S_1 and S_2 can be written as

$$\begin{aligned} S_1 &= \sum_{n=1}^{\infty} (-1)^n H_0^{(2)}(\mu R_n) \\ &= \sum_{n=1}^{\infty} (-1)^n H_0^{(2)}(2\pi p \sqrt{\epsilon^2 + n^2}) \\ &= \frac{1}{2\pi} \left[\frac{2ie^{-\pi\epsilon\sqrt{1-4p^2}}}{\sqrt{1-4p^2}} + 2i \sum_{n=1}^{\infty} \frac{e^{-\pi\epsilon\sqrt{(2n+1)^2-4p^2}}}{\sqrt{(2n+1)^2-4p^2}} + \right. \\ &\quad \left. \frac{e^{-\pi\epsilon\sqrt{(2n-1)^2-4p^2}}}{\sqrt{(2n-1)^2-4p^2}} - \pi H_0^{(2)}(2\pi\epsilon p) \right] \quad (12) \end{aligned}$$

and

$$\begin{aligned} S_2 &= \sum_{n=1}^{\infty} (-1)^n H_0^{(2)}\left(\frac{MknH}{\beta}\right) \\ &= \sum_{n=1}^{\infty} (-1)^n H_0^{(2)}(2\pi np) \\ &= \frac{1}{2\pi} \left\{ -\pi + 2i(\gamma + \log_e 2p) + 4i \sum_{n=1}^{\infty} \left[\frac{1}{\sqrt{(2n-1)^2-4p^2}} - \frac{1}{2n-1} \right] \right\} \quad (13) \end{aligned}$$

where Euler's constant $\gamma = 0.577215$.

Series S_3 may be evaluated by utilizing the expression for S_1 (eq. (12)) and integrating the resulting expression to obtain

$$S_3 = \int_0^{\infty} e^{-\frac{ik}{\beta^2}\xi} \sum_{n=1}^{\infty} (-1)^n H_0^{(2)} \left[\frac{kM}{\beta^2} \sqrt{\xi^2 + \beta^2(nH)^2} \right] d\xi \quad (14a)$$

$$\begin{aligned} S_3 &= -\frac{1}{2} \int_0^{\infty} e^{-\frac{ik}{\beta^2}\xi} H_0^{(2)} \left(\frac{kM\xi}{\beta^2} \right) d\xi + \\ &\quad \frac{2i\beta}{M} \sum_{n=0}^{\infty} \frac{1}{\sqrt{(2n+1)^2 \left(\frac{\pi\beta}{M} \right)^2 - (kH)^2}} \times \\ &\quad \int_0^{\infty} e^{-\xi \left[\frac{ik}{\beta^2} + \frac{M}{\beta^2 H} \sqrt{(2n+1)^2 \left(\frac{\pi\beta}{M} \right)^2 - (kH)^2} \right]} d\xi \quad (14b) \end{aligned}$$

$$\begin{aligned} S_3 &= -\frac{\beta}{\pi k} \log_e \frac{1+\beta}{M} + \\ &\quad \frac{2i\beta}{M} \sum_{n=0}^{\infty} \frac{1}{\left(\frac{\pi}{\beta H} \right)^2 [(2n+1)^2 - 4p^2] + \left(\frac{k}{\beta^2} \right)^2} \left[\frac{M}{\beta^2 H} - \right. \\ &\quad \left. i \frac{k/\beta^2}{\pi\beta \sqrt{(2n+1)^2 - 4p^2}} \right] \quad (14c) \end{aligned}$$

It is of interest to note that series S_3 may be employed in an alternative means of integrating equation (7). For application to wind-tunnel problems, where the ratio of tunnel height to wing semichord is small, or in application to cascade problems, the approximation employed in integrating equation (7) becomes less valid. It is possible to avoid the use of the approximation by writing the integral of equation (7) in a form which is identical to that of equations (14a) and (14b) with the exception of the upper limit. The integral containing the Hankel function can be evaluated by employing the tables of Schwarz (ref. 8). The second integral, containing only an exponential term, can be integrated in closed form, as was done to obtain equation (14c).

Series S_4 may be evaluated in a direct manner by employing tables of the Hankel function and by using for large values of the argument the approximation

$$H_1^{(2)}(\mu R_n) \approx \sqrt{\frac{2}{\pi \mu R_n}} e^{-i(\mu R_n - \frac{3}{4}\pi)} \quad (15)$$

With the aid of series S_1 , S_2 , S_3 , and S_4 , the kernel $K(M, z, H)$ may be evaluated.

METHOD OF SOLUTION

A method of using equation (8) to determine the aerodynamic forces on a wing oscillating in the presence of plane walls is now discussed. The method under consideration is one of collocation similar to that used by Possio (ref. 6) and Frazer (ref. 9) for the case of no walls. The approach involves the assumption of an appropriate series expression for the lift distribution, substitution of this series in the integral equation for the downwash, and calculation of the

downwash at arbitrarily selected points on the chord (control points). Thus equation (8) is reduced to a set of simultaneous equations, the unknowns of which are the coefficients of the assumed expression for the loading.

Expression for the loading.—The expression which is assumed for the lift distribution is a trigonometric series expansion which satisfies the Kutta condition at the trailing edge and which has the proper type of singularity at the leading edge. This expression is

$$\frac{L(x_0)}{\rho U^2} = A_0 \cot \frac{\theta_0}{2} + \sum_{n=1}^{\infty} A_n \sin n\theta_0 = L(\theta_0) \quad (16)$$

where $x_0 = -\cos \theta_0$ and the A_n 's are unknown coefficients to be determined in accordance with the downwash $w(x)$, which is known from the motion of the wing. It is desirable to rewrite equation (8) in terms of the variable θ_0 as follows:

$$w(x) = U k \left[\int_0^{\pi} L(\theta_0) K(M, z) \sin \theta_0 d\theta_0 + \int_0^{\pi} L(\theta_0) K(M, z, H) \sin \theta_0 d\theta_0 \right] \quad (17)$$

The first integral on the right-hand side of equation (17) is the integral expression first derived by Possio (ref. 6) for the condition of no walls. Its solution has been treated by several investigators (see, for example, ref. 9) and will not be discussed herein. It can be expressed entirely in terms of the unknown coefficients A_n of equation (16). The second integral of equation (17) may be evaluated by the use of equations (12), (13), (14), and (15).

Determination of the aerodynamic forces.—The integrals of equation (17) are determined for a selected number of control points and equated to the expression for the downwash. The expression relating the downwash to the motion of a wing translating (h) and pitching (α) about an axis located at x_a is

$$w(x) = \dot{h} + U\alpha + b(x - x_a)\dot{\alpha} \quad (18)$$

or, with the assumption of harmonic motion,

$$\frac{w(x)}{U} = ik \frac{h}{b} + [1 + ik(x - x_a)]\alpha \quad (19)$$

Equation (19) is used to calculate $w(x)$ for values of x appropriate to each of the selected control points. A set of simultaneous equations can then be written, the number of which corresponds to the number of control points employed and (conveniently) to the number of terms retained in the series for $L(\theta_0)$. The unknown coefficients may now be determined by solving these simultaneous equations. The total lift and moment about the midchord are given in terms of the coefficients A_n through the relations

$$\left. \begin{aligned} \frac{-L_a}{\pi \rho b U^2} &= \frac{1}{2} \left(A_0 + \frac{1}{2} A_1 \right) \\ \frac{M_a}{\pi \rho b^2 U^2} &= \frac{1}{8} \left(A_0 + \frac{1}{2} A_2 \right) \end{aligned} \right\} \quad (20)$$

Effect of the number of control points considered.—An investigation was made of the number of terms of the series for the lift distribution (eq. (16)) and thus of the number of control points required to obtain satisfactory accuracy. Calculations were performed for a particular case by increasing the number of control points and the number of terms of the loading series until the solutions were in reasonable agreement. For the case considered, three terms of the series for the lift and three control points at the quarter-, half-, and three-quarter-chord positions gave satisfactory results. The consideration of two additional control points at the leading and trailing edges, together with two additional terms of the lift series, made no significant change in the results. For high values of the reduced-frequency parameter k , the use of additional control points might be necessary.

The procedure just discussed involves consideration of a continuous distribution of pressure doublets over the chord. Calculations requiring much less computing can be made by considering the chordwise loading to be concentrated in a single doublet located at the quarter chord and by satisfying the downwash at the three-quarter chord. In the case of the lift, this approach has been found to give fairly good agreement with the results of the more elaborate calculations except in the vicinity of the resonant frequency.

THE ANALYTICALLY INDICATED RESONANCE PHENOMENON

Two-dimensional tunnel.—By examination of equations (12) and (13), it may be seen that the series S_1 and S_2 become infinite when

$$4p^2 = (2n-1)^2$$

or where

$$\frac{\omega \bar{H}}{a} = \pi \beta (2n-1) \quad (n=1, 2, 3, \dots) \quad (21)$$

At these critical values of the frequency parameter, the expression for the kernel $K(M, z, H)$ (eq. (11)) becomes infinite for all values of z . Physically, this condition represents a resonance in the tunnel involving a transverse oscillation of the moving air between the walls.

The fundamental or smallest critical values of $\omega \bar{H}/a$ corresponding to $n=1$ in equation (21) are shown plotted as functions of Mach number M in figure 1. Equation (21) and figure 1 show that finite values of the critical frequency exist for the condition $M=0$, $U=0$, and $a \neq \infty$. These conditions correspond to a compressible fluid at zero velocity in the tunnel. As the Mach number is increased, the critical-frequency parameter decreases rapidly and becomes zero at a Mach number of unity.

As indicated by equation (1), the product of the lift and the kernel function must remain equal to the vertical velocity over the wing; this velocity is defined by the motion of the wing and remains finite. The product of the lift and the kernel function can remain finite only if the lift approaches zero as the kernel becomes infinite. This condition in the tunnel is analogous to the well-known case of a simple undamped-spring-mass system for which, at the resonant frequency, theory predicts an infinite deflection of the mass occurring even with a forcing function of small amplitude.

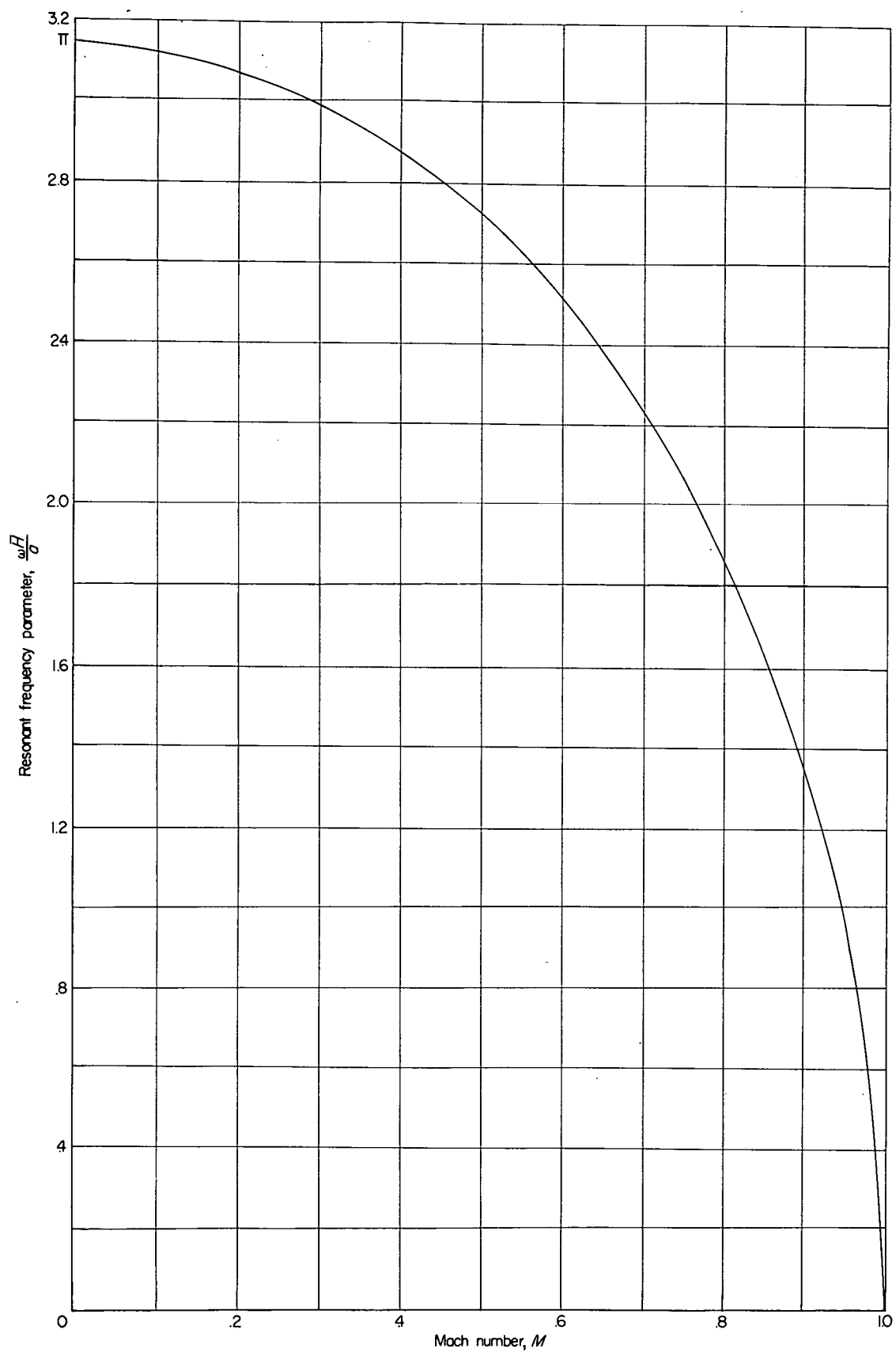


FIGURE 1.—Fundamental values of resonant frequency parameter $\frac{\omega \bar{H}}{a}$ as a function of Mach number.

Circular tunnel.—A resonance can also be demonstrated for the infinite circular tunnel. The nature of the boundary-value problem, for this case, makes it possible to separate variables; therefore, the governing partial-differential equation can be reduced to Bessel's equation. (See, for instance, ref. 10.) The resonant frequencies are then found as the roots of the equation

$$J_n' \left(\frac{\omega D}{2a\beta} \right) = 0 \quad (n=0, 1, 2, \dots)$$

or

$$\frac{\omega D}{2a} = \rho_n \beta$$

where J_n represents the Bessel function of the first kind, D is the tunnel diameter, and ρ_n is the root of the equation

$$J_n'(\rho_n) = 0$$

Values for ρ_n for the first several modes are $\rho_1=1.84$, 3.05 , and 4.17 . Note that, for a circular tunnel having a diameter equal to the height of a plane tunnel, the fundamental frequency is $3.68/\pi=1.17$ higher than resonant frequency in the plane tunnel discussed in this report.

EXPERIMENTAL INVESTIGATION

WIND TUNNEL

The experimental part of the investigation of the effect of tunnel walls on the forces acting on an oscillating airfoil was conducted in the Langley 2- by 4-foot flutter research tunnel. For these tests, a rectangular test section having dimensions of 2 feet by 3.8 feet was used. This tunnel is of the closed-throat, single-return type and employs either air or Freon-12 as a testing medium at pressures from 1 atmosphere down to about $\frac{1}{8}$ atmosphere.

It has been shown previously that the resonant frequency varies directly as the speed of sound. Inasmuch as Freon-12 has a speed of sound equal to about one-half that of air, the experiments to be discussed were conducted in Freon-12 so that the resonant frequency could be surveyed within the frequency limitations of the equipment.

MODEL AND OSCILLATING MECHANISM

Figure 2 is a schematic drawing of the test section with the model and oscillating mechanism installed. The model had a chord of 1 foot and an NACA 65-010 airfoil section; it completely spanned the 2-foot dimension of the test section. The gaps between the model and the tunnel wall were sealed by end plates which rotated with the model. The model, driven symmetrically from both ends, was oscillated in pitch about the midchord by a direct-drive eccentric-cam system powered by an induction motor with variable frequency supply.

INSTRUMENTATION

The lift and moment on the wing were obtained by electrical integration of the outputs of 12 model 49-TP

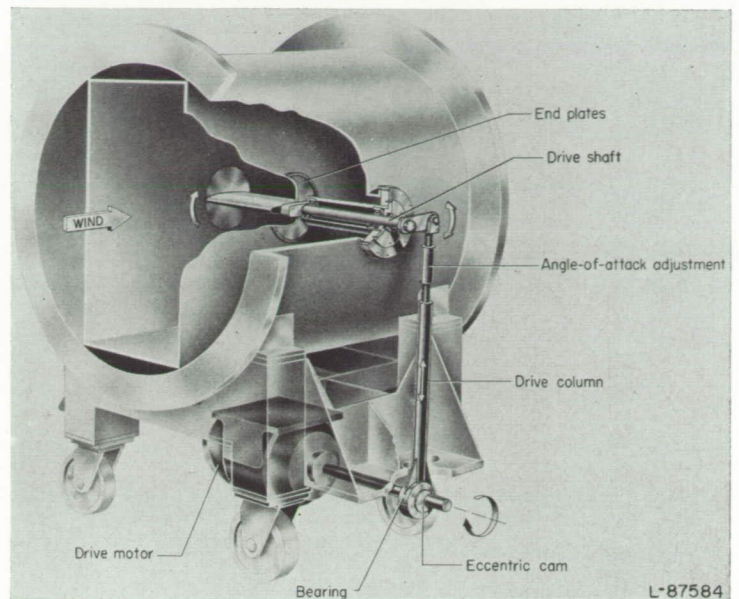


FIGURE 2.—Schematic drawing of test section with model and oscillating mechanism installed.

NACA miniature electrical pressure gages. The pressure gages, which are described in considerable detail in reference 11, were located at the center of the span at 2.5, 5, 10, 15, 20, 30, 40, 50, 60, 70, 80, and 90 percent of the chord. Each gage was arranged to indicate the difference in pressure between orifices on the upper and lower surfaces. Electrical integration techniques used in these experiments are discussed in reference 12. The so-called square-wave method of weighting was used; that is, the pressure indicated by each gage was assumed to represent the pressure acting over a portion of the chord extending one-half the distance to the next gage both forward and rearward. For example, the fraction of the chord assigned to the first gage was 3.75 percent and to the sixth gage was 10 percent. Some of the implications of this method of integration will be discussed in a subsequent section.

The angular displacement at the midspan position was indicated by resistance-wire strain gages attached to a torque rod running through the center of the hollow wing. One end of the torque rod was fixed to the center of the wing and the other end was fixed to the tunnel wall.

A schematic diagram of the instrumentation is shown in figure 3. The magnitude of the vector representing the fundamental component of lift or moment and angular displacement was indicated on an alternating-current vacuum-tube voltmeter attached to the output of a variable-frequency, narrow-pass-band filter. In essence, the filter performed the function of a Fourier analysis in that both random components and higher harmonics were removed from the signal. In order to measure the phase angle between lift or moment and the angular displacement, the output of the filter was fed into a pulse-shaping circuit designed to convert the sinusoidal signals into pulses corresponding in time to the "cross-over" points of the original signal. The pulses were then fed

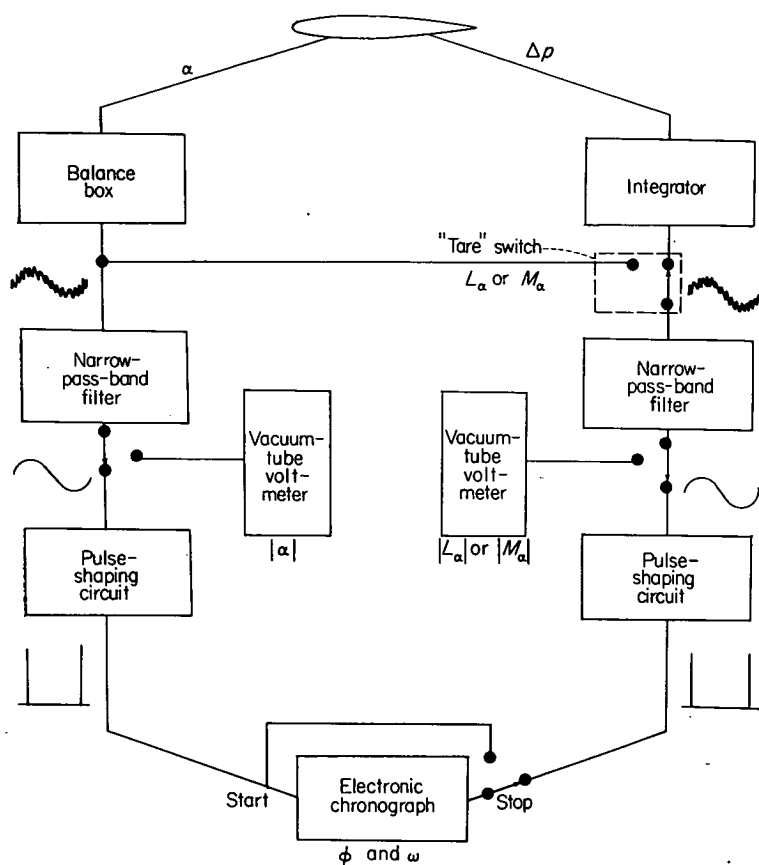


FIGURE 3.—Schematic diagram of instrumentation.

into an electronic chronograph that accurately indicated the time interval between the leading pulse which started the chronograph and the lagging pulse which stopped it. The ratio of this time interval to the period of oscillation, when multiplied by 360° , yields the phase angle in degrees. The period and frequency of oscillation were determined by starting and stopping the chronograph with the angular-displacement signal. In order to minimize the effects of small differences in components between the two circuits, a "tare" switch was provided which fed a single signal (the angular displacement) through both circuits. The resulting phase angle represented the phase shift introduced by the filters and pulse-shaping circuits.

TEST CONDITIONS

The Mach number of the tests was varied from $M=0.35$ to $M=0.7$ and the Reynolds number was held constant at about 5×10^6 by varying the density. The frequency of oscillation was varied from 0 to 60 cycles per second, and the magnitude of angular displacement was about 1.2° except for some lift data at $M=0.71$ which was obtained at an angular displacement of about 2.4° .

DISCUSSION OF RESULTS

The theory and calculation procedure and the experimental technique discussed previously for the determination of the forces acting on a wing oscillating between walls have been

applied to a number of specific examples. The investigation has been divided into three parts: (1) A comparison is made of analytical and experimental results obtained for the lift and moment on a pitching wing for several subsonic Mach numbers, (2) theoretical results for the effects of a variation in Mach number at constant tunnel height are given for a pitching wing and also for a wing undergoing vertical translation, and (3) theoretical results for the effects of a variation in the ratio of tunnel height to wing semichord are presented for particular values of Mach number.

COMPARISON OF THEORY AND EXPERIMENT

In figure 4 a comparison is made of analytical and experimental results for a wing oscillating in pitch about its mid-chord. Figures 4 (a), 4 (b), 4 (c), and 4 (d) apply, respectively, to Mach numbers of 0.35, 0.5, 0.6, and 0.7. The results apply to a ratio of tunnel height to wing semichord H of 7.60.

The plots on the left-hand side of each figure show the magnitudes of the forces and moments as a function of the frequency of oscillation, whereas those on the right-hand side show the corresponding phase angles. The magnitudes are presented as ordinates in the form of ratios $|L_\alpha/L_{\alpha'}|$ and $|M_\alpha/M_{\alpha'}|$. In these ratios, the quantities L_α and M_α are, respectively, the lift force and the moment on a wing in a tunnel; $L_{\alpha'}$ and $M_{\alpha'}$ are the theoretical lift and the theoretical moment on a wing in free air. The effect of the tunnel walls appears, therefore, as a deviation from unity of the ratios $|L_\alpha/L_{\alpha'}|$ and $|M_\alpha/M_{\alpha'}|$ when L_α and M_α are the theoretically derived forces and moments. When L_α and M_α represent the experimental forces and moments, the deviation from unity may not be completely attributed to the effect of tunnel walls because such factors as airfoil thickness and viscosity may cause deviation from the elementary theory. The abscissa in the figures is the ratio of the frequency of the pitching oscillation to a frequency calculated for the resonant condition.

Excellent agreement between theory and experiment is obtained for the phase angles, in most cases, for both the lift and the moment. Quantitatively, however, the agreement between theory and experiment for the magnitudes of the forces is not as good, although very similar trends are demonstrated; in most cases, a systematic difference appears. Some possible sources of the differences between theory and experiment are discussed in the following section.

Examination of figure 4 reveals that the theory predicted the resonant frequency very well. In all cases, the minimum lift and moment were found to lie very close to the analytically indicated resonant frequency. Theoretically, the lift and moment reduce to zero at the resonant condition. Under actual conditions, such as finite tunnel length, transmission of energy through the walls, nonlinearities at higher amplitudes, and turbulence in the flow that gives rise to damping, pure resonance is unobtainable. However, it may be seen by examining figure 4 (d) that the lift and moment were reduced to 20 percent of the values away from resonance.

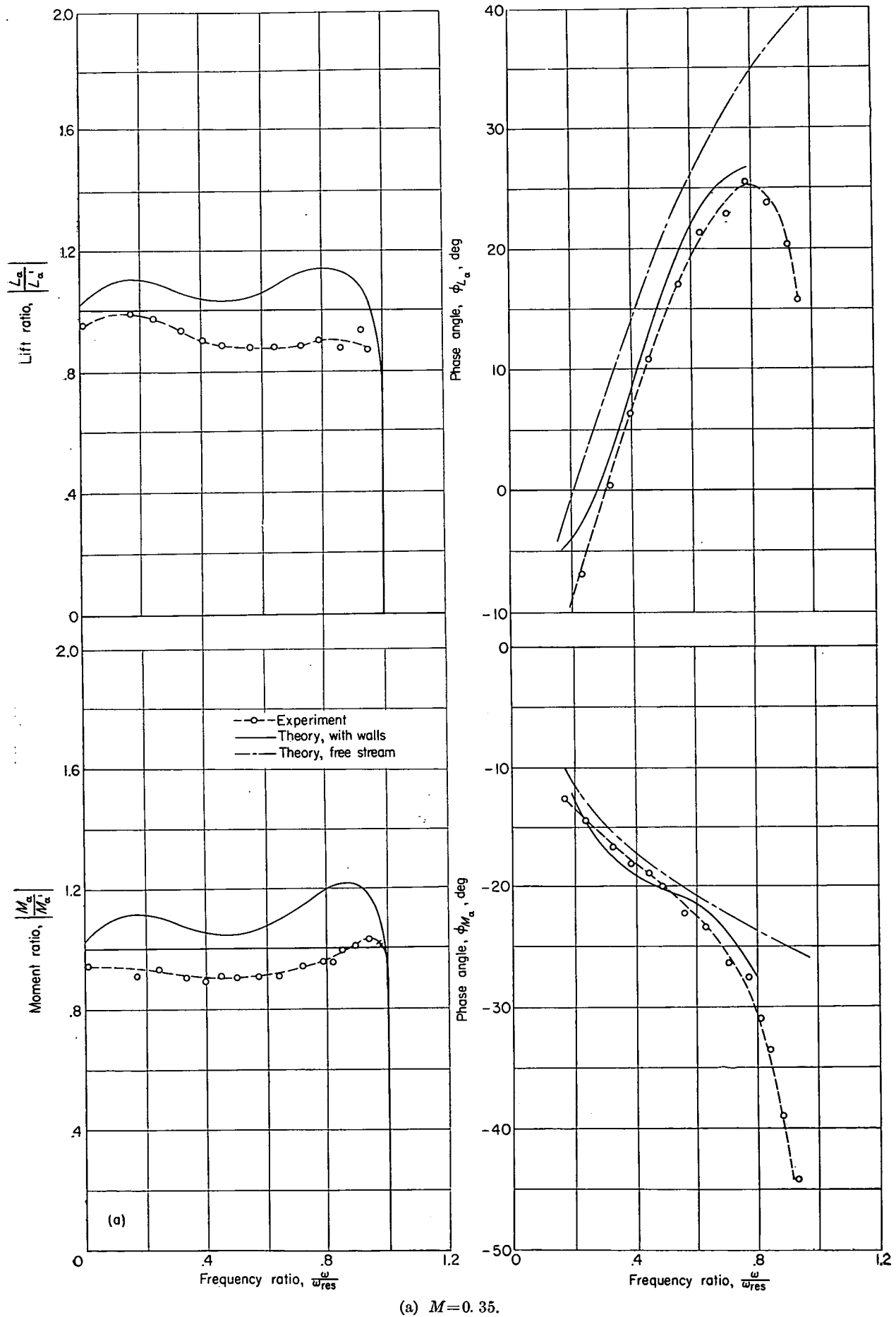


FIGURE 4.—Comparison of theoretical and experimental results for the magnitudes and phase angles of the lift and moment of a pitching wing. Height-semichord ratio $H=7.60$.

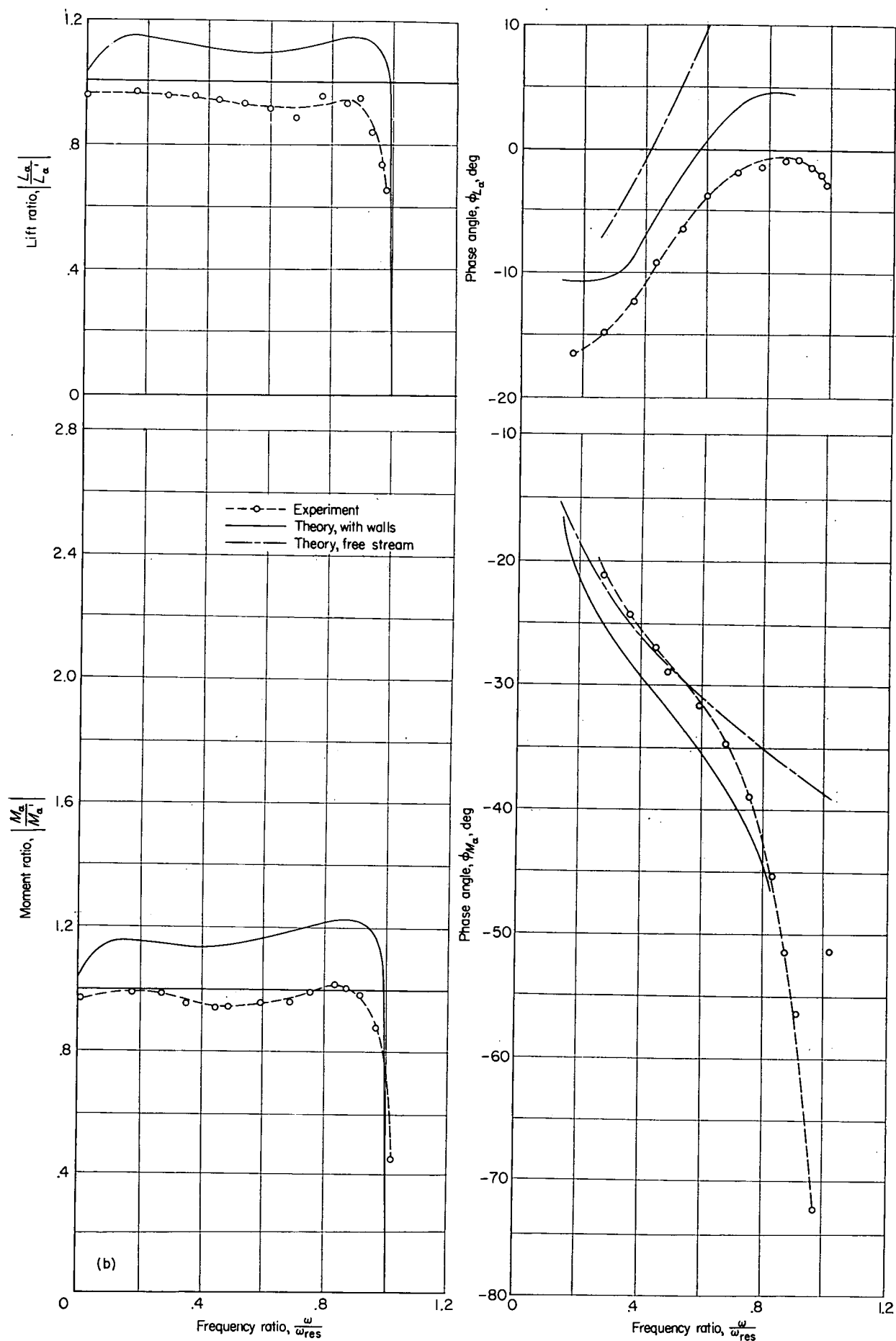


FIGURE 4.—Continued.

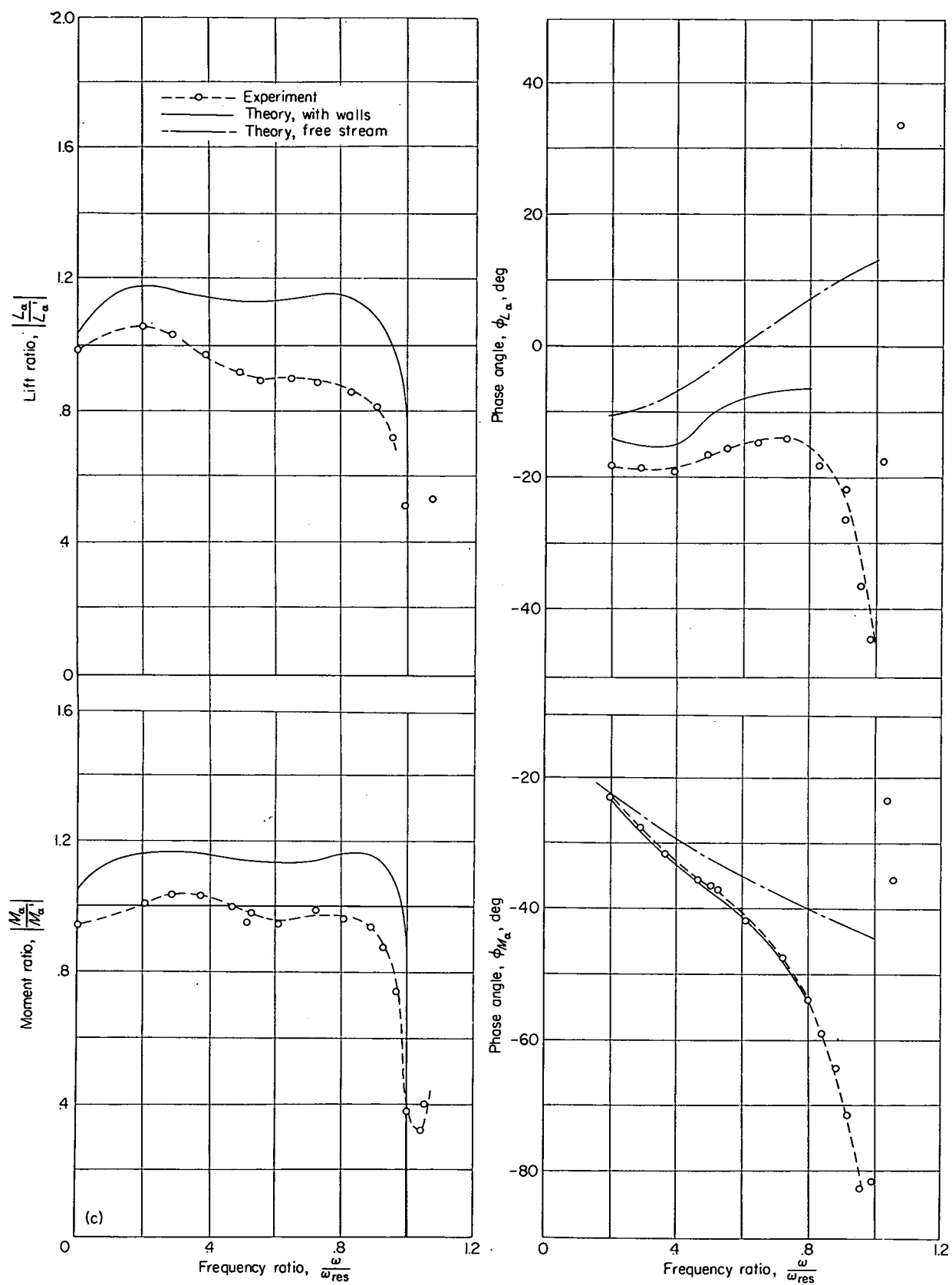
(c) $M=0.6$.

FIGURE 4.—Continued.

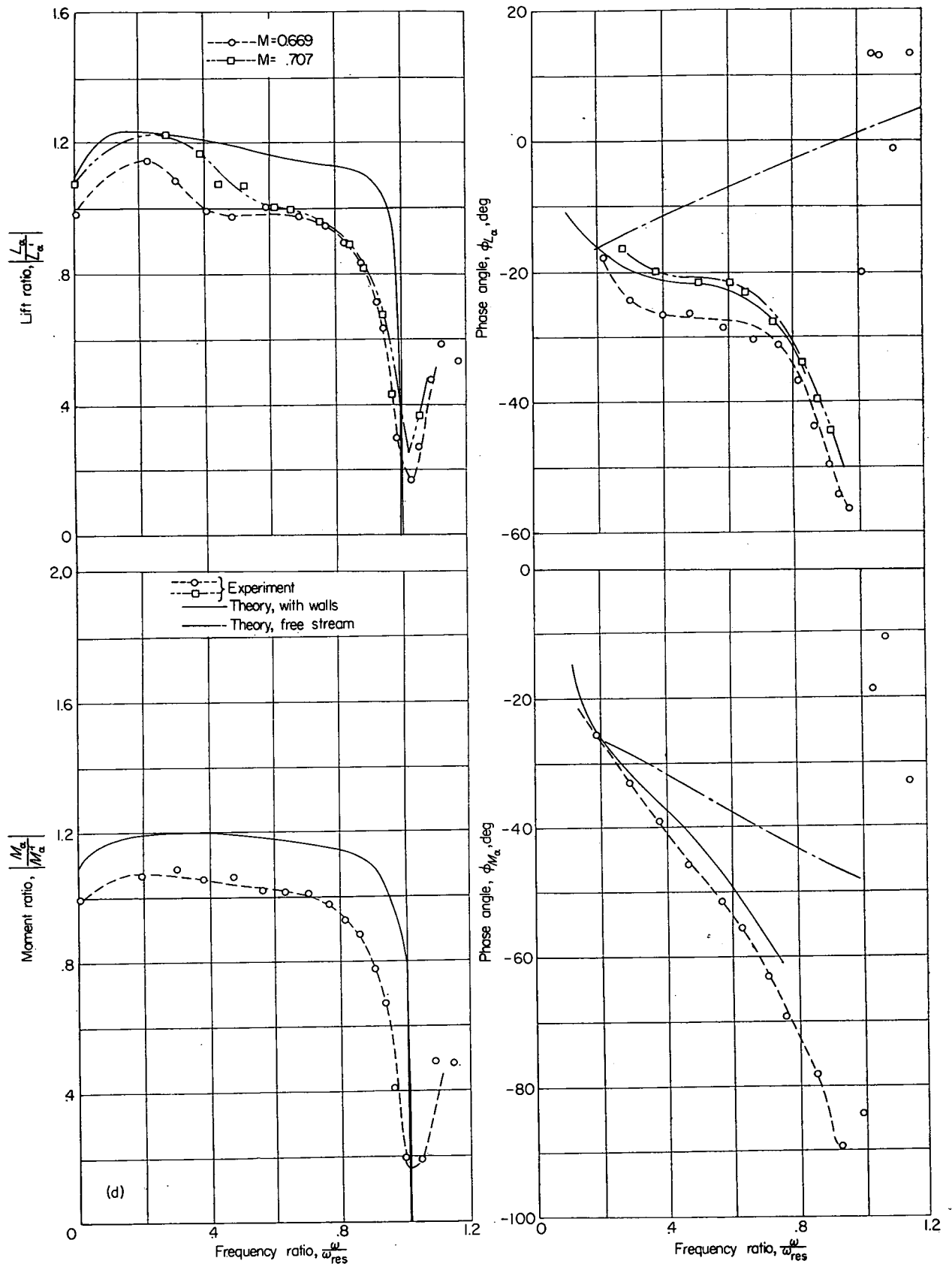
(d) $M=0.7$.

FIGURE 4.—Concluded.

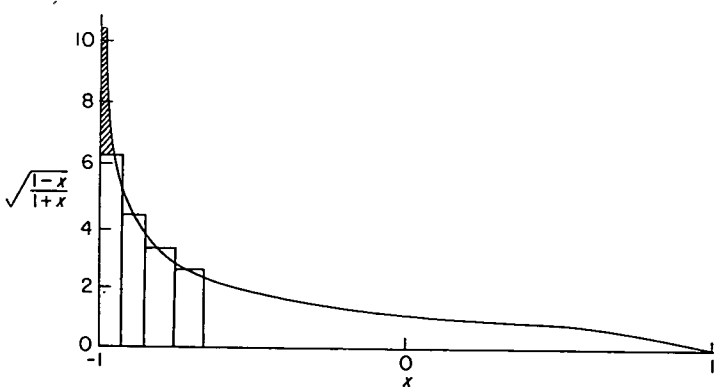
REMARKS ON SOME DIFFERENCES BETWEEN THEORY AND EXPERIMENT

In this section, some limitations and possible reasons for differences between theory and experiment are listed and discussed.

In the comparison between theory and experiment shown in figure 4, an almost constant difference of 10 to 15 percent between the magnitudes is to be noted, whereas the phase angles are in good agreement. Of the several possible reasons for these differences between theory and experiment, perhaps the more important ones are airfoil thickness, Reynolds number, finite tunnel length, transmission of energy through walls, dissipation of the pressure waves due to turbulence, and integration procedures. The effect of all these possibilities is not known for the oscillatory case. In the steady-state case, however, it is known that the effect of increasing thickness is to increase the slope of the lift curve.

In the considerations of the analytical integration, a collocation scheme was used to solve the integral equation. In general, the three collocation points used were found to be satisfactory as pointed out previously.

Twelve pressure cells were used for the experimental integration of the forces. A stepwise integration procedure was employed; that is, the pressure as recorded by the pressure cell was multiplied by an area of the wing over which it is assumed that the cell will give an average pressure. This procedure gives good results except possibly at the leading edge where the pressure variation is very great. Theoretically the pressure approaches infinity at the leading edge (as $\frac{1}{\sqrt{x}}$) and experimentally it is found to be very large. As a matter of fact, if a theoretical distribution of pressure is assumed to be $\cot \frac{\theta}{2} = \sqrt{\frac{1-x}{1+x}}$ as shown in the following sketch and this curve is integrated



in the same manner as the experimental curve was integrated (that is, by calculating the ordinate at the same value of the abscissa at which the pressure cells were located

for the experiment), it is found that the area as determined by the approximate method is 8 percent less than the area as determined by integrating $\cot \frac{\theta}{2}$ in closed form. It is apparent that the neglected area (shaded) can be appreciable. In the actual experiment, in which a fairly thick airfoil was used, the neglected area would probably be smaller but could perhaps contribute to the almost constant difference in magnitudes of lift and moment between the theoretical and experimental results. The effect of this integration difference on the phase angles, which have been shown to be in good agreement, would not be as pronounced.

EFFECT OF A VARIATION IN MACH NUMBER AT CONSTANT TUNNEL HEIGHT

An analytical investigation has been made of the effects of a variation in Mach number at constant tunnel height on the forces on an oscillating wing. Some of the results of the previous section are employed together with results of additional calculations. The magnitudes and associated phase angles of both the lift force and the moment have been determined for a pitching wing and also for a wing undergoing vertical translation. Calculations have been made for a constant value of the height-semichord ratio H of 7.60 and for Mach numbers of 0.3, 0.5, 0.7, and 0.8. Results of the calculations are shown in figures 5 and 6 for the lift and in figures 7 and 8 for the moment.

The magnitudes of the forces and moments are presented, as in the previous section, in the form of ratios: $|L_a/L_a'|$, $|M_a/M_a'|$, $|L_h/L_h'|$, and $|M_h/M_h'|$. The phase angles related to these ratios are presented as a difference between a wing in a tunnel and a wing in free air. The magnitudes and phase angles are plotted against a frequency parameter $\omega \bar{H}/a$, where ω is the circular frequency of oscillation of the wing, \bar{H} is the height of the tunnel, and a is the velocity of sound. At a particular value of the frequency parameter, a progressively larger effect of the walls is indicated as the Mach number increases. At all Mach numbers, the lift is reduced to zero at the resonant frequency. The dip in the curves against frequency ratio, which appears to be characteristic of the low Mach number cases, gradually disappears as the Mach number is increased. As in the case of the magnitude of the lift, the effect of the walls on the phase angle increases as the resonant frequency of the tunnel is approached and also as the Mach number is increased.

The magnitude of the moment about the midchord is shown in figures 7 and 8. The curves have the same shape as the lift-ratio curves and again decrease to zero at the resonant condition. The corresponding phase angles are shown in these figures. Note that in figures 5 to 8 only slight differences appear between results for pitch and those for translation.

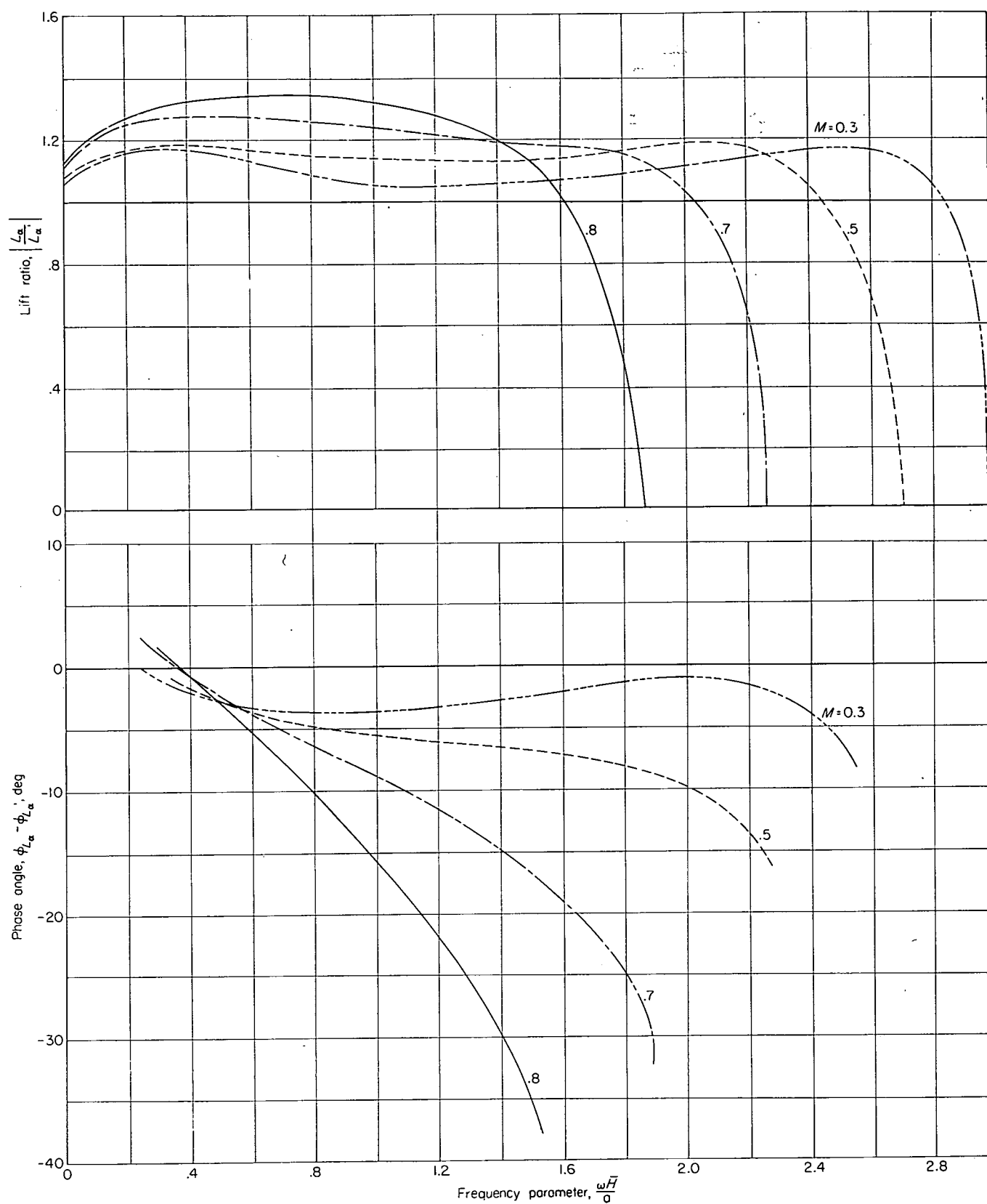


FIGURE 5.—Effect of variation in Mach number at constant height-semichord ratio $H=7.60$ on the magnitude and phase angle of the lift of a pitching wing.

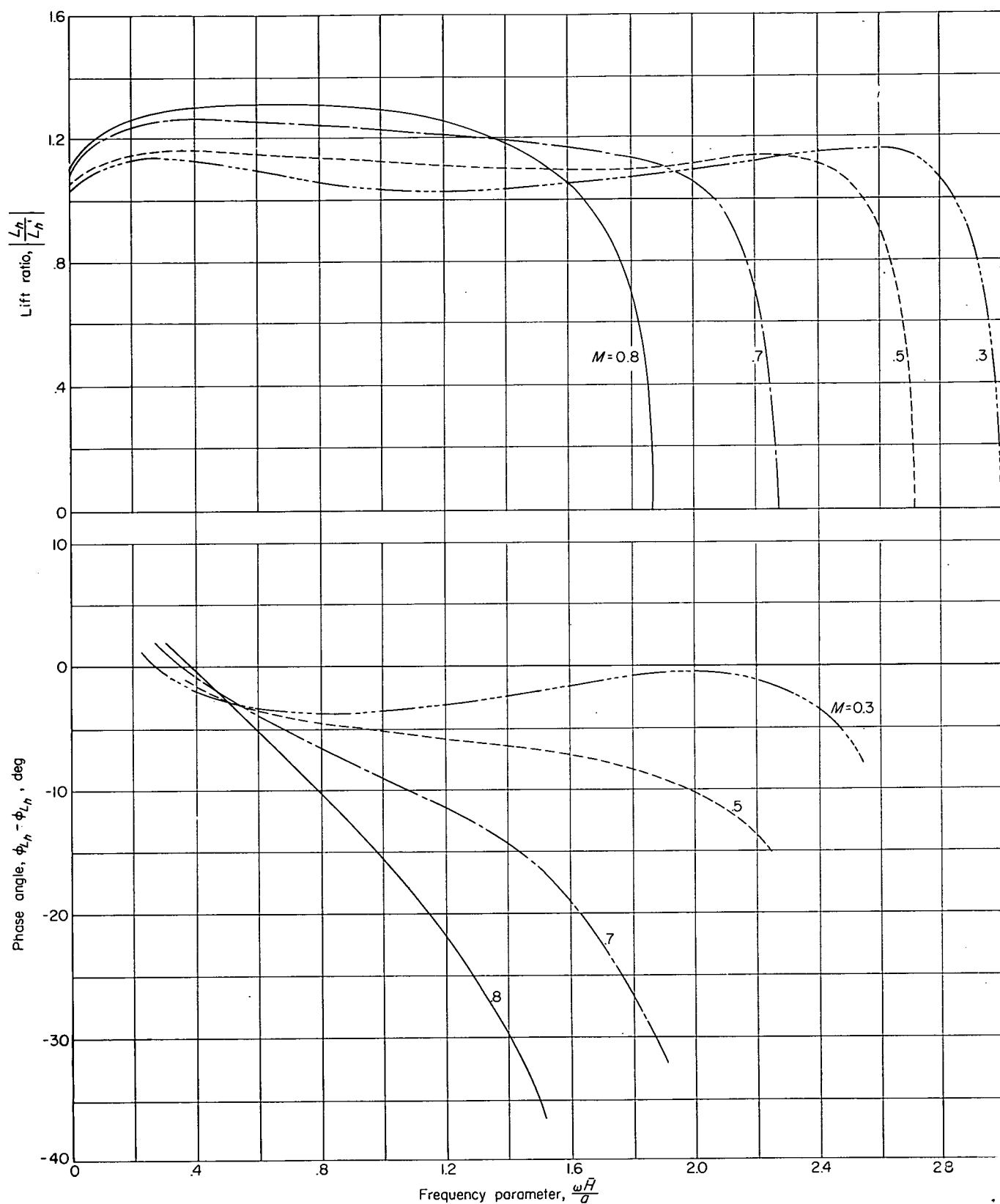


FIGURE 6.—Effect of variation in Mach number at constant height-semichord ratio $H=7.60$ on the magnitude and phase angle of the lift of a translating wing.

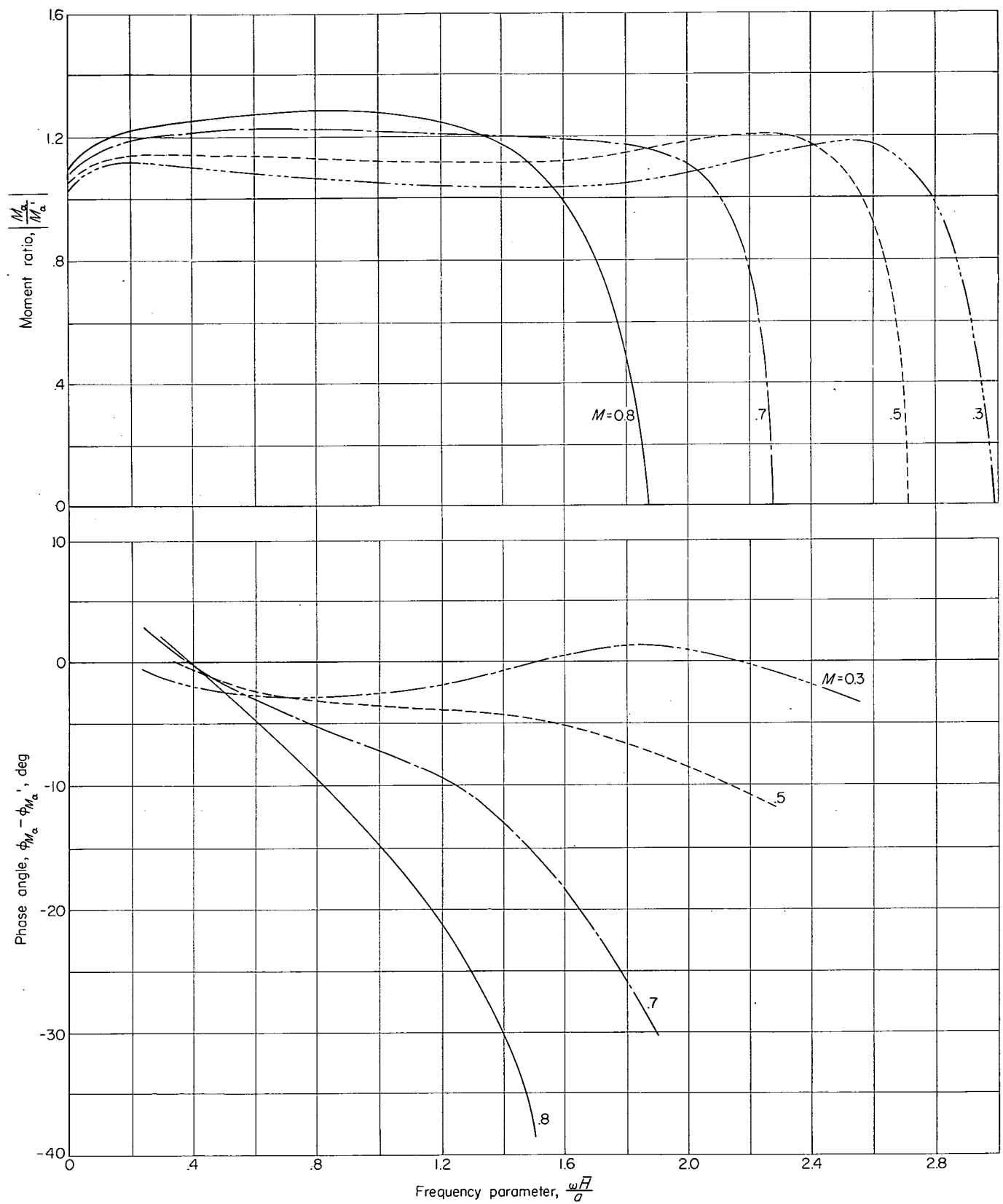


FIGURE 7.—Effect of variation in Mach number at constant height-semichord ratio $H=7.60$ on the magnitude and phase angle of the moment of a pitching wing.

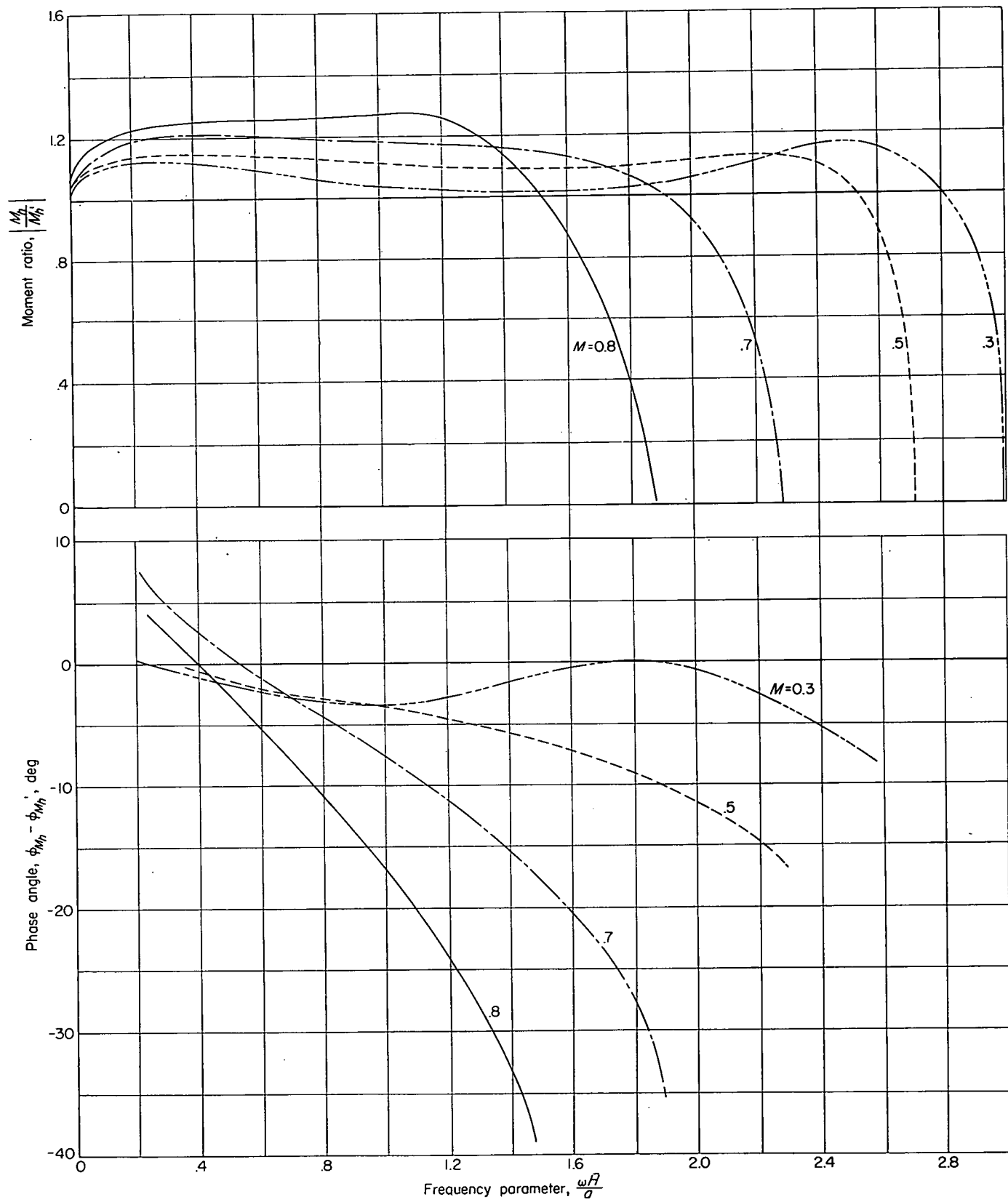


FIGURE 8.—Effect of variation in Mach number at constant height-semichord ratio $H=7.60$ on the magnitude and phase angle of the moment of a translating wing.

EFFECT OF VARIATION IN RATIO OF TUNNEL HEIGHT TO WING SEMICHORD

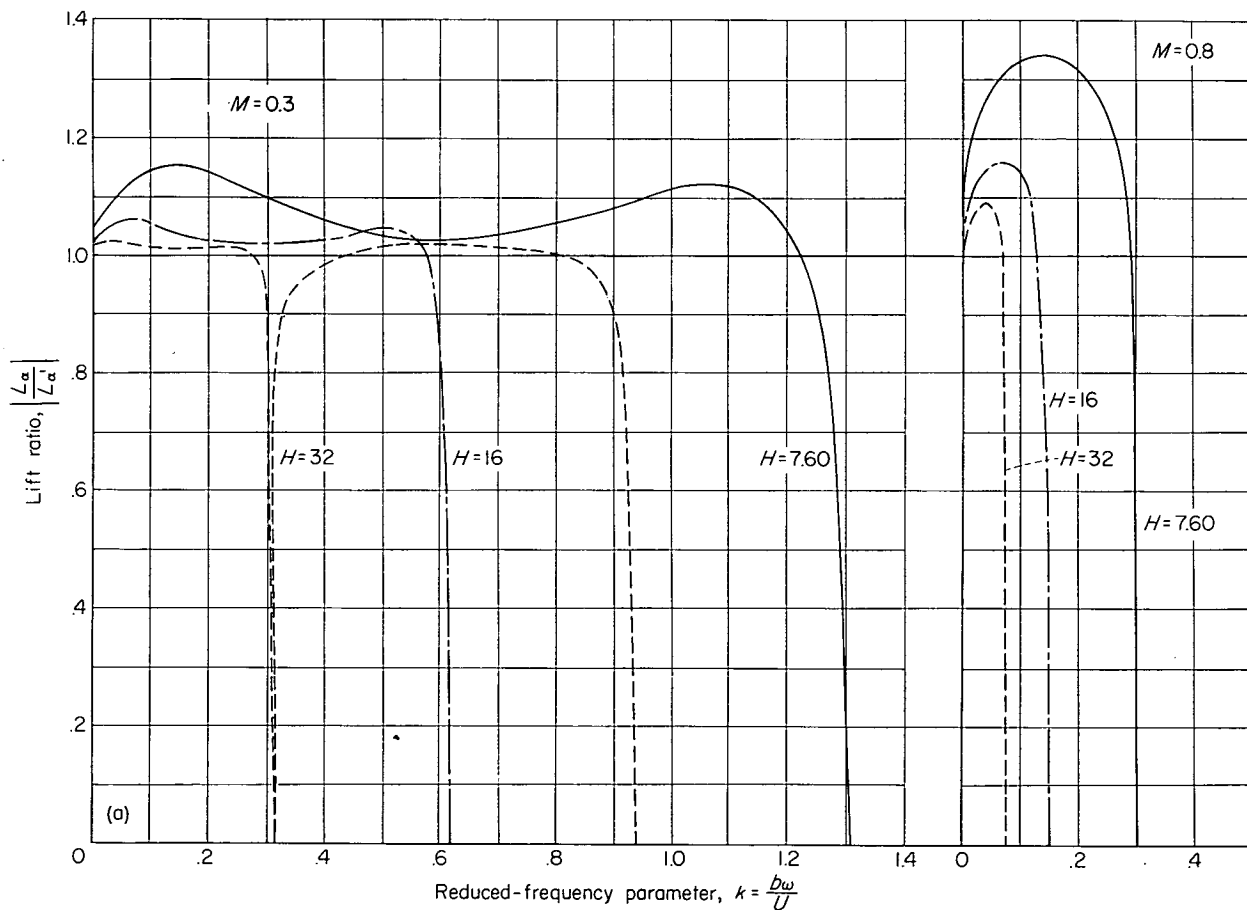
The effect on the lift-force ratio and on the associated phase angles of varying the ratio of tunnel height to wing semichord is illustrated in figure 9. The results presented in figures 7 and 8 have been based on the consideration of a distribution of pressure doublets over the chord of the airfoil and on satisfying the downwash condition at three chordwise stations. Results for figure 9 have been obtained by the simplified procedure of concentrating the loading in a single doublet at the quarter chord and satisfying the downwash condition at the three-quarter chord. This approach gives fairly good agreement with the results of the more elaborate procedure except near the resonant frequency.

Calculations have again been made for an airfoil oscillating in pitch about its midchord for values of the height-semichord ratio H of 7.60, 16, and 32 at $M=0.3$ and 0.8. In figure 9 (a) the lift ratio $|L_a/L_a'|$ is plotted against the reduced-frequency parameter $k=b\omega/U$. Plots for both Mach numbers are made to the same scale for ease of comparison. It is again apparent that the effect of reducing the Mach number is to reduce the effect of the tunnel walls and to raise the value of the critical frequency at which resonance can occur for a given tunnel. For example, for $H=7.60$, at $M=0.8$, the critical value of k is 0.30, whereas for $M=0.3$,

the critical value of k is increased to 1.31. Also, as was to be expected, increasing the height of the tunnel has a marked effect in reducing the influence of the tunnel walls for most of the frequency range. However, the critical frequency is reduced for increased tunnel height so that in the large tunnel the range of k below the fundamental resonance becomes smaller. This reduction in frequency would seem to be a disadvantage of the larger tunnels. However, the second branch of the curve for $H=32$ at $M=0.3$ shows that for frequencies between the first and second resonant points the effect of the walls on the magnitude of the lift is not greater than for frequencies below first resonance. Note also that the approach to resonance is quite abrupt; consequently, only a small range of frequencies very close to resonance would be critical and tests could then be conducted between the critical frequencies.

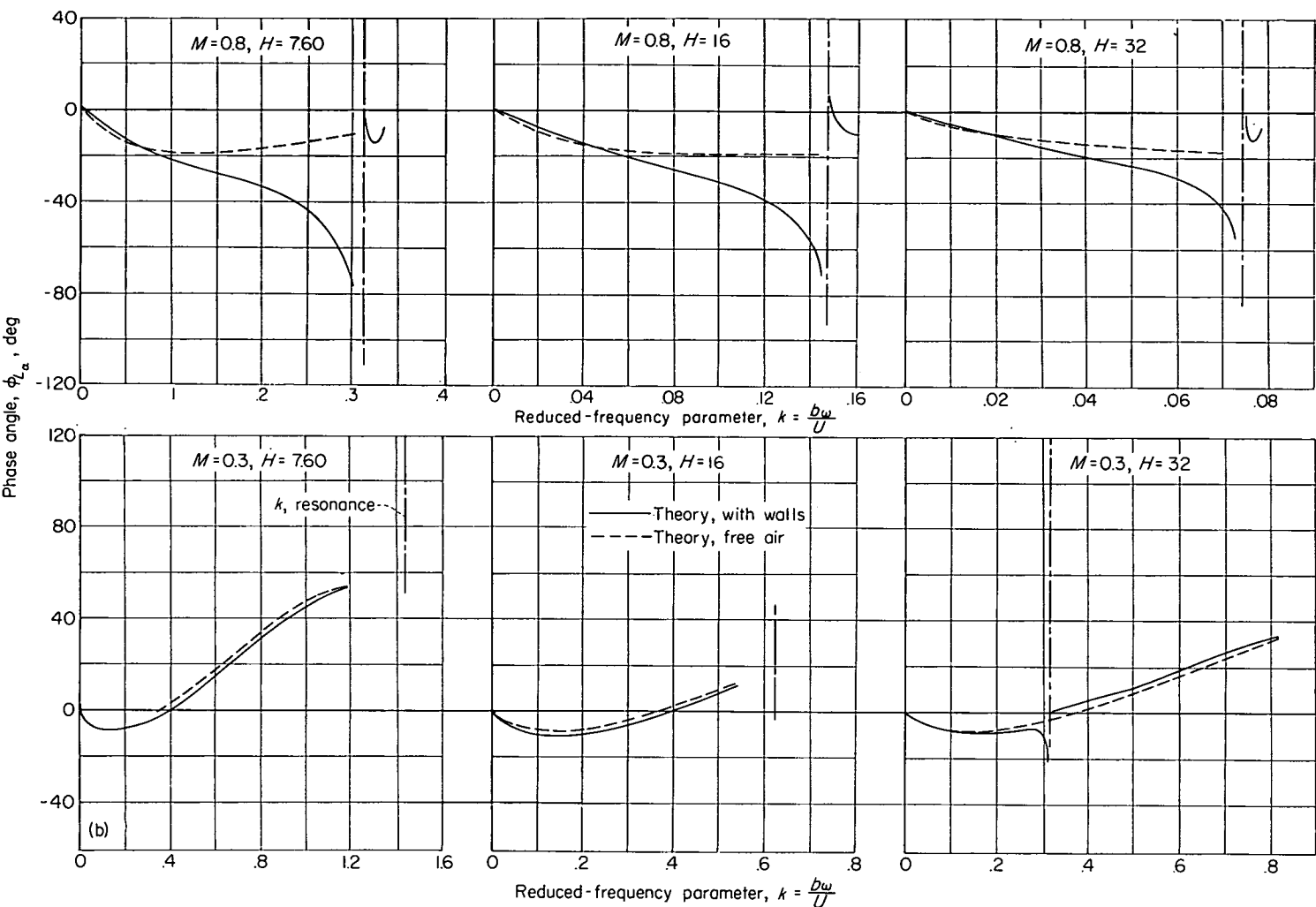
In figure 9 (b) the phase angles, associated with the results of figure 9 (a), for both the wing in a tunnel and for a wing in free air are shown as a function of reduced-frequency parameter k for values of height-semichord ratio H of 7.60, 16, and 32 at $M=0.3$ and 0.8.

At $M=0.3$, the effect of walls on the phase angle is generally very small; at $M=0.8$, the effect is small at low frequencies but increases greatly as the critical value of k is



(a) Magnitude of lift.

FIGURE 9.—Effect of a variation in tunnel height on the lift of a pitching wing for $M=0.3$ and $M=0.8$.

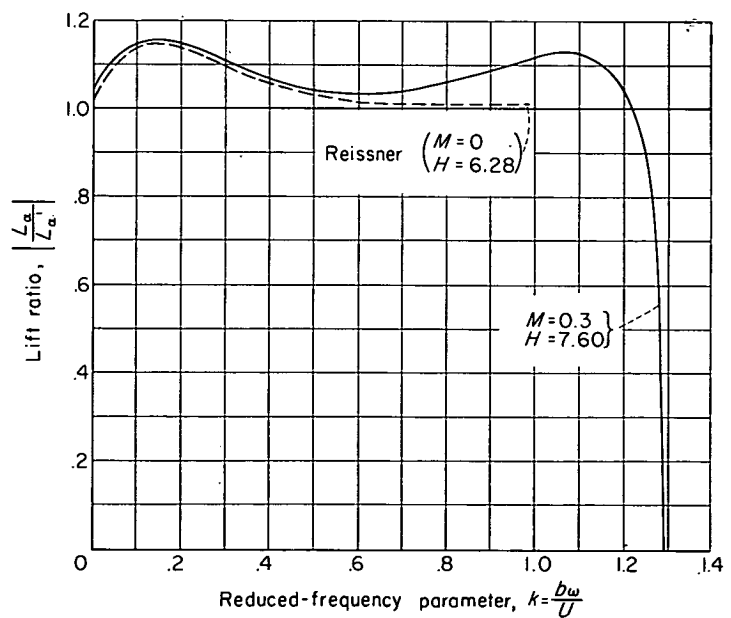


(b) Phase angle of the lift.

FIGURE 9.—Concluded.

approached. As the resonant frequency is approached, results at both Mach numbers show that the phase angle increases in negative value and appears to approach -90° . As the resonant condition is exceeded, there is a sudden shift in phase angle. This change is similar to that found for the scillation of a simple undamped spring-mass system where an abrupt change in phase angle of 180° is found as the resonant frequency is exceeded. Because of the complexity of the kernel, which involves an infinite series of Hankel functions, the phase angle at resonance has not been determined.

In figure 10, the plot from figure 9 (a) for $M=0.3$ and $H=7.60$ is compared with some results of Reissner (ref. 2) for the effect of walls on the lift-force ratio in incompressible flow. This curve for $M=0$ significantly duplicates the rather large wall effect at low values of k which is noted for the $M=0.3$ result. (At low values of k , the curves for the two different Mach numbers are almost coincident probably because of the fact that the slightly lower height semichord ratio $H=6.28$ used by Reissner counteracts the effect of decrease in Mach number.) For values of k greater than 0.5,

FIGURE 10.—Comparison of lift ratio for $M=0$ and $M=0.3$.

the curves for the two Mach numbers separate; the lift-force ratio at $M=0$ approaches unity and exhibits no effects of resonance because the resonant phenomenon arises only from the effects of compressibility.

CONCLUDING REMARKS

This report has dealt with the problem of an airfoil oscillating between plane walls in subsonic compressible flow. It constitutes a continuation of the work initiated in NACA Report 1150 in that a method of solving the integral equation is presented and some experimental results are compared with theory.

The comparison between theory and experiment for the phase angles between lift force or moment and position is shown to be very good, whereas the comparison between theory and experiment for the magnitudes of the lift and moment is not as good; however, the trends are all accurately predicted. In all cases the resonant frequency was accurately predicted. The cause of the apparent discrepancy between the theoretical and experimental lift and moment may be attributed to several factors such as dissipation of the pressure waves due to turbulence of the air flow and transmission of the energy through the tunnel walls. In addition,

the theoretical work was based on the concept of a very thin wing at infinite Reynolds number, whereas the experiments were made with a 10-percent-thick wing at a Reynolds number of approximately 5×10^6 . The effect of thickness and Reynolds number have not, as yet, been delineated for the oscillating case.

As would be expected, it is shown theoretically that the larger the tunnel the less the effect of the walls. The critical frequency, however, is also reduced as the tunnel height is increased, but it is shown that tests may be made above the resonant frequency with no larger tunnel-wall effect than is found below the resonance. In addition, the range of influence of the resonant region is greatly reduced so that only a small range of frequencies need be avoided. Wall effects are shown theoretically to be more pronounced as the Mach number is increased and at high Mach numbers are found to be large even at frequencies well removed from resonance.

LANGLEY AERONAUTICAL LABORATORY,
NATIONAL ADVISORY COMMITTEE FOR AERONAUTICS,
LANGLEY FIELD, VA., *January 12, 1955.*

APPENDIX

REDUCTION OF INTEGRAL EQUATION TO THE CASE OF ZERO FREQUENCY

In this appendix, the integral equation for the downwash for a wing oscillating in a compressible medium in the presence of wind-tunnel walls is reduced to the zero-frequency condition.

If equation (1) of the text is written as

$$w(x) = \lim_{\omega \rightarrow 0} \frac{b}{\rho U^2} \int_{-1}^1 L(x_0) [\omega K(M, z) + \omega K(M, z, H)] dx_0 \quad (A1)$$

and the limit taken as $\omega \rightarrow 0$, it will be found that all the terms of $\omega K(M, z)$ and $\omega K(M, z, H)$ vanish except terms involving $H_1^{(2)}$. These terms become infinite; however, as $\omega \rightarrow 0$, the asymptotic expansion for very small values of the argument may be used. Therefore,

$$H_1^{(2)}(\mu R_n) = -\frac{2}{\pi i \mu R_n}$$

and

$$\lim_{\omega \rightarrow 0} \omega e^{\frac{iz}{\beta^2}} H_1^{(2)}(\mu R_n) = \frac{M(x-x_0)}{R_n} = \frac{-2Ma\beta^2(x-x_0)}{\pi[(x-x_0)^2 + \beta^2(nH)^2]}$$

The vertical induced velocity may then be written as

$$w(x) = -\frac{Ma\beta b}{2\pi\rho U^2} \int_{-1}^1 L(x_0) \left[\frac{1}{x-x_0} + 2 \sum_{n=1}^{\infty} (-1)^n \frac{x-x_0}{(x-x_0)^2 + \beta^2(nH)^2} \right] dx_0 \quad (A2)$$

or

$$w(x) = -\frac{Mab}{2\rho U^2 H} \int_{-1}^1 L(x_0) \left[\frac{1}{\frac{\pi}{\beta H}(x-x_0)} + 2 \sum_{n=1}^{\infty} (-1)^n \frac{\frac{\pi(x-x_0)}{\beta H}}{\frac{\pi^2(x-x_0)^2}{\beta^2 H^2} + n^2 \pi^2} \right] dx_0 \quad (A3)$$

Equation (A3) may be written as

$$w(x) = \frac{-Mab}{2\rho U^2 H} \int_{-1}^1 L(x_0) \left[\operatorname{csch} \frac{\pi(x-x_0)}{\beta H} \right] dx_0 \quad (A4)$$

The additional induced velocity due to the presence of tunnel walls for the steady-state case in compressible flow is given by equation (40) of reference 13. Equation (A2)

can be reduced to the same form by making the approximation that the airfoil chord is small compared with the tunnel height.

REFERENCES

1. Jones, W. Pritchard: Wind Tunnel Interference Effect on the Values of Experimentally Determined Derivative Coefficients for Oscillating Aerofoils. R. & M. No. 1912, British A.R.C., Aug. 1943.
2. Reissner, E.: Wind Tunnel Corrections for the Two-Dimensional Theory of Oscillating Airfoils. Rep. No. SB-318-S-3, Cornell Aero. Lab., Inc., Apr. 22, 1947.
3. Timman, R.: The Aerodynamic Forces on an Oscillating Aerofoil Between Two Parallel Walls. Appl. Sci. Res. (The Hague), vol. A 3, no. 1, 1951, pp. 31-57.
4. Runyan, Harry L., and Watkins, Charles E.: Considerations on the Effect of Wind-Tunnel Walls on Oscillating Air Forces for Two-Dimensional Subsonic Compressible Flow. NACA Rep. 1150, 1953. (Supersedes NACA TN 2552.)
5. Woolston, Donald S., and Runyan, Harry L.: Some Considerations on the Air Forces on a Wing Oscillating Between Two Walls for Subsonic Compressible Flow. Jour. Aero. Sci., vol. 22, no. 1, Jan. 1955, pp. 41-50.
6. Possio, Camillo: L'Azione aerodinamica sul profilo oscillante in un fluido compressibile a velocità iposonora. L'Aerotecnica, vol. XVIII, fasc. 4, Apr. 1938, pp. 441-458. (Available as British Air Ministry Translation No. 830.)
7. Infeld, L., Smith, V. G., and Chien, W. Z.: On Some Series of Bessel Functions. Jour. Math. and Phys., vol. XXVI, no. 1, Apr. 1947, pp. 22-28.
8. Schwarz, L.: Untersuchung einiger mit den Zylinderfunktionen nullter Ordnung verwandter Funktionen. Luftfahrtforschung, Bd. 20, Lfg. 12, Feb. 8, 1944, pp. 341-372.
9. Frazer, R. A., and Skan, Sylvia W.: Possio's Subsonic Derivative Theory and Its Application to Flexural-Torsional Wing Flutter. Part I—Possio's Derivative Theory for an Infinite Aerofoil Moving at Subsonic Speeds. Part II—Influence of Compressibility on the Flexural-Torsional Flutter of a Tapered Cantilever Wing Moving at Subsonic Speed. R. & M. No. 2553, British A.R.C., 1942.
10. Morse, Phillip M.: Vibration and Sound. Second ed., McGraw-Hill Book Co., Inc., 1948.
11. Patterson, John L.: A Miniature Electrical Pressure Gage Utilizing a Stretched Flat Diaphragm. NACA TN 2659, 1952.
12. Helfer, Arleigh P.: Electrical Pressure Integrator. NACA TN 2607, 1952.
13. Allen, H. Julian, and Vincenti, Walter G.: Wall Interference in a Two-Dimensional-Flow Wind Tunnel, With Consideration of the Effect of Compressibility. NACA Rep. 782, 1944. (Supersedes NACA WR A-63.)

REPORT 1263

INVESTIGATION OF THE AERODYNAMIC CHARACTERISTICS OF A MODEL WING-PROPELLER COMBINATION AND OF THE WING AND PROPELLER SEPARATELY AT ANGLES OF ATTACK UP TO 90°†

By RICHARD E. KUHN and JOHN W. DRAPER

SUMMARY

An investigation of the aerodynamic characteristics of a model wing-propeller combination, and of the wing and propeller separately at angles of attack up to 90°, has been conducted in the Langley 300 MPH 7- by 10-foot tunnel. The tests covered thrust coefficients corresponding to free-stream velocities from zero forward speed to the normal range of cruising speeds. The results indicate that increasing the thrust coefficient increases the angle of attack for maximum lift and greatly diminishes the usual reduction in lift above the angle of attack for maximum lift.

Predicted characteristics of an assumed airplane designed for vertical take-off indicate that partial wing stalling would be encountered at certain attitudes but sufficient power was available for flight at any attitude. The effects of slipstream on the variation of lift-curve slope with thrust coefficient for this model could be satisfactorily estimated by means of a modified form of a method formulated by Smelt and Davies. The variation of propeller normal force with angle of attack compared favorably with calculated values. An appreciable direct pitching moment was found to exist on the propeller itself at high angles of attack. This pitching moment was approximately doubled when the propeller was operated in the presence of the wing and corresponded to a downward movement of the effective center of thrust of about 20 percent of the propeller radius.

INTRODUCTION

Numerous schemes have been suggested in an effort to design aircraft that would combine the take-off and landing characteristics of a helicopter with the high-speed potential of a conventional fixed-wing airplane. One of the proposed arrangements involves the use of large-diameter propellers as lifting rotors for the take-off and landing conditions. The cruising attitude is achieved by rotation of the wing-propeller combination through approximately 90°, with the wing providing the lift and the propellers (acting as conventional propellers) providing the thrust required for forward flight.

Results are presented of experimental data obtained with a semispan wing immersed in the slipstream of two large-diameter propellers, and a brief analysis of the application of the data to aircraft combining flight characteristics of the helicopter and conventional airplane. In addition, forces and moments measured on the propeller, when combined with the wing and when separated from the wing, are presented for an angle-of-attack range up to 90°.

SYMBOLS

With a wing operating in the slipstream of a propeller, large forces and moments can be produced even at very small free-stream velocities. In this condition, coefficients based on the free-stream dynamic pressure approach infinity and therefore become meaningless. It appears appropriate, therefore, to base the coefficients on the dynamic pressure in the propeller slipstream. For the present investigation, the coefficients based on this principle are indicated by the use of a double prime and are defined in the list that follows. The positive direction of forces, moments, and angles is indicated in figure 1.

C_L	lift coefficient, $\frac{\text{Lift}}{qS/2}$
C_L''	lift coefficient, $\frac{\text{Lift}}{q''S/2}$
C_m''	pitching-moment coefficient, $\frac{\text{Pitching moment}}{q''\bar{c}S/2}$
C_{m_p}''	pitching-moment coefficient of propeller, $\frac{\text{Propeller pitching moment}}{q''S\bar{c}}$
$\Delta C_m''$	increment of total model pitching moment due to propellers, calculated from the measured propeller data, $\left(C_{m_p}'' + C_{N_p}'' \frac{x_{c/4}}{\bar{c}}\right)_{\text{inboard}} + \left(C_{m_p}'' + C_{N_p}'' \frac{x_{c/4}}{\bar{c}}\right)_{\text{outboard}}$
C_{N_p}''	normal-force coefficient of propeller, $\frac{\text{Propeller normal force}}{q''S}$

†Supersedes NACA Technical Note 3304 by John W. Draper and Richard E. Kuhn, 1954.

C_P	power coefficient, $\frac{2\pi nQ}{\rho n^3 D^5}$
C_T	thrust coefficient, $\frac{T}{\rho n^2 D^4}$
$C_{x''}$	longitudinal-force coefficient, $\frac{\text{Longitudinal force}}{q'' S/2}$
T_c''	thrust coefficient, $\frac{T}{q'' \frac{\pi}{4} D^2}$
b	twice span of semispan wing, ft; also, propeller blade chord, ft
c	wing chord, ft
\bar{c}	mean aerodynamic chord, $\frac{2}{S} \int_0^{b/2} c^2 dy$, ft
D	propeller diameter, ft
d	diameter of the fully developed slipstream, ft
d_1	diameter of slipstream at any point, ft
h	propeller blade thickness, ft
K	$\frac{x/D}{\sqrt{\frac{1}{4} + \left(\frac{x}{D}\right)^2}}$ (See appendix B.)
N	number of propellers
n	propeller rotational speed, rps
P	propeller shaft power, $\frac{2\pi nQ}{550}$, hp
Q	torque, ft-lb
q	free-stream dynamic pressure, $\frac{1}{2} \rho V^2$, lb/sq ft
q''	slipstream dynamic pressure, $q + \frac{T}{\frac{\pi}{4} D^2}$, lb/sq ft
R	propeller tip radius, ft
r	radius to propeller blade element
S	twice area of semispan wing, sq ft
T	shaft thrust, per propeller, lb
V	free-stream velocity, ft/sec
V'	velocity at any point in slipstream, ft/sec
ΔV	increment of velocity in fully developed slipstream due to thrust, ft/sec
W	airplane weight, lb
x	longitudinal distance from propeller disk, ft
$x_{\bar{c}/4}$	value of x terminating at $\bar{c}/4$
y	spanwise distance from wing root, ft
α	angle of attack relative to free-stream velocity, deg
β	propeller blade angle, deg
$\beta_{.75R}$	propeller blade angle at 0.75 R , deg
η	propeller efficiency, $\frac{TV}{2\pi nQ}$
η''	static thrust efficiency, $\frac{T^{3/2}}{1100P \sqrt{\frac{\rho}{2} \frac{\pi}{4} D^2}}$
θ	angle of inclination of slipstream velocity, deg
λ	multiplication factor for increase of lift due to slipstream
ρ	mass density of air, slugs/cu ft
ϕ	angle of inclination of thrust axis with respect to free stream, deg
Subscripts:	
0	zero angle of attack
p	propeller

APPARATUS AND METHODS

MODEL

A semispan wing model of a hypothetical four-engine airplane was used in this investigation. The wing had an aspect ratio of 4.55, a taper ratio of 0.714, and an NACA 0015 airfoil section. A drawing of the model with pertinent dimensions is presented as figure 2 and a photograph of the model mounted for testing is shown as figure 3. The geometric characteristics of the model are given in the following table:

Wing:

Area (semispan), sq ft	5.125
Span (semispan), ft	3.416
Mean aerodynamic chord, \bar{c} , ft	1.514
Root chord, ft	1.75
Tip chord, ft	1.25
Airfoil section	NACA 0015
Aspect ratio	4.55
Taper ratio	0.714

Propellers:

Diameter, ft	2.0
Disk area, sq ft	3.14
Nacelle diameter, ft	0.33
Airfoil section	Clark Y

The wing was constructed on a steel spar, which served as the support for the two motor nacelles and for the mahogany blocks which form the wing contour. The wing was also equipped with plain flaps that were locked and sealed in the neutral position for this investigation.

The geometric characteristics of the three-blade aluminum-alloy propellers are given in figure 4. The propellers were driven by variable-frequency electric motors rated at 20 horsepower at 18,000 rpm. The motors were operated in parallel from one variable-frequency power supply.

The propeller diameter was too large to permit use of the high design rotational speed of the motors. During the tests, the rotational speed seldom exceeded 6,000 rpm or a propeller tip Mach number of 0.58. The speed of each motor was determined by observing a stroboscopic type of indicator, to which was fed the output frequency of a small alternator connected to the motor shaft. Because both motors were driven from a common power supply, their speeds were usually matched within 10 rpm.

The motors were mounted inside aluminum-alloy nacelles by means of strain-gage beams in order to measure the thrust, torque, normal force, and pitching moment of the propeller and spinner. A photograph of this installation is shown as figure 5.

TESTS

The investigation was conducted in the Langley 300 MPH 7- by 10-foot tunnel. The tests were made at various free-stream dynamic pressures and propeller thrusts so selected as to maintain a constant dynamic pressure of 8 pounds per square foot in the slipstream. Constant thrust on the inboard propeller was maintained by varying the motor speed throughout the angle-of-attack range of -10° to 90° . All data presented were obtained with the outboard propeller rotating in a clockwise direction and the inboard propeller rotating counterclockwise as viewed from behind the propeller. Also, the thrust determined from a given

thrust coefficient at $\alpha=0^\circ$ was held constant throughout the angle-of-attack range. The blade angle on the outboard propeller was adjusted slightly ($\pm 0.1^\circ$ or less) so as to develop the same thrust on this propeller as on the inboard propeller at zero angle of attack. During the tests, the thrust on the two propellers was matched within 0.25 pound for all conditions except for angles of attack above 60° at a thrust coefficient of 0.91. For higher angles of attack, the thrust on the outboard propeller exceeded that desired by as much as 4 pounds. The variations of thrust, dynamic pressure, velocities, and propeller blade angle with thrust coefficient (for each propeller) are tabulated as follows:

T_c''	T , lb	q'' , lb/sq ft	$V+\Delta V$, ft/sec	q/q''	$\frac{V}{V+\Delta V}$	β_{35R} , deg
0	0	8	82	1.00	1.000	20
.20	5.0	8	82	.80	.894	20
.50	12.5	8	82	.50	.707	8
.71	17.6	8	82	.29	.539	8
.91	22.6	8	82	.09	.300	8
1.00	25.0	8	82	0	0	8

The Reynolds number in the slipstream based on the mean aerodynamic chord of 1.514 feet was 0.8×10^6 .

The normal force, pitching moment, thrust, and torque were measured for each propeller at a point of intersection of the shaft center line and the blade axis. The pitching moment, lift, and drag of the complete wing-propeller configuration were measured at the quarter-chord point of the mean aerodynamic chord of the wing. It is emphasized that the wing-propeller data presented herein include the direct propeller forces as well as the forces on the wing.

The propeller-alone tests were made by mounting the propeller-nacelle assembly on a 3-inch-diameter sting, which was supported from the tunnel ceiling by a 3-inch tube located 3 feet behind the propeller disk. The mounting was such that the propeller remained in the center of the tunnel throughout the angle-of-attack range.

The static-thrust calibration of the propeller was made in a large room (18 ft by 42 ft by 10 ft) in order to minimize wall effects.

CORRECTIONS

The data presented have been corrected in the following manner. Approximate corrections for the effect of the tunnel walls on the velocity in the tunnel and in the slipstream were derived and are presented in appendix A. The derivation is based on the simple momentum theory and assumes the slipstream to be parallel to the free stream. For this condition these corrections are small. The applicability of the corrections thus derived for conditions approaching the static thrust and for the high angles of attack may be questionable; however, deviations are assumed to be relatively small and corrections to be fairly accurate for most of the test conditions.

The jet-boundary corrections applied to the angle of attack and longitudinal force were estimated by the method of reference 1. For a given model size, these corrections depend on the circulation about the wing; therefore, the corrections for a particular angle of attack with slipstream have been based on the lift of the wing at that angle of

attack without slipstream. The following relationships were used:

$$\alpha = \alpha_{\text{measured}} + 0.5 \frac{q}{q''} (C_L) \tau_c'' = c$$

$$C_{x''} = C_{x'' \text{ measured}} - 0.008 \frac{q}{q''} [(C_L) \tau_c'' = 0]^2$$

The correction to pitching-moment coefficient was estimated and found to be negligible.

Blockage corrections have not been applied to the data. These corrections were estimated by the method of reference 2 and, with the exception of the wake blockage correction which would become appreciable at the higher angles of attack, the blockage corrections were found to be small. The data can be corrected for the effects of wake blockage at the higher angles of attack by a method derived from reference 2, which can be written in the notation of the present report as follows:

$$q_{\text{corrected}} = q_{\text{measured}} \left[1 + \frac{0.036}{(1 - T_c'')} \left(C_{x''} - T_c'' \cos \alpha N \frac{\pi D^2}{S} \right) \right]$$

REDUCTION OF DATA

The type of flight operation for which the data of this investigation would be useful is one in which the wing-propeller combination is rotated as a unit. An example of this configuration is illustrated in figure 6. For this type of operation, the forward speed may drop to zero so that force and moment coefficients based on the free-stream velocity approach infinity and therefore become meaningless. For the condition in which the wing is largely immersed in the slipstream of a propeller, the forces on the wing would be expected to be largely determined by the dynamic pressure in the slipstream. It appears reasonable, therefore, to base the coefficients on the dynamic pressure in the slipstream.

For this investigation, the dynamic pressure in the slipstream is assumed to be related to the measured thrust by the following momentum-theory equations:

$$T = m_p \Delta V_0 = \rho \frac{\pi}{4} D^2 \left(V + \frac{\Delta V_0}{2} \right) \Delta V_0$$

where m_p is the mass flow through the propeller and ΔV_0 is the increment of slipstream velocity due to thrust at zero angle of attack. Rearranging terms gives

$$\frac{(\Delta V_0)^2}{2} + V(\Delta V_0) - \frac{T}{\rho \frac{\pi}{4} D^2} = 0$$

Solving by the quadratic equation yields

$$\Delta V_0 = -V \pm \sqrt{V^2 + 2 \frac{T}{\rho \frac{\pi}{4} D^2}}$$

$$(V + \Delta V_0)^2 = V^2 + 2 \frac{T}{\rho \frac{\pi}{4} D^2}$$

This equation may be expressed in terms of the dynamic

pressure as

$$q''_0 = q + \frac{T}{\frac{\pi}{4} D^2}$$

The above relationships have been derived for the condition of zero angle of attack of the model. The dynamic pressure in the slipstream would be expected to be a function of angle of attack; however, to include these effects would needlessly complicate the presentation.

For the purpose of presenting coefficients, therefore, the dynamic pressure in the slipstream can be defined as

$$q'' = q + \frac{T}{\frac{\pi}{4} D^2} \quad (1)$$

and the thrust coefficient as

$$T_c'' = \frac{T}{\frac{\pi}{4} D^2 q''}$$

or

$$T_c'' = \frac{T}{\frac{\pi}{4} D^2 q + T} \quad (2)$$

also

$$\frac{q}{q''} = \left(\frac{V}{V + \Delta V_0} \right)^2 = 1 - T_c'' \quad (3)$$

$$\left(\frac{V}{V + \Delta V_0} \right) = \sqrt{1 - T_c''} \quad (4)$$

For convenience, some values of the most used terms involving T_c'' have been tabulated in table I.

RESULTS AND DISCUSSION

BASIC DATA

Propeller characteristics.—The efficiency curves for the outboard propeller tested alone at various blade angles are presented in figure 7. The maximum efficiency reached (about 0.77) was obtained with a blade angle of 20°, the highest tested.

In order to minimize the time required, the operating conditions were chosen so that only two propeller blade-angle settings were required. A value of $\beta_{.75R}$ of 8° was found to be satisfactory for thrust coefficients of 0.91, 0.71, and 0.50 and $\beta_{.75R}$ of 20° for a thrust coefficient of 0.20.

The choice of blade angle for use at zero forward speed (vertical take-off or landing) cannot be made, however, on the basis of the efficiencies presented in the curves of figure 7. For this purpose, an efficiency factor based on the ability of the propeller to produce static thrust must be used. The static-thrust efficiency can be written in a manner analogous to the figure of merit of rotors:

$$\eta'' = \frac{T \frac{\Delta V_0}{2}}{550P}$$

which can be reduced to

$$\eta'' = \frac{T^{3/2}}{1100P \sqrt{\frac{\rho}{2} \frac{\pi}{4} D^2}}$$

TABLE I
FUNCTIONS OF T_c''

T_c''	$1 - T_c''$	$\sqrt{1 - T_c''}$	$\sqrt{1 - T_c''} - 1$	$1 + \sqrt{1 - T_c''}$	$1 - \sqrt{1 - T_c''}$
0	1	1	0	2	0
.1	.90	.949	-.051	1.949	.051
.2	.80	.894	-.106	1.894	.106
.3	.70	.837	-.163	1.837	.163
.4	.60	.774	-.226	1.774	.226
.5	.50	.707	-.293	1.707	.293
.6	.40	.632	-.365	1.632	.365
.7	.30	.548	-.452	1.548	.452
.8	.20	.447	-.553	1.447	.553
.9	.10	.316	-.684	1.316	.684
.92	.08	.283	-.717	1.283	.717
.94	.06	.245	-.755	1.245	.755
.96	.04	.200	-.800	1.200	.800
.98	.02	.141	-.859	1.141	.859
1.0	0	0	-1.000	1.000	1.000

The maximum static-thrust efficiency of 0.7 shown in figure 7 (diamond symbol) was obtained with a blade angle of 8°. With the propeller disks overlapped, the static-thrust efficiency was reduced to 0.65 as indicated in figure 8. A corresponding reduction in efficiency at forward speeds is indicated in figure 8. This loss in static-thrust efficiency with the propeller disks overlapped does not necessarily mean that overlapping is undesirable, however, because, for an airplane of a given size and with a given number of propellers, overlapping permits the use of larger diameter propellers, which can result in an increase in static thrust for a given horsepower, even though the efficiency is reduced somewhat by overlapping.

The variations of the propeller thrust coefficient C_T and power coefficient C_P with angle of attack are presented in figure 9. It should be remembered when use is made of these data that the thrust was held constant throughout the angle-of-attack range and the rotational speed and power were allowed to decrease with increasing angle of attack. In general, the data for the isolated propeller show somewhat lower values of C_T and C_P than the data for the propeller or propellers operating in the presence of the wing. The biggest differences, however, occur under conditions that are not likely to be of practical interest (high forward speed ($T_c'' = 0.2$) at high angles of attack). The corresponding variations of $\frac{V \cos \alpha}{nD}$ are presented in figure 10. The power required for a constant thrust condition through the angle-of-attack range is presented in figure 11. In general, the power decreased as the angle of attack increased.

The normal-force and pitching-moment coefficients of the outboard propeller are presented in figure 12. Similar data for the inboard propeller are not presented because of difficulties experienced with the instrumentation for the inboard propeller that resulted in excessive scatter and large shifts in the zero readings. The general trend of the data, however, was similar to that for the outboard propeller. The problems of obtaining reliable data were considerably increased because the strain-gage beams, which measured the normal force and pitching-moment loads, were also required to support the relatively heavy motor and carry the high thrust and torque loads.

Also presented in figure 12 are the theoretical variations of normal force obtained by the method of reference 3. The theoretical variation of propeller normal force with angle of

attack of reference 3 is intended to be applicable only at angles of attack near zero. The additional factors which contribute to the normal force at high angles of attack cannot readily be included in the theoretical treatment. It is interesting to note, however, that, for the configuration of this investigation, calculations of the normal-force coefficient using the q -factor (which accounts for the inflow to the propeller) based on the component of thrust in the free-stream direction rather than in the thrust direction, as assumed in reference 3, show relatively good agreement with the measured data.

The operation of both propellers in the presence of the wing is seen almost to double the pitching moment of the outboard propeller as compared with that of the propeller alone. This magnitude of increase cannot be attributed to an increase in wing-induced upwash at the propeller disk, because such an increase should produce corresponding increases in propeller normal force. It is probable that these increases in pitching moment are due to a change in the velocity through the upper and lower portions of the propeller disk (as referenced to the wing-chord plane). An increase in velocity over the wing (upper part of the propeller disk) would tend to decrease the thrust from the top part of the disk. Conversely, a decrease in velocity through the lower half would increase the thrust of this part of the propeller; thus an increase would occur in the nose-up pitching moment of the propeller with increasing angle of attack.

The propeller pitching moment can be regarded as being due to the fact that thrust of the propeller is applied at some distance from the center of rotation. The effective radial location of the thrust vector is presented in figure 13 and was determined from the pitching-moment data of figure 12 by the following relation

$$\frac{r}{R} = \frac{C_{m_p}'' S \bar{c}}{T_c'' \frac{\pi}{8} D^3}$$

For the most extreme condition, the effective location of the thrust vector is seen to move downward more than 20 percent of the propeller radius. (See sketch, fig. 13).

The significance of these propeller pitching moments can be judged from figure 14, which presents the total contribution of both propellers to the total model pitching moment. Because the data on the inboard propeller was unreliable, the data obtained for the outboard propeller was used for both the inboard and the outboard propellers in the summation represented by $\Delta C_m''$. The calculated variation was obtained by using the calculated values of normal-force coefficients (fig. 12) and letting the pitching-moment coefficient be zero. It can be seen that the usual procedure of basing the propeller contribution only on the propeller normal force accounts for less than half of the total contribution for this configuration at these thrust coefficients. Additional data on the normal force and pitching moments of isolated propellers are presented in references 4 and 5.

The contributions of the spinner (when not rotating) to the propeller normal force and pitching moment are presented in figure 15.

Wing characteristics.—Figure 16 presents the variation with angle of attack and thrust coefficient of the lift coefficient based on the dynamic pressure in the free stream. Figure 17 (a) presents the same data based on the dynamic pressure in the slipstream. The lift variation for a thrust coefficient of 1.0 (dashed line of fig. 17) cannot be presented in figure 16 because, if the free-stream dynamic pressure were used to obtain the coefficient, the lift coefficient at all angles of attack would be infinite. The disadvantage of basing the coefficients on the free-stream dynamic pressure is thus readily apparent.

Increasing the thrust coefficient, with either one propeller (fig. 18) or two propellers (fig. 17), results in an increase in the angle of attack at which maximum lift is reached and a more gradual variation of the lift with angle of attack above maximum lift. It should be remembered that these results are for constant thrust throughout the angle-of-attack range. If the power were held constant as the angle of attack was increased, the thrust would increase with angle of attack and an even more gradual variation of lift above maximum lift would be indicated.

The data at $T_c''=0$ (figs. 17 and 18) were obtained with the propellers removed. Data are compared in figure 19 for conditions of propeller removed, of zero thrust with the propeller on, and of propeller windmilling. Removing the propeller results in a small reduction in lift in the region of maximum lift. As would be expected from the propeller data discussed previously, removing the propellers appreciably decreases the unstable variation of pitching moment with angle of attack at the low angles of attack. These effects should be kept in mind when the propeller-off pitching-moment data of figures 17 and 18 are used.

The data of figure 20 indicate, as might be expected, that the nacelles disturb the flow over the wing so that the wing with nacelles stalls at a lower angle of attack and lower lift coefficient than the wing alone. As would be expected, the nacelles also cause a marked decrease in the static longitudinal stability (increase in $\frac{\partial C_m''}{\partial \alpha}$) below the stall.

The destabilizing effects of the propellers and nacelles at zero angle of attack are summarized in figure 21. These data show that, near zero angle of attack, there is only a small variation of stability, as indicated by the curve of $\frac{\partial C_m''}{\partial C_L''}$ against thrust coefficient.

Estimation of the lift-curve slope.—Reference 6 presents relationships for estimating the increase of lift due to a slipstream flowing over the wing. Rearranging the relationship to provide an expression for the lift-curve slope of the wing with slipstream and using the notation of the present report gives the following equation:

$$\frac{\partial C_L''}{\partial \alpha} = \left(\frac{\partial C_L}{\partial \alpha} \right)_{T_c''=0} (1 - T_c'') \left\{ 1 + \frac{d_1 c}{S} \left(\frac{V'}{V} - 1 \right) \left[\lambda - 0.6 \left(\frac{2\pi}{57.3} \right) \left(\frac{1}{(\partial C_L / \partial \alpha)_{T_c''=0}} \right) \left(\frac{\theta}{\alpha} \right) \right] \right\} \quad (5)$$

For the present configuration, λ can be taken as 1.0 (ref. 6),

$\left(\frac{V'}{V}-1\right)$ is obtained from equation (B5) of appendix B, $\frac{\theta}{\alpha} = \frac{\theta}{\phi}$ is obtained from equation (B7) of appendix B, and

$$0.6 \left(\frac{2\pi}{57.3} \right) \left(\frac{1}{(\partial C_L / \partial \alpha)_{T_c''=0}} \right) \approx 1$$

The lift-curve slope can be expressed as

$$\frac{\partial C_L''}{\partial \alpha} = \left(\frac{\partial C_L}{\partial \alpha} \right)_{T_c''=0} (1 - T_c'') \left[1 + \frac{d_1 c}{S} \left(\frac{1 - \sqrt{1 - T_c''}}{1 + \sqrt{1 - T_c''}} \right) (1 + K) \right] \quad (6)$$

where d_1 can be obtained from equation (B4) of appendix B. Calculation of the lift-curve slope by this equation underestimates the measured lift-curve slope (fig. 22).

If it is assumed that the inclination of the slipstream is zero ($\frac{\theta}{\alpha} = 0$), equation (5) reduces to

$$\frac{\partial C_L''}{\partial \alpha} = \left(\frac{\partial C_L}{\partial \alpha} \right)_{T_c''=0} (1 - T_c'') \left[1 + \frac{d_1 c}{S} \left(\frac{1 - \sqrt{1 - T_c''}}{2\sqrt{1 - T_c''}} \right) (1 + K) \right] \quad (7)$$

and much better agreement with the experimental data is obtained (fig. 22). This equation, in effect, is based on the assumption that the circulation around the wing is unchanged by the presence of the slipstream and the increase in lift is directly proportional to the increase in velocity across the circulation.

If it is further assumed that the wing is far enough behind the propeller so that the full slipstream velocity is developed ($K=1$) and that the wing is fully immersed in the slipstream ($\frac{d_1 c}{S} = 1$), the equation reduces to the simple form

$$\frac{\partial C_L''}{\partial \alpha} = \left(\frac{\partial C_L}{\partial \alpha} \right)_{T_c''=0} \sqrt{1 - T_c''} \quad (8)$$

According to equation 7, the fact that the lift-curve slope obtained for the configuration with two propellers is higher than that obtained for the configuration with one propeller is primarily due to the greater percentage of wing area that is immersed in the slipstream.

PERFORMANCE ESTIMATES

The procedure outlined in appendix C was used to estimate the performance of a hypothetical four-propeller airplane as it traversed the regime of flight represented in figure 6. The hypothetical airplane was assumed to have linear dimensions 6 times those of the model. Calculations were made for standard sea-level conditions, and the fuselage and other parts of the airplane not represented by the model were assumed to have a drag coefficient of 0.01.

The variation of the thrust coefficient required and the forward velocity reached in constant-altitude transition, as the wing attitude is lowered from 90° for take-off to conventional flight attitude, is shown in figure 23. The corresponding variation of thrust power required with forward velocity for an assumed wing loading of 40 pounds per square foot is shown in figure 24. The thrust power required is seen to decrease quite rapidly in the low speed range. The minimum thrust power required occurs in the normal flight range at a speed of 160 mph and a wing attitude of 8.5°. It

will be noted that (with the assumption that $\eta=0.75$ at high speed and $\eta''=0.65$ for static-thrust take-off), if this airplane were designed for a high speed of the order of 350 to 400 mph, sufficient power would be available for vertical take-off with the 12-foot-diameter propellers represented by the ones used on this model.

The untrimmed pitching moment and corresponding effective aerodynamic-center location, as indicated by $\frac{\partial C_m''}{\partial C_L''}$ for the conditions of this analysis, are indicated in figure 25. No allowance for the effects of trimming these moments was made in this analysis. These data are based on the assumption that the center of gravity of the airplane is located at the pivot axis of the wing and that this axis is located at the quarter-chord point of the mean aerodynamic chord. Figure 25 (c) indicates that a more forward location of the pivot axis would be desirable in reducing the out-of-trim moments. Figure 25 (a) indicates that, for the present configuration, a full-span, 30-percent-chord trailing-edge flap (ref. 7) would be ineffective in balancing the airplane. The complete loss in effectiveness in the angle-of-attack range from 56° to 77° indicates that the wing is partially stalled in this angle-of-attack range. Results of an unpublished investigation indicate that, with the propellers placed much closer to the wing, this reduction in control effectiveness may be greatly reduced.

CONCLUSIONS

An investigation of the aerodynamic characteristics of a wing-propeller combination and of the wing and propeller separately at angles of attack up to 90° indicates the following conclusions:

1. Increasing the thrust coefficient increased the angle of attack for maximum lift coefficient and greatly diminished the reduction of lift coefficient above the angle of attack for maximum lift. Analysis of the operation of a hypothetical airplane designed for vertical take-off indicated that partial wing stalling probably would be encountered in certain flight attitudes but sufficient power would be available for flights at any attitude.

2. The effects of slipstream on the variation of the lift-curve slope with thrust coefficient would be satisfactorily estimated for this model by means of a modified form of a method formulated by Smelt and Davies.

3. The variation of propeller normal force with angle of attack compared favorably with calculated values. There was also an appreciable direct pitching moment on the propeller itself. This pitching moment was approximately doubled when the propeller was operated in the presence of the wing and corresponded to a downward movement of the effective center of thrust of approximately 20 percent of the propeller radius.

4. Calculations for a hypothetical airplane, with a wing loading of 40 pounds per square foot and the relationship of the total propeller disk area to wing area represented by this model, indicate that airplanes designed for a high speed range of 350 to 400 mph will have sufficient power available for vertical take-off.

LANGLEY AERONAUTICAL LABORATORY,

NATIONAL ADVISORY COMMITTEE FOR AERONAUTICS,
LANGLEY FIELD, VA., August 13, 1954.

APPENDIX A

TUNNEL-WALL CORRECTIONS

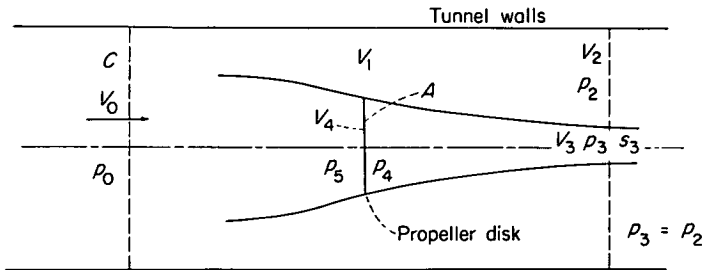
In order to correct the wind-tunnel data for tunnel-wall effects the following relations for velocities were obtained in a manner similar to that presented in reference 8. The symbols that are used in this appendix and which have not been defined previously are defined as follows:

A	propeller disk area, $\frac{\pi}{4} D^2$, sq ft
C	tunnel cross-sectional area, sq ft
s	slipstream cross-sectional area, sq ft
p	static pressure lb/sq ft
V	local velocity, ft/sec
K_1	ratio of free-stream velocity to slipstream velocity, $\frac{V_0}{V_3}$

Subscripts:

0	far ahead of propeller disk
1	in tunnel at propeller disk but outside of slipstream
2	in tunnel far behind propeller disk but outside of slipstream
3	in slipstream far behind propeller disk
4	immediately behind propeller disk
5	immediately ahead of propeller disk
x	at any station

The following sketch shows the relative location of the stations at which the velocities, pressures, and areas used in the following equations were obtained:



The relationships of pressure and velocity as determined by Bernoulli's equation for a station in front of the propeller, behind the propeller disk, and outside the slipstream tube are as follows:

Ahead of propeller:

$$p_0 + \frac{1}{2} \rho V_0^2 = p_5 + \frac{1}{2} \rho V_4^2 \quad (\text{A1})$$

Behind propeller:

$$p_4 + \frac{1}{2} \rho V_4^2 = p_3 + \frac{1}{2} \rho V_3^2 \quad (\text{A2})$$

Outside of propeller:

$$p_0 + \frac{1}{2} \rho V_0^2 = p_2 + \frac{1}{2} \rho V_2^2 \quad (\text{A3})$$

Also, assume

$$p_3 = p_2 \quad (\text{A4})$$

Solving for $\frac{1}{2} \rho V_4^2$ in equations (A1) and (A2) and equating gives

$$p_0 - p_5 + \frac{1}{2} \rho V_0^2 = p_3 - p_4 + \frac{1}{2} \rho V_3^2 \quad (\text{A5})$$

Also,

$$p_4 - p_5 = \Delta p = \frac{T}{A} \quad (\text{A6})$$

Solving for $p_4 - p_5$ in equation (A5) and substitution in equation (A6) gives

$$\frac{T}{A} = p_3 - p_0 + \frac{1}{2} \rho V_3^2 - \frac{1}{2} \rho V_0^2 \quad (\text{A7})$$

and, from equations (A3) and (A4),

$$p_3 - p_0 - \frac{1}{2} \rho V_0^2 = -\frac{1}{2} \rho V_2^2 \quad (\text{A8})$$

Then, from equations (A7) and (A8),

$$\frac{T}{A} = \frac{\rho}{2} (V_3^2 - V_2^2) \quad (\text{A9})$$

By definition,

$$T_c'' = \frac{T}{\frac{\rho}{2} A V_3^2} \quad (\text{A10})$$

and from equation (A9)

$$T_c'' = 1 - \left(\frac{V_2}{V_3} \right)^2 \quad (\text{A11})$$

From the continuity that $AV = A_x V_x$, the cross-sectional area of the slipstream can be obtained; thus

$$V_0 C = V_1 (C - A) + V_4 A = V_2 (C - s) + V_3 s$$

$$V_0 C = V_2 C - V_2 s + V_3 s$$

$$s = C \frac{(V_0 - V_2)}{(V_3 - V_2)} \quad (\text{A12})$$

Solution for the thrust from the equations for axial momentum is obtained by the use of the following equations:

$$T = s \rho V_3 (V_3 - V_0) - (C - s) \rho V_2 (V_0 - V_2) + C (p_2 - p_0) \quad (\text{A13})$$

Substituting for $(p_2 - p_0)$ from equation (A3) gives

$$T = s \rho V_3 (V_3 - V_0) - (C - s) (\rho V_2) (V_0 - V_2) + C \frac{\rho}{2} (V_0^2 - V_2^2) \quad (\text{A14})$$

Substituting for s from equation (A12) into equation (A14)

and solving for V_0 gives

$$V_0 = (V_3 + V_2) \pm \sqrt{V_3^2 - \frac{2T}{C\rho}} \quad (\text{A15})$$

Substitute $T = \frac{\rho}{2} A (V_3^2 - V_2^2)$ from equation (A9) into equation (A15) to obtain

$$V_0 = (V_3 + V_2) \pm \sqrt{V_3^2 - \frac{A}{C} (V_3^2 - V_2^2)} \quad (\text{A16})$$

But, from equation (A11), $V_3^2 = \frac{V_2^2}{1 - T_c''}$, so that substituting into equation (A16) and using the minus sign gives

$$V_0 = V_2 \left(\frac{1 + \sqrt{1 - T_c''} - \sqrt{1 - \frac{A}{C} T_c''}}{\sqrt{1 - T_c''}} \right) \quad (\text{A17})$$

Also,

$$V_0 = V_3 \left(1 + \sqrt{1 - T_c''} - \sqrt{1 - \frac{A}{C} T_c''} \right) \quad (\text{A18})$$

A simplification can be effected by assuming that

$$V_0 = V_3 K_1$$

Then,

$$V_0 = V_2 \frac{K_1}{\sqrt{1 - T_c''}}$$

where

$$K_1 = 1 + \sqrt{1 - T_c''} - \sqrt{1 - \frac{A}{C} T_c''} \quad (\text{A19})$$

The equations for slipstream area and velocities are then as

follows:

$$s = C \left(\frac{1 - \frac{\sqrt{1 - T_c''}}{K_1}}{\frac{1}{K_1} - \frac{\sqrt{1 - T_c''}}{K_1}} \right) = C \left(\frac{K_1 - \sqrt{1 - T_c''}}{1 - \sqrt{1 - T_c''}} \right) \quad (\text{A20})$$

$$s = C \frac{1 - \sqrt{1 - \frac{A}{C} T_c''}}{1 - \sqrt{1 - T_c''}} \quad (\text{A20})$$

From equation (A17)

$$V_2 = (\sqrt{1 - T_c''}) \frac{V_0}{K_1} \quad (\text{A21})$$

From equation (A18)

$$V_3 = \frac{V_0}{K_1} \quad (\text{A22})$$

From continuity, $V_4 A = V_3 s$ so that, with equations (A20) and (A22),

$$V_4 = \left(\frac{V_0}{K_1} \right) \left(\frac{C}{A} \right) \left(\frac{1 - \sqrt{1 - \frac{A}{C} T_c''}}{1 - \sqrt{1 - T_c''}} \right) \quad (\text{A23})$$

Since, from continuity,

$$V_0 C = V_4 A + V_1 (C - A)$$

equation (A23) can be used to obtain

$$V_1 = \frac{V_0 C \left[1 - \frac{1}{K_1} \left(\frac{1 - \sqrt{1 - \frac{A}{C} T_c''}}{1 - \sqrt{1 - T_c''}} \right) \right]}{C - A} \quad (\text{A24})$$

APPENDIX B

SLIPSTREAM CHARACTERISTICS

The following relationships concerning the character of the slipstream are helpful in analyzing the effects of slipstream on the aerodynamic characteristics of wings.

Diameter of the slipstream at any T_c'' and any distance behind the propeller.—Reference 6 gives a relation for the velocity at any point in the slipstream as

$$V' = V + \frac{\Delta V}{2} \left(1 + \frac{x/D}{\sqrt{\frac{1}{4} + \left(\frac{x}{D}\right)^2}} \right) = V + \frac{\Delta V}{2} (1 + K) \quad (\text{B1})$$

where V' is the velocity at distance x from the propeller disk. If the mass flow in the slipstream is assumed to be constant, then,

$$\rho \frac{\pi}{4} D^2 \left(V + \frac{\Delta V}{2} \right) = \rho \frac{\pi}{4} d_1^2 V' \quad (\text{B2})$$

$$d_1^2 = D^2 \frac{\left(V + \frac{\Delta V}{2} \right)}{V'} = D^2 \frac{1 + \frac{\Delta V}{2V}}{1 + \frac{\Delta V}{2V} (1 + K)}$$

where d_1 is the diameter of the slipstream at distance x

from the propeller disk and

$$K = \left(\frac{x/D}{\sqrt{\frac{1}{4} + \left(\frac{x}{D}\right)^2}} \right)$$

From equation (4) of the main body of this report,

$$\frac{\Delta V}{2V} = \frac{1 - \sqrt{1 - T_c''}}{2\sqrt{1 - T_c''}} \quad (\text{B3})$$

Equation (B3) can be substituted into equation (B2) and the result simplified to obtain

$$d_1^2 = D^2 \frac{1 + \sqrt{1 - T_c''}}{2 + (\sqrt{1 - T_c''} - 1)(1 - K)} \quad (\text{B4})$$

Also, from equations (B1) and (B3),

$$\frac{V'}{V} - 1 = \frac{\Delta V}{2V} (1 + K) = \frac{1 - \sqrt{1 - T_c''}}{2\sqrt{1 - T_c''}} (1 + K) \quad (\text{B5})$$

Inclination of the slipstream.—From reference 6 the following relationship for the inclination of the slipstream to the

free stream at small angles of attack can be obtained.

$$\Theta = \frac{\phi \frac{\Delta V}{2V}}{1 + \frac{\Delta V}{2V}} \quad (\text{B6})$$

From equations (B3) and (B6)

$$\frac{\Theta}{\phi} = \frac{1 - \sqrt{1 - T_c''}}{1 + \sqrt{1 - T_c''}} \quad (\text{B7})$$

where ϕ is the inclination of the thrust axis and Θ is the inclination of the slipstream at the propeller disk.

APPENDIX C

PERFORMANCE CALCULATIONS

Calculation of the performance by use of coefficients based on the dynamic pressure in the slipstream required some modification of conventional procedures. The thrust coefficient required for steady level flight at a particular attitude can be obtained by cross plotting the longitudinal force to determine the thrust coefficient for zero longitudinal force. Similar cross plots of lift coefficient can be used to determine the lift coefficient available at this thrust coefficient. The forward speed corresponding to this thrust coefficient and lift coefficient is calculated by the following equation

$$V_{mph} = \frac{60}{88} \sqrt{\left(\frac{W/S}{C_L''}\right) \frac{(1 - T_c'')}{\rho/2}} \quad (\text{C1})$$

The total thrust at this thrust coefficient is given by

$$NT = T_c'' \left(\frac{W/S}{C_L''}\right) \frac{\pi}{4} D^2 N \quad (\text{C2})$$

The thrust horsepower required for steady level flight can be calculated from momentum relations from the following basic equation:

$$\text{thp}_{\text{required}} = \frac{NTV \cos \alpha}{550} + \frac{NT \frac{\Delta V}{2}}{550} \quad (\text{C3})$$

where the first term represents the power required to overcome the drag and the second term represents the power in the slipstream. In the speed range of conventional airplanes the second term is negligible and $\cos \alpha$ is approximately unity. The power required equation then reduces to the conventional

$$\text{thp}_{\text{required}} = \frac{NTV}{550}$$

The increment of velocity in each slipstream due to thrust ΔV can be obtained from the momentum relation

$$T = m_p \Delta V = \rho \frac{\pi}{4} D^2 \left(V \cos \alpha + \frac{\Delta V}{2} \right) \Delta V$$

where m_p is the mass flow through the propeller and

$$\Delta V = \sqrt{V^2 \cos^2 \alpha + \frac{T}{\rho \frac{\pi}{4} D^2}} - V \cos \alpha \quad (\text{C4})$$

For vertical take-off and landing, V is zero and the power required (eq. (C3)) reduces to

$$\text{thp}_{\text{required}} = \frac{NT \frac{\Delta V}{2}}{550} = \frac{N(T)^{3/2}}{1100 \frac{D}{2} \sqrt{(\rho/2)\pi}} \quad (\text{C5})$$

For intermediate flight conditions at low speed, the power required (eq. (C3)) can be expressed as

$$\text{thp}_{\text{required}} = \frac{NTV}{550} \left(\frac{\cos \alpha + \sqrt{\cos^2 \alpha + \frac{T}{\frac{1}{2} \rho V^2 \frac{\pi}{4} D^2}}}{2} \right) \quad (\text{C6})$$

which can be expressed in terms of the thrust coefficient as

$$\text{thp}_{\text{required}} = \frac{NTV}{550} \left(\frac{\cos \alpha + \sqrt{\cos^2 \alpha + \frac{T_c''}{1 - T_c''}}}{2} \right) \quad (\text{C7})$$

REFERENCES

1. Gillis, Clarence L., Polhamus, Edward C., and Gray, Joseph L., Jr.: Charts for Determining Jet-Boundary Corrections for Complete Models in 7- by 10-Foot Closed Rectangular Wind Tunnels. NACA WR L-123, 1945. (Formerly NACA ARR L5G31.)
2. Herriot, John G.: Blockage Corrections for Three-Dimensional-Flow Closed-Throat Wind Tunnels, With Consideration of the Effect of Compressibility. NACA Rep. 995, 1950. (Supersedes NACA RM A7B28.)
3. Ribner, Herbert S.: Notes on the Propeller and Slipstream in Relation to Stability. NACA WR L-25, 1944. (Formerly NACA ARR L4I12a.)
4. Lesley, E. P., Worley, George F., and Moy, Stanley: Air Propellers in Yaw. NACA Rep. 597, 1937.
5. McLemore, H. Clyde, and Cannon, Michael D.: Aerodynamic Investigation of a Four-Blade Propeller Operating Through an Angle-of-Attack Range From 0° to 180°. NACA TN 3228, 1954.
6. Smelt, R., and Davies, H.: Estimation of Increase in Lift Due to Slipstream. R. & M. No. 1788, British A.R.C., 1937.
7. Kuhn, Richard E., and Draper, John W.: An Investigation of a Wing-Propeller Configuration Employing Large-Chord Plain Flaps and Large-Diameter Propellers for Low-Speed Flight and Vertical Take-Off. NACA TN 3307, 1954.
8. Glauert, H.: The Elements of Aerofoil and Airscrew Theory. Sec. ed., Cambridge Univ. Press, 1947. (Reprinted 1948.)

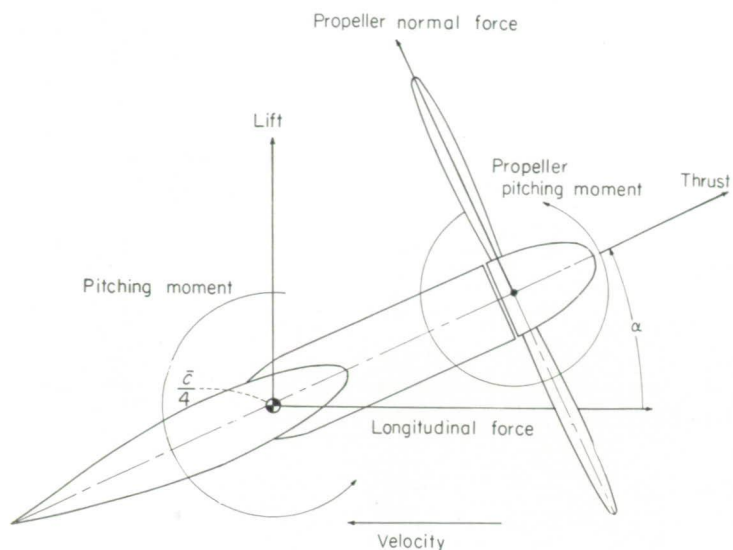


FIGURE 1.—System of axes showing positive direction of forces, moments, and angles.

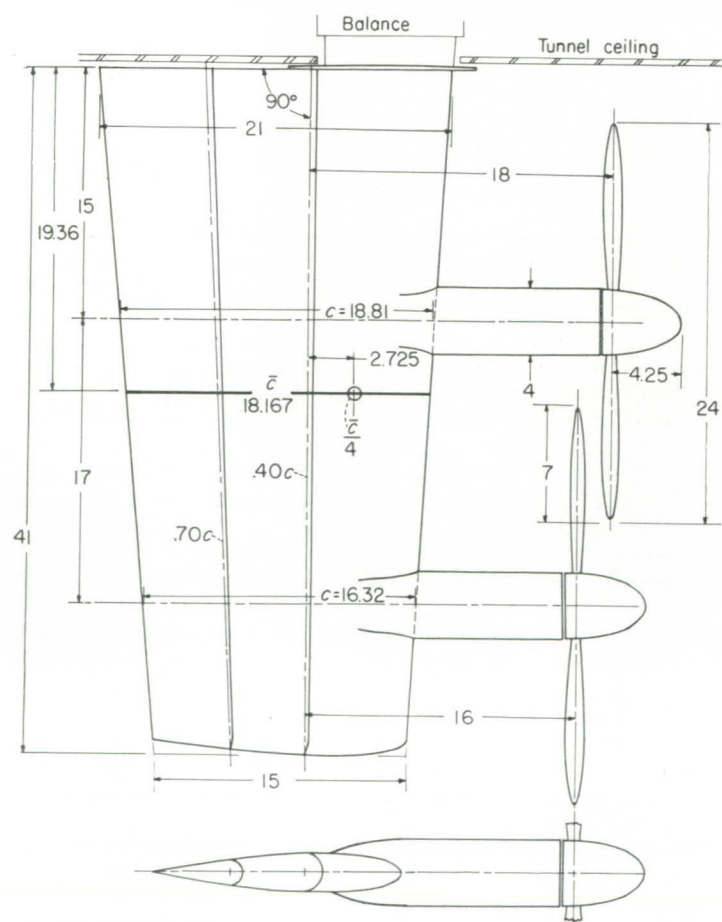


FIGURE 2.—Plan and cross-sectional views of model. (All dimensions are in inches.)

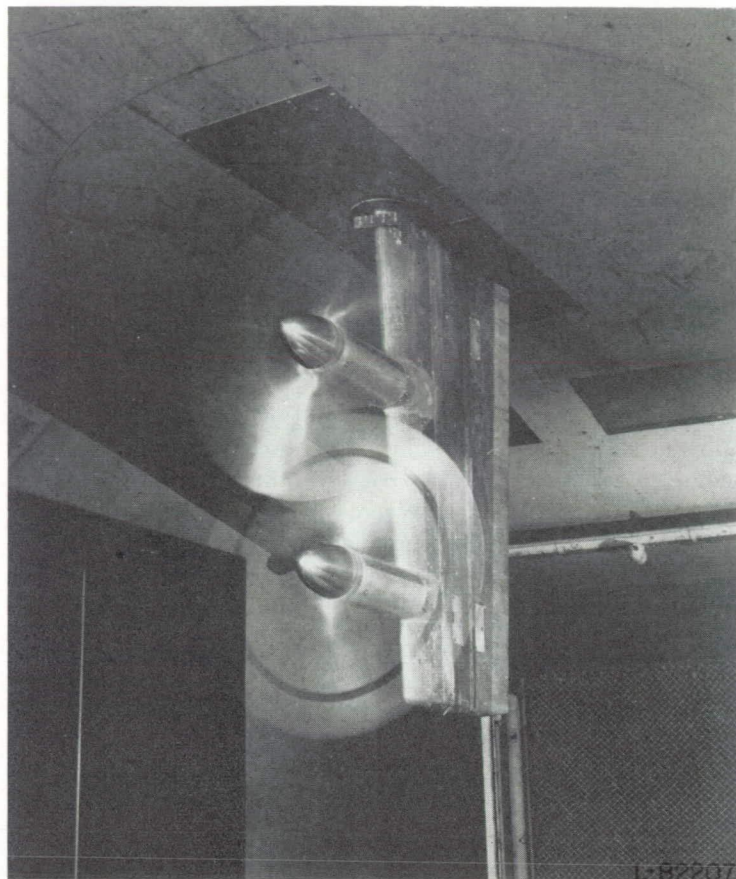


FIGURE 3.—Model installed in the test section of the Langley 300 MPH 7- by 10-foot tunnel.

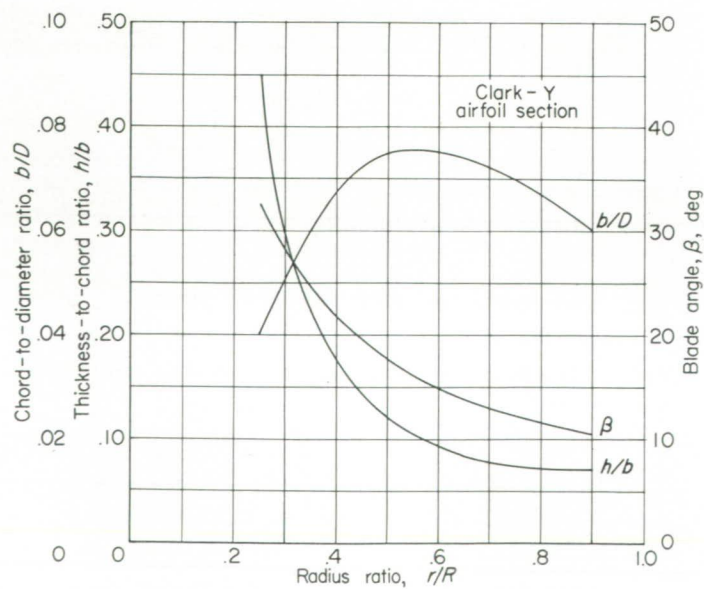
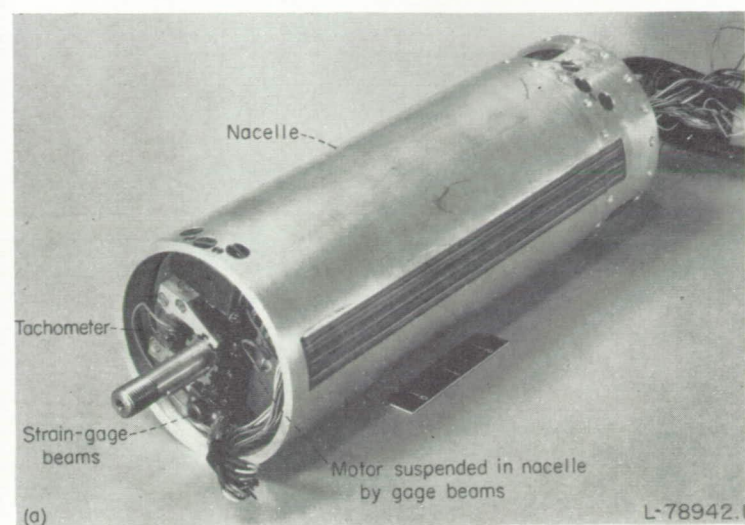
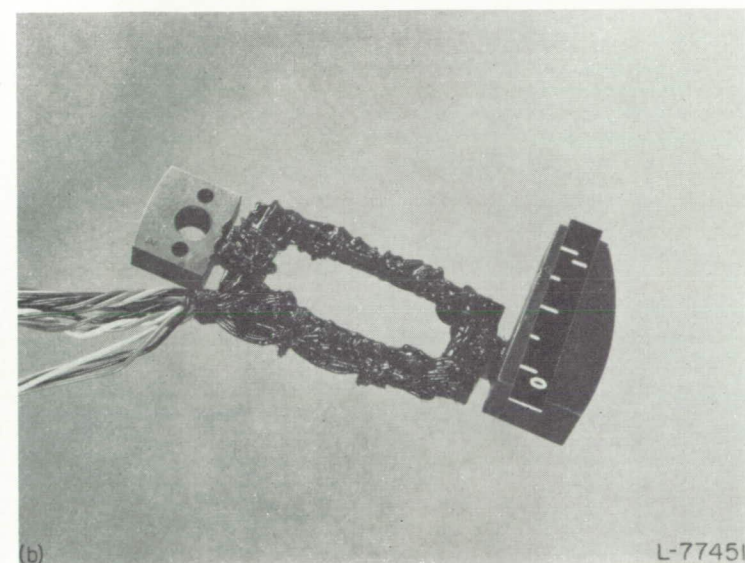


FIGURE 4.—Propeller-blade geometric characteristics.



(a) Complete motor balance.

FIGURE 5.—Motor-balance installation used for tests.



(b) Strain-gage beam used in measuring forces on propeller.

FIGURE 5.—Concluded.

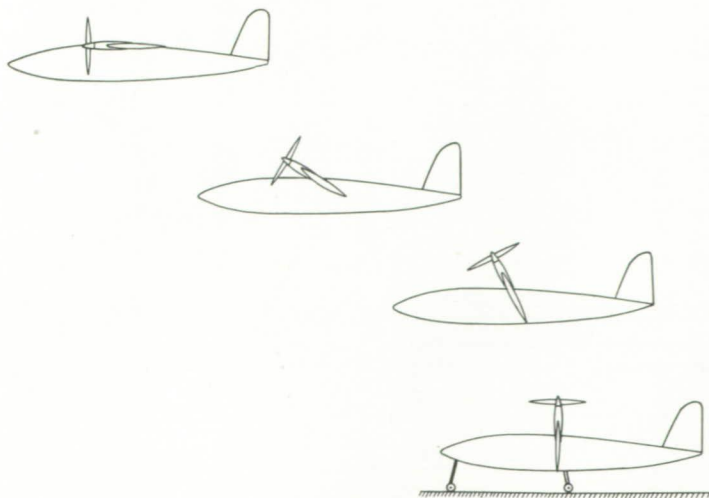


FIGURE 6.—Illustration of a method for vertical take-off and translation to horizontal flight for which data are applicable.

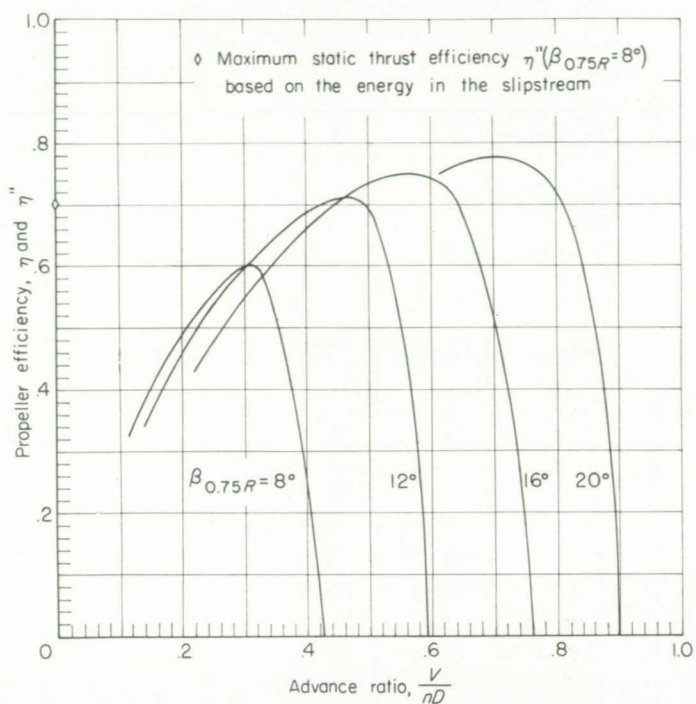
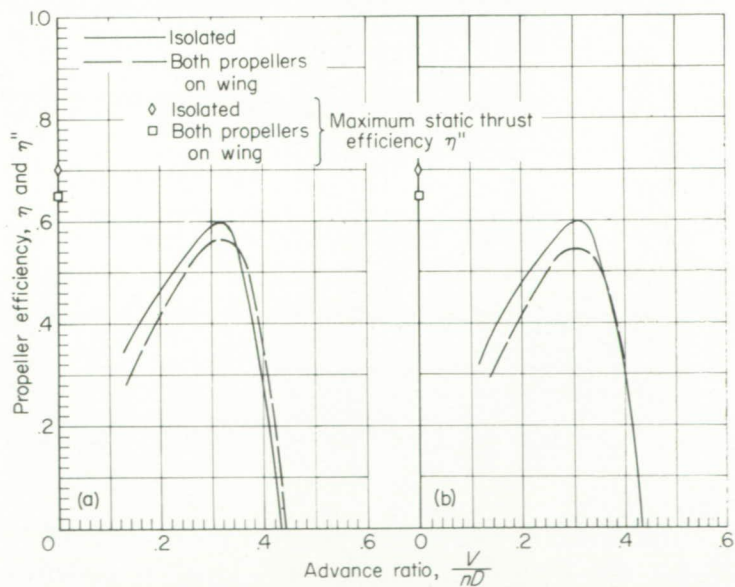


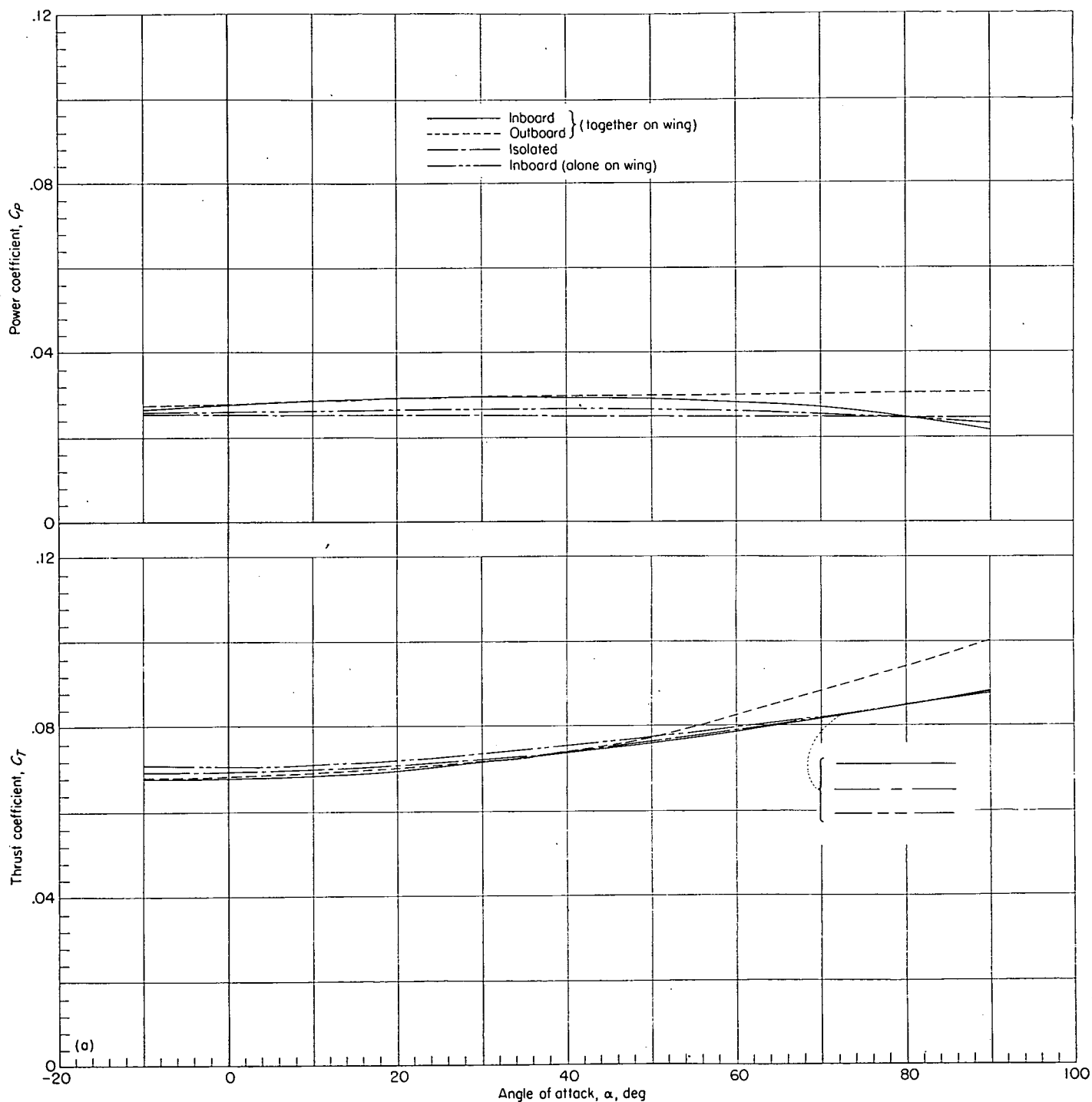
FIGURE 7.—Efficiency of the isolated propeller.



(a) Inboard propeller.

(b) Outboard propeller.

FIGURE 8.—Comparison of efficiency of the isolated propeller with that of two overlapping propellers mounted on the wing as shown in figure 2. $\beta_{0.75R} = 8^\circ$.



(a) $T_c'' = 0.91$; $\beta_{0.75R} = 8^\circ$.

FIGURE 9.—Propeller characteristics through angle-of-attack range with constant shaft thrust.

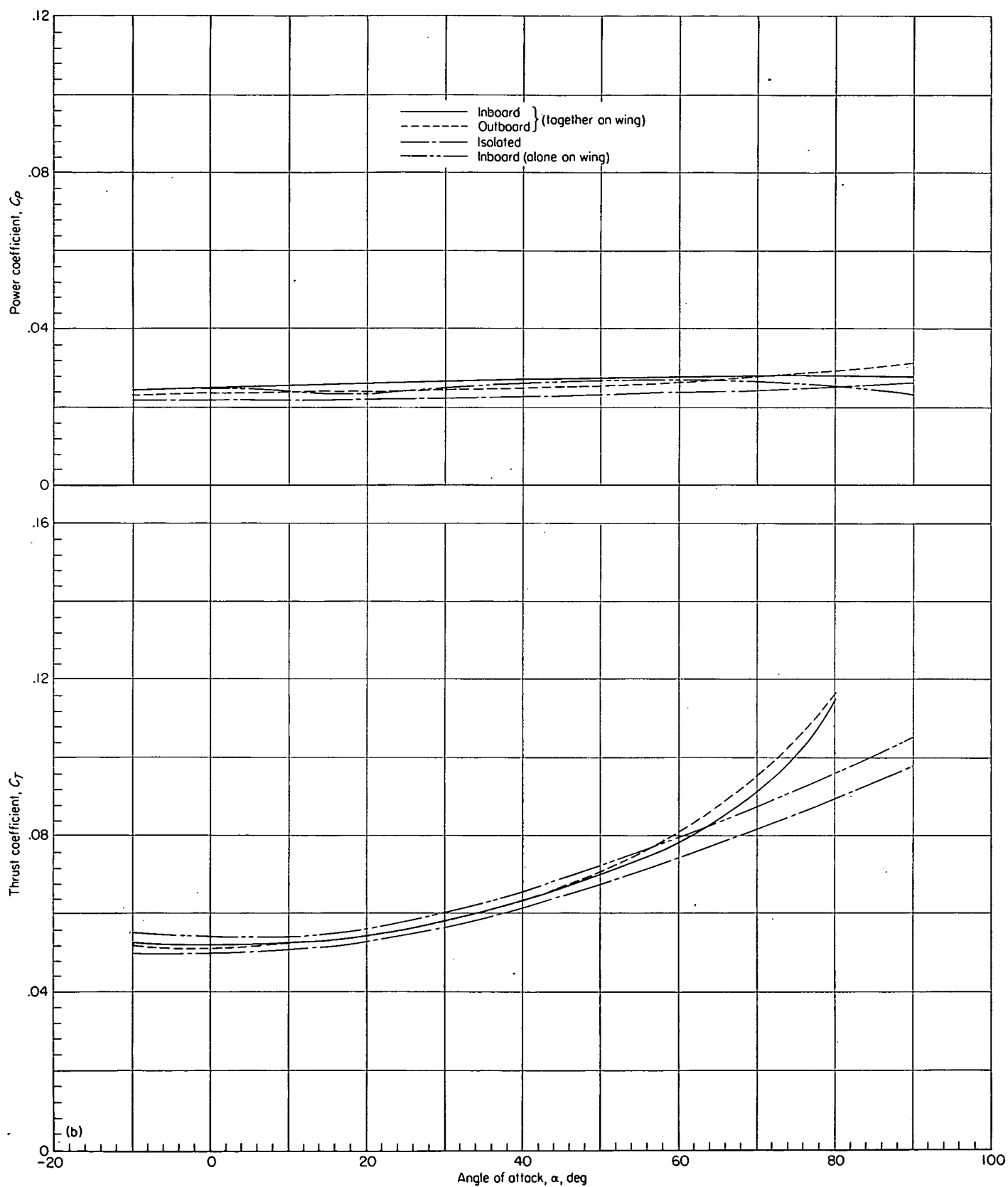
(b) $T_c'' = 0.71$; $\beta_{0.75R} = 8^\circ$.

FIGURE 9.—Continued.

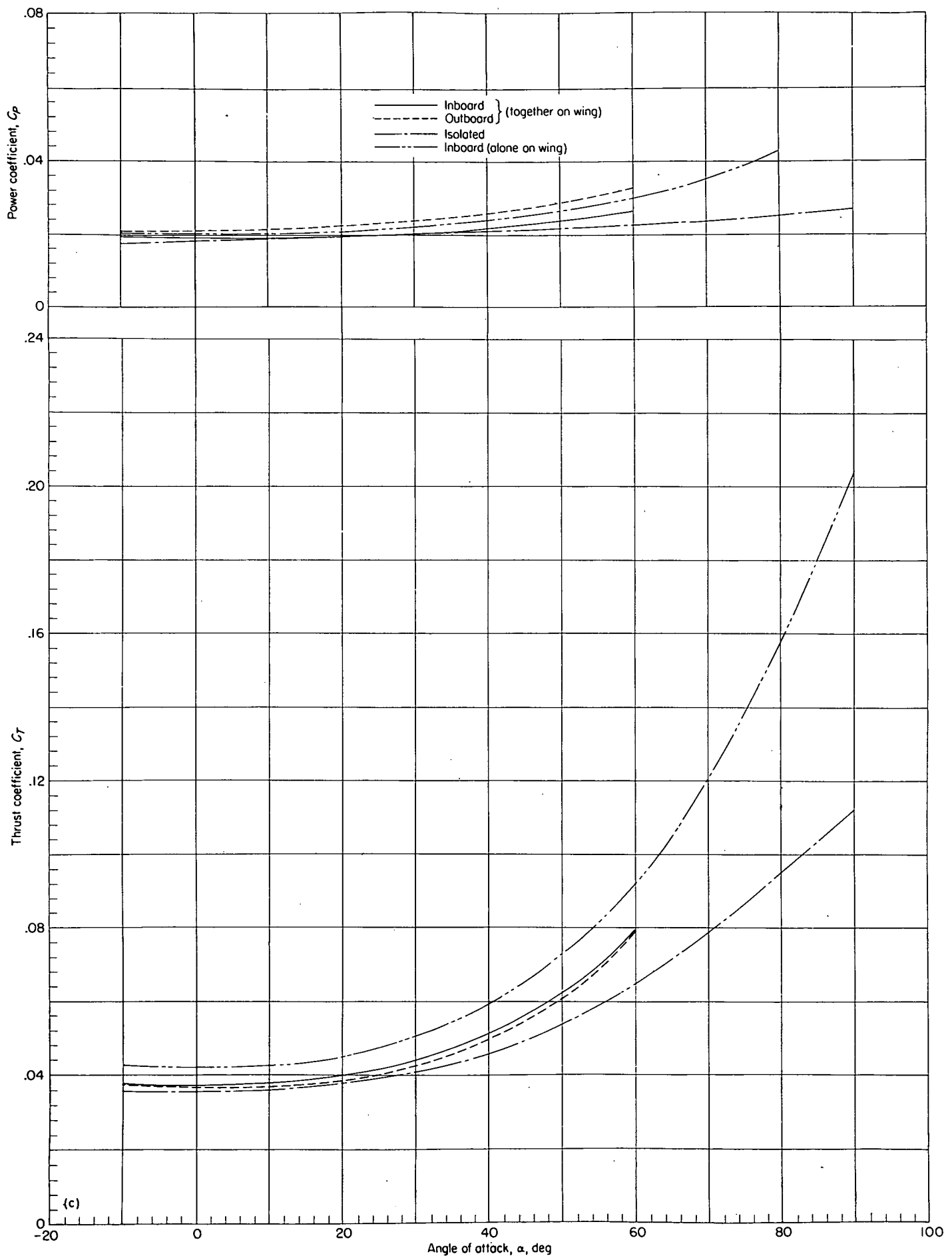
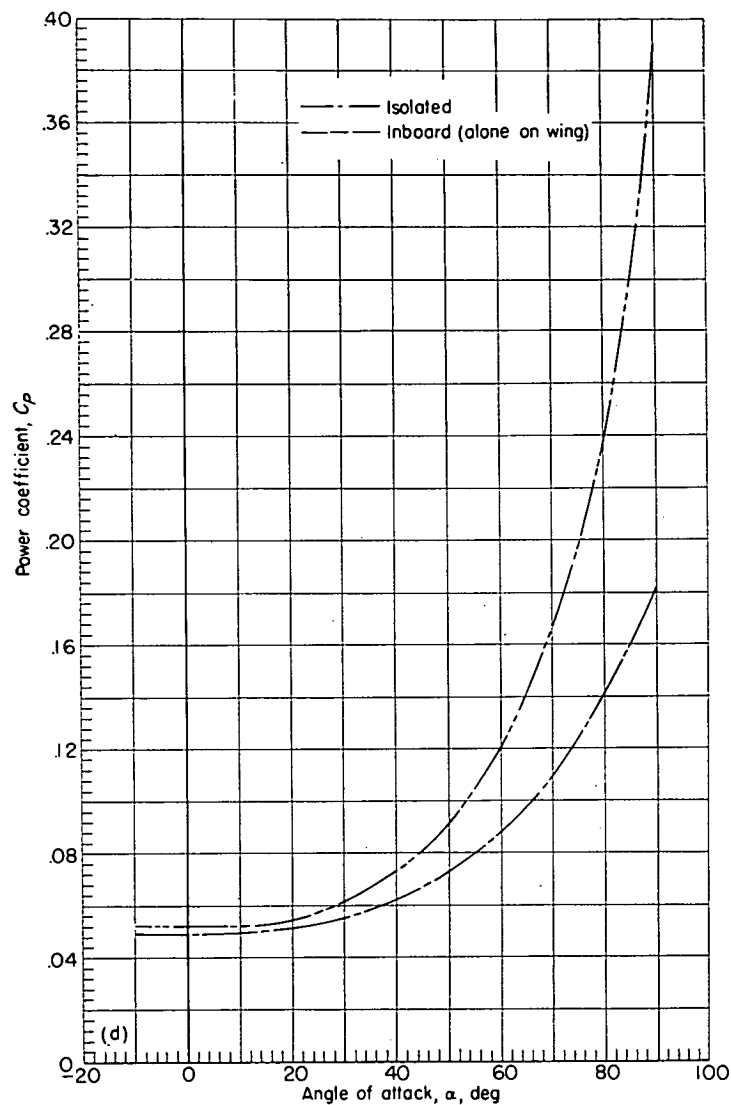
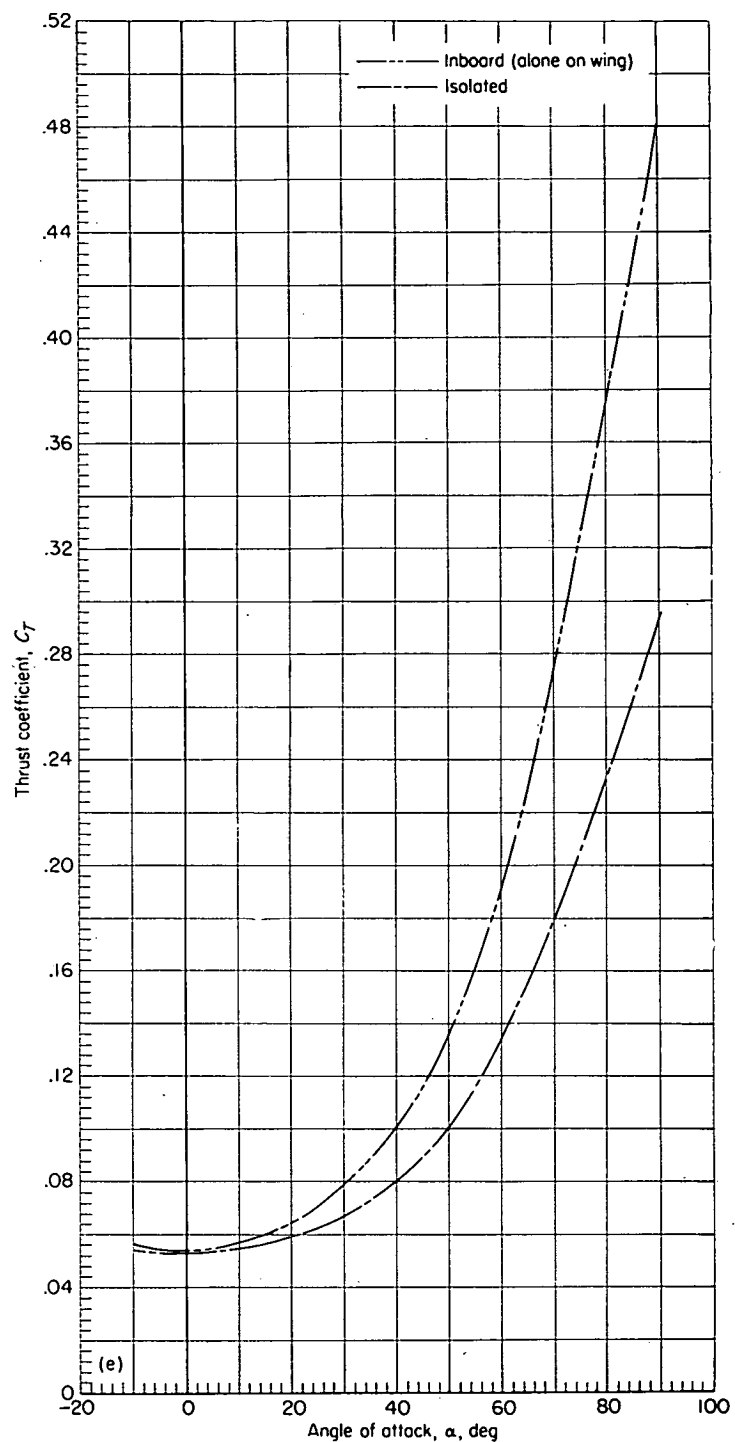
(c) $T_c'' = 0.50$; $\beta_{0.75R} = 8^\circ$.

FIGURE 9.—Continued.



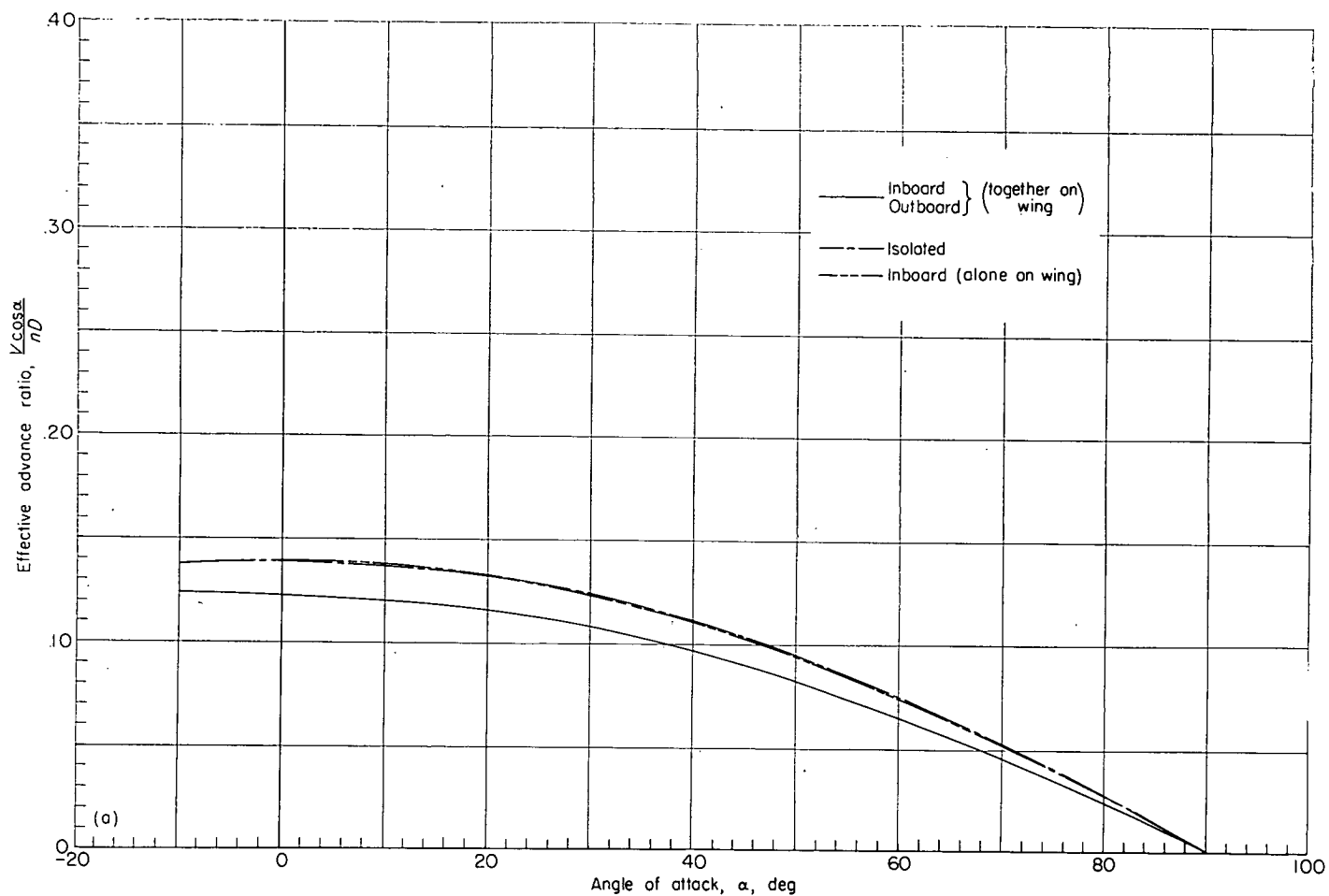
(d) $T_c'' = 0.20$; $\beta_{0.75R} = 20^\circ$.

FIGURE 9.—Continued.



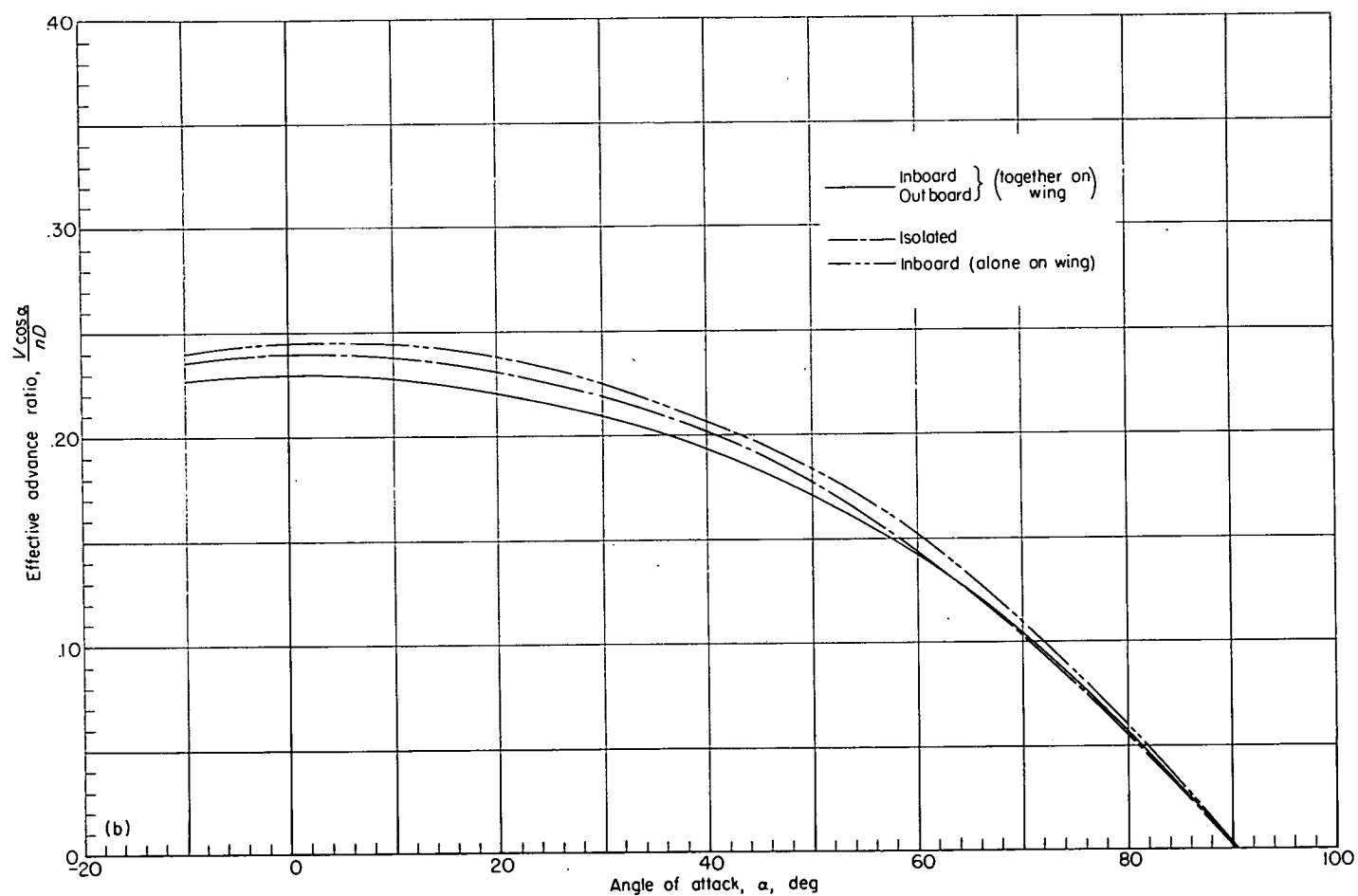
(e) $T_c'' = 0.20$; $\beta_{0.75R} = 20^\circ$.

FIGURE 9.—Concluded.



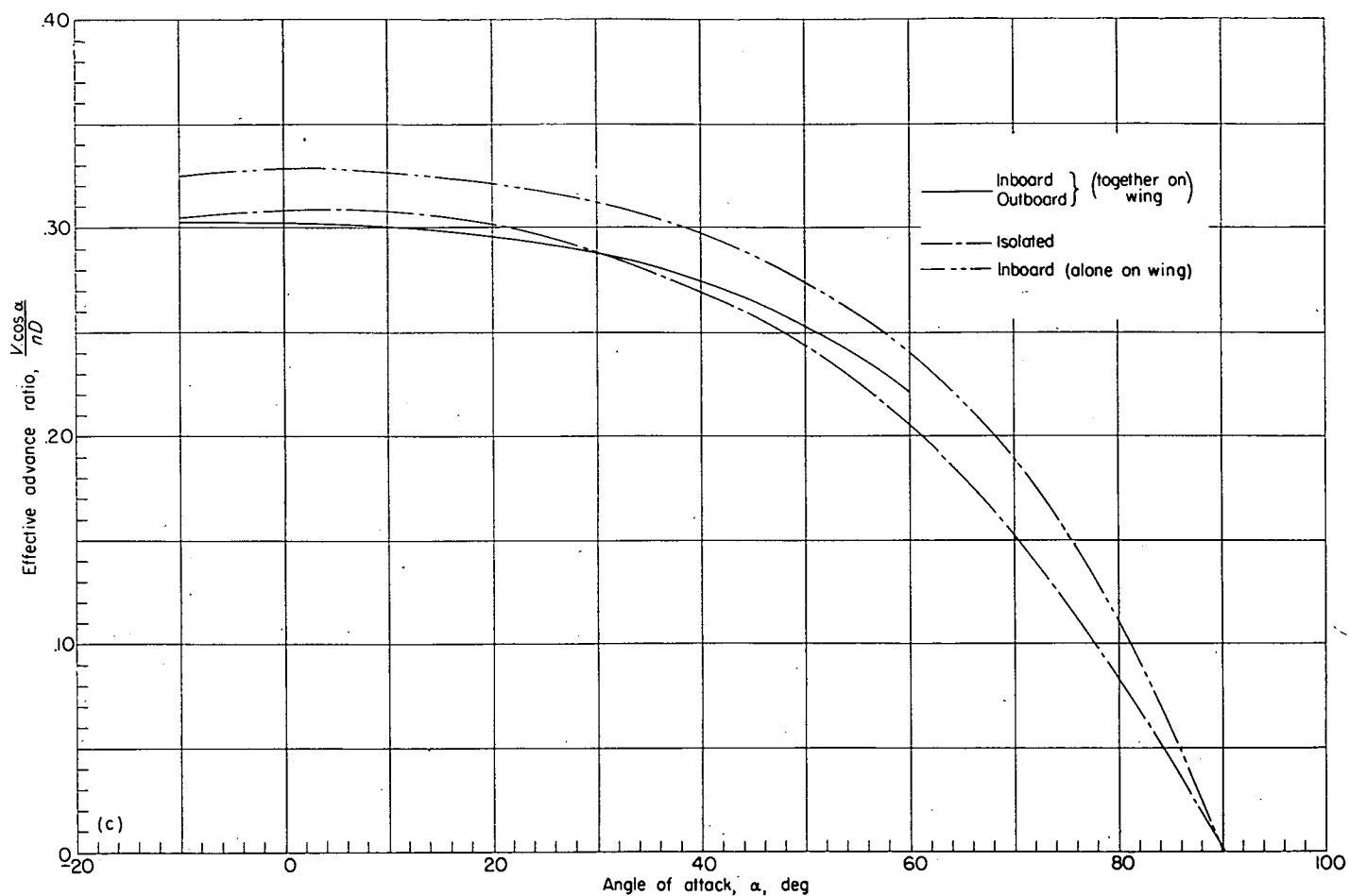
(a) $T_c'' = 0.91$; $\beta_{0.75R} = 8^\circ$.

FIGURE 10.—Comparison of advance ratios for various configurations at constant thrust through angle-of-attack range.



(b) $T_c'' = 0.71$; $\beta_{0.75R} = 8^\circ$.

FIGURE 10.—Continued.



(c) $T_c'' = 0.50$; $\beta_{0.75R} = 8^\circ$.

FIGURE 10.—Continued.

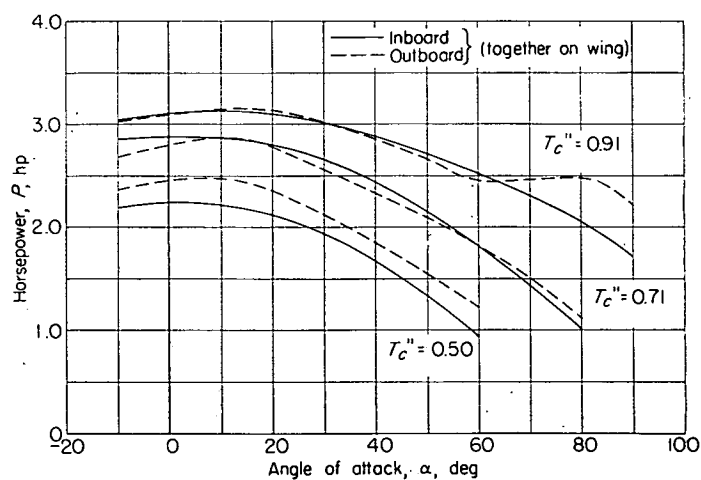
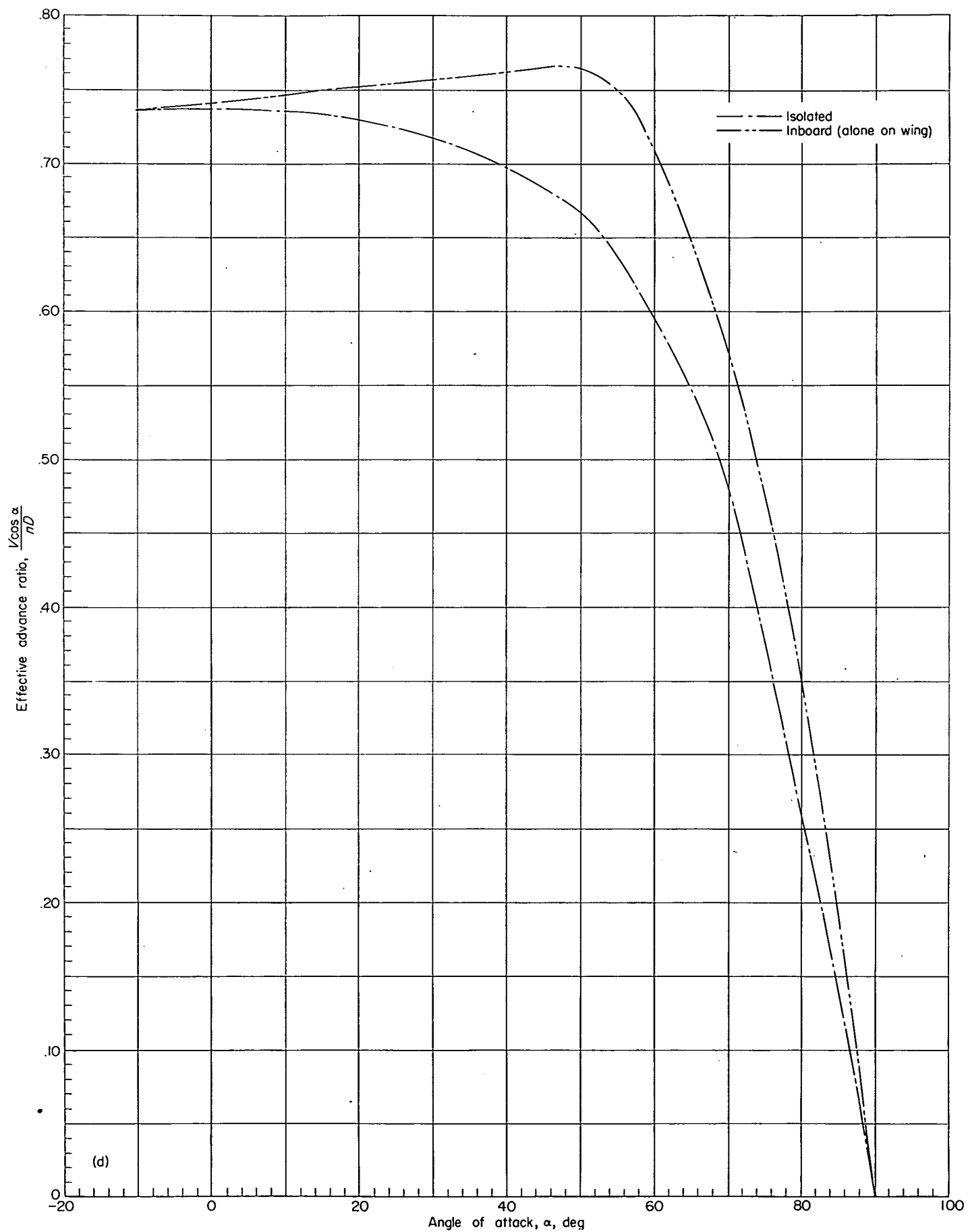


FIGURE 11.—Variation of horsepower required for constant thrust through angle-of-attack range. $\beta_{0.75R} = 8^\circ$.



(d) $T_e'' = 0.20$; $\beta_{0.75R} = 20^\circ$.

FIGURE 10.—Concluded.

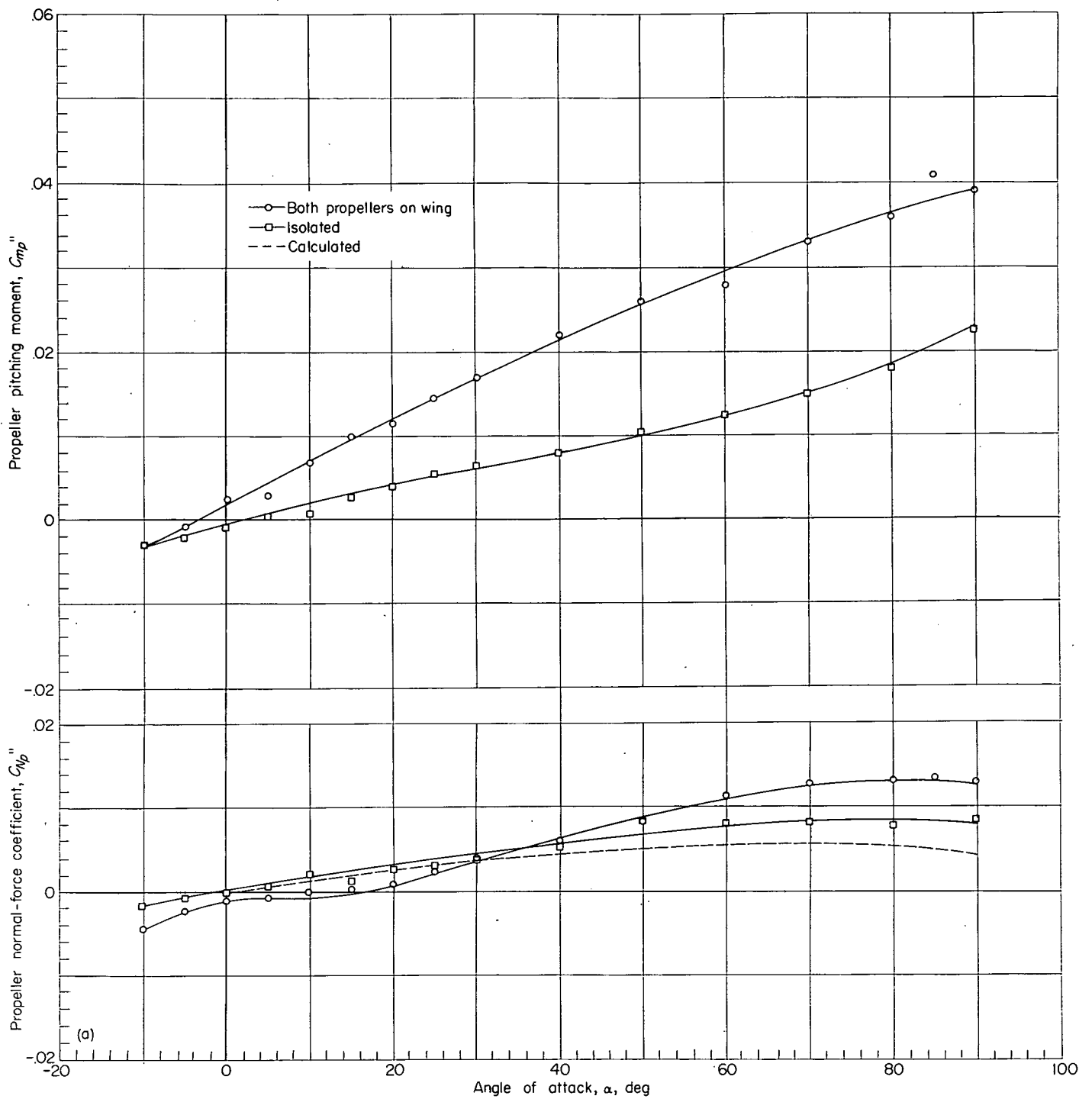


FIGURE 12.—Variation of direct pitching-moment and normal-force coefficients of the outboard propeller through angle-of-attack range.

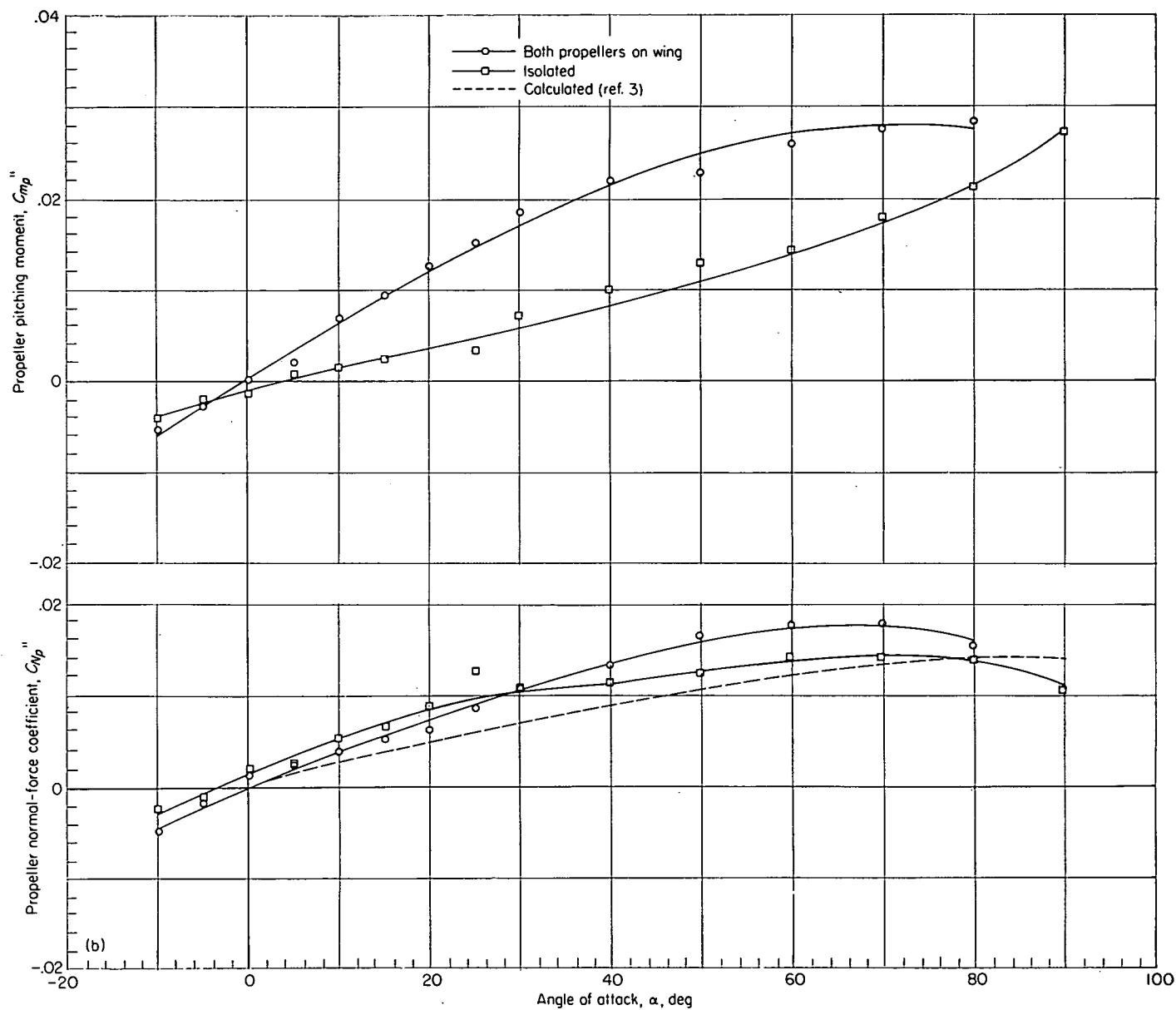
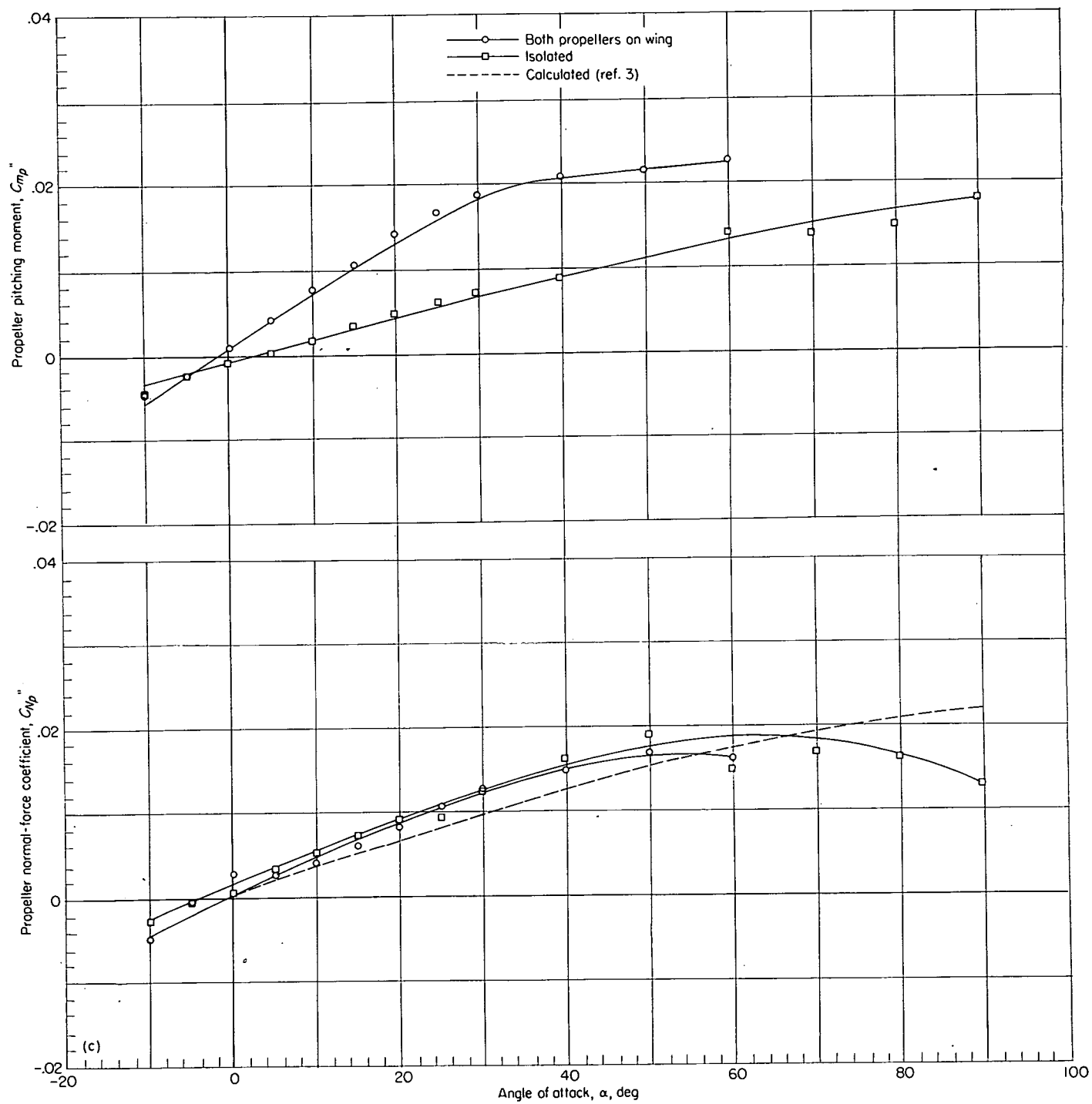
(b) $T_c'' = 0.71$.

FIGURE 12.—Continued.



(c) $T_e'' = 0.50$.

FIGURE 12.—Concluded.

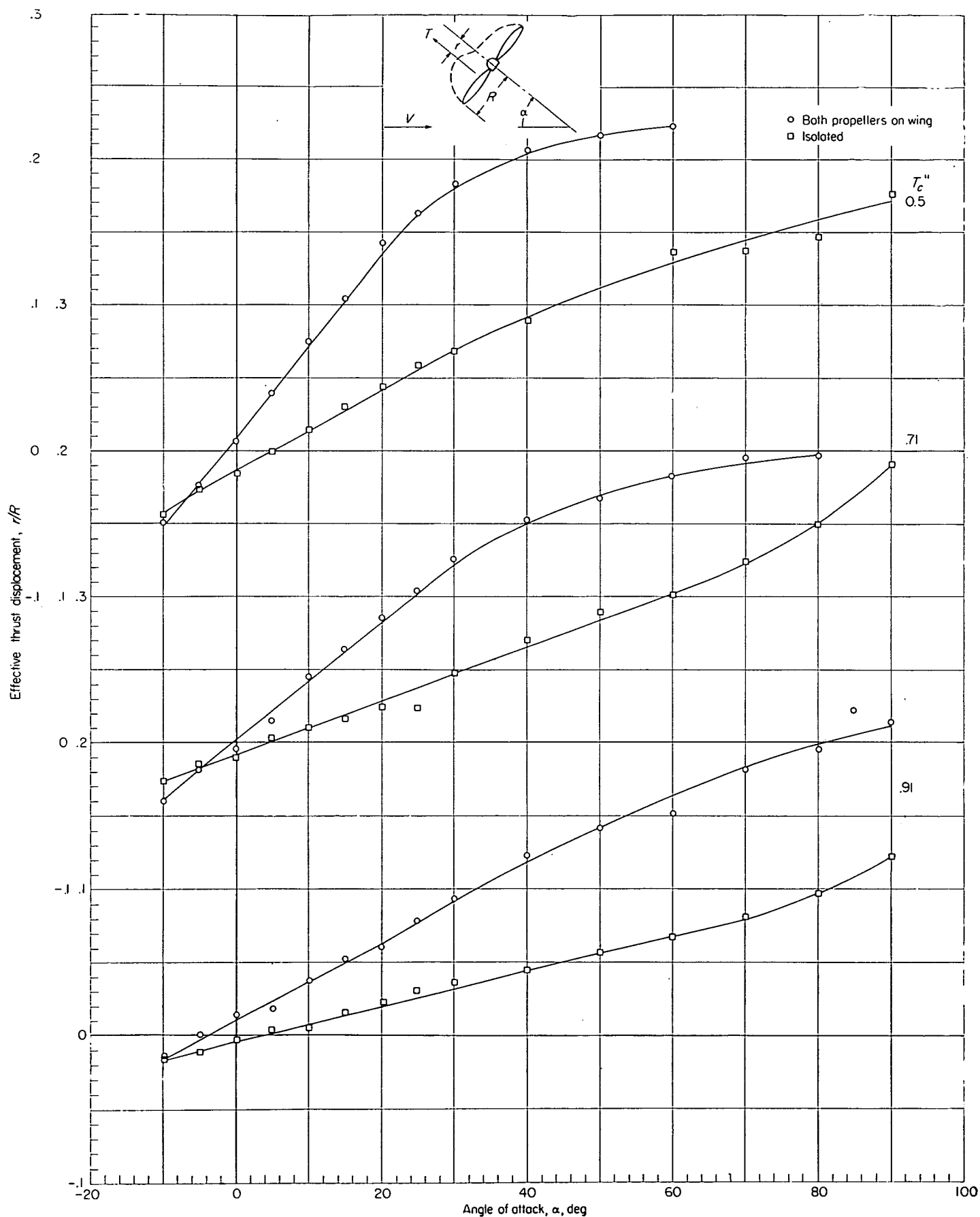


FIGURE 13.—Effect of angle of attack on effective thrust displacement from thrust axis as determined by $\frac{r}{R} = \frac{C_{m_p}'' S \bar{c}}{T_c'' \frac{\pi}{8} D^3}$ for outboard propeller.

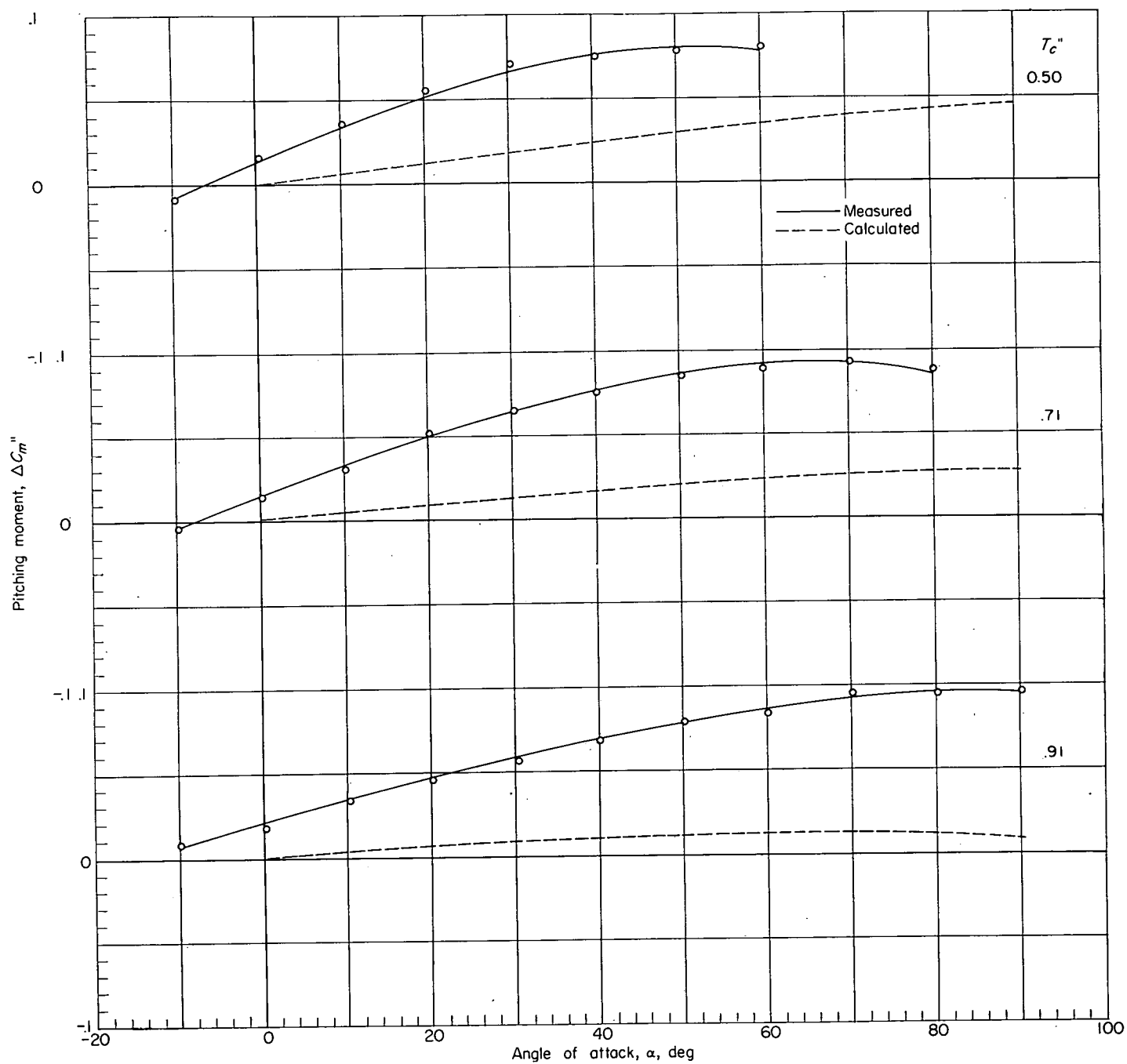


FIGURE 14.—Increment of model pitching moment due to the propellers (two propellers in operation).

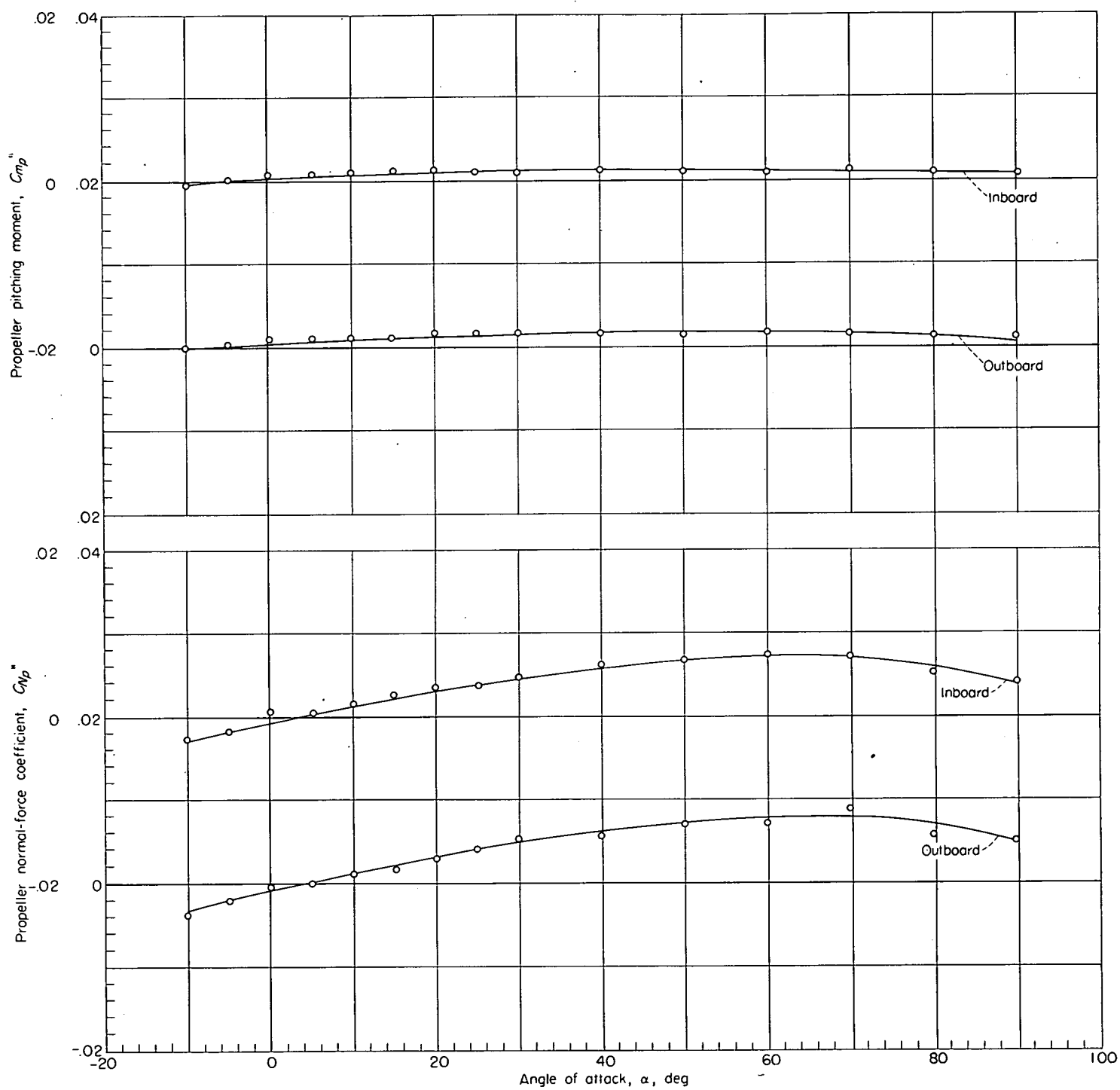


FIGURE 15.—Variation of the spinner characteristics with angle of attack. Propeller blades removed; spinner not rotating.

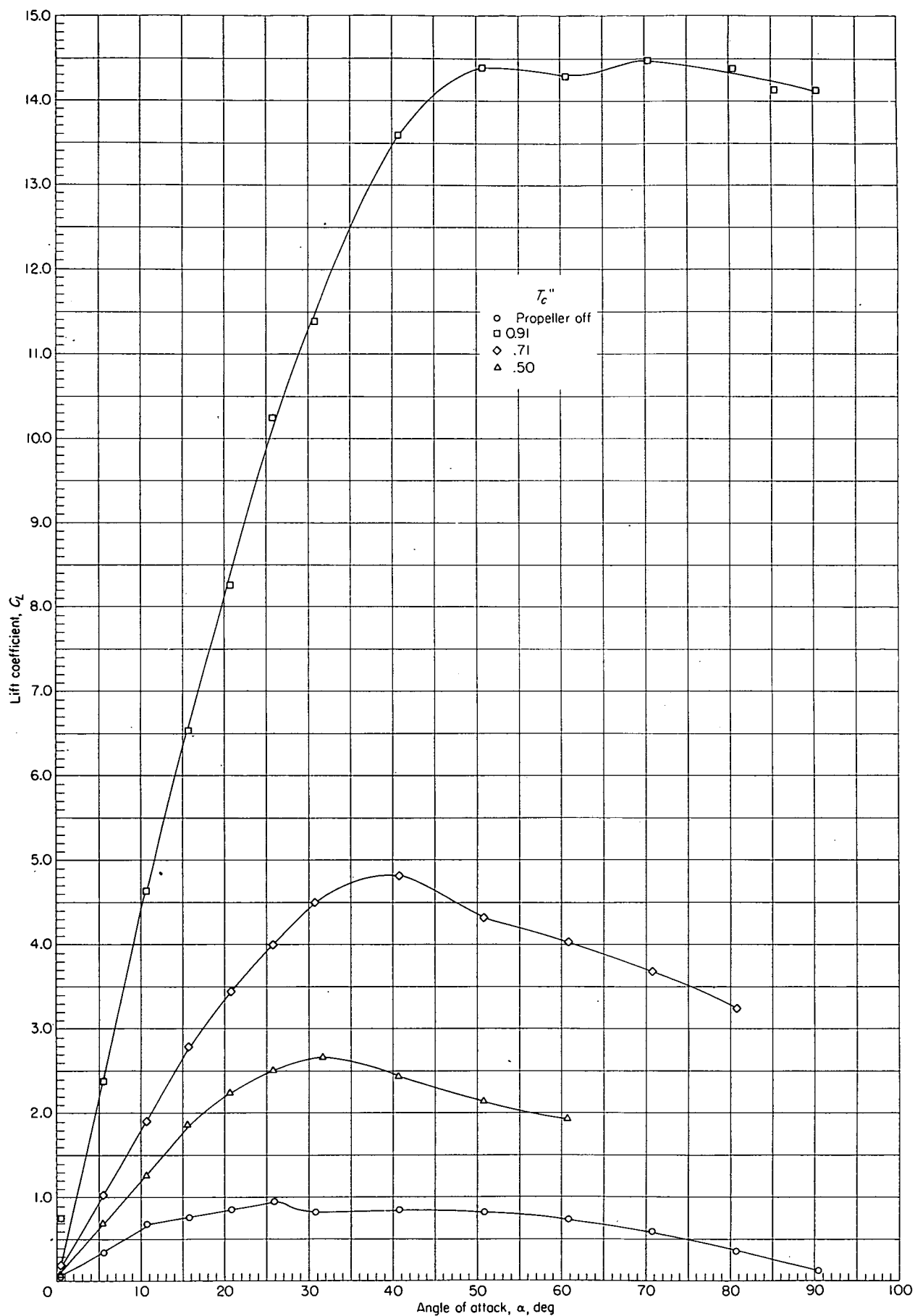
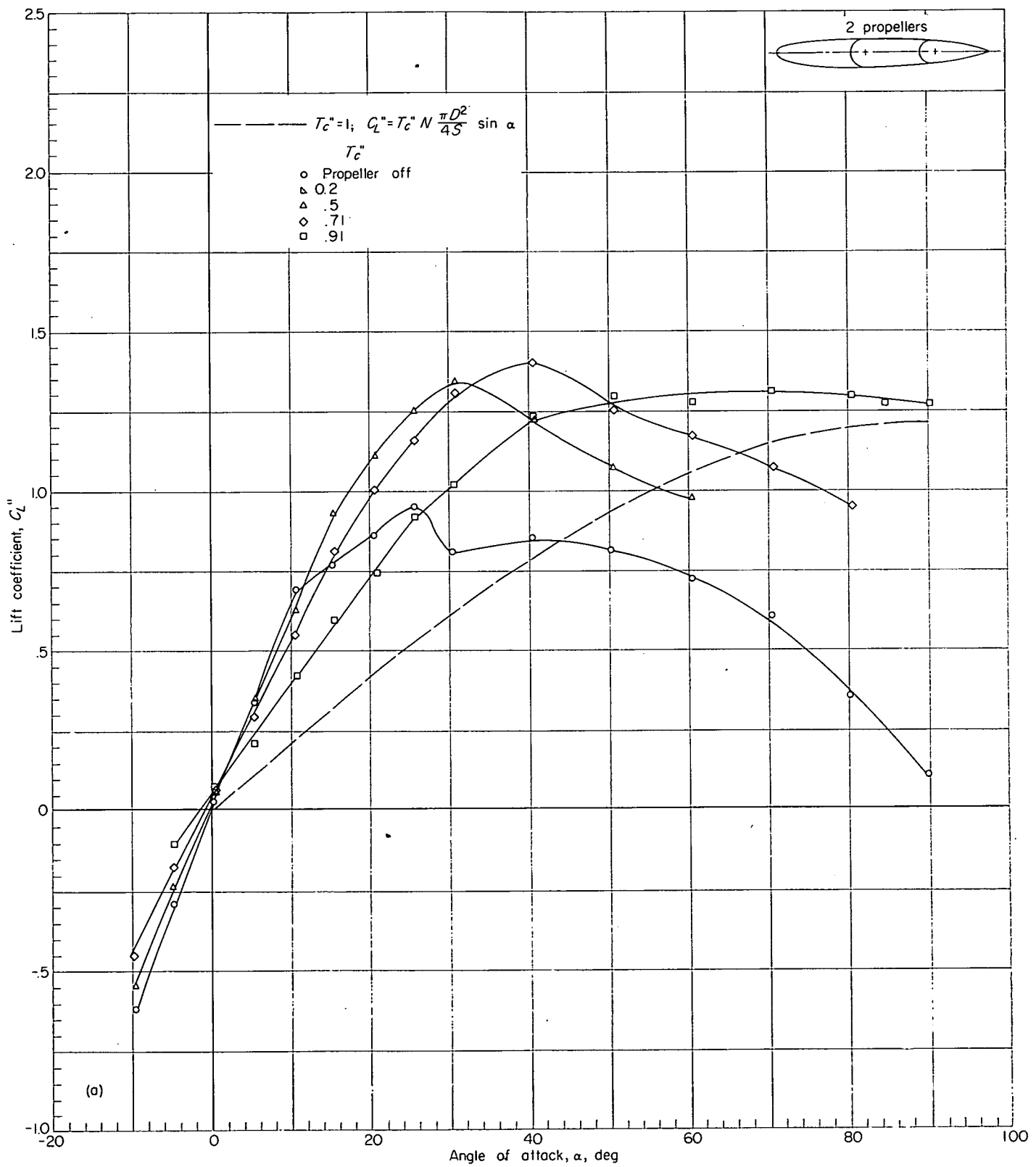
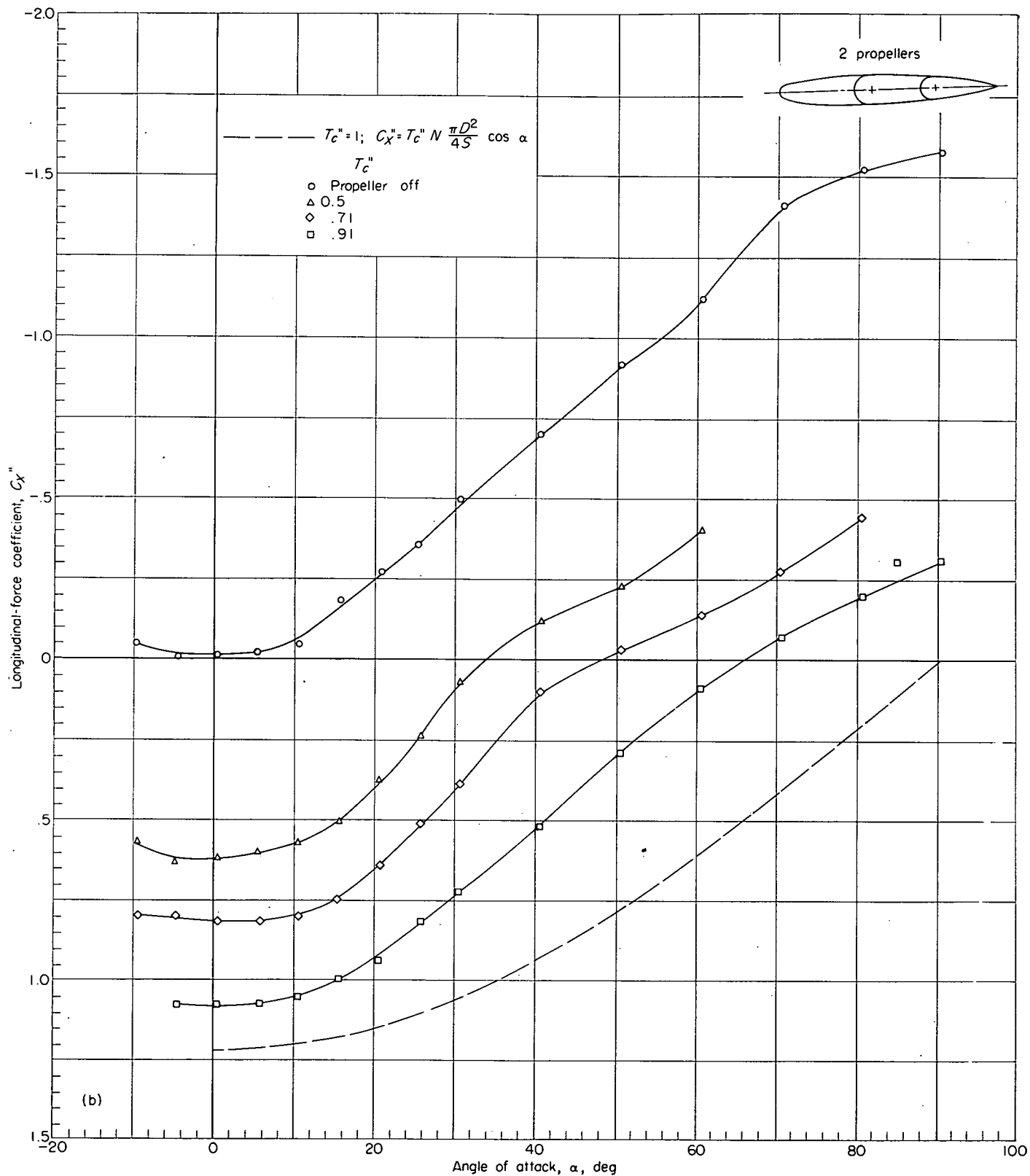


FIGURE 16.—Lift characteristics of model with various thrust coefficients. Lift coefficient based on free-stream dynamic pressure.



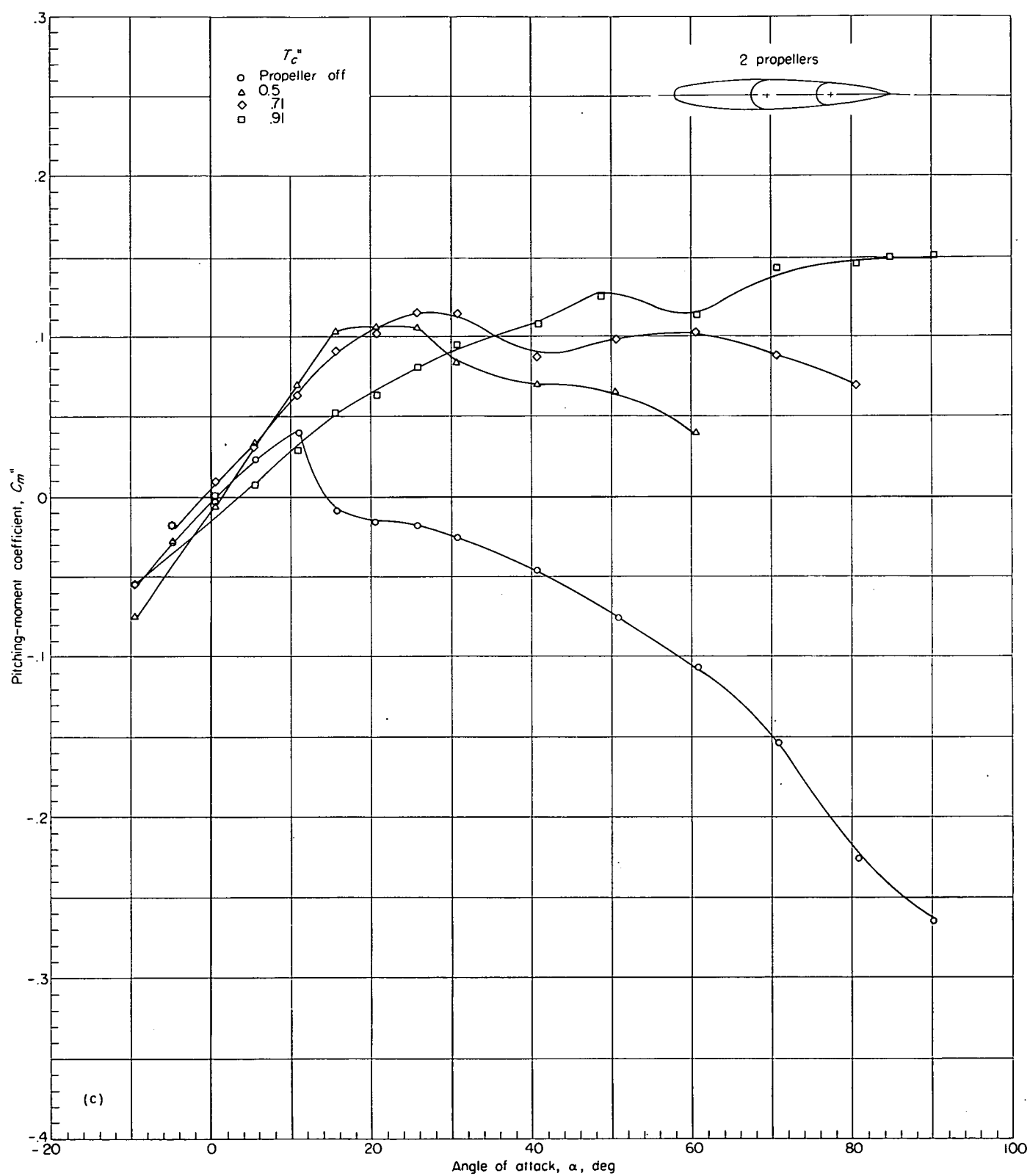
(a) Lift coefficient.

FIGURE 17.—Effect of thrust coefficient on aerodynamic characteristics of model with two propellers operating.



(b) Longitudinal-force coefficient.

FIGURE 17.—Continued.



(c) Pitching-moment coefficient.

FIGURE 17.—Concluded.

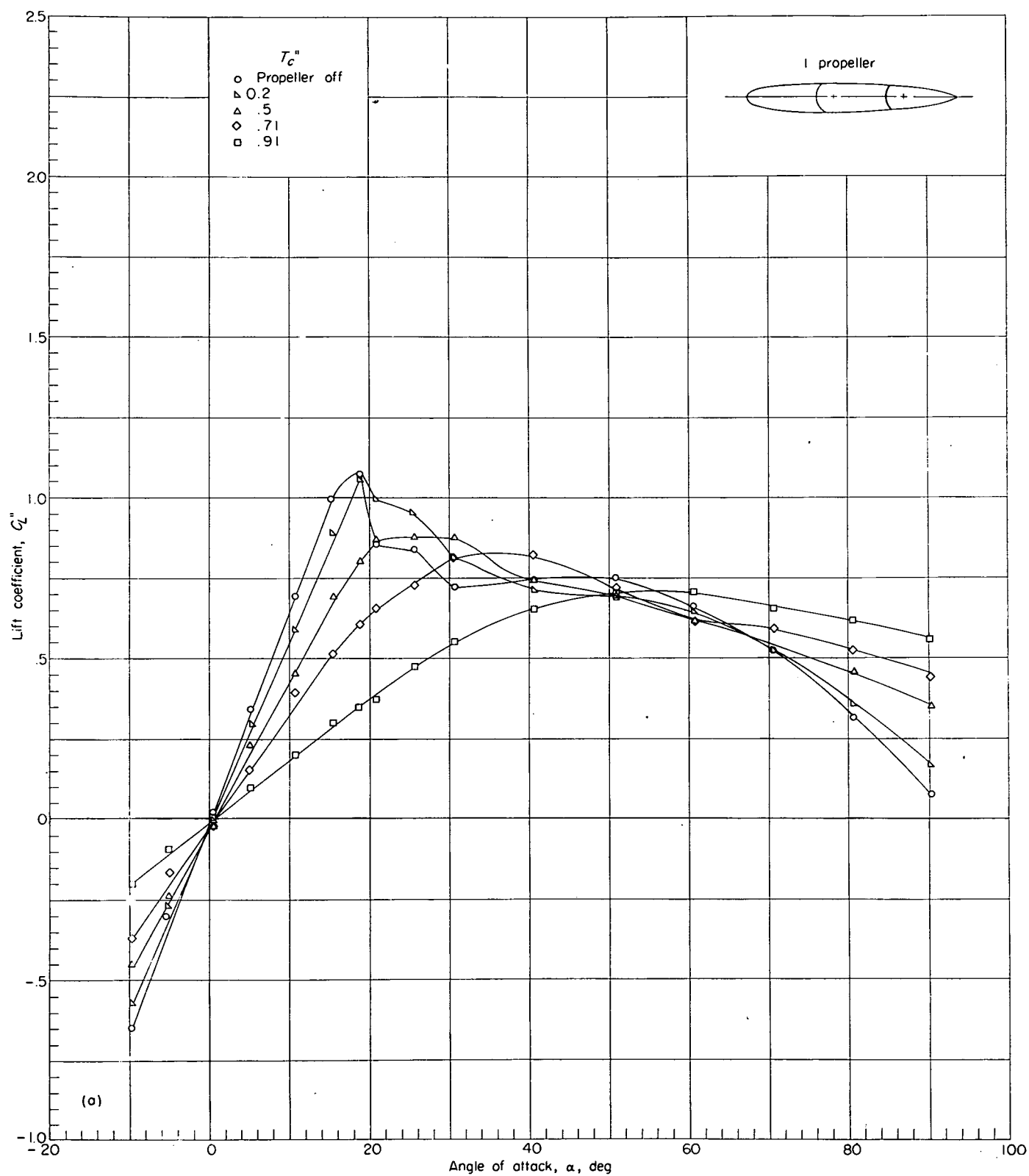
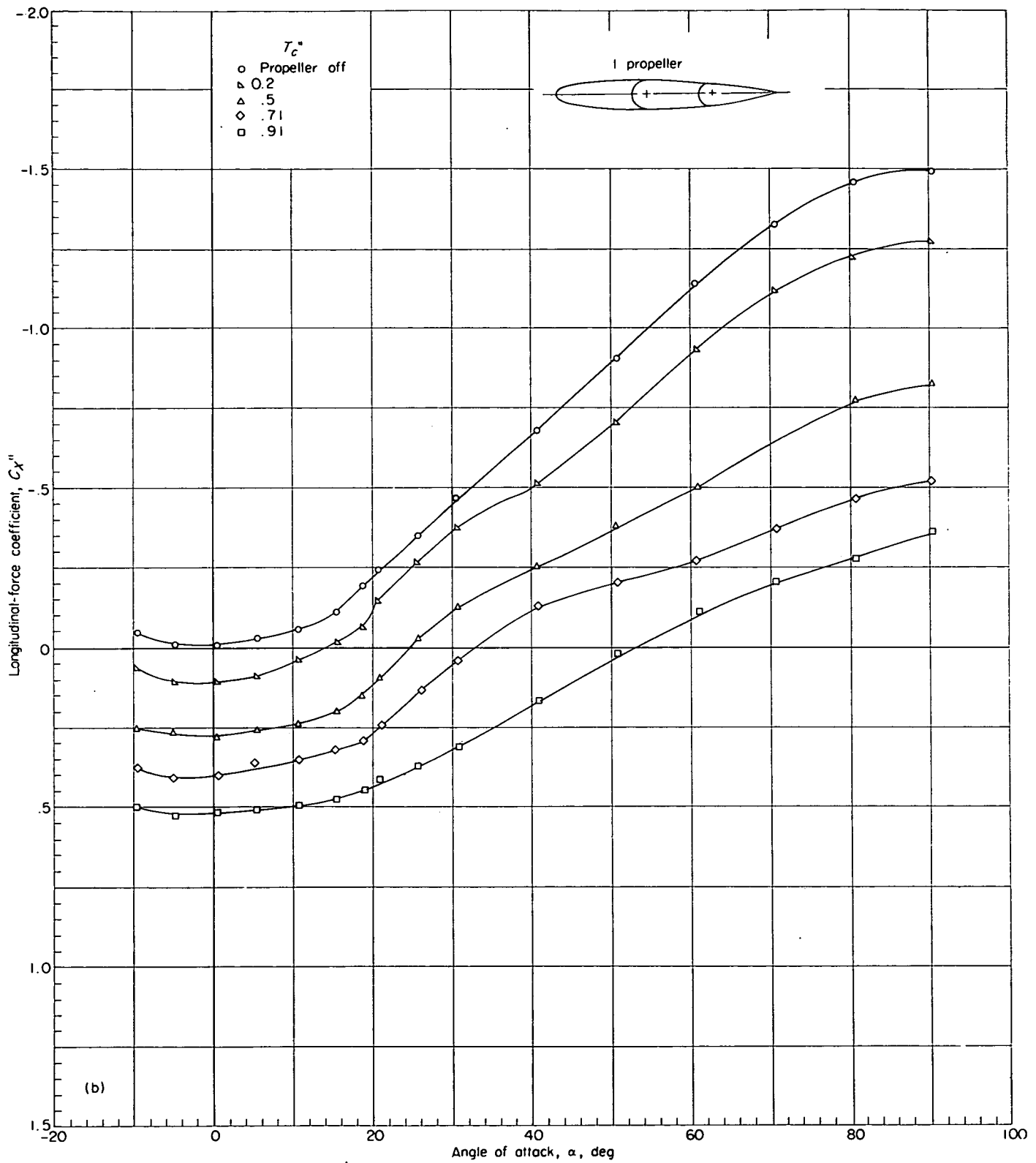
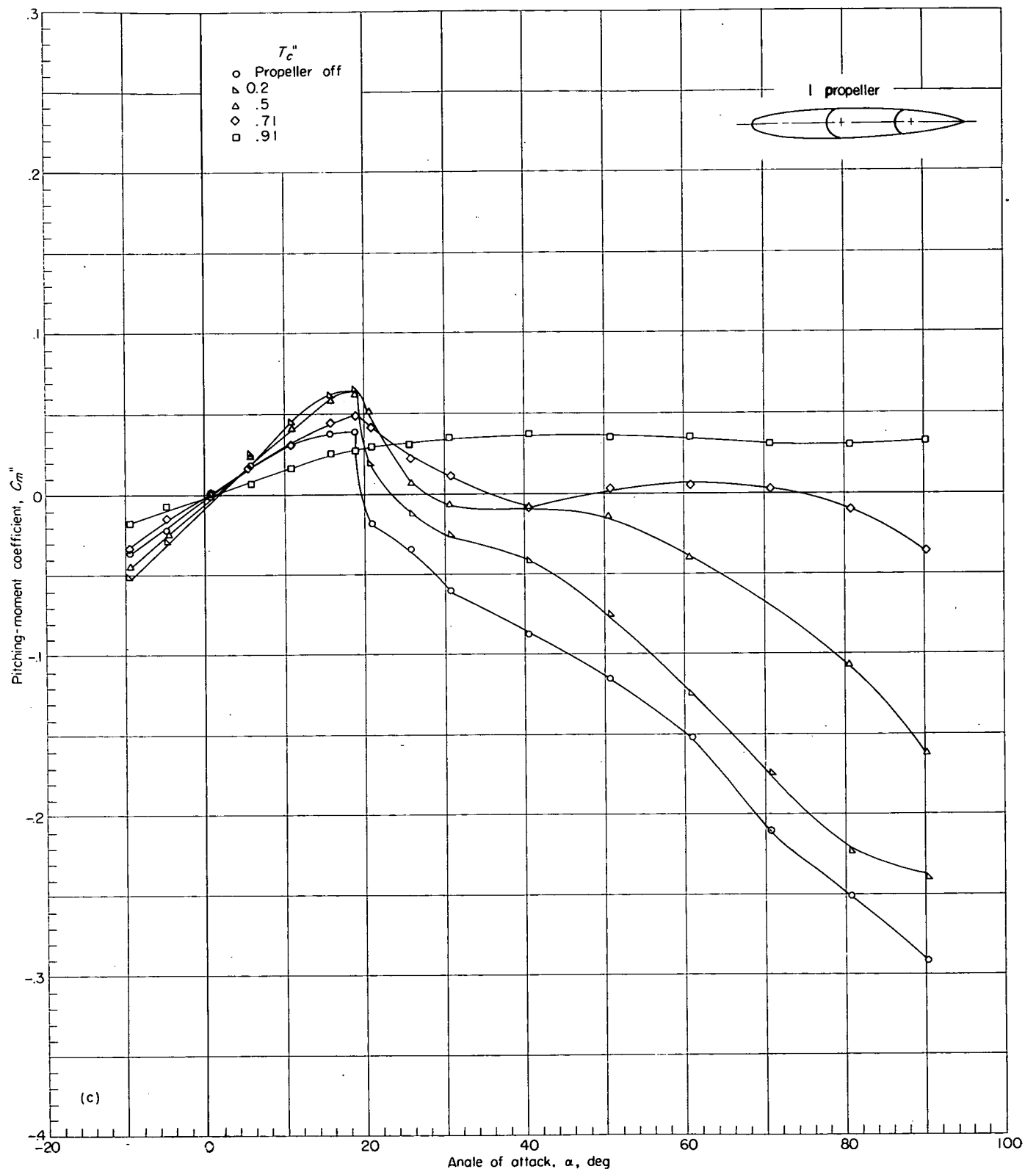


FIGURE 18.—Effect of thrust coefficient on aerodynamic characteristics of model with inboard propeller only.



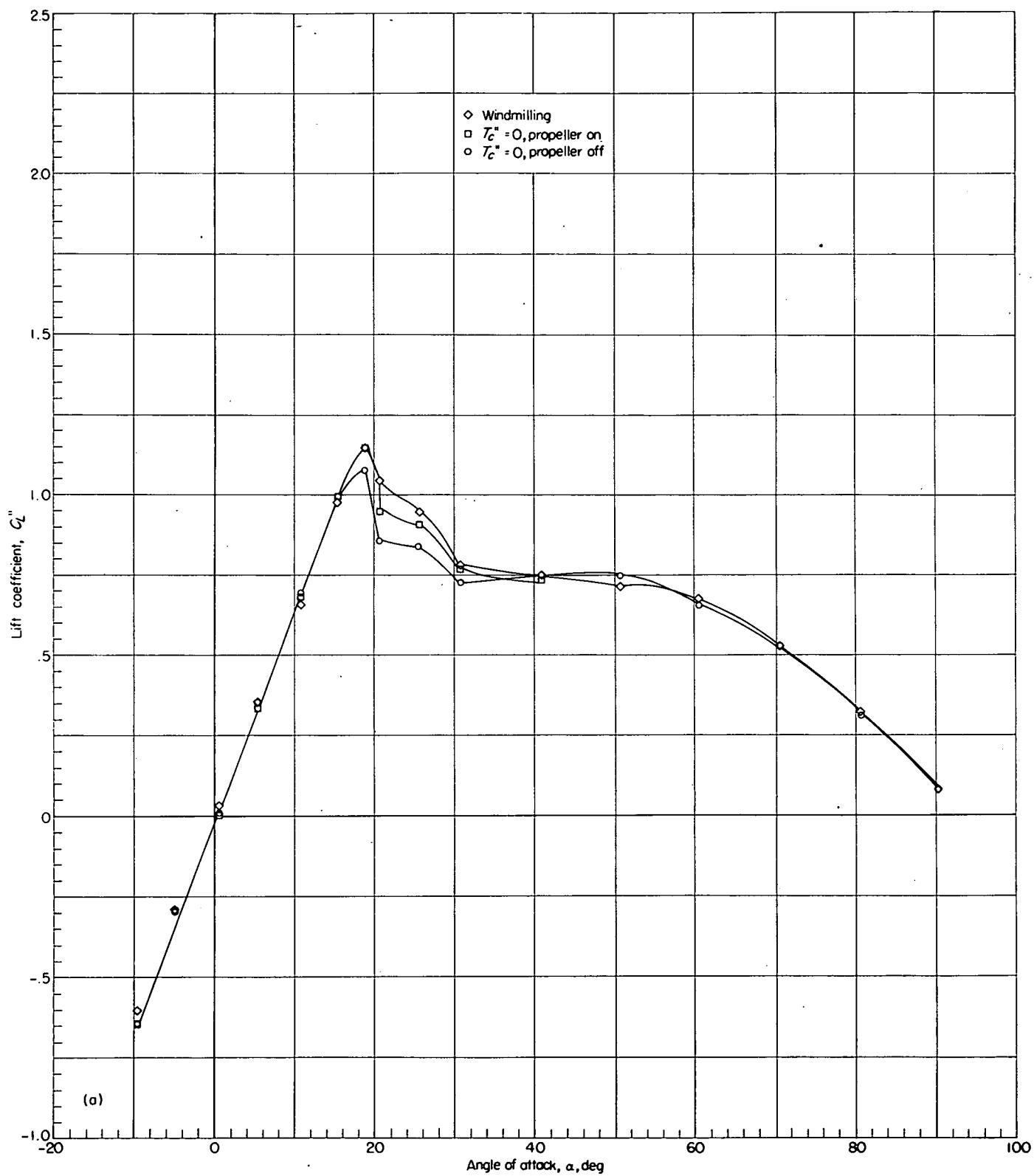
(b) Longitudinal-force coefficient.

FIGURE 18.—Continued.



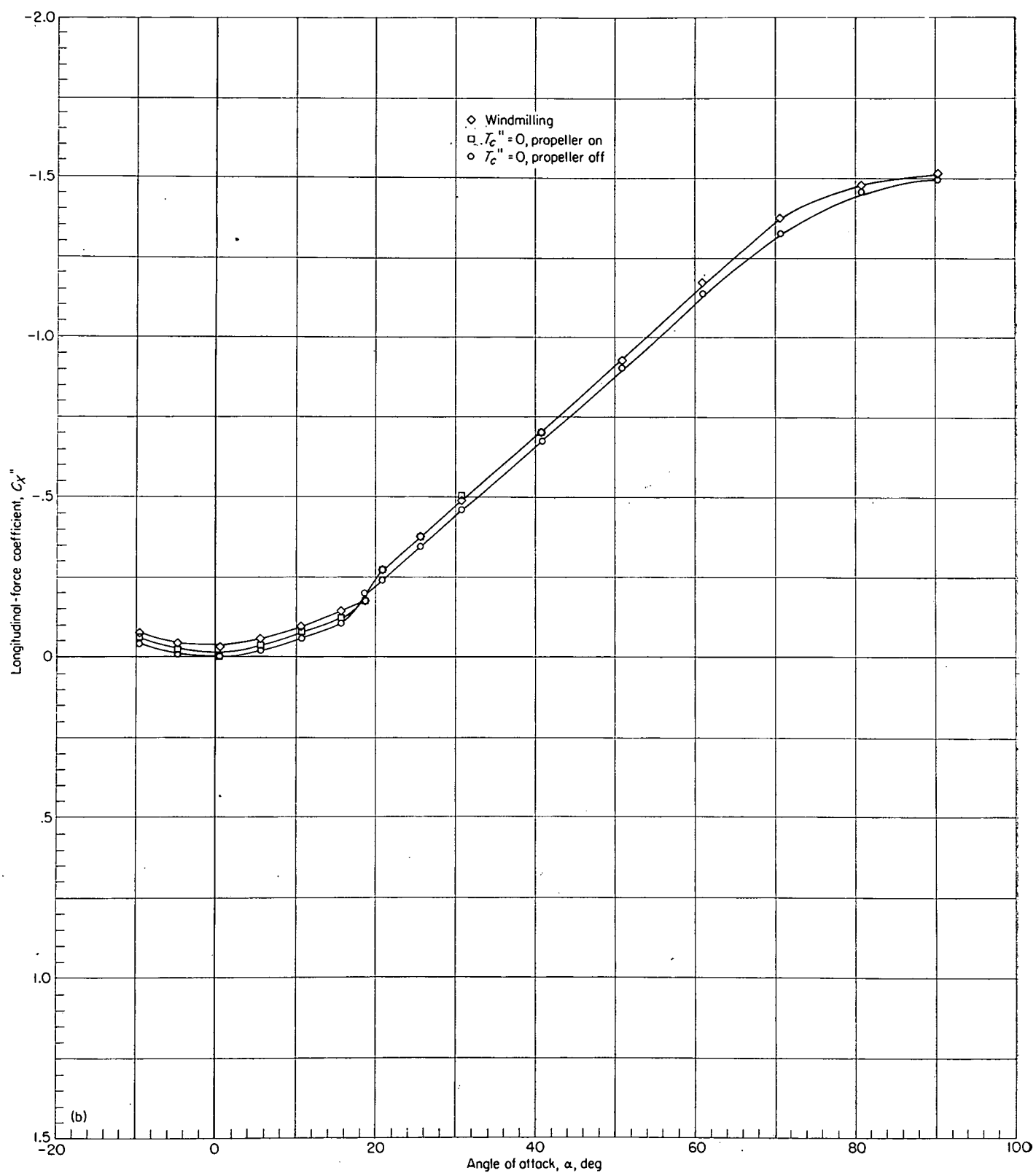
(c) Pitching-moment coefficient.

FIGURE 18.—Concluded.



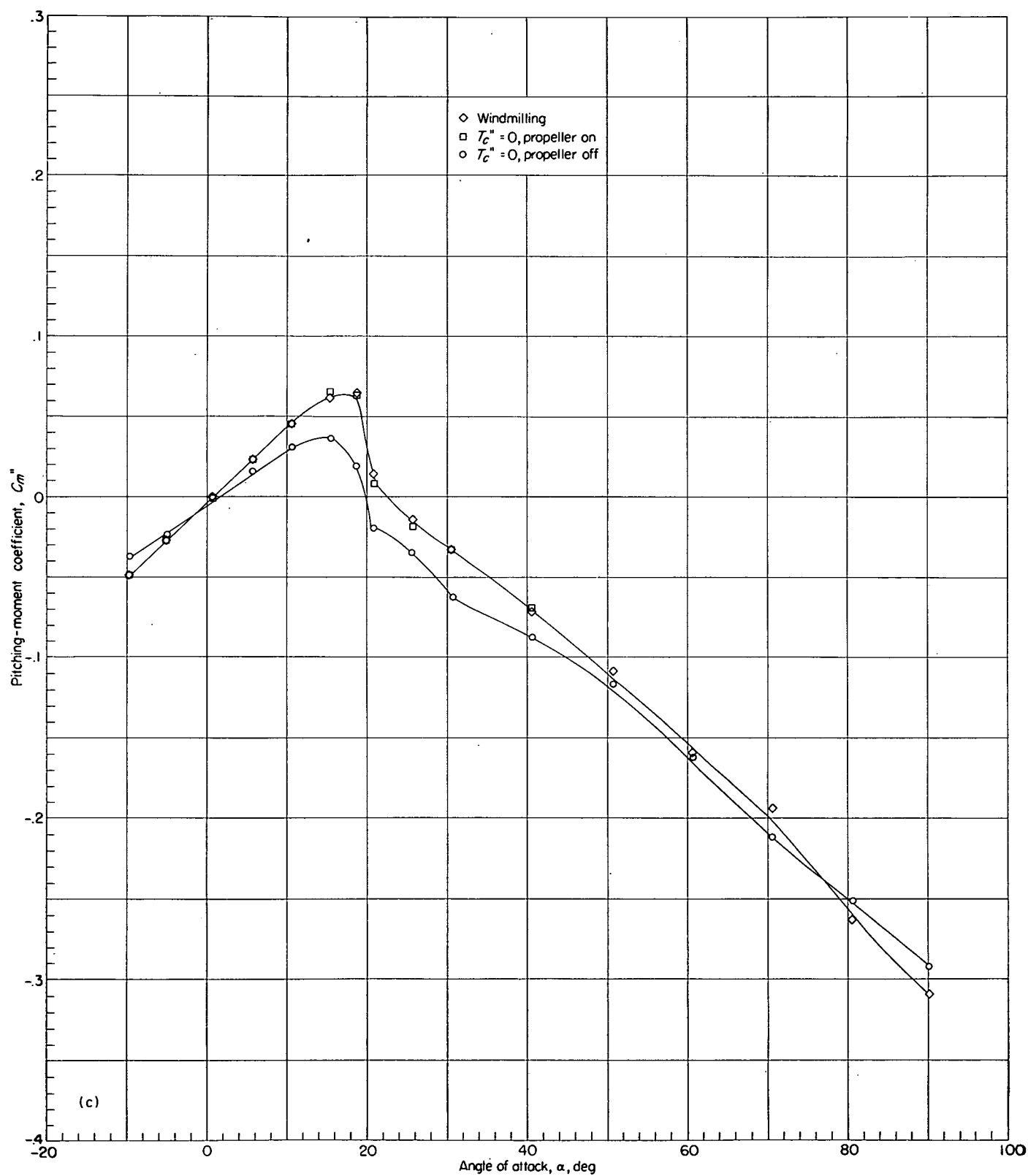
(a) Lift coefficient.

FIGURE 19.—Effect of propeller on aerodynamic characteristics of the model. Propeller windmilling, propeller at $T_c'' = 0$, and propeller-removed conditions.



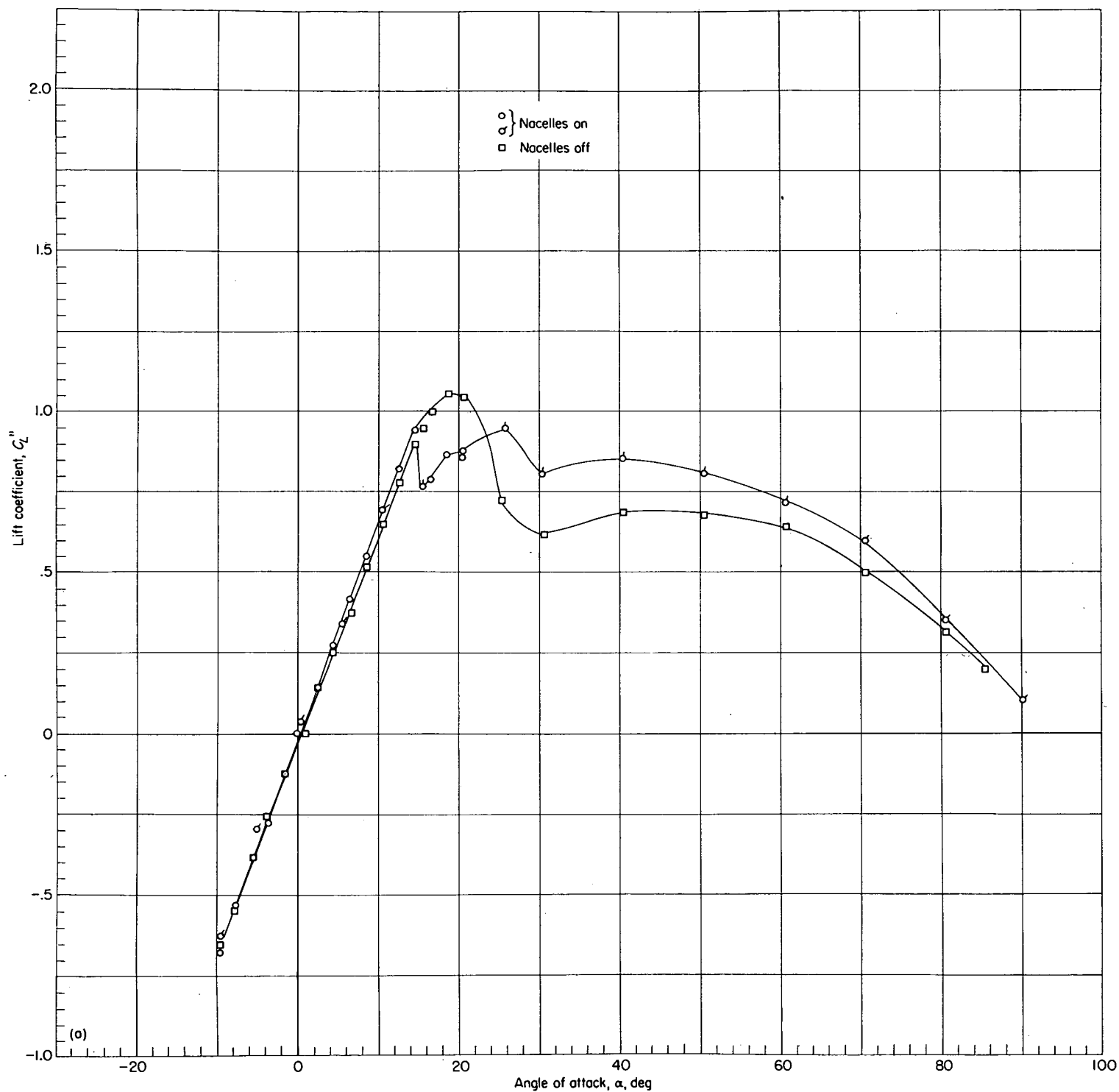
(b) Longitudinal-force coefficient.

FIGURE 19.—Continued.



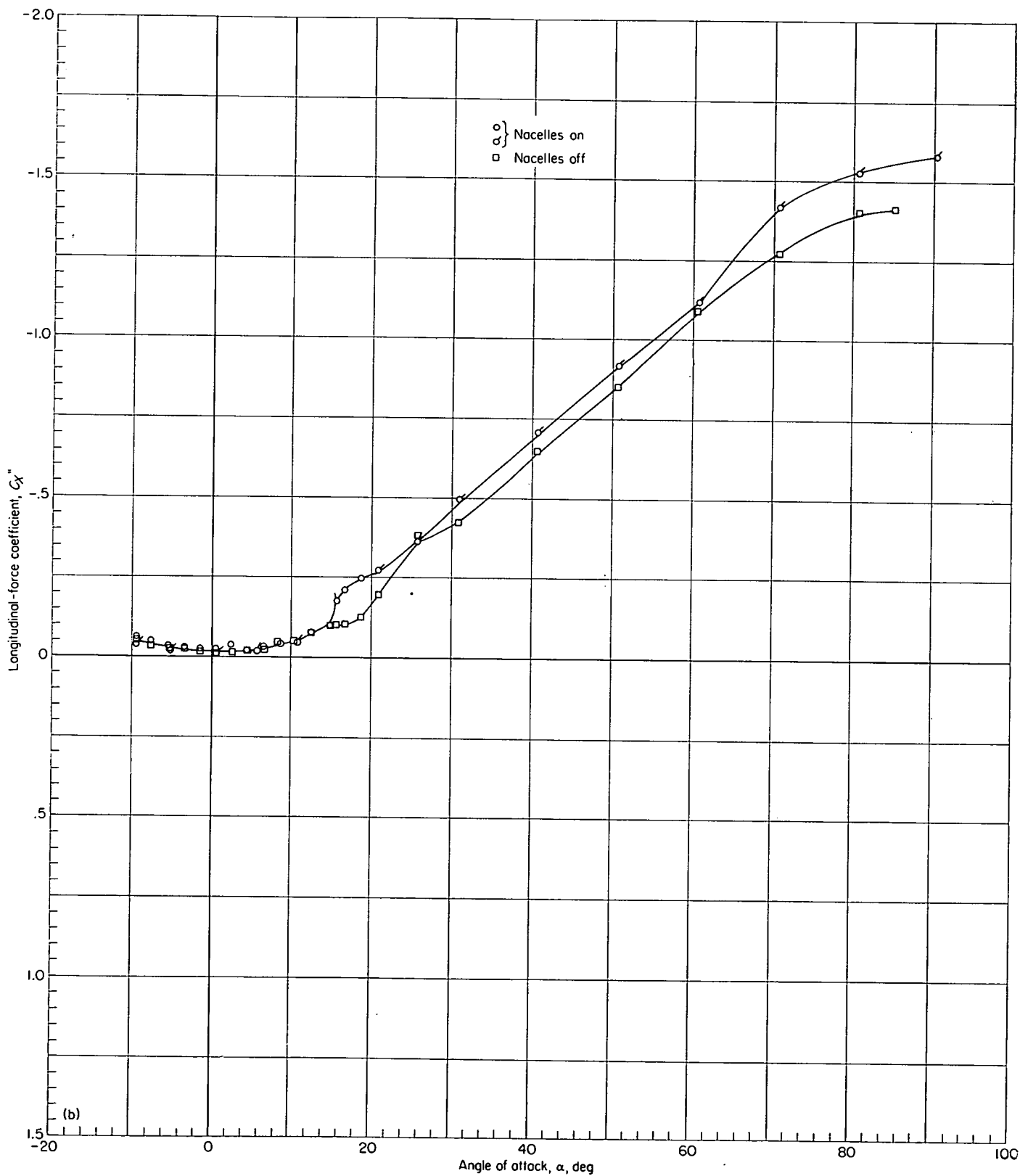
(c) Pitching-moment coefficient.

FIGURE 19.—Concluded.



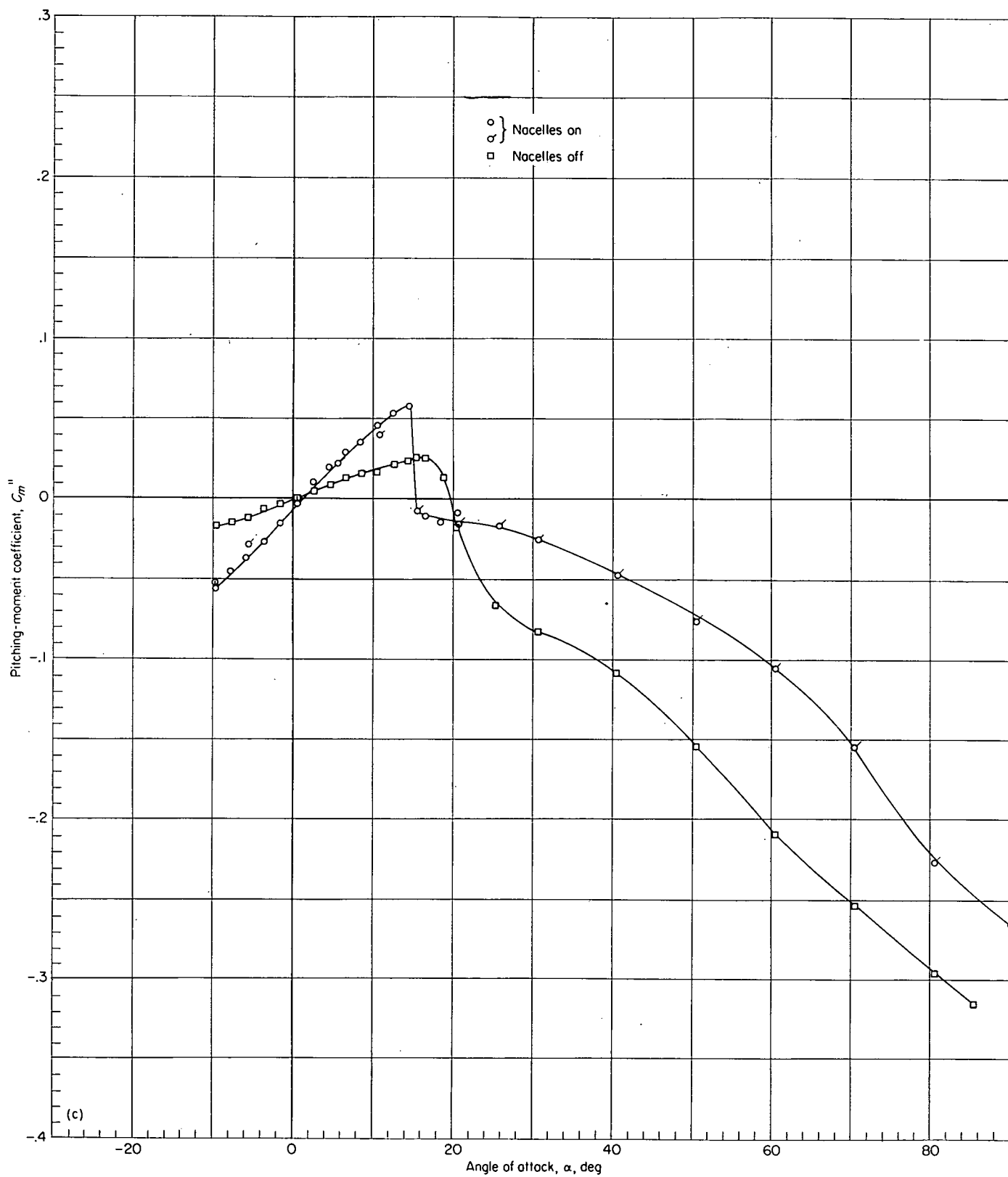
(a) Lift coefficient.

FIGURE 20.—Effect of nacelles on aerodynamic characteristics of the model with propellers off. (Flagged symbols indicate check tests.)



(b) Longitudinal-force coefficient.

FIGURE 20.—Continued.



(c) Pitching-moment coefficient.

FIGURE 20.—Concluded.

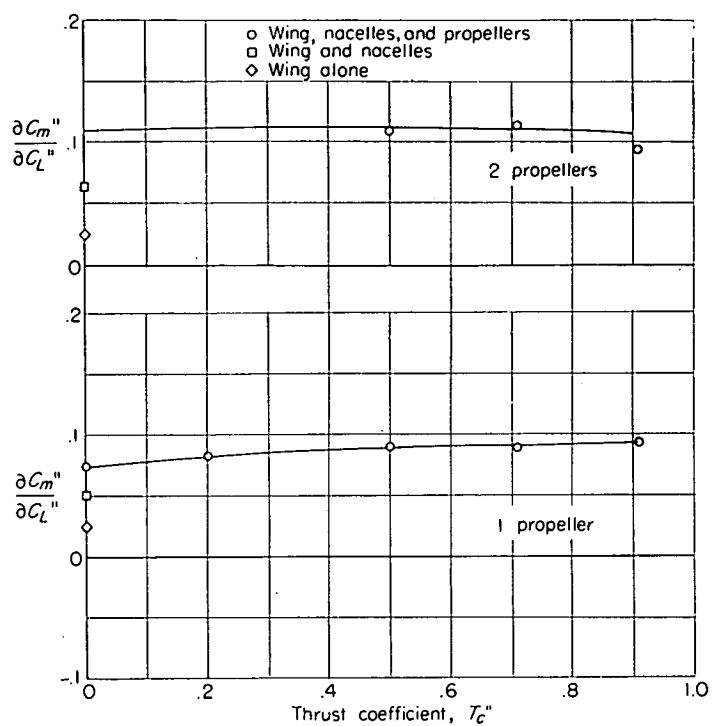


FIGURE 21.—Variation with thrust coefficient of longitudinal stability parameter $\partial C_m''/\partial C_L''$ near $\alpha=0^\circ$.

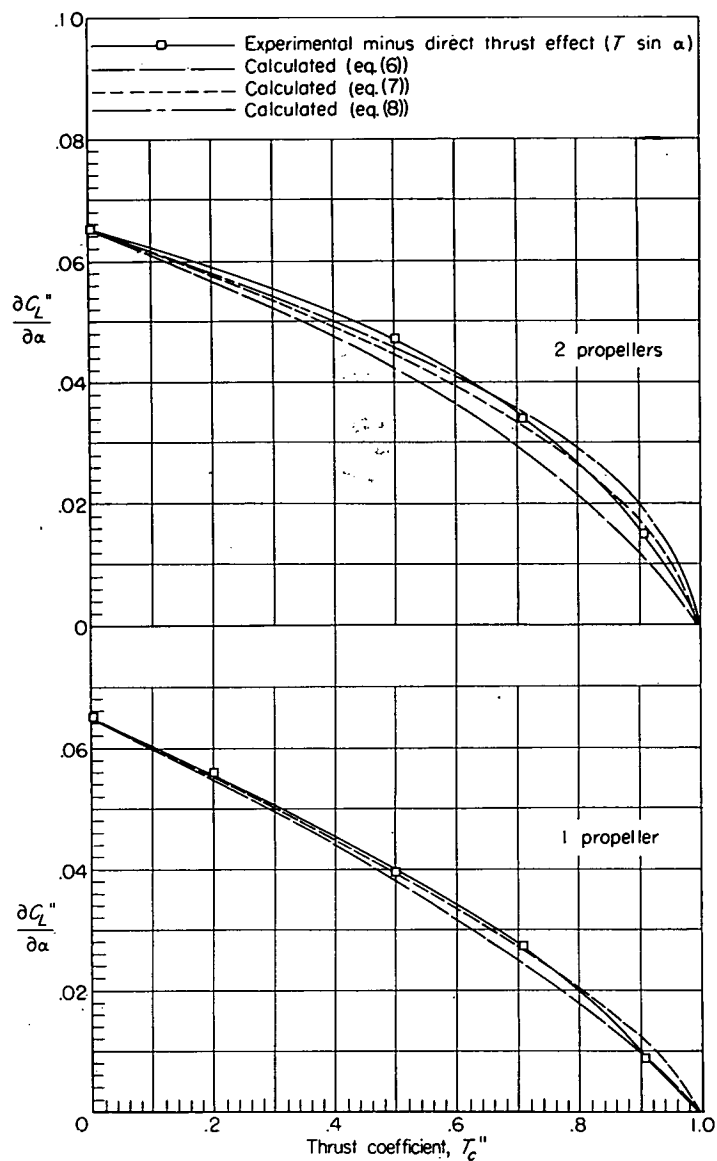


FIGURE 22.—Variation of $\partial C_L''/\partial \alpha$ with thrust coefficient near $\alpha=0^\circ$.

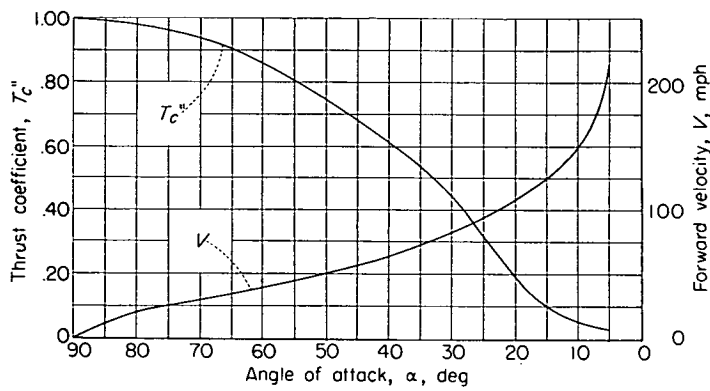


FIGURE 23.—Variation with angle of attack of thrust coefficient required and velocity attained in level flight by assumed airplane. $W/S=40$ pounds per square foot.

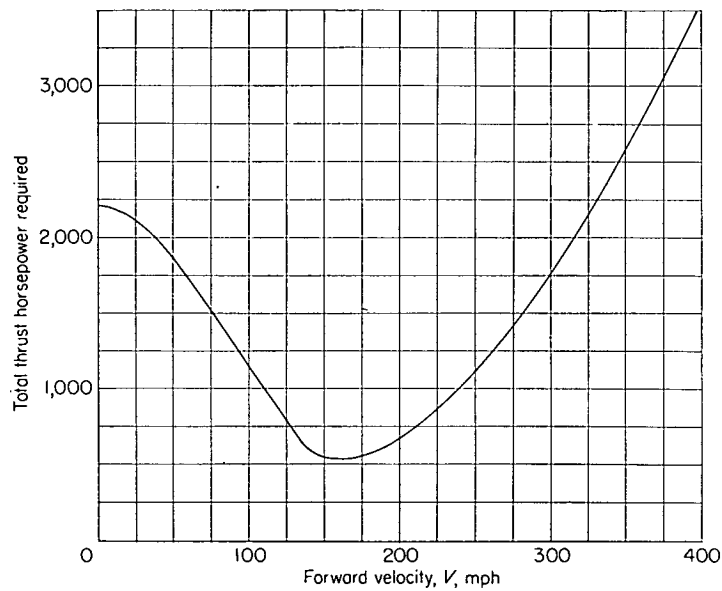
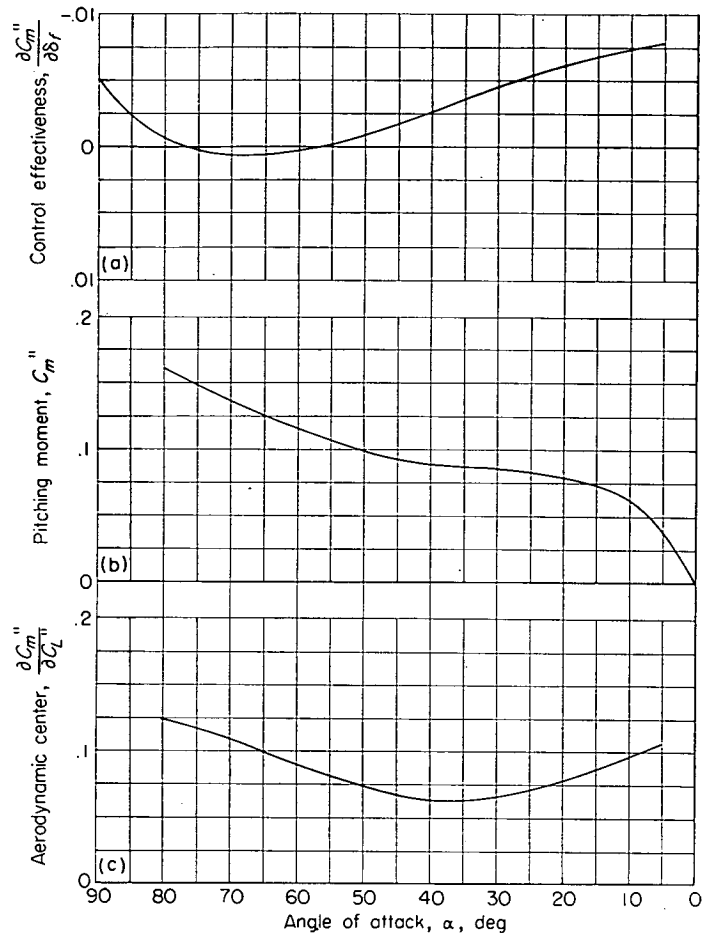


FIGURE 24.—Variation of thrust horsepower required for level flight for assumed airplane.



- (a) 30% full-span-flap effectiveness.
- (b) Untrimmed pitching moment.
- (c) Aerodynamic-center location.

FIGURE 25.—Pitching characteristics of assumed airplane through angle-of-attack range.

REPORT 1264

A THERMAL EQUATION FOR FLAME QUENCHING¹

By A. E. POTTER, Jr., and A. L. BERLAD

SUMMARY

An approximate thermal equation was derived for quenching distance based on a previously proposed diffusional treatment. The quenching distance was expressed in terms of the thermal conductivity, the fuel mole fraction, the heat capacity, the rate of the rate-controlling chemical reaction, a constant that depends on the geometry of the quenching surface, and one empirical constant.

The effect of pressure on quenching distance was shown to be inversely proportional to the pressure dependence of the flame reaction, with a small correction necessitated by the effect of pressure on flame temperature.

The equation was used with the Semenov equation for burning velocity to show that the quenching distance was inversely proportional to burning velocity and pressure at any given initial temperature and equivalence ratio.

In order to use the equation with experimental data, the rate-controlling reaction must be specified. Two choices were made: (1) the reaction between active particles and fuel (corresponding to the diffusional equation), and (2) the reaction between oxygen and fuel.

The two equations, one based on the active-particle—fuel reaction, the other based on the oxygen-fuel reaction, were tested using published data for the quenching of propane-oxygen-nitrogen flames. The data selected included the effect on quenching distance of oxygen-nitrogen ratio, propane concentration, and initial mixture temperature and pressure. A correlation of these data was obtained using each of the two equations, although both possessed shortcomings. The equation using the active-particle—fuel reaction did not correlate data for all rich mixtures; the equation using the oxygen-fuel reaction, while correlating data for both rich and lean mixtures, showed a larger deviation from the predicted linear relation than the other equation.

INTRODUCTION

The process of flame quenching is of interest, since it may be related to other combustion phenomena of engineering importance, such as flame stabilization, flammability limits, and the general behavior of flames near cold walls. Flame-quenching processes become especially important in turbojet combustion systems when operation at low pressure (i. e.,

high altitudes) is considered. Flame quenching is usually studied experimentally in terms of the quenching distance, which is defined as the minimum channel size that will allow a given flame to propagate. Most of the available quenching data have been obtained either by (1) observation of the minimum tube diameter or rectangular slot width that will allow a flame to flash back, or by (2) determination of the minimum distance between plane-parallel plates that will allow a flame to propagate from a spark of minimum ignition energy.

A rigorous theoretical treatment of the quenching process appears to be a most difficult task (refs. 1 and 2). Consequently, present theoretical treatments of quenching are necessarily approximate and seek primarily to correlate the quenching process with the variables that affect it, such as pressure, temperature, fuel type and concentration, inert-gas concentration, and quenching-surface geometry.

Approximate treatments of quenching have been based either on a thermal or a diffusional mechanism for the process (refs. 3 and 4). Such apparently different outlooks yield results consistent with experimental data because the equations for heat and mass transfer are formally identical, and because the thermodiffusivity and the molecular diffusivity are numerically nearly equal (ref. 5). Thus, each purely thermal approach to a combustion process has a diffusional analog.

A quenching-distance equation that successfully correlates lean quenching data (refs. 4, 6, and 7) is the diffusional equation given in reference 4. Unfortunately, the use of this equation in its present form is limited to stoichiometric or lean mixtures. The source of this difficulty appears to be the choice of the reaction kinetics.

Essentially, the objective of this paper is to extend, if possible, the useful range of the quenching concepts of reference 4 to include hydrocarbon-rich mixtures. Because of the similarities between heat and mass flow, it is to be expected that a thermal analog equation can be derived that will correlate data equally as well as the diffusional equation of reference 4. It is felt that such an alternate thermal equation is more susceptible to changes in the reaction kinetics than the original diffusional model. The result of such changes is an extension of the useful range of fuels and oxidants that may be treated.

¹ Supersedes NACA TN 3398, "A Thermal Equation for Flame Quenching," by A. E. Potter, Jr., and A. L. Berlاد, 1955.

This report contains the derivation of a thermal quenching equation in which the rate-controlling reaction is not specified. Two possible rate-controlling reactions are postulated, and the resulting two quenching equations are tested using published quenching data. It is shown that, if the oxygen-fuel reaction is assumed to be rate-controlling, quenching data are satisfactorily correlated for both rich and lean propane-oxygen-nitrogen flames. The pressure dependence of the quenching distance and the relation of quenching distance to burning velocity are also discussed.

THEORY

It is possible to obtain the thermal equation directly from the diffusional equation (if the initial assumption is slightly altered), but it is felt that the derivation presented below is more understandable and allows the assumptions involved to be clearly seen.

For a quenching equation, an initial postulate concerning the conditions under which a flame can exist inside a tube is necessary. A reasonable postulate is as follows: If the heat lost by the flame to the tube walls exceeds a critical value, the flame will be quenched. Since a definite amount of heat is produced in a given flame, an equivalent statement is that, in order for a flame to exist, the heat retained by it must be greater than a critical amount. It will be assumed that this critical amount is a constant fraction of the total heat produced in the flame. The criterion may be written as

$$H_r \geq FH_T \quad (1)$$

(Symbols are defined in the appendix.)

For the combustion of hydrocarbons, complete combustion of the fuel is assumed to occur for all mixture compositions. Consequently, the total heat produced by the process may be written as the product of the mole fraction of fuel in the unburned gas X_f and the heat produced upon the disappearance of 1 mole of fuel ΔH (as defined herein, ΔH is constant and equal to the heat of combustion to CO_2 and H_2O only for stoichiometric or lean mixtures; for rich mixtures, ΔH decreases as the oxygen concentration decreases). Thus, for hydrocarbon flames, equation (1) may be written as

$$H_r \geq FX_f \Delta H \quad (2)$$

The heat retained by the flame can be written in terms of heat capacity and average temperature of the flame in the tube

$$H_r = \bar{C}_p (\bar{T} - T_o) \quad (3)$$

Equation (2) can then be written as

$$\bar{C}_p (\bar{T} - T_o) \geq FX_f \Delta H \quad (4)$$

The average temperature of the flame may be found if it is assumed that heat flow to the walls follows a differential equation of the form

$$(T - T_o)'' = \frac{q}{\chi} \quad (5)$$

Here, q is the rate of temperature rise caused by chemical reaction, χ is the thermodiffusivity and primes refer to differentiation with respect to x .

The result of integrating and averaging equation (5) with the boundary condition $T = T_o$ at the wall is the equation

$$\bar{T} - T_o = \frac{d^2 q}{G_i \chi} \quad (6)$$

In this equation d is a characteristic dimension of the tube, and G_i is a constant associated with the geometric shape of the tube. Derivations of G_i values for various geometries are given in reference 7. Equations (4) and (6) may be combined to give

$$\frac{d^2}{G_i} \geq \frac{FX_f \Delta H \chi}{q} \quad (7)$$

In order for a flame to pass down a tube, the tube size, given by d^2/G_i , must be equal to or greater than the right side of equation (7). Since the quenching distance is the characteristic tube dimension that just quenches a given flame, equation (7) can be written as a quenching-distance equation by removing the inequality sign;

$$d^2 = \frac{FG_i X_f \Delta H \chi}{q} \quad (8)$$

Then the thermodiffusivity χ can be written as

$$\chi = \frac{\kappa_r RT}{PC_{p,r}} \quad (9)$$

The rate of temperature rise q can be written as

$$q = \frac{RT \Delta H w}{P \bar{C}_{p,r} N} \quad (10)$$

Here, w is the rate of disappearance of fuel, molecules per cubic centimeter per second.

Equations (8), (9), and (10) may be combined to give for the thermal quenching equation

$$d^2 = \frac{FG_i N \kappa_r X_f}{C_{p,r} w} \quad (11)$$

The most important fact concerning this equation is that the form for w is not specified; any reaction may be chosen as rate-controlling.

Equation (11) may be derived from the diffusional equation if it is assumed that the thermodiffusivity and diffusion

coefficient are equivalent, and if the criterion for flame propagation is assumed to be that the number of reaction events per cubic centimeter must be a critical fraction of the total number of events that normally occur in the unconfined flame.

In terms of the active-particle—fuel reaction (the reaction specified as rate-controlling in the diffusional equation of ref. 4), the reaction rate w is given by

$$w = k_i a_r \sum_i c_{i,r} \quad (12)$$

If a collision-theory-type temperature dependence is assigned to k_i , equation (12) becomes

$$w = B_i a_r \sum_i c_{i,r} T_r^{1/2} \exp\left(\frac{-E_i}{RT_r}\right) \quad (13)$$

Combination of equations (10) and (13) gives

$$d^2 = \frac{F G_i N_{\kappa_r} X_f}{C_{p,r} B_i a_r \sum_i c_{i,r} T_r^{1/2} \exp\left(\frac{-E_i}{RT_r}\right)} = \frac{F}{B_i} \psi_i \quad (14)$$

The choice of rate-controlling reaction is not limited to the active-particle—fuel reaction. For example, it is possible to follow Semenov (ref. 8) and assume the reaction in the combustion zone to be bimolecular and first-order with respect to fuel and oxygen. For this assumption, the real reacting species are obviously not fuel and oxygen molecules, but such an assumption is satisfactory if the concentrations of the reacting species are proportional to the fuel and oxygen concentrations. In this case, then, the rate of the reaction is given by

$$w = k_s a_r b_r \quad (15)$$

If a collision-theory-type temperature dependence is assigned to k_s , equation (15) becomes

$$w = B_s a_r b_r T_r^{1/2} \exp\left(\frac{-E_s}{RT_r}\right) \quad (16)$$

The combination of equations (10) and (16) gives

$$d^2 = \frac{F G_i N_{\kappa_r} X_f}{C_{p,r} B_s a_r b_r T_r^{1/2} \exp\left(\frac{-E_s}{RT_r}\right)} = \frac{F}{B_s} \psi_s \quad (17)$$

In order to test equations (14) and (17), data for the quenching of propane-oxygen-nitrogen flames were used. These data points include the effect on quenching distance of oxygen-nitrogen ratio, fuel concentration and pressure (ref. 6), and initial temperature (ref. 9).

In order to use equation (14), the assumptions made in reference 4 concerning the active-particle—fuel reaction were followed: T_r was taken to be $0.7 T_F$, the partial pressure of fuel in the reaction zone was assumed to be one-half the

partial pressure of fuel in the unburned gas, the partial pressures of the active particles (H atoms, OH radicals, and O atoms) in the reaction zone were assumed to be 0.7 times their partial pressure in the adiabatic equilibrium flame, and E_i was assumed to be 7 kilocalories per mole (ref. 10).

In order to use equation (17), the partial pressures of fuel and oxygen in the reaction zone were taken as equal to their values in the unburned gas and E_s was assumed to be 38 kilocalories per mole (ref. 11). In keeping with previous usage (refs. 4 and 6), T_r was chosen to be equal to $0.7 T_F$.

The thermal conductivities were calculated for the unburned gas mixture at $0.7 T_F$. The conductivities for oxygen, nitrogen, and propane were calculated at 1553° K, using the tables and data given in chapter 8 of reference 12. Conductivities at other temperatures were computed on the assumption of a $3/4$ -power temperature dependence. The thermal conductivities of the gas mixtures were calculated as the sum of the mole fraction times the thermal conductivity of each component, or,

$$\kappa = \sum_i X_i \kappa_i \quad (18)$$

It was felt that this simple linear mixing rule was adequate for systems largely composed of nitrogen and oxygen because of their similar conductivities.

The heat capacities were calculated for the unburned gas mixture at $0.7 T_F$ by the same linear mixing rule used for the thermal conductivities. Individual heat capacities for oxygen, nitrogen, and propane were calculated from data given in reference 13.

The equilibrium adiabatic flame temperatures and product compositions were calculated by the matrix method of reference 14 using the thermodynamic constants of reference 14 and the heat of formation of propane given in reference 13.

RESULTS AND DISCUSSION

CORRELATION OF QUENCHING-DISTANCE DATA

Inasmuch as the square of the quenching distance is predicted to be directly proportional to ψ_i (eq. (14)) or to ψ_s (eq. (17)), values of ψ_i and ψ_s were calculated for the pressure, equilibrium adiabatic flame composition and temperature, unburned gas composition and temperature, and tube geometry (assumed to be plane-parallel plates) which correspond to the quenching distances reported in references 6 and 9 for propane-oxygen-nitrogen flames. Plots of d^2 against ψ_i and ψ_s are shown in figures 1 (a) and (b), respectively. The ranges of the variables included were: pressure, 0.1 to 1.0 atmosphere; equivalence ratio, 0.33 to 1.90; mole fraction oxygen in the oxidant mixture, 0.21 to 0.70; and unburned gas temperature, 300° to 558° K. In figure 1 (a), it is shown that ψ_i (which is entirely analogous to the diffusional equation of ref. 4 except for the choice of quenching criterion) satisfactorily correlates the effect of these variables except for propane-rich mixtures where $\phi > 1.2$.

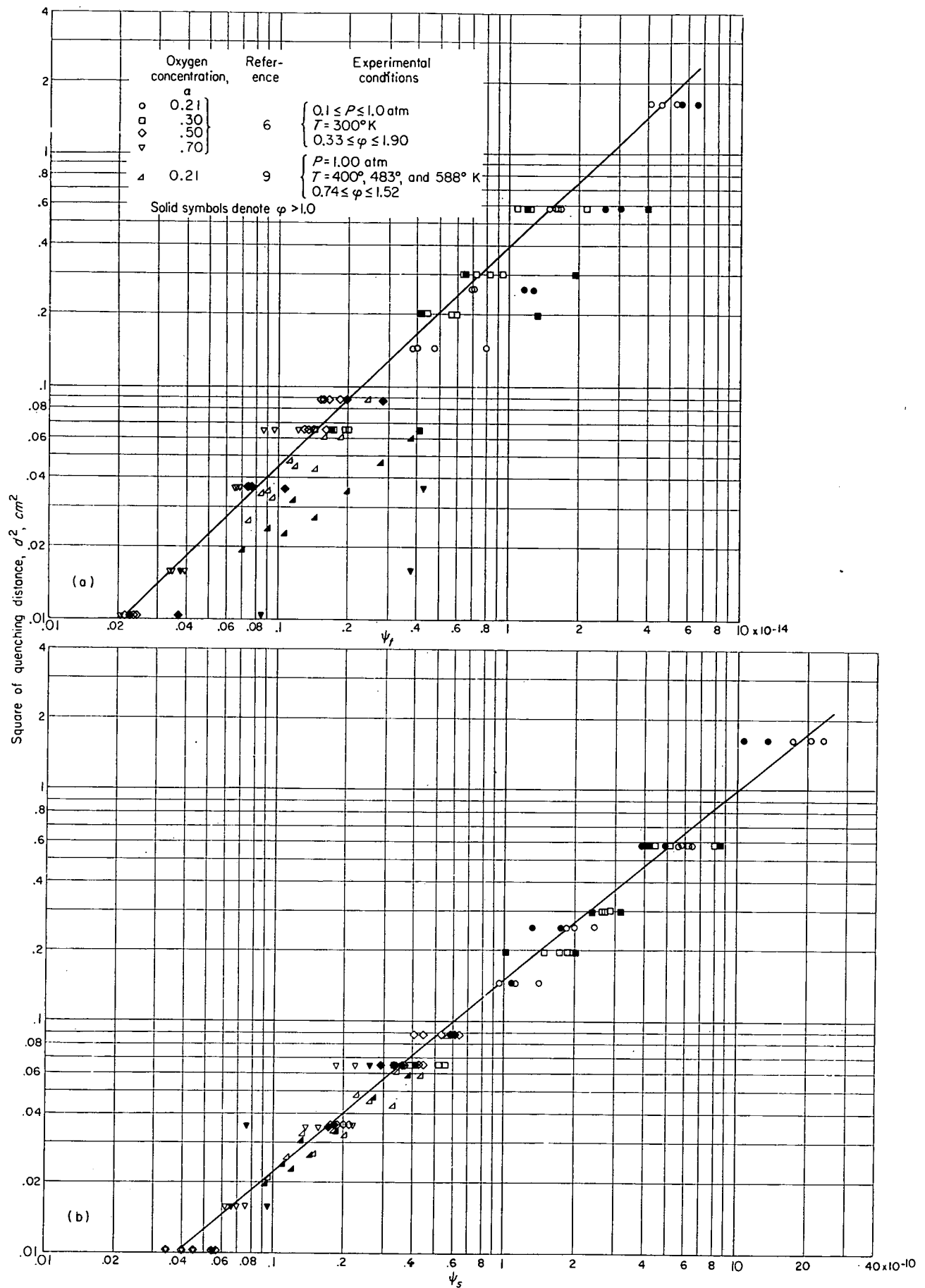


FIGURE 1.—Summary correlations of quenching data by thermal quenching equations.

Inspection of figure 1(b) reveals that ψ_s (which includes the oxygen-fuel reaction as the rate-determining step, rather than the active-particle—fuel reaction) correlates not only the propane-lean, but also all the propane-rich quenching data. Thus, it appears that by proper choice of the rate-controlling reaction, the quenching concepts of reference 4 may be extended in such a way as to include rich mixtures for the propane-oxygen-nitrogen system.

The same reaction-rate constants were used for mixtures both rich and lean in propane. This may not be possible for all hydrocarbons; it may be necessary to use different rate constants for rich and lean mixtures, since it is generally believed that the reaction mechanism changes in going from a lean to a rich hydrocarbon flame.

A mean line drawn through the data presented in figure 1 reveals that the predicted linear relation between d^2 and ψ_i and ψ_s does not hold exactly. Rather, the data are best correlated if $d^2 \propto (\psi_i)^{0.94} \propto (\psi_s)^{0.84}$. This difficulty is related, at least in part, to the choice of reaction mechanism, since the "best correlation" exponent is changed by a change in reaction mechanism.

PRESSURE DEPENDENCE OF QUENCHING DISTANCE

Examination of the equation for quenching distance (eq. (11)) reveals that all terms on the right side are independent of pressure except the reaction rate w . However, hydrocarbon flame temperatures change slightly with pressure because of changes in the extent of dissociation. Consequently, a pressure change indirectly affects temperature- and composition-dependent terms in the equation. This effect is quite small, so that the pressure dependence of the quenching distance may be regarded as primarily dependent on the pressure dependence of the initial chemical processes in the combustion wave.

The calculated pressure dependence of the quenching distance (including the indirect effect of pressure on flame temperature and composition) is compared in table I with the experimental values of reference 6. The average deviation of the calculated values from the observed values was found to be 10 percent for ψ_i and 17 percent for ψ_s . Reference 6 gives a value of 7 percent for the average deviation of values computed for the diffusional equation.

It is seen that ψ_s does not predict the pressure dependence as well as does ψ_i , except for the high-velocity flames at an oxygen fraction of 0.70. This is probably because the assumption of a simple second-order reaction between fuel and oxygen is a poor one. Concerning prediction of pressure dependence, a better choice of over-all order would be 1.7 rather than 2.0; this is in agreement with theoretical studies of the pressure dependence of burning velocity (ref. 12, p. 765), which indicate that the global reaction in most hydrocarbon flames ranges between first and second order. Such a choice would also tend to improve the linearity of the relation between d^2 (observed) and ψ_s (calculated).

QUENCHING DISTANCE AND BURNING VELOCITY

The relation of quenching distance to burning velocity has been discussed in references 3, 4, and 15. In reference 4, an

TABLE I.—COMPARISON OF OBSERVED PRESSURE DEPENDENCE OF QUENCHING DISTANCE WITH PREDICTED VALUES

Oxygen fraction, α	Equivalence ratio, φ	Exponent n describing pressure dependence, $d \propto p^{-n}$			
		Observed *	Diffusional *	Predicted	
				ψ_i	ψ_s
0.17	0.943	0.90	0.88	0.83	1.03
	1.000	.89	.85	.76	1.01
	1.340	.84	.75	.75	1.00
	1.530	.71	.75	.75	1.00
0.21	0.738	0.85	0.86	0.80	1.00
	.864	.84	.89	.84	1.03
	1.000	.89	.93	.89	1.03
	1.240	.95	.78	.79	1.02
0.30	1.490	.98	.76	.77	1.00
	0.566	0.76	0.87	0.87	1.01
	.662	.93	.89	.88	1.04
	.773	1.06	.92	.90	1.07
0.50	1.000	.98	.94	.90	1.09
	1.380	.93	.86	.84	1.06
	1.903	.74	.76	.76	1.01
	0.476	1.01	0.91	0.89	1.06
0.70	.544	1.01	.93	.91	1.07
	.680	.96	.96	.92	1.09
	1.000	.93	.97	.92	1.11
	1.358	.91	.95	.90	1.09
0.70	1.940	.88	.82	.81	1.05
	0.345	1.12	0.91	0.89	1.06
	.395	1.12	.93	.91	1.07
	.494	1.02	.96	.92	1.09
0.70	1.000	1.01	.98	.93	1.09
	1.234	1.07	.98	.92	1.11
	1.829	.60	.89	.86	1.08

* Ref. 6.

equation relating the two variables is derived on a purely diffusional basis. The thermal analog to this equation may be derived as follows:

According to reference 16, the Semenov equation for the burning velocity may be written as

$$U^2 = \frac{2\kappa_F \bar{W}}{a_o \rho_o \bar{C}_{p,F}} \left(\frac{n_1}{n_2} \right)^m \left(\frac{\kappa}{D C_p} \right)_F^m \quad (19)$$

Multiplying equation (11) by equation (19), converting specific heats to molar heat capacities, and writing a_o and ρ_o in the form

$$a_o = \frac{N X_F P}{R T_o} \quad (20a)$$

$$\rho_o = \frac{\bar{M} P}{R T_o} \quad (20b)$$

yield

$$d = \frac{R T_o}{U P} \sqrt{\frac{2\kappa_F \kappa_F F G_i \left(\frac{n_1}{n_2} \right)^m \left(\frac{\kappa R T}{D C_p P} \right)_F^m \bar{W}}{C_{p,\tau} \bar{C}_{p,F} w}} \quad (21)$$

If it is assumed that \bar{W} and w have the same pressure dependence, it follows from equation (21) that, at a given equivalence ratio,

$$U \propto \frac{1}{d P} \propto P^{-(n+1)} \quad (22)$$

From reference 6, it is seen that n decreases from about -0.9 to -1.05 as the percent oxygen in the oxidant mixture is increased from 21 to 70. Simultaneously, the burning velocity increases from about 40 centimeters per second to the order of 300 centimeters per second. Consequently, equation (22) predicts that the exponent describing the pressure dependence of U should increase from about -0.1 to 0.05 as U increases from 40 centimeters per second to about 300 centimeters per second. This result may be compared with the experimental findings of Lewis (ref. 17) (which indicate an increase of about -0.05 to 0.07 as burning velocity changes from 40 to 300 cm/sec) to confirm equation (22) qualitatively.

CONCLUDING REMARKS

The fact that reasonable agreement exists between experiment and quenching concepts based on either heat or mass transfer indicates only that these processes have the same formal laws and that the thermal and molecular diffusivities are either equal or remain directly proportional for the data considered in this study. No evidence for the preponderance of either heat or mass transfer in quenching can be deduced from these results. The principal advantage gained by formulation of the quenching concepts of reference 4 in a "thermal" form is that a change in reaction kinetics is much simpler from a conceptual point of view for the "thermal" form than for the "diffusional" form. This conceptual advantage might be useful in a discussion of bizarre fuel-oxidant systems for example, $\text{CS}_2\text{-F}_2$ flames. In addition, the actual calculations may be simplified, since by the proper choice of reaction mechanism, it may become unnecessary to calculate the equilibrium flame composition.

SUMMARY OF RESULTS

The results of an investigation into the possibility of extending quenching concepts previously proposed to include quenching of hydrocarbon-rich flames may be summarized as follows:

1. An equation for the critical quenching configuration of a channel was derived for hydrocarbon flames:

$$d^2 = \frac{FG_i N \kappa_r X_f}{C_{p,r} w}$$

where

$C_{p,r}$	heat capacity in reaction zone, cal/(°K) (mole)
d	characteristic dimension of tube geometry; quenching distance, cm
F	constant that relates total heat produced by combustion to heat which must be retained by flame for it to exist
G_i	dimensionless factor, dependent only on channel geometry
N	Avogadro's number
w	rate of reaction in reaction zone, molecules/(cc) (sec)
X_f	mole fraction of fuel in unburned gas
κ_r	mean thermal conductivity in reaction zone, cal/(cm) (sec) (°K)

2. Two possible flame-initiating reactions were considered in the detailed formulation of w : (1) the reaction between active particles and fuel molecules, and (2) the reaction between oxygen and fuel molecules.

3. The two equations resulting from the two reaction mechanism choices were tested using published data that included the effect of oxygen-nitrogen ratio, fuel concentration, pressure, and unburned gas temperature on the quenching distance for propane-oxygen-nitrogen flames. These variables were correlated reasonably well for both rich and lean flames by the equation involving the oxygen-fuel reaction. The equation involving the active-particle-fuel reaction was satisfactory primarily for lean flames.

4. It was concluded that, by the proper choice of reaction kinetics, the quenching concepts previously proposed may be cast in a form useful for the prediction of both propane-rich and -lean quenching data.

LEWIS FLIGHT PROPULSION LABORATORY

NATIONAL ADVISORY COMMITTEE FOR AERONAUTICS

CLEVELAND, OHIO, December 6, 1954

APPENDIX

SYMBOLS

The following symbols are used in this report:

a	fuel concentration, molecules/cc
B	Arrhenius constant
b	oxygen concentration, molecules/cc
C_p	heat capacity, cal/(°K) (mole)
$\bar{C}_{p,F}$	average heat capacity, T_o to T_F , cal/(°K) (mole)
c_i	concentration of i th active particle, molecules/cc
c_p	specific heat, cal/(°K) (g)
\bar{c}_p	average specific heat, T_o to T_F , cal/(°K) (g)
D	diffusion coefficient, sq cm/sec
d	characteristic dimension of tube geometry; quenching distance, cm
E	activation energy, cal/mole
F	constant that relates total heat produced by combustion to heat which must be retained by flame for it to exist
G_t	dimensionless factor, dependent only on tube geometry
ΔH	heat released upon consumption of 1 mole of fuel by combustion process, cal/mole
H_r	heat produced by chemical reaction in primary reaction zone, cal/mole
H_T	total heat produced by combustion of 1 mole of unburned gas, cal/mole
k	rate constant, (cc) (molecules)/sec
M	average molecular weight of unburned gas, g/mole
m	molecularity of flame reaction
N	Avogadro's number
n	exponent describing pressure dependence of quenching distance
n_1/n_2	moles of reactant per moles of product from stoichiometric equation
P	pressure, atm
q	rate of temperature rise, °K/sec
R	gas constant
T	temperature, °K
U	flame speed, cm/sec
\bar{W}	average reaction rate in flame front as defined by Semenov, molecules/(cc)(sec)
w	reaction rate in reaction zone, molecules/(cc)(sec)
X_f	mole fraction of fuel
x	distance, cm
α	mole fraction of oxidant in oxidant-inert mixture
κ	thermal conductivity, cal/(cm)(sec)(°K)
ρ	density, g/cc
φ	equivalence ratio
χ	thermodiffusivity, sq cm/sec

$$\psi_s = \frac{G_t N \kappa_r X_f}{C_{p,r} a_r b_r T_r^{1/2} \exp \frac{-E_s}{RT_r}}$$

$$\psi_i = \frac{G_t N \kappa_r X_f}{C_{p,r} a_r \sum c_{i,r} T_r^{1/2} \exp \frac{-E_i}{RT_r}}$$

Subscripts:

F	flame
i	active-particle species

o	unburned gas
r	reaction zone
s	involves reaction of oxygen and fuel molecules
t	involves reaction of active particles and fuel molecules

REFERENCES

1. von Kármán, Theodore, and Millán, Gregorio: Thermal Theory of a Laminar Flame Front Near a Cold Wall. Fourth Symposium (International) on Combustion, The Williams & Wilkins Co. (Baltimore), 1953, pp. 173-177.
2. Rosen, J. B.: Theory of Laminar Flame Stability. 1—Analytic Stability Condition. Jour. Chem. Phys., vol. 22, no. 4, Apr. 1954, pp. 733-748.
3. Lewis, Bernard, and von Elbe, Guenther: Combustion, Flames and Explosions of Gases. Academic Press, Inc. (New York), 1951.
4. Simon, Dorothy M., Belles, Frank E., and Spakowski, Adolph E.: Investigation and Interpretation of the Flammability Region for Some Lean Hydrocarbon-Air Mixtures. Fourth Symposium (International) on Combustion, The Williams & Wilkins Co. (Baltimore), 1953, pp. 126-138.
5. Friedman, Raymond, and Burke, Edward: Spark Ignition of Gas Mixtures. Jour. Chem. Phys., vol. 17, no. 7, July 1949, p. 667.
6. Berlad, A. L.: Flame Quenching by a Variable-Width Rectangular-Channel Burner as a Function of Pressure for Various Propane-Oxygen-Nitrogen Mixtures. Jour. Phys. Chem., vol. 58, no. 11, Nov. 1954, pp. 1023-1026.
7. Berlad, A. L., and Potter, A. E., Jr.: Prediction of the Quenching Effect of Various Surfaces Geometries. Fifth Symposium (International) on Combustion, Reinhold Pub. Corp., 1955, pp. 728-735.
8. Semenov, N. N.: Thermal Theory of Combustion and Explosion. III—Theory of Normal Flame Propagation. NACA TM 1026, 1942.
9. Friedman, Raymond, and Johnston, W. C.: The Wall-Quenching of Laminar Flames as a Function of Pressure, Temperature and Air-Fuel Ratio. Jour. Appl. Phys., vol. 21, no. 8, Aug. 1950, pp. 791-795.
10. Tanford, Charles: The Role of Free Atoms and Radicals in Burner Flames. Third Symposium on Combustion and Flame and Explosion Phenomena, The Williams & Wilkins Co. (Baltimore), 1949, pp. 140-146.
11. Jost, Wilhelm: Explosions and Combustion Processes in Gases. McGraw-Hill Book Co., Inc., 1946, p. 437.
12. Hirschfelder, Joseph O., Curtiss, Charles F., and Bird, R. Byron: Molecular Theory of Gases and Liquids. John Wiley & Sons, Inc., 1954.
13. Rossini, Frederick D., et al.: Selected Values of Properties of Hydrocarbons. Circular C461, Nat. Bur. Standards, Nov. 1947.
14. Huff, Vearl N., Gordon, Sanford, and Morrell, Virginia E.: General Method and Thermodynamic Tables for Computation of Equilibrium Composition and Temperature of Chemical Reactions. NACA Rep. 1037, 1951. (Supersedes NACA TN's 2113 and 2161.)
15. Friedman, Raymond: The Quenching of Laminar Oxyhydrogen Flames by Solid Surfaces. Third Symposium on Combustion and Flame and Explosion Phenomena, The Williams & Wilkins Co. (Baltimore), 1949, pp. 110-120.
16. Dugger, Gordon L., and Simon, Dorothy M.: Prediction of Flame Velocities of Hydrocarbon Flames. Fourth Symposium (International) on Combustion, The Williams & Wilkins Co. (Baltimore), 1953, pp. 336-345.
17. Lewis, Bernard: Selected Combustion Problems. Fundamentals and Aeronautical Applications, Butterworths Scientific Pub. (London), 1954, pp. 176-177.

REPORT 1265

A THEORY FOR STABILITY AND BUZZ PULSATION AMPLITUDE IN RAM JETS AND AN EXPERIMENTAL INVESTIGATION INCLUDING SCALE EFFECTS¹

By ROBERT L. TRIMPI

SUMMARY

A theory based on quasi-one-dimensional flow has been developed for determining factors affecting stable flow through ram jets with supersonic diffusers. Stable flow for such ram jets is shown to depend upon the instantaneous values of mass flow and total pressure recovery of the supersonic diffuser and immediate neighboring subsonic diffuser. Conditions for stable and unstable flow are considered. The theory is found to be in agreement with the experimental data of NACA TN 3506 and NACA RM L50K30. This theory indicates that the model assumed in the resonator analysis of NACA TN 3506 may be considered a rough approximation to the actual phenomena when applied for purposes of obtaining the general trends and orders of magnitude of frequency and amplitude of oscillation provided that the wave length of the highest frequency component of the oscillation be much larger than the length of the ram jet. The resonator analysis is not applicable to a determination of the initial instability of the inlet without combustion and should not be so applied to obtain such stability criteria.

A simple theory for predicting the approximate amplitude of small pressure pulsation in terms of mass-flow decrement from minimum-stable mass flow was developed and found to agree with experimental data.

Cold-flow tests at a Mach number of 1.94 of ram-jet models having scale factors of 3.15:1 and Reynolds number ratios of 4.75:1 with several supersonic diffuser configurations showed only small variations in performance between geometrically similar models. The predominant variation in steady-flow performance resulted from the larger boundary layer in the combustion chamber of the low Reynolds number models. The conditions at which buzz originated were nearly the same for the same supersonic diffuser (cowling-position angle) configurations in both large- and small-diameter models. There was no appreciable variation in stability limits of any of the models when the combustion-chamber length was increased by a factor of three. The unsteady-flow performance and wave patterns were also similar when considered on a reduced-frequency basis determined from the relative lengths of the model. The negligible effect of Reynolds number on stability of the off-design configurations was not anticipated in view of the importance of boundary layer to stability, and this result should not be construed to be generally applicable.

INTRODUCTION

The buzzing, or oscillation, of the shock configuration at the inlet of supersonic diffusers has been the subject of many investigations since 1944 when Oswatitsch (ref. 1) first encountered the phenomenon in axisymmetric inlets with central bodies. Recent research has shown that buzzing is not limited to axisymmetric conical center-body inlets but is also associated with scoop-type inlets and perforated convergent-divergent diffusers (ref. 2).

The operation of ram jets at off-design conditions due to flight speeds less than the design speed or due to various fuel-air ratios, as well as maneuvering at design speed, results in operation at reduced values of mass flow; in other words, the area of the stream tube swallowed by the inlet is smaller than the cross-sectional area of the inlet. In order to obtain this reduced mass flow there must be a change in the shock pattern of the inlet. In the axisymmetric center-body-type inlet any reduction in mass flow over that accomplished by the deflection of the stream lines across the conical shock can be obtained only as a result of the motion of the second or so-called "normal shock," which is usually at or to the rear of the cowling entrance at design Mach number. This shock moves forward to effect mass-flow spillage in the subsonic region existing just behind it. The mass-flow reduction in the various other types of inlet is also mainly dependent on the normal shock. Buzzing occurs when the flow pattern becomes unstable at the position to which the normal shock is forced to move in order to satisfy the particular mass-flow requirements of the ram jet.

The performance of a diffuser is reduced by instability (ref. 3) and in addition the resulting pressure fluctuations can produce serious combustion and structural problems depending on the oscillation amplitude. Consequently, it is essential for efficient operation that the buzzing be either eliminated, avoided, or its amplitude controlled at a small value.

Various criteria for determining the cause of instability have previously been reported. Reference 4 expounds the effects of a vortex-sheet induced separation as one cause, whereas reference 5 and others have shown separation on the central body to be another contributing factor in absence of combustion instability or rough burning. In addition

¹ Supersedes recently declassified NACA Research Memorandum L53G28 by Robert L. Trimpi, 1953.

to the aforementioned theories based on fundamental aerodynamic phenomena, a modified Helmholtz resonator concept (ref. 6) has been proposed to predict the onset of instability as a function of the slope of the mean pressure-recovery mass-flow curve.

In an investigation made at the Marquardt Aircraft Co. in 1951, W. J. Orlin and L. C. Dunsworth proposed a stability criterion, based only on the steady flow ahead of the cowling, in which a zero slope of the curve of cowling static pressure against mass flow predicts the start of buzz. Experimental results, however, have shown that the flow to the rear of the inlet lip can influence stability.

The mechanism for the continuation of the cold-flow-buzzing cycle, once it has been initiated, was investigated in reference 5 and the various traveling waves moving up and down the ram jet were theoretically computed on a quasi-one-dimensional basis and found to agree closely with experimental results. However, an experimental value of the strength of the initial wave had to be used as a starting point for the computations.

Since predictions of the buzzing phenomena by any of the methods described have not been infallible, the only recourse in determining the behavior of a particular ram jet has been to actually test the configuration. The testing of full-scale units is both difficult and costly so that the obvious solution is the testing of small-scale models, provided that the model behavior can be properly correlated with the actual ram jet for both steady and unsteady flow.

A possible method for predicting the amplitude of the pressure oscillations, based on a further modification of the Helmholtz resonator concept previously mentioned, was proposed in reference 7. Again an experimental point was used to get a basis from which to make further involved computations. Furthermore, the procedure required to obtain the amplitude by this method is quite involved and lengthy so that it would be advantageous to have a simple short method for amplitude prediction.

A theoretical and experimental investigation was conducted at Langley to gain further information regarding the cold-flow-stability limits for buzzing and regarding model scale effects in steady and time-dependent flow. In addition, a simple approximate theory for predicting pulsation amplitude was derived on a linearized one-dimensional acoustical basis.

SYMBOLS

a	local speed of sound
δa	perturbation to local speed of sound
f, g	functional solutions to wave equation
m	mass flow through model
m_b	mass flow through model at start of buzz
m_∞	mass flow at infinity through a stream tube of diameter equal to cowling-lip diameter
n	integer denoting number of wave traversals in each oscillation cycle (equivalent to quotient of oscillation wave length divided by twice ram-jet length)
p	pressure
$\Delta p, \delta p$	perturbations to pressure
r	radial distance measured from axis

r_i	maximum internal radius of model
r_o	radius of outer rake tube
r_1	radius of center-body surface
r_2	radius of cowling inner surface
t	time
w	turbulence velocity
x	axial distance measured from cowling lip
C_1, C_2, C_3, C_4	constants defined in equations
D	nominal (maximum internal) diameter of models
F, G	functional solutions to wave equation
L	length of model
M	Mach number
U	fluid speed in ram jet
$\Delta U, \delta U$	perturbations to fluid speed in ram jet
V	fluid speed in free stream
V_{max}	maximum fluid speed if fluid is expanded to zero pressure
α	angle of attack, deg
γ	ratio of specific heats, assumed equal to 1.40
ξ	axial coordinate in moving wave system
ρ	density
$\Delta \rho, \delta \rho$	perturbations to density
μ	viscosity
τ	period of oscillation
ω	frequency of oscillation
ϕ	velocity potential
$\delta \phi$	perturbation to potential

Subscripts indicate following states unless otherwise noted:

b	start of buzz
t	local stagnation conditions
∞	free stream
max	maximum value during cycle
min	minimum value during cycle

THEORY FOR APPROXIMATE PRESSURE AMPLITUDE OF BUZZ

A low-amplitude buzzing, while not beneficial to the performance of a propulsion unit, might under certain circumstances (such as a particular off-design operation encountered only for short-time periods) be less undesirable than the performance penalty required to avoid buzzing completely. It would then be advantageous to be able to predict the amplitude of buzzing as a function of mass flow. Reference 7 presents one method, based on resonator principles, which is quite lengthy and tedious and also yields a constant amplitude throughout the combustion chamber in contrast to experimental data which show varying amplitude. Consequently a simple linear theory has been derived to permit facile computations of the relation of pressure amplitude at various positions in the ram jet to mass flow.

A linearized equation of motion for small disturbances superimposed on a one-dimensional isentropic steady flow may be obtained by neglecting products of perturbations, of the derivatives of perturbations, of the perturbations and derivatives of perturbations, and so forth, in respect to the first power of said perturbations. Let the steady flow be defined by the parameters U, p, ρ , and a . Then the unsteady flow is defined by $U + \delta U(x, t)$, $p + \delta p(x, t)$, $\rho + \delta \rho(x, t)$, and $a + \delta a(x, t)$. For the above conditions and restrictions the equations of continuity and momentum become (when

subscripts denote partial differentiation)

$$\delta\rho_t + U \delta\rho_x + \rho \delta U_x = 0 \quad (1)$$

$$\delta U_t + U \delta U_x = -\frac{1}{\rho} \frac{dp}{d\rho} \delta\rho_x \quad (2)$$

Differentiating equation (1) with respect to x and equation (2) with respect to time gives

$$\delta\rho_{xt} + U \delta\rho_{xx} + \rho \delta U_{xx} = 0 \quad (3)$$

$$\delta U_{tt} + U \delta U_{xt} = -\frac{1}{\rho} \frac{dp}{d\rho} \delta\rho_{xt} \quad (4)$$

Combining equations (3) and (4) results in the following equation:

$$\frac{1}{\rho} \frac{dp}{d\rho} [U \delta\rho_{xx} + \rho \delta U_{xx}] = \delta U_{tt} + U \delta U_{xt} \quad (5)$$

Differentiating equation (2) with respect to x gives

$$\delta U_{xt} + U \delta U_{xx} = -\frac{1}{\rho} \frac{dp}{d\rho} \delta\rho_{xx} \quad (6)$$

Substituting equation (6) in equation (5) and rearranging, using $a^2 = \frac{dp}{d\rho}$, yields the following differential equations:

$$-U \delta U_{xt} - U^2 \delta U_{xx} + \frac{dp}{d\rho} \delta U_{xx} = \delta U_{tt} + U \delta U_{xt} \quad (7)$$

$$\delta U_{tt} = (a^2 - U^2) \delta U_{xx} - 2U \delta U_{xt} \quad (8)$$

It may be verified by substitution that solutions of equation (8) are to be found in the form

$$\delta U = f[x - (U+a)t] + g[x - (U-a)t] \quad (9)$$

The first term represents a wave moving with a velocity of $U+a$ and the second, a wave traveling with a velocity $U-a$.

These solutions are to be expected since if a potential $\phi = Ux + \delta\phi$ exists, where $\delta U = \delta\phi_x$, equation (8) becomes, after partial integration with respect to x ,

$$\delta\phi_{tt} = (a^2 - U^2) \delta\phi_{xx} - 2U \delta\phi_{xt} \quad (10)$$

Equation (10) could also have been obtained from the simple wave equation, $\phi_{\xi\xi} = \frac{1}{a^2} \phi_{tt}$, for a disturbance in a fluid at rest by a transformation of coordinates to account for the fluid motion. Solutions of the wave equation are known to be of the form $\delta U = f(\xi - at) + g(\xi + at)$, and replacing ξ by $x - Ut$ yields equations (9) and (10).

Substitution of equation (9) in equation (2) and integrating with respect to x yields the perturbation density

$$\frac{\delta\rho}{\rho} = \frac{f[x - (U+a)t] - g[x - (U-a)t]}{a} \quad (11)$$

Applying the isentropic relationships to determine the other perturbations yields

$$\frac{\delta p}{p} = \gamma \frac{\delta\rho}{\rho} = \gamma \frac{f[x - (U+a)t] - g[x - (U-a)t]}{a} \quad (12)$$

$$\frac{\delta a}{a} = \frac{\gamma-1}{2} \frac{\delta\rho}{\rho} = \frac{\gamma-1}{2} \frac{f[x - (U+a)t] - g[x - (U-a)t]}{a} \quad (13)$$

Equations (9), (11), (12), and (13) are the general equations applicable to a one-dimensional steady flow with unsteady perturbations.

If these equations are to be applied to the ram jet, considered as a constant area duct with a constriction at the exit, the proper boundary condition at the exit must be considered. In reference 5 it was shown that consistent with the assumption of a choked nozzle was the assumption of constant Mach number at the end of the duct for a given nozzle area.

Now, for $M = \text{Constant} = \frac{U}{a} = \frac{U+\delta U}{a+\delta a}$ at the exit,

$$M = \frac{U}{a} = \frac{U+\delta U}{a+\delta a} = \frac{U}{a} \left(1 + \frac{\delta U}{U} - \frac{\delta a}{a} + \dots \right) \quad (14)$$

Therefore, at $x=L$,

$$\begin{aligned} \frac{\delta U}{U} &= \frac{\delta a}{a} \\ \frac{f+g}{U} &= \frac{\gamma-1}{2} \left(\frac{f-g}{a} \right) \\ \frac{f(L,t)}{g(L,t)} &= \frac{\frac{\gamma-1}{2} M+1}{\frac{\gamma-1}{2} M-1} \end{aligned} \quad (15)$$

Equation (15) relating the strengths of the downstream and upstream waves at the exit is similar to equation (6) of reference 5 which gives the value of these waves for the exact characteristic solution.

Closed solutions satisfying equations (9) and (15) may be found in harmonic form. Since the sine wave form often occurs in buzzing, a simple expression for that type of wave is shown in the following equation, where C_1 is as yet an undetermined constant dependent on the amplitude and ω is the frequency of the oscillation:

$$\begin{aligned} \frac{\delta U}{C_1} &= \frac{\frac{\gamma-1}{2} M+1}{\frac{\gamma-1}{2} M-1} \sin \left\{ \frac{2\pi\omega}{(1-M^2)a} [(M-1)x + (1-M^2)at + L] \right\} + \\ &\sin \left\{ \frac{2\pi\omega}{(1-M^2)a} [(M+1)x + (1-M^2)at - L] \right\} \end{aligned} \quad (16)$$

Note that the boundary condition for $x/L=1$, equation (15), is identically satisfied for all times. Furthermore, if each cycle requires n waves to traverse the ram jet in both directions during a period τ , then

$$\frac{1}{\omega} = \tau = n \left(\frac{L}{U+a} + \frac{L}{a-U} \right) = \frac{2nL}{a(1-M^2)}$$

and

$$\begin{aligned} \frac{\delta U}{C_1} &= \frac{\frac{\gamma-1}{2} M+1}{\frac{\gamma-1}{2} M-1} \sin \left[(M-1) \frac{\pi x}{nL} + \frac{\pi}{n} + 2\pi \frac{t}{\tau} \right] + \\ &\sin \left[(M+1) \frac{\pi x}{nL} - \frac{\pi}{n} + \frac{2\pi t}{\tau} \right] \end{aligned} \quad (17)$$

From equation (17), where the first term on the right-hand side represents f and the second represents g , and equations (11) and (12), one finds the relationship between the perturbation amplitudes of pressure and density:

$$\frac{\delta \rho}{\rho} \frac{a}{C_1} = \frac{\delta p}{p} \frac{a}{\gamma C_1} = \frac{\frac{\gamma-1}{2} M+1}{\frac{\gamma-1}{2} M-1} \sin \left[(M-1) \frac{\pi x}{nL} + \frac{\pi}{n} + 2\pi \frac{t}{\tau} \right] - \sin \left[(M+1) \frac{\pi x}{nL} - \frac{\pi}{n} + 2\pi \frac{t}{\tau} \right] \quad (18)$$

Corresponding equations, though not in such simple form, may be found for any desired shape of a pressure-time curve by approximating the curve by straight-line segments for which the equations are linear in time.

The problem of determining the pressure perturbation at any time and at any value of x is then reduced to a determination of the constant C_1 . An approximation to this value for small amplitudes may be obtained in the following manner where perturbations are applied to the average mass flow which varies slightly from the incipient mass flow (at start of buzz). Time-averaged quantities are denoted by a bar and the following identities are employed:

$$\left. \begin{aligned} \bar{\rho} &\equiv \rho_b - \Delta \rho \\ \bar{U} &\equiv U_b - \Delta U \\ \bar{p} &\equiv p_b - \Delta p \end{aligned} \right\} \quad (19)$$

$$\bar{m} = \text{Average mass flow} = \bar{\rho} \bar{U} \quad (20)$$

$$\frac{\bar{m}}{m_b} = \frac{\bar{\rho}}{\rho_b U_b} = 1 - \frac{\Delta \rho}{\rho_b} - \frac{\Delta U}{U_b} \quad (21)$$

$$\frac{\bar{m}}{m_b} = 1 - \frac{\Delta p}{\gamma p_b} - \frac{\Delta U}{U_b} \quad (21a)$$

The assumption is then introduced that at the midpoint of the ram jet the maximum variations (amplitude) in pressure and velocity are equal to the difference between the incipient values and the average values, that is, at $x/L = 1/2$

$$\left. \begin{aligned} |\delta p|_{\max \text{ positive}} &= \Delta p \\ |\delta U|_{\max \text{ positive}} &= \Delta U \end{aligned} \right\} \quad (22)$$

Some justification for the pressure approximation has been found in experiments at both the Lewis and Langley Laboratories of the National Advisory Committee for Aeronautics. For example, figure 1 is a typical record obtained during the experiments of this investigation presented subsequently herein. These data show the peak pressure obtained at gage 3 ($x/L = 0.6$) to be approximately the incipient value for buzzing near the midpoint of the ram jet for small amplitudes in cold flow. Similar results have been reported from an investigation made in 1949 by James F. Connors and Albert H. Schroeder at the NACA Lewis Laboratory. When combustion is present, reference 3 and the aforementioned work of Connors and Schroeder show that the peak pressures

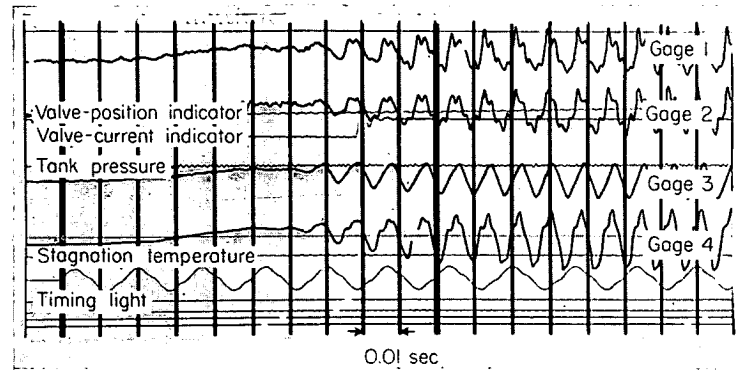


FIGURE 1.—Typical pressure record of start of buzz for configuration 1.278-14.91-44.2°. Time is increasing to right and pressure is positive upward.

are slightly below the cold-flow incipient value until a buzz giving optimum average static pressure (highest manometer pressure noted during buzzing) is reached, at which point the average pressure is equal to the optimum static pressure in cold flow (incipient pressure) less the amplitude of pressure pulsation.

No data are available for substantiation of the corresponding velocity assumption. However, it would seem logical to apply similar boundary conditions at the same point. Also, since at the midpoint of the ram jet the values of the velocity and pressure perturbation amplitude are between the maximum and minimum values existing at the extremities of the ducting, this midpoint would further appear to be the desirable place to evaluate amplitudes.

This assumption relating amplitudes to average and incipient values will apply only for small values of the oscillation and even then it is only an approximation in some cases. However, since it will give an easy method of determining the approximate pressure amplitudes, its use is justifiable providing the limits imposed are considered in analyzing results obtained. The weighted mass-flow values of U_b and a_b should be used in the computations where boundary-layer effects cause a nonuniformity in parameters across the channel.

Thus, the following approximation is determined:

$$\frac{\bar{m}}{m_b} = 1 - \frac{1}{\gamma} \left| \frac{\delta p}{p} \right|_{\max \text{ positive}} \bigg|_{x/L=1/2} - \left| \frac{\delta U}{U} \right|_{\max \text{ positive}} \bigg|_{x/L=1/2} \quad (23)$$

$$\frac{\bar{m}}{m_b} = 1 - \left| \frac{f-g}{a_b} \right|_{\max \text{ positive}} \bigg|_{x/L=1/2} - \left| \frac{f+g}{U_b} \right|_{\max \text{ positive}} \bigg|_{x/L=1/2} \quad (24)$$

In general, if f and g are replaced by $C_1 F$ and $C_1 G$ where F and G are representative only of the form of the waves of unit amplitude, then equations (9), (12), and (24) become:

$$\delta U = C_1 (F + G) \quad (25)$$

$$\frac{\delta p}{p} = \gamma C_1 \left(\frac{F - G}{a} \right) \quad (26)$$

$$1 - \frac{\bar{m}}{m_b} = \frac{C_1}{a_b} |F - G|_{\max \text{ positive}} \bigg|_{x/L=1/2} + \frac{C_1}{a_b} \frac{1}{M_b} |F + G|_{\max \text{ positive}} \bigg|_{x/L=1/2} \quad (27)$$

$$C_1 = \frac{\left(1 - \frac{\bar{m}}{m_b}\right)}{a \left|F - G\right|_{\max}^{positive} \frac{x}{L} = \frac{1}{2} + \frac{1}{M_b} \left|F + G\right|_{\max}^{positive} \frac{x}{L} = \frac{1}{2}} \quad (27a)$$

Equations (26) and (27a) permit the determination of the pressure-time variation for any given value of x/L , M_b , and $\frac{\bar{m}}{m_b}$ for a particular form F and G . In addition, an expression for the total amplitude for any given value of x/L and \bar{m}/m_b

may be obtained by maximizing equation (26):

$$\begin{aligned} \text{Total amplitude } \left(\frac{x}{L}, \frac{\bar{m}}{m_b}\right) &= \frac{p_{\max} - p_{\min}}{p_b} \\ &= \gamma \left(1 - \frac{\bar{m}}{m_b}\right) \frac{|F - G|_{\max}^{positive} \frac{x}{L} - |F - G|_{\max}^{negative} \frac{x}{L}}{|F - G|_{\max}^{positive} \frac{x}{L} = \frac{1}{2} + \frac{1}{M_b} |F + G|_{\max}^{positive} \frac{x}{L} = \frac{1}{2}} \end{aligned} \quad (28)$$

In particular for the sine wave oscillation previously mentioned, the closed form of the equation for total amplitude of pressure pulsation becomes

$$\begin{aligned} \frac{p_{\max} - p_{\min}}{p_b} &= 2 \frac{\Delta p}{p_b} \\ &= 2\gamma \left(1 - \frac{\bar{m}}{m_b}\right) \left\{ \left| \frac{\frac{\gamma-1}{2} M_b + 1}{\frac{\gamma-1}{2} M_b - 1} \sin \left[(M_b - 1) \frac{\pi x}{nL} + \frac{\pi}{n} + 2\pi \frac{t}{\tau} \right] - \sin \left[(M_b + 1) \frac{\pi x}{nL} - \frac{\pi}{n} + 2\pi \frac{t}{\tau} \right] \right|_{\max} \right\} \\ &\quad \left\{ \left| \frac{\frac{\gamma-1}{2} M_b + 1}{\frac{\gamma-1}{2} M_b - 1} \sin \left[(M_b - 1) \frac{\pi}{2n} + \frac{\pi}{n} + 2\pi \frac{t}{\tau} \right] - \sin \left[(M_b + 1) \frac{\pi}{2n} - \frac{\pi}{n} + 2\pi \frac{t}{\tau} \right] \right|_{\max} + \right. \\ &\quad \left. \frac{1}{M_b} \left| \frac{\frac{\gamma-1}{2} M_b + 1}{\frac{\gamma-1}{2} M_b - 1} \sin \left[(M_b - 1) \frac{\pi}{2n} + \frac{\pi}{n} + 2\pi \frac{t}{\tau} \right] + \sin \left[(M_b + 1) \frac{\pi}{2n} - \frac{\pi}{n} + 2\pi \frac{t}{\tau} \right] \right|_{\max} \right\}^{-1} \end{aligned} \quad (29)$$

The maximizing values of $2\pi \frac{t}{\tau}$ for equation (29) are expressed in equation (30). The upper signs in equation (30) apply to the first brace and first term in the second brace in equation (29) and the lower signs in equation (30) apply to the second term in the second brace in equation (29):

$$\tan \frac{2\pi t}{\tau} = \frac{\frac{\frac{\gamma-1}{2} M_b + 1}{\frac{\gamma-1}{2} M_b - 1} \cos \left[(M_b - 1) \frac{\pi x}{nL} + \frac{\pi}{n} \right] \mp \cos \left[(M_b + 1) \frac{\pi x}{nL} - \frac{\pi}{n} \right]}{\frac{\frac{\gamma-1}{2} M_b + 1}{\frac{\gamma-1}{2} M_b - 1} \sin \left[(M_b - 1) \frac{\pi x}{nL} + \frac{\pi}{n} \right] \mp \sin \left[(M_b + 1) \frac{\pi x}{nL} - \frac{\pi}{n} \right]} \quad (30)$$

The determination of the constant C_1 and the amplitudes is slightly more lengthy for waves not expressed in simple closed form (for any time and x/L) such as triangular pulses, and so forth. In these cases it may be necessary to plot the curves of $\frac{\delta U}{C_1}$ and $\frac{a}{\gamma C_1} \frac{\delta p}{p}$ against time at $x/L = \frac{1}{2}$ and at any other desired values of x/L to determine the value of the constant C_1 and the maximum value of the term $\frac{a}{\gamma C_1} \frac{\delta p}{p}$. However, computations have shown that the maximized values of the sum and difference of F and G for the same wave forms vary only slightly with M_b if $M_b \ll 1$. Consequently, if the amplitude is to be determined for several adjacent values of M_b the values of $|F \pm G|_{\max}$ need be computed for only one value of M_b . Then the total amplitude can be obtained from equation (28) employing these same values of $|F \pm G|_{\max}$ but varying M_b in the denominator.

For a given frequency and wave form the theory predicts:

(1) a linear increase in pressure amplitude with decrease in mass flow from the incipient value; (2) as n increases with resultant lower frequency for a given mass flow, the amplitude will increase; and (3) higher values of M_b result in larger amplitudes at the same value of n and mass-flow reduction.

APPARATUS

Tests of models of two different diameters were conducted in one of the blow-down jets of the Langley Gas Dynamics Branch which uses low humidity air from large pressure tanks. The models were tested at a Mach number of 1.94 ± 0.02 in a jet 5 inches high and 6 inches wide. The test Reynolds number based on cowl-inlet-diameter was 5.7×10^6 for the larger model. The majority of the testing for the small model was done at a Reynolds number of 1.2×10^6 . (Thus a Reynolds number ratio of 4.75:1 was obtained.) The test-section side walls extended past the end of the nozzle blocks so that the region in which the inlet was located was

open to the atmosphere on top and bottom while bounded laterally by the tunnel side walls. The test-section pressure was adjusted to approximately atmospheric pressure for tests of the large model to minimize disturbances near the cowlings which was located forward of the Mach lines originating at the ends of the nozzle block. For the small model the pressure was generally below atmospheric in order to lower the Reynolds number further but the flow near the cowlings was undisturbed since the shocks from the end of the nozzle intersected the model well behind the cowlings.

In the absence of the models, the turbulence level for pressure in the test section was measured by a sting-mounted inductance gage and found to be negligible for the lower test pressures used for the small model. However, the pressure fluctuations reached an amplitude of about 1.6 percent of the test-section pressure for the higher pressure runs.

Owing to misalignment of the model in the tunnel, tests of the large model were made at a positive angle of attack of 0.5° . Consequently, the majority of the small model tests were conducted at this angle of attack, and, in addition, a few pertinent runs were made at angles of attack of 0° and -0.5° .

Two intersecting piano wires were affixed to the outside of the tunnel windows to provide reference lines. The horizontal wire was aligned nearly parallel to the center-line flow whereas the vertical wire formed an angle of approximately $89^\circ 45'$ with the horizontal wire in the upper left quadrant.

The models which were constructed to be as geometrically similar as possible are shown schematically in figure 2 where dimensions are presented in terms of nominal combustion-chamber diameters. The diameter for the large model was 4.026 inches (the internal dimensions of 4-inch standard pipe) and for the small model was 1.278 inches (internal dimension of $1\frac{1}{4}$ -inch extra-strong pipe), which gives a scale factor of 3.15 for the two models.

The models will be denoted by three numbers. The first number gives the nominal diameter, the second the length-diameter ratio, and the third the cowling-position parameter (angle between ray from apex of cone to cowling lip and axis of ram jet). Thus, model 4.026-14.91- 44.2° would have a nominal diameter of 4.026 inches, a length-diameter ratio of 14.91, and a cowling-position angle of 44.2° . Omission of any of the numbers will cause no ambiguity since the diameters are 4.026 and 1.278, the length ratios 14.91 and 29.82, and cowling angles are between 40° and 48° . The models are closely similar in overall internal shape and in external shape in the region rearward as far as 3 diameters from the inlet. In order to use the same plug valve and exhaust system, a transition section was used at the rear of the small model (see fig. 2).

The removable center body was supported by three faired struts 120° apart and provision was made for varying the center-body position in an axial direction by the insertion of spacers between the center body and its strut support. The spacers required to give cowling-position angles of 48.1° , 44.2° , and 40.1° with tolerances of $\pm 0.05^\circ$ were determined by micrometer measurements. The critical shock angle for a 25° cone at a Mach number of 1.94 is $43^\circ 30'$. The ordinates, obtained by micrometer and surface table measurements, of the cowlings and center bodies are given in table I. The large center body had a conical half-angle of 25.1° and the small body, a conical half-angle of 25.2° . Fabrication limitations of the small model, rather than aerodynamic considerations, dictated the external cowling design and required an external lip angle of the cowling surface greater than the detachment angle for a Mach number of 1.94. The internal surface at the lip was chosen to be approximately parallel to the flow after the conical shock. Furthermore, the cowlings were not sharp-edged but had flats perpendicular to the model axis of about 0.01 inch and 0.001 inch, respectively, for

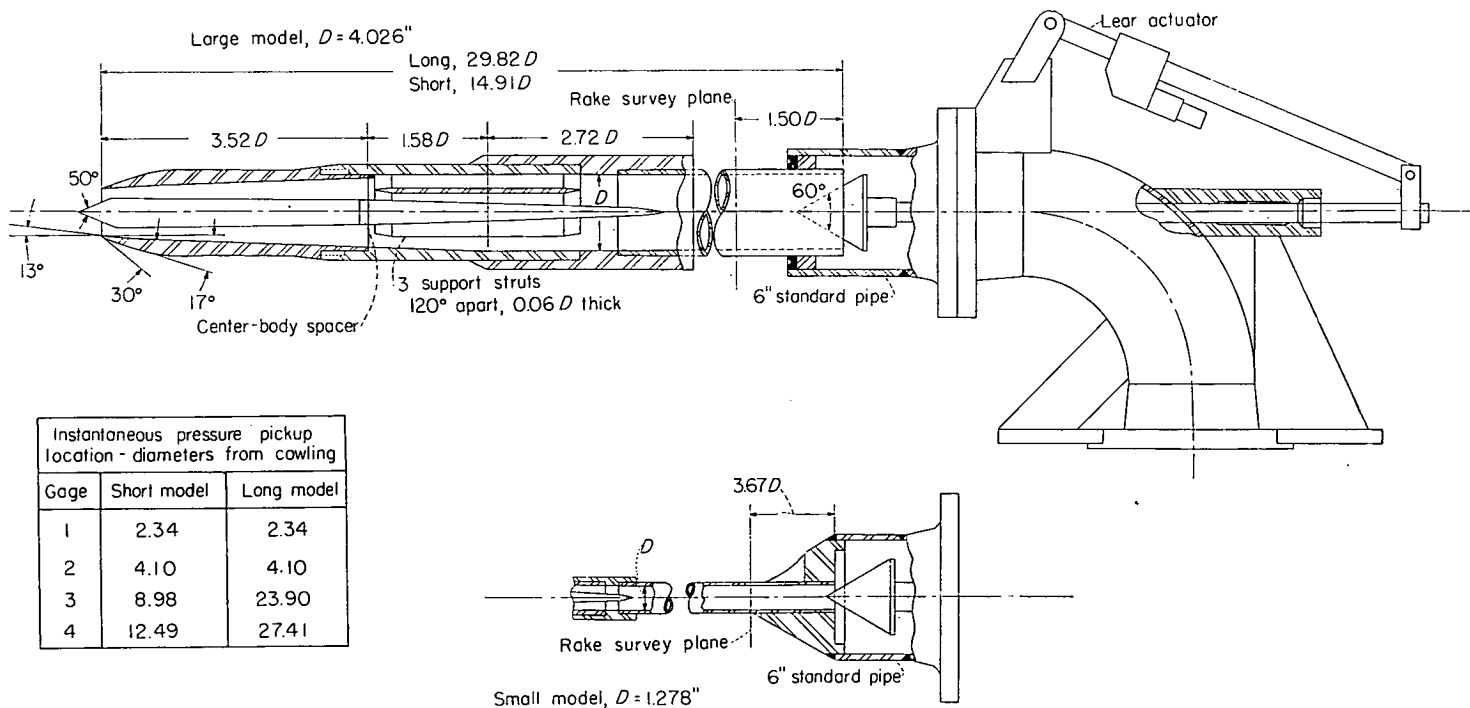


FIGURE 2.—Schematic diagram of models tested. Small model is similar to large model except for transition section at plug valve.

TABLE I.—ORDINATES OF MODELS

*Axial location, x/D	Radii of 4.026-inch-diameter model		Radii of 1.278-inch-diameter model	
	Center body	Inner cowling	Center body	Inner cowling
	r_1/r_i	r_2/r_i	r_1/r_i	r_2/r_i
-0.3095	0	0.601	0	0.599
0	0.290	0.611	0.294	0.608
.02	.308	.622	.313	.617
.04	.327	.631	.332	.626
.06	.345	.639	.350	.634
.08	.362	.647	.369	.643
.10	.377	.650	.386	.647
.11	.383	.653	.391	.651
.12	.389	.656	.395	.655
.13	.394	.660	.397	.658
.14	.397	.662	.400	.661
.15	.398	.665	.399	.664
.16	.398	.669	.399	.667
.18	.398	.673	.398	.675
.20	.397	.681		.684
.25	.396	.686		.688
.30	.395	.693		
.40	.393	.700		
.50	.391	.716		
.75	.385	.732		
1.00	.379	.765		
1.50	.368	.798		
2.00	.356	.830		
2.50	.345	.863		
3.00	.333	.892		
3.44	.324	.896		
3.50	.324	.899		
3.55	.324	.905		
3.65	.319	.916	Same as 4.026 model	Same as 4.026 model
3.82	.308	.929		
4.00	.297	.961		
4.50	.268	.994		
5.00	.239	1.0		
5.10	.233			
5.50	.209			
6.00	.180			
6.15	.171			
6.32	.162			
6.50	.151			
6.97	.124			
7.00	.124			
7.20	.099			
7.30	.079			
7.40	.037			
7.47	0	1.0		
To valve				

*Note: $\frac{x}{D}=0$ is taken at cowling lip

the large and small models. The variation of area normal to the internal flow with axial distance for cowling-position angle of 44.2° is shown in figure 3. The small model had a very slight amount of internal contraction just inside the cowling due to an 0.003-inch error in boring out the cowling in the first 0.1 inch of the model. The included conical angle

of the internal cowling is 3.75° rearward of $\frac{x}{D}=0.5$. The central body has a 1.2° included angle after the shoulder. The blockage of the support struts is only about 7 percent of the local cross-sectional area.

The plug valve was operated by a Lear model 440 actuator and the position of the valve was recorded electrically by means of a system employing an NACA control position transmitter, model 46C (slide-wire resistance), linked to the valve rod.

A nine-tube total-pressure rake with tubes alined in a vertical plane and positioned radially as shown in table II was employed in conjunction with a mercury-differential manometer to determine total-pressure profiles. The three equally spaced support struts were positioned such that the top strut was vertical. Hence, the upper tubes of the rake were in a strut wake, while the lower tubes were unobstructed. Two static orifices located at the rake station were independently connected to the manometer and also to Bourdon pressure gages. Pressure in the settling chamber of the nozzle was measured by both Bourdon and inductance gages while

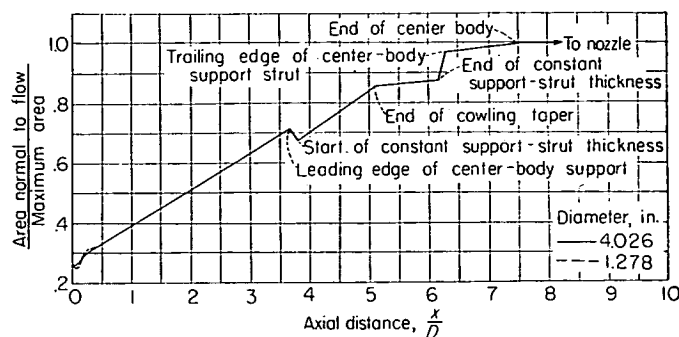


FIGURE 3.—Local flow area plotted against axial distance from cowling for models tested. Cowling-position angle, 44.2° .

the pressure in the reference tank of the induction gages was measured by a Bourdon gage.

Four 15-pound-per-square-inch NACA miniature electrical pressure gages were flush mounted with the diffuser wall at the axial stations given in figure 2. These gages were referenced to an air bottle to allow operation at high pressures. A fifth inductance gage was mounted in the settling chamber to compensate for the time lag which might be induced by the long tubing from the settling chamber to the Bourdon gage on the manometer board. In addition, a calibrated thermocouple was inserted into the settling chamber.

A General Electric B-H6 mercury lamp was used as the light source for instantaneous and high-speed motion-picture shadowgraphs. Motion pictures of the shadowgraph image appearing on a ground-glass screen were taken with a Wollensak Optical Company Fastax camera running approximately

TABLE II.—RAKE ORDINATES IN VERTICAL PLANE

Rake tube number	Ordinate = $\frac{\text{Rake radius}}{\text{Duct radius}}$	
	Large model	Small model
1, 9	0.910	0.889
2, 8	.694	.702
3, 7	.468	.468
4, 6	.231	.234
5	0	0

350 to 900 frames per second. Signals from the pressure gages were amplified by a Consolidated type 1-113 amplifier and then recorded on sensitized paper in a Consolidated type 5-114 recorder employing galvanometer elements. The frequency response of this system was flat from 2 to 300 cycles per second. In order to correlate movie film with the pressure records, a timing light was attached to one edge of the shadowgraph glass screen and the circuit energizing this light connected in parallel with one of the recording galvanometers so that every time the light flashed, a "blip" appeared on the pressure record. In order to reduce the labor of correlation, an interrupter was placed in the light circuit to stop the flow of current for a noticeable period four or five times a second and hence to provide blank spaces on the film and pressure record which could be easily counted.

The camera photographing the manometer board could be operated either manually or electronically. In the latter mode of operation a pressure pulse in the ram jet caused the camera solenoid to trip and concurrently put a marker on the pressure record.

TEST PROCEDURE

Tests of the various configurations were made in the following manner: After "no-flow" pressure and thermocouple zero traces had been recorded, the plug valve was retracted so that the mass flow through the model would be limited only by the supersonic diffuser configuration. Then, the tunnel was started and brought up to operating conditions. The valve was closed to a position below that which caused instability and a manometer picture and a short pressure record taken. After resetting the manometer camera, the Fastax camera and pressure recorder were then started and the valve closed as slowly as possible until buzz began. The valve was then varied further depending upon the type of run desired. A no-flow pressure trace was made after each run when possible.

Other runs were made to determine steady or, if buzzing, quasi-steady average values. In these cases the manometer and pressure records were taken at various fixed valve positions.

The differential inductance gages and valve-position indicator were calibrated daily. Both the larger and small models were tested at length-diameter ratios of 14.91 and 29.82 for each of the cowl-position parameters of 40.1°, 44.2°, and 48.1°. In addition, the small model was run with no central body in order to get a steady-flow calibration for the effective sonic area of the valve at various positions down to mass flows approaching zero. Such a series of runs was not made for the large model because of danger of choking the tunnel and, in addition, because it was felt that with a strong shock far ahead of the inlet that the model would not be free from wall effects.

METHOD OF DATA REDUCTION AND COMPUTATION

The nondimensional mass flow $\frac{\rho U}{\rho_{t\infty} V_{max}}$ at any rake radius

was computed (for steady flow or low amplitude buzzing) from the tank pressure and the local total pressure and static pressure with the assumption that the static pressure was constant across the rake survey plane and stagnation temperature was equal to that in the tank. The local mass flows were then integrated to yield the mass flow in the cross-sectional area bounded by the outer rake tubes. An incremental correction was applied to this mass flow to account for the additional mass flow between the outer rake tube and the wall. In order to determine the constant to be used for adjusting mass flow for the large model, the integrated mass flow was averaged over several runs for configurations 4.026–29.82–48.1° where a smooth symmetric velocity profile existed at the rake station and where the mass flow was known since both shocks were swallowed. The average of the local mass flows at the outer rake stations was also determined for these runs. The incremental constant for the large models was then determined as follows:

Incremental const.

$$= \frac{\left(\begin{array}{c} \text{Mass flow} \\ \text{for 100\% capture area} \end{array} \right) - \left(\begin{array}{c} \text{Av. integrated} \\ \text{mass flow} \end{array} \right)}{\text{Average local mass flow at outer rake}}$$

The adjusting factor to be applied to each of the integrated-mass-flow curves for the large model was then equal to the product of the incremental constant times the local mass flow value at the outer rake locations, that is:

$$\left(\begin{array}{c} \text{Total} \\ \text{mass flow} \end{array} \right) = \left(\begin{array}{c} \text{Integrated} \\ \text{mass flow} \end{array} \right) + \left(\begin{array}{c} \text{Incremental} \\ \text{const.} \end{array} \right) \times \left(\begin{array}{c} \text{Outer rake mass} \\ \text{flow for each run} \end{array} \right)$$

The product of the nondimensional local mass flow times pressure recovery $\left(\frac{\rho U p_t}{\rho_{t\infty} V_{max} p_{t\infty}} \right)$ was integrated similarly by using the correction constant obtained for the mass flow. Assuming the constant to be the same for both pressure recovery and mass flow introduces an error of about 0.1 percent in pressure recovery. The weighted average pressure recovery was determined as the quotient of the total area under the $\frac{\rho U p_t}{\rho_{t\infty} V_{max} p_{t\infty}}$ curve divided by the total area under the $\frac{\rho U}{\rho_{t\infty} V_{max}}$ curve.

A similar constant was obtained for use in the small-model computations by using the average values obtained from swallowed shock runs of configuration 1.278–29.82–48.1°.

The effective sonic area of the plug valve as it approached the fully closed position was computed for the small model from runs made with the central body removed, a configuration which did not buzz at any mass-flow value. A calibration curve of sonic area against valve position was thus obtained for low mass flow. This curve in conjunction with the average value of pressure recovery was used to determine the mass flow for the larger amplitude buzz of the small model. The static-pressure—total-pressure method used for steady-flow small-amplitude buzzing became inaccurate in this region since standing waves in the manometer tubing (see ref. 8) gave erroneous pressure readings which, even if small, have a large effect when the difference between static and total pressure becomes small also. This error in pressure would have only a small effect on mass flow computed on a sonic area and total-pressure basis.

The data plotted in figures 4 to 12 were obtained in the manner described above. An examination of figure 4 shows the computed total mass-flow ratios for the high L/D models with swallowed shock to vary only ± 1.0 percent from the 100-percent capture mass-flow ratio.

Typical steady-state mass-flow and Mach number profiles for the 29.82–48.1° configurations are presented in figures 13 and 14, respectively. Since the Mach number is so small these curves are also close approximations to the velocity profile. Because both the normal and conical shock are inside the cowl, the mass flow is known and the part of the curve between the outer rake and the wall was assumed to be approximately the cubic equation:

$$\frac{\rho U(r)}{\rho U(r_o)} = C_2 \left(1 - \frac{r}{r_t}\right) + C_3 \left(1 - \frac{r}{r_t}\right)^2 + C_4 \left(1 - \frac{r}{r_t}\right)^3$$

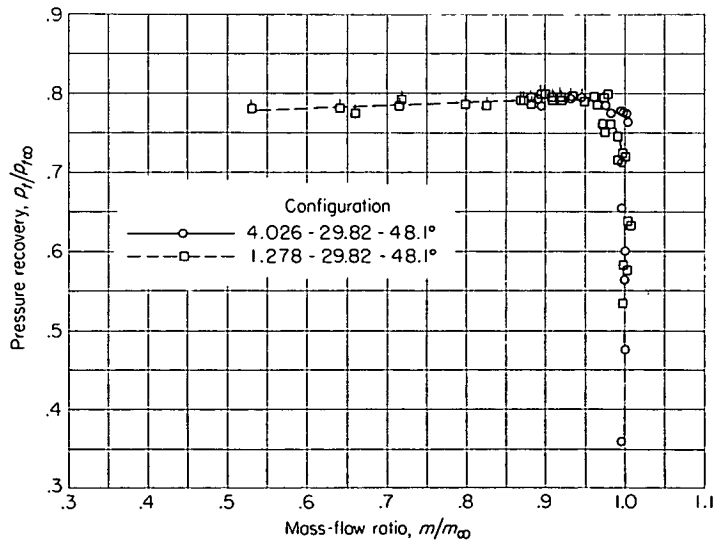


FIGURE 4.—Curves of pressure recovery plotted against mass-flow ratio for configurations 29.82–48.1°. Flagged symbols denote unsteady flow.

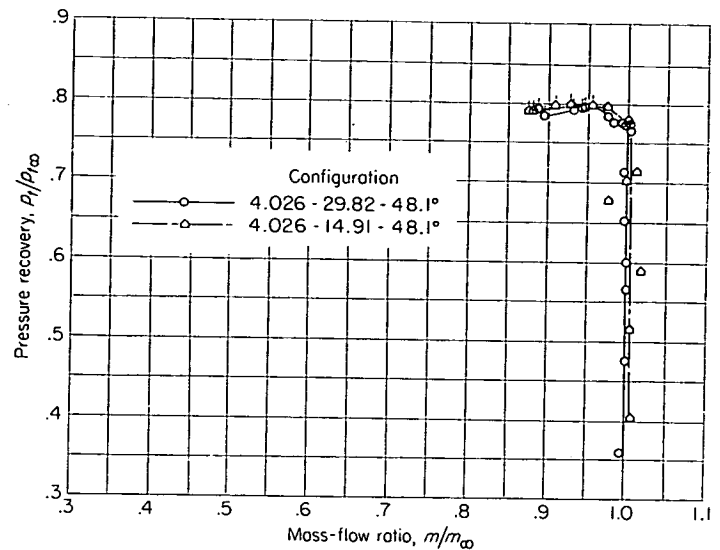


FIGURE 5.—Curves of pressure recovery plotted against mass-flow ratio for configurations 4.026–48.1°. Flagged symbols denote unsteady flow.

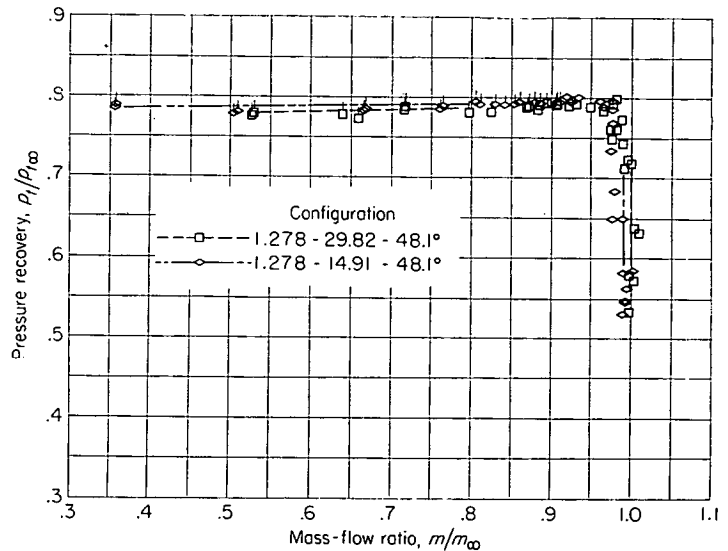


FIGURE 6.—Curves of pressure recovery plotted against mass-flow ratio for configurations 1.278–48.1°. Flagged symbols denote unsteady flow.

The constants C_2 , C_3 , and C_4 were determined to satisfy the boundary conditions of (1) a curve tangent at the outer rake position to the curve determined by the rake readings, (2) a prescribed mass flow, and (3) a curve which coincides with the outer rake points. The form of the equation inherently satisfies the zero velocity condition at the wall (assuming the density does not approach zero). The short-dash curves of figures 13 and 14 are drawn so that the total mass flow of the 1.278 model would give a mass-flow ratio of 1.000, and the long-short-dash curve is the one for which

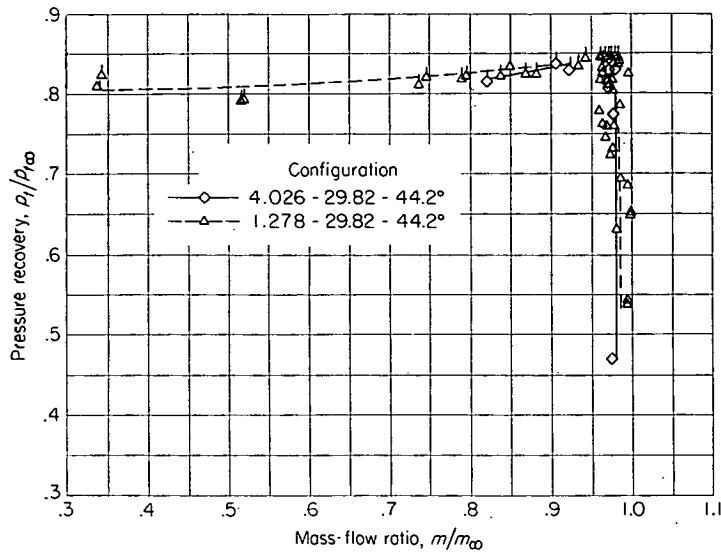


FIGURE 7.—Curves of pressure recovery plotted against mass-flow ratio for configurations 29.82-44.2°. Flagged symbols denote unsteady flow.

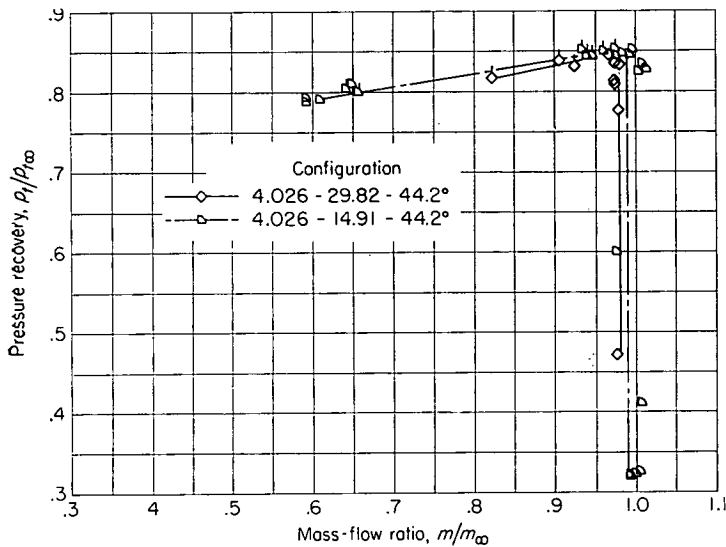


FIGURE 8.—Curves of pressure recovery plotted against mass-flow ratio for configurations 4.026-44.2°. Flagged symbols denote unsteady flow.

the integrated mass flow enclosed between the wall and the outer rake is equal to the "standard increment" applied in the general computations. The two curves coincide for the 4.026 model. The Mach number profile is then determined, since $M(r_o) \ll 1$, from

$$\frac{M(r)}{M(r_o)} = \frac{\rho U(r)}{\rho U(r_o)} \left[\frac{1 + \frac{\gamma-1}{2} M^2(r_o)}{1 + \frac{\gamma-1}{2} M^2(r)} \right]^{1/2}$$

$$\approx \frac{\rho U(r)}{\rho U(r_o)} \left\{ 1 + \frac{\gamma-1}{4} M^2(r_o) \left[1 - \frac{\rho^2 U^2(r)}{\rho^2 U^2(r_o)} \right] \right\}$$

The effective Mach numbers, defined as that Mach number which if invariant across the survey plane would give the measured values of mass flow, pressure, and so forth, of these runs were 0.209 and 0.219 for the 4.026 and 1.278 models, respectively. The average weighted pressure recoveries were 0.639 and 0.601.

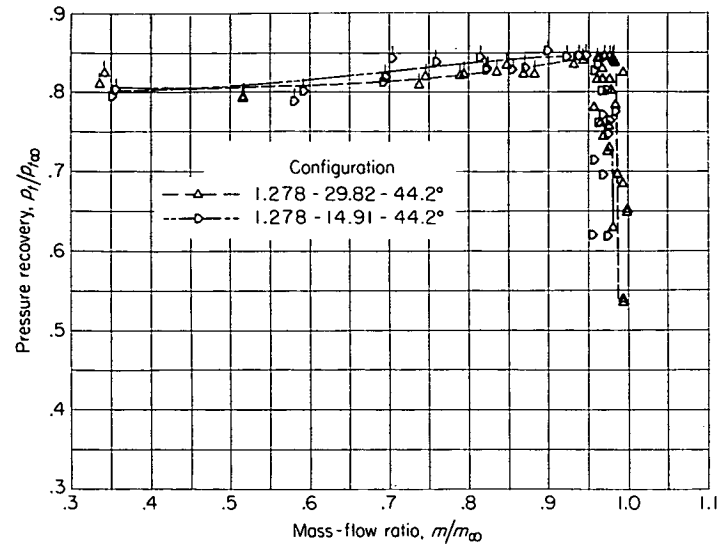


FIGURE 9.—Curves of pressure recovery plotted against mass-flow ratio for configurations 1.278-44.2°. Flagged symbols denote unsteady flow.

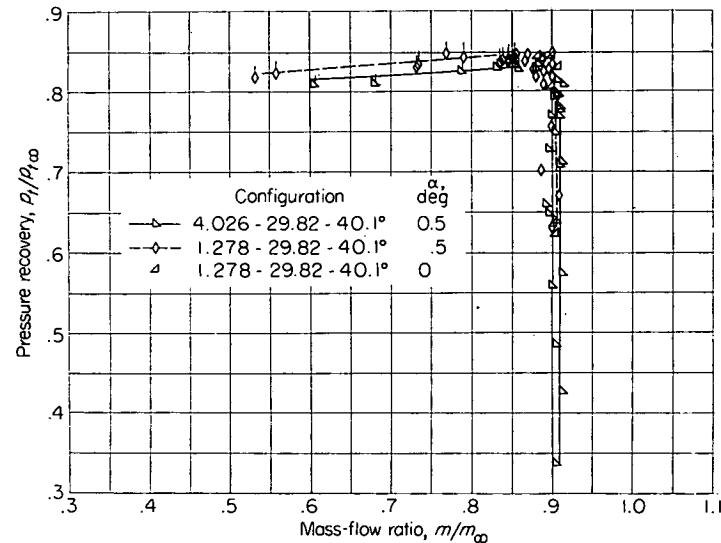


FIGURE 10.—Curves of pressure recovery plotted against mass-flow ratio for configurations 29.82-40.1°. Flagged symbols denote unsteady flow.

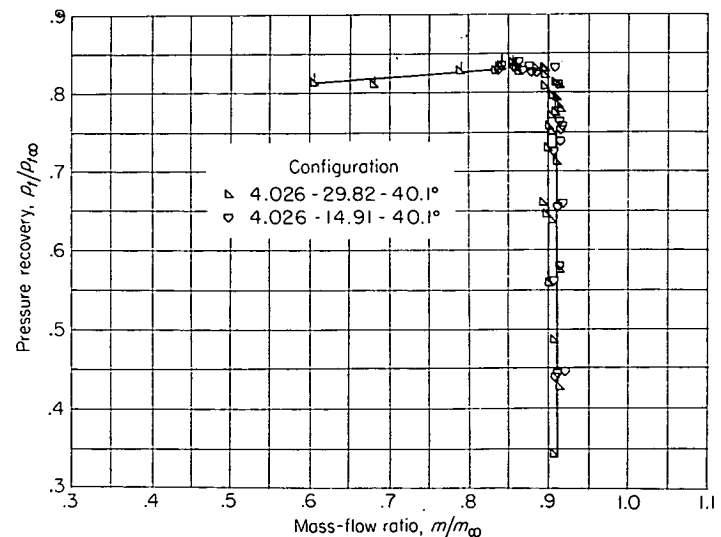


FIGURE 11.—Curves of pressure recovery plotted against mass-flow ratio for configurations 4.026-40.1°. Flagged symbols denote unsteady flow.

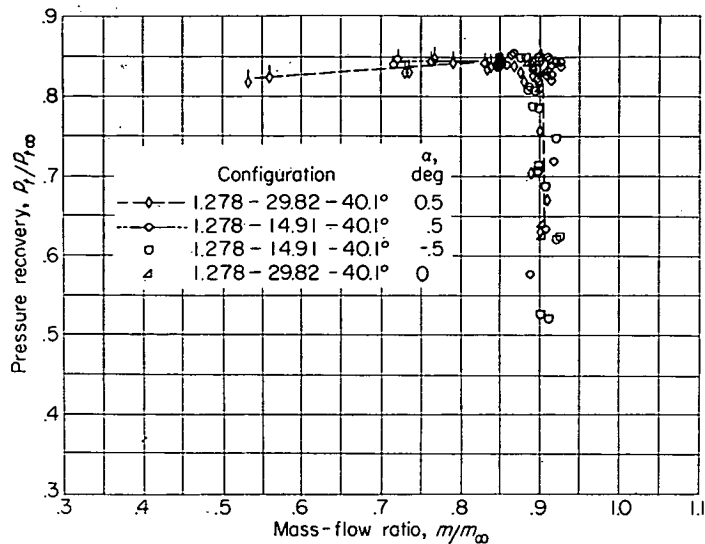


FIGURE 12.—Curves of pressure recovery plotted against mass-flow ratio for configurations 1.278-40.1°. Flagged symbols denote unsteady flow.

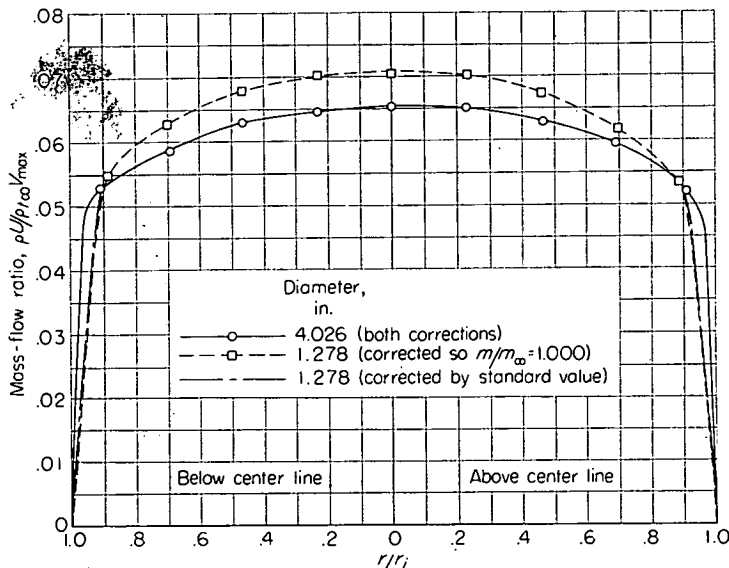


FIGURE 13.—Mass-flow profiles at rake survey station for configurations 29.82-48.1°.

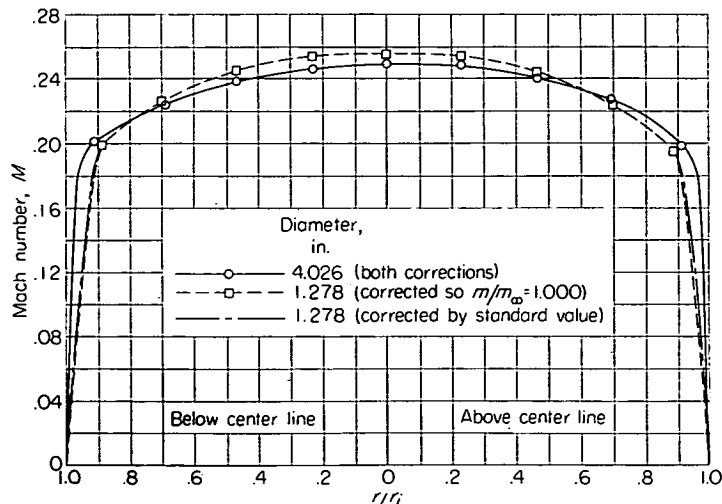


FIGURE 14.—Mach number profiles at rake survey station for configurations 29.82-48.1°.

The trace of the valve-position indicator was measured to an accuracy of 0.01 inch on the pressure record, which gave the indicated physical position of the valve to 0.005 inch. Some play in the linkage mechanism and change in the voltage applied to the slide-wire resistance reduced the accuracy of the position indicator for the large model. These factors were largely eliminated in the small model. There was also a lag of about 0.03 second in the response of the indicator so that for conditions of rapid throttling the valve readings were compensated for this time lag. The maximum valve speed obtained from the slope of valve position plotted against time was 0.55 inch per second.

In order to determine the values of static pressures and valve position at incipient mass flow, the corresponding values were read from the pressure-time or valve-position-time trace. Values were taken when either the high-speed motion pictures or the pressure traces showed instability. It was necessary to employ the motion pictures in some cases where the turbulence and hash level in the gages, especially the two forward ones, was high. The probable cause of the high hash level in the first two gages was separation in the subsonic diffusers.

Total amplitude measurements were taken by measuring peak-to-peak pressure fluctuations on the pressure-time curve.

The following are the estimated maximum probable errors arising when the flow is steady:

Mass-flow ratio:

For high length-diameter ratios..... ± 2 percent
For low length-diameter ratios..... ± 3 percent

Valve position:

For large model..... ± 0.01 in.
For small model..... ± 0.005 in.

Pressure recovery..... ± 1.0 percent

Static pressure..... ± 0.5 percent

Mach number in ram jet..... ± 0.002

RESULTS AND DISCUSSION

GENERAL RESULTS

Figures 4 to 12 show the performance curve of the inlets in terms of pressure recovery and mass flow. Experimental points having unsteady flow are denoted by flagged symbols. The ram jets with the higher value of length-diameter ratio were employed to give more accurate values of mass flow and pressure recovery for comparison purposes since in the larger models the velocity profile has become a smooth nearly symmetrical curve showing negligible effects of the center-body wake and angle of attack by the time the rake station has been reached. Each of the high-length-diameter-ratio configurations is compared separately with its two counterparts, namely: the same length-diameter-ratio model of different diameter and the shorter version of the same diameter. It is obvious from inspection that the accuracy is lower in the lower L/D models, but the curves for the high and low L/D models of the same diameter and cowling-position angle may be considered the same within the order of the expected experimental scatter.

Table III is a compilation of the values of mass-flow ratio, pressure recovery, valve position, and ratio of static pressure to tank pressure at the start of buzz. The incipient mass flow,

TABLE III.—VALUES OF PARAMETERS AT START OF BUZZ

Configuration	Mass-flow ratio	Pressure recovery	Static pressure Tank pressure		Valve position
			Gage 1	Gage 4	
1.278-14.91-48.1°	0.91	0.795	0.744	0.782	1.35
1.278-29.82-48.1°	.925	.790	.738	.778	1.345
4.026-14.91-48.1°	.955	.795	.727	.781	2.12
4.026-29.82-48.1°	.945	.790	.733	.782	2.12
1.278-14.91-44.2°	.98	.844	.805	.837	1.34
1.278-29.82-44.2°	.98	.844	.804	.835	1.34
4.026-14.91-44.2°	.98	.848	.804	.842	2.07
4.026-29.82-44.2°	.98	.844	.802	.838	2.06
1.278-14.91-40.1°	.85	.846	.817	.840	1.31
1.278-29.82-40.1°	.85	.846	.814	.844	1.31
4.026-14.91-40.1°	.86	.832	.806	.825	1.965
4.026-29.82-40.1°	.86	.832	.804	.829	1.96

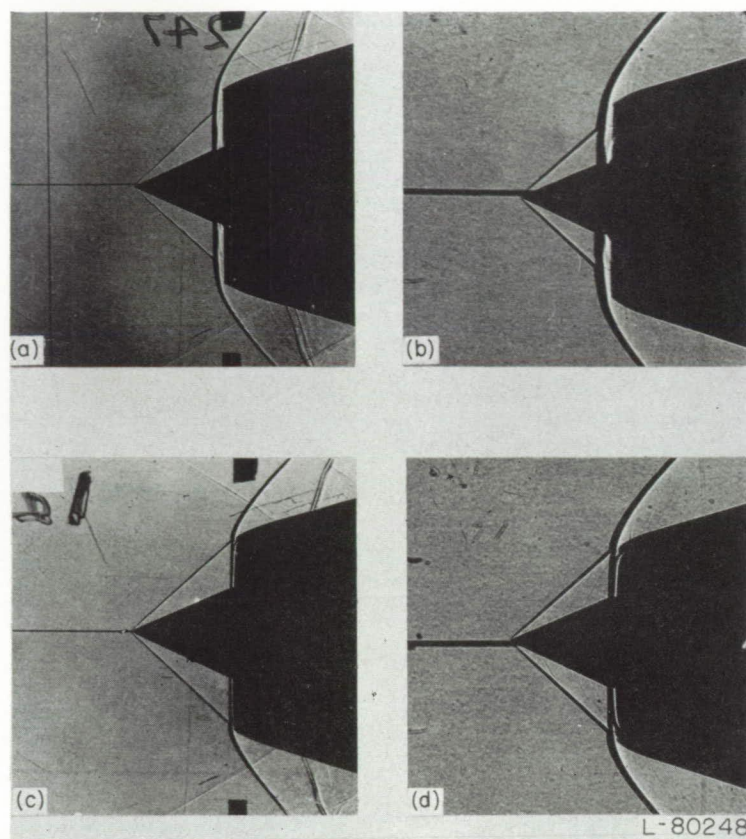
with one exception where the interval between the highest measured unsteady flow and lowest measured steady flow was large, was assumed equal to the largest value of mass flow at which unsteady flow was first recorded. This exception arose in the case of the 1.278-14.91-48.1° configuration where the unsteady flow was noted up to a mass-flow ratio of about 0.89 and the lowest measured steady flow was at a ratio of 0.915. The critical mass flow of 0.91 was determined by extrapolating a curve of pressure pulsation amplitude plotted against mass flow to zero amplitude.

The incipient pressure recovery was obtained from the faired curve of pressure-recovery mass flow at the incipient mass-flow value. The static-pressure—tank-pressure ratios and the valve positions, determined from the time-history records, are the average values of several runs.

Shadowgraphs of the critical-flow shock pattern for the various model configurations are given in figure 15. These pictures, with the exception of figure 15(g) which is for a negative angle of attack, are of the high length-diameter configurations at a positive angle of attack of 0.5°. The shadowgraphs of the models are adjusted to have approximately the same dimensions to facilitate comparison. The cowling lip was referenced by two pieces of opaque tape affixed to the tunnel glass at the top and bottom of the test section, but because of the enlarging procedure just mentioned the tape will show only in the large-diameter-model pictures.

The external shock pattern for the configurations with cowling-position angles of 44.2° and 48.1° appear unaffected by the slight angle of attack. For the 44.2° configuration three-dimensional effects are responsible for the apparent presence of the normal shock ahead of the cowling when in reality it is just at the lip, a fact which may be verified by the opaque-tape reference marks.

A difference in the flow configuration due to 0.5° angle of attack is noticeable for a cowling position angle of 40.1°. The normal shock on the leeward side of the cross flow induced by the angle of attack is advanced ahead of the cowling lip more than the shock on the windward side; and, in addition, the leeward shock may terminate in a lambda shock near the



(a) Configuration
4.026-29.82-48.1°; $\alpha=0.5^\circ$.
(c) Configuration
4.026-29.82-44.2°; $\alpha=0.5^\circ$.

(b) Configuration
1.278-29.82-48.1°; $\alpha=0.5^\circ$.
(d) Configuration
1.278-29.82-44.2°; $\alpha=0.5^\circ$.

FIGURE 15.—Instantaneous spark shadowgraphs of flow patterns for minimum stable mass flow.

cone. Proof that this phenomenon arises from the slight angle of attack is found in the shadowgraphs of the critical mass flow of the same supersonic diffuser configuration for an angle of attack of 0.5° (fig. 15(f)) and -0.5° (fig. 15(g)) which show the shock pattern to change with angle of attack. The cross flow of the boundary layer causes a boundary layer build-up on the leeward side which results in the asymmetric shock pattern.

Curves of Mach number at the center line of the rake plotted against steady-flow pressure recovery for configurations 4.026-29.82-48.1° and 1.278-29.82-48.1° are shown in figure 16. These curves are typical of the 44° and 40° configurations also. Values were not plotted for unsteady flow since such a procedure would make the plot multiple valued in pressure recovery.

SCALE EFFECTS

A dimensional analysis of the problem of testing buzzing models for correlation purposes yields the following results. The variables in the problem are: (1) pressure p or pressure perturbation Δp ; (2) stream velocity V ; (3) density ρ ; (4) length L or diameter D ; (5) viscosity μ ; (6) sonic velocity a ; (7) periodic time τ ; (8) turbulent velocity w and/or per-

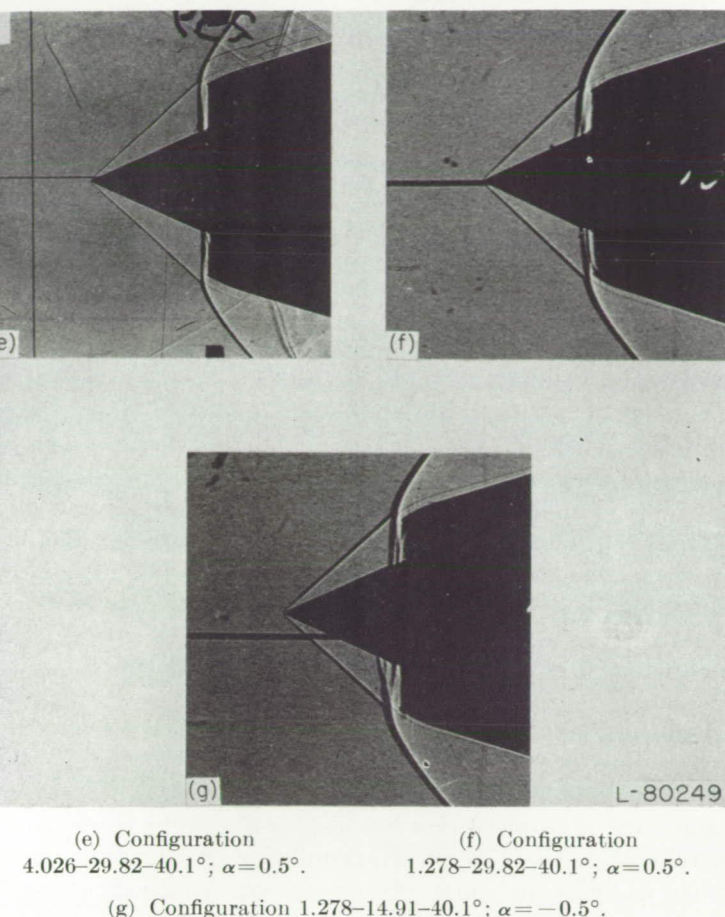


FIGURE 15.—Concluded.

turbation velocity ΔU . Then, the related nondimensional parameters in the mass-length-time system are: (1) Mach number $\frac{V}{a}$; (2) Reynolds number $\frac{\rho V L}{\mu}$, (3) wave length of model $\frac{L}{a\tau}$, (4) pressure coefficient $\frac{p}{\rho V^2}$ or $\frac{\Delta p}{\rho V^2}$, (5) turbulence or perturbation ratios $\frac{w}{V}$ or $\frac{\Delta U}{V}$. Thus, if models of different scale (L) are to be tested without maintaining constant Reynolds number, the effect of varying Reynolds number must be ascertained.

The importance of boundary-layer growth and separation to the stability of inlets in absence of combustion will be discussed in a later section of this report. If these viscous effects are to be a major factor in determining the stability of inlets, Reynolds number effects would then also be expected to be a major consideration.

Steady flow.—From the results presented the performance of the models to the start of buzz may be discussed. Figures 6, 8, 9, 11, and 12, in which pressure recovery plotted against mass-flow ratio of model pairs having the same diameter and cowling angle are compared, show the performance of such pairs to be nearly the same within experimental scatter. There does appear to be a tendency for the lower L/D models to have up to 1 percent higher pressure recovery

during buzzing, but this might be attributed to the different frequencies of the standing waves in the manometer tubing. Although the mass-flow measurements have a larger range of error in the low L/D models, the induction-gage pressures and valve-position indicator are not so affected. Hence, a good check of the conditions at start of buzz for the same diameter and cowling-position-angle models is found in table III, where the maximum variation of average valve position at start of buzz is found to be 0.005 inch and 0.01 inch for the 1.278- and 4.026-inch models, respectively, and of average static-to-tank pressure ratio at corresponding stations is found to be about 0.5 percent. An analysis of the high-speed motion pictures also revealed the shock patterns to be the same at the start of buzz independent of L/D ratio for the same diameter and cowling-lip angle.

A comparison of the performance of similar configurations having different diameters shows only a slight scale effect. The pressure recovery mass-flow curves of the 44.2° and 48.1° diffusers (figs. 4 and 7) are nearly identical for the two diameters. Instability appears at a slightly higher mass-flow ratio in the larger model of 48.1° lip angle than in the corresponding small model, but the 2-percent variation has little significance. The shadowgraphs of the flow patterns at the incipient point for the above configurations (figs. 15 (a) to 15 (d)) show no important differences in the flow for the different sized models.

It is to be noted that in the 40.1° inlets where, although the critical mass flows are nearly the same, the peak pressure recovery, critical pressure recovery, and the ratio of static pressure to tank pressure are higher in the small diameter model in spite of the lower Reynolds number of these models. See figure 10 and table III.

It was also found that the overall incipient values did not change when the angle of attack was reduced to 0° or made negative by 0.5° for the configurations 1.278-40.1° although the local conditions alternated with the shock pattern. Shadowgraphs in figures 15 (e) and 15 (f) at a positive angle of attack are nearly identical for the different sized models. Figure 15 (g) at an angle of attack -0.5° is not a mirror image of figure 15 (f), although the tendency of the leeward shock to advance and bifurcate is quite evident. For a configuration such as this, which is extremely sensitive to changes in angle of attack, such a variation could be attributed either to a failure to exactly match the positive angle with its negative counterpart or to a slight eccentricity of the central body which would alter the effective angle of attack of the cone.

The Reynolds number effects on the profiles of the models of large L/D are evident in figure 16; these profiles are typical of the curves for all the cowling-position angles. Although both models have profiles of turbulent pipe flow the greater relative viscous forces in the low Reynolds number tests result in a larger region of retarded flow contrasted to the much more fully developed flow of the high Reynolds number model (fig. 13).

The velocity and mass-flow profiles of the low L/D models showed the influence of the 0.5° angle of attack in varying

amounts in a majority of the runs. The pressure recovery and velocity were higher in that section of the survey plane behind the leeward cone surface for both large and small models. Two profiles for positive and negative angles of attack of configuration 1.278-14.91-40.1° which show the manner in which the asymmetry alternated with angle of attack are presented in figure 17. Oswatitsch (ref. 1) discovered the same phenomenon in certain of his tests at slightly larger angles of attack. Since the boundary layer tends to accumulate on the leeward side of the central body one might expect the poorer performance to occur in this region. For configurations 14.91-40.1° the shadowgraphs show external separation on the leeward side as the incipient mass flow is approached. There are several possible explanations for the measured distribution of total pressure. First, the lambda shock on the leeward side might increase the total pressure recovery of the fluid flowing through the upper bifurcations sufficiently to offset the adverse effect of the separation at the cone surface. Secondly, the flow on the inner surface of the windward cowling might separate to a greater degree than that on the leeward side of the central

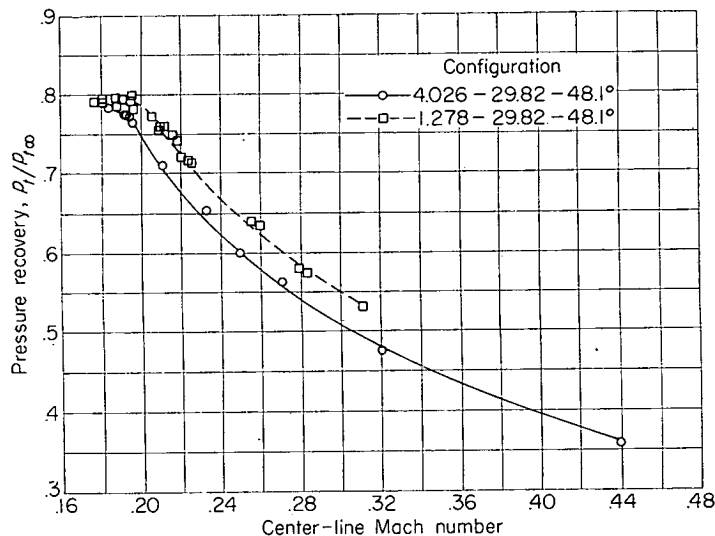


FIGURE 16.—Curves of average pressure recovery plotted against Mach number at center of rake survey station for configurations 29.82-48.1°.

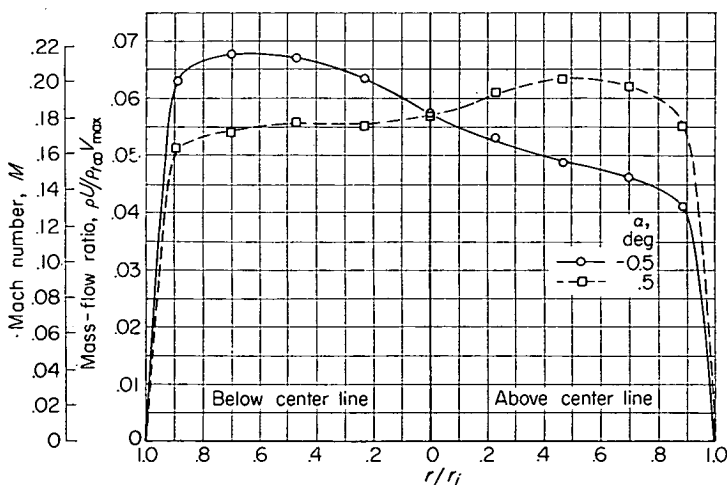


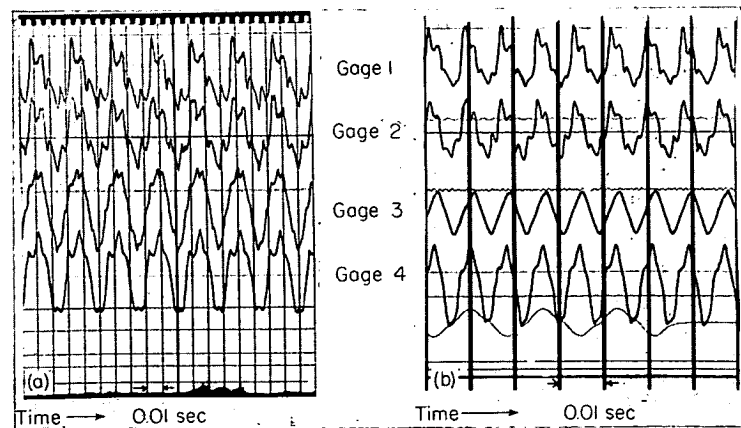
FIGURE 17.—Mass-flow and Mach number profiles at rake survey station for configuration 1.278-14.91-40.1° at angles of attack of $\pm 0.5^\circ$.

body. Finally, there is the possibility of a more violent separation occurring in the subsonic diffuser, either off the central body or cowling surface of the opposite side. In other words, the early flow separation on one side of the center body may prevent a more violent separation of the flow on the same side later in the subsonic diffuser.

The apparent lack of a strong Reynolds number effect in determining the stability of the 40.1° and 48.1° configurations (where the conical shock did not intersect the cowling lip) was not expected. Prior to conducting the tests it was thought that the Reynolds number effect would be small for those inlets which had the conical shock at the lip since the vortex sheet position would govern stability. For those inlets in which the central-body boundary layer was an important part of the governing mechanism for stability, the Reynolds number was thought to be a very important parameter. This negligible effect of Reynolds number should not be assumed to apply to inlets in general but rather to represent the effect only on the particular configurations investigated. It does, however, show that there is the possibility of testing cold-flow scaled models for approximate prediction of stability limits.

Unsteady flow.—The behavior of the comparative models during buzzing was also very similar. This similarity extended not only to the unsteady-flow cycles which were made up of multiple waves but also to the cycles dependent on random pulses. Typical examples of the first case are shown in figure 18 where the pressure-time records of configuration 4.026-14.91-44.2° at a mass flow ratio of 0.66 is compared to the curves of configuration 1.278-14.91-44.2° at a mass flow of 0.69. In spite of the 3-percent variation in mass flow it is obvious that the wave forms are quite similar if the time scale is modified by a factor equal to the length ratio. The pressure records of the 1.278 model were taken at a higher film speed to facilitate comparison. The vertical lines on the record indicate time intervals of 0.01 second.

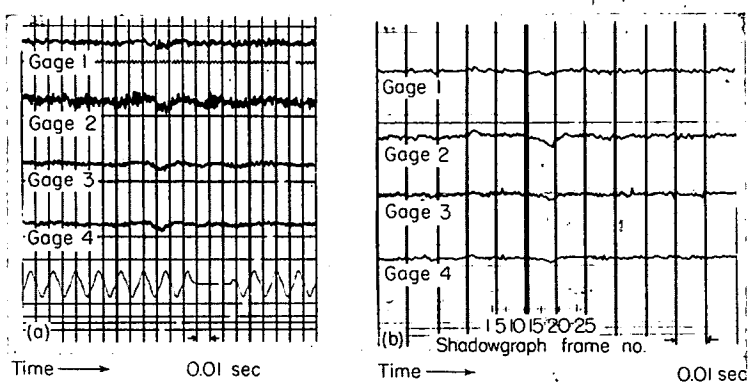
Figure 19 shows the pressure-time records of configurations 14.91-40.1° near the start of buzz where there is no regular cycle buzzing, instead the unsteady flow is characterized by spasmodic pulses separated by time intervals of various lengths. These latter curves show the unsteady behavior to be similar, even where irregular.



(a) Configuration 4.026-14.91-44.2° at a mass-flow ratio of 0.66. (b) Configuration 1.278-14.91-44.2° at a mass-flow ratio of 0.69.

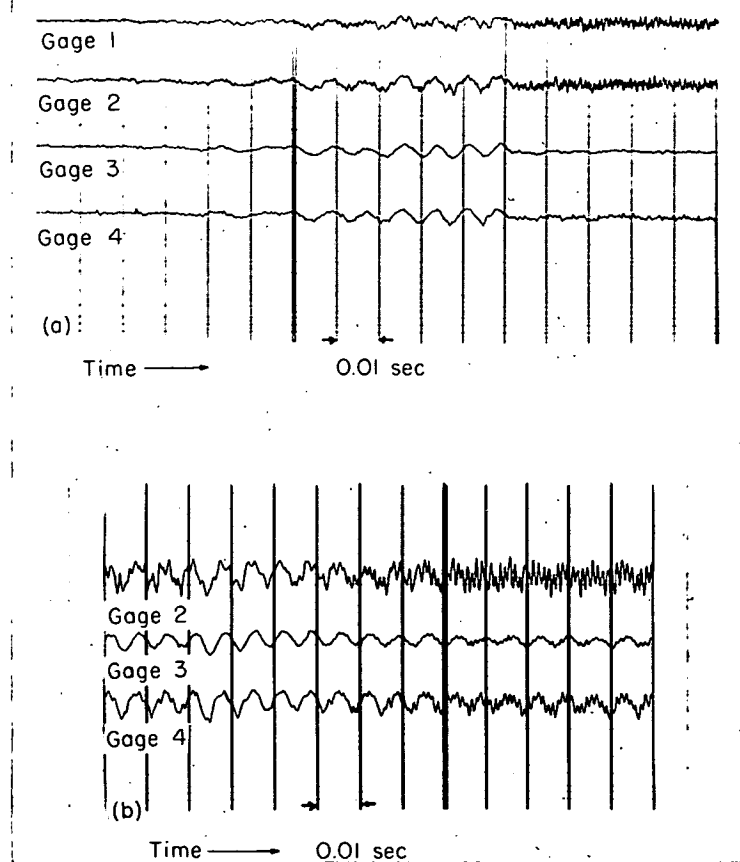
FIGURE 18.—Pressure time records showing similar regular pulses in buzzing of similar configurations. Pressure is positive upward.

The unsteady flow of configuration 1.278-14.91-40.1° was unstable at a mass-flow ratio of 0.72 and, as is shown in figure 20, changed from a relatively low frequency of 120 to 160 cycles per second, which was often found in most of the 1.278-14.91 configurations, to much higher frequencies, usually approximately 800, 900, or 1,400 cycles per second. The whole shock pattern oscillated at this frequency. With no change in valve position this high-frequency pattern would in time break down and revert back to the low fre-



(a) Configuration 4.026-14.91-40.1°. (b) Configuration 1.278-14.91-40.1°

FIGURE 19.—Pressure-time records showing similar isolated spasmodic pulse in buzzing of similar configurations. Pressure is positive upward.



(a) Slight valve motion.
(b) No valve motion.

FIGURE 20.—Pressure-time records showing transition from low-frequency to high-frequency buzzing in configuration 1.278-14.91-40.1°.

quency, and so forth. This conversion to high frequency is shown in figure 20. In figure 20 (b) (gage 1 is inoperative) there is no valve motion and the high frequency of 900 cycles per second is superimposed on the 160-cycle-per-second buzz. In figure 20 (a) the valve is slowly closing to the position of figure 20 (b), and in this case the high-frequency breakdown results in a 1400-cycle-per-second buzz with the elimination of most of the low-frequency pulses. An examination of other records and motion pictures at slightly higher mass flows showed a possibility that the frequency of oscillation of the bifurcated part of the shock to be about 900 cycles per second when the upper part of the shock was responding to the low frequency.

Figures 19 and 20 also prove the fact that the buzzing cycles are not necessarily repeatable, but that single pulses may occur or the cycle change drastically with no change in ram-jet geometry. Averaged results for the high and low frequency, obtained with no valve motion, similar to that in figure 20 showed a variation of less than ½ percent in pressure recovery and mass flow which is less than the scatter of the tests.

The flow of the longer 1.278-40.1° model did not break down completely into a high-frequency oscillation for periods longer than 0.02 second, but the pressure records did show evidence of such high frequency which was usually definitely subordinate to the low frequency. Previous unpublished data of tests at the Langley Aeronautical Laboratory have, however, shown the high-frequency oscillation to be present in high L/D models. Safety considerations, plus the doubt that large amplitude oscillations would be free from influence of the test-section boundaries, prevented all but a few runs of large pulsation amplitude for configuration 4.026-40.1°. No runs for the 14.91 L/D model were made at a low enough mass-flow ratio for the high frequency to appear predominant, though the oscillation frequency of the lambda shock was determined to be about 350 cycles per second compared to the 900 cycles per second of the model smaller by a factor of 1/3. A few runs were made at low mass flows for the 4.026-29.82-40.1° configuration and these also had high-frequency components subordinate to the low frequency.

Figure 21 is part of an 850-frame-per-second shadowgraph motion-picture film taken concurrently with the pressure record shown in figure 19 (b) of a single spasmodic pulse of configuration 1.278-14.91-40.1°. The shadowgraph frames are numbered to correspond to the numbers on the pressure record.

From these shadowgraphs it is evident that an appreciable part of the total shock motion, as well as almost all of the lambda shock motion, occurs between frames 9 and 10. This is in agreement with the pressure record of the gage at $x/L=0.275$ which shows, more sharply than the other gages, the break in pressure which for this particular gage occurs concurrently with shadowgraph frame number 10. The time lag, or time for a wave to travel from the cowl lip to $x/L=0.275$, is about one-half the time between frames. Thus, in this case, where it should be emphasized there was no valve movement whatsoever, it is evident that the overall

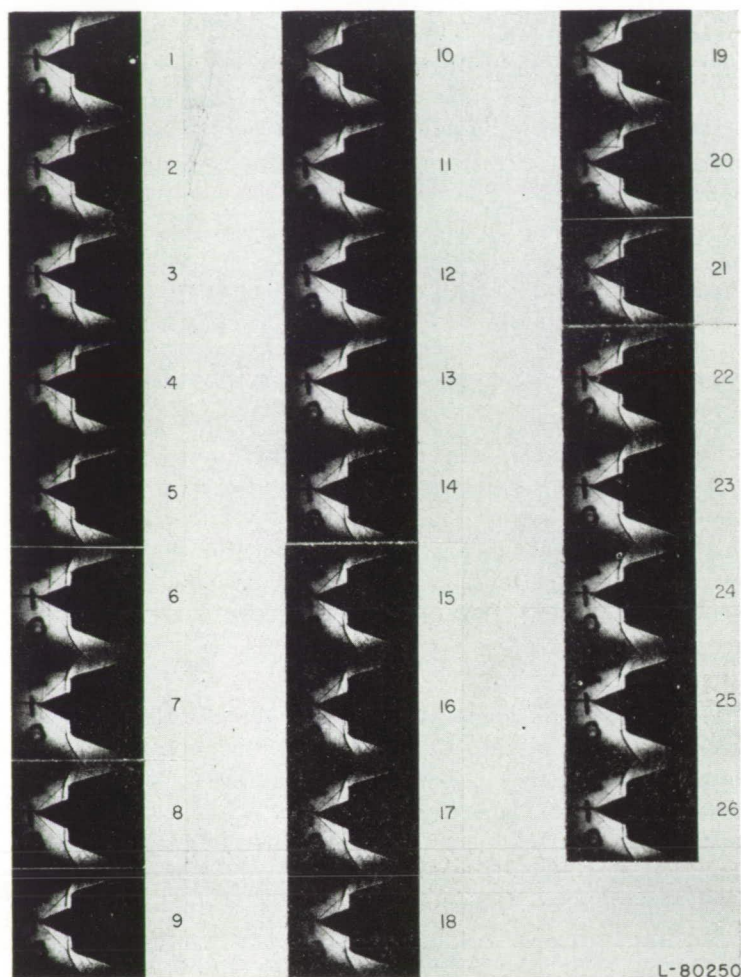


FIGURE 21.—High-speed motion-picture shadowgraphs of isolated spasmodic pulse in buzzing of configuration 1.278-14.91-40.1°.

ram-jet geometry can have no effect on the initial shock motion. This is substantiated by the fact that the initial shock motion, which is an appreciable part of the overall motion, has been completed before any waves which it generates at the inlet have had time to travel even 4 diameters downstream, let alone have had time to reflect from any significant geometrical or aerodynamic changes and return to the cowl to influence further motion. The reflection from the valve of the start of the initial expansion reaches the inlet at frame 12, but the shock does not start to retreat until frame 19 although expansion waves reflected from the nozzle are continuously hitting the shock during the interval between frames 12 to 19. The fact that the shock does not start to move rearward when the reflected expansion from the exit nozzle strikes it from behind indicates that there must be a flow phenomenon at or near the cowl which generates compressions to cancel the effect of the expansion. The above shock motion is not peculiar to this particular configuration but has been observed to occur in other tests. Although many of these tests may have a gradual throttling process, it is found that the shock is still out of equilibrium with the rearward part of the ram jet (that is, it moves faster than the low throttling rate would require).

Note also that the normal shock is slightly further advanced than the position of figure 15 (f) at the incipient mass flow. Thus for a short period of time the shock has an equilibrium position at a mass flow below the value for start of buzz.

The model pairs having the same diameter, supersonic diffuser, and subsonic diffuser configuration have approximately, within the expected maximum error, the same pressure recovery mass-flow curves (figs. 5, 6, 8, 9, 11, and 12). In the unsteady flow range there does appear a slight tendency for slightly higher pressure recoveries for the shorter L/D models. Now only the combustion-chamber volume varies in these comparable pairs. Since the combustion-chamber volume changes by a factor of about three between the 29.82 and 14.91 L/D models, according to the resonator theory of reference 6 the slope of the pressure recovery against mass-flow curve at the start of buzz for these configurations with continuous slopes should also vary so that the slope of the 14.91 L/D model should be three times the slope of the 29.82 L/D model since the absolute values of pressure recovery and mass flow at start of buzz are the same (table III). However, the experimental curves for the 40.1° and 48.1° configurations having continuous slopes show that the low L/D models generally have a smaller, not larger, slope.

DISCUSSION OF STABILITY CRITERIA

Since various contrasting theories (refs. 4 to 6) have been expounded regarding the start of instability of supersonic diffusers, there is a definite need for clarification of the subject. It will be advantageous to consider first the basic aerodynamic phenomena involved in the initiation and continuation of the buzz cycle.

Quasi-one-dimensional theory for originating mechanism.—The theory of reference 5 describes the buzzing cycle once it has been initiated and assumes the initiating mechanism to be some form of separation near the inlet. It was found that an unsteady-flow theory based on a quasi-one-dimensional analysis gave very close correlation to the experimental pressure-time records in the ram-jet model. The shortest model studied, with an L/D of about 16, was rather long for a ram jet; however, since the gage nearest the cowl, located about 5 diameters downstream from the cowl, showed excellent agreement with the plane wave theory, it may be assumed that plane wave theory holds for ram jets having L/D greater than 5 and probably even to lower values.

On a quasi-plane wave basis the buzzing cycle may be analyzed in the following manner: In the start of buzzing the normal shock moves outward away from the cowl and this shock motion requires compression waves to strike the downstream side of the shock. Since the pressure-time curves of reference 5 and figure 19 show that in the absence of rapid throttling there are no compression waves moving upstream inside the ram jet at any appreciable distance from the inlet, then the required compression waves must be generated

at or near the cowl entrance. Equation (2) of reference 5 shows that either a flow area decreasing with time or a flow entropy increasing with time is needed to generate upstream moving compression waves (that is, an increase of the parameter Q in eq. (2) of ref. 5). A separation, or even an unseparated boundary layer growing with time, satisfies both these requirements since the rate of displacement thickness growth produces a decreasing effective flow area while concurrently the entropy is increasing due to boundary-layer losses.

The entering of the vortex sheet from the conical-normal-shock intersection into the cowl will also result in both a reduced flow area for the flow inside the vortex sheet and, after mixing, an increased entropy. Moreover, the entrance of the vortex sheet must be violent and abrupt since the vortex sheet itself cannot stagnate on either the outer or inner surface of the cowl because of the total pressure difference existing across it. Thus, the entrance of the vortex sheet or the growing of the boundary layer (separation) have much the same effect as closing a throttling valve located near the inlet.

Thus, the mechanism of buzz initiation may be described as follows: The entrance of the vortex sheet, increasing separation, or boundary-layer growth (behind the shock), either on the central body or on the inner surface of the cowl, generates a compression wave which forces the normal shock outward. This initial growth may be very small and may result from the random fluctuations present in the flow. Such a case was illustrated in figure 19 for no valve motion. When buzzing arises during throttling, the compression waves generated by the throttling process force the shock to a position where either a random pulse at the inlet or the next small wave from the exit throttle may perturb the shock. In cases where the entrance of the vortex sheet into the cowl causes the initiation of buzz, the pulse generated by the abrupt motion of the vortex may also be augmented by separation on the cowl surface so that the compression wave generated is stronger and consequently the shock is generally forced out abruptly. Reference 4 explains that the case in which the vortex sheet enters the cowl without causing separation is a result of the mixing of the low and high energy air on each side of the vortex sheet before subsonic diffusion occurs. In addition, the pulse created by the vortex motion would be weakened for the inlets having sharper leading edges and thinner cowl thicknesses. These possibilities could explain the observed entrance of the vortex sheet into the cowl without causing buzz. In cases where separation on the central body initiates the buzz there is usually no such rapid growth of the separated region, instead a small growth of separation generates a compression wave which forces the shock out slightly. However, in this new forward position to which the shock has been forced, new flow conditions exist behind it which include a more adverse pressure gradient between the shock and the

cowl entrance. Consequently, additional separation may occur with consequent production of more compression waves to force the shock out farther, and so forth. This outward motion of the shock will continue until either (a) an equilibrium condition is reached in the region of flow between the shock and separation region, or (b) an expansion wave can strike the shock from behind to lower its back pressure so that it will retreat toward the cowl (see ref. 5).

It is to be noted that it is not necessary to "choke" the entering flow in the sense that sonic velocity must be obtained near the cowl entrance to start buzzing. The rate of effective-flow-area decrease and entropy increase are the important parameters, though it must also be emphasized that these factors will generate stronger waves when the Mach number is near unity.

Wave cycle.—Now that the basic phenomena involved in the initiation of buzzing have been described, the mechanism by which it is perpetuated will be reviewed (see ref. 5): The outward motion of the shock and the increasing boundary-layer displacement thickness reduce the mass flow through the diffuser. This reduced mass flow results in an expansion wave which moves down the subsonic diffuser and combustion chamber and lowers the pressure, density, and velocity. At the sonic exit nozzle, this downstream expansion is reflected as another expansion wave which moves upstream until it meets the shock. Whereupon the shock moves rearward and passes through the position it had at the start of buzz. The separation which originally caused the buzz is not as large at this time because the upstream expansion wave creates a favorable pressure gradient and the retreating shock results in reduced losses. In other words, as the shock passes the position from which buzz started the flow conditions are not the same. A change in flow pattern at the same shock position is shown in the instantaneous shadowgraphs, figure 22. Since the lambda pattern is known to exist in the outward motion, the other flow configuration probably occurs during the retreating shock motion. This would also be in accord with the effect of favorable pressure gradient just mentioned. The rearward shock motion generates a downstream compression wave, which in turn reflects as another compression wave moving upstream until it also strikes the shock.

In certain cases, since the strength of the waves reflected at the nozzle depends on the relative constriction of the nozzle area to combustion-chamber area, this reflected compression is strong enough to return the shock to the position at which buzzing began, and consequently another cycle starts immediately. The frequency is then nearly identical to that of an organ pipe closed at one end with a length equal to the ram jet.

In other cases the first reflection is weaker so that the shock is not moved far enough forward to reach the buzzing position. However, since the compression-wave—shock-wave interaction results in the generation of a downstream com-

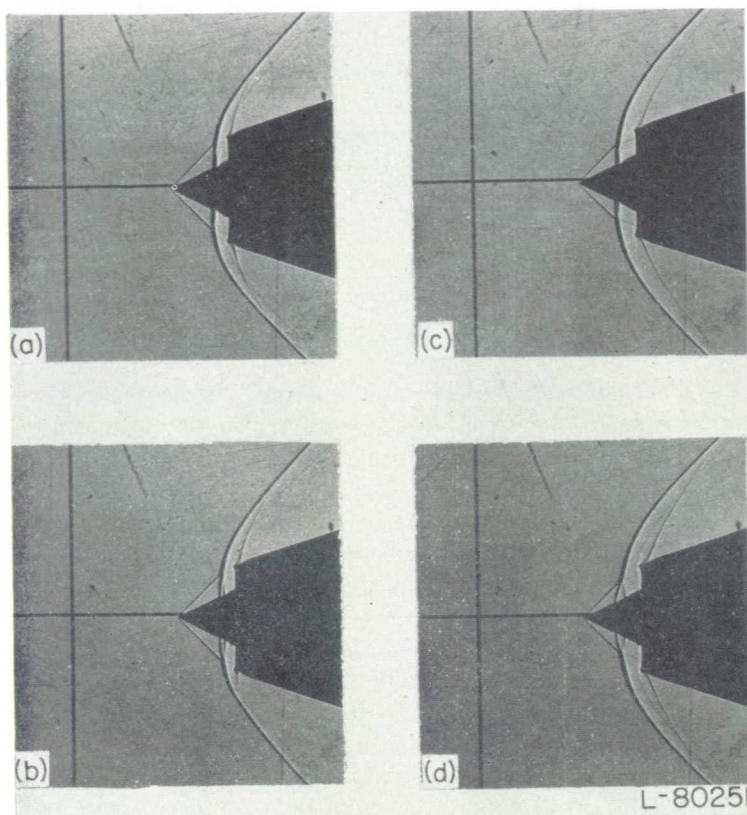


FIGURE 22.—Instantaneous shadowgraphs taken during buzzing of configuration 1.278–14.91–40.1° to show variation in flow pattern at foot of shock when outer part of shock is at same position.

pression which is in turn reflected at the nozzle as an upstream compression wave, this latter wave may move the shock out far enough for the next cycle to commence. If not, further compressions are generated and reflect until the shock is finally forced upstream to the point where it initially started to buzz. In reference 5 extremely close correlation between theory and experiment proved this behavior.

There are also cases where a reflected compression wave in itself is sufficient to push the shock ahead of its initial position, in which case the shock will move farther out in the next cycle than it did in the previous one. In this manner the amplitude of the oscillation may increase from its original one without further throttling.

In cases of a very high frequency buzz (fig. 20) which generally occurs at the lower mass flows of certain inlets there is insufficient time for any wave whatsoever to traverse the ram jet in the period of one cycle. Consequently the "source" of the buzz must be the flow in the immediate vicinity of the inlet, although the alteration or amplification of these pulses may depend on the overall ram-jet flow. In other words, the shock and boundary-layer oscillations ahead of the ram-jet ducting may be compared to a tuning fork at the mouth of an air column. For example, the oscillation frequency of the foot of the shock of configuration 1.278–14.91–40.1° appeared to be about 900 cycles per second while the remainder of the shock pattern oscillated at a much lower frequency. Since the fifth harmonic (second and fourth do not exist) of the ram-jet ducting considered as an organ pipe closed at one end is about 870 cycles per second, it is not at all surprising to find high-frequency buzzing in the range of 800 to 900 cycles per second as described previously. A

possible explanation for the mechanism of the source of the buzzing is the fact that the normal shock, which is in motion due to separation in its rear, will move far enough forward so that the cone boundary layer existing at its foot becomes small enough and possesses enough momentum to be able to withstand the pressure ratio of the shock without separating, or at least without separating as much. Now since it is the rate of increase in separation, boundary layer, or entropy which causes the upstream moving compression waves that keep the shock in motion, when this rate falls off, resultant expansion waves will travel upstream to start the shock moving rearward again. As the shock moves rearward the boundary layer becomes more susceptible to separation and a point is reached where the rate of change of the aforementioned variables become positive and the next cycle commences.

Proposed theory for stability criteria of supersonic inlet in cold flow.—It has been shown for axisymmetric conical center body supersonic inlets without heat addition that the pressure disturbances (in the absence of rapid throttling) originate at or near the cowl entrance. Furthermore, the sound wave traveling downstream and carrying the "news" of the initiation of buzz reaches the combustion chamber only after the second shock has completed a substantial part of its outward motion. Consequently, in these cases it is impossible for the mechanism which determines the stability to be located in the combustion chamber (in cold flow); instead, one is forced to look for the answer in the forward part of the ram jet at the supersonic diffuser and that part of the subsonic diffuser just behind it near the cowl entrance. It must also be noted that although the flow inside the ram jet may be very closely approximated by quasi-one-dimensional steady or unsteady flow, as in reference 5, the flow external to and ahead of the cowl cannot be so treated. The pressure pulses emerging from the cowl spread out into the whole region of flow behind the normal shock and are not "bound" by the streamline entering the cowl.

Thus, a possible explanation of the phenomenon may be examined qualitatively by considering the external flow ahead of the cowl. An insight into the overall reaction can be obtained by assuming quasi-one-dimensional flow although it must be remembered the flow ahead of the cowl is three-dimensional. In the one-dimensional-flow model, the stream tube entering the cowl is considered as a "channel" with flexible walls which expand at a rate sufficient to account for the spillage of mass flow around the cowl in the actual flow. Furthermore, any changes from the unperturbed state of entropy ahead of the cowl are assumed to occur not at the shock system but at the cowl. In other words, a distortion is introduced by considering that all of the generated waves are created at the cowl instead of in the whole region between the shock and cowl. The phenomena of increasing separation or boundary-layer thickness, which generates upstream moving compression waves and creates conditions of reduced mass flow and higher stagnation pressure immediately behind them, have been discussed. Now with the concept of a perturbation (that is, vortex entrance, increased boundary layer, separation) which decreases the effective flow area and increases the

entropy at the cowl entrance so that an upstream compression wave is generated at the inlet, the conditions for stability may be determined:

(a) Stable condition: If, as the shock is forced outward with decreasing mass flow, the expansion waves generated by the flexible walls (spreading out to accommodate the three-dimensional spillage) are of greater strength than the net sum of the initial compression wave and any additional waves generated at the cowl due to flow changes arising from the perturbed shock, then the shock will halt its outward motion and retreat toward the cowl. It should be noted that both a decrease in entropy rise through the shock system as well as a decrease in separation or boundary-layer thickness in the flow just after the shock (both conditions are associated with an increase in the conventional total pressure recovery) will result in the generation of expansion waves to aid those arising from the flexible wall in forcing the shock to retreat.

(b) Unstable condition: If, as the shock is forced outward with decreasing mass flow the expansion waves generated by the flexible walls are of less strength than the net sum of the initial compression wave and any additional waves generated at the cowl, then the shock will not immediately halt its outward motion. Instead it will move ahead of the cowl until it reaches an equilibrium with the flow in the cowl (that is, the conditions behind the last wave originating at the cowl are matched by a particular shock position) or until the net expansion wave (that is, the cumulative wave) generated on the downstream side of the separation "throttle" has an opportunity to reflect from the exit nozzle and return to the inlet. Both types of shock motion are demonstrated for the same diffuser configuration with different combustion chamber lengths in figures 9, 10, 15, and 16 of reference 5. Again it should be noted that an increase in entropy rise through the shock system and an increase in separation or boundary-layer height (corresponding to a decrease in the conventional total pressure recovery) will result in the generation of additional compression waves to help keep the shock in outward motion.

With these arguments in mind it is evident that the stability of a supersonic inlet is determined by the relation between the transient flow conditions behind the normal shock and the instantaneous flow existing in the cowl inlet of a conical diffuser. The fact that buzzing has been found experimentally to arise concurrently with a positive slope of the mean (time averaged) pressure recovery plotted against mass-flow curve (ref. 6) does not conflict with the above analysis. Moreover, since the instability criteria proposed previously in this section show that an instantaneous decrease in pressure recovery with mass flow at the inlet will generate destabilizing compression waves it would be surprising if the instantaneous values integrated over a buzzing cycle and then averaged did not yield values lower than the steady-flow value at the last stable position.

A similar stability criterion based on separation or boundary-layer growth could be applied to scoop inlets. Instead of the dependence of stability on the boundary-layer effects on the central body and cowl in the case of symmetric conical inlets, the dependence would be based on the boundary layer on the compression surface and the opposite wall.

The buzzing of convergent-divergent perforated inlets

(ref. 2) might also be explained on a similar, but less complicated, basis. Owing to lack of pressure-distance-time data it is impossible to definitely state the disturbance origin, but the following probable solution is presented. In contrast to the conical inlets where separation on the central body or inner cowl surfaces was the triggering mechanism, for convergent-divergent perforated inlets the probable mechanism is the thickening of the boundary layer on the outside of the cowl.

When a shock is located in the converging section of the inlet the mass flow passing through the shock is equal to that passing through the rearward perforations and through the throat. Now along the outer surface of the cowl the boundary layer thickens abruptly at the position of the internal shock because of the shock pressure differential which is transmitted through the perforations and also because of the increased mass-flow spillage through the perforations behind the shock (see fig. 19 of ref. 2). This thickening of the boundary layer causes an oblique compression wave to propagate into the free stream so that the pressure in this region is above free-stream static.

Now if a momentary thickening perturbation of this external boundary layer occurs, then the effective "ramp angle" of the layer will increase and the oblique compression wave increases in strength, the pressure increases, and the increasing pressure on the outer side of the perforations decreases the mass flow through them. The effect of pressure on the mass flow may be verified by the appendix of reference 2.

The reduced mass-flow spillage means that there must be an increase in the mass flow through the throat, but this is impossible without shock motion since the throat is choked at the original shock conditions. The shock must then move forward seeking to find another equilibrium condition matching the flow through the perturbed shock with the perturbed flow through the throat and perturbed spillage. As the shock moves upstream (usually) into regions of higher Mach number the losses across the shock will increase so the stability will depend upon whether the spillage flow can be increased enough to pass the added required mass flow. The external pressure is also increasing as the shock moves up because of increased shock strength and more spillage to produce a larger boundary layer with resultant stronger oblique compression waves.

In this case the stability of the inlet would then hinge on the perturbed relationship of mass flow through the throat and perforations and still be divorced from steady-state combustion-chamber pressures. The remainder of the buzzing cycle would follow and depend on reflections from the exit nozzle.

Discussion of Ferri-Nucci vortex-sheet theory.—The stability theory (ref. 4) based on a vortex sheet impinging on the cowl lip was found to be valid for the 44.2° configurations. Since the conical shock intersected the cowl lip, the vortex sheet struck the lip as soon as the normal shock emerged from the cowl and prevented any steady mass-flow reduction below the maximum attainable for this configuration. However, for cowl angles of 40.1° and 48.1° there was no vortex sheet approaching the cowl at the onset of buzzing and hence this criterion was not applicable in these cases. The instability of these two

models arose from separation on the central body at the foot of the shock. Since the cone surface Mach number was high (approximately 1.4), the pressure rise across the normal shock should be appreciable and separation should be expected. Thus, the vortex-sheet criterion appears to be inapplicable for inlets with high Mach numbers on the cone surface unless the vortex sheet at critical mass flow is quite near the cowl lip.

Other investigators have arrived at similar conclusions. The vortex criteria may also become fallible for inlets having very low rates of subsonic diffusion after the cowl lip.

Discussion of Sterbentz-Evvard resonator theory.—The theory of reference 6 is based on an analysis of the oscillation in the ram jet which considers a resonator model similar to that which might be obtained from a system composed of a mass with a weightless spring at each end. The "mass" is a "slug" of air in which compressibility is neglected and which is located in the diffusing region of the ram jet. This slug is assumed to oscillate as a unit parallel to the axis of the ram jet so that a region of "virtual separation" arises between the lateral boundaries of this slug and the diverging surfaces of the diffuser.

One of the "weightless springs" is the remainder of the air in the ram jet (mainly the air in the combustion chamber) where compressibility effects give rise to pressure changes to provide a force-displacement relationship. The pressure changes are assumed to result from the variation in the amount of air present in the combustion chamber as the flow of air entering from the diffuser and that leaving the choked-exit nozzle vary with time. The inertia of the air in the combustion chamber is neglected. The assumption is also made that the pressure in the combustion chamber may be considered constant throughout at any instant.

The other weightless spring is the external shock pattern which gives rise to pressure changes exerting a force on the upstream end of the slug. This spring has a spring constant that may be either positive or negative. It is assumed that total pressure, in lieu of static pressure, at the inlet produces accelerating forces. Furthermore, the variation of this total pressure from a mean value is assumed to be given by the product of the variation of the subsonic diffuser exit-mass flow from a mean value and of the mean slope of the curve for subsonic-diffuser-exit total pressure against diffuser-exit mass flow. In other words, it is assumed that the dynamic performance of the supersonic diffuser is equivalent to the mean (that is, quasi static) performance of the supersonic and subsonic diffuser combination.

The assumptions of constant density throughout the slug and constant pressure at any instant in the combustion chamber is equivalent to assuming that the wave length of the highest frequency component of the oscillation is much larger than the length of the ram jet. If the high-frequency components are to be ignored and only fundamental vibrations considered then the ram jet must have a length negligible compared to the fundamental wave length.

Since reference 5 has proven that quasi plane waves govern the buzzing cycle, it will be advantageous to attempt a correlation between these waves and the resonator model. The downstream spring is an approximation for the effect of the moving plane waves including those reflected from the

choked exit nozzle. The upstream spring then should be chosen as an approximation for the effect at the cowl lip of the waves traveling upstream as well as reflecting from the shock system and boundary layer at the cowl lip. However, by assuming the upstream "spring constant" to be given by mean values of the slope of the total pressure against the mass-flow curve measured at the subsonic diffuser exit, the approximation becomes dubious.

The oscillating slug of air in the diffuser neck is used to approximate the fluid in the ram jet which has the highest velocity perturbations. The plane-wave theory shows that the assumption of a choked nozzle results in the ram jet's acting much the same as an organ pipe closed (in regard to perturbations) at the exit so that the velocity perturbations are highest near the entrance. However, when the combustion chamber is much longer than the diffuser, the momentum perturbation in the combustion chamber cannot be neglected.

Now if the frequency of oscillation is low and of a simple harmonic type without higher frequency components so that the wave length of the oscillation is much larger than the length of the ram jet, then the relative pressure distribution along the ram jet at a particular instant of time, obtained by quasi-plane-wave theory, may be crudely approximated by the resonator model. Thus, under these conditions, the resonator model might be expected to give frequencies of the correct order of magnitude.

However, this resonator model would still be inapplicable for the determination of the correct stability parameters. The reason for the possible usefulness on one hand for frequency computations and the unsuitability for stability computations on the other hand lies in the importance of time effects and local flow conditions on stability.

It has been shown previously that the flow perturbations at the start of buzz originate at the inlet and grow to an appreciable size relative to their ultimate magnitude before the waves generated by the start of the growth can travel downstream to the combustion chamber. If waves traveling downstream with a speed equal to the sum of the sonic and the fluid speeds reach the combustion chamber only after such an appreciable growth, then it is obvious that any entropy discontinuities, which move with the speed of the fluid and which arise from the shock motion or boundary-layer variations at the cowl lip, must arrive at the combustion chamber at an even later time. Thus the springs of the resonator model, which approximate (for frequency purposes) the effect over a complete low frequency cycle of the waves in the ram jet, are not applicable at the start of buzz since the upstream waves are not present in the actual physical phenomenon.

If one were to set up a mass and spring model for stability purposes as an analogy to the stability criteria proposed in an earlier section of this report, the mass would be the slug of air between the normal shock and the boundary layer or entropy disturbance near the cowl lip inlet which gives rise to the upstream moving compression waves. The upstream spring would exert a force related to the instantaneous value of pressure recovery and mass flow through the shock and cowl lip system. There would be no downstream spring for stability determination since, as proved

previously, the initial motion of the slug would be unaffected by reflections from the rear of the ram jet. However, instead of the downstream spring acting on the rearward surface of the slug, there would be a forcing function representing the waves generated by the boundary-layer disturbance. The initial motion (stability) of the slug would then depend upon the relation between the forces exerted by the upstream spring and forcing function, where the forcing function is also affected by feedback of a magnitude dependent on the slug position. In this analogy the feedback forces represent the additional waves generated owing to changes of entropy, effective flow area, and spillage at the cowl inlet as the shock is displaced from its original position. The stable case would then occur when a random force arising at the rear face of the slug would move the slug only slightly before the spring ahead could stop the motion. The converse would then be true for cases of instability in which case the slug would continue to move outward until stopped by removal of the forcing function or (if enough time has elapsed in the equivalent ram jet to permit reflections from the exit nozzle) the application of another restoring force to the rear face.

The various assumptions employed in the resonator theory of reference 6 should also be weighed closely. The very critical assumption that the pressure on the upstream face of the slug can be given by a mean relation between total pressure recovery and mass flow at the diffuser exit is particularly susceptible to doubt. First there is the question of the indeterminacy of the slope of pressure recovery plotted against mass flow for inlets, operating with the conical shock at the lip of the cowl, which have no reduction in mass flow without buzzing. The slope of the curve is then discontinuous at the start of buzz (see fig. 7). Then there also arises the question of the relationship of static to dynamic properties. For example, if the shock velocity may be considered slow, the mass flow entering the cowl would be the same for cases similar to those shown in figures 22(a) and (b) and figures 22(c) and (d) where the shock pattern is quite similar except for the bifurcation at its foot. However, the similarity of pressure recovery in the combustion chamber could be markedly affected by the varying degrees of separation at the foot of the shock even though the mass flow was the same. If the shock velocity may not be considered slow, then there immediately arises a discrepancy in the assumption since the pressure recovery is different across advancing and retreating shocks when the mass flow behind them is the same. In addition, the assumption that the instantaneous static pressure at the inlet may be approximated by the quasi-steady total pressure at the diffuser exit not only ignores compressibility at the inlet (where the Mach number is high) but also disregards possible strong changes in the performance of the subsonic diffuser as the shock moves outward (usually) accompanied by separation either on the cowl or center-body surface.

Finally, there is the question whether it is correct to use mean values to describe quasi-steady-flow conditions for part of a cycle when there is never any possibility of equilibrium between the different parts of the flow. In other words, if strong waves or disturbances exist at any instant between the cowl and the subsonic diffuser exit, then the

pressure perturbation at the cowl cannot correctly be approximated as the product of the mean slope of the diffuser exit pressure-recovery mass-flow curve and diffuser exit mass-flow deviation from the mean. For example, for the configuration of figures 9 and 10 of reference 5 from the instant the first cycle of buzzing begins (with the normal shock at the cowl inlet) the conditions just behind the shock never reach an equilibrium with those at the inlet until the shock finally halts its motion and remains steady two-thirds of the way out on the spike. In other words the aforementioned equilibrium is never attained so that the quasi-steady state never exists with the shock a quarter of the way out, half the way out, and so forth. Yet a mean value as employed in reference 6 presumes that the flow is in equilibrium as it passes outward along the spike and that possible steady flows exist a quarter of the way out, half the way out, and so forth.

The neglect of the velocity perturbations in the combustion volume, when the combustion chamber is long relative to the diffuser length, must also be considered since the ratio of the combustion chamber area to slug cross-sectional area is usually between three and four. Thus neglecting these combustion-chamber perturbations relative to those in the slug roughly assumes that one-third or one-fourth is negligible compared to unity.

The wave length of the oscillation and its higher frequency harmonics in relation to the dimensions of the model must also be examined. For example, for the higher frequency oscillations of references 6, 7, and a British paper by C. F. Griggs and E. L. Goldsmith (not generally available), the wave length of the basic oscillations are only five to six times the length of the model (i. e., an equivalent n between 2.5 and 3) so that the constant pressure and density assumptions become inaccurate.

It should be noted that the resonator theory cannot possibly be applied to the very high frequency buzzing discussed in a previous section of this report and in the British paper. The wave length of the high-frequency oscillation in the latter paper, where the L/D ratios of the models were approximately 3 to 3½, was only twice that of the model. The highest frequency oscillation of configuration 1.278-14.91-40.1° had a wave length of less than half the model length. Furthermore, the resonator theory of reference 6 cannot account for an abrupt change in frequency of any significant magnitude with no significant change in valve position, mass flow, or pressure recovery.

Experimental data are compared with the resonator theory in references 6 and 7 as well as in the British paper. The experimental frequencies agree in regard to trend and order of magnitude. The arbitrary value of the geometric parameter denoting the end of the oscillating slug was chosen by Griggs and Goldsmith to give a minimum resonator frequency; yet the experimental values were always lower than the resonator frequency (except for the very high frequency cases) and errors ranged up to 50 percent of the experimental frequency. It should be noted that when the wave length of the oscillation was about five or six times as great as the ram-jet length, Griggs and Goldsmith reported theoretical frequencies consistently higher than experimental values whereas references 6 and 7 found theoretical fre-

quencies to be lower than experiment. Since a linearized theory, when stretched to the limits of its applicability, usually gives results consistently on one side of experimental data this irregular behavior is at present unexplainable.

The comparison between the slope of the diffuser pressure recovery against mass-flow curve at start of buzz predicted by the resonator theory and the experimental values of reference 6 and others is not conclusive. Griggs and Goldsmith state the magnitude of the slope to be so small for the models tested that the criterion of a positive slope appears to be sufficient for instability. The data of reference 6 indicate buzzing to occur with a positive slope, but the magnitude of the experimental slope sometimes exceeds and at other times is not as large as the theoretical slope.

It should be noted that there are major differences between the instantaneous relationship involving total pressure and mass flow at the cowling which was employed as a stability criterion in a previous section and the mean relationship obtained from the resonator theory of reference 6. First, the mean relationship is concerned with the whole-ram-jet geometry while the instantaneous one is concerned only with conditions local to the cowling. Secondly, changes in the combustion-chamber total pressure are the result of buzzing while the instantaneous variation at the cowling is a requisite condition for instability. The separation throttling and reduced mass flow generate expansion waves moving downstream into the combustion chamber which reduce the total pressure, and of course these waves are later followed by fluid of higher entropy. The fact that buzzing occurs only with a positive slope of the mean total-pressure against mean mass-flow curve has been explained in a previous section as resulting from a cyclic integration of the effect of the waves and entropy increase.

The amplitude computations of reference 7 are based on the same model as the frequency computations with the exception that the upstream spring constant may be nonlinear and is determined as the slope of an assumed steady flow relation between diffuser pressure recovery and mass flow. Thus these computations might be expected to also yield results showing the general trends and orders of magnitude. It has been stated previously in this report that the quasi-plane-wave solution for certain frequencies might be approximated by constant pressure in the combustion chamber at any instant of time. However, there is a variation in amplitude along this chamber which can be significant for amplitude considerations at higher frequencies. An examination of the experimental data of figure 4 of reference 7 reveals several facts pertinent to this argument. First the higher frequencies of each of the long and short models are inversely proportional to the model lengths, which substantiates the fact that quasi plane waves govern the oscillation. The wave length of the particular oscillation is about $5\frac{1}{4}$ times the length of the particular ram jet ($n \approx 2.9$). Now the experimental amplitudes were measured at different values of $\frac{x}{L}$ ($x/L \approx 0.8$ for small models, $x/L \approx 0.5$ for large)

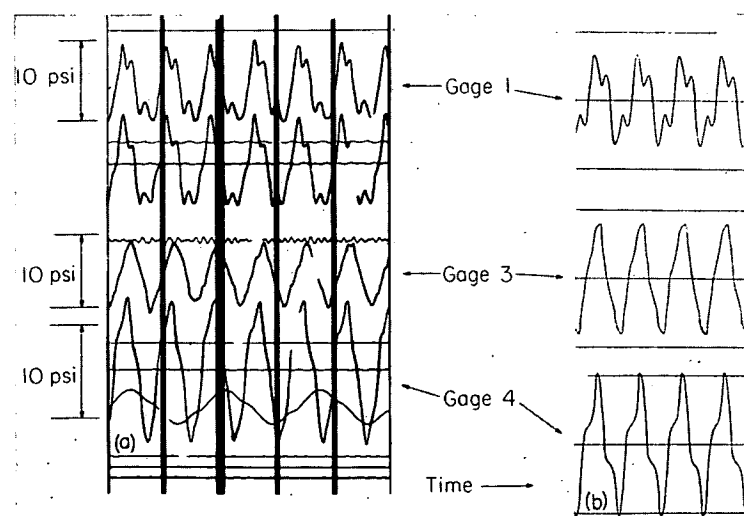
and consequently since quasi-plane-wave theory predicts and experiments show amplitudes increasing with x/L it is to be expected that the measured amplitudes would be higher for the shorter model. If the gages had been located

at the same value of x/L the amplitudes could be nearly equal. The result obtained by the resonator method which predicts higher amplitudes for the shorter model may be interpreted to reflect the fact that the longer-combustion-chamber length relative to total length of the larger volume ram jet yields an average pressure amplitude over that length which is less than the average pressure amplitude over the shorter relative length of the small-volume ram jet (since these lengths are taken from the exit of the ram jet and local amplitude increases as the exit is approached).

In conclusion it may be stated that the model assumed in the resonator analysis of references 6 and 7 may be considered a rough approximation to the actual phenomena when applied for purposes of obtaining the general trends and orders of magnitude of frequency and amplitude of oscillation providing the wave length of the highest frequency component of the oscillation be much larger than the length of the ram jet. The resonator analysis is not applicable when considering the initial instability of the inlet without combustion and should not be so applied to obtain such stability criteria.

COMPARISON BETWEEN THEORETICAL AND EXPERIMENTAL PRESSURE AMPLITUDES AND MASS FLOW

The theoretical approximation to determine pressure amplitude variation with mass flow was applied with the assumption that the shape of the pressure-time curve at $x/L=1$ be either sinusoidal or sawtooth with equal time intervals between peaks and valleys. The sinusoidal form is often found experimentally for the lower amplitudes. As the buzzing becomes more violent, the general form of the pressure-time curve usually becomes more highly peaked so that a sawtooth curve more nearly approximates the actual curve. Of course, the experimental pressure records at higher amplitudes are usually made up of many superimposed waves, but these pressure variations also can be approximated by adding simple curves. For example, figure 23 compares the pressure-time curve obtained experimentally for configuration 1.278-14.91-48.1° with the one obtained by



(a) Configuration 1.278-14.91-48.1°. (b) Computed sawtooth plus sine wave.

FIGURE 23.—Comparison of experimental pressure-time record with pressure-time record obtained by adding sine and sawtooth pulses.

adding a sinusoidal curve with $n=1$ to a sawtooth curve with an equivalent $n=3$ and amplitude about four times that of the sinusoidal curve (that is, a sawtooth curve which has a frequency one-third that of the sinusoidal curve). The small-perturbation-pressure-amplitude theory permits the addition of such pulses since the governing differential equation (eq. (8)) is linear, but it cannot predict the relative amplitudes of the waves having different frequencies without making some assumption regarding how much of the decrement in mass flow is due to each particular wave. Then a further assumption would be necessary regarding the phase relationship of the waves in order to obtain net peak values. Since there is no simple way of estimating these factors, they are ignored and the amplitudes computed as if the whole pressure and mass-flow variation were due to the lower frequency (higher value of n) oscillation. Note that the $n=1$ oscillation has a very small amplitude near the midpoint of the ram jet (see gage 3 at $x/L=0.602$ of fig. 23), which approaches zero as $x/L \rightarrow 1/2$ and $m_b \rightarrow 0$.

The variation of pressure amplitude coefficient with axial position along the ram jet for a value of $M_b=0.14$ is shown in figure 24 for both the sine curve and sawtooth curve. The sawtooth curve predicts amplitudes from 0 to 20 percent higher, other conditions being equal.

The variation of total amplitude coefficient with incipient Mach number is shown in figure 25 for various values of n at $x/L=0.838$. Since the experimental effective incipient Mach number for all configurations tested was close to $M_b=0.14$, this value was used as a basis to compare the

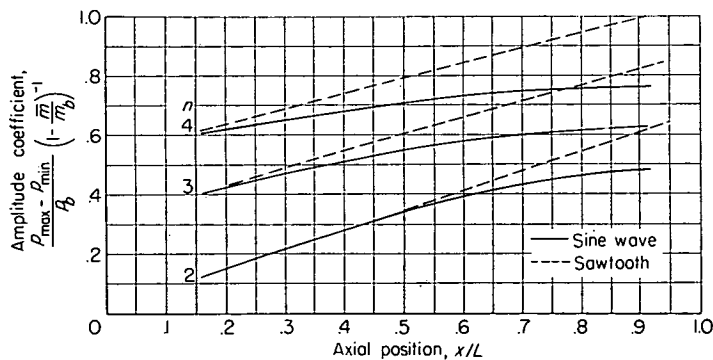


FIGURE 24.—Variation of pressure amplitude coefficient with axial position for $M_b=0.14$.

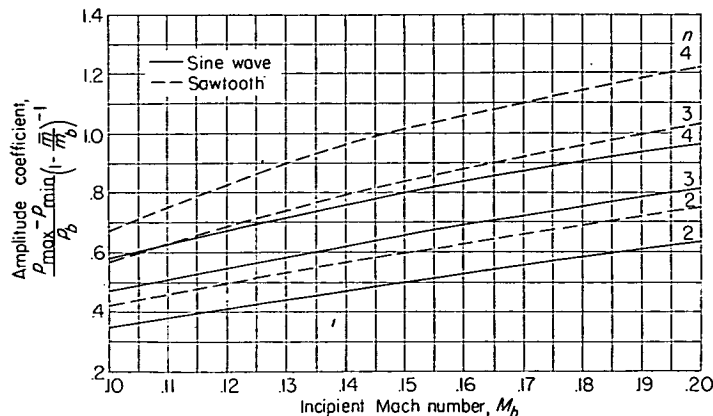


FIGURE 25.—Variation of pressure amplitude coefficient with Mach number at start of buzz for $x/L=0.838$.

theoretical and experimental trends of amplitude shown plotted against mass flow in figures 26 and 27. The theoretical curves are drawn for $x/L=0.838$; whereas the experimental points include values at $x/L=0.838$ and $x/L=0.919$ (gages 4 with $L/D=14.91$ and 29.82). However, from figure 24, it may be seen that there is only a slight difference in the predicted amplitude at the two stations. Reference

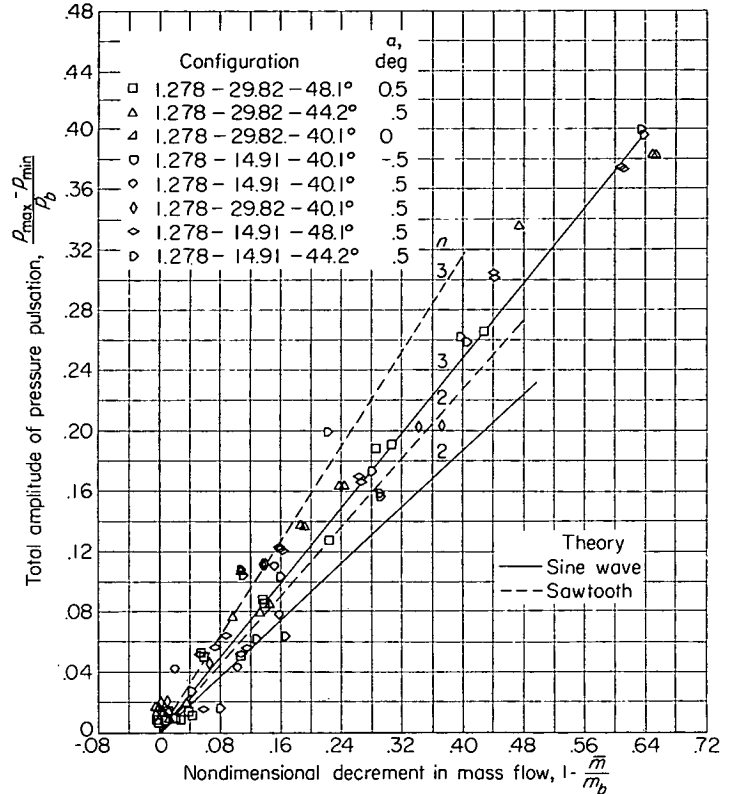


FIGURE 26.—Total amplitude of pressure pulsations at gage 4 plotted against nondimensional decrement in mass flow from minimum stable flow. Configurations 1.278.

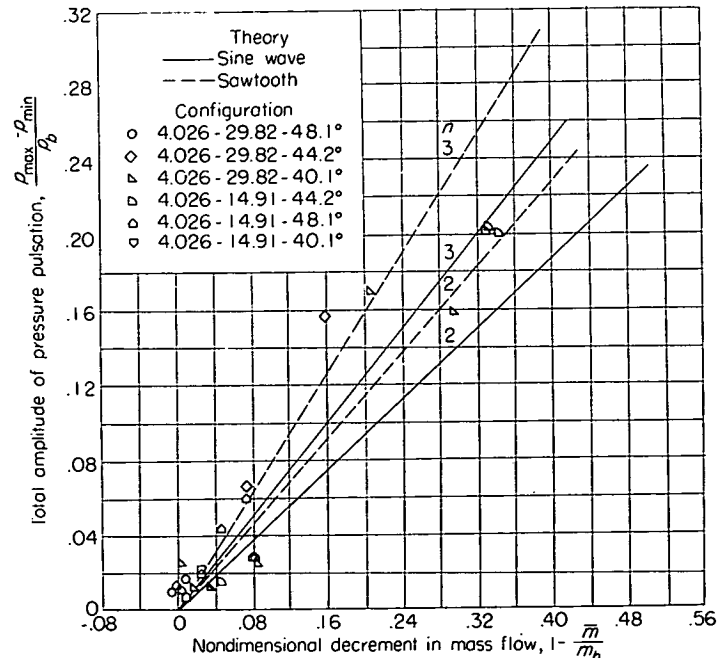


FIGURE 27.—Total amplitude of pressure pulsations at gage 4 plotted against nondimensional decrement in mass flow from minimum stable mass flow. Configurations 4.026: $\alpha=0.5^\circ$.

5 states that for buzzing other than the very high frequency type there is a minimum of two complete wave traversals per cycle (n must be equal to or greater than 2) and the pressure records of the present tests showed most of the runs to have frequencies corresponding to values of n between 2 and 3. Consequently, only the corresponding theoretical curves are shown for n equal to 2 and 3. The general agreement for the lower amplitudes tends to substantiate the theory and the assumptions involved, while the agreement at the higher amplitudes is only a coincidence and must not be construed to mean the theory is applicable to large amplitudes.

The experimental results indicate that the supersonic diffuser configurations, when used in conjunction with the same subsonic diffuser, yield similar curves of amplitude plotted against mass-flow decrement. The value of M_b , however, may often depend largely on the supersonic configuration.

A simplified method for predicting the mass-flow reduction below the value at start of buzz without exceeding a given small pressure amplitude may be obtained from the linearized theory. Since n usually decreases (frequency increases) as the mass flow is reduced (see refs. 5 and 6) for a given configuration, the value of n may be assumed to be 4 or greater at the start of buzz. Higher values of n will yield lower permissible mass-flow reductions for a given amplitude. In other words, the "factor of safety" of the prediction increases as the chosen value of n increases. Then employing values of m_b and M_b assumed from geometry of the ram jet or experimentally determined, the permissible reduction in mass flow for a given small amplitude of pressure pulsation may be obtained from equations (28), (29), and (30).

CONCLUSIONS

An analysis based on a quasi-one-dimensional-flow model has been made of the flow in a ram jet with supersonic diffuser. The results indicate the following conclusions:

1. From a theory developed on a quasi-one-dimensional-flow basis, it was found that the stability of the ram jet is dependent upon the instantaneous values of mass flow and total pressure recovery of the supersonic diffuser and immediate neighboring subsonic diffuser. Conditions for stable and unstable flow were presented.

2. The model assumed in the resonator analysis of NACA TN 3506 may be considered a rough approximation to the actual phenomena when applied for purposes of obtaining the general trends and orders of magnitude of frequency and amplitude of oscillation providing the wave length of the highest frequency component of the oscillation be much larger than the length of the ram jet. The resonator analysis is not applicable when considering the initial instability of the inlet without combustion and should not be so applied to obtain such stability criteria.

3. A simple theory for predicting the approximate amplitude of small pressure pulsation in terms of mass-flow decrement from minimum-stable mass flow was developed and found to agree with experiments.

In addition to the theoretical results, cold-flow tests at a Mach number of 1.94 of ram-jet models having scale factors of 3.15:1 and Reynolds number ratios of 4.75:1 with several supersonic diffuser configurations indicated the following results:

1. The predominant variation in steady-flow performance resulted from the larger boundary layer in the combustion chamber of the low Reynolds number model.

2. The conditions at which buzz originated were nearly the same for the same supersonic diffuser (cowling-position angle) configurations in both large and small diameter models. There was no appreciable variation in stability limits of any of the models when the combustion-chamber length was increased by a factor of three. The negligible effect of Reynolds number on stability of the off-design configurations was not anticipated in view of the importance of boundary layer to stability, and this result should not be construed to be generally applicable.

3. The unsteady-flow performance and wave patterns were also similar when considered on a reduced-frequency basis depending on the relative lengths of the model.

4. The velocity profile in the combustion chamber at both Reynolds numbers was appreciably influenced by an angle of attack of 0.5° . The external shock pattern was noticeably affected only for the lower cowling-position angles. The pressure recovery and mass-flow values at the start of buzz were not noticeably affected.

LANGLEY AERONAUTICAL LABORATORY,
NATIONAL ADVISORY COMMITTEE FOR AERONAUTICS,
LANGLEY FIELD, VA., July 28, 1953.

REFERENCES

1. Oswatitsch, Kl.: Der Druckrückgewinn bei Geschossen mit Rückstossantrieb bei hohen Überschallgeschwindigkeiten (Der Wirkungsgrad von Stossdiffusoren). Bericht Nr. 1005, Forsch. und Entwickl. des Heereswaffenamtes (Göttingen), 1944. (Available in English translation as NACA TM 1140.)
2. Hunczak, Henry R., and Kremzier, Emil J.: Characteristics of Perforated Diffusers at Free-Stream Mach Number 1.90. NACA RM E50B02, 1950.
3. Connors, James F.: Effect of Ram-Jet Pressure Pulsations on Supersonic-Diffuser Performance. NACA RM E50H22, 1950.
4. Ferri, Antonio, and Nucci, Louis M.: The Origin of Aerodynamic Instability of Supersonic Inlets at Subcritical Conditions. NACA RM L50K30, 1951.
5. Trimpi, Robert L.: An Analysis of Buzzing in Supersonic Ram Jets by a Modified One-Dimensional Nonstationary Wave Theory. NACA TN 3695, 1956. (Supersedes NACA RM L52A18.)
6. Sterbentz, William H., and Evvard, John C.: Criteria for Prediction and Control of Ram-Jet Flow Pulsations. NACA TN 3506, 1955. (Supersedes NACA RM E51C27.)
7. Sterbentz, William H., and Davids, Joseph: Amplitude of Supersonic Diffuser Flow Pulsations. NACA TN 3572, 1955. (Supersedes NACA RM E52I24.)
8. Kraushaar, Robert J.: Manometers in Pulsating Systems. Tech. Memo. NYU-14, U.S.N. and U. S. Air Force Project SQUID. New York Univ., Aug. 22, 1951.

REPORT 1266

CHARTS FOR ESTIMATING PERFORMANCE OF HIGH-PERFORMANCE HELICOPTERS

By ALFRED GESSOW and ROBERT J. TAPSCOTT

SUMMARY

Theoretically derived charts showing the profile-drag—thrust ratio are presented for helicopter rotors operating in forward flight and having hinged rectangular blades with a linear twist of 0° , -8° , and -16° . The charts, showing the profile-drag characteristics of the rotor for various combinations of pitch angle, ratio of thrust coefficient to solidity, and a parameter representing shaft power input, are presented for tip-speed ratios ranging from 0.05 to 0.50. Also presented in chart form are the ratio of thrust coefficient to solidity as a function of inflow ratio and blade pitch angle and the retreating-blade angles of attack as a function of inflow ratio and collective pitch and as a function of power and thrust coefficients.

The charts of this report differ from the rotor performance papers previously published by the National Advisory Committee for Aeronautics in that the theory on which the charts are based includes an approximate allowance for stall in the reversed-flow region and contains no small-angle assumptions regarding blade-section inflow angles and velocities. The charts of this report are therefore considered more accurate than previous ones for flight conditions involving high inflow velocities and large regions of reversed velocity that may be encountered by high-performance helicopters. The assumption is made, however, that outside of the reversed-velocity region, the section angles of attack are small; thus the angles can be replaced by their sine. In addition, other than including an approximate allowance for stall in the reversed-velocity region, the charts do not include stall and compressibility effects.

The charts may be used to study the effects of design changes on rotor performance and to indicate optimum performance conditions, as well as to estimate quickly rotor performance in forward flight. They are also useful in obtaining inflow-ratio and pitch-angle values for use in calculating flapping coefficients and spanwise loadings. The method of applying the charts to performance estimation is illustrated through sample calculation of a typical rotor-performance problem.

INTRODUCTION

Equations were presented in reference 1 from which the thrust, the accelerating and decelerating torque, and the profile-drag power of a hinged rotor operating at high tip-speed ratios and inflow angles could be calculated. Because the equations do not place any limitation on the magnitude of the inflow angle or on the rotor angle of attack, they are considered more accurate than previous analyses when applied to high-speed helicopters and to certain types of con-

vertible aircraft. This report is an extension of reference 1 in that the equations of that reference are used as the basis of a method for calculating the performance of lifting rotors over a wide range of operating conditions.

Because the basic equations are lengthy, the application of the method is considerably simplified by presenting the more lengthy equations in the form of charts from which rotor performance can be quickly estimated. The charts cover operation at any rotor angle of attack at tip-speed ratios varying from 0.05 to 0.50 for blades that are twisted 0° , -8° , and -16° (negative twists correspond to blade pitch angles at the tip which are lower than at the root). With the exception of an approximate allowance for stall in the reversed-velocity region, the charts do not include stall and compressibility effects.

Limit lines showing conditions for which blade angles of attack exceed specified values at given radial stations are included in the charts. These limit lines are useful in determining operating conditions at which stalling begins and for determining the limiting operating conditions.

SYMBOLS

- a slope of curve of section lift coefficient against section angle of attack, per radian (assumed equal herein to 5.73)
- b number of blades per rotor
- C_L rotor lift coefficient, $\frac{L}{\frac{1}{2}\rho V^2 \pi R^2}$
- C_P rotor-shaft power coefficient, $\frac{P}{\pi R^2 \rho (\Omega R)^3}$
- C_T rotor thrust coefficient, $\frac{T}{\pi R^2 \rho (\Omega R)^2}$
- c blade section chord, ft
- c_e equivalent blade chord (weighted on thrust basis), $\frac{\int_0^R cr^2 dr}{\int_0^R r^2 dr}$, ft
- c_{d_0} section profile-drag coefficient
- c_l section lift coefficient
- D_p helicopter parasite drag, lb
- $(D/L)_0$ rotor profile drag-lift ratio
- f parasite-drag area, $\frac{D_p}{\frac{1}{2}\rho V^2}$, sq ft
- I_1 mass moment of inertia of blade about flapping hinge, slug-ft²

¹ Supersedes NACA Technical Notes 3323 by Alfred Gessow and Robert J. Tapscott, 1955, and 3482 by Robert J. Tapscott and Alfred Gessow, 1955.

L	rotor lift, lb
P	rotor-shaft power, ft-lb/sec
P/L	shaft-power parameter, where P (in this ratio only) is equal to rotor-shaft power divided by velocity along flight path and is therefore also equal to drag force that could be overcome by shaft power at flight velocity
R	blade radius measured from center of rotation, ft
r	radial distance from center of rotation to blade element, ft
T	rotor thrust, lb
V	true airspeed of helicopter along flight path, fps
v	induced velocity at rotor (always positive), fps
W	helicopter gross weight, lb
x	ratio of blade-element radius to rotor-blade radius, r/R
α	rotor angle of attack; angle between axis of no feathering (that is, axis about which there is no cyclic-pitch change) and plane perpendicular to flight path, positive when axis is inclined rearward, deg
α_r	blade-element angle of attack, measured from line of zero lift, deg (when used in three-term drag polar in fig. 1 (b), α_r is expressed in radians)
$\alpha_{(x)(\psi)}$	blade-element angle of attack at any radial position x and at any blade azimuth angle ψ , deg; for example, $\alpha_{(1.0)(270^\circ)}$ is blade-element angle of attack at tip of retreating blade at 270° azimuth position
$\alpha_{(u_T=0.4)(270^\circ)}$	blade-element angle of attack at radius at which tangential velocity equals 0.4 tip speed and at 270° azimuth position, deg
γ	flight-path angle (positive in climb, negative in glide), deg
$\theta_{.75}$	blade-section pitch angle at 0.75 radius; angle between line of zero lift of blade section and plane perpendicular to axis of no feathering, deg
θ_i	difference between blade root and blade-tip pitch angles, positive when tip angle is larger, deg
λ	inflow ratio, $\frac{V \sin \alpha - v}{\Omega R}$
μ	tip-speed ratio, $\frac{V \cos \alpha}{\Omega R}$
ρ	mass density of air, slugs/cu ft
σ	rotor solidity, $bc_a/\pi R$
ψ	blade azimuth angle measured from downwind position in direction of rotation, deg
Ω	rotor angular velocity, radians/sec
Subscripts:	
c	climb
i	induced
o	profile
p	parasite
v	vertical component

METHOD OF ANALYSIS

The performance method presented herein utilizes the equations developed in reference 1 for blade-flapping coefficients, rotor thrust, torque, and profile-drag power and also, with some modifications, the energy performance analysis described in reference 2. Inasmuch as the performance

method described herein is based on the equations developed in reference 1, the assumptions and limitations incorporated in the reference equations also apply to the performance calculations. (The effects of the primary assumptions and limitations are discussed subsequently in the section entitled "Range of Application of Charts.")

In utilizing the equations of reference 1 to compute the section lift and drag contributions of the forward-velocity region, wherein stall effects were ignored, the section lift was calculated on the basis of constant lift-curve slope ($a=5.73$) and the section drag was calculated on the basis of a three-term drag polar ($c_{d_0}=0.0087-0.216\alpha+0.400\alpha^2$). These values are representative of "semismooth" blades and are the same values used in the construction of the charts of reference 2. For the reversed-velocity region, the values of c_l and c_{d_0} that were used are shown in figure 1. The values of c_l and c_{d_0} above the stall are based to some extent on wind-tunnel data given in reference 3 and are presented in figure 1 on the concept of a 360° angle-of-attack range. This concept is useful in the analysis because the angle of attack in the reversed-velocity region can exceed 180° .

By following the procedure of reference 1, it was assumed that the thrust, torque, and power contributions of the reversed-velocity region could be approximated by using constant lift and drag coefficients corresponding to a single representative section angle of attack. For each flight condition, the representative angle was computed at a radial station about one-third of the distance from the center of rotation to the outboard edge of the reversed-velocity region and at an azimuth angle of 270° . The forces at this radial station were found to represent approximately the average of the forces in the reversed-velocity region from plots of the radial distribution of the forces determined from step-by-step calculations for several sample cases. The values of c_l and c_{d_0} corresponding to the representative angle of attack were obtained from figure 1. Although some uncertainty as to the maximum value of c_{d_0} in the 90° angle-of-attack region exists, it was found that the use of a maximum value of 2.0, for example, instead of 1.6 had a negligible effect on the chart values over the range of applicability of the charts.

FUNDAMENTAL PERFORMANCE EQUATION

The power supplied at the rotor shaft of a helicopter is expended in overcoming the rotor profile-drag losses, the induced-drag losses, and the parasite-drag losses and in changing the potential energy of the aircraft in climb. The division of shaft power among the various sources can be written in coefficient form as

$$C_P = C_{P_o} + C_{P_i} + C_{P_p} + C_{P_e} \quad (1)$$

In presenting the relationship between C_P and C_{P_o} for various flight conditions in chart form, the resulting plots are greatly clarified if the power-coefficient ratios are divided by the thrust coefficient. Thus,

$$\frac{C_P}{C_T} = \frac{C_{P_o}}{C_T} + \frac{C_{P_i}}{C_T} + \frac{C_{P_p}}{C_T} + \frac{C_{P_e}}{C_T} \quad (2)$$

Each ratio of power coefficient to thrust coefficient in equation (2) may be considered alternately as either an equiva-

lent drag-thrust ratio (wherein the equivalent drag is equal to the drag force that would absorb the power at a velocity equal to ΩR) or as an efficiency factor representing power per unit thrust at a given tip speed.

Almost any problem in helicopter performance, whether it be to determine the shaft power required to maintain a steady-flight condition, the rate of climb at a given power condition, or the top speed of a given helicopter, can be solved by means of the fundamental power relation expressed by equation (2). It will be noted that the familiar P/L , $(D/L)_o$, . . . notation used in previous NACA helicopter performance papers is replaced herein by C_P/C_T , C_{P_o}/C_T , The power coefficients are based on the relatively constant ΩR instead of on V ; thus, the notation used herein avoids having the equivalent drag approach infinity as the forward speed approaches zero. For the same reason, rotor lift L —based on C_L , which is dependent on forward speed—is replaced by the rotor thrust T inasmuch as C_T is independent of forward speed. The conversion of one form of ratio to another is simply:

$$\left. \begin{aligned} \frac{C_P}{C_T} &= \frac{P}{L} \mu \\ \frac{C_{P_o}}{C_T} &= \left(\frac{D}{L}\right)_o \mu \\ &\dots \dots \end{aligned} \right\} \quad (3)$$

RELATIONS REQUIRED IN PERFORMANCE CALCULATIONS

Formulas that are necessary for evaluating helicopter performance by means of equation (2) are listed as follows:

$$T \cos(\alpha + \gamma) = W + D_p \sin \gamma \quad (4)$$

(Equation (4) is based on the assumption that the resultant rotor force acts along the axis of no feathering.)

$$\frac{C_P}{C_T} = \frac{P}{(\Omega R)T} \quad (5)$$

$$\frac{C_{P_o}}{C_T} = \frac{P_o}{(\Omega R)T} \quad (6)$$

$$\frac{C_{P_t}}{C_T} = \frac{C_T}{2\mu[1 + (\lambda/\mu)^2]^{1/2}} \quad (7)$$

$$\frac{C_{P_p}}{C_T} = \frac{1}{2C_T} \frac{f}{\pi R^2} \frac{\mu^3}{\cos^3 \alpha} \quad (8)$$

$$\frac{C_{P_c}}{C_T} = \sin \gamma \left[-\sin \gamma \frac{C_{P_p}}{C_T} \frac{\cos \alpha}{\mu} + \sqrt{1 - \cos^2 \gamma \left(\frac{C_{P_p}}{C_T} \right)^2 \frac{\cos^2 \alpha}{\mu^2}} \right] \frac{\mu}{\cos \alpha} \quad (9)$$

$$\tan \alpha = \frac{\lambda}{\mu} + \frac{C_T}{2\mu^2[1 + (\lambda/\mu)^2]^{1/2}} \quad (10)$$

These equations, with the exception of equation (9), are similar to those derived in chapter 9 of reference 4 except for the factor $\mu/\cos \alpha$. Equation (9) includes a drag term and is derived from a corresponding equation presented in the appendix of reference 5 by using a multiplying factor of $\mu/\cos \alpha$.

PERFORMANCE CHARTS

The calculation of the various C_P/C_T ratios in equations (5) to (9) can be greatly simplified by means of charts that relate the more lengthy ratios to the fundamental variables λ , $\theta_{.75}$, and μ and to each other. Such charts are presented in figures 2 to 7, and their use is demonstrated in succeeding sections of this report.

Each chart of figures 2, 3, and 4 gives $2C_T/\sigma a$ as a function of λ and $\theta_{.75}$ for fixed values of μ ranging from 0.05 to 0.50. In figures 5, 6, and 7, C_{P_o}/C_T is shown as a function of C_P/C_T , $2C_T/\sigma a$, and $\theta_{.75}$ for fixed values of μ ranging from 0.05 to 0.50. Also, stall limit lines, the significance of which is discussed in references 2 and 6, are shown in these plots. Figure 8 is a graphical presentation of equation (9) from

which the climb parameter $\frac{\cos \alpha}{\mu} \frac{C_{P_c}}{C_T}$ may be determined from the climb angle γ and the parasite-drag parameter $\frac{\cos \alpha}{\mu} \frac{C_{P_p}}{C_T}$.

OUTLINE OF PERFORMANCE METHOD UTILIZING CHARTS

The problem of computing helicopter performance may be thought of as one of finding the value of one variable for given values of other pertinent variables, the variables being related by a number of basic equations. The problem, in essence, thus becomes the solution of a number of simultaneous equations. The procedure can be greatly simplified by utilizing the performance charts presented in figures 2 to 7. The steps required in two typical types of performance calculations will be outlined and demonstrated by a sample calculation.

CALCULATION OF RATE-OF-CLIMB CURVES

If the rate of climb (or descent) is required, the calculating procedure would be as follows (for a given μ) for the known parameters P , W , σ , f , ΩR , and ρ :

- (1) Assume $T \approx W$ and calculate C_T .
- (2) Compute C_P/C_T from equation (5).
- (3) Find C_{P_o}/C_T and $\theta_{.75}$ from figure 5, 6, or 7.
- (4) Find λ from figure 2, 3, or 4.
- (5) Calculate α from equation (10).
- (6) Compute C_{P_d}/C_T and C_{P_p}/C_T from equations (7) and (8).
- (7) Compute C_{P_c}/C_T from equation (2).
- (8) Find γ from figure 8.
- (9) Compute V_c from the relationship $V_c = V \sin \gamma$.
- (10) If both γ and D_p are very large, a new C_T can be computed by means of equation (4) and the process repeated to find a new value of V_c .

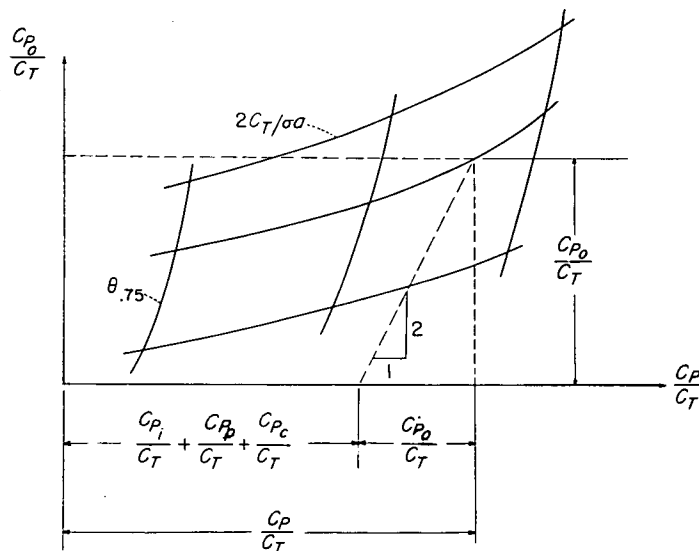
CALCULATION OF POWER-REQUIRED CURVES

A common performance calculation is to find the power required by a helicopter flying at a given airspeed and at a given rate of climb (or climb angle). The procedure would be as follows for the known parameters W , σ , f , γ , ΩR , ρ , and V :

- (1) Assume that $\alpha = 0^\circ$ and that $(\lambda/\mu)^2 \ll 1$; then, calculate T (and C_T) from equation (4).
- (2) Calculate μ from its definition.
- (3) Calculate C_{P_d}/C_T , C_{P_p}/C_T , and C_{P_c}/C_T from equations (7), (8), and (9), respectively. For convenience of application, equation (9) has been used to construct figure 8, from

which can be obtained, for example, values of C_{P_i}/C_T for given values of γ and C_{P_p}/C_T .

(4) On the appropriate chart of figure 5, 6, or 7, lay off the sum of C_{P_i}/C_T , C_{P_p}/C_T , and C_{P_c}/C_T along the C_P/C_T axis. Then, with that point as a base, construct a line having a slope of unity. (If C_{P_i}/C_T and C_{P_p}/C_T were drawn to the same scale in figures 5, 6, and 7, the construction line would be drawn at a 45° angle. For the actual scales of figures 5, 6, and 7, the line is constructed at an angle which has a tangent of 2.) The intersection of this line with the proper $2C_T/\sigma a$ line will yield values for C_{P_o}/C_T , C_P/C_T , and $\theta_{.75}$. This procedure is illustrated for a constant tip-speed ratio by the following sketch:



In order to avoid interpolation between tip-speed-ratio charts, the value of V can be chosen so that μ is an even multiple of 0.05; otherwise, the answer can be linearly interpolated between two successive charts.

(5) Since $2C_T/\sigma a$, $\theta_{.75}$, and μ are now known, λ can be found from figure 2, 3, or 4.

(6) Compute α from equation (10) and recompute μ from the equation $\mu = \frac{V \cos \alpha}{\Omega R}$.

(7) Recompute C_T , C_{P_i}/C_T , C_{P_p}/C_T , and C_{P_c}/C_T and find new values of C_P/C_T and C_{P_o}/C_T . If these values differ from the initially computed ones by more than a few percent, repeat the process. Normally one iteration is sufficient. However, when α is within the range of $\pm 20^\circ$ and $\mu \leq 0.50$, the initial assumptions that $\cos \alpha = 1$ and $(\lambda/\mu)^2 \ll 1$ are adequate and no iterations are needed.

SAMPLE PERFORMANCE CALCULATION

The performance calculations outlined in the preceding section will be illustrated by a sample problem: Calculate the power required by a helicopter traveling at 180 feet per second and climbing at a rate of 300 feet per minute. The following additional data are known: $W = 4,287$ pounds, $\sigma = 0.08$, $\Omega R = 600$ feet per second, $\rho = 0.00238$ slug per cubic foot, $R = 20$ feet, $\theta_1 = -8^\circ$, and $f = 12$ square feet.

(1) Assume that $\alpha = 0^\circ$ and $(\lambda/\mu)^2 \ll 1$. Also, $\gamma = \sin^{-1} \frac{V_o}{V} = \sin^{-1} \frac{5}{180} = 1.6^\circ$ and $D_p = \frac{f \rho V^2}{2} = 463$ pounds. Then, from equation (4), $T = 4,300$ pounds, and $C_T = 0.0040$.

(2) Then, $\mu = 180/600 = 0.30$.

(3a) From equation (7), $C_{P_i}/C_T = 0.0067$.

(3b) From equation (8), $C_{P_p}/C_T = 0.0322$.

(3c) Then, $\frac{\cos \alpha}{\mu} \frac{C_{P_p}}{C_T} = 0.107$. From figure 8, $\frac{\cos \alpha}{\mu} \frac{C_{P_c}}{C_T} = 0.028$. Thus, $\frac{C_{P_c}}{C_T} = 0.0084$.

(4a) $\frac{C_{P_i}}{C_T} + \frac{C_{P_p}}{C_T} + \frac{C_{P_c}}{C_T} = 0.0067 + 0.0322 + 0.0084 = 0.0473$.

(4b) For $\mu = 0.30$ and $2C_T/\sigma a = 0.018$, figure 6(e) gives:

$$\frac{C_{P_o}}{C_T} = 0.0315$$

$$\frac{C_P}{C_T} = 0.0788$$

$$\theta_{.75} = 9^\circ$$

(5) For $\theta_{.75} = 9^\circ$ and $2C_T/\sigma a = 0.018$, figure 3(e) gives $\lambda = -0.080$.

(6) The rotor angle of attack α can now be computed from equation (10) as follows:

$$\tan \alpha = \frac{-0.080}{0.30} + \frac{0.004}{0.18(1+0.0712)^{1/2}} = -0.245$$

$$\alpha = -13.8^\circ$$

(7a) Recomputing the power coefficients with the above values for α and λ results in changes that are within the accuracy of the computations; therefore, the originally computed values are sufficient.

(7b) The power required is then calculated as

$$\begin{aligned} \text{Power} &= \frac{C_P}{C_T} C_T \pi R^2 \rho (\Omega R)^3 \\ &= (0.079) (0.004) \pi (20)^2 (0.00238) (600)^3 \\ &= 204,000 \text{ ft-lb/sec} \\ &= 371 \text{ hp} \end{aligned}$$

(7c) The rotor profile-drag power is

$$\begin{aligned} \text{Profile power} &= \frac{0.031}{0.079} \times 204000 \\ &= 80,000 \text{ ft-lb/sec} \\ &= 146 \text{ hp} \end{aligned}$$

RANGE OF APPLICATION OF CHARTS

In the preparation of the charts, it was necessary to make some assumptions regarding the rotor physical parameters to be used with the theory. Some of the more pertinent effects of these assumptions as well as the effects of the re-

strictive assumptions of the theory are discussed in the succeeding sections.

BLADE CHARACTERISTICS

The sample rotors for which the charts presented herein were prepared were assumed to have hinged rectangular blades with a mass factor $\rho c a R^4/I_1$ equal to 15 and linear twists of 0° , -8° , and -16° . However, according to the error analysis made in reference 6, it would appear that the charts would be applicable to rotors having values of mass factors ranging from 0 to 25. Thus, although blade-flapping motion is sensitive to mass factor, average rotor forces are relatively insensitive to moderate changes in the flapping motion.

Although the charts were calculated for rotors having uniform-chord blades, previous experience has shown that, in general, the forward-flight performance of rotors with blades having as much as 3:1 taper ratio can be predicted with good accuracy by equations derived for uniform-chord blades, provided that the rotor solidity is based on the equivalent weighted chord c_e .

To determine the effects of blade twist on the theoretical values of C_{P_0}/C_T , a comparison of the values obtained from the charts for the different twists was made at several unstalled flight conditions. From the comparison, it appeared that for forward speeds ranging from the speed for minimum power to the maximum speeds of present-day helicopters (that is, for values of tip-speed ratio between approximately 0.05 and 0.30) the effects of twist on the profile power are small, particularly when considered as a percentage of the total power required. The importance of twist, however, is not primarily its effect on profile power but in the delay of stall. The effect of twist on stall limits is discussed in a later section of this report.

AIRFOIL SECTION CHARACTERISTICS

The three-term drag polar used in the preparation of the charts (see section entitled "Method of Analysis") is considered as representative of practical construction blades of conventional airfoil section having fairly accurate leading-edge profiles and rigid surfaces. The charts may be applied, however, to rough or poorly built blades of conventional section by multiplying the profile-drag—thrust ratio obtained from the charts by a constant "roughness" factor equal to the ratio of the average of the ordinates of the drag curve of the actual blade to the average of the ordinates of the drag curve used in the charts. If the drag curves do not have similar shapes, the determination of this factor should take into account the relative importance of different angles of attack; a basis for doing this by a method of "weighting" curves is discussed in reference 7. The angle of attack at which stall occurs will also be affected by the roughness of the blade surface, and consideration should be given to the surface condition when estimating the limits of validity of the theory.

STALL LIMITS

Satisfactory limits to the use of a theory in which stall is not considered are, for powered flight, the conditions at which the tip of the retreating blade reaches its stalling angle

of attack, as shown in references 2 and 6. For the autorotative case, limits to the theory are shown to consist of the conditions at which the velocity of the blade elements of the stalled inboard sections reach high enough values so that the contributions of these elements to the total thrust and torque of the rotor become significant. Therefore, following the procedure of previous NACA rotor papers (such as ref. 2), there are included on the charts of this report two sets of limit lines. One set corresponds to conditions at which a blade element at an azimuth angle of 270° with a relative velocity equal to 0.4 of the tip speed reaches angles of attack of 12° and 16° , whereas the other set corresponds to conditions at which the blade tip at an azimuth angle of 270° reaches angles of attack of 12° and 16° . These limit lines are designated by the symbols $\alpha_{(\mu_T=0.4)(270^\circ)}$ and $\alpha_{(1.0)(270^\circ)}$, respectively. The 12° and 16° lines represent a range of angles of attack in which conventional blade airfoils would be expected to stall. Also, since vibration and control limitations brought on by blade stall occur, in general, when the calculated stall angle is exceeded by about 4° , the difference between the 12° and 16° lines should also be useful in estimating the limits to practical operating conditions of a rotor. Moderate amounts of stall can be approximately accounted for by empirical corrections to the profile power when the limit lines on the charts are exceeded. The basis on which these corrections may be made is discussed in reference 8 and the procedure is summarized in reference 4 (pp. 266–267). The limit lines on the profile power charts, however, should be considered only as an indication of the limits of applicability of the charts. For estimating the limiting operating conditions the straight-line plots for thrust-coefficient—solidity ratio or the plots of figure 9 (a) should be used.

Theory indicates, and flight measurements have shown, that blade twist is effective in delaying stall. Twisting the blade so as to lower the pitch at the tip with respect to the pitch at the root tends to distribute the lift more evenly along the blades and therefore minimizes the high angles of attack in the tip region. Blade angles of attack of 12° and 16° at the specified stations are plotted in figure 9(a) as functions of λ and $\theta_{.75}$ for 0° , -8° , and -16° twist. For use in cases wherein it may be more convenient to determine the blade angles of attack in terms of power and thrust coefficients, combinations of C_P/C_T and $2C_T/\sigma a$ for which blade angles of attack at the specified station reach 12° and 16° for 0° , -8° , and -16° twist are plotted in figure 9(b). As would be expected, these plots show that higher values of C_T/σ can be attained with negative twist before retreating blade stall is encountered. Conversely, the greater the negative twist, the higher the tip-speed ratio that can be reached at a given C_T/σ before the onset of stall.

It should be noted that negative values of twist tend to decrease the angle of attack at the tip of the advancing blade. The advancing-blade-tip angle of attack is shown in figure 10 as a function of $2C_T/\sigma a$ and μ at several power conditions (as represented by the pitch values) for twists of -8° and -16° . Although the large negative angles of attack at the advancing-blade tip will adversely affect the performance, this effect is believed to be of less importance

than the benefits achieved by the delay in retreating blade stall. There is the possibility, however, that high negative advancing-blade-tip angles of attack would result in a contribution to blade stresses which should be considered for individual designs. These tip angles, however, were calculated on the basis of uniform inflow velocity, and the local upwash which tends to occur at the advancing tip should result in less negative values.

COMPRESSIBILITY LIMITS

The section lift and drag coefficients used in the preparation of the charts of this report do not vary with Mach number. It is expected that the primary effect of such variation would be an increase in the profile-drag power if the drag-divergence Mach number were approached or exceeded. Therefore, the charts underestimate the power required for a rotor operating within the range where compressibility effects are encountered. It is hoped that power losses due to compressibility may be taken into account by adding corrections to the charts in a manner similar to that done for the effects of stall. The corrections probably could be based on results of strip analyses or on experimental data. The operational limits imposed by Mach number, however, are yet to be determined.

CONCLUDING REMARKS

Charts based on rotor theory have been presented from which the profile-drag-thrust ratio of a rotor can be determined for various combinations of pitch angle, ratio of thrust coefficient to solidity, tip-speed ratio, and power input. The equations on which the charts are based have taken into account blade stall in the reversed-velocity region and are not limited by small-angle assumptions for blade pitch and inflow angles. For these reasons the method is believed to be more accurate than previous methods for cases wherein the rotor inflow velocity is relatively large, for rotors operating at steep rates of climb or descent, for flight at high tip-speed ratios, or for convertiplane transition attitudes.

In addition to providing a convenient means for quickly estimating rotor performance, the charts should be useful as a means for estimating the effects of changes in design variables and as a base to which corrections may be applied for the effects of stall and compressibility. Charts which indicate the stall condition of the rotor and which serve to indicate the limits to practical rotor operating conditions are also presented.

The method of using the charts for performance estimation is outlined and illustrated through computation of a sample problem.

LANGLEY AERONAUTICAL LABORATORY,
NATIONAL ADVISORY COMMITTEE FOR AERONAUTICS,
LANGLEY FIELD, VA., November 23, 1955.

REFERENCES

1. Gessow, Alfred, and Crim, Almer D.: An Extension of Lifting Rotor Theory To Cover Operation at Large Angles of Attack and High Inflow Conditions. NACA TN 2665, 1952.
2. Bailey, F. J., Jr., and Gustafson, F. B.: Charts for Estimation of the Characteristics of a Helicopter Rotor in Forward Flight. I—Profile Drag-Lift Ratio for Untwisted Rectangular Blades. NACA WR L-110, 1944. (Formerly NACA ACR L4H07.)
3. Pope, Alan: Summary Report of the Forces and Moments Over an NACA 0015 Airfoil Through 180° Angle of Attack. Aero Digest, vol. 58, no. 4, Apr. 1949, pp. 76-78, 100.
4. Gessow, Alfred, and Myers, Garry C., Jr.: Aerodynamics of the Helicopter. The Macmillan Co., c. 1952.
5. Gessow, Alfred: An Analysis of the Autorotative Performance of a Helicopter Powered by Rotor-Tip Jet Units. NACA TN 2154, 1950.
6. Bailey, F. J., Jr.: A Simplified Theoretical Method of Determining the Characteristics of a Lifting Rotor in Forward Flight. NACA Rep. 716, 1941.
7. Gustafson, F. B.: Effect on Helicopter Performance of Modifications in Profile-Drag Characteristics of Rotor-Blade Airfoil Sections. NACA WR L-26, 1944. (Formerly NACA ACR L4H05.)
8. Gustafson, F. B., and Gessow, Alfred: Effect of Blade Stalling on the Efficiency of a Helicopter Rotor As Measured in Flight. NACA TN 1250, 1947.

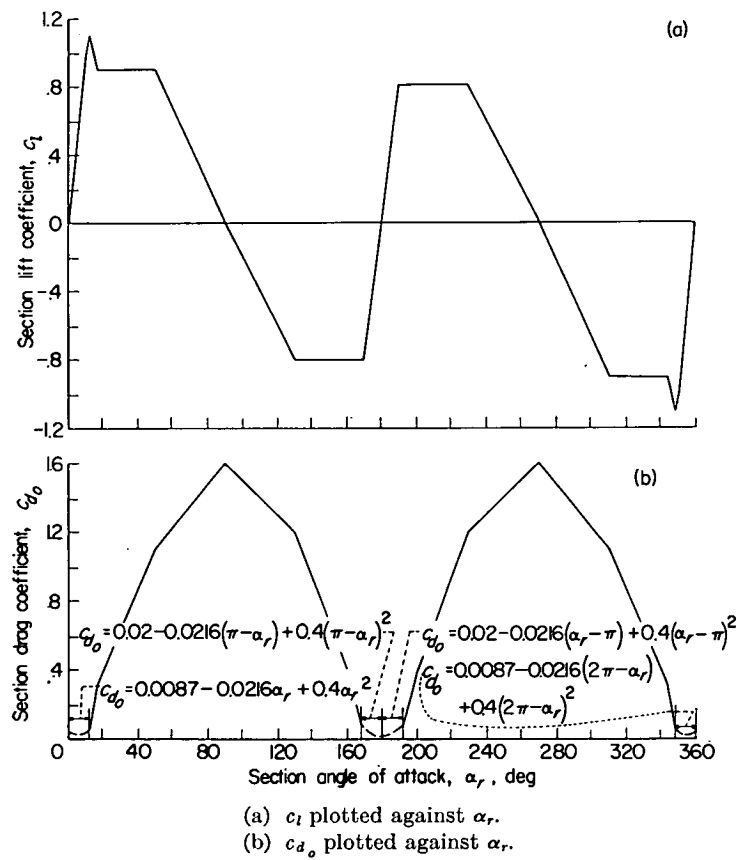


FIGURE 1.—Section lift and drag characteristics used in evaluation of reversed-velocity region.

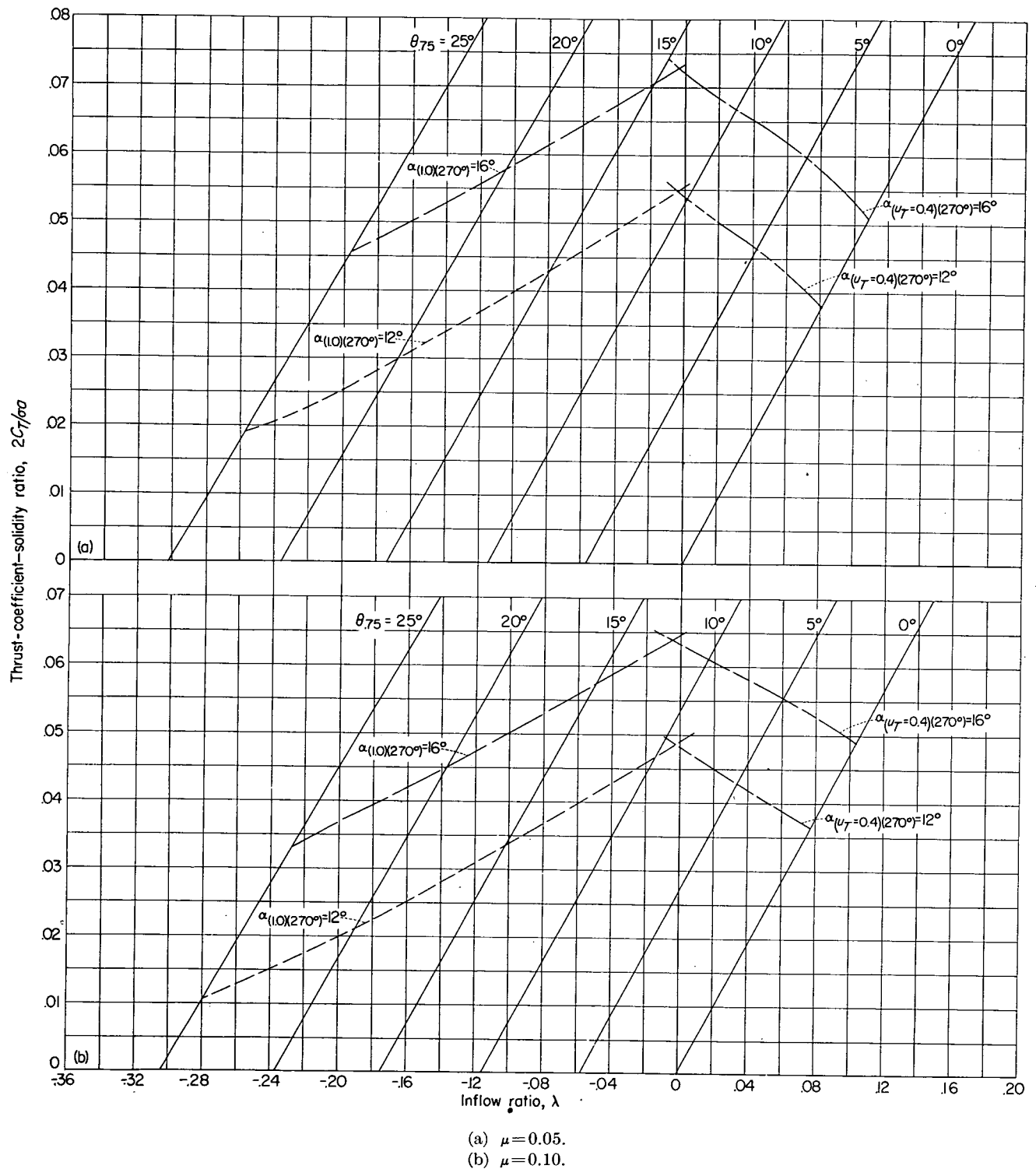


FIGURE 2.—Thrust-coefficient—solidity ratio as a function of inflow ratio and pitch angle for blades having 0° twist.

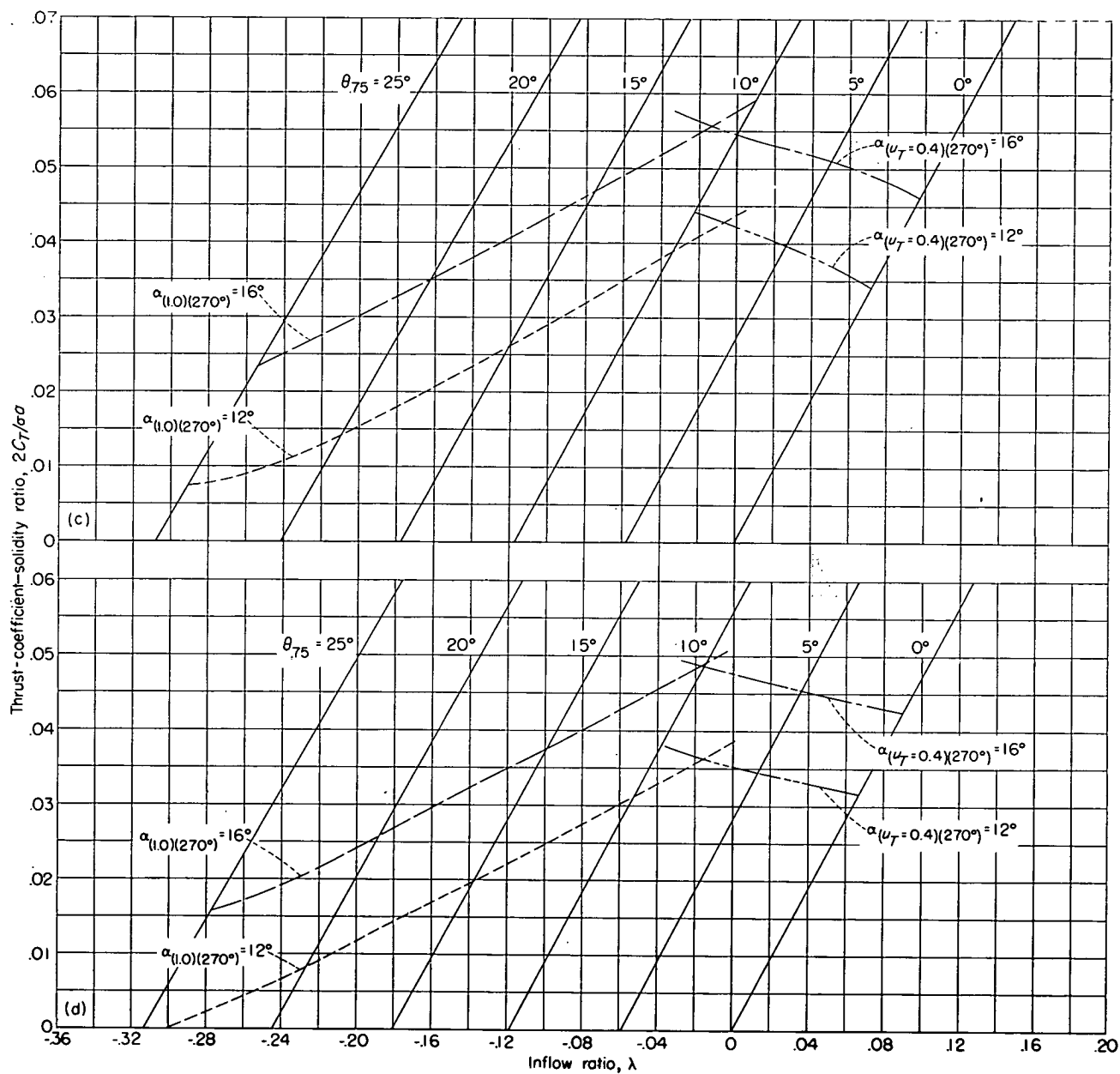
(c) $\mu = 0.15$.(d) $\mu = 0.20$.

FIGURE 2.—Continued.

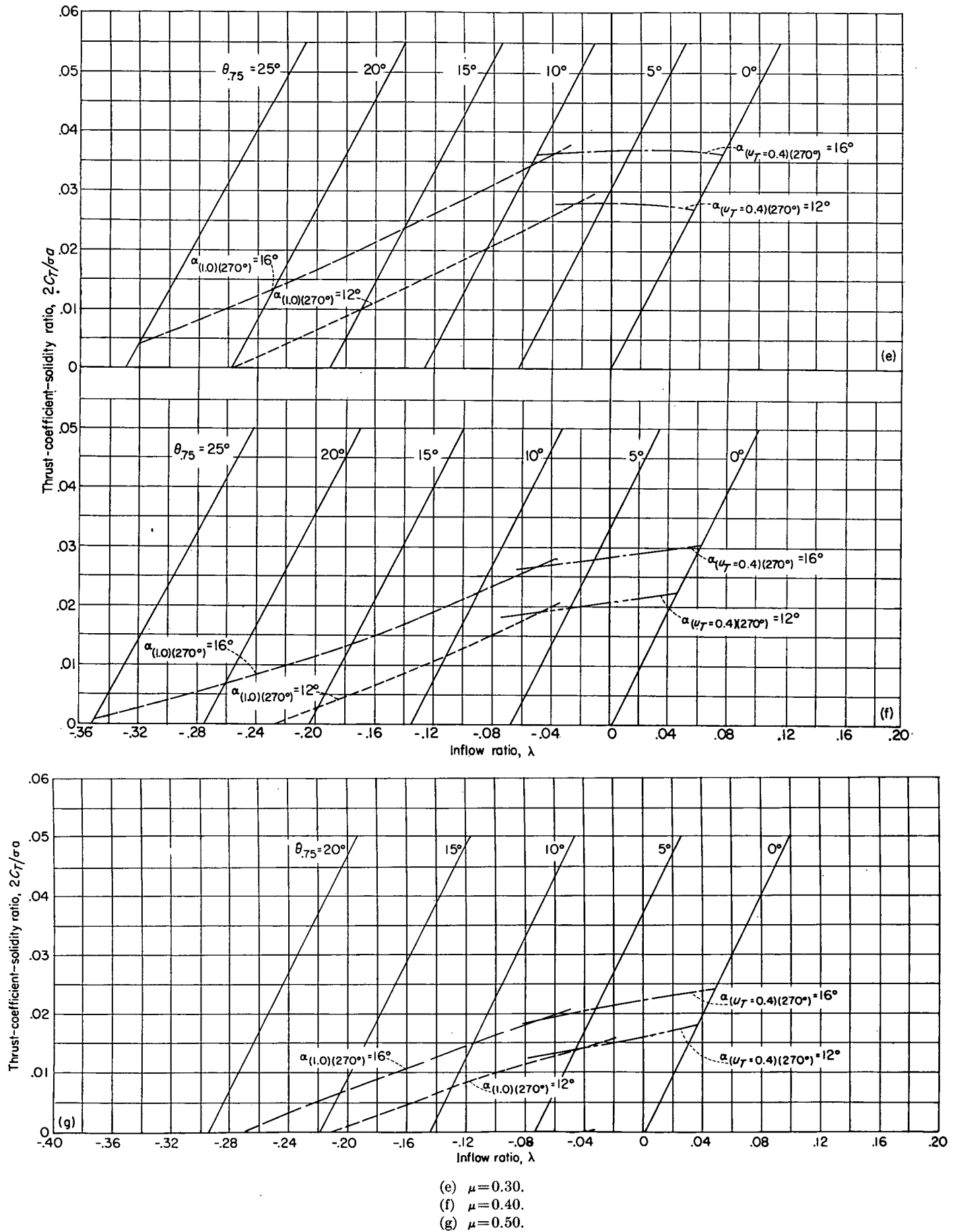
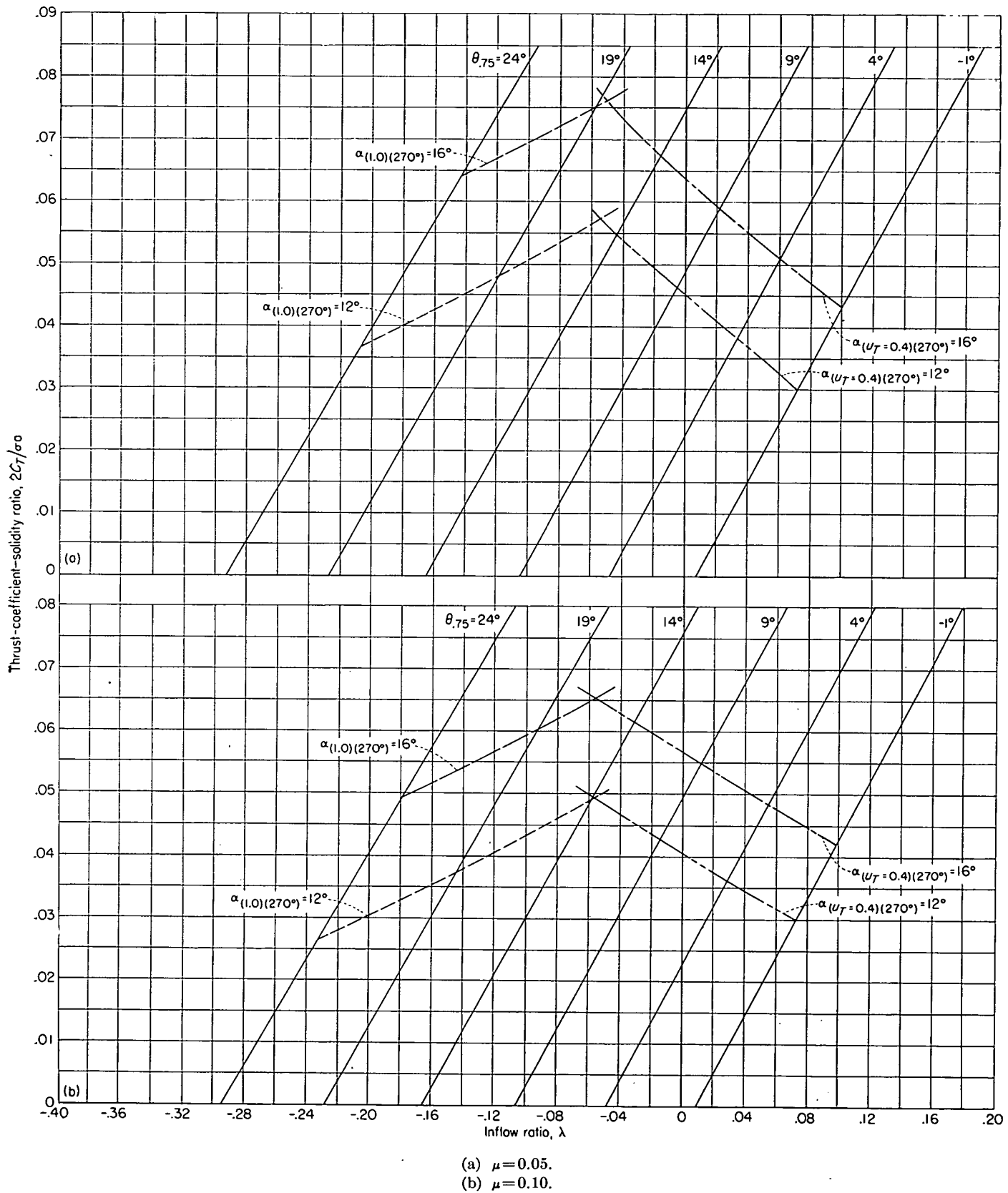


FIGURE 2.—Concluded.

FIGURE 3.—Thrust-coefficient—solidity ratio as a function of inflow ratio for blades having -8° twist.

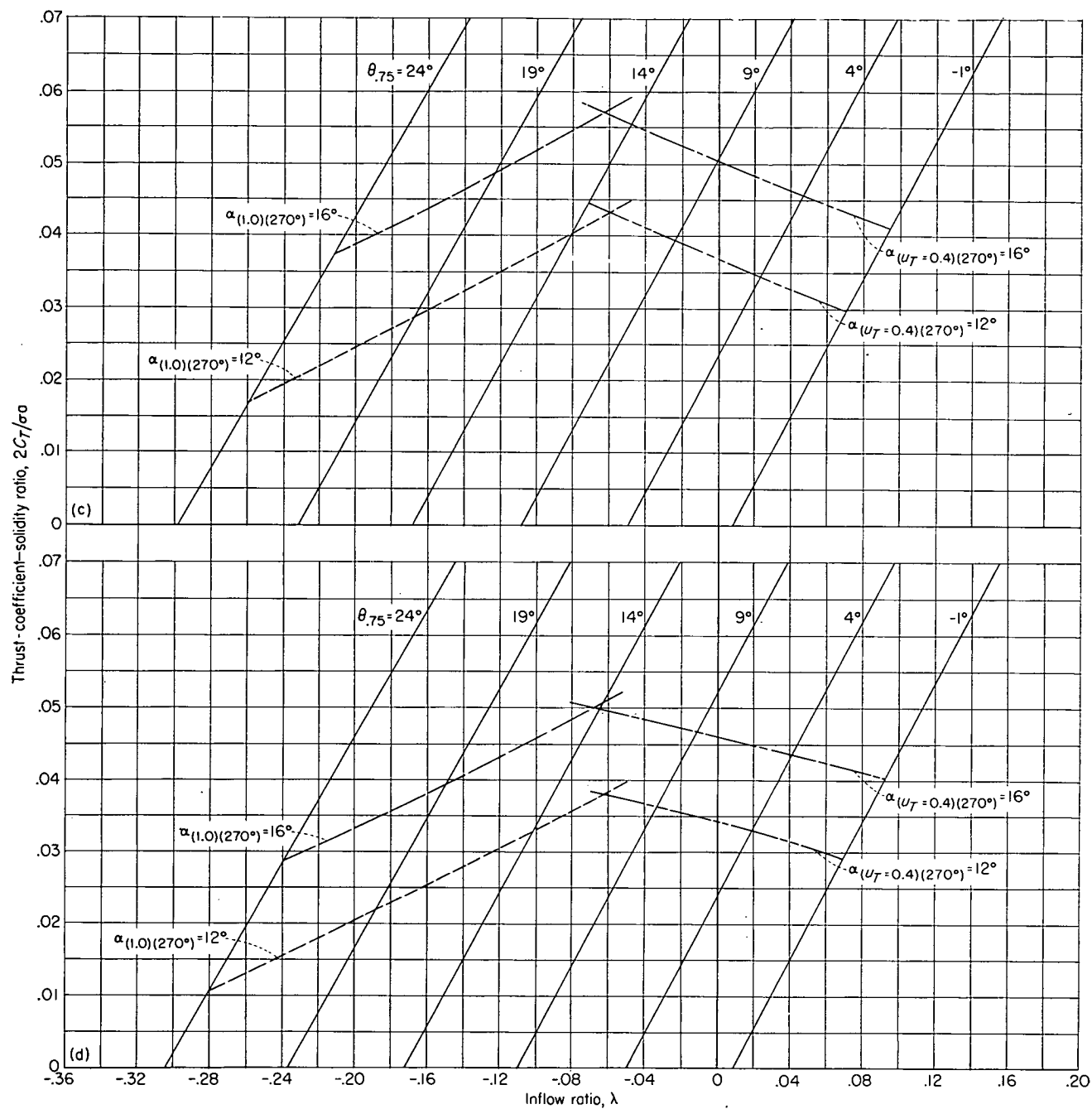
(c) $\mu = 0.15$.(d) $\mu = 0.20$.

FIGURE 3.—Continued.

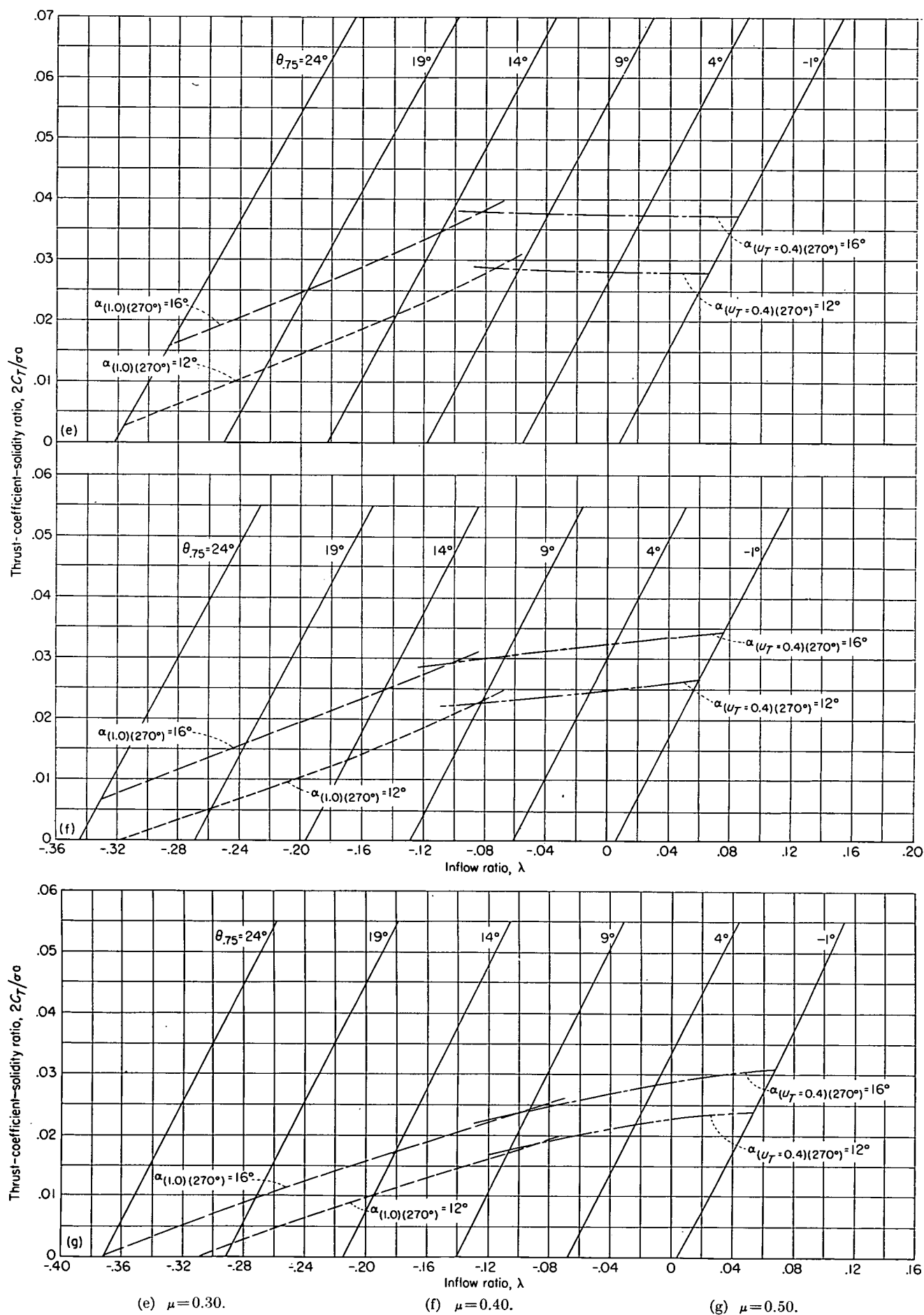
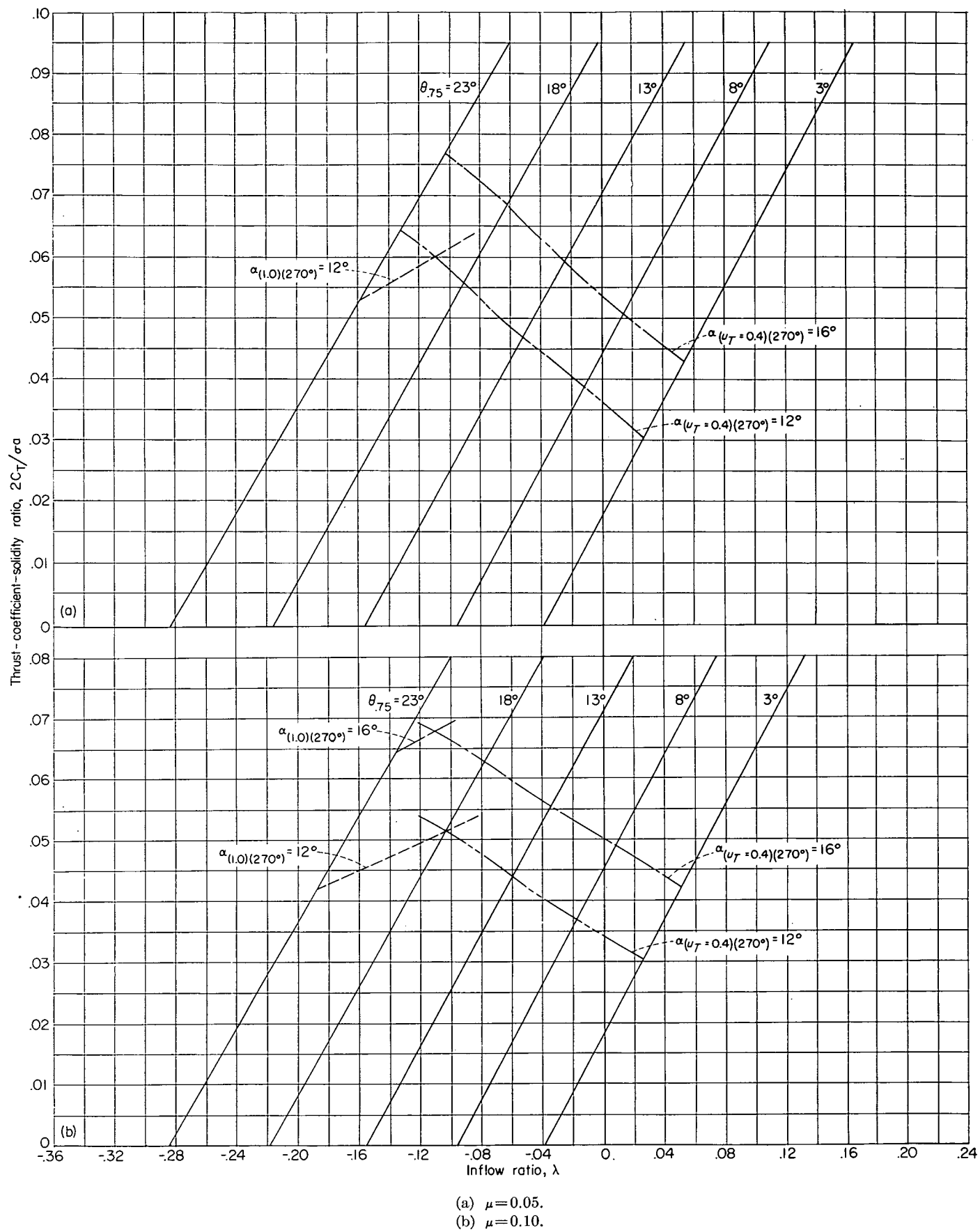


FIGURE 3.—Concluded.

FIGURE 4.—Thrust-coefficient—solidity ratio as a function of inflow ratio and pitch angle for blades having -16° twist.

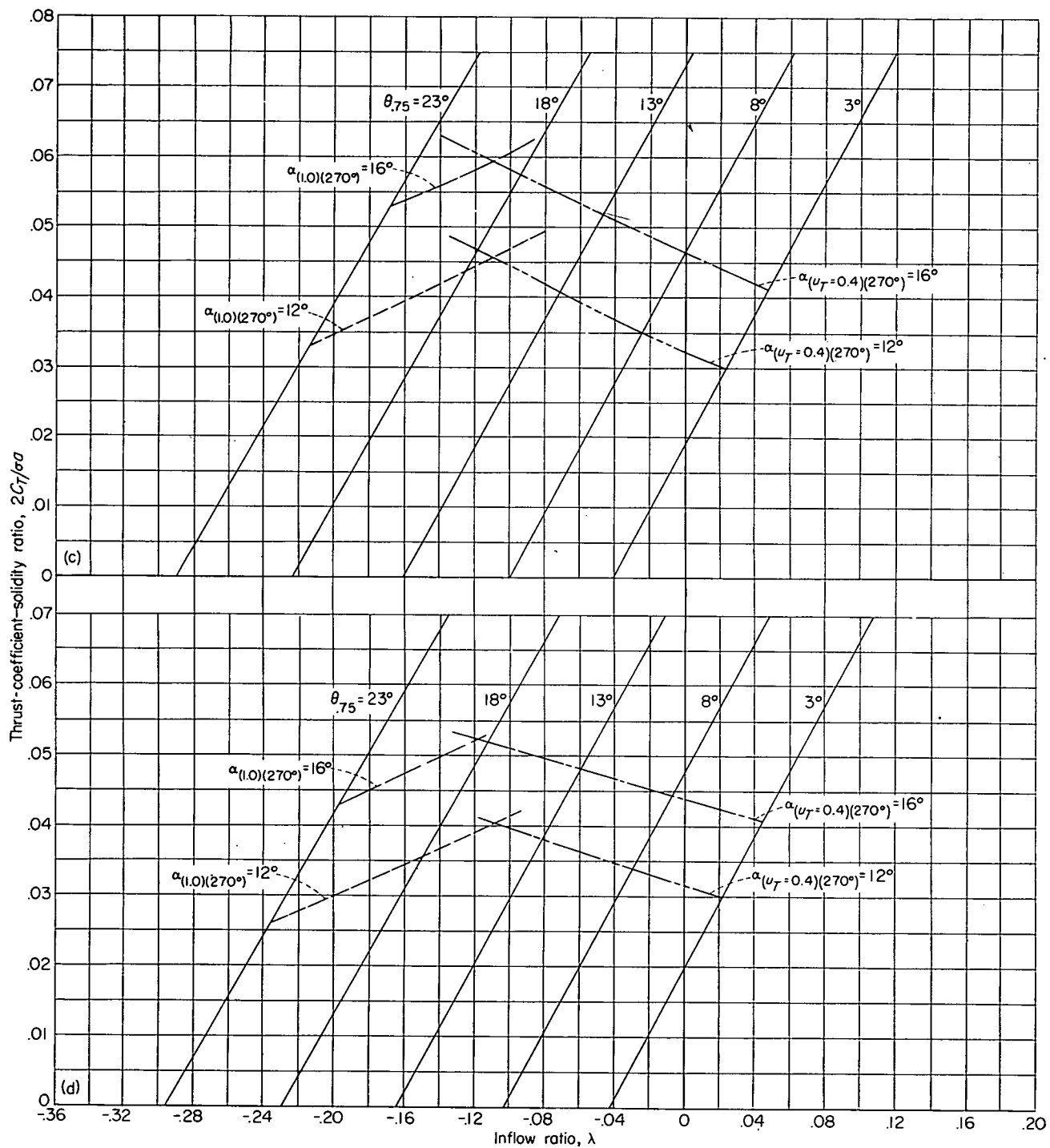
(c) $\mu = 0.15$.(d) $\mu = 0.20$.

FIGURE 4.—Continued.

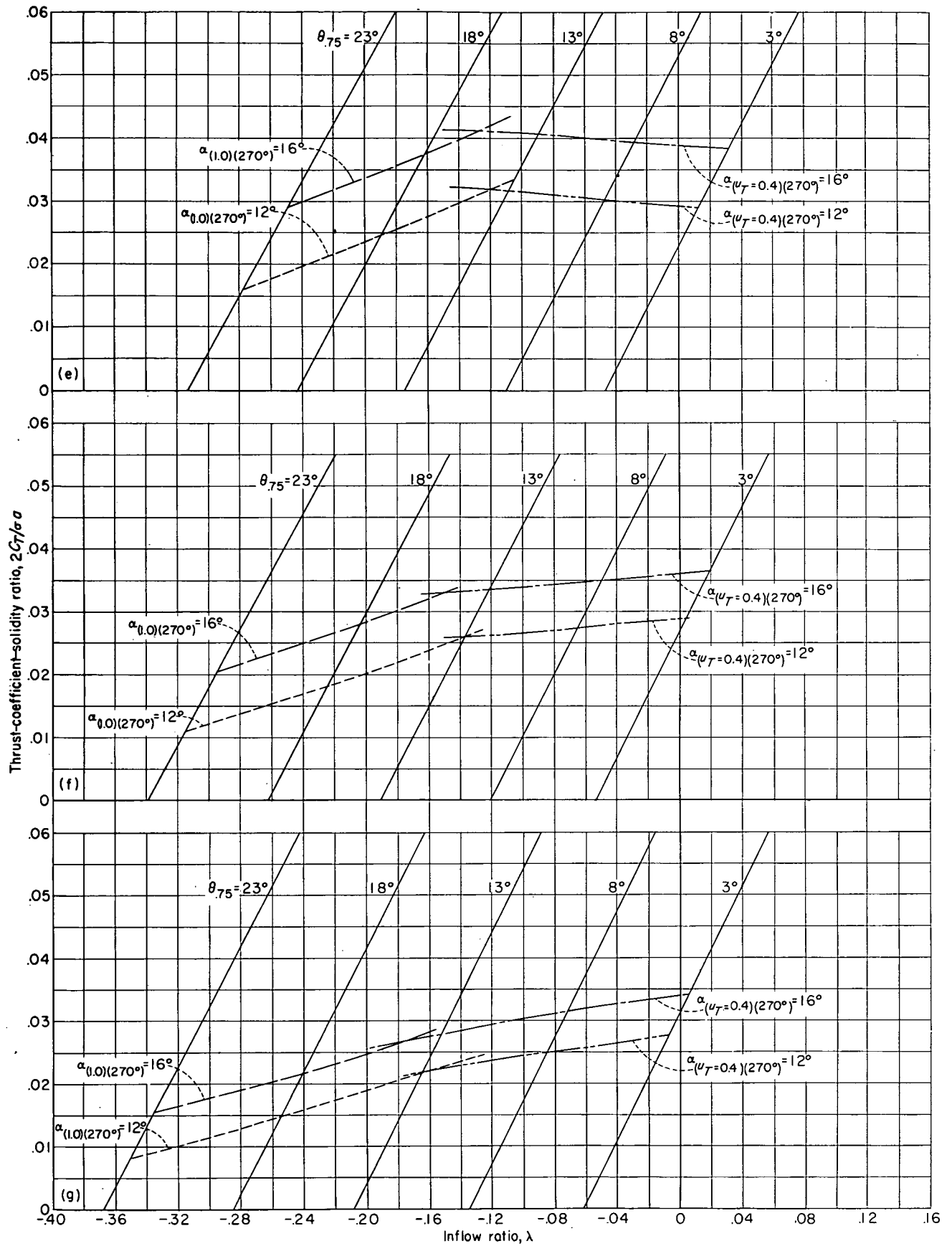
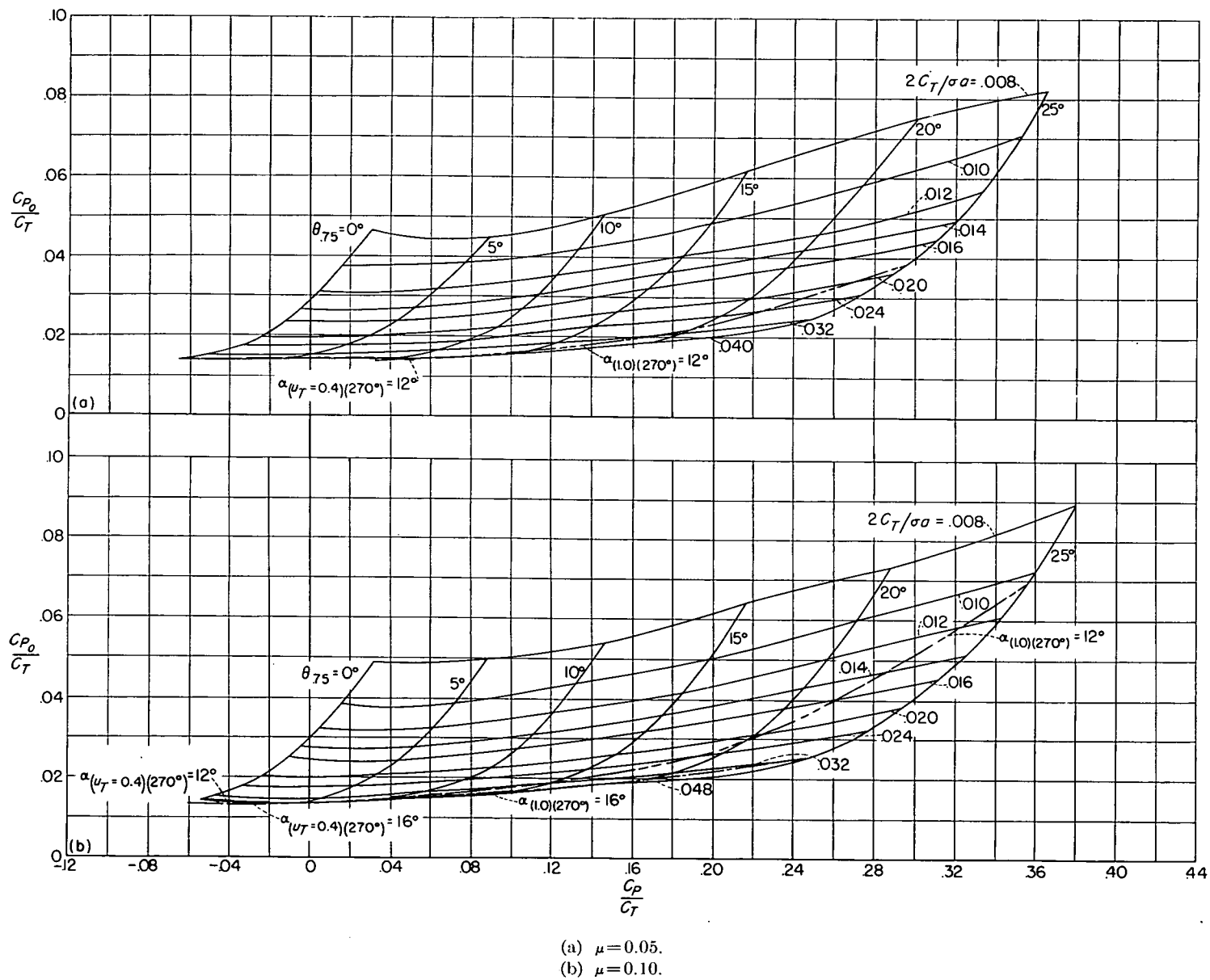


FIGURE 4.—Concluded.

FIGURE 5.—Profile-drag—thrust ratio for blades having 0° twist.

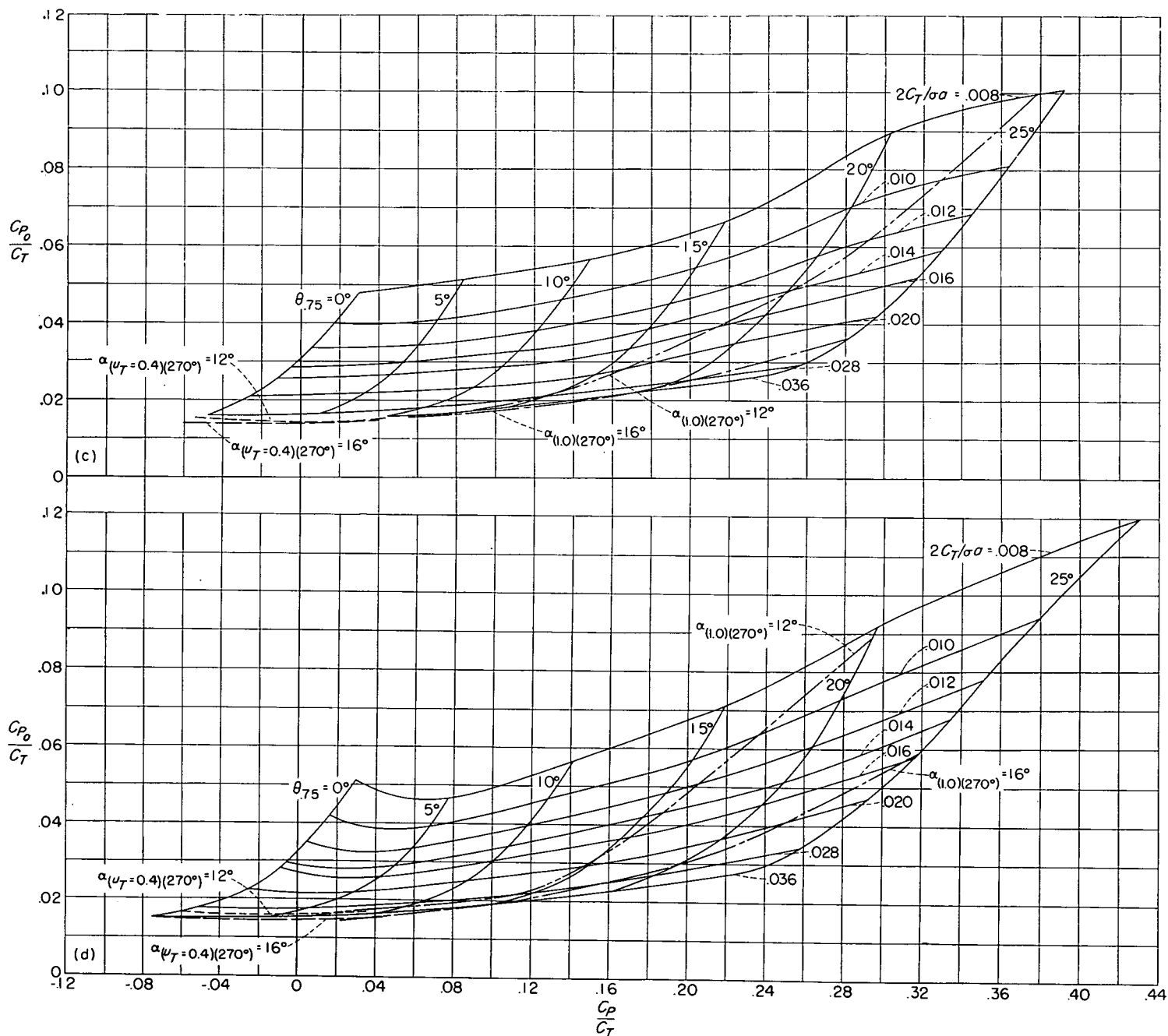
(c) $\mu = 0.15$.(d) $\mu = 0.20$.

FIGURE 5.—Continued.

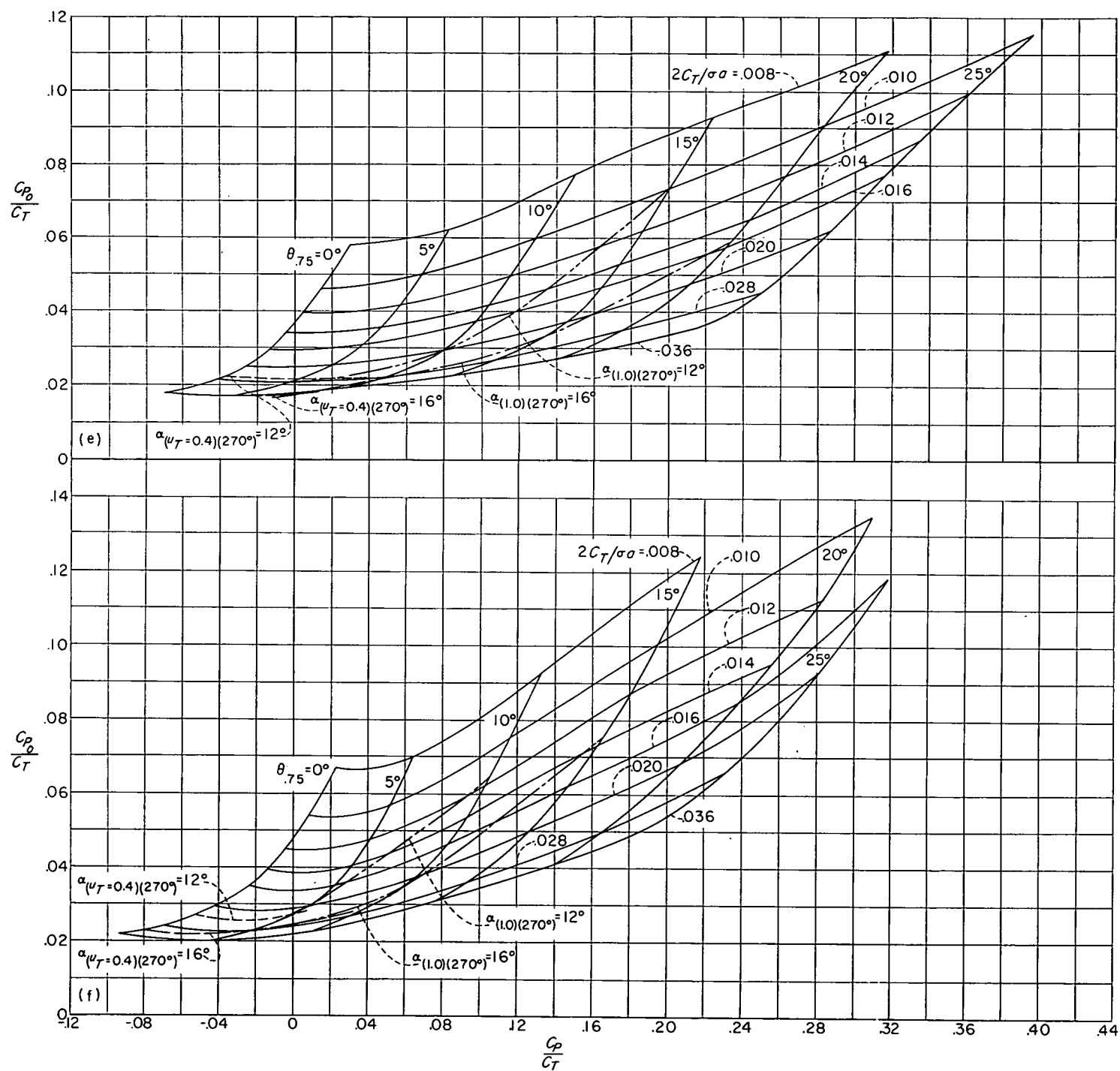
(e) $\mu = 0.30$.(f) $\mu = 0.40$.

FIGURE 5.—Continued.

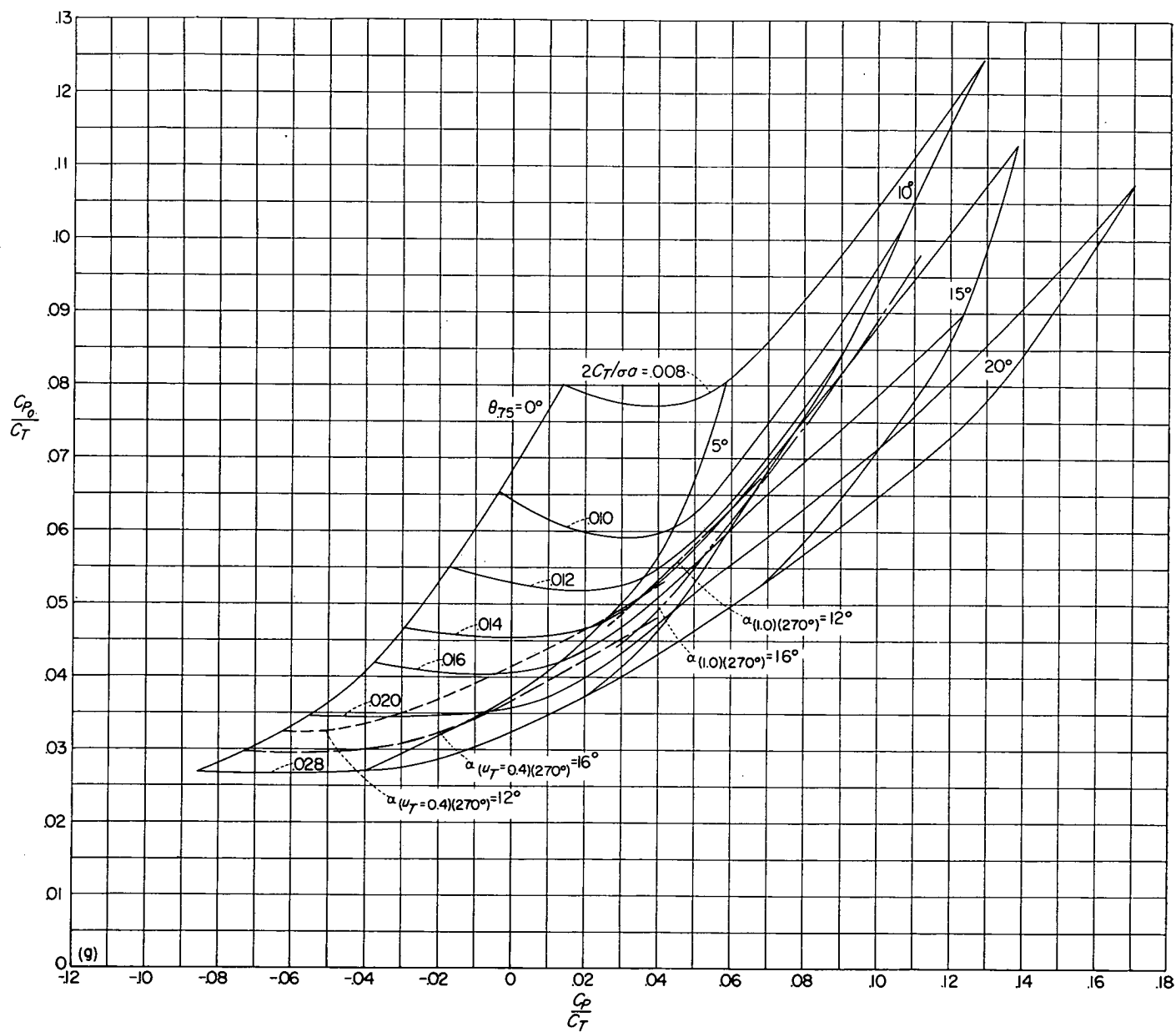
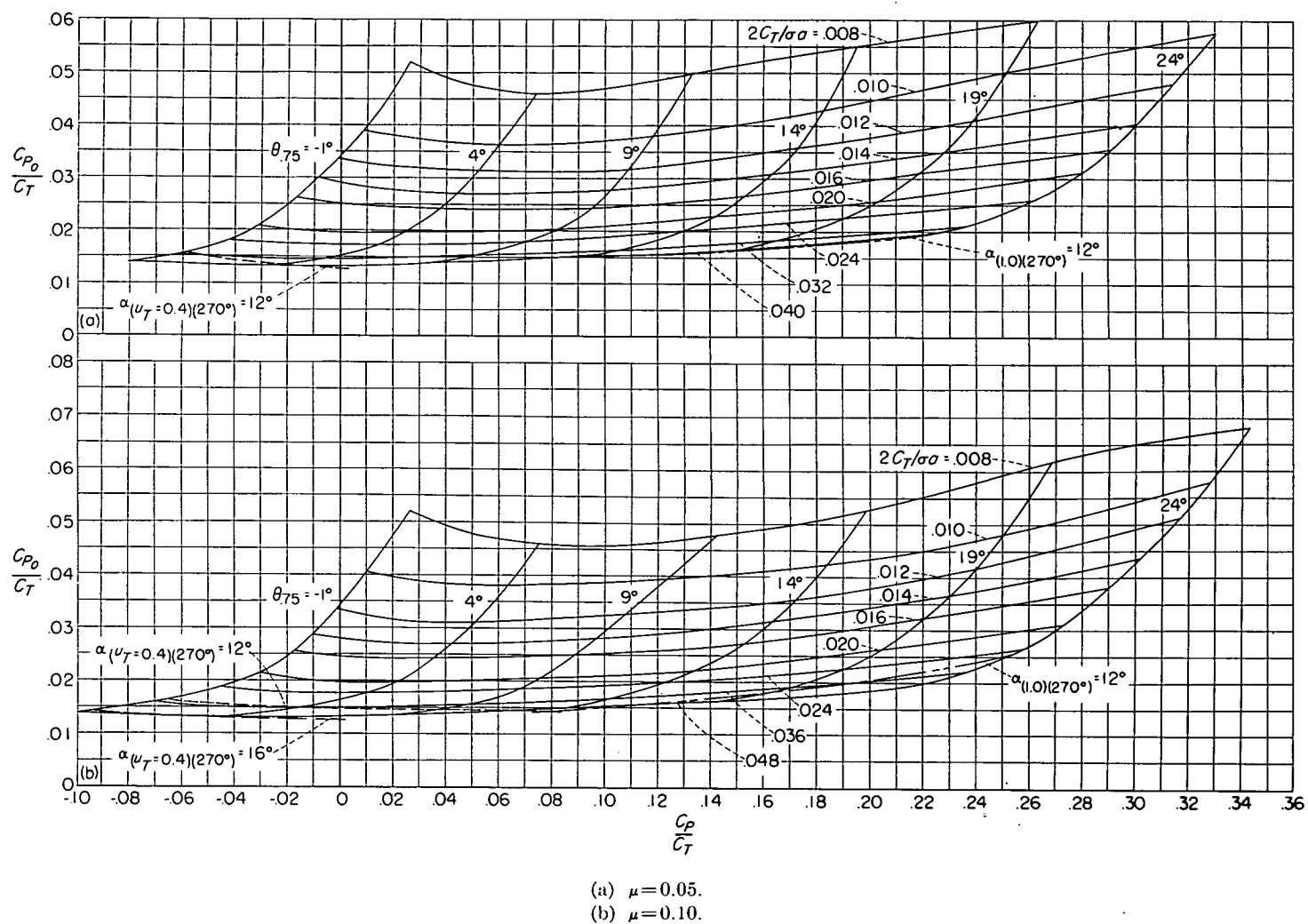
(g) $\mu = 0.50$.

FIGURE 5.—Concluded.

FIGURE 6.—Profile-drag—thrust ratio for blades having -8° twist.

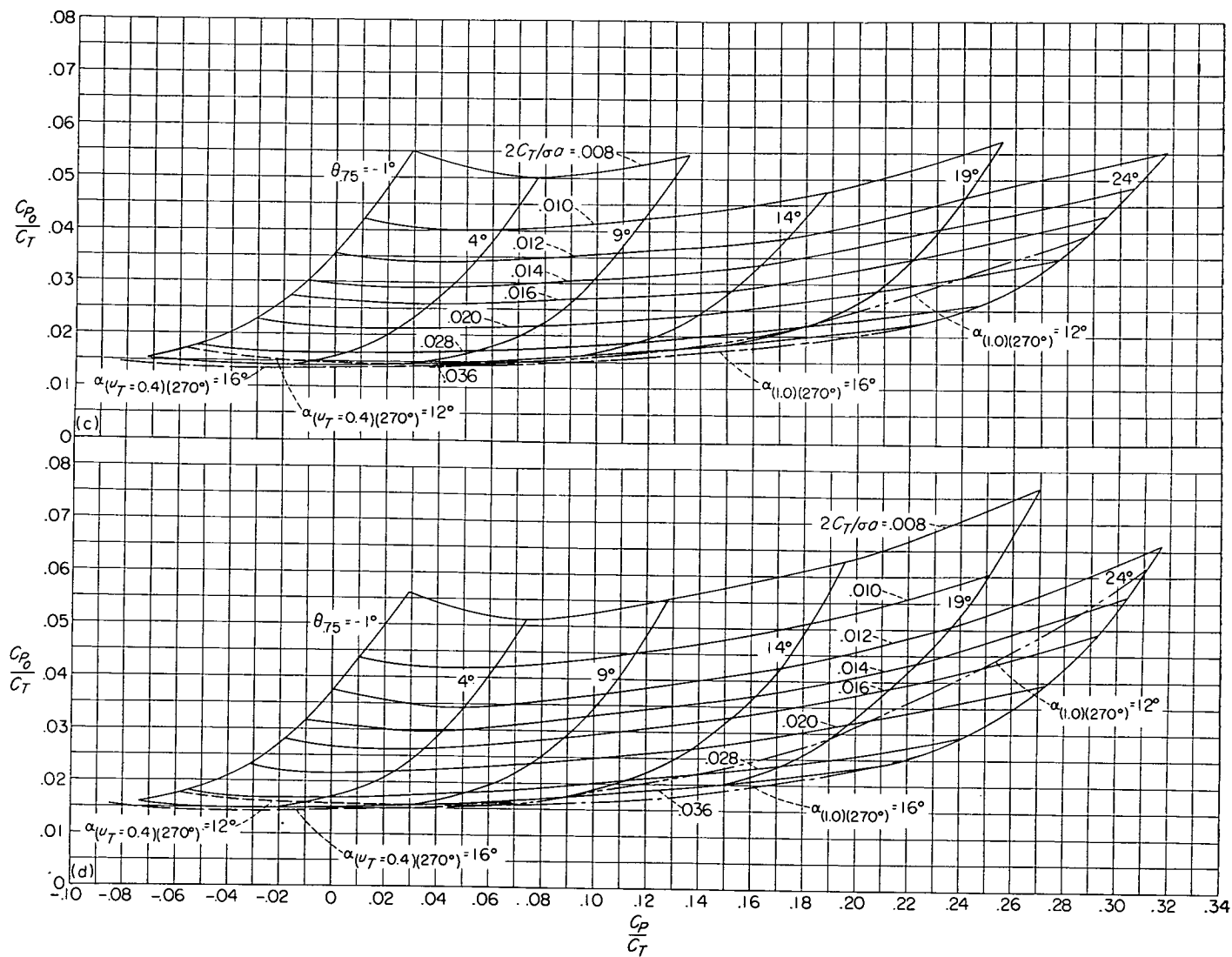
(c) $\mu = 0.15$.(d) $\mu = 0.20$.

FIGURE 6.—Continued.

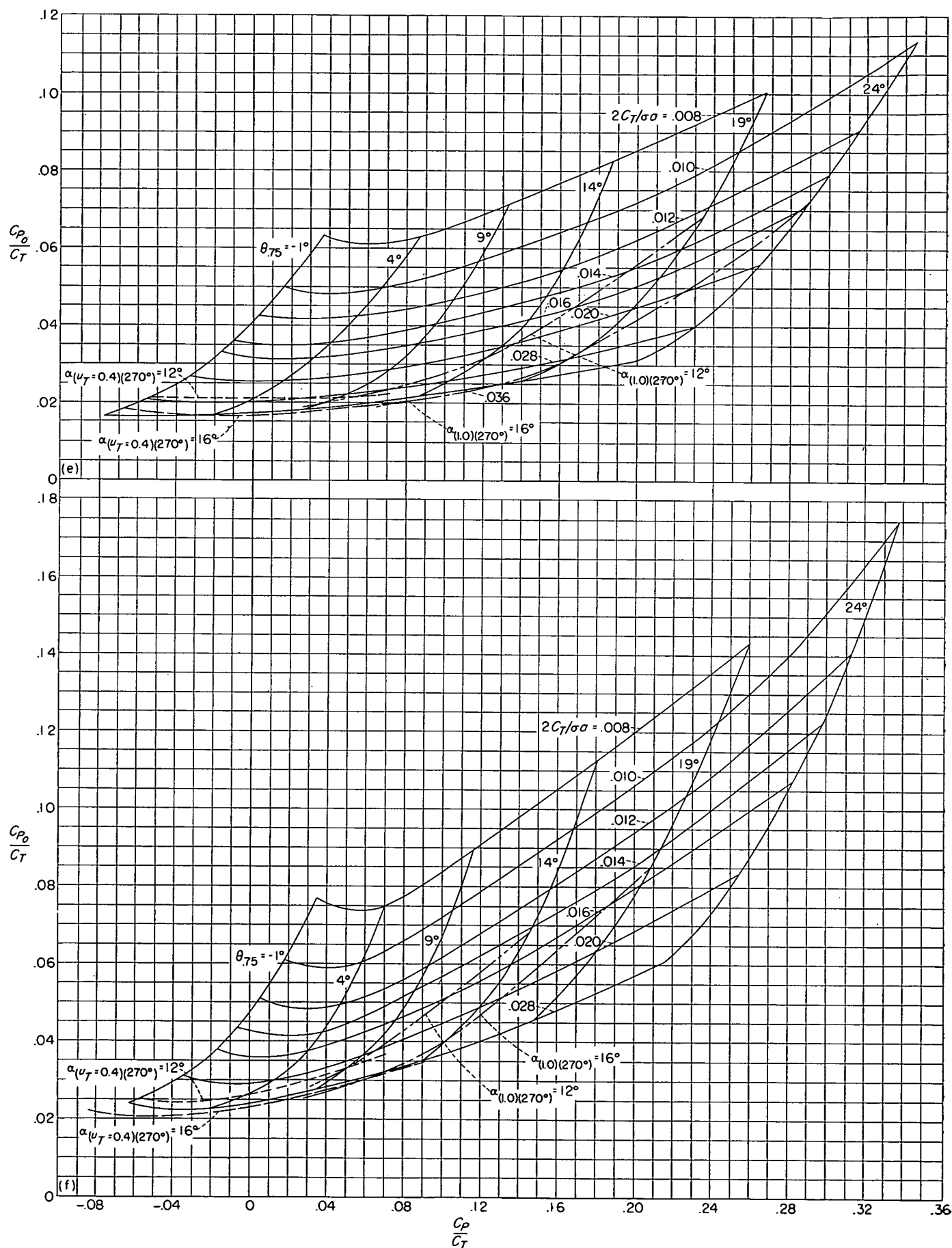
(e) $\mu = 0.30$.(f) $\mu = 0.40$.

FIGURE 6.—Continued.

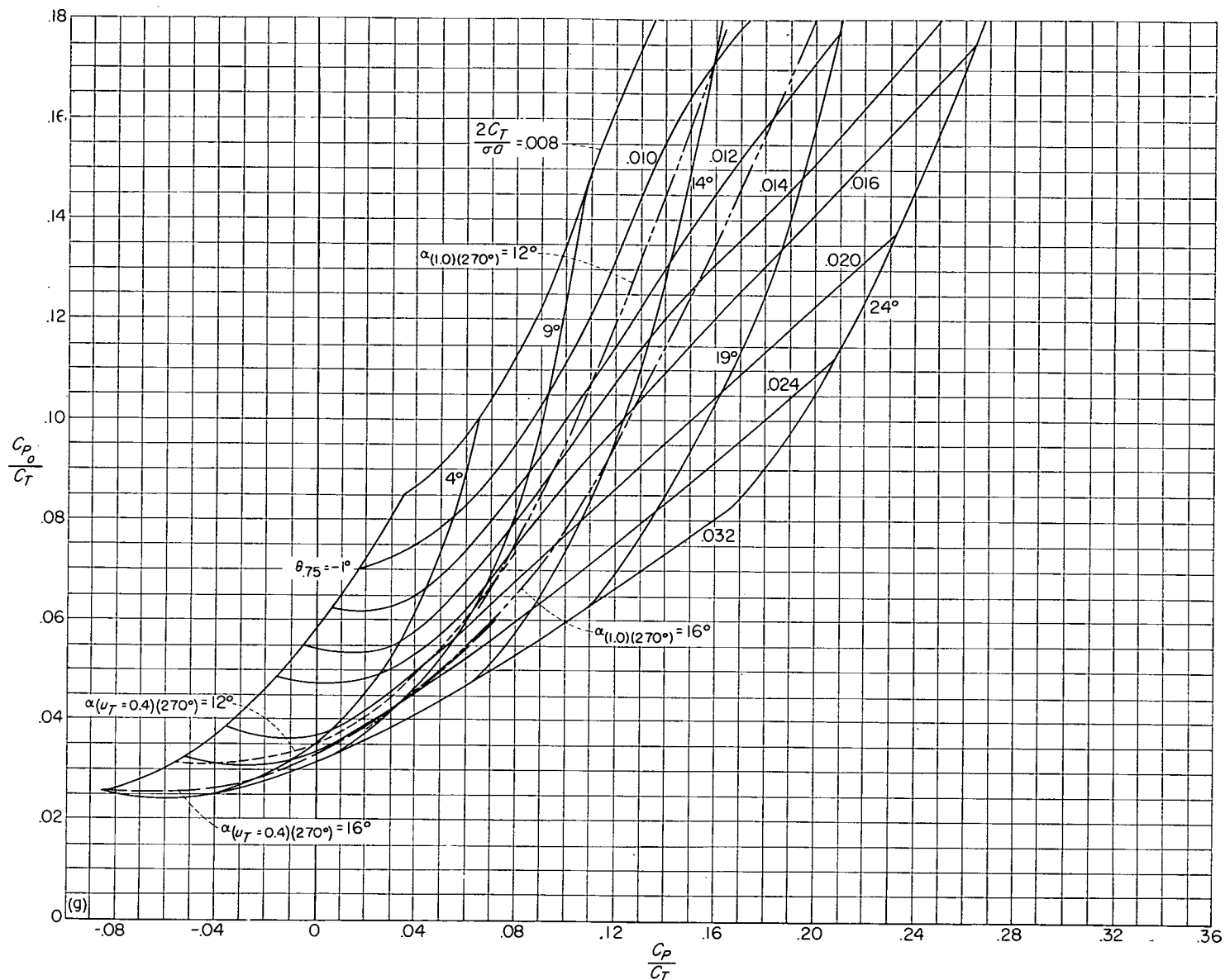
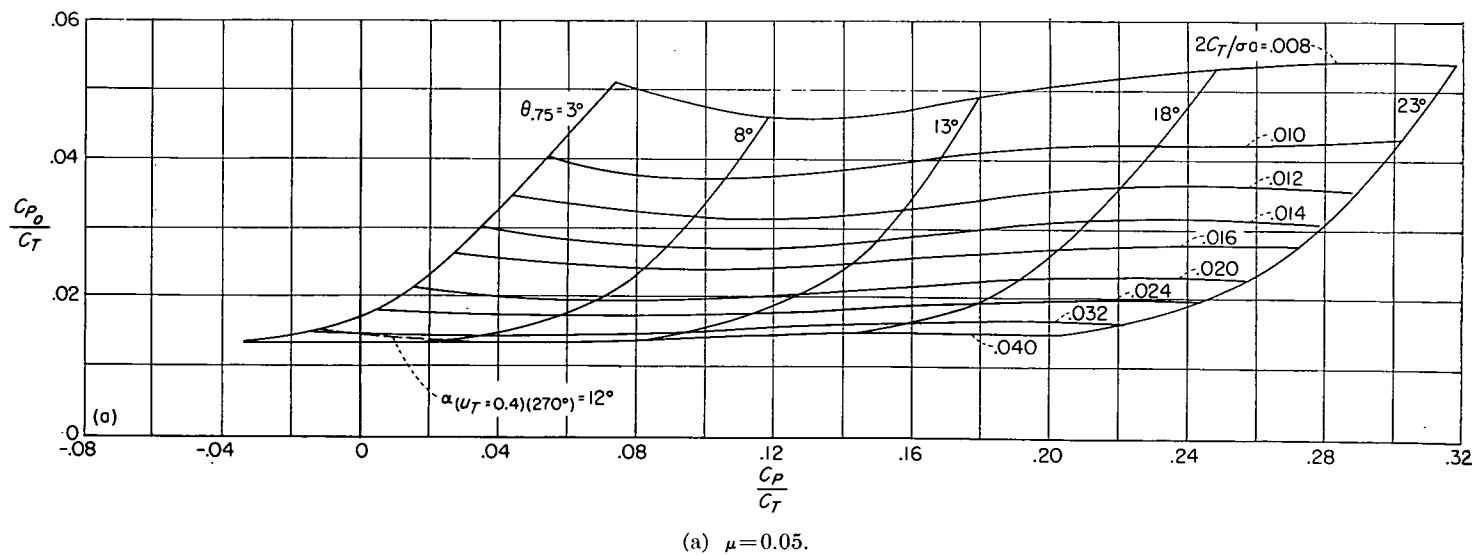


FIGURE 6.—Concluded.

FIGURE 7.—Profile-drag—thrust ratio for blades having -16° twist.

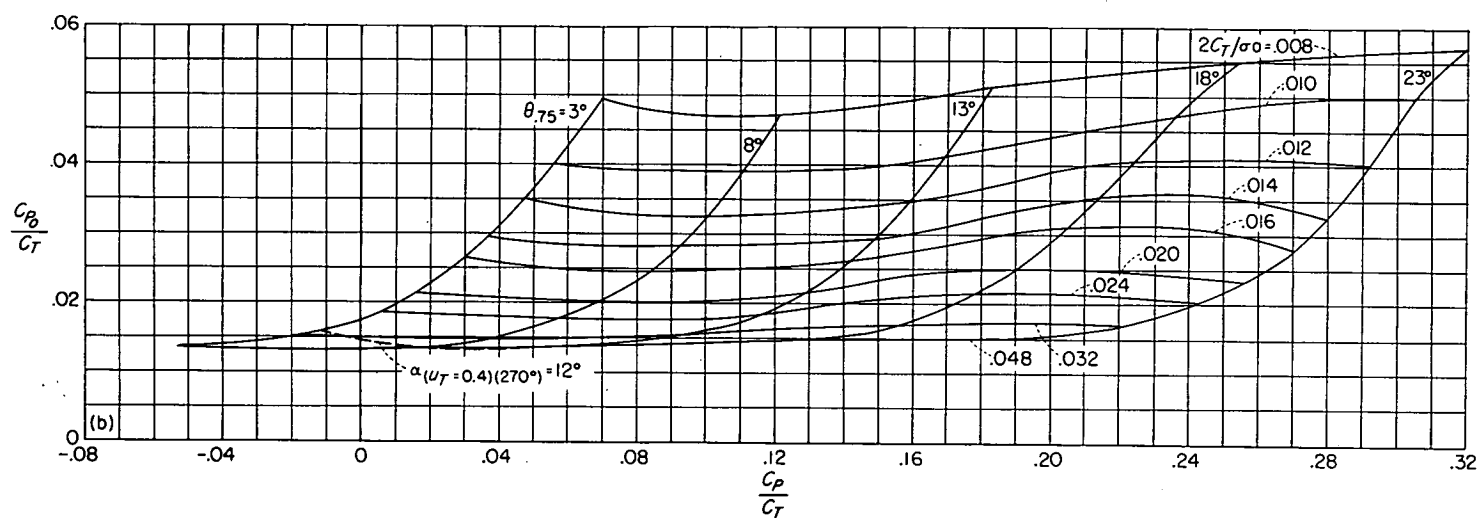
(b) $\mu = 0.10$.

FIGURE 7.—Continued.

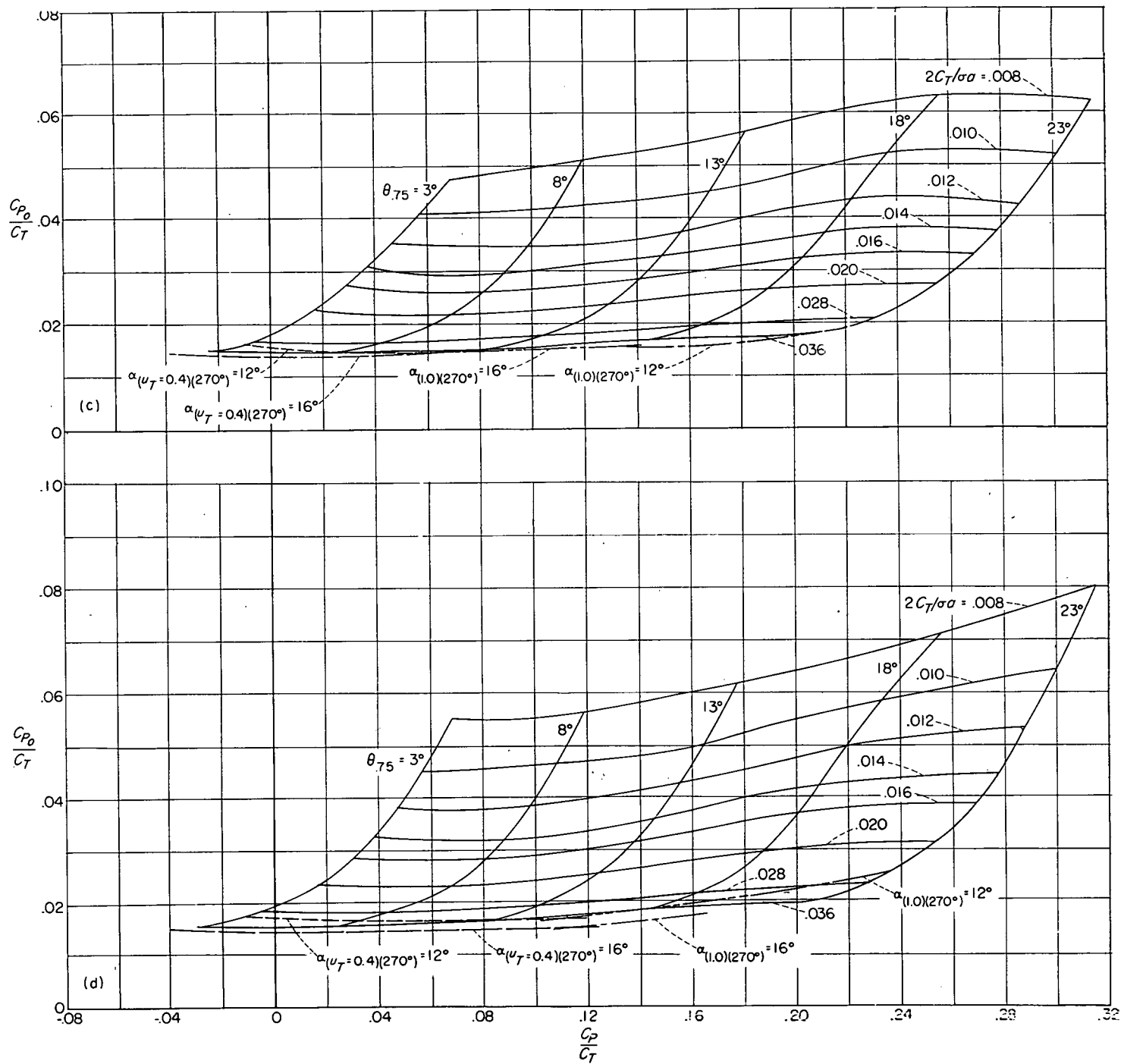
(c) $\mu = 0.15$.(d) $\mu = 0.20$.

FIGURE 7.—Continued.

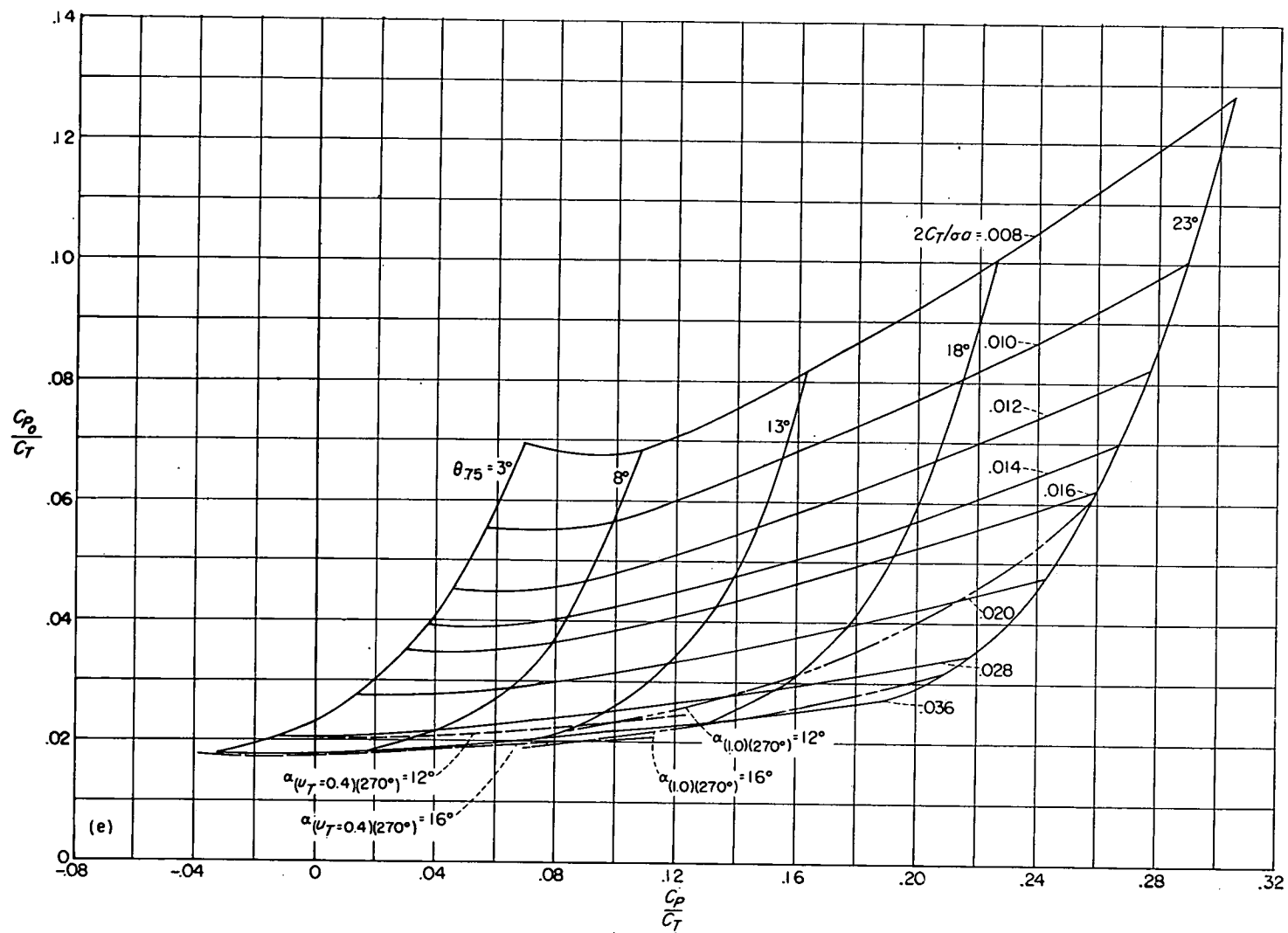
(e) $\mu=0.30$.

FIGURE 7.—Continued.

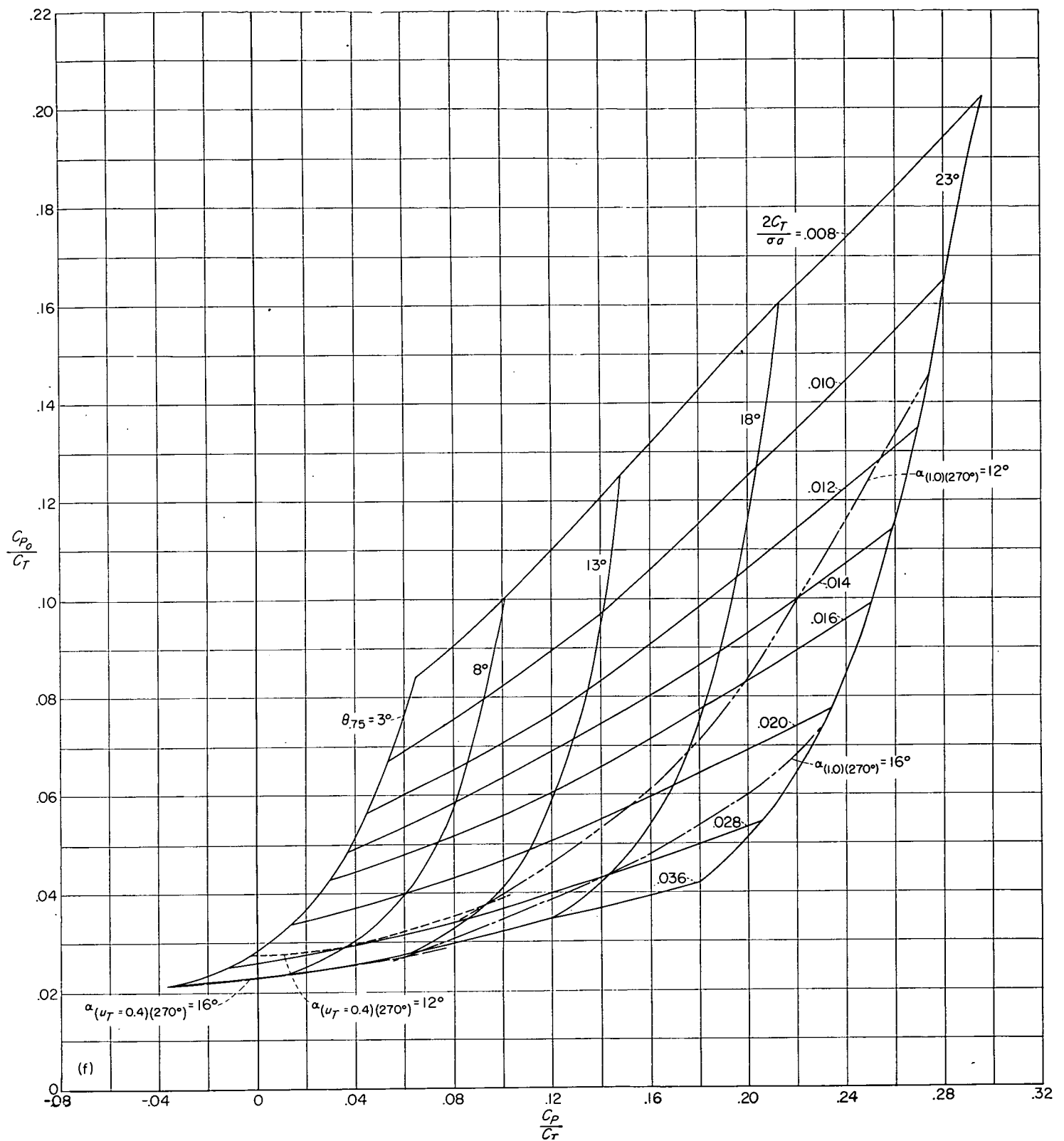
(f) $\mu = 0.40$.

FIGURE 7.—Continued.

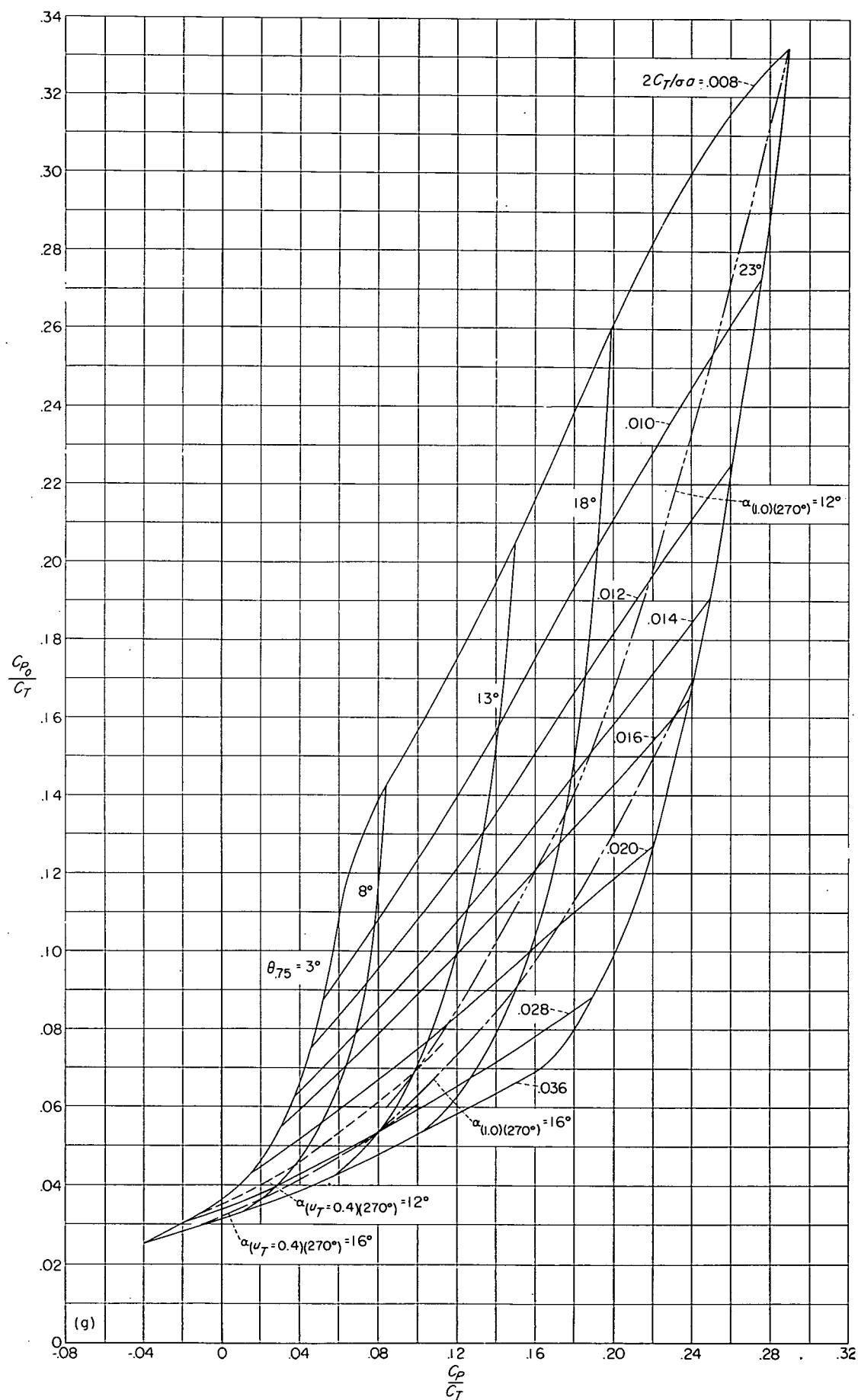
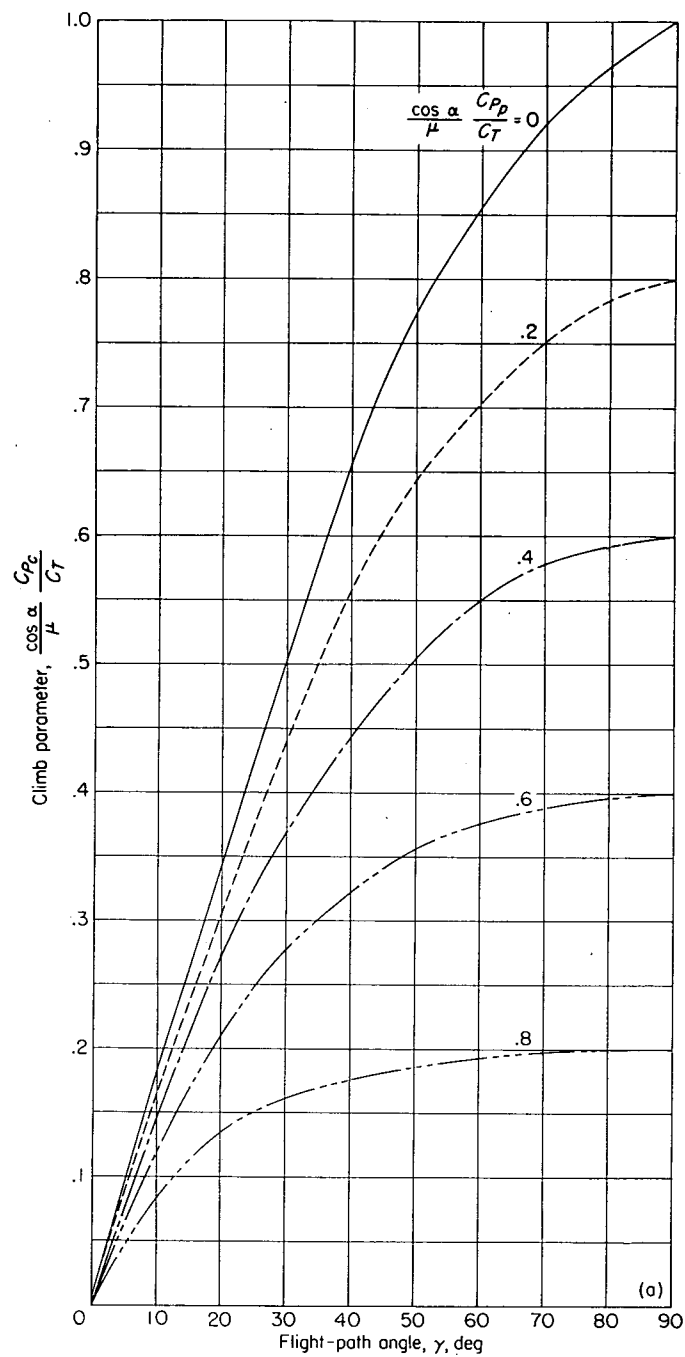


FIGURE 7.—Concluded.



(a) Climb (γ positive).

FIGURE 8.—Climb parameter $\frac{\cos \alpha}{\mu} \frac{C_{Pe}}{C_T}$ as a function of flight-path angle and parasite-drag parameter.

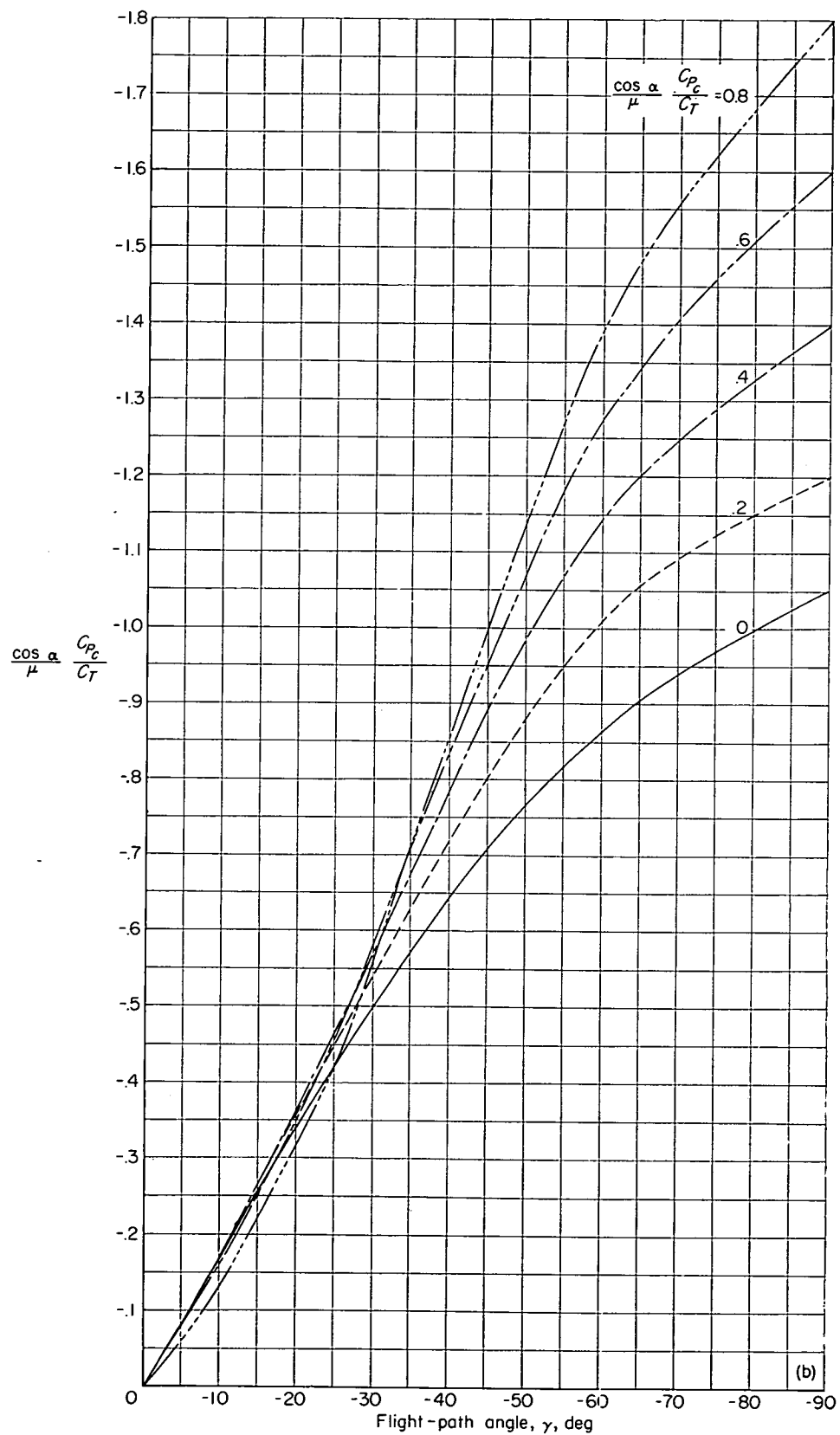
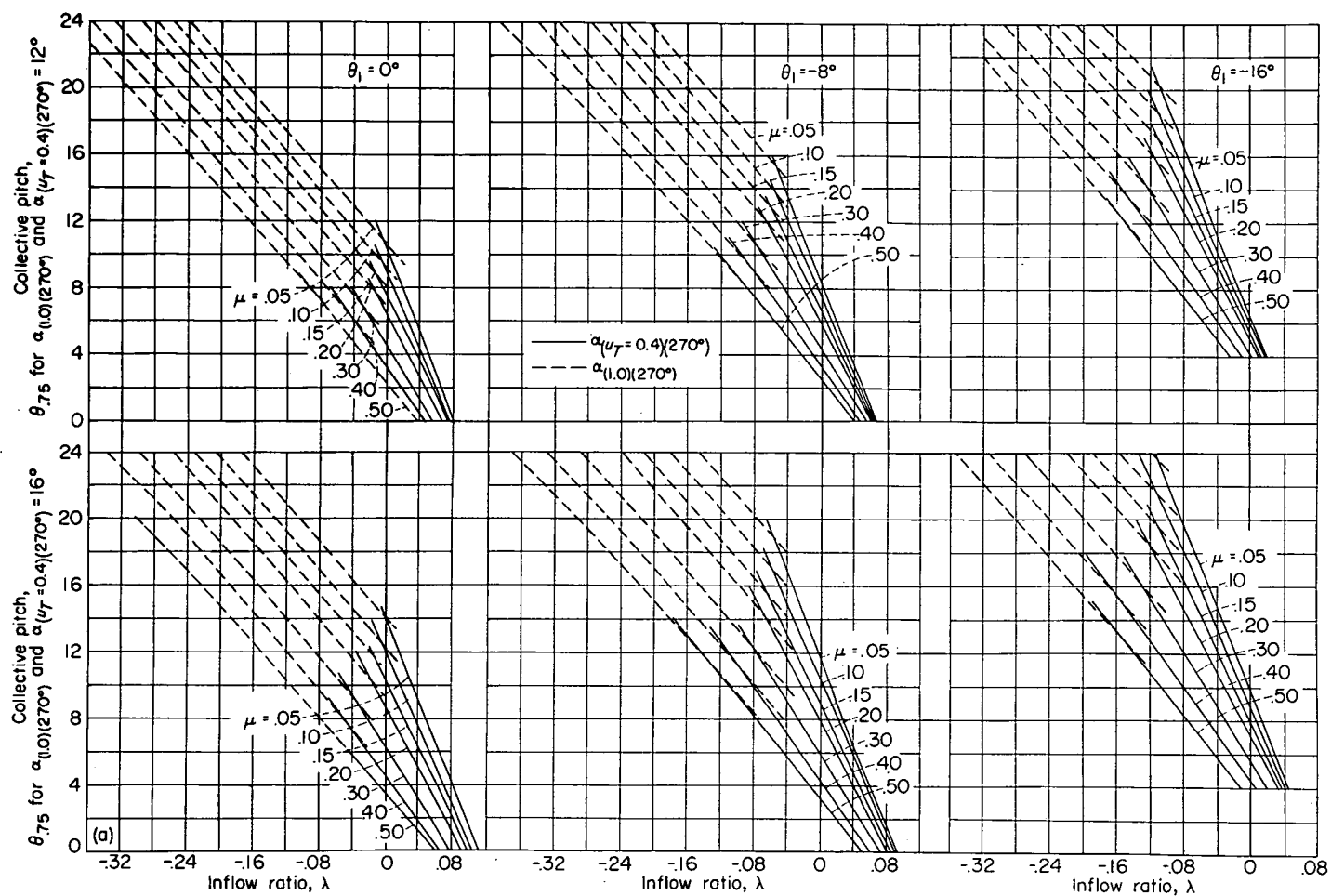
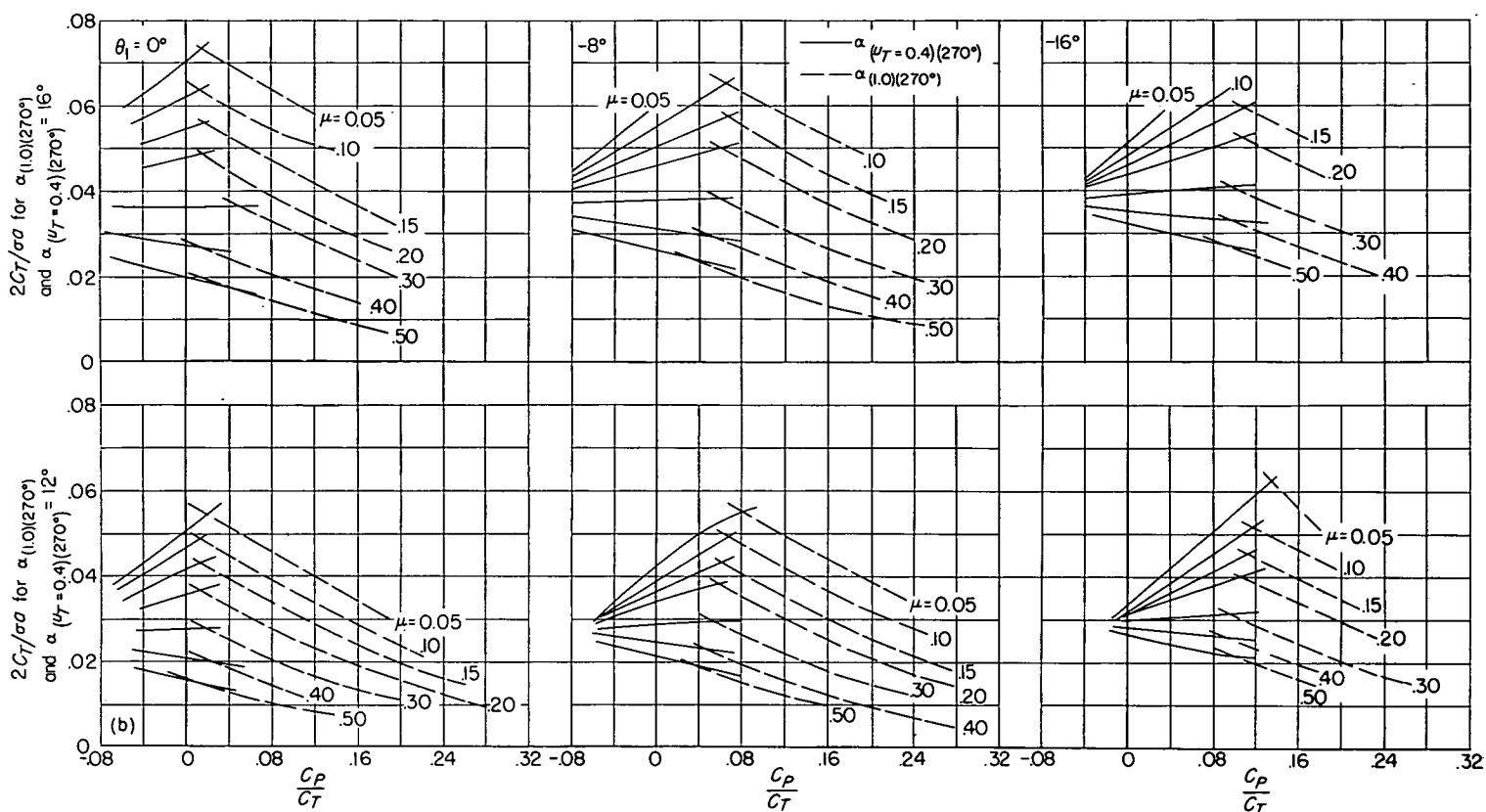
(b) Descent (γ negative).

FIGURE 8.—Concluded.



(a) Retreating-blade angle of attack as function of inflow ratio and collective pitch.

FIGURE 9.—Plots for estimating retreating-blade stall conditions.



(b) Retreating-blade angle of attack as function of thrust and power coefficients.

FIGURE 9.—Concluded.

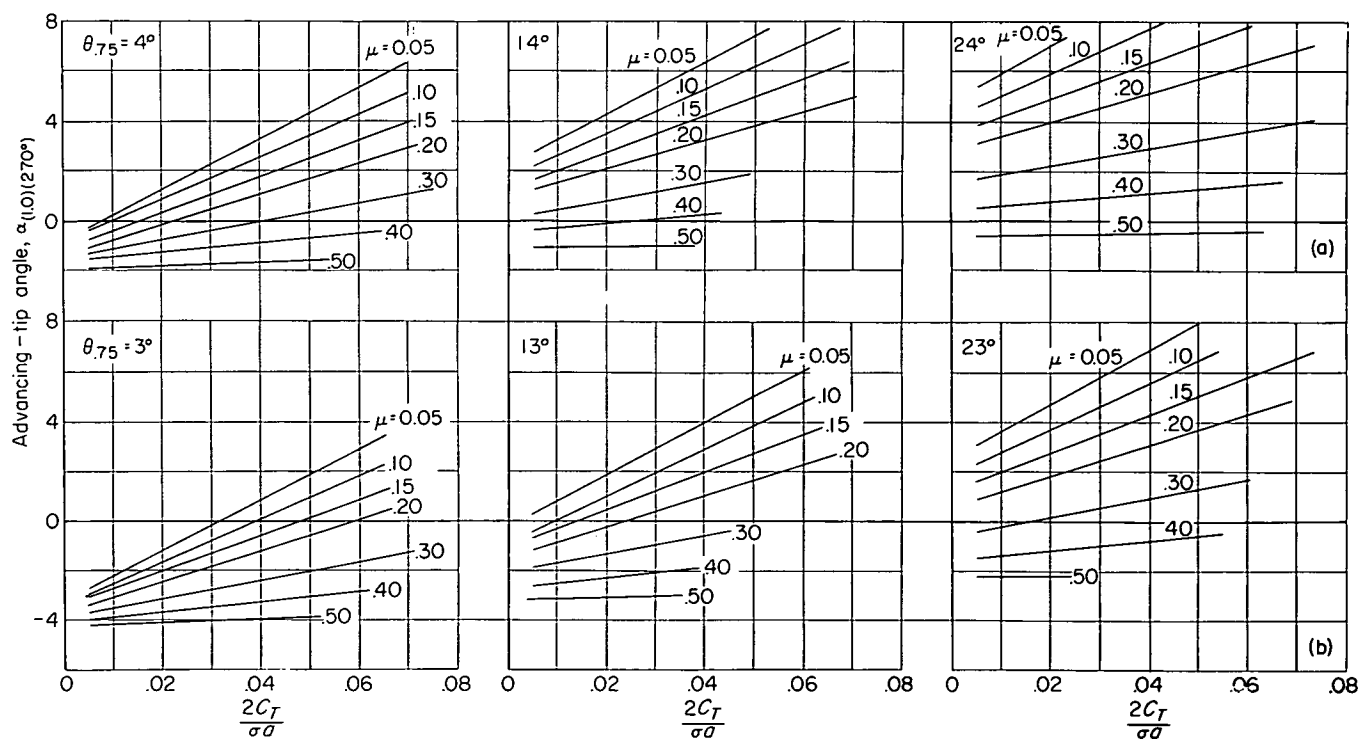
(a) $\theta_1 = -8^\circ$.(b) $\theta_1 = -16^\circ$.

FIGURE 10.—Plots for estimating advancing-tip angle of attack.

REPORT 1267

PLASTIC DEFORMATION OF ALUMINUM SINGLE CRYSTALS AT ELEVATED TEMPERATURES ¹

By R. D. JOHNSON, A. P. YOUNG, and A. D. SCHWOPE

SUMMARY

This report describes the results of a comprehensive study of plastic deformation of aluminum single crystals over a wide range of temperatures. The results of constant-stress creep tests have been reported for the temperature range from 400° to 900° F. For these tests, a new capacitance-type extensometer was designed. This unit has a range of 0.30 inch over which the sensitivity is very nearly linear and can be varied from as low a sensitivity as is desired to a maximum of 10 microinches per millivolt with good stability.

In constant-load creep tests at temperatures up to 1,100° F, four additional slip planes (the (100), (311), (110), and (211)) have been observed, besides the customary (111) plane. The (311) slip plane has been observed above 300° F; the (100), above 500° F; the (211), above 700° F; and the (110), only at 1,000° F.

The stress-strain curve has been determined in constant-load-rate tests at temperatures of 82°, 500°, and 1,100° F for single crystals of two purities, 99.99+ percent and 99.95 percent aluminum.

Experiments were carried out to investigate the effect of small amounts of prestraining, by two different methods, on the creep and tensile properties of these aluminum single crystals. Two high-resolution X-ray techniques used to detect and to follow the strain in these experiments showed a definite polygonization of the crystalline lattice during creep.

Light microscopy has been employed to observe the details of the process of kinking. Electron microscopy has been used with various replica techniques to investigate the complex nature of the slip bands resulting from plastic deformation at elevated temperatures. From these observations, it has been concluded that plastic deformation takes place predominantly by slip which is accompanied by the mechanisms of kinking and polygonization.

INTRODUCTION

This investigation has been directed toward the problem of determining the mechanisms of creep. This required that a number of different approaches be employed in attacking the problem. Reliable creep data had to be obtained over a wide range of temperatures. Then perturbations or small changes had to be introduced into the specimens to study their effects on the deformation characteristics. Examples

of such perturbations are a small change in purity or a small amount of prestraining. In addition, it was necessary to observe the changes in the specimens resulting from plastic deformation. This can be done on the surface by light microscopy, or, on an even finer scale, by electron microscopy. The deformation can be studied below the surface by high-resolution X-ray diffraction methods.

Previous portions of this investigation have included a survey of creep in metals (ref. 1), a study of the plastic and elastic properties of high-purity aluminum single crystals at room temperature (ref. 2), and a determination of the creep and tensile properties of these aluminum single crystals from room temperature to 400° F (ref. 3). This portion of the investigation has been concerned primarily with the plastic properties, both creep and tensile, over a wide range of temperatures up to and including 1,100° F.

Normal X-ray back-reflection Laue photographs were used for orientation determination. This same method can be used to identify the operative slip system when tests are conducted in the temperature range wherein more than one type of slip plane may operate. This was found to be necessary in aluminum, where the slip plane might be (111), (100), or (211) at elevated temperatures.

The use of electron microscopy in studying the deformation of metals on a submicroscopic scale is just coming into prominent and accepted use. Although research of this type has been carried on for the past few years, better and more reliable methods of replication have greatly enhanced the use of the electron microscope in this particular application. Most of these studies to date have been on polycrystalline materials deformed in tensile tests or by bending. This effort represents one of the first to study the plastic deformation of single-crystal specimens by creep with electron microscopy and replica techniques.

This investigation was conducted at Battelle Memorial Institute under the sponsorship and with the financial assistance of the National Advisory Committee for Aeronautics. The authors wish to thank Messrs. G. D. McDowell, W. B. Wilson, and J. R. Doig for performing the X-ray work throughout the course of the investigation. Thanks are also extended to Mr. C. L. Seale for his part in developing the capacitance strain gage and associated electronic equipment and to Mr. R. D. Smith for carrying out the testing program.

¹ Supersedes NACA TN 3351, "Plastic Deformation of Aluminum Single Crystals at Elevated Temperatures" by R. D. Johnson, A. P. Young, and A. D. Schwoppe, 1955.

SYMBOLS

$d=1+e$	
L	prefix to crystal number, indicating 99.95-percent purity
P, S	prefix to crystal number, indicating 99.99 ⁺ -percent purity
α, β, χ	angles between three cube planes and specimen axis
γ	resolved shear strain
ϵ	tensile strain
λ	angle between slip direction and specimen axis
σ	tensile stress
τ	resolved shear stress
ϕ	angle between normal to slip plane and specimen axis

EQUIPMENT

TESTING FACILITIES

The general equipment for performing creep tests and constant-load tests at elevated temperatures has been described in detail elsewhere (ref. 3). Three creep units were designed to employ direct axial loading through a fixed ball-seat arrangement. Two units were modified to allow loading through a lever arm with a 9:1 arm ratio. These units were used for constant-load-rate tests in which the load was applied by vibrating lead shot along a trough into a weight pan at the end of the lever arm at approximately a constant rate. This equipment was housed in a constant-temperature room in which the temperature was maintained at $82^{\circ} \pm 2^{\circ}$ F. Each creep unit was equipped with an electric-resistance-type furnace, either in one piece or of the split type. The power to each furnace was controlled by a Variac connected to a Honeywell controller.

CONSTANT-STRESS DEVICE

One of the creep units previously used for direct loading has been converted to a special lever-arm arrangement. The mechanics of this type of arrangement have been described by Cottrell and Aytakin (ref. 4). In the deformation of single crystals, the slip direction rotates toward the tension axis as extension takes place. In order to maintain a constant resolved shear stress, that is, the component of the tensile stress resolved in the slip plane in the slip direction, it is necessary to reduce the lever-arm ratio by the factor $\cos \lambda / [1 - \sin^2(\lambda/d^2)]^{1/2}$. Otherwise, the resolved shear stress increases as extension takes place.

The stress was transmitted from the weight pan to the lever arm and from the lever arm to the specimen through steel tapes which followed profiles. The profile on the end of the lever arm attached to the specimen with a 3-inch gage length was circular with a radius of 6 inches from the profile to the knife-edge suspension. Four profiles were made for the other end. Each was calculated to give an initial lever-arm ratio of 2:1 and then decrease according to the factor quoted above for extensions out to 15 percent. One was made for each of the initial angles of λ of 30° , 35° , 40° , and 45° , λ being the angle between the slip direction and the specimen axis. Since face-centered cubic crystals have 12 octahedral slip systems, this range of profiles was suitable for the most favorably oriented slip system in most crystals.

The lever-arm system had to be balanced so that its center of gravity was exactly at the center of rotation, so that no external moments other than the applied one would act after extension began. First, the profiles were made to weigh the same and to have approximately the same moments. Second, a small weight pan was attached to the specimen side of the lever arm for adjusting the moment to zero when the lever arm was in a horizontal position. Third, a threaded shaft was mounted directly above the point of the knife-edge suspension. Two threaded steel plates placed on this shaft enable a coarse and a fine adjustment to be made, so that the vertical position of the center of gravity of the whole lever-arm arrangement could be adjusted to the line of the knife-edge contact about which rotation takes place. Thus, the lever-arm arrangement remained balanced throughout the whole range of extension for which it was designed.

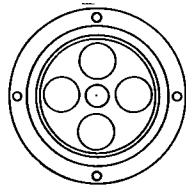
CAPACITANCE STRAIN GAGES

Two capacitance-type strain gages have been used in this investigation. The one containing flat parallel plates in the pickup has been described in reference 3. This unit has been redesigned slightly, so that now both capacitance plates are mounted on the same shaft. This increases the stability of the unit, while adding slightly to its weight. Although this unit has a very high sensitivity, the sensitivity is not linear over much of the range. The range can be increased with some sacrifice in sensitivity. Typical values from calibration curves indicate that, for a range of 0.02 inch, the sensitivity varies from 1.6 to 16 microinches per millivolt. For a range of 0.10 inch, the sensitivity varies from 4 to 50 microinches per millivolt. The unit can be rezeroed mechanically to increase the total range.

Because of the larger strains anticipated in these elevated-temperature tests, a new type of capacitance strain gage was developed. The pickup for this unit is a dual-capacitance type with cylindrical plates, as shown in figure 1. It is constructed so that, as extension takes place, the central cylinder moves within the concentrically located rings. Thus, the capacity increases in one section and decreases in the other. The capacitance pickup has a total electrical range of 10 to 50 micromicrofarads per section.

The outer shell and the end plates of this unit are made of Lucite, and the other parts are constructed of commercial 1100 (2S) aluminum. The center cylinder has four holes drilled through it to reduce its weight. The pickup is connected to the specimen by stainless-steel arms similar to those used with the flat parallel-plate pickup. One end of the specimen is connected to the Lucite case and the other end, to the push rod.

The four parts of the capacitance-measuring unit are shown in figure 2. The oscillator is a push-pull type employing the same tuned circuit for both grid and plate circuits. The variable condenser in this tuned circuit allows the sensitivity to be varied from approximately 10 microinches per millivolt to as low a sensitivity as is desired. The variation in sensitivity has little effect upon the range. The sensitivity is linear within approximately 2 percent over a range of 0.30 inch. A typical calibration curve is shown in figure 3.



Top view with top plate removed

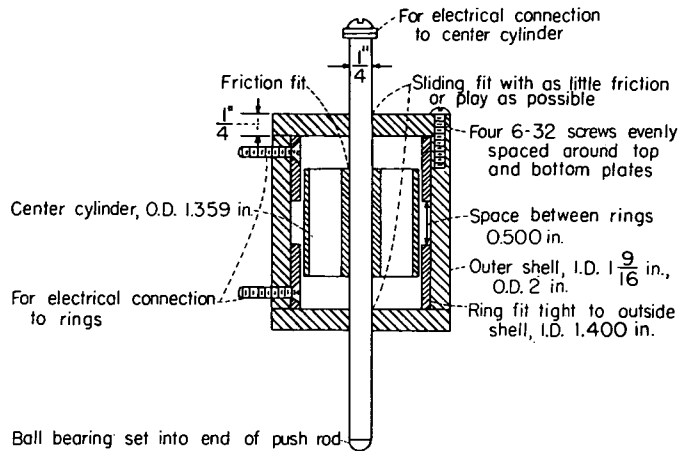


FIGURE 1.—Capacitance pickup with cylindrical plates. Materials: Cylindrical plates and push rod are commercial 1100(2S) aluminum; outside case is Lucite.

The oscillator is inductively coupled to two tuned circuits consisting of L_1 , L_2 , and the capacitance pickup. By means of discriminator action, the variations in capacitance of the pickup produce a proportional direct-current voltage across the two 100,000-ohm potentiometers at the output of the discriminator. The potentiometers are linear types and are ganged together. This facilitates rezeroing electrically in order to achieve high sensitivity over the entire range.

The output of the discriminator is amplified by the direct-current amplifier and applied to a recording instrument. The two 100-ohm resistors across which the output voltage is developed can be changed to match the input impedance of the recording device. The 1,000-ohm variable resistor in the cathode circuit of the 6N7GT tube is used to adjust the linearity of the stage. This control remains fixed after it is set initially, unless the tube is replaced. The fourth part of this measuring unit is the power supply.

The lead wire from the measuring unit to the pickup was 300-ohm television cable. However, since stray and lead-wire capacities have a large effect on the sensitivity of the instrument, it was necessary to calibrate the unit with the lead wires in the same position that they would be in during a

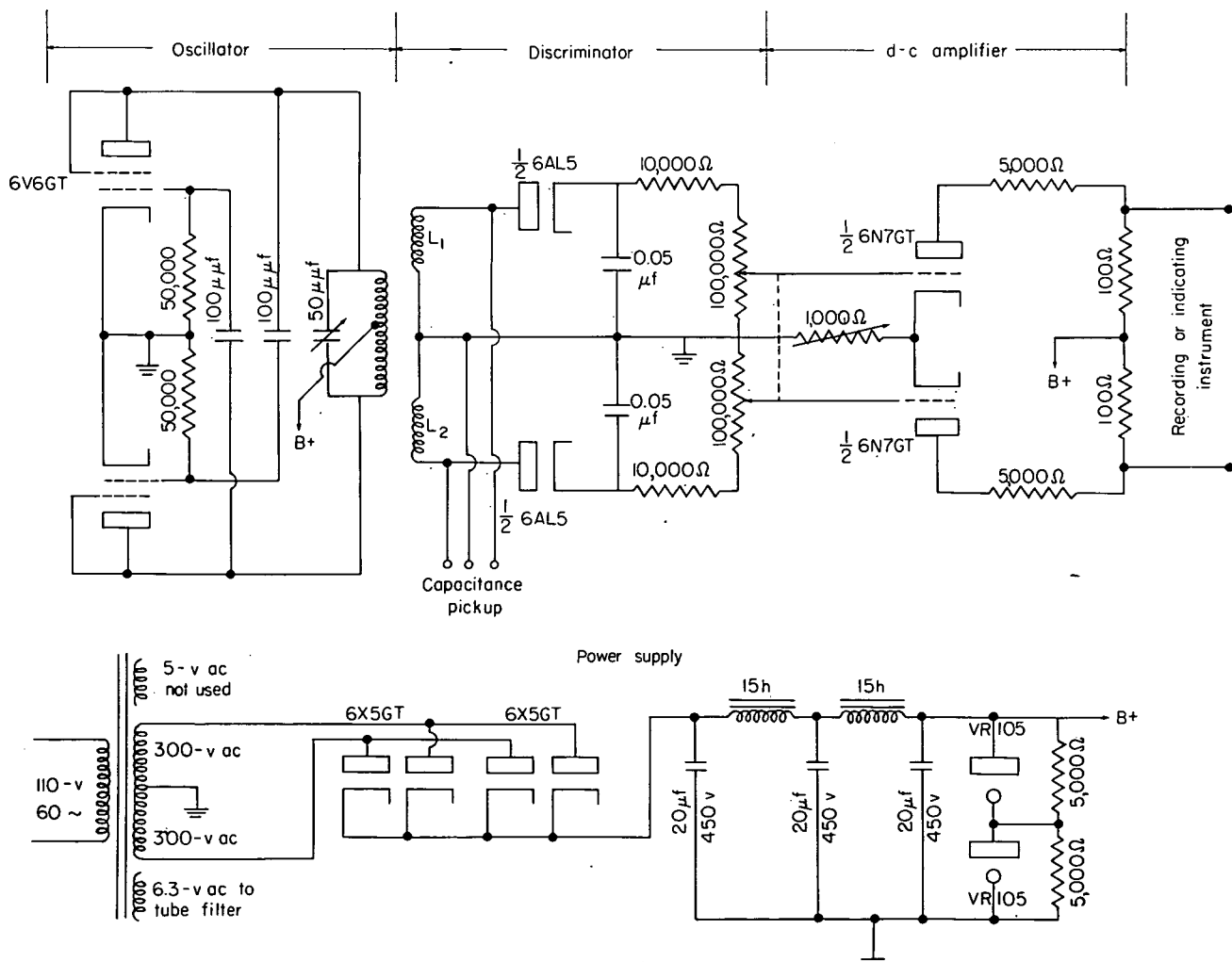


FIGURE 2.—Capacitance-measuring unit for cylindrical-plate pickup.

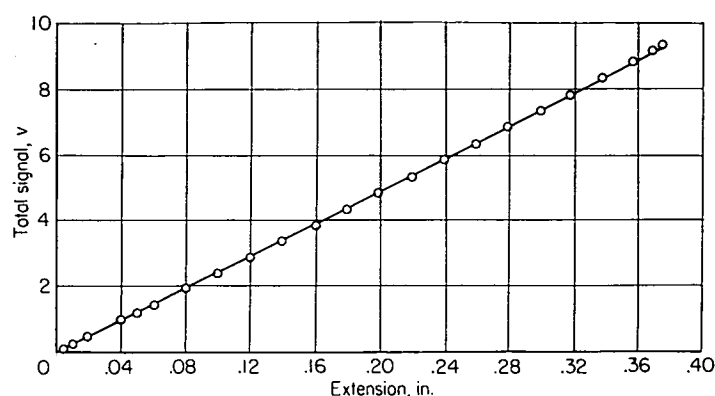


FIGURE 3.—Calibration plot for cylindrical-plate pickup. Sensitivity, 41 microinches per millivolt over a range of 0.30 inch.

test. Therefore, the cable was replaced by a 185-ohm shielded twin lead, with the shield used as the ground wire. For short lengths of approximately 2 feet, this wire does not exhibit the above shortcoming. The linear sensitivity and the extended range, which can also be increased by mechanically rezeroing the capacitance pickup, have been found to be extremely useful in this investigation.

EXPERIMENTAL PROCEDURE

PREPARATION OF CRYSTALS

The single crystals of aluminum were grown by the strain-anneal method in the form of tensile specimens with a 3-inch reduced section which had been machined to a 0.505-inch diameter. The method has been discussed at length in references 2 and 3. The crystals were grown primarily from high-purity (99.99+ percent) aluminum containing 17 parts per million of copper, 10 parts per million each of iron and silicon, 6 parts per million of sodium, 3 parts per million of magnesium, and no detectable manganese or calcium. A few crystals were also grown from a slightly lower purity aluminum, approximately 99.95 percent. This material contained 200 parts per million of silicon, 80 parts per million of iron, 50 parts per million of calcium, 30 parts per million each of manganese and magnesium, 8 parts per million of lead, and 5 parts per million of copper. These determinations were made by spectroscopic analysis.

In order to be able to increase the yield of large single crystals from the growth process, the amount of prestraining was varied to determine more accurately the critical value of the amount of prestraining. From the summary of the results of the two growths of 54 specimens each presented in table 1, it appears that 1- to 1¼-percent prestrain yields the maximum number of crystals throughout the entire 3-inch reduced section for the high-purity aluminum. Since a total of only 12 of the lower purity crystals was grown, the prestrain was not varied for these specimens. However, the critical amount of prestraining increases as the purity decreases. This prestraining follows a 6-hour anneal at 550° C for grain-size stabilization and precedes the final anneal, which takes 11 days, starting at 450° C and ending at 635° to 640° C.

After the crystals were grown, they were etched with a solution containing 50 parts hydrochloric acid, 48 parts nitric acid, and 2 parts hydrofluoric acid by volume. For

TABLE 1.—SUMMARY OF RESULTS OF CRYSTAL GROWTH

Crystal size, in.	Number of crystals at prestrain, percent, of—					Total
	2	1½	1¼	1	¾	
	First growth—54 specimens *					
1-----	b 4	5	-----	1	-----	10
1-----	b 4	11	-----	5	-----	20
2-----	b 2	3	-----	0	-----	5
3-----	b 2	12	-----	5	-----	19
Total.....	12	31	-----	11	-----	54
	Second growth—54 specimens *					
1-----	1	3	2	4	1	11
1-----	0	3	1	2	2	8
2-----	0	1	2	4	6	13
3-----	0	2	5	14	1	22
Total.....	1	9	10	24	10	54

* All from aluminum of 99.99+ percent purity unless otherwise indicated.

b From aluminum of 99.95 percent purity.

the most part, the specimens were electropolished according to the procedure mentioned in the section "Electron-Microscope Techniques."

The orientation of each specimen, or the largest crystal in the gage length, was determined by the Laue back-reflection X-ray technique. The orientations of the cube faces and the most probable slip systems are presented in table 2. The crystals have been grouped according to their use, although some crystals have been used for more than one test or observation. The angles α , β , and χ are the angles the three cube planes make with the specimen axis. The angle between the slip direction and the specimen axis is given as λ , and the angle between the normal to the slip plane and the specimen axis is given as ϕ . With but one exception, crystal S-64, the orientations of the slip planes reported are the three most favorable (111) types of planes. These are tabulated along with the values of λ for the associated [110] directions and the values of $\cos \phi \cos \lambda$. This is true for all but the last section of table 2, "Crystals for constant-load creep tests." In these specimens other slip planes have been important, so the reported plane may be a (111), (100), or (211), but the associated slip direction is still a [110] direction.

TESTING PROCEDURE

In the constant-load-rate tests, the load rate was held approximately constant throughout the test at a value between ½ pound per minute and 2 pounds per minute. This load rate could be varied by varying the power input to the vibrator which moved shot along a trough and into a container on the weight pan. This load was applied on the long portion of a lever arm with an arm ratio of 9:1. A spring scale was placed in the linkage between the lever arm and the weight pan for load measurements. The test was started after the lever-arm assembly had been balanced to give no net load on the specimen. A 2-inch gage length was used in these tests.

In the creep tests the loading was accomplished by releasing a hydraulic jack holding the weight pan. As a matter of technique, a 50-pound weight was placed between the weight pan and the jack to insure that the jack would release the load freely but without impact. The recording apparatus for the capacitance strain gage allowed the entire creep

TABLE 2.—CRYSTALLOGRAPHIC DATA FOR ALUMINUM SINGLE CRYSTALS

Crystal	Slip plane	α	β	χ	ϕ	λ	$\cos \phi \cos \lambda$
Crystals for constant-load-rate tests							
L-3	(111)	26.0	15.5	59.4	53.5	37.0	0.474
	(111)	---	---	---	25.7	65.5	.373
	(111)	---	---	---	66.0	23.5	.372
L-5	(111)	31.5	11.3	55.8	49.2	43.7	.470
	(111)	---	---	---	26.7	63.5	.398
	(111)	---	---	---	49.2	59.5	.330
L-12	(111)	32.0	8.0	56.5	45.0	46.7	.485
	(111)	---	---	---	30.0	60.5	.426
	(111)	---	---	---	45.0	61.5	.337
S-23	(111)	13.0	12.0	71.5	57.0	34.0	.450
	(111)	---	---	---	57.5	34.0	.445
	(111)	---	---	---	36.0	59.5	.410
S-56	(111)	57.5	7.8	31.3	45.3	46.3	.486
	(111)	---	---	---	30.0	60.1	.431
	(111)	---	---	---	45.3	62.0	.330
S-64	(111)	7.0	48.0	41.0	42.5	53.0	.445
	(111)	---	---	---	42.5	57.0	.402
	(211)	---	---	---	37.5	53.0	.477
Crystals for constant-stress creep tests							
S-6	(111)	5.8	71.7	17.0	49.8	42.0	0.480
	(111)	---	---	---	39.7	53.0	.462
	(111)	---	---	---	64.0	28.3	.371
S-7	(111)	12.0	63.0	22.0	51.5	38.0	.491
	(111)	---	---	---	30.0	61.0	.420
	(111)	---	---	---	65.5	24.0	.379
S-10	(111)	24.2	7.6	64.2	47.5	43.0	.493
	(111)	---	---	---	33.3	57.5	.448
	(111)	---	---	---	78.2	78.6	.397
S-14	(111)	28.5	56.7	15.5	52.5	39.0	.472
	(111)	---	---	---	24.0	66.5	.363
	(111)	---	---	---	69.0	21.5	.332
S-16	(111)	22.0	60.5	18.0	57.5	33.0	.450
	(111)	---	---	---	61.5	29.0	.417
	(111)	---	---	---	26.0	67.0	.350
S-25	(111)	37.0	49.5	13.0	48.5	45.0	.468
	(111)	---	---	---	48.5	54.0	.389
	(111)	---	---	---	23.0	68.0	.344
S-34	(111)	12.0	12.0	73.0	56.8	34.5	.452
	(111)	---	---	---	58.2	33.0	.440
	(111)	---	---	---	36.5	59.0	.413
S-35	(111)	55.0	31.0	12.5	49.0	43.5	.475
	(111)	---	---	---	26.0	64.5	.386
	(111)	---	---	---	49.0	60.0	.328
S-36	(111)	58.8	24.8	17.0	55.5	35.7	.460
	(111)	---	---	---	65.0	25.5	.381
	(111)	---	---	---	25.0	66.7	.358
S-50	(111)	38.0	48.7	12.6	48.5	46.5	.456
	(111)	---	---	---	48.5	53.9	.391
	(111)	---	---	---	23.1	67.9	.346
S-57	(111)	28.4	11.2	58.7	48.9	42.0	.488
	(111)	---	---	---	28.1	62.0	.414
	(111)	---	---	---	70.5	19.2	.315
S-66	(111)	12.0	57.5	30.0	49.5	42.0	.482
	(111)	---	---	---	26.5	63.5	.399
	(111)	---	---	---	49.5	60.0	.325
S-75	(111)	15.2	26.7	58.6	53.1	38.1	.472
	(111)	---	---	---	25.6	65.0	.382
	(111)	---	---	---	67.1	23.2	.357
Crystals for electron-microscope work							
L-6	(111)	63.0	7.8	25.8	46.7	43.7	0.495
	(111)	---	---	---	32.8	57.7	.449
	(111)	---	---	---	70.2	20.8	.315
L-11	(111)	20.0	18.5	62.0	58.5	31.0	.447
	(111)	---	---	---	60.0	30.5	.430
	(111)	---	---	---	27.5	66.5	.353
S-2	(111)	17.5	50.0	34.0	53.5	41.0	.447
	(111)	---	---	---	53.5	52.5	.361
	(111)	---	---	---	19.0	71.5	.299
S-9	(111)	63.5	22.5	13.0	52.0	38.0	.484
	(111)	---	---	---	30.5	62.0	.403
	(111)	---	---	---	65.0	26.0	.378
S-37	(111)	52.3	24.0	26.8	61.3	32.3	.404
	(111)	---	---	---	64.0	28.3	.385
	(111)	---	---	---	61.3	53.0	.288
S-38	(111)	2	36.2	52.5	36.2	55.5	.456
	(111)	---	---	---	36.2	56.0	.450
	(111)	---	---	---	36.2	65.0	.340
P-175	(111)	41.5	8.1	46.9	43.9	52.0	.444
	(111)	---	---	---	43.9	55.6	.407
	(111)	---	---	---	28.0	65.2	.370
P-181	(111)	15.9	27.0	57.5	53.6	37.8	.468
	(111)	---	---	---	24.0	66.2	.369
	(111)	---	---	---	67.7	22.8	.349
Crystals for prestrain experiments							
S-5	(111)	9.5	52.5	35.7	45.5	47.5	0.473
	(111)	---	---	---	27.7	63.5	.394
	(111)	---	---	---	45.5	58.2	.368
S-8	(111)	34.7	11.0	53.0	47.3	45.3	.475
	(111)	---	---	---	26.0	64.7	.383
	(111)	---	---	---	47.3	57.3	.364
S-12	(111)	47.5	38.2	15.5	51.5	44.5	.443
	(111)	---	---	---	51.5	51.2	.389
	(111)	---	---	---	20.5	70.2	.315

Crystal	Slip plane	α	β	χ	ϕ	λ	$\cos \phi \cos \lambda$
Crystals for prestrain experiments—Concluded							
S-17	(111)	10.7	39.5	48.2	46.5	49.0	0.451
	(111)	-----	-----	-----	46.5	54.3	.401
	(111)	-----	-----	-----	24.7	66.5	.361
S-43	(111)	23.3	45.3	35.2	59.0	38.5	.403
	(111)	-----	-----	-----	59.0	46.4	.355
	(111)	-----	-----	-----	72.5	24.0	.275
S-44	(111)	44.5	36.1	23.3	58.8	39.0	.402
	(111)	-----	-----	-----	58.8	46.0	.360
	(111)	-----	-----	-----	73.1	23.9	.266
S-58	(111)	29.6	21.3	52.0	58.2	35.5	.429
	(111)	-----	-----	-----	68.0	24.8	.341
	(111)	-----	-----	-----	18.1	72.6	.284
S-62	(111)	46.2	10.3	41.8	45.7	50.6	.443
	(111)	-----	-----	-----	45.7	53.5	.415
	(111)	-----	-----	-----	25.4	67.3	.349
S-67	(111)	59.6	20.0	21.7	58.8	31.7	.441
	(111)	-----	-----	-----	61.4	29.0	.419
	(111)	-----	-----	-----	24.8	68.1	.339
S-70	(111)	27.0	16.0	58.0	54.0	37.5	.466
	(111)	-----	-----	-----	24.5	66.5	.363
	(111)	-----	-----	-----	67.0	23.0	.360
S-73	(111)	9.7	37.0	50.7	45.7	47.9	.468
	(111)	-----	-----	-----	26.7	64.4	.386
	(111)	-----	-----	-----	45.7	56.9	.381
S-76	(111)	54.3	30.3	17.0	54.0	38.8	.458
	(111)	-----	-----	-----	21.8	68.6	.339
	(111)	-----	-----	-----	54.0	55.8	.330
S-78	(111)	9.7	25.7	62.0	48.5	42.0	.493
	(111)	-----	-----	-----	31.2	59.7	.432
	(111)	-----	-----	-----	69.2	21.3	.331
S-86	(111)	30.1	15.0	55.6	52.3	39.9	.469
	(111)	-----	-----	-----	23.9	66.5	.365
	(111)	-----	-----	-----	52.3	57.5	.329
S-94	(111)	6.5	37.0	52.0	42.3	50.2	.472
	(111)	-----	-----	-----	29.7	61.7	.411
	(111)	-----	-----	-----	42.3	59.5	.375
Crystal for X-ray work							
S-63	(111)	51.4	36.8	8.9	44.6	48.4	0.473
	(111)	-----	-----	-----	27.5	63.5	.396
	(111)	-----	-----	-----	44.6	58.0	.377
Crystals for constant-load creep tests							
P-149	(100)	22.3	36.7	44.6	45.4	46.1	0.486
	(211)	-----	-----	-----	51.3	40.0	.479
	(100)	-----	-----	-----	53.3	40.0	.458
	(111)	-----	-----	-----	58.0	40.0	.406
	(111)	-----	-----	-----	58.0	46.1	.367
P-159	(100)	25.3	44.3	34.9	45.7	45.1	.493
	(311)	-----	-----	-----	53.0	37.5	.477
	(111)	-----	-----	-----	60.8	37.5	.387
P-169	(100)	22.2	53.1	27.4	36.9	53.8	.473
	(111)	-----	-----	-----	59.4	34.0	.422
	(111)	-----	-----	-----	65.5	26.8	.371
S-1	(100)	27.7	47.5	29.0	42.5	47.7	.495
	(111)	-----	-----	-----	64.3	31.5	.368
	(111)	-----	-----	-----	65.5	30.0	.358
S-3	(111)	7	21.0	68.7	42.5	48.0	.493
	(111)	-----	-----	-----	41.0	49.7	.488
	(111)	-----	-----	-----	41.0	66.0	.306
S-13	(111)	5	28.7	61.0	39.0	51.3	.485
	(111)	-----	-----	-----	37.7	52.5	.480
	(111)	-----	-----	-----	39.0	69.7	.269
S-18	(211)	13.34	44.00	42.7	42.0	49.0	.487
	(100)	-----	-----	-----	46.0	50.0	.447
	(100)	-----	-----	-----	47.3	49.0	.443
	(111)	-----	-----	-----	49.3	49.0	.428
	(111)	-----	-----	-----	49.3	50.0	.419
S-20	(100)	26.0	54.0	23.0	36.0	54.0	.475
	(111)	-----	-----	-----	60.5	32.0	.417
	(111)	-----	-----	-----	64.0	28.0	.386
S-21	(100)	30.7	36.3	38.0	52.0	38.5	.481
	(311)	-----	-----	-----	53.7	37.0	.472
	(211)	-----	-----	-----	54.5	38.5	.454
	(111)	-----	-----	-----	58.5	37.0	.417
	(111)	-----	-----	-----	66.5	37.0	.318
	(111)	-----	-----	-----	66.5	38.5	.311
S-27	(211)	27.5	16.0	56.0	54.0	36.5	.472
	(111)	-----	-----	-----	56.0	36.5	.448
	(100)	-----	-----	-----	34.0	57.5	.445
	(111)	-----	-----	-----	68.0	22.5	.345
S-39	(211)	38.5	13.5	49.0	44.5	46.0	.496
	(111)	-----	-----	-----	49.0	46.0	.456
	(100)	-----	-----	-----	41.0	53.0	.454
	(111)	-----	-----	-----	49.0	53.0	.394
S-42	(211)	49.0	35.0	10.5	50.0	40.5	.489
	(100)	-----	-----	-----	41.0	51.2	.471
	(111)	-----	-----	-----	54.3	40.5	.443
	(111)	-----	-----	-----	54.3	51.2	.364
S-45	(100)	34.1	29.5	41.4	48.6	42.0	.491
	(211)	-----	-----	-----	55.9	35.0	.459
	(111)	-----	-----	-----	58.5	35.0	.428
	(111)	-----	-----	-----	65.0	35.0	.346
	(111)	-----	-----	-----	65.0	42.0	.314
S-46	(100)	30.4	26.9	46.7	43.3	47.2	.494
	(211)	-----	-----	-----	58.0	33.2	.444
	(111)	-----	-----	-----	62.8	33.2	.383
	(111)	-----	-----	-----	67.2	28.9	.340
S-51	(111)	70.5	19.2	.6	42.3	48.6	.489
	(111)	-----	-----	-----	43.1	48.0	.488
	(111)	-----	-----	-----	42.3	64.3	.321

TABLE 2.—CRYSTALLOGRAPHIC DATA FOR ALUMINUM SINGLE CRYSTALS—Concluded

Crystal	Slip plane	α	β	χ	ϕ	λ	$\cos \phi \cos \lambda$
Crystals for constant-load creep tests—Concluded							
S-60	(100)	α 29.0	α 35.5	41.0	α 49.0	41.0	0.495
	(100)	-----	-----	-----	54.5	α 36.0	.470
	(211)	-----	-----	-----	57.5	α 36.0	.434
	(111)	-----	-----	-----	65.0	α 36.0	.342
S-71	(111)	-----	-----	-----	65.0	41.0	.319
	(100)	α 33.1	α 40.7	30.7	49.3	α 41.4	.489
	(100)	-----	-----	-----	56.9	α 34.1	.452
	(111)	-----	-----	-----	66.3	α 34.1	.333
S-77	(111)	-----	-----	-----	69.1	30.7	.307
	(100)	α 23.5	39.0	41.0	α 49.0	43.0	.480
	(100)	-----	-----	-----	51.0	41.5	.471
	(111)	-----	-----	-----	59.0	41.5	.386
S-82	(111)	-----	-----	-----	59.0	43.0	.376
	(100)	α 36.1	38.2	30.9	α 51.8	38.7	.482
	(100)	-----	-----	-----	53.9	α 36.5	.474
	(111)	-----	-----	-----	66.4	α 36.5	.322
S-84	(111)	-----	-----	-----	66.4	38.7	.312
	(311)	α 41.3	18.8	42.3	45.5	α 45.7	.488
	(100)	-----	-----	-----	47.7	α 45.9	.468
	(211)	-----	-----	-----	47.3	α 45.7	.473
S-87	(111)	-----	-----	-----	54.0	α 45.7	.410
	(111)	-----	-----	-----	54.0	α 45.9	.409
	(110)	α 79.5	α 3.7	9.7	α 50.0	42.3	.475
	(111)	-----	-----	-----	51.0	42.3	.465

*Measured from left end of specimen; all others measured from right.

curve to be recorded continuously and automatically. In the constant-stress tests, the entire system was balanced with the specimen and capacitance strain gage in place. Then the weight pan and any additional weights would act as the applied load. In these constant-stress tests, a 3-inch gage length was employed, and only specimens with a single crystal throughout the entire 3-inch reduced section were used. The arms from the capacitance strain gage were attached to the shoulders of the specimen.

In the prestrain experiments, two different types of prestraining were employed. A rapid strain rate was obtained by dead-weight loading or essentially rapid initial elongation. A relatively slower strain rate was obtained in a constant-load-rate test. Since the initial extension could not be predicted reliably, this prestraining by dead-weight loading was carried out first on one specimen. Then prestraining in a constant-load-rate test could be carried out to the same shear strain on a second crystal, so that the effects of the two types of prestraining could be compared on the basis of the same shear strain.

In the prestraining operation, the extensometer was connected to the specimen on its shoulders. This prevented any damage resulting from the contact between the knife edges and the crystal in the 2-inch gage length used in the subsequent test. Specimens for which test results were to be compared directly were chosen to have approximately the same values of $\cos \phi \cos \lambda$, the factor which determines the fraction of the tensile stress which is resolved in the slip plane in the slip direction. When the prestraining was performed at elevated temperatures, a split furnace was used so that the furnace could be removed shortly after the prestraining operation had been completed. In the subsequent test upon which the effect of prestraining was being studied, an attempt was made to minimize and to equalize the heating periods. This tended to reduce and to standardize any recovery effects which may have been important at the temperature of the test.

X-RAY DIFFRACTION METHODS

A normal back-reflection Laue technique has been employed for the determination of crystal orientations. This method has been useful also for the determination of the operative slip plane in elevated-temperature tests. When the slip bands on a deformed crystal exhibited abnormally large shear strains, a back-reflection Laue photograph was taken normal to the shelf produced by the slip band. In this manner the operation of slip systems containing the (100) and the (211) slip planes was confirmed. However, the resolution of this technique is not sufficient to detect tensile strains less than about 2 percent, so it was necessary to use techniques with higher resolution to detect and to follow the strain throughout the various stages of a prestrain experiment.

The first of these techniques to be used was the "oblique Laue" method. The experimental arrangement for this method is presented in figure 4. An arrangement of two rectangular slits, each with one very small dimension in the vertical direction, was used to limit the area of the crystal to be photographed. Specimens studied by this method were crystals with a (100) plane nearly parallel to the crystal surface. With the arrangement of figure 4, each Laue spot from a perfect crystal is elongated into a streak composed of a continuous-radiation spectrum over the spectral range permitted by the geometrical divergence of the slits. With an imperfect crystal, the spectral band would be lengthened, but the sensitivity with respect to local orientation changes would not be very high. To improve the sensitivity, the angle of incidence of the X-ray beam upon the crystal was adjusted to superimpose the characteristic L-beta spectrum, from the second order of the (100) plane, upon the continuous-radiation streak. Different wavelengths are reflected from different parts of the irradiated area of the crystal at their respective Bragg angles. The ability of the crystal to resolve the individual lines in the tungsten L-beta spectrum gives a good indication of the regularity or perfection of the crystal lattice in the small region being photographed. In this method a single reflection is studied in detail before deformation, after prestraining, and then after a creep test.

The second method to be used was an X-ray reflection micrograph method. The experimental arrangement for this technique is presented in figure 5. Unfiltered copper radiation was employed. The crystal was oriented with the aid of a portable Geiger tube, so that the K-alpha wavelength was reflected by the (200) planes, which were approximately

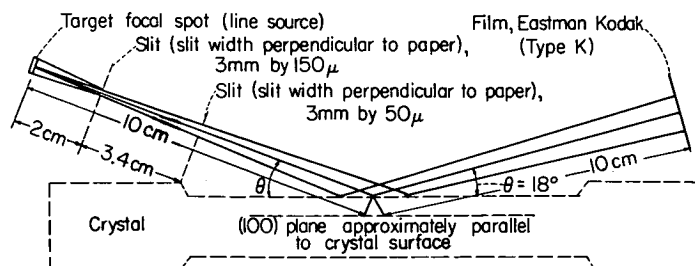


FIGURE 4.—Top view of experimental arrangement for oblique Laue photographs. (Not drawn to scale.)

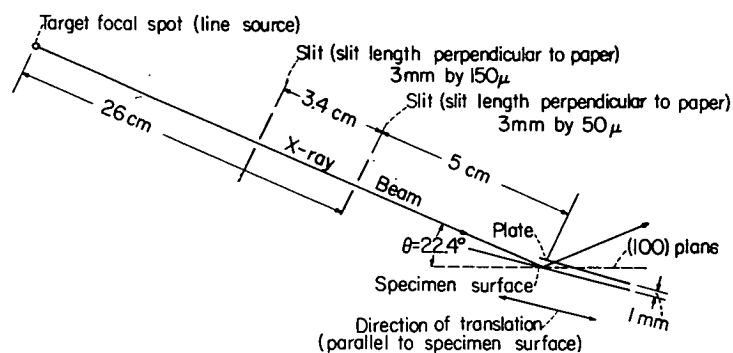


FIGURE 5.—Top view of experimental arrangement for X-ray reflection micrographs. (Not drawn to scale.)

parallel to the crystal surface. A slit-formed beam, well collimated in its short horizontal dimension, was reflected from the crystal. Because of the large distance between the X-ray source and the slits, some effective collimation was achieved in the long vertical dimension. The photographic plate and the crystal were translated without any relative motion between the two, in order that a larger area of the crystal could be examined. The translation extended the line image of the beam, defined by the slits, into a band. If the crystal were perfect, the band would be of uniform intensity. Any gross crystal imperfections would result in intensity deficiencies in the image. Hence, an X-ray micrograph of the lattice distortion was obtained. The high resolution of this method is a result of the large target-to-crystal distance (31 centimeters), the short crystal-to-plate distance (approximately 1 to 2 millimeters), and the fine slits (ref. 5). Exposures were made on either lantern slide or Type V-O photographic plates.

All exposures have been made with the X-ray tube operating at 10-milliampere current and a voltage of approximately 35 kilovolts.

ELECTRON-MICROSCOPE TECHNIQUES

Present-day electron microscopes require specimens thin enough to be permeable to an electron beam. Therefore, metal surfaces must be studied by means of replicas. Anodic-oxide replicas can be made from aluminum and aluminum alloys. The technique has been described by several investigators (refs. 6 and 7). Anodic-oxide replicas were used in the initial stages of this investigation. They were quite strong and held up well in the electron beam. Some difficulty was experienced in obtaining replicas of uniform thickness. Also, the replicas were quite likely to be dirty. Neither of these factors is too serious if the samples are easy to prepare, so that several sets of replicas can be prepared under varying conditions of anodization. However, it was not practicable to prepare a large number of creep specimens for electron microscopy. Therefore, a major portion of the effort in this investigation was devoted to developing a replica technique which would not destroy the creep specimen, thus making it possible to prepare several sets of replicas from one specimen.

The practicability of a specific replica technique depends on the nature of the surface to be replicated. The surface of the aluminum bars had to be prepared so that fine structure

in the slip bands after creep could be observed. During most of the investigation electropolishing, in a bath consisting of equal parts by volume of methanol alcohol and concentrated nitric acid, followed by etching in a modified aqua regia solution, appeared to be the best surface preparation.

The polished specimen surface was protected against oxidation during testing at elevated temperatures by one of two methods. One method was to perform the test in vacuum; the second was to coat the specimen with Dow Corning 710, a silicone oil. This was possible for temperatures up to 500° F or slightly higher. After testing, the oil could be dissolved in xylene.

The replica techniques, other than the oxide replicas, involved stripping a thick, plastic film from the aluminum bar. If this initial plastic was Zapon, then a positive plastic replica could be made by flowing Formvar on the surface of the Zapon. The Zapon was then dissolved in amyl acetate, leaving the Formvar, insoluble in amyl acetate, in the form of a positive replica. This technique has been described in detail elsewhere (refs. 8 and 9). However, these plastic replicas did not hold up well over the etch pits or over sharp corners in the slipped regions.

A method for preparing multiple aluminum oxide replicas from a single surface has been described by Hunter (ref. 10). He evaporated a thin film of aluminum on a stripped plastic replica. He then formed an oxide layer on the outer surface in an anodizing bath and dissolved away the aluminum and the plastic, leaving the oxide replica. It was felt that, for the purposes of this investigation, the surface of the aluminum adjacent to the plastic replica would have to be anodized. Several methods for separating the aluminum film from the plastic and then anodizing the inner surface were tried without much success. This technique is potentially good if some method can be devised for separating the soft aluminum film intact from the plastic.

During the latter part of the investigation, the formula for Alcoa R5 Bright Dip, a patented chemical polishing treatment licensed by Aluminum Company of America, was obtained. This chemical polish was followed by an etch of a few seconds' duration in a solution containing 10 cubic centimeters of concentrated hydrochloric acid, 30 cubic centimeters of concentrated nitric acid, and 20 cubic centimeters of a 5-percent ferric chloride solution to develop etch pits. The faces of etch pits developed by this solution represent (100) planes. With this surface preparation it was possible to make replicas consisting of a thin, evaporated, platinum film backed by an evaporated silica film. These replicas held up quite well over the small etch pits developed by the ferric chloride etch. As a result of the thinness of the platinum film and the large scattering cross section of platinum atoms for high-energy electrons, the contrast was sufficient to disclose fine structure in the slip bands.

This platinum-replica technique was developed at Battelle. The method was applied as follows: A strip of Faxfilm, wet on one side with acetone, was pressed onto the aluminum bar and then stripped when dry. Platinum was evaporated from two sources on opposite sides of the film and inclined at 45° angles to the film. One source was about double the

strength of the other, to give shadow contrast. Then silica was evaporated at normal incidence. The platinum-silica-coated plastic was cut into small squares. The squares were placed on specimen screens, and these, in turn, were placed on a coarse mesh in a glass container. Acetone was added barely to cover the coarse screen. After two or three changes of solvent, the plastic was dissolved and the replicas were ready for viewing in the microscope.

Faxfilm strippings have also been used to replicate the surfaces of these round aluminum single crystals for light microscopy. This produces a flat replica from a curved surface that ordinarily would be difficult to reproduce in a micrograph. The strippings can be used directly as replicas, or they can be shadowed with metal for better contrast.

EXPERIMENTAL RESULTS AND DISCUSSION

STRESS-STRAIN CURVE

Prior results (ref. 2) had shown that the critical resolved shear stress at room temperature increased by almost an order of magnitude when the purity was decreased from 99.99+ to 99.95 percent. Previous work (ref. 3) had also shown the stress-strain curve to be quite dependent on the test temperature. Therefore, stress-strain curves were determined in constant-load-rate tests at 82°, 500°, and 1,100° F for each of two purities, 99.99+ and 99.95 percent aluminum. These stress-strain curves were determined primarily to compare the effect of temperature and the effect of impurity content on the plastic properties of single crystals of aluminum over the range of temperature of interest. These stress-strain curves are presented in figure 6, along with two curves reported by Boas and Schmid

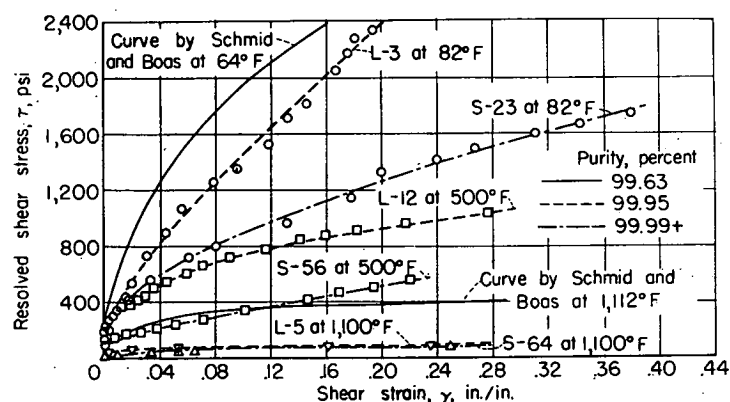


FIGURE 6.—Effects of temperature and purity on stress-strain curves of aluminum single crystals.

(ref. 11) at temperatures of 64° and 1,112° F for aluminum single crystals of 99.63-percent purity containing predominantly 0.23 percent iron and 0.14 percent silicon.

The data (stress σ versus strain ϵ) from these tests were converted to shear stress τ and shear strain γ and corrected for the rotation of the slip direction toward the tension axis during extension. For values of tensile strain less than 1 percent, the resolved shear stress is given within 1 percent by the equation:

$$\tau = \sigma \cos \phi \cos \lambda \quad (1)$$

With larger strains the resolved shear stress varies during extension according to the following equation (ref. 4):

$$\tau = \sigma \cos \phi \left(1 - \frac{\sin^2 \lambda}{d^2} \right)^{1/2} \quad (2)$$

For tensile strains of 1 percent or less the resolved shear strain is given within 1 percent by the relation:

$$\gamma = \epsilon / \cos \phi \cos \lambda \quad (3)$$

For larger strains the resolved shear strain is also affected by the lattice rotation. The shear strain has been described analytically in terms of the original orientation and the tensile strain ($d = 1 + \epsilon$) by Schmid and Boas (ref. 12) with the relation:

$$\gamma = \frac{1}{\cos \phi} [(d^2 - \sin^2 \lambda)^{1/2} - \cos \lambda] \quad (4)$$

A decrease in purity from 99.99+ to 99.95 percent has caused an increase in the stress required to produce a given strain. This increase in stress varies from approximately 40 to 85 percent for the curve at 82° F over the range of shear strain from 0.04 to 0.20. For the two curves at 500° F over a similar range of strains, the increase varies from 150 to 80 percent. For the two curves at 1,100° F, the increase varies from 50 percent to almost 0 percent over the same range of strains.

Concerning the magnitude of this increase produced by a small decrease in purity, the increase is quite important at 82° F and 500° F but becomes almost insignificant at 1,100° F. The effect of a still further decrease in purity to 99.63 percent is demonstrated by the curves reported by Boas and Schmid at 64° F and 1,112° F. Although the increase in the stress level at 64° F is appreciable, the important fact is that the stress level has been raised considerably at 1,112° F. Although not readily apparent from these curves, there is a large effect of the impurity content on the yield stress or the critical resolved shear stress, that is, the stress that marks the initiation of plastic deformation.

To observe the effect of temperature on the stress-strain curve, one need only to pick out the curves designated by the same type of line. When these data were plotted on logarithmic paper, a fairly linear range existed in the plots over the range of strains from 0.05 to 0.20 or more. The slopes of these curves are referred to ordinarily as the strain-hardening coefficients. Although the slopes decreased with increasing temperature for the 99.95-percent-pure crystals, no similar trend was apparent in the case of the 99.99+-percent-pure crystals. Therefore, no comparison of the effect of impurities on the strain-hardening coefficient as a function of temperature could be made.

These tests have been extremely useful in obtaining information on the flow stress required to produce a given strain in these aluminum single crystals at various temperatures. They have also given a good indication of the effect of alloying elements on the mechanical properties that might be expected with small amounts of alloying additions in elevated-temperature tests.

Because the processes or mechanisms of slip, kinking, and

polygonization are present in the total deformation process, it is felt that the effects of temperature and impurity content on the stress-strain curve are related directly to the manner in which these two variables affect the movement and generation of dislocations. However, this relationship is probably not a simple one. In this respect, Cottrell has discussed the effect of solute atoms on the behavior of dislocations (ref. 13). The primary effect of the solute or impurity atoms is to retard the movement of dislocations through the interaction of the stress fields associated with the solute atoms and the dislocations. An increase in temperature enhances the deformation process by increasing the internal thermal energy and thermal fluctuations, increasing the amplitude of vibration of the atoms, and decreasing the bonding energy between atoms. This eventually results in propagation of slip on planes other than the close-packed octahedral planes at elevated temperatures.

Work-hardening was first attributed to the interaction of dislocations by Taylor (ref. 14), who pointed out that dislocations exert forces on one another. Koehler has discussed the nature of work-hardening on the basis of interaction-hardening (ref. 15), which predominates at high strains, and on the basis of source-hardening (ref. 16), which predominates at low strains. The sources referred to are the so-called Frank-Read sources (ref. 17), which have been postulated by Frank and Read to explain the multiplication of dislocations during plastic deformation and to account for the occurrence of avalanches of slip on one plane. These sources are stopped when some dislocations become blocked at barriers and a back stress builds up.

In general, the initiation of plastic deformation is better understood than these later states of deformation involving work-hardening. The yield phenomenon in single-crystal and polycrystalline metals has been discussed by Cottrell (ref. 18). He attributed the yield point to the release of anchored dislocations. This takes place when the summation of the external or applied stress and any internal stresses, enhanced by thermal fluctuations, is sufficient to free the first anchored dislocations. Plastic deformation is not observed until these moving dislocations receive enough energy to surmount the barriers presented by the mosaic boundaries and other obstacles present in the metal, in order that slip can propagate through the bulk of the metal.

CREEP CURVE

The data from the constant-stress creep tests at elevated temperatures are presented in linear-coordinate plots of total shear strain versus time in figures 7 through 10. These data are presented in a summarized form in logarithmic plots in figure 11. Crystals used in these tests were specimens which contained a single crystal throughout the entire 3-inch reduced section. They had no favorably oriented high-temperature slip systems which might operate at the temperature of the test. This was necessary so that the operative slip system would be the one containing the (111) plane and the [110] direction with the highest resolved shear stress. By determining the operative slip system prior to testing, the correct profile could be chosen to maintain an approximately constant resolved shear stress throughout the test. The tensile strains have been converted to shear strains by

equation (3) for the strain-time plots presented. The creep curves have all been drawn on the same scale for easier visual comparison of the curves in various figures.

Prior to performing these elevated-temperature tests, it was necessary to determine whether an oxide layer might affect the reliability of the creep measurements. An oxide layer was formed on one crystal by anodizing at 70 volts and on another by annealing in air for 1 hour at 1,000° F. In neither case was any appreciable effect observed on the creep properties of these high-purity single crystals when tested at 300° F and 400-psi resolved shear stress. However, the result might be expected with single-crystal specimens $\frac{1}{2}$ inch in diameter, since most experiments designed to study the effect of oxide layers employ much smaller specimens. In smaller specimens the cross-sectional area of the oxide layer itself may be an appreciable fraction of the cross-sectional area of the specimen. Because of this result, it was not considered necessary to build vacuum-creep units to obtain reliable creep data at elevated temperatures.

The effect of the impurity content on the plastic properties, as detected in the stress-strain curves, has been checked also on the creep curve from the two specimens deformed in vacuum at 500° F for electron-microscopy observations. Specimen S-20 extended 12.4 percent in 25 hours at 300-psi resolved shear stress, as compared with a resolved shear stress of 970 psi (more than three times as large) which was necessary to extend crystal L-12 12.4 percent in 17 hours, both in constant-load creep tests.

The maximum strain for the highest stress at each temperature in the constant-stress tests has been limited by the range over which the profiles were designed to maintain a constant resolved shear stress. The range of temperatures investigated was from 400° to 900° F. In this range of temperatures recovery was definitely an important factor, although recrystallization was not observed, probably because the crystals were not sufficiently highly deformed.

Creep curves for three stresses at 500° F are shown in figure 7. These curves are similar to those obtained in the temperature range from room temperature to 400° F (ref. 3). They exhibit a continually decreasing slope. Although the slope appears to reach a constant value, which might be termed the steady-state or minimum creep rate, the magnitude of this slope depends on the time scale chosen. This

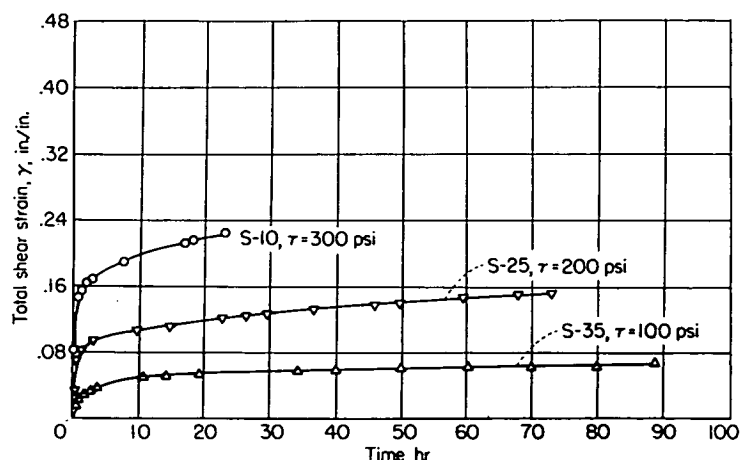


FIGURE 7.—Strain-time curves for three stresses at 500° F.

can be demonstrated by plotting the data on two time scales, one in units of seconds and the other in units of hours. Both plots will tend toward an approximately constant slope. However, the magnitudes of the slopes from the two time scales differ considerably, the slope from the plot with the second scale being approximately equal to the initial slope of the curve on the hour scale. This characteristic type of creep curve was observed also at the lowest stress, 50 psi, at 700° F (see fig. 8) and at 400 psi at 400° F (see fig. 10). A creep rate that continually decreases may be detected by plotting the creep curve logarithmically, as in figure 11. On such a plot, the slope of the line will be less than unity and will never increase, although a decrease in slope is possible. This type of curve, exhibiting a continually decreasing creep rate, has been observed also by Hazlett and Parker (ref. 19).

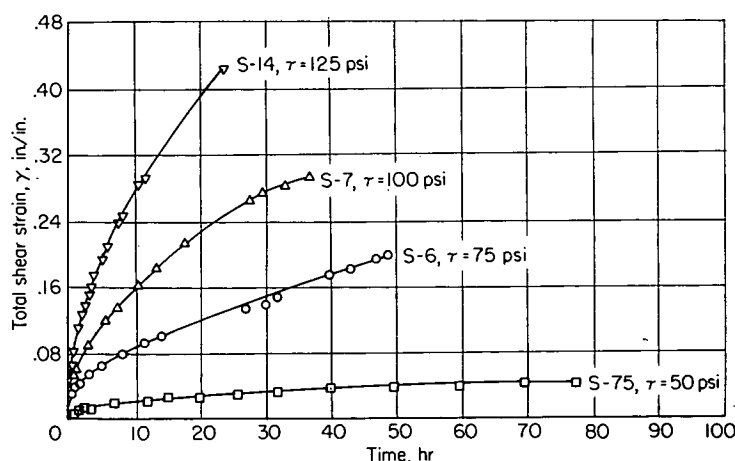


FIGURE 8.—Strain-time curves for four stresses at 700° F.

The remainder of the constant-stress creep curves from figures 8, 9, and 10 appear in figure 11 as curves which are convex downward, rather than straight lines. The reason for this curved plot has been the point of considerable controversy, as evidenced by the recent discussion by Roberts and Grant of Hazlett's and Parker's ideas (ref. 19). References have been quoted to back up both viewpoints. The viewpoint of Hazlett and Parker has been supported by the results of an independent investigation by Bhattacharya, Congreve, and Thompson (ref. 20). Likewise, Roberts is backed up by the bulk of the work by Andrade (ref. 21) and the more recent work of Cottrell and Aytakin (ref. 4).

Hazlett and Parker preferred to interpret this curvature to be a result of the time-independent strain occurring in the initial extension. They claimed that the initial extension should be subtracted from the total strain prior to plotting the data, in which case the logarithmic plot again assumed its linearity. This assumption appears to be reasonable since one would not expect that the initial extension would follow a relation involving the time. This method of plotting was tried on the data from several of the constant-stress creep tests in this investigation without complete success. An amount of strain usually could be found which, if subtracted from the total strain, would result in a linear logarithmic plot. However, this amount of strain was generally larger than the observed initial shear strain in the creep tests. This

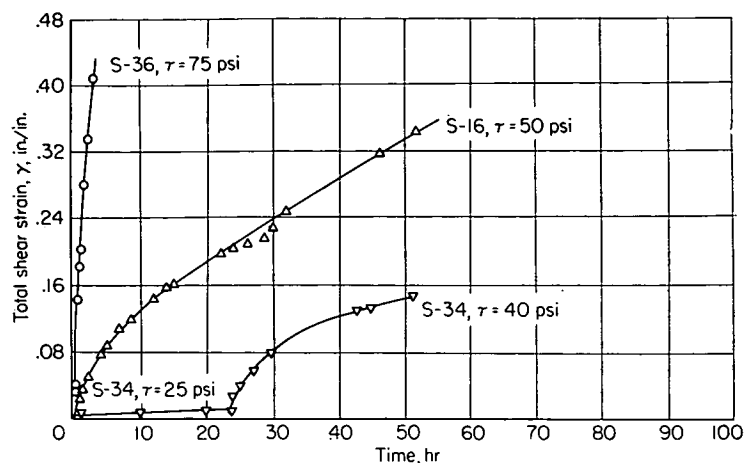


FIGURE 9.—Strain-time curves for four stresses at 900° F.

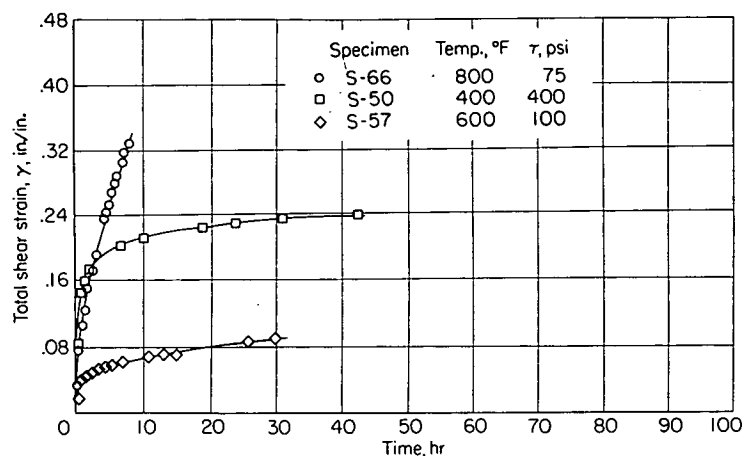


FIGURE 10.—Strain-time curves for various stresses and temperatures.

was especially true at the higher temperatures. Since much lower stresses had to be used at the higher temperatures to obtain comparable curves, the initial shear strains were correspondingly less. Hence, if the observed initial shear strain was subtracted from the total shear strain prior to plotting, many of the curves were still convex downward. The amount of curvature is more than can be accounted for by the fact that the shear strains were not corrected for rotation by equation (4). Therefore, unless the stress was not truly constant, it appears that the curvature in some of these logarithmic plots must be due to a decrease in the rate at which the creep rate is decreasing, if not to an approximately constant creep rate.

Concerning the characteristic creep curves presented in figure 11, some generalizations can be made. The linear plots are predominant at high stresses and low temperatures, whereas the plots which are convex downward are predominant at lower stresses and higher temperatures. These results are in agreement with the recent work of Roberts (ref. 22), who studied the creep behavior of extruded electrolytic magnesium in polycrystalline form. The two curves which are convex upward (100-psi resolved shear stress at 500° F and 50-psi resolved shear stress at 700° F) are, in both cases, for the lowest stress investigated at each temperature. The lowering of the first portion of the curve may have resulted from a small amount of accidental prestraining prior to

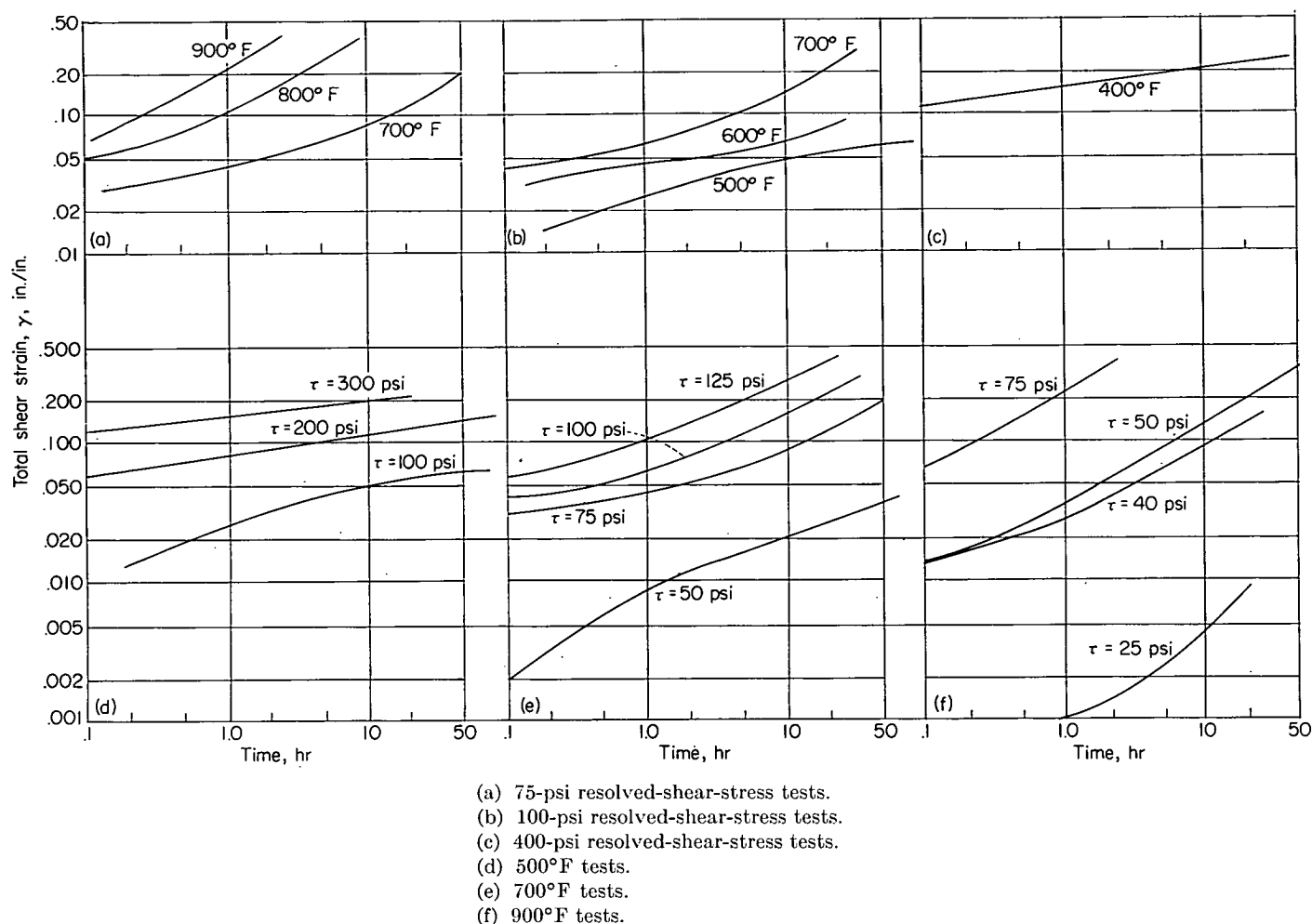


FIGURE 11.—Summary of constant-stress creep data on logarithmic plots.

testing. However, this strain should have been annealed out before the load was applied. On the other hand, the lowering of the later portion of the curve may have resulted from the onset of duplex slip, which is known to retard the creep process (ref. 3). In this investigation duplex slip has also been observed on a fine scale in the slip bands on crystals deformed during creep at elevated temperatures. It might also have resulted from the retarding effect of kink bands on the slip process, since slip bands have been observed to stop in the kink bands in this investigation. In the 900° F tests, the 25-psi and 40-psi tests were performed with the same crystal. This crystal was annealed for ½ hour at 900° F with the load removed after a shear strain of less than 1 percent in the 25-psi test.

Many investigators have employed various methods for analyzing and correlating creep data in empirical or mathematical forms in addition to those already mentioned. Wyatt (ref. 23) has analyzed transient creep in pure metals, and Cottrell (ref. 24) had discussed several of the time laws of creep. Sherby and Dorn (ref. 25) have correlated the creep data from alpha solid solutions of aluminum, and Johnson and Frost (refs. 26 and 27) have discussed the application of various relations to creep data from elevated-temperature tests. Most of these methods employ more than one empirical constant, and usually three constants,

to describe the time dependence of the creep process. The few theoretical attempts to describe creep have been discussed in references 1 and 3.

In the work reported here it has not been possible to describe accurately the time dependence of the results of the constant-stress creep tests summarized in figure 11 in a simple manner. Therefore, a complete mathematical analysis of the stress and temperature dependences of the creep process has not been obtained. It is felt that these results are indicative of the complex nature and the differing kinetics of the processes which make up the total deformation process, even in the case of creep of single crystals of high-purity aluminum. From a study of the inhomogeneity in creep deformation of coarse-grained high-purity aluminum, Chang and Grant (ref. 28) have concluded that any mathematical description of the creep curve must be considered to be a statistical summation of the equations describing the various component processes of creep. Since three mechanisms of deformation have been observed in this investigation, it is felt that the description and understanding of these basic mechanisms are more important than developing an empirical relationship which may describe the creep process mathematically without any physical insight regarding the creep process itself. Naturally, both would be desirable if they could be obtained.

PRESTRAIN EXPERIMENTS

Relatively little work has been reported on the effect of prestrain on creep, or, for that matter, any other type of plastic deformation. Probably the most complete investigation of this type has been reported by Kennedy (ref. 29), who studied the effect of instantaneous prestraining (of the order of 5 seconds) on constant-stress creep in polycrystalline lead. He investigated the effect of prestrains from 0 to 16 percent at temperatures of 100° C, 35° C, and -180° C on the creep curve at room temperature at three stress levels out to a total time of 3 hours. He fitted the resulting data to Andrade's law, involving two arbitrary constants β and k , by shifting the time scale of the strain-time plot. In this work he found that the amount the time scale had to be shifted increased with increasing amounts of prestrain and decreased with increasing temperature of the prestrain. For prestrains up to 10 percent the creep curve from a prestrained specimen could be made to coincide with the curve from an unstrained or control specimen by this shift in the time scale. However, for prestrains larger than 10 percent a decrease in one of the arbitrary constants k was necessary.

Bhattacharya and coworkers (ref. 20) have studied the effect of prior strain on creep of polycrystalline aluminum at 150° C under a constant tensile stress. As mentioned previously, they found that the creep strain (the total strain minus the initial strain upon loading) followed a power-law relationship with time, defined by two constants, a coefficient a and an exponent k for the time parameter. In a rather sketchy analysis, they found that the constant k increased and the constant a divided by the seventh power of the applied stress decreased with increasing prestrain out to 6 percent and that both were approximately constant with larger amounts of prestrain. The constant a was divided by the seventh power of the applied stress since the stress had to be raised to obtain similar rates of creep as the degree of prestrain was increased. The only points that the authors noted concerning these results were that the power-law relationship still existed for the prestrained specimens and that very small amounts of prior strain could well account for the unsatisfactory reproducibility often observed in the creep behavior of pure metals.

Other viewpoints have also been expressed on the effect of strain rate and temperature on plastic deformation. Brown (ref. 30) attempted to describe qualitatively an equation of state to explain the effects of a change in the temperature or in the strain rate during a tensile test; that is, a faster strain rate or a lower test temperature produced a higher stress-strain curve. Rosi and Mathewson (ref. 31) observed this effect of changing the temperature on the stress-strain curve of single crystals of high-purity aluminum at low strains up to 1-percent extension. Ellis and Greiner (ref. 32) found that the effect of decreasing the rolling temperature was to raise the stress-strain curve (i. e., increased flow strength and ultimate strength) at room temperature. They concluded that this observed effect was caused by simultaneous recovery during the rolling operation.

Following this brief review of the limited amount of material available on the effect of prestraining, the results of

this investigation, presented in figures 12 through 16, will now be discussed. The effects of prestraining to the same shear strain by a very rapid strain rate and by a comparatively slower strain rate on the room-temperature stress-strain curve are depicted in figure 12, along with the stress-strain curve from a control, or unstrained, specimen. The amount and the path of the prestrain have been included in both plots, so that the total shear strain and the resolved shear stress could be corrected for rotation. The two crystals that were prestrained had almost identical orientations. Still, only about two-thirds of the stress required in the rapid prestraining by dead-weight loading was required to produce the same shear strain in the slow prestraining in a constant-load-rate test. It was perhaps significant that no strain was detected in the subsequent constant-load-rate tests below the stress level to which the crystals had been prestrained. Therefore, no appreciable recovery had taken place at room temperature during the period of approximately 24 hours which elapsed between the time the crystals were prestrained and the time the stress-strain curves were obtained. The most important consequence of the prestraining was to increase the yield stress of the crystals. For comparable amounts of shear strain the rapid prestraining was more effective than the slow prestraining in raising the stress-strain curve.

The effect of increasing the amount of rapid prestraining at room temperature on the creep curve at 200° F and 400-psi resolved shear stress is shown in figure 13. The prestraining decreased the initial shear strain substantially. However, at this temperature strain-hardening was very predominant. Therefore, it was difficult to determine the effect of the prestraining on the later stages of creep, since the creep rate decreased rapidly even in the unstrained control specimen. An increase in the amount of the prestrain increased the observed effect; that is, the decrease in the initial shear strain and the lowering of the creep curve were more pronounced. In these and subsequent curves the amount of the prestrain has not been included in the total shear strain.

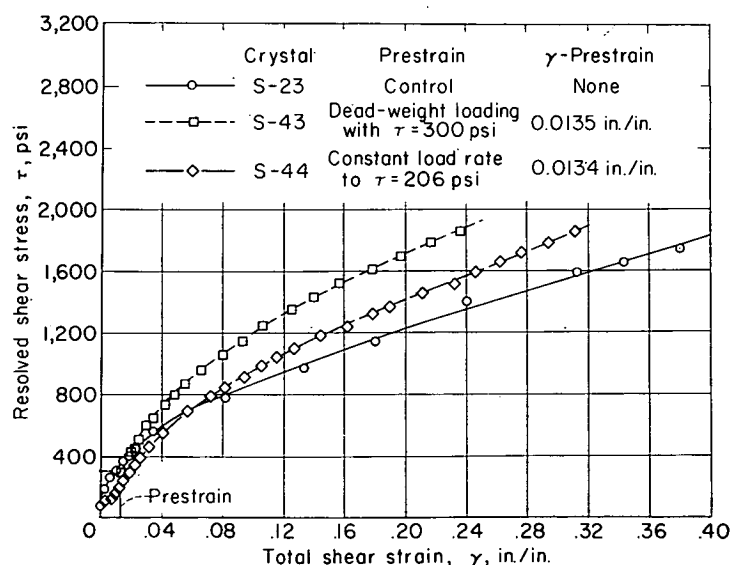


FIGURE 12.—Effect of prestraining by two different methods at 82° F on stress-strain curve at 82° F.

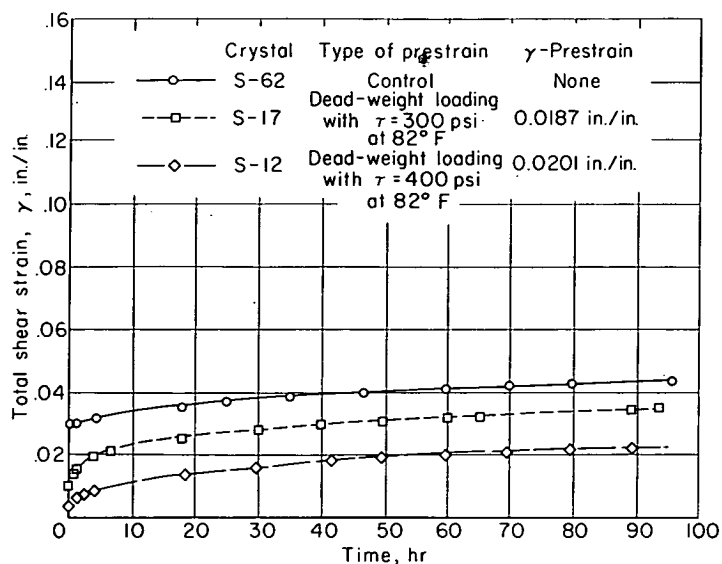


FIGURE 13.—Effect of rapid prestraining on creep curve at 200°F and 400-psi resolved shear stress.

The result of varying the temperature of the rapid prestraining and its effect on the creep curve at 300°F and 300-psi resolved shear stress are presented in figure 14. Increasing the temperature of the prestraining from room temperature to the testing temperature reduced the effect of the prestrain considerably. The effect of the prestraining at the elevated temperature was less for a larger amount of prestrain, although the stress required to produce this larger strain was slightly lower. Again, the primary effect of the prestrain was to reduce the initial shear strain and to lower the total shear strain and the level of the creep curve.

The effects of both rapid and slow prestraining at room temperature on the creep curve at 300°F and 400-psi resolved shear stress are shown in figure 15, along with a control curve from an unstrained crystal. Similar plots for both types of prestraining performed at 300°F to a larger shear strain are presented in figure 16. In addition to a reduced initial shear strain, the creep rate in the later stages of the creep process also was reduced. In prestraining at 300°F the faster strain rate was more effective in enhancing the

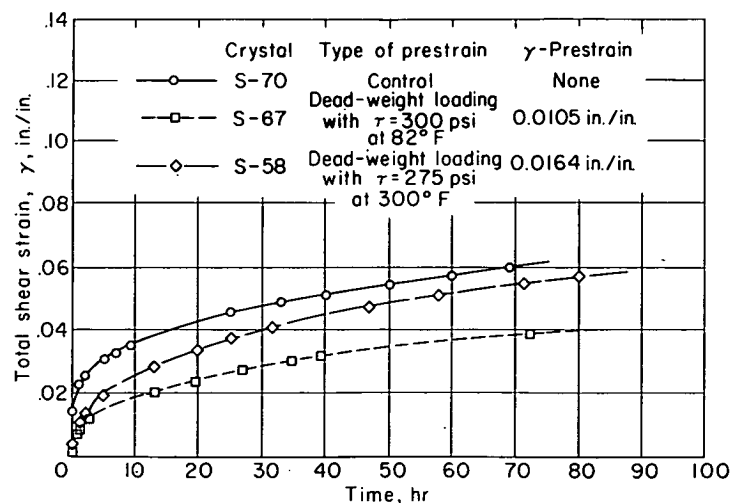


FIGURE 14.—Effect of temperature of rapid prestraining on curve at 300°F and 300-psi resolved shear stress.

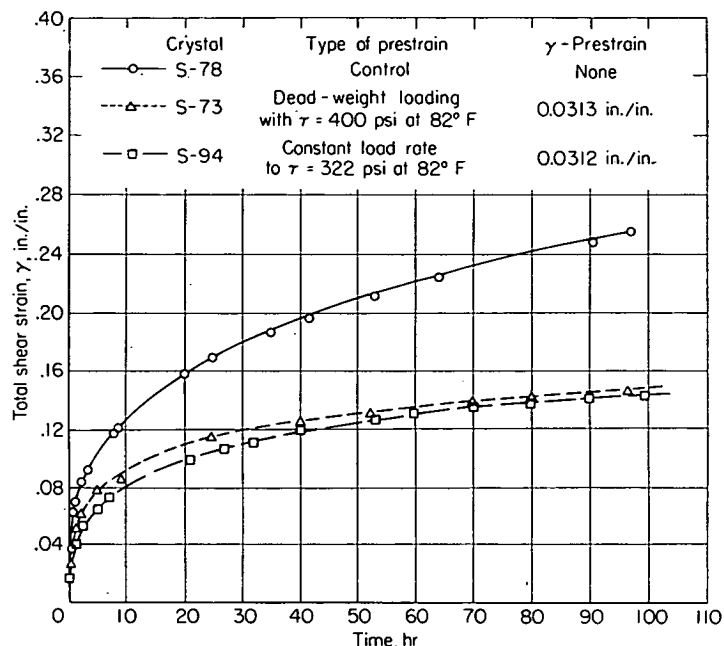


FIGURE 15.—Effects of two types of prestraining at 82°F on creep curve at 300°F and 400-psi resolved shear stress.

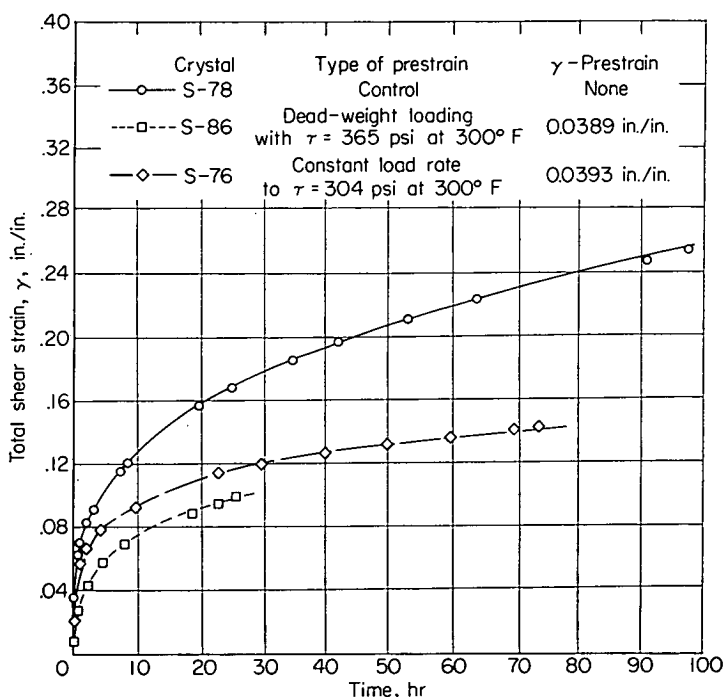


FIGURE 16.—Effects of two types of prestraining at 300°F on creep curve at 300°F and 400-psi resolved shear stress.

creep resistance of the single crystals. Although this trend was also observed in the stress-strain curves (see fig. 12), it was not observed with the room-temperature prestraining in figure 15. This may have resulted from some accidental prestraining of the crystal, S-94, in addition to the intentional slow prestraining. The crystals were extremely soft, and this particular crystal had to be handled more than most because of the X-ray pictures taken before and after prestraining and after the subsequent creep test.

Although not without exception, the effect of prior strain on the creep curve can be described. As determined in this

investigation, the effect of prestraining is to reduce the initial shear strain considerably, to remove a portion of the early or transient portion of the creep curve, and, in some instances, to reduce the creep rate in the later stage of creep. The larger the amount of the prestrain, the more the shape of the creep curve is affected. Also, increasing the temperature of the prestrain reduces its influence on the creep process. The most important observation that has been made is that the rapid prestraining obtained in dead-weight loading is more effective in hardening the crystals and increasing their resistance to plastic deformation than the slower prestraining obtained in a constant-load-rate method of deformation. Since the resolved shear stress required to produce the same shear strain is higher for the rapid prestraining than for the slower prestraining, dislocation theory provides a reasonable explanation for this behavior. The higher stress level involved in the rapid prestraining has used up more of the Frank-Read sources than were present in the crystal initially. The stress required to operate a Frank-Read source is Gb/l , where G is the shear modulus, b is the Burgers vector or unit slip distance in the slip direction, and l is the length of the source (ref. 33). Thus, the longest sources operate at the lowest stress level. Since a larger applied stress is required in the rapid prestraining to produce the same shear strain as that produced with the relatively slower prestraining, the sources would be effectively used up to a higher stress level by the rapid prestraining. The resulting increases in hardening of the crystals can be attributed to source-hardening, as defined by Koehler (ref. 16) in his analysis of stress-strain data at low strains.

The concept that more Frank-Read sources and, hence, more active slip planes are operative with the faster strain rate is consistent with the fact that the deformation is more uniform with the faster strain rate. This same observation has been made on crystals deformed at two relatively different strain rates at 1,100° F. Hence, the process of slip-band formation is related directly to the strain rate. This will be discussed further in a later section covering the observations of slip bands by light microscopy.

The above description of the effect of prestraining on the creep behavior of single crystals of aluminum has been stated in terms of trends purposely because of the difficulty encountered in obtaining reproducible results. This difficulty is due in part to the almost unavoidable amount of accidental prestraining which occurs during handling of these soft crystals, in part to the fact that the crystals do not have identical orientations, and in part to the inherent microscopic differences in the single crystals even in the annealed state. Regarding the latter cause, Parker and co-workers (ref. 34) have found that the yield stresses of zinc single crystals with identical orientations can be more than doubled by varying the annealing procedure prior to testing. They associate this result with the effect of subboundaries existing in the zinc crystals. The status of these subboundaries, which apparently can be changed by the annealing procedure, must play an important part in determining the plastic properties of metals. A fine substructure of the order of 1 micron in linear dimensions has been detected in this investigation in the annealed aluminum

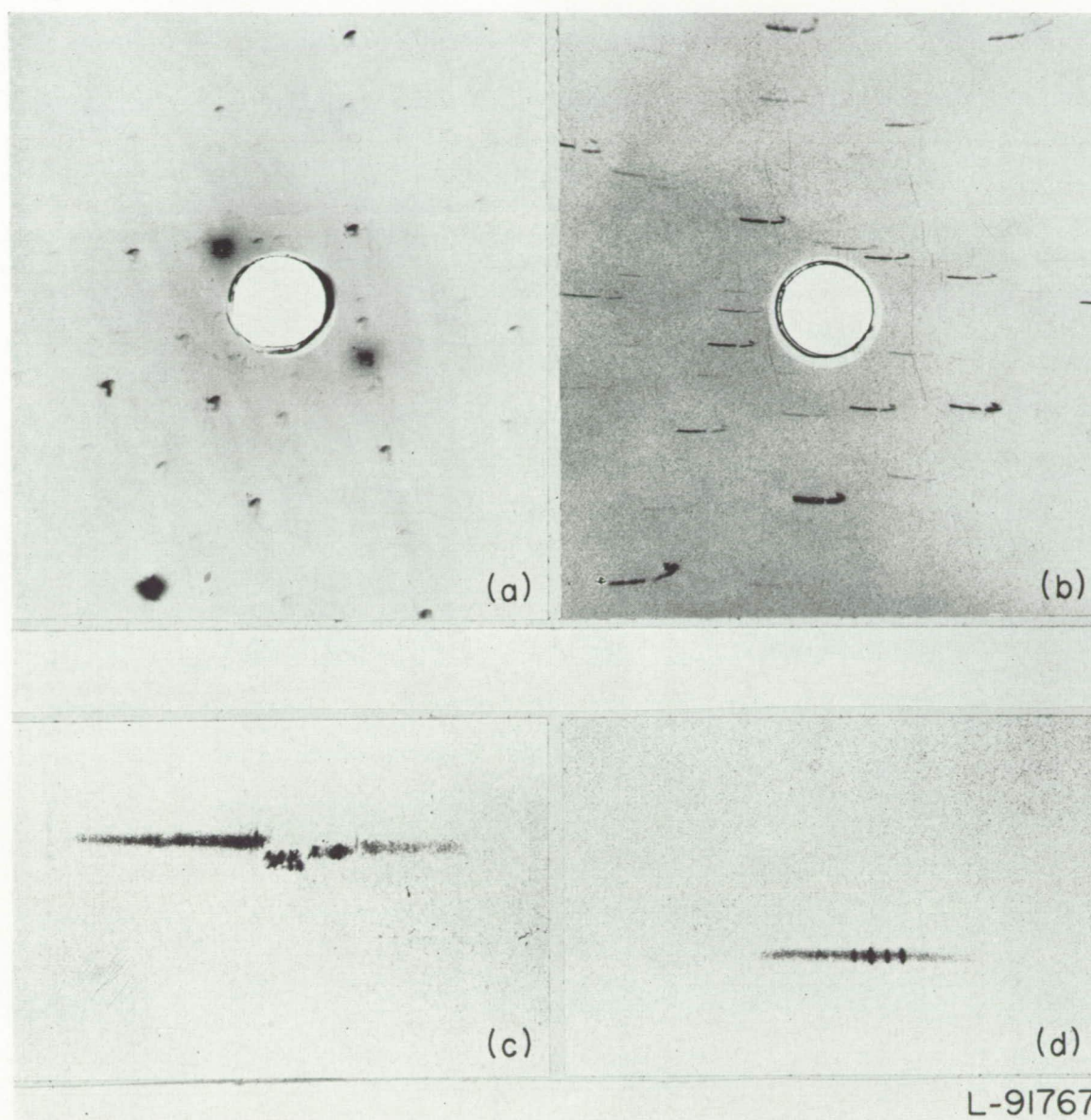
single crystals. Therefore, it is apparent that the effect of annealing procedure and deformation of this substructure will have to be understood before further experiments on the effect of prestraining are undertaken.

X-RAY DIFFRACTION INVESTIGATION

High-resolution X-ray diffraction techniques have been employed to obtain an indication of crystal perfection and to study the changes produced in the crystalline lattice by small amounts of prestraining and by subsequent deformation in creep. Since the oblique Laue technique was not a conventional one, photographs have been made by three methods from a crystal found to be imperfect after the growth process. The imperfect nature of the crystal was noticed first in the normal back-reflection Laue photograph in figure 17 (a) used for the determination of the crystal orientation. This photograph was made with the standard specimen-to-film distance of 3 centimeters and ordinary pinhole collimators with continuous tungsten radiation. When the large pinhole collimators were replaced by a collimating system consisting of a fine pinhole (150 microns in diameter) and a fine slit (3 millimeters by 150 microns), the photograph shown in figure 17 (b) was obtained. The use of the fine collimators increased the resolution and the detail observable in the individual reflections, although with the considerable increase in the required exposure time from 10 minutes to 12 hours.

A still further increase in resolution was obtained by observing the reflection of the tungsten L-beta spectrum of a single crystallographic plane with an increased specimen-to-film distance and the collimating arrangement for oblique Laue photographs, as shown in figure 4. A photograph of this type for the (200) planes of this same imperfect crystal is shown in figure 17 (c), and a comparison photograph of a relatively perfect single crystal, in figure 17 (d). The imperfect crystal exhibited fairly large differences in orientation in both the vertical and the horizontal directions in the area photographed, in addition to not being able to resolve the tungsten L-beta spectrum. However, the relatively perfect crystal, S-13, definitely resolved the individual lines in the tungsten L-beta spectrum. From a comparison of the photographs obtained in the three methods of photographing an imperfect crystal made up of regions of different orientations, one can visualize better what has taken place in deformed crystals which were originally relatively perfect, as indicated by an oblique Laue photograph such as that shown in figure 17 (d).

The theory of this oblique Laue method has been mentioned already under "Experimental Procedure." If the sample is a perfect crystal and is aligned properly, all the various tungsten L-beta wavelengths will be reflected from the same family of crystallographic planes, but at different positions along the length of the crystal. These characteristic reflections will strike the film at known consecutive positions along the film. As a matter of fact, from the relative intensities and the separations in the photograph in figure 17 (d), the various reflections can be identified as the L-beta-4, L-beta-6, L-beta-1, L-beta-3, and L-beta-2 wavelengths, respectively, from left to right. If a fine-grained polycrystalline sample were to be examined, each

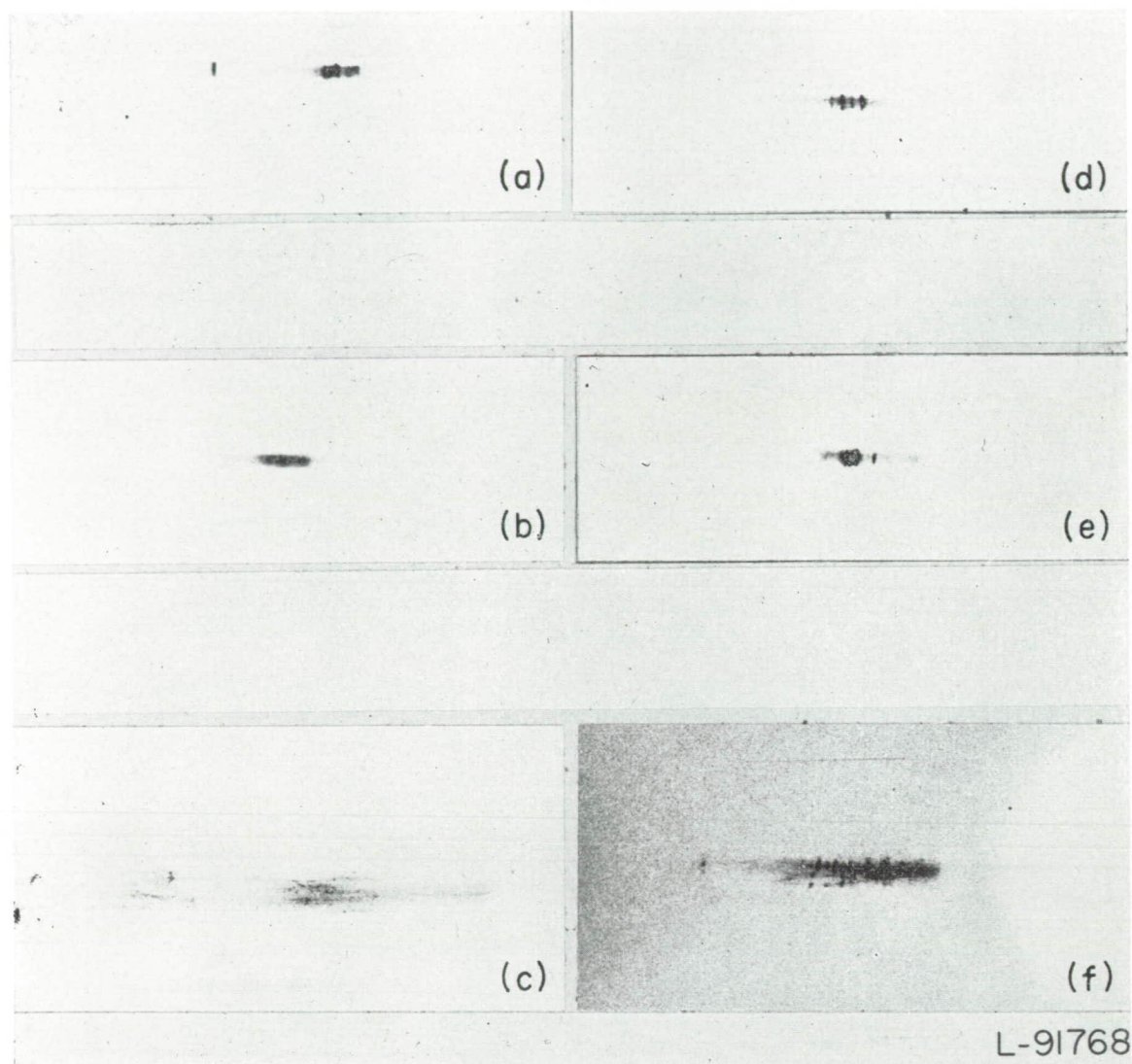


(a) Normal back-reflection Laue photograph of imperfect crystal S-63. Exposure time, 10 minutes; 1X.
 (b) Back-reflection photograph of imperfect crystal S-63 with a fine pinhole and slit collimation. Exposure time, 12 hours; 1X.
 (c) Oblique Laue photograph of (200) reflection from crystal S-63. Exposure time, 20 minutes; 2.5X.
 (d) Oblique Laue photograph of (200) reflection from crystal S-13. Exposure time, 10 minutes; 2.5X.

FIGURE 17.—Back-reflection Laue and oblique Laue photographs of imperfect crystal S-63 and oblique Laue photograph of relatively perfect crystal S-13.

wavelength would reflect continuously over a considerable portion of the reflection band. On the other hand, if the crystal were composed of crystallites having small disorientations from the average, not all the rays of any one wavelength would strike at the same position along the band. Hence, the relative intensities of the spots would be different from those of a perfect crystal, and the spots might not appear at the correct positions. The amount of disturbance of the oblique Laue photograph from the ideal condition yields a qualitative measure of the imperfections in the area photographed. The interpretation of asterism as being due to distortion or internal lattice strains and of discrete spots as being due to different orientations is the same as in normal back-reflection Laue photographs.

A series of oblique Laue photographs was taken from crystal S-5, initially, after rapid prestraining, and after a creep test at 300° F and 400-psi resolved shear stress. These photographs, shown in figures 18(a), 18(b), and 18(c), show the decreasing ability of the crystal to resolve the different wavelengths after successive deformations. A decrease in reflected intensity is also apparent from a consideration of exposure times. Figure 18(b), taken after prestraining, shows considerable distortion of the original pattern, although no discrete spots were found. This indicates that the lattice was strained, but no new crystallites had formed that could be detected. No difference in this reflection (i. e., no recovery) could be detected in a second photograph after 72 hours at room temperature. Figure 18(c) shows very definitely the



- (a) (200) reflection from undeformed crystal S-5 with experimental arrangement shown in figure 4. Exposure time, 10 minutes.
- (b) Same reflection after 1.63-percent extension by prestraining with 400-psi resolved shear stress for 3 minutes at 82°F. Exposure time, 10 minutes.
- (c) Same reflection after an additional 11.1-percent extension by creep with 400-psi resolved shear stress at 300°F to 575°F in 17 hours. Exposure time, 80 minutes.
- (d) (200) reflection from undeformed crystal S-8 with same experimental arrangement except a 150-micron pinhole was substituted for 150-micron slit. Exposure time, 100 minutes.
- (e) Same reflection after 1.53-percent extension by prestraining with 400-psi resolved shear stress for 3 minutes at 82°F. Exposure time, 100 minutes.
- (f) Same reflection after an additional 7.30-percent extension by creep with 400-psi resolved shear stress at 300°F for 64 hours. Exposure time, 12 hours.

FIGURE 18.—Oblique Laue photographs from (200) plane of two aluminum single crystals at various stages of deformation with tungsten radiation. 2.5X.

presence of many small crystallites, or the formation of a substructure. However, this crystal was found to be bent slightly during the course of this series of photographs and extensions. In addition, the failure of a temperature controller overnight allowed the test temperature to increase from 300° to 575° F, and the crystal extended until the weight pan came to rest on the jack used in loading, after which the crystal remained at temperature with essentially no applied stress. Because of these varying conditions, another experiment was performed.

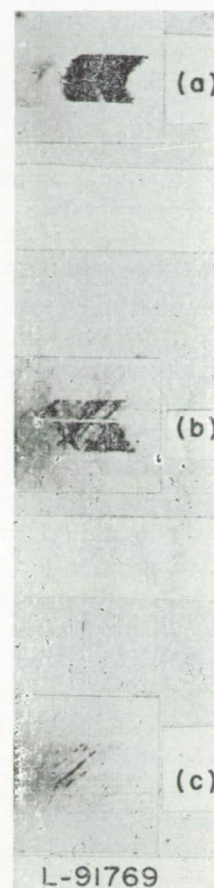
To increase the resolution of the arrangement shown in figure 4, the 150-micron slit was replaced by a 150-micron pinhole. This necessitated an increase in exposure times by

a factor of 10 but increased the sharpness of the reflections. A similar series of photographs was then made on crystal S-8, initially, after a rapid prestraining, and after a creep test at 300° F and 400-psi resolved shear stress. The resolution of this set of photographs, shown in figures 18(d), 18(e), and 18(f), was better, but the results are essentially the same. The initial status of the crystal was very good, as evidenced by the resolution of the five lines in the tungsten L-beta spectrum. The apparent difference in the lengths of the tungsten L-beta spectrum, as shown in figure 17(d) and figure 18(d), was a result of the fact that the crystal surfaces were at different angles with the incident beam. Again, the prestraining introduced considerable distortion, as evidenced

by the broadening of the characteristic reflections, but no new orientations were detected. After the subsequent creep test, many discrete spots were evident. However, the discrete reflections were larger than those obtained from crystal S-5 after creep. It appeared that some of the crystallites may have been large enough to reflect all or at least parts of the characteristic tungsten radiation from the L-beta spectrum.

The second high-resolution X-ray technique employed to detect and to follow the strain throughout the course of a prestrain experiment was the reflection-micrograph method. The experimental arrangement for this method is presented in figure 5. Although the method itself has been described by Honeycombe (ref. 5), the translational oscillation of the film and the specimen to increase the area under observation with this technique is believed to be new. However, this method does increase the exposure time considerably above that required with a stationary specimen. If a single crystal is properly oriented in this beam, a reflection of characteristic radiation will be obtained. Areas of either great or small disorientation in the crystal will not reflect. If the reflection is a low-order reflection, differences in intensity in the reflection may occur as a result of differences in extinction over the irradiated surface of the crystal. However, extinction would not be expected to produce sharp discontinuities in intensity. If the crystal is oriented so as to reflect the continuous radiation, differences in extinction may be observed, but small disorientations will not be observed.

The X-ray micrographs obtained from crystal S-94 initially after a slow prestrain at room temperature and after a creep test at 300° F and 400-psi resolved shear stress are presented in figure 19. The specimen was cross scratched to mark the area to be irradiated. The vertical and possibly the horizontal scratches can be seen in figure 19 (a), whereas the horizontal scratch shows up well in figure 19 (b). The original micrograph of the crystal before any deformation (fig. 19 (a)) showed no extra detail when examined at 100X. The continuous variations in intensity can be interpreted as differences in extinction. However, an attempt to correlate these variations with optically apparent irregularities in the electropolished surface of the crystal was not successful. In figure 19 (b), a micrograph of the specimen after prestraining, the reflection was still largely characteristic radiation. However, this figure shows large areas where the (200) reflecting planes have rotated relative to other portions of the crystal so that no characteristic reflection was possible. Traces of kink bands, which were quite apparent after the creep test, appear to run diagonally up and to the right in figure 19 (b). Therefore, the rotation observed in figure 19 (b) can be attributed to the early onset of kinking. After the creep test the lattice was so distorted that one of the entrance slits had to be removed to get an exposure in a reasonable length of time. Hence, the height of the micrograph was increased slightly in addition to the increase in the horizontal scanning which resulted from an increased translation. In all cases these micrographs appear to be approximately twice as large as calculated from the translation and the magnification. The



- (a) Deformation, none except a vertical and a horizontal scratch mark; exposure time, 6 hours; emulsion, type V-0; translation, 2 millimeters.
- (b) Deformation, 1.47-percent extension in constant-load-rate test to 327-psi resolved shear stress at 82°F in 15 minutes; exposure time, 6 hours; emulsion, type V-0; translation, 2 millimeters.
- (c) Deformation, an additional 6.94-percent extension by creep with 400-psi resolved shear stress 300°F in 118 hours; exposure time, 15 hours (with one entrance slit removed); emulsion, lantern slide; translation, 4 millimeters.

FIGURE 19.—X-ray reflection micrographs from (200) plane of aluminum single crystal S-94 at various stages of deformation with copper radiation. 2.5X.

micrograph given as figure 19 (c) shows considerable fine structure parallel to the slip lines in the reflections when viewed at 100X. Very little of the material in the irradiated area has been left intact to reflect the characteristic radiation because of the manner in which the crystal lattice has been broken up.

The manner in which the lattice breaks up during deformation has developed recently into a highly controversial issue. Wood and his English coworkers (refs. 35, 36, 37, 38, and 39) have supported a fragmentation theory, according to which the lattice breaks up immediately into subgrains in order to allow deformation to take place along the subgrains or crystallite boundaries. The size of the subgrains formed in a polycrystalline material was found to be a function of the strain rate and the temperature. On the other hand, numerous other workers, including Cahn (refs. 40 and 41), Greenough and Smith (refs. 42 and 43), and Servi, Norton, and Grant (ref. 44), have concluded from

similar experiments that the breakup of the crystalline lattice was a two-stage process in which plastic bending of the lattice planes was followed by polygonization. Polygonization is the process by which plastically bent and distorted regions can form a network of smaller regions which are relatively free of internal strains and which exhibit slight differences in orientation from one small region to the next. The plastic bending of the lattice produces an excess of dislocations of one sign. Then, at suitable temperatures, the stress-induced movement of the dislocations causes the dislocations to migrate along slip planes and to collect in localized regions to form an array of low-angle boundaries. Simultaneously, the segments of the lattice between the boundaries lose their curvature and elastic strain.

In a recent paper Gervais, Norton, and Grant (ref. 45) observed both types of subgrain formation. They found that the immediate fragmentation did take place in kinking but that most of the subgrain boundaries were formed by polygonization. They found little evidence of the flow along the subgrain boundaries predicted by Wood and his coworkers, but considerable rotation was observed to take place. In an investigation of the creep processes in coarse-grained aluminum (refs. 46, 47, and 48) McLean studied the formation of subgrains by using light microscopy and X-ray techniques. He observed no subboundaries during primary creep. Diffuse X-ray spots did not split into discrete spots until secondary creep had set in. From then on, the subgrain size decreased with increasing extension, being detected first near the grain boundaries and later in the interior of the grains. The disorientation of the subgrains also increased with extension. These disorientations were considerably larger than predicted by the observed subboundary movements. From this evidence McLean proposed a model in which the polygonization of the lattice into a substructure results in an observed extension. With this interpretation, polygonization, which contributes to the total deformation, can be termed a mechanism of deformation.

The X-ray work performed in this investigation, particularly the oblique Laue photographs, lends support to the views expressed by the second group of workers that the substructure is formed in a two-stage process. The oblique Laue photographs in figure 18 showed distortion of the lattice without any substructure formation after prestraining to a low extension at room temperature. The photographs taken after a creep test showed that a definite substructure had been formed during creep. The reflection micrographs in figure 19 also indicated considerable rotation after the prestraining, but no fine substructure was detected until after the creep test. This evidence for a two-stage process in the formation of a substructure and the large rotations observed support McLean's conclusion that polygonization was definitely a mechanism of deformation, rather than a result of the deformation.

OPERATIVE SLIP SYSTEMS AT ELEVATED TEMPERATURES

The operation of additional slip systems, especially at elevated temperatures, has been discussed by Chalmers

and Martius (ref. 49) on the basis of the energy of dislocations and their associated slip planes. The slip direction is the most closely packed direction. This corresponds to the movement of those dislocations with the shortest possible Burgers vector, that is, the shortest unit slip distance in the slip direction necessary to bring the crystal lattice back into registry. For face-centered-cubic metals, such as aluminum, this direction is a $[110]$ direction, and the unit slip distance is $a/(2)^{1/2}$, where a is the lattice parameter.

The energy of a dislocation must also depend on which slip plane is involved. Otherwise, any plane containing a $[110]$ direction might operate at any temperature. Chalmers and Martius have taken this dependence to be a function of the shear strain, with the dislocations of lowest energy producing the lowest shear strain in a unit slip process. The shortest distances to the next parallel planes for the (111) , (100) , and (211) planes are $a/(3)^{1/2}$, $a/2$, and $a/2(6)^{1/2}$, respectively. The tangents of the angles of shear for the unit slip process are 1.225, 1.414, and 3.464, respectively, for these three planes with their associated $[110]$ slip directions.

At room temperature only the (111) $[110]$ slip system has been observed. However, as the temperature of deformation is increased, other systems have been observed to operate. In the cases reported, the systems reported have been ones which have a low value of shear strain for the unit slip process. Boas and Schmid (ref. 50) have observed slip in the (100) plane in a $[110]$ direction in single crystals of aluminum at 450°C . More recently, Servi, Norton, and Grant (ref. 44) have shown that additional slip systems became operative during creep of high-purity coarse-grained aluminum at elevated temperatures. They found that the operative slip plane might be either a (100) plane or a (211) plane, in addition to the customary close-packed (111) plane. In all cases the associated slip direction was one of the $[110]$ close-packed directions located in the slip plane. However, the stress systems in polycrystalline materials are often quite complex.

With single-crystal specimens of known orientations it was possible to determine the effect of temperature on the operative slip system. Twenty-two crystals were deformed at temperatures from 300° to $1,100^\circ\text{F}$. All but one were deformed in constant-load creep tests, and 19 had one or more high-temperature slip systems containing a (100) , (211) , (311) , or (110) plane, at least one of which was oriented more favorably than the most favorable system containing a (111) slip plane. Therefore, the resolved shear stress, or the value of $\cos \phi \cos \lambda$ which determines the fraction of the applied tensile stress which was resolved in the slip plane in the slip direction, was higher for a system containing one of the four high-temperature slip systems than for any system containing an octahedral slip plane. The pertinent data on these tests, presented in table 3, include the conditions of the test, the type of the primary operative slip plane and its orientation factor $\cos \phi \cos \lambda$, and the ratio of the resolved shear stress in the most favorably oriented high-temperature slip system to that in the most favorably oriented low-temperature slip system.

The results are presented graphically in figure 20. The ratio of the resolved shear stress on the favorably oriented high-temperature slip system, containing a (211), (100), (311), or (110) slip plane, to that on the most favorably oriented octahedral slip system has been plotted for each test temperature. To the left of the straight line, the slip plane was always an octahedral plane. To the right of the line, the slip plane was one of the four observed planes ((211), (100), (311), or (110)) in the system on which the resolved shear stress was the highest. The boundary line delineating octahedral slip from high-temperature slip slopes down to the right from the lowest test temperature, 300° F, where a high-temperature slip system must be favored by approximately 40 percent to operate, to the point where a high-temperature slip system will operate at 900° F if it is equally favored or slightly more so. Because of the 12 slip systems containing a (111) plane and a [110] direction, one must be favored to some extent. Therefore, it is not possible to obtain crystals with high-temperature slip systems that are favored by more than 50 to 55 percent over the most favorably oriented octahedral slip system. The occurrence of slip on the (311) slip plane has been observed above 300° F; on the (100), above 500° F; on the (211), above 700° F; and on the (110) (one specimen), only at 1,000° F.

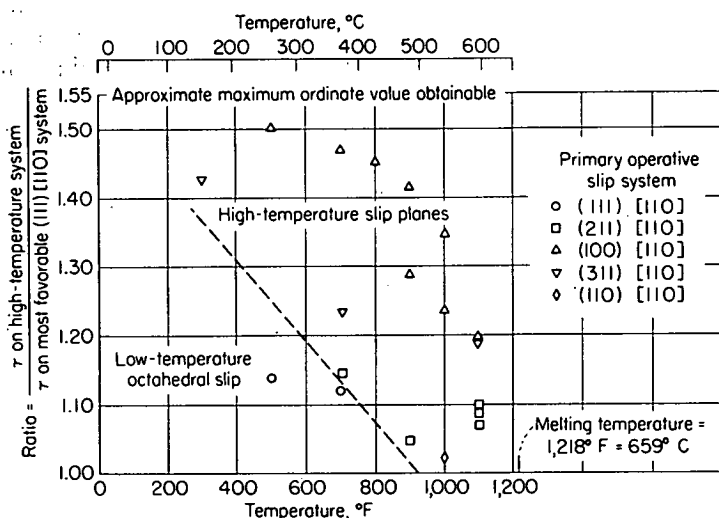


FIGURE 20.—Effect of orientation on operative slip system as function of temperature.

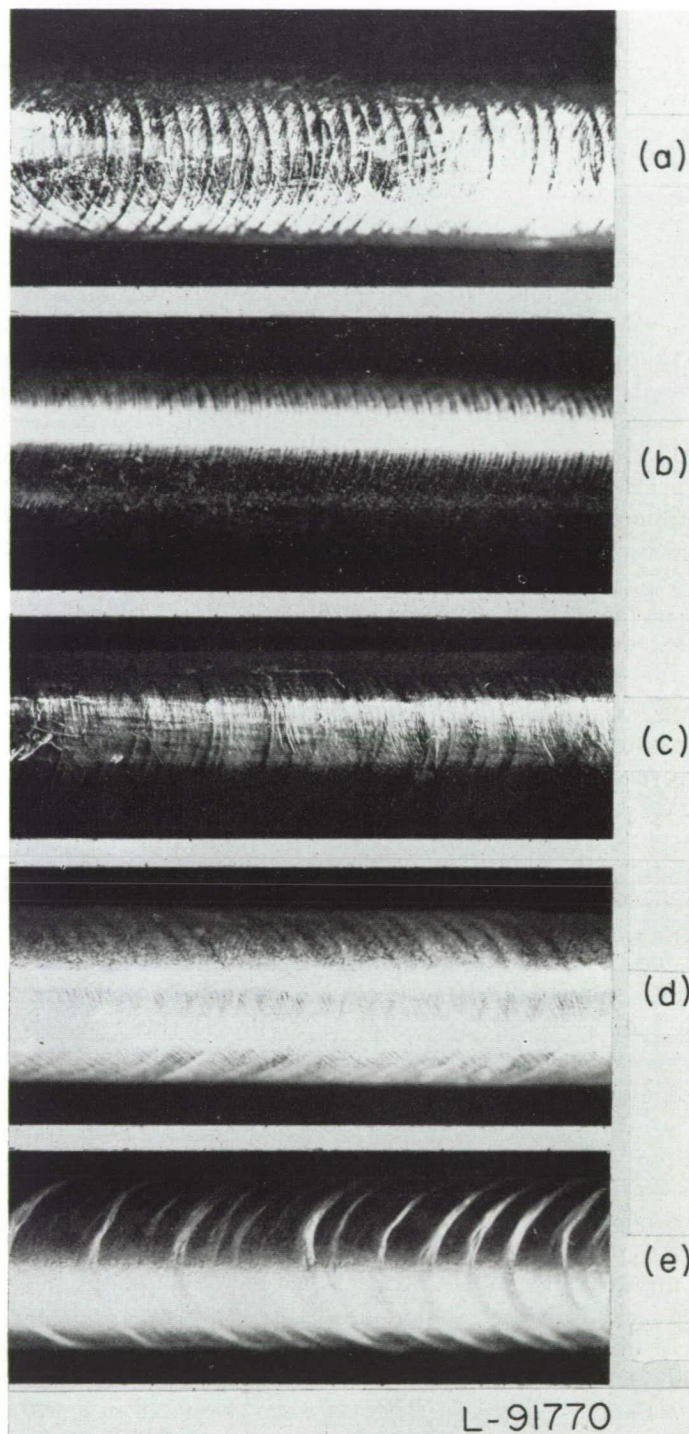
The onset of slip on these four high-temperature slip systems in aluminum demonstrates the increase in the ease of plastic deformation with the increase in the temperature at which the deformation takes place. As the temperature increases, the amplitude of vibration and the thermal energy of the atoms increase until the condition stated by Chalmers and Martius for the operative slip plane no longer holds. Then slip planes having slightly higher values of shear strain for the unit slip distance can operate also if they are oriented more favorably for slip than the most favorable system exhibiting the lowest value of shear strain for a unit slip distance. As the temperature is increased still further, the amount by which the high-temperature slip system must be favored decreases in accord with the results shown in figure 20 for single crystals of high-purity aluminum.

STRAIN MARKINGS BY LIGHT MICROSCOPY

The details of kinking and slip-band formation have been observed by light microscopy. However, the structure of the slip bands must be studied with electron microscopy by replica techniques, and this work will be discussed in the next section.

The microscopic strain markings observed on five representative crystals are presented in figure 21. These micrographs were taken in a direction perpendicular to a plane containing the specimen axis and approximately parallel to the plane containing the slip direction. In all cases, the crystals were positioned so that the ends of the ellipses formed by the intersection of the slip bands with the specimen surface appear convex to the left and the kink bands appear convex to the right. The kink bands were observed on almost all crystals deformed in creep from 300° to 1,100° F, with no apparent dependence on the orientation of the specimen axis. The amount of kinking appeared to depend on the amount of deformation, on the temperature at which the deformation took place, and possibly on the strain rate. The kink bands were very sharp in the temperature range from 300° to 500° F. In figure 21 (b), the observable bands are kink bands, which were much more prominent than the slip bands, which were not apparent in this micrograph. As the temperature was increased, the kink bands broadened out until they were barely noticeable in the creep specimen deformed at 1,100° F, as shown in figure 21 (e). The kink bands were approximately perpendicular to the slip direction; that is, the slip direction was normal to the plane of the kink bands. These observations did not appear to depend on the primary operative slip plane, which was a (111) in figure 21 (a), a (100) in figure 21 (b), and a (211) in figures 21 (c), 21 (d), and 21 (e).

Kinking presumably is the collection of an excess number of dislocations in a localized region. The physical appearance of the kink bands depends on the manner in which these dislocations are distributed, that is, whether they exist in a network or whether they have been collected in a boundary. Quite often the broad kink bands would either fade away or appear as a rumpled surface when viewed at higher magnifications. However, micrographs of the sharp kink bands were obtained at 100X from specimens deformed at 300° and 500° F. Three types of kink bands that were observed in a Faxfilm replica of the surface are presented in figure 22. The most typical form of a kink band runs diagonally down and to the right in figure 22 (a). Slip bands were observed to stop in the kink band, but no discrete difference in orientation was apparent. In figure 22 (b), the kink bands running diagonally up and to the right exhibited a sharp discontinuity in the surface in the kink band. When the specimen was viewed directly, instead of the replica, the difference in the reflections of light from the material on either side of the kink band provided evidence that there was a discrete difference in the orientation in this type of sharp kink band, which has been observed also by Gervais, Norton, and Grant (ref. 45). In the third type of kinking, duplex slip has been observed in the kink band in the upper-left-hand corner of figure 22 (c).



- (a) Crystal S-78; test, 400-psi resolved shear stress at 300°F; extension, 12.6 percent in 94 hours.
- (b) Crystal S-82; test, 450-psi resolved shear stress at 500°F; extension, 7.8 percent in 140 minutes.
- (c) Crystal S-18; test, 182-psi resolved shear stress at 700°F; extension, 12 percent in 46 minutes.
- (d) Crystal S-64; test, constant load rate at 1,100°F; extension, 13 percent in 6 minutes.
- (e) Crystal S-42; test, 27.6-psi resolved shear stress at 1,100°F; extension, 14 percent in 5.2 hours.

FIGURE 21.—Light micrographs of kink bands and slip bands on single crystals of aluminum deformed at various temperatures. 2X.

Kinking does not take place in single crystals of zinc deformed in pure shear (ref. 34), but it does in zinc single-crystal tension specimens (ref. 51). Therefore, the bending moment which acts on a crystal deformed by creep in tension must be responsible for the occurrence of kinking. In addition, the slip planes rotate toward the tension axis as extension takes place, and the lattice on the opposite side of the crystal must deform to accommodate this rotation. Chen and Mathewson (ref. 52) have observed the formation of kink bands in single crystals of aluminum that were very similar to the typical kink band shown in figure 22 (a).

Gervais, Norton, and Grant (ref. 53) have investigated the role of the bending moment in kink-band formation. They concluded that slip on a second system could relieve the bending moment and prevent kinking. In an attempt to check this hypothesis, three specimens, S-3, S-13, and S-51, each with two favorably oriented slip systems, were deformed at 500° F in constant-load creep tests. The test conditions for these specimens have been included at the end of table 3. In crystals S-3 and S-51 duplex slip was not observed on a gross scale but only locally in the kink bands, as shown in figure 22 (c). In crystal S-13, one slip system was operative on one end of the crystal and another on the other end. Kink bands were formed on each end of the specimen, and the only duplex slip on a gross scale was observed in the transition range between the two ends of the crystal. The deformation was too inhomogeneous to tell anything about kinking in this region. Because the specimens did not exhibit duplex slip on a gross scale, they did not prove or disprove whether duplex slip could eliminate kinking. However, they did indicate a tendency for duplex slip to take place on a fine, rather than a gross, scale at elevated temperatures. This tendency has also been observed in the electron-microscopy study of slip-band formation at elevated temperatures.

Low-magnification photographs of the slip bands are presented in figure 21. In general, the amount of shear on each slip band increased as the temperature was increased, that is, for a given strain. However, the most important observation to be made from these photographs is the difference between the slip bands formed at 1,100° F during a constant-load-rate test with a fairly rapid strain rate (see fig. 21 (d)) and those formed in a creep test with a relatively slower strain rate (see fig. 21 (e)). The slow deformation was much more inhomogeneous. These gross slip bands observed on the creep specimen were actually made up of a number of slip bands which could be resolved easily at 100X. Other light micrographs of slip bands on specimens of the two purities are presented in figure 23. The slip bands on the high-purity crystal S-2 appeared quite broad and wavy at 100X after an extension of 9.3 percent at 500° F in 1.5 hours with 400-psi resolved shear stress. The slip bands on the low-purity crystal L-12 appeared relatively straight and much narrower at 250X after an extension of 14.4 percent in a constant-load-rate test at 500° F in 19 minutes. In addition, duplex slip on a gross scale was quite apparent in

TABLE 3.—SUMMARY OF DATA ON OPERATIVE SLIP PLANE AT ELEVATED TEMPERATURES

Crystal	Temperature, °F	Test (a)	Strain, ϵ	Primary operative plane		
				Type	$\cos \phi \cos \lambda$	τ (high-temperature system)
						$\tau(111)$
S-21	300	400-psi RSS for 10 min.	0.005	(311)	0.454	1.43
S-20	500	300-psi RSS for 25.4 hr.	.124	(111)	.417	1.139
S-82	500	450-psi RSS for 140 min.	.078	(100)	.482	1.497
P-169	700	75-psi RSS for 67 hr.	.025	(111)	.422	1.121
P-159	700	100-psi RSS for 18.5 hr.	.098	(311)	.477	1.23
S-18	700	182-psi RSS for 46 min.	.12	(211)	.487	1.14
S-71	700	147-psi RSS for 5.3 hr.	.10	(100)	.489	1.468
S-60	800	109-psi RSS for 278 min.	.165	(100)	.495	1.447
S-27	900	79-psi RSS for 168 min.	.10	(211)	.472	1.054
S-46	900	75-psi RSS for 100 min.	.11	(100)	.494	1.290
S-45	900	71.0-psi RSS for 100 min.	.117	(100)	.491	1.418
S-87	1,000	50-psi RSS for 15 min.	.10	(110)	.475	1.02
S-77	1,000	62.2-psi RSS for 18 min.	.10	(100)	.480	1.244
S-1	1,000	67.3-psi RSS for 25 min.	.216	(100)	.495	1.345
S-64	1,100	CLR in 6 min.	.13	(211)	.477	1.072
S-39	1,100	27.2-psi RSS for 66 hr.	.129	(211)	.496	1.088
S-42	1,100	27.6-psi RSS for 5.2 hr.	.14	(211)	.489	1.104
S-84	1,100	28.8-psi RSS for 6 hr.	.20	(311)	.488	1.19
P-149	1,100	29.9-psi RSS for 20 hr.	.35	(100)	.486	1.197
S-3	500	400-psi RSS for 3.3 hr.	.115	(111)	.493	
S-13	500	400-psi RSS for 45 min.	.10	(111)	.485	
S-51	500	600-psi RSS for 1 min.	.15	(111)	.480	
					.489	

a RSS, resolved shear stress; CLR, constant load rate.

the lower purity specimen. These same observations were made in the electron micrographs at much higher magnifications.

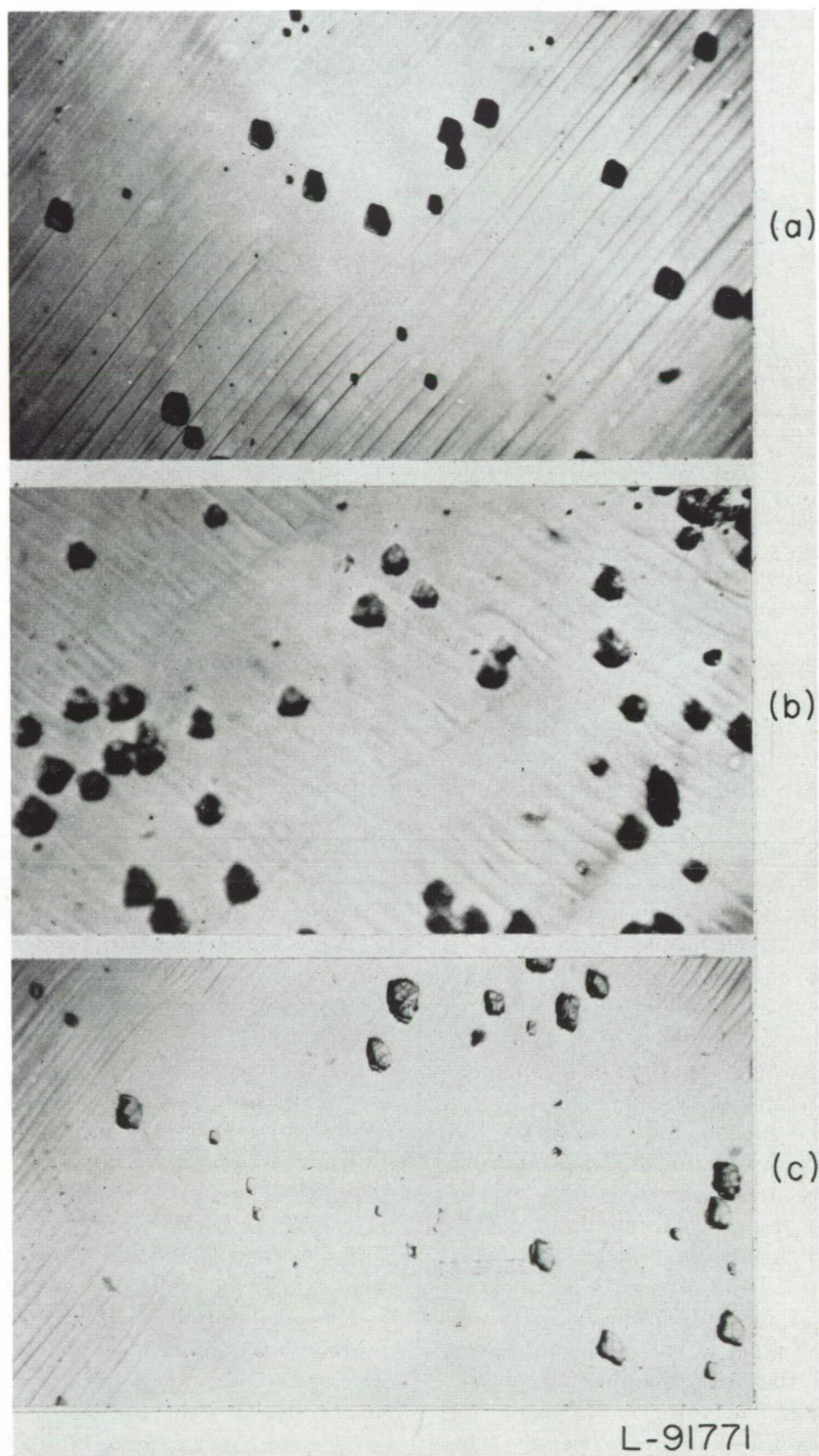
Several speculative viewpoints have been expressed on slip-band formation, considerable experimental work has been done, and conclusions have been drawn from this work. However, no complete physical explanation has been put forth to explain why slip bands form as they do. The propagation of slip in high-purity aluminum single crystals at room temperature has been observed and photographed with a moving-picture camera by Chen and Pond (ref. 54). However, Brown (refs. 30, 55, 56, and 57) probably has done the most work on this problem of slip-band formation. In reference 55 Brown states that he found that the average number of individual lines in a slip band after 15 percent deformation increased with temperature, while the spacing decreased. The slip distance on an individual slip line decreased only slightly with temperature and was approximately 2,000 Å at all temperatures from -180° to 500° C. In reference 30 Brown reports that the slip bands formed at room temperature were initially individual lines at low strains, and then the number of lines in a band increased as the strain was increased. He attempted to explain slip-band formation on the basis that slip took place in the regions of lowest hardness in the crystal and that a self-annealing process caused the hardness to be low in the region very close to the first and the subsequent slip lines in a slip band. This description must be considered weak, without any physical significance, until a physical picture of the self-annealing processes can be presented.

Recently, two suggestions for such a self-annealing process have been presented. Koehler (refs. 16 and 58) has suggested that the internal stresses resulting from thermal fluctuations can produce slip lamellae (individual lines) by allowing a screw dislocation to undergo cross slip and subsequent Frank-Read generation on a neighboring slip plane parallel to the initial locked lamella. This process would be dependent on the time involved in deformation, since longer times would allow more suitably large thermal fluctuations to

activate the process more times in the same slip band. As evidence for this time dependence, Koehler quoted Brown's results (ref. 30) that slip bands in aluminum strained rapidly at 450° C contained only 11 lamellae, whereas those formed in aluminum strained 1 percent per day at 450° C contained 50 lamellae.

The second suggestion for interpreting the structure of slip bands is based on a recovery model for the high-temperature creep process described by Sherby and Dorn (ref. 59). They have attributed the rate-controlling process to the recovery of barriers (to dislocation movement) by a self-diffusion process; that is, the barriers are reduced in strength, rather than being surmounted by thermally activated dislocations. At the temperatures at which diffusion is appreciable, it is also possible that a locked Frank-Read generator, such as the segment of an edge dislocation line in the slip plane, can climb perpendicular to the slip plane, by self-diffusion, to a neighboring plane, where it again can generate dislocations, resulting in another slip lamella in the slip band. This process would also be time dependent to the extent that specimens deformed in slow creep tests at high temperatures would be able to develop wide slip bands, whereas specimens deformed in relatively faster tensile tests would not have time to build up the large slip bands. These results are verified on a gross scale in figures 21 (d) and 21 (e). Details of the structure of the slip bands must be observed by electron microscopy. Regardless of the interpretation, the experimental results have shown that the structure of the slip bands at elevated temperature is dependent on the rate of straining. The relation is probably not simple but should be dependent on the recovery rate, which is a function of time, temperature, and possibly total strain.

Up to this point in the investigation, three mechanisms of creep, slip, kinking, and polygonization, have been observed. All three can be regarded as dislocation phenomena. They are probably all dependent on or interrelated to a recovery process involving either self-diffusion (ref. 59) or possibly the removal or redistribution of excess dislocations (ref. 60).



- (a) Crystal S-78; test, 400-psi resolved shear stress at 300°F; extension, 12.6 percent in 94 hours; typical kink band.
 (b) Crystal S-82; test, 450-psi resolved shear stress at 500°F; extension, 7.8 percent in 140 minutes; sharp kink bands.
 (c) Crystal S-51; test, 600-psi resolved shear stress at 500°F; extension, 15 percent in 1 minute; duplex slip in kink bands.

FIGURE 22.—Light micrographs of various types of kink bands observed on unshadowed Faxfilm replicas of deformed aluminum single crystals. 100X.

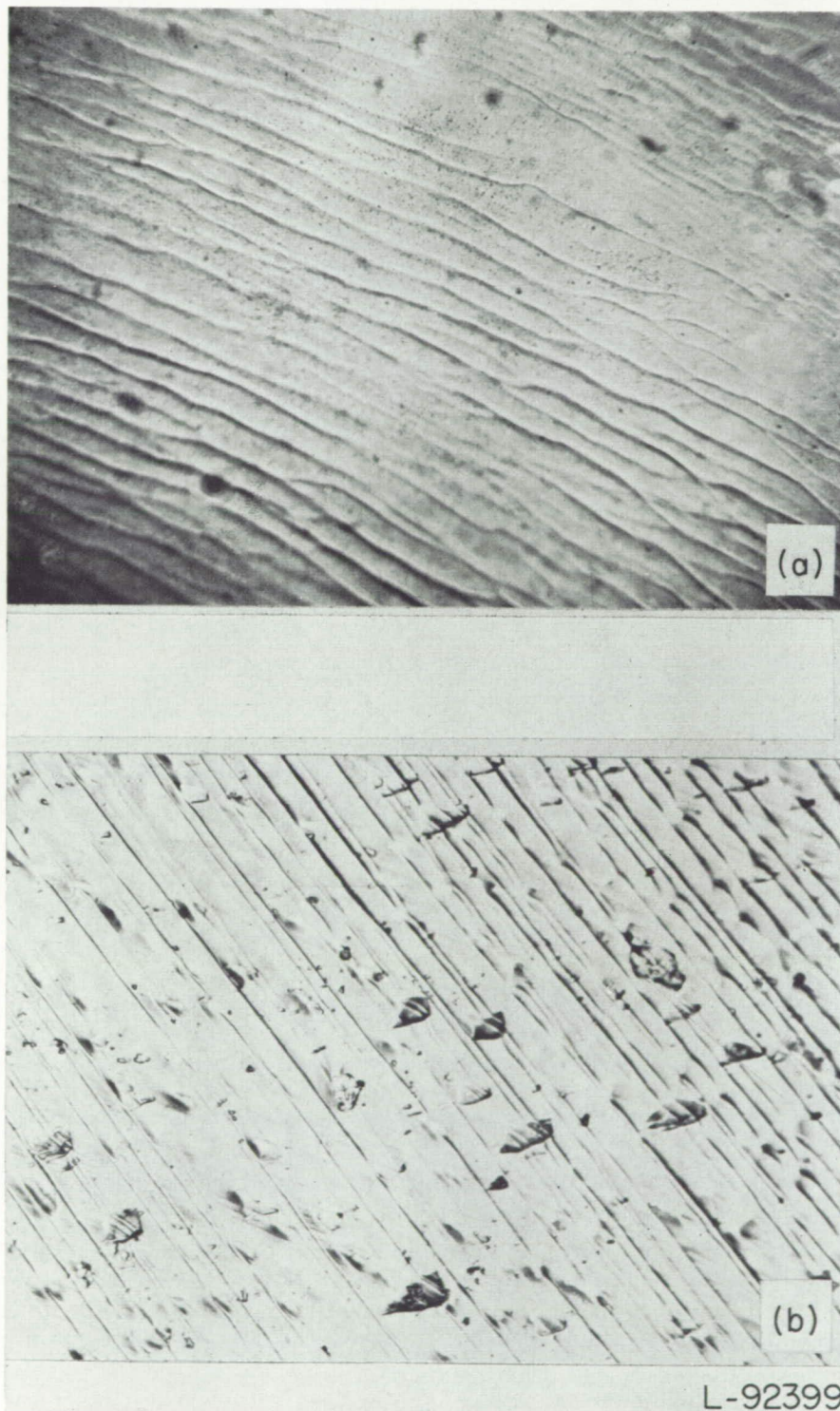
ELECTRON-MICROSCOPE OBSERVATIONS

The results of the electron-microscope work are presented in the form of 16 micrographs in figures 24, 25, 26, and 27. Light micrographs have already been shown in figure 23 from two of the crystals from which electron micrographs were made.

Figures 24 (a) and 24 (b) show the elementary slip-line structures in specimens with relatively low strain. These figures are not representative of most of the surface area of the specimen, since most of the area shows no strain markings at all. Areas with slip-line markings such as those in the figures are seen in only about 1 percent of the surface area

scanned. In figure 24 (a) the slip lines are nearly uniform, with the shear on each slip plane being about 400 Å. This is in agreement with the data of Kuhlmann-Wilsdorf and Wilsdorf (refs. 61 and 62) for the magnitude of the elementary structure which they observed covering the entire surface between slip bands at high strains at room temperature. As can be seen in figure 24 (a), even at low strain there is

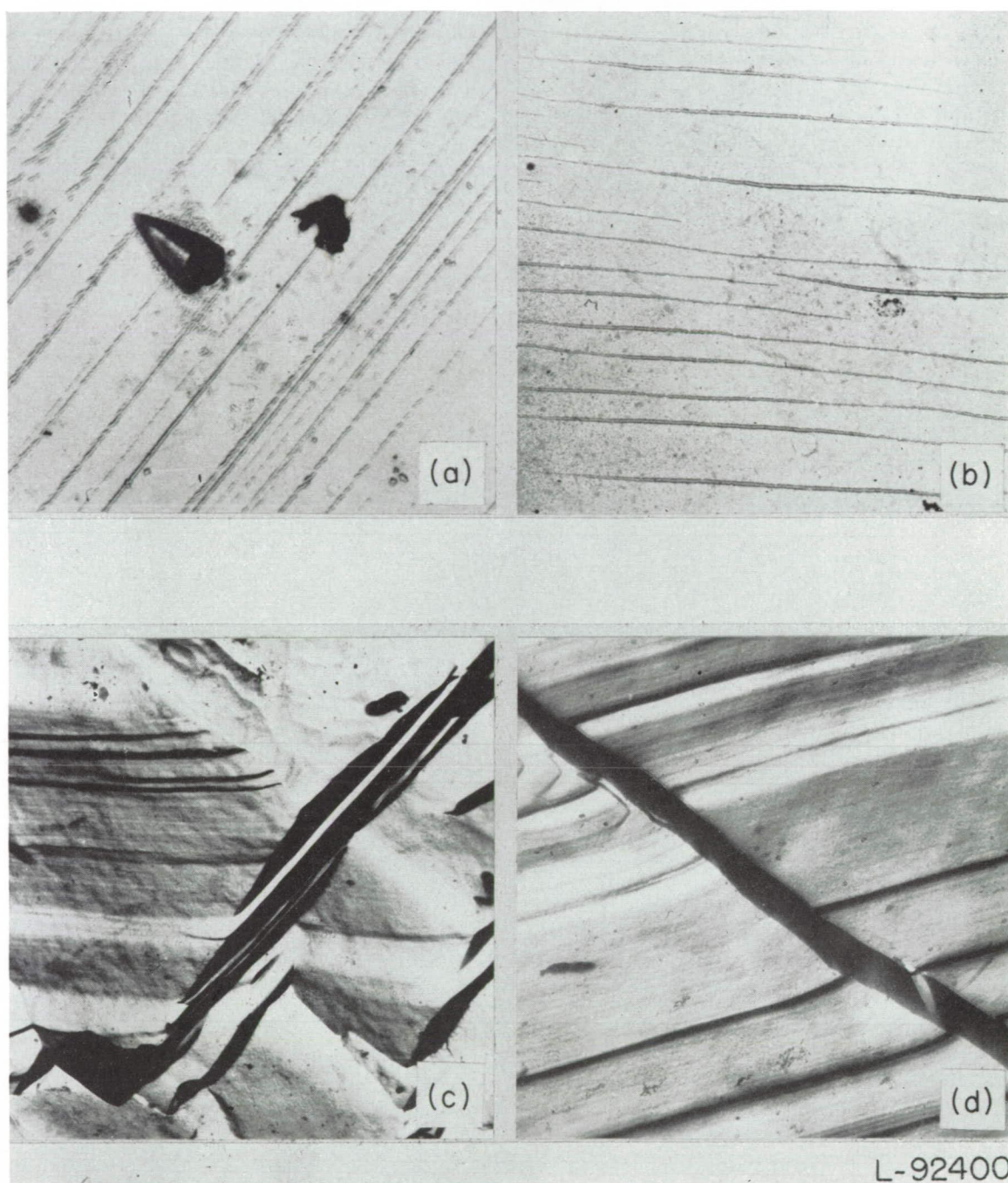
evidence of some duplex slip. It is not cross slip (i. e., slip on two planes in a common direction) because the slip directions are not the same in the two systems. This is consistent with the Kuhlmann-Wilsdorf hypothesis that aluminum contains many more possible Frank-Read sources (ref. 17) than can become active, because the dislocations from the different sources interfere strongly with each other's motion.



(a) Crystal S-2; 100X. (See fig. 26 for electron micrographs.)

(b) Crystal L-12; 250X. (See fig. 27 for electron micrographs.)

FIGURE 23.—Light micrographs of slip bands on deformed aluminum single crystals of two purities with chemically polished surfaces. Both micrographs are from unshadowed Faxfilm replicas.



- (a) Crystal P-181; test, 400-psi resolved shear stress at 82°F (10 minutes); extension, 0.90 percent; 13,500X.
 (b) Crystal P-175; test, tensile test at 400°F in vacuum; extension, 5 percent; 8,000X.
 (c) Test, bending at 82°F; deformation, heavily deformed; 3,500X.
 (d) Test, bending at 82°F; deformation, heavily deformed; 4,500X.

FIGURE 24.—Electron micrographs of aluminum-oxide replicas from electro-polished surfaces of deformed aluminum single crystals.

Therefore, the yield stress for duplex slip may not be appreciably greater than that for single slip, depending on the crystal orientation. The spacing and over-all distribution of the slip lines is not in agreement with the results of Kuhlmann-Wilsdorf and Wilsdorf. This may be due partly to the fact that their observations were made on polycrystalline, rather than single-crystal, specimens.

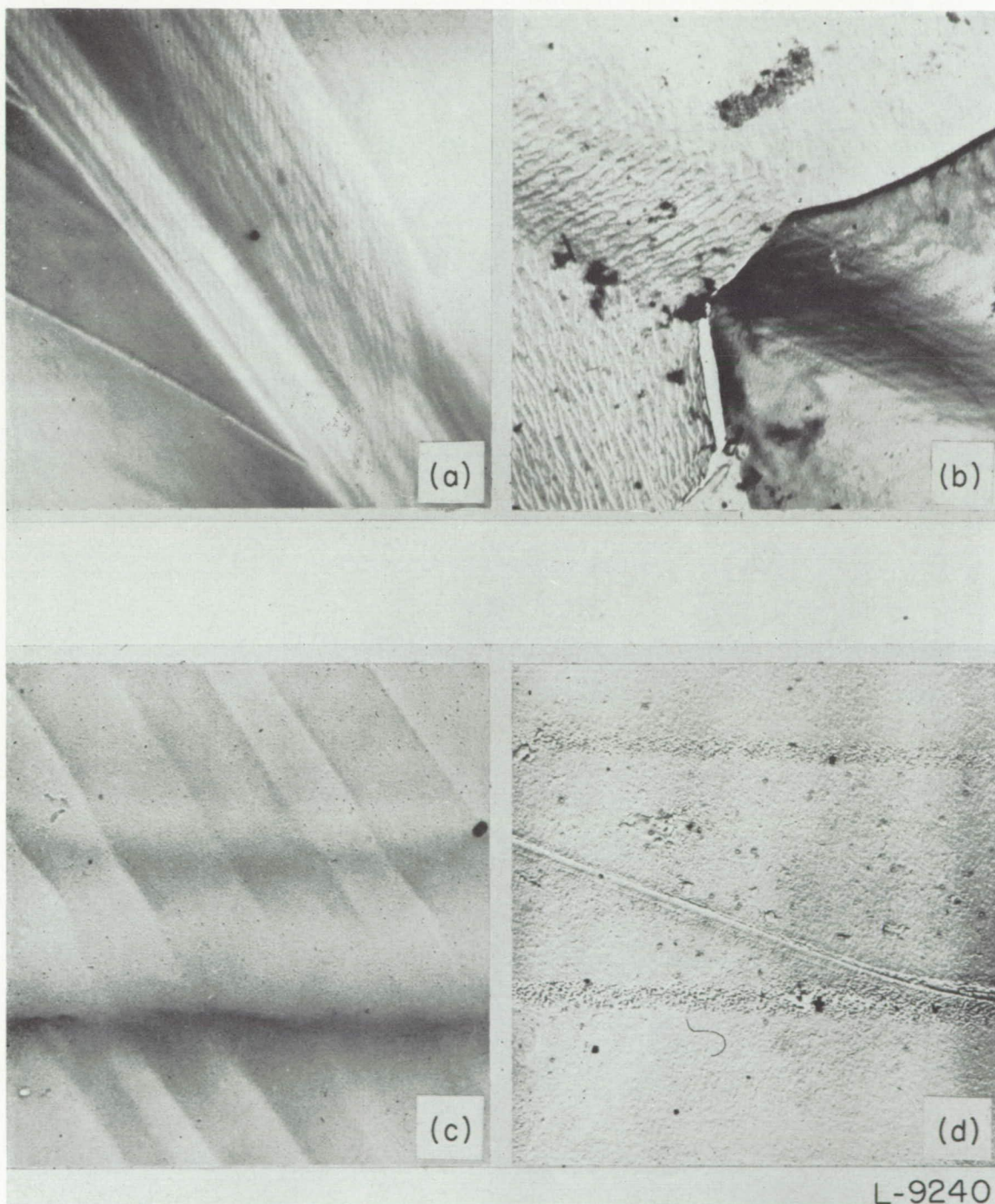
There is no evidence of the 400 Å elementary slip-line structure in any of the high-purity crystals deformed at elevated temperatures. The family of slip lines in figure 24 (b) appears to have been generated from Frank-Read

sources in the interior of the metal. In the widest portion of the slip lines the shear is probably between 1,500 Å and 2,000 Å. An accurate determination is difficult because there is no etch pit in the figure from which the orientation of the free surface can be calculated. The waviness of the slip lines at elevated temperatures is noticeable in figure 24 (b). This can be attributed to several causes. The first cause is curvature of the lattice. However, this does not seem likely at such a low strain. The second cause is bending of the replica, which might create the illusion of curved lines. In view of the irregularity of the waviness, this does not

appear to be likely. The most plausible explanation appears to be that these slip lines are not generated by a single Frank-Read source but by multiple sources on planes close together. It is entirely possible that a thinner replica, particularly a platinum replica, would disclose some fine structure in the wavy slip lines of figure 24 (b), which was made from an aluminum-oxide replica. It seems probable that the dynamics of slip-line or slip-band (multiple lines) formation at elevated temperatures are more complex than

the mechanisms based on Frank-Read sources and proposed by Fisher, Hart, and Pry (ref. 63) and other investigators.

The slip bands observed at low magnification after the deformation of high-purity aluminum at 500° F were also distinctly wavy, as shown in figure 23 (a). Kuhlmann-Wilsdorf and Wilsdorf have suggested that the special form of the slip bands (i. e., whether they are wavy or straight) is determined very early in the deformation process. This hypothesis, although interesting, is not very informative



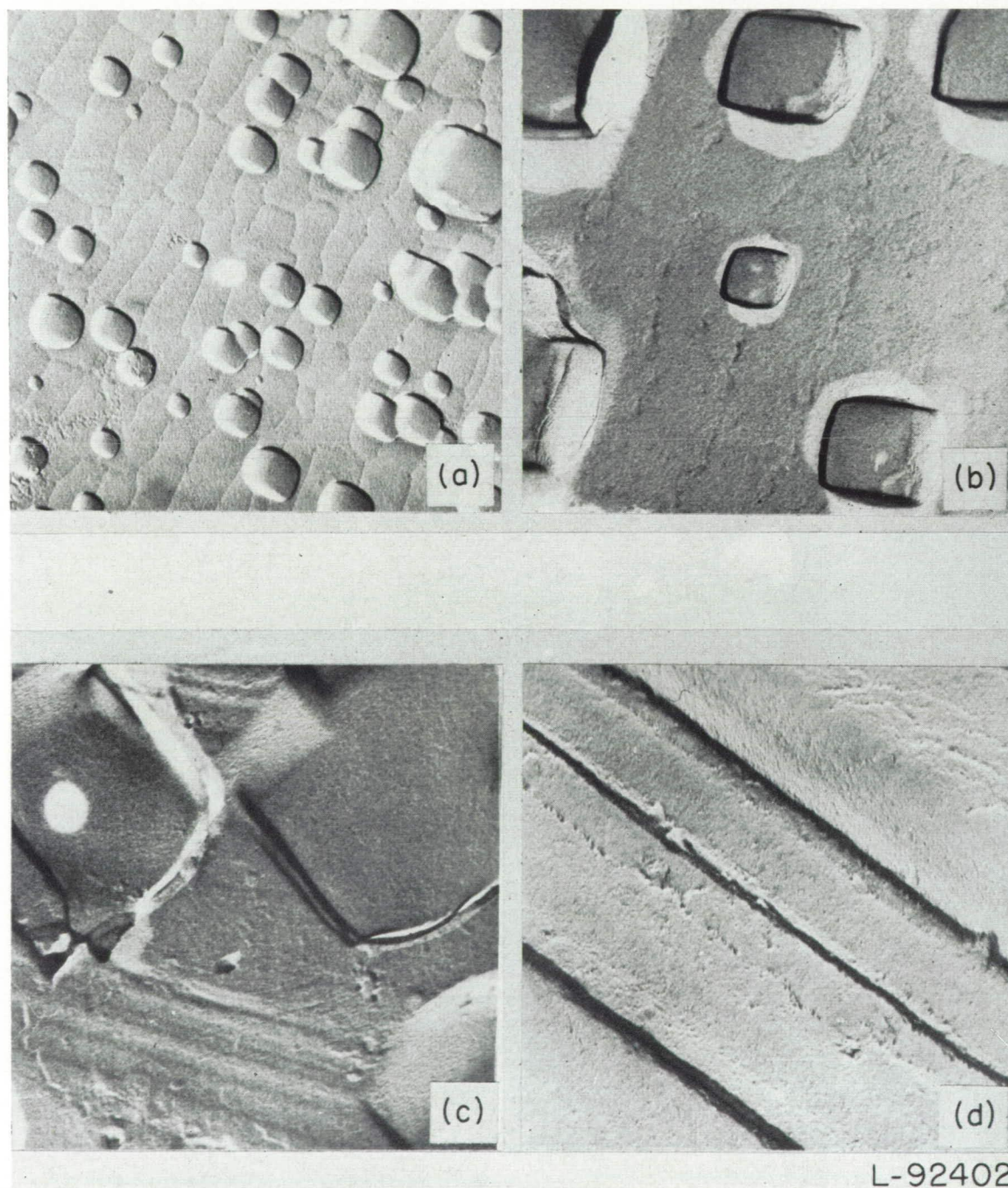
- (a) Crystal S-89 (unoriented); test, 800-psi tensile stress at 500°F in vacuum; extension, 11 percent in 19 hours; type replica, aluminum oxide; 7,500X.
 (b) Crystal S-56; test, constant load rate at 500°F with oil coating; extension, 22 percent in 16 minutes; type replica, aluminum oxide; 4,000X.
 (c) Crystal L-11; test, 970-psi resolved shear stress at 500°F in vacuum; extension, 12.4 percent in 17 hours; type replica, Formvar; 3,000X.
 (d) Crystal L-11; test, 970-psi resolved shear stress at 500°F in vacuum; extension, 12.4 percent in 17 hours; type replica, platinum; 4,000X.

FIGURE 25.—Electron micrographs of slip bands on various replicas from electro-polished surfaces of deformed aluminum single crystals.

with regard to the dynamics of the process. This hypothesis is apparently borne out for the most part in aluminum specimens that were heavily deformed at room temperature. The slip lines and slip bands in heavily deformed aluminum (deformed by bending) are straight, as shown by two examples in figures 24 (c) and 24 (d). The slip in the easily resolved slip lines (e. g., the group of three spaced quite close together and running from the bottom center diagonally up and to the right in fig. 24 (d)) exhibits a shear strain of 1,500 Å to 2,000 Å. However, there are evidently some

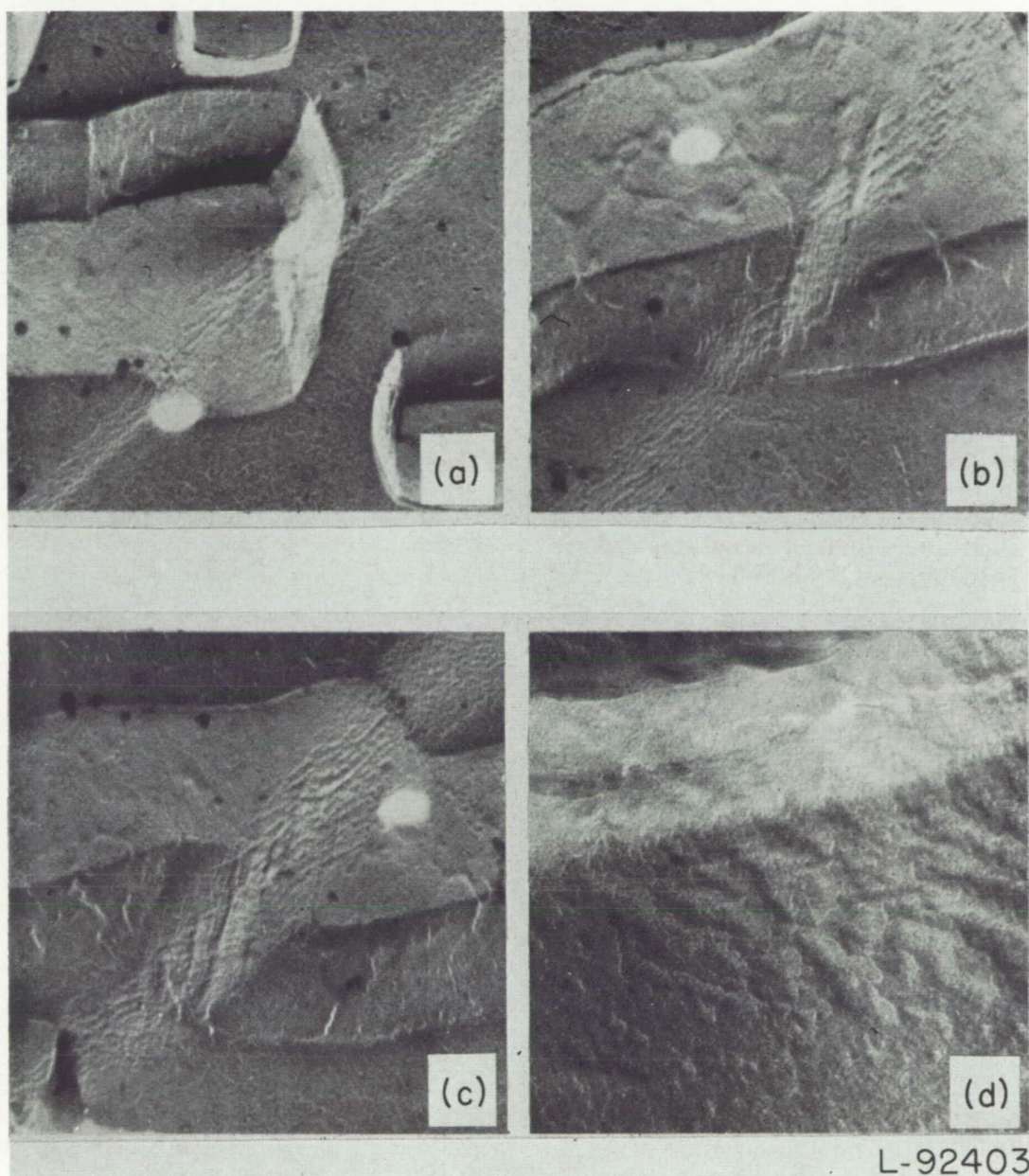
finer slip lines which are not resolvable at a magnification of 10,000X in these particular replicas. It appears from figures 24 (a), 24 (c), and 24 (d) that the shear along the slip plane in aluminum strained at room temperature varies from 400 Å to several thousand angstroms. This is in disagreement with Brown's result (ref. 57) that the shear is uniformly about 2,000 Å. It agrees with the observation of a considerable range in the shear on individual slip planes made by Kuhlmann-Wilsdorf and Wilsdorf (refs. 61 and 62).

Figures 25 (a), (25 (b), 26 (c), and 26 (d) show the surface



- (a) Crystal S-2; undeformed; surface, chemically polished and etched; 6,500X.
- (b) Crystal S-2; undeformed; surface, chemically polished and etched; 16,000X.
- (c) Crystal S-2; test, 400-psi resolved shear stress at 500°F with oil coating; extension, 9.3 percent in 1.5 hours; surface, chemically polished; 23,000X.
- (d) Crystal S-37; test, 50-psi resolved shear stress at 1,000°F in vacuum; extension, 12 percent in 1.4 hours; surface, electro-polished; 21,000X.

FIGURE 26.—Electron micrographs of platinum replicas of undeformed and deformed regions on aluminum single crystals.



- (a) 14,000X.
 (b) 14,000X.
 (c) 14,000X.
 (d) 50,000X.

FIGURE 27.—Electron micrographs of slip bands on a deformed aluminum single crystal with a chemically polished surface. Crystal L-12; test, constant load rate at 500°F with protective oil coating; extension, 14.4 percent in 19 minutes; type replica, platinum.

structures in high-purity aluminum crystals deformed at elevated temperature. All of the specimens strained at 500° F show evidence of duplex slip on different planes in varying degrees. This indicates, as previously mentioned, an excess of Frank-Read sources. The slip band in figure 26 (c) runs down and to the right. However, it should be mentioned that this structure was not typical of the surface. When the platinum replicas were examined under a vertical light microscope, slip bands were clearly visible. However, they almost always faded out when the objective lens current was turned on and the image enlarged and focused on the viewing screen. This is an indication that, when a high-purity aluminum crystal is deformed at elevated tempera-

tures, the slip is too fine to be visible in the electron microscope. The step heights are probably less than 200 Å. Only rarely was a band such as that one in figure 26 (c) visible at high magnification. Originally, the structure in figure 26 (c) was interpreted as a relatively fine slip on cubic planes (i. e., parallel to the side of the cubic etch pit in the lower right-hand corner) superimposed on a coarse slip on octahedral planes. However, in view of the fact that the slip bands are not generally visible at all in the electron microscope, this structure in figure 26 (c) can be construed probably better as a group of narrow sub-bands with octahedral slip too fine to be resolved superimposed on resolvable cube slip. In any event, the slip in most of the bands must

be fine slip because it was not generally visible in the electron microscope in replicas taken from high-purity crystals deformed in creep at elevated temperatures.

Bands in crystals deformed at 1,000° F sometimes appear straighter and narrower in the light microscope than bands in specimens strained at 500° F. The whole field in figure 26 (d) would appear to be single band in the light microscope at a magnification of 100X. The resolved shear stress at 1,000° F is only about one-eighth that required to give an equivalent creep curve at 500° F in the high-purity aluminum. Evidently slip on parallel planes may be easier than multiple slip at this temperature. This depends, in part, on the crystal orientation. However, more work is needed in the examination of band structures at high magnification as a function of both temperature and strain rate, as there are insufficient data available at present to test theories of slip-band formation.

Figure 27 shows micrographs of band structures in a lower purity aluminum crystal strained rapidly at 500° F. The bands in figures 27 (a), 27 (b), and 27 (c) run through etch pits. This band structure is quite complex. Apparently there are nearly equal slips on two sets of planes, giving a basket-weave structure. Which slip system appears more prominent depends on the orientation of the free surface. In some areas, such as in figure 27 (d), the surface becomes so rumpled that the pattern no longer appears to be crystallographic in nature. This can be attributed to a displacement of the slip lines by the lines of the second system. If there are more than two systems operating, or if the slip alternates on first one system and then the other, the pattern can become nearly unrecognizable as a slip-system pattern, particularly for certain orientations of the free surface.

In an investigation of deformed polycrystalline aluminum with both Formvar and aluminum-oxide replicas, Garrod, Suitor, and Wood (ref. 64) observed that wavy slip bands were typical at elevated temperatures but offered no explanation. Trotter (ref. 65) made the same observation on coarse-grained high-purity aluminum deformed at 200° C in creep. However, he attributed the wavy nature of the slip lines to the occurrence of intimate cross slip.

In the lower purity aluminum, the displacement per slip plane is about 500 Å, as compared with 2,000 Å for the primary slip system in high-purity aluminum. The bands are narrower and straighter in the lower purity aluminum, as can be seen in the light micrographs in figures 23 (a) and 23 (b). Also, in the lower purity aluminum, there is duplex slip between the bands, as shown in figure 23 (b) and in electron micrographs in figures 25 (c) and 25 (d). The indications are that there is still an excess of Frank-Read sources in the lower purity aluminum, so that most of the deformation takes place in the slip bands. However, the propagation of avalanches is hampered by the lattice defects around impurities, so that the strain per band is limited. If the strain is high enough, there is some cross slip between bands.

A subgrain structure in annealed polycrystalline aluminum was first noted by Robinson and Hunter (ref. 66) in electron micrographs from aluminum-oxide replicas of a chemically polished surface. This same structure has been revealed in figures 26 (a) and 26 (b) in platinum replicas from an unde-

formed aluminum single crystal. Although this crystal actually was deformed, the surface was prepared before the deformation, and these micrographs from undeformed sections of the crystal are characteristic of a crystal as grown by the strain-anneal method. Figure 26 (a) is probably the most striking of all the micrographs presented. All the smallest etch pits are located in subgrain or domain boundaries, whereas the somewhat larger ones are bisected by one of the boundaries. The facts that the boundaries are delineated by the chemical polish and that the etch pits originate in the boundaries indicate that these boundaries mark the sites of localized crystal imperfections of some sort. The most probable explanation is that they are the boundaries between small blocks slightly out of register. The continuous etching of the small boundaries might result from the elastically strained regions around the horizontal component of edge dislocations making up the straight boundaries. At higher magnification, such as in figure 26 (b), the boundaries do not always appear continuous.

The dimensions of these blocks range from about 3/4 micron to 3 microns, or of the order of 1 micron. This range of size is particularly difficult to detect, since the particles are too small to yield individual X-ray reflections in anything but the best of microbeam techniques, and they are too large to cause X-ray line broadening. This mosaic structure has been predicted in the theory of imperfect crystals (ref. 67), and there is reason to believe that all metals are made up of such a characteristic structure. This small substructure undoubtedly plays a large part in determining the mechanical properties of metals. Wyon and Crussard (ref. 68) and Parker and coworkers (ref. 34) have carried out experiments indicating that the boundaries of a fine substructure, at least at low strains, will act as barriers to deformation. How this fine substructure detected in this investigation varies with annealing procedure remains to be seen.

The presence of this mosaic structure in a supposedly single crystal brings up the question of the distribution of dislocations in the annealed crystal. According to the dislocation model of a grain boundary, nearly all of the dislocations could be concentrated in the boundaries. Vogel, Pfann, and Corey (ref. 69) have observed etch pits in a low-angle boundary between two subgrains in germanium. They found that the etch pits developed at regular intervals along the boundary, the spacing being related to the observed difference in orientations of the two subgrains. Therefore, they concluded that the etch pits started at the intersection of the line of the edge dislocations in the boundary with the surface. More recently, Amelinckz (ref. 70) has found that etch pits developed on slightly deformed aluminum along the slip lines, along grain boundaries, and randomly. From the results of this investigation, the classification of "randomly," in all probability, refers to the etch pits formed at small subgrain or mosaic boundaries, as shown in figure 26 (a).

At first sight, the hypothesis that all the dislocations are concentrated in the boundaries does not appear to be consistent with the presence of the elementary slip-line structure, as detected by Kuhlmann-Wilsdorf and Wilsdorf (refs.

61 and 62). They observed fine slip in aluminum with an average displacement of 300 Å to 400 Å per plane, with the lines spaced at approximately 400 Å. However, when it is considered that the structure observed in figure 26 (a) represents only the top layer and that there are many more layers below this one in offset positions, it is easy to see how the elementary lines can be so closely spaced, even if the dislocations and, hence, the Frank-Read sources are in these small boundaries, rather than inside the mosaic blocks. Again, regardless of the interpretation, any theory of slip-line formation must take into account the presence and the effect of this fine structure in the annealed crystals.

Some suggestions have been made in this section about future work. Basic to the theory of creep is the theory of slip-band formation. The electron microscope is probably the best single instrument for examination of slip bands. Improved surface-preparation and replica techniques enhance the value of this instrument. It probably would be advisable to use only high-purity aluminum in a fundamental study of slip-band formation. Crystals strained at various temperatures over a wide range of temperatures and with varying degrees of strain and strain rate would have to be examined. It probably would be profitable to examine the structure of a chemically polished surface after a low strain to see whether any relationship exists between the slip lines and the fine substructure, which indicates a definite ordering of at least one type of crystal imperfection.

SUMMARY OF RESULTS

The results of a study of plastic deformation of aluminum single crystals over a wide range of temperatures may be summarized as follows:

1. The effects of impurity content and temperature on the plastic properties of single crystals of aluminum have been observed in stress-strain curves determined by constant-load-rate tests at 82°, 500°, and 1,100° F on specimens of two purities.
2. The creep characteristics of high-purity aluminum single crystals have been determined for various stresses in the temperature range from 400° to 900° F under the condition of a constant resolved shear stress. No empirical relation has been obtained which could describe the creep data over the range of the variables investigated, presumably because of the differing kinetics of the mechanisms of deformation that have been observed.
3. The increased creep resistance provided by small amounts of prior strain was found to be determined by the details, such as temperature, strain rate, and amount of the prestrain.
4. The results of high-resolution X-ray techniques used to detect and to follow the internal strain throughout the various stages of a prestrain experiment showed the crystal-line lattice to break up by a two-stage process involving plastic bending and subsequent polygonization.
5. At temperatures of about 300° F and above the operative slip plane could be a (311), a (110), a (100), or a (211) plane. The operative plane was the plane in the system on which the resolved shear stress was the highest, assuming that the slip direction was a [110] direction in all cases.

6. The details of kinking and slip-band formation in plastic deformation of single crystals of aluminum have been observed and recorded in light micrographs. Kink bands always form along planes to which the slip direction is normal. The formation of gross slip bands at elevated temperature appeared to be a function of the rate of strain.

7. A fine substructure, disclosed by means of a chemical polish, has been detected in annealed single crystals of high-purity aluminum. This structure has linear dimensions of the order of 1 micron.

8. Etch pits have been observed to originate in the boundaries between these small domains.

9. On crystals deformed at room temperature, shear displacements from 400 Å to a few thousand angstroms have been observed on individual slip planes, or at least on fine slip bands which cannot be resolved at a magnification of 10,000X.

10. The amount of shear displacement per slip band has been observed to be considerably less in the lower purity specimens than in the high-purity specimens deformed to a comparable strain at the same elevated temperature.

11. Duplex slip has been observed within the band structure in specimens of both purities.

12. Duplex slip between the slip bands was much more apparent in the lower purity specimens in both the electron and the light micrographs.

13. The three mechanisms of plastic deformation by creep, slip, kinking, and polygonization that have been detected can all be interpreted as dislocation phenomena.

BATTELLE MEMORIAL INSTITUTE,
COLUMBUS, OHIO, *December 29, 1953.*

REFERENCES

1. Schwöpe, A. D., and Jackson, L. R.: A Survey of Creep in Metals. NACA TN 2516, 1951.
2. Schwöpe, A. D., Shober, F. R., and Jackson, L. R.: Creep in Metals. NACA TN 2618, 1952.
3. Johnson, R. D., Shober, F. R., and Schwöpe, A. D.: The Creep of Single Crystals of Aluminum. NACA TN 2945, 1953.
4. Cottrell, A. H., and Aytakin, V.: The Flow of Zinc Under Constant Stress. *The Jour. Inst. Metals*, vol. 77, 1950, pp. 389-423.
5. Honeycombe, R. W. K.: A Simple Method of X-Ray Microscopy and Its Application to the Study of Deformed Metals. *The Jour. Inst. Metals*, vol. 80, pt. 1, Sept. 1951, pp. 39-44.
6. Keller, F.: Electron Microscopy of Light Metal Alloys. Symposium on Metallurgical Applications of the Electron Microscope, *Inst. Metals (London)*, 1950, pp. 85-96.
7. Heidenreich, R. D., and Schockley, W.: Study of Slip in Aluminum Crystals by Electron Microscope and Electron Diffraction Methods. *Conf. on Strength of Solids, Phys. Soc. (London)*, 1948, pp. 57-75.
8. Schwartz, C. M., Austin, A. E., and Weber, P. M.: A Positive-Replica Technique for Electron Microscopy. *Jour. Appl. Phys.*, vol. 20, no. 2, Feb. 1949, pp. 202-205.
9. Austin, A. E., and Schwartz, C. M.: Modification of a Positive-Replica Technique for Electron Microscopy. *Jour. Appl. Phys.*, vol. 22, no. 6, June 1951, pp. 847-848.
10. Hunter, M. S., and Keller, F.: Techniques Used in Electron Microscopy of Aluminum Alloys. Symposium on Techniques for Electron Metallography, A. S. T. M., 1954, pp. 3-14.
11. Boas, W., and Schmid, E.: Über die Temperaturabhängigkeit der Kristallplastizität. *Zs. Phys.*, Bd. 71, 1931, pp. 703-714.

12. Schmid, E., and Boas, W.: Plasticity of Crystals With Special Reference to Metals. F. A. Hughes and Co., Ltd. (London). 1950, pp. 58-59. (A translation.)
13. Cottrell, A. H.: Effect of Solute Atoms on the Behavior of Dislocations. Conf. on Strength of Solids, Phys. Soc. (London), 1948, pp. 30-38.
14. Taylor, G. I.: The Mechanism of Plastic Deformation of Crystals. Proc. Roy. Soc. (London), ser. A, vol. 145, no. 855, July 2, 1934, pp. 362-404.
15. Koehler, J. S.: On Dislocation Theory and the Physical Changes Produced by Plastic Deformation. Am. Jour. Phys., vol. 10, no. 6, Dec. 1942, pp. 275-285.
16. Koehler, J. S.: The Nature of Work-Hardening. Phys. Rev., vol. 86, no. 1, Apr. 1, 1952, pp. 52-59.
17. Frank, F. C., and Read, W. T., Jr.: Multiplication Processes for Slow-Moving Dislocations. Phys. Rev., second ser., vol. 79, no. 4, Aug. 15, 1950, pp. 722-723.
18. Cottrell, A. H.: The Yield Point in Single Crystal and Polycrystalline Metals. Symposium on the Plastic Deformation of Crystalline Solids, Carnegie Inst. Tech. and Office of Naval Res., NAVEXOS-P-834, May 19-20, 1950, pp. 60-76.
19. Hazlett, Thomas H., and Parker, Earl R.: Nature of the Creep Curve. Jour. Metals, vol. 5, no. 2, sec. 2 (Trans. Supp.), Feb. 1953, pp. 318-323. (See also Discussion by C. S. Roberts and N. J. Grant, Jour. Metals, vol. 5, no. 11, sec. 2 (Trans.), Nov. 1953, pp. 1577-1579.)
20. Bhattacharya, S., Congreve, W. K. A., and Thompson, F. C.: The Creep/Time Relationship Under Constant Tensile Stress. The Jour. Inst. Metals, vol. 81, pt. 2, Oct. 1952, pp. 83-92.
21. Andrade, E. N. daC.: On the Viscous Flow in Metals and Allied Phenomena. Proc. Roy. Soc. (London), ser. A, vol. 84, no. 567, June 9, 1910, pp. 1-12.
22. Roberts, C. S.: Creep Behavior of Extruded Electrolytic Magnesium. Jour. Metals, vol. 5, no. 9, Sept. 1953, pp. 1121-1126.
23. Wyatt, O. H.: Transient Creep in Pure Metals. Proc. Phys. Soc. (London), ser. B, vol. 66, no. 402, pt. 6, June 1, 1953, pp. 459-480.
24. Cottrell, A. H.: The Time Laws of Creep. Jour. Mech. and Phys. of Solids, vol. 1, no. 1, Oct. 1952, pp. 56-63.
25. Sherby, O. D., and Dorn, J. E.: Creep Correlations in Alpha Solid Solutions of Aluminum. Jour. Metals, vol. 4, no. 9, Sept. 1952, pp. 959-964.
26. Johnson, A. E., and Frost, N. E.: Rheology of Metals at Elevated Temperatures. Jour. Mech. and Phys. of Solids, vol. 1, no. 1, Oct. 1952, pp. 37-52.
27. Johnson, A. E., and Frost, N. E.: The Temperature Dependence of Transient and Secondary Creep of an Aluminum Alloy to British Standard 2L42 at Temperatures Between 20° and 250° C and at Constant Stress. The Jour. Inst. Metals, vol. 81, pt. 2, Oct. 1952, pp. 93-107.
28. Chang, H. C., and Grant, N. J.: Inhomogeneity in Creep Deformation of Coarse Grained High Purity Aluminum. Jour. Metals, vol. 5, no. 9, sec. 2 (Trans.), Sept. 1953, pp. 1175-1180.
29. Kennedy, A. J.: The Effect of Instantaneous Pre-Strain on the Character of Creep in Lead Polycrystals. Proc. Phys. Soc. (London), ser. B, vol. 62, no. 356, pt. 8, Aug. 1, 1949, pp. 501-508.
30. Brown, A. F.: Slip Bands and Hardening Processes in Aluminum. The Jour. Inst. Metals, vol. 80, pt. 3, Nov. 1951, pp. 115-125.
31. Rosi, F. D., and Mathewson, C. H.: A Study of the Plastic Behavior of High-Purity Aluminum Single Crystals at Various Temperatures. Jour. Metals, vol. 188, no. 9, Sept. 1950, pp. 1159-1167.
32. Ellis, W. C., and Greiner, E. S.: The Effect of Prior Strain at Low Temperatures on the Properties of Some Close-Packed Metals at Room Temperature. Jour. Metals, vol. 4, no. 6, June 1952, pp. 648-650.
33. Mott, N. F.: A Theory of Work-Hardening of Metals, II. Flow Without Slip-Lines, Recovery, and Creep. Phil. Mag., ser. 7, vol. 44, no. 354, July 1953, pp. 742-765.
34. Li, Choh Hsien, Washburn, J., and Parker, Earl R.: Variation of Plastic Properties With Annealing Procedure in Zinc Single Crystals. Jour. Metals, vol. 5, no. 9, sec. 2 (Trans.), Sept. 1953, pp. 1223-1225.
35. Wood, W. A.: The Lower Limiting Crystallite Structure Size and Internal Strains in Some Cold-Worked Metals. Proc. Roy. Soc. (London), ser. A, vol. 172, no. 949, Aug. 3, 1949, pp. 231-241.
36. Wilms, G. R., and Wood, W. A.: Mechanism of Creep in Metals. The Jour. Inst. Metals, vol. 75, pt. 8, Apr. 1949, pp. 693-706.
37. Wood, W. A., and Rachinger, W. A.: The Mechanism of Deformation in Metals, With Special Reference to Creep. The Jour. Inst. Metals, vol. 65, pt. 3, Nov. 1949, pp. 237-253.
38. Wood, W. A., and Scrutton, R. F.: Mechanism of Primary Creep in Metals. The Jour. Inst. Metals, vol. 77, pt. 5, Jan. 1950, pp. 423-434.
39. Wood, W. A., Wilms, G. R., and Rachinger, W. A.: Three Basic Stages in the Mechanism of Deformation of Metals at Different Temperatures and Strain Rates. The Jour. Inst. Metals, vol. 79, pt. 3, May 1951, pp. 159-172.
40. Cahn, R. W.: Recrystallization of Single Crystals After Plastic Bending. The Jour. Inst. Metals, vol. 76, pt. 2, Oct. 1949, pp. 121-143.
41. Cahn, R. W.: Slip and Polygonization in Aluminum. The Jour. Inst. Metals, vol. 79, pt. 3, May 1951, pp. 129-158.
42. Greenough, G. B., and Smith, E. M.: The Mechanism of Creep as Revealed by X-Ray Methods. The Jour. Inst. Metals, vol. 77, pt. 5, Jan. 1950, pp. 435-445.
43. Greenough, G. B., Bateman, C. M., and Smith, E. M.: X-Ray Diffraction Studies in Relation to Creep. The Jour. Inst. Metals, vol. 80, pt. 10, June 1952, pp. 545-550.
44. Servi, I. S., Norton, J. T., and Grant, N. J.: Some Observations of Subgrain Formation During Creep in High-Purity Aluminum. Jour. Metals, vol. 4, no. 9, Sept. 1952, pp. 965-971.
45. Gervais, Andre M., Norton, John T., and Grant, Nicholas J.: Subgrain Formation in High-Purity Aluminum During Creep at High Temperatures. Jour. Metals, vol. 5, no. 9, sec. 2 (Trans.), Sept. 1953, pp. 1166-1174.
46. McLean, D.: Creep Processes in Coarse-Grained Aluminum. The Jour. Inst. Metals, vol. 80, pt. 9, May 1952, pp. 507-519.
47. McLean, D.: Crystal Fragmentation in Aluminum During Creep. The Jour. Inst. Metals, vol. 81, pt. 6, Feb. 1953, pp. 287-292.
48. McLean, D.: Grain-Boundary Slip During Creep of Aluminum. The Jour. Inst. Metals, vol. 81, pt. 6, Feb. 1953, pp. 293-300.
49. Chalmers, B., and Martius, U. M.: Slip Planes and the Energy of Dislocations. Proc. Roy. Soc. (London), ser. A, vol. 213, no. 1113, June 24, 1952, pp. 175-185.
50. Boas, W., and Schmid, E.: Über die Temperaturabhängigkeit der Kristallplastizität. (The Dependence of Crystal Plasticity on Temperature). III—Aluminum. Zs. Phys., Bd. 71, Heft 11-12, 1931, pp. 703-714.
51. Washburn, J., and Parker, E. R.: Kinking in Zinc Single-Crystal Tension Specimens. Jour. Metals, vol. 4, No. 10, Oct. 1952, pp. 1076-1078.
52. Chen, N. K., and Mathewson, C. H.: Structural Studies of Plastic Deformation in Aluminum Single Crystals. Jour. Metals, vol. 3, no. 8, Aug. 1951, pp. 653-660.
53. Gervais, A. M., Norton, J. T., and Grant, N. J.: Kink Band Formation in High-Purity Aluminum During Creep at High Temperature. Jour. Metals, vol. 5, no. 11, sec. 2 (Trans.), Nov. 1953, pp. 1487-1492.
54. Chen, N. K., and Pond, R. B.: Dynamic Formation of Slip Bands in Aluminum. Jour. Metals, vol. 4, no. 10, Oct. 1952, pp. 1085-1092.
55. Brown, A. F.: Fine Structure of Slip Zones in Aluminum. Nature, vol. 163, no. 4155, June 18, 1949, pp. 961-962.
56. Brown, A. F., and Honeycombe, R. W. K.: Micro-Slip in Metal Crystals. Phil. Mag., vol. 42, no. 333, Oct. 1951, pp. 1146-1149.
57. Brown, A. F.: Surface Effects in Plastic Deformation of Metals. Advances in Phys., vol. 1, no. 4, Oct. 1952, pp. 427-479.

58. Koehler, J. S.: Theory of Initial Stress-Strain Curves in Face-Centered Metals. *Acta Metallurgica*, vol. 1, no. 3, May 1953, p. 377.
59. Sherby, O. D., and Dorn, J. E.: A Recovery Model for the High Temperature Creep Process. Tech. Rep. 30, Ser. No. 22, Contract N7-onr-295, Task Order II, Project NR-031-048, Office of Naval Res. and Inst. Eng. Res., Univ. of Calif., Aug. 15, 1953.
60. Drouard, R., Washburn, J., and Parker, Earl R.: Recovery in Single Crystals of Zinc. *Jour. Metals*, vol. 5, no. 9, sec. 2 (Trans.), Sept. 1953, pp. 1226-1229.
61. Kuhlmann-Wilsdorf, D., Van der Merwe, J. H., and Wilsdorf, H.: Elementary Structure and Slip-Band Formation in Aluminum. *Phil. Mag.*, vol. 43, no. 341, June 1952, pp. 632-643.
62. Kuhlmann-Wilsdorf, Doris, and Wilsdorf, Heinz: The Surface Structures of Deformed Aluminum, Copper, Silver, and Alpha-Brass, and Their Theoretical Interpretation. *Acta Metallurgica*, vol. 1, no. 4, July 1953, pp. 394-413.
63. Fisher, J. C., Hart, E. W., and Pry, R. H.: Theory of Slip-Band Formation. *Phys. Rev.*, second ser., vol. 87, no. 6, Sept. 15, 1952, pp. 958-961.
64. Garrod, R. I., Suiter, J. W., and Wood, W. A.: An Electron-Microscope Study of the Effect of Temperature and Strain-Rate on the Mechanism of Deformation of Aluminum. *Phil. Mag.*, vol. 43, no. 341, June 1952, pp. 677-685.
65. Trotter, J.: Electron-Microscope Studies of Slip in Aluminum During Creep. *The Jour. Inst. Metals*, vol. 80, pt. 9, May 1952, pp. 521-523.
66. Hunter, M. S., and Robinson, D. L.: Revealing the Subgrain Structure of Aluminum. *Jour. Metals*, vol. 5, no. 5, sec. 2 (Trans. Supp.), May 1953, pp. 717-722.
67. Zachariasen, W. H.: Theory of X-Ray Diffraction in Crystals. John Wiley & Sons, Inc., 1945. p. 161.
68. Wyon, G., and Crussard, C.: Alterations of the Structure of Aluminum During Creep. *Rev. métallurgie*, vol. 48, pt. 2, Feb. 1951, pp. 121-130. (Translated by R. F. Flint, Fulmer Res. Inst., Ltd., Trans. No. 17.)
69. Vogel, F. L., Pfann, W. G., Corey, H. E., and Thomas, E. E.: Observations of Dislocations in Lineage Boundaries in Germanium. *Phys. Rev.*, second ser., vol. 90, no. 3, May 1, 1953, pp. 489-490.
70. Amelinckz, S.: Slip Lines and Etch Pits. *Phil. Mag.*, vol. 44, ser. 7., no. 356, Sept. 1953, pp. 1048-1049.

REPORT 1268

THEORETICAL CALCULATIONS OF THE PRESSURES, FORCES, AND MOMENTS AT SUPERSONIC SPEEDS DUE TO VARIOUS LATERAL MOTIONS ACTING ON THIN ISOLATED VERTICAL TAILS¹

By KENNETH MARGOLIS and PERCY J. BOBBITT

SUMMARY

Velocity potentials, pressure distributions, and stability derivatives are derived by use of supersonic linearized theory for families of thin isolated vertical tails performing steady rolling, steady yawing, and constant-lateral-acceleration motions. Vertical-tail families (half-delta and rectangular plan forms) are considered for a broad Mach number range. Also considered are the vertical tail with arbitrary sweepback and taper ratio at Mach numbers for which both the leading edge and trailing edge of the tail are supersonic and the triangular vertical tail with a subsonic leading edge and a supersonic trailing edge. For purposes of completeness, analogous expressions and derivatives for sideslip motion obtained primarily from other sources are included.

Expressions for potentials, pressures, and stability derivatives are tabulated. Curves which determine the stability derivatives for half-delta and rectangular tails are presented which enable rapid estimation of their values for given values of aspect ratio and Mach number. In order to indicate the importance of end-plate effects, several comparisons are shown of the derived results (based on a zero-end-plate analysis) with those corresponding to a complete-end-plate analysis.

INTRODUCTION

Detailed knowledge of the loading, forces, and moments acting on vertical tails undergoing various maneuvers is a necessary prerequisite for determining the lateral dynamic behavior of aircraft. The information presently available is, in many instances, insufficient to enable reliable estimates to be made of the vertical-tail contributions to airplane stability at supersonic speeds. Aside from calculations for several "slender" configurations, theoretical results to date have been concerned, for the most part, with tail configurations either subject to a constant sideslip attitude or performing a steady rolling motion (see refs. 1 to 13).

For the sideslip motion, the effects of Mach number and aspect ratio on the aerodynamic loads of a number of tail configurations with both one and two planes of cross-sectional symmetry have already been investigated extensively. The same effects on tail arrangements in a rolling motion

have also received considerable attention which has mainly been directed toward tails with two planes of symmetry such as cruciform arrangements. Additional theoretical analysis devoted to the evaluation of the Mach number and aspect-ratio effects on the forces and moments acting on tail systems in roll with one plane of cross-sectional symmetry is required. Tail arrangements performing a steady yawing motion or a constant-lateral-acceleration motion have received little attention to date in the literature. Yet the forces and moments produced by these motions are by no means negligible, and some indication of their magnitudes is necessary, particularly at supersonic speeds, in order to evaluate their relative importance on lateral stability.

The primary purpose of this report is to present the results of a theoretical investigation to determine at supersonic speeds the pressures, forces, and moments acting on several families of thin isolated vertical tails subject to various lateral disturbances. Three motions are treated: steady rolling, steady yawing, and constant lateral acceleration. A fourth motion, namely, constant sideslip, although analyzed previously, is included for purposes of completeness. The basic plan forms considered are: (a) half-delta tail with either a subsonic or supersonic leading edge, (b) rectangular tail, (c) general sweptback tail of arbitrary taper ratio with supersonic leading and trailing edges, and (d) triangular tail with a subsonic leading edge and a supersonic trailing edge. The half-delta and rectangular vertical tails are analyzed in detail in that forces and moments (expressed in the form of stability derivatives) and their variations with Mach number and aspect ratio are presented in a series of simple charts. Useful expressions and formulas are included for the other plan forms which enable similar calculations to be carried out.

A secondary objective, in view of the geometric nonplanar characteristics of tail arrangements, is to consider the estimation of the mutual aerodynamic interference that exists between the vertical and horizontal tails. In order to gain some insight into the possible effects of such interference, several of the derived results are compared with corresponding calculations based on a complete-end-plate analysis. (A complete-end-plate analysis implies that the horizontal tail acts as a perfect reflection plane.)

¹Supersedes NACA Technical Notes 3373 by Kenneth Margolis, 1955, and 3240 by Percy J. Bobbitt, 1954.

SYMBOLS

x, y, z	rectangular coordinates used in analysis (see fig. 2(a))	$K'(k)$	complete elliptic integral of first kind with modulus $\sqrt{1-k^2}$, $\int_0^{\pi/2} \frac{dn}{\sqrt{1-(1-k^2)\sin^2 n}}$
$\theta = z/x$		$\tau, \omega, \bar{\omega}$	arbitrary constants ($\bar{\omega} = \omega B m$)
ξ, ζ	rectangular coordinates of doublet	τ_p'	$-\frac{\sqrt{1+k^2}[k^2(1+k^2)K'(k) + (1-4k^2+k^4)E'(k)]}{(2-k^2)(1-2k^2)E'(k)^2 + k^2(1+k^2)K'(k)E'(k) - k^4K'(k)^2}$
$\sigma = \zeta/\xi$		ω_p'	$-\frac{(1+k^2)^{3/2}[(1+k^2)E'(k) - 2k^2K'(k)]}{2[(2-k^2)(1-2k^2)E'(k)^2 + k^2(1+k^2)K'(k)E'(k) - k^4K'(k)^2]}$
x_0, z_0	longitudinal and vertical distances, respectively, that origin is displaced relative to tail apex (see fig. 2(c))	τ_r'	$-\frac{k\sqrt{1+k^2}[(1+k^2)E'(k) - 2k^2K'(k)]}{(2-k^2)(1-2k^2)E'(k)^2 + k^2(1+k^2)K'(k)E'(k) - k^4K'(k)^2}$
u, v	perturbation velocities in x - and y -directions, respectively	ω_r'	$\frac{(1+k^2)^{3/2}[2(1-k^2+k^4)E'(k) - k^2(1+k^2)K'(k)]}{2k[(2-k^2)(1-2k^2)E'(k)^2 + k^2(1+k^2)K'(k)E'(k) - k^4K'(k)^2]}$
V	free-stream or flight velocity (see fig. 2)	ϵ	infinitesimally small quantity
M	Mach number, $V/\text{Speed of sound}$	γ	$\frac{x - B^2 z \sigma}{\sqrt{1-B^2 \sigma^2} \sqrt{x^2 - B^2(y^2 + z^2)}}$
$B = \sqrt{M^2 - 1}$		γ_0	expression for γ indicated at $y=0$, $\frac{1 - B^2 \sigma \theta}{\sqrt{1-B^2 \sigma^2} \sqrt{1-B^2 \theta^2}}$
p, r	angular velocities about x - and z -axes, respectively (see fig. 2)	ψ, ν	variables used for integrating purposes
β	angle of sideslip (see table I)	Y	side force
$\dot{\beta}$	rate of change of β with time, $d\beta/dt$	N	yawing moment
t	time	L'	rolling moment
ρ	density of air	C_Y	side-force coefficient, Y/qS
q	free-stream dynamic pressure, $\frac{1}{2} \rho V^2$	C_n	yawing-moment coefficient, N/qSb
$\Delta P/q$	coefficient of pressure difference between opposite sides of tail surface due to particular motion under consideration, positive in sense of positive side force (see fig. 2)	C_l	rolling-moment coefficient, L'/qSb
κ	constant determining degree of homogeneity of quasi-conical velocity field	$C_{Y\beta} = \left(\frac{\partial C_Y}{\partial \beta} \right)_{\beta \rightarrow 0}$	
φ	perturbation velocity potential due to particular motion under consideration evaluated on positive y -side of tail surface (see fig. 2)	$C_{n\beta} = \left(\frac{\partial C_n}{\partial \beta} \right)_{\beta \rightarrow 0}$	
$\Delta \varphi$	difference in perturbation velocity potential between two sides of tail surface, $\varphi(x, 0^+, z) - \varphi(x, 0^-, z)$	$C_{l\beta} = \left(\frac{\partial C_l}{\partial \beta} \right)_{\beta \rightarrow 0}$	
φ_D	potential of supersonic doublet distribution	$C_{Yp} = \left(\frac{\partial C_Y}{\partial \frac{pb}{V}} \right)_{p \rightarrow 0}$	
φ_L	potential of line of doublets	$C_{np} = \left(\frac{\partial C_n}{\partial \frac{pb}{V}} \right)_{p \rightarrow 0}$	
$A(x, z)$	doublet-strength function	$C_{lp} = \left(\frac{\partial C_l}{\partial \frac{pb}{V}} \right)_{p \rightarrow 0}$	
$f(\sigma)$	line-doublet-distribution function	$C_{Yr} = \left(\frac{\partial C_Y}{\partial \frac{rb}{V}} \right)_{r \rightarrow 0}$	
c_r	root chord of vertical tail	$C_{nr} = \left(\frac{\partial C_n}{\partial \frac{rb}{V}} \right)_{r \rightarrow 0}$	
b	span of vertical tail	$C_{lr} = \left(\frac{\partial C_l}{\partial \frac{rb}{V}} \right)_{r \rightarrow 0}$	
S	area of vertical tail	$C_{Y\dot{\beta}} = \left(\frac{\partial C_Y}{\partial \frac{\dot{\beta} b}{V}} \right)_{\dot{\beta} \rightarrow 0}$	
λ	taper ratio of vertical tail, Tip chord/Root chord		
A	aspect ratio of vertical tail, b^2/S		
m	slope of leading edge of tail; cotangent of sweepback angle of leading edge (see fig. 1)		
$k = \frac{1 - \sqrt{1 - B^2 m^2}}{B m}$			
$H(Bm) = \frac{\sqrt{2(1 - \sqrt{1 - B^2 m^2})}}{E'(k)}$			
$E'(k)$	complete elliptic integral of second kind with modulus $\sqrt{1-k^2}$, $\int_0^{\pi/2} \sqrt{1 - (1-k^2)\sin^2 n} \, dn$		

$$C_{n\dot{\beta}} = \left(\frac{\partial C_n}{\partial \dot{\beta} b} \right)_{\dot{\beta} \rightarrow 0}$$

$$C_{l\dot{\beta}} = \left(\frac{\partial C_l}{\partial \dot{\beta} b} \right)_{\dot{\beta} \rightarrow 0}$$

Subscripts:

- p refers to rolling condition
 r refers to yawing condition
 $r=1$ refers to unit-yawing condition
 β refers to sideslip condition
 $\beta=1$ refers to unit-sideslip condition
 $\dot{\beta}$ refers to constant-lateral-acceleration condition
 w based on wing dimensions
 $1,2$ components used for $\dot{\beta}$ derivatives

Abbreviations:

- L. E. leading edge
 T. E. trailing edge

All angles are measured in radians.

ANALYSIS

SCOPE

The vertical-tail plan forms considered herein are shown in figure 1. The leading edge has arbitrary sweepback and the trailing edge may be either sweptback or sweptforward. The permissible ranges of sweep, aspect ratio, and taper ratio for the supersonic-leading-edge configurations are determined by the conditions (indicated in fig. 1) that both the leading edges and trailing edges remain supersonic and that the Mach line emanating from the leading edge of the root chord does not intersect the tip chord. Also, the tip chord must be parallel to the root chord. For the subsonic leading-edge configurations, only the case of zero taper ratio is considered and the restriction to supersonic trailing edge is imposed.

Expressions based on linearized supersonic-flow theory are obtained for the perturbation velocity potentials and pressure distributions due to steady rolling, steady yawing, and constant lateral acceleration. For purposes of completeness, analogous results for constant sideslip motion obtainable, in general, from references 9 and 10 are included. The expressions, which are derived for the condition of zero geometric angle of attack and which are valid for low rates of angular velocities, small sideslip angles, and small angle-of-sideslip variation with time, are tabulated so that they may be utilized conveniently in the calculation of load distributions and the corresponding forces and moments.

Two important members of the family of vertical-tail plan forms are considered in detail. These are the rectangular tail and the triangular tail with an unswept trailing edge, that is, the half-delta tail. For these tails, closed-form expressions are derived for the side force, yawing moment, and rolling moment due to each motion. The resulting formulas are expressed in the form of stability derivatives and are tabulated; simple charts are presented which permit rapid estimation of the 12 stability derivatives for given values of aspect ratio and Mach number. Tabulation

of the derivatives for subsonic-edge triangular tails with trailing-edge sweep are also presented.

Three systems of body axes are employed in the present report. For plan-form integrations and in the derivation and presentation of velocity potentials and pressures, the conventional analysis system shown in figure 2 (a) is utilized. In order to maintain the usual stability system of positive forces and moments, the axes systems shown in figures 2 (b) and 2 (c) are used in formulating the stability derivatives. A table of transformation formulas is provided which enables the stability derivatives, presented herein with reference to a center of gravity (origin) located at the leading edge of the root chord (fig. 2(b)), to be obtained with reference to an arbitrary center-of-gravity location (fig. 2 (c)).

BASIC CONSIDERATIONS

The calculation of forces acting on the vertical tail essentially requires a knowledge of the distribution of the pressure difference between the two sides of the tail surface. This pressure-difference distribution is expressible in terms of the perturbation-velocity-potential difference or "potential jump across the surface" $\Delta\varphi$ by means of the linearized relationship

$$\frac{\Delta P}{q} = \frac{2}{V^2} \left(V \frac{\partial \Delta\varphi}{\partial x} + \frac{\partial \Delta\varphi}{\partial t} \right) \quad (1)$$

Inasmuch as for the present investigation thin isolated tail surfaces are considered and thus no induced effects are present from any neighboring surface, the perturbation velocity potentials on the two sides of the tail are equal in magnitude but are of opposite sign. Equation (1) may then be rewritten in terms of the perturbation velocity potential φ as follows:

$$\frac{\Delta P}{q} = \frac{4}{V^2} \left(V \frac{\partial \varphi}{\partial x} + \frac{\partial \varphi}{\partial t} \right) \quad (2)$$

where φ is evaluated on the positive y -side of the tail surface.

The basic problem, then, is to find for each motion under consideration the perturbation-velocity-potential function φ for the various tail regional areas formed either by plan-form or plan-form and Mach line boundaries. (See, for example, the sketch given in table I.)

For time-independent motions, such as steady rolling, steady yawing, and constant sideslip, the potential functions are of course independent of time (i. e., the last term in eqs. (1) and (2) vanishes) and may be determined for the subsonic-leading-edge cases by the doublet-distribution method of references 14 and 15. The details of the method and its application are given in the appendixes. The supersonic-leading edge configurations are analyzed by the well-known source-distribution method utilizing the area-cancellation—Mach line reflection technique of reference 16. The mathematical details are not presented herein, because it is felt that previous papers dealing with wing problems (e. g., refs. 17 to 20) have applied the basic method in sufficient detail. The main difference to be noted is that the root chord of the isolated vertical tail is, in effect, another free subsonic edge similar to the tip chord and must be treated accordingly. Actually, tail regions I and III (refer to the sketch in table I) are not affected by the additional

tip, and wing results in these regions for constant angle of attack (ref. 20), steady rolling (ref. 20), and steady pitching (ref. 18) are applicable to constant sideslip, steady rolling, and steady yawing motions, respectively, for the vertical tail, provided appropriate changes in coordinates are introduced and the proper sign convention is maintained.

The time-dependent motion considered in the present report, that is, constant lateral acceleration, can be analyzed in a manner analogous to that used for a wing surface undergoing constant vertical acceleration (e. g., refs. 21 to 23). By following this procedure, the basic expressions for the perturbation velocity potential and pressure coefficient (evaluated at time $t=0$) may be derived as follows:

$$\varphi = -\dot{\beta} \left[\frac{M^2}{B^2} \varphi_{r=1} - \left(t - \frac{M^2 x}{B^2 V} \right) \varphi_{\beta=1} \right] \quad (3)$$

$$\frac{\Delta P}{q} = -\frac{\beta}{B^2} \left[M^2 \left(\frac{\Delta P}{q} \right)_{r=1} + \frac{M^2 x}{V} \left(\frac{\Delta P}{q} \right)_{\beta=1} + \frac{4}{V^2} \varphi_{\beta=1} \right] \quad (4)$$

Equations (3) and (4) may be deduced directly from equations (1) and (2) of reference 23, provided the corresponding tail motion is substituted for each wing motion and, further, that care is exercised in preserving the conventional system of positive forces and moments. The choice of time $t=0$ in equation (4) was made for purposes of convenience and simplicity, inasmuch as the pressure due to constant sideslip is eliminated, and thus only the increment in pressure due to time rate of change of sideslip, that is, $\dot{\beta}$, remains.

The right-hand sides of equations (3) and (4) are composed of terms involving steady or time-independent motions, in particular, the motions previously discussed in this section. Thus, once the potentials and pressures are determined for steady yawing and constant sideslip, corresponding expressions may be obtained for constant lateral acceleration by use of equations (3) and (4).

Derivations of the potentials and pressures for the various regions of the tail plan forms under consideration have been carried out for each motion by using the methods and techniques discussed. Tabulations of the potential and pressure-distribution functions are given in tables I and II for constant sideslip, in tables III and IV for steady rolling, in tables V and VI for steady yawing, and in tables VII and VIII for constant lateral acceleration.

The forces and moments acting on the vertical tail due to each motion may be obtained by plan-form integrations of the appropriate potential and pressure functions and may be given as follows (the center of gravity is assumed to be at the leading edge of the root section):

$$Y = q \int_{\text{Root}}^{\text{Tip}} \int_{\text{L. E.}}^{\text{T. E.}} \frac{\Delta P}{q} dx dz \quad (5)$$

$$N = -q \int_{\text{Root}}^{\text{Tip}} \int_{\text{L. E.}}^{\text{T. E.}} \frac{\Delta P}{q} x dx dz \quad (6)$$

$$L' = q \int_{\text{Root}}^{\text{Tip}} \int_{\text{L. E.}}^{\text{T. E.}} \frac{\Delta P}{q} z dx dz \quad (7)$$

For steady motions, $\frac{\Delta P}{q} = \frac{4}{V} \frac{\partial \varphi}{\partial x}$ and thus the first integration with respect to x in equations (5) and (7) yields φ ; hence, equations (5) and (7), when applied to steady motions, reduce

to essentially a single integration involving the potential function.

The nondimensional force and moment coefficients and corresponding stability derivatives are directly obtainable from the definitions given in the list of symbols. For example,

$$\begin{aligned} C_{n_r} &= \left(\frac{\partial C_n}{\partial \frac{r\dot{\beta}}{V}} \right)_{r \rightarrow 0} \\ &= \left[\frac{\partial}{\partial \frac{r\dot{\beta}}{V}} \left(\frac{N}{qSb} \right) \right]_{r \rightarrow 0} \\ &= \left[\frac{\partial}{\partial \frac{r\dot{\beta}}{V}} \left(-\frac{1}{Sb} \int_{\text{Root}}^{\text{Tip}} \int_{\text{L. E.}}^{\text{T. E.}} \frac{\Delta P}{q} x dx dz \right) \right]_{r \rightarrow 0} \end{aligned}$$

Inasmuch as the various pressure coefficients are linear with reference to their respective angular velocities, attitude, or acceleration (i. e., linear in p , r , β , or $\dot{\beta}$), the partial derivative in the preceding example may be replaced by $\frac{1}{r\dot{\beta}/V}$ and the derivative C_{n_r} is then expressed as

$$C_{n_r} = -\frac{1}{Sb^2 \frac{r}{V}} \int_{\text{Root}}^{\text{Tip}} \int_{\text{L. E.}}^{\text{T. E.}} \frac{\Delta P}{q} x dx dz \quad (8)$$

Corresponding expressions for the 11 other derivatives C_{Y_β} , C_{n_β} , C_{l_β} , C_{Y_r} , C_{l_r} , C_{Y_p} , C_{n_p} , C_{l_p} , $C_{Y_{\dot{\beta}}}$, $C_{n_{\dot{\beta}}}$, and $C_{l_{\dot{\beta}}}$ may be obtained in an analogous manner.

In the present report, the triangular vertical tail with unswept trailing edge (half-delta) and the rectangular vertical tail have been analyzed in detail. The results obtained upon performing the plan-form integrations and other mathematical operations indicated in the previous discussion are tabulated in table IX. Table X presents similar results for the subsonic-edge triangular tails with trailing-edge sweep. For convenience, a table of transformation formulas is presented (table XI) which enables the derived results for the stability derivatives (tables IX and X) to be expressed with respect to an arbitrary center-of-gravity location.

Values of the elliptic-function parameters appearing in the subsonic-edge formulas are presented graphically in figure 3.

COMPUTATIONAL RESULTS AND DISCUSSION

The formulas for the stability derivatives given in tables IX and X are seen to be functions of the tail-aspect ratio A and the Mach number parameter $B = \sqrt{M^2 - 1}$. Use of the combined parameter AB for the abscissa variable and appropriate choice of derivative parameters for the ordinates allow the analytical results for most of the stability derivatives to be expressed graphically by means of a single simple curve; the stability derivatives due to $\dot{\beta}$ -motion require two curves. Figures 4 to 9 present the results for the half-delta tail and figures 10 to 14 present the analogous results for the rectangular tail. The lower limit $AB=1$ for the rectangular vertical tail corresponds to the condition where the Mach line from the leading edge of the root chord intersects the trailing edge of the tip chord. Values of the derivatives for the situation where the Mach line from the leading edge of the root chord intersects the tip chord, that is, values of $AB < 1$, cannot, in general, be obtained easily because of the

fact that the calculation involves the consideration of interacting external flow fields. The lower limit $AB=1$ in this case is not very restrictive except for very low aspect ratios at low supersonic Mach numbers.

In considering the curves given in figures 4 to 14, the following facts should be kept in mind: (a) The results are for a completely isolated vertical tail, (b) the center-of-gravity location is assumed to be at the tail apex, and (c) parameters used for nondimensionalizing purposes are the area and span of the vertical tail. For other center-of-gravity locations, analogous curves may be drawn by use of the presented data and the axes-transformation formulas given in table XI.

Thus far, only the isolated vertical tail has been considered, that is, the zero-end-plate solution. For comparison purposes, results for several of the derivatives based on a complete-end-plate analysis have been obtained and are presented in figures 15 and 16. The comparisons are shown for the side-force and yawing-moment derivatives due to constant sideslip, steady yawing, and constant lateral acceleration. The complete-end-plate results for these tail derivatives are obtainable from stability derivatives previously reported for symmetrical wings (refs. 18, 20, 23, and 24), provided modifications are introduced to account for (a) changes in nondimensionalizing parameters, (b) correspondence of wing and vertical-tail motions, and (c) preservation of sign convention for positive sense of motion, moments; and so forth. The transformations of symmetrical-wing derivatives into complete-end-plate derivatives for vertical tails having the same plan-form geometry as the half-wing may be summarized as follows:

$$C_{Y_{\beta}} = -1 \times (\text{Expression for } C_{L_{\alpha}} \text{ with wing aspect ratio replaced by } 2A)$$

$$C_{n_{\beta}} = -\frac{4}{3A} \frac{1+\lambda+\lambda^2}{(1+\lambda)^2} \times (\text{Expression for } C_{m_{\alpha}} \text{ with wing aspect ratio replaced by } 2A)$$

$$C_{Y_r} = \frac{2}{3A} \frac{1+\lambda+\lambda^2}{(1+\lambda)^2} \times (\text{Expression for } C_{L_q} \text{ with wing aspect ratio replaced by } 2A)$$

$$C_{n_r} = \frac{8}{9A^2} \frac{(1+\lambda+\lambda^2)^2}{(1+\lambda)^4} \times (\text{Expression for } C_{m_q} \text{ with wing aspect ratio replaced by } 2A)$$

$$C_{Y_{\dot{\beta}}} = -\frac{2}{3A} \frac{1+\lambda+\lambda^2}{(1+\lambda)^2} \times (\text{Expression for } C_{L_{\dot{\alpha}}} \text{ with wing aspect ratio replaced by } 2A)$$

$$C_{n_{\dot{\beta}}} = -\frac{8}{9A^2} \frac{(1+\lambda+\lambda^2)^2}{(1+\lambda)^4} \times (\text{Expression for } C_{m_{\dot{\alpha}}} \text{ with wing aspect ratio replaced by } 2A)$$

where $C_{L_{\alpha}}$, $C_{m_{\alpha}}$, C_{L_q} , C_{m_q} , $C_{L_{\dot{\alpha}}}$, and $C_{m_{\dot{\alpha}}}$ are conventionally defined wing derivatives (see, for example, ref. 23). Figures 15 and 16 indicate that for a given aspect ratio the effect of an end plate decreases with increasing Mach number and that for a given Mach number the effect of an end plate decreases with increasing aspect ratio. Although these conclusions apply specifically to those derivatives presented, it is felt that similar evidence would be found for the other derivatives as well. The percentage differences between zero- and complete-end-plate results vary of course with center-of-gravity location, as well as with Mach number and

aspect ratio, but in general are not too large for the side-force and yawing-moment derivatives considered except at the lower values of AB .

The stability derivatives as presented herein have been made nondimensional with respect to vertical-tail parameters such as tail span b , tail area S , and the angles pb/V , rb/V , and $\dot{\beta}b/V$. The magnitudes of the derivatives may, therefore, appear to be quite large with respect to the expected tail contributions to the derivatives for a complete airplane. The following factors should be used in converting the presented analytical and numerical results to corresponding derivatives (denoted in the following relationships by subscript w) based on wing area S_w , wing span b_w , and angles $pb_w/2V$, $rb_w/2V$, and $\dot{\beta}b_w/2V$:

$$\begin{aligned} (C_{Y_{\beta}})_w &= \frac{S}{S_w} C_{Y_{\beta}} \\ (C_{n_{\beta}})_w, (C_{l_{\beta}})_w &= \frac{S}{S_w} \frac{b}{b_w} (C_{n_{\beta}}, C_{l_{\beta}}) \\ (C_{Y_p})_w, (C_{Y_r})_w, (C_{Y_{\dot{\beta}}})_w &= 2 \frac{S}{S_w} \frac{b}{b_w} (C_{Y_p}, C_{Y_r}, C_{Y_{\dot{\beta}}}) \\ (C_{n_p})_w, (C_{l_p})_w, (C_{n_r})_w, (C_{l_r})_w, (C_{n_{\dot{\beta}}})_w, (C_{l_{\dot{\beta}}})_w \\ &= 2 \frac{S}{S_w} \left(\frac{b}{b_w}\right)^2 (C_{n_p}, C_{l_p}, C_{n_r}, C_{l_r}, C_{n_{\dot{\beta}}}, C_{l_{\dot{\beta}}}) \end{aligned}$$

CONCLUDING REMARKS

Velocity potentials, pressure distributions, and stability derivatives have been derived by use of supersonic linearized theory for families of thin isolated vertical tails performing steady rolling, steady yawing, and constant-lateral-acceleration motions. Vertical-tail families (half-delta and rectangular plan forms) are considered for a broad Mach number range. Also considered are the vertical tail with arbitrary sweepback and taper ratio at Mach numbers for which both the leading edge and trailing edge of the tail are supersonic and the triangular vertical tail with a subsonic leading edge and a supersonic trailing edge. For purposes of completeness, analogous expressions and derivatives for sideslip motion obtained primarily from other sources are included.

The effects of a complete end plate on several of the side-force and yawing-moment derivatives have been considered, and it appears that only for relatively small values of the aspect-ratio-Mach number parameter $A\sqrt{M^2-1}$ do the complete-end-plate and zero-end-plate values differ significantly enough to warrant further study of finite-end-plate corrections.

An additional point of interest pertinent to the present investigation is that the results obtained for the yawing-moment derivatives due to steady yawing and constant lateral acceleration C_{n_r} and $C_{n_{\dot{\beta}}}$ may be used to approximate the aerodynamic damping of the lateral oscillation in yaw to the first order in frequency. This approximation to the lateral damping is given by the expression $C_{n_r} - C_{n_{\dot{\beta}}}$ and can be rapidly calculated from the curves and formulas given herein.

LANGLEY AERONAUTICAL LABORATORY,
NATIONAL ADVISORY COMMITTEE FOR AERONAUTICS,
LANGLEY FIELD, VA., March 5, 1956.

APPENDIX A

DETERMINATION OF PRESSURE-DISTRIBUTION EXPRESSIONS FOR A SUBSONIC-EDGE TAIL UNDERGOING YAWING AND ROLLING MOTIONS

A method for solving supersonic-flow boundary-value problems governed by the classical, linearized, partial-differential equation

$$B^2 \frac{\partial^2 \varphi}{\partial x^2} - \frac{\partial^2 \varphi}{\partial y^2} - \frac{\partial^2 \varphi}{\partial z^2} = 0 \quad (A1)$$

has been developed in reference 14 and an application to rolling and pitching triangular wings is given in reference 15. This method allows the prediction of the disturbance-potential function φ , and hence the pressure distribution, for planar lifting surfaces. The analysis given in reference 15 is briefly summarized herein and is applied to the determination of the pressure distributions on a triangular-vertical-tail surface (fig. 2) performing rolling and yawing motions. (Yawing in the xz -plane is analogous to pitching in the xy -plane.)

DETERMINATION OF THE FORM OF THE VELOCITY POTENTIAL

As is well-known, the potentials of both the supersonic source and the supersonic doublet and their distributions represent solutions of equation (A1). For the determination of the potentials and pressure distributions of lifting surfaces with subsonic leading edges, a distribution of doublets that uniquely satisfies the prescribed boundary conditions is required. The boundary conditions on the vertical tail for the motions to be considered herein are as follows: On the rolling vertical tail,

$$v = pz = xp \frac{z}{x} = xp\theta \quad (A2)$$

and on the yawing vertical tail,

$$v = -rx \quad (A3)$$

In addition, the following relations must be valid on the surfaces of the tail:

For the rolling motion,

$$\frac{\partial \left(\frac{v}{x} \right)_p}{\partial \theta} = p \quad (A4)$$

$$\frac{\partial^2 \left(\frac{v}{x} \right)_p}{\partial \theta^2} = 0 \quad (A5)$$

and for the yawing motion,

$$\frac{\partial \left(\frac{v}{x} \right)_r}{\partial \theta} = 0 \quad (A6)$$

$$\frac{\partial^2 \left(\frac{v}{x} \right)_r}{\partial \theta^2} = 0 \quad (A7)$$

It is also necessary that the pressure along the streamwise edge be zero.

The potential in space produced by a distribution of doublets, for example, in the xz -plane, with the doublet axes normal to the plane is

$$\varphi_D(x, y, z) = \frac{\partial}{\partial y} \iint_S \frac{-A(\xi, \zeta) d\xi d\zeta}{\sqrt{(x-\xi)^2 - B^2(z-\zeta)^2 - B^2y^2}} \quad (A8)$$

where the area S is the region of the xz -plane intercepted by the forecone from the field point (x, y, z) .

The potential on the surface carrying the doublet distribution is given by

$$\varphi_D(x, z)_{y=\pm 0} = \lim_{y \rightarrow \pm 0} \left[\frac{\partial}{\partial y} \iint_S \frac{-A(\xi, \zeta) d\xi d\zeta}{\sqrt{(x-\xi)^2 - B^2(z-\zeta)^2 - B^2y^2}} \right]$$

As stated in reference 15, this surface potential is directly proportional to the doublet-strength function $A(x, z)$; that is,

$$\varphi_D(x, z)_{y=\pm 0} = \pm \pi A(x, z) \quad (A9)$$

The surface-pressure velocity $u(x, z)$ then becomes

$$u(x, z)_{y=\pm 0} = \frac{\partial \varphi_D(x, z)_{y=\pm 0}}{\partial x} = \pm \pi \frac{\partial A(x, z)}{\partial x} \quad (A10)$$

and the linearized pressure coefficient

$$\frac{\Delta P}{q} = \frac{4u(x, z)_{y=\pm 0}}{V} \quad (A11)$$

may be written as

$$\frac{\Delta P}{q} = \frac{4\pi}{V} \frac{\partial A(x, z)}{\partial x} \quad (A12)$$

The problem to be considered in this appendix is one in which the sidewash on the surface is prescribed (see eqs. (A2) and (A3)) and the surface velocity potential has to be determined. The doublet-strength function $A(x, z)$ then is an unknown and the determination of this quantity requires in general the solution of an integral equation. In some cases the general form of the surface-potential function $A(x, z)$ is known or can be obtained by inverting an integral equation. The problem then resolves simply into an evaluation of the arbitrary constants of the general solution by making use of the prescribed boundary conditions.

Brown and Adams in their analysis of rolling and pitching triangular wings with subsonic leading edges (ref. 15) were able to determine the function $A(x, z)$ by utilizing the concept that the conical properties of the produced flow gave rise to potentials and pressures in the crossflow planes that were similar in form to the potentials and pressures acting on flat finite segments in a two-dimensional flow; these segments correspond to a section of the wing in any crossflow plane. This remarkable connection between linearized supersonic

conical flow and incompressible two-dimensional flow is discussed by Busemann in reference 25.

A more general and rigorous approach to obtain the doublet-strength function may be formulated from an analysis presented in a later paper by Lomax and Heaslet (ref. 26) dealing also with conical and the so-called quasi-conical problems. In this analysis a general surface-pressure-coefficient expression has been determined for planar lifting surfaces with prescribed boundary conditions of the form

$$v \sim x^\kappa g\left(\frac{z}{x}\right) \quad (\text{A13})$$

This expression is

$$\frac{\Delta P}{q} = \left(\frac{x}{B}\right)^\kappa \sum_{i=0}^{\kappa+1} \frac{b_i \theta^i}{\sqrt{(m-\theta)(\theta-m_1)}} \quad (\text{A14})$$

where b_i are constants, $\theta = \frac{z}{x}$, κ is determined by the boundary-condition equation (eq. (A13)), and m and m_1 are the tangents of the apex angles of the two panels of the lifting surface. When $m_1 = m$, the lifting surface is symmetrical about the common root chord of the two panels, and when $m_1 \neq m$, the lifting surface is asymmetrical about this chord. From equations (A12), (A14), and (A9) the form of $A(x, z)$ or, synonymously, the form of the surface potential may be obtained by a simple integration. It should be mentioned at this point that reference 26 presents a method for deriving the arbitrary constants b_i in the pressure coefficient (eq. (A14)). This method is related to that of reference 15 which concerns itself with obtaining the arbitrary constants in the velocity potential.

By application of equation (A14) to the boundary problem of the triangular vertical tail ($m_1 = 0$) and by noting from the prescribed boundary conditions (see eqs. (A2) and (A3)) that $\kappa = 1$, the pressure coefficient for both the yawing and rolling motions is

$$\frac{\Delta P}{q} = \frac{x}{B} \frac{b_0 + b_1 \theta + b_2 \theta^2}{\sqrt{(m-\theta)\theta}} \quad (\text{A15})$$

The constant b_0 in this expression must be set equal to zero in order to satisfy the condition that along the streamwise edge the pressure must be zero.

The velocity potential on the vertical-tail surface is easily obtainable from the pressure expression by the formula

$$\varphi = \frac{V}{4} \int_{\text{L.E.}}^x \frac{\Delta P}{q} d\xi$$

and has been found to be

$$\varphi = \pi x^2 f\left(\frac{z}{x}\right) \quad (\text{A16})$$

where

$$f\left(\frac{z}{x}\right) = f(\theta) = (\tau\theta + \omega m) \sqrt{\theta(m-\theta)} \quad (\text{A17})$$

The arbitrary constants τ and ω in the so-called distribution function $f(\theta)$ are, in terms of b_1 and b_2 ,

$$\tau = \frac{V}{2\pi B} \left(\frac{2b_1}{3m^2} + \frac{b_2}{m} \right)$$

$$\omega = \frac{V}{2\pi B} \frac{b_1}{3m^2}$$

By relating equation (A16) to equation (A9), the doublet-strength function $A(x, z)$ is seen to be

$$A(x, z) = x^2 f\left(\frac{z}{x}\right) \quad (\text{A18})$$

A comparison of the potential given by equations (A16) and (A17) and the potential obtained for the slender, rolling, vertical tail reported in reference 5 shows, as expected, that both are of the same form.

EVALUATION OF THE CONSTANTS τ AND ω

The constants τ and ω in the expressions for the velocity potential given by equations (A16) and (A17) are still to be determined. As indicated previously, the expression for the pressure coefficient, and hence the velocity potential, can be determined completely through an application of the procedures developed in reference 26; however, many of the integrations and integrating procedures required in the method in reference 15 were already known to the junior author at the inception of this project and, for this reason, the analysis herein to determine the constants τ and ω closely parallels the procedures discussed in reference 15.

The determination of the constants τ and ω depends upon satisfying the boundary conditions associated with the vertical tail for the rolling and yawing motions. These boundary conditions are given by equations (A2) to (A7). The needed expressions for the prescribed velocities and their derivatives with respect to θ in terms of the distribution function $f(\sigma)$ are derived in appendix B.

For the rolling motion the constants τ and ω may be obtained by replacing $f(\sigma)$ by its equivalent (eq. (A17)) in the equations given in appendix B for v/x and $\frac{\partial(v/x)}{\partial\theta}$ and then applying the boundary conditions given by equations (A2) and (A4). When the integrations have been performed, the resulting equations may be solved simultaneously for τ_p and ω_p . The yawing constants are obtained in a like manner with equations (A3) and (A6) replacing equations (A2) and (A4), respectively.

In the calculation of the quantities v/x and $\frac{\partial(v/x)}{\partial\theta}$, any value of θ may be considered. It is advantageous for integration purposes to let this value of θ be zero. However, since one of the limits of integration is zero and since in several of the integrands a singular point exists at $\theta = \sigma = 0$, the integrations in which these singularities occur must be performed for θ arbitrary before θ can be set equal to zero.

Substituting equation (A17) into equation (B4) gives, for θ equal to zero,

$$\begin{aligned} \frac{v}{x} = \frac{1}{B} \int_0^{Bm} & \left[\frac{-3(\tau B\sigma + \omega Bm) \sqrt{B\sigma(Bm-B\sigma)} \tanh^{-1} \sqrt{1-B^2\sigma^2}}{(1-B^2\sigma^2)^{5/2}} + \frac{2(\tau B\sigma + \omega Bm) \sqrt{B\sigma(Bm-B\sigma)}}{(1-B^2\sigma^2)^2} \right] d(B\sigma) + \\ \lim_{\theta \rightarrow 0} & \left\{ \lim_{\epsilon \rightarrow 0} \left[\frac{1}{B} \int_0^{B(\theta-\epsilon)} \frac{(\tau B\sigma + \omega Bm) \sqrt{B\sigma(Bm-B\sigma)} (1-B^2\sigma\theta)^2 \sqrt{1-B^2\theta^2}}{(1-B^2\sigma^2)^2 (B\sigma-B\theta)^2} d(B\sigma) + \right. \right. \\ & \left. \left. \frac{1}{B} \int_{B(\theta+\epsilon)}^{Bm} \frac{(\tau B\sigma + \omega Bm) \sqrt{B\sigma(Bm-B\sigma)} (1-B^2\sigma\theta)^2 \sqrt{1-B^2\theta^2}}{(1-B^2\sigma^2)^2 (B\sigma-B\theta)^2} d(B\sigma) - \frac{2(\tau B\theta + \omega Bm) \sqrt{B\theta(Bm-B\theta)} \sqrt{1-B^2\theta^2}}{B^2\epsilon} \right] \right\} \end{aligned} \quad (A19)$$

Carrying out the integrations in equation (A19) yields

$$\frac{v}{x} = \frac{-\pi}{B\sqrt{1+k^2}(1-k^2)^2} \{K'(k)[2k^3\tau + \bar{\omega}k^2(1+k^2)] - E'(k)[\tau k(1+k^2) - \bar{\omega}(1-4k^2+k^4)]\} \quad (A20)$$

where

$$k = \frac{1 - \sqrt{1-B^2m^2}}{Bm} \quad (A21)$$

and

$$\bar{\omega} = \omega Bm = \omega \frac{2k}{1+k^2}$$

These integrations were accomplished with the aid of the tables in references 27 and 28 and are discussed in appendix C.

Substituting the distribution function into equation (B5) results in, for θ approaching zero,

$$\begin{aligned} \frac{\partial(v/x)}{\partial\theta} = & \int_0^{Bm} \left[\frac{3B\sigma(\tau B\sigma + \omega Bm) \sqrt{B\sigma(Bm-B\sigma)} \tanh^{-1} \sqrt{1-B^2\sigma^2}}{(1-B^2\sigma^2)^{5/2}} - \frac{3B\sigma(\tau B\sigma + \omega Bm) \sqrt{B\sigma(Bm-B\sigma)}}{(1-B^2\sigma^2)^2} \right] d(B\sigma) + \\ & \lim_{\theta \rightarrow 0} \left(\lim_{\epsilon \rightarrow 0} \left\{ \int_0^{B(\theta-\epsilon)} \left[\frac{B\theta(\tau B\sigma + \omega Bm) \sqrt{B\sigma(Bm-B\sigma)}}{\sqrt{1-B^2\theta^2} (B\sigma-B\theta)^2} - \frac{(\tau B\sigma + \omega Bm) \sqrt{B\sigma(Bm-B\sigma)}}{\sqrt{1-B^2\theta^2} (1-B^2\sigma^2) (B\sigma-B\theta)} + \right. \right. \\ & \left. \frac{2(\tau B\sigma + \omega Bm) \sqrt{B\sigma(Bm-B\sigma)} \sqrt{1-B^2\theta^2}}{(B\sigma-B\theta)^3} \right] d(B\sigma) + \int_{B(\theta+\epsilon)}^{Bm} \left[\frac{B\theta(\tau B\sigma + \omega Bm) \sqrt{B\sigma(Bm-B\sigma)}}{\sqrt{1-B^2\theta^2} (B\sigma-B\theta)^2} - \right. \\ & \left. \frac{(\tau B\sigma + \omega Bm) \sqrt{B\sigma(Bm-B\sigma)}}{\sqrt{1-B^2\theta^2} (1-B^2\sigma^2) (B\sigma-B\theta)} + \frac{2(\tau B\sigma + \omega Bm) \sqrt{B\sigma(Bm-B\sigma)} \sqrt{1-B^2\theta^2}}{(B\sigma-B\theta)^3} \right] d(B\sigma) - \\ & \left. \frac{2B\theta(\tau B\theta + \omega Bm) \sqrt{B\theta(B\theta-Bm)}}{B\epsilon \sqrt{1-B^2\theta^2}} - \frac{2[-4B^2\theta^2\tau + B\theta Bm(3\tau-2\omega) + \omega B^2m^2] \sqrt{1-B^2\theta^2}}{B\epsilon \sqrt{B\theta(B\theta-Bm)}} \right\} \end{aligned} \quad (A22)$$

By performing the integrations in equation (A22), the following expression is obtained:

$$\frac{\partial(v/x)}{\partial\theta} = \frac{\pi}{\sqrt{1+k^2}(1-k^2)^2} [k^2 K'(k)(\tau + \tau k^2 + 2\bar{\omega}k) + E'(k)(2\tau k^2 - 2\tau - \bar{\omega}k - 2\tau k^4 - \bar{\omega}k^3)] \quad (A23)$$

Consider the rolling case for which $\tau = \tau_p$ and $\omega = \omega_p$. Also from equations (A2) and (A4), for $\theta=0$, $v/x=0$ and $\frac{\partial(v/x)}{\partial\theta}=p$.

Solving equations (A20) and (A23) for τ_p and ω_p , with $\bar{\omega} = Bm\omega_p = \frac{2k}{1+k^2}\omega_p$, gives

$$\tau_p = \frac{-p\sqrt{1+k^2}[k^2(1+k^2)K'(k) + (1-4k^2+k^4)E'(k)]}{\pi[-k^4K'(k)^2 + k^2(1+k^2)K'(k)E'(k) + (2-k^2)(1-2k^2)E'(k)^2]} \quad (A24)$$

$$\omega_p = \frac{p(1+k^2)^{3/2}[2k^2K'(k) - (1+k^2)E'(k)]}{2\pi[-k^4K'(k)^2 + k^2(1+k^2)K'(k)E'(k) + (2-k^2)(1-2k^2)E'(k)^2]} \quad (A25)$$

For the yawing case $\tau = \tau_r$, $\bar{\omega} = \frac{2k}{1+k^2} \omega_r$, and, from equations (A3) and (A6) $\frac{v}{x} = -r$ and $\frac{\partial(v/x)_r}{\partial\theta} = 0$, respectively. Solving equations (A20) and (A23) simultaneously after making these substitutions yields

$$\tau_r = \frac{Brk\sqrt{1+k^2}[2k^2K'(k) - (1+k^2)E'(k)]}{\pi[-k^4K'(k)^2 + k^2(1+k^2)K'(k)E'(k) + (2-k^2)(1-2k^2)E'(k)^2]} \quad (\text{A26})$$

$$\omega_r = \frac{-Br(1+k^2)^{3/2}[k^2(1+k^2)K'(k) - 2(1-k^2+k^4)E'(k)]}{2\pi k[-k^4K'(k)^2 + k^2(1+k^2)K'(k)E'(k) + (2-k^2)(1-2k^2)E'(k)^2]} \quad (\text{A27})$$

It is convenient for plotting purposes and in expressing the aerodynamic coefficients to make the following definitions:

$$\left. \begin{aligned} \tau_r &= \tau_r' \frac{Br}{\pi} \\ \omega_r &= \omega_r' \frac{Br}{\pi} \\ \tau_p &= \tau_p' \frac{p}{\pi} \\ \omega_p &= \omega_p' \frac{p}{\pi} \end{aligned} \right\} \quad (\text{A28})$$

so that τ_r' , ω_r' , τ_p' , and ω_p' are functions of the Bm only. The variations of these four parameters with Bm are shown in figure 3.

The velocity potentials for the rolling and yawing motions, completely defined by equations (A16) and (A17) and the constants given in equations (A21), (A24), (A25), (A26), (A27), and (A28), may now be written as

$$\varphi_p = px^2(\tau_p'\theta + \omega_p'm)\sqrt{\theta(m-\theta)} \quad (\text{A29})$$

and

$$\varphi_r = Brx^2(\tau_r'\theta + \omega_r'm)\sqrt{\theta(m-\theta)} \quad (\text{A30})$$

The pressure coefficients for the rolling and yawing motions found from equations (A29), (A30), (A10), and (A11) are

$$\left(\frac{\Delta P}{q}\right)_p = \frac{2p}{V} \frac{\tau_p'mz^2 + 3m^2\omega_p'xz - 2m\omega_r'z^2}{\sqrt{z(mx-z)}} \quad (\text{A31})$$

and

$$\left(\frac{\Delta P}{q}\right)_r = \frac{2Br}{V} \frac{\tau_r'mz^2 + 3m^2\omega_r'xz - 2m\omega_r'z^2}{\sqrt{z(mx-z)}} \quad (\text{A32})$$

APPENDIX B

DEVELOPMENT OF EQUATIONS RELATING THE v -VELOCITY TO THE DISTRIBUTION FUNCTION $f(\sigma)$ IN THE $y=0$ PLANE

Equation (A8) gives the expression for the velocity potential (everywhere in space) resulting from a distribution of doublets in the xz -plane with the strength of each doublet in this distribution being governed by the doublet-strength function $A(x, z)$. The derivative of this velocity potential with respect to any one of the coordinates x , y , or z will give the perturbation velocity in that direction. Of primary interest herein is the v -velocity or the y -derivative of this potential

$$v(x, y, z) = \frac{\partial \varphi_D(x, y, z)}{\partial y} \quad (B1)$$

for points on the xz -plane. Brown and Adams in reference 15 have constructed the velocity potential in space of a distribution of doublets by the following approach. First, by using equations (A8) and (A18), the potential of a line of doublets in the xz -plane at an angle $\tan^{-1}\sigma$ to the x -axis is determined. This potential is given by

$$\varphi_L = -\frac{B^2 y (x - B^2 \sigma z)}{(1 - B^2 \sigma^2)^{5/2}} \left(3 \coth^{-1} \gamma - \frac{\gamma}{\gamma^2 - 1} \right) + \frac{2B^2 y \sqrt{x^2 - B^2(y^2 + z^2)}}{(1 - B^2 \sigma^2)^2} \quad (B2)$$

where

$$\gamma = \frac{x - B^2 \sigma z}{\sqrt{1 - B^2 \sigma^2} \sqrt{x^2 - B^2(y^2 + z^2)}}$$

The velocity potential of a distribution of line doublets (i. e., a surface distribution) in the xz -plane, on the vertical tail, with strengths governed by the distribution function $f(\sigma)$ may then be written as

$$\varphi = \int_0^m f(\sigma) \varphi_L d\sigma \quad (B3)$$

where $\tan^{-1}m$ is the apex angle of the vertical tail.

Substituting equation (B2) into equation (B3) and differentiating with respect to y yield the following equation for the v -velocity as $\beta y/x$ approaches zero (see ref. 15):

$$\begin{aligned} \frac{v}{x} = \lim_{\epsilon \rightarrow 0} \left\{ \int_0^{B(\theta-\epsilon)} \left[\frac{Bf(\sigma)\sqrt{1-B^2\theta^2}(1-B^2\sigma\theta)^2}{(1-B^2\sigma^2)^2(B\sigma-B\theta)^2} - \frac{3Bf(\sigma)(1-B^2\sigma\theta)\coth^{-1}\gamma_0}{(1-B^2\sigma^2)^{5/2}} + \frac{2Bf(\sigma)\sqrt{1-B^2\theta^2}}{(1-B^2\sigma^2)^2} \right] d(B\sigma) + \right. \\ \left. \int_{B(\theta+\epsilon)}^{Bm} \left[\frac{Bf(\sigma)\sqrt{1-B^2\theta^2}(1-B^2\sigma\theta)^2}{(1-B^2\sigma^2)^2(B\sigma-B\theta)^2} - \frac{3Bf(\sigma)(1-B^2\sigma\theta)\coth^{-1}\gamma_0}{(1-B^2\sigma^2)^{5/2}} + \frac{2Bf(\sigma)\sqrt{1-B^2\theta^2}}{(1-B^2\sigma^2)^2} \right] d(B\sigma) - \frac{2f(\theta)\sqrt{1-B^2\theta^2}}{\epsilon} \right\} \quad (B4) \end{aligned}$$

The singularity which occurs in the $\frac{\gamma}{\gamma^2-1}$ term of equation (B2) when y is set equal to zero has been accounted for in equation (B4).

By taking the first and second derivatives of equation (B4) with respect to θ , two other useful relations are obtained. They are given in the appendix of reference 15 as

$$\begin{aligned} \frac{\partial(v/x)}{\partial \theta} = \lim_{\epsilon \rightarrow 0} \left\{ \int_0^{B(\theta-\epsilon)} \left[\frac{3B^3\sigma f(\sigma) \coth^{-1} \gamma_0}{(1-B^2\sigma^2)^{5/2}} - \frac{B^2(3B\sigma+2B\theta+B\theta B^2\sigma^2)f(\sigma)}{\sqrt{1-B^2\theta^2}(1-B^2\sigma^2)^2} + \frac{B\theta B^2 f(\sigma)}{\sqrt{1-B^2\theta^2}(B\sigma-B\theta)^2} - \frac{B^2 f(\sigma)}{\sqrt{1-B^2\theta^2}(1-B^2\sigma^2)(B\sigma-B\theta)} + \right. \right. \\ \left. \frac{2B^2 f(\sigma)\sqrt{1-B^2\theta^2}}{(B\sigma-B\theta)^3} \right] d(B\sigma) + \int_{B(\theta+\epsilon)}^{Bm} \left[\frac{3B^3\sigma f(\sigma) \coth^{-1} \gamma_0}{(1-B^2\sigma^2)^{5/2}} - \frac{B^2(3B\sigma+2B\theta+B\theta B^2\sigma^2)f(\sigma)}{\sqrt{1-B^2\theta^2}(1-B^2\sigma^2)^2} + \frac{B\theta B^2 f(\sigma)}{\sqrt{1-B^2\theta^2}(B\sigma-B\theta)^2} - \right. \\ \left. \frac{B^2 f(\sigma)}{\sqrt{1-B^2\theta^2}(1-B^2\sigma^2)(B\sigma-B\theta)} + \frac{2B^2 f(\sigma)\sqrt{1-B^2\theta^2}}{(B\sigma-B\theta)^3} \right] d(B\sigma) - \frac{2B^2\theta f(\theta)}{\epsilon\sqrt{1-B^2\theta^2}} - \frac{4\sqrt{1-B^2\theta^2}f'(\theta)}{\epsilon} \right\} \quad (B5) \end{aligned}$$

and

$$\frac{\partial^2(v/x)}{\partial \theta^2} = \lim_{\epsilon \rightarrow 0} \left\{ 6\sqrt{1-B^2\theta^2} \int_0^{B(\theta-\epsilon)} \frac{B^3 f(\sigma)}{(B\sigma-B\theta)^4} d(B\sigma) + 6\sqrt{1-B^2\theta^2} \int_{B(\theta+\epsilon)}^{Bm} \frac{B^3 f(\sigma)}{(B\sigma-B\theta)^4} d(B\sigma) - \sqrt{1-B^2\theta^2} \left[\frac{6f''(\theta)}{\epsilon} + \frac{4f'(\theta)}{\epsilon^2} \right] \right\} \quad (B6)$$

The factor multiplying the $f''(\theta)$ term of the expression for $\frac{\partial^2(v/x)}{\partial \theta^2}$ as it appears in reference 15 is slightly in error and has been corrected in equation (B6). (The symbols $f'(\theta)$ and $f''(\theta)$ denote the first and second derivatives, respectively, with respect to θ .)

Considering equations (A5) and (A7), it is evident that equation (B6) must be zero for both the rolling and yawing cases. This equation has already been satisfied by $f(\theta)$ (eq. (A17)), since equation (B6) is in essence the integral equation which was inverted to obtain the general pressure expression from which $f(\theta)$ was derived (see ref. 26).

APPENDIX C

INTEGRATIONS TO OBTAIN v/x

The expression for v/x is, for θ approaching 0 (see eq. (A19)),

$$\begin{aligned} \frac{v}{x} = & \frac{1}{B} \int_0^{Bm} \left[\frac{\textcircled{1}}{(1-B^2\sigma^2)^{5/2}} \left(-3(\tau B\sigma + \omega Bm) \sqrt{B\sigma(Bm-B\sigma)} \tanh^{-1} \sqrt{1-B^2\sigma^2} \right) + \right. \\ & \left. \frac{\textcircled{2}}{(1-B^2\sigma^2)^2} \left(2(\tau B\sigma + \omega Bm) \sqrt{B\sigma(Bm-B\sigma)} \right) \right] d(B\sigma) + \\ & \lim_{\theta \rightarrow 0} \left\{ \lim_{\epsilon \rightarrow 0} \left[\frac{\textcircled{3a}}{(1-B^2\sigma^2)^2 (B\sigma-B\theta)^2} \int_0^{B(\theta-\epsilon)} (\tau B\sigma + \omega Bm) \sqrt{B\sigma(Bm-B\sigma)} (1-B^2\sigma\theta)^2 \sqrt{1-B^2\theta^2} d(B\sigma) + \right. \right. \\ & \left. \frac{\textcircled{3b}}{(1-B^2\sigma^2)^2 (B\sigma-B\theta)^2} \int_{B(\theta+\epsilon)}^{Bm} (\tau B\sigma + \omega Bm) \sqrt{B\sigma(Bm-B\sigma)} (1-B^2\sigma\theta)^2 \sqrt{1-B^2\theta^2} d(B\sigma) - \right. \\ & \left. \left. \frac{\textcircled{4}}{B^2\epsilon} \left(2(\tau B\theta + \omega Bm) \sqrt{B\theta(Bm-B\theta)} \sqrt{1-B^2\theta^2} \right) \right] \right\} \quad (C1) \end{aligned}$$

This expression has been broken into parts as indicated by the circled numbers with the third part being broken into two additional parts $\textcircled{3a}$ and $\textcircled{3b}$ because of the singularity in the integrand. Since $\textcircled{2}$ and $\textcircled{3}$ are elementary integrations similar to those found in most integral tables (see ref. 27), only $\textcircled{1}$ will be dealt with in detail. Performing the integrations $\textcircled{2}$ and $\textcircled{3}$ and combining the results yield

$$\begin{aligned} \frac{\sqrt{1-B^2\theta^2}}{B} \left\{ \frac{2(\tau B\theta + \bar{\omega}) \sqrt{B\theta(Bm-B\theta)}}{B\epsilon} - \frac{\pi[\tau(-7B\theta Bm - 2 + 10B\theta - Bm) + \bar{\omega}(4 - 7Bm + 4B\theta - B\theta Bm)]}{8\sqrt{1-Bm}(1-B\theta)} + \right. \\ \left. \frac{\pi[\tau(-2 - 10B\theta + Bm - 7B\theta Bm) + \bar{\omega}(-4 + 4B\theta - 7Bm + B\theta Bm)]}{8\sqrt{1+Bm}(1+B\theta)} \right\} \quad (C2) \end{aligned}$$

where $\bar{\omega} = \omega Bm$. The first term of expression (C2) exactly cancels $\textcircled{4}$, so that the total of $\textcircled{2}$, $\textcircled{3}$, and $\textcircled{4}$ for $\theta \rightarrow 0$ is

$$\frac{\pi}{8B} \left[\frac{\tau(2+Bm) - \bar{\omega}(4-7Bm)}{\sqrt{1-Bm}} + \frac{\tau(-2+Bm) - \bar{\omega}(4+7Bm)}{\sqrt{1+Bm}} \right] \quad (C3)$$

The following two integrals comprising $\textcircled{1}$ remain to be evaluated:

$$\frac{-3}{B} \int_0^{Bm} \frac{\tau B\sigma \sqrt{B\sigma(Bm-B\sigma)} \tanh^{-1} \sqrt{1-B^2\sigma^2}}{(1-B^2\sigma^2)^{5/2}} d(B\sigma) \quad (C4)$$

$$\frac{-3}{B} \int_0^{Bm} \frac{\bar{\omega} \sqrt{B\sigma(Bm-B\sigma)} \tanh^{-1} \sqrt{1-B^2\sigma^2}}{(1-B^2\sigma^2)^{5/2}} d(B\sigma) \quad (C5)$$

It might be mentioned at this point that the integrands of expressions (C4) and (C5) are finite and continuous over the interval 0 to Bm and therefore must yield a finite quantity when integrated.

The integration of expression (C4) by parts gives

$$\left[\frac{-\tau \sqrt{B\sigma(Bm-B\sigma)} \tanh^{-1} \sqrt{1-B^2\sigma^2}}{B(1-B^2\sigma^2)^{3/2}} \right]_0^{Bm} + \frac{\tau}{B} \left[\int_0^{Bm} \frac{(Bm-2B\sigma) \tanh^{-1} \sqrt{1-B^2\sigma^2}}{2(1-B^2\sigma^2)^{3/2} \sqrt{B\sigma(Bm-B\sigma)}} d(B\sigma) - \int_0^{Bm} \frac{\sqrt{B\sigma(Bm-B\sigma)}}{B\sigma(1-B^2\sigma^2)^2} d(B\sigma) \right] \quad (C6)$$

Integration of expression (C5) by parts gives

$$\left[\frac{-\bar{\omega} \sqrt{B\sigma(Bm-B\sigma)} \tanh^{-1} \sqrt{1-B^2\sigma^2}}{BB\sigma(1-B^2\sigma^2)^{3/2}} \right]_0^{Bm} - \int_0^{Bm} \frac{\bar{\omega} Bm \tanh^{-1} \sqrt{1-B^2\sigma^2}}{2BB\sigma(1-B^2\sigma^2)^{3/2} \sqrt{B\sigma(Bm-B\sigma)}} d(B\sigma) - \int_0^{Bm} \frac{\bar{\omega} \sqrt{B\sigma(Bm-B\sigma)}}{BB^2\sigma^2(1-B^2\sigma^2)^2} d(B\sigma) \quad (C7)$$

Combining expressions (C6) and (C7) results in

$$\textcircled{1} = \left[\frac{-(\tau B\sigma + \bar{\omega}) \sqrt{B\sigma(Bm - B\sigma)} \tanh^{-1} \sqrt{1 - B^2\sigma^2}}{BB\sigma(1 - B^2\sigma^2)^{3/2}} \right]_0^{Bm} - \int_0^{Bm} \frac{(\tau B\sigma + \bar{\omega}) \sqrt{B\sigma(Bm - B\sigma)}}{BB^2\sigma^2(1 - B^2\sigma^2)^2} d(B\sigma) + \int_0^{Bm} \frac{[\tau B\sigma(Bm - 2B\sigma) - \bar{\omega} Bm] \tanh^{-1} \sqrt{1 - B^2\sigma^2}}{2BB\sigma(1 - B^2\sigma^2)^{3/2} \sqrt{B\sigma(Bm - B\sigma)}} d(B\sigma) \quad (\text{C8})$$

The first term of equation (C8), when evaluated at the limits, is either zero or infinity. The integrand of $\textcircled{1}$, as was noted, is finite over the whole interval; therefore, infinities introduced as a result of parts integrations must, in the end, cancel themselves.

The second term of equation (C8) is an elementary integration which when evaluated (with infinities neglected) yields

$$\frac{\pi}{8B} \left(\frac{2\tau + 4\bar{\omega} - 3\tau Bm - 5\bar{\omega} Bm}{\sqrt{1 - Bm}} - \frac{-4\bar{\omega} - 5\bar{\omega} Bm + 2\tau + 3\tau Bm}{\sqrt{1 + Bm}} \right) \quad (\text{C9})$$

It is now convenient in integrating the third term in equation (C8) to introduce the variable substitution

$$B\sigma = \frac{\psi + k}{1 + k\psi} \quad (\text{C10})$$

so that Bm and k are related by

$$Bm = \frac{2k}{1 + k^2} \quad (\text{C11})$$

The third term in equation (C8) when transformed by equation (C10) may be written in the form

$$\frac{-1}{B\sqrt{1 + k^2}(1 - k^2)} \sum_{i=1}^7 I_i \quad (\text{C12})$$

where

$$\begin{aligned} I_1 &= \int_{-k}^k \frac{\tau(1 + k^4)\psi}{1 - \psi^2} F(\psi) d\psi \\ I_2 &= - \int_{-k}^k k(\tau + \bar{\omega}k^3) F(\psi) d\psi \\ I_3 &= \int_{-k}^k \frac{\tau k(1 + k^2) + 3\bar{\omega}k^2}{1 - \psi^2} F(\psi) d\psi \\ I_4 &= \int_{-k}^k \frac{\bar{\omega}k^4(k^2 - 2)}{k^2 - \psi^2} F(\psi) d\psi \\ I_5 &= \int_{-k}^k \frac{3\bar{\omega}k^3\psi}{k^2 - \psi^2} F(\psi) d\psi \\ I_6 &= \int_{-k}^k \frac{\bar{\omega}k^2(1 - k^2)}{(1 - \psi^2)(k^2 - \psi^2)} F(\psi) d\psi \\ I_7 &= - \int_{-k}^k \frac{\bar{\omega}k(1 - k^4\psi^2)\psi}{(1 - \psi^2)(k^2 - \psi^2)} F(\psi) d\psi \\ F(\psi) &= \frac{\tanh^{-1} \left(\frac{\sqrt{1 - k^2} \sqrt{1 - \psi^2}}{1 + k\psi} \right)}{\sqrt{(1 - \psi^2)(k^2 - \psi^2)}} \end{aligned}$$

The integrals I_1 , I_5 , and I_7 are elementary and may be determined by an integration by parts. If the multiplicative factor

before the summation sign in equation (C12) is neglected until all the components are totaled, these three components become

$$I_1 + I_5 + I_7 = \frac{-\tau k(1+k^4)\pi}{1-k^2} - \frac{\bar{\omega} k^2(1+k^2)\pi}{1-k^2} \quad (\text{C13})$$

Consider the integration required for I_2 , that is,

$$\int_{-k}^k \frac{\tanh^{-1} \left[\frac{\sqrt{(1-k^2)(1-\psi^2)}}{1+k\psi} \right] d\psi}{\sqrt{(1-\psi^2)(k^2-\psi^2)}} \quad (\text{C14})$$

Let $\psi = k \sin \theta$; then expression (C14) becomes

$$\int_{-\pi/2}^{\pi/2} \frac{\tanh^{-1} \left[\frac{\sqrt{(1-k^2)(1-k^2 \sin^2 \theta)}}{1+k^2 \sin \theta} \right] d\theta}{\sqrt{1-k^2 \sin^2 \theta}} \quad (\text{C15})$$

It can be shown that

$$\left. \begin{aligned} \tanh^{-1} \left[\frac{\sqrt{(1-k^2)(1-k^2 \sin^2 \theta)}}{1+k^2 \sin \theta} \right] &= \tanh^{-1} \frac{\sqrt{1-k^2}}{\sqrt{1-k^2 \sin^2 \theta}} - \tanh^{-1} \frac{\sqrt{1-k^2} \sin \theta}{\sqrt{1-k^2 \sin^2 \theta}} & 0 \leq \theta \leq \pi/2 \\ &= \tanh^{-1} \frac{\sqrt{1-k^2}}{\sqrt{1-k^2 \sin^2 \theta}} + \tanh^{-1} \frac{-\sqrt{1-k^2} \sin \theta}{\sqrt{1-k^2 \sin^2 \theta}} & 0 \geq \theta \geq -\pi/2 \end{aligned} \right\} \quad (\text{C16})$$

This fact allows expression (C15) to be written as

$$\int_{-\pi/2}^{\pi/2} \frac{\tanh^{-1} \left(\frac{\sqrt{1-k^2}}{\sqrt{1-k^2 \sin^2 \theta}} \right) d\theta}{\sqrt{1-k^2 \sin^2 \theta}} - \int_0^{\pi/2} \frac{\tanh^{-1} \left(\frac{\sqrt{1-k^2} \sin \theta}{\sqrt{1-k^2 \sin^2 \theta}} \right) d\theta}{\sqrt{1-k^2 \sin^2 \theta}} + \int_{-\pi/2}^0 \frac{\tanh^{-1} \left(\frac{-\sqrt{1-k^2} \sin \theta}{\sqrt{1-k^2 \sin^2 \theta}} \right) d\theta}{\sqrt{1-k^2 \sin^2 \theta}} \quad (\text{C17})$$

The last two integrals of expression (C17) cancel each other and leave

$$2 \int_0^{\pi/2} \frac{\tanh^{-1} \left(\frac{\sqrt{1-k^2}}{\sqrt{1-k^2 \sin^2 \theta}} \right) d\theta}{\sqrt{1-k^2 \sin^2 \theta}} \quad (\text{C18})$$

After the inverse hyperbolic tangent is replaced by its logarithmic equivalent and the additional variable transformation

$$\sin^2 \nu = \frac{1-k^2}{1-k^2 \sin^2 \theta} \quad (\text{C19})$$

is introduced, expression (C18) becomes

$$\int_{\sin^{-1} \sqrt{1-k^2}}^{\pi/2} \left(\log_e \frac{1+\sin \nu}{1-\sin \nu} \right) \frac{d\nu}{\sqrt{\sin^2 \nu - (1-k^2)}} \quad (\text{C20})$$

It is now convenient to make the substitution

$$\delta = \sin^{-1} \sqrt{1-k^2}$$

Expression (C20) then becomes

$$\int_{\delta}^{\pi/2} \left(\log_e \frac{1+\sin \nu}{1-\sin \nu} \right) \frac{d\nu}{\sqrt{\sin^2 \nu - \sin^2 \delta}} \quad (\text{C21})$$

which is exactly in the form of the fourth integration formula of table 335 in reference 28. This formula gives the value of expression (C21) as $\pi K'(k)$. The integration of I_2 may now be expressed as

$$I_2 = -k(\tau + \bar{\omega} k^3) \pi K'(k) \quad (\text{C22})$$

Using the same integrating procedure for I_3 , I_4 , and I_6 as just outlined for I_2 and the integration formulas in tables 335 and 336 of reference 28 leads to

$$I_3 = \frac{[\tau k(1+k^2) + 3\bar{\omega} k^3][1 + K'(k) - E'(k)]\pi}{1-k^2}$$

$$I_4 + I_6 = \pi \bar{\omega} (1 - k^2) k^2 \Pi \left[-(1 - k^2), \sqrt{1 - k^2}, \frac{\pi}{2} \right] - \bar{\omega} (1 - k^2) k^2 \pi K'(k) - \frac{\bar{\omega} k^2 \pi [1 + K'(k) - E'(k)]}{1 - k^2}$$

where $\Pi \left[-(1 - k^2), \sqrt{1 - k^2}, \frac{\pi}{2} \right]$ is a complete elliptic integral of the third kind with modulus $\sqrt{1 - k^2}$ and parameter $-(1 - k^2)$.

Summing all the various parts contributing to the third term in equation (C8), including the common factor, gives the following expression:

$$\frac{-1}{B(1 - k^2) \sqrt{1 + k^2}} \left\{ \pi \tau k^3 + \pi \bar{\omega} k^2 + \frac{\pi K'(k) [2k^3 \tau + \bar{\omega} k^2 (1 + k^2)]}{1 - k^2} - \frac{\pi E'(k) [2k^2 \bar{\omega} + \tau k (1 + k^2)]}{1 - k^2} + \bar{\omega} k^2 \pi (1 - k^2) \Pi \left[-(1 - k^2), 1 - k^2, \frac{\pi}{2} \right] \right\} \quad (C23)$$

The addition of expression (C23) to expression (C9) completely evaluates ①. Expression (C3) gives the evaluation of ②, ③, and ④. Before writing the total integration, that is the sum of expressions (C23), (C9), and (C3), it is desirable to combine expressions (C3) and (C9), which are functions of Bm , and transform them by equation (C11) to functions of k . This procedure yields

$$\frac{\pi (\bar{\omega} k^2 + \tau k^3)}{B \sqrt{1 + k^2} (1 - k^2)} \quad (C24)$$

The total integration may now be written in terms of the parameter k as

$$\frac{-\pi}{B \sqrt{1 + k^2} (1 - k^2)^2} \left\{ K'(k) [2k^3 \tau + \bar{\omega} k^2 (1 + k^2)] - E'(k) [2k^2 \bar{\omega} + \tau k (1 + k^2)] + \bar{\omega} k^2 (1 - k^2)^2 \Pi \left[-(1 - k^2), 1 - k^2, \frac{\pi}{2} \right] \right\} \quad (C25)$$

By use of the process commonly known as interchanging the amplitude and parameter (see pp. 133 to 141 of ref. 29) the elliptic integral of the third kind appearing in equation (C25) is found to be equivalent to $\frac{E'(k)}{k^2}$. This operation permits the expression for v/x (eq. (C25)) to assume the form given in equation (A20).

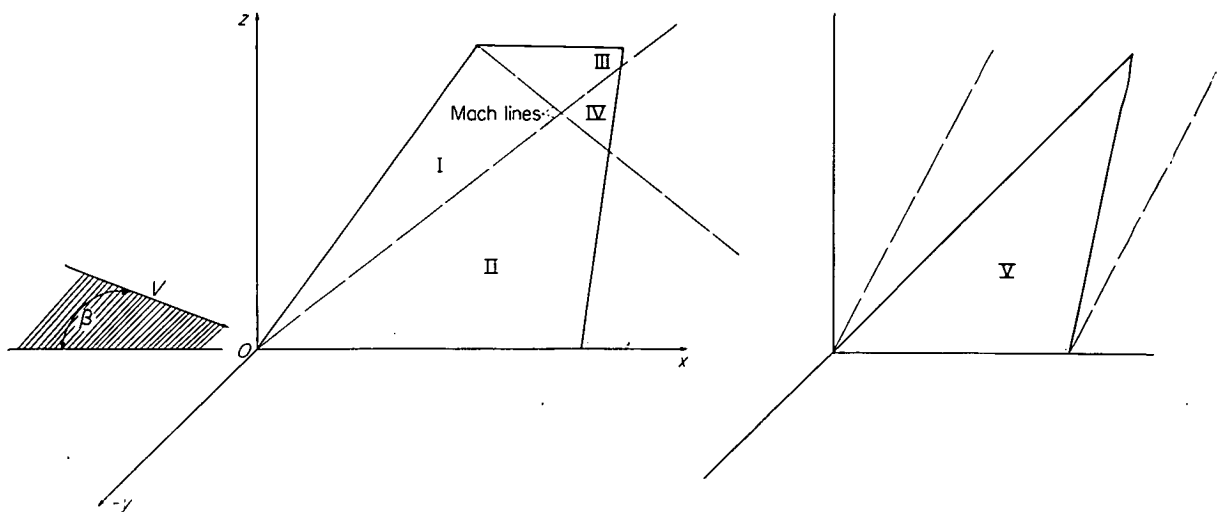
REFERENCES

1. Ribner, Herbert S.: The Stability Derivatives of Low-Aspect-Ratio Triangular Wings at Subsonic and Supersonic Speeds. NACA TN 1423, 1947.
2. Spreiter, John R.: The Aerodynamic Forces on Slender Plane- and Cruciform-Wing and Body Combinations. NACA Rep. 962, 1950. (Supersedes NACA TN's 1897 and 1662.)
3. Lomax, Harvard, and Heaslet, Max. A.: Damping-in-Roll Calculations for Slender Swept-Back Wings and Slender Wing-Body Combinations. NACA TN 1950, 1949.
4. Adams, Gaynor J.: Theoretical Damping in Roll and Rolling Effectiveness of Slender Cruciform Wings. NACA TN 2270, 1951.
5. Bobbitt, Percy J., and Malvestuto, Frank S., Jr.: Estimation of Forces and Moments Due to Rolling for Several Slender-Tail Configurations at Supersonic Speeds. NACA TN 2955, 1953.
6. Ribner, Herbert S.: Damping in Roll of Cruciform and Some Related Delta Wings at Supersonic Speeds. NACA TN 2285, 1951.
7. Martin, John C.: A Vector Study of Linearized Supersonic Flow Applications to Nonplanar Problems. NACA Rep. 1143, 1953. (Supersedes NACA TN 2641.)
8. Bleviss, Zegmund O.: Interference Effects in Supersonic Flow. Ph. D. Thesis, C.I.T., 1951.
9. Malvestuto, Frank S., Jr.: Theoretical Supersonic Force and Moment Coefficients on a Sideslipping Vertical- and Horizontal-Tail Combination With Subsonic Leading Edges and Supersonic Trailing Edges. NACA TN 3071, 1954.
10. Martin, John C., and Malvestuto, Frank S., Jr.: Theoretical Force and Moments Due to Sideslip of a Number of Vertical Tail Configurations at Supersonic Speeds. NACA TN 2412, 1951.
11. Heaslet, Max. A., Lomax, Harvard, and Jones, Arthur L.: Volterra's Solution of the Wave Equation as Applied to Three-Dimensional Supersonic Airfoil Problems. NACA Rep. 889, 1947. (Supersedes NACA TN 1412.)
12. Bryson, Arthur E., Jr.: Stability Derivatives for a Slender Missile With Application to a Wing-Body-Vertical-Tail Configuration. Jour. Aero. Sci., vol. 20, no. 5, May 1953, pp. 297-308.
13. Sacks, Alvin H.: Aerodynamic Forces, Moments, and Stability Derivatives for Slender Bodies of General Cross Section. NACA TN 3283, 1954.
14. Brown, Clinton E.: Theoretical Lift and Drag of Thin Triangular Wings at Supersonic Speeds. NACA Rep. 839, 1946. (Supersedes NACA TN 1183.)
15. Brown, Clinton E., and Adams, Mac C.: Damping in Pitch and Roll of Triangular Wings at Supersonic Speeds. NACA Rep. 892, 1948. (Supersedes NACA TN 1566.)
16. Evvard, John C.: Distribution of Wave Drag and Lift in the Vicinity of Wing Tips at Supersonic Speeds. NACA TN 1382, 1947.
17. Malvestuto, Frank S., Jr., Margolis, Kenneth, and Ribner, Herbert S.: Theoretical Lift and Damping in Roll at Supersonic Speeds of Thin Sweptback Tapered Wings With Streamwise Tips, Subsonic Leading Edges, and Supersonic Trailing Edges. NACA Rep. 970, 1950. (Supersedes NACA TN 1860.)
18. Martin, John C., Margolis, Kenneth, and Jeffreys, Isabella: Calculation of Lift and Pitching Moments Due to Angle of Attack and Steady Pitching Velocity at Supersonic Speeds for Thin Sweptback Tapered Wings With Streamwise Tips and Supersonic Leading and Trailing Edges. NACA TN 2699, 1952.
19. Margolis, Kenneth, Sherman, Windsor L., and Hannah, Margery E.: Theoretical Calculation of the Pressure Distribution, Span Loading, and Rolling Moment Due to Sideslip at Supersonic Speeds for Thin Sweptback Tapered Wings With Supersonic Trailing Edges and Wing Tips Parallel to the Axis of Wing Symmetry. NACA TN 2898, 1953.
20. Harmon, Sidney M., and Jeffreys, Isabella: Theoretical Lift and Damping in Roll of Thin Wings With Arbitrary Sweep and Taper at Supersonic Speeds—Supersonic Leading and Trailing Edges. NACA TN 2114, 1950.
21. Ribner, Herbert S., and Malvestuto, Frank S., Jr.: Stability Derivatives of Triangular Wings at Supersonic Speeds. NACA Rep. 908, 1948. (Supersedes NACA TN 1572.)
22. Malvestuto, Frank S., Jr., and Hoover, Dorothy M.: Supersonic Lift and Pitching Moment of Thin Sweptback Tapered Wings

- Produced by Constant Vertical Acceleration—Subsonic Leading Edges and Supersonic Trailing Edges. NACA TN 2315, 1951.
23. Cole, Isabella J., and Margolis, Kenneth: Lift and Pitching Moment at Supersonic Speeds Due to Constant Vertical Acceleration for Thin Sweptback Tapered Wings With Streamwise Tips—Supersonic Leading and Trailing Edges. NACA TN 3196, 1954.
24. Malvestuto, Frank S., Jr., and Margolis, Kenneth: Theoretical Stability Derivatives of Thin Sweptback Wings Tapered to a Point With Sweptback or Sweptforward Trailing Edges for a Limited Range of Supersonic Speeds. NACA Rep. 971, 1950.

- (Supersedes NACA TN 1761).
25. Busemann, Adolf: Infinitesimal Conical Supersonic Flow. NACA TM 1100, 1947.
26. Lomax, Harvard, and Heaslet, Max. A.: Generalized Conical-Flow Fields in Supersonic Wing Theory. NACA TN 2497, 1951.
27. Peirce, B. O.: A Short Table of Integrals. Third rev. ed., Ginn and Co., 1929.
28. De Haan, D. Bierens: Nouvelles Tables D'Intégrales Définies. G. E. Stechart & Co. (New York), 1939, pp. 475-477.
29. Cayley, Arthur: An Elementary Treatise on Elliptic Functions. Second ed., George Bell and Sons (London), 1895.

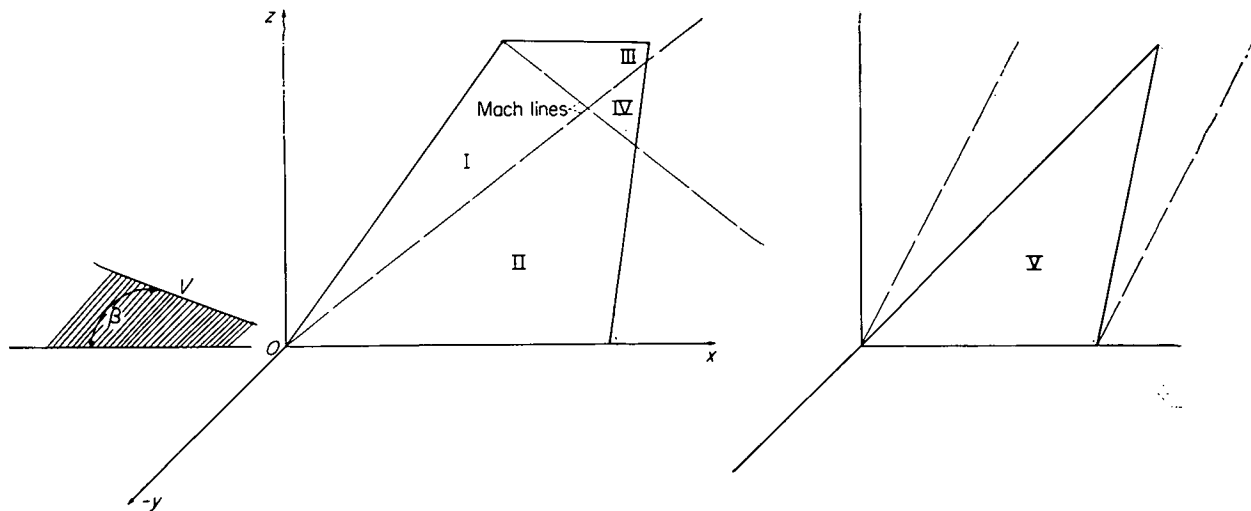
TABLE I
FORMULAS FOR POTENTIAL DISTRIBUTION DUE TO CONSTANT SIDESLIP



(Tail is in xz -plane; β is positive; V as shown is in xy -plane)

Region (see sketch)	$\varphi(x, 0^+, z)$
I	$-\frac{V\beta(mx-z)}{\sqrt{B^2m^2-1}}$
II	$-\frac{V\beta}{\pi\sqrt{B^2m^2-1}} \left[(mx-z) \cos^{-1} \frac{mx-z(2Bm-1)}{mx-z} + 2\sqrt{zm(x-Bz)(Bm-1)} \right]$
III	$-\frac{V\beta}{\pi\sqrt{B^2m^2-1}} \left\{ (mx-z) \cos^{-1} \frac{mx-z+2(1+Bm)(z-b)}{mx-z} + 2\sqrt{(z-b)(Bm+1)[b(1+Bm)-m(x+Bz)]} \right\}$
IV	$\Sigma (II+III-I)$
V	$-\frac{V\beta H(Bm)\sqrt{z(mx-z)}}{Bm}$

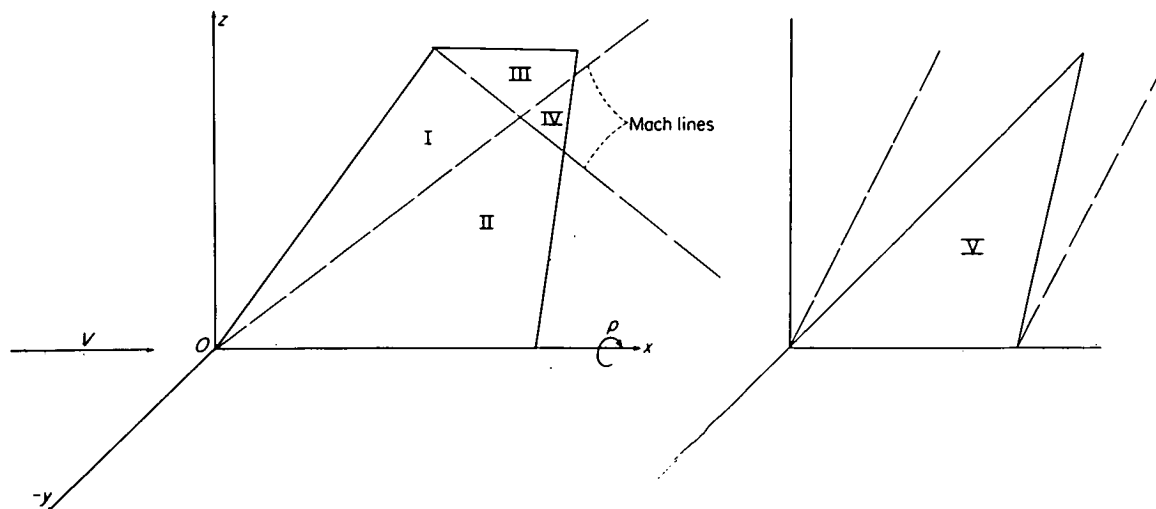
TABLE II
FORMULAS FOR PRESSURE-DIFFERENCE COEFFICIENT DUE TO CONSTANT SIDESLIP



(Tail is in xz -plane; β is positive; V as shown is in xy -plane)

Region (see sketch)	$\frac{\Delta P}{q}(x, z)$
I	$-\frac{4\beta m}{\sqrt{B^2 m^2 - 1}}$
II	$-\frac{4\beta m}{\pi \sqrt{B^2 m^2 - 1}} \cos^{-1} \frac{mx - z(2Bm - 1)}{mx - z}$
III	$-\frac{4\beta m}{\pi \sqrt{B^2 m^2 - 1}} \cos^{-1} \frac{mx - z + 2(1 + Bm)(z - b)}{mx - z}$
IV	$\Sigma (II + III - I)$
V	$-\frac{2\beta z H(Bm)}{B \sqrt{z(mx - z)}}$

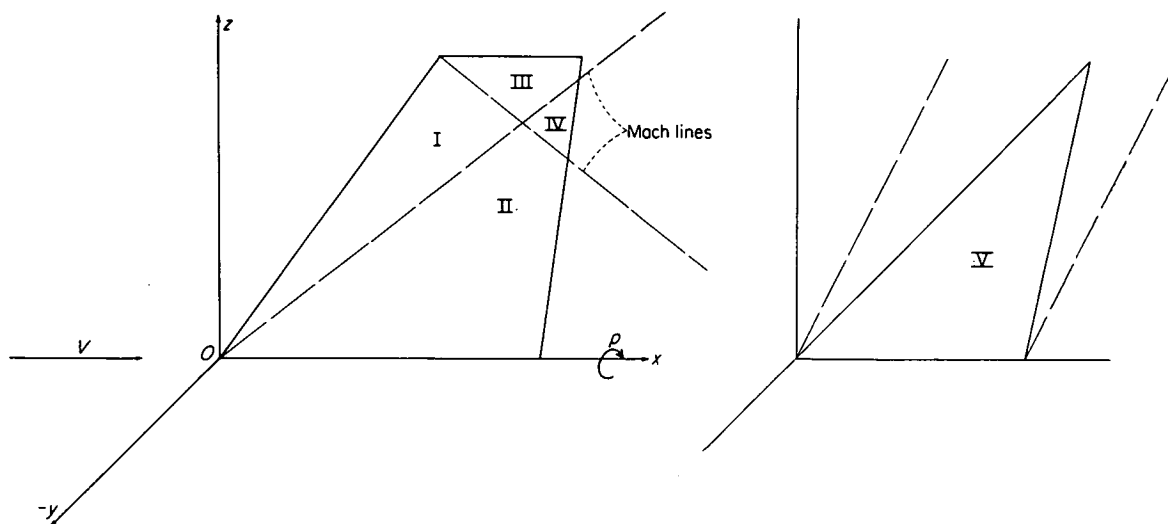
TABLE III
FORMULAS FOR POTENTIAL DISTRIBUTION DUE TO STEADY ROLLING



(Tail is in xz -plane; positive rolling)

Region (see sketch)	$\varphi(x, 0^+, z)$
I	$-\frac{p}{2(B^2m^2-1)^{3/2}} \left\{ (mx-z)[-mx+z(2B^2m^2-1)] \right\}$
II	$-\frac{p}{\pi} \left\{ \frac{mx(4Bm-1)+z(2B^2m^2-2Bm-3)}{3(B^2m^2-1)} \sqrt{\frac{mx(x-Bz)}{Bm+1}} - \frac{(mx-z)[mx-z(2B^2m^2-1)]}{2(B^2m^2-1)^{3/2}} \cos^{-1} \frac{mx+z(1-2Bm)}{mx-z} \right\}$
III	$-\frac{p}{\pi(B^2m^2-1)^{3/2}} \left\{ \frac{(mx-z)[-mx+z(2B^2m^2-1)]}{2} \cos^{-1} \frac{mx-z+2(1+Bm)(z-b)}{mx-z} - \frac{(mx-b)(4Bm-1)+(z-b)(3-2B^2m^2-2Bm)-6b(B^2m^2-1)}{3} \sqrt{(z-b)(Bm+1)[b(1+Bm)-m(x+Bz)]} \right\}$
IV	$\Sigma(\text{II} + \text{III} - \text{I})$
V	$p(\tau_p' z + \omega_p' mx) \sqrt{z(mx-z)}$

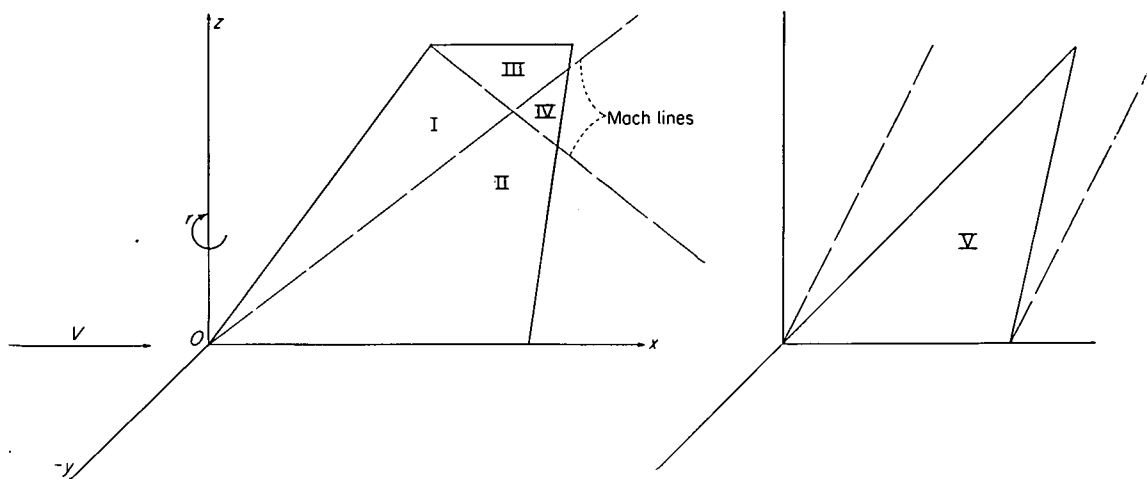
TABLE IV
FORMULAS FOR PRESSURE-DIFFERENCE COEFFICIENT DUE TO STEADY ROLLING



(Tail is in xz -plane; positive rolling)

Region (see sketch)	$\frac{\Delta P}{q}(x, z)$
I	$-\frac{4pm(B^2m^2z - mx)}{V(B^2m^2 - 1)^{3/2}}$
II	$-\frac{4p}{\pi V} \left[\frac{2Bm^2}{(B^2m^2 - 1)} \sqrt{\frac{zm(x - Bz)}{Bm + 1}} - \frac{m^2(x - B^2zm)}{(B^2m^2 - 1)^{3/2}} \cos^{-1} \frac{mx + z(1 - 2Bm)}{mx - z} \right]$
III	$-\frac{4pm}{\pi V(B^2m^2 - 1)^{3/2}} \left\{ (B^2m^2z - mx) \cos^{-1} \frac{mx - z + 2(1 + Bm)(z - b)}{mx - z} - 2Bm\sqrt{(z - b)(Bm + 1)[b(1 + Bm) - m(x + Bz)]} \right\}$
IV	$\Sigma(\text{II} + \text{III} - \text{I})$
V	$\frac{2p}{V} \frac{\tau_p' mz^2 + 3m^2\omega_p' xz - 2m\omega_p' z^2}{\sqrt{z(mx - z)}}$

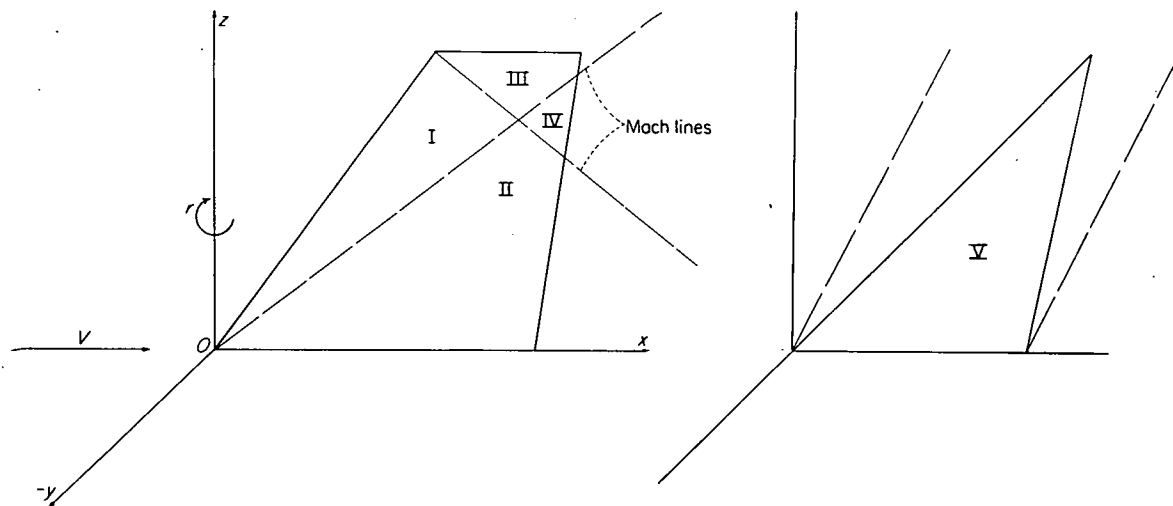
TABLE V
FORMULAS FOR POTENTIAL DISTRIBUTION DUE TO STEADY YAWING



(Tail is in xz -plane; positive yawing)

Region (see sketch)	$\varphi(x, 0^+, z)$
I	$\frac{r}{2(B^2 m^2 - 1)^{3/2}} [x^2(-2m + B^2 m^3) + 2xz - B^2 z^2 m]$
II	$\frac{r}{\pi} \left\{ \frac{x(5B^2 m^2 + 4Bm - 6) - B^2 m z(2Bm + 1)}{3(B^2 m^2 - 1)} \sqrt{\frac{mz(x - Bz)}{Bm + 1}} + \right.$ $\left. \frac{(mx - z)[mzB^2 + x(m^2 B^2 - 2)]}{2(B^2 m^2 - 1)^{3/2}} \cos^{-1} \frac{mx - z(2Bm - 1)}{mx - z} \right\}$
III	$\frac{r}{\pi} \left\{ \frac{mx(5B^2 m^2 - 4Bm - 6) + B^2 m^2(z - b)(2Bm - 1) + Bmb(4 + Bm)}{3m(B^2 m^2 - 1)^{3/2}} \sqrt{(z - b)(Bm + 1)[b(1 + Bm) - m(x + Bz)]} + \right.$ $\left. \frac{(mx - z)[B^2 m^2(mx + z) - 2mx]}{2m(B^2 m^2 - 1)^{3/2}} \cos^{-1} \frac{mx - z + 2(1 + Bm)(z - b)}{mx - z} \right\}$
IV	$\Sigma(\text{II} + \text{III} - \text{I})$
V	$Br(\tau_r' z + \omega_r' mx) \sqrt{z(mx - z)}$

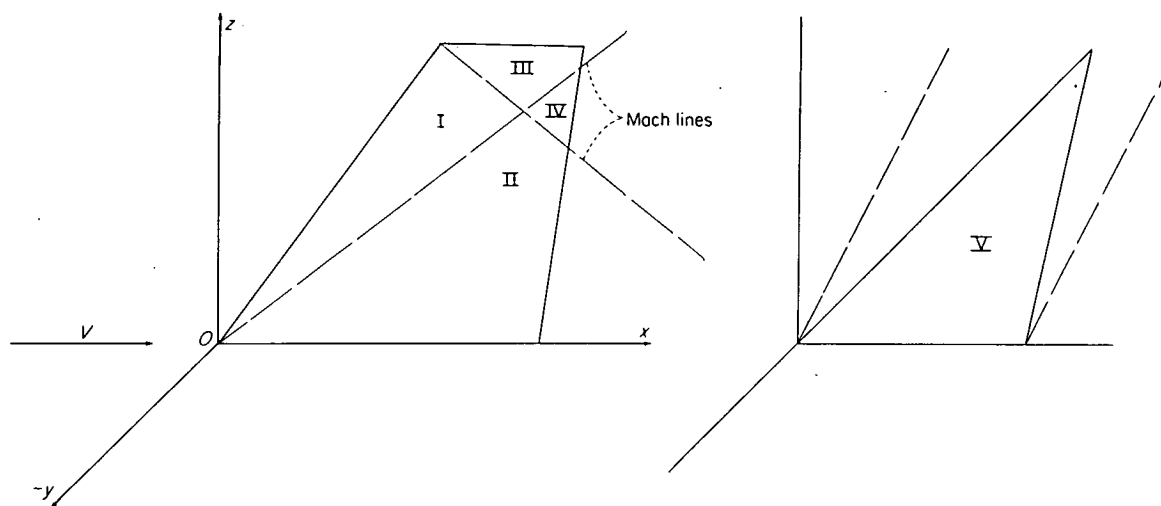
TABLE VI
FORMULAS FOR PRESSURE-DIFFERENCE COEFFICIENT DUE TO STEADY YAWING



(Tail is in xz-plane; positive yawing)

Region (see sketch)	$\frac{\Delta P}{q}(x, z)$
I	$\frac{4r}{V(B^2m^2-1)^{3/2}} [mx(B^2m^2-2) + z]$
II	$\frac{4r}{\pi V(B^2m^2-1)^{3/2}} \left\{ [mx(B^2m^2-2) + z] \cos^{-1} \frac{mx-z(2Bm-1)}{mx-z} + 2(B^2m^2+Bm-1) \sqrt{mz(Bm-1)(x-Bz)} \right\}$
III	$\frac{4r}{\pi V(B^2m^2-1)^{3/2}} \left\{ [z + mx(B^2m^2-2)] \cos^{-1} \frac{mx-z+2(1+Bm)(z-b)}{mx-z} + 2(B^2m^2-Bm-1) \sqrt{(z-b)(Bm+1)[b(1+Bm)-m(x+Bz)]} \right\}$
IV	$\Sigma(\text{II} + \text{III} - \text{I})$
V	$\frac{2Br}{V} \frac{\tau_r' m z^2 + 3m^2 \omega_r' x z - 2m \omega_r' z^2}{\sqrt{z(mx-z)}}$

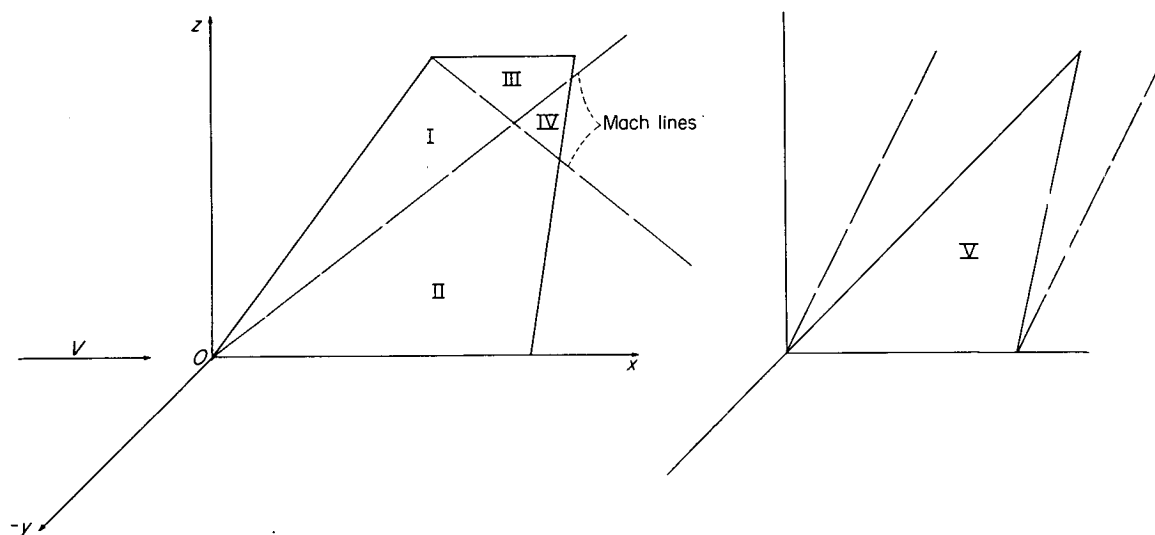
TABLE VII
FORMULAS FOR POTENTIAL DISTRIBUTION DUE TO CONSTANT LATERAL ACCELERATION



(Tail is in xz -plane; positive $\dot{\beta}$ in positive y -direction)

Region (see sketch)	$\varphi(x, 0^+, z)$
I	$-\frac{\dot{\beta}(mx-z)}{\sqrt{B^2m^2-1}} \left[tV - \frac{mM^2(mx-z)}{2(B^2m^2-1)} \right]$
II	$-\frac{\dot{\beta}}{\pi\sqrt{B^2m^2-1}} \left\{ \sqrt{mz(x-Bz)}(Bm-1) \left[2tV + \frac{M^2mx(4-Bm) - M^2mBz(2Bm+1)}{3B(B^2m^2-1)} \right] + \right. \\ \left. \left[\cos^{-1} \frac{mx-z(2Bm-1)}{mx-z} \right] \left[\frac{M^2m(z-mx)}{2(B^2m^2-1)} + tV \right] (mx-z) \right\}$
III	$-\frac{\dot{\beta}}{\pi\sqrt{B^2m^2-1}} \left\{ \sqrt{(z-b)(Bm+1)[b(1+Bm)-m(x+Bz)]} \left[2tV + \frac{M^2(4+Bm)(b-mx) + M^2Bm(z-b)(2Bm-1)}{3B(B^2m^2-1)} \right] + \right. \\ \left. \left[\cos^{-1} \frac{mx-z+2(1+Bm)(z-b)}{mx-z} \right] \left[tV + \frac{M^2m(z-mx)}{2(B^2m^2-1)} \right] (mx-z) \right\}$
IV	$\Sigma(\text{II} + \text{III} - \text{I})$
V	$-\dot{\beta}\sqrt{z(mx-z)} \left\{ \frac{(B^2+1)}{B} (\tau_r' z + \omega_r' mx) + \left[Vt - \frac{(B^2+1)x}{B^2} \right] \frac{H(Bm)}{Bm} \right\}$

TABLE VIII
FORMULAS FOR PRESSURE-DIFFERENCE COEFFICIENT DUE TO CONSTANT LATERAL ACCELERATION



(Tail is in xz -plane; positive β in positive y -direction)

Region (see sketch)	$\frac{\Delta P}{q}(x, z)$
I	$\frac{4\beta(mx-z)(1+m^2)}{V(B^2m^2-1)^{3/2}}$
II	$\frac{4\beta}{\pi B^2 V \sqrt{B^2m^2-1}} \left\{ \frac{B^2(1+m^2)(mx-z)}{B^2m^2-1} \cos^{-1} \frac{mx-z(2Bm-1)}{mx-z} + \right.$ $\left. 2 \left[1 - \frac{M^2(B^2m^2+Bm-1)}{B^2m^2-1} \right] \sqrt{zm(x-Bz)(Bm-1)} \right\}$
III	$\frac{4\beta}{\pi B^2 V \sqrt{B^2m^2-1}} \left\{ \frac{B^2(1+m^2)(mx-z)}{B^2m^2-1} \cos^{-1} \frac{mx-z+2(1+Bm)(z-b)}{mx-z} + \right.$ $\left. 2 \left[1 - \frac{M^2(B^2m^2-Bm-1)}{B^2m^2-1} \right] \sqrt{(z-b)(Bm+1)[b(1+Bm)-m(x+Bz)]} \right\}$
IV	$\Sigma(\text{II} + \text{III} - \text{I})$
V	$-\frac{2\beta}{B^2 \bar{V}} \left[\frac{(B^2+1)B(\tau_r' m z^2 + 3m^2 \omega_r' x z - 2m \omega_r' z^2)}{\sqrt{z(mx-z)}} - \right.$ $\left. \frac{(B^2+1)xzH(Bm)}{B\sqrt{z(mx-z)}} - \frac{2H(Bm)\sqrt{z(mx-z)}}{Bm} \right]$

TABLE IX
STABILITY DERIVATIVES FOR HALF-DELTA AND RECTANGULAR ISOLATED VERTICAL TAILS

Derivative (a)	Half-delta tails		Rectangular tails $AB \geq 1$
	$0 \leq AB < 2$	$AB \geq 2$	
C_{Y_β}	$-\frac{\pi}{B} H(Bm)$	$-\frac{4}{B} \sqrt{\frac{AB}{AB+2}}$	$-\frac{4}{B} \left(1 - \frac{1}{2AB}\right)$
C_{n_β}	$\frac{4\pi}{3AB} H(Bm)$	$\frac{16}{3AB} \sqrt{\frac{AB}{AB+2}}$	$\frac{2}{AB} \left(1 - \frac{2}{3AB}\right)$
C_{l_β}	$-\frac{\pi}{2B} H(Bm)$	$-\frac{4}{3B} \frac{AB+1}{\sqrt{AB(AB+2)}}$	$-\frac{2}{B} \left(1 - \frac{1}{2AB}\right)$
C_{Y_p}	$\frac{\pi AB}{4B} (\tau_p' + 2\omega_p')$	$-\frac{4}{3B} \frac{\sqrt{AB}(AB+3)}{(AB+2)^{3/2}}$	$-\frac{2AB-1}{AB^2}$
C_{n_p}	$-\frac{3\pi}{8} (\tau_p' + 2\omega_p')$	$\frac{2(AB+3)}{\sqrt{AB(AB+2)^{3/2}}}$	$\frac{3AB-2}{3A^2B^2}$
C_{l_p}	$\frac{\pi AB}{4B} \left(\frac{5}{8} \tau_p' + \omega_p'\right)$	$-\frac{2A^2B^2+6AB+3}{3B\sqrt{AB}(AB+2)^{3/2}}$	$-\frac{1+4AB-24A^2B^2+32A^3B^3}{24A^3B^4}$
C_{Y_r}	$\frac{\pi AB}{4} (\tau_r' + 2\omega_r')$	$\frac{8(2AB+5)}{3\sqrt{AB}(AB+2)^{3/2}}$	$\frac{2(3AB-1)}{3A^2B^2}$
C_{n_r}	$-\frac{3\pi B}{8} (\tau_r' + 2\omega_r')$	$-\frac{4B(2AB+5)}{[AB(AB+2)]^{3/2}}$	$-\frac{B(8AB-3)}{6A^3B^3}$
C_{l_r}	$\frac{\pi AB}{4} \left(\frac{5}{8} \tau_r' + \omega_r'\right)$	$\frac{2(3A^2B^2+9AB+5)}{3[AB(AB+2)]^{3/2}}$	$\frac{3AB-1}{3A^2B^2}$
$C_{Y_{\dot{\beta}}}$	$-\frac{AB\pi}{4} \left[\tau_r' + 2\omega_r' - \frac{16H(Bm)}{3A^2B^2}\right] -$ $\frac{AB\pi}{4B^2} \left[\tau_r' + 2\omega_r' - \frac{8H(Bm)}{A^2B^2}\right]$	$-\frac{8}{3B^2} \frac{B^2-AB-1}{\sqrt{AB}(AB+2)^3}$	$-\frac{2(B^2+2-3AB)}{3A^2B^4}$
$C_{n_{\dot{\beta}}}$	$\frac{\pi B}{4} \left[\frac{3}{2} \tau_r' + 3\omega_r' - \frac{8H(Bm)}{A^2B^2}\right] +$ $\frac{\pi}{4B} \left[\frac{3}{2} \tau_r' + 3\omega_r' - \frac{12H(Bm)}{A^2B^2}\right]$	$\frac{4}{B} \frac{B^2-AB-1}{\sqrt{A^3B^3}(AB+2)^3}$	$\frac{3B^2-8AB+6}{6A^3B^4}$
$C_{l_{\dot{\beta}}}$	$-\frac{AB\pi}{8} \left[2\omega_r' + \frac{5}{4} \tau_r' - \frac{6H(Bm)}{A^2B^2}\right] -$ $\frac{AB\pi}{8B^2} \left[2\omega_r' + \frac{5}{4} \tau_r' - \frac{8H(Bm)}{A^2B^2}\right]$	$\frac{2}{3B^2} \frac{B^2+A^2B^2+3AB+3}{\sqrt{A^3B^3}(AB+2)^3}$	$-\frac{B^2+2-3AB}{3A^2B^4}$

* Angular velocities and moments measured about the system of body axes shown in figure 2 (b).

TABLE X
STABILITY DERIVATIVES FOR TRIANGULAR ISOLATED VERTICAL TAILS
WITH SUBSONIC LEADING EDGE AND SUPERSONIC TRAILING EDGE

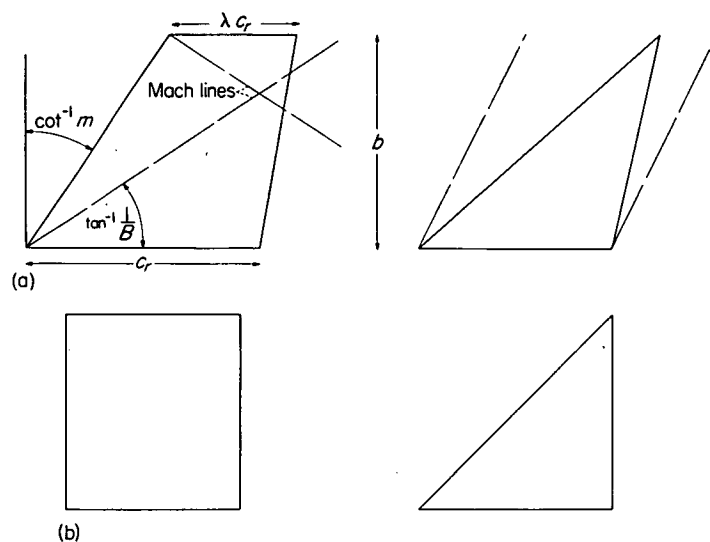
Derivative (a)	Formula (b)
$C_{Y\beta}$	$-\frac{\pi}{B}\sqrt{\frac{AB}{2Bm}} H(Bm)$
$C_{n\beta}$	$\frac{\pi(3AB+2Bm)}{6Bm\sqrt{2BmAB}} H(Bm)$
$C_{l\beta}$	$-\frac{\pi}{2B}\sqrt{\frac{AB}{2Bm}} H(Bm)$
C_{Yp}	$\frac{\pi}{B}\sqrt{2BmAB}\left(\frac{\tau_p'}{4}+\frac{\omega_p'}{4}+\frac{Bm}{2AB}\omega_p'\right)$
C_{n_p}	$-\pi\sqrt{2BmAB}\left[\tau_p'\left(\frac{5}{32Bm}+\frac{1}{16AB}\right)+\omega_p'\left(\frac{5}{32Bm}+\frac{1}{4AB}+\frac{3Bm}{8A^2B^2}\right)\right]$
C_{l_p}	$\frac{\pi}{16B}\sqrt{2BmAB}\left(\frac{5}{2}\tau_p'+\frac{5}{2}\omega_p'+\frac{3Bm}{AB}\omega_p'\right)$
C_{Yr}	$\pi\sqrt{2BmAB}\left(\frac{\tau_r'}{4}+\frac{\omega_r'}{4}+\frac{Bm}{2AB}\omega_r'\right)$
C_{n_r}	$-\pi B\sqrt{2BmAB}\left[\tau_r'\left(\frac{5}{32Bm}+\frac{1}{16AB}\right)+\omega_r'\left(\frac{5}{32Bm}+\frac{1}{4AB}+\frac{3Bm}{8A^2B^2}\right)\right]$
C_{l_r}	$\frac{\pi}{16}\sqrt{2BmAB}\left(\frac{5}{2}\tau_r'+\frac{5}{2}\omega_r'+\frac{3Bm}{AB}\omega_r'\right)$
$C_{Y\dot{\beta}}$	$-\pi\sqrt{2BmAB}\left[\frac{\tau_r'}{4}+\frac{\omega_r'}{4}\left(1+\frac{2Bm}{AB}\right)-\frac{H(Bm)}{4B^2m^2}-\frac{H(Bm)}{6BmAB}\right]-$ $\frac{\pi}{B^2}\sqrt{2BmAB}\left[\frac{\tau_r'}{4}+\frac{\omega_r'}{4}\left(1+\frac{2Bm}{AB}\right)-\frac{H(Bm)}{4B^2m^2}-\frac{H(Bm)}{2BmAB}\right]$
$C_{n\dot{\beta}}$	$\pi B\sqrt{2BmAB}\left[\tau_r'\left(\frac{5}{32Bm}+\frac{1}{16AB}\right)+\omega_r'\left(\frac{5}{32Bm}+\frac{1}{4AB}+\frac{3Bm}{8A^2B^2}\right)-$ $\left(\frac{5}{32B^3m^3}+\frac{1}{8B^2m^2AB}+\frac{1}{8BmA^2B^2}\right)H(Bm)\right]+$ $\frac{\pi}{B}\sqrt{2BmAB}\left[\tau_r'\left(\frac{5}{32Bm}+\frac{1}{16AB}\right)+\omega_r'\left(\frac{5}{32Bm}+\frac{1}{4AB}+\frac{3Bm}{8A^2B^2}\right)-$ $\left(\frac{5}{32B^3m^3}+\frac{1}{4B^2m^2AB}+\frac{3}{8BmA^2B^2}\right)H(Bm)\right]$
$C_{l\dot{\beta}}$	$-\frac{\pi}{32}\sqrt{2BmAB}\left[5\tau_r'+5\omega_r'+\frac{6Bm}{AB}\omega_r'-\left(\frac{5}{B^2m^2}+\frac{2}{BmAB}\right)H(Bm)\right]-$ $\frac{\pi}{32B^2}\sqrt{2BmAB}\left[5\tau_r'+5\omega_r'+\frac{6Bm}{AB}\omega_r'-\left(\frac{5}{B^2m^2}+\frac{6}{BmAB}\right)H(Bm)\right]$

^a Angular velocities and moments measured about the system of body axes shown in figure 2 (b).

^b Formulas valid for triangular plan forms with either sweptback or sweptforward trailing edge provided the edge is supersonic.

TABLE XI
TRANSFER-OF-AXES FORMULAS

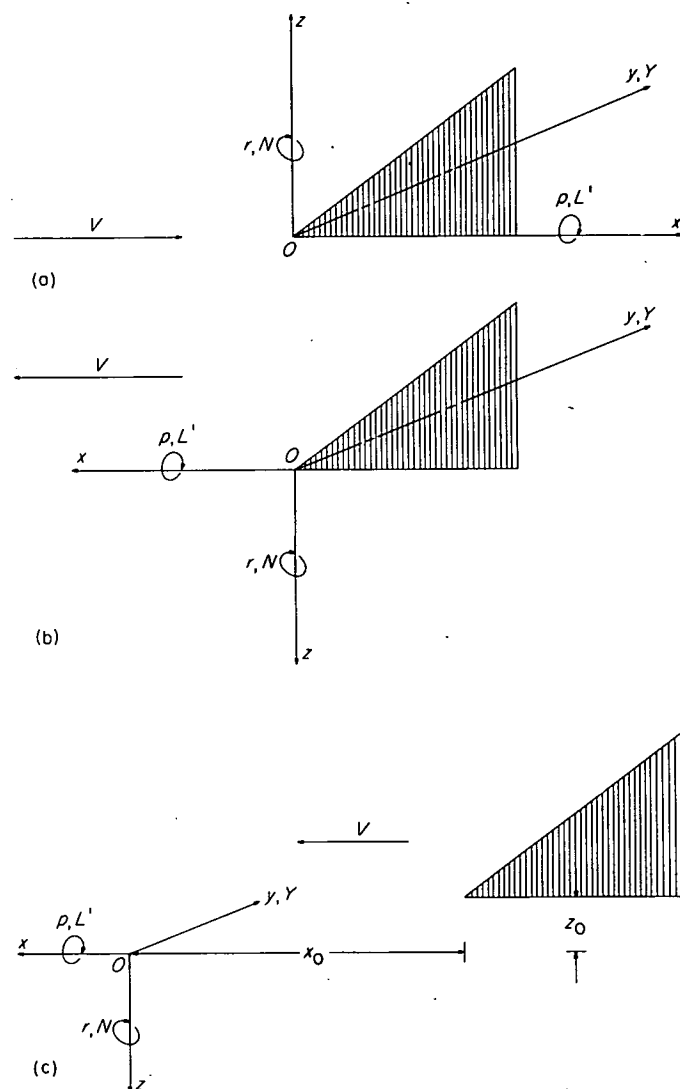
Stability derivatives in a body system of axes with origin at tail apex (see fig. 2 (b))	Formulas for transfer to a body system of axes with origin displaced dis- tances x_0 (positive forward) and z_0 (positive downward) from the tail apex (see fig. 2 (c))
$C_{Y\beta}$	$C_{Y\beta}$
$C_{n\beta}$	$C_{n\beta} - \frac{x_0}{b} C_{Y\beta}$
$C_{l\beta}$	$C_{l\beta} + \frac{z_0}{b} C_{Y\beta}$
C_{Y_p}	C_{Y_p}
C_{n_p}	$C_{n_p} - \frac{x_0}{b} C_{Y_p}$
C_{l_p}	$C_{l_p} + \frac{z_0}{b} C_{Y_p}$
C_{Y_r}	$C_{Y_r} - \frac{x_0}{b} C_{Y\beta}$
C_{n_r}	$C_{n_r} - \frac{x_0}{b} (C_{n\beta} + C_{Y_r}) + \left(\frac{x_0}{b}\right)^2 C_{Y\beta}$
C_{l_r}	$C_{l_r} + \frac{z_0}{b} C_{Y_r} - \frac{x_0}{b} C_{l\beta} - \left(\frac{z_0}{b}\right)\left(\frac{x_0}{b}\right) C_{Y\beta}$
$C_{Y\dot{\beta}}$	$C_{Y\dot{\beta}}$
$C_{n\dot{\beta}}$	$C_{n\dot{\beta}} - \frac{x_0}{b} C_{Y\dot{\beta}}$
$C_{l\dot{\beta}}$	$C_{l\dot{\beta}} + \frac{z_0}{b} C_{Y\dot{\beta}}$



(a) Plan forms of vertical tails analyzed. (Trailing edge may be either sweptback or sweptforward provided it remains supersonic.)

(b) Special cases (rectangular and half-delta vertical tails) for which stability-derivative curves are presented.

FIGURE 1.—Tail plan forms and associated data.



(a) Body-axes system used for analysis. Free-stream velocity V .

(b) Principal body-axes system used for presentation of stability derivatives. Entire system moving with flight velocity V .

(c) Same type of axes system as (b) with origin translated.

FIGURE 2.—Systems of body axes. Positive directions of axes, forces, and moments indicated by arrows.

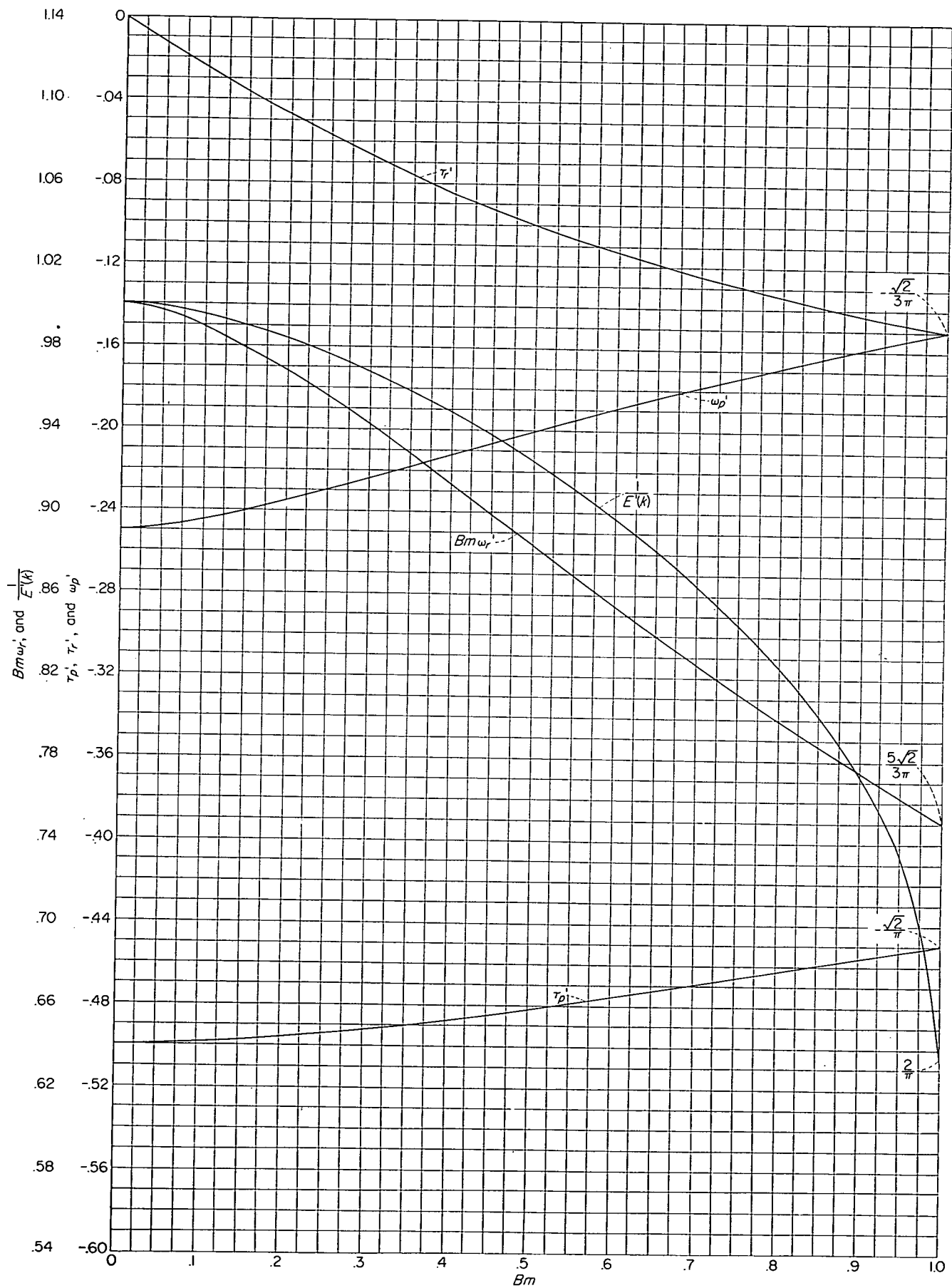


FIGURE 3.—Variation of the parameters $\frac{1}{E'(k)}$, ω_p' , $Bm\omega_r'$, τ_p' and τ_r' with Bm .

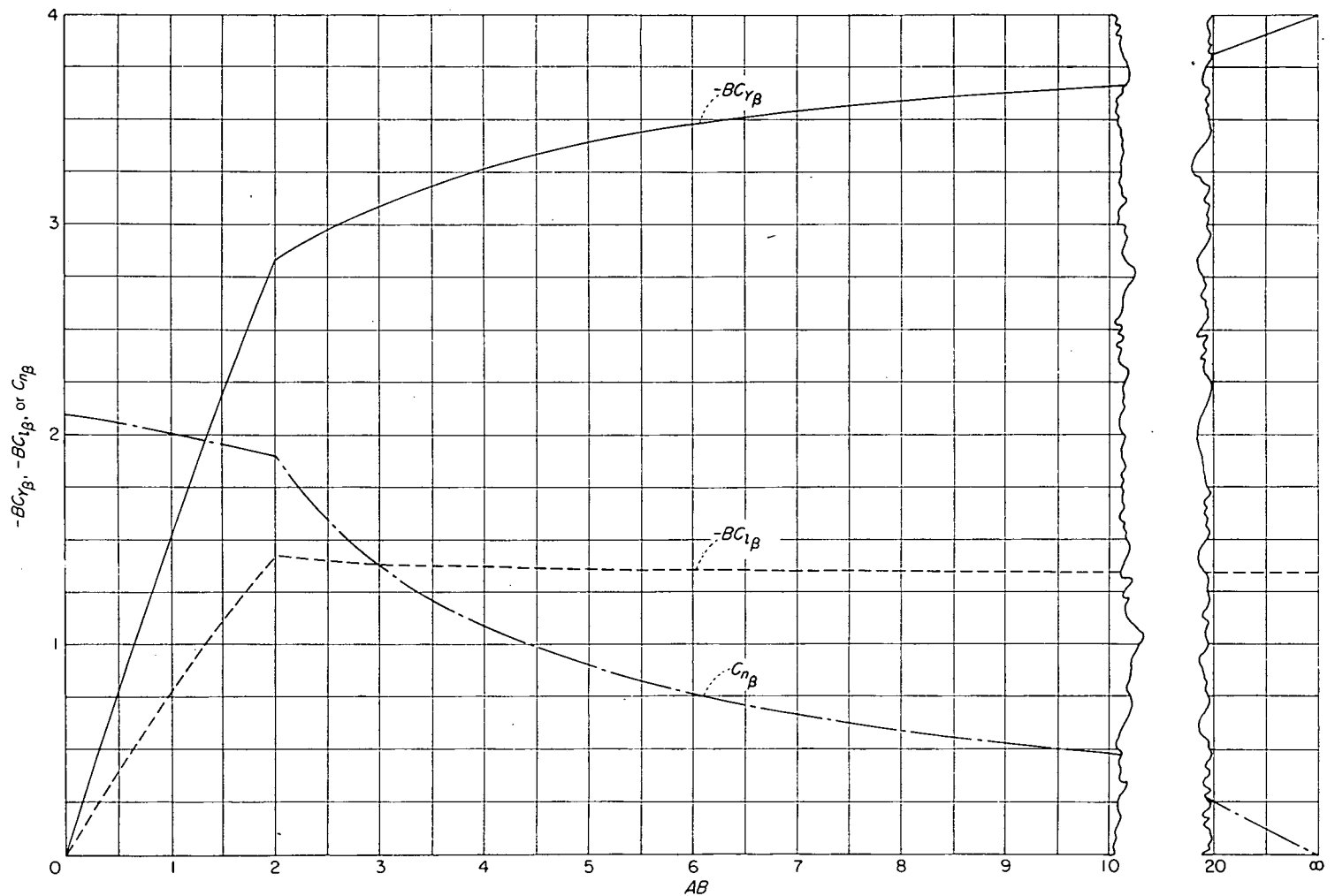


FIGURE 4.—Curves for determining the stability derivatives due to constant sideslip $C_{Y\beta}$, $C_{n\beta}$, and $C_{l\beta}$ for isolated half-delta vertical tails. Derivatives based on vertical-tail parameters b and S ; principal body-axes system with origin at leading edge of root section.

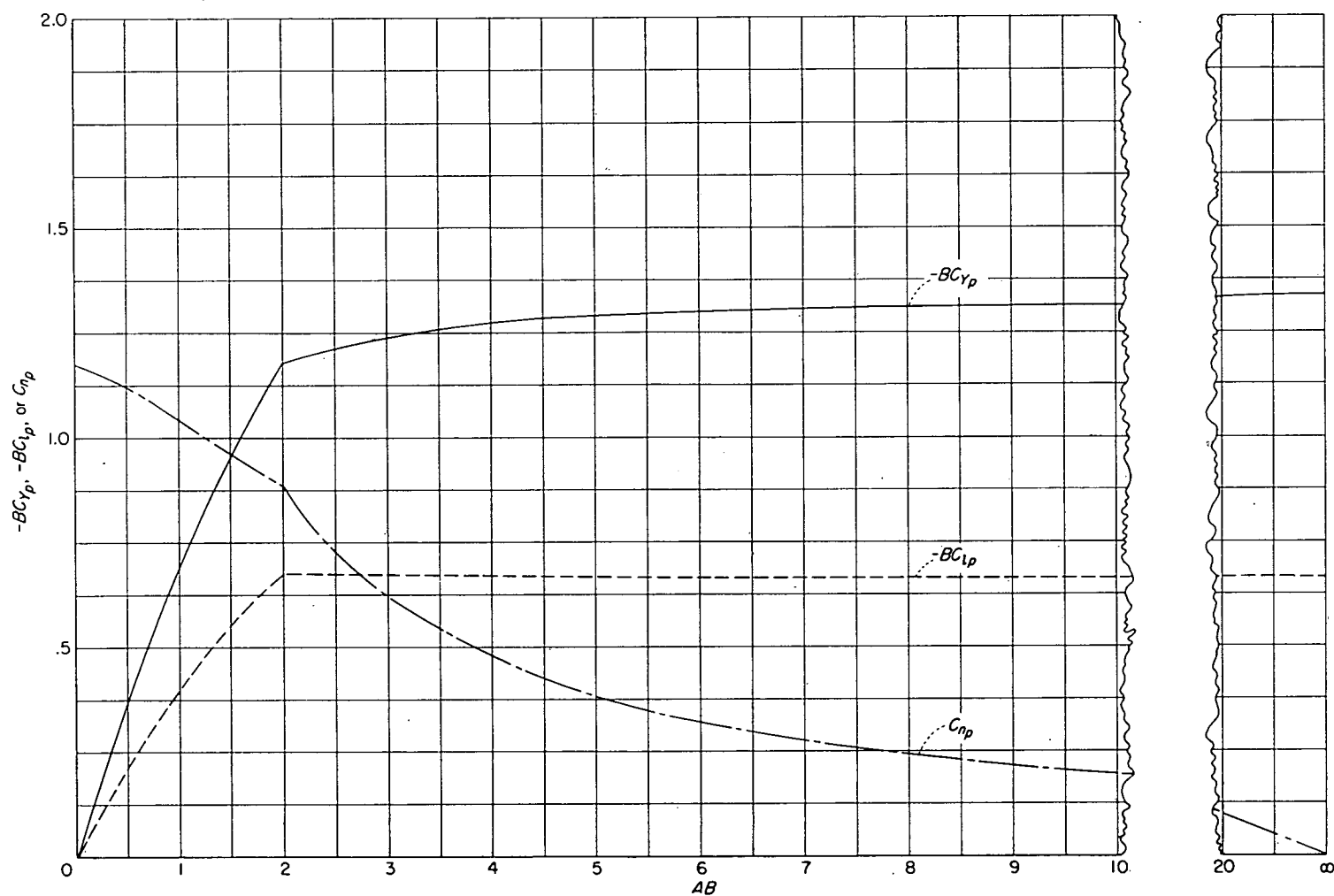


FIGURE 5.—Curves for determining the stability derivatives due to steady rolling C_{Y_p} , C_{n_p} , and C_{l_p} for isolated half-delta vertical tails. Derivatives based on vertical-tail parameters b , S , and angle pb/V ; principal body-axes system with origin at leading edge of root section.

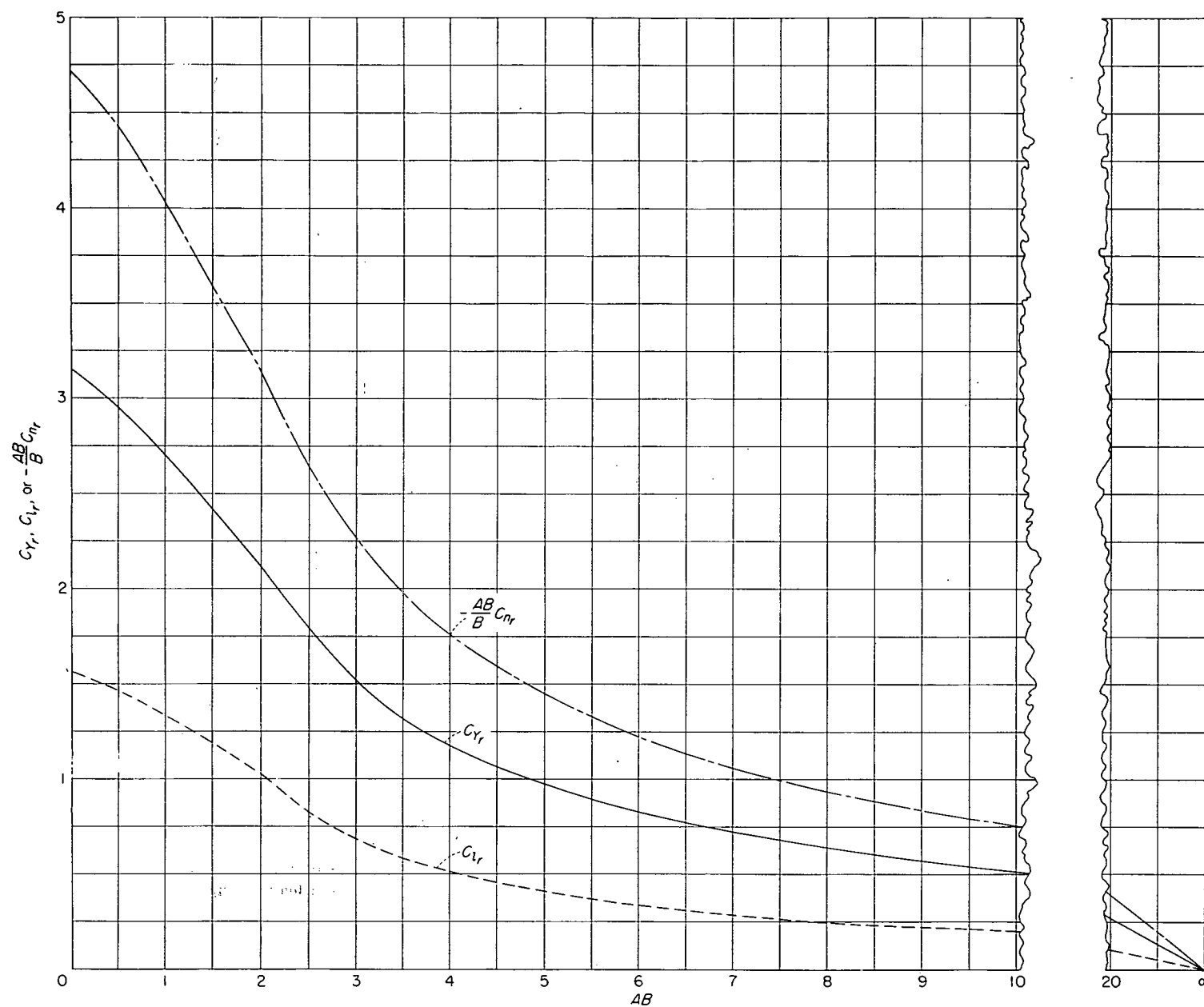


FIGURE 6.—Curves for determining the stability derivatives due to steady yawing C_Y , C_{n_r} , and C_{l_r} for isolated half-delta vertical tails. Derivatives based on vertical-tail parameters b , S , and angle rb/V ; principal body-axes system with origin at leading edge of root section.

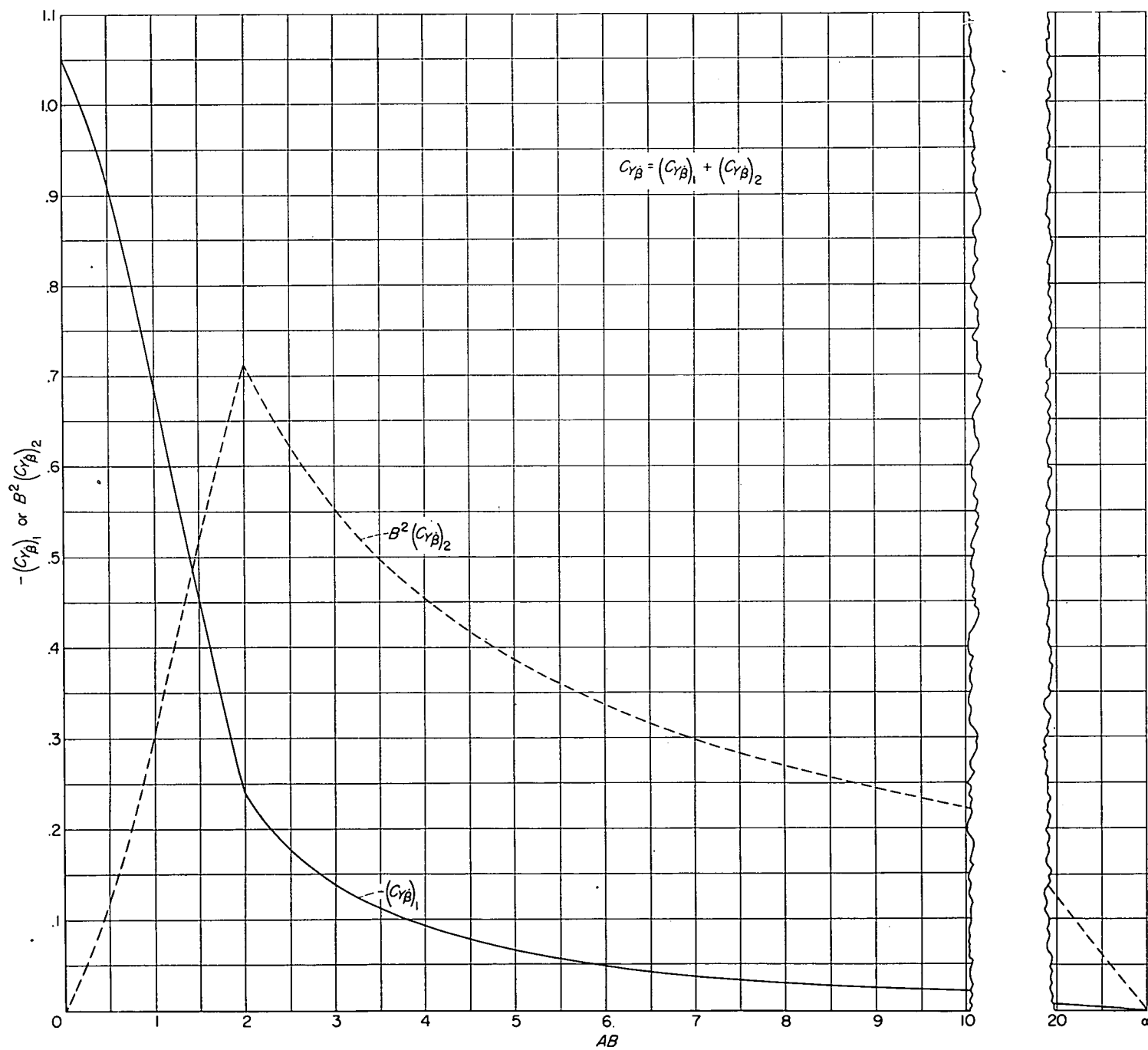


FIGURE 7.—Curves for determining the stability derivative due to constant lateral acceleration $C_{Y\beta}$ for isolated half-delta vertical tails. Derivative based on vertical-tail parameters b , S , and angle $\beta b/V$; principal body-axes system.

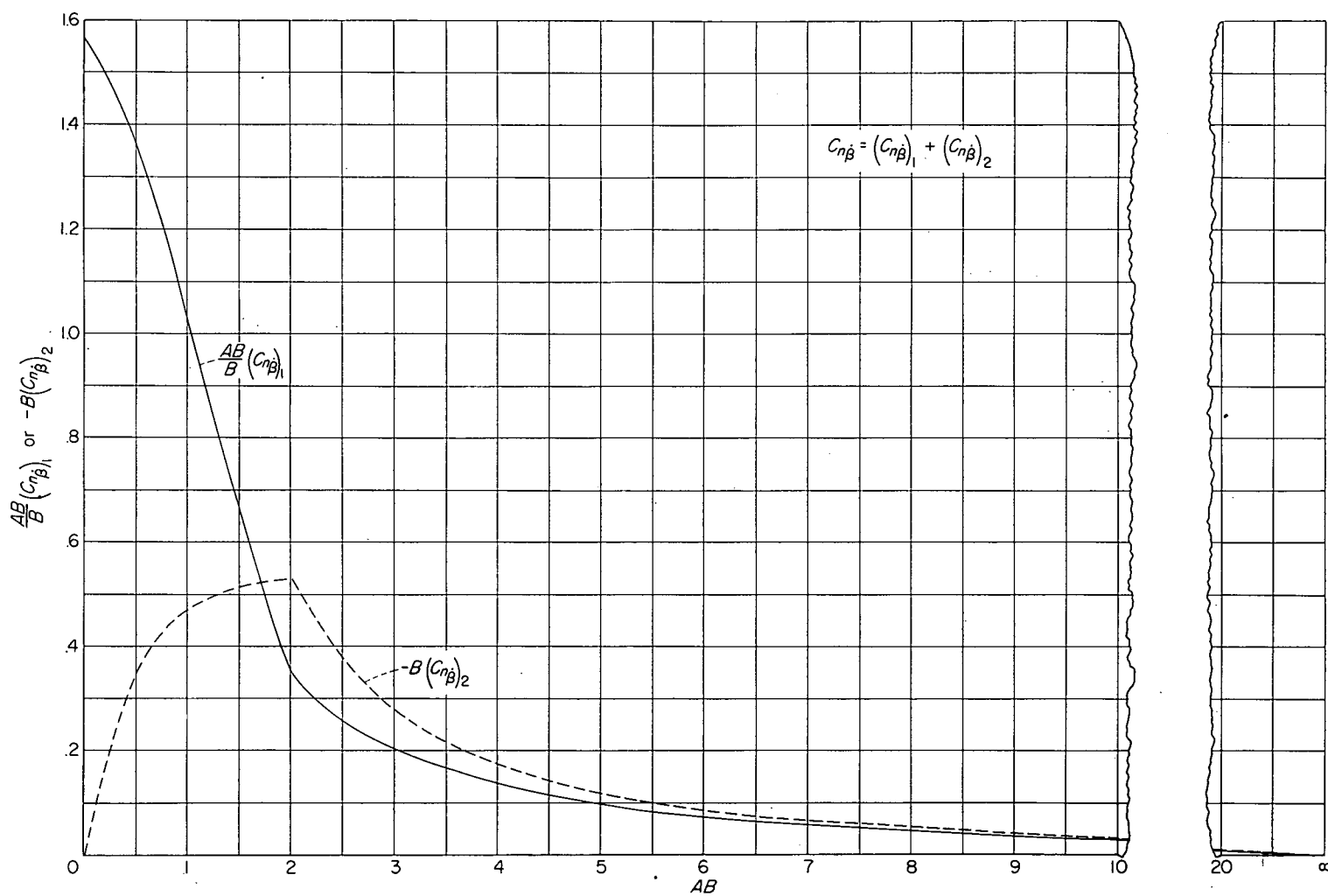


FIGURE 8.—Curves for determining the stability derivative due to constant lateral acceleration $C_{n\dot{\beta}}$ for isolated half-delta vertical tails. Derivative based on vertical-tail parameters b , S , and angle $\beta b/V$; principal body-axes system with origin at leading edge of root section.

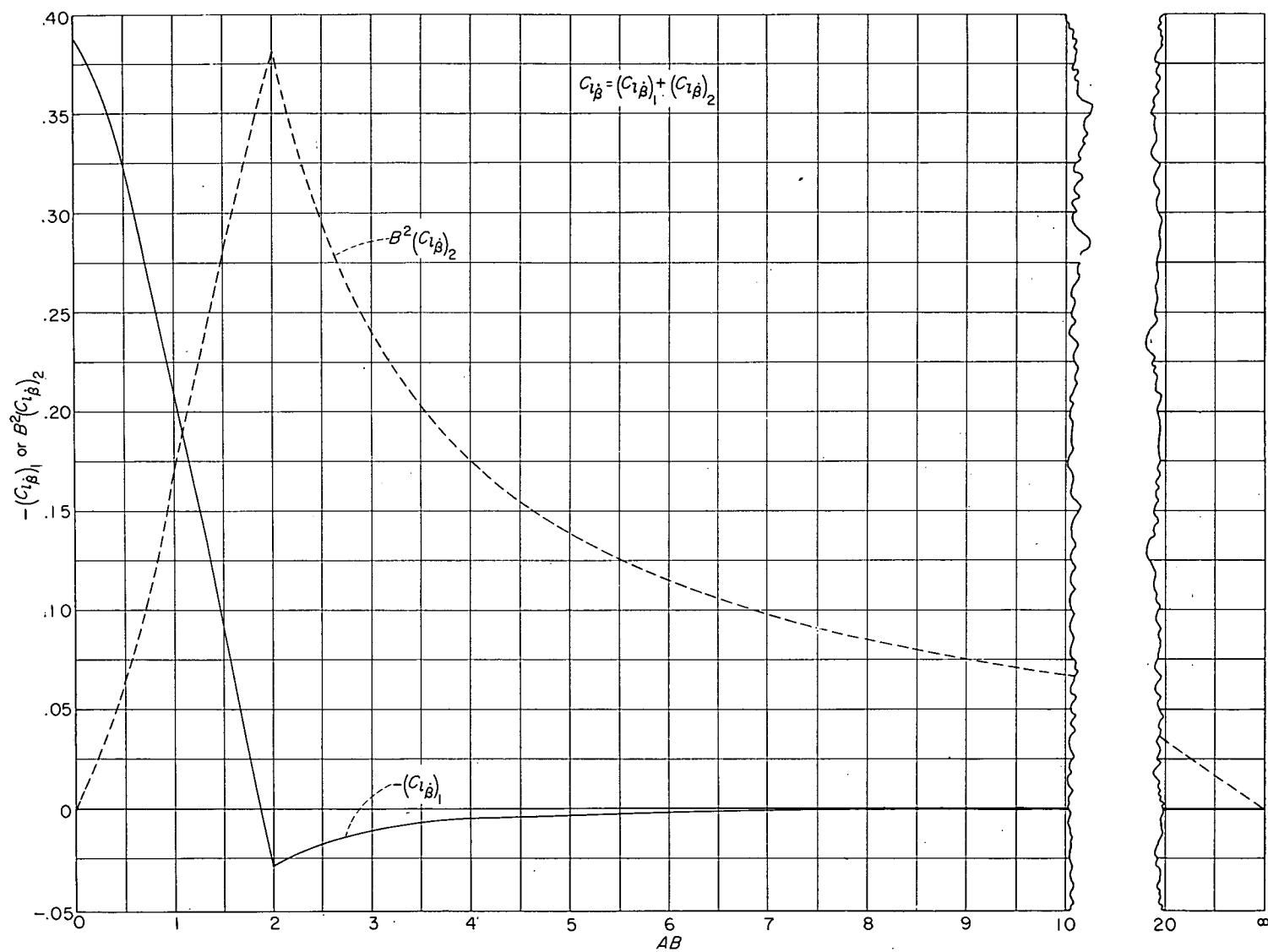


FIGURE 9.—Curves for determining the stability derivative due to constant lateral acceleration $C_{l\beta}$ for isolated half-delta vertical tails. Derivative based on vertical-tail parameters b , S , and angle $\beta b/V$; principal body-axes system with origin at leading edge of root section.

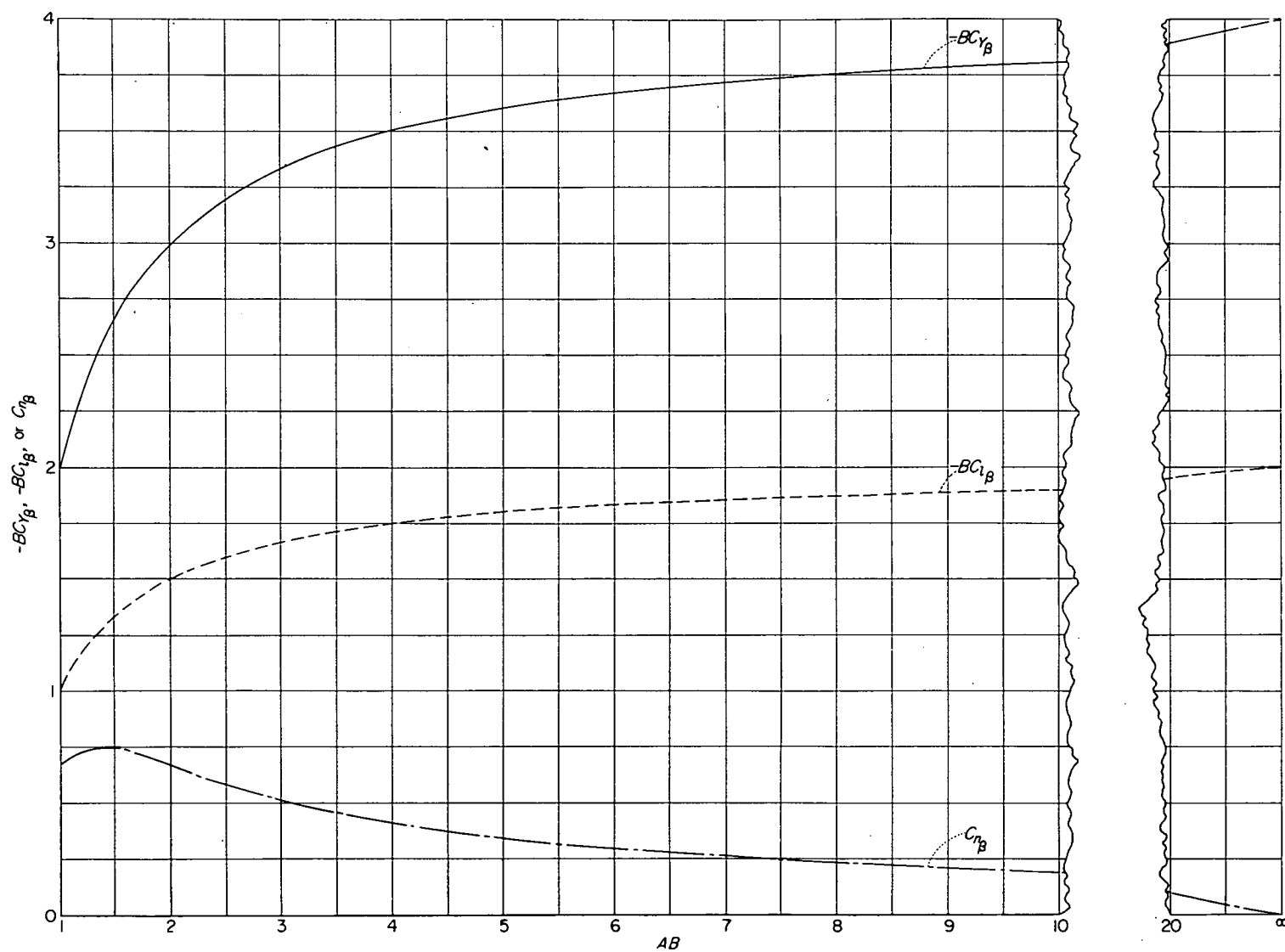


FIGURE 10.—Curves for determining the stability derivatives due to constant sideslip $C_{Y\beta}$, $C_{n\beta}$, and $C_{l\beta}$ for isolated rectangular vertical tails. Derivatives based on vertical-tail parameters b and S ; principal body-axes system with origin at leading edge of root section.

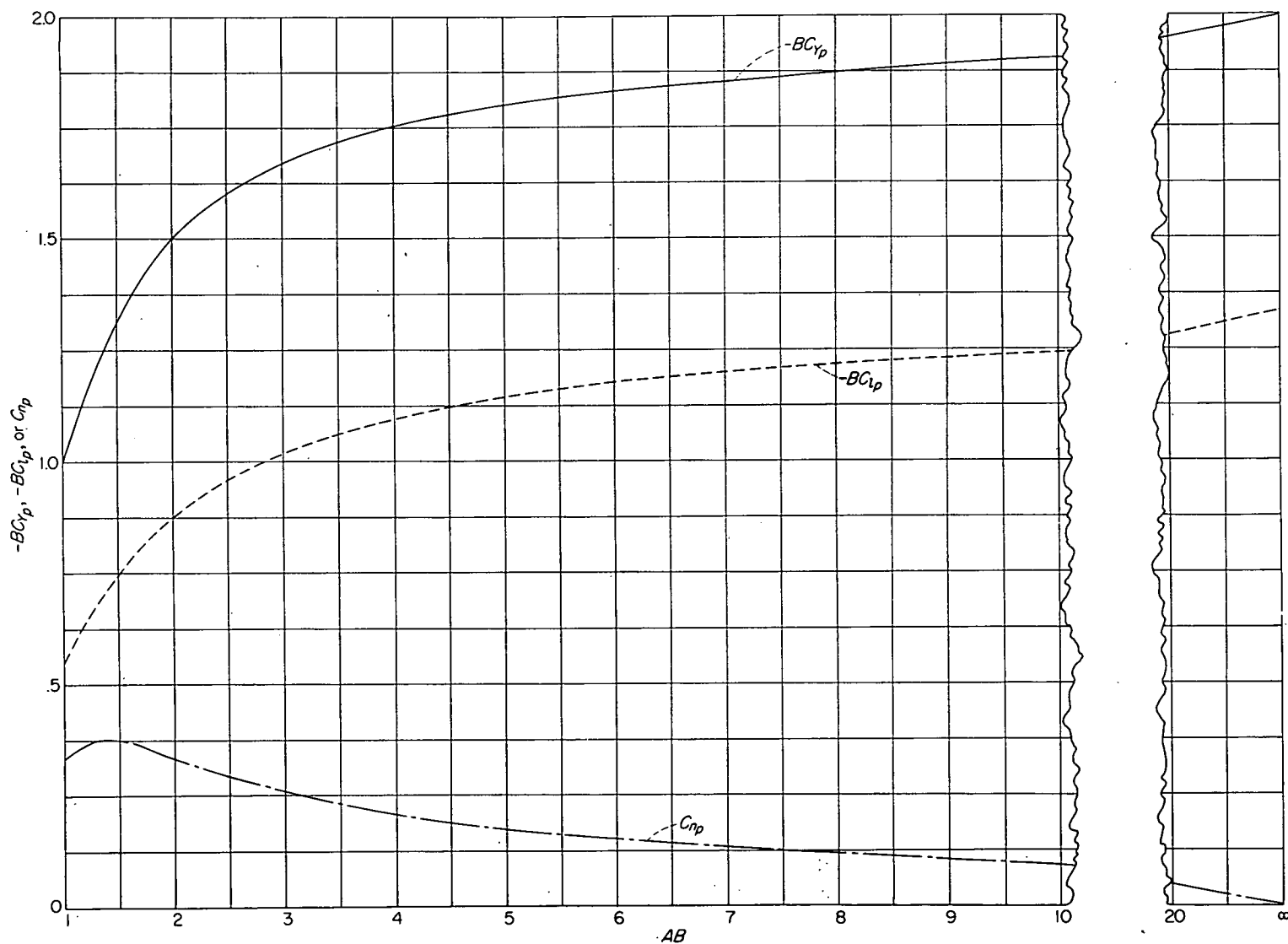


FIGURE 11.—Curves for determining the stability derivatives due to steady rolling C_{Yp} , C_{np} , and C_{lp} for isolated rectangular vertical tails. Derivatives based on vertical-tail parameters b , S , and angle pb/V ; principal body-axes system with origin at leading edge of root section.

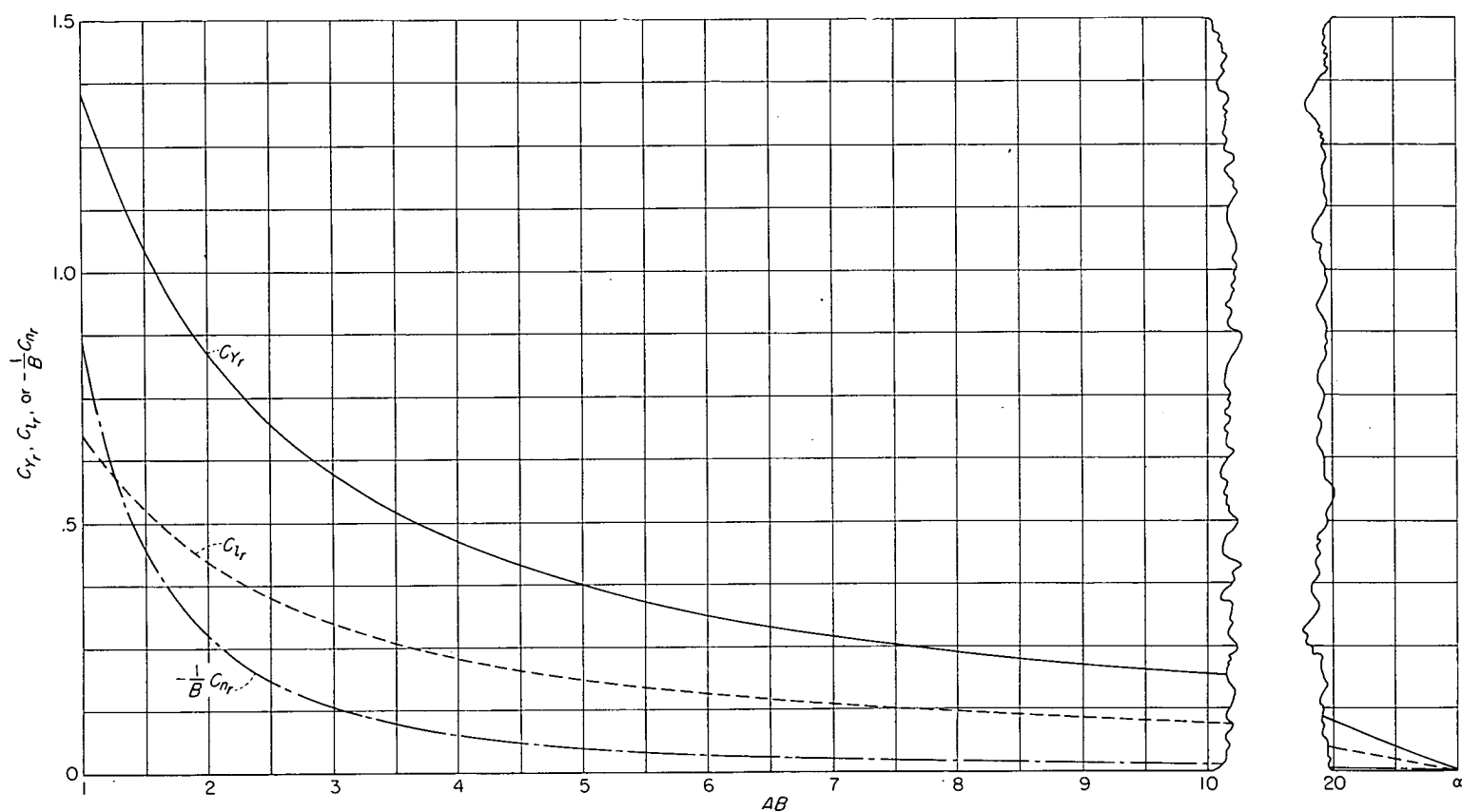


FIGURE 12.—Curves for determining the stability derivatives due to steady yawing C_Y , C_N , and C_L for isolated rectangular vertical tails. Derivatives based on vertical-tail parameters b , S , and angle rb/V ; principal body-axes system with origin at leading edge of root section.

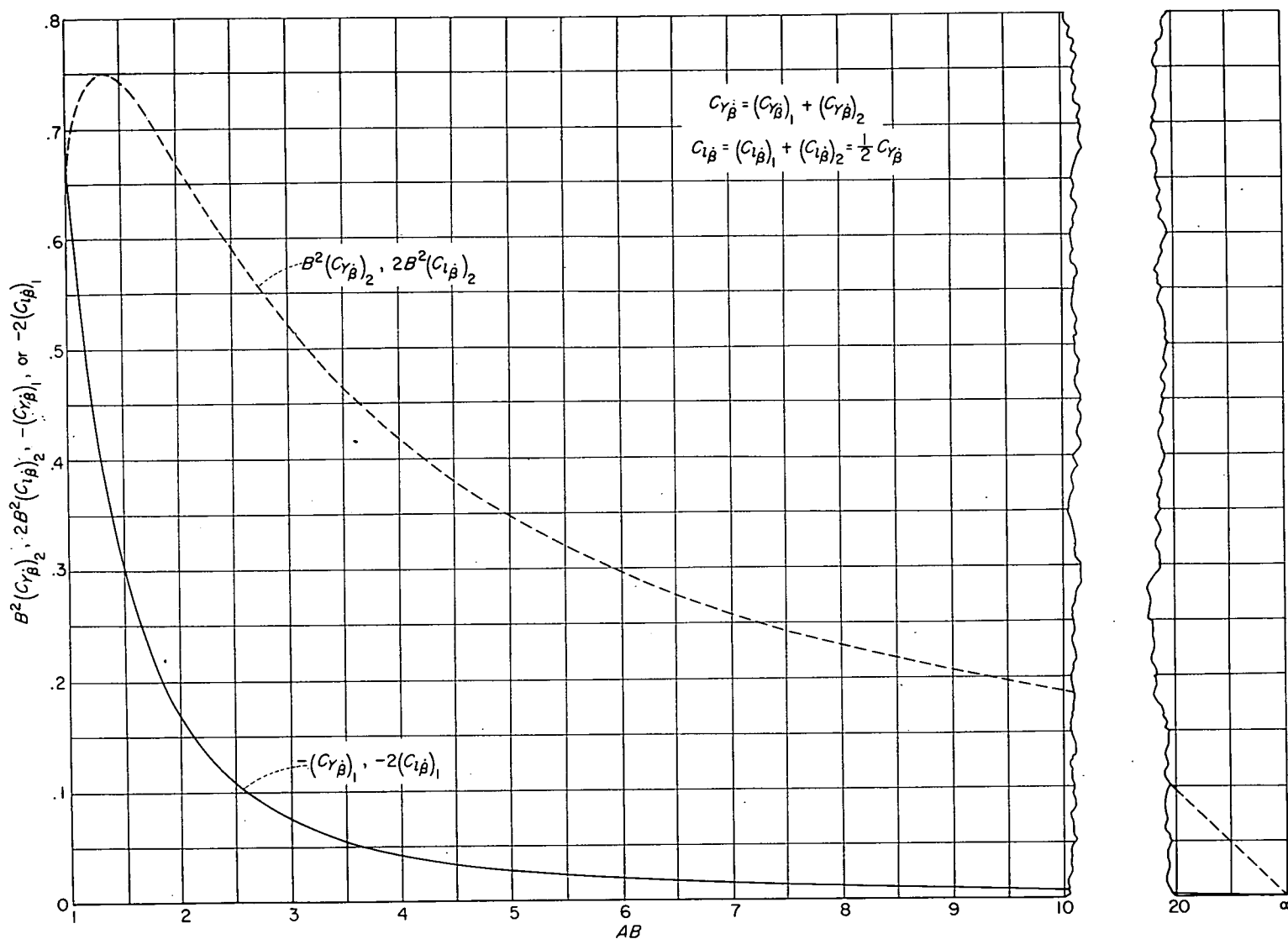
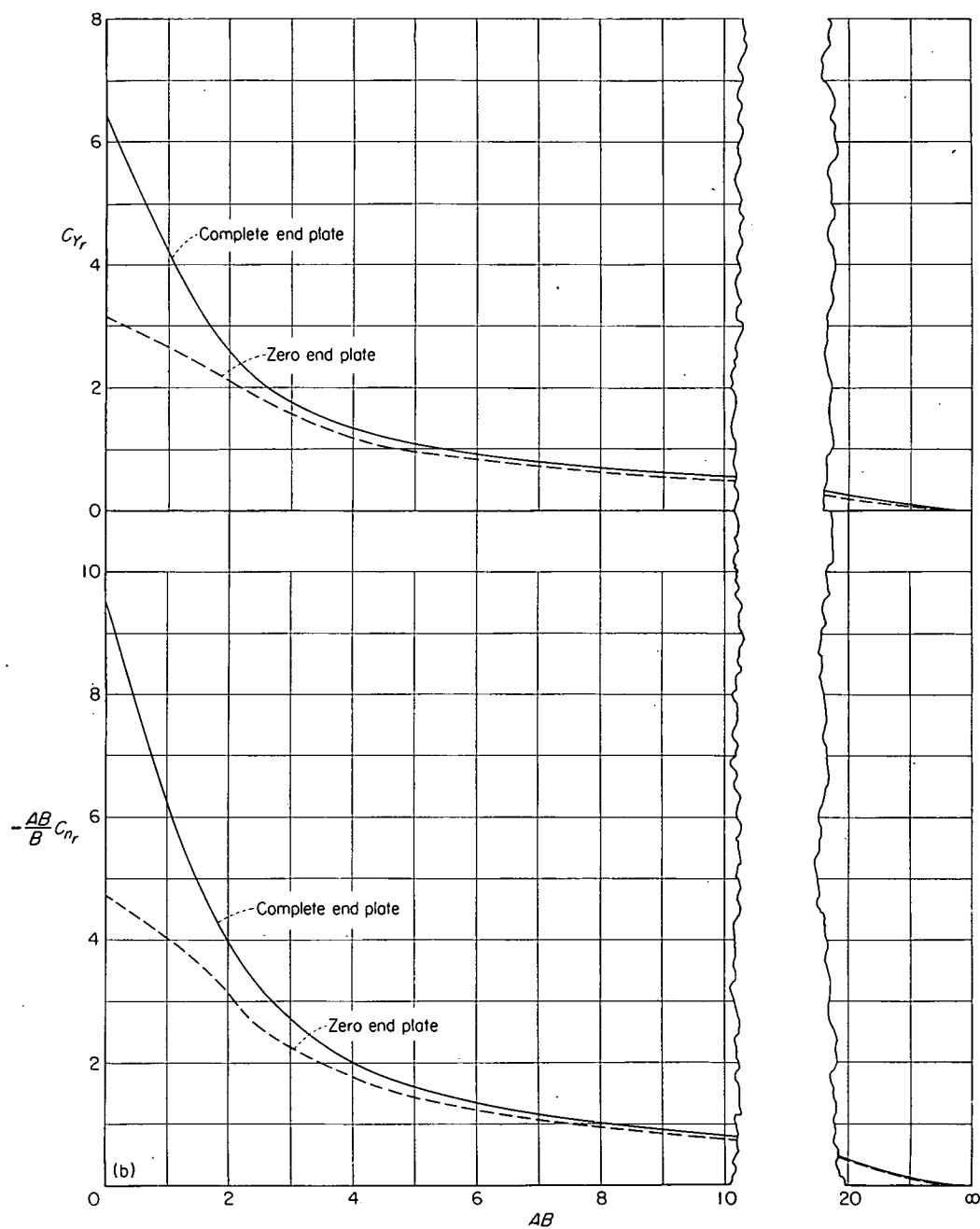
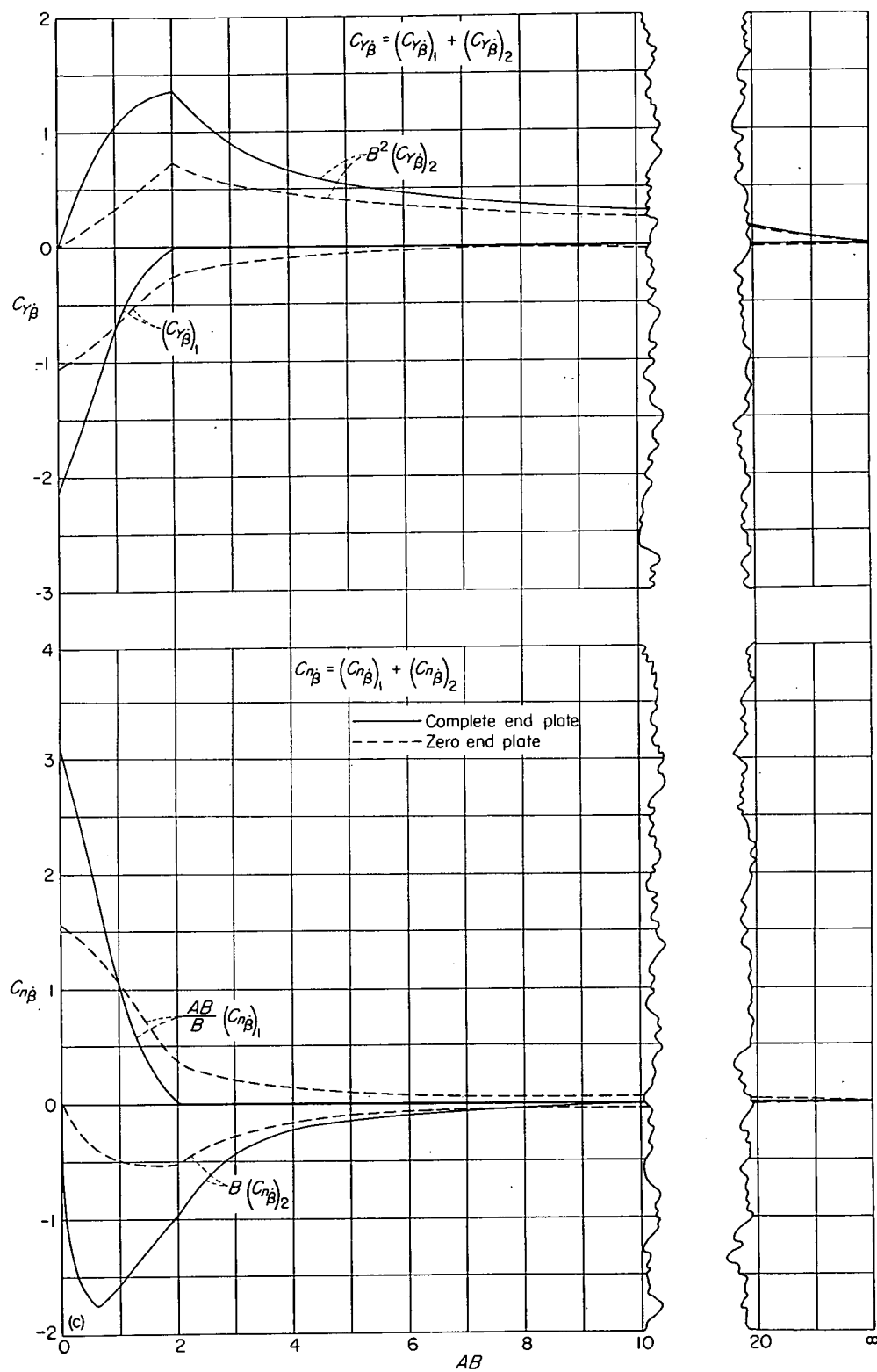


FIGURE 13.—Curves for determining the stability derivatives due to constant lateral acceleration $C_{Y_{\dot{\beta}}}$ and $C_{i_{\dot{\beta}}}$ for isolated rectangular vertical tails. Derivatives based on vertical-tail parameters b , S , and angle $\beta b/V$; principal body-axes system with origin at leading edge of root section.



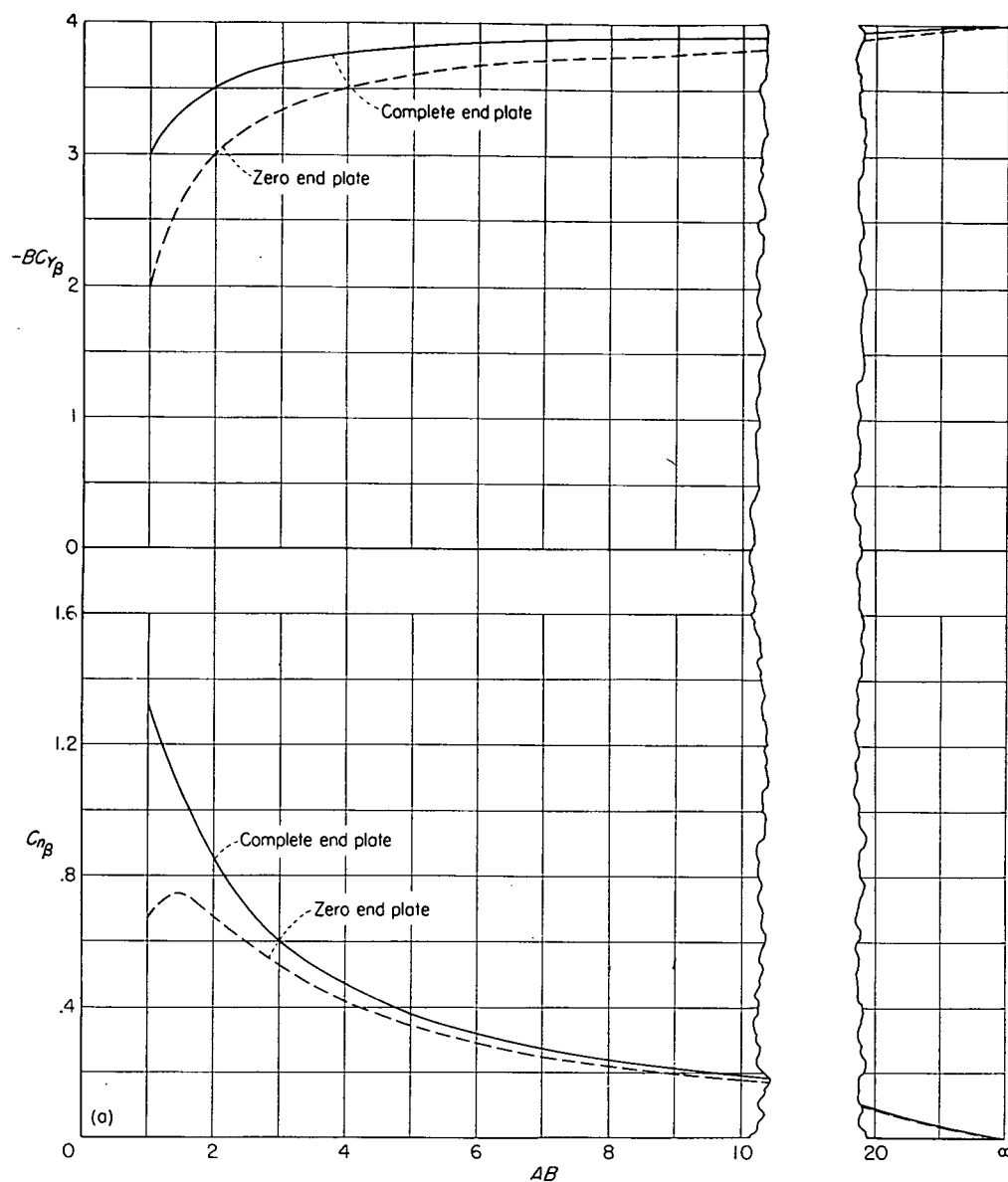
(b) Steady yawing.

FIGURE 15.—Continued.



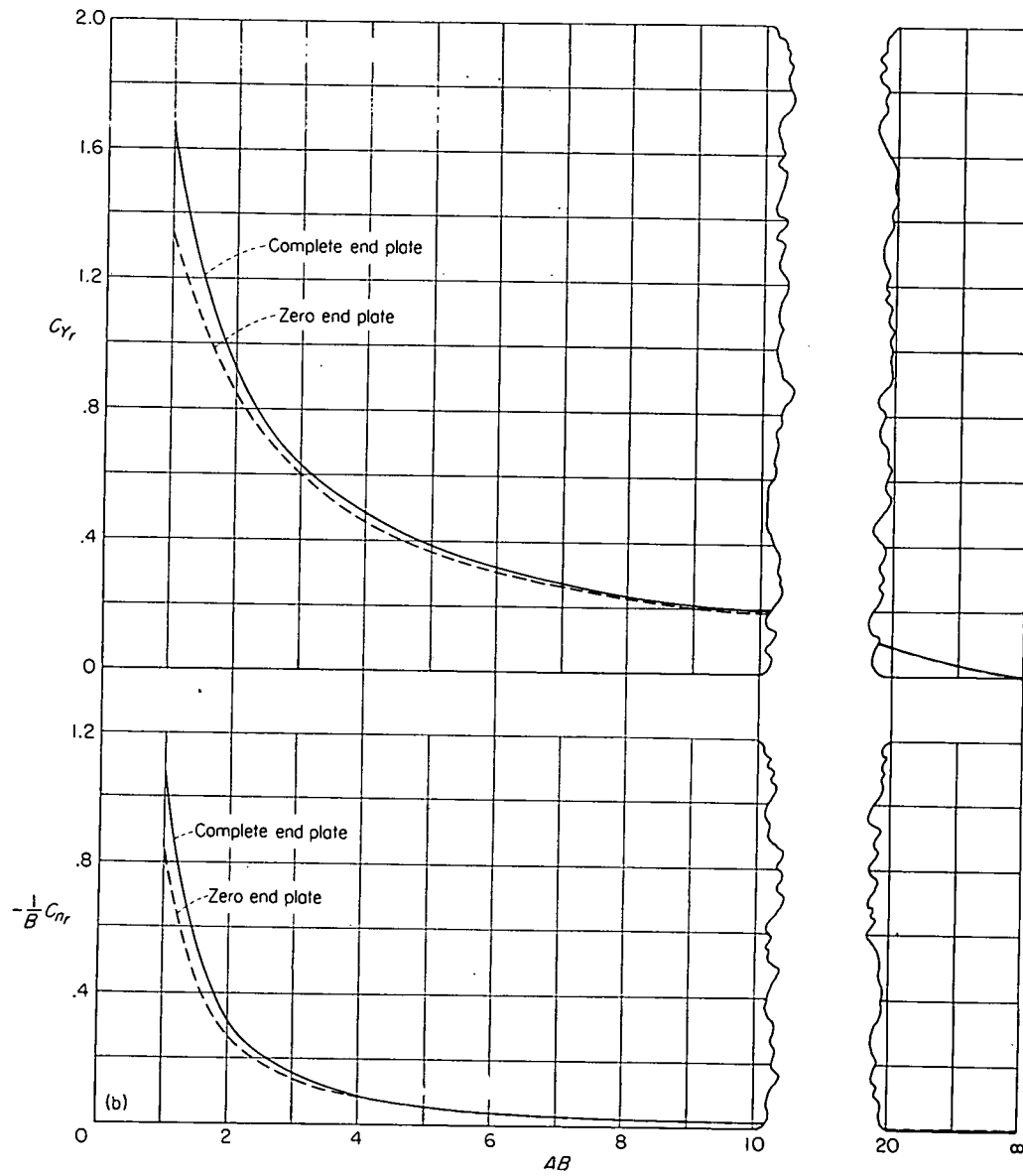
(c) Constant lateral acceleration.

FIGURE 15.—Concluded.



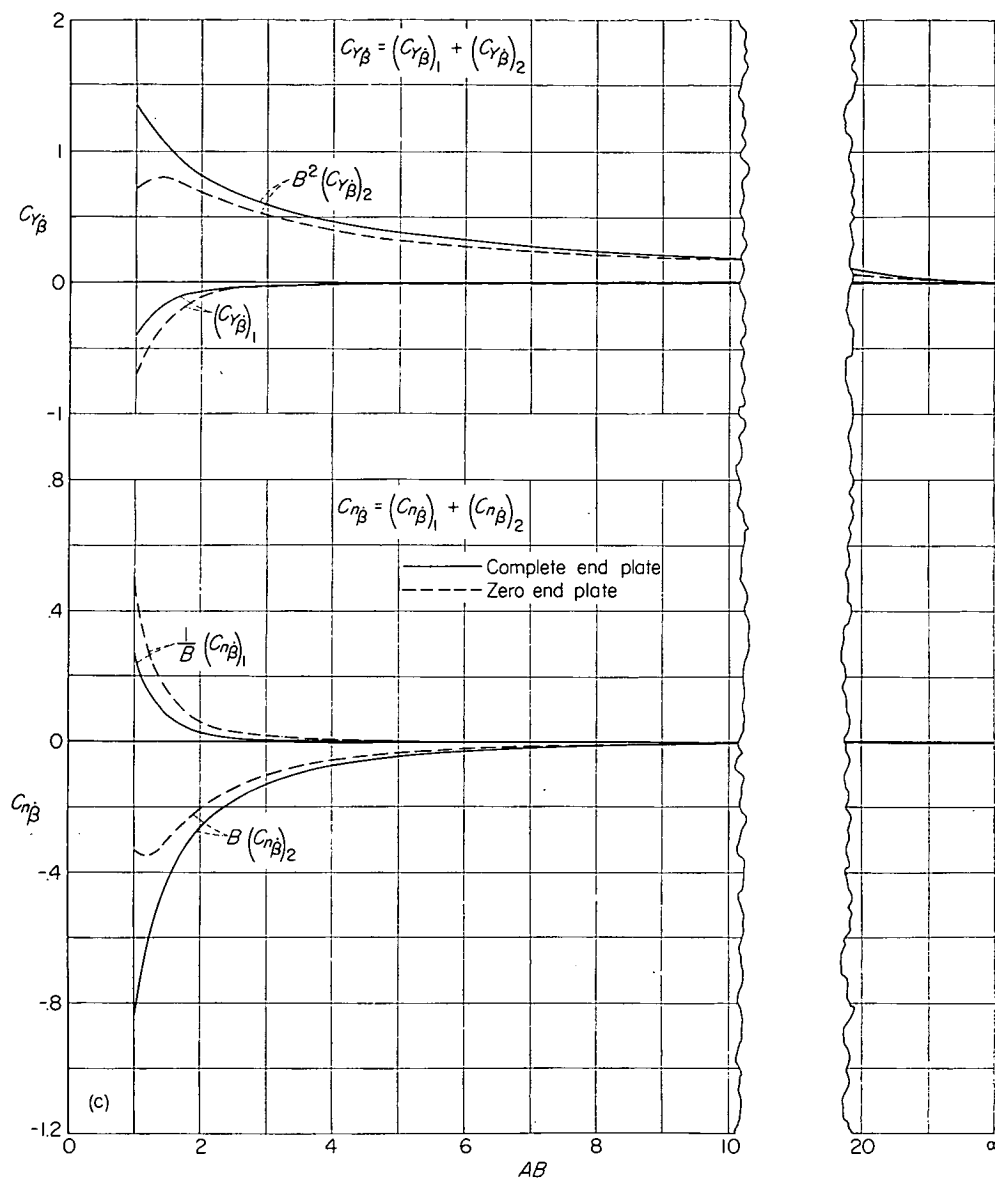
(a) Constant sideslip.

FIGURE 16.—Comparisons of zero- and complete-end-plate solutions for the side-force and yawing-moment derivatives due to several lateral motions for rectangular vertical tails. Derivatives based on vertical-tail parameters b , S , and angles pb/V , rb/V , and $\beta b/V$; principal body-axes system with origin at leading edge of root section.



(b) Steady yawing.

FIGURE 16.—Continued.



(c) Constant lateral acceleration.

FIGURE 16.—Concluded.

REPORT 1269

THEORETICAL SPAN LOAD DISTRIBUTIONS AND ROLLING MOMENTS FOR SIDESLIPPING WINGS OF ARBITRARY PLAN FORM IN INCOMPRESSIBLE FLOW ¹

By M. J. QUEIJO

SUMMARY

A method of computing span loads and the resulting rolling moments for sideslipping wings of arbitrary plan form in incompressible flow is derived. The method requires that the span load at zero sideslip be known for the wing under consideration. Because this information is available for a variety of wings, this requirement should not seriously restrict the application of the present method. The basic method derived herein requires a mechanical differentiation and integration to obtain the rolling moment for the general wing in sideslip. For wings having straight leading and trailing edges over each semispan, the rolling moment due to sideslip is given by a simple equation in terms of plan-form parameters and the lateral center of pressure of the lift due to angle of attack.

The mechanical differentiation and integration required to obtain the rolling moment for the general wing can be avoided by use of a step-load method which is also derived. Charts are presented from which the rolling-moment parameter $C_{l\beta}/C_L$ can be obtained for wings having straight leading and trailing edges over each semispan.

Calculated span loads and rolling-moment parameters are compared with experimental values. The comparison indicates good agreement between calculations and available experimental data.

INTRODUCTION

The span load distributions and rolling moments of a wing in sideslip are important in considering the structural and dynamic lateral-stability requirements of an aircraft and, hence, have been the subject of numerous experimental and theoretical studies. Most of the studies have been limited to the determination of the rolling moment due to sideslip $C_{l\beta}$; however, a few studies have been concerned with the span load distributions for wings in sideslip. (See refs. 1, 2, and 3, for example.) References 1 and 2 are theoretical studies: reference 1, for unswept wings; and reference 2, for sweptback wings. Comparisons between experimental and theoretical span loads for unswept wings showed good agreement (ref. 1). The few comparisons in reference 2 between theoretical and experimental span loads for swept wings indicated fair agreement over most of the semispan but poor agreement near the wing tip where the theory

indicated a rapid decrease in load and experiments indicated a rapid increase. The method of reference 1 does predict the rapid tip-load change with sideslip which has also been observed for unswept wings. Examination of reference 1 indicated that the basic concepts employed therein could be used in the calculation of span loads and rolling moments for swept wings in sideslip, provided sweep effects could be taken into account.

The purpose of the present report is to derive a method, using the basic concepts of reference 1 and introducing a means to account for sweep effects, which permits the calculation of the span load distribution and rolling moment for any wing in sideslip. The method requires that the span load distribution at zero sideslip angle be known. Since this information is available for a large variety of wings (see refs. 4 to 7, for example), this restriction is not believed to be serious.

The basic concepts used herein permit the determination of the span load and the resulting rolling-moment coefficient of a wing in sideslip by use of either an integration method and a continuous spanwise circulation distribution or a series summation in combination with a stepped circulation distribution. Both methods are developed herein.

SYMBOLS

A	aspect ratio, b^2/S
b	span
C_L	wing lift coefficient due to angle of attack, $\frac{\text{Wing lift due to } \alpha}{\frac{1}{2} \rho V^2 S}$
C_l	wing rolling-moment coefficient, $\frac{\text{Wing rolling moment}}{\frac{1}{2} \rho V^2 S b}$
$C_{l\beta} = \frac{\partial C_l}{\partial \beta}$	
c	chord, parallel to plane of symmetry
$\frac{cc_l}{\bar{c} C_L \beta} = \frac{\partial^2 \gamma}{\partial \beta \partial C_L}$	
\bar{c}	average chord, S/b
c_i	chord at inboard end of a vortex

¹ Supersedes NACA Technical Note 3605 by M. J. Queijo, 1955.

c_l	section lift coefficient, $\frac{\text{Section lift}}{\frac{1}{2} \rho V^2 c}$
$c_{l_\alpha} = \frac{\partial c_l}{\partial \alpha}$	
$(c_l)_\alpha$	section lift coefficient due to angle of attack
$(c_l)_\beta$	section lift coefficient due to sideslip
$(c_l)_{\beta=0}$	section lift coefficient at zero sideslip angle
c_o	chord at outboard end of a vortex
l	section lift (lift per unit span)
l'	rolling moment due to one horseshoe vortex
N	number of horseshoe vortices representing wing
n	index which indicates a specific horseshoe vortex
S	wing area
s	semispan of a horseshoe vortex
V	free-stream velocity
y	spanwise distance from plane of symmetry
\bar{y}	spanwise position of center of pressure due to angle-of-attack load on one semispan
z	distance along quarter-chord line, measured from plane of symmetry
α	geometric angle of attack, radians
α_i	induced angle of attack, radians
β	sideslip angle, radians
Γ_y	vortex strength in spanwise direction
$(\Gamma_y)_{\beta=0}$	vortex strength Γ_y for wing at zero sideslip angle
Γ_z	vortex strength along quarter-chord line
γ	section load parameter for total load on section, $\frac{cc_l}{c}$
$(\gamma)_\alpha$	section load parameter due to angle of attack
$(\gamma)_\beta$	section load parameter due to sideslip
$(\gamma)_{\beta=0}$	section load parameter at zero sideslip angle
$(\gamma)_\theta$	section load parameter due to twist
θ	local angle of attack due to twist, radians
κ	factor from reference 1
Λ	sweep of quarter-chord line, deg (positive for sweepback)
λ	taper ratio, $\frac{\text{Tip chord}}{\text{Root chord}}$
ρ	mass density of air

Superscript:

- * denotes that factor has been made nondimensional by dividing by $b/2$; for example, $c^* = \frac{c}{b/2}$

ANALYSIS

In making span-load calculations, the wing is generally represented by a system of vortices. For the case of zero sideslip, the unswept wing can be represented by a system of spanwise and chordwise vortices as shown in figure 1 (a). For wings of high aspect ratio, the spanwise vortices are generally replaced by a single vortex, and the resulting

system (fig. 1 (b)) is the common lifting-line-theory representation of a wing at zero sideslip angle.

Various systems of vortices have been considered for the representation of unswept wings in sideslip. One system is a modification of the lifting-line-theory representation and consists of a single spanwise vortex and a sheet of trailing vortices which are parallel to the free airstream (fig. 1 (c)). This system was used by Blenk (ref. 8); however, his calculated rolling moments due to sideslip were opposite in sign from those obtained experimentally.

The vortex system used by Weissinger for the unswept wing in sideslip is shown in figure 1 (d), and this system is also a modification of the lifting-line-theory representation at zero sideslip. The theoretical arguments for the system are given in reference 1 and, therefore, will not be repeated here. However, it should be noted here that the span load distributions and values of C_{l_β} computed by Weissinger for unswept wings are generally in very good agreement with experiment.

As stated in the introduction, the basic concepts used herein are the same as those of reference 1 and are applied directly to the swept wing. The swept wing in sideslip is represented by a system of vortices, as indicated in figure 2 (a), which consists of a vortex located along the wing quarter-chord line and a sheet of vortices emanating from this vortex. The vortices of the sheet are parallel to the wing plane of symmetry from the quarter-chord line to the trailing edge, and then they slant so as to be parallel to the relative wind direction. In the present report, the portion of the vortex sheet parallel to the plane of symmetry is referred to as being made up of chordwise-bound vortices, whereas the rest of the vortex sheet is considered to be made up of trailing-free vortices.

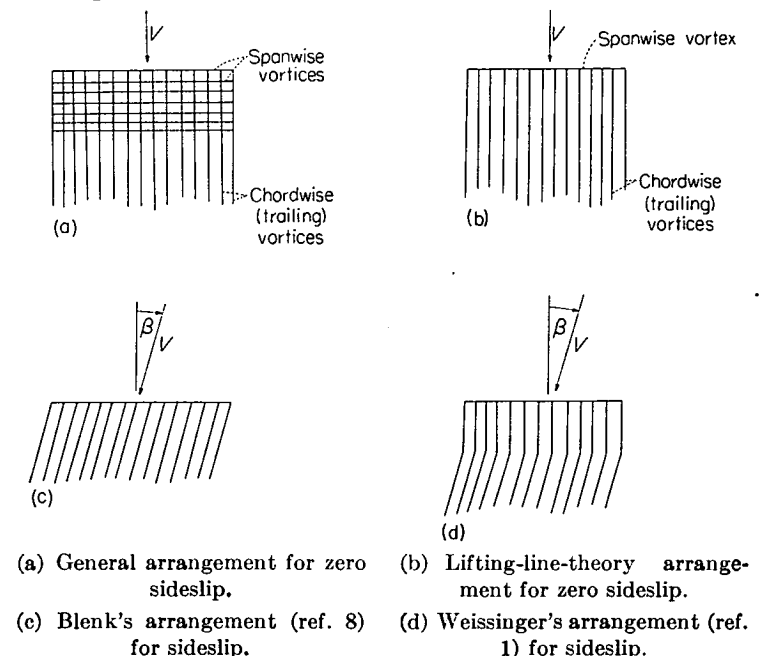


FIGURE 1.—Vortex systems used for representing unswept wings.

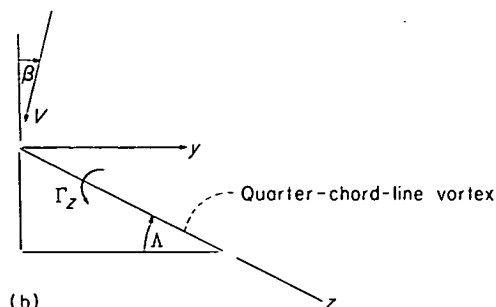
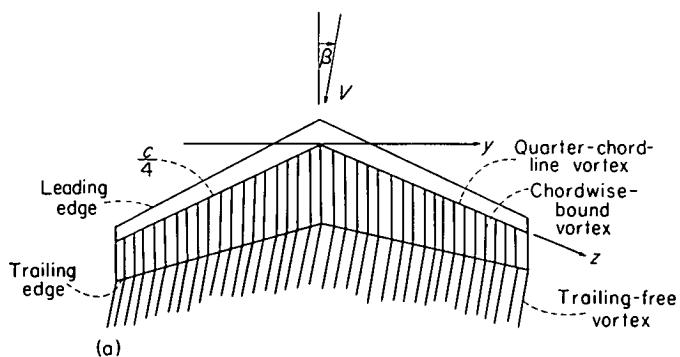
The lift produced by a unit length of vortex is given by the Kutta-Joukowski equation

$$l = \rho V_p \Gamma$$

where Γ is the vortex strength (or circulation) and V_p is the velocity component perpendicular to the vortex. As may be seen from figure 2 (a), the free-stream velocity has components perpendicular to the quarter-chord-line vortex and the chordwise-bound vortices and, hence, these vortices will produce lift in accordance with the Kutta-Joukowski equation. The trailing-free vortices are parallel to the relative wind and hence produce no lift. The strength of the chordwise-bound vortices is determined by the strength distribution of the quarter-chord-line vortex; therefore, the lift distribution of the wing in sideslip can be determined, provided the distribution of the strength of the quarter-chord-line vortex for the wing in sideslip is known.

The vortex strength would be made up of the circulation due to the basic-type loading (camber and/or twist), angle-of-attack loading, and some modification to the sum of these loadings as a result of sideslip. In general, the circulation at zero sideslip can be obtained from published reports (refs. 4, 5, and 6, for example), and the remaining unknown is the modification due to sideslip. An approximate method of evaluating this effect is as follows: with reference to figure 2 (b), which pertains to the right, or leading wing semispan, the lift per unit length of the quarter-chord-line vortex of a swept wing in sideslip is given by

$$l_1 = \rho V \cos(\Lambda - \beta) \Gamma_z$$



(a) Overall representation.
(b) Details of an element of the quarter-chord-line vortex.

FIGURE 2.—Representation of a wing by the vortex system used in analysis.

and also by

$$l_1 = \frac{1}{2} \rho V^2 \cos^2(\Lambda - \beta) c_{l_\alpha} \frac{\alpha - \alpha_i}{\cos(\Lambda - \beta)} c$$

so that the circulation Γ_z is

$$\Gamma_z = \frac{1}{2} V c c_{l_\alpha} (\alpha - \alpha_i)$$

Similarly, for the wing at zero sideslip, the circulation is given by

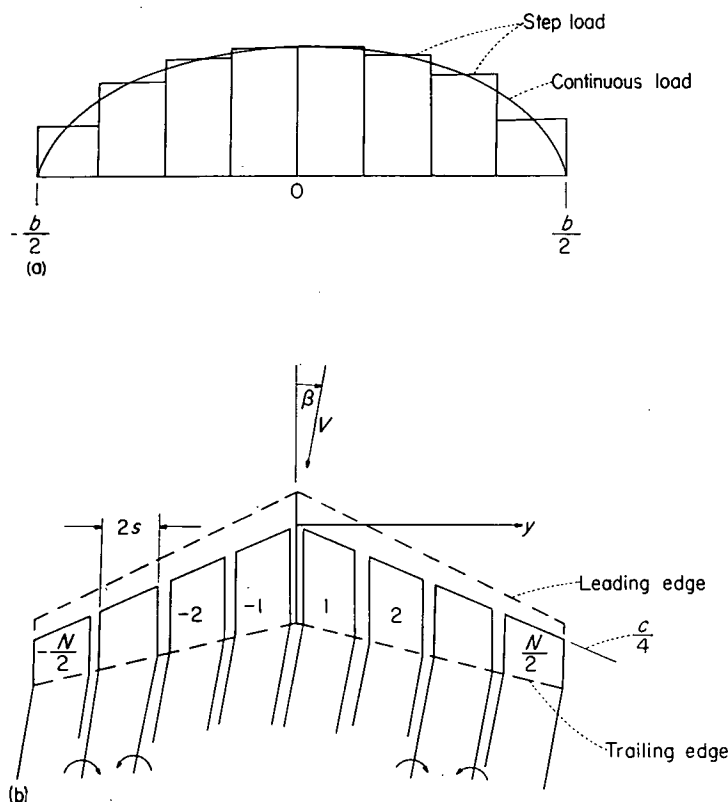
$$(\Gamma_z)_{\beta=0} = \frac{1}{2} V c c_{l_\alpha} (\alpha - \alpha_i)_{\beta=0}$$

Thus the circulation at a sideslip angle is related to the circulation at zero sideslip by

$$\Gamma_z = (\Gamma_z)_{\beta=0} \frac{\alpha - \alpha_i}{(\alpha - \alpha_i)_{\beta=0}}$$

It appears, therefore, that the local circulation of the quarter-chord-line vortex of a wing at a given angle of attack will be changed by sideslip only if sideslip changes the induced angle of attack. For infinite aspect ratio, the induced angle of attack is zero and, hence, Γ_z is exactly equal to $(\Gamma_z)_{\beta=0}$. For large aspect ratios, when α_i is small relative to α , a modification to α_i due to sideslip probably will have a negligible effect on the local circulation. Even for small aspect ratios, when α_i can be large relative to α , it does not appear that a small sideslip angle should affect α_i enough to change the local circulation appreciably. This argument is substantiated to some extent by calculations of the circulation distribution of unswept wings in sideslip made by Weissinger (ref. 1). These results showed that for unswept wings the change in circulation due to sideslip was small and resulted in an increment in C_{l_β}/C_L that was independent (for practical purposes) of aspect ratio and taper ratio for a fairly wide range of both parameters.

Because of the effort involved in actually computing the circulation distribution for wings in sideslip and because of the arguments given in the preceding paragraph, the analysis of the present report is based on the assumption that the circulation distribution for the wing in sideslip is the same as for the wing at zero sideslip. Span load distributions for the wing in sideslip can then be obtained by the methods derived in the appendix. The rolling moment due to sideslip can be obtained for any wing by integration of the span load due to sideslip, and this method is referred to herein as the integration method. For the most general case, the integration involved in this method cannot be made conveniently. In such instances a second method, wherein the wing is represented by a number of horseshoe vortices (see figs. 3 and 4), can be used. This method also is derived herein. The resulting values of the rolling-moment parameter C_{l_β} are obtained and a small correction to account for effects of sideslip on the circulation distribution (as determined in ref. 1 for unswept wings) is applied. Although this



(a) Approximation of continuous load by step load.
 (b) Representation of a wing by a finite number of horseshoe vortices.
 FIGURE 3.—Representation of wing when span load is assumed to be made up of spanwise step loadings.

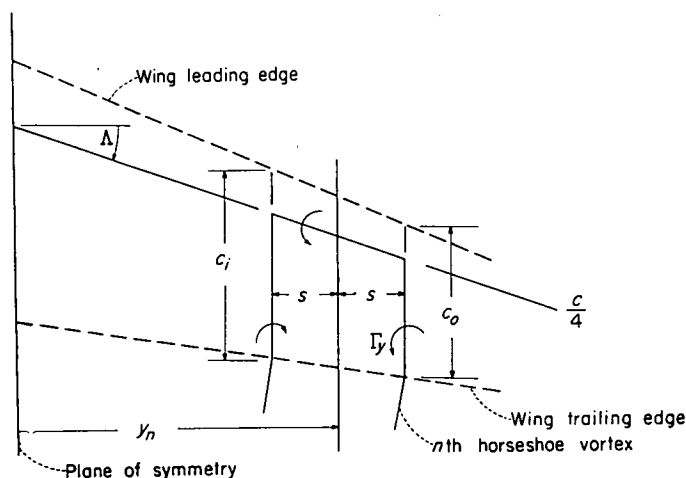


FIGURE 4.—Details of n th horseshoe vortex used in representing wing in sideslip by a number of horseshoe vortices.

final correction may not be strictly applicable to swept wings, it is a small quantity and should be of the right order of magnitude even for swept wings.

RESULTS AND DISCUSSION

GENERAL REMARKS

The general equations derived in the appendix can be used to obtain span loads and rolling moments for side-slipping wings of arbitrary plan form and twist in incompressible flow. The general equations have been used to determine equations which apply specifically to wings having straight leading and trailing edges and for wings of elliptic

plan form. Equations for specific types of wings not treated herein (for example, M, W, or cranked wings) can be obtained from the general equations with little difficulty. The span loads and rolling moments for wings in sideslip can be obtained by the methods presented herein, however, only if the span load at zero sideslip angle is known. This is not a serious restriction since such information is available for a large variety of wings. However, wings of odd plan form present an additional problem in that it will generally be necessary to compute the span load at zero sideslip before proceeding to the sideslip case. In such instances, the span load at zero sideslip can be computed by using a method such as that of references 7, 9, and 10.

In the following sections, some of the equations derived in the appendix are repeated and results obtained are discussed.

SPAN LOAD DISTRIBUTION IN SIDESLIP

The span load distribution of a wing in sideslip can be determined from the following general equation:

$$\gamma = (\gamma)_{\beta=0} (1 \pm \beta \tan \Lambda) - \frac{3}{4} \beta c^* \frac{d(\gamma)_{\beta=0}}{dy^*} \quad (1)$$

The load due to sideslip is given by

$$(\gamma)_{\beta} = (\gamma)_{\beta=0} (\pm \beta \tan \Lambda) - \frac{3}{4} \beta c^* \frac{d(\gamma)_{\beta=0}}{dy^*} \quad (2)$$

Wherever a choice of signs is indicated, a plus sign applies to the right or leading wing semispan, and a minus sign applies to the left or trailing wing semispan.

A study of equation (2) shows that, if a portion of the total wing load is symmetric over the wing span at zero sideslip, the change in that portion of the load due to sideslip will be antisymmetric (and, hence, will produce a resultant rolling moment). On the other hand, if a portion of the total wing load is antisymmetric over the wing span at zero sideslip, the change in that portion of the load due to sideslip is symmetric (and, hence, will produce no resultant rolling moment).

In order to illustrate the effects of sideslip on span loads, the parameter $\frac{cc_i}{cC_L\beta}$ has been computed for several rigid wings of aspect ratio 4.5. This parameter can be obtained readily by expanding equation (2); thus,

$$(\gamma)_{\beta} = \left[(\gamma)_{\theta} + \left(\frac{\gamma}{C_L} \right)_{\alpha} C_L \right] (\pm \beta \tan \Lambda) - \frac{3}{4} \beta c^* \left[\frac{d(\gamma)_{\theta}}{dy^*} + C_L \frac{d \left(\frac{\gamma}{C_L} \right)_{\alpha}}{dy^*} \right]$$

Inasmuch as the term $(\gamma)_{\theta}$ is independent of C_L due to angle of attack for rigid wings, differentiating with respect to β and C_L yields the desired parameter

$$\frac{cc_i}{cC_L\beta} = \left(\frac{cc_i}{cC_L} \right)_{\alpha} (\pm \tan \Lambda) - \frac{3}{4} c^* \frac{d \left(\frac{cc_i}{cC_L} \right)_{\alpha}}{dy^*} \quad (3)$$

For elliptic wings, equation (3) reduces to

$$\frac{cc_i}{cC_L\beta} = \pm \frac{32}{\pi^2 A} y^* \quad (4)$$

Computed values of $\frac{cc_i}{cC_L\beta}$ are shown in figure 5 for several wings. The span load due to sideslip is, of course, antisymmetric and, hence, results are presented only for the

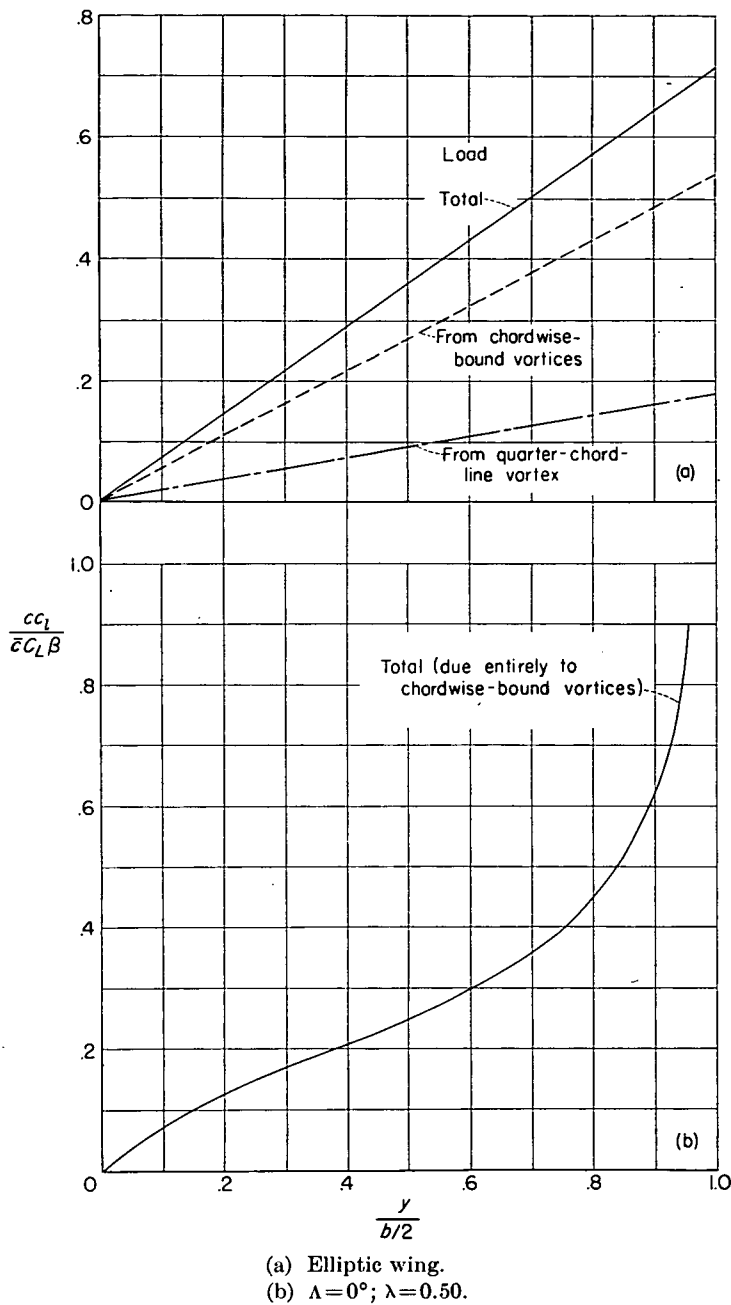


FIGURE 5.—Estimated span load due to sideslip for several plane wings. $A=4.5$.

right semispan. In each case the contributions of the quarter-chord-line vortex and chordwise-bound vortices are presented individually and are also combined. The results show that, for the true elliptic wing (unswept midchord line), the chordwise-bound vortices account for three-quarters of the local load coefficient and the local load coefficient varies linearly with spanwise position.

The results for the unswept wing are in qualitative agreement with the results given for unswept wings in reference 1 and indicate an infinite load coefficient at the wing tips. The effects of sweep can be seen by comparing figures 5 (b) and 5 (c). The local load due to sideslip associated with the quarter-chord-line vortex is, of course, a consequence of sweep and can contribute greatly to the load in sideslip.

Some comparisons between calculated and experimental span loads due to sideslip are shown in figure 6 for an un-

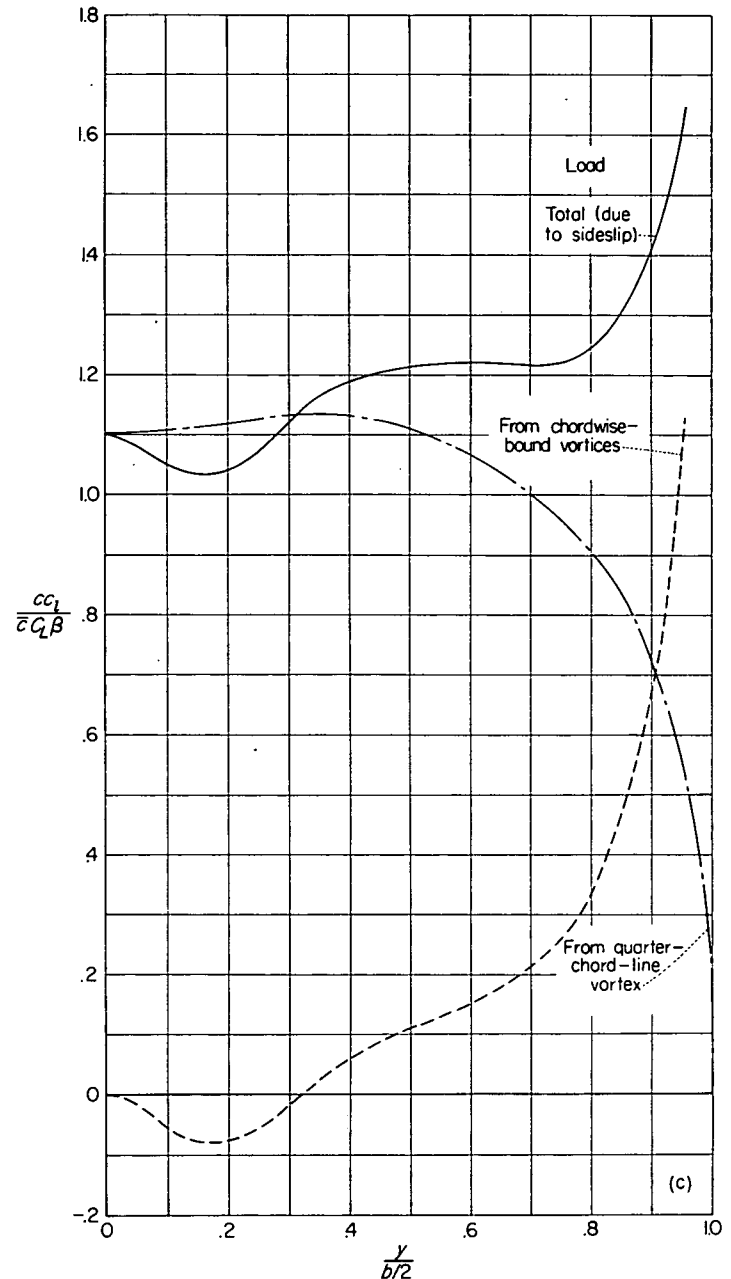


FIGURE 5.—Concluded.

tapered 45° sweptback wing of aspect ratio 5.16. The loads due to sideslip were computed from equation (2) and experimental values of $(\gamma)_{\beta=0}$. In general, the computed and experimental span loads due to sideslip are in very good agreement at low angles of attack.

ROLLING MOMENT DUE TO SIDESLIP

Integration method.—A general equation for the rolling moment due to sideslip is given in the appendix as

$$C_{l\beta} = -\frac{1}{4} \left\{ \int_{-1}^0 \left[(\gamma)_\theta \tan \Lambda + \frac{3}{4} c^* \frac{d(\gamma)_\theta}{dy^*} \right] y^* dy^* + \int_0^1 \left[(\gamma)_\theta \tan \Lambda - \frac{3}{4} c^* \frac{d(\gamma)_\theta}{dy^*} \right] y^* dy^* \right\} - \frac{1}{2} \int_0^1 \left[(\gamma)_\alpha \tan \Lambda - \frac{3}{4} c^* \frac{d(\gamma)_\alpha}{dy^*} \right] y^* dy^* + 0.05 C_L \quad (5)$$

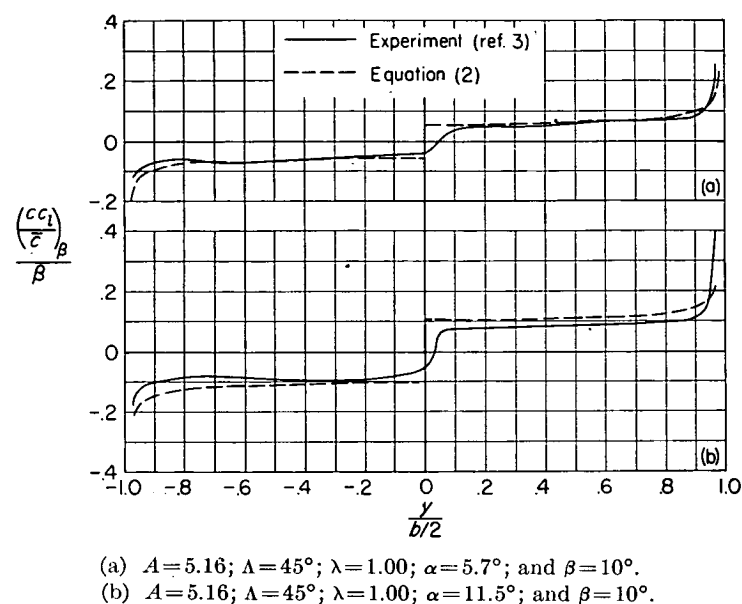


FIGURE 6.—Comparison of experimental and calculated span loads due to sideslip.

If the wing under consideration has symmetrical twist, equation (5) can be written as

$$C_{i\beta} = -\frac{1}{2} \int_0^1 \left\{ [(\gamma)_\theta + (\gamma)_\alpha] \tan \Lambda - \frac{3}{4} c^* \left[\frac{d(\gamma)_\theta}{dy^*} + \frac{d(\gamma)_\alpha}{dy^*} \right] \right\} y^* dy^* + 0.05 C_L \quad (6)$$

The rate of change of $C_{i\beta}$ with C_L for rigid wings is given by

$$\frac{C_{i\beta}}{C_L} = -\frac{1}{2} \bar{y}^* \tan \Lambda + \frac{3}{8} \int_0^1 c^* \frac{d\left(\frac{\gamma}{C_L}\right)_\alpha}{dy^*} y^* dy^* + 0.05 \quad (7)$$

which, for wings having straight leading and trailing edges over each semispan, reduces to

$$\frac{C_{i\beta}}{C_L} = -\frac{1}{2} \left\{ \frac{3}{A(1+\lambda)} + \bar{y}^* \left[\tan \Lambda - \frac{6}{A} \left(\frac{1-\lambda}{1+\lambda} \right) \right] \right\} + 0.05 \quad (8)$$

For elliptic wings (having unswept midchord lines), the parameter $C_{i\beta}/C_L$ is given by

$$\frac{C_{i\beta}}{C_L} = -\frac{16}{3\pi^2 A} + 0.05 \quad (9)$$

Equation (8) has been used to evaluate the parameter $C_{i\beta}/C_L$ for rigid wings covering a wide range of aspect ratio, taper ratio, and sweep, and having straight leading and trailing edges over each semispan. The values of \bar{y}^* used in equation (8) were obtained from references 4, 5, and 6. The results are given in figure 7.

Some comparisons of values of $C_{i\beta}/C_L$ computed from the equations presented herein with those of other theories are shown in figures 8, 9, and 10. The variation of $C_{i\beta}/C_L$ with aspect ratio for elliptic wings was computed by using equation (9) and is shown in figure 8. The computed values are somewhat greater than those given in equation (4) of

reference 1 with $\kappa=1.5$. The primary reason for the difference in the curves is that the effects of the quarter-chord-line vortex were not considered in reference 1. Omission of these effects in the present analysis yields a curve of $C_{i\beta}/C_L$ against aspect ratio which is in close agreement with Weissinger's curve. The remaining difference between the two curves (when the quarter-chord-line vortex is neglected) is present because, for elliptic wings, reference 1 evaluated the increment in $C_{i\beta}/C_L$ due to the small change in vortex strength associated with sideslip by an exact expression which is slightly different from the value of 0.05 used herein.

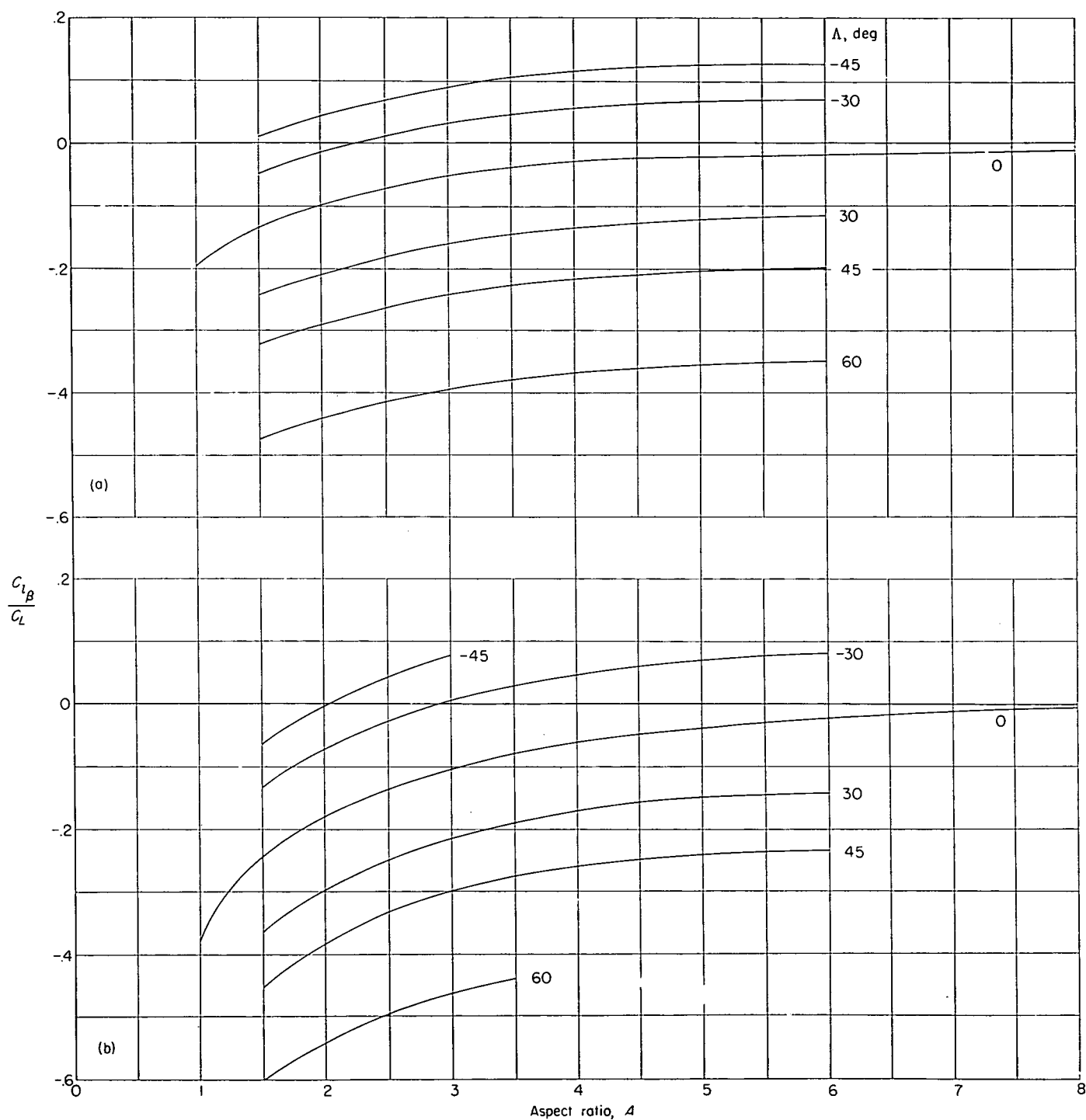
Values of $C_{i\beta}/C_L$ computed from equation (8) are compared in figure 9 with those from reference 1 for unswept wings having straight leading and trailing edges. In reference 1, Weissinger derives the following equation for this type of wing:

$$\frac{C_{i\beta}}{C_L} = -\frac{\kappa}{A} \frac{0.71\lambda + 0.29}{1+\lambda} + 0.05 \quad (10)$$

The reference also states that the exact theory fixes the value of κ at 1.5, but that, from comparison with experiment, a more practical value is $\kappa = 1.0$. The practice in the past therefore has been to use this equation with $\kappa = 1.0$ for unswept wings; and, in instances where sweep has been considered, the same equation generally has been used and an increment due to sweep then added. (See ref. 11, for example.) Tests of present-day wings generally have shown more negative values of $C_{i\beta}/C_L$ than those predicted by equation (10) with $\kappa = 1.0$, but these values are in good agreement with calculated values if $\kappa = 1.5$ is used. It appears likely that the value of κ considered practical by Weissinger was based on tests of wings which were in use at the time the investigation was made. These wings generally had rounded tips, which would tend to reduce the tip loading and, hence, also reduce $C_{i\beta}/C_L$.

Figure 9 presents a comparison of values of $C_{i\beta}/C_L$ from figure 7 (computed from eq. (8)) with theoretical values from reference 1 (computed from eq. (10)). Agreement between the values is good when $\kappa = 1.5$ is used in equation (10); in fact, with $\kappa = 1.5$, equations (8) and (10) are identical for a taper ratio of 1.0 and zero sweep.

Values of $C_{i\beta}/C_L$ computed from equation (8) for untapered 45° sweptback wings are compared in figure 10 with values from reference 11. The values from reference 11 are somewhat lower than those of the present report. Most of the difference is associated with the fact that the values of reference 11 are in part made up of the value for unswept wings determined by Weissinger's equation, equation (10), with $\kappa=1.0$. The remaining difference is associated with the contribution to $C_{i\beta}$ due to sweep. A comparison of equation (17) of reference 11 and equation (8) of the present report shows that the remaining difference is due to an induction factor $\frac{A+2 \cos \Lambda}{A+4 \cos \Lambda}$ used in reference 11 to account for induced effects because of the antisymmetric load due to sideslip. No such induction factor appears in the present report because it has been argued that the circulation remains symmetric even when the wing is sideslipping.

(a) $\lambda = 0$.(b) $\lambda = 0.25$ FIGURE 7.—Variation of $\frac{C_{l_B}}{C_L}$ with aspect ratio, taper ratio, and sweep.

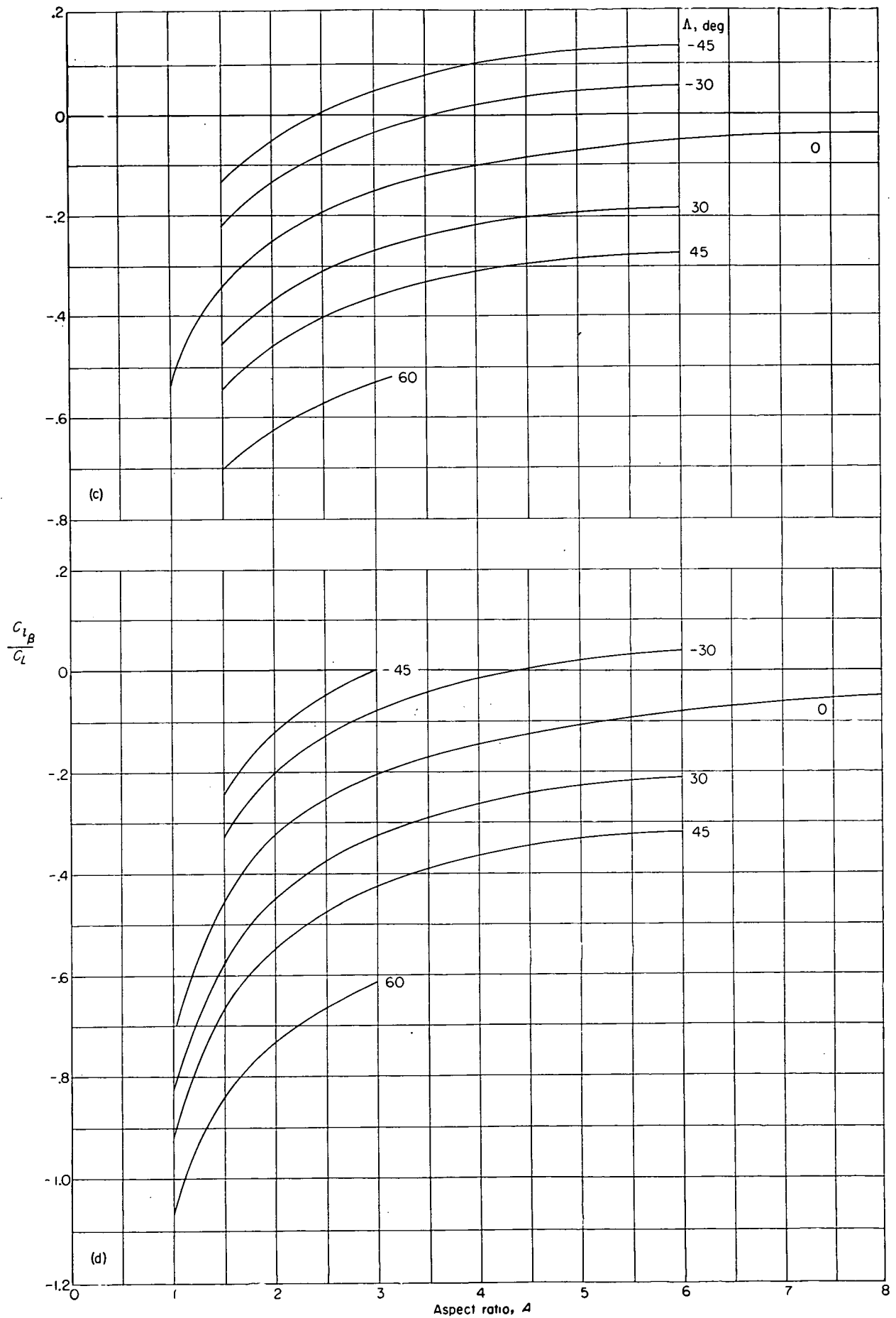
(c) $\lambda = 0.50$.(d) $\lambda = 1.00$.

FIGURE 7.—Continued.

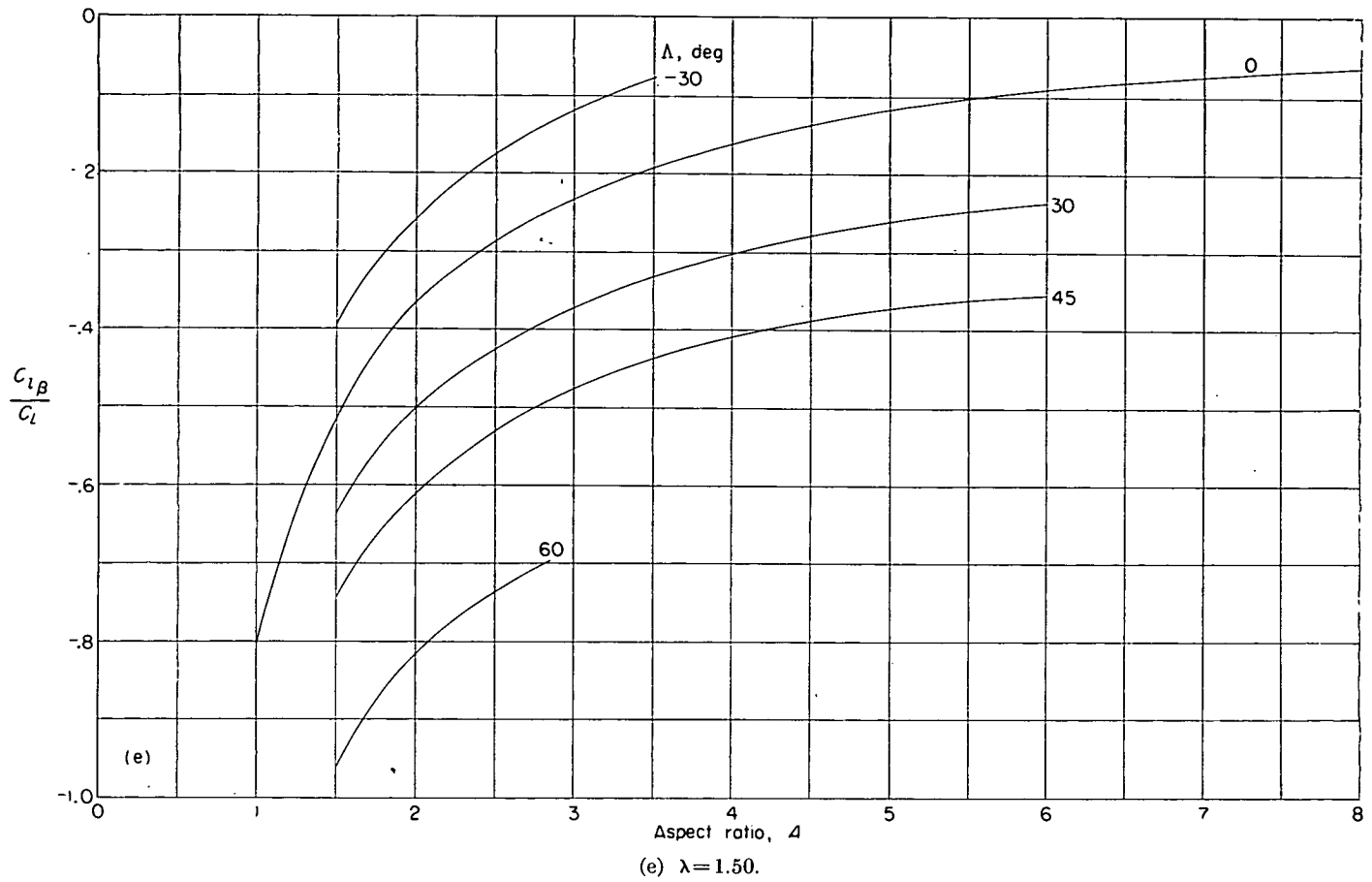


FIGURE 7.—Concluded.

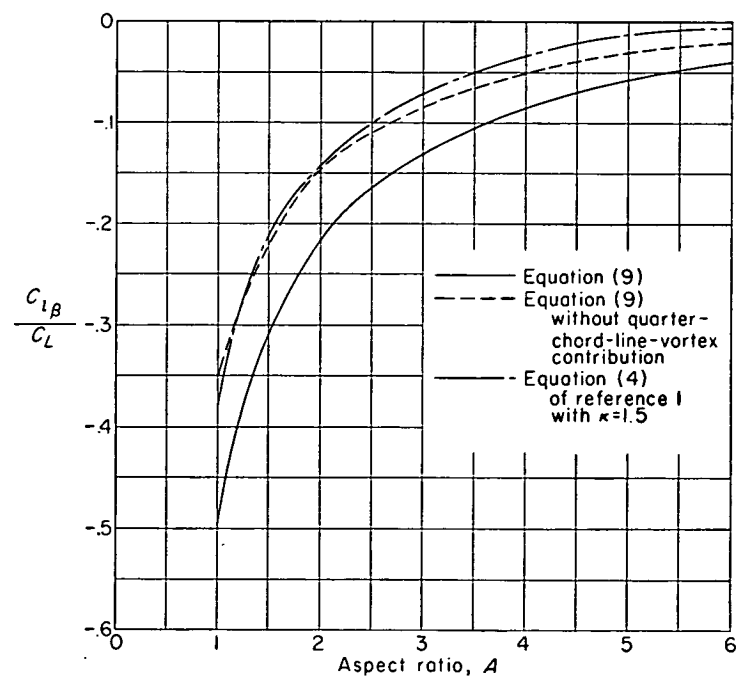


FIGURE 8.—Coefficient of rolling moment due to sideslip for elliptic wings.

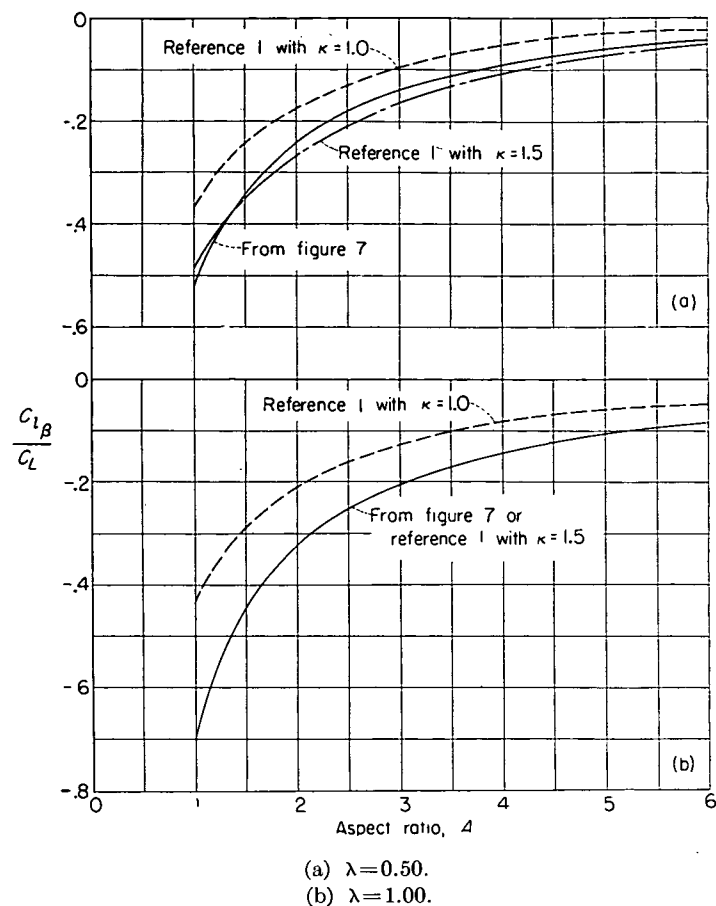


FIGURE 9.—Comparison of values of $\frac{C_{l\beta}}{C_L}$ from figure 7 with theoretical values from reference 1. $\Lambda=0^\circ$.

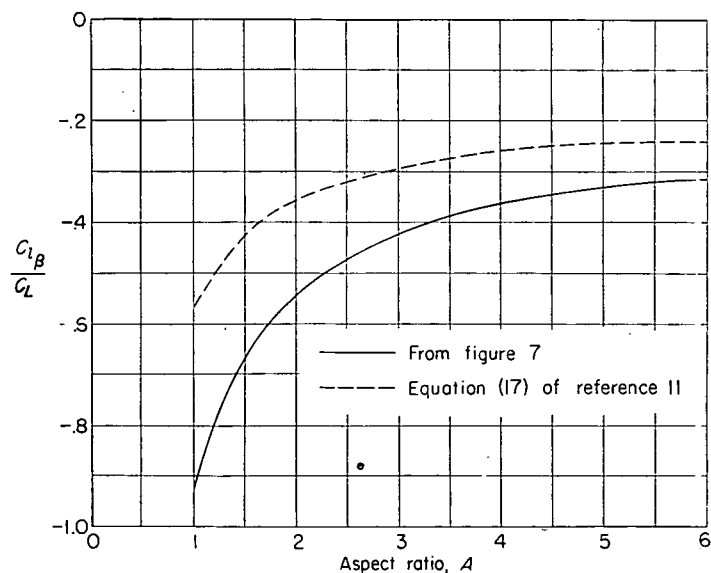
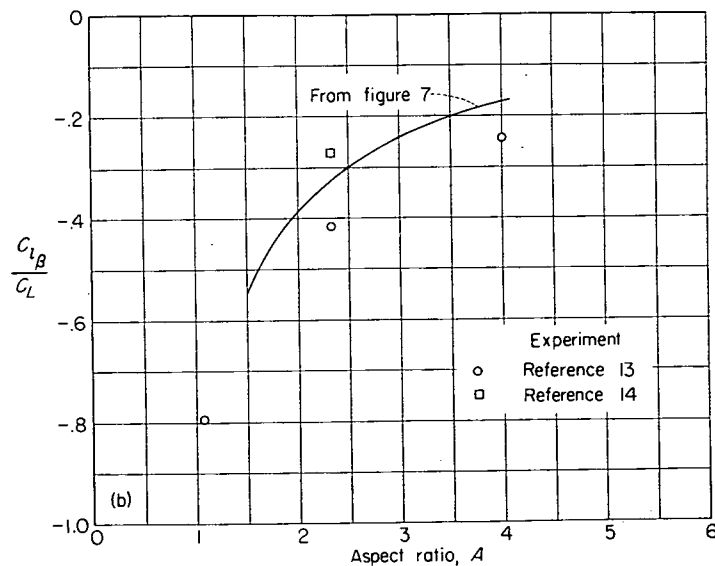
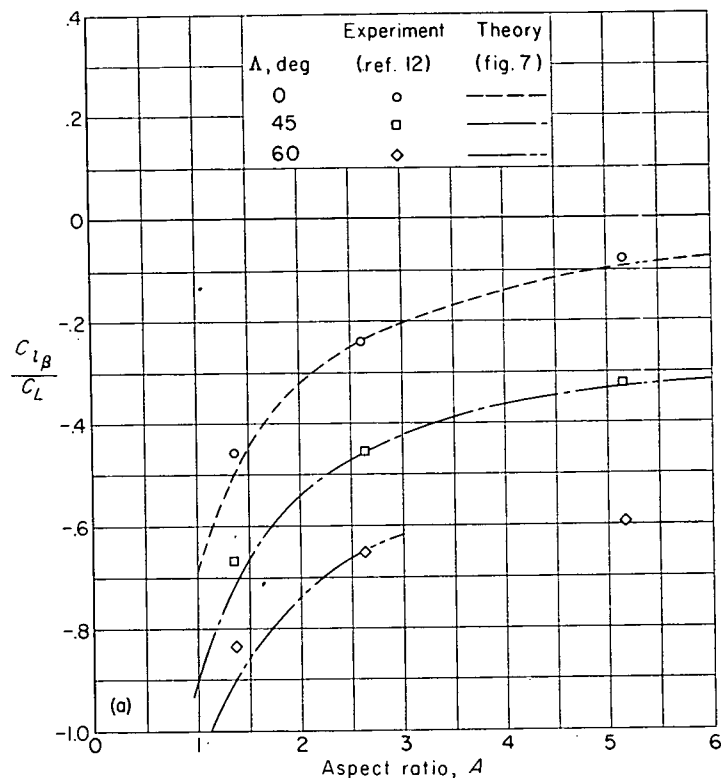


FIGURE 10.—Comparison of values of $\frac{C_{l\beta}}{C_L}$ from figure 7 with theoretical values from reference 11. $\Lambda=45^\circ$; $\lambda=1.00$.



(a) Untapered wings.

(b) Triangular wings.

FIGURE 11.—Comparison of experimental and calculated low-speed values of $\frac{C_{l\beta}}{C_L}$.

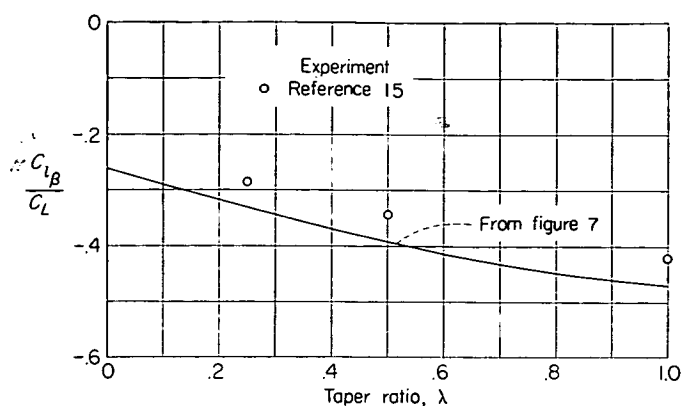


FIGURE 12.—Comparison of experimental and calculated effect of λ on $\frac{C_{l\beta}}{C_L}$. $A = 2.61$; $\Lambda = 45^\circ$.

Some comparisons of experimental and calculated low-speed values of $C_{l\beta}/C_L$ are shown in figures 11 and 12. The present theory correctly predicts effects of sweep, aspect ratio, and taper ratio, and the calculated values also generally agree quantitatively with experimental data from references 12 to 15.

Step-load method.—As stated previously, the advantage of using the step-load method instead of the integration method is that any integration or differentiation is avoided and, hence, the method is convenient to use for wings having the following characteristics: (1) chords which are not simple functions of spanwise position and (2) loads which are associated with twist.

The general equation for the rolling moment is derived in the appendix and is

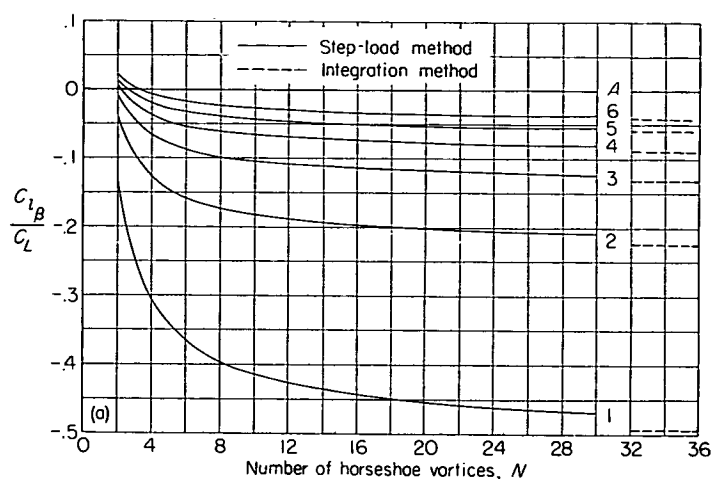
$$C_l = -\frac{1}{2N^2} \sum_{n=-N/2}^{n=-1} \left\{ (2n+1)(1-\beta \tan \Lambda) - \frac{3}{4} \beta N [nc_o^* - (n+1)c_i^*] \right\} [(\gamma)_{\beta=0}]_n - \frac{1}{2N^2} \sum_{n=1}^{n=N/2} \left\{ (2n-1)(1+\beta \tan \Lambda) + \frac{3}{4} \beta N [nc_o^* - (n-1)c_i^*] \right\} [(\gamma)_{\beta=0}]_n + 0.05\beta C_L \quad (11)$$

If the wing is symmetric, the rolling moment due to sideslip is

$$C_{l\beta} = -\frac{1}{N^2} \sum_{n=1}^{n=N/2} \left\{ (2n-1) \tan \Lambda + \frac{3}{4} N [nc_o^* - (n-1)c_i^*] \right\} [(\gamma)_{\beta=0}]_n + 0.05C_L \quad (12)$$

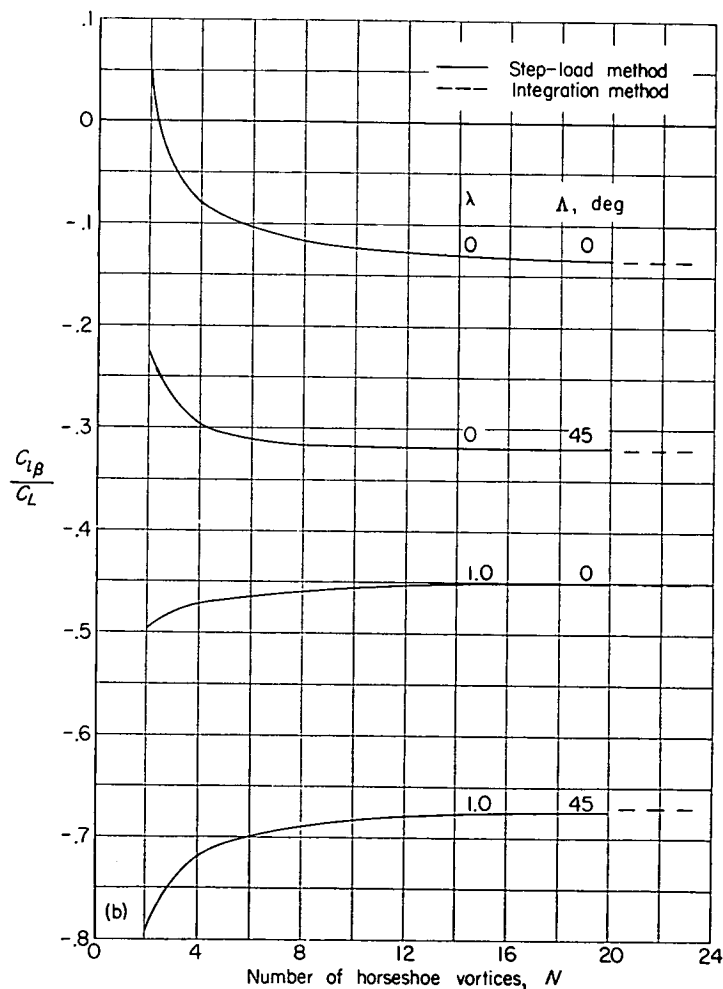
If in addition to being symmetric, the wing is also rigid, then the rate of change of $C_{l\beta}$ with C_L is given by

$$\frac{C_{l\beta}}{C_L} = -\frac{1}{N^2} \sum_{n=1}^{n=N/2} \left\{ (2n-1) \tan \Lambda + \frac{3}{4} N [nc_o^* - (n-1)c_i^*] \right\} \left[\left(\frac{\gamma}{C_L} \right)_\alpha \right]_n + 0.05 \quad (13)$$



(a) Elliptic wings.

FIGURE 13.—Effect of N on estimated value of $\frac{C_{l\beta}}{C_L}$.



(b) Tapered wings, $A = 1.5$.

FIGURE 13.—Concluded.

In order to determine the compatibility of the integration and step-load methods, values of $C_{l\beta}/C_L$ for several rigid symmetrical wings were computed and the results are presented in figure 13. The results show that values of $C_{l\beta}/C_L$ computed by the step-load method converge rapidly on the

values from the integration method as the number of horseshoe vortices used in the step-load method is increased. About 20 horseshoe vortices should be sufficient for a reasonable representation of a wing.

Equation (12) was used to compute the increment in $C_{l\beta}$ due to linear twist for a wing having an aspect ratio of 4.0, a taper ratio of 0.6, 45° sweep of the leading edge, and -6° maximum twist at the wing tips. Values of $(\gamma)_\theta$ used in the calculations were obtained by interpolation of the material in reference 6. The computed value of $C_{l\beta}$ due to twist at $\alpha=0^\circ$ was 0.05, a value which compares well with the experimental value of 0.04 (ref. 16).

CONCLUDING REMARKS

A method of computing span loads and the resulting rolling moments for sideslipping wings of arbitrary plan form in incompressible flow is derived. The method requires that the span load at zero sideslip be known for the wing under consideration. Since this information is available for a large variety of wings, this requirement should not seriously restrict the application of the present method. The basic

method derived herein requires a mechanical differentiation and integration to obtain the rolling moment for the general wing in sideslip. For wings having straight leading and trailing edges over each semispan, the rolling moment due to sideslip is given by a simple equation in terms of the planform parameters and the lateral center of pressure of the lift due to angle of attack.

The mechanical differentiation and integration required to obtain the rolling moment for the general wing can be avoided by a step-load method which is also derived herein.

Charts are presented from which the rolling-moment parameter $C_{l\beta}/C_L$ can be obtained for wings having straight leading and trailing edges over each semispan.

Calculated span loads and rolling-moment parameters are compared with experimental values. The comparison indicates good agreement between calculations and available experimental data.

LANGLEY AERONAUTICAL LABORATORY,
NATIONAL ADVISORY COMMITTEE FOR AERONAUTICS,
LANGLEY FIELD, VA., October 6, 1955.

APPENDIX

DERIVATION OF EQUATIONS

GENERAL EQUATIONS FROM INTEGRATION METHOD

In the following derivation, all equations refer to the right or leading wing semispan unless otherwise noted. The considerations presented in the section entitled "Analysis" permit lift to be obtained from the quarter-chord-line vortex and from the chordwise-bound vortices. By referring to figure 2(b), it is seen that, for the right (leading) wing semispan, the lift per unit length of the quarter-chord-line vortex of a swept wing in sideslip is given by

$$l_1 = \rho V \cos(\Lambda - \beta) \Gamma_z$$

or, per unit length of wing span, by

$$l_1 = \rho V \cos(\Lambda - \beta) \Gamma_z \frac{1}{\cos \Lambda}$$

The lift due to one chordwise-bound vortex is

$$l_2 = -\rho V \sin \beta \left(\frac{3}{4} c \right) \frac{d\Gamma_z}{dz}$$

For small sideslip angles such that $\sin \beta = \beta$ and $\cos \beta = 1.0$, the lift component per unit of wing span for the quarter-chord-line vortex is

$$l_1 = \rho V \Gamma_z (1 + \beta \tan \Lambda) \quad (A1)$$

and for the chordwise-bound vortex,

$$l_2 = -\frac{3}{4} \rho V c \beta \frac{d\Gamma_z}{dz} \quad (A2)$$

In general, span load or circulation distributions are presented in terms of the spanwise circulation strength Γ_y rather than the strength Γ_z along the quarter-chord line. The relationship between Γ_y and Γ_z can be determined readily from consideration of the lift on a wing at zero sideslip angle. The lift per unit span is given by

$$(l)_{\beta=0} = \rho V \Gamma_y \quad (A3)$$

and also by

$$(l)_{\beta=0} = \rho V \Gamma_z \cos \Lambda \frac{1}{\cos \Lambda}$$

from which it is seen that Γ_y and Γ_z are equal. Equations (A1) and (A2) therefore can be written as:

$$l_1 = \rho V \Gamma_y (1 + \beta \tan \Lambda) \quad (A4)$$

and

$$l_2 = -\frac{3}{4} \rho V c \beta \frac{d\Gamma_y}{dy} \quad (A5)$$

The vortex strength Γ_y is related to the section lift at zero sideslip by equation (A3) or, in coefficient form, by

$$\Gamma_y = \frac{1}{2} V c (c_l)_{\beta=0} \quad (A6)$$

Substituting equation (A6) into equations (A4) and (A5), adding the resulting equations, and nondimensionalizing yields the following general equation for determining the span load distribution:

$$\gamma = (\gamma)_{\beta=0} (1 + \beta \tan \Lambda) - \frac{3}{4} \beta c^* \frac{d(\gamma)_{\beta=0}}{dy^*} \quad (A7)$$

Similarly, for the left (or trailing) wing semispan, it can be shown that

$$\gamma = (\gamma)_{\beta=0} (1 - \beta \tan \Lambda) - \frac{3}{4} \beta c^* \frac{d(\gamma)_{\beta=0}}{dy^*} \quad (A8)$$

Equations (A7) and (A8) can be used to determine the span load on a wing in sideslip, provided that the load at zero sideslip is known. The load due to sideslip for the right semispan is

$$(\gamma)_{\beta} = (\gamma)_{\beta=0} \beta \tan \Lambda - \frac{3}{4} \beta c^* \frac{d(\gamma)_{\beta=0}}{dy^*} \quad (A9)$$

and for the left semispan,

$$(\gamma)_{\beta} = -(\gamma)_{\beta=0} \beta \tan \Lambda - \frac{3}{4} \beta c^* \frac{d(\gamma)_{\beta=0}}{dy^*} \quad (A10)$$

The parameter $(\gamma)_{\beta=0}$ is made up of the components $(\gamma)_{\theta}$ and $(\gamma)_{\alpha}$. For rigid wings, only $(\gamma)_{\alpha}$ varies with C_L , and, therefore, the rate of change of load due to sideslip with C_L is given by the following equation for the right wing semispan:

$$\frac{\partial(\gamma)_{\beta}}{\partial C_L} = \left(\frac{\gamma}{C_L} \right)_{\alpha} \beta \tan \Lambda - \frac{3}{4} \beta c^* \frac{d \left(\frac{\gamma}{C_L} \right)_{\alpha}}{dy^*}$$

A second differentiation, with respect to β , yields the following load parameters:

For the right semispan,

$$\frac{cc_i}{\bar{c} C_L \beta} = \left(\frac{cc_i}{\bar{c} C_L} \right)_{\alpha} \tan \Lambda - \frac{3}{4} c^* \frac{d \left(\frac{cc_i}{\bar{c} C_L} \right)_{\alpha}}{dy^*} \quad (A11)$$

For the left semispan,

$$\frac{cc_i}{\bar{c} C_L \beta} = - \left(\frac{cc_i}{\bar{c} C_L} \right)_{\alpha} \tan \Lambda - \frac{3}{4} c^* \frac{d \left(\frac{cc_i}{\bar{c} C_L} \right)_{\alpha}}{dy^*} \quad (A12)$$

The rolling moment of a wing in sideslip can be determined by an integration of the span load multiplied by the proper moment arm. A general form of a rolling-moment equation is obtained from equations (A7) and (A8), to which must be added the increment determined by Weissinger (ref. 1) for unswept wings and which is supposed to account for the small modification in circulation strength Γ_v due to sideslip. Thus, the rolling-moment equation is

$$C_l = \frac{1}{4} \left(\int_{-1}^0 \gamma y^* dy^* - \int_0^1 \gamma y^* dy^* \right) + 0.05 \beta C_L \quad (A13)$$

where γ for the left wing semispan is used in the first integral and γ for the right wing semispan is used in the second integral. The rolling moment due to sideslip is determined by substituting equations (A7) and (A8) into equation (A13) and differentiating with respect to β . The result can be shown to be, in expanded form,

$$C_{l\beta} = -\frac{1}{4} \left\{ \int_{-1}^0 \left[(\gamma)_{\theta} \tan \Lambda + \frac{3}{4} c^* \frac{d(\gamma)_{\theta}}{dy^*} \right] y^* dy^* + \int_0^1 \left[(\gamma)_{\theta} \tan \Lambda - \frac{3}{4} c^* \frac{d(\gamma)_{\theta}}{dy^*} \right] y^* dy^* \right\} - \frac{1}{2} \int_0^1 \left[(\gamma)_{\alpha} \tan \Lambda - \frac{3}{4} c^* \frac{d(\gamma)_{\alpha}}{dy^*} \right] y^* dy^* + 0.05 C_L \quad (A14)$$

The rate of change of $C_{l\beta}$ with C_L for a rigid wing is given by

$$\frac{C_{l\beta}}{C_L} = -\frac{1}{2} \int_0^1 \left[\left(\frac{\gamma}{C_L} \right)_{\alpha} \tan \Lambda - \frac{3}{4} c^* \frac{d \left(\frac{\gamma}{C_L} \right)_{\alpha}}{dy^*} \right] y^* dy^* + 0.05 \quad (A15)$$

Equation (A15) can be reduced by noting that the first term on the right-hand side can be integrated by inspection; that is,

$$\int_0^1 \left(\frac{\gamma}{C_L} \right)_{\alpha} \tan \Lambda y^* dy^* = \bar{y}^* \tan \Lambda \quad (A16)$$

The second term of equation (A15) can be simplified by integration by parts, so that equation (A15) becomes

$$\frac{C_{l\beta}}{C_L} = -\frac{1}{2} \bar{y}^* \tan \Lambda - \frac{3}{8} \int_0^1 \left(\frac{\gamma}{C_L} \right)_{\alpha} \left(c^* + y^* \frac{dc^*}{dy^*} \right) dy^* + 0.05 \quad (A17)$$

Equation (A17) can, of course, be further simplified if c^* is a simple function of spanwise position.

The differentiation and integration indicated in the various rolling-moment equations can be avoided by use of the step-load method which is developed in the following section.

GENERAL EQUATIONS FROM STEP-LOAD METHOD

The basic assumptions of the step-load method of determining the span load and rolling moment of a wing in sideslip are identical to those of the integration method. In the step-load method the span load distribution at zero sideslip angle is approximated by a number N of equal-span horseshoe vortices which are oriented and numbered as shown in figures 3 and 4. By considering one horseshoe vortex with its center at spanwise position y_n (see fig. 4 for details), it is readily seen that lift is produced by the quarter-chord-line-vortex segment and the two chordwise-bound vortices of the horseshoe vortex. The lift due to one horseshoe vortex on the right wing semispan is

$$\text{Lift} = \rho V \cos(\Lambda - \beta) \Gamma_v \frac{2s}{\cos \Lambda} + \rho V \sin \beta \Gamma_v \left(\frac{3}{4} c_o - \frac{3}{4} c_i \right)$$

or, when small sideslip angles are assumed,

$$\text{Lift} = 2s \rho V \Gamma_v (1 + \beta \tan \Lambda) + \frac{3}{4} \rho V \Gamma_v \beta (c_o - c_i) \quad (A18)$$

The step-load method results in a total load on each horseshoe vortex made up of a distributed load due to the quarter-chord-line-vortex segment and two concentrated loads (concentrated relative to spanwise position) due to the chordwise-bound vortices. It appears, therefore, that the step-load method does not lend itself to the determination of a continuous span load distribution.

The loads given by equation (A18) can, of course, be used to determine the rolling moment of the wing. The rolling moment due to each horseshoe vortex is obtained by multiplying the load on each lift-producing element by its moment arm; therefore,

$$l' = -2s\rho V\gamma\Gamma_v(1+\beta \tan \Lambda) - \frac{3}{4}\rho V\Gamma_v\beta[(y+s)c_o - (y-s)c_i]$$

This equation can be simplified to

$$l' = -\rho V\gamma\Gamma_v \left\{ 2s(1+\beta \tan \Lambda) + \frac{3}{4}\beta \left[\left(1+\frac{s}{y}\right)c_o - \left(1-\frac{s}{y}\right)c_i \right] \right\} \quad (\text{A19})$$

Substitution of equation (A6) into equation (A19) yields

$$l' = -\frac{1}{2}\rho V^2\gamma c(c_i)_{\beta=0} \left\{ 2s(1+\beta \tan \Lambda) + \frac{3}{4}\beta \left[\left(1+\frac{s}{y}\right)c_o - \left(1-\frac{s}{y}\right)c_i \right] \right\} \quad (\text{A20})$$

The spanwise distance to the center of a horseshoe vortex on the right wing semispan is given by

$$y = (2n-1)s$$

Therefore, equation (A20) can be written as

$$l' = -\frac{1}{2}\rho V^2 c(c_i)_{\beta=0} (2n-1)s \left\{ 2s(1+\beta \tan \Lambda) + \frac{3}{4}\beta \left[\left(1+\frac{1}{2n-1}\right)c_o - \left(1-\frac{1}{2n-1}\right)c_i \right] \right\}$$

This equation can be simplified further by algebraic manipulation to obtain

$$l' = -\rho V^2 c(c_i)_{\beta=0} s^2 \left\{ (2n-1)(1+\beta \tan \Lambda) + \frac{3}{4}\beta \left[\frac{nc_o}{s} - (n-1)\frac{c_i}{s} \right] \right\}$$

Similarly it can be shown that, for the left or trailing wing semispan, the rolling moment due to one vortex is given by

$$l' = -\rho V^2 c(c_i)_{\beta=0} s^2 \left\{ (2n+1)(1-\beta \tan \Lambda) - \frac{3}{4}\beta \left[\frac{nc_o}{s} - (n+1)\frac{c_i}{s} \right] \right\}$$

The horseshoe-vortex semispan is related to the wing span by $b=2Ns$; hence, the rolling moment per vortex on the right wing semispan can be written as

$$l' = -\rho V^2 c(c_i)_{\beta=0} \frac{b^2}{4N^2} \left\{ (2n-1)(1+\beta \tan \Lambda) + \frac{3}{4}\beta N [nc_o^* - (n-1)c_i^*] \right\} \quad (\text{A21})$$

and on the left wing semispan as

$$l' = -\rho V^2 c(c_i)_{\beta=0} \frac{b^2}{4N^2} \left\{ (2n+1)(1-\beta \tan \Lambda) - \frac{3}{4}\beta N [nc_o^* - (n+1)c_i^*] \right\} \quad (\text{A22})$$

The most general form for the rolling-moment coefficient is obtained by summing equations (A21) and (A22) over the wing span and adding the correction determined by Weisinger in reference 1. The result is

$$C_l = -\frac{1}{2N^2} \sum_{n=-N/2}^{n=N/2} \left\{ (2n+1)(1-\beta \tan \Lambda) - \frac{3}{4}\beta N [nc_o^* - (n+1)c_i^*] \right\} [(\gamma)_{\beta=0}]_n - \frac{1}{2N^2} \sum_{n=1}^{n=N/2} \left\{ (2n-1)(1+\beta \tan \Lambda) + \frac{3}{4}\beta N [nc_o^* - (n-1)c_i^*] \right\} [(\gamma)_{\beta=0}]_n + 0.05\beta C_L \quad (\text{A23})$$

If the wing is symmetrical, then it is necessary only to integrate over one semispan, multiply the result by two, and add the $0.05\beta C_L$ increment. The rolling moment due to sideslip for a symmetrical wing is given by

$$C_{l\beta} = -\frac{1}{N^2} \sum_{n=1}^{n=N/2} \left\{ (2n-1) \tan \Lambda + \frac{3}{4}N [nc_o^* - (n-1)c_i^*] \right\} [(\gamma)_{\beta=0}]_n + 0.05C_L \quad (\text{A24})$$

For rigid wings, the rate of change of $C_{l\beta}$ with C_L is given by

$$\frac{C_{l\beta}}{C_L} = -\frac{1}{N^2} \sum_{n=1}^{n=N/2} \left\{ (2n-1) \tan \Lambda + \frac{3}{4}N [nc_o^* - (n-1)c_i^*] \right\} \left[\left(\frac{\gamma}{C_L} \right)_\alpha \right]_n + 0.05 \quad (\text{A25})$$

The various equations can be simplified if c_o and c_i are simple functions of spanwise position.

EQUATIONS FOR SPECIFIC TYPES OF WINGS

Elliptic wings—integration method.—Elliptic wings have geometric and aerodynamic load characteristics at zero sideslip which can be defined by simple mathematical expressions; hence, some of their aerodynamic derivatives can be obtained readily. The following characteristics, which can be derived with little difficulty, are listed for reference:

$$\left(\frac{\gamma}{C_L} \right)_\alpha = \frac{4}{\pi} \sqrt{1-(y^*)^2}$$

$$c^* = \frac{8}{\pi A} \sqrt{1-(y^*)^2}$$

$$\tan \Lambda = \frac{2}{\pi A} \frac{y^*}{\sqrt{1-(y^*)^2}}$$

$$\frac{d\left(\frac{\gamma}{C_L} \right)_\alpha}{dy^*} = -\frac{4}{\pi} \frac{y^*}{\sqrt{1-(y^*)^2}}$$

These relationships can be used with equations (A9) and (A15) to obtain

$$\frac{d\gamma}{d\beta} = \frac{32}{\pi^2 A} y^* C_L \quad (\text{A26})$$

and

$$\frac{C_{l\beta}}{C_L} = -\frac{16}{3\pi^2 A} + 0.05 \quad (\text{A27})$$

Wings with straight leading and trailing edges—integration method.—The chord of a wing having straight leading and trailing edges over each semispan is given by

$$c^* = \frac{4}{A(1+\lambda)} [1 - (1-\lambda)y^*] \quad (\text{A28})$$

Equation (A28) can be used with equations (A9) and (A17) to obtain

$$\frac{d\gamma}{d\beta} = (\gamma)_\alpha \tan \Lambda - \frac{3}{A(1+\lambda)} [1 - (1-\lambda)y^*] \frac{d(\gamma)_\alpha}{dy^*} \quad (\text{A29})$$

and

$$\frac{C_{l\beta}}{C_L} = -\frac{1}{2} \left\{ \frac{3}{A(1+\lambda)} + \bar{y}^* \left[\tan \Lambda - \frac{6}{A} \left(\frac{1-\lambda}{1+\lambda} \right) \right] \right\} + 0.05 \quad (\text{A30})$$

Elliptic wing—step-load method.—The following characteristics of elliptic wings, when represented by horseshoe vortices, can be readily derived and are listed for reference. For the right semispan,

$$\left[\left(\frac{\gamma}{C_L} \right)_\alpha \right]_n = \frac{4}{\pi N} \sqrt{N^2 - (2n-1)^2}$$

$$(c_o^*)_n = \frac{8}{\pi N A} \sqrt{N^2 - 4n^2}$$

$$(c_i^*)_n = \frac{8}{\pi N A} \sqrt{N^2 - 4(n-1)^2}$$

$$(\tan \Lambda)_n = \frac{1}{\pi A} [\sqrt{N^2 - 4(n-1)^2} - \sqrt{N^2 - 4n^2}]$$

These relationships can be used with equation (A25) to obtain

$$\frac{C_{l\beta}}{C_L} = -\frac{4}{\pi^2 A N^3} \left\{ \sum_{n=1}^{n=N/2} [(4n+1) \sqrt{N^2 - 4n^2} - (4n-5) \sqrt{N^2 - 4(n-1)^2}] \sqrt{N^2 - (2n-1)^2} \right\} + 0.05 \quad (\text{A31})$$

Wings with straight leading and trailing edges—step-load method.—The local chord of a wing having straight leading and trailing edges over each semispan is given by equation (A28). The chords can also be expressed as

$$(c_o^*)_n = \frac{4}{A(1+\lambda)} \left[1 - (1-\lambda) \frac{2n}{N} \right]$$

and

$$(c_i^*)_n = \frac{4}{A(1+\lambda)} \left[1 - (1-\lambda) \frac{2n-2}{N} \right]$$

These expressions can be used with equation (A25) to obtain

$$\frac{C_{l\beta}}{C_L} = \frac{3}{A(1+\lambda)N^2} \left\{ \sum_{n=1}^{n=N/2} [(4n-2)(1-\lambda) - N - \frac{(2n-1)(1+\lambda)}{3} A \tan \Lambda] \left[\left(\frac{\gamma}{C_L} \right)_\alpha \right]_n \right\} + 0.05 \quad (\text{A32})$$

REFERENCES

1. Weissinger, J.: Der schiebende Tragflügel bei gesunder Strömung. Bericht S 2 der Lilienthal-Gesellschaft für Luftfahrtforschung, 1938-39, pp. 13-51.
2. Luckert, H. J.: Lift Distribution on Swept-Back Wings in Yaw. Reps. and Translations No. 741 (AGD Rep. No. 1066), British M.O.S. (A) Völknerode, Mar. 1947.
3. Jacobs, W.: Systematische Druckverteilungsmessungen an Pfeilflügeln konstanter Tiefe bei symmetrischer und unsymmetrischer Anströmung. Bericht 44/28, Aerodynamisches Institut der T. H. Braunschweig, Nov. 8, 1944.
4. DeYoung, John, and Harper, Chasles W.: Theoretical Symmetric Span Loading at Subsonic Speeds for Wings Having Arbitrary Plan Form. NACA Rep. 921, 1948.
5. Diederich, Franklin W., and Zlotnick, Martin: Calculated Spanwise Lift Distributions and Aerodynamic Influence Coefficients for Unswept Wings in Subsonic Flow. NACA TN 3014, 1953.
6. Diederich, Franklin W., and Zlotnick, Martin: Calculated Spanwise Lift Distributions and Aerodynamic Influence Coefficients for Swept Wings in Subsonic Flow. NACA TN 3476, 1955.
7. Diederich, Franklin W., and Latham, W. Owen: Calculated Aerodynamic Loadings of M, W, and A Wings in Incompressible Flow. NACA RM L51E29, 1951.
8. Blenk, Hermann: The Monoplane as a Lifting Vortex Surface. NACA TM 1111, 1947.
9. Campbell, George S.: A Finite-Step Method For the Calculation of Span Loadings of Unusual Plan Forms. NACA RM L50L13, 1951.
10. Gray, W. L., and Schenk, K. M.: A Method for Calculating the Subsonic Steady-State Loading on an Airplane With a Wing of Arbitrary Plan Form and Stiffness. NACA TN 3030, 1953.
11. Toll, Thomas A., and Queijo, M. J.: Approximate Relations and Charts for Low-Speed Stability Derivatives of Swept Wings. NACA TN 1581, 1948.
12. Goodman, Alex, and Brewer, Jack D.: Investigation at Low Speeds of the Effect of Aspect Ratio and Sweep on Static and Yawing Stability Derivatives of Untapered Wings. NACA TN 1669, 1948.
13. Jaquet, Byron M., and Brewer, Jack D.: Low-Speed Static-Stability and Rolling Characteristics of Low-Aspect-Ratio Wings of Triangular and Modified Triangular Plan Forms. NACA RM L8L29, 1949.
14. Goodman, Alex, and Thomas, David F., Jr.: Effects of Wing Position and Fuselage Size on the Low-Speed Static and Rolling Stability Characteristics of a Delta-Wing Model. NACA Rep. 1224, 1955. (Supersedes NACA TN 3063.)
15. Letko, William, and Cowan, John W.: Effect of Taper Ratio on Low-Speed Static and Yawing Stability Derivatives of 45° Sweptback Wings With Aspect Ratio of 2.61. NACA TN 1671, 1948.
16. Jaquet, Byron M.: Effect of Linear Spanwise Variations of Twist and Circular-Arc Camber on Low-Speed Static Stability, Rolling, and Yawing Characteristics of a 45° Sweptback Wing of Aspect Ratio 4 and Taper Ratio 0.6. NACA TN 2775, 1952.

REPORT 1270

REVIEW OF EXPERIMENTAL INVESTIGATIONS OF LIQUID-METAL HEAT TRANSFER¹

By BERNARD LUBARSKY and SAMUEL J. KAUFMAN

SUMMARY

The experimentally obtained results of various investigators of liquid-metal heat-transfer characteristics were examined and found to be not always directly comparable because of differences in experimental apparatus or in methods of calculation. The experimental data were therefore reevaluated using assumptions and methods as consistent as possible and then compared with each other and with theoretical results.

The reevaluated data for both local fully developed and average Nusselt numbers in the turbulent-flow region were still found to have considerable spread, with the bulk of the data being lower than predicted by existing analyses. An equation based on empirical grounds which best represents most of the fully developed heat-transfer data is

$$\bar{Nu} = 0.625 Pe^{0.4}$$

where Nu represents the Nusselt number and Pe , the Peclet number. The theoretical prediction of the heat transfer in the entrance region was found to give lower values, in most cases, than those found in the experimental work.

The theoretical and experimental results for the ratio of local Nusselt number to fully developed Nusselt number were integrated to obtain predictions for the ratio of average Nusselt number to fully developed Nusselt number for a range of Peclet numbers and length-diameter ratios. Most of the experimental data fall between 60 to 80 percent of the predicted values.

The experimental evidence was insufficient to serve as a basis for any conclusion concerning liquid-metal heat transfer in the laminar or transition flow regions.

INTRODUCTION

The use of liquid metals as heat-transfer media is presently of considerable interest. A number of theoretical and experimental investigations to determine the heat-transfer characteristics of liquid metals have been made by various investigators (refs. 1 to 26). In the literature, the results of the experimental investigations often have been compared with each other and with the results of theoretical investigations. During the course of investigations of liquid-metal heat-transfer characteristics at the NACA Lewis laboratory, the work of the various experimental investigators was carefully examined. It was found that different investigations were not always directly comparable because of differ-

ences in the experimental apparatus or in the methods of calculation. Some of the differences found were:

(1) Liquid-metal physical properties that differed from those currently accepted were sometimes used.

(2) At times, centerline temperatures in and out of the test section were measured rather than "mixing-cup" temperatures.

(3) Some of the experiments were conducted with uniform heat input to the wall of the test section, while others more closely approached constant wall temperature.

(4) Some investigators measured the combined heat-transfer coefficient in a tube and concentric annulus; different methods were used to obtain the individual coefficients.

(5) Some investigators measured local fully developed heat-transfer coefficients; others measured average over-all coefficients.

(6) The velocity profiles entering the test section varied; some approached a fully developed turbulent profile, while others were more nearly uniform.

(7) Different length-diameter ratios of the test section were used.

The differences in experimental apparatus of items (6) and (7) affect only the average heat-transfer coefficient and not the fully developed coefficient.

Because of the differences in experimental apparatus and methods of calculation listed, the experimental data of references 1 to 26 were reevaluated using consistent assumptions and methods in order to permit a better intercomparison of the experimental results and comparison with the results of theoretical investigations.

SYMBOLS

a	constant
c_p	specific heat, Btu/(lb)(°F)
D	equivalent or hydraulic diameter, ft
D_i	annulus inner diameter, ft
D_o	annulus outer diameter, ft
f	friction factor
G	weight flow per unit area, lb/(hr)(sq ft)
Gz	Graetz number, PeD/l or PeD/x
k	thermal conductivity, Btu/(hr)(sq ft)(°F/ft)
l	length of test section, ft
m	constant, eq. (10)
Nu	Nusselt number, UD/k
n	constant, eq. (10)

¹ Supersedes NACA TN 3336, "Review of Experimental Investigations of Liquid-Metal Heat Transfer," by Bernard Lubarsky and Samuel J. Kaufman, 1955.

Pe	Peclet number, $RePr$, GDc_p/k
Pr	Prandtl number, $c_p\mu/k$
Re	Reynolds number, GD/μ
St	Stanton number, U/c_pG
t_c	fluid centerline temperature, °F
t_m	fluid bulk temperature, °F ("bulk temperature" as used in this report is synonymous with "mixing-cup temperature" and "mixed mean temperature")
t_w	wall temperature, °F
U	heat-transfer coefficient, Btu/(hr)(sq ft)(°F)
x	distance along test section, ft
μ	fluid bulk viscosity, lb/(hr)(ft)
Subscripts:	
an	annulus
av	average
f	fully developed
x	at station x

PROCEDURE

The experimental data of the various references were reevaluated as consistently as possible, plotted as Nusselt number against Peclet or Graetz number or against both, and the results compared with theoretical predictions. These three steps will be discussed in reverse order, because some of the methods used in reevaluating the data were determined by theoretical considerations.

THEORETICAL INVESTIGATIONS OF LIQUID-METAL HEAT TRANSFER

The following discussion gives a brief description of some of the results of theoretical investigations and is not intended

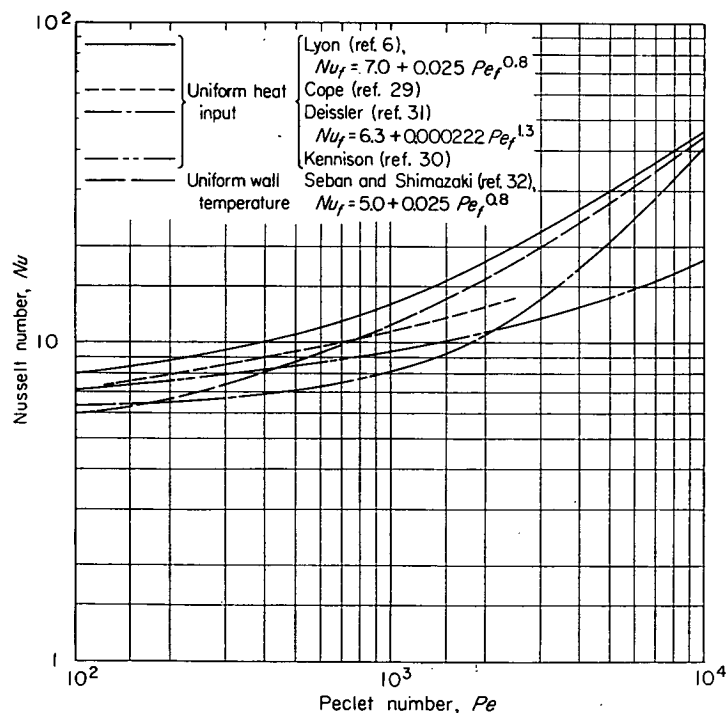


FIGURE 1.—Theoretical predictions of fully developed Nusselt numbers for heat transfer to liquid metals in turbulent flow in round tubes.

to be complete. All the theoretical investigations discussed consider only the turbulent-flow region.

Fully developed heat-transfer coefficients.—Heat-transfer coefficients for liquid metals in turbulent flow with fully developed velocity and temperature profiles have been predicted by a number of investigators using somewhat different assumptions:

(1) Uniform heat input to the wall; round tubes: The most frequently analyzed case is that of heat transfer to a round tube with uniform rate of heat input along the length of the tube. This case was investigated by Martinelli (ref. 27) using the "momentum transfer analogy." Lyon (ref. 6) found a simplified equation which approximated Martinelli's more complex relation. This equation, which is recommended by the Liquid-Metals Handbook (ref. 28), is

$$Nu_f = 7.0 + 0.025 Pe_f^{0.8} \quad (1)$$

Cope (ref. 29) investigated the possibility of assuming that the modified vorticity transfer analogy applied to the turbulent core of the fluid, while the momentum transfer analogy applied to the boundary layer and buffer layer. Kennison (ref. 30) assumed that the heat transfer is analogous to the transfer of vorticity for turbulent fluid flow in a long straight pipe. Deissler (ref. 31) modified the momentum transfer analogy to allow for heat transferred by conduction to or from a turbulent particle as it moves radially in the tube. Deissler's analysis is for a Prandtl number of 0.01.

Some of the results of these various investigations are shown in figure 1. The experimental results for fully developed heat transfer in a round tube with uniform heat

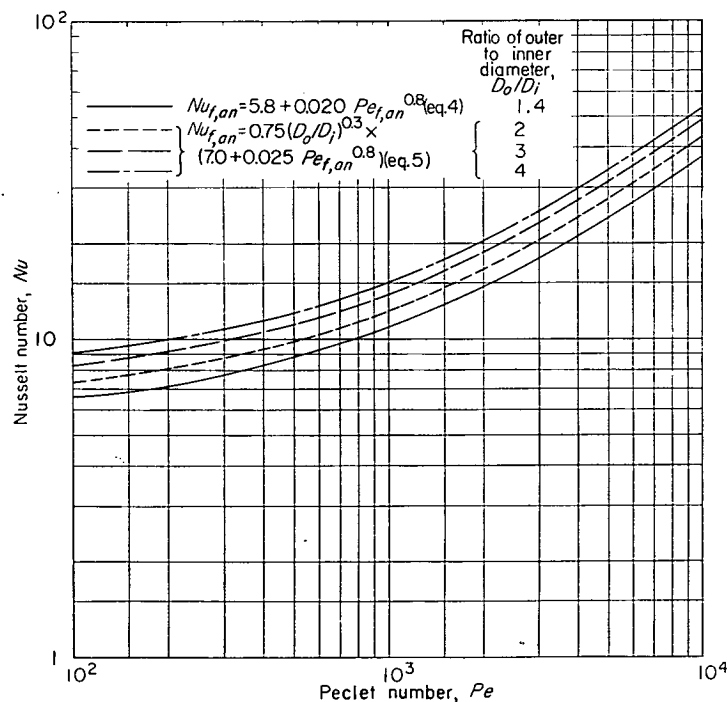


FIGURE 2.—Theoretical predictions of fully developed Nusselt numbers for heat transfer to liquid metals in turbulent flow in annuli and between flat plates.

input will be compared with Lyon's equation (eq. (1)) inasmuch as this is the equation recommended by the Liquid-Metals Handbook and most commonly used in practice.

(2) Uniform wall temperature; round tubes: The fully developed heat-transfer coefficient in turbulent flow in a round tube with a uniform wall temperature has been investigated by Seban and Shimazaki (ref. 32) using the momentum transfer analogy; they give, as an approximate relation, the equation

$$Nu_f = 5.0 + 0.025 Pe_f^{0.5} \quad (2)$$

This equation is also plotted in figure 1. The Liquid-Metals Handbook lists the equation as

$$Nu_f = 4.8 + 0.025 Pe_f^{0.5} \quad (3)$$

and gives the work of Seban and Shimazaki as a reference. The experimental results for fully developed heat transfer in a round tube with a uniform wall temperature will be compared with Seban and Shimazaki's equation (eq. (2)).

(3) Uniform heat input; annuli: Very little theoretical work has been done on the fully developed heat-transfer coefficient in annuli. For thin annuli (diameter ratio ≤ 1.4) the Liquid-Metals Handbook recommends the use of the theoretical relation proposed by Seban (ref. 33) for heat transfer to parallel plates with heat through one side only:

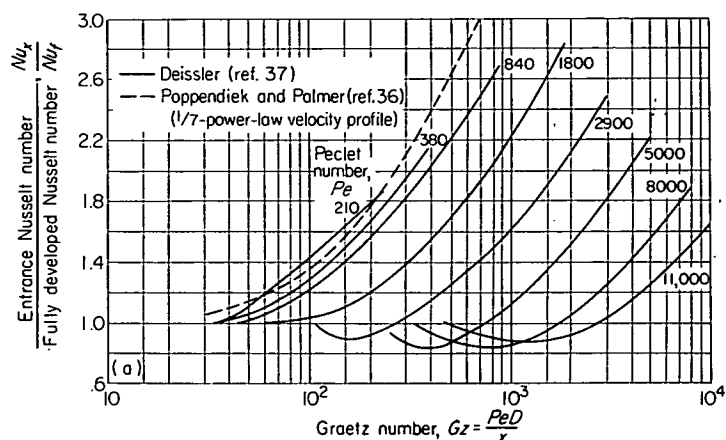
$$Nu_{f,an} = 5.8 + 0.020 Pe_{f,an}^{0.8} \quad \text{for } D_o/D_i \leq 1.4 \quad (4)$$

For annuli of diameter ratio greater than 1.4, the Liquid-Metals Handbook lists an equation which approximates the results of Bailey (ref. 34) and is of the form suggested by Werner, King, and Tidball (ref. 7):

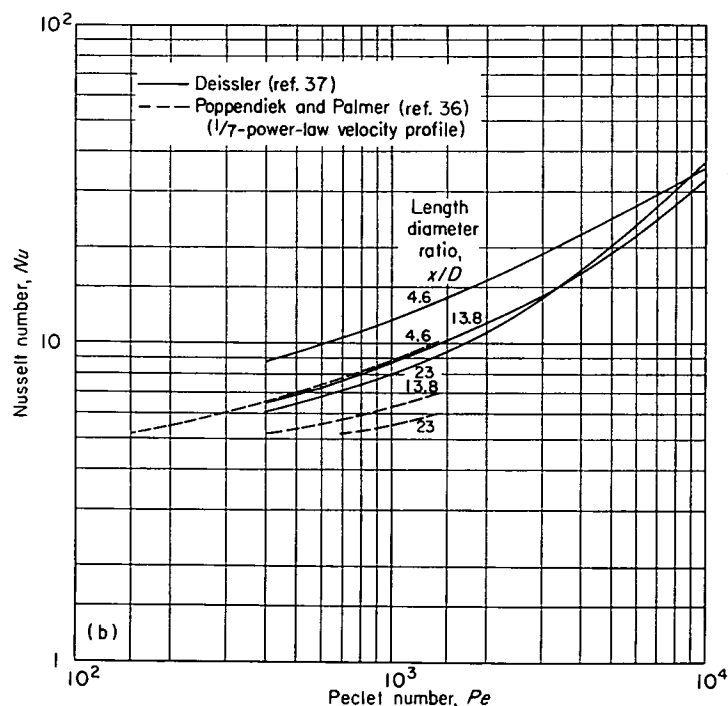
$$Nu_{f,an} = 0.75(D_o/D_i)^{0.3} (7.0 + 0.025 Pe_{f,an}^{0.8}) \quad \text{for } D_o/D_i > 1.4 \quad (5)$$

Equations (4) and (5) are plotted in figure 2. The experimental data on heat transfer in annuli will be compared with these equations.

Local heat-transfer coefficients in entrance region.—Heat-transfer coefficients in the entrance region have been calculated by several investigators for a number of different cases. Poppendiek, Palmer, and Harrison (refs. 26, 35, and 36) have analyzed the case of uniform wall temperature for various different entering velocity profiles; the analysis assumes that the eddy diffusivity of heat is negligible when compared with the molecular diffusivity and consequently is intended only for low Reynolds numbers. The analysis is independent of Prandtl number. Deissler (ref. 37) analyzed the case of uniform heat input at the wall, with a fully developed velocity profile at the entrance; the numerical calculations were carried out only for a Prandtl number of 0.01. Seban and Shimazaki (ref. 38) have made calculations for the case of uniform wall temperature and fully developed velocity profile at the entrance for a Prandtl number of 0.01 and Reynolds



(a) Ratio of entrance Nusselt number to fully developed Nusselt number against Graetz number.



(b) Nusselt number against Peclet number.

FIGURE 3.—Theoretical predictions of heat transfer to liquid metals in turbulent flow in round tubes.

numbers of 10^4 and 10^5 . The results of the analyses of Poppendiek and Palmer and of Deissler are shown in figure 3.

Average heat-transfer coefficients.—Predictions of average heat-transfer coefficients can be made by integrating the predictions for local heat-transfer coefficients over the length-diameter ratio of the tube in question. Heat transfer in the entrance region, however, has been analyzed for only relatively specialized cases. Therefore, the experimental results for average heat-transfer coefficients will first be compared with equations (1) and (2), even though these equations are derived for fully developed heat-transfer coefficients. Later in the report, a comparison will be made with the average heat-transfer coefficients on the basis of the analytical evidence.

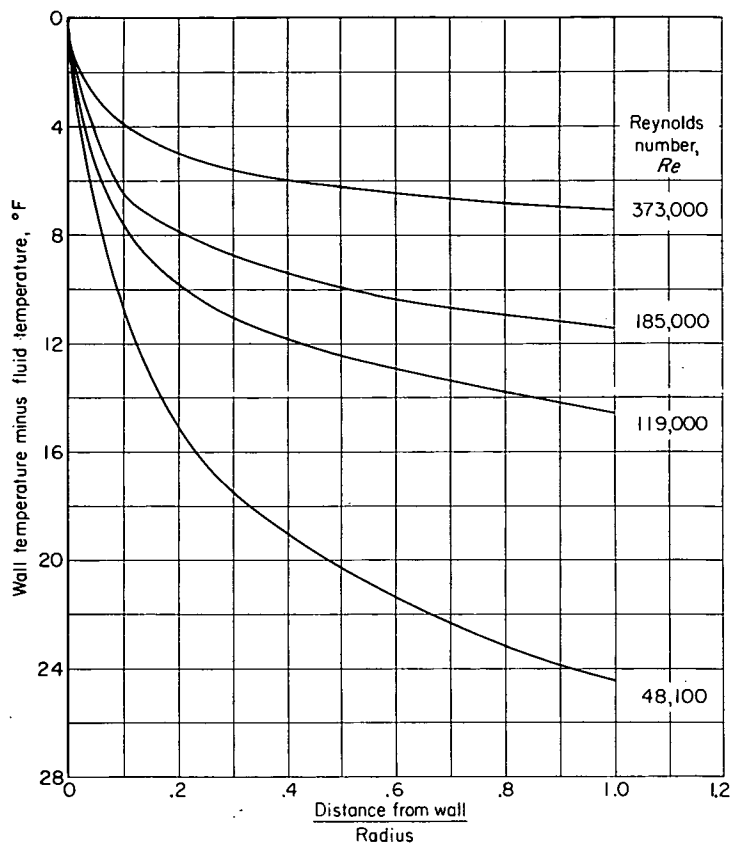
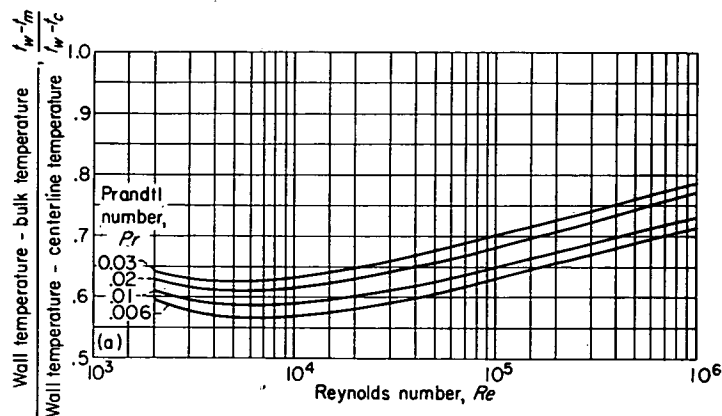
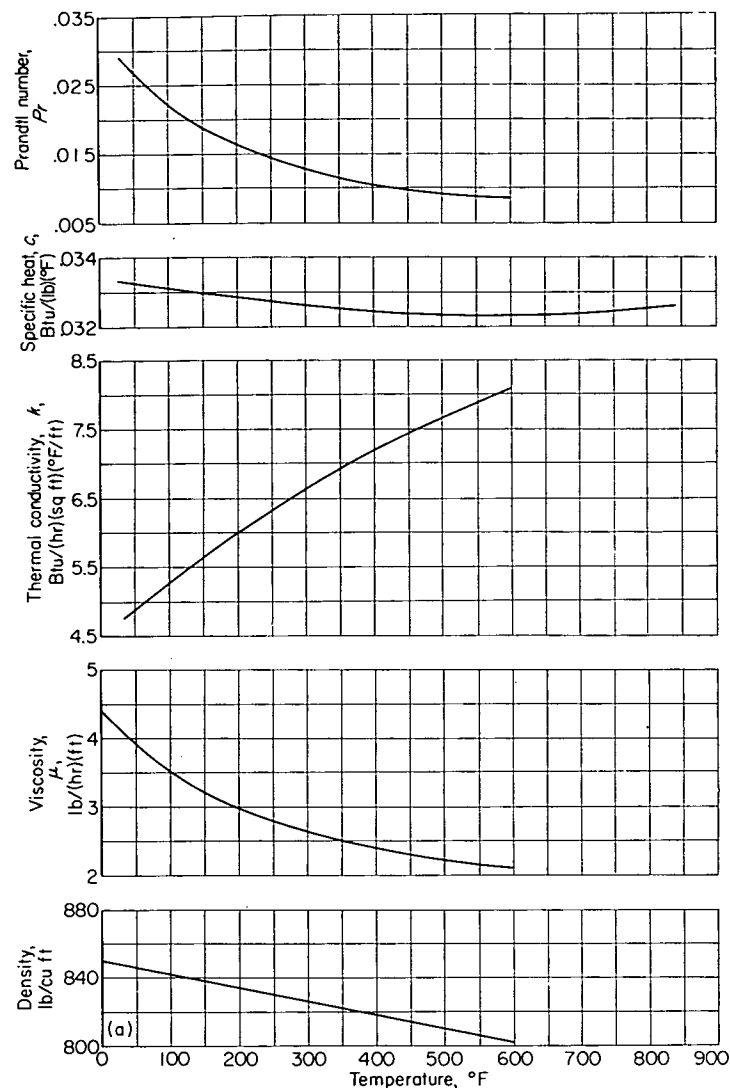


FIGURE 4.—Theoretical predictions of Martinelli (ref. 27) for fully developed temperature profiles for heat transfer to liquid metals in round tubes. Prandtl number, 0.022.

Temperature distribution.—The fully developed temperature distribution due to heat transfer to a liquid metal in turbulent flow in a round tube has been predicted on theoretical grounds by several investigators. The predictions of Martinelli (ref. 27) are shown in figure 4 for a Prandtl number of 0.022. Martinelli, using his own predicted values for the temperature distribution, calculated the ratio of the temperature differences $(t_w - t_m)/(t_w - t_c)$ as a function of Reynolds and Prandtl numbers. Martinelli's results are shown in figure 5(a) for Prandtl numbers pertinent to liquid metals. Martinelli also calculated values of $(t_w - t_m)/$



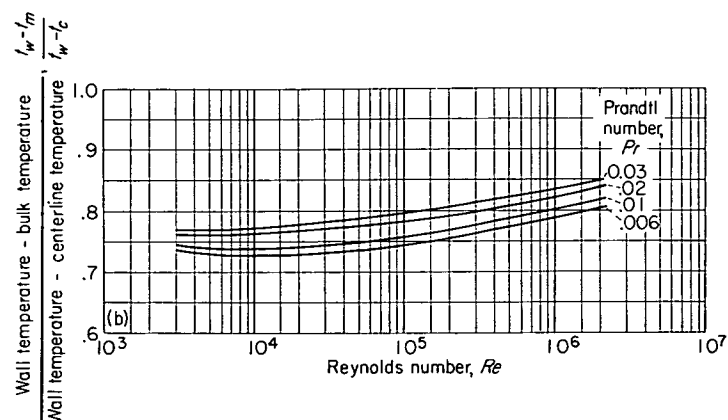
(a) In round tubes.



(a) Mercury.

FIGURE 6.—Physical properties of liquid metals (ref. 28).

$(t_w - t_c)$ for fully developed flow between flat plates with heat flow through both walls with uniform heat flux. These results are shown in figure 5(b).



(b) Between flat plates.

FIGURE 5.—Theoretical predictions of Martinelli (ref. 27) of ratio $(t_w - t_m)/(t_w - t_c)$ for heat transfer to liquid metals.

METHODS OF CALCULATION

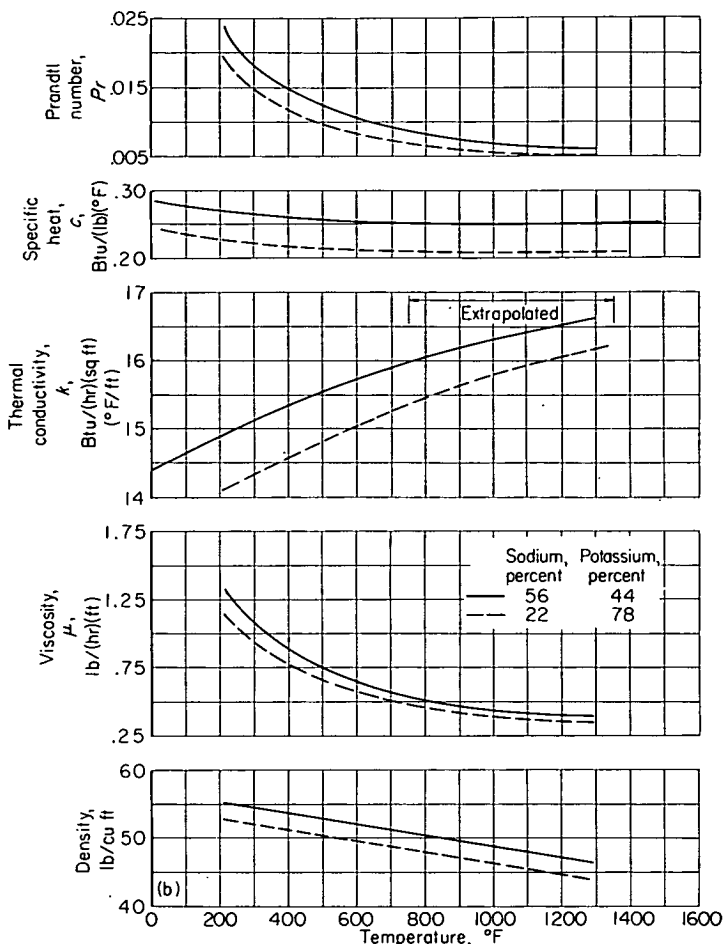
The heat-transfer parameters were evaluated using the same method of calculation for each individual reference as was used by the authors of that particular reference, with the following exceptions:

(1) All physical properties of liquid metals were taken from the second edition of the Liquid-Metals Handbook (ref. 28). These properties are shown in figure 6.

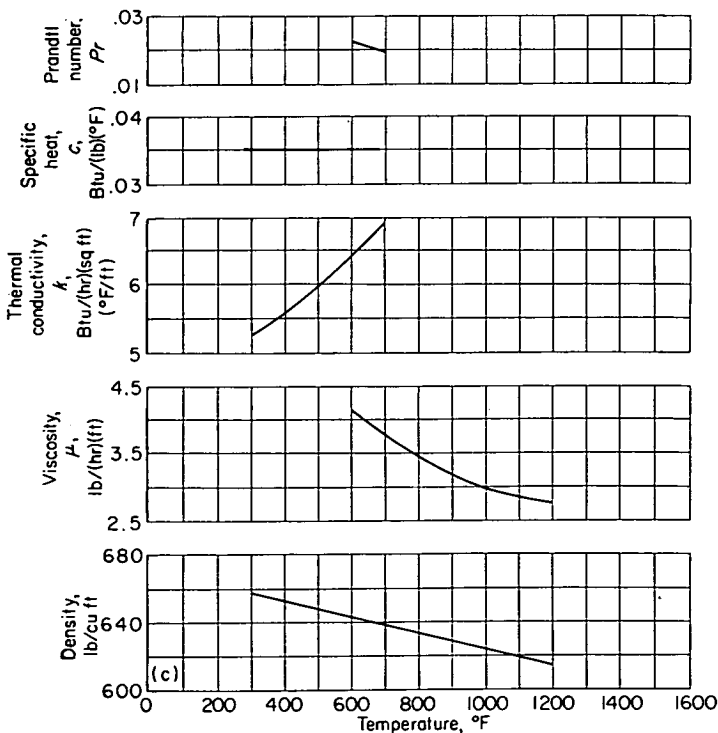
(2) When an investigator measured the combined liquid-metal heat-transfer coefficient in a tube and concentric annulus, the individual heat-transfer coefficients were obtained by assuming that the ratio of the Nusselt number in the tube to the Nusselt number in the annulus is determined by equations (1), (4), and (5):

$$\frac{Nu}{Nu_{an}} = \frac{7.0 + 0.025Pe^{0.8}}{5.8 + 0.020Pe_{an}^{0.8}} \quad \text{for } D_o/D_i \leq 1.4 \quad (6)$$

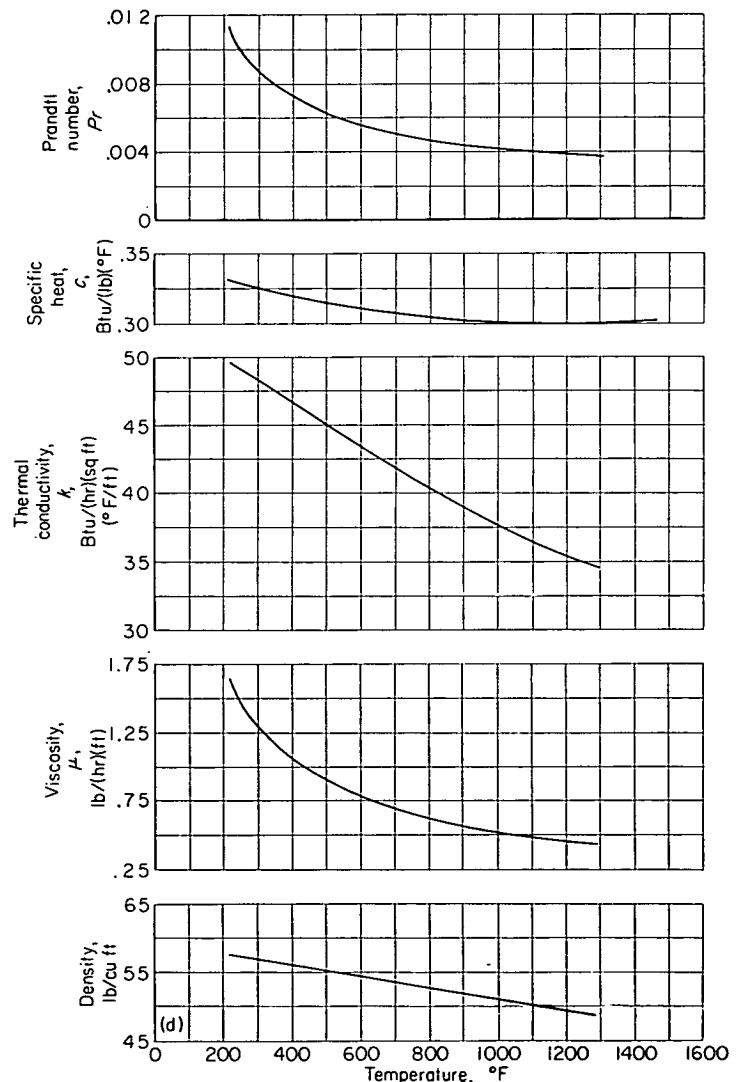
$$\frac{Nu}{Nu_{an}} = \frac{7.0 + 0.025Pe^{0.8}}{0.75(D_o/D_i)^{0.3}(7.0 + 0.025Pe_{an}^{0.8})} \quad \text{for } D_o/D_i > 1.4 \quad (7)$$



(b) Sodium-potassium alloy.



(c) Lead-bismuth eutectic.



(d) Sodium.

FIGURE 6.—Concluded. Physical properties of liquid metals (ref. 28).

Because of the lack of theoretical work on average heat-transfer coefficients, particularly in annuli, the same ratios which have been assumed for the fully developed Nusselt numbers will be assumed for the average Nusselt numbers.

It is important to note that in most of those tests in which the combined coefficient in a tube and concentric annulus was measured, the Reynolds number in the annulus was smaller than the Reynolds number in the tube. Quite often the flow in the annulus was in the transition flow region, while the flow in the tube was in the turbulent-flow region. Inasmuch as there are no predictions for liquid-metal heat transfer in the transition region, equations (6) and (7) will be used to separate the tube and annulus heat-transfer coefficients even when the flow in the annulus is in the transition region. This procedure is open to question, and the interpretation of the data calculated by this procedure may be inaccurate.

(3) In those tests in which the centerline temperature of the fluid was measured instead of the bulk temperature, the temperature difference between the wall and the bulk fluid will be calculated from Martinelli's relation for $(t_w - t_m)/(t_w - t_c)$ (fig. 5). Martinelli's prediction of $(t_w - t_m)/(t_w - t_c)$ for flat plates with heat flowing through both sides will be used for annuli inasmuch as no other predictions covering as broad range of Reynolds and Prandtl numbers are available.

REEVALUATION OF EXPERIMENTAL DATA

The experimental investigations of references 1 to 26 will first be discussed individually and then compared with each other and with theoretical investigations.

The experimental work of the various investigators will be discussed in a chronological order determined by the publication date of the original manuscript.

Styrikovich and Semenovker.—Styrikovich and Semenovker (ref. 1) investigated heat transfer to mercury as part of their investigation of the mercury-steam binary power cycle. They used a series of five tubes for test sections, each about 106 inches in length with 0.63-, 0.87-, 1.58-, 1.67-, and 1.97-inch diameters. The tubes were heated by external electric heaters. Thermocouples were placed 17.2 inches apart on the outside surface of each tube. The bulk fluid temperature in the test section was calculated by adding to the inlet temperature the temperature rise corresponding to the heat

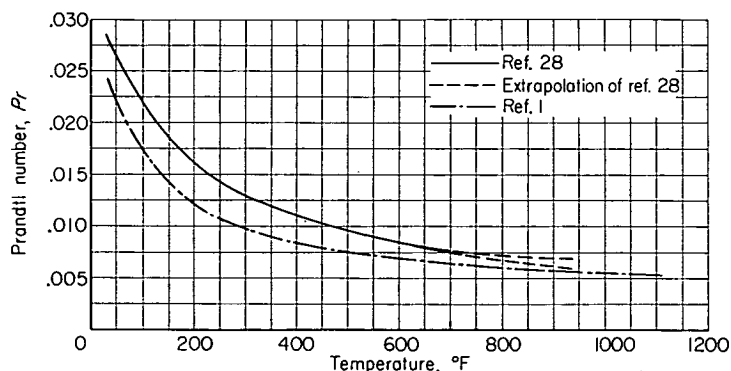


FIGURE 7.—Comparison of variations of Prandtl number of mercury with temperature of Liquid-Metals Handbook (ref. 28) and of Styrikovich and Semenovker (ref. 1).

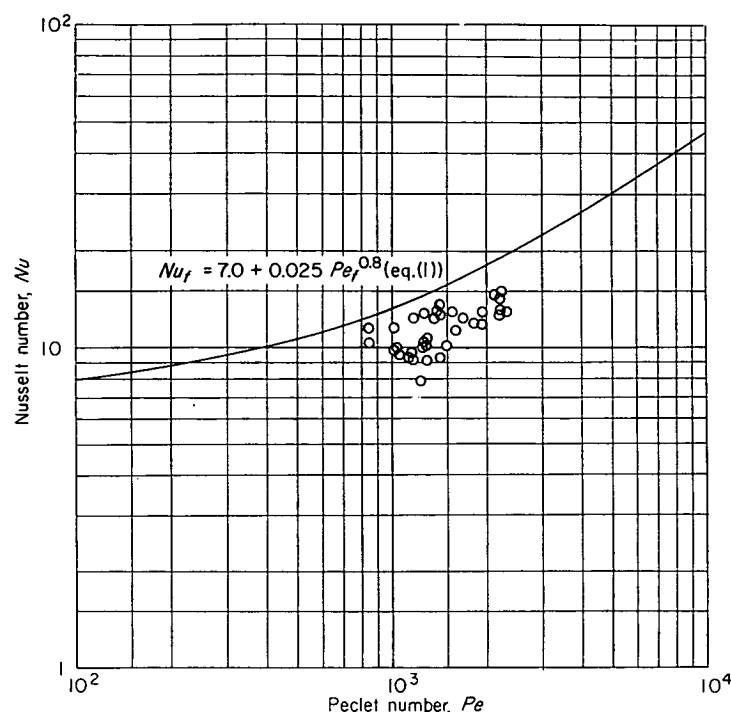


FIGURE 8.—Reevaluated data of Styrikovich and Semenovker (ref. 1) for fully developed heat transfer to mercury in round tubes.

input. The velocity profile of the mercury entering the test section was essentially fully developed. The method of heating the mercury approximated uniform heat input to the wall. The heat-transfer coefficient was calculated for only the central portion of the tube. The coefficients presented are essentially the fully developed heat-transfer coefficients.

The physical properties used in evaluating the heat-transfer coefficients are not listed, but the Prandtl number is tabulated over a range of temperature from 32° to 1112° F. These Prandtl numbers are lower than the values in reference 28, which lists values of Prandtl number for temperatures up to 600° F. The values of Prandtl number of Styrikovich and Semenovker and of reference 28 are shown in figure 7. Since the specific heat and viscosity in the temperature range used are essentially the same in reference 28 as those reported in the International Critical Tables (1929 edition), the inaccuracies in Prandtl number may be assumed due to incorrect values of thermal conductivity. It appears that Styrikovich and Semenovker used the thermal-conductivity data of Gelhoff and Neumeier, which have been found to be high (ref. 12). It was deemed advisable to recalculate the data of Styrikovich and Semenovker using the values of thermal conductivity from reference 28. The precise temperature level of the various data points is not reported, but the average temperature level is given as about 932° F. At this temperature, Styrikovich and Semenovker list a Prandtl number of 0.0056. Reference 28 presents Prandtl number data up to 600° F which when extrapolated to 932° F give a Prandtl number between 0.006 and 0.007. The data points were reevaluated using a Prandtl number of 0.0065 at 932° F. This increased the Nusselt and Peclet numbers of the data by about 16 percent. The reevaluated data of Styrikovich and Semenovker are shown in figure 8; also shown for comparison is equation (1).

Gilliland, Musser, and Page.—Gilliland, Musser, and Page (refs. 2 and 3) measured both heating and cooling coefficients for mercury. The heating test section had a 0.319-inch inside diameter and a 14-inch length; heat was added by dropwise condensation of steam on the outside of the test section. The cooling test section had a 0.319-inch inside diameter and a 51-inch length; it was cooled by water flowing on the outside in a direction opposite to that of the inside flow. Both test sections were made of nickel. The mercury and water bulk temperatures entering and leaving the test sections and the stream temperature and pressure entering the test section were measured. The velocity profile of the mercury was fully developed at the entrance to both test sections. The methods of heating and cooling the mercury were such that the heating tests approximated a constant wall temperature, while the cooling tests were somewhere between a constant wall temperature and a constant heat input. The heat-transfer coefficient measured was an over-all average coefficient.

Inasmuch as no wall temperatures were measured, it was necessary to separate the mercury heat-transfer coefficients from those of the steam and water. This was done by the Wilson plot method (see refs. 2 and 3).

(1) Heating: Tests were run with water in place of mercury, and the Wilson plot method was used to determine the combined resistance of the steam film and the wall. The range of water flows covered was sufficiently small and the scatter of the points sufficiently great that values of the combined resistance could be chosen ranging from 40 percent greater to 15 percent smaller than the value selected. An increase of 40 percent in steam and wall resistance, however, would increase the mercury coefficient only about 8 percent. An attempt was made to use the results of the mercury runs to confirm the steam and wall resistance, but in this case the range of mercury flows and data scatter permits selecting a value of resistance ranging from 200 percent greater to 50 percent lower than the value chosen. The slope of the Wilson plot for the runs with water can be compared with the slope predicted by the standard empirical relation for heat transfer to water (ref. 39, p. 168)

$$Nu = 0.023 Re^{0.8} Pr^{0.4} \quad (8)$$

The slope predicted by equation (8) turns out to be considerably higher than the slope best representing the experimental data.

(2) Cooling: At a given mercury flow rate, the water flow rate was varied and the combined mercury film and tube wall resistance determined by means of a Wilson Plot. The range and scatter of the data are such that the resistance of the mercury and the wall could be chosen 20 percent lower or 15 percent higher than the value actually chosen. The corresponding variation in mercury coefficient would be somewhat greater. Alternatively, cooling coefficients for mercury were calculated by evaluating the coefficients for water in an annulus using the following equation (ref. 39, p. 202):

$$St Pr^{2/3} = \frac{0.020 (D_o/D_i)^{0.53}}{Re^{0.2}} \quad (9)$$

The resulting mercury coefficients were approximately 40 percent lower than those derived by the Wilson plot method. The physical properties used by Gilliland, Musser, and Page are about the same as those of reference 28. In view of the possible inaccuracies in the method of evaluating the data, the reported results of Gilliland, Musser, and Page may not be very accurate. Their data are shown in figure 9 without change; shown for comparison are equations (1) and (2). The lower values for cooling coefficient may be due to the longer length-diameter ratio of the cooling section.

Elser.—Elser (ref. 4) measured cooling heat-transfer coefficients for mercury. Three different test sections were used: The test-section inner diameters were 0.317, 0.308, and 0.260 inch; the 0.317-inch-diameter test section was made of mild steel, and the other test sections were made of stainless steel. The test sections were all over 38 inches long, but measurements were made between two stations 10.2 and 38.3 inches from the entrance. The mercury was cooled by water flowing in a concentric annulus in a direction opposite to the flow of mercury. Two thermocouples imbedded in the wall measured the wall temperature at the two stations. Two other thermocouples immersed in the stream measured a temperature close to the fluid centerline temperature. The velocity profile of the mercury at the first station was fully developed. The cooling-water flow rate was such that a uniform heat input to the wall was approximated. The fully developed heat-transfer coefficient was measured.

The only mercury property listed by Elser is Prandtl number. These values are in agreement with the values of reference 28, and the other mercury properties will be assumed to be correct. The basic data are not presented by Elser. He presents a plot of Stanton number against Reynolds number

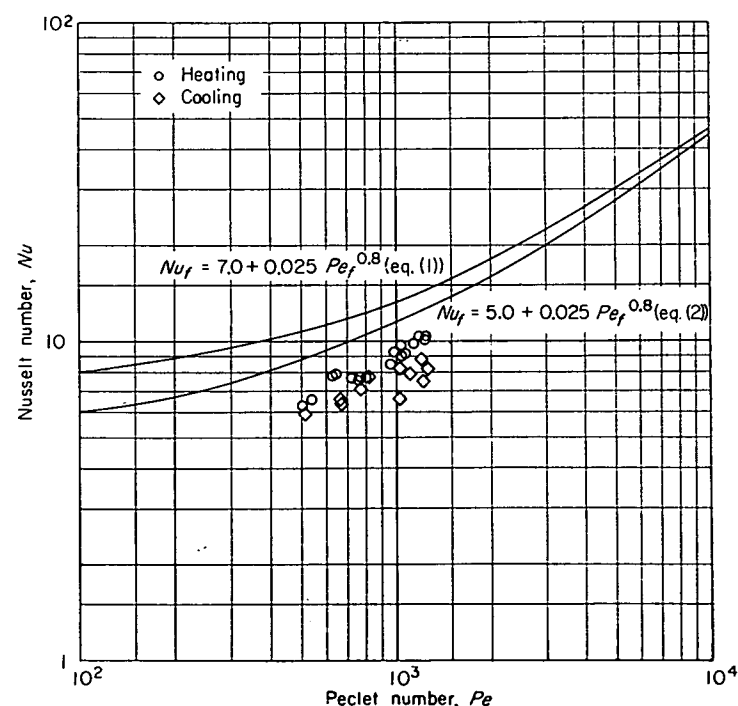


FIGURE 9.—Data of Gilliland, Musser, and Page (refs. 2 and 3) for average heat transfer to mercury in round tubes. Length-diameter ratio L/D : heating section, 45; cooling section, 160.

showing his data points. The values of Stanton number have been corrected by Elser to a common Prandtl number by approximating the data with a curve of the form

$$Nu_f = a Re_f^m Pr_f^n \quad (10)$$

He gives no values of n , so that it is impossible to return to the basic points.

Elser measured mercury flow by measuring the mercury pressure drop and assuming the following formula for friction factor:

$$4f = \frac{0.3164}{Re^{0.25}} \quad Re < 80,000 \quad (11)$$

$$\frac{1}{\sqrt{4f}} = 2 \log (Re \sqrt{4f}) - 0.8 \quad Re > 80,000 \quad (12)$$

Equation (11) is from Blasius; equation (12) from Kármán.

Elser's heat-transfer coefficients are based on the difference between wall and fluid centerline temperatures. He is not certain of the location (depth) of his wall thermocouples and states that the difference between a midwall and a wall surface location results in shifts of heat-transfer coefficients of 4, 7, and 18 percent, respectively, for the three tubes of 0.317-, 0.308-, and 0.260-inch diameter. In Elser's data, the wall thermocouple is assumed to be at the wall midpoint. Martinelli's predictions for the ratio of the temperature differences $(t_w - t_m)/(t_w - t_c)$ (fig. 5(a)) were used to change the heat-transfer coefficients of Elser so that they would be based on the difference between wall and fluid bulk temperatures. This increased the Nusselt number about 40 to 60 percent. In this reevaluation the wall thermocouples were assumed to be located at the wall midpoint. If the thermocouples were assumed at the wall surface, the Nusselt numbers would be somewhat increased. Figure 10 shows

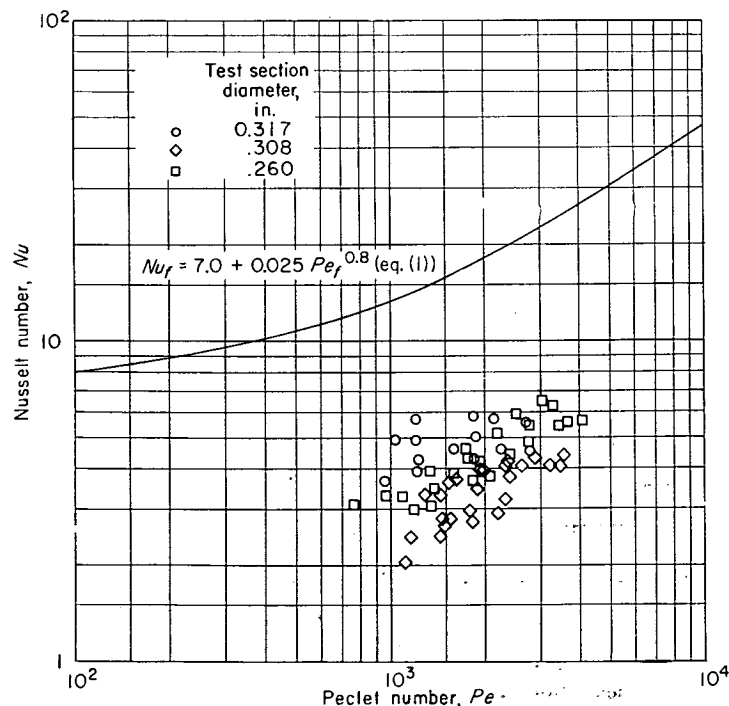


FIGURE 10.—Reevaluated data of Elser (ref. 4) for fully developed heat transfer to mercury in round tubes.

the reevaluation data of Elser; shown for comparison is equation (1).

Bailey, Cope, and Watson.—Bailey, Cope, and Watson (ref. 5) measured cooling coefficients for mercury. The test section was a mild-steel tube of 0.437-inch inner diameter. The central 18 inches of the tube was surrounded by a water jacket, with about 6 inches projecting at each end. These ends were enclosed in chambers in such a manner that the inlet and outlet mercury passed along the outside of the ends before entering and after leaving the test section. Fluid temperatures were measured at the inlet and outlet of the test section; wall temperatures were measured at four stations along the length of the water-jacketed section of the tube.

There is considerable question as to just what temperature was measured at the test-section outlet. First, there was no provision made for mixing before the exit temperature was measured. Second, inasmuch as the mercury was being cooled, the temperature distribution of the mercury was such that the temperature near the wall was lower than the bulk temperature. The mercury was discharged from the test section into a larger chamber, turned 180°, and passed over the end of the test section which projected from the water jacket. Because of the mixing in the discharge and turning processes, the mercury on the outside of the projecting end had a nearly flat temperature profile. Hence, the mercury on the outside of the projecting end of the test section was at about fluid bulk temperature, while the mercury on the inside of the projecting end (close to the wall) was at a temperature lower than fluid bulk temperature. Heat was therefore transferred from the outside to the inside; this tended to increase the measured mercury exit temperature and consequently decrease the observed heat-transfer coefficients. The combined effect on heat-transfer coefficient of the heat transferred through the projecting end and the lack of mixing before the exit temperature measurement is very difficult to estimate.

The velocity profile at the entrance to the water-jacketed section of the test section was close to fully developed. The method of cooling was such that uniform wall temperature was approximated at the lower mercury Peclet numbers, while uniform heat input to the wall was more nearly the case at high mercury Peclet numbers. Fully developed heat-transfer coefficients were measured.

The physical properties used by Bailey, Cope, and Watson were somewhat different from the values of reference 28; the Prandtl numbers were about 10 percent high. The data of Bailey, Cope, and Watson were therefore reevaluated, using the physical properties of reference 28, in two ways: First, it was assumed that the measured mercury exit temperature was equal to the fluid bulk temperature; second, it was assumed that the measured mercury exit temperature was equal to the fluid centerline temperature, and Martinelli's predictions of $(t_w - t_m)/(t_w - t_c)$ (fig. 5) were used to calculate the fluid bulk temperature. The results of both methods of computation are shown in figure 11; equations (1) and (2) are shown for comparison. Because of the uncertainties described in the measurement of mercury exit temperature, it is difficult to say whether either set of data in figure 11 is at all correct.

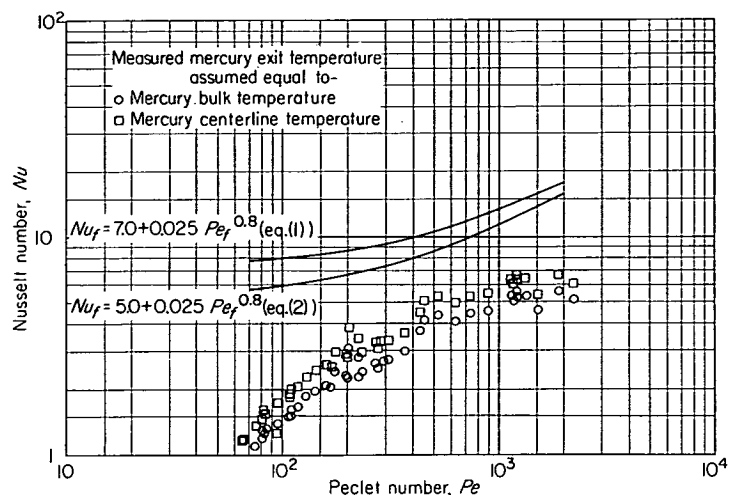


FIGURE 11.—Reevaluated data of Bailey, Cope, and Watson (ref. 5) for fully developed heat transfer to mercury in round tubes.

Lyon.—Lyon (ref. 6) used a tube and concentric annulus to measure the combined coefficient resulting from transferring heat from a sodium-potassium alloy (52 percent Na, 48 percent K) flowing in the annulus to the same fluid flowing in the tube. The weight flows in the tube and annulus are, necessarily, the same. This type of test section is often referred to as a “figure eight” and will be so referred to herein. Lyon used four different test sections made of nickel and having the following dimensions:

Test section	A	B	C	D
Tube inner diameter, D_i , in.	0.432	0.703	0.434	0.434
Annulus inner diameter, D_{ii} , in.	.500	.757	.500	.510
Annulus outer diameter, D_o , in.	.715	.931	.684	.684
Length, l , in.	48	69	33	69

Bulk fluid temperatures were measured at the inlet and outlet of the tube and annulus. The velocity profiles of the fluid entering the tube and the annulus were approximately flat (uniform velocity). The figure-eight test section with counterflow gives approximately constant heat input to the wall. The heat-transfer coefficients measured were over-all average coefficients.

Lyon used physical properties which were somewhat different from those of reference 28. The specific heat was about 12 percent higher and the thermal conductivity was about 6 percent higher. Use of the properties of reference 28 decreases both the Nusselt and Peclet numbers about 5 percent. Lyon assumed that the resistances of the walls of the four test sections were approximately constant, neglecting the differences in wall thickness. Lyon did not separate the experimental tube and annulus coefficients, but rather calculated a combined predicted coefficient using equation (1) for the tube and an equation approximating the results of Harrison and Menke (ref. 40)

$$Nu_{f,an} = 4.9 + 0.0175 Pe_{f,an}^{0.8} \quad (13)$$

for the annulus. The Liquid-Metals Handbook (ref. 28) mentions equation (13), but prefers equations (4) and (5) for heat transfer in an annulus.

Lyon's data were reevaluated using the physical properties of reference 28 and calculating exactly the resistance of the

wall. The over-all heat-transfer coefficient was divided into a tube coefficient and an annulus coefficient assuming that the Nusselt numbers in the tube and annulus are related as in equations (6) and (7), which are taken from equations (1), (4), and (5). The use of equations (4) and (5) rather than equation (13) for the annulus results in higher annulus heat-transfer coefficients and lower tube heat-transfer coefficients for the same over-all heat-transfer coefficient. The reevaluated data of Lyon are shown in figures 12 and 13; equations (1), (4), and (5) are shown for comparison.

Untermeyer.—The data of Untermeyer were obtained from unclassified material in a classified report. Untermeyer measured heating coefficients for a lead-bismuth eutectic with and without magnesium addition. The test section was a steel tube with a 0.25-inch inner diameter and 18-inch length. The test section was heated by passing electric current directly through it and the fluid it contained. Wall temperatures and fluid inlet and outlet temperatures were measured. The velocity profile at the test-section entrance was closer to flat than to fully developed. The method of heating most nearly approximated uniform heat input to the wall. Local fully developed coefficients were measured.

The physical properties used by Untermeyer are different from those of reference 28. The thermal conductivity used by Untermeyer was about 15 percent lower and the volumetric specific heat was about 8 percent higher. It is difficult to determine from the data whether the heat generated directly in the fluid has been subtracted from the total heat input. It is also difficult to determine whether a mixing chamber was used in the measurement of the fluid bulk temperature leaving the test section. Figure 14 shows the data of Untermeyer reevaluated using physical properties from reference 28.

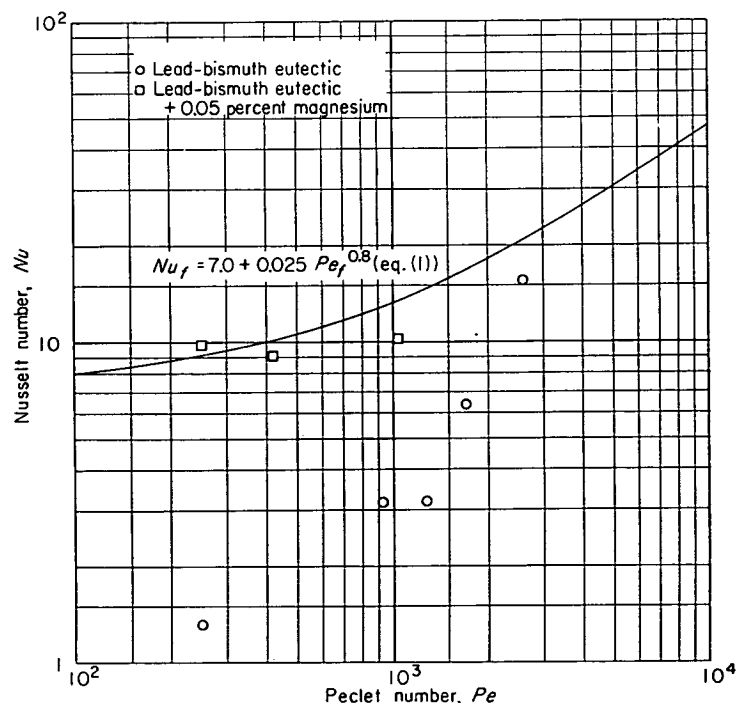


FIGURE 14.—Reevaluated data of Untermeyer for fully developed heat transfer to lead-bismuth eutectic, with and without magnesium addition, in round tubes.

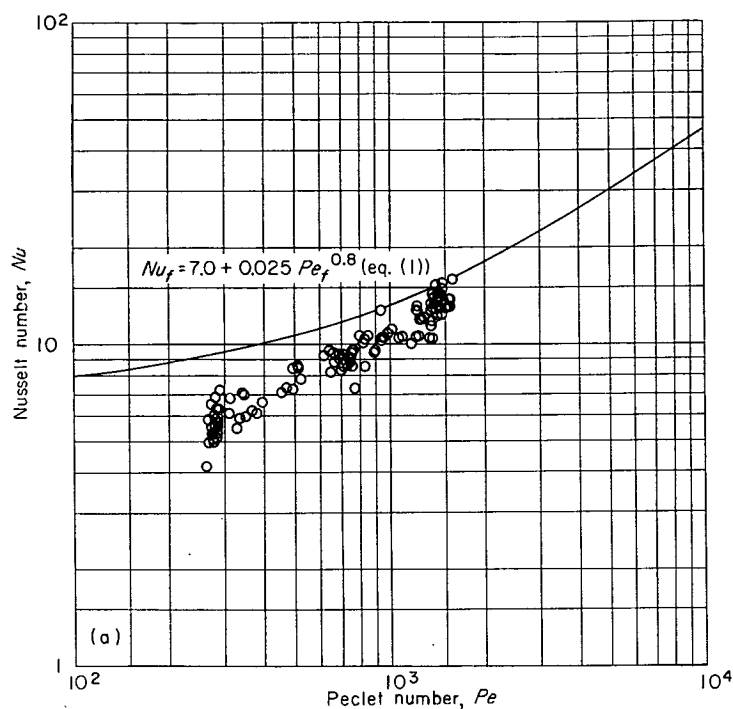
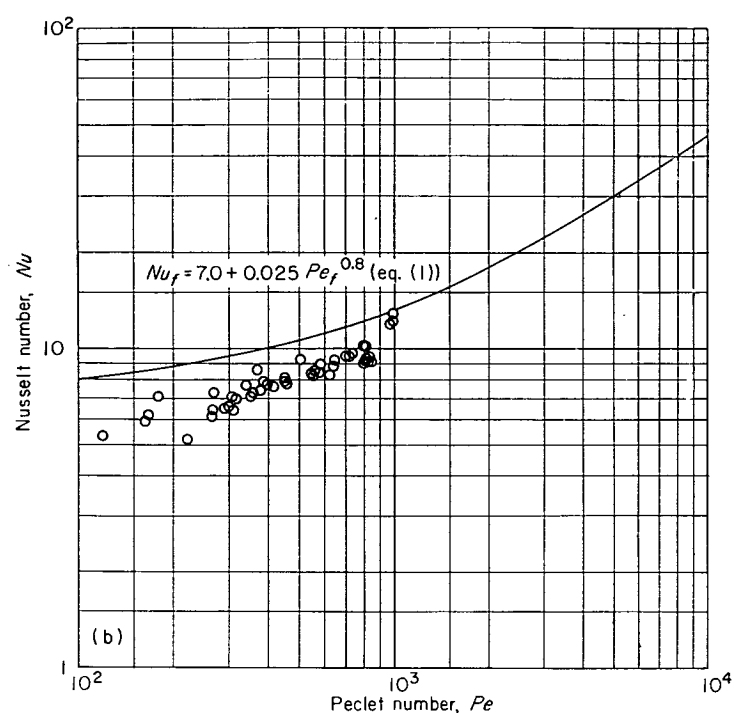
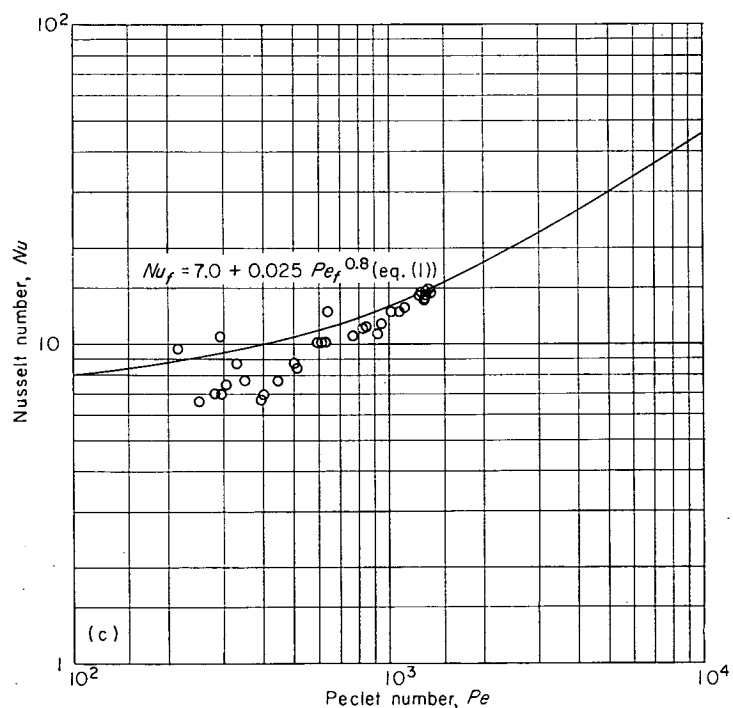
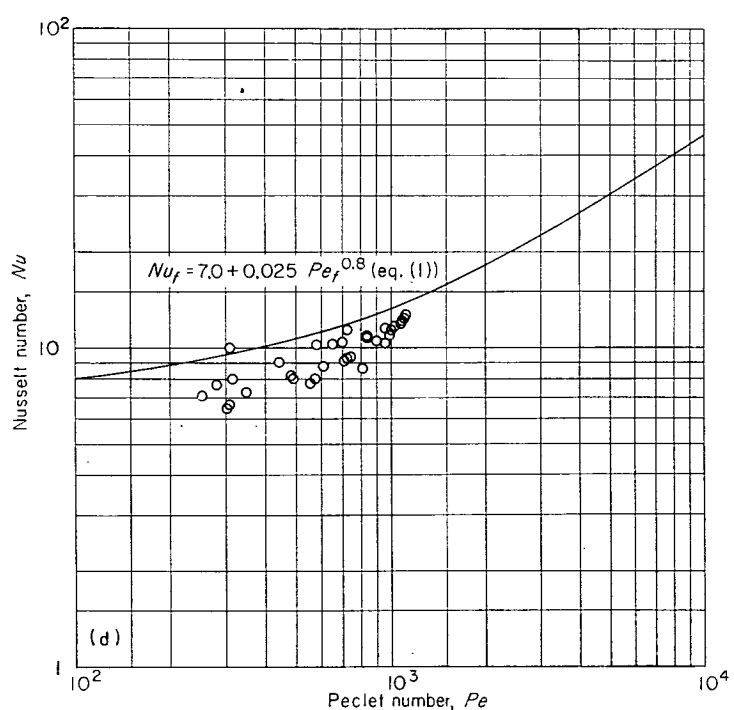
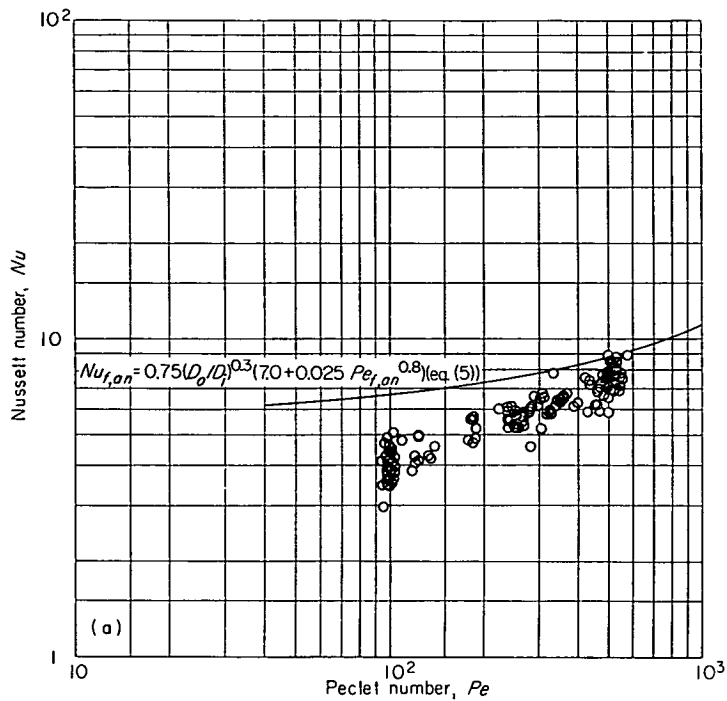
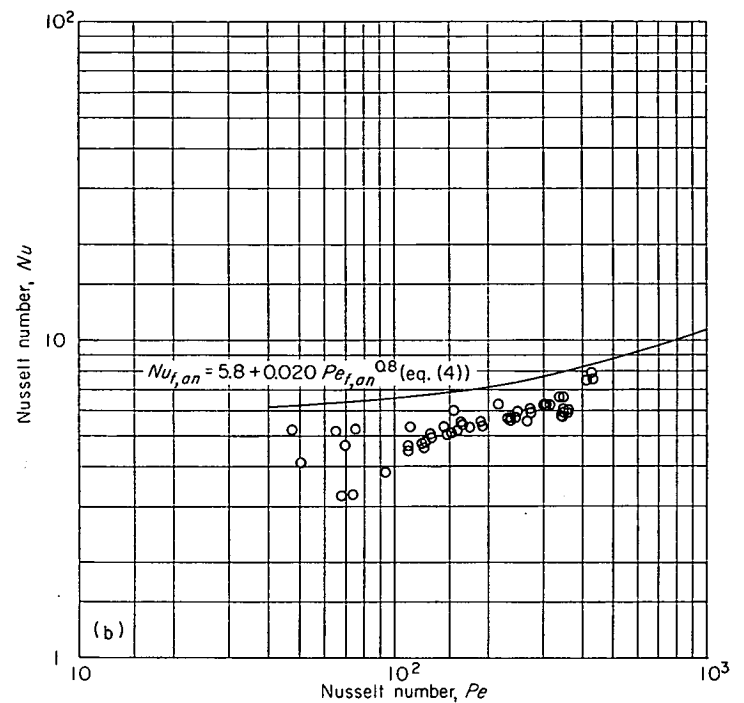
(a) Test section A (length-diameter ratio l/D , 111).(b) Test section B (length-diameter ratio l/D , 98).(c) Test section C (length-diameter ratio l/D , 76).(d) Test section D (length-diameter ratio l/D , 159).

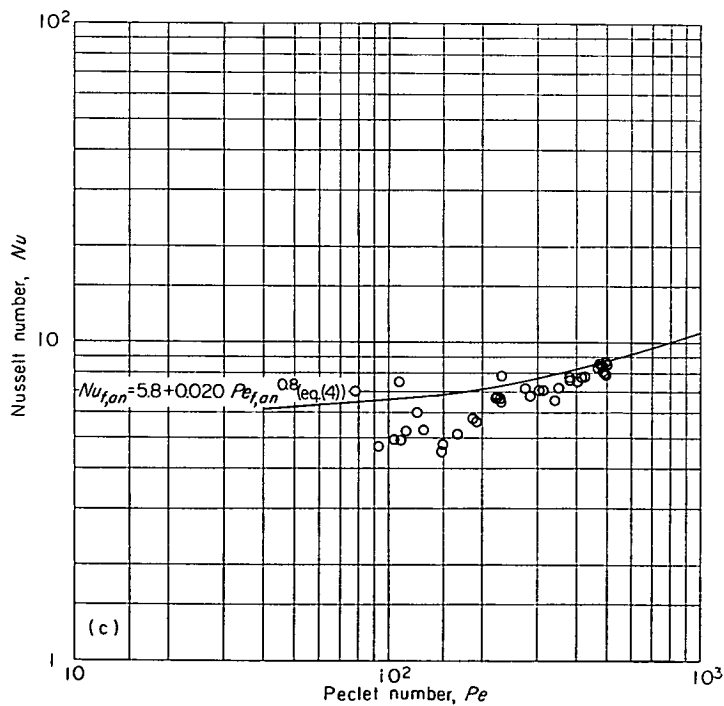
FIGURE 12.—Reevaluated data of Lyon (ref. 6) for average heat transfer to sodium-potassium alloy in round tubes.



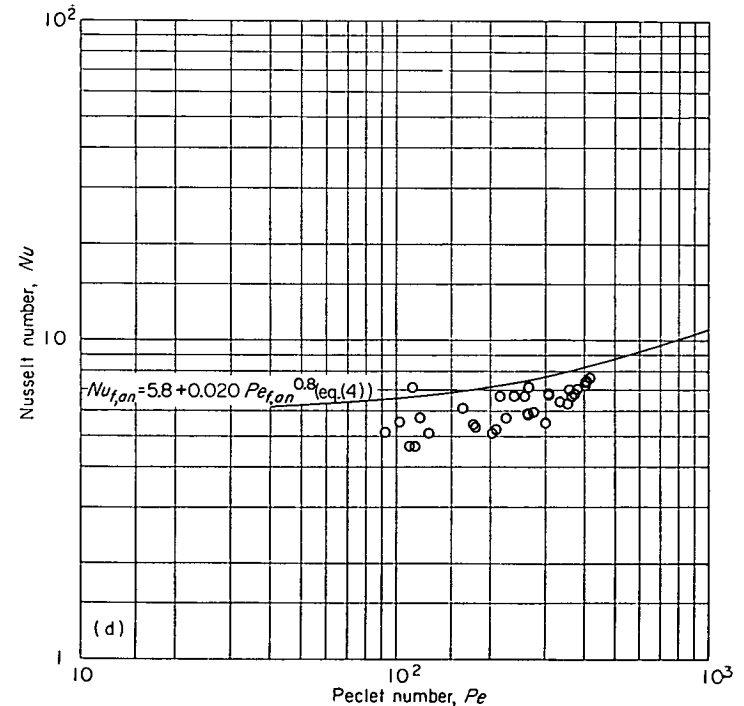
(a) Test section A (ratio of outer to inner diameter, 1.43; length-diameter ratio l/D , 223).



(b) Test section B (ratio of outer to inner diameter, 1.23; length-diameter ratio l/D , 397).



(c) Test section C (ratio of outer to inner diameter, 1.37; length-diameter ratio l/D , 179).



(d) Test section D (ratio of outer to inner diameter, 1.37; length-diameter ratio l/D , 375).

FIGURE 13.—Reevaluated data of Lyon (ref. 6) for average heat transfer to sodium-potassium alloy in annuli.

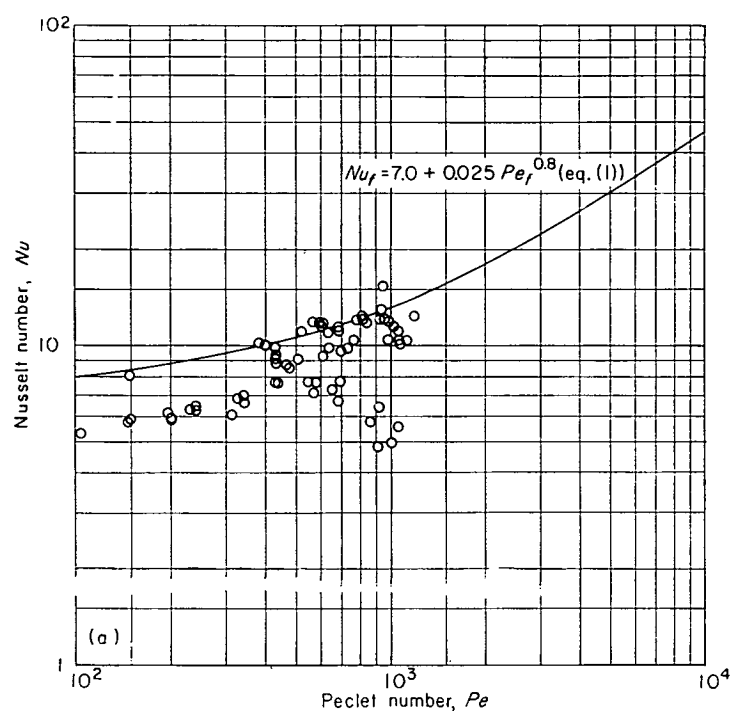
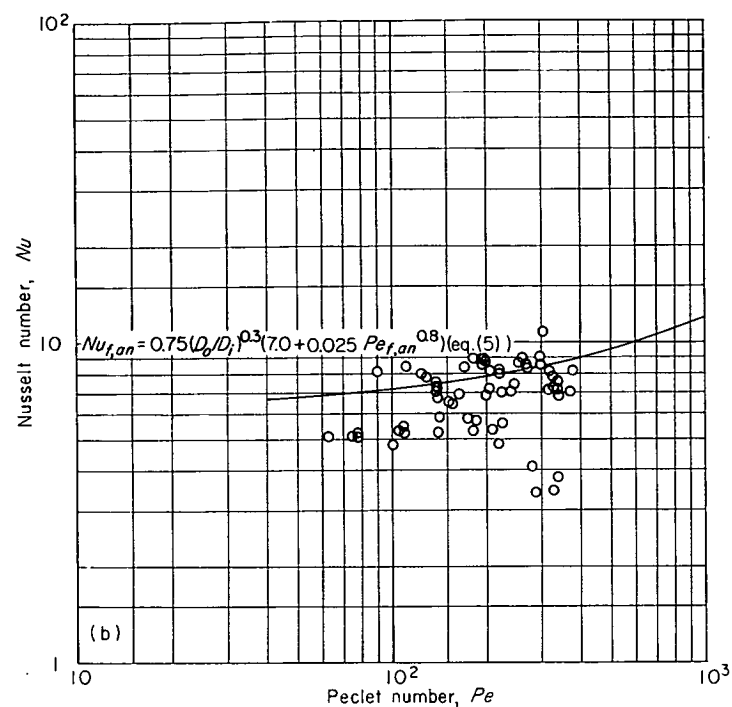
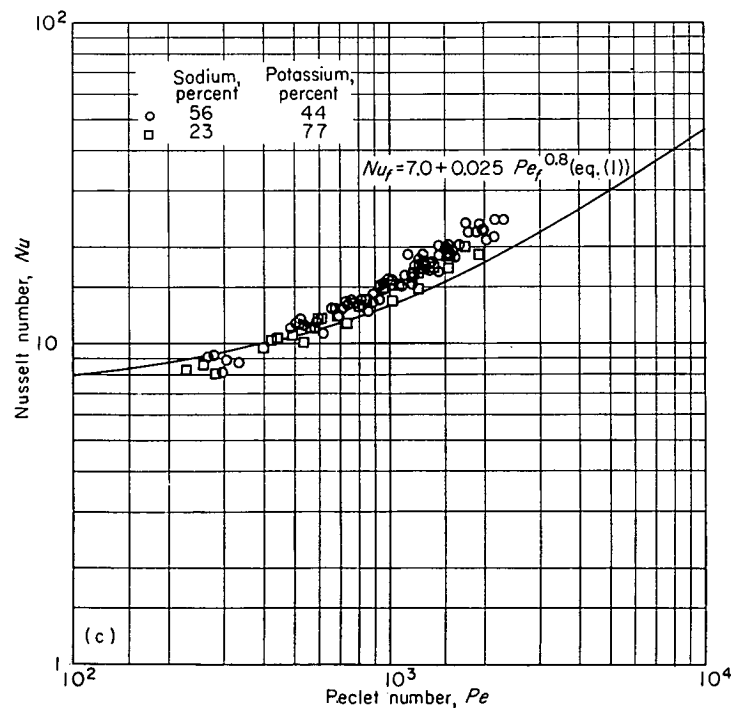
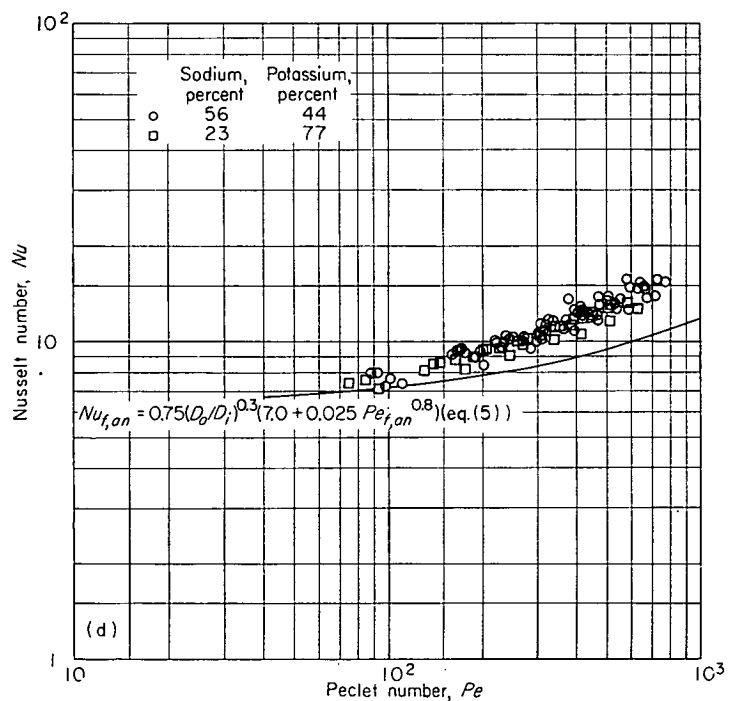
(a) In round tubes; test section A (length-diameter ratio l/D , 50).(b) In annuli; test section A (length-diameter ratio l/D , 54; ratio of outer to inner diameter, 1.83).(c) In round tubes; test section B (length-diameter ratio l/D , 48).(d) In annuli; test section B (length-diameter ratio l/D , 54; ratio of outer to inner diameter, 1.83).

FIGURE 15.—Reevaluated data of Werner, King, and Tidball (ref. 7) for average heat transfer to sodium-potassium alloy.

Werner, King, and Tidball.—Werner, King, and Tidball (ref. 7 and unclassified data from a classified report) used a figure-eight test section (tube and concentric annulus with same fluid in both) to measure heat-transfer coefficients for a sodium-potassium alloy. Cooling coefficients were measured in the tube and heating coefficients in the annulus. Two test sections having the following characteristics were used:

Test section	A	B
Tube inner diameter, D_i , in.	0.68	0.70
Annulus inner diameter, D_i , in.7575
Annulus outer diameter, D_o , in.	1.37	1.37
Length, l , in.	33.8	33.8
Material.	304 Stainless steel	Nickel

The tests in test section A were all run with an alloy of 56 percent sodium and 44 percent potassium. The tests in test section B were run with alloys of both 56 percent sodium plus 44 percent potassium and 23 percent sodium plus 77 percent potassium. Fluid temperatures were measured at the inlet and outlet of the tube and of the annulus. In test section A no provision was made for mixing the fluid before measuring the outlet temperatures of the tube or the annulus, except that the fluid turned one right-angle bend before each thermocouple. The outlet temperatures measured in test section A were, therefore, somewhere between fluid bulk temperature and fluid centerline temperature, probably closer to fluid centerline temperature. In test section B, mixing baffles were used to mix the fluid before measuring outlet temperatures, and the temperatures measured were fluid bulk temperatures. The velocity profiles of the fluid entering the tube and the annulus were essentially flat in test section B, and between flat and fully developed in test section A. The figure-eight test section with counterflow gives approximately uniform heat input to the wall. The heat-transfer coefficients measured were over-all average coefficients.

Werner, King, and Tidball used physical properties which were about the same as those of reference 28. However, the relation used to divide the over-all heat-transfer coefficient in the test section into separate coefficients for the tube and annulus is somewhat different from that recommended by the Liquid-Metals Handbook (eq. (7)).

The experimental data of Werner, King, and Tidball were reevaluated using equation (7) to separate the over-all heat-transfer coefficient into tube and annulus coefficients. In addition, the predictions of Martinelli for the ratio of the temperature differences $(t_w - t_m)/(t_w - t_c)$ for the tube and the annulus (fig. 5) were used to make allowance for the lack of mixing of the fluid before the outlet thermocouples of test section A. The reevaluated data of Werner, King, and Tidball are shown in figure 15; equations (1) and (5) are shown for comparison.

Sineath.—Sineath (ref. 8) ran heat-transfer tests with mercury in rectangular channels. Sineath's test section was of the figure-eight type except that, instead of a tube and concentric annulus, he had two rectangular channels with one common wall. Heat was added to the mercury in one channel and removed from the mercury in the other. The common wall of the two channels was 4 inches high

by $\frac{1}{4}$ inch thick and was made of mild steel. The channel gap was $\frac{1}{4}$ inch and the length, 25 inches. Fluid temperatures were measured at the inlet and outlet of the two channels. No attempt was made to provide any mixing of the fluid before the outlet temperatures were measured except that the abrupt transition from a 4- by $\frac{1}{4}$ -inch rectangular channel to the $\frac{3}{4}$ -inch pipes which carried the fluid to and away from the test section probably resulted in considerable mixing. The pipe entered the channels at right angles to the direction of flow in the channels; there was no smooth transition piece between the pipes and the channels. The fluid temperatures measured were probably close to the bulk temperature. However, the abrupt change of section at the entrance to the channels probably caused some of the heat-transfer surface to be relatively less effective as a result of poor local flow distribution. The figure-eight test section with counterflow approximated uniform heat input to the wall. The heat-transfer coefficients measured were over-all average coefficients.

Sineath ran four sets of tests. The first three sets were inconclusive because of experimental difficulties with air entrainment and with deposition of mercurous oxide on the wall through which heat was being transferred. These problems were partially eliminated in the fourth set of runs. There was probably no air entrainment during the fourth set of runs; the wall through which heat was being transferred was carefully cleaned at the beginning of the runs but was covered with a thin layer of scale at the end.

Sineath used physical properties similar to those of reference 28. The temperatures in the two channels were sufficiently close that the heat-transfer coefficients in both channels could be assumed the same.

The data of the fourth set of runs of Sineath are shown unchanged in figure 16; equation (4) is shown for comparison. The data of Sineath are undoubtedly lower than they should

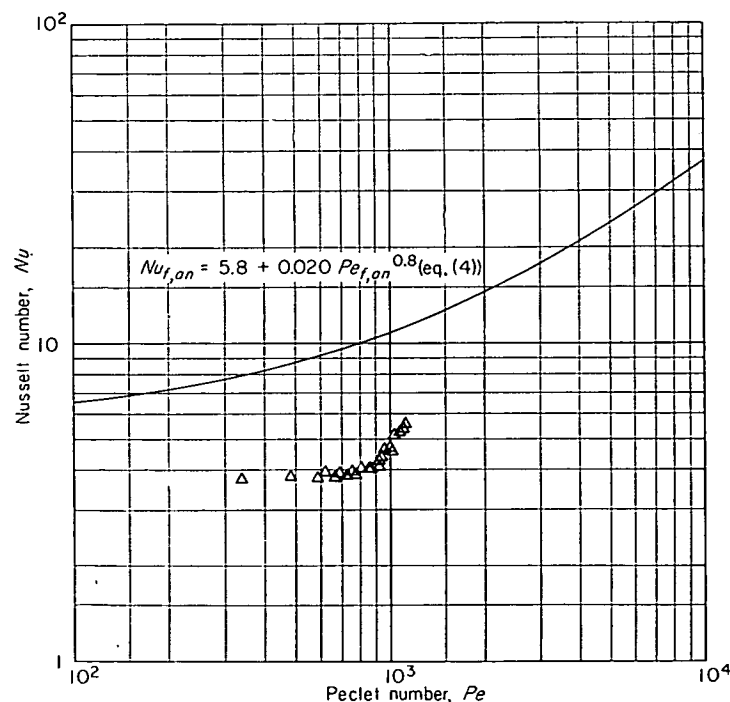


FIGURE 16.—Data of Sineath (ref. 8) for average heat transfer to mercury in rectangular ducts. Length-diameter ratio l/D , 50.

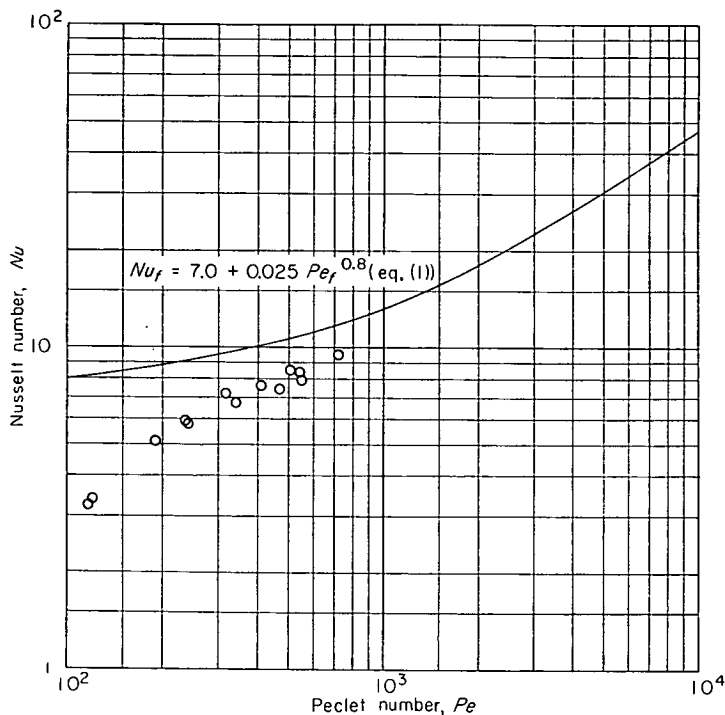


FIGURE 17.—Data of English and Barrett (refs. 9 and 10) for fully developed heat transfer to mercury in round tubes.

be as a result of the deposit of an oxide film on the heat-transfer surface and of the abrupt change of cross section at the entrance to the channels, which makes a portion of the heat-transfer surface ineffective. It is difficult, however, to estimate the magnitude of these effects.

English and Barrett.—English and Barrett (refs. 9 and 10) measured heating coefficients for mercury. The test sections were of nickel and stainless steel with a 0.051-inch inner diameter, a 0.059-inch outer diameter, and a 1.9-inch length. A copper coating was bonded to the outside of the

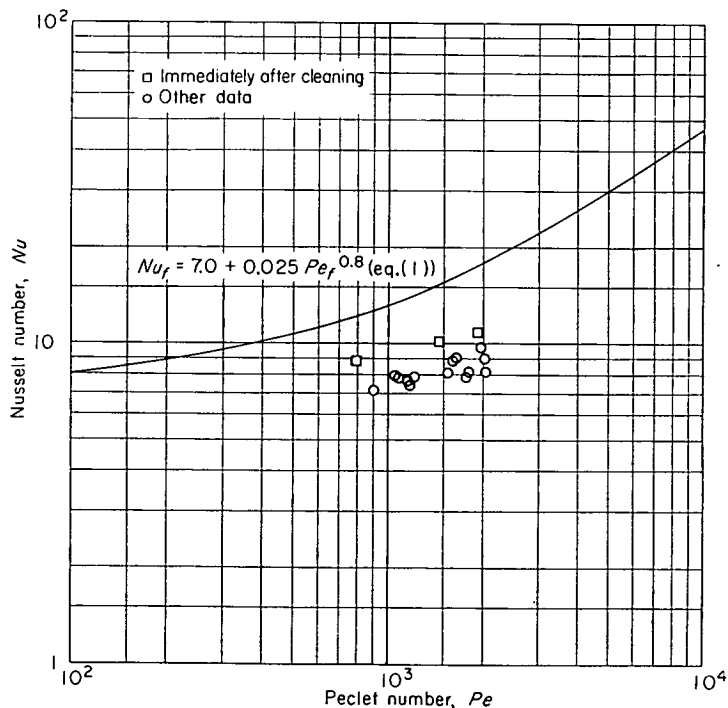


FIGURE 19.—Data of Seban (ref. 11) for fully developed heat transfer to lead-bismuth eutectic in round tubes.

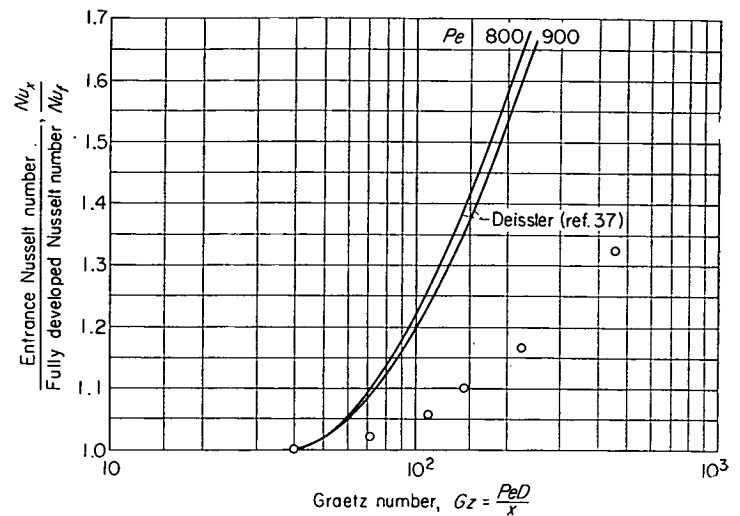


FIGURE 18.—Data of English and Barrett (ref. 9) for entrance-region heat transfer to mercury in round tubes. Peclet number, 800 to 900.

test section; the outer diameter of the copper was 0.0825 inch. The test section was heated by passing electricity directly through it. The inlet and outlet mercury bulk temperatures were measured, as was the outside-wall temperature along the test section; the voltage distribution along the test section was also measured. The velocity profile at the test-section entrance was fully developed. The method of heating most nearly approximated uniform heat input to the wall. English and Barrett measured local heat-transfer coefficients along the test section and present the local fully developed coefficients for all runs. For one run, the local coefficient along most of the tube is presented.

The physical properties used by English and Barrett are the same as those of reference 28 except that the viscosity is slightly high at low temperatures. This will probably not affect the fully developed heat-transfer coefficients, but the entrance-region Reynolds numbers should be increased 3 to 4 percent.

The fully developed heat-transfer coefficients of English and Barrett are shown unchanged in figure 17; equation (1) is shown for comparison. The entrance heat-transfer

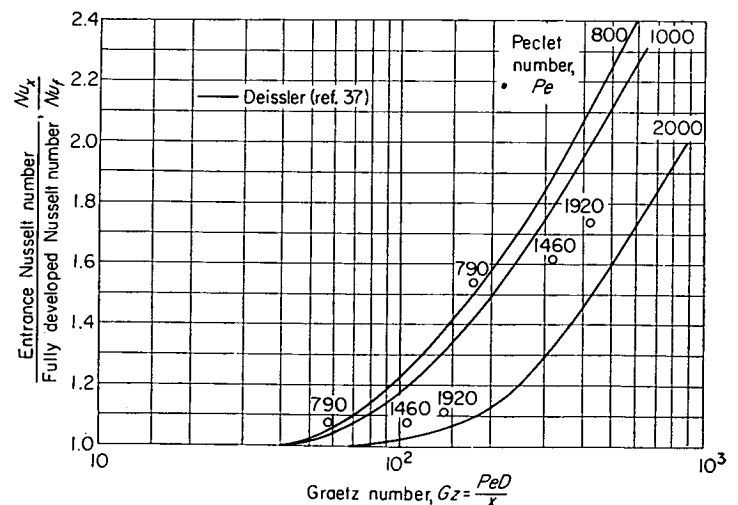


FIGURE 20.—Data of Seban (ref. 11) for entrance-region heat transfer to lead-bismuth eutectic in round tubes.

coefficients for the one run presented are shown in figure 18; Deissler's predicted curves for a Prandtl number of 0.01 and the same Peclet number range are shown for comparison.

Seban.—Seban (ref. 11) measured heat-transfer coefficients with lead-bismuth eutectic in two different types of test section. One was the figure-eight type with a tube and concentric annulus; the other was a copper-coated tube heated by external electric heaters. Only combined heat-transfer coefficients for the tube and annulus of the figure-eight test section are presented in reference 11. Not enough basic data (specifically, fluid temperatures) are presented to separate the tube and annulus coefficients. Accordingly, only the electrically heated test section will be discussed. The test section had a 0.652-inch inner diameter and a 48-inch length. The copper coating was for the purpose of containing the wall thermocouples in a region of relatively low temperature gradient and of smoothing out the non-uniformities of heat input of the external electric heaters. The fluid bulk temperatures were measured at the inlet and outlet of the test section, and the wall temperatures were measured at eight stations along the tube. The velocity profile was close to fully developed at the entrance to the test section. The method of heating approximates very closely uniform heat input to the wall. Local heat-transfer coefficients were measured. The local fully developed coefficients are presented for all the runs; entrance coefficients are presented for a few of the runs.

The physical properties of Seban are the same as those given in reference 28. Seban had some trouble with fouling, which caused the heat-transfer coefficients to decrease with time. Figure 19 shows unchanged the fully developed heat-transfer coefficients of Seban; equation (1) is shown for comparison. Those points taken immediately after cleaning have higher heat-transfer coefficients than the others. The entrance heat-transfer coefficients presented by Seban are shown in figure 20; predicted curves of Deissler (see fig. 3) for the same range of Peclet number and for a Prandtl number of 0.01 are shown for comparison.

Trefethen.—Trefethen (refs. 12 and 13) used a figure-eight type of test section to measure heat-transfer coefficients with mercury. Six different tubes, described in the following table, were used in the tube and concentric annulus test section:

Test section	A	B	C	D	E	F
Tube inner diameter, D_i , in.	0.711	0.737	0.585	0.523	0.308	0.429
Annulus inner diameter, D_i , in.	.749	.748	.629	.627	.378	.500
Annulus outer diameter, D_o , in.	.874	.874	.874	.874	.874	.874
Length, l , in.	39.3	39.3	39.3	39.3	39.3	39.3
Tube material.	Stainless steel.	Stainless steel.	Stainless steel.	Copper.	Copper.	Copper.

Heating and cooling tests were run in both the tube and the annulus. Trefethen measured the fluid bulk temperature at the inlet and outlet of the tube and annulus. He also measured the wall temperature of the outside of the annulus. The velocity profiles were between flat and fully developed at the entrance to the test section, probably a little closer to flat. The counterflow figure-eight test section approximated a uniform heat input to the wall.

Trefethen presents a fully developed heat-transfer coefficient for the central section of his tube (from 10.2 to 29.4 in. from the entrance.) In his calculations he assumed that the temperature difference between the fluid in the tube and in the annulus remains the same as the temperature difference at the entrance to the tube and annulus, and that the fluid bulk temperature gradient along the length of the tube center section is the same as the temperature gradient along the annulus outer-wall center section. Trefethen separates the tube and annulus coefficients in a manner different from that resulting from the use of equations (6) and (7).

The physical properties used by Trefethen are about the same as those of reference 28 for the range of temperature covered by his experiments. (The values of thermal conductivity at high temperature (extrapolated by Trefethen to correct the data of Styrikovich and Semenovker) are lower than those of the Liquid-Metals Handbook by about 6 percent at 212°, 14 percent at 392°, and 20 percent at 662° F.)

The data of Trefethen for fully developed heat-transfer coefficients were recalculated using equations (6) and (7) to separate the coefficients of the tube and annulus. The reevaluated data for the tube are shown in figure 21; equation (1) is shown for comparison. Trefethen gives enough data to permit the calculation of over-all average heat-transfer coefficients for the tube and annulus. These coefficients also were calculated using equations (6) and (7) to separate the individual coefficients in the tube and annulus. These data are shown in figure 22; equations (1), (4), and (5) are shown for comparison.

Doody and Younger.—Doody and Younger (refs. 14 and 15) measured both heating and cooling coefficients for mercury with and without sodium additions. The test section was a steel tube 0.493 inch in inner diameter and 61

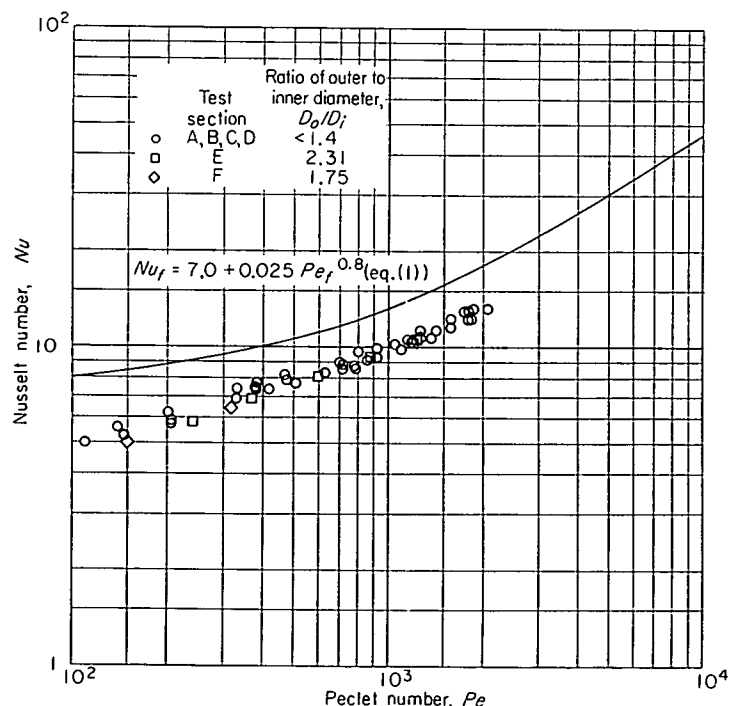


FIGURE 21.—Reevaluated data of Trefethen (refs. 12 and 13) for fully developed heat transfer to mercury in round tubes.

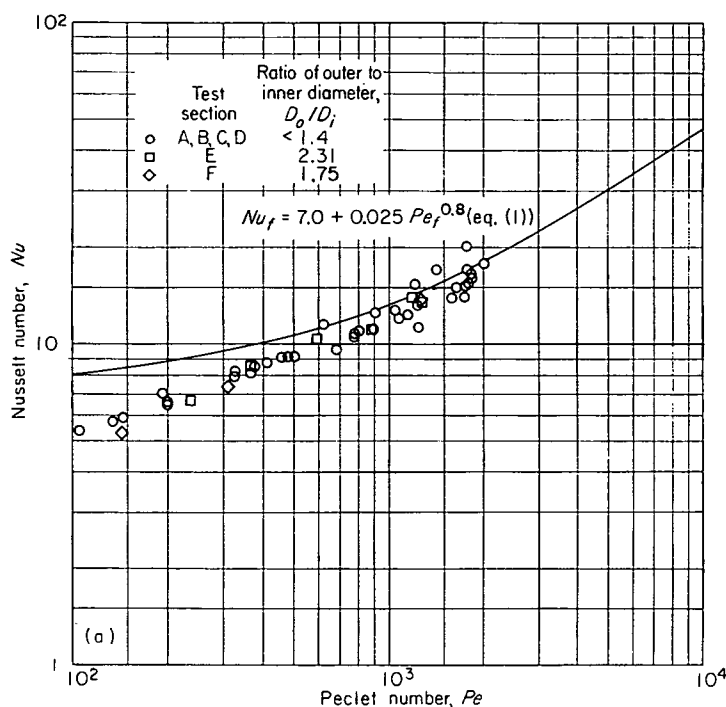
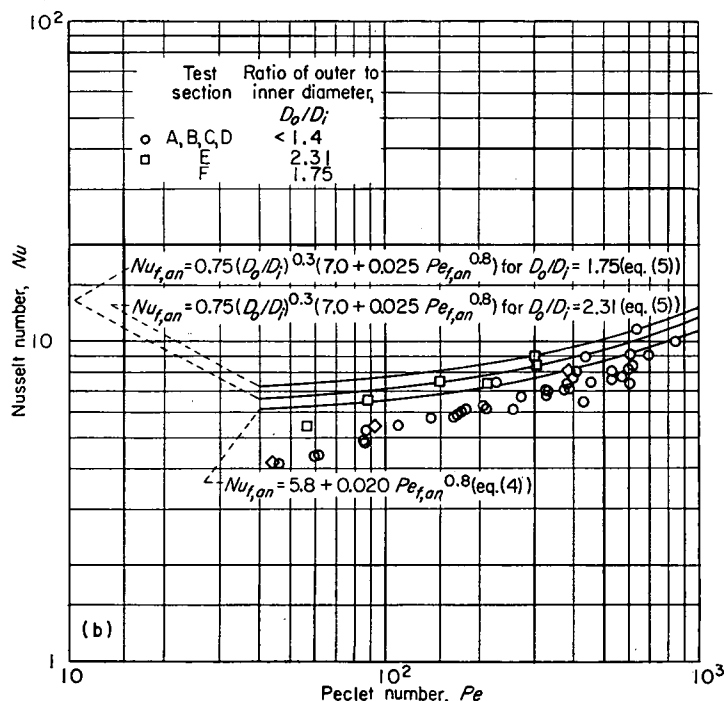
(a) In round tubes; length-diameter ratio l/D , 53 to 128.(b) In annuli; length-diameter ratio l/D , 79 to 334.

FIGURE 22.—Reevaluated data of Trefethen (refs. 12 and 13) for average heat transfer to mercury.

inches long. The test section was heated or cooled by water flowing in a concentric annulus. Both parallel and counterflow runs were made. The annulus was 61 inches long, but the annulus entrance and exit were each 6 inches from the ends of the test section; therefore, the length of the test section between the annulus entrance and exit was 49 inches. Tube wall temperatures were measured at five stations starting $\frac{1}{2}$ inch downstream of the annulus inlet

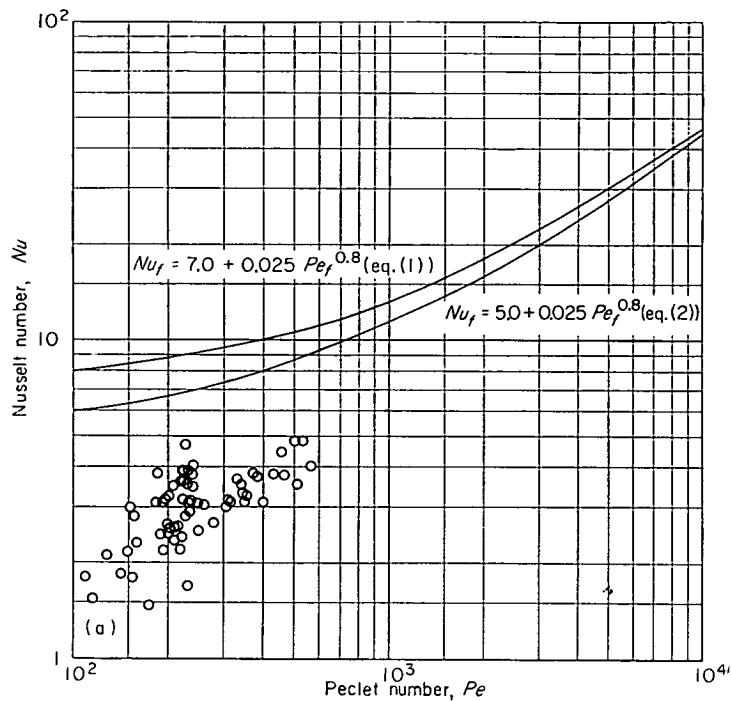
and ending 3 inches upstream of the annulus outlet (inlet and outlet refer to the parallel-flow case); the measurements covered $45\frac{1}{2}$ inches of the test section. The mercury temperature was measured at the inlet and outlet of the test section. The measurement of test-section exit temperature was made without any preliminary mixing of the fluid, and the exit temperature measured is closer to the fluid centerline temperature than to the fluid bulk temperature. The mercury velocity profile at the test-section entrance was probably closer to flat than it was to fully developed. The method of heating resulted in a wall condition somewhere between uniform heat input and uniform wall temperature for the counterflow runs. The parallel-flow runs resulted in a wall condition where the rate of heat input varied even more rapidly than for the condition of uniform wall temperature.

The physical properties used by Doody and Younger are the same as those of reference 28 except for the thermal conductivity. The values of thermal conductivity used by Doody and Younger are low by about 1 to 14 percent in the temperature range of the investigation. Because of the location of the annulus entrance and exit as described, some effective length of test section between 49 and 61 inches must be selected. Doody and Younger used a method due to Sherwood and Petrie (ref. 41) and arrived at an effective length of 56 inches. Since the wall temperatures at the ends of the test section were not measured, Doody and Younger extrapolated the wall temperature measurements to cover a length of 56 inches, the "effective" length of their test section. Inasmuch as this extrapolation necessarily neglects end effects, the data of Doody and Younger represent something between over-all average and fully developed heat-transfer coefficients.

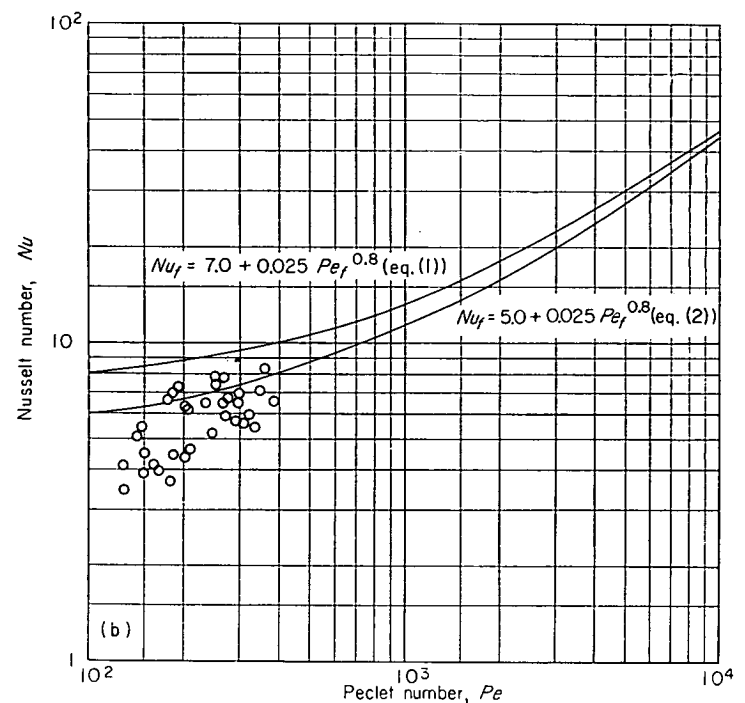
The heat balances of Doody and Younger show deviations as great as 140 percent, with deviations between 40 and 100 percent being quite common. Flow was measured by an orifice, and the orifice calibration showed variations as great as 50 percent. The end temperature differences between the wall and the fluid found by the previously mentioned extrapolation were very small, varying from about 0.3° to 8° F, with values of 2° F or less being extremely common. Small errors in temperature measurement can therefore result in large errors in log mean temperature difference.

Doody and Younger attempted to check their experimental apparatus by running heat-transfer experiments with butanol. Unfortunately, most of these data were in the transition region. Some of the data were in the laminar-flow region, and these data were 25 to 75 percent higher than the predictions of the Colburn equation for laminar flow (ref. 39, p. 191).

In view of the difficulties mentioned, the data of Doody and Younger may not be very accurate. The data of Doody and Younger were reevaluated using the physical properties of reference 28 and the predictions of Martinelli for the ratio $(t_w - t_m)/(t_w - t_c)$ to determine the value of the temperature differences between the wall temperature and the fluid bulk temperature at the test-section exit. The original data on wall temperature are not presented in either reference 14 or 15; therefore the extrapolated end temperature will be used for the wall temperature at the test-section



(a) Without sodium addition.



(b) With small sodium additions.

FIGURE 23.—Reevaluated data of Doody and Younger (refs. 14 and 15) for heat transfer to mercury in round tubes.

inlet and outlet. The reevaluated data of Doody and Younger are shown in figure 23; equations (1) and (2) are shown for comparison.

Lubarsky.—Lubarsky (ref. 16) used a figure-eight type of test section to measure heating coefficients in a tube and cooling coefficients in a concentric annulus for lead-bismuth eutectic with and without magnesium additions. The test section was 40.2 inches long, with a 0.402-inch tube inner diameter, a 0.50-inch annulus diameter, and a 0.625-inch annulus outer diameter. The fluid bulk temperatures at

the inlet and outlet of the tube and annulus were measured. The entering velocity profile was approximately flat. The figure-eight-type heat exchanger with counterflow approximated uniform heat input to the wall. Over-all average heat-transfer coefficients were measured.

Lubarsky used physical properties which were the same as those of reference 28. He used equation (6) to separate the heat-transfer coefficients in the tube and the annulus. Lubarsky's data are shown unchanged in figure 24; equations (1) and (4) are shown for comparison.

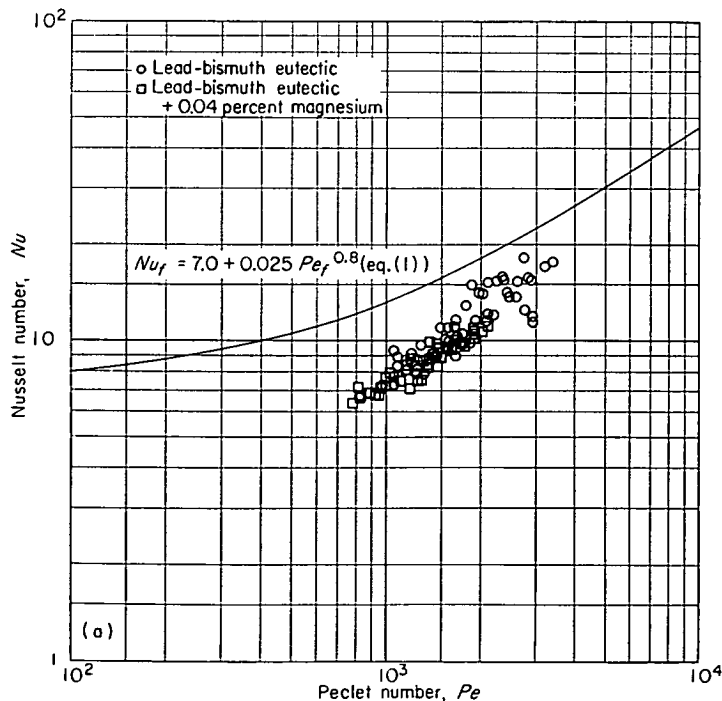
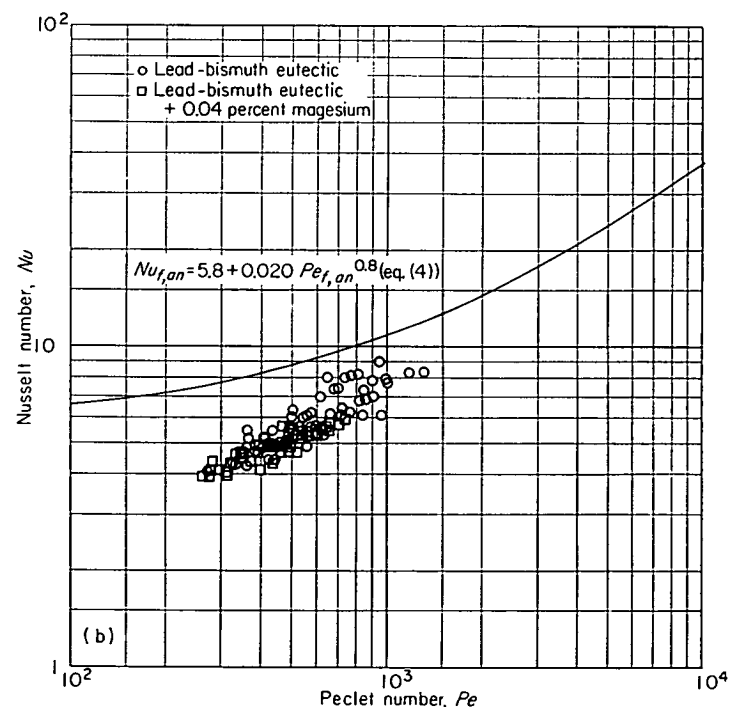

 (a) In round tubes; length-diameter ratio l/D , 100.

 (b) In annuli; length-diameter ratio l/D , 322.

FIGURE 24.—Data of Lubarsky (ref. 16) for average heat transfer to lead-bismuth eutectic.

Johnson, Hartnett, and Clabaugh (lead-bismuth tests).— Johnson, Hartnett, and Clabaugh (refs. 17 and 18) measured heating coefficients for lead-bismuth eutectic in an aluminum-coated tube heated externally by electric heaters. The test section was very similar to that of Seban (ref. 11) described previously, except that an aluminum coating was used instead of a copper one. The test-section inner diameter was 0.652 inch and its length 48 inches. The fluid bulk temperature was measured at the inlet and outlet of the test section, and the wall temperature was measured at eight stations along

the wall. The inlet velocity profile was very close to fully developed. The method of heating very closely approximated uniform heat input to the wall. Local heat-transfer coefficients are presented for both the fully developed region and the entrance region.

Physical properties the same as those of reference 28 were used. The data on fully developed heat-transfer coefficients are shown unchanged in figure 25; equation (1) is shown for comparison. The data on entrance heat-transfer coefficients are shown unchanged in figure 26; predicted curves of Deissler (fig. 3(b)) for the same length-diameter ratio x/D and a

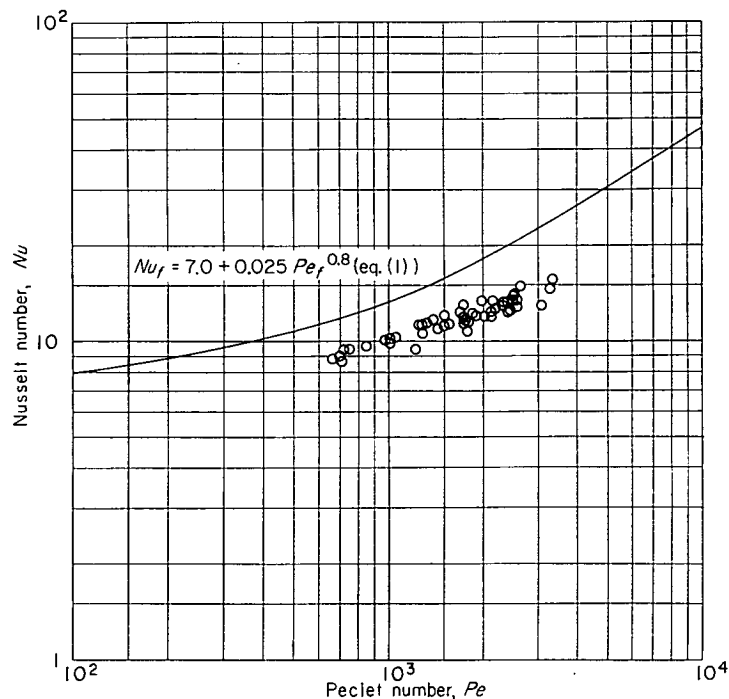
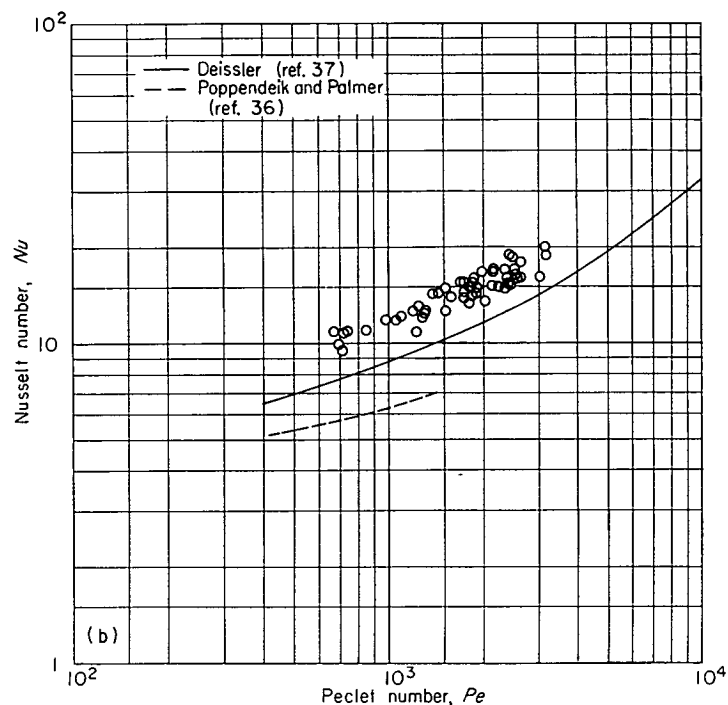
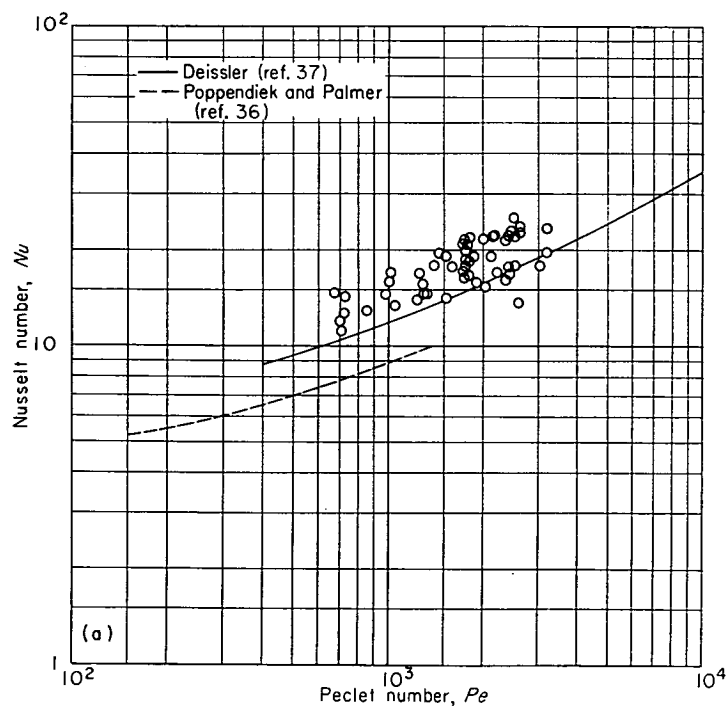


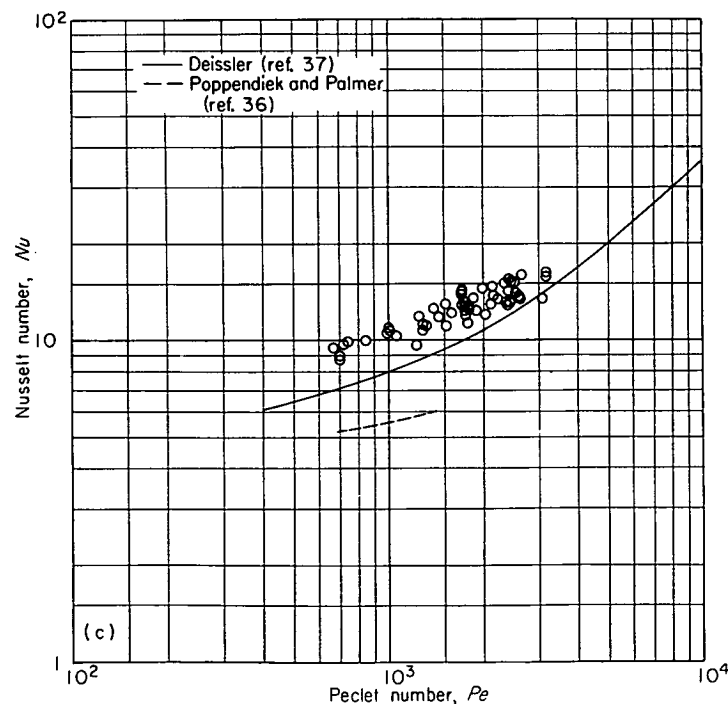
FIGURE 25.—Data of Johnson, Hartnett, and Clabaugh (refs. 17 and 18) for fully developed heat transfer to lead-bismuth eutectic in round tubes.



(b) Length-diameter ratio x/D , 13.8.



(a) Length-diameter ratio x/D , 4.6.



(c) Length-diameter ratio x/D , 23.

FIGURE 26.—Data of Johnson, Hartnett, and Clabaugh (refs. 17 and 18) for entrance-region heat transfer to lead-bismuth eutectic in round tubes.

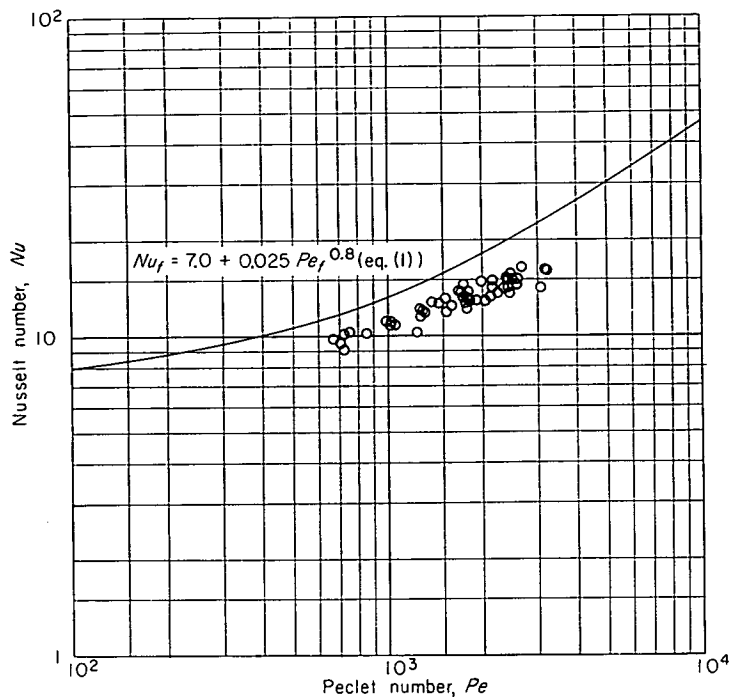


FIGURE 27.—Data of Johnson, Hartnett, and Clabaugh (refs. 17 and 18) for average heat transfer to lead-bismuth eutectic in round tubes. Length-diameter ratio l/D , 74.

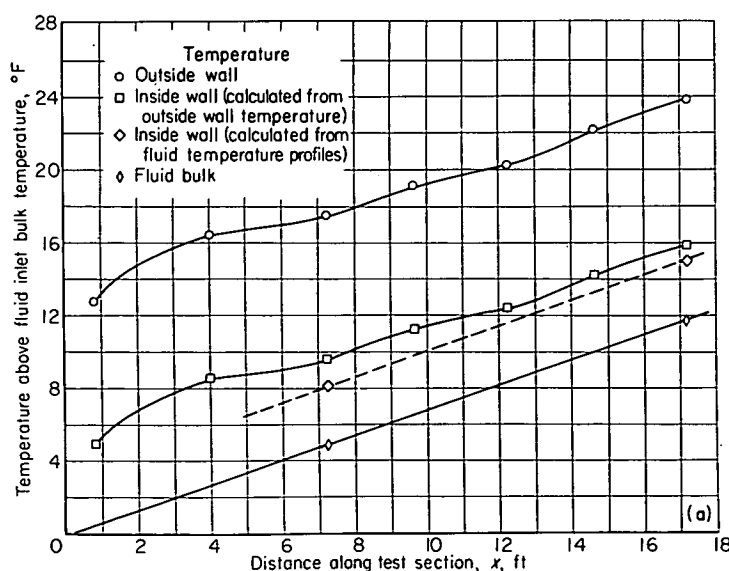
Prandtl number of 0.01 are shown for comparison. The predictions of Poppendiek and Palmer (fig. 3(b)) for low Reynolds numbers are also shown in figure 26. From the local data of Johnson, Hartnett, and Clabaugh, it is possible to determine an approximate over-all average coefficient by plotting and integrating the local coefficients. The results of this procedure are shown in figure 27; equation (1) is shown for comparison.

Isakoff and Drew.—Isakoff and Drew (refs. 19 and 20) measured heating coefficients with mercury. The test section was a stainless-steel tube with a 0.127-inch wall thickness, 1.5-inch inner diameter, and about 223-inch length, heated externally by electric heaters. The fluid bulk temperature was measured at the test-section inlet and outlet, and the

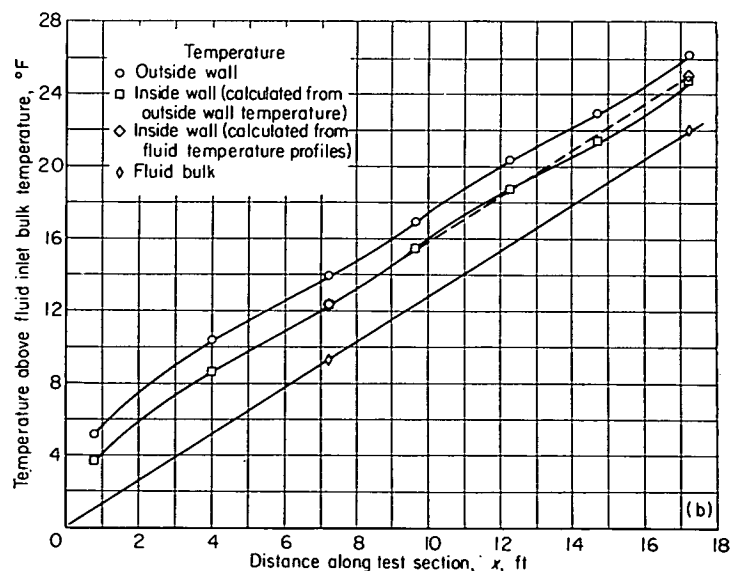
outside wall temperature was measured at seven stations along the tube. Velocity and temperature profiles in the fluid were measured at three stations along the tube ($x/D = 58, 98$, and 138). The entrance velocity profile was very close to flat. The method of heating approximated very closely uniform heat input to the wall. Local fully developed heat-transfer coefficients were measured at the stations of $x/D = 98$ and $x/D = 138$. The heat-transfer coefficients measured at the $x/D = 58$ are still in the entrance region.

The physical properties used by Isakoff and Drew are the same as those of reference 28. The inside wall temperature was calculated in two ways: one was to extrapolate the temperature profile in the fluid to the wall; the other was to use the measured outside wall temperature to calculate the temperature drop through the wall. When this calculation was made, the two inside wall temperatures were found to coincide for only three of the total of 12 experimental runs. For the other nine runs, the inside wall temperature calculated from the outside wall temperatures was higher than the inside wall temperature as extrapolated from the fluid temperature profile. Fluid and wall temperatures for two typical runs are shown in figure 28.

This discrepancy between the two methods of determining inside wall temperature may be due to inaccuracies in the measurement of outside wall temperature. The outside wall temperature was measured by eight thermocouples at each station. The temperature readings of these thermocouples varied as much as 25 percent from each other in the high-flux region. The deviation may have been due to the proximity of the thermocouples to the electric heaters. At any rate, the order of magnitude of the variation of the thermocouple readings on the outside wall is as great as the magnitude of the differences in temperature resulting from the two methods of calculating inside wall temperature. It is interesting to note, however, that the inside wall temperature as calculated from the outside wall temperature is greater (for nine cases out of twelve) than that extrapolated from the fluid temperature profile. This effect is that which would be noted if



(a) Run 3.



(b) Run 12.

FIGURE 28.—Test-section temperatures from two typical runs of Isakoff and Drew (refs. 19 and 20).

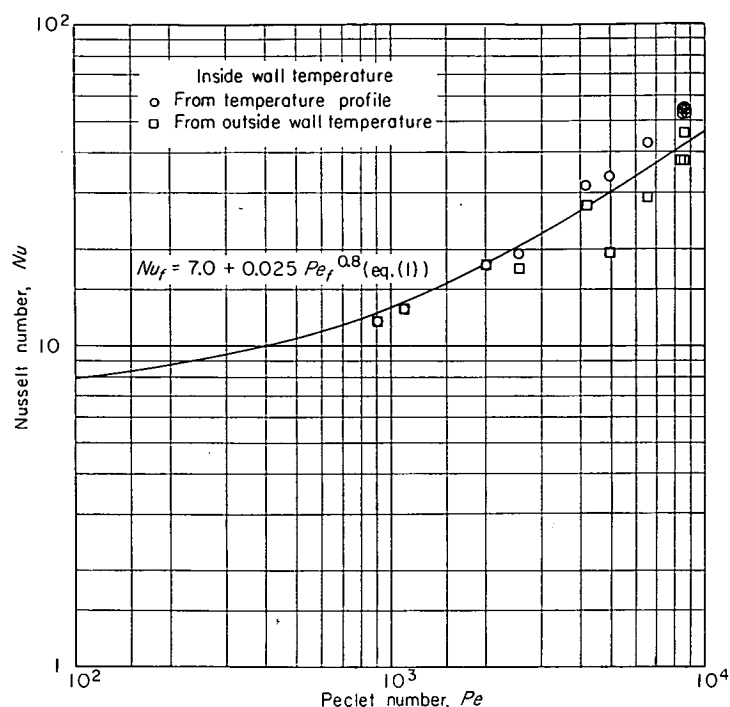


FIGURE 29.—Data of Isakoff and Drew (refs. 19 and 20) for fully developed heat transfer to mercury in round tubes. Length-diameter ratio x/D , 138.

there were some form of interfacial resistance between the fluid and the tube. However, because of the circumferential variation of outside wall temperature and because three of the runs showed no difference in the inside wall temperature calculated by the two methods, no conclusions can be reached.

The data of Isakoff and Drew are shown in figure 29 for the fully developed heat-transfer coefficient ($x/D=138$); the coefficient is shown for both methods of calculating inside wall temperature; equation (1) is shown for comparison. The entrance data at $x/D=58$ are shown in figure 30; inasmuch as the ordinate in this figure is a ratio, both methods of calculating the inside wall temperature give the same

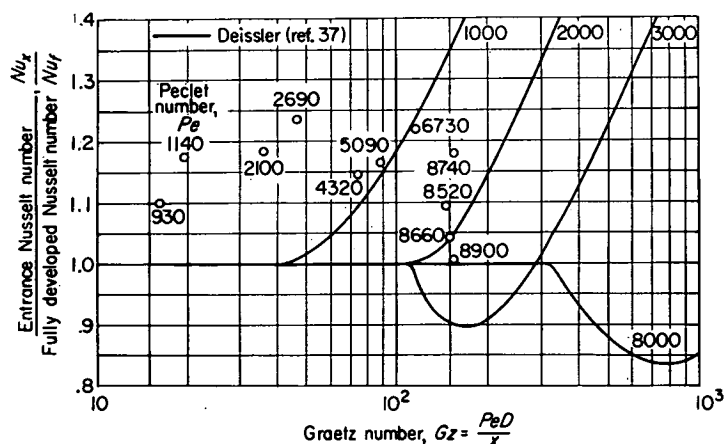


FIGURE 30.—Data of Isakoff and Drew (refs. 19 and 20) for entrance-region heat transfer to mercury in round tubes (inside wall temperatures extrapolated from fluid temperature profile). Length-diameter ratio x/D , 58.

results; Deissler's predicted curves (fig. 3) are shown for comparison. The outside wall temperature was measured at a sufficient number of stations along the tube (see fig. 28) to permit the estimate of an over-all average heat-transfer coefficient. The average over-all coefficient from $x/D=6.3$ to $x/D=138$, based on inside wall temperatures calculated from the outside temperature, is shown in figure 31. These average coefficients are actually lower than the fully developed coefficients because the average outside wall temperature at the second station from the test-section entrance is higher than might be expected from the other measured temperatures. Whether this might be a result of the local temperature gradients caused by the external electric heaters cannot be determined.

The temperature profiles in the fluid at $x/D=138$ are shown in figure 32 and compared with the predictions of Martinelli (ref. 27).

Stromquist.—Stromquist (ref. 21) measured heating coefficients for mercury with and without sodium additions. The test section was a steel tube heated by passing electricity directly through the tube. The following four different test sections were used:

Test section	A	B	C	D
Inner diameter, D_i , in.	0.380	0.488	0.753	0.787
Outer diameter, D_o , in.753	1.002	1.500	1.501
Length, l , in.	47.25	48.25	50.25	50.25

Fluid bulk temperatures were measured at the test-section inlet and outlet, and the outside wall temperatures were measured at 12 stations along the length of the test section.

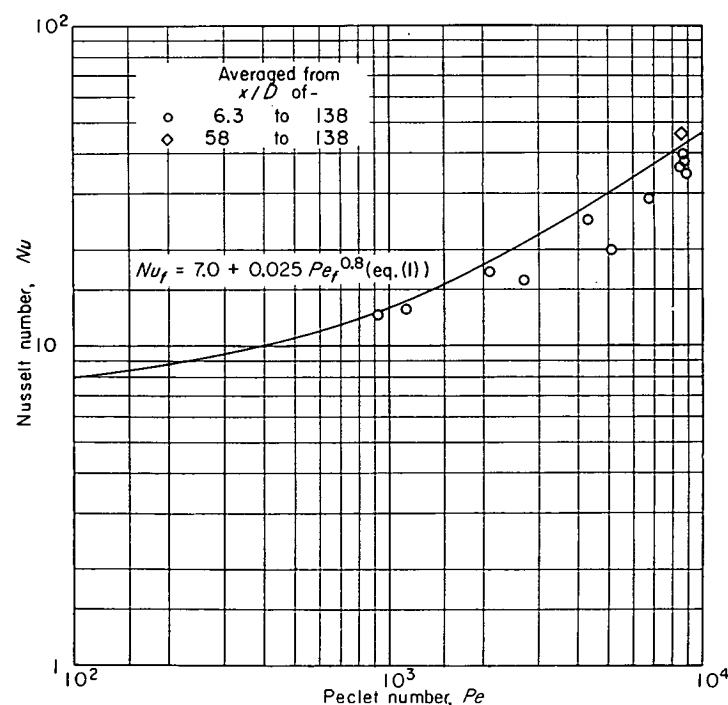


FIGURE 31.—Data of Isakoff and Drew (refs. 19 and 20) for average heat transfer to mercury in round tubes (inside wall temperatures calculated from outside wall temperatures).

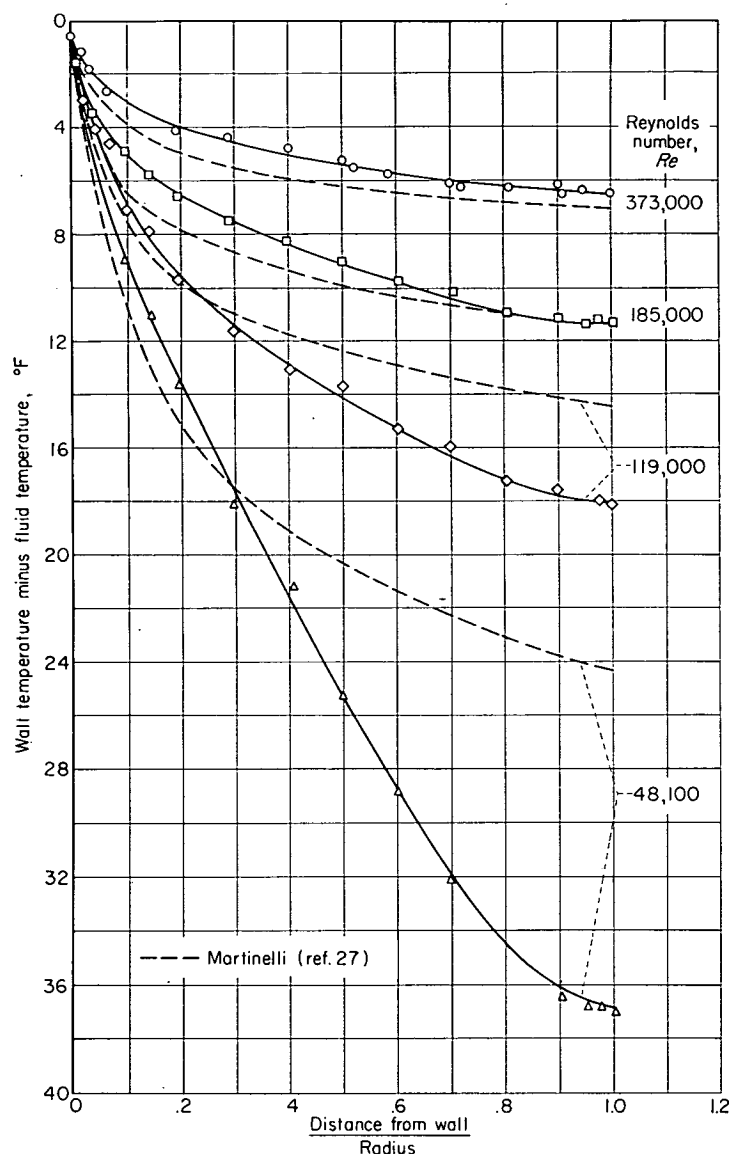


FIGURE 32.—Data of Isakoff and Drew (refs. 19 and 20) for fully developed temperature distribution for heat transfer to mercury in round tubes. Length-diameter ratio x/D , 138.

The entrance velocity profile to the test section was somewhere between flat and fully developed. The method of heating more nearly approximated uniform heat input than it did uniform wall temperature. Local heat-transfer coefficients, both entrance and fully developed, were measured.

Stromquist used physical properties which were the same as those of reference 28. Figure 33 shows the fully developed heat-transfer coefficients of Stromquist unchanged; equation (1) is included for comparison. The unchanged entrance heat-transfer coefficient data of Stromquist are shown in figure 34; Deissler's predicted curves (fig. 3(a)) are shown for comparison. The predictions of Poppendiek and Palmer (fig. 3(a)) for low Reynolds numbers are shown in figure 34(a).

MacDonald and Quittenton.—MacDonald and Quittenton (refs. 22 and 23) measured heating coefficients with sodium. The test section consisted of a monel tube with a copper

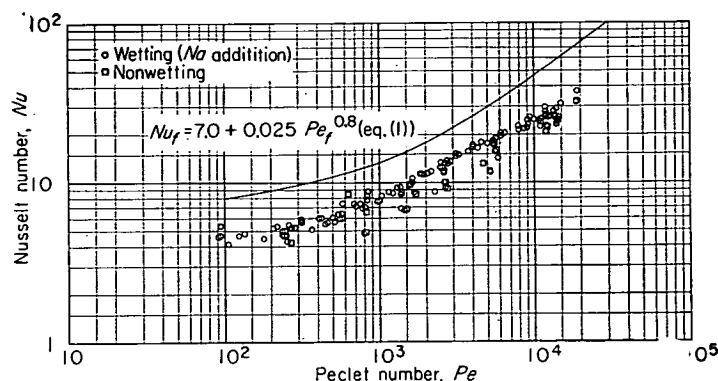


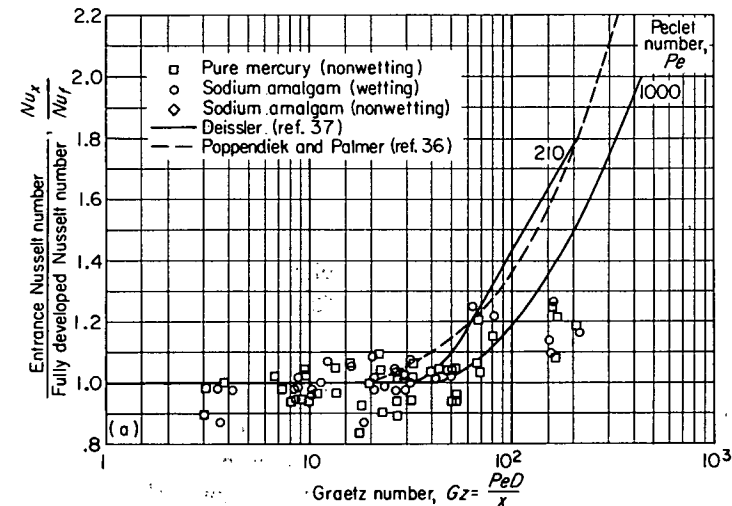
FIGURE 33.—Data of Stromquist (ref. 21) for fully developed heat transfer to mercury, with and without sodium additions, in round tubes.

jacket bonded to the outside. The test section of 0.625-inch inner diameter and 60.05-inch length was heated externally by electric heaters. The purpose of the copper jacket was the same as the purpose of the copper coating used by Seban (ref. 11) and described in a previous section entitled "Seban." The fluid bulk temperature was measured at the inlet and outlet of the test section, and the wall temperatures were measured at 11 stations along the test section. The entrance velocity profile was close to fully developed if the length of piping in the diagram shown in figure 1 of reference 23 is drawn to scale. The method of heating very closely approximated uniform heat input to the walls. Local heat-transfer coefficients were measured; the authors present fully developed heat-transfer coefficients for a length of the tube from 47.3 to 54.8 inches downstream of the tube entrance.

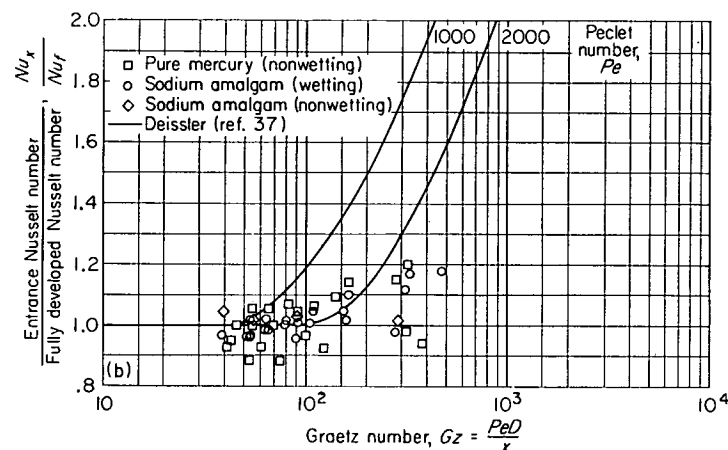
MacDonald and Quittenton used the same physical properties as those in reference 28. The data for fully developed heat-transfer coefficients are shown unchanged in figure 35; equation (1) is shown for comparison. The data show a great amount of scatter. Consecutive runs at identical Peclet numbers and similar temperature levels vary as much as 120 percent in Nusselt number, with variations of 30 to 60 percent in consecutive runs being common. In view of this scatter, the entrance coefficients and over-all average coefficients have not been calculated, although the data were sufficient to make these calculations possible.

Johnson, Clabaugh, and Hartnett (mercury tests).—Johnson, Clabaugh, and Hartnett (ref. 24) measured heating coefficients for mercury. The test section was almost identical to the test section described previously under the section "Johnson, Hartnett, and Clabaugh (lead-bismuth tests)." The test section was an aluminum-coated tube with a 0.652-inch inner diameter and a 48-inch length. The fluid bulk temperatures were measured at the inlet and outlet of the test section; the wall temperatures were measured at eight stations along the test section. The entrance velocity profile was close to fully developed. The method of heating approximated very closely uniform heat input to the wall. Local heat-transfer coefficients, both fully developed and entrance, are presented.

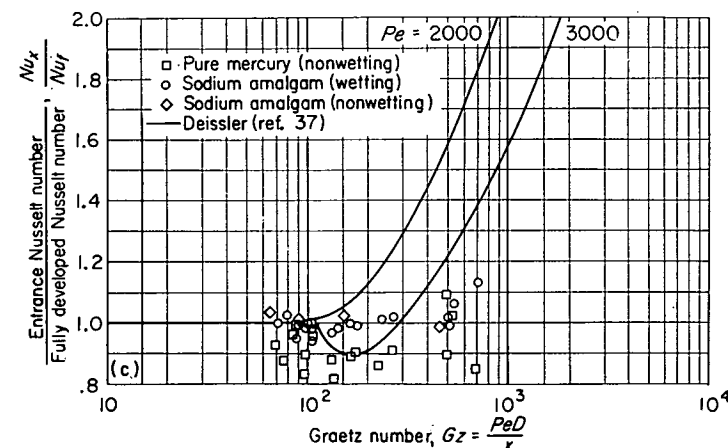
The physical properties used by Johnson, Clabaugh, and Hartnett are the same as those of reference 28. The fully developed heat-transfer coefficients of Johnson, Clabaugh, and Hartnett are shown unchanged in figure 36; equation (1) is shown for comparison. The entrance heat-transfer coefficients are shown in figure 37. Deissler's predicted



(a) $170 < \text{Peclet number} < 1000$.



(b) $1000 < \text{Peclet number} < 2000$.



(c) $2000 < \text{Peclet number} < 3000$.

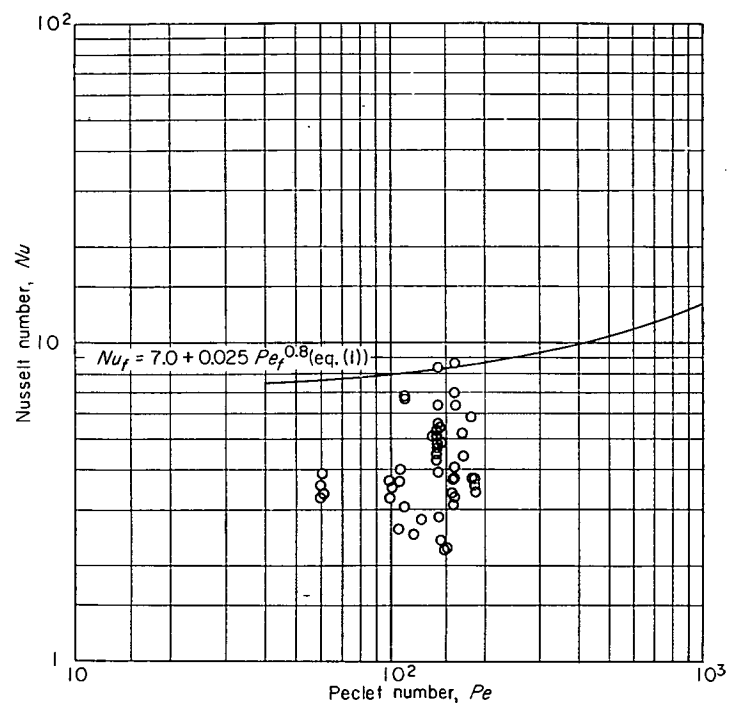
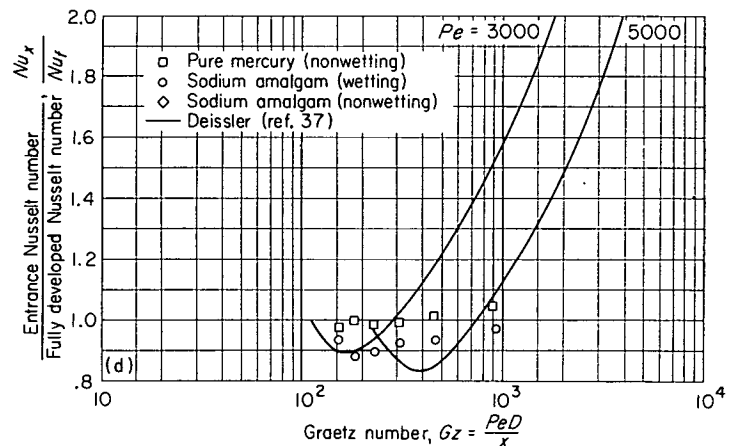
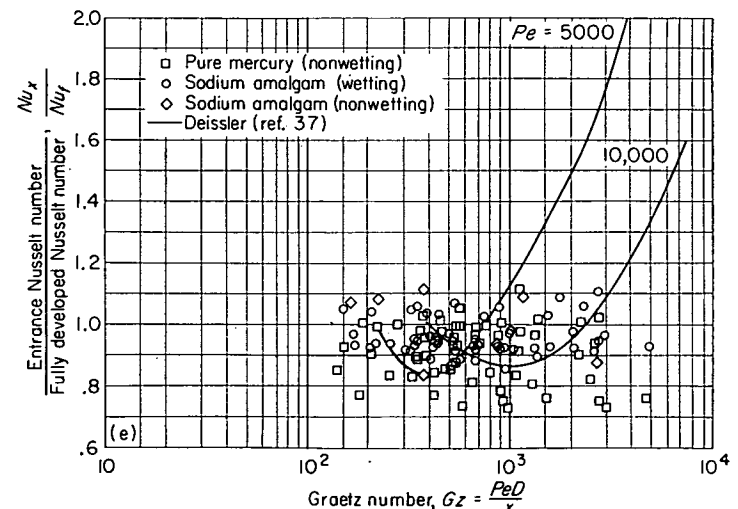


FIGURE 35.—Data of MacDonald and Quittenton (refs. 22 and 23) for fully developed heat transfer to sodium in round tubes.



(d) $3000 < \text{Peclet number} < 5000$.



(e) $5000 < \text{Peclet number} < 20,000$.

FIGURE 34.—Data of Stromquist (ref. 21) for entrance-region heat transfer to mercury, with and without sodium additions, in round tubes.

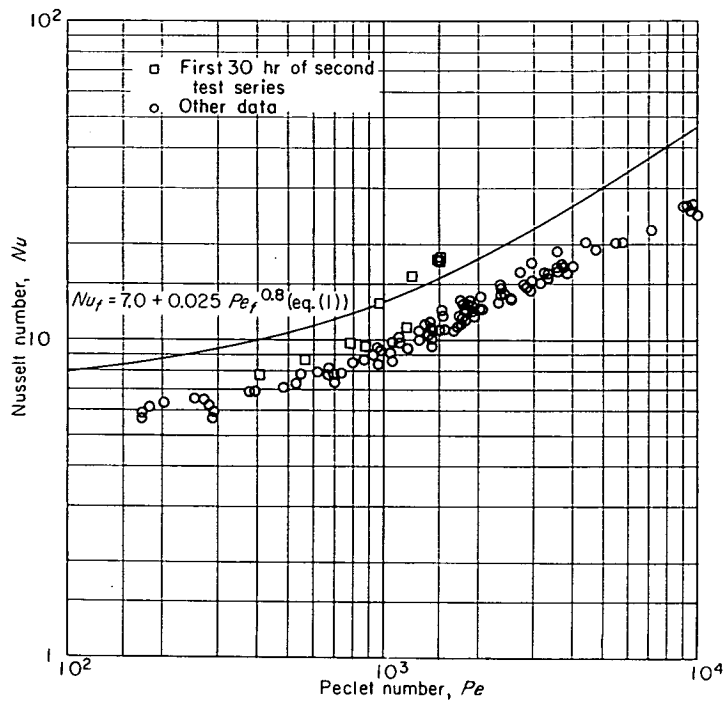
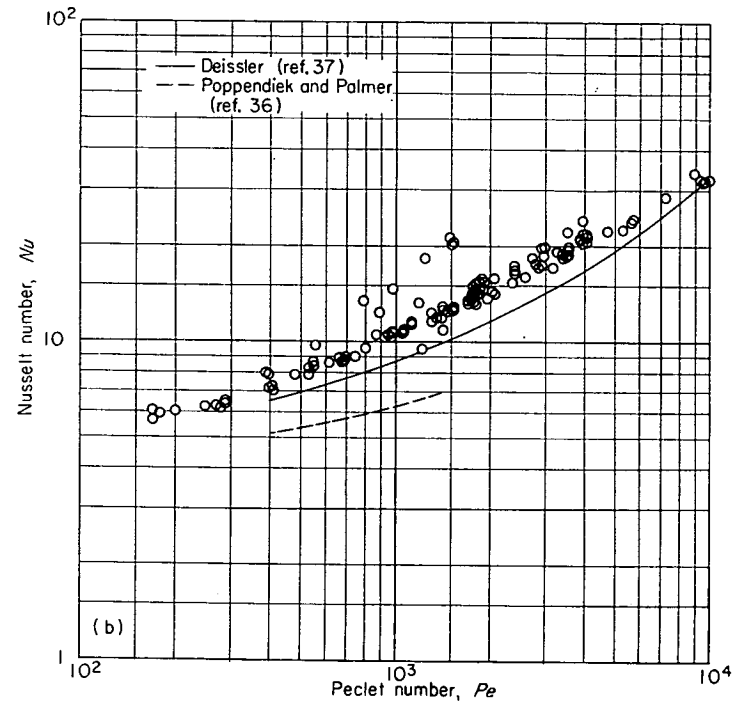


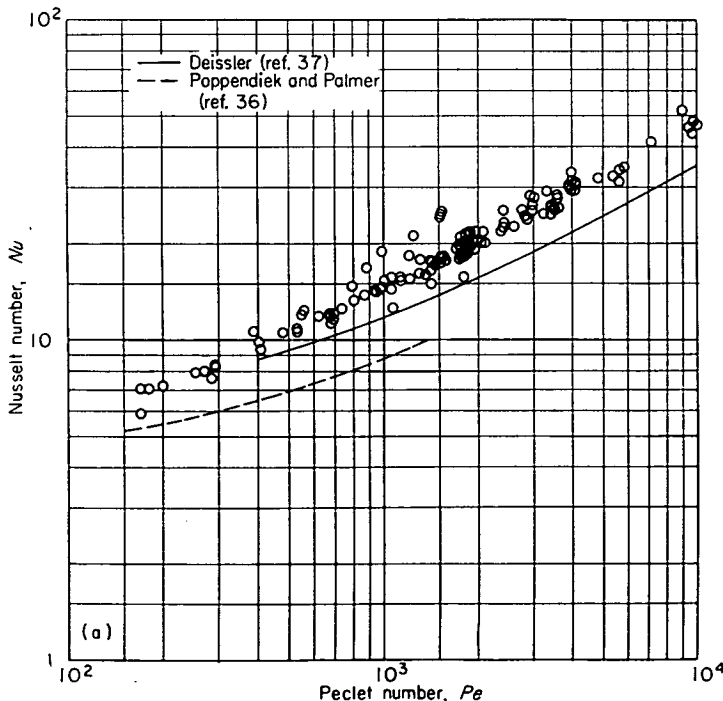
FIGURE 36.—Data of Johnson, Clabaugh, and Hartnett (ref. 24) for fully developed heat transfer to mercury in round tubes.

curves (fig. 3(b)) are shown for comparison; the predictions of Poppendiek and Palmer (fig. 3(b)) for low Reynolds number are also shown in figure 37. From the experimentally determined entrance and fully developed heat-transfer coefficients, it is possible to determine by integration the over-all average coefficient. The resulting over-all average heat-transfer coefficients are shown in figure 38; equation (1) is shown for comparison.

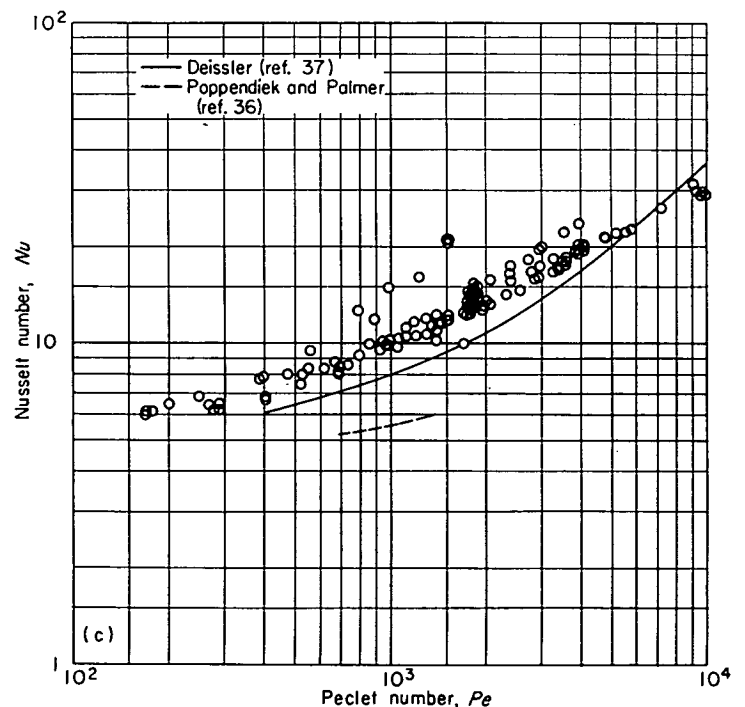
Johnson, Hartnett, and Clabaugh (laminar and transition ow).—Johnson, Hartnett, and Clabaugh (ref. 25) have measured heating coefficients for lead-bismuth eutectic and mercury in the laminar and transition flow regions. The test section used was identical to the test sections used in the investigations of lead-bismuth eutectic and mercury in the turbulent-flow region by Johnson, Hartnett, and Clabaugh (see the preceding sections entitled “Johnson, Hartnett, and Clabaugh (lead-bismuth tests)” and “Johnson, Clabaugh, and Hartnett (mercury tests)”). The test sec-



(b) Length-diameter ratio x/D , 13.8.



(a) Length-diameter ratio x/D , 4.6.



(c) Length-diameter ratio x/D , 23.

FIGURE 37.—Data of Johnson, Clabaugh, and Hartnett (ref. 24) for entrance-region heat transfer to mercury in round tubes.

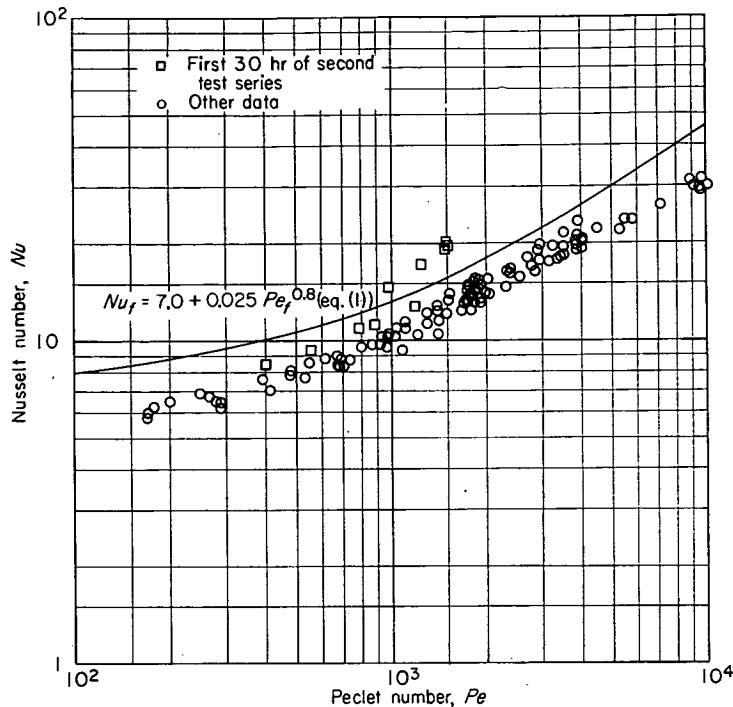


FIGURE 38.—Data of Johnson, Clabaugh, and Hartnett (ref. 24) for average heat transfer to mercury in round tubes. Length-diameter ratio l/D , 74.

tion was an aluminum-coated tube of 0.652-inch inner diameter and a 48-inch length. The fluid bulk temperatures were measured at the inlet and outlet of the test section, and the wall temperatures were measured at eight stations along the test section. The entrance velocity profile was in doubt, since the flow was mostly in the transition region. The method of heating approximated very closely uniform heat input to the wall. Local heat-transfer co-

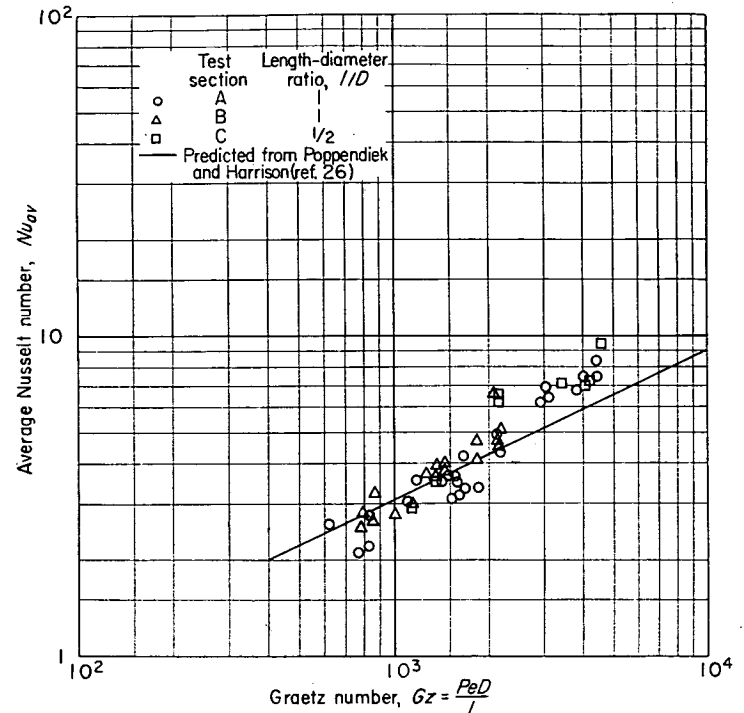
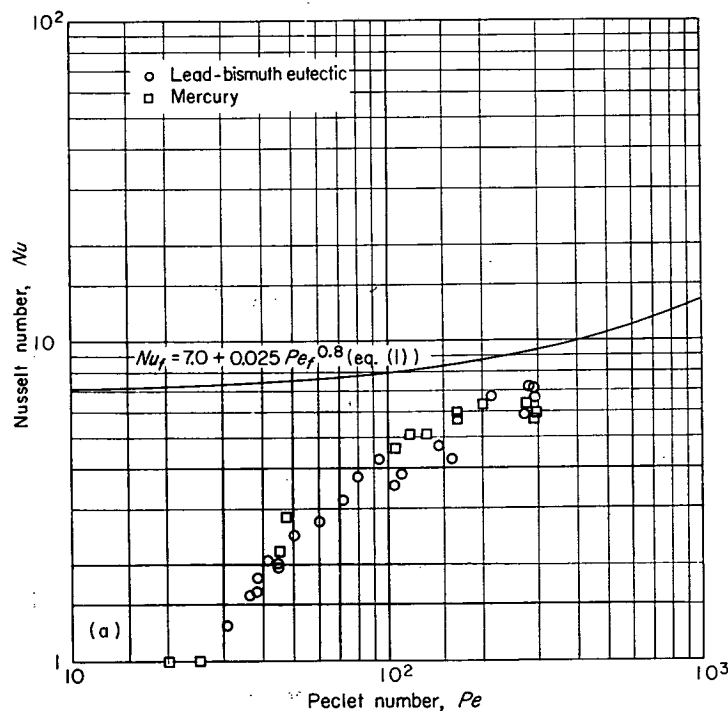


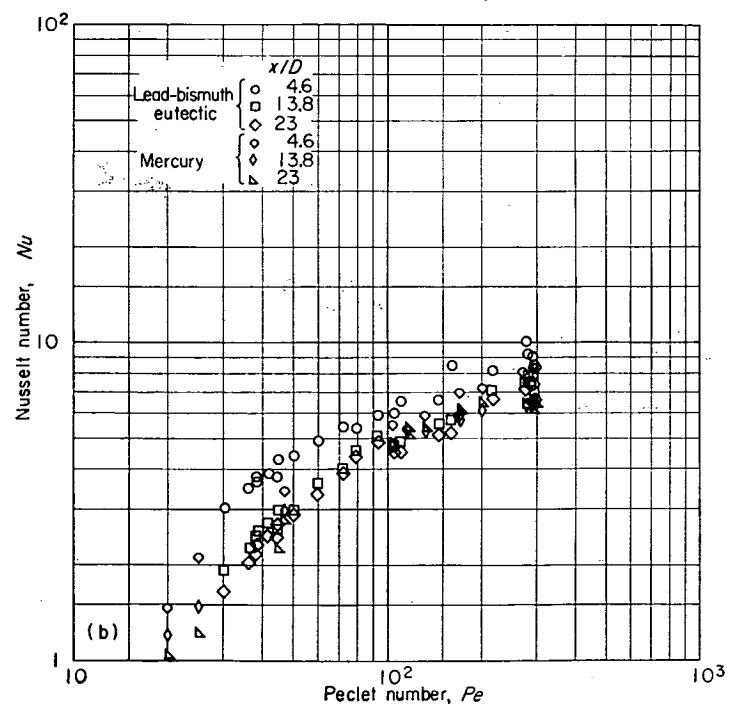
FIGURE 40.—Data of Poppendiek and Harrison (ref. 26) for average heat transfer to mercury in very short round tubes.

efficients, both fully developed and entrance, were measured.

The physical properties used by Johnson, Hartnett, and Clabaugh are the same as those of reference 28. The fully developed heat-transfer coefficients are shown in figure 39(a); equation (1) is shown for comparison. The entrance-region heat-transfer coefficients are shown in figure 39(b). There has been no theoretical work on entrance-region heat transfer in the transition flow region; therefore no curves can be shown for purposes of comparison.



(a) Fully developed heat transfer.



(b) Entrance-region heat transfer.

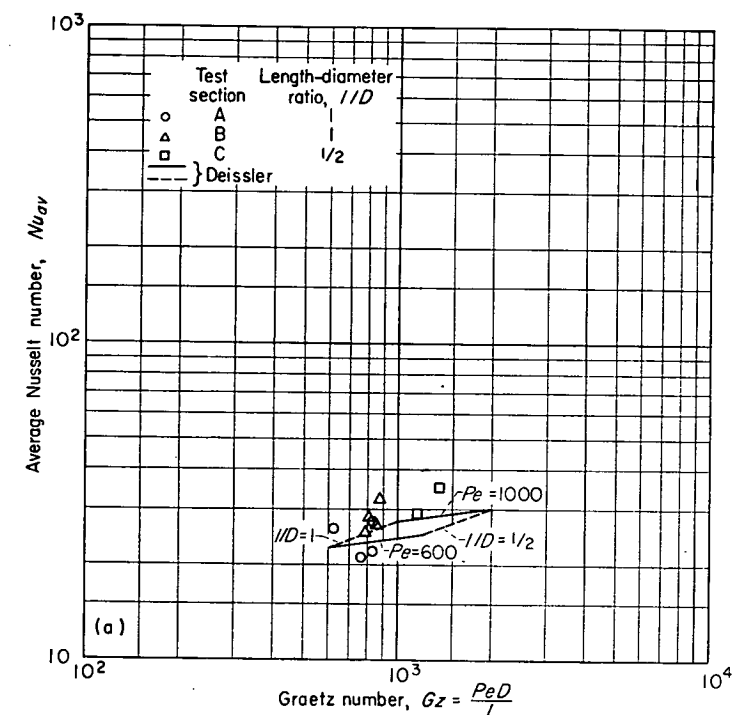
FIGURE 39.—Data of Johnson, Hartnett, and Clabaugh (ref. 25) for heat transfer to lead-bismuth eutectic and mercury in round tubes in laminar and transition flow regions.

Poppendiek and Harrison.—Poppendiek and Harrison (ref. 26) have measured average heating coefficients with mercury in very short test sections. The test section was a small hole along the axis of a copper disk of 3-inch outer diameter heated on the outside with water. An unheated starting length was used so that the entrance velocity profile was very close to fully developed. Three different test sections were used:

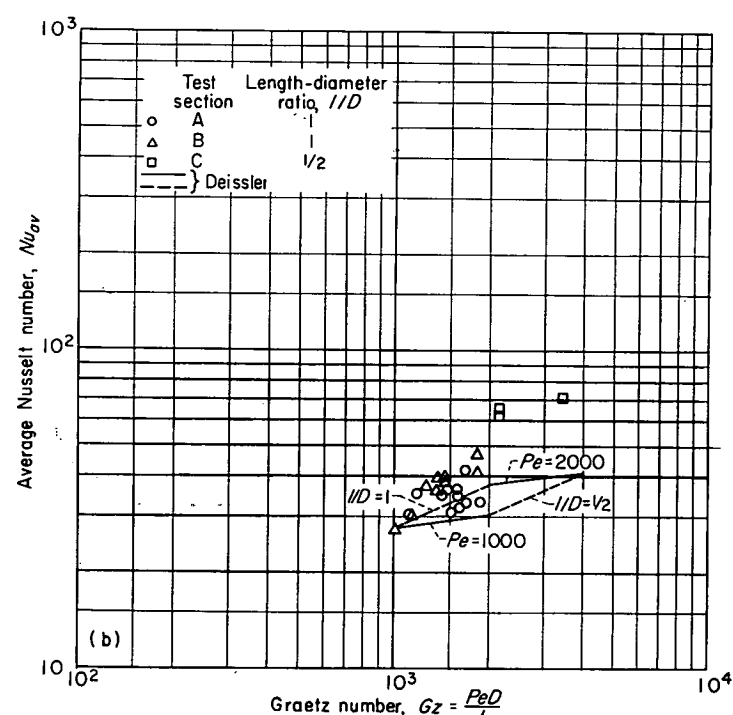
Test section	A	B	C
Inner diameter, D_i , in.....	$\frac{1}{8}$	$\frac{1}{16}$	$\frac{1}{8}$
Length, l , in.....	$\frac{1}{8}$	$\frac{1}{16}$	$\frac{1}{8}$

The fluid bulk temperatures of the mercury were measured at the inlet and outlet of the test section. Wall temperatures were measured at several radial stations in the test section. The method of heating approximated constant wall temperature.

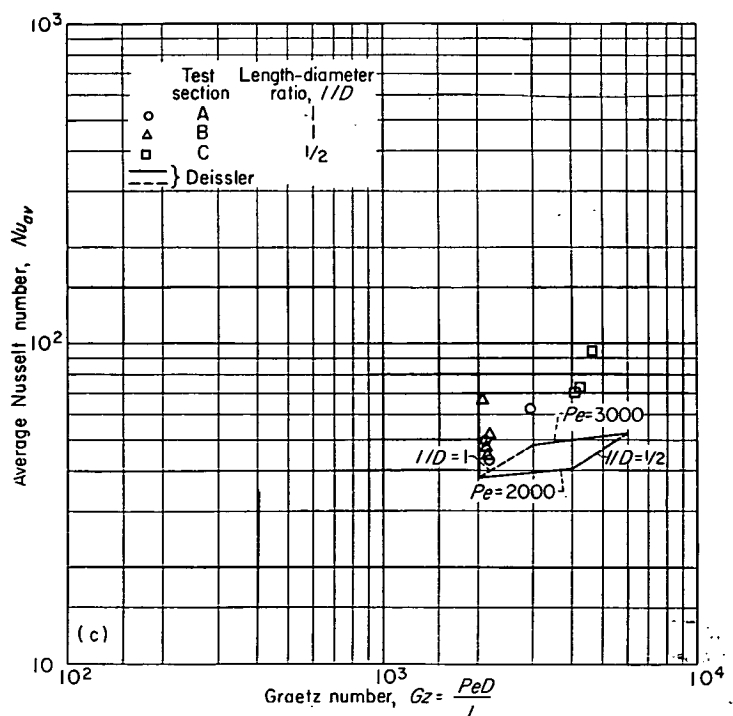
The properties used by Poppendiek and Harrison are the same as those of reference 28. The over-all average heat-transfer coefficients are shown in figure 40. Also shown is a predicted curve of Poppendiek and Harrison (ref. 26) for average coefficients. They obtained the curve by integrating the local coefficients predicted by Poppendiek and Palmer for low Peclet numbers (fig. 3).



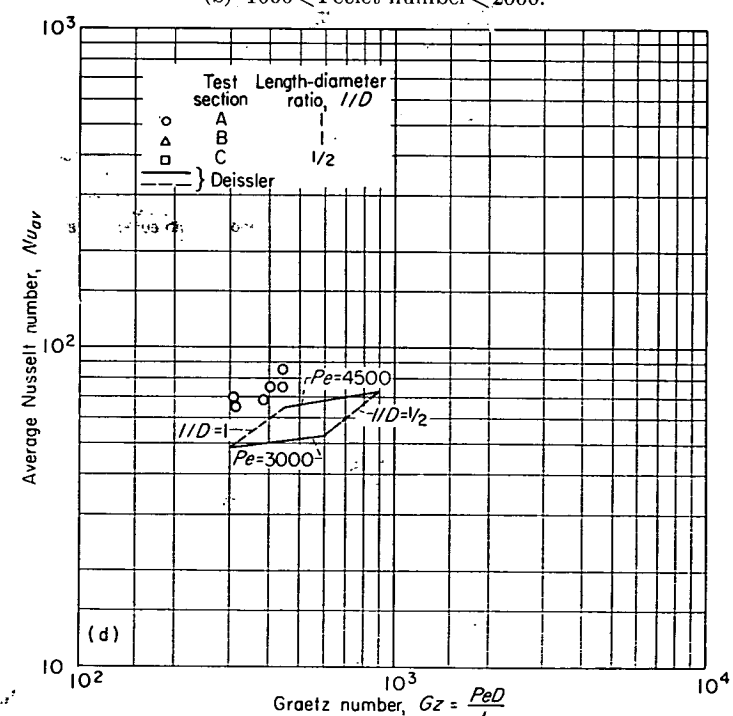
(a) $600 < \text{Peclet number} < 1000$.



(b) $1000 < \text{Peclet number} < 2000$.

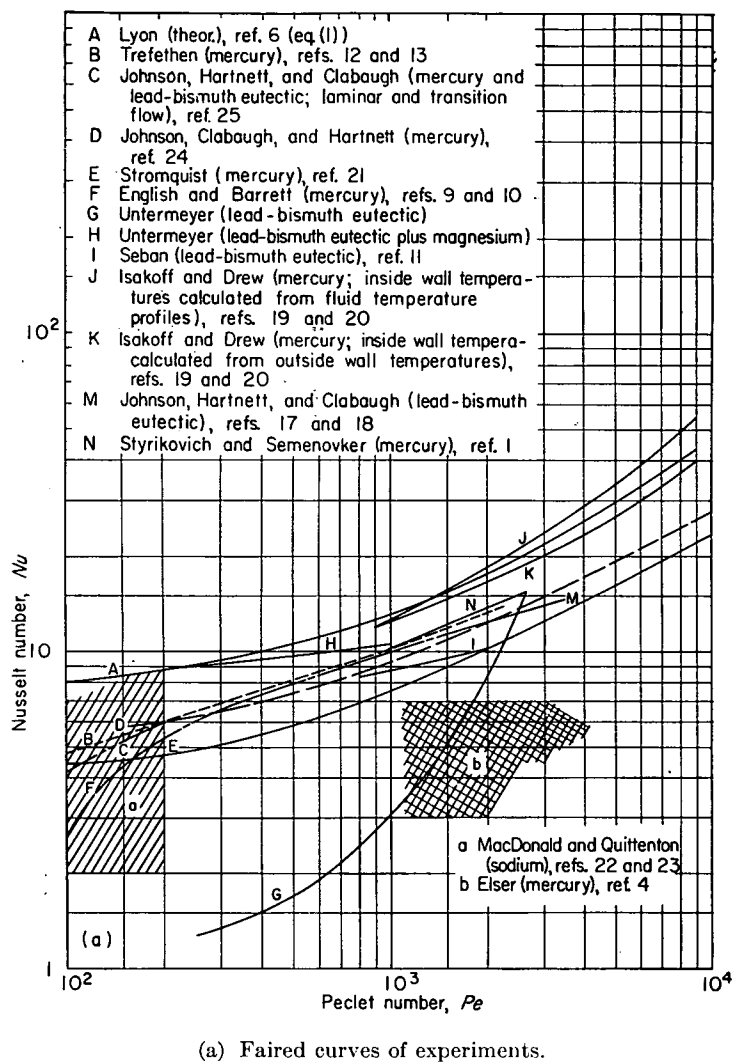


(c) $2000 < \text{Peclet number} < 3000$.



(d) $3000 < \text{Peclet number} < 4500$.

FIGURE 41.—Data of Poppendiek and Harrison (ref. 26) for average heat transfer to mercury in very short round tubes compared with predictions of Deissler (ref. 37).



So that the data could be compared with the predictions of Deissler (fig. 3), the local heat-transfer predictions of Deissler were integrated to obtain predictions for average Nusselt number for short length-diameter ratios. In figure 41 the data of Poppendiek and Harrison for average Nusselt number are compared with the predictions of Deissler for the average Nusselt number for small length-diameter ratios.

INTERCOMPARISON OF EXPERIMENTAL RESULTS AND COMPARISON WITH THEORY

The experimental results of the various investigators will be compared with each other and with theoretical predictions. The arrangement of the subjects to be considered will be the same as in the section Theoretical Investigations of Liquid-Metal Heat Transfer.

Fully developed heat-transfer coefficients.—Fully developed heat-transfer coefficients for the case of uniform heat input to the wall were measured by the following investigators from the group of 20 investigations reviewed: Styrikovich and Semenovker; Elser; Untermeyer; English and Barrett; Seban; Trefethen; Johnson, Hartnett, and Clabaugh (lead-bismuth tests); Isakoff and Drew; Stromquist; MacDonald and Quittenton; Johnson, Clabaugh, and Hartnett (mercury); and Johnson, Hartnett, and Clabaugh (laminar and transition flow). Curves representing mean lines through the data of these various investigators are shown in figure 42(a); when the amount of scatter of a set of data is so great that no mean line can be drawn through it, a cross-hatched area is used to represent the data; equation (1) is shown in figure 42(a) for purposes of comparison. The spread of all the data in figure 42(a) is extremely great. However, the following data are not considered:

- (1) Data below a Peclet number of 200: These data, being

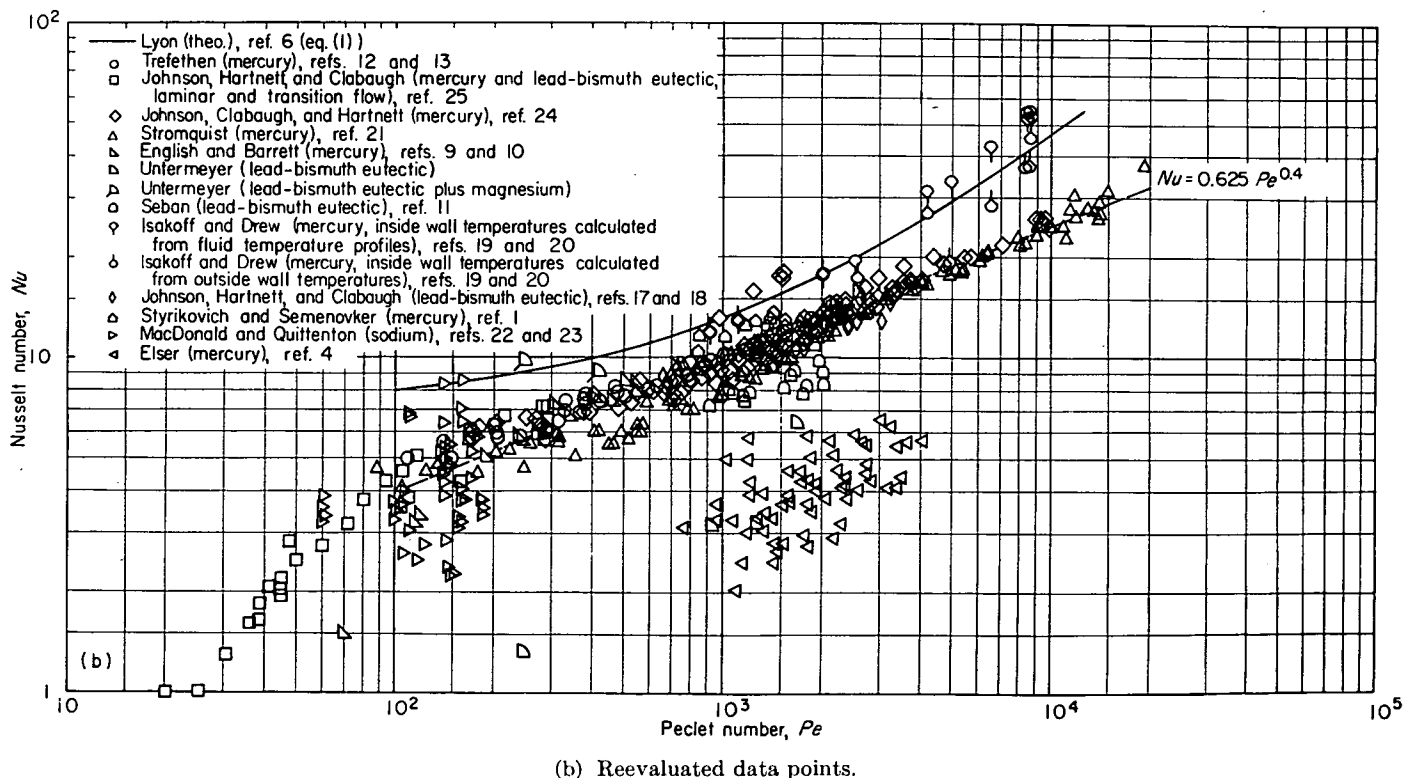


FIGURE 42.—Comparison of measured and predicted fully developed Nusselt numbers in round tubes with constant heat input to wall.

below a Reynolds number of 10,000 and therefore in the transition flow region, are not intended to be represented by equation (1).

(2) Data of Elser, and MacDonald and Quittenton: These are less reliable because of the very large scatter of the data.

(3) Data of Untermeyer: Severe corrosion throughout the duration of the tests caused large changes in the physical dimensions of the test section, as well as possibly contaminating the fluid and the heat-transfer surface.

The Nusselt number of the remaining data can be compared with the predicted values of equation (1) as follows:

Peclet number, Pe	200	500	1000	2000	5000	9000
Range of ratio of measured values to predicted values.	0.54 to 0.69	0.55 to 0.75	0.57 to 0.96	0.57 to 1.04	0.55 to 1.13	0.50 to 1.26

Another method of comparing the data for the fully developed heat transfer is to show on a single plot the actual corrected data of all the investigators (fig. 42(b)). If the same data are considered valid in this figure as in figure 42(a), a line given by the following equation would best represent most of the data:

$$Nu = 0.625 Pe^{0.4} \quad (14)$$

This equation is purely empirical and does not in any way suggest that the theoretical predictions are faulty. However, inasmuch as there is a considerable amount of scatter and since most of the data agree fairly well with this line, it would seem preferable for the designer to use equation (14) until further experiment reduces the uncertainty as to the precise values of liquid-metal heat-transfer coefficients.

Local heat-transfer coefficients in entrance region.—Entrance-region heat-transfer coefficients have been measured by the following investigators from the group of 20 investigations reviewed: English and Barrett; Seban; Johnson, Hartnett, and Clabaugh (lead-bismuth eutectic); Isakoff and Drew; Stromquist; Johnson, Clabaugh, and Hartnett (mercury); Johnson, Hartnett, and Clabaugh (laminar and transition flow); and Poppendiek and Harrison. The bulk of the data on heat transfer in the entrance region is in the reports of Johnson, Hartnett, and Clabaugh (lead-bismuth eutectic); Stromquist; Johnson, Clabaugh, and Hartnett (mercury); and Poppendiek and Harrison; and is presented in figures 26, 34, 37, and 41.

There is considerable scatter in most of the entrance heat-transfer data presented. The predictions of Deissler (fig. 3) agree well with the data of Stromquist (fig. 34), but fall slightly low when compared with the remaining data (figs. 26, 37, and 41).

English and Barrett, Seban, and Isakoff and Drew present a small amount of entrance-region heat-transfer data. As may be seen from figure 18, the data of English and Barrett are considerably lower than the predictions of Deissler. The data of Seban (fig. 20) agree reasonably well with the predictions of Deissler. The data of Isakoff and Drew (fig. 30) are considerably higher than the predictions of Deissler, which may be, in part, due to the fact that the entrance velocity profile of Isakoff and Drew was very

nearly flat, while in the analyses of Deissler a fully developed velocity profile was assumed at the entrance.

Average heat-transfer coefficients.—Theoretical predictions of the over-all average heat-transfer coefficient can be made from the information on local heat-transfer coefficients. The predictions of Deissler for the ratio Nu_f/Nu_x were integrated mechanically, and the values of the ratio of average Nusselt number to fully developed Nusselt number Nu_{av}/Nu_f are shown plotted against length-diameter ratio x/D for various Peclet numbers in figure 43.

Values of average Nusselt number were determined from the values of the ratio Nu_{av}/Nu_f in figure 43 and the values of fully developed Nusselt number Nu_f of equation (1). The results are shown in figure 44, which gives the variation of average Nusselt number with Peclet number for several length-diameter ratios.

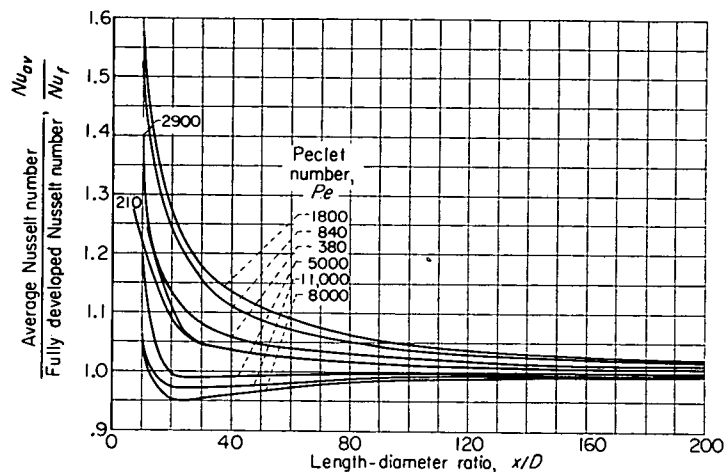


FIGURE 43.—Predictions of Deissler (ref. 37) for variation of ratio of average Nusselt number to fully developed Nusselt number with length-diameter ratio for various Peclet numbers (Prandtl number, 0.01).

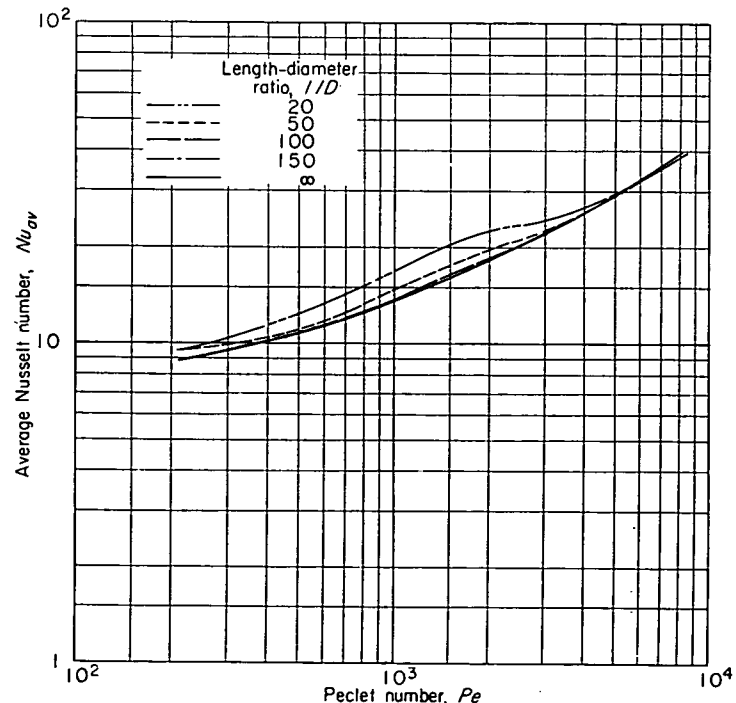


FIGURE 44.—Variation of average Nusselt number with Peclet number for several length-diameter ratios as determined from figure 43 and equation (1).

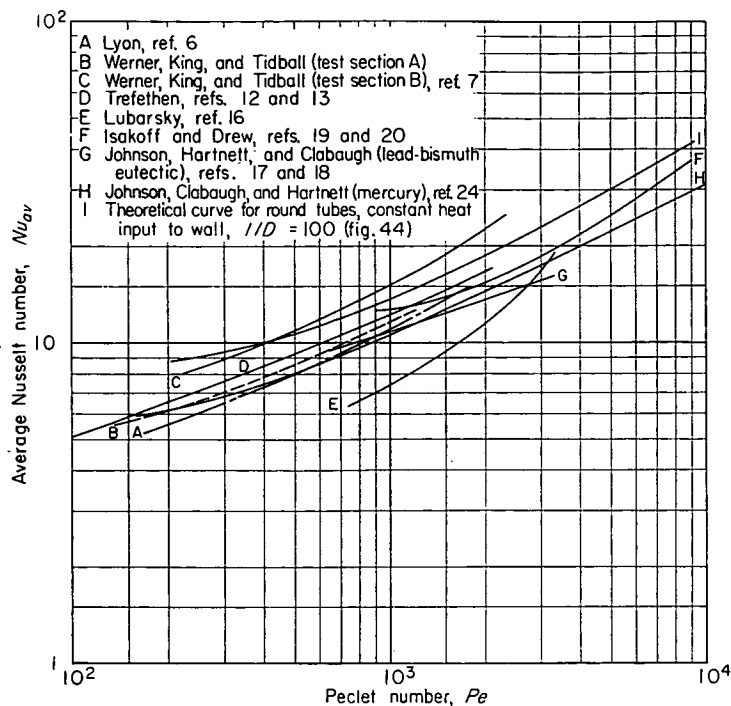


FIGURE 45.—Comparison of measured and predicted average Nusselt numbers in round tubes with uniform heat input to wall.

The measured average heat-transfer coefficients are described as follows:

(1) Uniform heat input to the wall; round tubes: Average heat-transfer coefficients in round tubes with constant heat input to the walls were measured by Lyon; Werner, King, and Tidball; Trefethen; Lubarsky; Johnson, Hartnett, and Clabaugh (lead-bismuth); Isakoff and Drew; and Johnson, Clabaugh, and Hartnett (mercury). Curves representing mean lines through the data of these various investigators are shown in figure 45. Also shown is the relation for average Nusselt number ($l/D=100$) from figure 44. The Nusselt numbers of the data compare with the predicted values for a length-diameter ratio of 100 as follows (values below a Peclet number of 200 are not considered because they fall in the transition flow region):

Peclet number, Pe	200	500	1000	2000	5000	9000
Range of ratio of measured values to predicted values.	0.64 to 0.88	0.75 to 1.03	0.54 to 1.10	0.61 to 1.21	0.75 to 0.83	0.70 to 0.88

(2) Uniform wall temperature; round tubes: Average heat-transfer coefficients in round tubes with uniform wall temperatures or with wall conditions somewhere between uniform wall temperature and uniform heat input were measured by Gilliland, Musser, and Page; and by Doody and Younger. In figure 46 are curves representing mean lines through the data of Gilliland, Musser, and Page; the data of Doody and Younger are represented by a cross-hatched area because of scatter. Also shown in figure 46 are the relations for average Nusselt number ($l/D=100$) calculated from equations (1) and (2) and figure 44. The following data are not considered:

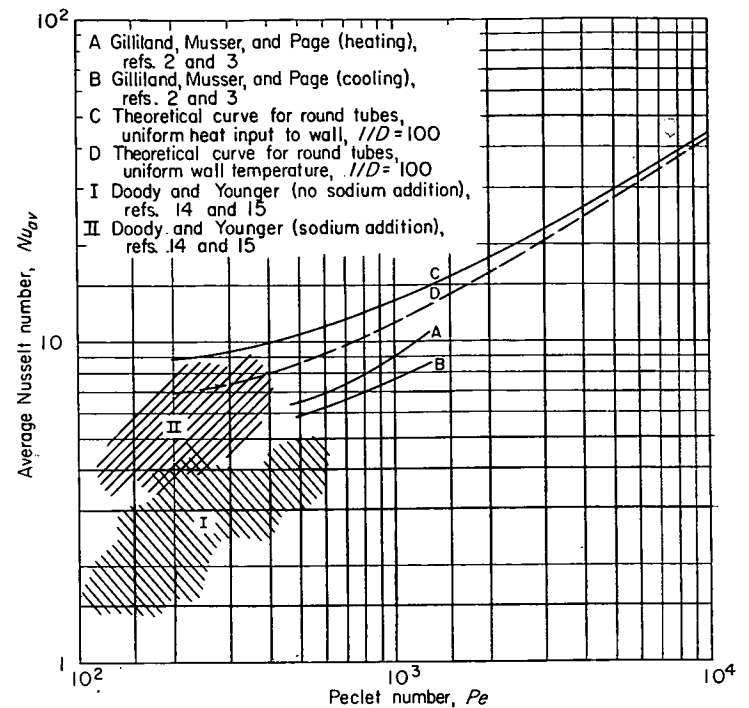


FIGURE 46.—Comparison of measured and predicted average Nusselt numbers in round tubes with uniform wall temperature or with a wall condition somewhere between uniform wall temperature and uniform heat input.

(a) Data below a Peclet number of 200: These data are in the transition flow region.

(b) Data of Doody and Younger: The scatter is large.

The Nusselt number of the remaining data can be compared with the predicted values for an l/D of 100 as follows (values of Nusselt number halfway between the values of the two theoretical curves in fig. 46 will be used for comparison):

Peclet number, Pe	500	1000
Range of ratio of measured values to predicted values.....	0.63 to 0.69	0.61 to 0.72

(3) Annuli: Average heat-transfer coefficients in annuli or between flat plates with constant heat input to the wall were measured by Lyon; Werner, King, and Tidball; Sineath; Trefethen; and Lubarsky. Figure 47 shows curves representing mean lines through the data of these various investigators; also shown are the relations for average Nusselt number ($l/D=100$) calculated from equations (4) and (5) and figure 44. The Nusselt numbers of the data compare with the predicted Nusselt numbers (average of the Nusselt numbers of the two theoretical curves of fig. 47) as follows (values below a Peclet number of 200 are not considered because they fall in the transition flow region):

Peclet number, Pe	200	500	1000
Range of ratio of measured values to predicted values.	0.69 to 1.21	0.39 to 1.37	0.39 to 0.67

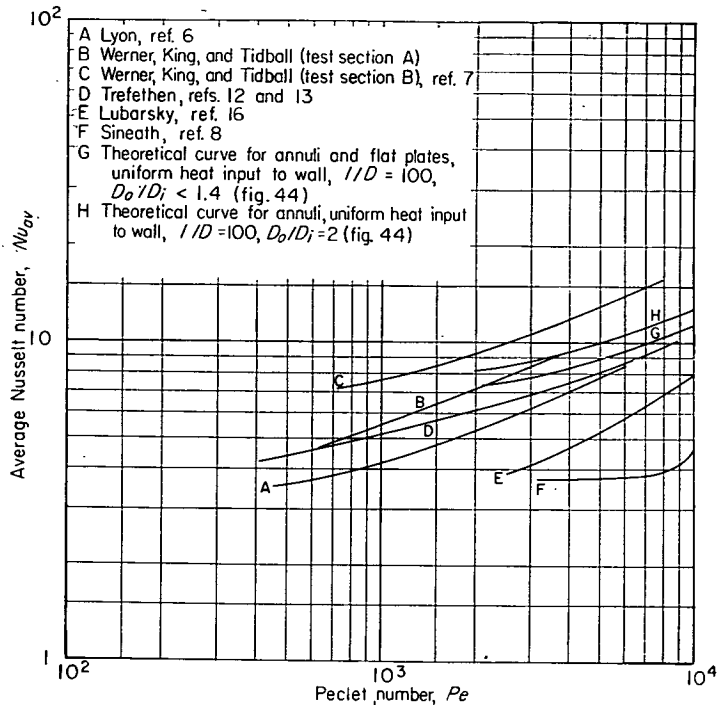


FIGURE 47.—Comparison of measured and predicted average Nusselt numbers in annuli and between flat plates with uniform heat input to wall.

Temperature distribution.—The only experimental data on temperature distribution are those of Isakoff and Drew. Plots of the temperature distributions measured by them are shown in figure 32; Martinelli's predicted temperature distributions are shown for comparison. It is possible to use Isakoff and Drew's temperature and velocity profiles (the measured velocity profiles check quite well with the predicted velocity profiles) to calculate the values of the ratio $(t_w - t_m)/(t_w - t_c)$ shown in figure 48. Martinelli's predictions (fig. 5) for the ratio $(t_w - t_m)/(t_w - t_c)$ are also shown. The measured values are smaller than the predicted values. The predicted values of Martinelli for $(t_w - t_m)/(t_w - t_c)$ were used to calculate the fluid bulk temperature in those cases in which fluid centerline temperature was measured (Elser; Doody and Younger; Werner, King, and Tidball (test section A)). If the values of $(t_w - t_m)/(t_w - t_c)$ are actually lower than predicted by Martinelli, the Nusselt numbers of these cases would increase.

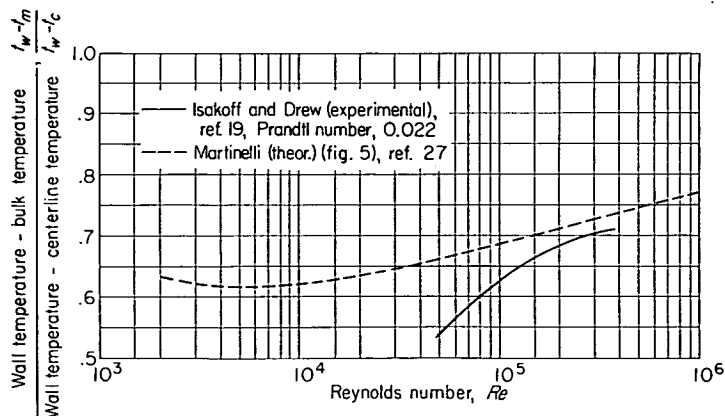


FIGURE 48.—Comparison of measured and predicted values of ratio $(t_w - t_m)/(t_w - t_c)$ in round tubes with uniform heat input to wall.

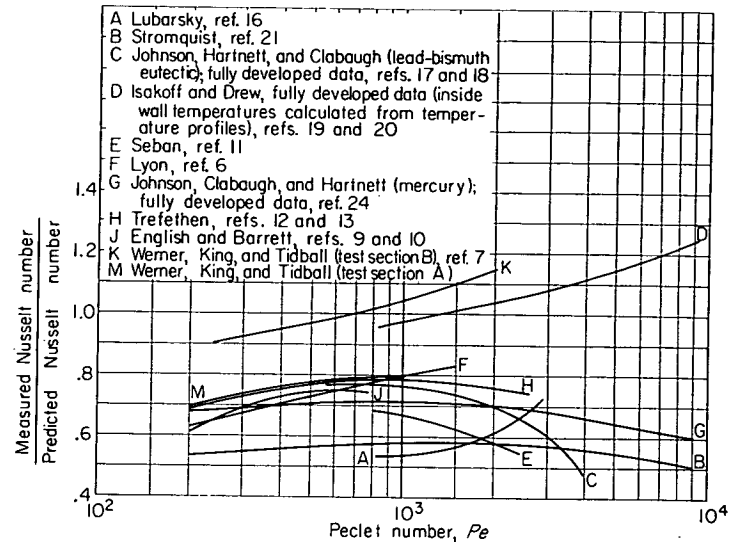


FIGURE 49.—Variation of ratio of measured Nusselt number to predicted Nusselt number with Peclet number.

Final comparison of heat-transfer data.—The experimental data of all the investigators for fully developed and average heat-transfer coefficients have been compared with the appropriate prediction, and the results are shown in table I.

The variation of the ratio of measured to predicted Nusselt number with Peclet number is shown in figure 49 for some of the data of table I. The results which are not shown in figure 49 were not included for the following reasons:

- (1) There is large scatter of data.
- (2) Obvious uncertainties exist as to the accuracy of the data.
- (3) The measurements are of average heat-transfer coefficients which were made concurrently with the measurements of fully developed coefficients; the fully developed coefficients are shown in figure 49.
- (4) The measurements are of annulus heat-transfer coefficients which were made concurrently with the measurements of round-tube coefficients; the round-tube coefficients are shown in figure 49.

On the basis of the results shown in table I and figure 49, it can be seen that most of the measured values of fully developed and average Nusselt numbers for turbulent flow (as given by eqs. (1), (2), (4), and (5) and fig. 43) fall between 60 to 80 percent of their predicted values.

SUGGESTED EXPERIMENTAL WORK

It is suggested that the type of experiment most likely to reduce the uncertainties with respect to liquid-metal heat transfer would be one in which velocity and temperature profiles were measured in the fluid, somewhat like the experiment of Isakoff and Drew. The experiment of Isakoff and Drew could be improved by the use of a thick, high-conductivity metallic coating around the test section similar to the one used by Seban or Johnson, Hartnett, and Clabaugh; this would probably eliminate the uncertainties in the measurements of outside wall temperature.

The experimental data are insufficient to lead to any conclusion concerning liquid-metal heat transfer in the laminar

and transition flow regions. Such data are greatly needed, because the small amount of data in these flow regions disagrees considerably with theoretical predictions.

SUMMARY OF RESULTS

The review of the experimental investigations of liquid-metal heat transfer may be summarized as follows:

1. The experimental data of the various investigators were reevaluated using assumptions and methods as consistent as possible, and the results were compared with each other and with theoretical values.

2. The reevaluated experimental data for fully developed Nusselt number in the turbulent-flow region were found still to have considerable spread, and most of the data are lower than predicted theoretically.

3. An equation based on empirical grounds, which best represents most of the fully developed heat-transfer data, is

$$Nu = 0.625 Pe^{0.4}$$

where Nu and Pe represent Nusselt number and Peclet number, respectively.

4. The theoretical predictions of heat transfer in the entrance region were found to give lower values, in most cases, than those found in the experimental work.

5. Integrating the theoretical and experimental results for the ratio Nu_x/Nu_f gave predictions for the value of the ratio Nu_{ax}/Nu_f over a range of Peclet number and length-diameter ratio.

6. The small amount of data on temperature distribution disagreed with the theoretical predictions, the discrepancy increasing with decreasing Reynolds number.

7. The experimental evidence is insufficient to lead to any conclusion about liquid-metal heat transfer in the laminar and transition flow regions.

LEWIS FLIGHT PROPULSION LABORATORY

NATIONAL ADVISORY COMMITTEE FOR AERONAUTICS

CLEVELAND, OHIO, November 4, 1954

REFERENCES

1. Styrikovich, M. A., and Semenovker, I. E.: Heat Exchange at Very Low Prandtl Numbers. *Jour. Tech. Phys. (USSR)*, vol. X, no. 16, 1940, pp. 1324-1330.
2. Gilliland, E. R., Musser, R. J., and Page, W. R.: Heat Transfer to Mercury. General Discussion on Heat Transfer, *Inst. Mech. Eng. and A. S. M. E.*, 1951, pp. 402-404.
3. Musser, R. J., and Page, W. R.: Heat Transfer to Mercury. M. S. Thesis, M. I. T., 1947.
4. Elser, D. (Ronald Kay, trans.): Heat Transfer Measurements with Mercury. *Eng. Res. Proj.*, Univ. Calif., May 10, 1949.
5. Bailey, D. L. R., Cope, W. F., and Watson, G. G.: Heat Transfer to Mercury. *Heat Div. Paper No. 13*, Mech. Eng. Res. Lab., East Kilbride (Glasgow), July 1952.
6. Lyon, Richard N.: Forced Convection Heat Transfer Theory and Experiments with Liquid Metals. ORNL 361, Tech. Div., Eng. Res. Section, Oak Ridge Nat. Lab., Apr. 1949. (Contract No. W-7405, eng. 26.)
7. Werner, Robert C., King, Earle C., and Tidball, Robert A.: Heat Transfer with Sodium-Potassium Liquid Alloys. Paper presented at meeting of Am. Inst. Chem. Eng., Pittsburgh (Penn.), Dec. 5, 1949.
8. Sineath, Henry H.: Heat Transfer to Mercury—The Asymmetric Case. M. S. Thesis, Univ. of Tenn., 1949.
9. English, D., and Barrett, T.: Heat Transfer Properties of Mercury. A. E. R. E. E/R 547, Atomic Energy Res. Est., Ministry of Supply, Harwell, Berks, June 1950.
10. English, D., and Barrett, T.: Heat-transfer Properties of Mercury. General Discussion of Heat Transfer, *Inst. Mech. Eng. and A. S. M. E.*, 1951, pp. 458-460.
11. Seban, R. A.: Heat Transfer Measurements on Lead Bismuth Eutectic in Turbulent Pipe Flow. *Inst. Eng. Res.*, Univ. Calif., June 15, 1950. (Contract N7-onr-29523, Phase (2), Proj. NR 035 324.)
12. Trefethen, Lloyd MacGregor: Heat Transfer Properties of Liquid Metals. NP 1788, Tech. Info. Service, United States Atomic Energy Comm., July 1, 1950.
13. Trefethen, Lloyd M.: Liquid Metal Heat Transfer in Circular Tubes and Annuli. General Discussion on Heat Transfer, *Inst. Mech. Eng. and A. S. M. E.*, 1951, pp. 436-438.
14. Doody, T. C., and Younger, Andrew H.: Heat Transfer Coefficients for Liquid Mercury and Dilute Solutions of Sodium in Mercury in Forced Convection. Preprints of papers presented at meeting of Am. Inst. Chem. Eng., Atlantic City (New Jersey), Dec. 5, 1951, pp. 77-98.
15. Younger, A. H.: Heat Transfer for Liquid Mercury and Dilute Solutions of Sodium in Mercury. Doctoral Thesis, Purdue Univ., Jan. 1951.
16. Lubarsky, Bernard: Experimental Investigation of Forced-Convection Heat-Transfer Characteristics of Lead-Bismuth Eutectic. NACA RM E51G02, 1951.
17. Johnson, H. A., Hartnett, J. P., and Clabaugh, W. J.: Heat Transfer to Molten Lead-Bismuth Eutectic in Turbulent Pipe Flow. Final Rep., Univ. Calif., *Inst. Eng. Res.*, Nov. 15, 1951. (Contract A. E. C. No. AT-(40-1)-1061 Pt. 2.)
18. Johnson, H. A., Hartnett, J. P., and Clabaugh, W. J.: Heat Transfer to Molten Lead-Bismuth Eutectic in Turbulent Pipe Flow. *Trans. A. S. M. E.*, vol. 75, no. 6, Aug. 1953, pp. 1191-1198.
19. Isakoff, Sheldon E., and Drew, Thomas B.: Heat and Momentum Transfer in Turbulent Flow of Mercury. General Discussion on Heat Transfer, *Inst. Mech. Eng. and A. S. M. E.*, 1951, pp. 405-409.
20. Isakoff, Sheldon E.: Heat and Momentum Transfer in Turbulent Flow of Mercury. Ph. D. Thesis, Columbia Univ., May 1952.
21. Stromquist, W. K.: Effect of Wetting on Heat Transfer Characteristics of Liquid Metals. ORO-93, Tech. Info. Service, U. S. Atomic Energy Commission, Mar. 1953. (Contract No. AT-(40-1)-1310.)
22. MacDonald, W. C., and Quittenton, R. C.: A Critical Analysis of Metal "Wetting" and Gas Entrainment in Heat Transfer to Molten Metals. Preprint No. 8, Am. Inst. Chem. Eng., 1953.
23. Quittenton, Richard Charles: The Direct Measurement of the Film Coefficient of Heat Transfer to Molten Sodium Metal in Forced Convection. Ph. D. Thesis, Univ. of Toronto, 1953.
24. Johnson, H. A., Clabaugh, W. J., and Hartnett, J. P.: Heat Transfer to Mercury in Turbulent Pipe Flow. *Inst. Eng. Res.*, Univ. Calif., July 1953. (Contract AT-11-1-GEN 10, Proj. 5, Phase II.)
25. Johnson, H. A., Hartnett, J. P., and Clabaugh, W. J.: Heat Transfer to Lead-Bismuth and Mercury in Laminar and Transition Pipe Flow. *Inst. Eng. Res.*, Univ. Calif., Aug. 1953. (Contract AT-11-1-GEN 10, Proj. 5, Phase II.)
26. Poppendiek, H. F., and Harrison, W. B.: Remarks on Thermal Entrance-Region Heat Transfer in Liquid-Metal Systems. Preprint No. 7, Am. Inst. Chem. Eng., 1953.
27. Martinelli, R. C.: Heat Transfer to Molten Metals. *Trans. A. S. M. E.*, vol. 69, no. 8, Nov. 1947, pp. 947-959.
28. Lyon, Richard N., ed.: Liquid-Metals Handbook. Second ed., Atomic Energy Comm., Dept. Navy, June 1952.
29. Cope, W. F.: Heat Transfer to Mercury. General Discussion on Heat Transfer, *Inst. Mech. Eng. and A. S. M. E.*, 1951, pp. 453-458.

30. Kennison, R. G.: Vorticity Heat Transfer in Molten Metals. Knolls Atomic Power Lab., General Electric Co., Apr. 11, 1952.
31. Deissler, Robert G.: Analysis of Fully Developed Turbulent Heat Transfer at Low Peclet Numbers in Smooth Tubes with Application to Liquid Metals. NACA RM E52F05, 1952.
32. Seban, R. A., and Shimazaki, T. T.: Heat Transfer to a Fluid Flowing Turbulently in a Smooth Pipe with Walls at Constant Temperature. Paper No. 50-A-128, A. S. M. E., 1950.
33. Seban, R. A.: Heat Transfer to a Fluid Flowing Turbulently Between Parallel Walls with Asymmetric Wall Temperatures. Trans. A. S. M. E., vol. 72, no. 6, Aug. 1950, pp. 789-795.
34. Bailey, Raymond V.: Heat Transfer to Liquid Metals in Concentric Annuli. ORNL 521, Tech. Div., Eng. Res. Section, Oak Ridge Nat. Lab., June 13, 1950. (Contract No. W-7405, eng. 26.)
35. Poppendiek, H. F.: Forced Convection Heat Transfer in Thermal Entrance Regions, pt. I. ORNL 913, Reactor Tech. Div., Oak Ridge Nat. Lab., Mar. 1951. (Contract No. W-7405, eng. 26.)
36. Poppendiek, H. F., and Palmer, L. D.: Forced Convection Heat Transfer in Thermal Entrance Regions, pt. II. ORNL 914, Reactor Exp. Eng. Div., Oak Ridge Nat. Lab., May 26, 1952. (Contract No. W-7405, eng. 26.)
37. Deissler, Robert G.: Analysis of Turbulent Heat Transfer and Flow in Entrance Regions of Smooth Passages. NACA TN 3016, 1953.
38. Seban, R. A., and Shimazaki, T.: Calculations Relative to the Thermal Entry Length for Fluids of Low Prandtl Number. Inst. Eng. Res., Univ. Calif., Jan. 10, 1950. (Contract No. N7-onr-29523, Phase (2), NR 035 324.)
39. McAdams, William H.: Heat Transmission. Second ed., McGraw-Hill Book Co., Inc., 1942.
40. Harrison, W. B., and Menke, J. R.: Heat Transfer to Liquid Metals Flowing in Asymmetrically Heated Channels. Trans. A. S. M. E., vol. 71, no. 7, Oct. 1949, pp. 797-803.
41. Sherwood, T. K., and Petrie, J. M.: Heat Transmission to Liquids Flowing in Pipes. Ind. and Eng. Chem., vol. 24, no. 7, July 1932, pp. 736-745.

TABLE I.—COMPARISON OF HEAT-TRANSFER DATA

Investigation	Ref.	Type of heat-transfer coefficient measured	Theoretical eq. used for comparison	Ratio of measured Nusselt number to predicted Nusselt number for Peclet number of—			
				200	500	1000	2000
Styrikovich and Semenovker.	1	Round tube, fully developed, uniform heat input.	$Nu_f = 7.0 + 0.025 Pe_f^{0.5}$ -----	--	--	0.80	0.77
Gilliland, Musser, and Page (heating data).	2, 3	Round tube, over-all av., uniform wall temperature.	$Nu_f = 5.0 + 0.025 Pe_f^{0.5}$, * corrected for $l/D = 44$.	--	0.69	0.72	--
Gilliland, Musser, and Page (cooling data).	2, 3	Round tube, over-all av., between uniform heat input and uniform wall temperature.	$Nu_f = 6.0 + 0.025 Pe_f^{0.5}$, (av. of eqs. (1) and (2)), corrected for $l/D = 160$.	--	0.63	0.61	--
Elser -----	4	Round tube, fully developed, uniform heat input.	$Nu_f = 7.0 + 0.025 Pe_f^{0.5}$ -----	--	--	--	0.17 .40
Bailey, Cope, and Watson.	5	Round tube, fully developed, between uniform heat input and uniform wall temperature	$Nu_f = 6.0 + 0.025 Pe_f^{0.5}$, (av. of eqs. (1) and (2)).	0.36	0.46	0.39	0.35
Lyon (tube data) -----	6	Round tube, over-all av., uniform heat input.	$Nu_f = 7.0 + 0.025 Pe_f^{0.5}$, corrected for $l/D = 110$.	0.63	0.72	0.80	--
Lyon (annulus data) -----	6	Annulus, over-all av., uniform heat input.	$Nu_{f,an} = 5.8 + 0.020 Pe_{f,an}^{0.5}$, corrected for $l/D = 225$.	0.74	0.90	--	--
Untermeyer (without magnesium additions).	---	Round tube, fully developed, uniform heat input.	$Nu_f = 7.0 + 0.025 Pe_f^{0.5}$ -----	--	0.16	0.23	0.48
Untermeyer (with magnesium additions).	---	Round tube, fully developed, uniform heat input.	$Nu_f = 7.0 + 0.025 Pe_f^{0.5}$ -----	--	0.92	0.80	--
Werner and King (heat exchanger A, tube data).	---	Round tube, over-all av., uniform heat input.	$Nu_f = 7.0 + 0.025 Pe_f^{0.5}$, corrected for $l/D = 49$.	0.69	0.76	0.79	--
Werner and King (heat exchanger A, annulus data).	---	Annulus, over-all av., uniform heat input.	$Nu_{f,an} = 0.75(D_o/D_i)^{0.3} \times (7.0 + 0.025 Pe_{f,an}^{0.5})$, $D_o/D_i = 1.83$, corrected for $l/D = 55$.	0.90	--	--	--
Werner, King, and Tidball (heat exchanger B, tube data).	7	Round tube, over-all av., uniform heat input.	$Nu_f = 7.0 + 0.025 Pe_f^{0.5}$, corrected for $l/D = 49$.	--	0.97	1.04	1.14
Werner, King, and Tidball (heat exchanger B, annulus data).	7	Annulus, over-all av., uniform heat input.	$Nu_{f,an} = 0.75(D_o/D_i)^{0.3} \times (7.0 + 0.025 Pe_{f,an}^{0.5})$, $D_o/D_i = 1.83$, corrected for $l/D = 55$.	1.15	1.29	--	--
Sineath -----	8	Rectangular ducts, over-all av., uniform heat input.	$Nu_f = 5.8 + 0.020 Pe_{f,an}^{0.5}$, corrected for $l/D = 50$.	--	0.41	0.40	--
English and Barrett.	9, 10	Round tube, fully developed, uniform heat input.	$Nu_f = 7.0 + 0.025 Pe_f^{0.5}$ -----	0.61	0.74	--	--
Seban -----	11	Round tube, fully developed, uniform heat input.	$Nu_f = 7.0 + 0.025 Pe_f^{0.5}$ -----	--	--	0.67	0.58
Trefethen (fully developed tube data).	12, 13	Round tube, fully developed, uniform heat input.	$Nu_f = 7.0 + 0.025 Pe_f^{0.5}$ -----	0.68	0.77	0.78	0.76
Trefethen (over-all average tube data).	12, 13	Round tube, over-all av., uniform heat input.	$Nu_f = 7.0 + 0.025 Pe_f^{0.5}$, corrected for $l/D = 65$.	0.74	0.83	0.86	0.87

* "Corrected for l/D " means that the fully developed Nusselt number found from the eq. was multiplied by the ratio Nu_{av}/Nu_f from fig. 43.

TABLE I. COMPARISON OF HEAT-TRANSFER DATA—Concluded

Investigation	Ref.	Type of heat-transfer coefficient measured	Theoretical eq. used for comparison	Ratio of measured Nusselt number to predicted Nusselt number for Peclet number of—					
				200	500	1000	2000	5000	9000
Trefethen (over-all average annulus data).	12, 13	Annulus, over-all av., uniform heat input.	Average of $Nu_f = 5.8 + 0.020 Pe_f^{0.8}$ and $Nu_f = 0.75 (D_o/D_i)^{0.3} (7.0 + 0.025 Pe_{f,an}^{0.8})$, $\frac{D_o}{D_i} = 2$, corrected for $l/D = 200$.	0.81	0.87	--	--	--	--
Doody and Younger (data with no sodium additions).	14, 15	Round tube, over-all av., between uniform heat input and uniform wall temperature.	$Nu_f = 6.0 + 0.025 Pe_f^{0.8}$, (average of eqs. (1) and (2)), corrected for $l/D = 114$.	0.22 .51	0.33 .53	--	--	--	--
Doody and Younger (data with sodium additions).	14, 15	Round tube, over-all av., between uniform heat input and uniform wall temperature.	$Nu_f = 6.0 + 0.025 Pe_f^{0.8}$, (average of eqs. (1) and (2)), corrected for $l/D = 114$.	0.50 .92	--	--	--	--	--
Lubarsky (tube data)----	16	Round tube, over-all av., uniform heat input.	$Nu_f = 7.0 + 0.025 Pe_f^{0.8}$, corrected for $l/D = 100$.	--	--	0.54	0.61	--	--
Lubarsky (annulus data)	16	Annulus, overall av., uniform heat input.	$Nu_{f,an} = 5.8 + 0.020 Pe_{f,an}^{0.8}$, corrected for $l/D = 320$.	--	0.59	0.72	--	--	--
Johnson, Hartnett, and Clabaugh (lead-bismuth eutectic, fully developed data).	17, 18	Round tube, fully developed, uniform heat input.	$Nu_f = 7.0 + 0.025 Pe_f^{0.8}$ -----	--	--	0.76	0.70	--	--
Johnson, Hartnett, and Clabaugh (lead-bismuth eutectic, over-all average data).	17, 18	Round tube, over-all av., uniform heat input.	$Nu_f = 7.0 + 0.025 Pe_f^{0.8}$, corrected for $l/D = 74$.	--	--	0.77	0.72	--	--
Isakoff and Drew (fully developed data, inside wall temperature calculated from fluid temperature profile).	19, 20	Round tube, fully developed, uniform heat input.	$Nu_f = 7.0 - 0.025 Pe_f^{0.8}$ -----	--	--	0.97	1.05	1.14	1.25
Isakoff and Drew (fully developed data, inside wall temperature calculated from outside wall temperature).	19, 20	Round tube, fully developed, uniform heat input.	$Nu_f = 7.0 + 0.025 Pe_f^{0.8}$ -----	--	--	0.95	0.94	0.90	0.91
Isakoff and Drew (over-all average data, inside wall temperature calculated from outside wall temperature).	19, 20	Round tube, over-all av., uniform heat input.	$Nu_f = 7.0 + 0.025 Pe_f^{0.8}$, corrected for $l/D = 138$.	--	--	0.93	0.84	0.84	0.86
Stromquist-----	21	Round tube, fully developed, uniform heat input.	$Nu_f = 7.0 + 0.025 Pe_f^{0.8}$ -----	0.54	0.55	0.57	0.58	0.54	0.51
MacDonald and Quitten-ton.	22, 23	Round tube, fully developed, uniform heat input.	$Nu_f = 7.0 + 0.025 Pe_f^{0.8}$ -----	1.0 .26	--	--	--	--	--
Johnson, Clabaugh, and Hartnett (mercury, fully developed data).	24	Round tube, fully developed, uniform heat input.	$Nu_f = 7.0 + 0.025 Pe_f^{0.8}$ -----	0.68	0.70	0.71	0.70	0.65	0.60
Johnson, Clabaugh, and Hartnett (mercury, over-all average data).	24	Round tube, over-all av., uniform heat input.	$Nu_f = 7.0 + 0.025 Pe_f^{0.8}$, corrected for $l/D = 74$.	0.70	0.73	0.75	0.76	0.76	0.69
Johnson, Hartnett and Clabaugh (laminar and transition flow).	25	Round tube, fully developed, uniform heat input.	$Nu_f = 7.0 + 0.025 Pe_f^{0.8}$ -----	0.68	--	--	--	--	--

REPORT 1271

ON BOATTAIL BODIES OF REVOLUTION HAVING MINIMUM WAVE DRAG¹

By KEITH C. HARDER and CONRAD RENNEMANN, JR.

SUMMARY

The problem of determining the shape of slender boattail bodies of revolution for minimum wave drag has been reexamined. It was found that minimum solutions for Ward's slender-body drag equation can exist only for the restricted class of bodies for which the rate of change of cross-sectional area at the base is zero. In order to eliminate this restriction, certain higher order terms must be retained in the drag equation and isoperimetric relations. The minimum problem for the isoperimetric conditions of given length, volume, and base area is treated as an example. According to Ward's drag equation, the resulting body shapes have slightly less drag than those determined by previous investigators.

INTRODUCTION

An approximate expression for the wave drag of slender bodies of revolution having zero rate of change of cross-sectional area at the base was first given by Von Kármán (ref. 1). By using this expression, together with the calculus of variations, several investigators (refs. 1 to 3) have determined minimum-wave-drag bodies for various isoperimetric conditions. Later, Ward (ref. 4) derived the slender-body approximation for the drag of bodies with a nonzero rate of change of cross-sectional area at the base.

In reference 5, Adams considered several minimum-wave-drag problems on the basis of Ward's equation. In each case he concluded that the minimum-drag body had zero slope at the base. This conclusion implied that the minimum shapes for Ward's equation are the same as those for Von Kármán's. Recently, Parker (ref. 6) presented a different expression for the wave drag of slender bodies and showed that the optimum body having given length and base area has a finite slope at the base. Clearly, this result is not in agreement with that obtained by Adams.

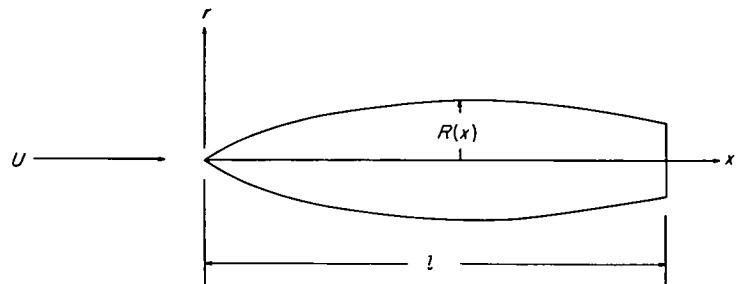
In the present report, the problem of determining minimum-drag boattail bodies of revolution on the basis of linear theory is reexamined with particular emphasis on the choice of drag equation, isoperimetric relations, and method of calculating the body shape. The minimum problem for the isoperimetric conditions of given length, volume, and base area is treated as an example.

DISCUSSION OF MINIMUM-WAVE-DRAG PROBLEM

Within the approximations of linear theory, the supersonic flow past slender bodies of revolution can be represented by a distribution of sources along the axis of the body. The wave drag D of the body may be related to the source distribution (ref. 1) by

$$\frac{4\pi D}{\rho U^2} = - \int_0^l \int_0^l f'(x)f'(\xi) \log_e |x-\xi| dx d\xi \quad (1)$$

provided the source distribution $f(x)$ is zero at the nose and the base (i. e., $f(0)=f(l)=0$) where ρ is the stream density and U is the stream velocity. The coordinate system is shown in the following sketch:



In the slender-body approximation, the source strength is related to the body cross-sectional-area distribution $A(x)$ by

$$f(x) = \frac{dA}{dx} = 2\pi R(x)R'(x) \quad (2)$$

and the restriction that $f(l)=0$ implies that either the body is closed ($R(l)=0$) or that the body has zero slope at the base ($R'(l)=0$).

Several investigators (refs. 1 to 3) have determined minimum-wave-drag bodies for various isoperimetric conditions by applying the calculus of variations to equation (1). However, as a result of the restriction that $f(l)=0$, these shapes can be considered optimum only for the restricted class of bodies having zero rate of change of cross-sectional area at the base.

¹ Supersedes NACA Technical Note 3478 by Keith C. Harder and Conrad Rennemann, Jr., 1955.

WARD'S DRAG EQUATION

An equation which does not have the restriction that $f(l)=0$ was proposed by Ward (ref. 4) on the basis of slender-body theory as

$$\frac{4\pi D}{\rho U^2} = - \int_0^l \int_0^l f''(x)f''(\xi) \log_e |x-\xi| dx d\xi + 2f(l) \int_0^l f''(\xi) \log_e (l-\xi) d\xi - f^2(l) \log_e \frac{\beta R(l)}{2} \quad (3)$$

where $\beta = \sqrt{M^2 - 1}$ and M is the Mach number. The source strength is again related to the body geometry by equation (2).

The problem of determining the source distribution which minimizes the drag given by equation (3) for given isoperimetric conditions without specifying the value of $f(l)$ at the outset is a variable end-point problem of the calculus of variations. In appendix A this problem is considered for a general type of isoperimetric condition where it is shown that, if a mathematical minimum exists, it satisfies the condition $f(l)=0$. The significance of the mathematical solution obtained by the variational procedure warrants further consideration since the variational procedure assumes the existence of a solution at the outset and, consequently, can lead only to necessary conditions for the attainment of an extremum. Three mutually exclusive possibilities must be considered:

(1) A minimum for Ward's equation exists for the class of bodies having all values of the slope at the base and satisfies the condition $f(l)=0$.

(2) A minimum for Ward's equation exists only for the restricted class of bodies for which $f(l)=0$.

(3) No minimum exists for Ward's equation.

A single example, not satisfying the condition $f(l)=0$ but having less drag than the shape obtained by the variational procedure, is sufficient to eliminate the first possibility. Perhaps the simplest example is the cone which, for given length and base area, has less drag than the variational minimum (Von Kármán's ogive) for $\beta \frac{R(l)}{l} \geq 0.164$. However, a more illuminating example is given by the body

$$A(x) = \frac{A(l)}{l + \epsilon \log_e \frac{\epsilon}{l'}} \left[x + (l' - x) \log_e \left(1 - \frac{x}{l'} \right) \right] \quad (0 \leq x \leq l) \quad (4)$$

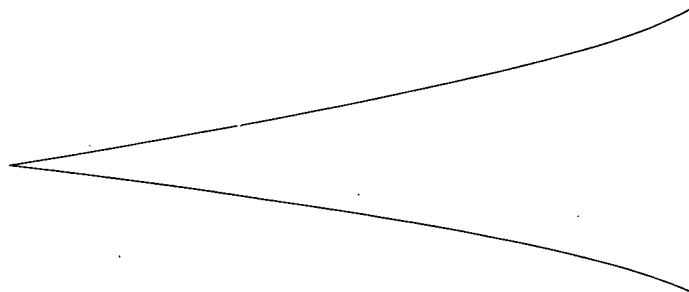
where $A(l)$ is the base area, $l' = l + \epsilon$, and ϵ is a parameter related to the slope at the base $R'(l)$ by

$$R'(l) = \frac{R(l) \log_e \frac{l'}{\epsilon}}{2 \left(l + \epsilon \log_e \frac{\epsilon}{l'} \right)}$$

For this body, Ward's equation (eq. (3)) gives the result that, for small ϵ ,

$$\frac{4\pi D}{\rho U^2} = - \left[\frac{A(l)}{l + \epsilon \log_e \frac{\epsilon}{l'}} \right]^2 \left(\log_e \frac{\epsilon}{l'} \right)^2 \left\{ \log_e \left[\frac{\beta R(l)}{2l'} \left(\frac{l'}{\epsilon} \right)^{\frac{2}{3}} \right] + O \left(\frac{\epsilon/l'}{\log_e \frac{\epsilon}{l'}} \right) \right\}$$

which approaches minus infinity as ϵ approaches zero; that is, as the slope and curvature at the base both approach infinity. (The mathematical symbol $O(\)$ denotes the order of a function.) The body shape for $\epsilon=0$ is shown in the following sketch:



In order to decide between the second and third possibilities, it would be necessary to prove the existence or non-existence of a minimum solution for Von Kármán's drag equation (eq. (1)). Such a study is beyond the scope of the present report; however, it should be noted that the minimum solutions obtained for Von Kármán's equation have provided a useful guide in the search for low-drag shapes. It is in this same vein that, later in the report, minimum problems are considered on the basis of a different drag equation. Since existence proofs are not attempted, the most that can be claimed is that, if a solution exists, it must have a certain mathematical form. However, in order to avoid the repetition of this qualifying remark in the remainder of the report, solutions obtained by the calculus of variations are referred to as minimum solutions.

The problem under discussion has been previously considered by Adams (ref. 5) who correctly determined the necessary conditions for a minimum. His interpretation of these conditions was that the optimum boattail body has zero rate of change of cross-sectional area at the base. However, the proper interpretation is that, if a minimum exists, it exists only for the restricted class of bodies having zero rate of change of cross-sectional area at the base.

PARKER'S DRAG EQUATION

From the preceding discussion, it is clear that Ward's drag equation (eq. (3)) cannot be used to determine minimum-drag boattail bodies.² Parker (ref. 6) has shown that application of the calculus of variations to the drag equation

$$\frac{4\pi D}{\rho U^2} = \int_0^{1-\beta R(l)} \int_0^{1-\beta R(l)} f'(\xi) f'(x) \cosh^{-1} \left| \frac{(l-\xi)(l-x) - \beta^2 R^2(l)}{\beta R(l)(x-\xi)} \right| dx d\xi \quad (5)$$

which he obtained on the basis of linear theory, yields a minimum without the restriction that $f(l)=0$ for the isoperimetric conditions of given length and base area. The body shape so determined has a finite slope at the base and less drag than the mathematical minimum for equation (3).

Equation (5) contains some higher order terms which are not included in the slender-body approximation to the drag (eq. (3)) since Parker did not make the slender-body approximation to the velocity potential in the derivation. Apparently, the additional terms are necessary in order to obtain minimum-drag shapes without the restriction that $f(l)=0$. However, it should not be inferred that equation (5) necessarily gives a better estimate of the drag of bodies satisfying the assumptions of slender-body theory than equation (3). Lighthill (ref. 8) has shown that the slender-body equations (eqs. (2) and (3)) are fully as accurate as the linearized differential equations of motion for sufficiently smooth bodies. Consequently, the slender-body results are theoretically equivalent to those obtained without making the slender-body approximation.

ISOPERIMETRIC CONDITIONS

The isoperimetric conditions most commonly considered have been those of fixed length, volume, and base area. In order to carry out the mathematical details of determining the source strength which minimizes the drag, the isoperimetric conditions must be directly related to the source strength. The simplest relations would appear to be those given by slender-body theory. However, in order to carry out the analysis on the basis of Parker's equation, certain higher order terms must be retained in the isoperimetric relations. In particular, the limits of integration in the isoperimetric relations must be the same as those in the drag equation. Furthermore, the analysis can sometimes be simplified by including certain additional higher order terms in the integrand of the isoperimetric relations.

The relation between the isoperimetric conditions and source strength used in the example to be treated in the present report is obtained by approximately satisfying the boundary conditions on a cone passing through the nose

² Essentially the same arguments can be used to show that Lighthill's drag equation (ref. 7), which was derived for slender shapes with discontinuities in slope, cannot be used to determine minimum-drag bodies with corners.

and base. The linear-theory expression for $A'(x)$ is

$$A'(x) = \int_0^{x-\beta r} \frac{(x-\xi) f'(\xi) d\xi}{\sqrt{(x-\xi)^2 - \beta^2 r^2}} \quad (6)$$

where r is on the body surface. Equation (6) is approximately satisfied by evaluating the integral on the cone $r=R(l) \frac{x}{l}$. Then,

$$A'(x) \approx \int_0^{x \left[1 - \beta \frac{R(l)}{l} \right]} \frac{(x-\xi) f'(\xi) d\xi}{\sqrt{(x-\xi)^2 - \beta^2 \frac{R^2(l)}{l^2} x^2}} \quad (7)$$

from which, with $\delta = \beta \frac{R(l)}{l}$,

$$A(x) \approx \int_0^{x(1-\delta)} f'(\xi) \sqrt{(x-\xi)^2 - \delta^2 x^2} d\xi$$

and

$$A(l) \approx \int_0^{l(1-\delta)} f'(\xi) \sqrt{(l-\xi)^2 - \delta^2 l^2} d\xi \quad (8)$$

where use has been made of the condition $f(0)=0$. Similarly, the volume V is given approximately by

$$V \approx \frac{1}{2} \int_0^{l(1-\delta)} (l-\xi) f'(\xi) \sqrt{(l-\xi)^2 - \delta^2 l^2} d\xi \quad (9)$$

In the derivation of equations (8) and (9) from equation (7), terms of the order of $\delta^2 \log \delta$ have been neglected. The slender-body approximation to the isoperimetric relations is obtained by equating δ to zero in equations (8) and (9).

CALCULATION OF BODY SHAPE

When the calculus of variations is applied to the drag equation and isoperimetric relations, the resulting source strength for minimum drag contains several constants to be determined from the isoperimetric conditions. The calculation of these constants and the body shape can be treated independently of the minimization process.

Since higher order terms have been retained in the drag equation and isoperimetric relations, the question arises as to whether similar terms should be retained in the body-shape calculation. Theoretically, the inclusion of these terms does not affect the accuracy of the result for shapes satisfying the assumptions of slender-body theory. Even so, it is interesting to compare the various body shapes obtained from the source distribution

$$f(\xi) = K \sqrt{\xi[l + \beta R(l) - \xi]} \quad (10)$$

found by Parker to give minimum drag for the isoperimetric conditions of given length and base area. In equation (10), K is a constant to be determined from the isoperimetric

conditions. The numerical value of K depends on the method used to calculate the body shape.

Parker calculated the body shape from this source distribution without making the slender-body approximation by numerically solving the integral equation

$$\pi R^2(x) = \int_0^{x-\beta R(x)} f'(\xi) \sqrt{(x-\xi)^2 - \beta^2 R^2(x)} d\xi \quad (11)$$

The body shape calculated from equation (10) by means of the slender-body expression $A'(x) = f(x)$ is

$$A(x) = \frac{Kl^2}{2(1+c)^2} [t\sqrt{1-t^2} + \cos^{-1}(-t)] \quad (-1 \leq t \leq c) \quad (12)$$

where

$$\frac{x}{l} = \frac{1+t}{1+c}, \quad \frac{Kl^2}{2(1+c)^2} = \frac{A(l)}{c\sqrt{1-c^2} + \cos^{-1}(-c)}, \quad \text{and} \quad c = \frac{l-\beta R(l)}{l+\beta R(l)}.$$

When the expression $A'(x) = f(x)$ is altered to take partially into account the fact that a given point on the body is influenced only by sources in the upstream Mach cone by equating

$$\frac{dA(x)}{dx} = f\left(x \left[1 - \beta \frac{R(l)}{l}\right]\right) \quad (13)$$

the body shape is given by

$$A(x) = \frac{l^2 K}{4c(1+c)} [t\sqrt{1-t^2} + \cos^{-1}(-t)] \quad (-1 \leq t \leq 2c-1) \quad (14)$$

where

$$t = \frac{2cx}{l} - 1$$

and

$$\frac{l^2 K}{4c(1+c)} = \frac{A(l)}{2(2c-1)\sqrt{c(1-c)} + \cos^{-1}(1-2c)}$$

The body shapes calculated by means of equations (11), (12), and (14) for $\beta \frac{R(l)}{l} = 0.2$ are compared in figure 1. The differences between the shapes are small even for this rather large value of $\beta \frac{R(l)}{l}$. For smaller values of $\beta \frac{R(l)}{l}$, the differences are even less and the shapes become coincident as $\beta \frac{R(l)}{l}$ approaches zero. Similar body-shape calculations based on

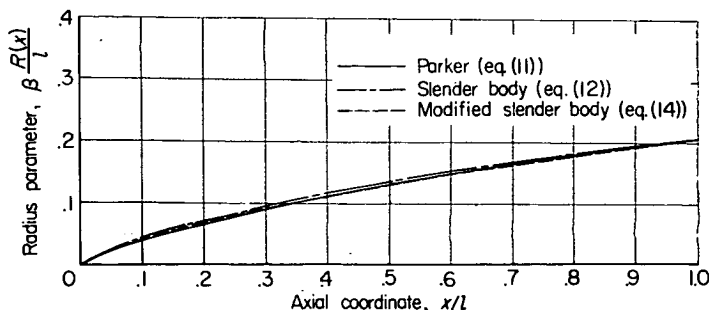


FIGURE 1.—Comparison of body shapes calculated from source distribution given by equation (10) by various methods for $\beta \frac{R(l)}{l} = 0.2$.

equations (2) and (13) for the source strength that is derived in the example (fixed volume, length, and base area) were performed for $\beta \frac{R(l)}{l} = 0.05$ and several values of $\beta^2 \frac{V}{l^3}$, where V is the volume. This comparison is not presented since the body shapes obtained by the two methods are almost identical. Evidently, the difference in body shape is appreciable only for shapes that cannot be considered slender. Consequently, the simpler slender-body relation is preferable.

The discussion concerning the inclusion of higher order terms is briefly summarized as follows: Higher order terms must be retained in the drag equation in order to obtain the minimum-drag boattail body; having done this, higher order terms must also be retained in the isoperimetric relations in order to perform the analysis. Once the source strength for minimum drag has been determined within several undetermined constants, higher order terms need not be retained in the calculation of the shape and drag of bodies satisfying the assumptions of slender-body theory.

PROBLEM OF LENGTH, VOLUME, AND BASE AREA

The problem of determining the body shape that gives minimum wave drag for fixed length, volume, and base area is treated in order to illustrate the ideas developed in the preceding sections. The minimum-drag body having given length and base area or given length and volume can be obtained as special cases of the problem under consideration.

The source distribution for minimum drag is obtained by applying the calculus of variations to equations (5), (8), and (9), and as shown in appendix B, this leads to the source distribution

$$f(\xi) = (a + b\xi)\sqrt{\xi[l - \xi + \beta R(l)]} \quad (15)$$

where a and b are constants to be determined from the isoperimetric conditions.

As discussed in the previous section, the body shape is determined on the basis of the slender-body equations. Integration of $A'(x) = f(x)$ gives

$$A(x) = \frac{l^2}{(1+c)^2} \left\{ \frac{A}{2} [t\sqrt{1-t^2} + \cos^{-1}(-t)] - \frac{B}{3} (1-t^2)^{3/2} \right\} \quad (-1 \leq t \leq c) \quad (16)$$

where

$$\frac{x}{l} = \frac{1+t}{1+c}, \quad c = \frac{l-\beta R(l)}{l+\beta R(l)}, \quad B = \frac{l+\beta R(l)}{2} b$$

and

$$A = a + \frac{l+\beta R(l)}{2} b$$

The base area is given by

$$A(l) = \frac{l^2}{(1+c)^2} \left\{ \frac{A}{2} [c\sqrt{1-c^2} + \cos^{-1}(-c)] - \frac{B}{3} (1-c^2)^{3/2} \right\} \quad (17)$$

The volume is obtained from equation (16) as

$$V = \frac{l^3}{2(1+c)^3} \left\{ A \left[c \cos^{-1}(-c) + \sqrt{1-c^2} - \frac{1}{3} (1-c^2)^{3/2} \right] - \frac{B}{4} \left[\frac{2c}{3} (1-c^2)^{3/2} + c\sqrt{1-c^2} + \cos^{-1}(-c) \right] \right\} \quad (18)$$

Equation (16) for $A(x)$ (with the use of eqs. (17) and (18)) reduces to the minimum-drag body shape given by Haack (ref. 3) and Adams (ref. 5) when $c=1$. In this case, $A(x)$ is given by

$$A(x) = \frac{A(l)}{\pi} [t\sqrt{1-t^2} + \cos^{-1}(-t)] + \frac{8}{3\pi} \left[\frac{2V}{l} - A(l) \right] (1-t^2)^{3/2} \quad (-1 \leq t \leq 1) \quad (19)$$

where

$$\frac{x}{l} = \frac{1+t}{2}$$

This body was obtained by Haack on the basis of Von Kármán's drag equation (eq. (1)) and by Adams on the basis of Ward's drag equation and is referred to in the remainder of the report as the Haack-Adams body.

The constants A and B in the equation for the body shape (eq. (16)) are determined from equations (17) and (18) in terms of l , β , $R(l)$, and V . The solution may be expressed as

$$\beta^2 A = A_1 - A_2 \beta^2 \frac{V}{l^3} \quad (20)$$

and

$$\beta^2 B = B_1 - B_2 \beta^2 \frac{V}{l^3} \quad (21)$$

where A_1 , A_2 , B_1 , and B_2 are functions of $\beta \frac{R(l)}{l}$. Values of A_1 , A_2 , B_1 , and B_2 are given in table I for values of $\beta \frac{R(l)}{l}$ between 0.01 and 0.10.

A direct comparison of the drag of the body of the present report with that of the Haack-Adams body is made on the basis of Ward's drag equation. From equation (3), the drag of the source distribution given by equation (15) is

$$\frac{D}{\rho U^2} = \frac{1}{8\pi} \frac{l^2}{(1+c)^2} \left(A^2 \{ [\cos^{-1}(-c)]^2 + 2c\sqrt{1-c^2} \cos^{-1}(-c) - (1-c^2) \} - 4AB(1-c^2)[c + \sqrt{1-c^2} \cos^{-1}(-c)] + \frac{B^2}{2} [(2-5c^2)(1-c^2) + 2c\sqrt{1-c^2}(2c^2-1)\cos^{-1}(-c) + (\cos^{-1}(-c))^2] + 2(A+Bc)^2(1-c^2) \log_e [4(1+c)] \right) \quad (22)$$

TABLE I
COEFFICIENTS OF EQUATIONS (20) AND (21)

$\beta \frac{R(l)}{l}$	$\beta^2 A = A_1 - A_2 \beta^2 \frac{V}{l^3}$ (eq. (20))		$\beta^2 B = B_1 - B_2 \beta^2 \frac{V}{l^3}$ (eq. (21))	
	A_1	A_2	B_1	B_2
0.10	0.080572	0.76164	0.26804	18.0291
.09	.064852	.66854	.21938	18.1466
.08	.050946	.57666	.17531	18.2780
.07	.038807	.48644	.13590	18.4255
.06	.028390	.39843	.10121	18.5919
.05	.019652	.31338	.071357	18.7809
.04	.012554	.23231	.046443	18.9973
.03	.0070607	.15669	.026623	19.2482
.02	.0031450	.088843	.012091	19.5439
.01	.00079066	.032849	.0031002	19.8686

The drag of the Haack-Adams body is

$$\frac{D}{\rho U^2} = \frac{2l^2}{\pi} \left\{ 9 \frac{A^2(l)}{l^4} + 32 \frac{V}{l^3} \left[\frac{V}{l^3} - \frac{A(l)}{l^2} \right] \right\} \quad (23)$$

The form of equations (20), (21), and (22) indicates that $\frac{\beta^2 D}{\rho U^2 l^2}$ is a function of $\beta^2 \frac{V}{l^3}$ and $\beta \frac{R(l)}{l}$. In figure 2, the drag of the Haack-Adams body (eq. (23)) and the drag given by equation (22) are plotted on a logarithmic scale for several values of $\beta \frac{R(l)}{l}$. To help orient the reader, several body shapes are shown for $\beta=1$, $\frac{R(l)}{l}=0.05$. The drag given by equation (22) is somewhat less than that of the Haack-Adams body for most values of $\beta^2 \frac{V}{l^3}$. For example, for $\beta \frac{R(l)}{l}=0.05$ and $\beta^2 \frac{V}{l^3}=0.01$, which represents a fuselage-type shape, the body given by equation (16) has approximately 7½ percent less drag than the Haack-Adams body. Each drag curve begins at a particular value of $\beta^2 \frac{V}{l^3} > 0$; for a given value of $\beta \frac{R(l)}{l}$, smaller values of $\beta^2 \frac{V}{l^3}$ give rise to negative body areas.

For a given value of $\beta \frac{R(l)}{l}$, the slope at the base of the body is positive for small values of $\beta^2 \frac{V}{l^3}$ and is negative for large values. The two drag curves become nearly tangent at intermediate values of $\beta^2 \frac{V}{l^3}$ for which the body slope at the base is near zero. Actually, the Haack-Adams body must have less drag for this condition since this body gives minimum drag for Ward's equation for the class of bodies which have zero slope at the base.

The value of $\beta^2 \frac{V}{l^3}$ for minimum drag is obtained, for a given value of $\beta \frac{R(l)}{l}$, by equating B to zero in equations (17) and (18). This procedure gives the optimum body having a given length and base area.

In figure 3 the body shape of the present report is compared with the Haack-Adams body for $\beta \frac{R(l)}{l}=0.05$ and $\beta^2 \frac{V}{l^3}=0.003$ and 0.02. The bodies are plotted to an expanded vertical scale (expanded 5 times) to illustrate the differences which for the most part are small. The most significant difference occurs near the base for the larger values of $\beta^2 \frac{V}{l^3}$ where the body given by equation (16) does not exhibit the reflex shape of the afterbody characteristic of the Haack-Adams body.

The effect of Mach number on body shape is illustrated in figure 4 where the optimum shapes (vertical scale enlarged 2½ times) for $\frac{R(l)}{l}=0.05$ and $\frac{V}{l^3}=0.02$ are compared for $M=\sqrt{2}$ and $M=\sqrt{5}$. The body shape of the present report exhibits a small dependence on Mach number, whereas the Haack-Adams body is independent of Mach number.

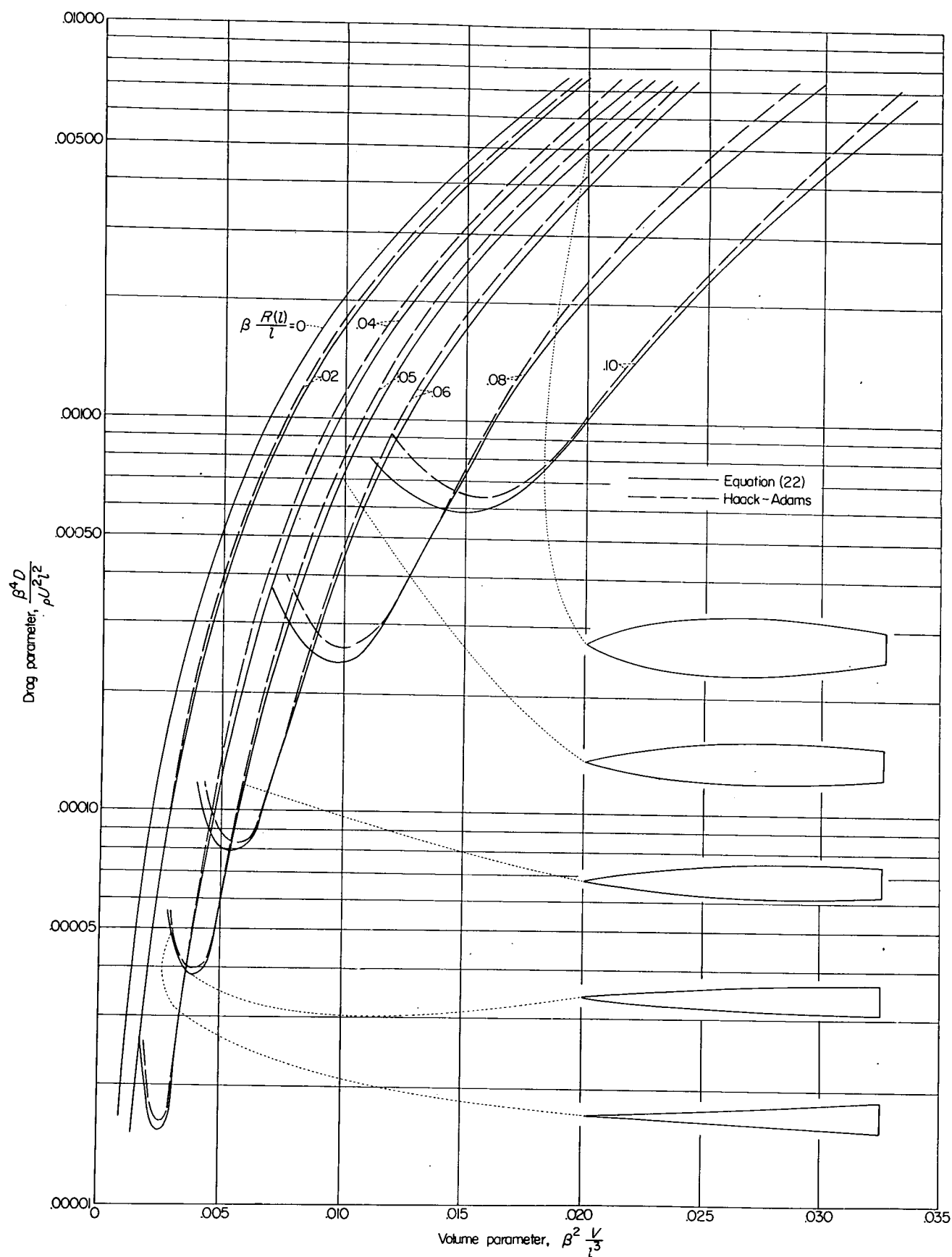


FIGURE 2.—Comparison of drag given by Ward's equation for Haack-Adams body and body given by equation (22). Body shapes shown are

$$\text{for } \beta \frac{R(l)}{l} = 0.05.$$

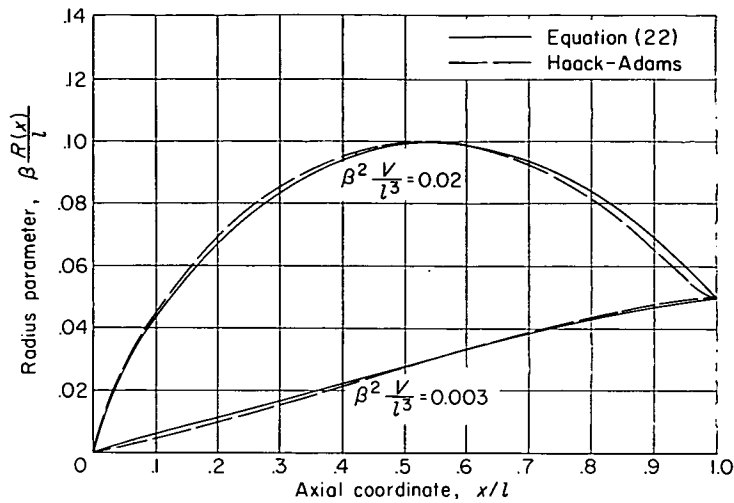


FIGURE 3.—Comparison of Haack-Adams body with that given by equation (22) for $\beta \frac{R(l)}{l} = 0.05$.

CONCLUSIONS

The problem of determining the shape of slender boattail bodies of revolution for minimum wave drag has been re-examined and the following conclusions are indicated:

1. Minimum solutions for Ward's drag equation can exist only for the restricted class of bodies for which the rate of change of cross-sectional area at the base is zero.
2. In order to eliminate this restriction, certain higher order terms must be retained in the drag equation and isoperimetric relations. However, higher order terms need not be retained in the calculation of drag and body shape from the source distribution.

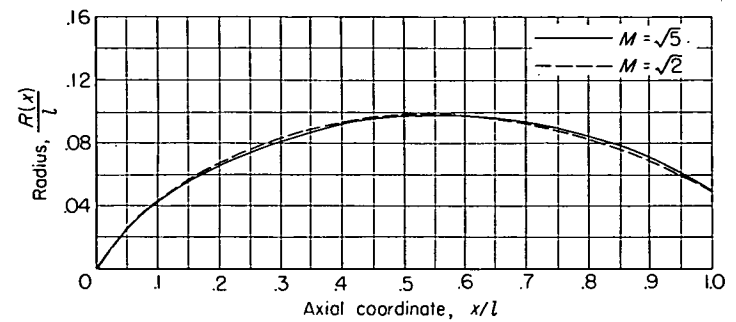


FIGURE 4.—Effect of Mach number on body shape given by equation (22) for $\beta \frac{V}{l^3} = 0.02$ and $R = \frac{R(l)}{l} = 0.05$.

3. Adams in NACA Technical Note 2550 correctly determined the necessary conditions for a minimum for Ward's drag equation. His interpretation of these conditions was that the optimum boattail body has zero rate of change of cross-sectional area at the base. However, the proper interpretation is that, if a minimum exists, it exists only for the restricted class of bodies having zero rate of change of cross-sectional area at the base.

4. Application of the ideas expressed in conclusion 2 to the minimum problem of given length, volume, and base area led to body shapes which have slightly less drag than the Haack-Adams body.

LANGLEY AERONAUTICAL LABORATORY,
NATIONAL ADVISORY COMMITTEE FOR AERONAUTICS,
LANGLEY FIELD, VA., June 8, 1955.

APPENDIX A

APPLICATION OF CALCULUS OF VARIATIONS TO WARD'S DRAG EQUATION

In this appendix the calculus of variations is applied to Ward's drag equation (eq. (3)) for a general type of isoperimetric condition to determine the source strength for minimum drag when the source strength at the base $f(l)$ is not specified at the outset. From equation (3), Ward's drag equation is

$$\frac{4\pi D}{\rho U^2} = - \int_0^l \int_0^l f'(x) f'(\xi) \log_e |x - \xi| dx d\xi + 2f(l) \int_0^l f'(\xi) \log_e (l - \xi) d\xi - f^2(l) \log_e \beta \frac{R(l)}{2} \quad (A1)$$

The usual isoperimetric conditions considered may be related to the source strength by expressions of the form

$$I_i = \int_0^l f(\xi) g_i(\xi) d\xi \quad (A2)$$

For example, $g(\xi) = 1$ for fixed base area and $g(\xi) = (l - \xi)$ for fixed volume. In the subsequent analysis, it is assumed that one of the isoperimetric conditions is that of fixed base area. This assumption simplifies the analysis without restricting its generality.

In the derivation of equation (A1) it is assumed that

$$f(0) = 0 \quad (A3)$$

Equation (A3) gives one of the end-point conditions to be satisfied by the minimizing source distribution. At the other end point, $x = l$, the value of $f(x)$ is not prescribed.

The source distribution for minimum drag is obtained by considering the variation of the function

$$J = \frac{4\pi D}{\rho U^2} + \sum \lambda_i I_i \quad (A4)$$

where the Lagrange multipliers λ_i are determined from the isoperimetric conditions. The variation of equation (A4) is obtained by considering the one-parameter family of comparison functions (see ref. 9, for example)

$$f(x) = F(x) + \epsilon \eta(x) \quad (A5)$$

where $F(x)$ is the function which minimizes equation (A4), ϵ is the parameter of the family, and $\eta(x)$ is an arbitrary function within the condition

$$\eta(0) = 0 \quad (A6)$$

This condition arises since all the comparison functions must satisfy the same end-point condition as the minimizing function. Since no end-point condition is prescribed at $x=l$, $\eta(l)$ is arbitrary.

From equations (A4) and (A5), J is a function of ϵ and the source strength for minimum drag is determined from the condition

$$\left. \frac{dJ}{d\epsilon} \right|_{\epsilon=0} = 0 = \int_0^l \eta(\xi) \left[-\frac{d}{d\xi} \int_0^l \frac{F(x)dx}{x-\xi} + \sum \frac{\lambda_i}{2} g_i(\xi) \right] d\xi + \eta(l) \left[\lim_{\xi \rightarrow l} F(l) \log_e \frac{2(l-\xi)}{\beta R(l)} \right] \quad (A7)$$

where the equation has been simplified by several integrations by parts and use of equations (A3) and (A6).

Since equation (A7) must hold for all choices of $\eta(\xi)$ consistent with equation (A6), it must in particular hold for

those choices of $\eta(\xi)$ for which $\eta(l)=0$. For such $\eta(\xi)$,

$$\int_0^l \eta(\xi) \left[-\frac{d}{d\xi} \int_0^l \frac{F(x)dx}{x-\xi} + \sum \frac{\lambda_i}{2} g_i(\xi) \right] d\xi = 0$$

and from the basic lemma of the calculus of variations (ref. 8),

$$\frac{d}{d\xi} \int_0^l \frac{F(x)dx}{x-\xi} = \sum \frac{\lambda_i}{2} g_i(\xi) \quad (A8)$$

With this result, and for general $\eta(\xi)$ once again, that is, $\eta(l)$ not necessarily equal to zero, the end-point condition obtained is that

$$\lim_{\xi \rightarrow l} \left[F(l) \log_e \frac{2(l-\xi)}{\beta R(l)} \right] = 0 \quad (A9)$$

In order to satisfy this condition, $F(l)$ must equal zero. Consequently, the body shapes which give a mathematical minimum for Ward's equation, if they exist, must have zero rate of change of cross-sectional area at the base.

APPENDIX B

APPLICATION OF CALCULUS OF VARIATIONS TO PARKER'S DRAG EQUATION

The source distribution for minimum drag for the isoperimetric condition of given length, volume, and base area is obtained by considering the variation of the function

$$J = \frac{4\pi D}{\rho U^2} + \lambda_1 A(l) + \lambda_2 V \quad (B1)$$

where D , $A(l)$, and V are given by equations (5), (8), and (9), respectively, and λ_1 and λ_2 are Lagrange multipliers. By proceeding in the same manner as in appendix A, the variation of equation (B1) is obtained by considering the one-parameter family of comparison functions.

$$f(x) = F(x) + \epsilon \eta(x) \quad (B2)$$

where $F(x)$ is the function which minimizes equation (B1), ϵ is the parameter of the family, and $\eta(x)$ is an arbitrary function within the condition $\eta(0)=0$.

The source strength for minimum drag is then determined from the condition

$$\left. \frac{dJ}{d\epsilon} \right|_{\epsilon=0} = 0 = - \int_0^{l-\beta R(l)} \eta(\xi) \frac{d}{d\xi} \left\{ 2 \int_0^{l-\beta R(l)} \frac{F(x) \sqrt{(l-\xi)^2 - \beta^2 R^2(l)}}{x-\xi \sqrt{(l-x)^2 - \beta^2 R^2(l)}} dx + \left[\lambda_1 + \frac{\lambda_2}{2} (l-\xi) \right] \sqrt{(l-\xi)^2 - \beta^2 R^2(l)} \right\} d\xi + \eta(l-\beta R(l)) \lim_{\xi \rightarrow l-\beta R(l)} \left\{ 2 \int_0^{l-\beta R(l)} \frac{F(x) \sqrt{(l-\xi)^2 - \beta^2 R^2(l)}}{x-\xi \sqrt{(l-x)^2 - \beta^2 R^2(l)}} dx + \left[\lambda_1 + \frac{\lambda_2}{2} (l-\xi) \right] \sqrt{(l-\xi)^2 - \beta^2 R^2(l)} \right\} \quad (B3)$$

where the equation has been simplified by several integrations by parts and use of the conditions

$$F(0) = \eta(0) = 0$$

Since equation (B3) must hold for all choices of $\eta(\xi)$ consistent with $\eta(0)=0$, it must in particular hold for those choices of $\eta(\xi)$ for which $\eta[l-\beta R(l)]=0$. For such $\eta(\xi)$,

$$\int_0^{l-\beta R(l)} \eta(\xi) \frac{d}{d\xi} \left\{ 2 \int_0^{l-\beta R(l)} \frac{F(x) \sqrt{(l-\xi)^2 - \beta^2 R^2(l)}}{x-\xi \sqrt{(l-x)^2 - \beta^2 R^2(l)}} dx + \left[\lambda_1 + \frac{\lambda_2}{2} (l-\xi) \right] \sqrt{(l-\xi)^2 - \beta^2 R^2(l)} \right\} d\xi = 0$$

and from the basic lemma of the calculus of variations,

$$2 \int_0^{l-\beta R(l)} \frac{F(x) \sqrt{(l-\xi)^2 - \beta^2 R^2(l)}}{x-\xi \sqrt{(l-x)^2 - \beta^2 R^2(l)}} dx + \left[\lambda_1 + \frac{\lambda_2}{2} (l-\xi) \right] \sqrt{(l-\xi)^2 - \beta^2 R^2(l)} = N \quad (B4)$$

where N is a constant. With this result, and for general $\eta(\xi)$, the end-point condition is obtained as

$$\lim_{\xi \rightarrow l - \beta R(l)} \left\{ 2 \int_0^{l - \beta R(l)} \frac{F(x) \sqrt{(l - \xi)^2 - \beta^2 R^2(l)}}{x - \xi \sqrt{(l - x)^2 - \beta^2 R^2(l)}} dx + \left[\lambda_1 + \frac{\lambda_2}{2} (l - \xi) \right] \sqrt{(l - \xi)^2 - \beta^2 R^2(l)} \right\} = 0 \quad (B5)$$

Since equation (B4) must hold for all values of ξ , and in particular for $\xi \rightarrow l - \beta R(l)$, from equation (B5), $N=0$. Hence, $\sqrt{(l - \xi)^2 - \beta^2 R^2(l)}$ can be canceled from each term of equation (B4) and the following integral equation is obtained for the source strength:

$$2 \int_0^{l - \beta R(l)} \frac{F(x)}{x - \xi} \frac{dx}{\sqrt{(l - x)^2 - \beta^2 R^2(l)}} = -\lambda_1 - \frac{\lambda_2}{2} (l - \xi) \quad (B6)$$

The solution of equation (B6) satisfying the condition $F(0) = 0$ is

$$F(\xi) = f(\xi) = (a + b\xi) \sqrt{\xi[l - \xi + \beta R(l)]} \quad (B7)$$

where a and b are constants related to λ_1 and λ_2 .

REFERENCES

1. Von Kármán, Th.: The Problem of Resistance in Compressible Fluids. *R. Accad. d'Italia, Cl. Sci. Fis., Mat. e Nat.*, vol. XIV, 1936.
2. Sears, William R.: On Projectiles of Minimum Wave Drag. *Quarterly Appl. Math.*, vol. IV, no. 4, Jan. 1947, pp. 361-366.
3. Haack, W.: Projectile Shapes for Smallest Wave Drag. Translation No. A9-T-3, Contract W33-038-ac-15004 (16351), ATI No. 27736, Air Materiel Command, U. S. Air Force, Brown Univ., 1948.
4. Ward, G. N.: Supersonic Flow Past Slender Pointed Bodies. *Quarterly Jour. Mech. and Appl. Math.*, vol. II, pt. 1, Mar. 1949, pp. 75-97.
5. Adams, Mac C.: Determination of Shapes of Boattail Bodies of Revolution for Minimum Wave Drag. NACA TN 2550, 1951.
6. Parker, Hermon M.: Minimum-Drag Ducted and Pointed Bodies of Revolution Based on Linearized Supersonic Theory. NACA Rep. 1213, 1955. (Supersedes NACA TN 3189.)
7. Lighthill, M. J.: Supersonic Flow Past Slender Bodies of Revolution the Slope of Whose Meridian Section is Discontinuous. *Quarterly Jour. Mech. and Appl. Math.*, vol. I, pt. 1, Mar. 1948, pp. 90-102.
8. Lighthill, M. J.: Supersonic Flow Past Bodies of Revolution. *R. & M. No. 2003*, British A. R. C., 1945.
9. Weinstock, Robert: *Calculus of Variations*. First ed., McGraw-Hill Book Co., Inc., 1952.

REPORT 1272

A REEVALUATION OF DATA ON ATMOSPHERIC TURBULENCE AND AIRPLANE GUST LOADS FOR APPLICATION IN SPECTRAL CALCULATIONS ¹

By HARRY PRESS, MAY T. MEADOWS, and IVAN HADLOCK

SUMMARY

The available information on the spectrum of atmospheric turbulence is first briefly reviewed. On the basis of these results, methods are developed for the conversion of available gust statistics normally given in terms of counts of gusts or acceleration peaks into a form appropriate for use in spectral calculations. The fundamental quantity for this purpose appears to be the probability distribution of the root-mean-square gust velocity. Estimates of this distribution are derived from data for a number of load histories of transport operations; also, estimates of the variation of this distribution with altitude and weather condition are derived from available data and the method of applying these results to the calculation of airplane gust-response histories in operations is also outlined.

INTRODUCTION

During the last few years, advances have been made in the analysis of airplane behavior in rough air through the application of the theory of random processes and the techniques of generalized harmonic analysis (refs. 1 to 7). The application of these techniques is based upon the representation of atmospheric turbulence as a continuous random disturbance characterized by power-spectral-density functions and certain probability distributions. The power spectrum of the turbulence is then used along with the airplane response characteristics to determine the power spectra and other statistical characteristics of the airplane loads or motions in rough air. The application of this approach to the problem of calculating load and other histories for operational flight requires detailed information on the spectrum of turbulence in the atmosphere. The information required may be considered of two types: detailed information on the spectrum of turbulence and its variations, and information on the probability of encountering the various spectra.

A few measurements of the power spectrum of atmospheric turbulence have so far been made and are briefly reviewed in the report. These measurements indicate that, over most of the frequency range of interest, the spectra are inversely proportional to the square of the frequency and may be approximated by simple analytic expressions such as have been used in wind-tunnel studies of isotropic turbulence.

Also, the intensity of the turbulence as given by the root-mean-square gust velocity varied appreciably with the weather conditions. These results thus appear to provide some information on the power spectrum and its variations. They do not, however, provide any information of the second type required, that is, information on the probability of encountering the various spectra in actual operations. The purpose of this report is to provide information of this second type, that is, information on the probabilities of encountering the various conditions of turbulence.

The only source of information on the probability of encountering the various conditions of atmospheric turbulence appears to be the considerable amount of statistical data concerning atmospheric turbulence and airplane loads in rough air that has been collected by the National Advisory Committee for Aeronautics in the last 20 years. (See, for example, refs. 8 to 12.) These data have been obtained, in most cases, from airplane acceleration measurements in normal operations, although in some instances (ref. 10) the data were obtained in special flight investigations. These data are generally given in the form of the number of peak accelerations or effective (or "derived") gust velocities per second which exceed given values and in this form do not appear applicable to spectral methods of analysis.

Fortunately, in the theory of random processes, relations have been derived (ref. 13) between peak counts (such as have been made for normal acceleration) and the associated power spectra. These relations apply to the case of a stationary Gaussian random process, the stationarity of the process implying that its characteristics do not change with time and the term Gaussian designating a process characterized by a Gaussian probability distribution for the amplitude of the disturbance as well as for its time derivatives. The approximately Gaussian character of turbulent velocity fluctuations has been noted and, for the case of atmospheric turbulence, results reported, for example in reference 3, appear to support such an assumption. Inasmuch as the intensity of turbulence is known to vary widely with weather conditions, the overall gust and load experience in operations cannot be considered a stationary Gaussian process. If the operational gust history is

¹ Supersedes NACA Technical Notes 3362 by Harry Press, May T. Meadows, and Ivan Hadlock, 1955, and 3540 by Harry Press and May T. Meadows, 1955.

considered to be a nonstationary Gaussian process varying only in intensity or root-mean-square gust velocity, the problem of specifying the gust history is reduced to that of specifying the probability distribution of the root-mean-square gust velocity. For this case, it appears possible to extend the results of reference 13 for the stationary Gaussian process in order to derive a basis for estimating the distribution of root-mean-square gust velocity from counts of acceleration peaks.

On the basis of the foregoing considerations, techniques are developed in this report for the estimation of the probability distributions of the root-mean-square acceleration and root-mean-square gust velocity from data on peak gust accelerations. Two approaches are considered: first, that the root-mean-square gust velocity takes on only a few discrete values and, secondly and more realistically, that the root-mean-square values cover a continuous range of values. These techniques are then applied to available gust-load data obtained from a number of transport operations and the associated probability distributions of root-mean-square gust velocity are derived. Also, available data are used to estimate the variations in this distribution with altitude and weather condition. The method of application of these results to the calculation of gust-load and other airplane response histories in operations is outlined and some of the limitations of the present results are indicated.

SYMBOLS

$\bar{A}_1 = \frac{\rho V S m}{2W} \sqrt{\frac{I(K,s)}{\pi}}$	
a_n	acceleration, g units
a_1, a_2, a_3	scale parameters in distributions, $f(\sigma_{a_n})$
b_1, b_2, b_3	scale parameters in distributions, $\hat{f}(\sigma_U)$
\bar{c}	average chord, ft
$f(\sigma_{a_n})$	probability density distribution of σ_{a_n}
$\hat{f}(\sigma_U)$	probability density distribution of σ_U
$\hat{F}(\sigma_U)$	cumulative probability distribution of σ_U
g	acceleration due to gravity, 32.2 ft/sec ²
$\left[\frac{I(K,s)}{\pi} \right]^{1/2}$	airplane gust-response factor
K	airplane mass parameter, $\frac{4W}{g\rho\pi S\bar{c}}$
L	scale of turbulence
$\bar{M}(a_n)$	average number of maximums per second exceeding given value of a_n in operations
m	slope of lift curve per radian
$N()$	average number of maximums per second exceeding given value of specified argument for Gaussian disturbance

$$N_0 = \frac{1}{2\pi} \left[\frac{\int_0^\infty \omega^2 \Phi(\omega) d\omega}{\int_0^\infty \Phi(\omega) d\omega} \right]^{1/2}$$

$N_2 = N_0 e^{-2}$	
P	proportion of total flight time
S	wing area, sq ft
s	ratio of chord to turbulence scale, \bar{c}/L
T	specified time, sec
$T(\omega)$	amplitude of airplane acceleration response to unit sinusoidal gusts of frequency ω
t	time, sec
V	true airspeed, fps
V_w	wind speed, fps
W	airplane weight, lb
$y(t)$	random function of time
\bar{Z}^2	mean-square normal acceleration, ft/sec ²
ρ	air density, slugs/cu ft
σ	root-mean-square deviation, $(\overline{y^2(t)})^{1/2}$
$\Phi(\omega)$	power-spectral-density function, $\lim_{T \rightarrow \infty} \frac{1}{2\pi T} \left \int_{-T}^T y(t) e^{-i\omega t} dt \right ^2$
λ	gust wavelength, ft
ω	frequency, radians/sec
Ω	reduced frequency, $2\pi/\lambda$, radians/ft
Subscript:	
U	gust velocity

SPECTRAL CHARACTERISTICS OF ATMOSPHERIC TURBULENCE

In the way of background for the present analysis, it will be helpful to review the available measurements of the power spectrum of atmospheric turbulence. Figure 1 contains a summary of most of the available airplane measurements of the power spectrum of atmospheric turbulence. The first of these measurements was made by Clementson at the Massachusetts Institute of Technology (ref. 4), and subsequent measurements were made by the National Advisory Committee for Aeronautics (refs. 5 and 7), Douglas Aircraft Company, Inc. (ref. 14), Massachusetts Institute of Technology (ref. 15), and Cornell Aeronautical Laboratory (refs. 16 and 17). The curves shown represent the various power spectra which were obtained under different weather conditions. The abscissa is the frequency argument Ω which has the dimensions of radians per foot and is equal to 2π divided by λ , the gust wavelength. (The data shown cover a range of gust wavelengths from about 10 feet to 5,000 feet.)

The spectra in all but one case are for the vertical or lateral component of the turbulence. In one case marked by the letter H , the spectrum is for the horizontal or longitudinal component of turbulence. Examination of these results indicates that the spectral shapes appear to be relatively consistent; in all cases, the power decreases rapidly with increasing frequency. In fact, in most cases, the spectra appear to be inversely proportional to the square of the frequency. This spectral shape of $1/\Omega^2$ is in reasonable agreement with theoretical results obtained for the spectral shape at the

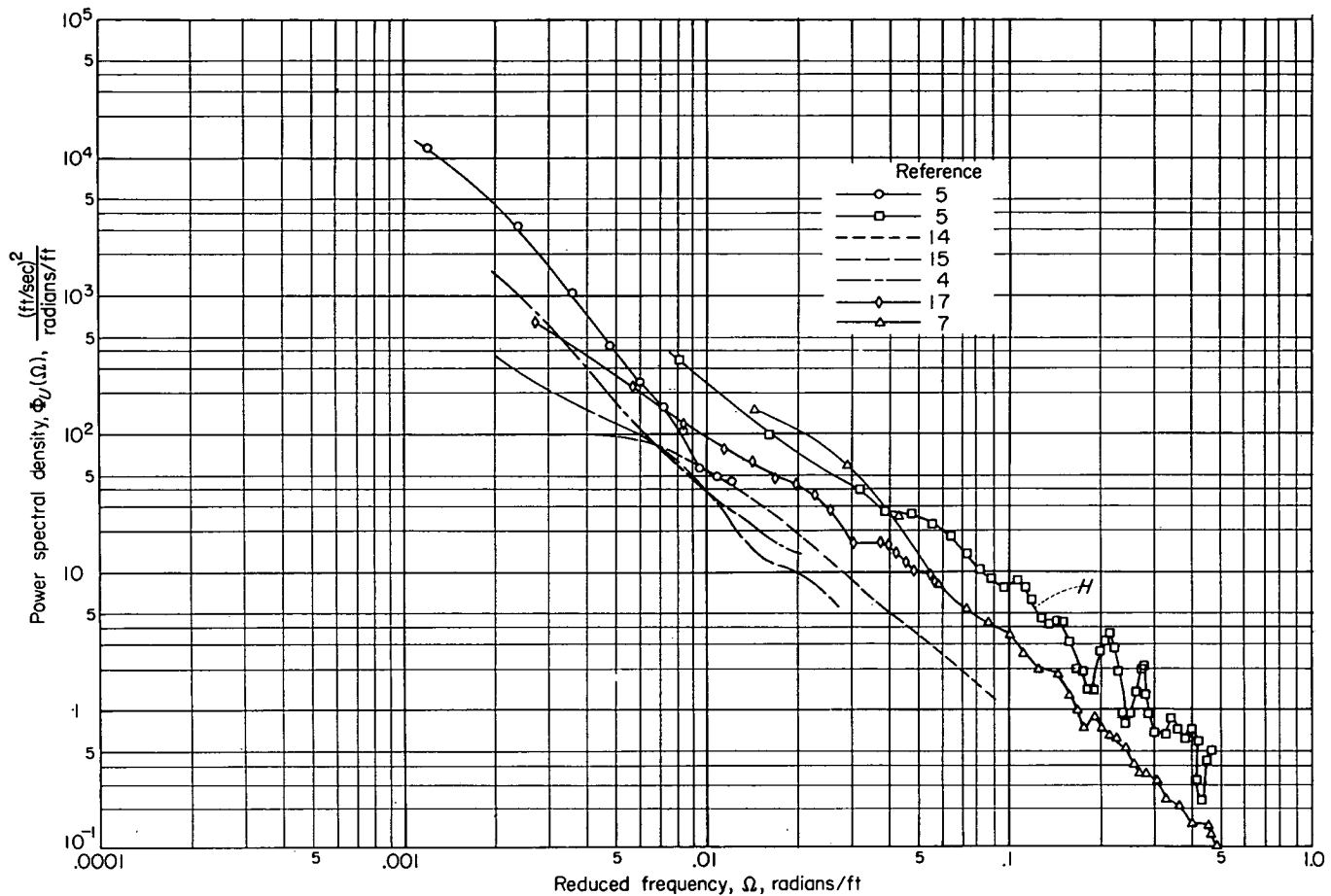


FIGURE 1.—Summary of airplane measurements of the power spectrum of atmospheric turbulence.

higher frequencies in the theory of isotropic turbulence. At the lower frequencies, the situation is not as clear, few measurements being available for frequencies $\Omega < 0.002$. Some additional measurements obtained at the Cornell Aeronautical Laboratory and at the NACA (ref. 18) do cover these lower frequencies and indicate a flattening of the spectrum at frequencies $\Omega < 0.001$.

In addition to these variations in spectral shape, the various measurements also differ in turbulence intensity. The individual root-mean-square values are estimated to vary from roughly 1.5 to perhaps 8 feet per second, which, as will be seen, represent the relatively light-to-moderate levels of atmospheric turbulence.

Another source of information on the spectral characteristics of atmospheric turbulence is the measurements at lower altitudes made from meteorological towers. A large number of such spectral measurements have now been obtained. A few representative measurements obtained at an elevation of about 300 feet and for various conditions of average wind speed V_w (ref. 19) are shown in figure 2. These measurements extend to lower frequencies (longer gust wavelengths) than do most of the available airplane measurements. At the higher frequencies, these results approximate the same form $1/\Omega^2$ that is characteristic of the airplane

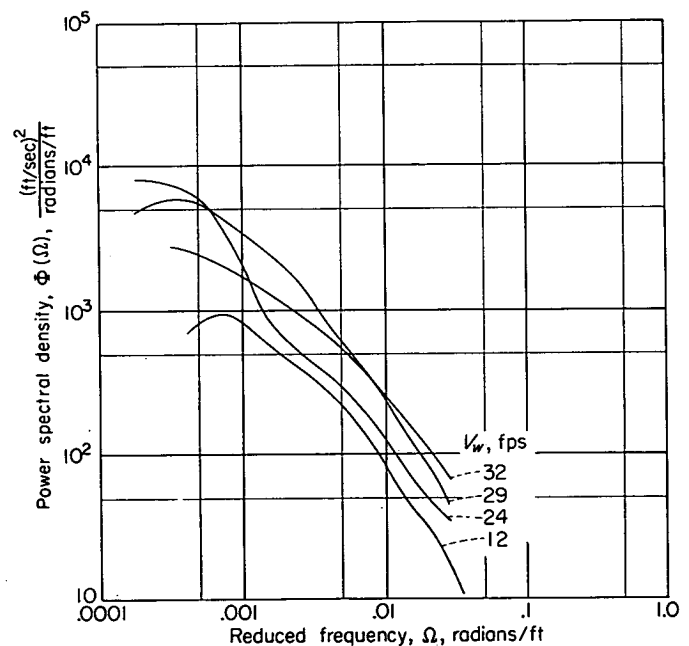


FIGURE 2.—Measurements of the power spectrum of atmospheric turbulence obtained at 300 feet from a meteorological tower (ref. 19).

measurements. In addition, at the lower frequencies, a definite tendency toward a flattening of the spectra can be noted. The variation in the spectrum intensity with wind speed V_w should also be noted.

Because of the general characteristics of these spectral measurements, it has been convenient in theoretical studies to use the following analytical expression for the turbulence spectrum

$$\Phi(\Omega) = \sigma_v^2 \frac{L}{\pi} \frac{1 + 3\Omega^2 L^2}{(1 + \Omega^2 L^2)^2} \quad (1)$$

where $\Omega = 2\pi/\lambda$ and λ is the gust wavelength. This expression has been useful in wind-tunnel studies of turbulence and has the general characteristics of the measured spectra of atmospheric turbulence. The equation has two parameters: the mean-square gust velocity σ_v^2 which describes the overall intensity, and the so-called scale of turbulence L which, in a sense, can be considered to be proportional to the average eddy size. Curves for this expression are shown in figure 3 for values of L of 200, 600, 1,000, and 2,000 feet. At higher frequencies, these curves all approach a shape of $1/\Omega^2$ but differ in the frequency at which the flattening occurs. For increasing values of L , the curves flatten out at lower frequencies. Comparison of these curves with those of figures 1 and 2 and other measurements of the spectrum for atmospheric turbulence has indicated that the values of L for atmospheric turbulence are of the order of 1,000 feet. A value of 1,000 feet is used as a representative average value in the subsequent analysis.

For design purposes, the overall gust experience in operations is of concern. Presumably, the overall experience consists of various exposure times to each of the spectra shown in figures 1 and 2 as well as to other spectra associated with different weather conditions. It thus appears important to determine the proportion of flight time spent under these various conditions of turbulence. In the next section methods are developed for obtaining information on this problem from available gust statistics. These methods are then applied in a subsequent section.

DERIVATION OF CONVERSION TECHNIQUES

BASIC METHOD

In the present analysis, use will be made of some concepts and results in the theory of random processes. The theory of random processes is a recently developed branch of probability theory and the aspects of the theory pertinent to the present applications are described in some detail in reference 13. In particular, the relations between peak counts and spectra for a stationary Gaussian random process which will be used in the present study are derived therein. Some general aspects of random-process theory are also covered in references 20 and 21.

In many recent studies of airplane behavior in rough air, atmospheric turbulence is generally considered a stationary Gaussian random process. The assumption that turbulence is a Gaussian random process appears warranted by the approximately Gaussian character of turbulent velocity fluctuations. The assumption of stationarity implies that

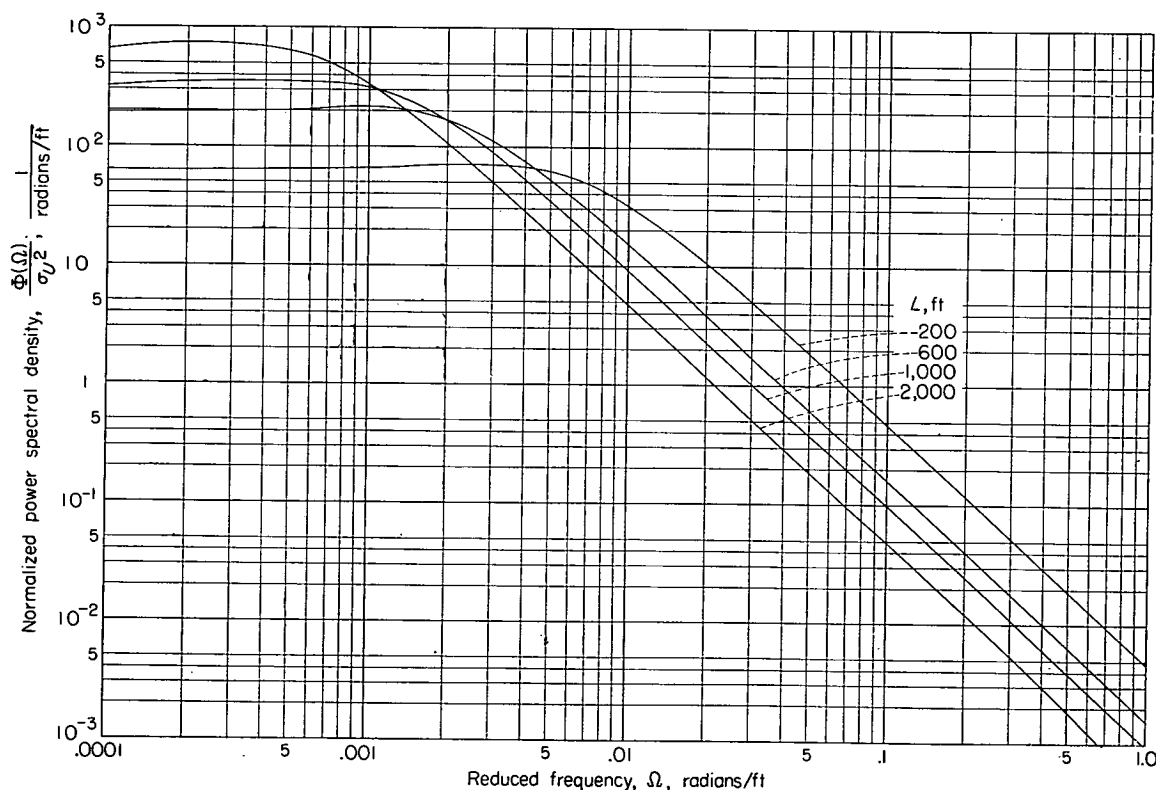


FIGURE 3.—Analytic representation of the spectrum of atmospheric turbulence.

$$\Phi(\Omega) = \sigma_v^2 \frac{L}{\pi} \frac{1 + 3\Omega^2 L^2}{(1 + \Omega^2 L^2)^2}$$

the statistical characteristics of the turbulence are invariant with space and time and also appears warranted for many purposes. For present purposes (in which the overall gust and load experiences of an airplane in operational flight are of concern), however, the process cannot be considered a simple stationary one, inasmuch as the turbulence characteristics of the atmosphere vary widely with weather conditions, particularly in regard to the intensity of the turbulence.

In order to account for the variations in atmospheric turbulence with weather condition, it will be assumed that turbulence is only locally Gaussian and stationary; that is, its statistical characteristics are Gaussian and invariant in a given restricted region and for a short time but vary, particularly in intensity, from time to time and place to place. This assumption implies that the region or time is small relative to the entire flight path or flight duration but large enough for statistical equilibrium to be achieved. The Gaussian character for the turbulent velocity fluctuations for a given weather condition will be used as a building block to construct the operational gust history, which must cover many weather conditions and, in the overall, is not a stationary Gaussian process. On this basis, the overall turbulence experienced by an airplane in given operations is taken to consist of the summation for appropriate exposure times to a series of elemental stationary Gaussian processes.

If the airplane response to turbulence is linear, as assumed in the present analysis, the response, such as the load history to each elemental turbulence process, is likewise a Gaussian process and the overall operational load history may in turn also be considered to consist of a summation of the loads for the various elemental Gaussian turbulence disturbances. This scheme serves to yield a reasonable approximation of the actual airplane load history and, further, has the particular advantage for present purposes of permitting the use of relations between peak counts and spectra derived for the stationary Gaussian case in reference 13.

The foregoing considerations form the basis for the present analysis. They will be applied in order to estimate the probability distribution of root-mean-square acceleration from operational data on peak accelerations. These estimates of the distribution of root-mean-square acceleration will then be used in order to obtain the associated probability distributions of root-mean-square gust velocity by taking into account the airplane dynamics.

RELATIONS BETWEEN NUMBER OF PEAKS AND SPECTRA

Simple Gaussian case.—The asymptotic relation between the average number of maximums per second exceeding a given value and the spectrum of a stationary Gaussian disturbance $y(t)$ has been derived in reference 13 and is for large values of y given by (see appendix)

$$N(y) = \frac{1}{2\pi} \left[\frac{\int_0^\infty \omega^2 \Phi(\omega) d\omega}{\int_0^\infty \Phi(\omega) d\omega} \right]^{1/2} e^{-y^2/2\sigma^2} \quad (2)$$

where

$N(y)$ average number of maximums per second exceeding given values of y
 ω frequency, radians/sec
 $\Phi(\omega)$ power-spectral-density function of random disturbance $y(t)$

$$\sigma^2 = \int_0^\infty \Phi(\omega) d\omega$$

Equation (2) is the exact expression for the number of crossings per second with positive slope of given values of y but is an approximate expression for the number of maximums above a given value of y . For present purposes, however, equation (2) appears to be an adequate approximation of the number of peaks, as indicated in the appendix, and forms the basis for the present analysis.

Examination of equation (2) indicates that the number of peaks per second above given values depends upon σ^2 , which is the area under the spectrum, and upon the second moment of the spectrum about the origin. If it is assumed that the spectral shape of turbulence is invariant with weather conditions (as suggested by available measurements) and varies only in intensity or root-mean-square gust velocity, the output spectrum $\Phi_{a_n}(\omega)$ for acceleration $a_n(t)$ for a given airplane under given operating conditions (fixed speed, weight, altitude, etc.) is likewise invariant in shape. Under these conditions, the coefficient of the exponential term in equation (2) is a fixed constant and equation (2) may be written as

$$N(a_n) = N_0 e^{-a_n^2/2\sigma^2} \quad (3)$$

where the constant N_0 is given by

$$N_0 = \frac{1}{2\pi} \left[\frac{\int_0^\infty \omega^2 \Phi_{a_n}(\omega) d\omega}{\int_0^\infty \Phi_{a_n}(\omega) d\omega} \right]^{1/2} \quad (4)$$

The constant N_0 gives the expected number of times per second that $a_n(t)$ crosses the value zero with a positive slope. Because of the invariance of the shape of $\Phi_{a_n}(\omega)$, the quantity N_0 is independent of the turbulence intensity. It has the dimensions of a frequency and can be considered a characteristic frequency of the airplane acceleration response to turbulence.

If the logarithm of both sides of equation (3) is taken, the following relation is obtained:

$$\log N(a_n) = \log N_0 - \frac{a_n^2}{2\sigma^2} \quad (5)$$

Equation (5) indicates that the $\log N(a_n)$ is a linear function of a_n^2 with slope equal to $-1/2\sigma^2$. Thus, for a stationary Gaussian disturbance, the root-mean-square value σ may be obtained simply from the slope of the line for the number of peaks when plotted on semilogarithmic paper as a function of a_n^2 . Because of the linearity of the relationship, this plotting arrangement is found useful.

A representative distribution of the number of peak accelerations per second (both positive and negative peaks) obtained from operations of a transport airplane is shown as the solid curve of figure 4 as a function of a_n^2 . The data are given, as is generally the case, for a threshold value of $0.3g$. The distribution appears concave upward and departs considerably from the straight lines that would be expected for a simple stationary Gaussian disturbance in this plot. It is thus clear that the overall distribution of peak accelerations cannot be adequately represented by the simple Gaussian case. A method for obtaining a more adequate representation of the load history is explored in the following paragraphs. For this purpose, the idea of a combination or composite of Gaussian processes is used and equation (2), which

expresses the relation between peak counts and the power spectrum for the simple Gaussian case, is extended to this composite condition.

Composite Gaussian case.—If the overall operational load history (in terms of the average number of acceleration peaks per second exceeding given values) is considered to consist of various exposure times to different Gaussian gust disturbances, the average number of peaks per second exceeding given values is given by

$$\overline{M}(a_n) = \sum_{i=1}^k P_i N_i(a_n) \quad (6)$$

where P_i is the proportion of total flight at the i th condition and $N_i(a_n)$ is the number of peak accelerations per second

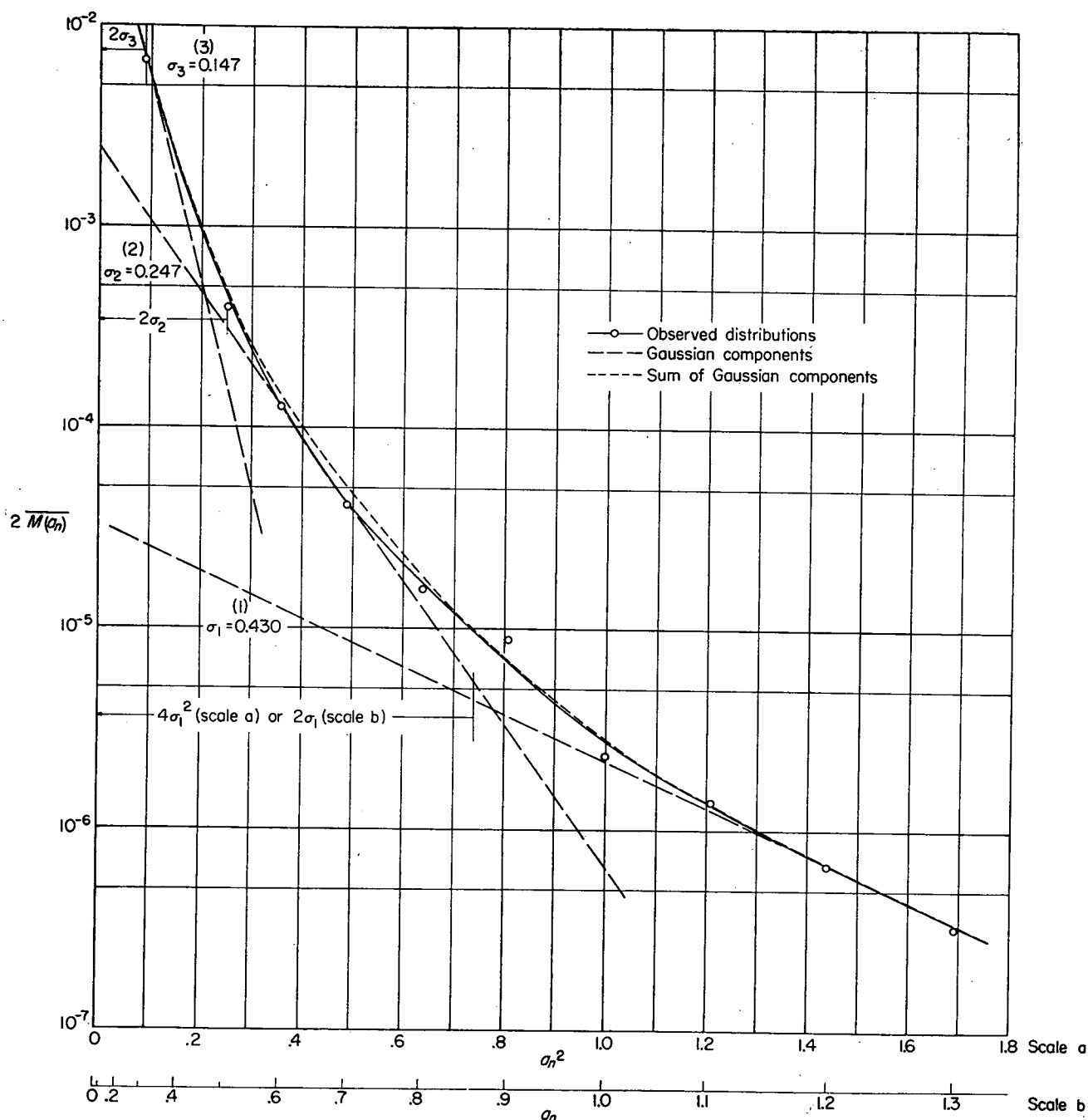


FIGURE 4.—Illustrative example of graphical separation into Gaussian components of distribution of peak acceleration (operation 1).

exceeding given values of acceleration for the i th condition. In this form, equation (6) is general and permits accounting not only for variation in the spectrum of turbulence but also for variations in the airplane response characteristics.

If equation (3) is substituted into equation (6), there is obtained

$$\overline{M(a_n)} = \sum_{i=1}^k (N_0)_i P_i e^{-a_n^2/2\sigma_i^2} \quad (7)$$

It will be assumed, as previously indicated, that the spectrum of atmospheric turbulence is invariant in shape but varies in intensity or in root-mean-square gust velocity. This assumption is suggested by the available measurements of turbulence spectra and appears reasonable for present purposes. Further, if the response characteristics for a particular airplane in operation are represented by a single-response function, such as obtained for average values of the airplane, and operating parameters, such as the weight, airspeed, and density, equation (7) may be written for this (the discrete) case as

$$\overline{M(a_n)} = N_0 \sum_{i=1}^k P_i e^{-a_n^2/2\sigma_i^2} \quad (8)$$

where the quantity N_0 is, as in equation (3), fixed for a given airplane.

Continuous case.—If the airplane is now assumed to encounter turbulence of all intensities (continuous variations in the root-mean-square gust velocity) but of the same spectral shape (fixed value of L for present applications), equation (8) may be extended for the continuous case to yield the following relation:

$$\overline{M(a_n)} = N_0 \int_0^\infty f(\sigma_{a_n}) e^{-a_n^2/2\sigma_{a_n}^2} d\sigma_{a_n} \quad (9)$$

In this case, the sum of the terms of equation (8) becomes a continuous integral. The expression for the continuous case contains the same characteristic frequency N_0 , which is independent of the turbulence intensity, the same exponential term as the earlier expressions, and, in addition, the function $f(\sigma_{a_n})$. This function is the counterpart of the ratios P_1, P_2, \dots, P_k in equation (8) and is the probability-density distribution of σ_{a_n} which defines the proportion of time spent at various values of σ_{a_n} ; the quantity $f(\sigma_{a_n})d\sigma_{a_n}$ gives the proportion of flight time spent at values of σ_{a_n} between σ_{a_n} and $\sigma_{a_n} + d\sigma_{a_n}$.

The relations between the number of peaks and the root-mean-square values of the random process given by equation (8) for the discrete case and by equation (9) for the continuous case are the basic relations in the present analysis. These two relations are applied in the following sections and methods are developed for estimating the distribution of the root-mean-square acceleration from operational gust-load data generally available in the form of peak counts $\overline{M(a_n)}$. Then, the transformation of these distributions of root-mean-square acceleration to distribution of root-mean-square gust velocity is considered.

DISTRIBUTION OF ROOT-MEAN-SQUARE ACCELERATION FOR DISCRETE CASE

As previously indicated, the operational load history for a particular airplane in terms of the number of peaks per second exceeding given values is given by equation (8). Each of the terms of the summation of equation (8) is given by

$$\overline{M_i(a_n)} = N_0 P_i e^{-a_n^2/2\sigma_i^2} \quad (10)$$

which, as previously noted, yields a straight line of slope $-1/2\sigma_i^2$ if $\log \overline{M(a_n)}$ is plotted as a function of a_n^2 . This condition suggests that the overall operational loads for a given operation when plotted in this specified form can be built up of straight-line or Gaussian components. A simple trial for a sample load history shown in figure 4 indicates that a good approximation to $\overline{M(a_n)}$ can be obtained with only a few components. (Note that the ordinate of figure 4 is $2\overline{M(a_n)}$ inasmuch as both acceleration peaks and acceleration minimums have been included in the operational data.) The values for the three components shown add up to give the short-dash curve which is seen to be a close approximation to the overall load history. The procedure devised for the determination of these straight-line components consists of the following steps: First, line (1) is obtained by taking a tangent to the tail of the observed distribution; line (2) is then taken from the point on line (1) which underestimates the observed distribution by one-half and is drawn tangent to the upper part of the overall load-history curve. The third line, if required, is then obtained from line (2) in the same manner that line (2) was obtained from line (1). The sum of the values of the lines obtained in this manner will generally yield a good approximation to the observed distribution, as will be seen subsequently.

The procedure outlined in the preceding paragraph for obtaining the linear components of the observed distribution is somewhat arbitrary. Several alternative procedures were also considered and discarded. These procedures included the selection of the first component at the upper end of the curve and the use of specified combinations of slopes corresponding to given values of root-mean-square gust velocities (which might be considered averages for various weather conditions such as clear-air turbulence and thunderstorms). These alternative procedures appeared to offer no significant advantages and had the additional undesirable characteristic of yielding a poorer approximation at the larger values of acceleration which are of greatest interest.

It will be recalled that the slopes of the lines in figure 4 are equal to $-1/2\sigma_1^2$, $-1/2\sigma_2^2$, and $-1/2\sigma_3^2$ where σ_1 , σ_2 , and σ_3 , respectively, represent the root-mean-square acceleration for the three effective Gaussian components. The values for the case represented in figure 4 are $\sigma_1=0.430$, $\sigma_2=0.247$, and $\sigma_3=0.147$. These values σ_1 , σ_2 , and σ_3 for the acceleration components are used subsequently to obtain the associated root-mean-square gust velocities for these Gaussian components.

In order to estimate the values of the proportion of total flight time P_i for the i th condition, it will be noted from

equation (10) that for each component

$$P_i = \frac{\overline{M_i(a_n)}}{N_0 e^{-a_n^2/2\sigma_i^2}} \quad (11)$$

where $\overline{M_i(a_n)}$ is the number of accelerations per second exceeding a_n for the i th condition or component. The numerator of equation (11) may be obtained directly from the line for each component in figure 4. The denominator of equation (11), as would be expected, is the total number of peak accelerations per second exceeding a_n that would be experienced if the airplane spent all its flight time at the indicated root-mean-square acceleration value. The value of the denominator is seen to depend upon the value of the constant N_0 .

The values of N_0 and the denominator of equation (11) may be determined in a number of ways. They may be determined from their relation to the power spectrum as given in equations (3) and (4), but this procedure is not very practical for present purposes because the acceleration spectrum cannot be determined from the type of records available. The value of these quantities can also be determined in a number of ways from short sections of flight record in homogeneous rough air. The most direct way is to make use of the property that N_0 is equal to the average number of times per second that $a_n(t)$ crosses the value zero with positive slope. Unfortunately, the film speed of the records available (2 to 8 feet per hour) was frequently too slow to permit such counts with the desired degree of reliability.

Another method of determining the value of N_0 and the denominator of equation (11) from sample flight records involves the use of the property of equation (3) of defining the average number of peaks or crossings per second above given values of a_n . If a_n is set equal to $k\sigma$ in equation (3), the quantity $N(k\sigma)$ gives the average number of peaks per second that have a value of a_n greater than $k\sigma$ where σ is the value of the root-mean-square acceleration for the record. Thus, from equations (3) and (4) $N(k\sigma)$, which is designated as N_k for brevity, is given by

$$N_k = \frac{1}{2\pi} \left[\frac{\int_0^\infty \omega^2 \Phi(\omega) d\omega}{\int_0^\infty \Phi(\omega) d\omega} \right]^{1/2} e^{-k^2/2}$$

or

$$N_k = N_0 e^{-k^2/2} \quad (12)$$

Inasmuch as the average number of peaks (or crossings) per second exceeding a value of $a_n = k\sigma$ can be estimated from the available sample records, equation (12) provides a useful method for determining the value of N_0 and the denominator of equation (11). Care should be taken in such applications to insure that the record section used approximates a Gaussian disturbance.

On this basis, the proportion of flight spent in rough air

yielding a root-mean-square acceleration above $k\sigma_i$ is from equation (11) given by

$$P_i = \frac{\overline{M_i(k\sigma_i)}}{N_k} \quad (13)$$

where $\overline{M_i(k\sigma_i)}$ is the average number of peaks per second exceeding the value $k\sigma_i$ for the linear component. This relation is used in the subsequent analysis of the operational loads data. In order to avoid the errors associated with the expression for the number of peaks at small values of k , a value of k of 2 was generally used. For the illustration of figure 4, the values of $2\overline{M_1(2\sigma_1)}$, $2\overline{M_2(2\sigma_2)}$, and $2\overline{M_3(2\sigma_3)}$ are indicated by ticks on the figure and are 4.3×10^{-6} , 3.2×10^{-4} , and 7.4×10^{-3} . The sum of the P 's will in any case be less than one, the remaining time being in either smooth air or very light rough air which does not contribute many peak values above the threshold value.

DISTRIBUTION OF ROOT-MEAN-SQUARE ACCELERATION FOR CONTINUOUS CASE

The representation of the load experience in the previous section in terms of a few discrete values of root-mean-square acceleration is a simplification, since atmospheric turbulence may actually be expected to cover a continuous variation in intensity. In this section, the problem of estimating the associated continuous distribution of root-mean-square acceleration from the overall peak counts will be considered.

The determination of the actual probability distribution of root-mean-square acceleration $f(\sigma)$ from a given peak-load history requires the solution of the integral equation given by equation (9). Since it does not, in general, appear possible to represent the load experience in terms of the number of peak accelerations above given values by a simple function, an effort was made instead to estimate $f(\sigma)$ directly in simple form, based on the results obtained in the application of the methods for the discrete case. Equation (9) is then integrated and the results obtained are presented in chart form for use in comparison with operational data.

Experience with the analysis of gust-load data, wherein the foregoing discrete-case methods have been used, has indicated that the distribution of σ decreases rapidly with increasing values of σ and might be approximated by simple exponential distributions. On this basis, three exponential-type probability density functions were considered, namely,

$$\left. \begin{array}{l} \text{Case a:} \\ \text{Case b:} \\ \text{Case c:} \end{array} \right\} \begin{array}{l} f_1(\sigma) = \frac{1}{a_1} \sqrt{\frac{2}{\pi}} e^{-\sigma^2/2a_1^2} \\ f_2(\sigma) = \frac{1}{a_2} e^{-\sigma/a_2} \\ f_3(\sigma) = \frac{1}{2a_3^2} e^{-\sqrt{\sigma}/a_3} \end{array} \quad (14)$$

where in each case $\sigma \geq 0$.

For each case, a is a scale parameter, larger values of a representing more severe load histories. The three distributions are shown in figure 5 for values of $a=1$ and, in order, are seen to have increasingly larger areas at the higher values of σ . These functions, by the definition of a probability density function, all have unit area.

Case a.—If it is assumed that $f(\sigma)$ is given by case a, equation (9) may be integrated in closed form and yields the following result for $\overline{M}(a_n)/N_0$:

$$\frac{\overline{M}(a_n)}{N_0} = e^{-a_n/a_1} \quad (15)$$

The function $\overline{M}(a_n)/N_0$ gives the proportion of peak accelerations exceeding given values of a_n and is thus a cumulative probability distribution. Figure 6(a) shows the distribution $\overline{M}(a_n)/N_0$ for a range of values of a_1 . Equation (15) yields a simple result for the proportion of peak accelerations per second exceeding given values of a_n , in terms of the single-scale parameter of the distribution of σ_{a_n} . The value of the parameter a_1 is inversely proportional to the slope of the line for $\overline{M}(a_n)/N_0$ when plotted on semilogarithmic paper and also gives the value of σ_{a_n} below which 68 percent of the airplane flight time is spent. The linear variation with a_n of the $\log \overline{M}(a_n)$ given by equation (15) is of considerable interest because gust-load flight-test data on peak accelerations under some conditions, particularly where a limited range of weather conditions is represented, tend to exhibit linear trends when plotted on semilogarithmic paper ($\log \overline{M}(a_n)$ as a function of a_n). This condition, however, does not generally apply to operational data.

Case b.—The distributions of $\overline{M}(a_n)$ observed from operational flights frequently exhibit a nonlinear trend and

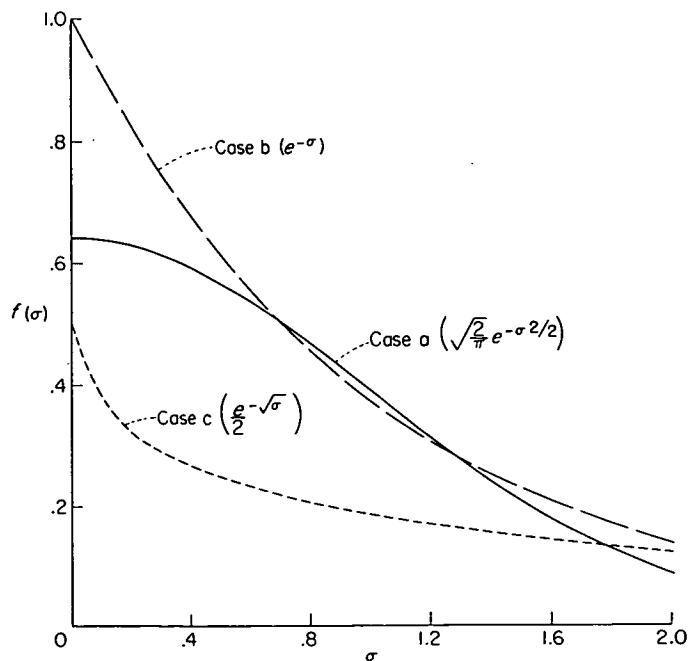


FIGURE 5.—Comparison of three assumed distributions.

a concave upward form when the $\log \overline{M}(a_n)$ is plotted against a_n . This form implies that the distributions of $f(\sigma)$ for these cases might more adequately be represented by case b or case c. Substituting the expression for case b in equation (9) yields the following expression for the number of maximums exceeding a_n :

$$\overline{M}(a_n) = \int_0^\infty \frac{N_0}{a_2} e^{-\frac{a_n^2}{2\sigma^2} - \frac{\sigma}{a_2}} d\sigma \quad (16)$$

A closed-form evaluation of the integral could not be found. Numerical evaluations of the integral, however, are made readily. If the substitution $\sigma = sa_2$ is made into equation (16) and both sides of the equation are divided by N_0 , the following result is obtained:

$$\frac{\overline{M}(a_n)}{N_0} = \int_0^\infty e^{-\frac{a_n^2}{2a_2^2} \frac{1}{s^2} - s} ds \quad (17)$$

Equation (17) was evaluated for various values of $a_n^2/2a_2^2$ so that $\overline{M}(a_n)/N_0$ could be determined for various values of a_2 . The results obtained are shown plotted in figure 6(b). Operational gust-load data can be plotted conveniently in figure 6(b) in order to determine whether they adhere to the present distribution shape and, if so, to obtain the appropriate value of the scale parameter a_2 . (The plotting requires the determination of the value of N_0 which may be estimated from flight records as described previously.) The points shown in the figure represent operational gust-load data which are discussed in a subsequent section.

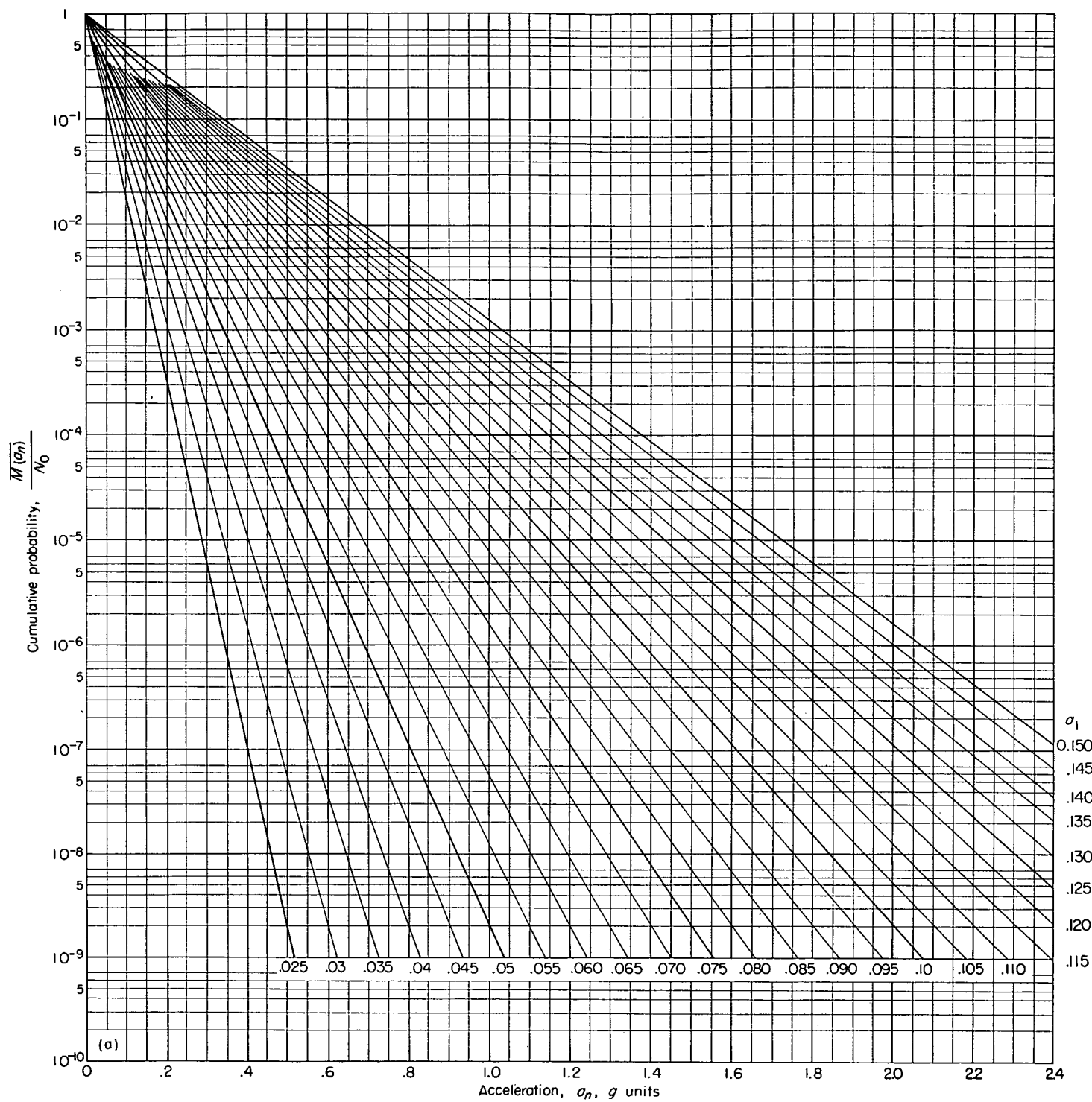
Case c.—For case c, equation (9) becomes

$$\frac{\overline{M}(a_n)}{N_0} = \frac{1}{2a_3^2} \int_0^\infty e^{-\frac{a_n^2}{2\sigma^2} - \frac{\sqrt{\sigma}}{a_3}} d\sigma \quad (18)$$

Equation (18) could not be evaluated in closed form but was evaluated numerically for various values of a_3 . The results obtained for a range of values of a_3 are shown in figure 6(c). Operational gust-load data can also be plotted conveniently in figure 6(c) in order to determine whether they adhere to the present distribution shape and, if so, to obtain the appropriate value of the parameter a_3 .

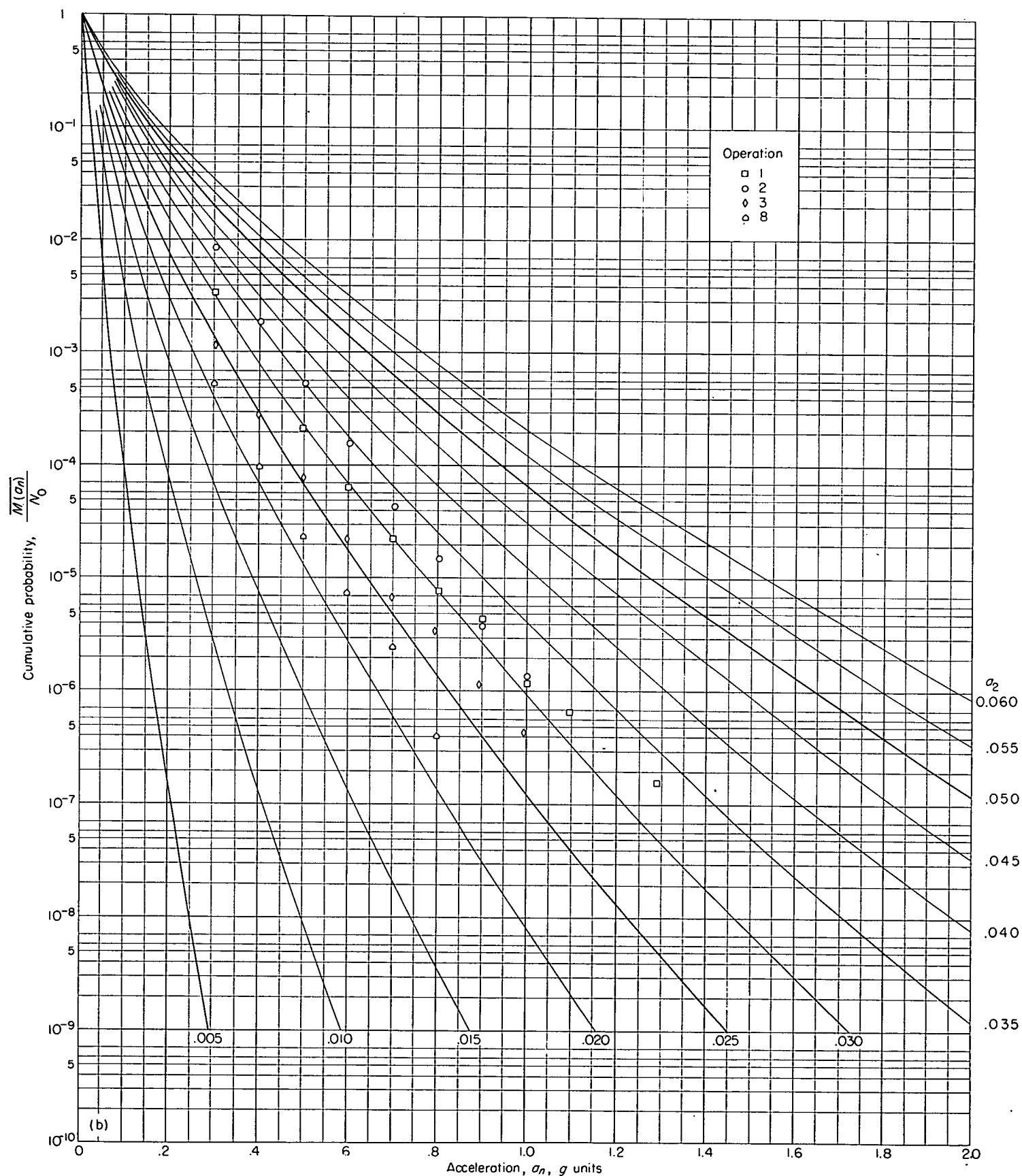
In general, a good representation of the observed distribution of peak values can be obtained by comparison of the data with the three charts of figure 6.² The choice of the appropriate case and the value of the scale parameter then specify the probability distribution of the root-mean-square acceleration in accordance with equations (14). As will be seen in the section entitled "Application to Gust-Load Statistical Data," these three distributions appear, in most cases, to be adequate for the representation of the types of data so far considered. However, other distribution forms appear worth investigating in future studies.

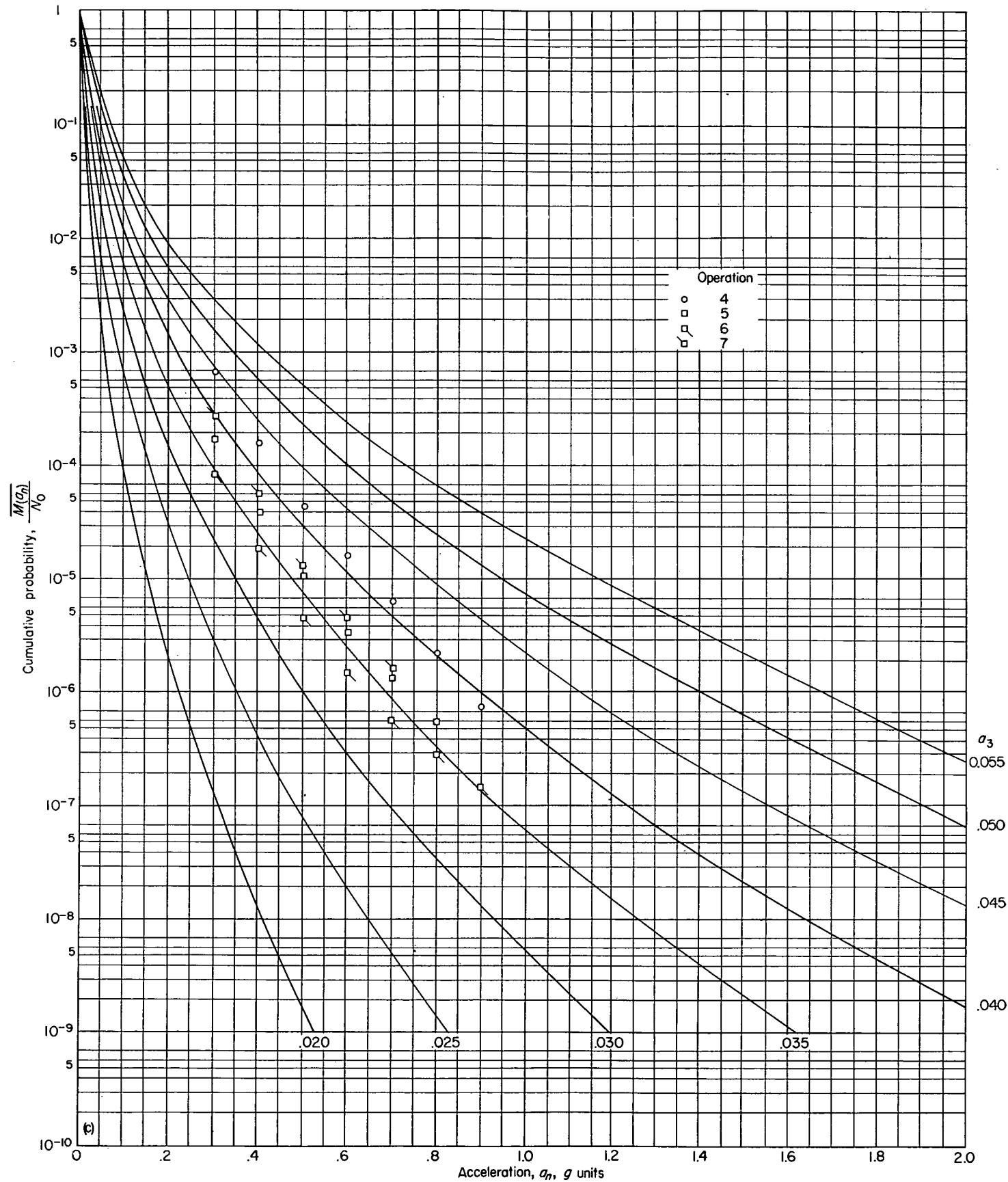
² The charts of figures 6(b) and 6(c) contain extensions and revisions to the charts presented earlier in Technical Note 3362.



(a) Case a.

FIGURE 6.—Cumulative probability of a peak acceleration exceeding given values of a_n .





(c) Case c.

FIGURE 6.—Concluded.

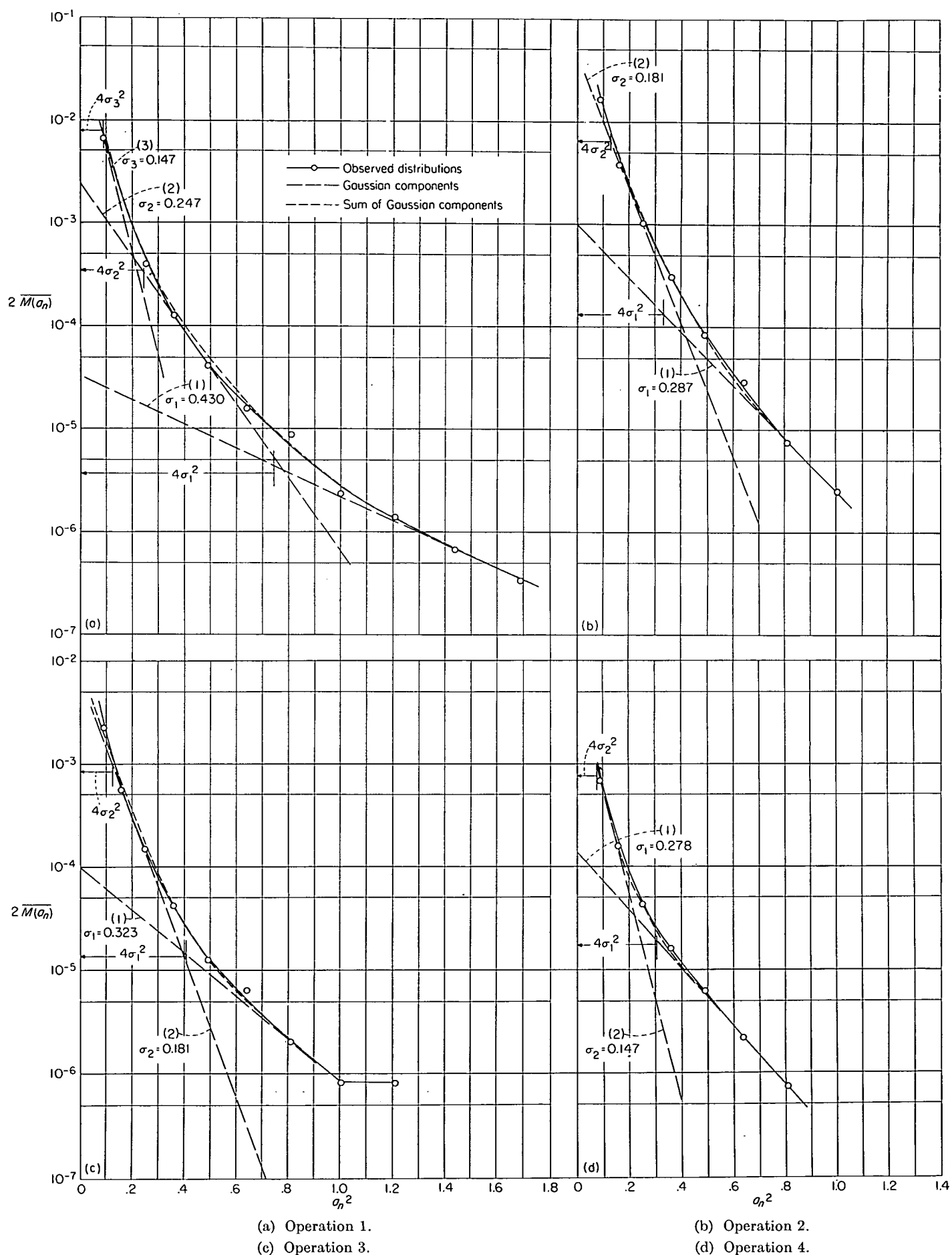


FIGURE 8.—Graphical separation into Gaussian components of distribution of peak acceleration.

DIRECT TRANSFER OF GUST LOADS FROM ONE AIRPLANE TO ANOTHER

It may on occasion be desirable to transfer the gust loads directly from one airplane to another without recourse to first determining the probability distributions of root-mean-square acceleration and gust velocity. The following analysis indicates a simple direct manner of performing this transfer.

Consider airplanes i and j . Assume that the gust loads have been measured on airplane i under fixed operating conditions and that it is desired to determine the load experience for airplane j under fixed operating conditions and with the same turbulence experience as that of airplane i . For airplane i ,

$$\overline{M_i(a)} = (N_0)_i \int_0^\infty f_i(\sigma_i) e^{-a^2/2\sigma_i^2} d\sigma_i \quad (25)$$

where the subscripts for acceleration have been omitted for brevity. Similarly, for airplane j

$$\overline{M_j(a)} = (N_0)_j \int_0^\infty f_j(\sigma_j) e^{-a^2/2\sigma_j^2} d\sigma_j \quad (26)$$

If the turbulence experience is the same for both airplanes, then

$$\sigma_j = \frac{\overline{A_j}}{\overline{A_i}} \sigma_i \quad (27)$$

by virtue of equation (22) or (22a). Substituting equation (27) into equation (26) and making use of the relation for the change of variables for probability distributions yields

$$\overline{M_j(a)} = (N_0)_j \int_0^\infty f_i(\sigma_i) e^{-\left(\frac{a\overline{A_i}}{\overline{A_j}}\right)^2/2\sigma_i^2} d\sigma_i \quad (28)$$

The integral on the right-hand side is, from equation (25), equal to the quantity

$$\overline{M_i\left(\frac{\overline{A_i}}{\overline{A_j}}a\right)} / (N_0)_i \quad (29)$$

Thus,

$$\overline{M_j(a)} = \frac{(N_0)_j}{(N_0)_i} \overline{M_i\left(\frac{\overline{A_i}}{\overline{A_j}}a\right)} \quad (30)$$

Equation (30) indicates that, in order to obtain the load history $\overline{M_j(a)}$, it is only necessary to take the value of measured distribution $\overline{M_i(\cdot)}$ at the acceleration value $\left(\frac{\overline{A_i}}{\overline{A_j}}a\right)$ and multiply the result by the ratio of the characteristic frequencies $(N_0)_j/(N_0)_i$. Essentially, the operation involves only a change of the abscissa scale and a multiplication of the ordinate value by the ratio of the characteristic frequencies.

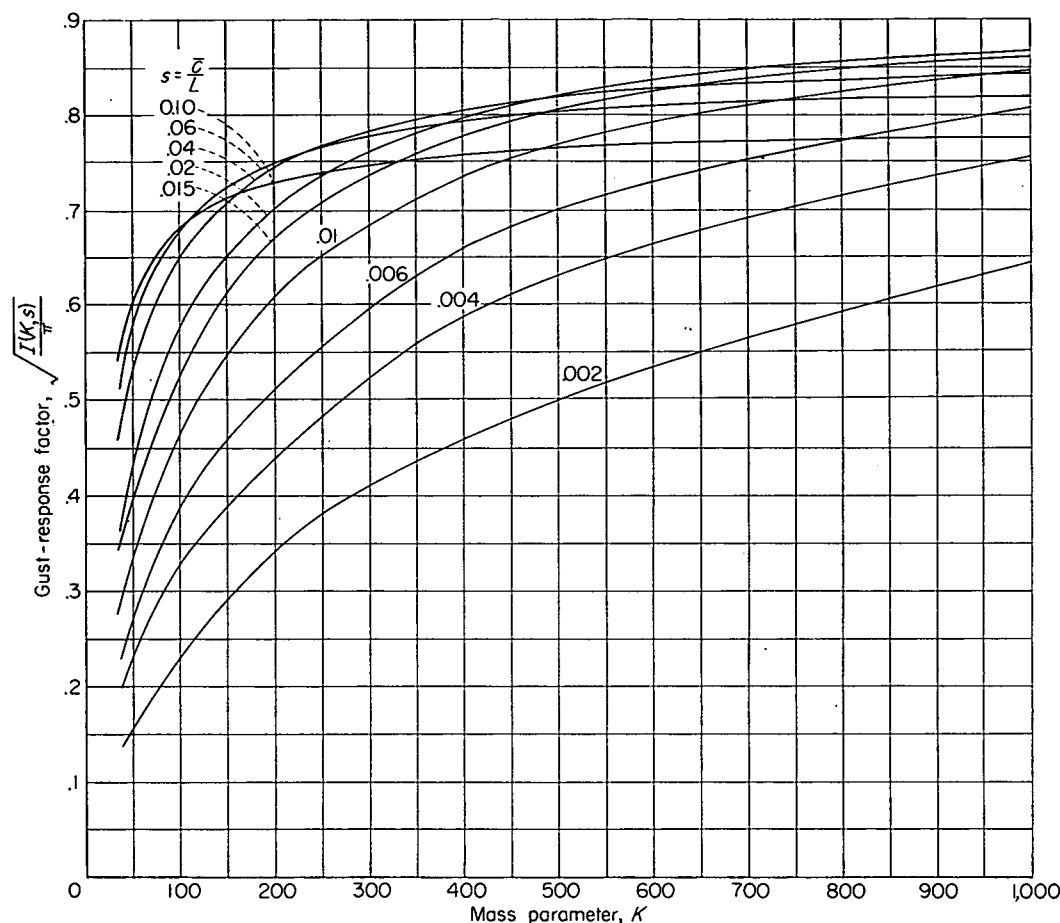
It should be noted that the values of \overline{A} need not necessarily be restricted to the one-degree-of-freedom case considered in the present conversion of the acceleration data to gust velocities. In many cases, it may be desirable to consider a more complete dynamic analysis in determining the quantities N_0 and \overline{A} .

APPLICATION TO GUST-LOAD STATISTICAL DATA

In this section, the methods developed in the section on derivation of conversion techniques are applied to available gust-load statistical data in order to convert the statistical data in terms of peak counts of accelerations and gusts into distribution of root-mean-square gust velocity. The data to be considered are of two types: first, data obtained from a number of different transport operations, and, then, in order to obtain a description of the turbulence that is more flexible than the operational gust experience and that is applicable to arbitrary flight plans, available data on the variation of turbulence with altitude and with weather condition. For the operational data, both the discrete and continuous methods are applied; whereas, only the continuous case is considered for the other data.

OPERATIONAL GUST-LOAD HISTORIES

Discrete case.—The graphical procedure outlined in an earlier section is applied to a series of eight operational load histories obtained from NACA VGH records. The scope of the data considered is summarized in table I. The data were obtained from six different types of transport airplanes with operations 5, 6, and 7 representing the same airplane type flown by different operators. The pertinent airplane characteristics and operating conditions are given in table II. These data include estimates of the overall average flight altitude, average flight speed, and average weight. The overall distributions of peak accelerations measured in flight are given in table III. Because of the limited data available, no effort was made to consider breakdowns of the overall data by flight condition or altitude. Values of N_0 and N_2 , given in table IV, were estimated in accordance with equation (12) from sections of record obtained in continuous rough air by counting the number of peak accelerations exceeding 2σ . These values contain some revisions of the values presented earlier in NACA Technical Note 3362 but owing to the nature of the records available are still considered crude estimates. The measured distributions of acceleration increments for the eight operations are shown in figures 8 (a) to 8 (h). (The illustration previously considered in figure 4 is operation 1 which is also shown in fig. 8 (a).) The subdivision of the distribution into Gaussian components in the manner previously described is also indicated by the long-dash lines in each case. The values of σ_i and P_i for each operation obtained from the slopes of the linear components and the values of $2\overline{M}(2\sigma_i)$ were determined in each case and are summarized in table IV.

FIGURE 7.—Gust-response factor $\sqrt{\frac{I(K,s)}{\pi}}$.

or for the gust spectrum assumed herein

$$\bar{A} = \left[\frac{L}{\pi} \int_0^\infty \frac{1 + 3\Omega^2 L^2}{(1 + \Omega^2 L^2)^2} T^2(\Omega) d\Omega \right]^{1/2} \quad (22c)$$

In these cases, the amplitude of the airplane frequency response function $T(\Omega)$ will depend upon additional aerodynamic, geometric, and structural parameters of the airplane rather than upon those considered in the single-degree-of-freedom case.

For the case of discrete values of σ_{a_n} , equation (22) permits the direct evaluation of the associated values of root-mean-square gust velocity σ_U for the single-degree-of-freedom case.

For the case of a continuous distribution of root-mean-square acceleration, the appropriate distribution of root-mean-square gust velocity is obtained from equation (22) or (22a) by the relation for a change of variables for probability distributions and in terms of $f(\sigma_{a_n})$ is given by

$$\hat{f}(\sigma_U) = \bar{A}_1 f(\bar{A}_1 \sigma_U) \quad (\sigma_{a_n} = \bar{A}_1 \sigma_U) \quad (23a)$$

$$\hat{f}(\sigma_U) = \bar{A} f(\bar{A} \sigma_U) \quad (\sigma_{a_n} = \bar{A} \sigma_U) \quad (23b)$$

Thus, for the three acceleration distributions considered, the distributions of root-mean-square gust velocity are given by the following equations:

Case a:

$$\hat{f}_1(\sigma_U) = \frac{1}{b_1} \sqrt{\frac{2}{\pi}} e^{-\sigma_U^2 / 2b_1^2}$$

where

$$b_1 = \frac{a_1}{\bar{A}_1}$$

Case b:

$$\hat{f}_2(\sigma_U) = \frac{1}{b_2} e^{-\sigma_U / b_2}$$

where

$$b_2 = \frac{a_2}{\bar{A}_1}$$

Case c:

$$\hat{f}_3(\sigma_U) = \frac{1}{2b_3^2} e^{-\sqrt{\sigma_U} / b_3}$$

where

$$b_3 = \frac{a_3}{\sqrt{\bar{A}_1}}$$

(24)

DISTRIBUTION OF ROOT-MEAN-SQUARE GUST VELOCITY

In the foregoing sections, methods have been given for converting the overall load histories from counts of peak accelerations into several discrete root-mean-square values of acceleration and their associated percentage exposure times to each level or into a continuous distribution of root-mean-square acceleration. The problem of the conversion of these results into the airplane gust experience is now considered.

The root-mean-square gust acceleration in rough air is related to the turbulence spectrum and the airplane response characteristics by the following equation:

$$\begin{aligned}\sigma_{a_n}^2 &= \int_0^\infty \Phi_U(\omega) T^2(\omega) d\omega \\ &= \int_0^\infty \Phi_{a_n}(\omega) d\omega\end{aligned}\quad (19)$$

where

$\Phi_U(\omega)$ power spectrum of vertical gust velocity
 $T(\omega)$ amplitude of airplane acceleration response to sinusoidal gusts of unit amplitude
 $\Phi_{a_n}(\omega)$ power spectrum of airplane normal acceleration

Since the root-mean-square acceleration obtained by the preceding evaluation is seen to depend on both the spectrum of turbulence and the airplane response characteristics, the root-mean-square acceleration is apparently not sufficient to fix the turbulence spectrum. Several procedures appear possible for the analysis of load measurements for the present purpose of deducing root-mean-square gust velocities. These include the actual measurement of acceleration spectra and the calculation of the airplane frequency-response function. The turbulence spectrum is then given by

$$\Phi_U(\omega) = \frac{\Phi_{a_n}(\omega)}{T^2(\omega)} \quad (20)$$

This procedure is extremely laborious and requires extensive calculations for the output spectrum $\Phi_{a_n}(\omega)$; the reliability of the results, in turn, depends upon the reliability of the calculated airplane transfer functions. At the present time, it is unlikely that the large amount of work involved in this approach is warranted even if the available records were in a form which would permit this type of analysis. Actually, the film speed used for the available records was far too slow to permit this type of analysis.

As an alternative, some simplifications appear warranted. As a preliminary effort in this direction, it will be assumed that:

- (1) The airplane is rigid.
- (2) The airplane is free to move vertically only (not pitch.)
- (3) The spectrum of vertical gust velocity is given by

$$\Phi_U(\Omega) = \sigma_U^2 \frac{L}{\pi} \frac{1 + 3\Omega^2 L^2}{(1 + \Omega^2 L^2)^2}$$

where Ω is a reduced frequency ω/V in radians per foot and L is the scale of turbulence.

These assumptions, although crude, should nevertheless provide some reasonable approximations of the gust histories. The possible magnitude of the errors introduced by these assumptions is considered in the section entitled "Reliability of Results."

For the foregoing conditions, a useful result obtained by Y. C. Fung (ref. 2) is that

$$\bar{Z}^2 = \sigma_U^2 \frac{16V^2}{\pi \bar{c}^2 (1+K)^2} I(K, s) \quad (21)$$

where

\bar{Z}^2 mean-square acceleration
 \bar{c} mean chord
 K airplane mass parameter, $\frac{4W}{g\pi\rho S\bar{c}}$
 s ratio of mean chord to scale of turbulence, \bar{c}/L
 Since $K \gg 1$ in almost all cases of concern, equation (21) may be simplified to yield

$$\begin{aligned}\sigma_{a_n} &= \sigma_U \frac{\rho V S m}{2W} \sqrt{\frac{I(K, s)}{\pi}} \\ \bar{A}_1 &= \bar{A}_1 \sigma_U\end{aligned}\quad (22)$$

where

$$\bar{A}_1 = \frac{\rho V S m}{2W} \sqrt{\frac{I(K, s)}{\pi}}$$

and $\sqrt{\frac{I(K, s)}{\pi}}$ is an airplane gust-response factor defined in reference 2 and is shown in figure 7 as a function of K for various values of $s = \bar{c}/L$.

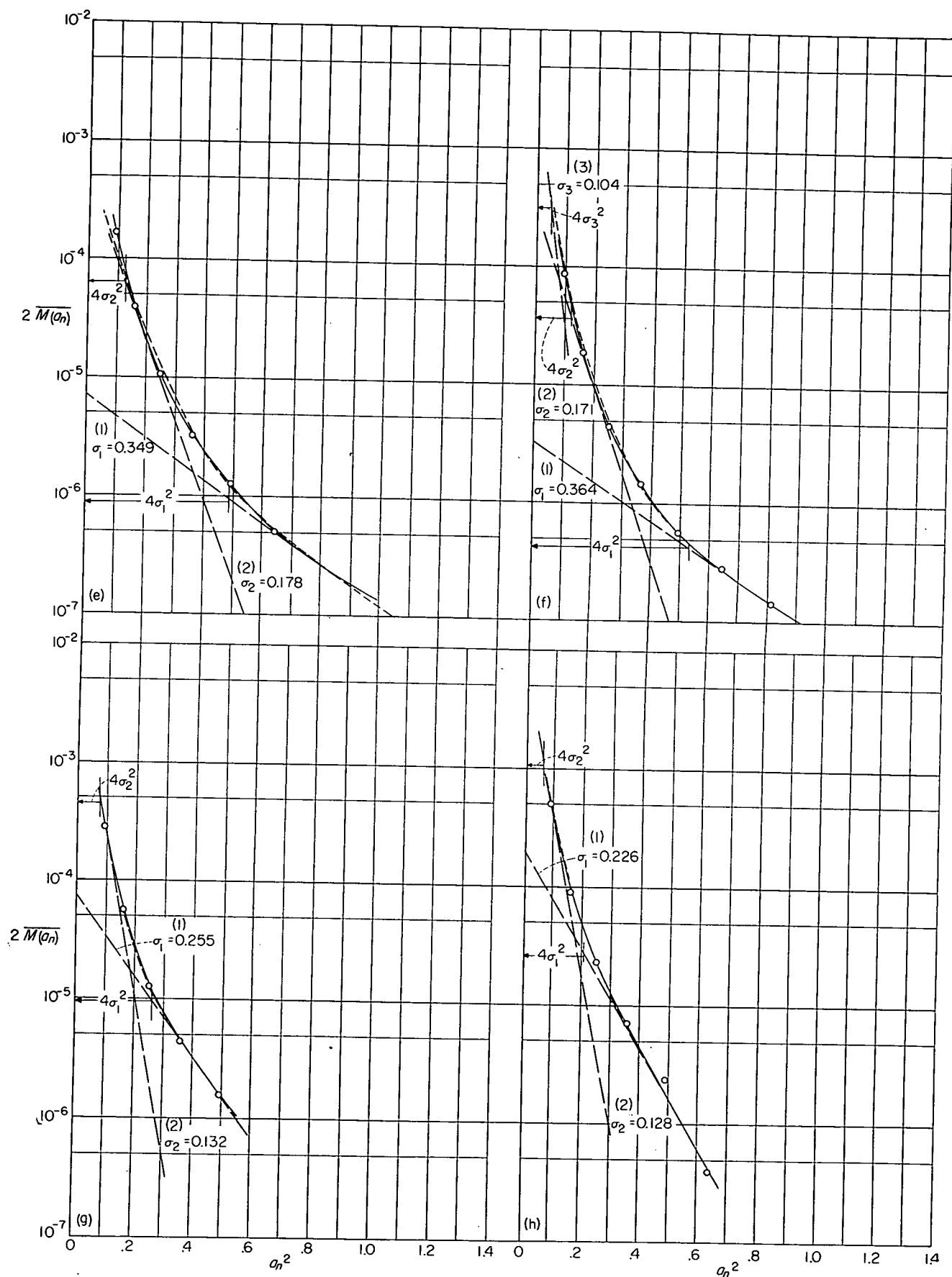
In this representation, the three-dimensional slope of the lift curve m has been used to replace 2π in order to account for the overall three-dimensional aerodynamic effects. In this form, observed values of σ_{a_n} may be used directly with the values of the airplane parameters to determine σ_U . This calculation requires the determination of the value of \bar{A}_1 . For this purpose, it would appear adequate to use average values of ρ , V , and W as well as an average value of K for a given operation or, if greater precision is required, for portions of an operation. Thus, the quantity \bar{A}_1 may be treated as a constant for a given operation (or portion of an operation).

It should be noted that the direct proportionality between the root-mean-square gust velocity and acceleration as given by equation (22) is not restricted to the one-degree-of-freedom case but may be generalized to cover as many degrees of freedom as desirable. In general,

$$\sigma_{a_n} = \bar{A} \sigma_U \quad (22a)$$

where, from equation (19), \bar{A} is defined by

$$\bar{A} = \frac{1}{\sigma_U} \left[\int_0^\infty \Phi_U(\Omega) T^2(\Omega) d\Omega \right]^{1/2} \quad (22b)$$



(e) Operation 5.

(g) Operation 7.

(f) Operation 6.

(h) Operation 8.

FIGURE 8.—Concluded.

The results of figure 8 and table IV indicate that the operational load histories can, in most cases, be reproduced by numbers of the order of 1 percent of the flight time at $\sigma_{a_n}=0.15g$ and 0.05 percent of the flight time at $\sigma_{a_n}=0.3g$. In some cases, three components were found desirable. Actually, the total flight time in rough air is considerably higher than the 1 percent indicated by these values, as previously mentioned, and should perhaps include as much as 10 percent at a lower value of σ_{a_n} of the order of 0.05g. This flight time would yield the primary contribution to the number of peak accelerations at values of a_n below 0.3g but contributes only a few peak accelerations above the threshold value of 0.3g used in the data evaluations considered herein.

The conversion of the root-mean-square accelerations to root-mean-square gust velocities requires the determination of the value of the quantity \bar{A}_1 for each operation, as defined in equation (22),

$$\bar{A}_1 = \frac{\rho V S m}{2W} \sqrt{\frac{I(K,s)}{\pi}}$$

For this purpose, the airplane characteristics given in table II were used along with the average values of air density, airspeed, and airplane weight. In determining the gust response factor, average values of weight and air density were also used along with a value of L of 1,000 feet. The values of \bar{A}_1 obtained for the eight operations and the resultant values obtained for σ_U are given in table IV. It is of interest to note that a change in the value of L by a factor of 2 results in root-mean-square gust velocities that are increased by about 25 percent if L is doubled ($L=2,000$ feet) or decreased by about 25 percent if L is halved ($L=500$ feet).

Continuous case.—In order to determine the appropriate continuous distribution of root-mean-square acceleration, the tabulated distributions of table III were compared with curves of figure 6. Operations 1, 2, 3, and 8 appeared to follow case b best and are shown in figure 6 (b). (The measured distribution of peaks which included positive and negative peaks was divided by 2 for this comparison.) The appropriate values of a_2 can be obtained from the figure by interpolation and are given in table IV. The distribution of σ_a for these operations is, from equations (14), given by

$$f_2(\sigma_a) = \frac{1}{a_2} e^{-\sigma_a/a_2} \quad (\sigma \geq 0)$$

It is of interest to note that all three of the two-engine aircraft in low-altitude operations, operations 1, 2, and 3, are best represented by this case.

The remaining four operations had a slower rate of decrease in $\bar{M}(a_n)/N_0$ with increasing a_n ; this condition suggested that case c might be more appropriate. The data for these operations are shown plotted in figure 6 (c) and are in fair agreement with the curves for case c. Again, one-half the measured distributions are plotted to be comparable with

the calculated curves. The acceleration histories for these operations are thus described by the probability distribution for case c (eqs. (14))

$$f_3(\sigma_a) = \frac{1}{2a_3^2} e^{-\sqrt{\sigma_a}/a_3}$$

where the appropriate value of a_3 determined by interpolation from figure 6 (c) for each operation is given in table IV.

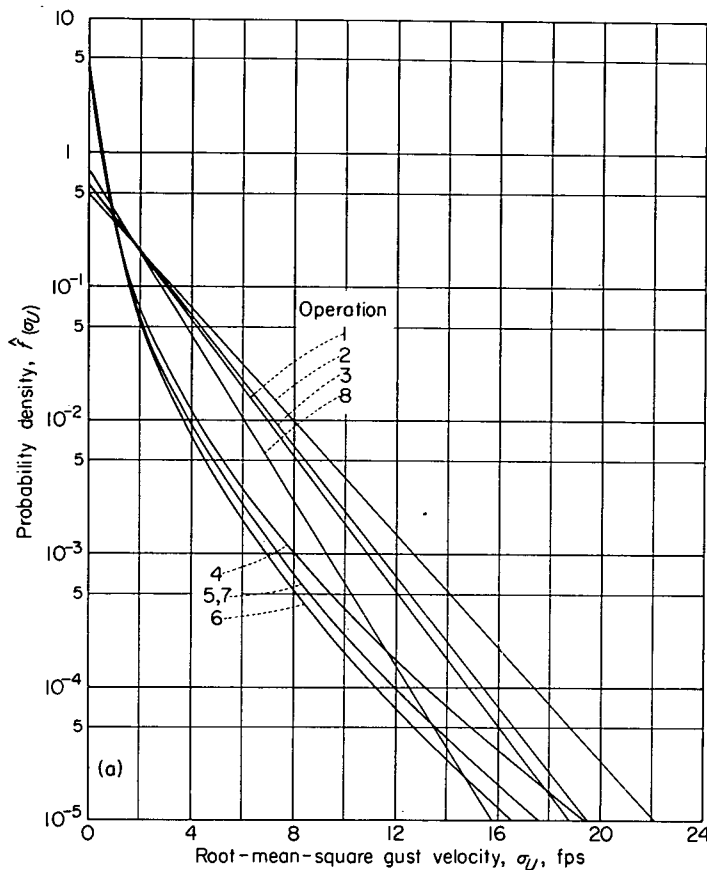
In some of the foregoing cases, the acceleration histories are not too well represented by the analysis. Better representations, if desirable, can be obtained, however, by considering combinations of the three distributions or more complicated distribution forms.

The conversion of these distributions to distributions of root-mean-square gust velocities only requires the determination of the values of b defined in equations (24). The appropriate values of b (b_2 or b_3) were determined by use of the values of \bar{A}_1 for each operation and are given in table IV. These values apply to the associated distributions which are given by equations (24). The probability distributions obtained for each of the operations are shown in figure 9 (a). Because of the changes in the values of N_0 and several other minor changes, these results also differ in some cases from those presented in NACA Technical Note 3362. The cumulative probability distributions, which are obtained by integrating the probability distributions, are given in figure 9 (b) and define the proportion of total flight time spent in turbulence exceeding given values of σ_U .

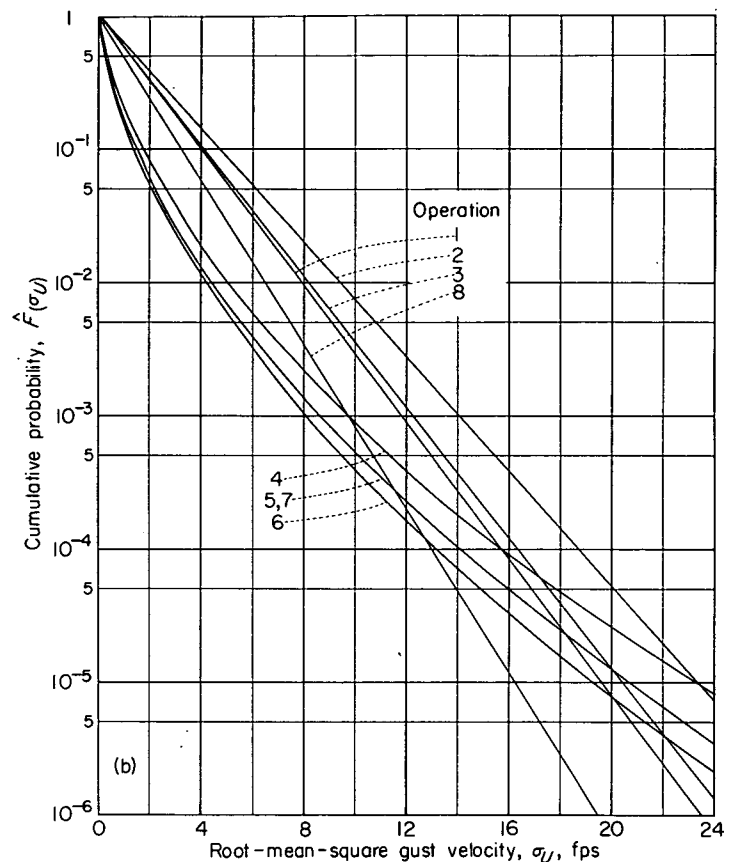
The description of the gust experience in this form is directly applicable to load calculations for other airplanes in similar operations by reversing the procedures used in obtaining these results. However, direct application of these results would apply only to similar operations. In order to obtain results that are more flexible and applicable to arbitrary flight plans, it would be desirable to determine the variations in these distributions with altitude, weather condition, and, perhaps, geography. Preliminary results obtained in this respect are described in the next sections.

VARIATION WITH ALTITUDE

Conversion of data.—In order to arrive at some rough estimates of the variation of $\hat{f}(\sigma_U)$ with altitude, use was made of the summary of gust statistics given in reference 22. Figure 6 of reference 22 presents estimates of the average gust experience at various altitudes that are representative of contemporary types of transport operations. In order to estimate the associated distributions of root-mean-square gust velocity, these results which are in terms of the frequencies of derived gust velocities were, for convenience, first converted to acceleration peaks by using the conventional gust-response equation as given, for example, in reference 12, and the characteristics of a representative transport airplane. The charts of figure 6 could then be used to estimate the appropriate distribution form and the scale value a .



(a) Probability density.



(b) Cumulative probability.

FIGURE 9.—Probability distribution of the root-mean-square gust velocity for eight operations.

The airplane and operating parameters used for this conversion to accelerations are given in table V. The acceleration histories as defined by the cumulative probability distribution of peak accelerations $\overline{M(a_n)}/N_0$ obtained on this basis are shown in figure 10 (a) for each 10,000-foot altitude bracket with the exception of the lowest altitude bracket. Also shown in the figure are curves for $\overline{M(a_n)}/N_0$ corresponding to the probability distribution of root-mean-square acceleration $f_3(\sigma_{a_n})$ as given in figure 6 (c). It will be noted that, except for the lowest altitude bracket, the acceleration histories can be reasonably well approximated by members of this family of distributions. The appropriate values of a_3 obtained by interpolation on the figure for these altitudes are given in table V. For the lowest altitude bracket, 0 to 10,000 feet, a better representation was needed. A few trials indicated that a very good approximation for the data for the lowest altitude bracket could be obtained by the following two-term probability distribution:

$$f(\sigma_{a_n}) = (0.99) \frac{1}{0.026} e^{-\sigma_{a_n}/0.026} + (0.01) \frac{1}{0.050} e^{-\sigma_{a_n}/0.050} \quad (31)$$

The distribution of peak accelerations $\overline{M(a_n)}/N_0$ corresponding to this distribution for σ_{a_n} is shown in figure 10 (b) as the short-dash curve and is seen to be in excellent agreement with the data points for this altitude bracket. The contribution

of each of the two terms of the right-hand side of equation (31) to the total curve is indicated by the two long-dash curves.

By applying the values of A_1 for each altitude bracket in table V and the foregoing results in equation (23a), the following distributions $\hat{f}(\sigma_U)$ were obtained for the various altitude brackets:

For the altitude bracket of 0 to 10,000 feet,

$$\hat{f}(\sigma_U) = 0.99 \frac{1}{1.48} e^{-\sigma_U/1.48} + 0.01 \frac{1}{2.84} e^{-\sigma_U/2.84} \quad (32)$$

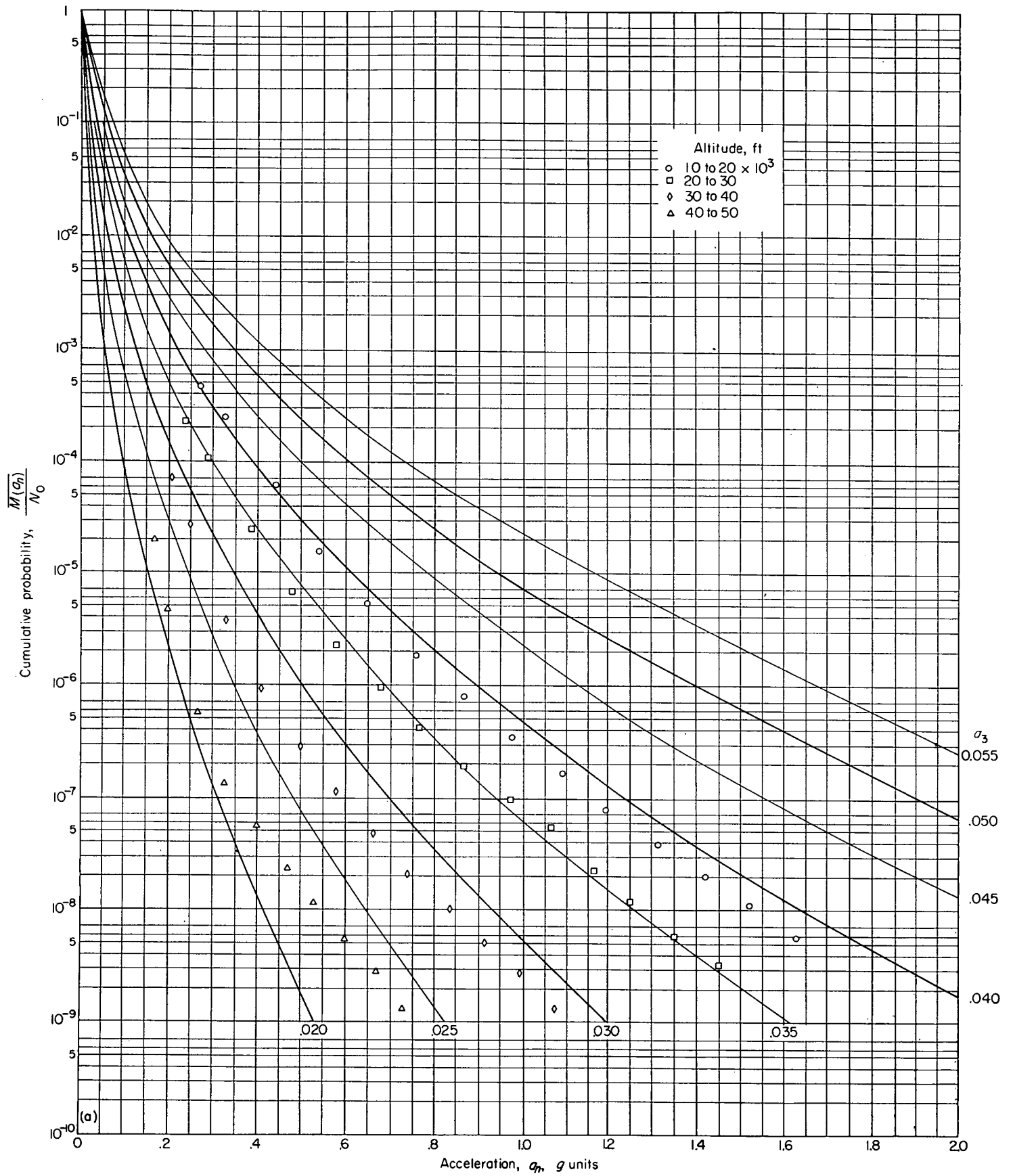
for both altitude brackets of 10,000 to 20,000 feet and 20,000 to 30,000 feet,

$$\hat{f}(\sigma_U) = \frac{1}{2(0.32)^2} e^{-\sqrt{\sigma_U}/0.32} \quad (33)$$

and for both altitude brackets of 30,000 to 40,000 feet and 40,000 to 50,000 feet,

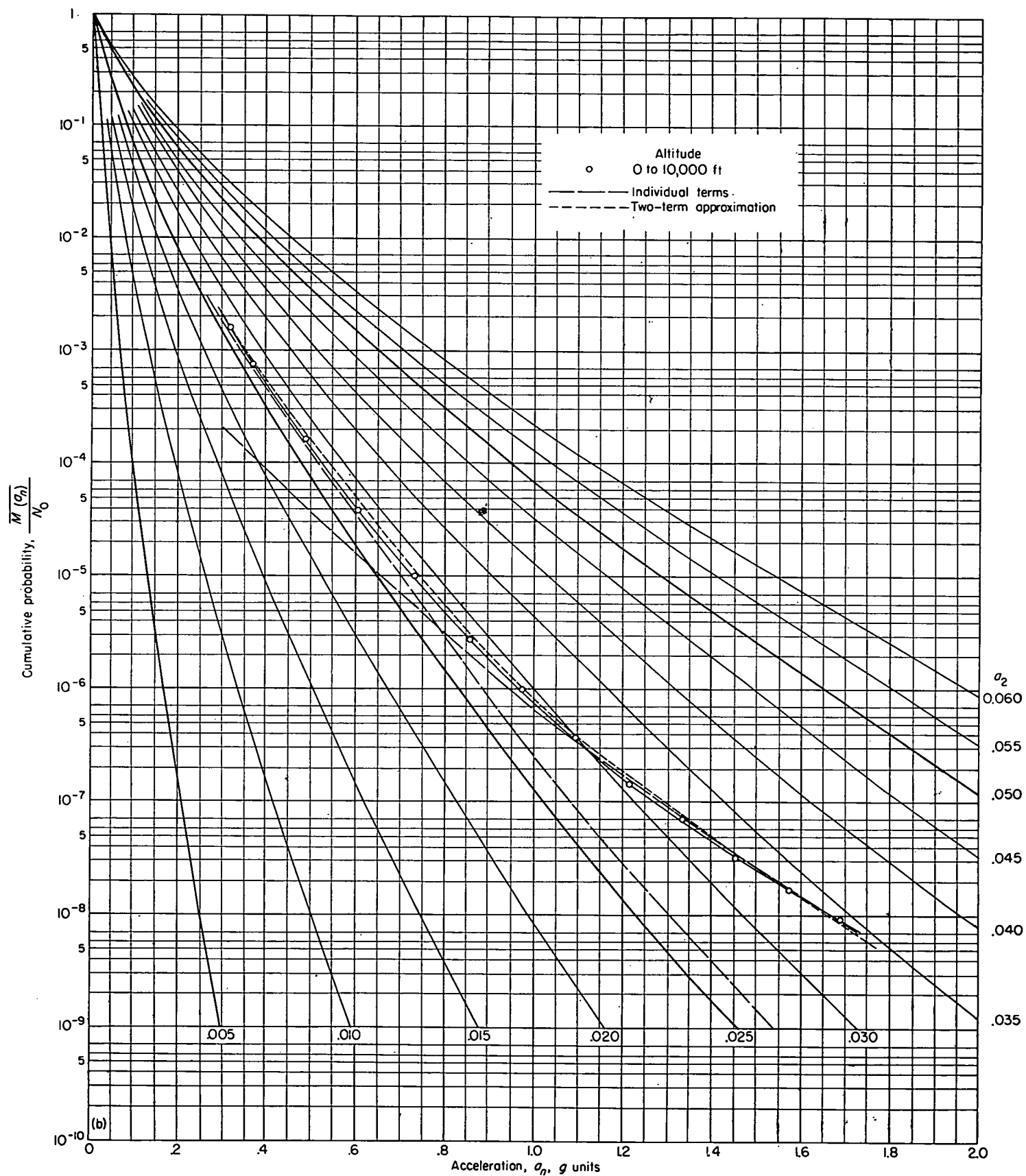
$$\hat{f}(\sigma_U) = \frac{1}{2(0.29)^2} e^{-\sqrt{\sigma_U}/0.29} \quad (34)$$

In both equations (33) and (34) average values of b_3 are given for the two 10,000-foot intervals covered. These distributions are shown in figure 11 (a). The cumulative distributions are shown in figure 11 (b) and give the probability of exceeding given values of σ_U .



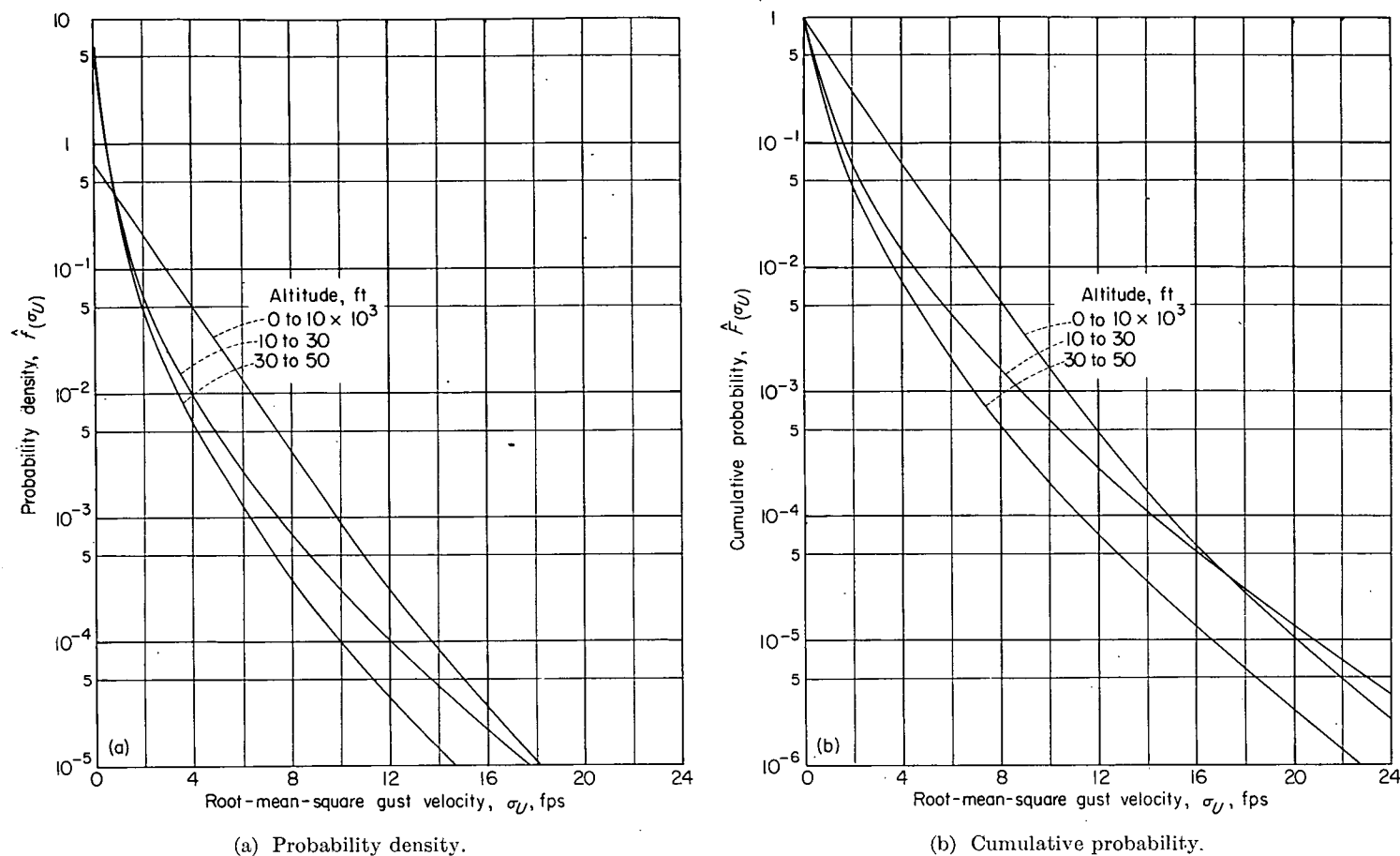
(a) 10,000 to 50,000 feet.

FIGURE 10.—Probability of a peak acceleration exceeding a given value of a_n for a representative transport in flight at various altitude brackets.



(b) 0 to 10,000 feet.

FIGURE 10.—Concluded.

FIGURE 11.—Distribution of σ_U with altitude for routine operations.

Perhaps the most important points to be noted from figure 11 (b) are the relatively large amount of time spent in essentially smooth air at the higher altitudes ($\sigma_U < 2$ feet per second 93 to 96 percent of the time) and the relatively large amount of time spent in light to severe turbulence at the lowest altitude bracket ($\sigma_U > 2$ feet per second 25 percent of the time). The time spent above 5 feet per second for the lowest altitude bracket is roughly five to ten times as great as that for the higher altitude brackets.

It should be remembered that these results are in terms of true gust velocity. If equivalent gust velocities which are more directly related to the airplane response are used, the decrease in turbulence intensity with altitude would, of course, be even more pronounced than is indicated herein.

Method of application.—The method of application of these results to the calculation of response histories for arbitrary flight is based on the following relation:

$$\overline{M(a_n)} = N_0 \int_0^{\infty} \hat{f}(\sigma_U) e^{-\frac{a_n^2}{2(\bar{A}\sigma_U)^2}} d\sigma_U \quad (35)$$

which is obtained by substituting equations (22a) and (23b) into equation (9). The procedure involves the division of the operational flight plan into homogeneous portions or segments in regard to flight altitude and operating conditions such as airspeed and airplane weight. The appropriate distribution of the root-mean-square gust velocity is

selected for each flight segment from figure 11 (a) and equation (35) is then evaluated for each segment. Actual numerical calculations are facilitated by the use of the charts of figure 6. The sequence of steps involved in such application is as follows:

- (1) The operational flight plan is divided into homogeneous segments in regard to flight altitude (10,000-foot altitude brackets) and operating conditions such as airspeed and weight.
- (2) The appropriate distribution of $\hat{f}(\sigma_U)$ is selected for each altitude bracket from figure 11 (a).
- (3) The values of \bar{A} are determined for each significant segment of the flight plan in accordance with equation (22) or (22c).
- (4) In order to obtain the associated distributions of acceleration $f(\sigma_{a_n})$, each of the distributions of $\hat{f}(\sigma_U)$ is transformed by the relation

$$f(\sigma_{a_n}) = \frac{1}{\bar{A}} \hat{f}(\sigma_U)$$

where

$$\sigma_U = \sigma_{a_n} / \bar{A}$$

- (5) The values of N_0 are most easily determined from flight records, if available, by the methods already indicated. For new designs N_0 must be estimated analytically.

From equations (4) and (20)

$$N_0 = \frac{1}{2\pi} \left[\frac{\int_0^\infty \omega^2 \Phi_U(\omega) T^2(\omega) d\omega}{\int_0^\infty \Phi_U(\omega) T^2(\omega) d\omega} \right]^{1/2}$$

The reliable estimation of N_0 from this relation is a difficult problem inasmuch as the value depends heavily on the reliability of both the gust spectrum and the airplane frequency response function at the higher frequencies. In order to obtain reliable estimates of this quantity, it appears necessary to account for the effects of spanwise variations in turbulence which act strongly to attenuate the airplane response at these higher frequencies. The effects of the spanwise variations of turbulence on the airplane response have been studied in references 6 and 23 and will have to be considered further in order to establish how best to account for these effects in estimating the value of N_0 by analytical means.

(6) The distributions of σ_{a_n} and the values of N_0 are then used in equation (9) to derive the number of peak accelerations per second or per mile for each condition. These calculations are facilitated by the use of charts such as given in figure (6).

(7) The results obtained in step 6 are then weighted in accordance with the flight distance in each condition or segment and then summed for all conditions in order to obtain the overall acceleration history.

VARIATION WITH WEATHER CONDITION

In the preceding discussion, the variation in the gust experience with flight altitude was considered. Another breakdown of the gust experience which may be useful in some problems is the variation in gust experience with weather conditions. Figure 12 (a) shows estimates of the variations in $\hat{f}(\sigma_U)$ that have been obtained from data for several types of turbulent weather conditions (ref. 24). The curve for clear-air turbulence was based on data obtained in flight through clear and turbulent air at the lower altitudes. The curve for cumulus clouds was based on data obtained in flight under moderate convective conditions such as represented by bulging cumulus clouds. Finally, the curve for thunderstorms was based on data obtained in flight in the immediate vicinity of or within severe thunderstorms. Inasmuch as the data of reference 24 showed a linear variation of the logarithmic gust frequency with gust intensity, the probability distributions of σ_U is given by case a (fig. 6 (a)). The curves of figure 12 (a) are thus given by the equation for case a:

$$\hat{f}(\sigma_U) = \frac{1}{b_1} \sqrt{\frac{2}{\pi}} e^{-\sigma_U^2/2b_1^2} \quad (\sigma_U \geq 0)$$

The values obtained for b_1 are as follows:

For clear-air turbulence,

$$b_1 = 3.15$$

for cumulus clouds,

$$b_1 = 6.28$$

and for thunderstorms,

$$b_1 = 10.05$$

A simple linear measure of the relative intensity of the turbulence for these conditions may be obtained by comparing the values of b_1 . It will be noted that the values of b_1 for the cumulus and thunderstorm conditions are roughly two and three times that for the clear-air condition. The cumulative probability distributions for the three weather conditions are shown in figure 12 (b).

It has been estimated that contemporary transport operations spend about 10 percent of their flight time in this clear-air-turbulence condition, 1 percent in the cumulus condition, and perhaps 0.05 percent in thunderstorms. These results may therefore be applied in evaluating the effects on the overall load experience of operational procedures which would tend to modify this weather experience. For example, the introduction of airborne radar for weather avoidance may be expected to reduce the exposure time to the severe turbulence conditions of thunderstorms. Also, high rates of climb and descent through the lower and more turbulent altitude layers may cause a drastic reduction in the 10 percent of the flight time attributed to clear-air-turbulence conditions and thereby cause a marked reduction in the overall gust experience.

RELIABILITY OF RESULTS

The foregoing analysis has indicated that, under reasonable assumptions, available gust statistics in the form of counts of acceleration and gust peaks may be converted into a form suitable for applications in spectral calculations of airplane responses. The appropriate form for this purpose is the probability distribution of the root-mean-square gust velocity. Estimates of this distribution are derived from data for a number of transport operations, and the variation of this distribution with altitude and weather condition is also given. In the derivation of these results, a number of assumptions were made and these assumptions may affect the reliability of the results obtained and their method of application in response calculations. The reliability of the results and the method of applying these results are discussed in this section.

The principal errors in the present analysis stem from the following sources:

(1) The assumption of the form of the turbulence spectrum and the assumed value of 1,000 feet for the scale of the turbulence

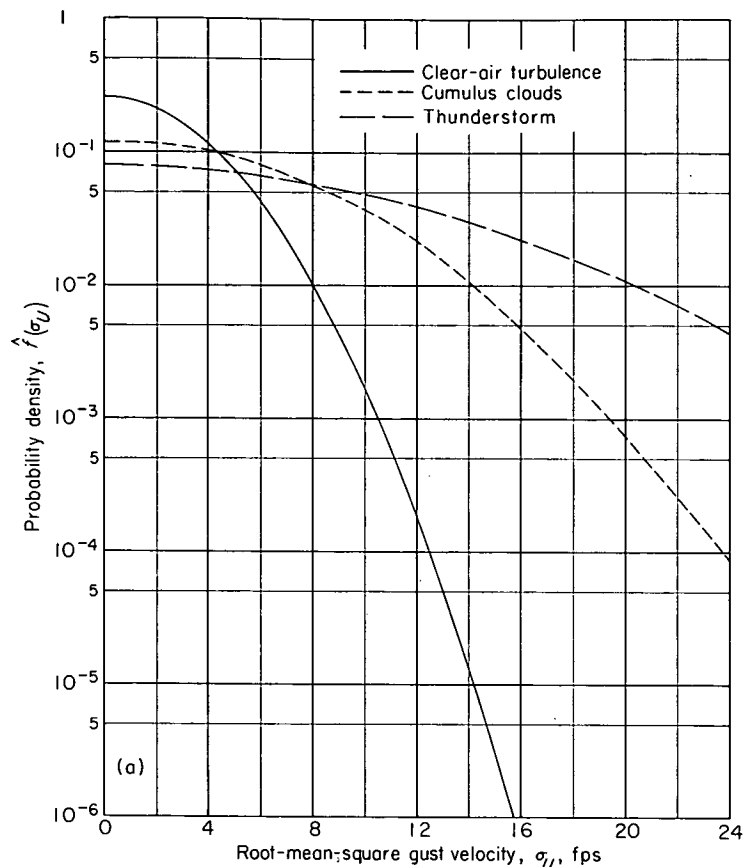
(2) The assumption of average values of weight, altitude, and airspeeds in the reduction of the data

(3) The restriction of the airplane dynamics to the one-degree-of-freedom case in the conversion of the results from acceleration to gust velocity

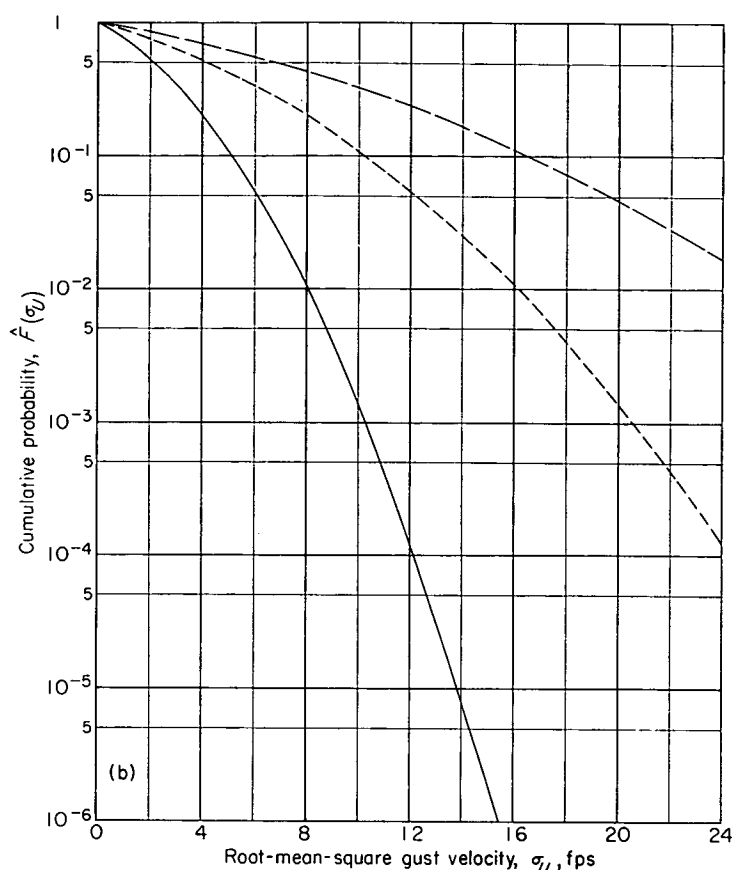
(4) The assumption that the gusts are uniform across the span

(5) The statistical sampling errors that arise from the limited data considered.

The magnitude of the errors resulting from each of these sources is considered in turn.



(a) Probability density.



(b) Cumulative probability.

FIGURE 12.—Distribution of root-mean-square gust velocity with weather condition.

Turbulence spectra.—The assumed spectral shape given by equation (1) appears to be a reasonable representation of the spectra measurements reviewed in figures 1 and 2 for the region of gust wavelengths covered (10 feet to perhaps 10,000 feet). At the shorter gust wavelengths, the spectrum probably approaches zero at a faster rate than that assumed. However, the contribution of these higher frequencies to the total power is very small and appears negligible.

At the very low frequencies (say, gust wavelengths greater than 3,000 feet), the spectrum is not yet adequately defined although the available measurements suggest a flattening of the spectrum in this region and values of L of the order of 1,000 feet. It may be expected that the value of L varies somewhat with weather condition and, as previously indicated, such variations would affect the reliability of the derived root-mean-square gust velocities. This assumption thus appears to be a possible source of error in the distributions of root-mean-square gust velocities derived herein.

The consequences of such possible errors in the scale of turbulence and in the root-mean-square gust velocities on the reliability of load and other response calculations will vary depending upon the airplane response characteristics and have to be evaluated in each case. For many airplanes, the errors in the calculated loads may be largely compensating inasmuch as the errors in the values of root-mean-square gust velocity will be balanced by the error due to the use of the erroneous value of L ($L=1,000$ feet) in the calculation of the quantity \bar{A} . This condition can be verified in a concrete fashion for the one-degree-of-freedom case by some trial calculations by use of the curves for the gust response factor of

figure 7 and consideration of possible variations in the value of the scale of turbulence. For example, representative values of the mass parameter and the mean chord for the airplanes used to collect the gust data are 100 and 10 feet, respectively. For these values and the scale of turbulence of 1,000 feet, the value of $s=\frac{\bar{c}}{L}$ is 0.01 and the value of the gust response factor $\sqrt{\frac{I(K,s)}{\pi}}$ is 0.465. If the true value of the scale of turbulence is 2,000 feet, the value of $\sqrt{\frac{I(K,s)}{\pi}}$ is about 0.36. The use of the higher value of the gust response factor would, from equation (22), yield a root-mean-square gust velocity that is about 29 percent too low. However, the determination of the value of \bar{A}_1 for the airplane for which the loads are being calculated would, in turn, be high by about the same amount for many cases. For example, for the same mean chord but with a mass parameter of 200, the value obtained for the gust response factor in figure 7 is about 0.61 for $L=1,000$ feet, as compared with the value of 0.48 for the scale of turbulence of 2,000 feet. Thus, the use of a value of $L=1,000$ feet in the load calculation yields a compensating error of about 27 percent. Thus, at least for limited variations in the airplane parameters, the net errors in the load calculation due to variation in the scale of turbulence from the assumed value of 1,000 feet would be small.

Average values of airplane parameters.—The effects of assuming average conditions of weight, altitude, and speed may also be expected to introduce some errors in the derived root-mean-square gust velocities given in figure 9 for the

various operations. The errors resulting from the assumptions of average weight and altitude may be expected to be small because these errors should largely average out. The effects of speed variations are in a somewhat different category inasmuch as efforts are normally made to reduce speed in rough air. For the operations considered herein (fig. 9), it appears that the reductions in speed from normal operating speeds were generally small and negligible at the lighter levels of turbulence. At the more severe levels of turbulence, the airspeeds were, on the average, somewhat lower than normal operating speeds, but the reductions in most cases were small, about 5 to 10 percent. Thus, the distribution of σ_u at the higher levels may be biased to this extent.

In deriving the results on the variation of the distributions of root-mean-square gust velocity with altitude and weather condition, figures (11) and (12), the assumption of an average speed was not necessary inasmuch as the original distributions of derived gust of reference 8 were largely based on data in which the actual speeds were taken into account. However, average conditions of altitude and weight were assumed both in the derivation of the basic data and in the present reductions. The errors due to these sources should be largely self-balancing and therefore small.

Airplane dynamics.—In the derivation of the root-mean-square gust velocities, the airplane was assumed to be rigid and restrained in pitch although free to move vertically. These assumptions are admittedly rough approximations and their effects on the derived gust data require additional study. Extensions of the present results to include the effects of these two additional degrees of freedom appear possible although they would involve a considerably larger number of airplane and operating parameters. It should, however, be possible in the meantime to make some rough overall corrections to the root-mean-square gust velocities for some of these effects. For example, available information suggests that the neglect of the dynamic structural-response effects on the center-of-gravity accelerations might be expected to have resulted in roughly a 10-percent overestimation of the root-mean-square gust velocities for most of the airplanes considered in the present study. The effects of the airplane pitching motions on the root-mean-square gust velocities for the present airplanes are also generally considered small. Recent studies suggest that the pitching motions for the present airplanes would tend to decrease the gust accelerations and thus tend to lead to some underestimation of the root-mean-square gust velocities. A rough estimate of about 10 percent appears reasonable for this effect for the airplanes considered. Thus, it is suggested that the overall effects of pitch and flexibility might largely cancel each other. However, additional study of these effects is needed.

Effect of spanwise variations in turbulence.—In the present analysis, no consideration has been given to the effects of gust averaging introduced by the finite span. If the ratio of the span to the scale of turbulence is large, these effects, as has been indicated in reference 6, may be appreciable. For example, for a span of 150 feet and a value of $L=1,000$ feet, the results of reference 6 suggest that the root-mean-square value of σ_u may be underestimated in the present analysis by perhaps as much as 5 to 10 percent. For smaller values of the ratio of the span to the scale of

turbulence, the magnitude of this discrepancy is considerably smaller. If desirable, the incorporation of these effects on an average basis would also appear straightforward.

Statistical reliability of results.—Since the present results are based on relatively small operational samples (of the order of 1,000 hours), the statistical reliability of the desired distributions of root-mean-square value is dependent upon the statistical reliability of the acceleration data. Past experience has indicated that these distributions are reliable for samples of this size at the lower levels of acceleration (0.3g to 0.5g) but have poor statistical reliability at the higher acceleration values. As a consequence, it may be expected that the derived probabilities for the higher root-mean-square gust velocities are only rough estimates and should be used only as a guide. More reliable information regarding the higher root-mean-square gust velocities, requires more extensive flight data although it may be possible to supplement the present results by use of available NACA V-G records. The extension of the present applications to include such other data is, however, beyond the scope of the present report.

Applicability of results.—In view of the foregoing considerations, the distribution of root-mean-square gust velocity given herein may be considered a reasonable first-order estimate of the characteristics of atmospheric turbulence that are essentially independent of the characteristics of the airplanes involved. Thus, these gust spectra and root-mean-square gust-velocity distributions can be reasonably applied in gust-load calculations in which the effects of pitching motions and flexibility are included in the determination of the airplane transfer functions.

A final word of caution is appropriate in regard to the limitations of the present results, particularly figure 11, for response calculations. Inasmuch as the basic data on which the present results are based were largely obtained from conventional American transport-type operations, they are representative of such operations in regard to such factors as geography, turbulence avoidance procedures, and terrain clearance. As a consequence, the present results may require modification for operations that differ in a significant fashion from those considered herein.

CONCLUDING REMARKS

The foregoing analysis has served to demonstrate that the gust statistics may, under reasonable assumptions, be converted into a form appropriate for spectral-type calculations. The significant and fundamental quantity, for this purpose, appears to be the probability distribution of the root-mean-square gust velocity. The results obtained in defining the variations of this function with type of operation, flight altitude, and weather condition provide at least a starting basis for their application to response calculations in arbitrary operations. These results should serve to supplement the discrete-gust techniques in current use and be particularly appropriate in problems requiring a more detailed accounting for the airplane dynamics than is possible by discrete-gust techniques.

LANGLEY AERONAUTICAL LABORATORY,
NATIONAL ADVISORY COMMITTEE FOR AERONAUTICS,
LANGLEY FIELD, VA., March 5, 1956.

APPENDIX

RELATIONS BETWEEN PEAK COUNTS AND SPECTRA FOR A GAUSSIAN RANDOM PROCESS

In the present analysis, use is made of the relations between the number of maximums per second and the spectra for a Gaussian random process. These relations are derived in reference 13 and are summarized herein in order to permit the examination of the reliability of the approximate expression used in the body of the report.

NUMBER OF MAXIMUMS

The probability p_m that a Gaussian random process $y(t)$ will have a maximum intensity ranging from y_1 to $y_1 + dy_1$ in the time interval t to $t + dt$ is given in reference 13 as

$$p_m = dy_1 dt \frac{(2\pi)^{1/2}}{M_{33}} \left[|M|^{1/2} e^{-M_{11}y_1^2/2|M|} + M_{13}y_1 \left(\frac{\pi}{2M_{33}} \right)^{1/2} e^{-y_1^2/2\psi_0} \left(1 + \operatorname{erf} \frac{M_{13}y_1}{(2|M|M_{33})^{1/2}} \right) \right] \quad (\text{A1})$$

where the error function is

$$\operatorname{erf} Z_1 = \frac{2}{\sqrt{\pi}} \int_0^{Z_1} e^{-Z^2} dZ$$

and the coefficients M_{ij} can be expressed in terms of the value at zero of the autocorrelation function $\psi(\tau)$ and its derivatives as

$$\left. \begin{aligned} M_{11} &= -\psi_0''\psi_0^{(4)} \\ M_{13} &= (\psi_0'')^2 \\ M_{33} &= -\psi_0\psi_0'' \\ |M| &= -\psi_0''[\psi_0\psi_0^{(4)} - (\psi_0'')^2] \end{aligned} \right\} \quad (\text{A2})$$

where

$$\psi(\tau) = \lim_{T \rightarrow \infty} \frac{1}{2T} \int_{-T}^T y(t)y(t+\tau)dt$$

and ψ_0'' and $\psi_0^{(4)}$ are, respectively, the values at 0 of the second and fourth derivative of the autocorrelation function $\psi(\tau)$. The values at zero of the autocorrelation function and its derivatives are in turn related to the power-spectral-density function $\Phi(\omega)$ by the following relations:

$$\left. \begin{aligned} \psi_0 &= \int_0^\infty \Phi(\omega) d\omega \\ -\psi_0'' &= \int_0^\infty \omega^2 \Phi(\omega) d\omega \\ \psi_0^{(4)} &= \int_0^\infty \omega^4 \Phi(\omega) d\omega \end{aligned} \right\} \quad (\text{A3})$$

Equation (A1) is rather unwieldy, but two simple results of interest may be obtained from it. The first result—the expected number of maximums per second N_p —is obtained

by integrating over y_1 from $-\infty$ to ∞ and over t for a time of 1 second to obtain

$$N_p = \frac{1}{2\pi} (\psi_0^{(4)}/-\psi_0'')^{1/2} = \frac{1}{2\pi} \left[\frac{\int_0^\infty \omega^4 \Phi(\omega) d\omega}{\int_0^\infty \omega^2 \Phi(\omega) d\omega} \right]^{1/2} \quad (\text{A4})$$

The second result is an asymptotic expression for large y_1 for the number of maximums per second $N(y_1)$ exceeding given values of y_1 , which can be obtained by integrating an asymptotic approximation to p_m from y_1 to ∞ ; the result, given in reference 13, is

$$N(y_1) = \frac{1}{2\pi} (-\psi_0''/\psi_0)^{1/2} e^{-y_1^2/2\psi_0} = \frac{1}{2\pi} \left[\frac{\int_0^\infty \omega^2 \Phi(\omega) d\omega}{\int_0^\infty \Phi(\omega) d\omega} \right]^{1/2} e^{-y_1^2/2\psi_0} \quad (\text{A5})$$

It is of interest to note that the right-hand side of equation (A5) is also the exact expression for the number of crossings per second with positive slope of given values of y_1 .

Equation (A5) is the basic relation used in the present analysis for the number of peaks per second exceeding given values of y_1 . Since it is an approximation for this purpose, the magnitude of the errors introduced in the present analysis by its use is of interest and is considered in the remainder of the appendix.

RELIABILITY OF THE APPROXIMATION

Past experience has indicated that in gust-load applications, the approximation given by equation (A5) is in most cases good for values of $y_1/\sigma > 2$. For values of $y_1/\sigma < 2$, equation (A5) tends to underestimate the number of peak loads to some extent. The magnitude of these errors does not, however, appear to be large and, as will be indicated, has only a very small effect on the reliability of the present analysis.

The magnitude of the error introduced by the approximation for small values of y_1/σ may be indicated by considering the ratio $N(0)$ to the total number of peaks N_p . From equations (A4) and (A5), this ratio is given by

$$\frac{N(0)}{N_p} = \frac{\int_0^\infty \omega^2 \Phi(\omega) d\omega}{\left(\int_0^\infty \omega^4 \Phi(\omega) d\omega \right)^{1/2} \left(\int_0^\infty \Phi(\omega) d\omega \right)^{1/2}} \quad (\text{A6})$$

For a low-pass filter, which appears to describe roughly the response of a relatively rigid airplane to turbulence, equation (A6) reduces to

$$\frac{N(0)}{N_p} = \frac{\sqrt{5}}{3} \approx 0.75 \quad (\text{A7})$$

The quantity N_p , which gives all the maximums, includes some maximums at negative values of y_1 . For the low-pass-filter case, the results of reference 13 indicate that about 15 percent of all maximums are at negative values of y_1 . Thus, the approximation of equation (A5) appears to be roughly 10 percent low for the low-pass-filter case at $y_1/\sigma=0$. For increasing values of y_1/σ , this error decreases rapidly and is less than 3 percent at $y_1/\sigma=0.5$.

For moderately flexible airplanes of the type considered in the present study, the degree of underestimation of the asymptotic formula is somewhat larger than for the band-pass case. In this case, calculations indicate that equation (A5) appears to underestimate the number of peaks by about 30 percent at $y_1/\sigma=0$, 10 to 15 percent at $y_1/\sigma=1$, and 2 to 3 percent at $y_1/\sigma=2$. The effect of these errors is, however, considerably mitigated in the present applications for the following reason. The total number of peak accelerations exceeding given values is seen from equation (9) to depend in principle upon the whole distribution of root-mean-square values. Actually, for the particular exponential-type functions for $f(\sigma)$ considered in the present analysis, the principal contributions to $\bar{M}(a_n)$ arise from values of a_n/σ_{a_n} that range from about 1.0 to 4.0. Thus, the asymptotic expression is being applied principally over the region where the underestimation is only a few percent. Therefore, the errors introduced in the present analysis by the use of the asymptotic formula (eq. (A5)) can be considered negligible.

REFERENCES

1. Liepmann, H. W.: On the Application of Statistical Concepts to the Buffeting Problem. *Jour. Aero. Sci.*, vol. 19, no. 12, Dec. 1952, pp. 793-800, 822.
2. Fung, Y. C.: Statistical Aspects of Dynamic Loads. *Jour. Aero. Sci.*, vol. 20, no. 5, May 1953, pp. 317-330.
3. Press, Harry, and Mazelsky, Bernard: A Study of the Application of Power-Spectral Methods of Generalized Harmonic Analysis to Gust Loads on Airplanes. NACA Rep. 1172, 1954. (Supersedes NACA TN 2853.)
4. Clementson, Gerhardt C.: An Investigation of the Power Spectral Density of Atmospheric Turbulence. Ph. D. Thesis, M.I.T., 1950.
5. Press, Harry, and Houbolt, John C.: Some Applications of Generalized Harmonic Analysis to Gust Loads on Airplanes. *Jour. Aero. Sci.*, vol. 22, no. 1, Jan. 1955, pp. 17-26.
6. Diederich, Franklin W.: The Dynamic Response of a Large Airplane to Continuous Random Atmospheric Disturbances. Preprint No. 548, S.M.F. Fund Paper, Inst. Aero. Sci., Jan. 1955.
7. Chilton, Robert G.: Some Measurements of Atmospheric Turbulence Obtained From Flow-Direction Vanes Mounted on an Airplane. NACA TN 3313, 1954.
8. Press, Harry, and McDougal, Robert L.: The Gust and Gust-Load Experience of a Twin-Engine Low-Altitude Transport Airplane in Operation on a Northern Transcontinental Route. NACA TN 2663, 1952.
9. Pratt, Kermit G., and Walker, Walter G.: A Revised Gust-Load Formula and a Re-Evaluation of V-G Data Taken on Civil Transport Airplanes From 1933 to 1950. NACA Rep. 1206, 1954. (Supersedes NACA TN's 2964 by Kermit G. Pratt and 3041 by Walter G. Walker.)
10. Bineckley, E. T., and Funk, Jack: A Flight Investigation of the Effects of Compressibility on Applied Gust Loads. NACA TN 1937, 1949.
11. Coleman, Thomas L., Copp, Martin R., Walker, Walter G., and Engel, Jerome N.: An Analysis of Accelerations, Airspeeds, and Gust Velocities From Three Commercial Operations of One Type of Medium-Altitude Transport Airplane. NACA TN 3365, 1955.
12. Coleman, Thomas L., and Walker, Walter G.: Analysis of Accelerations, Gust Velocities, and Airspeeds From Operations of a Twin-Engine Transport Airplane on a Transcontinental Route From 1950 to 1952. NACA TN 3371, 1955.
13. Rice, S. O.: Mathematical Analysis of Random Noise. Pts. I and II. *Bell Syst. Tech. Jour.*, vol. XXIII, no. 3, July 1944, pp. 282-332; Pts. III and IV, vol. XXIV, no. 1, Jan. 1945, pp. 46-156.
14. Connor, Roger J., Hawk, John, and Levy, Charles: Dynamic Analyses for the C-47 Airplane Gust Load Alleviation System. Rep. No. SM-14456, Douglas Aircraft Co., Inc., July 29, 1952.
15. Summers, Robert A.: A Statistical Description of Large-Scale Atmospheric Turbulence. Sc. D. Thesis, M.I.T., 1954. (Also Rep. T-55, Instrumentation Lab., M.I.T., May 17, 1954.)
16. Lappi, U. O.: A Direct Method of Utilizing Flight Data To Determine Space and Spectrum Gust Velocity Distributions and Airplane Gust Performance Function (Low Level Turbulence Study). Rep. No. GM-776-T-45 (Contract AF 18(600)-1550), Cornell Aero. Lab., Inc., Aug. 1955.
17. Notess, Charles B., and Eakin, Grady J.: Flight Test Investigation of Turbulence Spectra at Low Altitude Using a Direct Method for Measuring Gust Velocities. Rep. No. VC-839-F-1 (Contract AF 33(616)174), Cornell Aero. Lab., Inc., July 1, 1954.
18. Crane, Harold L., and Chilton, Robert G.: Measurements of Atmospheric Turbulence Over a Wide Range of Wave Lengths for One Meteorological Condition. NACA TN 3702, 1956.
19. Panofsky, H. A.: Statistical Properties of the Vertical Flux and Kinetic Energy at 100 Meters. Scientific Rep. No. 2 (Contract No. AF19(604)-166), Div. of Meteorology, Pennsylvania State College, July 1, 1953.
20. Lawson, James L., and Uhlenbeck, George E., eds.: Threshold Signals. McGraw-Hill Book Co., Inc., 1950, ch. 3.
21. James, Hubert M., Nichols, Nathaniel B., and Phillips, Ralph S.: Theory of Servomechanisms. McGraw-Hill Book Co., Inc., 1947, ch. 6.
22. McDougal, Robert L., Coleman, Thomas L., and Smith, Philip L.: The Variation of Atmospheric Turbulence With Altitude and Its Effect on Airplane Gust Loads. NACA RM L53G15a, 1953.
23. Liepmann, H. W.: Extension of the Statistical Approach to Buffeting and Gust Response of Wings of Finite Span. Rep. No. SM-15172, Douglas Aircraft Co., Inc., Feb. 1954.
24. Press, Harry: An Approach to the Prediction of the Frequency Distribution of Gust Loads on Airplanes in Normal Operations. NACA TN 2660, 1952.

TABLE I.—SCOPE OF OPERATIONS

Operation	Route	Flight hours	Flight miles
1	Northern transcontinental.....	834	188,000
2	Rocky Mountains—North and South.....	331	55,500
3	Southern transcontinental.....	676	130,000
4	90 percent east of Mississippi River.....	771	202,000
5	New York to Europe—New York to South America.....	1,079	284,000
6	San Francisco to Honolulu.....	1,953	486,000
7	Northern transcontinental.....	876	235,500
8	Southern transcontinental.....	706	193,500

TABLE II.—AIRPLANE AND OPERATIONAL CHARACTERISTICS

Operation	Gross weight, W , lb	Average weight, \bar{W} , lb	Wing area, S , sq ft	Average chord, \bar{c} , ft	Average flight altitude, ft	Average air density, ρ , slugs/cu ft	Airspeed, V , ft/sec	m , per radian	Mass parameter, K	$L=1,000$; $\sqrt{\frac{I(K,s)}{\pi}}$
1.....	39,900	33,915	864	10.1	5,000	0.002049	327	5.0	75.00	0.411
2.....	25,200	21,420	987	10.4	8,000	.001869	246	4.92	44.14	.318
3.....	40,500	34,425	817	9.7	5,000	.002049	281	5.03	83.83	.426
4.....	107,000	90,950	1,650	14.7	10,000	.001756	384	4.93	84.55	.385
5.....	142,500	121,125	1,720	12.9	12,500	.001622	386	5.12	133.08	.567
6.....	142,500	121,125	1,720	12.9	12,500	.001622	366	5.12	133.08	.567
7.....	142,500	121,125	1,720	12.9	12,500	.001622	394	5.12	133.08	.567
8.....	89,900	76,415	1,463	13.7	12,100	.001653	402	4.95	91.20	.495

TABLE III.—NUMBER OF ACCELERATION PEAKS EXCEEDING GIVEN VALUES

a_n	Cumulative frequency for various operations ¹							
	1	2	3	4	5	6	7	8
0.3.....	20,609	19,483	5,593	1,888	659	612	909	1,287
0.4.....	-----	4,632	1,350	427	152	132	178	232
0.5.....	1,203	1,288	365	118	40	31	40	60
0.6.....	377	370	104	44	13	10	14	18
0.7.....	124	100	31	17	5	4	5	6
0.8.....	47	35	16	6	2	2	2	1
0.9.....	26	9	5	2	1	1	-----	-----
1.0.....	7	3	2	-----	1	-----	-----	-----
1.1.....	4	-----	2	-----	1	-----	-----	-----
1.2.....	2	-----	-----	-----	-----	-----	-----	-----
1.3.....	1	-----	-----	-----	-----	-----	-----	-----
Total flight hours..	834	331.1	676.5	770.8	1,078.5	1,953.4	875.5	706.5

¹ Number includes both positive and negative peaks.

TABLE IV.—RESULTS FOR VARIOUS OPERATIONS

(a) Summary of acceleration experience

	Acceleration experience for operation—							
	1	2	3	4	5	6	7	8
$\sigma_{a_{n_1}}$	0.430	0.287	0.323	0.278	0.349	0.364	0.255	0.226
$\sigma_{a_{n_2}}$	0.247	0.181	0.181	0.147	0.178	0.171	0.132	0.128
$\sigma_{a_{n_3}}$	0.147					0.104		
$\frac{2\overline{M}_1(2\sigma_1)}{2\overline{M}_2(2\sigma_2)}$	4.3×10^{-6}	1.35×10^{-4}	1.35×10^{-3}	1.9×10^{-3}	9.5×10^{-7}	4.6×10^{-7}	9.5×10^{-6}	2.85×10^{-3}
$\frac{2\overline{M}_2(2\sigma_2)}{2\overline{M}_3(2\sigma_3)}$	3.2×10^{-4}	6.2×10^{-3}	8.8×10^{-4}	8.2×10^{-4}	6.6×10^{-3}	3.7×10^{-3}	5.4×10^{-4}	1.15×10^{-3}
$\frac{2\overline{M}_3(2\sigma_3)}{N_0}$	7.4×10^{-3}					3.0×10^{-4}		
N_0	1.0	1.0	1.0	0.5	0.5	0.5	0.5	0.5
$2N_2$	0.270	0.270	0.270	0.135	0.135	0.135	0.135	0.135
P_1	1.59×10^{-3}	4.99×10^{-4}	5.00×10^{-3}	1.41×10^{-4}	7.04×10^{-6}	3.41×10^{-6}	7.04×10^{-3}	2.11×10^{-4}
P_2	1.18×10^{-3}	2.29×10^{-3}	3.15×10^{-3}	6.07×10^{-3}	4.89×10^{-4}	2.74×10^{-4}	4.00×10^{-3}	8.52×10^{-3}
P_3	2.74×10^{-2}					2.22×10^{-3}		
a_2	0.030	0.034	0.026					0.022
a_3				0.041	0.036	0.034	0.037	

(b) Summary of gust experience for $L=1,000$ ft

	Gust experience for operation—							
	1	2	3	4	5	6	7	8
\overline{A}_1	0.01755	0.0166	0.0146	0.0146	0.0129	0.0122	0.0132	0.0156
σ_{U_1}	24.501	17.289	22.063	19.041	27.033	29.787	19.347	14.515
σ_{U_2}	14.074	10.904	12.363	10.068	13.788	13.993	10.015	8.221
σ_{U_3}	8.376					8.511		
b_1	1.709	2.048	1.781					1.410
b_2				.339	0.317	0.308	0.322	

TABLE V.—AIRPLANE AND OPERATIONAL CHARACTERISTICS USED FOR DISTRIBUTION OF σ_U WITH ALTITUDE[$\overline{W}=76,415$ lb; $S=1,463$ sq ft; $\overline{c}=13.7$ ft; $V_1=401.5$ ft/sec; $m=4.95$ per radian; $N_0=0.5$ per sec]

Altitude, ft	Air density, ρ , slugs/cu ft	Mass parameter, K	$\sqrt{\frac{I(K, s)}{\pi}}$	\overline{A}_1	a_2	a_3	b_2	b_3
0 to 10×10^3	0.002049	73.4	0.451	0.01758	0.026 .050		1.479 2.844	
10 to 20	.001496	100.5	.524	.01491		0.040		0.327
20 to 30	.001065	141.2	.583	.01181		.035		.313
30 to 40	.000736	204.5	.659	.00907		.0275		.289
40 to 50	.000458	328.4	.741	.00638		.0225		.282

REPORT 1273

A STUDY OF THE ZERO-LIFT DRAG-RISE CHARACTERISTICS OF WING-BODY COMBINATIONS NEAR THE SPEED OF SOUND ¹

By RICHARD T. WHITCOMB

SUMMARY

Comparisons have been made of the shock phenomena and drag-rise increments for representative wing and central-body combinations with those for bodies of revolution having the same axial developments of cross-sectional areas normal to the airstream. On the basis of these comparisons, it is concluded that near the speed of sound the zero-lift drag rise of a low-aspect-ratio thin-wing and body combination is primarily dependent on the axial development of the cross-sectional areas normal to the airstream. It follows that the drag rise for any such configuration is approximately the same as that for any other with the same development of cross-sectional areas.

Investigations have also been made of representative wing-body combinations with the body so indented that the axial developments of cross-sectional areas for the combinations were the same as that for the original body alone. Such indentations greatly reduced or eliminated the zero-lift drag-rise increments associated with the wings near the speed of sound.

INTRODUCTION

In the interpretation of the zero-lift drag-rise characteristics of configurations near the speed of sound, the transonic similarity rules and linear theory have been applied in limited analyses. However, no general means is available for directly explaining quantitatively the variations of the transonic drag rise associated with the numerous changes in wing plan form and section considered by airplane designers even for the simplified case of a wing alone. More important, even a qualitative understanding of the large and highly variable zero-lift drag interferences near the speed of sound associated with practical combinations of wings and bodies has been lacking. A logical means for interpreting the drag-rise values for bodies with thin low-aspect-ratio wings is discussed herein.

The results presented in reference 1 indicate that, for a representative swept-wing and central-body combination, the zero-lift drag rise is due primarily to shock losses. A study of these results also indicates that the shock formations about this relatively complex configuration at zero lift near the speed of sound are similar to those that would be

expected for a body of revolution with the same axial development of cross-sectional areas normal to the airstream. Further, the drag-rise characteristics for this wing-body combination at zero lift are about the same as those for a body of revolution (ref. 2) with approximately the same axial development of cross-sectional areas. On the basis of these facts and a preliminary consideration of the general physical nature of the flow about configurations, it has been reasoned that near the speed of sound the zero-lift drag rise of a wing-body configuration generally should be primarily dependent on the axial development of the cross-sectional areas normal to the airstream.

In order to ascertain the soundness of this concept, measurements have been made of the flow fields and drag-rise characteristics for four representative wing—central-body combinations and for bodies of revolution with the same axial developments of cross-sectional areas normal to the airstream. The results, obtained at Mach numbers from 0.85 to 1.10 in the Langley 8-foot transonic tunnel, are compared and analyzed herein. In order to illustrate possibilities for improving airplane performance at transonic speeds, zero-lift drag coefficients for three special wing-body combinations are also presented.

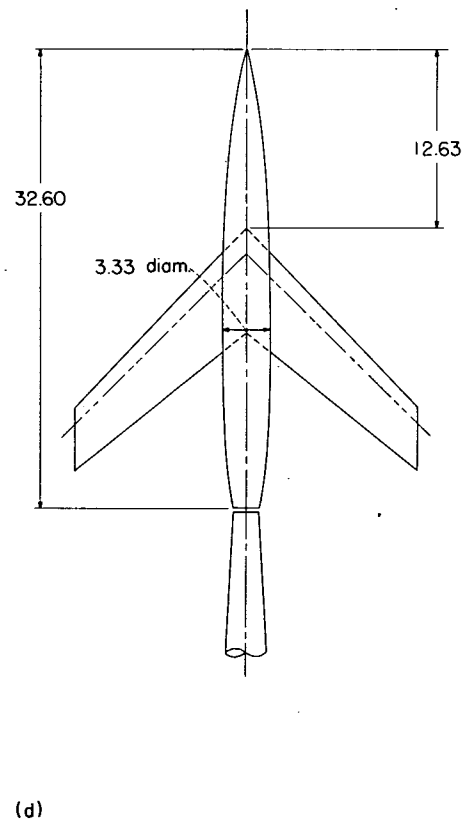
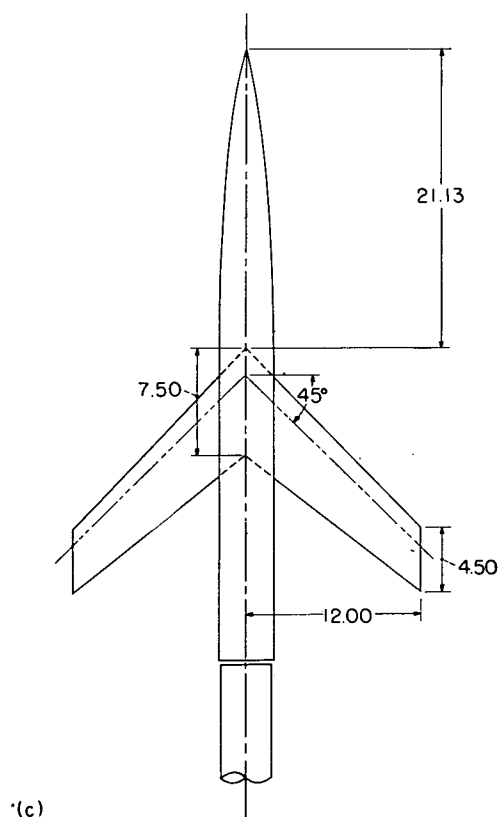
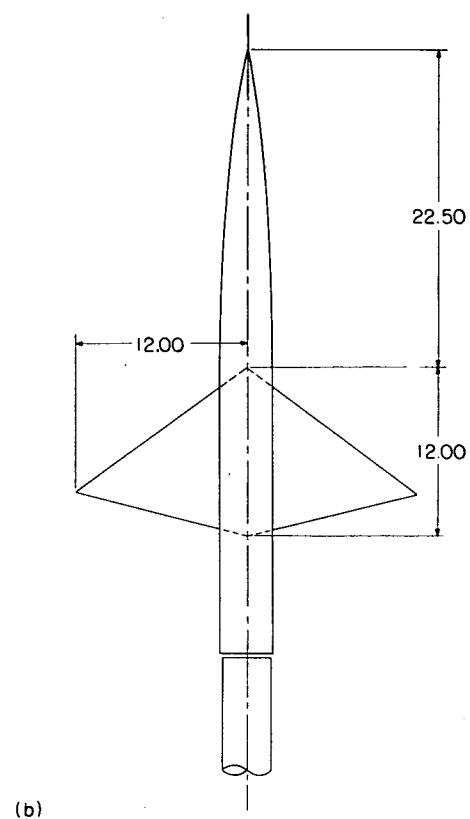
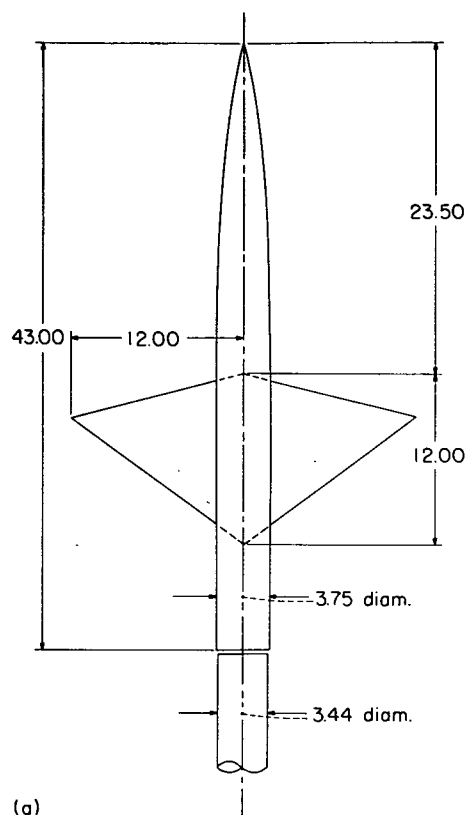
EXPERIMENTS AND PROCEDURE

CONFIGURATIONS

Basic bodies.—The major part of the results discussed herein were obtained for three wings in conjunction with the body of revolution shown in figures 1 (a), 1 (b), and 1 (c). The body is normally cylindrical in the region of the wing and has a forebody of the same shape as that of the body described in reference 1. The radii of the cylindrical body are given in table I. The swept wing was also investigated in conjunction with the body having a curved afterbody as shown in figure 1 (d). This combination is the same model used in studies in reference 1. Radii of the curved body are also given in table I. The maximum diameter of this curved body is somewhat less than that of the cylindrical body.

Wings.—The wing for which the most extensive results were obtained has 0° sweep of the quarter-chord line, an

¹ Supersedes recently declassified NACA Research Memorandum L52H08 by Richard T. Whitcomb, 1952



(a) Unswept wing, cylindrical body.
(c) Swept wing, cylindrical body.

(b) Delta wing, cylindrical body.
(d) Swept wing, curved body.

FIGURE 1.—Wing-body combinations used in investigation. (All dimensions are in inches.)

aspect ratio of 4.0, and a taper ratio of 0. The streamwise sections of the wing are symmetrical, are 4 percent thick, and consist of circular arcs with the maximum thickness at the 40-percent-chord stations. This configuration (fig. 1 (a)) is referred to as the "unswept" wing. Results were also obtained with this wing reversed so that the 75-percent-chord line is unswept, as shown in figure 1 (b). The leading-edge sweep of this wing is 37° . This configuration has almost a delta plan form and, therefore, is referred to as the "delta" wing. Finally, investigations were made with a wing which has 45° sweep of the quarter-chord line, an aspect ratio of 4.0, a taper ratio of 0.6, and an NACA 65A006 airfoil section parallel to the airstream. This configuration (figs. 1 (c) and 1 (d)) is referred to as the "swept" wing.

Special bodies.—Bodies of revolution with the same axial developments of cross-sectional areas as the wing-body combinations were obtained by altering the original bodies. The radii of these revised bodies of revolution are given in table II. Special indented bodies of revolution were investigated in conjunction with the three wings and these bodies were also obtained by altering the original cylindrical body. The radii of these bodies in the region of the wing are presented in table III.

MEASUREMENTS

Schlieren surveys were obtained with a temporary schlieren system. In order to obtain side-view schlieren surveys of the fields at distances from the model center lines with the horizontal symmetrically oriented schlieren system, the various models were displaced downward from the center line of the tunnel, as shown in figure 2 (a). In every case the displacements for the comparable bodies of revolution were the same as for the wing-body combination. Plan-view schlieren surveys for the unswept-wing—body configuration were obtained by rotating the model 90° and displacing it farther from the center line of the tunnel. Wall Mach number distributions were obtained from pressures measured at the rows of orifices placed along the center lines of panels of the test section adjacent to the top and bottom panels as shown in figure 2 (a). The relative radial locations of the wall Mach number measurement stations with respect to

TABLE II.—ORDINATES OF COMPARABLE BODIES OF REVOLUTION

[All dimensions are in inches]

Comparable to unswept wing on cylindrical body		Comparable to delta wing on cylindrical body	
Station	Radius	Station	Radius
22.500	1.875	22.500	1.875
23.500	1.875	24.000	1.875
24.500	1.892	24.500	1.882
25.000	1.939	25.000	1.894
25.500	2.012	25.500	1.911
26.000	2.087	26.000	1.934
26.500	2.155	26.500	1.968
27.000	2.182	27.000	1.992
27.500	2.185	27.500	2.019
28.000	2.174	28.000	2.054
28.500	2.145	28.500	2.086
29.000	2.113	29.000	2.113
29.500	2.086	29.500	2.145
30.000	2.054	30.000	2.174
30.500	2.019	30.500	2.185
31.000	1.992	31.000	2.182
31.500	1.968	31.500	2.155
32.000	1.934	32.000	2.087
32.500	1.911	32.500	2.012
33.000	1.894	33.000	1.939
33.500	1.882	33.500	1.892
34.000	1.875	34.500	1.875
43.000	1.875	43.000	1.875

Comparable to swept wing on cylindrical body		Comparable to swept wing on curved body	
Station	Radius	Station	Radius
22.500	1.875	14.000	1.573
23.125	1.875	14.300	1.580
24.125	1.907	14.625	1.595
25.125	1.957	15.625	1.670
26.125	2.024	16.625	1.747
27.125	2.080	17.625	1.836
28.125	2.117	18.625	1.903
29.125	2.143	19.625	1.943
30.125	2.135	20.625	1.966
31.125	2.107	21.625	1.949
32.125	2.083	22.625	1.901
33.125	2.071	23.625	1.857
34.125	2.045	24.625	1.822
35.125	2.001	25.625	1.756
36.125	1.946	26.625	1.664
37.125	1.899	27.625	1.545
38.125	1.876	28.625	1.413
38.375	1.875	29.625	1.292
43.000	1.875	29.875	1.260
		30.000	1.251
		32.000	1.010
		32.605	0.940

TABLE I.—ORDINATES OF BASIC BODY

[All dimensions are in inches]

Cylindrical body		Curved body	
Station	Radius	Station	Radius
0	0	0	0
.225	.04	.200	.092
.338	.134	.300	.119
.563	.193	.500	.171
1.125	.325	1.000	.289
2.250	.542	2.000	.482
3.375	.726	3.000	.645
4.500	.887	4.000	.788
6.750	1.167	6.000	1.037
9.000	1.391	8.000	1.236
11.250	1.559	10.000	1.386
13.500	1.683	12.000	1.496
15.750	1.770	14.000	1.573
18.000	1.828	16.000	1.625
20.250	1.864	18.000	1.657
22.500	1.875	20.000	1.667
43.000	1.875	22.000	1.652
		24.000	1.610
		26.000	1.537
		28.000	1.425
		30.000	1.251
		32.000	1.010
		32.605	0.940

TABLE III.—ORDINATES OF INDENTED BODIES

[All dimensions are in inches]

With unswept wing		With delta wing		With swept wing	
Station	Radius	Station	Radius	Station	Radius
22.500	1.875	22.500	1.875	22.500	1.875
24.000	1.875	24.000	1.875	23.125	1.875
24.500	1.857	24.500	1.868	24.125	1.842
25.000	1.807	25.000	1.856	25.125	1.787
25.500	1.720	25.500	1.837	26.125	1.710
26.000	1.622	26.000	1.812	27.125	1.641
26.500	1.521	26.500	1.773	28.125	1.592
27.000	1.476	27.000	1.743	29.125	1.560
27.500	1.470	27.500	1.710	30.125	1.572
28.000	1.487	28.000	1.664	31.125	1.611
28.500	1.533	28.500	1.642	32.125	1.640
29.000	1.580	29.000	1.580	33.125	1.656
29.500	1.642	29.500	1.533	34.125	1.688
30.000	1.664	30.000	1.487	35.125	1.740
30.500	1.710	30.500	1.470	36.125	1.802
31.000	1.743	31.000	1.476	37.125	1.850
31.500	1.773	31.500	1.521	38.125	1.874
32.000	1.812	32.000	1.622	38.375	1.875
32.500	1.837	32.500	1.720	43.000	1.875
33.000	1.856	33.000	1.807		
33.500	1.868	33.500	1.857		
34.000	1.875	34.000	1.875		
43.000	1.875	43.000	1.875		

the model are also indicated in this figure. For the side-view schlieren surveys, the distances from the model center lines to these stations were 35.5 and 52.8 inches; for the plan-view surveys, they were 31.2 and 58.0 inches. Drag measurements were obtained by internal strain-gage balances. Base pressures were also measured.

PRESENTATION OF RESULTS

Detailed flow surveys.—Composites of the schlieren photographs and the distributions of wall Mach number M_w for the unswept-wing and cylindrical-body combination, the comparable body of revolution, and the cylindrical body alone are presented in figure 2 for several stream Mach numbers M_∞ . The schlieren photographs presented above the diagrams of the three configurations show the side views; those below the wing-body configuration show the plan views. The plan-view schlieren surveys for the wing-body configurations were not duplicated for the bodies of revolution. The relative orientations and sizes of the photographs with respect to the configuration outlines are the same as those of the schlieren fields with respect to the test model. (See sketches in fig. 2 (a).)

The wall Mach number distributions shown above the composites for the three configurations were obtained during side-view schlieren surveys; those below the composites for the wing-body combination are from plan-view surveys. (See sketches in fig. 2 (a).) These two Mach number distributions presented on a given set of ordinates (fig. 2) are for the two measurement stations that are shown by the circle and square symbols labeled in the top sketch of figure 2 (a). The Mach number distributions are placed on the composites so that the distances from the center line of the model to the M_∞ points on the Mach number scales are equal relatively to the distances from the model to the lower-wall Mach number measurement stations, as indicated by the circle symbol in the sketch in figure 2 (a). The horizontal scale of the wall Mach number distributions is the same as that for the model outline.

The stream Mach numbers M_∞ at which the various schlieren photographs and wall Mach number distributions were obtained varied by as much as ± 0.005 from the mean values for each of the composites. However, the maximum difference between the stream Mach number for the directly comparable side-view photographs for the wing-body combination and for the comparable body of revolution was approximately 0.003.

Drag coefficients.—The zero-lift drag coefficients C_{D_0} for the wing-body combinations, the comparable bodies of revolution, and the basic bodies alone, as presented in the various figures such as figure 3, are all based on wing areas of 1 square foot. These coefficients have been corrected to a condition at which the base pressure is equal to the stream static pressure. The drag-coefficient increments ΔC_{D_0} , as presented in figure 3, have been obtained by subtracting the drag-coefficient values measured at a Mach number of approximately 0.85 from those measured at the higher Mach numbers. This subtraction nearly eliminated the effects of differences in the skin friction of the comparable configur-

ations on the comparisons of the drag characteristics for these configurations.

The maximum error of the absolute drag coefficients presented is approximately ± 0.0005 . The effects of wall-reflected disturbances on the drag results have been essentially eliminated at all Mach numbers except those near a value of about 1.05. This elimination has been accomplished by displacing the model from the tunnel center line, by using a cylindrical afterbody on the larger body, and by correcting for the base-pressure variations. No results were obtained for Mach numbers near 1.05.

Schlieren photographs.—The schlieren fields for the delta- and swept-wing configurations (fig. 4, for example) were oriented with respect to the configurations as indicated by the lowest schlieren photographs and configuration outlines.

RESULTS AND DISCUSSION

In the discussion that follows, the basic comparisons and analyses are made for the unswept-wing—cylindrical-body combination. The results for the other combinations indicate the effects of several variations of the wing and body configurations on the phenomena.

UNSWEPT WING AND CYLINDRICAL BODY

Shock phenomena.—The wall Mach number distributions and schlieren photographs presented in figures 2 (a) to 2 (d) indicate that the extensive shock formations produced by the unswept-wing—cylindrical-body combination at the test Mach numbers near the speed of sound are almost exactly the same as those caused by the body of revolution with the same axial development of cross-sectional areas, except in the local region directly downstream of the wing. In this locality, the shock formations, while not as closely similar as at greater distances from the configurations, are at least approximately comparable. (The incompatible shock crossing the downstream, plan-view schlieren photograph (fig. 2 (d)), at a Mach number of 1.03 is a weak reflection of a disturbance of the configuration from the tunnel wall.) At a Mach number of 1.10 (fig. 2 (e)), the similarities of the schlieren photographs for the comparable configurations are less close than at Mach numbers near 1.0.

A study of the physical nature of the flow indicates that the similarities of the extensive shock formations produced by the wing-body combination and a body of revolution with the same axial development of cross-sectional areas near the speed of sound can logically be attributed primarily to two basic factors: the negligible variations of stream-tube areas with changes in velocity (ref. 3) and the concentration of the effects of a disturbance in a plane nearly normal to the airstream. (These two factors are basically related.) It is apparent that, because of the second factor, the streamwise locations of the effects of the disturbances of the wing should be essentially the same as those for the corresponding effects produced by the body of revolution with the same axial distribution of disturbances. Also, because of the second factor, the analysis of the lateral similarities of the fields of the comparable configurations may be greatly simplified by considering the flow changes in each normal plane independently.

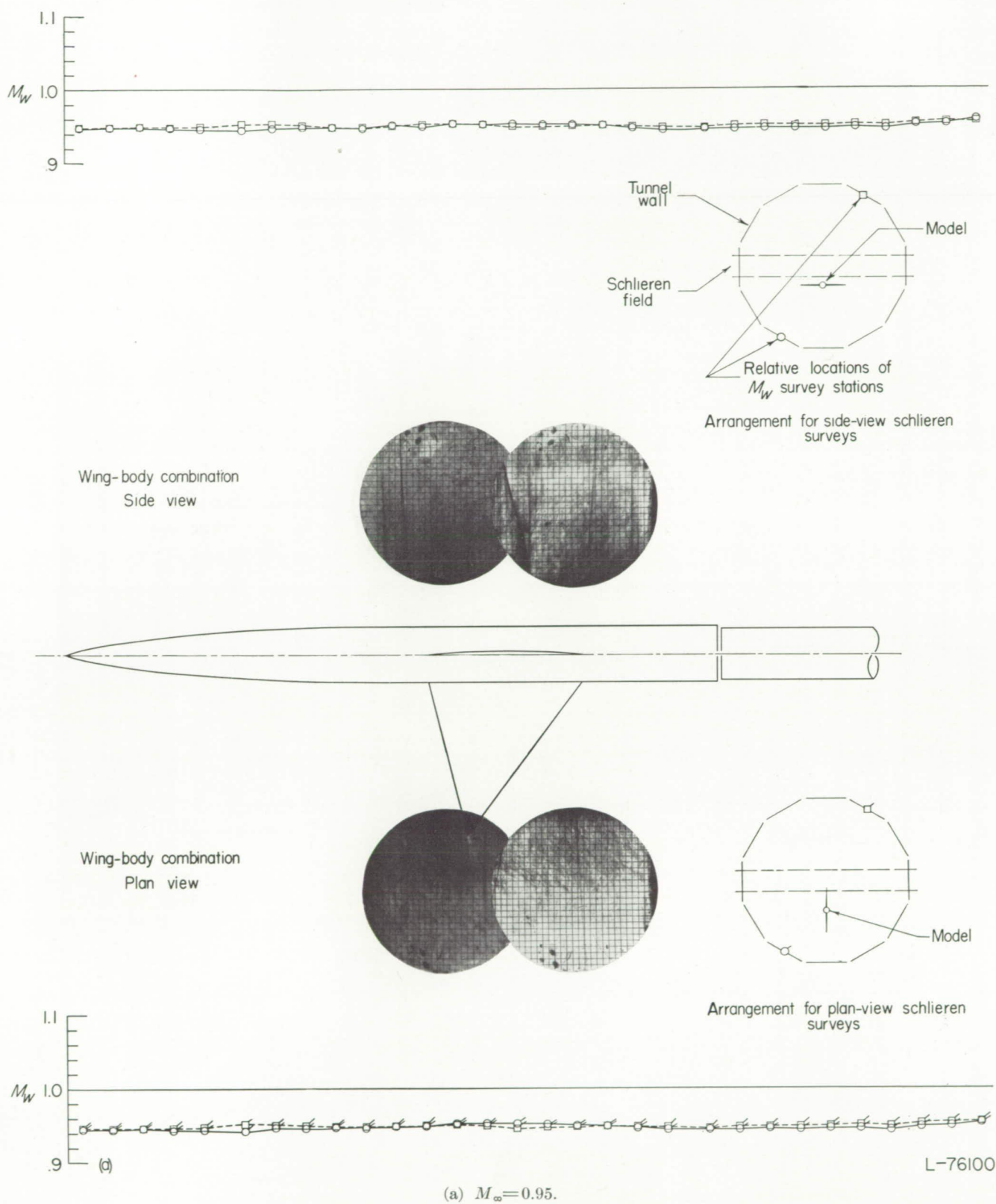
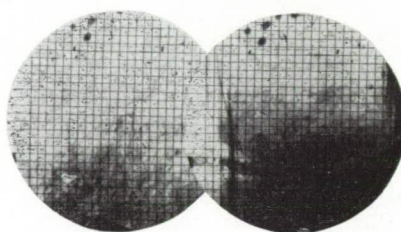
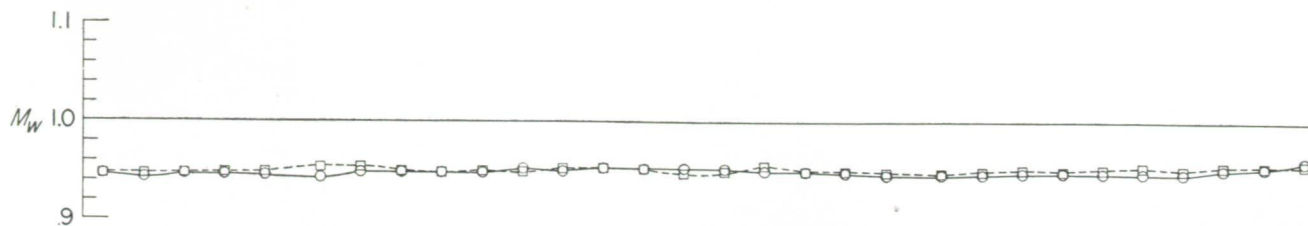
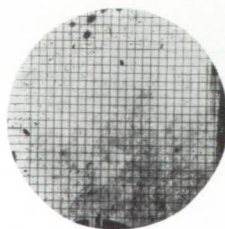
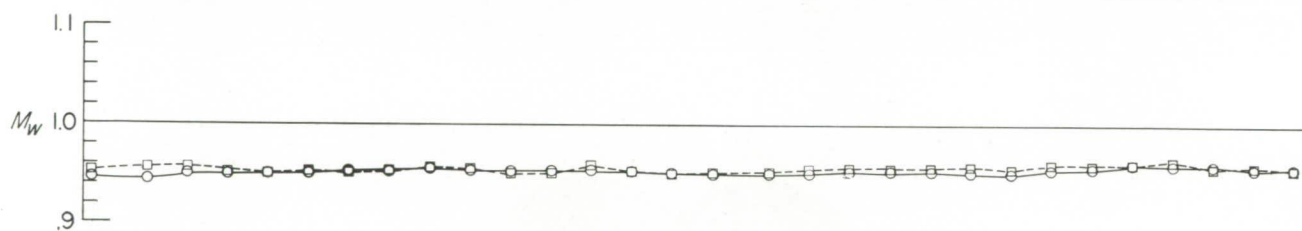


FIGURE 2.—Comparisons of the shock phenomena for the unswept-wing and cylindrical-body combination with those for the comparable body of revolution and the cylindrical body alone.



Comparable body of revolution
Side view



Cylindrical body
Side view

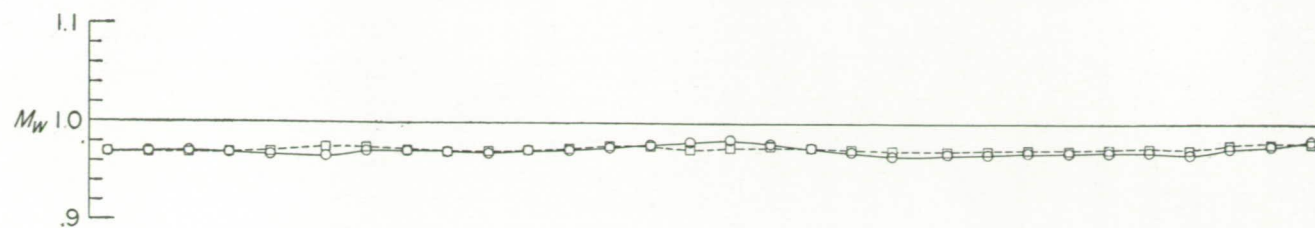


(d)

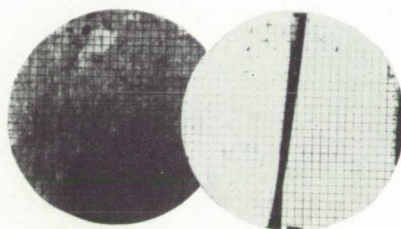
L-76101.1

(a) $M_\infty = 0.95$. Concluded.

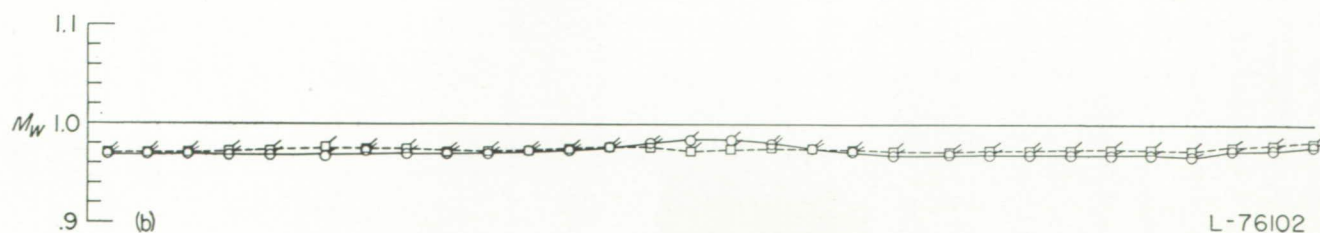
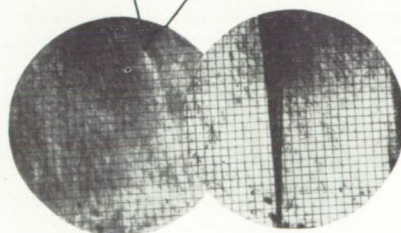
FIGURE 2.—Continued.



Wing-body combination
Side view



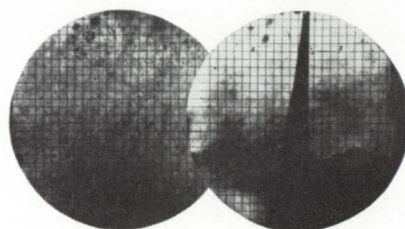
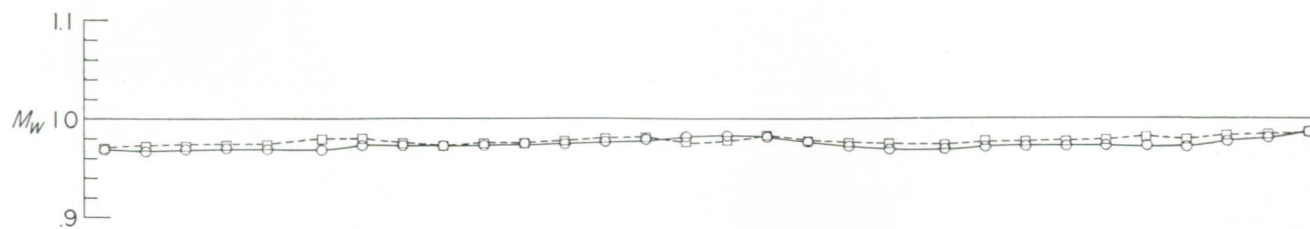
Wing-body combination
Plan view



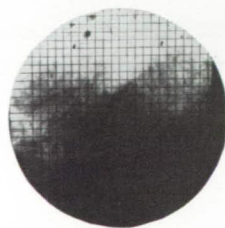
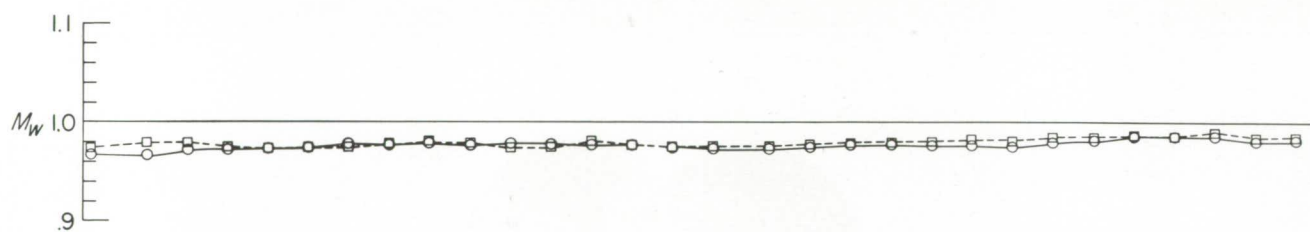
(b) $M_\infty = 0.98$. See figure 2 (a) for test-point arrangement.

L-76102

FIGURE 2.—Continued.



Comparable body of revolution
Side view



Cylindrical body
Side view

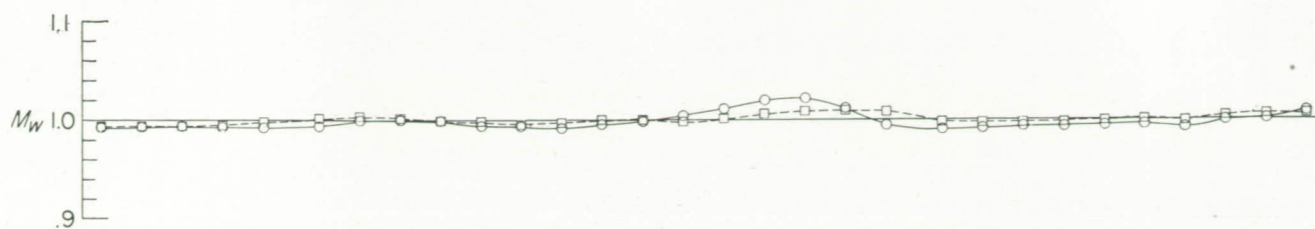


(b)

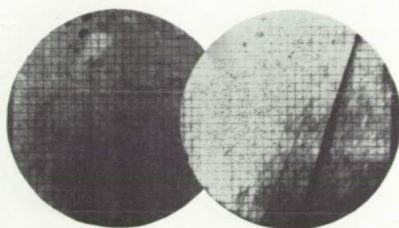
(b) $M_\infty = 0.98$. Concluded.

FIGURE 2.—Continued.

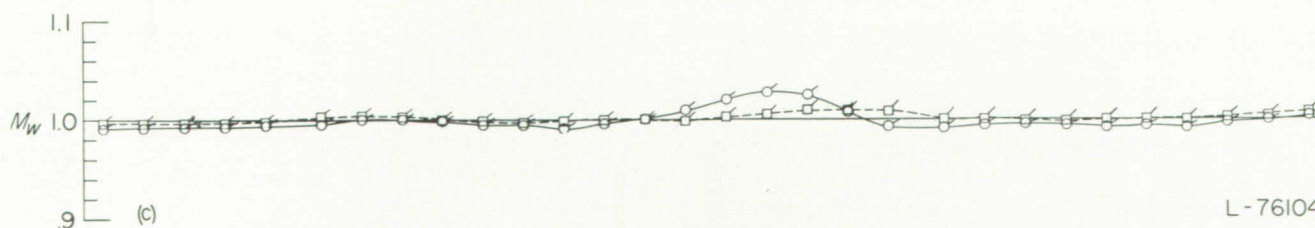
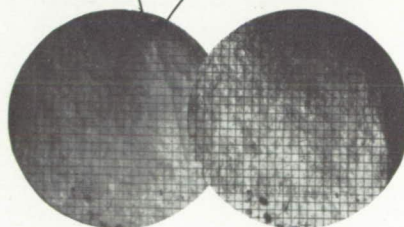
L-76103



Wing-body combination
Side view



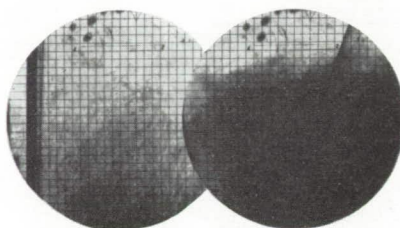
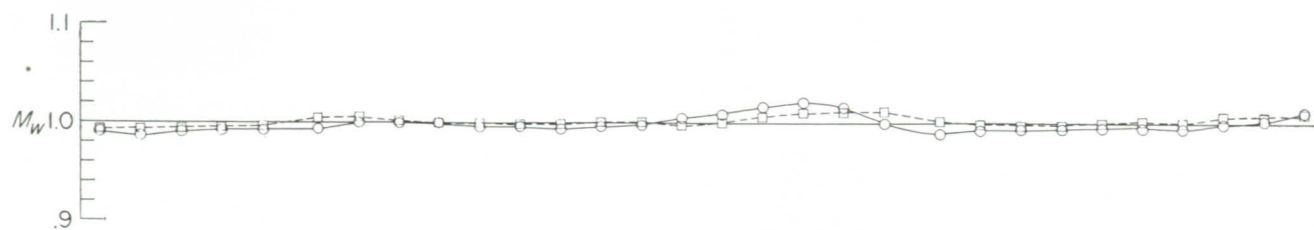
Wing-body combination
Plan view



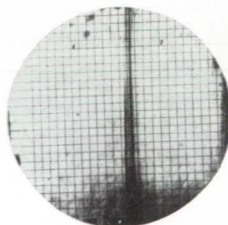
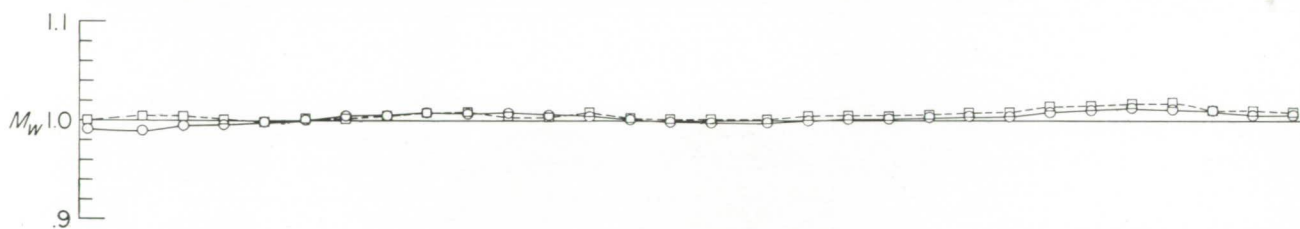
L-76104

(c) $M_\infty = 1.00$. See figure 2 (a) for test-point arrangement.

FIGURE 2.—Continued.



Comparable body of revolution
Side view



Cylindrical body
Side view

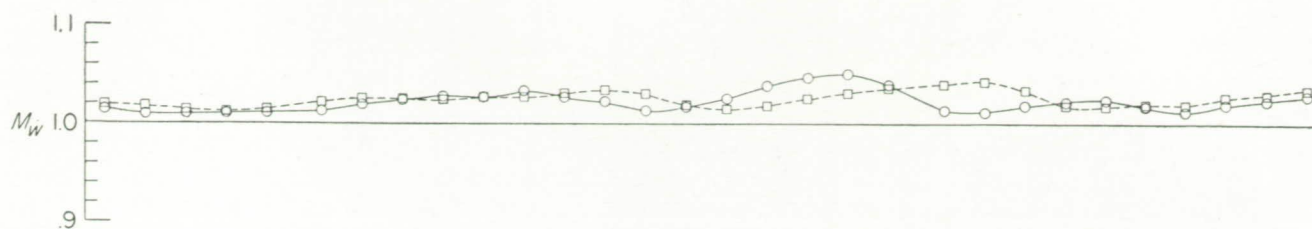


(c)

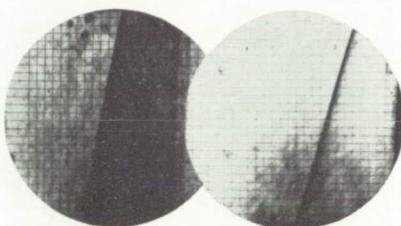
L-76105

(c) $M_\infty = 1.00$. Concluded.

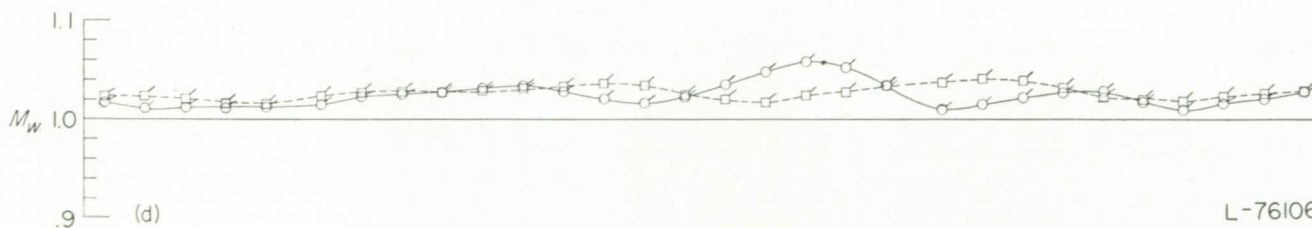
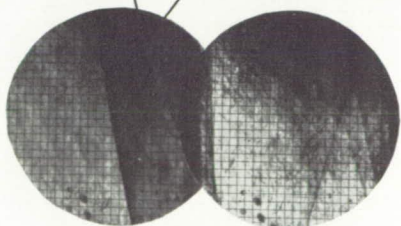
FIGURE 2.—Continued.



Wing-body combination
Side view



Wing-body combination
Plan view

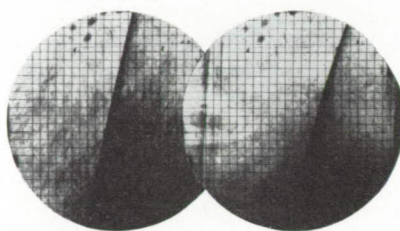
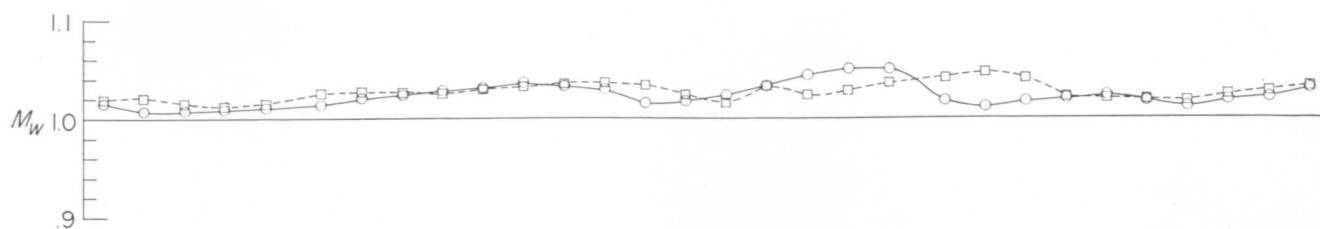


(d)

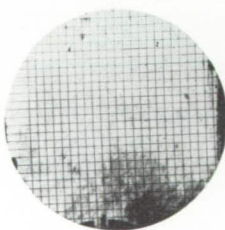
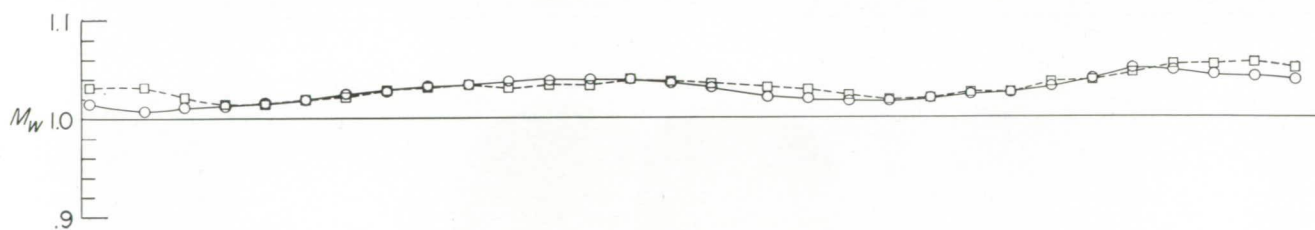
L-76106

(d) $M_\infty = 1.03$. See figure 2 (a) for test-point arrangement.

FIGURE 2.—Continued.



Comparable body of revolution
Side view



Cylindrical body
Side view

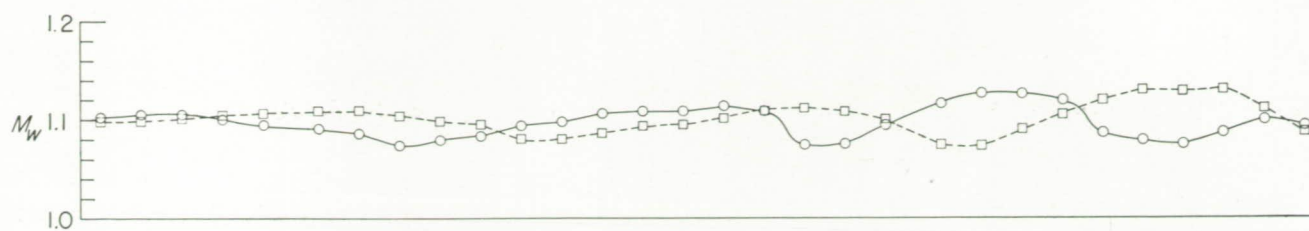


(d)

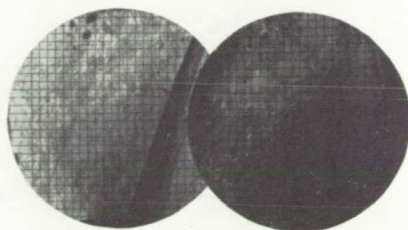
(d) $M_\infty = 1.03$. Concluded.

FIGURE 2.—Continued.

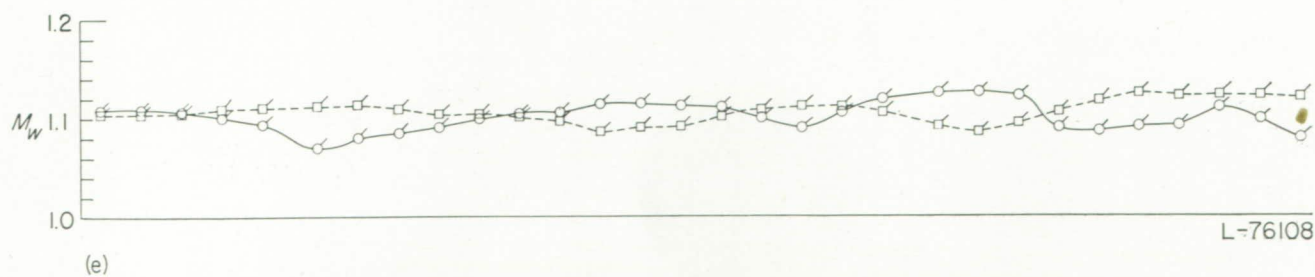
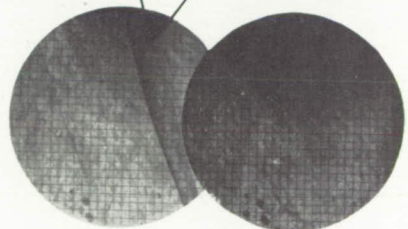
L-76107



Wing-body combination
Side view



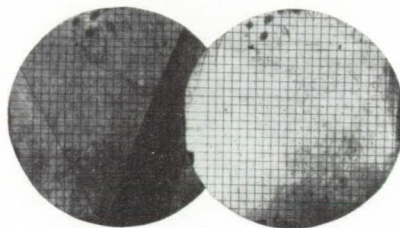
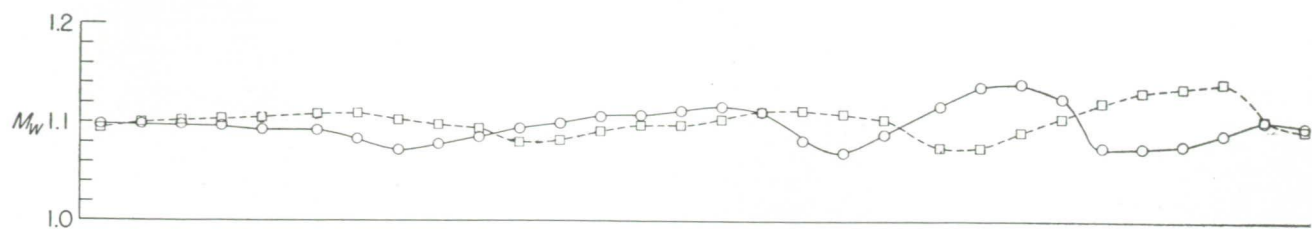
Wing-body combination
Plan view



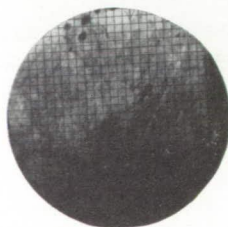
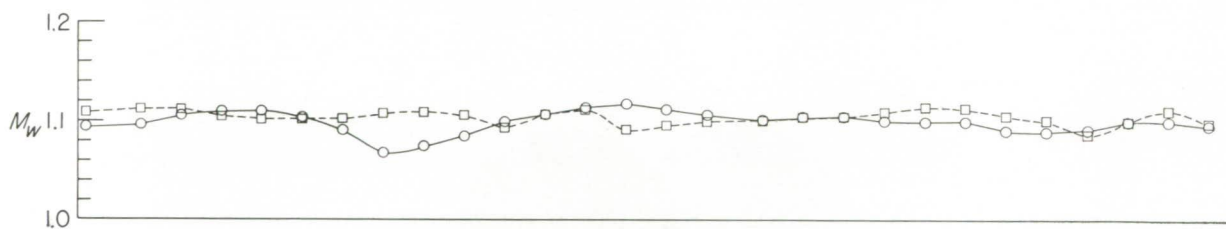
L-76108

(e) $M_\infty = 1.10$. See figure 2 (a) for test-point arrangement.

FIGURE 2.—Continued.



Comparable body of revolution
Side view



Cylindrical body
Side view



(e)

L-76109

(e) $M_\infty = 1.10$. Concluded.

FIGURE 2.—Concluded.

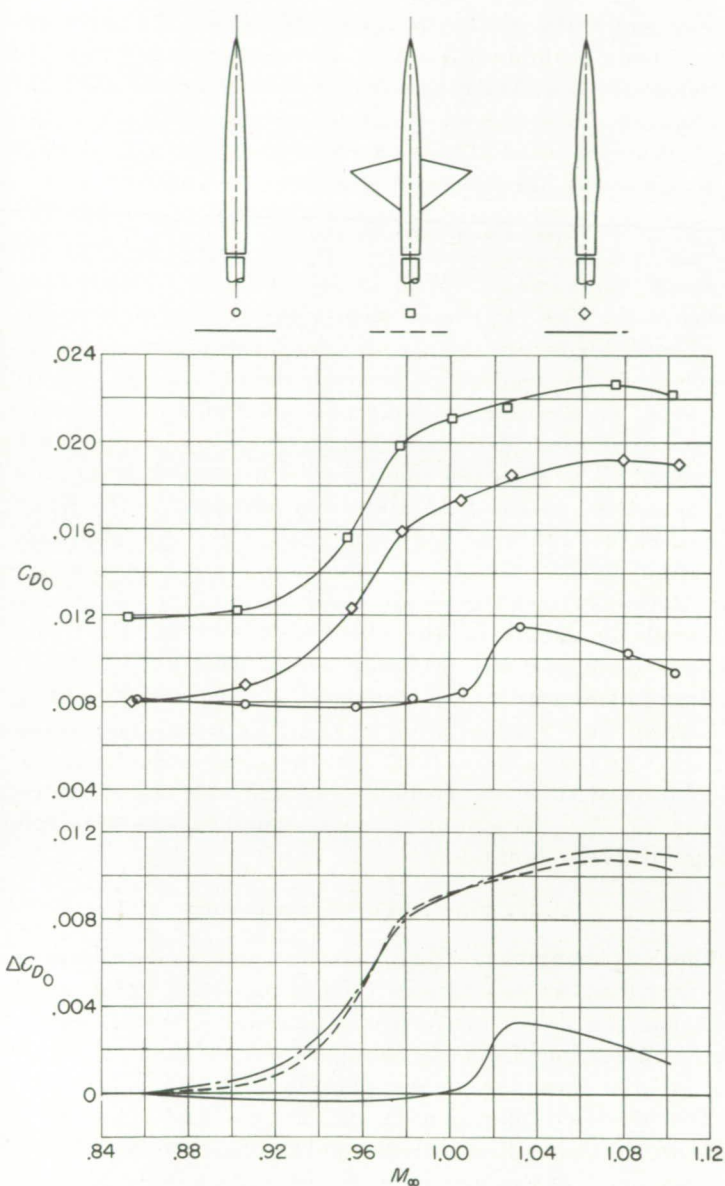


FIGURE 3.—Comparisons of the drag rise for the unswept-wing and cylindrical-body combination with that for the comparable body of revolution and the cylindrical body alone.

As a starting point for the analysis of the lateral similarities, consider the flow about the comparable configurations in a given normal plane at a circle, concentric to the axis of symmetry, outside the tip of the wing. As a result of the essential invariance of the stream tubes, the total radial deviations of the fields at this circle are essentially the same as the displacements of the surfaces of the configurations in the same plane. Since the total surface displacements for the two configurations are the same, the total flow deviations at the circle must be essentially equal. However, circumferential variations of these deviations may exist for the wing-body configuration. The essential irrotationality of the flow leads to reductions of these circumferential variations with increase in distance from the configuration. Because of the invariance of the stream-tube areas, these reductions are relatively rapid. This invariance causes the outer field to be relatively inflexible, and as a result, it reacts strongly to the circumferential variations of the radial deviations; this reaction produces pronounced circumferential pressure gradients. These gradients cause deviations in the

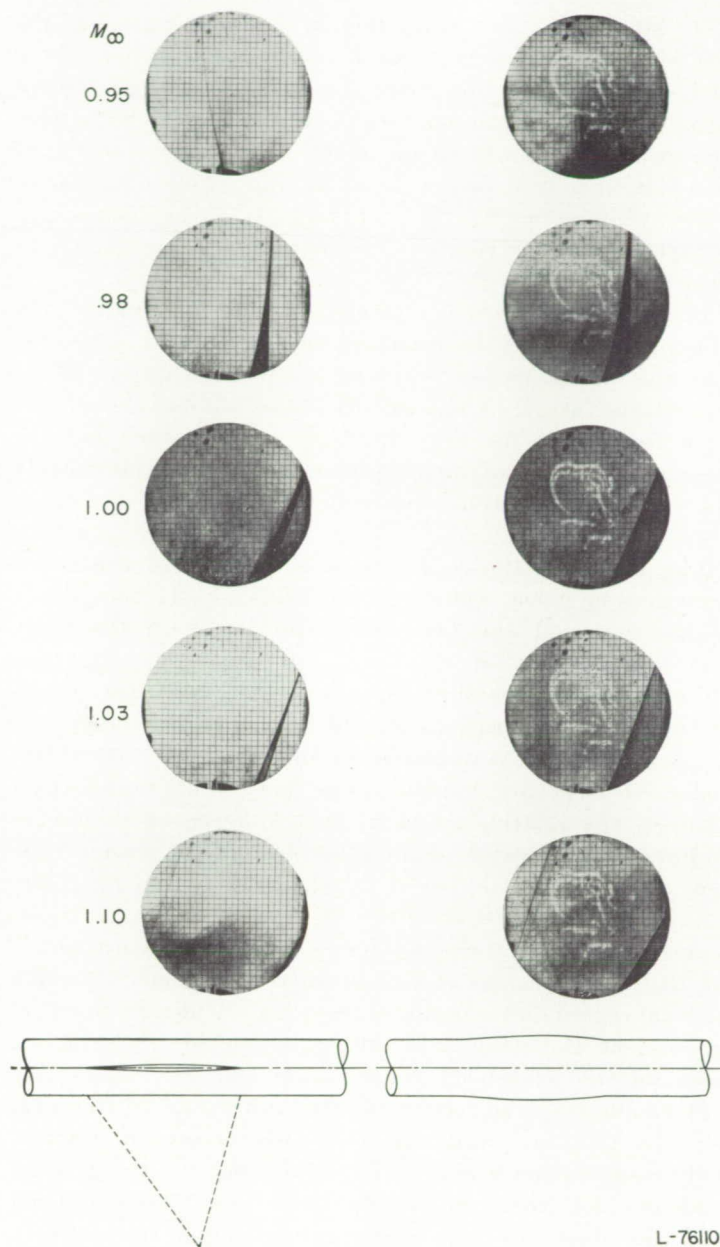


FIGURE 4.—Comparisons of the shock phenomena for the delta-wing and cylindrical-body combination with those for the comparable body of revolution. Side views.

circumferential direction which markedly reduce the variations of the radial deviations. Such effects lead to an essential elimination of the circumferential variations of radial deviations at a relatively short distance from the configuration. Also, any initial circumferential deviations associated with the asymmetry of the wing-body combination are rapidly dissipated with increase in radial distance. As a consequence of the rapid dissipation of both the circumferential deviations and the variations of radial deviations with radial distance, the deviations in a given plane at a short distance from the wing-body configuration are nearly the same as the axially symmetric effects produced by the comparable body of revolution. Such likenesses for the various normal planes are substantiated by the observed similarities of the strong shock formations for the wing-body combination and the comparable body of revolution at a distance from the configurations.

The strong reactions of the flow in the outer regions of the field of the wing-fuselage combination to deviations from axial symmetry, as previously described, converge toward the axis of symmetry and reduce the asymmetrical deviations, even in the immediate region of the wing. These reactions force the inner field into at least an approximate similarity to the axially symmetric field of the body of revolution with the same axial distribution of disturbances, as shown in figure 2.

As the Mach number is increased to supersonic values, the fields of the various disturbances become conical. Also, at these speeds, changes in velocities result in variations of the stream-tube areas. Consequently, the similarities of the shock formations for the wing-body combination and the comparable body of revolution should be progressively lessened as the Mach number is increased beyond the speed of sound.

Drag characteristics.—The close similarity of the shock formations in most regions of the fields for the wing-body combination and the body of revolution with the same axial development of cross-sectional areas suggests that in these regions the energy losses associated with the shocks for the two configurations should be nearly the same. In the locality directly downstream of the wing, the shock losses for the two configurations may differ somewhat; however, the relative effect of such differences should be unimportant. Because of the invariance of the stream-tube areas near a Mach number of 1.0, the fields of flow for these, or any, configurations are relatively extensive. As a result, the greater part of the shock losses for the configurations is due to the large areas of significantly strong shock outside the local region downstream of the wing. Thus, in the local region near the wing, the differences between the shock losses for the wing-body combination and the comparable body should result in relatively small differences of the total losses for the two configurations. Also, because of the low thickness ratio and aspect ratio of the wing and the gradual curvature for the comparable body, the shock-induced separation losses for these configurations should be relatively small, although probably not negligible, and any differences of these losses should be small. Therefore, the drag rise for the combination should be approximately the same as that for the comparable body of revolution.

The measured increments of drag coefficient for the unswept-wing—body combination are the same as those for the comparable body of revolution within the probable accuracy of the data (fig. 3). (The absolute drag coefficients for the comparable configurations differ somewhat, primarily because of differences in skin friction.)

The exact agreement of the drag-rise increments for the unswept-wing—body combination with those for the comparable body of revolution suggests that the secondary separation losses, as well as the primary shock losses, are essentially the same for the two configurations. This apparent agreement can logically be attributed to the fact that the relationships between the shocks and boundary layers for the wing-body combination and the comparable bodies are approximately the same.

The similarity of the drag-rise values for the unswept-wing—body combination and the comparable body of revolution at a Mach number of 1.10 indicates that the perceptible deviations of the shock formations for the two configurations noted at this Mach number (fig. 2 (e)) result in insignificant differences of the shock losses.

DELTA WING AND CYLINDRICAL BODY

Shock phenomena.—Wall Mach number distributions indicate that, as for the unswept-wing—body combination, the flow fields for the delta-wing—body combination at a distance from the configuration are generally almost exactly the same as those for the body of revolution with the same axial distribution of cross-sectional area for all test Mach numbers. The schlieren photographs presented in figure 4 indicate that, in the field above the aft part of the wing, the shocks for the wing-body combination are approximately the same as those for the comparable body. As is the case for the unswept-wing—body combination, the most pronounced deviations of the shock patterns for the comparable configurations probably occur behind the wing.

Drag Characteristics.—The measured variation of the drag coefficient with Mach number for the delta-wing—body combination is the same as that for the comparable body of revolution within the probable accuracy of the measurements (fig. 5). This result was also found for the unswept-wing—body combination.

SWEPT WING AND CYLINDRICAL BODY

Shock phenomena.—Wall Mach number distributions indicate that, as was true for the unswept-wing—body combination, the flow fields for the swept-wing—body combination at a distance from the configuration are almost exactly the same as those for the comparable body of revolution.

The schlieren photographs of figure 6 and reference 1 indicate that near the speed of sound the swept wing produces a weak shock at the trailing edge of the wing-body juncture and a strong shock behind the trailing edge of the juncture. At a Mach number of 1.03, an additional weak shock is also present between these two shocks. The losses in the two weak shocks are insignificant and may be neglected in a comparison of the total shock losses. The side-view schlieren photographs presented in figure 6 indicate that the main shock produced by the wing appears to be approximately the same as the shock caused by the comparable body in the region above the combination. However, the shock produced by the wing is generally somewhat rearward of that produced by the body. At a Mach number of 1.00, this shock for the wing is just visible in the schlieren photograph. Plan-view schlieren surveys not presented herein indicate that near the wing tip the main shock produced by the wing is somewhat different from that caused by the comparable body, particularly at a Mach number of 1.10. (The shock in this region is similar to that for the same wing on the curved body (ref. 1).)

Drag characteristics.—The drag-coefficient increments for the swept-wing—cylindrical-body combination are approximately 0.001 greater than those for the comparable body of

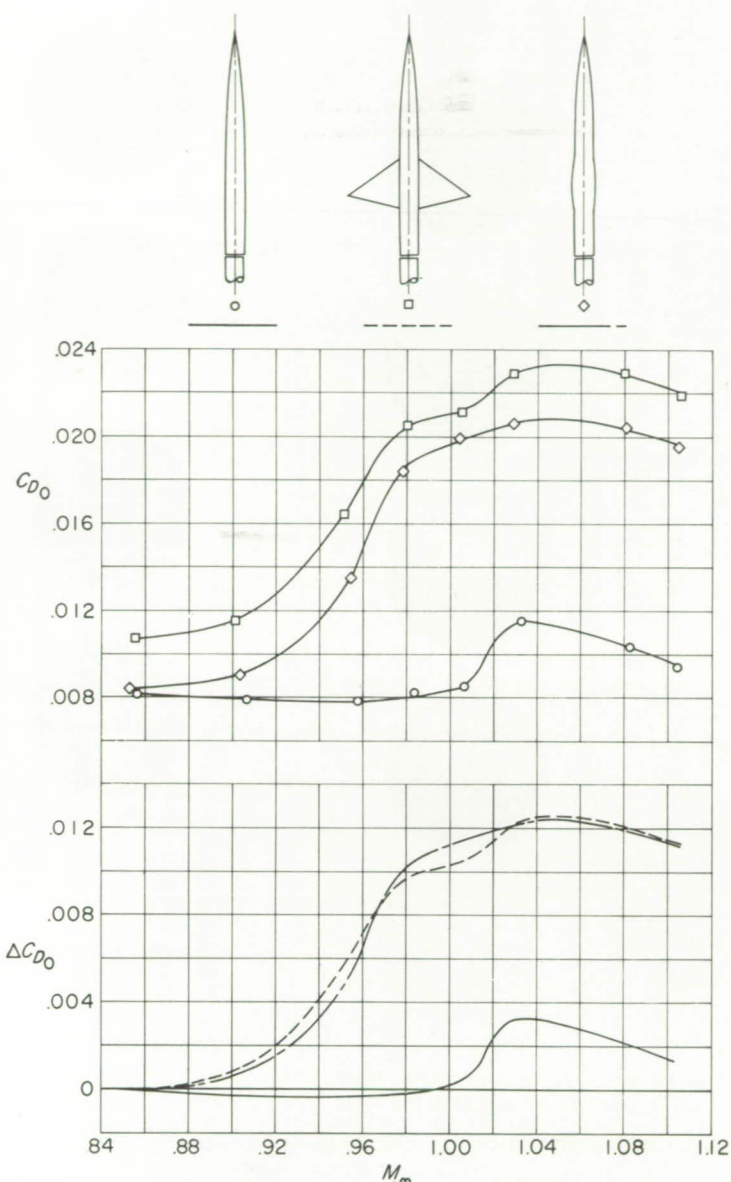


FIGURE 5.—Comparisons of the drag rise for the delta-wing and cylindrical-body combination with that for the comparable body of revolution and the cylindrical body alone.

revolution at Mach numbers up to approximately 1.02 (fig. 7). This difference is approximately the same as the total of the possible maximum errors of the drag measurements. However, if this discrepancy shown is assumed to be real, it can logically be attributed to differences in the shock formations and associated boundary-layer separation. At higher Mach numbers, the differences between the drag increments for the comparable configurations increase primarily because of the more pronounced deviations of the shock formations. The greater differences between the drag-rise increments for this swept-wing—body combination and the comparable body of revolution in comparison with those for the unswept wing may be attributed primarily to the greater thickness ratio and smaller taper of the swept wing.

SWEPT WING AND CURVED BODY

Shock phenomena.—The shock formations as indicated in the side-view schlieren photograph for the swept-wing—

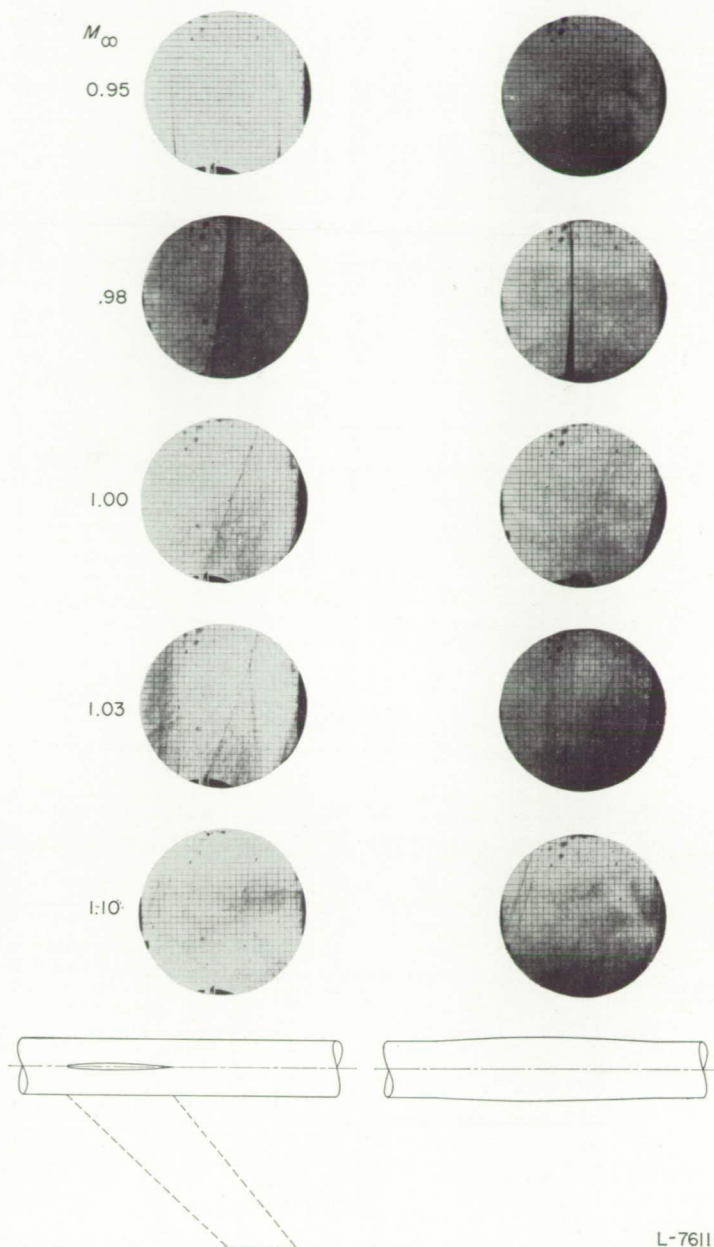


FIGURE 6.—Comparisons of the shock phenomena for the swept-wing and cylindrical-body combination with those for the comparable body of revolution. Side views.

curved-body combination (fig. 8) are similar to, but apparently stronger than, those for the swept-wing—cylindrical-body configuration (fig. 6). The differences between the shock formations produced by the swept-wing—curved-body configuration (fig. 8 and ref. 1) and those for the comparable body of revolution are also similar to the differences for the swept-wing—cylindrical-body combination.

Drag characteristics.—Combination of the swept wing and curved body results in a severe adverse drag interference between the wing and body near the speed of sound (fig. 9). The drag-coefficient rise for the swept wing in combination with this body near the speed of sound is approximately 0.012 as compared with a value of 0.004 for the wing in conjunction with the essentially interference-free cylindrical body. (See figs. 7 and 9.) (These differences in the drag-rise values may be due in part to the difference in the

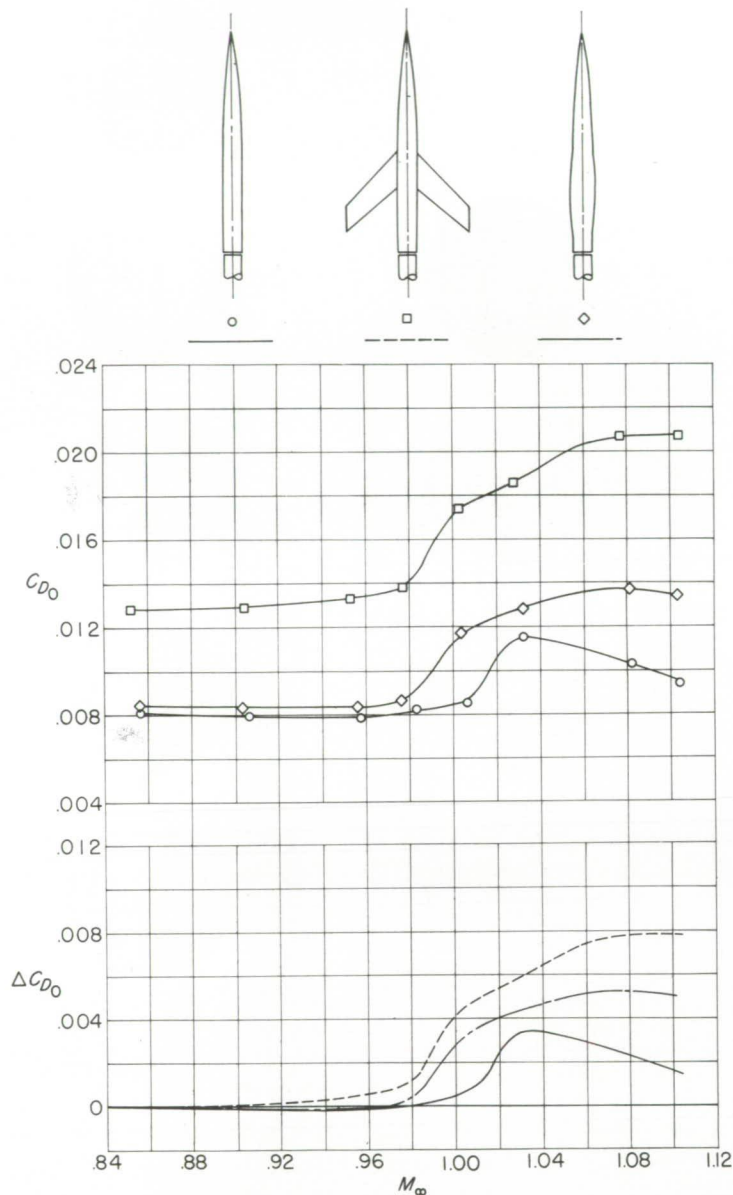


FIGURE 7.—Comparisons of the drag rise for the swept-wing and cylindrical-body combination with that for the comparable body of revolution and the cylindrical body alone.

maximum body diameter as well as the large variation of the curvature of the afterbody.)

The pronounced drag-rise increments for the swept-wing and curved-body configuration are approximately 0.003 greater than those for the comparable body near the speed of sound (fig. 9). The maximum drag rise for the combination, as measured at a Mach number of 1.03, is approximately 15 percent greater than that for the comparable body of revolution. These differences can be attributed to the same factors which caused the similar but smaller differences for the swept-wing—cylindrical-body combination.

Of particular importance is the fact that the relative increase in the drag rise for the swept-wing—curved-body combination as compared with that for the swept-wing—cylindrical-body configuration is approximately the same as the relative increase for the comparable bodies of revolution.

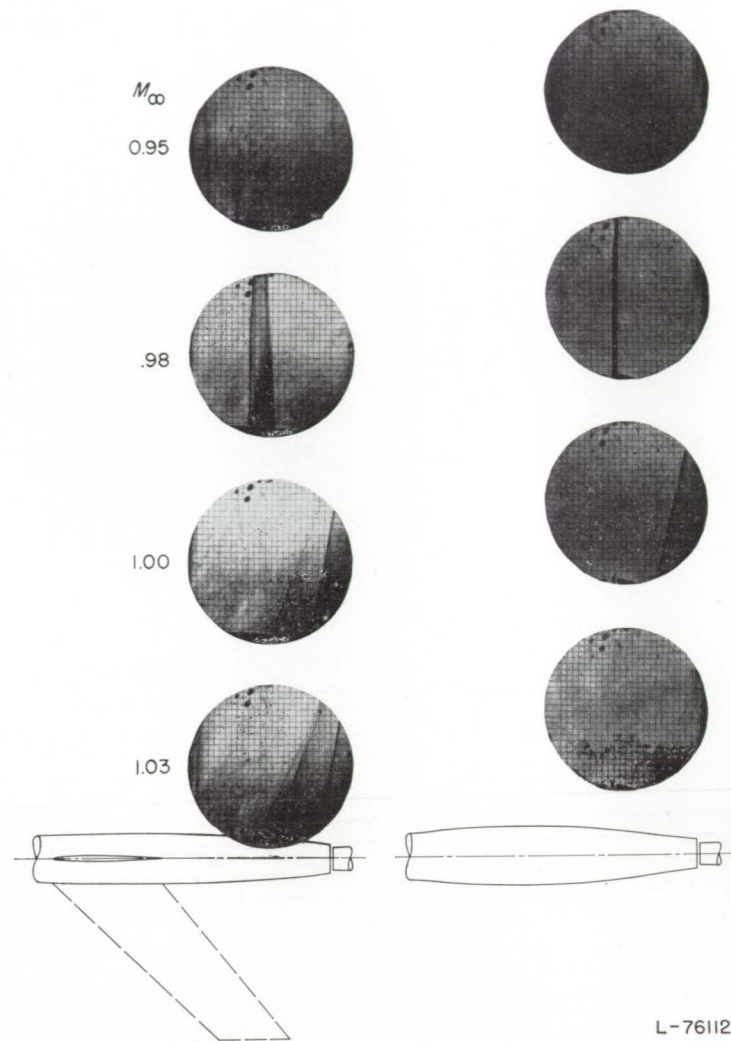


FIGURE 8.—Comparisons of the shock phenomena for the swept-wing and curved-body combination with those for the comparable body of revolution. Side views.

GENERALIZATION

The results presented indicate that, near the speed of sound, the shock formations and the associated drag-rise characteristics for the various wing and central-body combinations investigated are, to the first order, the same as those for the bodies of revolution with the same axial developments of cross-sectional areas normal to the airstream. These bodies of revolution are simple axial developments of cross-sectional areas. Therefore, on the basis of the results presented, it may logically be concluded that, near the speed of sound, the zero-lift drag rise of a low-aspect-ratio thin-wing—body combination is primarily dependent on the axial development of cross-sectional areas normal to the airstream. It follows that the drag rise for any such configuration is approximately the same as that for any other with the same development of cross-sectional areas.

It may be assumed that this concept is also valid for wings alone, wings or wing-body combinations with moderate twist or camber, or yawed configurations; however, no directly

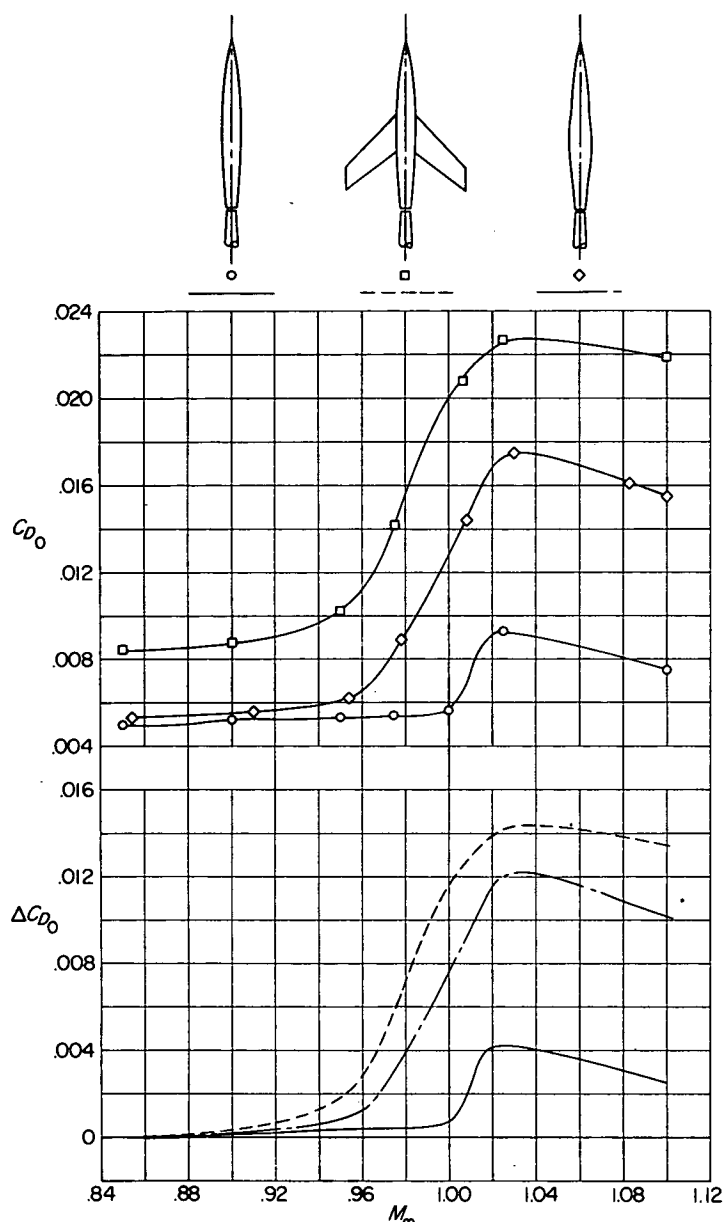


FIGURE 9.—Comparisons of the drag rise for the swept-wing and curved-body combination with that for the comparable body of revolution and the curved body alone.

comparable experimental results are available to substantiate these conjectures. Linear theory (ref. 4) and experiments (ref. 5) have indicated that a similar relation is valid for slender noncircular bodies at supersonic as well as at transonic speeds. A similar relationship for the wave drag of wing-body combinations is implicit in the linear supersonic theory of reference 6.

APPLICATIONS OF TRANSONIC DRAG-RISE CONCEPT

Correlation of drag-rise characteristics.—The accuracy of a quantitative correlation of the drag rise of a conventional wing-body combination by using the proposed concept should be lessened by increasing the thickness ratio, aspect ratio, or taper ratio of the wing. The effects of enlarging these variables should become greater as the Mach number is increased beyond the speed of sound. The results presented

herein indicate that usual variations of the shape of the body should have little effect on the accuracy of a quantitative correlation. The magnitudes of the section thickness ratios, aspect ratios, and taper ratios for the wings of contemporary transonic and supersonic aircraft generally lie between the values for the unswept and swept wings used in the present investigation. It may be assumed, therefore, that the accuracies of quantitative correlations of the drag-rise increments for these real configurations would be between those for the models investigated.

Because of the lack of knowledge as to the effects of detailed changes in the axial developments of cross-sectional areas on the drag-rise characteristics, quantitative correlations as presented herein are not generally feasible. However, it has been possible to correlate qualitatively all the available reliable drag-rise results for wings and wing-body combinations (refs. 7 and 8, for example) by use of the available information for the effects of general changes in body shape on the transonic drag rise (refs. 2 and 9, for example). It appears that the concept should be generally useful in comparing the approximate relative effects of various design alterations.

A preliminary analysis of the available information defining the effects of nacelle position on the interference between the nacelle and the wing at transonic speeds (ref. 10) indicated that this interference can be correlated qualitatively, at least, on the basis of the concept proposed. However, further specific experimental comparisons are required to define the exact applicability of this concept to the correlation of such interference.

An idea, similar to that proposed herein, was presented in reference 11 for predicting the critical speeds of wing-body combinations.

Interpretation of variations of drag-rise characteristics.—Analyses of the available drag-rise characteristics indicate that variations in wing configurations which result in less rapid rates of development of cross-sectional areas, as well as reductions of the relative magnitude of the maximum areas, decrease the drag-rise increments near the speed of sound. For example, the rates of development and maximum value of the cross-sectional areas for the swept wing of the present investigation are less than those for the unswept wing (table II). As a result, the drag rise for the swept wing is less pronounced (figs. 3 and 7).

Reversing the unswept wing to form the delta wing (fig. 1) reduced the rate of expansion of cross-sectional areas for the forward part of the wing but increased the rate of contraction of areas for the rearward part (table II). These variations resulted in increases of the drag-rise increments for the delta wing (figs. 3 and 5). On the basis of this comparison, as well as the results presented in reference 2, it may be assumed that, near the speed of sound, a given rate of decrease in cross-sectional area generally results in a greater drag rise than does a similar increase.

On the basis of the proposed concept, adverse zero-lift drag interference between wings and bodies, as for the swept-wing-body combination investigated (fig. 9), can generally

be attributed basically to greater rates of development of the cross-sectional areas for the combinations compared with those for the components (table II). These more rapid variations of area generally result in higher induced velocities and considerably stronger shocks in the fields of the combinations. (For example, compare figs. 6 and 8.) Obviously the interference drags, associated with the increased shock losses, are directly produced by changes in the pressures on the body and wing. (For example, see ref. 1.) The favorable effects of various changes in body shape on the interference between the wing and body, as shown in reference 8, can be attributed to reductions in the rates of development of the cross-sectional areas.

Reductions of the drag-rise increments of wing-body combinations.—On the basis of the concept proposed, it would be expected that indenting the body of a wing-body combination, so that the combination has the same axial distribution of cross-sectional area as the original body alone, would result in a large reduction or elimination of the drag rise associated with the wing. This type of indentation was used on the cylindrical body investigated in combination with the unswept, delta, and swept wings. (See fig. 1.)

As shown in figure 10, indenting the body reduced the drag-rise increments associated with the unswept and delta wings by approximately 60 percent near the speed of sound. This alteration eliminated the drag rise associated with the swept wing at Mach numbers up to 1.04. At higher Mach numbers, the effects of the indentations gradually decreased. Even for these relatively unconventional configurations, the proposed concept predicts correctly the qualitative effects of design modifications on the drag-rise characteristics near the speed of sound.

The incomplete effects of indenting the bodies with the unswept and delta wings may be attributed in part to local induced flows and to the displacement of the stream tubes by the boundary layer, which were neglected in the design of the indentations. For the swept wing, these effects are less important because of the more gradual axial development of the indentation. Minor modifications of the indentations of the body to account for these factors should further reduce the drag-rise increments associated with the unswept and delta wings. The reductions of the effects of these indentations at supersonic Mach numbers are associated with the change in the nature of the flow field at the higher speeds, as described in the discussion of the shock phenomena for the unswept wing.

At lift coefficients up to approximately 0.3, the indentations of the bodies result in drag reductions similar to those shown. Although these indentations have not completely eliminated the near-sonic drag-rise increments associated with all the wings investigated, they have at least greatly reduced the increments in every case.

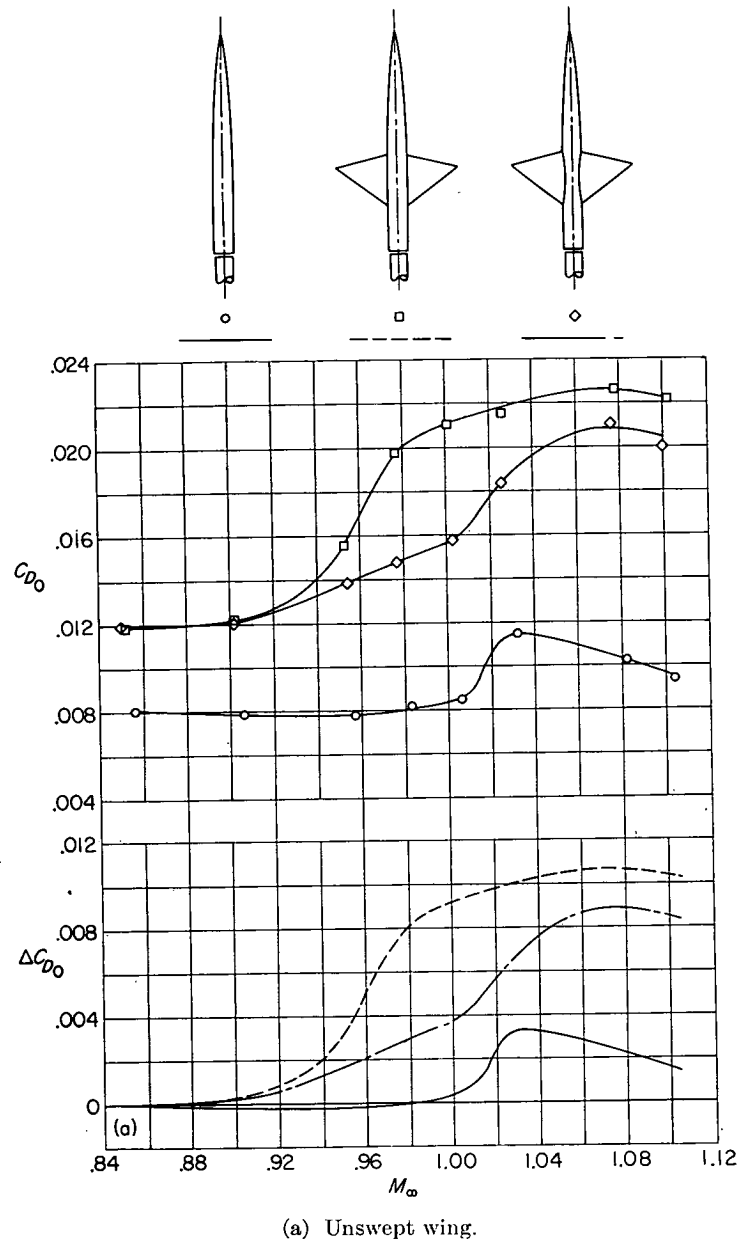


FIGURE 10.—The effects on transonic drag obtained by indenting the bodies of three wing-body combinations.

On the basis of this concept it would be expected that the minimum transonic drag rise for an airplane could be obtained by shaping the fuselage so that the development of cross-sectional area for the airplane approaches that for a low-drag body of revolution with the highest feasible fineness ratio.

CONCLUSIONS

Comparisons of the shock phenomena and drag-rise increments for representative wing and central-body combinations with those for bodies of revolution having the same

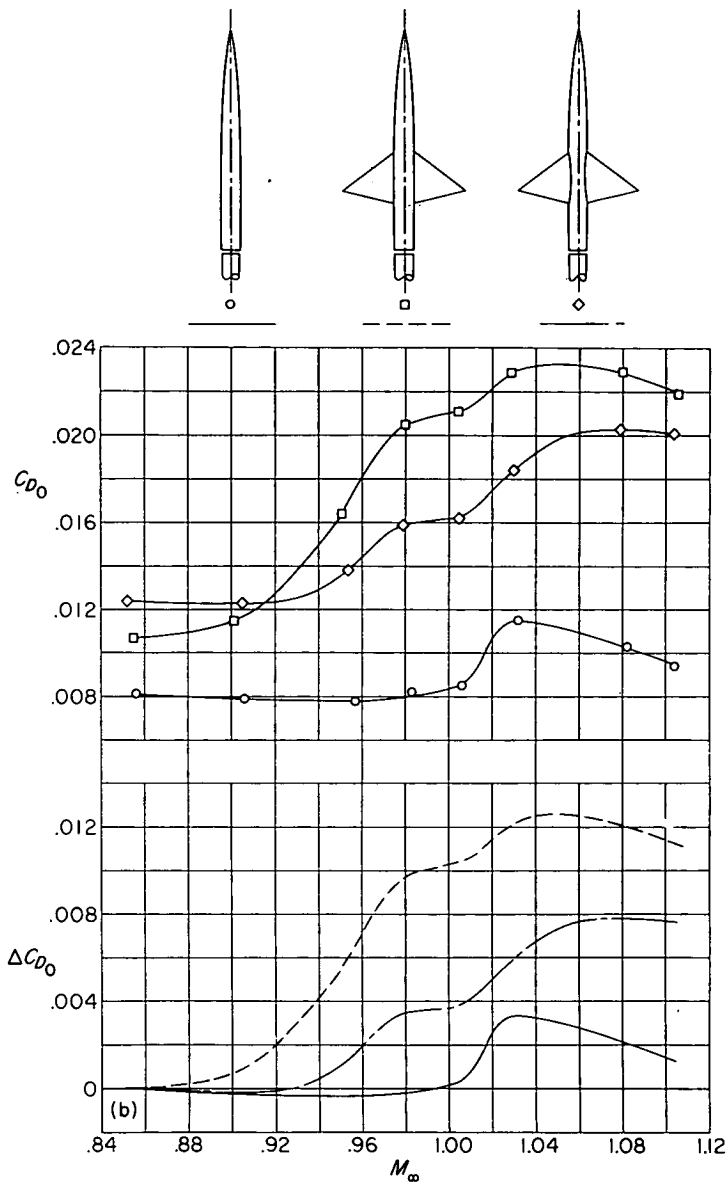


FIGURE 10.—Continued.

axial developments of cross-sectional areas normal to the airstream have indicated the following conclusions:

1. The shock phenomena and drag-rise increments measured for these representative wing and central-body combinations at zero lift near the speed of sound are essentially the same as those for the comparable bodies of revolution.
2. Near the speed of sound, the zero-lift drag rise of a low-aspect-ratio thin-wing—body combination is primarily dependent on the axial development of the cross-sectional areas normal to the airstream. Therefore, it follows that

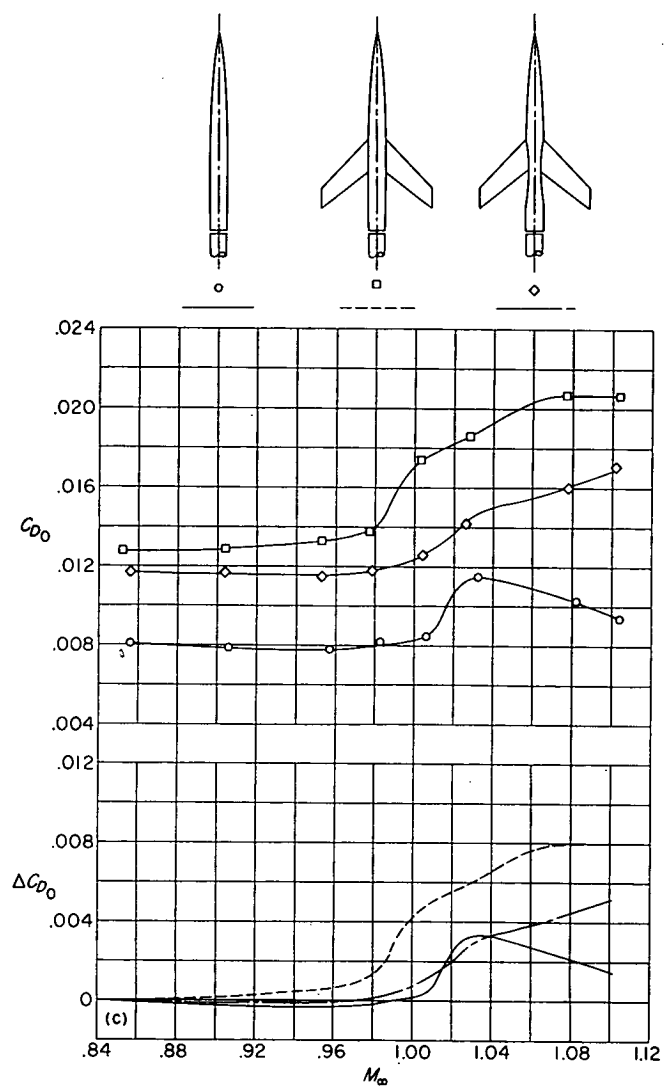


FIGURE 10.—Concluded.

the drag rise for any such configuration is approximately the same as that for any other with the same development of cross-sectional areas.

Further results have indicated that indenting the bodies of three representative wing-body combinations, so that the axial developments of cross-sectional areas for the combinations were the same as for the original body alone, greatly reduced or eliminated the zero-lift drag-rise increments associated with wings near the speed of sound.

LANGLEY AERONAUTICAL LABORATORY,
NATIONAL ADVISORY COMMITTEE FOR AERONAUTICS,
LANGLEY FIELD, VA., August 1, 1952.

REFERENCES

1. Whitecomb, Richard T., and Kelly, Thomas C.: A Study of the Flow Over a 45° Sweptback Wing-Fuselage Combination at Transonic Mach Numbers. NACA RM L52D01, 1952.
2. Thompson, Jim Rogers, and Kurbjun, Max C.: Drag Measurements at Transonic Speeds of Two Bodies of Fineness Ratio 9 With Different Locations of Maximum Body Diameter. NACA RM L8A28b, 1948.
3. Busemann, Adolf: Application of Transonic Similarity. NACA TN 2687, 1952.
4. Graham, Ernest W.: The Pressure on a Slender Body of Non-Uniform Cross-Sectional Shape in Axial Supersonic Flow. Rep. No. SM-13346-A, Douglas Aircraft Co., Inc., July 20, 1949.
5. Stoney, William E., Jr., and Putland, Leonard W.: Some Effects of Body Cross-Sectional Shape, Including a Sunken-Canopy Design, on Drag As Shown by Rocket-Powered-Model Tests at Mach Numbers From 0.8 to 1.5. NACA RM L52D07, 1952.
6. Hayes, Wallace D.: Linearized Supersonic Flow. Rep. No. AL-222, North American Aviation, Inc., June 18, 1947.
7. Nelson, Warren H., and McDevitt, John B.: The Transonic Characteristics of 22 Rectangular, Symmetrical Wing Models of Varying Aspect Ratio and Thickness. NACA TN 3501, 1955. (Supersedes NACA RM A51A12.)
8. Pepper, William B.: The Effect on Zero-Lift Drag of an Indented Fuselage or a Thickened Wing-Root Modification to a 45° Sweptback Wing-Body Configuration As Determined by Flight Tests at Transonic Speeds. NACA RM L51F15, 1951.
9. Thompson, Jim Rogers: Measurements of the Drag and Pressure Distribution on a Body of Revolution Throughout Transition From Subsonic to Supersonic Speeds. NACA RM L9J27, 1950.
10. Pepper, William B., Jr., and Hoffman, Sherwood: Comparison of Zero-Lift Drags Determined by Flight Tests at Transonic Speeds of Symmetrically Mounted Nacelles in Various Spanwise Positions on a 45° Sweptback Wing and Body Combination. NACA RM L51D06, 1951.
11. Robinson, Russell G., and Wright, Ray H.: Estimation of Critical Speeds of Airfoils and Streamline Bodies. NACA ACR, Mar. 1940.

REPORT 1274

SECOND-ORDER SUBSONIC AIRFOIL THEORY INCLUDING EDGE EFFECTS ¹

By MILTON D. VAN DYKE

SUMMARY

Several recent advances in plane subsonic flow theory are combined into a unified second-order theory for airfoil sections of arbitrary shape. The solution is reached in three steps: The incompressible result is found by integration, it is converted into the corresponding subsonic compressible result by means of the second-order compressibility rule, and it is rendered uniformly valid near stagnation points by further rules. Solutions for a number of airfoils are given and are compared with the results of other theories and of experiment. A straightforward computing scheme is outlined for calculating the surface velocities and pressures on any airfoil at any angle of attack.

INTRODUCTION

Thin-airfoil theory provides a useful first approximation to the incompressible flow past two-dimensional airfoils, and the results can be immediately extended to subsonic compressible flow by the Prandtl-Glauert rule. It is natural to attempt to improve this simple theory by successive approximations so as to increase its accuracy for thicker airfoils and higher subsonic Mach numbers. There results a series expansion of the flow quantities in powers (supplemented by logarithms in the fourth and higher approximations) of the airfoil thickness ratio, camber ratio, and angle of attack.

For incompressible flow, the higher-order theory has been studied by various writers, in particular Riegels and Wittich (refs. 1 and 2) and Keune (ref. 3). A less straightforward series of approximations was developed by Goldstein (ref. 4). Perhaps the most concise exposition of higher-order incompressible thin-airfoil theory is given by Lighthill (ref. 5).

For subsonic compressible flow, the corresponding analysis was first undertaken by Görtler (ref. 6), followed by Hantzsche and Wendt (refs. 7 and 8), Schmieden and Kawalki (ref. 9), Kaplan (refs. 10 and 11), Imai and Oyama (refs. 12 and 13) and others. These investigators treated only specific simple shapes by rather laborious analysis. Later, it was discovered that particular integrals of the second-order iteration equation can be expressed in terms of the first approximation (refs. 14 and 15). This permits the second-order subsonic solution for any profile to be given in terms of integrals (refs. 15 and 16). However, the resulting solutions are sometimes incorrect everywhere for airfoils with stagnation points, for reasons to be discussed later.

Recently Hayes (ref. 17), improving on a result of Imai (ref. 18), has given a second-order similarity rule for surface pressure that implies a second-order extension of the Prandtl-Glauert rule (ref. 19). This remarkable result was overlooked by earlier investigators because they did not calculate surface pressures, but were content with finding surface speeds, for which the second-order compressibility rule is more complicated. These rules reduce the second-order problem of subsonic compressible flow past airfoils to the corresponding incompressible problem.

However, the solution by successive approximations breaks down near leading and trailing edges if there are stagnation points. The result is therefore merely a formal series expansion, which fails to converge near the edges. In first-order theory spurious singularities arise at stagnation edges, but it is known how they can be taken into account, since they are integrable. In the second approximation, however, these singularities are intensified, so that at round edges they are no longer integrable. In any case, the calculated speeds and pressures are incorrect near such edges, and more so in the second approximation than the first. Moreover, in subsonic compressible flow the second approximation may be incorrect everywhere as a consequence of the defects in the first approximation.

For round edges in incompressible flow, previous investigators have shown how these defects can be corrected. Riegels (ref. 2) gave a simple rule that renders the first-order thin-airfoil solution valid near the edge. Lighthill (ref. 5) gave an equivalent rule for the second approximation. Recently, corresponding rules have been developed for higher approximations, for sharp as well as round edges, and for subsonic compressible flow (ref. 20).

It is the aim of this paper to combine these recent advances into a unified theory. There results a uniform second approximation to subsonic flow past any profile at angle of attack, expressed in terms of integrals that can, if necessary, be evaluated numerically. It may be noted that, except possibly for certain particular shapes at isolated Mach numbers, the resulting solution is now generally believed to be valid only below the critical Mach number—that is, for purely subsonic flows. Although only flow quantities at the airfoil surface are considered here in detail, the entire flow field could be treated in the same way.

For numerical computation, the most useful method appears to be that initiated by Riegels and Wittich (refs. 1 and 2) and independently by Germain (ref. 21), with

¹ Supersedes NACA TN 3390, "Second-Order Subsonic Airfoil-Section Theory and its Practical Application," 1955, and portions of NACA TN 3343, "Subsonic Edges in Thin-Wing and Slender-Body Theory," 1954.

extensions by Watson (ref. 22), Thwaites (ref. 23), and Weber (ref. 24 and 25). It requires a knowledge only of the airfoil ordinates at a specified set of points. In this report a straightforward scheme, based on an extension of this method, is given for computing the second-order subsonic solution for any airfoil. The reader interested only in calculating a specific case, without necessarily understanding the details of the theory, can turn directly to the section "PRACTICAL NUMERICAL COMPUTATION."

The author is indebted to R. T. Jones for many helpful discussions throughout the course of this work.

THEORY

From the preceding remarks it is clear that the solution is reached in three steps. First, the formal second-order incompressible solution is found by integration. Second, this is converted into the corresponding subsonic compressible solution by means of the second-order compressibility rule. Third, this is modified near stagnation points by the appropriate rules for round or sharp edges. These three steps will be considered successively.

FORMAL INCOMPRESSIBLE SOLUTION

The expansion of the velocity components in a formal series of powers of the airfoil thickness ratio, camber ratio, and angle of attack has been discussed in detail by Lighthill (ref. 5). It will suffice here to summarize his results for the second approximation. We mainly follow his notation except to make it more mnemonic, and to suppress his parameter ϵ characteristic of the airfoil thickness, which is only convenient in the detailed analysis.

Accordingly, consider an airfoil of moderate thickness and camber at a moderate angle of attack to a uniform subsonic stream (fig. 1). It is essential that the x axis be chosen to pass through both the leading and trailing edges. Let the upper and lower surfaces of the airfoil be described by

$$y = Y(x) = C(x) \pm T(x) \quad (1)$$

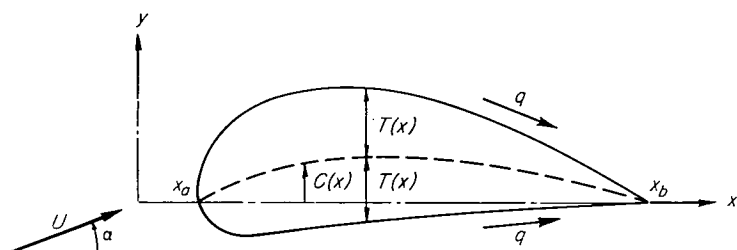


FIGURE 1.—Notation for airfoil.

where $C(x)$ describes the mean camber line and $T(x)$ the thickness. The airfoil extends over the interval $x_a \leq x \leq x_b$, which is usually conveniently taken to be either $-1 \leq x \leq 1$ or $0 \leq x \leq 1$. All symbols are defined in Appendix A.

First-order solution.—In the first approximation of thin-airfoil theory, the condition of tangent flow at the airfoil surface is imposed on the two sides of the chord line $y=0$ rather than at the surface, and requires that

$$\left. \frac{v_1}{U} \right|_{y=0} = Y'(x) = C'(x) \pm T'(x) \quad (2)$$

The corresponding horizontal velocity disturbance on the chord line, which is required for calculating the surface pressure, consists of a term associated with the airfoil thickness, and another associated with its camber and angle of attack. For the thickness

$$\frac{u_{1t}}{U} = \frac{1}{\pi} \oint_{x_a}^{x_b} \frac{T'(\xi) d\xi}{x - \xi} \quad (3)$$

and for the camber and angle of attack

$$\frac{u_{1c}}{U} = \left(\frac{x_b - x}{x - x_a} \right)^{1/2} \left[\alpha + \frac{1}{\pi} \oint_{x_a}^{x_b} \left(\frac{\xi - x_a}{x_b - \xi} \right)^{1/2} \frac{C'(\xi) d\xi}{x - \xi} \right] \quad (4)$$

The latter result is due to Munk (ref. 26) and the former was first given by Pistolesi (ref. 27). Cauchy principal values are indicated in each integral.

The surface speed is then given to a first approximation by

$$\frac{q_1}{U} = 1 + \frac{u_{1t}}{U} \pm \frac{u_{1c}}{U} \quad (5)$$

Second-order solution.—In the second approximation, the tangency condition is transferred from the airfoil surface to the chord line by Taylor series expansion. The condition on the second-order increment in vertical velocity is thus found to be

$$\left. \frac{v_2}{U} \right|_{y=0} = C'_2(x) \pm T'_2(x) \quad (6a)$$

where

$$\left. \begin{aligned} C_2(x) &= \frac{u_{1t}}{U} C + \frac{u_{1c}}{U} T \\ T_2(x) &= \frac{u_{1t}}{U} T + \frac{u_{1c}}{U} C \end{aligned} \right\} \quad (6b)$$

(We depart here from Lighthill's notation in order to emphasize that the functions C_2 and T_2 are effectively the camber and thickness for some fictitious airfoil.) The problem is identical with that in first-order theory except for the condition at infinity, which is readily disposed of. Thus, corresponding to T_2 is the increment in horizontal velocity

$$\frac{u_{2t}}{U} = \frac{1}{\pi} \oint_{x_a}^{x_b} \frac{T'_2(\xi) d\xi}{x - \xi} - \frac{1}{2} \alpha^2 \quad (7)$$

and corresponding to C_2

$$\frac{u_{2c}}{U} = \frac{1}{\pi} \left(\frac{x_b - x}{x - x_a} \right)^{1/2} \oint_{x_a}^{x_b} \left(\frac{\xi - x_a}{x_b - \xi} \right)^{1/2} \frac{C'_2(\xi) d\xi}{x - \xi} \quad (8)$$

The velocity components on the surface of the airfoil include also terms arising from the transfer from the chord line to the surface, which is again effected by Taylor series expansion. Hence the surface speed is given to a second approximation by

$$\frac{q_2}{U} = 1 + \frac{u_{1t}}{U} \pm \frac{u_{1c}}{U} + \frac{u_{2t}}{U} \pm \frac{u_{2c}}{U} + (C \pm T)(C'' \pm T'') + \frac{1}{2} (C' \pm T')^2 \quad (9)$$

and the surface pressure coefficient by

$$C_{p2} = -2 \left(\frac{q_2}{U} - 1 \right) - \left(\frac{u_{1t}}{U} \pm \frac{u_{1c}}{U} \right)^2 \quad (10)$$

Higher-order solutions can be found by continuing this process. Lighthill gives explicit formulas for the third-order solution.

Airfoil integrals.—The incompressible solution to second order (or, indeed, to any order) is thus reduced to a succession of "airfoil integrals" typified by equations (3), (4), (7), and (8). Goldstein (ref. 28) emphasizes that in first-order theory these integrals can be evaluated analytically for practically every profile for which formulas have ever been proposed. In second-order theory this appears to true to a somewhat lesser extent, although the labor of calculation becomes great except for simple shapes. Often the integrals are most readily evaluated by guessing $(u-iv)$ as a function of the complex variable $(x+iy)$ that has the required behavior on the chord line. A short table of airfoil integrals useful for finding second-order solutions is given in Appendix B. Other can be found in references 28, 29, and 30.

For complicated profiles, exact analytic evaluation of the integrals may be impossible or excessively laborious. Then numerical integration may be resorted to, or the profile can be approximated by a simpler shape that can be treated analytically. The most useful numerical procedure is apparently that originated independently by Riegels and Germain and simplified and extended by Watson, Thwaites, and Weber. In this method the airfoil ordinates are approximated by the trigonometric polynomial

$$Y \approx k_0 + \sum_{r=1}^{N-1} (k_r \cos r\theta + t_r \sin r\theta) + k_N \cos N\theta$$

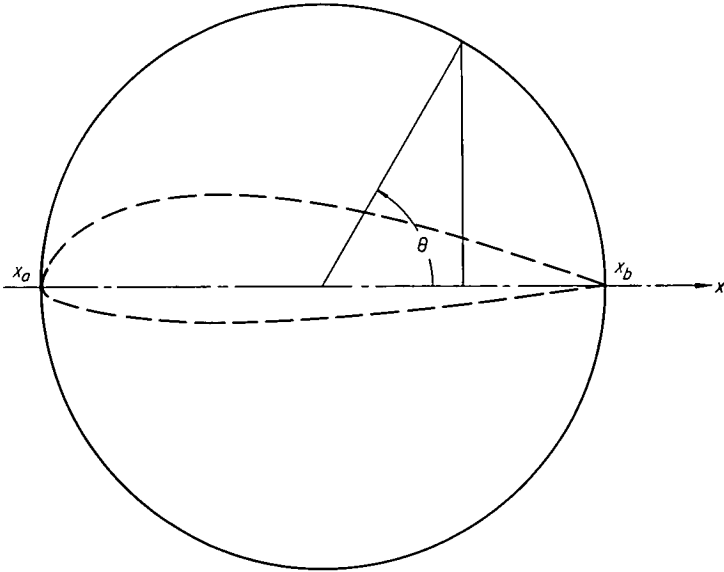


FIGURE 2.—Parametric angle θ .

where θ is the angle indicated in figure 2. The coefficients k_r (for camber) and t_r (for thickness) are chosen to give the actual ordinates at the $2N$ points for which $\theta = m\pi/N$. In this way it is found that the airfoil integrals can be expressed approximately as sums of the airfoil ordinates at certain pivotal points multiplied by standard influence coefficients. The details of this method, as adapted to second-order thin-airfoil theory, are given in Appendix C. The numerical computing procedure is outlined in the last section of this paper.

SECOND-ORDER COMPRESSIBILITY RULE

The second-order counterpart of the Prandtl-Glauert compressibility rule is implicit in an extension of transonic similitude that was initiated by Imai (ref. 18) and carried to completion by Hayes (ref. 17). Imai sought to improve the transonic similarity rule by retaining in its derivation all terms proportional to the square of the airfoil thickness except one appearing in the condition of tangent flow at the surface. The correlation of experimental data was not appreciably improved, which led him to suggest that the neglected second-power term should also be included. This probably cannot be done for the whole flow field. However, in attempting merely to reproduce Imai's result as announced before publication, Hayes actually included that term in a second-order rule for surface pressure.

Hayes' result is that for two-dimensional subsonic or supersonic flow the ratio of the second-order to first-order pressure term on the surface is proportional to the parameter

$$\frac{\tau}{(1-M^2)^{3/2}} \left[\frac{\gamma+1}{2} M^4 + 2(1-M^2) \right] \quad (11)$$

where τ is some measure of the thickness, camber, or angle of attack. Now at subsonic speeds the first-order pressure term is related to its value in incompressible flow by the Prandtl-Glauert rule. Combining these two results yields the second-order compressibility rule (ref. 19).

In incompressible flow the second-order surface-pressure coefficient has the form

$$C_{p_0}(x) = C_{p_1}(x) + \Delta C_{p_2}(x) \quad (12a)$$

where the first-order term C_{p_1} contains linear terms in thickness, camber, and angle of attack, and the second-order increment ΔC_{p_2} contains their squares and products. Then for the same airfoil in subsonic compressible flow, according to the compressibility rule, the pressure coefficient is

$$C_{p_M} = K_1 C_{p_1} + K_2 (\Delta C_{p_2}) \quad (12b)$$

where

$$\left. \begin{aligned} K_1 &= \frac{1}{\sqrt{1-M^2}} = \frac{1}{\beta} \\ K_2 &= \frac{(\gamma+1)M^4 + 4\beta^2}{4\beta^4} \end{aligned} \right\} \quad (12c)$$

The corresponding compressibility rule for surface speed is readily found from the above rule for pressure by considering the small-disturbance series form of Bernoulli's equation for compressible flow. Thus it is found that if the surface speed ratio in incompressible flow is

$$\frac{q_0}{U} = 1 + \frac{\Delta q_1}{U} + \frac{\Delta q_2}{U} \quad (13a)$$

where Δq_1 contains linear terms in thickness, camber, and angle of attack, and Δq_2 their squares and products, then at subsonic speeds

$$\frac{q_M}{U} = 1 + K_1 \frac{\Delta q_1}{U} + K_2 \frac{\Delta q_2}{U} + \frac{K_2-1}{2} \left(\frac{\Delta q_1}{U} \right)^2 \quad (13b)$$

with

$$\frac{K_2 - 1}{2} = M^2 \frac{(\gamma + 1)M^2 + 4\beta^2}{8\beta^4} \quad (13c)$$

This rule is seen to lack the fundamental simplicity of the rule for pressure.

EDGE CORRECTIONS

Thin-airfoil theory is known to fail near leading and trailing edges if there is a stagnation point. The flow is actually brought to rest, but thin-airfoil theory predicts infinite speeds instead. If r is the distance from the edge, the velocity contains powers of $r^{-1/2}$ for a round edge and for any leading edge with flow around it (associated with angle of attack), and powers of $\ln r$ for a sharp edge. First-order theory contains first powers of these singularities, second-order theory their squares and products, and so on, so that the formal thin-airfoil series diverges in some neighborhood of the edge. Not only are the velocities and pressure incorrect near stagnation edges, but nonintegrable singularities appear in the higher-order expressions for aerodynamic forces on round edges.

False subsonic solutions.—Even more serious difficulties may arise in subsonic compressible flow, where the infection spreads in some cases so that the formal second-order solution is incorrect not only near the edges but over the entire airfoil surface. Thus, using the particular integral of reference 14, Harder and Klunker gave an expression for the second-order solution for any symmetric airfoil at zero angle of attack (ref. 16). However, they noted that their expression does not apply to round-edged airfoils, for which it contains divergent integrals. A more deceptive defect appears if their expression is applied to a sharp-edged airfoil such as a biconvex section; then the predicted surface speeds are finite (except near the edges) but incorrect everywhere by a term proportional to M^2 . This defect arises from the fact that near sharp edges the first-order source distribution is not approximately the airfoil slope, as is assumed in thin-airfoil theory. The second-order solution involves the derivative of the source strength which, as indicated in figure 3, has infinite peaks that are missed by thin-airfoil

theory. It is enough to take account of this shortcoming in even the crudest fashion. Thus, if the region of integration is extended an infinitesimal distance beyond the edges to include the pulses (Dirac delta functions) of the thin-airfoil approximation, Harder and Klunker's expression yields a solution that is correct to second order except in the vicinity of the edges.

Keune has discovered an alternative particular integral containing the stream function rather than the velocity potential, and so has obtained another expression for the second-order solution (ref. 15). Because the tangency condition is one degree smoother for the stream function than the velocity potential, his expression yields the correct result (except near stagnation edges) for sharp-edged shapes. It fails, however, for round-edged shapes, so that his solution for subsonic flow past an ellipse is incorrect everywhere.

Both these expressions can be manipulated by partial integration so as to be correct except near stagnation edges. However, the result is simply that obtained by applying the second-order compressibility rule to the expressions for second-order incompressible flow. Hence these more serious difficulties are of no further concern here. They do serve, however, to warn of the danger of false second-order solutions in more complicated problems.

The role of edge corrections.—Thin-airfoil theory fails near stagnation edges because there the basic assumption of small disturbances is violated. It might be feared that uniformly valid solutions could be found only by abandoning that assumption, which leads to such great mathematical simplification. Fortunately, however, Riegels and Lighthill have shown that for round edges in incompressible flow all the results of small-disturbance theory can be salvaged. They have given simple rules to be applied to the formal thin-airfoil solution that render it uniformly valid near the edge.

For present purposes, corresponding rules are required for subsonic as well as incompressible flows, for sharp as well as round edges, and for cambered round edges, for which Lighthill's rule is correct only to first order. It is believed that neither Riegels' nor Lighthill's technique can be extended to these cases. Instead, a different technique is used here, which is particularly suited to the study of edges. It consists in comparing the exact and thin-airfoil solutions for simple shapes that approximate the airfoil in the vicinity of the edge. This technique was first applied in reference 20 to the surface velocity on airfoil sections, three-dimensional wings, and bodies of revolution. It is reproduced here insofar as it applies to second-order theory for airfoil sections, and is extended to treat surface pressures as well as velocities.

Round edges in incompressible flow.—Most subsonic airfoil sections have finite leading-edge radius, and many are actually analytic (except at the trailing edge). This means that all derivatives are continuous, so that, with s the abscissa measured from the edge into the airfoil, the upper and lower surfaces are described by

$$y = \pm T_0 s^{1/2} + C_1 s \pm T_1 s^{3/2} + C_2 s^2 + \dots \quad (14)$$

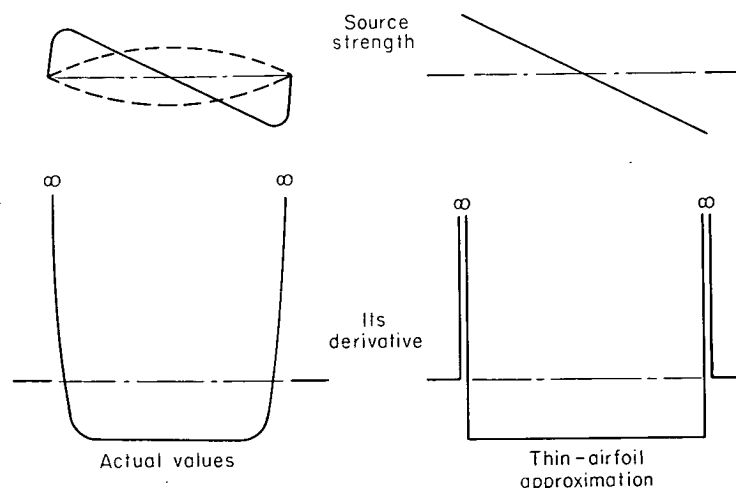


FIGURE 3.—Source strength for biconvex airfoil.

Here the T_n and C_n are coefficients for the thickness and camber, respectively (fig. 1). Thus T_0 determines the nose radius, C_1 the initial camber, and so on.

Thin-airfoil theory breaks down close to the edge where s is of the order of the leading-edge radius ρ . Now ρ is proportional to the square of the thickness ratio τ , so that thin-airfoil theory fails where $s=O(\tau^2)$. In this small region the airfoil is described to second order by the first two terms of equation (14). In terms of the leading-edge radius ρ and initial slope λ of the camber line, the airfoil is given by

$$y = \pm \sqrt{2\rho s} + \lambda s \quad (15a)$$

This is the equation of an inclined parabola, described in rotated coordinates by

$$\tilde{y} = \pm \sqrt{2\rho \tilde{s}} \quad (15b)$$

where the two origins of coordinates are separated by a negligible distance, and the difference between ρ and $\tilde{\rho}$ can also be ignored.

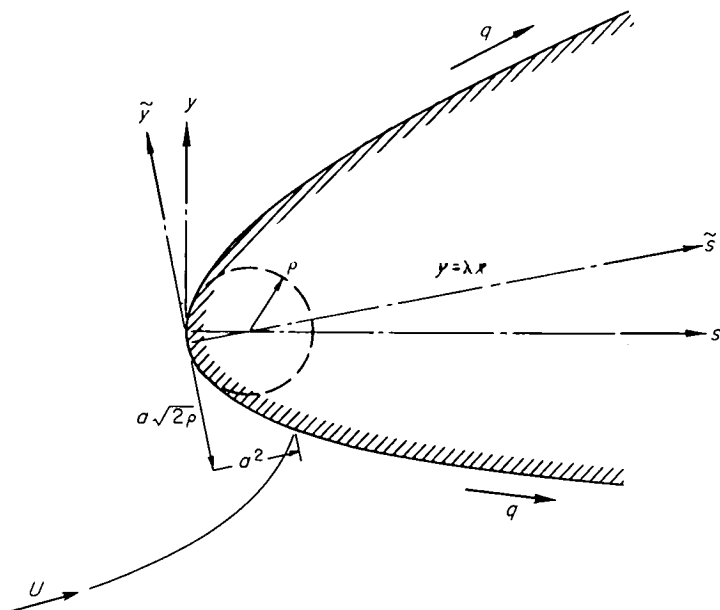


FIGURE 4.—Flow past inclined parabola.

The exact velocity on this parabola in a uniform stream is found, from conformal mapping or otherwise, to be given by

$$\frac{q}{U} = \left(\frac{\tilde{s}}{\tilde{s} + \rho/2} \right)^{1/2} \left(1 \pm \frac{a}{\sqrt{\tilde{s}}} \right) \quad (16)$$

where the signs refer to the upper and lower surfaces. Here a has the physical interpretation that the stagnation point lies at $\tilde{s} = a^2$ and $\tilde{y} = -a\sqrt{2\rho}$ (fig. 4). When the flow past the parabola is related to that near an airfoil nose, a is some moderate multiple of the angle of attack measured from the "ideal" angle—the angle at which the stagnation point coincides with the vertex. The factor of proportionality depends on the entire airfoil shape (and the trailing-edge condition), but its value is not required here. Expanding this expression for small ρ/\tilde{s} yields, to second order, the formal series

$$\frac{q_2}{U} = 1 \pm \frac{a}{\sqrt{\tilde{s}}} - \frac{\rho}{4\tilde{s}} + \dots \quad (17)$$

and, as it must be, this is the second-order thin-airfoil solution for a parabola. It is clear from this formal expansion how the singularity arises at the leading edge.

The ratio of the exact speed on the parabola to its formal series expansion serves as a multiplicative correction factor for other shapes having the same nose radius. Thus the second-order thin-airfoil solution q_2 for any airfoil of leading-edge radius ρ is converted into an approximation \bar{q} that is uniformly valid near the edge by

$$\frac{\bar{q}}{U} = \frac{\left(\frac{\tilde{s}}{\tilde{s} + \rho/2} \right)^{1/2} \left(1 \pm \frac{a}{\sqrt{\tilde{s}}} \right)}{1 \pm \frac{a}{\sqrt{\tilde{s}}} - \frac{\rho}{4\tilde{s}}} \frac{q_2}{U} \quad (18)$$

Simplifying this insofar as possible without destroying its validity near the edge, and retaining only second-order terms, gives the rule

$$\bar{q} = \left(\frac{\tilde{s}}{\tilde{s} + \rho/2} \right)^{1/2} \left(\frac{q_2}{U} + \frac{\rho}{4\tilde{s}} \right) \quad (19)$$

It might be supposed that since the airfoil nose was fitted to second order, this rule yields a solution that is uniformly valid to second order. Comparison with various exact solutions indicates that this is true, in the sense that the velocity disturbance and hence the pressure coefficient are correct to second order everywhere (except near the trailing edge, where additional modification is required). This will be indicated by replacing \bar{q} by \bar{q}_2 .

The oblique abscissa \tilde{s} can be expressed in terms of the original abscissa s , since on the surface of the parabola

$$\tilde{s} = s \pm \lambda \sqrt{2\rho s} + \dots \quad (20)$$

Hence the rule becomes finally

$$\frac{\bar{q}_2}{U} = \left(\frac{s \pm \lambda \sqrt{2\rho s}}{s \pm \lambda \sqrt{2\rho s} + \rho/2} \right)^{1/2} \left(\frac{q_2}{U} + \frac{\rho}{4s} \right) \quad (21)$$

In the special case $\lambda=0$ this reduces to Lighthill's rule (ref. 5).

The corresponding rule for surface pressure coefficient is found by proceeding in the same way with the exact pressure on the parabola, which is found from equation (16) using Bernoulli's equation. Again expanding formally for small ρ/s and taking the ratio as a multiplicative correction factor yields the rule

$$\bar{C}_{p_2} = \frac{s \pm \lambda \sqrt{2\rho s}}{s \pm \lambda \sqrt{2\rho s} + \rho/2} C_{p_2} \quad (22)$$

Airfoils of the NACA four- and five-digit series are not analytic at the nose. Their thickness distribution $T(x)$ consists initially of the ordinates of a parabola minus those of a wedge, so that the airfoil is described by

$$y = \pm T_0 s^{1/2} + C_1 s \mp T_1 |s| + \dots \quad (23)$$

These airfoils are fitted only to first order by an inclined parabola, and it follows that the preceding rules render the thin-airfoil solution uniformly valid only to first order near the

edge, though it remains correct to second order elsewhere. An appropriate second-order rule would require finding the conformal mapping for a parabola minus a wedge.

First-order theory; Riegels' rules.—In the first-order theory, the terms in λ can be neglected, so that the rule for pressure, equation (22), simplifies to

$$\bar{C}_{p1} = \frac{s}{s + \rho/2} C_{p1} \quad (24)$$

The last term in equation (21) is also of second order, so that the rule for speed becomes

$$\frac{\bar{q}_1}{U} = \left(\frac{s}{s + \rho/2} \right)^{1/2} \frac{q_1}{U} \quad (25)$$

This is not precisely Riegels' rule. However, for a parabola

$$\left(\frac{s}{s + \rho/2} \right)^{1/2} = \cos \eta \quad (26)$$

where η is the angle of the surface. Hence an alternative form of equation (25) is

$$\frac{\bar{q}_1}{U} = \cos \eta \frac{q_1}{U} \quad (27)$$

and this is Riegels' rule (ref. 2). The corresponding rule for pressure is

$$\bar{C}_{p1} = (\cos \eta)^2 C_{p1} \quad (28)$$

These alternative forms suffer the defect of falsely implying that the nose exerts an influence even at remote points if the local airfoil slope is appreciable (for example, at the trailing edge). To this extent they fail to render the solution uniformly valid. However, it happens that they are exact for ellipses as well as parabolas, and are accordingly much more accurate for most airfoils, as indicated by the example of figure 5.

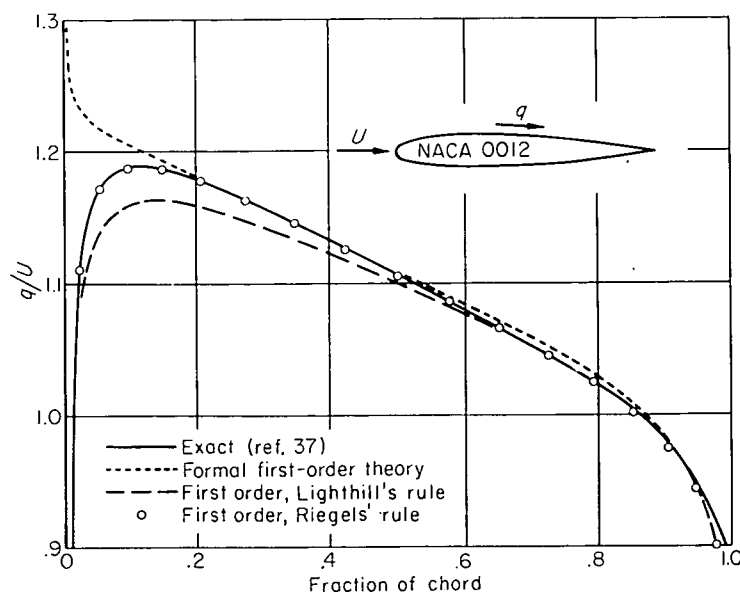


FIGURE 5.—Comparison of Lighthill's and Riegels' rules for incompressible flow past NACA 0012 airfoil.

The second-order rules can be manipulated into the form of Riegels' rule (ref. 20), but the slight advantages of accuracy and simplicity then scarcely offset their defects. The same is true of the rules for compressible flow given later. Hence Riegels' rules are recommended only for first-order incompressible-flow theory.

Round edges in subsonic flow.—The previous rules can be extended to subsonic speeds simply by considering subsonic rather than incompressible flow past an inclined parabola. Although no exact solution of this problem is known, existing approximate solutions by the Janzen-Rayleigh method are probably sufficiently accurate, at least at the ideal angle of attack, and could, in principle be refined indefinitely. Alternatively, one could use experimental measurements on a parabola.

The problem is defined by ρ and a and the free-stream Mach number M . (The adiabatic exponent γ also enters, but is assumed fixed at 7/5.) Therefore, dimensional reasoning shows that the surface speed is given by

$$\frac{q}{U} = Q \left(\frac{\tilde{s}}{\rho/2}, \pm \frac{a}{\sqrt{\rho/2}}, M \right) \quad (29)$$

where, as usual, the upper and lower signs apply to the upper and lower surfaces. (Choosing $\rho/2$ rather than ρ as the reference length leads to later simplification.) Expanding this function formally for x large compared with ρ and a^2 would yield the thin-airfoil series, which is, to second order

$$\frac{q_2}{U} = 1 \pm K_1 \frac{a}{\sqrt{s}} - K_2 \frac{\rho}{4s} + \frac{K_2 - 1}{2} \frac{a^2}{\tilde{s}} \quad (30)$$

where K_1 and K_2 are the compressibility factors of equation (12c). Again the ratio of Q to its series expansion serves as a multiplicative correction factor to be applied to any rounded airfoil. Simplifying as before, and replacing \tilde{s} by s according to equation (20), gives the rule²

$$\frac{\bar{q}_2}{U} = Q \left(\frac{s \pm \lambda \sqrt{2\rho s}}{\rho/2}, \pm \frac{a}{\sqrt{\rho/2}}, M \right) \times \left[\frac{q_2}{U} \mp K_1 \frac{a}{\sqrt{s}} \frac{q_1}{U} + \frac{K_2 \rho}{4s} + \left(K_1^2 - \frac{K_2 - 1}{2} \right) \frac{a^2}{s} \right] \quad (31)$$

where q_1/U is the first-order thin-airfoil solution. Here a must be identified as the coefficient of $\pm K_1/\sqrt{s}$ in the second-order solution, as is clear from equation (30). (The physical interpretation of a shown in fig. 4 is valid only at zero Mach number.)

The corresponding rule for pressure is found by considering the exact pressure coefficient for the parabola, which must have the form

$$C_p = \Pi \left(\frac{\tilde{s}}{\rho/2}, \pm \frac{a}{\sqrt{\rho/2}}, M \right) \quad (32)$$

² As $M \rightarrow 0$ this reduces not to the rule given previously for incompressible flow, but to an alternative that is equivalent up to terms of second order. The difference arises from the fact that in the incompressible case the dependence of q/U upon a is given explicitly by the factor $(1 \pm a/\sqrt{s})$ in equation (16), which is used to cancel a corresponding term in the denominator of equation (18).

Its series expansion would give the thin-airfoil result

$$C_{p2} = \mp 2K_1 \frac{a}{\sqrt{s}} + K_2 \left(\frac{\rho}{2s} - \frac{a^2}{s} \right) \quad (33)$$

Hence the rule for any airfoil is

$$\bar{C}_{p2} = P \left(\frac{s \pm \lambda \sqrt{2\rho s}}{\rho/2}, \pm \frac{a}{\sqrt{\rho/2}}, M \right) C_{p2} \quad (34a)$$

where

$$P \left(\frac{s}{\rho/2}, \pm \frac{a}{\sqrt{\rho/2}}, M \right) = \frac{\Pi \left(\frac{s}{\rho/2}, \pm \frac{a}{\sqrt{\rho/2}}, M \right)}{\mp 2K_1 \frac{a}{\sqrt{s}} + K_2 \left(\frac{\rho}{2s} - \frac{a^2}{s} \right)} \quad (34b)$$

In this case a is the coefficient of $\mp 2K_1/\sqrt{s}$ in the second-order pressure coefficient.

Imai has recently calculated the Janzen-Rayleigh solution for a parabola at the ideal angle of attack including terms in M^4 (ref. 31). Thus, his results give

$$Q \left(\frac{s}{\rho/2}, 0, M \right) = q_0 + M^2 q_1 + M^4 q_2 + O(M^6) \quad (35)$$

where the q_n are increasingly complicated functions of $s/(\rho/2)$. In reference 20 an attempt was made to increase the accuracy of this approximation by modifying it so that for large $s/(\rho/2)$ it tends exactly to the second-order thin-airfoil solution of equation (30). However, the third-order thin-airfoil solution has since been calculated by Kaplan (ref. 32):

$$\frac{q_3}{U} = 1 - \frac{1}{2} K_2 \left(\frac{\rho}{2s} \right) + \frac{1}{2} K_3 \left[\left(\frac{\rho}{2s} \right)^{3/2} + \frac{4\beta}{\pi} \left(\frac{\rho}{2s} \right)^2 \ln \left(2\beta \sqrt{\frac{\rho}{2s}} \right) \right] + O \left(\frac{\rho}{2s} \right)^2$$

where

$$K_3 = \frac{\pi M^2}{2 \beta^3} \left[1 + \frac{\gamma+1}{8} \frac{M^2}{\beta^2} \left(1 + \frac{\gamma+1}{4} \frac{M^2}{\beta^2} \right) (8 - M^2) \right]$$

(It is a matter of taste whether the logarithmic term included here is regarded as being of third or fourth order.) The comparison with this result shown in figure 6 suggests that the modification was detrimental, and that Imai's solution is adequate for practical purposes.³ A short table of the function $Q[s/(\rho/2), 0, M]$ calculated from equation (35) is given below:

$$Q \left(\frac{s}{\rho/2}, 0, M \right)$$

$M \backslash s/(\rho/2)$	0	0.5	1	2	4	10	20	50
0	0	0.5774	0.7071	0.8165	0.8944	0.9535	0.9759	0.9901
.4	0	.5570	.6874	.8002	.8829	.9473	.9724	.9855
.5	0	.5449	.6752	.7893	.8753	.9431	.9699	.9874
.6	0	.5295	.6592	.7758	.8648	.9371	.9664	.9858
.7	0	.5104	.6388	.7574	.8508	.9290	.9616	.9835
.8	0	.4870	.6133	.7338	.8324	.9182	.9551	.9805
.85	0	.4737	.5982	.7197	.8213	.9116	.9512	.9788
.9	0	.4590	.5816	.7039	.8083	.9042	.9466	.9765

³ The table on p. 11 of ref. 20 also involves an error in computing the q_2 of eq. (35).

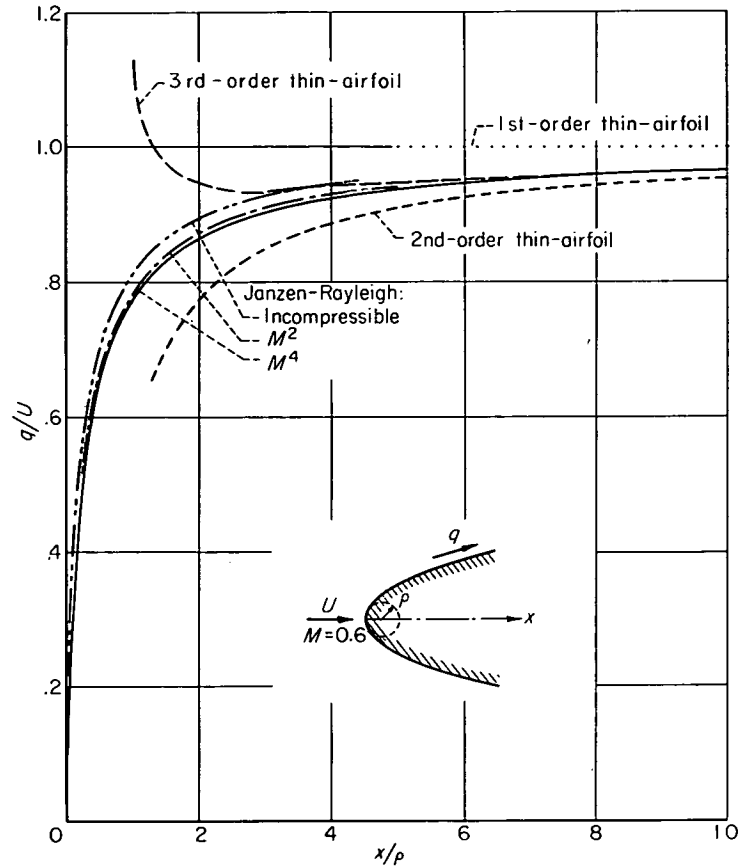


FIGURE 6.—Various approximations for velocity on parabola at $M=0.6$.

The corresponding table of the function $P[s/(\rho/2), 0, M]$ appearing in equation (34) is:

$$P \left(\frac{s}{\rho/2}, 0, M \right)$$

$M \backslash s/(\rho/2)$	0.5	1	2	4	10	20	50
0	0.3333	0.5000	0.6667	0.8000	0.9091	0.9524	0.9804
.4	.2924	.4444	.6018	.7339	.8502	.9015	.9402
.5	.2623	.4019	.5500	.6779	.7958	.8507	.8950
.6	.2189	.3391	.4703	.5881	.7025	.7587	.8073
.7	.1607	.2523	.3500	.4531	.5528	.6044	.6517
.8	.0918	.1466	.2111	.2742	.3427	.3797	.4155
.85	.0578	.0932	.1357	.1783	.2256	.2518	.2774
.9	.0284	.0463	.0682	.0906	.1162	.1305	.1437

For other angles of attack, the function Q to order M^2 can be extracted by a limiting process from Kaplan's Janzen-Rayleigh solution (ref. 33) for an inclined ellipse. This gives, with $s/(\rho/2) = X$, $a/\sqrt{\rho/2} = A$

$$Q(X, A, M) = \frac{\sqrt{X} + A}{\sqrt{1+X}} - \frac{M^2}{2(1+X)^{3/2}} \left\{ (1-A^2)\sqrt{X} - A(X+A^2) + \frac{1+A^2}{1+X} \left[\left(\sqrt{X} + \frac{1}{2} AX - \frac{1}{2} A \right) \ln \frac{1+X}{4} + (1-X+2A\sqrt{X}) \tan^{-1} \sqrt{X} \right] \right\} \quad (36)$$

The corresponding approximation for the pressure coefficient is

$$\Pi(X, A, M) = \frac{1 - 2A\sqrt{X} - A^2}{1 + X} + \frac{M^2}{(1 + X)^2} \left\{ \frac{1}{4} (1 - 2A\sqrt{X} - A^2)^2 + (1 - A^2)(X + A\sqrt{X}) - A(X + A^2)(\sqrt{X} + A) + \frac{(1 + A^2)(\sqrt{X} + A)}{1 + X} \left[\left(\sqrt{X} + \frac{1}{2}AX - \frac{1}{2}A \right) \ln \frac{1 + X}{4} + (1 - X + 2A\sqrt{X}) \tan^{-1} \sqrt{X} \right] \right\} \quad (37a)$$

and for the function P , according to equation (34b)

$$P(X, A, M) = \frac{\Pi(X, A, M)}{-2K_1 \frac{A}{\sqrt{X}} + K_2 \left(\frac{1}{X} - \frac{A^2}{X} \right)} \quad (37b)$$

The error involved in retaining only terms of order M^2 can be estimated from figure 6 in the special case $\alpha = 0$. At other angles of attack the error may be greater; in particular, neither the Janzen-Rayleigh expansion nor the thin-airfoil expansion is believed to converge if the local Mach number exceeds unity.

Sharp edges.—The corrections for sharp edges can be found by considering flow in an angle. At a trailing edge with Kutta condition enforced, or a leading edge at ideal angle of attack, the surface and the dividing streamline meet at slightly less than a straight angle, as indicated on the

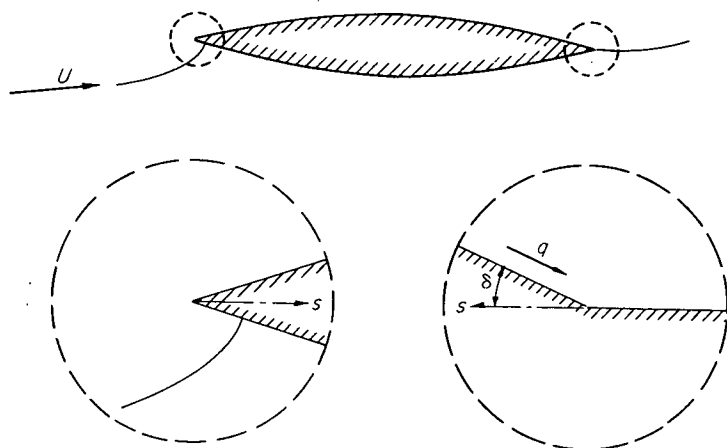


FIGURE 7.—Flow near sharp edges.

right of figure 7. For incompressible flow, the surface speed is found from conformal mapping to be given by

$$\frac{q}{U} = cs^{\frac{\delta}{\pi - \delta}} \quad (38)$$

where δ is the semivertex angle, and s is again measured into the edge. In fixing the constant c , the difficulty that in the angle flow the velocity increases indefinitely upstream can be circumvented by requiring that at any point the velocity must approach that of the free stream as the angle δ tends to zero. Thus it is seen that c is unity except for terms of order δ .

The connection with thin-airfoil theory follows from the fact that for small ϵ

$$s^\epsilon = 1 + \epsilon \ln s + \frac{1}{2} \epsilon^2 \log^2 s + \dots \quad (39)$$

though this relation is not uniformly valid near $s = 0$. Hence, the thin-airfoil series for flow in an angle is, to second order.

$$\frac{q_2}{U} = c \left[1 + \frac{\delta}{\pi} \ln s + \frac{\delta^2}{\pi^2} \left(\ln s + \frac{1}{2} \ln^2 s \right) \right] \quad (40)$$

and it is clear how the spurious logarithmic singularities arise.

Comparing these expressions gives a rule that renders the second-order thin-airfoil solution for any sharp-nosed profile uniformly valid:

$$\frac{\bar{q}_2}{U} = s^{\frac{\delta}{\pi - \delta}} \left[\frac{q_2}{U} - \frac{\delta}{\pi} \frac{q_1}{U} \ln s - \frac{\delta^2}{\pi^2} \left(\ln s - \frac{1}{2} \ln^2 s \right) \right] \quad (41)$$

For a leading edge not at the ideal angle of attack, the flow includes a circulatory component, as indicated at the left of figure 7. For incompressible flow, conformal mapping gives the surface speed associated with this component as

$$\frac{q}{U} = \pm as^{-\frac{\pi - 2\delta}{2(\pi - \delta)}} \quad (42)$$

and its thin-airfoil expansion is

$$\frac{q_2}{U} = \pm \frac{a}{\sqrt{s}} \left(1 + \frac{\delta}{2\pi} \ln s \right) \quad (43)$$

Comparing these yields a rule for correcting the circulatory component:

$$\frac{\bar{q}_2}{U} = s^{\frac{\delta}{2(\pi - \delta)}} \left(\frac{q_2}{U} - \frac{\delta}{2\pi} \frac{q_1}{U} \ln s \right) \quad (44)$$

The second-order thin-airfoil solution can be treated by splitting off the terms that are singular at least as $s^{-1/2}$ near the leading edge, applying equation (44) to this circulatory component, applying equation (41) to the remainder, and recombining.

These rules could be extended to subsonic speeds, in the case of ideal angle of attack, by calculating the Janzen-Rayleigh solution for flow in an angle. However, at other angles the Janzen-Rayleigh approximation certainly fails, because it would predict infinite speeds that are tolerable only in an incompressible fluid. In any case, the correction is negligible for most practical purposes, because it is significant in only a minute neighborhood of the edge, and, furthermore, sharp edges are usually trailing edges, in which case the details of the flow are masked by viscous effects. For these reasons, no correction for sharp edges is included in the computing scheme given later.

Combined edges.—Airfoils with two stagnation edges are treated by applying the appropriate corrections in turn at

each edge by shifting the origin. Thus, consider an airfoil with round leading and trailing edges of radii ρ_a and ρ_b located at $x=x_a$ and $x=x_b$, respectively, and initial and final camber angles λ_a and λ_b . Assume that the Kutta condition

is imposed at the trailing edge. Applying equation (31) twice, identifying s successively with $x-x_a$ and x_b-x , and then simplifying to keep no more than second-order terms gives

$$\frac{\bar{q}_2}{U} = Q \left[\frac{x-x_a \pm \lambda_a \sqrt{2\rho_a(x-x_a)}}{\rho_a/2}, \pm \frac{a}{\sqrt{\rho_a/2}}, M \right] Q \left[\frac{x_b-x \mp \lambda_b \sqrt{2\rho_b(x_b-x)}}{\rho_b/2}, 0, M \right] \times \\ \left[\frac{q_2}{U} \mp K_1 \frac{a}{\sqrt{x-x_a}} \frac{q_1}{U} + \frac{K_2}{4} \left(\frac{\rho_a}{x-x_a} + \frac{\rho_b}{x_b-x} \right) + \left(K_1^2 - \frac{K_2-1}{2} \right) \frac{a^2}{x-x_a} \right] \quad (45)$$

(The simpler form of this equation for incompressible flow is given as equation (24) of reference 20.) The corresponding rule for pressure coefficient is

$$\bar{C}_{p_2} = P \left[\frac{x-x_a \pm \lambda_a \sqrt{2\rho_a(x-x_a)}}{\rho_a/2}, \pm \frac{a}{\sqrt{\rho_a/2}}, M \right] \times \\ P \left[\frac{x_b-x \mp \lambda_b \sqrt{2\rho_b(x_b-x)}}{\rho_b/2}, 0, M \right] C_{p_2} \quad (46)$$

Similar rules can be found for combinations of a round and a sharp edge, or two sharp edges. For example, for incompressible flow past two sharp edges of equal angle, both with Kutta condition imposed (as for a symmetrical biconvex airfoil at zero angle of attack) and located at $x=\pm 1$, the combined rule has the form of equation (41) with s replaced by $(1-x^2)$.

EXAMPLES: COMPARISON WITH EXPERIMENT AND OTHER THEORIES

INCOMPRESSIBLE FLOW

It has been seen that the solution for subsonic flow depends on that for incompressible flow. It is therefore pertinent to test the second-order theory in the case of incompressible flow, where it can be checked against the exact results of conformal mapping.

Ellipse.—Consider an ellipse of thickness ratio τ with the interval $-1 \leq x \leq 1$ as chord line. It is described by

$$y = \pm \tau \sqrt{1-x^2}, \quad -1 \leq x \leq 1 \quad (47)$$

Suppose that the Kutta condition is satisfied—the rear stagnation point coincides with the end of the major axis. Then the first-order solution for surface speed is found, from equations (3), (4), and (5), together with Appendix B, to be

$$\frac{q_1}{U} = 1 + \tau \pm \alpha \sqrt{\frac{1-x}{1+x}} \quad (48a)$$

Proceeding with equations (6) to (9) gives the formal second-order result

$$\frac{q_2}{U} = 1 + \tau \pm \alpha \sqrt{\frac{1-x}{1+x}} - \frac{1}{2} \tau^2 \frac{x^2}{1-x^2} \pm \alpha \tau \sqrt{\frac{1-x}{1+x}} - \frac{1}{2} \alpha^2 \quad (48b)$$

This can be checked by expanding the exact result, which is

$$\frac{q}{U} = (1+\tau) \frac{\sqrt{1-x^2} \cos \alpha \pm (1-x) \sin \alpha}{\sqrt{1-x^2 + \tau^2 x^2}} \quad (49)$$

The formal second-order solution clearly breaks down near the ends of the ellipse. It is converted into a uniformly

valid second approximation by applying equation (21) twice in succession, or using the combined rule of equation (24) of reference 20, which gives

$$\frac{\bar{q}^2}{U} = \sqrt{\frac{1-x^2}{1-x^2 + \tau^2}} \left[(1+\tau) \left(1 \pm \alpha \sqrt{\frac{1-x}{1+x}} \right) + \frac{1}{2} (\tau^2 - \alpha^2) \right] \quad (48c)$$

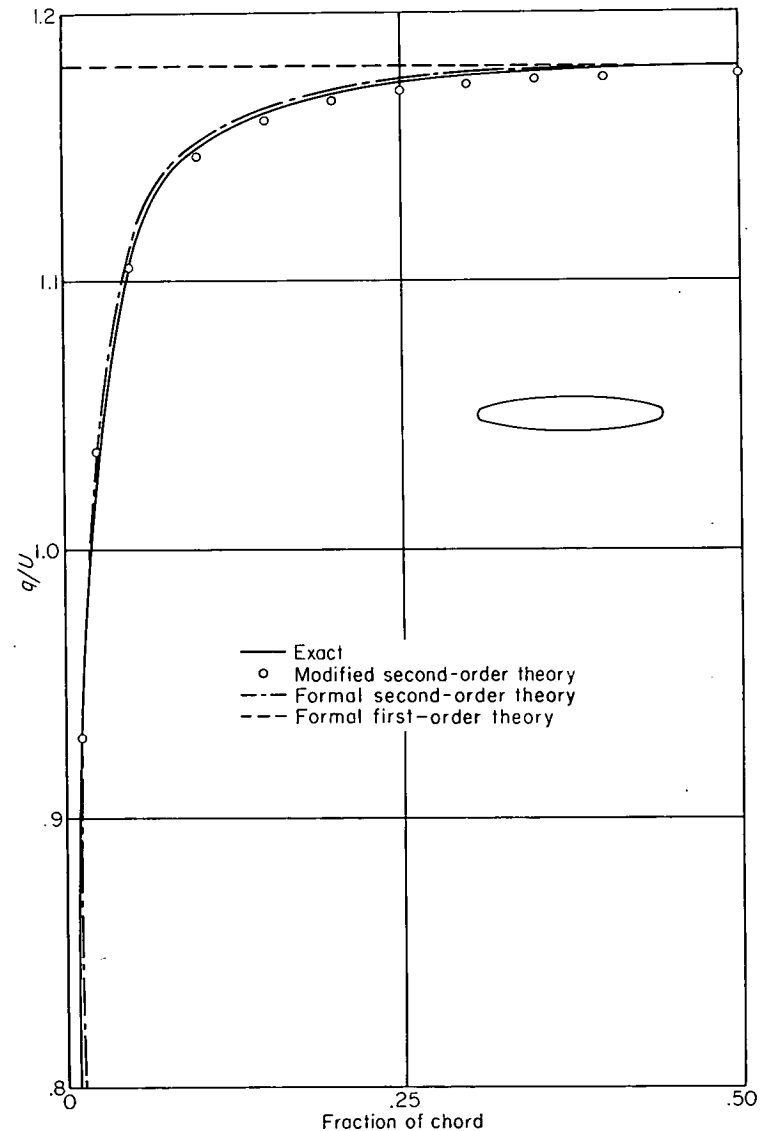


FIGURE 8.—Speed on 18-percent-thick ellipse at zero angle of attack in incompressible flow.

These approximations are compared in figure 8 with the exact solution for an 18-percent-thick ellipse (which has nearly the same nose radius as an NACA 0012 airfoil) at zero angle of attack. The precipitate descent of the formal

TABLE III.—INFLUENCE COEFFICIENTS FOR SLOPE

(a) $N=8$

e_{ns} (slope due to thickness)							
$s \backslash n$	1	2	3	4	5	6	7
1	-6.3086	-4.9932	1.5307	-0.8284	0.6340	-0.6636	1.0824
2	17.0479	-1.4142	-4.7183	2.0000	-1.4046	1.4142	-2.2658
3	-8.9218	8.0547	-4.4483	-4.8284	2.6131	-2.3978	3.6955
4	5.6568	-4.0000	5.6568	0	-5.6568	4.0000	-5.6568
5	-3.6955	2.3978	-2.6131	4.8284	.4483	-8.0547	8.9218
6	2.2658	-1.4142	1.4046	-2.0000	4.7183	1.4142	-17.0479
7	-1.0824	.6636	-.6340	.8284	-1.5307	4.9932	6.3086

f_{ns} (slope due to camber)							
$s \backslash n$	1	2	3	4	5	6	7
1	6.3086	-9.2262	3.6955	-2.1648	1.5307	-1.2262	1.0824
2	9.2262	1.4142	-6.1648	2.8284	-1.8352	1.4142	-1.2262
3	-3.6955	6.1648	.4483	-5.2262	2.6131	-1.8352	1.5307
4	2.1648	-2.8284	5.2262	0	-5.2262	2.8284	-2.1648
5	-1.5307	1.8352	-2.6131	5.2262	-.4483	-6.1648	3.6955
6	1.2262	-1.4142	1.8352	-2.8284	6.1648	-1.4142	-9.2262
7	-1.0824	1.2262	-1.5307	2.1648	-3.6955	9.2262	-6.3086

(b) $N=16$

e_{ns} (slope due to thickness)															
$s \backslash n$	1	2	3	4	5	6	7	8	9	10	11	12	13	14	15
1	-25.7693	-17.9172	4.7035	-2.0162	1.1036	-0.7061	0.5063	-0.3978	0.3383	-0.3098	0.3054	-0.3269	0.3875	-0.5353	1.0196
2	68.9411	-6.3086	-14.9078	4.9932	-2.4992	1.5307	-1.0708	.8284	-.6974	-.6340	-.6222	-.6636	-.7848	1.0824	-2.0598
3	-38.1441	31.4204	-2.6938	-12.6356	4.8436	-2.6799	1.7802	-1.3964	1.1036	-.9906	-.9635	-1.0213	1.2027	-1.6541	3.1428
4	26.4874	-17.0479	20.4685	-1.4142	-11.2241	4.7183	-2.8162	2.0000	-1.5982	1.4046	-1.3470	1.4142	-1.6545	2.2658	-4.2947
5	-20.0462	11.7984	-10.8489	15.5194	-.8036	-10.4112	4.7035	-2.9632	2.2587	-1.9184	1.8000	-1.8625	2.1580	-2.9372	5.5482
6	15.8356	-8.9218	7.4108	-8.0547	12.8540	-.4483	-10.0428	4.8284	-3.2607	2.6131	-2.3685	2.3978	-2.7393	3.6955	-6.9465
7	-12.7972	7.0334	-5.5482	5.4180	-6.5445	11.3181	-.2028	-10.0547	5.1258	-3.6748	3.1428	-3.0748	3.4394	-4.5808	8.5508
8	10.4525	-5.6568	4.3296	-4.0000	4.3296	-5.6568	10.4525	0	-10.4525	5.6568	-4.3296	4.0000	-4.3296	5.6568	-10.4525
9	-8.5508	4.5808	-3.4394	3.0748	-3.1428	3.6748	-5.1258	10.0547	2028	-11.3181	6.5445	-5.4180	5.5482	-7.0334	12.7972
10	6.9465	-3.6955	2.7393	-2.3978	2.3685	-2.6131	3.2607	-4.8284	10.0428	-.4483	-12.8540	8.0547	-7.4108	8.9218	-15.8356
11	-5.5482	2.9372	-2.1580	1.8625	-1.8000	1.9184	-2.2587	2.9632	-4.7035	10.4112	.8036	-15.5194	10.8489	-11.7984	20.0462
12	4.2947	-2.2658	1.6545	-1.4142	1.3470	-1.4046	1.5982	-2.0000	2.8162	-4.7183	11.2241	1.4142	-20.4685	17.0479	-26.4874
13	-3.1428	1.6541	-1.2027	1.0213	-.9635	.9906	-1.1036	1.3964	-1.7802	2.6799	-4.8436	12.6356	2.6938	-31.4204	38.1441
14	2.0598	-1.0824	.7848	-.6636	.6222	-.6340	-.6974	-.8284	1.0708	-1.5307	2.4992	-4.9932	14.9078	6.3086	-68.9411
15	-1.0196	.5353	-.3875	.3269	-.3054	.3098	-.3383	.3978	-.5063	.7061	-1.1036	2.0162	-4.7035	17.9172	25.7693

f_{ns} (slope due to camber)															
$s \backslash n$	1	2	3	4	5	6	7	8	9	10	11	12	13	14	15
1	25.7693	-35.1459	13.3944	-7.3078	4.7035	-3.3439	2.5455	-2.0392	1.7009	-1.4668	1.3018	-1.1849	1.1036	-1.0500	1.0196
2	35.1459	6.3086	-21.6427	9.2262	-5.4302	3.6955	-2.7443	2.1648	-1.7874	1.5307	-1.3518	1.2262	-1.1394	1.0824	-1.0500
3	-13.3944	21.6427	2.6938	-16.0820	7.2490	-4.4565	3.1428	-2.4054	1.9482	-1.6472	1.4419	-1.2999	1.2027	-1.1394	1.1036
4	7.3078	-9.2262	16.0820	1.4142	-13.1982	6.1648	-3.9061	2.8284	-2.2168	1.8352	-1.5839	1.4142	-1.2999	1.2262	-1.1849
5	-4.7035	5.4302	-7.2490	13.1982	.8036	-11.5683	5.5482	-3.5999	2.6643	-2.1316	1.8000	-1.5839	1.4419	-1.3518	1.3018
6	3.3439	-3.6955	4.4565	-6.1648	11.5683	-.4483	-10.6614	5.2262	-3.4616	2.6131	-2.1316	1.8352	-1.4419	1.5307	-1.4669
7	-2.5455	2.7443	-3.1428	3.9061	-5.5482	10.6614	.2028	-10.2517	5.1258	-3.4616	2.6643	-2.2108	1.9482	-1.7874	1.7009
8	2.0392	-2.1648	2.4054	-2.8284	3.5999	-5.2262	10.2517	0	-10.2517	5.2262	-3.5999	2.8284	-2.4054	2.1648	-2.0392
9	-1.7009	1.7874	-1.9482	2.2168	-2.6643	3.4616	-5.1258	10.2517	-.2028	-10.6614	5.5482	-3.9061	3.1428	-2.7443	2.5455
10	1.4669	-1.5307	1.6472	-1.8352	2.1316	-2.6131	3.4616	-5.2262	10.6614	-.4483	-11.5683	6.1648	-4.4565	3.6955	-3.3439
11	-1.3018	1.3518	-1.4419	1.5839	-1.8000	2.1316	-2.6643	3.5999	-5.5482	11.5683	-.8036	-13.1982	7.2490	-5.4302	4.7035
12	1.1849	-1.2262	1.2999	-1.4142	1.5839	-1.8352	2.2168	-2.8284	3.9061	-6.1648	13.1982	-16.0820	9.2262	-7.3078	13.3944
13	-1.1036	1.1394	-1.2027	1.2999	-1.4419	1.6472	-1.9482	2.4054	-3.1428	4.4565	-7.2490	16.0820	-21.6427	35.1459	-25.7693
14	1.0500	-1.0824	1.1394	-1.2262	1.3518	-1.5307	1.7874	-2.1648	2.7443	-3.6955	5.4302	-9.2262	21.6427	-35.1459	68.9411
15	-1.0196	.5353	-1.1036	1.1849	-1.3018	1.4668	-1.7009	2.0392	-2.5455	3.3439	-4.7035	7.3078	-13.3944	35.1459	-25.7693

TABLE IV.—INFLUENCE COEFFICIENTS FOR SECOND DERIVATIVE

(a) $N=8$

g_{ns} (second derivative due to thickness)							
$s \backslash n$	1	2	3	4	5	6	7
1	-414.392	106.260	-12.686	3.587	-1.373	-0.250	11.314
2	99.478	-160.000	62.406	-11.314	3.896	0	-23.032
3	46.627	76.529	-97.608	50.469	-11.314	2.019	35.314
4	-46.882	-11.314	54.056	-84.000	54.056	-11.314	-46.882
5	35.314	2.019	-11.314	50.469	-97.608	76.529	46.627
6	-23.032	0	3.896	-11.314	62.406	-160.000	99.478
7	11.314	-250	-1.373	3.587	-12.686	106.260	-414.392

h_{ns} (second derivative due to camber)							
$s \backslash n$	1	2	3	4	5	6	7
1	-760.098	144.152	-24.000	9.373	-6.059	6.476	-16.000
2	286.658	-184.000	70.481	-16.000	8.382	-8.000	18.479
3	-73.941	93.446	-103.902	54.627	-16.000	11.927	-24.000
4	36.686	-104.000	59.314	-88.000	59.314	-104.000	36.686
5	-24.000	11.927	-16.000	54.627	-103.902	93.446	-73.941
6	18.479	-8.000	8.382	-16.000	70.481	-184.000	286.658
7	-16.000	6.476	-6.059	9.373	-24.000	144.152	-760.098

(b) $N=16$

g_{ns} (second derivative due to thickness)															
$s \backslash n$	1	2	3	4	5	6	7	8	9	10	11	12	13	14	15
1	-6276.99	1485.50	-151.34	35.17	-12.16	5.36	-2.78	1.62	-1.01	0.63	-0.36	-0.15	1.23	-5.63	50.47
2	1292.86	-2162.47	725.61	-106.26	31.16	-12.69	6.31	-3.59	2.21	-1.37	.68	.25	-2.44	11.31	-101.83
3	944.06	963.60	-1072.52	442.15	-78.01	26.29	-11.91	6.43	-3.85	2.38	-1.23	-.23	3.59	-17.10	155.04
4	-977.99	-99.48	548.07	-672.00	314.31	-62.41	23.14	-11.31	6.44	-3.90	2.10	0	-4.61	23.03	-211.17
5	844.58	-20.73	-98.84	365.76	-489.21	250.21	-54.10	21.55	-11.12	6.46	-3.59	.63	5.40	-29.12	271.50
6	-710.24	46.63	26.13	-76.53	276.74	-397.53	218.21	-50.47	21.25	-11.31	6.29	-2.02	-5.73	35.31	-337.63
7	594.40	-50.14	-4.98	27.00	-62.10	231.18	-353.29	206.15	-50.47	22.15	-11.70	4.94	5.13	-41.42	411.61
8	-496.08	46.88	-2.50	-11.31	24.21	-54.06	210.07	-340.00	210.07	-54.06	24.21	-11.31	-2.50	46.88	-496.08
9	411.61	-41.42	5.13	4.94	-11.70	22.15	-50.47	206.15	-353.29	231.18	-62.10	27.00	-4.98	-50.14	594.40
10	-337.63	35.31	-5.73	-2.02	6.29	-11.31	21.25	-50.47	218.21	-397.53	276.74	-76.53	26.13	46.63	-710.24
11	271.50	-29.12	5.40	.63	-3.59	6.46	-11.12	21.55	-54.10	250.21	-489.21	365.76	-98.84	-20.73	844.58
12	-211.17	23.03	-4.61	0	2.10	-3.90	6.44	-11.31	23.14	-62.41	314.31	-672.00	548.07	-99.48	-977.99
13	155.04	-17.10	3.59	-.23	-1.23	2.38	-3.85	6.43	-11.91	26.29	-78.01	442.15	-1072.52	963.60	944.06
14	-101.83	11.31	-2.44	.25	.68	-1.37	2.21	-3.59	6.31	-12.69	31.16	-106.26	725.61	-2162.47	1292.86
15	50.47	-5.63	1.23	-.15	-.36	.63	-1.01	1.62	-2.78	5.36	-12.16	35.17	-151.34	1485.50	-6276.99

h_{ns} (second derivative due to camber)															
$s \backslash n$	1	2	3	4	5	6	7	8	9	10	11	12	13	14	15
1	-11694.53	2027.02	-286.66	86.14	-36.69	19.36	-11.93	8.32	-6.48	5.62	-5.48	6.16	-8.38	15.45	-54.63
2	4281.83	-2508.18	820.21	-144.15	50.25	-24.00	13.95	-9.37	7.11	-6.06	5.83	-6.48	8.73	-16.00	56.32
3	-1049.15	1209.89	-1143.53	471.77	-93.45	35.72	-18.48	11.57	-8.38	6.90	-6.48	7.06	-9.37	16.97	-59.31
4	483.45	-286.66	603.90	-696.00	327.17	-70.48	28.93	-16.00	10.73	-8.38	7.56	-8.00	10.38	-18.48	63.88
5	-286.66	127.49	-144.15	385.71	-500.17	257.28	-59.31	25.92	-15.28	11.00	-9.37	9.50	-11.93	20.71	-70.48
6	194.70	-73.94	63.73	-93.45	286.24	-403.83	223.01	-54.63	25.37	-16.00	12.51	-11.93	14.30	-24.00	79.90
7	-144.15	49.69	-36.69	41.56	-70.48	236.89	-357.78	210.19	-54.63	27.07	-18.48	16.10	-18.09	28.94	-93.45
8	113.41	-36.69	24.53	-24.00	31.70	-59.31	214.35	-344.00	214.35	-59.31	31.70	-24.00	24.53	-36.69	113.41
9	-93.45	28.94	-18.09	16.10	-18.48	27.07	-54.63	210.19	-357.78	236.89	-70.48	41.56	-36.69	49.69	-144.15
10	79.90	-24.00	14.30	-11.93	12.51	-16.00	25.37	-54.63	223.01	-403.83	286.24	-93.45	63.73	-73.94	194.70
11	-70.48	20.71	-11.93	9.50	-9.37	11.00	-15.28	25.92	-59.31	257.28	-500.17	385.71	-144.15	127.49	-286.66
12	63.88	-18.48	10.38	-8.00	7.56	-8.38	10.73	-16.00	28.93	-70.48	327.17	-696.00	603.90	-483.45	1049.15
13	-59.31	16.97	-9.37	7.06	-6.48	6.90	-8.38	11.57	-18.48	35.72	-78.01	442.15	-1072.52	963.60	944.06
14	56.32	-15.45	8.73	-6.48	5.83	-6.06	7.11	-9.37	13.95	-24.00	50.25	-24.00	15.45	-2508.18	4281.83
15	-54.63	15.45	-8.38	6.16	-5.48	5.62	-6.48	8.32	-11.93	19.36	-36.69	86.14	-286.66	2027.02	-11694.53

TABLE V.—COMPRESSIBILITY FACTORS ($\gamma=7/5$)

M	K_1	K_2	K_2-1	$\frac{K_2-1}{2}$	M	K_1	K_2	K_2-1	$\frac{K_2-1}{2}$	M	K_1	K_2	K_2-1	$\frac{K_2-1}{2}$
0	1.0000	1.0000	0	0	0.56	1.2070	1.5821	0.58212	0.29106	0.76	1.5386	3.4893	2.4893	1.2447
.05	1.0013	1.0025	.00251	.00126	.57	1.2171	1.6202	.62023	.31012	.77	1.5673	3.7291	2.7291	1.3645
.10	1.0050	1.0102	.01016	.00508	.58	1.2276	1.6611	.66112	.33056	.78	1.5980	4.0019	3.0019	1.5009
.15	1.0114	1.0233	.02334	.01167	.59	1.2385	1.7051	.70506	.35253	.79	1.6310	4.3142	3.3142	1.6571
.20	1.0206	1.0427	.04271	.02135	.60	1.2500	1.7523	.75234	.37617	.80	1.6667	4.6741	3.6741	1.8370
.25	1.0328	1.0693	.06933	.03467	.61	1.2620	1.8033	.80332	.40166	.81	1.7052	5.0917	4.0917	2.0458
.30	1.0483	1.1048	.10477	.05238	.62	1.2745	1.8584	.85838	.42919	.82	1.7471	5.5802	4.5802	2.2901
.35	1.0675	1.1513	.15129	.07565	.63	1.2877	1.9180	.91796	.45898	.83	1.7929	6.1565	5.1565	2.5783
.40	1.0911	1.2122	.21224	.10612	.64	1.3014	1.9826	.98255	.49128	.84	1.8430	6.8434	5.8434	2.9217
.45	1.1198	1.2926	.29260	.14630	.65	1.3159	2.0527	1.0527	.52637	.85	1.8983	7.6708	6.6708	3.3354
.46	1.1262	1.3116	.31161	.15581	.66	1.3311	2.1292	1.1292	.56460	.86	1.9597	8.6504	7.6504	3.8402
.47	1.1329	1.3318	.33177	.16588	.67	1.3471	2.2126	1.2126	.60632	.87	2.0702	9.9300	8.9300	4.4650
.48	1.1399	1.3532	.35315	.17658	.68	1.3639	2.3040	1.3040	.65200	.88	2.1054	11.502	10.502	5.2512
.49	1.1472	1.3759	.37586	.18793	.69	1.3816	2.4043	1.4043	.70213	.89	2.1832	13.520	12.520	6.2598
.50	1.1547	1.4000	.40000	.20000	.70	1.4003	2.5146	1.5146	.75732	.90	2.2942	16.168	15.168	7.5839
.51	1.1626	1.4257	.42568	.21284	.71	1.4200	2.6365	1.6365	.81827	.91	2.4119	19.741	18.741	9.3707
.52	1.1707	1.4530	.45303	.22651	.72	1.4410	2.7716	1.7716	.88580	.92	2.6184	24.729	23.729	11.865
.53	1.1792	1.4822	.48218	.24109	.73	1.4632	2.9218	1.9218	.96091	.93	2.7206	31.993	30.993	15.496
.54	1.1881	1.5133	.51330	.25665	.74	1.4868	3.0895	2.0895	1.0448	.94	3.0196	43.166	42.166	21.083
.55	1.1974	1.5465	.54654	.27327	.75	1.5119	3.2776	2.2776	1.1388	.95	3.2026	61.065	60.065	30.332

REPORT 1275

THE PROPER COMBINATION OF LIFT LOADINGS FOR LEAST DRAG ON A SUPERSONIC WING¹

By FREDERICK C. GRANT

SUMMARY

Lagrange's method of undetermined multipliers is applied to the problem of properly combining lift loadings for the least drag at a given lift on supersonic wings. The method shows the interference drag between the optimum loading and any loading at the same lift coefficient to be constant. This is an integral form of the criterion established by Robert T. Jones for optimum loadings.

The best combination of four loadings on a delta wing with subsonic leading edges is calculated as a numerical example. The loadings considered have finite pressures everywhere on the plan form. Through the sweepback range the optimum combination of the four nonsingular loadings has about the same drag coefficient as a flat plate with leading-edge thrust.

INTRODUCTION

The problem of minimizing the supersonic drag for a given lift on a fixed plan form has been approached in different ways. Jones, in references 1 and 2, makes use of reverse-flow theorems to derive several simple properties of the optimum load distribution and to present as well the optimum distribution for elliptic plan forms. Graham, in reference 3, shows how the proper use of orthogonal loadings can reduce the drag at fixed lift. Orthogonal loadings are loadings of zero interference drag. The interference drag between two loadings is the total drag of each in the downwash field of the other. In reference 4, theorems concerning orthogonality and reverse flow are developed, whereas in references 5 and 6 numerical examples of drag reduction by use of orthogonal loadings are given. For delta wings with conical camber the optimum shapes are derived by Ritz's method in reference 7.

In this report Lagrange's method of undetermined multipliers is applied to the problem of properly combining loadings for the least drag at a given lift. By use of this method a simply expressed property of the optimum loading is found which is an integral form of a property established by Jones in reference 1 for reversible flows. Jones' property of the optimum loading is that the downwash on the plan form is constant in the combined forward- and reverse-flow fields. The best combination of four types of nonsingular loading on a delta wing is calculated as a numerical example of the use of the method.

SYMBOLS

A	loading strength parameter
b	span
c	local chord
C_D	drag coefficient
$C_{D,i}$	drag coefficient of i th loading
$C_{D,ij}$	drag coefficient of interference between i th and j th component loadings
C_L	lift coefficient
$C_{L,i}$	lift coefficient of i th loading
C_p	lifting pressure coefficient
M	Mach number
m	tangent of semiapex angle
N	number of loadings
$n = \beta m$	sweepback-speed parameter
R	functions of θ and n (see appendix)
S	wing area
X', Y'	arbitrary Cartesian coordinates
l	loading on an arbitrary line, $\int_l C_p dX'$
s, t	integers
x, y, z	Cartesian coordinates of lifting surface (see fig. 2)
α	local angle of attack of lifting surface
$\beta = \sqrt{M^2 - 1}$	
ϵ	small positive number
$\theta = \frac{y}{mx}$	
λ	Lagrange's multiplier
τ	plan form
$1 - \mu$	root chord of arrow wing
Subscripts:	
i, j	i th, j th loading component
M	minimum among all loadings
0	minimum among N loadings
X	arbitrary loading

ANALYSIS

THEORY

Consider a superposition of N loadings of the form

$$C_p = A_1 C_{p,1} + A_2 C_{p,2} + A_3 C_{p,3} + \dots + A_N C_{p,N} \quad (1)$$

¹ Supersedes NACA Technical Note 3533 by Frederick C. Grant, 1955.

REPORT 1275

THE PROPER COMBINATION OF LIFT LOADINGS FOR LEAST DRAG ON A SUPERSONIC WING¹

By FREDERICK C. GRANT

SUMMARY

Lagrange's method of undetermined multipliers is applied to the problem of properly combining lift loadings for the least drag at a given lift on supersonic wings. The method shows the interference drag between the optimum loading and any loading at the same lift coefficient to be constant. This is an integral form of the criterion established by Robert T. Jones for optimum loadings.

The best combination of four loadings on a delta wing with subsonic leading edges is calculated as a numerical example. The loadings considered have finite pressures everywhere on the plan form. Through the sweepback range the optimum combination of the four nonsingular loadings has about the same drag coefficient as a flat plate with leading-edge thrust.

INTRODUCTION

The problem of minimizing the supersonic drag for a given lift on a fixed plan form has been approached in different ways. Jones, in references 1 and 2, makes use of reverse-flow theorems to derive several simple properties of the optimum load distribution and to present as well the optimum distribution for elliptic plan forms. Graham, in reference 3, shows how the proper use of orthogonal loadings can reduce the drag at fixed lift. Orthogonal loadings are loadings of zero interference drag. The interference drag between two loadings is the total drag of each in the downwash field of the other. In reference 4, theorems concerning orthogonality and reverse flow are developed, whereas in references 5 and 6 numerical examples of drag reduction by use of orthogonal loadings are given. For delta wings with conical camber the optimum shapes are derived by Ritz's method in reference 7.

In this report Lagrange's method of undetermined multipliers is applied to the problem of properly combining loadings for the least drag at a given lift. By use of this method a simply expressed property of the optimum loading is found which is an integral form of a property established by Jones in reference 1 for reversible flows. Jones' property of the optimum loading is that the downwash on the plan form is constant in the combined forward- and reverse-flow fields. The best combination of four types of nonsingular loading on a delta wing is calculated as a numerical example of the use of the method.

SYMBOLS

A	loading strength parameter
b	span
c	local chord
C_D	drag coefficient
$C_{D,i}$	drag coefficient of i th loading
$C_{D,ij}$	drag coefficient of interference between i th and j th component loadings
C_L	lift coefficient
$C_{L,i}$	lift coefficient of i th loading
C_p	lifting pressure coefficient
M	Mach number
m	tangent of semiapex angle
N	number of loadings
$n = \beta m$	sweepback-speed parameter
R	functions of θ and n (see appendix)
S	wing area
X', Y'	arbitrary Cartesian coordinates
l	loading on an arbitrary line, $\int_l C_p dX'$
s, t	integers
x, y, z	Cartesian coordinates of lifting surface (see fig. 2)
α	local angle of attack of lifting surface
$\beta = \sqrt{M^2 - 1}$	
ϵ	small positive number
$\theta = \frac{y}{mx}$	
λ	Lagrange's multiplier
τ	plan form
$1 - \mu$	root chord of arrow wing
Subscripts:	
i, j	i th, j th loading component
M	minimum among all loadings
0	minimum among N loadings
X	arbitrary loading

ANALYSIS

THEORY

Consider a superposition of N loadings of the form

$$C_p = A_1 C_{p,1} + A_2 C_{p,2} + A_3 C_{p,3} + \dots + A_N C_{p,N} \quad (1)$$

¹Supersedes NACA Technical Note 3533 by Frederick C. Grant, 1955.

where A is the strength parameter and C_p is the resultant lifting pressure coefficient at a point on the plan form. The corresponding local angle of attack may be written as

$$\alpha = A_1\alpha_1 + A_2\alpha_2 + A_3\alpha_3 + \dots + A_N\alpha_N \quad (2)$$

The local drag coefficient $C_{p,i}$ is a quadratic in A which may be integrated over the plan form τ to give the drag coefficient of the wing. Thrust-loaded singularities at the leading edge are therefore excluded from the drag. This exclusion is merely for convenience and is not necessary. A formula for the drag coefficient is

$$C_D = \frac{1}{S} \int_{\tau} C_p \alpha^2 dS = \frac{1}{2} \sum_{i=1}^N \sum_{j=1}^N C_{D,ij} A_i A_j \quad (3)$$

where

$$C_{D,ij} = C_{D,ji} = \frac{1}{S} \int_{\tau} (C_{p,i}\alpha_j + C_{p,j}\alpha_i) dS$$

The average lifting pressure coefficient on the plan form is the lift coefficient, which is

$$C_L = \frac{1}{S} \int_{\tau} C_p dS = \sum_{i=1}^N C_{L,i} A_i \quad (4)$$

The problem is to find the set of A 's which yields the minimum value of C_D subject to the condition that C_L is constant. Because of the quadratic nature of C_D and the linear form of C_L , Lagrange's method of undetermined multipliers is particularly suitable for the solution as it leads to a set of linear algebraic equations.

As shown in reference 8, a function of the A coefficients $F = C_D + \lambda C_L$ is formed, where λ is Lagrange's multiplier. The minimum value of F as determined by the N linear algebraic equations $\frac{\partial F}{\partial A_i} = 0$ plus condition (4) is Lagrange's solution. In matrix form these equations are:

$$\begin{bmatrix} 2C_{D,1} & C_{D,12} & C_{D,13} & \dots & C_{D,1N} & C_{L,1} \\ C_{D,12} & 2C_{D,2} & C_{D,23} & \dots & C_{D,2N} & C_{L,2} \\ C_{D,13} & C_{D,23} & 2C_{D,3} & \dots & C_{D,3N} & C_{L,3} \\ \vdots & \vdots & \vdots & \ddots & \vdots & \vdots \\ C_{D,1N} & C_{D,2N} & C_{D,3N} & \dots & 2C_{D,N} & C_{L,N} \\ C_{L,1} & C_{L,2} & C_{L,3} & \dots & C_{L,N} & 0 \end{bmatrix} \begin{bmatrix} A_1 \\ A_2 \\ A_3 \\ \vdots \\ A_N \\ \lambda \end{bmatrix} = \begin{bmatrix} 0 \\ 0 \\ 0 \\ \vdots \\ 0 \\ C_L \end{bmatrix} \quad (5)$$

The equations may be written more simply if first the interference drag between the optimum loading and the i th component of the loading is computed. From equations (1) and (2), the following expressions may be written:

$$\left. \begin{aligned} C_{p,0}\alpha_i &= A_1 C_{p,1}\alpha_i + A_2 C_{p,2}\alpha_i + A_3 C_{p,3}\alpha_i + \dots + \\ &\quad A_i C_{p,i}\alpha_i + \dots + A_N C_{p,N}\alpha_i \\ \alpha_0 C_{p,i} &= A_1 \alpha_i C_{p,i} + A_2 \alpha_i C_{p,i} + A_3 \alpha_i C_{p,i} + \dots + \\ &\quad A_i \alpha_i C_{p,i} + \dots + A_N \alpha_i C_{p,i} \end{aligned} \right\} \quad (6)$$

Adding equations (6) and integrating over the plan form gives

$$\begin{aligned} C_{D,0i} &= \frac{1}{S} \int_{\tau} (C_{p,0}\alpha_i + \alpha_0 C_{p,i}) dS = A_1 C_{D,1i} + A_2 C_{D,2i} + \\ &\quad A_3 C_{D,3i} + \dots + 2A_i C_{D,i} + \dots + A_N C_{D,Ni} \\ &= \sum_{j=1}^N A_j C_{D,ji} \end{aligned} \quad (7)$$

This expression for $C_{D,0i}$ is a part of the left-hand side of the i th equation of the linear set which is now written as

$$C_{D,0i} + \lambda C_{L,i} = 0 \quad (8)$$

A simple property of the optimum load distribution may now be derived. First $C_{D,0}$ is rewritten by use of equation (7):

$$C_{D,0} = \frac{1}{2} \sum_{i=1}^N A_i C_{D,0i} \quad (9)$$

or using equations (8) and (4)

$$C_{D,0} = -\frac{1}{2} \lambda C_L \quad (10)$$

Substituting equation (10) into equation (8) gives

$$C_{D,0i} = 2 \frac{C_{D,0}}{C_L} C_{L,i} \quad (11)$$

Since equation (11) holds for any number of loadings, let the number of components increase without limit to include all possible loadings. For an arbitrary loading X and the absolute minimum M , equation (11) may be written as

$$C_{D,MX} = 2 \frac{C_{D,M}}{C_L} C_{L,X} \quad (12)$$

The meaning of equation (12) may be simply expressed as follows: The interference drag between the optimum loading and any loading at the same lift coefficient is constant. If the reversibility theorem is applicable, equation (12) is an integral equivalent of a condition established by Jones in reference 1. Jones' condition states that for the optimum loading the downwash on the plan form is constant in the combined forward- and reverse-flow fields. Barred variables will represent the reverse flow which has the same lift loading on the plan form but, in general, a different surface shape. Then, by reversibility,

$$\int_{\tau} C_{p,M} \alpha_X dS = \int_{\tau} \bar{C}_{p,M} \alpha_X dS = \int_{\tau} \bar{\alpha}_M C_{p,X} dS \quad (13)$$

By definition, $C_{D,MX}$ is

$$C_{D,MX} = \frac{1}{S} \int_{\tau} (C_{p,M} \alpha_X + \alpha_M C_{p,X}) dS$$

Therefore, equation (12) may be written as

$$\int_{\tau} C_{p,X} (\alpha_M + \bar{\alpha}_M) dS = 2 \frac{C_{D,M}}{C_L} \int_{\tau} C_{p,X} dS \quad (14)$$

Since $C_{p,X}$ is arbitrary, $\alpha_M + \bar{\alpha}_M$ must be constant. Hence,

$$\alpha_M + \bar{\alpha}_M = 2 \frac{C_{D,M}}{C_L} \quad (15)$$

This is the condition derived by Jones in reference 1. Equation (12) is then an equivalent integral form of this condition.

Equation (12) shows the orthogonality of the optimum loading to, and only to, zero lift loadings. This result, which was stated by Graham in reference 3, is seen to be a special case of a more general interference drag property given by equation (12).

COMPARISON WITH THE METHOD OF ORTHOGONAL LOADINGS

If two loadings are to be combined, it may be shown that Graham's method of orthogonal loadings (ref. 3) and the present method are equivalent. If the resultant combination of two loadings is combined by the method of reference 3 with a third loading, the lift ratio of the first two loadings is unchanged in the best combination of the three. If $n > 2$ loadings are successively combined in the manner of reference 3, the first $n-1$ loadings are not allowed to adjust their relative strengths upon addition of the n th. In the present Lagrangian method every loading has equal freedom to adjust. For this reason, the Lagrangian method should be more rapidly convergent.

NUMERICAL EXAMPLE

Tucker in reference 9 presents formulas for the surface coordinates of delta and arrow wings which support four types of pressure distribution. The formulas are given for subsonic leading edges and supersonic trailing edges. In the notation of this report (fig. 1) a combination of the four loadings may be written:

$$C_p = A_1 + A_2 x + A_3 \frac{|y|}{m} + A_4 \frac{y^2}{m^2} \quad (16)$$

Formulas for the $C_{D,ij}$ quantities may be derived from equation (16) and the surface formulas given in reference 9, by integrations over the plan form. Details are given in the appendix.

The optimum-drag results are presented in figure 2 along with the corresponding drag values for a flat delta wing with and without leading-edge thrust (ref. 10). The drag values for the four component loadings taken alone are also shown. In addition, the drag of the conically cambered optimum delta wing (ref. 7) and Jones' absolute minimum for narrow wings (ref. 1) are plotted. The optimum A values are tabulated in the appendix.

Noteworthy in figure 2 is the closeness with which all the optimum drags agree with each other and with the drag of a flat delta wing which has a thrust-loaded leading edge. The close approach of the present optimum of four loadings to Jones' absolute minimum for narrow wings is also evident. The data indicate that the relatively low drag of the flat

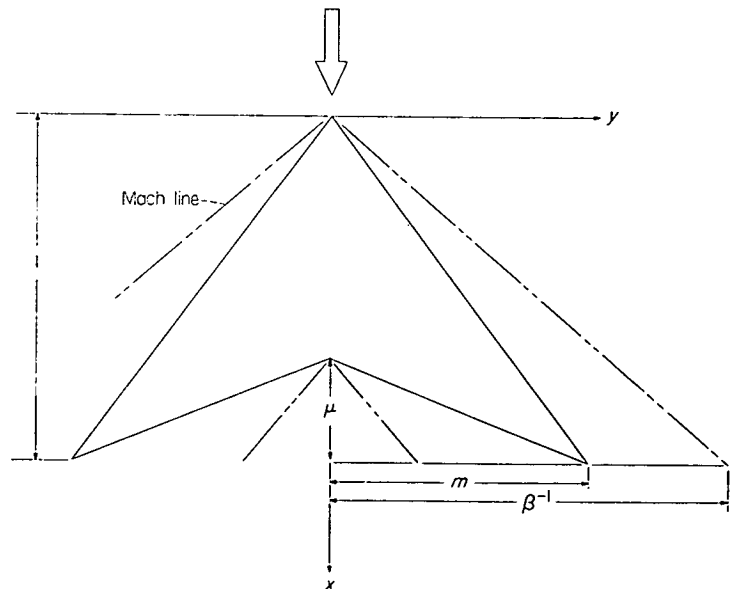


FIGURE 1.—Arrow plan form.

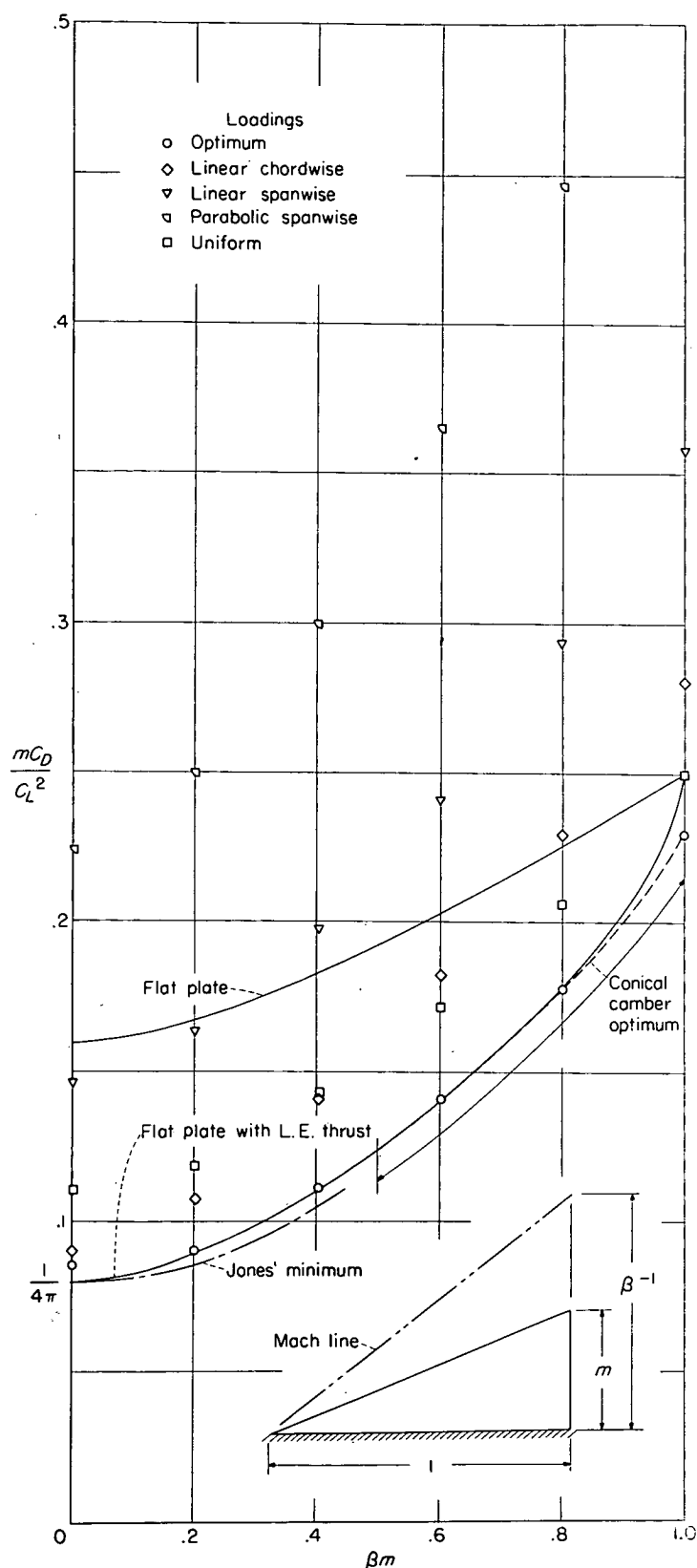
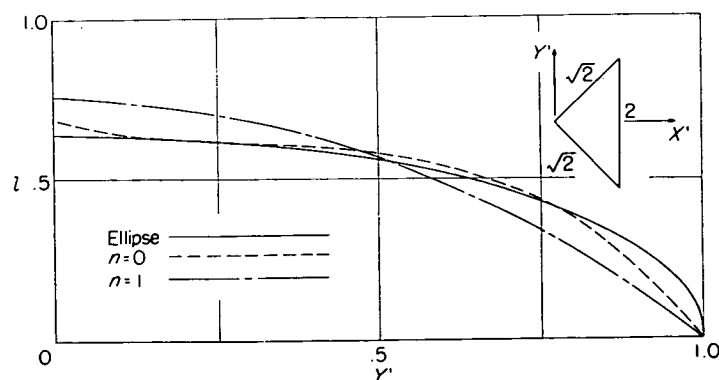


FIGURE 2.—Comparative drags on a delta plan form.

delta wing with leading-edge thrust can be equalled by properly combining a few loadings having finite pressures everywhere on the plan form. A plausible speculation suggested by the data is that it is possible to come very close to the minimum drag on a delta wing with but a few steps in a series approximation. Perhaps, too, a restricted minimum, such as the one for conical camber, gives a close approximation to the absolute minimum drag if the restriction is not too unnatural.

Since the vortex drag of a wing at any Mach number depends only on the spanwise loading, a departure from the elliptic spanwise loading is a measure of the vortex drag in excess of the least possible drag. In figure 3 the spanwise loading of the optimum combination is shown at the extremes of the sweepback range. There is good agreement with the elliptic loading especially for the case of extreme sweepback ($n=0$). Because for extreme sweepback the wave drag vanishes, a direct comparison of the vortex drag of the optimum combination and the elliptic spanwise loading is given by figure 2 at $n=0$. The elliptic spanwise loading has the drag parameter value $\frac{1}{4\pi}$.

It is shown in reference 2 that the wave drag due to lift depends on all the lift loadings $l(Y')$ where $l = \int_r C_p dX'$ and X' is an arbitrary direction inclined to the free stream at more than the Mach angle. The coordinate Y' is perpendicular to X' . A sufficient condition for minimum wave drag is shown to be that $l(Y')$ is an ellipse. In figure 4 the loading of lines perpendicular to the free stream, or chordwise loading, is shown for the optimum combination with a sonic leading edge ($n=1$). Agreement with the elliptical loading is poor. For the case of extreme sweepback ($n=0$) no chordwise loading for the optimum combination is shown in figure 4 because it is partially arbitrary. (See appendix.) The allowable variations of the optimum loading at $n=0$ correspond to changes in the oblique loadings that do not change the spanwise loading. This result emphasizes the vanishing of the wave drag with extreme sweepback.

FIGURE 3.—The loading of lines parallel to the free stream for the optimum combination. $m=C_L=1$.

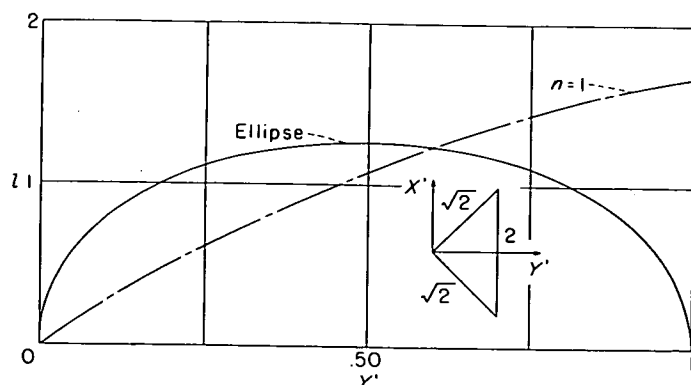


FIGURE 4.—The loading of lines perpendicular to the free stream for the optimum combination. $m=C_L=1$.

CONCLUDING REMARKS

Lagrange's method of undetermined multipliers is applied to the problem of properly combining lift loadings for the least drag at a given lift on supersonic wings.

The method shows the interference drag between the optimum loading and any loading at the same lift coefficient to be constant. This is an integral form of the criterion established by Robert T. Jones for optimum loadings.

The best combination of four loadings on a delta wing with subsonic leading edges is calculated as a numerical example. The loadings considered have finite pressures everywhere on the plan form. At each Mach number the optimum combination of these four nonsingular loadings has nearly the same drag coefficient as a flat plate with leading-edge thrust.

LANGLEY AERONAUTICAL LABORATORY,

NATIONAL ADVISORY COMMITTEE FOR AERONAUTICS,

LANGLEY FIELD, VA., July 27, 1955.

APPENDIX

DETAILS OF NUMERICAL EXAMPLE

INTERFERENCE DRAG FORMULAS

Inasmuch as the pressure coefficient C_p and corresponding angle of attack α are given by

$$\left. \begin{aligned} C_p &= A_1 + A_2 x + A_3 \frac{|y|}{m} + A_4 \frac{y^2}{m^2} \\ \alpha &= A_1 \alpha_1 + A_2 \alpha_2 + A_3 \alpha_3 + A_4 \alpha_4 \end{aligned} \right\} \quad (A1)$$

then the local drag coefficient may be written as

$$\begin{aligned} C_{D,i} &= A_1^2 (\alpha_1) + A_1 A_2 (x \alpha_1 + \alpha_2) + A_1 A_3 \left(\frac{|y|}{m} \alpha_1 + \alpha_3 \right) + \\ &+ A_1 A_4 \left(\frac{y^2}{m^2} \alpha_1 + \alpha_4 \right) + A_2^2 (x \alpha_2) + A_2 A_3 \left(\frac{|y|}{m} \alpha_2 + x \alpha_3 \right) + \\ &+ A_2 A_4 \left(\frac{y^2}{m^2} \alpha_2 + x \alpha_4 \right) + A_3^2 \left(\frac{|y|}{m} \alpha_3 \right) + \\ &+ A_3 A_4 \left(\frac{y^2}{m^2} \alpha_3 + \frac{|y|}{m} \alpha_4 \right) + A_4^2 \left(\frac{y^2}{m^2} \alpha_4 \right) \end{aligned} \quad (A2)$$

The required $C_{D,i}$ functions are the averages over the plan form (fig. 1) of the quantities in parentheses in equation (A2). Rather than α_i itself, reference 9 gives the surface ordinate z_i which is the chordwise integrated value of α_i :

$$z_i = - \int \alpha_i dx \quad (A3)$$

The values given for z_i are

$$\left. \begin{aligned} z_1 &= \frac{x}{m} R_1 \\ z_2 &= \frac{x^2}{m} R_2 \\ z_3 &= \frac{x^2}{m} R_3 \\ z_4 &= \frac{x^3}{m} R_4 \end{aligned} \right\} \quad (A4)$$

The values of R_i are functions of $\theta = \frac{y}{mx}$ tabulated in reference 9 for different values of n . The equations for R_i are

$$\begin{aligned} R_1 &= \frac{1}{4\pi} \left[2\sqrt{1-n^2\theta^2} - 2 \cosh^{-1} \left| \frac{1}{n\theta} \right| + \right. \\ &\quad \left. \sqrt{1-n^2} (1+\theta) \cosh^{-1} \left| \frac{1+n^2\theta}{n(1+\theta)} \right| + \right. \\ &\quad \left. \sqrt{1-n^2} (1-\theta) \cosh^{-1} \left| \frac{1-n^2\theta}{n(1-\theta)} \right| \right] \end{aligned} \quad (A5a)$$

$$\begin{aligned} R_2 &= -\frac{1}{4\pi} \left\{ \sqrt{1-n^2\theta^2} - 2\theta^2 \cosh^{-1} \left| \frac{1}{n\theta} \right| + \right. \\ &\quad \frac{1}{\sqrt{1-n^2}} \left[\frac{n^2(1-\theta^2)}{2} + \theta + \theta^2 \right] \cosh^{-1} \left| \frac{1+n^2\theta}{n(1+\theta)} \right| + \\ &\quad \left. \frac{1}{\sqrt{1-n^2}} \left[\frac{n^2(1-\theta^2)}{2} - \theta + \theta^2 \right] \cosh^{-1} \left| \frac{1-n^2\theta}{n(1-\theta)} \right| \right\} \end{aligned} \quad (A5b)$$

$$\begin{aligned} R_3 &= -\frac{1}{4\pi} \left[\frac{5}{2} \sqrt{1-n^2\theta^2} - \left(1 + 3\theta^2 - \frac{1}{2} n^2\theta^2 \right) \cosh^{-1} \left| \frac{1}{n\theta} \right| + \right. \\ &\quad \frac{(1+\theta)^2 + 2(1-n^2)(\theta + \theta^2)}{2\sqrt{1-n^2}} \cosh^{-1} \left| \frac{1+n^2\theta}{n(1+\theta)} \right| + \\ &\quad \left. \frac{(1-\theta)^2 - 2(1-n^2)(\theta - \theta^2)}{2\sqrt{1-n^2}} \cosh^{-1} \left| \frac{1-n^2\theta}{n(1-\theta)} \right| \right] \end{aligned} \quad (A5c)$$

$$\begin{aligned} R_4 &= \frac{1}{4\pi} \left\{ \frac{(1-n^2\theta^2)^{3/2}}{3(1-n^2)} + \frac{12-10n^2}{3n^2(1-n^2)} n^2\theta^2 \sqrt{1-n^2\theta^2} - 6\theta^2 \cosh^{-1} \left| \frac{1}{n\theta} \right| + \right. \\ &\quad \frac{1}{(1-n^2)^{3/2}} \left[\frac{6-9n^2+2n^4}{2} (\theta^2 + \theta^3) + \frac{2-3n^2}{2} (\theta - \theta^3) - \right. \\ &\quad \left. \frac{n^2}{6} (1+\theta^3) \right] \cosh^{-1} \left| \frac{1+n^2\theta}{n(1+\theta)} \right| + \frac{1}{(1-n^2)^{3/2}} \left[\frac{6-9n^2+2n^4}{2} (\theta^2 - \theta^3) - \right. \\ &\quad \left. \frac{2-3n^2}{2} (\theta - \theta^3) - \frac{n^2}{6} (1-\theta^3) \right] \cosh^{-1} \left| \frac{1-n^2\theta}{n(1-\theta)} \right| \left. \right\} \end{aligned} \quad (A5d)$$

For terms in equation (A2) of the type $(y/m)^s \alpha_i$, a spanwise integration of z_i gives the following average on the plan form:

$$\begin{aligned} \frac{1}{S} \int_{\tau} \left(\frac{y}{m} \right)^s \alpha_i dS &= \frac{2}{1-\mu} \frac{1}{m} \left[\frac{R_i(1)}{s+t+1} - \right. \\ &\quad \left. (1-\mu)^{s+t+1} \int_0^1 \frac{\theta^s R_i(\theta)}{(1-\mu\theta)^{s+t+2}} d\theta \right] \end{aligned} \quad (A6)$$

For terms of the type $x \alpha_i$ an additional integration by parts in the x direction is required to maintain the R_i functions intact under the integral signs. The result for this case is

$$\begin{aligned} \frac{1}{S} \int_{\tau} x \alpha_i dS &= \frac{2}{1-\mu} \frac{1}{m} \left[\frac{R_i(1)}{t+2} - (1-\mu)^{t+2} \int_0^1 \frac{R_i(\theta)}{(1-\mu\theta)^{t+3}} d\theta + \right. \\ &\quad \left. \frac{(1-\mu)^{t+2}}{t+2} \int_0^1 \frac{R_i(\theta)}{(1-\mu\theta)^{t+2}} d\theta \right] \end{aligned} \quad (A7)$$

In formulas (A6) and (A7) the value of t for each i is as follows:

i	t
1	1
2	2
3	2
4	3

By applying formulas (A6) and (A7) to the integration of (A2), the following equations for $C_{D,ij}$ are derived:

$$2mC_{D,1} = \frac{2}{1-\mu} R_1(1) - 4(1-\mu) \int_0^1 \frac{R_1(\theta)}{(1-\mu\theta)^3} d\theta \quad (\text{A8a})$$

$$mC_{D,12} = \frac{2}{3(1-\mu)} [R_1(1) + R_2(1)] + \frac{2(1-\mu)^2}{3} \int_0^1 \frac{R_1(\theta)}{(1-\mu\theta)^3} d\theta - 2(1-\mu)^2 \int_0^1 \frac{R_1(\theta)}{(1-\mu\theta)^4} d\theta - 2(1-\mu)^2 \int_0^1 \frac{R_2(\theta)}{(1-\mu\theta)^4} d\theta \quad (\text{A8b})$$

$$mC_{D,13} = \frac{2}{3(1-\mu)} [R_1(1) + R_3(1)] - 2(1-\mu)^2 \int_0^1 \frac{\theta R_1(\theta)}{(1-\mu\theta)^4} d\theta - 2(1-\mu)^2 \int_0^1 \frac{R_3(\theta)}{(1-\mu\theta)^4} d\theta \quad (\text{A8c})$$

$$mC_{D,14} = \frac{1}{2(1-\mu)} [R_1(1) + R_4(1)] - 2(1-\mu)^3 \int_0^1 \frac{\theta^2 R_1(\theta)}{(1-\mu\theta)^5} d\theta - 2(1-\mu)^3 \int_0^1 \frac{R_4(\theta)}{(1-\mu\theta)^5} d\theta \quad (\text{A8d})$$

$$2mC_{D,2} = \frac{R_2(1)}{1-\mu} - 4(1-\mu)^3 \int_0^1 \frac{R_2(\theta)}{(1-\mu\theta)^5} d\theta + (1-\mu)^3 \int_0^1 \frac{R_2(\theta)}{(1-\mu\theta)^4} d\theta \quad (\text{A8e})$$

$$mC_{D,23} = \frac{1}{2(1-\mu)} [R_2(1) + R_3(1)] - 2(1-\mu)^3 \int_0^1 \frac{\theta R_2(\theta)}{(1-\mu\theta)^5} d\theta - 2(1-\mu)^3 \int_0^1 \frac{R_3(\theta)}{(1-\mu\theta)^5} d\theta + \frac{1}{2}(1-\mu)^3 \int_0^1 \frac{R_3(\theta)}{(1-\mu\theta)^4} d\theta \quad (\text{A8f})$$

$$mC_{D,24} = \frac{2}{5(1-\mu)} [R_2(1) + R_4(1)] - 2(1-\mu)^4 \int_0^1 \frac{\theta^2 R_2(\theta)}{(1-\mu\theta)^6} d\theta - 2(1-\mu)^4 \int_0^1 \frac{R_4(\theta)}{(1-\mu\theta)^6} d\theta + \frac{2}{5}(1-\mu)^4 \int_0^1 \frac{R_4(\theta)}{(1-\mu\theta)^5} d\theta \quad (\text{A8g})$$

$$2mC_{D,3} = \frac{R_3(1)}{1-\mu} - 4(1-\mu)^3 \int_0^1 \frac{\theta R_3(\theta)}{(1-\mu\theta)^5} d\theta \quad (\text{A8h})$$

$$mC_{D,34} = \frac{2}{5(1-\mu)} [R_3(1) + R_4(1)] - 2(1-\mu)^4 \int_0^1 \frac{\theta^2 R_3(\theta)}{(1-\mu\theta)^6} d\theta - 2(1-\mu)^4 \int_0^1 \frac{\theta R_4(\theta)}{(1-\mu\theta)^6} d\theta \quad (\text{A8i})$$

$$2mC_{D,4} = \frac{2}{3(1-\mu)} R_4(1) - 4(1-\mu)^5 \int_0^1 \frac{\theta^2 R_4(\theta)}{(1-\mu\theta)^7} d\theta \quad (\text{A8j})$$

The required $C_{L,t}$ functions are simple integrals over the plan form which yield

$$\left. \begin{aligned} C_{L,1} &= 1 \\ C_{L,2} &= \frac{2-\mu}{3} \\ C_{L,3} &= \frac{1}{3} \\ C_{L,4} &= \frac{1}{6} \end{aligned} \right\} \quad (\text{A9})$$

NUMERICAL CALCULATIONS

The integrals in equations (A8) were, in general, evaluated numerically. However, several of the integrands in equations (A8) have the form $\frac{R_1(\theta)}{(1-\mu\theta)^i}$ and $\frac{R_3(\theta)}{(1-\mu\theta)^i}$. These functions have an infinite discontinuity at $\theta=0$. For such a discontinuity, numerical methods break down. Near zero the following approximation is integrated analytically:

$$\left. \begin{aligned} R_1(\theta) &\approx R_1(\epsilon) + \frac{1}{2\pi} \cosh^{-1} \frac{1}{n\epsilon} - \frac{1}{2\pi} \cosh^{-1} \frac{1}{n\theta} \\ R_3(\theta) &\approx R_3(\epsilon) - \frac{1}{4\pi} \cosh^{-1} \frac{1}{n\epsilon} + \frac{1}{4\pi} \cosh^{-1} \frac{1}{n\theta} \end{aligned} \right\} 0 < \theta \leq \epsilon \ll 1 \quad (\text{A10})$$

The integrals for the region $0 \leq \theta \leq \epsilon$ can then be approximated:

$$\left. \begin{aligned} \int_0^\epsilon \frac{R_1(\theta)}{(1-\mu\theta)^i} d\theta &\approx f(\epsilon) \left[R_1(\epsilon) + \frac{1}{2\pi} \cosh^{-1} \frac{1}{n\epsilon} \right] - \frac{I(\epsilon)}{2\pi} \\ \int_0^\epsilon \frac{R_3(\theta)}{(1-\mu\theta)^i} d\theta &\approx f(\epsilon) \left[R_3(\epsilon) - \frac{1}{4\pi} \cosh^{-1} \frac{1}{n\epsilon} \right] + \frac{I(\epsilon)}{4\pi} \end{aligned} \right\} \quad (\text{A11})$$

where

$$f(\epsilon) = \int_0^\epsilon \frac{d\theta}{(1-\mu\theta)^i} = \epsilon \left[1 + \frac{t}{1} \mu \frac{\epsilon}{2} + \frac{t(t+1)}{2!} \frac{\mu^2 \epsilon^2}{3} + \frac{t(t+1)(t+2)}{3!} \frac{\mu^3 \epsilon^3}{4} + \dots \right] \quad (\text{A12})$$

and

$$I(\epsilon) = \int_0^\epsilon \frac{\cosh^{-1} \frac{1}{n\theta}}{(1-\mu\theta)^i} d\theta \quad (\text{A13})$$

The integral in equation (A13) may be evaluated by expanding the denominator by the binomial theorem and writing $I(\epsilon)$ as an infinite series

$$I(\epsilon) = a_0 i_0 + a_1 i_1 + a_2 i_2 + a_3 i_3 + \dots \quad (\text{A14})$$

where

$$a_0 = 1 \quad (\text{A15a})$$

$$a_1 = \frac{t}{1} \mu \quad (\text{A15b})$$

$$a_2 = \frac{t(t+1)}{2!} \mu^2 \quad (\text{A15c})$$

$$a_3 = \frac{t(t+1)(t+2)}{3!} \mu^3 \quad (\text{A15d})$$

$$a_s = \frac{t(t+1) \dots (t+s-1)}{s!} \mu^s \quad (\text{A15e})$$

$$i_0 = \int_0^\epsilon \cosh^{-1} \frac{1}{n\theta} d\theta \quad (\text{A15f})$$

$$i_1 = \int_0^\epsilon \theta \cosh^{-1} \frac{1}{n\theta} d\theta \quad (\text{A15g})$$

$$i_2 = \int_0^\epsilon \theta^2 \cosh^{-1} \frac{1}{n\theta} d\theta \quad (\text{A15h})$$

$$i_s = \int_0^\epsilon \theta^s \cosh^{-1} \frac{1}{n\theta} d\theta \quad (\text{A15i})$$

The i_s integrals of equations (A15) are evaluated by use of the relation

$$\int \theta^s \cosh^{-1} \frac{1}{n\theta} d\theta = \frac{\theta^{s+1}}{s+1} \cosh^{-1} \frac{1}{n\theta} + \frac{1}{s+1} \int \frac{\theta^s}{\sqrt{1-n^2\theta^2}} d\theta \quad (\text{A16})$$

EXACT CALCULATIONS

At the extremes of the sweepback range, equations (A8) may be evaluated exactly. For the case of extreme sweepback ($n=0$), there results:

$$R_1 = \frac{1}{4\pi} \left(2 + \log_e \frac{\theta^2}{1-\theta^2} + \theta \log_e \frac{1-\theta}{1+\theta} \right) \quad (\text{A17a})$$

$$R_2 = -\frac{1}{4\pi} \left(1 + \theta \log_e \frac{1-\theta}{1+\theta} + \theta^2 \log_e \frac{\theta^2}{1-\theta^2} \right) \quad (\text{A17b})$$

$$R_3 = -\frac{1}{4\pi} \left[\frac{5}{2} + (1+3\theta^2) \log_e \frac{\theta}{\sqrt{1-\theta^2}} + 2\theta \log_e \frac{1-\theta}{1+\theta} \right] \quad (\text{A17c})$$

$$R_4 = \frac{1}{4\pi} \left[\frac{1}{3} + 4\theta^2 + (\theta+2\theta^3) \log_e \frac{1-\theta}{1+\theta} + 3\theta^2 \log_e \frac{\theta^2}{1-\theta^2} \right] \quad (\text{A17d})$$

$$2mC_{D,1} = \frac{\log_e 2}{\pi} \quad (\text{A18a})$$

$$mC_{D,12} = \frac{\frac{2}{3} + \frac{4}{3} \log_e 2}{4\pi} \quad (\text{A18b})$$

$$mC_{D,13} = \frac{\frac{4}{3} - \frac{4}{3} \log_e 2}{4\pi} \quad (\text{A18c})$$

$$mC_{D,14} = \frac{\frac{4}{3} \log_e 2 - \frac{5}{6}}{4\pi} \quad (\text{A18d})$$

$$2mC_{D,2} = \frac{1}{4\pi} \quad (\text{A18e})$$

$$mC_{D,23} = \frac{\frac{4}{3} - \frac{4}{3} \log_e 2}{4\pi} \quad (\text{A18f})$$

$$mC_{D,24} = \frac{\frac{4}{5} \log_e 2 - \frac{2}{5}}{4\pi} \quad (\text{A18g})$$

$$2mC_{D,3} = \frac{\frac{4}{3} - \frac{4}{3} \log_e 2}{4\pi} \quad (\text{A18h})$$

$$mC_{D,34} = \frac{\frac{1}{30} + \frac{4}{15} \log_e 2}{4\pi} \quad (\text{A18i})$$

$$2mC_{D,4} = \frac{\frac{4}{5} \log_e 2 - \frac{2}{5}}{4\pi} \quad (\text{A18j})$$

Equations (18) provide the interference drag coefficients required to calculate the vortex drag due to any combination of A values.

In the solution for the optimum A values, the parameters A_1 , A_2 , and A_3 are found to be linearly related and one of them may therefore be chosen arbitrarily. Choosing A_1 yields:

$$A_1 = A_1 \quad (\text{A19a})$$

$$A_2 = \frac{3(4a-1)}{1+a} - 2A_1 \quad (\text{A19b})$$

$$A_3 = A_1 - \frac{3(38a-26a^2-11)}{(2-3a)(1+a)} \quad (\text{A19c})$$

$$A_4 = \frac{30(3a-a^2-1)}{(2-3a)(1+a)} \quad (\text{A19d})$$

$$C_{D,0} = \frac{9}{8\pi} \frac{(4a-1)(3-2a)(1-2a)}{(2-3a)(1+a)} \quad (\text{A19e})$$

where

$$a = \frac{4}{3} (1 - \log_e 2)$$

The spanwise loading may be written as

$$l(y) = \left[\left(A_1 + \frac{A_2}{2} \right) + y \left(\frac{A_2}{2} + A_3 \right) + y^2 (A_4) \right] (1-y) \quad y > 0 \quad (\text{A20})$$

when $m = C_L = 1$. Substitution of the A values given in equations (A19) shows that $l(y)$ is independent of the variations in A_1 , A_2 , and A_3 .

For the case of a sonic leading edge ($n = 1$),

$$R_1 = \frac{1}{4\pi} \left(2\sqrt{1-\theta^2} - 2 \cosh^{-1} \frac{1}{\theta} \right) \quad (\text{A21a})$$

$$R_2 = -\frac{1}{4\pi} \left(2\sqrt{1-\theta^2} - 2\theta^2 \cosh^{-1} \frac{1}{\theta} \right) \quad (\text{A21b})$$

$$R_3 = -\frac{1}{4\pi} \left(\frac{7}{2} \sqrt{1-\theta^2} - \left(1 + \frac{5}{2} \theta^2 \right) \cosh^{-1} \frac{1}{\theta} \right) \quad (\text{A21c})$$

$$R_4 = \frac{1}{4\pi} \left[\left(\frac{2}{9} + \frac{52}{9} \theta^2 \right) \sqrt{1-\theta^2} - 6\theta^2 \cosh^{-1} \frac{1}{\theta} \right] \quad (\text{A21d})$$

$$2mC_{D,1} = \frac{1}{2} \quad (\text{A22a})$$

$$mC_{D,12} = \frac{1}{3} \quad (\text{A22b})$$

$$mC_{D,13} = \frac{1}{6\pi} + \frac{1}{12} \quad (\text{A22c})$$

$$mC_{D,14} = \frac{1}{16} \quad (\text{A22d})$$

$$2mC_{D,2} = \frac{1}{4} \quad (\text{A22e})$$

$$mC_{D,23} = \frac{1}{6\pi} + \frac{1}{16} \quad (\text{A22f})$$

$$mC_{D,24} = \frac{7}{120} \quad (\text{A22g})$$

$$2mC_{D,3} = \frac{1}{4\pi} \quad (\text{A22h})$$

$$mC_{D,34} = \frac{1}{48} + \frac{7}{90\pi} \quad (\text{A22i})$$

$$2mC_{D,4} = \frac{11}{360} \quad (\text{A22j})$$

CALCULATED VALUES OF A

The table that follows contains the calculated values of A for the optimum combination through the sweepback range. Four significant figures are given, since the tabulated values of R have four decimals. Values of $C_{D,0}$ for $m = C_L = 1$ are also shown:

n	A_1	A_2	A_3	A_4	$C_{D,0}$
0	-----	-----	-----	1.654	0.0830
.2	1.993	-2.586	1.435	1.517	.0899
.4	1.977	-2.571	1.590	1.244	.1105
.6	1.781	-2.147	1.472	.9568	.1398
.8	1.641	-1.818	1.364	.6957	.1766
1.0	1.357	-1.201	1.259	.1406	.2295

REFERENCES

1. Jones, Robert T.: The Minimum Drag of Thin Wings in Frictionless Flow. *Jour. Aero. Sci.*, vol. 18, no. 2, Feb. 1951, pp. 75-81.
2. Jones, Robert T.: Theoretical Determination of the Minimum Drag of Airfoils at Supersonic Speeds. *Jour. Aero. Sci.*, vol. 19, no. 12, Dec. 1952, pp. 813-822.
3. Graham, E. W.: A Drag Reduction Method for Wings of Fixed Plan Form. *Jour. Aero. Sci.*, vol. 19, no. 12, Dec. 1952, pp. 823-825.
4. Rodriguez, A. M., Lagerstrom, P. A., and Graham, E. W.: Theorems Concerning the Drag Reduction of Wings of Fixed Plan Form. *Jour. Aero. Sci.*, vol. 21, no. 1, Jan. 1954, pp. 1-7.
5. Walker, Kelsey, Jr.: Examples of Drag Reduction for Rectangular Wings. Rep. No. SM-14446, Douglas Aircraft Co., Inc., Jan. 15, 1953.
6. Beane, Beverly: Examples of Drag Reduction for Delta Wings. Rep. No. SM-14447, Douglas Aircraft Co., Inc., Jan. 12, 1953.
7. Tsien, S. H.: The Supersonic Conical Wing of Minimum Drag. Ph. D. Thesis, Cornell Univ., June 1953.
8. Courant, R.: Differential and Integral Calculus. Vol. II. Interscience Publishers, Inc. (New York), 1952, pp. 183-199.
9. Tucker, Warren A.: A Method for the Design of Sweptback Wings Warped To Produce Specified Flight Characteristics at Supersonic Speeds. NACA Rep. 1226, 1955. (Supersedes NACA RM L51F08, 1951.)
10. Brown, Clinton E.: Theoretical Lift and Drag of Thin Triangular Wings at Supersonic Speeds. NACA Rep. 839, 1946. (Supersedes NACA TN 1183.)

REPORT 1276

WIND-TUNNEL AND FLIGHT INVESTIGATIONS OF THE USE OF LEADING-EDGE AREA SUCTION FOR THE PURPOSE OF INCREASING THE MAXIMUM LIFT COEFFICIENT OF A 35° SWEEP-WING AIRPLANE ¹

By CURT A. HOLZHAUSER and RICHARD S. BRAY

SUMMARY

An investigation was undertaken to determine the increase in maximum lift coefficient that could be obtained by applying area suction near the leading edge of a wing. This investigation was performed first with a 35° swept-wing model in the wind tunnel, and then with an operational 35° swept-wing airplane which was modified in accord with the wind-tunnel results.

The wind-tunnel and flight tests indicated that the maximum lift coefficient was increased more than 50 percent by the use of area suction. Good agreement was obtained in the comparison of the wind-tunnel results with those measured in flight.

INTRODUCTION

It has been observed in numerous investigations that the maximum lift coefficient of thin wings and wings with sweepback are frequently limited by air-flow separation from the leading edge of the wing. This type of air-flow separation is the result of large adverse pressure gradients developed over the forward portion of the airfoil at an angle of attack. The magnitude of these adverse pressure gradients can be reduced by the use of leading-edge camber or increased leading-edge radius, either of which tends to delay leading-edge air-flow separation to higher angles of attack, and consequently to higher values of lift coefficient. Another manner in which leading-edge separation can be delayed is to stabilize the boundary layer in the region of the leading edge so that these large adverse gradients can be tolerated. Two methods of stabilizing the boundary layer are to re-energize the boundary layer by blowing high-energy air into it, or to remove the low-energy portion of the boundary layer by means of suction.

A theoretical analysis made by Thwaites in 1946 (ref. 1) suggested that air-flow separation from the leading edge of an airfoil could be delayed by the use of only small quantities of suction air when distributed over a porous area. To distinguish this method of applying suction from that of suction through a slot, it is hereafter referred to as area suction. The two-dimensional experimental investigations reported in references 2 to 5 indicated that area suction could be applied at the leading edge of the airfoil to delay

air-flow separation from the leading edge and that the suction flow quantities required were small. Because of the increases in maximum lift coefficient indicated to be possible with low suction flow quantities, a three-dimensional investigation was planned to obtain the information necessary for designing a porous leading edge for an airplane.

The three-dimensional investigation was to be performed in two phases; the first in the wind tunnel, and the second in flight. The purpose of the wind-tunnel test was to determine the effect of chordwise extent of porous area on the maximum lift coefficient as well as on suction requirements. These results were to be used to demonstrate the increases in maximum lift coefficient obtainable with area suction, and to make a comparison with the chordwise extents and suction flow quantities computed by the method set forth by Thwaites. The results were also to be used as a basis for the design of a porous leading edge and pumping system for the flight test vehicle. In addition to checking the wind-tunnel results, the purposes of the flight test were to evaluate and compare the flight characteristics of an airplane having leading-edge area suction with those of other high lift devices, namely a slatted leading edge and a leading edge modified to have increased camber and radius at the leading edge. The flight tests would also be used to ascertain the existence of possible limitations to the use of a porous leading-edge installation which could not be revealed by wind-tunnel tests.

In order to accomplish satisfactorily these objectives, an operational airplane was chosen as the basic vehicle for both the wind-tunnel and the flight investigations. This airplane was the F-86 which has a 35° swept-back wing and horizontal tail. The wing panels and horizontal tail of an F-86 airplane were modified and mounted on a research fuselage and tested in the Ames 40- by 80-foot wind tunnel in 1951. At the completion of the test, North American Aviation, Inc., received a contract from the United States Air Force to modify an F-86F airplane for the application of area suction at the leading edge of the wing. The design of the porous leading-edge installation was based on the wind-tunnel results. The airplane was then turned over to the NACA in 1954 for further instrumentation and flight testing. A standard F-86A airplane was used to obtain comparative flight characteristics of the airplane having a

¹ Supersedes NACA RM A52G17 by Curt A. Holzhauser and Robert K. Martin, 1952, and RM A55C07 by Richard S. Bray and Robert C. Innis, 1955.

normal leading edge, a slatted leading edge, and a leading edge having increased camber and radius. The results of the wind-tunnel and the flight tests are included in this report.

NOTATION

b	wing span, ft
c	chord, measured parallel to the plane of symmetry, ft
\bar{c}	mean aerodynamic chord, $\frac{\int_0^{b/2} c^2 dy}{\int_0^{b/2} c dy}$, ft
C_D	drag coefficient, $\frac{\text{drag}}{qS}$
c_l	section lift coefficient, $(1/c) \oint P dx \cos \alpha - (1/c) \oint P dz \sin \alpha$
C_L	lift coefficient, $\frac{\text{lift}}{qS}$
$C_{L_{max}}$	maximum lift coefficient
C_m	pitching-moment coefficient, referred to quarter-chord line, $\frac{\text{pitching moment}}{qS\bar{c}}$
C_Q	flow coefficient, $\frac{Q}{US}$
h_i	total pressure at pump inlet, lb/sq ft
l	surface length of porous material, measured parallel to the plane of symmetry, ft
H	ratio of displacement thickness to momentum thickness of boundary layer, $\frac{\delta^*}{\theta}$
p	free-stream static pressure, lb/sq ft
p_a	static pressure in duct, lb/sq ft
p_i	local surface static pressure, lb/sq ft
p_p	static pressure in plenum chamber, lb/sq ft
P	airfoil pressure coefficient, $\frac{p_i - p}{q}$
P_a	duct pressure coefficient, $\frac{p_a - p}{q}$
P_p	pressure coefficient measured in plenum chamber of model or at pump inlet of airplane, $\frac{p_p - p}{q}$ or $\frac{h_i - p}{q}$, respectively
q	free-stream dynamic pressure, lb/sq ft
Q	volume of air removed through porous surface, based on free-stream density at test altitude, cu ft/sec
R	Reynolds number, $\frac{Uc}{\nu}$
S	wing area, sq ft
t	thickness of porous material, in.
u	velocity in the boundary layer, ft/sec
U	free-stream velocity, ft/sec
U_i	local velocity outside of the boundary layer, ft/sec
$U_{i_{max}}$	maximum local velocity outside of the boundary layer, ft/sec
w	suction-air velocity, normal to surface, ft/sec
$\frac{W}{S}$	wing loading of airplane, lb/sq ft

x	chordwise distance parallel to plane of symmetry, ft
y	spanwise distance perpendicular to plane of symmetry, ft
z	vertical distance, ft
α	angle of attack referred to fuselage center line, deg
δ^*	displacement thickness of boundary layer, ft
δ_f	flap deflection, deg
Δp	pressure drop across porous material, lb/sq ft
η	fraction of semispan, $\frac{2y}{b}$
θ	momentum thickness of boundary layer, ft
ν	kinematic viscosity of air, sq ft/sec

DESIGN OF THE POROUS LEADING EDGE

PRINCIPLE OF AREA SUCTION—THWAITES ANALYSIS

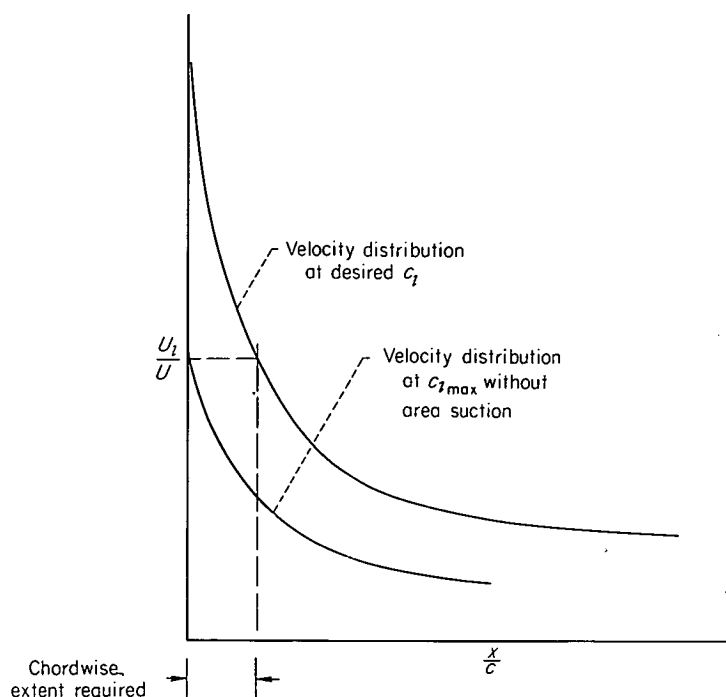
The use of area suction to delay leading-edge type of air-flow separation was suggested by Thwaites in reference 1. This report presented a method by which the chordwise extent of porous area required to prevent leading-edge air-flow separation was estimated, and it presented equations whereby the suction quantities required for area suction and slot suction were calculated and compared. It was concluded in Thwaites' analysis that the application of area suction near the leading edge of an airfoil would delay leading-edge air-flow separation by the use of suction flow quantities only a small fraction of those required for suction through a slot.

It was reasoned by Thwaites that it is necessary to have porous suction extend chordwise on an airfoil only to the point where at the desired lift coefficient, the adverse velocity gradient is no more severe than the maximum velocity gradient reached prior to leading-edge air-flow separation without area suction. Since it is difficult to estimate the required chordwise extent of area suction by a comparison of velocity gradients, the simplifying assumption has been made that area suction is required in the region of the adverse velocity gradient where the ratio of local to free-stream velocity is greater than the maximum value reached without area suction. An example of this latter approximation is given in the following sketch. It has been found that the chordwise extents estimated by this simplified method are slightly greater than those estimated by a comparison of the pressure gradients.

In order to calculate the suction quantities required to delay leading-edge air-flow separation, use was made of the basic momentum equation for boundary-layer flow:

$$U \frac{dU}{dx} (\delta^* + 2\theta) + U^2 \frac{d\theta}{dx} = w(x)U + \nu \left(\frac{du}{dy} \right)_{y=0}$$

To simplify solution of this equation, Thwaites specified that the suction velocity, $w(x)$, be constant in the chordwise direction. He also specified that the velocity distribution through the boundary layer with suction applied would be maintained similar to that of a Blasius profile. With these simplifying specifications it was possible to find a chordwise distribution of velocity for which a Blasius boundary-layer profile could be supported with a given suction-air velocity.



The suction-air velocity required at any desired lift coefficient could then be calculated from the equation:

$$\frac{w}{U} = \sqrt{K \left(\frac{U_1}{U} \right)_{\max} \frac{1}{R}}$$

In this equation, K is determined from a comparison of the chordwise velocity distribution of the airfoil at the desired lift coefficient with the chordwise velocity distribution which would support a Blasius profile with a particular suction-air velocity (ref. 1).

Since it was specified that the suction velocity be constant in the chordwise direction, and since the chordwise extent required was obtained previously, the suction quantity required for the desired lift coefficient of the airfoil section can be computed.

TWO-DIMENSIONAL APPLICATIONS OF AREA SUCTION

Several experimental investigations have been made with area suction near the leading edge of two-dimensional airfoils. The results of these tests are reported in references 2 to 5. These results indicated that applying area suction near the leading edge of the airfoil delayed air-flow separation and increased the maximum lift coefficient of the sections. In these tests, it was noted that the increases in the maximum lift coefficients obtained with area suction appeared to be limited by air-flow separation occurring either at the trailing edge of the airfoil or from the tunnel walls.

An application of Thwaites' analysis to the results of the tests reported in references 2 to 5 indicated that the method used to estimate the chordwise extent of porous area was valid. However, the suction quantities required for the two-dimensional tests were 10 to 15 times greater than the values computed by the equations derived by Thwaites. Further, for some lift coefficients, near the maximum values obtained with suction, the ratio of suction flow quantity to free-stream velocity had to be increased as the free-stream

velocity was increased (refs. 4 and 5); whereas Thwaites' analysis indicated that this ratio should decrease.

At the present time, it cannot be determined to what extent the results of the two-dimensional tests were affected by the flow separation that occurred either at the trailing edge of the airfoil or from the tunnel walls.

THREE-DIMENSIONAL APPLICATION OF AREA SUCTION

An exploratory test performed on a 63° sweptback wing in the Ames 40- by 80-foot wind tunnel in 1949 showed that area suction was effective in delaying the leading-edge air-flow separation. When Thwaites' analysis was applied to the airfoil sections near the tip of this sweptback wing, the location of initial air-flow separation, the results were similar to those for two-dimensional sections in that the chordwise extents of porous area could be estimated but the suction-air velocities were about 10 times the values computed to be necessary. However, when Thwaites' analysis was applied to the sections inboard of the tip, it was found that the minimum chordwise extents found necessary for the tests were less than those estimated to be necessary; as on the wing tip, the minimum suction-air velocities used on the inboard sections were about 10 times the values computed to be necessary. The result that the chordwise extents of porous area inboard were less than the values indicated to be necessary is believed to be caused by a spanwise boundary-layer flow similar to that noted to exert a strong effect on the section maximum lift coefficients of the 45° swept wing of reference 6.

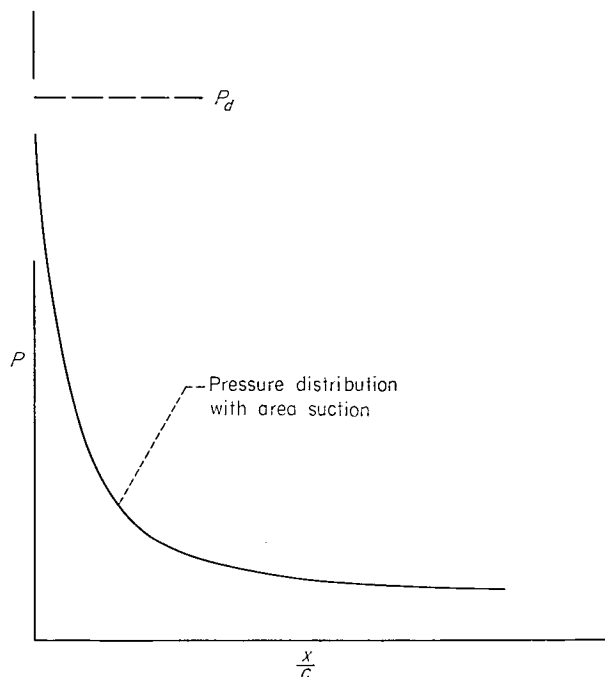
Although a lack of agreement existed between the theoretical and experimental results, it appeared that Thwaites' analysis could be modified to provide a first approximation in the design of the porous leading-edge installation. The manner in which this was done for the tests reported herein is described in the following paragraphs.

Tests were first performed on the 35° swept-wing model without boundary-layer control in order to obtain the force and pressure-distribution data for the basic model. A lift coefficient of 1.93 with flaps deflected was then chosen as the lift coefficient desired without air-flow separation, and a free-stream velocity of 112 feet per second was chosen for the test velocity. The section lift coefficients and the corresponding chordwise velocity distributions for four spanwise stations were then obtained for a wing lift coefficient of 1.93 by linear extrapolation of the measured data without area suction to an angle of attack corresponding to the wing lift coefficient of 1.93. This procedure was followed rather than the use of theoretical values or values obtained from two-dimensional tests because it was felt that linear extrapolation of the measured data provided more accurate values of the spanwise section lift variation and the chordwise and spanwise velocity distributions, particularly when the partial-span trailing-edge flap was deflected. The chordwise extents of porous area required at four spanwise stations were then obtained by a comparison of the individual velocity diagrams at section lifts corresponding to a wing lift coefficient of 1.93 with the comparable diagrams at the maximum section lift coefficients without area suction. The suction-air velocities at the same four spanwise stations were then computed for the desired wing lift coefficient of 1.93 and free-stream

velocity of 112 feet per second by using the equations set forth by Thwaites and the velocity diagrams at the desired section lift coefficient for each of the stations. The values of these requirements and the expected section lift coefficients are tabulated below:

Spanwise station, $2y/b$	Section lift coefficient, c_l	Chordwise extent, x/c	Ratio of suction-air to free-stream velocity, w/U
0.25	1.95	0.027	0.0030
.45	2.11	.023	.0033
.65	1.90	.020	.0040
.85	1.76	.020	.0048

These values were then used in the design of the porous leading edge for the wind-tunnel model as follows. The chordwise extent of porous area was approximately doubled to allow ample freedom in adjusting the porous-area opening by trial and error. The suction-air velocities required were assumed to be 12 times the values computed (as an average between the factors of 10 to 15 noted in the previous tests). It was assumed that the suction-air velocities required to control separation should be constant in the chordwise direction. Since the external surface pressures vary in the chordwise direction whereas the internal duct pressure is constant, as shown in the following sketch, a porous material whose porosity varied along the chord was used to maintain



approximately constant suction-air velocities over the chordwise extent of porous area. It should be pointed out that Thwaites specified that the suction-air velocities be constant in the chordwise direction to simplify solution of the equations, and it is not known whether a constant suction-air velocity is necessary or even desirable for the lowest flow quantities.

The design of the porous leading edge of the flight vehicle, the F-86F airplane, was based on the results of the wind-tunnel tests of the 35° swept-wing model. The desired lift coefficient was 1.81 with flaps deflected and the free-stream velocity was 148 feet per second. It should be pointed out that the flight lift coefficient of 1.81 corresponds to an un-

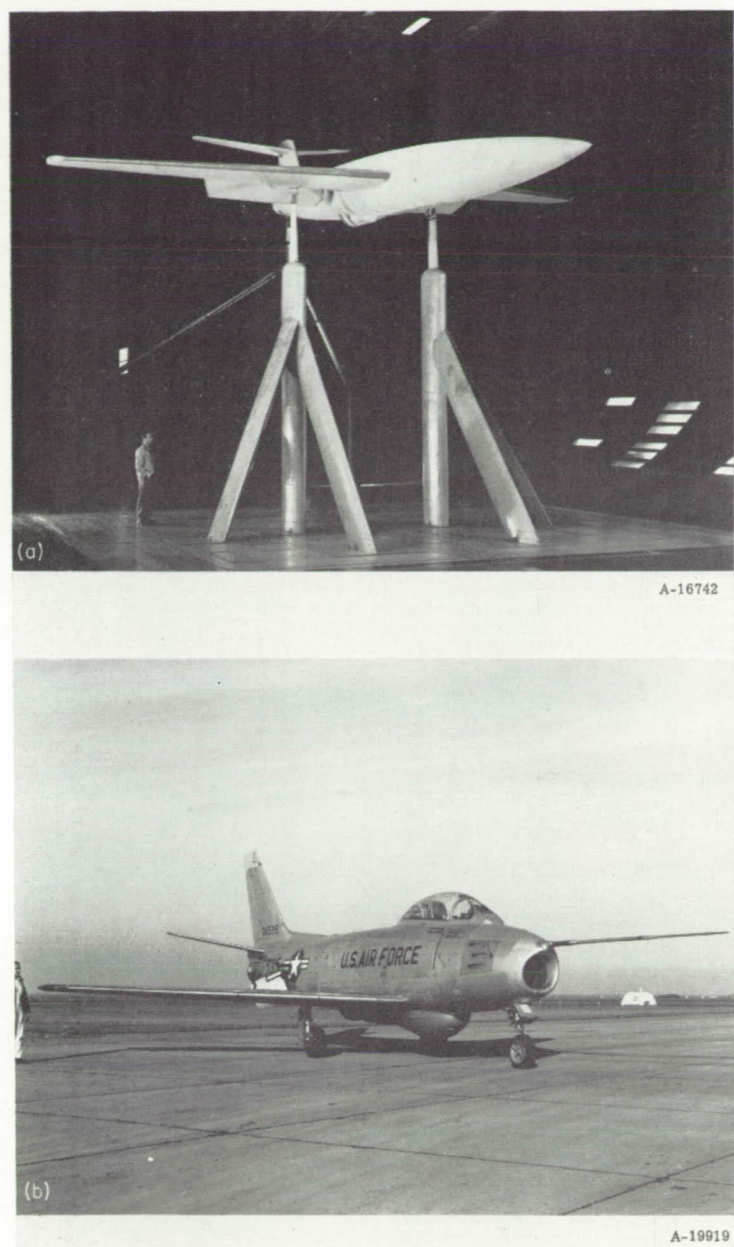
trimmed lift coefficient of 1.93 measured in the wind-tunnel test. These values were chosen on the basis of the characteristics of the suction pump used and the wing loading of the airplane; further details may be found in reference 7. The suction-air velocities at the design condition were chosen as 16 times the values computed, in contrast to the factor of 12 used for the wind-tunnel investigation. The higher factor for the flight airplane was used to allow for the possibility of unknown adverse effects that might occur in flight. It was again specified that the suction-air velocities should be constant in the chordwise direction, and therefore the porous material used had a porosity that varied in the chordwise direction.

DESCRIPTION OF RESEARCH VEHICLES, INSTRUMENTATION, AND TESTS

WIND-TUNNEL MODEL

Since the wind-tunnel investigation was to be the basis of the design of an area-suction installation on an F-86 airplane, the wing panels and horizontal-tail surface of an F-86 were utilized on the model. These surfaces were mounted on a circular fuselage in the same relative location to each other as on an F-86 airplane. The general arrangement of this model is shown in the photograph of the model mounted in the tunnel, figure 1 (a), and in the two-view drawing, figure 2 (a). Additional dimensions of the model are provided in table I.

The wing had 35° of sweepback measured at the quarter-chord line and had an airfoil section of approximately 11 percent thickness normal to the quarter-chord line (coordinates of the airfoil are given in table II). The structure ahead of the front spar was replaced by the porous surface and ducting to enable application of area suction (figs. 3 (a) and 4 (a)). The porous surface near the leading edge of the wing consisted of an outer surface of metal mesh which was backed with a porous, hard wool felt material. The metal mesh had a thickness of 0.008 inch and had 11-percent open area (4225 square holes per square inch with each side of the hole about 0.005 inch long). This mesh extended from the 5-percent chord station on the upper surface to the 3-percent chord station on the lower surface of the wing, and from the intersection of the wing and fuselage ($2y/b = 0.10$) to the beginning of the wing tip fairing ($2y/b = 0.96$). The wool felt backing the mesh outer surface was tapered in the chordwise direction to provide the varying porosity required to compensate for the surface pressure distribution in order to obtain a constant suction-air velocity in the chordwise direction. The spanwise distribution of suction-air velocity specified for the design condition is shown in figure 5. The tapered wool felt was cut from ½-inch-thick material weighing about 9 pounds per square yard. This ½-inch-thick material had the pressure-drop variation with suction-air velocity shown in figure 6; for the range of suction-air velocities of interest, the pressure drop at a given suction-air velocity was proportional to the thickness of the felt. The thickness variations of the felt backing used in the wing are given in figure 7. It will be noted from this figure that while a continuously varying chordwise porosity was realized, the spanwise variation was made in four steps

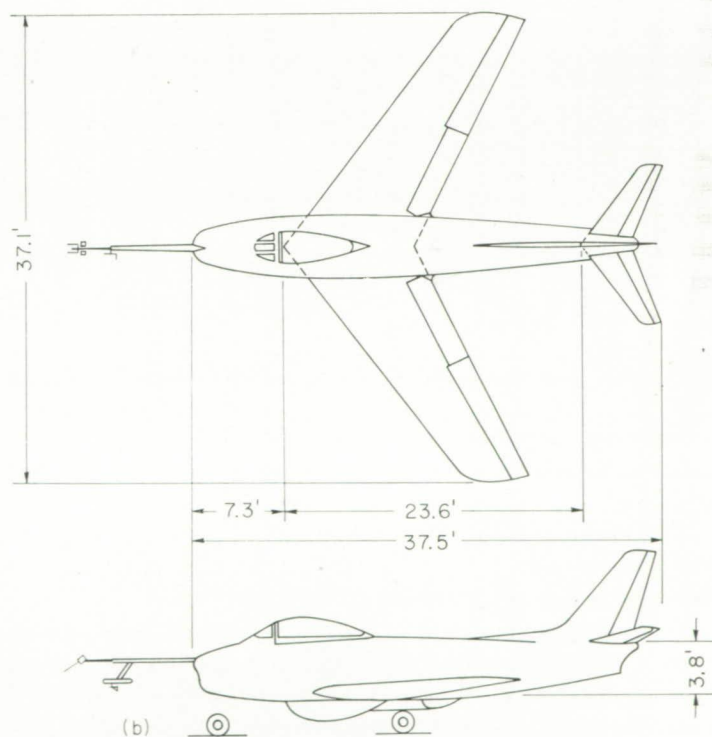
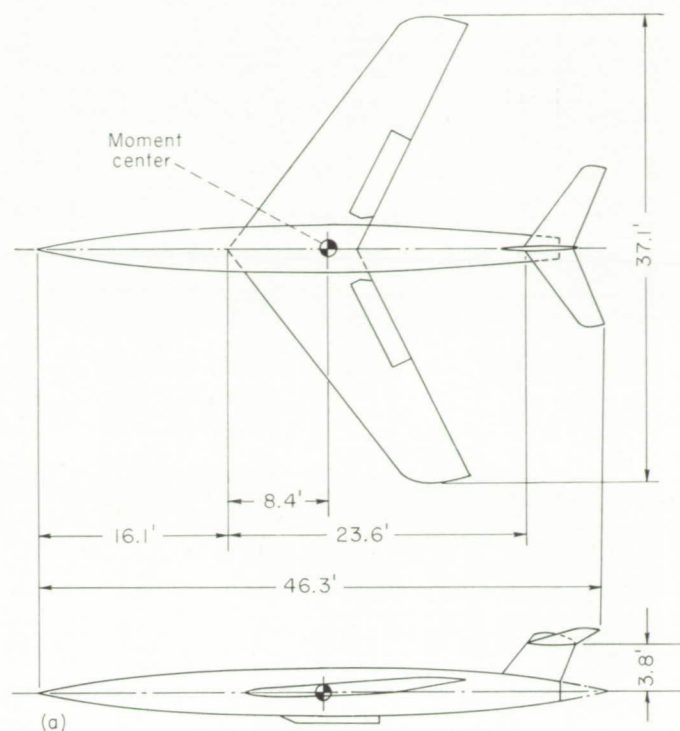


(a) The 35° swept-wing model mounted in 40- by 80-foot wind tunnel.
(b) The F-86F airplane.

FIGURE 1.—Photos of the model and the airplane equipped with a porous leading-edge installation.

rather than continuously as specified in figure 5; this approximation was adopted since the specified variation was relatively small. Chordwise and spanwise extents of porous area were controlled by sealing with a nonporous cellulose tape 0.003 inch thick. In order to simulate the leading edge of an F-86 with slats retracted, the porous leading edge was completely taped. Partial taping of the porous leading edge provided the four spanwise distributions of chordwise extents studied in the wind-tunnel tests, configurations A, B, C, and D, shown in figure 8.

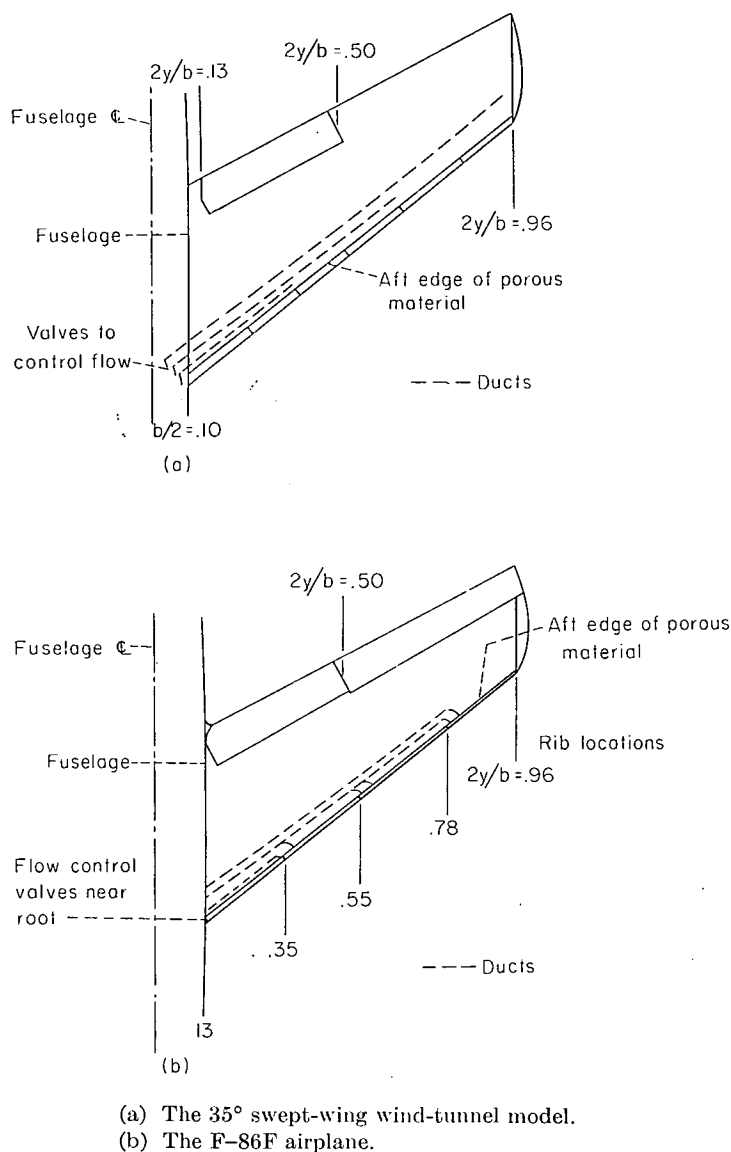
The normal F-86 ailerons and single-slotted flaps were retained on the model. The ailerons were locked in a neutral position, and the flaps were either undeflected or fully deflected, a deflection of 38° measured normal to the flap hinge line.



(a) The 35° swept-wing wind-tunnel model.
(b) The F-86F airplane.

FIGURE 2.—General arrangements of test vehicles equipped with porous leading-edge installations.

The fuselage used was circular in cross section and the radius, in feet, is defined by the equation $1.84 \left[1 - \left(\frac{x}{23} - 1 \right)^2 \right]^{3/4}$. This fuselage has a larger fineness ratio (11.5 as compared to 6.9) and a smaller width (0.10 $b/2$ as compared to 0.13 $b/2$) than the fuselage of the F-86 airplane. Use of this



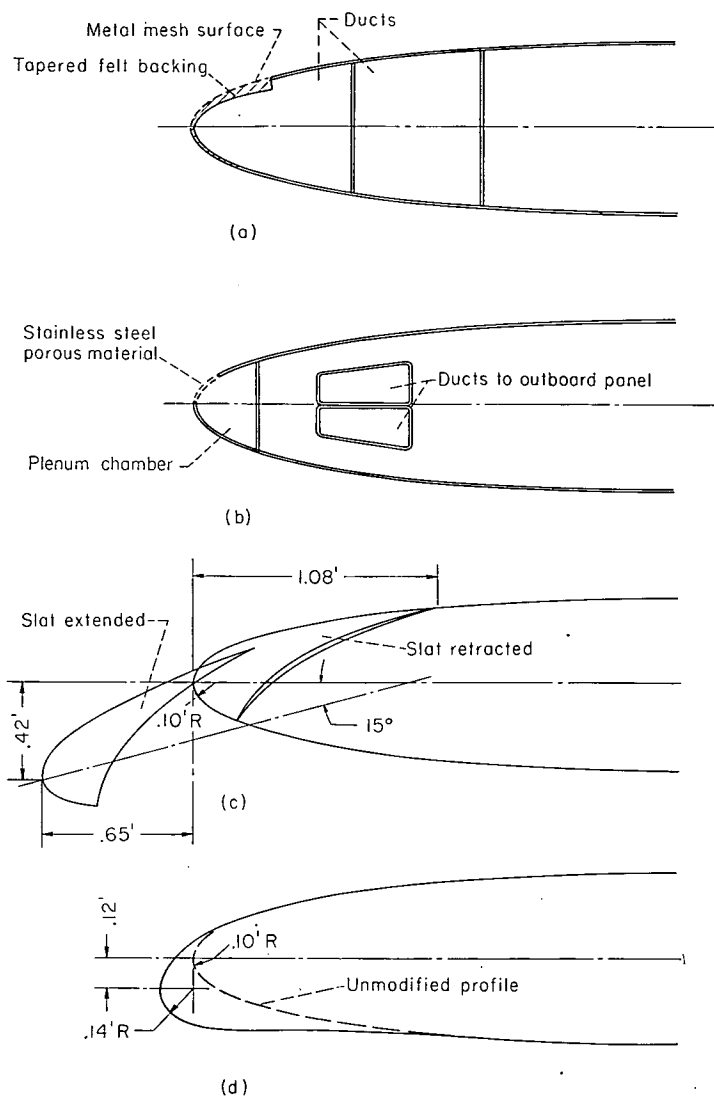
(a) The 35° swept-wing wind-tunnel model.
(b) The F-86F airplane.

FIGURE 3.—Plan view of wings with porous leading-edge installations.

fuselage necessitated mounting the wings in a midwing location in contrast to the low wing position of the F-86 airplane.

The horizontal tail, which had 35° of sweep measured at the quarter chord line, was set at 0° incidence with the elevators set at 0° deflection.

The pumping equipment for the porous leading edge was housed in the fuselage. The pump consisted of the compressor portion of a turbosupercharger, and was driven by a 300-horsepower variable-speed electric motor. This pump induced the required suction flow quantities through the porous surface and then into ducts in the wing which had individual valves near the root of the wing to control the flow (see fig. 3 (a)). The air then dumped into a plenum chamber in the fuselage prior to entering the pump and was discharged from the pump through a duct in the bottom of the fuselage (see fig. 2 (a)). In order to measure the suction flow quantities, a survey rake was located at the exit on the bottom of the fuselage. This rake consisted of 54 total-pressure tubes, 9 static-pressure tubes, and 1 thermocouple and was calibrated against a standard ASME orifice



(a) Porous leading edge for wind-tunnel model.
(b) Porous leading edge for F-86F airplane.
(c) Slatted leading edge for F-86A airplane.
(d) Cambered leading edge for F-86A airplane.

FIGURE 4.—Cross sections of the various leading edges. Sections are normal to the quarter-chord line at the $0.47b/2$ station.

meter. The power input to the suction pump was measured with a wattmeter.

To measure the external surface pressure distributions, static pressure orifices were installed on the upper and lower surfaces of the left wing in streamwise rows at $2y/b = 0.25$, 0.45, 0.65, and 0.85; the chordwise locations of these orifices are given in table III. Orifices were also located in the ducts of the wing, as well as in the plenum chamber, in order to permit evaluation of the pumping requirements and duct losses.

WIND-TUNNEL TESTS AND CORRECTIONS

Force measurements were made for all configurations throughout an angle-of-attack range of -4° to 30° , at an angle of sideslip of 0° . The free-stream velocity was 112 feet per second which corresponded to a Reynolds number of 5.8×10^6 based on the mean aerodynamic chord. The spanwise distributions of chordwise extent of porous area, configurations A, B, C, and D, were obtained by trial and

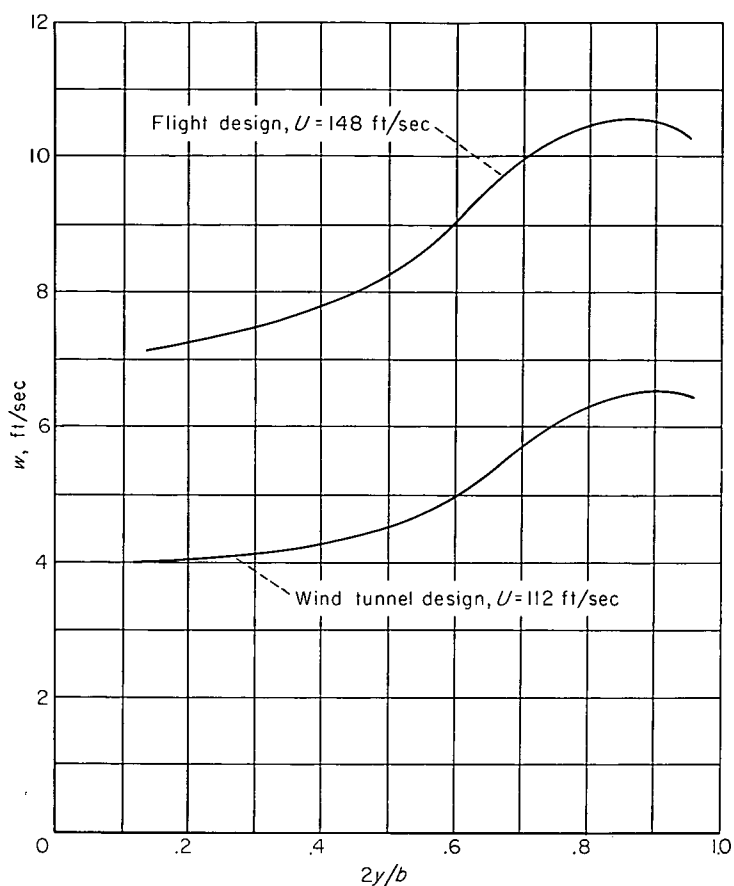


FIGURE 5.—Spanwise variation of the suction-air velocities desired for the porous-leading-edge installations.

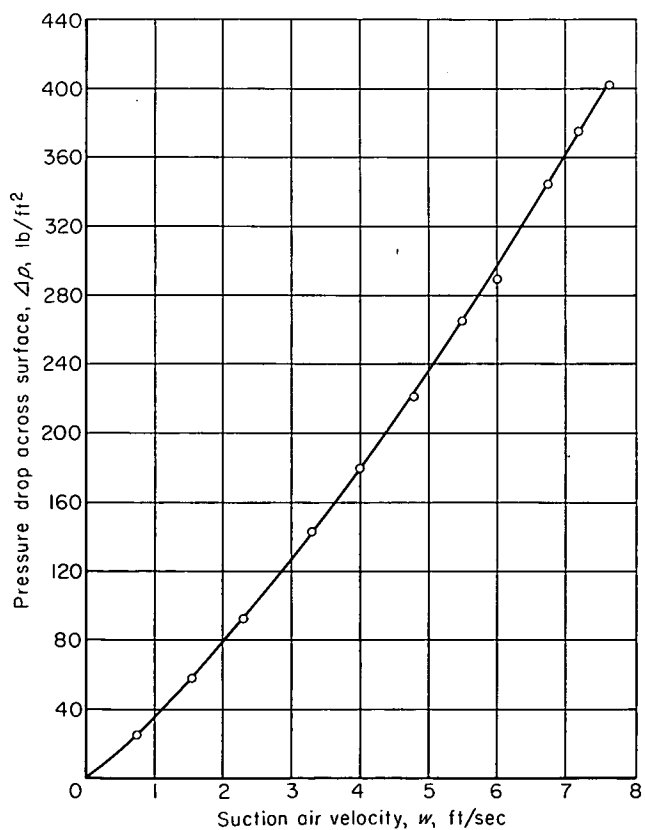


FIGURE 6.—Calibration of suction-air velocities for the porous mesh sheet backed with $\frac{1}{2}$ -inch wool felt.

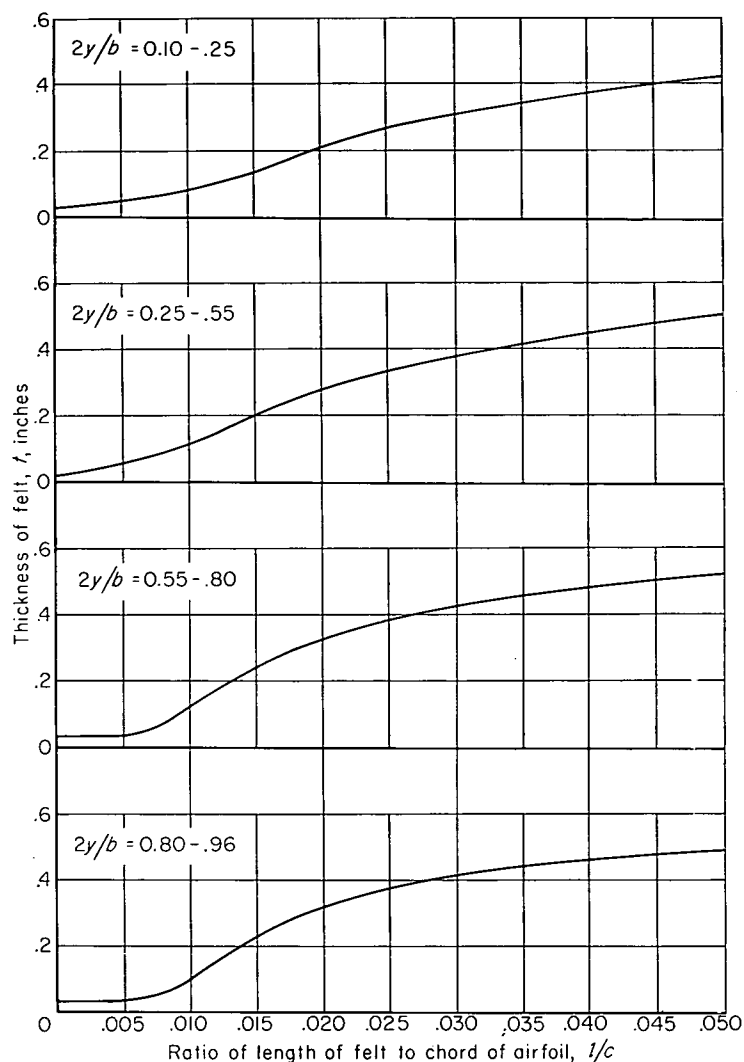


FIGURE 7.—Thickness variation of wool-felt backing used for porous leading edge of wind-tunnel model.

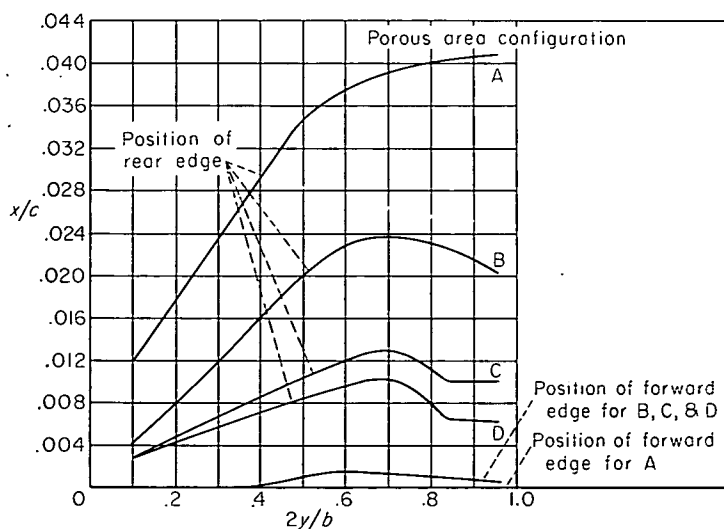


FIGURE 8.—The four spanwise distributions of the chordwise extents of porous area tested on the wind-tunnel model.

error in the following manner: the lower surface of the porous leading edge was taped from the leading edge ($x/c=0$) to the rear edge of the porous surface ($x/c=0.03$); this area was taped for the entire test. Next, the upper surface was taped so that a constant width opening was obtained with the chordwise extent of porous area on the outboard portion of the wing approximating the value calculated to be necessary for the design lift coefficient of 1.93. For this configuration, a polar was run and the maximum lift coefficient and the flow coefficient required were measured. Then the rear edges of the inboard openings were progressively taped until a further reduction in chordwise extents would reduce the maximum lift coefficient. This procedure was repeated for the forward edge of the porous area and then for the tip of the wing. The resulting distribution of porous area was such that any further reduction in porous area extent anywhere along the span of the wing would result in a reduction in the maximum lift coefficient from the original value measured; this distribution of porous area was that of configuration B. A similar, although less extensive, procedure was followed in arriving at the distributions of porous area providing a higher maximum lift coefficient and two lower maximum lift coefficients. In order to determine the effects of free-stream velocity as well as to simulate the flow conditions of the F-86 airplane in a landing and a take-off configuration, additional measurements were made at free-stream velocities corresponding to wing loadings of 30, 40, and 50 pounds per square foot. These latter tests were made by changing the dynamic pressure of the wind tunnel for each angle of attack so that $C_L \times q$ was constant and equal to the wing loading, W/S . The maximum velocity at which these tests were performed was 180 feet per second which corresponded to a Reynolds number of 9.3×10^6 . The various configurations and test conditions are summarized in table IV.

Standard tunnel-wall corrections for a straight wing of the same area and span as the sweptback wing were applied to the force data measured. No corrections were made for the strut interference, and no tares were applied to the pitching moment since they were believed to be negligible for the data of interest. Calculations indicated that the effect of the thrust of the exhausting air on the force characteristics was negligible.

The suction requirements (flow coefficients, duct and plenum chamber pressure coefficients, and power supplied to the blower) were measured for all configurations of the model with suction applied. However, only near the maximum lift coefficient were sufficient data taken with different values of suction flow coefficient to be able to define the minimum values of suction flow coefficient required to obtain the measured lift coefficient with the porous area installation tested. All values of flow coefficient presented were corrected to standard sea-level conditions. Limited measurements indicated that leakage resulting from the method of construction of the model was less than 10 percent of the total flow coefficient, and the values of flow coefficients were not corrected for this leakage. All values of the measured power input to the pump included pump losses and leakage. The duct losses were determined from pressure measurements in

the duct behind the porous leading edge and in the plenum chamber just ahead of the compressor, and the pump losses were obtained from the characteristics of the pump. Consequently, the suction power required to compress the air from inside the wing ducts to a free-stream condition was then computed by subtracting from the measured power input the sum of the duct and pump losses.

Wool yarn tufts were taped to the upper surface of the wing during some of the tests to observe the boundary-layer flow characteristics as the stall was encountered.

FLIGHT TEST AIRPLANES

F-86F airplane with porous leading edge.—The general arrangement of the F-86F airplane is shown in the photograph, figure 1 (b), and in the two-view-drawing, figure 2 (b). The airplane was a standard F-86F modified to incorporate a porous leading-edge installation. Dimensions of the airplane are given in table I.

The wing had 35° of sweepback at the quarter-chord line, and the structure forward of the front spar was modified to incorporate the porous leading edge and ducting in a manner similar to that of the wind-tunnel model (figs. 3 (b) and 4 (b)). However, the method of construction differed since it was desired to place no restriction on the operation of the airplane. The porous leading edge was constructed of panels of sintered, porous stainless steel having a constant thickness of about 0.050 inch, and having a varying porosity to provide a chordwise varying pressure drop in order to maintain the desired constant suction-air velocities over the chordwise extent at each spanwise station. The spanwise distribution of the suction-air velocity used for the design is shown in figure 5. Ground tests indicated that the pressure-drop characteristics of the leading-edge panels deviated locally from the design values a maximum of 30 percent. The spanwise distribution of the chordwise extent of the porous area used was that of configuration B (fig. 8), which was obtained by sealing portions of the porous leading edge with lacquer. The porous leading edge was stiffened by nose ribs only at the junctures of the porous panels. For each wing panel, these junctures, which are shown in figure 3 (b), formed four plenum chambers which were individually ducted to the vicinity of the wing root where they were joined in a single duct leading to the pump. Valves were located in each of the eight ducts to adjust the spanwise suction-flow distribution; these valves were closed to prevent flow through the pump and ducts when the pump was not being operated.

The pump used in this installation was a modified Thompson Products, Inc., B-31 turbosupercharger operated by high-pressure air bled from the compressor of the airplane's J-47 engine. The pump was mounted beneath the fuselage and was covered with a streamlined fairing (figs. 1 (b) and 2 (b)). A valve located in the bleed-air duct was adjusted by the pilot to control the pump speed. Due to limitations on the amount of air that could be taken from the engine, the maximum pump speed and resultant suction-flow quantity were dependent upon the engine speed. The suction-flow quantities were measured with a rake located at the pump inlet. This rake consisted of two total-pressure tubes

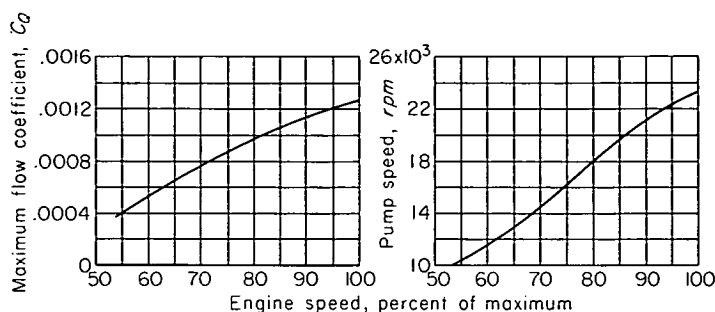


FIGURE 9.—Characteristics of the area-suction pumping system at the stalling speeds of the airplane; 7000 foot altitude.

and two static-pressure tubes and was calibrated against a standard ASME orifice meter. In figure 9 is shown the effect of engine speed on the maximum suction pump speed and on the maximum flow coefficient corresponding to conditions at the stalling speeds of the airplane at an altitude of 7,000 feet.

F-86A airplane.—The general arrangement and dimensions of the F-86A airplane were the same as the F-86F, except no pump and pod existed on the bottom of the fuselage. The F-86A was equipped with leading-edge slats which are shown in figure 4 (c). These slats could be locked in the retracted position or they could be allowed to extend automatically.

By removing the forward portion of the wing, the slatted leading edge was replaced with the cambered leading edge shown in figure 4 (d). This cambered leading edge also incorporated an increased leading-edge radius. The coordinates of this cambered leading edge are given in table II.

FLIGHT TESTS AND CORRECTIONS

F-86F airplane with porous leading edge.—Measurements of the low-speed characteristics of the test airplane were taken at an altitude of 7,000 feet to permit complete stalling of the airplane without undue hazard. The data included in this report were taken from time-history records obtained in the following manner: with engine power and pump speed set at appropriate constant values, and starting at an airspeed above the suction-off stall speed, the nose of the airplane was slowly elevated in such a manner as to decelerate at a rate not exceeding 1 knot per second. The records were terminated when the pilot felt that the airplane was no longer controllable. The majority of these stalls were performed at 85-percent engine rpm in the interest of consistency in evaluating the stalling characteristics of the airplane. However, since the maximum flow coefficient obtainable at 85-percent engine rpm was about 0.0011, it was necessary to perform several stalls at 100-percent engine rpm to determine the lift characteristics of the porous leading edge with the maximum available flow coefficient of 0.0012. These flight tests were performed with the trailing-edge flaps undeflected as well as deflected 38° . The chordwise extent of the porous area on the leading edge of the airplane for all of the flights was that of configuration B (fig. 8). In addition to the tests with suction applied, tests were also made with suction off and the duct valves closed. During some of the tests, wool yarn tufts were taped to the upper surface of the wing; the behavior of the tufts at the stall was recorded photographically.

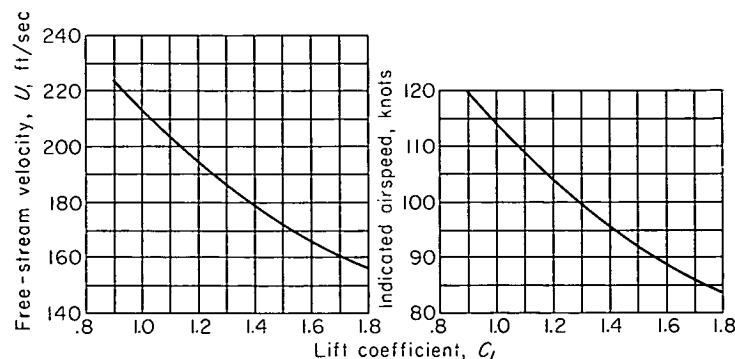


FIGURE 10.—Variation of free-stream velocity and indicated airspeed with lift coefficient for the conditions of the flight tests; 7000 foot altitude.

The variations of the indicated airspeed and free-stream velocities with lift coefficients for the average conditions of the tests are shown in figure 10. These relationships correspond to an average wing loading of about 45 pounds per square foot. The values of lift coefficients presented in this report are values corrected for the effect of the engine thrust; the values of engine thrust used were obtained from data provided by the manufacturer of the J-47 engine.

The flow coefficients measured were corrected to the static conditions at the test altitude. Limited measurements indicated that a negligible amount of leakage resulted from the method of construction of the porous leading-edge installation.

In addition to the quantitative tests previously mentioned, several qualitative tests were made with the airplane. These tests included evaluation of the landing and take-off performance as affected by the suction equipment. Several flights were also made in which the airplane was flown up to a Mach number of 0.9 and up to an altitude of 35,000 feet. These flights were conducted with the F-86F airplane with the porous leading edge and with a standard leading edge, in order to obtain comparative values with the pump installed and operating. Maximum speed and buffet characteristics were of primary interest in this phase of the investigation.

F-86A airplane.—Measurements of the low-speed characteristics of this test airplane were also taken at 7,000 feet, and the data presented in the report were obtained and corrected in the same manner as those for the F-86F airplane. These data were obtained with the slatted leading edge automatically extended, as well as locked in the retracted position. Similar data were also obtained for the airplane with the cambered leading edge.

The wing loadings of the F-86A were approximately the same as for the F-86F, and therefore the flight speed variation with lift coefficient presented in figure 10 is also applicable for the F-86A.

RESULTS AND DISCUSSION

WIND-TUNNEL TESTS

Static longitudinal characteristics of model without suction applied.—The three-component force data of the 35° swept-back wing model without suction are shown in figure 11 with the trailing-edge flaps fully deflected (38°) and undeflected

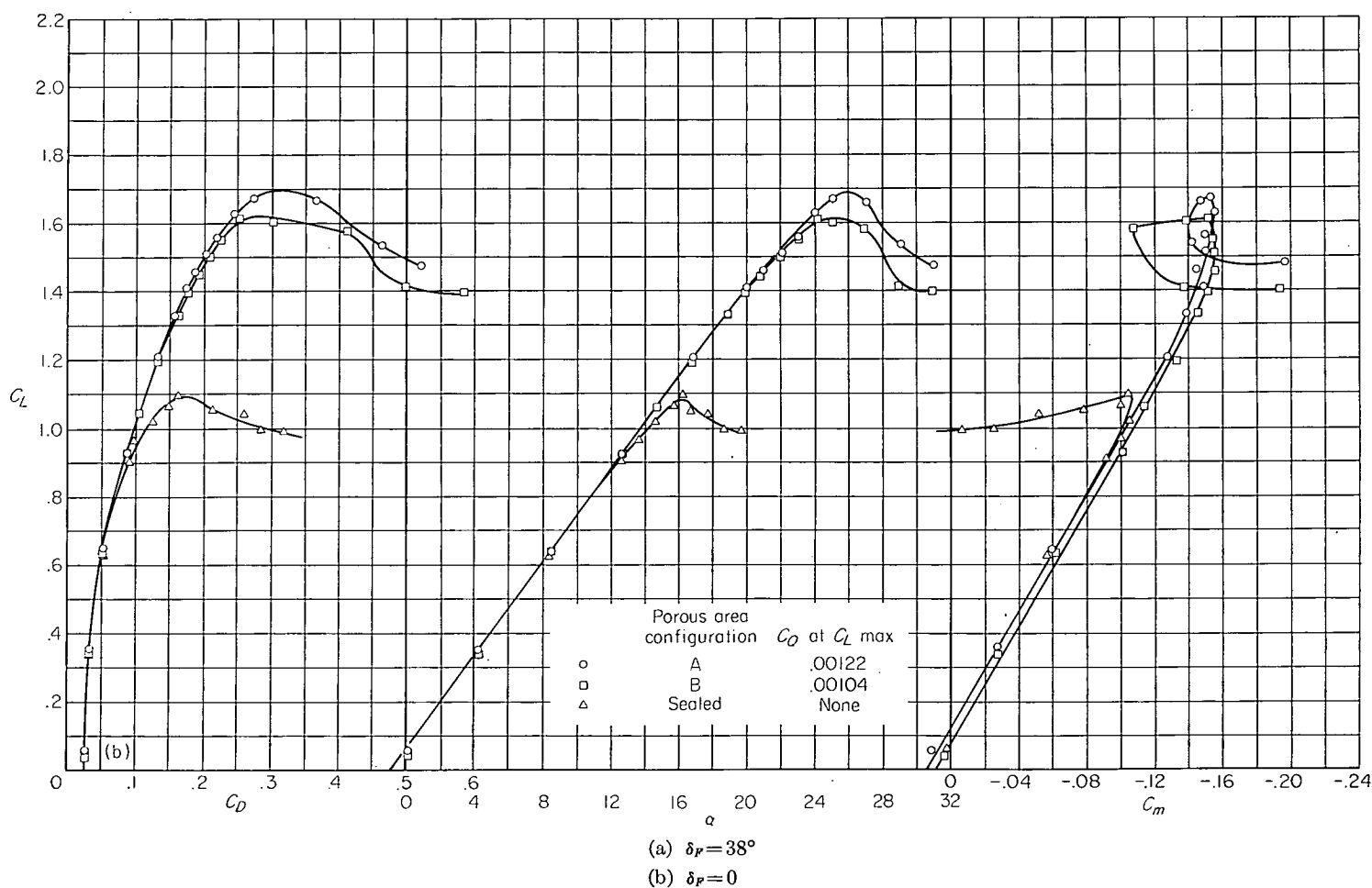
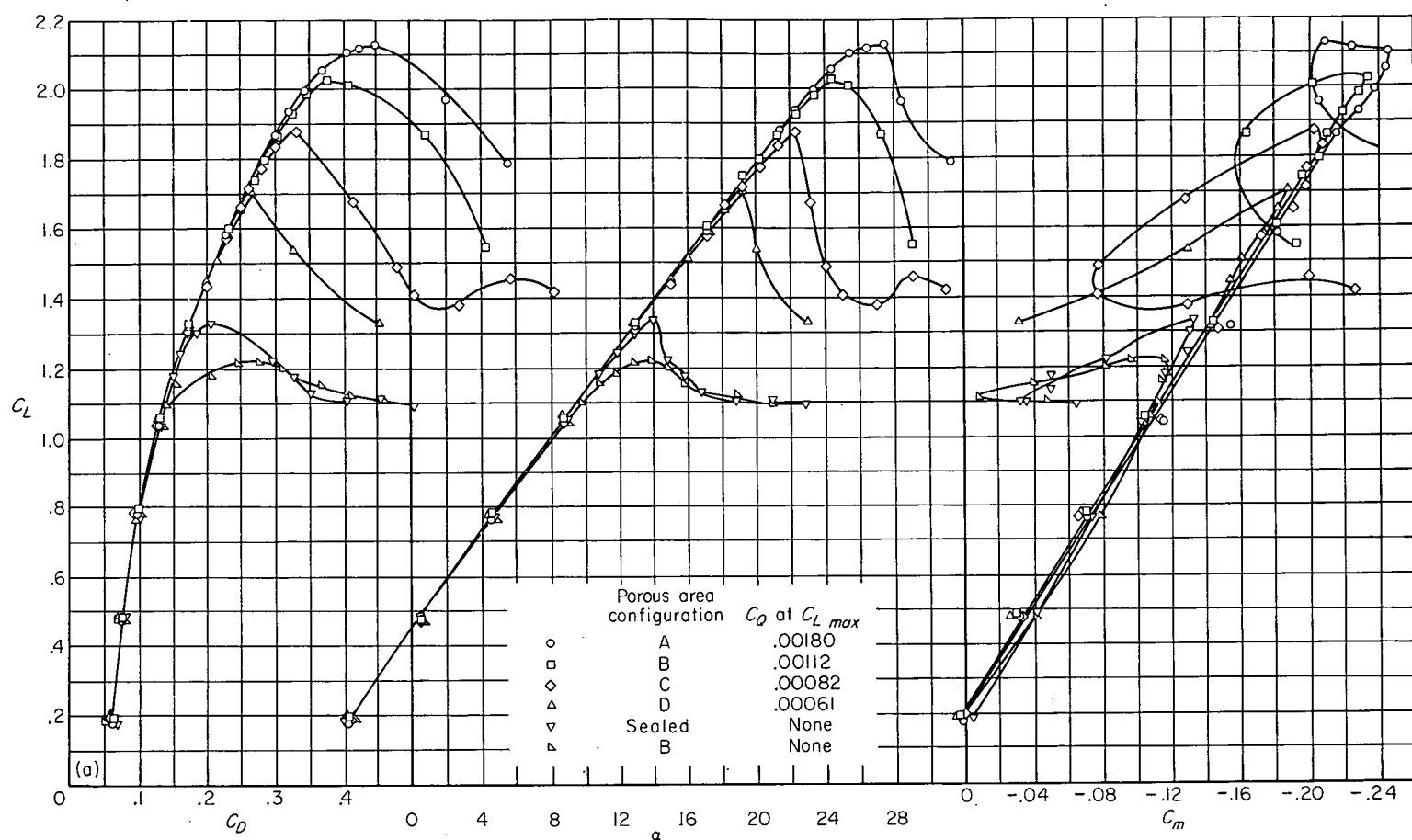


FIGURE 11.—Aerodynamic characteristics of 35° swept-wing model with several chordwise extents of porous area; $U = 112$ feet per second.

(0°). The force characteristics with the porous leading edge sealed simulate the operational airplane with the slats closed. Also shown in figure 11(a) are the force characteristics for the model with the porous area open but with no suction, simulating the condition that would exist for the porous leading-edge installation when the suction pump is inoperative. The data of this figure show that the air circulating through the porous surface had a detrimental effect on the maximum lift coefficient of the model.

Static longitudinal characteristics of model with area suction.—Three-component force data of the 35° swept-wing model with several chordwise extents of area suction along the full span of the leading edge are shown in figure 11. Included in the figure are the values of flow coefficients required at the maximum lift coefficients for the different chordwise extents of area suction. The extensions of the linear portion of the lift and pitching-moment curves and of the drag parabola indicate that the use of area suction at the leading edge delayed air-flow separation. External surface pressure distributions with and without suction applied at 13° and 17° angle of attack are shown in figure 12. These distributions show that the pressure distributions were not changed when suction was applied at an angle of attack below that at which separation occurred without suction; whereas at larger angles of attack, the pressure distributions were changed from distributions indicating separation to ones indicating that the separation was eliminated by area suction. The effectiveness of area suction in delaying air-flow separation and, hence, increasing the lift coefficient of the wing is more clearly shown in figure 13 in which the section lift coefficients, obtained from integration of pressure distributions, are plotted as a function of angle of attack. The complete pressure distributions presented in graphical form at the end of this report (figs. 24 and 25) show the spanwise progression of the air-flow separation. The pressure distributions presented with suction applied are for the porous-area configuration B with flaps deflected; however, the effects of area suction on the pressure distributions were similar for the other configurations tested. The force and pressure data presented in figures 11, 12, 24, and 25 were for a free-stream velocity of 112 feet per second; however, it was found that increasing the free-stream velocity to 180 feet per second (the maximum velocity of the test) did not significantly alter these characteristics.

Suction requirements of porous leading edge.—In figure 11 values of flow coefficient required at the maximum lift coefficients measured with the different porous-area configurations are listed. These values of flow coefficient are indicative of the lowest values of flow coefficient which could be used for each of the openings tested and yet maintain the values of maximum lift coefficients shown in figure 11. For each of the configurations, a reduction in the maximum lift coefficient was measured when the flow coefficient was somewhat reduced; whereas, in contrast, doubling the flow coefficient from the values presented had a negligible effect on the maximum lift coefficient or on the angle of attack for the maximum lift coefficient. Thus, it is seen that the angle of attack and the maximum lift coefficient to which the air-flow separation could be delayed were determined

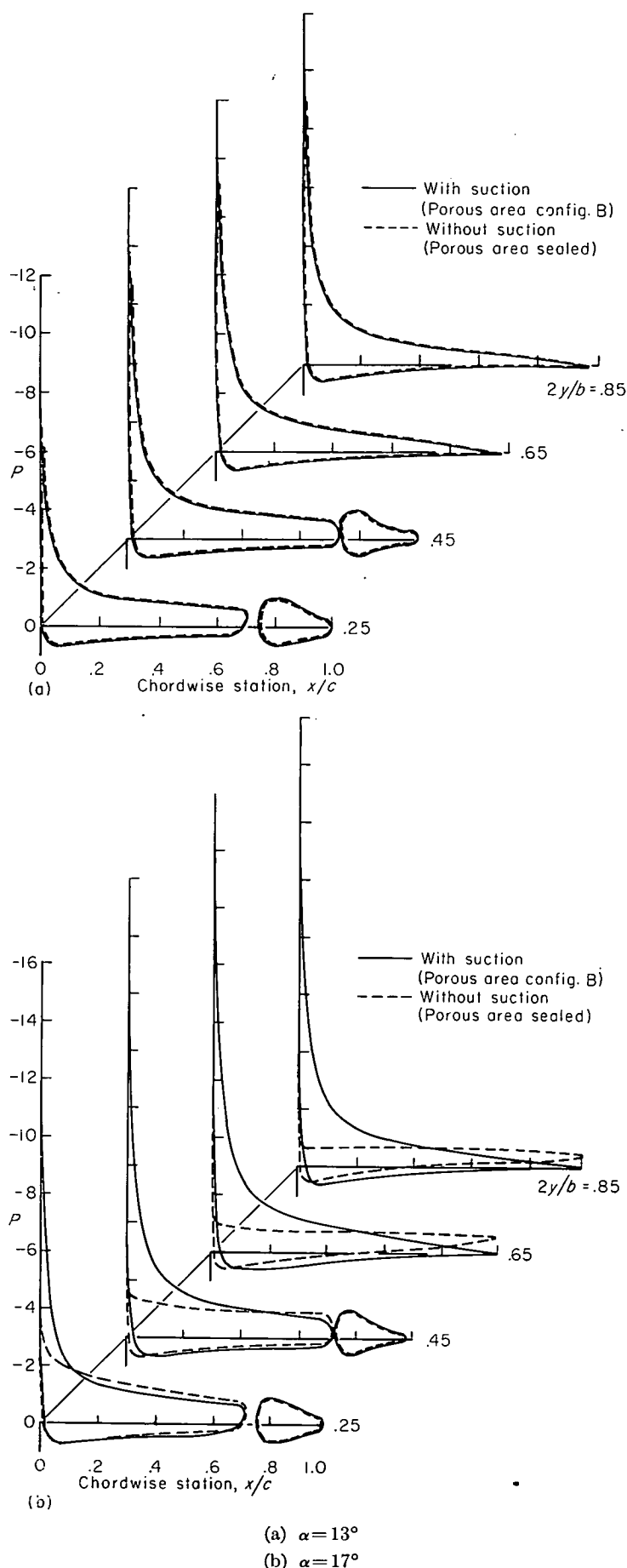


FIGURE 12.—Effect of area suction on the pressure distributions of the 35° swept-wing model; $\delta_F = 38^\circ$, $U = 112$ feet per second.

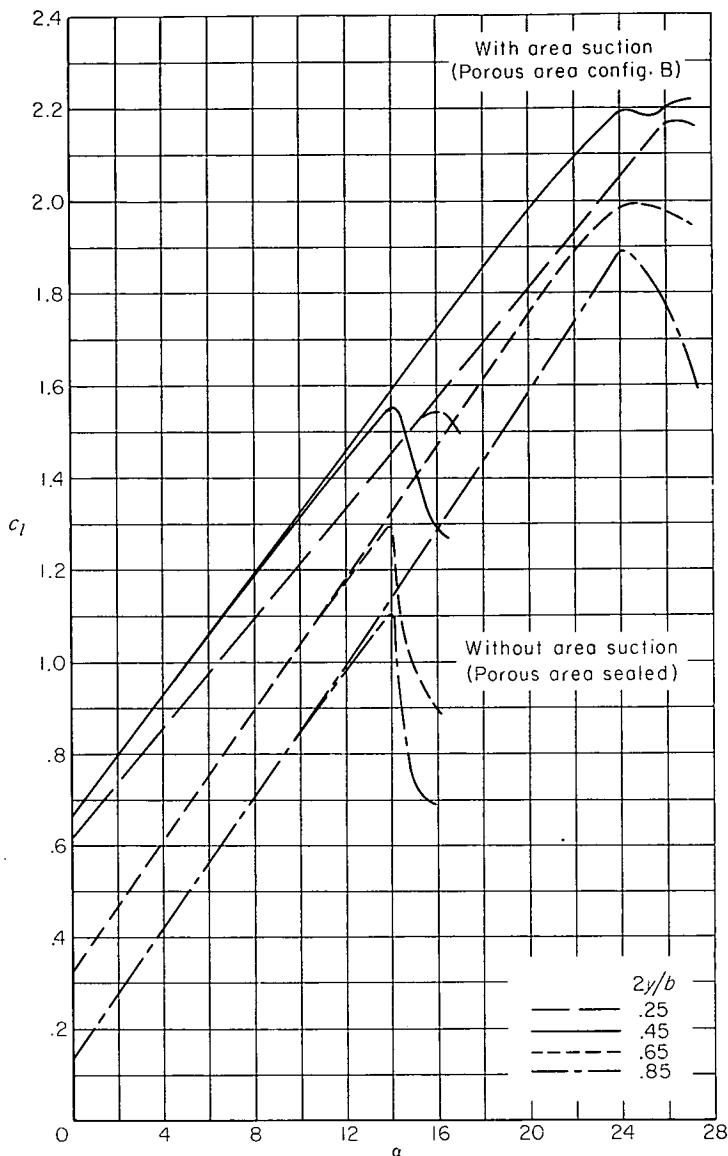


FIGURE 13.—Variation of section lift coefficients with angle of attack, with and without area suction; $\delta_F = 38^\circ$, $U = 112$ feet per second.

primarily by the chordwise extent of porous area. Further, it should be pointed out that only a small increase in the maximum lift coefficient was obtained when configuration A was used in place of configuration B, even though the chordwise extent of porous area and the suction flow coefficients were approximately doubled. Based on these results, as well as on the pressure distributions, it is believed that air-flow separation from the trailing edge of the wing limited the maximum lift coefficient obtained with configuration A, and that further large increases in the maximum lift coefficient would not be expected by the use of area suction only at the leading edge.

The data presented in figure 14 show the variation of flow coefficient and duct pressure coefficient with lift coefficient for the different porous-area configurations tested at a free-stream velocity of 112 feet per second. Since the effects of free-stream velocity on the suction requirements were not known, additional data were obtained at higher free-stream velocities with porous-area configuration B and with the flaps deflected 38° . These data were obtained at free-stream

velocities corresponding to those obtained at constant wing loadings in order to simulate the suction requirements of an airplane during a landing or take-off maneuver. These data are presented in figure 15 and in table V. Figure 15 shows the variation of suction flow coefficient and duct pressure coefficient with lift coefficient, and table V summarizes the measured power inputs and division of losses for several lift coefficients. It should be noted that the suction requirements presented in figures 14 and 15 are probably not the minimum values required at all of the lift coefficients. There are several reasons for this statement. First, a range of flow coefficients was run only at angles of attack near the maximum lift coefficient, thus the flow coefficients presented at lower lift coefficients are probably greater than those required to prevent air-flow separation. Second, the spanwise control of the duct pressures was very limited, and the duct pressure for the inboard sections of the wing could not be adequately reduced to compensate for the variation in peak surface pressures resulting from the span load distribution. Third, theoretically, a particular distribution of porosity exists for each lift coefficient and free-stream velocity to obtain a minimum flow coefficient; whereas in these tests only one design was used for all lift coefficients and free-stream velocities.

The data presented in figure 14 show that the flow requirements increased with increasing lift coefficients, and that for each porous area configuration, a particular value of lift coefficient was reached which could not be increased by increased suction; this lift coefficient was the maximum lift coefficient shown in figure 11. These data also show that for a given lift coefficient, the suction flow coefficient increased with increasing porous area extent, and the dashed curve in figure 14 (a) represents the probable variation of the minimum flow coefficient required to reach any given lift coefficient with the design of porous material tested. Further, it can be seen that for a given lift coefficient, the duct pressure coefficient remained essentially unchanged when the extent of porous area was increased, even though the required flow coefficient was increased. This resulted because the pressure drop through the porous material for all of the required suction-air velocities was relatively small at the chordwise location of the maximum surface pressure coefficient. Thus the duct pressure coefficient was essentially equal to the maximum surface pressure coefficient which was primarily a function of the angle of attack.

The data of figure 15 indicate that increasing the free-stream velocity did not affect the flow coefficient or duct pressure coefficient at a particular lift coefficient. Therefore, the suction power required should vary as the cube of the free-stream velocity; this is verified by the data given in table V.

Comparison of experimental results with those computed by Thwaites' method.—In figure 16 the experimentally minimized chordwise extents are compared with those predicted to be necessary for the same maximum lift coefficients. A comparison of the experimental and predicted chordwise extents of porous areas show that the chordwise extents for the maximum lift coefficients of 1.71, 1.87, and 2.03 were reasonably well predicted for the outboard portions

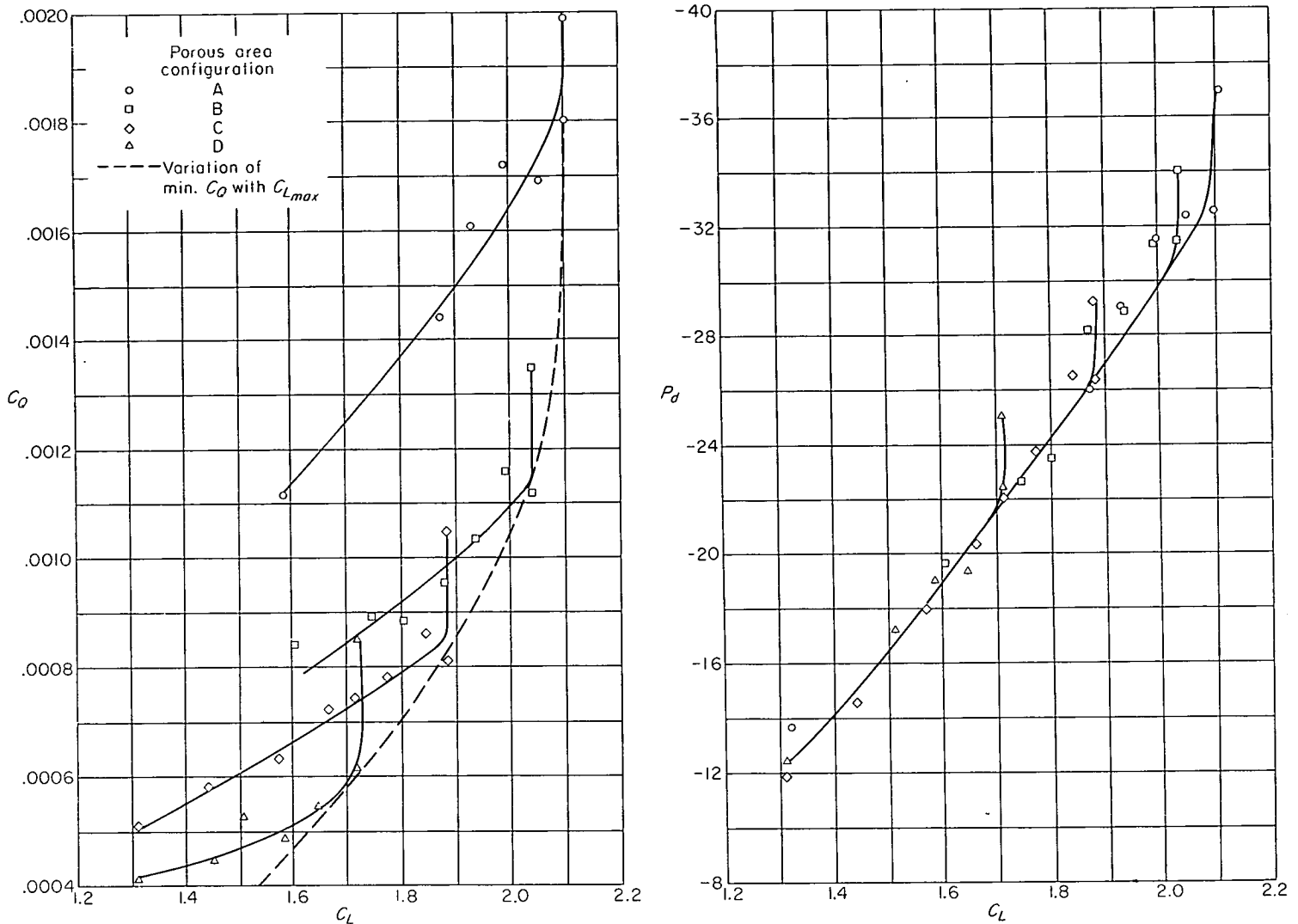


FIGURE 14.—Variation of suction requirements with lift coefficient for several porous area configurations on 35° swept-wing model; $U=112$ feet per second; $\delta p=38^\circ$.

of the wing where the initial separation occurred. The chordwise extents of porous area required for the inboard portions of the wing were considerably less than those predicted to be necessary. This difference is believed to be attributable to the spanwise flow of the boundary layer and its effect on the maximum lift characteristics of the airfoil sections on a sweptback wing; this effect is discussed in reference 6 for a 45° sweptback wing.

The chordwise extent required on the outboard portion of the wing for a maximum lift coefficient of 2.13 was about twice that predicted to be necessary. It was noted in a previous section that it was believed this maximum lift coefficient was limited by air-flow separation from the trailing edge of the wing rather than from the leading edge; hence, the chordwise extent required was greater than that predicted to be necessary based on considerations of leading-edge separation alone.

The variation of the experimental flow coefficient with lift coefficient is compared in figure 17 with the values computed to be necessary. The experimental curve used in this figure is the envelope of the curves of figure 14 (a) for a free-stream velocity of 112 feet per second. Two curves are shown for the computed values; one curve is for the values computed

from the predicted chordwise extents of porous area and the suction-air velocities calculated to be necessary by the equations set forth by Thwaites. The other curve is 12 times the flow coefficient computed to be necessary, and this curve represents the magnitude of the difference between the computed and experimental results. Figure 18 is presented to show the spanwise distribution of the average suction-air velocities at a lift coefficient of 1.93 and a free-stream velocity of 112 feet per second. These suction-air velocities were calculated from the measured external and duct pressures at each of the four spanwise measuring stations. Included in figure 18 for comparative purposes is the spanwise distribution of suction-air velocity used for the design of the porous material. It can be seen in this figure that on the outboard portion of the wing the average suction-air velocities were of the order of those expected to be necessary (based on previous tests with area suction), values about 12 times those computed from Thwaites' equations. However, on the inboard portion of the wing, the suction-air velocities were considerably higher than had been anticipated. It is believed that these higher values were caused by the inadequate control of the spanwise duct pressure that was available on the model. Thus, it can be surmised that it was fortuitous

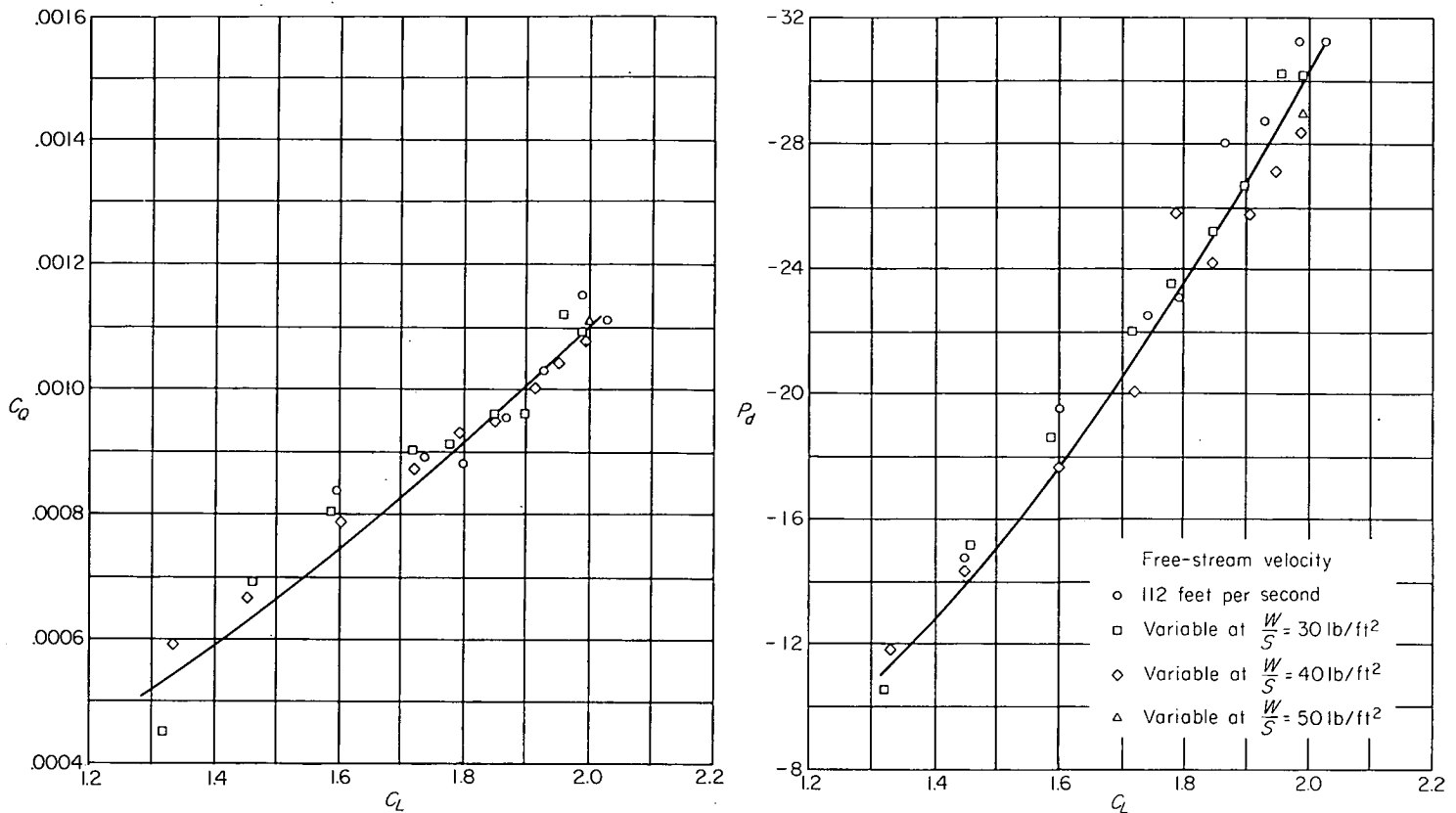


FIGURE 15.—Effect of free-stream velocity on the variation of suction flow coefficient and duct pressure coefficient with lift coefficient for 35° swept-wing model; porous area configuration B, $\delta_F = 38^\circ$.

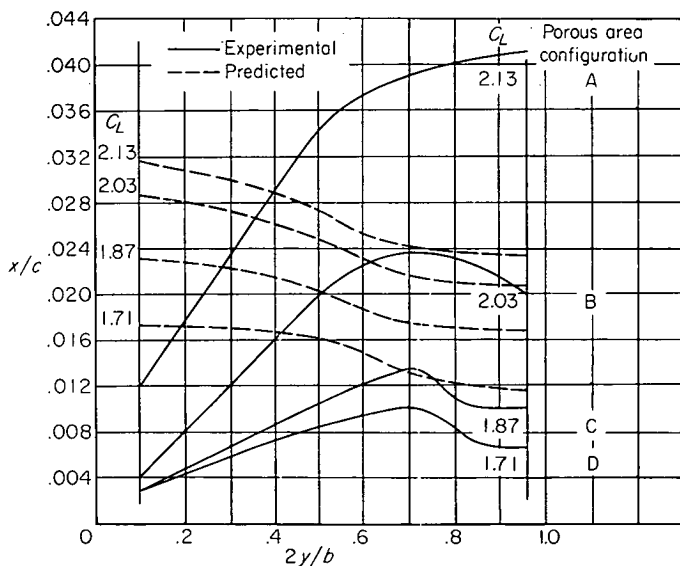


FIGURE 16.—Comparison of experimentally minimized chordwise extents of porous areas with those predicted to be necessary; $\delta_F = 38^\circ$.

that the total flow coefficient was 12 times the computed value (fig. 17).

It is also of interest to compare the chordwise distribution of suction-air velocity with that used in the design of the porous leading edge. For this purpose, the 0.85 semispan station was chosen, and the chordwise distribution of suction-air velocity at three flow coefficients is shown in figure 19 for the design lift coefficient of 1.93 and free-stream velocity of 112 feet per second. These flow coefficients represent values above the minimum required, the minimum required,

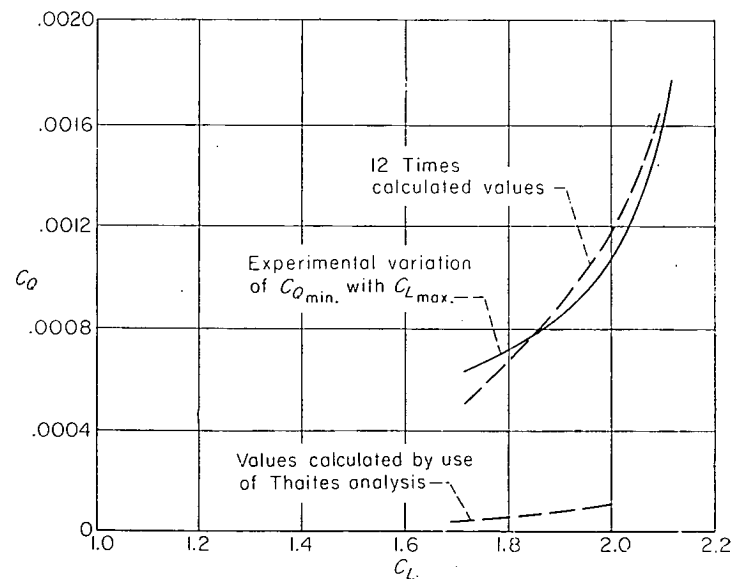


FIGURE 17.—Comparison of experimental and predicted flow coefficients for the model; $\delta_F = 38^\circ$. $U = 112$ feet per second.

and a value below the minimum required. Also included in this figure are the lift coefficients measured at these three flow coefficients. It can be seen from this figure that a loss in lift was encountered when the flow coefficient was reduced to the point where the suction-air velocity near the leading edge was less than the value used in the design. It cannot be determined, however, whether the suction-air velocities aft of the leading edge could have been reduced by redesigning the porous material.

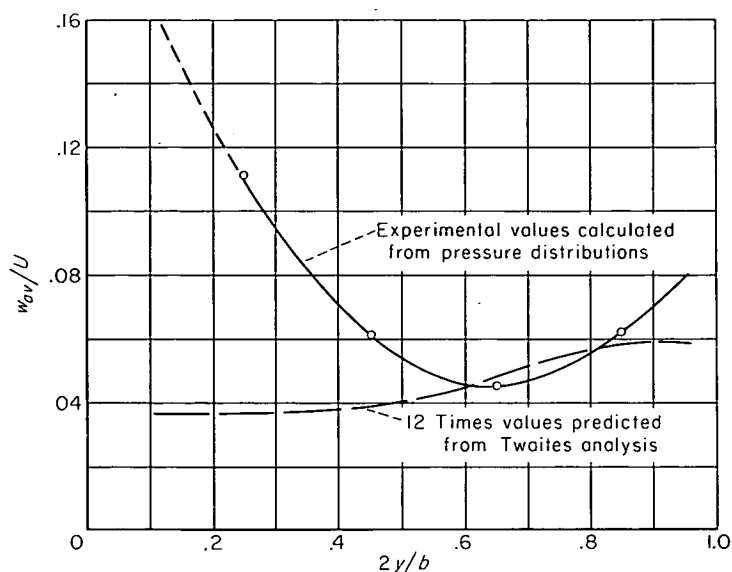


FIGURE 18.—Comparison of experimental and theoretical ratios of average suction-air velocity to free-stream velocity; $C_L=1.93$; $U=112$ feet per second.

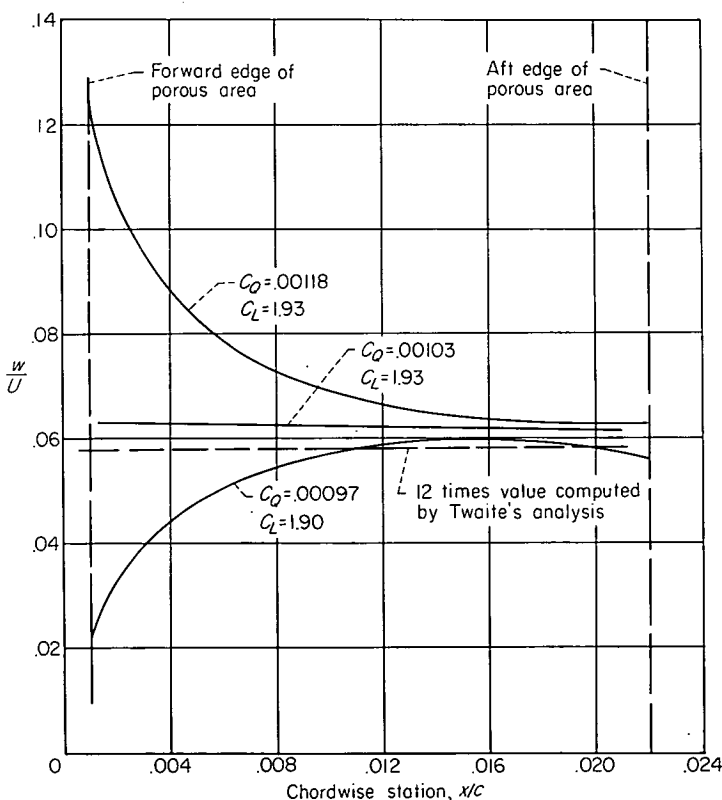


FIGURE 19.—Ratio of suction-air to free-stream velocity at 0.85 semi-span station, computed from surface pressure distributions; $\alpha=22.2^\circ$, $U=112$ feet per second, porous area configuration B, flap deflected 38° .

FLIGHT TESTS

Lift characteristics of the airplane with a porous leading edge.—The lift characteristics of the test airplane with the full-span porous leading edge are shown in figure 20 for conditions of maximum available suction flow, and for suction off with the porous surface open and the ducts closed. Also included in this figure for comparative purposes are the results of the wind-tunnel investigation for a similar

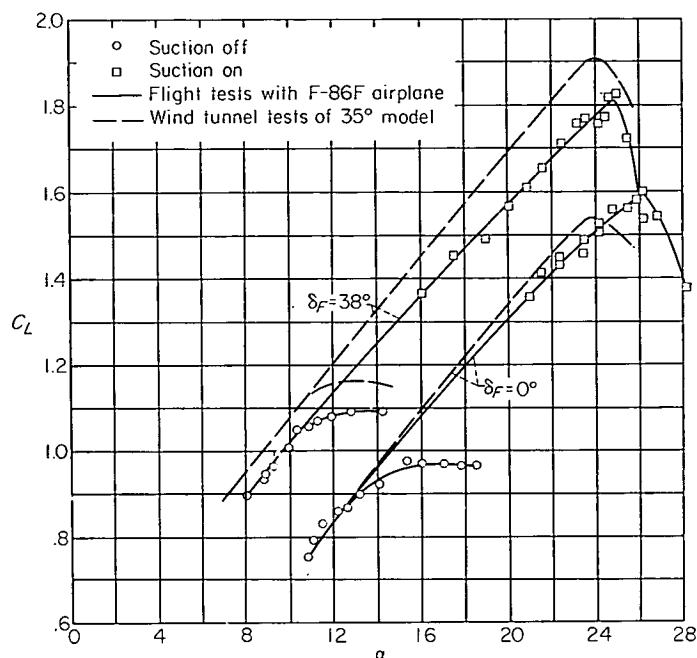


FIGURE 20.—Comparison of flight results with those obtained in the wind tunnel; porous area configuration B.

configuration (porous-area configuration B). It should be pointed out that the wind-tunnel data have been corrected to trimmed conditions for a center-of-gravity position similar to that of the flight tests. For the flaps-retracted condition, good agreement is obtained between the flight and wind-tunnel results, with the flight installation providing a slightly higher value of maximum lift coefficient. For the flaps-down condition, the agreement is less satisfactory, with the flight data showing lower lift throughout the angle-of-attack range. This difference might be explained partially by differences in the configurations of the wind-tunnel model and the F-86 airplane. The wind-tunnel model had no landing gear, but in its place were the model support struts; in addition, the landing-gear wells were closed. The fuselage of the wind-tunnel model bore no resemblance to that of the F-86 airplane; it had a circular cross section with a smaller width and a higher fineness ratio, and the wing of the model was mounted on the fuselage center line instead of the low position. Flight tests with the landing gear of the airplane extended and retracted indicated that the major portion of the difference in lift at the lower angles of attack is the result of a loss of flap effectiveness due to the extended gear and open gear wells.

The stall with suction, despite the extremely nose-high attitude due to angle of attack and the relatively high engine power required, was not considered objectionable by the pilot, but a lack of stall warning was noted. Although the stall was abrupt, the accompanying roll-off and pitch-up were of a controllable magnitude. With flaps and gear retracted, the stall was considered extremely mild and was characterized by a slight pitch-up and no roll-off. Just prior to the stall with maximum suction power, tufts on the wing surface indicated a strong spanwise flow in the boundary layer over the ailerons. With an increase in angle of attack, the flow at the outboard portions of the trailing edge appeared to separate, the area of separation rapidly spreading

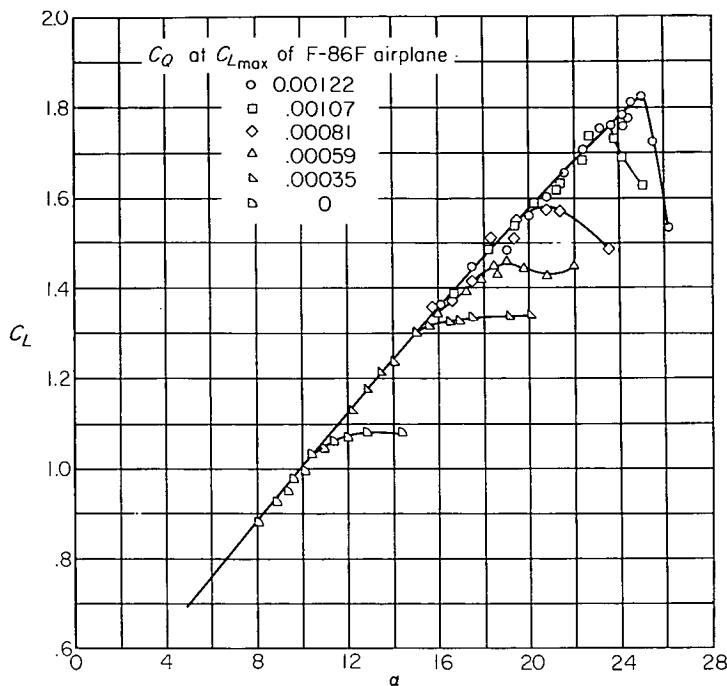


FIGURE 21.—Variation of lift coefficient with angle of attack for several values of suction flow coefficient; $\delta_F=38^\circ$, porous area configuration B.

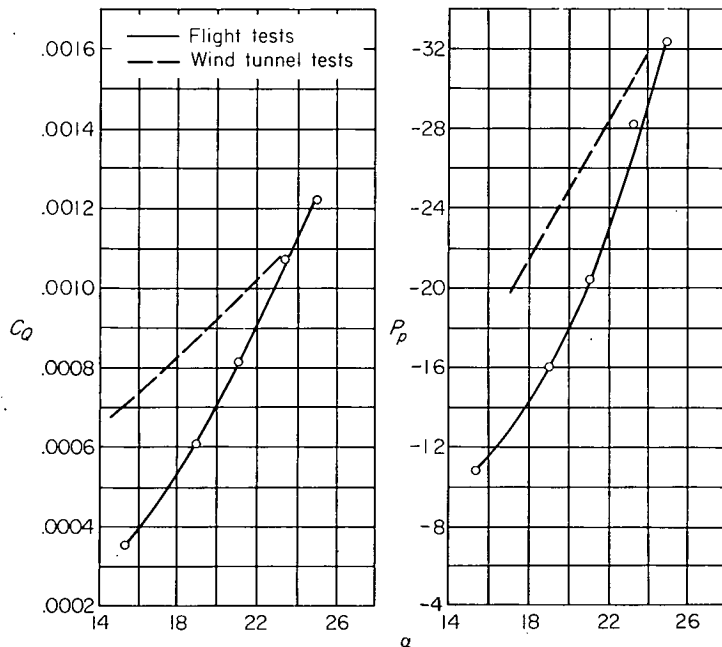


FIGURE 22.—Comparison of suction pumping requirements in the flight tests and wind-tunnel tests; $\delta_F=38^\circ$, porous area configuration B.

forward and inboard as the stall was approached. However, it appeared that while a trailing-edge type of stall was imminent, the final complete flow separation was triggered by a disturbance occurring at the leading edge at about the 70-percent semispan station. Based on these observations, as well as on the wind-tunnel results with a larger open chordwise extent of porous area, it seems doubtful that further increases in suction flow or refinements of the porous-area configuration would produce large increases in maximum lift coefficient. In contrast to the stall with area suction, the pilot was not able to define the stall point of the airplane

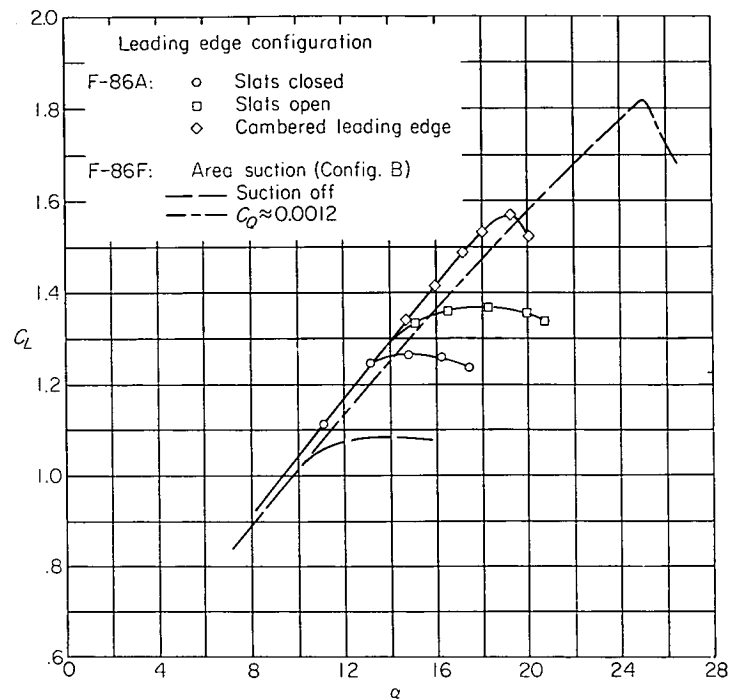


FIGURE 23.—Comparison of lift coefficients obtained with various leading-edge high-lift devices; $\delta_F=38^\circ$.

with suction off. Buffeting and lateral unsteadiness appeared at a speed corresponding to an angle of attack of 11° and increased gradually with increasing angle of attack. Due to the lack of reference with which to gage rate of sink, it was not obvious to the pilot that the airplane was beyond the maximum lift coefficient at angles of attack above 13° . With suction off, tufts indicated that flow separation appeared first from the leading edge at mid-semispan and spread slowly outboard and inboard.

The effects of varying flow coefficient upon the lift characteristics of the airplane with flaps deflected are shown in figure 21. With a reduction in flow coefficient, the stalling behavior of the airplane gradually changed from the abrupt stall exhibited at maximum flow to the mild type of stall that occurred with suction off.

Suction requirements of porous leading edge.—The variations of flow coefficient and pump inlet pressure coefficient with angle of attack are shown in figure 22 for porous-area configuration B with the trailing-edge flaps deflected. To obtain a further comparison of the flight-test and wind-tunnel-test results, figure 22 also includes the suction requirements, measured in the wind tunnel for porous-area configuration B with flaps deflected, at a wing loading of 40 pounds per square foot. These suction requirements are compared on the basis of angle of attack rather than lift coefficient because of the previously noted differences in lift coefficient. Comparison of the flight and wind-tunnel suction requirements indicates a close agreement near the maximum effectiveness of the leading-edge suction installation; however, for angles of attack below 24° , the flight installation appeared to require considerably less flow than was required in the wind tunnel. The exact reason for this discrepancy is not known; however, in the flight tests there was a better spanwise control of the duct pressure distribution. In addition, as was noted previously, the minimum

suction requirements were not completely evaluated in the wind tunnel at angles of attack below those for maximum lift coefficient.

Comparison of lift characteristics of various leading-edge-type high-lift devices.—The lift characteristics of the F-86A airplane having the trailing-edge flap deflected with a slatted leading edge extended and retracted and with a leading edge modified to include increased camber and leading-edge radius are compared in figure 23 with those of the F-86F airplane having the porous leading edge. Although slight differences were obtained in the lifts measured at angles of attack below the respective maximum lift coefficients, it is felt that a comparison of the maximum lift coefficients is indicative of the relative lift capabilities of the various leading-edge devices. These maximum lift coefficients, $C_{L_{max}}$, are compared in the following table along with the pilot's opinions of the stalling characteristics of each device:

Configuration	$C_{L_{max}}$	Stalling characteristics
Porous leading edge, suction on.	1.82	Controllable, but no stall warning.
Cambered leading edge-----	1.58	Not controllable and no stall warning.
Normal leading edge, slats extended.	1.36	Controllable and adequate stall warning.
Normal leading edge, slats closed.	1.27	Controllable and adequate stall warning.
Porous leading edge, suction off.	1.08	Controllable and adequate stall warning.

It is evident that the area-suction leading edge is a considerably more effective means of increasing the maximum lift of a wing than the other high-lift devices. It can also be seen that there was a reduction in the maximum lift coefficient when the normal leading edge (slats closed) was replaced by the porous leading edge and no suction was applied. A similar loss was measured in the wind-tunnel tests and was attributed to circulation of air through the porous material.

Landing and take-off performance.—The effects of the porous leading-edge installation upon the landing and take-off characteristics of the F-86F airplane are reported here only in terms of a pilot's preliminary evaluation; no precise measurements of speeds or distances were taken. The performances quoted refer to the F-86A and F-86F airplanes without external stores at normal take-off and landing weights. This evaluation is subject to the following factors which apply to the F-86 airplane as a type: (1) The airplane is limited to a maximum ground angle of attack of about 15° and has no protective tail bumper, and (2) at the highest angles of attack which were attainable in the landing approach with the suction equipment, visibility was objectionably limited.

The take-off characteristics of the F-86F airplane with the porous leading-edge installation were considered very similar to those of the normal F-86A or F-86F with slatted leading edge. At normal gross weight for take-off, the nose wheel lifted off at about 90 knots, indicated airspeed, and the airplane became airborne at about 105 knots. After take-off, however, an extremely nose-high attitude could be attained which resulted in a steep angle of climb. At a climb speed of 110 knots, flaps and gear up, under no-wind conditions, an altitude of 1,000 feet could be easily attained before reaching the end of an 8,000-foot runway.

The main advantage of the high maximum lift due to suction in the landing approach was the increased ability to maneuver; however, the high engine speed required to maintain adequate suction (about 70 percent of the maximum) made it difficult to lose altitude and still approach at a low airspeed. The best approach speed for a normal descending type of approach seemed to be 112 knots. For a power-on, carrier-type approach, a favorable speed was 105 knots. Comparable speeds for the F-86A or F-86F airplane with slats are about 120 and 115 knots, respectively. The touch-down speed with suction applied was about 104 knots and was limited by poor visibility and a fear of dragging the tail pipe. It is obvious that the reduction in stalling speed afforded by this leading-edge-suction installation cannot be fully utilized on this airplane to decrease the landing speed.

High-speed performance.—Several flights were made at altitudes up to 35,000 feet and speeds up to those corresponding to a Mach number of 0.9 in order to check the effects of the suction equipment and porous leading edge under these conditions. Determination of the effects of the porous leading edge on the high-speed drag of the airplane was made difficult by the fact that the contribution of drag from the pump pod was unknown and apparently varied with operation of the suction equipment. Therefore, drag measurements were obtained with the porous leading edge, suction on and suction off, and with a production leading edge installed, and the pump operative and inoperative. The results of these tests indicated that flow through the porous leading edge had little effect on the high-speed flight drag of the test airplane.

A check of the buffeting characteristics of the airplane in turns at 35,000 feet revealed no measurable change in the buffet boundary due to the porous leading edge, suction on or off, from that of an F-86 airplane with a slatted leading edge. At Mach numbers from 0.60 to 0.80 and at lift coefficients above the buffet boundary, there was some evidence of an increase in buffet amplitude with the suction equipment operating at maximum power. A low-frequency buffeting (7 to 8 cycles per second) accompanied an apparent stalling of the pump and surging of the static pressure in the duct which resulted in intermittent flow separation on the wing. A similar condition could be found in turns at low altitudes at indicated airspeeds of 200 to 300 knots. This phenomenon has not been fully explained; however, it is not considered particularly significant since the conditions are well beyond the design operating range of the pumping equipment.

Serviceability of the porous leading edge.—During the early tests with the porous leading edge, disappointingly low values of maximum lift coefficient were obtained. An examination of the behavior of tufts on the wing showed that the stall was being precipitated by a premature localized flow separation which appeared immediately behind the juncture of the two outer porous panels on the right wing. Yawing the airplane to the right duplicated this condition on the left wing. Removal of portions of the nose ribs at the junctures of the leading-edge panels, effectively eliminating discontinuities in the porous area which were about $\frac{3}{4}$ of an inch in width, resulted in an increase in maximum lift

coefficient from 1.45 to 1.82. In contrast to the sensitivity of the installation to small areas of reduced porosity was its apparent insensitivity to wing surface condition near the leading edge. In the original condition, numerous large defects in contour existed in the modified portion of the leading edge. During the course of the tests, a major portion of the defects was removed by refairing the surface immediately aft of the porous area; however, no changes in the aerodynamic characteristics of the wing were noted.

One flight was devoted to a determination of the effects of rain on the operation of the suction equipment and upon the lift of the wing. A series of stalls made in moderate to heavy rain revealed no significant effects on either the lift coefficient for the stall or the power required. Unfortunately, these flights were made early in the program, before the highest lifts were being obtained, so any small effects of rain might have been masked.

After approximately six months of operation of the aircraft (60 hours of flight), flow-quantity and pressure measurements revealed no evidence of decreasing porosity of the leading-edge material. Other than covering the leading edges when the airplane was inactive, little special attention was given to their maintenance.

CONCLUDING REMARKS

The results of the wind-tunnel and flight tests of a 35° sweptback wing airplane having area suction applied to the leading edge of the wing showed that the use of area suction increased the maximum lift coefficient more than 50 percent. Although the maximum lift coefficients were obtained with relatively low flow coefficients, relatively high pumping pressure ratios were required. Good agreement was obtained in the comparison of the wind-tunnel results with those measured in flight. The increase in the maximum lift coefficient obtained with area suction applied to the leading edge of the wing of the airplane was greater than that obtained by the use of a slatted leading edge or a leading edge having camber and increased leading-edge radius. Further, there appeared to be no detrimental effects of the area-suction installation on the operation or performance of the airplane.

AMES AERONAUTICAL LABORATORY

NATIONAL ADVISORY COMMITTEE FOR AERONAUTICS

MOFFETT FIELD, CALIF., March 2, 1956

REFERENCES

1. Thwaites, B.: A Theoretical Discussion of High-Lift Aerofoils With Leading-Edge Porous Suction. R. & M. No. 2242, British A. R. C., July, 1946.
2. Nuber, Robert J., and Needham, James R., Jr.: Exploratory Wind-Tunnel Investigation of the Effectiveness of Area Suction in Eliminating Leading-Edge Separation over an NACA 64A212 Airfoil. NACA TN 1741, 1948.
3. Pankhurst, R. C., Raymer, W. G., and Devereux, A. N.: Wind-Tunnel Tests of the Stalling Properties of an 8-Percent Thick Symmetrical Section With Continuous (Distributed) Nose Suction. R. & M. No. 2666, British A. R. C., 1953.
4. Dannenberg, Robert E., and Weiberg, James A.: Section Characteristics of a 10.5-Percent-Thick Airfoil With Area Suction as Affected by Chordwise Distribution of Permeability. NACA TN 2847, 1952.

5. Weiberg, James A., and Dannenberg, Robert E.: Section Characteristics of an NACA 0006 Airfoil With Area Suction Near the Leading Edge. NACA TN 3285, 1954.
6. Hunton, Lynn W.: Effects of Finite Span on the Section Characteristics of Two 45° Sweptback Wings of Aspect Ratio 6. NACA TN 3008, 1953.
7. Campbell, G. W., Peskin, B. A., and Przybylowicz, J. A.: Boundary Layer Control by Porous Area Suction on the Wing Leading Edges of an F-86F Airplane. WADC TR 54-290, Wright Air Development Center, June 1954

TABLE I.—DIMENSIONS OF THE TEST VEHICLES

Wing	
Total area, sq ft.....	287.9
Span, ft.....	37.1
Aspect ratio.....	4.79
Taper ratio.....	0.51
Mean aerodynamic chord (wing station 98.7 in.), \bar{c} , ft.....	8.1
Dihedral angle, deg.....	3.0
Sweepback of leading edge, deg.....	37.7
Sweepback of 0.25-chord line, deg.....	35.0
Aerodynamic and geometric twist, deg.....	2.0
Root airfoil section (normal to 0.25-chord line).....	NACA 0012-64 (modified)
Tip airfoil section (normal to 0.25-chord line).....	NACA 0011-64 (modified)
Horizontal tail	
Total area, sq ft.....	35.0
Span, ft.....	12.7
Aspect ratio.....	4.65
Taper ratio.....	0.45
Dihedral angle, deg.....	10.0
Mean aerodynamic chord (horizontal-tail station 33.54 in.) ft.....	2.9
Sweepback of 0.25-chord line, deg.....	34.6
Airfoil section (parallel to center line).....	NACA 0010-64
Vertical tail of the F-86 airplanes	
Total area, sq ft.....	34.4
Span, ft.....	7.5
Aspect ratio.....	1.74
Taper ratio.....	0.36
Sweepback of 0.25-chord line, deg.....	35.0
Distance between wing $\frac{c}{4}$ and horizontal tail $\frac{c}{4}$, ft.....	18.1

TABLE II.—COORDINATES OF THE WING AIRFOIL SECTIONS NORMAL TO THE WING QUARTER-CHORD LINE AT TWO SPAN STATIONS

(a) Coordinates for normal F-86 wing

Section at 0.467 semispan			Section at 0.857 semispan		
Chord-wise station in.	z, in.		Chord-wise station in.	z, in.	
	Upper surface	Lower surface		Upper surface	Lower surface
0	0.231	-----	0	-.098	-----
.119	.738	-0.307	.089	.278	-0.464
.239	.943	-.516	.177	.420	-.605
.398	1.127	-.698	.295	.562	-.739
.597	1.320	-.895	.443	.701	-.879
.996	1.607	-1.196	.738	.908	-1.089
1.992	2.104	-1.703	1.476	1.273	-1.437
3.984	2.715	-2.358	2.952	1.730	-1.878
5.976	3.121	-2.811	4.428	2.046	-2.176
7.968	3.428	-3.161	5.903	2.290	-2.401
11.952	3.863	-3.687	8.855	2.648	-2.722
15.936	4.157	-4.064	11.806	2.911	-2.944
19.920	4.357	-4.364	14.758	3.104	-3.102
23.904	4.480	-4.573	17.710	3.244	-3.200
27.888	4.533	-4.719	20.661	3.333	-3.250
31.872	4.525	-4.800	23.613	3.380	-3.256
35.856	4.444	-4.812	26.564	3.373	-3.213
39.840	4.299	-4.758	29.516	3.322	-3.126
43.825	4.081	-4.638	32.467	3.219	-2.989
47.809	3.808	-4.452	35.419	3.074	-2.803
51.793	3.470	-4.202	38.370	2.885	-2.574
55.777	3.066	-3.891	41.322	2.650	-2.302
59.761	2.603	-3.521	44.273	2.374	-1.986
* 63.745	2.079	-3.089	* 47.225	2.054	-1.625
83.681	-.740	-----	63.031	.321	-----
Leading edge radius: 1.202; center at 1.201, 0.216			Leading edge radius: 0.822; center at 0.822, -0.093		

TABLE II.—COORDINATES OF THE WING AIRFOIL SECTIONS NORMAL TO THE WING QUARTER-CHORD LINE AT TWO SPAN STATIONS

(b) Coordinates for the cambered leading edge of the F-86A airplane

Section at 0.467 semispan			Section at 0.857 semispan		
Chord-wise station in.	z, in.		Chord-wise station in.	z, in.	
	Upper surface	Lower surface		Upper surface	Lower surface
-1.692	-1.445	-----	-1.250	-1.359	-----
-1.273	-.348	-2.552	-.934	-.495	-2.192
-.855	-.222	-2.898	-.619	-.099	-2.454
-.436	.629	-3.114	-.304	.197	-2.609
-.018	.969	-3.272	.011	.456	-2.701
.400	1.266	-3.391	.326	.675	-2.769
.819	1.527	-3.473	.641	.867	-2.796
1.237	1.760	-3.523	.956	1.040	-2.813
1.655	1.952	-3.549	1.272	1.189	-2.821
1.992	2.104	-----	1.476	1.273	-----
2.074	-----	-3.552	1.587	-----	-2.813
2.911	-----	-3.531	2.217	-----	-2.787
4.166	-----	-3.481	3.163	-----	-2.742
6.258	-----	-3.472	4.739	-----	-2.709
8.350	-----	-3.542	6.314	-----	-2.712
10.442	-----	-3.657	7.890	-----	-2.751
14.626	-----	-3.956	9.466	-----	-2.808
15.936	-----	-4.064	11.042	-----	-2.885
			11.806	-----	-2.944
Leading edge radius: 1.674; center at -0.018, -1.445			Leading edge radius: 1.261; center at 0.011, -1.359		

TABLE III.—LOCATION OF SURFACE PRESSURE ORIFICES ON WIND-TUNNEL MODEL

[Position of orifices, fraction of streamwise chord]

0.25 $\frac{b}{2}$ station		0.45 $\frac{b}{2}$ station		0.65 $\frac{b}{2}$ and 0.85 $\frac{b}{2}$ station	
Upper surface	Lower surface	Upper surface	Lower surface	Upper surface	Lower surface
0	-----	0	-----	0	-----
.0025	0.0025	.0025	0.0025	.0025	0.0025
.005	.005	.005	.005	.005	.005
.01	.01	.01	.01	.01	.01
.015	.015	.015	.015	.015	.015
.02	.02	.02	.02	.02	.02
.025	.025	.025	.025	.025	.025
.035	.035	.035	.035	.035	.035
.05	.05	.05	.05	.05	.05
.075	.075	.075	.075	.075	.075
.1	.1	.1	.1	.1	.1
.15	.15	.15	.15	.15	.15
.2	.2	.2	.2	.2	.2
.3	.3	.3	.3	.3	.3
.4	.4	.4	.4	.4	.4
.5	.5	.5	.5	.5	.5
.6	.6	.6	.6	.6	.6
.7	.7	.7	.7	.7	.7
.765	.8	.74	.82	.8	.8
.78	.915	.755	.98	.9	.9
.81	.98	.788	-----	.975	.975
.92	-----	.85	-----		
.98	-----	.98	-----		

TABLE IV.—CONFIGURATIONS OF THE WIND-TUNNEL MODEL TESTED AND THE TEST CONDITIONS

Porous-leading-edge configuration	δ , deg	Suction or no suction	U, ft/sec	W/S lb/sq ft
Sealed	0	-----	112	varied
Sealed	38	-----	112	varied
B, root valves closed	38	none	112	varied
A	38	suction	112	varied
B	38	suction	112	varied
B	38	suction	112 to 162	30
B	38	suction	129 to 180	40
B	38	suction	145 to 180	50
C	38	suction	112	varied
D	38	suction	112	varied
A	0	suction	112	varied
B	0	suction	112	varied

TABLE V.—POWER REQUIREMENTS FOR 35° SWEEP-WING MODEL WITH POROUS-AREA CONFIGURATION B AND FLAPS DEFLECTED 38°

C_L	U, ft/sec	C_q	Measured power input, hp	Suction power, hp	Pump loss, hp	Duct loss, hp
Wing loading, 30 lb/sq ft						
1.99	112	0.00109	56	36	17	3
1.85	116	.00096	44	30	12	2
1.72	121	.00090	35	23	10	2
1.59	126	.00080	30	20	8	2
Wing loading, 40 lb/sq ft						
1.99	129	.00108	81	47	27	7
1.85	134	.00095	70	41	23	6
1.72	140	.00087	57	35	17	5
1.60	145	.00079	49	30	14	5
Wing loading, 50 lb/sq ft						
1.99	145	.00111	160	80	63	17

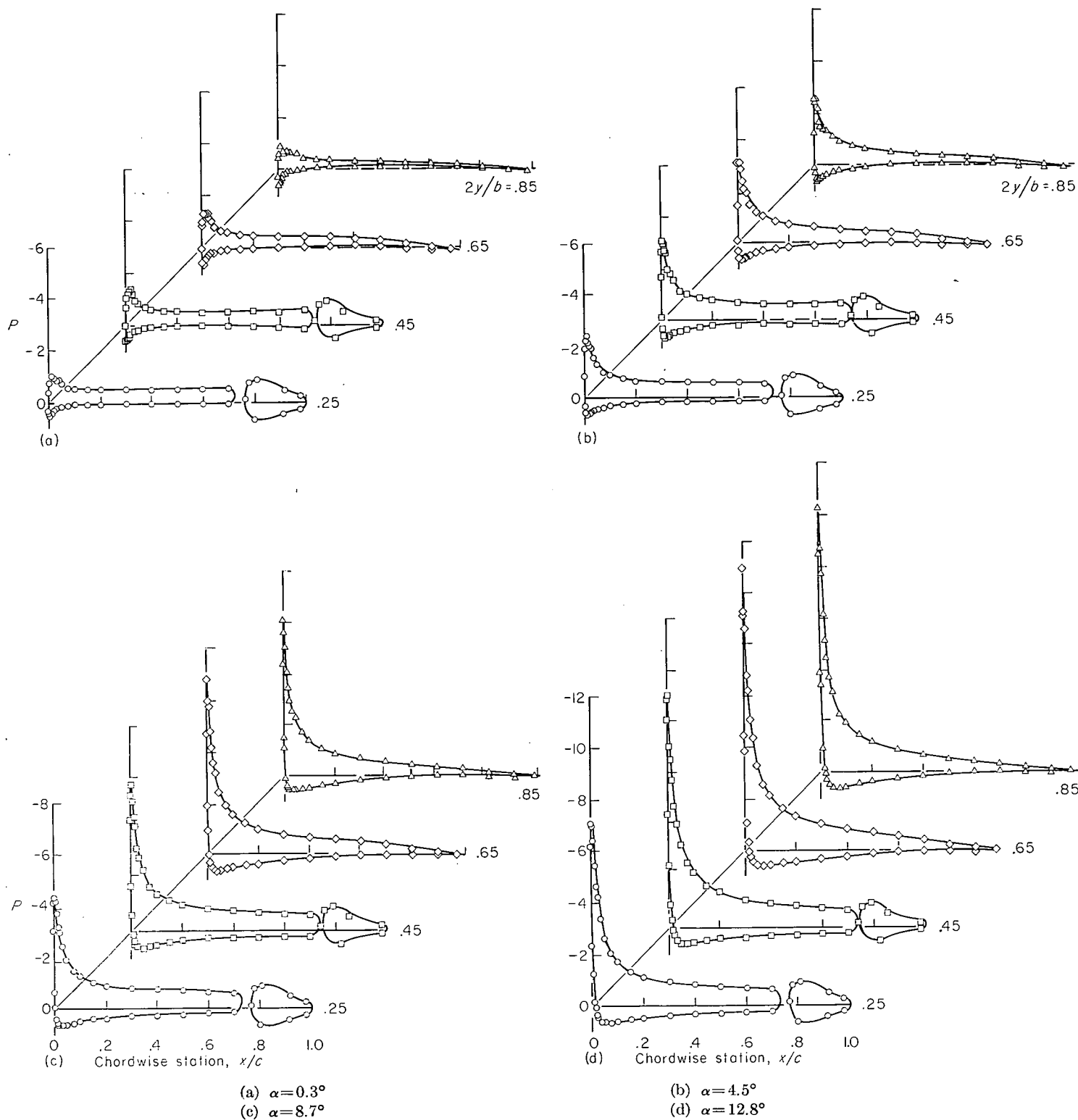


FIGURE 24.—Chordwise pressure distributions of the 35° swept-wing model with porous leading edge sealed; $\delta_F = 38^\circ$, $U = 112$ feet per second.

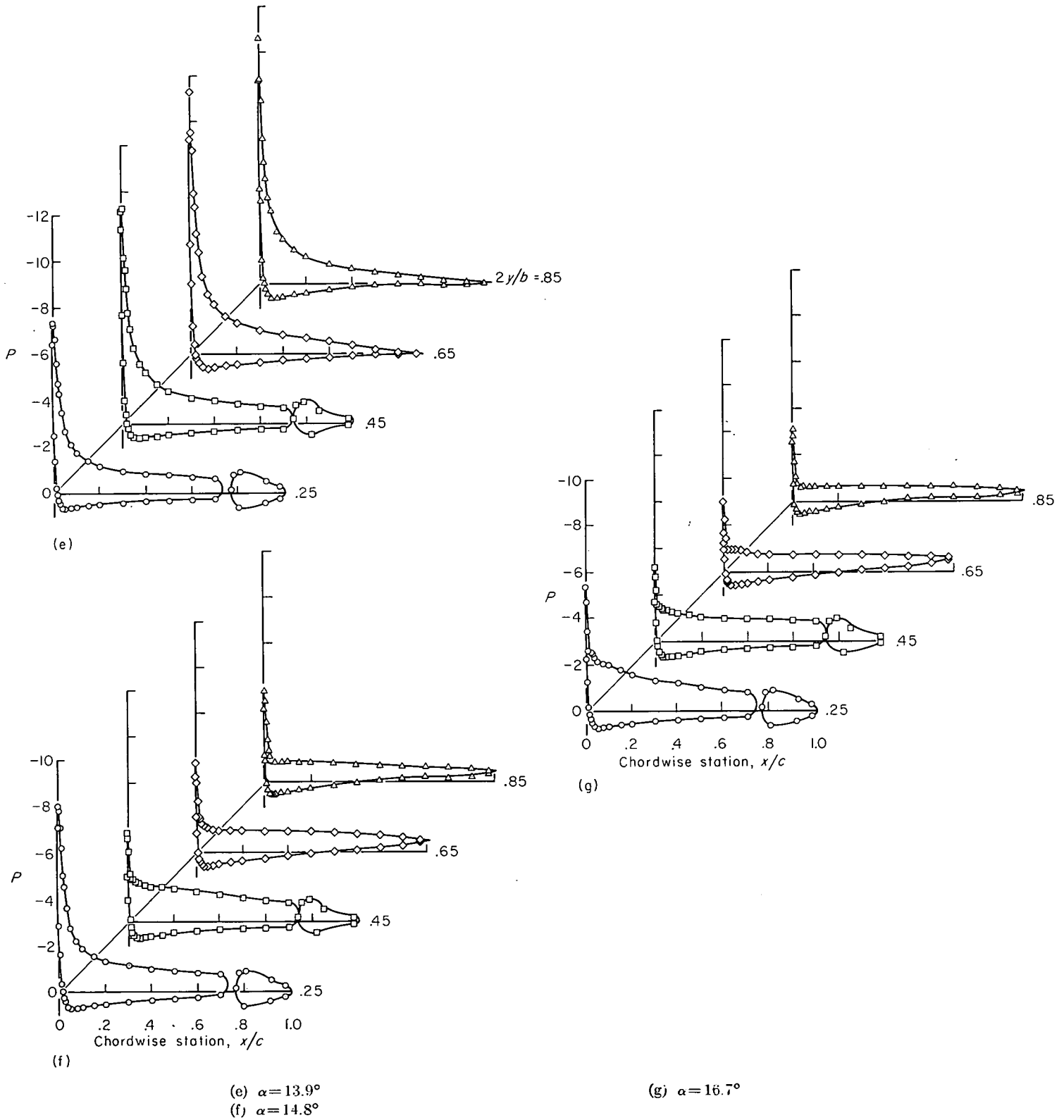


FIGURE 24.—Concluded.

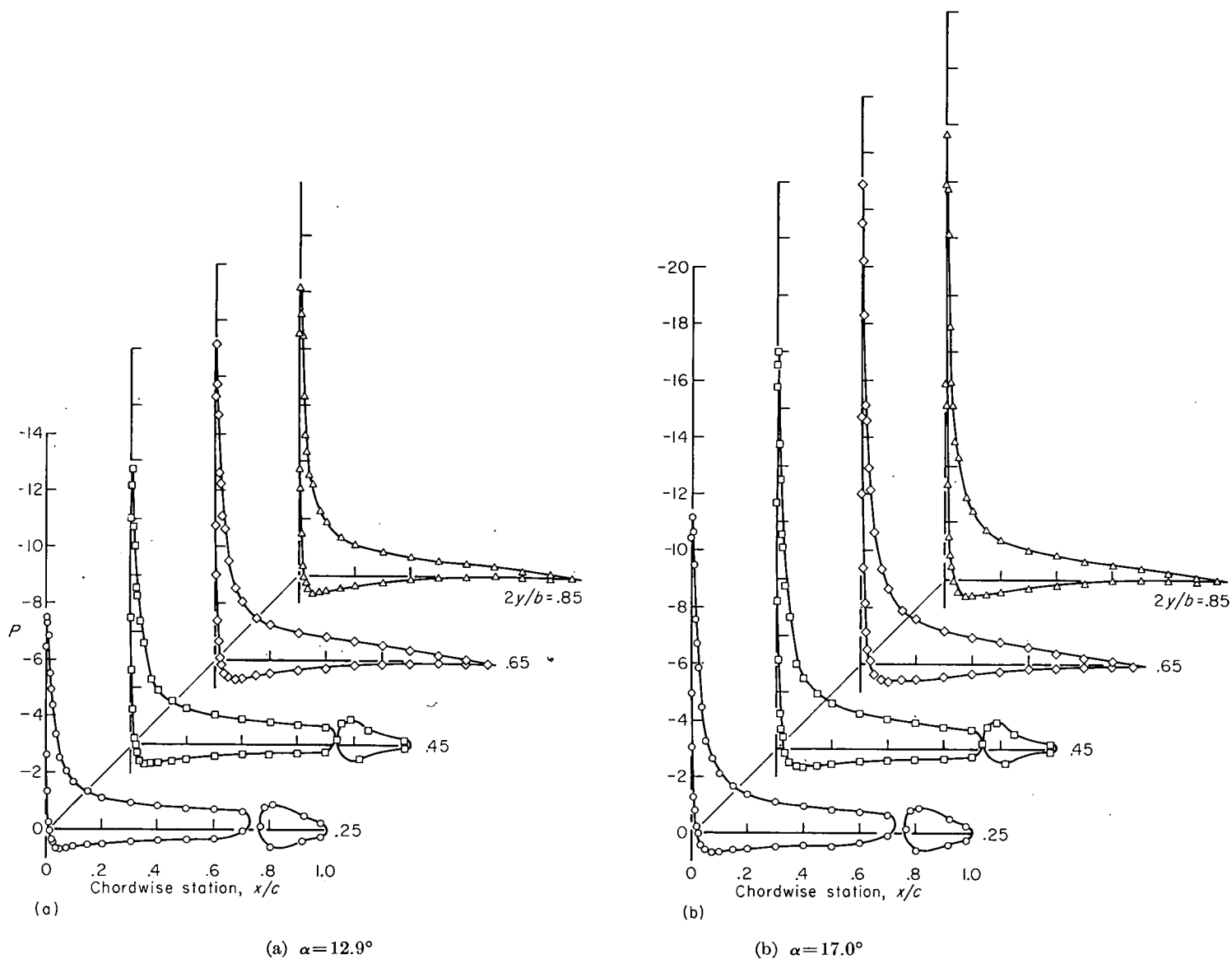


FIGURE 25.—Chordwise pressure distributions of the 35° swept-wing model with area suction applied and $\delta_F = 38^\circ$; porous area configuration B. $U = 112$ feet per second.

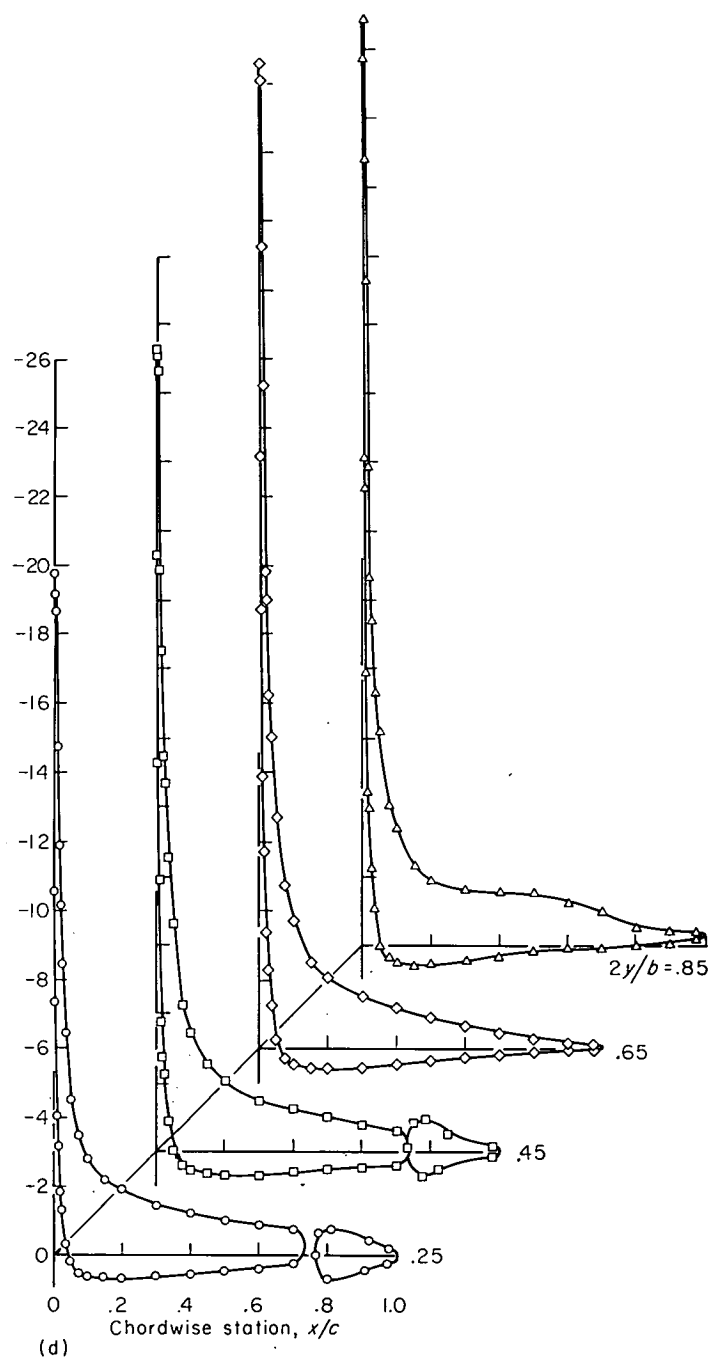
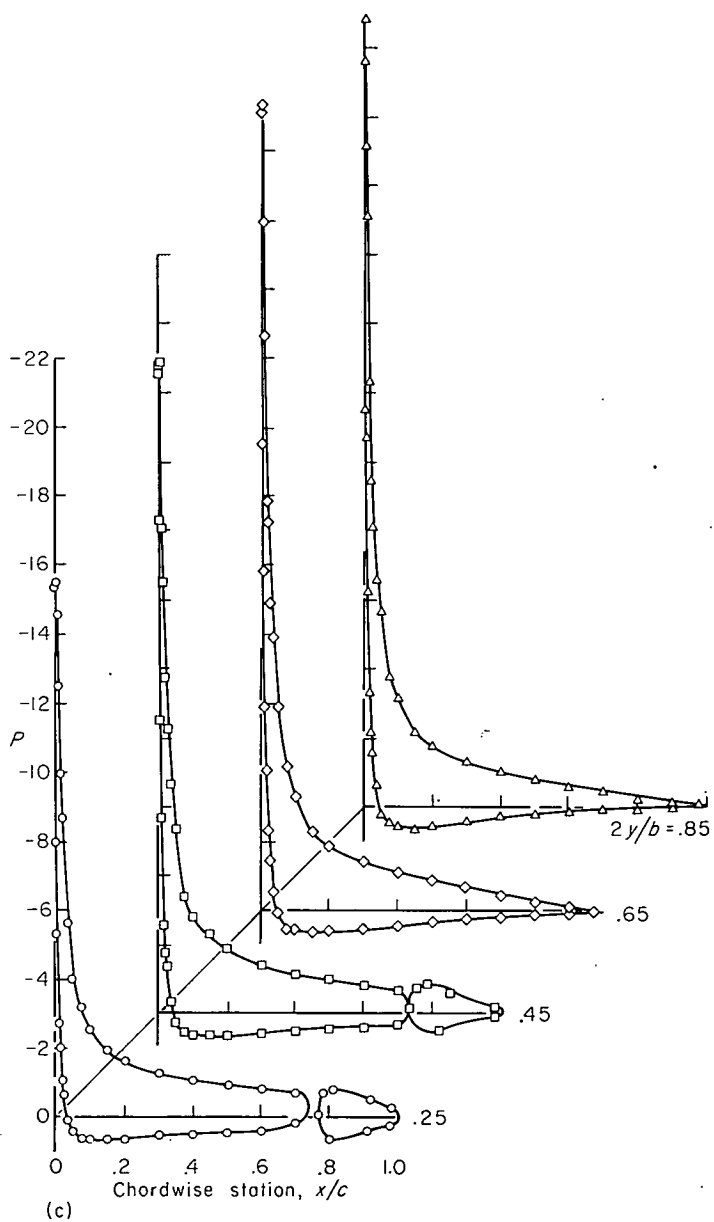


FIGURE 25.—Continued.

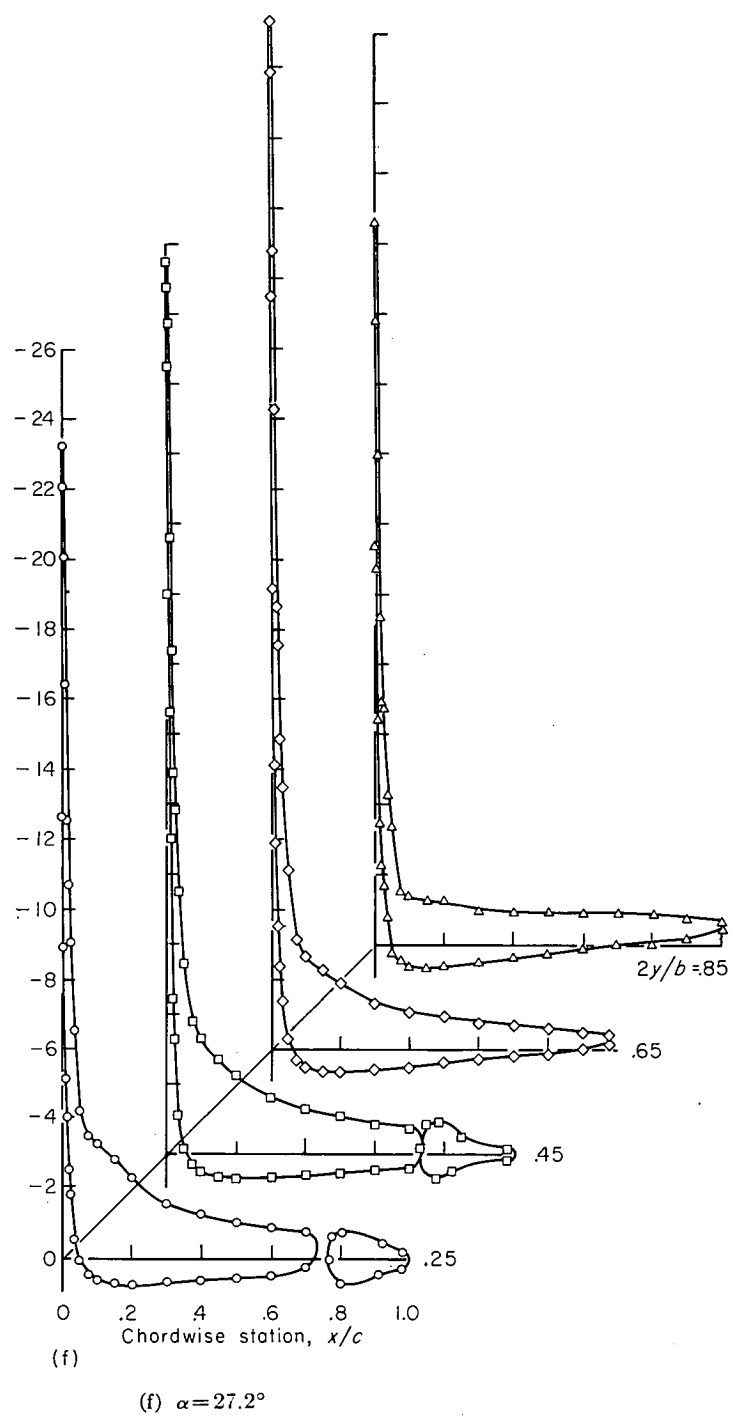
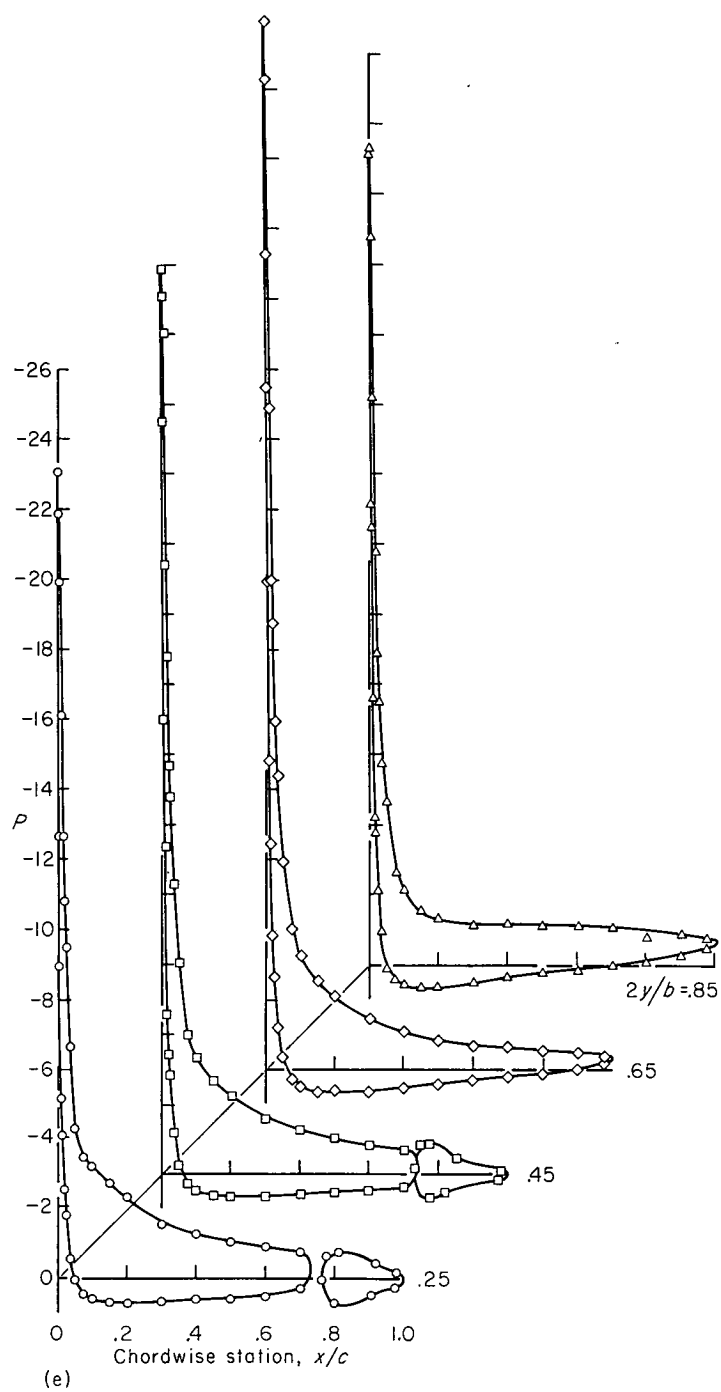


FIGURE 25.—Concluded.

REPORT 1277

INTERACTION OF A FREE FLAME FRONT WITH A TURBULENCE FIELD¹

By MAURICE TUCKER

SUMMARY

Small-perturbation spectral-analysis techniques are used to obtain the root-mean-square flame-generated turbulence velocities and the attenuating pressure fluctuations stemming from interaction of a constant-pressure flame front with a field of isotropic turbulence in the absence of turbulence decay processes.

The anisotropic flame-generated turbulence velocities are found to be of about the same intensity as those of the incident isotropic turbulence, the lateral turbulence velocities being always lower, but the longitudinal velocity is somewhat increased for flame-temperature ratios over 7. The small-perturbation analysis indicates that the incremental turbulent flame speed is a second-order quantity composed of two parts. One part represents the root-mean-square area of the turbulent flame front; the other represents the contribution of the transverse velocity fluctuations resulting from the flame-front distortion. Directly at the flame front, the noise-pressure levels of the pressure fluctuations are fairly intense (59 to 81 db referred to 0.0002 dyne/sq cm) even at moderate approach-flow turbulence intensities.

INTRODUCTION

Development of high-output jet engines has stimulated interest in the role played by turbulence in combustion phenomena. In the earliest studies of flame-turbulence interaction, Damkohler (ref. 1) and Shelkin (ref. 2) utilized mixing-length theories of turbulence to obtain semiquantitative relations for predicting flame speeds. Damkohler introduced the concept that turbulence of a scale large relative to the flame-front thickness increases the average flame speed by increasing the instantaneous flame surface area. The relations of references 1 and 2 were not confirmed by the experimental values of turbulent flame speed in Bunsen burners obtained in reference 3. Experiments on flames stabilized in channels (ref. 4) suggested that approach-flow turbulence had little effect on burning velocity and that the disturbances affecting turbulent flame speed were primarily flame-generated. A similar conclusion was drawn in reference 5.

In an attempt to obtain agreement between theory and experiment, Karlovitz, Denniston, and Wells (ref. 6) and Scurlock and Grover (ref. 7) have incorporated the concept of flame-generated disturbances in their recent theories of

turbulent flame speed which utilize G. I. Taylor's one-dimensional theory of diffusion by continuous movements. The somewhat arbitrary assumption is made in the analyses of both references 6 and 7 that these flame-generated disturbances constitute additional turbulence only. In reference 6 the energy of the flame-generated turbulence is taken as the difference between the kinetic energy of the burned gas in the absence of turbulence and the kinetic energy obtained by using the average velocity of the burned gas normal to the turbulent flame front. In reference 7 the flame-generated turbulence energy is obtained from a momentum balance of unburned and burned gases before and after an assumed mixing of the burned gas.

The data obtained in reference 8 on pentane-air flames baffle-stabilized in a rectangular duct suggest that the methods of references 6 and 7 considerably overestimate the turbulence generated by flame-turbulence interaction. Apart from the question of validity of such methods of calculating flame-generated turbulence, objections have been raised (ref. 9) to calculations of flame speed made on the basis of a hypothetical upstream turbulence compounded from approach-stream turbulence and turbulence generated downstream of the flame as was done in reference 7 and implied in reference 6.

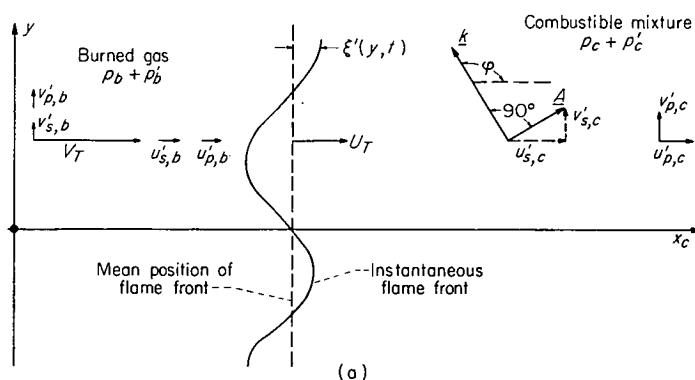
The present analysis is primarily concerned with the turbulence velocities and other fluctuation quantities associated with the linearized interaction of a free flame (not influenced by bounding walls) with turbulence present in the combustible mixture. Such turbulence will be referred to as approach-flow turbulence. The flame is treated as a discontinuity specified by the appropriate fundamental (laminar) flame speed and flame temperature. The interaction of such a flame front with a transverse plane wave, that is, a vorticity wave or shear wave, of arbitrary inclination relative to the front is first analyzed. The effects of an entire spectrum of transverse plane waves constituting a weak field of turbulence are then developed from the single-wave results. The statistical or root-mean-square fluctuation quantities describing the pressure fields and the anisotropic flame-generated turbulence resulting from interaction of the flame front with isotropic approach-flow turbulence are obtained for the limiting case of constant-pressure combustion. Some discussions of turbulent flame speed and of combustion noise are also presented.

¹ Supersedes NACA TN 3407, "Interaction of a Free Flame Front with a Turbulence Field," by Maurice Tucker, 1955.

FLAME—TURBULENCE INTERACTION PROCESS

Turbulent motion may be regarded as a Fourier superposition of a very large number of different-sized and randomly oriented component plane-wave motions. The customary assumptions concerning the turbulence (see ref. 10) are also made in the present analysis, namely, that turbulent decay effects are negligible and that the density fluctuations associated with the turbulence are also small enough to be neglected. The first assumption, which implies inviscid flow and very small turbulent velocity fluctuations, permits linear superposition of the component waves. With the second assumption, the continuity equation requires that these Fourier waves be transverse plane waves, that is, vorticity or shear waves. For each of these waves the local velocity vector \underline{A} is perpendicular to the vector \underline{k} , normal to the wave front. The vector \underline{k} is termed the wave-number vector; its magnitude k is termed the wave number, which is defined as 2π divided by the wavelength. All symbols are defined in appendix A. Any one of the parallel planes containing both the local velocity vector \underline{A} and the wave-number vector \underline{k} is called the "polarization plane."

Because of the assumed linear superposition of the component waves, the complete interaction results can be obtained from the study of the interaction of a plane flame front with a single-component transverse wave of the turbulence field. For simplicity, this typical vorticity wave will first be taken as a two-dimensional wave. Generalization to the three-dimensional case will be made later. The configuration considered is shown in sketch (a):



A flame front moves with mean velocity U_T into an inviscid combustible mixture. This mixture is at rest, but contains a vorticity wave with velocity vector \underline{A} (components $u_{s,c}$ and $v_{s,c}$) and with wave-number vector \underline{k} inclined at an angle ϕ to the positive direction of the x_c -axis. In the absence of any perturbation interaction, the plane front propagates into the combustible mixture with velocity U (the laminar flame speed). As indicated in appendix B, the motion of the burned gas, whose velocity V is constant, is away from the

flame front. The flame front is assumed to be of infinite extent in directions transverse to the direction of the x_c -axis.

A weak inviscid disturbance field may be resolved into a stationary component and a moving component, both relative to the mean local flow (refs. 11 and 12). The moving component is an irrotational isentropic pressure-velocity disturbance. The stationary component, which is convected by the mean local flow, is a constant-pressure disturbance containing any vorticity fluctuations and entropy fluctuations present in the disturbance field. Thus, the interaction of the flame front with the vorticity wave would be expected to generate both an irrotational disturbance with velocity components $u'_{p,b}$, $v'_{p,b}$ and a rotational disturbance with velocity components $u'_{s,b}$, $v'_{s,b}$ in the burned gas, and an irrotational disturbance with velocity components $u'_{p,c}$, $v'_{p,c}$ in the combustible mixture. The resulting velocity fluctuations, which include both the irrotational and rotational disturbances, are designated as u'_c , v'_c and u'_b , v'_b for the combustible mixture and the burned gas, respectively. The flame front is displaced by an amount $\xi'(y, t)$ from its mean or unperturbed position as a result of the interaction.

The diagrams of figure 1, which are similar to those used in reference 12, may prove helpful in visualizing the interaction process. Suppose that at some instant t_1 the flame intersects a front of the vorticity wave at point P_1 of figure 1(a). At a later time $t_1 + \delta t$, the flame has moved a distance $U\delta t$ and now intersects the stationary vorticity wave front at point P_2 . A vorticity wave with front parallel to line QP_2 is then produced in the burned gas. A cylindrical sound wave is generated at point P_1 at time t_1 and propagates at speed a_b into the burned gas while being convected with velocity $-V$. Another cylindrical wave is generated at point P_1 at time t_1 and propagates into the combustible mixture with speed a_c . The cylindrical wave fronts thus generated form envelopes (Mach lines) in both the combustible mixture and the burned gas, which constitute plane sound waves.

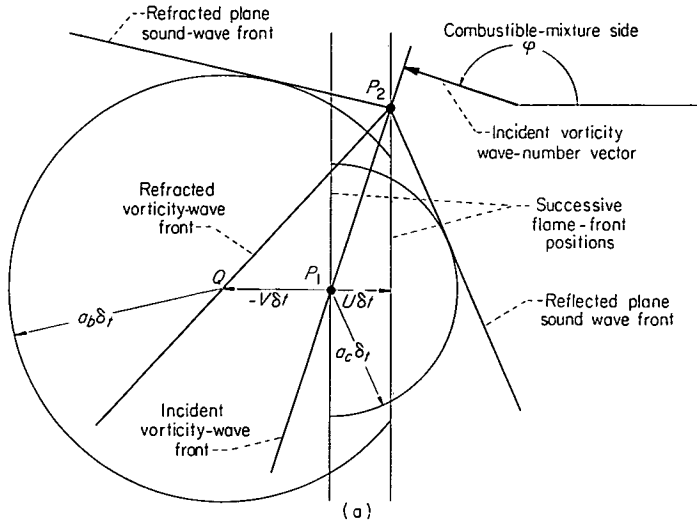
For the wave-inclination angle ϕ shown in figure 1(b), an envelope cannot be formed on the burned-gas side of the flame front. The cylindrical sound waves thus expand independently and are thereby attenuated. On the combustible-mixture side of the front, the cylindrical sound waves meet at the common tangent point P_2 . For inclination angles less than the critical angle shown, attenuating pressure waves are also produced in the combustible mixture until another critical angle $180^\circ - \phi$ is reached. Below this second critical angle, plane sound waves are again obtained. These critical angles may be obtained from the geometry of

figure 1(b). For small flame Mach numbers where $M \equiv \frac{U}{a_c}$,

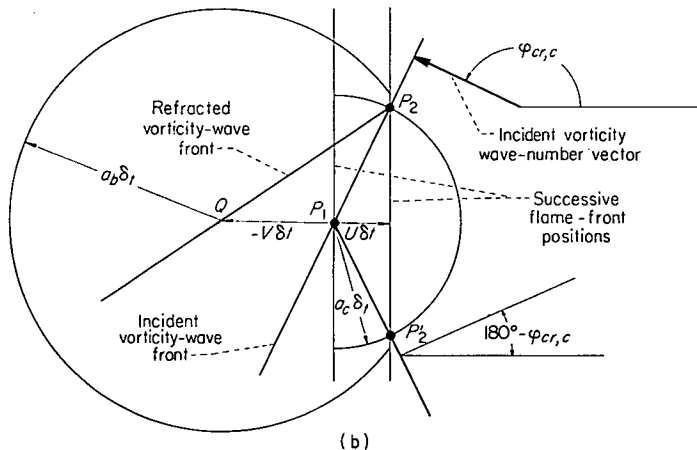
$$\phi_{cr,c} = \sin^{-1} M$$

$$\phi_{cr,b} = \sin^{-1} \frac{M}{\sqrt{\tau}}$$

As the flame Mach number M decreases, attenuating waves are produced for a wider range of inclination angle. In the limiting case of very slow flow (constant-pressure combustion),² only attenuating pressure waves appear in combination with the vorticity waves if $0^\circ < \varphi < 180^\circ$. Quantities associated with the pressure wave vanish when $\varphi = 0^\circ$ or 180° because the incident vorticity wave then passes through the combustion front without distorting the front.



(a)



(b)

- (a) Interaction for wave-number vector inclinations generating plane sound waves.
 (b) Interaction for wave-number vector inclinations generating non-coalescing cylindrical sound waves.

FIGURE 1.—Wave formation arising from interaction of flame front with vorticity wave.

SINGLE-WAVE ANALYSIS

TWO-DIMENSIONAL FORMULATION

The interaction process described in the preceding section is now formulated analytically for the passage of a combustion front through a single weak two-dimensional vorticity

² It can be shown that the static-pressure ratio across a flame front is given by $p_u/p_c = 1 - \gamma(\tau - 1)M^2 + \dots$

wave of constant density inclined to the flame front. The case of a vorticity wave in three dimensions is considered later.

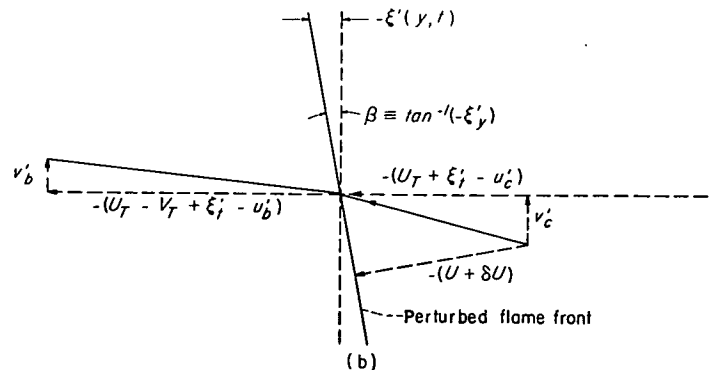
The combustion front is assumed to be completely specified by its laminar flame velocity U and the ratio of stagnation temperatures τ in the burned gas and in the combustible mixture, respectively. In the absence of any perturbations, the equations for conservation of momentum, energy, and mass-flow rate, respectively, as written for a reference frame moving with the flame front, are

$$\left. \begin{aligned} p_c + \rho_c U^2 &= p_b + \rho_b (U - V)^2 \\ \tau \left(\frac{\gamma R_g}{\gamma - 1} T_c + \frac{1}{2} U^2 \right) &= \frac{\gamma R_g}{\gamma - 1} T_b + \frac{1}{2} (U - V)^2 \\ \rho_c U &= \rho_b (U - V) \end{aligned} \right\} \quad (1)$$

where subscripts c and b designate stations in the combustible mixture and in the burned gas, respectively. For simplicity it has been assumed that the combustion process does not entail a change in the number of moles per unit mass of gas; also, differences in the ratio of specific heats for the burned and unburned gas are ignored. The quantity $(\tau - 1)$ is then indicative of the increase in stagnation enthalpy or heat release.

For the interaction problem the resulting flame-front distortion $\xi'(y, t)$ must be considered in addition to the generated disturbances previously mentioned. Thus, both the flame-front perturbation velocity $\frac{\partial \xi'}{\partial t} \equiv \xi'_v$ and the instan-

taneous flame-front slope $\frac{\partial \xi'}{\partial y} \equiv \xi'_y$ will appear in the equations of motion. The conservation equations may still be applied in a coordinate system moving instantaneously with the distorted flame front since extreme gradients occur across the front and small disturbances are postulated. The various perturbation quantities (designated by primes) are assumed to have zero space or time averages. The flame speed U_T (see sketch (b)) will thus include any time-



(b)

independent contributions arising from the perturbations. Conservation of normal and tangential momentum, energy, and mass-flow rate provides the following relations:

$$(p_c + p'_c)[1 + (\xi'_y)^2] + (\rho_c + \rho'_c)[(U_T + \xi'_i - u'_c)^2 + (v'_c)^2(\xi'_y)^2 + 2(U_T + \xi'_i - u'_c)v'_c\xi'_y]$$

$$= (p_b + p'_b)[1 + (\xi'_y)^2] + (\rho_b + \rho'_b)[(U_T - V_T + \xi'_i - u'_b)^2 + (v'_b)^2(\xi'_y)^2 + 2(U_T - V_T + \xi'_i - u'_b)v'_b\xi'_y] \quad (2a)$$

$$(U_T + \xi'_i - u'_c)\xi'_y - v'_c = (U_T - V_T + \xi'_i - u'_b)\xi'_y - v'_b \quad (2b)$$

$$(\tau + \tau') \left[\frac{\gamma R_g}{\gamma - 1} (T_c + T'_c) + \frac{1}{2} (U_T + \xi'_i - u'_c)^2 + \frac{1}{2} (v'_c)^2 \right] = \frac{\gamma R_g}{\gamma - 1} (T_b + T'_b) + \frac{1}{2} (U_T - V_T + \xi'_i - u'_b)^2 + \frac{1}{2} (v'_b)^2 \quad (2c)$$

$$(\rho_c + \rho'_c)(U_T + \xi'_i - u'_c + v'_c\xi'_y) = (\rho_b + \rho'_b)(U_T - V_T + \xi'_i - u'_b + v'_b\xi'_y) \quad (2d)$$

Small-perturbation techniques are used to make the interaction problem amenable to analysis. Then, if the velocity perturbations are assumed to be small relative to the flame speed U_T and the flame-front slope ξ'_y is also assumed to be very small so that terms of the second order in the fluctuation quantities may be neglected, application of the linearized state equation $\frac{p'}{p} = \frac{\rho'}{\rho} + \frac{T'}{T}$ and utilization of equations (1) permit the following boundary conditions at the flame front to be obtained from equations (2):

$$\frac{p'_b}{p_b} + B_1 \frac{\rho'_b}{\rho_b} + B_2 \frac{\xi'_i - u'_b}{U} = B_3 \frac{p'_c}{p_c} + B_2 \frac{\xi'_i - u'_c}{U} \quad (3a)$$

$$\frac{v'_b}{U} = \frac{v'_c}{U} + E_1 \xi'_y \quad (3b)$$

$$\frac{p'_b}{p_b} - \frac{\rho'_b}{\rho_b} + K_1 \frac{\xi'_i - u'_b}{U} = K_2 \frac{p'_c}{p_c} + K_3 \tau' + K_4 \frac{\xi'_i - u'_c}{U} \quad (3c)$$

$$\frac{\rho'_b}{\rho_b} + D_1 \frac{\xi'_i - u'_b}{U} = \frac{\xi'_i - u'_c}{U} + \frac{1}{\gamma} \frac{p'_c}{p_c} \quad (3d)$$

where

$$\left. \begin{aligned} B_1 &\equiv \frac{\gamma U^2}{a_b^2} \left(\frac{U - V}{U} \right)^2, \quad B_2 \equiv \frac{2\gamma U^2}{a_b^2} \left(\frac{U - V}{U} \right), \quad B_3 \equiv \frac{U - V}{U} \left(\frac{U^2}{a_b^2} \right) \left(1 + \frac{a_c^2}{U^2} \right), \quad D_1 \equiv \frac{U}{U - V}, \quad E_1 \equiv \frac{-V}{U} \\ K_1 &\equiv (\gamma - 1) \frac{U^2}{a_b^2} \left(\frac{U - V}{U} \right), \quad K_2 \equiv \frac{\gamma - 1}{\gamma} \tau \frac{a_c^2}{a_b^2}, \quad K_3 \equiv \left(\frac{c_p T_{s,c}}{U^2} \right) (\gamma - 1) \frac{U^2}{a_b^2}, \quad K_4 \equiv (\gamma - 1) \tau \frac{U^2}{a_b^2} \\ a_c^2 &\equiv \gamma R_g T_c, \quad a_b^2 \equiv \gamma R_g T_b \end{aligned} \right\} \quad (4)$$

It has also been assumed that the flow upstream of the flame is isentropic. It will be shown in the section TURBULENT FLAME SPEED that $U_T = U$ is correct through first-order terms.

Another relation is required at the flame front. For the two-dimensional case under consideration, the local instantaneous normal propagation velocity $U + \delta U$ of the distorted flame front into the combustible mixture at rest (see sketch (b)) is

$$U + \delta U = \frac{U_T + \xi'_i - u'_c + v'_c\xi'_y}{\sqrt{1 + (\xi'_y)^2}}$$

The incremental propagation velocity δU will be determined from existing information on laminar flames. Some support for this procedure is given in reference 13. As reported therein, radiant flux-intensity measurements on laminar and turbulent propane-air flames suggest that a small surface element of a turbulent flame is chemically and physically the same as that of a corresponding laminar flame.

The propagation speed of a laminar flame is affected by both the ambient pressure and temperature. Although the functional relations have not been rigorously determined, preliminary indications are that the pressure effect is much smaller than the temperature effect. In the present analysis

the local flame-propagation speed is assumed to depend only upon the temperature of the combustible mixture, that is,

$$\delta U = \frac{dU}{dT_c} dT_c = \left(\frac{dU}{dT_c} \right) T'_c$$

With the empirical relation obtained in reference 14 as a guide, it is assumed that $U = r_1 + r_2 T_c^n$ where r_1 , r_2 , and n are constants which depend upon the fuel and oxidant under consideration. Thus,

$$\delta U = n r_2 T_c^n \left(\frac{T'_c}{T_c} \right) = n r_2 \left(\frac{\gamma - 1}{\gamma} \right) T_c^n \left(\frac{p'_c}{p_c} \right) = U \Lambda \frac{p'_c}{p_c}$$

and

$$U \left(1 + \Lambda \frac{p'_c}{p_c} \right) \sqrt{1 + (\xi'_y)^2} = U_T + \xi'_i - u'_c + v'_c\xi'_y$$

Correct through first-order terms wherein $U_T = U$, the following boundary condition is obtained at the flame front:

$$\frac{\xi'_i - u'_c}{U} = \Lambda \frac{p'_c}{p_c} \quad (3e)$$

In a coordinate system fixed in space, the equations of motion for the two-dimensional fluctuation quantities in

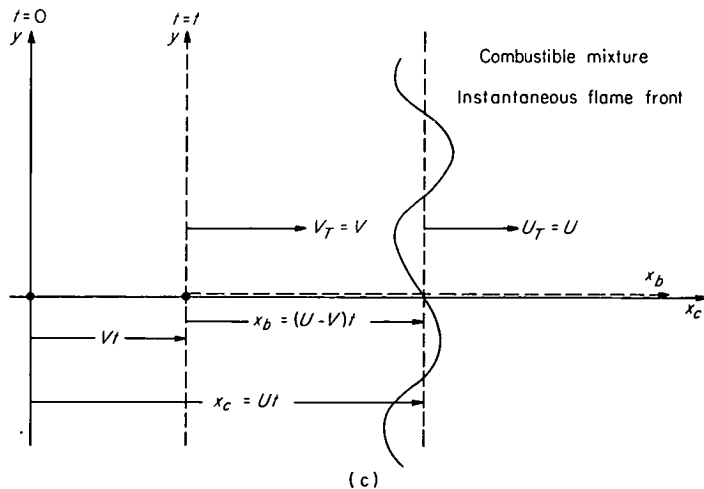
the burned gas with terms of the second order neglected are

$$\begin{aligned}\frac{\partial u'_b}{\partial t} + V \frac{\partial u'_b}{\partial x_c} &= -\frac{1}{\rho_b} \frac{\partial p'_b}{\partial x_c} \\ \frac{\partial v'_b}{\partial t} + V \frac{\partial v'_b}{\partial x_c} &= -\frac{1}{\rho_b} \frac{\partial p'_b}{\partial y} \\ \frac{\partial \rho'_b}{\partial t} + V \frac{\partial \rho'_b}{\partial x_c} + \rho_b \left(\frac{\partial u'_b}{\partial x_c} + \frac{\partial v'_b}{\partial y} \right) &= 0 \\ \rho_b c_v \frac{\partial T'_b}{\partial t} + \rho_b c_v V \frac{\partial T'_b}{\partial x_c} + p_b \left(\frac{\partial u'_b}{\partial x_c} + \frac{\partial v'_b}{\partial y} \right) &= 0\end{aligned}$$

For a coordinate system moving with constant velocity V , the preceding equations reduce to the same form as the corresponding equations for the fluctuation quantities in the combustible mixture relative to a coordinate system fixed in space. Thus, the flow equations for both the combustible-mixture fluctuations and the burned-gas fluctuations may be written, with appropriate subscripts c or b , as

$$\left. \begin{aligned}\frac{\partial u'}{\partial t} &= -\frac{1}{\rho} \frac{\partial p'}{\partial x} \\ \frac{\partial v'}{\partial t} &= -\frac{1}{\rho} \frac{\partial p'}{\partial y} \\ \frac{\partial \rho'}{\partial t} &= -\rho \left(\frac{\partial u'}{\partial x} + \frac{\partial v'}{\partial y} \right) \\ \rho c_v \frac{\partial T'}{\partial t} &= -\rho \left(\frac{\partial u'}{\partial x} + \frac{\partial v'}{\partial y} \right)\end{aligned}\right\} \quad (5)$$

The coordinate systems x_c, y and x_b, y for the first-order analysis are indicated in sketch (c).



A two-dimensional vorticity wave in the combustible mixture with velocity vector of magnitude A that has its wave-number vector \underline{k} inclined at an angle φ to the positive direction of the x_c -axis may be written in the form

$$\frac{u'_{s,c}}{U} = (A \sin \varphi) e^{i\nu}, \quad \frac{v'_{s,c}}{U} = (-A \cos \varphi) e^{i\nu}$$

where $\nu \equiv k'_1 x_c + k'_2 y$, and k'_1 and k'_2 are components of the wave-number vector \underline{k} in the x_c - and y -directions, respectively, with $k'_2/k'_1 = \tan \varphi$. As a result of the linear boundary conditions of equations (3), obtaining a unique solution of the interaction problem requires that the arguments of all disturbance waves match at the flame front. This matching requirement together with provision for differences in phase angle yields the following form for the vorticity wave present in the burned gas:

$$\frac{u'_{s,b}}{U} = (G_1 + iG_2) e^{i\psi}, \quad \frac{v'_{s,b}}{U} = (I_1 + iI_2) e^{i\psi}$$

where

$$\psi \equiv \left(\frac{U}{U-V} \right) k'_1 x_b + k'_2 y$$

Pressure fluctuations generated by the interaction must satisfy the following wave equation, with appropriate subscripts c or b , which is obtainable from equations (5):

$$\frac{\partial^2 p'}{\partial t^2} - a^2 \left(\frac{\partial^2 p'}{\partial x^2} + \frac{\partial^2 p'}{\partial y^2} \right) = 0 \quad (6)$$

The present analysis will be concerned with the limiting case of very slow flow (constant-pressure combustion). It is clear from the relations given for the critical wave-inclination angles $\varphi_{cr,c}$ and $\varphi_{cr,b}$ that, for very slow flows, only the irrotational isentropic pressure waves described in the section FLAME-TURBULENCE INTERACTION PROCESS will be generated by the interaction. The form of these pressure waves that satisfies equation (6) has already been established in reference 12 in terms of the variables η and ζ , where

$$\left. \begin{aligned}\eta_c &\equiv (f_c)(x_c - Ut) \\ \zeta_c &\equiv b_c x_c + c_c y + U d_c t \\ \eta_b &\equiv (f_b)[-x_b + (U - V)t] \\ \zeta_b &\equiv b_b x_b + c_b y + U d_b t\end{aligned}\right\} \quad (7)$$

The variable η is proportional to the distance from the flame front. At the front, $\eta_c = \eta_b = 0$; upstream of the flame, η_c is positive; and downstream of the flame, η_b is positive. The equation $\zeta = \text{constant}$ defines planes moving with constant velocity $(Ud)_{c,b}$ at an angle $\tan^{-1}(c/b)_{c,b}$ to the flame velocity U . Equation (6) takes the form of the Laplace equation

$$\left(\frac{\partial^2}{\partial \eta^2} + \frac{\partial^2}{\partial \zeta^2} \right) \frac{p'}{p} = 0$$

when

$$\left. \begin{aligned}\left(\frac{\partial \eta}{\partial t} \right)^2 - \left(\frac{\partial \zeta}{\partial t} \right)^2 &= a^2 \left[\left(\frac{\partial \eta}{\partial x} \right)^2 - \left(\frac{\partial \zeta}{\partial x} \right)^2 - \left(\frac{\partial \zeta}{\partial y} \right)^2 \right] \\ \frac{\partial \eta}{\partial t} \frac{\partial \zeta}{\partial t} &= a^2 \frac{\partial \eta}{\partial x} \frac{\partial \zeta}{\partial x}\end{aligned}\right\} \quad (8)$$

Matching arguments of the pressure and vorticity waves at the combustion front where $\eta = 0$ and satisfying the require-

ments of equations (8) provide the following values for the constants of equations (7):

$$\left. \begin{aligned} c_c = c_b = k'_2, b_c = -\frac{k'_1 M^2}{1-M^2}, b_b = \frac{-k'_1 \left(\frac{U-V}{U}\right) \frac{U^2}{a_b^2}}{1-\left(\frac{U-V}{U}\right)^2 \frac{U^2}{a_b^2}}, d_c = \frac{k'_1}{1-M^2} \\ d_b = -\frac{k'_1}{1-\left(\frac{U-V}{U}\right)^2 \frac{U^2}{a_b^2}}, f_c^2 = \frac{b_c^2 + c_c^2 - d_c^2 M^2}{1-M^2}, f_b^2 = \frac{b_b^2 + c_b^2 - d_b^2 \frac{U^2}{a_b^2}}{1-\left(\frac{U-V}{U}\right)^2 \frac{U^2}{a_b^2}} \end{aligned} \right\} \quad (9)$$

In addition to the boundary condition from equations (3), the pressure fluctuations will be required to satisfy the boundary condition $\frac{p'}{p} = 0$ at $\eta = \infty$. Utilizing equations (36) and (37) of reference 12 yields

$$\frac{p'_c}{p_c} = (R_1 + iR_2)e^{i\zeta_c - \eta_c} \quad (10a)$$

$$\frac{p'_b}{p_b} = (J_1 + iJ_2)e^{i\zeta_b - \eta_b} \quad (10b)$$

In the combustible mixture, density fluctuations are associated only with the pressure fluctuations according to the isentropic relation $\frac{\rho'_c}{\rho_c} = \frac{1}{\gamma} \frac{p'_c}{p_c}$. In the burned gas, density fluctuations may also be caused by entropy fluctuations generated by flame distortion and heat-release fluctuations, if present, as well as by pressure fluctuations. Velocity fluctuations are associated with both pressure fluctuations and vorticity fluctuations. It is convenient to deal with the pressure coefficient $p'/\rho_c U^2$. Thus, the disturbances arising from the interaction of the flame front and incident vorticity wave take the following forms:

$$\frac{p'_c}{\rho_c U^2} = \frac{1}{\gamma M^2} (R_1 + iR_2)e^{i\zeta_c - \eta_c} \equiv (R^{(1)} + iR^{(2)})e^{i\zeta_c - \eta_c} \quad (10c)$$

$$\frac{p'_b}{\rho_c U^2} = \frac{p_b}{\rho_c U^2} (J_1 + iJ_2)e^{i\zeta_b - \eta_b} \equiv (J^{(1)} + iJ^{(2)})e^{i\zeta_b - \eta_b} \quad (10d)$$

$$\frac{\rho'_b}{\rho_b} = \frac{1}{\gamma} (J_1 + iJ_2)e^{i\zeta_b - \eta_b} + (L_1 + iL_2)e^{i\psi} \quad (10e)$$

$$\frac{u'_b}{U} = (N_1 + iN_2)e^{i\zeta_b - \eta_b} + (G_1 + iG_2)e^{i\psi} \quad (10f)$$

$$\frac{v'_b}{U} = (P_1 + iP_2)e^{i\zeta_b - \eta_b} + (I_1 + iI_2)e^{i\psi} \quad (10g)$$

$$\frac{u'_c}{U} = (W_1 + iW_2)e^{i\zeta_c - \eta_c} + (A \sin \varphi)e^{i\psi} \quad (10h)$$

$$\frac{v'_c}{U} = (X_1 + iX_2)e^{i\zeta_c - \eta_c} - (A \cos \varphi)e^{i\psi} \quad (10i)$$

The flame displacement velocity may be written

$$\frac{\xi'_t}{U} = (H_1 + iH_2)e^{i(k'_1 U t + k'_2 y)} \equiv (H_1 + iH_2)e^{i\sigma} \quad (10j)$$

To satisfy the requirements that the arguments of all disturbance quantities match at the flame front and that $\frac{\partial^2 \xi}{\partial t \partial y} = \frac{\partial^2 \xi}{\partial y \partial t}$, the flame-front slope must take the form

$$\xi'_y = (H_1 + iH_2)(\tan \varphi)e^{i\sigma} \quad (10k)$$

Integration of equation (10j) with respect to time t gives the flame displacement as

$$\xi' = \frac{1}{k'_1} (H_2 - iH_1)e^{i\sigma} = \frac{\tan \varphi}{k'_2} (H_2 - iH_1)e^{i\sigma} \quad (10l)$$

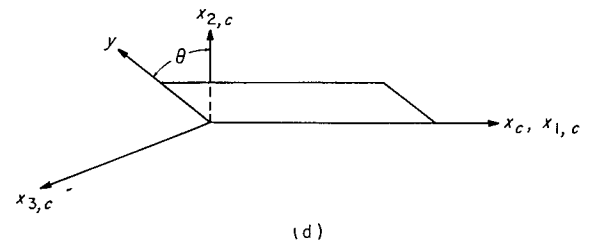
EXTENSION TO THREE-DIMENSIONAL DISTURBANCES

Equations (10) describe the interaction of a flame front with a constant-density vorticity wave having velocity components

$$\frac{u'_{s,c}}{U} = (A \sin \varphi)e^{i\psi} \text{ and } \frac{v'_{s,c}}{U} = (-A \cos \varphi)e^{i\psi}$$

in the x_c - and y -directions, respectively. The vorticity wave may be considered to have a third velocity component $\frac{w'_{s,c}}{U} = Ce^{i\psi}$ in the z -direction. In the preceding linearized analysis, the amplitude C was not prescribed. This component, which is normal to both the u' and v' components and parallel to the plane of the flame front, then is associated with a corresponding component of the vorticity wave in the burned gas $\frac{w'_{s,b}}{U} = Ce^{i\psi}$.

Inasmuch as turbulence fields are three-dimensional, the interaction equations must be revised accordingly for application to the spectral analysis which follows. Assume, as shown in sketch (d), that the polarization plane which will contain the wave-number vector \underline{k} is inclined at some angle θ to the $x_{1,c}, x_{2,c}$ -plane of a new coordinate system $x_{1,c}, x_{2,c}, x_{3,c}$ fixed in space for the combustible mixture.



The corresponding coordinate system $x_{1,b}, x_{2,b}, x_{3,b}$ for the burned gas is assumed to be moving with mean flow velocity V . Components k_1, k_2 , and k_3 of the wave-number vector \underline{k} in the directions of $x_{1,c}, x_{2,c}$, and $x_{3,c}$, respectively, are

$$\left. \begin{aligned} k_1 &= k \cos \varphi \\ k_2 &= k \sin \varphi \cos \theta \\ k_3 &= k \sin \varphi \sin \theta \end{aligned} \right\} \quad (11)$$

With primed perturbation vector quantities referring to the original coordinates x_c, x_b, y, z and unprimed perturbation vector quantities referring to the $x_{1,c}, x_{2,c}, x_{3,c}$ and $x_{1,b}, x_{2,b},$

$x_{3,b}$ -coordinate systems, the following transformation relations apply:

$$\left. \begin{aligned} u_{1,c} &= u'_c & u_{1,b} &= u'_b \\ u_{2,c} &= v'_c \cos \theta - w'_c \sin \theta & u_{2,b} &= v'_b \cos \theta - w'_b \sin \theta \\ u_{3,c} &= v'_c \sin \theta + w'_c \cos \theta & u_{3,b} &= v'_b \sin \theta + w'_b \cos \theta \\ \xi &= \xi' \\ \xi_i &= \xi'_i \\ \xi_{x_{2,c}} &= \xi'_v \cos \theta \\ \xi_{x_{3,c}} &= \xi'_v \sin \theta \end{aligned} \right\} \quad (12)$$

This notation refers only to equations (12).

With the use of equations (10) and (12), the interaction fluctuation quantities (again designated by primes) referred to the coordinate axes $x_{1,c}$, $x_{2,c}$, $x_{3,c}$ and $x_{1,b}$, $x_{2,b}$, $x_{3,b}$ may be written as

$$\left. \begin{aligned} \frac{p'_c}{\rho_c U^2} &= (R^{(1)} + iR^{(2)})e^{i\xi_c - \eta_c} \\ \frac{p'_b}{\rho_b U^2} &= (J^{(1)} + iJ^{(2)})e^{i\xi_b - \eta_b} \\ \frac{\rho'_c}{\rho_c} &= \frac{1}{\gamma} (R_1 + iR_2)e^{i\xi_c - \eta_c} \\ \frac{\rho_b}{\rho_b} &= \frac{1}{\gamma} (J_1 + iJ_2)e^{i\xi_b - \eta_b} + (L_1 + iL_2)e^{i\psi} \\ \frac{u'_{1,c}}{U} &= (W_1 + iW_2)e^{i\xi_c - \eta_c} + (A \sin \varphi)e^{i\psi} \\ \frac{u'_{2,c}}{U} &= (X_1 + iX_2)(\cos \theta)e^{i\xi_c - \eta_c} - (A \cos \varphi \cos \theta + C \sin \theta)e^{i\psi} \\ \frac{u'_{3,c}}{U} &= (X_1 + iX_2)(\sin \theta)e^{i\xi_c - \eta_c} - (A \cos \varphi \sin \theta - C \cos \theta)e^{i\psi} \\ \frac{u'_{1,b}}{U} &= (N_1 + iN_2)e^{i\xi_b - \eta_b} + (G_1 + iG_2)e^{i\psi} \\ \frac{u'_{2,b}}{U} &= (P_1 + iP_2)(\cos \theta)e^{i\xi_b - \eta_b} + [(I_1 + iI_2)\cos \theta - C \sin \theta]e^{i\psi} \\ \frac{u'_{3,b}}{U} &= (P_1 + iP_2)(\sin \theta)e^{i\xi_b - \eta_b} + [(I_1 + iI_2)\sin \theta + C \cos \theta]e^{i\psi} \\ \frac{\xi'_i}{U} &= (H_1 + iH_2)e^{i\sigma} \\ \xi'_{x_{2,c}} &= (H_1 + iH_2)(\tan \varphi \cos \theta)e^{i\sigma} \\ \xi'_{x_{3,c}} &= (H_1 + iH_2)(\tan \varphi \sin \theta)e^{i\sigma} \\ \xi' &= \frac{(H_2 - iH_1)e^{i\sigma}}{k'_1} \end{aligned} \right\} \quad (13)$$

The fluctuation amplitude coefficients of equation (10) or (13) may be determined from equations (3) and (5). Details of the solution are given in appendixes B and C. The general

solution for the attenuating pressure-wave regime is indicated in appendix B. Inasmuch as the flame Mach number $M \equiv \frac{U}{a_c}$ is generally much less than 0.01, the limiting case of very slow flow (constant-pressure combustion) provides a reasonable simplification of the problem and only the attenuating-wave solution need be considered. The amplitude coefficients for this limiting case are given in appendix C (eqs. (C8)).

Equations (13) and (C8) describe the linearized interaction of a constant-pressure flame front with a single vorticity wave or shear wave having its wave-number vector \underline{k} inclined at an angle φ to the direction of travel of the undisturbed flame front and having its plane of polarization inclined at an angle θ to the $x_{1,c}$, $x_{2,c}$ -plane of the coordinate axes $x_{1,c}$, $x_{2,c}$, $x_{3,c}$. The wave-number vector of the shear wave generated in the burned gas makes an angle $\varphi_b = \tan^{-1}(\tau \tan \varphi)$ with the direction of propagation of the undisturbed flame front. Attenuating potential fields are generated in both the combustible mixture and the burned gas. Physical quantities associated with these fields attenuate exponentially with increasing distance from the flame front. The amplitude coefficients for a given heat release (a prescribed τ) and a given inclination angle φ and a polarization angle θ depend upon both the intensity of the incident vorticity wave and the heat-release perturbation parameter τ'/τ . In the absence of such heat-release perturbations, there are no density fluctuations in the burned gas (correct to order M^2).

These single-wave results may be used to determine the interaction of a constant-pressure combustion front with a turbulence field of constant density for the case of negligible turbulence decay. The turbulence field will contain an infinite number of transverse plane waves with all wavelengths and planes of polarization. The spectral analysis technique used in obtaining such a superposition of waves will be discussed briefly before proceeding with the interaction problem.

SPECTRAL ANALYSIS

GENERAL CONSIDERATIONS

A turbulence field satisfying the incompressible-flow continuity equation may be represented by the following superposition of plane transverse waves:

$$\underline{u}(\underline{x}, t) = \iiint_{-\infty}^{\infty} e^{i\underline{k} \cdot \underline{x}} d\underline{Z}(\underline{k}, t)$$

where \underline{x} is a position vector, \underline{k} is a wave-number vector, t is the time, and $d\underline{Z}(\underline{k}, t)$ is the random amplitude vector of a component wave. The quantity $d\underline{Z}(\underline{k}, t)e^{i\underline{k} \cdot \underline{x}}$ represents the contribution to the velocity field from a volume element $d\underline{k}$ in wave-number space. When, as in the present case, the equations of motion are linear there is no modulation or interference between component waves, and the various statistical quantities describing a random field may be obtained from the results of a single-wave analysis. To avoid the interpretative difficulties associated with the random variable $\underline{Z}(\underline{k}, t)$, which is nondifferentiable with respect to \underline{k} , use is made of the techniques of references 10 and 15, which utilize correlation spectra rather than amplitude spectra in the analysis of homogeneous turbulence.

A velocity correlation is defined as the ensemble average $\overline{u_i(\underline{x}, t) u_j(\underline{x}', t)}$ of the product of a fluctuation-velocity component u_i at \underline{x} and a component u_j at $\underline{x}' = \underline{x} + \underline{r}$ where \underline{r} is a separation vector. The subscripts i and j take on the values 1, 2, and 3. The ensemble average, designated by a bar, may be regarded as the result of averaging the product $u_i(\underline{x}, t) u_j(\underline{x}, t)$ at a given instant over a very large number of statistically similar fields. The nine velocity correlations $u_i u_j$ constitute the velocity correlation tensor $T_{ij}(\underline{x}, \underline{x}', t)$. For a homogeneous field, T_{ij} depends only on \underline{r} so that the tensor may be written $T_{ij}(\underline{r}, t)$.

As shown in references 10 and 15, the velocity correlation tensor has the following Fourier integral expansion:

$$T_{ij}(\underline{r}, t) = \iiint_{-\infty}^{\infty} e^{i(\underline{k} \cdot \underline{r})} dF_{ij}(\underline{k}, t) = \iiint_{-\infty}^{\infty} e^{i(\underline{k} \cdot \underline{r})} \Phi_{ij}(\underline{k}, t) d\mathbf{k} \quad (14)$$

where $F_{ij}(\underline{k}, t)$ is the spectral tensor function, $\Phi_{ij}(\underline{k}, t)$ is the spectral tensor density of a homogeneous turbulence field, and

$$\Phi_{ij}(\underline{k}, t) d\mathbf{k} = \overline{dZ_i^*(\underline{k}, t) dZ_j(\underline{k}, t)} \quad (15)$$

where $dZ_i^*(\underline{k}, t)$ denotes the complex conjugate of $dZ_i(\underline{k}, t)$. For $r=0$ and $i=j$, equation (14) may be written

$$T_{ii}(0, t) = \overline{u_i^2} = \iiint_{-\infty}^{\infty} \overline{dZ_i^*(\underline{k}, t) dZ_i(\underline{k}, t)} \quad (16)$$

For homogeneous turbulence fields, wherein ensemble averages and space averages are identical, equations (15) and (16) provide the basis for obtaining the spatial mean-square velocity components from the single-wave results given by equations (13) and (C8). Equations (15) and (16) are also applicable to scalar fields. In the absence of viscosity, as postulated, the shear-velocity fields present in the combustible mixture and in the burned gas are homogeneous, and application of equation (16) presents no complications. The corresponding potential-flow fields, although spatially inhomogeneous, are homogeneous in the given x_2, x_3 -planes. It has been shown in reference 16 that equation (16), in effect, may be applied for such fields to obtain the mean-square fluctuations pertaining to a given plane of homogeneity.

As a result of the preceding discussion, the single-wave interaction results for constant-pressure combustion will be used to obtain the spectral densities of the fluctuation quantities at the flame front where the attenuation factors $e^{-\eta_c}$ and $e^{-\eta_b}$ are unity and $\zeta_c = \zeta_b = \sigma = \psi = \nu$. For conciseness, define $RA \sin \varphi \equiv R^{(1)} + iR^{(2)}$, $WA \sin \varphi \equiv W_1 + iW_2$,

$GA \sin \varphi \equiv G_1 + iG_2$, $NA \sin \varphi \equiv N_1 + iN_2$, $HA \sin \varphi \equiv H_1 + iH_2$, and $C^1 A \sin \varphi \equiv C$. With the notation

$$\overline{u_{1,s,c}^2} \equiv \iiint_{-\infty}^{\infty} \overline{dZ_{1,c}^* dZ_{1,c}}$$

and, for example,

$$\overline{\left(\frac{p'_c}{\rho_c U^2}\right)^2} = \iiint_{-\infty}^{\infty} d\left(\frac{p'_c}{\rho_c U^2}\right)^* d\left(\frac{p'_c}{\rho_c U^2}\right)$$

as in equation (16), the following equations are obtained by analogy with equations (13) and (C8) for the case where heat-release perturbations are absent, that is, $\tau' = 0$:

$$\left. \begin{aligned} d\left(\frac{p'_c}{\rho_c U^2}\right) &= d\left(\frac{p'_b}{\rho_c U^2}\right) = R dZ_{1,c} \\ d\left(\frac{u'_{1,c}}{U}\right) &= W dZ_{1,c} + dZ_{1,c} \\ d\left(\frac{u'_{2,c}}{U}\right) &= -iW \cos \theta dZ_{1,c} - (\cot \varphi \cos \theta + C^1 \sin \theta) dZ_{1,c} \\ d\left(\frac{u'_{3,c}}{U}\right) &= -iW \sin \theta dZ_{1,c} - (\cot \varphi \sin \theta - C^1 \cos \theta) dZ_{1,c} \\ d\left(\frac{u'_{1,b}}{U}\right) &= N dZ_{1,c} + G dZ_{1,c} \\ d\left(\frac{u'_{2,b}}{U}\right) &= iN \cos \theta dZ_{1,c} - \left(\frac{\cot \varphi \cos \theta}{\tau} G + C^1 \sin \theta\right) dZ_{1,c} \\ d\left(\frac{u'_{3,b}}{U}\right) &= iN \sin \theta dZ_{1,c} - \left(\frac{\cot \varphi \sin \theta}{\tau} G - C^1 \cos \theta\right) dZ_{1,c} \\ d(\xi') &= -\frac{iH}{k_1} dZ_{1,c} = -\frac{iH}{k \cos \varphi} dZ_{1,c} \\ d\left(\frac{\xi_t}{U}\right) &= H dZ_{1,c} \\ d(\xi'_{x_2,c}) &= H \tan \varphi \cos \theta dZ_{1,c} \\ d(\xi'_{x_3,c}) &= H \tan \varphi \sin \theta dZ_{1,c} \end{aligned} \right\} \quad (17)$$

In the velocity ratios of equations (17), the first term on the right side represents the potential-flow contributions $\frac{u_{1,p,c}}{U}$ or $\frac{u_{1,p,b}}{U}$; the second term represents the shear-flow contributions $\frac{u_{1,s,c}}{U}$ or $\frac{u_{1,s,b}}{U}$. The subscript i takes on the values 1, 2, and 3.

At a given instant the spatial mean-square potential- and shear-flow contributions of the disturbance fields are obtained from equations (17):

$$\left. \begin{aligned}
 \overline{\left(\frac{p'_c}{\rho_c U^2}\right)^2} &= \overline{\left(\frac{p'_b}{\rho_c U^2}\right)^2} = \iiint_{-\infty}^{\infty} (R^* R) \overline{dZ_{1,c}^* dZ_{1,c}} \\
 \overline{\left(\frac{u_{1,s,c}}{U}\right)^2} &= \iiint_{-\infty}^{\infty} \overline{dZ_{1,c}^* dZ_{1,c}} \\
 \overline{\left(\frac{u_{2,s,c}}{U}\right)^2} + \overline{\left(\frac{u_{3,s,c}}{U}\right)^2} &= \iiint_{-\infty}^{\infty} \overline{dZ_{2,c}^* dZ_{2,c}} + \overline{dZ_{3,c}^* dZ_{3,c}} \\
 \overline{\left(\frac{u_{1,p,c}}{U}\right)^2} &= \overline{\left(\frac{u_{2,p,c}}{U}\right)^2} + \overline{\left(\frac{u_{3,p,c}}{U}\right)^2} = \iiint_{-\infty}^{\infty} (W^* W) \overline{dZ_{1,c}^* dZ_{1,c}} \\
 \overline{\left(\frac{u_{1,s,b}}{U}\right)^2} &= \iiint_{-\infty}^{\infty} (G^* G) \overline{dZ_{1,c}^* dZ_{1,c}} \\
 \overline{\left(\frac{u_{2,s,b}}{U}\right)^2} + \overline{\left(\frac{u_{3,s,b}}{U}\right)^2} &= \overline{\left(\frac{u_{2,s,c}}{U}\right)^2} + \overline{\left(\frac{u_{3,s,c}}{U}\right)^2} + \iiint_{-\infty}^{\infty} \left(\frac{\cot \varphi}{\tau}\right)^2 (G^* G - \tau)^2 \overline{dZ_{1,c}^* dZ_{1,c}} \\
 \overline{\left(\frac{u_{1,p,b}}{U}\right)^2} &= \overline{\left(\frac{u_{2,p,b}}{U}\right)^2} + \overline{\left(\frac{u_{3,p,b}}{U}\right)^2} = \iiint_{-\infty}^{\infty} (N^* N) \overline{dZ_{1,c}^* dZ_{1,c}}
 \end{aligned} \right\} \quad (18)$$

The mean-square flame-front quantities are

$$\begin{aligned}
 \overline{\left(\frac{\xi_t}{U}\right)^2} &= \iiint_{-\infty}^{\infty} (H^* H) \overline{dZ_{1,c}^* dZ_{1,c}} \\
 \overline{\xi^2} &= \iiint_{-\infty}^{\infty} \frac{(H^* H)}{k^2 \cos^2 \varphi} \overline{dZ_{1,c}^* dZ_{1,c}} \\
 \overline{\xi_{x2,c}^2} + \overline{\xi_{x3,c}^2} &= \iiint_{-\infty}^{\infty} (H^* H) \tan^2 \varphi \overline{dZ_{1,c}^* dZ_{1,c}}
 \end{aligned}$$

From equations (C8) of appendix C with $\tau' = 0$:

$$\left. \begin{aligned}
 R^* R &= \frac{(\tau-1)^2 (\tau \tan^2 \varphi - 1)^2}{\Delta \sin^2 \varphi} \\
 W^* W &= \frac{(\tau-1)^2 (\tau \tan^2 \varphi - 1)^2}{\Delta} \\
 G^* G &= \frac{\tau^2 \sec^2 \varphi [\Delta - 4\tau(\tau-1) \tan^2 \varphi]}{\Delta(1 + \tau^2 \tan^2 \varphi)} \\
 N^* N &= \frac{\tau^2 (\tau-1)^2 (\tau \tan^2 \varphi - 1)^2 \sec^2 \varphi}{\Delta(1 + \tau^2 \tan^2 \varphi)} \\
 H^* H &= \frac{4\tau^2 \sec^2 \varphi}{\Delta}
 \end{aligned} \right\} \quad (19)$$

MEAN-SQUARE FLUCTUATIONS FOR INITIAL ISOTROPIC TURBULENCE

For a given combustion process (τ and U prescribed), the spatial mean-square fluctuations of equations (18) depend

upon the quantity $\overline{dZ_{1,c}^* dZ_{1,c}}$, which is specified by the type of turbulence present in the combustible mixture. The results obtained in reference 16 for the interaction of axisymmetric turbulence with a shock wave suggest that for the present problem, the degree of anisotropy of the incident turbulence field may not be critical. For simplicity, the turbulence in the combustible mixture is assumed isotropic.

As indicated in reference 10, the spectral density tensors for any isotropic turbulence field satisfying the incompressible-flow continuity equation are

$$\Phi_{ij}(k) = \Omega(k)(k^2 \delta_{ij} - k_i k_j) \quad (20)$$

where $k^2 = k_1^2 + k_2^2 + k_3^2$; $\delta_{ij} = 1$ for $i = j$; $\delta_{ij} = 0$ for $i \neq j$; and $\Omega(k)$ is the scalar amplitude function defining the spectral density tensor. From equations (15), (20), and (11),

$$\overline{dZ_{1,c}^* dZ_{1,c}} = \Omega(k) k^2 \sin^2 \varphi dk$$

or, transforming to spherical polar coordinates k, θ, φ , wherein $d\mathbf{k} = dk_1 dk_2 dk_3 = k^2 \sin \varphi dk d\theta d\varphi$, yields

$$\left. \begin{aligned} \overline{dZ_{1,c}^* dZ_{1,c}} &= \Omega(k) k^4 dk d\theta \sin^3 \varphi d\varphi \\ \overline{dZ_{2,c}^* dZ_{2,c}} &= \Omega(k) k^4 dk d\theta \sin \varphi [\cos^2 \varphi + \sin^2 \varphi \sin^2 \theta] d\varphi \\ \overline{dZ_{3,c}^* dZ_{3,c}} &= \Omega(k) k^4 dk d\theta \sin \varphi [\cos^2 \varphi + \sin^2 \varphi \cos^2 \theta] d\varphi \\ \overline{dZ_{2,c}^* dZ_{2,c}} + \overline{dZ_{3,c}^* dZ_{3,c}} &= \Omega(k) k^4 dk d\theta \sin \varphi [1 + \cos^2 \varphi] d\varphi \end{aligned} \right\} \quad (21)$$

The mean-square velocity components of the incident isotropic turbulence field are then given by

$$\left. \begin{aligned} \left(\frac{u_{1,s,c}}{U} \right)^2 &= \int_0^\infty \Omega(k) k^4 dk \int_0^{2\pi} d\theta \int_0^\pi \sin^3 \varphi d\varphi = \frac{8\pi}{3} \int_0^\infty \Omega(k) k^4 dk \\ \left(\frac{u_{2,s,c}}{U} \right)^2 + \left(\frac{u_{3,s,c}}{U} \right)^2 &= \int_0^\infty \Omega(k) k^4 dk \int_0^{2\pi} d\theta \int_0^\pi \sin \varphi (1 + \cos^2 \varphi) d\varphi \\ &= \frac{16\pi}{3} \int_0^\infty \Omega(k) k^4 dk \end{aligned} \right\} \quad (22)$$

The remaining spatial mean-square fluctuation quantities, referred to the intensities of equations (22) in order that the scale need not be specified, are given by

$$\frac{\left(\frac{p'_c}{\rho_c U^2} \right)^2}{\left(\frac{u_{1,s,c}}{U} \right)^2} = \frac{\left(\frac{p'_b}{\rho_b U^2} \right)^2}{\left(\frac{u_{1,s,c}}{U} \right)^2} = \frac{3}{4} (\tau - 1)^2 \int_0^\pi \frac{\sin \varphi}{\Delta} (\tau \tan^2 \varphi - 1)^2 d\varphi \quad (23a)$$

$$\frac{\left(\frac{u_{1,p,c}}{U} \right)^2}{\left(\frac{u_{1,s,c}}{U} \right)^2} = \frac{\left(\frac{u_{2,p,c}}{U} \right)^2 + \left(\frac{u_{3,p,c}}{U} \right)^2}{\left(\frac{u_{1,s,c}}{U} \right)^2} = \frac{3}{4} (\tau - 1)^2 \int_0^\pi \frac{\sin^3 \varphi}{\Delta} (\tau \tan^2 \varphi - 1)^2 d\varphi \quad (23b)$$

$$\frac{\left(\frac{u_{1,s,b}}{U} \right)^2}{\left(\frac{u_{1,s,c}}{U} \right)^2} = \frac{3\tau^2}{4} \int_0^\pi \frac{[\Delta - 4\tau(\tau^2 - 1)\tan^2 \varphi] \sin \varphi \tan^2 \varphi}{\Delta(1 + \tau^2 \tan^2 \varphi)} d\varphi \quad (23c)$$

$$\frac{\left(\frac{u_{2,s,b}}{U} \right)^2 + \left(\frac{u_{3,s,b}}{U} \right)^2}{\left(\frac{u_{2,s,c}}{U} \right)^2 + \left(\frac{u_{3,s,c}}{U} \right)^2} = 1 - \frac{3}{8} (\tau^2 - 1) \int_0^\pi \frac{(\Delta + 4\tau \sec^2 \varphi) \sin^3 \varphi}{\Delta(1 + \tau^2 \tan^2 \varphi)} d\varphi \quad (23d)$$

$$\frac{\left(\frac{u_{1,p,b}}{U} \right)^2}{\left(\frac{u_{1,s,c}}{U} \right)^2} = \frac{\left(\frac{u_{2,p,b}}{U} \right)^2 + \left(\frac{u_{3,p,b}}{U} \right)^2}{\left(\frac{u_{1,s,c}}{U} \right)^2} = \frac{3}{4} \tau^2 (\tau - 1)^2 \int_0^\pi \frac{(\tau \tan^2 \varphi - 1)^2 \sin \varphi \tan^2 \varphi}{\Delta(1 + \tau^2 \tan^2 \varphi)} d\varphi \quad (23e)$$

$$\frac{\left(\frac{\xi_t}{U} \right)^2}{\left(\frac{u_{1,s,c}}{U} \right)^2} = 3\tau^2 \int_0^\pi \frac{\sin \varphi \tan^2 \varphi}{\Delta} d\varphi \quad (23f)$$

$$\frac{\xi_{2,c}^2 + \xi_{3,c}^2}{\left(\frac{u_{1,s,c}}{U} \right)^2} = 3\tau^2 \int_0^\pi \frac{\tan^4 \varphi \sin \varphi}{\Delta} d\varphi \quad (23g)$$

$$\frac{\xi^2}{\left(\frac{u_{1,s,c}}{U} \right)^2} = 3\tau^2 \left[\frac{\int_0^\infty \Omega(k) k^2 dk}{\int_0^\infty \Omega(k) k^4 dk} \right] \int_0^\pi \frac{\sin^3 \varphi}{\Delta \cos^4 \varphi} d\varphi \quad (23h)$$

The subscript 1 designates a longitudinal component; subscripts 2 and 3 designate the lateral components. Of the remaining subscripts, s denotes a shear-flow component; p denotes a potential-flow component; c refers to the combustible mixture; and b refers to the burned gas. Equations (23a) to (23g) have been integrated numerically using Simpson's rule with the following increments for π : 2° intervals from 0° to 20° , 5° intervals from 20° to 70° , 2° intervals from 70° to 90° , and so forth. Numerical results are listed in table I.

TABLE I.—FLAME—TURBULENCE INTERACTION FLUCTUATION RATIOS

τ	$\sqrt{\frac{\left(\frac{u_{1,s,b}}{U} \right)^2}{\left(\frac{u_{1,s,c}}{U} \right)^2}}$ (eq. (23c))	$\sqrt{\frac{\left(\frac{u_{2,s,b}}{U} \right)^2 + \left(\frac{u_{3,s,b}}{U} \right)^2}{\left(\frac{u_{2,s,c}}{U} \right)^2 + \left(\frac{u_{3,s,c}}{U} \right)^2}}$ (eq. (23d))	$\sqrt{\frac{\left(\frac{u_{1,p,b}}{U} \right)^2}{\left(\frac{u_{1,s,c}}{U} \right)^2}}$ (eq. (23e))	$\sqrt{\frac{\left(\frac{u_{1,p,c}}{U} \right)^2}{\left(\frac{u_{1,s,c}}{U} \right)^2}}$ (eq. (23b))	$\sqrt{\frac{\left(\frac{p'_c}{\rho_c U^2} \right)^2}{\left(\frac{u_{1,s,c}}{U} \right)^2}}$ (eq. (23a))	$\sqrt{\frac{\left(\frac{\xi_t}{U} \right)^2}{\left(\frac{u_{1,s,c}}{U} \right)^2}}$ (eq. (23f))	$\frac{\xi_{2,c}^2 + \xi_{3,c}^2}{\left(\frac{u_{1,s,c}}{U} \right)^2}$ (eq. (23g))	$\frac{-\frac{u_{2,c}}{U} \xi_{2,c} - \frac{u_{3,c}}{U} \xi_{3,c}}{\left(\frac{u_{1,s,c}}{U} \right)^2}$ (eq. (26))
1	1.0000	1.0000	0	0	0	1.0000	∞	1.0000
1.5	.8868	.9380	—	—	—	—	6.0062	1.9553
2	.8814	.9120	.7024	.6833	.7146	.6109	2.2942	1.4270
2.25	—	—	—	—	—	—	1.6501	1.2626
3	.9103	.8904	.8235	.7823	.8358	.4686	.7974	.9439
3.5	—	—	—	—	—	—	.5559	.8098
5	.9676	.8772	.9325	.8604	.9416	.3307	.2521	.5697
7	1.0067	.8727	.9876	.8956	.9943	.2599	.1236	.4094
10	1.0452	.8700	1.0352	.9234	1.0397	.1995	.0592	.2884
15	1.0833	.8682	1.0786	.9463	1.0813	.1462	.0260	.1936
∞	1.2247	.8660	1.2247	1.0000	1.2247	0	0	0

DISCUSSION OF RESULTS

Mean-square fluctuation quantities generated by the linearized interaction of a constant-pressure combustion front with a weak isotropic turbulence field satisfying the continuity equation for incompressible flow are given by equations (23) in terms of the incident-turbulence-velocity components. Equations (23a), (23b), and (23e) apply only at the flame front where the attenuation factors are unity. This restriction does not apply to equations (23c) and (23d) in the assumed absence of turbulent decay processes.

VELOCITY FLUCTUATIONS

Potential-flow fluctuations.—The root-mean-square velocities associated with the attenuating pressure fields generated in the combustible mixture (eq. (23b)) and in the burned gas (eq. (23e)) are plotted in figure 2. Since these

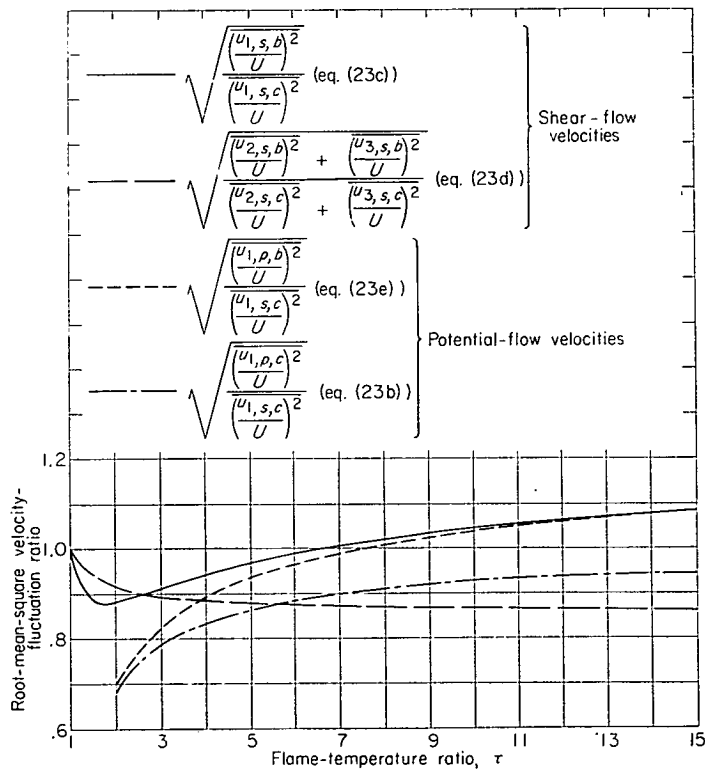


FIGURE 2.—Effect of flame-temperature ratio on shear-flow and potential-flow velocity fluctuations.

ratios apply only at the flame front where the exponential attenuation factors are unity, they represent maximum values. As is to be expected from the boundary-condition requirement of equal pressure fluctuations with differing densities on each side of the flame front, potential-flow velocity components in the burned gas exceed those in the combustible mixture. Both ratios increase with increasing flame-temperature ratio, reaching asymptotic values of $\sqrt{3/2}$ in the burned gas and 1 in the combustible mixture. Hot-wire instrumentation will respond to these fluctuation velocities as well as to the shear-flow fluctuation velocities. In view of their exponential attenuation characteristics, however, such contributions would not be of importance unless measurements were made at stations very close to the flame, that is, within

a distance of the order of incident-turbulence scale. For the low flame Mach numbers encountered in combustion, the contribution to the hot-wire signal voltage of the unattenuated sound waves described in the section FLAME—TURBULENCE INTERACTION PROCESS should be quite small.

Flame-generated turbulence.—The shear flow in the burned gas (eqs. (23c) and (23d)) constitutes the flame-generated turbulence occasioned by the presence of approach-flow turbulence. These velocities, referred to the incident turbulence velocities, are also plotted in figure 2. A slight amplification of the longitudinal component occurs for values of τ over 7. In the limit, as τ becomes very large the longitudinal and lateral velocity ratios approach asymptotic values of $\sqrt{3/2}$ and $\frac{1}{2}\sqrt{3}$, respectively.

The diagrams of figure 1 indicate that a pressure wave interacting with the flame front can also bring about a shear flow in the burned gas. Although the reflection and the consequent impingement of the pressure fields described by equation (23a) upon the flame front are possible, any additions to the flame-generated turbulence level through the reflection process would probably be negligible because of the attenuating nature of the pressure field. Thus, contrary to the predictions of references 6 and 7 that the flame-generated turbulence intensity should be many times greater than the intensity of the incident field, the present analysis indicates that the two intensities are about equal.

It is interesting to note that a stream contraction (ref. 17) increases the downstream velocity of the mean flow (as does the flame front also) while exercising a different selective effect upon an incident isotropic turbulence field. For example, with a sevenfold increase in the downstream velocity of the mean flow, the longitudinal velocity ratio (in the absence of decay effects) is 1.01 for the flame front and 0.31 for the contraction. The corresponding lateral velocity ratios are 0.87 and 2.29, respectively.

TURBULENT FLAME SPEED

The higher mass-flow burning rate of a turbulent flame as compared with that of the corresponding laminar flame is generally described in terms of a turbulent flame speed U_T . The flame-speed ratio U_T/U is generally assumed to be equivalent to the ratio of turbulent-to-laminar flame surface area.

Calculation of the turbulent flame speed requires consideration of second-order terms. The local instantaneous normal propagation velocity $U + \delta U$ of the distorted flame front into the combustible mixture at rest is

$$U + \delta U = \frac{U_T + \xi'_1 - u'_{1,c} + \xi'_{2,c} u'_{2,c} + \xi'_{3,c} u'_{3,c}}{\sqrt{1 + \xi'^2_{2,c} + \xi'^2_{3,c}}} \quad (24)$$

Let $U_T = U + U_I + U_{II} + \dots$ where U_N represents a steady-state contribution to the flame speed of order N . The perturbation quantities, for example, are written as

$$\xi'_i = \xi'_i^I + \xi'_i^{II} + \dots$$

$$u'_{i,c} = u'_{i,c}^I + u'_{i,c}^{II} + \dots$$

The superscript on a fluctuation quantity ξ_i^N indicates the order of the perturbation. As before, $\delta U/U$ is taken as

$$\frac{\delta U}{U} = \frac{nr_2 T_c^n}{U} \frac{T_c'}{T_c} = \frac{(\gamma-1)nr_2}{\sqrt{\gamma R_g}} (T_c)^{n-\frac{1}{2}} M \frac{p_c'}{\rho_c U^2} \equiv \Gamma \frac{p_c'}{\rho_c U^2}$$

Substitution of this expression into equation (24) and performing the indicated expansions yield the following relation, which is correct through second-order terms:

$$\underbrace{\Gamma \left(\frac{p_c'}{\rho_c U^2} \right)}_{\text{first-order terms}} + \underbrace{\left\{ \Gamma \frac{p_c''}{\rho_c U^2} + \frac{1}{2} [(\xi_{x_2,c}^I)^2 + (\xi_{x_3,c}^I)^2] \right\}}_{\text{second-order terms}} \\ = \underbrace{\left(\frac{U_I}{U} + \frac{\xi_i^I}{U} - \frac{u_{1,c}^I}{U} \right)}_{\text{first-order terms}} + \underbrace{\left(\frac{U_{II}}{U} + \frac{\xi_i^{II}}{U} - \frac{u_{1,c}^{II}}{U} + \frac{u_{2,c}^I}{U} \xi_{x_2,c}^I + \frac{u_{3,c}^I}{U} \xi_{x_3,c}^I \right)}_{\text{second-order terms}}$$

$$-\frac{\overline{u_{2,c}^I}}{U} \xi_{x_2,c}^I - \frac{\overline{u_{3,c}^I}}{U} \xi_{x_3,c}^I = \frac{3\tau}{2} \int_0^\pi \left\{ [\tau(\tau-1) \tan^4 \varphi + (\tau^2+1) \tan^2 \varphi + (\tau+1)] \frac{\sin^3 \varphi}{\Delta} + iQ \right\} d\varphi \quad (26)$$

The imaginary term has not been written out inasmuch as it does not contribute to the integral. The results of the indicated integrations are listed in table I.

Equation (25) for the flame-speed ratio U_T/U may also be written in the form

$$\frac{U_T}{U} = 1 + S \frac{\overline{u_{1,s,c}^2}}{U^2} \quad (27)$$

where the flame-speed parameter S is obtained from the values listed in table I from equations (23g) and (26). The variation of this parameter with the flame-temperature ratio τ shown in figure 3 suggests, on the assumption that the flame-front slopes $\xi_{x_2,c}$ and $\xi_{x_3,c}$ govern contributions to the right side of equation (25), that the flame front with the higher heat release is distorted less by a given intensity of turbulence. For the degenerate case $\tau=1$ (no heat release), the parameter S becomes infinite—a condition compatible with this viewpoint.

The present analysis requires that the flame-front slopes, as well as the other perturbation quantities, be small. The preceding discussion suggests that the incremental flame-speed ratio $(U_T-U)/U$ may be of the second order as a result of this restriction to small flame-front slopes.

COMBUSTION NOISE

The root-mean-square pressure-fluctuation coefficient $\sqrt{\overline{p_c'^2}}/\rho_c U^2$, which applies directly at the flame front, is plotted in figure 4 for the limiting case of constant-pressure combustion. The pressure fluctuations are a measure of the random noise generated by the interaction of the flame front with the incident turbulence. In acoustical measurements, the noise level in decibels is usually given with respect to a reference pressure of 0.0002 dyne per square centimeter

Averaging this equation yields

$$\frac{U_I}{U} = 0$$

$$\frac{U_{II}}{U} = \Gamma \frac{\rho_c^{II}}{\rho_c U^2} + \frac{1}{2} [(\overline{\xi_{x_2,c}^I})^2 + (\overline{\xi_{x_3,c}^I})^2] - \frac{\overline{u_{2,c}^I}}{U} \xi_{x_2,c}^I - \frac{\overline{u_{3,c}^I}}{U} \xi_{x_3,c}^I$$

For the limiting case of constant-pressure combustion, $\Gamma=0$. Thus, the ratio of turbulent-to-laminar flame speeds can be written for this case as

$$\frac{U_T}{U} = 1 + \frac{1}{2} [(\xi_{x_2,c}^I)^2 + (\xi_{x_3,c}^I)^2] - \left(\frac{\overline{u_{2,c}^I}}{U} \xi_{x_2,c}^I + \frac{\overline{u_{3,c}^I}}{U} \xi_{x_3,c}^I \right) \quad (25)$$

The first two terms on the right side of equation (25) represent the ratio of averaged turbulent-to-laminar flame surface area. The third term is a correlation coefficient representing the transverse-velocity-fluctuation contribution to the turbulent flame speed caused by flame-front distortion. It is interesting to note that only the transverse velocity fluctuations appear explicitly. The second term has already been determined (eq. (23g)). The third term may be obtained from equations (C8) as

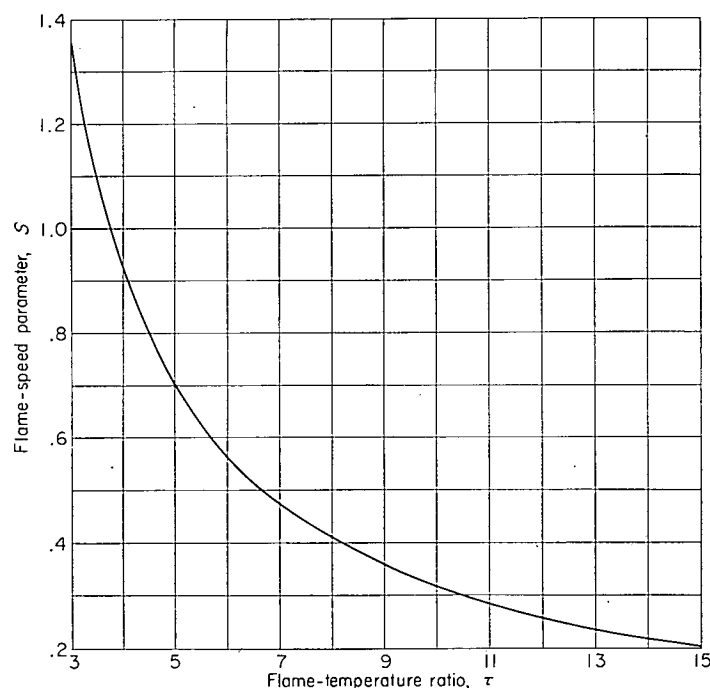


FIGURE 3.—Effect of flame-temperature ratio on flame speed for incident isotropic turbulence.

(ref. 18), which corresponds approximately to the pressure amplitude of a plane sound wave of minimum audible intensity at a frequency of 1000 cycles per second. The noise-pressure level in decibels is defined by the relation

$$\text{Noise-pressure level} \equiv 20 \log_{10} \left(\frac{\sqrt{\overline{p_c'^2}}}{0.0002} \right) = 74 + 20 \log_{10} \sqrt{\overline{p_c'^2}} \quad (28)$$

where the pressure fluctuations in the combustible mixture are given in dynes per square centimeter.

TABLE II.—HYDROCARBON-AIR FLAME DATA AT SPECIFIED CONDITIONS

[Static pressure and temperature of combustible mixture, 760 mm Hg and 25° C, respectively.]

	Propane, C ₃ H ₈		Ethylene, C ₂ H ₄		Acetylene, C ₂ H ₂	
	At stoichiometric	At maximum <i>U</i>	At stoichiometric	At maximum <i>U</i>	At stoichiometric	At maximum <i>U</i>
Fuel-air ratio.....	0.0638	0.0721	0.0676	0.0757	0.0753	0.1040
Fuel in air, percent by volume.....	4.04	4.54	6.54	7.65	7.75	10.70
Laminar flame speed, <i>U</i> , cm/sec.....	37.5	39	64	68	123.5	141
Adiabatic flame-temperature ratio, τ	7.70	7.45	7.95	8.00	8.64	8.71

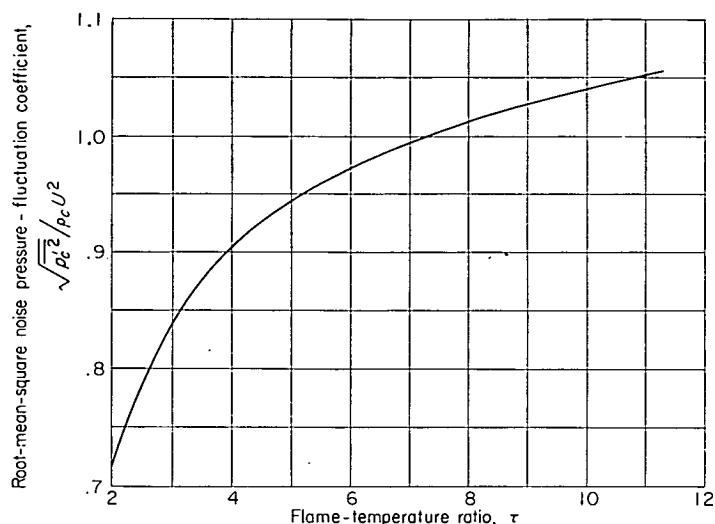


FIGURE 4.—Effect of flame-temperature ratio on random pressure fluctuations generated at flame front.

Equations (23a) and (28) indicate that the noise level should be particularly dependent upon flame speed. Propane-air and acetylene-air combustions, which are characterized by a low flame speed and a fairly high flame speed, respectively, will be considered for illustrative purposes. Pertinent data for these flames at maximum-flame-speed and stoichiometric conditions for an ambient temperature of 25° C and a pressure of 760 millimeters of mercury are given in table II. The adiabatic equilibrium flame temperatures, at which the total enthalpy of the fuel and oxidant equals the total enthalpy of the products of reaction, were calculated using the procedure of reference 19. (Total enthalpy includes the chemical contributions to the internal energy.) Flame-speed data were obtained from references 20 and 21.

If the flame-front turbulence intensity $\sqrt{u_{i,s,c}^2}/U$ is assumed equal to 10 percent, noise-pressure levels of 59 and 81 decibels are obtained for propane-air flames and acetylene-air flames, respectively, under conditions for maximum laminar flame speed. At an approach-flow velocity of 1225 centimeters per second, which is in the range of velocities usually encountered in combustion experiments, the corresponding intensity of the approach-flow turbulence would be about 0.3 percent for the propane-air mixture and about 1 percent for the acetylene-air mixture.

Thus, the pressure fluctuations generated at the flame front when the incident turbulence is of low intensity, although small compared with ambient pressure, are apparently of fairly high acoustical intensity for constant-pressure combustion. Because of the exponential attenuation of these pressure fields, the "far-field" acoustic intensity (the intensity at distances very far from the flame front) approaches zero. For cases other than constant-pressure combustion, a finite "far-field" intensity is obtained.

CONCLUDING REMARKS

The present linearized analysis has treated the interaction of a field of isotropic turbulence with a free flame front under constant-pressure combustion conditions with no turbulence decay processes or heat-release fluctuations. The interaction produces an anisotropic turbulence field in the burned gas which has axisymmetry about the mainstream direction. Contrary to the results predicted by several current theories of turbulent flame speed, the flame-generated turbulence velocities caused by approach-flow turbulence do not differ greatly from the turbulence velocities of the incident field.

The incremental flame-speed ratio $(U_\tau - U)/U$ as obtained from the present analysis is a second-order quantity consisting of two parts. One part represents the root-mean-square area of the turbulent flame front; the other represents the contribution of the transverse velocity fluctuations which result from the flame-front distortion. The flame-speed ratio U_τ/U for a given level of incident turbulence intensity $\sqrt{u_{i,s,c}^2}/U$ is found to decrease with increasing heat-release rates (increasing values of τ).

Random pressure fluctuations generated in both the combustible mixture and the burned gas, although small compared with ambient pressure, give rise to appreciable noise levels (59 to 81 db) directly at the flame front even for very moderate intensities of approach-flow turbulence (flame-front turbulence intensities of 10 percent). For the limiting case of constant-pressure combustion, the pressure waves attenuate exponentially with distance from the flame front, so that the "far-field" intensity approaches zero.

LEWIS FLIGHT PROPULSION LABORATORY
NATIONAL ADVISORY COMMITTEE FOR AERONAUTICS
CLEVELAND, OHIO, January 25, 1955

APPENDIX A

SYMBOLS

A	magnitude of two-dimensional vorticity-wave velocity vector in combustible mixture	R	$(R^{(1)} + R^{(2)})/A \sin \varphi$
\underline{A}	two-dimensional vorticity-wave velocity vector in combustible mixture	R_g	gas constant
a	speed of sound	R_1, R_2	amplitude coefficients of pressure wave in combustible mixture
B_1, B_2, B_3	coefficients defined in eqs. (4)	$R^{(1)}, R^{(2)}$	$R^{(1)} \equiv R_1/\gamma M^2, R^{(2)} \equiv R_2/\gamma M^2$, eq. (10c)
b	constant defined in eqs. (7) and (9)	\underline{r}	separation vector
C	amplitude of combustible mixture shear-wave component parallel to $x_{3,c}$ -axis	r_1, r_2	constants used in representation of laminar flame speed as function of combustible-mixture static temperature
c	constant defined in eqs. (7) and (9)	S	flame-speed parameter, eq. (27)
c_p	specific heat at constant pressure	T	static temperature
c_v	specific heat at constant volume	$T_{ij}(\underline{r}, t)$	velocity correlation tensor for homogeneous turbulence
D_1	$U/(U - V)$, eqs. (4)	T_s	stagnation temperature
d	constant defined in eqs. (7) and (9)	t	time
E_1	$-V/U$, eqs. (4)	U	laminar or fundamental flame speed
$F_{ij}(\underline{k}, t)$	spectral tensor function	U_T	mean turbulent flame speed
f	constant defined in eqs. (7) and (9)	u'	longitudinal component of velocity perturbation
G	$(G_1 + iG_2)/A \sin \varphi$	$u_{1,c}, u_{2,c}, u_{3,c}$	velocity perturbation components in combustible mixture parallel to $x_{1,c}, x_{2,c}, x_{3,c}$ -coordinate axes, respectively
G_1, G_2	amplitude coefficients of shear-wave longitudinal component in burned gas	$u_{1,b}, u_{2,b}, u_{3,b}$	velocity perturbation components in burned gas parallel to $x_{1,b}, x_{2,b}, x_{3,b}$ -coordinate axes, respectively
H	$(H_1 + iH_2)/A \sin \varphi$	V	mean velocity of burned gas
H_1, H_2	amplitude coefficients of flame-front displacement	V_T	mean velocity of burned gas in turbulent combustion
h_1, h_2, \dots, h_{10}	groupings defined in eqs. (B16)	v'	lateral component of velocity perturbation
I_1, I_2	amplitude coefficients of shear-wave transverse component in burned gas	W	$(W_1 + iW_2)/A \sin \varphi$
J_1, J_2	amplitude coefficients of pressure wave in burned gas	W_1, W_2	amplitude coefficients of longitudinal velocity component associated with pressure wave in combustible mixture
$J^{(1)}, J^{(2)}$	$J^{(1)} \equiv \frac{p_b}{\rho_c U^2} J_1; J^{(2)} \equiv \frac{p_b}{\rho_c U^2} J_2$, eq. (10d)	w'	lateral component of velocity perturbation (component parallel to plane of unperturbed flame front and normal to u' and v' components)
K_1, K_2, K_3, K_4	coefficients defined in eqs. (4)	X_1, X_2	amplitude coefficients of lateral velocity component associated with pressure wave in combustible mixture
k	magnitude of wave-number vector \underline{k}	\underline{x}	position vector
k	wave-number vector of shear wave in combustible mixture with components k'_1, k'_2 in x_c, y -coordinate system, with components k_1, k_2, k_3 in $x_{1,c}, x_{2,c}, x_{3,c}$ -coordinate system	x_b	coordinate in x_b, y -system measured in direction of unperturbed flame-front travel relative to which burned gas is at rest
L_1, L_2	amplitude coefficients of density associated with shear entropy wave in burned gas	x_c	coordinate in x_c, y -system measured in direction of unperturbed flame-front travel relative to which combustible mixture is at rest
M	flame-front Mach number, $M \equiv U/a_c$	$x_{1,b}$	coordinate in $x_{1,b}, x_{2,b}, x_{3,b}$ -system measured in direction of unperturbed flame-front travel relative to which burned gas is at rest
m^2	$a_2/\gamma U^2$, eq. (B16)	$x_{2,b}$	coordinate orthogonal to $x_{1,b}$ and $x_{3,b}$ and making angle θ with y -coordinate
N	$(N_1 + iN_2)/A \sin \varphi$	$x_{3,b}$	coordinate orthogonal to $x_{1,b}$ and $x_{2,b}$
N_1, N_2	amplitude coefficients of longitudinal velocity component associated with pressure wave in burned gas		
n	exponent used in representation of laminar flame speed as function of combustible-mixture static temperature		
P_1, P_2	amplitude coefficients of lateral velocity component associated with pressure wave in burned gas		
p	static pressure		
p'	static-pressure perturbation		
Q	term not contributing to the integral in eq. (26)		

$x_{1,c}$	coordinate in $x_{1,c}, x_{2,c}, x_{3,c}$ -system measured in direction of unperturbed flame-front travel relative to which combustible mixture is at rest	$\xi'_{x_{2,c}}$	flame-front slope with respect to $x_{2,c}$ -coordinate
$x_{2,c}$	coordinate orthogonal to $x_{1,c}$ and $x_{3,c}$ and making angle θ with y -coordinate	$\xi'_{x_{3,c}}$	flame-front slope with respect to $x_{3,c}$ -coordinate
$x_{3,c}$	coordinate orthogonal to $x_{1,c}$ and $x_{2,c}$	ξ'_y	flame-front slope with respect to y -coordinate
y	coordinate orthogonal to x_c and x_b	ρ	static density
$d\underline{Z}_i(k, t)$	random amplitude vector of shear-field Fourier component	ρ'	static-density perturbation
z	coordinate orthogonal to x_c and y	σ	$k'_1 U t + k'_2 y$, eq. (10j)
$\alpha_1, \alpha_2 \dots \alpha_5$	grouping defined in eqs. (B18)	τ	flame-temperature ratio, $T_{s,b}/T_{s,c}$
Γ	$\frac{(\gamma-1)nr_2(T_c)^{n-\frac{1}{2}}M}{\sqrt{\gamma R_g}}$	$\Phi_{ij}(k, t)$	spectral density tensor
γ	ratio of specific heats	φ	angle between wave-number vector of incident shear wave and direction of unperturbed flame-front travel, $\tan \varphi \equiv k'_2/k'_1$
Δ	$\tau^2(\tau-1)^2 \tan^4 \varphi + 2\tau(\tau^2+2\tau-1) \tan^2 \varphi + (\tau+1)^2$	ψ	$\left(\frac{U}{U-V}\right) k'_1 x_b + k'_2 y$
$\delta_1, \delta_2 \dots \delta_6$	grouping defined in eqs. (B24)	Ω	scalar amplitude function defining spectral density tensor
$\epsilon_1, \epsilon_2 \dots \epsilon_{10}$	grouping defined in eqs. (B21)	Subscripts:	
ζ	variable upon which pressure wave depends, eqs. (7)	b	burned gas
η	variable upon which pressure wave depends, eqs. (7)	c	combustible mixture
θ	angle between polarization plane of incident shear wave and $x_{1,c}, x_{2,c}$ -plane	cr	critical
Λ	coefficient defined in eq. (3e)	p	potential-flow velocity component
ν	$k'_1 x_c + k'_2 y$	s	shear-flow velocity component
$\xi'(y, t)$	flame-front displacement	1, 2, 3	orthogonal coordinate designation
$\dot{\xi}$	flame-front displacement velocity	I, II	designates order of steady-flow quantity
		Superscripts:	
		I, II	designates order of fluctuation quantity
		*	denotes complex conjugate
		'	denotes fluctuation quantity except where otherwise specified

APPENDIX B

ATTENUATING-WAVE SOLUTION FOR SINGLE-WAVE INTERACTION

The arguments of the various fluctuation quantities are equal at the flame front where $x_c = Ut$ and $x_b = (U-V)t$. Therefore, substituting equations (10) into equations (3) and (5) and separately equating the real terms and the imaginary terms provide the following set of equations:

$$\left. \begin{aligned} J_1 \left(1 + \frac{B_1}{\gamma}\right) + B_1 L_1 - B_2 N_1 - B_2 G_1 = \\ -B_2 A \sin \varphi - B_2 W_1 + B_3 R_1 \\ J_2 \left(1 + \frac{B_1}{\gamma}\right) + B_1 L_2 - B_2 N_2 - B_2 G_2 = -B_2 W_2 + B_3 R_2 \end{aligned} \right\} \quad (B1)$$

$$\left. \begin{aligned} J_1 \left(1 - \frac{1}{\gamma}\right) - L_1 - K_1 N_1 - K_1 G_1 = -K_4 W_1 - \\ K_4 A \sin \varphi + K_2 R_1 + K_3 \tau' - (K_1 - K_4) H_1 \\ J_2 \left(1 - \frac{1}{\gamma}\right) - L_2 - K_1 N_2 - K_1 G_2 = \\ -K_4 W_2 + K_2 R_2 - (K_1 - K_4) H_2 \end{aligned} \right\} \quad (B2)$$

$$\left. \begin{aligned} \frac{1}{\gamma} J_1 + L_1 + (D_1 - 1) H_1 - D_1 N_1 - D_1 G_1 = \\ -W_1 - A \sin \varphi + \frac{1}{\gamma} R_1 \\ \frac{1}{\gamma} J_2 + L_2 + (D_1 - 1) H_2 - D_1 N_2 - D_1 G_2 = -W_2 + \frac{1}{\gamma} R_2 \end{aligned} \right\} \quad (B3)$$

$$\left. \begin{aligned} P_1 + I_1 = X_1 - \frac{k'_1}{k'_2} A \sin \varphi + \frac{k'_2}{k'_1} E_1 H_1 \\ P_2 + I_2 = X_2 + \frac{k'_2}{k'_1} E_1 H_2 \end{aligned} \right\} \quad (B4)$$

$$\left. \begin{aligned} -f_b \left(\frac{U-V}{U}\right) N_1 - d_b N_2 = m^2 (-f_b J_1 + b_b J_2) \\ d_b N_1 - f_b \left(\frac{U-V}{U}\right) N_2 = m^2 (-b_b J_1 - f_b J_2) \end{aligned} \right\} \quad (B5)$$

$$\left. \begin{aligned} -f_b \left(\frac{U-V}{U}\right) P_1 - d_b P_2 = m^2 c_b J_2 \\ d_b P_1 - f_b \left(\frac{U-V}{U}\right) P_2 = -m^2 c_b J_1 \end{aligned} \right\} \quad (B6)$$

$$\left. \begin{aligned} -k_1 \left(\frac{U}{U-V}\right) G_2 = k_2 I_2 \\ -k_1 \left(\frac{U}{U-V}\right) G_1 = k_2 I_1 \end{aligned} \right\} \quad (B7)$$

$$\left. \begin{aligned} f_c W_1 - d_c W_2 &= \frac{1}{\gamma M^2} (f_c R_1 + b_c R_2) \\ d_c W_1 + f_c W_2 &= \frac{1}{\gamma M^2} (-b_c R_1 + f_c R_2) \end{aligned} \right\} \quad (B8)$$

$$\left. \begin{aligned} f_c X_1 - d_c X_2 &= \frac{1}{\gamma M^2} c_c R_2 \\ d_c X_1 + f_c X_2 &= -\frac{1}{\gamma M^2} c_c R_1 \end{aligned} \right\} \quad (B9)$$

$$\left. \begin{aligned} H_1 - W_1 - A \sin \varphi &= \Lambda R_1 \\ H_2 - W_2 &= \Lambda R_2 \end{aligned} \right\} \quad (B10)$$

From equations (B5), (B6), (B8), (B9), and (B10),

$$\left. \begin{aligned} N_1 &= h_1(h_2 J_1 - h_3 J_2) \\ N_2 &= h_1(h_3 J_1 + h_2 J_2) \end{aligned} \right\} \quad (B11)$$

$$\left. \begin{aligned} P_1 &= h_1(-h_4 J_1 - h_5 J_2) \\ P_2 &= h_1(h_5 J_1 - h_4 J_2) \end{aligned} \right\} \quad (B12)$$

$$\left. \begin{aligned} W_1 &= h_6(h_7 R_1 + h_8 R_2) \\ W_2 &= h_6(-h_8 R_1 + h_7 R_2) \end{aligned} \right\} \quad (B13)$$

$$\left. \begin{aligned} X_1 &= h_6(-h_9 R_1 + h_{10} R_2) \\ X_2 &= h_6(-h_{10} R_1 - h_9 R_2) \end{aligned} \right\} \quad (B14)$$

$$\left. \begin{aligned} H_1 &= \Lambda R_1 + A \sin \varphi + h_6(h_7 R_1 + h_8 R_2) \\ H_2 &= \Lambda R_2 + h_6(-h_8 R_1 + h_7 R_2) \end{aligned} \right\} \quad (B15)$$

where

$$\left. \begin{aligned} h_1 &\equiv \frac{m^2}{f_b^2/D_1^2 + d_b^2} & h_6 &\equiv \frac{1}{\gamma M^2(f_c^2 + d_c^2)} \\ h_2 &\equiv \frac{f_b^2}{D_1} - b_b D_b & h_7 &\equiv f_c^2 - b_c d_c \\ h_3 &\equiv \frac{b_b f_b}{D_1} + d_b f_b & h_8 &\equiv b_c f_c + d_c f_c \\ h_4 &\equiv c_b d_b & h_9 &\equiv c_c d_c \\ h_5 &\equiv \frac{c_b f_b}{D_1} & h_{10} &\equiv c_c f_c \\ m^2 &\equiv a_b^2/\gamma U^2 \end{aligned} \right\} \quad (B16)$$

From equations (B4), (B7), (B12), (B14), and (B15),

$$\left. \begin{aligned} G_1 &= \alpha_1 R_1 - \alpha_2 R_2 - \alpha_3 J_1 - \alpha_4 J_2 + \alpha_5 A \sin \varphi \\ G_2 &= \alpha_2 R_1 + \alpha_1 R_2 + \alpha_4 J_1 - \alpha_3 J_2 \end{aligned} \right\} \quad (B17)$$

where

$$\left. \begin{aligned} \alpha_1 &\equiv \frac{k'_2}{k'_1 D_1} \left[\frac{-k'_2 E_1}{k'_1} (\Lambda + h_6 h_7) + h_6 h_9 \right] \\ \alpha_2 &\equiv \frac{k'_2}{k'_1 D_1} \left[\frac{k'_2 E_1}{k'_1} h_6 h_8 + h_6 h_{10} \right] \\ \alpha_3 &\equiv \frac{k'_2}{k'_1 D_1} h_1 h_4 \\ \alpha_4 &\equiv \frac{k'_2}{k'_1 D_1} h_1 h_5 \\ \alpha_5 &\equiv \frac{1}{D_1} \left[1 - \frac{(k'_2)^2}{(k'_1)^2} E_1 \right] \end{aligned} \right\} \quad (B18)$$

Then, from equation (B2),

$$\left. \begin{aligned} L_1 &= J_1 \left[1 - \frac{1}{\gamma} - K_1(h_1 h_2 - \alpha_3) \right] + J_2 [K_1(h_1 h_3 + \alpha_4)] + \\ &\quad R_1 [K_1(h_6 h_7 - \alpha_1) - K_2 + (K_1 - K_4)\Lambda] + \\ &\quad R_2 [K_1(h_6 h_8 + \alpha_2)] + A \sin \varphi [K_1(1 - \alpha_5)] - K_3 \tau' \\ L_2 &= -J_1 [K_1(h_1 h_3 + \alpha_4)] + J_2 \left[1 - \frac{1}{\gamma} - K_1(h_1 h_2 - \alpha_3) \right] - \\ &\quad R_1 [K_1(h_6 h_8 + \alpha_2)] + R_2 [K_1(h_6 h_7 - \alpha_1) - K_2 + \\ &\quad (K_1 - K_4)\Lambda] \end{aligned} \right\} \quad (B19)$$

The various disturbance amplitude coefficients of equations (10) have now been obtained in terms of the coefficients R_1 , R_2 , J_1 , J_2 and the parameters $A \sin \varphi$ and τ' . From equations (B1) and (B3),

$$\left. \begin{aligned} J_1 \epsilon_1 + J_2 \epsilon_2 + R_1 \epsilon_3 + R_2 \epsilon_4 &= \epsilon_5 \\ -J_1 \epsilon_2 + J_2 \epsilon_1 - R_1 \epsilon_4 + R_2 \epsilon_3 &= 0 \\ J_1 \epsilon_6 + J_2 \epsilon_7 + R_1 \epsilon_8 + R_2 \epsilon_9 &= \epsilon_{10} \\ -J_1 \epsilon_7 + J_2 \epsilon_6 - R_1 \epsilon_9 + R_2 \epsilon_8 &= 0 \end{aligned} \right\} \quad (B20)$$

where

$$\left. \begin{aligned} \epsilon_1 &\equiv 1 + B_1 - (B_1 K_1 + B_2)(h_1 h_2 - \alpha_3) \\ \epsilon_2 &\equiv (B_1 K_1 + B_2)(h_1 h_3 + \alpha_4) \\ \epsilon_3 &\equiv (B_1 K_1 + B_2)(h_6 h_7 - \alpha_1) + B_1(K_1 - K_4)\Lambda - B_3 - B_1 K_2 \\ \epsilon_4 &\equiv (B_1 K_1 + B_2)(h_6 h_8 + \alpha_2) \\ \epsilon_5 &\equiv B_1 K_3 \tau' - A \sin \varphi [(B_1 K_1 + B_2)(1 - \alpha_5)] \\ \epsilon_6 &\equiv 1 - (D_1 + K_1)(h_1 h_2 - \alpha_3) \\ \epsilon_7 &\equiv (D_1 + K_1)(h_1 h_3 + \alpha_4) \\ \epsilon_8 &\equiv (D_1 + K_1)(h_6 h_7 - \alpha_1) + (D_1 - 1)\Lambda - K_2 + \frac{1}{\gamma} + (K_1 - K_4)\Lambda \\ \epsilon_9 &\equiv (D_1 + K_1)(h_6 h_8 + \alpha_2) \\ \epsilon_{10} &\equiv K_3 \tau' - A \sin \varphi (D_1 + K_1)(1 - \alpha_5) \end{aligned} \right\} \quad (B21)$$

$$\left. \begin{aligned} J_1 &= \frac{R_1(\epsilon_1\epsilon_9 - \epsilon_4\epsilon_6) - R_2(\epsilon_1\epsilon_8 - \epsilon_3\epsilon_6)}{\epsilon_2\epsilon_6 - \epsilon_1\epsilon_7} \\ J_2 &= \frac{R_1(\epsilon_2\epsilon_9 - \epsilon_4\epsilon_7) - R_2(\epsilon_2\epsilon_8 - \epsilon_3\epsilon_7)}{\epsilon_2\epsilon_6 - \epsilon_1\epsilon_7} \end{aligned} \right\} \quad (\text{B22})$$

$$\left. \begin{aligned} R_1 &= \frac{\delta_2\delta_6 - \delta_3\delta_5}{\delta_2\delta_4 - \delta_1\delta_5} \\ R_2 &= \frac{\delta_1\delta_6 - \delta_3\delta_4}{\delta_2\delta_4 - \delta_1\delta_5} \end{aligned} \right\} \quad (\text{B23})$$

where

$$\left. \begin{aligned} \delta_1 &\equiv \epsilon_1(\epsilon_1\epsilon_9 - \epsilon_4\epsilon_6) + \epsilon_3(\epsilon_2\epsilon_6 - \epsilon_1\epsilon_7) - \epsilon_2(\epsilon_4\epsilon_7 - \epsilon_2\epsilon_9) \\ \delta_2 &\equiv \epsilon_1(\epsilon_1\epsilon_8 - \epsilon_3\epsilon_6) - \epsilon_4(\epsilon_2\epsilon_6 - \epsilon_1\epsilon_7) - \epsilon_2(\epsilon_3\epsilon_7 - \epsilon_2\epsilon_8) \\ \delta_3 &\equiv \epsilon_5(\epsilon_2\epsilon_6 - \epsilon_1\epsilon_7) \\ \delta_4 &\equiv \epsilon_6(\epsilon_1\epsilon_9 - \epsilon_4\epsilon_6) + \epsilon_8(\epsilon_2\epsilon_6 - \epsilon_1\epsilon_7) - \epsilon_7(\epsilon_4\epsilon_7 - \epsilon_2\epsilon_9) \\ \delta_5 &\equiv \epsilon_6(\epsilon_1\epsilon_8 - \epsilon_3\epsilon_6) - \epsilon_7(\epsilon_3\epsilon_7 - \epsilon_2\epsilon_8) - \epsilon_9(\epsilon_2\epsilon_6 - \epsilon_1\epsilon_7) \\ \delta_6 &\equiv \epsilon_{10}(\epsilon_2\epsilon_6 - \epsilon_1\epsilon_7) \end{aligned} \right\} \quad (\text{B24})$$

Equations (B11) to (B15), (B17), (B19), (B22); and (B23) provide the formal solution of equations (B1) to (B10).

APPENDIX C

ATTENUATING-WAVE SOLUTION FOR CONSTANT-PRESSURE COMBUSTION

If terms of order M^2 are retained, equations (1) provide the following relations for the unperturbed-flow quantities:

$$\begin{aligned} \frac{p_b}{p_c} &= 1 - \gamma(\tau - 1)M^2 + \dots \\ \frac{\rho_c}{\rho_b} &= \frac{U - V}{U} = \tau \left[1 + \frac{\gamma + 1}{2}(\tau - 1)M^2 + \dots \right] \\ \frac{c_p T_{s,c}}{U^2} &= \frac{1}{2} + \frac{1}{(\gamma - 1)M^2} \\ \frac{U^2}{a_b^2} &= \frac{2M^2}{\tau[2 - (\gamma - 1)(\tau - 1)M^2 - (\gamma^2 - 1)\tau(\tau - 1)M^4 + \dots]} \end{aligned}$$

With these relations, equations (4) take the form

$$\left. \begin{aligned} B_1 &= \gamma\tau M^2, B_2 = 2\gamma M^2, B_3 = 1 + [1 + \gamma(\tau - 1)]M^2 \\ D_1 &= \frac{1}{\tau} \left[1 - \frac{\gamma + 1}{2}(\tau - 1)M^2 \right], E_1 = (\tau - 1) \left[1 + \frac{\gamma + 1}{2}\tau M^2 \right] \\ K_1 &= K_4 = (\gamma - 1)M^2, K_2 \\ &= \frac{\gamma - 1}{\gamma} \left[1 + \frac{\gamma - 1}{2}(\tau - 1)M^2 \right], K_3 = \frac{1}{\tau} + \frac{\gamma - 1}{2}M^2 \end{aligned} \right\} \quad (\text{C1})$$

and equations (9) may be written

$$\left. \begin{aligned} b_c &= b_b = -k'_1 M^2, c_c = c_b = k'_2, d_c = k'_1(1 + M^2), d_b = k'_1(1 + \tau M^2) \\ f_c^2 &= (k'_2)^2 - [(k'_1)^2 - (k'_2)^2]M^2, f_b^2 = (k'_2)^2 - \left[\frac{(k'_1)^2 - \tau^2(k'_2)^2}{\tau} \right]M^2 \end{aligned} \right\} \quad (\text{C2})$$

If only the leading terms in powers of M^2 are retained, equations (B16) and (B18) provide the following relations:

$$\left. \begin{aligned} h_1 h_2 &= h_1 h_5 = \frac{\tau^2 \tan^2 \varphi}{\gamma M^2 (1 + \tau^2 \tan^2 \varphi)}, h_1 h_3 = h_1 h_4 = \frac{\tau \tan \varphi}{\gamma M^2 (1 + \tau^2 \tan^2 \varphi)} \\ h_6 h_7 &= h_6 h_{10} = \frac{\sin^2 \varphi}{\gamma M^2}, h_6 h_8 = h_6 h_9 = \frac{\sin \varphi \cos \varphi}{\gamma M^2} \end{aligned} \right\} \quad (\text{C3})$$

and

$$\left. \begin{aligned} \alpha_1 &= \frac{\tau \sin^2 \varphi}{\gamma M^2} [1 - (\tau - 1) \tan^2 \varphi] \\ \alpha_2 &= \frac{\tau^2 \sin^2 \varphi \tan \varphi}{\gamma M^2} \\ \alpha_3 &= \frac{\tau^2 \tan^2 \varphi}{\gamma M^2 (1 + \tau^2 \tan^2 \varphi)} \\ \alpha_4 &= \frac{\tau^3 \tan^3 \varphi}{\gamma M^2 (1 + \tau^2 \tan^2 \varphi)} \\ \alpha_5 &= \tau [1 - (\tau - 1) \tan^2 \varphi] \end{aligned} \right\} \quad (\text{C4})$$

From these relations:

$$\left. \begin{aligned} h_1 h_3 + \alpha_4 &= \frac{\tau \tan \varphi}{\gamma M^2}, h_6 h_7 - \alpha_1 = \frac{(\tau - 1) \sin^2 \varphi (\tau \tan^2 \varphi - 1)}{\gamma M^2} \\ h_1 h_2 - \alpha_3 &= 0, h_6 h_8 + \alpha_2 = \frac{\sin \varphi \cos \varphi (1 + \tau^2 \tan^2 \varphi)}{\gamma M^2} \end{aligned} \right\} \quad (\text{C5})$$

From equations (B21) and (C5),

$$\left. \begin{aligned} \epsilon_1 \epsilon_9 - \epsilon_4 \epsilon_6 &= \frac{\sin \varphi \cos \varphi (1 + \tau^2 \tan^2 \varphi)}{\gamma M^2 \tau} \\ \epsilon_1 \epsilon_8 - \epsilon_3 \epsilon_6 &= \frac{(\tau - 1) \sin^2 \varphi (\tau \tan^2 \varphi - 1)}{\gamma M^2 \tau} \\ \epsilon_3 \epsilon_7 - \epsilon_2 \epsilon_8 &= \epsilon_2 \epsilon_6 - \epsilon_1 \epsilon_7 = -\frac{\tan \varphi}{\gamma M^2}, \epsilon_4 \epsilon_7 - \epsilon_2 \epsilon_9 = 0 \end{aligned} \right\} \quad (\text{C6})$$

and from equations (B21), (B24), and (C6):

$$\left. \begin{aligned} \delta_1 &= \frac{\sin \varphi \cos \varphi}{\gamma M^2 \tau} [(\tau+1)(1+\tau \tan^2 \varphi) - \\ &\quad 2 \tan^2 \varphi (\tau-1) \tau (\tau \tan^2 \varphi - 1)] \\ \delta_2 &= \frac{\sin^2 \varphi}{\gamma M^2 \tau} [(\tau-1)(\tau \tan^2 \varphi - 1) + 2(\tau+1) \tau (\tau \tan^2 \varphi + 1)] \\ \delta_3 &= -\tan \varphi [\tau' - 2(\tau-1)(\tau \tan^2 \varphi - 1) A \sin \varphi] \\ \delta_4 &= \frac{-(\tau-1) \tan \varphi \sin^2 \varphi (\tau \tan^2 \varphi - 1)}{\gamma^2 M^4 \tau} \\ \delta_5 &= \frac{(\tau+1)(\tau \tan^2 \varphi + 1) \sin^2 \varphi}{\gamma^2 M^4 \tau} \\ \delta_6 &= -\frac{\tan \varphi}{\gamma M^2 \tau} [\tau' - (\tau-1)(\tau \tan^2 \varphi - 1) A \sin \varphi] \end{aligned} \right\} \quad (C7)$$

Since for constant-pressure combustion $R^{(1)} \equiv R_2/\gamma M^2$, $R^{(2)} \equiv R_2/\gamma M^2$, and so forth, the coefficients $R^{(1)}$, $R^{(2)}$, $J^{(1)}$, and $J^{(2)}$ are obtained from equations (B22), (B23), (C6), and (C7). With these coefficients determined, the remainder are obtained from equations (B7), (B11) to (B14), (B17), and (B19). The amplitude coefficients are

$$\left. \begin{aligned} R^{(1)} &= \frac{-1}{\Delta} \left\{ (\tau-1)^2 (\tau \tan^2 \varphi - 1)^2 A \sin \varphi - [\tau^2 (\tau^2 + 2\tau - 1) \tan^2 \varphi + \tau (\tau^2 + 1)] \frac{\tau'}{\tau} \right\} \\ R^{(2)} = J^{(2)} &= -\frac{1}{\Delta \tan \varphi} \left\{ (\tau^2 - 1)(\tau^2 \tan^4 \varphi - 1) A \sin \varphi + [\tau^3 (\tau - 1) \tan^4 \varphi - 2\tau^3 \tan^2 \varphi - \tau (\tau + 1)] \frac{\tau'}{\tau} \right\} \\ J^{(1)} &= -\frac{1}{\Delta} \left\{ (\tau-1)^2 (\tau \tan^2 \varphi - 1)^2 A \sin \varphi + \tau^2 [\tau (\tau - 1)^2 \tan^4 \varphi + (\tau^2 + 2\tau - 1) \tan^2 \varphi + 2] \frac{\tau'}{\tau} \right\} \\ L_1 &= -\frac{\tau'}{\tau}, \quad L_2 = 0 \\ N_1 &= \frac{\tau}{\Delta(1 + \tau^2 \tan^2 \varphi)} \left\{ (\tau-1)(\tau \tan^2 \varphi - 1)[(\tau+1)(\tau \tan^2 \varphi + 1) - \tau(\tau-1) \tan^2 \varphi (\tau \tan^2 \varphi - 1)] A \sin \varphi - \right. \\ &\quad \left. \tau \left\{ \tau^2 \tan^2 \varphi [\tau (\tau - 1)^2 \tan^4 \varphi + \tau (\tau + 1) \tan^2 \varphi + 4] + (\tau + 1) \right\} \frac{\tau'}{\tau} \right\} \\ N_2 &= \frac{-\tau(\tau-1) \tan \varphi}{\Delta(1 + \tau^2 \tan^2 \varphi)} \left\{ (\tau \tan^2 \varphi - 1)[\tau(\tau+1)(\tau \tan^2 \varphi + 1) + (\tau-1)(\tau \tan^2 \varphi - 1)] A \sin \varphi + \right. \\ &\quad \left. \tau^2 [\tau(2\tau-1) \tan^4 \varphi - (\tau-1) \tan^2 \varphi - 1] \frac{\tau'}{\tau} \right\} \\ G_1 &= \frac{\tau}{\Delta(1 + \tau^2 \tan^2 \varphi)} \left\{ [(\tau+1)^2 (\tau \tan^2 \varphi + 1)^2 + \tau(\tau-1)^2 \tan^2 \varphi (\tau \tan^2 \varphi - 1)^2] A \sin \varphi - \right. \\ &\quad \left. \tau(\tau-1) \tan^2 \varphi [\tau(\tau^2 + 2\tau - 1) \tan^2 \varphi + (\tau^2 + 1)] \frac{\tau'}{\tau} \right\} \\ G_2 &= \frac{(\tau-1) \tan \varphi}{\Delta(1 + \tau^2 \tan^2 \varphi)} \left\{ (\tau^2 - 1)(\tau \tan^2 \varphi - 1)(\tau \tan^2 \varphi + 1) A \sin \varphi + [\tau^3 (\tau - 1) \tan^4 \varphi - 2\tau^3 \tan^2 \varphi - \tau(\tau + 1)] \frac{\tau'}{\tau} \right\} \\ P_1 &= -N_2, \quad P_2 = N_1 \\ I_1 &= \frac{G_1}{\tau \tan \varphi}, \quad I_2 = \frac{-G_2}{\tau \tan \varphi} \\ W_1 &= -\frac{1}{\Delta} \left\{ (\tau-1)(\tau \tan^2 \varphi - 1)[\tau(\tau-1) \tan^2 \varphi + (\tau+1)] A \sin \varphi - [\tau^2 (3\tau-1) \tan^2 \varphi + \tau(\tau+1)] \frac{\tau'}{\tau} \right\} \\ W_2 &= -\frac{\tau(\tau-1) \tan \varphi}{\Delta} \left\{ 2(\tau \tan^2 \varphi - 1) A \sin \varphi + \tau [\tau \tan^2 \varphi + 1] \frac{\tau'}{\tau} \right\} \\ X_1 &= H_2 = W_2, \quad X_2 = -W_1 \\ H_1 &= \frac{\tau}{\Delta} \left\{ 2(\tau+1)(\tau \tan^2 \varphi + 1) A \sin \varphi + [\tau(3\tau-1) \tan^2 \varphi + (\tau+1)] \frac{\tau'}{\tau} \right\} \end{aligned} \right\} \quad (C8)$$

For constant-pressure combustion, $\zeta_c = \zeta_b = k'_1 U t + k'_2 y$, $\eta_c = k'_2(x_c - U t)$, $\eta_b = k'_2[-x_b + (U - V)t]$, $v = k'_1 x_c + k'_2 y$, $\psi = \frac{k'_1 x_b}{\tau} + k'_2 y$, and $\sigma = k'_1 U t + k'_2 y$. At the flame front where $x_c = U t$ and $x_b = (U - V)t$, $\eta_c = \eta_b = 0$, the attenuation factors $e^{-\eta_c}$ and $e^{-\eta_b}$ are 1, and the arguments of the disturbance waves have the form $(k'_1 U t + k'_2 y)$.

The procedure of reference 23 is utilized in reference 22 to treat a similar interaction problem for consideration of flame-front stability. It is assumed that there are first-order perturbations in the laminar flame speed U (in the present notation). Reference 22 presents results only for the special case where the plane of polarization of the incident shear wave is in the plane $x_{1,c} - x_{2,c} (\theta = 0^\circ)$ and the wave-number vector is parallel to the unperturbed flame front ($\varphi = 90^\circ$). The results of the present analysis were compared with those of reference 22 for the case of an absence of first-order perturbations in the laminar flame speed and for the special case of $\theta = 0^\circ$ and $\varphi = 90^\circ$ without heat-release perturbations. Although agreement as to sign and magnitude is obtained for the shear-field velocity components, apparently differences in sign occur for the potential-field velocity-component amplitudes as indicated in the following table:

	Present analysis	Analysis of ref. 22
$\frac{u'_{p,c}}{U}$	$-A$	$-A$
$\frac{v'_{p,c}}{U}$	iA	$-iA$
$\frac{u'_{p,b}}{U}$	A	$-A$
$\frac{v'_{p,b}}{U}$	iA	iA

Consideration of conservation of momentum across the flame front indicates that $v'_{p,c}/U$ and $v'_{p,b}/U$ should be of the same sign. The present analysis is in agreement with this consideration.

REFERENCES

1. Damköhler, Gerhard: The Effect of Turbulence on the Flame Velocity in Gas Mixtures. NACA TM 1112, 1947.
2. Shelkin, K. I.: On Combustion in a Turbulent Flow. NACA TM 1110, 1947.
3. Bollinger, Lowell M., and Williams, David T.: Effect of Reynolds Number in the Turbulent-Flow Range on Flame Speeds of Bunsen Burner Flames. NACA Rep. 932, 1949. (Supersedes NACA TN 1707.)
4. Williams, G. C., Hottel, H. C., and Scurlock, A. C.: Flame Stabilization and Propagation in High Velocity Gas Streams. Third Symposium on Combustion and Flame and Explosion Phenomena, The Williams & Wilkins Co. (Baltimore), 1949, pp. 21-40.
5. Markstein, G. H.: Interaction of Flame Propagation and Flow Disturbances. Third Symposium on Combustion and Flame and Explosion Phenomena, The Williams & Wilkins Co. (Baltimore), 1949, pp. 162-167.
6. Karlovitz, Béla, Denniston, D. W., Jr., and Wells, F. E.: Investigation of Turbulent Flames. Jour. Chem. Phys., vol. 19, no. 5, May 1951, pp. 541-547.
7. Scurlock, A. C., and Grover, J. H.: Propagation of Turbulent Flames. Fourth Symposium (International) on Combustion, The Williams & Wilkins Co. (Baltimore), 1953, pp. 645-658.
8. Westenberg, Arthur A.: Flame Turbulence Measurements by the Method of Helium Diffusion. Jour. Chem. Phys., vol. 22, no. 5, May 1954, pp. 814-823.
9. Wohl, K., Shore, L., Von Rosenberg, H., and Weil, C. W.: The Burning Velocity of Turbulent Flames. Fourth Symposium (International) on Combustion, The Williams & Wilkins Co. (Baltimore), 1953, pp. 620-635.
10. Batchelor, G. K.: The Theory of Homogeneous Turbulence. Cambridge Univ. Press, 1953.
11. Carrier, G. F., and Carlson, F. D.: On the Propagation of Small Disturbances in a Moving Compressible Fluid. Quarterly Appl. Math., vol. 4, no. 1, Apr. 1946, pp. 1-12.
12. Moore, Franklin K.: Unsteady Oblique Interaction of a Shock Wave with a Plane Disturbance. NACA Rep. 1165, 1954. (Supersedes NACA TN 2879.)
13. Clark, Thomas P., and Bittker, David A.: A Study of the Radiation from Laminar and Turbulent Open Propane-Air Flames as a Function of Flame Area, Equivalence Ratio, and Fuel Flow Rate. NACA RM E54F29, 1954.
14. Dugger, Gordon L.: Effects of Initial Mixture Temperature on Flame Speed of Methane-Air, Propane-Air, and Ethylene-Air Mixtures. NACA Rep. 1061, 1952. (Supersedes NACA TN's 2170 and 2374.)
15. Moyal, J. E.: The Spectra of Turbulence in a Compressible Fluid; Eddy Turbulence and Random Noise. Proc. Cambridge Phil. Soc., vol. 48, pt. 2, Apr. 1952, pp. 329-344.
16. Ribner, H. S.: Shock-Turbulence Interaction and the Generation of Noise. NACA TN 3255, 1954.
17. Ribner, H. S., and Tucker, M.: Spectrum of Turbulence in a Contracting Stream. NACA Rep. 1113, 1953. (Supersedes NACA TN 2606.)
18. Morse, Philip M.: Vibration and Sound. Second ed., McGraw-Hill Book Co., Inc., 1948.
19. Hottel, H. C., Williams, G. C., and Satterfield, C. N.: Thermodynamic Charts for Combustion Processes, pt. I. John Wiley & Sons, Inc., 1949.
20. Gerstein, Melvin, Levins, Oscar, and Wong, Edgar L.: Fundamental Flame Velocities of Pure Hydrocarbons. I - Alkanes, Alkenes, Alkynes, Benzene, and Cyclohexane. NACA RM E50G24, 1950.
21. Levine, Oscar, and Gerstein, Melvin: Fundamental Flame Velocities of Pure Hydrocarbons. III - Extension of Tube Method to High Flame Velocities - Acetylene-Air Mixtures. NACA RM E51J05, 1951.
22. Markstein, George H.: Interaction of a Plane Flame Front with a Plane Sinusoidal Shear Wave. Jour. Aero. Sci., vol. 20, no. 8, Aug. 1953, pp. 581-582.
23. Ribner, H. S.: Convection of a Pattern of Vorticity Through a Shock Wave. NACA Rep. 1164, 1954. (Supersedes NACA TN 2864.)

REPORT 1278

EFFECT OF INTERACTION ON LANDING-GEAR BEHAVIOR AND DYNAMIC LOADS IN A FLEXIBLE AIRPLANE STRUCTURE¹

By FRANCIS E. COOK and BENJAMIN MILWITZKY

SUMMARY

The effects of interaction between a landing gear and a flexible airplane structure on the behavior of the landing gear and the loads in the structure have been studied by treating the equations of motion of the airplane and the landing gear as a coupled system. The landing gear is considered to have nonlinear characteristics typical of conventional gears, namely, velocity-squared damping, polytropic air-compression springing, and exponential tire force-deflection characteristics. For the case where only two modes of the structure are considered, an equivalent three-mass system is derived for representing the airplane and landing-gear combination, which may be used to simulate the effects of structural flexibility in jig drop tests of landing gears.

As examples to illustrate the effects of interaction, numerical calculations, based on the structural properties of two large airplanes having considerably different mass and flexibility characteristics, are presented. For the particular cases considered, it was found that the effects of interaction can result in appreciable reductions in the magnitude of the landing-gear force, particularly when the flexibility of the airplane structure is large and the natural frequency is small. Thus, neglect of interaction effects, that is, the use of the landing-gear forcing function for a rigid airplane, in a dynamic analysis of a flexible airplane can lead to the calculation of excessive loads in the airplane structure.

In the case of one of the airplanes considered, the structural loads calculated from the interaction solutions are greater than those for a completely rigid airplane treatment (rigid structure subjected to rigid-body forcing function) because the effects of dynamic magnification more than overcome the reduction in landing-gear force due to interaction. In the case of the second airplane, because of the relatively large natural period of the structure in comparison with the duration of the impact pulse, the dynamic magnification factor is appreciably less than unity. This effect, coupled with the reductions in landing-gear force due to interaction, results in structural loads that are less than those for a rigid airplane.

INTRODUCTION

In the design of landing gears it is usually assumed that the airplane is a rigid body and development tests are

frequently carried out in a drop-test jig with a landing gear attached to a concentrated mass. In so doing, it is tacitly assumed that the interaction between the motions of the landing gear and the deformations of the airplane structure has little or no effect on the behavior of the landing gear. Also, load time histories obtained on a rigid-body basis are often used as the forcing function in a dynamic analysis to determine the inertia loads and stresses in flexible airplane structures, again under the assumption that the behavior of the landing gear is independent of the effects of airplane flexibility. Although it has been recognized that this assumption is not altogether valid, the errors involved have not been considered particularly significant in the past because: (a) The errors were thought to be on the conservative side and (b) until comparatively recently main landing gears have generally been located very close to the nodes of the fundamental bending mode of the wing, and the airplane therefore closely approximated a rigid body insofar as the behavior of the landing gear is concerned. However, the trend toward increased size of airplanes, the disposition of large concentrated masses in outboard locations in the wings, the use of thinner wings, and the development of unconventional configurations tend to increase the flexibility of the airplane structure and reduce the natural frequencies of vibration. These characteristics tend to cause an increase in the amplitudes of the oscillatory motions of the landing-gear attachment points relative to the center of gravity of the flexible system during impact so that the effects of interaction are increased, both with regard to the behavior of the landing gear and the dynamic loads in the structure, particularly when the natural period of the fundamental mode of the structure approaches the time duration of the impact pulse.

A number of analytical studies and some simplified model tests (refs. 1 to 5) which have been made to evaluate the effects of structural flexibility on landing-gear loads have indicated some reduction in landing-gear force due to the effects of structural deformation. However, in view of the fact that these previous investigations considered only rather highly idealized linear-spring landing gears with either no damping at all or viscous damping, a further study of the effects of interaction between the landing gear and

¹ Supersedes NACA Technical Note 3467 by Francis E. Cook and Benjamin Milwitzky, 1955.

the airplane structure has been made with a more realistic representation of the landing gear. In the present analysis, as in reference 6, the landing gear is considered to have velocity-squared damping, polytropic air-compression springing, and exponential tire force-deflection characteristics, as is the case with conventional oleo-pneumatic landing gears in current use. The particular purposes of this investigation are to evaluate the effects of interaction on the behavior of the landing gear and to study the errors introduced into the calculated loads in the structure (applied loads, accelerations, bending moments, and shears) when a dynamic analysis is made on the basis of applying the landing-gear forcing function for a rigid body to a flexible airplane. For these purposes, case-history studies, based on the structural properties of two large airplanes having considerably different mass and flexibility characteristics, are presented. In order to cover a range of parameters, the landing gear of each airplane was assumed to be located at three arbitrary spanwise positions in addition to its original location. Only symmetrical impact conditions are considered.

The basic analysis of the landing gear and the airplane structure as a coupled system is presented in a general form. In the numerical examples presented, however, the system is simplified by considering the motions of the airplane in its first two structural modes only. With these restrictions, the combination of airplane and landing gear can also be represented by an equivalent three-mass system which may be used in jig drop tests of landing gears to simulate the primary effects of structural flexibility. A similar type of concentrated-mass system was used in the study of the hydrodynamic impact of a flexible seaplane in reference 7.

SYMBOLS

GENERAL

g	gravitational constant
K_L	lift factor, L_{tot}/W_{tot}
L_{tot}	total lift force (half the airplane)
t	time after initial contact
τ	time variable of integration
T	time to maximum landing-gear force
t'	time after maximum landing-gear force
V_{V_0}	vertical velocity at initial contact
W_{tot}	total weight (half the airplane)
Ω	circular frequency of sine pulse
Ω_i	circular frequency of cosine pulse
λ	any variable
λ_p	value of any variable λ at end of p th interval subsequent to beginning of numerical integration procedure

LANDING GEAR

A_a	pneumatic area of shock strut
A_h	hydraulic area of shock strut, $A_1 - A_p$
A_1	internal cross-sectional area of shock-strut inner cylinder
A_n	net orifice area of shock strut, $A_o - A_p$
A_o	area of fixed opening in orifice plate
A_p	cross-sectional area of metering pin or rod in plane of orifice

C_d	orifice discharge coefficient
F_{V_s}	vertical component of force in shock strut subsequent to beginning of shock-strut deflection
$F_{V_g}(z_u)$	vertical force applied to tire at ground
m_u	unsprung mass below shock strut
m, r, m'	constants in tire force-deflection relationship
n	polytropic exponent for air-compression process in shock strut
p_{a_0}	air pressure in shock strut when fully extended
ρ	mass density of hydraulic fluid
v_0	air volume of shock strut when fully extended
s	shock-strut stroke
t_i	duration of impact pulse
θ	angle between shock-strut axis and vertical
W_u	weight of unsprung mass below shock strut
z_f	vertical displacement of landing-gear attachment point from position at initial contact
z_u	vertical displacement of axle from position at initial contact

DISTRIBUTED STRUCTURE

a_n	generalized coordinate for n th mode
φ	angle of twist of transverse station
φ_n	modal function for torsion in n th mode
w	vertical displacement of elastic axis from position at initial contact
w_n	modal function of elastic axis for bending in n th mode
ζ	vertical displacement of station mass centers from position at initial contact
ζ_n	modal function of station mass centers for coupled bending torsion in n th mode
ξ_n	modal amplitude of landing-gear attachment point for coupled bending-torsion in n th mode
ϵ	chordwise distance between elastic axis and station mass center
b	wing span
M_B	bending moment
F	vertical component of applied landing-gear force
f_1	natural frequency of first deflection mode
I_o	polar moment of inertia of wing cross section about station mass center
I_{ea}	polar moment of inertia of wing cross section about elastic axis
K	radius of gyration of wing station about elastic axis
L	lift force per unit length of span
m	mass per unit length of span
M_n	generalized mass for n th mode (half the airplane)
ω_n	circular frequency of n th mode
Q_n	generalized force in n th mode
S	shear
t_n	natural period of n th mode
x	chordwise distance between elastic axis and any arbitrary point
x_f	chordwise distance between elastic axis and landing-gear attachment point
y	spanwise distance from airplane center plane to any transverse station

y_g	spanwise distance from airplane center plane to landing-gear station
z	vertical displacement of any point from position at initial contact
z_f	vertical displacement of landing-gear attachment point from position at initial contact
z_u	vertical displacement of axle from position at initial contact
δa_n	virtual displacement of generalized coordinate of n th mode
δW_n	virtual work in n th mode

EQUIVALENT THREE-MASS SYSTEM

a_0	vertical displacement of center of gravity of spring-connected masses from position of initial contact
k	spring constant
L_f	lift force acting on mass m_f
L_s	lift force acting on mass m_s
m_f	mass acting directly on landing gear
m_s	elastically supported mass
ω_1	natural frequency of vibration of spring-connected masses
u	deflection of spring
W_f	weight of mass acting directly on landing gear
W_s	weight of elastically supported mass
z_f	vertical deflection of landing-gear attachment point
z_s	vertical deflection of elastically supported mass
z_u	vertical displacement of axle from position at initial contact

AERODYNAMIC

A	total wing area (half the airplane)
A_i	wing area assumed concentrated at station i
C_L	lift coefficient
C_{L_0}	lift coefficient at instant of initial contact
C_{L_α}	lift-curve slope
γ	flight-path angle
γ_0	flight-path angle at instant of initial contact
ρ	mass density of air
V_L	landing speed of airplane

Subscripts:

a	aerodynamic
f	landing-gear attachment point
g	landing-gear station
i	any spanwise station
n	pertaining to the n th mode
0	zero or rigid-body mode
τ	at instant of initial shock-strut motion
T	at instant of maximum landing-gear force
max	maximum

The use of dots over symbols indicates differentiation with respect to time t or τ . All translations are positive downward (see figs. 1 to 3). The absolute value of any term () is indicated by |()|.

ANALYSIS

In order to study the behavior of a landing gear and a flexible airplane structure as mutually interacting elements of a coupled system, the equations for the landing-gear

force are combined with the equations of motion of the structure. The motions of the structure are treated by the mode-superposition approach, wherein the deflections of the structure are expanded in terms of its natural modes of vibration. The effects of interaction between the landing gear and the structure are introduced by expressing the landing-gear force in terms of the motions of the landing-gear attachment point and the wheel axle (or unsprung mass) rather than as an arbitrary function of time.

Because conventional oleo-pneumatic shock struts do not begin to deflect until some finite time after initial contact of the tire with the ground, the impact is treated in two parts, namely, the phases prior to and subsequent to the beginning of shock-strut deflection, where the initial conditions for the second phase are determined from the terminal conditions for the first phase.

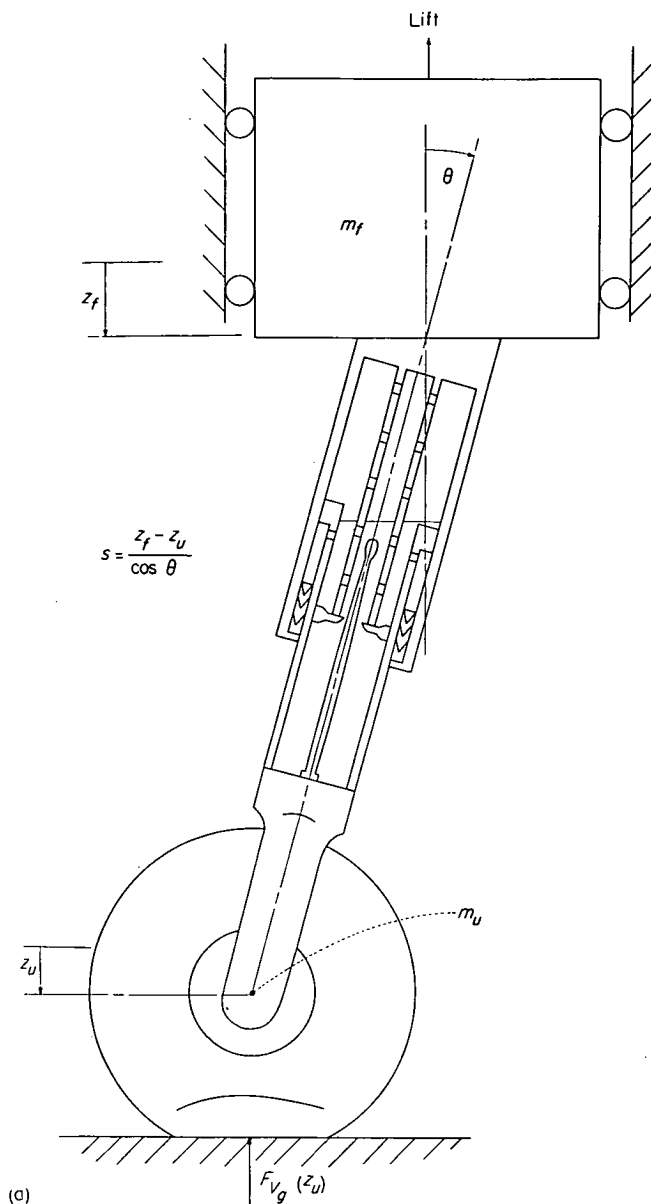
In the first part of the analysis, the equations for the landing-gear force are presented. Then, the deflections of the structure are expanded in terms of coupled modes and the resulting equations of motion for the system are presented in a general form. For the purpose of indicating the quantitative effects of interaction, however, the system used in the numerical trend studies has been simplified by restricting consideration of the structural deflections to the first two modes of the expansion. Within the framework of this two-mode treatment, it is also shown that the airplane structure can be represented by an equivalent system of spring-connected concentrated masses, which may be used to simulate the effects of structural flexibility in jig drop tests of landing gears.

LANDING-GEAR FORCE

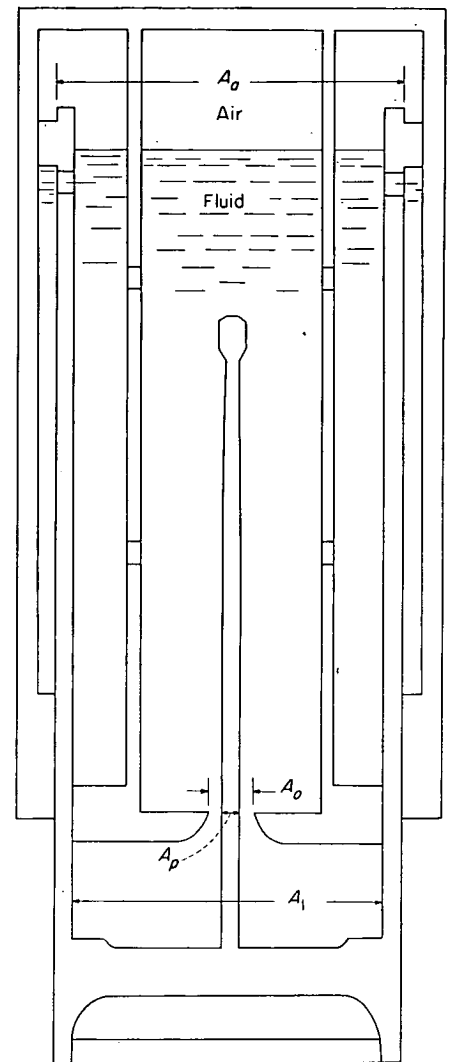
An analysis of the behavior of the conventional type of oleo-pneumatic landing gear was presented in reference 6. In this study the mass above the landing gear was considered as a rigid body; the system treated therefore had two degrees of freedom and is schematically represented in figure 1. The analysis of the landing gear considered the velocity-squared damping of the metering orifice, the air-compression springing of the shock strut, the nonlinear force-deflection characteristics of the tire, and the internal shock-strut friction forces. Calculated time histories of the landing-gear forces and the motions of the system were in good agreement with experimental data obtained in drop tests.

In the present study the rigid mass is replaced by a flexible airplane structure, but the treatment of the landing gear is essentially the same as that in reference 6. However, since conventional landing gears are inclined forward so as to minimize normal forces and bending moments due to the combination of vertical and drag forces, it will be assumed that the resultant force on the landing gear lies along the axis of the shock strut so that strut bending moments and resulting internal friction forces are neglected in the present analysis.

In view of the fact that conventional oleo-pneumatic shock struts are preloaded with air and therefore do not begin to deflect until some finite time t_r after initial contact of the tire with the ground, the impact must be treated in two phases. In the first phase, since the strut is effectively rigid,



(a) System with two degrees of freedom.



(b)

(b) Schematic representation of shock strut.

FIGURE 1.—Dynamical system (rigid airplane) considered in reference 6.

the landing gear has only one degree of freedom and the motion of the complete system of the landing gear and airplane is governed by the force between the tire and the ground. This ground force arises from the deflection of the tire and, in general, may be written as

$$F_{vg} = F_{vg}(z_u) \quad (1)$$

the exact variation depending on the particular tire force-deflection characteristics. Prior to the beginning of shock-strut deflection

$$F_{vg} = F_{vg}(z_f) \quad (t \leq t_r) \quad (1a)$$

since $z_u = z_f$. (This relationship is exact when the landing gear is vertical and holds very closely when the gear is inclined.)

The shock strut starts to deflect at the time t_r when the force exerted on the airplane by the shock strut becomes equal

to the air-pressure preloading force in the strut. At this instant the free-body equation for the unsprung mass of the landing gear is

$$m_u \ddot{z}_{f_r} + F_{vg}(z_{f_r}) = p_{a_0} A_a \cos \theta + W_u \quad (t = t_r) \quad (2)$$

Equation (2) provides the relationship between the terminal conditions for the first phase of the impact which, in conjunction with the solution of the equations of motion for the complete system prior to shock-strut deflection, determines the time t_r when the shock strut begins to deflect and, thus, the terminal values of the variables for the first phase of the impact. These values then serve as the initial conditions for the second phase of the impact.

After the shock strut begins to deflect, the landing gear has two degrees of freedom, since the motions of the landing-gear attachment point and the motions of the unsprung mass are no longer the same. The equation for the vertical

component of the force transmitted to the airplane by the landing gear after the shock strut starts to deflect is (see ref. 6)

$$F_{v_s} = \left[\frac{\dot{s}}{|\dot{s}|} \frac{\rho A_n^3}{2(C_d A_n)^2} \dot{s}^2 + p_{a_0} A_a \left(\frac{v_0}{v_0 - A_a \dot{s}} \right)^n \right] \cos \theta \quad (t \geq t_r) \quad (3)$$

where

$$s = \frac{z_f - z_u}{\cos \theta}$$

$$\dot{s} = \frac{\dot{z}_f - \dot{z}_u}{\cos \theta}$$

The equation of motion of the unsprung mass is

$$m_u \ddot{z}_u + F_{v_g}(z_u) = F_{v_s} + W_u \quad (t \geq t_r) \quad (4)$$

In equation (3) the first term represents the hydraulic force in the shock strut, where the factor $\frac{\dot{s}}{|\dot{s}|}$ indicates the change in sign required between the compression and extension strokes. (During the extension stroke of the shock strut, because of the action of the rebound check valve or "snubber" incorporated in most landing gears, the net orifice area A_n will generally be smaller and the orifice discharge coefficient C_d will be different from the values which apply during the compression stroke.) The second term of equation (3) expresses the air-compression force in the strut, based on a polytropic pressure-volume relationship. In equation (4), the force arising from the deflection of the tire may be expressed as $F_{v_g}(z_u) = m z_u^r$ for the usual types of pneumatic tires, where m and r are constants for each regime of the tire-deflection process (see ref. 6).

EQUATIONS OF MOTION OF THE AIRPLANE

Differential equations of airplane structure.—In the mode-superposition approach, the structure is considered to deflect in its natural modes of vibration and the total displacement of any point in the system is the sum of the displacements of the point in all the modes considered. With this approach the motions are separated into functions which depend only on the space coordinates and functions which depend on the time variable.

In the case of a landing impact the process is discontinuous at the instant t_r when the shock strut begins to deflect. In the first phase of the impact the shock strut is effectively rigid, so that the motion of the unsprung mass of the landing gear is essentially the same as the motion of the landing-gear attachment point and the force transmitted by the landing gear to the airplane is the vectorial sum of the ground force due to tire deflection, the inertia reaction of the unsprung mass, and the weight of the unsprung mass. In the second phase of the impact, the motion of the unsprung mass is not the same as the motion of the landing-gear attachment point and the force applied to the airplane is governed by the relative motion between the landing-gear attachment point and the unsprung mass, as given by equation (3).

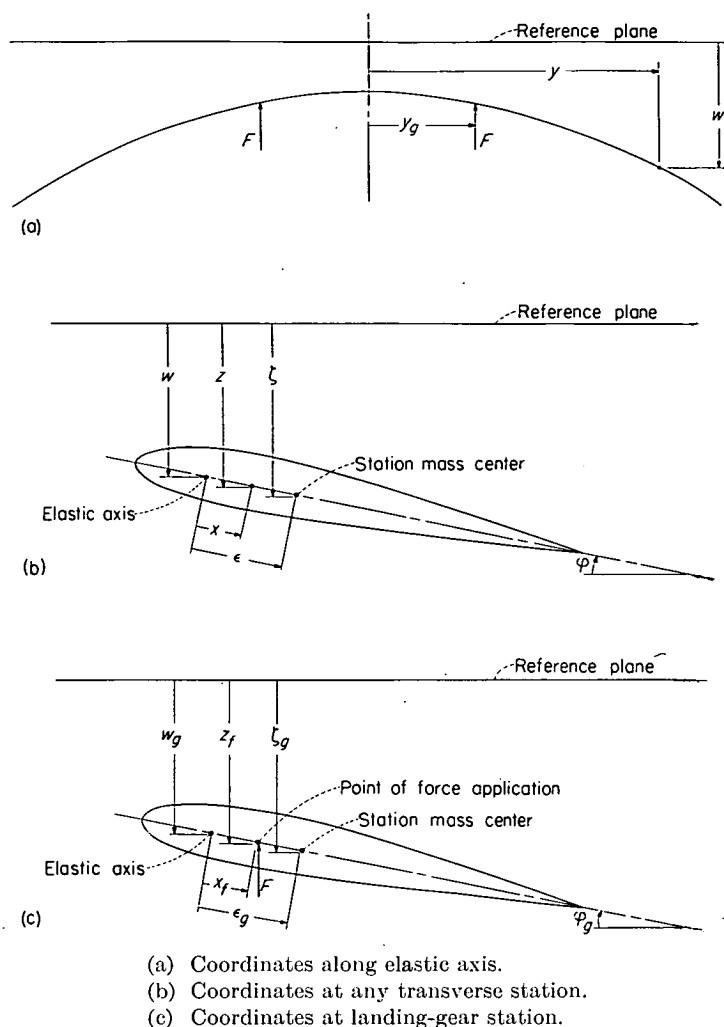


FIGURE 2.—Coordinates for airplane structure.

The notation employed in the analysis is indicated in figure 2. A typical transverse station located at a spanwise distance y from the airplane center plane is considered. The mass per unit length of span is designated by m . The translation of the elastic axis at the station is denoted by w ; ζ is the translation of the station mass center; ϵ is the chordwise distance between the station mass center and the elastic axis; and ϕ is the angle of twist of the station. The translation of an arbitrary point located at a chordwise distance x from the elastic axis is designated by z . The spanwise distance from the center plane of the airplane to the landing-gear station is indicated by y_g . The translation of the landing-gear attachment point, or force-application point, is designated z_f ; the distance between the landing-gear attachment point and the elastic axis is denoted by x_f .

In the most general case, the expansion of the deflection of the structure in terms of its natural coupled modes of vibration may be written as

$$w(y, t) = \sum_{n=0}^{\infty} a_n(t) w_n(y) \quad (5)$$

and

$$\phi(y, t) = \sum_{n=0}^{\infty} a_n(t) \phi_n(y) \quad (6)$$

where the subscript n denotes the order of any mode, a_n is the generalized coordinate in the n th mode, and w_n and φ_n are the corresponding modal functions for bending and torsion, respectively.

For later use it is convenient to introduce expressions for the displacements at other points in the structure. Since the translation of the station mass centers is given by $\zeta = w + \epsilon\varphi$, it follows that

$$\zeta(\epsilon, y, t) = \sum_{n=0}^{\infty} a_n(t) \zeta_n(y) \quad (7)$$

where the modal function $\zeta_n = w_n + \epsilon\varphi_n$. The translation of any arbitrary point along the chord is given by $z = w + x\varphi$; therefore,

$$z(x, y, t) = \sum_{n=0}^{\infty} a_n(t) z_n(y) \quad (8)$$

where the modal function $z_n = w_n + x\varphi_n$. The translation of the landing-gear attachment point is given by $z_f = w + x_f\varphi$; therefore,

$$z_f(x_f, y_f, t) = \sum_{n=0}^{\infty} a_n(t) \xi_n(y_f) \quad (9)$$

where the modal amplitude $\xi_n = w_n + x_f\varphi_n$.

By application of Lagrange's equation and the orthogonality relationships between coupled modes, it can be shown (see, for example, refs. 8 to 10) that the equation of motion for the airplane in the n th mode may be written as

$$M_n \ddot{a}_n + M_n \omega_n^2 a_n = Q_n \quad (n=0, 1, 2, \dots) \quad (10)$$

where M_n is termed the generalized mass for the n th mode and Q_n is the generalized force, as determined from virtual-work considerations. For a continuous system,

$$\left. \begin{aligned} M_n &= \int_0^{b/2} m w_n^2 dy + 2 \int_0^{b/2} m \epsilon \varphi_n w_n dy + \int_0^{b/2} m K^2 \varphi_n^2 dy \\ &= \int_0^{b/2} m \zeta_n^2 dy + \int_0^{b/2} I_o \varphi_n^2 dy \end{aligned} \right\} \quad (11)$$

In practice the spanwise mass distribution is often approximated by breaking up the distribution into discrete masses which are concentrated at a finite number of stations along the span. With this approach equation (11) may be written as

$$\left. \begin{aligned} M_n &\approx \sum_i (m_i w_{ni}^2 + 2m_i \epsilon_i \varphi_{ni} w_{ni} + m_i K_i^2 \varphi_{ni}^2) \\ &\approx \sum_i (m_i \zeta_{ni}^2 + I_{oi} \varphi_{ni}^2) \end{aligned} \right\} \quad (11a)$$

where the subscript i denotes any spanwise station.

For $n=0$ (rigid-body mode), since $w_0 = \zeta_0 = 1$ and $\varphi_0 = 0$,

$$M_0 = \int_0^{b/2} m dy \approx \sum m_i$$

The relationship between Q_n and the external forces can be determined by application of virtual-work principles. By definition, the work done in the n th mode by the generalized force acting through a virtual displacement of the generalized coordinate of the mode is equal to the work done by the external forces acting through virtual displacements of their points of application in the mode. Thus, the virtual work done by the generalized force in the n th mode is

$$\delta W_n = Q_n \delta a_n \quad (12)$$

In the case of an airplane during landing, the external forces are the distributed lift forces $L(y)$, the distributed weights $gm(y)$, and the force F transmitted by the landing gear. The virtual work done by these external forces in the n th mode is therefore given by

$$\begin{aligned} \delta W_n &= - \left(\int_0^{b/2} L \delta a_n z_n dy - g \int_0^{b/2} m \delta a_n \zeta_n dy + F \delta a_n \xi_n \right) \\ &= - \delta a_n \left(\int_0^{b/2} L z_n dy - g \int_0^{b/2} m \zeta_n dy + F \xi_n \right) \end{aligned} \quad (13)$$

Equating equations (12) and (13) gives the following relationship for Q_n :

$$Q_n = - \left(\int_0^{b/2} L z_n dy - g \int_0^{b/2} m \zeta_n dy + F \xi_n \right)$$

Therefore, the equation of motion of the structure in the n th mode is

$$M_n \ddot{a}_n + M_n \omega_n^2 a_n = -F \xi_n - \int_0^{b/2} L z_n dy + g \int_0^{b/2} m \zeta_n dy \quad (n=0, 1, 2, \dots) \quad (14)$$

For the rigid-body mode ($n=0$), since $\omega_0 = 0$ and $z_0 = \zeta_0 = \xi_0 = 1$, equation (14) becomes

$$M_0 \ddot{a}_0 = -F - \int_0^{b/2} (L - gm) dy$$

subject to the initial conditions

$$a_0(0) = 0$$

and

$$\dot{a}_0(0) = V_{v_0}$$

If the airplane is assumed to be free of oscillations at the time of initial contact,

$$\dot{a}_n(0) = \ddot{a}_n(0) = 0 \quad (n \neq 0)$$

At the instant of initial contact, the airplane may be accelerating, that is, $\ddot{a}_0(0) \neq 0$, if the total lift is not exactly equal to the total weight. Consideration of the balance of forces on the unsprung mass as a free body leads to the following equation for the force applied to the airplane by

the landing gear at the instant of contact:

$$F(0) = W_u \left[\frac{\ddot{a}_0(0)}{g} - 1 \right]$$

Substitution of this relationship into the equation of motion for the rigid-body mode gives

$$\begin{aligned} \ddot{a}_0(0) &= \frac{W_u - \int_0^{b/2} (L - gm) dy}{M_0 + m_u} = \frac{W_{tot} - L_{tot}}{W_{tot}/g} \\ &= (1 - K_L)g \end{aligned}$$

where

$$K_L = \frac{L_{tot}}{W_{tot}}$$

so that

$$F(0) = -K_L W_u$$

With this definition of $F(0)$ and the initial conditions for the modes $n \neq 0$, equation (14) applied to the instant $t=0$ gives

$$a_n(0) = \frac{1}{M_n \omega_n^2} \left(g \int_0^{b/2} m \xi_n dy - \int_0^{b/2} L z_n dy + K_L W_u \xi_n \right) \quad (n \neq 0)$$

This relationship indicates that, in general, a finite static deflection in the flexible modes will be present at the time of initial contact. At any subsequent time the deflection will be equal to this initial static deflection plus an additional deflection a_{n_t} , which varies with time; that is, $a_n = a_n(0) + a_{n_t}$. This substitution permits equation (14) to be written as

$$M_n \ddot{a}_{n_t} + M_n \omega_n^2 a_{n_t} = -(F + K_L W_u) \xi_n \quad (n \neq 0) \quad (15)$$

subject to the initial conditions

$$a_{n_t}(0) = \dot{a}_{n_t}(0) = 0$$

In the remainder of the report, for the sake of simplicity of notation, the subscript t will be dropped, with the understanding that a_n represents the time-varying part of the displacement of the n th mode, so that equation (15) is written as

$$M_n \ddot{a}_n + M_n \omega_n^2 a_n = -(F + K_L W_u) \xi_n \quad (n \neq 0) \quad (15a)$$

If the external forces are specified solely as functions of time, the equations of motion for each mode of the system are uncoupled and can be solved individually. However, when the external forces depend on the motions of the system, as in the case of the landing-gear force during a landing impact, the relationships between the external forces and the motions in the modes serve to couple the equations of motion so that they must be solved simultaneously. Furthermore, in the case of landing impact, since the process has two

phases, as previously discussed, the equations of motion for each phase must be solved separately, where the initial conditions for the second phase are the same as the terminal conditions for the first phase.

Motion prior to beginning of shock-strut deflection.—Since the shock strut is effectively rigid in the first phase of the impact, the force transmitted by the landing gear to the airplane, F in equation (15a), is equal to the ground force $F_{V_g}(z_f)$ less the inertia reaction of the unsprung mass and the weight of the unsprung mass, as may be seen by considering the unsprung mass as a free body; thus,

$$F_{t \leq t_r} = F_{V_g}(z_f) + m_u \ddot{z}_f - W_u$$

so that the motions of the system during the first phase of the impact are governed by the following set of differential equations:

$$\left. \begin{aligned} M_0 \ddot{a}_0 &= -[F_{V_g}(z_f) + m_u \ddot{z}_f + W_{tot}(K_L - 1)] \\ M_1 \ddot{a}_1 + M_1 \omega_1^2 a_1 &= -[F_{V_g}(z_f) + m_u \ddot{z}_f + W_u(K_L - 1)] \xi_1 \\ &\vdots \\ M_m \ddot{a}_m + M_m \omega_m^2 a_m &= -[F_{V_g}(z_f) + m_u \ddot{z}_f + W_u(K_L - 1)] \xi_m \end{aligned} \right\} \quad (t \leq t_r) \quad (16)$$

where

$$z_f = \sum_{n=0}^m a_n \xi_n$$

and the m th mode is the highest mode considered.

The initial conditions for equations (16) are the conditions at the instant of initial contact, namely,

$$a_0(0) = 0$$

$$\dot{a}_0(0) = V_{V_o}$$

and

$$a_n(0) = \dot{a}_n(0) = 0 \quad (n \neq 0)$$

As previously indicated, the first phase of the impact terminates at the time t_r when the force in the shock strut becomes equal to the air-pressure preload force. The terminal conditions at this instant, as determined by consideration of the unsprung mass as a free body, are given by equation (2), namely,

$$m_u \ddot{z}_{f_r} + F_{V_g}(z_{f_r}) = p_{a_o} A_a \cos \theta + W_u$$

The solution of equations (16) in conjunction with equation (2) permits the determination of the time t_r when the shock strut begins to deflect and the values of the motion variables at this instant; these values then serve as the initial conditions for the second phase of the impact.

Motion subsequent to beginning of shock-strut deflection.—In the second phase of the impact the force transmitted by the landing gear, F in equation (15a), is the vertical component of the shock-strut force F_{V_s} , as given by

equation (3). Thus, the motions of the system during the second phase of the impact are governed by the following set of differential equations:

$$\left. \begin{aligned} M_0 \ddot{a}_0 &= -(F_{V_s} + W_u) - W_{tot}(K_L - 1) \\ M_1 \ddot{a}_1 + M_1 \omega_1^2 a_1 &= -(F_{V_s} + K_L W_u) \xi_1 \\ &\vdots \\ M_m \ddot{a}_m + M_m \omega_m^2 a_m &= -(F_{V_s} + K_L W_u) \xi_m \end{aligned} \right\} \quad (t > t_r) \quad (17)$$

and

$$m_u \ddot{z}_u + F_{V_g}(z_u) = F_{V_s} + W_u$$

where

$$F_{V_s} = F_{V_g}(z_f - z_u, \dot{z}_f - \dot{z}_u)$$

as given by equation (3); and

$$z_f = \sum_{n=0}^m a_n \xi_n$$

The first m equations of equations (17) represent the motions of the airplane structure in its first m modes, whereas the last equation of the set is the equation of motion of the unsprung mass of the landing gear as previously given by equation (4). The initial conditions for equations (17) are the terminal conditions for equations (16) as previously discussed. In view of the fact that the landing-gear forcing term F_{V_g} is highly nonlinear, analytical solution of the system of equations (17) does not appear possible, so that it is necessary to resort to numerical-integration or analog methods.

SIMPLIFIED SYSTEM CONSIDERED IN NUMERICAL STUDIES

The preceding section has presented the equations of motion for a flexible airplane coupled to a landing gear, which permit calculation of the motions of the system during a landing impact with consideration of as many modes as may be desired. For the study of the effects of interaction between the landing gear and the structure, however, it appears that the primary effects of structural flexibility on the behavior of the landing gear can be represented by considering only the first deflection mode in addition to the rigid-body mode.² This simplification, which greatly reduces the amount of computational work, is felt to be justified for the purposes of the present investigation since both theoretical considerations and experimental data indicate that the higher modes should have relatively little effect on the landing-gear performance. With this assumption the equa-

² In a dynamic analysis, stresses in the structure due to excitation of the higher modes can be approximated by calculating the response of such modes, individually, to the forcing function determined for the landing gear coupled with the rigid-body and first deflection modes. This procedure should be a considerable improvement over the use of the rigid-body forcing function as a basis for response calculations in cases where the landing-gear attachment points experience appreciable deflections relative to the mass center of the system.

tions of motion reduce to

$$M_0 \ddot{a}_0 = -[F_{V_g}(z_f) + m_u \ddot{z}_f + W_{tot}(K_L - 1)] \quad (18a)$$

$$M_1 \ddot{a}_1 + M_1 \omega_1^2 a_1 = -[F_{V_g}(z_f) + m_u \ddot{z}_f + W_u(K_L - 1)] \xi_1 \quad (18b)$$

and

$$M_0 \ddot{a}_0 = -(F_{V_s} + W_u) - W_{tot}(K_L - 1) \quad (19a)$$

$$M_1 \ddot{a}_1 + M_1 \omega_1^2 a_1 = -(F_{V_s} + K_L W_u) \xi_1 \quad (19b)$$

$$m_u \ddot{z}_u + F_{V_g}(z_u) = F_{V_s} + W_u \quad (19c)$$

where

$$z_f = a_0 + a_1 \xi_1$$

and

$$m_u \ddot{z}_{f_r} + F_{V_g}(z_{f_r}) = p_{a_0} \cos \theta + W_u \quad (t = t_r)$$

The solution of equations (18) and the determination of the conditions at the time t_r when the shock strut begins to deflect, which serve as the initial conditions for equations (19), are treated in appendix A. With these initial conditions, equations (19) may be solved by numerical integration or analog methods.

From the time-history solutions for the motions of the system thus obtained, the accelerations and inertia loads at any point in the structure can be calculated from the equations presented in appendix B.

EQUIVALENT THREE-MASS SYSTEM

It is of interest to note that the equations of motion previously given not only represent the distributed system of the airplane but can also be used to define equivalent systems of spring-connected masses, where the number of masses above the landing gear is equal to the number of modes considered. For the particular case where two modes are considered, the equivalent system is one containing three masses, one of which is the unsprung mass of the landing gear. The use of such a three-mass system provides a relatively simple means for simulating the primary effects of structural flexibility in actual drop tests of landing gears in a drop-test jig.

In the equivalent three-mass system (see fig. 3), m_f represents the mass to which the landing gear is directly attached and m_s is the elastically connected mass. The displacement of m_f relative to its position at the instant of initial contact is denoted by z_f ; the displacement of m_s is designated z_s , whereas the displacement of the axle or unsprung mass m_u is z_u . The spring constant of the elastic member is denoted by k . Separate lift forces L_s and L_f will be considered to act on the masses m_s and m_f .

In order that the three-mass system represents the airplane properly, z_f , z_u , m_u , and, of course, the landing-gear characteristics must be the same for the two systems, so that the

$$\frac{M_1}{\xi_1} \ddot{a}_1 + \frac{M_1}{\xi_1} \omega_1^2 a_1 + K_L W_u = -F \quad (23b)$$

Thus, the problem is reduced to determining the constants for the three-mass system so as to make equations (22) identically equivalent to equations (23). This may be done in any of several different ways. For example, since the structure is taken as linear, let

$$z_s = a_0 + a_1 \beta$$

where β is a constant to be determined. Substituting for z_f and z_s in equations (22a) and (22b) and eliminating \ddot{a}_0 between these equations gives

$$m_f(\xi_1 - \beta) \ddot{a}_1 + \frac{k}{m_s}(\xi_1 - \beta)(m_f + m_s)a_1 + L_f - W_f + \frac{m_f}{m_s}(W_s - L_s) = -F \quad (24)$$

whereas subtracting equation (22a) from equation (22b), with the same substitutions, gives

$$\ddot{a}_0 + \beta \ddot{a}_1 + \frac{k}{m_s}(\beta - \xi_1)a_1 + \frac{L_s}{m_s} - g = 0 \quad (25)$$

Equation (24) is directly comparable with equation (23b). Combining equations (23a) and (23b) so as to eliminate F and to make the coefficient of \ddot{a}_0 equal to unity gives the following equation with which equation (25) may be directly compared:

$$\ddot{a}_0 - \frac{M_1}{M_0 \xi_1} \ddot{a}_1 - \frac{M_1 \omega_1^2}{M_0 \xi_1} a_1 + (K_L - 1)g = 0 \quad (26)$$

In order to evaluate the constants for the three-mass system, each term in equations (24) and (25) is set equal to the corresponding term in equations (23b) and (26), respectively. This procedure gives six simultaneous equations, the solution of which yields the following expressions for the constants in the three-mass system:

$$m_s + m_f = M_0 \quad (27)$$

$$L_s + L_f = K_L W_{101} \quad (28)$$

$$m_s = \frac{M_0^2 \xi_1^2}{M_1 + M_0 \xi_1^2} \quad (29)$$

$$m_f = \frac{M_1 M_0}{M_1 + M_0 \xi_1^2} \quad (30)$$

$$\frac{m_s}{m_f} = \frac{M_0 \xi_1^2}{M_1} \quad (31)$$

$$k = M_1 \omega_1^2 \left(\frac{M_0 \xi_1}{M_1 + M_0 \xi_1^2} \right)^2 \quad (32)$$

$$L_s = K_L g \left(\frac{M_0^2 \xi_1^2}{M_1 + M_0 \xi_1^2} \right) \quad (33)$$

and

$$L_f = K_L g \left(\frac{M_1 M_0}{M_1 + M_0 \xi_1^2} + m_u \right) \quad (34)$$

where

$$\beta = -\frac{M_1}{M_0 \xi_1} \quad (35)$$

and

$$m_f \ddot{z}_f + m_s \ddot{z}_s = M_0 \ddot{a}_0 \quad (36)$$

With the foregoing substitutions, equations (22) are identically equivalent to equations (23); thus, the three-mass system with the specified values of m_s , m_f , k , L_s , and L_f can be considered to be equivalent to the airplane in its first two modes during both the first and second stages of the impact. Equations (27) and (28) are required to satisfy the equations of motion for the airplane as a rigid body, whereas equations (29) to (34) are required for proper representation of the airplane in its first flexible mode. With this approach the structural properties of the airplane are defined by three parameters: the total mass above the landing gear M_0 , the mass ratio m_s/m_f , and the natural frequency ω_1 .

The solution of the equations of motion during the first phase of the impact and the determination of the conditions at the instant of initial shock-strut deflection t_r are treated in appendix A. With these conditions as initial conditions, the equations of motion for the second phase of the impact can be solved by numerical-integration or analog methods. From the time-history solutions for the motion of the three-mass system, the inertia loads and bending moments at any point in the airplane structure can be calculated by use of the equations in appendix B.

SOLUTION OF EQUATIONS OF MOTION

In view of the fact that the equations of motion subsequent to time t_r are highly nonlinear and therefore cannot be solved in closed form, it is necessary to resort to numerical-integration or analog methods. Various numerical-integration procedures are given in references 11 to 13. Appendix A of reference 6 illustrates the application of several such methods to the problem of the impact of a landing gear attached to a rigid mass. One of these methods, which may be termed the "quadratic procedure," was used to obtain those numerical results presented in this report which could not be obtained analytically.

In this procedure, which involves a step-by-step solution of the equations of motion, the following difference equations

(ref. 11, p. 16) based on a quadratic variation of displacement over successive finite time intervals are used to replace the derivatives in the equations of motion:

$$\dot{\lambda}_p = \frac{\lambda_{p+1} - \lambda_{p-1}}{2 \Delta t}$$

and

$$\lambda_p = \frac{\lambda_{p+1} - 2\lambda_p + \lambda_{p-1}}{(\Delta t)^2}$$

where λ_p is the value of any variable at the end of the p th interval subsequent to the beginning of the process and Δt is the time interval. The difference equations of motion obtained by substituting these expressions into the differential equations of the system then become essentially extrapolation formulas which permit calculation of the displacements to come from the values of displacement already calculated, the whole procedure starting out with the initial conditions of the process; that is, the conditions at the instant $t=t_r$ when the shock strut first begins to deflect. With the displacement time histories thus calculated, the velocities and accelerations are then determined from the foregoing difference equations.

CALCULATED RESULTS AND DISCUSSION

CASES CONSIDERED

In order to investigate the effects of structural flexibility on the behavior of the landing gear and the loads in the airframe, several case-history studies are presented which cover a range of airplane mass ratios m_s/m_f . The calculations are based on the structural properties of two large airplanes having considerably different mass and flexibility characteristics. Airplane A is representative of a four-engine propeller-driven World War II bomber having a gross weight of 47,200 pounds and a natural frequency of vibration in the first coupled bending-torsion mode of 3.37 cycles per second. The structural characteristics used for airplane B are representative of a present-day swept-wing six-jet-engine bomber having a gross weight of 125,000 pounds and a natural frequency of 1.29 cycles per second in the first coupled bending-torsion mode. The landing-gear characteristics used for airplane A were based on the manufacturer's data, whereas for airplane B, because information was not available, the shock-strut characteristics were chosen so as to yield a landing gear which is essentially a scaled-up model of the landing gear of airplane A. The pertinent numerical data for airplanes A and B are given in tables I and II, respectively; the modal functions for the first coupled bending-torsion mode are plotted in figure 4.

The main landing gears of airplane A were located in the inboard engine nacelles very close to the nodes of the first coupled bending-torsion mode; in the case of airplane B the

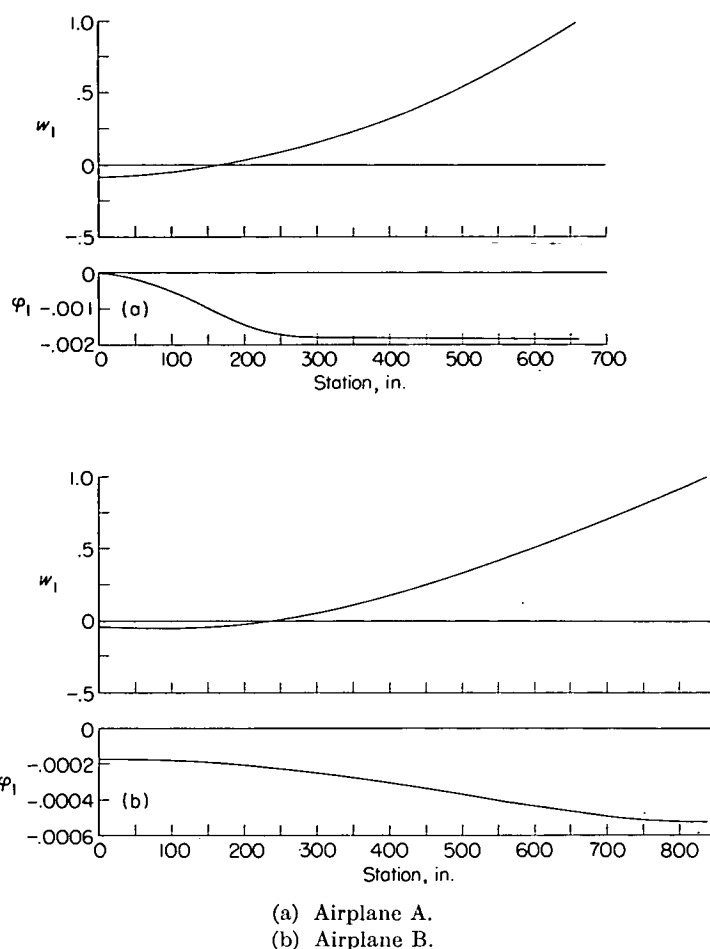


FIGURE 4.—Modal functions for bending and torsion.

landing gear is of the bicycle type and is located in the airplane center plane. The position of the landing gear (since it determines the value of the modal amplitude ξ_1) in conjunction with the values of M_0 and M_1 governs the value of the mass ratio m_s/m_f for each case. (See eq. (31).)

In order to represent a broader range of mass and flexibility effects, the calculations for each airplane were made for four mass ratios corresponding to three arbitrary landing-gear positions in addition to the original landing-gear location. In practice, of course, a change in landing-gear location would probably necessitate a modification of the wing structure and result in some change in the modal characteristics and, thus, the mass ratio. The main purpose of the calculations, however, is to indicate the effect of mass ratio on the behavior of the system, and the exact locations of the landing gear which correspond to the mass ratios used are of secondary interest.

In the calculation of the mass ratio m_s/m_f , the landing-gear force was assumed to pass through the mass center of the landing-gear station. Since the modal characteristics

used were for the complete airplane including the unsprung mass of the landing gear m_u , it was assumed that the unsprung mass was rigidly connected to the mass m_f in the equivalent three-mass system, as in the first phase of the impact, so that

$$\frac{m_s}{m_f + m_u} = \frac{M_0 \xi_1^2}{M_1}$$

where M_0 , M_1 , and ξ_1 include the effects of the unsprung mass as part of the airplane mass distribution. The mass ratios considered and the corresponding landing-gear locations are as follows:

Airplane A		Airplane B	
Landing-gear location at—	Mass ratio, m_i/m_f	Landing-gear location at—	Mass ratio, m_i/m_f
Station 0.....	0.24	Station 0.....	0.22
Nodes.....	0	Nodes.....	0
Station 245.....	.52	Station 420.....	.85
Station 307.....	3.33	Station 504.....	2.84

When the landing gear is located at the node of the first flexible mode, this mode, of course, is not excited and, since higher modes are not considered in the numerical calculations, the airplane behaves as though it were a rigid body, its motion being governed by equation (23a). As might be expected, the farther away the landing gear is from the nodes, the larger is the effective flexibility of the system and, thus, the mass ratio.

In the calculation of the time histories of the motions of the system, the lift force was assumed to be constant during the impact and equal to the total weight of the airplane, that is, $K_L=1$. This assumption corresponds to the condition that

$$L_s = W_s$$

and

$$L_f = W_f + W_u$$

in the equivalent three-mass system.

TABLE I.—CHARACTERISTICS OF AIRPLANE A

(a) Structure

[Data taken from ref. 8]

Station, in.	$\frac{m_i}{\text{lb-sec}^2 \text{ in.}}$	$I_{ea_i}, \text{ lb-in.-sec}^2$	$\epsilon_i, \text{ in.}$	W_{1_i}	φ_{1_i}
0	28.5	---	0	-0.078	0
133	16.3	85,234	-39.26	-.031	-.00084
217	5.27	1,288	0	-.047	-.0016
307	9.15	61,717	-62.19	.164	-.00183
428	.974	536	0	.374	-.00185
548	.686	287	0	.670	-.00187
638	.153	34.1	0	.936	-.00188

$M_0, \frac{\text{lb-sec}^2}{\text{in.}}$	61.033
$M_1, \frac{\text{lb-sec}^2}{\text{in.}}$	1.607
$f_1, \text{ cps}$	3.365

(b) Shock strut

[Manufacturer's data]

$A_h, \text{ sq ft}$	0.163
$A_a, \text{ sq ft}$	0.214
$A_n, \text{ sq ft}$	0.00173
$v_o, \text{ cu ft}$	0.2597
$p_{a_o}, \text{ lb/sq ft}$	30,528
$p, \text{ slugs/cu ft}$	1.626

(c) Unsprung mass

[Manufacturer's data]

$W_u, \text{ lb}$	700
Tires (one per landing gear).....	56-inch smooth contour
Tire pressure, lb/sq in.	70
$m, \text{ lb/ft}$	85,309
r	1.22

TABLE II.—CHARACTERISTICS OF AIRPLANE B

(a) Structure

[Unpublished data]

Station, in.	$\frac{m_i}{\text{lb-sec}^2 \text{ in.}}$	$I_{ea_i}, \text{ lb-in.-sec}^2$	$\epsilon_i, \text{ in.}$	W_{1_i}	φ_{1_i}
0	109.534	4,475,280	200.37	-0.0585	-0.000176
84	4.695	3,046	-4.65	-.0579	-.000187
168	4.920	19,490	-24.20	-.0350	-.000204
252	22.177	278,942	-101.22	.0037	-.000231
336	2.560	2,161	2.44	.090	-.000272
420	2.557	1,988	2.60	.1842	-.000322
504	1.773	1,136	.92	.3253	-.000379
588	3.269	2,474	-14.79	.4772	-.000435
672	8.628	8,439	-26.88	.6369	-.000482
756	1.144	500	.60	.8181	-.000514
840	.520	186	5.48	1.000	-.000526

$M_0, \frac{\text{lb-sec}^2}{\text{in.}}$	161.775
$M_1, \frac{\text{lb-sec}^2}{\text{in.}}$	6.9096
$f_1, \text{ cps}$	1.29

(b) Shock strut

[Values estimated from generalized curves of ref. 6]

$\frac{\rho A_h^3}{2(C_d A_n)^2}, \text{ slugs/ft}$	17,900
$A_a, \text{ sq ft}$	0.585
$v_o, \text{ cu ft}$	0.7095
$p_{a_o}, \text{ lb/sq ft}$	30,528

(c) Unsprung Mass

[Manufacturer's data]

$W_u, \text{ lb}$	2,300
Tires (two per landing gear).....	56×16
m per landing gear, lb/ft.....	280,180
r	1.21

On the basis of the calculations in reference 6, the shock-strut orifice discharge coefficient C_d was assumed as 0.9 and the polytropic exponent n for the air-compression process was taken as 1.12.

EFFECT OF INTERACTION ON BEHAVIOR OF SYSTEM

Time-history solutions for the motions of the system during impact at an initial vertical velocity of 10 feet per second have been made for the eight configurations previously mentioned. Figures 5 to 8 show the variation during impact of the more important quantities, such as the landing-gear force F , the responses \ddot{a}_0/g , \ddot{a}_1/g , \ddot{z}_1/g , \ddot{z}_s/g , the landing-gear-motion variables, and the accelerations at the mass centers of several stations along the span. Comparison of the calculated results for the flexible cases with those for the airplane as a rigid body (or landing gear at nodes, $m_s/m_f=0$) indicates that the interaction between the flexible structure and the landing gear can result in an appreciable reduction in the applied landing-gear force (and thus, the nodal acceleration), the largest reductions occurring at the highest mass ratios. Furthermore, the reductions in landing-gear force at the higher mass ratios are greater for airplane B, because of its lower natural frequency, than for airplane A.

Consideration of the calculated time histories of the motion of the landing gear indicates how the interaction between the flexible structure and the landing gear affects the loads produced in the landing gear. Because of the flexibility of the structure, the landing-gear attachment point deflects upward relative to the nodes, or instantaneous center of mass of the system, as the applied force builds up and the deceleration of the landing-gear attachment point is greater than in the case of the rigid airplane. Thus, the downward velocity of the shock-strut outer cylinder is more rapidly dissipated and the displacement of the outer cylinder is smaller throughout most of the impact. The tire deflection is also smaller; however, because of the high stiffness of the tire, the decrease in tire deflection is smaller than the decrease in outer-cylinder displacement. The net result is a reduction in strut stroke during that part of the impact when the maximum force occurs and an accompanying reduction in the strut telescoping velocity. Since the maximum landing-gear force is primarily due to the hydraulic resistance in the strut (because the strut stroke, and thus the air-compression force, is generally small at the time of maximum telescoping velocity), the decrease in telescoping velocity results in a decrease in shock-strut force.

In the case of airplane A with landing gear at station 307, the effect of interaction is a marked change in the shape, as well as in the magnitude, of the time histories. Because of the superimposed vibrations of the structure, the shock-strut telescoping velocity (see fig. 5) has acquired an os-

cillatory character with two peaks of the same amplitude. However, since the second telescoping-velocity peak occurs when the stroke is large, the superposition of the high air-compression force on the hydraulic-force results in a total-force time history the second peak of which is much higher than the first (see Force-time curves, fig. 5) and which is also higher than might be expected from the results for the smaller mass ratios, which have a considerably different appearance. In the case of airplane B, because of the lower natural frequency, this double-peaked characteristic does not appear even for the largest mass ratio, all mass ratios yielding time histories similar in shape, the maximum force decreasing in a regular manner with increasing mass ratio.

The extent to which the first flexible modes of airplanes A and B are excited by the impacts may be observed by examining the time histories of a_1 , \dot{a}_1 , and \ddot{a}_1 . As may be expected, the higher the mass ratio, the greater is the degree of excitation.

From the calculated values of \ddot{a}_0/g and \ddot{a}_1/g or \ddot{z}_1/g and \ddot{z}_s/g , the acceleration at any point along the span may be computed by means of the equations in appendix B. Figures 6 and 8 show time histories of the acceleration at the mass centers of several stations for each of the landing-gear locations considered. Because of the combined effects of the changes in the landing-gear forcing function and in the degree of excitation of the flexible modes, a given change in landing-gear location may result in an increase in acceleration at some stations and a reduction in acceleration at other stations.

Figures 5 and 7 also show time histories of the acceleration \ddot{z}_s/g which would be experienced by the elastically connected mass m_s in the equivalent three-mass system, as in a drop test. The reduction in acceleration with increasing mass ratio is evident. As previously indicated, if such a drop test were made, the measured accelerations \ddot{z}_1/g and \ddot{z}_s/g could be used to calculate the accelerations and stresses that would result at any point in the corresponding airplane structure by means of the equations presented in appendix B.

Figure 9 (a) presents a summary graph showing the effects of structural flexibility and interaction on the maximum landing-gear force for the various configurations considered. As previously indicated, the reductions in landing-gear force are greater for airplane B than for airplane A because of the lower natural frequency of airplane B. For the range of mass ratios representative of existing and proposed large airplanes, for example, values up to about 0.5, reductions in landing-gear force up to between 15 and 20 percent may be possible. Along the same lines, figure 9 (b) shows the effects of interaction on the acceleration response of the landing-gear attachment point and on the acceleration of the elastically connected mass in the equivalent three-mass system.

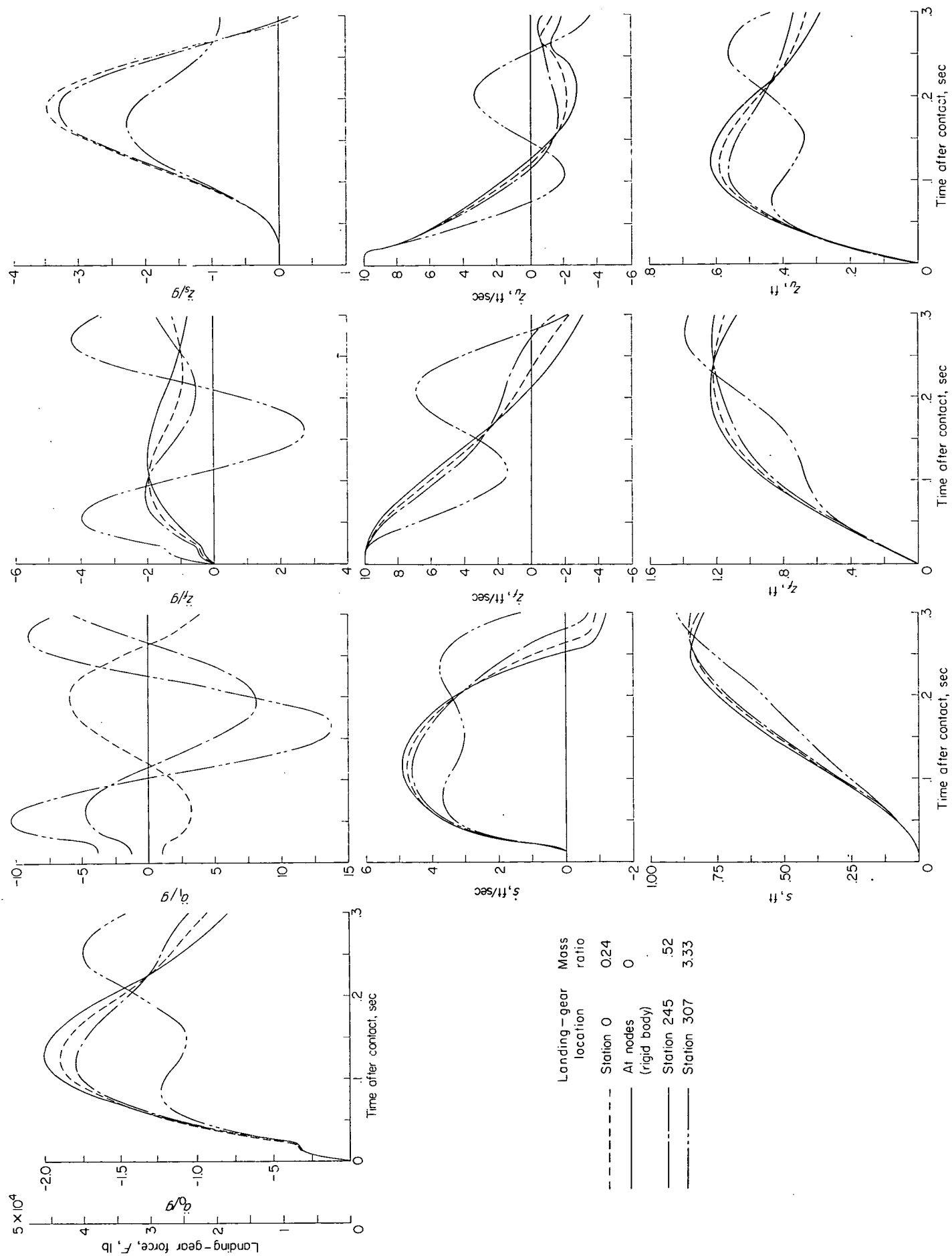
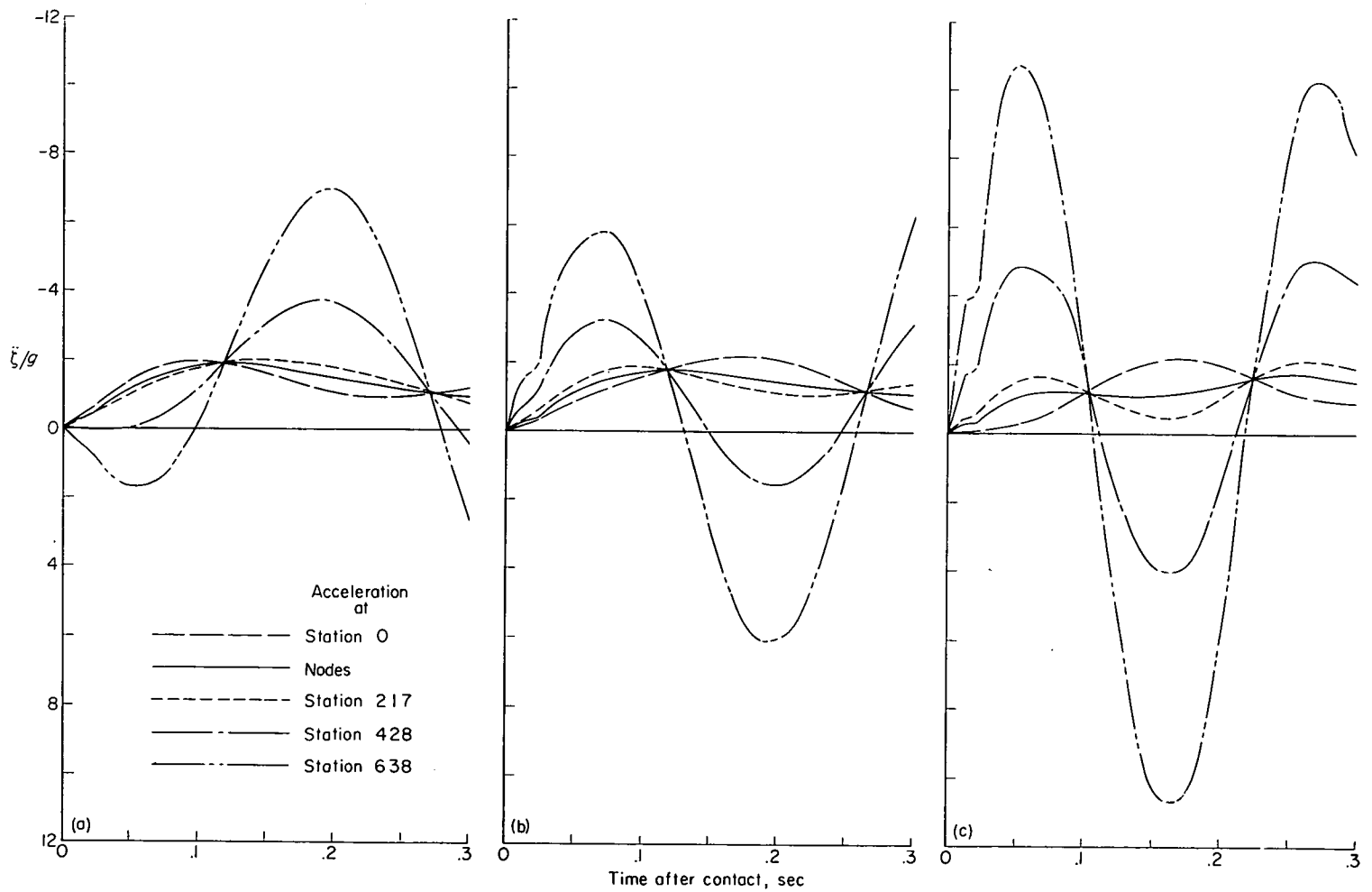


FIGURE 5.—Time histories of motions of airplane A during impact.



(a) Landing gear at station 0.

(b) Landing gear at station 245.

(c) Landing gear at station 307.

FIGURE 6.—Time histories of accelerations at various stations along the span of airplane A.

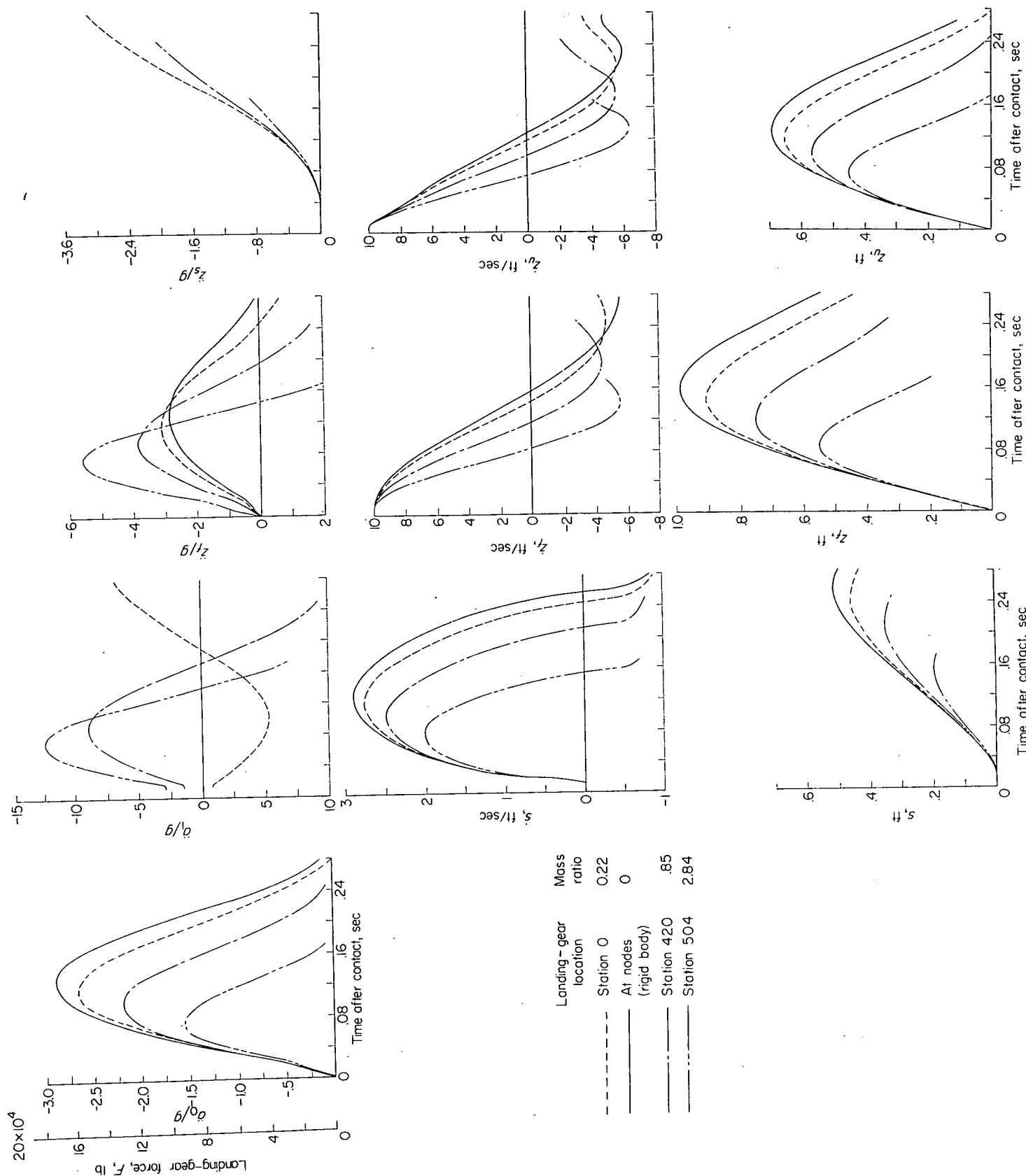


FIGURE 7.—Time histories of motions of airplane B during impact.

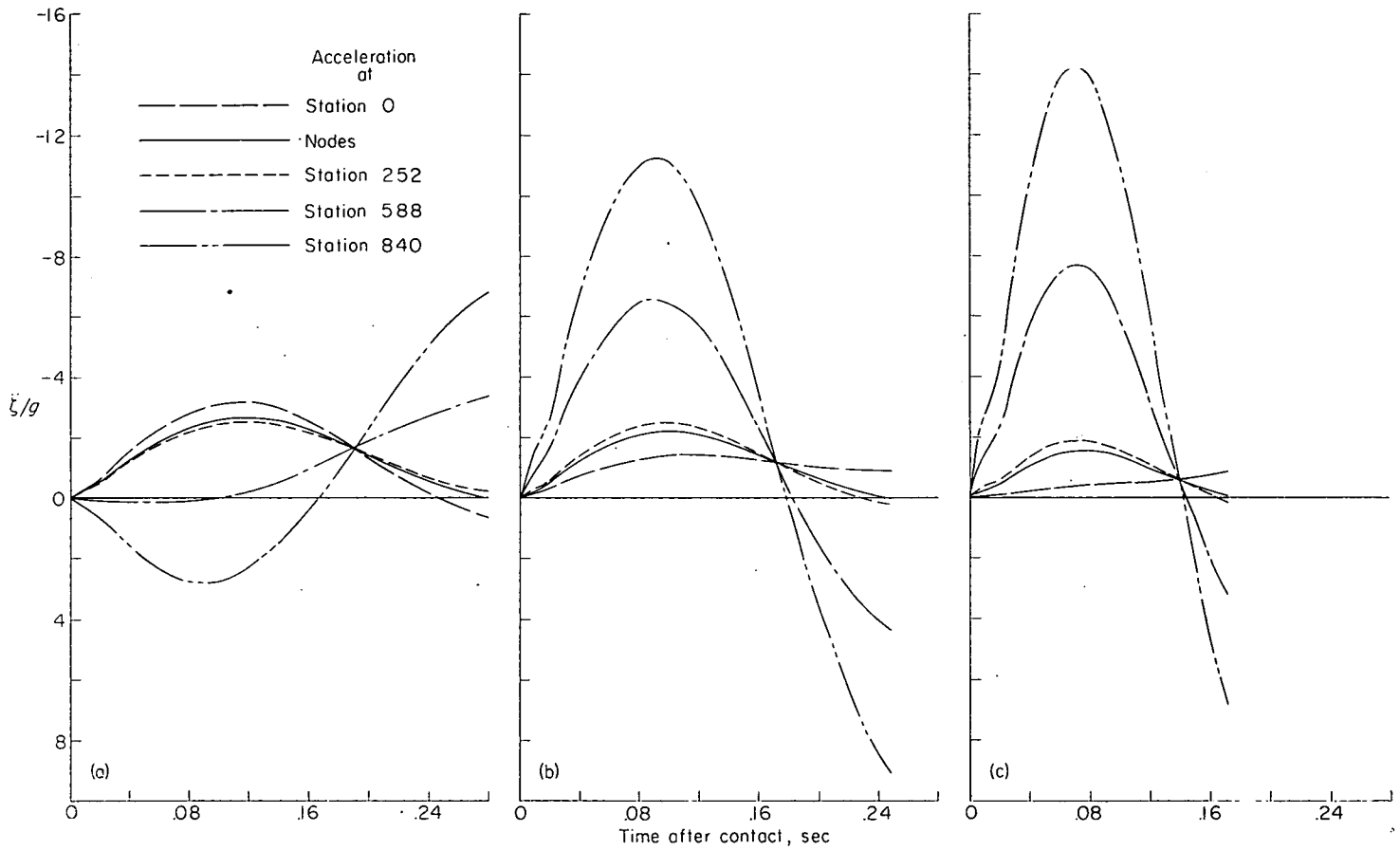
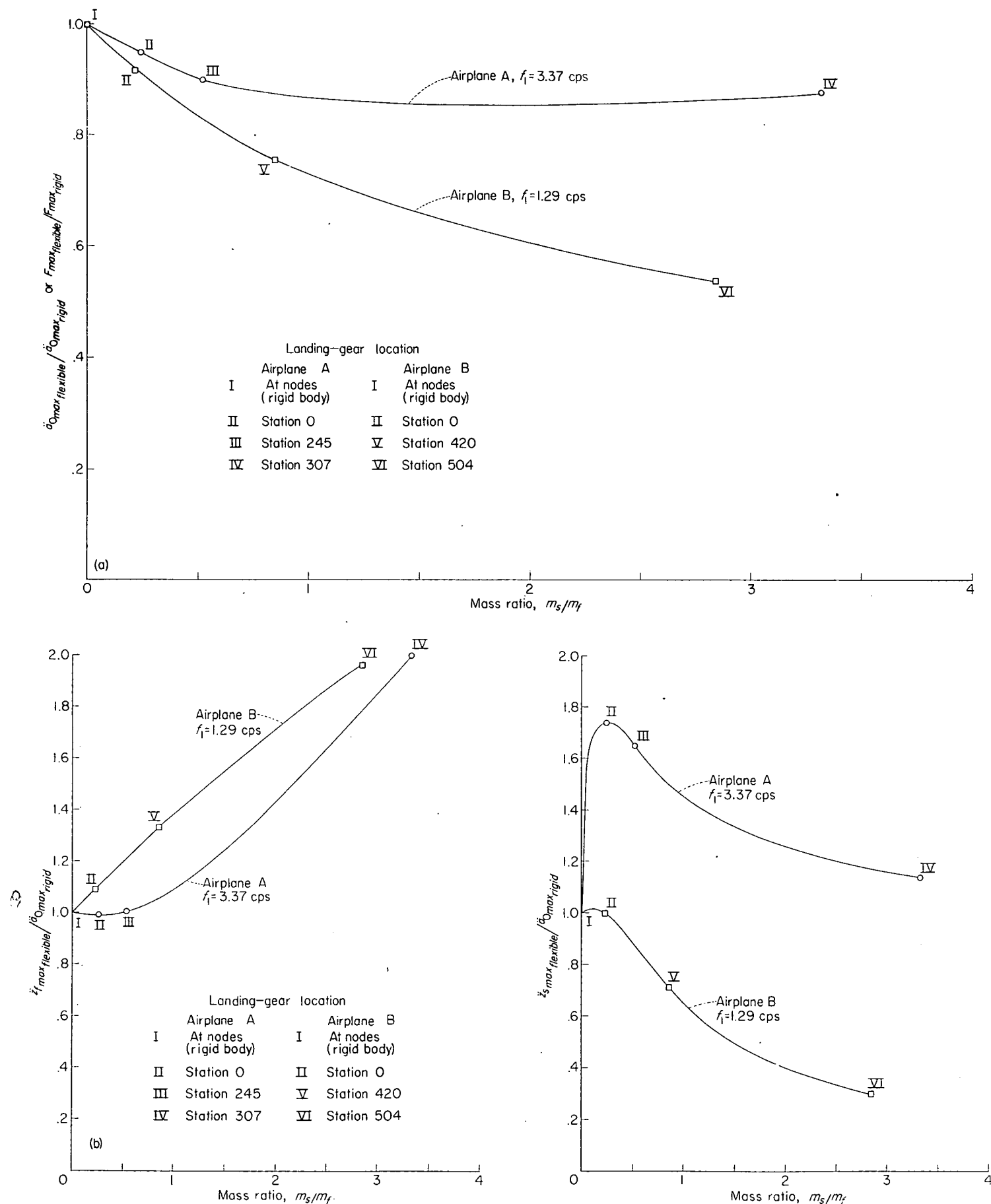


FIGURE 8.—Time histories of accelerations at various stations along the span of airplane B.



(a) Landing-gear force.

(b) Accelerations of landing-gear attachment point and elastically connected mass.

FIGURE 9.—Effects of interaction.

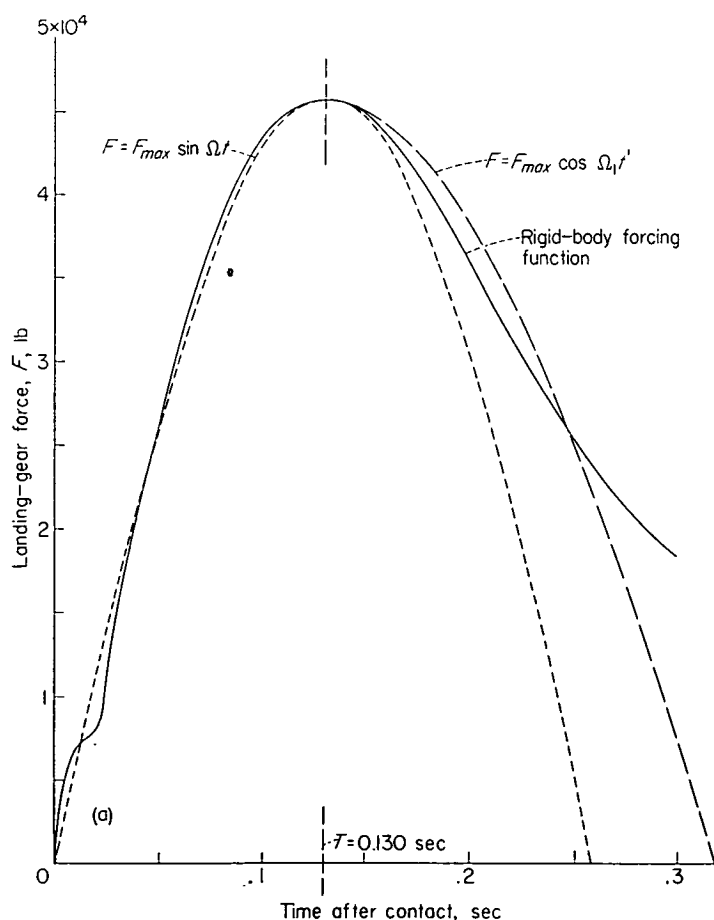
EFFECTS OF NEGLECTING INTERACTION IN THE
CALCULATION OF DYNAMIC LOADS

In the usual procedures of dynamic analysis of landing loads it is customary to neglect the effects of interaction on the landing-gear forcing function and to determine the dynamic loads in the structure by calculating the response of the structure to the forcing function which would be obtained if the airplane were a rigid body, this rigid-body forcing function being either calculated or, more frequently, determined on the basis of drop tests of the landing gear with a rigid mass. In practice, either the actual rigid-body forcing function or some simplified analytical approximation of it (see, for example, fig. 10) is used.

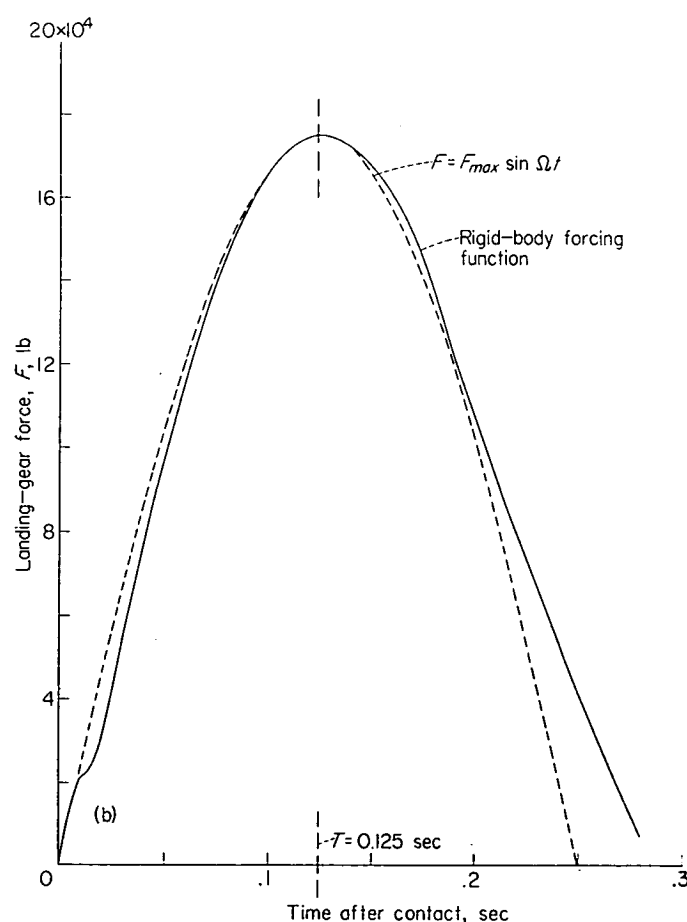
In order to evaluate the errors introduced by neglect of interaction effects, the root bending moments and shears determined from the interaction solutions for airplanes A and B are compared in figures 11 and 12 with those determined by calculating the response of the various configurations to the rigid-body forcing functions previously presented and to simple analytical approximations to the rigid-body forcing functions. These bending moments and shears are total values due to both inertia and aerodynamic forces, the latter being included to permit comparison with the steady-flight values. For reference purposes, figures 11 and 12 also show the root bending moments and shears which would be experienced by a completely rigid airplane.

The calculation of the response of systems with two degrees of freedom to predescribed forcing functions is treated in appendix C. The response of the various configurations to the rigid-body forcing function was calculated by application of the numerical-integration procedure previously described, whereas the response to the analytical forcing functions was obtained in closed form. The rigid-body forcing functions for airplanes A and B and their approximations are shown in figure 10. In the case of airplane A, the rigid-body forcing function was approximated by a pulse composed of sine and cosine segments; for airplane B, a simple sine pulse was used. The equations for calculating the inertia moments and shears from the response of the system are given in appendix C; simplified expressions for calculating the moments and shears due to the aerodynamic forces are given in appendix D.

From figures 11 and 12 it can be seen that the bending moments and shears calculated from the response to the rigid-body forcing function are larger than those determined from the interaction solutions, the differences being greater for the higher mass ratios where the effects of interaction result in a greater reduction in the magnitude of the landing-gear forcing function. From these particular examples, it appears that neglect of the effects of interaction on the landing-gear forcing function can lead to overconservatism in design not only of the landing gear but also of the structure,

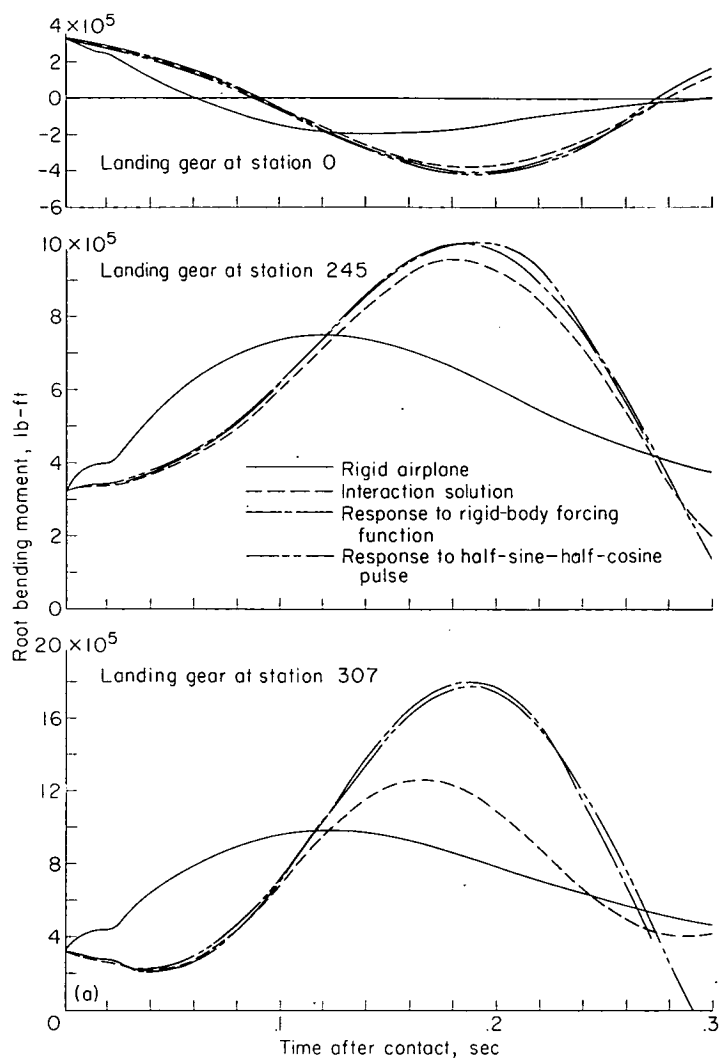


(a) Airplane A. $\Omega = 12.08$ radians/second; $\Omega_1 = 8.27$ radians/second.



(b) Airplane B. $\Omega = 12.57$ radians/second.

FIGURE 10.—Rigid-body forcing functions and simple analytical approximations.



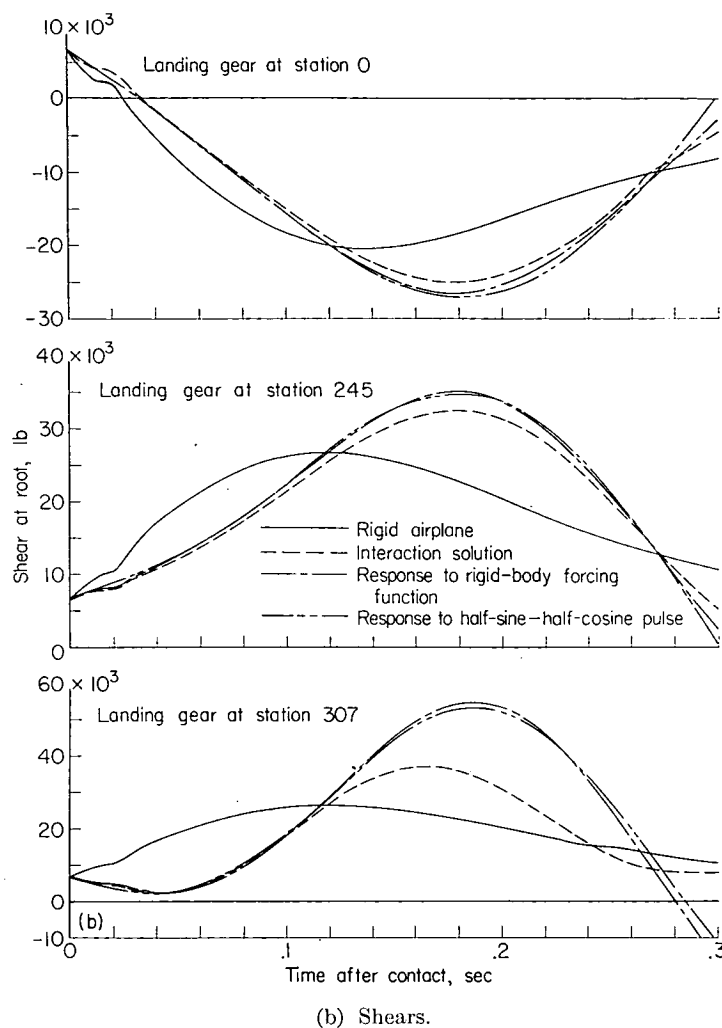
(a) Bending moments.

FIGURE 11.—Dynamic loads in airplane A.

particularly for very flexible configurations with high mass ratios. As might be expected, there was relatively little difference in the loads calculated from the response to the analytical approximations and from the response to the rigid-body forcing function.

It is of interest to note that in the case of airplane A the loads calculated from the interaction solutions are greater than those calculated for the completely rigid airplane, whereas, for airplane B, the converse is true. This result for airplane B is due to two factors: (a) the dynamic amplification factor is less than unity because of the relatively large natural period of the airplane compared with the duration of the impact pulse ($t_i/t_n \approx 0.3$), and (b) there is considerable reduction in the magnitude of the landing-gear force because of the effects of interaction. In the case of airplane A, the natural period is of about the same duration as the impact pulse ($t_i/t_n \approx 1.1$) so that the dynamic magnification factor is considerably greater than unity and more than overcomes the effect of the reduction in landing-gear force.

From the preceding results, it can be seen that the effects of structural flexibility are twofold; namely, (a) a change in

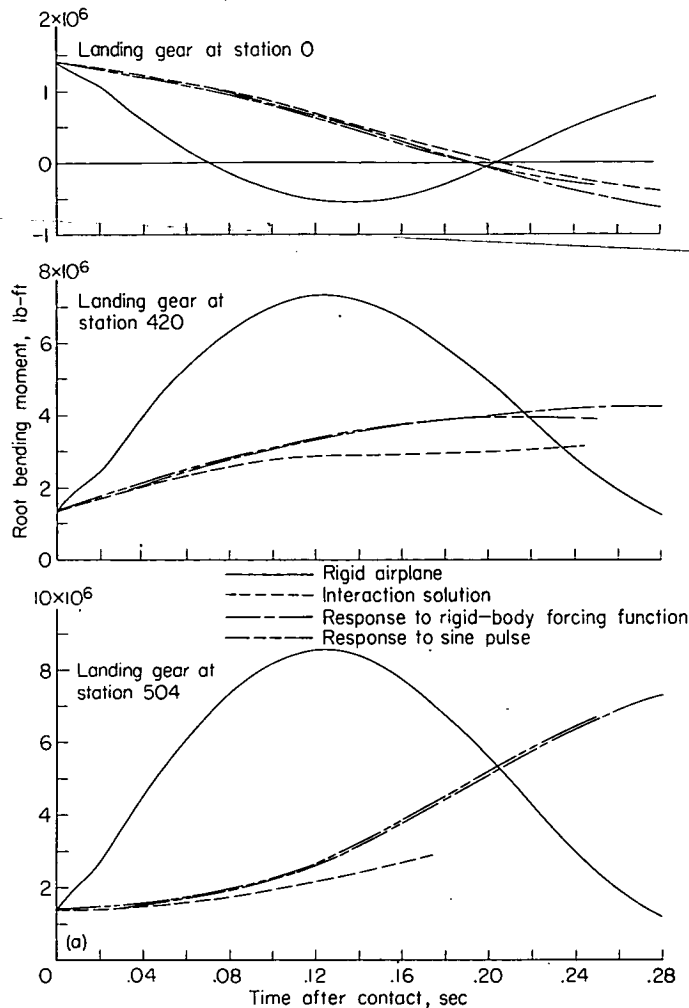


(b) Shears.

FIGURE 11.—Concluded.

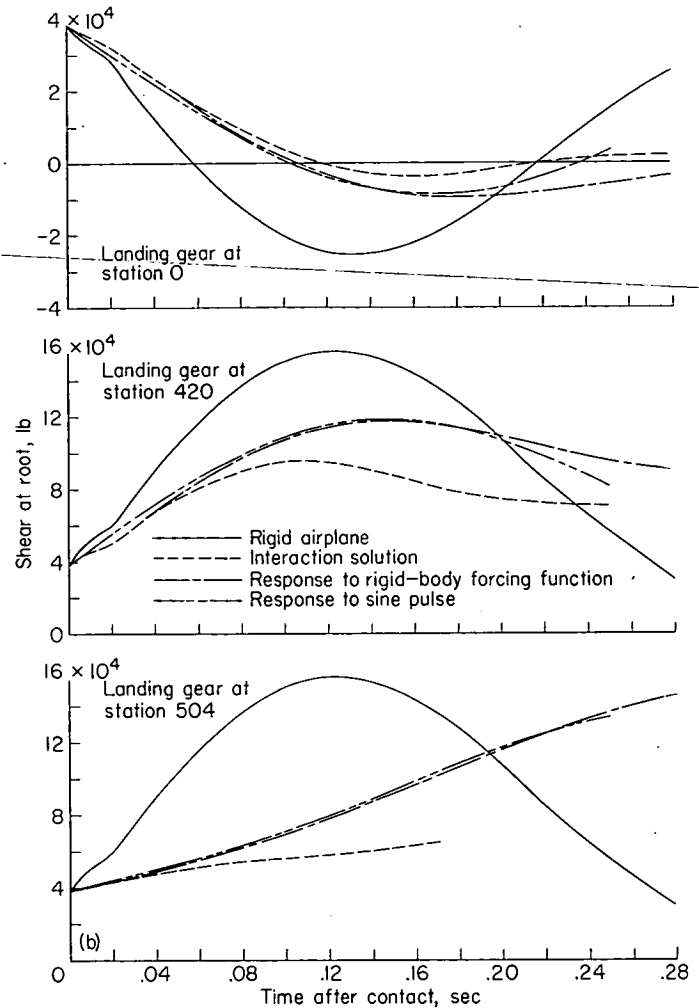
the magnitude of the applied landing-gear force due to interaction, the amount depending on the natural frequency of the structure, the mass ratio m_s/m_f , and the landing-gear characteristics, and (b) either dynamic amplification or attenuation of the loads in the structure compared with those for a rigid body, depending largely on the ratio of the duration of the impact pulse to the natural period of the structure. In the particular examples considered, the landing-gear force was reduced by the effects of interaction; it is conceivable, however, that, for some combinations of landing-gear and airplane characteristics, perhaps when the natural period of the structure is smaller than the duration of the impact pulse and the mass ratio is large, interaction might result in an increase in the maximum landing-gear force over that for a rigid airplane because of the superposition of oscillations of the landing-gear attachment point on the motions of the shock strut. Such an unfavorable effect of structural flexibility of the applied force was indicated for certain cases of seaplane impact in reference 7.

In view of the foregoing observations it would appear worthwhile to consider the effects of interaction in dynamic analyses of landing loads when the landing gear is located at points in the airplane that experience appreciable deflections relative to the mass center of the system.



(a) Bending moments.

FIGURE 12.—Dynamic loads in airplane B.



(b) Shears.

FIGURE 12.—Concluded.

CONCLUSIONS

The effects of interaction between a landing gear and a flexible airplane structure on the behavior of the landing gear and the loads in the structure have been studied by treating the equations of motion of the airplane and the landing gear as a coupled system. The landing gear is considered to have nonlinear characteristics typical of conventional gears, namely, velocity-squared damping, polytropic air-compression springing, and exponential tire force-deflection characteristics. For the case where only two modes of the structure are considered, an equivalent three-mass system is derived for representing the airplane and landing-gear combination, which may be used to simulate the effects of structural flexibility in jig drop tests of landing gears.

As examples to illustrate the effects of interaction, numerical calculations, based on the structural properties of two large airplanes having considerably different mass and flexibility characteristics, are presented. In order to cover a range of parameters, the landing gear of each airplane was assumed to be located at three arbitrary spanwise positions in addition to its original location. For the particular cases considered, it was found that

1. The effects of interaction can result in appreciable reductions in the magnitude of the landing-gear force, particularly when the flexibility of the airplane structure is

large and the natural frequency of the structure is small.

2. Neglect of interaction effects, that is, the use of the landing-gear forcing function for a rigid airplane in a dynamic analysis of a flexible airplane, can lead to the calculation of excessive loads in the airplane structure.

3. In the case of one of the airplanes, the structural loads calculated from the interaction solutions are greater than those for a completely rigid airplane treatment (rigid structure subjected to rigid-body forcing function) because of the fact that the effects of dynamic magnification more than overcome the reduction in landing-gear force due to interaction. In the case of the second airplane, because of the relatively large natural period of the structure in comparison with the duration of the impact pulse, the dynamic magnification factor is appreciably less than unity. This effect, coupled with the reductions in landing-gear force due to interaction, results in structural loads that are less than those for a rigid airplane. It thus appears desirable to consider the effects of interaction in dynamic analyses of landing loads for large airplanes, particularly when the landing-gear attachment points experience large deflections relative to the mass center of the airplane.

LANGLEY AERONAUTICAL LABORATORY,
NATIONAL ADVISORY COMMITTEE FOR AERONAUTICS,
LANGLEY FIELD, VA., May 5, 1955.

APPENDIX A

CONDITIONS AT BEGINNING OF SHOCK-STRUT MOTION

Since the shock strut does not begin to deflect until the preloading force imposed by the internal air pressure is overcome by the inertia forces, the shock strut is essentially rigid during the interval between the instant of initial contact with the ground and the beginning of shock-strut motion at some time $t=t_r$. During this interval, since the deflection of the tire is essentially the same as the displacement of the landing-gear attachment point, the system used in the numerical calculations to represent the airplane and landing-gear combination has only two degrees of freedom, namely, the rigid-body or zero-mode displacement and the deflection in the first flexible mode, the higher modes being neglected. The purpose of this appendix is to consider the motions of the system prior to the beginning of shock-strut deflection in order to determine the conditions which exist at the instant the shock strut first begins to move; these motions then serve as the initial conditions for the equations of motion of the system during the main part of the impact. For this purpose it may be reasonably assumed that the tire force-deflection relationship is linear for the relatively small range of deflection prior to the beginning of shock-strut motion and that, therefore, $F_{V_g}(z_f) = m' z_f$. In order to avoid a step jump in the time-history solution at the time t_r , the constant m' should be determined so that

$$m' z_{f,r} = m z_{f,r} \quad (A1)$$

DISTRIBUTED SYSTEM

Prior to time t_r the equations of motion for the airplane and landing gear are given by equations (18) with initial conditions:

$$z_f(0) = a_0(0) = a_1(0) = 0$$

$$\dot{z}_f(0) = \dot{a}_0(0) = V_{v_o}$$

$$\dot{a}_1(0) = 0$$

Since $a_1 = \frac{z_f - a_0}{\xi_1}$, equations (18) can be written as

$$M_0 \ddot{a}_0 = -m' z_f - m_u \ddot{z}_f - W_{tot}(K_L - 1) \quad (A2a)$$

$$\frac{M_1}{\xi_1^2} \ddot{a}_0 + \frac{M_1 \omega_1^2}{\xi_1^2} a_0 = \left(\frac{M_1}{\xi_1^2} + m_u \right) \ddot{z}_f + \left(\frac{M_1 \omega_1^2}{\xi_1^2} + m' \right) z_f + W_u(K_L - 1) \quad (A2b)$$

The exact solution of equations (A2) can be shown to be

$$z_f(t) = \frac{1}{A^2 - B^2} \left\{ V_{v_o} \left(\frac{A^2 - C}{A} \sin At - \frac{B^2 - C}{B} \sin Bt \right) + D \left[\frac{A^2 - C}{A^2} \cos At - \frac{B^2 - C}{B^2} \cos Bt + C \left(\frac{1}{A^2} - \frac{1}{B^2} \right) \right] \right\} \quad (A3)$$

where

$$A = \sqrt{\frac{E - \sqrt{E^2 - 4F}}{2}}$$

$$B = \sqrt{\frac{E + \sqrt{E^2 - 4F}}{2}}$$

$$C = \frac{M_1 \omega_1^2 (M_0 + m_u)}{G}$$

$$D = (K_L - 1)g$$

$$E = \frac{m' (M_1 + M_0 \xi_1^2)}{G} + C$$

$$F = \frac{m' M_1 \omega_1^2}{G}$$

$$G = M_1 (M_0 + m_u) + m_u M_0 \xi_1^2$$

By successive differentiation of equation (A3), the higher derivatives of $z_f(t)$ are found to be

$$\dot{z}_f(t) = \frac{1}{A^2 - B^2} \left\{ V_{v_o} [(A^2 - C) \cos At - (B^2 - C) \cos Bt] + D \left[\left(\frac{B^2 - C}{B} \right) \sin Bt - \left(\frac{A^2 - C}{A} \right) \sin At \right] \right\} \quad (\text{A4})$$

$$\ddot{z}_f(t) = \frac{1}{A^2 - B^2} \left\{ V_{v_o} [B(B^2 - C) \sin Bt - A(A^2 - C) \sin At] + D [(B^2 - C) \cos Bt - (A^2 - C) \cos At] \right\} \quad (\text{A5})$$

$$\ddot{z}_f(t) = \frac{1}{A^2 - B^2} \left\{ V_{v_o} [B^2(B^2 - C) \cos Bt - A^2(A^2 - C) \cos At] + D [A(A^2 - C) \sin At - B(B^2 - C) \sin Bt] \right\} \quad (\text{A6})$$

At the time t_r , the equation of motion of the unsprung mass of the landing gear as a free body is given by equation (2) which, with $F_{v_g} = m' z_{f_r}$, may be written as

$$m_u \ddot{z}_{f_r} + m' z_{f_r} = p_{a_o} A_a \cos \theta + W_u \quad (\text{A7})$$

Substituting for z_{f_r} and \ddot{z}_{f_r} in equation (A7) gives a relationship between t_r and m' :

$$\frac{1}{A^2 - B^2} \left\{ V_{v_o} \left[\frac{A^2 - C}{A} (m' - m_u A^2) \sin At - \frac{B^2 - C}{B} (m' - m_u B^2) \sin Bt \right] + D \left[\frac{A^2 - C}{A^2} (m' - m_u A^2) \cos At - \frac{B^2 - C}{B^2} (m' - m_u B^2) \cos Bt + m' C \left(\frac{1}{A^2} - \frac{1}{B^2} \right) \right] \right\} = p_{a_o} A_a \cos \theta + W_u \quad (\text{A8})$$

Because equation (A8) is transcendental in both t_r and m' (m' being involved in the constants A and B), in order to obtain an explicit solution for t_r or m' , some approximation to the trigonometric terms is necessary, the order of the approximation depending on the accuracy required. For the determination of t_r and m' it will generally be sufficient to assume first-order approximations for the trigonometric terms where only the first terms of their series expansions are used. With these approximations the solution of equation (A8) for t_r is

$$t_r = \frac{G(p_{a_o} A_a \cos \theta + K_L W_u)}{m' M_1 M_0 V_{v_o}} \quad (\text{A9})$$

As indicated previously, m' cannot be chosen arbitrarily but must be determined in accordance with equation (A1), which may be written as

$$m' = m z_{f_r}^{r-1}$$

The first-order approximation for z_{f_r} , obtained from equation (A3), is

$$z_{f_r} = V_{v_o} t_r \quad (\text{A10})$$

With these substitutions equation (A9) may be written as

$$t_r = \frac{1}{V_{v_o}} \left[\frac{G(p_{a_o} A_a \cos \theta + K_L W_u)}{m M_1 M_0} \right]^{1/r} \quad (\text{A11})$$

and the equation for m' becomes

$$m' = m^{1/r} \left[\frac{G(p_{a_o} A_a \cos \theta + K_L W_u)}{M_1 M_0} \right]^{\frac{r-1}{r}} \quad (\text{A12})$$

The first-order approximations for the derivatives of z_f at time t_r , from equations (A4) to (A6), are

$$\dot{z}_{f_r} = V_{v_o} - Dt_r \quad (\text{A13})$$

$$\ddot{z}_{f_r} = V_{v_o}[C - (A^2 + B^2)]t_r - D \quad (\text{A14})$$

and

$$\ddot{\ddot{z}}_{f_r} = (V_{v_o} - Dt_r)[C - (A^2 + B^2)] \quad (\text{A15})$$

With the values of t_r and m' calculated from equations (A11) and (A12), the values of $z_{f_r} = z_{u_r}$, $\dot{z}_{f_r} = \dot{z}_{u_r}$, and $\ddot{z}_{f_r} = \ddot{z}_{u_r}$ can be calculated from equations (A10), (A13), and (A14), respectively. These values provide two-thirds of the initial conditions for the process subsequent to the beginning of shock-strut deflection (eq. 19). The remaining initial conditions, for example, a_{0_r} , \dot{a}_{0_r} , and \ddot{a}_{0_r} , can be obtained by manipulation of the differential equations (A2). From equation (A2b) it can be seen that

$$a_{0_r} = \frac{\xi_1^2}{M_1 \omega_1^2} \left[\left(\frac{M_1}{\xi_1^2} + m_u \right) \ddot{z}_{f_r} + \left(\frac{M_1 \omega_1^2}{\xi_1^2} + m' \right) z_{f_r} - \frac{M_1}{\xi_1^2} \ddot{a}_{0_r} + W_u(K_L - 1) \right] \quad (\text{A16})$$

By differentiation,

$$\dot{a}_{0_r} = \frac{\xi_1^2}{M_1 \omega_1^2} \left[\left(\frac{M_1}{\xi_1^2} + m_u \right) \ddot{\ddot{z}}_{f_r} + \left(\frac{M_1 \omega_1^2}{\xi_1^2} + m' \right) \dot{z}_{f_r} - \frac{M_1}{\xi_1^2} \ddot{\ddot{a}}_{0_r} \right] \quad (\text{A17})$$

where, from equation (A2a),

$$\left. \begin{aligned} \ddot{a}_{0_r} &= - \frac{m' z_{f_r} + m_u \ddot{z}_{f_r} + W_{tot}(K_L - 1)}{M_0} \\ &= - \frac{p_{a_0} A_a \cos \theta + W_{tot}(K_L - 1) + W_u}{M_0} \end{aligned} \right\} \quad (\text{A18})$$

Differentiating equation (A2a) gives

$$\ddot{\ddot{a}}_{0_r} = - \frac{m' \dot{z}_{f_r} + m_u \ddot{\ddot{z}}_{f_r}}{M_0} \quad (\text{A19})$$

The substitution of equations (A18) and (A19) and the initial conditions previously determined (z_{f_r} , \dot{z}_{f_r} , \ddot{z}_{f_r} , and $\ddot{\ddot{z}}_{f_r}$) into equations (A16) to (A18) provides the remaining initial conditions for the second phase of the impact.

EQUIVALENT THREE-MASS SYSTEM

The equations of motion for the equivalent three-mass system prior to the time t_r are equations (20) with initial conditions

$$z_f(0) = z_s(0) = 0$$

and

$$\dot{z}_f(0) = \dot{z}_s(0) = V_{v_o}$$

Since it has been shown that equations (20) are identically equivalent to equations (18) for the distributed system when the relationships between the constants of the two systems are as defined by equations (27) to (34), it follows that equations (A3) to (A15) are equally valid for the three-mass system when the constants are redefined in accordance with equations (27) to (34). The redefined constants, in terms of the properties of the three-mass system, may be written as

$$C = \frac{m_f \omega_1^2 (M_0 + m_u)}{M_0 (m_f + m_u)}$$

$$D = (K_L - 1)g$$

$$E = \frac{m'}{m_f + m_u} + C$$

$$F = \frac{m_f m' \omega_1^2}{M_0 (m_f + m_u)}$$

where

$$M_0 = m_f + m_s$$

and

$$\omega_1 = \sqrt{\frac{kM_0}{m_fm_s}}$$

The equations for t_r and m' , equations (A11) and (A12), become

$$t_r = \frac{1}{V_{v_o}} \left[\frac{H(p_{a_o} A_a \cos \theta + K_L W_u)}{m} \right]^{1/r} \quad (\text{A20})$$

and

$$m' = m^{1/r} \left[H(p_{a_o} A_a \cos \theta + K_L W_u) \right]^{\frac{r-1}{r}} \quad (\text{A21})$$

where

$$H = \frac{m_f + m_u}{m_f}$$

The values of t_r and m' given by these equations permit the calculation of $z_{f_r} = z_{u_r}$, $\dot{z}_{f_r} = \dot{z}_{u_r}$, and $\ddot{z}_{f_r} = \ddot{z}_{u_r}$ by means of equations (A10), (A13), and (A14). The remaining initial conditions for the second phase of the impact, z_s and its derivatives at the time t_r , can be obtained by manipulation of the differential equations (20). Solving equation (20a) for z_s at time t_r gives

$$z_{s_r} = \frac{1}{k} \left[(m_f + m_u) \ddot{z}_{f_r} + (k + m') z_{f_r} + L_f + W_f - W_u \right] \quad (\text{A22})$$

Differentiating equation (20a) and substituting $F_{v_g}(z_f) = m' z_f$ gives

$$\dot{z}_{s_r} = \frac{1}{k} \left[(m_f + m_u) \ddot{z}_{f_r} + (k - m') \dot{z}_{f_r} \right] \quad (\text{A23})$$

An expression for \ddot{z}_{s_r} can easily be obtained from equation (20b) as follows:

$$\ddot{z}_{s_r} = -\frac{1}{m_s} \left[(m_f + m_u) \ddot{z}_{f_r} + m' z_{f_r} + (L_s + L_f) - (W_s + W_f + W_u) \right] \quad (\text{A24})$$

Equations (A22) to (A24), in conjunction with the values of z_{f_r} , \dot{z}_{f_r} , and \ddot{z}_{f_r} previously determined, supply all the initial conditions for the second phase of the impact of the equivalent three-mass system.

APPENDIX B

DYNAMIC LOADS IN AIRPLANE STRUCTURE

The equations of motion of the airplane have been previously presented in several forms so that solutions for the motions of the structure can be obtained in terms of the variables a_0 and a_1 , a_0 and z_f , or z_f and z_s . The purpose of this appendix is to present equations from which the accelerations, bending moments, and shears at any point on the airplane structure can be calculated once the time-history solutions for the basic variables have been obtained.

ACCELERATION

At any point.—The absolute displacement at any point on the structure (see fig. 2) is

$$z = w + x\varphi$$

Since

$$w = a_0 + a_1 w_1$$

and

$$\varphi = a_1 \varphi_1$$

where w_1 and φ_1 are the modal functions for bending and torsion, respectively,

$$z = a_0 + a_1(w_1 + x\varphi_1)$$

and

$$\ddot{z} = \ddot{a}_0 + \ddot{a}_1(w_1 + x\varphi_1) \quad (\text{B1})$$

Since

$$\ddot{a}_1 = \frac{\ddot{z}_f - \ddot{a}_0}{\xi_1}$$

the acceleration at any point may also be written as

$$\ddot{z} = \ddot{a}_0 + (\ddot{z}_f - \ddot{a}_0) \frac{w_1 + x\varphi_1}{\xi_1} \quad (\text{B2})$$

Since, from equation (36),

$$\ddot{a}_0 = \frac{m_f \ddot{z}_f + m_s \ddot{z}_s}{M_0}$$

the acceleration can also be written as

$$\ddot{z} = \frac{1}{M_0} \left[m_f \ddot{z}_f + m_s \ddot{z}_s + m_s (\ddot{z}_f - \ddot{z}_s) \frac{w_1 + x\varphi_1}{\xi_1} \right] \quad (\text{B3})$$

Along elastic axis.—At the elastic axis, the displacement is designated w and $x=0$ so that equation (B1) becomes simply

$$\ddot{w} = \ddot{a}_0 + \ddot{a}_1 w_1 \quad (\text{B4})$$

Equation (B2) becomes

$$\ddot{w} = \ddot{a}_0 + (\ddot{z}_f - \ddot{a}_0) \frac{w_1}{\xi_1} \quad (\text{B5})$$

Equation (B3) becomes

$$\ddot{w} = \frac{1}{M_0} \left[m_f \ddot{z}_f + m_s \ddot{z}_s + m_s (\ddot{z}_f - \ddot{z}_s) \frac{w_1}{\xi_1} \right] \quad (\text{B6})$$

Along station mass centers.—At the mass center of any station the displacement is designated ξ and $x=\epsilon$ so that equation (B1) becomes

$$\xi = \ddot{a}_0 + \ddot{a}_1 \xi_1 \quad (\text{B7})$$

where ξ_1 is the modal function for the station mass center and is equal to $w_1 + \epsilon\varphi_1$. Equation (B2) becomes

$$\xi = \ddot{a}_0 + (\ddot{z}_f - \ddot{a}_0) \frac{\xi_1}{\xi_1} \quad (\text{B8})$$

Equation (B3) becomes

$$\xi = \frac{1}{M_0} \left[m_f \ddot{z}_f + m_s \ddot{z}_s + m_s (\ddot{z}_f - \ddot{z}_s) \frac{\xi_1}{\xi_1} \right] \quad (\text{B9})$$

BENDING MOMENTS

Outboard of landing gear.—The bending moment at any spanwise station y_j outboard of the landing-gear station y_s is readily determined by summing up the inertia moments produced by the accelerations of the mass centers of all stations i between station y_j and the tip. Thus,

$$M_{B(y_i \geq y_s)} = \sum_{i=j}^{\text{tip}} m_i \ddot{\xi}_i (y_i - y_j) \quad (\text{B10})$$

Inboard of landing gear.—The bending moment at any spanwise station y_j inboard of the landing-gear station y_s is equal to the sum of the inertia moments produced by the accelerations of the mass centers of all stations i between station y_j and the tip plus the moment produced by the landing-gear force. Thus,

$$M_{B(y_i \leq y_s)} = \sum_{i=j}^{\text{tip}} m_i \ddot{\xi}_i (y_i - y_j) + F(y_s - y_j) \quad (\text{B11})$$

where

$$F = -[M_0 \ddot{a}_0 + W_{tot}(K_L - 1) + W_u]$$

SHEARS

Outboard of landing gear.—The vertical shear at any spanwise station y_j outboard of the landing-gear station y_s is simply the sum of the inertia reactions due to the accelerations of the mass centers of all stations i between station y_j and the tip. Thus,

$$S_{(y_i \geq y_s)} = \sum_{i=j}^{\text{tip}} m_i \ddot{\xi}_i \quad (\text{B12})$$

Inboard of landing gear.—The vertical shear at any spanwise station y_j inboard of the landing-gear station y_s is the sum of the inertia reactions due to the accelerations of the mass centers of all stations i between station y_j and the tip, plus the landing-gear force. Thus,

$$\begin{aligned} S_{(y_i \leq y_s)} &= \sum_{i=j}^{\text{tip}} m_i \ddot{\xi}_i + F \\ &= \sum_{i=j}^{\text{tip}} m_i \ddot{\xi}_i - [M_0 \ddot{a}_0 + W_{tot}(K_L - 1) + W_u] \end{aligned} \quad (\text{B13})$$

APPENDIX C

RESPONSE TO GIVEN FORCING FUNCTIONS

In this appendix equations are presented for the acceleration response of the airplane structure to predetermined forcing functions applied by the landing gear. The cases considered are the arbitrary forcing function, the sine pulse, and a pulse made up of sine and cosine segments. For the particular case where the landing-gear forcing function can be represented by a single sine pulse,

$$F(t) = F_{max} \sin \Omega t$$

where Ω is the circular frequency of the applied sine pulse and is expressed by

$$\Omega = \frac{\pi}{2T}$$

where T is the time to reach F_{max} .

If the forcing pulse is not symmetrical in time about its maximum value, it may be represented by a combined pulse consisting of a sine function up to the time T and a cosine function subsequent to the time T . This latter function may be written as

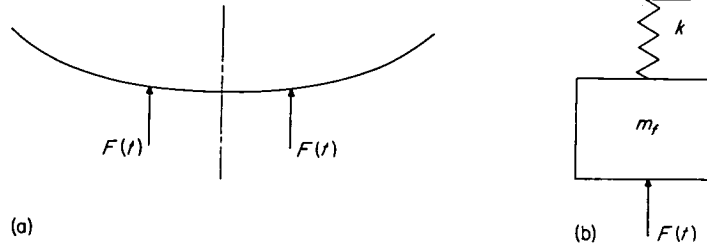
$$F(t') = F_{max} \cos \Omega_1 t' \quad (t' \geq 0)$$

where

$$t' = t - T$$

and Ω_1 is the circular frequency of the cosine pulse; the initial conditions are the same as the conditions at the time $t = T$ determined from the response to the sine-function segment of the pulse.

The solutions are presented for the distributed system of the airplane (sketch a) and for the equivalent concentrated-mass system (sketch b)



DISTRIBUTED SYSTEM

The acceleration response of the rigid body or zero mode is immediately evident from the equation of motion for $n=0$, namely,

$$\ddot{a}_0 = -\frac{F(t) + W_{tot}(K_L - 1) + W_u}{M_0}$$

The response of the deflection modes follows.

Arbitrary forcing function.—When the landing-gear forcing function is predetermined and arbitrary, the equation of motion for the n th mode (eq. (15a)) can be written as

$$M_n \ddot{a}_n + M_n \omega_n^2 a_n = -[F(t) + K_L W_u] \xi_n \quad (n \neq 0) \quad (C1)$$

where $F(t)$ is an arbitrary function of time and a_n is the generalized coordinate of the n th mode.

The general solution of equation (C1) may be written as

$$a_n(t) = -\frac{\xi_n}{M_n \omega_n} \int_0^t F(\tau) \sin \omega_n(t - \tau) d\tau + \frac{K_L W_u \xi_n}{M_n \omega_n^2} (\cos \omega_n t - 1) + a_n(0) \cos \omega_n t + \frac{\dot{a}_n(0)}{\omega_n} \sin \omega_n t \quad (C2)$$

The acceleration response is obtained by double differentiating equation (C2) as follows:

$$\ddot{a}_n(t) = \frac{\xi_n}{M_n} \left[F(t) - \omega_n \int_0^t F(\tau) \sin \omega_n(t - \tau) d\tau + K_L W_u \cos \omega_n t \right] - a_n(0) \omega_n^2 \cos \omega_n t - \dot{a}_n(0) \omega_n \sin \omega_n t \quad (C3)$$

Equations (C2) and (C3) are general solutions to equation (C1) and thus represent the response of any mode to an arbitrary forcing function $F(t)$. In the present study of landing impact, the initial conditions are

$$a_n(0)=0$$

and

$$\dot{a}_n(0)=0$$

Sine-pulse forcing function.—For the particular case where the forcing function is a sine pulse, the acceleration response, as determined from equation (C3), is

$$\ddot{a}_n(t) = F_{max} \frac{\xi_n}{M_n} \left[\frac{\omega_n}{\Omega^2 - \omega_n^2} (\Omega \sin \omega_n t - \omega_n \sin \Omega t) - \sin \Omega t \right] - \left[\frac{K_L W_u \xi_n}{M_n} + a_n(0) \omega_n^2 \right] \cos \omega_n t - \dot{a}_n(0) \omega_n \sin \omega_n t \quad (C4)$$

where, again, $a_n(0)=0$ and $\dot{a}_n(0)=0$.

Half-sine—half-cosine pulse.—In this case the response up to time T is given by equation (C4). Subsequent to time T the acceleration response, determined from equation (C3), may be written as

$$\ddot{a}_n(t') = F_{max} \frac{\xi_n}{M_n} \left[\frac{\omega_n^2}{\Omega_1^2 - \omega_n^2} (\cos \omega_n t' - \cos \Omega_1 t') - \cos \Omega_1 t' \right] - \left[\frac{K_L W_u \xi_n}{M_n} + a_n(0) \omega_n^2 \right] \cos \omega_n t' - \dot{a}_n(0) \omega_n \sin \omega_n t' \quad (C5)$$

where

$$t' = (t - T) \geq 1$$

$$a_n(0) = a_{nT}$$

$$\dot{a}_n(0) = \dot{a}_{nT}$$

EQUIVALENT CONCENTRATED-MASS SYSTEM

The equations of motion for the concentrated-mass system subject to an arbitrary forcing function are (see eqs. (22))

$$\left. \begin{aligned} m_f \ddot{z}_f - k(z_s - z_f) + L_f - W_f &= -F(t) \\ m_f \ddot{z}_f + m_s \ddot{z}_s + (L_f + L_s) - (W_s + W_f) &= -F(t) \end{aligned} \right\} \quad (C6)$$

Introducing the new variable

$$u = z_s - z_f$$

permits the combination of equations (C6) into a single equation in one variable:

$$m_f \ddot{u} + k \left(1 + \frac{m_f}{m_s} \right) u = F(t) + J \quad (C7)$$

where

$$J = L_f - W_f - \frac{m_f}{m_s} (L_s - W_s)$$

The solution of equation (C7), by analogy with equation (C1), can be written as

$$u(t) = \frac{1}{m_f \omega_1} \int_0^t F(\tau) \sin \omega_1(t - \tau) d\tau + \frac{J}{m_f \omega_1^2} (1 - \cos \omega_1 t) + u(0) \cos \omega_1 t + \frac{\dot{u}(0)}{\omega_1} \sin \omega_1 t \quad (C8)$$

where

$$\omega_1^2 = k \frac{M_0}{m_f m_s}$$

By substituting $u(t)$ for $z_s - z_f$ in equations (C6) and combining, the following equations for the responses \ddot{z}_s and \ddot{z}_f can be obtained:

$$\ddot{z}_s(t) = -\frac{k}{m_s} \left[\frac{1}{m_f \omega_1} \int_0^t F(\tau) \sin \omega_1(t-\tau) d\tau + \frac{J}{m_f \omega_1^2} (1 - \cos \omega_1 t) + u(0) \cos \omega_1 t + \frac{\dot{u}(0)}{\omega_1} \sin \omega_1 t \right] + \frac{W_s - L_s}{m_s} \quad (C9)$$

and

$$\ddot{z}_f(t) = \frac{1}{m_f} \left\{ -[F(t) + (L_f - W_f)] + k \left[\frac{1}{m_f \omega_1} \int_0^t F(\tau) \sin \omega_1(t-\tau) d\tau + \frac{J}{m_f \omega_1^2} (1 - \cos \omega_1 t) + u(0) \cos \omega_1 t + \frac{\dot{u}(0)}{\omega_1} \sin \omega_1 t \right] \right\} \quad (C10)$$

In equations (C9) and (C10), $u(0) = \dot{u}(0) = 0$ for the present application to landing impact.

Sine-pulse forcing function.—For the case where the forcing term is a sine pulse, equations (C9) and (C10) become

$$\ddot{z}_s(t) = -\frac{k}{m_s} \left[\frac{F_{max}(\Omega \sin \omega_1 t - \omega_1 \sin \Omega t)}{m_f \omega_1 (\Omega^2 - \omega_1^2)} + \frac{J}{m_f \omega_1^2} (1 - \cos \omega_1 t) + u(0) \cos \omega_1 t + \frac{\dot{u}(0)}{\omega_1} \sin \omega_1 t \right] + \frac{W_s - L_s}{m_s} \quad (C11)$$

and

$$\ddot{z}_f(t) = \frac{1}{m_f} \left\{ F_{max} \left[\frac{k(\Omega \sin \omega_1 t - \omega_1 \sin \Omega t)}{m_f \omega_1 (\Omega^2 - \omega_1^2)} - \sin \Omega t \right] - (L_f - W_f) + \frac{Jk(1 - \cos \omega_1 t)}{m_f \omega_1^2} + k \left[u(0) \cos \omega_1 t + \frac{\dot{u}(0)}{\omega_1} \sin \omega_1 t \right] \right\} \quad (C12)$$

where, again, $u(0) = \dot{u}(0) = 0$.

Half-sine—half-cosine pulse.—The response up to time T is given by equations (C11) and (C12). Subsequent to time T , the responses (eqs. (C9) and (C10)) become

$$\ddot{z}_s(t') = -\frac{k}{m_s} \left[\frac{F_{max}(\cos \omega_1 t' - \cos \Omega t')}{m_f (\Omega_1^2 - \omega_1^2)} + \frac{J}{m_f \omega_1^2} (1 - \cos \omega_1 t') + u(0) \cos \omega_1 t' + \frac{\dot{u}(0)}{\omega_1} \sin \omega_1 t' \right] + \frac{W_s - L_s}{m_s} \quad (C13)$$

and

$$\ddot{z}_f(t') = \frac{1}{m_f} \left\{ F_{max} \left[\frac{k(\cos \omega_1 t' - \cos \Omega_1 t')}{m_f (\Omega_1^2 - \omega_1^2)} - \cos \Omega_1 t' \right] - (L_f - W_f) + \frac{Jk(1 - \cos \omega_1 t')}{m_f \omega_1^2} + k \left[u(0) \cos \omega_1 t' + \frac{\dot{u}(0)}{\omega_1} \sin \omega_1 t' \right] \right\} \quad (C14)$$

where

$$t' = t - T = 0$$

$$u(0) = u_T$$

$$\dot{u}(0) = \dot{u}_T$$

APPENDIX D

AERODYNAMIC AND WEIGHT MOMENTS AND SHEARS

In appendix B equations were presented for the bending moments and shears due to the combination of the inertia forces arising from the accelerations of the masses distributed along the span and the landing-gear force. In the calculation of the total moments and shears, however, consideration must be given to the aerodynamic lift and weight forces. This appendix presents equations for estimating these aerodynamic and weight moments and shears which, although only first approximations, are considered sufficiently accurate for the purposes of the present study.

If it is assumed that the lift coefficient is constant along the span and equal to the average lift coefficient of the wing C_L , the lift force at any station y_i is equal to $C_L \frac{\rho}{2} V_L^2 A_i$ where A_i is the area assumed to be concentrated at the station.

The moment at any station y_j due to the lift and weight forces at each station i outboard of station y_j is

$$M_{a(y_j)} = C_L \frac{\rho}{2} V_L^2 \sum_{i=j}^{\text{tip}} A_i (y_i - y_j) - g \sum_{i=j}^{\text{tip}} m_i (y_i - y_j) \quad (\text{D1})$$

If unsteady-state lift effects are neglected, the instantaneous lift coefficient is related to the lift coefficient at the instant of initial contact by the expression

$$\begin{aligned} C_L &= C_{L_0} + C_{L_\alpha} (\gamma - \gamma_0) \\ &= C_{L_0} + C_{L_\alpha} \left(\frac{\dot{a}_0 - V_{v_0}}{V_L} \right) \end{aligned}$$

Inasmuch as the total lift at the instant of contact is $K_L W_{tot}$,

$$C_{L_0} = \frac{K_L W_{tot}}{\frac{\rho}{2} A V_L^2}$$

so that

$$M_{a(y_j)} = \left[\frac{K_L W_{tot}}{A} + C_{L_\alpha} (\dot{a}_0 - V_{v_0}) \frac{\rho}{2} V_L \right] \sum_{i=j}^{\text{tip}} A_i (y_i - y_j) - g \sum_{i=j}^{\text{tip}} m_i (y_i - y_j) \quad (\text{D2})$$

Similarly, the shear at any station y_j is

$$S_{a(y_j)} = \left[\frac{K_L W_{tot}}{A} + C_{L_\alpha} (\dot{a}_0 - V_{v_0}) \frac{\rho}{2} V_L \right] \sum_{i=j}^{\text{tip}} A_i - g \sum_{i=j}^{\text{tip}} m_i \quad (\text{D3})$$

REFERENCES

1. Fairthorne, R. A.: The Effects of Landing Shock on Wing and Undercarriage Deflexion. R. & M. No. 1877, British A.R.C., 1939.
2. Stowell, Elbridge Z., Houbolt, John C., and Batdorf, S. B.: An Evaluation of Some Approximate Methods of Computing Landing Stresses in Aircraft. NACA TN 1584, 1948.
3. McPherson, Albert E., Evans, J., Jr., and Levy, Samuel: Influence of Wing Flexibility on Force-Time Relation in Shock Strut Following Vertical Landing Impact. NACA TN 1995, 1949.
4. Pian, T. H. H., and Flomenhoft, H. I.: Analytical and Experimental Studies on Dynamic Loads in Airplane Structures During Landing. Jour. Aero. Sci., vol. 17, no. 12, Dec. 1950, pp. 765-774, 786.
5. O'Brien, T. F., and Pian, T. H. H.: Effect of Structural Flexibility on Aircraft Loading. Part 1. Ground-Loads. AF Tech. Rep. No. 6358, pt. 1, WADC, U. S. Air Force, M.I.T., July 1951.
6. Milwitzky, Benjamin, and Cook, Francis E.: Analysis of Landing-Gear Behavior. NACA Rep. 1154, 1953. (Supersedes NACA TN 2755.)
7. Mayo, Wilbur L.: Hydrodynamic Impact of a System With a Single Elastic Mode. I—Theory and Generalized Solution With an Application to an Elastic Airframe. NACA Rep. 1074, 1952. (Supersedes NACA TN 1398.)
8. Biot, M. A., and Bisplinghoff, R. L.: Dynamic Loads on Airplane Structures During Landing. NACA WR W-92, 1944. (Formerly NACA ARR 4H10.)
9. Lawrence, H. R.: The Dynamics of a Swept Wing. Jour. Aero. Sci., vol. 14, no. 11, Nov. 1947, pp. 643-650.
10. Isakson, G.: A Survey of Analytical Methods for Determining Transient Stresses in Elastic Structures. Contract No. N5 ori-07833, Office Naval Res. (Project NR-035-259), M.I.T. Mar. 3, 1950.
11. Southwell, R. V.: Relaxation Methods in Theoretical Physics. The Clarendon Press (Oxford), 1946.
12. Scarborough, James B.: Numerical Mathematical Analysis. Second ed., The Johns Hopkins Press (Baltimore), 1950.
13. Levy, H., and Baggott, E. A.: Numerical Solutions of Differential Equations. First Am. ed., Dover Pub. Inc., 1950.

REPORT 1279

THEORETICAL ANALYSIS OF INCOMPRESSIBLE FLOW THROUGH A RADIAL-INLET CENTRIFUGAL IMPELLER AT VARIOUS WEIGHT FLOWS¹

By JAMES J. KRAMER, VASILY D. PRIAN, and CHUNG-HUA WU

SUMMARY

A method for the solution of the incompressible nonviscous flow through a centrifugal impeller, including the inlet region, is presented. Several numerical solutions are obtained for four weight flows through an impeller at one operating speed. These solutions are refined in the leading-edge region. The results are presented in a series of figures showing streamlines and relative velocity contours. A comparison is made with the results obtained by using a rapid approximate method of analysis.

INTRODUCTION

In order to provide the fundamental information about the internal flow necessary for the rational design of efficient centrifugal compressors, two-dimensional solutions of the potential flow through centrifugal compressors on both blade-to-blade and meridional surfaces are obtained by means of relaxation methods in references 1 to 4. In addition, a three-dimensional potential-flow solution is obtained by similar means in reference 5. However, all these solutions are for impellers with inducer sections extended infinitely far upstream or to the axis of the impeller and thus yield no information concerning the flow behavior ahead of and at the entrance to blades of finite thickness or blades which are not aligned with the inlet stream.

A rapid approximate method is developed in reference 6 that will predict the blade surface velocities in centrifugal impellers. The accuracy of this method is investigated herein for the region downstream of the inducer section. However, because of the lack of an exact solution of the flow in the inlet region, there has been no verification of the approximate method in that region.

Consequently, a method for analyzing the flow in a centrifugal impeller, including the inlet region, by numerical solution of the partial differential equation governing the flow was developed at the NACA Lewis laboratory and is presented herein. This method was applied to a 48-inch-diameter centrifugal impeller for both design and off-design flow conditions. The impeller is similar to that discussed in references 7 and 8. The results of the exact solution are compared with the results of the rapid approximate method of reference 6.

In addition, the flow in the region of the leading edge of the blade was determined in more detail than that obtained in the original solution. This refinement of the original solution is obtained by solving the partial differential equation in that region by relaxation methods using a grid of much finer mesh. More detailed information concerning the flow behavior near the leading edge than that obtained in the original solution is desirable, because a knowledge of the velocity gradients in this region is helpful in avoiding boundary-layer separation caused by rapidly decelerating flow. The magnitude of losses caused by boundary-layer separation at the leading edge is discussed in references 9 and 10 for sharp-nosed blades, but the manner in which the losses occur is not discussed.

ANALYSIS

The formulation of the problem and the proposed method of solution of the problem are discussed in this section.

STATEMENT OF PROBLEM

The basic assumptions which are made concerning the physical nature of the flow determine the partial differential equation governing the flow. The assigning of proper boundary conditions to the problem then determines the particular solution of the partial differential equation.

Assumptions.—The flow is assumed to be steady, incompressible, and nonviscous. The assumption of steady nonviscous flow is customary in compressor flow analyses. Several solutions have been obtained taking compressibility into account (e. g., refs. 1 and 2). The addition of the condition of compressibility complicates the solution by a factor which was considered to be out of proportion with its value in this case. Therefore, the fluid was assumed incompressible.

The further assumption is made that the flow is constrained to a blade-to-blade surface of revolution which is symmetrical about the impeller axis. Although the flow is constrained to this surface, a variation in the thickness of the stream sheet provides a closer approximation to the actual case. The shape of the stream surface in the axial-radial plane as well as the thickness variation are defined as functions of radial position, which are specified at the beginning of the solution.

¹ Supersedes NACA TN 3448, "Theoretical Analysis of Incompressible Flow Through a Radial-Inlet Centrifugal Impeller at Various Weight Flows. I—Solution by a Matrix Method and Comparison with an Approximate Method," by Vasily D. Prian, James J. Kramer, and Chung-Hua Wu, 1955; and TN 3449, "Theoretical Analysis of Incompressible Flow Through a Radial-Inlet Centrifugal Impeller at Various Weight Flows. II—Solution in Leading-Edge Region," by James J. Kramer, 1955.

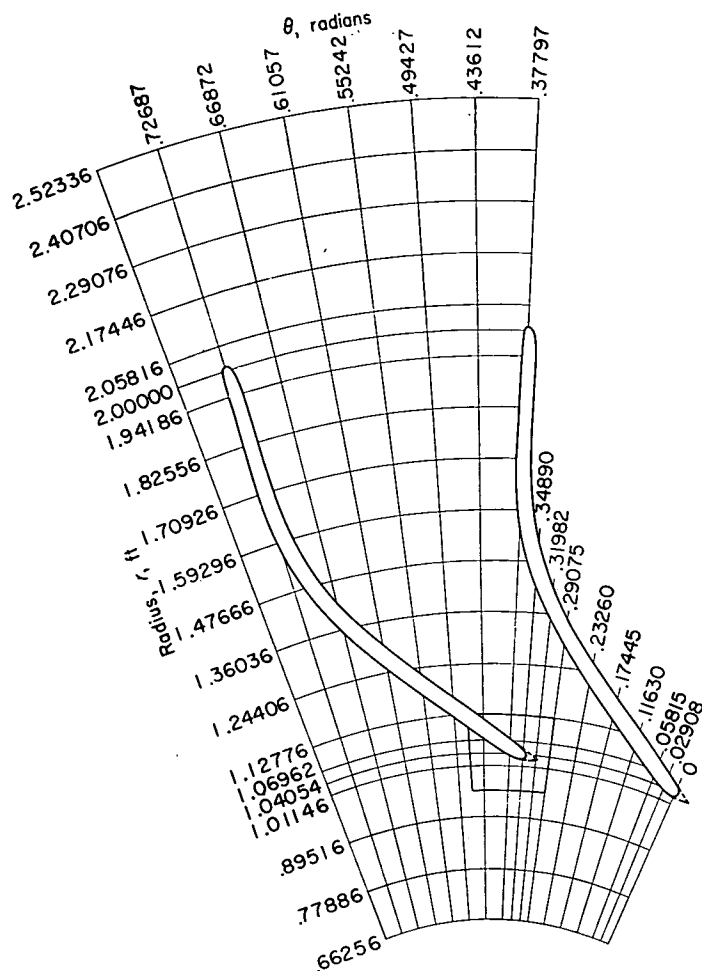


FIGURE 1.—Grid system for over-all solution.

The rear stagnation point is assumed to be located at the blade tip. The Kutta condition states that for a noncuspidate blade with a sharp trailing edge the rear stagnation point occurs at the tip. However, for an impeller with a rounded trailing edge the location of the rear stagnation point cannot be predicted. It is necessary, therefore, to assume the location of the rear stagnation point.

For the refined solution it is assumed that the values of the stream function obtained in the original solution along the boundaries of the region in which the refined solution is obtained remain unchanged during the numerical procedure of obtaining the refined solution.

Differential equation.—In this analysis, the cylindrical coordinates r , θ , and z (see figs. 1 and 2) are used. (All symbols are defined in the appendix.) The angular velocity of the impeller is denoted by ω and the fluid density by ρ . The stream-sheet thickness in the z -direction is represented by b . The trace of the stream surface in the axial-radial plane is given by specifying z as a function of r . The slope dr/dz of this curve is equal to the tangent of the angle between the axis of rotation and the tangent to the trace of the stream surface in the axial-radial plane and is denoted by λ (see fig. 2). Thus, the resultant velocity w is given by

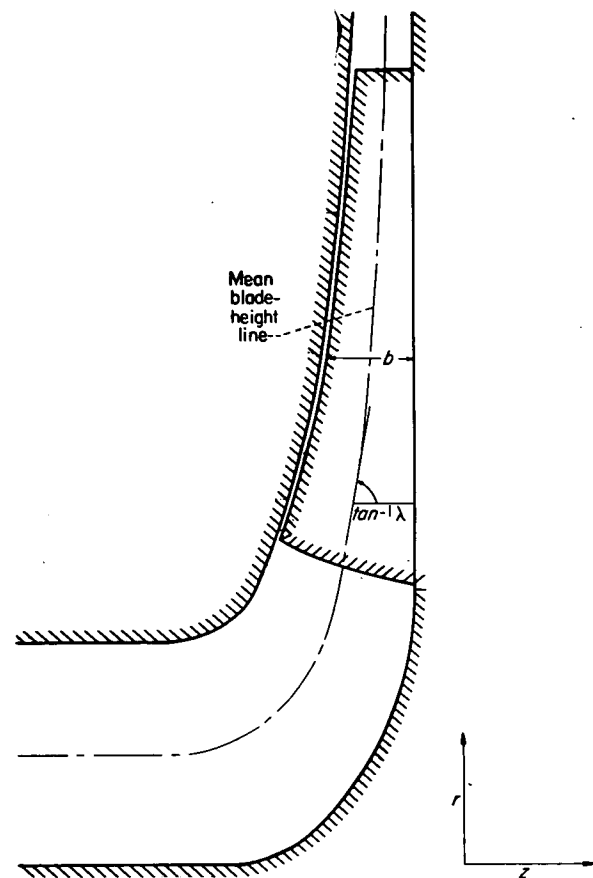


FIGURE 2.—Axial-radial plane view of 48-inch-diameter centrifugal impeller.

$$w^2 = w_r^2 + w_\theta^2 \left(1 + \frac{1}{\lambda^2} \right)$$

where the subscripts r and θ indicate components in the r and θ -directions, respectively.

The stream function Ψ is defined by the following differential equations:

$$\frac{\partial \Psi}{\partial r} = -b \rho w_\theta \quad (1a)$$

$$\frac{\partial \Psi}{\partial \theta} = r b \rho w_r \quad (1b)$$

In this report all derivatives with respect to r shall be understood to mean derivatives with respect to r on the stream surface; that is, $\partial/\partial r$ in this report shall correspond to the boldfaced $\partial/\partial r$ of reference 11, in which the differential equation for the type flow considered herein is derived. With these

definitions and assumptions, the differential equation of the flow becomes (see ref. 11, p. 35)

$$\frac{\partial^2 \Psi}{\partial r^2} + \left(\frac{1}{r} - \frac{\partial \ln b}{\partial r} \right) \frac{\partial \Psi}{\partial r} + \frac{1}{r^2} \left(1 + \frac{1}{\lambda^2} \right) \frac{\partial^2 \Psi}{\partial \theta^2} = 2\omega b \rho \quad (2)$$

This equation, together with the boundary conditions, mathematically determines the problem.

Boundary conditions.—This analysis of the flow is a boundary-value problem of the first kind or a Dirichlet problem. Certain boundaries of the flow and the values of the stream function on these boundaries are specified. Furthermore, the flow is assumed to vary periodically in the circumferential direction, completing a cycle in one pitch angle, the angular distance between two adjacent blade mean lines. The rotational speed of the impeller and the weight flow through the compressor are also specified. The domain of the solution is extended sufficiently far upstream and downstream so that the flow is assumed to be uniform at the upstream and downstream boundaries. With the addition of these conditions, the problem is determined mathematically.

For the refined solution the boundary conditions are obtained from the original solution. The value of the stream function, expressed as a dimensionless ratio of the weight flow through a single passage, on the blade surface is equal to 1; the values along the other boundaries are obtained from cross plots of the original data. The error involved in reading values from the cross plots was less than 0.0003 with values of Ψ/M ranging from 0 to 1.

METHOD OF OBTAINING SOLUTION FOR FLOW THROUGH ENTIRE BLADE PASSAGE

Superposition of four basic solutions.—The differential equation (eq. (2)) was solved by a superposition of four basic solutions. These four basic solutions form a set of linearly independent solutions such that all possible flows (including all tip speeds) are expressible as linear combinations of these basic solutions. The first of these, designated ψ_0 , is a solution of equation (2) with the condition that no flow crosses the upstream and downstream boundaries and $\omega = \omega_0 \neq 0$.

The other three basic solutions, designated ψ_1 , ψ_2 , and ψ_3 , are solutions of the linear homogeneous equation obtained by equating the left side of equation (2) to zero. Thus, if

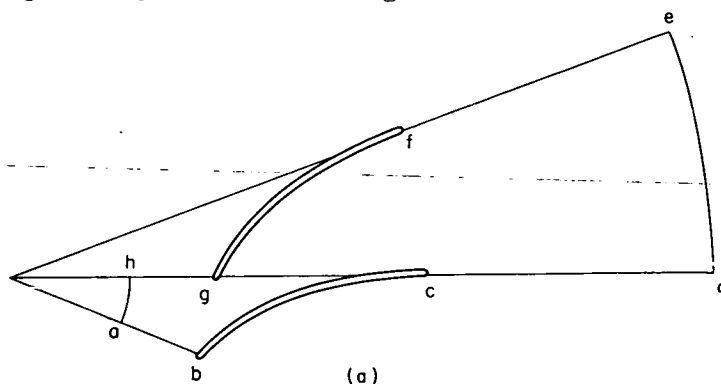
$$L = \frac{\partial^2}{\partial r^2} + \left(\frac{1}{r} - \frac{\partial \ln b}{\partial r} \right) \frac{\partial}{\partial r} + \frac{1}{r^2} \left(1 + \frac{1}{\lambda^2} \right) \frac{\partial^2}{\partial \theta^2}$$

then ψ_1 , ψ_2 , and ψ_3 are solutions of

$$L(\psi) = 0$$

Because L is a linear operator, ψ_0 plus linear combinations of ψ_1 , ψ_2 , and ψ_3 will satisfy equation (2) for $\omega = \omega_0$.

Boundary conditions for four basic solutions.—The flow region is represented by abcdefgh in sketch (a):



The upstream and downstream boundaries, ah and de, respectively, are placed sufficiently far from the blades so that flow conditions can be assumed uniform at these stations. The angular distance from a to h and from d to e is one pitch angle. For all the basic solutions, the condition that the flow is periodic about the axis of rotation with a period of one pitch angle makes it possible to obtain the solutions without a knowledge of the stream function along ab and gh. The finite-difference equation for points along these lines is obtained in the same manner as in reference 12. For the solution ψ_0 in which the flow is that induced only by the rotation of the impeller without any through flow, the value of ψ along ah and de is specified zero, indicating no flow crossing the upstream and downstream boundaries. The values along the blade surfaces bc and gf are also specified as zero. The solution to equation (2) for these boundary conditions is designated ψ_0 .

The through-flow solution, that is, the flow through the stationary blade row, is obtained from linear combinations of three basic solutions to the homogeneous equation obtained by equating the left side of equation (2) to zero. All possible flows through the stationary blade row can be represented by linear combinations of these basic solutions. It can be seen from the boundary conditions shown in the following table that these three basic solutions are linearly independent:

Basic solution	Boundary values at point—			
	a	d	e	h
ψ_0	0	0	0	0
ψ_1	0	0	1	1
ψ_2	-1	0	1	0
ψ_3	-1	-1	0	0

The value of ψ along the trailing face is specified as zero and along the driving face as 1 for all three solutions. That these independent solutions are sufficient for the construction of all possible through flows can be seen from the following consideration.

Any flow is determined when the upstream and downstream flow conditions are specified. The velocity is assumed to be constant at stations ah and de. Hence, the stream function varies linearly from a to h and from d to e. Since the angular distance from a to h and from d to e is one pitch angle and the flow is assumed to vary periodically about the axis with a period of one pitch angle, the specification of conditions at points a, d, and h fixes the solution. The value of ψ is constant along both the driving and trailing faces, with the difference between the function values being equal to $\psi_h - \psi_a$. The choice of 0 and ± 1 as the values of ψ at points a, h, d, and e and along bc and gf represents no restriction since these three basic solutions remain solutions to the homogeneous equation when changed by a multiplicative or additive constant.

Coefficients of ψ_0 , ψ_1 , ψ_2 , and ψ_3 in linear combinations.—The final solution Ψ for any weight flow or rotational speed will be obtained from an equation of the form

$$\Psi = A_0\psi_0 + A_1\psi_1 + A_2\psi_2 + A_3\psi_3 \quad (3)$$

The coefficients A_0 , A_1 , A_2 , and A_3 are determined by the specification of four independent physical conditions: (1) the rotational speed, (2) the weight flow, (3) the location of the rear stagnation point, and (4) the irrotationality of the absolute flow.

The coefficient A_0 is determined by the rotational speed and is given by

$$A_0 = \frac{\omega}{\omega_0} \quad (4)$$

That is, A_0 is the ratio of the rotational speed ω for the desired solution to that used in obtaining the basic solution ω_0 .

The change in Ψ across one blade passage is equal to the weight flow through a single passage. Therefore,

$$A_1 + A_2 + A_3 = M \quad (5)$$

where M is the weight flow through a single passage.

The rear stagnation point is assumed to be at the blade tip. Thus, at the tip

$$w_{\theta, t} = 0$$

or

$$\left(\frac{\partial \Psi}{\partial r}\right)_t = 0 \quad (6)$$

This derivative is expressed in finite-difference form for the grid point at the blade tip and with equation (3) yields a linear relation in A_0 , A_1 , A_2 , and A_3 .

The absolute flow is irrotational; therefore, if r_1 and r_2 are radial stations upstream of the blade row, the following equation holds:

$$\int_0^{2\pi} (w_{\theta, 2} + \omega r_2) r_2 d\theta - \int_0^{2\pi} (w_{\theta, 1} + \omega r_1) r_1 d\theta = 0 \quad (7)$$

where the subscripts 1 and 2 indicate values along the lines $r=r_1$ and $r=r_2$, respectively. If r_1 is chosen equal to the value of r at the upstream boundary, equation (7) becomes

$$\int_0^{2\pi} r_2 w_{\theta, 2} d\theta = -2\omega \pi r_2^2 \quad (8)$$

since $w_{\theta, 1}$ is equal to $-\omega r_1$. When the stream-function definition (eq. (1a)) is introduced, equation (8) becomes

$$\int_0^{2\pi} \frac{\partial \Psi}{\partial r} d\theta = 2\pi \omega p b_2 r_2 \quad (9)$$

Equation (9) can be integrated numerically to yield a linear relation in A_0 , A_1 , A_2 , and A_3 .

Equations (4) to (6) and (9) form a system of four independent simultaneous linear equations in four unknowns, A_0 , A_1 , A_2 , and A_3 .

Numerical method of obtaining basic solutions.—The region of solution was covered with a network of grid lines whose intersections form grid or nodal points, as shown in figure 1.

The solution for a given set of boundary conditions of the differential equation was obtained at each of these grid points by solving the set of linear simultaneous equations obtained when the differential equation is written in finite-difference form for each grid point. A five-point system was used in the finite-difference approximation of the derivatives. This procedure is equivalent to approximating the stream function by a fourth-degree polynomial in the neighborhood of the grid point. The solution of the set of n linear simultaneous equations was obtained on high-speed digital computers by the matrix method outlined in reference 12. Since there were four basic solutions, four sets of n simultaneous linear equations were solved by this process.

METHOD OF OBTAINING REFINED SOLUTION IN LEADING-EDGE REGION

Relaxation method.—The solution of equation (2) was obtained by means of relaxation techniques (ref. 13) in the region outlined by the bold lines in figure 1. The residuals of the relaxation process were reduced to a value indicating unit change in the fifth decimal place of the stream function. This degree of accuracy is consistent with the accuracy of the cross plots used to obtain the boundary values.

Grid.—The grid used in the relaxation process is shown in figure 3. The density of the grid lines is greatest in the region of the leading edge and decreases gradually in both directions. This type of grid assured greatest accuracy in the region of main interest. The ratio of the grid spacing in either direction at a point is never greater than 2.5 and usually less than or equal to 2.0. The intersections of the grid lines are called grid points. The grid points in the interior of the boundaries are the points at which the numerical solution is obtained. There were 138 interior grid points for this problem.

Finite-difference approximation.—The derivatives of equation (2) were written in finite-difference form with a three-point system used. In the original solution a five-point

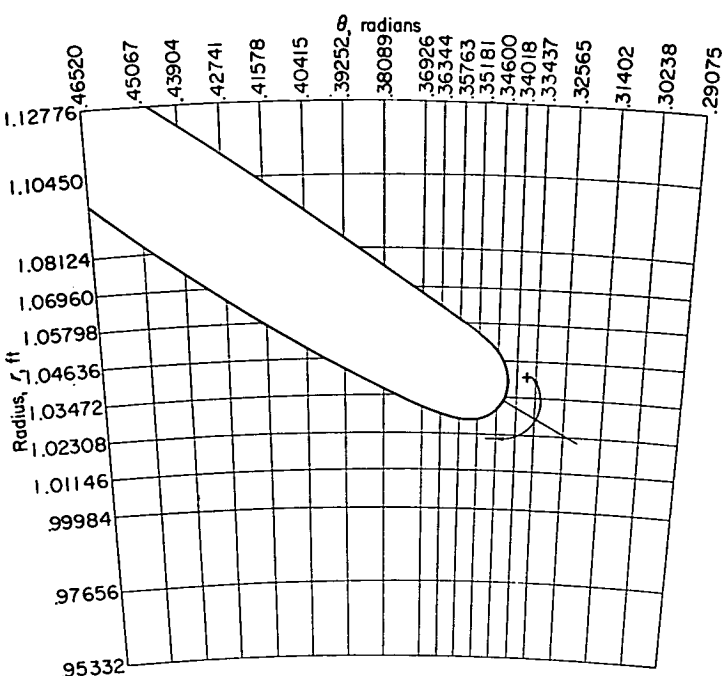


FIGURE 3.—Grid system for refined solution.

system was used. Because of the fineness of the grid, a three-point system was considered adequate for this problem.

NUMERICAL EXAMPLE

The previously outlined methods were applied in order to analyze the flow in a 48-inch-diameter radial-inlet centrifugal impeller. A description of the geometry of the impeller and the operating conditions for which the analysis was carried out follow.

Geometry of impeller.—The impeller investigated was a 48-inch-tip-diameter radial-inlet centrifugal impeller having 18 blades, similar to the one discussed in references 7 and 8. The sharp leading edge and blunt trailing edge were rounded as shown in figure 1 because of practical computing considerations. The blade coordinates are given in table I. The solution was obtained on the surface generated by rotating the mean blade-height line about the axis of rotation. This line was approximated by the following function:

$$z = \frac{-0.041456}{(r-0.40828)} + \text{constant} \quad (10)$$

The streamline spacing in the axial-radial plane is not known. Therefore, the stream-sheet thickness b in the z -direction was approximated by the blade height in the z -direction. This parameter was approximated by the following function:

$$b = 0.07208 + 1.01517e^{-1.54601r} \quad (11)$$

The parameter λ is equal to dr/dz of the stream-surface trace in the axial-radial plane and from equation (10) is given by

$$\frac{1}{\lambda} = \frac{0.041456}{(r-0.40828)^2} \quad (12)$$

Operating conditions.—Four solutions were obtained corresponding to four weight flows at a tip speed of 700 feet per second. These four weight flows, which are the same as those of reference 7, are shown in the following table:

Case	Weight flow, M , lb/sec
A	14. 00
B	26. 25
C	32. 10
D	44. 00

RESULTS AND DISCUSSION

The results of the solutions obtained by the application of the previously outlined methods are presented in figures 4 to 11, which show streamlines and constant relative velocity contours. The over-all solution for the entire blade passage as obtained by the matrix method is shown in the (a) part of each figure and the refined solution for the leading-edge region in the (b) part. Figures 4 to 11 are projections on the $r\theta$ -plane; that is, the curvature of the stream surface in the axial-radial plane is neglected. The comparison with the results of the approximate method described in reference 6 is made in figure 12.

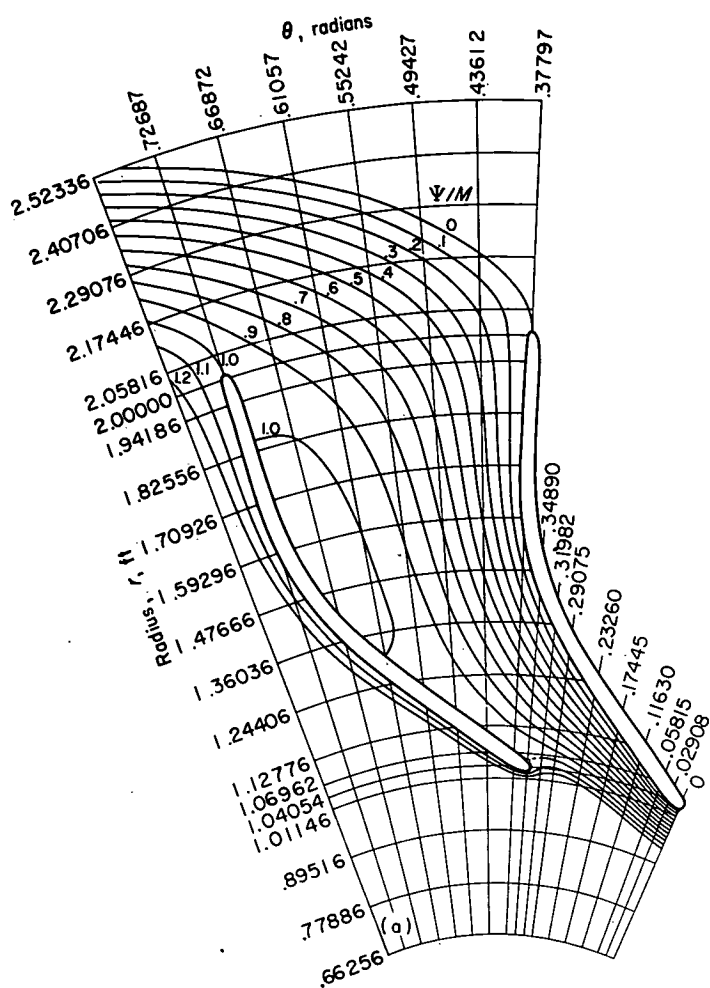
STREAMLINES

The distribution of stream function is shown by means of contours of constant stream-function ratio Ψ/M in figures 4 to 7 for the four weight flows investigated. The impeller tip speed was 700 feet per second for all four cases.

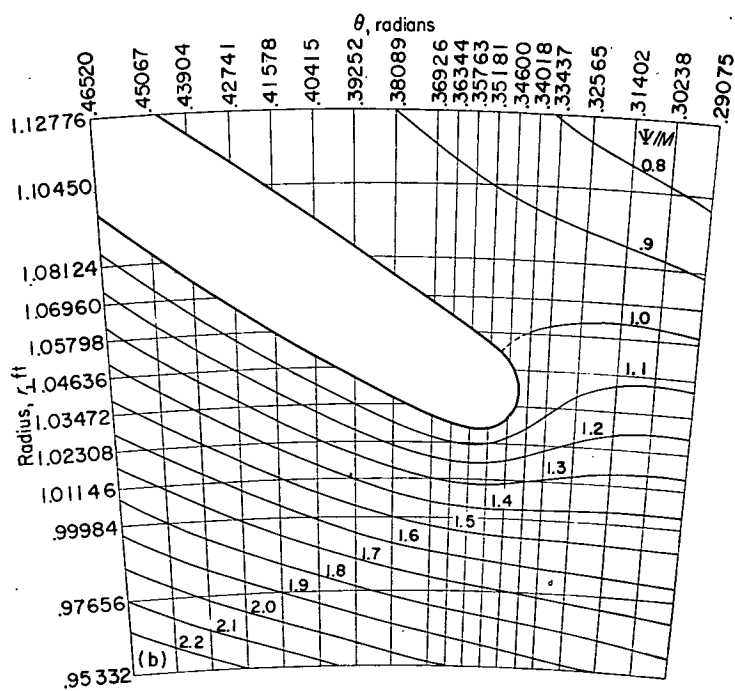
Case A.—In figure 4 the streamlines for a weight flow of 14 pounds per second are shown. This condition is the incipient surge weight flow for the experimental case (ref. 7). A large eddy attached to the driving face of the blade extends from $r \sim 1.31$ to $r \sim 1.84$ and almost one-third the distance across the passage between blades at its widest point. The major part of the flow is concentrated in the region near the trailing face, while the eddy and other relatively low-momentum fluid occupy half the channel.

The inlet stagnation point occurs on the driving face of the blade at $r \sim 1.05$, and the local angle of attack is 80° . The local angle of attack is defined as the angle between the tangents to the blade mean line and the stagnation streamline. The sign convention for angle of attack, shown in figure 3, is chosen so that flow directed at the driving face results in a positive angle of attack. The slip factor, the ratio of the mass-averaged absolute tangential velocity of the fluid at the tip to the absolute tip speed, is equal to 0.874.

Case B.—The streamline pattern for a weight flow of 26.25 pounds per second is shown in figure 5. This weight flow is sufficiently high to eliminate the eddy on the driving face of the blade. However, a fairly large concentration of low-momentum air is still present, so that halfway through the impeller 50 percent of the fluid occupies more than two-thirds the available flow area. The slip factor at the impeller tip is 0.873, and the local angle of attack is approximately 6° .

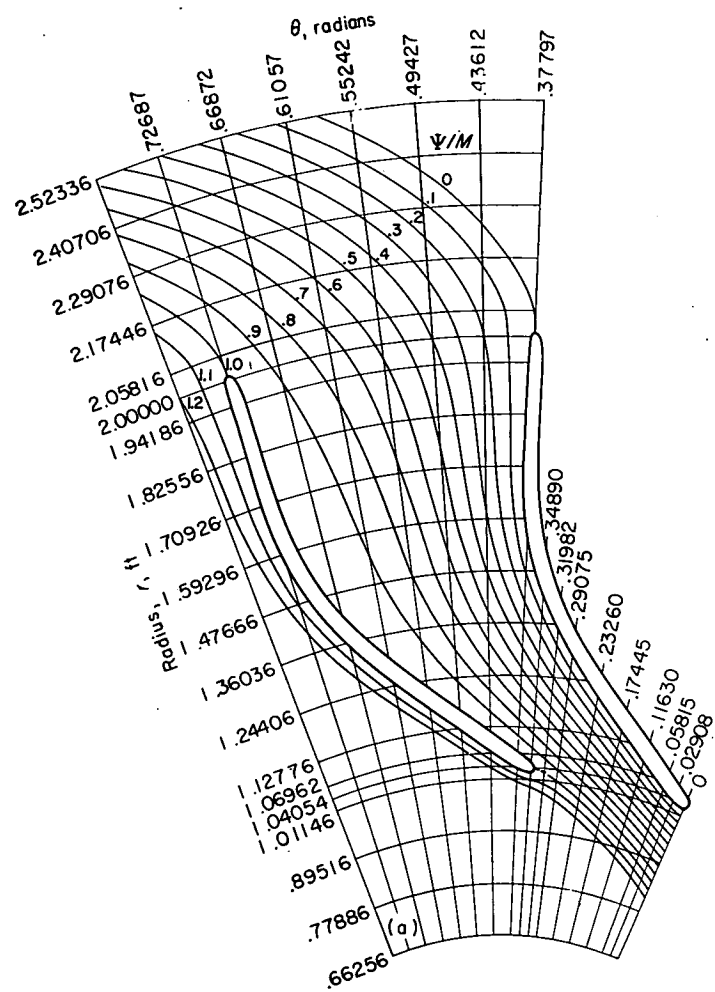


(a) Entire blade passage.

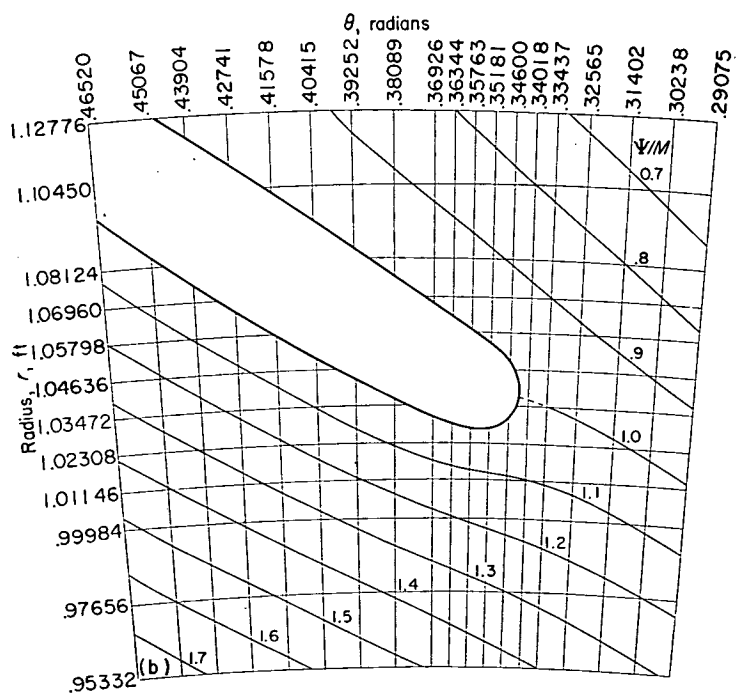


(b) Leading-edge region.

FIGURE 4.—Streamlines for weight flow of 14 pounds per second (case A).

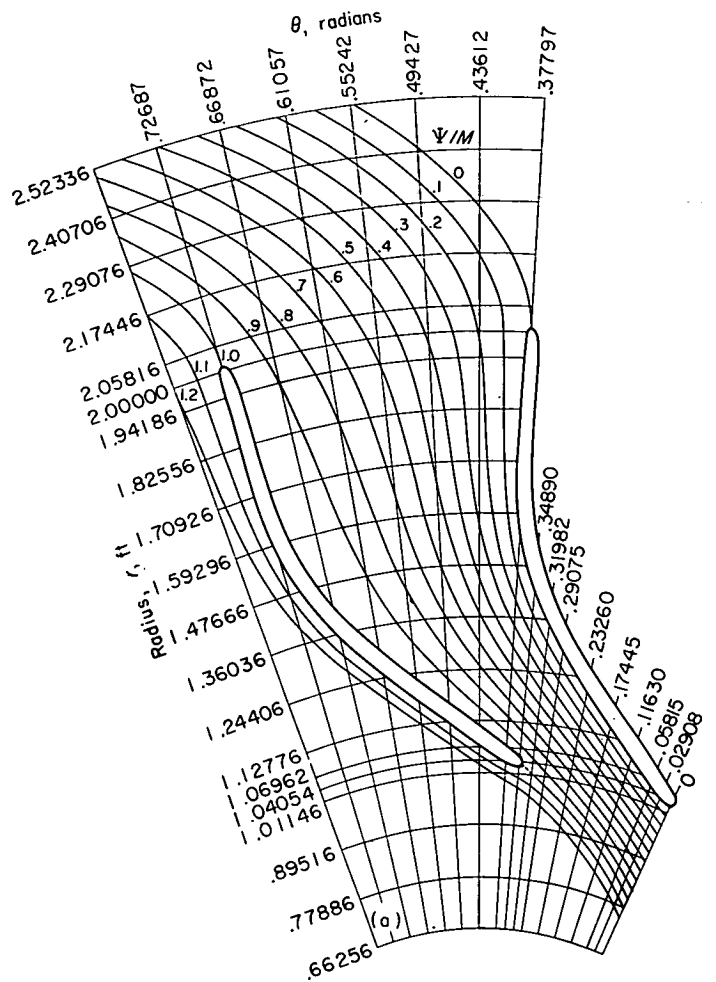


(a) Entire blade passage.

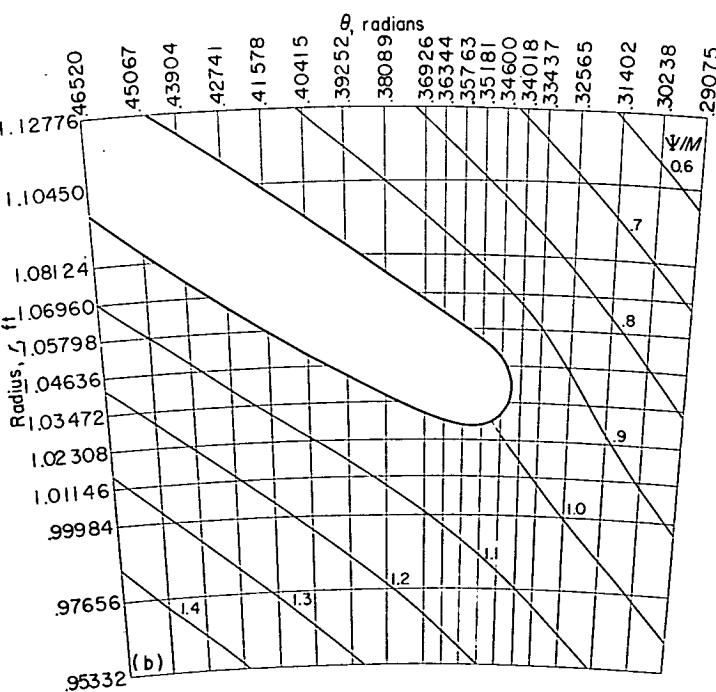


(b) Leading-edge region.

FIGURE 5.—Streamlines for weight flow of 26.25 pounds per second (case B).

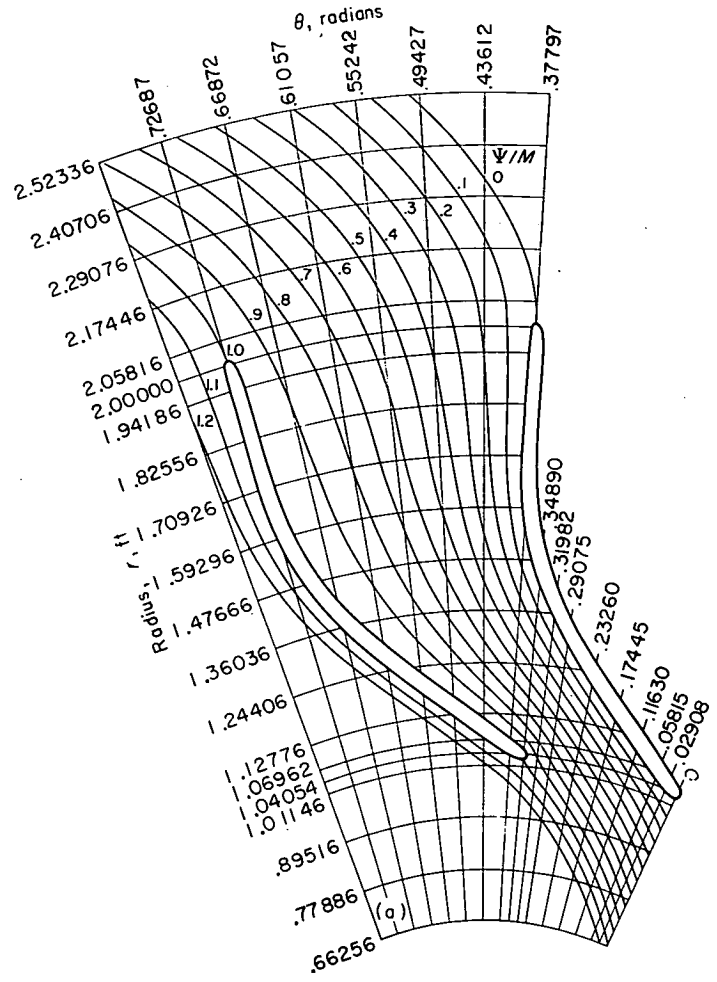


(a) Entire blade passage.

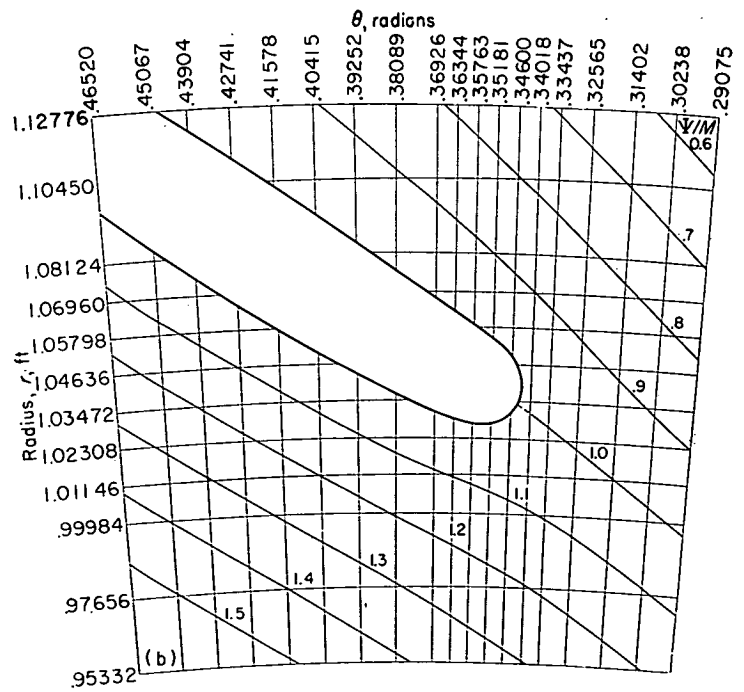


(b) Leading-edge region.

FIGURE 6.—Streamlines for weight flow of 32.10 pounds per second (case C).

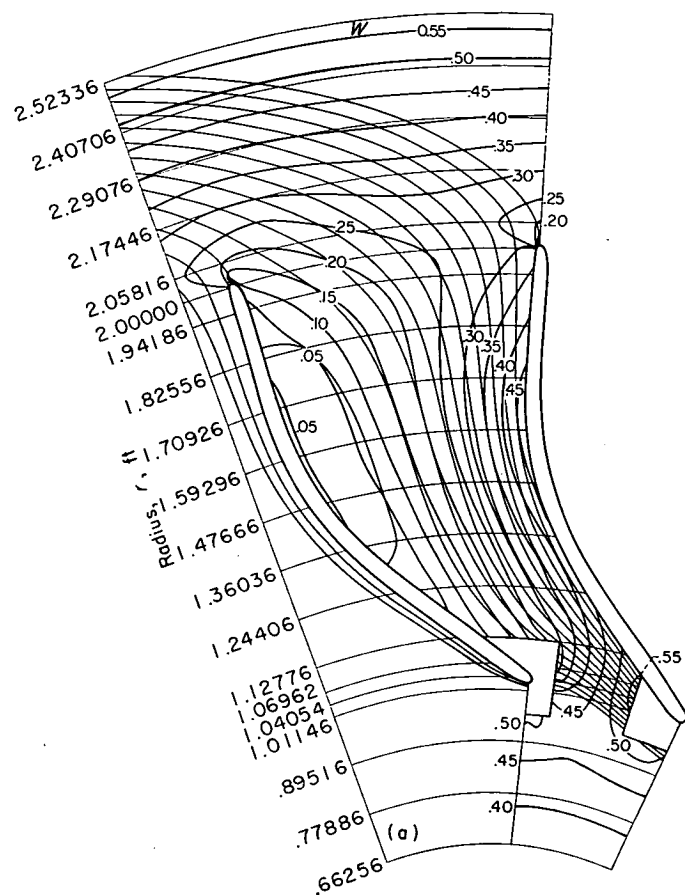


(a) Entire blade passage.

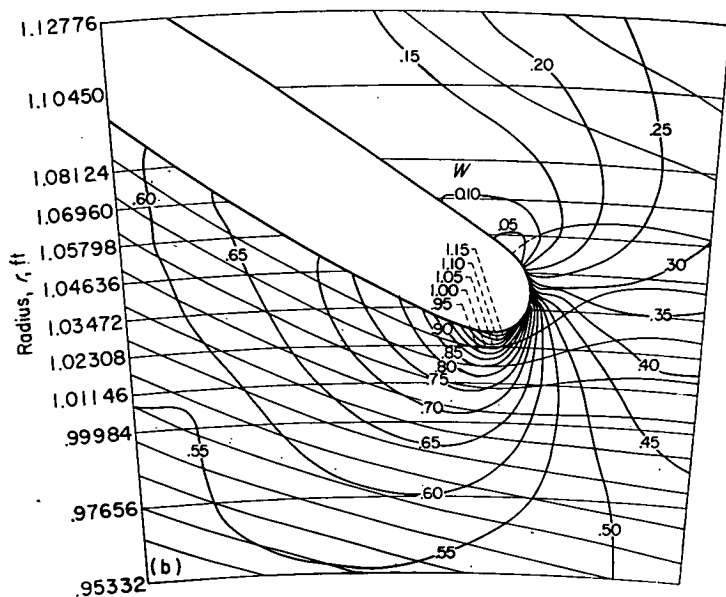


(b) Leading-edge region.

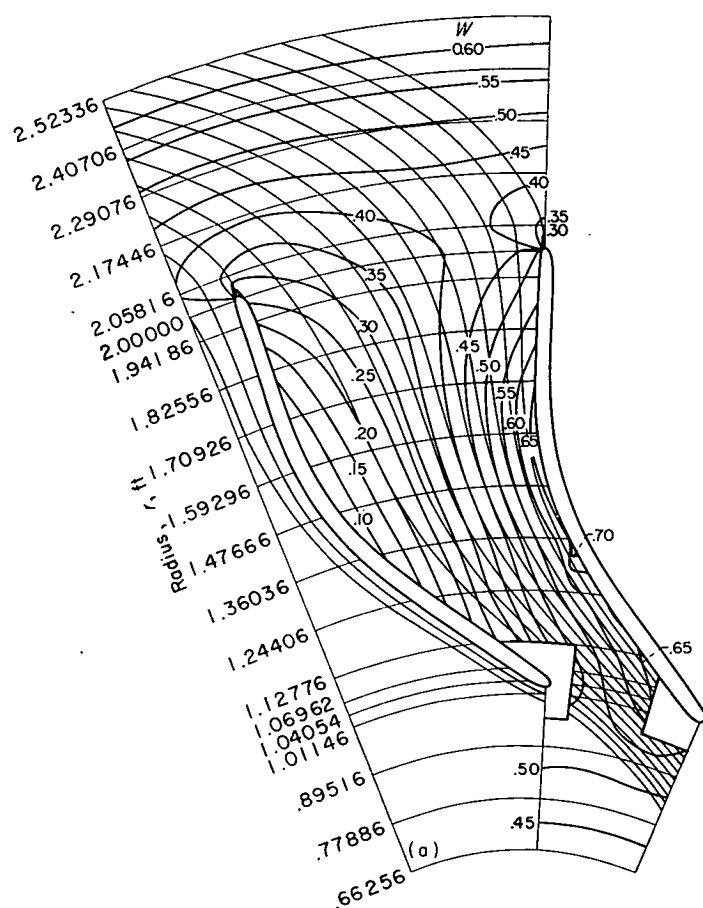
FIGURE 7.—Streamlines for weight flow of 44 pounds per second (case D).



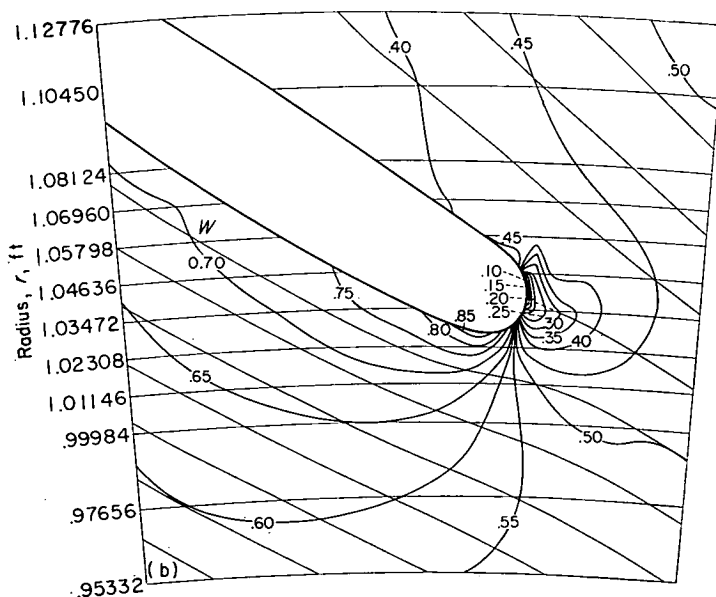
(a) Entire blade passage.



(b) Leading-edge region.

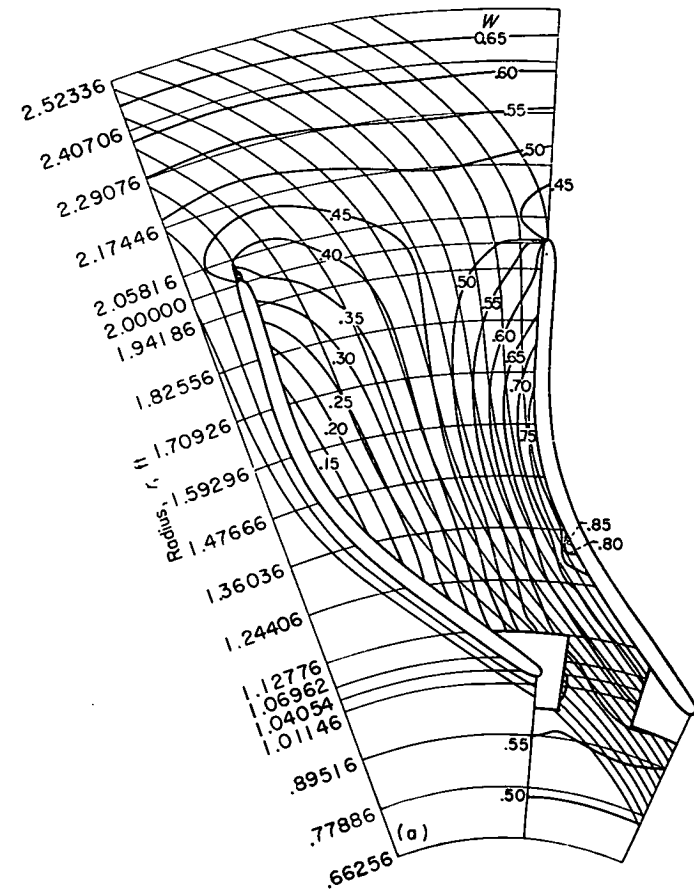
FIGURE 8.—Contours of constant relative velocity ratio W for weight flow of 14 pounds per second (case A).

(a) Entire blade passage.

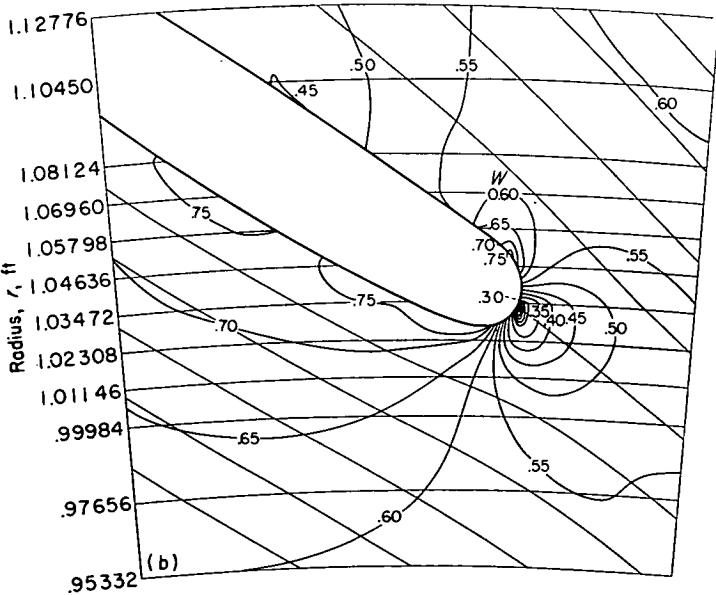


(b) Leading-edge region.

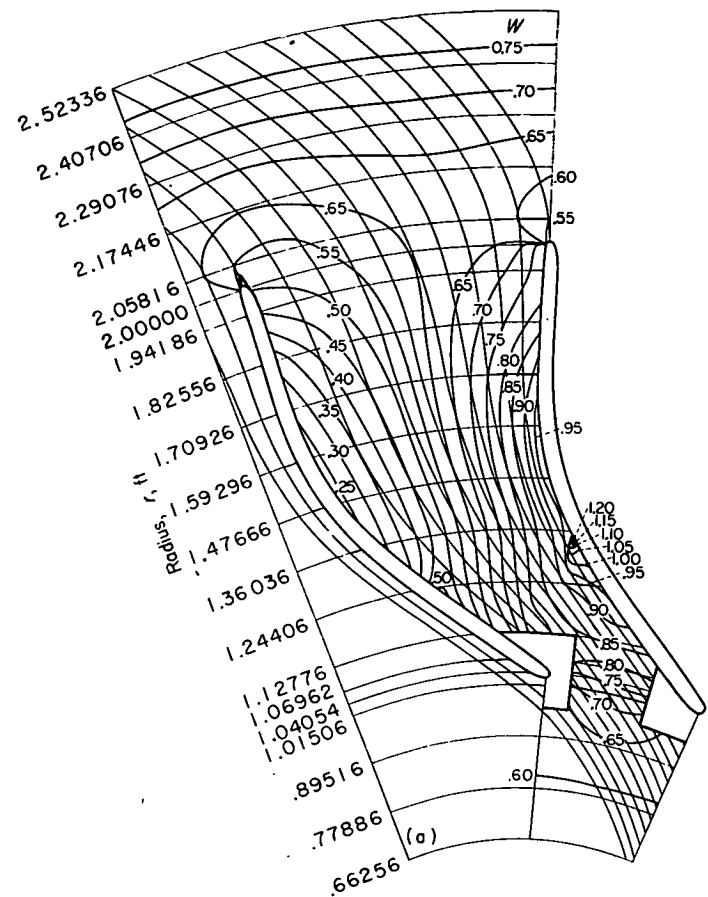
FIGURE 9.—Contours of constant relative velocity ratio W for weight flow of 26.25 pounds per second (case B).



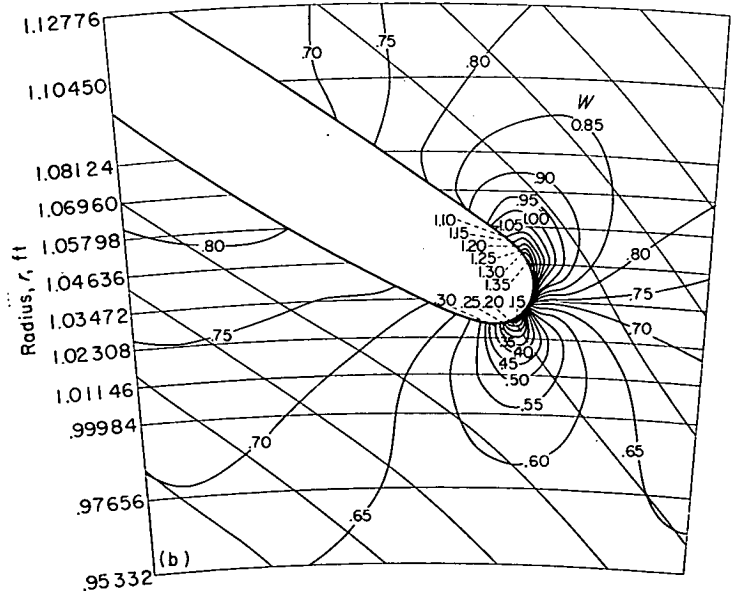
(a) Entire blade passage.



(b) Leading-edge region.

FIGURE 10.—Contours of constant relative velocity ratio W for weight flow of 32.10 pounds per second (case C).

(a) Entire blade passage.



(b) Leading-edge region.

FIGURE 11.—Contours of constant relative velocity ratio W for weight flow of 44 pounds per second (case D).

Case C.—The streamline pattern for a weight flow of 32.10 pounds per second (fig. 6) is similar to that for 26.25 pounds per second because of the comparatively small change in weight flow. However, the local angle of attack changes considerably, from 6° for case B to -7° for case C. This sensitivity of local angle of attack to weight flow changes is quite marked over the entire weight flow range investigated. The weight flow for zero local angle of attack is about 29 pounds per second.

The flow continues to shift toward the driving face, and the slip factor at the tip is 0.871.

Case D.—In figure 7, the streamline pattern is shown for a weight flow of 44 pounds per second. In the investigation reported in reference 7, this represented the maximum weight flow. The flow is distributed across the passage more nearly uniformly than in the other examples. The flow ceases to be perfectly guided at $r \sim 1.5$, as occurred for all other weight flows. The slip factor at the tip for this condition is 0.859, so that the total variation in slip factor from surge to maximum weight flow as determined in reference 7 is 0.015. The inlet stagnation point occurs on the trailing face at $r \sim 1.028$. Thus, the stagnation point shifts about 0.022 foot as the weight flow increases from 14 to 44 pounds per second. The local angle of attack for case D is -28° so that the total range of local angle of attack investigated was from 80° to -28° .

RELATIVE VELOCITY

Contours of constant relative velocity ratio W (relative velocity divided by tip speed) are shown in figures 8 to 11. In the figures showing the entire blade passage ((a) parts), the velocities near the leading edge are not shown. Reference should be made to the figures showing the leading-edge region only ((b) parts).

Case A.—For a weight flow of 14 pounds per second (fig. 8) a stagnation point occurs where the eddy begins to form at $r \sim 1.31$ on the driving face. Velocities are low along the entire driving face with slightly negative velocities in the eddy region. A rapid acceleration followed by a less rapid deceleration occurs on the leading edge and the trailing face because of the large positive local angle of attack.

Case B.—In figure 9 the velocity contours for a weight flow of 26.25 pounds per second are shown. Downstream of the leading-edge region the velocity along the trailing face is nearly constant (except for a small acceleration and deceleration at $r \sim 1.3$ to $r \sim 1.7$). In the leading-edge region, small local decelerations occur on both the driving and trailing faces with the one on the trailing face being the larger. Flow conditions in the leading-edge region are better for this weight flow than for any of the other weight flows investigated.

Case C.—The velocity contours for a weight flow of 32.10 pounds per second are presented in figure 10. At $r \sim 1.3$ on the trailing face, a slight acceleration occurs followed by a rapid deceleration. This velocity peak is caused by the beginning of more rapid blade curvature at that point.

For case C a larger deceleration occurs on the driving face than for case B. Decelerations are probably more serious on the driving face than on the trailing face because the low-momentum air caused by the deceleration aggravates the secondary-flow conditions. These secondary flows transport the low-momentum fluid on the driving face to the trailing

face. This type of motion is discussed in more detail in reference 14.

It was previously noted that the weight flow for zero local angle of attack is about 29 pounds per second. However, zero local angle of attack is not necessarily desirable for rounded leading edges such as the one considered herein. In view of the velocity contours of the 26.25- and 32.10-pound-per-second cases, a slight positive local angle of attack seems desirable. For a weight flow of 29 pounds per second, a greater deceleration would probably occur on the driving face than that which occurs for a weight flow of 26.25 pounds per second. This appears to be the case since the leading edge is shaped so that at zero local angle of attack the flow on the blade surfaces would be roughly symmetrical about the blade mean line. Consequently, it seems advisable to design the leading-edge regions in the manner suggested in reference 15 and further discussed in reference 16. These leading-edge contours are characterized by very little curvature of the driving face so that flow aligned with the driving face would produce little or no local deceleration.

Case D.—The velocity contours for a weight flow of 44 pounds per second are plotted in figure 11. The flow along the driving and trailing faces is similar to that for case C, because in both cases the inlet flow is directed toward the trailing face. The local acceleration and deceleration on the trailing face at $r \sim 1.3$ is more pronounced for this case.

A very large deceleration occurs on the driving face just downstream of the leading edge. This deceleration is about the same size as that which occurred on the trailing face in case A. The deceleration is probably more serious on the driving face because of its contribution to the buildup of secondary flows. Also, at sufficiently high weight flows the separation following a rapid deceleration will induce choking before the theoretical maximum weight flow is attained.

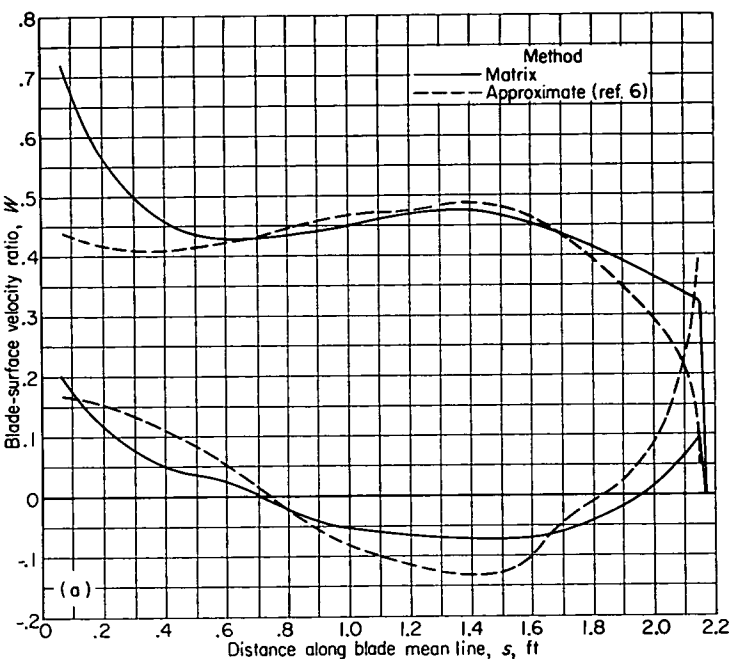
MEAN ANGLE OF ATTACK

The approximate mean angle of attack, that is, the angle between the mean flow direction at the inlet and the tangent to the blade mean line, was computed from the rotational speed and the average inlet velocity. The average inlet velocity was computed from the weight flow and the annular area. Two values were used for the annular area: (1) the total annular area with no blade blockage assumed, and (2) the total annular area minus the blockage caused by the blades. The thickness of the blades used in the latter computation was that at the 1.04-foot radius, which was approximately the radius at which maximum blade thickness in the tangential direction occurred. The mean angle of attack across the passage at the 1.04-foot radius was also computed from the exact solution. These are compared in the following table:

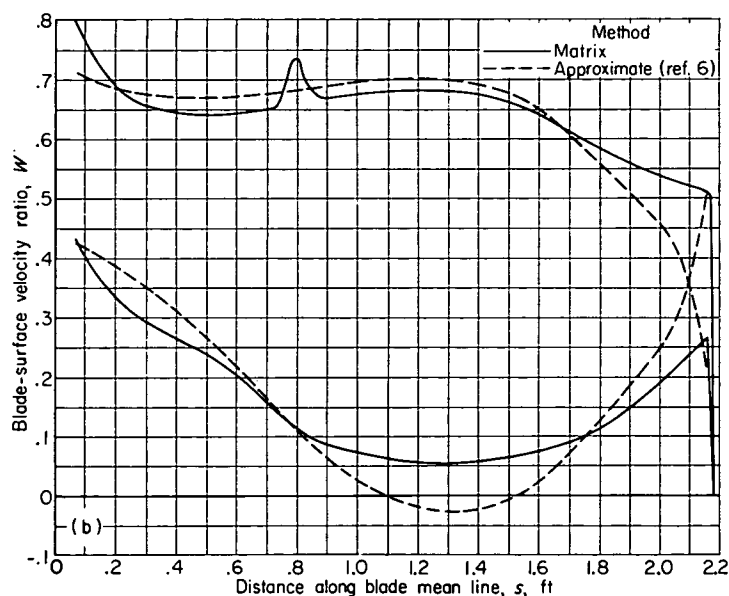
Weight flow, M , lb/sec	Mean angle of attack, deg, based on—		
	Unblocked annulus	Blocked annulus	Exact solution
14.00	12.3	9.2	0
26.25	.1	-4.6	-5.3
32.10	-4.9	-10.0	-9.0
44.00	-13.6	-19.0	-15.4

The sign convention for the angle of attack is such that a positive angle of attack indicates flow directed toward the driving face of the blade. From the comparison of these angles of attack, it is apparent that the mean angle of attack is best predicted by basing the calculations on the annular area with blade blockage considered. The poor agreement between the mean angle of attack of the exact solution and that based on the blocked-inlet annular area at the lowest weight flow is probably caused by the eddy. It appears that

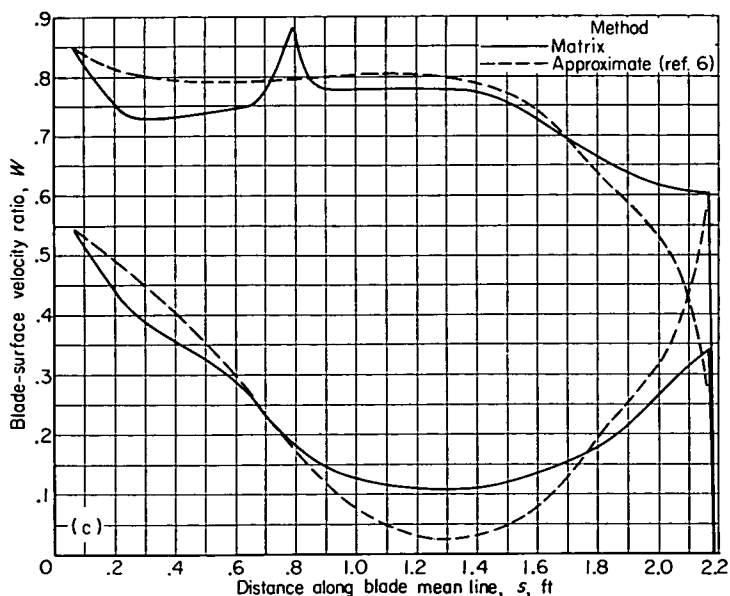
inlet flow aligned with the driving face results in good flow conditions in the leading-edge region. The blade angle of the driving face just downstream of the rounded leading edge is 57° , whereas the angle between the mean line and the radial direction is 62° . Thus, for case B the average inlet flow angle would approximately equal the driving-face blade angle. Flow conditions in the leading-edge region for case B seemed to be the best of the conditions investigated.



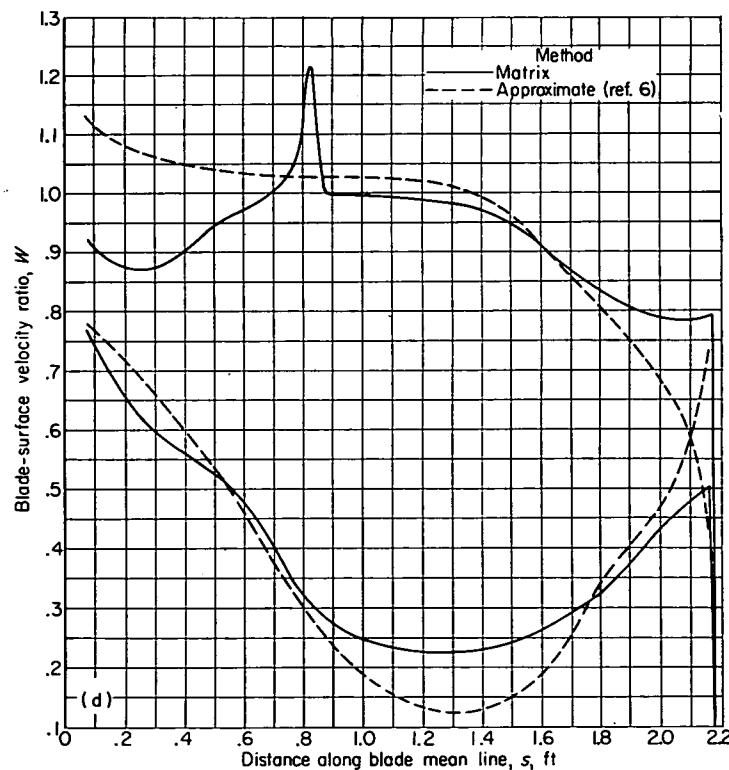
(a) Weight flow, 14 pounds per second (case A).



(b) Weight flow, 26.25 pounds per second (case B).

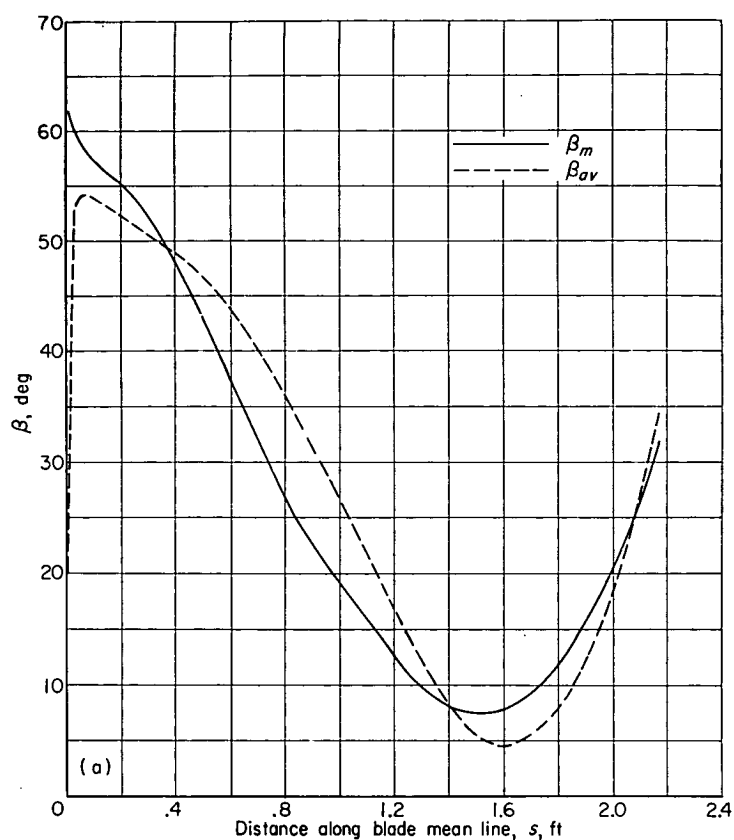


(c) Weight flow, 32.10 pounds per second (case C).

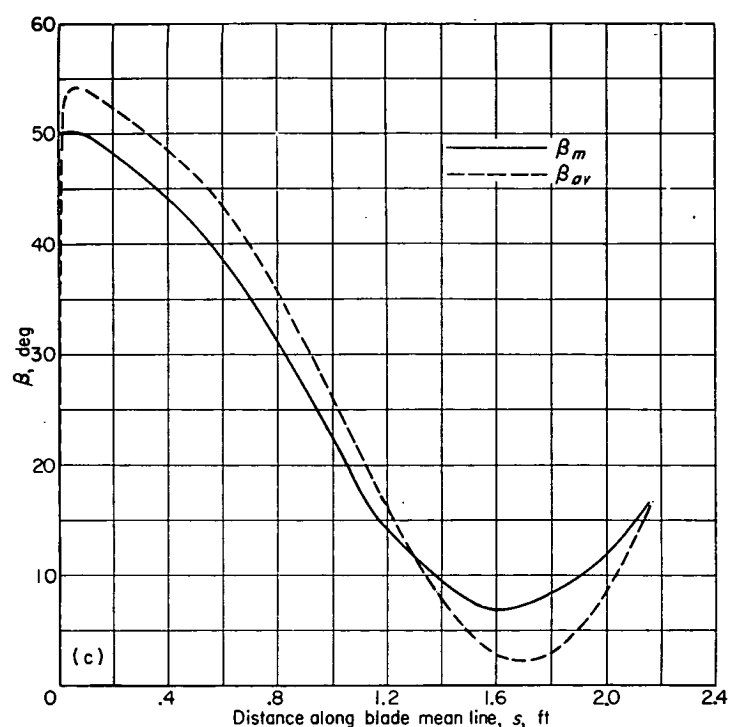


(d) Weight flow, 44 pounds per second (case D).

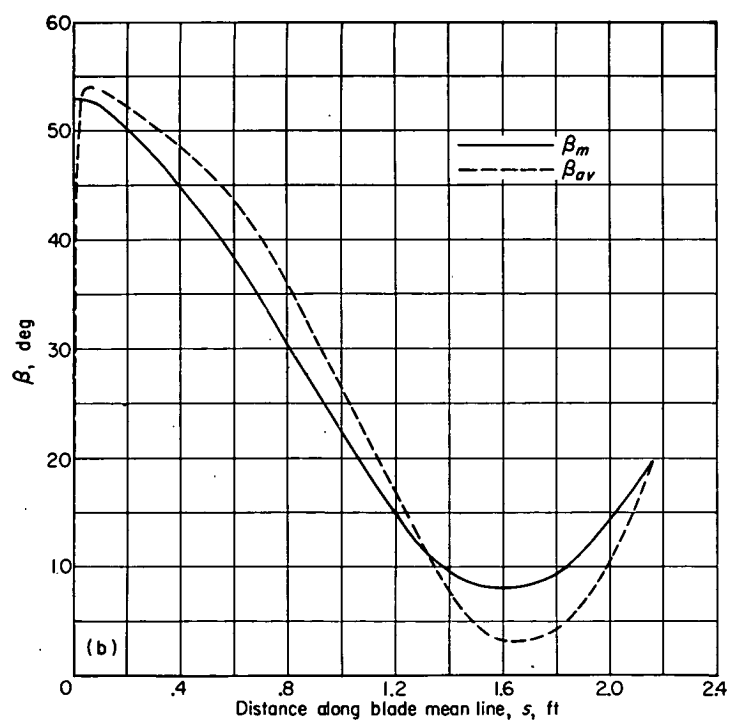
FIGURE 12.—Comparison of blade-surface velocity ratios obtained by approximate and matrix methods.



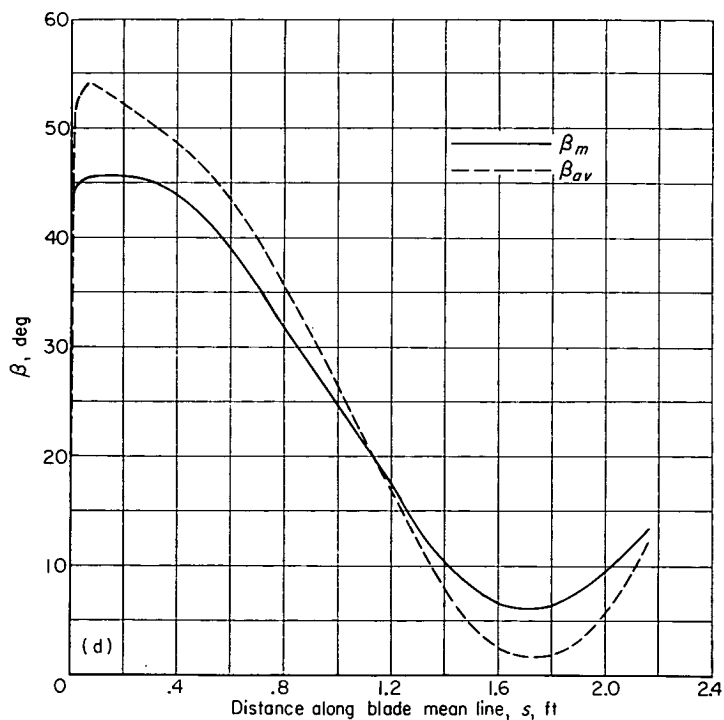
(a) Weight flow, 14 pounds per second (case A).



(c) Weight flow, 32.10 pounds per second (case C).



(b) Weight flow, 26.25 pounds per second (case B).



(d) Weight flow, 44 pounds per second (case D).

FIGURE 13.—Comparison of mass-averaged flow angle of exact solution β_m with approximation of β_m used in approximate method β_{av} .

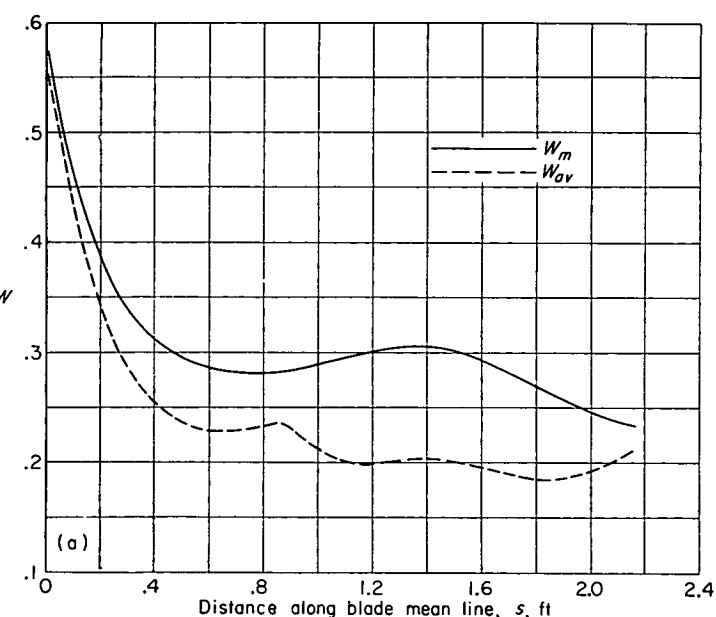
COMPARISON WITH APPROXIMATE METHOD

The blade surface velocities for the four weight flows were computed by the rapid approximate method of reference 6 in order to determine the accuracy of the approximate method, especially in the inlet region, by comparison with the matrix solution. In figure 12, the surface velocity ratios as computed by the approximate method are compared with the surface velocity ratios as determined by the matrix method. The velocity ratios are plotted against distance s along the blade mean line.

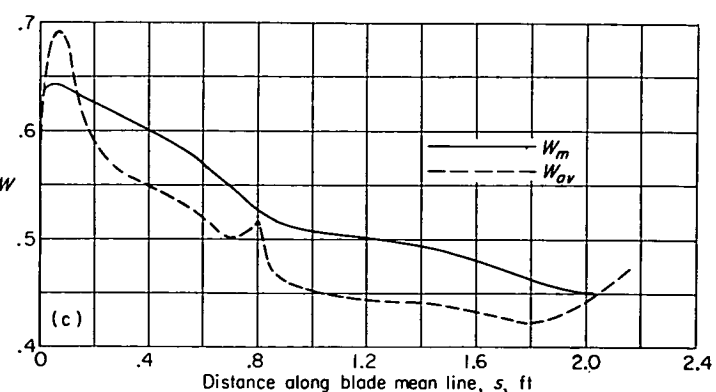
In the approximate method the "average" values of W and β are values which satisfy the one-dimensional continuity equation. The "average" velocity ratio is assumed equal to the average of the blade surface velocity ratios W_{av} . The "average" flow angle is assumed equal to β_{av} , the average of the blade surface angles, for values of $s \leq 1.34$. For $s > 1.34$,

the "average" flow angle is approximated by a parabolic variation (with r) between the average of the blade surface angles at $s=1.34$ and the flow angle at the tip as determined by the slip factor. The slope $d\beta_{av}/dr$ at $s=1.34$ is used as the third condition to determine the parabola. The approximate flow angle as given by the parabolic variation is also denoted by β_{av} . It is difficult to evaluate these assumptions separately. In order to get some idea of their validity, the mass-averaged flow angle β_m is compared with β_{av} in figure 13, and the mass-averaged velocity ratio W_m is compared with W_{av} in figure 14.

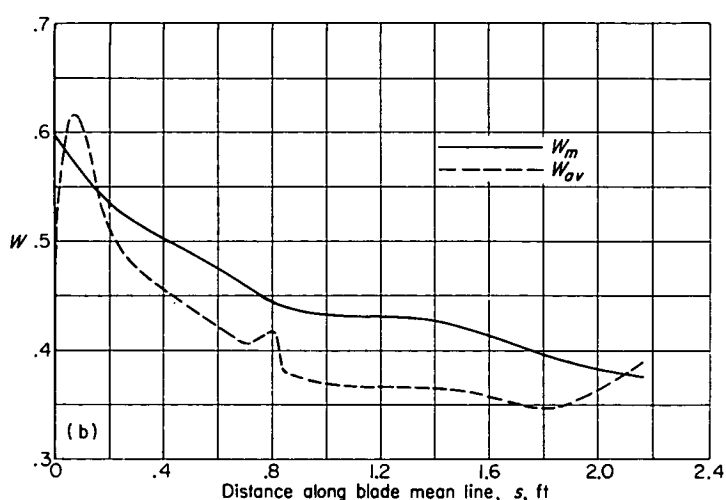
It was impossible to obtain meaningful results in the region of the rounded leading edge. This failure of the approximate method is caused by the invalidity of the assumption that β_m is equal to β_{av} . For values of s such that $0.07 \leq s \leq 0.6$, the surface velocities are predicted adequately for cases B and C but poorly for cases A and D. For case A the failure



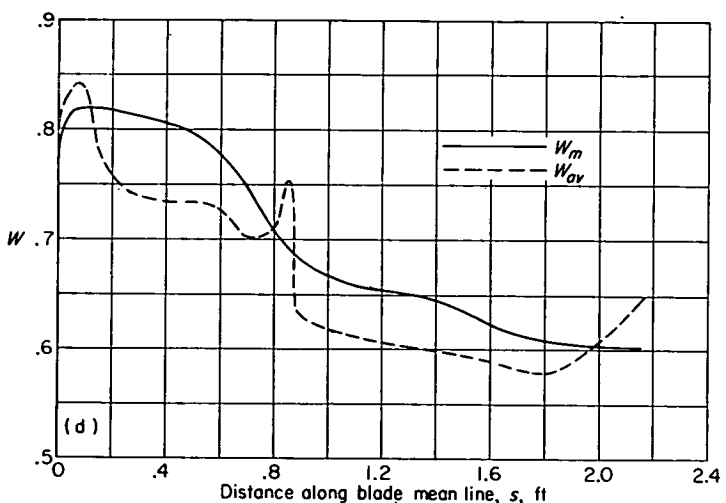
(a) Weight flow, 14 pounds per second (case A).



(c) Weight flow, 32.10 pounds per second (case C).



(b) Weight flow, 26.25 pounds per second (case B).



(d) Weight flow, 44 pounds per second (case D).

FIGURE 14.—Comparison of mass-averaged relative velocity ratio W_m with average of blade-surface velocity ratios W_{av} .

is probably caused by the change in the relative size of β_{av} and β_m . At $s=0.6$, β_{av} is greater than β_m but then becomes less than β_m as s decreases. This trend is not followed in the other cases. For case D the agreement of W_{av} with W_m and of β_{av} with β_m is poorer for $s < 0.6$ than for the other cases. The trends for case D, however, were the same as for cases B and C.

In the region $0.6 \leq s \leq 1.8$, the agreement between the approximate solution and the exact solution is adequate (except in the neighborhood of $s=0.8$ for cases B, C, and D) for approximately predicting both the velocity and the velocity gradients for all four weight flows. Such good agreement is surprising for case A, because the agreement between W_m and W_{av} and between β_m and β_{av} is not nearly so good for case A as it is for the other cases; the eddy attached to the driving face for case A is the cause of this poor agreement.

For $s > 1.8$, the agreement between the approximate method and the exact method is poor, and β_{av} is less than β_m for all four cases except near the tip in case A. This reverse in trend, together with the fact that the blade surface angles differ by a large amount, probably is the reason for the failure of the approximate method near the tip. In the region $s > 1.34$, β_{av} is determined by a parabolic approximation to β_m . Since β_{av} and β_m agree fairly well at $s=1.34$ and at the tip, the failure of the parabolic approximation must be attributed to incorrect values of $d\beta_{av}/dr$ at $s=1.34$ or to the inadequacy of a parabolic approximation.

SUMMARY OF RESULTS

A method for the solution of the incompressible nonviscous flow through a centrifugal impeller (including the inlet region) is presented and is applied to a 48-inch-diameter centrifugal impeller. Solutions for the entire blade passage were obtained for four weight flows ranging from incipient surge to maximum as determined by actual impeller tests. In addition, these solutions were refined in the leading-edge

region. The blade surface velocities obtained by the matrix solutions for the entire blade passage were compared with those obtained by a rapid approximate method of analysis. The following results were noted:

1. A large eddy formed on the driving face of the blade at the incipient surge weight flow but was not present for the three higher weight flows.
2. The slip factor varied from 0.874 to 0.859 as the weight flow increased.
3. For weight flows of 26.25, 32.10, and 44 pounds per second, a local acceleration followed by a rapid deceleration occurred on the trailing face of the blades at a radius of about 1.3 feet, that is, where the blade begins to curve more rapidly.
4. The stagnation point shifted from the driving to the trailing face of the blade as the weight flow increased, while the local angle of attack varied from 80° to -28° .
5. A small positive local angle of attack seems desirable for rounded leading-edge blades.
6. Of the four weight flows investigated, flow conditions around the blade nose were the best for the weight flow corresponding to an angle of attack of -4.6° computed from blade speed and an upstream radial-axial velocity for which blade blockage had been taken into account.
7. The rapid approximate method was adequate in the inlet region just downstream of the leading edge for weight flows of 26.25 and 32.10 pounds per second. These weight flows corresponded to mean angles of attack of -5.3° and -9.0° , respectively.
8. The mean angle of attack was best predicted by basing the approximate computation on the weight flow, the tip speed, and the annular area minus the blockage of the blades.

LEWIS FLIGHT PROPULSION LABORATORY

NATIONAL ADVISORY COMMITTEE FOR AERONAUTICS

CLEVELAND, OHIO, March 4, 1955

APPENDIX

SYMBOLS

The following symbols are used in this report:

$A_0, A_1,$ A_2, A_3	coefficients in eq. (3)
b	stream-sheet thickness in z -direction, ft
M	weight flow through single passage, lb/sec
r	radial distance, ft
s	distance along blade mean line, ft
W	ratio of relative velocity to tip speed
w	relative velocity, ft/sec
z	axial distance, ft
β	flow angle, deg
θ	angular coordinate in relative system, radians
λ	slope of trace of stream surface in axial-radial plane

ρ	fluid density, lb/cu ft
Ψ	stream function, eqs. (1)
$\psi_0, \psi_1,$ ψ_2, ψ_3	basic solutions
ω	angular velocity of impeller, radians/sec
Subscripts:	
av	approximation to averaged value used in approximate method
m	mass-averaged value
r	component in radial direction
t	impeller tip
θ	component in tangential direction
0	value in basic solution of eq. (2)
1,2	conditions along $r=r_1$ and $r=r_2$, respectively

REFERENCES

- Stanitz, John D., and Ellis, Gaylord O.: Two-Dimensional Compressible Flow in Centrifugal Compressors with Straight Blades. NACA Rep. 954, 1950. (Supersedes NACA TN 1932.)
- Ellis, Gaylord O., and Stanitz, John D.: Two-Dimensional Compressible Flow in Centrifugal Compressors with Logarithmic-Spiral Blades. NACA TN 2255, 1951.
- Ellis, Gaylord O., Stanitz, John D., and Sheldrake, Leonard J.: Two Axial-Symmetry Solutions for Incompressible Flow Through a Centrifugal Compressor with and without Inducer Vanes. NACA TN 2464, 1951.
- Stanitz, John D., and Ellis, Gaylord O.: Two-Dimensional Flow on General Surfaces of Revolution in Turbomachines. NACA TN 2654, 1952.
- Ellis, Gaylord O., and Stanitz, John D.: Comparison of Two- and Three-Dimensional Potential-Flow Solutions in a Rotating Impeller Passage. NACA TN 2806, 1952.
- Stanitz, John D., and Prian, Vasily D.: A Rapid Approximate Method for Determining Velocity Distribution on Impeller Blades of Centrifugal Compressors. NACA TN 2421, 1951.
- Michel, Donald J., Ginsburg, Ambrose, and Mizisin, John: Experimental Investigation of Flow in the Rotating Passages of a 48-Inch Impeller at Low Tip Speeds. NACA RM E51D20, 1951.
- Prian, Vasily D., and Michel, Donald J.: An Analysis of Flow in Rotating Passage of Large Radial-Inlet Centrifugal Compressor at Tip Speed of 700 Feet Per Second. NACA TN 2584, 1951.
- Kramer, James J., and Stanitz, John D.: Prediction of Losses Induced by Angle of Attack in Cascades of Sharp-Nosed Blades for Incompressible and Subsonic Compressible Flow. NACA TN 3149, 1955.
- Wright, Linwood C.: Approximate Effect of Leading-Edge Thickness, Incidence Angle, and Inlet Mach Number on Inlet Losses for High-Solidity Cascades of Low Cambered Blades. NACA TN 3327, 1954.
- Wu, Chung-Hua: A General Theory of Three-Dimensional Flow in Subsonic and Supersonic Turbomachines of Axial-, Radial-, and Mixed-Flow Types. NACA TN 2604, 1952.
- Wu, Chung-Hua, and Brown, Curtis A.: A Theory of the Direct and Inverse Problems of Compressible Flow Past Cascade of Arbitrary Airfoils. Jour. Aero. Sci., vol. 19, no. 3, Mar. 1952, pp. 183-196.
- Southwell, R. V.: Relaxation Methods in Theoretical Physics. Clarendon Press (Oxford), 1946.
- Hamrick, Joseph T., Mizisin, John, and Michel, Donald J.: Study of Three-Dimensional Internal Flow Distribution Based on Measurements in a 48-Inch Radial-Inlet Centrifugal Impeller. NACA TN 3101, 1954.
- Weinig, F.: Die Strömung um die Schaufeln von Turbomaschinen. Johann Ambrosius Barth (Leipzig), 1935.
- Stanitz, John D.: Effect of Blade-Thickness Taper on Axial-Velocity Distribution at the Leading Edge of an Entrance Rotor-Blade Row with Axial Inlet, and the Influence of This Distribution on Alinement of the Rotor Blade for Zero Angle of Attack. NACA TN 2986, 1953.

TABLE I.—MODIFIED BLADE COORDINATES

Driving face		Trailing face	
r , ft	θ , radians	r , ft	θ , radians
1. 0405	0. 34256	1. 0285	0. 34890
1. 0521	. 34890	1. 0352	. 37797
1. 0696	. 37224	1. 0405	. 38604
1. 0740	. 37797	1. 0518	. 40705
1. 1190	. 43612	1. 0696	. 43273
1. 1278	. 44633	1. 0971	. 46520
1. 1711	. 49427	1. 1278	. 49939
1. 2324	. 55242	1. 1511	. 52335
1. 2441	. 56242	1. 2144	. 58150
1. 3095	. 61057	1. 2441	. 60413
1. 3604	. 63995	1. 2974	. 63965
1. 4262	. 66872	1. 3525	. 66872
1. 4767	. 68476	1. 3604	. 67227
1. 5930	. 70726	1. 4283	. 69780
1. 7093	. 71497	1. 4767	. 71113
1. 8256	. 71601	1. 5600	. 72687
1. 9419	. 71601	1. 5930	. 73041
2. 0000	. 72080	1. 7093	. 73583
2. 0123	. 72687	1. 8256	. 73416
		1. 9419	. 73312
		2. 0000	. 73145
		2. 0123	. 72687

REPORT 1280

THEORETICAL INVESTIGATION OF FLUTTER OF TWO-DIMENSIONAL FLAT PANELS WITH ONE SURFACE EXPOSED TO SUPERSONIC POTENTIAL FLOW¹

By HERBERT C. NELSON and HERBERT J. CUNNINGHAM

SUMMARY

A Rayleigh type analysis involving chosen modes of the panel as degrees of freedom is used to treat the flutter of a two-dimensional flat panel supported at its leading and trailing edges and subjected to a middle-plane tensile force. The panel has a supersonic stream passing over its upper surface and still air below. The aerodynamic forces due to the supersonic stream are obtained from the theory for linearized two-dimensional unsteady flow and the forces due to the still air are obtained from acoustical theory.

In order to study the effect of increasing the number of modes in the analysis, two and then four modes are employed. The modes used are the first four natural modes of the panel in a vacuum with no tensile force acting. The analysis includes these variables: Mach number, structural damping, tensile force, density of the still air, and edge fixity (clamped and pinned). For certain combinations of these variables, stability boundaries are obtained which can be used to determine the panel thickness required to prevent flutter for any panel material and altitude.

In contrast to some previous panel-flutter investigations, the results of the present analysis show that sufficiently thick panels are flutter free for the Mach numbers treated and suggest that this is true throughout the supersonic speed range.

A comparison of results from the present theory for flat panels and from a criterion developed by R. P. Isaacs for the static stability of buckled panels is made with a few experimental results on flat and buckled panels clamped at leading and trailing edges.

INTRODUCTION

The flutter of thin metal plates or panels, such as compose the covering or skin of missiles and other craft intended for high-speed flight, has recently become of increased concern. Such panels may be initially flat or curved and may be small or fairly large in aspect ratio. In addition, they may be prestressed and will probably become warped in flight by aerodynamic heating. If one or more of the panels on a particular configuration are vibrating, the basic structure supporting them can usually be considered rigid. The fixity at the edges of the panels ranges between clamped and pinned, depending on the construction. Some preliminary experimentation and analytical work suggests that this type of instability is of concern only at supersonic speeds.

The problem of panel flutter embraces so many possible factors as to discourage general treatment, and previous papers on the subject (for example, refs. 1 to 7) have employed various simplifying assumptions in order to obtain specific solutions to what might perhaps be considered different phases of the problem. In all the references cited, the main assumption made is that a panel and the flow over it are two-dimensional. Other assumptions common to the reference papers are that small-deflection plate theory and linearized flow theory may be used.

References 1 to 4 examine the case of a panel buckled by a constant shortening and held at its leading and trailing edges, with a supersonic stream over its upper surface and no perturbation pressures on its lower surface. In reference 1 steady-state air forces and in reference 2 quasi-stationary air forces, which include the first order of the frequency of oscillation, are used. Both these references consider the dynamic stability of the buckled panel. Reference 3 and the more exhaustive reference 4 examine the static stability of the buckled panel and propose that motion (flutter) is the result when static equilibrium is not possible. Reference 5 and a section of reference 2 treat the case of a flat panel pinned at its leading and trailing edges. Reference 5 uses exact linearized unsteady aerodynamic forces and therefore, in contrast to reference 2, imposes no limitations on the order of the frequency. In references 1, 2, and 5 a generalized-coordinate approach involving chosen modes of the panel as degrees of freedom is employed. Reference 6, on the other hand, indicates how the problem of a vibrating membrane in a supersonic stream can be treated by means of Laplace transforms and suggests that similar treatment can be given to the plate problem. Reference 7 treats the case of a two-dimensional panel on many equally spaced simple supports with compressible air flowing over the upper surface and dead air below the panel, and the results indicate that the possible panel instabilities are divergence for subsonic flow and flutter for supersonic flow. Some questionable features of the results obtained in references 2, 5, and 7 are examined in the section entitled "Results and Discussion" in the present report.

A Rayleigh type flutter analysis is developed herein by means of Galerkin's process for a two-dimensional flat panel held in some manner at its leading and trailing edges and acted on by a middle-plane or axial force (which, in the case of tension, introduces a restoring force similar to that for the membrane). The upper surface of the panel is subjected to

¹ Supersedes NACA Technical Note 3465 by Herbert C. Nelson and Herbert J. Cunningham, 1955.

a supersonic stream and the lower surface to an unconfined mass of stationary compressible air. The normal modes of the panel with no middle-plane force acting are used as degrees of freedom in the analysis. As in reference 5, exact linearized unsteady aerodynamic forces are employed. In the reference paper the integrals yielding these forces are evaluated analytically. In the present report these integrals are evaluated numerically.

Numerical results are presented in order to examine some effects of including two and then four modes in the analysis and to determine effects of Mach number, density of the supersonic stream, panel mass and stiffness, edge fixity (to some extent), structural damping, axial load, and density of the still air below the panel. In appendix A an alternative solution by means of Laplace transforms is developed for the plate problem just described. No numerical results are obtained by this method, however.

A comparison of results from the theory presented herein for flat panels and from a criterion of reference 3 for the static stability of buckled panels is made with a few experimental results for flat and buckled panels clamped at the leading and trailing edges.

SYMBOLS

a	speed of sound in undisturbed medium
A_{mn}, B_{mn}, C_{mn}	structural and aerodynamic integrals defined after equation (13)
c	panel chord
D	local flexural stiffness, $\frac{E\tau^3}{12(1-\nu^2)}$
E	Young's modulus of elasticity of panel material
f	tension parameter, $F/c^2 m_A \omega_1^2$
f_λ	functions defined in equation (24)
F	external force per unit width acting in midplane of panel (tensile force positive)
g	structural damping coefficient
G_{mn}	matrix elements defined in equation (13)
$H_0^{(2)}(u)$	Hankel function of second kind, of zero order, (notation of ref. 18)
$I_{mn}, \bar{I}_{mn}, \bar{\bar{I}}_{mn}$	aerodynamic integrals defined after equation (23)
$J_p(u), Y_p(u)$	Bessel functions of order p of first and second kind, respectively, (notation of ref. 18)
k	reduced frequency, $c\omega/2U$
k_1	stiffness parameter (reduced first natural frequency), $c\omega_1/2U$
K_n	eigenvalues defined after equations (16) and (17) and given for first four panel modes in table I
$L(u), \bar{L}(u)$	aerodynamic functions defined after equation (21)
$\bar{\bar{L}}_\tau(u)$	aerodynamic functions defined after equation (B16)

m_A	panel mass per unit surface area, $\sigma\tau$
M	Mach number, U/a
N_1, N_2	coefficients in mode-shape equations (16) and (17), given for first four panel modes in table I
$p(x, t)$	net perturbation pressure, positive downward
$p_n(x)$	pressure coefficient associated with mode shape Z_n , defined in equation (20)
p_u, p_l	upper- and lower-surface contributions to perturbation pressure, respectively
p_∞, p_0	pressures in undisturbed supersonic stream and still-air region, respectively
$P_n(x), \bar{P}_n(x), \bar{\bar{P}}_n(x)$	components of $p_n(x)$ defined after equation (22)
q	dynamic pressure, $\frac{1}{2} \rho U^2$
s_r	coefficients of equations (28) and (B15) tabulated in appendix B for first four modes of panel with clamped edges
t	time
U	velocity of supersonic stream
x, y, z	coordinates defined in figure 1
$z(x, t)$	vertical displacement of panel
$Z(x)$	flutter mode shape
$Z_n(x)$	n th natural mode shape for panel vibrating in vacuo
μ	panel-air mass ratio, $m_A/\rho c$
ν	Poisson's ratio
ρ, ρ_0	densities in undisturbed supersonic stream and still-air region, respectively
σ	density of panel material
τ	local thickness of panel
ϕ	disturbance-velocity potential
ω	frequency of oscillation
ω_n	frequency associated with mode shape Z_n
$\bar{\omega}$	frequency parameter, $2kM^2/\beta^2$
Ω	frequency ratio squared $\left(\frac{\omega_1}{\omega}\right)^2$, except in flutter calculations where $\Omega = \left(\frac{\omega_1}{\omega}\right)^2 (1 + ig)$
[]	square matrix
{ }	column matrix
Subscripts:	
u	upper-surface contribution
l	lower-surface contribution
Primes denote differentiation with respect to the argument.	

ANALYSIS

STATEMENT OF PROBLEM

A thin isotropic, two-dimensional plate (beam) of constant thickness, as shown in figure 1, is considered herein. The plate is undergoing simple harmonic motion and is acted on by a middle-plane or axial force F (tension or compression); its upper surface is subjected to a supersonic stream of velocity U , pressure p_∞ , and density ρ , and its

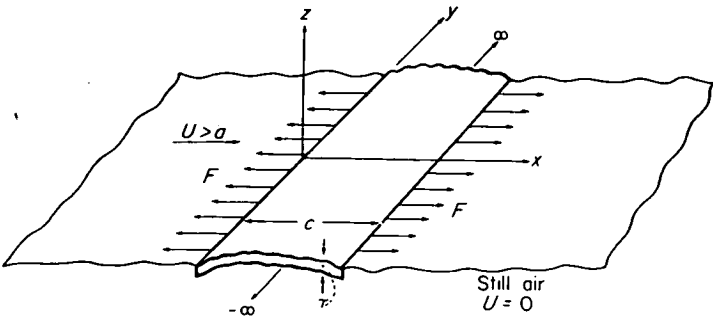


FIGURE 1.—Sketch of flexible two-dimensional panel.

lower surface is subjected to still air with pressure p_0 and density ρ_0 . The differential equation of motion for the plate may be written as

$$D \frac{\partial^4 z}{\partial x^4} + m_A \frac{\partial^2 z}{\partial t^2} - F \frac{\partial^2 z}{\partial x^2} + (p_\infty - p_0) + p(x, t) = 0 \quad (1)$$

where, in the present case, the vertical displacement of the plate $z(x, t)$ may be expressed as $Z(x)e^{i\omega t}$, ω is the circular frequency of oscillation, $p(x, t)$ is the net perturbation pressure (positive downward) arising from the motion of the plate, m_A is the plate mass per unit surface area, and the local flexural stiffness D is given by $E\tau^3/12(1-\nu^2)$. For the case where $p(x, t) = 0$, equation (1) may be obtained, with appropriate changes in notation, from reference 8.

In the remaining development the constant-pressure term $p_\infty - p_0$ of equation (1) is considered to be zero. This in no way affects the generality of the results for the oscillating plate, since inclusion of the constant-pressure term as nonzero would result only in adding a particular solution which represents a static vertical deflection. In addition, the coordinate x of equation (1) is divided by the plate chord c and henceforth is employed in this nondimensional sense. Thus, equation (1) multiplied by $e^{-i\omega t}$ becomes

$$\frac{D}{c^4} Z'''' - \omega^2 m_A Z - \frac{F}{c^2} Z'' + p(x, t) e^{-i\omega t} = 0 \quad (2)$$

where the primes denote differentiation with respect to the argument x .

In order to obtain a specific solution of equation (2), four boundary conditions are required. The plate is considered to be held at its leading and trailing edges as shown in figure 1, and this assumption leads to the conditions for pinned edges:

$$Z(0) = Z(1) = Z''(0) = Z''(1) = 0 \quad (3)$$

and for clamped edges:

$$Z(0) = Z(1) = Z'(0) = Z'(1) = 0 \quad (4)$$

In a later section of the analysis the boundary-value problems, as exemplified by equations (2) and (3) or (2) and (4), are solved by Galerkin's method. Also considered in

appendix A are the solutions to these problems by means of Laplace transforms.

NET PERTURBATION PRESSURE $p(x, t)$

The net pressure $p(x, t)$, as mentioned previously, arises from the oscillatory motion of the plate. It is this pressure which damps, or in the case of flutter sustains, the oscillation. The pressure on the upper surface is obtained from the theory for linearized unsteady supersonic flow and the pressure on the lower surface from acoustical theory. The perturbation pressure in terms of the pressures p_u on the upper surface and p_l on the lower surface is

$$p(x, t) = p_u - p_l \quad (5)$$

where

$$p_u = \rho \left(\frac{\partial \phi_u}{\partial t} + \frac{U}{c} \frac{\partial \phi_u}{\partial x} \right) \quad (6)$$

and

$$p_l = \rho_0 \frac{\partial \phi_l}{\partial t} \quad (7)$$

From reference 9 the velocity potential for the upper surface can be obtained in the form

$$\phi_u = \frac{ce^{i\omega t}}{\beta} \int_0^x \left[i\omega Z(\xi) + \frac{U}{c} \frac{dZ}{d\xi} \right] e^{-i\bar{\omega}(x-\xi)} J_0 \left[\frac{\bar{\omega}}{\bar{M}}(x-\xi) \right] d\xi \quad (8)$$

where

$$\bar{\omega} = \frac{2kM^2}{\beta^2} \quad \beta = \sqrt{M^2 - 1} \quad k = \frac{\omega c}{2U}$$

Based on reference 10, the velocity potential for the lower surface can be obtained, as shown in appendix B, in the form

$$\phi_l = -\frac{\omega c e^{i\omega t}}{2} \int_0^1 Z(\xi) H_0^{(2)}(2kM|x-\xi|) d\xi \quad (9)$$

where $H_0^{(2)}(x)$ is the Hankel function of the second kind, of zero order.

SOLUTION BY GALERKIN'S METHOD

Outline of method.—The boundary-value problems considered earlier (eqs. (2) and (3) for the pinned-edge plate and equations (2) and (4) for the clamped-edge plate) are now solved by means of Galerkin's method. (A detailed account of Galerkin's method may be found in ref. 11.) As a first step, the flutter mode shape $Z(x)$ is approximated by a linear combination of the form

$$Z(x) = c \sum_{n=1}^N a_n Z_n(x) \quad (10)$$

where the coefficients a_n may represent complex amplitudes and where the functions $Z_n(x)$ are the mode shapes for the plate vibrating in a vacuum without an axial force F acting. The function Z_1 is the fundamental mode shape associated with the lowest natural frequency ω_1 , and the remaining functions Z_2, Z_3, \dots, Z_N are consecutively the higher modes

shapes. The shapes Z_n satisfy the pinned-edge or clamped-edge boundary conditions (Z_n replacing Z in eqs. (3) and (4)) and the differential equation

$$\frac{D}{c^4} Z_n'''' - \omega_n^2 m_A Z_n = 0 \quad (11)$$

where ω_n is the frequency of oscillation for which Z_n is the mode shape.

The remainder of the Galerkin process for solving the aforementioned boundary-value problems consists of determining the coefficients a_n of equation (10) in the following manner: Substitute equation (10) into equation (2), replace the term $\frac{D}{c^4} Z_n''''$ by $\omega_n^2 m_A Z_n$ in accordance with equation (11), multiply by one of the mode shapes Z_n , integrate the result from $x=0$ to $x=1$, and equate to zero. When n is made 1, 2, . . . N in succession, N linear equations are obtained which determine the unknowns a_n . These equations can be written in the form

$$\begin{bmatrix} G_{11} & G_{12} & \dots & G_{1N} \\ G_{21} & G_{22} & \dots & G_{2N} \\ \cdot & \cdot & \dots & \cdot \\ G_{N1} & G_{N2} & \dots & G_{NN} \end{bmatrix} \begin{Bmatrix} a_1 \\ a_2 \\ \cdot \\ a_N \end{Bmatrix} = \begin{Bmatrix} 0 \\ 0 \\ \cdot \\ 0 \end{Bmatrix} \quad (12)$$

The matrix elements are given by

$$G_{mn} = \mu \left\{ A_{mn} - \Omega \left[\left(\frac{\omega_m}{\omega_1} \right)^2 A_{mn} + f B_{mn} \right] \right\} - C_{mn} \quad (13)$$

where

$$\begin{aligned} \mu &= \frac{m_A}{\rho c} & A_{mn} &= \int_0^1 Z_m Z_n dx \\ \Omega &= \left(\frac{\omega_1}{\omega} \right)^2 & B_{mn} &= \int_0^1 Z_m' Z_n' dx \\ f &= \frac{F}{c^2 m_A \omega_1^2} & C_{mn} &= \int_0^1 Z_m p_n(x) dx \end{aligned}$$

and where $p_n(x)$ is the pressure $p(x, t)$, obtained from equations (5) to (9) with Z replaced by Z_n , multiplied by $e^{-i\omega t}/\rho c \omega^2$. In equation (13) ω_1 and ω_n are the first and the n th natural frequency, respectively, of the plate with no axial force acting.

Flutter determinant.—The flutter condition or condition of harmonic vibration, which is given by the nontrivial solution for the coefficients a_n , is obtained from equation (12) by setting the determinant of the matrix G_{mn} equal to zero.

Thus the flutter condition may be expressed in the form

$$\begin{vmatrix} G_{11} & G_{12} & \dots & G_{1N} \\ G_{21} & G_{22} & \dots & G_{2N} \\ \cdot & \cdot & \dots & \cdot \\ G_{N1} & G_{N2} & \dots & G_{NN} \end{vmatrix} = 0 \quad (14)$$

Remarks on alternative procedure.—The procedure from equation (11) to equation (13) is, in general, not the most accurate that could be followed for values of F other than zero. A generally more accurate procedure would be to use, instead of equation (11), the differential equation for the panel with tension:

$$\frac{D}{c^4} Z_n'''' - \omega_n^2 m_A Z_n - \frac{F}{c^2} Z_n'' = 0 \quad (15)$$

When equation (15) is solved, subject to the appropriate boundary conditions, the frequencies ω_n are found to be functions of F for both pinned and clamped edges, but the mode shapes Z_n do not vary with F for pinned edges. The use of equation (15) rather than equation (11) would mean that in equation (13) the term $f B_{mn}$ would not appear and the frequencies and mode shapes would be those that satisfy equation (15).

Equation (11) rather than equation (15) has been used herein for the following reasons: For pinned-edge panels there is no difference in the mode shapes or in the final numerical flutter results; for clamped-edge panels the determination of the values of Z_n and ω_n that satisfy equation (15) is laborious and must be carried out for every desired value of F . Elimination of the term $f B_{mn}$ from the matrix elements, through use of equation (15), does not compensate for the labor of determining the natural frequencies and mode shapes as functions of F . The differences in final numerical flutter results for the clamped-edge panel approach zero as the number of modes in the analysis is increased and are expected to be small even when only a few modes are used.

EVALUATION OF TERMS IN FLUTTER DETERMINANT

Structural integrals A_{mn} and B_{mn} and frequencies ω_n .—Consideration will now be given to the evaluation of the mode-shape integrals and frequencies in the elements of equation (15). The mode shapes Z_n and associated natural frequencies ω_n obtained from equation (12) are:

For the pinned-edge plate,

$$\left. \begin{aligned} Z_n &= N_1 \sin K_n x \\ \omega_n &= K_n^2 \sqrt{\frac{D}{m_A c^4}} \end{aligned} \right\} \quad (16)$$

where K_n is obtained from the frequency equation

$$\sin K_n = 0$$

For the clamped-edge plate,

$$\left. \begin{aligned} Z_n &= N_1 [\cos K_n x - \cosh K_n x + N_2 (\sin K_n x - \sinh K_n x)] \\ \omega_n &= K_n^2 \sqrt{\frac{D}{m_A c^4}} \end{aligned} \right\} \quad (17)$$

where K_n is obtained from the frequency equation

$$\cos K_n \cosh K_n = 1$$

In equations (16) and (17) the factor N_1 is used to produce unit deflection at the center of the plate ($x=0.5$) for modes that are symmetric about the center and at the point of maximum deflection between the leading edge ($x=0$) and the center of the plate for modes that are antisymmetric about the center. The factor N_2 in equation (17) is established by the boundary condition requiring zero deflection at $x=1$ and is expressed by

$$N_2 = -\frac{\cos K_n - \cosh K_n}{\sin K_n - \sinh K_n} \quad (18)$$

The quantities ω_1 , ω_n/ω_1 , A_{nn} , and B_{nn} required in equation (14) can be determined directly from equations (16) or (17). First, however, values must be established for N_1 and K_n in the case of the pinned-edge plate and for N_1 , N_2 , and K_n in the case of the clamped-edge plate. Table I includes values of all these quantities for the first four modes of vibration.

The values for A_{mn} shown in table I are zero when $m \neq n$ because of the orthogonality of the mode shapes Z_n of equations (16) and (17). For the pinned-edge case the slopes

TABLE I.—MODE-SHAPE FACTORS, EIGENVALUES, FREQUENCY RATIOS, AND STRUCTURAL INTEGRALS FOR FIRST FOUR NORMAL MODES

(a) Pinned-edge plate ^a

Mode, n	N_1	N_2	K_n	ω_n/ω_1	A_{nn}	B_{nn}
1	1	-----	π	1	0.5	$0.5\pi^2$
2	1	-----	2π	4	.5	$2.0\pi^2$
3	1	-----	3π	9	.5	$4.5\pi^2$
4	1	-----	4π	16	.5	$8.0\pi^2$

^a $A_{mn} = B_{mn} = 0$ ($m \neq n$)

(b) Clamped-edge plate ^{b, c}

Mode, n	N_1	N_2	K_n	ω_n/ω_1	A_{nn}	B_{nn}
1	-0.629699	-0.98250	4.730	1	0.396	4.88
2	-.66260	-1.000778	7.853204625	2.7566	.440	21.2
3	.7109645	-.99997	10.99560784	5.404	.506	49.8
4	-.66120074	-1.0000145	14.13716549	8.933	.432	76.4

^b $A_{mn} = 0$ ($m \neq n$)

$B_{13} = B_{31} = 4.362$

$B_{31} = B_{13} = -8.360$

Other $B_{mn} = 0$ ($m \neq n$)

^c The significant figures shown were used to avoid small-difference errors in mode shapes

Z_n' of the mode shapes are also orthogonal and, consequently, B_{mn} is zero when $m \neq n$. For the clamped-edge case, even though the slopes Z_n' are not orthogonal, the integrand of B_{mn} is antisymmetric about $x=0.5$ when m and n are not both even or both odd and, consequently, B_{mn} is zero when $m \neq n$ except for B_{13} , B_{31} , B_{24} , and B_{42} (for the first four modes).

Aerodynamic integrals C_{mn} .—The remaining term in the elements of equation (14) that requires evaluation is the integral

$$C_{mn} = \int_0^1 Z_m p_n(x) dx \quad (19)$$

As mentioned previously, $p_n(x)$ is the pressure $p(x, t)$, obtained from equations (5) to (9) with Z replaced by Z_n , multiplied by $e^{-i\omega t}/\rho c \omega^2$. The quantity $p_n(x)$ is therefore given by

$$\begin{aligned} p_n(x) = & \frac{1}{\beta} \left(\int_0^x \left[-Z_n(\xi) + \frac{i}{2k} \frac{dZ_n}{d\xi} \right] e^{-i\bar{\omega}(x-\xi)} J_0 \left[\frac{\bar{\omega}}{M} (x-\xi) \right] d\xi + \right. \\ & \left. \frac{-i}{2k} \frac{d}{dx} \left\{ \int_0^x \left[-Z_n(\xi) + \frac{i}{2k} \frac{dZ_n}{d\xi} \right] e^{-i\bar{\omega}(x-\xi)} J_0 \left[\frac{\bar{\omega}}{M} (x-\xi) \right] d\xi \right\} \right)_u + \\ & \frac{\rho_0}{\rho} \left[\frac{i}{2} \int_0^1 Z_n(\xi) H_0^{(2)}(2kM|x-\xi|) d\xi \right]_l \end{aligned} \quad (20)$$

where the contributions from the upper and lower surfaces of the plate are designated by subscripts u and l , respectively. Upon elimination of the derivatives in the integrands of the upper-surface contribution through integration by parts, performance of the indicated differentiation of the second integral, and extraction of the singularity at $\xi=x$ in the Hankel function of the lower-surface contribution, equation (20) may be written in the form

$$p_n(x) = \frac{1}{\beta} \left[\int_0^x Z_n(\xi) L(x-\xi) d\xi + \frac{i}{2k} \frac{M^2 - 2}{\beta^2} Z_n(x) + \frac{1}{4k^2} Z_n'(x) \right]_u + \frac{\rho_0}{\rho} \left[\int_0^1 Z_n(\xi) \bar{L}(x-\xi) d\xi + \frac{1}{\pi} \int_0^1 Z_n(\xi) \log_e(kM|x-\xi|) d\xi \right]_l \quad (21)$$

where

$$L(u) = \left[-\frac{M^2+2}{2\beta^4} J_0\left(\frac{\bar{\omega}}{M}u\right) + i\frac{2M}{\beta^4} J_1\left(\frac{\bar{\omega}}{M}u\right) + \frac{M^2}{2\beta^4} J_2\left(\frac{\bar{\omega}}{M}u\right) \right] e^{-i\bar{\omega}u}$$

$$\bar{L}(u) = \frac{i}{2} J_0(2kM|u|) + \frac{1}{2} Y_0(2kM|u|) - \frac{1}{\pi} \log_e(kM|u|)$$

$$\bar{L}(0) = \frac{\gamma}{\pi} + \frac{i}{2} \quad \gamma = 0.577216 \text{ (Euler's constant)}$$

The quantities J_p and Y_p are the Bessel functions of order p , of the first and second kind, respectively.

For convenience $p_n(x)$ is considered in three parts, namely,

$$p_n(x) = P_n(x) + \bar{P}_n(x) + \bar{\bar{P}}_n(x) \quad (22)$$

where

$$P_n(x) = \frac{1}{\beta} \left[\int_0^x Z_n(\xi) L(x-\xi) d\xi + \frac{i}{2k} \frac{M^2-2}{\beta^2} Z_n(x) + \frac{1}{4k^2} Z_n'(x) \right]$$

$$\bar{P}_n(x) = \frac{\rho_0}{\rho} \int_0^1 Z_n(\xi) \bar{L}(x-\xi) d\xi$$

$$\bar{\bar{P}}_n(x) = \frac{\rho_0}{\rho} \frac{1}{\pi} \int_0^1 Z_n(\xi) \log_e(kM|x-\xi|) d\xi$$

Hence, equation (19) may be put in the form

$$C_{mn} = I_{mn} + \bar{I}_{mn} + \bar{\bar{I}}_{mn} \quad (23)$$

where

$$I_{mn} = \int_0^1 Z_m P_n(x) dx$$

$$\bar{I}_{mn} = \int_c^1 Z_m \bar{P}_n(x) dx$$

$$\bar{\bar{I}}_{mn} = \int_0^1 Z_m \bar{\bar{P}}_n(x) dx$$

The first integral I_{mn} represents the effect of the supersonic stream passing over the upper surface of the plate; the other two integrals represent the effect of the still air below the plate.

Before further development of the method of the present report for determining C_{mn} , the aerodynamic treatments of references 1, 2, and 5, which deal with the pinned-edge plate, will be examined. These references consider only the effects of the supersonic stream, the air below the plate being treated, in essence, as massless; that is, ρ_0/ρ is taken to

be zero and the integrals \bar{I}_{mn} and $\bar{\bar{I}}_{mn}$ are omitted. In references 1 and 2 the aerodynamic effects are accounted for as if the integral I_{mn} has been expanded as a power series in the frequency of oscillation; reference 1 retains only the steady-state or zero-order frequency term and reference 2 adds the first-order frequency term. In reference 5, on the other hand, the integral I_{mn} is evaluated exactly with regard to the frequency. This is possible because the modal functions Z_n for the pinned-edge plate are sine waves (see eq. (16)) so that I_{mn} can be obtained in terms of the functions (sometimes called Schwarz functions)

$$f_\lambda(a, b) = \frac{1}{b^{\lambda+1}} \int_0^b u^\lambda e^{-iu} J_0\left(\frac{u}{a}\right) du \quad (\lambda=0, 1) \quad (24)$$

where

$$a = \frac{M}{\bar{\omega}} b$$

and b has the four values

$$b = \bar{\omega} + \left\{ \begin{matrix} \pm m \\ \pm n \end{matrix} \right\} \pi$$

A similar result could be obtained for the clamped-edge plate by approximating the modal functions Z_n (see eq. (17)) by a finite sine series

$$Z_n \approx \sum_{r=1}^R d_r \sin r\pi x$$

For either pinned or clamped edges, the arguments a and b of the Schwarz functions f_λ would range from large positive to large negative values, particularly for the higher modes, and would thus require extensive tabulation of f_0 and f_1 . The exact expression for the pressure term $p_n(x)$ is employed in the present report but, because the necessary tables of f_0 and f_1 are not available, for convenience, a numerical method of integration is used to evaluate $p_n(x)$ and the aerodynamic integrals I_{mn} , \bar{I}_{mn} , and $\bar{\bar{I}}_{mn}$ of equation (23).

The numerical method is based on the following integration rules for parabolic arcs:

$$\int_{x_1}^{x_2} y(x) dx = \frac{\Delta x}{12} [5y(x_1) + 8y(x_2) - y(x_3)] \quad (25a)$$

$$\int_{x_2}^{x_3} y(x) dx = \frac{\Delta x}{12} [-y(x_1) + 8y(x_2) + 5y(x_3)] \quad (25b)$$

where $x_2 = x_1 + \Delta x$ and $x_3 = x_2 + \Delta x$. The range of integration in equation (19), $0 \leq x \leq 1$, is, for convenience, divided into an even number of equal segments. From the standpoint of accuracy the number of segments needed depends on the number of nodes in the highest mode and on the value of

$\bar{\omega}$ for which $p_n(x)$ is evaluated. For the numerical applications of the present report, 10 segments were found to be adequate, and the method of integration is illustrated for this number of segments in the equations to follow.

The use of 10 segments would, in general, require the determination of $p_n(x)$ in equation (19) at 11 points on the plate. However, the integrand of C_{mn} at $x=0$ and $x=1$ is zero since the mode shapes Z_m are zero at these points, and therefore $p_n(x)$ need be evaluated at only the 9 interior points (equally spaced between $x=0$ and $x=1$). The values of the terms P_n , \bar{P}_n , and $\bar{\bar{P}}_n$ of equation (22) for these points may be arranged in matrix form as follows:

$$\begin{Bmatrix} P_n(1) \\ P_n(2) \\ P_n(3) \\ P_n(4) \\ P_n(5) \\ P_n(6) \\ P_n(7) \\ P_n(8) \\ P_n(9) \end{Bmatrix} = \frac{1}{120\beta} \begin{bmatrix} 8L(0) & -L(-.1) & 0 & 0 & 0 & 0 & 0 & 0 & 0 \\ 13L(1) & 7L(0) & -L(-.1) & 0 & 0 & 0 & 0 & 0 & 0 \\ 13L(2) & 12L(1) & 7L(0) & -L(-.1) & 0 & 0 & 0 & 0 & 0 \\ 13L(3) & 12L(2) & 12L(1) & 7L(0) & -L(-.1) & 0 & 0 & 0 & 0 \\ 13L(4) & 12L(3) & 12L(2) & 12L(1) & 7L(0) & -L(-.1) & 0 & 0 & 0 \\ 13L(5) & 12L(4) & 12L(3) & 11L(2) & 15L(1) & 4L(0) & 0 & 0 & 0 \\ 13L(6) & 12L(5) & 12L(4) & 11L(3) & 14L(2) & 12L(1) & 5L(0) & 0 & 0 \\ 13L(7) & 12L(6) & 12L(5) & 11L(4) & 14L(3) & 11L(2) & 13L(1) & 5L(0) & 0 \\ 13L(8) & 12L(7) & 12L(6) & 11L(5) & 14L(4) & 11L(3) & 12L(2) & 13L(1) & 5L(0) \end{bmatrix} \begin{Bmatrix} Z_n(1) \\ Z_n(2) \\ Z_n(3) \\ Z_n(4) \\ Z_n(5) \\ Z_n(6) \\ Z_n(7) \\ Z_n(8) \\ Z_n(9) \end{Bmatrix} + \frac{i(M^2-2)}{2k\beta^3} \begin{Bmatrix} Z_n(1) \\ Z_n(2) \\ Z_n(3) \\ Z_n(4) \\ Z_n(5) \\ Z_n(6) \\ Z_n(7) \\ Z_n(8) \\ Z_n(9) \end{Bmatrix} + \frac{1}{4k^2\beta} \begin{Bmatrix} Z_n'(1) \\ Z_n'(2) \\ Z_n'(3) \\ Z_n'(4) \\ Z_n'(5) \\ Z_n'(6) \\ Z_n'(7) \\ Z_n'(8) \\ Z_n'(9) \end{Bmatrix} \quad (26)$$

$$\begin{Bmatrix} \bar{P}_n(1) \\ \bar{P}_n(2) \\ \bar{P}_n(3) \\ \bar{P}_n(4) \\ \bar{P}_n(5) \\ \bar{P}_n(6) \\ \bar{P}_n(7) \\ \bar{P}_n(8) \\ \bar{P}_n(9) \end{Bmatrix} = \frac{\rho_0/\rho}{120} \begin{bmatrix} \bar{L}(0) & \bar{L}(1) & \bar{L}(2) & \bar{L}(3) & \bar{L}(4) & \bar{L}(5) & \bar{L}(6) & \bar{L}(7) & \bar{L}(8) \\ \bar{L}(1) & \bar{L}(0) & \bar{L}(1) & \bar{L}(2) & \bar{L}(3) & \bar{L}(4) & \bar{L}(5) & \bar{L}(6) & \bar{L}(7) \\ \bar{L}(2) & \bar{L}(1) & \bar{L}(0) & \bar{L}(1) & \bar{L}(2) & \bar{L}(3) & \bar{L}(4) & \bar{L}(5) & \bar{L}(6) \\ \bar{L}(3) & \bar{L}(2) & \bar{L}(1) & \bar{L}(0) & \bar{L}(1) & \bar{L}(2) & \bar{L}(3) & \bar{L}(4) & \bar{L}(5) \\ \bar{L}(4) & \bar{L}(3) & \bar{L}(2) & \bar{L}(1) & \bar{L}(0) & \bar{L}(1) & \bar{L}(2) & \bar{L}(3) & \bar{L}(4) \\ \bar{L}(5) & \bar{L}(4) & \bar{L}(3) & \bar{L}(2) & \bar{L}(1) & \bar{L}(0) & \bar{L}(1) & \bar{L}(2) & \bar{L}(3) \\ \bar{L}(6) & \bar{L}(5) & \bar{L}(4) & \bar{L}(3) & \bar{L}(2) & \bar{L}(1) & \bar{L}(0) & \bar{L}(1) & \bar{L}(2) \\ \bar{L}(7) & \bar{L}(6) & \bar{L}(5) & \bar{L}(4) & \bar{L}(3) & \bar{L}(2) & \bar{L}(1) & \bar{L}(0) & \bar{L}(1) \\ \bar{L}(8) & \bar{L}(7) & \bar{L}(6) & \bar{L}(5) & \bar{L}(4) & \bar{L}(3) & \bar{L}(2) & \bar{L}(1) & \bar{L}(0) \end{bmatrix} \begin{Bmatrix} 13Z_n(1) \\ 12Z_n(2) \\ 12Z_n(3) \\ 11Z_n(4) \\ 14Z_n(5) \\ 11Z_n(6) \\ 12Z_n(7) \\ 12Z_n(8) \\ 13Z_n(9) \end{Bmatrix} \quad (27)$$

$$\begin{Bmatrix} \bar{\bar{P}}_n(1) \\ \bar{\bar{P}}_n(2) \\ \bar{\bar{P}}_n(3) \\ \bar{\bar{P}}_n(4) \\ \bar{\bar{P}}_n(5) \\ \bar{\bar{P}}_n(6) \\ \bar{\bar{P}}_n(7) \\ \bar{\bar{P}}_n(8) \\ \bar{\bar{P}}_n(9) \end{Bmatrix} = \frac{\rho_0/\rho}{4} \begin{bmatrix} \bar{\bar{L}}_1(1) & \bar{\bar{L}}_2(1) & \bar{\bar{L}}_3(1) & \bar{\bar{L}}_4(1) & \bar{\bar{L}}_5(1) & \bar{\bar{L}}_6(1) & \bar{\bar{L}}_7(1) & \bar{\bar{L}}_8(1) & \bar{\bar{L}}_9(1) & \bar{\bar{L}}_{10}(1) \\ \bar{\bar{L}}_1(2) & \bar{\bar{L}}_2(2) & \bar{\bar{L}}_3(2) & \bar{\bar{L}}_4(2) & \bar{\bar{L}}_5(2) & \bar{\bar{L}}_6(2) & \bar{\bar{L}}_7(2) & \bar{\bar{L}}_8(2) & \bar{\bar{L}}_9(2) & \bar{\bar{L}}_{10}(2) \\ \bar{\bar{L}}_1(3) & \bar{\bar{L}}_2(3) & \bar{\bar{L}}_3(3) & \bar{\bar{L}}_4(3) & \bar{\bar{L}}_5(3) & \bar{\bar{L}}_6(3) & \bar{\bar{L}}_7(3) & \bar{\bar{L}}_8(3) & \bar{\bar{L}}_9(3) & \bar{\bar{L}}_{10}(3) \\ \bar{\bar{L}}_1(4) & \bar{\bar{L}}_2(4) & \bar{\bar{L}}_3(4) & \bar{\bar{L}}_4(4) & \bar{\bar{L}}_5(4) & \bar{\bar{L}}_6(4) & \bar{\bar{L}}_7(4) & \bar{\bar{L}}_8(4) & \bar{\bar{L}}_9(4) & \bar{\bar{L}}_{10}(4) \\ \bar{\bar{L}}_1(5) & \bar{\bar{L}}_2(5) & \bar{\bar{L}}_3(5) & \bar{\bar{L}}_4(5) & \bar{\bar{L}}_5(5) & \bar{\bar{L}}_6(5) & \bar{\bar{L}}_7(5) & \bar{\bar{L}}_8(5) & \bar{\bar{L}}_9(5) & \bar{\bar{L}}_{10}(5) \\ \bar{\bar{L}}_1(6) & \bar{\bar{L}}_2(6) & \bar{\bar{L}}_3(6) & \bar{\bar{L}}_4(6) & \bar{\bar{L}}_5(6) & \bar{\bar{L}}_6(6) & \bar{\bar{L}}_7(6) & \bar{\bar{L}}_8(6) & \bar{\bar{L}}_9(6) & \bar{\bar{L}}_{10}(6) \\ \bar{\bar{L}}_1(7) & \bar{\bar{L}}_2(7) & \bar{\bar{L}}_3(7) & \bar{\bar{L}}_4(7) & \bar{\bar{L}}_5(7) & \bar{\bar{L}}_6(7) & \bar{\bar{L}}_7(7) & \bar{\bar{L}}_8(7) & \bar{\bar{L}}_9(7) & \bar{\bar{L}}_{10}(7) \\ \bar{\bar{L}}_1(8) & \bar{\bar{L}}_2(8) & \bar{\bar{L}}_3(8) & \bar{\bar{L}}_4(8) & \bar{\bar{L}}_5(8) & \bar{\bar{L}}_6(8) & \bar{\bar{L}}_7(8) & \bar{\bar{L}}_8(8) & \bar{\bar{L}}_9(8) & \bar{\bar{L}}_{10}(8) \\ \bar{\bar{L}}_1(9) & \bar{\bar{L}}_2(9) & \bar{\bar{L}}_3(9) & \bar{\bar{L}}_4(9) & \bar{\bar{L}}_5(9) & \bar{\bar{L}}_6(9) & \bar{\bar{L}}_7(9) & \bar{\bar{L}}_8(9) & \bar{\bar{L}}_9(9) & \bar{\bar{L}}_{10}(9) \end{bmatrix} \begin{Bmatrix} s_1 \\ s_2 \\ s_3 \\ s_4 \\ s_5 \\ s_6 \\ s_7 \\ s_8 \\ s_9 \\ s_{10} \end{Bmatrix} \quad (28)$$

where $L(u)$ and $\bar{L}(u)$ are defined after equation (21) and $\bar{\bar{L}}_r(u)$ and s_r are defined in appendix B (eqs. (B16) and (B15)).

The rows of the square matrix in equation (26), down to the row pertaining to $P_n(.5)$, were obtained by applying the integration rule given by equation (25a). In the remaining rows the contributions from the region $x > 0.5$ were obtained by applying equation (25b). In equation (27) the integrating factors multiplying Z_n in the column matrix were obtained by using equation (25a) between $x=0$ and $x=0.5$ and equation (25b) between $x=0.5$ and $x=1.0$. In appendix B the singular integral $\bar{P}_n(x)$ presented after equation (22) is evaluated and the form of \bar{P}_n leading to equation (28) is derived.

Equations (26), (27), and (28) are summed in accordance with equation (22) to obtain the column matrix $\{p_n(x)\}$. By use of this column matrix and the integration rules of equation (25), the aerodynamic term C_{mn} is obtained in the form

$$C_{mn} = \frac{1}{120} [13p_n(.1)Z_m(.1) + 12p_n(.2)Z_m(.2) + 12p_n(.3)Z_m(.3) + 11p_n(.4)Z_m(.4) + 14p_n(.5)Z_m(.5) + 11p_n(.6)Z_m(.6) + 12p_n(.7)Z_m(.7) + 12p_n(.8)Z_m(.8) + 13p_n(.9)Z_m(.9)] \quad (29)$$

where the integrating factors 13, 12, . . . 12, 13 were obtained in the same manner as those in equation (27). By means of equation (29), C_{mn} can be evaluated for a given edge fixity and for particular values of M , k , and ρ_0/ρ .

SOLUTION OF FLUTTER DETERMINANT

As previously stated, the conditions for flutter are determined from the nontrivial solutions of equation (14). Since equation (14) is complex, it may be solved directly for one complex unknown or two real unknowns. For a specific edge fixity the variables (see eq. (13)) in equation (14) are $1/\mu$ (the inverse of μ is preferred because μ becomes infinite for $\rho=0$), Ω , f , M , k , and ρ_0/ρ . It is convenient to interpret the Ω of equation (13) as the complex quantity $(\omega_1/\omega)^2(1+ig)$ rather than $(\omega_1/\omega)^2$, where g may be regarded as a structural damping coefficient. (For this use of g , see, for example, refs. 12 and 13.) Each of the various quantities on which equation (14) is dependent was varied to some extent, as will be discussed in the next section. A particular calculation was performed by setting values for $1/\mu$, M , k , f , and ρ_0/ρ and solving for Ω . Then, because it was one of the more easily varied parameters, $1/\mu$ was changed and again Ω was solved for. This procedure was continued until curves of $1/\mu$ and $(R.P.\Omega)^{1/2}$ plotted against g passed through $g=0$. The value for k was then changed and the procedure repeated. After sufficient variation of $1/\mu$ and k , curves could be established of $1/\mu$ against $2k_1=2k(R.P.\Omega)^{1/2}$ for particular values of the other parameters M , g , f , and ρ_0/ρ .

RESULTS AND DISCUSSION

In the preceding sections a method of flutter analysis has been developed for a two-dimensional flat panel or plate held at its leading and trailing edges. The variables in the

analysis are the number of modes or degrees of freedom the panel is assumed to have, Mach number (greater than 1.0), $1/\mu$, $2k_1=2k(R.P.\Omega)^{1/2}$, g , f , ρ_0/ρ , and edge fixity. The analysis conveniently yields stability boundaries in terms of $1/\mu$ and $2k_1$, which are used as the coordinates of most of the figures presented. These two parameters are given in terms of the properties of the panel and supersonic stream by

$$\left. \begin{aligned} \frac{1}{\mu} &= \frac{\rho}{\sigma} \frac{c}{\tau} \\ 2k_1 &= \frac{\omega_1 c}{U} = \frac{K_1^2}{\sqrt{24(1-\nu^2)}} \frac{\tau}{c} \sqrt{\frac{\rho}{\sigma} \frac{E}{q}} \end{aligned} \right\} \quad (30)$$

where σ is panel density, q is dynamic pressure, and K_1 is the first-mode eigenvalue given in table I for clamped and pinned edges. Inasmuch as the various parameters in the analysis contain implicitly the panel properties (E , σ , ν , and τ/c), axial force F , air density, and speed of sound, the effects of varying these implicit properties can be obtained only by cross-plotting.

Some effects of the number of modes used in the analysis are studied by using two and then four modes of the clamped-edge panel with selected values of M , g , f , and ρ_0/ρ . In addition, M , g , f , and ρ_0/ρ are varied in order to study their effects. To a lesser extent the pinned-edge panel is investigated for comparison with certain clamped-edge results.

The following table lists the conditions for which stability boundaries are given:

Mach number, M	Degrees of freedom	Structural damping coefficient, g	Tension parameter, f	Density ratio, ρ_0/ρ
Clamped edge				
1.3	2	0	0	0
			0, 0.1, 0.5, 1.0	1.0
	4	0, 0.005, 0.025, 0.03, 0.05	0	0
$\sqrt{2}$		0	0, 0.1, 0.5, 1.0	0
	2	0, 0.002, 0.00375, 0.05	0	0
	4	0	0	0
Pinned edge				
$\sqrt{2}$	2	0, 0.003, 0.00475, 0.05	0	0

The results are first grouped according to Mach number and are later summarized and compared.

RESULTS FOR MACH NUMBER OF 1.3

Effects of two and four modes.—Figure 2 gives the results for the clamped-edge panel for the simple case of two degrees of freedom (first and second modes) with $g=f=\rho_0/\rho=0$. The abscissa is the stiffness parameter $\omega_1 c/U=2k_1$ and the ordinate is the mass ratio $1/\mu$. An ordinate of zero represents the limiting case of $\rho=0$, or, in other words, the plate is vibrating in a vacuum. The two solid curves are the first- and second-mode stability boundaries as indicated. It was

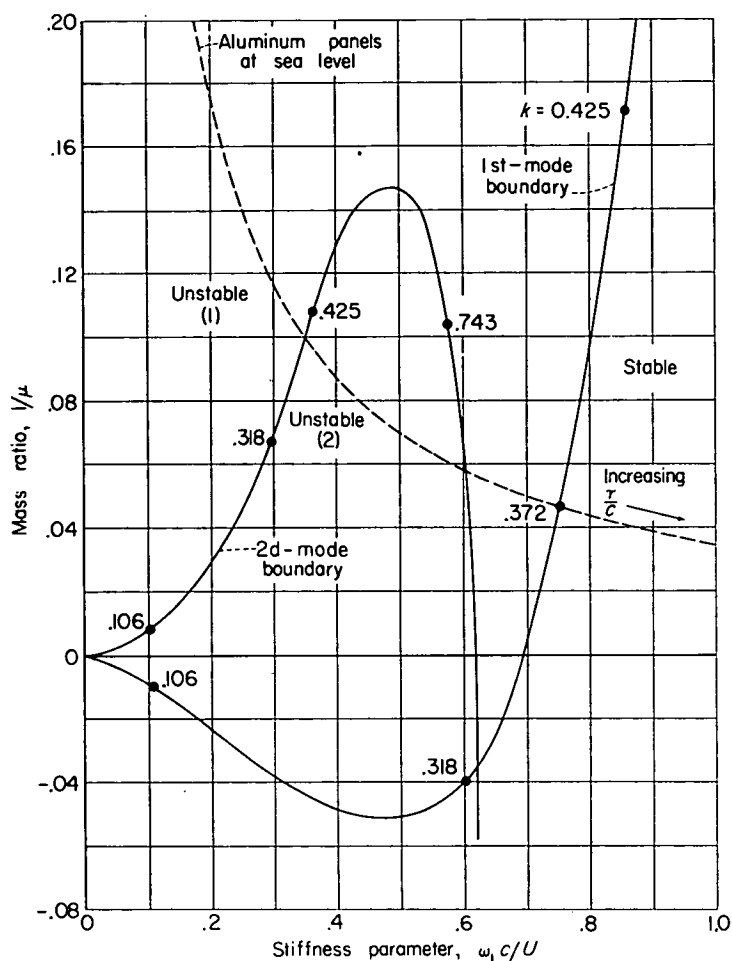


FIGURE 2.—Stability boundaries from a two-mode analysis for clamped-edge panels. $M=1.3$; $g=f=\frac{\rho_0}{\rho}=0$.

established by application of the Nyquist criterion (see, for example, ref. 14) as well as by interpretation of structural-damping results that the region to the right of the first mode boundary is stable, whereas the region to the left is unstable; furthermore, the region within the second-mode boundary is doubly unstable as indicated (unstable with regard to both boundaries). Values of the reduced frequency k are indicated along both curves. The points at which the curves cross the abscissa correspond to vibration in a pure normal mode (flutter at the limiting condition of $\rho=0$).

It can be seen from equations (30), by taking the product of $1/\mu$ and $2k_1$, that a specified panel material, air density, and speed of sound are represented by a hyperbola such as the dashed curve of figure 2 with the panel thickness-chord ratio τ/c increasing to the right. The intersection of the hyperbola with the stability boundary fixes the value of τ/c for neutral stability. Thicker panels are stable and thinner panels are unstable. (The particular hyperbola shown is for aluminum panels in air with standard sea-level properties. For denser panels or less dense air, the hyperbola would be below the one shown.)

Some effects of the number of modes in the analysis were

studied by including the first four normal modes, and the results are shown as the solid curves of figure 3. The dashed curves are the results for two modes from figure 2. With the addition of the third and fourth modes, the first-mode boundary is moved very slightly to the left (except where it crosses the abscissa) and is still the "critical" or decisive stability boundary separating the stable from the unstable region. The second-mode boundary is also only moderately affected. Within the already unstable region there now exist third-mode and fourth-mode boundaries which are closely analogous in appearance and character to the first- and second-mode boundaries, respectively. The unstable region is divided by three of the boundaries, into regions of different degrees of instability as indicated by the numbers in parentheses ranging from (1) to (4). (The points at which the

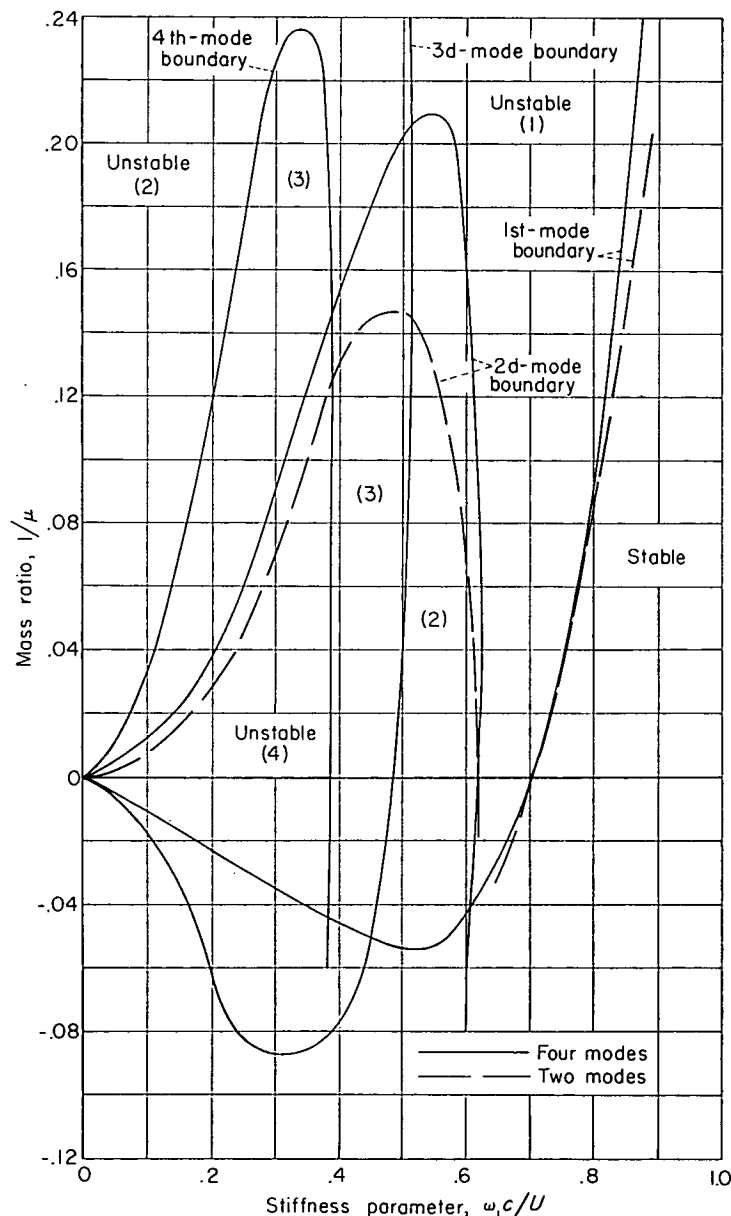


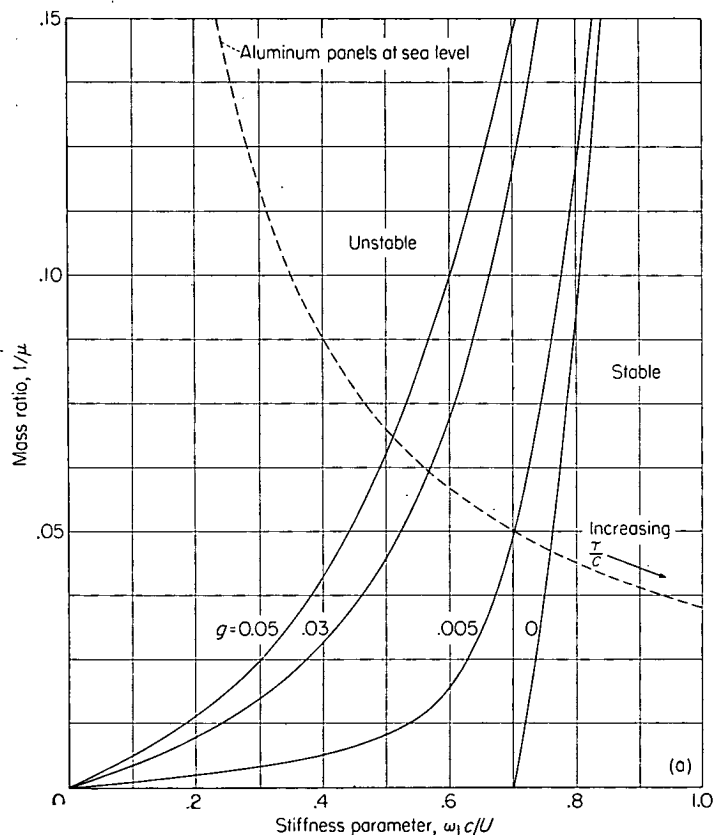
FIGURE 3.—Stability boundaries from two-mode and four-mode analyses for clamped-edge panels. $M=1.3$; $g=f=\frac{\rho_0}{\rho}=0$.

various boundaries cross the abscissa have the same significance as before.) These results indicate that two modes give a decisive stability boundary which is a close approximation to that for a large number of modes, at least for the conditions $g=f=\rho_0/\rho=0$ and $M=1.3$.

Effects of structural damping coefficient g .—Figures 4 (a) and 4 (b) show the first-mode and second-mode boundaries (from a four-mode analysis) for various values of g (taken to be the same for all modes). Third- and fourth-mode boundaries are affected by g in a manner similar to that of the first and second modes, respectively, and are not shown. The second-mode boundary of figure 4 (b) vanishes completely when g becomes slightly greater than 0.025, and for all positive values of g it remains in the unstable region to the left of the first-mode boundary. Included in figure 4 is the dashed hyperbola from figure 2. Since the thickness-chord ratio τ/c decreases to the left in the figure, the abscissas of the intersections of the hyperbola with the stability boundaries in figure 4 (a) show the proportional reduction in thickness required to prevent flutter as g increases.

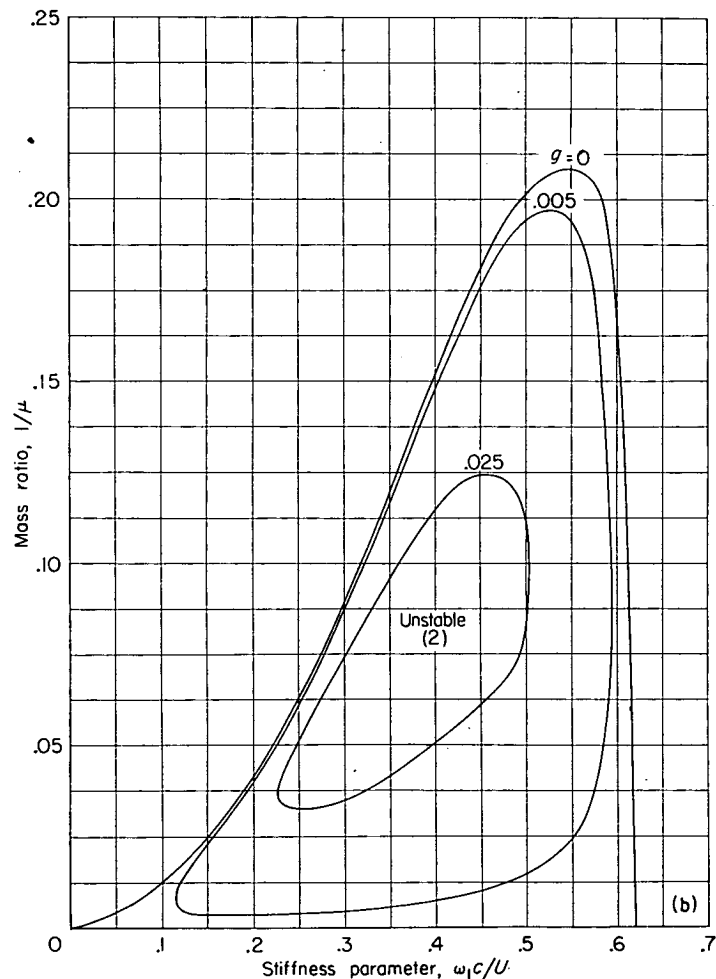
Effects of tension.—Tension has a marked effect on the

stability boundaries, as shown in figures 5 (a) and 5 (b). Figure 5 (a) shows the pertinent segments of the first-, second-, third-, and fourth-mode stability boundaries for $g=0$ and for the three values 0.1, 0.5, and 1.0 of the tension parameter f . As f increases, all the boundaries move to the left, and the thickness required to prevent flutter is decreased. Furthermore, as f increases, the first-mode boundary moves to the left more rapidly than the higher mode boundaries so that the rightmost boundary, separating stable from unstable regions, is one of the higher mode boundaries. For example, for $f=1.0$ in figure 5 (a), the third-mode boundary is farthest to the right. This trend is not surprising since application of tension to the clamped-edge plate causes the largest percentage increase in the first natural frequency, the next largest in the second natural frequency, and so on. Thus, it appears that the inclusion of only two modes in a flutter analysis may not be sufficient when the plate is subjected to tension. Inasmuch as the stiffness parameter $2k_1$ and the tension parameter f are both



(a) First-mode boundary.

FIGURE 4.—First-mode and second-mode stability boundaries from a four-mode analysis for clamped-edge panels for various values of structural damping coefficient g . $M=1.3$; $f=\frac{\rho_0}{\rho}=0$.



(b) Second-mode boundary.

FIGURE 4.—Concluded.

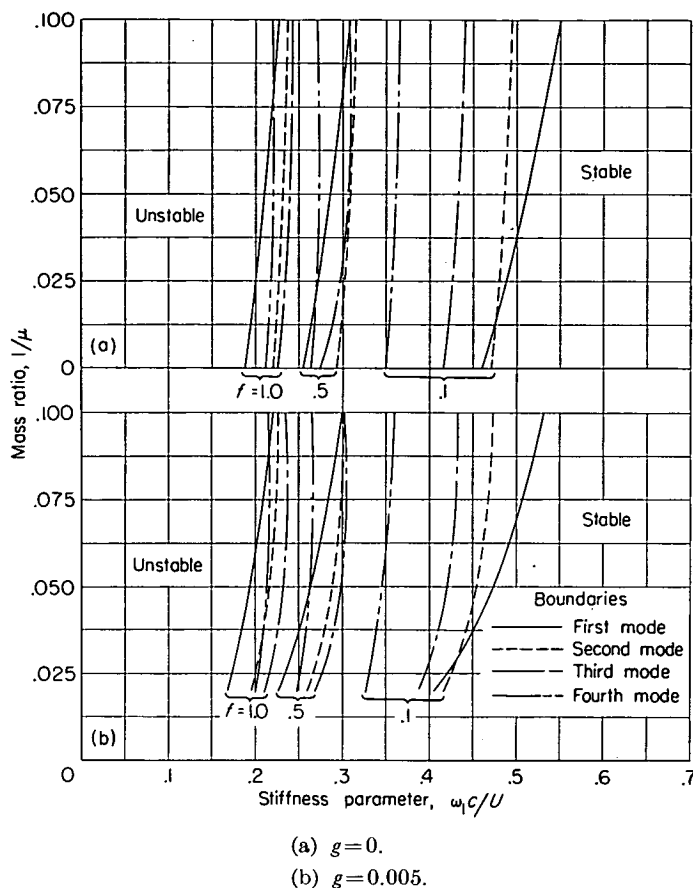


FIGURE 5.—Stability boundaries from a four-mode analysis for clamped-edge panels for three values of the tension parameter f . $M=1.3$; $\rho_0/\rho=0$.

based on the first natural frequency of the panel without tension, the shift of the boundaries is due solely to the tensile force F .

Figure 5 (b) shows segments of the first-, second-, third-, and fourth-mode boundaries with $f=0.1, 0.5$, and 1.0 for $g=0.005$. By comparing figures 5 (b) and 5 (a) it can be seen that g has a marked effect for the smaller values of f but its effect diminishes as f increases.

Effects of still air below panel.—The one remaining parameter to be considered at $M=1.3$ is ρ_0/ρ , the ratio of the density of the still air below the panel to the density of the supersonic stream above. In the preceding results this ratio was zero. The effect of increasing ρ_0/ρ to 1.0 will now be examined. For the sake of simplicity and convenience, only a two-mode analysis is made. Effects of structural damping and tension are also included.

Figure 6 (a) shows first- and second-mode boundaries for $\rho_0/\rho=1$ as solid curves and, for comparison, the dashed boundaries for $\rho_0/\rho=0$ from figure 2. Just as with the other results, the points where the boundaries cross the abscissa

correspond to pure-mode resonance in a vacuum. At these crossings the imaginary part of C_{nn} passes through zero. This imaginary part is a measure of aerodynamic damping. In the previous calculations C_{nn} consisted only of I_{nn} , whereas, for $\rho_0/\rho=1.0$, C_{nn} also contains $\bar{I}_{nn} + \bar{I}_{nn}$ (see eq. (23)). By comparison of the solid and dashed curves on figure 6 (a) it can be seen that, as a consequence, the first-mode boundary has moved to the left by about 20 percent but the second-mode boundary has changed relatively little.

Such an effect of still air might be expected since, for the same maximum panel amplitude, a first-mode vibration radiates into the still-air region a greater amount of energy per cycle than does a second-mode vibration. (With regard to the radiation of sound from a piston in a plane wall, specifically for the case of a piston with nonrigid face, p. 336 of ref. 15 gives the result that, at frequencies which are small compared with the ratio of the speed of sound to 2π times the piston radius, the pressure on the piston is approximately uniform and nearly proportional to the average velocity of the piston. Since the average velocity of the second mode and all other antisymmetric modes is zero, the pressure due to these modes is nearly zero and, accordingly, almost no work is being done on the still air.) From the fact that net energy can never pass from the still air into the panel, it does not follow, however, that the still air necessarily has a stabilizing effect in all cases. Conceivably, the still air could act to modify the flutter mode so that more energy would be extracted from the supersonic stream, and thus contribute toward an instability. Apparently such is the case in figure 6 (a), where the solid second-mode curve is above the dashed second-mode curve. The fact that dissipation of energy into the still air is not necessarily stabilizing should not be surprising, inasmuch as another means of energy dissipation, structural damping, is usually stabilizing but sometimes destabilizing.

As can be observed in figure 6 (a), the first-mode boundary has moved to the left of the second-mode boundary in the region of small mass ratio; in this region the second-mode boundary becomes critical.

Figure 6 (b) shows the effects of structural damping on the first-mode boundary, which for $g=0$ is shown more completely in figure 6 (a). Curves are included for $g=0, 0.005, 0.03$, and 0.05 . For values of g larger than about 0.025 the second-mode boundary vanishes as it did previously with $\rho_0/\rho=0$ in figure 4 (b), and only the first-mode boundary remains. The dashed hyperbola for aluminum at sea level is included in figure 6 (b), and it can be seen that a plate with zero structural damping would have to be about 30 percent thicker than one with $g=0.05$ in order to prevent flutter.

Figure 7 shows the effects of the tension parameter f for $\rho_0/\rho=1$ and $g=0$. Both first- and second-mode boundaries are shown for $f=0, 0.1, 0.5$, and 1.0 . In this case, just as

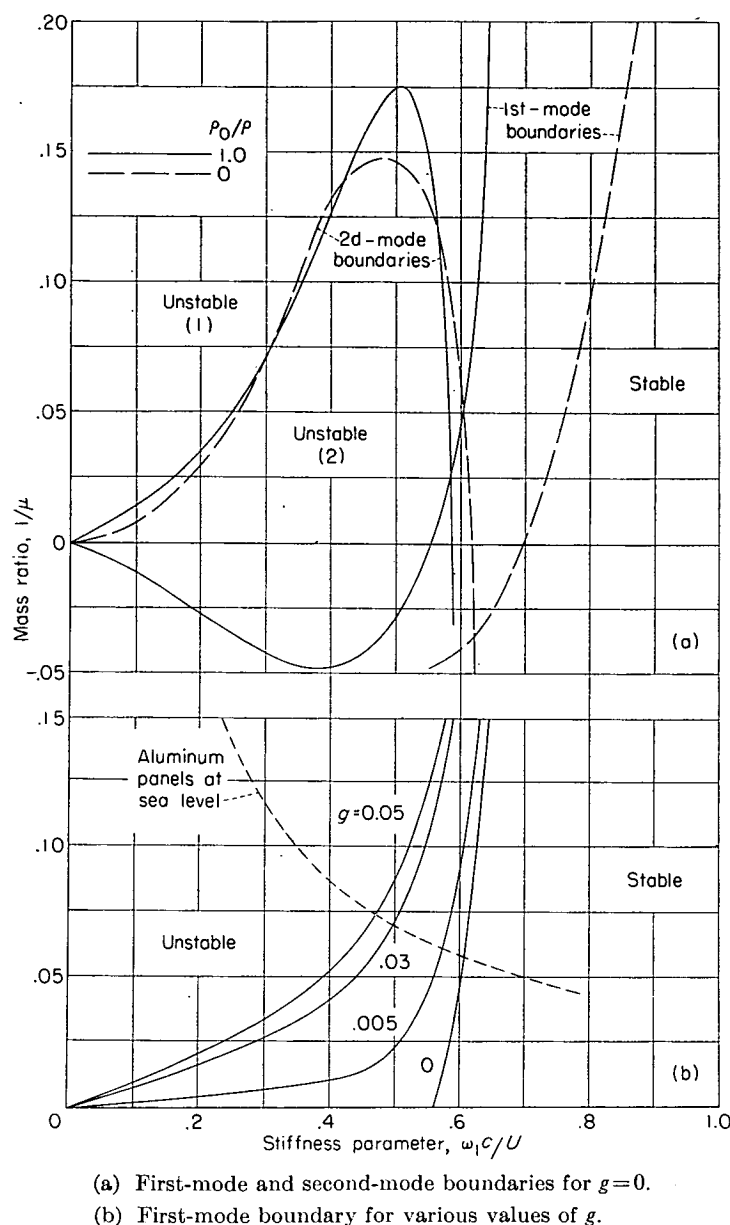


FIGURE 6.—Stability boundaries from a two-mode analysis for clamped-edge panels for various values of g . $M=1.3$; $f=0$; $\frac{\rho_0}{\rho}=0$ and 1.0.

with $\rho_0/\rho=0$, tension causes a marked reduction in the thickness required to prevent flutter. Furthermore, if more than two modes had been included, tension would have resulted in a higher mode boundary farther to the right than the curves shown for the higher values of f .

RESULTS FOR MACH NUMBER OF $\sqrt{2}$

Clamped-edge panels.—Figure 8 (a) shows the stability boundaries obtained from a two-mode analysis for clamped-edge panels at $M=\sqrt{2}$ with $f=\rho_0/\rho=0$ for various values of g . Included in the figure is the dashed hyperbola appropriate to this Mach number for aluminum panels in sea-level air. From a comparison of figure 2 and the curves of figure 8 (a)

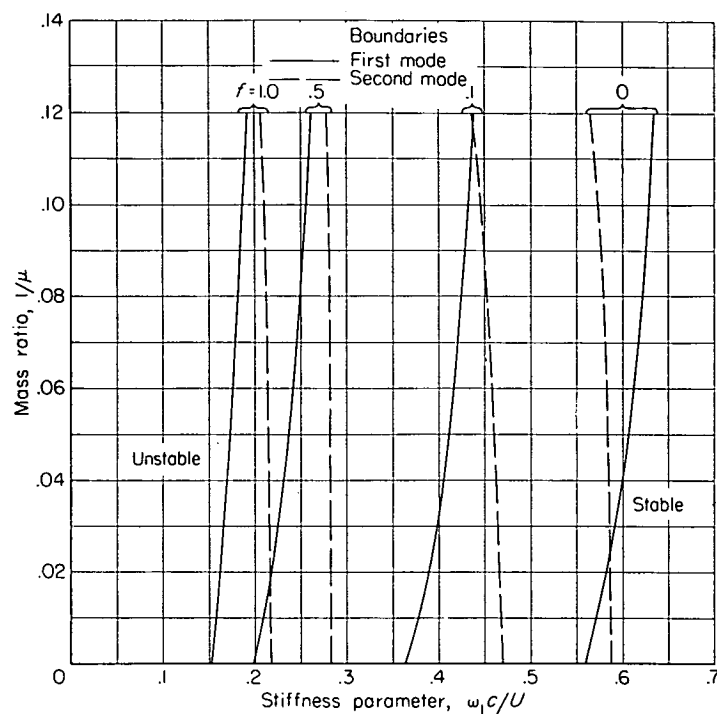


FIGURE 7.—Stability boundaries from a two-mode analysis for clamped-edge panels for various values of f . $M=1.3$; $g=0$; $\frac{\rho_0}{\rho}=1.0$.

for $g=0$, the first-mode boundary of figure 2 appears to have moved into the positive mass-ratio region and the second-mode boundary appears to be moving toward the negative mass-ratio region. Such is the case, but, inasmuch as the flutter frequencies on the upper boundary of figure 8 (a) are about midway between the first and second natural frequencies, this boundary can now be referred to only loosely as a "first-mode" boundary. The lower boundary is still readily identified as a second-mode boundary and the intersection with the abscissa corresponds to vibration in a pure second mode.

In contrast to the situation at $M=1.3$, the second-mode boundary for $g=0$ is now decisive for panels represented by the dashed hyperbola. Values of thickness to the right of the second-mode boundary are stable and, in addition, a small range of thickness values is stable between the upper and second-mode boundaries.

The curves in figure 8 (a) for positive values of g show that the region of instability within the second-mode boundary is reduced for small values of g (as for $M=1.3$) and vanishes when g is slightly greater than 0.00375, but that small values of g increase the region of instability associated with the upper boundary. This effect of g on the upper boundary is in marked contrast to its effect on the first-mode boundary at $M=1.3$. (See fig. 4 (a).) The differing effects of structural damping at $M=1.3$, $M=\sqrt{2}$, and $M=1.56$ are considered further in the section on "Variations With Mach Number."

Pinned-edge panels.—In order to indicate effects of edge

fixity, boundaries are shown in figure 8 (b) for conditions identical to those of figure 8 (a) except that the edges are pinned rather than clamped. The boundaries for $g=0$, which are given incompletely in reference 5 and thereby lead to the conclusion that only a small range of panel thickness is stable at $M=\sqrt{2}$, have been extended to higher frequencies with the result that sufficiently thick panels are also found to be stable. The effect of structural damping on both boundaries in figure 8 (b) is very similar to that in figure 8 (a). The dashed hyperbola appropriate to pinned-edge aluminum panels in sea-level air is included in the figure. The hyperbolas of figures 8 (a) and 8 (b) are located differently because of the different values for the first-mode eigenvalue K_1 of equation (30) for pinned and clamped edges. (See table I.) From the intersection of the dashed hyperbolas with the stability boundaries in the two figures, it can be determined that a pinned-edge panel must be somewhat thicker than a clamped-edge panel in order to be flutter free but not nearly as thick as might be expected from a simple comparison of the first natural frequencies. Values of the reduced fre-

quency k are indicated along each of the boundaries of figure 8.

Based on what occurred at $M=1.3$ (see fig. 3), there is the possibility that for $g=0$ the fourth-mode boundary from a four-mode analysis would alter the stability picture in both figures 8 (a) and 8 (b) in the relatively unimportant narrow range of stability between the boundaries shown for $g=0$. This minor effect of the fourth-mode boundary is expected to disappear for values of g greater than about 0.005 and, therefore, a four-mode analysis was not made for this Mach number.

RESULTS FOR MACH NUMBER OF 1.56

Effects of two and four modes.—As in the case of $M=1.3$, stability boundaries were obtained first for two and then for four degrees of freedom with $g=f=\rho_0/\rho=0$. These boundaries appear in figure 9 as dashed curves for two modes and solid curves for four modes. Values of the reduced frequency k are indicated along the boundaries. The stable region is again to the right, and on the left the degree of instability is indicated in parentheses for the four-mode analysis.

The two-mode results in figure 9 continue the trend noted in the preceding section from comparison of the curves of figure 2 and those of figure 8 (a) for $g=0$. The second-mode

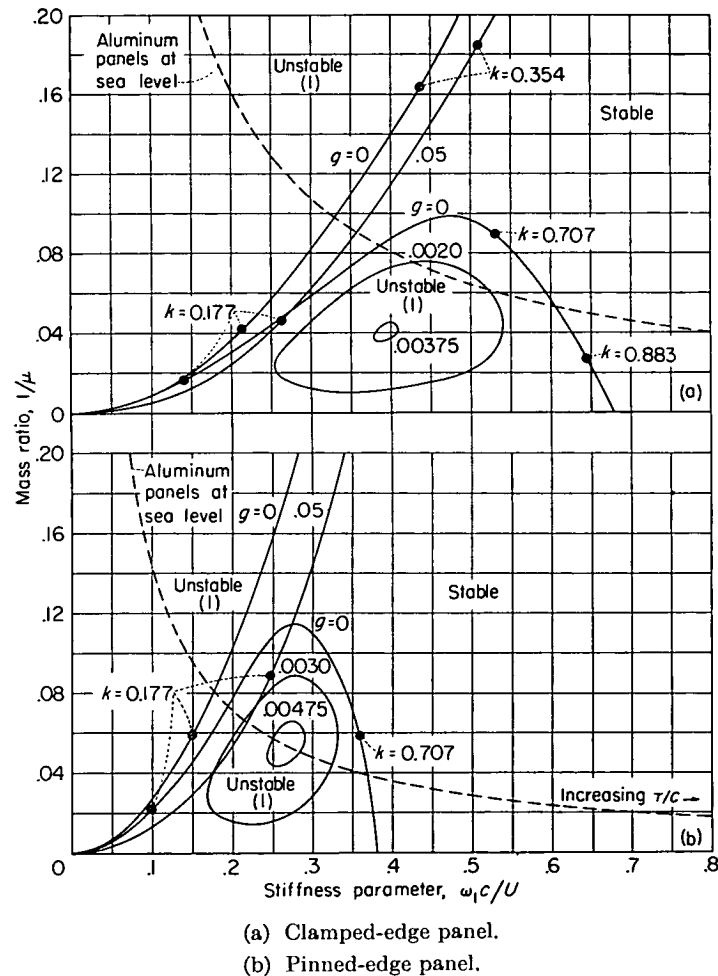


FIGURE 8.—Stability boundaries from a two-mode analysis for clamped-edge and pinned-edge panels for various values of g . $M=\sqrt{2}$; $f=\frac{\rho_0}{\rho}=0$.

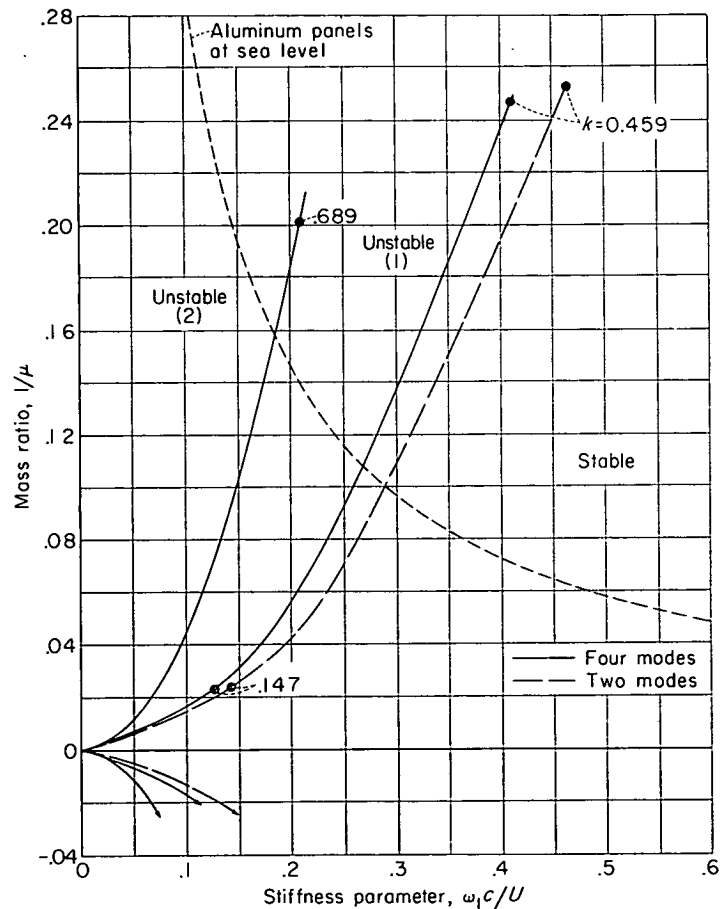


FIGURE 9.—Stability boundaries from two-mode and four-mode analyses for clamped-edge panels. $M=1.56$; $g=f=\frac{\rho_0}{\rho}=0$.

boundary has moved entirely into the negative mass-ratio region. The upper boundary has moved higher in the positive mass-ratio region, and the flutter frequencies along it, which in figure 8 (a) were midway between the first and second natural frequencies, are now closer to the second. For this reason the upper boundary, which was loosely identified as a "first-mode" boundary in the discussion of figure 8 (a), will now be referred to as a "second-mode" boundary.

A further point of difference between the results at $M=1.3$ and $M=1.56$ is that the addition of the third and fourth modes at $M=1.56$ shifts the decisive stability boundary to the left by about 10 percent, whereas at $M=1.3$ the shift is insignificant. (Compare figs. 3 and 9.) Although this shift indicates that the two-mode result is not well converged, the two-mode boundary is conservative; that is, it requires a greater thickness to prevent flutter. (As with two modes, when four modes are used, half of the stability boundaries fall in the negative mass-ratio region.)

Effects of structural damping coefficient g .—No curves are shown to indicate effects of structural damping at a Mach number of 1.56, the reason being that, for moderate values of the coefficient g , ranging at least up to 0.05, the stability boundaries fall virtually on top of those for $g=0$. The major effect of structural damping is a moderate change in flutter frequency.

Effects of tension and of still air below panel.—Effects of tension have not been determined, but tension is expected to have essentially the same favorable stiffening effect at all Mach numbers as at $M=1.3$. The effect of still air behind the panel has also not been determined, but this effect is expected to be less than at $M=1.3$ for two reasons: First, the air beneath the panel acts primarily as an energy absorber and one means of energy absorption, structural damping, has been found ineffective in shifting the stability boundaries. Second, on the decisive boundary the flutter mode appears to be predominantly the second natural panel mode, and it was found that at $M=1.3$ the second-mode boundary is changed only slightly by increasing ρ_0/ρ from 0 to 1.

VARIATIONS WITH MACH NUMBER

The foregoing results have been presented for particular Mach numbers. In an effort to clarify some of the anomalies that have been noted in these results, figures 10 to 12 are presented. Figure 10 shows the panel thickness-chord ratio required to prevent flutter as a function of M for clamped-edge panels with $g=f=\rho_0/\rho=0$. The curves apply to aluminum panels in standard sea-level air. The values at $M=1.3$, $\sqrt{2}$, and 1.56 were obtained from figures 2 and 8 (a) and the two-mode results of figure 9. The shape of the curves between these known points is estimated. The stable region is above or to the right of the shaded boundaries.

The boundary which is labeled "first-mode" on one end and "second-mode" on the other has flutter frequencies which progress from slightly above the first natural frequency to somewhat below the second natural frequency as the Mach number is increased. (See previous discussions con-

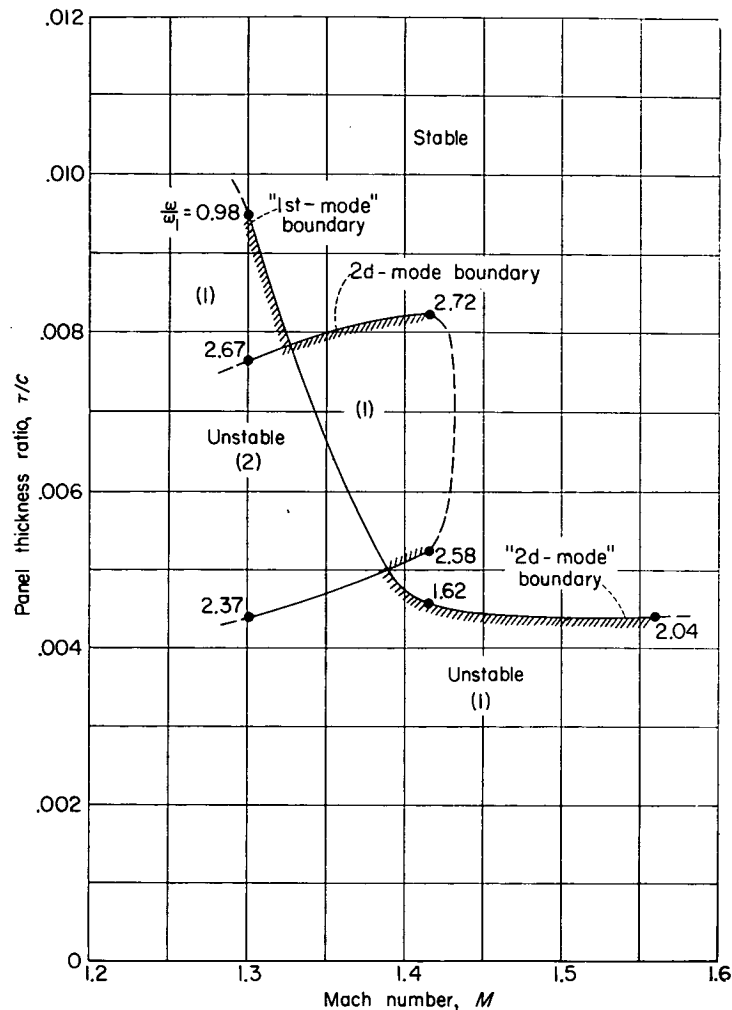


FIGURE 10.—Minimum panel thickness ratio τ/c required to prevent flutter as a function of Mach number for clamped-edge aluminum panels in sea-level air. $g=f=\frac{\rho_0}{\rho}=0$.

cerning figs. 2, 8 (a), and 9.) The boundary labeled "second-mode" has flutter frequencies slightly below the second natural frequency throughout.

Figure 10 shows the second-mode stability boundary to be decisive in the Mach number range from slightly above 1.30 to slightly above $\sqrt{2}$. As the structural damping g is increased from zero, the second-mode boundary shrinks to the left leaving the "first-mode"—"second-mode" boundary decisive throughout the range of M shown. For example, for a value of g slightly greater than 0.0038 the second-mode boundary does not exist at $M=\sqrt{2}$ (see fig. 8 (a)), and for a value of g slightly greater than 0.025 it does not exist at $M=1.3$ (see fig. 4 (b)).

These effects of g on the second-mode boundary are illustrated in figure 11, which contains cross plots of g against τ/c obtained from the intersections of the dashed hyperbolas (for aluminum panels in sea-level air) with the boundaries for constant g such as shown in figures 4, 8 (a), and 9. Figure 11 also shows that an increase in g from

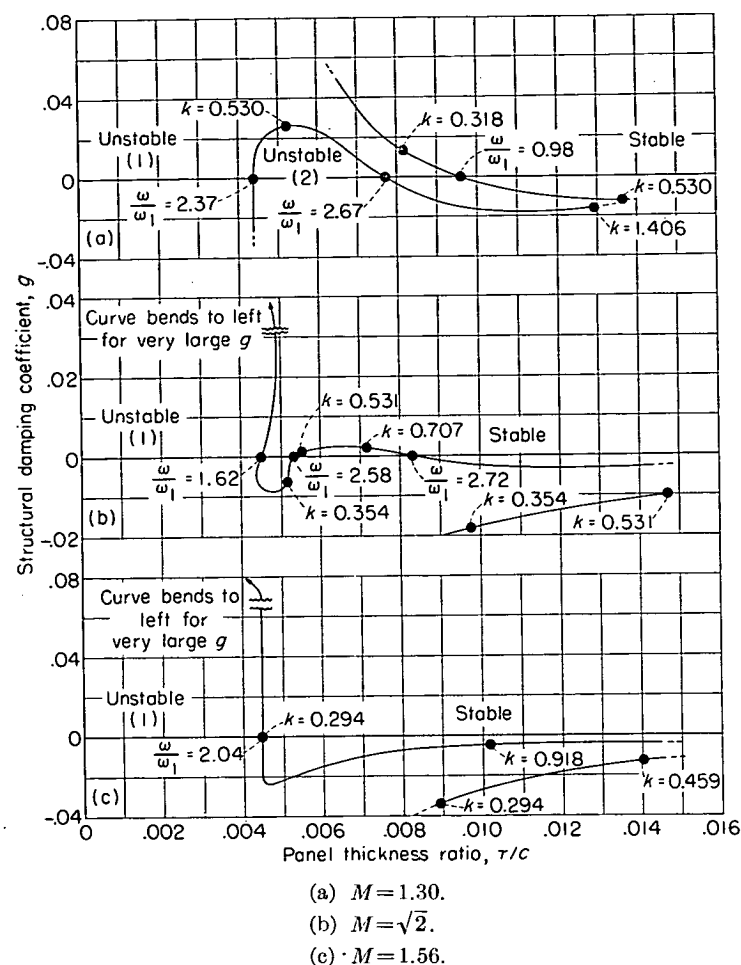


FIGURE 11.—Structural damping coefficient g as a function of panel thickness ratio τ/c from a two-mode analysis for clamped-edge aluminum panels in sea-level air. $f = \frac{p_0}{\rho} = 0$. (Refer to dashed hyperbolas in figs. 2, 8 (a), and 9.)

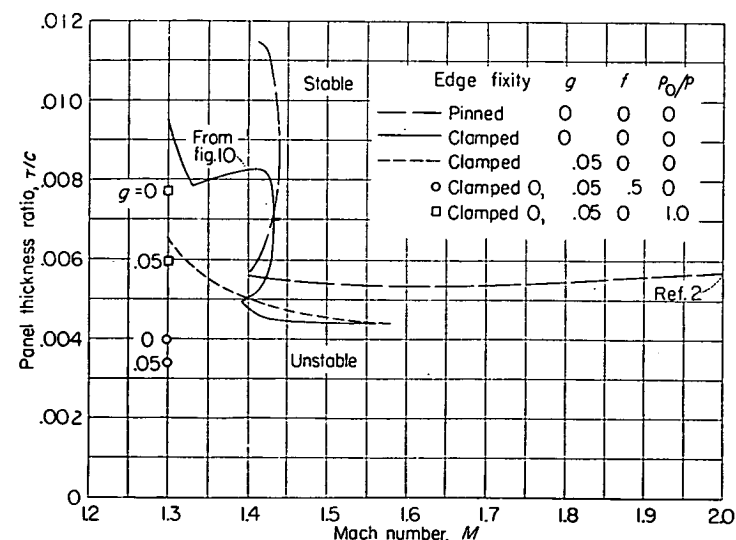


FIGURE 12.—Minimum panel thickness ratio τ/c required to prevent flutter as a function of Mach number for aluminum panels in sea-level air.

zero would cause the “first-mode”—“second-mode” boundary of figure 10 to drop markedly at $M=1.3$, rise slightly at $M=\sqrt{2}$, and remain essentially unchanged at $M=1.56$. The ratios of flutter frequency to the first natural frequency ω/ω_1 are indicated for each of the crossings and tend to show more clearly the connection between figures 10 and 11. (Values of ω/ω_1 near ω_2/ω_1 , which is approximately 2.76, are associated with the second-mode boundary and values between 1.0 and 2.05 are associated with the “first-mode”—“second-mode” boundary.) A complete understanding of the manner in which the curves change character and position with Mach number, particularly between $M=1.3$ and $M=\sqrt{2}$, requires more calculation than presented herein.

Figure 12, which has the same ordinates as figure 10, is presented for the purpose of summarizing some effects of all the parameters investigated. The results shown are based on two modes, except in the case of tension where only four-mode results are known. The results again apply to aluminum panels in sea-level air. The figure shows as a solid curve the shaded boundary from figure 10 for clamped-edge panels and as a short-dash curve the effect on this boundary of increasing g from 0 to 0.05. The third (long-dash) curve is for pinned-edge panels with $g=0$, the value at $M=2$ having been obtained from reference 2. The points at $M=\sqrt{2}$ were obtained from figure 8 (b) and the upper (second-mode) curve was patterned after that for clamped-edge panels. As a matter of interest, points are included in figure 12 at $M=1.3$ for clamped-edge panels and indicate the effects of tension ($f=0.5$) and of still air below the panel ($p_0/p=1.0$) for $g=0$ and $g=0.05$.

Some effects of the various parameters can be assessed from figure 12. The overall result is that τ/c is highest in the low supersonic Mach number range and suggests that this range is the more critical from a design standpoint. Structural damping is seen to have a large favorable effect near and below $M=\sqrt{2}$. Although rather influential at $M=1.3$, the still air below the panel is expected to have less effect at $M=\sqrt{2}$ and 1.56. Tension, which is seen to have a large favorable effect at $M=1.3$, is expected to be similarly effective for all Mach numbers. In this connection, it might be mentioned that one means of producing tension is by a static-pressure difference between the upper and lower panel surfaces, particularly for the case where the panel leading and trailing edges are prevented from moving toward each other. A comparison of the results for the edge fixities, pinned and clamped, is of interest because the edge fixity of actual panels falls somewhere between.

COMPARISON WITH OTHER THEORETICAL WORK

In reference 2 the conclusion is reached that all panels, regardless of thickness, are unstable for supersonic Mach numbers less than $\sqrt{2}$. This result and the more plausible results of reference 2 for $M > \sqrt{2}$ are based on air forces expanded to the first power of the frequency of oscillation. In reference 5 the necessity of including higher order frequency terms for Mach numbers near $\sqrt{2}$ is pointed out, and

stability boundaries, based on exact linearized unsteady air forces, are presented for $M=\sqrt{2}$ and $M=2$. One boundary is obtained at $M=2$ which agrees well with the comparable result from reference 2, whereas two boundaries are obtained at $M=\sqrt{2}$. The boundaries at $M=\sqrt{2}$, because they are not carried high enough in frequency, are interpreted in reference 5 as showing that stability is possible only for a small range of panel thickness at this Mach number. The results of reference 2 for $M<\sqrt{2}$ are not questioned in reference 5.

In the present report, stability boundaries are computed for $M=\sqrt{2}$ and for Mach numbers above and below this value (namely, $M=1.3$ and $M=1.56$). In view of the findings of references 2 and 5, perhaps the most noteworthy result of the present investigation is that, for the Mach numbers treated and probably throughout the supersonic range, sufficiently thick panels are stable.

In references 2 and 5 and the present report, $M=\sqrt{2}$ appears as a transitional value. The transition is evidenced herein by the contrasting behavior of the stability boundaries at $M=1.3$ and $M=1.56$. Some understanding of why a Mach number of $\sqrt{2}$ is transitional can be had by examining matrix equation (26). The term $\frac{i(M^2-2)}{2k\beta^3} \{Z_n\}$ of equation

(26), being the entire first-order frequency contribution to the damping, is dominant at low frequencies. This term appears to control the slope, at low frequencies, of the eventually decisive stability boundary and changes sign as M passes through $\sqrt{2}$. When $M<\sqrt{2}$, the slope is negative for low frequencies, but as the frequency increases the slope eventually becomes positive because of the higher order frequency effects (for example, in fig. 2). Because only first-order frequency effects are included, in essence only the beginning portions of the stability boundaries for $M<\sqrt{2}$ are obtained in reference 2, and, as a consequence, the conclusion is reached that all panels are unstable below this Mach number. For $M>\sqrt{2}$ the slope of the decisive stability boundary starts out positive and becomes more so as the frequency increases. (See fig. 9.) If aspect ratio were included in the present treatment (by considering three-dimensional rather than two-dimensional panels), a reduction in aspect ratio would probably tend to eliminate the initial negative slope of the eventually decisive stability boundary for $M<\sqrt{2}$ and increase the initial positive slope for $M>\sqrt{2}$. This effect of aspect ratio is expected because, in general, a reduction in aspect ratio results in an increase in aerodynamic damping with a consequent enlargement of regions of stability.

In reference 7, which treats a different problem (namely, an infinite two-dimensional panel on equally spaced supports), the result was also obtained that somewhere in the supersonic Mach number range a panel will flutter regardless of its thickness. The conclusion was reached that stability is not possible at supersonic Mach numbers less than about 1.25 and that at higher Mach numbers a sufficient increase in thickness will always render a stable panel unstable. However, it was observed that over a large portion of the predicted region of instability the flutter was of an extremely

mild character, since a large number of oscillations were required to double the amplitude. With the hope of eliminating the large region of mild instability, small amounts of viscous damping were included. Contrary to expectations, thick panels remained unstable for the example given at $M=1.8$.

As part of the viscous-damping investigation, the results were interpreted so as to determine regions of stability and instability. As shown in figure 10 of reference 7, an apparent conflict with the results of Nyquist diagrams was found. (The Nyquist diagram concept is used in general in reference 7 for determining stability.) This conflict is based on the assumption that most investigators interpret structural-damping results according to the concept that removal of damping tends to destabilize. This assumption is incorrect, however, and no such simple criterion holds true for interpreting structural-damping results. A feature to be noted in the example chosen in reference 7 to illustrate the apparent conflict is the existence of infinite singularities in the air forces at the end points of the boundaries ($g=0, 0.01$, and 0.03) on the right in figure 9 of the reference (designated type B loci therein). By way of explanation, such singularities occur in the linearized-flow treatment because a traveling wave of panel deflection is moving at a speed corresponding to $M=1$ relative to the air above or below the panel.

In this analysis the question of stability was investigated by means of both the structural-damping concept and the Nyquist diagram concept. The structural-damping results in every case agreed with the Nyquist diagram results. Incidentally, in using the Nyquist concept, knowledge of the aerodynamic forces for all frequencies from minus infinity to plus infinity is required. Thus, the concept is not applicable, in general, when the air forces are approximated by a few terms of a power-series expansion in the frequency of oscillation.

COMPARISON WITH EXPERIMENT

A few experimental results on the flutter of flat and buckled panels are available for comparison with the theory of the present report for flat panels and that of reference 3 for buckled panels. Reference 16 gives experimental results at $M=1.3$ for panels 11.62 inches long in the stream direction and 8 inches wide that were held by clamping the leading and trailing edges. In figure 13, the results of reference 16 at $M=1.3$, together with data more recently obtained in the Langley supersonic flutter apparatus on both flat and buckled panels at other Mach numbers, are compared with theory. The results are presented in terms of the thickness-chord ratio τ/c needed to prevent flutter of aluminum-alloy panels at an altitude of 25,000 feet as a function of Mach number. These points were obtained from tests of panels of different thicknesses (see, for example, ref. 16) and represent the thinnest panels which did not flutter. (Where necessary, experimental data were adjusted to a pressure altitude of 25,000 feet with the relation $\tau/c = (\tau/c)_r (q/q_r)^{1/3}$. The subscript r refers to the experimental conditions.)

In figure 13, the solid curve is the flutter boundary for flat panels obtained from the present theory and the square symbols are the corresponding experimental results. The

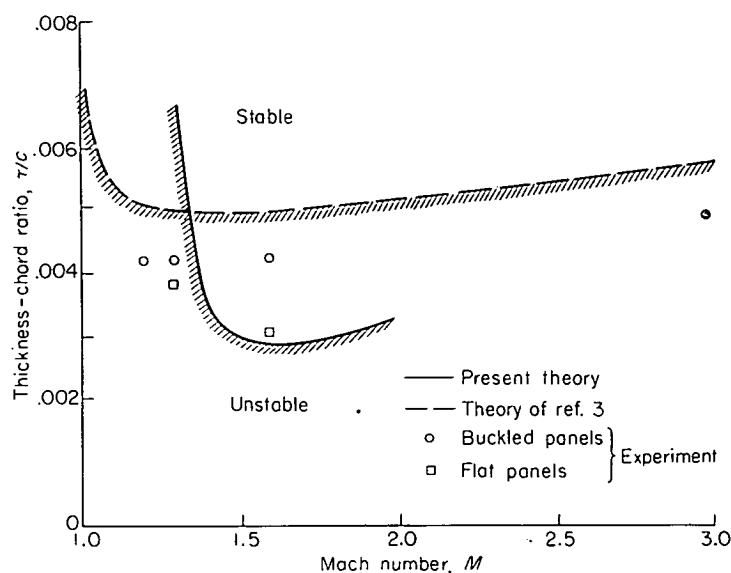


FIGURE 13.—Minimum panel thickness ratio τ/c required to prevent flutter of aluminum-alloy panels at 25,000-ft altitude.

dashed curve is the static-stability boundary for buckled panels, proposed as a flutter boundary in reference 3, and the circles are the associated experimental results. The theoretical curves are seen to increase rather sharply near Mach number 1.0. For buckled panels the increase is due to the use of steady-state linearized air forces which become infinite at $M=1$. For flat panels the increase is thought to be associated with a change in flutter mode and decreased aerodynamic damping. The curve for flat panels would have a finite ordinate at $M=1.0$.

As can be seen from figure 13, buckled panels have been fluttered up to a Mach number of 3. Flat panels were not fluttered over the same range because buckled panels appeared to be more susceptible to flutter, in general, and during a test it was difficult to prevent the thin, flat panels from buckling due to heating. (A temperature rise of 5° to 10° F was sufficient to induce buckling in many panels.)

The agreement between theory and experiment for both flat and buckled panels is surprisingly good, inasmuch as the experiments were made on panels with a width-length ratio of 0.69, whereas the theories are for two-dimensional panels.

CONCLUDING REMARKS

A Rayleigh type analysis involving chosen modes of the panel as degrees of freedom has been used to treat the flutter of a two-dimensional flat panel supported at its leading and trailing edges and subjected to a middle-plane tensile force. The panel had a supersonic stream passing over its upper surface and still air below. The aerodynamic forces due to the supersonic stream were obtained from the theory for linearized two-dimensional unsteady flow and the forces due to the still air were obtained from acoustical theory. The still air beneath the panel was treated on the assumption that the still-air reservoir extended to infinity. Accordingly, once acoustic energy was radiated into this region, none of it was ever reflected. Such a situation is, of course, not the

same as for a panel on a closed body but represents a first approximation for many practical cases.

In order to study the effect of increasing the number of modes in the analysis, two and then four modes were employed. The modes used were the first four natural modes of the panel in a vacuum with no tensile force acting. The analysis included the variables: Mach number M , structural damping, tensile force, density of the still air, and edge fixity (clamped and pinned). For certain combinations of these variables, stability boundaries were obtained which can be used to determine the panel thickness required to prevent flutter for any panel material and altitude.

In contrast to some previous panel flutter investigations, the present results show that sufficiently thick panels are flutter free for the Mach numbers treated and suggest that this is true throughout the supersonic speed range. The low supersonic Mach numbers were found to be most critical from a design standpoint in the range examined (from $M=1.3$ to $M=2.0$). Tension was shown at $M=1.3$ to have a marked favorable effect (also expected at all Mach numbers) in reducing the thickness required to prevent flutter, and it was pointed out that one means of producing tension is by a static pressure difference between the upper and lower surfaces of the panel. Small amounts of structural damping were found to have a pronounced beneficial effect near and below $M=\sqrt{2}$ and essentially no effect at $M=1.56$. In the neighborhood of $M=\sqrt{2}$ a small change in either Mach number or structural damping was found to cause an abrupt change in the thickness required to prevent flutter. At $M=\sqrt{2}$ a pinned-edge panel must be somewhat thicker than a clamped-edge panel in order to be flutter free: Still air below the panel was taken into account only at $M=1.3$ and was shown to have a moderate beneficial effect. For $M>\sqrt{2}$ the still air is expected to have little effect because for this Mach number range the flutter mode is predominantly the second natural mode, which radiates very little energy into the still air.

The theories of the present report for flat panels and of Isaacs for buckled panels were compared with a few experimental results on panels clamped at leading and trailing edges over the Mach number range 1.2 to 3.0. The agreement was surprisingly good inasmuch as the experiments were made on panels with a width-length ratio of 0.69, while the theories are for two-dimensional panels. Over the Mach number range of the experiments it was found that buckled panels had to be thicker than flat panels in order not to flutter. The effect of restraining flat or buckled panels on all four edges has not been investigated. Such restraint together with variation of width-length ratio will probably have a significant effect on the thickness required to prevent flutter. Another factor which requires investigation is built-in curvature of the panel in the streamwise or cross-stream direction.

LANGLEY AERONAUTICAL LABORATORY,
NATIONAL ADVISORY COMMITTEE FOR AERONAUTICS,
LANGLEY FIELD, VA., April 20, 1955.

APPENDIX A

SOLUTION BY MEANS OF LAPLACE TRANSFORMS

In a recent paper (ref. 6), a procedure is outlined for obtaining by means of Laplace transforms the exact solution for the flutter of a two-dimensional membrane which is subjected to a supersonic stream on one side and stagnant air on the other. This solution is called exact, inasmuch as the equation of motion for the system is solved directly without any limitation being imposed on the mode shape or frequency of flutter. Reference 6 also mentions that pure bending of a plate and the more general case in which plate bending and membrane stretching are combined could be treated in the same manner. The present report treats the latter case; namely, the flutter of a panel (plate) acted on by a middle-plane or axial force, such as tension, or compression less than the buckling load. In the body of the report this problem is solved by the generalized-coordinate approach, and the coordinates used are the normal modes of the panel with no axial force acting. In this appendix, for the sake of completeness, the solution to the same problem is derived by means of Laplace transforms to the point where numerical calculations can be made. The feasibility of applying the Laplace transform solution is examined, but no numerical results are obtained.

The integrodifferential equation to be solved is given by equation (2) which, upon substitution of the expression for $p(x,t)$ obtained from equations (5) to (9), may be written as

$$\frac{D}{c^4} Z'''' - \omega^2 m_A Z - \frac{F}{c^2} Z'' + \frac{\rho U^2}{c} \left\{ \frac{1}{\beta} \left[i2k \int_0^x w_u(\xi) I_u(x-\xi) d\xi + \frac{d}{dx} \int_0^x w_u(\xi) I_u(x-\xi) d\xi \right] - \frac{i}{2} \frac{\rho_0}{\rho} \left[i2k \int_0^1 w_l(\xi) I_l(x-\xi) d\xi \right] \right\} = 0 \quad (A1)$$

or alternatively as

$$\frac{D}{c^4} Z'''' - \omega^2 m_A Z - \frac{F}{c^2} Z'' + \frac{\rho U^2}{c} \left\{ \frac{1}{\beta} \left[w_u(0) I_u(x) + \int_0^x I_u(x-\xi) \left(\frac{d}{d\xi} + i2k \right) w_u(\xi) d\xi \right] - \frac{i}{2} \frac{\rho_0}{\rho} \left[i2k \int_0^1 w_l(\xi) I_l(x-\xi) d\xi \right] \right\} = 0 \quad (A2)$$

where

$$w_u(x) = Z'(x) + i2kZ(x)$$

$$w_l(x) = i2kZ(x)$$

$$I_u(x) = e^{-i\omega x} J_0 \left(\frac{\bar{\omega}}{M} x \right)$$

$$I_l(x) = H_0^{(2)}(2kM|x|)$$

Dividing equation (A2) by $m\omega^2$ yields

$$\alpha Z'''' - \delta Z'' - Z + \frac{1}{\mu} \frac{1}{4k^2} \left\{ \frac{1}{\beta} \left[w_u(0) I_u(x) + \int_0^x I_u(x-\xi) \left(\frac{d}{d\xi} + i2k \right) w_u(\xi) d\xi \right] + \frac{-i}{2} \frac{\rho_0}{\rho} \left[i2k \int_0^1 w_l(\xi) I_l(x-\xi) d\xi \right] \right\} = 0 \quad (A3)$$

where

$$\alpha = \frac{1}{K_1^4} \left(\frac{\omega_1}{\omega} \right)^2 = \frac{1}{K_1^4} \Omega$$

$$\delta = \frac{F}{m_A c^2 \omega_1^2} \left(\frac{\omega_1}{\omega} \right)^2 = f \Omega$$

The quantity ω_1 in the formulas for α and δ is the first natural frequency of the plate vibrating in a vacuum with no axial force F acting and K_1 is the associated eigenvalue. (See table I.) In the case of the membrane, ω_1 would be the first natural frequency of the membrane, α would be zero (D is negligible for the membrane), and f would be $\left(\frac{1}{\pi} \right)^2$.

Applying the Laplace transform

$$L\{Z(x)\} = \bar{Z}(s) = \int_0^\infty e^{-sx} Z(x) dx$$

to equation (A3) (using in the process pairs 4 and 7, p. 294, ref. 17) yields the transformed problem in the form

$$\alpha(s^4\bar{Z}-s^3z_0-s^2z_1-sz_2-z_3)-\delta(s^2\bar{Z}-sz_0-z_1)-\bar{Z}+\frac{1}{4k^2\mu}\left(\frac{1}{\beta}[(s^2+i4ks-4k^2)\bar{Z}-(s+i2k)z_0]\bar{I}_u(s)+\frac{i}{2}\frac{\rho_0}{\rho}4k^2L\left\{\int_0^1Z(\xi)I_l(x-\xi)d\xi\right\}\right)=0 \quad (\text{A4})$$

where $z_0=Z(0)$, $z_1=Z'(0)$, $z_2=Z''(0)$, $z_3=Z'''(0)$, and $\bar{I}_u(s)$ is the Laplace transform of $I_u(x)$. The Laplace transform in equation (A4) involving ρ_0/ρ as a multiplier is the contribution of the perturbation pressure on the lower surface of the panel. Unfortunately, this transform does not appear to be obtainable here where the deflection Z is unknown. In the body of the report the effect of including the air below the panel is found to be moderate at a Mach number of 1.3 and reasons are given why this effect is expected to be even smaller at the higher Mach numbers investigated. In view of these facts and in view of the difficulty of handling the lower-surface term in equation (A4), this term will be omitted in the rest of this appendix—that is, treated as if ρ_0 were zero.

Equation (A4) can therefore be reduced to

$$[(\alpha s^4-\delta s^2-1)+\epsilon(s+i2k)^2\bar{I}_u(s)]\bar{Z}(s)=\alpha(s^2z_1+sz_2+z_3)-\delta z_1 \quad (\text{A5})$$

where $\epsilon=1/4k^2\mu\beta$ and z_0 has been dropped because it is zero for the present boundary-value problems. Thus the integro-differential equation (A1) has been reduced to the algebraic equation (A5).

Now by means of pair 11, p. 294, and pair 55, p. 298, of reference 17 there is obtained

$$\bar{I}_u(s)=\left[(s+i\bar{\omega})^2+\left(\frac{\bar{\omega}}{\bar{M}}\right)^2\right]^{-1/2} \quad (\text{A6})$$

Therefore, from equation (A5), after some algebraic manipulation

$$\bar{Z}(s)=\frac{M(s)}{Q(s)}+\frac{N(s)}{Q(s)}\bar{I}_u(s) \quad (\text{A7})$$

where

$$\begin{aligned} Q(s) &= (\alpha s^4 - \delta s^2 - 1)^2 \left[(s+i\bar{\omega})^2 + \left(\frac{\bar{\omega}}{\bar{M}}\right)^2 \right] - \epsilon^2 (s+i2k)^4 \\ M(s) &= (\alpha s^4 - \delta s^2 - 1) \left[(s+i\bar{\omega})^2 + \left(\frac{\bar{\omega}}{\bar{M}}\right)^2 \right] [\alpha(s^2z_1+sz_2+z_3)-\delta z_1] \\ N(s) &= -\epsilon(s+i2k)^2 \left[(s+i\bar{\omega})^2 + \left(\frac{\bar{\omega}}{\bar{M}}\right)^2 \right] [\alpha(s^2z_1+sz_2+z_3)-\delta z_1] \end{aligned}$$

In polynomial form the quantities Q , M , and N are

$$Q(s)=\sum_{r=0}^{10}q_rs^{10-r} \quad (\text{A8})$$

$$M(s)=z_1\sum_{r=0}^8m_r^{(1)}s^{8-r}+z_2\sum_{r=0}^7m_r^{(2)}s^{7-r}+z_3\sum_{r=0}^6m_r^{(3)}s^{6-r} \quad (\text{A9})$$

$$N(s)=z_1\sum_{r=0}^6n_r^{(1)}s^{6-r}+z_2\sum_{r=0}^5n_r^{(2)}s^{5-r}+z_3\sum_{r=0}^4n_r^{(3)}s^{4-r} \quad (\text{A10})$$

The coefficients of the various series are given in the following table:

r	q_r	$m_r^{(1)}$	$m_r^{(2)}$	$m_r^{(3)}$	$n_r^{(1)}$	$n_r^{(2)}$	$n_r^{(3)}$
0	α^2	α^2	α^2	α^2	$-\alpha\epsilon$	$-\alpha\epsilon$	$-\alpha\epsilon$
1	$i2\bar{\omega}\alpha^2$	$i2\bar{\omega}\alpha^2$	$i2\bar{\omega}\alpha^2$	$i2\bar{\omega}\alpha^2$	$-i2\bar{\omega}\alpha\epsilon\left(1+\frac{\beta^2}{M^2}\right)$	$-i2\bar{\omega}\alpha\epsilon\left(1+\frac{\beta^2}{M^2}\right)$	$-i2\bar{\omega}\alpha\epsilon\left(1+\frac{\beta^2}{M^2}\right)$
2	$-\left(2\alpha\delta+\alpha^2\frac{\beta^2\bar{\omega}^2}{M^2}\right)$	$-\left(2\alpha\delta+\alpha^2\frac{\beta^2\bar{\omega}^2}{M^2}\right)$	$-\left(\alpha\delta+\alpha^2\frac{\beta^2\bar{\omega}^2}{M^2}\right)$	$-\left(\alpha\delta+\alpha^2\frac{\beta^2\bar{\omega}^2}{M^2}\right)$	$\delta\epsilon+\alpha\epsilon\frac{\beta^2\bar{\omega}^2}{M^2}\left(5+\frac{\beta^2}{M^2}\right)$	$\alpha\epsilon\frac{\beta^2\bar{\omega}^2}{M^2}\left(5+\frac{\beta^2}{M^2}\right)$	$\alpha\epsilon\frac{\beta^2\bar{\omega}^2}{M^2}\left(5+\frac{\beta^2}{M^2}\right)$
3	$-i4\bar{\omega}\alpha\delta$	$-i4\bar{\omega}\alpha\delta$	$-i2\bar{\omega}\alpha\delta$	$-i2\bar{\omega}\alpha\delta$	$i2\epsilon\left[\bar{\omega}\delta\left(1+\frac{\beta^2}{M^2}\right)+2\alpha\frac{\beta^4\bar{\omega}^3}{M^4}\right]$	$i4\alpha\epsilon\frac{\beta^4\bar{\omega}^3}{M^4}$	$i4\alpha\epsilon\frac{\beta^4\bar{\omega}^3}{M^4}$
4	$\delta^2-2\alpha+\alpha\delta\frac{2\beta^2\bar{\omega}^2}{M^2}$	$\delta^2-\alpha+2\alpha\delta\frac{\beta^2\bar{\omega}^2}{M^2}$	$-\alpha+\alpha\delta\frac{\beta^2\bar{\omega}^2}{M^2}$	$-\alpha+\alpha\delta\frac{\beta^2\bar{\omega}^2}{M^2}$	$-\epsilon\frac{\beta^2\bar{\omega}^2}{M^2}\left[\alpha\frac{\beta^4\bar{\omega}^2}{M^4}+\delta\left(5+\frac{\beta^2}{M^2}\right)\right]$	$-\alpha\epsilon\frac{\beta^6\bar{\omega}^4}{M^6}$	$-\alpha\epsilon\frac{\beta^6\bar{\omega}^4}{M^6}$
5	$i2\bar{\omega}(\delta^2-2\alpha)$	$i2\bar{\omega}(\delta^2-\alpha)$	$-i2\bar{\omega}\alpha$	$-i2\bar{\omega}\alpha$	$-i4\delta\epsilon\frac{\beta^4\bar{\omega}^3}{M^4}$	0	
6	$2\delta-\epsilon^2-(\delta^2-2\alpha)\frac{\beta^2\bar{\omega}^2}{M^2}$	$\delta-(\delta^2-\alpha)\frac{\beta^2\bar{\omega}^2}{M^2}$	$\alpha\frac{\beta^2\bar{\omega}^2}{M^2}$	$\alpha\frac{\beta^2\bar{\omega}^2}{M^2}$	$\delta\epsilon\frac{\beta^6\bar{\omega}^4}{M^6}$		
7	$i(4\bar{\omega}\delta-8k^2\epsilon^2)$	$i2\bar{\omega}\delta$	0				
8	$1-2\delta\frac{\beta^2\bar{\omega}^2}{M^2}+24k^2\epsilon^2$	$-\delta\frac{\beta^2\bar{\omega}^2}{M^2}$					
9	$i(2\bar{\omega}+32k^3\epsilon^2)$						
10	$-\left(\frac{\beta^2\bar{\omega}^2}{M^2}+16k^4\epsilon^2\right)$						

The exact inverse transform of equation (A7) requires the determination of the roots of $Q(s)$ (eq. (A8)). Since $Q(s)$ is a tenth-order polynomial, its roots can be solved only approximately for specific values of the coefficients q_r . An alternative procedure is to expand the quantity $[Q(s)]^{-1}$ in a Maclaurin's series (a procedure used in ref. 18), with the result that it may be expressed in the form

$$\frac{1}{Q(s)} = \frac{1}{s^{10}} \sum_{n=0}^{\infty} \frac{T_n}{s^n} \quad (\text{A11})$$

where

$$q_0 T_0 = 1$$

$$q_0 T_n = - \sum_{r=1}^{10} q_r T_{n-r} \quad (n \geq 1)$$

and T with a negative subscript is to be interpreted as zero.

When the series expansion for $[Q(s)]^{-1}$ (eq. (A11)) is substituted into equation (A7), the transform $\bar{Z}(s)$ becomes the sum of infinite series with terms of the two distinct types

$$\frac{A}{s^m}$$

and

$$\frac{B}{s^m} \bar{I}_u(s)$$

where m is a positive integer. The inverse Laplace transform of the first type of term is (see pair 3, p. 295 of ref. 17)

$$L^{-1} \left\{ \frac{A}{s^m} \right\} = \frac{Ax^{m-1}}{(m-1)!} \quad (\text{A12})$$

and of the second is (see pair 7, p. 294 of ref. 17)

$$L^{-1} \left\{ \frac{B}{s^m} \bar{I}_u(s) \right\} = \frac{B}{(m-1)!} \int_0^x (x-\xi)^{m-1} I_u(\xi) d\xi \quad (\text{A13})$$

where $I_u(x)$ is defined following equation (A2).

Upon substituting equations (A9), (A10), and (A11) into equation (A7) and using equations (A12) and (A13) to obtain the inverse transform of the resultant expression, $Z(x)$ is given by

$$Z(x) = h_1(x)z_1 + h_2(x)z_2 + h_3(x)z_3 \quad (\text{A14})$$

where

$$\begin{aligned} h_1(x) &= \sum_{n=0}^{\infty} \sum_{r=0}^8 \frac{T_n m_r^{(1)} x^{n+r+1}}{(n+r+1)!} + \sum_{n=0}^{\infty} \sum_{r=0}^6 \frac{T_n n_r^{(1)}}{(n+r+3)!} \int_0^x (x-\xi)^{n+r+3} I_u(\xi) d\xi \\ h_2(x) &= \sum_{n=0}^{\infty} \sum_{r=0}^7 \frac{T_n m_r^{(2)} x^{n+r+2}}{(n+r+2)!} + \sum_{n=0}^{\infty} \sum_{r=0}^5 \frac{T_n n_r^{(2)}}{(n+r+4)!} \int_0^x (x-\xi)^{n+r+4} I_u(\xi) d\xi \\ h_3(x) &= \sum_{n=0}^{\infty} \sum_{r=0}^6 \frac{T_n m_r^{(3)} x^{n+r+3}}{(n+r+3)!} + \sum_{n=0}^{\infty} \sum_{r=0}^4 \frac{T_n n_r^{(3)}}{(n+r+5)!} \int_0^x (x-\xi)^{n+r+5} I_u(\xi) d\xi \end{aligned}$$

In deriving equation (A14) only one boundary condition—namely, $z_0 = Z(0) = 0$ —has been used thus far. In order to obtain the solution for a plate restrained in a particular manner, it is necessary to impose three additional boundary conditions. These additional conditions for the plate with pinned and clamped edges are given in equations (3) and (4), respectively. By their use, one of the terms of equation (A14) is eliminated and two homogeneous equations in the two remaining unknown z_i 's are obtained. The borderline condition of harmonic oscillation, or the point at which flutter occurs, is obtained by setting the determinant of the coefficients of these equations equal to zero. Thus, the flutter determinant for the pinned-edge plate is

$$\begin{vmatrix} h_1(1) & h_3(1) \\ h_1''(1) & h_3''(1) \end{vmatrix} = 0 \quad (\text{A15})$$

and for the clamped-edge plate is

$$\begin{vmatrix} h_2(1) & h_3(1) \\ h_2'(1) & h_3'(1) \end{vmatrix} = 0 \quad (\text{A16})$$

where the determinant elements are given by

$$\begin{aligned} h_1(1) &= \sum_{n=0}^{\infty} \sum_{r=0}^8 \frac{T_n m_r^{(1)}}{(n+r+1)!} + \sum_{n=0}^{\infty} \sum_{r=0}^6 \frac{T_n n_r^{(1)}}{(n+r+3)!} \int_0^1 (1-\xi)^{n+r+3} I_u(\xi) d\xi \\ h_1''(1) &= m_0^{(1)} \sum_{n=1}^{\infty} \frac{T_n}{(n-1)!} + \sum_{n=0}^{\infty} \sum_{r=1}^8 \frac{T_n m_r^{(1)}}{(n+r-1)!} + \sum_{n=0}^{\infty} \sum_{r=0}^6 \frac{T_n n_r^{(1)}}{(n+r+1)!} \int_0^1 (1-\xi)^{n+r+1} I_u(\xi) d\xi \\ h_2(1) &= \sum_{n=0}^{\infty} \sum_{r=0}^7 \frac{T_n m_r^{(2)}}{(n+r+2)!} + \sum_{n=0}^{\infty} \sum_{r=0}^5 \frac{T_n n_r^{(2)}}{(n+r+4)!} \int_0^1 (1-\xi)^{n+r+4} I_u(\xi) d\xi \\ h_2'(1) &= \sum_{n=0}^{\infty} \sum_{r=0}^7 \frac{T_n m_r^{(2)}}{(n+r+1)!} + \sum_{n=0}^{\infty} \sum_{r=0}^5 \frac{T_n n_r^{(2)}}{(n+r+3)!} \int_0^1 (1-\xi)^{n+r+3} I_u(\xi) d\xi \\ h_3(1) &= \sum_{n=0}^{\infty} \sum_{r=0}^6 \frac{T_n m_r^{(3)}}{(n+r+3)!} + \sum_{n=0}^{\infty} \sum_{r=0}^4 \frac{T_n n_r^{(3)}}{(n+r+5)!} \int_0^1 (1-\xi)^{n+r+5} I_u(\xi) d\xi \\ h_3'(1) &= \sum_{n=0}^{\infty} \sum_{r=0}^6 \frac{T_n m_r^{(3)}}{(n+r+2)!} + \sum_{n=0}^{\infty} \sum_{r=0}^4 \frac{T_n n_r^{(3)}}{(n+r+4)!} \int_0^1 (1-\xi)^{n+r+4} I_u(\xi) d\xi \\ h_3''(1) &= \sum_{n=0}^{\infty} \sum_{r=0}^6 \frac{T_n m_r^{(3)}}{(n+r+1)!} + \sum_{n=0}^{\infty} \sum_{r=0}^4 \frac{T_n n_r^{(3)}}{(n+r+3)!} \int_0^1 (1-\xi)^{n+r+3} I_u(\xi) d\xi \end{aligned}$$

Each of the preceding elements contains integrals of the form

$$I_m(M, \bar{\omega}) = \int_0^1 (1-\xi)^m I_u(\xi) d\xi \quad (\text{A17})$$

which can be written in terms of the Schwarz functions $f_\lambda(M, \bar{\omega})$ (see ref. 9 or eq. (24)) as

$$I_m(M, \bar{\omega}) = \sum_{\lambda=0}^m \frac{(-1)^\lambda m!}{(m-\lambda)! \lambda!} f_\lambda(M, \bar{\omega}) \quad (\text{A18})$$

where

$$f_\lambda = \int_0^1 \xi^\lambda I_u(\xi) d\xi$$

Examination of the series in the elements of equations (A15) and (A16) reveals that λ of equation (A18) ranges at least between 0 and $n+7$ and at most between 0 and $n+9$. In order to obtain accuracy to four significant figures, at least the first eight terms of each series and the consequent ranging of λ between 0 and 16 are probably required. Inasmuch as the Schwarz functions f_λ have been tabulated for only the first few values of λ , the use of equation (A18) would require the determination of a rather extensive series of f_λ 's. An alternative and perhaps more efficient procedure would be to evaluate directly the integrals I_m as given in equation (A17) rather than to resort to the expanded form in equation (A18).

Attention will now be given to the solution of the determinantal equations (A15) and (A16). A method of solution for parameters that were sought in the generalized-coordinate approach of the body of the report (that is, $1/\mu$ and $2k_1=2k (R.P.\Omega)^{1/2}$) will be outlined here.

The elements of equations (A15) and (A16) are complex functions of the five parameters M , k , Ω (with $g=0$), f , and $1/\mu$. The most difficult parts of these elements to evaluate are the integrals generically represented by I_m in equation (A17), which are functions of the parameters M and k . Therefore, a convenient method of solution would be to fix the parameters M and k and preferably f and vary the remaining parameters Ω and $1/\mu$ in the left-hand side (hereinafter referred to as Δ) of equation (A15) or of equation (A16). By varying Ω and $1/\mu$ over sufficiently broad ranges, an indefinitely large number of combinations of Ω and $1/\mu$ which cause Δ to vanish could be found. Each combination would define a point on separate stability boundaries, such as those shown in figure 3. Each boundary could then be determined as completely as desired by varying k over a sufficient range and repeating for each chosen value of k the process of finding combinations of Ω and $1/\mu$ which cause Δ to vanish.

As can be surmised, the numerical calculations would be extremely lengthy even apart from two other questions which arise; namely, which is the stable side of each boundary, and has the critical boundary been found which separates stable and unstable regions and thereby defines the thinnest panel that is stable? In the present report, therefore, the stability boundaries shown in figures 2 to 9 were calculated exclusively on the basis of the generalized-coordinate or modal approach.

APPENDIX B

VELOCITY POTENTIAL ϕ_i AND RELATED INTEGRAL \bar{P}_n VELOCITY POTENTIAL ϕ_i

The velocity potential ϕ_i given in equation (9), which applies to the lower surface of the two-dimensional panel shown in figure 1, will now be derived. The system consists of a panel of width c , which is part of an otherwise rigid surface of infinite extent, oscillating harmonically with stationary air extending to infinity below. Thus, over the panel the normal velocity on the lower surface is $w_i = i\omega Z(x)e^{i\omega t}$, while over the rest of the plane $w_i = 0$.

According to reference 10 the solution to this problem can be obtained from

$$\phi = -\frac{1}{2\pi} \iint w_i \frac{e^{-i\frac{\omega}{a}r}}{r} dS \quad (B1)$$

where w_i is the given normal velocity at the element of area dS of the plane and ϕ is the velocity potential at a point P which is at a distance r from dS . From equation (B1) the velocity potential at the surface of the panel may be obtained, in terms of the coordinates of figure 1, as

$$\phi_i = -\frac{i\omega e^{i\omega t}}{2\pi} \int_0^c Z(\xi) d\xi \int_{-\infty}^{\infty} \frac{e^{-i\frac{\omega}{a}\sqrt{(x-\xi)^2+y^2}}}{\sqrt{(x-\xi)^2+y^2}} dy \quad (B2)$$

Upon making the substitution $y = |x - \xi| \cosh \theta$, the integral with respect to y in equation (B2) may be written in the form

$$I(x - \xi) = \int_{-\infty}^{\infty} \frac{e^{-i\frac{\omega}{a}\sqrt{(x-\xi)^2+y^2}}}{\sqrt{(x-\xi)^2+y^2}} dy = \int_{-\infty}^{\infty} e^{-i\frac{\omega}{a}|x-\xi| \cosh \theta} d\theta \quad (B3)$$

By means of equation (11) on page 180 of reference 19, equation (B3) becomes

$$I(x - \xi) = -i\pi H_0^{(2)}\left(\frac{\omega}{a}|x - \xi|\right) \quad (B4)$$

Substitution of equation (B4) into equation (B2) yields

$$\phi_i = -\frac{\omega e^{i\omega t}}{2} \int_0^c Z(\xi) H_0^{(2)}\left(\frac{\omega}{a}|x - \xi|\right) d\xi \quad (B5)$$

If the coordinates x and ξ are nondimensionalized by dividing by the panel chord c , the form for ϕ_i given in equation (9) is obtained.

INTEGRAL \bar{P}_n

The third term on the right-hand side of equation (22), namely,

$$\bar{P}_n(x) = \frac{\rho_0}{\rho} \frac{1}{\pi} \int_0^1 Z_n(\xi) \log_e (kM|x - \xi|) d\xi \quad (B6)$$

contains the singularity of the Hankel function in equation (20).

As a first step in the evaluation of the improper integral in equation (B6), let

$$\left. \begin{aligned} \xi &= \frac{1}{2}(1 - \cos \zeta) \\ x &= \frac{1}{2}(1 - \cos \psi) \end{aligned} \right\} \quad (B7)$$

and

$$Z_n(\xi) = \sum_{m=1}^{\infty} S_m \sin m\zeta \quad (B8)$$

where

$$S_m = \frac{2}{\pi} \int_0^{\pi} Z_n(\zeta) \sin m\zeta d\zeta$$

In terms of equations (B7) and (B8), equation (B6) becomes

$$\bar{P}_n(x) = \frac{\rho_0}{\rho} \frac{1}{2\pi} I(\psi) \quad (B9)$$

where

$$I(\psi) = \sum_{m=1}^{\infty} S_m \int_0^{\pi} \sin \zeta \sin m\zeta \log_e \left(\frac{kM}{2} |\cos \zeta - \cos \psi| \right) d\zeta \quad (B10)$$

Taking the derivative of equation (B10) with respect to ψ and making use of reference 20 to evaluate the resulting improper integrals yields

$$\begin{aligned} \frac{dI}{d\psi} &= \frac{1}{2} \sum_{m=1}^{\infty} S_m \int_0^{\pi} \frac{\cos(m-1)\zeta - \cos(m+1)\zeta}{\cos \zeta - \cos \psi} \sin \psi d\zeta \\ &= \frac{\pi}{2} \sum_{m=1}^{\infty} S_m [\sin(m-1)\psi - \sin(m+1)\psi] \end{aligned} \quad (B11)$$

Integration of equation (B11) gives

$$I(\psi) = \frac{\pi}{2} \left\{ \frac{1}{2} S_1 \cos 2\psi + \sum_{m=2}^{\infty} S_m \left[\frac{\cos(m+1)\psi}{m+1} - \frac{\cos(m-1)\psi}{m-1} \right] \right\} + K \quad (B12)$$

The integration constant K in equation (B12) is determined by setting ψ equal to $\pi/2$ in equations (B10) and (B12) and equating the two resultant expressions. By so doing, it is found that

$$K = \frac{\pi}{2} S_1 \log_e \frac{kM}{4} \quad (B13)$$

By means of equations (B12) and (B13), equation (B9) becomes

$$\begin{aligned} \bar{P}_n(x) &= \frac{\rho_0}{\rho} \frac{1}{4} \left\{ \left(\log_e \frac{kM}{4} + \frac{1}{2} \cos 2\psi \right) S_1 + \right. \\ &\quad \left. \sum_{m=2}^{\infty} S_m \left[\frac{\cos(m+1)\psi}{m+1} - \frac{\cos(m-1)\psi}{m-1} \right] \right\} \end{aligned} \quad (B14)$$

The mode shapes Z_n in equation (B6) are now approximated by the finite sine series

$$Z_n(\xi) \approx \sum_{r=1}^{10} s_r \sin rx \quad (\text{B15})$$

The constants S_m in equation (B14) are obtained from the expression following equation (B8), with the result that equation (B14) can be written as

$$\bar{P}_n(x) = \frac{\rho_0}{\rho} \frac{1}{4} \sum_{r=1}^{10} \bar{L}_r(x) s_r \quad (\text{B16})$$

where

$$\bar{L}_1(x) = \log_e \frac{kM}{4} + \frac{1}{2} \cos 2\psi$$

$$\bar{L}_r(x) = \frac{1}{r+1} \cos(r+1)\psi - \frac{1}{r-1} \cos(r-1)\psi \quad (r \geq 2)$$

and, as in equation (B7),

$$x = \frac{1}{2} (1 - \cos \psi)$$

The form given in equation (B16) was used to obtain equation (28). Of interest is the fact that only \bar{L}_1 depends on k and M . The term \bar{P}_n is therefore comparatively simple to include in equation (22).

The coefficients s_r in equations (B15) and (B16) for the first four modes of the plate with clamped edges are given in the following table:

	Mode 1	Mode 2	Mode 3	Mode 4
s_1	0.66613	0	-0.32917	0
s_2	0	0.64119	0	0.40890
s_3	-0.29503	0	-0.50867	0
s_4	0	-0.46861	0	0.27852
s_5	0.039764	0	0.61134	0
s_6	0	0.098515	0	-0.61524
s_7	0.001315	0	-0.18746	0
s_8	0	-0.003411	0	0.25500
s_9	0.000396	0	0.021697	0
s_{10}	0	0.002858	0	-0.028044

The coefficients s_{10} for the second and fourth modes were obtained by forcing the slope of Z_n , as given by equation (B15), to be zero at $\psi=0$ (that is, at $x=0$). A similar table can be easily calculated for the pinned-edge plate.

REFERENCES

- Hayes, W.: A Buckled Plate in a Supersonic Stream. Rep. No. AL-1029, North American Aviation, Inc., May 10, 1950.
- Miles, John W.: Dynamic Chordwise Stability at Supersonic Speeds. Rep. No. AL-1140, North American Aviation, Inc., Oct. 18, 1950.
- Isaacs, R. P.: Transtability Flutter of Supersonic Aircraft Panels. U. S. Air Force Project RAND P-101, The Rand Corp., July 1, 1949.
- Fung, Y. C.: The Static Stability of a Two-Dimensional Curved Panel in a Supersonic Flow, With an Application to Panel Flutter. Jour. Aero. Sci., vol. 21, no. 8, Aug. 1954, pp. 556-565.
- Shen, S. F.: Flutter of a Two-Dimensional Simply-Supported Uniform Panel in a Supersonic Stream. Contract No. N5ori-07833, Office of Naval Res., Dept. Aero. Eng., M.I.T., Aug. 6, 1952.
- Goland, Martin, and Luke, Yudell L.: An Exact Solution for Two-Dimensional Linear Panel Flutter at Supersonic Speeds. Jour. Aero. Sci. (Readers' Forum), vol. 21, no. 4, Apr. 1954, pp. 275-276.
- Hedgepeth, John M., Budiansky, Bernard, and Leonard, Robert W.: Analysis of Flutter in Compressible Flow of a Panel on Many Supports. Jour. Aero. Sci., vol. 21, no. 7, July 1954, pp. 475-486.
- Reissner, Eric, and Stein, Manuel: Torsion and Transverse Bending of Cantilever Plates. NACA TN 2369, 1951.
- Garrick, I. E., and Rubinow, S. I.: Flutter and Oscillating Air-Force Calculations for an Airfoil in a Two-Dimensional Supersonic Flow. NACA Rep. 846, 1946. (Supersedes NACA TN 1158.)
- Rayleigh, (Lord): The Theory of Sound. First American ed., vol. II, sec. 302, Dover Publications, 1945, p. 162.
- Duncan, W. J.: Galerkin's Method in Mechanics and Differential Equations. R. & M. No. 1798, British A.R.C., 1937.
- Theodorsen, Theodore, and Garrick, I. E.: Mechanism of Flutter—A Theoretical and Experimental Investigation of the Flutter Problem. NACA Rep. 685, 1940.
- Scanlan, Robert H., and Rosenbaum, Robert: Introduction to the Study of Aircraft Vibration and Flutter. The Macmillan Co., 1951.
- Dugundji, John: A Nyquist Approach to Flutter. Jour. Aero. Sci. (Readers' Forum), vol. 19, no. 6, June 1952, pp. 422-423.
- Morse, Philip M.: Vibration and Sound. Second ed., McGraw-Hill Book Co., Inc., 1948.
- Sylvester, Maurice A., and Baker, John E.: Some Experimental Studies of Panel Flutter at Mach Number 1.3. NACA RM L52I16, 1952.
- Churchill, Ruel V.: Modern Operational Mathematics in Engineering. McGraw-Hill Book Co., Inc., 1944.
- Runyan, Harry L., and Watkins, Charles E.: Flutter of a Uniform Wing With an Arbitrarily Placed Mass According to a Differential-Equation Analysis and a Comparison With Experiment. NACA Rep. 966, 1950. (Supersedes NACA TN 1848.)
- Watson, G. N.: A Treatise on the Theory of Bessel Functions. Second ed., The Macmillan Co., 1944.
- Glauert, H.: The Elements of Aerofoil and Airscrew Theory. Second ed., Cambridge Univ. Press, 1947 (Reprinted 1948), pp. 92-93.

REPORT 1281

FLIGHT DETERMINATION OF DRAG OF NORMAL-SHOCK NOSE INLETS WITH VARIOUS COWLING PROFILES AT MACH NUMBERS FROM 0.9 TO 1.5¹

By R. I. SEARS, C. F. MERLET, and L. W. PUTLAND

SUMMARY

Free-flight tests were made with normal-shock nose-inlet models with NACA 1-series, parabolic, and conic cowlings profiles to investigate the external drag characteristics at an angle of attack of 0°. The Mach number range of the tests was from 0.9 to 1.5, the mass-flow ratio was from 0.7 to 1.0, and the Reynolds number based on body maximum diameter varied from 2.5×10^6 to 5.5×10^6 . Two related nonducted bodies were also tested for comparison purposes.

At the maximum flow rate the inlet models had about the same external drag at a Mach number of approximately 1.1 but at higher Mach numbers the conic cowling had the least drag. Blunting or beveling the lip of the conic cowling while keeping the fineness ratio constant resulted in a slightly higher drag than for the sharp-lip conic cowling at maximum flow rate, but at a mass-flow rate of 0.8 the blunt-, beveled-, and sharp-lip conic cowlings and the parabolic cowling all had about the same drag. The higher drag of the NACA 1-49-300 cowling compared with the blunt-lip conic cowling is associated with the greater fullness back of the inlet.

INTRODUCTION

Because the total-pressure recoveries attainable with normal-shock nose inlets at Mach numbers up to about 1.4 are as good as, or better than, those for other types of inlets, normal-shock inlets are of real interest for aircraft at low supersonic speeds. The Pilotless Aircraft Research Division of the Langley Laboratory has therefore undertaken a program to investigate the drag characteristics of normal-shock nose inlets of various nose geometry. The first phase of this program is concerned with the effects of nose profile and the results are reported herein. A flight technique, differing from that previously used for ducted models, was developed in order to obtain a little information from each of many models rather than more extensive information about only a few models.

Two related nonducted bodies were tested for purposes of comparison with the normal-shock nose-inlet data. Although the models of the present investigation are all nose-inlet models, it is expected that many of the results might also be applicable in the design of scoop inlets.

SYMBOLS

A	area, sq ft
A_{cr}	critical area (area at which sonic velocity will be obtained, assuming one-dimensional isentropic process), sq ft
C_D	drag coefficient, $\frac{D}{\frac{1}{2} \rho_{\infty} V_{\infty}^2 A_F}$
C_p	pressure coefficient, $\frac{p - p_{\infty}}{\frac{1}{2} \rho_{\infty} V_{\infty}^2}$
D	drag, lb
g	acceleration of gravity, 32.2 ft/sec ²
M	Mach number
m/m_{∞}	ratio of mass flow of air through the duct to mass flow of air through a free-stream tube of area equal to inlet area
p	static pressure, lb/sq ft
p_t	total pressure, lb/sq ft
p_t'	pitot stagnation pressure, lb/sq ft
R	Reynolds number, based on 7.00-inch body diameter
r	radius, in.
t	time, sec
V	velocity, fps
W	weight of the model, lb
x	longitudinal distance, measured from the maximum-diameter station, positive downstream, in.
γ	ratio of specific heats, 1.40 for air
ρ	air density, slugs/cu ft
θ	flight-path angle, deg

Subscripts:

∞	free stream
1	first minimum-area station
e	exit
ext	external
F	frontal
i	inlet, at lip leading edge
int	internal
t	total

¹ Supersedes recently declassified NACA Research Memorandum L53125a by R. I. Sears, C. F. Merlet, and L. W. Putland, 1953.

MODELS

Ducted-nose-inlet models having six different cowlings shapes were tested as part of the investigation reported herein. Three models of each cowling shape were tested; each model had a different flow rate. The only difference in the external geometry of the three models for each cowling shape was a slight difference in length, the afterbody being cut off at the station required to give the desired exit area.

Five of the cowlings were of fineness ratio 3 and had an inlet area 24 percent of the body frontal area. The sixth cowling was of fineness ratio 2.5 and had an inlet area 16 percent of the body frontal area. Two related nonducted bodies of revolution were tested—one for each cowling fineness ratio investigated.

The general arrangement of the three model configurations tested for a typical cowling of fineness ratio 3.0 and the related nonducted body is shown in figure 1. Similar information is presented in figure 2 for the cowling models of fineness ratio 2.5. All models had identical fins and afterbody lines.

The afterbody, defined by a parabolic arc with its vertex at the maximum-diameter station, is similar to that used in the inlet investigation reported in reference 1. The coordinates are listed in table I. All afterbodies were spun on the same die from 0.09-inch magnesium and finished to a smooth fair contour and formed the afterportion of the duct. The length at which the afterbody was cut off for each flow rate is shown in figures 1 and 2.

Each model was stabilized by four 60° delta fins having a total exposed area 3.2 times the body frontal area. The airfoil section was hexagonal and was fabricated from 1/8-inch magnesium sheet by beveling the leading and trailing edges.

The nonducted models shown in figures 1 and 2 were related to the ducted models in that coordinates of the duct lips were also coordinates of the nonducted bodies. Thus, the nonducted forebody was defined by a parabolic arc with its vertex at the maximum diameter and passing through the inlet lip. Coordinates are listed in table I.

Details of the various cowling shapes tested are shown in figure 3, and coordinates are given in table I. The external profiles shall be designated by Roman numerals, whereas the internal configurations shall be referred to by Arabic numbers. Cowling I had the NACA 1-49-300 profile (ref. 2). Cowling II had a parabolic profile which was obtained by cutting off at the inlet station the nose of the nonducted body A shown at the top of figure 1. The external lip angle was 9.8°. Cowlings III, IV, and V are called conic because all of cowling III and the major part of the contour of cowlings IV and V were defined by a truncated cone. The cone half-angle was 4.9° for cowling III and 4.4° for cowlings IV and V. Cowling III had sharp lips with an external lip angle of 4.9°. Cowling IV had a beveled lip of external angle 9.8°; the contour in the region of the lips was identical with that of the parabolic cowling II. Cowling V had blunt lips with an external lip angle of 90°. The contour in the region of the lips was identical with that of cowling I of the NACA 1-series. Cowling VI had the NACA 1-40-250 profile.

The external profiles in the region of the lips of the five cowlings of fineness ratio 3.0 are better compared in figure 4.

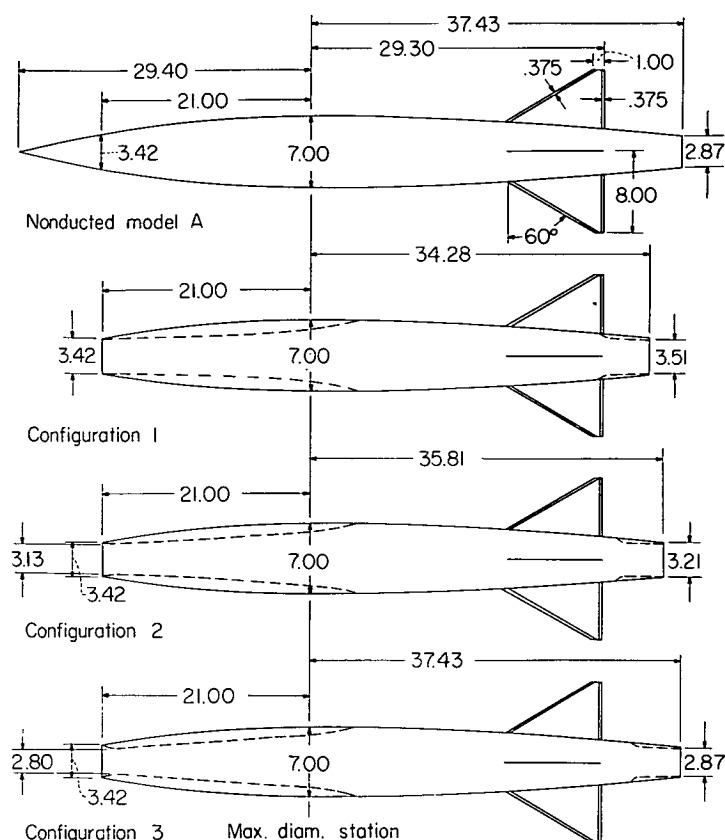


FIGURE 1.—General arrangement of ducted models with cowlings of fineness ratio 3.0 and related nonducted model. All dimensions are in inches.

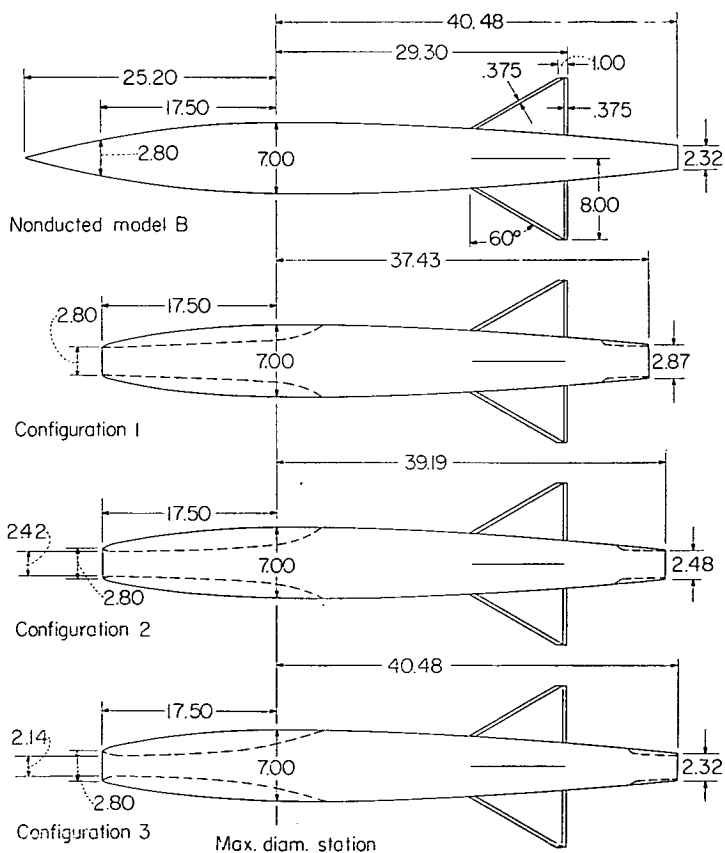


FIGURE 2.—General arrangement of ducted models with cowlings of fineness ratio 2.5 and related nonducted model. All dimensions are in inches.

TABLE I.—EXTERNAL COORDINATES

Nonducted model (from maximum diameter)

Model A forebody		Model B forebody		Afterbody	
x , in.	r , in.	x , in.	r , in.	x , in.	r , in.
-29.40	0	-25.20	0	0	3.50
-28.90	.12	-24.20	.27	5.60	3.45
-28.40	.23	-23.20	.53	10.27	3.34
-28.00	.33	-22.20	.78	15.87	3.14
-27.00	.55	-21.20	1.02	21.47	2.84
-25.00	.97	-20.20	1.25	24.27	2.65
-20.00	1.88	-18.20	1.67	30.80	2.15
-15.00	2.59	-15.20	2.23	35.70	1.68
-10.00	3.10	-10.20	2.93	42.70	.90
-5.00	3.40	-5.20	3.35		
0	3.50	0	3.50		

Normal-shock nose-inlet models—forebody (from maximum diameter)

Cowling I		Cowling II		Cowling III	
x , in.	r , in.	x , in.	r , in.	x , in.	r , in.
-21.00	1.71	-21.00	1.71	-21.00	1.71
-20.79	1.90	-20.00	1.88	-10.00	2.65
-20.37	2.04	-19.00	2.04	0	3.50
-19.95	2.15	-18.00	2.19		
-17.85	2.52	-17.00	2.33		
-14.70	2.87	-15.00	2.59		
-10.50	3.19	-10.00	3.10		
-6.30	3.39	-5.00	3.40		
0	3.50	0	3.50		

Cowling IV		Cowling V		Cowling VI	
x , in.	r , in.	x , in.	r , in.	x , in.	r , in.
-21.00	1.71	-21.00	1.71	-17.50	1.40
-20.00	1.88	-20.92	1.83	-17.40	1.57
-19.00	2.04	-20.79	1.90	-17.24	1.67
0	3.50	0	3.50	-17.06	1.75
				-16.63	1.91
				-14.88	2.35
				-10.50	2.97
				-5.25	3.37
				0	3.50

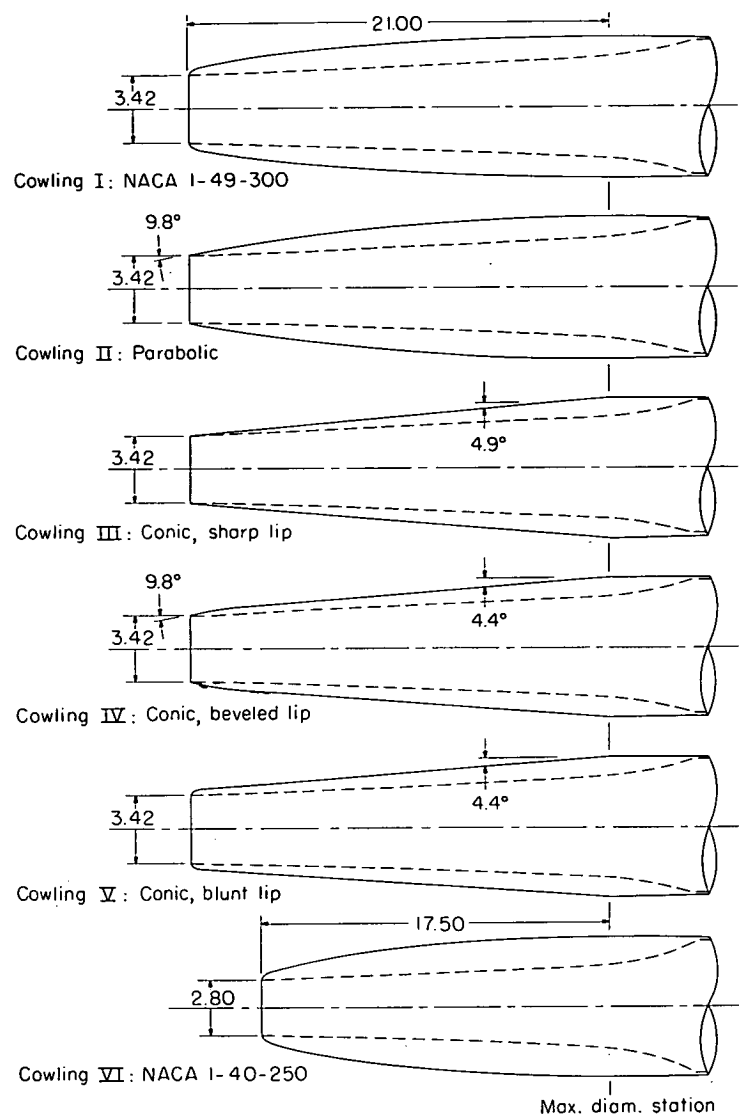


FIGURE 3.—Details of cowling shapes. All dimensions are in inches

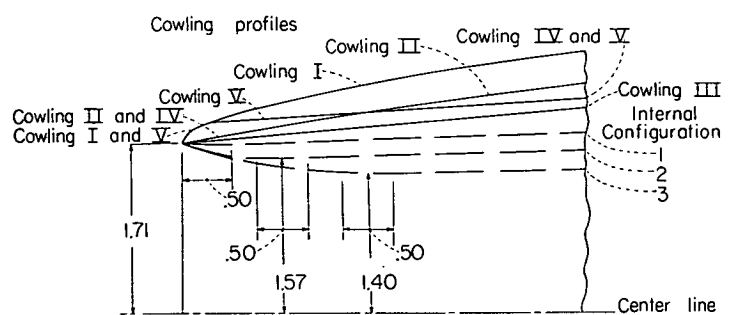


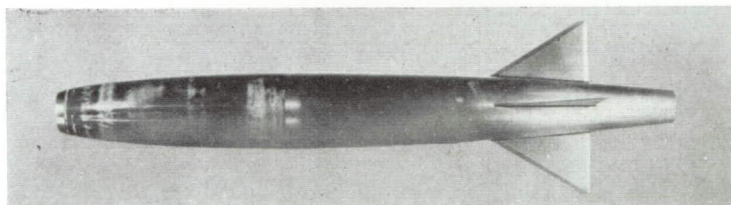
FIGURE 4.—Details of lip shapes of cowlings of fineness ratio 3. All dimensions are in inches.

The three arrangements of internal lines in the region of the inlet designated by the configuration numbers 1, 2, and 3 and used with each cowling shape to regulate the internal air flow are also shown in figure 4. For each cowling shape the internal contraction ratios used were 1.00, 0.83, and 0.67 for configurations 1, 2, and 3, respectively. A similar arrangement, using contraction ratios of 1.00, 0.75, and 0.56, was used for cowling VI which had a smaller inlet area. The minimum section of all models was a cylindrical section $\frac{1}{2}$ -inch long, and the internal lips of the models with a contraction ratio less than 1.00 were parabolic from the lip to the minimum section. No attempt was made to measure total-pressure recovery. Details of the diffuser shape are not considered pertinent to this drag investigation and are not presented.

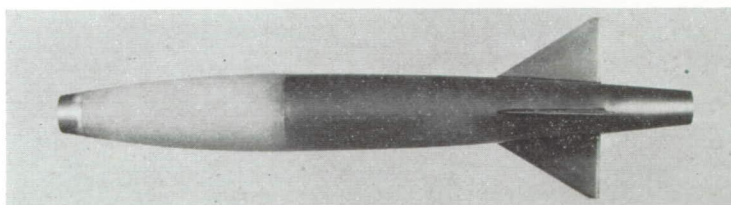
Photographs of the models showing each cowling shape and nonducted body tested are given in figure 5, and the major physical characteristics of the models are presented in table II.

TESTS AND TECHNIQUES

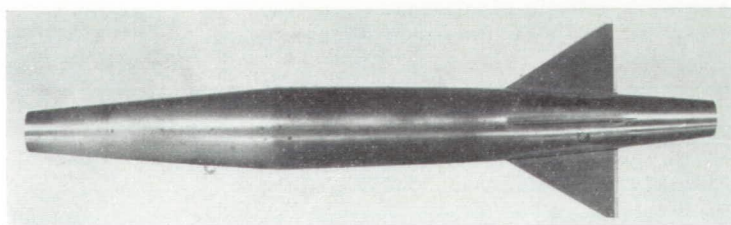
Three models were flown for each normal-shock inlet-cowling shape in order to obtain the variation of C_D with m/m_∞ . Different rocket motors were used during the course of the investigation; this fact largely accounts for the different maximum Mach numbers to which data were obtained for the various models. The range of variation of Reynolds number with Mach number is shown in figure 6 for the models tested. All models were flown on a zero-lift trajectory and the data presented are for an angle of attack of 0° .



Cowling I: NACA 1-49-300 L-72410.1



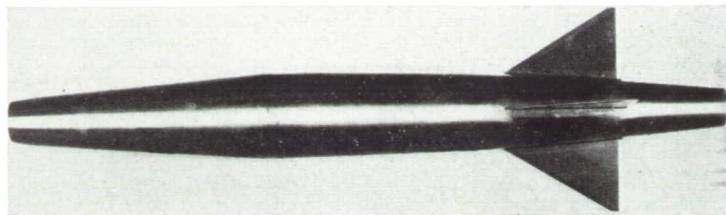
Cowling II: Parabolic L-71587.1



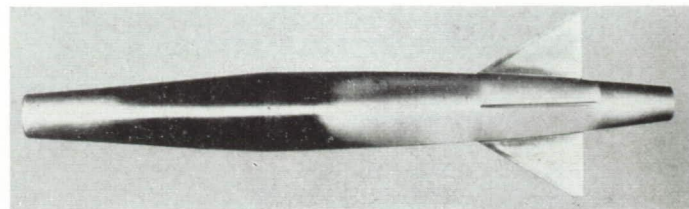
Cowling III: Conic, sharp lip L-73586.1

(a) General views of ducted models.

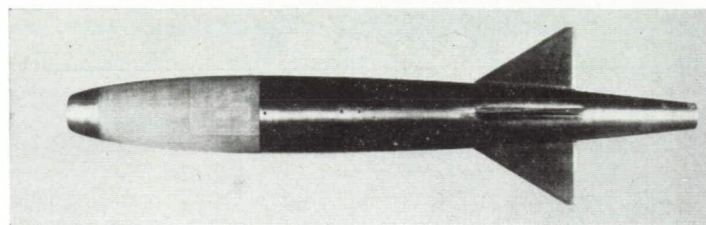
FIGURE 5.—Photographs of models.



Cowling IV: Conic, beveled lip L-73636.1



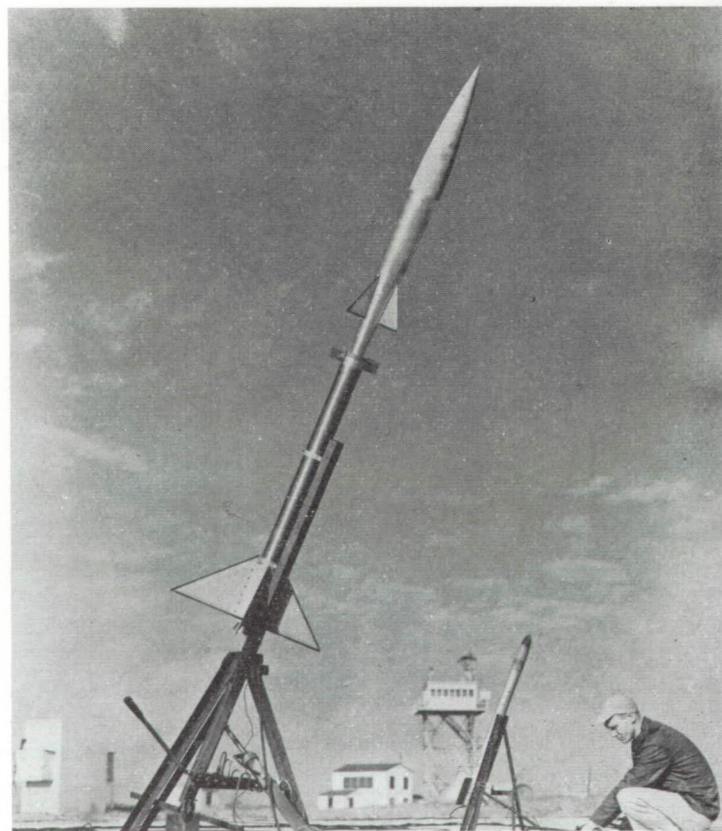
Cowling V: Conic, blunt lip L-75157.1



Cowling VI: NACA 1-40-250 L-75361.1

(a) Concluded.

FIGURE 5.—Continued.



(b) Nonducted model A on the launcher. L-73803.1

FIGURE 5.—Concluded.

TABLE II.—PHYSICAL CHARACTERISTICS OF THE MODELS

Designation	Forebody profile	Forebody fineness ratio	External lip angle, deg	Inlet contraction ratios tested for configurations—		
				1	2	3
Cowling I.....	NACA 1-49-300.....	3.0	90	1.0	0.83	0.67
Cowling II.....	Parabolic.....	3.0	9.8	1.0	.83	.67
Cowling III.....	Sharp lip conic, 4.9° half-angle.....	3.0	4.9	1.0	.83	.67
Cowling IV.....	Beveled lip conic, 4.4° half-angle.....	3.0	9.8	1.0	.83	.67
Cowling V.....	Blunt lip conic, 4.4° half-angle.....	3.0	90	1.0	.83	.67
Cowling VI.....	NACA 1-40-250.....	2.5	90	1.0	.75	.56
Nonducted model A.....	Parabolic.....	4.2	-----	---	---	---
Nonducted model B.....	Parabolic.....	3.6	-----	---	---	---

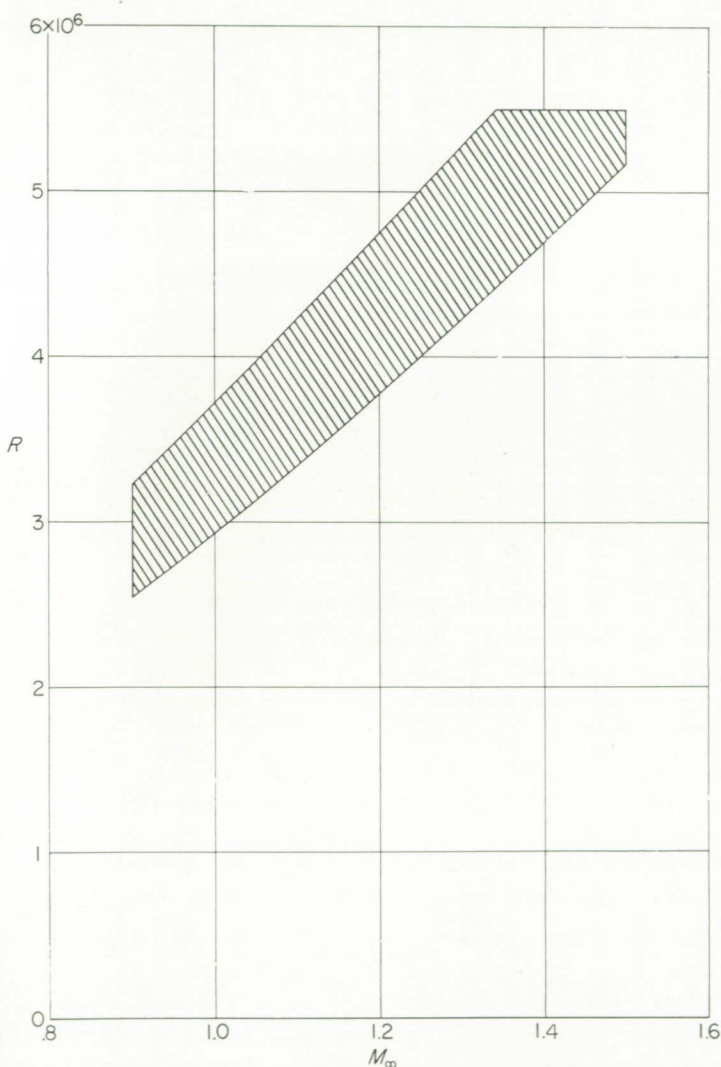


FIGURE 6.—Range of variation of Reynolds number, based on body maximum diameter, with Mach number for models tested.

In order to facilitate the building and flight testing of models of many different inlet contours, all but three of the models were built without telemeters. Total drag coefficients were obtained over the flight Mach number range from computations based on the CW Doppler radar velocity measurements, the flight path indicated by the NACA modified SCR 584 tracking radar, and radiosonde observations. Corrections were made for the horizontal component of the wind

velocity and for flight-path curvature. A telemeter was used with a model (cowling II, configuration 3) to measure the static pressures at the inlet minimum-area station, the exit, and at two stations on the afterbody. Telemeter measurements were also made of three afterbody static pressures on a second model (cowling VI, configuration 3) and of the base pressure on nonducted model B.

The internal contour of the model was made so that at supersonic speeds the inlet was started or choking occurred at the minimum area just back of the inlet, while the exit was choked for all cases. The exit area of each ducted model was made equal to 1.05 times the inlet minimum area in order that the exit would stay choked to as low a free-stream Mach number as possible to permit evaluation of the internal drag. The duct was made cylindrical for at least 1.2 exit diameters ahead of the exit to aid in providing uniform static pressure at the exit. The fairly large contraction of at least 4 to 1 from near the maximum-diameter station to the exit assured sonic rather than supersonic exit velocities and also helped in providing uniform total pressure at the exit. The entering mass flow and the internal drag can, therefore, be calculated for the Mach number range over which these choking conditions existed. The method used for making these calculations is presented in the appendix.

Figure 7 compares the values of $C_{D, int}$ and m/m_∞ calculated as indicated in the appendix with the values computed from measurements made with a telemetered model (cowling II, configuration 3). The good agreement shown is believed to justify use of the calculated results at $M_\infty \geq 0.9$, although at subsonic speeds some of the assumptions involved are not quite fulfilled.

ACCURACY OF DATA

The accuracy of the data is estimated to be within the following limits:

m/m_∞ , for $M_\infty \geq 1.0$	± 0.01
$C_{D, exit}$	± 0.01
C_p	± 0.015
M_∞	± 0.01

RESULTS AND DISCUSSION

EFFECT OF AFTERBODY LENGTH

Because the afterbody length was slightly greater for the models admitting lesser mass flow, it is necessary to examine the differences in $C_{D, exit}$ associated with differences in model length. Figure 8 presents measured afterbody pressure

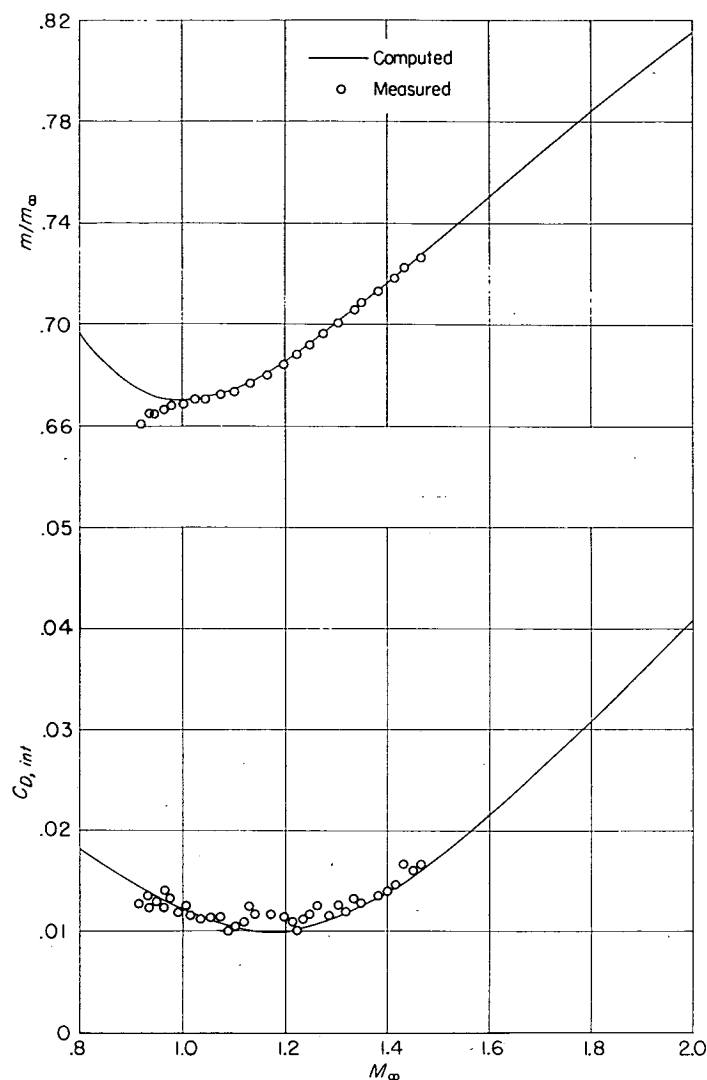
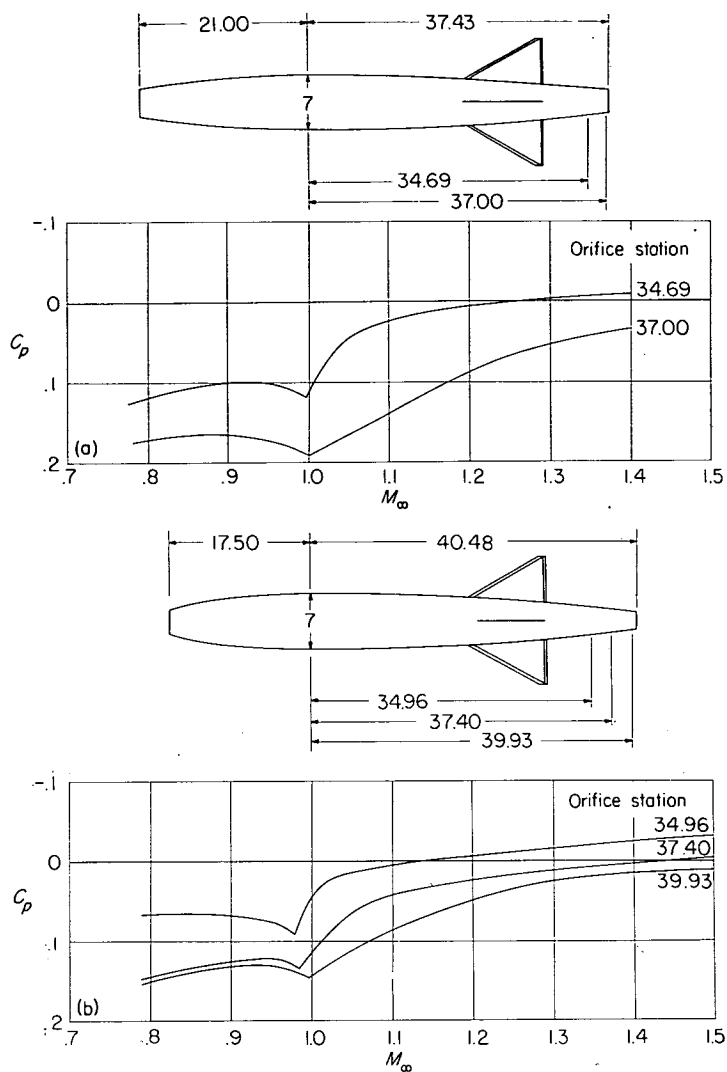


FIGURE 7.—Variation of internal drag coefficient and mass-flow ratio with Mach number for models with telemeter.

coefficients for two ducted models as a function of Mach number. The static-pressure orifices were located at the body stations on a longitudinal line that passed midway between two fins (see fig. 8).

The data of reference 3 indicate that large changes in nose shape have negligible effect on the pressures over the rearward portion of the body length. It is, therefore, assumed that the differences in C_p shown in figure 8 are caused primarily by the differences in afterbody length and by the effects of the exit and of the jet propagating upstream through the boundary layer at supersonic Mach numbers or through the subsonic flow field at the exit in the lower range of test Mach numbers.

Integration of the measured pressures to obtain a pressure drag coefficient for the portion of each model rearward of station 34 (where both models had nearly the same pressure coefficient) gave the same value for each model, within $\Delta C_D = 0.001$. The coefficient of skin-friction drag acting on



(a) Cowling II: parabolic; configuration 3.

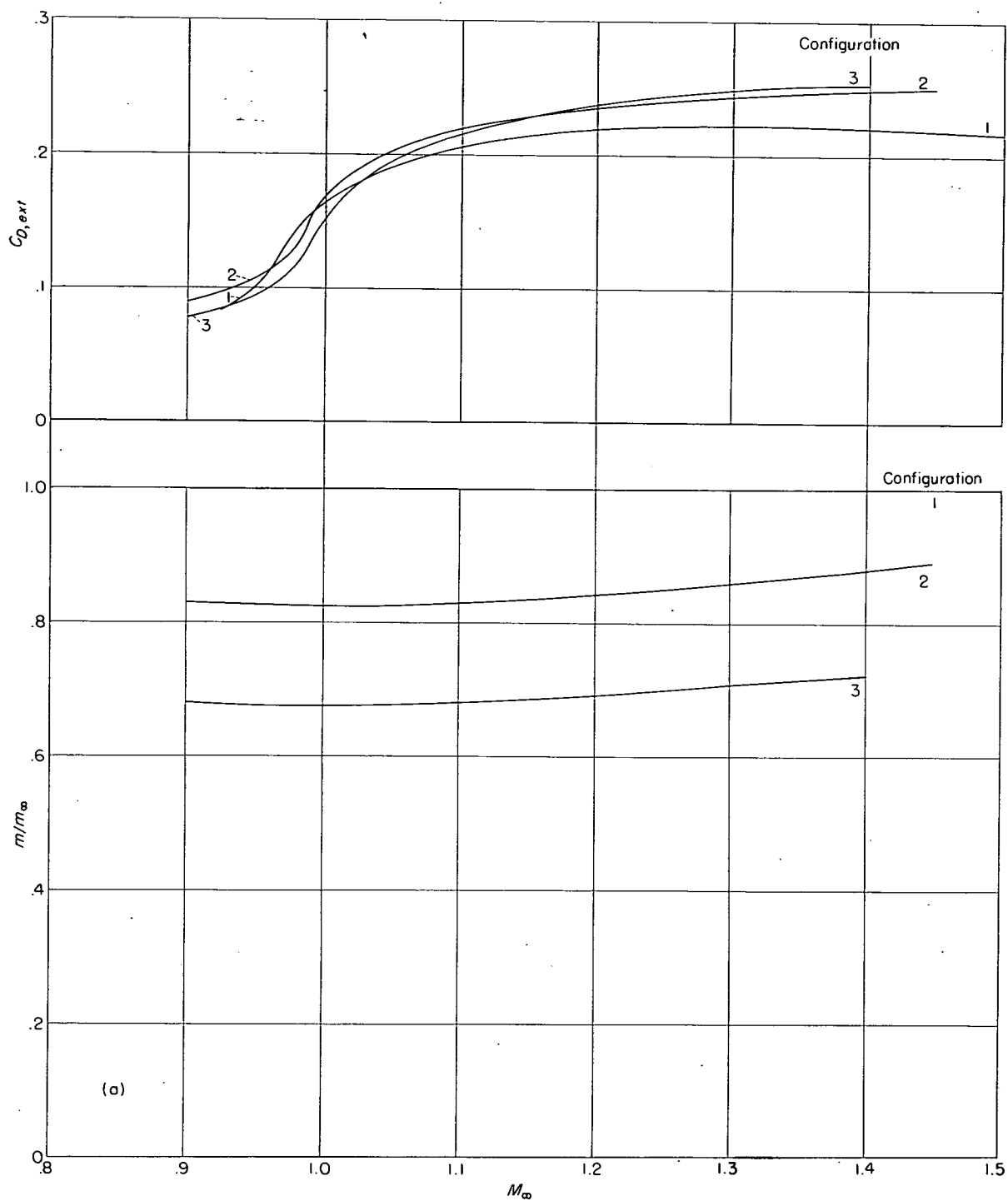
(b) Cowling VI: NACA 1-40-250; configuration 3.

FIGURE 8.—Variation of pressure coefficient with Mach number at several afterbody stations for two ducted models. All dimensions are in inches.

the incremental surface area of the longer afterbody is estimated to be 0.002. Any differences in $C_{D,ext}$ caused by varying the length of the afterbody, therefore, are believed to be small and well within the accuracy of $C_{D,ext}$.

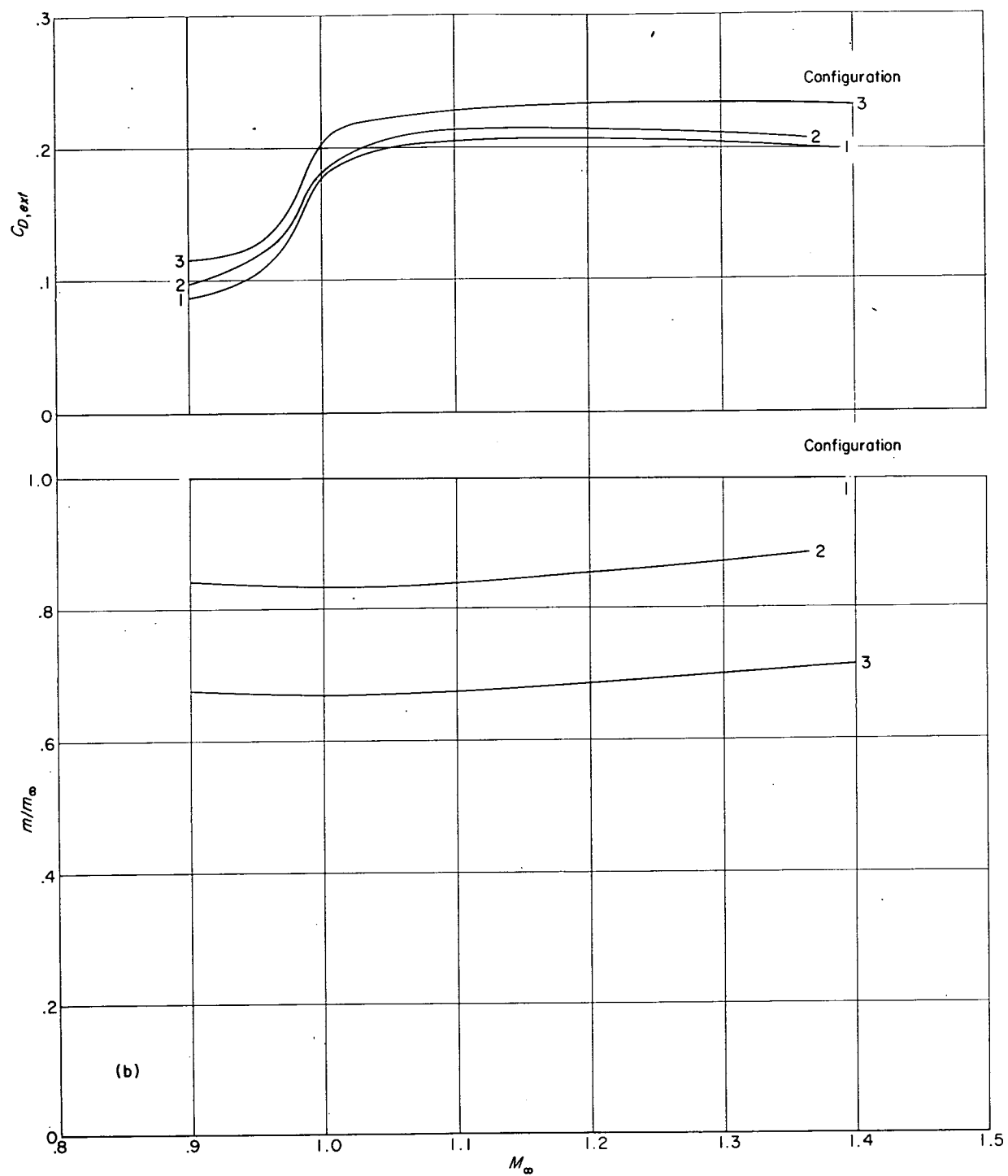
BASIC DATA

The curves of external drag for each ducted model are presented in figure 9. The mass-flow ratio associated with each drag curve is also given. For configuration 1 with each cowling the mass-flow ratio was unity at all Mach numbers; that is, no air was spilled. An increasing amount of air was spilled with configurations 2 and 3. The inlet-contraction ratios of configurations 2 and 3 were too great to permit the inlets to start in the test Mach number range.



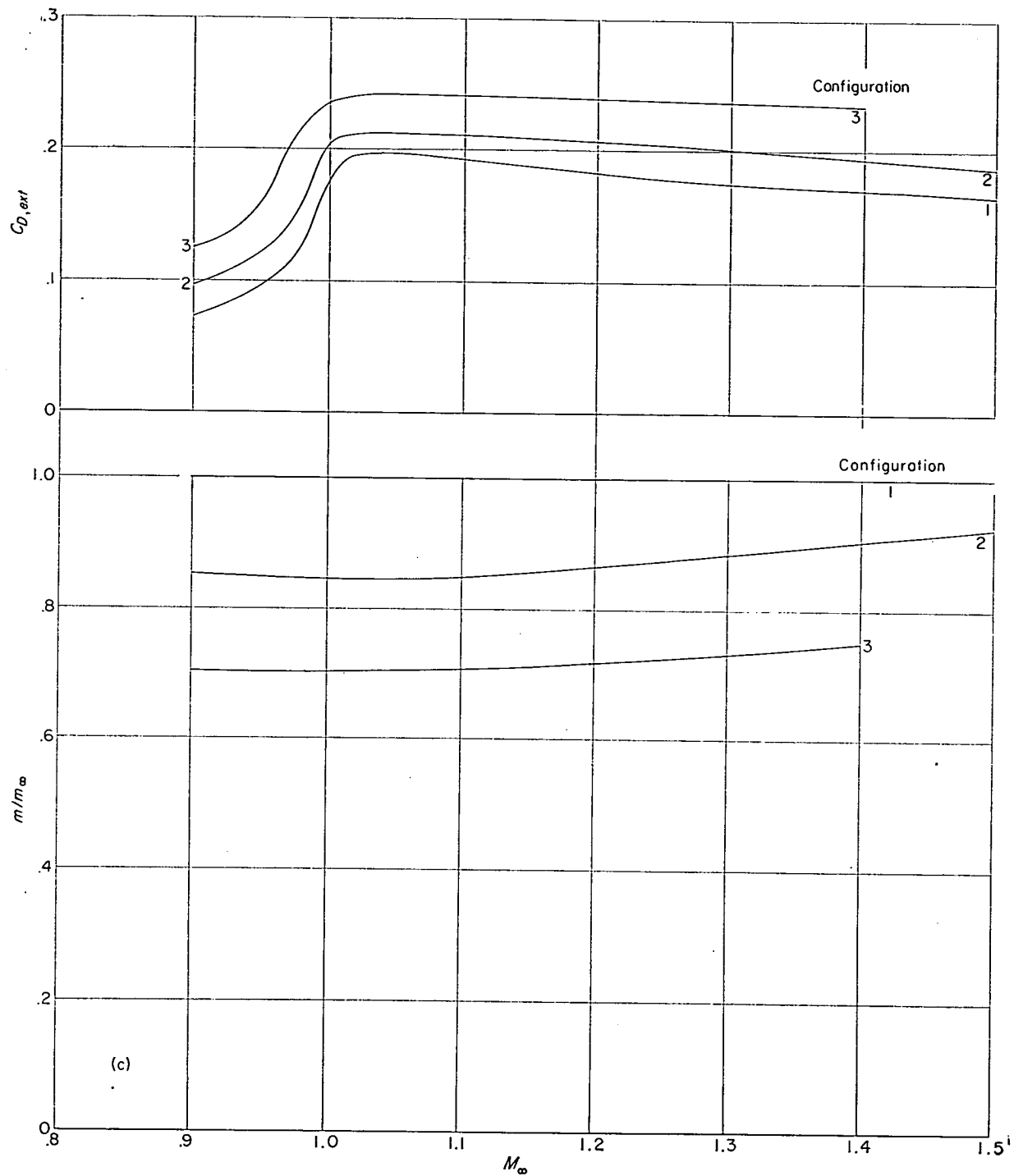
(a) Cowling I: NACA 1-49-300.

FIGURE 9.—Variation of external drag coefficient and mass-flow ratio with Mach number for the models with various cowling shapes.



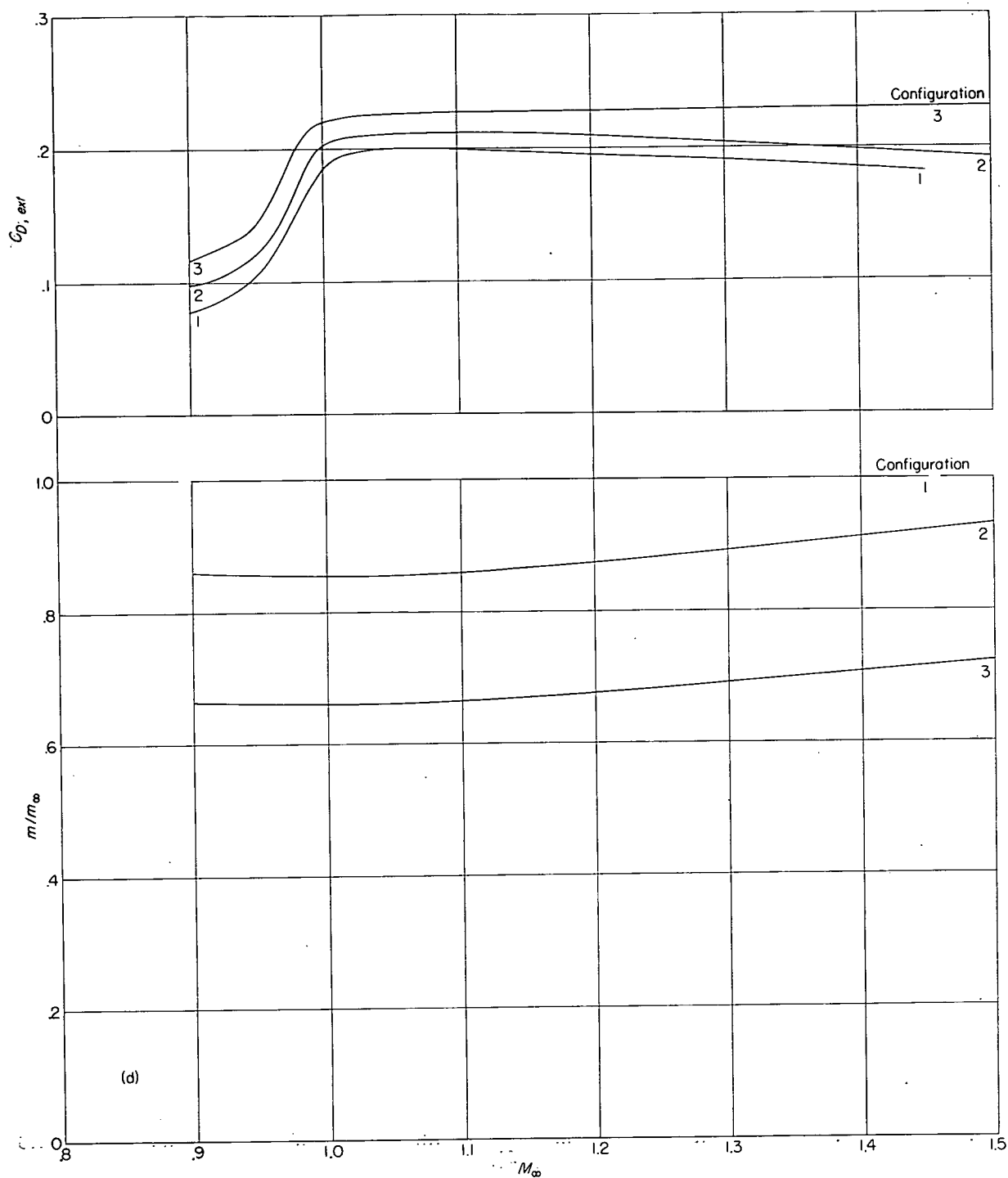
(b) Cowling II: parabolic.

FIGURE 9.—Continued.



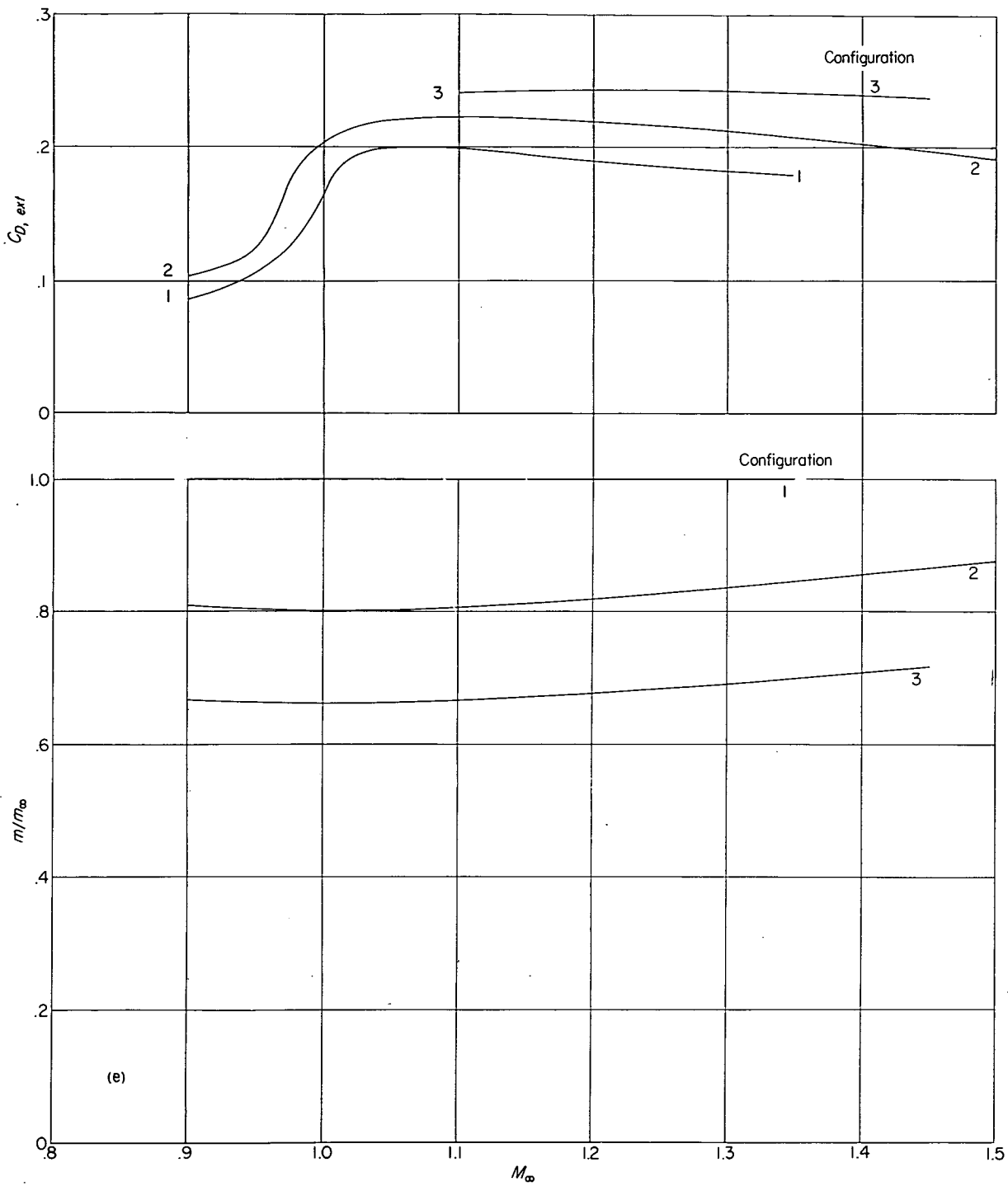
(c) Cowling III: conic, sharp lip.

FIGURE 9.—Continued.



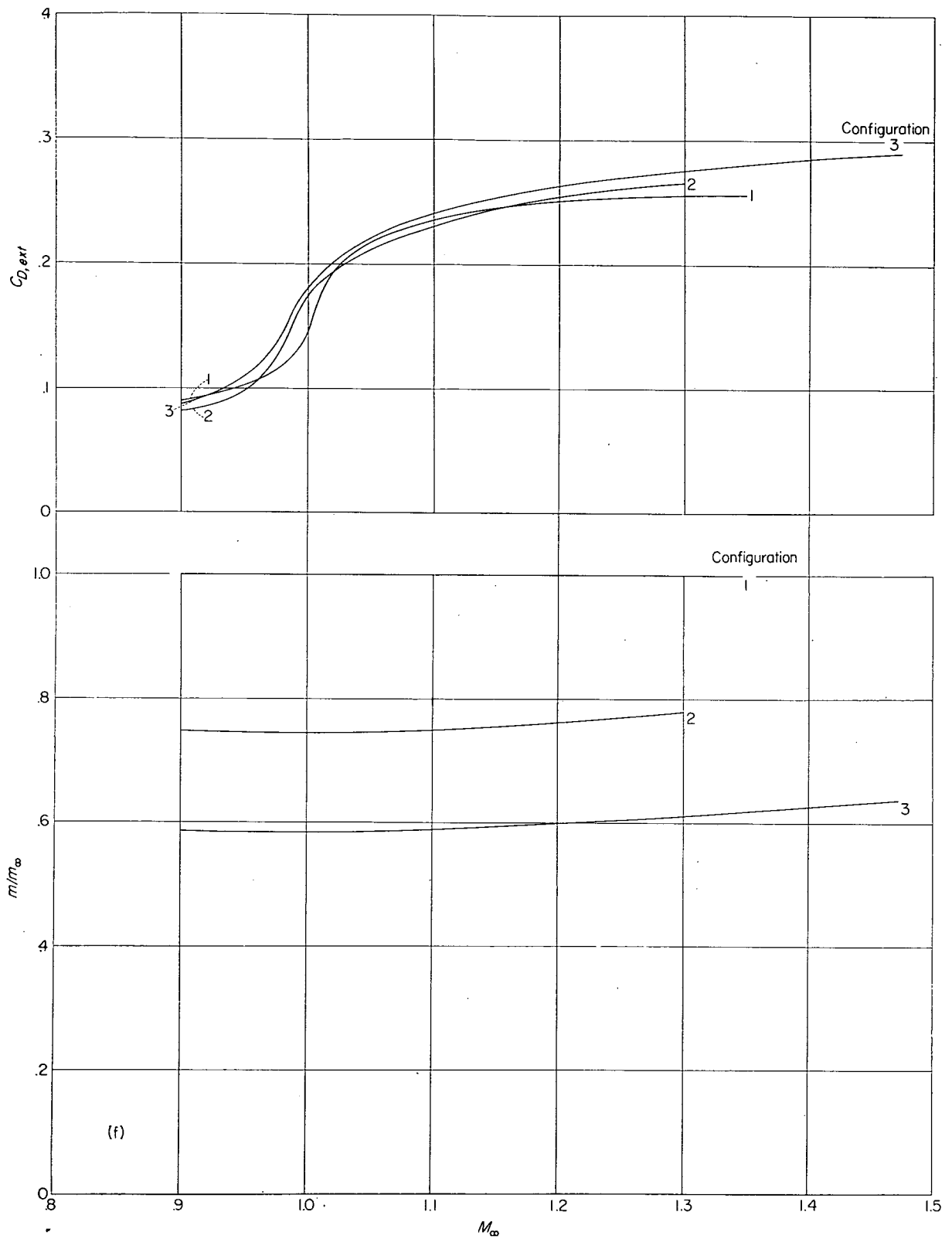
(d) Cowling IV: conic, beveled lip.

FIGURE 9.—Continued.



(e) Cowling V: conic, blunt lip.

FIGURE 9.—Continued.



(f) Cowling VI: NACA 1-40-250.

FIGURE 9.—Concluded.

The curves of total drag coefficient as a function of Mach number are given in figure 10 for the two nonducted models. Base drag coefficient was measured for nonducted model B only and is also shown in figure 10.

EFFECT OF COWLING SHAPE

The drag-coefficient curves at $m/m_\infty=1.0$ for the various normal-shock inlet models with cowlings of fineness ratio 3.0 are shown superimposed in figure 11 for comparison purposes. Also shown is the curve for the total-minus-base drag coefficient for solid body model A. The base drag coefficient of model A was obtained by using the measured base pressure coefficient of model B.

Inspection of figure 11 indicates that in the transonic range below $M_\infty \approx 1.1$ all the ducted models with cowlings of fineness ratio 3.0 have about the same drag coefficient. As the Mach number increases the curves diverge; the sharp-lip conic cawling has the least drag and the NACA 1-series cawling has the greatest drag. Comparison of the drag of the three conic cawling models at $M_\infty > 1.2$ indicates that, for these cowlings of constant fineness ratio, beveling or blunting the lip caused a small increase in drag over that of the sharp-lip conic cawling. It should be noted, however, that, of the two conic cowlings which were identical except for lip shape (cowlings IV and V), the blunt-lip conic cawling had slightly lower drag than the beveled-lip conic cawling. Thus, it appears that the effect of lip bluntness on drag is critically dependent on the manner of blunting the lip. Because the NACA 1-series cawling and the blunt-lip conic cawling had the same external lines in the region of the inlet lip, it is apparent that the higher drag of the NACA 1-series cawling is associated with its greater fullness farther rearward.

The drag of the pointed nonducted body is greater than the external drag of all the inlet models in the transonic range and at $M_\infty > 1.2$ is about equal to that of the cawling which was defined by the same parabolic arc. At all test Mach numbers greater than 1.05, the external drag of the conic-cawling models was less than drag of the solid body for mass-flow ratios greater than 0.9. The data of reference 4 indicate that the solid body is a low-drag configuration at supersonic speeds. The lower drags obtained with the conic cowlings indicate therefore that these also must be considered as low-drag configurations.

The variation of external drag coefficient with mass-flow ratio at $M_\infty=1.3$ is shown for the various cowlings in figure 12 by cross plotting the data of figure 9. The increase in drag with spillage is different for each cawling and is greatest for the conic cawling with sharp lips and least for the NACA

1-series cawling I. At $m/m_\infty=0.8$, the three conic cowlings and the parabolic cawling all have about the same drag. The NACA 1-series cawling has the greatest drag at all flow rates tested because of its high drag at maximum-flow rate.

The rate of increase of drag coefficient with spillage for the various cowlings is better compared in figure 13 where the slopes of the curves of figure 12 and similar ones for other Mach numbers are shown for each cawling. The slope of the additive drag curve computed by assuming one-dimensional flow is also shown as a function of Mach number. The departure of the curves of figure 13 from the additive drag curve is caused by the reductions in cawling pressure drag with spillage. The data indicate very little change in cawling pressure drag with spillage for the sharp-lip inlet and large reductions for the NACA 1-series inlet. This trend is consistent with previous experiences with leading-edge suction for wings at angle of attack. Cawling pressure distributions at several flow rates are shown in reference 3 for NACA 1-series cowlings.

NACA 1-40-250 COWLING

The models with the NACA 1-40-250 cawling and the related nonducted body B were tested for purpose of comparison of results with those results reported in reference 1. These models and those of reference 1 differed only in fin geometry and overall length. The flight-test technique for obtaining the data was considerably different from that reported herein. Comparison of the data of figures 9(f) and 10 with those presented in reference 1 indicates that, when allowance is made for the differences in fin drag, the measured drag coefficients of the present tests are essentially the same as those of reference 1 for both the ducted and nonducted models. A comparison of the results for the ducted models is shown in figure 14 for several Mach numbers. The solid curve is the external drag coefficient, as presented in reference 1, which was extrapolated to $m/m_\infty=1.0$. The points are the measured values obtained for cawling VI of this investigation. The long dashed curve was obtained by correcting the data of reference 1 for the difference in fin-plus-interference drag. The difference in fin-plus-interference drag was obtained by subtracting the total-minus-base drag of nonducted model B from the total-minus-base drag of the solid body of reference 1.

Comparison of the minimum drag of the NACA 1-40-250 nose-inlet model with the minimum drag of the NACA 1-49-300 model (cawling I) shows that the subsonic drags were essentially the same, but, for $M_\infty > 1.02$, the shorter, blunter, NACA 1-40-250 cawling had the higher drag.

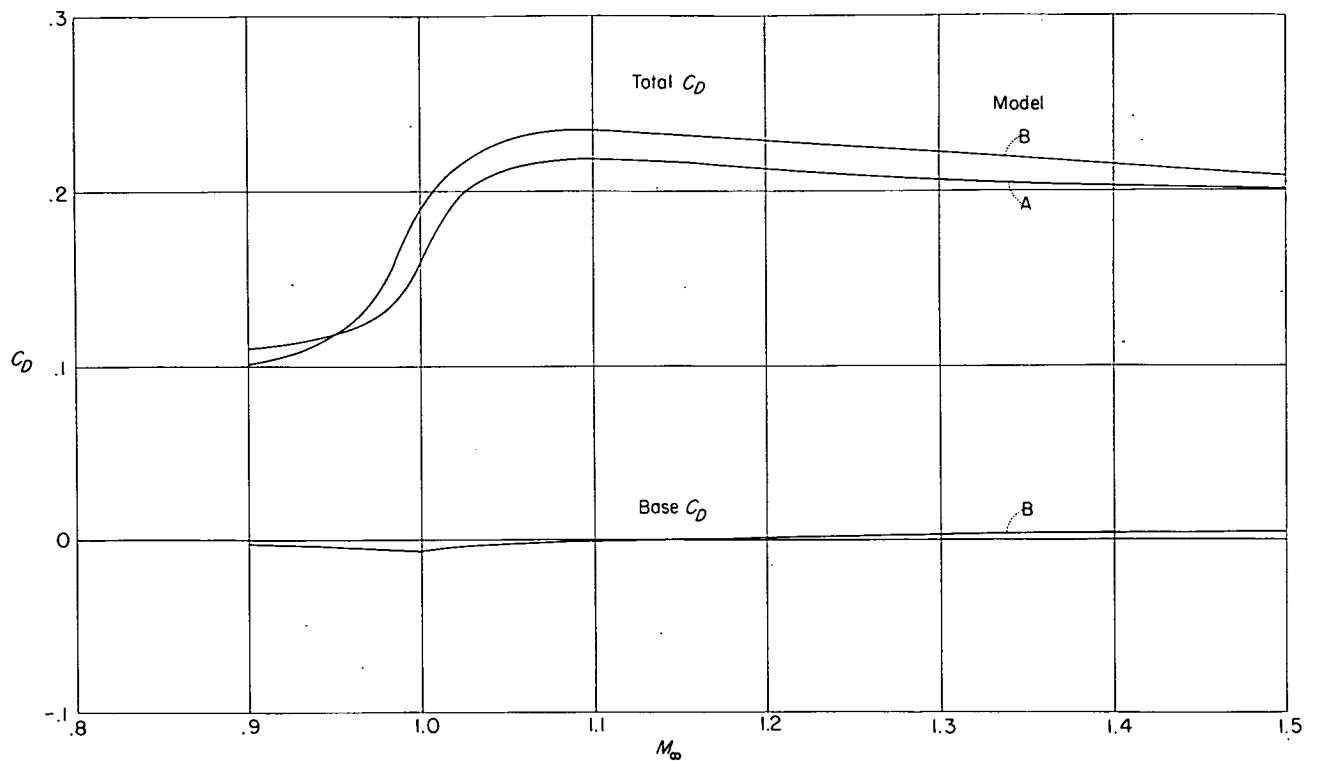


FIGURE 10.—Variation of total and base drag coefficients with Mach number for the nonducted models.

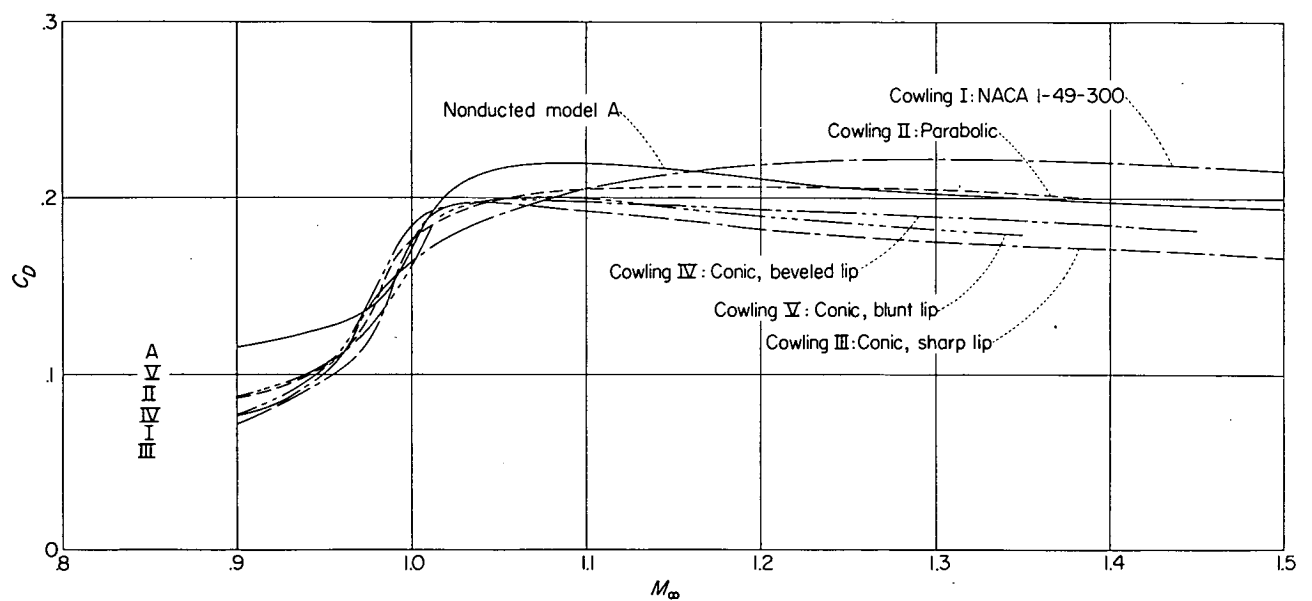
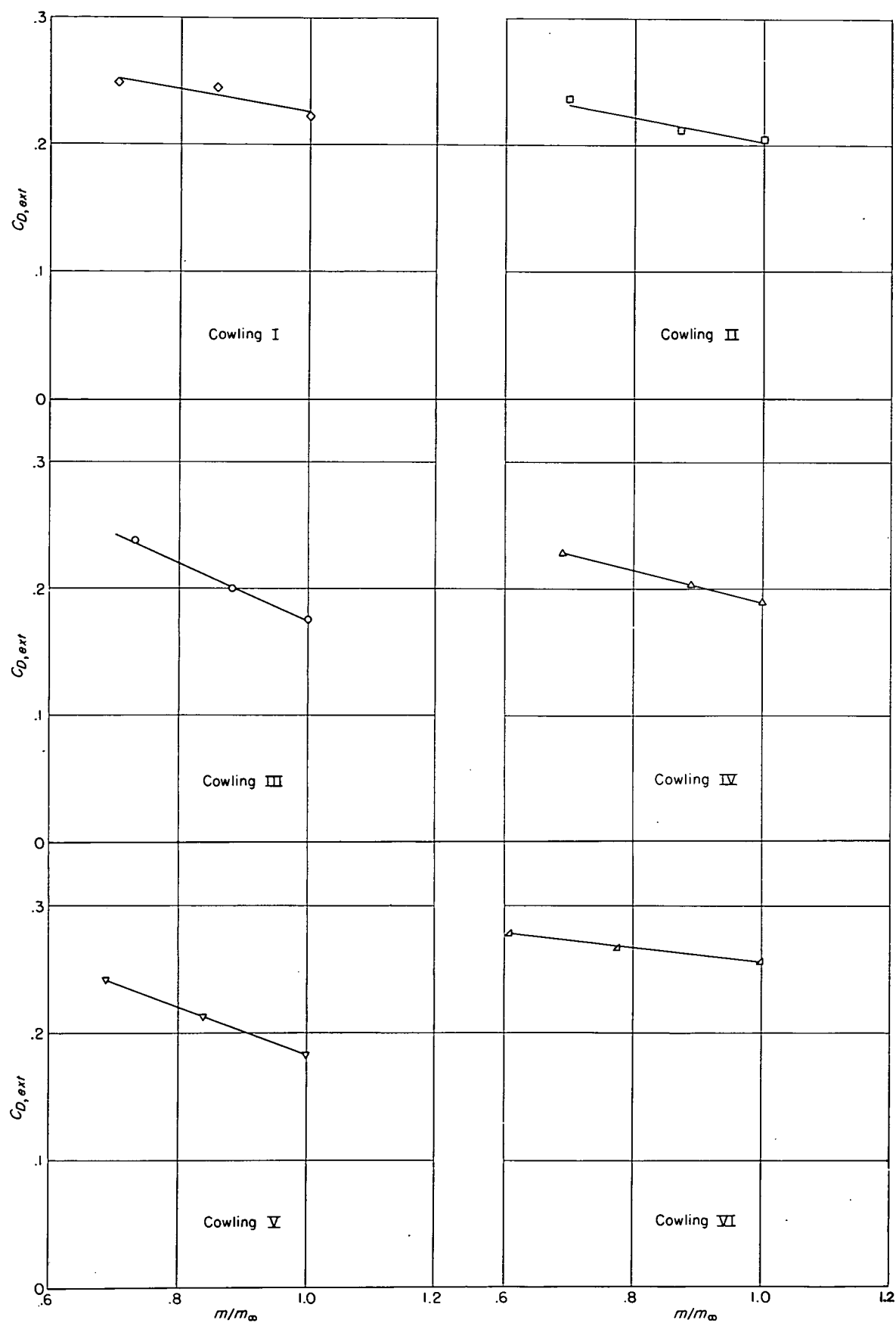


FIGURE 11.—Variation with Mach number of external drag coefficient for ducted models with various cowlings of fineness ratio 3.0 and total minus base drag coefficient for nonducted model A. $\frac{m}{m_\infty} = 1.0$.


 FIGURE 12.—Variation of external drag coefficient with mass-flow ratio at $M_\infty = 1.3$.

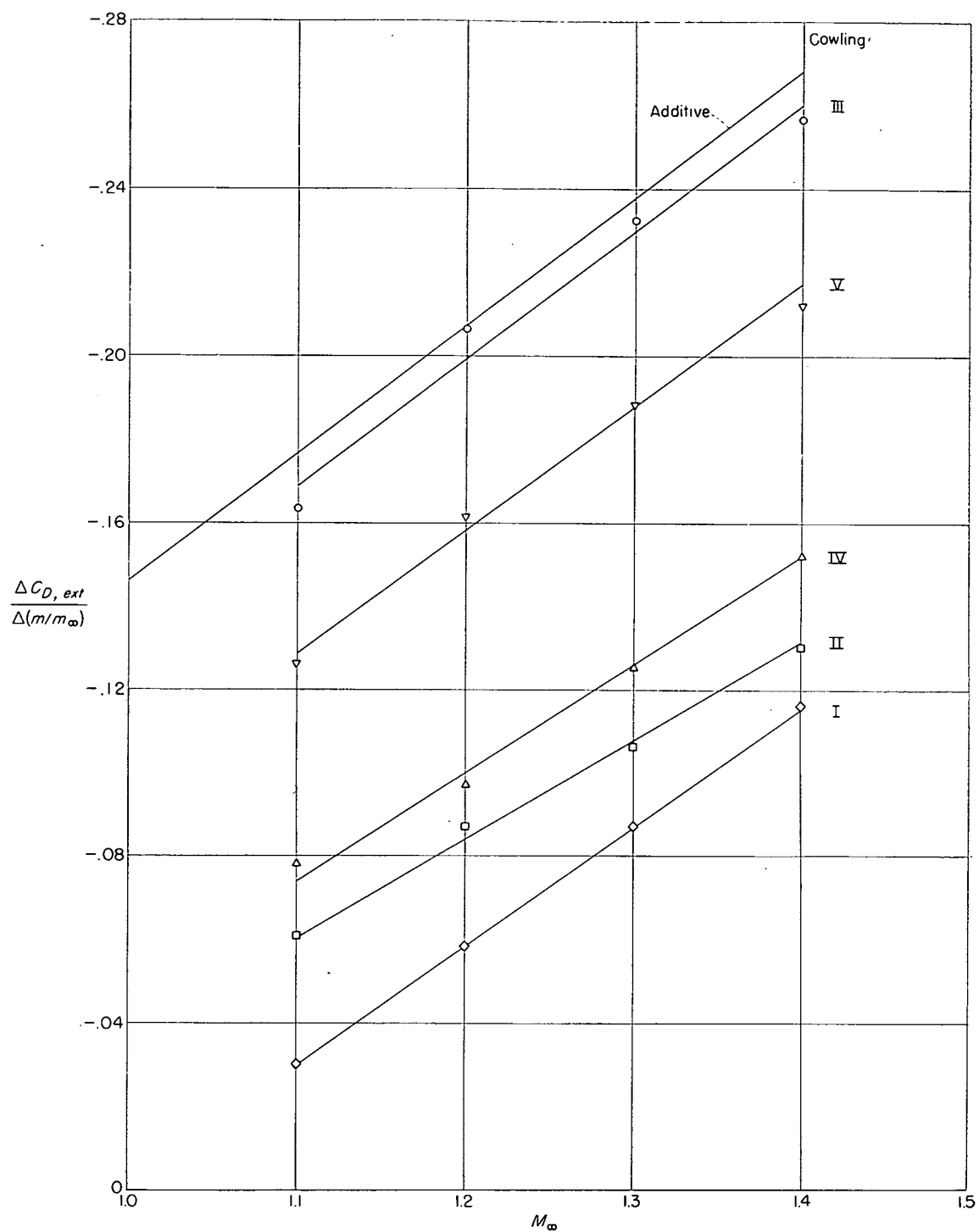


FIGURE 13.—Variation with Mach number of the change in external drag coefficient with change in mass-flow ratio for models with various cowlings of fineness ratio 3.0.

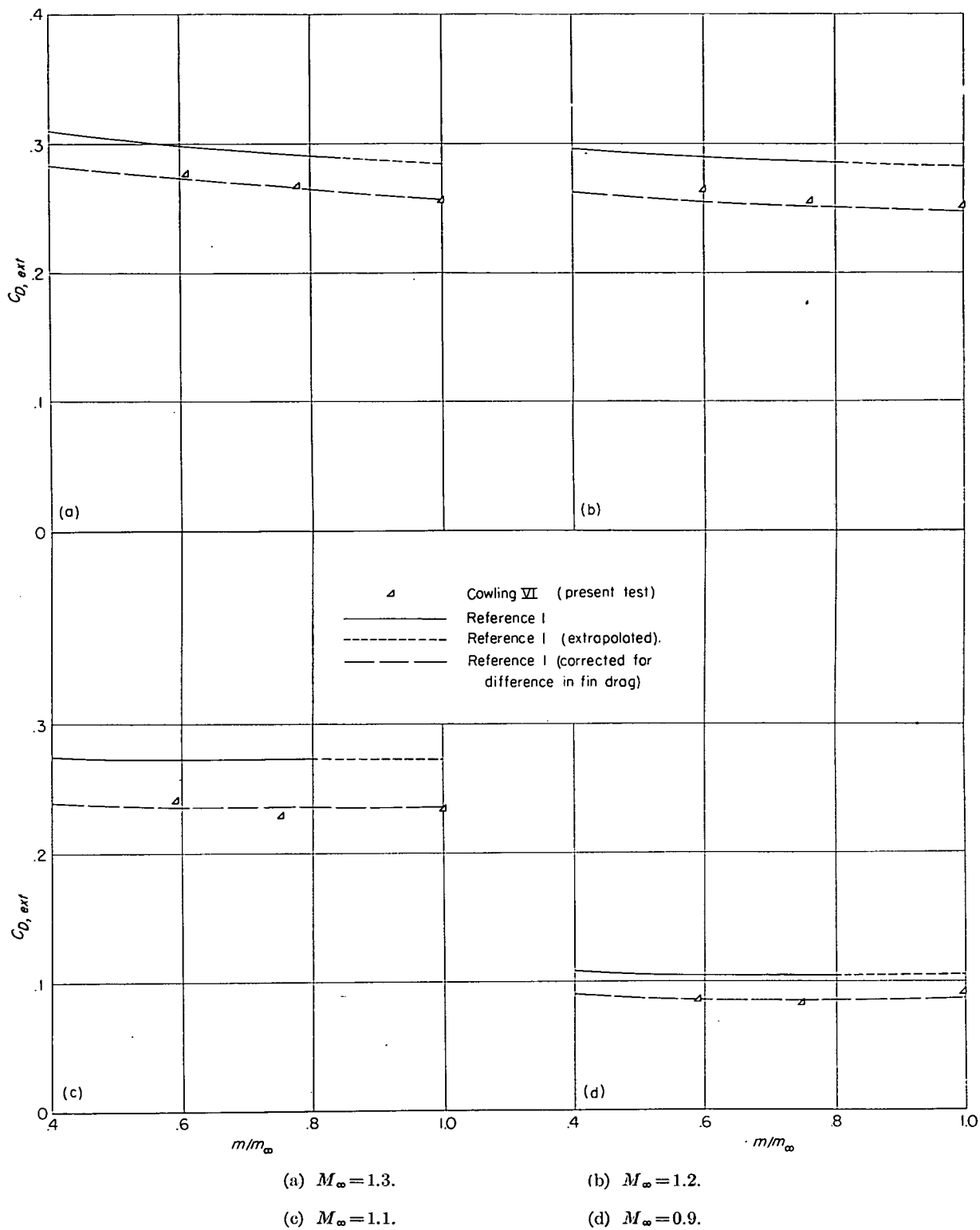


FIGURE 14.—Comparison of the external drag coefficient of cowling VI (NACA 1-40-250) with reference 1 at various Mach numbers.

CONCLUSIONS

Models having normal-shock nose inlets with NACA 1-series, parabolic, and conic cowlings have been tested at free-stream Mach numbers from 0.9 to 1.5 and flow ratio from 0.7 to 1.0 at an angle of attack of 0° . Two related nonducted bodies were also tested for comparison purposes. Within the range of the tests, the following conclusions apply:

1. At the maximum flow rate, the conic, parabolic, and NACA 1-series cowlings all had about the same external drag at a Mach number of approximately 1.1. At higher Mach numbers, the drag of the conic cowling was appreciably less than that of the parabolic or NACA 1-series cowlings.

2. Blunting or beveling the lip of the conic cowling while keeping the cowling fineness ratio constant resulted in drag coefficients slightly higher than for the sharp-lip conic cowling at maximum flow rate. At a mass-flow ratio of about 0.8, the conic cowlings with sharp, blunt, or beveled lips and the parabolic cowling all give about the same drag. The higher drag of the NACA 1-49-300 cowling compared with the

blunt-lip conic cowling is associated with its greater fullness back of the inlet.

3. The sharp-lip conic cowling experienced only small reductions in cowling pressure drag with air spillage, whereas the NACA 1-series cowling had large reductions. Because of its high drag at maximum flow rate, however, the NACA 1-series cowling gave the greatest drag at all flow rates of the cowlings tested at Mach numbers greater than 1.1.

4. The drag of the conic-cowling models at high mass-flow rates was less than that of a related parabolic nonducted model at Mach number greater than 1.05. At Mach number greater than 1.2, the drag of the parabolic-cowling model was about the same as that of the nonducted model.

LANGLEY AERONAUTICAL LABORATORY,
NATIONAL ADVISORY COMMITTEE FOR AERONAUTICS,
LANGLEY FIELD, VA., *September 8, 1953.*

APPENDIX

METHOD USED TO DETERMINE THE DRAG AND MASS-FLOW RATIO FOR NORMAL-SHOCK NOSE INLETS

The total drag was obtained from the CW Doppler radar and the SCR 584 tracking radar measurements of velocity and flight path, respectively. Thus,

$$D_t = -W \left(\frac{1}{g} \frac{dV}{dt} + \sin \theta \right) \quad (\text{A1})$$

The external drag is defined, in the usual manner, as the sum of the dragwise component of the aerodynamic pressure and viscous forces acting on the external surface of the body plus the dragwise component of the aerodynamic pressure forces acting on the external contour of the entering stream-tube. Thus, the external drag is obtained by subtracting the internal drag from the total drag:

$$D_{ext} = D_t - D_{int} \quad (\text{A2})$$

The internal drag is obtained from the following equation by applying the momentum equation between the free stream ahead of the inlet and the duct exit:

$$D_{int} = \gamma p_\infty M_\infty^2 A_\infty - \gamma p_e M_e^2 A_e - (p_e - p_\infty) A_e \quad (\text{A3})$$

where the unknowns M_e , p_e , and A_∞ are obtained in the following manner. Since the exit is assumed to be choked (i.e., $M_e = 1.0$),

$$p_e = 0.528 p_{t, \infty} \frac{A_\infty}{A_e} \left(\frac{A_e}{A} \right)_\infty \quad (\text{A4})$$

where M_∞ is less than M_∞ necessary to start the inlet, if it is assumed that $M_1 = 1.0$ and $p_{t, 1} = p_{t, \infty}$,

$$A_\infty = \frac{p_{t, \infty}' / p_{t, \infty}}{(A_{cr}/A)_\infty} A_1 \quad (\text{A5a})$$

and where M_∞ is equal to or greater than M_∞ necessary to start the inlet,

$$A_\infty = A_1 \quad (\text{A5b})$$

The mass-flow ratio is

$$m/m_\infty = \frac{\rho_\infty A_\infty V_\infty}{\rho_\infty A_1 V_\infty} = \frac{A_\infty}{A_1} \quad (\text{A6})$$

Obviously the mass flow and internal drag can be properly evaluated in the manner indicated only for the range of M_∞ for which the flow follows the assumed pattern. The minimum Mach number for which the inlet and exit will be choked depends on the relative size of the minimum area at the inlet and exit and on the internal losses. The models of the present investigations were designed to choke at both the inlet and exit at Mach numbers from slightly above sonic to the maximum attained.

One ducted model with pressure instrumentation and telemetry was flight tested in order to determine the minimum Mach number at which the assumed choking conditions existed at the inlet and exit. The measured inlet and exit static pressures together with the pitot stagnation pressure at the inlet were used to evaluate the internal drag and mass flow for this model. The method of reducing these data was the same as that discussed in reference 1 for ducted-nose-inlet models with telemeters.

The pressure measurements indicated that the inlet and exit were choked for values of M_∞ greater than 1.03 and 1.08, respectively. The data of figure 7, however, show that the mass flow and internal drag computed according to equations (A3) to (A6) is in excellent agreement with the measured values at all supersonic Mach numbers. At $M_\infty = 0.9$ the computed $C_{D, int}$ is still in good agreement with the measured value and the computed m/m_∞ is about 0.015 greater than that measured. It is, therefore, believed that the method of calculation gives the correct values of $C_{D, int}$ and m/m_∞ at $M_\infty > 1.03$. For Mach numbers from 0.9 to 1.03, a small error is introduced in the magnitude of m/m_∞ only.

REFERENCES

1. Sears, R. I., and Merlet, C. F.: Flight Determination of the Drag and Pressure Recovery of an NACA 1-40-250 Nose Inlet at Mach Numbers From 0.9 to 1.8. NACA TN 3218, 1955. (Supersedes NACA RM L50L18.)
2. Baals, Donald D., Smith, Norman F., and Wright, John B.: The Development and Application of High-Critical-Speed Nose Inlets. NACA Rep. 920, 1948. (Supersedes NACA ACR L5F30a.)
3. Pendley, Robert E., and Robinson, Harold L.: An Investigation of Several NACA 1-Series Nose Inlets With and Without Protruding Central Bodies at High-Subsonic Mach Numbers and at a Mach Number of 1.2. NACA TN 3436, 1955. (Supersedes NACA RM L9L23a.)
4. Hart, Roger G., and Katz, Ellis R.: Flight Investigations at High-Subsonic, Transonic, and Supersonic Speeds to Determine Zero-Lift Drag of Fin-Stabilized Bodies of Revolution Having Finesness Ratios of 12.5, 8.91, and 6.04 and Varying Positions of Maximum Diameter. NACA RM L9I30, 1949.

If equation (4) is placed into equation (3) and r is assumed to be large, the potential induced by a source is

$$\varphi_{r \rightarrow \infty} = -\frac{1}{2\pi\sqrt{2\beta r}} \int_{-L_0}^{x_0} \frac{a_0(\xi)d\xi}{\sqrt{x_0-\xi}} \quad (5)$$

and the induced velocities are

$$\varphi_x(x,r,\theta) = -\frac{1}{2\pi\sqrt{2\beta r}} \int_{-L_0}^{x_0} \frac{a_0'(\xi)d\xi}{\sqrt{x_0-\xi}} \quad (6a)$$

$$\varphi_r(x,r,\theta) = -\beta\varphi_x \quad (6b)$$

MULTIPOLES

Lamb, in reference 2, page 527, has presented a general solution to equation (1) consisting of an infinite set of basic singular solutions. These basic singularities, referred to as multipoles, can be distributed along a line and weighted so as to reproduce certain body shapes enclosing the line. The expression for the perturbation velocity potential for a distribution of n th-order ($n=0,1,2,\dots$) multipoles starting at $-L_0$ and continuing along the x axis can be written in terms of a cylindrical coordinate system (fig. 1) as

$$\varphi_n(x,r,\theta) = -\frac{r^n}{2\pi} \left(\frac{1}{r} \frac{\partial}{\partial r} \right)^n \int_{-L_0}^{x-\beta r} \frac{[a_n(\xi) \cos n\theta + b_n(\xi) \sin n\theta] d\xi}{\sqrt{(x-\xi)^2 - \beta^2 r^2}} \quad (7)$$

The operator $\left(\frac{1}{r} \frac{\partial}{\partial r} \right)^2$ is defined as

$$\left(\frac{1}{r} \frac{\partial}{\partial r} \right)^2 = \frac{1}{r} \frac{\partial}{\partial r} \left(\frac{1}{r} \frac{\partial}{\partial r} \right) = -\frac{1}{r^3} \frac{\partial}{\partial r} + \frac{1}{r^2} \frac{\partial^2}{\partial r^2}$$

and the definition of $\left(\frac{1}{r} \frac{\partial}{\partial r} \right)^n$ follows by induction. If the notation⁴

$$\left(\frac{\partial}{\partial x} \right)^n \int_a^x \frac{A(y)dy}{\sqrt{x-y}} = (-1)^n \frac{(1)(3)\dots(2n-1)}{2^n} \int_a^x \frac{A(y)dy}{(x-y)^{(2n+1)/2}}$$

is introduced, where the symbol \int is read "finite part of the integral," equation (7) becomes

$$\varphi_n(x,r,\theta) = -\frac{r^n \beta^{2n} (2n)!}{2^{n+1} \pi (n)!} \int_{-L_0}^{x-\beta r} \frac{[a_n(\xi) \cos n\theta + b_n(\xi) \sin n\theta] d\xi}{[(x-\xi)^2 - \beta^2 r^2]^{(2n+1)/2}} \quad (8)$$

and the general expressions for the induced velocities become—writing only the term involving the cosine, since the result for the sine is directly analogous

$$\varphi_x(x,r,\theta) = \sum_{n=0}^{\infty} \frac{r^n \beta^{2n} (2n+2)!}{2^{2n+2} \pi (n+1)!} \int_{-L_0}^{x+\beta r} \frac{(x-\xi) a_n(\xi) \cos n\theta d\xi}{[(x-\xi)^2 - \beta^2 r^2]^{(2n+3)/2}} \quad (9a)$$

$$\varphi_r(x,r,\theta) = -\sum_{n=0}^{\infty} \frac{\beta^{2n} r^{n-1} (2n)!}{2^{n+1} \pi (n)!} \int_{-L_0}^{x-\beta r} \frac{[n(x-\xi)^2 + (n+1)\beta^2 r^2] a_n(\xi) \cos n\theta d\xi}{[(x-\xi)^2 - \beta^2 r^2]^{(2n+3)/2}} \quad (9b)$$

$$\frac{1}{r} \varphi_\theta(x,r,\theta) = \sum_{n=0}^{\infty} \frac{n r^{n-1} \beta^{2n} (2n)!}{2^{n+1} \pi (n)!} \int_{-L_0}^{x-\beta r} \frac{a_n(\xi) \sin n\theta d\xi}{[(x-\xi)^2 - \beta^2 r^2]^{(2n+1)/2}} \quad (9c)$$

Another very useful way of developing these multipole solutions evolves from an application of operational tech-

niques. To begin with, rewrite equation (1) in terms of a polar coordinate system, thus

$$\beta^2 \frac{\partial^2 \varphi}{\partial x^2} - \frac{\partial^2 \varphi}{\partial r^2} - \frac{1}{r} \frac{\partial \varphi}{\partial r} - \frac{1}{r^2} \frac{\partial^2 \varphi}{\partial \theta^2} = 0 \quad (10)$$

Next, define the Laplace transform of $\varphi(x,r,\theta)$ by

$$\bar{\varphi}(s,r,\theta) = \int_0^\infty \varphi(x,r,\theta) e^{-xs} dx \quad (11)$$

and apply this transform to equation (10). There results (for a proof see Appendix A).

$$\beta^2 s^2 \bar{\varphi} - \frac{\partial^2 \bar{\varphi}}{\partial r^2} - \frac{1}{r} \frac{\partial \bar{\varphi}}{\partial r} - \frac{1}{r^2} \frac{\partial^2 \bar{\varphi}}{\partial \theta^2} = 0 \quad (12)$$

Now, if a general solution to equation (12) is expressed in the form

$$\bar{\varphi}(s,r,\theta) = f(r) \cos n\theta$$

then $f(r)$ must satisfy the equation

$$\frac{d^2 f}{dr^2} + \frac{1}{r} \frac{df}{dr} - \left(\frac{n^2}{r^2} + \beta^2 s^2 \right) f = 0$$

Solutions to this are given by

$$f(r) = \bar{C}_n(s) I_n(\beta r s) + \bar{A}_n(s) K_n(\beta r s)$$

where I_n and K_n are modified Bessel functions as defined in reference 4, page 77. Hence, if $\bar{\varphi}$ is to vanish as r goes to infinity, a general solution to equation (10) can be written in the form

$$\bar{\varphi}(s,r,\theta) = -\frac{1}{2\pi} \sum_0^\infty [\bar{A}_n(s) \cos n\theta + \bar{B}_n(s) \sin n\theta] K_n(\beta r s) \quad (13)$$

The above result will be transformed back to the physical plane in two ways. First, apply the identity (ref. 4, p. 79)

$$K_n(z) = (-1)^n \left(\frac{1}{z} \frac{d}{dz} \right)^n K_0(z)$$

and re-express equation (13) as (only the coefficient of the $\cos n\theta$ term is written since the treatment of the sine term is identical)

$$\bar{\varphi}(s,r,\theta) = -\frac{1}{2\pi} \sum_0^\infty (-1)^n \cos n\theta \frac{\bar{A}_n(s)}{\beta^n s^n} r^n \left(\frac{1}{r} \frac{d}{dr} \right)^n K_0(\beta r s)$$

The inverse Laplace transform of $K_0(\beta r s)$ —see reference 5—is

$$L^{-1}[K_0(\beta r s)] = \begin{cases} 0 & , \quad x < \beta r \\ \frac{1}{\sqrt{x^2 - \beta^2 r^2}} & , \quad x > \beta r \end{cases}$$

So, since

$$\int_{-L_0}^x dx_1 \int_{-L_0}^{x_1} dx_2 \dots \int_{-L_0}^{x_{n-1}} dx_n A_n(x_n) =$$

$$\frac{1}{(n-1)!} \int_{-L_0}^x (x-x_1)^{n-1} A_n(x_1) dx_1 \quad (14)$$

⁴ For a detailed discussion of the finite-part concept as used in this report see reference 3.

airplane shape having low wave drag finds the real definition of his problem somewhat obscure. In a sense his first problem is, literally, to pose a problem; that is, to impose a minimum number of arbitrary but pertinent restraints within the framework of which the wave drag is to be minimized. Even when this has been done, he still is concerned with the question of uniqueness, since optimum shapes are not necessarily unique even when several restraints are imposed. Consider, for example, the problem of finding the Busemann biplane which will have minimum wave drag at a given Mach number for a fixed section strength, volume, and wetted area. If the design Mach number is 1.41, one such design (on the basis of linearized theory) is shown in figure 3 where the chord-gap ratio, h/c , is equal to $\frac{1}{2}$. The resulting variation of the wave drag is shown in the upper part of figure 4. However, when the gap is closed to the point where h/c equals $\frac{1}{4}$, the variation of wave drag, shown in the lower part of figure 4, is the same within the interval $1.28 \leq M \leq 1.66$ and everywhere else is lower. It is likely that one would have first discovered the former solution, yet to the accuracy of the theory used, the latter is obviously preferable.

With the above observations always in mind, attention will be directed in this report to the analysis of simplified configurations composed of two distinct types of volume: planar types, that is, wing-like volumes, thin in one dimension and bounded by surfaces that never deviate far from a reference plane; and rectilinear types, that is, fuselage-like volumes longer in one dimension than in the other two and disposed more or less symmetrically about a straight line.

In particular the following problem is posed:

Given a thin nonlifting wing, what is the shape of an adjoining fuselage, the stream surface of which is simulated by a line of multipoles in the same plane as the wing, that will minimize the wave drag of the combination at a given Mach number?

BASIC CONCEPTS

A LINE OF SOURCES

The velocity potential induced at the point x, r, θ by a group of sources distributed along the x axis, starting at $-L_0$, is well known to be given by

$$\varphi(x, r, \theta) = -\frac{1}{2\pi} \int_{-L_0}^{x-\beta r} \frac{a_0(\xi) d\xi}{\sqrt{(x-\xi)^2 - \beta^2 r^2}} \quad (3)$$

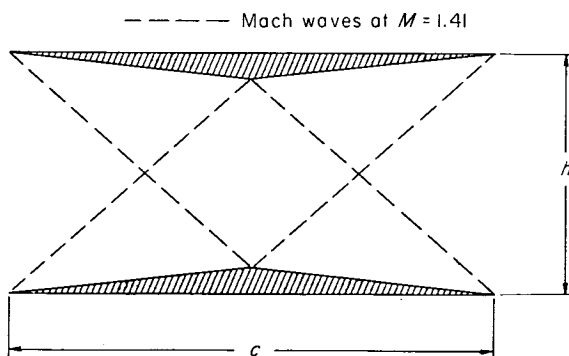


FIGURE 3.—Busemann biplane.

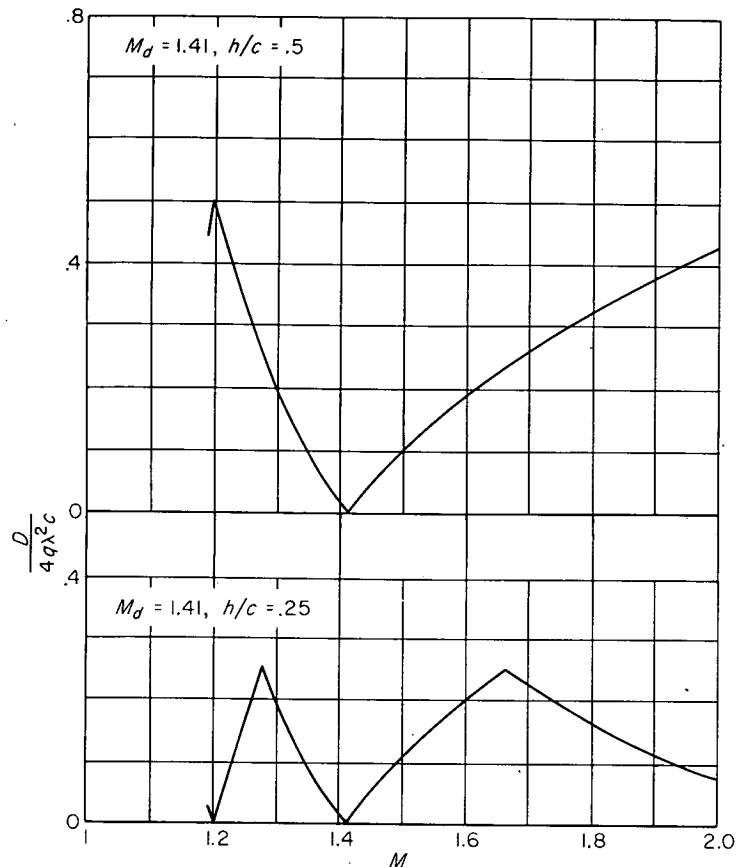


FIGURE 4.—Drag variation for double-wedge Busemann biplanes.

where $a_0(\xi)$ is the source strength per unit of length. In order to calculate wave drag one needs only the value of φ as r approaches infinity. This asymptotic value is simple enough to find provided it is observed that, as r is increased, x should also be increased so the potential can be studied in the vicinity of the Mach waves radiating from the disturbing object. Hence, set

$$x = x_0 + \beta r \quad (4)$$

so for a given r , x_0 measures the streamwise distance of the point x, r, θ from the Mach wave emanating from the origin and, in particular, the foremost wave is located at $x_0 = -L_0$. (See figure 5.)

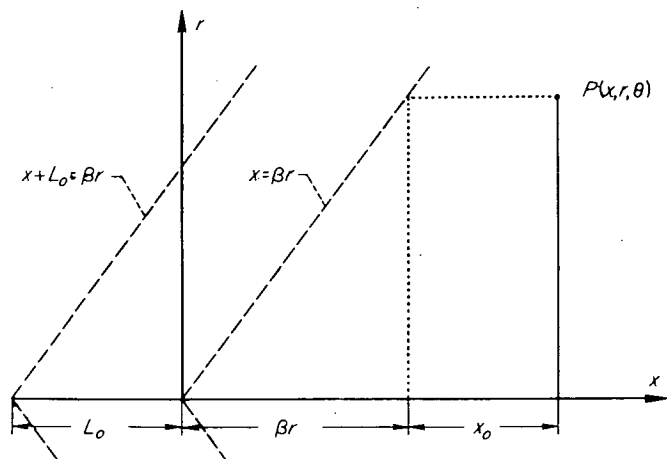


FIGURE 5.—Coordinates introduced in equations (4) and (5).

vicinity, different classes of real objects and, by means of equation (2), finds optimum combinations of these solutions from the viewpoint of low wave drag. The analysis involved in solving this problem has, in general, a distinct mathematical advantage over the problem of calculating the drag of a given object; namely, that the immediate problem of finding a shape with a relatively low wave drag is divorced from any detailed reference to the shape itself. It is true, of course, that the stream surface representing this shape must eventually be found and, in fact, a limitation on the applicability of the method is given by the requirement that this shape be real. However, the problem of finding the shape of the object when φ is known is a matter of direct calculation.³ One should also be careful to notice that the optimum solutions obtained by this procedure are not necessarily true optimums but purely relative to the choice of solutions used in the analysis.

LIST OF IMPORTANT SYMBOLS

A	wing aspect ratio
$A_n(x)$	$(-\beta)^n$ times the n th derivative of the n th multipole distribution $a_n(x)$ (See eq. 16.)
a	semi-root-chord of elliptic wing
$a_n(x)$	strength of n th-order multipole distribution multiplying $\cos n\theta$
$B_n(x)$	$(-\beta)^n$ times the n th derivative of the n th multipole distribution $b_n(x)$
b	semispan of elliptic wing
$b_n(x)$	strength of n th-order multipole distribution multiplying $\sin n\theta$
C_D	drag coefficient, $\frac{D}{qS}$
C_p	pressure coefficient, local pressure minus static pressure divided by q
D	wave drag
\bar{D}_n	wave drag associated with n th-order cancellation multipole distribution (See eq. (59).)
L'_o, L_o	maximum fore-and-aft extent of wing equivalent multipole distribution
$L'(\theta), L(\theta)$	maximum fore-and-aft extent of wing equivalent multipole distribution for angle θ
M	free-stream Mach number
q	free-stream dynamic pressure, $\frac{\rho_o U_o^2}{2}$
\bar{r}	$\frac{\beta R}{L_o}$
\bar{r}_e	see equation (46)
R	radius of body
S	area of wing plan form
$S_w(x, \theta)$	normal projection of wing cross-sectional area measured in oblique planes
t	maximum thickness of wing root chord
U_o	speed of free stream
V	volume
x, y, z	Cartesian coordinate system, x parallel to free-stream direction
x, r, θ	cylindrical coordinate system, x parallel to free-stream direction

³ From a mathematical point of view the essence of the method outlined above is that the analysis involves the solution to direct problems, that is, problems of integration. Calculating the drag of a given body, on the other hand, involves the solution to inverse problems, that is, problems involving the inversion of integral equations.

$\alpha_n(x)$	strength of n th-order optimum cancellation multipoles (See eq. (36).)
β	$\sqrt{M^2 - 1}$
λ_u	slope of wing upper surface measured relative to free-stream direction
μ	$\tan^{-1}(\beta \cos \theta)$
ρ_o	free-stream density
φ	perturbation velocity potential

DEFINITION OF THE PROBLEM

The problem of designing an airplane to have a minimum wave drag must be stated quite precisely. If the aerodynamicist is approached with the question, "Given an aerodynamic shape, can its wave drag be lowered?" he can always reply that any volume of material having a wave drag can always be reshaped within a space of finite dimensions so that it will have less wave drag at a given Mach number. Such an answer is interesting but, at present, not very useful to the airplane designer. There is first, of course, the basic criterion that the total drag should be minimized at a given lift and minimizing a component part of this total without holding the other parts fixed does not necessarily yield the lowest possible drag for a given set of restraints. For example, the configuration illustrated in figure 2 has no wave

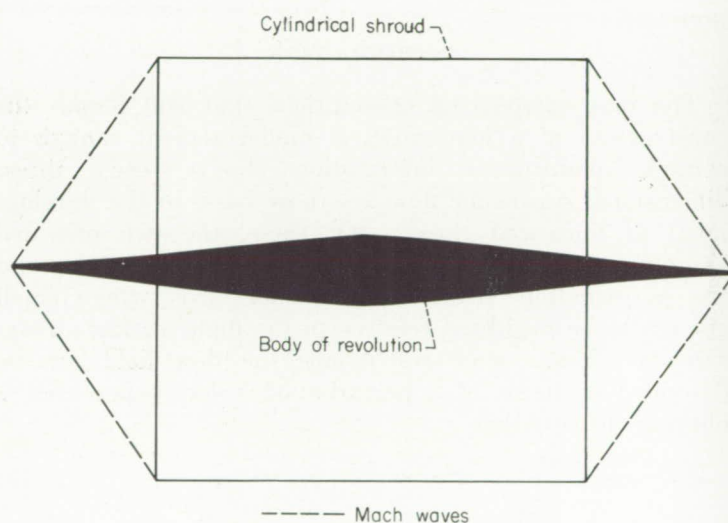


FIGURE 2.—Body and shroud with zero wave drag.

drag when traveling at zero angle of attack; but it has a relatively high friction drag, because of the large amount of wetted area, and its drag due to lift could also be relatively high. Completely aside from all such performance considerations, however, are many other important considerations that are unfortunately more or less vaguely defined from an aerodynamic point of view. For example, an airplane must contain a certain amount of usable volume, the shaping of individual parts is limited by structural requirements, and the arrangement of these parts must not seriously harm the airplane stability and control. The interrelation of all such separate demands presents an extremely complex design problem making it difficult to deviate too far from the reliable shapes set by experience.

As a result of the above-mentioned difficulties, the aerodynamicist who is concerned with discovering a practical

REPORT 1282

A SPECIAL METHOD FOR FINDING BODY DISTORTIONS THAT REDUCE THE WAVE DRAG OF WING AND BODY COMBINATIONS AT SUPERSONIC SPEEDS¹

By HARVARD LOMAX and MAX. A. HEASLET

SUMMARY

For a given wing and supersonic Mach number, the problem of shaping an adjoining fuselage so that the combination will have a low wave drag is considered. Only fuselages that can be simulated by singularities (multipoles) distributed along the body axis are studied. However, the optimum variations of such singularities are completely specified in terms of the given wing geometry. An application is made to an elliptic wing having a biconvex section, a thickness-chord ratio equal to 0.05 at the root, and an aspect ratio equal to 3. A comparison of the theoretical results with a wind-tunnel experiment is also presented.

INTRODUCTION

The most simplifying assumptions that still permit the construction of a mathematical model general enough to contain quantitative information about steady three-dimensional supersonic flow are those basic to the development of linearized theory. Of these, the two principal assumptions are that the viscosity effects are negligible and the perturbation velocities are almost everywhere small enough to be neglected relative to the flight or free-stream velocity. Under such restrictions the flow field can be described in terms of a perturbation velocity potential φ obeying the equation

$$\beta^2 \varphi_{xx} - \varphi_{yy} - \varphi_{zz} = 0 \quad (1)$$

where $\beta^2 = M^2 - 1$ and the reference coordinate system² is shown in figure 1. Further, the wave drag of any object in a flow field governed by equation (1) can be evaluated (see, e. g., ref. 1) by means of the equation

$$D = -\rho_0 \int_{-\infty}^{\infty} dx \int_0^{2\pi} d\theta \left[\lim_{r \rightarrow \infty} (r \varphi_r \varphi_x) \right] \quad (2)$$

where x , r , and θ are cylindrical coordinates also defined in figure 1.

General solutions to equation (1) are numerous and classical. In applying these solutions to the interpretation of physical phenomena the usual approach is to fit them to the given boundary conditions, that is, to make the flow field simulated by them conform to the shape of the disturbing object as well as to a uniform free stream at infinity. Hence,

from this point of view, the choice of a type of general solution to be used in analyzing a particular problem with the least mathematical effort depends on the geometric form of the object under consideration. For example, general solutions based on Green's theorem are well adapted to the study of forces on single planar wings in a steady supersonic flow. On the other hand, the general solution given by Lamb (ref. 2)—which is composed of an infinite set of multipole distributions disposed along a line—is well adapted to the study of the flow around fuselage-like objects.

In this report use is made of certain general solutions to equation (1) but with a deviation from the usual approach mentioned above. One considers, in fact, two different kinds of solutions which represent separately, in a given

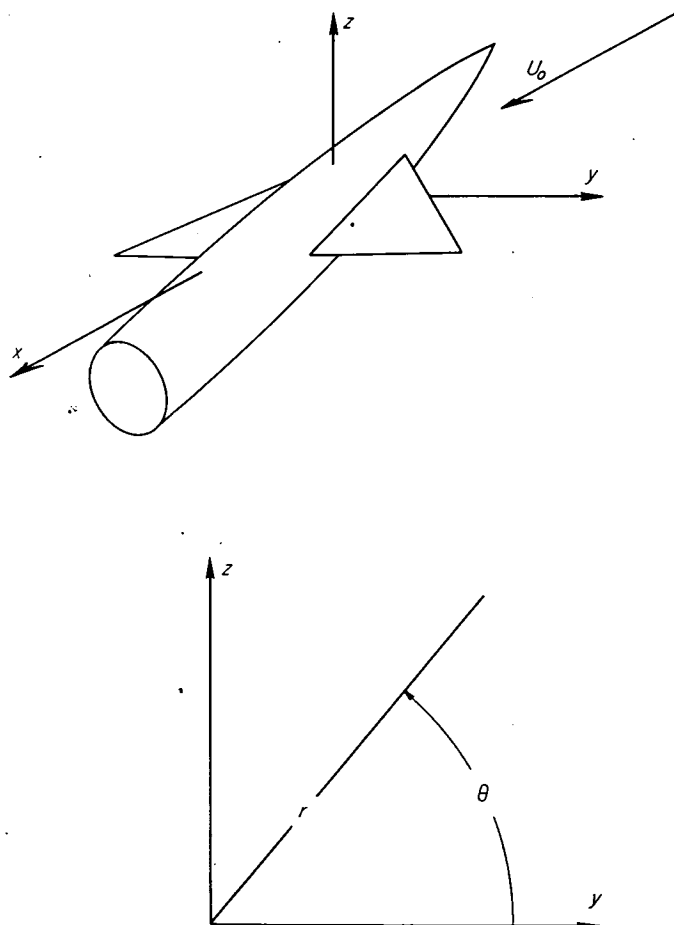


FIGURE 1.—Reference coordinate systems.

¹ Supersedes NACA RM A55B16 by Harvard Lomax and Max. A. Heaslet, 1955.
² It should be stressed that the x axis is parallel to the free-stream direction (wind axes) so a body of revolution can be symmetrical about this axis only at zero angle of attack.

an application of the convolution integral and other standard operational techniques yields

$$\varphi(x, r, \theta) = -\frac{1}{2\pi} \left\{ \int_{-L_0}^{x-\beta r} \frac{A_0(\xi) d\xi}{\sqrt{(x-\xi)^2 - \beta^2 r^2}} + \sum_{n=1}^{\infty} r^n \left(\frac{1}{r} \frac{d}{dr} \right)^n \int_{-L_0}^{x-\beta r} \frac{\left[\frac{(-1)^n}{\beta^n (n-1)!} \int_{-L_0}^{\xi} (\xi-x_1)^{n-1} A_n(x_1) dx_1 \right]}{\sqrt{(x-\xi)^2 - \beta^2 r^2}} d\xi \right\} \quad (15)$$

From comparison of equations (8) and (15), the relation between the strengths $a_n(x)$ and $A_n(x)$ for the two different forms of the solution is found to be

$$\left. \begin{aligned} a_0(x) &= A_0(x), & n=0 \\ (-\beta)^n a_n(x) &= \frac{1}{(n-1)!} \int_{-L_0}^x (x-x_1)^{n-1} A_n(x_1) dx_1, & n>0 \end{aligned} \right\} \quad (16a)$$

or

$$(-\beta)^n a_n^{(n)}(x) = A_n(x) \quad (16b)$$

where $a_n^{(n)}(x)$ symbolizes the operation $\frac{d^n}{dx^n} a_n(x)$ and where use is made of the conditions

$$a_n^{(n)}(-L_0) = a_n^{(n-1)}(-L_0) = \dots = a_n(-L_0) = 0 \quad (17)$$

Another way to transform equation (13) back to the physical plane is to do so directly. In this way one finds (from ref. 5)

$$L^{-1}K_n(\beta rs) = \begin{cases} 0, & x < \beta r \\ \frac{\cosh \left[n \cosh^{-1} \left(\frac{x}{\beta r} \right) \right]}{\sqrt{x^2 - \beta^2 r^2}}, & x > \beta r \end{cases}$$

from which equation (13) reduces immediately to

$$\varphi(x, r, \theta) = -\frac{1}{2\pi} \sum_{n=0}^{\infty} \cos n\theta \int_{-L_0}^{x-\beta r} \frac{A_n(\xi) \cosh \left[n \cosh^{-1} \left(\frac{x-\xi}{\beta r} \right) \right]}{\sqrt{(x-\xi)^2 - \beta^2 r^2}} d\xi \quad (18)$$

The perturbation velocities in the field represented by this potential are readily calculated. Thus

$$\varphi_x(x, r, \theta) = -\frac{1}{2\pi} \sum_{n=0}^{\infty} \cos n\theta \int_{-L_0}^{x-\beta r} \frac{A_n'(\xi) \cosh \left[n \cosh^{-1} \left(\frac{x-\xi}{\beta r} \right) \right]}{\sqrt{(x-\xi)^2 - \beta^2 r^2}} d\xi \quad (19a)$$

$$\frac{1}{r} \varphi_\theta(x, r, \theta) = \frac{1}{2\pi r} \sum_{n=0}^{\infty} n \sin n\theta \int_{-L_0}^{x-\beta r} \frac{A_n(\xi) \cosh \left[n \cosh^{-1} \left(\frac{x-\xi}{\beta r} \right) \right]}{\sqrt{(x-\xi)^2 - \beta^2 r^2}} d\xi \quad (19b)$$

and by taking the derivative of equation (13) with respect to r , one finds

$$\bar{\varphi}_r = \frac{1}{2\pi} \left\{ \beta s \bar{A}_0(s) K_1(\beta rs) + \frac{1}{2} \sum_{n=1}^{\infty} \beta s \bar{A}_n(s) [K_{n-1}(\beta rs) + K_{n+1}(\beta rs)] \right\}$$

which transforms to

$$\varphi_r(x, r, \theta) = \frac{1}{\pi} \left(\int_{-L_0}^{x-\beta r} \frac{(x-\xi) A_0'(\xi) d\xi}{r \sqrt{(x-\xi)^2 - \beta^2 r^2}} + \frac{\beta}{2} \sum_{n=1}^{\infty} \cos n\theta \int_{-L_0}^{x-\beta r} \frac{A_n'(\xi) \left\{ \frac{x-\xi}{\beta r} \cosh \left[n \cosh^{-1} \left(\frac{x-\xi}{\beta r} \right) \right] \right\}}{\sqrt{(x-\xi)^2 - \beta^2 r^2}} d\xi \right) \quad (19c)$$

If the relation between the functions $a_n(x)$ and $A_n(x)$ is given by equation (16), the velocities represented by equations (9) and (19) are, of course, identical.

In order to obtain limiting values induced by multipoles distributed along the x axis starting at $-L_0$, one returns to either equation (8) or (18) and calculates the leading term in a $1/r$ expansion. As in the derivation of equation (5), it is necessary to observe that as r is increased, x should also be increased so φ is given in the vicinity of the foremost Mach cone created by the multipole distributions. Hence, using equation (4), one finds for equation (18)

$$\varphi = -\frac{1}{2\pi} \sum_{n=0}^{\infty} \cos n\theta \int_{-L_0}^{x_0} \frac{A_n(\xi) \cosh \left[n \cosh^{-1} \left(1 + \frac{x_0 - \xi}{\beta r} \right) \right]}{\sqrt{2\beta r(x_0 - \xi) \left(1 + \frac{x_0 - \xi}{2\beta r} \right)}} d\xi$$

which has the leading term as r goes to infinity

$$\varphi_{r \rightarrow \infty} = -\frac{1}{2\pi \sqrt{2\beta r}} \sum_{n=0}^{\infty} \cos n\theta \int_{-L_0}^{x_0} \frac{A_n(\xi) d\xi}{\sqrt{x_0 - \xi}} \quad (20)$$

Similarly, the perturbation velocities reduce to

$$\varphi_x)_{r \rightarrow \infty} = -\frac{1}{2\pi \sqrt{2\beta r}} \sum_{n=0}^{\infty} \cos n\theta \int_{-L_0}^{x_0} \frac{A_n'(\xi) d\xi}{\sqrt{x_0 - \xi}} \quad (21a)$$

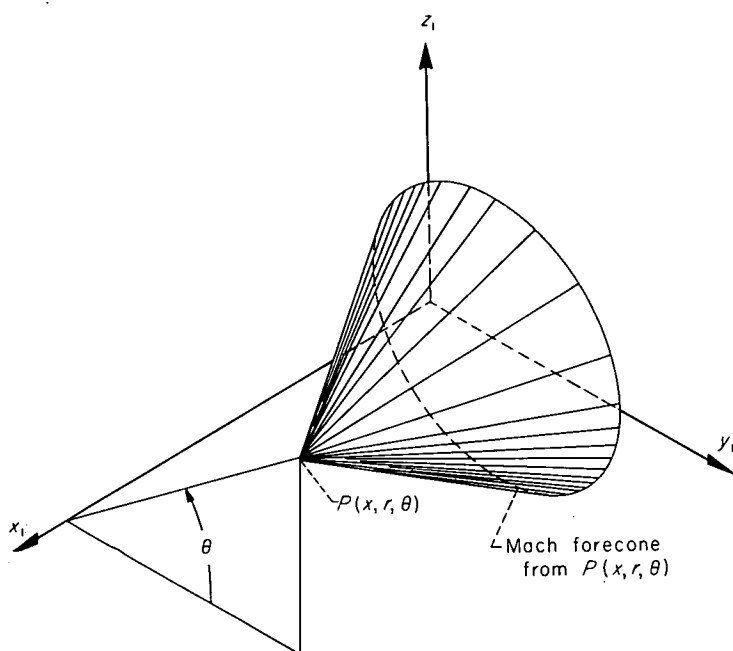
$$\varphi_r)_{r \rightarrow \infty} = -\beta \varphi_x \quad (21b)$$

$$\left(\frac{1}{r} \varphi_\theta \right)_{r \rightarrow \infty} = \frac{1}{2\pi \sqrt{2\beta r}} \sum_{n=0}^{\infty} n \sin n\theta \int_{-L_0}^{x_0} \frac{A_n(\xi) d\xi}{\sqrt{x_0 - \xi}} \quad (21c)$$

In calculating the wave drag using equation (2) only the velocity components $\varphi_x)_{r \rightarrow \infty}$ and $\varphi_r)_{r \rightarrow \infty}$ are necessary. Hence, from comparison of equations (21a) and (21b) with (6a) and (6b), it follows that at a given θ a series of multipoles induce the same momentum flux on an infinite cylindrical control surface as a line of sources having a strength variation $a_0(x)$ equal to $\sum_{n=0}^{\infty} \cos n\theta A_n'(\xi)$. If one identifies a line of sources with a body of revolution, then it is apparent that, at a given θ , a dragwise equivalence has been established between a line of multipoles and a body of revolution.

HAYES' THEOREM AND ITS APPLICATION

In the previous section a relation was found between multipole and source strengths which produce, at a fixed θ ,

FIGURE 6.—Mach forecone from x, r, θ in x_1, y_1, z_1 space.

equivalent momentum transport across a cylinder of infinite radius. By using a theorem attributable to Hayes (ref. 6) one can derive the strength relationship between any distribution of singularities throughout space and a line of sources which gives the same equivalence.

The essence of Hayes' theorem is that, for a fixed θ , the velocities induced on a cylinder of infinite radius by singular solutions to equation (1) (e. g., sources and doublets) are invariant to displacements of the singularities along certain oblique planes. In order to be specific, the equation of these oblique planes is next derived.

Consider the point x, r, θ in a flow field having a supersonic free stream moving parallel to the x axis. Figure 6 shows the Mach forecone (by definition the Mach forecone is the boundary of the region within which a disturbance in a supersonic stream can affect the flow at the cone apex) from x, r, θ in x_1, y_1, z_1 space. The equation of the forecone is

$$x_1 = x - \beta \sqrt{(r \cos \theta - y_1)^2 + (r \sin \theta - z_1)^2} \quad (22)$$

One wishes to let r become very large and find the shape of the forecone as it passes through regions close to the origin of the x_1, y_1, z_1 coordinate system, regions in which the objects creating the wave drag are located. From equation (4) and the expansion of equation (22) for large r , it follows that

$$\begin{aligned} x_1 &= x_0 + \beta r - \beta r \left[1 - \frac{2}{r} (y_1 \cos \theta + z_1 \sin \theta) + \frac{y_1^2 + z_1^2}{r^2} \right]^{1/2} \\ &= x_0 + \beta (y_1 \cos \theta + z_1 \sin \theta) - \frac{\beta}{2r} (y_1 \sin \theta - z_1 \cos \theta)^2 + \dots \end{aligned}$$

and when r goes to infinity

$$x_1 = x_0 + \beta y_1 \cos \theta + \beta z_1 \sin \theta \quad (23)$$

which is the equation of the oblique plane mentioned above. It should be noted that the envelope formed from these planes by fixing x_0 and varying θ between 0 and 2π coincides

with the Mach forecone and aftercone from the point $x_0, 0, 0$. Hayes' result can now be stated ⁵

To the lowest order in $1/r$, as r tends to infinity, the magnitude of the perturbation velocity potential and its gradients at a fixed angle θ is invariant to a finite translation of sources (or any other singular solution to the wave equation) on planes parallel to that given by equation (23).

Consider the application of Hayes' theorem to planar distributions of sources lying in the $z_1=0$ plane. As is well known, such a distribution simulates a wing symmetrically disposed about the horizontal ($z_1=0$) plane. In fact, if $\lambda_u(x_1, y_1)$ is the local slope of the wing upper surface, the local source strength per unit area (according to thin airfoil theory) required to simulate the wing is $-U_o \lambda_u / \pi$ and the velocity potential of the disturbed flow field is given by

$$\varphi(x, y, z) = -\frac{U_o}{\pi} \int_{\tau} \int \frac{\lambda_u(x_1, y_1) dx_1 dy_1}{\sqrt{(x-x_1)^2 - \beta^2(y-y_1)^2 - \beta^2 z^2}} \quad (24)$$

where τ is the area of integration bounded by the wing edge and the trace in the $z_1=0$ plane of the Mach forecone from the point x, y, z . Next introduce the new coordinates ξ_1 and η_1 such that ξ_1 lies along the x_1 axis and η_1 lies along the intersection of the $z_1=0$ plane and the plane given by equation (23) (see fig. 7). Set

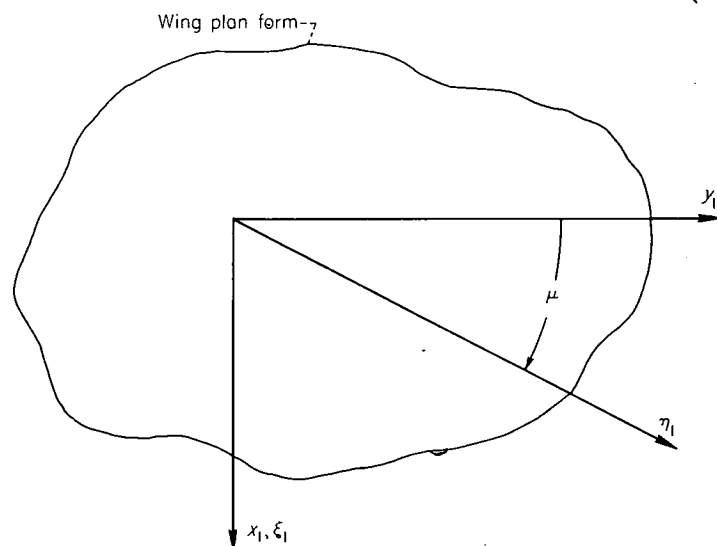
$$\tan \mu = \beta \cos \theta \quad (25)$$

and

$$\left. \begin{aligned} \xi_1 &= x_1 - y_1 \tan \mu \\ \eta_1 &= y_1 \sec \mu \\ x_1 &= \xi_1 + \eta_1 \sin \mu \\ y_1 &= \eta_1 \cos \mu \end{aligned} \right\} \quad (26)$$

Then, in terms of the ξ_1, η_1 system, equation (24) becomes

$$\varphi(x, y, z) = -\frac{U_o}{\pi} \int_{\tau} \int \frac{\lambda_u(\xi_1 + \eta_1 \sin \mu, \eta_1 \cos \mu) \cos \mu d\xi_1 d\eta_1}{\sqrt{(x-\xi_1-\eta_1 \sin \mu)^2 - \beta^2(y-\eta_1 \cos \mu)^2 - \beta^2 z^2}} \quad (27)$$

FIGURE 7.—Orientation of x_1, y_1 and ξ_1, η_1 coordinates.

⁵ For proofs, see Hayes' original derivation (ref. 6) or, if more convenient, reference 1.

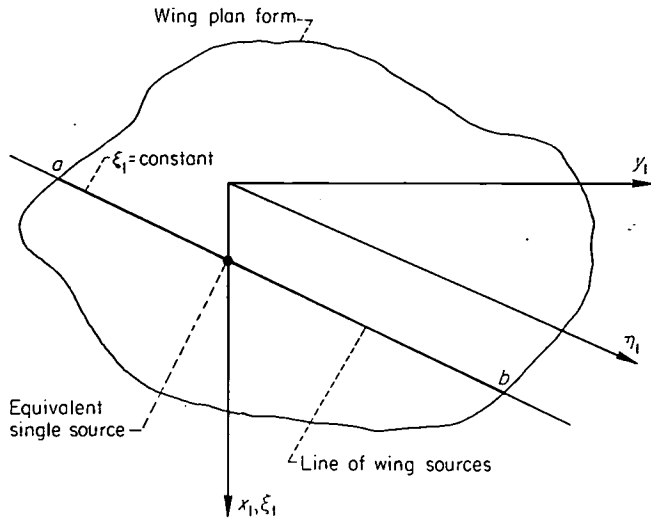


FIGURE 8.—Position of wing sources and equivalent single source.

As before, the asymptotic value of φ as $r = \sqrt{y^2 + z^2} \rightarrow \infty$ is to be calculated. Accordingly, one can apply Hayes' theorem and sum up all the sources along a line $\xi_1 = \text{constant}$ (e. g., between a and b in fig. 8) and place them as a single source on the axis. The strength of this equivalent single source is given by

$$U_o S_w'(\xi_1, \theta) = 2U_o \cos \mu \int_{\text{wing}} \lambda_w(\xi_1 + \eta_1 \sin \mu, \eta_1 \cos \mu) d\eta_1 \quad (28)$$

where the integration is taken across the complete wing along the line $\xi_1 = \text{constant}$ and $S_w'(\xi_1, \theta) = \frac{\partial}{\partial \xi_1} S_w(\xi_1, \theta)$.

The term $S_w(x, \theta)$ has a clear geometrical interpretation (see fig. 9), being simply the normal projection of the wing area intercepted by the oblique plane $x_1 = x + \beta y_1 \cos \theta$.

The above defines the strength variation of a line of sources (and, therefore, a body of revolution) which induces, for large r and a fixed θ , a potential field identical to that

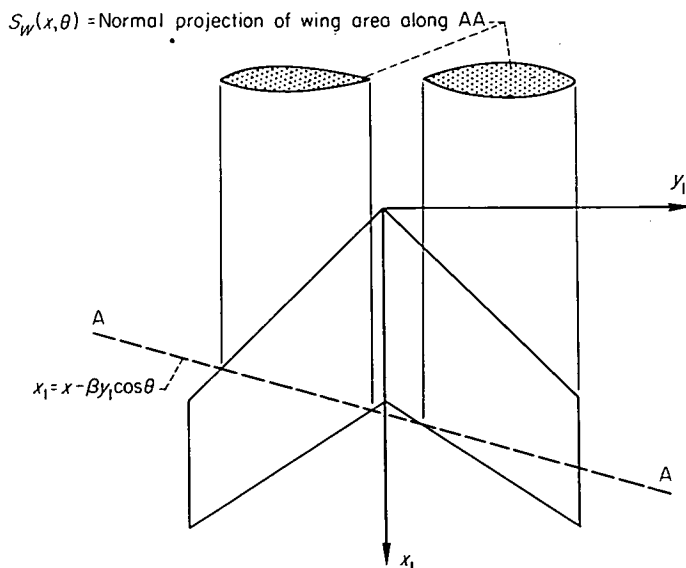


FIGURE 9.—Wing area intercepted by oblique plane.

* The true oblique plane is given by equation (23) but the wing is so close to the $z_1 = 0$ plane that the variation with z_1 can be neglected.

induced by a given wing. Hence, the results given in equation (6) yield

$$\varphi_x)_{r \rightarrow \infty} = -\frac{U_o}{2\pi\sqrt{2\beta r}} \int_{-L'(\theta)}^{x_o} \frac{S_w''(\xi_1, \theta) d\xi_1}{\sqrt{x_o - \xi_1}} \quad (29a)$$

$$\varphi_r)_{r \rightarrow \infty} = -\beta \varphi_x \quad (29b)$$

A similar result exists for a planar doublet distribution (see ref. 1 or 6) but, in this report, only problems in which the wings have no loading (local lift) will be considered. Lifting effects have been treated in a similar fashion in reference 7.

CANCELLATION MULTIPOLES AND DRAG MINIMIZATION

Since the flow field is governed by a linear partial differential equation the velocities induced by different solutions to it are additive. Therefore, the drag of an object simulated by various multipoles distributed along the x_1 axis and a sheet of sources in the $z_1 = 0$ plane is given by

$$D = -\rho_o \int_0^{2\pi} d\theta \int_{-\infty}^{\infty} dx \left\{ \lim_{r \rightarrow \infty} r [(\varphi_r)_m + (\varphi_r)_w] [(\varphi_x)_m + (\varphi_x)_w] \right\}$$

where the subscripts m and w refer to the multipoles and wing sources, respectively. But equations (21) and (29) identify, for a fixed θ , these velocities with those induced by equivalent line sources. Hence, for any given θ , one can immediately apply Kármán's drag formula (ref. 8) and then for the total drag, integrate θ from 0 to 2π . This leads to

$$D = -\frac{\rho_o}{8\pi^2} \int_0^{2\pi} d\theta \int_{-L'(\theta)}^{L(\theta)} dx_1 \int_{-L'(\theta)}^{L(\theta)} dx_2 \left\{ U_o S_w''(x_1, \theta) + \sum_0^{\infty} (-\beta)^n [a_n^{(n+1)}(x_1) \cos n\theta + b_n^{(n+1)}(x_1) \sin n\theta] \right. \\ \left. \left\{ U_o S_w''(x_2, \theta) + \sum_0^{\infty} (-\beta)^n [a_n^{(n+1)}(x_2) \cos n\theta + b_n^{(n+1)}(x_2) \sin n\theta] \right\} 1n|x_1 - x_2| \right\}$$

However, since both the wing and multipoles are in the same plane (interpreted physically, the wing is centrally mounted on the fuselage) and the wing is simulated by sources only (has no twist or camber), one can show the optimum value of each $b_n^{(n+1)}(x_1)$ is identically zero.⁷ Hence, one can write

$$D = -\frac{\rho_o}{8\pi^2} \int_0^{2\pi} d\theta \int_{-L'(\theta)}^{L(\theta)} dx_1 \int_{-L'(\theta)}^{L(\theta)} dx_2 \left[U_o S_w''(x_1, \theta) + \sum_0^{\infty} (-\beta)^n a_n^{(n+1)}(x_1) \cos n\theta \right] \\ \left[U_o S_w''(x_2, \theta) + \sum_0^{\infty} (-\beta)^n a_n^{(n+1)}(x_2) \cos n\theta \right] 1n|x_1 - x_2| \quad (30)$$

⁷ By symmetry

Hence

$$S_w''(x, \theta) = S_w''(x, 2\pi - \theta)$$

$$\int_0^{2\pi} \sin n\theta S_w''(x, \theta) d\theta = 0$$

and any positive or negative variation of $b_n^{(n+1)}(x_1)$ can only increase the drag.

Next expand the term $S_w''(x, \theta)$ in a Fourier series. One finds

$$U_o S_w''(x, \theta) = \sum_0^{\infty} (-\beta)^n \alpha_n^{(n+1)}(x) \cos n\theta \quad (31)$$

where

$$\alpha_o(x) = \frac{U_o}{2\pi} \int_0^{2\pi} S_w'(x, \theta) d\theta \quad (32)$$

$$\alpha_n^{(n)}(x) = \frac{U_o}{\pi(-\beta)^n} \int_0^{2\pi} S_w'(x, \theta) \cos n\theta d\theta \quad (33)$$

Place these expressions in equation (30), integrate with respect to θ —using the orthogonal property of the trigonometric series—and one finds

$$D = 2D_o + \sum_1^{\infty} D_n \quad (34)$$

where

$$\begin{aligned} \frac{D_n}{q} = & -\frac{\beta^{2n}}{4\pi U_o^2} \int_{-L_o}^{L_o} dx_1 \int_{-L_o}^{L_o} dx_2 [\alpha_n^{(n+1)}(x_1) + \alpha_n^{(n+1)}(x_2)] \\ & [\alpha_n^{(n+1)}(x_2) + \alpha_n^{(n+1)}(x_1)] 1n|x_1 - x_2| \end{aligned} \quad (35)$$

Since one can show⁸

$$I = - \int_{-L_o}^{L_o} dx_1 \int_{-L_o}^{L_o} dx_2 f'(x_1) f'(x_2) 1n|x_1 - x_2| \geq 0$$

the minimum value of D as expressed by equation (34) is given when each D_n is itself a minimum. In other words, each D_n can be minimized separately. Further, it follows that the value of the minimum itself is zero and occurs when

$$\begin{aligned} a_n^{(n+1)}(x) = & -\alpha_n^{(n+1)}(x) \\ = & \begin{cases} -\frac{U_o}{2\pi} \int_0^{2\pi} S_w''(x, \theta) d\theta, & n=0 \\ -\frac{U_o}{\pi(-\beta)^n} \int_0^{2\pi} S_w''(x, \theta) \cos n\theta d\theta, & n>0 \end{cases} \end{aligned} \quad (36)$$

Equation (36) is the mathematical definition of the optimum cancellation multipoles; namely, those multipoles which are just equal in magnitude and opposite in sign to the wing equivalent multipoles—equivalent in the sense that they induce an identical momentum flux across a cylinder of infinite radius.

Obviously, if all the optimum cancellation multipoles were used, the wave drag of the combination would be zero. This result must, however, be properly interpreted with regard to the simulated shape. In order that the multipole lines can represent the distortion of a real fuselage, one must assume a cylindrical body exists upstream from the Mach cone $x + L_o = \beta r$ (the effects of the nose are being neglected). This body forms the initial boundary of the stream tube which represents the physical fuselage in the vicinity of the wing and multipole lines. Clearly, the area enclosed by this initial boundary can be small enough for the subsequent stream surface to cross itself and represent, therefore, a physically unreal body. Hence, the fact that the wave drag of the wing and multipole combination can

be reduced to zero is quite valid, but in the over-all picture not only have the inevitable nose and tail drags been neglected but also the shape simulated by the combination can be unrealistic.

SOME PROPERTIES OF THE CANCELLATION MULTIPOLES

Let us consider next some of the restrictions necessarily imposed on cancellation-multipole distributions and some of the particular properties of those given by equation (36). In the first place, if $a_n(x)$ is any multipole distribution that generates a potential field given by equation (8) or (15), it follows from equation (17) that the value of $a_n(x)$ and its first n derivatives should be everywhere continuous. Further, if $a_n(x)$ is a constant behind some point, say L_o (i. e., for $\infty > x > L_o$), the induced flow field would simulate expanding streamlines in the case $n=0$ or some form of vorticity in the case $n>0$; the former case is to be avoided since any simulated body is assumed to have a finite area at $x = \infty$, and the latter case is to be avoided if there are no resultant forces normal to the free stream.

One can show that all the above properties are satisfied by $\alpha_n(\xi)$, the optimum cancellation-multipole distribution as defined by equation (36). First, notice that $\alpha_n^{(n+1)}(\xi)$ must be zero everywhere outside the wing-enclosing Mach forecone and aftercone, that is, for $-\infty < \xi < -L_o'$ and $L_o' < \xi < \infty$ (see fig. 10). (Any multipoles in these regions cannot combine with the wing equivalent multipoles and must, therefore, increase the drag.) Hence, one can set

$$\begin{aligned} \alpha_n^{(n)}(-L_o') &= \alpha_n^{(n-1)}(-L_o') \\ &= \dots \alpha_n(-L_o') \\ &= 0 \end{aligned}$$

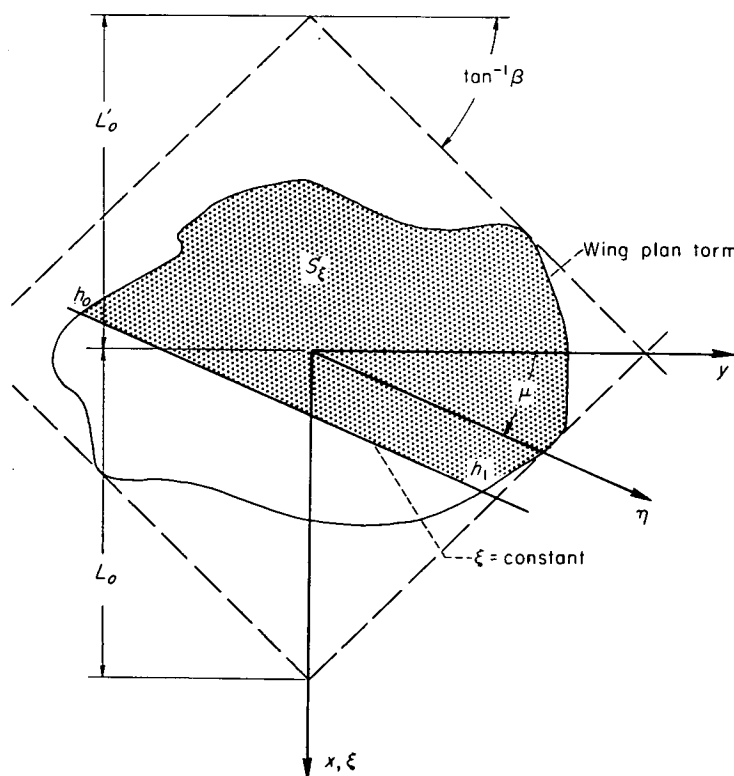


FIGURE 10.—Symbols used in study of multipole properties.

⁸ Set $f(x) = \sum_1^{\infty} A_n \sin n\psi$, $x = -L_o \cos \psi$. Integration gives $I = \frac{\pi^2}{2} \sum_1^{\infty} n A_n^2$ which can never be negative.

Then the condition of continuity is automatically satisfied for $\alpha_n^{(m)}(\xi)$ in the entire interval $-\infty < \xi < \infty$ if $S_w'(\xi, \theta)$ is derived from a wing having finite wave drag (in particular, from a wing having no blunt edges along which the normal component of the free-stream Mach number is unity or greater). It follows immediately that $\alpha_n^{(m)}(\xi)$, $m < n$, is continuous since the latter is found by integrating (further smoothing) $\alpha_n^{(n)}(\xi)$.

The proof that $\alpha_n(L_o)$ as given by equation (36) is zero requires more consideration. One can show, however, that $\alpha_n^{(m)}(L_o) = 0$ where $0 \leq m \leq n$. First, the equality $\alpha_n^{(n)}(L_o) = 0$ follows from the fact that the wing closes and $S_w'(L_o, \theta)$ itself is zero. Next consider the definition of $\alpha_n^{(m)}(\xi)$. Thus

$$\alpha_n^{(m)}(\xi) = \frac{-U_o}{(-\beta)^n \pi} \int_0^{2\pi} S_w'(\xi, \theta) \cos n\theta d\theta$$

$$= \frac{-2U_o}{(-\beta)^n \pi} \int_0^{2\pi} \cos \mu \cos n\theta d\theta \int_{h_o(\theta, \xi)}^{h_1(\theta, \xi)} \lambda_u(\xi + \eta \sin \mu, \eta \cos \mu) d\eta$$

where use has been made of equation (28) for the definition of $S_w'(\xi, \theta)$ and h_o and h_1 are defined in figure 10. Since

$$\alpha_n^{(m)}(\xi) = \frac{1}{\Gamma(n-m)} \int_{-L_o}^{\xi} (\xi - \xi_1)^{n-m-1} \alpha_n^{(n)}(\xi_1) d\xi_1 \quad (37)$$

one has

$$\alpha_n^{(m)}(\xi) = \frac{-2U_o}{(-\beta)^n \pi \Gamma(n-m)} \int_0^{2\pi} \cos n\theta d\theta$$

$$\int_{-L_o}^{\xi} d\xi_1 \int_{h_o(\theta, \xi_1)}^{h_1(\theta, \xi_1)} d\eta (\xi - \xi_1)^{n-m-1} \lambda_u(\xi_1 + \eta \sin \mu, \eta \cos \mu) \cos \mu$$

Change the ξ_1, η coordinates back to the x, y system by means of equation (26) and this becomes

$$\alpha_n^{(m)}(\xi) = \frac{-2U_o}{(-\beta)^n \pi \Gamma(n-m)} \int_0^{2\pi} \cos n\theta d\theta \int_{S_\xi} (\xi - x + \beta y \cos \theta)^{n-m-1} \lambda_u(x, y) dx dy$$

The area S_ξ , shown in figure 10, becomes independent of θ when $\xi = L_o$ (being then just the area of the wing itself), therefore

$$\alpha_n^{(m)}(L_o) = \frac{-2U_o}{(-\beta)^n \pi \Gamma(n-m)} \iint_S \lambda_u(x, y) dx dy$$

$$\int_0^{2\pi} (L_o - x + \beta y \cos \theta)^{n-m-1} \cos n\theta d\theta = 0$$

since, for $m < n$.

$$\int_0^{2\pi} \cos m\theta \cos n\theta d\theta = 0$$

Hence, for the $\alpha_n(\xi)$ defined by equation (36)

$$\alpha_n^{(n)}(L_o) = \alpha_n^{(n-1)}(L_o) = \alpha_n^{(n-2)}(L_o) = \dots = \alpha_n(L_o) = 0 \quad (38)$$

AIRPLANE SHAPE

In the previous section a connection was established between multipole distributions and their resulting wave drag.

Further, this connection was direct and relatively simple if the strengths and positions of the distributions were given. Unfortunately the connection between the multipoles and the shape of the simulated surface is generally not so simple. Such a relation does certainly exist, however, and if the strengths of the multipoles are known, the relationship is again direct. That is, a given distribution of multipoles yields directly, by the formulas given in the previous section, the induced velocities everywhere in the flow field, these, in turn, fix the stream surfaces along any one of which (since, of course, the theory neglects viscosity) a physical surface can be imagined.

In general, if

$$\left. \begin{aligned} F_c(x, y, z) &= 0 \\ F_p(x, r, \theta) &= 0 \end{aligned} \right\} \quad (39)$$

are the equations of a stream surface in cartesian and polar coordinates, respectively, then the equations

$$\left. \begin{aligned} (U_o + \varphi_z) \frac{\partial F_c}{\partial x} + \varphi_y \frac{\partial F_c}{\partial y} + \varphi_z \frac{\partial F_c}{\partial z} &= 0 \\ (U_o + \varphi_z) \frac{\partial F_p}{\partial x} + \varphi_r \frac{\partial F_p}{\partial r} + \frac{1}{r^2} \varphi_\theta \frac{\partial F_p}{\partial \theta} &= 0 \end{aligned} \right\} \quad (40)$$

must hold.

For example, in studies of thin wings lying in a plane, the particular form of equation (39)

$$z - h(x, y) = 0$$

is assumed and equation (40) becomes

$$-(U_o + \varphi_z) \frac{\partial h}{\partial x} - \varphi_y \frac{\partial h}{\partial y} + \varphi_z = 0$$

or, neglecting second-order effects,

$$\frac{\partial h}{\partial x} = \frac{1}{U_o} \varphi_z$$

which is the familiar boundary condition used in thin-airfoil theory. On the other hand, if the equation of the body shape is written in the form

$$r - R(x, \theta) = 0$$

then equation (40) becomes, for linearized theory,

$$U_o \frac{\partial R}{\partial x} = \varphi_r - \frac{\varphi_\theta}{R^2} \frac{\partial R}{\partial \theta} \quad (41)$$

If the flow field is radially symmetrical or if the body surface is quasi-cylindrical, equation (41) reduces to

$$\frac{\partial R}{\partial x} = \frac{1}{U_o} \varphi_r \quad (42)$$

which is the familiar boundary condition used in the study of quasi-cylindrical bodies or bodies of revolution.

In general, a nonlinear partial differential equation of the first order such as equation (41) can be reduced to two simul-

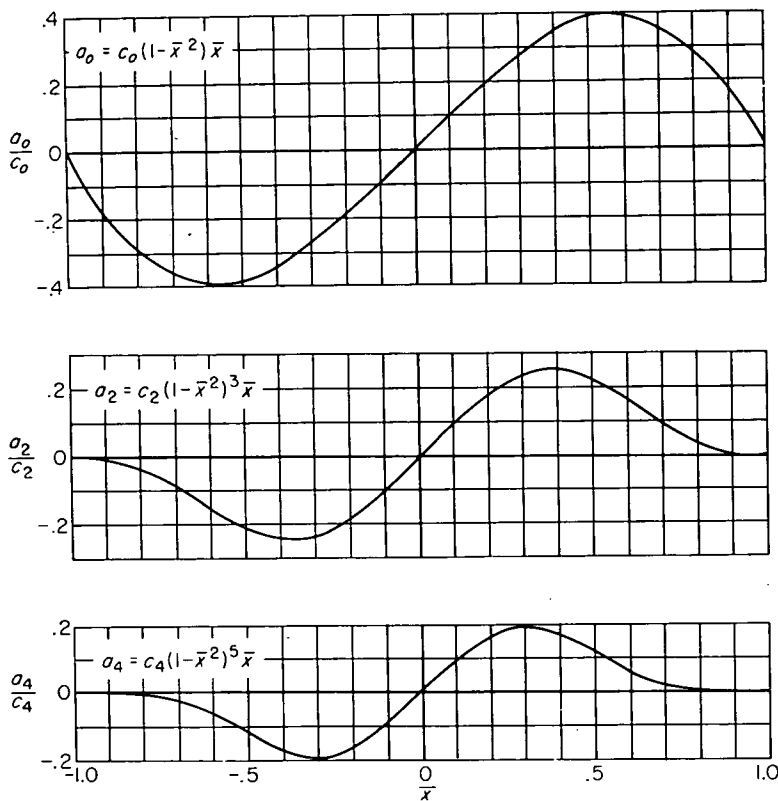
taneous, ordinary, nonlinear differential equations of the first degree (see, e. g., ref. 9). Thus equation (41) becomes

$$\left. \begin{aligned} \frac{d\theta}{dx} &= \frac{1}{U_o R^2} \varphi_\theta(x, R, \theta) \\ \frac{dR}{dx} &= \frac{1}{U_o} \varphi_r(x, R, \theta) \end{aligned} \right\} \quad (43)$$

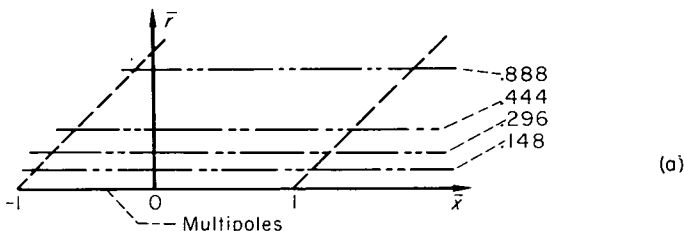
and if φ_θ and φ_r are known functions of x , R , and θ , these can be solved numerically.

If the strengths of all rectilinear multipoles and source sheets are given, equation (19) or (24) can be used to find φ_r and φ_θ at arbitrary field points. Hence, the first step in finding the body shapes reduces to that of integrating such equations. However, these integrations are difficult and tedious even when entirely numerical procedures are employed and the results still have to be interpreted in terms of the body shape according to equations (43). Therefore, from a practical viewpoint, it is necessary to study certain approximate methods for obtaining the velocity field.

Let attention be concentrated on the disturbances created by a line of multipoles. In particular, consider the fields

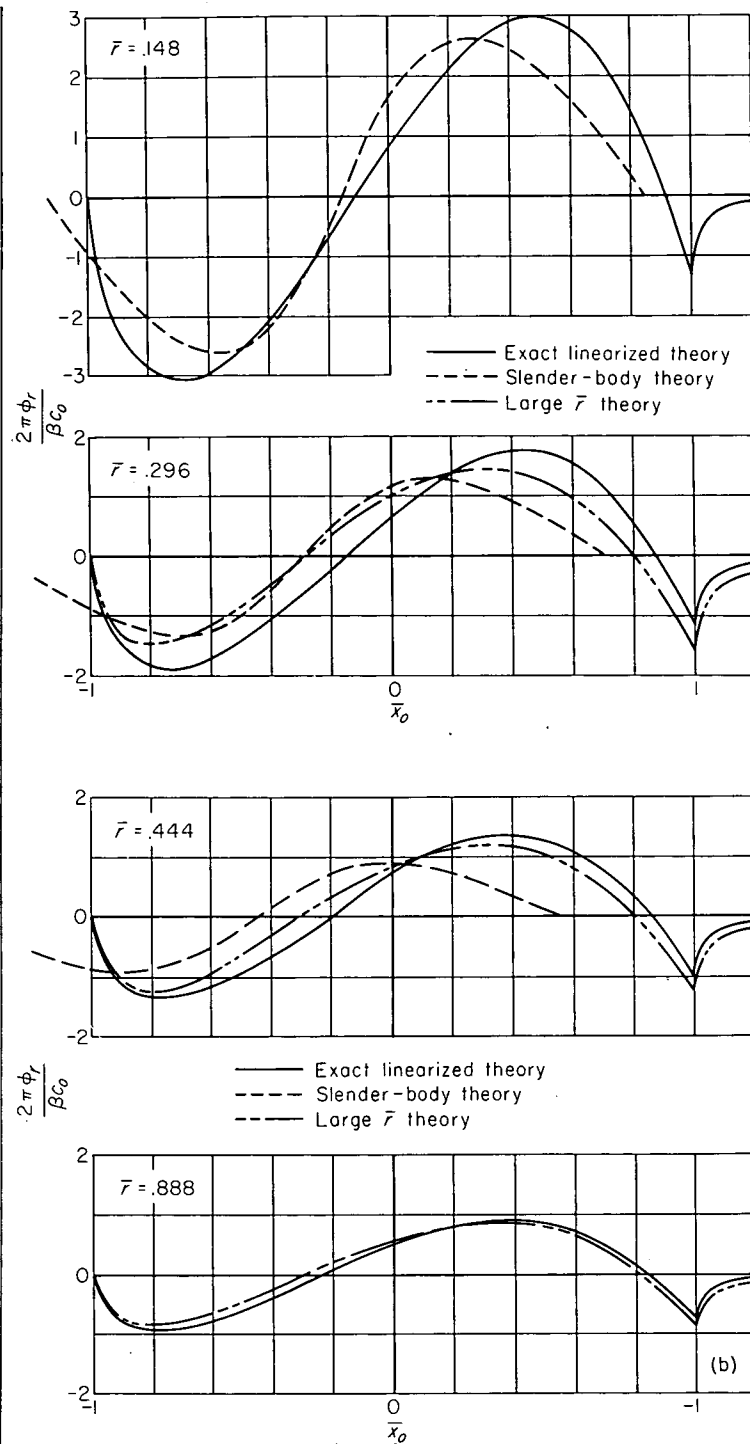


--- Radii at which velocities ϕ_r and ϕ_θ are presented



(a) Multipole distributions.

FIGURE 11.—Radial and tangential velocities induced by three different multipole distributions at four radii.



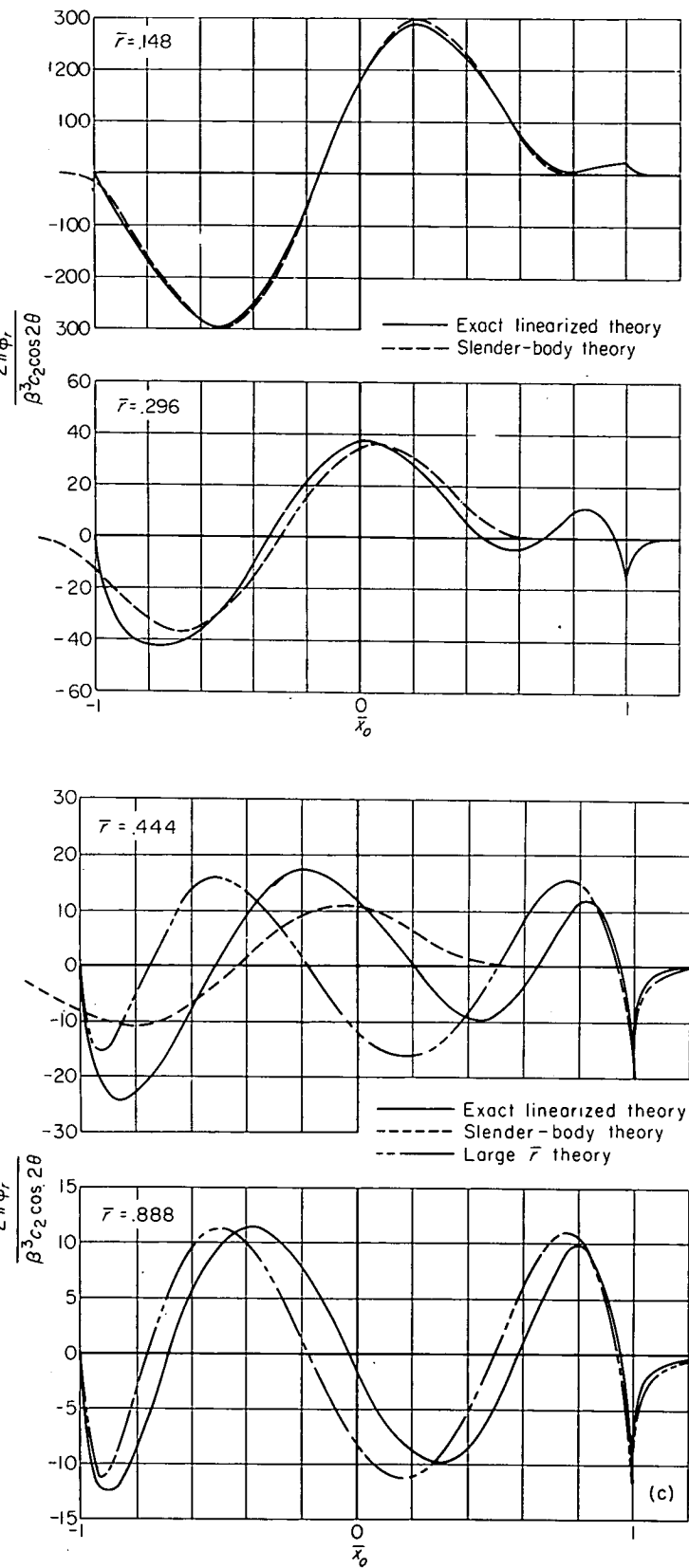
(b) Velocities, ϕ_r .

FIGURE 11.—Continued.

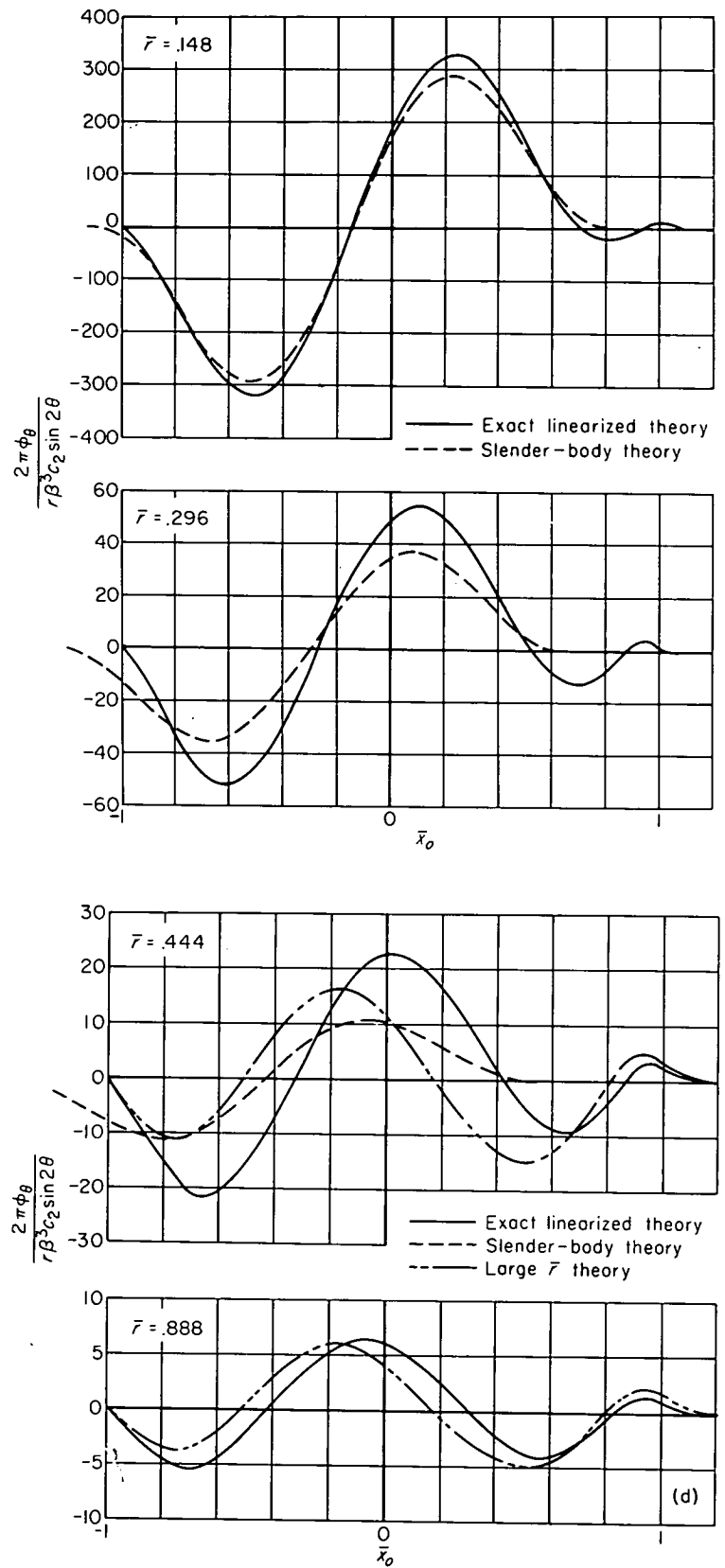
induced by simple polynomial distributions satisfying, in each case, the end conditions given by equation (17). For particular variations set

$$\left. \begin{aligned} a_0(\bar{x}) &= c_0(1-\bar{x}^2)\bar{x} \\ a_2(\bar{x}) &= c_2(1-\bar{x}^2)^3\bar{x} \\ a_4(\bar{x}) &= c_4(1-\bar{x}^2)^5\bar{x} \end{aligned} \right\} \quad (44)$$

where c_0 , c_2 , and c_4 are constants determining the amplitudes and $\bar{x} = x/L_o$. Figure 11 (a) shows the variations of these coefficients with \bar{x} , and figures 11(b) through 11(f) show



(c) Velocities, φ_{2r} .
FIGURE 11.—Continued.



(d) Velocities, $\varphi_{2\theta}$.
FIGURE 11.—Continued.

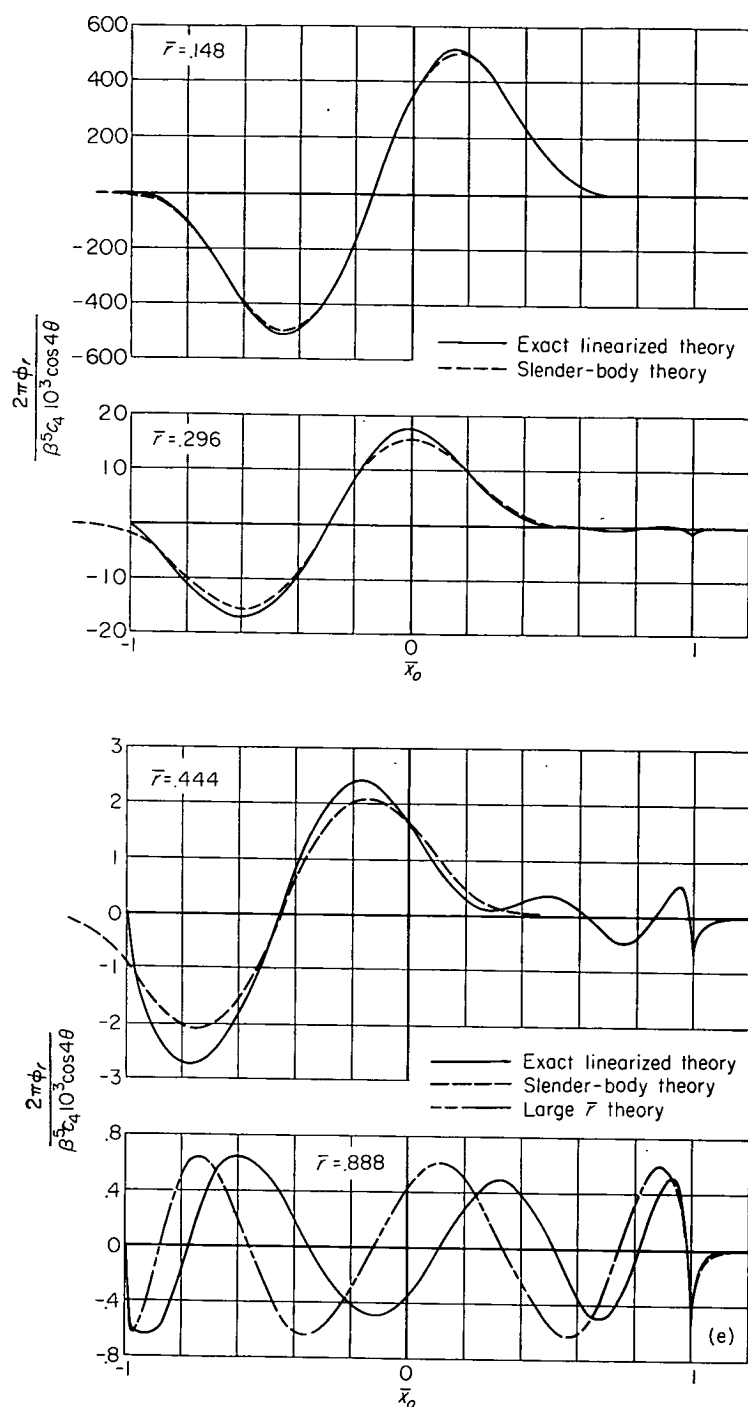
(e) Velocities, ϕ_{1r} .

FIGURE 11.—Continued.

how velocities induced by these distributions vary with \bar{x}_0 ($\bar{x}_0 = \bar{x} - \beta\bar{r}$) and \bar{r} ($\bar{r} = \beta r/L_0$). The results have been compared with those for large \bar{r} given by equation (21) and with those for small \bar{r} given by slender-body theory. Values for the latter theory are determined from equations (9) or (19) by expanding the expressions in powers of r and neglecting all but the first terms. Thus it can be shown

$$\phi_{nr})_{r \rightarrow 0} = \begin{cases} \frac{a_0(x)}{2\pi r}, & n=0 \\ \frac{(-2)^n n! a_n(x) \cos n\theta}{4\pi r^{n+1}}, & n>0 \end{cases} \quad (45a)$$

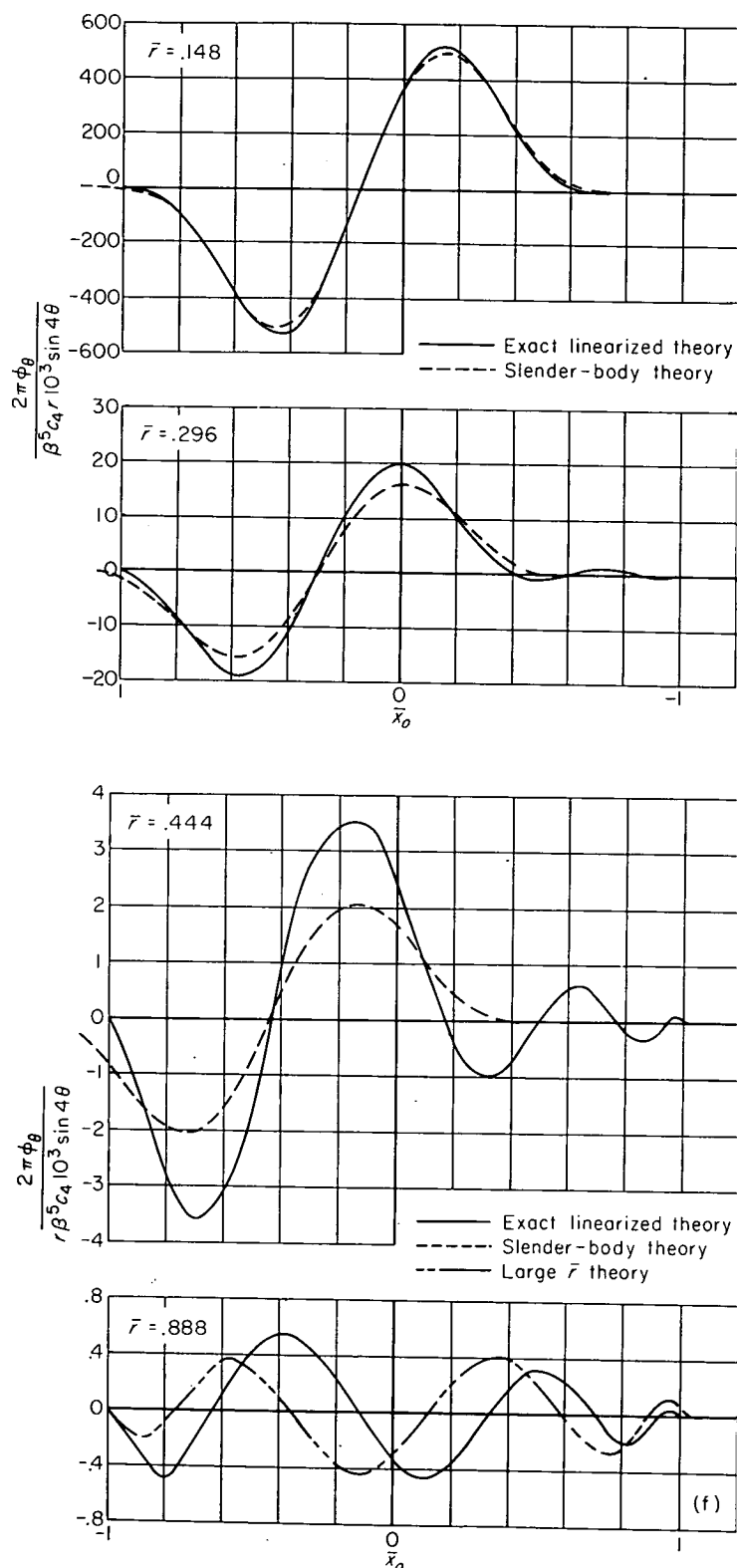
(f) Velocities, $\phi_{1\theta}$.

FIGURE 11.—Concluded.

$$\frac{1}{r} \phi_{n\theta})_{r \rightarrow 0} = \frac{(-2)^n n! a_n(x) \sin n\theta}{4\pi r^{n+1}}, \quad n \geq 0 \quad (45b)$$

The significance of figure 11 with regard to practical applications is more or less obvious. The first step in its use is to find the effective length of the cancellation-multipole distributions. Since the wing is given, the streamwise variation of the cancellation multipoles can be calculated. Actually

this variation will extend between the apexes of the enclosing Mach forecone and aftercone, a distance of $L_o + L'_o$ (see fig. 10). However, depending on the wing plan form and section, the effective lengths of the distributions (the interval of principal variation) can be considerably less as illustrated in figure 12. Designate this effective length as $2L_e$ and the

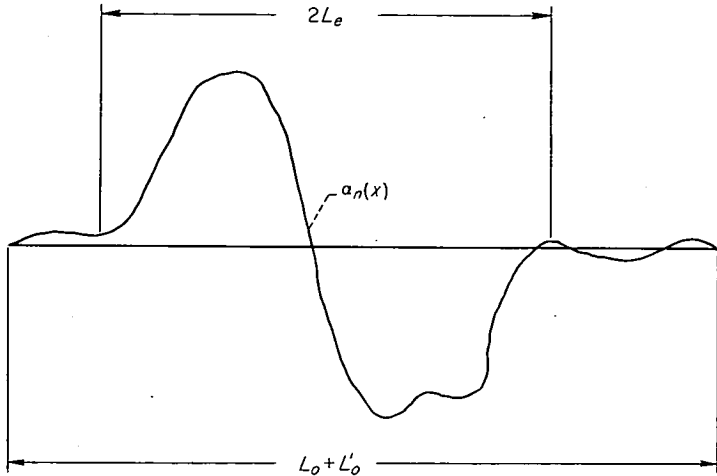
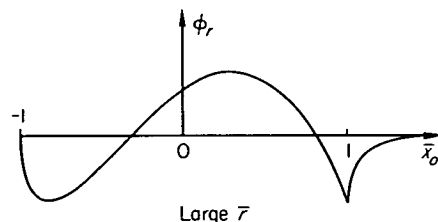
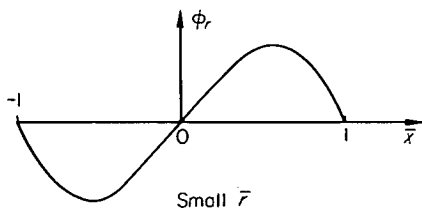
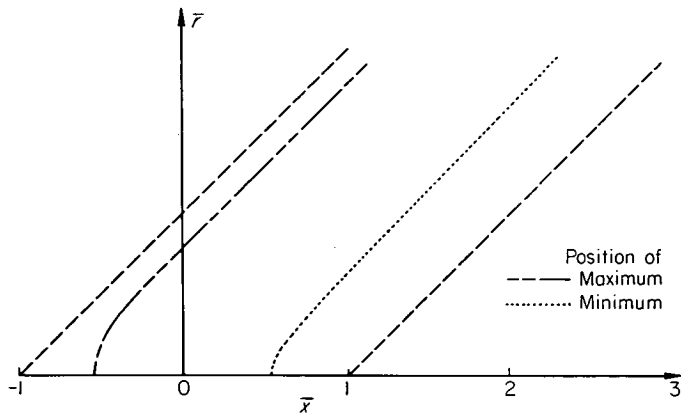


FIGURE 12.—Effective length of multipole distribution.



(a) Radial velocities induced by sources.

FIGURE 13.—Positions of crests of waves created by multipole distributions shown in figure 11.

distance to the vicinity of the body surface as r_e , and one can define the parameter \bar{r}_e thus

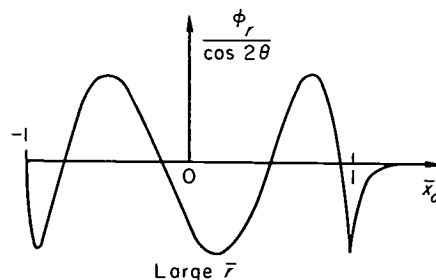
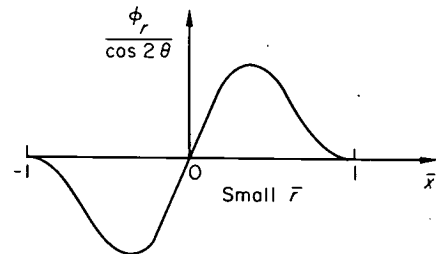
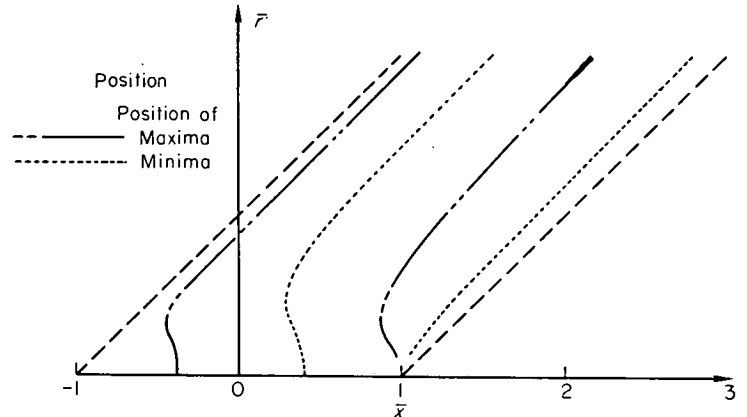
$$\bar{r}_e = \frac{\beta r_e}{L_e} \quad (46)$$

Using figure 11 and the parameter \bar{r}_e , one can now estimate the error incurred by the use of various approximate methods for calculating the body shape. A convenient way to carry out these estimations is to study the magnitude of the first crest of the waves shown in figures 11 (b) through 11 (f), and the distance this crest lies from the foremost Mach cone. Graphs showing the variations of these quantities with \bar{r} are given in figures 13, 14, and 15.

By means of the above concepts, let us study briefly four different approximate methods that can be used to calculate a body shape.

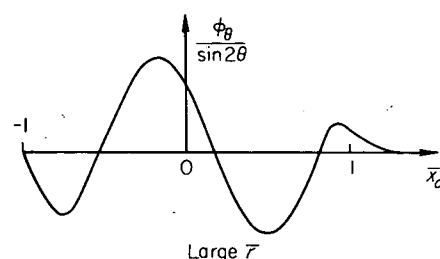
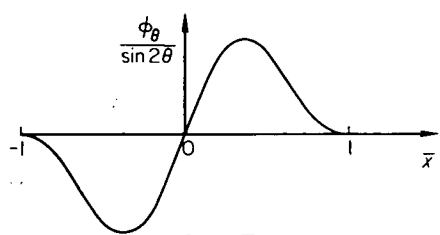
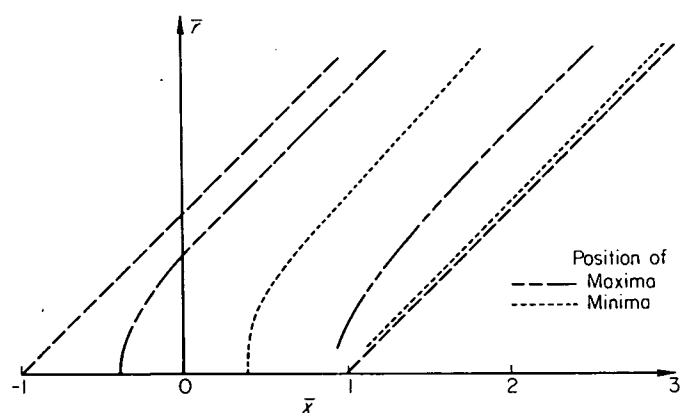
SLENDER-BODY THEORY

Slender-body theory is represented in figure 14 by the straight lines having the slopes, on the log-log scale, equal to $-(n+1)$ where n is the order of the multipole. Since this theory amounts to an expansion of the equations for the velocities in powers of \bar{r} , it obviously represents a good approximation when \bar{r}_e is sufficiently small. Notice that for a given percentage error the limiting value of \bar{r}_e for which the method applies increases as the order of the multipoles in-



(b) Radial velocities induced by second-order multipoles.

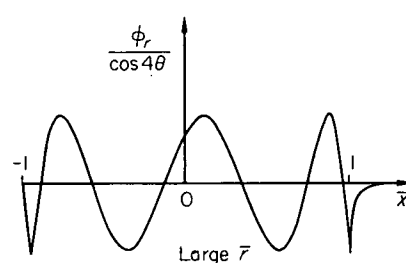
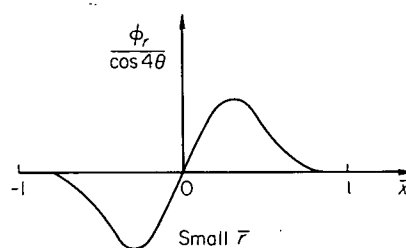
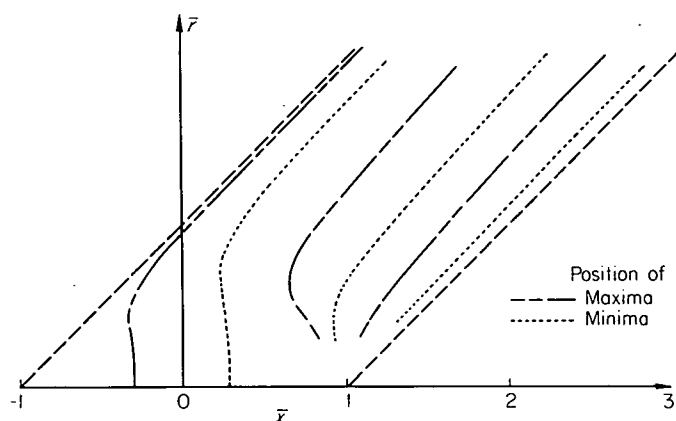
FIGURE 13.—Continued.



(c) Tangential velocities induced by second-order multipoles.

FIGURE 13.—Continued.

creases. For example, when $\bar{r}_e = 0.2$, φ_{θ} , as given by slender-body theory is 19 percent less than that given by exact linearized theory for the case shown, whereas φ_r is only 3 percent less. Correspondingly, the positions of the wave crests follow the path predicted by slender-body theory to larger values of \bar{r} as the order of the multipoles increases. The latter trend is illustrated by figure 15.



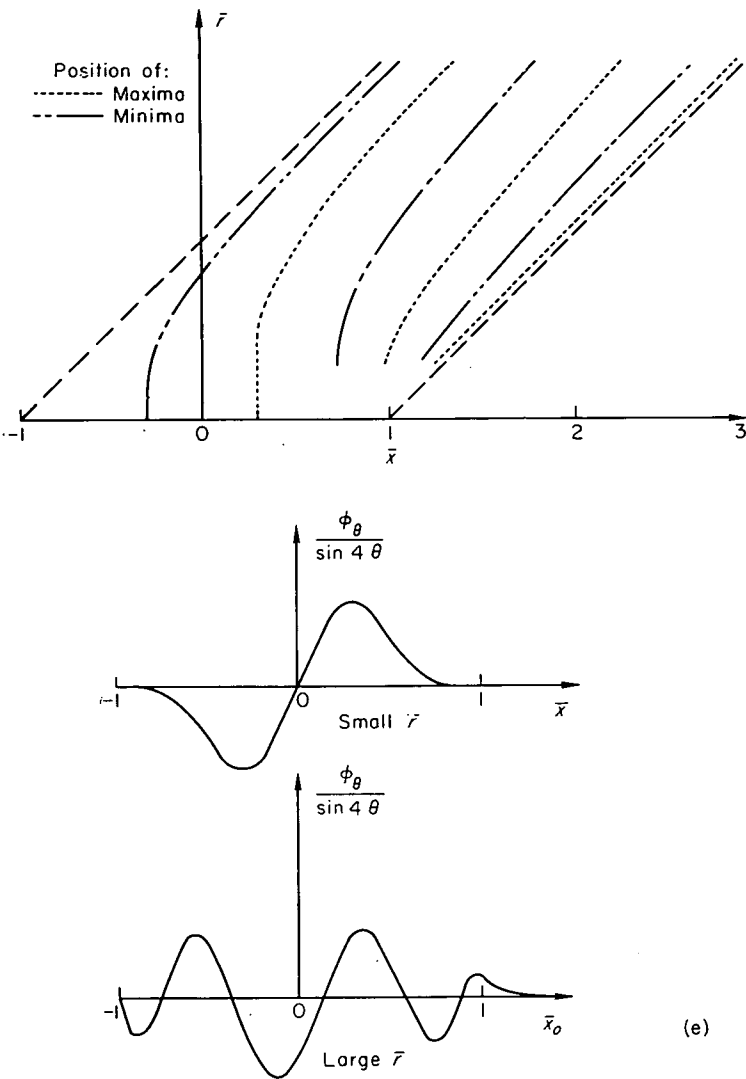
(d) Radial velocities induced by fourth-order multipoles.

FIGURE 13.—Continued.

If for a particular problem r_e is small enough for slender-body theory to be considered a good approximation, the equation for the body shape, $r = R(x, \theta)$, corresponding to the combined wing and optimum cancellation multipoles defined in equation (36) is determined by the expressions (using equations (45), (36), and (14) together with equation (42))

$$\frac{d\theta}{dx} = \left[\frac{\varphi_{\theta}(x, R, \theta)}{U_o R^2} \right]_{wing} + \sum_0^{\infty} \frac{\left(\frac{2}{\beta}\right)^n \sin n\theta}{4\pi^2 R^{n+2}} \int_0^{2\pi} d\psi \int_{-L_o}^x dx_1 (x-x_1)^n \cos n\psi S_w''(x_1, \psi) \quad (47a)$$

$$\frac{dR}{dx} = \left[\frac{\varphi_r(x, R, \theta)}{U_o} \right]_{wing} + \sum_0^{\infty} \frac{\left(\frac{2}{\beta}\right)^n \cos n\theta}{4\pi^2 R^{n+1}} \int_0^{2\pi} d\psi \int_{-L_o}^x dx_1 (x-x_1)^n \cos n\psi S_w''(x_1, \psi) \quad (47b)$$



(e) Tangential velocities induced by fourth-order multipoles.
FIGURE 13.—Concluded.

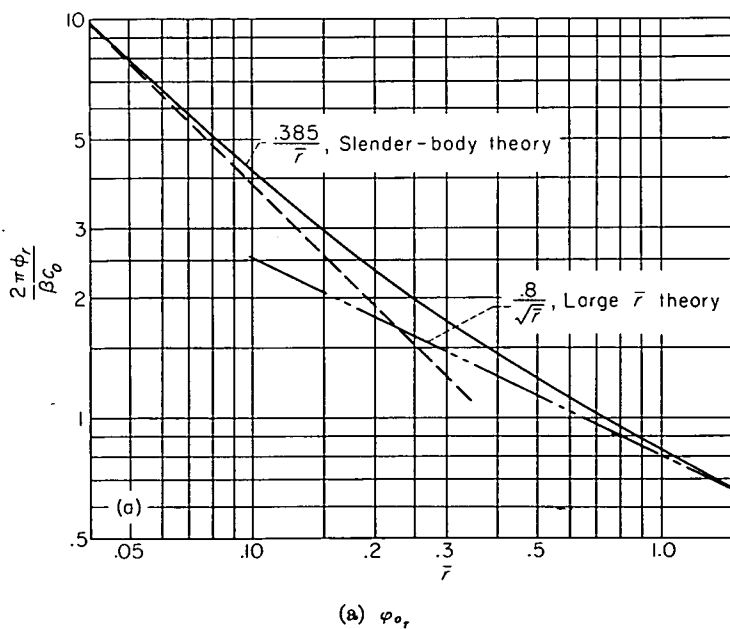
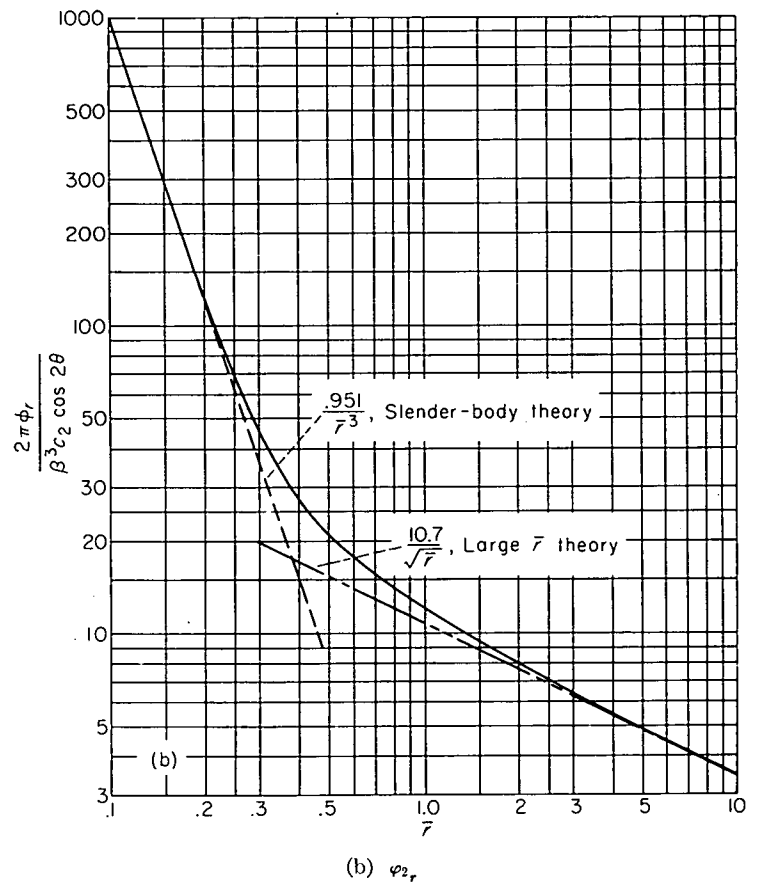
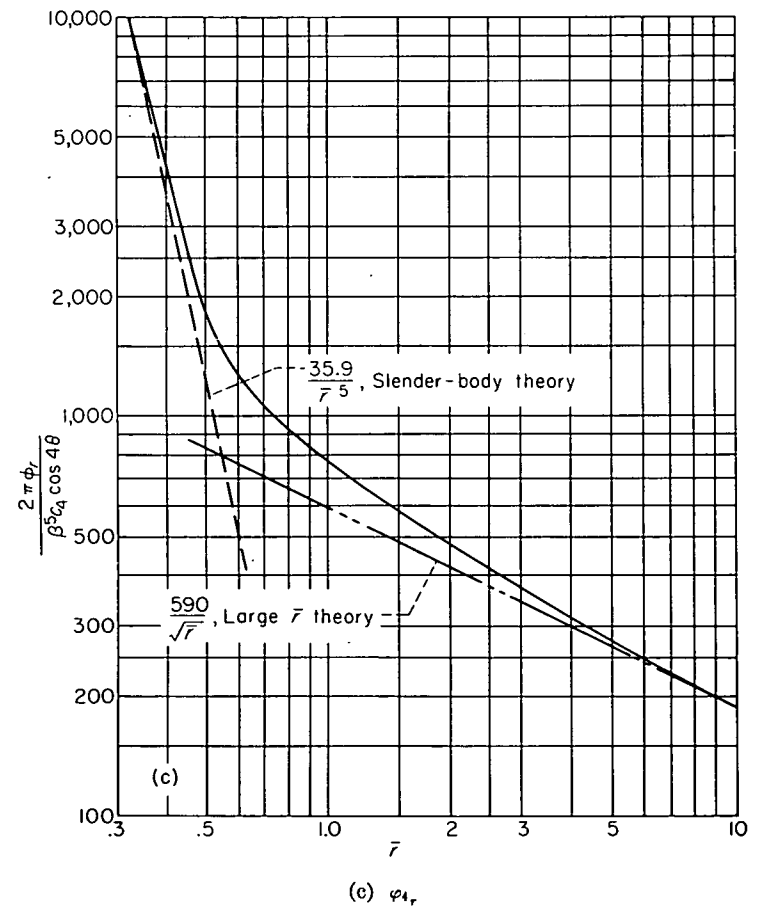


FIGURE 14.—Attenuation of first crest of waves created by multipole distributions shown in figure 11.



(b) φ_{2r}
FIGURE 14.—Continued.



(c) φ_{4r}
FIGURE 14.—Continued.

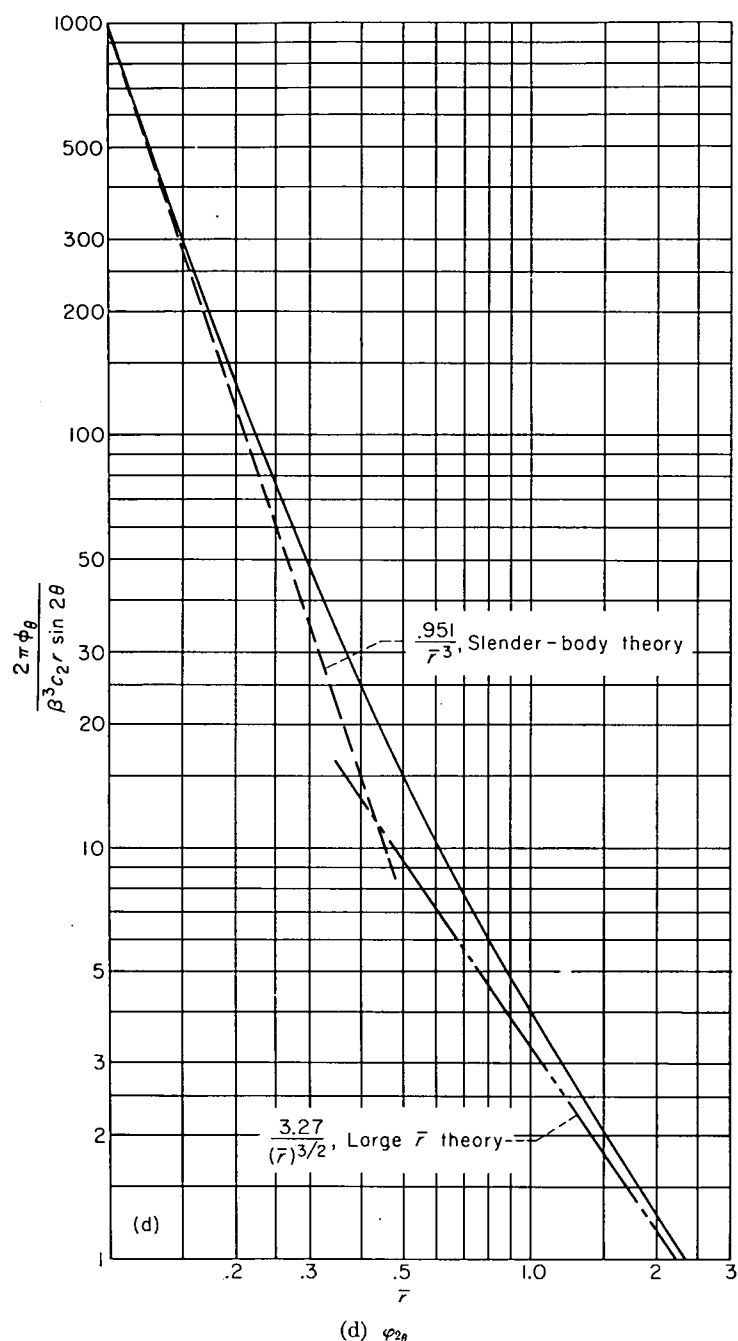


FIGURE 14.—Continued.

Approximate methods for finding $(\varphi_{\theta}/U_o R)_{wing}$ and $(\varphi_r/U_o)_{wing}$, the velocities induced by the wing, can often be used also; but these apply to individual cases and cannot be discussed here.

THEORY FOR LARGE \bar{r}_e

The asymptotic values for magnitude and position of the first wave crest obtained by placing equations (44) into

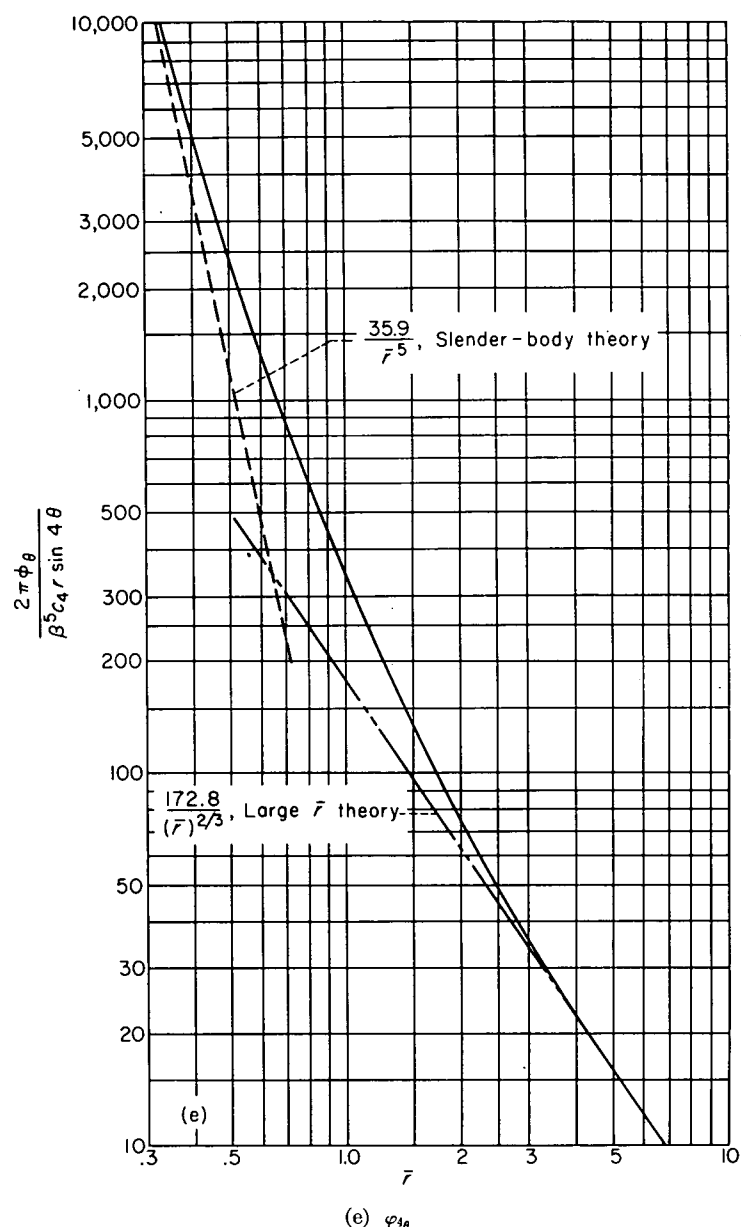
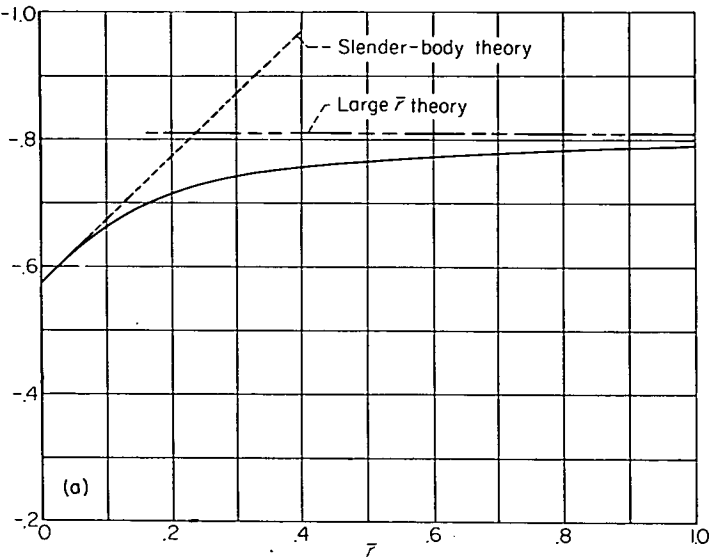


FIGURE 14.—Concluded.

equations (21) are also shown in figures 13, 14, and 15. For $n \leq 4$ it is clear that this theory can be used when \bar{r}_e is greater than about 2.

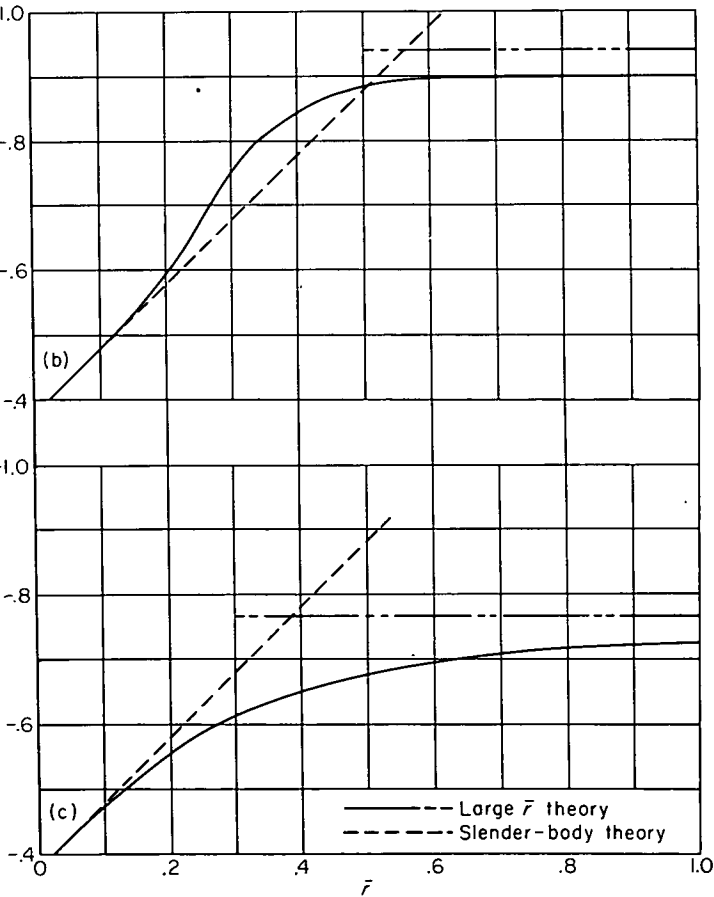
CONTROL-SURFACE THEORY

The approximations inherent in ordinary control-surface theory can also be estimated by inspecting figures 14 and 15, where by control-surface theory one means that the



(a) Radial velocities induced by sources.

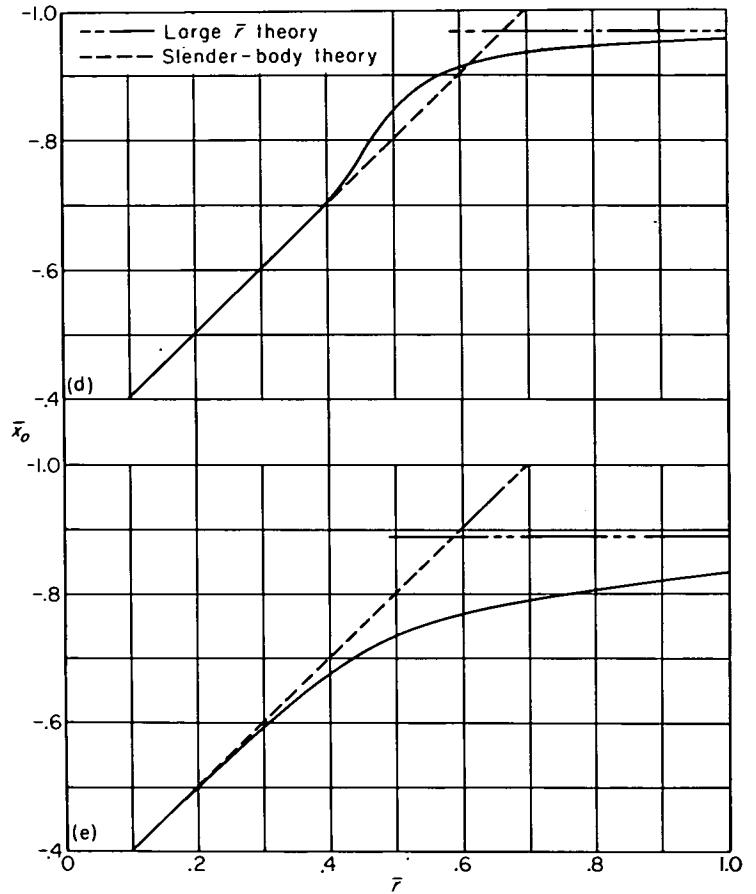
FIGURE 15.—Position of first crest of waves created by multipole distributions shown in figure 11.



(b) Radial velocities induced by second-order multipoles.

(c) Tangential velocities induced by second-order multipoles.

FIGURE 15.—Continued.



(d) Radial velocities induced by fourth-order multipoles.

(e) Tangential velocities induced by fourth-order multipoles.

FIGURE 15.—Concluded.

exact linearized theory is used to evaluate induced velocities along a given surface and these values are assumed constant for all \bar{r} in the vicinity of the surface. As shown in figure 16, this amounts to assuming φ_r and φ_θ are given by a straight horizontal line in figure 14 and by straight lines with a unit negative slope in figure 15. Obviously, the error in the body shape calculated by this theory increases as the amplitudes of the disturbing multipoles increase and as the radius of the control surface diminishes.

One of the simplest applications of control-surface theory arises in the study of quasi-cylindrical bodies. In such cases the expression for the body surface can be derived immediately from equation (42). Thus, if the amplitudes of the cancellation multipoles are small enough and R_c , the radius of the control surface, is large enough for control-surface theory to be considered a good approximation, the body shape, $r=R(x,\theta)$, corresponding to the combined wing and optimum cancellation multipoles is determined by using equations (19c), (16b), and (36) together with equation (42)

$$\frac{dR}{dx} = \left[\frac{\varphi_r(x, R_c, \theta)}{U_o} \right]_{wing} + \sum_0^{\infty} \frac{\sigma_n \cos n\theta}{4\pi^2 R_c} \int_{-L_o}^{x-\beta R_c} \frac{(x-\xi) \cosh \left(n \cosh^{-1} \frac{x-\xi}{\beta R_c} \right) d\xi}{\sqrt{(x-\xi)^2 - \beta^2 R_c^2}} \int_0^{2\pi} S_w''(\xi, \psi) \cos n\psi d\psi \quad (48)$$

where $\sigma_n = 1$ for $n=0$ and $\sigma_n = 2$ for $n > 0$.

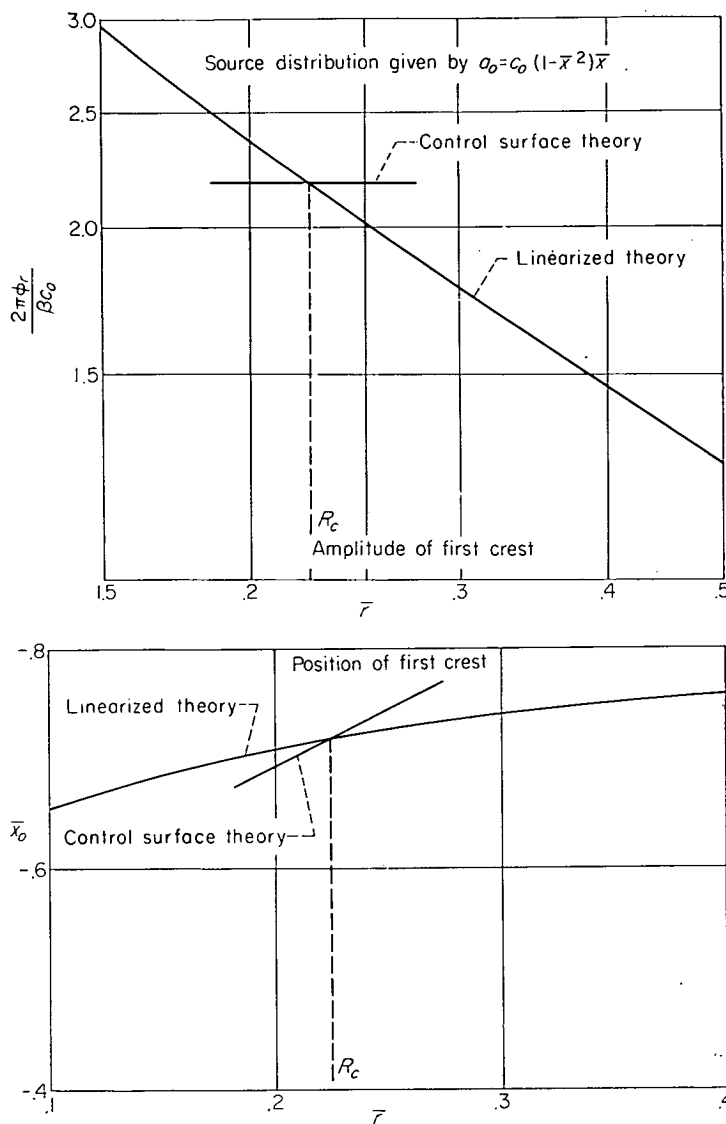


FIGURE 16.—Comparison of velocity fields given by exact-linearized and control-surface theory.

A study of optimum fuselage shapes using control-surface theory has been carried out by Nielsen (ref. 10) for a constant-chord sweptback wing having a biconvex section and a sonic leading edge. The set of interfering singularities used in reference 10 are equivalent (the singularities are limited to the x axis) to the multipoles used herein. The fuselage shapes calculated by Nielsen are thus the same—within the accuracy of control-surface theory—as those given by equation (48).

MODIFIED CONTROL-SURFACE THEORY

A method of modifying control-surface theory to increase its accuracy is illustrated in figure 17. Induced velocities computed by this method are based on those calculated along a given control surface but are extended away from this surface by varying their magnitude as $(\bar{r})^{\gamma_n}$ where the value of γ_n is fixed by the slope of the curves in figure 14 at $\bar{r} = \bar{r}_e$, \bar{r}_e being defined by equation (46) (fig. 17). With this modification equation (48) becomes

$$\frac{dR}{dx} = \left[\frac{\phi_r(x, R_c, \theta)}{U_0} \right]_{\text{wing}} + \sum_0^{\infty} \left(\frac{R_c}{R} \right)^{\gamma_n} \frac{\sigma_n \cos n\theta}{4\pi^2 R_c}$$

$$\int_{-L_0}^{x-\beta R_c} \frac{(x-\xi) \cosh \left(n \cosh^{-1} \frac{x-\xi}{\beta R_c} \right) d\xi}{\sqrt{(x-\xi)^2 - \beta^2 R_c^2}} \int_0^{2\pi} S_w''(\xi, \psi) \cos n\psi d\psi \quad (49)$$

which can be solved using numerical techniques.

A further refinement of equation (49) can be obtained if the position of the induced velocities is also varied according to the slope (again at $\bar{r} = \bar{r}_e$) of the curves in figure 15. Defining this slope as δ_n , see figure 17, and x_δ as

$$x_\delta = x - \beta(1 + \delta_n)(R - R_c)$$

one can see this refinement simply amounts to replacing the value of x in the right-hand term of equation (49) by x_δ .

ILLUSTRATIVE EXAMPLE—ELLIPTIC WING

In order that one may be able to assess the practical significance of the preceding sections, the concepts presented therein will now be applied to the solution of a particular problem. For the basic wing plan form in this particular

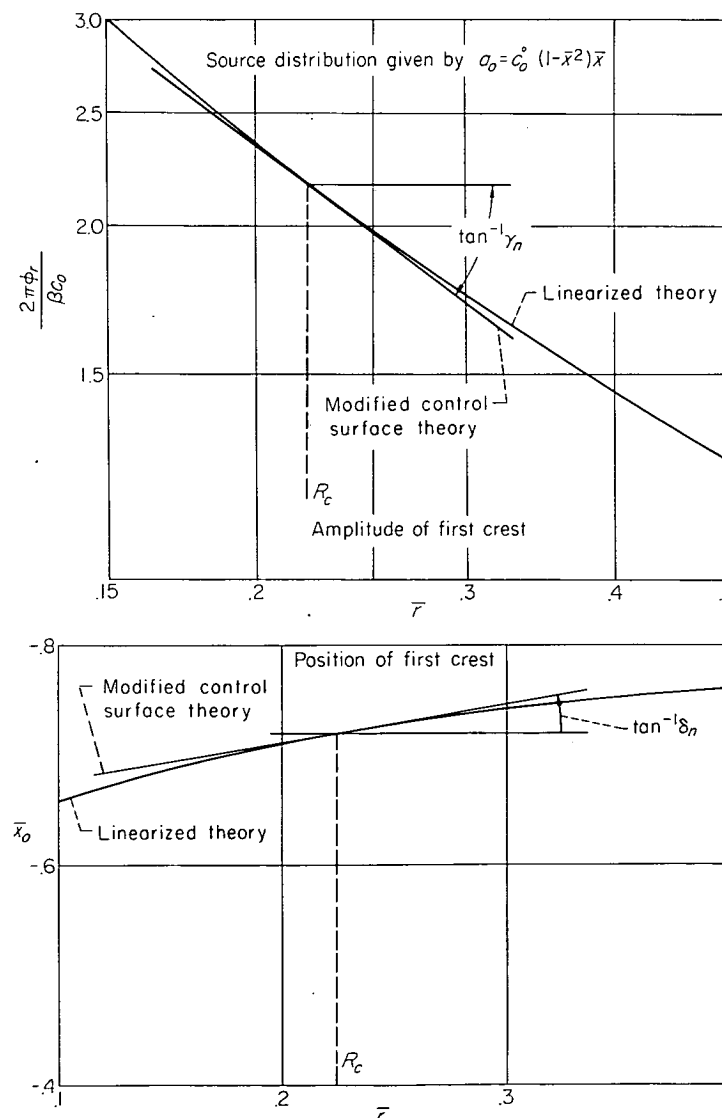


FIGURE 17.—Comparison of velocity fields given by exact-linearized and modified control-surface theory.

example an ellipse will be chosen. There are two good reasons for this choice; first, the ellipse is effectively unswept and places a severe test on the role of body interference in reducing the wave drag at a supersonic speed, and, second, for a given volume, the optimum section (i. e., the one yielding minimum wave drag) for these wings when considered separately has been discovered (see ref. 11) so the reduction in wave drag brought about by the body will reduce the minimum value possible for such wings when flying alone. The drag reductions for the first few cancellation-multipole distributions will be calculated and compared with the total drag of the wing alone, the wing mounted on an infinite cylinder, and the wing mounted on a basic body of revolution. Finally the details of calculating a body shape simulated by the wing source sheet, a source line representing a basic body of revolution, and the first two optimum cancellation-multipole distributions will be carried out.

THE ELLIPTIC WING

Consider the elliptic lens specified by the equation

$$z = \pm \frac{t}{2} \left(1 - \frac{x^2}{a^2} - \frac{y^2}{b^2} \right) \quad (50)$$

where the thickness, span, and chord are shown in figure 18. The streamwise slope of the upper surface is seen to be

$$\left. \frac{\partial z}{\partial x} \right|_u = \lambda_u(x, y) = -\frac{tx}{a^2} \quad (51)$$

and the total wing plan-form area S and volume V are, respectively,

$$\left. \begin{aligned} S &= \pi ab \\ V &= \frac{\pi}{2} tab \end{aligned} \right\} \quad (52)$$

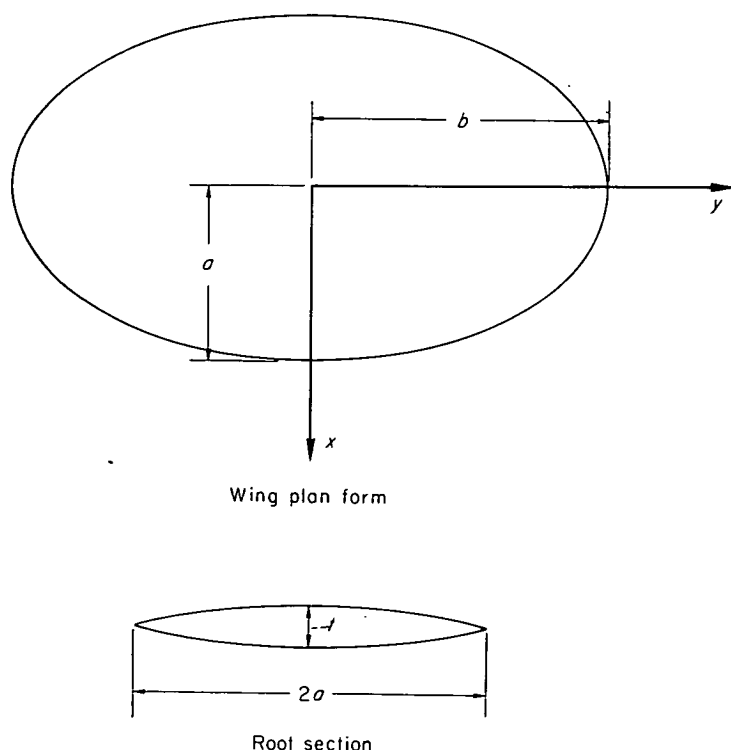


FIGURE 18.—Definition of parameters used to study elliptic wing.

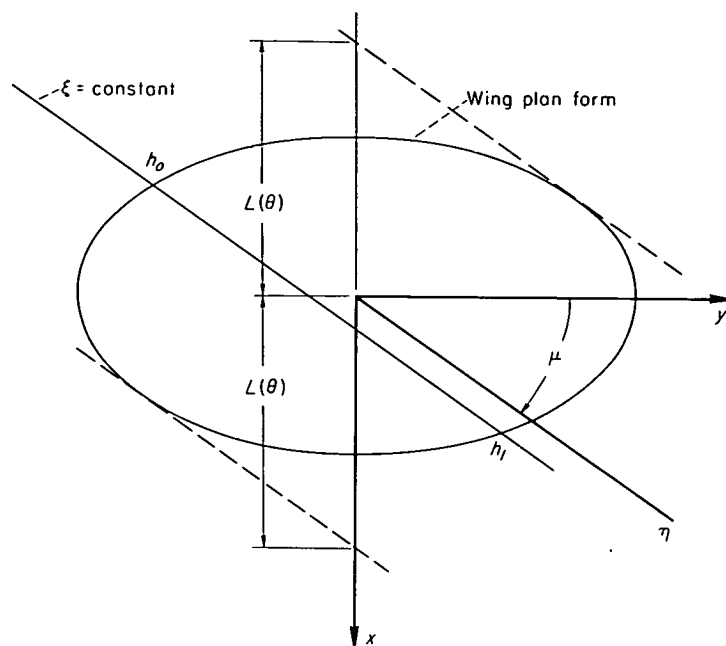


FIGURE 19.—Elliptic wing in ξ, η coordinates.

Wave drag.—The wave drag of the elliptic wing represented by equation (50) can be calculated by means of equation (30) in which, since one wishes now to find the wave drag of the wing alone, the a_n 's are set equal to zero. The value of $S_w'(x, \theta)$ follows by placing equation (51) into equation (28) and integrating. Thus

$$U_o S_w'(x, \theta) = 2U_o \cos \mu \int_{h_o}^{h_1} \left(-\frac{t}{a^2} \right) (\xi + \eta \sin \mu) d\eta = -\frac{2tU_o \cos \mu}{a^2} \left(\xi \eta + \frac{\eta^2 \sin \mu}{2} \right)_{h_o}^{h_1}$$

where, by referring the equation of the plan form to the ξ, η coordinates (see eq. (26)) and solving for the points where the straight line $\xi = \text{constant}$ intersects the wing edges, one finds—see figure 19

$$\left. \begin{aligned} h_1 \\ h_o \end{aligned} \right\} = \frac{-b^2 \xi \sin \mu \pm ab \sqrt{a^2 \cos^2 \mu + b^2 \sin^2 \mu - \xi^2 \cos^2 \mu}}{a^2 \cos^2 \mu + b^2 \sin^2 \mu}$$

Hence,

$$S_w'(x, \theta) = -\frac{4xtab}{(a^2 + b^2 \beta^2 \cos^2 \theta)^2} \sqrt{a^2 + b^2 \beta^2 \cos^2 \theta - x^2} \quad (53)$$

From the relation

$$L^2(\theta) = a^2 + b^2 \beta^2 \cos^2 \theta \quad (54)$$

the wave drag can be expressed in the form (integrating once by parts)

$$\frac{D}{q} = -\frac{1}{4\pi^2} \int_0^{2\pi} d\theta \int_{-L(\theta)}^{L(\theta)} d\xi_1 \int_{-L(\theta)}^{L(\theta)} d\xi_2 \left[\frac{4tab}{L^4(\theta)} \right] \left[\frac{L^2(\theta) - 2\xi_1^2}{\sqrt{L^2(\theta) - \xi_1^2}} \right] \frac{\xi_2 \sqrt{L^2(\theta) - \xi_2^2}}{\xi_1 - \xi_2}$$

Further integration yields

$$\frac{D}{q} = t^2 a^2 b^2 \int_0^{2\pi} \frac{d\theta}{(a^2 + b^2 \beta^2 \cos^2 \theta)^2}$$

Values of ϕ_r/U_0

Point number	Exact linearized theory	Ackeret wave — $t(x-r)/a^2$
1	.044	.050
2	-.053	-.050
3	-.102	-.100
4	-.104	-.100

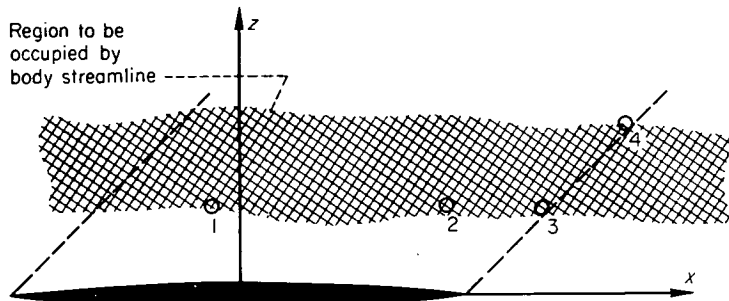


FIGURE 20.—Points at which exact-linearized theory was compared with an Ackeret wave in plane of symmetry for elliptic wing.

Finally, the wave drag can be expressed in coefficient form, based on the total wing area πab , as

$$C_D = \frac{4}{\beta} \left(\frac{t}{2a} \right)^2 \frac{1 + 2 \left(\frac{a}{b\beta} \right)^2}{\left[1 + \left(\frac{a}{b\beta} \right)^2 \right]^{3/2}} \quad (55)$$

Equation (55) represents the lowest value of wave drag possible for a wing having an elliptic plan form and fixed volume. This equation was first derived by Jones in reference 11.

The velocities induced by the wing source sheet in the vicinity of the fuselage.—Later, when one wishes to calculate a stream surface in the presence of the source sheet that simulates the wing given by equation (50), it is necessary to know the velocities induced by these sources at the body surface. Hence, the value of ϕ_r induced by the source sheet was calculated at the four points indicated in figure 20. As it turns out, these values are so close (see the figure for a numerical comparison) to those obtained by assuming the source sheet to be two-dimensional with a chordwise intensity identical to that along the root section of the elliptical sheet (i. e., using the Ackeret wave generated by the root section) that the effect of the wing can be assumed to be given everywhere in the vicinity of the body by the latter velocity field if (as will be the case in subsequent application) the surface of the body passes through the region shaded in the figure. That is, the effect of the wing in the equations for the fuselage shape (such as eqs. (47), (48), or (49)) is assumed to be

$$\left. \begin{aligned} \frac{1}{U_0} \phi_r &= \mp \frac{t}{a^2} (x \mp \beta r \sin \theta) \sin \theta, & \begin{cases} - \text{for } 0 \leq \theta \leq \pi \\ + \text{for } \pi \leq \theta \leq 2\pi \end{cases} \\ \frac{1}{rU_0} \phi_\theta &= \mp \frac{t}{a^2} (x \mp \beta r \sin \theta) \cos \theta, & \begin{cases} - \text{for } 0 < \theta < \pi \\ + \text{for } \pi < \theta < 2\pi \end{cases} \end{aligned} \right\} \quad (56)$$

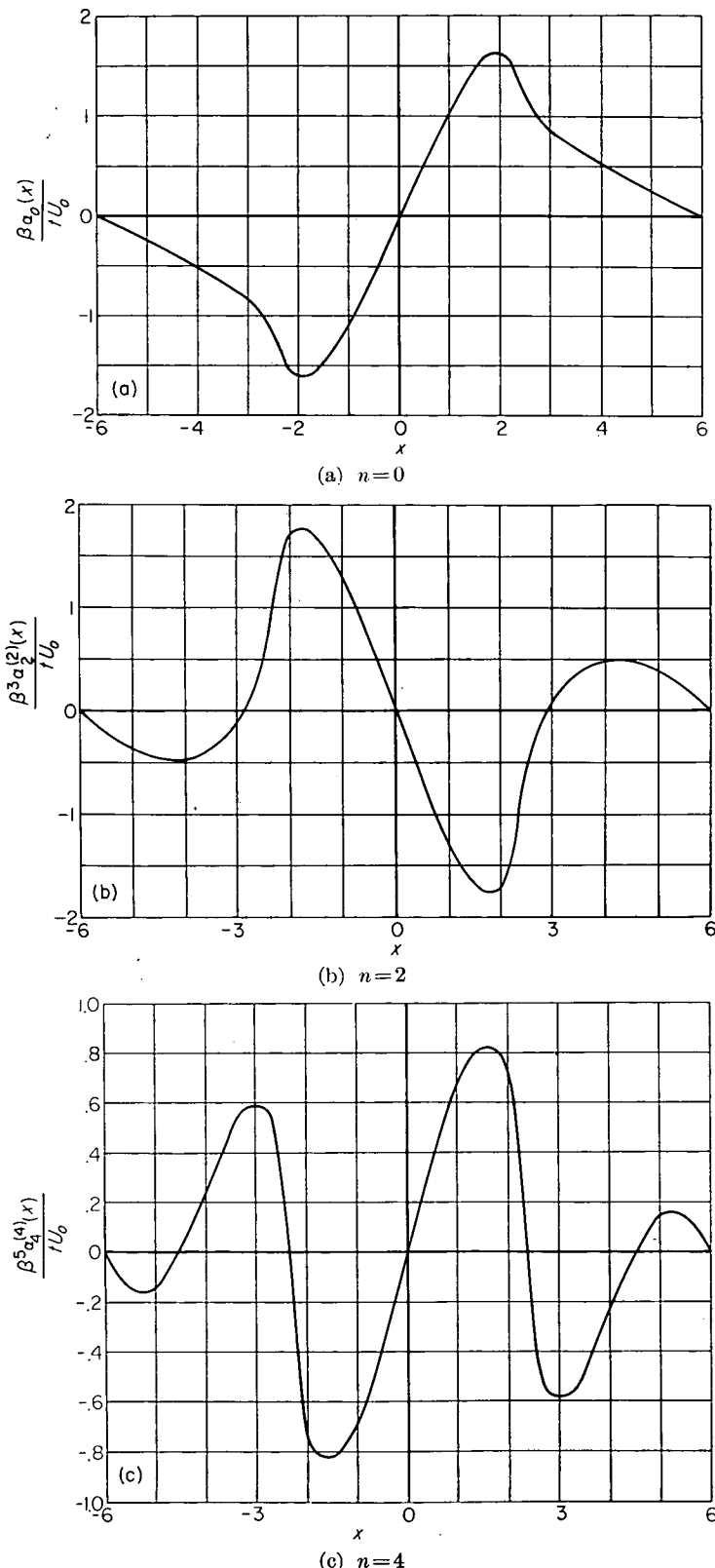
THE OPTIMUM CANCELLATION MULTIPOLES

One can now find the strengths of the multipoles along the x axis which induce around a cylinder of infinite radius a momentum field identical to that created there by the elliptic wing. The negatives of these variations are, according to

equation (36), the optimum cancellation multipoles. Hence, combining equations (53) and (36)

$$\alpha_n^{(n)}(x) = -\sigma_n \frac{2tabU_0x}{\pi(-\beta)^n} \int_0^{2\pi} \frac{\sqrt{a^2 + b^2\beta^2 \cos^2 \theta - x^2}}{(a^2 + b^2\beta^2 \cos^2 \theta)^2} \cos n\theta d\theta \quad (57)$$

where $\sigma_n = 1$ for $n = 0$ and $\sigma_n = 2$ for $n > 0$. Particular variations of $\alpha_n^{(n)}(x)$ are shown in figure 21. These results are

FIGURE 21.—Variation of n th derivative of n th-order cancellation multipoles for elliptic wing.

for $n=0, 2$, and 4 , since $\alpha_n^{(m)}(x)$ for any odd n is zero by symmetry, and apply when the wing plan for and free-stream Mach number are related by

$$\frac{a}{b\beta} = \frac{4}{3\pi} \quad (58)$$

which contains the particular case for which the Mach number is $\sqrt{2}$ and the aspect ratio is 3. It is apparent that there are at least $n+1$ roots to $\alpha_n^{(m)}(x)$ for $-L_o < x < L_o$. This follows immediately from equation (38) and is true in general. As a result the curves for the higher values of n

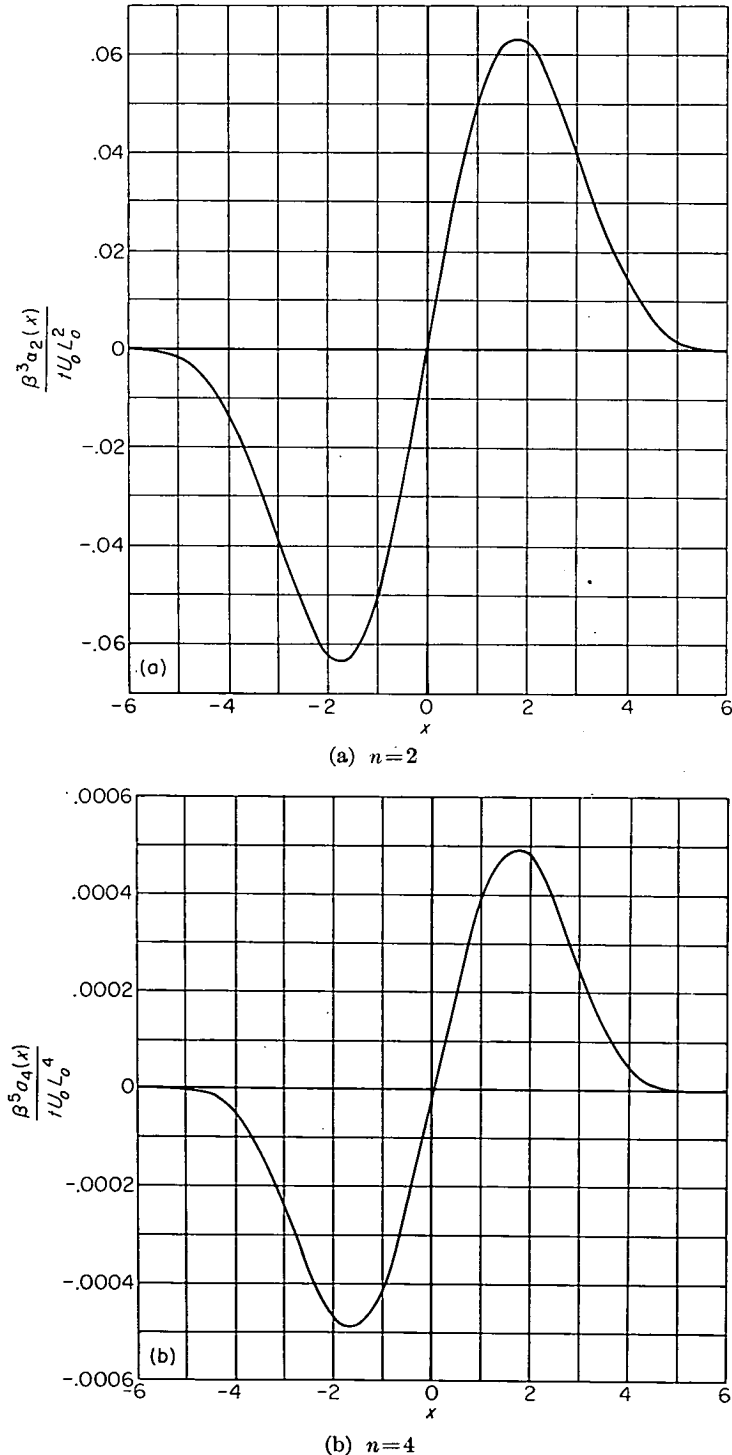


FIGURE 22.—Variation of n th-order cancellation multipoles for elliptic wing.

become increasingly wavy and, correspondingly, increasingly difficult to evaluate numerically.

Figure 22 presents the values of $\alpha_n(x)$ for the same elliptic-wing Mach number relation given by equation (58). Notice that each of these curves has only one root (they necessarily have at least one) in the interval $-L_o < x < L_o$ and is increasingly smooth with increasing n . The latter follows from equation (37) and the fact that the first n derivatives of these curves must, in general, be continuous. For example at $x = \pm L_o$ the first four derivatives of $\alpha_4(x)$ must vanish.

Wave drag.—One can now calculate how much the wing-alone drag is reduced when combined with each successive optimum cancellation-multipole distribution. If \bar{D}_n denotes the drag saved by the n th-order cancellation multipoles, then by equation (35)

$$\frac{\bar{D}_n}{q} = -\frac{\beta^{2n}}{4\pi U_o^2} \int_{-L_o}^{L_o} dx_1 \int_{-L_o}^{L_o} dx_2 \alpha_n^{(n+1)}(x_1) \alpha_n^{(n+1)}(x_2) \ln|x_1 - x_2| \quad (59)$$

where L_o is the maximum value of $L(\theta)$ as given by equation (54)

$$L_o^2 = a^2 + b^2\beta^2 \quad (60)$$

The total drag saved by means of the first m multipole distributions, would, by equation (34), be

$$\bar{D} = 2\bar{D}_o + \sum_1^m \bar{D}_n \quad (61)$$

Using equations (53) and (36) to define the $\alpha_n^{(n+1)}(x)$ in equation (59), reversing the order of integration, and integrating once by parts, one finds

$$\begin{aligned} \frac{\bar{D}_n}{q} &= \frac{-4}{\pi^2} \int_0^{\pi/2} \cos n\theta_1 d\theta_1 \int_0^{\pi/2} \cos n\theta_2 d\theta_2 \int_{-L(\theta_1)}^{L(\theta_1)} d\xi_1 \int_{-L(\theta_2)}^{L(\theta_2)} d\xi_2 \\ &\quad \frac{(4tab)^2}{L^4(\theta_1)L^4(\theta_2)} \frac{L^2(\theta_1) - 2\xi_1^2}{\sqrt{L^2(\theta_1) - \xi_1^2}} \frac{\xi_2 \sqrt{L^2(\theta_2) - \xi_2^2}}{\xi_1 - \xi_2} \\ &= -\frac{64(tab)^2}{\pi^3} \int_0^{\pi/2} \cos n\theta_1 d\theta_1 \int_0^{\pi/2} \cos n\theta_2 d\theta_2 \\ &\quad \begin{cases} -\pi^2/4L^4(\theta_2), & L^2(\theta_1) \leq L^2(\theta_2) \\ -\pi^2/4L^4(\theta_1), & L^2(\theta_1) \geq L^2(\theta_2) \end{cases} \end{aligned}$$

It is apparent from figure 23 that this can be written

$$\begin{aligned} \frac{\bar{D}_n}{q} &= \frac{16(tab)^2}{\pi} \left[\int_0^{\pi/2} \frac{\cos n\theta_1 d\theta_1}{L^4(\theta_1)} \int_{\theta_1}^{\pi/2} \cos n\theta_2 d\theta_2 + \right. \\ &\quad \left. \int_0^{\pi/2} \cos n\theta_1 d\theta_1 \int_0^{\theta_1} \frac{\cos n\theta_2}{L^4(\theta_2)} d\theta_2 \right] \end{aligned}$$

or

$$\frac{\bar{D}_n}{q} = \frac{32(tab)^2}{\pi} \int_0^{\pi/2} \frac{\cos n\theta_1 d\theta_1}{(a^2 + b^2\beta^2 \cos^2\theta_1)^2} \int_{\theta_1}^{\pi/2} \cos n\theta_2 d\theta_2 \quad (62)$$

The total drag saved by using all the cancellation multipoles is, by definition,

$$\frac{\bar{D}}{q} = \frac{16(tab)^2}{\pi} \int_0^{\pi/2} \frac{d\theta_1}{(a^2 + b^2\beta^2 \cos^2\theta_1)^2} \left(\frac{\pi}{2} - \theta_1 \sum_{n=1}^{\infty} \frac{1}{n} \sin 2n\theta_1 \cos 2n\theta_1 \right)$$

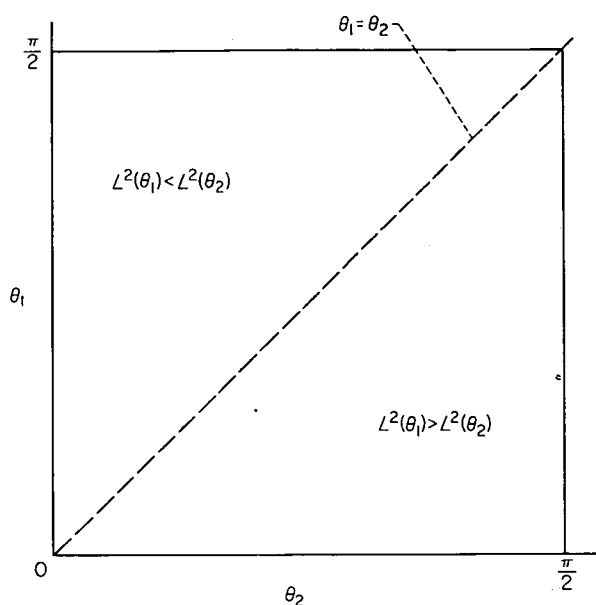


FIGURE 23.—Regions used in developing equation (62).

and since

$$x = \frac{\pi}{4} - \sum_{n=1}^{\infty} \frac{1}{n} \sin 2nx \cos 2nx$$

this is equal to the drag of the wing alone, as it, of course, should be.

The reduction in wave drag as the wing is combined with the first three optimum cancellation multipoles is presented in figure 24. In studying figure 24, one sees, as the Mach number approaches 1 (i. e., $\beta \rightarrow 0$), more and more of the original wing wave drag is destroyed by a line of simple sources alone. Further, the value of \bar{r}_e which can be written—see equations (46), (54), and figures 21 and 22—

$$\bar{r}_e = \frac{\beta r_e}{\sqrt{a^2 + b^2 \beta^2}} \quad (63)$$

tends (for a fixed average distance to the body surface r_e) to zero as the Mach number approaches 1; and this, in turn, means that as β goes to zero the effect of the multipole strengths on the body shape can be calculated using slender-body theory.

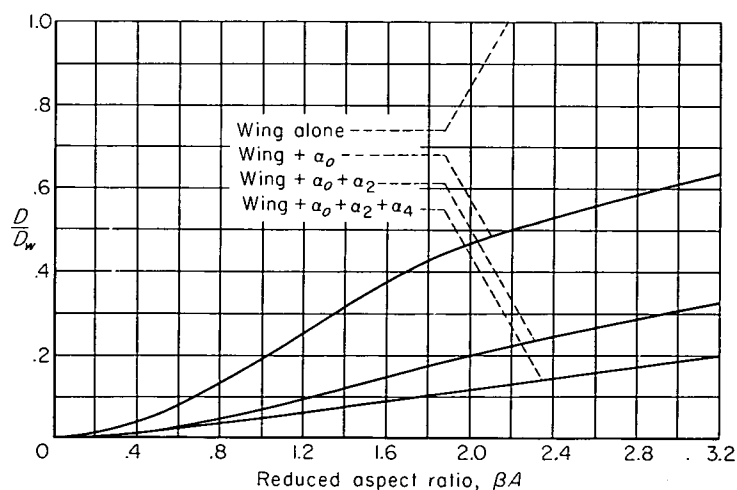
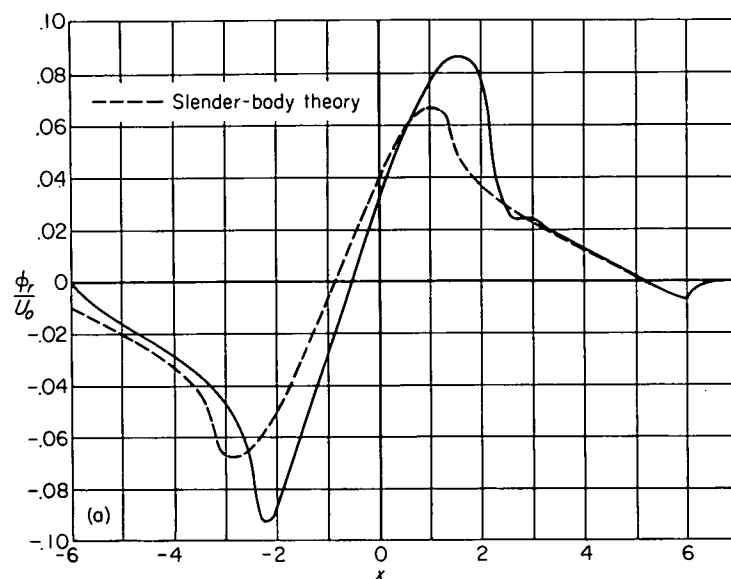


FIGURE 24.—Portions of elliptic-wing wave drag created by various equivalent multipole distributions.



(a) Radial velocities induced by sources.

FIGURE 25.—Velocities induced by the elliptic-wing cancellation multipoles at the control surface where $\beta R/L_o = 0.148$.

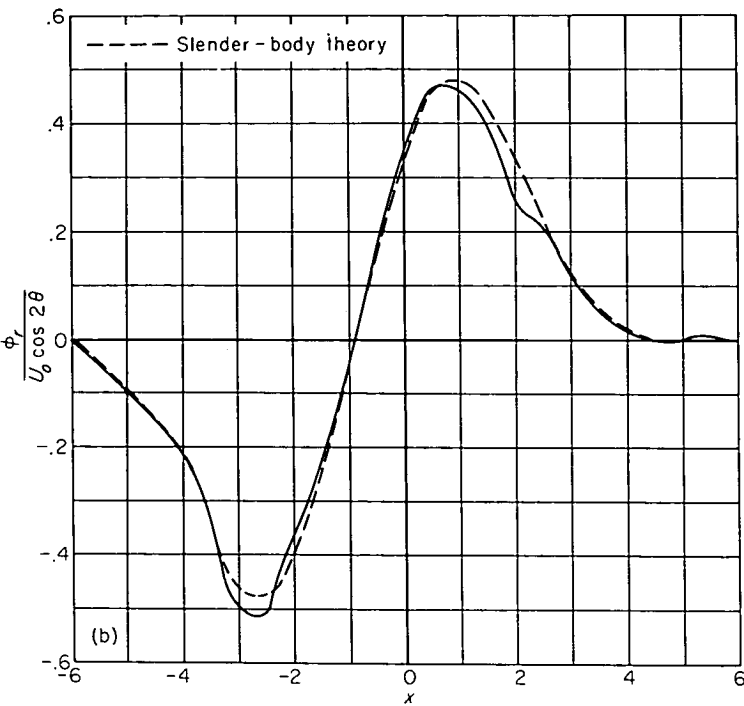
When various orders of multipoles are distributed along a line, one can show the cross-sectional area normal to the free stream of the simulated body as given by slender-body theory is a function of the source distribution only (see Appendix B). Coupled with the discussion in the preceding paragraph, this can be used to demonstrate that, for Mach numbers close to 1, the "supersonic area rule" proposed by Jones (ref. 12) and Whitcomb and discussed in reference 13 gives a good approximation for the wave drag of an elliptic wing and body combination which is symmetrical with respect to the plane of the wing.

The induced velocity field.—A method for calculating the velocity field induced by the multipoles when $\alpha_n(x)$ is given numerically is presented in Appendix C. By means of this method, velocities induced by the α_0 and α_2 multipole distributions shown in figure 22 have been calculated for \bar{r} equal to 0.148 and the results are shown in figure 25. Since the distributions in figure 22 were for the particular case $a/b\beta = 4/3\pi$, it is evident from equation (63) that the values in figure 25 apply to the case r_e/b equal to 0.161; that is, when the body radius is about 16 percent of the wing semispan.

For comparative purposes, the values given by slender-body theory are also shown in figure 25. The degree of agreement between the two curves is consistent with the results shown in figures 14 and 15.

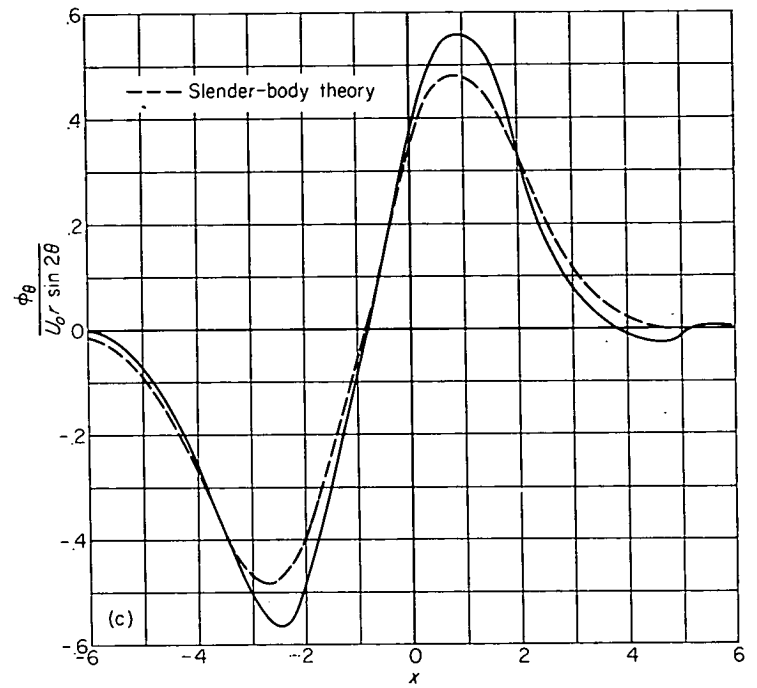
INTERPRETATION OF DRAG REDUCTIONS

Comparison with wing mounted on a circular cylinder.—With regard to figure 24 one should be careful to notice that the drag of the wing alone has been used for the reference drag. The drag reductions shown, therefore, represent gains brought about by interfering with the velocity field induced by a planar source sheet, or, in terms of a combination with an upstream cylindrical stream surface, gains made by modifying a body, shown in figure 26, which bulges behind the wing leading-edge Mach wave in accordance with the velocities induced there by the source sheet.



(b) Radial velocities induced by second-order multipoles.

FIGURE 25.—Continued.



(c) Tangential velocities induced by second-order multipoles.

FIGURE 25.—Concluded.

Obviously, from this viewpoint, a considerable reduction in drag can be brought about merely by eliminating the bulge, thereby making the body a circular cylinder throughout. Mathematically, such a procedure amounts to using a certain set⁹ of cancellation multipoles along the x axis behind the point $-L_0$, and, if the drag of this resulting combination were used as a reference, the gains shown in figure 24 would be diminished.

An approximate way to estimate the drag of a wing mounted on a circular cylinder is illustrated in figure 27 and consists merely of subtracting from the wing source sheet those sources blanketed by the body. Using the subscripts 1, 2, and 3 to designate the wave drags of the individual wings as indicated in figure 27, Jones (ref. 15) has shown that if wing 1 is an elliptic wing with a bi-convex section and wing 2 lies entirely within the plan form of wing 1, then

$$D_3 = D_1 \left(1 + \frac{2V_2}{V_1} \right) + D_2 \quad (64)$$

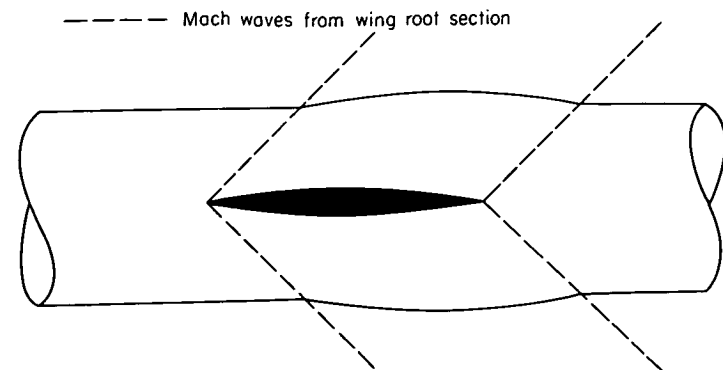


FIGURE 26.—Wing and stream tube simulated by planar sheet of sources.

⁹ The exact evaluation of multipole distributions necessary to simulate a circular cylinder for the entire body length has been studied in reference 14.

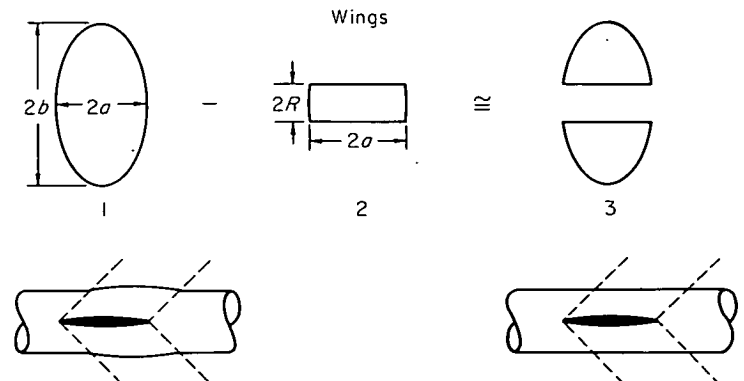
where V_2 and V_1 are the volumes of wings 1 and 2, respectively.

For a supersonic Mach number, D_2 is closely approximated by the wave drag of a rectangular wing having the same section and aspect ratio. If A_2 , $4Ra$, and τ_2 are, respectively, the aspect ratio, plan-form area, and thickness ratio of the rectangular wing, its drag can be expressed in the form

$$\frac{\beta D_2}{q \tau_2^2} = 4Ra N_2 \quad (65)$$

where

$$N_2 = \begin{cases} \frac{16}{\pi} \beta A_2 \left[\frac{2}{3} \frac{\sin^{-1} \beta A_2}{\beta A_2} - \frac{\sqrt{1 - \beta^2 A_2^2}}{6} + \left(1 - \frac{\beta^2 A_2^2}{6} \right) \cosh^{-1} \frac{1}{\beta A_2} \right], & \beta A_2 \leq 1 \\ \frac{16}{3}, & \beta A_2 \geq 1 \end{cases} \quad (66)$$



Equivalent wing-body combinations

FIGURE 27.—Method of approximating wing mounted on a cylinder

Further, if A_1 is the aspect ratio of the elliptic wing, one can show—see figure 27 and equation (52)—

$$\beta A_2 = \frac{\pi}{4} \left(\frac{R}{b} \right) \beta A_1 \quad (67)$$

The drag of the elliptic wing follows from equation (55) and can be written

$$\frac{\beta D_1}{q \tau_2^2} = 4abN_1 \quad (68)$$

where

$$N_1 = \pi \frac{1 + 2 \left(\frac{4}{\pi \beta A_1} \right)^2}{\left[1 + \left(\frac{4}{\pi \beta A_1} \right)^2 \right]^{3/2}} \quad (69)$$

Finally, therefore, equation (64) can be put in the form

$$\frac{D_3}{D_1} = \left[1 - \frac{32}{3\pi} \left(\frac{R}{b} \right) \right] + \frac{R}{b} \frac{N_2}{N_1} \quad (70)$$

and the ratio N_2/N_1 is a function of the parameters R/b and βA_1 only.

By means of equation (70), the dashed curves shown in figure 28—

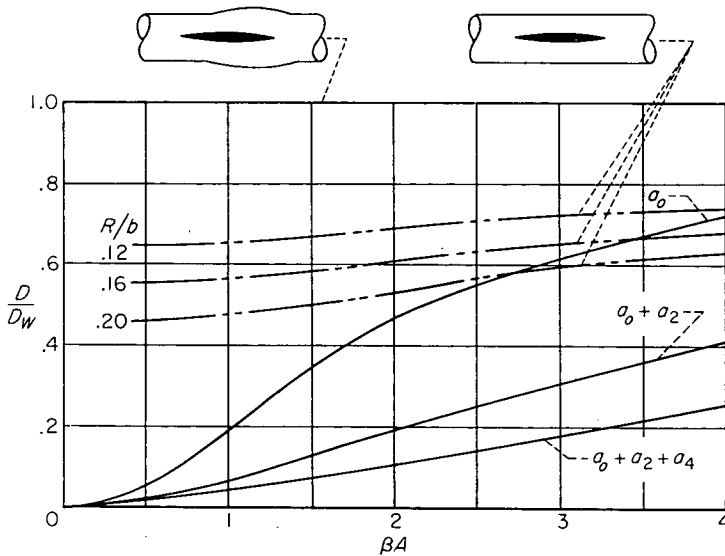


FIGURE 28.—Drag of various multipole distributions compared with drag of wing mounted on circular cylinder.

representing approximately the wave drag of a wing mounted centrally on a circular cylinder—were calculated. Though considerable drag reduction is indicated by adding just those multipoles necessary to make the body cylindrical, it is apparent the total wave drag can be reduced further, for the range of parameters shown, by using only the first two optimum cancellation-multipole distributions, $\alpha_0(x)$ and $\alpha_2(x)$, given by equation (36).

Comparison with wing mounted on a basic body of revolution.—Figure 28 shows the effect on the wave drag of adding the optimum cancellation multipoles either to the wing alone or to the combination of an infinite circular cylinder and a centrally mounted wing. Estimates of their effect when added to a wing mounted on a basic body of revolution can also be carried out. In order to present these

estimates, however, the results of the following two theorems due to R. T. Jones (ref. 15) are needed.

1. Designate the closed body of revolution which, by slender-body theory, has a minimum drag for a fixed volume and length as a Sears-Haack body. Then the total wave drag of a Sears-Haack body and any other body of revolution or any centrally mounted thin wing which lie entirely within the Sears-Haack body's enclosing Mach forecone and aftercone is given by the equation

$$D = D_{SH} \left(1 + \frac{2V_2}{V_{SH}} \right) + D_2 \quad (71)$$

where:

D_{SH} wave drag of Sears-Haack body alone

D_2 wave drag of other body or (exposed) wing alone

V_{SH} volume of Sears-Haack body

V_2 volume of other body or (exposed) wing

2. Designate the body of revolution which, by slender-body theory, has a minimum drag for a fixed base diameter and length as a Kármán ogive. Then the total wave drag of a Kármán ogive and any other slender body of revolution or any centrally mounted thin wing which lie entirely within the ogive's enclosing Mach forecone and aftercone is given by the equation

$$D = D_K + D_2 \quad (72)$$

where:

D_K wave drag of Kármán ogive alone

D_2 wave drag of other body or (exposed) wing alone

In order that the theoretical results could be tested by wind-tunnel experiments, a basic body of revolution having a finite base area was chosen. Such a body can be simulated by a combination of the source distributions which produce,¹⁰ separately, the Sears-Haack body and the Kármán ogive. Thus, if $2l$ is to be the body length, the line of sources

$$\frac{a_0(x)}{U_\infty} = \frac{2}{\pi l^3} \left(V_K - 4V_{SH} \frac{x}{l} \right) \sqrt{l^2 - x^2} \quad (73)$$

simulates (by slender-body theory) a body of revolution having a total volume V equal to $V_{SH} + V_K$, a cross-sectional area given by

$$S(x) = \frac{V_K}{\pi l^3} \left[x \sqrt{l^2 - x^2} + l^2 \left(\frac{\pi}{2} + \sin^{-1} \frac{x}{l} \right) \right] + \frac{8V_{SH}}{3\pi l^4} (l^2 - x^2)^{3/2}, \quad -l \leq x \leq l \quad (74)$$

and a base area $S(l)$ equal to V_K/l .

The wave drag of a wing mounted on this basic, unmodified body will now be calculated. Just as was the case in studying the wing attached to an infinite cylinder, the assumption is made that the wave drag of this combination is the same as the wave drag on the configuration simulated by superimposing the singularity distributions which create sepa-

¹⁰ The source distributions simulate the Sears-Haack body and the Kármán ogive only when slender-body theory is used to calculate the body shapes. If linearized theory is used instead, the body shape will, of course, be somewhat different. However, the subsequent results and conclusions are by no means limited by the assumptions pertaining to slender-body theory. The latter theory is used only to obtain an estimate of the body volumes or to study cases for which it gives results that are not significantly different from those given by linearized theory.

rately the exposed wing panels and the body of revolution. With this assumption, the wave drag can be written explicitly in terms of the wing and body geometry by applying equations (71) and (72). Hence,

$$D = D_K + D_{SH} \left(1 + \frac{2V_3}{V_{SH}} \right) + D_3 \quad (75)$$

where D_3 is the drag of the exposed wing panels alone, given by equation (70) and shown for various values of R/b in figure 28, and V_3 is their volume (see fig. 27)

$$V_3 = tab \left(\frac{\pi}{2} - \frac{8}{3} \frac{R}{b} \right) \quad (76)$$

Since D_K and D_{SH} , the wave drags of a Kármán ogive and a Sears-Haack body flying alone, are well known to be

$$\left. \begin{aligned} D_K &= \frac{q}{\pi} \frac{V_K^2}{l^4} \\ D_{SH} &= \frac{8q}{\pi} \frac{V_{SH}}{l^4} \end{aligned} \right\} \quad (77)$$

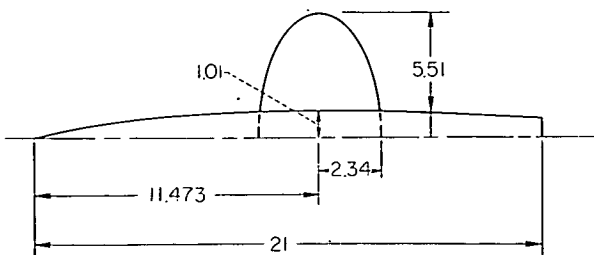
the wave drag coefficient of the unmodified combination, based on the complete wing area πab , can be expressed as

$$\frac{D}{q\pi ab} = C_D = \frac{V_K^2 + 8V_{SH}^2}{\pi^2 l^4 ab} + \frac{16tV_{SH}}{\pi^2 l^4} \left(\frac{\pi}{2} - \frac{8}{3} \frac{R}{b} \right) + \frac{t^2 N_1}{\pi a^2 \beta} \left[\left(1 - \frac{32}{3\pi} \frac{R}{b} \right) + \frac{R}{b} \frac{N_2}{N_1} \right] \quad (78)$$

where N_1 and N_2 are defined in terms of Mach number and wing-body geometry in equations (66) and (69). An example of the variation of C_D with Mach number for the particular combination shown in figure 29 (R/b was set equal to 0.181) is given by the dashed line in figure 30.

It is now possible to find how much the drag of this unmodified combination can be reduced by means of the optimum cancellation-multipole distributions used to derive the results shown in figure 24. Again applying equations (71) and (72), one can show

$$D = D_K + D_{SH} \left(1 + \frac{2V_4}{V_{SH}} \right) + D_4 \quad (79)$$



Maximum thickness of wing
along center line, $t = 0.234$

Total volume of body = 44.60
 $V_{SH} = 31.72$
 $V_K = 12.88$

FIGURE 29.—Dimensions of wing-body combination analyzed.

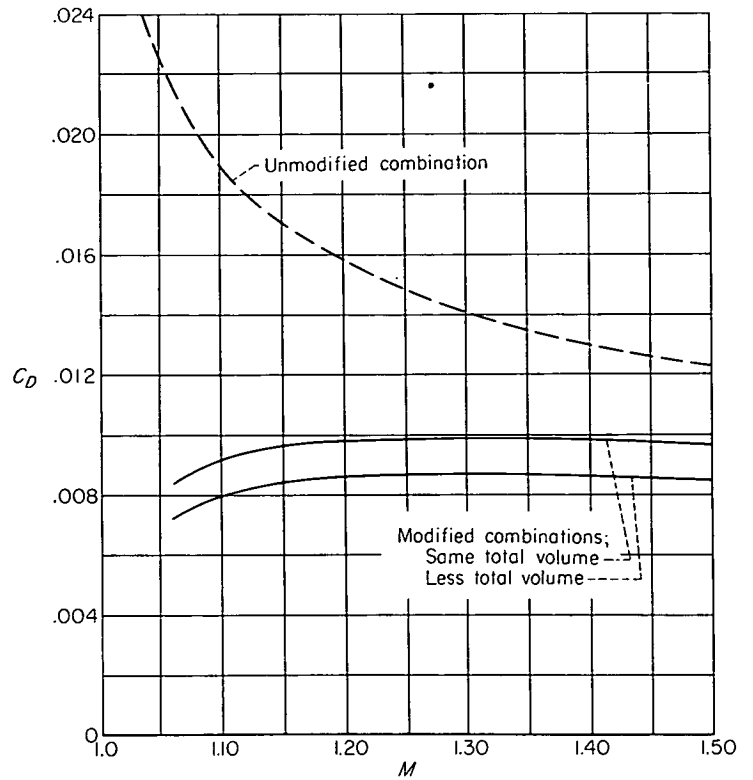


FIGURE 30.—Drag variation for modified and unmodified wing-body combinations.

where V_4 is the total volume and D_4 the total wave drag pertaining to the wing (now the complete wing including the portion blanketed by the body) and the multipoles. However, within the accuracy of the approximation—being, in fact, exact within slender-body theory, see Appendix B—the volume added by the wing is subtracted from the basic body by the optimum cancellation-source distribution so that V_4 is zero. Further, if N_4 is the value of D/D_w read from figure 24 for a specific value of βA_1 and a specific number of multipole types, one can readily show

$$D_4 = \frac{t^2 b q}{\beta a} N_1 N_4 \quad (80)$$

where N_1 is defined in equation (69). Hence, the drag of the unmodified combination can be reduced to either

$$\frac{D}{q\pi ab} = C_D = \frac{1}{\pi^2 ab l^4} \left\{ V_K^2 + 8 \left[V_{SH} + tab \left(\frac{\pi}{2} - \frac{8}{3} \frac{R}{b} \right) \right]^2 \right\} + \frac{t^2}{\pi a^2 \beta} N_1 N_4 \quad (81)$$

if the same total volume is maintained (maintained, as is obvious from an inspection of the equation, by increasing the value of the Sears-Haack portion of the basic body an amount equal to the volume of the exposed wing) or to

$$C_D = \frac{1}{\pi^2 ab l^4} (V_K^2 + 8V_{SH}^2) + \frac{t^2}{\pi a^2 \beta} N_1 N_4 \quad (82)$$

if the volume of the fuselage is reduced by an amount equal to the wing volume.

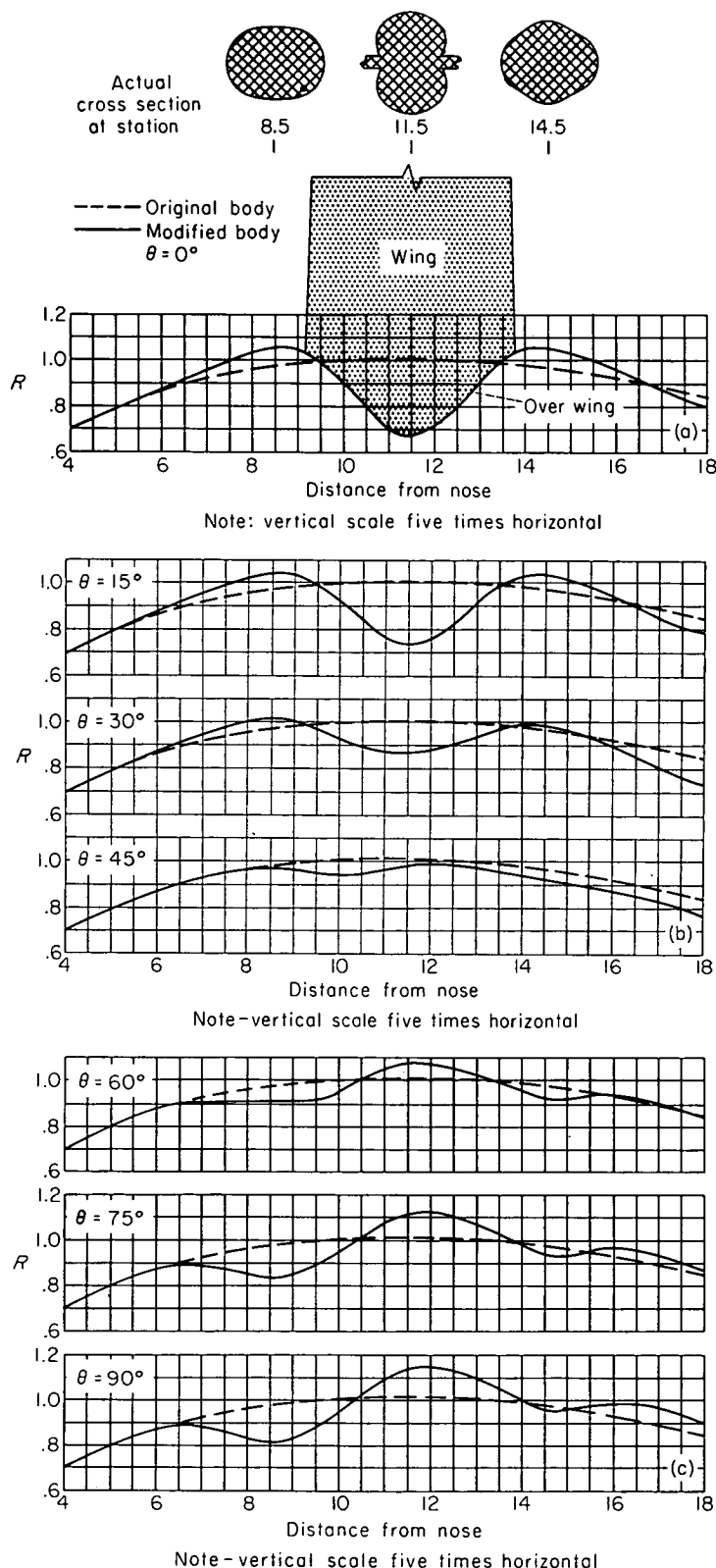


FIGURE 31.—Body shape having favorable interference wave drag at $M=1.41$ when combined with elliptic wing.

The results expressed by equations (80) and (81), when applied to the first two optimum cancellation-multipole distributions, are shown for the geometrical parameters presented in figure 29 by the solid curves in figure 30. The value of R/b used for the solid curves was 0.161 instead of the 0.181 value used to calculate the dashed curve. The smaller value was used since the modified body is drawn in along the

sides by the cancellation multipoles (see fig. 31), decreasing the average body radius in the wing region from about 1.00 to about 0.89. One must be careful to notice that the solid curves represent minimum (relative to the special method being discussed) values which can be obtained by a specific design at a specific Mach number and do not represent the variation of wave drag with Mach number for any given combination.

THE BODY SHAPE—FIRST CALCULATION

The final step in studying the effect of the optimum cancellation multipoles, defined in equation (36), is to find the distorted body shape which they produce in combination with the wing and a basic body. The decision was made to calculate a body shape which would be optimum at a Mach number equal to $\sqrt{2}$. The details of the wing and body geometry are given in figure 29 and the basic body parameters V_K and V_S were interpreted in terms of source strength by equation (73).

It was apparent from the results of figure 25 that, for the values of r_e and b given by figure 29, the velocity field induced by the first two optimum multipole distributions can be calculated with good accuracy using slender-body theory. Combining the values of φ_r and φ_θ so calculated with those induced by the wing, given by equation (56), and those induced by the basic body, using also slender-body theory to interpret equation (73), one can find the body shape by solving the two simultaneous nonlinear differential equations presented as equations (43). These were solved numerically by the method outlined in Appendix D and the results were, unfortunately, unrealistic. Figure 32 shows an example of a streamline close to the $\theta=0$ plane and the crossing of such streamlines obviously invalidates the solution.

BODY SHAPE—SECOND CALCULATION

The failure observed in the first calculation has a simple enough interpretation. For the chosen wing the basic body was too small in diameter at the wing-body juncture to permit the use of the first two cancellation multipoles in their entirety.

Several avenues of approach are yet available. One could, for example, maintain the same wing and basic body but reduce the Mach number, one could start with a larger basic body, or one could lower the thickness ratio or aspect ratio of the wing, thus diminishing the strength of the cancellation multipoles. All of these, however, are modifications of the basic conditions or basic restraints and as soon as such

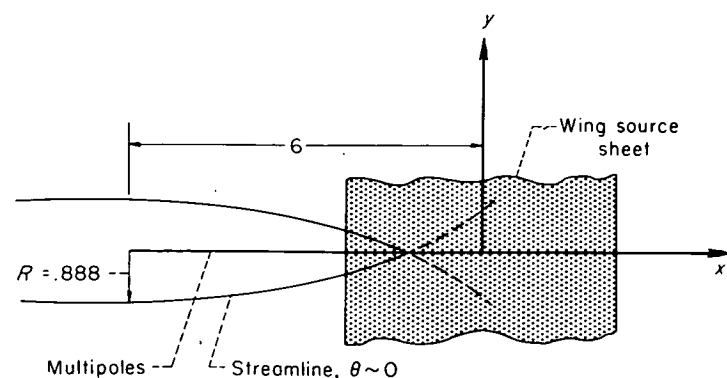


FIGURE 32.—Streamline when starting body radius is too small.

restrictions are abandoned it must be remarked that no matter how low the wave drag of a set of nonlifting, volume-enclosing surfaces has been made, another arrangement of the same volume within a finite space will give a lower value, unless, of course, the wave drag of the first arrangement is already zero. Therefore, instead of modifying any of the initial restraints, consider the following alternative:

How much can the drag be reduced by using only a portion of the first two cancellation multipoles so that a real body would still be simulated?

In order to answer the above question, examine briefly the first calculation. Notice, from figure 25, that the cause of the body collapse is attributable to the large values of φ_r and φ_θ induced by the second-order cancellation multipoles, $\alpha_2(x)$. Hence, let $\alpha_0(x)$ be maintained at its full value and reductions permitted only in the magnitude of $\alpha_2(x)$. To carry out such a procedure efficiently, one must be able to determine the effect of a given variation of $\alpha_2(x)$ on the body shape. Fortunately, Graham, in reference 16, has developed a method by means of which the relation between $\alpha_2(x)$ and body shape can be quickly estimated. Graham has shown if

1. a rectilinear distribution of second-order multipoles of strength $\alpha_2(x)$ is placed along the x axis (see fig. 33) in a supersonic stream ($M=\sqrt{2}$)
2. slender-body theory is used to evaluate φ_r and φ_θ ,
3. $R=R_c$ is the radius of a circularly cylindrical tube for $-L_o > x > -\infty$,

$$4. F^*(x) = \frac{4}{\pi U_o R_c^4} \int_{-L_o}^x \alpha_2(x_2) dx_2$$

then

$$R = R_c \left\{ \frac{1 + 2F^*(x) \cos 2\theta + \sqrt{1 + 4F^*(x) \cos 2\theta + 4[F^*(x)]^2}}{2} \right\}^{1/4} \quad (83)$$

is the continuation of the stream tube for $x > -L_o$.

Since the initial strengths of the cancellation multipoles are negative, $F^*(x)$ is negative and the critical value of R

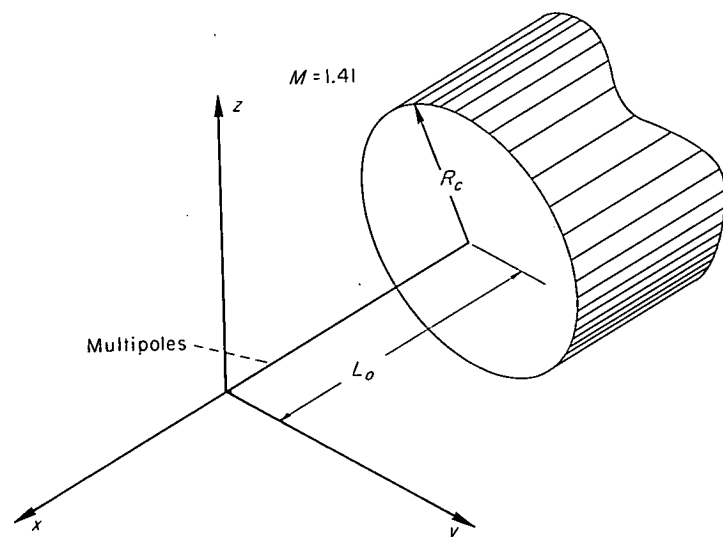


FIGURE 33.—Definition of parameters used to study effect of second-order multipoles on fuselage shape.

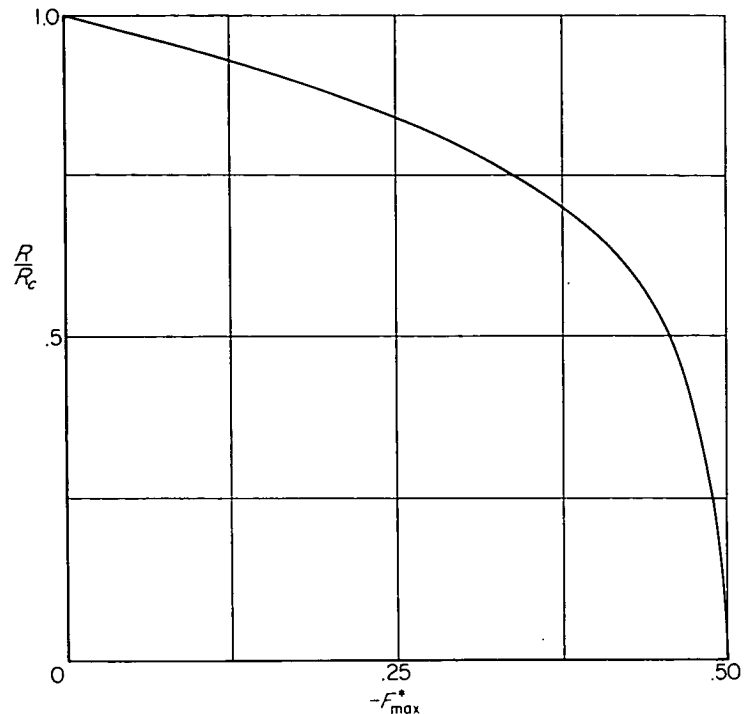


FIGURE 34.—Variation of R/R_c with $-F^*_{max}$.

occurs along the plane $\theta=0$ or π . The variation of R/R_c with F^*_{max} is given in figure 34 from which one can see that the maximum value of $|F^*|$ must be less than 0.5 if the simulated stream tube behind the plane $x=-L_o$ is to be real.

The problem can now be continued, using Graham's result as a guide, by assuming the critical body radius in the more complicated source and multipole arrangement is principally determined by $F^*(0)$ —the parameter governing the body indentation at the center of the cutout and at the wing-body juncture. In the first place, since there is no interference between different orders of multipoles, it is necessary to consider only the drag produced by the second-order multipole. Appendix E presents a method for finding the optimum distribution of the second-order cancellation multipoles for a given wing and a fixed value of $F^*(0)$. The resulting wave drag is given in equation (E11). At a Mach number equal to $\sqrt{2}$ and for the basic wing and body parameters presented in figure 29, $F_w^*(0)$ (defined by eq. (E8)) equals -2.90 and the reduction in \bar{D}_2/qS , the amount of drag caused by the wing second-order multipoles alone—see equation (62) and figure 24—is shown in figure 35 for a range of $F^*(0)$. Variations on the strength of various combinations of second-order multipoles are shown in figure 36. It is important to notice that for a given percentage reduction in the maximum strength of the multipoles the resulting percentage reduction in \bar{D}_2 is much larger.

The strengths of $\alpha_2(x)$ shown in figure 36 must now be combined with the zero-order multipoles and wing source sheet, and the combined velocity field used to calculate the shape of the new body. Using again slender-body theory to evaluate the velocity field induced by the multipoles and the numerical methods given in Appendix D to compute the streamlines, one finds, by restricting the distribution and strength of the second-order cancellation multipoles to their

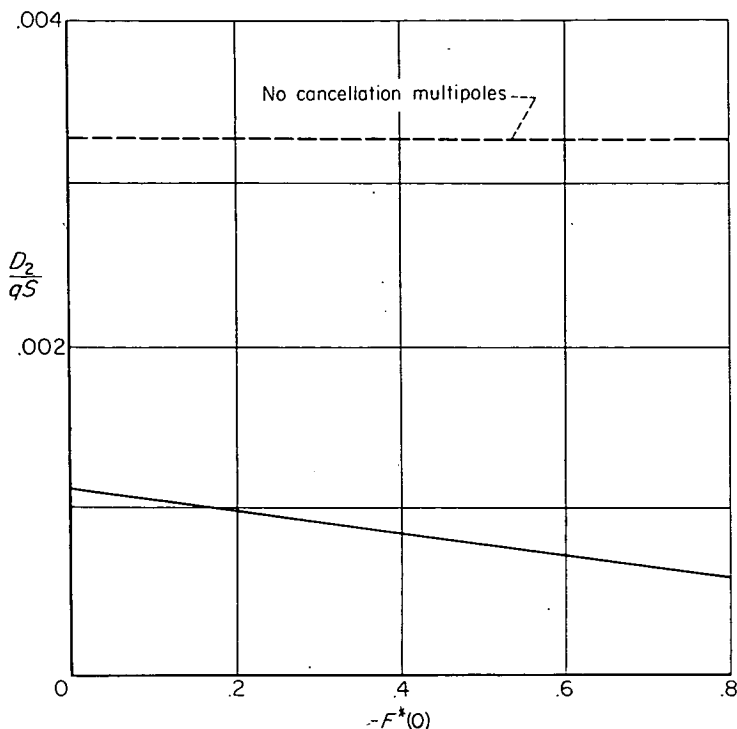
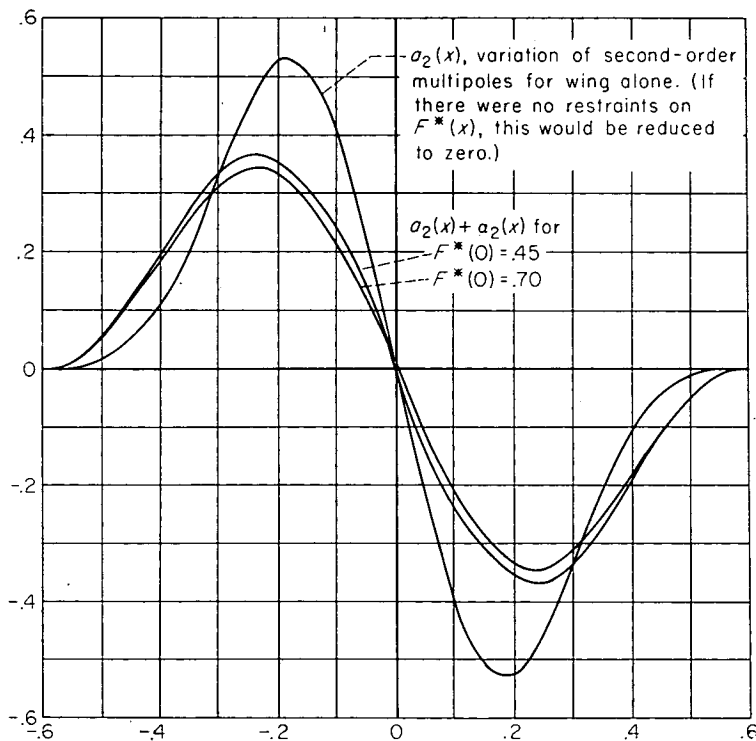


FIGURE 35.—Reduction in drag caused by second-order multipoles.

FIGURE 36.—Variation of second-order multipoles for several values of $F^*(0)$.

optimum values corresponding to the restraint¹¹ $F^*(0) = -0.6$, that a real as well as reasonable body shape results. The details of this shape are presented in figure 31 and their general interpretation is discussed in the next section. Finally, using the value $F^*(0) = -0.6$, the drag curves shown in figure 30 were reinterpreted, and the results—which rep-

¹¹ Figure 34 gives 0.5 as the maximum permissible value of $-F^*(x)$. However, that value is based on a distribution of $a_2(x)$ alone, and in our more general case the added velocity field caused by the presence of the other singularities permits the larger value.

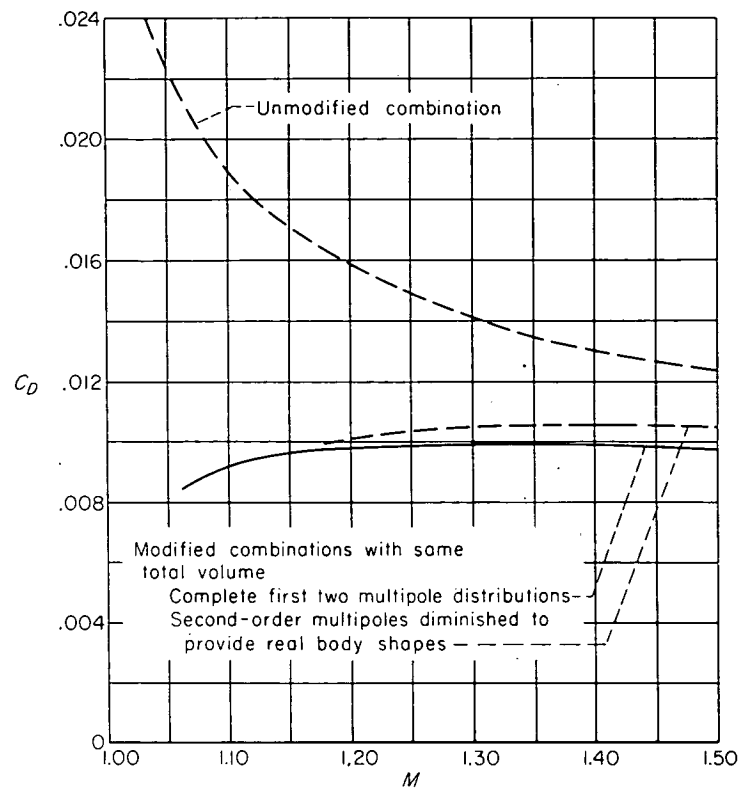


FIGURE 37.—Drag of unmodified and modified combinations with real body shapes.

resent an estimate of the amount the wave drag of an elliptic wing mounted on a basic body of revolution can be reduced by realistic body distortions—are shown in figure 37.

DISCUSSION OF RESULTS

It is possible to gain some insight into the reasons for the various body distortions shown in figure 31 by inspecting, in another light, the body shape first calculated. Consider first the elliptic wing at the top of figure 38. The air over the forward part of this wing, when it is alone in a supersonic stream, is compressed (mathematically, the sign of φ_x is negative), the compression being greatest near the leading edge. On the other hand, the air over the after portion of the wing is undergoing an expansion, the magnitude of which is greatest near the trailing edge. Consider now, in combination with this wing, a body which is to have a shape providing favorable interference. It is apparent that the body should cast expansion waves over the forward portion of the wing, destroying the compression there, and absorb the expansion waves coming from the wing afterportion. Or in another light, the positive pressure on the forward region of the wing (one can use the equation $C_p = (p - p_o)/q = -2\varphi_x/U_o$ for the pressure coefficient) should be reduced as far as possible by a wave shed from the body and having large negative pressures where it comes in contact with the wing forward region.

Since waves in a supersonic flow field are fundamentally associated with the slope of the disturbing surface, the aforementioned favorable interference fields would be created by a body having, longitudinally along its surface, slopes such as those shown in the lower part of figure 38. This is exactly what the solution obtained from the calculation of the

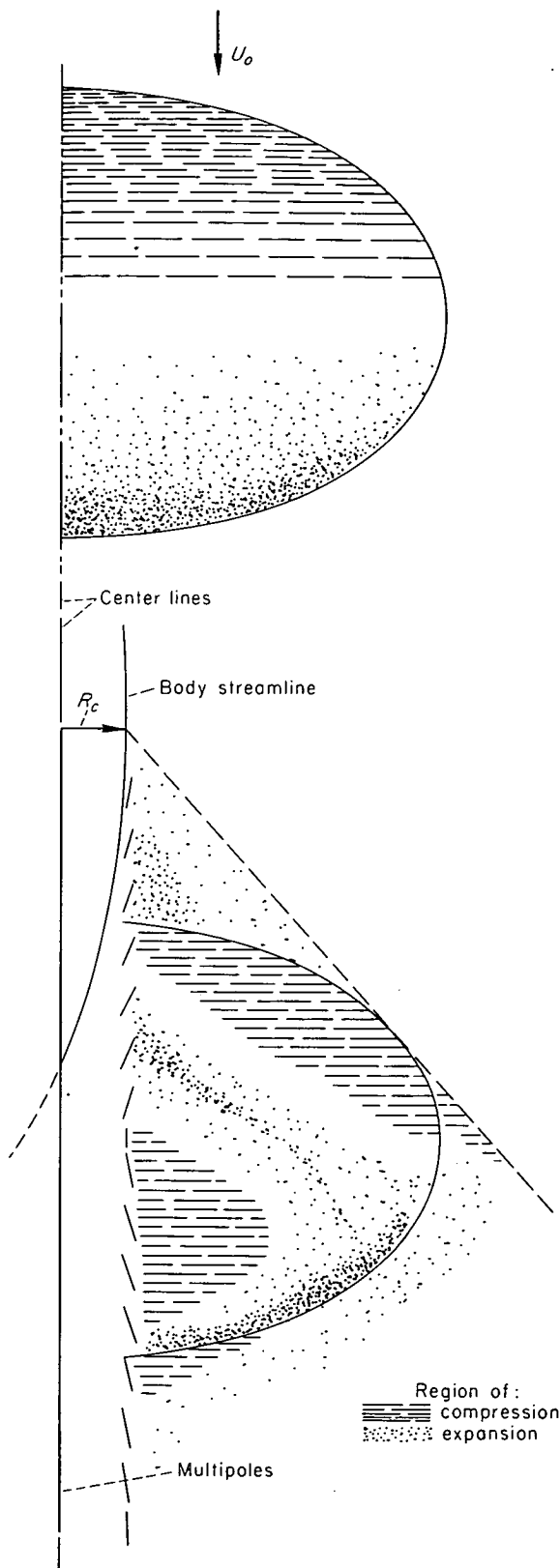


FIGURE 38.—Regions of expansion and compression on wing with unmodified and modified fuselage.

first body shape tried to establish since the fuselage near the plane of the wing (the portion most strongly affecting and being affected by the pressures on the wing) and ahead of the wing chordwise center line was distorted in a manner that caused an expansion across the wing entire forward portion. The difficulty arose because the fuselage was not wide enough

to provide the longitudinal extent of favorable slopes necessary to create the positive pressure called for by the wing forward compression region, and the body streamline near the wing root, following a path such as that shown by the line in figure 38, crossed the body center line before it reached the wing chordwise center.

Consider now the second body calculated in the previous section. In this case an additional restraint was imposed which, effectively, fixed the maximum body indentation. Subject to such a condition, an optimum interference field was discovered. If the resulting fuselage shape is inspected near the plane of the wing, surface slopes are found similar to those shown in figure 39. The following discussion is intended to show that, from a physical viewpoint, this arrangement is reasonable.

Most of the wing pressure drag occurs on the wing inboard portions. Hence, for a fixed maximum fuselage indentation, it is beneficial, from an over-all point of view, to create initially a compression wave, which increases the pressure drag on the forward portion of the wing tip but provides a

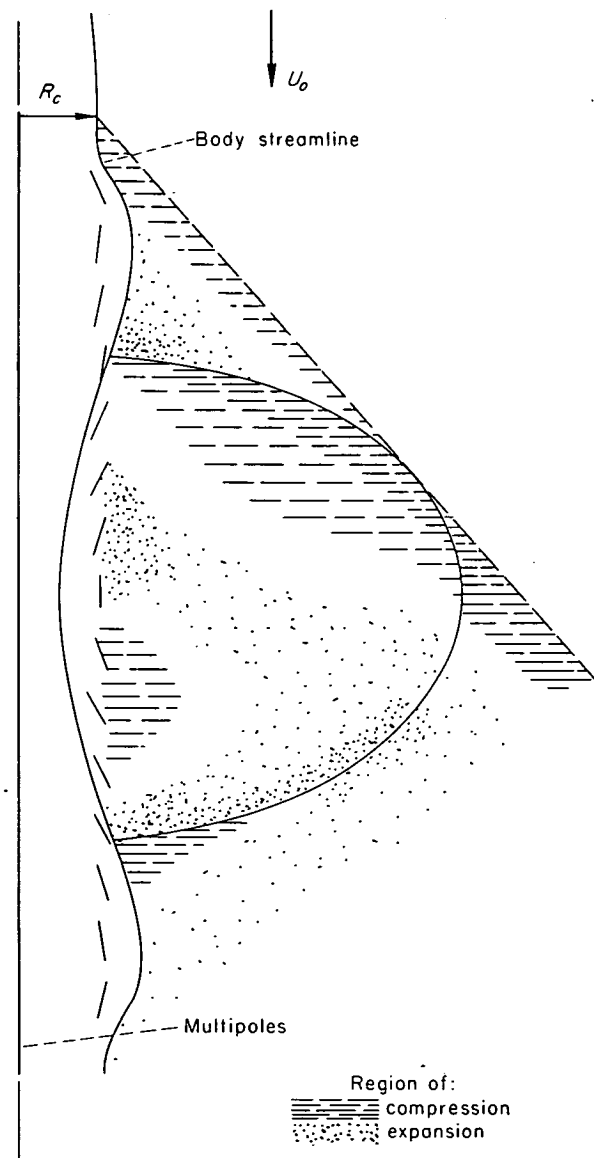


FIGURE 39.—Regions of expansion and compression on wing with fuselage distortion shown.

succeeding extent of fuselage having slopes that generate a strong expansion wave over the forward portion of the wing inboard section. Similarly, the final portion of the body is forced to have a region of unfavorable interferences where the expansion waves from the wing tips combine with body expansion waves to increase the local drag (i. e., increase the local suction pressure) in order that the over-all interference effects are as beneficial, under the given restraints, as possible. This arrangement (i. e., unfavorable interference near the wing tip and favorable interference near the wing root) is given further support by the attenuation property inherent in three-dimensional waves. Thus the pressures induced by the body on the wing tips are not as strong, for a given generating surface slope, as those induced on the inner portion of the wing, simply because the tips are farther from the disturbing surface.

Although these considerations are somewhat oversimplified (the shape of the upper part of the body has been completely ignored in estimating the effect of the waves), the longitudinal variation of surface slopes near the plane of the wing and the resulting body streamlines there are, from a physical point of view, reasonable.

In order to support the above conclusions, the source and multipole distributions simulating the final modified body shown in figure 31 were used to calculate (see Appendix C) u/U_o in the plane of the wing near the root section. The values of u/U_o induced by the wing sources along these sections were assumed to be the same as those induced by a two-dimensional biconvex section having the same local chord; that is, tip effects were neglected. These values for body and wing were added and the resulting pressure distribution, shown in figure 40 ($C_p = -2 u/U_o$), were obtained.

The results are similar to the estimates presented in figure 39. The large drag saving near the root section is illustrated in figure 40 by the graph showing the low values of section drag coefficient along the inner portion of the wing.

Another important characteristic of wing-body combinations designed to have low wave drag is also illustrated in figure 40. As shown in the graph of u/U_o over the surface of a two-dimensional biconvex section the air is everywhere accelerating in the streamwise direction. In studies concerning the effects of viscosity on the fluid flow and, in particular, studies concerning the boundary layer, this positive fluid acceleration is referred to as a favorable pressure gradient. If the flow is laminar in the vicinity of the leading edge of a smooth wing and the pressure gradient is everywhere favorable, the flow tends to remain laminar and unseparated over most of the wing chord. Notice that the modified wing-body combination has a line of zero pressure gradient extending along a Mach line downstream from a point near the body and wing leading-edge juncture. Immediately behind this line the pressure gradient is unfavorable which gives rise to the possibility of flow separation or, at least, transition from laminar to turbulent flow there.

COMPARISON WITH EXPERIMENT

The modified wing-body combination shown in figure 31 was tested in the Ames 2- by 2-foot transonic wind tunnel. The Reynolds number of the test, based on the mean aerodynamic chord, was approximately 1.5×10^6 . This combination had an exposed wing volume of 3.44 cubic inches and a body volume equal to 44.60 cubic inches, for a total volume of 48.04 cubic inches. As a control, an unmodified combination composed of the same elliptic wing mounted on a body of revolution (the area distribution of which was determined from equation (74) with $l=10.5$, $V_K=12.88$, and $V_{SH}=29.02$ cubic inches) was tested. The exposed wing area in the unmodified combination was 3.32 cubic inches and the body volume was 41.90 cubic inches, for a total volume of 45.22 cubic inches. Thus, the unmodified combination had the same body length as the modified one but less volume.

The wave drag at $M=1.41$ of the combination shown in figure 31 has already been calculated and presented in figure 37 by the curve pertaining to real body shapes. By use, in equation (78), of the values of V_K and V_{SH} mentioned above and a value of 0.176 for R/b , the wave drag for the unmodified body was calculated throughout a supersonic Mach number range. The theoretical results obtained for body configurations are shown by the dashed curves in figure 41.

The wind-tunnel results for the total drag on both configurations are shown in figure 42 for $0.6 \leq M \leq 1.4$. Notice that three groups of data are shown. The lower one represents the unmodified body alone, the middle one represents the modified and unmodified combinations with no fixed transition, and the upper one represents both combinations with transition fixed along the leading edge. The models tested with natural transition did not show the predicted drag reduction. As was pointed out in the discussion of figure 40, however, the adverse pressure gradients on the modified model could be inducing transition in the vicinity of

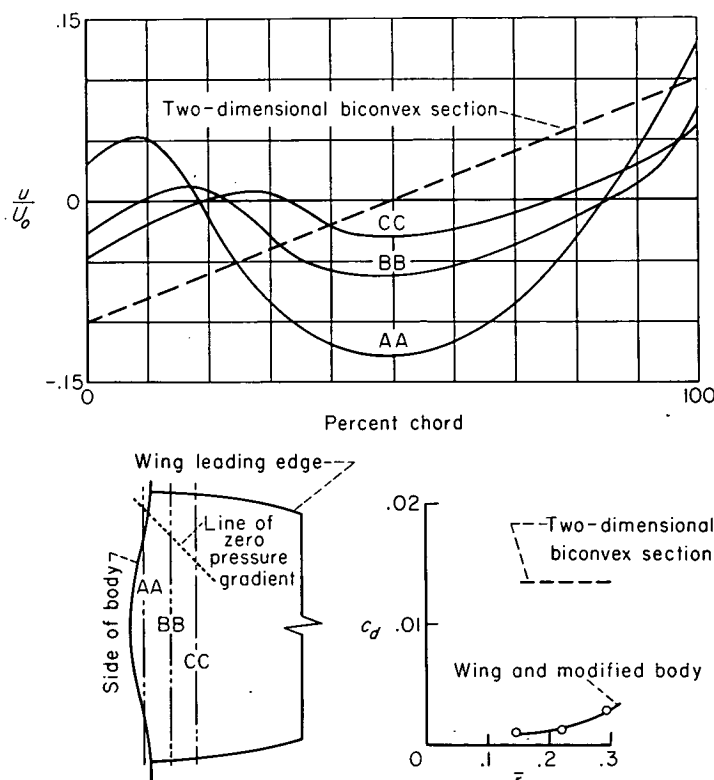


FIGURE 40.—Variation of pressure and section-drag coefficient on sections indicated.

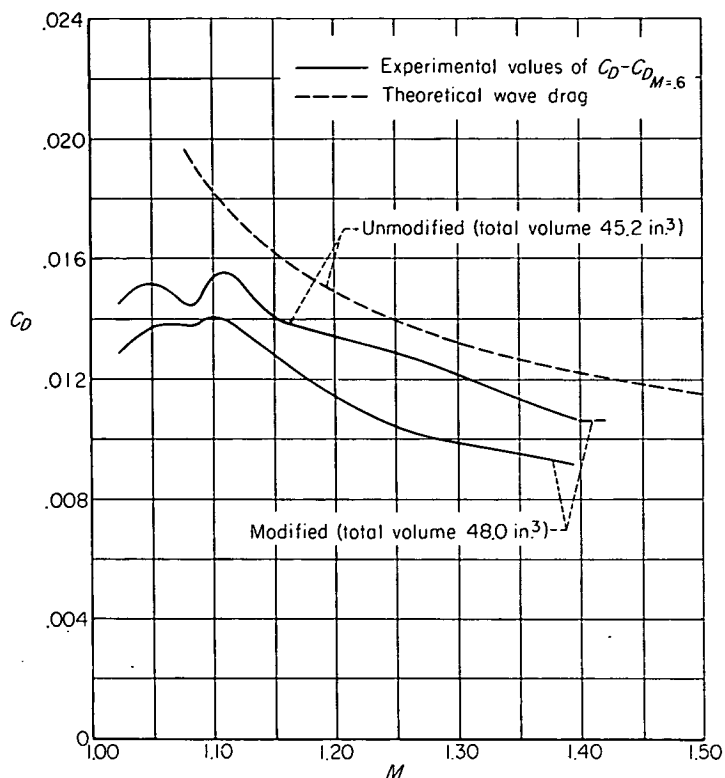


FIGURE 41.—Variation with Mach number of theoretically and experimentally determined drag coefficient.

the 45° line behind the juncture of the wing leading edge with the fuselage. This, in turn, would cause the wing of the modified model to have a larger area covered with a turbulent boundary layer and, hence, cause the drag of the model to increase. In order to separate the potential and viscous effects, the transition-fixed tests were made. If the experimental wave drag is taken to be the difference between the drag at a supersonic Mach number and the drag at

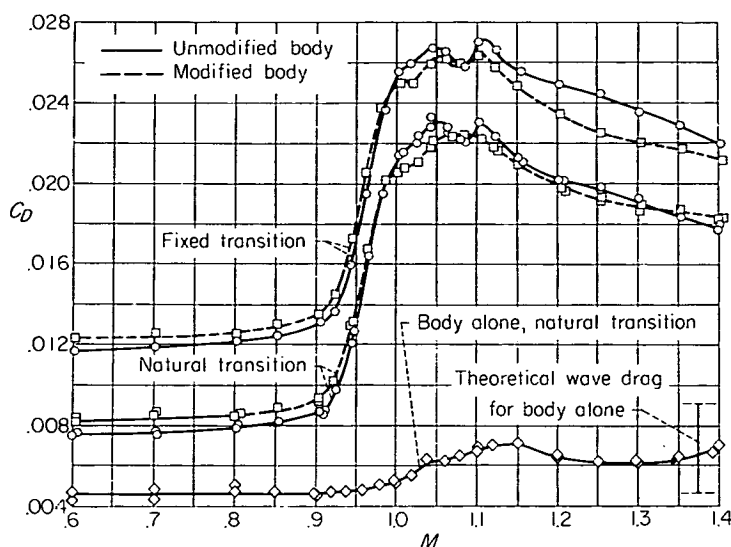


FIGURE 42.—Experimental values for drag coefficient.

$M=0.6$, the resulting values of experimental wave drag are as shown in figure 41.

Figure 41 shows that the experimental reduction in wave drag brought about by the modification agrees with that predicted by theory. Both theory and experiment show a reduction of about 0.0015 in the drag coefficient at the design Mach number (1.41), and the experiment further shows an average reduction of 0.0020 over the Mach number range $1.2 < M < 1.4$. A further study of figure 42 shows that the difference between the experimental and theoretical wave drags shown in figure 41 for the wing-body combinations is nearly the same as the difference between experiment and theory for the body alone.

AMES AERONAUTICAL LABORATORY

NATIONAL ADVISORY COMMITTEE FOR AERONAUTICS

MOFFETT FIELD, CALIF., May 16, 1956

APPENDIX A

DERIVATION OF THE OPERATIONAL FORM OF THE WAVE EQUATION

For convenience, take the normalized form of the wave equation in Cartesian coordinates, thus

$$\frac{\partial^2 \varphi}{\partial x^2} - \frac{\partial^2 \varphi}{\partial y^2} - \frac{\partial^2 \varphi}{\partial z^2} = 0 \quad (A1)$$

and define the Laplace transform of $\varphi(x, y, z)$ by

$$\bar{\varphi}(s, y, z) = \int_0^\infty e^{-sx} \varphi(x, y, z) dx \quad (A2)$$

Now if $x=f(y, z)$ is the equation of the foremost Mach cone or Mach cone envelope and $f(y, z) \geq 0$, it is apparent

$$\frac{\partial^2 \bar{\varphi}}{\partial y^2} = \frac{\partial^2}{\partial y^2} \int_f^\infty \varphi(x, y, z) e^{-sx} dx = \int_f^\infty e^{-sx} \frac{\partial^2 \varphi}{\partial y^2} dx - \frac{\partial f}{\partial y} e^{-sf} \left(\frac{\partial \varphi}{\partial y} \right)_{x=f} \quad (A3)$$

since $(\varphi)_{x=f}$ is, but $\left(\frac{\partial \varphi}{\partial y} \right)_{x=f}$ is not, necessarily zero. From equation (A3) we see

$$\int_0^\infty e^{-sx} \frac{\partial^2 \varphi}{\partial y^2} dx = \frac{\partial^2 \bar{\varphi}}{\partial y^2} + \frac{\partial f}{\partial y} e^{-sf} \left(\frac{\partial \varphi}{\partial y} \right)_{x=f} \quad (A4)$$

$$\int_0^\infty e^{-sx} \frac{\partial^2 \varphi}{\partial z^2} dx = \frac{\partial^2 \bar{\varphi}}{\partial z^2} + \frac{\partial f}{\partial z} e^{-sf} \left(\frac{\partial \varphi}{\partial z} \right)_{x=f} \quad (A5)$$

Further, integrating by parts gives

$$\int_0^\infty e^{-sx} \frac{\partial^2 \varphi}{\partial x^2} dx = s^2 \bar{\varphi} - e^{-sf} \left(\frac{\partial \varphi}{\partial x} \right)_{x=f} \quad (A6)$$

Hence,

$$\int_0^\infty e^{-sx} \left(\frac{\partial^2 \varphi}{\partial x^2} - \frac{\partial^2 \varphi}{\partial y^2} - \frac{\partial^2 \varphi}{\partial z^2} \right) dx = s^2 \bar{\varphi} - \frac{\partial^2 \bar{\varphi}}{\partial y^2} - \frac{\partial^2 \bar{\varphi}}{\partial z^2} - e^{-sf} \left(\frac{\partial \varphi}{\partial x} + \frac{\partial \varphi}{\partial y} \frac{\partial f}{\partial y} + \frac{\partial \varphi}{\partial z} \frac{\partial f}{\partial z} \right)_{x=f} \quad (A7)$$

The last term on the right is the directional derivative of the perturbation potential along the surface $x=f(y, z)$. This is, of course, along the so-called conormal. Since φ is a constant on the forward envelope, its gradient along the envelope is zero and

$$\int_0^\infty e^{-sx} \left(\frac{\partial^2 \varphi}{\partial x^2} - \frac{\partial^2 \varphi}{\partial y^2} - \frac{\partial^2 \varphi}{\partial z^2} \right) dx = s^2 \bar{\varphi} - \frac{\partial^2 \bar{\varphi}}{\partial y^2} - \frac{\partial^2 \bar{\varphi}}{\partial z^2} = 0 \quad (A8)$$

APPENDIX B

ON THE VOLUME OF BODIES CALCULATED USING SLENDER-BODY THEORY

The following proof shows that in a rectilinear distribution of singularities, only the sources contribute to the total cross-sectional area of the simulated body and, hence, to its volume.

According to slender-body theory, the velocities induced in the field by distributions of multipoles along the x axis can be written

$$\varphi_{n_r} = \begin{cases} \frac{a_0(x)}{2\pi r}, & n=0 \\ \frac{(-2)^n n! a_n(x) \cos n\theta}{4\pi r^{n+1}}, & n>0 \end{cases} \quad (B1a)$$

$$\frac{1}{r} \varphi_{n_\theta} = \frac{(-2)^n n! a_n(x) \sin n\theta}{4\pi r^{n+1}} \quad (B1b)$$

Further, we have derived—see equation (41)—neglecting only second-order effects, the equation representing the boundary condition for the body, thus

$$U_0 \frac{\partial R}{\partial x} = \left(\varphi_r - \frac{\varphi_\theta}{r^2} \frac{\partial R}{\partial \theta} \right)_{r=R(x, \theta)} \quad (B2)$$

Combine equations (B1) and (B2)

$$2\pi U_0 R \frac{\partial R}{\partial x} = a_0(x) + \sum_{n=1}^{\infty} (-2)^n n! a_n(x) \left(\frac{\cos n\theta}{R^n} - \frac{\sin n\theta}{R^{n+1}} \frac{\partial R}{\partial \theta} \right)$$

multiply by $d\theta$, and integrate

$$2\pi U_0 \frac{\partial}{\partial x} \int_0^{2\pi} \frac{R^2}{2} d\theta = 2\pi a_0(x) + \sum_{n=1}^{\infty} (-2)^n n! a_n(x) \int_0^{2\pi} \left(\frac{R \cos n\theta - \sin n\theta \frac{\partial R}{\partial \theta}}{R^{n+1}} \right) d\theta$$

or

$$2\pi U_0 \frac{\partial}{\partial x} S(x) = 2\pi a_0(x) + \sum_{n=1}^{\infty} (-2)^n (n-1)! a_n(x) \int_0^{2\pi} \frac{d}{d\theta} \left(\frac{\sin n\theta}{R^n} \right) d\theta \quad (B3)$$

Since the integrand in equation (B3) is a periodic function in θ , we have

$$\frac{\partial S}{\partial x} = \frac{a_0(x)}{U_0} \quad (B4)$$

which shows the simulated-body normal cross-sectional area to be dependent only on the source strength. Further, the total volume is given by

$$V = \int_{-l}^{l'} S(x) dx = \int_{-l}^{l'} (l' - x) S'(x) dx + (l' + l) S(-l)$$

and when $S(l') = S(-l) = 0$, there results

$$V = -\frac{1}{U_0} \int_{-l}^{l'} x a_0(x) dx \quad (B5)$$

APPENDIX C

ON THE CALCULATION OF VELOCITIES INDUCED BY ARBITRARY SOURCE DISTRIBUTIONS

The potential and velocity fields represented by equations (18) and (19) are difficult to evaluate analytically even if $A_n(\xi)$ is a simple function. However, the calculations can be reduced to a relatively simple process. First, let equation (18) be expressed in terms of the dimensionless variables \bar{x} , $\bar{\xi}$, and \bar{r} where

$$\left. \begin{aligned} \bar{x} &= x/L_o \\ \bar{\xi} &= \xi/L_o \\ \bar{r} &= \beta r/L_o \end{aligned} \right\} \quad (C1)$$

Then

$$\varphi_o(\bar{x}, \bar{r}, \theta) = -\frac{1}{2\pi} \int_{-1}^{\bar{x}-\bar{r}} \frac{A_o(\bar{\xi}) d\bar{\xi}}{\sqrt{(\bar{x}-\bar{\xi})^2 - \bar{r}^2}} \quad (C2a)$$

$$\varphi_2(\bar{x}, \bar{r}, \theta) = -\frac{\cos 2\theta}{2\pi} \int_{-1}^{\bar{x}-\bar{r}} \frac{A_2(\bar{\xi}) [2(\bar{x}-\bar{\xi})^2 - \bar{r}^2] d\bar{\xi}}{\bar{r}^2 \sqrt{(\bar{x}-\bar{\xi})^2 - \bar{r}^2}} \quad (C2b)$$

and so forth. Consider next the variation of $A_n(\bar{\xi})$ shown in figure 43 and represented by the equation

$$A_n(\bar{\xi}) = \begin{cases} (190n - 360m) + (390n - 760m)\bar{\xi} + (200n - 400m)\bar{\xi}^2, & -1 \leq \bar{\xi} \leq -0.9 \\ n, & -0.9 \leq \bar{\xi} \end{cases} \quad (C3)$$

As seen in the figure, A_n vanishes at $\bar{\xi} = -1$, is a parabola between -1 and -0.9 (assuming the values m at $\bar{\xi} = -0.95$ and n at $\bar{\xi} = -0.9$), and the straight line, $A_n(\bar{\xi}) = n$, for $\bar{\xi}$

greater than -0.9 . The velocities induced by a multipole distribution given by equation (C3) can be calculated in a straightforward manner in the two regions $-1 + \bar{r} \leq \bar{x} \leq -0.9 + \bar{r}$ and $-0.9 + \bar{r} \leq \bar{x}$. For example, if

$$\frac{\pi \bar{r} M_{o\tau}(\bar{x})}{200} = \begin{cases} -(\bar{x} + 0.9) \sqrt{(\bar{x} + 1.0)^2 - \bar{r}^2} + \bar{r}^2 n \frac{\bar{x} + 1.0 + \sqrt{(\bar{x} + 1.0)^2 - \bar{r}^2}}{\bar{r}}, & -1 + \bar{r} < \bar{x} < -0.9 + \bar{r} \\ -(\bar{x} + 0.9) \sqrt{(\bar{x} + 1.0)^2 - \bar{r}^2} + (\bar{x} + 1.0) \sqrt{(\bar{x} + 0.9)^2 - \bar{r}^2} + \bar{r}^2 n \frac{\bar{x} + 1.0 + \sqrt{(\bar{x} + 1.0)^2 - \bar{r}^2}}{\bar{x} + 0.9 + \sqrt{(\bar{x} + 0.9)^2 - \bar{r}^2}}, & -0.9 + \bar{r} < \bar{x} \end{cases} \quad (C4)$$

$$\frac{\pi \bar{r} N_{o\tau}(x)}{100} = \begin{cases} (\bar{x} + 0.95) \sqrt{(\bar{x} + 1.0)^2 - \bar{r}^2} - \bar{r}^2 n \frac{\bar{x} + 1.0 + \sqrt{(\bar{x} + 1.0)^2 - \bar{r}^2}}{\bar{r}}, & -1 + \bar{r} < \bar{x} < -0.9 + \bar{r} \\ (\bar{x} + 0.95) \sqrt{(\bar{x} + 1.0)^2 - \bar{r}^2} - (\bar{x} + 1.05) \sqrt{(\bar{x} + 0.9)^2 - \bar{r}^2} - \bar{r}^2 n \frac{\bar{x} + 1.0 + \sqrt{(\bar{x} + 1.0)^2 - \bar{r}^2}}{\bar{x} + 0.9 + \sqrt{(\bar{x} + 0.9)^2 - \bar{r}^2}}, & -0.9 + \bar{r} < \bar{x} \end{cases} \quad (C5)$$

then $\varphi_{o\tau}$ can be written

$$\varphi_{o\tau} = m M_{o\tau}(\bar{x}) + n N_{o\tau}(\bar{x}) \quad (C6)$$

Now, if one is given a distribution of sources that is composed of, or is adequately approximated by, a series of 20 equally spaced parabolic arcs, equation (C6) can be used for each individual arc and the results superimposed for the complete solution. To this effect, define m_i and n_i in terms of $A_o(x)$ by

$$\left. \begin{aligned} m_i &= A_o\left(\frac{i-0.5}{10} - 1\right) - A_o\left(\frac{i-1}{10} - 1\right) \\ n_i &= A_o\left(\frac{i}{10} - 1\right) - A_o\left(\frac{i-1}{10} - 1\right) \end{aligned} \right\} \quad (C7)$$

so they represent the magnitudes shown in figure 44. Then, if $[\bar{x}]$ denotes the greatest integer contained in \bar{x} (e. g., [6.34] equals 6), the equation for the radial velocity becomes

$$\varphi_{o\tau} = \sum_{i=1}^{[10(\bar{x}-\bar{r})+11]} \left[m_i M_{o\tau}\left(\bar{x} - \frac{i-1}{10}\right) + n_i N_{o\tau}\left(\bar{x} - \frac{i-1}{10}\right) \right] \quad (C8)$$

Values of $M_{o\tau}$ and $N_{o\tau}$ are tabulated in table I for \bar{r} equal to 0.074, 0.148, 0.222, and 0.296. The asymptotic magnitudes of these functions are given by slender-body theory. Hence, one can easily show for large \bar{x}

$$\left. \begin{aligned} M_{o\tau} &\approx 0 \\ N_{o\tau} &\approx \frac{1}{2\pi\bar{r}} \end{aligned} \right\} \quad (C9)$$

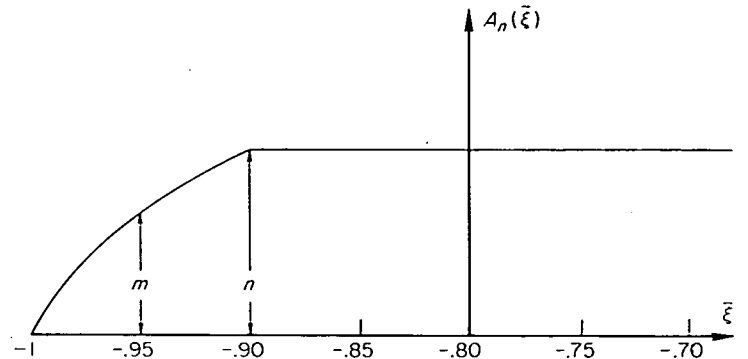


FIGURE 43.—Definition of symbols used in equations (C3) and (C6).

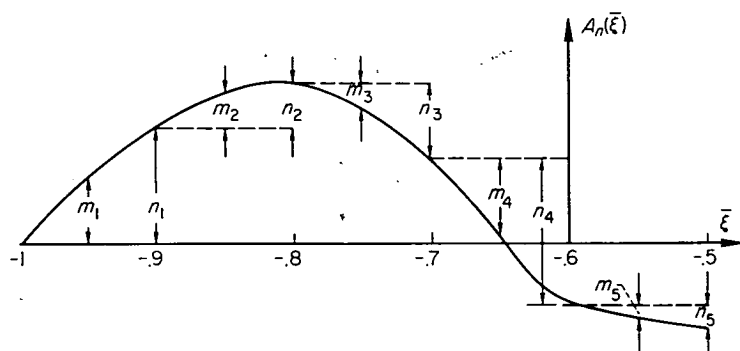


FIGURE 44.—Definition of symbols used in equation (C7).

Notice that both functions have essentially reached their asymptotic values for large x by the time $\bar{x} = -1 + \bar{r} + 0.5$. By applying simple tabulative procedures to equation (C8)—for example, listing m_i and n_i in reverse order and accumulating multiplications of adjacent terms—the value of $\varphi_{o\bar{r}}$ for any $A_o(\bar{x})$ representable by equation (C7) is readily calculated.

The velocities induced by higher order multipoles can be calculated in a similar fashion. Because of the asymptotic behavior of the M 's and N 's, however, one is led into the numerically inefficient process of obtaining small numbers from differences of large numbers. For the velocities φ_r and φ_θ , the following is a method for circumventing this difficulty.

It follows from equations (9) or (19), that for small \bar{r} , $\varphi_{n\bar{r}}$ and $\varphi_{n\theta}$ can be expressed in terms of the multipole strengths $a_n(\bar{x})$ —as defined by equation (7)—by the equations

$$r^{n+1} \left(\frac{\varphi_{n\bar{r}}}{\cos n\theta} \right) = C_o + C_1 r + \dots + C_\nu r^\nu + \dots \quad (\text{C10a})$$

$$r^{n+1} \left(\frac{\varphi_{n\theta}}{r \sin n\theta} \right) = D_o + D_1 r + \dots + D_\nu r^\nu + \dots \quad (\text{C10b})$$

where for $\nu \leq n$, $n \geq 1$

$$C_\nu = \begin{cases} \frac{(-1)^{n+\frac{\nu}{2}} \beta^\nu 2^{n-\nu}}{4\pi} \frac{(n-\nu)\Gamma\left(n-\frac{\nu}{2}\right)}{\Gamma\left(1+\frac{\nu}{2}\right)} a_n^{(\nu)}(x), & \nu \text{ even} \\ 0, & \nu \text{ odd} \end{cases} \quad (\text{C11a})$$

$$D_\nu = \begin{cases} \frac{(-1)^{n+\frac{\nu}{2}} \beta^\nu 2^{n-\nu}}{4\pi} \frac{n\Gamma\left(n-\frac{\nu}{2}\right)}{\Gamma\left(1+\frac{\nu}{2}\right)} a_n^{(\nu)}(x), & \nu \text{ even} \\ 0, & \nu \text{ odd} \end{cases} \quad (\text{C11b})$$

Consider now the velocities $\varphi_{2\bar{r}}$ and $\varphi_{2\theta}$ induced by the multipole strength defined by equation (C3); thus

$$\frac{\varphi_{2\bar{r}}}{\cos 2\theta} = m M_{2\bar{r}}(\bar{x}) + n N_{2\bar{r}}(\bar{x}) \quad (\text{C12a})$$

$$\frac{\varphi_{2\theta}}{r \sin 2\theta} = m M_{2\theta}(\bar{x}) + n N_{2\theta}(\bar{x}) \quad (\text{C12b})$$

where values of the M 's and N 's are listed in tables II and III. Their asymptotic values, as given by equations (C10) and (C11), are

$$\left. \begin{aligned} M_{2\bar{r}} &= \frac{19+20\bar{x}}{150\pi\bar{r}^3} \\ N_{2\bar{r}} &= \frac{150\bar{x}^2+275\bar{x}+126}{150\pi\bar{r}^3} \\ M_{2\theta} &= \frac{19+20\bar{x}}{150\pi\bar{r}^3} \\ N_{2\theta} &= \frac{150\bar{x}^2+275\bar{x}+126}{150\pi\bar{r}^3} - \frac{1}{2\pi\bar{r}} \end{aligned} \right\} \quad (\text{C13})$$

and these are also given in the tables.

As the tables show, equations (C13) are sufficiently accurate approximations to M and N for practical calculating purposes when $\bar{x} > -1 + \bar{r} + 0.5$. Hence, the velocities at the point \bar{x}, \bar{r} induced by the multipoles in the interval $-1 < \bar{x} < \bar{x} - \bar{r} - 0.5$ can be calculated using equations (C13). In terms of the distribution for $A_2(\xi)$ —which is equal to $a_2^{(2)}(\xi)$, see equation (16)—this means the multipole distribution shown in the upper part of figure 45 can be calculated by means of the asymptotic formulas and the result added to that obtained for the distribution shown in the lower part of figure 45 by use of equations (C12b) and tables II and III in a manner identical to the one represented by equations (C6), (C7), and (C8).

The value of $\varphi_{2\theta}(\bar{x}, \bar{r})$ induced by a multipole distribution such as that shown in the upper part of figure 45 is, on the basis of equations (C10) and (C11),

$$\frac{\varphi_{2\theta}}{r \sin 2\theta} = H(\bar{x}, \bar{r}) = \frac{2}{\pi\bar{r}^3} \int_{-1}^{\bar{x}} (\bar{x} - \xi) A_2(\xi) d\xi - \frac{A_2(\bar{x})}{2\pi\bar{r}}$$

so

$$H(\bar{x}, \bar{r}) = \frac{2}{\pi\bar{r}^3} a_2(\bar{x} - \bar{r} - \bar{x}_i) + \frac{2(\bar{r} + \bar{x}_i)}{\pi\bar{r}^3} a_2^{(1)}(\bar{x} - \bar{r} - \bar{x}_i) + a_2^{(2)}(\bar{x} - \bar{r} - \bar{x}_i) \left[\frac{(\bar{r} + \bar{x}_i)^2}{\pi\bar{r}^3} - \frac{1}{2\pi\bar{r}} \right] \quad (\text{C14})$$

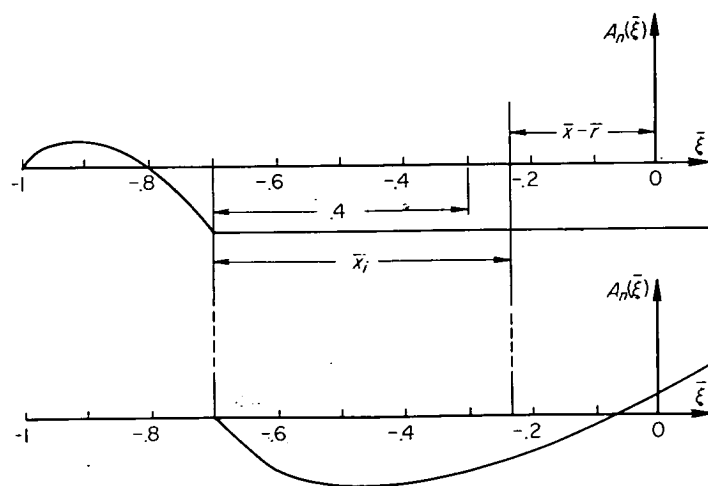


FIGURE 45.—Range of application of equations (C12) and (C13).

where $\beta^2 a_2^{(2)}(x) = A_2(x)$ and x_i is shown in figure 45 and defined by the equation

$$\bar{x}_i = 0.4 + \bar{x} - \bar{r} - \frac{[10(\bar{x} - \bar{r})]}{10} \quad (C15)$$

the symbol $[10(\bar{x} - \bar{r})]$ meaning, as before, the highest integer value contained in $10(\bar{x} - \bar{r})$. A similar result can be derived for $\varphi_{2\bar{r}}$ and one has finally for $-1 \leq [10(\bar{x} - \bar{r}) + 11] \leq 5$

$$\frac{\varphi_{2\theta}(\bar{x})}{\bar{r} \sin 2\theta} = \sum_1^{[10(\bar{x} - \bar{r}) + 11]} \left[m_i M_{2\theta} \left(\bar{x} - \frac{i-1}{10} \right) + n_i N_{2\theta} \left(\bar{x} - \frac{i-1}{10} \right) \right] \quad (C16a)$$

$$\frac{\varphi_{2\bar{r}}(\bar{x})}{\cos 2\theta} = \sum_1^{[10(\bar{x} - \bar{r}) + 11]} \left[m_i M_{2\bar{r}} \left(\bar{x} - \frac{i-1}{10} \right) + n_i N_{2\bar{r}} \left(\bar{x} - \frac{i-1}{10} \right) \right] \quad (C16b)$$

and for $[10(\bar{x} - \bar{r}) + 11] \geq 6$

$$\frac{\varphi_{2\theta}(\bar{x})}{\bar{r} \sin 2\theta} = \sum_{[10(\bar{x} - \bar{r}) + 11] - 5}^{[10(\bar{x} - \bar{r}) + 11]} \left[m_i M_{2\theta} \left(\bar{x} - \frac{i-1}{10} \right) + n_i N_{2\theta} \left(\bar{x} - \frac{i-1}{10} \right) \right] + H(\bar{x}, \bar{r}) \quad (C17a)$$

$$\frac{\varphi_{2\bar{r}}(\bar{x})}{\cos 2\theta} = \sum_{[10(\bar{x} - \bar{r}) + 11] - 5}^{[10(\bar{x} - \bar{r}) + 11]} \left[m_i M_{2\bar{r}} \left(\bar{x} - \frac{i-1}{10} \right) + n_i N_{2\bar{r}} \left(\bar{x} - \frac{i-1}{10} \right) \right] + H(\bar{x}, \bar{r}) - \frac{A_2(\bar{x} - \bar{r} - \bar{x}_i)}{2\pi\bar{r}} \quad (C17b)$$

The streamwise gradients of induced velocities can also be defined in terms of M 's and N 's as were the velocities $\varphi_{\bar{r}}$ and $\frac{1}{\bar{r}} \varphi_{\theta}$. Thus

$$\varphi_{\theta\bar{x}} = m M_{\theta\bar{x}} + n N_{\theta\bar{x}}$$

$$\frac{\varphi_{2\bar{x}}}{\cos 2\theta} = m M_{2\bar{x}} + n N_{2\bar{x}}$$

Values of $M_{\theta\bar{x}}$, $N_{\theta\bar{x}}$, $M_{2\bar{x}}$, and $N_{2\bar{x}}$ for \bar{r} equal to 0.148, 0.222, and 0.296 are given in tables IV and V.

APPENDIX D

NUMERICAL METHOD USED TO CALCULATE BODY SHAPE

The method used to calculate the body shape was a standard step-by-step solution to the two simultaneous total differential equations (eq. (43) in the text)

$$\left. \begin{aligned} \frac{d\theta}{dx} &= \frac{1}{U_o R^2} \varphi_{\theta}(x, R, \theta) \\ \frac{dR}{dx} &= \frac{1}{U_o} \varphi_r(x, R, \theta) \end{aligned} \right\} \quad (D1)$$

The essentials of the process are recognized from the following computing-sheet heading set up for initial values of θ and \bar{R} equal to 30° and 0.148, respectively, where $\bar{x} = x/L_o$ and $\bar{R} = \beta R/L_o$

①	②	③	④	⑤	⑥	⑦
n	\bar{x}	$\frac{\textcircled{10}_n \times 0.05 + \textcircled{10}_{n-1}}{\theta}$	$\frac{\textcircled{10}_n \times 0.05 + \textcircled{10}_{n-1}}{\bar{R}}$	$\left(\frac{1}{U_o} \frac{\partial \varphi}{\partial \theta} \right)$ for ⑤ and ④	$\left(\frac{d\theta}{d\bar{x}} \right)_1$ $\frac{\textcircled{10}}{\textcircled{10}^2}$	$\left(\frac{1}{U_o} \frac{\partial \varphi}{\partial \bar{r}} \right)$ for ⑤ and ④
0	-0.852	0.524	0.148	-----	-----	-----
1	-.802	-----	-----	-----	-----	-----
2	-.752	-----	-----	-----	-----	-----
⑧	⑨	⑩	⑪	⑫	⑬	⑭
$\frac{\textcircled{10}_{n-1} \times 0.05 + \textcircled{10}_{n-1}}{\theta_1}$	$\frac{\textcircled{10}_{n-1} \times 0.05 + \textcircled{10}_{n-1}}{\bar{R}_1}$	$\left(\frac{1}{U_o} \frac{\partial \varphi}{\partial \theta} \right)$ for ⑩ and ⑧	$\left(\frac{d\theta}{d\bar{x}} \right)_2$ $\frac{\textcircled{10}}{\textcircled{10}^2}$	$\left(\frac{1}{U_o} \frac{\partial \varphi}{\partial \bar{r}} \right)$ for ⑩ and ⑧	$\left(\frac{d\theta}{d\bar{x}} \right)_{**}$ $\frac{\textcircled{10}_{n-1} + \textcircled{10}_n}{2}$	$\left(\frac{d\bar{R}}{d\bar{x}} \right)_{**}$ $\frac{\textcircled{10}_{n-1} + \textcircled{10}_n}{2}$
-----	-----	-----	-----	-----	-----	-----

APPENDIX E

OPTIMUM VARIATION OF $\alpha_2(x)$ FOR A FIXED VALUE OF $\int_{-L_o}^0 \alpha_2(x) dx$

Given

$$D_2 = -\frac{q}{4\pi U_o^2} \int_{-L_o}^{L_o} \int_{-L_o}^{L_o} [a_2^{(3)}(x_1) + \alpha_2^{(3)}(x_1)] [a_2^{(3)}(x_2) + \alpha_2^{(3)}(x_2)] \frac{1}{n} \left| \frac{x_1 - x_2}{L_o} \right| dx_1 dx_2 \quad (E1)$$

where the variation of $a_2^{(3)}(x)$ is fixed, pose the restraint

$$\frac{1}{U_o} \int_{-L_o}^0 \alpha_2(x) dx = F^*(0) \frac{\pi}{4} R_c^4 = \text{constant} \quad (E2)$$

and ask for the function $\alpha_2(x)$ which minimizes D_2 for a given value of the constant.

If $f(x) = f(-x)$, then

$$\begin{aligned} & \int_{-1}^1 \int_{-1}^1 f(x_1) f(x_2) 1/n |x_1 - x_2| dx_1 dx_2 \\ &= 2 \int_{-1}^0 \int_{-1}^0 f(x_1) f(x_2) 1/n |x_1^2 - x_2^2| dx_1 dx_2 \end{aligned}$$

and since $\alpha_2(-L_o) = \alpha_2^{(1)}(-L_o) = \alpha_2^{(2)}(-L_o) = 0$

$$\int_{-L_o}^0 \alpha_2(x) dx = -\frac{1}{6} \int_{-L_o}^0 x^3 \alpha_2^{(3)}(x) dx$$

Therefore, the standard variational problem

$$\delta \left[D_2 + \lambda \int_{-L_o}^0 \frac{\alpha_2(x) dx}{U_o} \right] = 0 \quad (E3)$$

reduces to

$$\delta \left\{ \frac{-q}{2\pi U_0^2} \int_{-L_0}^0 \int_{-L_0}^0 [a_2^{(3)}(x_1) + \alpha_2^{(3)}(x_1)] [a_2^{(3)}(x_2) + \alpha_2^{(3)}(x_2)] \right. \\ \left. 1n \left| \frac{x_1^2 - x_2^2}{L_0^2} \right| dx_1 dx_2 - \frac{\lambda}{6U_0} \int_{-L_0}^0 x_1^3 \alpha_2^{(3)}(x_1) dx_1 \right\} = 0$$

and this becomes

$$\int_{-L_0}^0 \delta \left[\frac{\alpha_2^{(3)}(x_1)}{U_0} \right] dx_1 \left\{ \frac{q}{\pi U_0} \int_{-L_0}^0 [\alpha_2^{(3)}(x_2) + \alpha_2^{(3)}(x_2)] \right. \\ \left. 1n \left| \frac{x_1^2 - x_2^2}{L_0^2} \right| dx_2 + \frac{\lambda x_1^3}{6} \right\} = 0$$

Integrating three times by parts, using the relations

$$\delta \alpha_2(-L_0) = \delta \alpha_2^{(1)}(-L_0) = \delta \alpha_2^{(2)}(-L_0) = 0$$

$$\delta \alpha_2(0) = \delta \alpha_2^{(2)}(0) = 0, \text{ by symmetry}$$

and

$$\lim_{x_1 \rightarrow 0} \frac{\partial}{\partial x_1} \int_{-L_0}^0 [a_2^{(3)}(x_2) + \alpha_2^{(3)}(x_2)] 1n \left| \frac{x_1^2 - x_2^2}{L_0^2} \right| dx_2 \\ = \lim_{x_1 \rightarrow 0} 2x_1 \int_{-L_0}^0 \frac{a_2^{(3)}(x_2) + \alpha_2^{(3)}(x_2)}{x_1 - x_2} dx_2 = 0$$

yields

$$\int_{-L_0}^0 \delta \left[\frac{\alpha_2(x_1)}{U_0} \right] dx_1 \frac{\partial^3}{\partial x_1^3} \left\{ \int_{-L_0}^0 [a_2^{(3)}(x_2) + \alpha_2^{(3)}(x_2)] \right. \\ \left. 1n \left| \frac{x_1^2 - x_2^2}{L_0^2} \right| dx_2 + U_0 \lambda_0 x_1^3 \right\} = 0$$

where

$$\lambda_0 = \frac{\lambda \pi}{6q} \quad (\text{E4})$$

By the fundamental lemma of the calculus of variations

$$\frac{\partial^3}{\partial x_1^3} \left\{ \int_{-L_0}^0 [a_2^{(3)}(x_2) + \alpha_2^{(3)}(x_2)] 1n \left| \frac{x_1^2 - x_2^2}{L_0^2} \right| dx_2 + U_0 \lambda_0 x_1^3 \right\} = 0, \\ 0 > x_1 > -L_0$$

One can also show

$$\frac{\partial^3}{\partial x_1^3} \left\{ \int_0^{L_0} [a_2^{(3)}(x_2) + \alpha_2^{(3)}(x_2)] 1n \left| \frac{x_1^2 - x_2^2}{L_0^2} \right| dx_2 - U_0 \lambda_0 x_1^3 \right\} = 0, \\ L_0 > x_1 > 0$$

Hence,

$$\int_{-L_0}^0 \frac{\alpha_2^{(3)}(x_2)}{U_0} 1n \left| \frac{x_1^2 - x_2^2}{L_0^2} \right| dx_2 = \gamma_0 + \gamma_2 x_1^2 - \lambda_0 x_1^3 \\ \int_{-L_0}^0 \frac{a_2^{(3)}(x_2)}{U_0} 1n \left| \frac{x_1^2 - x_2^2}{L_0^2} \right| dx_2 \quad (\text{E5})$$

Integrating by parts and changing the notation so that

$$\eta_2 = \frac{x_2^2}{L_0^2}, \quad f(\eta_2) = \frac{a_2^{(2)}(x_2)}{U_0} \\ \eta_1 = \frac{x_1^2}{L_0^2}, \quad g(\eta_2) = \frac{a_2^{(2)}(x_2)}{U_0}$$

one has

$$\int_0^1 \frac{f(\eta_2) d\eta_2}{\eta_1 - \eta_2} = \gamma_0 + \gamma_2 \eta_1 - \lambda_0 \eta_1^{3/2} - \int_0^1 \frac{g(\eta_2) d\eta_2}{\eta_1 - \eta_2} \quad (\text{E6})$$

Equation (E6) is the familiar singular integral equation known, in aerodynamic applications, as the airfoil equation. Its inversion is discussed, for example, in reference 3. If one solves equation (E6) and applies the conditions

$$a_2^{(2)}(0) = a_2^{(2)}(L_0) = 0$$

then

$$\gamma_0 = -\frac{4\lambda_0 L_0^3}{15\pi}, \quad \gamma_2 = \frac{48\lambda_0 L_0}{15\pi}$$

and

$$\frac{\alpha_2(x)}{U_0} + \frac{a_2(x)}{U_0} = \frac{\lambda_0 L_0^4 x}{60\pi^2} \left\{ \left[10 \left(\frac{x}{L_0} \right)^2 - 4 \right] \sqrt{1 - \left(\frac{x}{L_0} \right)^2} \right. \\ \left. 3 \left(\frac{x}{L_0} \right)^4 1n \frac{L_0 - \sqrt{L_0^2 - x^2}}{L_0 + \sqrt{L_0^2 - x^2}} \right\} \quad (\text{E7})$$

Now set

$$\int_{-L_0}^0 \frac{a_2(x)}{U_0} dx = F_w^*(0) \frac{\pi}{4} R_c^4 \quad (\text{E8})$$

so that $F_w^*(0)$ is a known constant. Then

$$\int_{-L_0}^0 \frac{\alpha_2(x) dx}{U_0} = F^*(0) \frac{\pi}{4} R_c^4 = -F_w^*(0) \frac{\pi}{4} R_c^4 + \frac{2\lambda_0 L_0^6}{225\pi^2} \quad (\text{E9})$$

Using the above expressions, one can show

$$\frac{\alpha_2(x)}{U_0} + \frac{a_2(x)}{U_0} = \frac{15\pi R_c^4 x}{32L_0^2} [F^*(0) + F_w^*(0)] \\ \left\{ \left[10 \left(\frac{x}{L_0} \right)^2 - 4 \right] \sqrt{1 - \left(\frac{x}{L_0} \right)^2} + 3 \left(\frac{x}{L_0} \right)^4 1n \frac{L_0 - \sqrt{L_0^2 - x^2}}{L_0 + \sqrt{L_0^2 - x^2}} \right\} \quad (\text{E10})$$

The wave drag can be calculated by combining equations (E5) and (E1).

$$D_2 = -\frac{q}{2\pi} \int_0^{L_0} (\gamma_0 + \gamma_2 x_1^2 - \lambda_0 x_1^3) \left[\frac{a_2^{(3)}(x_1)}{U_0} + \frac{\alpha_2^{(3)}(x_1)}{U_0} \right] dx_1$$

Integrate three times by parts and there results, finally

$$D_2 = \frac{675}{32} q L_0^2 \pi^3 \left(\frac{R_c}{L_0} \right)^4 [F^*(0) + F_w^*(0)]^2 \quad (\text{E11})$$

REFERENCES

1. Heaslet, Max. A., Lomax, Harvard, and Spreiter, John R.: Linearized Compressible-Flow Theory for Sonic Flight Speeds. NACA Rep. 956, 1950.
2. Lamb, Horace: Hydrodynamics. Sixth ed., Dover Publications (New York), 1945.
3. Lomax, Harvard, Heaslet, Max. A., and Fuller, Franklyn B.: Integrals and Integral Equations in Linearized Wing Theory. NACA Rep. 1054, 1951.
4. Watson, G. N.: A Treatise on the Theory of Bessel Functions. Second ed., Cambridge Univ. Press (Cambridge, England), 1952.

5. Erdélyi, Arthur: Table of Integral Transforms. Vol. I, McGraw-Hill Book Co., Inc., 1954.
6. Hayes, Wallace D.: Linearized Supersonic Flow. North American Aviation, Inc., Rep. No. AL-222, June 1947.
7. Lomax, Harvard, and Heaslet, Max. A.: Recent Developments in the Theory of Wing-Body Wave Drag. IAS Preprint 617, 1956.
8. von Kármán, Th.: The Problem of Resistance in Compressible Fluids. (Fifth Volta Congress) Roma Reale Accademia D'Italia 1936.
9. Webster, Arthur Gordon: Partial Differential Equations of Mathematical Physics. Second ed., Hafner Publishing Co., Inc. (New York), 1950.
10. Nielsen, Jack N., and Pitts, William C.: General Theory of Wave-Drage Reduction for Combinations Employing Quasi-Cylindrical Bodies With an Application to Swept Wing and Body Combinations. NACA TN 3722, 1956. (Formerly NACA RM A55B07).
11. Jones, Robert T.: Theoretical Determination of the Minimum Drag of Airfoils at Supersonic Speeds. Jour. Aero. Sci., vol. 19, no. 12, Dec. 1952, pp. 813-822.
12. Jones, Robert T.: Theory of Wing-Body Drag at Supersonic Speeds. NACA RM A53H18a, 1953.
13. Lomax, Harvard: The Wave Drag of Arbitrary Configurations in Linearized Flow as Determined by Areas and Forces in Oblique Planes. NACA RM A55A18, 1955.
14. Nielsen, Jack N., and Pitts, William C.: Wing-Body Interference at Supersonic Speeds With an Application to Combinations With Rectangular Wings. NACA TN 2677, 1952.
15. Jones, Robert T.: Some Recent Developments in the Aerodynamics of Wings for High Speeds. Zeitschrift Für Flugwissenschaften, 4. Jahr., Heft 8, Aug. 1956, pp. 257-262.
16. Graham, Ernest W.: The Pressure on a Slender Body of Non-Uniform Cross-Sectional Shape in Axial Supersonic Flow. Douglas Aircraft Co., Inc., Rep. No. SM-13346-A, July 1949.

TABLE I.—VALUES OF $M_{\sigma\tau}$ AND $N_{\sigma\tau}$.

\bar{z}	$M_{\sigma\tau}$		$N_{\sigma\tau}$		\bar{z}	$M_{\sigma\tau}$		$N_{\sigma\tau}$	
	Exact	Asymp- totic	Exact	Asymp- totic		Exact	Asymp- totic	Exact	Asymp- totic
$\bar{r}=0.074$					$\bar{r}=0.148$				
-0.926	0	----	0	----	-0.852	0	----	0	----
-876	3.16	----	.56	----	-802	2.00	----	.42	----
-826	-2.96	----	4.86	----	-752	-2.26	----	3.24	----
-776	-.24	----	2.52	----	-702	-.22	----	1.60	----
-726	-.03	----	2.34	----	-652	-.10	----	1.30	----
-676	-.04	----	2.26	----	-602	-.06	----	1.20	----
-626	-.02	----	2.22	----	-552	-.04	----	1.18	----
-576	-.02	----	2.20	----	-502	-.02	----	1.14	----
-526	-.02	0	2.20	2.15	-452	-.02	0	1.14	1.08
-476	0	0	2.18	2.15	-402	0	0	1.12	1.08
-426	0	0	2.18	2.15	-352	0	0	1.10	1.08
$\bar{r}=0.222$					$\bar{r}=0.296$				
-0.778	0	----	0	----	-0.704	0	----	0	----
-728	1.56	----	.34	----	-654	1.32	----	.30	----
-678	-1.90	----	2.62	----	-604	-1.66	----	2.24	----
-628	-.22	----	1.12	----	-554	-.20	----	.92	----
-578	-.10	----	.94	----	-504	-.03	----	.78	----
-528	-.06	----	.88	----	-454	-.06	----	.70	----
-478	-.04	----	.84	----	-404	-.04	----	.66	----
-428	-.02	----	.80	----	-354	-.02	----	.64	----
-378	-.02	0	.78	0.72	-304	-.02	0	.62	0.54
-328	-.02	0	.78	.72	-254	-.02	0	.60	.54
-278	0	0	.76	.72	-204	0	0	.60	.54

TABLE II.—VALUES OF $M_{\tau\tau}$ AND $N_{\tau\tau}$.

\bar{z}	$M_{\tau\tau}$		$N_{\tau\tau}$		\bar{z}	$M_{\tau\tau}$		$N_{\tau\tau}$	
	Exact	Asymp- totic	Exact	Asymp- totic		Exact	Asymp- totic	Exact	Asymp- totic
$\bar{r}=0.074$					$\bar{r}=0.148$				
-0.926	0	----	0	----	-0.852	0	----	0	----
-876	9.77	----	-.16	----	-802	3.86	----	2.31	----
-826	10.61	----	8.31	----	-752	.68	----	4.38	----
-776	18.09	----	15.53	----	-702	3.11	----	4.73	----
-726	23.44	----	28.41	----	-652	3.85	----	6.97	----
-676	23.72	----	45.32	----	-602	4.53	----	9.77	----
-626	33.95	----	66.17	----	-552	5.19	----	13.05	----
-576	39.15	----	90.98	----	-502	5.85	----	16.90	----
-526	44.38	44.41	119.70	119.66	-452	6.51	6.52	21.20	21.17
-476	49.62	49.64	152.35	152.32	-402	7.17	7.17	26.01	25.98
-426	54.87	54.88	188.91	188.89	-352	7.83	7.83	31.30	31.23
$\bar{r}=0.222$					$\bar{r}=0.296$				
-0.778	0	----	0	----	-0.704	0	----	0	----
-728	2.49	----	.26	----	-654	1.90	----	.25	----
-678	-.60	----	3.20	----	-604	-.92	----	2.62	----
-628	1.11	----	2.66	----	-554	.51	----	1.86	----
-578	1.38	----	3.46	----	-504	.67	----	2.22	----
-528	1.61	----	4.47	----	-454	.78	----	2.72	----
-478	1.81	----	5.65	----	-404	.87	----	3.29	----
-428	2.01	----	6.99	----	-354	.96	----	3.93	----
-378	2.21	2.22	8.47	8.44	-304	1.05	1.06	4.64	4.60
-328	2.40	2.41	10.10	10.07	-254	1.13	1.14	5.42	5.39
-278	2.60	2.61	11.88	11.86	-204	1.22	1.22	6.26	6.23

TABLE III.—VALUES OF $M_{2\theta}$ AND $N_{2\theta}$.

\bar{z}	$M_{2\theta}$		$N_{2\theta}$		\bar{z}	$M_{2\theta}$		$N_{2\theta}$	
	Exact	Asymp- totic	Exact	Asymp- totic		Exact	Asymp- totic	Exact	Asymp- totic
$\bar{r}=0.074$					$\bar{r}=0.148$				
-0.926	0	----	0	----	-0.852	0	----	0	----
-876	6.62	----	-.73	----	-802	1.86	----	-.19	----
-826	13.59	----	3.42	----	-752	2.93	----	1.11	----
-776	18.38	----	12.97	----	-702	3.34	----	3.25	----
-726	23.43	----	26.12	----	-652	3.93	----	5.65	----
-676	28.70	----	43.10	----	-602	4.58	----	8.55	----
-626	33.92	----	63.97	----	-552	5.22	----	11.91	----
-576	39.15	----	88.80	----	-502	5.89	----	15.74	----
-526	44.47	44.41	117.45	117.51	-452	6.49	6.52	20.07	20.09
-476	49.63	49.64	150.15	150.17	-402	7.16	7.17	24.89	24.90
-426	54.85	54.88	186.77	186.74	-352	7.83	7.83	30.18	30.20
$\bar{r}=0.222$					$\bar{r}=0.296$				
-0.778	0	----	0	----	-0.704	0	----	0	----
-728	.93	----	-.09	----	-654	.58	----	-.05	----
-678	1.29	----	.59	----	-604	.74	----	.37	----
-628	1.32	----	1.54	----	-554	.71	----	.93	----
-578	1.45	----	2.51	----	-504	.76	----	1.45	----
-528	1.66	----	3.60	----	-454	.83	----	2.02	----
-478	1.85	----	4.82	----	-404	.91	----	2.63	----
-428	2.04	----	6.18	----	-354	.98	----	3.29	----
-378	2.23	2.22	7.69	7.72	-304	1.06	1.06	4.03	4.07
-328	2.42	2.41	9.33	9.35	-254	1.15	1.14	4.82	4.85
-278	2.61	2.61	11.11	11.14	-204	1.23	1.22	5.67	5.69

TABLE IV.—VALUE OF $M_{\sigma\bar{z}}$ AND $N_{\sigma\bar{z}}$.

\bar{z}	$M_{\sigma\bar{z}}$		$N_{\sigma\bar{z}}$		\bar{z}	$M_{\sigma\bar{z}}$		$N_{\sigma\bar{z}}$	
	Exact	Asymp- totic	Exact	Asymp- totic		Exact	Asymp- totic	Exact	Asymp- totic
$\bar{r}=0.148$					$\bar{r}=0.222$				
-0.852	0	0	0	0	-0.778	0	0	0	0
-802	-1.663	-.442	-.723	-1.379	-728	-1.379	-.360	-.654	-1.204
-752	2.529	-3.024	-.678	2.051	-678	2.051	-2.435	-.604	1.769
-702	.369	-1.019	-.623	.297	-628	.297	-.859	-.554	.255
-652	.191	-.723	-.578	.155	-578	.155	-.620	-.504	.133
-602	.121	-.572	-.528	.099	-528	.099	-.498	-.454	.085
-552	.035	-.477	-.478	.070	-478	.070	-.420	-.404	.061
-502	.063	-.410	-.423	.053	-423	.053	-.365	-.354	.046
-452	.049	-.361	-.378	.042	-378	.042	-.324	-.304	.036
-402	.040	-.323	-.323	.034	-323	.034	-.292	-.254	.030
-352	.033	-.292	-.278	.023	-278	.023	-.266	-.204	.025
-302	.027	-.267	-.223	.024	-223	.024	-.243	-.154	.021
-252	.023	-.245	-.178	.020	-178	.020	-.226	-.104	.018
-202	.020	-.227	-.128	.018	-128	.018	-.210	-.054	.016
-152	.018	-.212	-.078	.015	-78	.015	-.197	-.004	.014
-102	.015	-.199	-.023	.014	-.023	.014	-.185	.046	.012
-52	.014	-.187	.022	.012	.022	.012	-.174	.096	.011
-0.02	.012	-.176	.072	.011	.072	.011	-.165	.146	.010
.045	.011	-.167	.122	.010	.122	.010	-.157	.196	.009
.098	.010	-.158	.172	.009	.172	.009	-.149	.246	.008
.145	.009	-.151	.222	.008	.222	.008	-.142	.296	.007
.198	.008	-.144	.272	.007	.272	.007	-.136	.346	.007
.245	.007	-.138	.322	.007	.322	.007	-.131	.396	.006
.298	.007	-.132	.372	.006	.372	.006	-.125	.446	.006
.345	.006	-.127	.422	.006	.422	.006	-.120	-----	-----
.398	.006	-----	-----	-----	-----	-----	-----	-----	-----
.445	.005	-.117	-----	-----	-----	-----	-----	-----	-----

TABLE V.—VALUES OF $M_{2\bar{z}}$ AND $N_{2\bar{z}}$.

\bar{z}	$M_{2\bar{z}}$		$N_{2\bar{z}}$		\bar{z}	$M_{2\bar{z}}$		$N_{2\bar{z}}$		\bar{z}	$M_{2\bar{z}}$		$N_{2\bar{z}}$	
	Exact	Asymp- totic	Exact	Asymp- totic		Exact	Asymp- totic	Exact	Asymp- totic		Exact	Asymp- totic	Exact	Asymp- totic
$\bar{r}=0.148$					$\bar{r}=0.222$					$\bar{r}=0.296$				
-0.852	0	-----	0	-----	-0.778	0	-----	0	-----	-0.704	0	-----	0	-----
-.802	-3.16	-----	-.31	-----	-.723	-2.18	-----	-.29	-----	-.654	-1.72	-----	-.27	-----
-.752	.92	-----	-4.05	-----	-.678	1.22	-----	-3.04	-----	-.604	1.25	-----	-2.52	-----
-.702	-.85	-----	-3.23	-----	-.623	-.30	-----	-2.05	-----	-.554	-.11	-----	-1.52	-----
-.652	-.93	-----	-3.91	-----	-.578	-.38	-----	-2.27	-----	-.504	-.19	-----	-1.60	-----
-.602	-.95	-----	-4.61	-----	-.523	-.41	-----	-2.56	-----	-.454	-.22	-----	-1.74	-----
-.552	-.96	-----	-5.23	-----	-.478	-.42	-----	-2.86	-----	-.404	-.23	-----	-1.90	-----
-.502	-.96	-----	-6.04	-----	-.423	-.42	-----	-3.18	-----	-.354	-.23	-----	-2.07	-----
-.452	-.96	-0.97	-6.76	-6.75	-.378	-.42	-0.43	-3.49	-3.48	-.304	-.24	-0.24	-2.24	-2.23
-.402	-.97	-.97	-7.49	-7.43	-.323	-.43	-.43	-3.81	-3.80	-.254	-.24	-.24	-2.42	-2.41
-.352	-.97	-.97	-8.21	-8.21	-.278	-.43	-.43	-4.13	-4.12	-.204	-.24	-.24	-2.60	-2.59

REPORT 1283

EXTRAPOLATION TECHNIQUES APPLIED TO MATRIX METHODS IN NEUTRON DIFFUSION PROBLEMS¹

By ROBERT R. MCCREADY

SUMMARY

A general matrix method is developed for the solution of characteristic-value problems of the type arising in many physical applications. The scheme employed is essentially that of Gauss and Seidel with appropriate modifications needed to make it applicable to characteristic-value problems. An iterative procedure produces a sequence of estimates to the answer; and extrapolation techniques, based upon previous behavior of iterates, are utilized in speeding convergence. Theoretically sound limits are placed on the magnitude of the extrapolation that may be tolerated.

This matrix method is applied to the problem of finding criticality and neutron fluxes in a nuclear reactor with control rods. The two-dimensional finite-difference approximation to the two-group neutron-diffusion equations is treated. Results for this example are indicated.

The calculations were performed on the IBM card-programmed calculator.

INTRODUCTION

A general matrix method is developed for the solution of characteristic-value problems of a type arising in many physical applications. The method of this paper is essentially that of Gauss and Seidel (ref. 1), which itself is but a special case of the method of conjugate gradients (ref. 2). The adaptation of the Gauss-Seidel technique to the characteristic-value problem calls for a means of computing successive estimates of the characteristic value as well as the vector. This calculation is made to rely upon Turner's technique (ref. 3) for assigning a meaning to the ratio of two vectors.

Extrapolation techniques are also employed to speed up the convergence of the iterative process. One of these is based on Turner's original formula (ref. 3), and the other is a slightly more complicated modification.

The number of iterations required for convergence is not studied theoretically here as in the "n-step" methods, but the minimization of a suitable form at each step is derived.

The method is applied to two-group neutron-diffusion equations. The calculations were performed at the NACA Lewis laboratory.

SYMBOLS

The following symbols are used in this report:

A, B, L, U	matrices
B_z^2	axial leakage
D, E, F, G, J, X	vectors
h	grid dimension
i, j, k	indices
k_{th}	thermal multiplication constant
L_f^2	average square slowing down length for fast neutrons
L_{th}^2	average square diffusion length for thermal neutrons
N	number of nuclei per cc
p_{th}	resonance escape probability
r	radial coordinate
r_c	core radius
$\operatorname{sgn} u =$	$\begin{cases} 1 & u > 0 \\ -1 & u < 0 \\ 0 & u = 0 \end{cases}$
t	reflector thickness
w, ω	weight functions
γ	characteristic value
$\Delta_{k+1}^{(i)}$	deviation at i th point of k th iteration (eq. (80))
$\delta_{k+1}^{(i)}$	difference $X_{k+1}^{(i)} - X_k^{(i)}$
λ	actual damping rate
τ	bulk damping rate
$\varphi, \psi, \varphi_{th}, \varphi_f$	neutron fluxes

Parameter groupings:

$$\begin{aligned}
 a &= \frac{1}{L_{f0}^2} + B_z^2 & a' &= \frac{1}{L_{f0}^2} \\
 b &= \frac{\lambda_{tr, th0}}{\lambda_{tr, f0}} k_{th0} \frac{1}{L_{th0}^2} \\
 c &= \frac{1}{L_{th0}^2} + B_z^2 & c' &= \frac{1}{L_{th0}^2} \\
 \bar{d} &= \frac{\lambda_{tr, f0}}{\lambda_{tr, th0}} p_{th0} \frac{1}{L_{f0}^2} \\
 f &= \frac{1}{L_{f1}^2} + B_z^2 & f' &= \frac{1}{L_{f1}^2}
 \end{aligned}$$

¹ Supersedes NACA TN 3511, "Extrapolation Techniques Applied to Matrix Methods in Neutron Diffusion Problems," by Robert R. McCready, 1955.

$$g = \frac{1}{L_{ih_1}^2} + B_i^2 \quad g' = \frac{1}{L_{ih_1}^2}$$

$$m = \frac{\lambda_{ir,f_1}}{\lambda_{ir,ih_1}} p_{ih_1} \frac{1}{L_{f_1}^2}$$

Subscripts:

f	fast
th	thermal
tr	transport
0	reactor
1	reflector
2	rod

THE METHOD

MATRIX FORMULATION

Consider the matrix equation

$$AX = \gamma BX \quad (1)$$

where A and B are $n \times n$ matrices, X is an n -component vector, and the characteristic value of γ is a scalar to be determined. A may be separated into the sum of two triangular matrices L and U , where L contains all the diagonal elements of the original matrix A .

This separation, which anticipates the Gauss-Seidel process, is effected in the following manner:

$$A = L + U \quad (2)$$

$$l_{ij} = a_{ij} \quad j \leq i; \quad l_{ij} = 0 \quad j > i \quad (3)$$

$$u_{ij} = a_{ij} \quad j > i; \quad u_{ij} = 0 \quad j \leq i \quad (4)$$

If L is a nonsingular matrix (always true if $l_{ii} \neq 0$ for all i), equation (1), modified to

$$(L + U)X = \gamma BX \quad (5)$$

may be multiplied by L^{-1} , giving

$$(I + L^{-1}U)X = \gamma L^{-1}BX \quad (6)$$

For a given X , the quantities $L^{-1}UX$ and $L^{-1}BX$ of equation (6) may be calculated without the actual formation of L^{-1} . This fact, which is very helpful for systems containing matrices, arises in the following manner and depends upon the triangular nature of L . Let D be the vector defined by

$$D = L^{-1}UX \quad (7)$$

Then

$$LD = UX = C \quad (8)$$

whence

$$l_{11}d_1 = c_1 \quad (9)$$

gives d_1 , since all the c_i can be computed from U and X in equation (8). Then

$$l_{21}d_1 + l_{22}d_2 = c_2 \quad (10)$$

gives d_2 , and

$$l_{31}d_1 + l_{32}d_2 + l_{33}d_3 = c_3 \quad (11)$$

gives d_3 , and so forth, so that L^{-1} need not be computed in order to obtain $L^{-1}UX$. The same argument applies to $L^{-1}BX$.

ITERATIVE SCHEME

Equation (6) may be written

$$X = \gamma L^{-1}BX - L^{-1}UX \quad (12)$$

which may be interpreted as defining the iterative scheme

$$X_{k+1} = \gamma_{k+1} L^{-1}BX_k - L^{-1}UX_k \quad (13)$$

in which γ_{k+1} is an estimate to γ that can be calculated from X_k . To obtain γ_{k+1} , form the inner product of the vector $\text{sgn } L^{-1}BX_k$ with each side of equation (6); thus,

$$\gamma_{k+1} = \frac{(\text{sgn } L^{-1}BX_k, (I + L^{-1}U)X_k)}{(\text{sgn } L^{-1}BX_k, L^{-1}BX_k)} \quad (14)$$

Equations (13) and (14) are the basic equations of the iterative scheme. Given any X_k , γ_{k+1} is computed from equation (14) and γ_{k+1} and X_k are placed in (13) to yield the next iterant X_{k+1} . This process is repeated until X_k and γ_{k+1} converge.

Some normalization is necessary in problems of a homogeneous nature. The simplest method of normalization is to adjust a permanently specified coordinate of X_k to unity before beginning each iteration. This is accomplished by dividing each element of the vector by the specified coordinate.

The ratio defined by equation (14) was chosen for simplicity of calculation on available punched-card equipment. That ratio can be compared to the Rayleigh quotient (for eq. (13))

$$\gamma'_{k+1} = \frac{(J_k, G_k)}{(J_k, J_k)} \quad (15)$$

where

$$J_k = L^{-1}BX_k \quad (16)$$

$$G_k = (I + L^{-1}U)X_k \quad (17)$$

by noting that each of the relations (14) and (15) constitute a weighted sum of local (point by point) values $\gamma_{k+1}^{(i)}$ of γ'_{k+1} . These local values are defined by

$$\gamma_{k+1}^{(i)} = \gamma_{k+1}^{(i)} = g_k^{(i)} / j_k^{(i)} \quad (18)$$

where $g_k^{(i)}$ and $j_k^{(i)}$ are the i th components of G_k and J_k respectively. The weighted average associated with (15) is

$$\gamma'_{k+1} = \sum_i w_i \gamma_{k+1}^{(i)} \quad (19)$$

where

$$w_i = \frac{[j_k^{(i)}]^2}{\sum_m [j_k^{(m)}]^2} \quad (20)$$

while the weighted average associated with (14) is

$$\gamma_{k+1} = \sum_i \omega_i \gamma_{k+1}^{(i)} \quad (21)$$

where

$$\omega_i = \frac{|j_k^{(i)}|}{\sum_m |j_k^{(m)}|} \quad (22)$$

Equation (15) selects that value of γ'_{k+1} which minimizes the sum of the squares of the residuals of equation (6) where that quantity is thought of as a function of γ'_{k+1} . The sum

of the squares of the residuals is not, of course, the only quadratic form that is suitable for minimization (ref. 2). Consider the expression

$$p = p(\gamma_{k+1}) = \sum_i \left\{ \frac{g_k^{(i)} \operatorname{sgn} j_k^{(i)}}{[j_k^{(i)} \operatorname{sgn} j_k^{(i)}]^{1/2}} - \gamma_{k+1} [j_k^{(i)} \operatorname{sgn} j_k^{(i)}]^{1/2} \right\}^2 \quad (23)$$

which is zero for $X_k = X$ and $\gamma_{k+1} = \gamma$. This generally positive quantity can be minimized (made closer to its ultimate value zero) by setting

$$\gamma_{k+1} = \frac{(\operatorname{sgn} J_k, G_k)}{(\operatorname{sgn} J_k, J_k)} \quad (24)$$

which is equation (14) expressed in terms of J and G .

EXAMPLE

To illustrate the convergence of this method in a special case, consider the problem of equation (1) with

$$A = \begin{pmatrix} 3 & -1 & -1 & 0 \\ 0 & 2 & -1 & -1 \\ 0 & -1 & 3 & -1 \\ 0 & -1 & -2 & 3 \end{pmatrix} \quad (25)$$

and

$$B = \begin{pmatrix} 0 & 1 & 0 & 0 \\ 0 & 0 & 1 & 0 \\ 1 & 0 & 0 & 0 \\ 0 & 0 & 0 & 0 \end{pmatrix} \quad (26)$$

which has the real solution $X^{(1)} = 1.020070$, $X^{(2)} = 1.329658$, $X^{(3)} = 1.000000$, $X^{(4)} = 1.109886$; $\gamma = 0.549429$ and two solutions with complex characteristic values. This solution was found by the ordinary process of solving the characteristic equation.

This problem was solved in 15 iterations starting with an initial guess of $X_0 = (10, 100, 1, 1000)$. The values of successive iterants, together with those of γ , are listed in the following table. The iterants are normalized so that $X_k^{(3)} = 1$ at the start of each iteration:

k	$X_k^{(1)}$	$X_k^{(2)}$	$X_k^{(4)}$	γ_{k+1}
0	10	100	1000	
1	-0.692996	1.069635	1.023212	-10.634589
2	.271412	.438315	.812771	-1.352353
3	.848870	1.565152	1.188384	-.097105
4	1.132470	1.360721	1.120240	.526554
5	1.006120	1.292707	1.097568	.592807
6	1.010639	1.337044	1.112348	.538366
7	1.024544	1.331918	1.110639	.547271
8	1.019872	1.328104	1.109368	.551383
9	1.019593	1.329848	1.109949	.549107
10	1.020236	1.329788	1.109929	.549291
11	1.020078	1.329596	1.109865	.549510
12	1.020048	1.329660	1.109886	.549423
13	1.020076	1.329665	1.109889	.549422
14	1.020071	1.329656	1.109885	.549432
15	1.020070	1.329658	1.109886	.549430

EXTRAPOLATION TECHNIQUE

If, instead of four components, the iterant vector has many components, techniques of extrapolation are usually desirable to speed convergence of the process. The technique employed here, which is due to Turner (ref. 3), attempts to

evaluate a bulk damping rate that describes in an average way the over-all trend of the individual components of the iterant vectors.

Assume that each iterant X_k is made up of the sum of the solution X and two error vectors E_k and F_k satisfying the damping relations

$$E_{k+1} + \tau E_k \quad (27)$$

and

$$F_{k+1} = -\tau F_k \quad (28)$$

Then the following relations hold:

$$X_0 = X + E_0 + F_0 \quad (29)$$

$$X_1 = X + \tau E_0 - \tau F_0 \quad (30)$$

$$X_2 = X + \tau^2 E_0 + \tau^2 F_0 \quad (31)$$

$$X_3 = X + \tau^3 E_0 - \tau^3 F_0 \quad (32)$$

One may compute

$$\tau^2 = \frac{X_3 - X_2}{X_1 - X_0} \quad (33)$$

The "vector division" implied in equation (33) is possible because, under the initial assumption of error behavior (eqs. (27) and (28)), the vectors $X_3 - X_2$ and $X_1 - X_0$ are collinear and therefore differ only in length.

If the error vectors are eliminated from equations (30) and (32), one obtains

$$X = \frac{X_3 - \tau^2 X_1}{1 - \tau^2} \quad (34)$$

which gives the answer as a linear combination of the alternate iterants X_1 and X_3 .

The preceding analysis suggests that a formula analogous to (34) be used to estimate the answer. The difficulty here is that equation (33) may be meaningless when equations (29) to (32) do not hold. To circumvent this difficulty, a method of computing τ^2 is needed. Toward this end, define $\delta_{k+1}^{(j)}$ by means of

$$\delta_{k+1}^{(j)} = X_{k+1}^{(j)} - X_k^{(j)} \quad (35)$$

and define τ^2 by means of

$$\tau^2 = \frac{\sum_j \delta_1^{(j)} \operatorname{sgn} \delta_1^{(j)}}{\sum_j |\delta_1^{(j)}|} \quad (36)$$

The direct analogy to equation (14) will be noticed. Equation (36) permits computation, in an average way, of the damping of the error vectors. With τ^2 available, the extrapolated value X' of X is computed from

$$X' = \frac{X_3 - \tau^2 X_1}{1 - \tau^2} \quad (37)$$

In case the error is damping exactly as assumed in (27) and (28), equation (36) gives the value indicated by (33), and equation (37) reduces to (34); that is, X' becomes the answer X .

Since the ideal damping behavior is rarely an actuality, it is of interest to examine the effect of the preceding process on

error components. Suppose that X_0 is more adequately represented by

$$X_0 = X + \sum_{i=1}^n E_0^{(i)} \quad (38)$$

where $E_0^{(i)}$ has a damping rate (positive or negative) of λ_i . Then

$$X_3 = X + \sum_{i=1}^n \lambda_i^3 E_0^{(i)} \quad (39)$$

and

$$X_1 = X + \sum_{i=1}^n \lambda_i E_0^{(i)} \quad (40)$$

hold. The extrapolation indicated in equation (37) now yields the following relation between the estimate X' and the answer X :

$$X' = X + \sum_{i=1}^n \frac{\lambda_i(\lambda_i^2 - \tau^2)}{1 - \tau^2} E_0^{(i)} \quad (41)$$

This interpretation is useful, since it indicates the damping effect upon the errors of three iterations and one extrapolation.

If, for simplicity, one of the errors $E_0^{(i)}$ and its damping rate λ_i are designated by E and λ , respectively, then

$$R(\lambda, \tau) = \frac{(\lambda^2 - \tau^2)\lambda^{j-2}}{1 - \tau^2} \quad (42)$$

gives the damping of this error component as a result of j iterations and one extrapolation. The "extreme" value of R (actually that value farthest from zero; i. e., farthest from maximum damping) may be found by setting

$$\frac{dR}{d\lambda} = \frac{j\lambda^{j-1} - \tau^2(j-2)\lambda^{j-3}}{1 - \tau^2} = 0 \quad (43)$$

This yields

$$\lambda^2 = \left(\frac{j-2}{j}\right) \tau^2 \quad (44)$$

as the equation to be solved for the values of λ which are associated with the errors that receive the minimum damping from the process of j iterations and one extrapolation. Equations (42) and (44) give $R_{ext}(\tau)$, the extreme value of R , as a function only of τ and j :

$$R_{ext}(\tau) = \frac{-2\tau^j}{1 - \tau^2} \frac{1}{j-2} \left(\frac{j-2}{j}\right)^{j/2} \quad (45)$$

To find the value of τ^2 so that this function (R_{ext}) cannot exceed the bounds ± 1 [i. e., so that the slowest damping component (and hence all components) cannot increase through extrapolation], τ must be less in absolute value than the least of the roots of

$$\pm \left(\frac{2}{j-2}\right) \left(\frac{j-2}{j}\right)^{j/2} \tau^j - \tau^2 + 1 = 0 \quad (46)$$

If only such τ^2 are used, the convergence of the process cannot be impaired by the extrapolation.

Suppose now that the previous value of $R(\lambda, \tau)$ is replaced by the formula

$$\tilde{R}(\lambda, \tau) = \frac{\lambda^{j-4}(\lambda^2 - \tau^2)}{1 - \tau^2} \frac{\lambda^2 - \frac{j-2}{j} \tau^2}{1 - \frac{j-2}{j} \tau^2} \quad (47)$$

In formula (47), $j \geq 4$. The second factor places a zero (maximum damping) at just the points of minimum damping, that is, at the values of λ determined by (44). If now $d\tilde{R}/d\lambda$ is taken as zero and the limit ± 1 is placed upon the resulting $R_{ext}(\tau^2)$, the limiting safe values of τ^2 are obtained by finding the least of the roots of

$$[j\tau^j - 2(j-1)\tau^{j-2} + (j-2)\tau^{j-4}] \tau^j \pm [j - 2(j-1)\tau^2 + (j-4)\tau^4] = 0 \quad (48)$$

where τ^2 satisfies

$$\tau^2 = \frac{(j-1)(j-2) \pm \sqrt{5j^2 - 12j + 4}}{j^2} \quad (49)$$

The revised formula (47) has both the effect of ensuring that no component will be impaired in its damping by the extrapolation and also that the least rapidly damping component receives a zero contribution in the extrapolation.

Since, as before, for some error component E ,

$$X_j = X + \lambda^j E \quad (50)$$

$$X_{j-2} = X + \lambda^{j-2} E \quad (51)$$

$$X_{j-4} = X + \lambda^{j-4} E \quad (52)$$

in which X represents the answer, the specification of (47) as a damping formula implies

$$X' = X + \frac{j\lambda^j - 2(j-1)\tau^2\lambda^{j-2} + (j-2)\tau^4\lambda^{j-4}}{j - 2(j-1)\tau^2 + (j-2)\tau^4} E \quad (53)$$

where X' is the extrapolated value of X_j . If $\lambda^j E$, $\lambda^{j-2} E$, and $\lambda^{j-4} E$ are eliminated from (53) using the relations (50), (51), and (52), then

$$X' = \frac{jX_j - 2(j-1)\tau^2 X_{j-2} + (j-2)\tau^4 X_{j-4}}{j - 2(j-1)\tau^2 + (j-2)\tau^4} \quad (54)$$

Comparison of (42) (with $j=3$) with (37) on one hand and of (47) with (54) on the other hand leads to the following valid rule of thumb to obtain the extrapolated value of X for a given damping function: Replace the power λ^j of λ in the damping function by X_j ; the resulting linear combination of alternate iterants is the formula for the extrapolated X . It is easily verified that the validity of this arises from the manner in which the error vectors are assumed to behave.

The smallest roots of equations (46) and (48) are listed in the following tables:

Eq. (46)	
j	τ^2
4	0.8284
6	.8941
8	.9233
10	.9399

Eq. (48)	
j	τ^2
4	0.6667
6	.8745
8	.9213
10	.9427

These are the upper limits of the "safe" values of τ^2 within the framework of the definition.

APPLICATION TO REACTOR THEORY

GENERAL REMARKS

Multigroup reactor equations can be solved, in principle, by the present method. The number of components in the vector solution, to be discussed in detail later, is approximately equal to the product of the number of grid points and the number of groups in the multigroup scheme. An extreme increase in the number of these elements lengthens the problem considerably. The calculations here are performed in accordance with two-group neutron-diffusion theory.

The two-dimensional reactor with control rods, which is considered later, is suited to two-group calculations, since the control rods are particularly effective on the thermal group, and two-group calculations are good for thermal assemblies.

The following illustration is introduced to show the general principles of the matrix setup in detail. These principles do not change for the more complicated two-dimensional problem that is treated later. A relatively simple one-dimensional problem has been chosen to illustrate the detailed setup and the consequent matrix.

EXAMPLE OF TWO-GROUP DIFFUSION EQUATIONS

The one-dimensional diffusion equations for a reflected thermal reactor of slab geometry are (ref. 4)

$$\frac{d^2\varphi_f}{dx^2} - a'\varphi_f = -\gamma b\varphi_{th} \quad (55)$$

and

$$\frac{d^2\varphi_{th}}{dx^2} - c'\varphi_{th} + \bar{d}\varphi_f = 0 \quad (56)$$

for the core, and

$$\frac{d^2\varphi_f}{dx^2} - f'\varphi_f = 0 \quad (57)$$

and

$$\frac{d^2\varphi_{th}}{dx^2} - g'\varphi_{th} + m\varphi_f = 0 \quad (58)$$

for the reflector.

The parameters a' , b , c' , \bar{d} , f' , g' , and m are defined in the list of symbols; γ is the characteristic value of the system and equals 1 for criticality. When γ converges to a value other than unity, the uranium concentration is adjusted and the process repeated.

The differential equations (55) to (58) are replaced by finite-difference equations; the operation $d^2\varphi/dx^2$ is estimated by means of the approximate formula

$$h^2 \frac{d^2\varphi}{dx^2} \Big|_{x=x_j} = \varphi_{j+1} + \varphi_{j-1} - 2\varphi_j \quad (59)$$

where the points of the region are numbered in order as grid points of a finite-difference net, and h is the distance between successive points. In the following, r_c is the core radius, r_{c+i} the complete reactor radius, and point 6 lies on the interface:

$$\begin{array}{cccccccccc} & & & & & & & & & \\ & & & & & & & & & \\ & & & & & & & & & \\ & & & & & & & & & \\ & & & & & & & & & \\ 0 & 1 & 2 & 3 & 4 & 5 & 6 & 7 & 8 & 9 \\ & & & & & & & & & \\ & & & & & & & & & \end{array}$$

The boundary conditions are that the fast and thermal fluxes have zero current across the plane of symmetry ($x=0$). This condition

$$-\lambda_{ir} \frac{d\varphi}{dx} \Big|_{x=0} = 0 \quad (60)$$

can be approximated by

$$\frac{\varphi_1 - \varphi_0}{h} = 0 \quad (60a)$$

for both φ_f and φ_{th} . The condition of continuity of currents at the interface is met by approximating the derivatives in the expression

$$-\lambda_{ir,0} \frac{d\varphi}{dx}(r_c-0) = -\lambda_{ir,1} \frac{d\varphi}{dx}(r_c+0) \quad (61)$$

for both the fast and thermal fluxes. The remaining condition is that the flux be zero at the outer boundary. If the fast flux is designated by φ and the thermal by ψ , the system becomes:

Equation

$$\left. \begin{array}{ll} j & \\ 0 & \frac{\varphi_1 - \varphi_0}{h} = 0 \\ 1-5 & \frac{\varphi_{j+1} + \varphi_{j-1} - 2\varphi_j}{h^2} - a'\varphi_j = -\gamma b\psi_j \\ 6 & \gamma_{ir,0} \frac{\varphi_6 - \varphi_5}{h} = \lambda_{ir,1} \frac{\varphi_7 - \varphi_6}{h} \\ 7 & \frac{\varphi_8 + \varphi_6 - 2\varphi_7}{h^2} - f'\varphi_7 = 0 \\ 8 & \frac{\varphi_7 - 2\varphi_8}{h^2} + f'\varphi_8 = 0 \text{ which incorporates } \varphi_9 = 0 \end{array} \right\} \quad (62)$$

for the fast-balance equations and, for the thermals:

$$\left. \begin{array}{ll} i & \\ 0 & \psi_1 - \psi_0 = 0 \\ 1-5 & \frac{\psi_{i+1} + \psi_{i-1} - 2\psi_i}{h^2} - c'\psi_i + \bar{d}\varphi_i = 0 \\ 6 & \lambda_{ir,0} \frac{\psi_6 - \psi_5}{h} = \lambda_{ir,1} \frac{\psi_7 - \psi_6}{h} \\ 7 & \frac{\psi_8 + \psi_6 - 2\psi_7}{h^2} - g'\psi_7 + m\varphi_7 = 0 \\ 8 & \frac{\psi_7 - 2\psi_8}{h^2} - g'\psi_8 + m\varphi_8 = 0 \text{ which incorporates } \psi_9 = 0 \end{array} \right\} \quad (63)$$

The variables φ_0 to φ_8 and ψ_0 to ψ_3 may now be written as X_0 to X_8 and X_9 to X_{17} , respectively. The matrix formulation of these equations is presented in figure 1. The following symbols have been introduced:

$$I_h = 1/h^2 \quad (64)$$

$$A_h = 2/h^2 + a \quad (65)$$

$$F_h = 2/h^2 + f \quad (66)$$

$$C_h = 2/h^2 + c \quad (67)$$

$$G_h = 2/h^2 + g \quad (68)$$

$$L = \frac{\lambda_{tr, f0}}{\lambda_{tr, f1}} \quad (69)$$

$$S = \frac{\lambda_{tr, th0}}{\lambda_{tr, th1}} \quad (70)$$

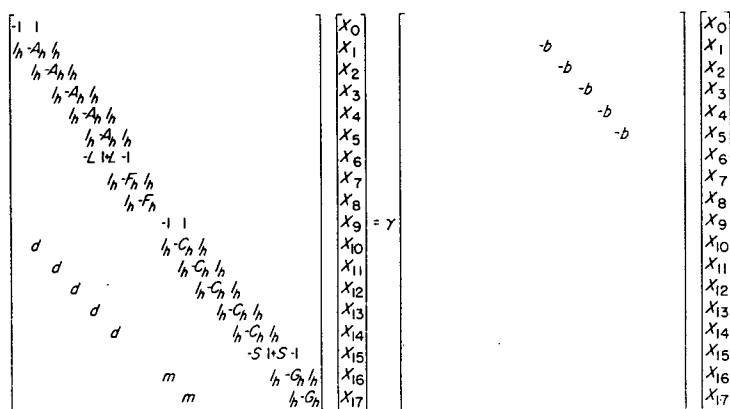


FIGURE 1.—Matrix formulation of equations (62) and (63).

RECAPITULATION

To review the general application of the method to two-group reactor equations, consider the following broad outline of this process:

- (1) Write the two-group equations with the parameter γ introduced as a multiplier of the production term of the fast-balance equations.
- (2) Express the differential equations by their finite-difference approximations so that they become a linear algebraic set of the type associated with equation (1).
- (3) Perform such iterations and extrapolations as necessary to obtain well-converged values of γ and X .
- (4) Adjust the uranium concentration and repeat step (3) using the original answer from (3) for the initial guess X_0 . The concentration should be changed so that $\gamma \rightarrow 1$.
- (5) Repeat (3) and (4) until γ converges. If criticality is desired, change the concentration so that the converged values of $\gamma \rightarrow 1$.

TWO-DIMENSIONAL REACTOR WITH CONTROL RODS

GEOMETRY OF REACTOR

The reactor (see fig. 2) is cylindrical and water-reflected with a core composed of aluminum, water, and uranium, which are assumed to be homogeneously mixed. The height of the reactor is 70 centimeters, the outside radius 50 centimeters, and the core radius 32 centimeters. Nine

cadmium control rods are inserted in the core; one, a cylindrical rod of 2-centimeter radius, is centered along the axis of the reactor. The remaining eight rods are equally spaced on a radius of 24 centimeters and are shaped so as to be bounded by coordinate surfaces. Each of these rods extends over a radial distance of 4 centimeters and subtends a central angle of 9° .

The symmetry of this assembly is an important factor in making solution of the reactor problem feasible. The flux in the 45° sector indicated in figure 2 is adequate to represent the flux in the entire reactor; in fact, additional symmetry within the sector implies that only half the sector need be considered. The three-dimensional problem is made two-dimensional (computation-wise) by estimating the neutron leakage in the axial direction due to the finite height of the reactor. This is based upon an axial cosine distribution similar to the bare pile solution (eq. (75)).

COMPOSITION AND NUCLEAR PARAMETERS

The core volume is proportioned between the water (density, 1 g/cc) and aluminum by assuming a volume ratio of aluminum to water of 0.76. The nuclear diffusion constants for the core and reflector are listed in the following tables. The subscripts 0, 1, and 2 refer to the core, reflector, and rod regions of the reactor, respectively:

Fast		
Zone	L_f^2	λ_f
0	64	3.78
1	33	3.43
2	---	4.35

Thermal				
Zone	L_{th}^2	λ_{th}	p_{th}	k_{th}
0	3.471	0.815	0.95	1.675
1	8.3	.43	.98	---

Parameters for the rod regions are unnecessary because of the simplified treatment of the rod, in which the thermal neutron flux is assumed to vanish on the rod boundary and the radial and axial leakages are assumed to balance in the absence of fast-neutron absorption processes. The thermal parameters in the preceding table are those associated with an atom ratio of N^H/N^u of 350; these, of course, change for different uranium concentrations.

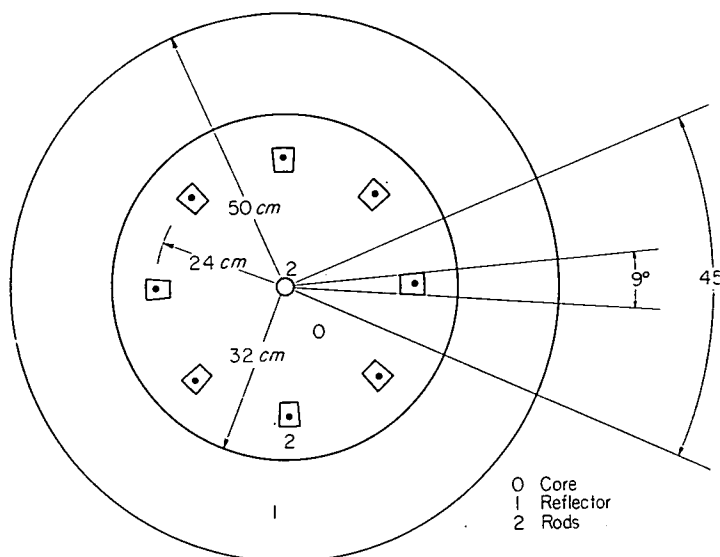


FIGURE 2.—Two-dimensional reactor.

For two-dimensional cylindrical geometry, the operation of the form $\nabla^2\varphi$ is given by

$$\nabla^2 = \frac{\partial^2}{\partial r^2} + \frac{1}{r} \frac{\partial}{\partial r} + \frac{\partial^2}{\partial \theta^2} \quad (76)$$

This form is to be replaced by a difference operation that relates each point to its four nearest neighbors. If the point in question is designated by the subscript zero and the others are

$$\begin{array}{c} 1 \\ \cdot \\ h_r \\ 4 \cdot h_\theta \cdot 0 \cdot h_\theta \cdot 2 \quad r \uparrow \theta \rightarrow \\ \cdot \\ h_r \\ \cdot \\ 3 \end{array}$$

where h_r and h_θ are the grid widths in the r and θ directions, respectively, then at $\varphi = \varphi_0$ the following approximation is used:

$$\nabla^2\varphi = \left(\frac{1}{h_r^2} + \frac{1}{2rh_r}\right)\varphi_1 + \left(\frac{1}{h_r^2} - \frac{1}{2rh_r}\right)\varphi_3 + \frac{1}{r^2h_\theta^2}(\varphi_2 + \varphi_4) - \left(\frac{2}{h_r^2} + \frac{2}{h_\theta^2r^2}\right)\varphi_0 \quad (77)$$

With this designation (and barring certain exceptional points to be discussed later), one may move from point to point on the grid and write equations of neutron balance for each of the two neutron groups.

The following equations may be taken as typical illustrations:

Thermal-balance equation 93 (see fig. 4):

$$\left(\frac{1}{h_r^2} + \frac{1}{2rh_r}\right)X_{89} + \left(\frac{1}{h_r^2} - \frac{1}{2rh_r}\right)X_{97} + \frac{1}{r^2h_\theta^2}(X_{92} + X_{94}) - \left(\frac{2}{h_r^2} + \frac{2}{h_\theta^2r^2} + \frac{1}{L_{i0}^2} + B_2^2\right)X_{93} + \frac{\lambda_{tr, f0}}{\lambda_{tr, i0}}p_{i0}\frac{1}{L_{f0}^2}X_{234} = 0 \quad (78)$$

Fast-balance equation 234:

$$\left(\frac{1}{h_r^2} + \frac{1}{2rh_r}\right)X_{228} + \left(\frac{1}{h_r^2} - \frac{1}{2rh_r}\right)X_{240} + \frac{1}{r^2h_\theta^2}(X_{233} + X_{235}) - \left(\frac{2}{h_r^2} + \frac{2}{h_\theta^2r^2} + \frac{1}{L_{f0}^2} + B_2^2\right)X_{234} = -\gamma \frac{\lambda_{tr, i0}}{\lambda_{tr, f0}}k_{i0}\frac{1}{L_{i0}^2}X_{93} \quad (79)$$

In contradistinction to equations (78) and (79), there are certain special equations that hold at the exceptional points referred to earlier. These equations result from one or more of the following conditions:

- (1) Continuity of currents at interfaces
- (2) Zero flux at the outside boundary
- (3) Zero current across planes of symmetry
- (4) Change in grid dimensions

Condition (1) is treated by matching a suitable ratio of normal derivatives from either side of the interface. Each of these derivatives is evaluated by a five-point differentiation formula. Condition (2) is treated by writing the difference approximation to the diffusion equation for points adjacent to the outside boundary with zero replacing the flux at the boundary point.

Condition (3) is accounted for by writing the diffusion equation of a point on the plane assuming the same flux at grid points on either side of the plane. For condition (4) θ -wise interpolation formulas are used to define flux at the points marked X on figure 4, and these are utilized where needed, in writing diffusion equations in the finer mesh. If each equation of the set is written in order and the production terms are isolated as illustrated in equation (71), then the matrix equation constructed from the approximate finite difference may be written in the form of equation (1).

The matrix B is singular, largely consisting of zero elements with an essentially diagonal group of nonzero terms somewhat off the leading diagonal. The matrix A has a substantial number of nonzero elements crowded quite close to the leading diagonal. This latter situation is numerically desirable, as elements far from the leading diagonal tend to slow the convergence of numerical processes.

If criticality is desired, the concentration of fissionable material is adjusted, after γ and X have converged, and a whole new set of calculations is run until a new value for γ is reached. This process may be continued until $\gamma = 1$.

The method can also be used to compute reactivity changes; the calculation time is again shortened considerably if flux distributions are not demanded.

SOLUTIONS OF TWO-DIMENSIONAL PROBLEM

The results of the calculations of the supercritical ($\gamma = 0.948$) case are shown in figures 5 to 7. Figure 5 gives the fast flux as a function of r for $\theta = 0^\circ, 9^\circ$, and 18° . The control rods have no substantial effect on the fast flux. Figure 6 gives the corresponding thermal flux and shows the localized effect of the control rods. Figure 7 presents isoflux contours of the thermal flux. The 0.19 contour in the reflector and the 0.234 contour in the core represent relative maximums.

COMMENTS ON APPLICATION OF THE METHOD

A number of numerical quantities may be examined in an attempt to evaluate the degree of convergence of a system. One of the most natural of these quantities is the sum of the squares of the residuals. Another may be formed by considering the fact that, as the limit is approached, the rate

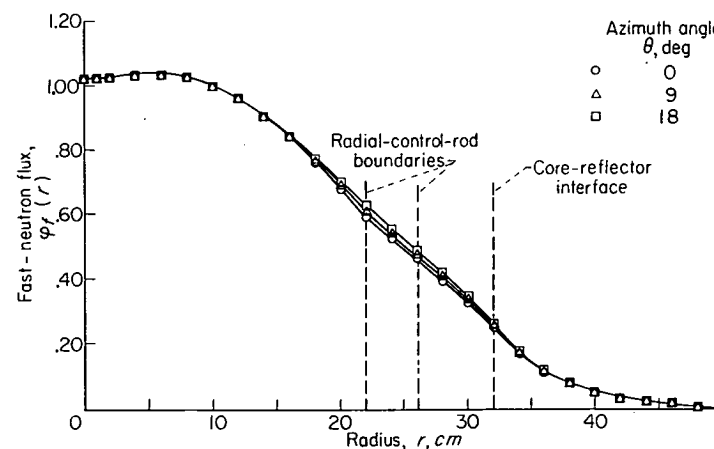


FIGURE 5.—Fast-neutron flux for azimuth angles of 0° , 9° , and 18° .

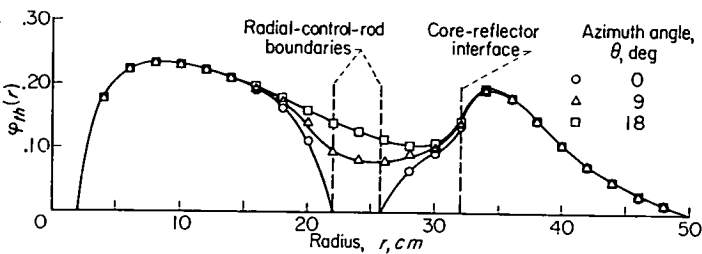


FIGURE 6.—Thermal-neutron flux for azimuth angles of 0°, 9°, and 18°.

$\Delta_{k+1}^{(i)}/\gamma_{k+1}$ must tend toward unity. This means that the deviation defined by

$$\Delta_{k+1}^{(i)} = 1 - \frac{\gamma_{k+1}^{(i)}}{\gamma_{k+1}} \quad (80)$$

must tend toward zero. The average absolute value of the deviation, summed over all points of the reactor, is

$$|\overline{\Delta_{k+1}^{(i)}}| = \frac{\sum_{i=1}^n \left| 1 - \frac{\gamma_{k+1}^{(i)}}{\gamma_{k+1}} \right|}{n} \quad (81)$$

where n is the number of reactor points.

An illustration of the behavior of this quantity is given in the following table:

$k+1$	$ \overline{\Delta_{k+1}^{(i)}} $	$ \Delta_{k+1}^{(i)} _{\max}$
6	0.02199	0.2133
15	.02551	.3156
22	.00254	.0147
31	.00130	.0113
40	.000793	.0061
49	.00028	.0027

The iterants listed are those which just precede the extrapolation process. These are chosen so as to minimize the effect of fluctuations introduced by the extrapolation technique.

These illustrative values come from the second general process; that is, after γ had converged to 1.2064, the concentration (and hence elements of the matrices A and B) was changed and a new series of iterations begun. This converged (more rapidly than the first run) to a value of 0.948.

To estimate the value of uranium concentration needed for the new run, the equation

$$1.2064 k_{th}(\text{old}) = k_{th}(\text{new}) \quad (82)$$

was used to compute a new k_{th} from which to obtain a new concentration. This formula is an approximation, since the influence of a change in concentration upon L_{th}^2 is appreciable. The better rate of convergence of the second run is due to the fact that the flux is relatively independent of the characteristic value, so that the initial estimate for the second run was a relatively good one.

The quantity $|\overline{\Delta_{k+1}^{(i)}}|$ reflects the convergence of γ , which is faster than that of the vector X .

In order to determine the degree of convergence of X , consider the quantities

$$d_{k+1} = \sum_{i=1}^n |\delta_{k+1}^{(i)}| = \sum_{i=1}^n |X_{k+1}^{(i)} - X_k^{(i)}| \quad (83)$$

$$|\overline{\delta_{k+1}^{(i)}}| = \frac{d_{k+1}}{n} \quad (84)$$

and the maximum $|\delta_{k+1}^{(i)}|$ designated by $|\delta_{k+1}^{(i)}|_{\max}$. Typical values of these quantities are as follows:

$\gamma = 1.206$				$\gamma = 0.948$			
$k+1$	d_{k+1}	$ \overline{\delta_{k+1}^{(i)}} $	$ \delta_{k+1}^{(i)} _{\max}$	$k+1$	d_{k+1}	$ \overline{\delta_{k+1}^{(i)}} $	$ \delta_{k+1}^{(i)} _{\max}$
111	0.0099	0.000034	0.000269	6	0.3299	0.001137	0.00918
122	.0083	.000028	.000176	15	.2139	.000735	.00530
133	.0049	.000017	.000157	22	.0223	.000077	.000204
144	.0028	.000010	.0000904	31	.0044	.000015	.0000666
155	.0022	.000008	.0000709	40	.0020	.000007	.0000245

The sums of the squares of the residuals for the two cases $\gamma = 1.206$ and $\gamma = 0.948$ are as follows:

$\gamma = 1.206$		$\gamma = 0.948$	
$k+1$	$\sum R_i^2$	$k+1$	$\sum R_i^2$
111	9.44×10^{-7}	6	1.53×10^{-3}
122	4.98×10^{-7}	15	3.51×10^{-4}
133	2.66×10^{-7}	22	1.80×10^{-4}
144	8.60×10^{-8}	31	1.22×10^{-4}
155	5.37×10^{-8}	40	1.99×10^{-4}

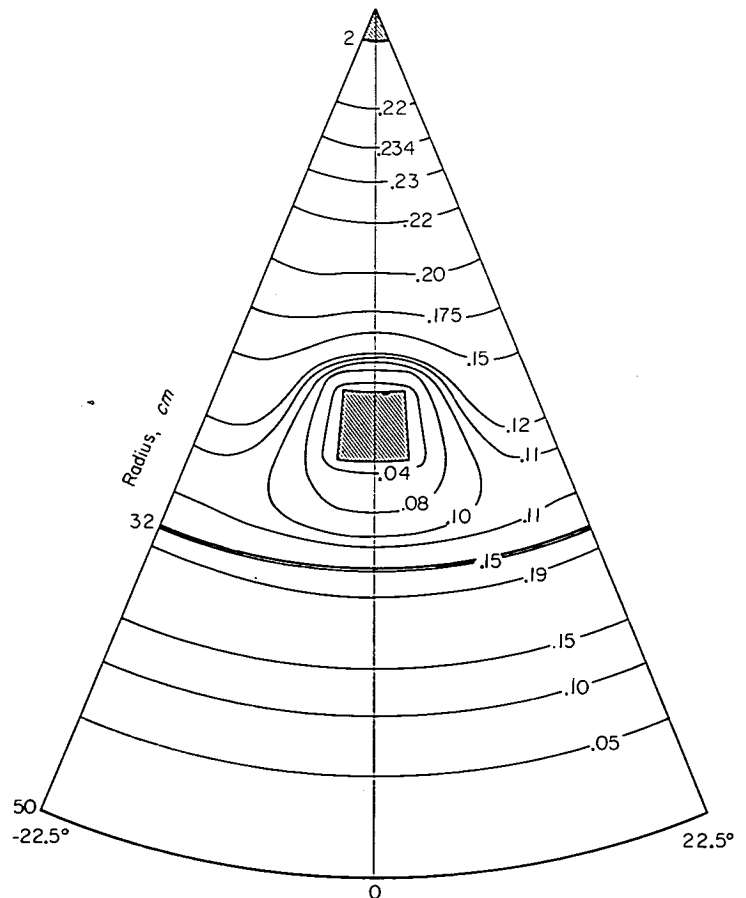


FIGURE 7.—Contour lines for thermal flux.

Several general observations can be made about the process:

(1) The number of iterations in this problem starting from an initial guess to a well-converged value of X was about 150 to 175.

(2) In general, 8 to 10 iterations between extrapolations seem desirable, as the use of too few iterations does not allow the establishment of a fairly uniform damping rate.

(3) The extrapolation formula of equation (37) seems best for rough estimates where error components are being damped rapidly; that of equation (54) seems to be superior for later extrapolations where one is closer to the solution.

(4) When computed values of τ^2 exceed the upper limit, they may be replaced by the limit from the tables giving roots of equations (46) and (48) and then the extrapolation may be carried out, or two more iterations performed with τ^2 recomputed until it falls within prescribed limits.

The following table gives the sum of the squares of the residuals for (a) direct iteration from X_{31} to X_{49} , (b) eight iterations from X_{31} followed by extrapolation with " τ^2 safe" when " τ^2 computed" was too large, then iteration to X_{49} , (c) eight iterations from X_{31} followed by two iterations and

a test until " τ^2 computed" was less than " τ^2 safe," then extrapolation followed by iteration to X_{49} :

Case	$\sum R_i^2$
(a)	1.35×10^{-7}
(b)	3.44×10^{-9}
(c)	1.68×10^{-3}

LEWIS FLIGHT PROPULSION LABORATORY

NATIONAL ADVISORY COMMITTEE FOR AERONAUTICS

CLEVELAND, OHIO, May 12, 1955

REFERENCES

1. Whittaker, E. T., and Robinson, G.: The Calculus of Observations. Fourth ed., Blackie and Son (London), 1949.
2. Hestenes, Magnus R., and Stiefel, Eduard: Methods of Conjugate Gradients for Solving Linear Systems. RP 2379, Jour. Res. Nat. Bur. Standards, vol. 49, no. 6, Dec. 1952, pp. 409-436.
3. Turner, L. Richard: Improvement in the Convergence of Method of Successive Approximation. International Business Machines Corp., 1951. (Reprinted from Proc. Computation Seminars, Dec. 1949.)
4. Glasstone, Samuel, and Edlund, Milton C.: The Elements of Nuclear Reactor Theory. D. Van Nostrand Co., Inc., 1952.

REPORT 1284

THEORY OF WING-BODY DRAG AT SUPERSONIC SPEEDS¹

By ROBERT T. JONES

SUMMARY

The relation of Whitcomb's "area rule" to the linear formulas for wave drag at slightly supersonic speeds is discussed. By adopting an approximate relation between the source strength and the geometry of a wing-body combination, the wave-drag theory is expressed in terms involving the areas intercepted by oblique planes or Mach planes. The resulting formulas are checked by comparison with the drag measurements obtained in wind-tunnel experiments and in experiments with falling models in free air. Finally, a theory for determining wing-body shapes of minimum drag at supersonic Mach numbers is discussed and some preliminary experiments are reported.

DISCUSSION

At subsonic speeds the pressure drag arising from the thickness of the body or wings is negligible so long as the shapes are sufficiently well streamlined to avoid flow separation. In that range there exists no possibility of either favorable or adverse interference on the pressure distributions themselves. If one body is so placed as to receive a drag from the pressure field of another then the second body is sure to receive a corresponding increment of thrust from the first.

At supersonic speeds this tolerance which was permitted the designer disappears, and the drag becomes sensitive to the shape and arrangement of the bodies. To be sure, the primary factor here is the thickness ratio, but nevertheless there exist arrangements in which a large cancellation of drag occurs. Examples of the latter are the sweptback wing and the Busemann biplane.

Recently R. T. Whitcomb (ref. 1) has shown how the drag at transonic speeds may be reduced to a surprising extent by simply cutting out a portion of the fuselage to compensate for the area blocked by the wing. The purpose of the present paper is to discuss some of the theoretical aspects of this method of drag reduction and to show how the basic idea may be extended to higher speeds in the supersonic range.

Whitcomb's deduction of the "area rule" was based on considerations of stream-tube area and the phenomenon of "choking"—which follow from one-dimensional-flow theory. Each individual stream tube of a three-dimensional-flow field must obey the law of one-dimensional flow. While we cannot actually determine the three-dimensional field on this basis alone, nevertheless it provides a good starting point for our thinking. The results demonstrate again the effectiveness of basic and simple considerations.

While one-dimensional-flow theory thus provides a clue to the area rule, the necessary principle appears more specifically in the three-dimensional-flow theory. Thus, the formulas for wave drag given by linear theory, if followed toward the limit as M approaches 1.0 (from above), show that the wave drag of a system of wings and bodies depends solely on the longitudinal area distribution of the system as a whole. This was first noted by W. D. Hayes in his 1946 thesis (ref. 2). However, because of the limitations of the theory at transonic speeds, this result was not thought to be of practical significance. Later G. N. Ward (ref. 3), E. W. Graham (ref. 4), and others, restricting themselves to very narrow shapes, expressed the wave drag in terms of the longitudinal area distribution for Mach numbers above 1.0, where the linear theory has a better justification.

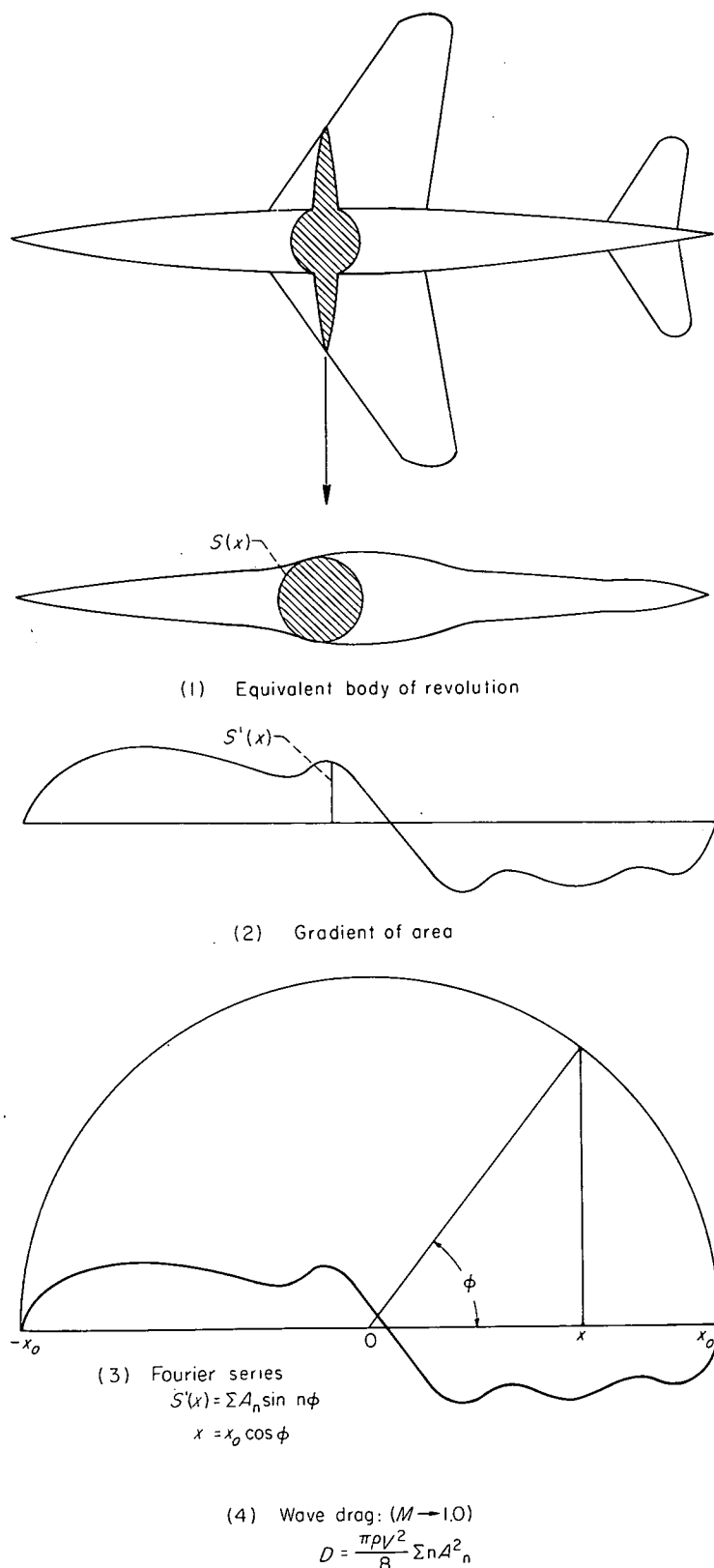
It should be noted, however, that both of the problems cited are limiting cases of the more general problem of supersonic drag and it should be borne in mind that only in certain cases has it been possible to reduce the general theoretical formulas to the form of an area rule. It can be shown that the flow field about any system of bodies may be created by a certain distribution of sources and sinks over the surfaces of the bodies. Hayes' formula and the formulas given in reference 5 relate the drag of such a system to the distribution of these singularities. To obtain a formula for the wave drag in terms of area distributions we have to adopt a simplified relation between the source strength and the geometry of the bodies, namely, that the source strength is proportional to the normal component of the stream velocity at the body surface. There are examples (e. g., Busemann biplanes and ducted bodies) for which this assumption is not valid. If, on the other hand, we limit ourselves to thin symmetrical wings mounted on vertically symmetrical fuselages, there are indications that a good estimate of the wave drag at supersonic speeds can be obtained on the basis of the simplified relation assumed.

Following Hayes' method of calculation, we find that at $M=1.0$ the expression for the wave drag of a system of wings and bodies reduces to Kármán's well-known formula (ref. 6) for the wave drag of a slender body of revolution, that is,

$$D_{M=1} = -\frac{\rho V^2}{4\pi} \int_{-x_0}^{+x_0} \int_{-x_0}^{+x_0} S''(x) S''(x_1) \log |x-x_1| dx dx_1$$

Here $S(X)$ represents the total cross-sectional area intercepted by a plane perpendicular to the stream at the station

¹Supersedes NACA RM A53H18a by Robert T. Jones, 1953.

FIGURE 1.—Steps in the calculation of wave drag for $M \rightarrow 1.0$.

x (see fig. 1) and $S''(x)$ is the second derivative of S with respect to x . Following Sears (ref. 7) we may expand $S'(x)$ in a Fourier series and obtain in this way a formula for the drag which is completely analogous to the well-known formula for the induced drag of a wing in terms of its spanwise load distribution. Thus, if we write

$$x = x_0 \cos \phi$$

and

$$S'(x) = \sum A_n \sin n\phi$$

we obtain for the wave resistance

$$D = \frac{\pi \rho V^2}{8} \sum n A_n^2$$

Of all the terms of the series, each contributes to the drag, but only A_1 and A_2 contribute to the volume or the base area of the system. Thus, to achieve a small drag with a given base area, or with a given over-all volume within the given length, the higher harmonics in the curve $S'(x)$ should be suppressed. This formula enables us to characterize the smoothness of a given shape in a quantitative fashion.

To extend these considerations to supersonic speeds we have to consider a series of cross sections of the system made not by planes perpendicular to the stream, but by planes inclined at the Mach angle, or "Mach planes." By means of

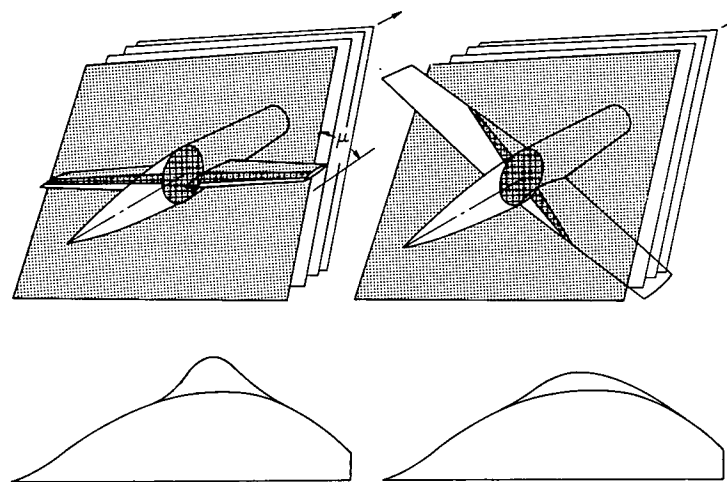


FIGURE 2.—Area distribution given by intersections of Mach planes.

a set of parallel Mach planes (see fig. 2) we construct an "equivalent body of revolution," using the intercepted areas, and compute the drag by von Kármán's formula. The theoretical basis of this step is the fact that the complete three-dimensional disturbance field may be constructed by the superposition of elementary one-dimensional disturbances in the form of plane waves (ref. 8). It is evident that the set of parallel Mach planes may be placed at various angles around the x axis. In constructing the flow field it is necessary to superimpose disturbances at all of these angles and, in computing the drag, to consider the drags of all the equivalent bodies of revolution. The final value of the drag is simply the average of the values obtained through a complete rotation of the Mach planes.

In order to make these statements more specific, we may write the equation of one such Mach plane as follows:

$$X = x - y' \cos \theta - z' \sin \theta$$

where $y' = \sqrt{M^2 - 1} y$, $z' = \sqrt{M^2 - 1} z$, and θ is the angle of rotation of the Mach plane. By assigning different values to X while keeping θ constant, we obtain a series of parallel

planes at the same angle θ around the x axis. By assigning different values to θ while keeping X a constant, we obtain a set of planes enveloping that Mach cone whose apex lies at the point $x=X$.

Selecting a value of θ , we cut through the wing-body system with a series of planes corresponding to different values of X . The total intercepted area in each plane is then equated to the area intercepted by this plane passing through the equivalent body of revolution. If we denote the area intercepted obliquely by $s(X, \theta)$, then the area $S(X, \theta)$ is defined by

$$S = s \sin \mu$$

where μ is the Mach angle (i. e., $\sin \mu = 1/M$). Thus, S is the area intercepted by normal planes passing through the equivalent body of revolution on the assumption that this body is slender. Again, we write

$$S'(X, \theta) = \frac{\partial}{\partial X} S(X, \theta) = \sum A_n \sin n\phi$$

with

$$\cos \phi = \frac{X}{X_0}$$

Here, however, both the length $2X_0$ and the shape of the equivalent body vary with the angle θ . The drag of each equivalent body of revolution, which we may denote by $D'(\theta)$ is then determined by applying Sears' formula:

$$D'(\theta) = \frac{\pi \rho V^2}{8} \sum n A_n^2$$

The total drag of the wing-body system is the average of all these values between $\theta=0$ and $\theta=2\pi$, that is,

$$D = \frac{1}{2\pi} \int_0^{2\pi} D'(\theta) d\theta$$

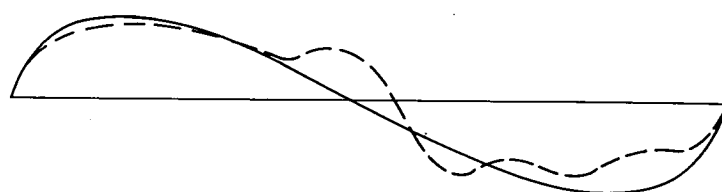
In general, the coefficients A_n will be functions of the angle of projection θ . However, calculation shows that the first two coefficients A_1 and A_2 are again related in a simple way to the base area and the volume v . Thus,

$$A_1 = \frac{2}{\pi} \frac{S(X_0)}{X_0}$$

$$A_2 = 2A_1 - \frac{4}{\pi} \frac{v}{X_0^2}$$

None of the higher coefficients contribute to the base area or volume, but they invariably contribute to the drag.

The rules for obtaining a low wave drag now reduce to the rule that each of the equivalent bodies obtained by the oblique projections should be as smooth and slender as possible, the "smoothness" again being related to an absence of higher harmonics in the series expression for $S'(X)$. Thus in the case of given length and volume the series should contain only the term $A_2 \sin 2\phi$ (see fig. 3). It should be noted that in this theory, the equivalent bodies of revolution do not have a physical significance. The concept is simply an aid in visualizing the magnitude of the drag of the complete system.



$$S'(x) = A_2 \sin 2\phi$$

(Sears-Haack body)

FIGURE 3.—Optimum area distribution for given length and volume.

To check the agreement between these theoretical formulas for the wave drag and experimental values, we have compared our calculations with the results of tests made by dropping models from a high altitude. This comparison was made by George H. Holdaway of Ames Laboratory, who supplied the accompanying illustration (fig. 4). In some of these cases it was found necessary to retain more than 20 terms of the Fourier series in order to obtain a convergent expression for the drag.

Considering the variety of the shapes represented here, the agreement is certainly as good as we ought to expect from our linear simplifications. The agreement is naturally better in those interesting cases in which the drag is small.

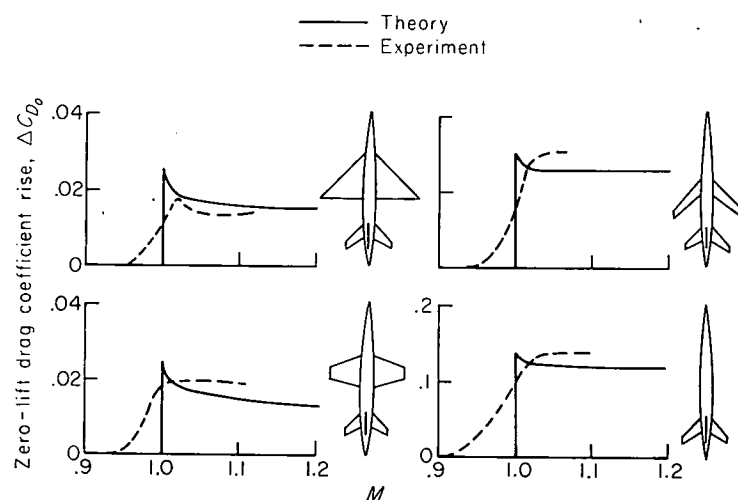


FIGURE 4.—Comparison of theory with results of Ames Laboratory drop tests.

Figure 5 shows an analysis of one of Whitcomb's experiments. The linear theory, of course, shows the transonic drag rise simply as a step at $M=1.0$. We may expect such a variation to be approached more closely as the thickness vanishes. To represent actual values here a nonlinear theory would be needed. For many purposes it will be sufficient to estimate roughly the width of the transonic zone by considerations such as those given in reference 9. In the present case it will be noted that agreement with the linear theory is reached at Mach numbers above about 1.08, and the linear theory clearly shows the effect of the modification.

For further theoretical studies of wing-body drag, shapes have been selected which are especially simple analytically, namely, the Sears-Haack body and biconvex wings of elliptic

plan form, having aspect ratios of 2.54 and 0.635. Figure 6 shows the effect of wing proportions on the variation of wave drag with Mach number, both with and without the Whitcomb modification. In each case the modification has the effect of reducing the wave drag to that of the body alone at $M=1.0$. In the case of the low-aspect-ratio wing this drag reduction remains effective over a considerable range of higher Mach numbers. With the higher aspect ratio, however, the drag increases sharply at higher speeds, so that at $M=1.6$ the modification nearly doubles the wave drag.

The rapid increase of drag in the case of the high-aspect-ratio wing is, of course, the result of the relatively abrupt curvatures introduced into the fuselage lines by the cutout. Such abrupt cutouts are necessarily associated with wings having small fore and aft dimensions, that is, unswept wings of high aspect ratio.

These considerations led to the problem of determining a fuselage shape for such wings that is better adapted to the higher Mach numbers. The first step in this direction is, obviously, simply to lengthen the region of the cutout—thus avoiding the rapid increase of drag with Mach number. The problem of actually determining the best shape for the fuselage cutout at any specified Mach number has been under-

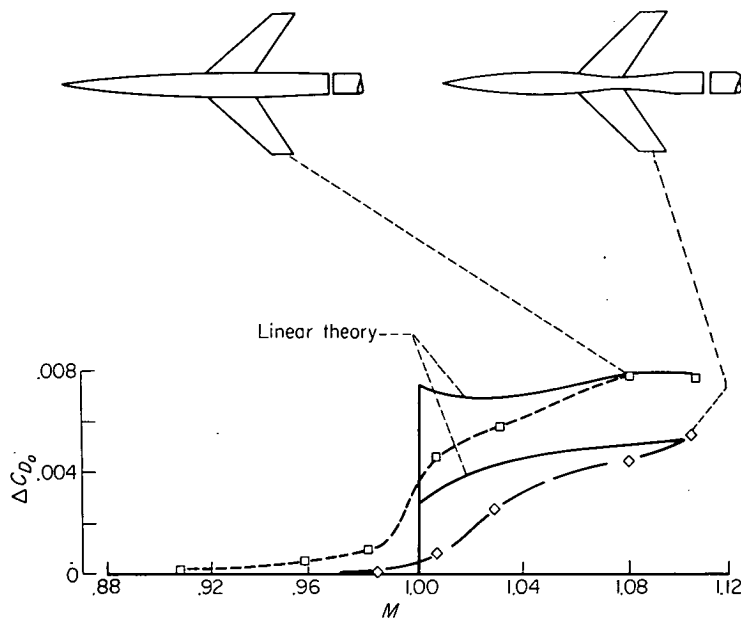


FIGURE 5.—Comparison of Whitcomb's experiments with theory.

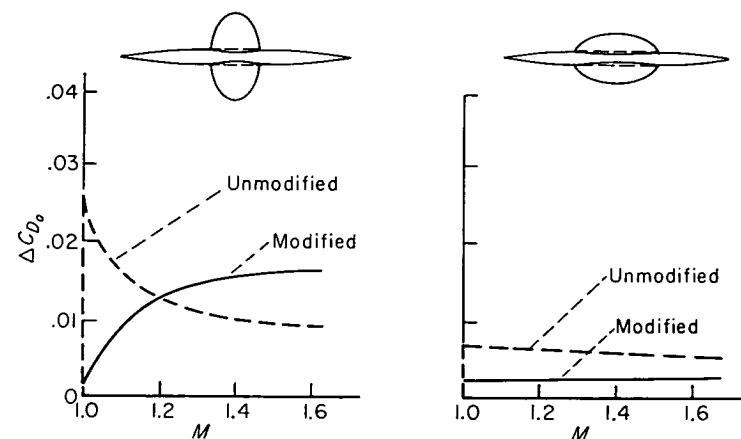


FIGURE 6.—Effect of Whitcomb modification on calculated wave drag.

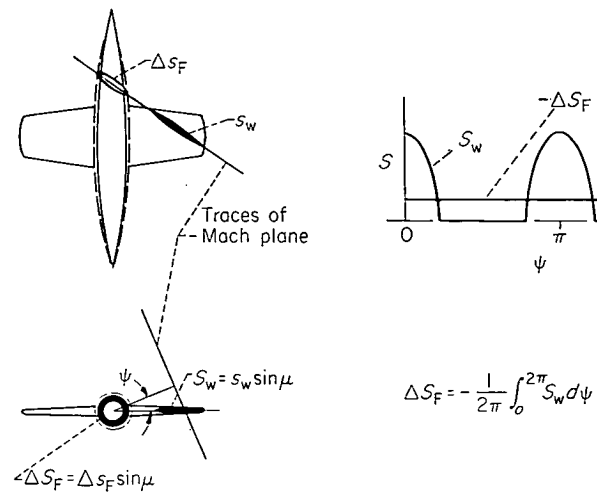


FIGURE 7.—Design of fuselage modification for specified Mach number.

taken by Harvard Lomax and Max. A. Heaslet at Ames Laboratory (ref. 10). Their solution of this problem provides a definite method for determining the distribution of sources and sinks along the fuselage axis that will achieve a minimum value of the drag for a given *wing shape* at any specified Mach number. Furthermore, by admitting singularities of higher order—quadrupoles, etc., which would distort the rotational symmetry of the fuselage—they have been able to show that the wave drag of a wing-body system can be reduced, in principle at least, to a minimum value associated with the given overall length and volume of the system, that is, to the value for a simple Sears-Haack body containing the whole volume of the system.²

By adopting our simplified relation between the source strength and the body shape, we may describe the result of this theory by a relatively simple concept, which is illustrated in figure 7. For modifications of the first type, the problem is to determine the area ΔS_F to be removed from the fuselage to best compensate for a given wing. (See fig. 7.) Selecting a station along the fuselage axis and a Mach plane passing through this station, we revolve this plane around the axis, measuring at each angle ψ the normal projection, or frontal projection, of the area intercepted where the plane cuts through the wing. After plotting these areas against ψ and integrating between 0 and 2π , we obtain ΔS_F as the average of the values of S_w . At any Mach number the total volume to be subtracted from the fuselage is equal to the wing volume. At higher Mach numbers, since the modification extends over a greater length, the area subtracted at individual cross sections becomes less.

Figure 8 shows the calculated result of designing the fuselage cutout for a specific Mach number, 1.2 in this case. The lower curve is an envelope showing the minimum values that can be achieved by such a radially symmetric cutout.

Figure 9 shows the magnitude of the gain that is theoretically possible by higher order modifications of the fuselage shape. There are three lower bounds here, and the symbols a_0 , a_2 , etc., attached to them refer to a representation of the fuselage shape by singularities of increasingly higher order.

² This value is, of course, not an absolute minimum for a given volume since, as shown by Ferrari, the wave drag of a body can be reduced to zero by special volume distributions (see ref. 11).

The curve labeled a_0 is that given on the previous figure and shows the maximum effect of radially symmetric modifications. While the fuselage shapes for the other curves have not actually been determined, the curve labeled $a_0 + a_2$ may be thought of as referring to a cutout with an additional elliptic modification.

In order to test this theory of determining optimum body shapes we have started a program using models similar to those investigated theoretically. Several of these models have already been tested in the Ames 2- by 2-foot wind tunnel, with results that agree quite well with calculations made on the assumptions given earlier. Shown in figure 10 are the experimental and theoretical curves. It is evident that the calculated differences are all reproduced approximately in the experimental values.

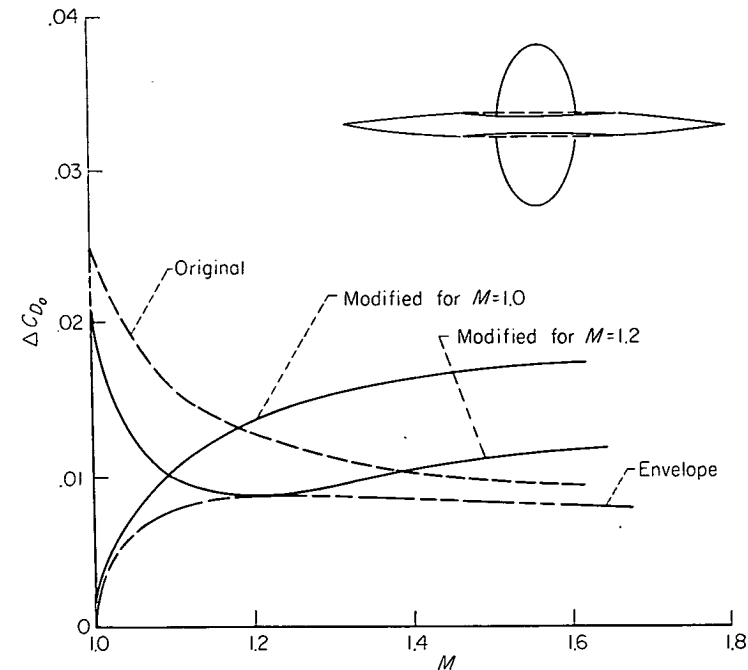


FIGURE 8.—Effect of modification designed for a specified Mach number.

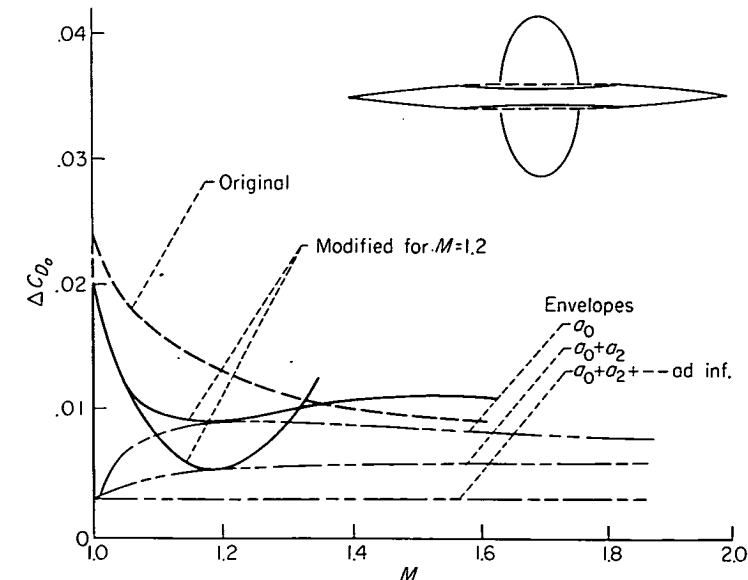
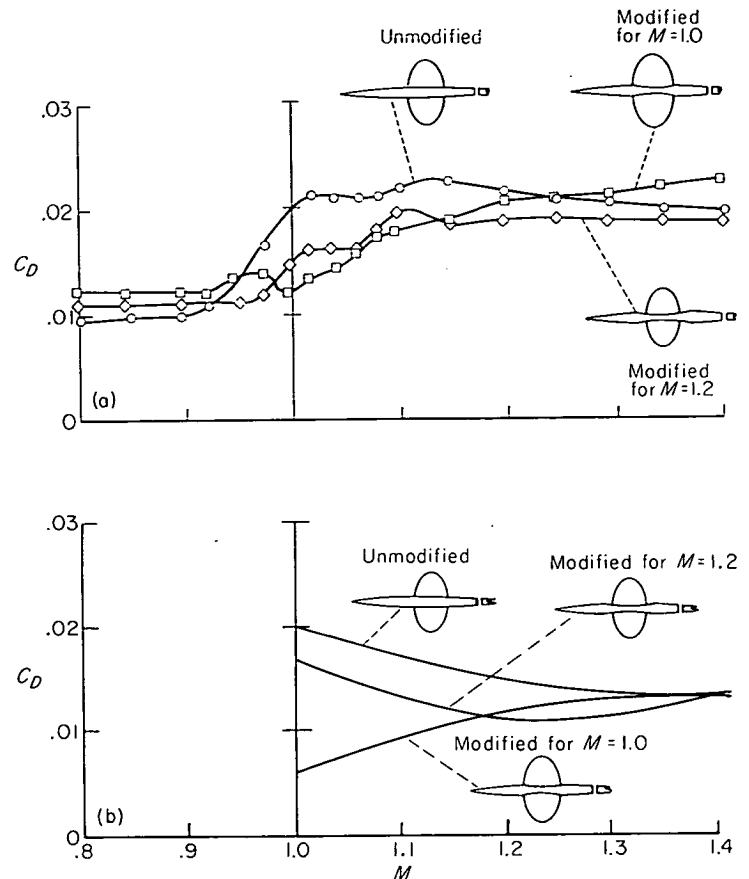


FIGURE 9.—Envelopes for drag at design Mach number.



(a) Experimental values.
(b) Calculated values.

FIGURE 10.—Drag of bodies with elliptic wings.

There are, of course, examples of wing-body systems which would hardly benefit by any change in shape of the fuselage. It is easy to decide whether a gain is possible, or worthwhile, by comparing the actual wave drag of the system with that of a Sears-Haack body containing the over-all volume of the system. In the case of 63° the wing-body combination, which has been described in several previous reports, this comparison yields 0.0045 as a lower bound for the wave-drag coefficient and 0.005 for the actual value. In such cases, for which the wave drag is initially very low, further reduction by reshaping the fuselage is not worthwhile.

It is clear from the foregoing, however, that appreciable savings in drag can be made in many cases by a suitable shaping of the fuselage. Unswept wings of high aspect ratio are benefited most and require the most careful consideration of the fuselage shape.

These new developments illustrate, again, the fact that the disturbance fields at transonic and supersonic speeds are essentially three-dimensional phenomena. It was not long ago that our ideas concerning the wing section—which had their origin in the older incompressible flow theory—had to be relinquished because of the predominating effects of the wing plan form. Now we must learn how to design the wing and the fuselage together.

AMES AERONAUTICAL LABORATORY

NATIONAL ADVISORY COMMITTEE FOR AERONAUTICS
MOFFETT FIELD, CALIF., July 8, 1953

APPENDIX A

SIMPLIFIED CALCULATION OF DRAG IN SPECIAL CASES

If special shapes such as the Sears-Haack body (ref. 7) and the elliptic wing (ref. 8) are selected for exploratory studies, then the calculation of drag can be greatly simplified.

The radius r of the Sears-Haack body at any station X is given by

$$\frac{r}{r_{max}} = \left[1 - \left(\frac{x}{x_0} \right)^2 \right]^{3/4} \quad (A1)$$

For this shape

$$S'(X) = A_2 \sin 2\phi \quad (A2)$$

and the drag has a minimum value for the given volume and length. The value of the drag is given by

$$C_D = \frac{D}{\frac{\rho}{2} V^2 S_{max}} = \frac{9}{8} \pi^2 \frac{(r_{max})^2}{x_0^2} \quad (A3)$$

The elliptic wing has symmetrical biconvex sections, with ordinates z given by

$$\frac{z}{z_{max}} = 1 - \frac{x^2}{a^2} - \frac{y^2}{b^2} \quad (A4)$$

where a and b are the semiaxes. The area distribution for every angle of projection is similar to that of the Sears-Haack body, but the projected length varies with the angle. The wing thus yields a minimum value of the wave drag consistent with a given volume and the elliptic plan form. The value of this drag is:

$$C_D = \frac{D}{\frac{\rho}{2} V^2 S} = 4 \frac{(z_{max})^2}{a^2} \frac{1}{\sqrt{M^2 - 1 + \frac{a^2}{b^2}}} \left(2 - \frac{M^2 - 1}{M^2 - 1 + \frac{a^2}{b^2}} \right) \quad (A5)$$

where S is the plan area of the wing.

By making use of the reversal theorem for drag we may compute the wave drag of any body from the fictitious pressure field obtained by superimposing the perturbation velocities for forward and reversed motion (refs. 12 and 13). This process leads to some interesting relations for the shapes selected. Thus in the case of the Sears-Haack body it may be shown that the combined pressure distribution \bar{p} consists of a uniform gradient of pressure over the whole interior R of its "characteristic envelope" defined by the Mach cone from the nose together with the reversed Mach cone from the tail. (See fig. 11.)

By thinking of the characteristic region R as a region of uniform horizontal buoyancy, and of the body b in terms of a certain volume, ν_b , we see that the drag is simply the product

$$D_{bb} = \nu_b \frac{d\bar{p}_b}{dx} \quad (A6)$$

The existence of a constant pressure gradient makes the computation of interference drag particularly simple for such shapes, provided the interfering body lies entirely within the characteristic region R . Thus the additional drag of an airfoil a placed within the double cone of the fuselage will be given by

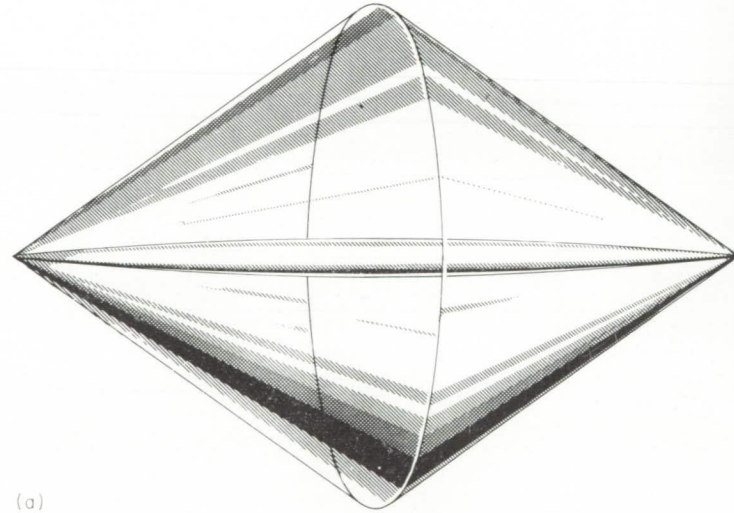
$$D_{ab} = \nu_a \frac{D_{bb}}{\nu_b} \quad (A7)$$

Now, by the mutual drag theorem (ref. 13) we have

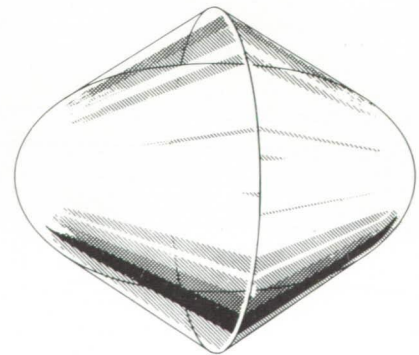
$$D_{ab} = D_{ba} \quad (A8)$$

or, "the drag of the fuselage caused by the presence of the wing is equal to the drag of the wing caused by the presence of the fuselage." In this way we obtain the general formula

$$D(a+b) = D_{bb} + 2D_{ab} + D_{aa} \quad (A9)$$



(a)



(b)

(a) Body of revolution.

(b) Elliptic wing.

FIGURE 11.—Characteristic envelopes.

and for the special shapes selected:

$$D(a+b) = D_{bb} \left(1 + 2 \frac{v_a}{v_b} \right) + D_{aa} \quad (A10)$$

The effect of an indentation or cutout in the fuselage may be calculated by introducing a second "body," c , shorter than the fuselage, and having a negative volume equal to the volume subtracted by the indentation. In order to simplify the situation as much as possible it will be assumed that the wing lies entirely within the characteristic region of the indentation, and furthermore that the latter may be represented by a "negative" Sears-Haack body with volume equal to that of the wing.

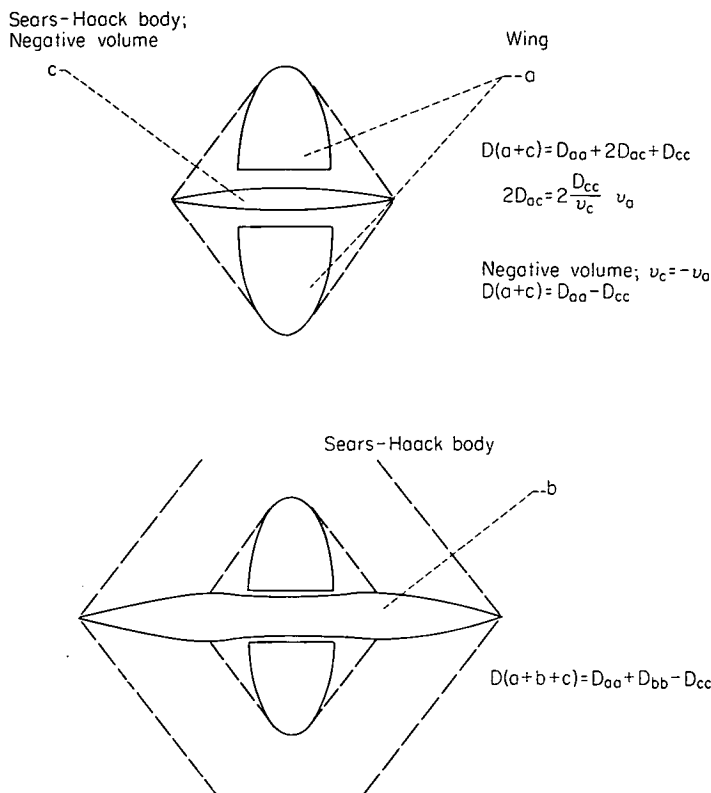


FIGURE 12.—Simplified calculation of interference drag.

The calculation of drag in this case is illustrated in figure 12. For the airfoil and cutout we have

$$\left. \begin{aligned} D(a+c) &= D_{aa} + 2D_{ac} + D_{cc} \\ 2D_{ac} &= -2D_{cc} \\ D(a+c) &= D_{aa} - D_{cc} \end{aligned} \right\} \quad (A11)$$

Now, the combination $(a+c)$ may be placed inside the characteristic region of the body b without interference, since $v_a + v_c = 0$. Hence,

$$D(a+b+c) = D_{aa} + D_{bb} - D_{cc} \quad (A12)$$

This formula yields the minimum drag for the shapes selected under the assumption that v_{b+c} is fixed. In this case the drag saving is equal to the drag of the indentation alone.

The negative Sears-Haack body is not the optimum shape of the indentation c for the elliptic wing, as shown by the result of Heaslet and Lomax quoted earlier (ref. 10). Again, however, in the case of the optimum shape for c , our previous equation holds. However, the calculation of D_{cc} is more complex in this case and its value is somewhat greater.

REFERENCES

1. Whitecomb, Richard T.: A study of the Zero-Lift Drag Rise Characteristics of Wing-Body Combinations Near the Speed of Sound. NACA RM L52H08, 1952.
2. Hayes, W. D.: Linearized Supersonic Flow. North American Aviation, Inc., Rep. No. AL-222, June 1947, pp. 94-95.
3. Ward, G. N.: Supersonic Flow Past Slender Pointed Bodies. Quart. Jour. Mech. and Appl. Math., vol. II, pt. 1, 1949.
4. Graham, E. W.: Pressure and Drag on Smooth Slender Bodies in Linearized Flow. Douglas Aircraft Co., Rep. SM-13417, 1949.
5. Heaslet, Max. A., Lomax, Harvard, and Spreiter, John R.: Linearized Compressible Flow Theory for Sonic Flight Speeds. NACA Rep. 956, 1950.
6. de Kármán, Th.: The Problem of Resistance in Compressible Fluids. Estratto dagli Atti del V Convegno della Fondazione Alessandro Volta, 1935, Rome, Reale Accademia d'Italia, 1936.
7. Sears, W. R.: On Projectiles of Minimum Wave Drag. Quart. Appl. Math., vol. IV, no. 4, Jan. 1947.
8. Jones, Robert T.: Theoretical Determination of the Minimum Drag of Airfoils at Supersonic Speeds. Jour. Aero. Sci., vol. 19, no. 12, Dec. 1952.
9. Busemann, A.: Application of Transonic Similarity. NACA TN 2687, 1952.
10. Lomax, Harvard, and Heaslet, Max. A.: A Special Method for Finding Body Distortions That Reduce the Wave Drag of Wing and Body Combinations at Supersonic Speeds. NACA Rep. 1282, 1956.
11. Ferri, Antonio: Application of the Method of Characteristics to Supersonic Rotational Flow. NACA Rep. 841, 1946.
12. Munk, Max M.: The Reversal Theorem of Linearized Supersonic Airfoil Theory. Jour. Appl. Phys., vol. 21, no. 2, Feb. 1950, pp. 159-161.
13. Jones, Robert T.: The Minimum Drag of Thin Wings in Frictionless Flow. Jour. Aero. Sci., vol. 18, no. 2, Feb. 1951, pp. 75-81.

REPORT 1285

SUMMARY OF DERIVED GUST VELOCITIES OBTAINED FROM MEASUREMENTS WITHIN THUNDERSTORMS ¹

By H. B. TOLEFSON

SUMMARY

This report presents the available data on the derived gust velocities in thunderstorms for altitudes up to 34,000 feet. The gust-velocity measurements were obtained from investigations made by the National Advisory Committee for Aeronautics in the vicinity of Langley Field, Va., in 1941 and 1942 and from the operations of the thunderstorm project in 1946 and 1947. The derived gust velocities were obtained from the previously evaluated effective gust velocities through use of a conversion factor that is a function of airplane characteristics and altitude. The results indicate that the intensity of the derived gust velocities in thunderstorms is essentially constant for altitudes up to about 20,000 feet and that an approximate 10-percent reduction in the intensity occurs as altitude is increased from 20,000 to 30,000 feet. These results apply to the data available for both convective and frontal types of storms.

INTRODUCTION

A revised gust-load formula with a new gust or alleviation factor (ref. 1) has been adopted for use in gust studies in order to account, in part, for the variations with altitude of the airplane response to gusts. The new gust factor is based on airplane mass ratio and on a gust profile represented by a one-minus-cosine curve whereas the previous alleviation factor was based on airplane wing loading and on a linear-gradient gust profile. The gust velocities obtained in evaluating flight measurements of the airspeed and vertical acceleration of an airplane by use of the revised formula are called the derived gust velocities and correspond to the maximum equivalent velocity for the assumed gust profile; the gust velocities previously obtained, the so-called effective gust velocities, represented only a fraction of this velocity. The derived gust velocities are accordingly numerically larger for the same turbulence than the effective gust velocities. The ratio of the derived to the effective gust velocities would also differ for the same turbulence at different altitudes since the airplane mass ratio is a function of air density.

Since the revised gust-load formula is now being used in the routine evaluation of gust data, the large amounts of effective-gust-velocity data available from V-G records on civil transport airplanes from 1933 to 1950 were converted to derived gust velocities and are summarized in reference 1.

Examples of the more detailed data on the derived gust velocities obtained from VGH records taken during scheduled airline operations are given in reference 2.

In addition to these data for routine airline operations, a large amount of data on the effective gust velocities is also available from special NACA flight investigations of thunderstorms. The effective gust velocities obtained from the earlier thunderstorm investigations in the vicinity of Langley Field, Va., in 1941 and 1942 are presented in reference 3. Parts of the data on the effective gust velocities obtained from the larger scale operations of the thunderstorm project in 1946 and 1947 are presented in references 3 to 8, although the complete gust data for this investigation have not been published. This report converts all the available data on the effective gust velocities in thunderstorms to derived gust velocities and summarizes the results in a form suitable for gust-load studies. In presenting the reevaluated data, particular attention is given to the question of the variation with altitude of the derived gust velocities in thunderstorms.

SYMBOLS

A	aspect ratio, b^2/S
a_n	vertical or normal acceleration, g units
b	wing span, ft
\bar{c}	mean wing chord, ft
g	acceleration due to gravity, ft/sec ²
K	gust alleviation factor (function of W/S)
K_g	gust factor (function of μ_g)
M	Mach number
m	slope of wing lift curve, per radian
S	wing area, sq ft
U_{de}	derived gust velocity, $\frac{2a_n W/S}{\rho_0 m V_e K_g}$, fps
U_e	effective gust velocity, $\frac{2a_n W/S}{\rho_0 m V_e K}$, fps
V_e	equivalent airspeed, fps
W	airplane weight, lb
μ_g	airplane mass ratio, $\frac{2W/S}{\rho g m \bar{c}}$
ρ	mass density of air, slugs/cu ft
ρ_0	mass density of air at sea level, slugs/cu ft

¹ Supersedes NACA Technical Note 3538 by H. B. Tolefson, 1955.

SCOPE OF DATA

The scope of the data is summarized in table I in terms of the flight miles traveled during the recording of gust data at various altitudes within thunderstorms.

Most of the thunderstorms represented by the data for the 1941-42 investigation in the vicinity of Langley Field, Va., resulted from convective activity. The bulk of these flight data recorded within the active portions of the storms was taken at altitudes from about 10,000 to 30,000 feet. For altitudes above 30,000 feet, a total of 117 flight miles was actually recorded. As indicated by the mileage values in table I, however, only 54 miles were associated with thunderstorms; the remainder represented clear-air and cirrus-cloud conditions. The data recorded during only the 54 miles of thunderstorm flying are considered in the subsequent analysis of the derived gust velocities for the highest altitudes. A considerable number of the records for altitudes below 10,000 feet were also taken in some of the lower intensities of turbulence in small cumuliform clouds or in clear air in the vicinity of these clouds, but the large variety of weather conditions represented precluded an accurate breakdown of the records to include only thunderstorms. The data for the lowest altitude range for the 1941-42 flights are accordingly biased toward the less turbulent conditions. The effective gust velocities evaluated from the flight records for this investigation are given in reference 3.

The data for the investigations in 1946 and 1947 were obtained from the operations of the thunderstorm project in Florida and Ohio (ref. 4). The thunderstorms were caused primarily by convective activity for the 1946 investigation in Florida, while squall-line and frontal-type storms were also represented by the 1947 investigation in Ohio. The records for the 1946 investigation contained a small amount of flight distance in clear-air turbulence in the immediate vicinity of the thunderstorms. For the 1947 investigation, however, only the portion of records taken within the cloud could be determined. Parts of the data on the effective gust velocities for these tests are given in references 3 to 8.

The investigations made in the vicinity of Langley Field in 1941 and 1942 as well as the operations of the thunder-

storm project in 1946 and 1947 represent surveys through thunderstorms which developed to altitudes between about 25,000 feet and 45,000 feet. Although in most cases the intention was to make the surveys at the time of maximum thunderstorm intensity, all stages of cloud development are included in the tests. The results from the flights summarized in table I can be used, therefore, to give only an overall indication of the variation of the turbulence in the storms in relation to altitudes above sea level and not in relation to such factors as cloud height or the state of the physical processes within the clouds.

METHOD OF CONVERSION AND RESULTS

From the definition of U_e and U_{de} , it may be seen that the two gust velocities differ only in regard to the factors K and K_g . The effective gust velocities may accordingly be converted to derived gust velocities simply by the relation

$$U_{de} = U_e \frac{K}{K_g}$$

The large number of effective gust velocities evaluated from the thunderstorm investigations were available in the form of cumulative frequency distributions of effective gust velocities above a threshold of 4 feet per second for given altitude ranges. Rather than converting the individual values of the effective gust velocity to derived gust velocities by the previous relation, the work was simplified considerably by converting the distribution for each altitude to a distribution of derived gust velocities. Check calculations indicated that this simplification introduced only very small errors in the resulting distributions of derived gust velocities. An average value of the ratio K/K_g was determined for each altitude from the values of K previously used in the evaluation of effective gust velocities and from the values of K_g computed for individual thunderstorm traverses. Minor variations occurred in the ratio K/K_g for separate traverses within a given altitude range because of slight variation in Mach number, altitude, or airplane weight; however, for both the 1941-42 and the thunderstorm-project data, the variations from the average were less than 1 percent for about 90 percent of the cases and none were greater than about 3 percent. The average values of Mach number, Mach number correction to the lift-curve slope, mass ratio, and gust factors for each altitude range are given in table II.

In the original calculations for the effective gust velocities for the 1941-42 investigation, no correction was made for the effect of compressibility on the lift-curve slope. Inasmuch as most subsequent gust work, including the evaluation of the effective gust velocities for the 1946-47 operations of the thunderstorm project, included the usual compressibility factors, this additional correction was made to the lift-curve slope for the 1941-42 data in order to place all results on a consistent basis. As noted in table II, this correction increased the lift-curve slope from 1 to 4 percent for the 1941-42 investigation for altitudes from 5,000 to 34,000 feet.

TABLE I

SCOPE OF DATA IN TERMS OF FLIGHT MILES TRAVELED DURING RECORDING OF GUST DATA AT VARIOUS ALTITUDES WITHIN THUNDERSTORMS

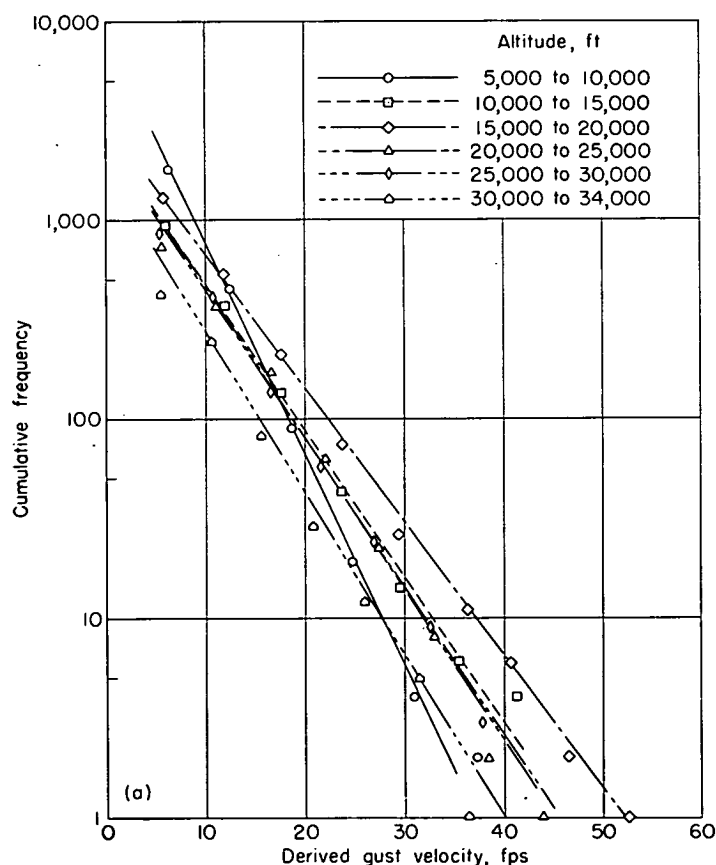
1941-42 investigation		1946 investigation		1947 investigation	
Altitude, ft	Flight miles	Altitude, ft	Flight miles	Altitude, ft	Flight miles
5,000 to 10,000	247	6,000	993	5,000	757
10,000 to 15,000	130	11,000	1,565	10,000	1,340
15,000 to 20,000	180	16,000	1,716	15,000	1,612
20,000 to 25,000	114	21,000	1,422	20,000	1,208
25,000 to 30,000	180	26,000	1,064	25,000	939
30,000 to 34,000	54				

TABLE II
VALUES USED FOR CALCULATIONS

Altitude, ft	Flight Mach number	Mach number correction to lift-curve slope, $\frac{A+2}{A\sqrt{1-M^2}+2}$	Airplane mass ratio, μ_g	Gust factors		
				K_g	K	K/K_g
1941-42 investigation						
5, 000 to 10, 000	0. 17	1. 010	18. 7	0. 686	1. 078	1. 57
10, 000 to 15, 000	. 20	1. 015	23. 6	. 718	1. 070	1. 49
15, 000 to 20, 000	. 23	1. 020	27. 5	. 738	1. 074	1. 46
20, 000 to 25, 000	. 26	1. 030	32. 1	. 755	1. 070	1. 42
25, 000 to 30, 000	. 29	1. 035	37. 7	. 771	1. 070	1. 39
30, 000 to 34, 000	. 31	1. 040	44. 0	. 785	1. 070	1. 36
1946-47 investigation						
5, 000 to 6, 000	0. 23	1. 020	26. 4	0. 733	1. 180	1. 61
10, 000 to 11, 000	. 29	1. 035	30. 0	. 748	1. 179	1. 58
15, 000 to 16, 000	. 31	1. 040	34. 6	. 763	1. 179	1. 54
20, 000 to 21, 000	. 33	1. 045	41. 1	. 779	1. 179	1. 51
25, 000 to 26, 000	. 34	1. 050	48. 6	. 793	1. 178	1. 49

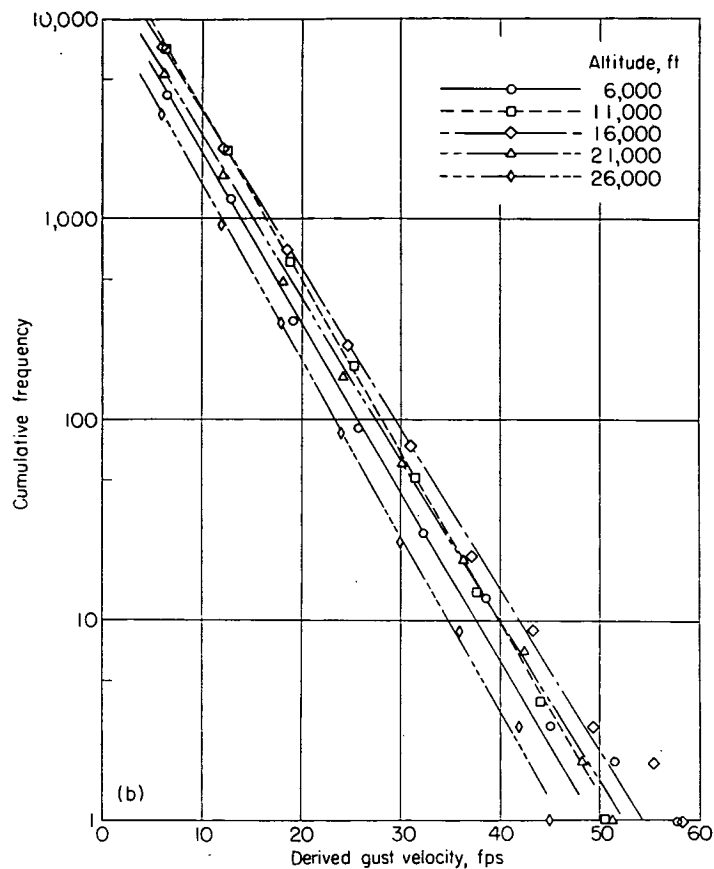
The cumulative frequency distributions of derived gust velocities are shown in figure 1 for the different altitudes of the 1941-42 investigation and the thunderstorm-project investigation. It will be noted in the figure that the gust-velocity intervals for each set of data vary somewhat between the different altitudes because of the differences in the ratio K/K_g . The dropoff in the gust frequency at the lowest gust velocity in some cases is due to incomplete evaluation of all gusts near the threshold value. Some scatter also occurs in the plotted points for the higher gust velocities at several altitudes because the infrequent encounters with the more severe turbulence result in only a small number of the larger gusts. In figure 1 (c) in particular, the scatter at the higher gust velocities for an altitude of 15,000 feet is entirely due to four gusts greater than 55 feet per second encountered during a single traverse through a thunderstorm. The trend of the data in all instances, however, is very nearly linear, and a straight line was faired through each set of data to represent the distribution. Since the bulk of the data in each case is represented by the gust velocities less than about 40 feet per second, most weight was given to these points in fairing the lines.

In order to obtain basic distributions of derived gust velocity in a form suitable for other studies, the numbers of gusts within common class intervals of 5 feet per second were obtained from the curves in figure 1. The results are tabulated in table III for the flight altitudes of each data sample. The flight mileage represented by each distribution is also given in table III for completeness.



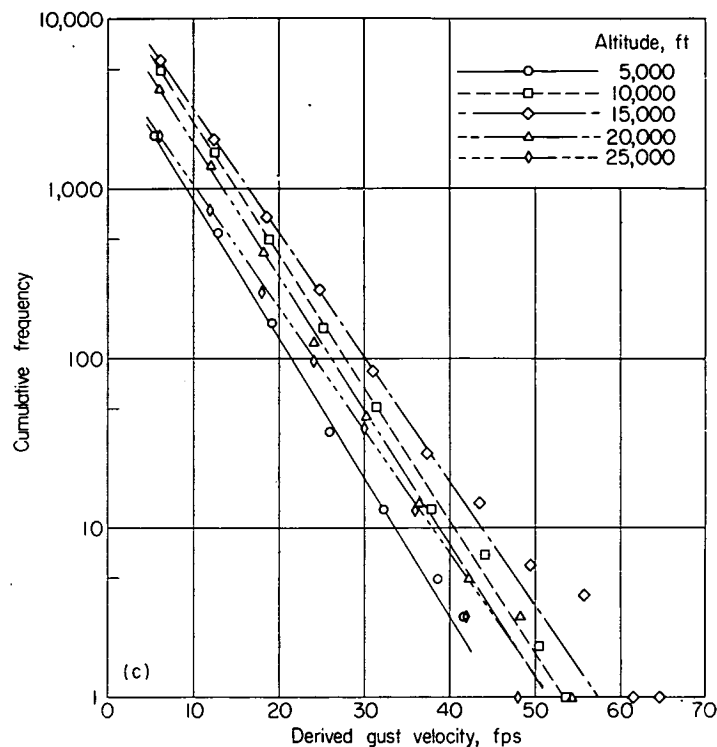
(a) 1941-42 investigation.

FIGURE 1.—Cumulative frequency distributions of derived gust velocities for thunderstorm investigations.



(b) 1946 investigation.

FIGURE 1.—Continued.



(c) 1947 investigation.

FIGURE 1.—Concluded.

TABLE III
FREQUENCY DISTRIBUTIONS OF DERIVED GUST VELOCITY

U_{ac} , fps	1941-42 investigation						1946 investigation					1947 investigation				
	Frequency of gusts at altitude (ft) of—															
	5,000 to 10,000	10,000 to 15,000	15,000 to 20,000	20,000 to 25,000	25,000 to 30,000	30,000 to 34,000	6,000	11,000	16,000	21,000	26,000	5,000	10,000	15,000	20,000	25,000
5 to 10 -----	1, 855	635	860	570	640	410	3, 560	6, 000	5, 180	3, 920	2, 570	1, 430	3, 700	4, 000	2, 810	1, 370
10 to 15 -----	552	283	376	249	279	171	1, 385	2, 230	2, 020	1, 590	940	510	1, 495	1, 720	1, 135	620
15 to 20 -----	166	114	180	111	111	67	500	870	840	635	342	210	595	720	454	260
20 to 25 -----	47	50	84	46	46	26	187	313	338	245	126	79	248	321	180	113
25 to 30 -----	14	22	37	19	20	10	74	117	132	96	45	31	95	138	72	51
30 to 35 -----	4	9	18	9	8	3	27	44	54	39	17	12	40	57	29	20
35 to 40 -----	2	4	8	3	4	3	11	16	22	15	6	5	16	25	12	10
40 to 45 -----	---	3	4	3	2	---	4	6	8	6	4	3	7	11	5	3
45 to 50 -----	---	---	2	---	---	---	2	3	4	4	---	---	2	4	2	3
50 to 55 -----	---	---	1	---	---	---	---	1	2	---	---	---	2	2	1	---
55 to 60 -----	---	---	---	---	---	---	---	---	---	---	---	---	---	2	---	---
Totals -----	2, 640	1, 120	1, 570	1, 010	1, 110	690	5, 750	9, 600	8, 600	6, 550	4, 050	2, 280	6, 200	7, 000	4, 700	2, 450
Flight miles --	247	130	180	114	180	54	993	1, 565	1, 716	1, 422	1, 064	757	1, 340	1, 612	1, 208	939

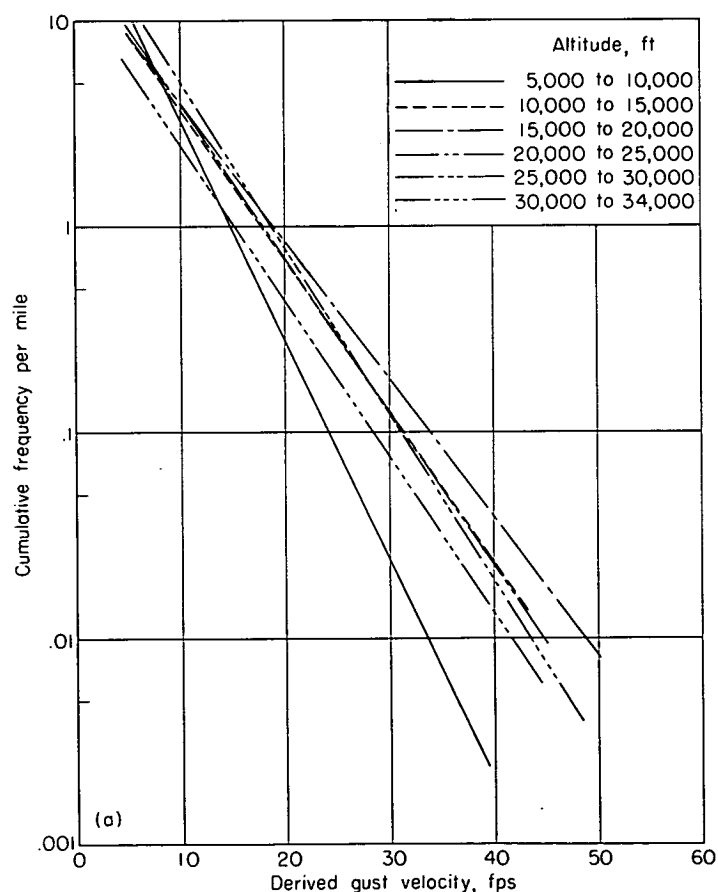
The distributions of table III or figure 1 cannot be used directly for comparing the gust velocities for the different investigations or for the different altitudes because each distribution represents a different flight mileage. In order to provide a common basis for such comparisons, the cumulative frequency distributions of figure 1 were divided by the pertinent flight mileage in table I to obtain the number of gusts greater than given values per mile of flight. These results are shown in figure 2.

As a simple measure of the relative intensity of the turbulence at the different altitudes, the gust velocity which was exceeded on the average a given number of times per mile of flight was read from figure 2 for each of the flight altitudes. A frequency level (ordinate value of fig. 2) of 0.04 gust per mile for the 1941-42 flights, 0.007 gust per mile for those of 1946, and 0.01 gust per mile for those of 1947 was selected in order to obtain derived gust velocities of about 40 feet per second for each investigation. The results are plotted at the midpoint of each altitude range in figure 3. The corresponding effective gust velocities are also shown in figure 3 for comparison. A curve has been faired through the points for the derived and effective gust velocities to indicate an estimated overall variation in these quantities

with altitude. In fairing the curves, consideration was given both to the sample sizes and the conditions under which the data were taken. For example, the data point for the lowest altitude range (5,000 to 10,000 feet) for the 1941-42 investigation was disregarded because of the fairly large proportion of data taken in clear air or smaller clouds. The curves are dashed for altitudes above 28,000 feet because of the small data sample and uncertainty of the results at the highest altitude.

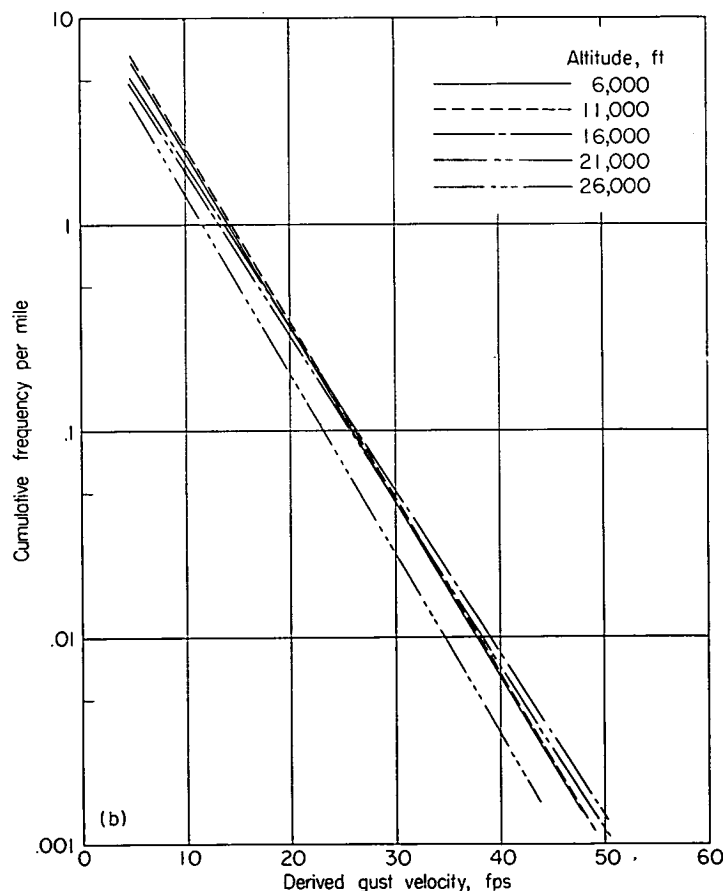
DISCUSSION

Inspection of figure 2 indicates no consistent or large variations in the magnitude of the derived gust velocities for the different altitudes of each set of data if altitudes below 10,000 feet are neglected in the 1941-42 investigation. For a frequency level corresponding to the larger gust velocities, which are of primary interest from a loads standpoint, figure 2 indicates that differences of about 5 to 7 feet per second occur in the magnitude of the derived gust velocities for the different altitudes of each investigation. A comparison of the three sets of distributions in figure 2 also indicates that the derived gust velocities for the 1946 and 1947 thunderstorm investigations were of almost equal intensity, whereas the gust velocities for the 1941-42 investigation were somewhat greater.



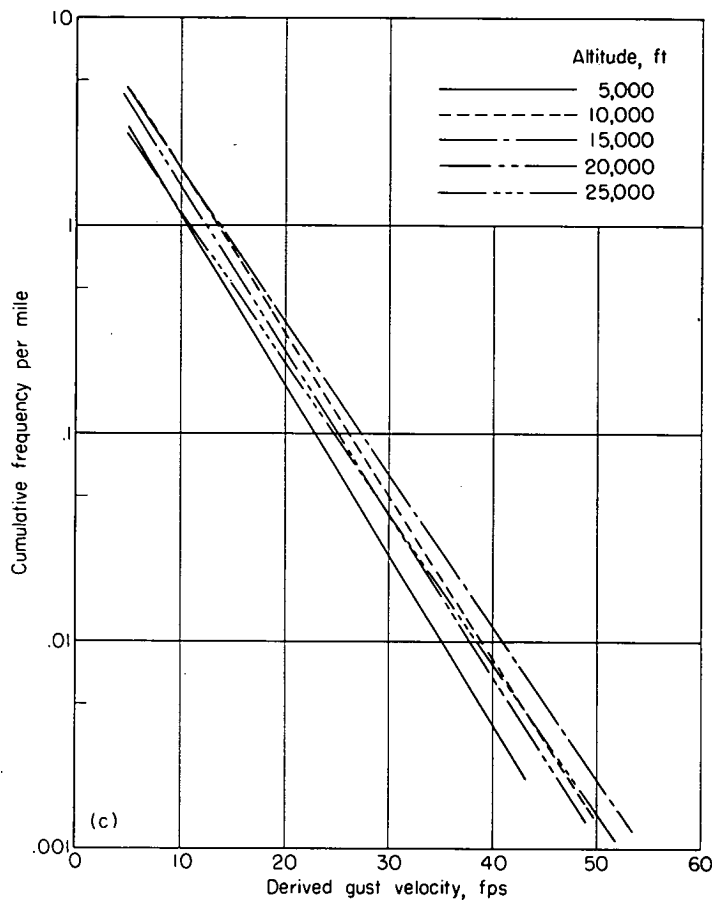
(a) 1941-42 investigation.

FIGURE 2.—Average frequency of exceeding given values of derived gust velocity per mile of flight at different altitudes within thunderstorms.



(b) 1946 investigation.

FIGURE 2.—Continued.



(c) 1947 investigation.

FIGURE 2.—Concluded.

In addition to the observations from figure 2 on the intensity of the turbulence at different altitudes, calculations were made to check whether the differences noted between the distributions for the separate altitudes resulted from differences in the turbulence intensities or from random or sampling fluctuations in the data. These results, based on a comparison of the confidence limits for each distribution at a gust velocity of about 40 feet per second, indicated that a scatter of only about 1 foot per second would be ascribed to sampling errors. The differences in the derived gust velocities of 5 to 7 feet per second at the different altitudes accordingly reflect the differences in the turbulence intensities.

A better indication of the magnitude of the derived gust velocities measured at the separate altitudes in thunderstorms can be seen in figure 3. Although the points scatter somewhat from altitude to altitude, the overall trend of the data indicates that the values of the derived gust velocities remain essentially constant for altitudes up to about 20,000 feet and then decrease slightly at the higher altitudes. On the basis of the faired curve in the figure, the magnitude of this decrease is from about 39 feet per second at 20,000 feet to 35 feet per second at 30,000 feet, or a decrease of approximately 10 percent in 10,000 feet. Other similar plots were made to check this variation with altitude at gust-velocity levels of about 20 and 30 feet per second. These results indicated substantially the same type of variation with altitude as shown in figure 3.

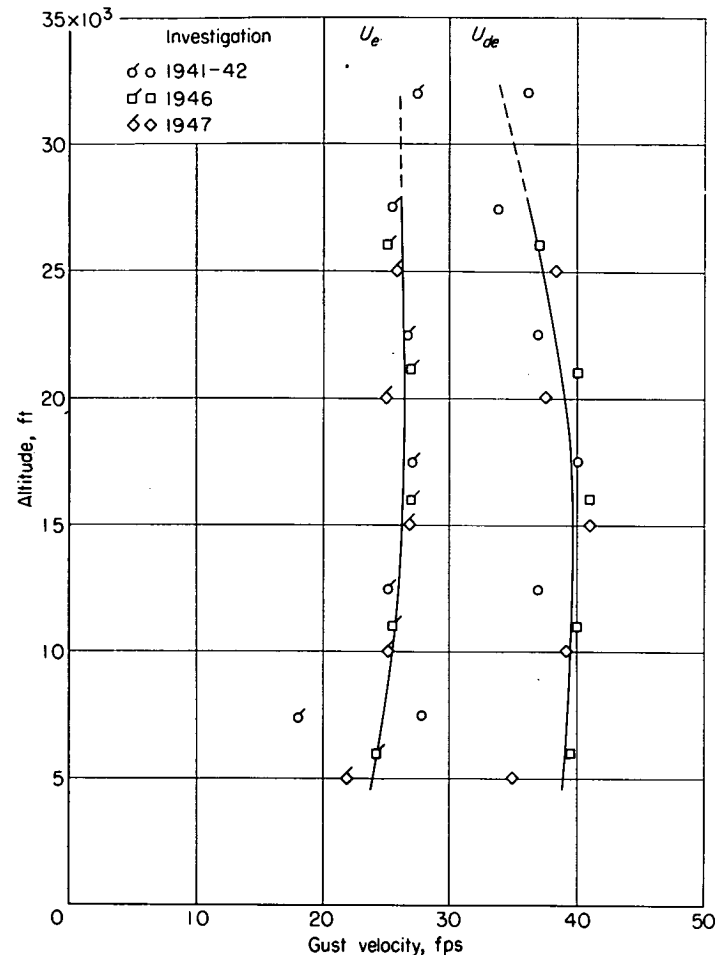


FIGURE 3.—Derived and effective gust velocities exceeded on the average a given number of times per mile of flight at various altitudes within thunderstorms.

A comparison of the derived gust velocities with the effective gust velocities in figure 3 illustrates the effect of altitude on the ratio K/K_g . It will be noted from the figure that the effective gust velocities are essentially constant with altitude, whereas the decrease in the ratio K/K_g at the higher altitudes leads to the decrease in derived gust velocities of about 10 percent from 20,000 to 30,000 feet.

In an attempt to determine whether variations existed in the turbulence intensities for different types of thunderstorms, the gust-velocity measurements taken in convective types of storms were compared with those taken in frontal types of storms for the 1947 investigation. Reference 4 indicated that five of the thunderstorms for which records were obtained in 1947 were of convective origin. Ten thunderstorms were associated with frontal activity, either squall-line or surface-front condition. A comparison of the distributions of the derived gust velocity for the convective types of storms with those for the frontal types of storms indicated only negligible differences in either the overall intensity of the turbulence or in the variation of the intensity with altitude. As has also been noted in connection with figure 2, the overall intensity of the turbulence for the convective types of storms investigated in 1946 was about equal to that for the combined convective and frontal types of storms investigated in 1947. These examinations of the

data accordingly indicated no real variations between the derived gust velocities for the two storm types.

CONCLUSIONS

A study of the available data on the derived gust velocities within thunderstorms indicates the following:

1. The intensity of the derived gust velocity which was exceeded a given number of times per mile of flight within thunderstorms remains essentially constant for altitudes up to about 20,000 feet. An approximate 10-percent reduction in the intensity of the derived gust velocities occurs as altitude is increased from 20,000 to about 30,000 feet.

2. For the convective and frontal types of thunderstorms represented by the data, no differences that could be ascribed to storm type were indicated in either the overall intensity of the turbulence or in the variation of the intensity with altitude.

LANGLEY AERONAUTICAL LABORATORY,
NATIONAL ADVISORY COMMITTEE FOR AERONAUTICS,
LANGLEY FIELD, VA., *July 27, 1955.*

REFERENCES

1. Pratt, Kermit G., and Walker, Walter G.: A Revised Gust-Load Formula and a Re-Evaluation of V-G Data Taken on Civil Transport Airplanes From 1933 to 1950. NACA Rep. 1206, 1954. (Supersedes NACA TN's 2964 by Kermit G. Pratt and 3041 by Walter G. Walker.)
2. Coleman, Thomas L., and Walker, Walter G.: Analysis of Accelerations, Gust Velocities, and Airspeeds From Operations of a Twin-Engine Transport Airplane on a Transcontinental Route From 1950 to 1952. NACA TN 3371, 1955.
3. Tolefson, H. B.: An Analysis of the Variation With Altitude of Effective Gust Velocity in Convective-Type Clouds. NACA TN 1628, 1948.
4. Anon.: The Thunderstorm. U. S. Dept. of Commerce, June 1949.
5. Donely, Philip: Summary of Information Relating to Gust Loads on Airplanes. NACA Rep. 997, 1950. (Supersedes NACA TN 1976.)
6. Tolefson, Harold B.: Preliminary Analysis of NACA Measurements of Atmospheric Turbulence Within a Thunderstorm—U. S. Weather Bureau Thunderstorm Project. NACA TN 1233, 1947.
7. Press, Harry: A Statistical Analysis of Gust-Velocity Measurements As Affected by Pilots and Airplanes. NACA TN 1645, 1948.
8. Thompson, J. K., and Lipscomb, V. W.: An Evaluation of the Use of Ground Radar for Avoiding Severe Turbulence Associated With Thunderstorms. NACA TN 1960, 1949.

REPORT 1286

PROPAGATION OF A FREE FLAME IN A TURBULENT GAS STREAM¹

By WILLIAM R. MICKELSEN and NORMAN E. ERNSTEIN

SUMMARY

Effective flame speeds of free turbulent flames were measured by photographic, ionization-gap, and photomultiplier-tube methods, and were found to have a statistical distribution attributed to the nature of the turbulent field. The effective turbulent flame speeds for the free flame were less than those previously measured for flames stabilized on nozzle burners, Bunsen burners, and bluff bodies. The statistical spread of the effective turbulent flame speeds was markedly wider in the lean and rich fuel-air-ratio regions, which might be attributed to the greater sensitivity of laminar flame speed to flame temperature in those regions. Values calculated from the turbulent free-flame-speed analysis proposed by Tucker apparently form upper limits for the statistical spread of free-flame-speed data. Hot-wire anemometer measurements of the longitudinal velocity fluctuation intensity and longitudinal correlation coefficient were made and were employed in the comparison of data and in the theoretical calculation of turbulent flame speed.

INTRODUCTION

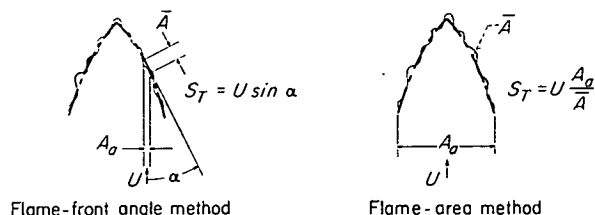
The high volumetric heat-release rate required in present and future jet-engine combustors has placed an ever-growing emphasis on turbulent combustion research. The theory of turbulent flame propagation is as yet in a formative stage, partly because of the lack of reliable experimental methods for determining the effect of turbulence on the rate of flame propagation. The purpose of this investigation was to explore a new experimental method believed to approximate more nearly a theoretical, or ideal, flame model than previous methods.

The major portion of experimental data on turbulent flame speeds has been taken in open flames stabilized on Bunsen burners (refs. 1 to 3) or on Mache type burners (refs. 4 and 5). A substantial amount of experimental data has also been obtained from flames confined in a duct and stabilized on bluff bodies (refs. 6 to 8). Another experimental method consists in measuring the speed of a flame advancing into a turbulent fuel-air mixture flowing through a tube (ref. 9). In general, the definition of turbulent flame speed used in these methods is that given in reference 8:

$$S_T = U \frac{A_g}{A} \quad (1)$$

(All symbols are defined in appendix A.) Equation (1) has been used for local measurements by the flame-front angle method and for over-all flame-speed measurements by the

flame-area method. These two methods are shown in the following sketches:



Turbulent-flame-speed values obtained by these methods may be significantly affected by conditions external to the flame front itself, such as

- (1) Large fluctuations in instantaneous flame-front position that introduce uncertainty in the determination of mean position in long-time-exposure photographs of stabilized flames (ref. 10)
- (2) Existence of piloting zones at the rims of Bunsen burners, immediately downstream of bluff bodies, or in the boundary layer of flame tubes, which may affect the burning rate of the flames near such zones (refs. 7 and 10)
- (3) Large velocity differences between unburned and burned gas flows, which may introduce considerable turbulence in stabilized flames (refs. 2, 6, 7, and 11)
- (4) Curvature of unburned-gas stream lines at the flame front, which may introduce substantial error in flame speeds measured in stabilized flames by the angle method (refs. 7 and 12)
- (5) Variations in local flame speeds along the flame envelope, which may introduce substantial error in average flame speeds measured by the flame-area method

This investigation was conducted to determine the effect of turbulence on the growth of a free flame. It was thought that the free flame would not be subject to the complicating conditions present in stabilized flames such as those listed. In addition, the free-flame growth could take place entirely in a homogeneous, isotropic, turbulent field away from boundary layers and bluff-body wakes, thus providing a more nearly fundamental flame model.

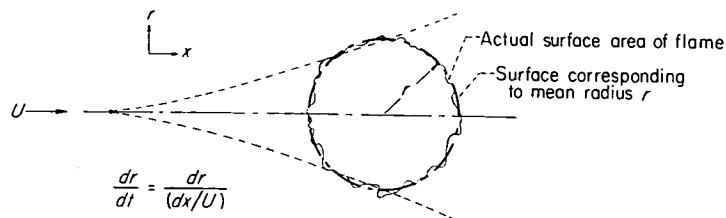
The method used in the present investigation is an extension of the "soap-bubble" technique (ref. 13) and consists of the observation of the growth of a free-flame globule as it is carried downstream in a flowing, turbulent, homogeneous mixture of gaseous fuel and air. The flame globule was initiated by a single spark, and its growth was recorded by three separate methods, high-speed motion-picture photography, ionization-gap probes, and photomultiplier-tube signals.

¹ Supersedes NACA TN 3456, "Propagation of a Free Flame in a Turbulent Gas Stream," by William R. Mickelsen and Norman E. Ernstein, 1955.

The flame-globule growth was characterized by an effective turbulent flame speed S_T , which is defined by a mass-balance equation similar to that derived in reference 13:

$$S_T = \frac{\rho_F}{\rho_a} \frac{dr}{dt} \quad (2)$$

Equation (2) can be clarified by the following sketch:



The rate of change of the globule radius was measured over periods of time less than the characteristic time of the turbulence. This means that, on the average, the flame front traveled through less than one turbulent eddy during the time of observation. In the past, average turbulent flame speeds have generally been measured from photographs of flames having long exposure times compared with the characteristic time of the turbulence.

The experimental work was carried out in two phases. The first phase was initiated and carried out at the NACA Lewis laboratory and is reported in reference 14. (Because of its limited circulation, considerable portions of the work reported in ref. 14 are included in this report.) Turbulent-flame-speed measurements were obtained from high-speed motion-picture records of the growth of the free-flame globule as it was swept downstream in an enclosed tunnel. The turbulent field was introduced by means of a wire grid placed at the tunnel inlet some distance upstream of the spark-electrode position. The turbulent field was characterized by hot-wire-anemometer measurements.

The effective turbulent flame speeds determined by the photographic method varied for runs made under identical fuel-air and mean stream conditions. The variation was concluded to be due to the statistical nature of the turbulent field. Statistical analysis of groups of 30 or more runs made at identical fuel-air and mean stream conditions showed that the data for each group approximated a normal probability distribution. When plotted on the basis of cumulative probability of occurrence, the effective turbulent-flame-speed data showed a consistent increase with increasing turbulence intensity.

The second phase of the investigation was carried out in a free jet with a technique whereby the cumulative probability of occurrence of turbulent flame speed could be determined from flame groups consisting of thousands of separate flame globules. This technique utilized ionization-gap probes and counters, which indicated directly the percentage of flames reaching or exceeding any given diameter at a series of stations downstream of the spark electrodes. By this method, flame speeds were measured over a range of fuel-air weight ratios from 0.053 to 0.090 and a range of mean stream velocities from 35 to 142 feet per second at a stream static pressure of 1 atmosphere and a stream static temperature of 85° F. The stream turbulence was varied

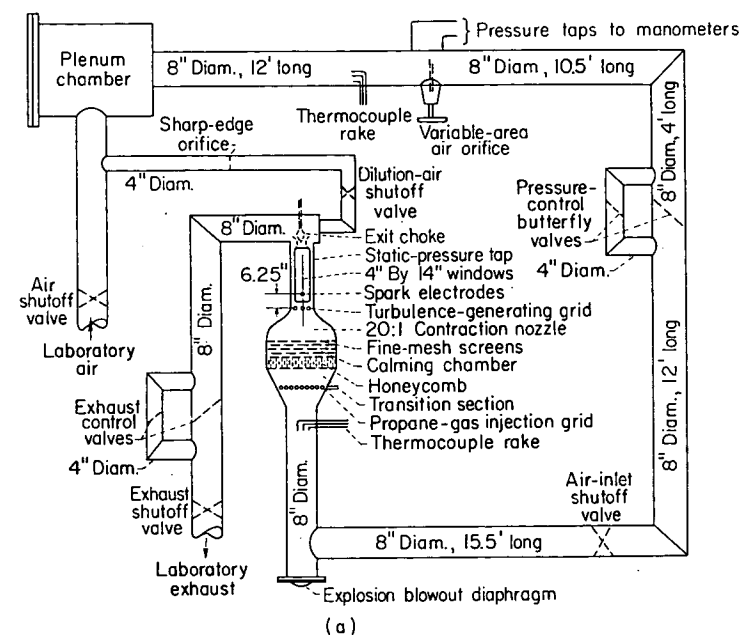
by the use of three interchangeable grids, and the parameters of the turbulence were measured with constant-temperature hot-wire-anemometer instrumentation.

The investigation was carried out at the Lewis laboratory as a part of the combustion research program.

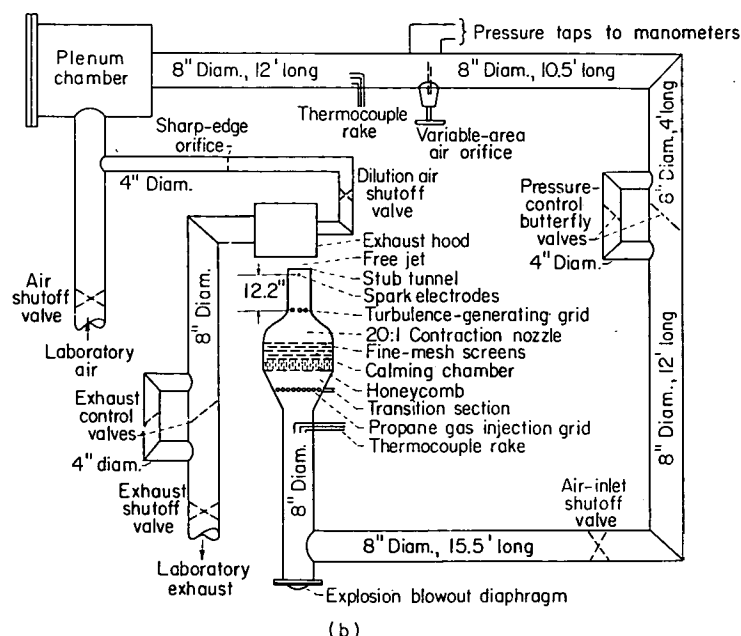
APPARATUS

AIR-DUCTING, WIND-TUNNEL, AND AIRFLOW INSTRUMENTATION

The air-ducting, wind-tunnel, and airflow instrumentation used in the first phase of the investigation and reported in reference 14 is shown in figure 1(a). Alterations made to the apparatus for the second phase of the investigation are shown in figure 1(b). The alterations essentially converted the system from an enclosed tunnel to a free jet.



(a) Enclosed-tunnel installation.



(b) Free-jet installation.

FIGURE 1.—Air-ducting, wind-tunnel, and mean airflow instrumentation.

Air supplied from the laboratory air facility was metered with a standard variable-area orifice and controlled with the butterfly and gate valves shown in figure 1. Static pressures and temperatures were measured with conventional manometers and thermocouples.

The ducting approach to the tunnel was designed from principles used in conventional low-turbulence wind tunnels. The transition section was followed by a honeycomb and turbulence-damping screen in the calming section to reduce the turbulence present in the air-supply flow. The entrance to the enclosed tunnel (or free jet) was a nozzle with a contraction ratio of 20, and provisions were made at the tunnel throat for the insertion of turbulence-producing grids. Three grids were used for the investigation, all having a mesh to wire-diameter ratio of 5. The grid wire diameters were 0.0313, 0.063, and 0.125 inch.

The enclosed-tunnel installation was equipped with an adjustable plug and nozzle by which critical flow could be maintained at the tunnel exit, so that the tunnel flow field could be isolated from pressure disturbances in the laboratory exhaust facility. The free-jet installation was equipped with an exhaust hood into which diluting room air could be drawn in addition to the free-jet flow.

FUEL SYSTEM

The propane fuel used throughout the investigation had the following composition by liquid volume:

Propane, percent.....	97.76
Ethane, percent.....	1.72
Isobutane, percent.....	0.51

The propane fuel system is shown in figure 2 and was identical for both the enclosed-tunnel and free-jet installations. Propane was supplied from a laboratory facility and metered with standard rotameters. Pressure, temperature, and flow controls are shown in figure 2. The propane was injected into the airstream through a grid having 60 equally spaced, 0.040-inch-diameter holes. The injection grid was installed at a station upstream of the calming chamber as shown in figure 1.

IGNITION SYSTEM

The flame-globule ignition system consisted of a pair of spark electrodes protruding into the tunnel stream from opposing walls and an electrical energy source. The spark electrodes used in the enclosed tunnel were carefully streamlined to a fineness ratio of 5 with a thickness tapering from 0.019 inch at the tunnel center to 0.038 inch at the tunnel wall. The spark electrodes used in the free-jet installation were of circular cross section with a diameter tapering from 0.015 inch at the stub tunnel center to 0.075 inch at the stub tunnel wall. The spark-gap spacing was 0.015 and 0.030 inch for the enclosed-tunnel and free-jet installations, respectively. The spark-electrode positions for the two installations are shown in figure 1.

The spark-energy source was of the capacitive type and produced single sparks synchronized with the camera operation in the enclosed-tunnel installation or successive sparks at the rate of 3 per second in the free-jet installation. The spark energy could be varied by changing capacitors.

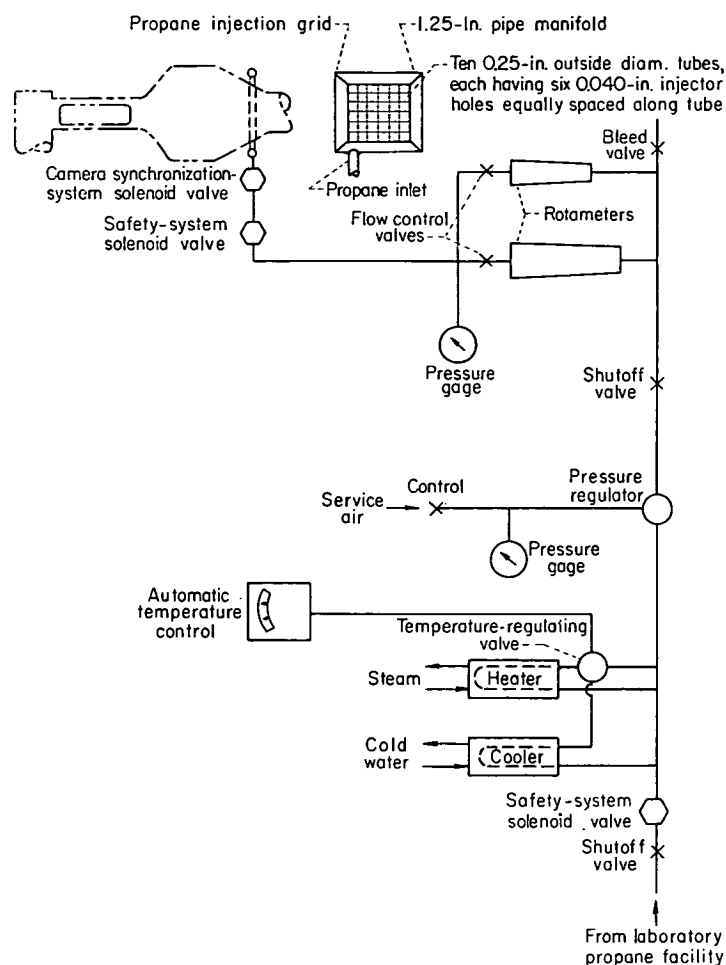


FIGURE 2.—Fuel system.

FLOW-FIELD INSTRUMENTATION

In general, the flow-field instrumentation was adaptable to point measurements in either the enclosed-tunnel or free-jet streams. Mean-stream-velocity measurements were made with a conventional pitot-static probe and micromanometer. Fuel-air ratio was measured directly by a mixture analyzer. Stream samples were drawn through a sharp-edged 0.125-inch-inside-diameter sampling probe to the analyzer, which indicated fuel-air ratio directly by the thermal-conductivity-bridge method.

Turbulence measurements were made with constant-temperature hot-wire-anemometer equipment, which is described in appendix B. Sound pressure levels were measured with a conventional microphone and a sound-pressure-level meter, also described in appendix B.

FREE-FLAME-GROWTH MEASUREMENT

Photographic instrumentation.—The growth of the free-flame globule was recorded photographically in the enclosed-tunnel installation with the optical system shown in figure 3. The photographic records were taken with a 16-millimeter Fastax camera operated at approximately 3600 frames per second and located at the end point of the parallel-beam schlieren system. The enclosed-tunnel windows were striation-free plate glass. The light source was a mercury-vapor BH-6 lamp operated with a high-voltage direct-current power supply.

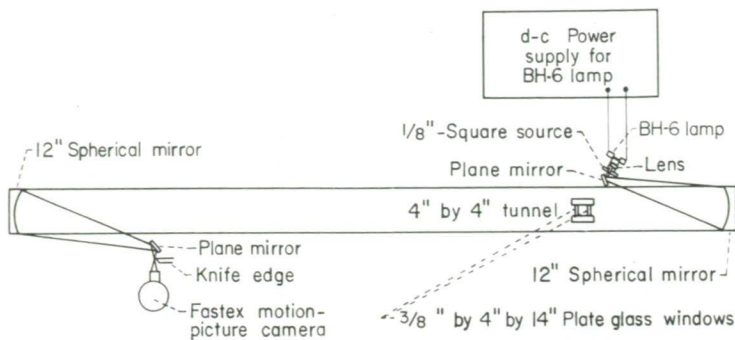
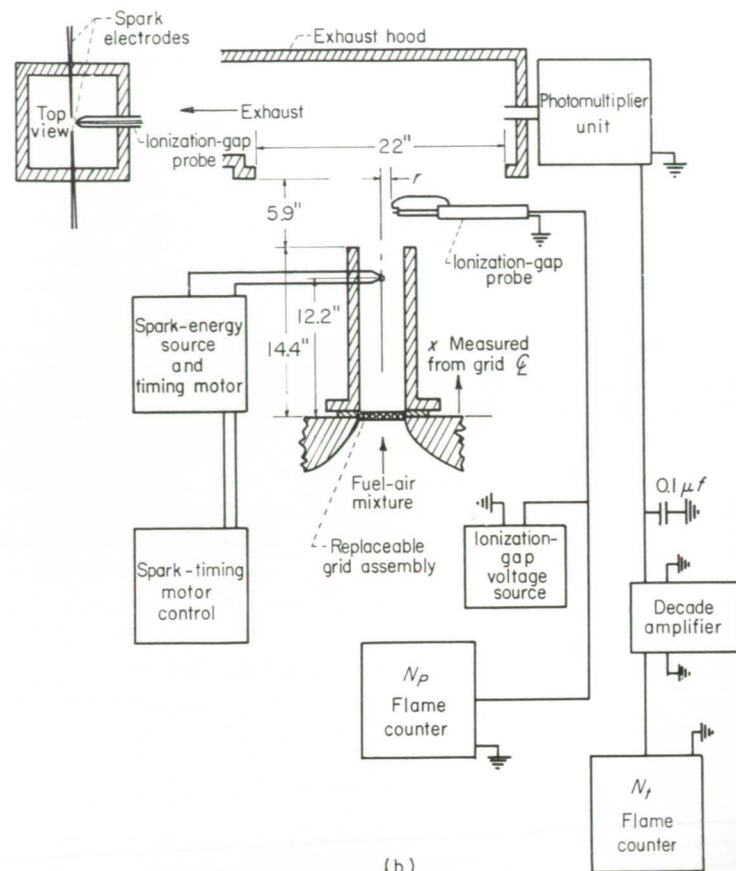


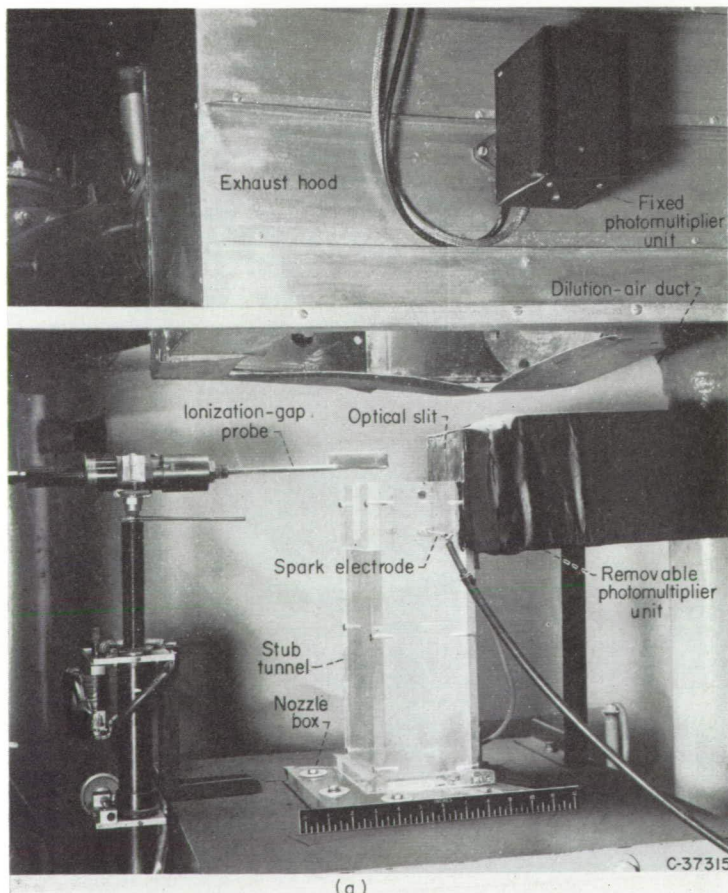
FIGURE 3.—Photographic instrumentation for measurement of free-flame growth in enclosed-tunnel installation.

Ionization-gap instrumentation.—The growth of the free-flame globule was measured in the free-jet installation with an ionization-gap probe, a photomultiplier flame sensing unit, and two flame counters. The physical orientation of these instrumentation components is shown in figures 4(a) and (b). The photomultiplier unit and its accompanying flame counter recorded the total number of flames that occurred during any particular run. The ionization-gap probe and its accompanying flame counter recorded the number of flames that grew to a radius of r or greater at the axial station x during any particular run.

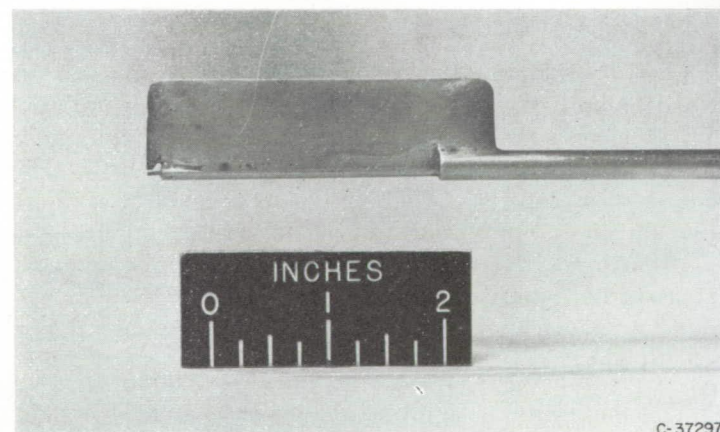
The photomultiplier unit consisted of a 931A photomultiplier vacuum tube with a fixed-plate voltage supply. The ionization-gap probe is shown in detail in figures 4(c) and (d). The brass fairing along the probe tip prevented



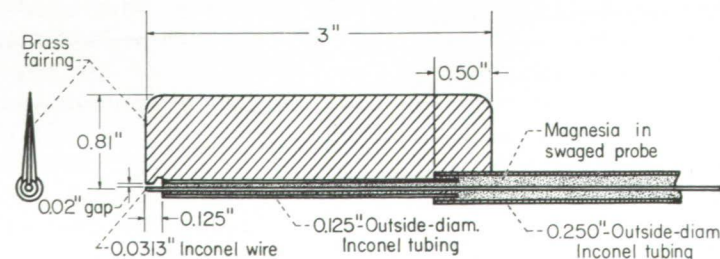
(b) Instrumentation.



(a) Over-all view of installation.



(c)



(d)

(c) Ionization-gap probe.

(d) Construction details of ionization-gap probe.

FIGURE 4.—Ionization-gap instrumentation for measurement of free-flame growth in free-jet installation.

flame seating on the probe both by flame quenching and by elimination of the recirculation zone. Because of the convoluted form of each flame globule, the voltage signal from the ionization gap usually contained multiple peaks, which caused spurious counts in the flame counter. In order to smooth these peaks, resistors, capacitors, and diodes were included in the 360-volt direct-current battery circuit for the ionization gap.

In order to prevent spurious counts arising from small fluctuations in the voltage signal from both the photomultiplier unit and the ionization-gap probe, a long time constant was included in the flame-counter design. These flame counters employed thyratron-controlled relays and solenoids which actuated a mechanical counter.

Photomultiplier instrumentation.—Simultaneous measurements of the spark light intensity and ensuing free-flame-globule growth were made in the free-jet installation with the photomultiplier instrumentation shown in figure 5. The photomultiplier unit consisted of a 931A photomultiplier tube with an adjustable-plate voltage supply. Light emitted from the spark and ensuing flame passed through the narrow slit to the photomultiplier unit. The voltage signal from the photomultiplier unit was recorded on 35-millimeter film from an oscilloscope trace. The photomultiplier instrumentation and the assumption required to relate output voltage to flame speed are discussed in appendix C.

PROCEDURE

The test schedule was as follows:

Grid, in.		Stream velocity, U , ft/sec	Propane-air weight ratio	Distance downstream of grid, x , in.
Wire diam.	Mesh			
Free jet				
0.125	0.625	35 to 105	0.07	15.2 to 16.2
.125	.625	70	.056 to .090	15.2 to 16.2
.063	.313	70	.058 to .084	15.2 to 16.2
.0313	.156	70	.053 to .084	15.2 to 16.2
Enclosed tunnel				
0.125	0.625	35 to 140	0.045 (approx.)	6.3 to 15.3

ENCLOSED-TUNNEL INSTALLATION

Room air was supplied to the enclosed tunnel and exhausted at critical flow through an exit choke by means of the altitude exhaust facility. Tunnel static pressures and temperatures were measured by manometers and thermocouple rakes as shown in figure 1(a). Fuel was injected into the airstream and metered through a standard rotameter, after which dilution air was admitted downstream of the choke. The tunnel stream velocity was then measured with a Pitot-static probe and micromanometer.

The sequential schlieren photographs of the propagation of the free-flame globule in the fuel-air mixture were obtained by actuating a single switch which synchronized the following operations: fuel shutoff (producing a semi-infinite fuel slug),

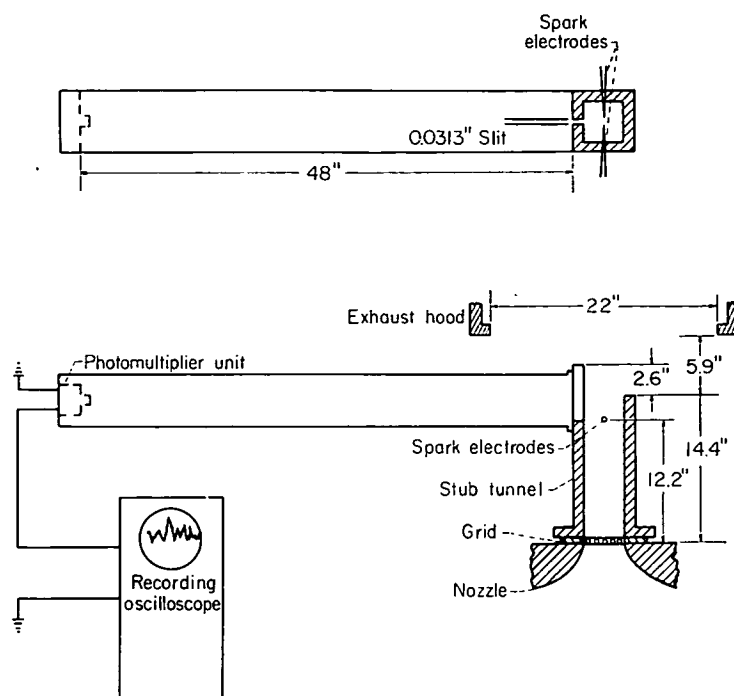


FIGURE 5.—Photomultiplier instrumentation for simultaneous measurement of free-flame growth and spark light intensity.

camera start, ignition by a single spark, and camera stop after an appropriate interval.

FREE-JET INSTALLATION

An exhaust airflow rate of approximately 500 pounds per minute was initiated, and dilution air was admitted to the hood. Laboratory pressurized air and propane were admitted into the stub tunnel, after which the fuel-air ratio was adjusted to the desired value by means of a probe and the NACA mixture analyzer; the stream velocity was determined from Pitot-tube measurements.

The ionization-gap probe was positioned at a station x downstream of the spark electrodes and at a radial distance r from the tunnel centerline. A series of flame globules was initiated by the ignition system, firing at the rate of 3 sparks per second. The number of flame globules N_p intercepting the ionization-gap probe and the total number of flame globules ignited N_t were read from instrumentation shown in figure 4(b).

FLOW-FIELD MEASUREMENTS

In order to check the uniformity of the flow field, velocity profiles were measured in both the enclosed-tunnel and free-jet installations. The mean stream velocity for both installations was essentially constant over the core of interest, as shown by figure 6. Similar measurements were made to check the uniformity of the propane-air ratio in both installations. The propane-air ratio was found to be constant over the major portion of the enclosed-tunnel flow field, and typical profiles measured in the free-jet installation are shown in figure 7.

In order to establish the characteristics of the turbulent field, extensive measurements of the turbulence intensity $\sqrt{u^2}$, the spectrum function F , and the correlation coefficient f were made in both the enclosed-tunnel and the free-jet

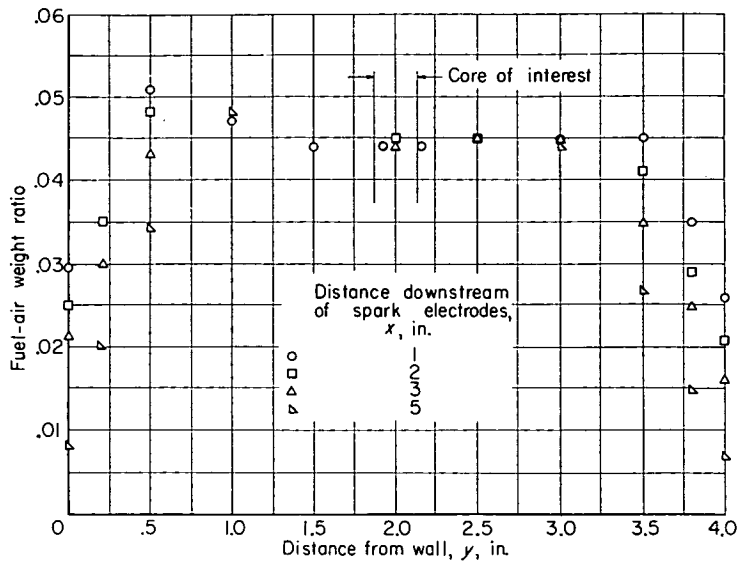


FIGURE 7.—Typical fuel-air-ratio profiles in free-jet installation.

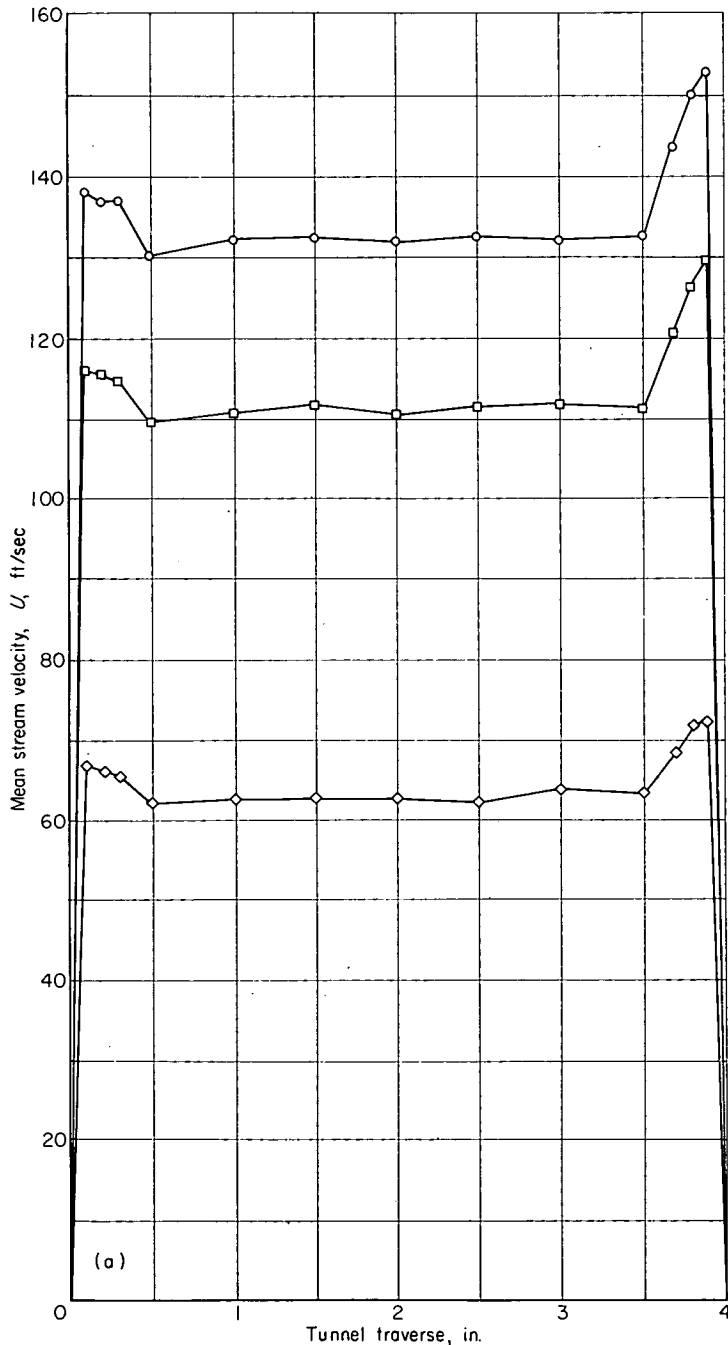
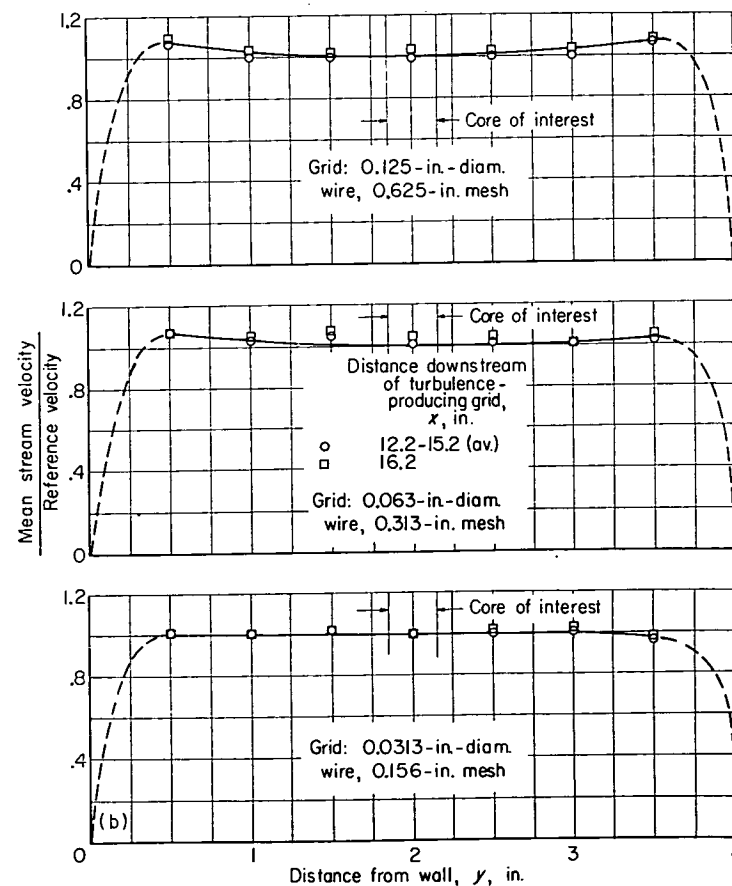


FIGURE 8.—Longitudinal turbulence intensity measured in enclosed tunnel installation.

installations. The definitions of these quantities and the instrumentation used to measure them are discussed in appendix B.

ENCLOSED-TUNNEL TURBULENCE MEASUREMENTS

Longitudinal turbulence intensity measurements made in the enclosed-tunnel installation are shown in figure 8. The data shown in the figure agree well with the von Kármán



(a) Enclosed-tunnel installation. Measured 10.75 inches downstream of grid of 0.125-inch-diameter wire by 0.625-inch mesh.
 (b) Free-jet installation. Reference velocity equals velocity at $y=0.5$ inch and $x=1.0$ inch downstream of spark electrodes.

FIGURE 6.—Typical mean-stream velocity profiles.

data quoted in reference 15 and show a substantial decrease in turbulence intensity from the electrode position ($x/d=50$) to the end of the flame-growth observation field ($x/d=122$). Longitudinal intensity profiles measured in the tunnel centerplane perpendicular to the observation plane were essentially flat over the core of interest. Turbulent energy spectra were measured in the enclosed-tunnel installation as described in appendix B. The scale of turbulence was estimated by comparison of experimental data with a grid of spectrum density curves based on an exponential form of the longitudinal correlation coefficient $f=\exp(\xi/L_T)$. A typical measured spectrum is shown in figure 9, and the estimated turbulence scales are listed in table I.

FREE-JET TURBULENCE MEASUREMENTS

Conversion of the enclosed tunnel to a free jet resulted in an intense sound field originating in the dilution air and exhaust hood and piping. As described in reference 16, velocity fluctuations associated with sound waves contribute to the hot-wire-anemometer measurements through the relation

$$\sqrt{u^2} = \sqrt{u_r^2 + u_s^2} \quad (3)$$

with the assumption that no correlation exists between the turbulence and sound velocity fluctuations. In order to determine the applicability of equation (3) in the free jet, longitudinal velocity fluctuation intensities were measured both with and without the intense sound field. These measurements are shown in figure 10 for each of the three turbulence grids used in the investigation. The velocity fluctuation intensity was definitely increased with the presence of the sound field for each of the three turbulence-generating grids.

The sound pressure level in the free jet was measured with the instrumentation described in appendix B and was found to be 136 decibels, which corresponds to a sound velocity

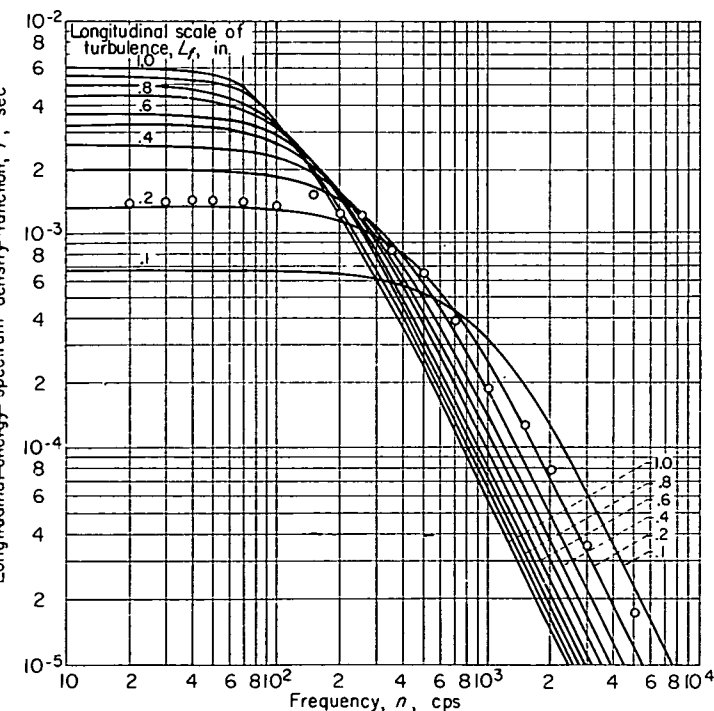


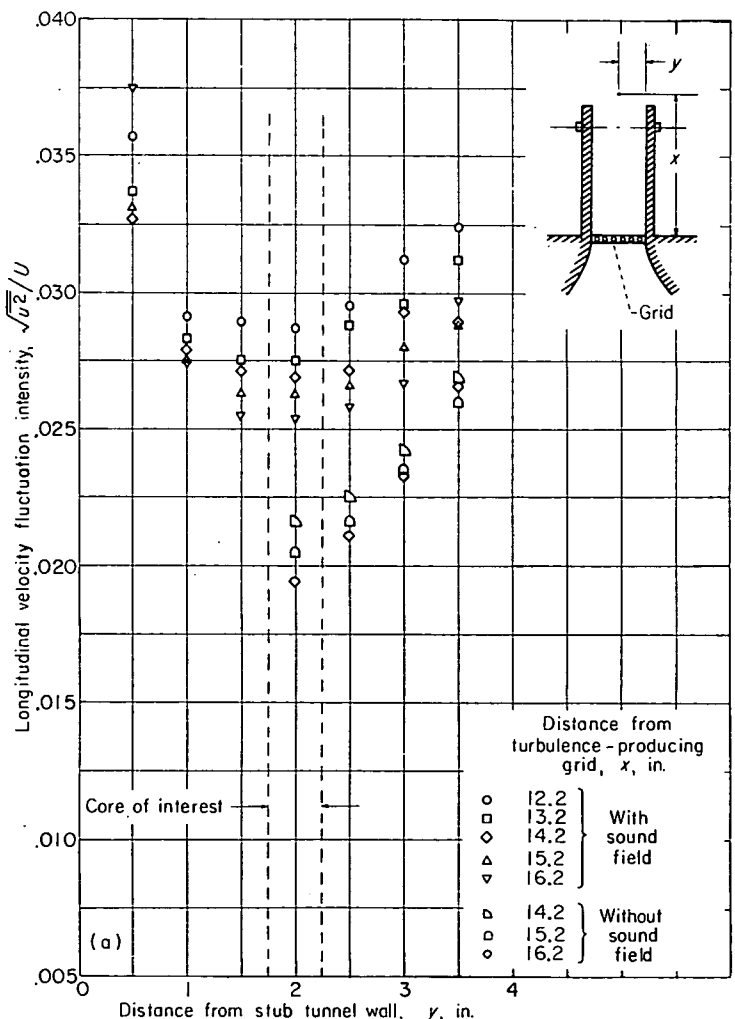
FIGURE 9.—Typical longitudinal energy spectrum of turbulence in enclosed-tunnel installation. Mean stream velocity, 50 feet per second.

fluctuation $\sqrt{u_s^2}$ of 0.96 foot per second. Values of the sound velocity fluctuation $\sqrt{u_s^2}$ were also calculated from the data of figure 10 by the use of equation (3). These values of $\sqrt{u_s^2}$ are compared in table II with the value of $\sqrt{u_s^2}$ corresponding to the sound pressure level of 136 decibels; good agreement is shown in every case.

The kinetic-energy spectrum of the sound field alone is shown in figure 11; it has a generally continuous form with peaks, or periodicities, at 57, 110, 140, 170, 230 to 285, 600 to 870, 1050, 1500, 2400, 3000, 4000 to 5600, and 7000 to 9000 cycles per second. Periodicities observed in the sound spectrum were generally found again in the longitudinal velocity fluctuation energy spectra measured in the free-jet installation, as shown by the typical spectrum in figure 12.

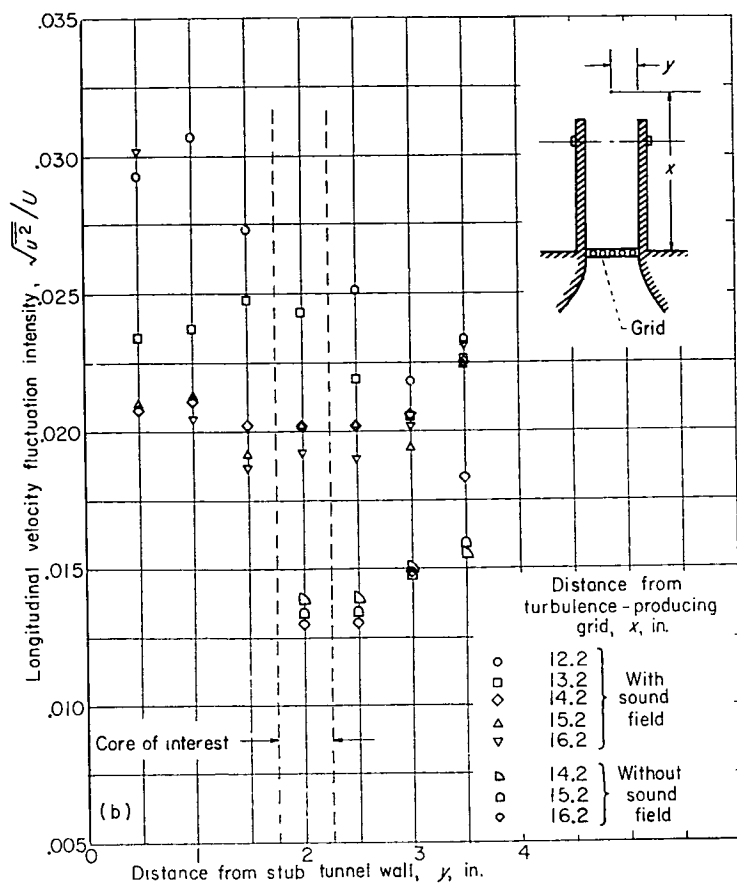
Longitudinal double-velocity correlation coefficients f measured in the free-jet installation are shown in figure 13 for each of the three turbulence-producing grids. The irregular form of the correlation-coefficient curves is attributed to the periodic nature of a considerable portion of the velocity fluctuations. The correlation coefficients were measured by the special methods described in appendix B and are defined by the relation

$$f = \frac{\overline{u_o u_\xi}}{u^2} \quad (4)$$

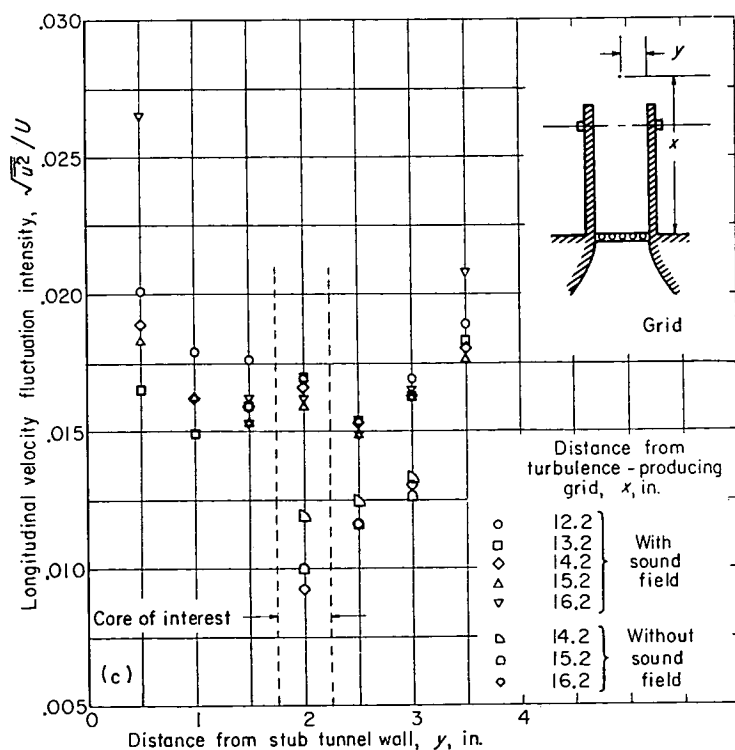


(a) Grid: 0.125-inch-diameter wire, 0.625-inch mesh.

FIGURE 10.—Longitudinal velocity fluctuation intensity in free-jet installation.



(b) Grid: 0.063-inch-diameter wire, 0.313-inch mesh.



(c) Grid: 0.0313-inch-diameter wire, 0.156-inch mesh.

FIGURE 10.—Concluded. Longitudinal velocity fluctuation intensity in free-jet installation.

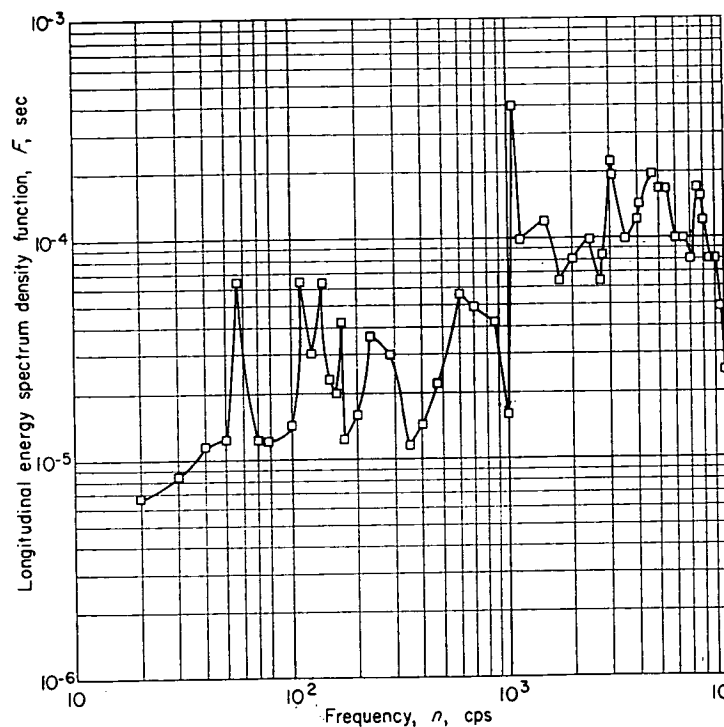


FIGURE 11.—Longitudinal kinetic-energy spectrum of free-jet sound field.

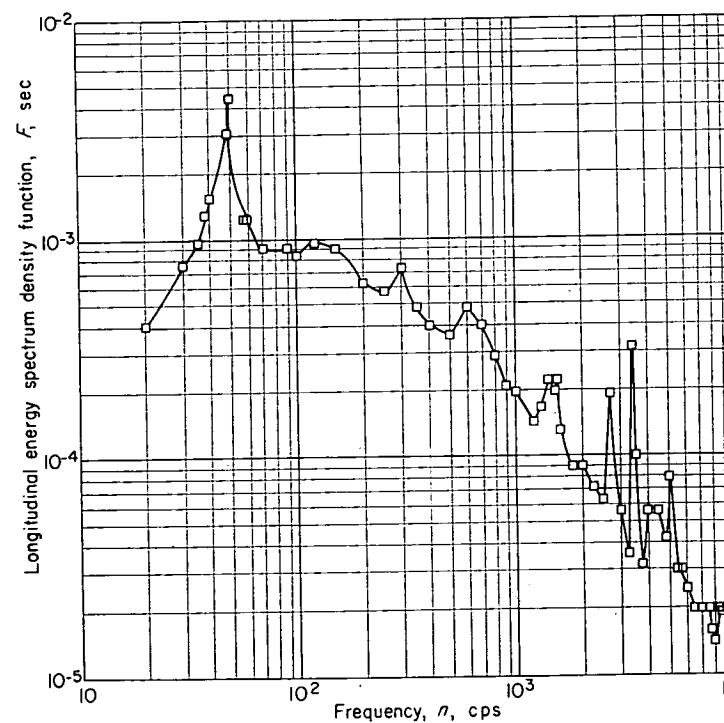
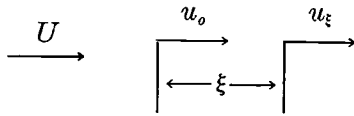


FIGURE 12.—Typical longitudinal velocity fluctuation energy spectrum measured in free-jet installation. Grid: 0.125-inch-diameter wire, 0.625-inch mesh; distance downstream of spark electrodes, 4 inches; mean stream velocity, 68.5 feet per second; static pressure, 29 inches of mercury absolute; static temperature, 545° R.

where the symbols are defined by the following vector diagram:



The longitudinal turbulence scale is usually defined by the relation

$$L_f = \int_0^{\infty} f d\xi \quad (5)$$

Because of the periodic nature of the combined turbulence and sound fields, the longitudinal correlation coefficient did not approach zero within the range of measurement. Therefore, equation (5) could not be used to define the turbulence scale. Since the growth of the flame globule was observed over times comparable with ξ of 0.1 inch, only the first portions of the correlation curves shown in figure 13 were considered relevant to the experiment. As a part of the calculations involved in the Scurlock-Grover analysis, values of the lateral scale of turbulence L_g were calculated as described in appendix D. These calculated values of L_g are listed in the table in the RESULTS section.

DETERMINATION OF FLAME SPEED

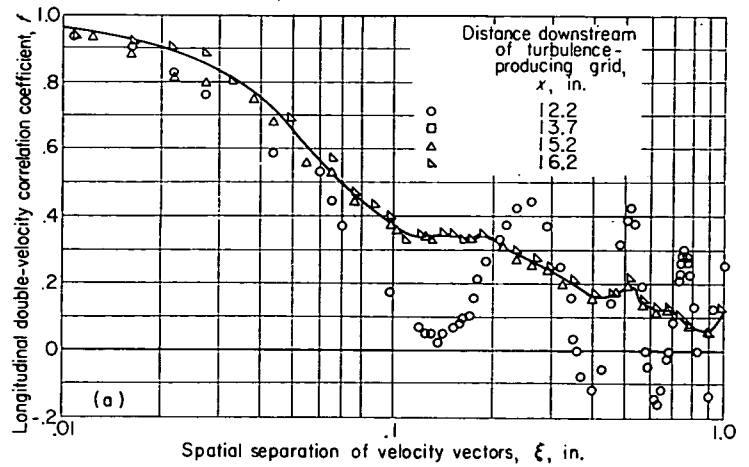
FUNDAMENTAL CONSIDERATIONS

The relation between flame speed and free-flame-globule expansion rate is derived in reference 13 for a constant-pressure laminar free flame propagating in a quiescent fuel-air mixture. This relation was obtained by equating the mass flow of the unburned gases entering a flame front of infinitesimal thickness to the mass flow of the burned gases leaving the flame front. In a physical sense, equation (2) accounts for both the flame-front motion due to flame propagation and the motion due to thermal expansion of the burned gases. The following modification of this equation to account for a finite flame-front thickness δ is presented in reference 14:

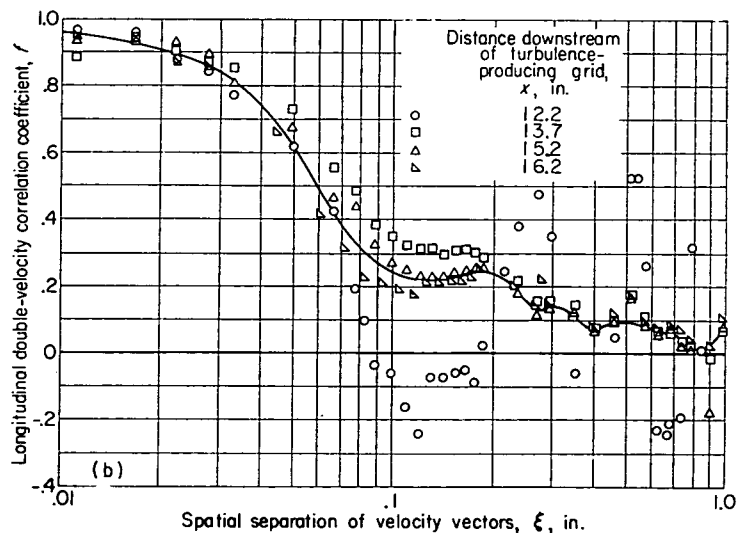
$$S_T = \frac{\rho_F}{\rho_a} \frac{dr}{dt} \left(\frac{r - \delta/2}{r + \delta/2} \right)^2 \quad (6)$$

For this investigation, the thickness of the flame front was considered negligible compared with the radius r so that equation (2) was used to analyze the data. The values of ρ_a , computed from R_a and T_a , were obtained from measurements of tunnel approach-stream flow. The values of ρ_F , computed from R_F and T_F for each fuel-air ratio, were taken from references 17 and 18, respectively. The value of ρ_F/ρ_a varied from 0.12 to 0.14 in the present investigation. A number of assumptions are necessary to the definition of effective turbulent flame speed as given by equation (2). The definition requires that—

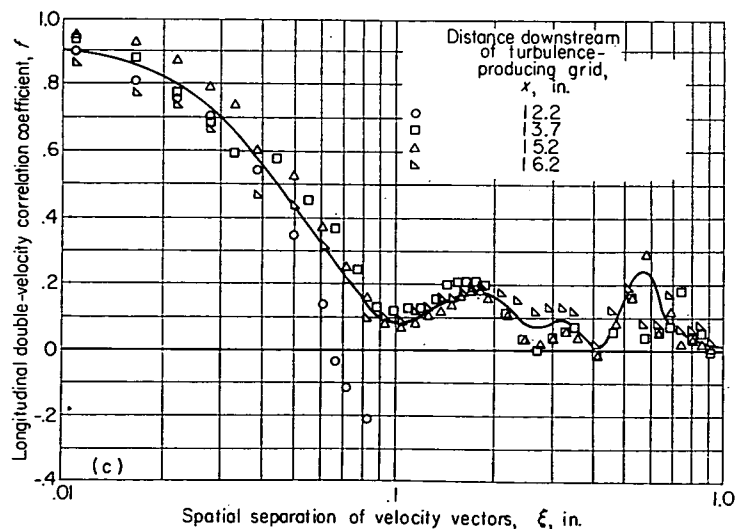
- (1) The free-flame globule grow uniformly in all radial directions
- (2) The combustion proceed in a constant-pressure field



(a) Grid: 0.125-inch-diameter wire, 0.625-inch mesh.



(b) Grid: 0.063-inch-diameter wire, 0.313-inch mesh.



(c) Grid: 0.0313-inch-diameter wire, 0.153-inch mesh.

FIGURE 13.—Longitudinal double-velocity correlation coefficients measured in free-jet installation. Mean stream velocity, 68.5 feet per second.

- (3) The flame globule be swept downstream at the stream velocity
- (4) No circumferential flow exist about the flame globule
- (5) Variations in spark energy not affect the globule propagation rate

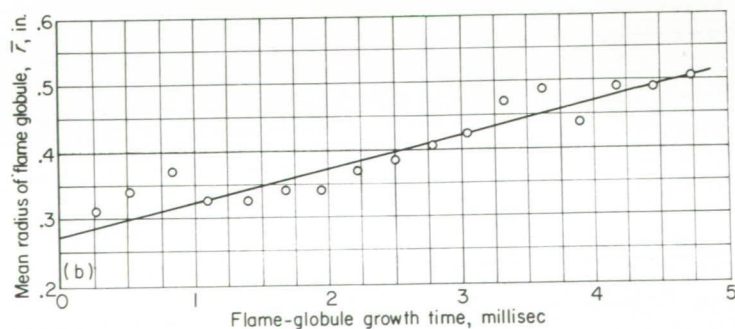
The validity of the assumptions was established by special tests described later in this section.

PHOTOGRAPHIC METHOD

Photographic data obtained in the enclosed tunnel were analyzed by projecting the 16-millimeter motion-picture film record of each flame-globule expansion onto a film viewer. A typical photographic record is shown in figure 14(a). The outline of each globule was traced in order to permit planimetering its area and calculating a mean radius. The mean radius was plotted against time for each flame globule of the sequence, as shown in figure 14(b).



(a) Typical photographic record. Film speed, approximately 3600 frames per second.



(b) Flame-globule expansion history.

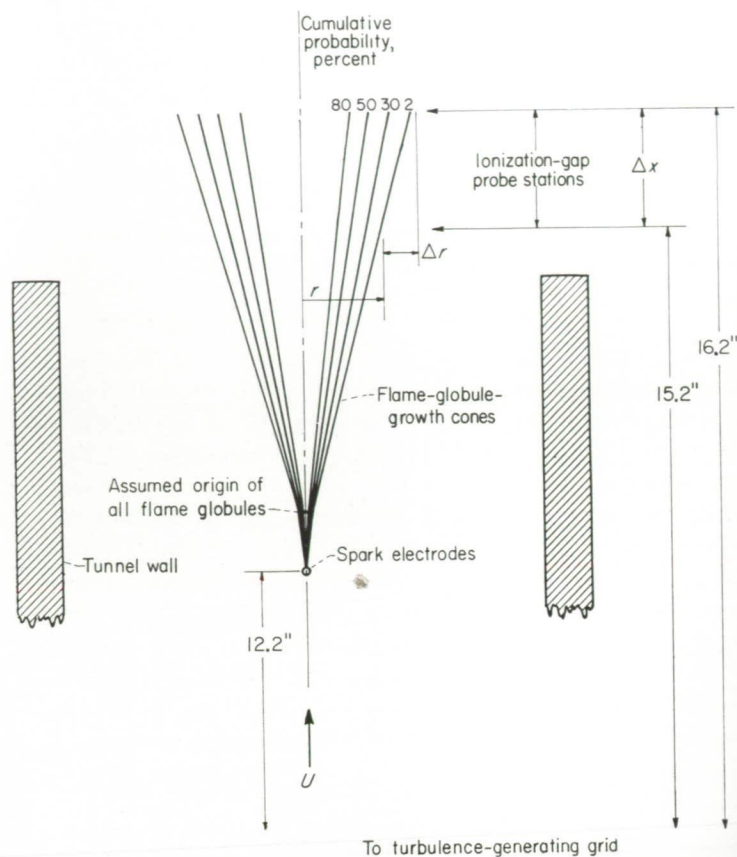
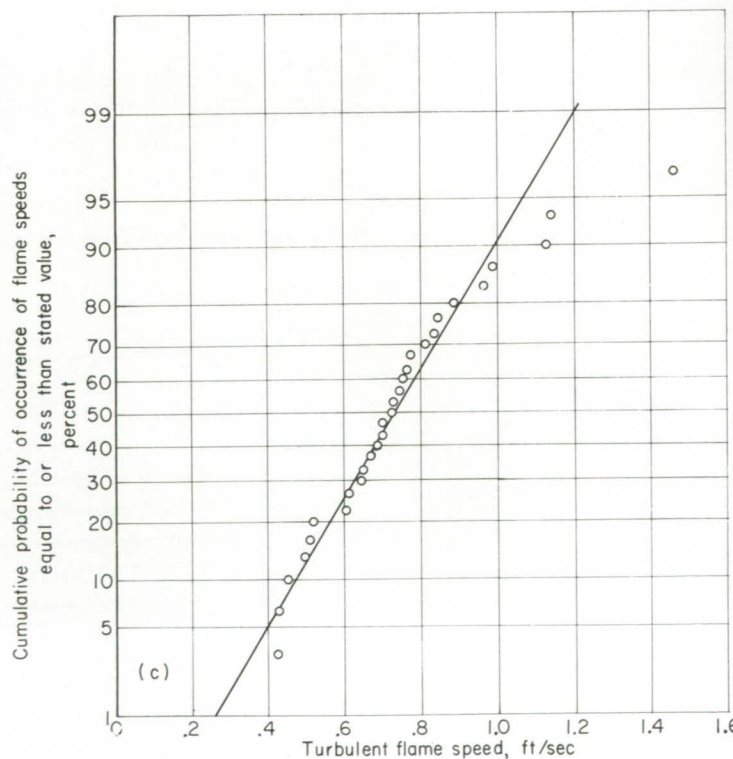


FIGURE 15.—Flame-globule-growth measurement with ionization-gap instrumentation. $S_T = \frac{\Delta r}{\Delta x/u} \frac{R_a T_a}{R_f T_f}$



(c) Cumulative probability of turbulent flame speed. Mean stream velocity, 60 feet per second; propane-air ratio, approximately 0.04 by weight; static pressure, 26 inches of mercury absolute; temperature, 540° R.

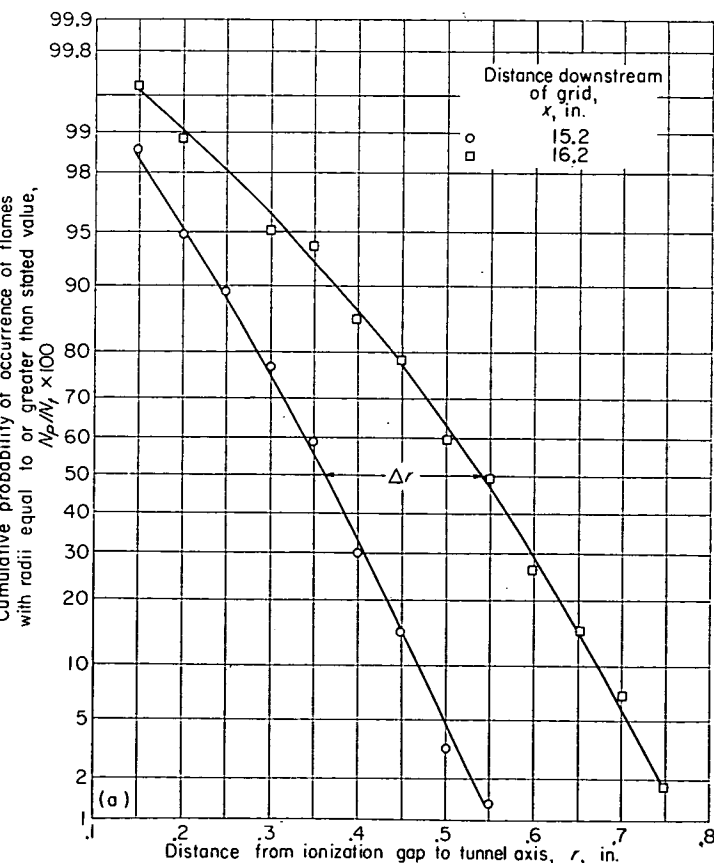
FIGURE 14.—Typical turbulent-flame-speed data from enclosed-tunnel installation.

The slope of a straight line faired through such a series of experimental points is dr/dt . The effective turbulent flame speed was then calculated by multiplying dr/dt by the expansion factor ρ_F/ρ_a , as shown in equation (2).

From sets of 30 or more flame speeds obtained in this manner for identical fuel-air flow conditions, the cumulative probability of occurrence of flames having these flame speeds was calculated. In order to illustrate the statistical nature of these data, the turbulent flame speeds of a typical set of data have been plotted against cumulative probability of occurrence in figure 14(c). Each datum point represents the effective flame speed of a single free flame. Cumulative probability of occurrence is defined as the percentage of flames having flame speeds greater than a given value.

IONIZATION-GAP METHOD

In order to obtain a set of turbulent flame speeds for a particular condition of turbulent approach-stream intensity and fuel-air ratio in the free-jet installation, the ionization-gap probe was positioned consecutively at two stations $x=15.2$ and 16.2 inches, as outlined diagrammatically in figure 15. For each chosen position r , at least 1000 flames N_t were ignited. The ionization-gap counter recorded the number of flames N_p intercepting the probe. The ratio N_p/N_t was the cumulative probability of a flame globule having a radius at least as great as that indicated by the probe setting r . The ratio N_p/N_t was then plotted on probability coordinates against r and a curve was faired through



(a) Fuel-air ratio, 0.056; mean stream velocity, 68.3 feet per second.

each of the two sets of data as shown in figure 16. The difference Δr was obtained from the curves for the cumulative probabilities of 2, 20, 50, 80, and 98 percent. Equation (2) was then employed to determine the flame speeds corresponding to the five probability percentages.

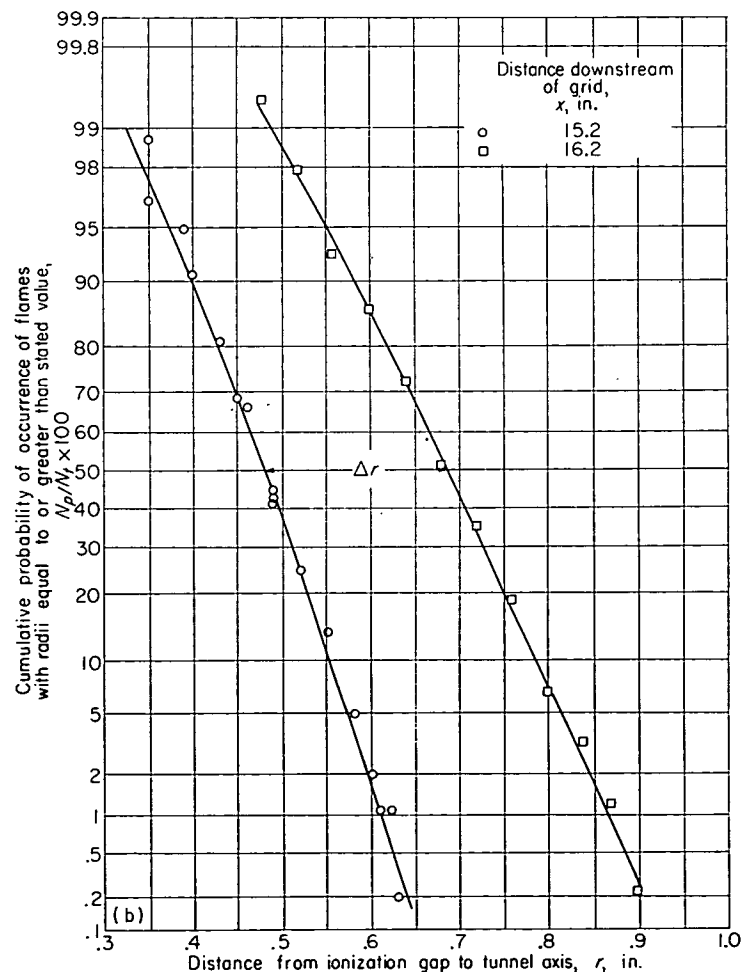
PHOTOMULTIPLIER METHOD

The photomultiplier method was used to obtain values proportional to the effective flame speed. The method essentially consists of measuring the free-flame-globule growth rate along the axial diameter of the globule. The method is described in the APPARATUS section and in appendix C. The instrumentation is shown in figure 5.

VERIFICATION OF EXPERIMENTAL METHOD

The discussion of equation (2) in a preceding section includes a number of assumptions necessary to the derivation of the equation. Since equation (2) essentially expresses the experimental method used in the investigation, the assumptions were verified by tests that are described in the following paragraphs.

Uniformity of globule growth.—Photographic data of the flame-globule growth in the enclosed tunnel were analyzed to determine whether the globules had preferential growth directions. This analysis was made by measuring globule



(b) Fuel-air ratio, 0.070; mean stream velocity, 69.6 feet per second.

FIGURE 16.—Typical cumulative probability of flame-globule size measured with ionization-gap instrumentation in free-jet installation. Grid: 0.125-inch-diameter wire, 0.625-inch mesh; static pressure, 29.3 inches of mercury absolute; static temperature, 545° R.

diameters (see fig. 17) at four angles of rotation from the tunnel axis. While each globule had different growth rates along the four diameters, no consistent relation between growth rate and direction was found. This observation supports the use of a mean radius in the photographic method of flame-speed measurement, the use of a single radial direction in the ionization-gap method, and the use of a single diameter in the photomultiplier method of flame-growth observation.

Pressure pulsations.—In order to determine whether the fluctuations in flame-globule-growth rates, illustrated by figure 14(b), were due to pressure fluctuations in the enclosed tunnel, data as shown in figure 17 were inspected for possible phase relations between the fluctuations in growth rate along the four diametral directions. Since no frequency-phase relation was found from these data, it was concluded that pressure fluctuations were not responsible for the fluctuations in globule-growth rate. Additional measurements with a wall-mounted pressure pickup indicated the absence of significant pressure pulsations in the enclosed tunnel.

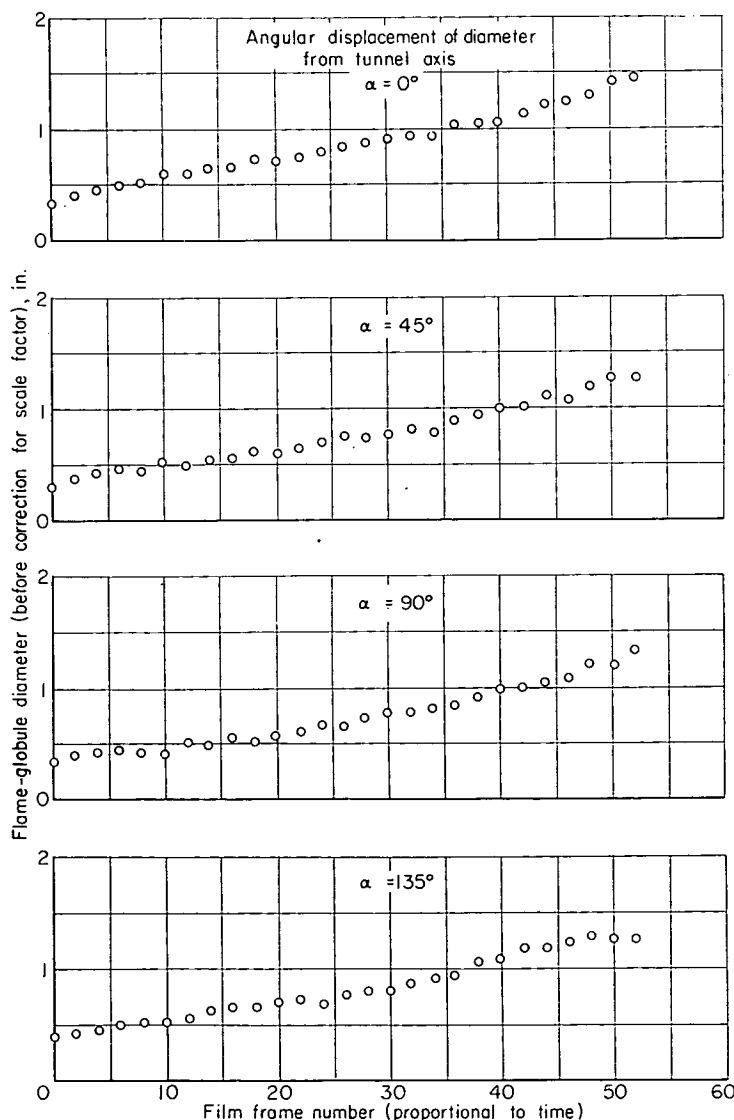


FIGURE 17.—Typical flame-globule-diameter histories measured in enclosed-tunnel installation.

Axial velocity of flame globule.—The effect of buoyancy of the hot flame globule on its axial velocity was determined by measuring the distance from the spark electrodes to the globule center on each frame of photographic sequences such as shown in figure 14(a). The axial velocities calculated from such measurements agreed closely in all cases with the measured stream velocity, which indicated that the buoyancy effect was negligible.

Unburned-gas motion.—As shown by equation (2), the rate of thermal expansion of the flame globule is from 7 to 8 times as great as the effective turbulent flame speed. In order to determine whether the unburned-gas motion caused by this thermal expansion was purely radial (from the globule center), simultaneous oscillograph records were made in the free-jet installation with the ionization-gap probe and a shielded hot-wire-anemometer probe as shown by the typical oscillograph and probe position diagram in figure 18. The ionization-gap trace indicated the flame globule passage, and the anemometer trace was proportional to the instantaneous stream velocity. Inspection of 60 such records indicated no axial change in mean stream velocity and therefore no circumferential flow of unburned gases about the sphere. The marked decrease in amplitude of velocity fluctuations at the time of flame-globule passage is interpreted as being due to the radial translation of the free-jet stream core by the thermal expansion of the flame globule.

Effect of spark energy.—In order to determine the effect of spark energy on the flame-globule growth, two series of runs were made in the free-jet installation under identical stream and fuel conditions but with spark source energies differing by a factor of 2.5. As shown in figure 19, cumulative probabilities of flame-globule sizes were measured at a series of axial positions with the ionization-gap instrumentation for the two spark source capacitors of 0.0004 and 0.0010 microfarads. The data of figure 19 show an increase in initial flame-globule size, but no change in turbulent flame speed between the axial positions $x=15.2$ and 16.1 inches.

Effect of spark light intensity.—Additional information on the relation between the spark characteristics and the flame globule growth was obtained with the photomultiplier in

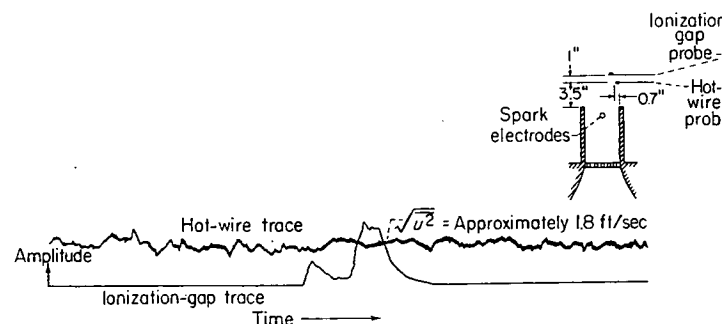


FIGURE 18.—Typical oscillograph of ionization-gap and hot-wire signals in free-jet stream at time of flame-globule passage. Grid, 0.125-inch-diameter wire, 0.625-inch mesh; stream velocity, 70 feet per second; static pressure, 29 inches of mercury absolute; temperature, 80° F.

umentation shown in figure 5. With this instrumentation, oscillographs were obtained in a free-jet installation showing spark light intensity and flame light intensity as a function of time for 151 consecutive flame globules at constant mean stream and fuel conditions. Typical oscillographs obtained by this method are shown in figure 20. As shown in appendix C, the portion of the trace due to the spark light intensity was proportional to spark current, and statistical analysis of the magnitudes of the peak spark light intensity indicated that this parameter approximated normal probability distribution. The flame speed of the globule was taken as proportional to the slope of the portion of the oscillograph trace due to flame light intensity, as discussed in appendix C.

The group of 151 consecutive runs is shown in figure 21, in which peak spark light intensity is plotted against flame speed for each particular flame globule. The statistical correlation coefficient for this data was determined with Pearson's product moment formula (ref. 19) and was found to have an absolute value of $|0.17|$ for a possible range of zero to $|1.0|$. The low value of the statistical correlation coefficient is interpreted to indicate that variations in spark current had no effect on turbulent flame speed.

Additional verification of statistical variation of turbulent flame propagation.—The cumulative probability of occurrence of slopes measured from the series of 151 photo-

multiplier oscillographs is shown in figure 22. The statistical distribution of flame speeds measured by this method is interpreted as additional proof of the randomness of the phenomena.

Validity of common-origin assumption.—The ionization-gap method, described earlier in this section, assumes that all flame globules have a common origin point, as shown in figure 15. In order to determine the error introduced by this assumption, "origin points" were measured from the series of 151 photomultiplier traces by extrapolating the slope of the flame light intensity trace to the time axis, as shown in figure 20. The origin points showed a statistical deviation in position, and the theoretical error introduced into flame speeds determined by the ionization-gap method

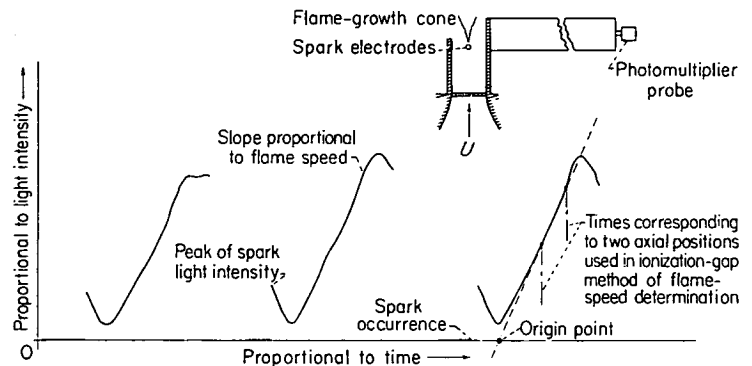


FIGURE 20.—Typical oscillographs of photomultiplier probe trace depicting spark occurrence and growth of flame globule in free-jet stream.

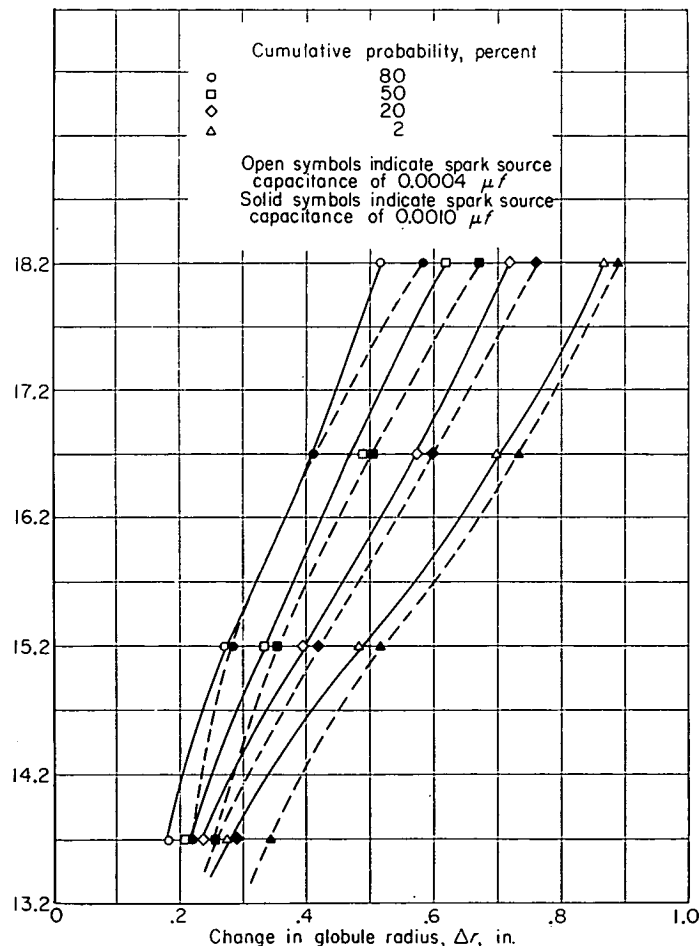


FIGURE 19.—Effect of spark source energy on flame-globule growth.

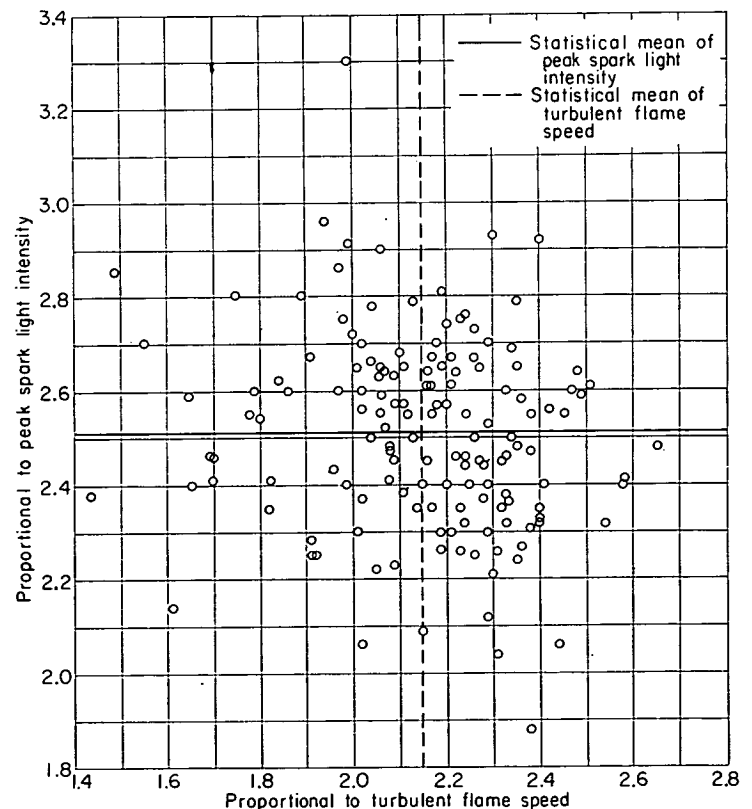


FIGURE 21.—Correlation between spark light intensity and turbulent flame speed for 151 consecutive flame globules at identical mean stream and fuel conditions.

was calculated to be ± 2.5 percent or less, within one standard deviation of origin positions. The error in flame speed due to shift in origin point is small compared with the deviations in flame speed actually measured by the photographic (fig. 14(c)), the ionization-gap, and the photomultiplier-tube methods (fig. 22).

PRECISION OF DATA

Ionization-gap measurements.—Each datum point plotted as cumulative probability against flame radius, such as shown in figure 16, represents information from at least 1000 flames. As shown in reference 20, samples consisting of 1000 flames

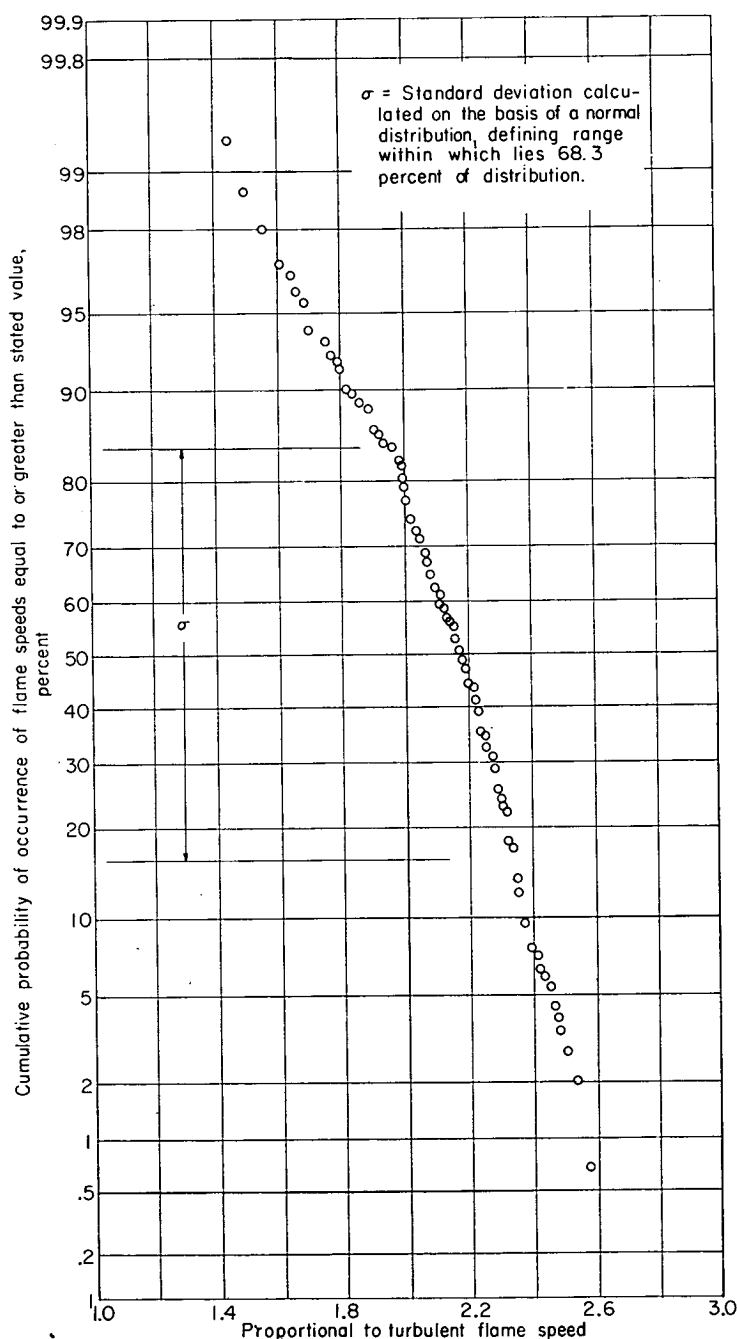


FIGURE 22.—Statistical variation of flame speed as determined from photomultiplier oscillograms.

would have the following accuracy in the cumulative probability value:

Cumulative probability, percent	Possible error, percent
50	± 5
20	± 7
2	± 29

The possible errors listed correspond to 1.28 standard deviations of the error distribution and therefore should hold 80 percent of the time. The general consistency of the data throughout the lower probability region such as shown in figure 16 seems to justify greater confidence in the lower cumulative probability range than that shown in the preceding table.

The reliability of the curves faired through the plotted experimental data, such as presented in figure 16, may be estimated from the deviation of data points from the fitted curves.

The greatest divergence was found in results for the 0.125-inch-diameter wire. For the 98-percent probability level the maximum data scatter from a faired curve was 20 percent; for the 50-percent level, 7.8 percent; and for the 2-percent level, 3 percent. The maximum scatter for the 0.063-inch-diameter wire was 5.3 percent at 98-percent probability, and for the 0.0313-inch-diameter wire, it was 1.5 percent at the 98-percent level.

As discussed earlier in this section, the value of flame temperature used in the equation for turbulent flame speed was a calculated theoretical value. It may be of interest to note that flame temperature has a much greater effect on the laminar flame speed than on the calculation leading to effective turbulent flame speed. As shown by reference 21, a decrease of theoretical adiabatic flame temperature from 4000° to 3900° R would result in a laminar flame speed decrease of 43 percent. In contrast, this change in flame temperature would cause only a 2.5-percent decrease in the turbulent flame speed calculated from equation (2). It appears, then, for the purpose of this investigation, that the effect of a small error in actual flame temperature is negligible in calculating the density ratio.

Other sources of inaccuracy may be found in the instrumentation and equipment. The positioning of the ionization gap probe involved an error not exceeding 0.5 percent. Measurement of the fuel-air ratio was accurate within 1 percent. Flow measurements were made with a precision of 3 percent. For the measurements characterizing the turbulence parameters, an estimated value of ± 5 percent is suggested for the probable limit of error.

Photomultiplier method.—A treatment of the sources of error present in flame-speed measurement by the photomultiplier method is presented in appendix C.

Photographic method.—In addition to the errors introduced by the equipment and instrumentation, sources of error peculiar to the photographic method must be considered. Such factors as adjustment of the projected image to one-to-one correspondence, timing, optical resolution, and

scale factor are all considered significant and have been thoroughly treated in reference 22, which assigns a relative maximum error of 10 percent to the photographic-reduction technique.

RESULTS

Effective turbulent flame speeds were measured in the enclosed-tunnel and free-jet installations over a range of propane-air and turbulence conditions as shown in the following table:

Grid, in.		Stream velocity, U , ft/sec	Longitudinal velocity fluctuation intensity, $\sqrt{u^2}$, ft/sec	Lateral turbulence scale, L_s , in.	Propane-air weight ratio	Distance downstream of grid, x , in.
Diam.	Mesh					
Free jet						
0.125	0.625	35 to 105	1.18 to 2.60	0.0645	0.07	15.2 to 16.2
.125	.625	70	1.69	.0645	.056 to .09	15.2 to 16.2
.063	.313	70	1.34	.0587	.058 to .084	15.2 to 16.2
.0313	.156	70	1.17	.0437	.053 to .084	15.2 to 16.2
Enclosed tunnel						
0.125	0.625	35 to 140	0.81 to 3.51	0.08 to 0.13	0.045 (approx.)	6.3 to 15.3

The lateral turbulence scales L_g for the enclosed tunnel were obtained from the values of L_f shown in table I by using equation (B1c) of appendix B. The values of L_g for the free jet were obtained by fitting an exponential curve to the lateral correlation coefficient g as described in appendix D. Both methods for evaluation of L_g are based on the assumption of isotropy, which was not proven because of the lack of turbulence measurements in the lateral direction.

The effective turbulent flame speeds, plotted in figure 23, were measured in the free-jet installation at a fixed propane-air ratio of 0.07 over a range of mean stream velocities with the 0.125-inch wire diameter by 0.625-inch mesh turbulence-generating grid. The data are plotted as a function of longitudinal velocity fluctuation intensity $\sqrt{u'^2}$ with cumulative probability as a parameter. Since turbulence measurements were made at only one stream velocity, and since the sound pressure level was inde-

TABLE I.—SUMMARY OF LONGITUDINAL TURBULENCE SCALES

[Estimated from longitudinal energy spectra in enclosed-tunnel installation. Mean stream velocity, 50 ft/sec; static pressure, 26 in. Hg abs; static temperature, 540° R. Comparative values calculated through the isotropic turbulence relation $L_f = 2L_t$ from lateral scale of turbulence data reported in ref. 15.]

Distance downstream of grid, x , in.	Longitudinal scale of turbulence, L_f , in.	
	Present investigation	Ref. 15
6.3	0.16	-----
9.3	.21	-----
12.3	.25	0.17
15.3	.25	.21

pendent of stream velocity, the data of table II and the following equation were employed to calculate the longitudinal velocity fluctuation intensity:

$$\sqrt{u'^2} = \sqrt{\left[U \left(\frac{\sqrt{u'^2}}{U} \right) \right]^2 + u_s^2} \quad (7)$$

The turbulence intensity $(\sqrt{u'^2}/U)$ was assumed constant throughout the range of stream velocity U (see ref. 15), and u_s corresponded to the measured sound pressure level of 136 decibels.

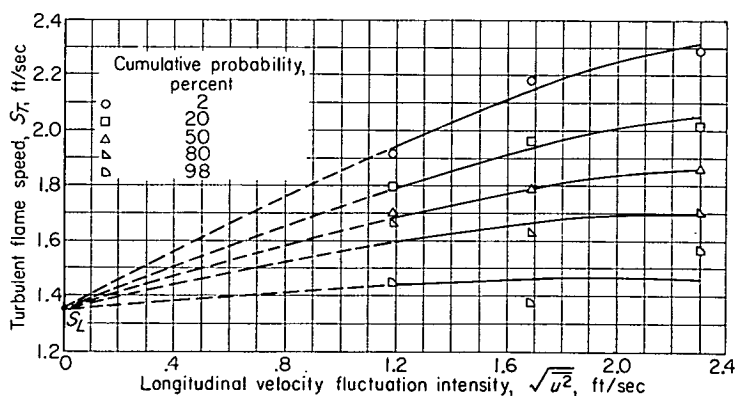


FIGURE 23.—Turbulent flame speed as a function of longitudinal velocity fluctuation intensity with cumulative probability of occurrence as a parameter. Propane-air weight ratio, 0.070; stream static temperature, 545° R; static pressure, 29.3 inches of mercury absolute; grid: 0.125-inch-diameter wire, 0.625-inch mesh; free-jet installation.

TABLE II.—COMPARISON OF VELOCITY FLUCTUATIONS IN TURBULENT STREAM WITH AND WITHOUT INTENSE SOUND FIELD

[Velocity fluctuations measured along duct axis. Measured value of sound pressure level, 136 db; stream velocity, 68.5 ft/sec.]

Grid, in.		Distance downstream of turbulence-producing grid, x , in.	Stream velocity fluctuations, ft/sec		Calculated values of sound field		Measured values of sound field	
Diam.	Mesh		With sound field, $\sqrt{u'^2}$	Without sound field, $\sqrt{u'^2}$	$\sqrt{u_s^2} = \sqrt{u'^2 - u'^2}$, ft/sec	Sound pressure level, db	$\sqrt{u_s^2}$, ft/sec	Sound pressure level, db
0.125	0.625	3	1.81	1.40	1.15	137.5	0.96	136
		4	1.75	1.32	1.15	137.5	.96	136
0.063	0.313	3	1.32	0.926	0.94	135.5	0.96	136
		4	1.41	.892	1.10	137.0	.96	136
0.0313	0.156	3	1.12	0.688	0.89	135.0	0.96	136
		4	1.22	.619	1.05	136.5	.96	136

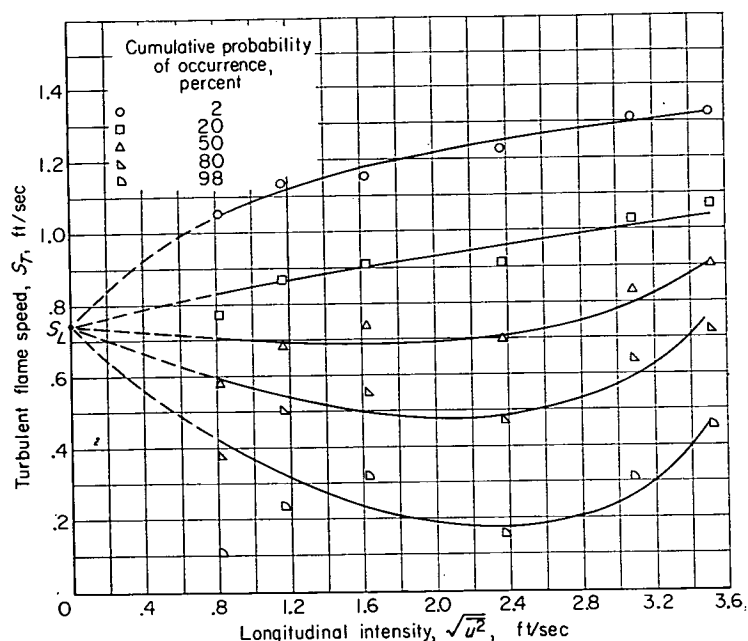


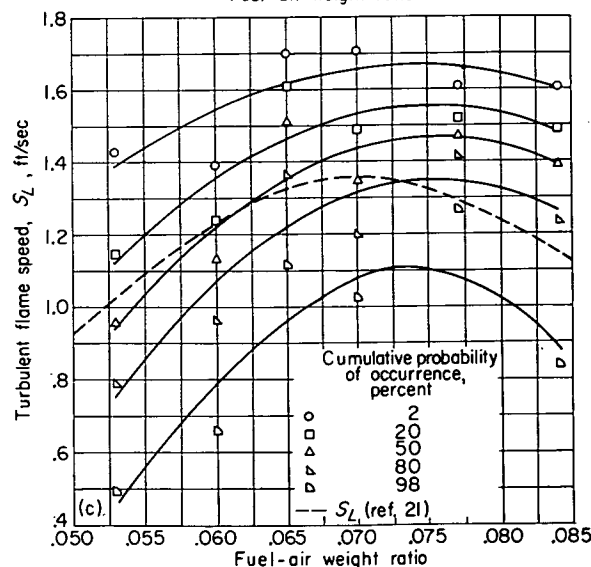
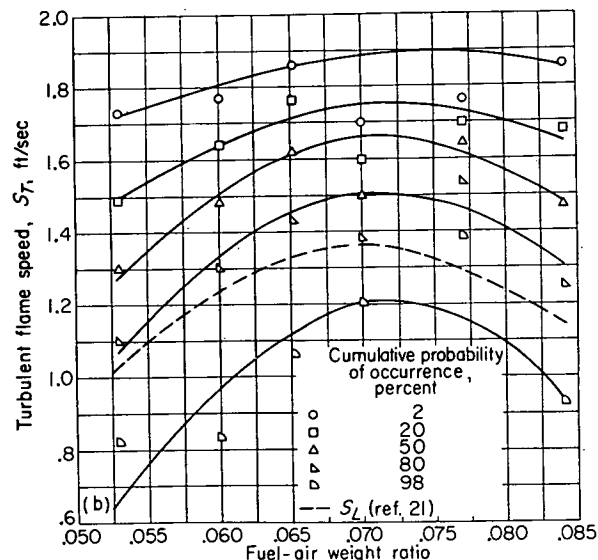
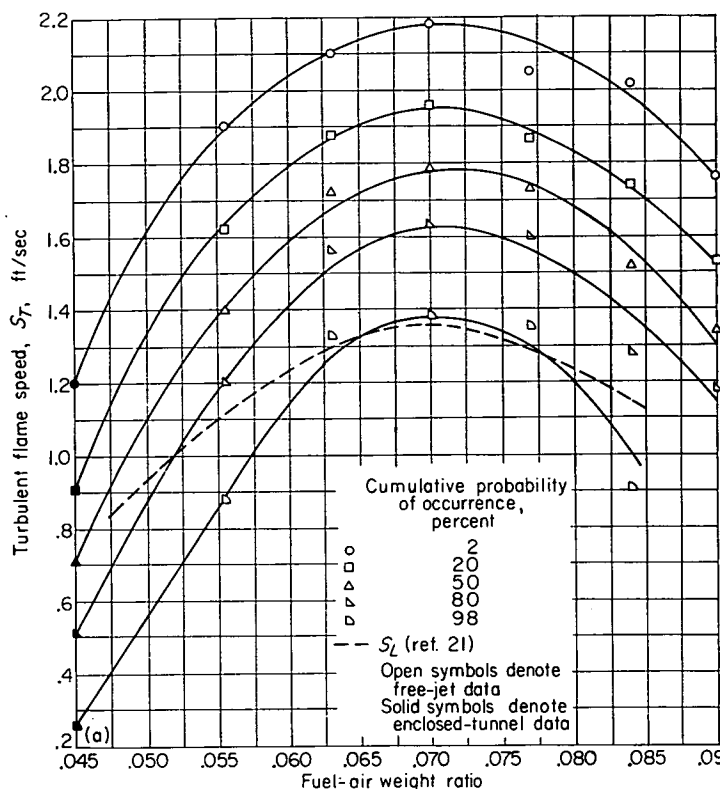
FIGURE 24.—Turbulent flame speed as a function of turbulence intensity. Propane-air weight ratio, approximately 0.045; stream temperature, 540° R; static pressure, 26 inches of mercury absolute; enclosed-tunnel installation; grid: 0.125-inch-diameter wire, 0.625-inch mesh.

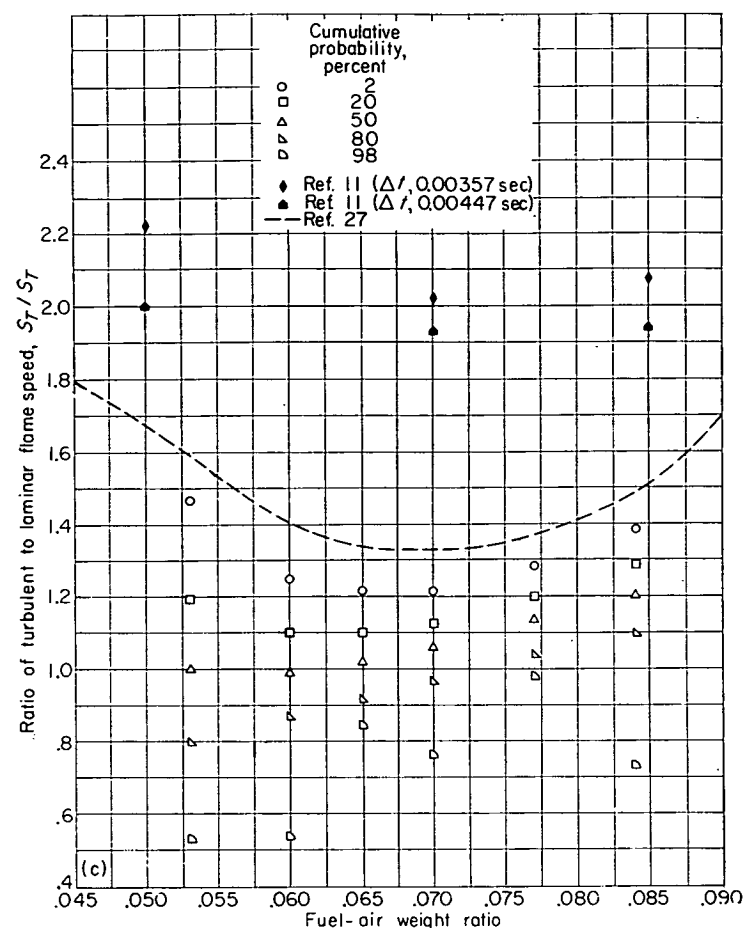
Effective turbulent flame speeds measured in the enclosed-tunnel installation at a fixed propane-air ratio of approximately 0.045 are plotted in figure 24 as a function of the longitudinal velocity fluctuation intensity $\sqrt{u^2}$ with cumulative probability as a parameter. The data show a consistent increase of effective turbulent flame speed with velocity fluctuation intensity. These data were obtained downstream of the 0.125-inch-diameter-wire by 0.625-inch-mesh grid over a range of stream velocities from 30 to 140 feet per second. As shown by the data of figure 8, the decay of the turbulence intensity was quite severe over the range of interest ($x/d=50$ to 122). A turbulence intensity of $(\sqrt{u^2}/U)=0.027$ was taken as a representative value and assumed constant to obtain values of $\sqrt{u^2}$ over the stream-velocity range.

The effects of propane-air ratio and turbulence scale on the propagation rate of the free flame were investigated in the free-jet installation by measuring the turbulent flame speed downstream of the three turbulence-generating grids over a range of propane-air ratio from 0.053 to 0.090. (The variations in turbulence scale are listed in the table at the beginning of this section.) These data are shown in figure 25 along with a dashed line representing laminar flame-speed data reported in reference 21. Turbulent flame speeds from the enclosed tunnel are included in figure 25(a) and were evaluated by interpolating the data of figure 24 at a velocity fluctuation intensity equal to that of the free-jet data in figure 25(a).

- (a) Grid: 0.125-inch-diameter wire, 0.625-inch mesh.
- (b) Grid: 0.063-inch-diameter wire, 0.313-inch mesh.
- (c) Grid: 0.0313-inch-diameter wire, 0.156-inch mesh.

FIGURE 25.—Turbulent flame speed as function of fuel-air ratio with cumulative probability of occurrence as parameter. Mean stream velocity, 70 feet per second; stream static pressure, 1 atmosphere; static temperature, 85° F.





(c) Grid: 0.0313-inch-diameter wire, 0.156-inch mesh.

FIGURE 30.—Concluded. Comparison of turbulent-flame-speed data with theories from references 11 and 27.

The data of the present investigation fall below the values of S_T/S_L predicted by the modified Scurlock-Grover analysis. The data follow the Scurlock-Grover analysis more closely for the largest turbulence scale (fig. 30(a)), and the agreement

becomes progressively worse as the turbulence scale becomes smaller (figs. 30(b) and (c)). This type of relation may be due to an increasing diffusive action of the turbulence as the scale becomes smaller, as discussed previously in this section.

The data agree somewhat better with the Scurlock-Grover analysis than with the Tucker theory in the extremes of the lean and rich fuel-air-ratio regions. This probably is due to the increasing $\sqrt{u^2}/S_L$ in those regions that tend to exceed the limits of the assumptions made in the Tucker analysis discussed in a preceding paragraph.

In summary, values from both the Tucker and the Scurlock-Grover analysis seem to form an upper limit to the data of the present investigation, except in the extremes of the lean and rich fuel-air-ratio regions.

CONCLUSIONS

From the results of the investigation, the following conclusions are made:

1. The propagation rate of a free flame in a turbulent field with intense random sound velocity fluctuations is a statistical variable having a probability of occurrence band bounded by a zero propagation rate and possibly an upper propagation rate well above the laminar flame speed.
2. The propagation rate of a free turbulent flame is substantially less than those previously measured for stabilized flames.
3. The statistical spread of free-flame propagation rates is markedly wider in both the lean and rich fuel-air-ratio regions.
4. Values calculated from the Tucker analysis for free-flame propagation rates apparently form an upper limit for the statistical spread of free-flame propagation rates in the regions where the velocity fluctuation intensity is low.

LEWIS FLIGHT PROPULSION LABORATORY
NATIONAL ADVISORY COMMITTEE FOR AERONAUTICS
CLEVELAND, OHIO, May 7, 1956

APPENDIX A

SYMBOLS

A	cross-sectional area	x	distance downstream of turbulence-producing grid, in.
\bar{A}	smoothed time-average surface area of turbulent flame	y	distance from tunnel wall, in.
B	constant in Shelkin equation	α	angle, deg
C	constant	β	power band width of wave analyzer, cps
D	turbulent diffusion coefficient, sq ft/sec	δ	flame-front thickness, ft
d	wire diameter of turbulence-producing grid, in.	ξ	spatial separation of velocity vectors comprising correlation coefficient, in.
\bar{E}	d-c voltage, v	ρ	density, lb/cu ft
$\sqrt{\bar{E}^2}$	rms of a-c complex wave voltage, v	σ	one standard deviation
F	longitudinal energy-spectrum density function, sec	τ	ratio of flame temperature to unburned-gas temperature, T_F/T_a
f	longitudinal double-velocity correlation coefficient	φ	equivalence ratio, fuel-air ratio/stoichiometric fuel-air ratio
g	lateral double-velocity correlation coefficient	Ω	hot-wire resistance at stream conditions, ohms
i	hot-wire current at stream conditions, amp		
K	gain of decade amplifier		
L_f	longitudinal scale of turbulence, in.		
L_g	lateral scale of turbulence, in.		
\mathcal{L}	Lagrangian scale of turbulence, in.		
N	number of flame globules		
n	frequency, cps		
R	gas constant		
\mathcal{R}	Lagrangian double-velocity correlation coefficient		
r	radial distance from tunnel axis, in.		
S	flame speed, ft/sec		
SPL	sound pressure level, db		
T	temperature, °R		
t	time, sec		
U	mean stream velocity, ft/sec		
u	longitudinal velocity fluctuation, ft/sec		
v, w	lateral velocity fluctuations, ft/sec		
X	fluid particle displacement due to turbulent motion, ft		

Subscripts:

a	ambient, or approach stream
F	flame
f	pertaining to correlation coefficient f
g	pertaining to correlation coefficient g
L	laminar
n	pertaining to a frequency interval
o	no-flow condition in anemometry, or reference point in space or time double-velocity correlation coefficients
P	pertaining to number of flames of a given radius or greater
s	sound
T	turbulent
t	total, or time
ξ	at a distance ξ from zero position

APPENDIX B

TURBULENCE AND SOUND INSTRUMENTATION AND ANALYSIS

THEORETICAL BACKGROUND

Turbulent fields are generally defined by the two parameters intensity and correlation coefficient. The turbulence intensity is defined as the rms value of the turbulent velocity fluctuations $\sqrt{\bar{u}^2}$, $\sqrt{\bar{v}^2}$, and $\sqrt{\bar{w}^2}$. The double-velocity correlation coefficient may be represented by a second-order tensor which for a homogeneous, isotropic field of turbulence can be reduced to two components as shown in reference 28. These two components are the longitudinal and lateral double-velocity correlation coefficients defined as follows:

$$\text{Longitudinal: } f = \frac{\overline{u_o u_\xi}}{\bar{u}^2} \quad \left| \begin{array}{c} u_o \\ \leftarrow \xi \rightarrow \\ u_\xi \end{array} \right| \quad (4)$$

$$\text{Lateral: } g = \frac{\overline{v_o v_\xi}}{\bar{v}^2} \quad \left| \begin{array}{c} v_o \\ \leftarrow \xi \rightarrow \\ v_\xi \end{array} \right| \quad (4a)$$

where f and g are the longitudinal and the lateral correlation coefficients, respectively, u is turbulent velocity fluctuation, ξ is the spatial separation between the points of measurement of the u , and the bar signifies a long time average.

Longitudinal and lateral turbulence scales have been defined by the relations

$$L_f = \int_0^\infty f d\xi \quad (5)$$

$$L_g = \int_0^\infty g d\xi \quad (5a)$$

These scales are intended to represent a mean turbulent eddy size, and for homogeneous, isotropic turbulence may be related through the equation (ref. 28)

$$f + \frac{\xi}{2} \frac{\partial f}{\partial \xi} = g \quad (\text{B1a})$$

which, by integration, becomes

$$L_f + \frac{1}{2} \int_0^\infty \xi \frac{\partial f}{\partial \xi} d\xi = L_g \quad (\text{B1b})$$

For the commonly observed exponential form of $f = \exp\left(-\frac{\xi}{L_f}\right)$, equation (B1b) becomes

$$L_f = 2L_g \quad (\text{B1c})$$

Taylor has shown (ref. 29) that the one-dimensional turbulence energy spectral density function F is the Fourier transform of the longitudinal correlation coefficient f

$$f = \int_0^\infty F \cos \frac{2\pi n x}{U} dn \quad (\text{B2})$$

where F is defined by the relations

$$\overline{u^2} = \int_0^\infty \overline{u_n^2} F dn$$

and

$$\int_0^\infty F dn = 1$$

where $\overline{u^2}$ represents the total kinetic energy in the longitudinal direction, and $\overline{u_n^2}$ represents the kinetic energy contained in the frequency interval n to $n+dn$.

HOT-WIRE ANEMOMETRY

The constant-temperature hot-wire anemometry equipment is shown diagrammatically in figure 31, and for the most part has been described in references 16 and 30. The equation relating the rms voltage $\sqrt{E_i^2}$ measured by the average square computer to the turbulence intensity has been discussed in reference 16 and is as follows:

$$\sqrt{\overline{u^2}} = \frac{4iU}{(2K)\Omega(i^2 - i_0^2)} \sqrt{E_i^2} \quad (\text{B3})$$

The spectrum density function F was measured from the tape-recorder playback signal by the following equation which is given in reference 16:

$$F = \frac{\overline{E_n^2}}{\beta \overline{E_i^2}} \quad (\text{B4})$$

where $\overline{E_n^2}$ is the square of the rms voltage reading of the wave analyzer.

The double-velocity correlation coefficient f was determined from a double-channel magnetic-tape recording of the

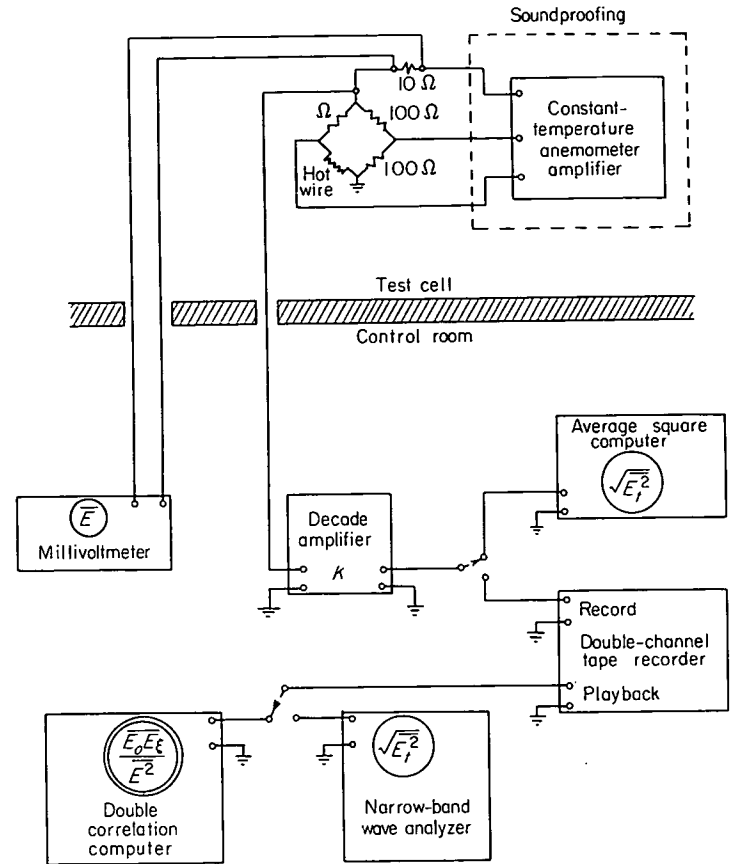


FIGURE 31.—Hot-wire anemometer and auxiliary instrumentation.

instantaneous voltage signal from the hot-wire anemometer. The double-channel tape was played back into a double correlation computer which electronically performed the instantaneous multiplication of velocity fluctuations indicated in equation (4). The variable separation ξ between velocity vectors was attained by the use of a movable and a fixed playback head. The separation ξ between the velocity vectors was equal to the separation between the heads multiplied by the ratio of the stream velocity to the tape speed. The equivalence of the correlation coefficient measured by this method and by the two-probe method was proven as a part of a research program reported in reference 31.

SOUND-FIELD INSTRUMENTATION

The sound instrumentation consisted of a standard microphone and sound-level meter from which sound-pressure level could be determined. The microphone signal was also impressed on the wave analyzer to obtain the sound kinetic energy spectrum through equation (B4). The relation between sound pressure level SPL and sound velocity fluctuations $\sqrt{\overline{u_s^2}}$ is given in reference 32 (for simple harmonic waves) as

$$SPL = 20 \log (\rho_a \sqrt{\overline{u_s^2}}) + 74 \quad (\text{B5})$$

APPENDIX C

PHOTOMULTIPLIER INSTRUMENTATION

RELATION BETWEEN FLAME LIGHT INTENSITY AND FLAME SPEED

Assumptions.—The conditions assumed in relating flame light intensity as indicated by the voltage output of a photomultiplier tube to the surface area of a flame are treated in reference 33. They may be summarized as follows:

(1) It is postulated that, if a point source of light is increased to a finite size but the distance from the light source to the detector is constant and large in comparison with the maximum dimension of the flame, the light flux impinging on the detector will obey the inverse square law. Under this condition, a change in the surface area of the flame will produce an approximately linear change in the flux intensity registered by the detector.

(2) The flame must consist of a homogeneous cloud of nonabsorbing emitters.

If the propagation of a free-flame globule moving in a gas stream at stream velocity is observed by a detector through a long slit placed axially with respect to globule travel, some additional requirements are:

(3) The detector must have an essentially flat light response over the entire field of view.

(4) The slit must be narrow enough in relation to flame-globule diameter to approximate a diameter of the projected spheroid.

(5) The flame-globule center must not suffer any appreciable radial displacement from the tunnel centerline.

(6) The flame globule must not have a preferential growth direction.

(7) The flame temperature must be constant for all the flame globules.

Conditions (1) and (4) were met by suitable placement and dimensioning of the apparatus. For condition (3), it was determined that the photomultiplier unit had a maximum light response error of 5 percent over the total light acceptance angle. Photographic evidence obtained in the preliminary phase of the investigation indicated satisfactory fulfillment of requirements (5) and (6). Assumption (7) has been previously treated in the section MEASUREMENTS OF PRESENT INVESTIGATION.

Description of apparatus.—A 931A-type photomultiplier having an adjustable-plate voltage power supply was mounted in a light-tight box behind a 0.25-inch-diameter

aperture. This detector unit was positioned in an enclosed tunnel 4 feet from the free-jet stub tunnel, as shown in figure 5. The detector aperture was centrally located with respect to the slit in the machined aluminum plate, which replaced an upper portion of one wall of the stub tunnel. The voltage output of the photomultiplier was amplified and fed to an oscilloscope. Oscillograms were taken by high-speed, continuous motion-picture technique.

Oscillograms.—As shown in figure 20, the oscillograph trace of the ignition and growth of a single flame consists of two portions, a spark light amplitude decay curve and a flame light amplitude growth curve whose slope at any point is equal to the change of diameter of the flame globule with time, governed by the considerations listed previously. This slope $2dr/dt$ is proportional to turbulent flame speed S_T as given by equation (2).

RELATION BETWEEN SPARK LIGHT INTENSITY AND SPARK CURRENT

Standring and Looms (ref. 34), using short-duration sparks produced by a lightly damped oscillatory current, have shown that the light emitted by a given spark gap depends on the current in the gap and its time variation.

In order to determine the effect of a long-duration, direct-current pulsed spark on the current-spark light relation, an auxiliary investigation was undertaken in collaboration with Clyde C. Swett, Jr. The spark production and recording apparatus is fully described in reference 35. The photomultiplier detector apparatus was as described previously except that the detector unit was mounted at one end of a rectangular tube 2 feet in length. The field of view of the photomultiplier tube was limited by a 0.0625- by 2-inch aperture in the other end of the tube. A Polaroid Land Camera was used to make oscillograms.

A series of oscillograms was taken of sparks ignited in still air and in an airstream having a velocity of 50 feet per second. Spark duration was about 600 microseconds, spark energy was of the order of 17 millijoules, and peak spark current approximated 0.23 amperes. A comparison of spark light amplitude-time curves with the current-time curves obtained in the apparatus designed by Swett showed a marked similarity of shape between the sets. It was concluded from this information that, at least for a first-order approximation, spark light intensity was roughly proportional to spark current.

APPENDIX D

CALCULATION OF FLAME SPEED FROM SCURLOCK-GROVER ANALYSIS

The basic equation in the Scurlock-Grover theory (ref. 11) is obtained by assuming that the increase of flame speed is due to the wrinkling of the flame front in the form of right circular cones, so that

$$\frac{S_T}{S_L} = \frac{A_T}{A_L} = \left[1 + C_1 \left(\frac{\overline{X^2}}{L_g^2} \right) \right]^{1/2} \quad (\text{D1})$$

where $\sqrt{\overline{X^2}}/L_g$ is assumed proportional to the ratio of cone height to base diameter and $C_1=4$ is a constant. The mean square particle displacement is assumed to depend on three effects:

- (1) Turbulent mixing, which increases the flame-front area
- (2) Laminar flame propagation, which decreases the flame-front area
- (3) Flame-generated turbulence, which increases the turbulent mixing

The first effect on $\overline{X^2}$ is given by

$$\frac{d\overline{X_T^2}}{dt} = 2\overline{u^2} \int_0^t \mathcal{R} g_t dt \quad (\text{D2})$$

where \mathcal{R} is the Lagrangian correlation coefficient and g_t is the Eulerian correlation coefficient. The second effect is given by

$$\frac{d\sqrt{\overline{X_L^2}}}{dt} = C_2 S_L \left\{ \left[1 + C_1 \left(\frac{\overline{X_T^2}}{L_g^2} \right) \right]^{1/2} - 1 \right\} \quad (\text{D3})$$

where $C_2=1/4$ is a constant. The combination of the first two effects is then

$$\frac{d\sqrt{\overline{X^2}}}{dt} = \frac{1}{\sqrt{\overline{X_T^2}}} \frac{d\overline{X_T^2}}{dt} - \frac{d\sqrt{\overline{X_L^2}}}{dt} \quad (\text{D4})$$

Since the Lagrangian correlation coefficient cannot be measured directly, Scurlock and Grover assumed it to be of the form given in reference 15:

$$\mathcal{R} = \exp \left(-\frac{\sqrt{\overline{u^2}} t}{\mathcal{L}} \right) \quad (\text{D5})$$

where \mathcal{L} is the Lagrangian scale of turbulence and was assumed to be equal to $1/2 L_g$. In the present analysis, \mathcal{R} was assumed to be related to f through the independent variable

transformation $\xi = 0.6 \sqrt{\overline{u^2}} t$ (ref. 36). Isotropy was assumed, so that g was obtained from f through the relation (ref. 28)

$$g = f + \frac{\xi}{2} \frac{df}{d\xi} \quad (\text{D6})$$

The correlation coefficient g_t was then obtained from the independent variable transformation $\xi = S_L t$. The turbulence scale L_g was calculated by matching the curve $\exp(-\xi/L_g)$, $g = e^{-\xi/L_g}$, $\ln g = L_g \xi$ to the g plot previously calculated from f by equation (D6).

All integrations and differentiations were done graphically, and the calculation procedure followed the following order:

- (1) Calculate g from equation (D6).
- (2) Transform $f(\xi)$ to $\mathcal{R}[\xi/(0.6\sqrt{\overline{u^2}})]$
- (3) Transform $g(\xi)$ to $g_t(\xi/S_L)$.
- (4) Calculate

$$\frac{d\overline{X_T^2}}{dt} = 2\overline{u^2} \int_0^t \mathcal{R} g_t dt$$

- (5) Calculate

$$\sqrt{\overline{X_T^2}} = \left[\int_0^t \left(\frac{d\overline{X_T^2}}{dt} \right) dt \right]^{1/2}$$

- (6) Calculate

$$\frac{d\sqrt{\overline{X_L^2}}}{dt} = \frac{S_L}{4} \left\{ \left[1 + 4 \left(\frac{\sqrt{\overline{X_T^2}}}{L_g} \right)^2 \right]^{1/2} - 1 \right\}$$

- (7) Calculate

$$\frac{d\sqrt{\overline{X^2}}}{dt} = \frac{1}{2\sqrt{\overline{X_T^2}}} \frac{d\overline{X_T^2}}{dt} - \frac{d\sqrt{\overline{X_L^2}}}{dt}$$

- (8) Calculate

$$\sqrt{\overline{X^2}} = \int_0^{\Delta t} \left(\frac{d\sqrt{\overline{X^2}}}{dt} \right) dt$$

- (9) Calculate

$$\frac{S_T}{S_L} = \frac{A_T}{A_L} = \left[1 + 4 \left(\frac{\overline{X^2}}{L_g^2} \right) \right]^{1/2}$$

As mentioned in the DISCUSSION section, flame-generated turbulence has been assumed negligible, and the final form of the Scurlock-Grover theoretical equation is as given previously.

REFERENCES

1. Hottel, H. C., Williams, G. C., and Levine, R. S.: The Influence of Isotropic Turbulence on Flame Propagation. Fourth Symposium (International) on Combustion, The Williams & Wilkins Co. (Baltimore), 1953, pp. 636-644.
2. Karlovitz, Béla, Denniston, D. W., Jr., and Wells, F. E.: Investigation of Turbulent Flames. *Jour. Chem. Phys.*, vol. 19, no. 5, May 1951, pp. 541-547.
3. Bollinger, Lowell M., and Williams, David T.: Effect of Reynolds Number in Turbulent-Flow Range of Flame Speeds of Bunsen Burner Flames. NACA Rep. 932, 1949. (Supersedes NACA TN 1707.)
4. Wright, F. H.: Measurements of Flame Speed and Turbulence in a Small Burner. Prog. Rep. No. 3-21, Jet Prop. Lab., C. I. T., June 6, 1950.
5. Bowditch, F. W.: Some Effects of Turbulence on Combustion. Fourth Symposium (International) on Combustion, The Williams & Wilkins Co. (Baltimore), 1953, pp. 674-682.
6. Scurlock, A. C.: Flame Stabilization and Propagation in High-Velocity Gas Streams. Meteor Rep. 19, Fuels Res. Lab., M. I. T., May 1948. (Contract NOrd 9661.)
7. Williams, G. C., Hottel, H. C., and Scurlock, A. C.: Flame Stabilization and Propagation in High Velocity Gas Streams. Third Symposium on Combustion and Flame and Explosion Phenomena, The Williams & Wilkins Co. (Baltimore), 1949, pp. 21-40.
8. Wohl, Kurt, Shore, L., von Rosenberg, H., and Weil, C. W.: The Burning Velocity of Turbulent Flames. Fourth Symposium (International) on Combustion, The Williams & Wilkins Co. (Baltimore), 1953, pp. 620-635.
9. Leason, D. B.: Turbulence and Flame Propagation in Premixed Gases. *Fuel*, vol. XXX, no. 10, Oct. 1951, pp. 233-238; discussion, pp. 238-239.
10. Caldwell, Frank R., Ruegg, Fillmer W., and Olsen, Lief D.: Combustion in Moving Air. Paper presented at meeting SAE and Air Transport (New York City), Apr. 13-15, 1948.
11. Scurlock, A. C., and Grover, J. H.: Propagation of Turbulent Flames. Fourth Symposium (International) on Combustion, The Williams & Wilkins Co. (Baltimore), 1953, pp. 645-658.
12. Ball, George A.: Combustion Aerodynamics—A Study of a Two-Dimensional Flame. Dept. Eng. Sci. and Appl. Phys., Harvard Univ., July 1951. (Army Ord. Dept. Contract No. W-19-020-ORD-6509.)
13. Stevens, F. W.: A Constant Pressure Bomb. NACA Rep. 176, 1923.
14. Mickelsen, William R.: The Propagation of a Free Flame Through a Turbulent Gas Stream. M. S. Thesis, Case Inst. Tech., 1953.
15. Dryden, Hugh L.: A Review of the Statistical Theory of Turbulence. *Quart. of Appl. Math.*, vol. 1, no. 1, Apr. 1943, pp. 7-42.
16. Mickelsen, William R., and Laurence, James C.: Measurement and Analysis of Turbulent Flow Containing Periodic Flow Fluctuations. NACA RM E53F19, 1953.
17. Hottel, H. C., Williams, G. C., and Satterfield, C. N.: Thermodynamic Charts for Combustion Processes, Pt. II. John Wiley & Sons, Inc., 1949.
18. Anon.: Annual Program Report. Proj. Squid, U. S. Navy, U. S. Army, Jan. 1, 1949.
19. Worthing, Archie G., and Geffner, Joseph: Treatment of Experimental Data. John Wiley & Sons, Inc., 1943, p. 275.
20. Lusser, Robert: A Study of Methods for Achieving Reliability of Guided Missiles. Tech. Report No. 75, U. S. Naval Air Missile Test Center, July 10, 1950.
21. Dugger, Gordon L.: Effect of Initial Mixture Temperature on Flame Speed of Methane-Air, Propane-Air, and Ethylene-Air Mixtures. NACA Rep. 1061, 1952. (Supersedes NACA TN's 2170 and 2374.)
22. Bolz, Ray E., and Burlage, Henry, Jr.: The Influence of Turbulence on Flame Propagation Rates. *Jet Prop.*, vol. 25, no. 6, June 1955, pp. 265-275.
23. Taylor, G. I.: Diffusion by Continuous Movements. *Proc. London Math. Soc.*, vol. 20, 1922, pp. 196-212.
24. Botha, J. P., and Spalding, D. B.: The Laminar Flame Speed of Propane/Air Mixtures with Heat Extraction from the Flame. *Proc. Roy. Soc. (London)*, ser. A, vol. 225, no. 1160, Aug. 6, 1954, pp. 71-95.
25. Damköhler, Gerhard: The Effect of Turbulence on the Flame Velocity in Gas Mixtures. NACA TM 1112, 1947.
26. Shelkin, K. I.: On Combustion in a Turbulent Flow. NACA TM 1110, 1947.
27. Tucker, Maurice: Interaction of a Free Flame Front with a Turbulence Field. NACA TN 3407, 1955.
28. von Kármán, Theodore, and Howarth, Leslie: On the Statistical Theory of Isotropic Turbulence. *Proc. Roy. Soc. (London)*, ser. A, vol. 164, Jan. 21, 1938, pp. 192-215.
29. Taylor, G. I.: The Spectrum of Turbulence. *Proc. Roy. Soc. (London)*, ser. A, vol. 164, Feb. 18, 1938, pp. 476-490.
30. Laurence, James C., and Landes, L. Gene: Auxiliary Equipment and Techniques for Adapting the Constant-Temperature Hot-Wire Anemometer to Specific Problems in Air-Flow Measurements. NACA TN 2843, 1952.
31. Laurence, James C.: Intensity, Scale, and Spectra of Turbulence in Mixing Region of Free Subsonic Jet. NACA Rep. 1292, 1956. (Supersedes TN's 3561 and 3576.)
32. Morse, Philip M.: *Vibration and Sound*. Second ed., McGraw-Hill Book Co., Inc., 1948.
33. Clark, Thomas P., and Bittker, David A.: A Study of the Radiation from Laminar and Turbulent Open Propane-Air Flames as a Function of Flame Area, Equivalence Ratio, and Fuel Flow Rate. NACA RM E54F29, 1954.
34. Standring, W. G., and Looms, J. S. T.: Light Output from a Spark "Point Source". *Nature*, vol. 165, no. 4192, Mar. 4, 1950, p. 358.
35. Swett, Clyde C., Jr.: Effect of Gas Stream Parameters on the Energy and Power Dissipated in a Spark and on Ignition. Third Symposium on Combustion and Flame and Explosion Phenomena, The Williams & Wilkins Co. (Baltimore), 1949, pp. 353-361.
36. Mickelsen, William R.: An Experimental Comparison of the Lagrangian and Eulerian Correlation Coefficients in Homogeneous Isotropic Turbulence. NACA TN 3570, 1955.

REPORT 1287

SPARK IGNITION OF FLOWING GASES

By CLYDE C. SWETT, Jr.

SUMMARY

Research conducted at the NACA Lewis laboratory on ignition of flowing gases by means of long-duration discharges is summarized and analyzed. Data showing the effect of a flowing combustible mixture on the physical and electrical characteristics of spark discharges and data showing the effects of variables on the spark energy required for ignition of the combustible mixture are presented. A theory of ignition that has been developed to predict the effect of many of the gas-stream and spark variables is described and applied to a limited amount of experimental data.

The trends observed for ignition in flowing gases were similar to those observed in quiescent gases with the exception that increasing velocity and turbulence increased the ignition energy requirements. Lengthening of the discharge path by the flowing stream results in less energy being available to the important part of the discharge length. Flow also causes multiple discharges which should be avoided since they represent an energy loss. Less energy is required for ignition with an "arc" discharge than with a "glow" discharge. Effects of most of the variables on ignition energy requirements were predicted by theoretical equations; the effects of fuel-air ratio, however, required an empirical correction to the equations.

INTRODUCTION

Spark discharges are ordinarily used as the ignition source in aircraft engines. While such discharges are normally reliable sources of ignition, difficulty in starting jet engines has been encountered under these conditions:

- (1) Ground starting in cold climates
- (2) Altitude starting of auxiliary engines
- (3) Altitude restarting of engines after flame blowout

Basic information on spark ignition of flowing gases might indicate the reasons for these ignition problems and might lead to the development of lighter weight, more efficient, and more reliable ignition systems.

For these reasons, the NACA Lewis laboratory has studied spark ignition in flowing gases; the object has been to promote understanding of the ignition process. The results of this work are reported in references 1 to 6. The present report summarizes and analyzes these results and points out their significance in relation to practical ignition problems.

The fundamental aspects of ignition of flowing combustible gases are considered in three sections of the report. First,

the effect of gas velocity on the spark discharge is considered. The voltage necessary to form a spark, the physical shape of the spark discharge, and the electrical characteristics of the discharge under flow conditions are discussed. Second, the energy required to ignite flowing gases is considered. The parameters that affect the energy required for ignition are presented. The trends observed are compared with those observed with quiescent gases. Third, a theory which relates the factors affecting ignition is described. Correlations of experimental data based on the theory are presented. The concluding section points out the significance of the research in relation to practical ignition problems.

The following characteristics and parameters were investigated experimentally:

- (1) Spark characteristics:
 - Breakdown voltage
 - Spark-discharge length
 - Multiple discharges
 - Current
 - Voltage
 - Voltage distribution
 - Spark duration
 - Energy
 - Energy distribution
- (2) Ignition energy parameters:
 - Velocity
 - Pressure
 - Fuel-air ratio
 - Temperature
 - Turbulence
 - Spark duration
 - Electrode spacing
 - Electrode diameter
 - Electrode configuration
 - Type of discharge
 - Electrode material
- (3) Ignition theory parameters:
 - Velocity
 - Pressure
 - Fuel-air ratio
 - Temperature
 - Turbulence
 - Spark duration
 - Electrode spacing

Most of the research was conducted at pressures of 2 to 5 inches of mercury absolute. Limitations of energy-measurement equipment precluded operation at higher pressures where the energy requirements would be reduced. The research was conducted with two types of apparatus: (1) simple flow equipment that had no provisions for controlling turbulence and (2) equipment that had complete control of turbulence level. Only one combustible gas, a propane-air mixture, was used. This gas was ignited by a single long-duration spark discharge obtained from a resistance-capacitance ignition system.

SYMBOLS

a	constant
$c_1, c_2, c_3,$	constants
c_4, c_5	
c_p	specific heat at constant pressure
d_q	quenching distance of quiescent mixtures
E_{act}	energy of activation
E_c	energy in cathode region
E_{l_s}	energy in line source of ignition
E'_{l_s}	theoretical energy in line source of ignition required to heat ignition zone to flame temperature
E_p	energy in positive column
E_s	total energy of spark discharge
$f(\sqrt{u^2})$	functions of intensity of turbulence
$f'(\sqrt{u^2})$	
i	current in discharge
J	conversion factor, heat to electrical energy
L_x	longitudinal scale of turbulence
m	mesh size of turbulence promoter
n	constant
P_{av}	average power in total spark discharge
P_{l_s}	average power in line source of ignition
p	static pressure
Q	heat of combustion of fuel
R	gas constant
r	radius of heated zone caused by energy in line source of ignition
s	electrode spacing
T_{am}	ambient temperature
T_F	flame temperature
\mathcal{T}_{re}	thickness of reaction zone across which the temperature change is $T_F - T_{am}$
t	time
t_s	spark duration
U	stream velocity
$\sqrt{u^2}$	intensity of turbulence
v_c	cathode voltage drop
v_t	total voltage of discharge
X_f	mole fraction of fuel
X_o	mole fraction of oxygen
x	distance from turbulence promoter to spark electrodes
κ	thermal conductivity
ρ	density
Φ	work function of electrode

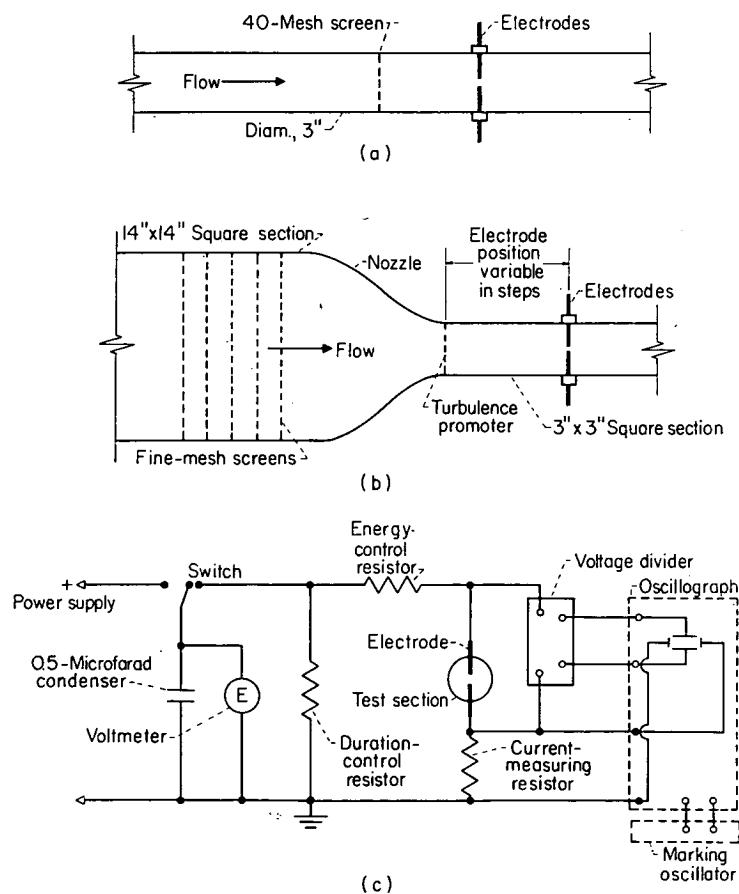
APPARATUS AND PROCEDURE

FLOW APPARATUS

The important features of the flow apparatus used are shown in figures 1(a) and (b). The complete systems are described in detail in references 2 to 6. Basically, the apparatus produced controlled-flow conditions of premixed propane and air in a test section in which the spark electrodes were located. Provisions were made for observing the spark and the flame. The criterion for ignition was appearance of flame downstream from the electrodes. In the simple flow apparatus (fig. 1(a)), the pressure, temperature, and velocity of flow were controlled. No attempt was made to vary the turbulence. The controlled-turbulence flow apparatus (fig. 1(b)) had a series of fine mesh screens to reduce the turbulence in a large section, a nozzle to accelerate the flow into the test section, a plate for installing different turbulence promoters upstream of the electrodes, and movable electrodes for varying the distance between the electrodes and the turbulence promoter.

IGNITION SYSTEM AND ENERGY MEASUREMENT

The ignition and energy-measuring systems used are described in detail in reference 3; they are shown schematically in figure 1(c). The condenser is charged and then discharged through a combination of resistors to cause a spark discharge.



(a) Simple flow apparatus.

(b) Controlled-turbulence flow apparatus.

(c) Ignition and energy-measuring equipment.

FIGURE 1.—Important features of flow apparatus and electrical equipment used for investigating spark ignition of flowing gases.

The energy and duration depend upon the relative values of condenser capacity, the voltage, and the resistances.

The voltage of the discharge was reduced by means of a balanced resistance-capacitance voltage divider (ref. 3) and applied to the vertical plates of the oscillograph. A current-measuring resistance placed in series with the spark gap produced a voltage that was applied to the horizontal plates. These two voltages in conjunction with timing marks supplied by an oscillator gave an oscillogram from which energy and duration of the discharge could be determined.

The procedure used with this apparatus was as follows: the desired flow conditions were set, and a spark discharge was passed between the electrodes. Tests were run with varying amounts of energy until the minimum amount of energy that would cause ignition was determined. Then one or more oscillograms were obtained depending upon reproducibility at the particular condition. A more detailed description of the procedure used to obtain and analyze the ignition data is presented in references 1 to 6.

TURBULENCE MEASUREMENT

Descriptions of the hot-wire anemometer apparatus and methods used to measure the turbulence are included in reference 7. Single-wire probes measured the velocity fluctuations in the longitudinal direction, and \times -wire probes measured the velocity fluctuations in the lateral direction. A difference circuit was used in the lateral measurements to obtain the difference in velocity fluctuations from the two wires of the \times -wire probes. The spectrum of the turbulence was analyzed by means of a wave analyzer. An average-square computer totaled the kinetic energy in the velocity fluctuations to give the intensity of turbulence.

Measurements of the turbulence were made as follows: With the spark electrodes removed, the probe was inserted into the test section and located so that the hot wire would be at the center of the duct. After flow conditions were established using air in place of the combustible mixture, the intensity of turbulence was determined and a spectrum analysis made to determine the scale of the turbulence.

CHARACTERISTICS OF SPARK DISCHARGES IN FLOWING GASES

The characteristics of spark discharges in flowing gases were determined using air or a propane-air mixture. The ignition and energy-measuring system (fig. 1(c)) was used except for the breakdown voltage test, for which a simple power supply was used.

BREAKDOWN VOLTAGE

The breakdown voltage, or the lowest voltage that will cause a spark to be established between two electrodes, is one of the primary considerations in selecting an ignition system. The breakdown voltage of a spark gap in quiescent gas increases with electrode spacing and gas density and, to some extent, is dependent on the electrode configuration (ref. 8). The effect of gas velocity on voltage must also be known, since in aircraft jet engines a flowing fuel-air mixture must be ignited.

Figure 2 shows the effect of velocity and pressure on the direct-current breakdown voltage of $\frac{1}{16}$ - and $\frac{3}{16}$ -inch-diameter

electrodes in air. These electrodes result in experimental data obtained under nonuniform (distorted) electrostatic field conditions. These data lie below Paschen's curve obtained for uniform or undistorted fields (ref. 8). For the larger electrode there is no effect of velocity on breakdown voltage. For the smaller electrode there may be a slight effect of velocity; however, for practical purposes the effect is negligible. Hence, it may be concluded that flowing gases do not have an adverse effect on the breakdown voltage of a spark gap.

SPARK-DISCHARGE LENGTH

The spark discharge established in a flowing gas ionizes a small channel of the gas. This ionized channel is subject to the motion of the stream. Therefore, the discharge should move with a velocity identical to the stream velocity.

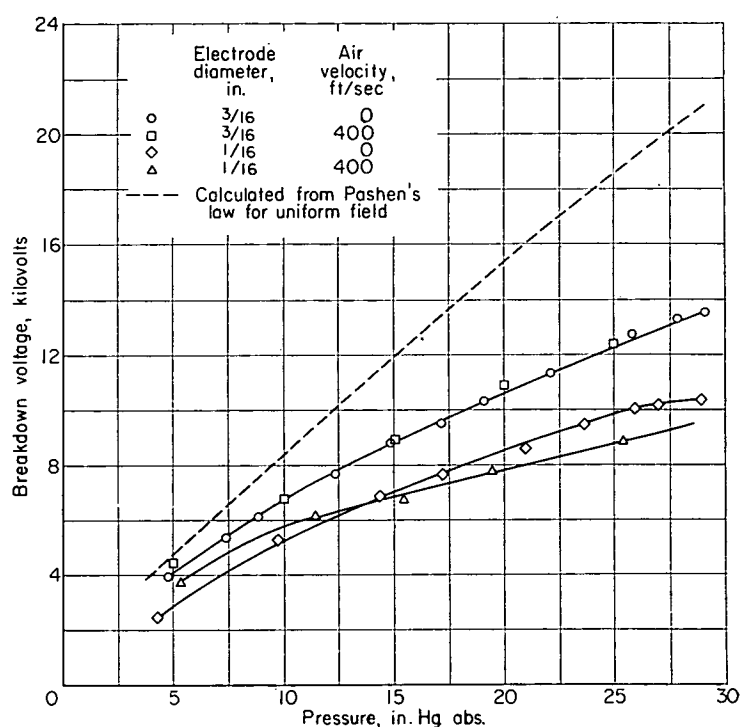


FIGURE 2.—Effect of pressure on direct-current breakdown voltage of spark gap in air. Temperature, 80° F; electrode spacing, 0.250 inch. (Data from ref. 1.)

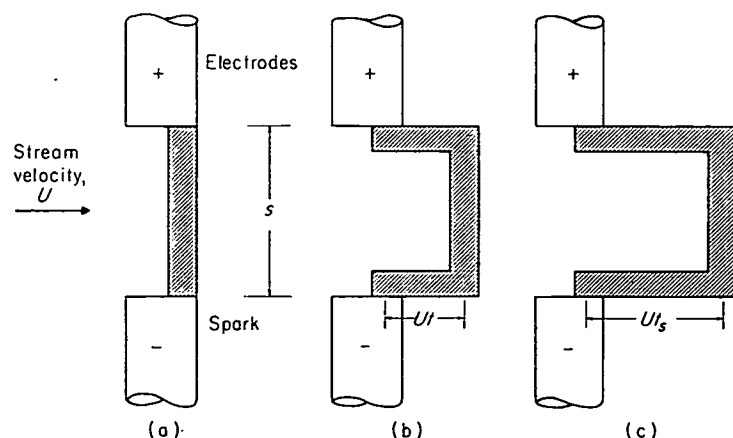


FIGURE 3.—Model of spark discharge in flowing gas showing lengthening of discharge path with time. (t , time; t_s , spark duration.)

The length of the discharge then varies with time and the shape approximates that shown in figure 3. At the instant the discharge is first established ($t=0$) in the flowing stream of velocity U , the discharge passes in a straight line between the electrodes. However, at some later times t and t_s (the instant the discharge ceases), the ionized path moves downstream and the discharge has the forms shown in figure 3. The paths shown in figure 3 are idealized; actually, considerable rounding of the discharge where the horizontal and vertical portions intersect would be expected. In theoretical analyses presented herein such rounding is neglected.

The distance traveled by the discharge at any time t is Ut , and the maximum distance traveled by the discharge is Ut_s . Some visual measurements have been made of the effect of U on the maximum distance traveled (fig. 4). The distances agree within 12 percent with the values calculated by multiplying U and t_s . The reasons for this large discrepancy may be that the technique for measuring durations was not fully developed at the time this particular set of data was obtained and that visual measurements were not very accurate.

The total spark length is made up of the horizontal and vertical lengths of the discharge and is equal to $s+2Ut$ for any time less than the discharge duration and $s+2Ut_s$ for the discharge duration. The value $s+2Ut_s$ is the maximum length that the discharge attains; rounding at the corners (fig. 3) shortens the length.

MULTIPLE DISCHARGES

The length and, hence, the resistance of the spark discharge are directly proportional to the stream velocity and time, so that for constant current the discharge voltage must increase with Ut_s . If this voltage increase is large enough to reach the breakdown voltage of the spark gap, a second spark is established directly between the electrodes, and the new discharge in turn also moves downstream. The first discharge ceases at the formation of the second discharge. The number of sparks that can be formed in this manner

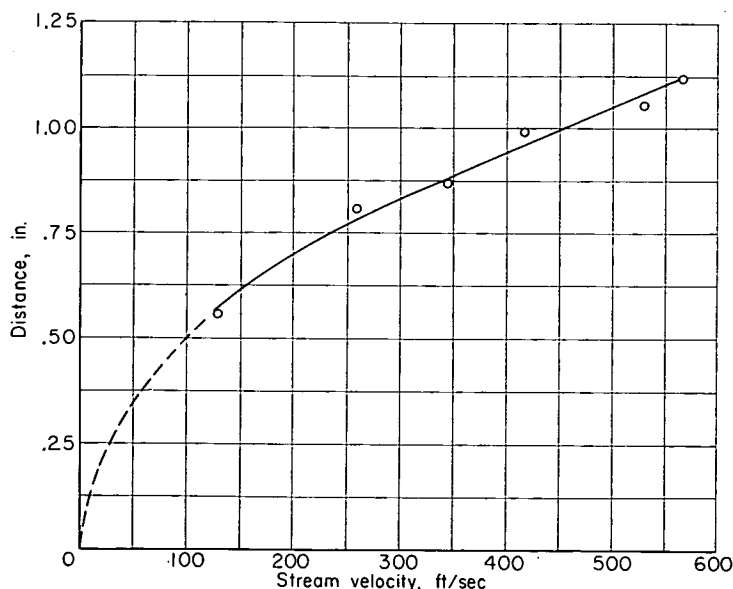


FIGURE 4.—Effect of airstream velocity on observed downstream displacement. Pressure, 11.36 inches of mercury absolute; temperature, 80° F; electrode spacing, 0.250 inch; electrode diameter, $\frac{3}{16}$ inch. (Data from ref. 1.)

depends upon Ut_s and also on the voltage output characteristics of the spark source. These multiple discharges should be distinguished from the repetitive discharges deliberately produced by commercial ignition systems. Such discharges may occur many times per second.

Table I shows the number of additional sparks formed after the initial spark for various conditions of air velocity, electrode spacing, electrode diameter, and pressure for one spark source. The number of sparks increases with increasing velocity, decreasing spacing, and decreasing pressure. For the data presented in table I, electrode diameter was unimportant. Increasing the duration of the discharge or the output voltage should also increase the number of sparks formed.

TABLE I.—NUMBER OF SPARKS AFTER INITIAL SPARK FOR VARIOUS CONDITIONS OF AIR VELOCITY, ELECTRODE SPACING, ELECTRODE DIAMETER, AND PRESSURE

[Data from ref. 1.]

Electrode spacing, 0.250 in.						Electrode spacing, 0.125 in.					
Air velocity, ft/sec	Pressure, in. Hg abs.					Air velocity, ft/sec	Pressure, in. Hg abs.				
	5.26	11.36	15.36	19.36	25.36		5.26	11.36	15.36	19.36	25.36
Electrode diameter, $\frac{1}{8}$ in.											
0	0	0	0	0	0	0	0	0	0	0	0
200	0	0	0	0	0	200	2	1	0	0	0
300	1	0	0	0	0	300	3	2	1	1	0
400	2	1	0	0	0	400	5	3	2	1	1
450	---	---	---	---	0	450	---	---	---	---	1
480	---	---	---	---	0	485	---	---	---	---	1
500	2	1	0	0	---	500	7	5	3	2	---
550	3	1	1	0	---	550	8	5	4	2	---
Electrode diameter, $\frac{3}{16}$ in.											
0	0	0	0	0,0	---	0	0	0	0	0	0
200	0	0	0	0	---	200	2	2	1	1	1,0
250	---	---	---	0	---	300	4	2	2	1	1
300	*1,1	0	0	*0,0	---	400	7	4	3	*3,2	1
400	1	1	0	0	*0,0,0	450	---	---	---	---	1
485	---	---	---	---	*0,0,0	480	---	---	---	---	3
500	*3,3	1	0	*0,1,0,0	---	500	9	4	3	3	---
550	3	1	---	---	---	550	---	*6,6	4	---	---
565	---	---	*1,0	*0,0,0,0	---	555	---	5	---	---	---
570	---	---	---	0	---	565	---	---	---	3	---
---	---	---	---	---	---	575	9	---	---	---	---

* More than one observation made at this condition.

Multiple sparks are probably not desirable for ignition since the discharge energy is then distributed over too many separate channels or volumes. More energy is contained in the first of the multiple discharges than in the others, and that energy should be responsible for ignition.

CURRENT

The current of a spark discharge is determined largely by the impedance of the ignition source and to some extent by factors of the spark gap, especially in the case of long-duration discharges generated by a high-impedance source.

It can be shown that the current in the spark discharge using the ignition source shown in figure 1(c) should decrease exponentially during the life of the discharge if the gap resistance is constant. Actually, the resistance does vary somewhat so that the current does not decrease quite exponentially during the latter stages of the discharge, even under quiescent conditions. Also, as noted previously, the lengthening of the discharge under flow conditions increases the resistance so rapidly that there is a marked decrease in the

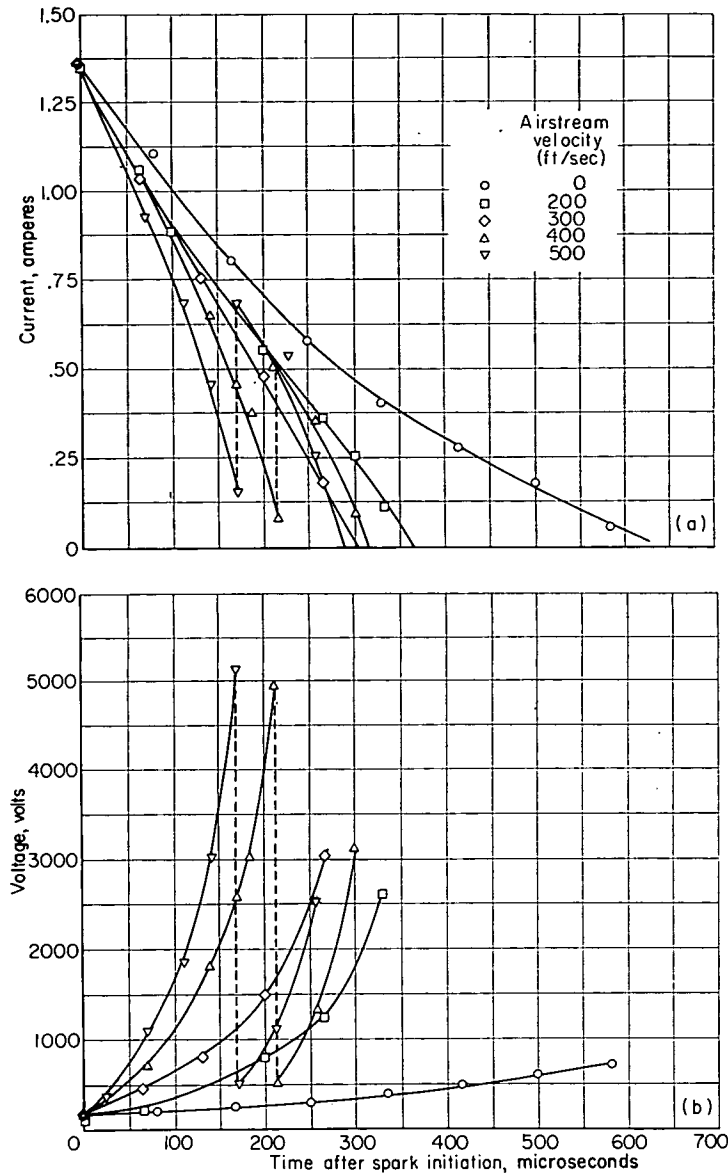


FIGURE 5.—Variation of voltage and current of spark discharge with time for various airstream velocities. Pressure, 11.36 inches of mercury absolute; temperature, 80° F; electrode spacing, 0.250 inch; electrode diameter, $\frac{1}{16}$ inch. (Data from ref. 1.)

current. These effects are shown in figure 5(a), which compares the current and time characteristics of five discharges at various air velocities. At zero velocity the current decays almost exponentially. With flow the current decreases at a greater rate, the higher velocities causing greater decreases. Secondary spark discharges are formed at 400 and 500 feet per second as indicated by breaks in the curves (fig. 5(b)). The average rate of current decrease for the highest velocity is about twice that for no flow.

VOLTAGE

The total voltage of a discharge varies to a much greater extent with velocity than does the current. Total voltage also depends upon current, type of discharge, gas density, electrode spacing, and gas; it does not vary uniformly along the length of the discharge. Because this nonlinearity may have some bearing on the ignition process in combustible mixtures, this section discusses the component parts of the

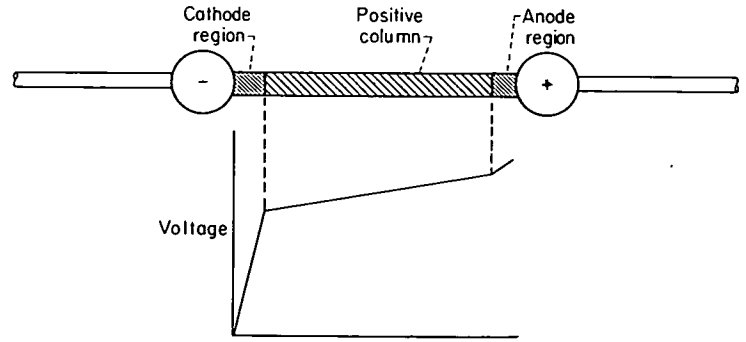


FIGURE 6.—Variation of voltage along constant-current discharge.

total voltage in addition to considering factors affecting the total voltage.

Component parts of the total voltage.—The total voltage of a discharge is the sum of the voltage drops in a number of specific regions along the length of the discharge. Consider the voltage along the discharge at any instant of time (fig. 6). At the negative or cathode end of the discharge there is a voltage change defined as the cathode drop. This drop can represent a considerable portion of the total voltage, and it occurs within an extremely short distance from the cathode. Next to the cathode-drop region is a region known as the positive column that occupies most of the discharge length. The voltage increases linearly with distance in this region. Between the end of the positive column and the anode there is another voltage change defined as the anode drop. This drop also occurs close to the electrode and has a magnitude approximately equal to the ionization potential of the gas (10 to 15 volts). Actually, both the anode and cathode regions contain one or more regions, but such division is unimportant for the present discussion. Reference 8 discusses all the regions in detail.

The cathode voltage drop determines the type of discharge that exists. Figure 7 shows how the cathode drop varies qualitatively with current and shows the general regions of the various types of discharges. The current of the spark discharge is continuously varying with time and therefore defines some portion of this curve. As the current is in-

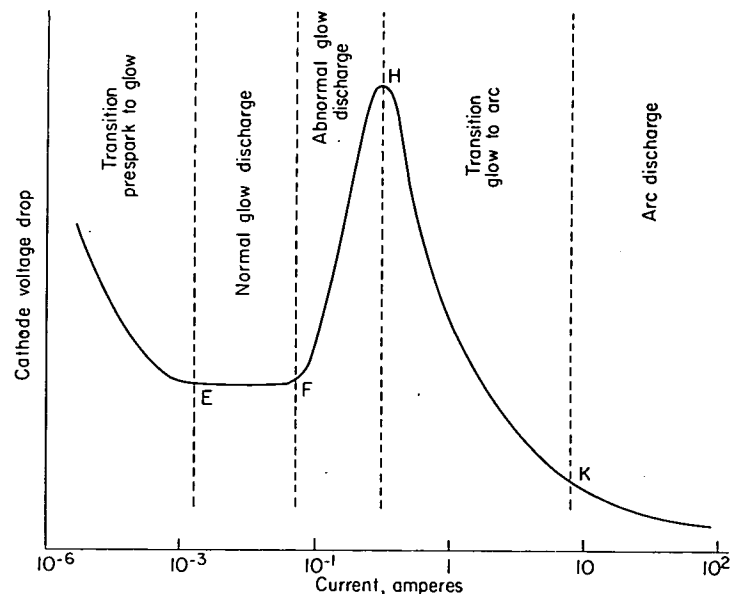


FIGURE 7.—Effect of discharge current on cathode voltage drop. (Data from ref. 16.)

creased from point E the voltage remains constant to point F. The region between E and F is defined as the normal glow discharge region. From F to H the voltage increases; this region is defined as the abnormal glow discharge region. From H to K the voltage decreases through a transition region with an arc discharge originating at point K. The cathode drop in the arc discharge can decrease to the order of magnitude of the ionization potential (10 to 15 volts). Frequently, the curve may be discontinuous between H and K, or the peak at H may not be observed; that is, the discharge may change from an arc to a normal glow without passing through the abnormal glow region.

Most of the ignition data reported herein were obtained with glow discharges. Therefore, the discussion is primarily concerned with the glow discharge, although many of the trends observed also apply to the arc discharge.

Methods are given in references 3 and 6 for determining cathode voltage drops experimentally at no flow and with flow, respectively. These methods assume the anode drop to be negligibly small. Figure 8 shows the cathode voltage drop determined for five electrode materials. The cathode drop is independent of current for the brass and cadmium electrodes. This effect is typical for the glow discharge (fig. 7). The cathode drop for the other metals is not independent of current, possibly because of the tendency of the discharge to be an abnormal glow discharge. The effect may also be partially due to experimental errors in the determination of the voltage.

The cathode-drop data shown in figure 8 correlate to a certain degree with the work function of the electrode material. The work function is a measure of the work required

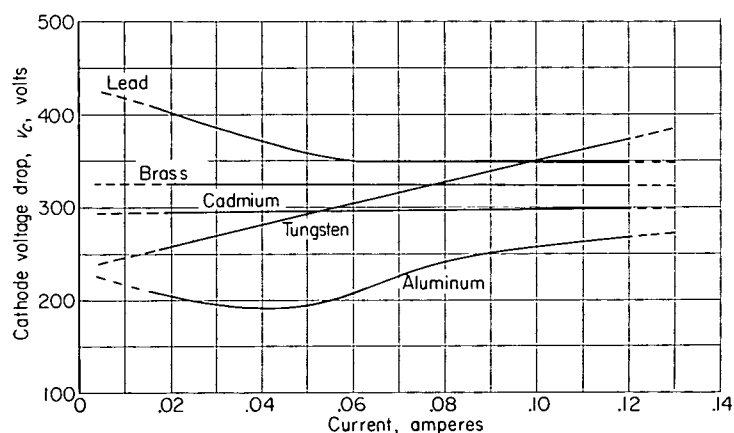


FIGURE 8.—Effect of current on cathode voltage drop for five electrode materials. Pressure, 3.0 inches of mercury absolute; temperature, 80° F; fuel-air ratio, 0.0835; gas stream velocity, 5.0 feet per second; duration of discharge, approximately 600 microseconds. (Data from ref. 3.)

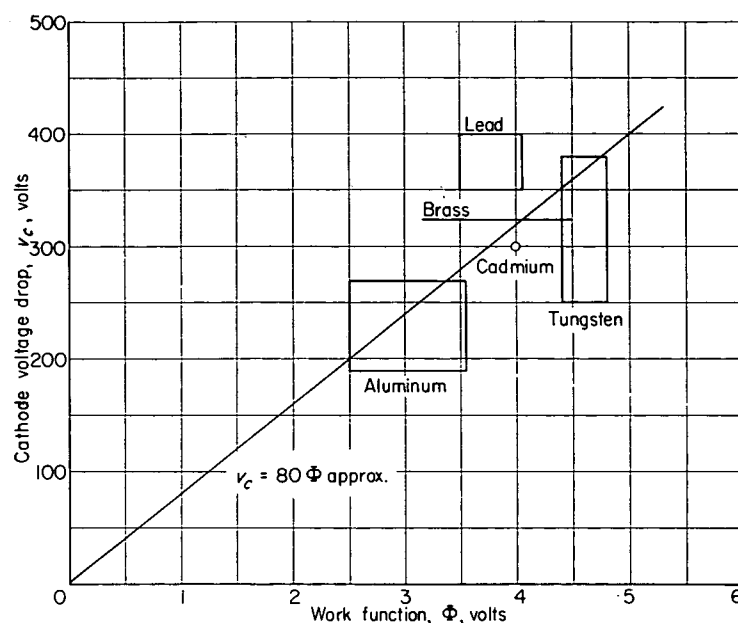


FIGURE 9.—Effect of work function on cathode voltage drop. Range of voltage drops from figure 8; range of work functions from reference 9.

to extract from the electrode the electrons that are necessary for maintaining the discharge. The correlation is shown in figure 9. The limits of the data cover the range of work functions found in the literature (ref. 9) and the range of cathode drops shown in figure 8.

The positive-column voltage is obtained by subtracting the cathode drop from the total voltage drop. The individual voltage drops, together with instantaneous-current data, determine the energies dissipated in the cathode region and in the positive column.

Total voltage.—The variation in voltage of a discharge with time is shown in figure 5(b). At zero velocity there is a gradual increase in voltage with time as the current decreases (fig. 5(a)). This effect is the result of the negative characteristic, that is, increasing voltage with decreasing current, typical of an arc discharge (fig. 7). With flow the rate of voltage increase is much greater because of lengthening of the discharge path. When the voltage reaches the breakdown voltage of the gap, approximately 5000 volts for the 400-foot-per-second curve, a new spark forms directly between the electrodes. The voltage then immediately falls to a low value and begins to increase again as the second discharge moves downstream.

With a glow discharge at high flow, the same trend found for the arc discharge is observed; however, at low or no flow the trend is opposite. That is, the voltage decreases as the

current decreases during the life of the discharge. In this respect the glow discharge behaves somewhat like a resistance.

At the present time, the total voltage of a discharge cannot be predicted by any theoretical considerations. Empirically, the factors which determine the total voltage v_t have been shown to be related by the following equation:

$$v_t = v_c + 360s + 3460si \quad (1)$$

where v_c is the cathode drop, and the units are volts, amperes, and inches. A plot of this empirical equation is presented in figure 10. The total voltage varies linearly with spacing s when the current i is constant. In like manner, the total voltage varies linearly with current when the spacing is constant.

SPARK-DISCHARGE ENERGY

The most important characteristic of a discharge insofar as ignition is concerned is the energy dissipated in the discharge. The effect of several operating and design variables on the total energy and the division of total energy into its component parts are considered in this section.

Effect of variables on total energy.—The effect of velocity and pressure on total energy are shown in figure 11 for constant settings of ignition system. Temperature, 80° F; electrode spacing, 0.125 inch; electrode diameter, $\frac{3}{16}$ inch. (Data from ref. 1.)

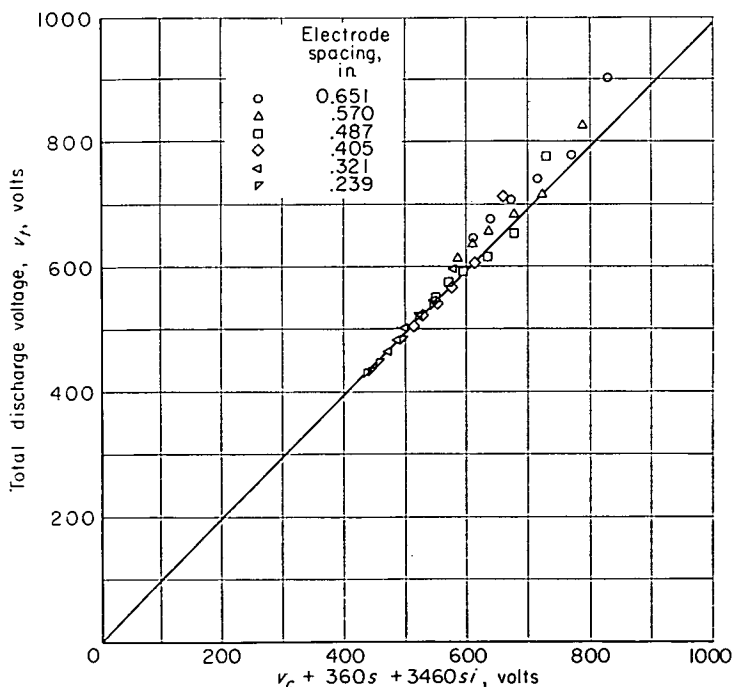


FIGURE 10.—Empirical correlation of total discharge voltage with cathode drop, electrode spacing, and spark current. Type of discharge, glow; electrode spacing s , inches; current i , amperes; cathode drop v_c , volts (325 for brass). (Data from ref. 3.)

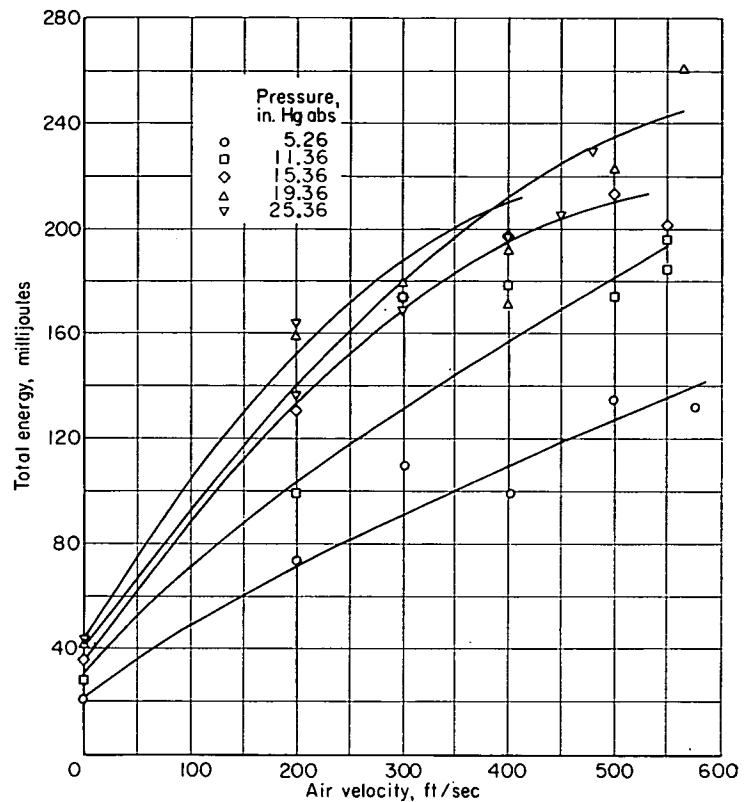


FIGURE 11.—Effect of air velocity and pressure on total discharge energy for constant settings of ignition system. Temperature, 80° F; electrode spacing, 0.125 inch; electrode diameter, $\frac{3}{16}$ inch. (Data from ref. 1.)

the discharge increases with flow velocity, it is also distributed over a lengthening path. As is shown earlier, the path length of the discharge increases from s at no flow to $2Ut_s + s$ with flow.

The effect of temperature on total energy has been shown to be negligible over the range -67° to 80° F (ref. 1). An increase in electrode spacing with constant settings of the ignition system increases the energy because the discharge resistance increases without affecting the current markedly. The effect of electrode diameter is negligible.

Separation of total energy into its component parts.—The total energy of a spark discharge can be separated into its component parts when the voltage drop of each specific region along the discharge length is known. The voltage drop, determined as a function of time, is used with instantaneous-current values to determine energy. Since only two regions, cathode and positive-column, are considered, only the cathode energy need be determined. The positive-column energy is then the difference between the cathode energy and the total energy. The cathode energy represents a substantial part of the total energy. For example, reference 3 shows that one-third to one-half of the total energy is dissipated in the cathode region for a typical ignition condition.

SPARK DURATION

The duration of a spark discharge is primarily dependent on the relative values of resistance and capacitance in the ignition source, although factors of the gas stream do have

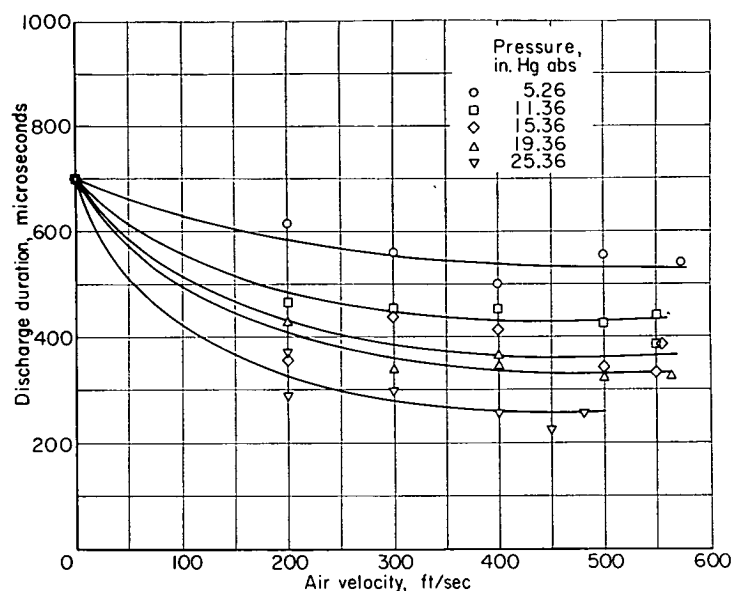


FIGURE 12.—Effect of air velocity and pressure on duration of discharge for constant settings of ignition system. Temperature, 80° F; electrode spacing, 0.125 inch; electrode diameter, $\frac{3}{16}$ inch. (Data from ref. 1.)

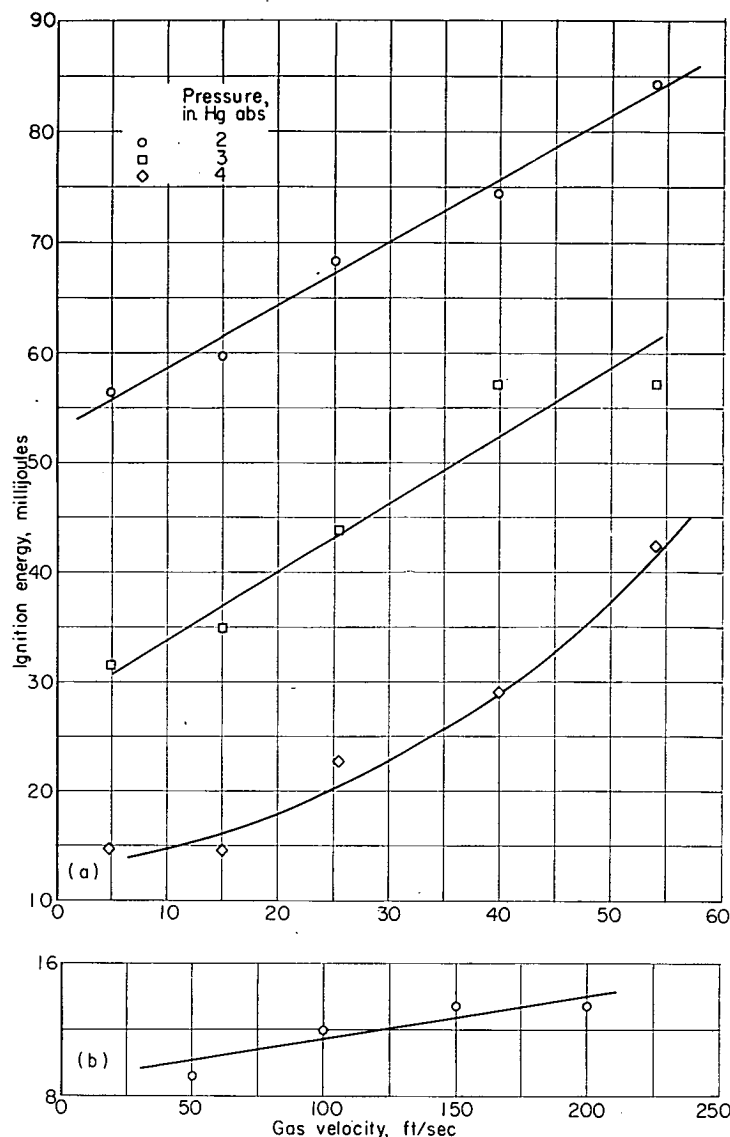
some effect. Figure 12 shows that the duration of the spark discharge is decreased by increasing the velocity and the pressure. Both of these factors increase the electrical resistance of the discharge and result in a larger voltage requirement. The maximum voltage of the spark source is reached in a shorter time (fig. 5(b)), and the discharge then ceases. Increasing the electrode spacing also causes the same result because it increases the length of the discharge.

EFFECT OF PARAMETERS ON IGNITION ENERGY REQUIREMENTS OF FLOWING GASES

The most important spark characteristic determining the ease of ignition is energy. If ignition is considered as a thermal mechanism, energy determines the amount of heat added, and hence the temperature rise of a volume of the combustible mixture. This section discusses the effects on ignition energy requirements of a number of variables that may be encountered in jet-engine operation. Some of the data to be presented were obtained at electrode spacings less than the quenching distance and so do not represent the minimum energy that would have been required with an optimum spacing. These data are indicated on the figures as having been obtained within the quenching distance.

VELOCITY

The effect of velocity on ignition energy is shown in figure 13. The required energy increases approximately linearly with velocity for both sets of data. The slopes of the curves are not directly comparable because of differences in pressure and electrode spacing. For example, figure 13(a) shows that an increase in mixture velocity from 5.0 to 54.2 feet per second required approximately a 300-percent increase in energy, whereas figure 13(b) shows that the energy increase is only about 50 percent for a velocity increase from 50 to 200 feet per second.



(a) Gas velocity and pressure. Data obtained in simple flow apparatus; electrode spacing, 0.25 inch (less than quenching distance); spark duration, approximately 600 to 800 microseconds. (Data from ref. 2.)

(b) Gas velocity. Data obtained in controlled-turbulence apparatus; electrode spacing, 0.37 inch; electrode diameter, 0.0225 inch; spark duration, approximately 500 microseconds. (Data from ref. 5.)

FIGURE 13.—Effect of gas velocity and pressure on energy required for ignition. Temperature, 80° F; fuel-air ratio, 0.0835.

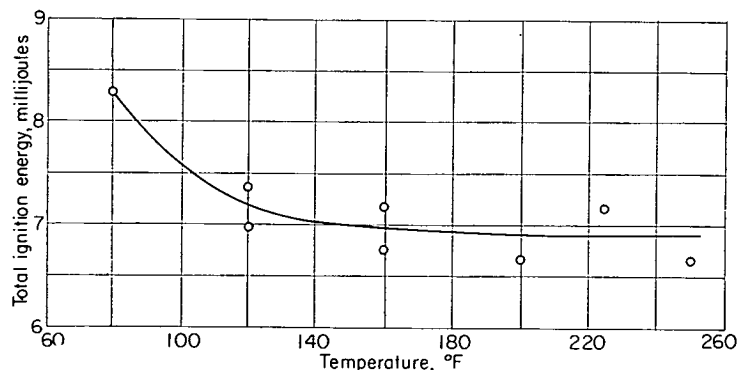


FIGURE 14.—Effect of initial temperature on total ignition energy. Pressure, 5.0 inches of mercury absolute; fuel-air ratio, 0.0835; gas velocity, 50 feet per second; electrode spacing, 0.37 inch; spark duration, 440 microseconds. (Data from ref. 6.)

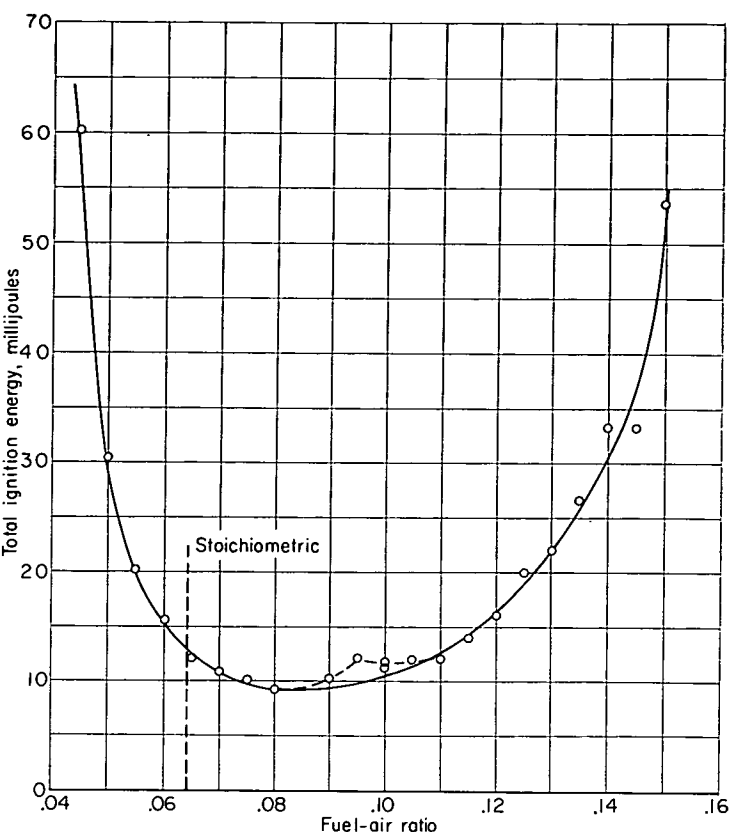


FIGURE 15.—Effect of fuel-air ratio on total ignition energy. Pressure, 5.0 inches of mercury absolute; temperature, 80° F; gas velocity, 50 feet per second; electrode spacing, 0.723 inch; spark duration, approximately 440 microseconds. (Data from ref. 6.)

PRESSURE AND TEMPERATURE

The effect of pressure on ignition energy is shown in figure 13(a). Energy decreases with increasing pressure in the same manner as found for ignition under quiescent conditions (ref. 10). The relation for ignition under flow conditions is $E \propto \frac{1}{p^n}$. The exponent n varies from about 1 to 2 for these data.

The effect of temperature (fig. 14) is also consistent with the trend found for quiescent gases (ref. 11) in that ignition energy decreases with increasing temperature.

FUEL-AIR RATIO

The effect of fuel-air ratio on ignition energy of flowing gases (fig. 15) is consistent with the trend observed for quiescent gases except that energy requirements are greater with a flowing mixture. The same fuel-air-ratio limits and minimum-energy point are observed. Close examination of the data points on the rich side of the minimum shows that the data might be better represented by the dashed line. Such double lobes have been observed in flammability-limit investigations with quiescent mixtures (ref. 12). The existence of a double lobe in figure 15 is questionable, however, and no great significance is attached to it.

TURBULENCE

If a turbulence promoter such as a wire screen is placed upstream of the spark electrodes, the ignition energy requirement varies with the mesh size and the distance between promoter and electrodes. The trends are illustrated

in figure 16, and the data are listed in table II. The ignition energy increases with increasing mesh size and with decreasing promoter-to-electrode distance.

TABLE II.—TURBULENCE AND IGNITION ENERGY DATA

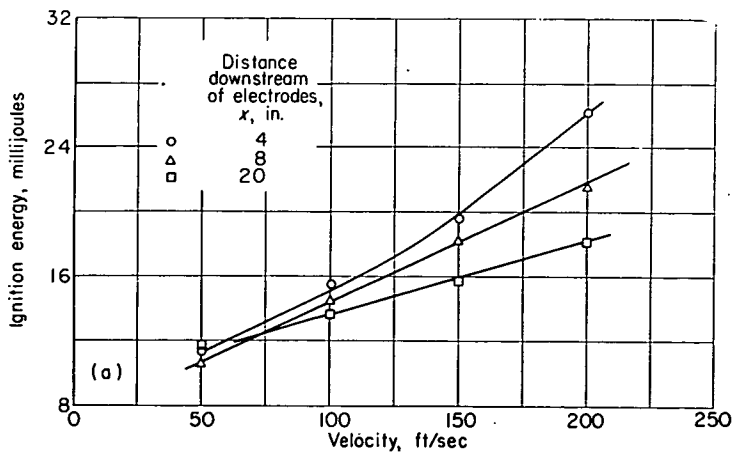
[Pressure, 5.0 in. Hg abs; temperature, 80° F; data from ref. 5.]

Mesh size of turbulence promoter, in.	Velocity, U , ft/sec	Distance downstream, x , in.	Intensity of turbulence, $\sqrt{u^2}$, ft/sec (a)	Scale of turbulence, L_x , in. (b)	Spark duration, t_s , microsec	Ignition energy, E_i , millijoules (c)
0.235	50	4	2.16	0.13	395	11.3
		8	1.19	.20	381	10.6
		20	.638	.35	415	11.6
	100	4	2.49	0.20	346	15.6
		8	1.88	.20	346	14.6
		20	.991	.30	325	13.7
	150	4	4.17	0.14	277	19.7
		8	2.35	.19	277	18.4
		20	1.26	.20	311	15.7
	200	4	5.76	0.15	277	26.4
		8	2.89	.20	277	21.7
		20	1.79	.30	249	18.27
0.525	50	4	3.44	0.17	464	11.0
		12	1.28	.26	450	10.6
		20	.868	.30	415	9.55
	100	4	7.34	0.20	415	21.2
		8	3.72	.23	381	16.5
		20	1.66	.30	388	14.1
	150	4	9.6	0.20	346	29.5
		8	5.25	.20	346	19.5
		20	2.62	.27	332	15.8
	200	4	11.8	0.19	318	46.4
		8	6.18	.20	346	25.2
		20	2.51	.30	318	23.0
0.625	50	4	4.0	-----	415	10.7
		8	2.03	-----	415	11.4
		20	1.03	-----	415	10.8
	100	4	7.04	-----	346	30.6
		8	3.61	-----	346	14.9
		20	1.76	-----	277	9.93
	150	4	9.08	-----	311	36.5
		8	5.68	-----	277	20.9
		20	2.55	-----	242	14.7
	200	4	11.8	-----	346	-----
		8	6.92	-----	277	34.6
		20	3.35	-----	208	23.2
No promoter	50	-----	-----	-----	346	9.28
	100	-----	-----	-----	311	12.0
	150	-----	-----	-----	242	13.5
	200	-----	-----	-----	208	13.5

• Obtained using air.

• Obtained using air. Data uncorrected for length of hot wire.

• Fuel, propane; fuel-air ratio, 0.0835 (by weight); electrode spacing, 0.37 in.



(a) Mesh size, 0.235 inch.

FIGURE 16.—Effect of velocity on ignition energy for various sizes and locations of turbulence promoters. Pressure, 5.0 inches of mercury absolute; temperature, 80° F; fuel-air ratio, 0.0835; electrode spacing, 0.37 inch; electrode diameter, 0.0225 inch; spark duration, approximately 500 microseconds. (Data from ref. 5.)

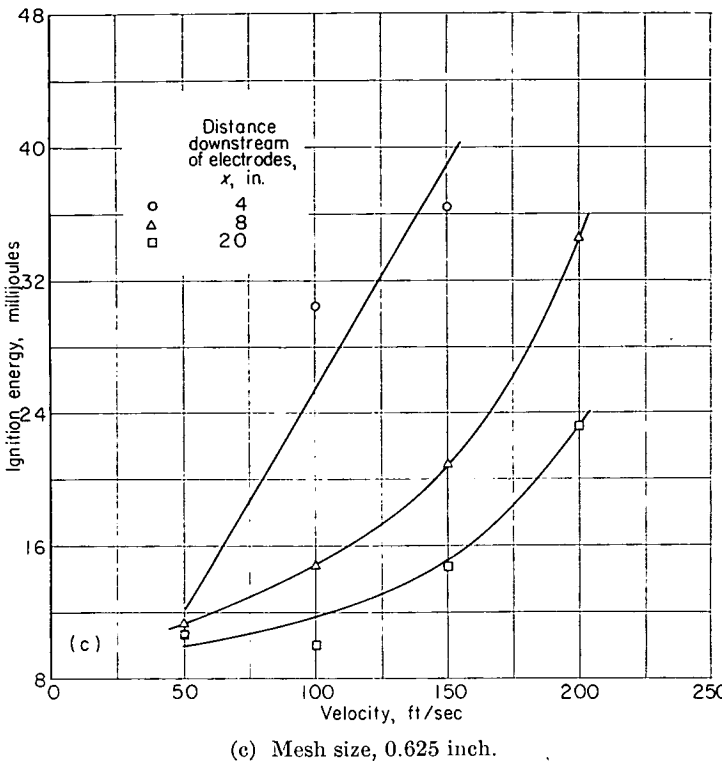
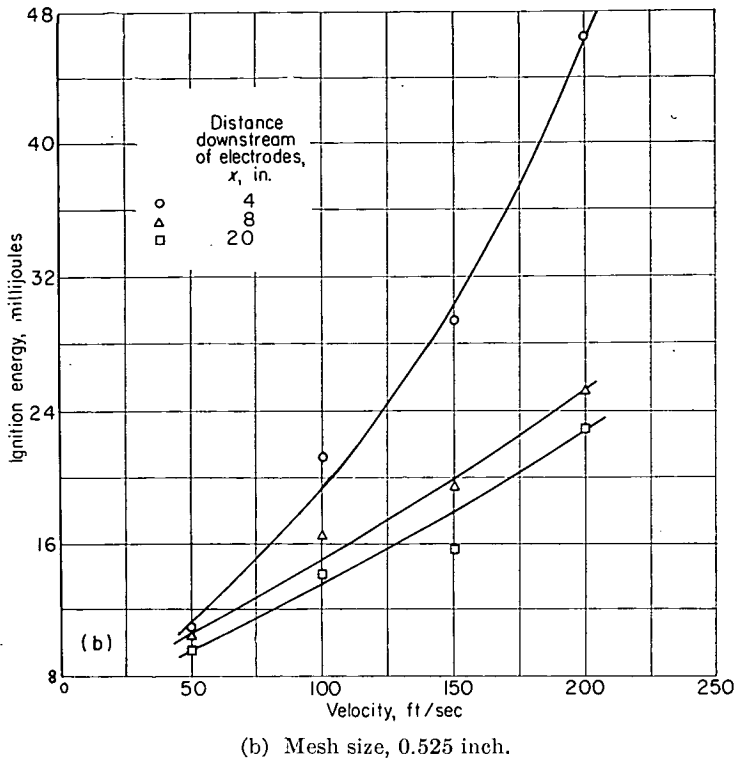


FIGURE 16.—Concluded. Effect of velocity on ignition energy for various sizes and locations of turbulence promoters. Pressure, 5.0 inches of mercury absolute; temperature, 80° F; fuel-air ratio, 0.0835; electrode spacing, 0.37 inch; electrode diameter, 0.0225 inch; spark duration, approximately 500 microseconds. (Data from ref. 5.)

Attempts have been made to analyze the effects of turbulence promoters on ignition energy in terms of the characteristics of the turbulence produced. Figure 17 shows the effect of velocity, distance, and mesh size on the experimentally measured values of intensity of turbulence. As the ratio of distance to mesh size x/m is decreased, the intensity of turbulence increases. Comparison of the data of figures 16 and 17 indicates that the minimum ignition energy required increases with an increase in turbulence.

Another turbulence factor that must be considered is the scale of turbulence, which can be important in eddy diffusion. Table II shows values of scales and intensities of turbulence and ignition energies for various mesh sizes, promoter-electrode distances, and velocities. The scale of turbulence has no apparent effect on energy if data at constant velocity and at approximately constant intensity are compared, as in table III. Hence, for conditions covered by this work, scale of turbulence may be neglected.

SPARK DURATION

The effect of spark duration on the energy required for ignition at velocities of 5.0 and 54.2 feet per second and

TABLE III.—EFFECT OF SCALE OF TURBULENCE ON LINE-SOURCE AND TOTAL IGNITION ENERGIES

[Pressure, 5.0 in. Hg abs; temperature, 80° F; data from ref. 5.]

Mesh size of turbulence promoter, in.	Distance downstream, x , in.	Velocity, U , ft/sec	Intensity of turbulence, $\sqrt{u^2}$, ft/sec	Scale of turbulence, L_z , in.	Line-source energy, E_L , millijoules	Total ignition energy, E_t , millijoules (a)
0.235 .525	8	50	1.19	0.17	6.9	10.6
	12		1.28	.26	6.6	10.6
0.235 .525	4	200	5.76	0.15	11.2	26.4
	8		6.18	.20	9.6	25.2

* Fuel-air ratio, 0.0535; electrode spacing, 0.37 in.

pressures of 3 and 4 inches of mercury absolute is shown in figure 18. As the spark duration was reduced from about 25,000 microseconds to about 100 microseconds, which was the limit of the measuring apparatus, the required energy decreased. The relation between energy and duration is not linear and is of the form $H \propto t^n$, where $n < 1$. The decrease in energy with the shorter durations may be explained in terms of the spark-discharge length. Decreasing the dura

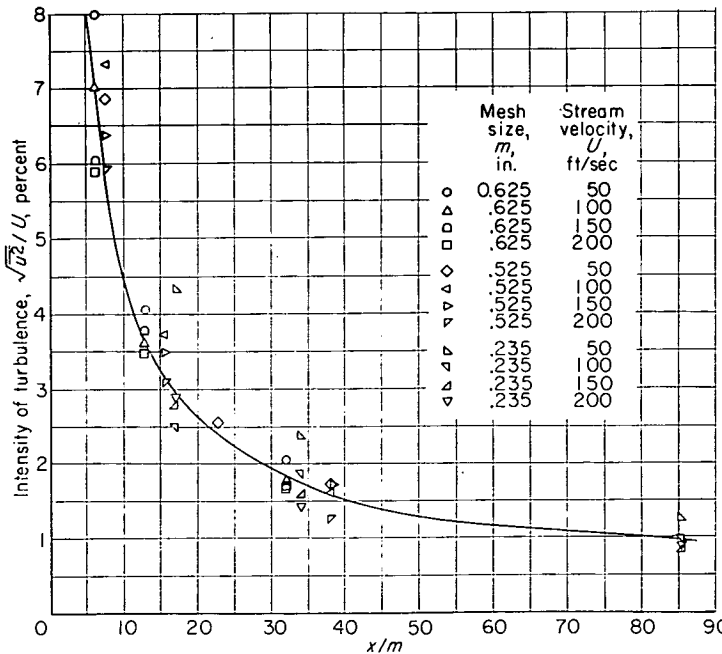


FIGURE 17.—Effect of x/m on $\sqrt{u^2}/U$ for various values of mesh size and velocity. (Data from ref. 5.)

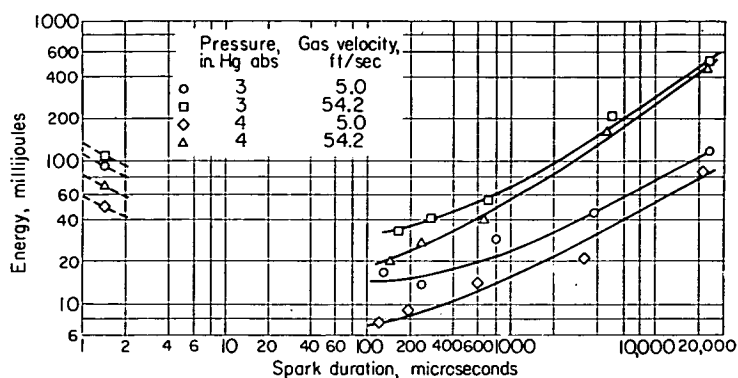


FIGURE 18.—Effect of spark duration on energy required for ignition. Temperature, 80° F; fuel-air ratio, 0.0835; electrode spacing, 0.25 inch (less than quenching distance). (Data from ref. 2.)

tion reduces the length of the discharge and thereby distributes the energy over a smaller volume. This distribution should result in a more effective ignition source.

An attempt was made to define minimum ignition requirements for very short duration discharges. A capacitance spark, that is, one obtained by discharging a condenser directly into the gap, was used. The energy values obtained in this manner, for a spark duration of 1.5 microseconds, are shown in figure 18. The fact that these energies are higher than those for longer duration sparks is contrary to the trends observed for spark durations between 100 and 25,000 microseconds. The discrepancy is explained in reference 3 as possibly being due to differences in the way the energy is distributed along the discharge length. It is not due to the fact that the data were obtained with electrode spacing less than quenching distance, since reference 3 shows the same trend with spacing equal to quenching distance.

ELECTRODE SPACING

As shown in figure 19, the effect of electrode spacing on ignition of flowing gases is similar to that observed for quiescent gases (ref. 10). As the electrode spacing was increased from about 0.25 inch, the energy required decreased for a variety of electrodes. With the smaller electrodes the spacing for minimum energy was not sharply defined. The increase in energy at spacings less than 0.65 inch is attributed to quenching of the initial flame zone by the electrodes. At the optimum spacing (0.65 in.), or arbitrarily assumed quenching distance, the quenching effect is a minimum. This quenching distance is the same as found for quiescent mixtures for the particular pressure and fuel-air-ratio conditions (ref. 10). The energy requirement increased at spacings greater than 0.65 inch for the same reason that the energy requirement increased with increased flow velocity, that is, the lengthening of the discharge path.

ELECTRODE DIAMETER AND CONFIGURATION

The effects of electrode diameter and configuration are also shown in figure 19. The data show that at the quenching distance (0.65 in.) the size or shape of the electrodes has no significant effect. However, at shorter spacings the larger electrodes require more energy for ignition because of their larger surface area for flame quenching. This same trend has been observed for capacitance sparks in quiescent mixtures (ref. 10). The fact that the sharp-needle electrodes

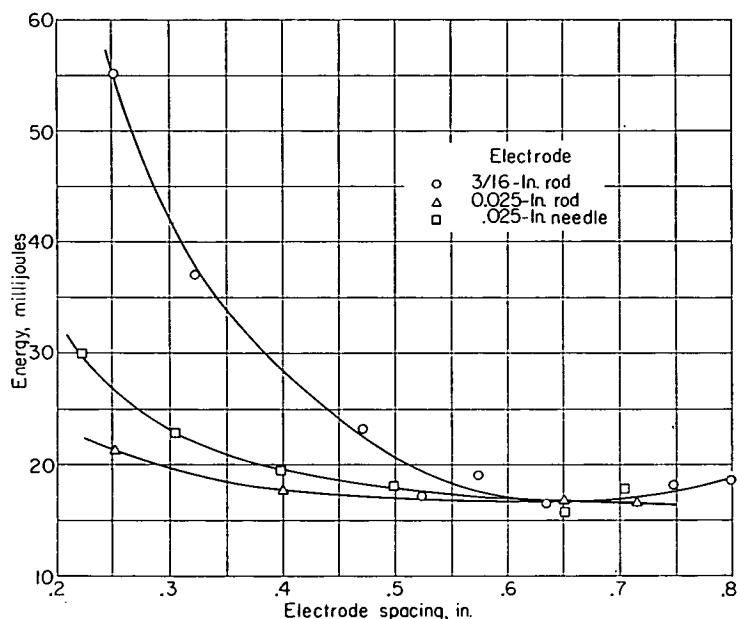


FIGURE 19.—Effect of electrode diameter, configuration, and spacing on ignition energy. Pressure, 3 inches of mercury absolute; temperature, 80° F; fuel-air ratio, 0.0835; velocity, 5.0 feet per second. (Data from ref. 3.)

required slightly higher energy in spite of smaller surface area may possibly be due to differences in the manner in which the energy is distributed along the length of the discharge for sharp points and rods.

TYPE OF DISCHARGE

The type of discharge used affects the energy required. Figure 20 shows data obtained with stainless steel electrodes that resulted in a glow discharge and data obtained with cadmium electrodes that resulted in a discharge designated as an arc-glow discharge. This discharge started as an arc discharge but changed into a glow discharge. For most of its life it was an arc discharge, however. The glow discharge required a higher ignition energy than did the arc discharge. This effect was not due to differences in electrode material, for after many trials a glow discharge was obtained with the cadmium electrodes. The energy value so obtained was comparable to that obtained with the stainless steel electrodes.

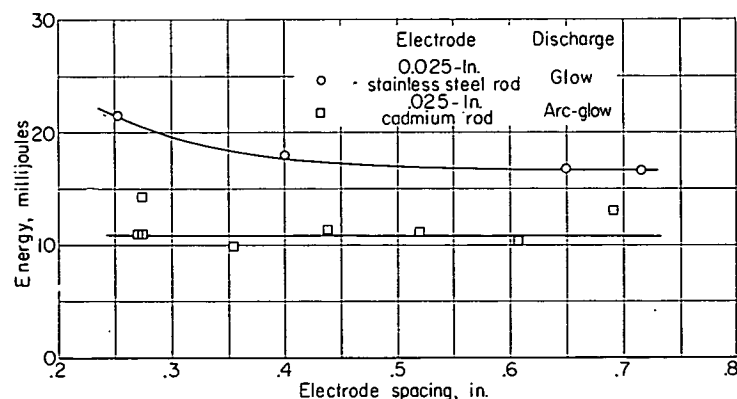


FIGURE 20.—Effect of electrode material and spacing on ignition energy. Pressure, 3 inches of mercury absolute; temperature, 80° F; fuel-air ratio, 0.0835; velocity, 5.0 feet per second. (Data from ref. 3.)

The fact that the arc discharge has lower cathode and total energy may indicate that the positive-column energies of both arc and glow discharges were equal and that the ignition occurred in the positive column. There are no experimental measurements of cathode energies for the arc-glow discharge; the experimental method used for the glow discharge failed when such measurements were attempted because the transition between arc and glow upset cross-plotting techniques. Therefore, positive-column energies of the two discharges cannot be compared at the present time.

ELECTRODE MATERIAL

Investigations such as those reported in reference 13 indicate that electrode material has an effect on ignition in quiescent mixtures. The data show that decreasing density of the electrode material generally decreased the amount of energy required to ignite a flammable mixture. However, the type of discharge, that is, arc or glow, was not determined, and the observed effect may have been due to the type of discharge and not to the electrode material.

The effect of electrode material on ignition of flowing gases is reported in reference 3, which shows that at least for the glow discharge the ignition energy is negligibly affected by electrode material. Data reported in reference 3 may be summarized as follows:

Metal	Ignition energy, millijoules *
Lead.....	17.1±0.5
Brass.....	17.8±0.5
Cadmium.....	18.6±0.5
Aluminum.....	19.4±0.7
Tungsten.....	19.6±0.9

* Obtained with $\frac{3}{8}$ -inch-diam. spheres spaced 0.65 inch apart; pressure, 3.0 in. Hg abs; temperature, 80° F; velocity, 5.0 ft/sec; fuel-air ratio, 0.0335; spark duration, 600 μ sec.

DEVELOPMENT AND TESTS OF A THEORY OF IGNITION OF FLOWING GASES

It is shown previously that a large number of variables affect not only the physical and electrical characteristics of a spark discharge but also the ease of ignition of a flowing combustible gas. Theoretical equations that show how these variables may be related for both nonturbulent and turbulent flow are discussed in this section. Experimental data that are available are then applied to these relations.

CONCEPT OF LINE SOURCE OF ENERGY

Most investigations of ignition of combustible gases consider total energy of the discharge as the experimental variable. It is noted earlier, however, that the total energy is not distributed uniformly along the length of the discharge and that the distribution may be important to ignition. Ignition may conceivably proceed from only a portion of the discharge length, and the energy contained in this length must then be the basis for theoretical analysis. The model used to develop a theory for the ignition of flowing gases is shown in figure 21. After a spark discharge moves downstream and is extinguished at time t_s , there exists a heated zone larger in diameter than the discharge itself but in a

path coincident with that of the discharge. The vertical portion of the discharge (fig. 21) moves at stream velocity so that the same volume of gas is continuously heated, whereas the legs of the discharge lengthen with time so that fresh gas is continuously being heated at the electrode ends of the discharge. Hence, it may be considered that the zone surrounding the vertical portion of the discharge is at a much higher temperature than the legs and, therefore, constitutes a more probable zone of ignition. This vertical zone, or line source of ignition, is used in the development of the theory of ignition of flowing gases.

The line source of energy consists of a portion of the positive column of the discharge. The energy dissipated in the cathode region is assumed to be unimportant to the ignition process. This is a reasonable assumption, since, according to reference 8, in a glow discharge almost all of the cathode energy is lost to the cathode.

The energy in the line source of ignition can be calculated if two assumptions are made. The first assumption is that the total amount of energy in the discharge at any time varies linearly with time. Actually, for the ignition data presented herein the energy goes into the discharge somewhat more rapidly during the first part of the discharge; however, the assumption of uniform energy release is believed sufficiently accurate for practical use. The second assumption is that the power per unit length of discharge at any time is constant. The power can be based on either the total power if the cathode energy is assumed uniformly distributed throughout the gap or on the power in the positive column. Actually, in order to agree with the concept of the line source of energy, the power should be based on the positive column only; but for practical reasons involved in measurement of cathode energies, total power is used in most of the analysis. Correction of the data to include positive-column energies only is discussed later.

The average power P_{av} of the total energy E_s is E_s/t_s , where t_s is the spark duration. This average power is divided into two portions: the line source and the legs of the discharge. The relative amounts dissipated in each region depend upon the respective lengths of the legs and, hence, on time and gas velocity. The amount of power available for the line source at any instant is

$$P_{ls} = \frac{s}{2Ut + s} P_{av}$$

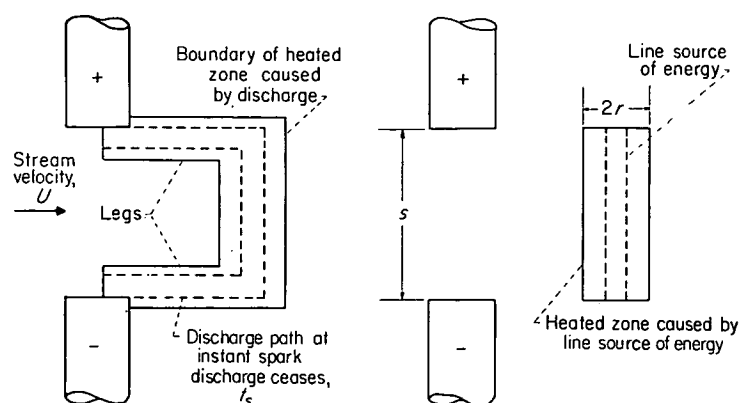


FIGURE 21.—Model used to develop concept of line source of energy.

The energy of the line source E_{i_s} is the integral of this instantaneous power with respect to time taken over the discharge duration or

$$\begin{aligned} E_{i_s} &= \int_0^{t_s} P_{i_s} dt \\ &= \int_0^{t_s} \frac{s}{2Ut+s} \frac{E_s}{t_s} dt \\ &= \frac{E_s s}{2Ut_s} \ln \frac{2Ut_s+s}{s} \end{aligned} \quad (2)$$

Equation (2) assumes the cathode and anode energies to be uniformly distributed over the whole length of the discharge. If the cathode energy is assumed to be lost to the electrode, E_s in equation (2) may be replaced by E_p where $E_p = E_s - E_c$:

$$E_{i_s} = \frac{E_p s}{2Ut_s} \ln \frac{2Ut_s+s}{s} \quad (3)$$

Equation (2) is used herein because E_c , and hence E_p , are difficult to measure accurately.

DEVELOPMENT OF THEORETICAL EQUATIONS

The process of establishing steady burning of a homogeneous fuel-air mixture from a long-duration discharge is visualized as follows: The line source of ignition is assumed to supply the heat necessary to raise the temperature of the heated zone to flame temperature. The initial flame then propagates if the heated zone is of proper volume to fulfill the condition that the rate of heat generation in the volume be equal to or greater than the rate of heat loss from the volume. An additional requirement is that the electrode spacing be equal to the quenching distance in order to preclude quenching effects. No heat losses from the heated zone either to the electrodes or to the gas during the spark duration are considered; also, no heat is considered to be supplied from any chemical reaction during this period.

The relation between ignition energy and operating variables can be determined by comparing the line-source energy with the theoretical amount of energy necessary to raise the temperature of the volume under consideration to flame temperature. The radius r of the heated volume (fig. 21) is the unknown dimension of the volume. Since both the rate of heat generation and the rate of heat loss are functions of the radius, equating these rates results in a value for the critical radius. The rate of heat generation in this heated zone is dependent upon the size of the volume and upon a reaction-rate term, whereas the rate of heat loss not only depends upon the size of the zone but also upon the method of heat transfer, that is, thermal conduction or eddy diffusion. According to the concept of a line source of energy, the zone is moving at stream velocity and, therefore, may be considered as a zone in a quiescent mixture if no turbulence is present. Heat is, therefore, lost from the zone by thermal conduction (neglecting radiation). If turbulence

is present, heat can be lost by both thermal conduction and eddy diffusion. The equations have been developed for two cases: (1) heat transfer by thermal conduction when intensity of turbulence is low and (2) heat transfer by eddy diffusion when intensity of turbulence is high. In the latter case it was assumed that thermal conduction is negligible compared to eddy diffusion.

Nonturbulent flow.—The equations for the rate of heat generation and the rate of heat loss are those of reference 11 converted from the spherical to the cylindrical case:

$$\text{Rate of heat generated} = \pi r^2 d_q Q X_f X_o \rho^2 a e^{-\frac{E_{act}}{RT_F}} \quad (4)$$

$$\begin{aligned} \text{Rate of heat loss} &= \frac{2\pi r d_q k (T_F - T_{am})}{\mathcal{J}_{re}} \\ &= \frac{2\pi r d_q k (T_F - T_{am})}{c_1 r} \end{aligned} \quad (5)$$

The term $c_1 r$ has been substituted for \mathcal{J}_{re} as done in reference 11. This substitution is an approximation; proof for its use is as follows: Equating equations (4) and (5) and solving for r give

$$r = \sqrt{\frac{2k(T_F - T_{am})}{c_1 Q X_f X_o \rho^2 a e^{-\frac{E_{act}}{RT_F}}}} \quad (6)$$

Equation (6) gives the critical size of the zone and indicates that r is inversely proportional to the square root of reaction rate. In a flame front the thickness of the reaction zone \mathcal{J}_{re} is approximately inversely proportional to the square root of the reaction rate; hence, r must be proportional to \mathcal{J}_{re} . The amount of energy necessary to increase the temperature of the zone from T_{am} to T_F is

$$\begin{aligned} E'_{i_s} &= J \pi r^2 d_q \rho c_p (T_F - T_{am}) \\ &= \frac{2\pi J k d_q c_p (T_F - T_{am})^2}{c_1 Q X_f X_o \rho a e^{-\frac{E_{act}}{RT_F}}} \end{aligned} \quad (7)$$

The theoretical energy should be equal to the line-source energy,

$$\begin{aligned} E'_{i_s} &= E_{i_s} \\ \frac{2\pi J k d_q c_p (T_F - T_{am})^2}{c_1 Q X_f X_o \rho a e^{-\frac{E_{act}}{RT_F}}} &= \frac{E_s d_q}{2Ut_s} \ln \left(\frac{2Ut_s + d_q}{d_q} \right) \end{aligned}$$

or

$$\frac{4\pi J U t_s k c_p (T_F - T_{am})^2}{c_1 E_s Q X_f X_o \rho a e^{-\frac{E_{act}}{RT_F}}} = \ln \left(\frac{2Ut_s + d_q}{d_q} \right) \quad (8)$$

Turbulent flow.—For turbulent flow the rate of heat loss depends on the rate at which mass is transferred by eddy diffusion through the cylindrical surface of area $2\pi r d_q$.

The two factors that control the diffusion process are the intensity and the scale of turbulence. When the scale of turbulence is large compared to the flame-front thickness as it is for this problem, the effect of scale on the diffusion process is negligible compared to the effect of intensity of turbulence; hence, the effect of scale is not included in the analysis that follows.

The rate of heat loss is a function of the product of surface area, density, specific heat, temperature difference, and a term representing the velocity with which heat moves through the surface. The velocity term can be represented by some function of the intensity of turbulence, or $f'(\sqrt{u^2})$. The function involves the first power of $\sqrt{u^2}$ in order to be correct dimensionally. Thus,

$$\text{Rate of heat loss} = 2\pi r d_q \rho c_p (T_F - T_{am}) f'(\sqrt{u^2}) \quad (9)$$

For ignition conditions equation (9) equals equation (4). Solving for r gives

$$r = \frac{2c_p(T_F - T_{am})}{\frac{E_{act}}{RT_F}} f'(\sqrt{u^2})$$

$$QX_f X_o \rho a e \frac{RT_F}{RT_F}$$

The theoretical energy required to increase the temperature of the heated zone to flame temperature under turbulent-flow conditions is

$$E'_{ls} = J\pi r^2 d_q c_p \rho (T_F - T_{am})$$

$$= \frac{4\pi J d_q c_p^3 (T_F - T_{am})^3}{\frac{2E_{act}}{RT_F}} f(\sqrt{u^2})$$

$$Q^2 X_f^2 X_o^2 \rho a^2 e \frac{RT_F}{RT_F}$$

where $f(\sqrt{u^2})$ is a new function of the intensity of turbulence.

The relation between the theoretical and the line-source energies is therefore

$$\frac{4\pi J d_q c_p^3 (T_F - T_{am})^3}{\frac{2E_{act}}{RT_F}} f(\sqrt{u^2}) = \frac{E_s d_q}{2U t_s} \ln \left(\frac{2U t_s + d_q}{d_q} \right) \quad (10)$$

$$Q^2 X_f^2 X_o^2 \rho a^2 e \frac{RT_F}{RT_F}$$

or

$$\frac{E_s Q^2 X_f^2 X_o^2 \rho a^2 e \frac{RT_F}{RT_F}}{8\pi U t_s J c_p^3 (T_F - T_{am})^3} \ln \left(\frac{2U t_s + d_q}{d_q} \right) = f(\sqrt{u^2}) \quad (11)$$

APPLICATION OF THEORETICAL EQUATIONS TO EXPERIMENTAL DATA

Only limited data are available to verify the theoretical equations. Although a considerable amount of data has been obtained, much of it cannot be used in the equations because of differences in type of discharge or because electrode spacings were less than the quenching distance. The data used with the equations following are those obtained with glow discharges and with spacing equal to the quenching distance.

Nonturbulent flow.—Data to be applied to the nonturbulent-flow equation were obtained with one fuel and one fuel-air ratio; hence, equation (8) may be reduced to

$$\frac{c_2 U t_s \kappa c_p T_F (T_F - T_{am})^2}{p E_s e^{-\frac{E_{act}}{RT_F}}} = \ln \frac{2U t_s + d_q}{d_q} \quad (12)$$

where $\rho \propto \frac{p}{T_F}$. A plot of this relation is shown in figure 22

along with a table of the operating conditions and references for each point. The correlation is satisfactory for the limited data available.

Equation (8) indicates that there is an effect of fuel-air ratio. The data of figure 15 were applied to this equation which, for the operating conditions of the figure and for $\rho \propto 1/T_F$, reduces to

$$\ln \frac{E_s X_f X_o \ln \frac{2U t_s + d_q}{d_q}}{T_F (T_F - T_{am})^2} = c_3 + c_4 \left(\frac{1}{T_F} \right) \quad (13)$$

A plot of the data using equation (13) is shown in figure 23. A single straight line, which would be predicted by the theory was not obtained. There is a factor of about 2 between the values for the rich and lean ends of the curve. Possible reasons for this discrepancy are discussed later.

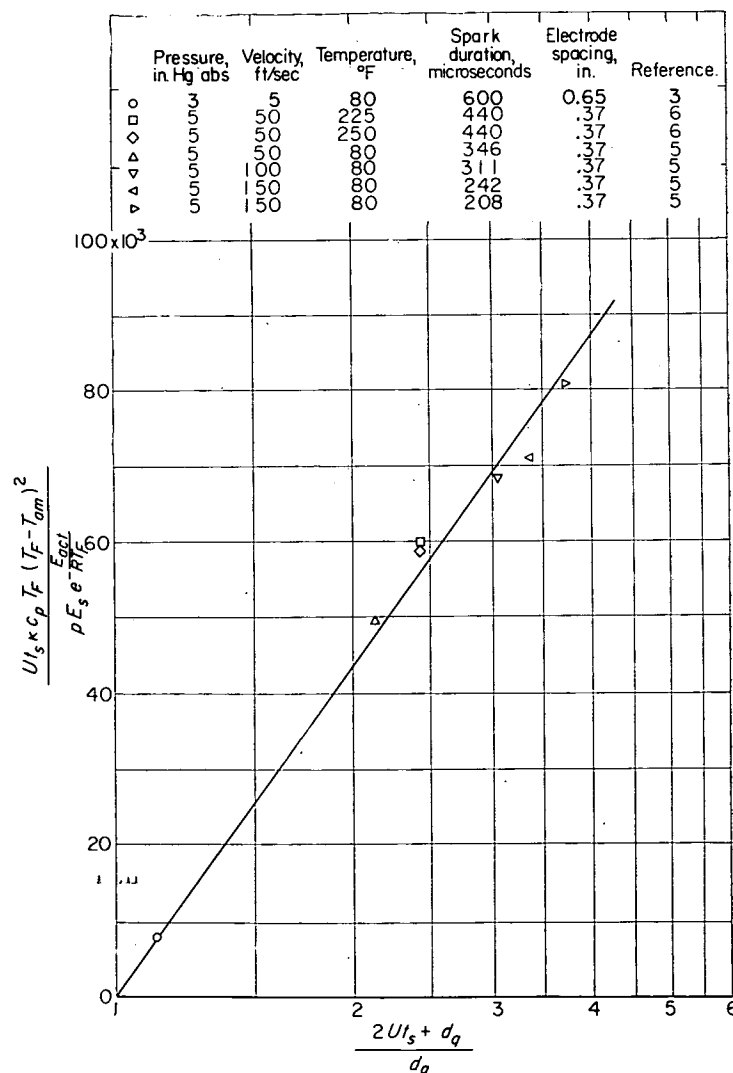


FIGURE 22.—Correlation of nonturbulent-flow data at fuel-air ratio of 0.0835.

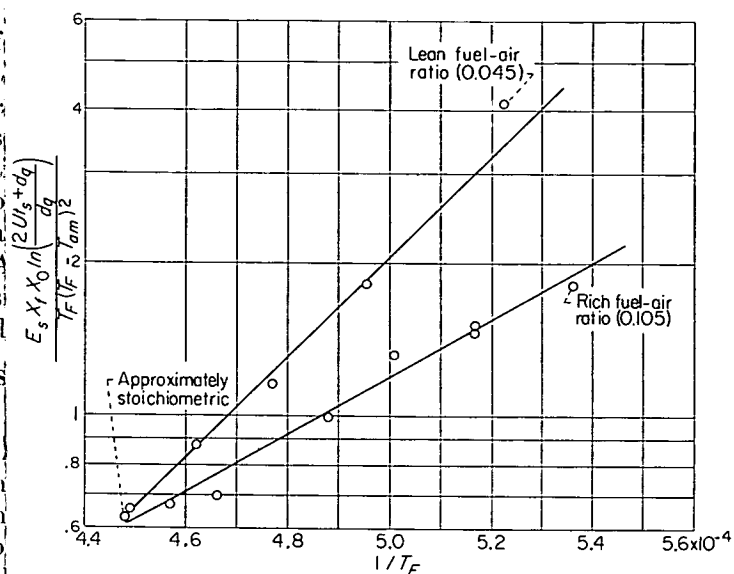


FIGURE 23.—Curve obtained by applying ignition-energy and fuel-air-ratio data to equation (13). (Data (fuel-air ratio 0.045 to 0.105) from fig. 15.)

Turbulent flow.—The data used to verify the turbulent flow equation (11) are those presented in figure 16. For the conditions used to obtain these data, equation (11) may be reduced to

$$\frac{E_s}{U t_s} \ln \frac{2U t_s + d_q}{d_q} = c_s f(\sqrt{u^2}) \quad (14)$$

Data calculated according to this relation are plotted in figure 24, which shows that a reasonably good correlation exists among the variables: energy required for ignition, stream velocity, and intensity of turbulence. The data correlated with an average deviation of 11 percent and a maximum deviation of 35 percent.

In developing the theory, the effect of scale of turbulence was considered unimportant. Experimental verification of this fact is indicated in table III, which shows a comparison of both line-source and total ignition energies at approximately constant intensities of turbulence but varying scales of turbulence. With the experimental errors involved and small variation in scale investigated, it must be concluded that the effect of scale, if any, is small.

DISCUSSION OF THEORY

The theory that is described in the preceding section and its experimental verification mark the first attempt to treat ignition of flowing gases and, as such, are greatly simplified. The many approximations and assumptions that are made may be summarized as follows:

- (1) The analysis is based on a second-order reaction for the rate of heat generation.
- (2) Diffusion processes are neglected.
- (3) Radiation from the ignition zone is neglected.
- (4) An approximation is made of thickness of the reaction zone.
- (5) The average power of the discharge is assumed to be constant.
- (6) The discharge is assumed to take the shape of a square-cornered U ; rounding effects at the corners are neglected.

(7) Cathode energy is assumed evenly distributed along the length of the discharge.

(8) There are no heat losses from the heated zone left by the spark during the duration of the discharge.

(9) There is no heat resulting from chemical reaction in the heated zone during the duration of the discharge.

Many of these assumptions could be removed from the theory, but the theoretical treatment would be unduly complicated.

The data used to verify the theory are limited in scope. This is the result of using data from one type of discharge (glow). Glow discharges are mostly obtained at low pressures, and arc discharges are obtained at higher pressures. Energy measurements cannot be made at higher pressures, because the small amount of energy required for ignition at high pressures becomes comparable to the energy stored in the capacitance of the voltage divider. This latter energy is not measured by the oscillographic technique used.

The effects on ignition energy of all operating variables except fuel-air ratio were correlated by the theoretical relations. Other investigators have also encountered inconsistencies in variable-fuel-air-ratio data. For example, in reference 10, which describes an ignition theory of quiescent gases that is separate and distinct from the one described herein, data obtained over a range of fuel-air ratios did not correlate with theoretical relations. The trends observed with the two theories may be compared by calculating the ratios of theoretical to experimental energy for the two sets of data. The term

$$\frac{4\pi JU t_s \kappa c_p (T_F - T_{am})^2}{c E_s Q X_f X_o \rho a e^{-\frac{E_{act}}{RT_F}} \ln \frac{2U t_s + d_q}{d_q}}$$

derived from equation (8) represents the ratio of theoretical to experimental energy for the data contained in this report. The values of κ and c_p in this equation were assumed constant, and a value of 26 kilocalories per mole was used for E_{act} . The energy ratios for the two sets of data were multiplied by constants in order to adjust the energy ratios to a

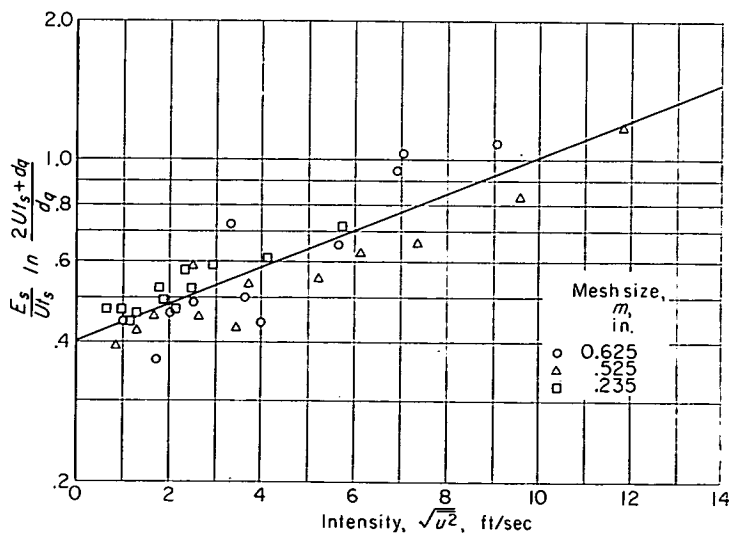


FIGURE 24.—Correlation of ignition data with intensity of turbulence. Pressure, 5.0 inches of mercury absolute; temperature, 80° F; fuel-air ratio, 0.0835. (Data from ref. 5.)

establish a spark discharge in a flowing stream as in a quiescent one. No voltage limitation is, therefore, imposed on an ignition system when it is used to ignite a flowing gas.

Finally, the significance of the theoretical research is in predicting how ignition energy requirements will be affected by a number of parameters. Exact values of energy may not be given by the theory, but at least the order of magnitude of energy change can be predicted. The results confirm the concept of a line source of ignition.

This research may be summarized to give the following ideal environmental conditions for ignition by electrical discharges:

- (1) Low gas-stream velocity
- (2) High pressure
- (3) Location of discharge in best mixture composition
- (4) High gas-stream temperature
- (5) Low turbulence in gas stream
- (6) Optimum spark duration as dictated by gas-velocity condition
- (7) Electrode spacing maintained at quenching distance
- (8) Small electrodes, if electrode spacing is less than quenching distance
- (9) Arc discharge in preference to glow discharge

These conditions are desirable from ignition considerations only. For over-all engine operation, all of the conditions may not be practical.

LEWIS FLIGHT PROPULSION LABORATORY

NATIONAL ADVISORY COMMITTEE FOR AERONAUTICS

CLEVELAND, OHIO, *June 20, 1956*

REFERENCES

1. Swett, Clyde C., Jr.: Investigation of Spark Gaps Subjected to Altitude and Air-Velocity Conditions. NACA RM E8I17, 1948.
2. Swett, Clyde C., Jr.: Spark Ignition of Flowing Gases. I—Energies to Ignite Propane-Air Mixtures in Pressure Range of 2 to 4 Inches Mercury Absolute. NACA RM E9E17, 1949.
3. Swett, Clyde C., Jr.: Spark Ignition of Flowing Gases. II—Effect

- of Electrode Parameters on Energy Required to Ignite a Propane-Air Mixture. NACA RM E51J12, 1951.
4. Swett, Clyde C., Jr., and Donlon, Richard H.: Spark Ignition of Flowing Gases. III—Effect of Turbulence Promoter on Energy Required to Ignite a Propane-Air Mixture. NACA RM E52J28, 1953.
5. Swett, Clyde C., Jr.: Spark Ignition of Flowing Gases. IV—Theory of Ignition in Nonturbulent and Turbulent Flow Using Long-Duration Discharges. NACA RM E54F29a, 1954.
6. Swett, Clyde C., Jr.: Spark Ignition of Flowing Gases. V—Application of Fuel-Air-Ratio and Initial-Temperature Data to Ignition Theory. NACA RM E55I16, 1955.
7. Mickelsen, William R., and Laurence, James C.: Measurement and Analysis of Turbulent Flow Containing Periodic Flow Fluctuations. NACA RM E53F19, 1953.
8. Cobine, James Dillon: Gaseous Conductors. McGraw-Hill Book Co., Inc., 1941.
9. Becker, J. A.: Thermionic Electron Emission and Absorption. Pt. I. Thermionic Emission. Rev. Mod. Phys., vol. 7, no. 2, Apr. 1935, pp. 95–128.
10. Lewis, Bernard, and von Elbe, Guenther: Combustion, Flames and Explosions of Gases. Academic Press, Inc., 1951.
11. Fenn, John B.: Lean Inflammability Limit and Minimum Spark Ignition Energy. Ind. and Eng. Chem., vol. 43, no. 12, Dec. 1951, pp. 2865–2868.
12. DiPiazza, James T., Gerstein, Melvin, and Weast, Robert C.: Flammability Limits of Hydrocarbon-Air Mixtures. Reduced Pressures. Ind. and Eng. Chem., vol. 43, no. 12, Dec. 1951, pp. 2721–2725.
13. Thornton, W. M.: The Reaction between Gas and Pole in the Electrical Ignition of Gaseous Mixtures. Proc. Roy. Soc. (London), ser. A, vol. XCII, no. A634, Oct. 1, 1915, pp. 9–22.
14. Jackson, Joseph L., and Brokaw, Richard S.: Variation of Spontaneous Ignition Delays with Temperature and Composition for Propane-Oxygen-Nitrogen Mixtures at Atmospheric Pressure. NACA RM E54B19, 1954.
15. Brokaw, Richard S., and Jackson, Joseph L.: Effect of Temperature, Pressure, and Composition on Ignition Delays for Propane Flames. Fifth Symposium (International) on Combustion, The Reinhold Pub. Corp., 1955, pp. 563–569.
16. Druyvesteyn, M. J., and Penning, F. M.: The Mechanism of Electrical Discharges in Gases of Low Pressure. Rev. Mod. Phys., vol. 12, no. 2, Apr. 1940, pp. 87–174.

There are probably other factors that may be responsible for the observed discrepancy. Preferential diffusion of the deficient reactant in the combustible mixture could be a contributing factor, as discussed in reference 10. Or possibly some cool flame mechanism that results in different activation energy in lean and rich mixtures may be present. Both of these items are qualitatively in the right direction to account for this difference between lean and rich data. Actually, a combination of the above factors may be responsible for the discrepancy. Further research on all the factors discussed is indicated.

SIGNIFICANCE OF RESULTS IN RELATION TO PRACTICAL IGNITION PROBLEMS

Most research on spark ignition reported in the literature has been conducted with quiescent gases; the work contained herein comprises the bulk of information that is available on ignition of flowing gases. The purpose of this section of the report is to point out the significance of this latter information with relation to practical ignition problems.

The experimental data on ignition of flowing gases show that the energy required for ignition is low even under severe velocity, pressure, and turbulence conditions. The amount of energy is measured in millijoules, whereas in aircraft operation an amount of 3 joules or more is not uncommon. It is obvious that there is room for improvement in ignition. Any means whereby lower ignition energies would be obtained would lead to the development of simpler, lighter weight, more efficient, and possibly, more reliable ignition systems.

One cause of the high ignition energy requirement in engines must be the mixture composition, which is quite different from the homogeneous composition used herein. The fuel-air ratio near the line source of ignition in an engine depends upon the degree of atomization of the fuel, on fuel-spray and air-flow patterns, and on the rate of vaporization of the fuel. This localized fuel-air ratio varies with operating conditions, and at any one operating condition, varies with time because of the fluctuating flow patterns that are inherently present in combustors. With these nonsteady heterogeneous mixture conditions, the ignition energy requirements may be many times greater than energy values reported herein. Temperature may also be important in ignition of the heterogeneous mixture, for some energy is needed to vaporize the liquid drops, the colder drops requiring more energy than warmer drops. Decreasing fuel volatility should also increase the energy requirements. All these factors can have adverse effects on ignition and, therefore, pose problems in the design of ignition systems.

Ignition in an engine should occur preferably in a sheltered region, that is, a region where low turbulence and low velocity exist. Such a region is difficult to find in the practical jet-engine combustor. The high mass-flow rates together with the air-entry-hole arrangements required to achieve high combustion efficiencies and uniform outlet temperature profiles make it difficult to provide such regions. Although turbulence is not desirable for easy ignition, it appears to be necessary for propagation of the initial flame throughout the combustor. Therefore, ignition systems must be designed for

the necessary turbulent condition. However, turbulence by itself, as shown herein, does not result in excessive energies if the mixture conditions are suitable.

Low velocities and short spark durations are desirable because they result in short spark-discharge length. Spark-discharge length is responsible for many of the trends observed. It determines current, voltage, energy and energy distribution, occurrence of multiple discharges, and ignition characteristics. The current and the voltage have little practical significance, but the other factors are important.

Increased discharge length due to either velocity or time increases the resistance of the discharge and thereby changes the division of energy among the legs of the discharge, the line source of ignition, and the impedance of the ignition source. The larger the discharge resistance, the smaller the loss in the impedance of the ignition source; hence, the efficiency of the ignition system is actually increased by increased discharge length. For a low-impedance source this increase in efficiency may be insignificant, however.

Although the efficiency of the system is improved, the amount of energy that goes into the line source of ignition is actually decreased as velocity is increased. Larger portions of the energy are then wasted in the legs of the discharges. Thus, as the length is increased with flow velocity and time, it becomes necessary to increase the total amount of energy if ignition is to be obtained.

Lengthening of the discharge path is also responsible for the occurrence of multiple discharges. Multiple discharges should normally be avoided because only one of the discharges may be expected to cause ignition. The energy in the other discharges is wasted. In the case of homogeneous mixtures, the first of the multiple discharges should cause ignition because it contains more energy than subsequent discharges. In the case of heterogeneous mixtures found in engines, however, one of the subsequent discharges might occur in a better fuel-air mixture and so cause ignition even though it has an energy somewhat smaller than the energy of the first discharge. Ease of ignition depends upon the actual variation of fuel-air ratio with time. Without knowledge of this variation, it is impossible to conclude that multiple discharges are desirable. It is also impossible to determine what the energy content and sparking rate should be for the repetitive discharges produced by commercial ignition systems. A reduction in the fuel-air-ratio fluctuations would lead to lower energies and lower sparking rates.

It is noted previously that the smaller the discharge length, that is, the lower the velocity and the shorter the spark duration, the smaller is the amount of energy required for ignition. However, the ignition energy at extremely short durations is higher than that found at somewhat longer durations. This, however, has only been observed under low-velocity conditions. With high velocities the short-duration discharge would be expected to require less energy than the long-duration discharge because of the reduced discharge length.

This research has indicated another significant fact which may not be generally known; namely, the breakdown voltage is not affected by the flowing stream. It is just as easy to

establish a spark discharge in a flowing stream as in a quiescent one. No voltage limitation is, therefore, imposed on an ignition system when it is used to ignite a flowing gas.

Finally, the significance of the theoretical research is in predicting how ignition energy requirements will be affected by a number of parameters. Exact values of energy may not be given by the theory, but at least the order of magnitude of energy change can be predicted. The results confirm the concept of a line source of ignition.

This research may be summarized to give the following ideal environmental conditions for ignition by electrical discharges:

- (1) Low gas-stream velocity
- (2) High pressure
- (3) Location of discharge in best mixture composition
- (4) High gas-stream temperature
- (5) Low turbulence in gas stream
- (6) Optimum spark duration as dictated by gas-velocity condition
- (7) Electrode spacing maintained at quenching distance
- (8) Small electrodes, if electrode spacing is less than quenching distance
- (9) Arc discharge in preference to glow discharge

These conditions are desirable from ignition considerations only. For over-all engine operation, all of the conditions may not be practical.

LEWIS FLIGHT PROPULSION LABORATORY

NATIONAL ADVISORY COMMITTEE FOR AERONAUTICS

CLEVELAND, OHIO, *June 20, 1956*

REFERENCES

1. Swett, Clyde C., Jr.: Investigation of Spark Gaps Subjected to Altitude and Air-Velocity Conditions. NACA RM E8I17, 1948.
2. Swett, Clyde C., Jr.: Spark Ignition of Flowing Gases. I—Energies to Ignite Propane-Air Mixtures in Pressure Range of 2 to 4 Inches Mercury Absolute. NACA RM E9E17, 1949.
3. Swett, Clyde C., Jr.: Spark Ignition of Flowing Gases. II—Effect of Electrode Parameters on Energy Required to Ignite a Propane-Air Mixture. NACA RM E51J12, 1951.
4. Swett, Clyde C., Jr., and Donlon, Richard H.: Spark Ignition of Flowing Gases. III—Effect of Turbulence Promoter on Energy Required to Ignite a Propane-Air Mixture. NACA RM E52J28, 1953.
5. Swett, Clyde C., Jr.: Spark Ignition of Flowing Gases. IV—Theory of Ignition in Nonturbulent and Turbulent Flow Using Long-Duration Discharges. NACA RM E54F29a, 1954.
6. Swett, Clyde C., Jr.: Spark Ignition of Flowing Gases. V—Application of Fuel-Air-Ratio and Initial-Temperature Data to Ignition Theory. NACA RM E55I16, 1955.
7. Mickelsen, William R., and Laurence, James C.: Measurement and Analysis of Turbulent Flow Containing Periodic Flow Fluctuations. NACA RM E53F19, 1953.
8. Cobine, James Dillon: Gaseous Conductors. McGraw-Hill Book Co., Inc., 1941.
9. Becker, J. A.: Thermionic Electron Emission and Absorption. Pt. I. Thermionic Emission. Rev. Mod. Phys., vol. 7, no. 2, Apr. 1935, pp. 95–128.
10. Lewis, Bernard, and von Elbe, Guenther: Combustion, Flames and Explosions of Gases. Academic Press, Inc., 1951.
11. Fenn, John B.: Lean Inflammability Limit and Minimum Spark Ignition Energy. Ind. and Eng. Chem., vol. 43, no. 12, Dec. 1951, pp. 2865–2868.
12. DiPiazza, James T., Gerstein, Melvin, and Weast, Robert C.: Flammability Limits of Hydrocarbon-Air Mixtures. Reduced Pressures. Ind. and Eng. Chem., vol. 43, no. 12, Dec. 1951, pp. 2721–2725.
13. Thornton, W. M.: The Reaction between Gas and Pole in the Electrical Ignition of Gaseous Mixtures. Proc. Roy. Soc. (London), ser. A, vol. XCII, no. A634, Oct. 1, 1915, pp. 9–22.
14. Jackson, Joseph L., and Brokaw, Richard S.: Variation of Spontaneous Ignition Delays with Temperature and Composition for Propane-Oxygen-Nitrogen Mixtures at Atmospheric Pressure. NACA RM E54B19, 1954.
15. Brokaw, Richard S., and Jackson, Joseph L.: Effect of Temperature, Pressure, and Composition on Ignition Delays for Propane Flames. Fifth Symposium (International) on Combustion, The Reinhold Pub. Corp., 1955, pp. 563–569.
16. Druyvesteyn, M. J., and Penning, F. M.: The Mechanism of Electrical Discharges in Gases of Low Pressure. Rev. Mod. Phys., vol. 12, no. 2, Apr. 1940, pp. 87–174.

REPORT 1288

COOPERATIVE INVESTIGATION OF RELATIONSHIP BETWEEN STATIC AND FATIGUE PROPERTIES OF WROUGHT N-155 ALLOY AT ELEVATED TEMPERATURES¹

BY NACA SUBCOMMITTEE ON POWER-PLANT MATERIALS

SUMMARY

Extensive data were obtained relating properties of wrought N-155 alloy under static, combined static and dynamic, and completely reversed dynamic stress conditions. Time periods for fracture ranged from 50 to 500 hours at room temperature, 1,000°, 1,200°, 1,350°, and 1,500° F. Correlation of the data showed:

1. Increasingly higher percentages of dynamic stress superimposed on the steady loads for rupture in 50, 150, and 500 hours were required to change rupture strength appreciably as the temperature increased. At 1,500° F the dynamic stresses approached the completely reversed fatigue strength before a substantial reduction in fracture time occurred.

2. A given amount of superimposed dynamic stress had decreasingly less effect on the rupture time as the steady stress was reduced to increase rupture time.

3. Completely reversed stress tests showed fatigue strengths which were of the order of 40 to 60 percent of the static tensile strength over the entire temperature range. As the temperature and time periods considered were increased, the fatigue strengths increased relative to static rupture strengths to values twice the rupture strength for 500 hours at 1,500° F. This means that the material can tolerate a cyclic load of larger magnitude than the steady load for fracture in time periods longer than some limiting value under conditions where creep occurs.

4. Limited data indicated that under combined stresses up to 27 percent of the steady load at 1,350° and 1,500° F the fatigue stress did not appreciably alter the creep characteristic through the second stage of creep. Apparently superimposed fatigue stresses exerted their main influence during the third stage of creep, at least for this particular test material and these test conditions.

5. Properties evaluated on the basis of number of cycles to failure differed from those evaluated on a time basis only when the properties were time dependent. Thus two fatigue machines operating at different cyclic speeds gave differing values on a cyclic basis when a fatigue limit was not attained. This was particularly evident in combined stress tests at 1,350° and 1,500° F.

6. Increasing amounts of fatigue loading decreased elongation from the rupture test progressively to very low values in completely reversed stress tests.

7. Bending tests gave slightly higher fatigue strengths than completely reversed axial stress tests. The difference decreased

with increasing test temperature so that the two types of tests gave comparable results at 1,500° F. There seemed to be little definite effect from variation in cyclic speed. Axial tests did not show the "knee" typical of many S-N curves. The knee also tended to disappear with increasing temperatures in all tests.

8. Surface-finish effects decreased with increasing temperature. Apparently residual stress was the main variable. Polished specimens gave higher strengths than ground specimens at low temperatures. This may have been a factor in the difference between bending and axial stress tests.

Limited data are reported on dynamic stress-strain properties, damping characteristics, and the influence of notches in rotating cantilever beam tests.

INTRODUCTION

Data are presented and correlated to relate the fatigue and static properties of wrought N-155 alloy over a wide range of temperatures. The work was undertaken on a cooperative basis to help clarify the principles governing the load-carrying ability of heat-resistant alloys at temperatures and conditions where both creep and fatigue can occur simultaneously. In view of the uncertainty in interpreting the results of various types of fatigue tests, duplicate data were obtained from as many types of fatigue testing machines as could be arranged.

In the major part of the program, extensive efforts were used to eliminate variations in test specimens as a factor. One cooperator did study surface-finish effects in reversed bending. Another cooperator obtained creep data under static tension and combined dynamic axial loading. This cooperator also measured damping and dynamic elasticity properties and carried out reversed bending tests on notched specimens.

The program was undertaken by the NACA Subcommittee on Power-Plant Materials in view of the uncertainties of the principles involved at high temperatures where materials are subjected to fatigue or fatigue and creep simultaneously. A Special Panel was appointed by the Subcommittee to investigate the relationships between static and fatigue properties of heat-resistant alloys at high temperatures. The fragmentary nature of available fatigue data at high temperatures made it nearly impossible to develop such

¹ Supersedes NACA TN 3216, "Cooperative Investigation of Relationship Between Static and Fatigue Properties of Wrought N-155 Alloy at Elevated Temperatures" by NACA Subcommittee on Power-Plant Materials, 1955.

relationships. The Panel decided that the best procedure was to organize a cooperative testing program to obtain reasonably complete data for one representative alloy.

Cooperation was obtained from the following organizations:

- (1) The Elliott Company
- (2) General Motors Corporation, Research Laboratories Division
- (3) National Advisory Committee for Aeronautics by contract with Battelle Memorial Institute
- (4) National Advisory Committee for Aeronautics, Lewis Flight Propulsion Laboratory
- (5) National Advisory Committee for Aeronautics by contract with the Engineering Research Institute, University of Michigan
- (6) Office of Naval Research, U. S. Navy, by contract with Battelle Memorial Institute
- (7) Rolls-Royce Limited, Research Laboratory, England
- (8) U. S. Naval Engineering Experiment Station
- (9) Westinghouse Electric Corporation, Research Laboratories
- (10) Wright Air Development Center, Materials Laboratory, by contract with the Institute of Industrial Research, Syracuse University
- (11) Wright Air Development Center, Materials Laboratory, by contract with the Institute of Technology, University of Minnesota

A progress report previously issued presented part of the data included in this report (ref. 1).

PROCEDURE

A Special Panel of the NACA Subcommittee on Power-Plant Materials arranged the cooperative program. The general objective was to obtain data which would define the load-carrying ability of a typical heat-resistant alloy at high temperatures as a function of mean and alternating stresses from static rupture tests to completely reversed fatigue tests. The temperatures selected were 1,000°, 1,200°, 1,350°, and 1,500° F to cover a wide range of temperature effects. In addition, some data were established at room temperature for comparative purposes. In general, tests were aimed to cover time periods for fracture of 50 to 500 hours so that the results could be expressed in terms of both time and cycles to failure. An attempt was made to obtain data from as many types of test machines as possible and particularly to have as many data as possible duplicated by two types of machines.

A procedure was adopted to reduce variations from test material and surface finish to a minimum because the program was set up to obtain objective data on the relation between static and dynamic properties at elevated temperatures. Low-carbon N-155 alloy bar stock solution-treated for 1 hour at 2,200° F, water-quenched, and then aged for 16 hours at 1,400° F was selected because it met two requirements. One was that this material treated in this manner had the most uniform properties at high temperatures of any representative "superalloy" known to the Panel. Secondly, it was metallurgically similar to several forged alloys of the type of interest for application in the gas turbines of jet engines. An additional factor in the choice was that there

was more experimental metallurgical background available for this alloy than for any other choice. The NACA purchased 271 feet of 1-inch round bar stock for the test program.

In order to insure uniformity of test specimens, the NACA sponsored the preparation of the specimens at the Engineering Research Institute of the University of Michigan. A system of sampling was set up so that any lot of specimens sent to a cooperator was made from material representative of the complete length of the original ingot. This avoided misleading trends which might have occurred from segregation effects in specimens taken from one hot-rolled length of bar stock. The bar stock was cut to the lengths required for specimens and heat-treated. All specimens were prepared using elaborate procedures to keep the surface of the gage sections constant regardless of shape.

Arrangements were made to have all fractured specimens examined. Westinghouse, Syracuse University, University of Minnesota, and the Lewis Laboratory of the NACA elected to examine the specimens which they tested. All others except those tested by Rolls-Royce were returned to the University of Michigan for visual and metallographic examination under sponsorship of the NACA.

Under sponsorship of the NACA, the Engineering Research Institute of the University of Michigan served as secretary to the Panel to compile data and prepare reports.

TEST MATERIAL

Two hundred and seventy-one feet of 1-inch round bar stock from one ingot of heat A-1726 were supplied as 26 mill-length bars in the as-rolled condition.

The chemical analysis of heat A-1726 was as follows:

Chemical composition, weight percent									
C	Mn	Si	Cr	Ni	Co	Mo	W	Cb	N
Supplier's heat analysis									
0.13	1.64	0.42	21.22	19.00	19.70	2.90	2.61	0.84	0.13
Univ. of Michigan check on bar stock									
0.14	1.43	0.35	20.80	18.80	19.65	3.00	2.00	0.99	0.135

The manufacturing conditions were reported to be as described in the appendix.

Coupons about 1 inch long were cut from both ends and the center of each bar, heated at 2,200° F for 1 hour, water quenched, and then aged at 1,400° F for 16 hours. The Brinell hardness was then determined on the surface of each coupon and at the center of the cross section. The hardness values shown in table I indicate good uniformity. Metallographic examination showed that specimens cut from the top, middle, and bottom bars of the ingot had similar structures after the heat treatment.

COOPERATING LABORATORIES AND TESTING METHODS

STATIC TESTS

The NACA sponsored short-time tensile tests and rupture tests at the University of Michigan. Testing temperatures were 1,000°, 1,200°, 1,350°, and 1,500° F. In addition

tensile tests were also run at room temperature. All tests were conducted in accordance with A.S.T.M. Recommended Practices on standard 0.505-inch-diameter specimens. Tensile specimens were held at temperature 1 hour before testing. The rupture specimens were brought to temperature over a 24-hour period before loading. Stress-strain data for the tensile tests and creep data from the rupture tests were measured with an optical lever extensometer system attached to the specimens.

DYNAMIC AXIAL STRESS FATIGUE AND CREEP TESTS

The Materials Laboratory, WADC, sponsored dynamic creep tests at 1,350° and 1,500° F at Syracuse University. Specimens having an equivalent uniform-diameter gage length of 2 inches (fig. 1 (a)) were tested under combinations of steady axial stress with superimposed axial dynamic stress. Loads were applied by a constant-force spring mechanism, the alternating stress being applied at 3,600 cpm. Temperatures were measured and controlled from thermocouples attached to the specimens.

Creep data were measured during the tests. In order to use the uniform-diameter gage-length specimens, the stresses had to be kept in tension. Consequently creep data were limited to ratios of alternating to mean stress of 0, 0.25, and 0.67. Combinations of stress were used to give fracture times out to several thousand hours.

The Materials Laboratory, WADC, also sponsored tests at high ratios of alternating to mean stress at Syracuse University and later at the University of Minnesota. Tests

were carried out in the same machines at ratios of alternating to mean stress of 1.64 and ∞ at 1,350° and 1,500° F and at ratios of 2 and ∞ at room temperature and 1,000° F. A profile specimen (fig. 1 (b)) was used to prevent buckling. The gage section was made the same as that of the specimens tested at Battelle Memorial Institute in Krouse machines at high alternating stresses. Creep data could not be obtained from this type of specimen.

Difficulty was encountered from heating of the specimen by damping during the application of the load in the tests at room temperature and 1,000° F. Attempts were made to control this by using an air blast to cool the specimens and by loading the specimens before they were brought to temperature. The most successful procedure, however, was to load the specimens at reduced cyclic speed and then gradually bring the specimens up to 3,600 cpm as a function of temperature.

In addition to the tests carried out on specimens prepared and furnished by the NACA through the University of Michigan, completely reversed stress tests were made at 1,500° F on specimens heat-treated and made at the University of Minnesota. The stock for the specimens was obtained from the producer in the form of bars rolled from the same heat at the same time as were the bars furnished to the NACA. Similar specimens were also used for part of the tests at 1,000° F.

The testing machine and details of procedure are described in references 2, 3, and 4.

KROUSE AXIAL FATIGUE TESTS

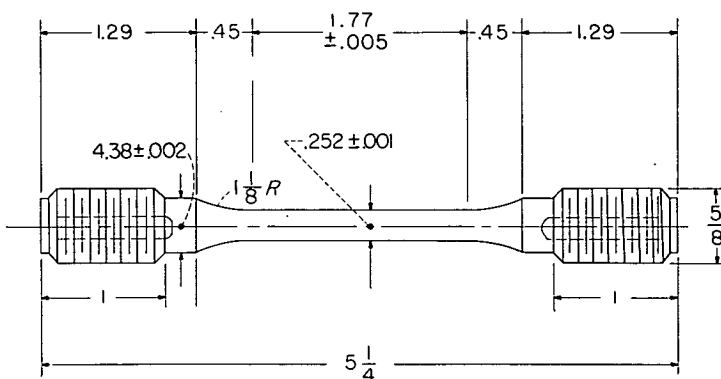
The Office of Naval Research and the NACA sponsored axial fatigue tests at Battelle Memorial Institute. Profile specimens (fig. 1(c)) were tested in a Krouse machine at 1,200°, 1,350°, and 1,500° F with varying mean stresses for constant superimposed axial fatigue loads of $\pm 7,500$, $\pm 15,000$, and $\pm 25,000$ psi. A modified specimen (fig. 1 (d)) was used for tests going into compression and for completely reversed stress tests at 1,350° and 1,500° F.

Constant axial loads are applied by the Krouse machine through a load maintainer, and constant-amplitude alternating axial loads at 1,500 cpm are applied through a crank mechanism. Special adapters had to be developed for the tests going into compression. Some difficulty in obtaining axially for the tests going into compression was encountered, but was corrected by redesigning grips.

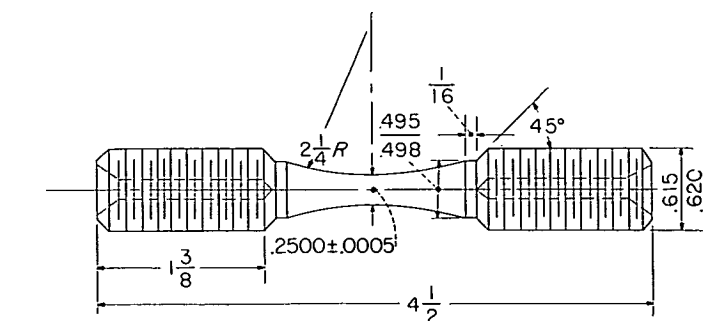
SONNTAG SF-4 AXIAL FATIGUE TESTS

The Elliott Company carried out tests in which combinations of steady axial and alternating axial stresses were applied. The alternating stresses were restricted to values which did not permit the combined stress to go into compression. The testing program was selected to provide the following data:

- Establish the alternating stresses to cause fracture at room temperature for a mean stress of 75,000 psi.
- Obtain curves of alternating stress versus rupture time out to 500 hours at 1,000° F for mean stresses of 75,000, 60,000, 45,000, and 40,000 psi.
- Establish the influence of superimposed alternating stress on the rupture time for tests with the mean stress equal



(a)

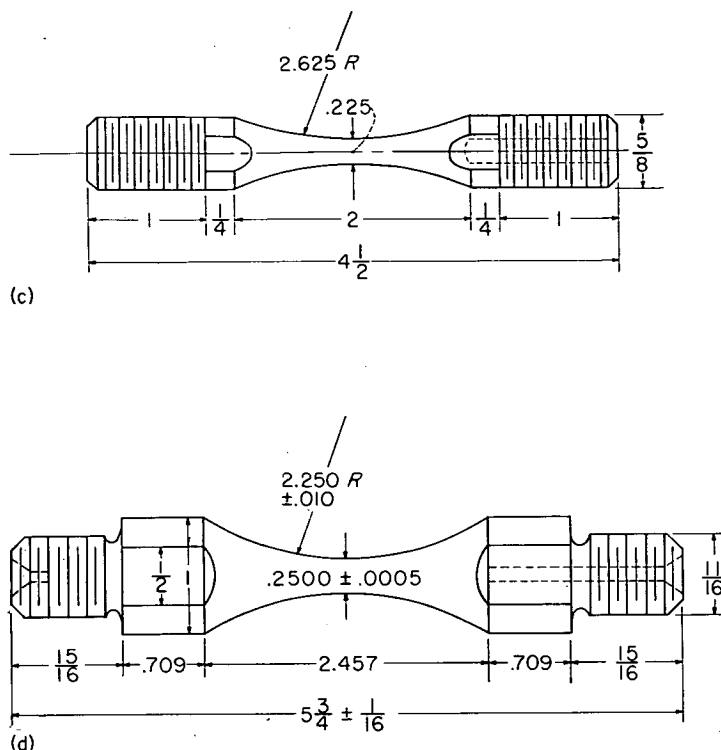


(b)

(a) Axial stress dynamic creep test specimen.

(b) Axial stress radius fatigue specimen.

FIGURE 1.—Fatigue specimens used by cooperators. R indicates radius. (All dimensions are in inches.)



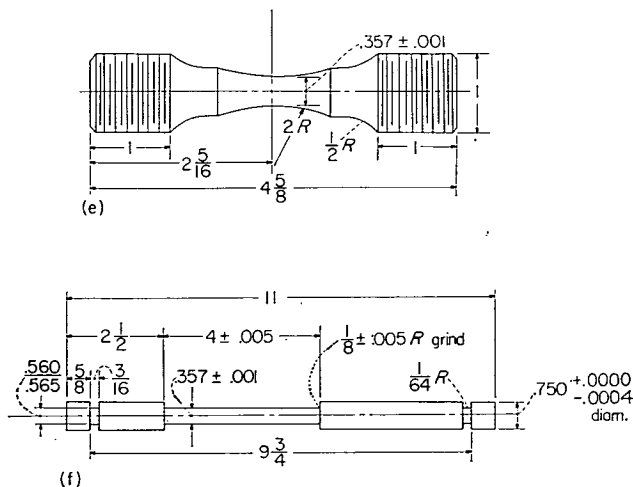
(c) Krouse machine axial stress fatigue specimen.
(d) Krouse machine axial stress fatigue specimen for tests in compression.

Figure 1.—Continued.

to the static rupture strength for 175 hours at 1,350° F (28,000 psi).

The Sonntag SF-4 machine applies constant-force loads through a spring mechanism. It operates at 3,600 cpm. Temperatures were measured and controlled by thermocouples in the furnace adjacent to the specimen. Eccentricity difficulties required new grips for the higher stress tests at 1,000° F.

The test specimen (fig. 1(e)) was profiled to a minimum diameter. A few of the specimens tested at 1,000° F were machined by the Elliott Company from blanks heat-treated at Michigan.



(e) Sonntag SF-4 axial stress fatigue specimen.
(f) Specimen for rupture tests with superimposed rotating bending stress.

Figure 1.—Continued.

RUPTURE TESTS WITH SUPERIMPOSED ALTERNATING BENDING STRESS

The Research Laboratories Division of the General Motors Corporation conducted tests at 1,350° F with combined rotating bending and steady axial tension stresses. A uniform diameter gage-length specimen (fig. 1(f)) was loaded in steady axial tension under 28,000-psi stress (stress to cause rupture in 175 hours) and then rotating bending stress was applied at 10,800 cpm by causing one end of the system to rotate in a circle. The specimen was heated by gas flames. Temperatures were measured by thermocouples welded to the gage length of the specimen.

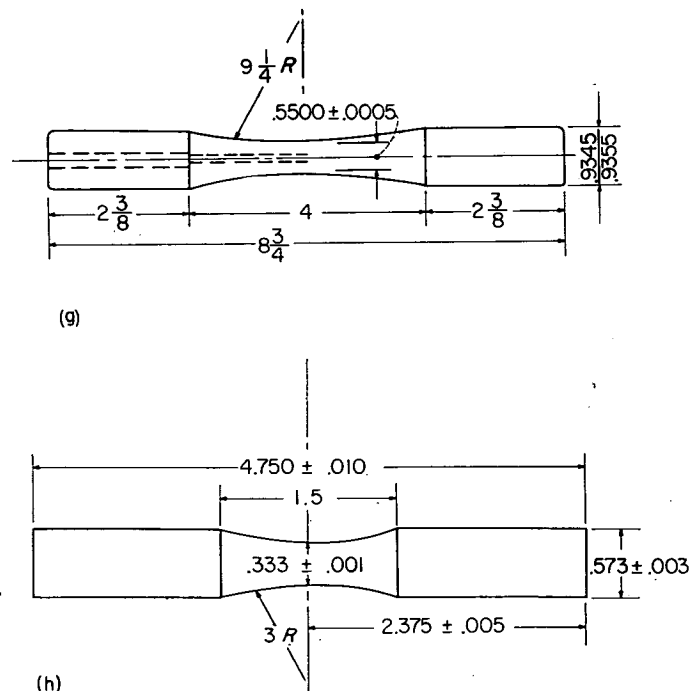
WESTINGHOUSE REVERSED BENDING FATIGUE TESTS

The Research Laboratories of the Westinghouse Electric Corporation conducted completely reversed bending tests at room temperature, 1,000°, 1,200°, 1,350°, and 1,500°. Round-profile specimens (fig. 1 (g)) were tested in the Westinghouse 7,200-cpm electronic fatigue machine. The specimens were vibrated electrically at resonance in one plane so that maximum stress occurred on the surface at two diametrically opposite points. Temperatures were measured and controlled by thermocouples welded to the specimens.

In addition to a complete set of tests on specimens machined at Michigan with the controlled machining procedure, check tests were made on specimens simply turned and hand polished at Michigan. The object of these tests was to obtain some information regarding the influence of surface finish.

EFFECT OF SURFACE FINISH ON WESTINGHOUSE REVERSED BENDING FATIGUE TESTS

The Lewis Laboratory of the NACA investigated the influence of surface finish on fatigue properties at room temperature and 1,350° F in the Westinghouse reversed bending fatigue machine described previously. A smaller specimen (fig. 1 (h)) was used by the NACA. Three types of finish



(g) Westinghouse reversed bending fatigue specimen.
(h) NACA modified Westinghouse reversed bending fatigue specimen.

FIGURE 1.—Continued.

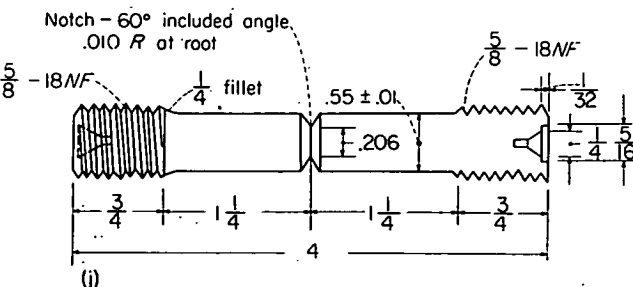
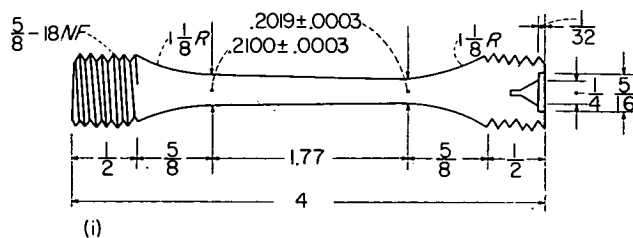
were utilized for the main tests: (1) ground and polished, (2) ground only, and (3) ground, partly polished, and then deliberately roughened with emery cloth. The influence of a stress relief for 4 hours at 1,400° F on the fatigue properties at room temperature was also established. In addition, tests were carried out at 1,350° F on specimens turned and polished. The polished specimens had about the same surface roughness as that of the specimens machined at Michigan. The specimens were machined at the Lewis Laboratory from blanks heat-treated by Michigan.

Temperatures were measured and controlled from thermocouples welded to the specimen.

FATIGUE, DAMPING, AND ELASTICITY PROPERTIES FROM ROTATING CANTILEVER BEAM TESTS ON UNNOTCHED AND NOTCHED SPECIMENS

The Materials Laboratory, WADC, sponsored tests at the University of Minnesota which provided fatigue, damping, and dynamic modulus data for room temperature, 1,350°, and 1,500° F. A special testing machine rotated specimens under cantilever beam loads. Targets mounted on the rotating extension arm, loading weight, and specimen assembly were used to measure vertical and horizontal deflections from which the damping and elastic values were calculated. Tapered specimens (fig. 1 (i)) resulted in equal maximum bending stresses along the gage length.

All tests were conducted under variable speeds of rotation. A speed of 20 rpm was used for the first 500 cycles. In general, the speed was then increased to 50 rpm until several thousand cycles were imposed, after which the highest speed between readings was about 400 rpm for the elevated-temperature tests and various speeds up to 1,500 rpm for the tests at room temperature. All deflection readings were taken at 20 rpm. Temperatures were measured and controlled from thermocouples attached to the specimens.



(i) Rotating cantilever beam specimen for fatigue, damping, and elasticity tests.

(j) Notched rotating cantilever beam specimen for fatigue, damping, and elasticity tests.

Figure 1.—Continued.

Tests were made on notched specimens (fig. 1 (j)) as well as on the unnotched specimens. The theoretical stress concentration factor was 2.6 according to Neuber's analysis. Approximate damping and dynamic elasticity properties were measured (ref. 5) but have not been included in this report.

The unnotched specimens were prepared at Michigan with the controlled surface-finish procedures. The notched specimens were prepared for Minnesota by the John Stulen Company.

The testing machine and procedures are described in detail in reference 5.

ROLLS-ROYCE ROTATING CANTILEVER BEAM TESTS

Rolls-Royce Limited of Derby, England, conducted rotating cantilever beam tests at their Research Laboratory. Tests were made at 1,200°, 1,350°, and 1,500° F. The testing machine was of their own design and operated at 5,500 rpm.

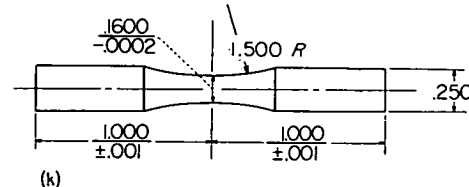
Temperatures were measured by thermocouples located 1/32 inch from the critical section of the test specimen. Data were submitted which showed that the maximum temperature difference between the specimen and the measuring thermocouple was 5.85° F; temperatures were reproducible to 1.8° F; and at any instant during the test the error in temperature measurement due to heat produced in the specimen from damping was less than 32.9° F.

The specimens used (fig. 1 (k)) were profiled to a minimum diameter. They were machined by Rolls-Royce from heat-treated stock supplied to them. Their specimen was small enough so that they quartered the bar stock in making specimens.

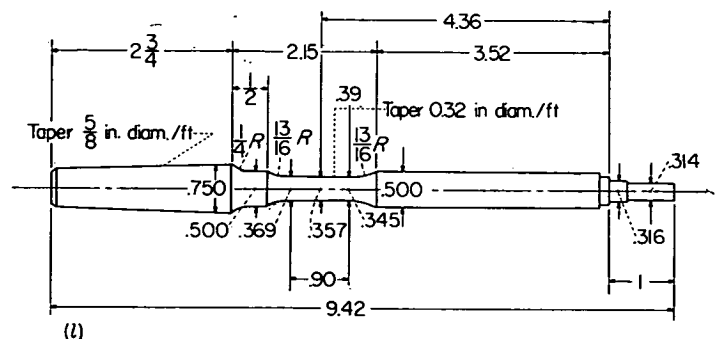
NEES ROTATING CANTILEVER BEAM FATIGUE TESTS

The Naval Engineering Experiment Station conducted completely reversed fatigue tests at 1,350° F in a rotating cantilever beam machine of their own design.

Tapered gage-length specimens (fig. 1 (l)) were loaded at one end and rotated at 1,700 cpm.



(k)



(l)

(k) Rolls-Royce rotating cantilever beam fatigue specimen.

(l) NEES rotating cantilever beam fatigue specimen.

Figure 1.—Concluded.

SPECIMEN PREPARATION

In an effort to keep surface finish constant, all the specimens except as noted later were prepared for the NACA by the Production Engineering Department of the University of Michigan. Procedures were developed which would meet requirements of constant surface roughness and constant surface cold-work for all types of specimens included in the program. The objective was to avoid variable surface-finish effects which would influence the results from the various types of tests. A third variable arising from specimen preparation (surface stresses) should also have been constant since the surface preparation was duplicated regardless of the shape and size of the specimen.

The surface roughness was maintained at 2 to 4 microinches root mean square. This quality of surface finish was established to meet the most severe specification of the several cooperators.

The amount of cold-work on the surface after finishing was not measured. Extreme precautions, however, were taken to reproduce the method of metal removal on all specimens in order to keep surface cold-work constant. This requirement imposed severe restrictions because the very close dimensional tolerances of the specimens had to be met with a fixed procedure for metal removal. The result was that the specimen preparation was very time consuming and expensive. Because emphasis was placed on reproducibility of surface finish on the various specimens and not on minimizing cold-work or surface roughness, the following details of machining and finishing operations should not be accepted as the most desirable for preparing fatigue specimens for testing at high temperatures.

MACHINING PROCEDURE

All of the several types of test specimens submitted to the University of Michigan for machining were processed by substantially traditional methods. All gage sections were turned on a lathe with the exception of the Krouse machine specimen for tests in compression (fig. 1 (d)). This specimen was turned on a milling machine in a setup wherein the specimen was mounted between centers in the spindle and the cutting tool was mounted on a rotary table which in turn was mounted on the table of the milling machine; the rotary table was rotated manually through a worm gearset for the feeding motion. All turning tools were 18-4-1 high-speed steel machine ground to the following shape: 10° back rake angle, 15° side rake angle, 10° relief angle, and 0.010-inch nose radius. All cutting speeds were confined to the range 30 to 40 feet per minute; the depth of cut was selected in a descending sequence ranging from the maximum of 0.030 inch to a minimum of 0.005 inch, while the feed rate was held constant at 0.005 inch per revolution in every case except for manual feed where an attempt was made to keep the feed above a minimum of 0.005 inch per revolution.

The above conditions were set up in the belief that the amount of cold flow was directly proportional to the size of cut. Consequently, it was expected that the progressively decreasing series of depth of cut used consistently would establish a degree of control as well as lead to a minimum of cold flow. The unique characteristics of the specimen material make it unusually susceptible to burnishing and

related effects resulting from dull cutting edges, especially at light feed rates. This latter reason was the basis for establishing a minimum feed rate.

FINISHING PROCEDURE

The original finishing setup was on a Kent-Owens 2-20 milling machine. The milling-machine setup was characterized by a continuous belt and was unique in that a system of counterbalances was used in an attempt to minimize and control the pressure between the cloth-backed abrasive and the specimen. However, irregularities developed and the mass of the counterbalance system made it impossible to achieve control over the pressure between the abrasive and the specimen.

The Krouse machine specimens (see fig. 1 (c)) were finished on the Kent-Owens setup using only cloth-backed abrasives as belts down through 500 grit, wherein the final step involved the use of a chrome-oxide polishing stick rubbed on thoroughly worn 500-grit belts. Irregularities of the belts and the light pressures used made it impossible to improve the accuracy of the machined specimens and it is probable in some cases that the runout and out-of-roundness increased as a consequence of the finishing process.

The Westinghouse specimens were finished on a special setup wherein strips of cloth-backed abrasive were fastened to the surface of an oscillating sector while the specimen was mounted between centers and rotated. By this time all attempts to control finishing pressure by counterbalancing had been abandoned in favor of precision positioning of the specimens relative to the abrasive so that greater accuracy could be obtained. Pressure control was achieved somewhat arbitrarily by holding back on the rate of cutting so that the specimen did not heat. The finishing procedure used on the Westinghouse specimens is considered to be the most satisfactory in terms of the original objective, although it was very slow and very expensive as a consequence of the relatively small amount of abrasive available during each setup.

All subsequent specimens were finished by one of two arrangements of a final setup shown schematically in figure 2. The specimen was mounted between centers and rotated. A continuous belt was operated over a system of driving and idler pulleys with the motion of the belt oriented long

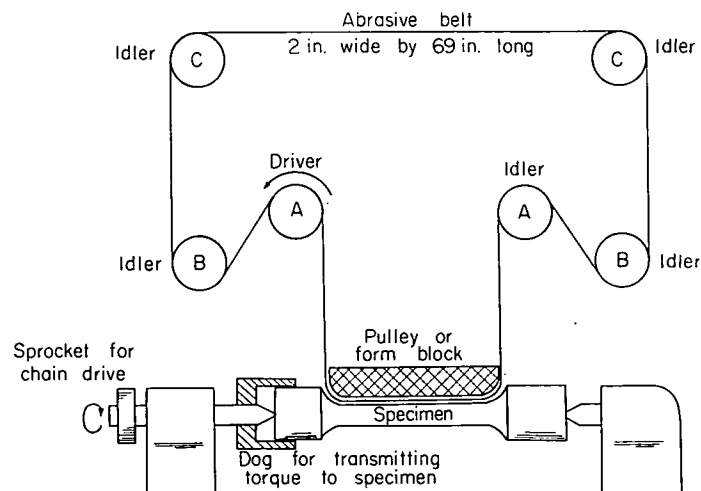


FIGURE 2.—Polishing machine.

radially to the specimen. When the longitudinal section of the specimen was a radius, a pulley or wheel with a corresponding radius was mounted in place of the form block shown in the sketch although a form block could be used for these specimens. The pulley or wheel was substituted for the form block in this case so as to reduce the heat arising from friction between the belt and the form block. Control of both pressure and size, to the extent that it was achieved, was obtained through screw adjustments of the position of the axis of the specimen relative to the form block or wheel.

The procedure for finishing specimens involved the use of continuous abrasive belts used in sequence of decreasing grain size with the following grain sizes: 60, 120, 240, 320, 400, and 500. This was followed by a final step wherein a standard tallow stick such as is used for grease polishing was smeared on a well-worn 500-grit belt to inhibit further its cutting action. It is vitally important to use this belt at highly specific operating conditions.

It is possible with such a combination to produce a highly finished surface by exerting considerable pressure between the belt and the specimen to be finished. However, much less cold flow and an even smoother finish can be obtained by using a very light pressure between the belt and the specimen. So far as is known now, this is a unique property of the type of specimen material.

It is significant that, as mentioned earlier in this report, chrome oxide was first used for this final step, although tallow was later used. From experimentation it became apparent that the chrome-oxide stick had little or no value as an abrasive but rather that the beneficial effects arose from the ability of the stearate base or bond to inhibit the abrasive and cutting action of the belt. It was this experience which led to the final practice of using tallow on a well-worn 500-grit belt for the final finishing step.

The belts were made from commercial rolls of Behr-Manning cloth-backed abrasive. Appropriate lengths were cut on a bias and the belt was formed with a butt joint backed up with a manila paper of about 0.006-inch thickness and cemented with a commercial grinding disk cement (Gardner No. 2 Disc Wheel cement).

SPECIMENS PREPARED BY COOPERATORS

Certain cooperators prepared their own specimens from stock heat-treated at the University of Michigan. In general, such specimens were for special purposes as follows:

(1) The Lewis Laboratory of the NACA prepared their own specimens because they were interested in studying surface-finish effects. The gage section was made by form-grinding in a cylindrical grinder with a 60-grit aluminum-oxide, vitrified bonded wheel of grade J and density 5. The grinding wheel speed was maintained between 5,000 and 7,000 surface feet per minute and the specimen speed for the finish cut was maintained between 200 and 300 surface feet per minute. The "polished" finish was prepared by polishing the ground surface with successively finer grades of emery cloth and paper, finishing in the longitudinal direction of the specimen with paper grade 20. The "rough" finish was prepared by semipolishing the ground specimens to remove the grinding scratches and then roughening the surface by hold-

ing a strip of 46-grit abrasive cloth against a slowly rotating specimen, causing circumferential finish marks. The "ground" specimens had the finish obtained in grinding, the finish marks being circumferential. One lot of specimens was turned in a lathe which gave the same finish as that described for the "polished" specimens.

(2) The notched specimens for the rotating cantilever beam tests at the University of Minnesota were prepared separately. It seemed impossible to duplicate the surface finish of the other specimens in a notch. The John Stulen Company made the specimens for the University of Minnesota using the following procedure:

- (a) Rough turned to 0.070 inch oversize in diameter
- (b) Rough ground to 0.025 inch oversize in diameter; feed, 0.040 inch per minute
- (c) Rough ground to 0.007 inch oversize in diameter; feed, 0.020 inch per minute
- (d) Finish ground to size; feed, 0.010 inch per minute

(3) Part of the specimens used for axial fatigue tests at 1,000° F and 1,500° F at the University of Minnesota were heat-treated and machined by the University of Minnesota. These specimens are designated in table IV by "N . . . F" rather than the "J . . ." designation used for specimens prepared at Michigan. The specimens were taken from the same stock as that used for the specimens prepared at Michigan but the stock was obtained directly from the supplier. Apparently, the machining procedure approximated that used at Michigan (ref. 3).

(4) A few specimens were prepared by the Elliott Company from blanks heat-treated at Michigan.

(5) Rolls-Royce prepared their own specimens from heat-treated blanks furnished to them.

TEST DATA

Test data from each individual cooperator have been included separately in the report. An effort was made to present the data exactly as reported. In general, the fatigue curves have been drawn as nearly as possible the way the cooperator drew them in submitting the data. In a few instances, curves were redrawn to present the data on a time basis rather than a number-of-cycle basis. In such cases, however, care was exercised to maintain the fatigue strength reported by the cooperator.

This procedure has been used because in several cases where there was duplication of tests it is probable that the curves would have been drawn differently if all the data had been considered. It seemed evident in considering the data that this feature was significant.

The data for each cooperator are explained in the following sections and any significant features recorded.

STATIC TENSILE AND RUPTURE TESTS

There was little variation in yield strengths between 1,000° and 1,500° F (see table II), although the tensile strength decreased appreciably over the same temperature range. Ductility also decreased with temperature. The agreement between check tests was quite close.

The original stress-rupture data obtained are given in table III and figure 3. The points fell on straight lines of logarith-

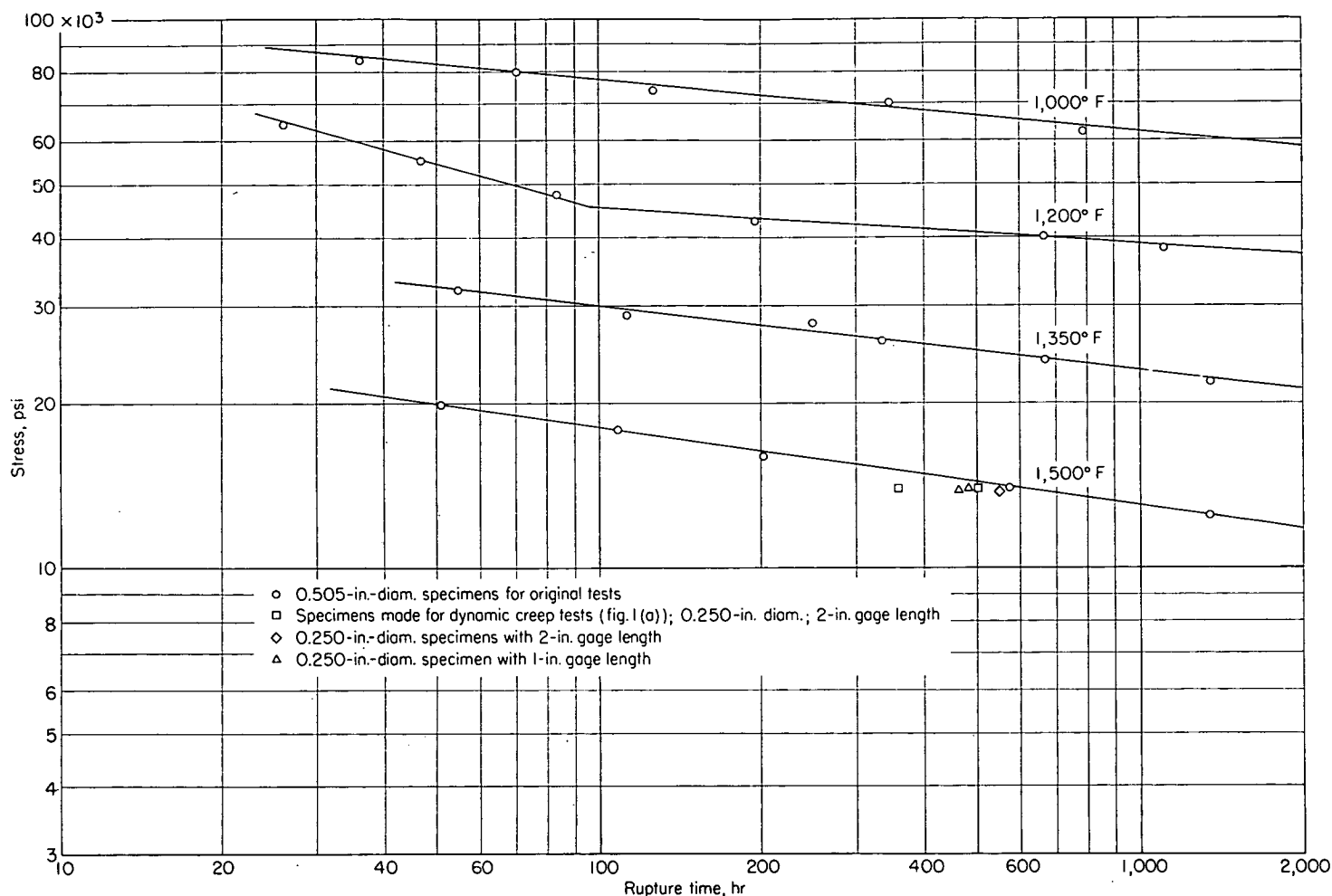


FIGURE 3.—Curves of stress against rupture time for static tests at 1,000°, 1,200°, 1,350°, and 1,500° F.

mic stress against logarithmic rupture time with no more scatter than usual even though the specimens were taken at random from the original mill lengths of bar stock. The curve for 1,200° F exhibited a decrease in slope at about 100 hours and 45,000 psi, which is somewhat unusual. Elongation and reduction-of-area values appeared to show more scatter than did the rupture times. They tended to decrease with time for rupture and were lowest at 1,200° F.

When the data for static tests in the dynamic creep test unit at Syracuse University became available, their slightly lower rupture strengths were evident. Certain check tests were made to try to determine the cause (table III and fig. 3).

Two specimens from the original group heat-treated and machined for Syracuse (fig. 1 (a)) were tested at Michigan. The results of one test fell closer to the Syracuse data than to the data from the original tests at Michigan (JX4). The data from the other one were closer to the original data (JR5). Two check tests were made on new specimens using a 1-inch gage length 0.250 inch in diameter to see if specimen size and surface preparation were responsible. The fracture times were slightly less than those for the original curve for 0.505-inch-diameter specimens. One additional test was made on a 0.250-inch-diameter specimen with a 2-inch gage length to see if the 2-inch gage length of the Syracuse specimens was a factor. A perfect check of the original data on 0.505-inch-diameter specimens was obtained. These results tend to indicate that variation in properties of the individual speci-

mens (JX4) could have been a contributing cause and probably was combined with some factor in testing technique. Specimen size or surface finish was apparently not a factor. One possible reason for a consistent variation in specimen properties might have been that all of the original specimens tested at Michigan were taken from the end of the mill lengths, whereas the Syracuse specimens were taken farther along the bars.

Creep data from the rupture tests in the form of curves of stress against testing time for 0.5 and 2 percent deformation are shown in figure 4. Minimum creep rates measured are included as curves of stress against creep rate in figure 5. These data are limited to 1,200°, 1,350°, and 1,500° F because deformation upon loading at 1,000° F exceeded deformations of interest.

DYNAMIC AXIAL STRESS FATIGUE AND CREEP TESTS

The dynamic creep test machine stresses a specimen axially with combinations of steady and alternating stress ranging from steady-load creep tests with no fatigue load through combinations of fatigue and steady stresses to completely reversed stress fatigue tests. The test data obtained are given in table IV. It will be noted that a series of tests was made at several constant ratios of alternating to mean stress (both alternating and mean stress were varied at a constant ratio). The primary graphical treatment was curves of mean stress against time for fracture for each constant ratio (see

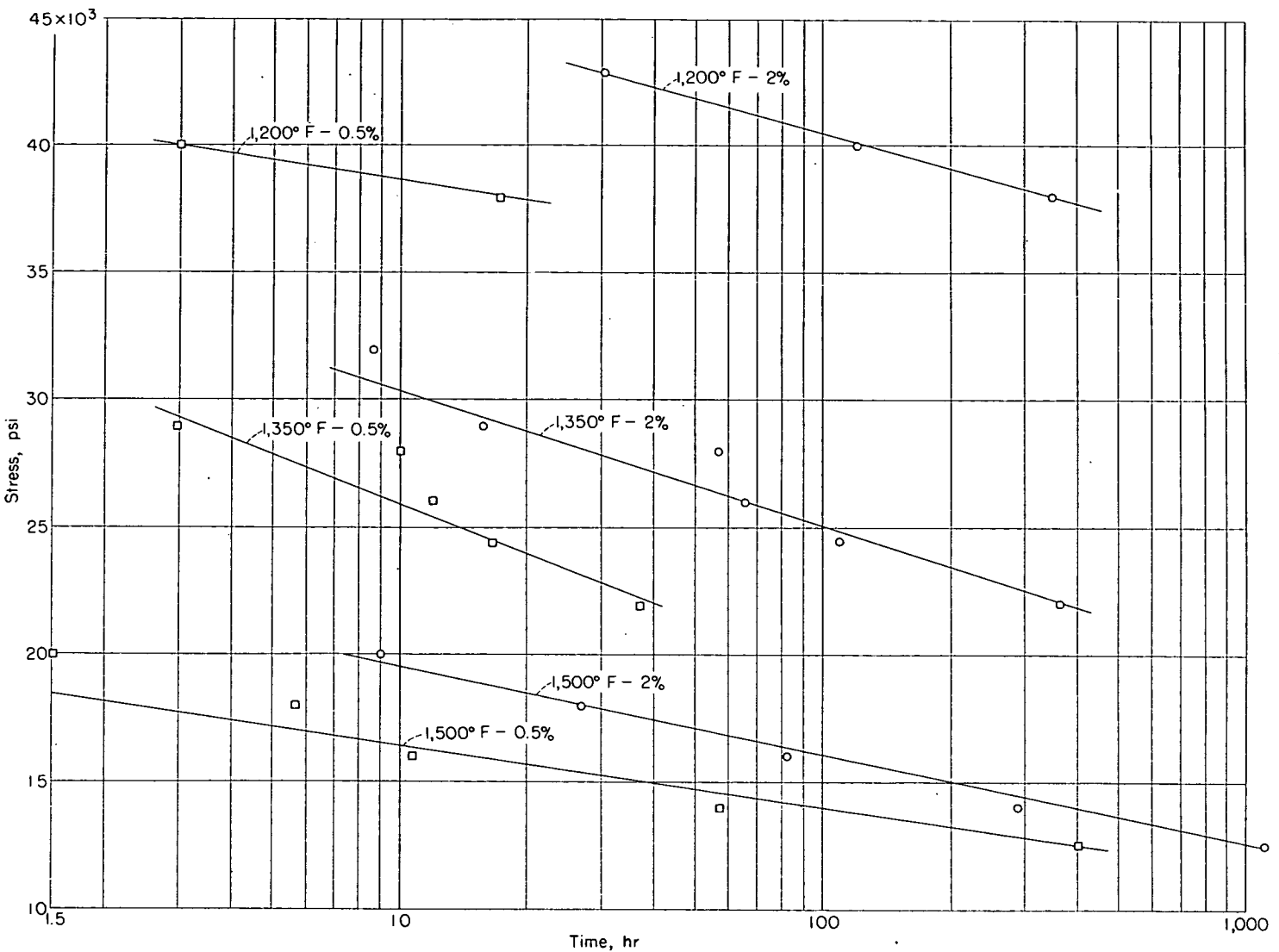


FIGURE 4.—Curves of stress against time for total deformation of 0.5 and 2 percent from static rupture tests at 1,200°, 1,350°, and 1,500° F.

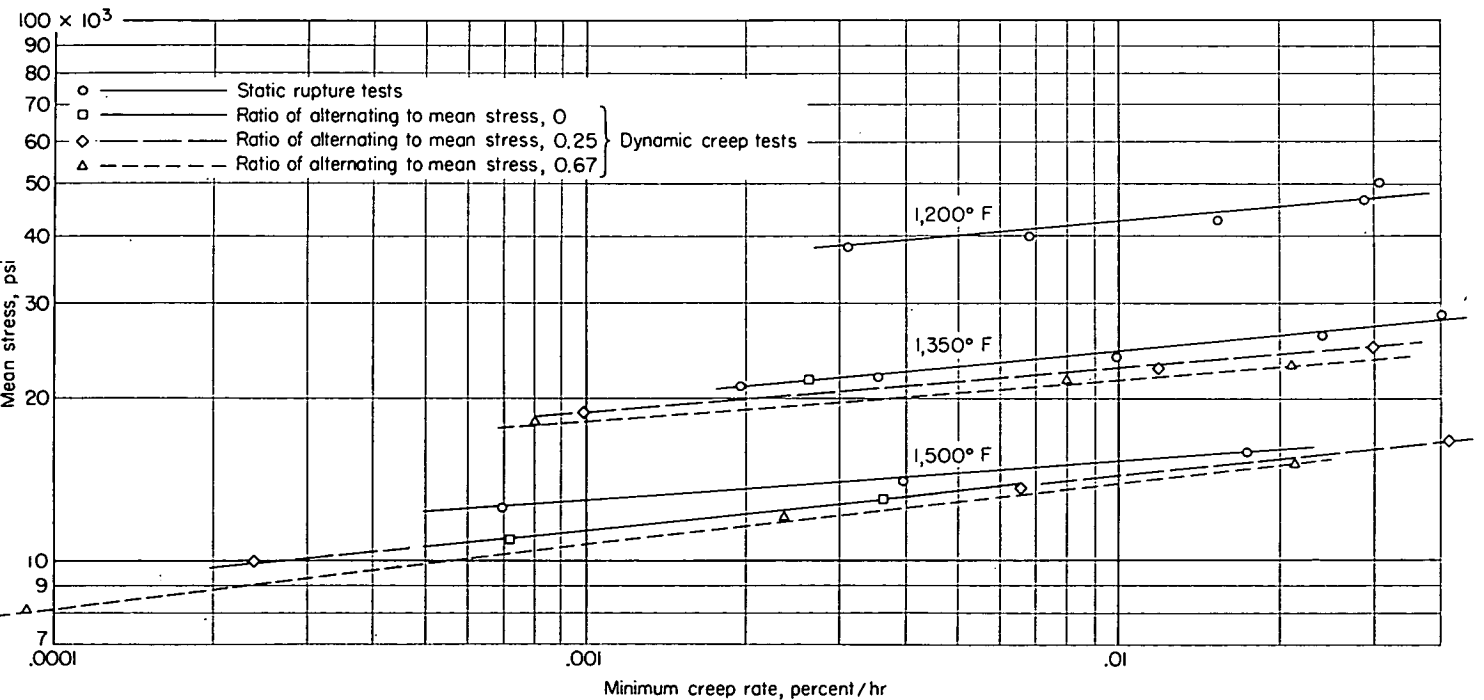


FIGURE 5.—Curves of stress against minimum creep rate from static rupture tests at 1,200°, 1,350°, and 1,500° F and for dynamic creep tests at 1,350° and 1,500° F.

fig. 6) or of maximum stress against time for fracture (see fig. 7). The former method is most convenient for low ratios of stress and the latter, for high ratios.

Ratios of alternating to mean stress of 2 and ∞ were used at room temperature and 1,000° F. At 1,350° and 1,500° F the ratios were 0, 0.25, 0.67, 1.64, and ∞ . A ratio of ∞ involves completely reversed stress fatigue tests, while a ratio of 0 indicates a steady-load rupture test.

Creep data were also measured for the tests which did not go into compression (stress ratios of 0, 0.25, and 0.67). The specimens had a 2-inch gage length of uniform diameter. Figure 6 includes curves of mean stress versus time for total deformations of 0.5 and 2.0 percent for these stress ratios. Elongations of the fractured specimens are included in table IV. Minimum creep rates are compared with those for rupture tests in figure 5.

In the tests in which the alternating stress went into compression (stress ratios of 1.64, 2.0, and ∞), it was necessary to use a profile specimen with a minimum diameter to avoid buckling. Two tests were made at a ratio of 0.67 and 1,500° F to check the results from the two types of specimens. The agreement was quite good (see fig. 6). Creep data could not be obtained from profile specimens, however. By agreement, the gage section of these specimens was made identical to that of the high-alternating-stress specimens in the Krouse

machine. The following features of the data should be recognized:

(1) Rather complete data were obtained for establishing the curves at 1,350° and 1,500° F.

(2) Subsequent to the establishment of the original curve with specimens machined for the NACA at Michigan, the University of Minnesota conducted additional tests at 1,500° F for a stress ratio of ∞ on specimens which they heat-treated and machined. The latter data yielded a curve which was of a considerably higher stress level than the original curve. For this reason two curves are included in figure 7 for a ratio of ∞ at 1,500° F. The specimens were made from bar stock from the same ingot as that used for specimens made at Michigan but were not part of the stock supplied to Michigan by the producer.

(3) Tests were also made at 1,000° F on specimens heat-treated and machined at Minnesota. The data, however, are inconclusive as to whether there was a difference in the properties of the two groups of specimens.

(4) The data are very sparse at room temperature and 1,000° F. The curves shown in figure 7 are very approximate. Both a shortage of specimens and considerable testing difficulty were encountered, as detailed in the notes to table IV. The points in figure 7 for which there were extenuating circumstances have been starred. The shortage of speci-

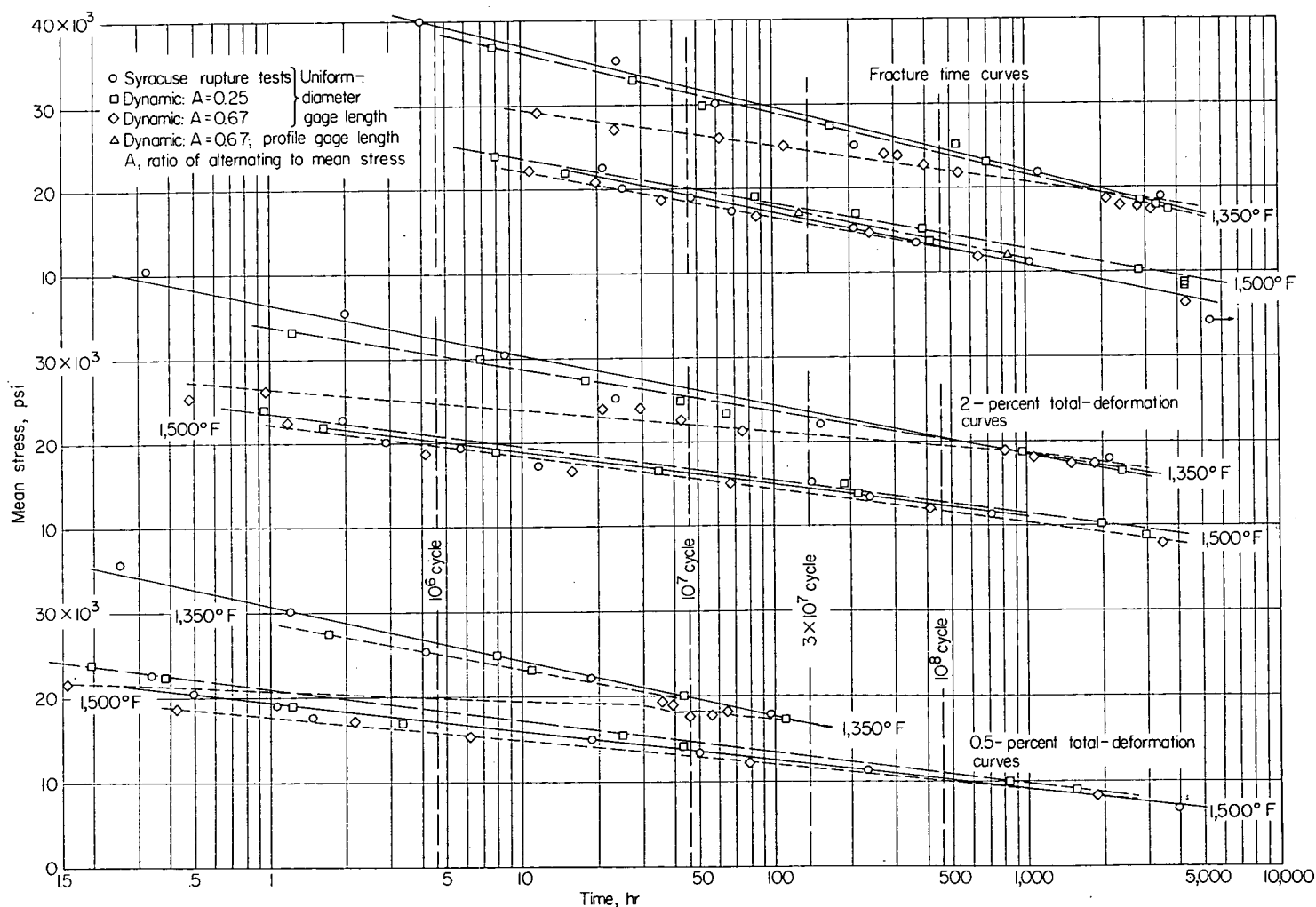


FIGURE 6.—Curves of mean stress against time for fracture and time for total deformations of 0.5 and 2 percent at 1,350° and 1,500° F for axial stress dynamic creep tests.

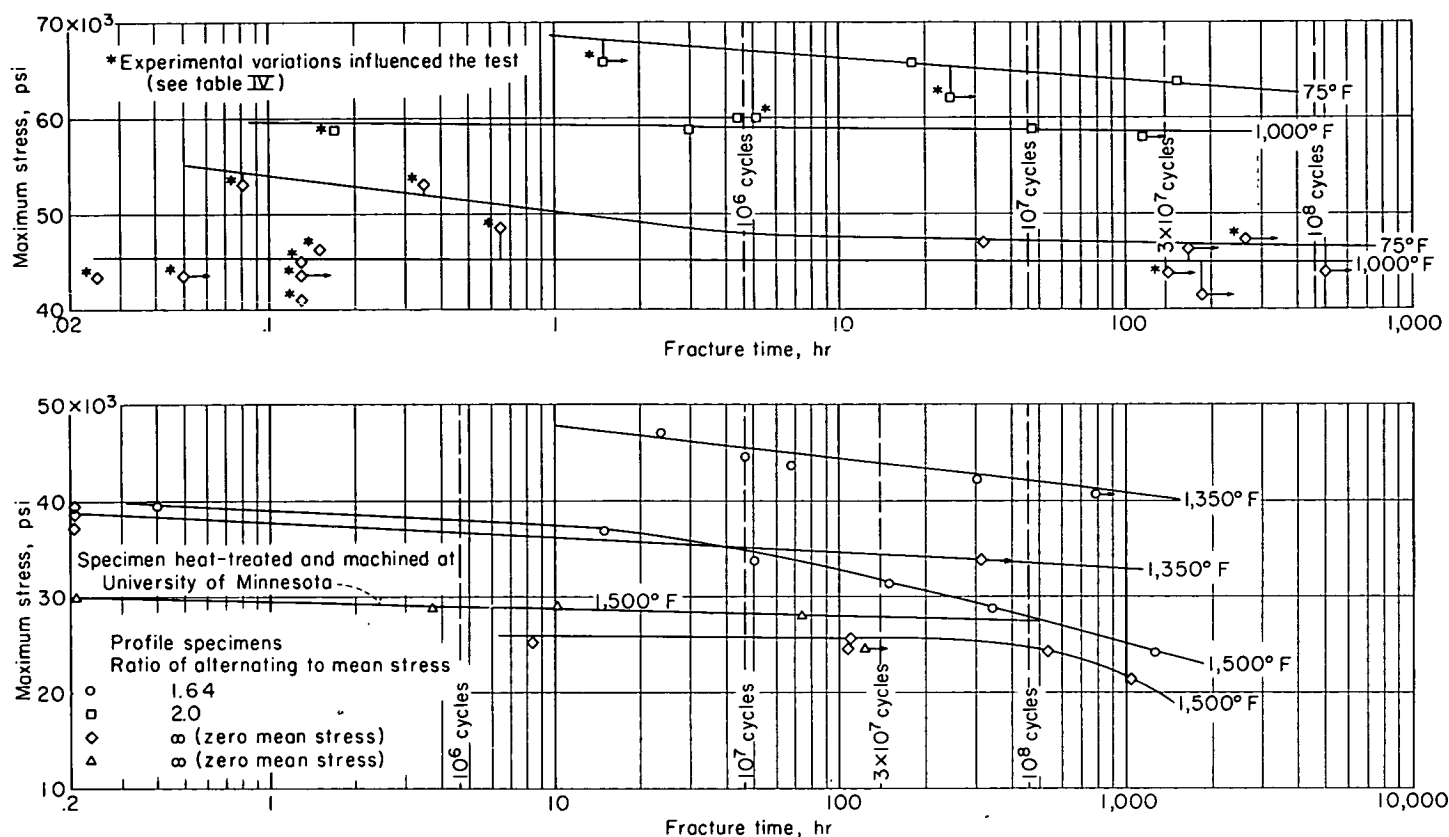


FIGURE 7.—Curves of maximum stress against fracture time for indicated ratios of alternating to mean stress at room temperature, 1,000°, 1,350°, and 1,500° F in axial dynamic stress creep testing machine.

mens led to retesting unbroken specimens at higher stresses after varying times of testing with a consequent uncertainty of the effect of prior history. Secondly, a good deal of difficulty from overheating due to damping while the load was being applied was encountered, particularly at 1,000° F. Those tests carried out at reduced cyclic speeds during loading to prevent overheating are indicated in table IV. It was also noted that stresses below $\pm 40,000$ psi gave no difficulty. A small amount of overheating at 1,350° F was also noted for the high-stress tests at zero mean stress.

The data presented are published and discussed in detail in references 3 and 4 except for the ∞ stress-ratio tests at 1,500° F for specimens heat-treated and machined at Minnesota.

KROUSE AXIAL FATIGUE TESTS

Data were obtained in a Krouse machine for combinations of steady axial stress and superimposed axial dynamic stress at 1,200°, 1,350°, and 1,500° F (see table V and fig. 8). A series of tests was made with varying mean stress with constant amounts of alternating stress, which led to curves of stress versus rupture time for the various constant alternating-stress values. The tests at 1,200° F were stopped at $\pm 25,000$ psi because of load limitations of the test machine. Tests were carried out at increasing alternating-stress values at 1,350° and 1,500° F to completely reversed zero mean stresses.

Most of the curves with varying mean stress were reasonably well established in the range of 50 to 500 hours and were fairly consistent. The completely reversed stress curves are, however, based on very meager data. There was no

evident effect from changing the dimensions of the specimens for the high-dynamic-stress tests. Some difficulty in alignment from grips was encountered for the high-stress tests. This was corrected and only the successful tests have been plotted in figure 8. No overheating during application of the loads was reported.

It will be noted that increasing amounts of alternating stress reduced strength as measured by mean stress. The reduction, however, decreased with increasing temperature so that there was little effect at 1,500° F.

The curves for completely reversed stress tests at 1,350° and 1,500° F were very nearly horizontal. Apparently, in this type of test there is a characteristic maximum stress above which fracture occurs immediately and below which fracture is prolonged indefinitely.

SONNTAG SF-4 AXIAL FATIGUE TESTS

The influence of varying alternating axial stresses on the time for fracture under constant mean stresses was established at room temperature, 1,000°, and 1,350° F in the Sonntag SF-4 machine (see table VI and fig. 9). The data show:

(1) For time periods of 10 hours or less at 1,000° F, the magnitude of the alternating stress rather than the mean stress in the range from 40,000 to 60,000 psi appeared to govern fracture. The approach to a common value of $\pm 30,000$ psi for fracture for these mean stresses suggests that the fatigue load governed fracture.

As the alternating stress was reduced, the curves diverged, indicating that mean stress became increasingly important in governing fracture time.

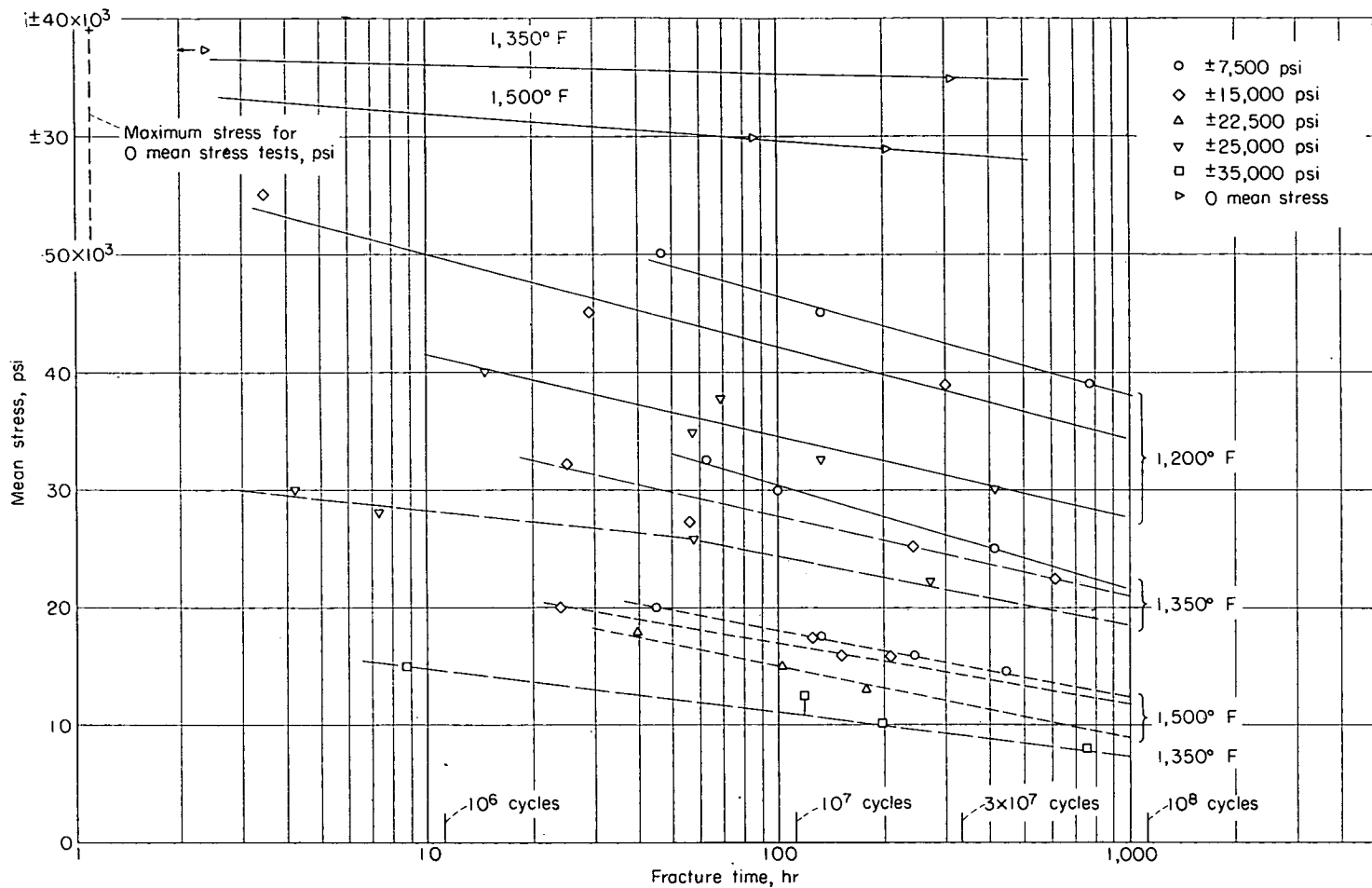


FIGURE 8.—Curves of mean stress against fracture time for Krouse axial fatigue tests at 1,200°, 1,350°, and 1,500° F.

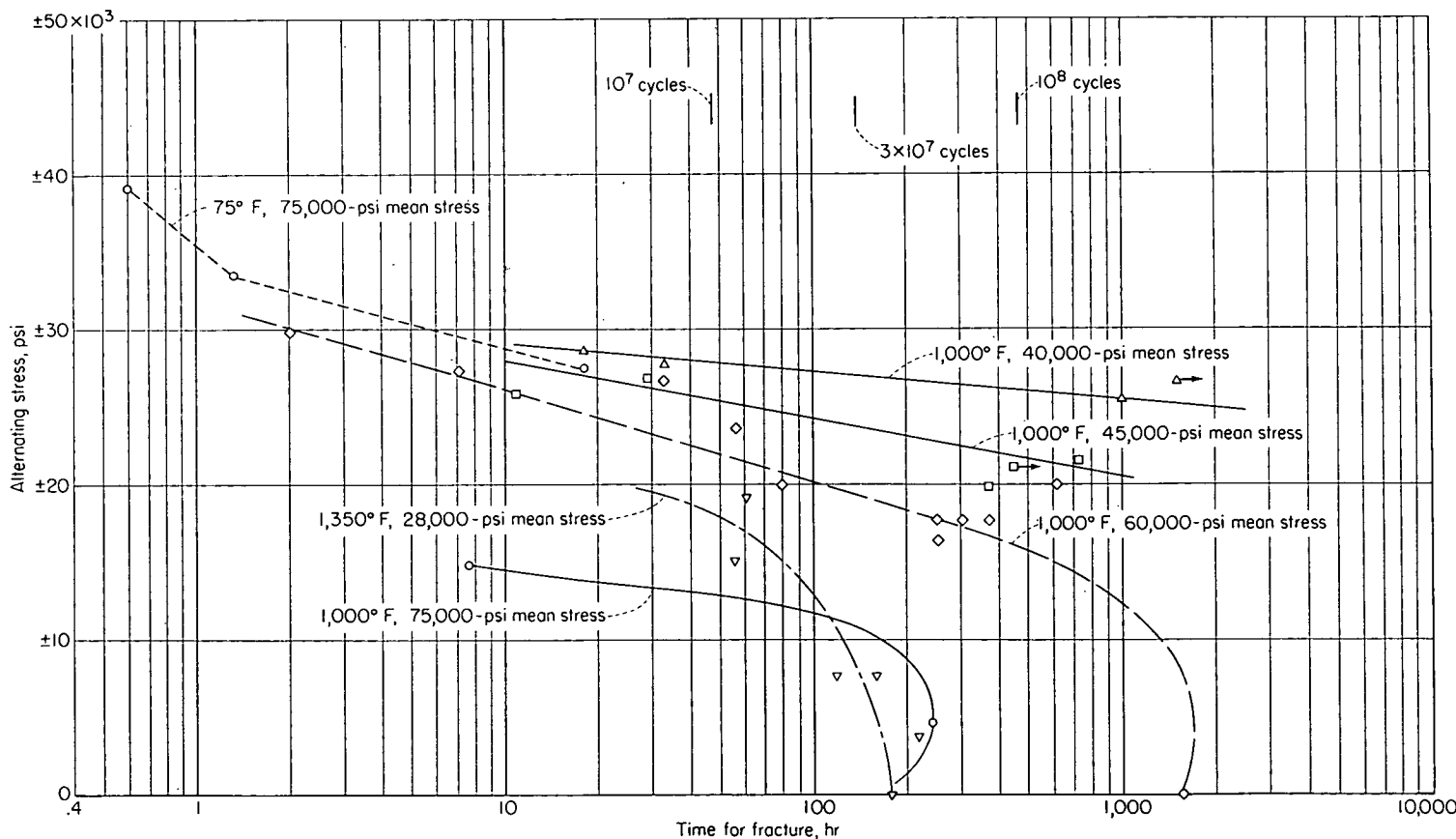


FIGURE 9.—Effect of superimposed alternating stress in Sonntag SF-4 3,600-cpm fatigue tester on time for fracture at room temperature, 1,000°, and 1,350° F at constant mean stresses.

The necessity for the curves to drop rather abruptly to the rupture time from rather high levels of alternating stress indicates that there is a range of low alternating stresses which has little effect on fracture time. Thus, there appear to have been three types of response to the test conditions:

- (a) Nearly pure fatigue at high values of alternating stress
- (b) Fatigue and creep both governing life at intermediate values of alternating stress
- (c) Nearly pure creep at low values of alternating stress and prolonged times for fracture

(2) The tests at 75,000-psi mean stress indicate that when there is a high level of mean stress small amounts of alternating stress result in an excessive maximum stress and short life.

(3) The data at 1,350° F follow the pattern of other tests in that as the temperature increased larger amounts of alternating stress were required to shorten life from a given static rupture time.

(4) The data at room temperature are sparse but suggest approach to a fatigue limit at 75,000 psi \pm approximately 27,000 psi.

(5) Fairly extensive testing problems were encountered for tests at high mean-stress values. The combination of this factor together with correction of eccentricity part way through the testing program makes it difficult to analyze causes for abnormal test results. These factors masked any effect, if one was present, from specimens machined at Michigan and the Elliott Company. It is suggested that the combined influence of both fatigue and creep at intermediate alternating-stress values could in itself have been a source of erratic data.

(6) The measuring and control of temperature by thermocouples measuring furnace temperature could have masked overheating effects. This could have been responsible for apparently low strengths at high alternating stresses, as will be discussed later.

RUPTURE TESTS WITH SUPERIMPOSED ROTATING BENDING STRESS

A series of tests was carried out at 1,350° F with 10,800-cpm rotating bending stresses superimposed on a steady axial stress of 28,000 psi (see table VII and fig. 10).

All the specimens in the combined stress tests had less than one-third the life of those in the rupture steady-stress test. In the three lowest alternating stress tests the specimens failed by rupture at points remote from the point of calculated maximum stress. Only the highest alternating stress gave fracture at the point of maximum stress, and this was a fatigue failure.

The pronounced reduction in life from as small an alternating stress as $\pm 5,000$ psi was considerably different from behavior of specimens in axial combined stress tests. The axial tests showed either no reduction or an increase in life from small alternating stresses. The reason for the effect as well as the fracturing at points other than those of maximum stress is uncertain. The most likely explanation points to some material and testing-machine effect rather than to the presence of rotating bending stresses.

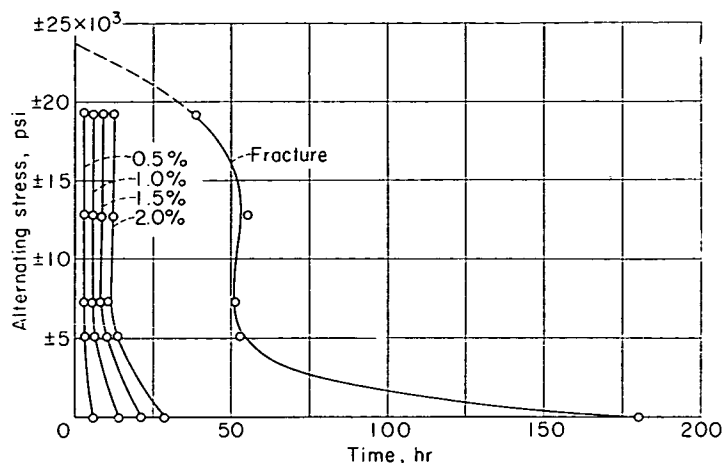


FIGURE 10.—Influence of rotating bending stress at 1,350° F on time for 0.5-, 1.0-, 1.5-, and 2-percent total deformation and fracture time under a steady axial stress of 28,000 psi.

Superimposed alternating stresses of small magnitude can increase strength for a given mean stress, as indicated by other tests. This does not appear to be an adequate explanation of the abnormal fractures because it is difficult to see how the point of maximum stress could have been strengthened while the life could have been lowered by one-third in other parts of the gage length, where the bending stresses were less. It was reported that other materials had always fractured at the point of maximum stress, so that some material characteristic apparently entered into the abnormal results.

Creep data obtained during the test and included in figure 10 as total-deformation curves were apparently influenced less than the rupture time by the bending stresses. The much longer times required for fracture than for total deformations of 2 percent were rather striking.

WESTINGHOUSE REVERSED BENDING FATIGUE TESTS

The Westinghouse machine bends a specimen in one plane at 7,200 cpm. The results of the tests carried out at room temperature, 1,000°, 1,200°, 1,350°, and 1,500° F are given in table VIII and shown as S-N curves in figure 11.

Fatigue limits were established by 5×10^6 cycles at room temperature, 1,000°, 1,200°, and 1,350° F. A fatigue limit was not established in 10^8 cycles at 1,500° F. There was no apparent difference in fatigue life between specimens finished by the specially controlled practice and those simply turned and hand polished.

EFFECT OF SURFACE FINISH ON REVERSED BENDING FATIGUE PROPERTIES AT ROOM TEMPERATURE AND 1,350° F

The effect of surface finish on reversed bending fatigue properties at room temperature and 1,350° F is shown in table IX and figure 12. Plain ground specimens were found to have considerably lower fatigue strength than polished or roughened specimens at room temperature in the Westinghouse reversed bending fatigue machine. The difference was considerably reduced at 1,350° F, although the polished specimens were still slightly stronger.

Stress-relieving at 1,400° F for 4 hours did not reduce the strength of the polished specimens at room temperature and may have increased it slightly at high stress values (see

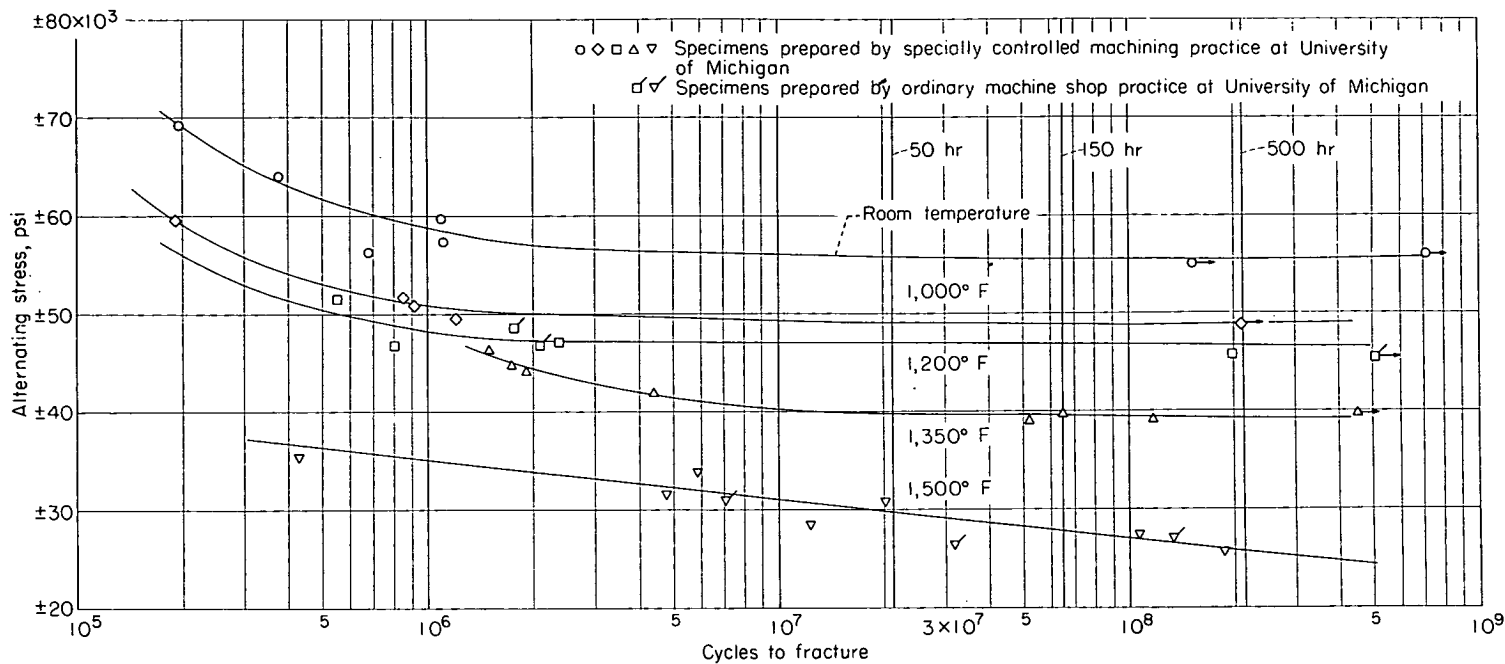


FIGURE 11.—Reversed bending S-N fatigue curves at room temperature, 1,000°, 1,200°, 1,350°, and 1,500° F from Westinghouse 7,200-cpm fatigue tester. Westinghouse data for 0.550-inch-diameter specimens.

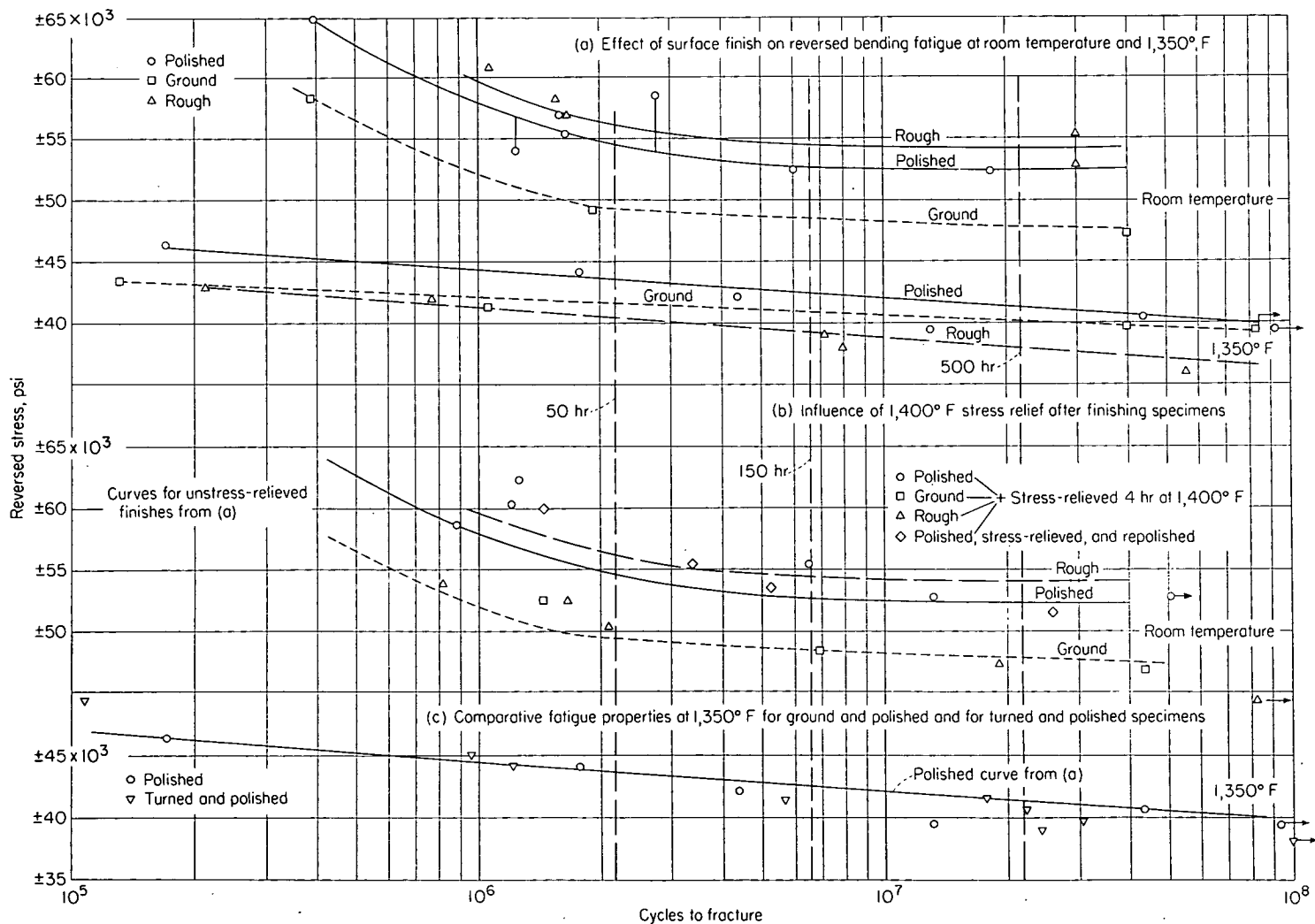


FIGURE 12.—Influence of surface finish on reversed bending fatigue at room temperature and 1,350° F.

table IX and fig. 12). Repolishing after stress-relieving did not alter the strength. The strength of the roughened specimens was, however, reduced to that of the ground specimens, and the ground specimens were not affected.

The turned and polished specimens had the same fatigue characteristics at 1,350° F as those of the ground and polished specimens. (See table IX and fig. 12.) The values reported for fatigue strength of polished specimens at room temperature were slightly lower than those reported by Westinghouse, although it is doubtful if the difference is justified in view of scatter of data. There was no difference in reported strength from the two laboratories for 1,350° F.

FATIGUE, DAMPING, AND ELASTICITY PROPERTIES FROM VARIABLE-SPEED ROTATING CANTILEVER BEAM TESTS ON NOTCHED AND UNNOTCHED SPECIMENS

The fatigue data from variable-speed cantilever beam tests on notched and unnotched specimens are given in table X and plotted in figure 13. Figure 13 also shows curves for the "first evidence of crack" for the notched specimens as obtained from changes in damping and stiffness behavior. It was not possible to obtain evidence of cracking prior to fracture from the damping and deflection data for the unnotched specimens. Such values would, however, be so close to the fracture curve as nearly to coincide with it.

The fatigue curves were considered approximate because of the small number of points. The approximate fatigue strengths were:

Type of specimen	Temp., ° F	Stress, psi, for fracture in indicated cycles		Effective stress concentration factor * at 3×10^7 cycles
		10^7	3×10^7	
Unnotched	Room	$\pm 53,000$	$\pm 53,000$	
	1,350	$\pm 40,000$	$\pm 40,000$	
	1,500	$\pm 29,000$	$\pm 29,000$	
Notched	Room	$\pm 25,000$	$\pm 23,500$	2.2
	1,350	$\pm 22,000$	$\pm 21,500$	1.85
	1,500	$\pm 19,500$	$\pm 19,000$	1.50

*Theoretical stress concentration factor according to Neuber's analysis was 2.6.

It is evident from these data and the curves of figure 13 that the notch drastically reduced strength. In fact, the notched specimens at room temperature were weaker than the unnotched at 1,500° F for stresses below $\pm 31,500$ psi. Also there was very little difference in strength of notched specimens from room temperature to 1,500° F for 10^7 cycles. The difference in cycles for the first evidence of a crack and actual fracture for the notched specimens was large.

Because the cyclic speeds were so nonuniform in these tests, the significance of the times for fracture (table X and fig. 14) is uncertain. It would seem that considerable information ought to be available from these data regarding influence of cyclic-speed effects. However, the data are so few and scatter so much that any possible conclusions are

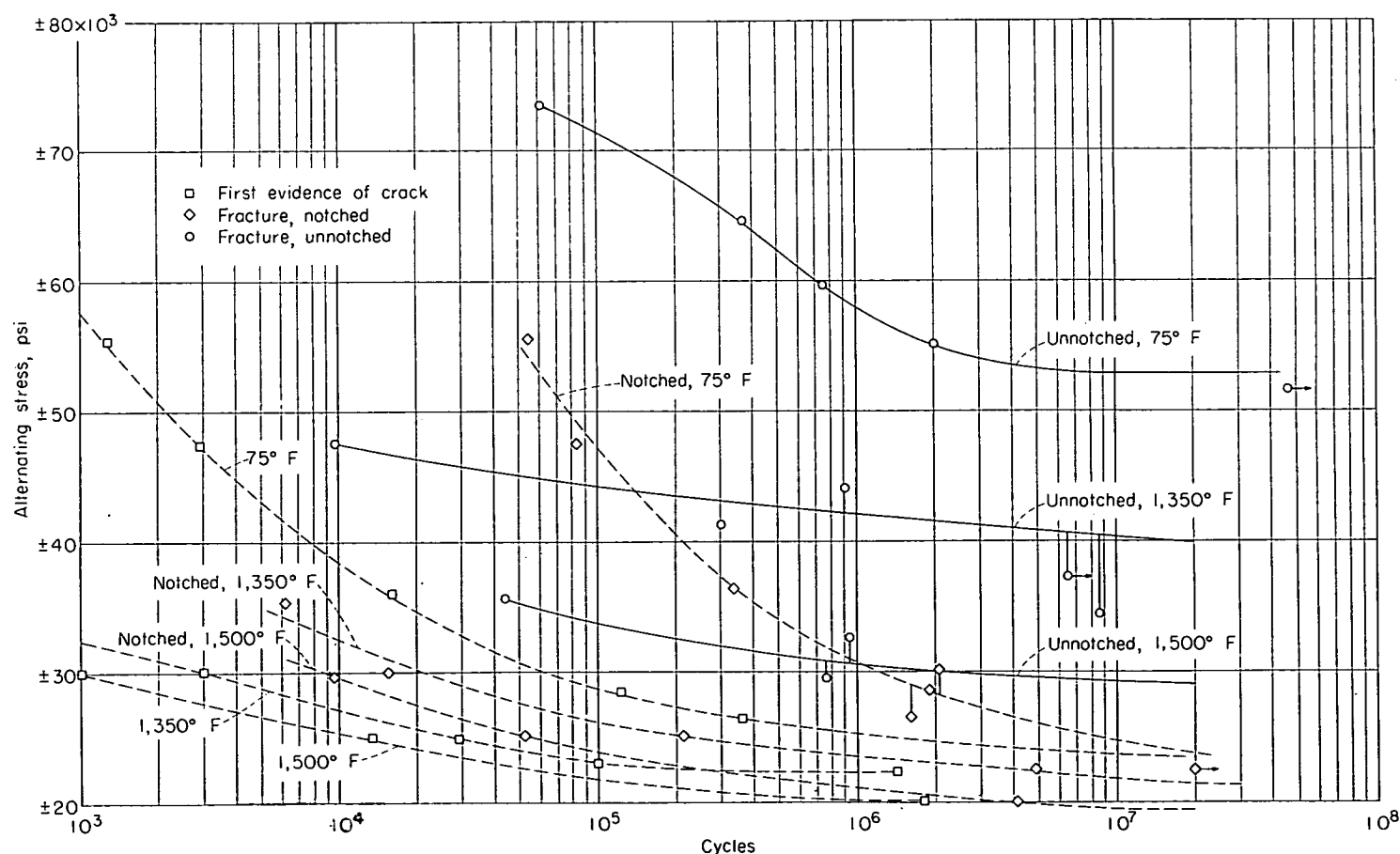


FIGURE 13.—S-N curves for fracture of unnotched and notched specimens and for first evidence of crack for notched specimens at room temperature, 1,350°, and 1,500° F in variable-speed rotating cantilever beam tests.

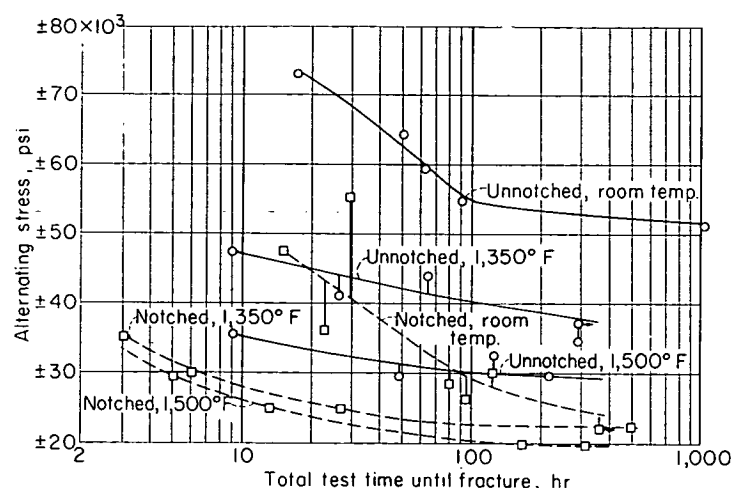


FIGURE 14.—Curves of alternating stress against fracture time for unnotched and notched specimens in variable-speed rotating cantilever beam tests. (See table X for cyclic speeds.)

masked. It is evident that cyclic-speed variations caused two points for notched specimens to deviate far more widely than they would on the basis of number of cycles. Observations other than this are masked by data scatter.

In addition to the fatigue data, damping and dynamic modulus-of-elasticity data were obtained by the cooperator.

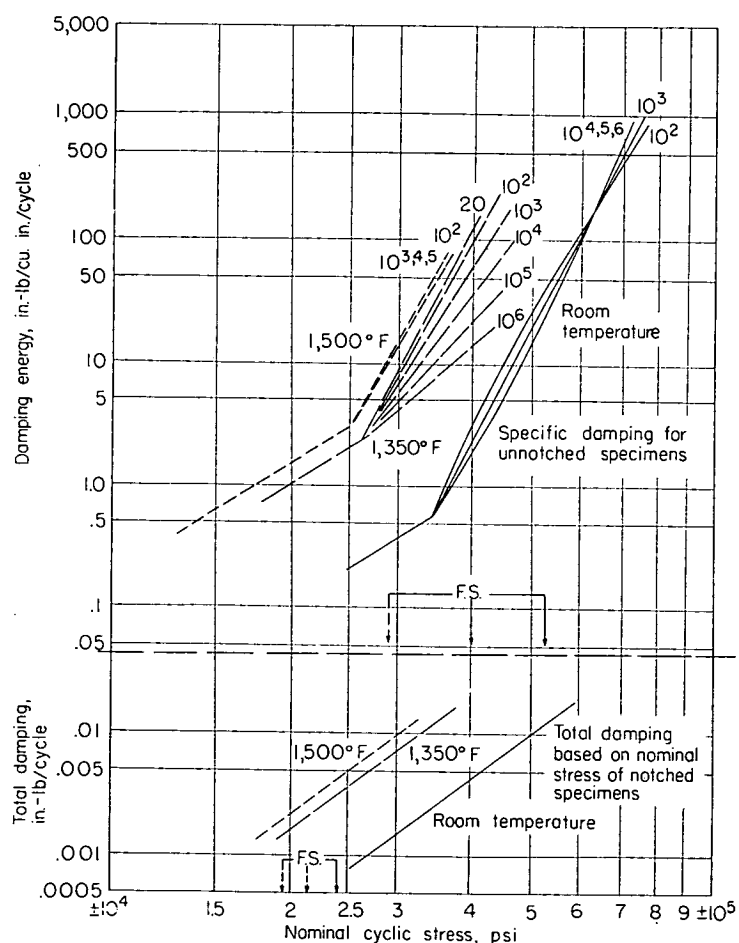


FIGURE 15.—Effect of stress magnitude and constant cyclic-stress history on damping energy for unnotched and notched specimens at room temperature, 1,350°, and 1,500° F. F. S. indicates fatigue strength at 2×10^7 cycles; numbers on curves identify damping lines, after 20, 10^2 , 10^3 , . . . cycles of stress.

These data are thoroughly presented and analyzed in reference 5. The more important trends discernible from the data were:

(1) Damping increased with stress and temperature in a complex manner, depending on the stress level, number of cycles, and temperature. Figure 15 shows the specific damping (inch-pounds of energy absorbed per cubic inch of metal per cycle for uniform stress) as a function of stress for the three test temperatures.

(2) The greater damping with increasing temperature for the temperatures considered at a given stress is evident.

(3) The increase in damping with stress became sensitive to the number of cycles above certain limiting stresses at each temperature:

(a) Room temperature—The damping decreased with number of cycles at stresses between $\pm 34,000$ and $\pm 60,000$ psi. Above $\pm 60,000$ psi the damping increased with number of cycles.

(b) 1,350° F—Damping decreased with number of cycles above $\pm 26,000$ psi.

(c) 1,500° F—There was little effect from number of cycles.

(4) The rather high damping capacity at high stresses is noteworthy. The values are much higher for the engineering stress range than would be indicated from the low stress measurements and the usually accepted value of 3 for the exponent of the curves of damping capacity versus stress.

Data on damping for notched specimens did not show cyclic-stress sensitivity. Perhaps the most important point to be noticed from the damping data from the notched specimens is the very small volume of metal absorbing energy and the consequent low energy-absorbing capacity in the presence of a notch.

The results of the measurements of dynamic modulus are summarized in figure 16. As in the damping measurements,

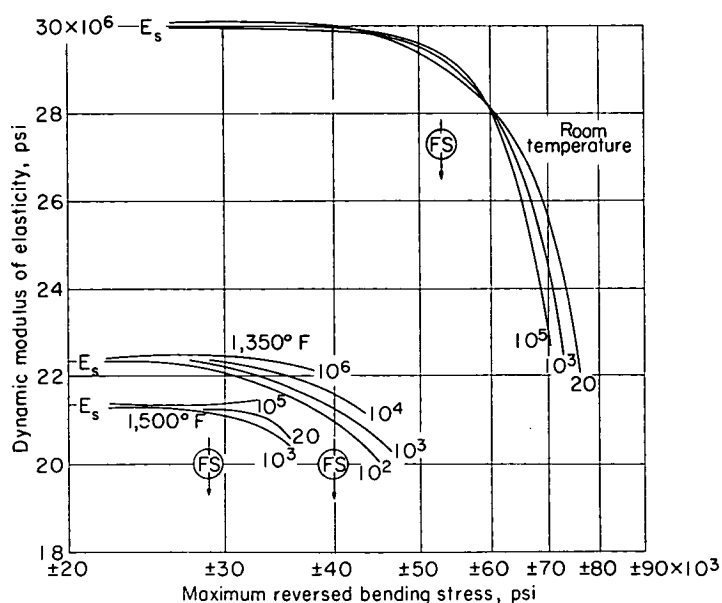


FIGURE 16.—Dynamic moduli of elasticity at room temperature, 1,350°, and 1,500° F after different numbers of cycles of reversed bending stress. E_s , initial static modulus; F.S., fatigue strength at 2×10^7 cycles; numbers on curves identify modulus lines after 20, 10^2 , 10^3 , . . . cycles of stress.

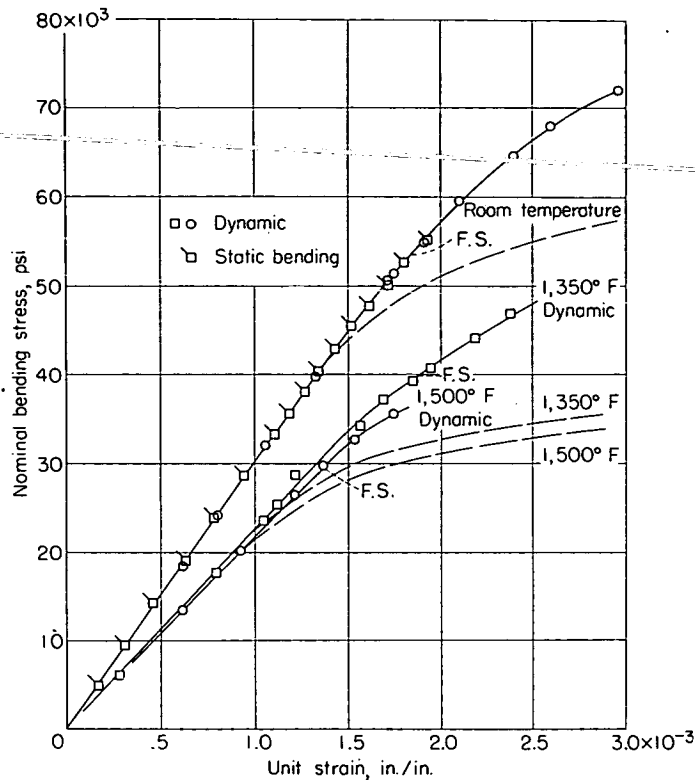


FIGURE 17.—Static and dynamic stress-strain curves in bending for unnotched specimens. Dashed lines are static tension data; values are based on static modulus of 30×10^6 psi; fatigue strengths (F.S.) are given for 2×10^7 cycles.

to the static tension curves shown by the dashed lines, data from one static bending test are shown at room temperature. The bending data checked the dynamic values above the proportional limit rather than the static tension curves. It will be noted that:

(1) The dynamic proportional limit was above the static tension values. This might have been influenced by the sensitivity of the strain measurements and the use of separate specimens for each point.

(2) At room temperature and 1,350° F the fatigue strength was above the dynamic proportional limit and was very close at 1,500° F.

ROLLS-ROYCE ROTATING CANTILEVER BEAM TEST

Completely reversed stress tests were conducted on small specimens rotated at 5,500 rpm with a cantilever beam load. The specimens were profiled to a minimum diameter. The heat-treated bar stock furnished to Rolls-Royce was quartered and the specimens were machined from the quarters. Because of this procedure and the short length of the specimens, a number of tests were obtained from a single bar furnished to them with the coding system established by Michigan.

The data obtained from the tests at 1,200°, 1,350°, and 1,500° F are recorded in table XI and shown as S-N curves in figure 18. The following observations should be recognized:

(1) Fatigue limits were apparently attained by 10^7 cycles at 1,200° and 1,350° F. Apparently, a limit was not reached in 10^8 cycles at 1,500° F.

(2) There appeared to be two distinct curves at 1,500° F. The higher curve was defined mainly by specimens from bars JP14 and JS15. The lower curve was based mainly on specimens from bar JR16, although there were test points on this curve from bars JP14 and JS15. Rolls-Royce suggested that this was evidence of appreciable variation along the length of the bars. Comparison of the data with those

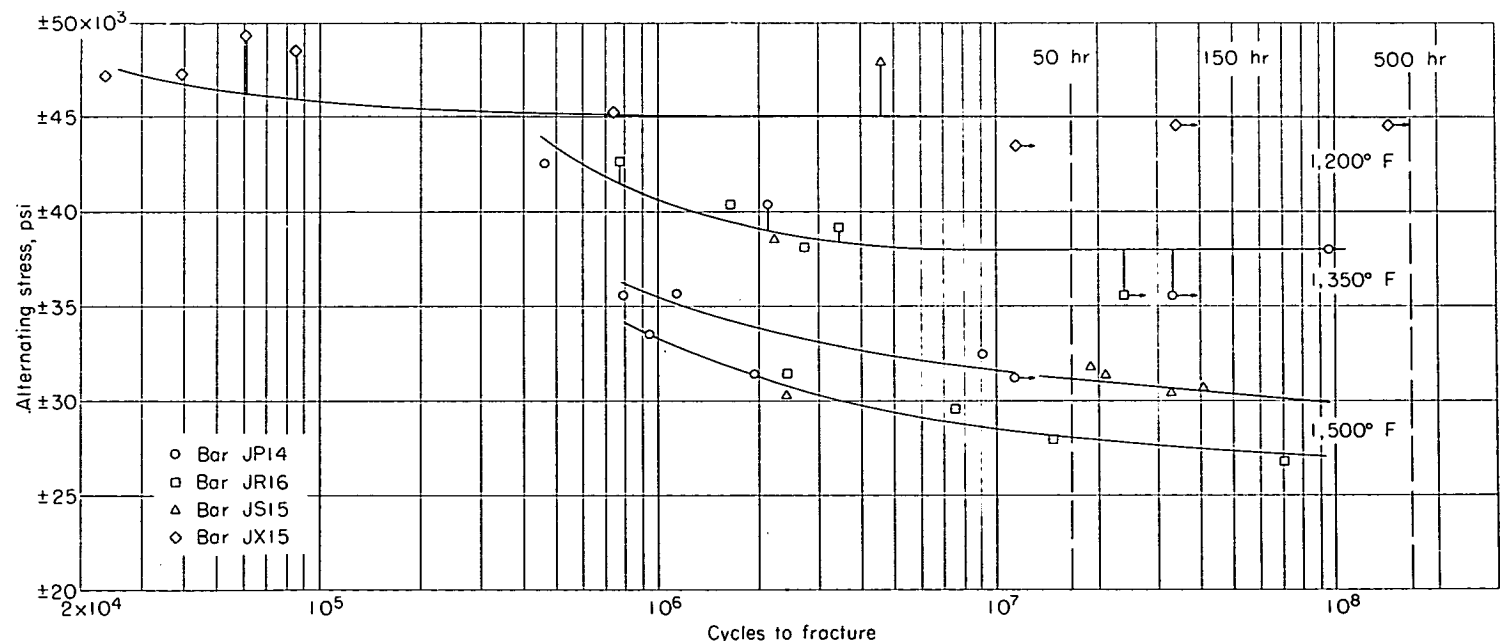


FIGURE 18.—S-N curves at 1,200°, 1,350°, and 1,500° F for Rolls-Royce rotating cantilever beam fatigue tests.

obtained in the Westinghouse machine, however, shows that the total scatter was about the same. Thus, there may have been an appreciable contribution to the scatter from bar-to-bar variations.

Bar JR came from a point in the ingot intermediate to bars JP and JS, so that this does not appear to be a cause of variation. Also, all three bars involved were taken from about the same location along the length of the original mill length.

(3) The quartered specimens used by Rolls-Royce gave the same fatigue strengths as those obtained from other reversed bending tests in which the gage section was in the center of the original bar.

NEES ROTATING CANTILEVER BEAM FATIGUE TESTS

Tapered specimens having uniform stress in the gage length were tested at 1,350° F in the 1,700-cpm rotating cantilever machine of the Naval Engineering Experiment Station. (See table XII and fig. 19.) The S-N curve of figure 19 indicates a lower fatigue strength than those obtained in the other reversed stress tests. Actually, however, the scatter of points is the same as that in the other tests. Thus, the fatigue results in this test checked with those from other machines even though the NEES preferred to report a curve at the lower range of the test points. As with other

reversed stress tests at 1,350° F, a fatigue limit was attained at 10^6 cycles.

FRACTURE CHARACTERISTICS

The results of extensive studies of fractured specimens are summarized as follows:

(1) Fatigue nuclei can appear in fractures of specimens tested at 1,350° and 1,500° F when an alternating stress of approximately 67 percent of the mean stress is applied. (See fig. 20.) The appearance of nuclei under combined stress apparently increases with alternating stress to a limit where the maximum stress (at a given mean stress) exceeds the limit the material can withstand for even a short time, and a tensile-type fracture results. This occurred in the 1- and 2-minute tests for dynamic creep with completely reversed axial stresses at 1,350° F and accounts for those specimens at the outer range of alternating stress in combined tests which did not show fatigue nuclei.

For the lower values of alternating stress, the mean stress, at least, can be reduced to values where no nucleus appears and failure occurs entirely by creep rupture. This is equivalent to saying that, as the time for fracture is increased by decreasing the mean stress, fatigue nuclei tend to disappear and the failure is characteristic of a creep-rupture test.

At 1,000° F fatigue nuclei apparently occur at lower ratios of combined stress than at the higher temperatures. On the other hand, tests at 1,200° F in the Krouse machine did not show fatigue nuclei when the alternating stress was nearly equal to the mean stress.

All completely reversed stress tests showed fatigue nuclei, except for a few very high stress tests of very short duration in which the specimens appeared to have failed entirely by excessive deformation.

(2) In the longer time tests at 1,350° F there was more of a tendency to fracture with a fatigue nucleus than in the tests at 1,500° F at the same ratios of alternating to mean stress. Apparently at higher temperatures there is more of

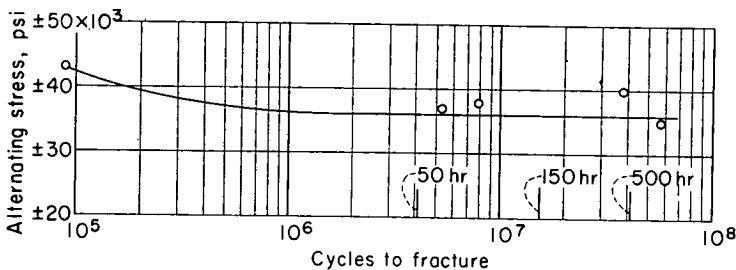


FIGURE 19.—S-N curve at 1,350° F for NEES rotating cantilever beam fatigue tests.

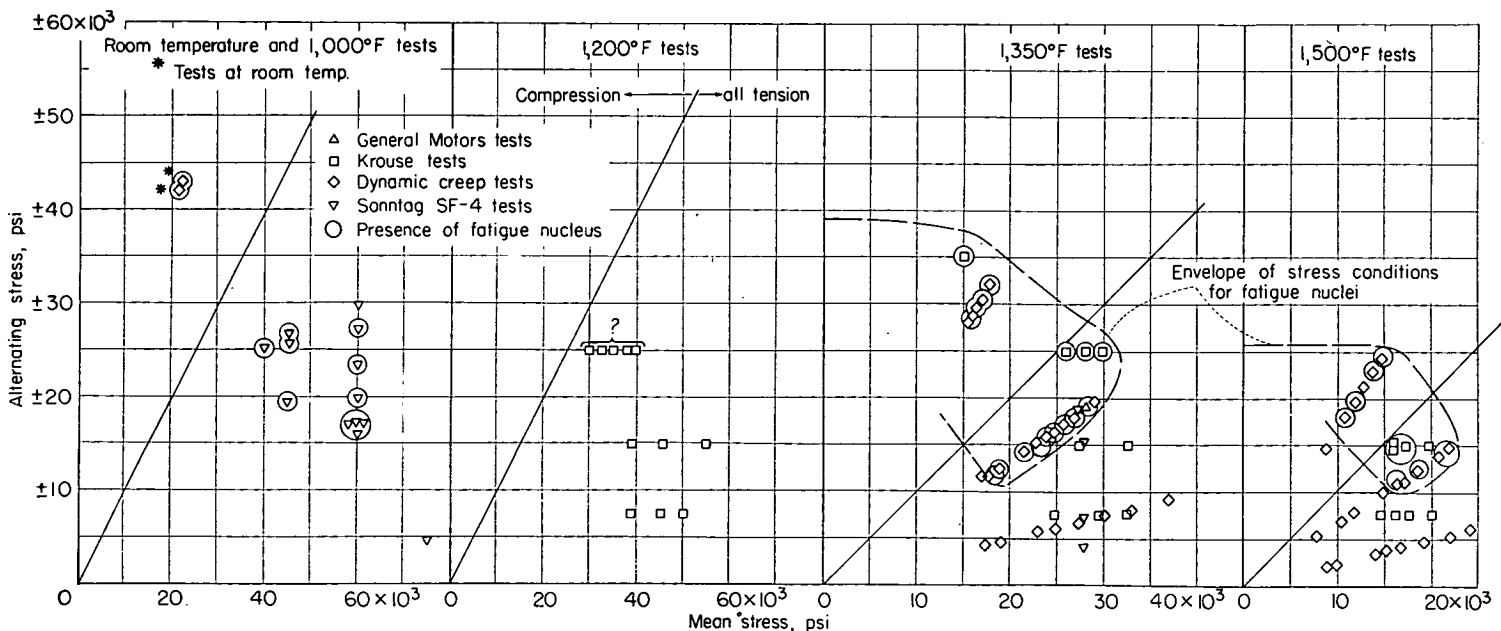


FIGURE 20.—Graphical representation relating presence or absence of fatigue nuclei on fractures of combined stress test specimens to conditions of loading.

a tendency for fracture by creep rupture than by fatigue for the same times for fracture.

(3) The fractures in the fatigue nuclei were straight, transgranular, and showed no evidence of deformation.

In those specimens which failed in a short time with a fatigue nucleus, the remaining area of fracture outside the nucleus resembled short-time tensile fractures. As the time for fracture increased, the fracture area outside the nucleus tended to resemble rupture test fractures at the same time period; that is, the fractures became increasingly intergranular. Even the completely reversed axial fatigue specimens showed substantial amounts of intergranular fracture at the longer time periods at 1,350° and 1,500° F. Low mean stresses and high alternating stresses reduced the tendency for a creep-rupture type of failure and often resulted in what appeared to be a combination of fatigue-nucleus, creep-rupture, and rapid tensile-type fractures. High mean stresses and low alternating stresses favored the creep-rupture type of fracture even for the same time for fracture.

(4) Fatigue nuclei appeared both internally and at the surface of axial fatigue specimens.

(5) Creep-rupture specimens normally show intergranular cracks adjacent to the main fracture, particularly at the surface. This tendency normally increases with both temperature and time for fracture. This tendency was reduced by high alternating stresses, although intergranular cracking at the surface was found even in the longer duration completely reversed axial stress tests at 1,350° and 1,500° F. A longer time for fracture or a higher temperature seems to be required to produce a given state of crack formation under fatigue loading.

(6) No evidence was found to show that an intergranular creep-rupture crack initiated a fatigue nucleus. In fact, it was not possible to determine whether the fatigue nucleus or the creep-rupture type of fracture occurred first or whether they developed simultaneously in the combined stress tests.

(7) There is some scatter in the data relating fatigue nuclei to stress in figure 20. The scatter, however, seems related to some extent to the type of test machine. This is mainly evident in the comparison of the dynamic creep test data and the Krouse machine data at 1,350° and 1,500° F. While the data are very few, it appears that alternating stresses for fatigue need to be slightly higher for the Krouse specimens to develop fatigue nuclei. This may have been related to the use of profiled specimens, as compared with uniform-diameter specimens, in the dynamic creep specimens. It seems possible, however, that the higher cyclic speed may have been a factor in the greater nucleus-forming tendency of the dynamic creep specimens. This is partially supported by the one good test in the 10,800-cpm General Motors machine at 1,350° showing a fatigue nucleus whereas the tests in the 3,600-cpm dynamic creep test and Sonntag SF-4 machines did not. Again, however, this might have been due to the rotating bending in the high-speed machine instead of axial fatigue loading in the slower machines.

(8) A very detailed study of fractures was carried out at Syracuse and Minnesota on their test specimens. (See refs. 6 and 7.) In general, their findings agreed with those of others. It was found, however, that a prohibitive amount of

work would have been necessary to duplicate their quantitative measurements of percentage intergranular fracture in all specimens. As they found, it is difficult to estimate such values reliably. For this reason this report has been restricted to qualitative observation and is nowhere as detailed in description of fractures.

Typical microstructures for the original material, fracture at a fatigue nucleus, and a rupture fracture are included as figure 21. The reader is, however, referred to the remarkable composite photographs of complete fracture profiles in reference 7 for more complete pictures of fracture.

Reference 7 also indicates that structural changes are slightly increased in rate by stress. High alternating stress was reported to increase the rate of breakdown of an intergranular precipitate which occurs in the test alloy at prolonged times at 1,350° and 1,500° F.

DISCUSSION

The data obtained show the relationships between static and fatigue properties of the test material over a wide range of temperatures. Test conditions ranged from ordinary tensile and creep-rupture tests through combinations of steady and fatigue loads to completely reversed fatigue tests. The features of the relationships between steady and fatigue loads will be correlated in the following sections.

RUPTURE AND FATIGUE STRENGTHS

The influence of superimposed fatigue loads on curves of stress versus rupture time was as follows:

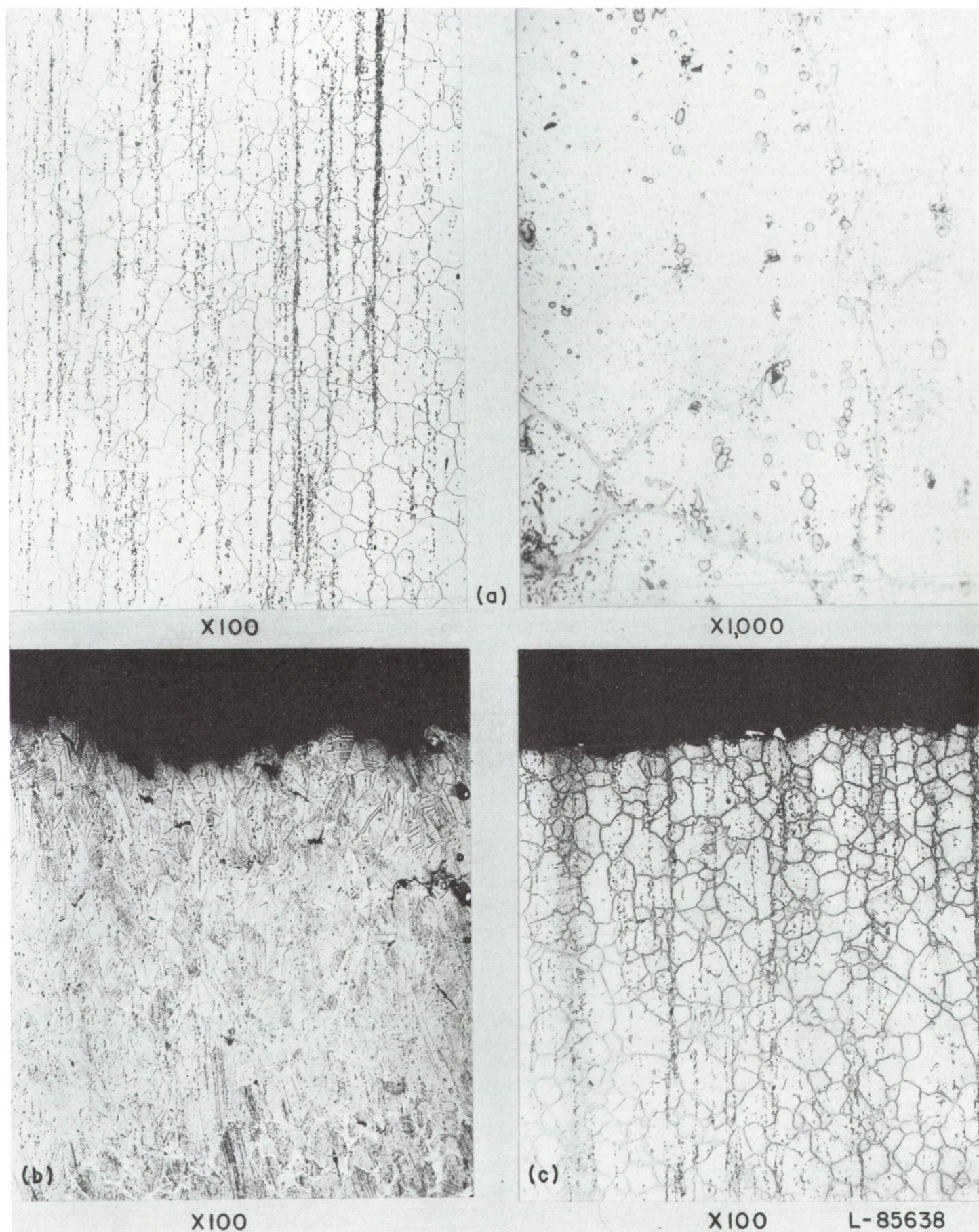
(1) As the temperature increased, larger amounts of fatigue loading could be added without appreciably affecting the curve of stress versus rupture time. (See figs. 6 and 8.) At a high temperature for the alloy (1,500° F) fatigue stresses as large as 67 percent of the steady stress did not change the curve of stress versus rupture time appreciably.

(2) As the temperature was lowered, less and less fatigue load could be tolerated without reducing strength. At 1,350° F fatigue loads up to $\pm 15,000$ psi had little effect, while at 1,200° F loads above $\pm 7,500$ psi reduced strength. (See fig. 8.)

(3) The reduction in strength due to superimposed fatigue loads tends to be greater at short time periods than at long time periods. This is evident in the tendency of the curves of stress versus rupture time for the higher superimposed alternating stresses to converge at long time periods in figures 6 and 8.

(4) At high ratios of alternating to mean stress, the curves of mean stress against rupture time tend to flatten out. This behavior would be expected inasmuch as the completely reversed stress curve would necessarily have to be horizontal at zero mean stress. The major influence of temperature is to control the alternating-stress level at which the flattening occurs and the resulting degree of strength as is evident in the curves of figures 6 and 8.

(5) Completely reversed stress and high ratios of alternating to mean stress are more realistically presented in terms of maximum stress, as in figures 7 and 8. It is evident that these high-stress fatigue curves based on maximum stress cross or lie above the curves for smaller amounts of



(a) Original material.

(b) Typical creep-rupture fracture; 248 hours at 1,350° F under 28,000 psi.

(c) Typical fatigue nucleus; 369 hours at 1,350° F. under $\pm 40,000$ psi.

FIGURE 21.—Typical microstructures of original test material and fractures of test specimens.

superimposed dynamic stress at the longer time periods when both are considered on a maximum-stress basis.

These trends in the relationship between static and dynamic rupture-strength characteristics are summarized by the values of alternating stress versus mean stress for fracture in 50, 150, and 500 hours in table XIII and figure 22. The tendency for the decreasing influence of alternating stress with increasing temperature is evident. The decreasing influence of alternating stress with increasing time for fracture is also evident, though it is not so striking as in the curves of stress versus rupture time previously discussed. Perhaps the most significant feature of figure 22 is the fact that at 1,500° F superimposed alternating stresses had to be increased to the nearly completely reversed level to change strength appreciably. The indication of slight strengthening from small superimposed fatigue loads apparently was real.

Ratio	Loading	Room temp.	1,000°	1,200°	1,350°	1,500° F
Fatigue strength Tensile strength	Axial Bending	0.38 .46	0.48 .52	0.58 .65	0.58 .65	0.54 to 0.68 .57 to 0.66
Fatigue strength 50-hr rupture strength	Axial Bending	---	.54 .59	---	1.09 1.22	1.3 to 1.56 1.5
Fatigue strength 150-hr rupture strength	Axial Bending	---	.61 .66	1.05 1.38	1.23 1.38	1.5 to 1.8 1.6
Fatigue strength 500-hr rupture strength	Axial Bending	---	.67 .73	1.13 1.6	1.43 1.6	1.7 to 2.0 1.9

The ratio of completely reversed strength to tensile strength tended to increase from about 0.4 to 0.68 with temperature. The ratios of fatigue strength to static rupture strength also remained at about 0.6 at 1,000° F. However, at the higher temperatures, the fatigue strengths were

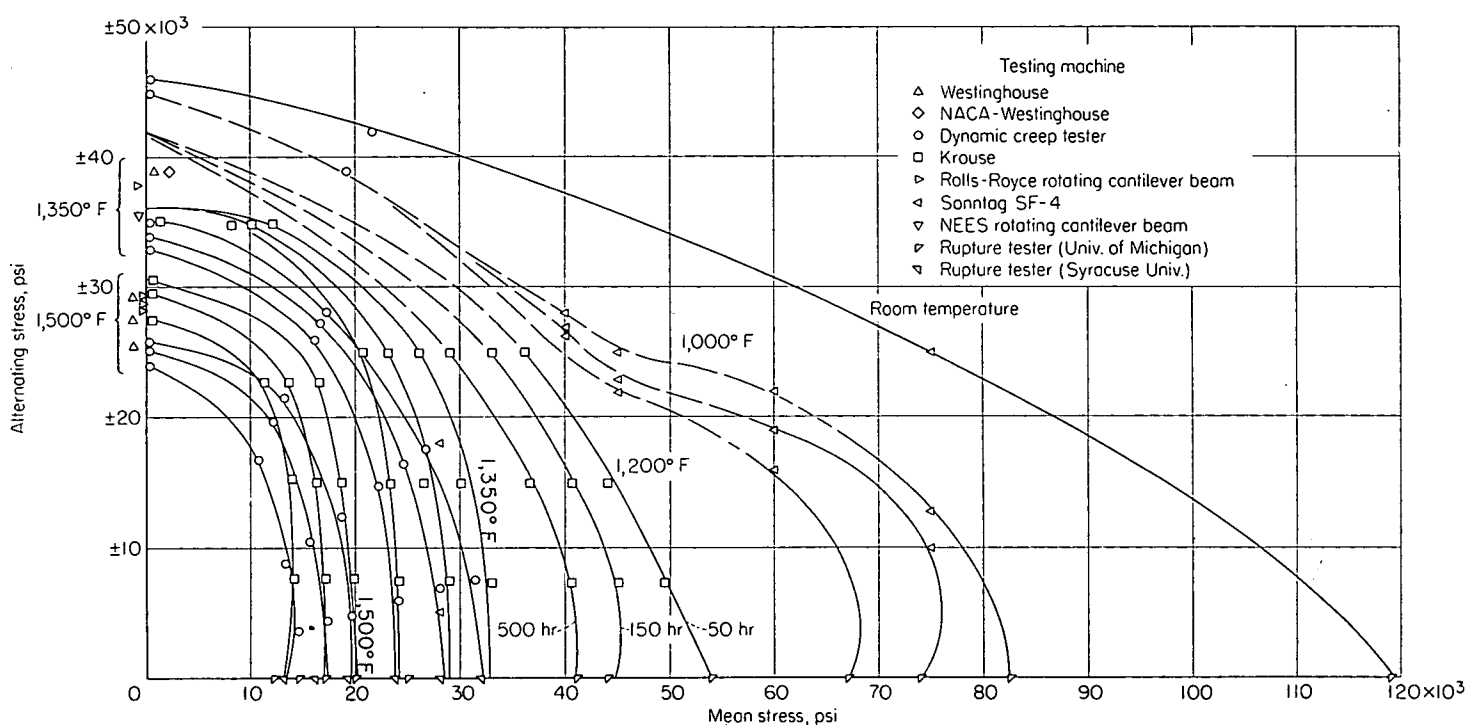
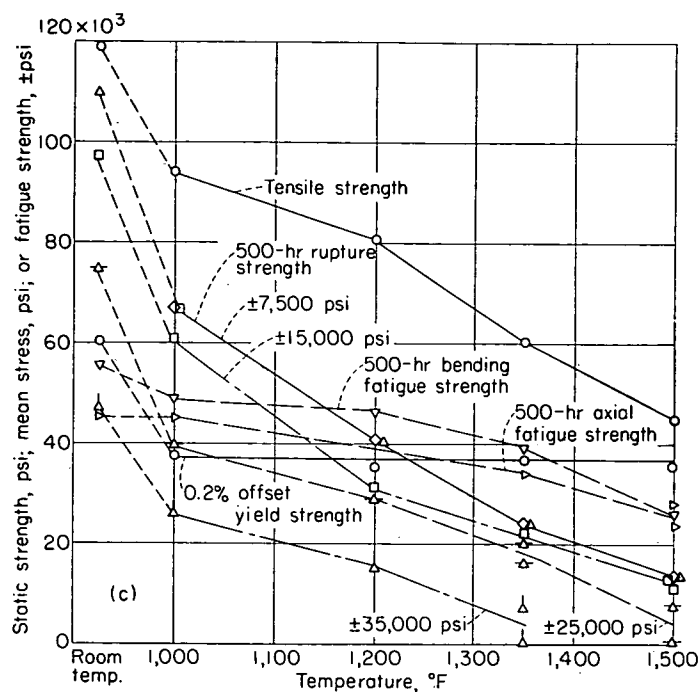


FIGURE 22.—Curves of alternating stress against mean stress for fracture in 50, 150, and 500 hours at room temperature, 1,000°, 1,200°, 1,350°, and 1,500° F.

The relative strengths under static and fatigue loads are further compared in figure 23. This figure shows the influence of temperature on static tensile, 0.2-percent-offset yield strength and the 50-, 150-, and 500-hour rupture strengths, as compared with the completely reversed fatigue strengths and the mean stresses for superimposed fatigue loads of $\pm 7,500$, $\pm 15,000$, $\pm 25,000$, and $\pm 35,000$ psi for the time periods of 50, 150, and 500 hours. These curves show clearly the temperatures for the various time periods where the controlling property shifts from fatigue to static stresses. It is interesting to note that, insofar as static strength is concerned, the yield strength would govern allowable stress up to 1,325° F for 50 hours and up to 1,225° F for 500 hours. Some of the ratios involved are also of interest:

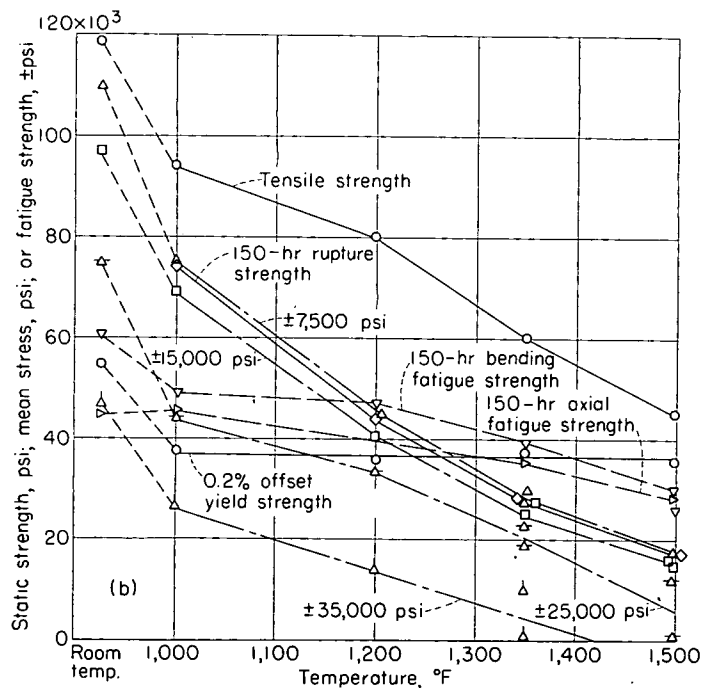
higher than the static rupture strength, the ratios ranging up to the maximum value of 2 for 1,500° F and 500 hours. There were variations in the data from different tests, which will be discussed later. The general trends, however, appear valid for the data and should not be confused by the small difference due to test machines.

The relationships between static and dynamic properties appear to be controlled by the relative predominance of creep or fatigue damage as influenced by temperature, stress level, and time. At high stress levels rapid repetitions of a given stress were more damaging than a steady stress from a static load. At temperatures where creep occurred, a static stress eventually became more damaging than the same stress repeatedly applied. Consequently, conditions



(a) 50 hours for fracture.

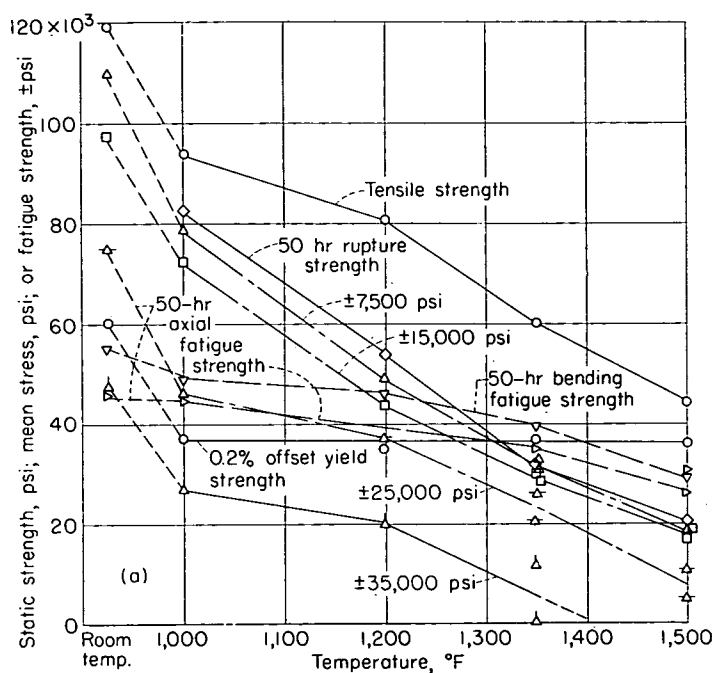
FIGURE 23.—Comparative static and fatigue strengths for fracture in 50, 150, and 500 hours from room temperature to 1,500° F. Curves designated with $\pm 7,500$, $\pm 15,000$, $\pm 25,000$, or $\pm 35,000$ psi show mean stress for rupture with indicated alternating stress superimposed.



(b) 150 hours for fracture.

Figure 23.—Continued

were reached at which the static strength was less than the fatigue strength. This was true at shorter time periods and increasingly higher stresses as the temperature was increased. For these reasons, fatigue strengths were always lower than static rupture strengths where creep was not involved and for all except relatively short time periods were higher at high temperatures where creep did occur.



(c) 500 hours for fracture.

Figure 23.—Concluded.

FATIGUE STRENGTHS BASED ON CYCLES TO FAILURE

The fatigue strengths based on cycles to failure were the same as those based on time to failure when fatigue limits were established. The two differ because of variation of cyclic speed in different test machines when the time periods involved were less than those required to establish a fatigue limit or when a definite fatigue limit was not obtained. The stresses for fracture established for the arbitrarily selected values of 10^7 , 3×10^7 , and 10^8 cycles (table XIII and fig. 24) show such deviations. The features of figure 24 are:

(1) At 1,350° and 1,500° F the 3,600-cpm dynamic creep test unit and the 1,500-cpm Kröuse machine gave considerably different values at low superimposed fatigue stresses. The strengths were time dependent under these conditions because of the predominating effect of creep, so that higher values were obtained in the 3,600-cpm unit than in the slower, 1,500-cpm, machine.

(2) The agreement for the two axial-type units was improved at high values of superimposed stresses, but it was not perfect. The reason for this is not apparent from the data.

INFLUENCE OF SUPERIMPOSED FATIGUE LOADS ON CREEP

Fatigue stresses superimposed on steady static loads appear to have the same effects on total deformation as they do on rupture properties. (See figs. 6 and 25.) The data do not cover so wide a range of combinations of stresses as for rupture, but up to ratios of alternating to mean stress of 0.67 the behavior had the same general characteristics. The most significant difference was the substantial decrease in time for the total-deformation curves of figure 6 to converge at 1,350° F, where the stress ratio was high enough to reduce strength at the shorter time periods. The following tabulation gives the time periods beyond which there

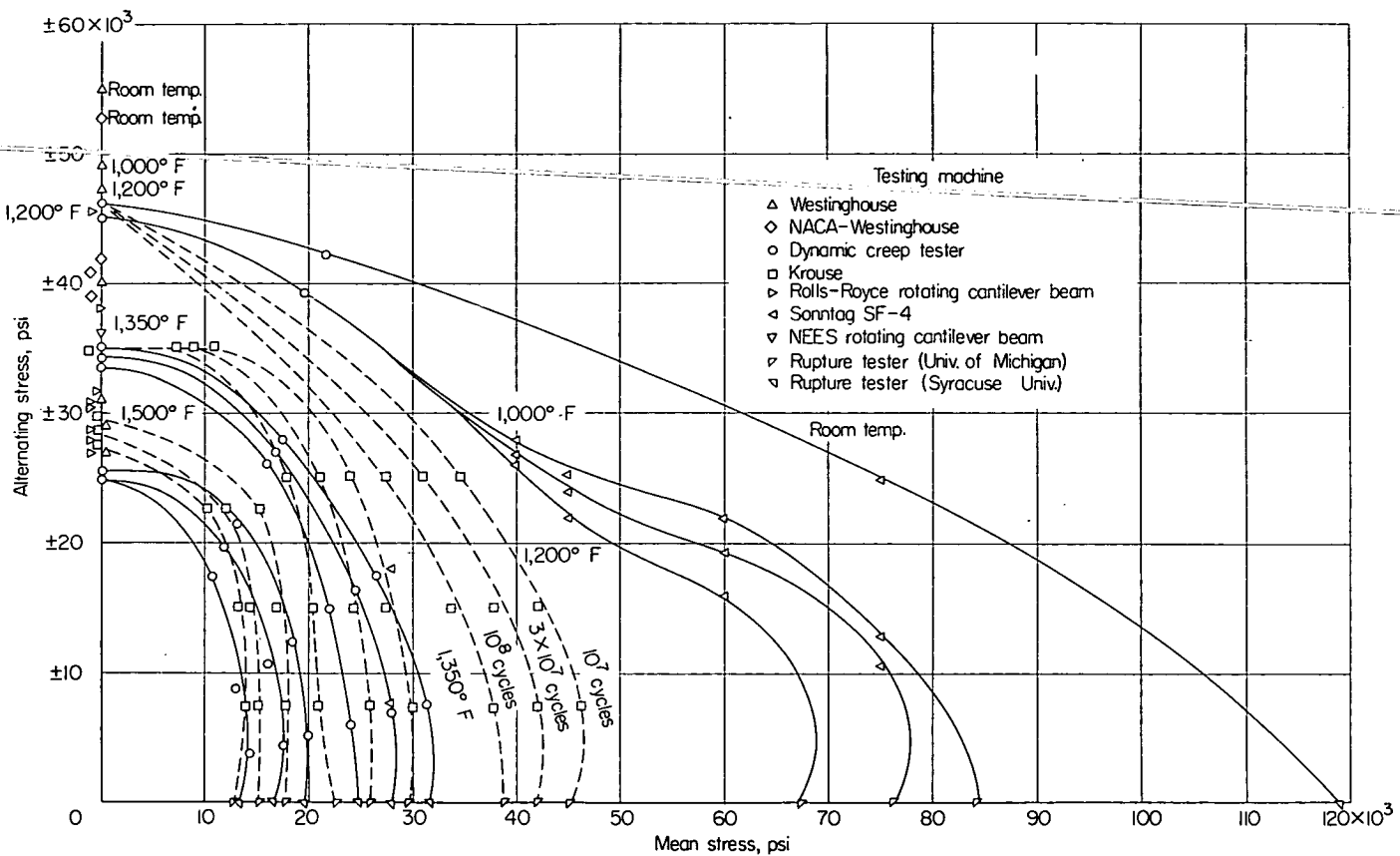


FIGURE 24.—Curves of alternating stress against mean stress for fracture in 10^7 , 3×10^7 , and 10^8 cycles at room temperature, $1,000^\circ$, $1,200^\circ$, $1,350^\circ$, and $1,500^\circ$ F.

was no appreciable effect from superimposed stress at $1,350^\circ$ F:

Deformation	Time to reach equal strengths at ratios of alternating to mean stress of 0, 0.25, and 0.67, hr
Rupture.....	2,000
2.0-percent total deformation.....	800
0.5-percent total deformation.....	100

This illustrates strikingly the degree to which the effects of fatigue loads were reduced for limited amounts of creep. Superimposed alternating loads must have had less effect on creep than on fracture characteristics. Another way of expressing this effect would be to state that superimposed fatigue loads probably had little effect until third-stage creep occurred.

The lack of an appreciable effect of superimposed fatigue loads on creep prior to the third stage is emphasized by the almost complete absence of any effect on minimum creep rates for stress ratios up to 0.67 at $1,350^\circ$ and $1,500^\circ$ F. (See fig. 5.) In reference 3 it was shown that there was no effect of alternating stress on total creep up to the start of third-stage creep for the same data.

The data for total deformations reported for the General Motors rupture tests with superimposed rotating bending (fig. 10) differ from those established by the dynamic axial creep tests (fig. 6). The main difference is that the General

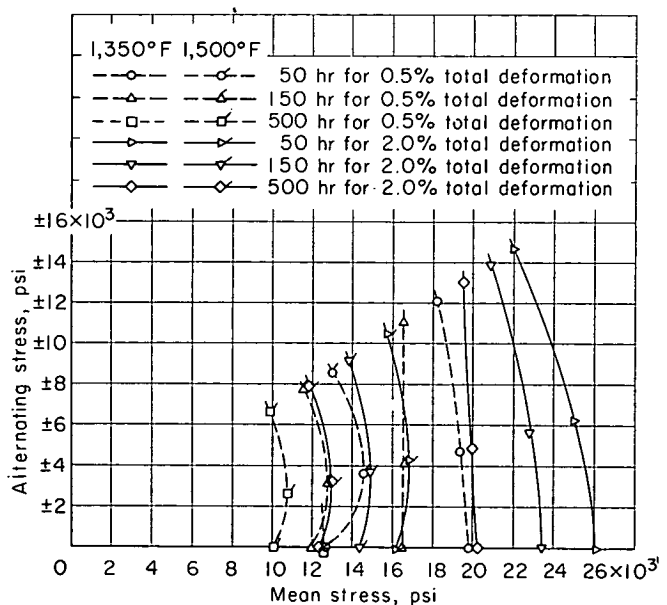


FIGURE 25.—Influence of superimposed fatigue stress on mean stress for total deformation of 0.5 and 2.0 percent in 50, 150, and 500 hours.

Motors tests show appreciable times for limited deformations at $28,000 \pm 18,800$ psi, whereas the dynamic creep tests show that 0.5-percent deformation was exceeded upon loading to this stress and 2-percent deformation was reached in a very short time period. The two sets of data agree very well at $28,000 \pm 7,000$ psi and for static tests. It will be noted that, at the high mean stress of 28,000 psi, a small amount of

superimposed fatigue loading reduced total-deformation strength. The General Motors data indicate no effect from substantial further increases in fatigue stress, while the dynamic creep tests indicate continued decrease in time to reach the deformation.

INFLUENCE OF SUPERIMPOSED FATIGUE STRESS ON ELONGATION IN THE RUPTURE TEST

Elongations were reduced from those exhibited by static tests in increasing amounts (table V and fig. 26) by fatigue loading:

(1) At 1,350° F when ratios of dynamic to static stress were 0.67, 1.64, and ∞

(2) At 1,500° F when stress ratios were 1.64 and ∞

There was also some tendency for the elongations to be reduced at shorter time periods for the smaller dynamic loadings.

As would be expected, there was very little elongation in completely reversed stress tests. The values of 2 percent at 1,500° F were, in fact, surprisingly high. It is uncertain if this latter effect was due to error in measuring matched fractures or represented a real effect from more creep in tension than in compression.

It was interesting to note that the high values of superimposed stress apparently eliminated the time dependency of elongation characteristic of static tests. There was also a slight tendency for improved elongation at the longer time periods for the lowest dynamic loads (stress ratio of 0.25).

This influence of alternating stress on total elongation contrasts sharply with the absence of an effect for limited creep deformations or total creep through second-stage creep discussed in the previous section. While it is true that the limited total-creep effects were restricted to stress ratios of 0.25 and 0.67, it appears that for these ratios, at least, superimposed dynamic stress effects are largely limited to third-stage creep.

STRESS-STRAIN CHARACTERISTICS UNDER FATIGUE LOADING

Completely reversed stress tests (fig. 17) in a rotating cantilever beam type of test indicated that static tensile proportional limits fell below the dynamic bending proportional limits. Apparently this is not necessarily a characteristic result, inasmuch as data for mild steel showed the opposite effect (ref. 5).

Static bending tests gave load-deflection curves at room temperature which coincided with those for the dynamic

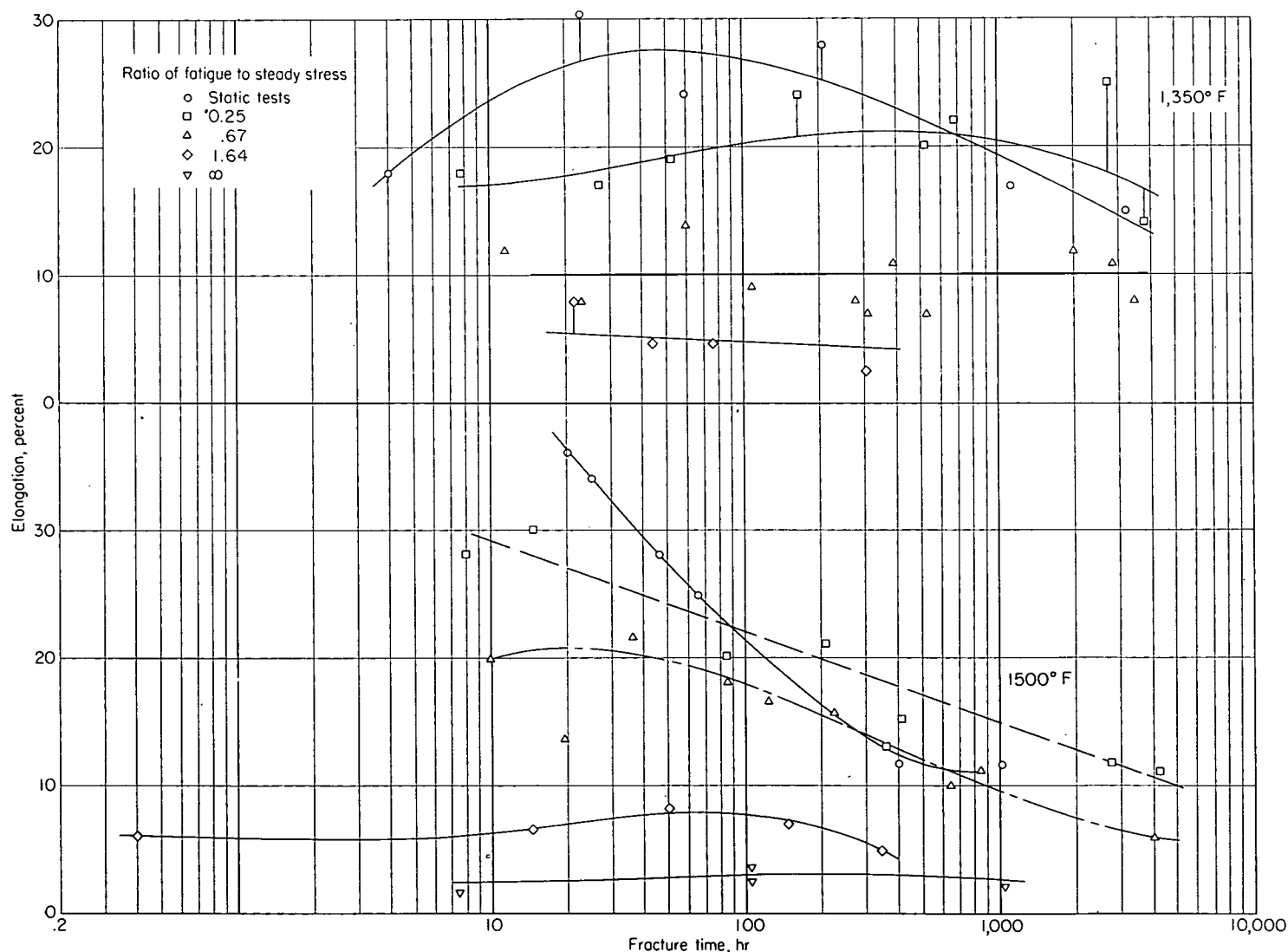


FIGURE 26.—Curves of elongation against fracture time for combined steady and superimposed fatigue.

ending tests. The more gradual deviation from proportionality for the bending curves is related to the restriction of plastic yielding to the higher stressed surface layers in the bending tests. The reason for the higher proportional limit under bending conditions is not so clear. Possibly testing technique, particularly sensitivity of strain measuring equipment, could be involved.

Perhaps the most important point from the dynamic modulus data regarding the relationship between static and dynamic properties is that static or low-stress modulus data can be very misleading in computing resonance effects. At least for the material tested, the tendency for dynamic moduli to decrease with stress is reduced by increasing temperature and also with increased numbers of cycles. Variations of dynamic moduli of the type shown by figure 16 could be a source of considerable shift in vibration response on both a stress and a number-of-cycle basis. Such variations are, however, considerably less for stresses below the fatigue limit than for those above the fatigue limit.

DAMPING EFFECTS

The actual data on specific damping (fig. 15) were discussed previously from the viewpoint of actual stress and stress history. In addition, damping characteristics as evidenced in heating of test specimens were mentioned for several of the axial-stress-type tests.

From the viewpoint of the relationship between static and fatigue properties, damping characteristics probably alter the relationships between static and fatigue properties in a manner that is not evident from this investigation.

Insofar as actual fatigue is concerned either in practice or in testing, one important feature of the data is the very evident excessive temperatures which can be induced by high damping under high fatigue loads. For the test material involved damping can be much higher at engineering stress levels than would be expected from low-stress data. It may also increase or decrease with the number of cycles of applied stress. The surprising large damping at high stress levels is probably related to the overheating problem encountered in a number of the tests in axial stress machines, since the energy absorbed where the whole specimen is being stressed can be quite large. This effect seems to be critically influenced by cyclic speed and stress level in a nonuniform manner. This observation is based on the extremely rapid temperature increases reported for axial tests at room temperatures and 1,000° F above certain stress levels. Further, it seemed that the machines operated at 3,600 cpm were more subject to such heating than was the 1,500-cpm machine. In fact, reduction of cyclic speed during loading seemed necessary to control the heating. Apparently, these critical effects diminish with temperature since no one reported overheating at 1,500° F even though damping increased with temperature.

High damping tends to reduce notch sensitivity. A notch is very detrimental, however, when material damping is important because the volume of metal at high stress in the notch is too small to absorb much energy.

Apparently, damping characteristics can vary in different alloys to a considerable extent (ref. 5).

INFLUENCE OF CYCLIC SPEED ON FATIGUE PROPERTIES

The major emphasis in this report has been placed on properties from a time viewpoint. The main problem has been to relate fatigue properties to the rupture properties which are expressed in terms of the static stress for rupture in a specified time.

Cyclic-speed effects in the fatigue tests would be expected to:

(1) Show a difference in strength for a given number of cycles where the speeds of the machines differ and the fatigue properties are time dependent (i. e., no fatigue limit as at high temperatures or at stresses above fatigue limit).

(2) Show a difference in fatigue strength where the cyclic speed itself influences properties.

The data obtained show the following effects regarding cyclic speed:

(1) Tests carried out at low values of superimposed alternating stress and at high temperature where creep occurs show differences in strength between the 3,600-cpm and 1,500-cpm machine data on the basis of number of cycles. There was little difference in strength on a time basis (compare figs. 22 and 24) at 1,350° and 1,500° F.

(2) Comparisons based on number of cycles did not eliminate the differences between the two axial tests at high alternating-stress values. (See figs. 22 and 24 at 1,350° and 1,500° F.) Both machines indicated fatigue limits, so that there was little difference between comparison based on time or cycles. The 1,500-cpm machine gave the higher strengths although it is doubtful that cyclic-speed differences were responsible.

(3) There were differences in fatigue strength for completely reversed stress tests. It is difficult to determine if this was due to cyclic-speed variation or to other causes. Data scatter tended to obscure such effects. There were a few trends which may be due to cyclic speed:

(a) The Westinghouse 7,200-cpm machines tended to require higher stresses than the other machines to cause fracture in a given number of cycles. (See fig. 24.) This was not so evident at room temperature as at temperatures of 1,200° F and higher.

(b) In the short-time tests in the variable-speed rotating cantilever tests the specimens tended to fracture at shorter times than did those in the tests in the Westinghouse machines. The short-time tests were run at very slow cyclic speeds. This, however, is not a definitely established effect, inasmuch as some of the other tests also tended to show the same behavior.

(c) In view of the relatively small differences between the fatigue strengths for the variable-speed cantilever tests and the other higher speed machines, it seems doubtful that the cyclic speed alone had much effect; possibly the very slow speeds resulted in low strength for short time periods.

The lowest fatigue strengths were obtained in axial stress test machines. This, however, is apparently due to other causes than cyclic speed.

A possible relation between cyclic speed and overheating was discussed under damping effects. High cyclic speeds unquestionably increase overheating from damping.

The possibility exists that fatigue nuclei may be expected in fractures from combined stress at somewhat lower stress

ratios for higher speed machines. This may be the reason for the slight overlap of the stress conditions for the appearance of nuclei in figure 20. This does not seem unreasonable because the slower speed machines require longer times for fracture and there is a time-depending effect on the time of fracture at 1,350° and 1,500° F.

INFLUENCE OF NOTCHES ON FATIGUE

No data were accumulated for notched specimens under static stresses. The variable-speed rotating cantilever beam fatigue tests indicate the very pronounced reduction of fatigue strength which can result from a notch. (See figs. 13 and 14.) The indications that there is little difference in the fatigue strength for notched material over a wide range of temperatures were somewhat surprising. Notch weakening was reduced by increasing temperature, although there still was a substantial difference between notched and unnotched specimens even at 1,500° F.

The very much longer time required for fracture of notched specimens after the first evidence of a crack was also surprising. This is particularly true in view of the very short time difference for unnotched specimens. This should be an interesting phenomenon for both stress analysis and fracture study.

SURFACE FINISH

The most important general result of the NACA Lewis Laboratory studies of the effects of surface finish is the evidence that such effects decrease with increasing temperature. Very little effect remained at 1,350° F, in spite of the fact that there was a substantial effect at room temperature. This checks the cooperators' results on another heat of low-carbon N-155 alloy (ref. 8), although the other heat showed lower strengths and lower temperatures of disappearance of the effect of surface finish.

The influence of surface finish seems to be related more to the procedure used in finishing the specimens than to surface roughness (ref. 8). Polished surfaces apparently have higher strength than plain ground specimens at low temperatures. This, however, does not appear to be related to less surface roughness, inasmuch as the rough surface was even stronger. Reference 8 attributed the main effect to the compressive stresses induced by polishing or by the roughening procedure, offsetting the fatigue stresses and requiring higher applied stresses for fracture. The reduced effect of increasing temperature was attributed to stress relief.

The data obtained for this report do not substantiate the stress-relief theory so definitely as the previous work on the same alloy with a lower fatigue strength. Heating at 1,400° F did not change the fatigue strength at room temperature for either the ground or the polished specimens. The rough specimens were, however, reduced to the level of the ground specimens.

All surfaces were cold-worked by the finishing procedures. Cold-working definitely alters strength at both low and high temperatures and ductility characteristics as well. It seems improbable, therefore, that residual-stress effects alone control the effect of surface finish. The ground surface should have had the least cold-work and particularly a very shallow depth of penetration. The polished and rough surfaces should

have had increasing effects. A 4-hour treatment at 1,400° F would not be expected to remove the effects of such cold-work, although it should considerably decrease the strength and increase the ductility. It is probable that a complete evaluation will show a complex relation between residual stress, strength, and ductility, as reflected in fatigue properties. Thus, different alloys, different heat treatments of the same alloy, and different response of the same alloy to treatment (see low fatigue strength of N-155 alloy in ref. 8) all probably alter surface-finish effects.

Polished specimens of the material used for this investigation prepared by different laboratories showed no significant difference in fatigue characteristics at 1,000°, 1,200°, 1,350°, or 1,500° F. It would appear, therefore, either that there was little difference in surface finishes or that fatigue properties of the alloy at these temperatures were not sensitive to variations in polishing. The NACA Lewis Laboratory data suggested that there ought to have been an effect at 1,000° and 1,200° F if there were differences in surface finish. Their data show slight effects at 1,350° F, and, if true, this would indicate greater effects at lower temperatures. Possibly their data at 1,350° F were not outside the scatter band and there actually was no great effect even at 1,000° F, as was indicated by their data in reference 8.

The indication of an absence of surface-finish effects on fatigue at high temperatures should not be accepted as general until a much wider range of response of alloys to cold-work and stress-concentration effects has been studied. In view of the known sensitivity of other properties of heat-resistant alloys at high temperatures to cold-work, it seems unlikely that all alloys will be free of such effects. This seems particularly true for bending fatigue, where stresses are a maximum on the surface.

There is one very interesting feature of the NACA Lewis Laboratory data. The ground specimens had a fatigue strength about 5,000 psi less than that of the polished specimens. This is the same order of magnitude as the difference between axial and reversed bending fatigue tests. Axial fatigue tests would probably be much less sensitive to surface-finish effects. The ground specimens were considered to have low strength because they were relatively free of surface-finish effects. This suggests that a major contributing cause for the difference between the two types of tests was the increased strength imparted to bending tests by polishing. The decrease in difference with increasing temperature also parallels the influence of surface finish found by the Lewis Laboratory.

TYPES OF TESTING MACHINES

There were four general types of stress applied by the various testing machines:

(1) Axial with superimposed axial fatigue load: In general, this type of test gave lower results than the bending-type tests for completely reversed stresses. This is shown by the data of table XIII and figures 22, 23, and 24. The actual S-N curves of figure 27 clearly show the tendency to be lower. As was pointed out in the surface-finish studies, this difference may have largely been due to high compression stresses in the surface of the bending specimens. The general absence of a "knee" in the S-N curves for axial tests was also evident.

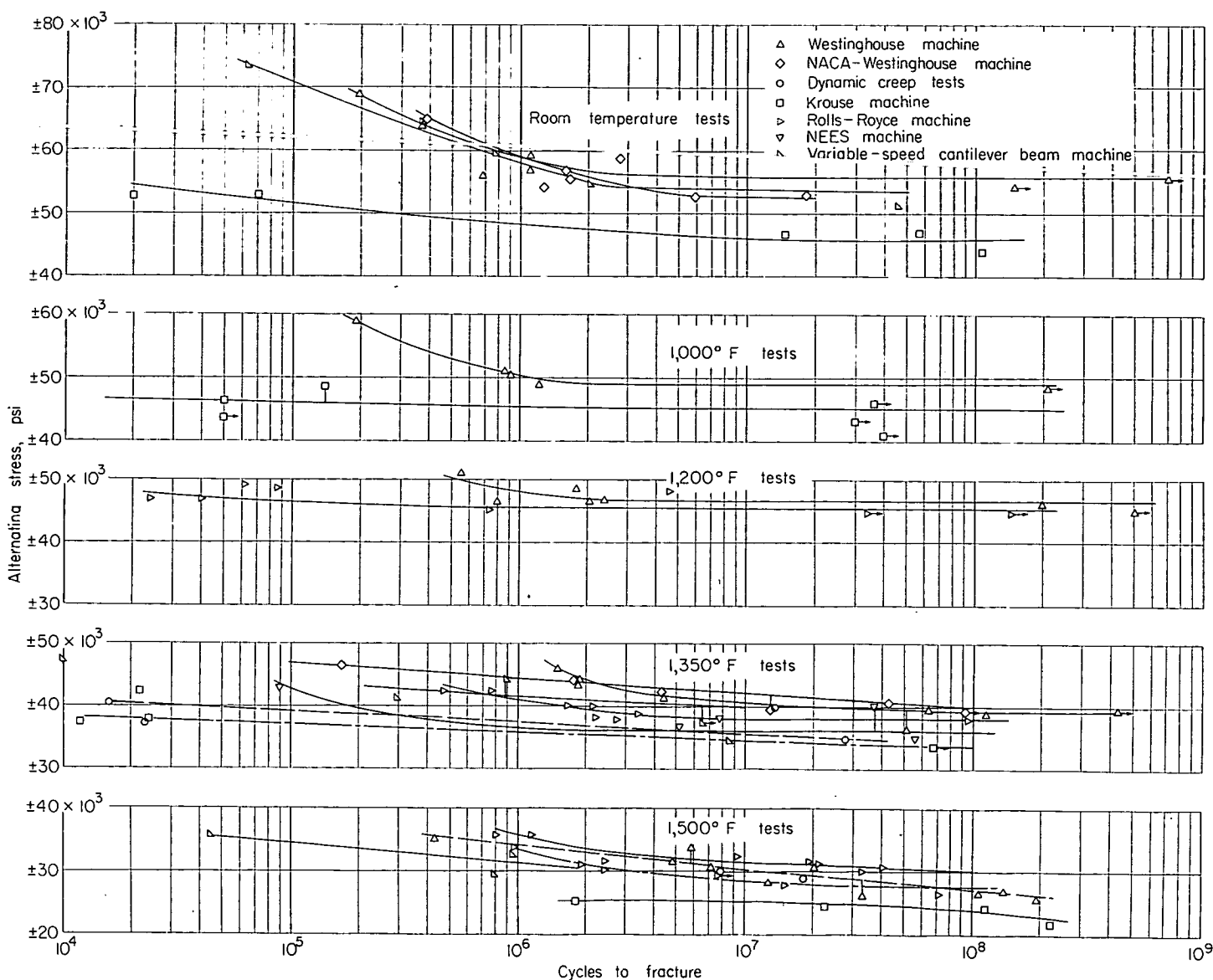


FIGURE 27.—Comparison of S-N curves from different types of test machines operated with completely reversed stresses.

The difference between the two types of tests tends to disappear at the longer times at the higher temperatures. This is more evident on a time than on a cyclic basis.

As discussed elsewhere, the data from the two axial-type test machines did not agree too well over the range of superimposed stresses from static to completely reversed stress tests. Apparently, some variable in the characteristics of the two machines is the most logical reason. Differences in cyclic speed do not seem to be the answer.

The curves of alternating versus mean stress for fracture at 50, 150, and 500 hours (fig. 22) at 1,000° F were irregular and approached closer to the 1,200° F curves than would be expected. No evident reason was found to explain the difference. It was noted that the specimens tested at 1,000° F showed fatigue nuclei at rather low stress ratios, whereas those tested at 1,200° F showed the opposite effect. It also could be noted that the Krouse machine tended to give higher strengths than the dynamic creep machine. It is possible that the Sonntag machine gives lower strengths than the Krouse machine, pulling the curves together at 1,000° F and 1,200° F.

(2) Steady axial loads with superimposed rotating bending fatigue loads: Only a few tests were made with this type of machine and only one specimen fractured at the point of maximum stress. This one test agreed very well with those made in the axial fatigue machines. The very little evidence indicates agreement between the two types of stressing. The reason some of the specimens fractured away from the point of maximum stress in this test remains unexplained.

(3) Cantilever beam tests, vibrating in one plane with completely reversed stress: Only one machine of this type was involved, although it was used by two laboratories. Different-sized specimens were used in the two laboratories. While there were minor variations in the reported fatigue strength, it is doubtful that the differences were outside the normal scatter of the data.

(4) Rotating cantilever beam tests: Some variation in reported fatigue strengths existed between the various rotating beam tests and the fixed bending tests. (See table XIII and figs. 22, 24, and 27.) It is difficult to determine whether such variations were real or reflected data scatter.

There was a slight tendency for the rotating test machines to give lower strengths than the Westinghouse fixed bending machine. The low curve at 1,350° F reported for the NEES tests was largely due to the cooperator's drawing the curve on the low side of sparse data. The test points (fig. 27) agree reasonably well with those for the other tests.

In the very slow variable-speed rotating tests the specimens tended to fracture at short time periods at the higher stress (fig. 27). This suggests a possible reduction in strength at low cyclic speeds. Otherwise, the results of the variable-speed tests agreed reasonably well with those of the other tests.

LIMITATIONS OF FINDINGS

The major limitation of the relationships developed in this report is their restriction to one alloy with one heat treatment. It is expected that the trends are characteristic of static and fatigue tests. It is, however, reasonably certain that the characteristic effects will vary in temperature, time period, and magnitude for various alloys or for the same alloy with varying heat treatments. The data in this report indicate that increased creep resistance will increase the temperatures and time to which fatigue will control properties. This, however, will probably be altered by fracture characteristics at least and probably by other characteristics not immediately evident. For instance, factors which minimize third-stage creep ought to minimize the effects of superimposed fatigue or steady loads. Alloys may differ considerably in sensitivity to surface-finish effects. Likewise, the

detrimental effect of large grain size on fatigue resistance is reported to be important.

Many of the fatigue-strength values reported, particularly for the high alternating-stress axial tests, are based on very limited data and are only approximate. The reported difficulties from overheating by damping in these types of tests also raise the question as to how much influence from this source is reflected in the data.

The Rolls-Royce data suggest that an appreciable amount of scatter in the data may have been due to variations from specimen to specimen. The substantial difference in fatigue strength for completely reversed axial stress tests at 1,500° F on specimens prepared at Michigan and those prepared at Minnesota also points to the possibility of some contribution to scatter from variations in heat treatment.

There are minor differences in data due to peculiarities of test machines, although presumably the machines applied the same combinations of stresses. These differences do not, and should not, complicate the overall trends. They simply point out that characteristics of different machines alter the results of the tests to a minor degree. These could at least be related to the actual shape of the stress pattern, the way the stresses are applied, or to some of the evident difficulties of calibration.

NACA HEADQUARTERS,

WASHINGTON, D. C., *June 15, 1953.*

APPENDIX

PROCESSING OF LOW-CARBON N-155 1-INCH ROUND BAR STOCK

The Universal-Cyclops Steel Corporation reported the processing of the low-carbon N-155 bar stock to be as follows.

An ingot was hammer-cogged and then rolled to bar stock under the following conditions:

- (1) Hammer-cogged to a 13-inch square from a 15½-inch ingot
Furnace temperature, 2,210° to 2,220° F
Three heats—Starting temperature on die, 2,050° to 2,070° F
Finish temperature on die, 1,830° to 1,870° F
- (2) Hammer-cogged to a 10¾-inch square
Furnace temperature, 2,200° to 2,220° F
Three heats—Starting temperature on die, 2,050° to 2,070° F
Finish temperature on die, 1,790° to 1,800° F
- (3) Hammer-cogged to a 7-inch square
Furnace temperature, 2,200° to 2,220° F
Three heats—Starting temperature on die, 2,050° to 2,070° F
Finish temperature on die, 1,790° to 1,890° F
Billets ground to remove surface defects
- (4) Hammer-cogged to a 4-inch square
Furnace temperature, 2,190° to 2,210° F
Three heats—Starting temperature on die, 2,040° to 2,060° F
Finish temperature on die, 1,680° to 1,880° F
Billets ground to remove surface defects
- (5) Hammer-cogged to a 2-inch square
Furnace temperature, 2,180° to 2,210° F
Three heats—Starting temperature on die, 2,050° to 2,065° F
Finish temperature on die, 1,730° to 1,870° F
Billets ground to remove surface defects
- (6) 1-inch rounds were rolled from 2-inch square billets in one heat.
The 2-inch bars were heated in a furnace at 2,100° to 2,115° F; the temperature at the start of rolling was 2,050° to 2,060° F; and the finishing temperatures were from 1,820° to 1,840° F.
The bars were numbered in order of their position in the ingot.
- (7) Bars were assigned letters from A through Z, bar A representing the extreme bottom of the ingot and bar Z the extreme top position.
All billets were kept in number sequence throughout all processing, so that ingot position of any bar could be determined by its letter.
- (8) All bars were cooled on the bed and no anneal or stress relief was applied after rolling.

REFERENCES

- NACA Subcommittee on Heat-Resisting Materials: Cooperative Investigation of Relationship Between Static and Fatigue Properties of Heat-Resistant Alloys at Elevated Temperatures. NACA RM 51A04, 1951.
- Lazan, B. J.: Dynamic Creep and Rupture Properties of Temperature-Resistant Materials Under Tensile Fatigue Stress. Proc. A.S.T.M., vol. 49, 1949, pp. 757-787.
- Lazan, B. J., and Westberg, E.: Properties of Temperature-Resistant Materials Under Tensile and Compressive Fatigue Stress. WADC TR 52-227, Nov. 1952.
- Lazan, B. J., and DeMoney, F.: Investigation of Axial Loading Fatigue Properties of Heat-Resistant Alloy N-155. WADC TR 52-226, pt. 1, Mar. 1953.
- Lazan, B. J., and Demer, L. J.: Damping, Elasticity, and Fatigue Properties of Temperature-Resistant Materials. WADC TR 52-243, Nov. 1952.

6. Morral, F. R., and Lazan, B. J.: Metallographic Studies on N-155 Specimens Exposed to Static and Dynamic Stress at Elevated Temperatures. WADC TR 52-253, Dec. 1952.
7. DeMoney, Fred W.: Investigation of Axial Loading Fatigue Properties of Heat-Resistant Alloy N-155. Part 2. An Exploratory Investigation of the Effect of Temperature, Time, and Stress on Fracture Characteristics and Metallographic Structure of N-155 and Hardness of N-155 and S-816. WADC TR 52-226, pt. 2, Feb. 1953.
8. Ferguson, Robert R. Effect of Surface Finish on Fatigue Properties at Elevated Temperatures. I—Low-Carbon N-155 With Grain Size of A.S.T.M. 1. NACA RM E51D17, 1951.

TABLE I.—BRINELL HARDNESS RANGES OF TEST STOCK

[Heat treatment: 2,200° F for 1 hr, water-quenched, and 16 hr at 1,400° F: NACA data from University of Michigan]

Bar ^a	Brinell hardness ^b		
	Surface	Cross section	Range
JA	207-220	217-218	207-220
JB	197-212	207-214	197-214
JC	210-212	214-216	210-216
JD	207-208	210-214	207-213
JE	204-216	212-217	204-217
JF	199-214	212-214	199-214
JG	198-215	201-216	198-216
JH	203-212	205-212	203-212
JI	192-215	201-213	192-215
JJ	209-212	210-211	209-212
JK	203-208	205-213	203-213
JL	211-214	211-215	211-215
JM	203	200	200-203
JN	205-208	213-214	205-214
JO	206-208	212-214	206-214
JP	201-213	211-211	201-213
JQ	201-215	213-216	201-216
JR	211-215	212-216	211-216
JS	206-211	208-212	206-212
JT	205-211	206-210	205-211
JU	204-208	213-215	204-215
JV	205-207	211-212	205-212
JW	208-208	210-216	208-216
JX	203-211	210-214	203-214
JY	211-212	211-216	211-216
JZ	202-205	209-211	202-211
Overall range	192-220	200-218	192-220

^a Specimens taken from 26 bars marked A through Z. A represents bottom bar from ingot, and Z, top bar from ingot, with the others lettered consecutively in between.

^b Hardness values were taken on samples cut from center and each end of every bar.

TABLE II.—TENSILE TEST DATA

[NACA data from University of Michigan]

Specimen	Test temp., °F	Tensile strength, psi	Proportional limit, psi	Offset yield strengths, psi				Elongation, percent in 2 in.	Reduction of area, percent
				0.01 percent	0.02 percent	0.10 percent	0.20 percent		
JM1	Room	119,100	41,000	46,000	48,700	56,100	59,500	45.0	46.2
JY1	Room	119,000	40,000	47,600	50,500	58,500	61,500	42.5	45.5
JF1	1,000	91,250	26,750	31,750	32,500	34,800	35,800	44.5	49.3
JW1	1,000	93,900	26,000	31,750	34,000	38,750	40,000	39.5	45.7
JM4	1,000	94,250	26,250	32,500	33,800	37,000	37,750	42.0	47.1
JP1	1,200	81,200	25,750	29,500	30,500	34,250	35,250	35.0	38.0
JG1	1,200	79,600	26,000	29,500	31,000	34,900	35,800	33.0	34.5
JX1	1,350	60,250	22,250	27,500	29,750	34,750	36,500	27.5	28.5
JN1	1,350	60,125	23,500	28,750	30,750	35,250	37,200	2.65	28.5
JF1	1,500	45,600	20,000	26,250	28,500	33,800	35,800	19.5	26.8
JR1	1,500	43,625	20,500	26,800	28,500	33,200	35,800	25.5	27.1

TABLE III.—RUPTURE TEST DATA

[NACA data from University of Michigan]

Specimen	Test temp., °F	Stress, psi	Rupture time, hr	Elongation, percent in 2 in.	Reduction of area, percent
J110	1,000	85,000	36	24	28
JT9		80,000	70	25	25
JH9		75,000	128	17	17
JP10		70,000	345	14	13
JL9		63,000	790	12	13
JX8	1,200	65,000	26	12	14
JB12		55,000	47	10	11
JA1		50,000	61	10	11
JM2		47,000	83	16	10
JQ1		43,000	195	15	8.5
JM8		40,000	663	10	16
JD1		38,000	1,107	20	18
JS1	1,350	32,000	55	20	23
JC1		29,000	112	37	40
JB1		28,000	248	25	35
JJ1		26,000	336	30	43
JT1		24,000	665	20	30
J11		22,000	1,361	12	20
JU1	1,500	20,000	51	34	37
JK1		18,000	108	28	32
JO1		16,000	203	25	37
JH1		14,000	575	26	33
JS10		12,500	1,361	13	20
• JX4	1,500	14,000	358	13	17
• JR5		14,000	502		
• JA21		14,000	484	25	24
• JA16		14,000	470	22	26
• JR17		14,000	554	18	26

• Specimens made for dynamic creep tests at Syracuse.

• 0.250-in.-diam. specimens with 1-in. gage length.

• 0.250-in.-diam. specimen with 2-in. gage length.

TABLE IV.—AXIAL FATIGUE DATA FROM 3,600-CPM DYNAMIC CREEP TEST MACHINE

[Materials Laboratory, WADC, data from Syracuse University and University of Minnesota]
(a) Room temperature and 1,000° F

Specimen	Test temp., °F	Stress ratio	Stress, psi	Cycles to fracture	Time for fracture, hr
Profile specimens					
JU-23	Room	2.0	21,000±41,200	5.3×10 ⁶	^b 24.6
JB-23			21,500±42,200	32.8	152.0
JE-21			22,100±43,200	.3	^c 1.5
JF-20			22,000±43,400	3.9	18.2
JT-22(1)	Room	∞	0±44,200	108.5	^d 502.0
JW-21			0±47,000	15.0	32.5
JT-22(2)			0±47,200	57.6	^d 267.5
JP-19			0±52,900	.02	^e .08
JT-22(3)			0±52,900	.07	^e .35
N1231F(1)	1,000	2.0	19,300±38,700	25.3	^b 117.0
N1230F	1,000	1.8	21,000±37,900	.004	^e .018
JL19	1,000	2.0	19,700±39,300	.65	3.0
N1233F			19,700±39,300	.04	^e .17
N1234F			19,700±39,300	10.6	48.1
N1231F(2)			20,000±40,000	1.1	^e 5.1
N1232F			20,000±40,000	.95	4.4
JC20(1)	1,000	∞	0±39,000	58.5	^d 270.9
JJ18(1)			0±41,000	40.4	^f 187.4
JJ22			0±41,000	.03	^e .13
JS-21			0±43,400	.002	^e .008
JC20(2)			0±43,400	.005	^e .025
JJ18(2)			0±43,500	.003	^e .13
N1226F			0±43,500	.01	^e .05
N1227F(1)			0±43,500	30.7	^d 142.0
N1228F			0±45,000	.03	^e .15
N1227F(2)			0±46,000	36.3	^d 168.0
N1235F			0±46,500	.03	^e .15
N1227F(3)			0±48,500	.14	^e .65

• Specimen numbers with J prefix prepared by Michigan. Specimen numbers with N prefix prepared by Minnesota.

• Flexplate (machine part) failed which bent specimen and stopped test.

• Specimen fractured in threads.

• Test stopped before specimen ruptured.

• Previous stress history. See JT-22(1) for previous testing of same specimen.

• Test section of specimen attained dull red-heat color with consequent elongation of specimen, which stopped test.

• Previous stress history. See JT-22(1) and (2). Specimen temperature rose from 75° to approximately 400° F during time of test.

• Test stopped before specimen ruptured. Variable-speed start-up procedure used to control damping heat.

• Specimen ruptured before machine attained 3,600 cpm. Stress calculated on basis of maximum speed attained. Variable-speed start-up procedure used to control damping heat.

• Specimen temperature rose 20° from 1,000° F within 20 sec after machine attained 3,600 cpm. Variable-speed start-up procedure used to control damping heat.

• Previous stress history. See N1231F(1).

• Test stopped before specimen ruptured. Air blast used to control specimen heating at approximately 825° F.

• Specimen temperature rose from 800° to approximately 1,130° F within 30 sec after machine attained 3,600 cpm.

• Previous stress history. See JC20(1). Specimen temperature rose from 900° to approximately 1,126° F within 90 sec after machine attained 3,600 cpm.

• Previous stress history. See JJ18(1). Specimen temperature rose from 900° to approximately 1,150° F after machine attained 3,600 cpm. Thermocouple failure occurred 2 min after starting test. Air blast used.

• Specimen temperature rose from 950° to approximately 1,040° F in about 20 sec. Air blast used.

• Variable-speed start-up procedure used to control damping heat.

• Specimen temperature rose from 1,000° to 1,100° F in approximately 30 sec. Variable-speed start-up procedure used; specimen ruptured before machine attained 3,600 cpm. Stress calculated on basis of maximum speed attained.

• Previous stress history. See N1227F(1). Variable speed start-up procedure used to control specimen damping heat.

• Specimen temperature rose from 1,000° to 1,030° F at time of rupture. Variable-speed start-up procedure used.

• Previous stress history. See N1227F(1) and (2). Specimen temperature rose from 1,000° to 1,030° F at time of rupture. Variable-speed start-up procedure used.

TABLE IV.—AXIAL FATIGUE DATA FROM 3,600-CPM DYNAMIC CREEP TEST MACHINE—Continued

(b) 1,350° F.

Specimen	Test temp., °F	Ratio of alternating to mean stress	Stress, psi	Cycles to fracture	Time for fracture, hr	Elongation, percent (*)
Uniform-diameter gage length, 2 in. long						
JJ-6	1,350	0	40,000±0	-----	4.0	18.4
JY-6			35,000±0	-----	22.8	31.4
JM-22			30,000±0	-----	58.3	24.7
JA-20			25,000±0	-----	208.8	28.5
JC-5			22,000±0	-----	1,114.7	17.9
JZ-16			17,500±0	-----	3,185.0	15.0
JN-6	1,350	.25	37,000±9,200	1.64 ×10 ⁶	7.6	18.5
JB-13			33,000±8,250	5.88	27.2	17.4
JK-13			30,000±7,500	11.3	52.2	19.0
JC-10			27,500±6,875	35.8	165.7	24.9
JF-11			25,000±6,250	112	518.3	20.8
JG-5			23,200±5,800	147.2	682.2	22.3
JV-13			19,000±4,750	580	2,683	25.8
JQ-5			17,500±4,400	817	3,783	14.0
JK-5	1,350	.67	29,000±19,332	2.44	11.3	12.6
JZ-19			27,000±18,000	4.97	23.0	8.7
JO-4			26,000±17,332	12.96	60.0	14.5
JP-5			24,000±16,000	60.0	278.0	8.0
JM-20			25,000±16,666	23.55	109.0	9.8
JZ-20			24,000±16,000	65.5	303.6	7.5
JY-4			22,800±15,200	85.75	397.2	11.9
JA-19			26,001±14,400	114.5	530.0	7.9
JI-12			19,000±12,600	456.0	2,107	12.0
JD-13			18,000±12,000	540.0	b 2,500	-----
JX-6			17,500±11,700	609.0	2,821	11.0
JQ-14			17,500±11,700	724.0	3,349	8.0
Profile specimens						
JN-5	1,350	1.64	15,500±25,400	17.16 ×10 ⁶	c 795.0	-----
JW-10			16,000±26,200	66.5	308.0	2.4
JO-9			16,500±27,100	14.6	67.7	4.8
JP-11			17,000±27,900	9.55	44.2	4.8
JV-15			18,000±29,500	5.08	23.5	8.0
JX-10	1,350	∞	0±33,600	6.80	c 315.0	.2
JO-5			0±37,900	.024	4 min	.2
JT-14			0±38,800	.012	2 min	.4
JV-14			0±39,700	.005	1 min	1.0

* Elongations for uniform-diameter specimens were measured over a 2-in. gage length. For profile specimens, elongations were obtained by a suitable factor to give equivalent percentage of values. (See ref. 3.)

b Controller failure at 2,126 hr. Estimated rupture time was 2,500 hr.

c Test stopped before failure because of too long time for fracture.

TABLE IV.—AXIAL FATIGUE DATA FROM 3,600-CPM DYNAMIC CREEP TEST MACHINE—Concluded

(c) 1,350° and 1,500° F

Specimen	Test temp., °F	Ratio of alternating to mean stress	Stress, psi	Cycles to fracture	Time for fracture, hr	Elongation, percent (*)
Uniform-diameter gage length, 2 in. long						
JP-12	1,500	0	7,000±0	-----	(b)	-----
JI-5			11,000±0	-----	1,004.6	11.6
JE-5			13,000±0	-----	398.5	11.7
JH-10			15,000±0	-----	c 221.2	17.0
JV-8			17,500±0	-----	67.2	25.2
JA-16			19,000±0	-----	47.9	28.0
JO-6			20,000±0	-----	24.9	34.4
JB-5			22,500±0	-----	20.7	36.4
JR-10	1,500	.25	8,800±2,200	889.0 ×10 ⁶	4,117.0	11.1
JH-5			10,000±2,500	603.0	2,790.0	11.9
JF-5			14,000±3,500	88.8	410.9	15.4
JT-5			15,200±3,800	82.6	c 382.3	9.6
JE-12			16,800±4,200	45.2	209.5	21.3
JL-5			19,200±4,800	18.0	83.4	19.9
JM-21			22,000±5,500	3.2	14.9	30.0
JW-4			24,000±6,000	1.7	8.0	28.1
JS-5	1,500	.67	8,000±5,300	880.0	4,066.0	5.9
JT-11			12,000±8,000	138.0	640.0	10.2
JW-6			15,000±10,000	49.0	226.5	15.8
JD-5			16,800±11,200	18.4	85.1	18.3
JL-10			18,600±12,400	78.4	36.3	21.8
JG-12			21,000±14,000	4.3	d 19.7	13.7
JV-13			22,200±14,800	2.4	10.9	19.9
Profile specimens						
JL-8	1,500	0.67	12,000±8,000	181.0 ×10 ⁶	837.5	11.4
JI-14			16,800±11,200	27.0	125.1	16.8
JY-9	1,500	1.64	9,000±14,800	275.0	1,273.0	-----
JK-11			11,000±18,000	74.1	343.7	5.0
JY-10			12,000±19,700	32.4	150.0	7.0
JS-13			13,000±21,800	10.9	50.7	8.0
JW-9			14,000±23,000	3.2	14.7	6.5
JR-14			15,000±24,600	.08	.4	6.0
JX-9	1,500	∞	0±21,800	226.0	1,048.0	2.8
JO-14			0±24,300	115.6	536.1	-----
JI-15			0±24,600	22.9	106.1	3.4
JH-15			0±25,300	23.0	106.9	2.4
JS-14			0±25,300	1.8	8.3	1.6
Profile specimens heat-treated and machined at Minnesota						
N1236F(1)	1,500	∞	0±25,300	24.1 ×10 ⁶	e 111.5	-----
N1236F(2)			0±28,000	3.39	15.7	-----
N1248F			0±28,000	16.1	74.5	-----
N1240F			0±28,500	.80	3.7	-----
N1238F			0±29,000	2.18	10.1	-----
N1237F			0±30,000	.048	.2	-----

* Elongations for uniform-diameter specimens were measured over a 2-in. gage length. For profile specimens, elongations were obtained by a suitable factor to give equivalent percentage of values. (See ref. 3.)

b Discontinued; unbroken at 5,000 hr.

c Test stopped before failure, because of either too long time for fracture or experimental difficulties.

d Temperature 20° F low for 2 hr at beginning of test.

e Statically loaded for 100 hr at 14,000 psi prior to dynamic loading.

f Previously tested for 111.5 hr at ±25,300 psi before this test.

TABLE V.—KROUSE AXIAL 1,500-CPM
FATIGUE TEST DATA

[Office of Naval Research and NACA data from Battelle Memorial Institute]

Specimen	Test temp., °F	Stress, psi (a)	Cycles to fracture	Time to fracture, hr
JL7	1,200	40,000±25,000	1.32 × 10 ⁶	14.7
JD2		38,000±25,000	6.16	68.5
JP2		35,000±25,000	5.27	58.6
JG7		35,000±25,000	5.63	62.5
JI2		32,500±25,000	11.90	132
JT7		30,000±25,000	37.10	412
JE7	1,200	55,000±15,000	.31	3.45
JV6		45,000±15,000	2.63	29.2
JJ2		39,000±15,000	27.04	300.5
JC3	1,200	50,000±7,500	4.18	46.4
JQ2		45,000±7,500	11.79	131
JQ6		39,000±7,500	69.01	767
b JD12	1,350	0±45,000	.005	.055
b JC9		0±42,500	.022	.244
b JV12		0±41,000	.016	.18
b JK12		0±40,000	13.19	146.5
JJ14		0±37,500	.023	.25
JT16		0±35,000	28.021	311.3
JO8	1,350	15,000±35,000	.8	8.8
JB15		12,500±35,000	10.638	118.2
JQ11		10,000±35,000	17.94	197
JU8		8,000±35,000	67.436	749
JP7	1,350	30,000±25,000	.378	4.2
JC7		28,000±25,000	.66	7.3
JG2		26,000±25,000	5.23	58.2
JF14		22,000±25,000	24.441	271.6
JI18	1,350	32,500±15,000	2.25	25
JN2		27,500±15,000	5.10	56.6
JR2		25,000±15,000	22.0	244
JD8		22,500±15,000	55.0	611
JZ6	1,350	32,500±7,500	5.62	62.4
JZ8		30,000±7,500	9.04	100.3
JK2		25,000±7,500	36.67	408
JV19	1,500	0±30,000	7.702	85.6
JV9		0±29,000	18.247	202.6
JW16		0±27,000	° 8.752	° 97.2
JO14		0±20,000	d 84.59	d 940
JY15	1,500	18,000±22,500	° .28 × 10 ⁶	° 3.12
JK16		18,000±22,500	3.639	40.0
JH16		17,000±22,500	f 11.320	f 125.9
JK15		15,000±22,500	9.318	103.5
JL14		13,000±22,500	15.979	177.5
JM6	1,500	20,000±15,000	2.15	23.9
JS2		17,500±15,000	11.58	128.7
JA12		16,000±15,000	18.72	208
JK7		16,000±15,000	13.63	151.5
JT2	1,500	20,000±7,500	4.0	44.4
JH7		17,500±7,500	11.8	131
JV3		16,000±7,500	21.91	244
JZ13		14,500±7,500	39.78	442

* Tests at ±7,500, ±15,000, and ±25,000 psi were made with specimen having configuration shown by fig. 1(c); all other tests were made on specimens shown by fig. 1(d).

b Tests not plotted because results could not be checked by subsequent tests.

c Result of test appears to have been affected by bearing failure and replacement during the test.

d Test discontinued because of probable fracture time being excessive.

e Defective bearing.

f Test discontinued because of test-machine failure.

TABLE VI.—SONNTAG SF-4 3,600-CPM
AXIAL FATIGUE TEST DATA

[Elliott Company data]

Specimen	Test temp., °F	Stress, psi	Cycles to fracture	Time to fracture, hr
a JL21	75	75,000±39,350	0.13 × 10 ⁶	0.60
a JC22		75,000±33,880	.0279	1.30
a JY23		75,000±27,880	3.85	17.8
JX5	1,000	75,000±14,470	1.646	7.63
JV11		75,000±4,840	51.504	239.0
JT10	1,000	60,000±29,880	.421	1.95
a b JB24		60,000±27,350	1.49	6.90
a b JJ19		60,000±23,350	12.176	56.3
JS11		60,000±19,910	17.156	79.5
a c JI24		60,000±19,910	130.8	605.0
a b d JY22		60,000±17,410	77.818	360.0
a b e JS22		60,000±17,410	62.341	288.0
a b e JP20		60,000±17,410	53.886	249
JW5		60,000±16,430	53.707	249
JY5	1,000	45,000±26,880	6.181	28.6
a JP21		45,000±25,840	2.230	10.3
JN9		45,000±21,410	151.249	701
a e JC21		45,000±21,170	f 94.708	f 439
e JRS		45,000±19,410	77.242	357
a JF21	1,000	40,000±28,880	3.824	17.7
a JL20		40,000±27,380	6.993	32.4
a JJ20		40,000±26,380	f 316.761	f 1,460
a JE23		40,000±25,380	203.402	980
JE11	1,350	28,000±24,000	(e)	
JG11		28,000±24,000	(b)	
JI11		28,000±19,080	12.844	59.5
JCS		28,000±15,039	11.667	54
JD11		28,000±7,469	33.878	157
JHS		28,000±7,469	25.751	119
JF10		28,000±3,969	46.938	217

* Tests run after reducing eccentricity of grips.

b Specimen machined by Elliott Company.

c Test considered probably to be untrustworthy; only known difficulty was slight reductions of alternating stress for 2 hr due to slippage in a flexible coupling.

d Temperature found 60° F low just prior to fracture.

e Tests interrupted two or three times because of power failures or machine shut-down.

f Discontinued.

g Broke upon starting.

h Excessive creep upon starting.

TABLE VII.—STRESS-RUPTURE TESTS WITH SUPER-
IMPOSED ROTATING BENDING STRESS

[Research Laboratories Division, General Motors Corporation, machine and data]

Specimen	Test temp., °F	Steady axial stress, psi	10,800-cpm bending stress, psi	Cycles to fracture	Time to fracture, hr	Elongation, percent
JV17	1,350	28,000	±19,250	24.6 × 10 ⁶	a 38.0	6.78
JX14		28,000	±12,800	35.3	b 54.5	117.5
JW12		28,000	±5,100	34	c 52.5	130.5
JO11		28,000	±7,250	33	b 51.0	139.5
JW14		28,000	±0	0	d (>180)	153.7

a Fatigue failure at point of maximum stress (¾ in. above lower shoulder of specimen).

b Rupture failure at thermocouple strap weld remote from point of maximum stress (1½ in. from upper shoulder of specimen).

c Rupture failure remote from point of maximum stress and thermocouple welds.

d Specimen deformation reached limit of machine at 180 hr; creep data indicated failure before 200 hr.

TABLE VIII.—REVERSED BENDING FATIGUE DATA FROM WESTINGHOUSE 7,200-CPM MACHINE

[Westinghouse data for 0.550-in.-diam. specimens]

Test temp., °F	Alternating stress, psi	Cycles to fracture	Time to fracture, hr
Room	± 69,000	0.195 × 10 ⁶	0.45
	± 64,000	.37	.86
	± 59,500	1.1	2.55
	± 57,000	1.1	2.55
	± 56,000	.69	1.6
	± 55,500	^a 711	^a 1,645
	± 54,500	^a 150	^a 347
1,000	± 59,000	.19	.44
	± 51,000	.85	1.97
	± 50,500	.90	2.08
	± 49,000	1.22	2.82
	± 48,500	^a 210	^a 487
1,200	± 51,000	.55	1.27
	± 47,000	2.35	5.44
	± 46,500	.79	1.8
	± 46,000	200	463
	^b ± 48,500	1.77	4.1
	^b ± 46,500	2.05	4.75
	^b ± 45,000	^a 508	^a 1,175
1,350	± 46,000	1.5	3.47
	± 44,000	1.75	4.05
	± 43,500	1.88	
	± 41,500	4.4	10.17
	± 39,500	64	148
	± 39,500	^a 430	^a 994
	± 39,000	115.8	268
1,500	± 38,500	52	120
	± 35,000	.43	.99
	± 33,500	5.9	13.7
	± 31,500	4.9	11.3
	± 30,500	20.5	47.5
	± 28,000	12.8	29.6
	± 26,500	109	252
	± 25,500	190	440
	^b ± 30,500	7.2	16.7
	^b ± 27,000	138	320
	^b ± 26,000	33.45	77.4

^a Discontinued.

^b Specimens machined by ordinary shop practice.

TABLE IX.—EFFECT OF SURFACE FINISH ON REVERSED BENDING FATIGUE DATA FROM WESTINGHOUSE 7,200-CPM MACHINE

[Lewis Laboratory, NACA, data for 0.333-in.-diam. specimen]

Specimen	Test temp., °F	Alternating stress, psi	Cycles to fracture	Time to fracture, hr	
Polished finish: 4-5 microin. rms					
JB20	Room	±65,000	0.39×10 ⁶	0.90	
JS20		±58,800	2.76	6.4	
JC19		±57,100	1.60	3.7	
JK21		±55,700	1.64	3.8	
JI10		±54,100	1.25	3.0	
		±52,700	18.14	42.6	
		±52,500	6.0	13.9	
JT20		1,350	±46,400	.17	.4
JI20			±44,100	1.77	4.1
JL17			±42,200	4.36	10.1
JE20	±40,700		43.3	100.2	
	±39,500		13.0	30.1	
		±39,500	*92	212	
Ground finish: 20-25 microin. rms					
-----	Room	±58,500	0.31×10 ⁶	0.72	
		±49,700	1.92	4.45	
		±47,500	40.0	92.5	
-----	1,350	±43,500	.13	.3	
		±41,300	1.07	2.47	
		±39,800	40.0	92.5	
		±39,500	*82	190	
Rough finish: 70-80 microin. rms					
-----	Room	±62,000	1.08×10 ⁶	2.5	
		±58,200	1.55	3.6	
		±57,000	1.60	3.7	
		±55,700	30.0	69.4	
		±52,800	30.0	69.4	
-----	1,350	±43,000	.215	.28	
		±42,000	.77	.41	
		±39,200	7.1	16.4	
		±38,200	8.0	18.5	
		±36,200	55.0	115.5	
Specimens turned to shape and polished					
JY11	1,350	±49,700	0.108×10 ⁶	0.25	
JK14		±45,000	.95	2.2	
JI16		±44,000	1.21	2.8	
JW11		±41,500	5.57	12.8	
JO10		±41,700	17.58	40.7	
JP17		±40,600	22.12	51.2	
JU16		±39,700	30.15	69.8	
JV16		±38,900	24.62	57.0	
JJ13		±38,100	*123.55	286.7	
Polished and stress-relieved for 4 hr at 1,403° F					
-----	Room	±62,700	1.25×10 ⁶	2.9	
		±60,600	1.20	2.8	
		±58,900	.88	2.0	
		±55,500	6.4	14.8	
		±52,900	13	30.1	
		±52,900	*52	120	
Polished, stress-relieved for 4 hr at 1,400° F, and repolished					
-----	Room	±60,000	1.45×10 ⁶	3.35	
		±55,500	3.55	7.75	
		±53,700	5.2	12.0	
		±51,700	24.5	56.8	

TABLE IX.—EFFECT OF SURFACE FINISH ON REVERSED BENDING FATIGUE DATA FROM WESTINGHOUSE 7,200-CPM MACHINE—Continued

Specimen	Test temp., °F	Alternating stress, psi	Cycles to fracture	Time to fracture, hr
Ground and stress-relieved for 4 hr at 1,400° F				
-----	Room	±52,700	1.45×10 ⁶	3.35
		±48,500	6.9	16.0
		±47,000	44	102
Roughened and stress-relieved after 4 hr at 1,400° F				
-----	Room	±54,000	0.82×10 ⁶	1.9
		±52,500	1.65	3.8
		±50,500	2.1	4.8
		±47,300	19	44
		±44,500	83	192

* Unbroken.

TABLE X.—FATIGUE DATA FROM VARIABLE-SPEED ROTATING CANTILEVER BEAM TESTS ON UNNOTCHED AND NOTCHED SPECIMENS

[Materials Laboratory, WADC, data from University of Minnesota]

Specimen	Test temp., °F	Alternating stress, psi	Cycles to fracture	Time to fracture, hr	Average cyclic speed, cpm
Unnotched specimens					
J119	Room	* ±76,600	3,650	-----	-----
JE15		±73,500	62,000	18	5.73
JH19		±64,600	386,500	50	122.5
JJ15		±59,500	761,500	62	205
JE17		±54,900	2,028,000	90	451
JT18		±51,400	^b 46,000,000	^b 1,032	7,500
JY16	1,350	±47,400	9,750	9	18
JY17		±44,100	890,000	64	241.5
JT17		±41,250	^c 296,000	26	190
JW18		±37,200	^c 6,470,000	288	375
JX20		±34,450	8,500,000	287	493
JP16	1,500	±35,600	^d 43,950	9	81.7
J119		±32,700	945,000	123	127.5
JF17		±29,500	781,000	48	272
JS17		* ±29,800	172,000	216	133
Notched specimens					
JH20	Room	±55,700	55,850	29	32.1
JC16		±47,400	84,500	14	100.5
JF16(2)		* ±45,900	114,900	22	87
JO15		* ±39,700	213,500	76	46.8
JL15		±36,100	342,500	23	248
JV19		±30,000	2,112,000	121	291
JX21		±28,600	1,926,000	80	400
JC17		±26,500	1,656,000	95	291
JF16(1)		±22,600	^b 20,300,000	^b 358	945
J118	1,350	±35,100	6,600	3	36.7
JU21		±30,000	15,500	6	43
JN10		±25,000	218,000	27	135
JE16		±22,500	4,970,000	548	151.5
JO16		±19,960	* 1,086,000	163	111
JF15	1,500	±29,900	9,700	5	32.3
JL16		±25,000	52,200	13	66.8
JL15		±19,960	4,166,000	311	223

* Previously run at lower stresses.

^b Test discontinued.^c Test difficulties.^d Bent suddenly.

TABLE XI.—ROTATING CANTILEVER BEAM FATIGUE DATA FROM ROLLS-ROYCE 5,500-CPM MACHINE

[Rolls-Royce data for 0.160-in.-diam. ground specimens from quartered 1-in.-diam. bars]

Specimen	Test temp., °F(*)	Alternating stress, psi	Cycles to fracture	Time to fracture, hr
JX15	1,203	±49,200	^a 0.062×10 ⁶	0.79
JX15	1,203	±48,600	^b 0.086	.26
JS15	1,203	±48,100	4.60	13.9
JX15	1,203	±47,000	^b 0.040	.12
JX15	1,203	±47,000	^b 0.024	.07
JX15	1,203	±45,200	.740	2.24
JX15	1,203	±44,700	^c 34.24	104
JX15	1,203	±44,700	^c 145.97	441
JX15	1,203	±43,600	^c 11.56	35
JX15	1,203	±38,600	^c 24.00	73
JP14	1,355	±42,500	.47	1.42
JR16	1,355	±42,500	.77	2.33
JR16	1,355	±40,200	1.68	5.09
JP14	1,355	±40,200	2.15	6.51
JR16	1,355	±39,100	3.43	10.4
JS15	1,355	±38,600	2.23	6.76
JR16	1,355	±38,000	2.73	8.27
JP14	1,355	±38,000	96.27	292
JR16	1,355	±35,750	^c 24.2	73
JP14	1,355	±35,750	^c 34.00	103
JP14	1,504	±35,750	1.15	3.48
JP14	1,504	±35,750	.80	2.42
JP14	1,504	±33,500	.96	2.91
JP14	1,504	±32,400	9.24	28
JS15	1,504	±31,800	19.27	64
JR16	1,504	±31,400	2.45	7.45
JS15	1,504	±31,300	21.35	61
JP14	1,504	±31,300	1.93	5.85
JP14	1,504	±31,300	^c 11.72	35
JS15	1,504	±30,700	41.0	124
JS15	1,504	±30,200	2.41	7.3
JS15	1,504	±30,200	33.12	100
JR16	1,504	±29,600	7.63	23
JR16	1,504	±27,900	15.02	46
JR16	1,504	±26,800	71.36	216

* 1,203°±3° F; 1,355°±3° F; 1,504°±3° F.

^b Preliminary tests; endurance only approximate because of motor overrun at failure.^c Specimen unfractured.

TABLE XII.—NEES ROTATING CANTILEVER BEAM FATIGUE TEST DATA

[U. S. Naval Engineering Experiment Station 1,700-cpm machine and data]

Specimen	Test temp., °F	Alternating stress, psi	Cycles to fracture	Time to fracture, hr
JX12	1,350	±43,000	0.09×10 ⁶	0.88
JJ15		±40,000	37.69	369
JY13		±38,000	7.79	76.3
JW12		±37,000	5.22	51.1
JX13		±35,000	56.75	556.4

TABLE XIII.—COMPARATIVE STRESSES FOR FRACTURE IN FIXED TIMES OR AFTER FIXED NUMBERS OF CYCLES FOR VARIOUS TESTS

Type of test	Test machine	Test temp., °F	Stress, psi, for fracture in—			Stress, psi, for fracture in—		
			50 hr	150 hr	500 hr	10 ⁷ cycles	3—10 ⁷ cycles	10 ⁸ cycles
Axial.....	3,600-cpm dynamic creep.....	75	±46,500	±46,500	±46,500	±46,500	±46,500	±46,500
Reverse bending.....	7,200-cpm Westinghouse.....	75	±55,500	±55,500	±55,500	±55,500	±55,500	±55,500
Reverse bending.....	7,200-cpm NACA-Westinghouse.....	75	±54,800	±52,900	±52,500	±52,600	±52,500	±52,400
Rotating beam.....	Variable-speed.....	75	±62,500	±54,300	±52,600	±53,000	±53,000	±53,000
Axial.....	3,600-cpm dynamic creep.....	75	21,200±42,400	21,200±42,400	21,200±42,400	21,200±42,400	21,200±42,400	21,200±42,400
Axial.....	3,600-cpm Sonntag.....	75	75,000±25,000	75,000±25,000	75,000±25,000	75,000±25,000	75,000±25,000	75,000±25,000
Rupture.....	3,600-cpm dynamic creep.....	1,000	82,500	74,000	67,000	-----	-----	-----
Axial.....	3,600-cpm dynamic creep.....	1,000	±45,000	±45,000	±45,000	±45,000	±45,000	±45,000
Reverse bending.....	7,200-cpm Westinghouse.....	1,000	±49,500	±49,200	±49,000	±49,500	±49,300	±49,200
Axial.....	3,600-cpm dynamic creep.....	1,000	19,700±39,300	19,700±39,300	19,700±39,300	19,700±39,300	19,700±39,300	19,700±39,300
Axial.....	3,600-cpm Sonntag.....	1,000	75,000±12,000	75,000±10,000	-----	75,000±13,000	75,000±10,500	-----
		1,000	60,000±22,000	60,000±19,000	60,000±16,000	60,000±22,000	60,000±19,500	60,000±16,000
		1,000	45,000±25,500	45,000±23,500	45,000±22,000	45,000±25,500	45,000±24,000	45,000±22,000
		1,000	40,000±28,000	40,000±27,000	40,000±27,000	40,000±28,000	40,000±27,000	40,000±26,000
Rupture.....	7,200-cpm Westinghouse.....	1,200	54,000	44,000	41,000	-----	-----	-----
Reverse bending.....	7,200-cpm Westinghouse.....	1,200	±47,000	±46,900	±46,800	±47,000	±47,000	±46,800
Rotating beam.....	5,500-cpm.....	1,200	±45,000	±45,000	±45,000	±45,000	±45,000	±45,000
Axial.....	1,500-cpm Krouse.....	1,200	49,000±7,500	45,000±7,500	40,600±7,500	46,400±7,500	42,000±7,500	37,700±7,500
		1,200	44,800±15,000	41,000±15,000	36,900±15,000	41,900±15,000	38,100±15,000	33,900±15,000
		1,200	36,800±25,000	33,400±25,000	29,900±25,000	34,500±25,000	31,000±25,000	27,500±25,000
		1,350	32,000	28,500	25,000	-----	-----	-----
Rupture.....	3,600-cpm dynamic creep.....	1,350	32,000	28,000	23,750	-----	-----	-----
Axial.....	3,600-cpm dynamic creep.....	1,350	±35,000	±34,000	±33,000	±35,000	±34,500	±33,500
Axial.....	1,500-cpm Krouse.....	1,350	±35,000	±35,000	±35,000	±35,000	±35,000	±35,000
Reverse bending.....	7,200-cpm Westinghouse.....	1,350	±40,000	±39,800	±39,500	±40,000	±39,800	±39,700
Reverse bending.....	7,200-cpm NACA-Westinghouse.....	1,350	±43,600	±42,500	±41,300	±42,000	±41,000	±39,500
Rotating beam.....	Variable-speed.....	1,350	±42,300	±39,700	±37,000	±40,400	±40,000	-----
Rotating beam.....	5,500-cpm.....	1,350	±38,000	±38,000	±38,000	±38,000	±38,000	±38,000
Rotating beam.....	1,700-cpm.....	1,350	±36,000	±36,000	±36,000	±36,000	±36,000	±36,000
Axial.....	3,600-cpm dynamic creep.....	1,350	31,250±7,800	28,000±7,000	24,000±6,000	31,200±7,800	28,000±7,000	24,000±6,000
		1,350	26,500±17,700	24,500±16,400	22,000±14,700	26,500±17,750	24,500±16,400	22,000±14,750
		1,350	17,000±28,000	16,500±27,000	16,000±26,000	17,200±28,200	16,700±27,300	15,900±26,100
		1,350	28,000±17,500	28,000±5,000	-----	28,000±18,000	28,000±7,500	-----
Axial.....	3,600-cpm Sonntag.....	1,350	33,100±7,500	28,900±7,500	24,400±7,500	30,000±7,500	26,000±7,500	21,000±7,500
		1,350	30,000±15,000	26,500±15,000	23,000±15,000	27,500±15,000	24,300±15,000	20,600±15,000
		1,350	25,900±25,000	23,200±25,000	20,200±25,000	24,100±25,000	21,200±25,000	18,000±25,000
		1,350	12,000±35,000	10,300±35,000	8,300±35,000	11,000±35,000	9,000±35,000	7,200±35,000
Rupture.....	3,600-cpm dynamic creep.....	1,500	20,000	17,000	14,500	-----	-----	-----
		1,500	19,000	16,250	12,750	-----	-----	-----
Axial.....	3,600-cpm dynamic creep.....	1,500	±25,900	±25,500	±25,500	±25,500	±25,500	±24,800
Axial.....	1,500-cpm Krouse.....	1,500	±30,500	±28,900	±28,000	±29,500	±28,400	±27,500
Reverse.....	7,200-cpm Westinghouse.....	1,500	±29,500	±28,000	±26,000	±31,000	±29,000	±27,000
Rotating beam.....	5,500-cpm.....	1,500	±31,200	±30,400	±30,000	±31,700	±30,700	±29,900
Rotating beam.....	Variable-speed.....	1,500	±28,100	±27,400	±27,000	±28,500	±27,700	±27,000
Axial.....	3,600-cpm dynamic creep.....	1,500	±31,500	±30,000	-----	±29,300	-----	-----
		1,500	19,750±4,900	17,250±4,300	14,500±3,600	20,000±5,000	17,500±4,400	14,500±3,600
		1,500	18,500±12,300	15,500±10,400	13,000±8,700	18,500±12,300	16,000±10,700	13,000±8,700
		1,500	13,100±21,400	12,000±19,600	10,500±17,100	13,200±21,600	11,900±19,600	10,600±17,400
Axial.....	1,500-cpm Krouse.....	1,500	19,750±7,500	16,500±7,500	14,300±7,500	18,000±7,500	15,200±7,500	14,000±7,500
		1,500	18,500±15,000	15,500±15,000	13,500±15,000	17,000±15,000	14,400±15,000	13,300±15,000
		1,500	17,000±22,500	13,000±22,500	11,000±22,500	15,100±22,500	11,800±22,500	10,300±22,500

REPORT 1289

CONTRIBUTIONS ON THE MECHANICS OF BOUNDARY-LAYER TRANSITION¹

By G. B. SCHUBAUER and P. S. KLEBANOFF

SUMMARY

The manner in which flow in a boundary layer becomes turbulent was investigated on a flat plate at wind speeds generally below 100 feet per second. Hot-wire techniques were used, and many of the results are derived from oscillograms of velocity fluctuations in the transition region. Following a presentation of the more familiar aspects of transition, there are presented the very revealing facts discovered while studying the characteristics of artificially produced turbulent spots. These are: (1) Oscillograms of natural transition are identical to oscillograms of spot passage. (2) Transition starts from perturbations in the laminar flow as spots which then grow in accordance with the general concept proposed by Emmons. (3) Turbulence always moves downstream followed by laminar flow. (4) The following flow is in a state of calm for a period during which transition will not occur.

INTRODUCTION

The present paper presents the principal results of an experimental investigation performed in the boundary layer of a flat plate in an attempt to supply much-needed information about the process of transition from laminar to turbulent flow. In spite of the fact that a great deal was known about stability and the general circumstances surrounding transition, little was known about the actual mechanics of transition and its immediate cause. Consequently, it has been difficult to explain why flows known to be unstable do not necessarily become turbulent and flows calculated to be stable do not always remain laminar. The engineer has had disappointing results in his attempts to maintain laminar flow, and he has often been unable to locate the source of the trouble. The theorist has not been able to come to grips with the problem for want of a physical model.

Experiments have failed to agree on a consistent picture of transition. The water-table experiment of Emmons showed isolated patches of turbulence which suggested to him the theory of transition by formation and growth of turbulent spots, as described in references 1 and 2. Hot-wire probes used in boundary layers in air generally could not confirm this picture. The same was generally true of short-exposure schlieren and shadowgraph observations. For example, in the recent experiments of Evvard, Tucker, and Burgess on a 10° cone at supersonic speeds (ref. 3),

evidence for the growth of turbulent spots was seldom seen. While their results did not preclude a mechanism of transition involving turbulent spots, they indicated transition to be abrupt and fluctuating and followed by flow that was predominantly turbulent. One might even suspect that nature has confused the issue by providing more than one transition pattern.

The present investigation employed the same flat plate and wind tunnel as were used for the investigation of laminar-boundary-layer oscillations described in reference 4. The plate, which was a $\frac{1}{4}$ -inch rolled aluminum sheet with a sharpened leading edge, was 12 feet long and completely spanned the $4\frac{1}{2}$ -foot distance across the test section of the tunnel. The top speed of the tunnel was around 140 feet per second, but most of the work was done below 100 feet per second in order to place the transition region at a convenient location on the plate. The pressure gradient was adjustable between moderate limits and, unless otherwise specified, was zero.

Except for the measurement of pressures and mean-velocity profiles, for which static- and total-head tubes were used, all measurements were made with hot-wire probes and the associated amplifying and recording equipment. Only hot-wire arrangements sensitive to the longitudinal component of the fluctuations were employed, but in many cases the signals from two wires or two probes were observed simultaneously. While certain mean quantities, such as the root-mean-square value of the fluctuations, were useful, records of the actual wave form of the fluctuations turned out to be by far the more meaningful; hence film recording from a cathode-ray oscilloscope yielded most of the significant information.

The cases studied included free transition with various amounts of free-stream turbulence, transition induced by the so-called trip wire, the turbulence wedge behind a three-dimensional roughness element, and spark-initiated transition and subsequent growth of the turbulent spot. Only after the last of these was it possible to appreciate the real significance of what had been observed in all previous cases. In short, a transition region was found to be a region of spot growth as had been concluded by Emmons from his water-table observations. The seemingly futile attempts to reach and study phenomena at a transition point, all of which turned out to be steps toward a final picture, together with the confirming experiments are described in the following sections.

¹ Supersedes NACA TN 3489, "Contributions on the Mechanics of Boundary-Layer Transition," by G. B. Schubauer and P. S. Klebanoff, 1955.

This investigation was conducted at the National Bureau of Standards under the sponsorship and with the financial assistance of the National Advisory Committee for Aeronautics. The authors wish to acknowledge the assistance of Mr. K. D. Tidstrom and Miss Z. W. Diehl in conducting these experiments and in the analysis and processing of data.

SYMBOLS

c	velocity of spot growth
c_r	velocity of laminar-boundary-layer wave
R_{δ^*}	Reynolds number, $U_1 \delta^* / \nu$
U	mean velocity in x -direction at any point
U_1	mean velocity of free stream
u	x -component of velocity fluctuation
u'	root-mean-square value of u
x	distance from leading edge of plate
y	distance from surface
z	coordinate normal to xy -plane
α	half-angle of turbulent spot-growth envelope
γ	intermittency factor
δ	boundary-layer thickness
δ^*	displacement thickness
θ	half-angle for leading edge of turbulent spot
ν	kinematic viscosity
σ	standard deviation in Gaussian distribution

NONSTATIONARY CHARACTER OF TRANSITION

If a hot-wire probe sensitive to the velocity fluctuation u is placed sufficiently close to the surface in a transition region, the wave form of the output signal appears as shown in figure 1. This figure shows sample records made by photographing the screen of a cathode-ray oscilloscope with a continuously moving film. The film speed in these cases is about 5 feet per second and the progression of events is from right to left. Upward displacement of the trace corresponds to an increase in velocity at the location of the probe. The wire length and diameter were, respectively, 0.03 inch and

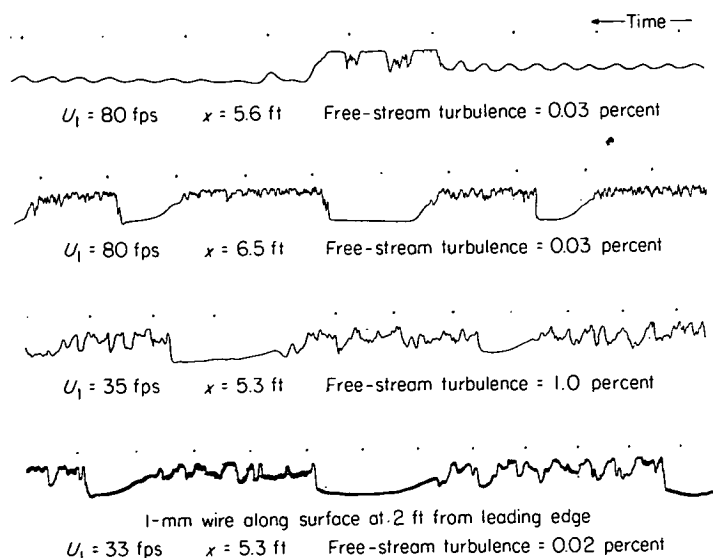


FIGURE 1.—Oscillograms of u -fluctuation in transition regions with hot-wire probe 0.013 inch from surface. Time interval between dots, 1/60 second.

0.0001 inch. Since the lag was too small to be of concern here, the lag compensation, usually introduced during amplification, was omitted in obtaining these records. The distance of the wire from the surface was about 0.013 inch in these cases.

The top record was made 5.6 feet from the leading edge of the plate which was near the beginning of the transition region when the free-stream turbulence was low ($u'/U_1 = 0.03$ percent) and the velocity of the free stream was 80 feet per second. Here the regular laminar-boundary-layer oscillations are followed by a burst of turbulence and this in turn is followed by laminar flow. The flat-topped character of the turbulent section is caused by overloading of the amplifier. The second record was made farther into the transition region where the flow was turbulent about 70 percent of the time. In the third and fourth records the position was selected so that the flow was again turbulent about 70 percent of the time, but in these cases the disturbance level was raised, in the third case by increasing the free-stream turbulence to 1.0 percent and in the fourth case by placing a 1-millimeter wire along the surface 2 feet from the leading edge.

In all cases the flow was laminar for some distance (even downstream from the 1-millimeter wire) but contained low frequency fluctuations, generally consisting of amplified sinusoidal waves when the stream turbulence was low or fluctuations of a less regular nature when the disturbance level was high. This was followed by the transition region usually around 2 feet in length, in which increasing amounts of turbulence were observed and finally by the completely turbulent regime. Throughout the transition region the mean characteristics of the layer change gradually from those characterizing laminar flow to those characterizing fully developed turbulent flow.

Records similar to those shown in figure 1 have often been used in the past as proof that transition occurs suddenly and that the observed gradual change in mean flow through a transition region is due to the varying position of the sudden change. The concept most commonly held was that transition occurred abruptly along an irregular line which separated the laminar flow ahead from turbulent flow behind and that this line surged upstream and downstream. In 1951 Emmon (refs. 1 and 2) introduced the idea of turbulent spots which formed at random and grew while moving downstream until they finally encompassed the entire field. There is a very basic difference between these two points of view and one on which much of the mechanics of transition hangs. The true state of affairs proved to be very illusive, but once the key to the mystery was found the answer was clearly displayed in all records. Figure 1 therefore contains much more significant information about transition than had previously been supposed. This information is the manner in which the turbulent section begins and ends. This feature will be referred to repeatedly in subsequent sections.

From numerous records such as those shown in figure 1 it is possible to determine the fraction of the total time that the flow is turbulent at any point in the transition region. This fraction, defined as an intermittency factor γ , is shown in figure 2 for several cases where conditions leading to transition were varied. The length of the region was different

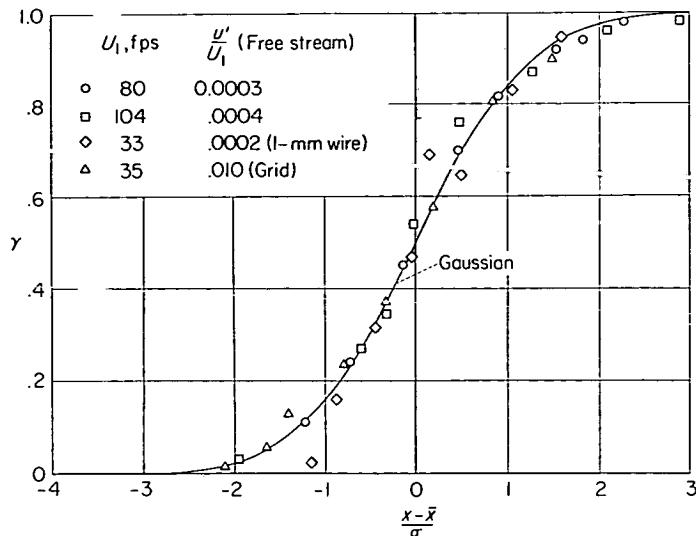


FIGURE 2.—Intermittency factor γ in transition regions. Range of standard deviation σ , 0.3 to 0.8 foot. Curve is Gaussian integral curve matched at $\gamma=0.5$.

in all of these cases, but the distributions were similar. In order to obtain a common basis of comparison, Gaussian integral curves were fitted to the cases separately and the standard deviation σ was determined for each case. All could then be represented to a common scale in units of σ and, when superimposed at the point $\gamma=0.5$, they appear as shown in figure 2. Here x is the distance from the leading edge of the plate, \bar{x} being the distance to the point where $\gamma=0.5$. The curve is a Gaussian integral curve. Values of σ ranged from 0.3 to 0.8 foot.

It is probably of some significance that transition regions are statistically similar whether long or short and whether disturbances are strong or weak and irrespective of whether they are introduced from the free stream or from a roughness element on the surface. It does not follow that transition regions would show the same distribution of γ in the presence of a pressure gradient. The close resemblance to a Gaussian integral curve would seem to indicate a near randomness, which may indicate that transition depends on random perturbations superimposed on the more or less regular amplified oscillations in the boundary layer. The skewness evidenced by the departure from the curve at the downstream end of the region may be related in some way to the structure of a transition region as discussed in the section "Structure of Transition Region and Nature of Transition."

CHANGES IN MEAN CHARACTERISTICS THROUGH TRANSITION REGION

Some of the more familiar progressive changes occurring through a transition region are examined next. The first and best known is the gradual change in mean-velocity profile which is shown in figure 3. Here the transition region begins at 5.25 feet from the leading edge of the plate and ends at 8 feet. The profiles up to the 5.25-foot position are of the Blasius type characteristic of the laminar boundary layer with zero pressure gradient. From this point on the profiles change progressively and reach that characteristic of a fully developed boundary layer at 8 feet. These

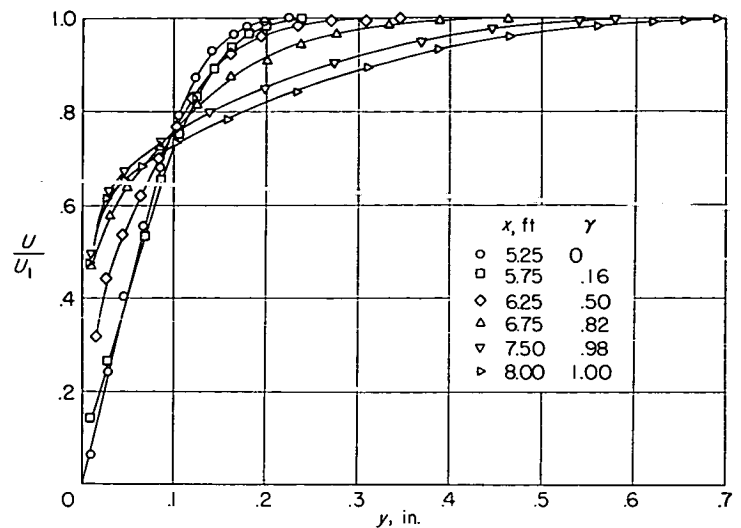


FIGURE 3.—Mean-velocity profiles through transition region. $U_1=80$ feet per second; free-stream turbulence, 0.03 percent.

measurements were made in the conventional manner with a small total-head tube. The free-stream velocity was 80 feet per second, and the stream turbulence level was about 0.03 percent. It should be remarked that the position of transition would shift somewhat from day to day, and check runs had to be made to be sure that this did not occur during a set.

Observe next the change in the fluctuation profiles shown in figure 4. Here u' is the root-mean-square value of the x -component of the velocity fluctuations, measured by conventional hot-wire techniques employing a wire 0.0001 inch in diameter and 0.03 inch long. In this case the turbulence level of the free stream was again about 0.03 percent, and under this condition fluctuations in the laminar layer near the beginning of the transition region consist mainly of the strongly amplified oscillations. These account for the fluctuation level at the 5- and 5.25-foot positions. As the transition region is entered the fluctuation level increases markedly near the surface and develops a strong maximum around $y \approx 0.03$ inch. Referring to figure 1, it is noticed that there is an abrupt step-up in velocity from a laminar region to a turbulent region, indicating that the transition

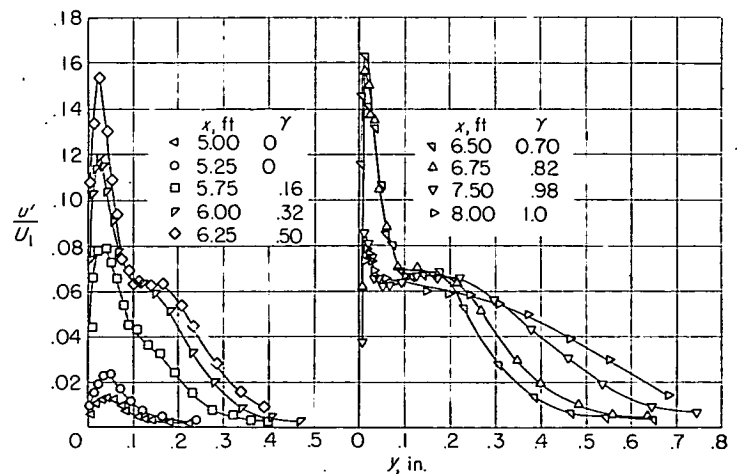


FIGURE 4.—Profiles of u'/U_1 through transition region. $U_1=80$ feet per second; free-stream turbulence, 0.03 percent.

region contains a mixture of the two distinct mean-velocity profiles, one pertaining to the laminar flow and the other pertaining to the turbulent flow. The steps from the one to the other register on the hot-wire as fluctuations and account largely for the high fluctuation level in the vicinity of the maximum. Referring to figure 3, it is seen that the step between laminar and turbulent profiles disappears around 0.1 inch and is small percentagewise at greater distances. This is about the location of the foot of the peak in figure 4. It is seen also that the peak subsides as the downstream end of the transition region is approached. The fluctuation profile at 8 feet is similar to that observed for fully developed turbulent flow.

It is clear that turbulent characteristics are fully developed at the end of the transition region. This is perhaps not surprising since this is already far from many points of initial transition. An interesting question is, how close to the point of actual breakdown are the steady-state characteristics of turbulent profiles to be found? At this stage of the investigation it appeared that the real obstacle to obtaining the answer to this question, as well as to studying the mechanism of transition itself, was the fluctuating character of transition which made measurements at a transition point practically impossible. Since the well-known wedge of turbulence behind a single roughness element appeared to offer the possibility of a sharp line of transition well away from the disturbing element, attention was turned to this case.

TURBULENCE WEDGE

If a particle of sufficient size is placed on the surface in a region of laminar flow, transition occurs at the particle, and a wedge-shaped region of turbulent flow extends downstream. Such wedges have frequently been observed on airfoils starting from particles of dirt or similar surface irregularities. It has also been observed that when the particle size or the velocity is reduced, the wedge may begin some distance downstream from the particle. In any case the particle introduces disturbances which cause breakdown of the laminar flow.

It appears that various observers agree on nearly the same value for the half-angle of the wedge and report values in the neighborhood of 10° . Thus, the width of the turbulent region increases more rapidly and is always much wider than the wake of the object initiating the wedge. Charters (ref. 5) appears to have been the first to call attention to this more rapid spreading and termed the effect "transverse contamination."

The wedge was introduced into the present investigation mainly in the hope that it would provide a reasonably sharp, stationary line of demarcation between laminar and turbulent flow at which phenomena at the position of changeover could be studied. However, it was soon discovered that the previously reported sharp outline was only an average condition and that the wedge was in reality bounded by an intermittent region as shown in figure 5. It was further found that only when the particle was sufficiently large or the velocity was sufficiently high did the sides become straight and the angle attain a constant value. When these conditions were not met, even though transition occurred at

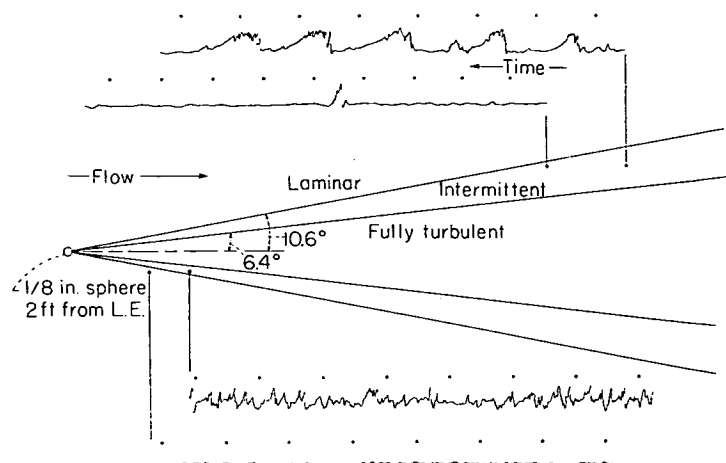


FIGURE 5.—Turbulence wedge produced by three-dimensional roughness element ($\frac{1}{8}$ -inch sphere) on surface. Time interval between dots, $\frac{1}{60}$ second; $U_1 = 80$ feet per second.

the particle, the sides initially curved outward, approaching the proper angle asymptotically.

Figure 5 shows a fully established wedge produced at a free-stream velocity of 80 feet per second by a $\frac{1}{8}$ -inch sphere cemented on the surface of the plate 2 feet from the leading edge. This case was investigated in some detail with a hot-wire probe and a total-head tube. Beyond a fully turbulent core, subtending a half-angle of 6.4° , was a region in which the turbulence was intermittent, as illustrated by the oscillograms in the figure. The outer limit of the intermittent region subtended a half-angle of 10.6° . It is interesting to note that this value agrees reasonably well with the value of $9\frac{1}{2}^\circ$ found by Charters to be the angle of transverse contamination.

Since one purpose in using the wedge was to learn how soon after abrupt transition the fully developed, steady-state condition would be found, mean-velocity profiles were determined with a total-head tube. Within the turbulent core the profiles were those characteristic of a fully developed turbulent boundary layer. While the so-called transition in this case was not sharp, the intermittent region was short compared with that found in free transition on a flat plate. Thus it appears that the only requirement for the existence of the fully developed character is that the flow be turbulent all of the time.

The oscillograms in figure 5 show typical conditions at several points. Here, as in figure 1, the time scale runs from right to left, and the interval between timing dots is $\frac{1}{60}$ second. The top record shows the sudden velocity step-up at the beginning of a turbulent region and the ending followed by a slow fall in velocity which was always characteristic of a record obtained with a hot-wire close to the surface. A possible explanation of the regular repetition of turbulent bursts is given in the section "Artificially Initiated Turbulent Spot." The second record shows a very short pulse near the outer limit having a suggestion of the characteristic shape. The third record obtained near the apex of the wedge, although giving the appearance of being composed largely of spikes jutting upward, has traces of the characteristic shape. The fourth record shows disturbances in the laminar layer caused by the presence of the wedges. With-

but the wedge no visible disturbance would have appeared there for the same signal amplification.

At this stage two facts had become clear. One was that the so-called transition point could not be made stationary. The other was that all records in a transition region, except those pertaining to the intermittent region very near the apex of the wedge, showed two very distinct features, namely, the beginning of a turbulent section with an abrupt velocity increase and the ending followed by a slow, exponential-like velocity decrease. The reason for these facts was unknown. It was, of course, not unreasonable that a transition point should be bobbing about, but the characteristic features of the records were very puzzling. It was conjectured that the abrupt rise might mean that the flow somehow tumbled and that the turbulence was the result of the tumbling. However, there was no definite evidence of a momentarily large disturbance in the laminar flow to cause the tumbling. In particular, it was noted that deep in a transition region, where the flow was turbulent for a large percentage of the time, oscillations in the remaining laminar regions were conspicuously absent.

Much time was spent in attempts to find evidence of momentary flow separation in transition regions. The most trustworthy method consisted of emitting iodine vapor from a small hole in the plate and noting by the discoloration of a starch film on the surface whether vapors ever traveled upstream. No evidence of separation could be found in any part of a transition region.

Bits of information like this, while so far not proving anything, aroused the suspicion that all was not well with the concept of breakdown along a wobbly line which fluctuated randomly upstream and downstream. Perhaps patches of turbulence like those observed on a water table by Emmons (ref. 1) and later by Mitchner (ref. 6) were actually being encountered. This would at least explain why a transition point could never be held stationary.

Early in the investigation a number of film records had been obtained of the simultaneous response of two hot-wire probes placed one behind the other with a spacing of from 3 to 5 inches. Some offsetting was necessary to avoid interference. Inspection of a large number of records showed that only very rarely was turbulence absent at the downstream station when it was present at the upstream station. In these few cases it appeared as though turbulent patches might have moved across the probes, striking the upstream one first and the downstream one second; but, because of the rarity of this occurrence, turbulent patches seemed to be the exception rather than the rule. As previously mentioned, a similar condition was found by Evvard, Tucker, and Burgess (ref. 3) in their studies of transition on a 10° cone at supersonic speeds. In a few cases their short-exposure schlieren photographs showed regions of turbulent boundary layer followed downstream by laminar flow. As a rule transition appeared to occur abruptly at various points, followed downstream by flow that was predominately turbulent.

While these experiments showed that isolated turbulent spots could exist, they were interpreted as evidence against a mechanics of transition involving the growth of spots.

This interpretation, in addition to being wrong, had the unfortunate effect of delaying the crucial experiment described in the next section.

ARTIFICIALLY INITIATED TURBULENT SPOT

If a particle which produces a turbulence wedge is suddenly removed, the turbulence will recede downstream followed by laminar flow. If a particle or equivalent disturbance appears only for a brief instant, a turbulent spot is produced which moves downstream. Both Emmons and Mitchner had shown that spots could readily be produced in their water-table experiments by allowing, say, a drop of water to strike the surface. Mitchner (ref. 7) had also shown that a spot could be initiated in a boundary layer by an electric spark, and he was able to study its form and rate of propagation. He commented, however, that the ability to produce a spot artificially did not offer a complete verification of Emmon's theory by any means and that considerable work remained to be done. The investigation of the spot was undertaken here with the feeling that, whether or not it had any significant connection with natural transition, it was unquestionably a phenomenon of intrinsic interest. Fortunately, it turned out to be most fruitful.

A spark was made to jump to the flat plate from a fine needle placed $\frac{1}{4}$ inch or less from the surface. Short duration was obtained by discharging a condenser previously charged from a high-voltage source. Sparks were produced one at a time while a hot-wire probe was placed in various locations to detect the passage of the spot. From film records containing $\frac{1}{60}$ -second timing marks, the times for the spot to reach and pass over the probe were readily determined. Figure 6 shows the velocities and shape of the spot as derived from such records. Included in the figure is a sample record of the passage of a spot over a hot-wire 0.015 inch from the surface. The electrical disturbance from the spark picked up by the circuit showed on the trace in all cases and served as a convenient and accurate means of indicating the time of discharge.

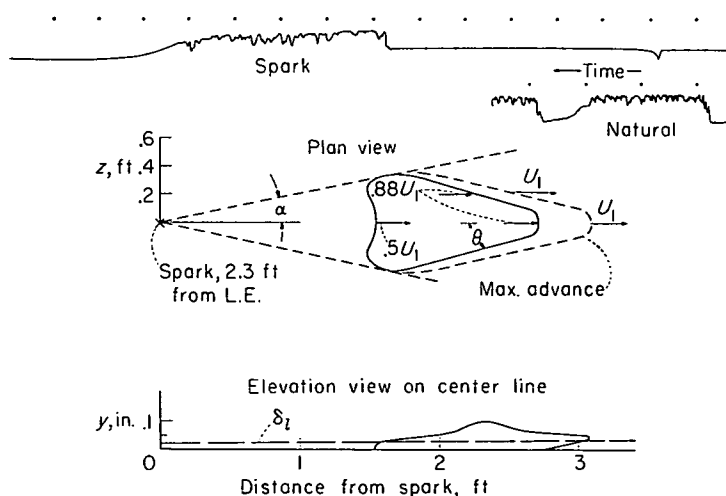


FIGURE 6.—Turbulent spot initiated by electric spark between needle electrode and surface. Oscillograms with 1/60-second timing dots shown at top of figure; time progression from right to left; upper record shows spark discharge on right and spot passage on left; lower record shows natural transition; $\alpha = 11.3^\circ$; $\theta = 15.3^\circ$.

The records were at once seen to contain much more information than the time of passage of a spot. The first significant fact recognized was that these records had the same features as all records previously obtained in transition regions, namely, the start of the turbulent section with an abrupt set-up in velocity and the ending of the section with a slow exponential-like fall. For comparison a typical record of natural transition is included in figure 6. This feature was characteristic of the passage of a spot. The abrupt rise occurred when the spot met the wire, and the slow fall occurred when it left. This was not proof that all turbulence actually originated at points and grew into spots, as did the spark-initiated spot of figure 6, but it was almost indisputable evidence that what had been observed in transition regions was the passage of turbulent patches as they moved downstream. This subject will again be considered in the section "Structure of Transition Region and Nature of Transition" where experiments will be described that completely confirmed this evidence.

The characteristics of the spot shown in figure 6 were derived from detailed observations at free-stream velocities of 30 feet per second and at positions 2.7 and 4.7 feet downstream from the spark with the spark 2.3 feet from the leading edge. Measurements at a free-stream velocity of 50 feet per second showed the same behavior. Additional information was obtained on the velocity of propagation at various distances along the center line and on the angle α when the spark was 3 inches from the leading edge.

The center-line observations showed that the streamwise propagation velocity of the leading end of the spot (downstream end) was independent of distance from the spark but that the velocity of the trailing end (upstream end) apparently decreased somewhat for distances less than 1.7 feet. However, the accuracy was low within 1 foot because of the shortness of the time interval and the uncertainty in defining the beginning and ending of a spot. Furthermore, a duration of the effect of the spark of only 0.005 second, such as might have arisen from the size of the initial disturbance, would have produced an apparent reduction in velocity of the trailing end at short distances of the amount observed. Accordingly, it was concluded that the reduction was apparent rather than real. The velocities were further found to be directly proportional to the free-stream velocity U_1 . The values at the surface were: At the trailing end, $(0.50 \pm 0.01)U_1$ and, at the leading end, $(0.88 \pm 0.02)U_1$.

As indicated by the shape of the trailing end shown in the elevation view of figure 6, the velocity of this end was independent of y out to about the normal thickness of the laminar layer δ_1 . The velocity of the leading end was at first thought to be about the same as U_1 , but more detailed observations revealed that it varied from a value of $0.88U_1$ at the surface to U_1 at the end of the overhanging tip shown in figure 6. The turbulence is, in fact, transported downstream with the free-stream velocity, and the lag at the surface is due to the time required for propagation inward through the slower moving air of the laminar layer. Probably the chief significance of the slower progress near the surface is that it gives rise to an overhanging leading edge. Since the velocity at the surface evidently depends on the

time required to reach the surface, it is not clear that it should bear a constant ratio to U_1 nor, correspondingly, that the overhang should remain proportional to the length of the spot. Dependence on the thickness of the laminar layer would also be expected. Nevertheless, the ratio was constant and proportions were preserved as far as could be ascertained for the limited range covered in the investigation.

Only on the center line were sufficient data taken to define the thickness distribution of the spot. The position of the outer edge was determined from the known positions of the hot-wire and spark and the time required for the spot to meet and pass over the wire for different values of y . In this way rates of propagation of the edges were determined, and from the rates the relative positions could be found. As far as could be determined from the measurements, the general shape shown in the elevation view of figure 6 was preserved as the spot grew. So far there is no ready explanation for the existence of the hump; but, using the top of the hump as a measure of the thickness of the spot, it was found that the thickness increased with distance like a fully developed turbulent boundary layer with an initial thickness equal to that of the laminar layer at the position of the spark.

The plan form of the spot was determined in detail by placing the hot-wire at different distances z from the center line. A fixed distance, $y=0.015$ inch, was chosen as being sufficiently close to the surface to give results indicative of the condition at the surface. As far as could be ascertained, the shape remained similar as the spot grew. Except for some degree of bluntness near the center line, the leading sides (or edges) were on the average straight lines extending to about the maximum width, and the angle θ had a constant value of 15.3° . The downstream propagation velocity was everywhere the same along these sides and equal to the velocity at the center. The trailing edge was found to preserve the somewhat indented appearance shown in figure 6; and, except for a slight variation in velocity to account for this shape, the velocity was essentially constant along the trailing edge and equal to $0.5U_1$, the value on the center line. The shape of the spot shown here is qualitatively like that found by Mitchner (ref. 7). With respect to the velocity of propagation, it is interesting to note in reference 8 that turbulent bursts, which were attributed to surface roughness, were observed on a body of revolution at a Mach number of 3.5. The velocity was estimated from the shock wave emanating from the upstream edge of the burst and reported to be 60 percent of the free-stream velocity:

In discussing this problem with Dr. Hugh L. Dryden, he suggested that it would be interesting to find out whether a spot would grow laterally when the Reynolds number based on the displacement thickness of the laminar layer was below the critical value of about 450, for which complete stability is predicted on the basis of small-perturbation theory. Accordingly, the growth envelope, corresponding to the wedge of angle α in figure 6, was investigated when the spark was fired 3 inches from the leading edge of the plate at free-stream velocities of 10 and 30 feet per second. At 10 feet per second the Reynolds number was below critical for a distance of about 1 foot from the spark. There was,

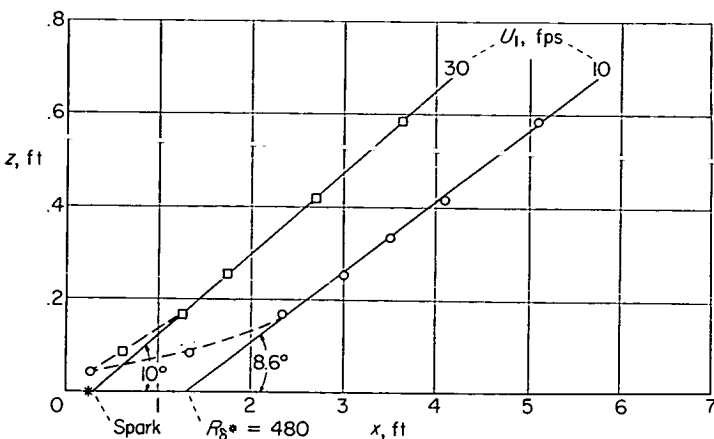


FIGURE 7.—Envelopes of spot growth. R_{δ^*} , Reynolds number based on laminar-boundary-layer displacement thickness.

however, a small favorable pressure gradient in this region which probably extended the stable range.

The envelopes corresponding to 10 and 30 feet per second are shown in figure 7. Beginning from the initial size of the disturbance, the growth is at first slow but approaches a linear increase in both cases with inclinations 10° and 8.6° , respectively, for 30 and 10 feet per second. If the 8.6° line is extrapolated to the axis, the apparent origin is at a position corresponding to a Reynolds number of 480. This is better agreement with stability theory than could have been expected under the circumstances and may be partly fortuitous. However, there is definitely a lag in growth for the extent of the stable range.

The difference between $\alpha = 10^\circ$ in figure 7 and $\alpha = 11.3^\circ$ in figure 6 may be accounted for by the fact that in the latter the initial size of the spot was neglected. However, the difference between α at 30 and 10 feet per second probably reflects the effect of Reynolds number. Mitchner's value of α , which was found at a Reynolds number in this low range, was 8.6° .

The remarkable similarity between the growth envelope of a spot and the turbulence wedge and the agreement between the angles in the two cases is evidently far more than mere coincidence. It will be noted in figure 5 that the occurrence of alternately turbulent and laminar flow has a striking regularity. It is known, furthermore, that the manner of beginning and ending of turbulent sections signifies passage downstream of turbulent regions. These facts suggest that the turbulence wedge may be something on the order of a succession of turbulent spots telescoped one into the other just far enough to form the fully turbulent core.

A more plausible connection with spots may be found in an important phenomenon associated with receding turbulence. This is the stable state left in the laminar flow following the passage of turbulence. The existence of this phenomenon was suspected when it was noted from the ending of turbulent records that the velocity near the surface was left high after the passage of turbulence and then decreased to its normal value. It was concluded that this meant that the entire velocity profile of the laminar layer was left turbulentlike and then gradually changed back to a normal type of profile. While the layer was in this state, it

was highly stable and no breakdown was likely to occur. This interval will be termed "the recovery trail." The remarkable calm following this trail and some of the consequences of it will be discussed in the section "Calming Effect." For the present it is merely noted that receding turbulence is automatically followed by laminar flow at least in this trail unless overtaken by another spot. Applying this to the turbulence wedge and realizing that the sides will move downstream unless held by transverse spreading, it appears that any irregularity will grow into a sequence of turbulent protuberances moving downstream and separated from one another by the length of the recovery trail. The record of figure 5 would certainly support this conclusion.

Returning to a consideration of the spot, the streamwise propagation may be rationalized as follows: The leading end is projected downstream with the free-stream velocity and the turbulent state penetrates the slower moving air of the laminar layer causing the lag of increasing amounts toward the surface. The movement of the trailing end may be visualized as just the reverse, namely, a blowing away of the turbulence by the outer stream and a lagging behind of the turbulence in the slower moving air near the surface. The mean-velocity profile here is such that air traveling slower than the trailing edge constitutes a very thin layer near the surface in which turbulence is not self-sustained. In other words, it dissipates rapidly because of both viscosity and diffusion outward. Because of the stability of the profile, the turbulence diffused outward cannot sustain itself in the outer strata. If this were not the case, the velocity of the trailing end would be fixed by the velocity of air which was never turbulent, namely, the velocity at the height of the laminar sublayer, which is about $0.3U_1$.

The triangular shape of the spot with vertex pointing downstream may be accounted for by the fact that the downstream end does not have the time that the upstream end has in which to grow laterally. It was noted by Dr. Dryden that a rate of spot expansion could be estimated in the following way: Assuming a mean velocity of the spot to be the average of $0.50U_1$ and $0.94U_1$, where $0.94U_1$ is the mean of $0.88U_1$ and U_1 , a value of $0.72U_1$ is obtained. Denoting a velocity of spot growth by cU_1 , the value of c upstream and downstream becomes the difference between the value 0.72 and that of the two ends, or $c = 0.22$. Since the vertex angle of the leading edge is 15.3° , one should find $c = 0.72 \sin 15.3^\circ = 0.19$. While these values are in reasonable agreement, the meaning of the first value of c is vague because of the different conditions at the leading and trailing edges. It is felt that more information must be obtained on the factors controlling spot growth before this problem is understood.

By this time there seemed to be little doubt that a transition region consisted of turbulent patches going downstream and finally merging to form the completely turbulent region. It was pertinent therefore to inquire whether two spots side by side would merge at their normal rate of growth or whether they would close in more rapidly because of a mutual effect on the flow between them. Accordingly, two sparks separated in the z -direction were set off simultaneously and spot growth was studied. As far as could be detected, the two behaved independently, and the mutual effect, if any, was

small. Evidence of this fact had been obtained earlier by observing that two intersecting turbulence wedges showed little tendency to affect one another.

STRUCTURE OF TRANSITION REGION AND NATURE OF TRANSITION

Before concluding that a transition region consists of patches of turbulence going downstream, one item of contradictory evidence must be disposed of. Why had it been inferred from earlier experiments that laminar flow was rarely to be found downstream from turbulent flow? If present ideas are right, just the opposite is the rule in a transition region. In order, therefore, to confirm these ideas, it must be possible to detect turbulence at an upstream point before it arrives at a downstream point.

In the earlier experiments the hot-wire probes were separated longitudinally from 3 to 5 inches and displaced in the z -direction about $\frac{1}{4}$ inch to avoid interference. Consequently, much could happen in the space between them. Accordingly, new experiments were arranged in which the separation was 1 inch with one wire directly behind the other. In this case interference was avoided by making the leading wire longer than the rear wire and using very fine prongs. Both wires were 0.016 inch from the surface. Runs in which the signals from the two wires were recorded simultaneously by photographing the screen of a dual-beam oscilloscope were made in a natural transition region. Since the time to travel 1 inch was short and the film speed was limited to about 8 feet per second, the spacing between events was small. A representative sample of the record obtained at a free-stream velocity of 80 feet per second is shown in figure 8. Turbulence is seen to arrive first at the upstream wire and a short time later at the downstream wire and to leave first at the upstream wire and later at the downstream wire. Many such records were inspected. Except for a few cases where terminations were poorly defined, all showed the same phenomenon. Furthermore, the velocities for the leading and trailing edges calculated from the time delay checked those for the spot to about 10 percent. No better accuracy would be expected with such small time resolutions.

While this completely confirmed the passage of turbulent patches, a further experiment was performed to see whether spot characteristics in the y -direction could be detected.

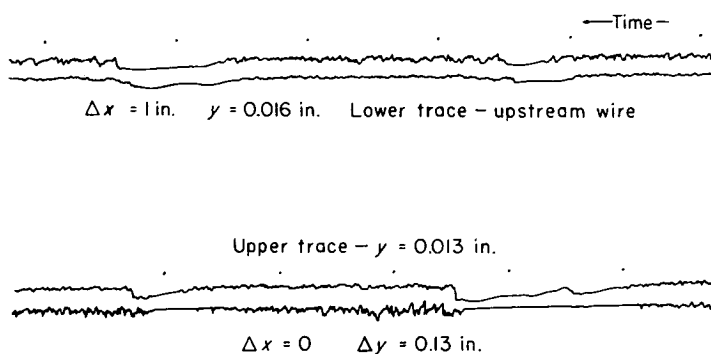


FIGURE 8.—Simultaneous signals from two hot-wires in region of natural transition. Time progression from right to left; time interval between dots, 1/60 second; upper record, 1-inch separation in x ; lower record, 0.13-inch separation in y .

Two wires were placed at the same x -position but at distances of 0.013 and 0.143 inch from the surface. The simultaneous records are shown by the second sample in figure 8. It is clearly seen that the turbulence arrives first and leaves first at the outermost wire. This was all around confirmation not only that a transition region consists of patches of turbulence moving downstream but that the patches behave as do artificially produced spots. This statement does not infer that the patches have the shapes shown in figure 6; for granted that they may have had this shape early in their history, they would sooner or later merge and give a resultant of almost any shape.

It now becomes completely clear that what were always seen in a transition region were patches of turbulence moving downstream. Points of initial breakdown were rarely if ever seen. The term "transition," meaning the change from the laminar to turbulent state, may be retained, but it must now be recognized that it has two parts: (1) The initial breakdown of laminar flow due to a perturbation and (2) the growth of turbulence into the surrounding laminar region.

Since the first part was universally missed in surveying a transition region, one can so far only infer something about it from circumstantial evidence. First, the mere fact that it was missed means that the probability of having a probe at the point where the event occurred was small. This is evidence that the breakdown is pointlike as opposed to a simultaneous breakdown along a line or over a considerable area. If the breakdown is pointlike, then there exists the opportunity for lateral growth. Of this there is ample evidence. For example, observed times of arrival of large patches at two points separated laterally by as little as $\frac{1}{2}$ inch were markedly different, and the same was true of times of leaving. This indicates that patches have edges at least as sloping as those of the single spot of figure 6. Sloping sides automatically mean the occurrence of lateral spreading. The existence of lateral spreading also explains why, when two probes were separated longitudinally by several inches, the downstream probe so rarely showed laminar flow when the upstream probe showed turbulent flow. The opportunity for conditions to be otherwise was simply made small by the cross feeding of turbulence into the space between the two probes. The same explanation can be applied to the appearance of schlieren photographs of transition on a body of revolution at supersonic speeds. Here the silhouette view of phenomena along only one generator of the body would rarely show the result of laminar breakdown along this generator but, in general, the turbulence that reached this generator from the sides. If the breakdown had occurred in the form of a line, say a ring or partial ring around the body, the chances for observing gaps of laminar flow would have been increased.

The concept of transition along a continuous line stems from the old idea of a front dividing the laminar and turbulent regimes. The argument was that, if the flow was sufficiently unstable to break down at a given value of x , it would be even more unstable at a greater value of x and therefore would be completely turbulent up to the first point. It has now been shown that this argument is false. It is nevertheless true that the amplitude of amplified waves

is on the average greater at the greater values of x ; and, therefore, if these cause the breakdown, it should generally have occurred at the downstream point. The explanation of this apparent inconsistency is to be found in the observed interference patterns which produce trains of high and low amplitude advancing in the x -direction. In regions of high amplitude isolated peaks are found, usually jutting toward the higher velocities. From observations made with two wires spaced $\frac{3}{4}$ inch in the z -direction, it appears that these irregularities occur in a spotty fashion over the xz -plane. Local breakdown, probably at the peaks, would be expected to be equally spotty.

Peaks are observed when the hot-wire is close to the surface, say 0.01 or 0.02 inch away, and indicate a momentary increase in velocity near the surface. Closely spaced peaks found near the apex of a turbulence wedge give the records a one-sided, spiked appearance. Some interesting observations were made in an adverse pressure gradient strong enough to shorten the transition region to a few inches. Here amplitudes increased rapidly with x and developed short trains in which the frequency was approximately doubled and the mean level of the group was shifted toward the higher velocity. This shift, whether accompanying a pulse or a train, evidently means that shearing stresses are brought into play which increase the velocity near the surface much as do the stresses in turbulent flow. Not only must such phenomena be out of the linear range, but one would suppose that they would be three dimensional as well. The next step is the appearance of turbulence, but what is involved in this step is still unknown.

It may be remarked that momentary flow separation, which has been postulated as a prelude to transition, is ruled out by the evidence available in these cases. While it is true that the velocity near the surface could reverse during part of a cycle when the amplitude is high, this apparently is prevented by the action of the shearing stresses which become high at the same time.

Since the present evidence for pointlike breakdown is circumstantial, this must be left an open question. The possibility that conditions for breakdown may be met practically simultaneously over a region of some extent cannot be ruled out. Cases may differ in this respect. It is hoped that further experiments will provide a definite answer to this question. It is known, however, that the breakdown is moving downstream as it is occurring. In short, all parts of the process, the wave and the breakdown as well as the resulting spot or patch, are moving downstream.

Having disposed of the mechanism of initial breakdown as best as can be done with the meager information at hand, attention is now turned to the structure of the transition region. At a given value of x_1 , defined as the beginning of the transition region, points of breakdown begin. While this position may vary somewhat, it is fairly definite. From here on spots form, grow, and merge with one another. At the position x_1 waves and irregular disturbances in the laminar flow are much in evidence. After x_1 waves and general perturbations in the laminar regions are less in evidence, and finally in about the last half of the transition region they are nearly absent in what is left of laminar flow.

The beginning of the disappearances can be attributed to the spotty nature of waves, regions of high amplitude having been taken out by breakdowns. The more complete disappearance in the later stages is the result of a calming effect which will be discussed more fully in the next section. This effect has already been mentioned in connection with the outline of the turbulence wedge. It will be found that trailing each turbulent patch is a region of calm by virtue of which the patch prohibits a fresh breakdown behind it.

Thus finally a transition region is found divided roughly into two parts: (1) An initial stage where initial breakdowns occur and spots form and begin to grow; (2) a final stage consisting primarily of spot growth with new breakdowns prohibited. The change from one to the other is, of course, progressive. Patches of irregular shape form from the merging of spots. The stable trail of a patch does not prevent the leading edge of a following patch from overtaking it. Finally, all patches close and the transition region is ended.

The striking fact is that turbulence is always moving downstream and in a very real sense tends to blow away. In a manner of speaking, it experiences a struggle for survival and can only maintain itself by fresh breakdowns in the following laminar flow. It will be seen in the next section that it does not maintain itself when one interferes with the struggle for survival.

CALMING EFFECT

The brief reference to the recovery trail and the attention called to trailing effects in the two preceding sections have perhaps given some hint that this subject deserves further attention. Its importance stems from the fact that a boundary layer passed over by a recovery trail is left in a state of calm for a period until the disturbed condition again sets in. Transition will not occur within this period.

The possible existence of such an effect was anticipated because of the highly stable condition of the recovery trail. A probably more logical argument runs as follows: At the trailing edge of receding turbulence the flow becomes laminar, but the velocity near the surface is higher than it would be for a boundary layer in its normal state. The normal state returns in a relatively short interval termed the recovery trail. The normal layer that results is a reconstructed layer, built for the most part of old properties contributed by the oncoming flow but of only those old properties that have arrived. Since the reconstructed layer is laid down at the rate of one-half the free-stream velocity and the disturbances travel at a slower rate, there is a progressively widening interval in which the layer lacks the disturbances. According to stability theory and experiment (ref. 4) two-dimensional waves travel downstream at a velocity around one-third the free-stream velocity, the exact value depending on the Reynolds number, boundary-layer thickness, and wave length.

Having made the foregoing prediction, it was decided to try an experiment in which a recovery trail would be made to pass through a region of natural transition. What was desired was an instantaneous line source of turbulence which would span a considerable distance z and so sweep over a considerable width of the layer. Presumably a row

of simultaneously fired sparks would have produced this result; but, since the necessary equipment was not at hand, a single spark was fired sufficiently far upstream to grow into a large spot by the time it reached the transition region. The conditions were free-stream turbulence, 0.03 percent; $U_1=80$ feet per second; beginning of transition, 5.5 feet; and spark, 0.25 feet from the leading edge. The maximum lateral width of the spot was calculated to be 2 feet at the 5.5-foot position.

Oscillograph records were obtained with a hot-wire about 0.015 inch from the surface on the center line at 5.5, 7, 8, and 8.5 feet from the leading edge. Examples are shown in figure 9. The first record of each set shows the natural condition; the second shows the passage of the trail. The record pertaining to 5.5 feet shows the period of calm fol-

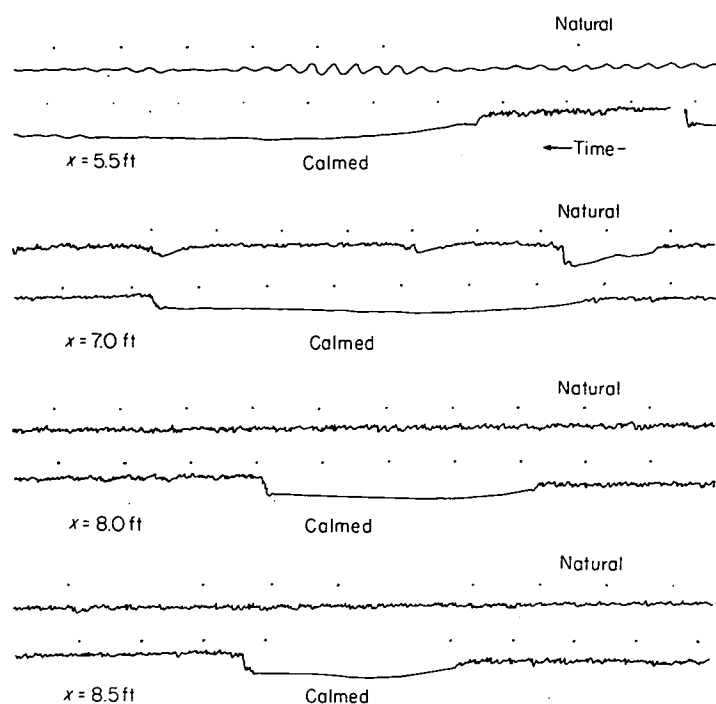


FIGURE 9.—Oscillograms comparing natural and calmed conditions. Time progression from right to left; time interval between dots, 1/60 second; $U_1=80$ feet per second.

lowing the recovery trail. The other records show how laminar flow is brought to 7, 8, and 8.5 feet. The laminar condition lasts until the flow again breaks down at some upstream position and the leading edge of the resulting turbulence reaches the point under observation. The position is assumed to be that for the beginning of natural transition, which in this case is 5.5 feet. Since the leading edge is traveling with a velocity 1.76 times that of the trail it catches up and progressively shortens the laminar section.

From the length of the laminar sections at 7, 8, and 8.5 feet the period of calm at 5.5 feet during which transition did not occur was estimated on the basis of the velocities of trailing and leading edges of a spot as given in figure 6. These came out to be 0.122 second from 7 feet, 0.098 second from 8 feet, and 0.078 second from 8.5 feet. The progressively decreasing time is an indication of systematic error or is evidence of edge effects from the turbulent field about

the relatively narrow laminar strip. Judging by the record at 5.5 feet, the period of calm was probably around 0.1 second.

If the starting point for the wave reaching the 5.5-foot position were known, its velocity could be calculated. One needs to know the nearest upstream point outside of the growth envelope of the spot from which a wave can arrive at the center line at the 5.5-foot position. If it is assumed that a wave cannot travel on a diagonal course and therefore had to start at the origin of the spot, it would be required to travel a distance of 5.25 feet. If it started to follow the spot immediately, its time of travel would be the time for the trailing edge of the spot to reach the 5.5-foot position plus the 0.1-second period of calm. The time is found to be 0.231 second. The wave velocity c , is found to be 23 feet per second, or $c/U_1=0.29$. If, on the other hand, a wave does travel on a diagonal, say 10° to the mean flow, or about as the half-angle of a turbulence wedge, then it would be required to travel only 3 feet in a time of 0.175 second; c/U_1 is then found to be 0.21. While the present conditions differed considerably, the results are of the same order.

Because of the foregoing uncertainties an attempt was made to produce a breakdown of short duration along a line and to obtain a trail of considerable extent in the z -direction. A piece of twine about 0.03 inch in diameter was attached at the floor and ceiling of the tunnel by rubber bands and was thus held under tension about an inch from the plate. This was drawn out like the string of a bow and allowed to slap the plate. The object was to make the twine enter the boundary layer, disrupt the flow, and then leave. Since the twine would vibrate like any plucked string, damping was required.

A position about 4 feet from the leading edge was chosen. At a free-stream velocity of 78 feet per second the twine contacted the surface at 4.17 feet along a line of about 2 feet in extent in the z -direction. At this position and this velocity waves were already well developed. On this particular occasion the beginning of natural transition appeared to be at 6 feet. Two observations were made with the hot-wire at 5 feet and three were made at 9 feet where the layer was completely turbulent. Some calming was noted at 5 feet, but the duration was uncertain. A period of laminar flow was observed at 9 feet for each of the three trials. From these the times that the flow remained calm at 6 feet without transition were 0.067, 0.06, and 0.05 second.

Since the wave was already present at the 4.17-foot position, it was assumed that the wave continued to progress from this point and that it approached the 6-foot position during the time that the trailing end of the receding turbulence traveled from 4.17 feet to 6 feet plus the estimated calm period at 6 feet. The values of c/U_1 were calculated from the three trials to be 0.21, 0.22, and 0.24.

These values agree fairly well with those obtained with the spot. The mean of all is 0.23 with a maximum deviation of 13 percent. While this value seems rather definite, it should be remembered that it depends on assumptions that may be questionable. If the value 0.23 represents a wave velocity, it is apparently lower than that of the two-dimensional wave

calculated in stability theory. Furthermore, one should probably be comparing group velocity which for boundary-layer waves should be somewhat higher than that for a single wave. There exists also the possibility that the calming may have other effects which lengthen the period before breakdown is resumed.

Obviously much more study is required in order to clarify this subject. The properties of three-dimensional waves about which little is known should be examined. The waves may be required to be three dimensional, or to have a three-dimensional perturbation superposed on them, to produce breakdown. There also remains the question of the extent of calming when the impressed disturbances are already large, as occurs when the free-stream turbulence is high or when roughness elements are present on the surface. Cases where pressure gradients exist also need to be investigated.

The calming effect interrupts the formation of spots and thus allows established turbulence to pass on downstream. The results can be an extension of laminar flow. It has already been noted in the preceding section that breakdowns are prohibited by this effect in the latter part of the transition region. This results in a lengthening of the transition region. The action here, however, is reduced to a minor role because of the rapidity with which upstream patches overrun the regions of calm. If turbulence, initially in the form of a line, were made to sweep over the transition region from its beginning, then the calming effect would be fully effective. Obviously the extent of laminar regime following the line depends on the length of time during which a state of calm exists. This in turn depends on where one chooses to initiate the line and on the difference between the velocity of the trailing edge of the resulting turbulent strip ($0.5U_1$) and that of the following wave.

When the velocity of the wave is sufficiently small, say of the order of $0.25U_1$, it appears to be possible to derive a net gain in the average extent of laminar flow by artificially starting turbulence along a line somewhere ahead of a region of natural transition, provided the turbulence so introduced

begins as a line (negligible width at the start) and passes downstream with velocities of leading and trailing edges as given for the spot. However, until more is known about this effect, any attempt to assess potential benefits is purely in the realm of speculation. It is interesting to note, however, that turbulence properly injected at proper time intervals can in principle ~~alleviate the severity of the turbulence~~ "disease." The parallel to medical practice is obvious. The difficulty here is that the patient will suffer just as much from the mild cases as from the disease proper if the periods of immunity are too short.

NATIONAL BUREAU OF STANDARDS,

WASHINGTON, D. C., *February 28, 1955.*

REFERENCES

1. Emmons, H. W.: The Laminar-Turbulent Transition in a Boundary Layer—Part I. *Jour. Aero. Sci.*, vol. 18, no. 7, July 1951, pp. 490-498.
2. Emmons, H. W., and Bryson, A. E.: The Laminar-Turbulent Transition in a Boundary Layer—Part II. *Proc. First U. S. Nat. Cong. Appl. Mech.* (June 1951, Chicago, Ill.), A. S. M. E., 1952, pp. 859-868.
3. Evvard, John C., Tucker, Maurice, and Burgess, Warren C.: Transition-Point Fluctuations in Supersonic Flow. *Jour. Aero. Sci.*, vol. 21, no. 11, Nov. 1954, pp. 731-738. See also, *Statistical Study of Transition-Point Fluctuations in Supersonic Flow*. NACA TN 3100, 1954.
4. Schubauer, G. B., and Skramstad, H. K.: Laminar-Boundary-Layer Oscillations and Transition on a Flat Plate. NACA Rep. 909, 1948. (Supersedes NACA ACR, 1943.)
5. Charters, Alex C., Jr.: Transition Between Laminar and Turbulent Flow by Transverse Contamination. NACA TN 891, 1943.
6. Mitchner, Morton: The Propagation of Turbulence Into a Laminar Boundary Layer. *Interim Tech. Rep. No. 3*, Combustion Tunnel Lab., Harvard Univ., June 1952.
7. Mitchner, Morton: Propagation of Turbulence From an Instantaneous Point Disturbance. *Readers' Forum, Jour. Aero. Sci.*, vol. 21, no. 5, May 1954, pp. 350-351.
8. Jedlicka, James R., Wilkins, Max E., and Seiff, Alvin: Experimental Determination of Boundary-Layer Transition on a Body of Revolution at $M=3.5$. NACA TN 3342, 1954.

REPORT 1290

DEVELOPMENT OF CRAZE AND IMPACT RESISTANCE IN GLAZING PLASTICS BY MULTIAXIAL STRETCHING

By G. M. KLINE, I. WOLOCK, B. M. AXILROD, M. A. SHERMAN, D. A. GEORGE, and V. COHEN

SUMMARY

The loss of strength of cast polymethyl methacrylate plastic as a result of crazing is of considerable importance to the aircraft industry. Because of the critical need for basic information on the nature of crazing and the effects of various treatments and environmental conditions on its incidence and magnitude, an investigation of this phenomenon was undertaken.

In the course of this study of crazing the following factors were examined: (1) The effect of stress-solvent crazing on tensile strength of polymethyl methacrylate; (2) the critical stress and strain for onset of crazing at various temperatures; (3) the effect of molecular weight on crazing; and (4) the effect of multiaxial stretching on crazing of polymethyl methacrylate and other acrylic glazing materials.

It was found that moderate stress-solvent crazing of polymethyl methacrylate results in a loss in tensile strength of approximately 30 percent. Stress crazing develops at 80 to 95 percent of the tensile strength in the standard tensile test in the temperature range of 23° to 70° C. Craze resistance increases slightly with increasing molecular weight of the polymer. Multiaxial stretching of polymethyl methacrylate markedly increased its craze resistance. Material stretched 150 percent did not craze in short-time tensile tests and the crazing threshold was increased several fold in stress-solvent crazing tests. The strain at failure was increased several fold (up to 60 percent strain), thus imparting toughness to the stretched sheets. The orientation of the large molecules of this high-polymeric material transforms the amorphous, brittle cast sheets into laminar, tough products that are resistant to shattering under impact loads. Multiaxial stretching of other acrylic plastics, including polymethyl alpha-chloroacrylate, gave comparable results.

The improvement in the crazing resistance of acrylic plastic sheets produced by multiaxial stretching indicates that enclosures made from stretched sheets have crazing and strength properties superior to those of enclosures formed with little or no stretching. As an alternative to the use of prestretched material to achieve improved craze resistance and toughness in acrylic enclosures, there is the possibility of preparing a more highly stretched enclosure directly, such as by forming a larger and more deeply drawn enclosure than required and then using only the central portion of the formed piece. Either method would improve the craze resistance, particularly at the rim, where there

is likely to be stress concentration and where contact with solvents of adhesives used to seal the enclosure is quite likely; in a normally formed enclosure, the craze resistance is a minimum at the rim. The laminar structure of the stretched acrylic sheets also offers the possibility of obtaining resistance to shattering of pressurized acrylic canopies by shrapnel without the necessity of employing the heavier and more expensive acrylic laminate made with a safety-glass type of vinyl interlayer.

INTRODUCTION

Acrylic-plastic glazing has been used for many years in astrodomes, gun turrets, antenna covers, and other transparent curved enclosures in military aircraft. However, in spite of its good weathering and optical properties and the ease with which it can be formed into shapes with compound curvature, this material has several disadvantages such as low impact strength and craze cracking. Perhaps the most serious of these is its tendency to craze under stress, especially in the presence of organic solvents. This results not only in reduced visibility but also in lowered resistance to both steady and impact loads. Because of the critical need for basic information on the nature of crazing and the effects of various treatments and environmental conditions on its incidence and magnitude, an investigation of this phenomenon was conducted at the National Bureau of Standards under the sponsorship and with the financial assistance of the National Advisory Committee for Aeronautics.

In the course of this study of crazing the following factors were examined: (1) The effect of stress-solvent crazing on tensile strength of polymethyl methacrylate; (2) the critical stress and strain for onset of crazing at various temperatures; (3) the effect of molecular weight on crazing; and (4) the effect of multiaxial stretching on crazing of polymethyl methacrylate and other acrylic glazing materials. It was found that craze-resistant glazing materials could be produced by the multiaxial-stretching process; furthermore, the orientation of the large molecules of these high polymeric materials transforms the amorphous, brittle, cast sheets into laminar, tough products that are resistant to shattering when subjected to gunfire.

The results obtained in the various phases of the investigation of crazing are presented in this report.

EFFECT OF STRESS-SOLVENT CRAZING ON TENSILE STRENGTH OF POLYMETHYL METHACRYLATE

The loss of strength of tensile specimens of polymethyl methacrylate as a result of stress-solvent crazing at 23° C and 50-percent relative humidity was investigated (ref. 1). The materials tested were commercial cast polymethyl methacrylate sheets of both heat-resistant and general-purpose grades from each of two manufacturers. Most of the tests were made on samples 0.15 inch thick and covered with masking paper on one side only. The tensile specimens were artificially crazed by applying benzene to the central portion of the reduced section while under stress, as described in footnotes c and e of table I and in appendix A, and were subsequently broken. Specimens for controls were treated identically except that no benzene was applied. Among the factors studied were the effect of the masking paper on the crazing and the relative effect on tensile strength of a few large craze cracks compared with that of more numerous finer cracks. The coarse crazing was produced by applying a larger amount of benzene and a smaller stress than were used to create the fine crazing. The results are summarized in table I.

The crazing treatment that produced up to two coarse cracks per square millimeter with a crack length and depth of roughly 1 and 0.15 millimeter, respectively, caused a loss of strength that averaged approximately 35 percent for all materials. The loss in strength produced by the fine crazing averaged roughly 27 percent for all materials. It should be noted that, in order to produce this loss in strength, a higher stress was used in crazing the heat-resistant grade than was used in crazing the general-purpose material. This result agrees with the well-known fact that the threshold stress for

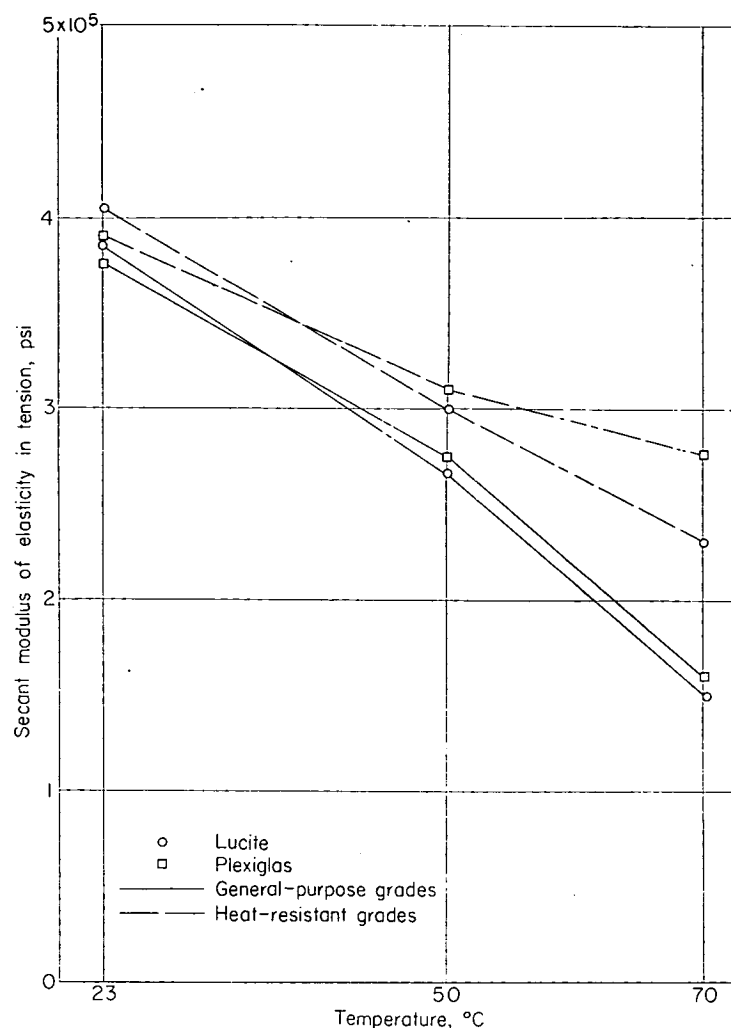


FIGURE 2.—Variation of tensile secant modulus of elasticity with temperature for acrylic plastics. Stress range is zero to about one-half of tensile strength.

solvent crazing is higher for the heat-resistant than for the general-purpose cast material. The masking paper had no statistically significant effect on the loss of strength resulting from crazing.

The crazed specimens were more variable than the controls, the coefficients of variation for tensile strength averaging about 15 and 5 percent, respectively, for all samples. In addition, although the crazing treatment was done in a controlled manner, there was a significant daily variation in treatment that contributed an additional 15 percent to the coefficient of variation for the crazed specimens. It was not found possible to predict the tensile strength of a crazed specimen from its appearance.

STRESS AND STRAIN AT ONSET OF CRAZING OF POLYMETHYL METHACRYLATE AT VARIOUS TEMPERATURES

The stress and strain at the onset of crazing of polymethyl methacrylate were determined at 23°, 50°, and 70° C (ref. 2). The materials tested were commercial cast polymethyl methacrylate sheets of both general-purpose and heat-resistant grades. Most of the tests were made on samples 0.15 inch thick. The standard tensile test described in appendix A was used with the exception that when the strain gage was

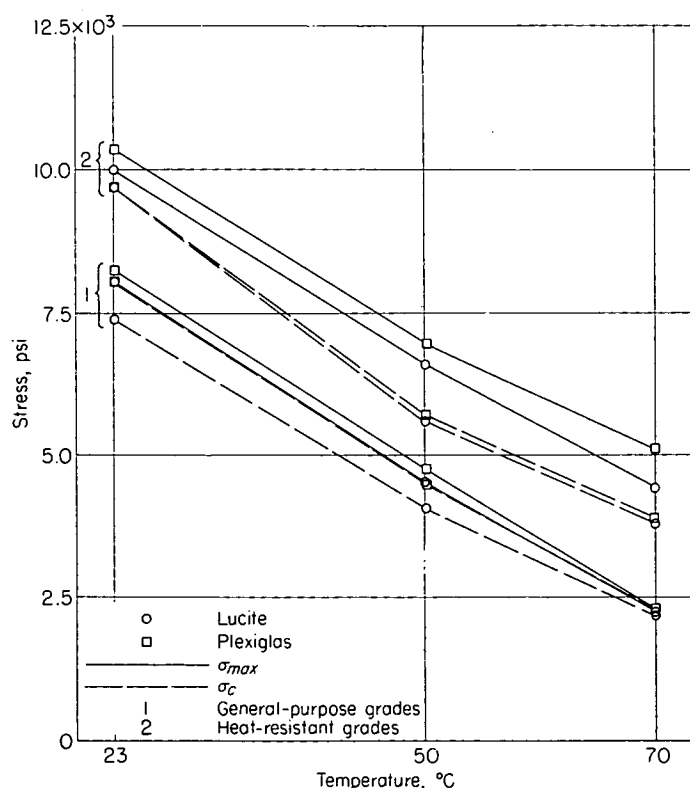


FIGURE 1.—Variation of tensile strength σ_{max} and stress at onset of crazing σ_c with temperature for acrylic plastics.

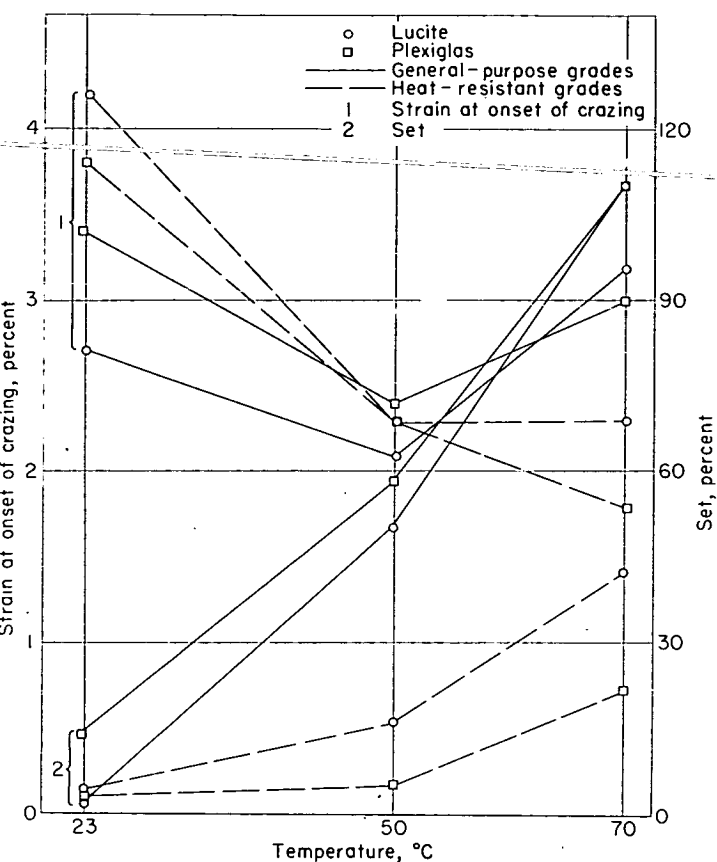


FIGURE 3.—Variation of strain at onset of crazing and permanent set with temperature for acrylic plastics.

removed the testing speed was increased to about 0.6 inch per minute.

The average values of tensile strength and of stress at the onset of crazing for the four materials tested are shown graphically in figure 1, the secant modulus values, in figure 2, and the values of the strain at the onset of crazing and of permanent set, in figure 3.

Polymethyl methacrylate did not begin to craze at the same strain for all temperatures; in general, the strain decreased with increase in temperature. For three of the four samples tested the strain at crazing was statistically significantly lower at 50° C, when the samples were still well below the glass transition point, than it was at 23° C. No consistent trend is evident between 50° and 70° C.

The ratio of stress at the threshold of crazing to the maximum stress was, in general, between 80 and 95 percent for all the samples tested at 23°, 50°, and 70° C.

The tensile strength and secant modulus of elasticity decrease approximately linearly with increase in temperature. The strengths at 70° C of the general-purpose and heat-resistant grades of polymethyl methacrylate were reduced to about 30 and 50 percent, respectively, of the strengths at 23° C. The modulus values at 70° C were correspondingly reduced to about 40 and 70 percent of the values at 23° C.

EFFECT OF MOLECULAR WEIGHT ON CRAZING OF POLYMETHYL METHACRYLATE

Tensile and crazing properties were determined for five cast polymethyl methacrylate sheets in which the viscosity-

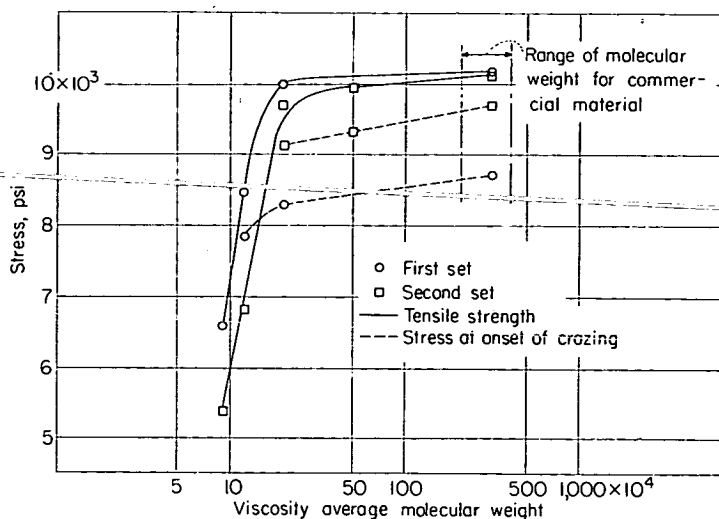


FIGURE 4.—Variation of tensile strength and stress at onset of crazing with molecular weight.

average molecular weights of the resin were 90,000, 120,000, 200,000, 490,000, and 3,160,000, respectively (ref. 3). Both stress crazing and stress-solvent crazing tests were conducted by the methods described in appendix A. The results are shown in figures 4 and 5. In the first set of stress-solvent crazing tests the solvent was applied by the blotter method with benzene as the solvent. In the second set of tests, both the brush and blotter methods were used with both benzene and isopropanol as solvents. For a given molecular weight, no significant differences in threshold values were observed among the various methods used in the second set of tests.

It was found that the tensile strength and strain at failure increase rapidly with increasing molecular weight at the lower molecular weights and begin to level off at molecular weights of approximately 200,000 and 500,000, respectively. There was no change in the modulus of elasticity over the range of molecular weights studied. The specimens with molecular weights of 90,000 and 120,000 broke at low strains without crazing. For the higher molecular weights, the stress and the strain at which crazing occurred increased with increasing molecular weights. In the stress-solvent

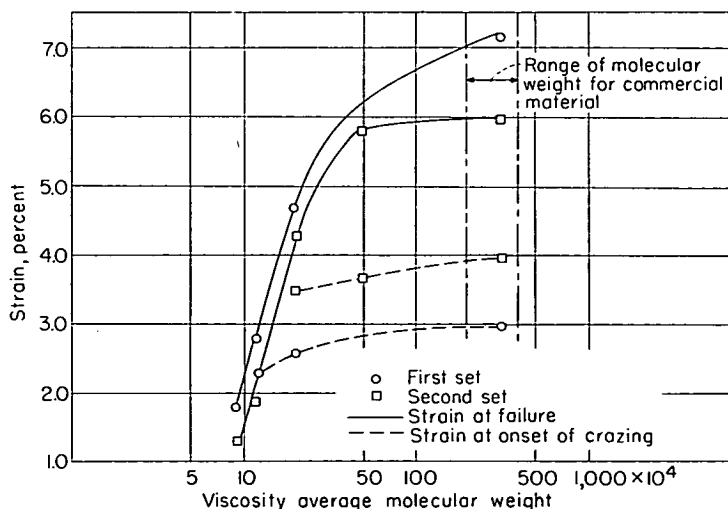


FIGURE 5.—Variation of strain at failure and strain at onset of crazing with molecular weight.

crazing tests, the materials with the three lowest molecular weights broke immediately upon crazing, usually at an observed craze crack. For the materials with the two highest molecular weights the craze resistance increased slightly with increase in molecular weight.

EFFECTS OF MULTIAXIAL STRETCHING ON CRAZING AND OTHER PROPERTIES OF TRANSPARENT PLASTICS

Improvement in the resistance of transparent plastics to crazing was sought by multiaxial stretch forming. The initial tests were conducted with general-purpose and heat-resistant grades of polymethyl methacrylate stretched 50 percent (ref. 4). A marked increase in the strain at the onset of crazing was noted in the standard short-time tensile test; in fact, most of the stretched specimens tested showed no crazing. The threshold stress for stress-solvent crazing with benzene applied by brush increased 70 to 80 percent. In long-time tensile tests (7 days), the threshold stress for stress crazing increased 40 to 50 percent. The tensile strength was unaffected, but the strain at failure was increased from 10 percent to about 60 percent. This considerable increase in strain at failure suggested that enclosures made from multiaxially stretched acrylic sheets might have not only greatly improved crazing resistance but also sufficient toughness and resistance to gunfire to obviate the need for the use of the heavier laminated acrylic materials.

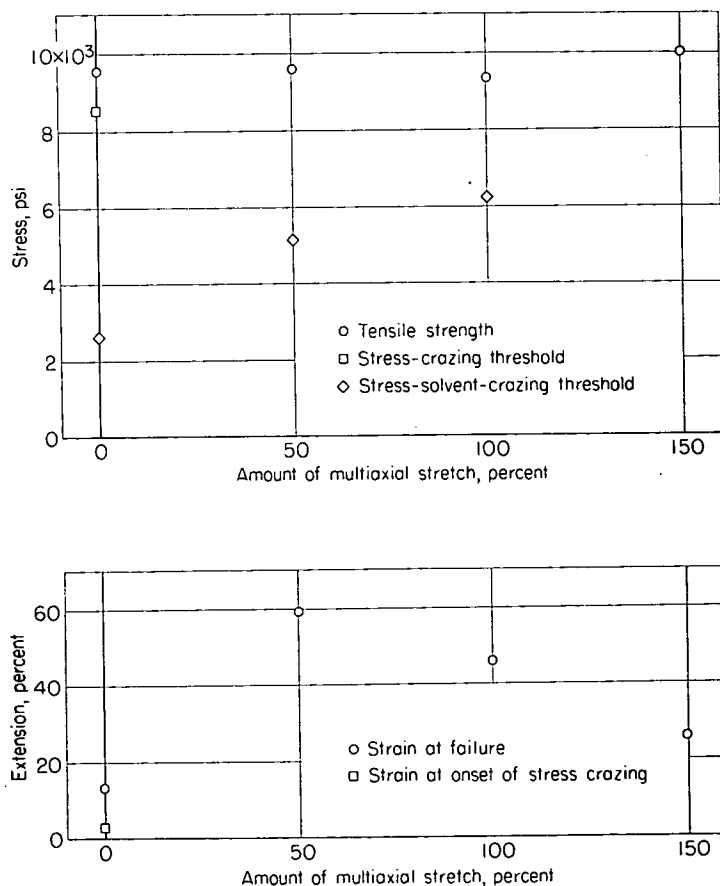


FIGURE 6.—Effect of multiaxial stretching on tensile properties of heat-resistant polymethyl methacrylate at 23° C. None of stretched specimens crazed in the stress-crazing test.

In view of these favorable results with polymethyl methacrylate stretched 50 percent, the effects of 100- and 150-percent multiaxial stretching were investigated (ref. 5). The tests were conducted with both general-purpose and heat-resistant grades of the acrylic plastic and the results are shown in figure 6. The tensile strength did not change for the 100-percent-stretched material but increased 6 to 12 percent for the 150-percent-stretched material. The strain at failure increased from approximately 7 percent for the unstretched material to 50 and 25 percent for the 100- and 150-percent-stretched materials, respectively. None of the stretched specimens crazed in the short-time tensile test. The threshold stress for stress-solvent crazing with benzene applied by blotter increased from approximately one-fourth of the strength for the unstretched material to approximately three-fourths for the 100-percent-stretched material. Most of the 150-percent-stretched specimens did not solvent craze even at tensile stresses very close to the ultimate strength. These observations indicate that the resistance to crazing increases markedly with increasing degrees of multiaxial stretching.

Tests were then conducted to determine the effects of multiaxial stretching on various properties of three heat-resistant transparent plastics, namely, polymethyl methacrylate (Lucite HC-222), modified polymethyl methacrylate (Plexiglas 55), and polymethyl alpha-chloroacrylate (Gafite and resin C). The properties measured for samples of these materials unstretched and multiaxially stretched approximately 50, 100, and 150 percent, depending upon the stretching limitations of the particular material, were as follows: Tensile strength including crazing threshold stress, strain at failure, secant modulus of elasticity, stress-solvent crazing with ethylene dichloride applied by blotter, dimensional stability at elevated temperatures, and resistance to abrasion. The method of stretching the samples and the testing procedures are described in appendices A and B.

These tests, discussed in reference 6, showed that polymethyl methacrylate and polymethyl alpha-chloroacrylate can be multiaxially stretched at least 150 percent, whereas Plexiglas 55 (modified polymethyl methacrylate) cannot be stretched more than 85 percent with the apparatus used.

Multiaxial stretching causes the following general effects on the properties of the transparent plastics studied:

- (1) Large increases in resistance to stress crazing and to stress-solvent crazing. This resistance increases with increasing degrees of stretching (table II).
- (2) A slight increase in tensile strength (table II).
- (3) A large increase in strain at failure (table II).
- (4) Little effect on the tensile secant modulus of elasticity (table II).
- (5) A decrease in the resistance to surface abrasion (table III).

Annealing increases the tensile strength of the stretched materials slightly and has the same effect for some of the unstretched materials. The resistance of both unstretched and stretched materials to stress-solvent crazing is usually increased markedly by annealing. However, the stress-crazing behavior of the unstretched materials is not affected

by annealing in most cases. Resistance of the stretched materials to surface abrasion is not affected by annealing.

As an alternative to the use of prestretched material to achieve improved craze resistance and toughness in acrylic enclosures, there is the possibility of preparing a more highly stretched enclosure directly, such as by forming a larger and more deeply drawn enclosure than required and then using only the central portion of the formed piece. Either method would improve the craze resistance, particularly at the rim, where there is likely to be stress concentration and where contact with solvents of adhesives used to seal the enclosure is quite likely; in a normally formed enclosure, the craze resistance is a minimum at the rim.

STRESS-STRAIN BEHAVIOR OF STRETCHED ACRYLICS

Typical stress-strain diagrams for unstretched and stretched heat-resistant polymethyl methacrylate and polymethyl alpha-chloroacrylate are presented in figures 7 and 8. The shape of the stress-strain curve of polymethyl methacrylate is not appreciably altered by the stretching, but that of polymethyl alpha-chloroacrylate is markedly affected. The unstretched polymethyl alpha-chloroacrylate failed before reaching a yield point; the stretched materials, however, show yield points.

In the tests conducted on stretched polymethyl methacrylate, very little increase in tensile strength was observed for the stretched materials over that of the unstretched. However, there was a marked decrease in the cross section of tensile specimens of the stretched material prior to failure at high strains, whereas the unstretched material broke at low strains with little change in cross section. Thus, the true stress at failure was probably much greater for the stretched specimens than that based on the original area.

For this reason, several tests were conducted on specimens of stretched heat-resistant polymethyl methacrylate without increasing the speed of testing when the strain reached 10 percent and the strain gage was removed. A speed of 0.05 inch per minute was used up to failure. Starting at

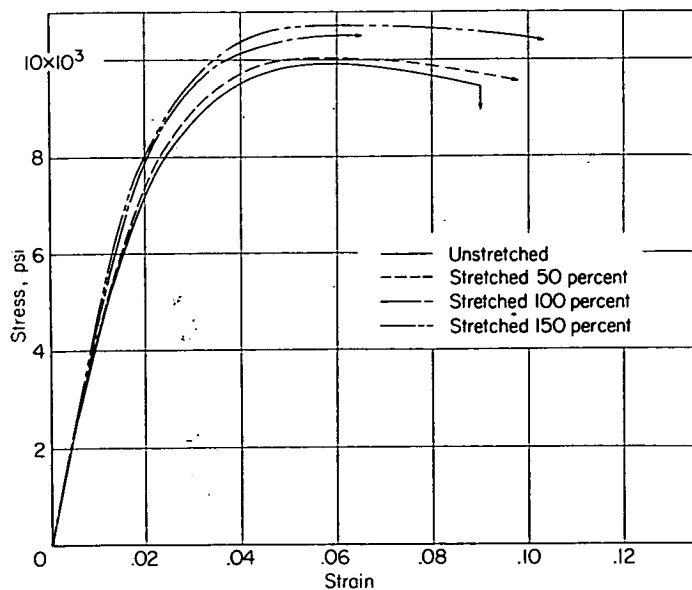


FIGURE 7.—Stress-strain diagrams of heat-resistant polymethyl methacrylate.

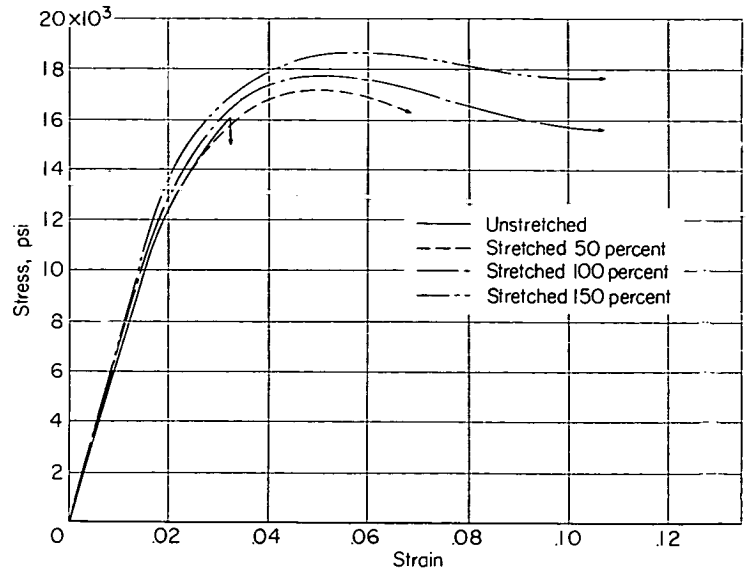


FIGURE 8.—Stress-strain diagrams of polymethyl alpha-chloroacrylate.

10-percent strain and continuing at intervals of 10-percent strain until failure, the width and thickness of the test specimens were measured with micrometer calipers to the nearest thousandth of an inch. The load was observed at each reading. From these data, the true stress at various strains could be calculated. Since most of the specimens of the stretched chloroacrylate materials broke at strains of 20 percent or less with little decrease in cross section, no measurements of this type were made on these specimens.

A typical true stress-strain diagram for the stretched polymethyl methacrylate is shown in figure 9. The results show that the true stress at the yield point is approximately 10 percent greater than the tensile strength because of the reduction in the cross-sectional area. The materials with the highest tensile strength did not have the highest true stress at failure. The 50-percent-stretched materials, which elongated the most and thus decreased the most in area, had the highest values for true stress at failure. That is, for each material, the true stress at failure was related to the strain at failure. The true stress at failure varied from approximately 25 to 50 percent greater than the tensile strength.

From the measurements made in the above tests of the changes in dimensions of the tensile specimens of the stretched

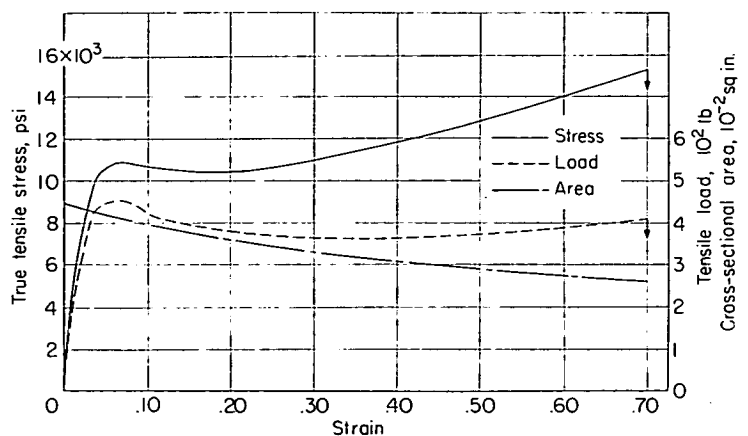


FIGURE 9.—Stress-strain diagram of heat-resistant polymethyl methacrylate multiaxially stretched 50 percent.

materials, it was possible to calculate values for Poisson's ratio. This is the ratio of lateral strain to axial strain. These values were calculated from changes in width and changes in thickness for each specimen, starting at 10 percent axial strain, at intervals of 10 percent strain to failure. The results show that Poisson's ratio is initially approximately 0.4 to 0.5 and decreases to approximately 0.3 to 0.4 as the strain increases. The reported value for Poisson's ratio for unstretched polymethyl methacrylate is 0.35.

RETENTION OF STRUCTURE ON HEATING OF STRETCHED ACRYLICS

The stretched materials will recover gradually if heated to a high enough temperature. The higher the heat-distortion point of the unstretched material, the lower is the extent of recovery of the stretched material at any given temperature within the range investigated. For any material, the higher the degree of stretching, the greater is the extent of recovery at a given temperature. Most of the recovery occurs in the first 2 hours (table IV).

The retention of the structure of stretched acrylic plastics when heated while restrained was also investigated by conducting stress-solvent crazing tests on tapered tensile specimens of heat-resistant polymethyl methacrylate that had been multiaxially stretched and then heated while restrained. Three disks were prepared at 50-percent, 100-percent, and 150-percent stretch. One disk at each degree of stretch was heated for 17 hours at 90° C, one for 6 hours at 115° C, and one for $\frac{3}{4}$ hour at 130° C. The heating period at each temperature was determined experimentally as the maximum period that the formed pieces could be heated without tearing.

The results of these tests are presented in table V. The data indicate that heating while restrained does not affect the structure of multiaxially stretched acrylic plastic appreciably, as measured by crazing resistance.

In addition, the degree of stretch of each formed disk was observed by measuring the distance between points drawn on each sheet prior to forming. There was no significant change in these distances during the heating periods, indicating that the degree of stretching was not changing.

Thus, there is no apparent reorientation of the polymer chains if the stretched material is restrained while it is heated above the glass transition temperature for the times and temperatures investigated. From a practical point of view, this means that multiaxially stretched material can be heated for forming without a change in its structure or loss of orientation if it is restrained at the edges.

APPEARANCE OF CRAZED SPECIMENS

The patterns of crazing appearing on stress-crazed and stress-solvent-crazed specimens of polymethyl methacrylate are shown in figure 10. The stress crazing of polymethyl methacrylate is apparent in figure 11 as a rather uniform blushing of the surface, which is common for this material. The crazing of the modified polymethyl methacrylate, although not nearly so uniform nor so dense, also appeared on the surface only. The stress crazing of the polymethyl alpha-chloroacrylate specimens was rather uniform and

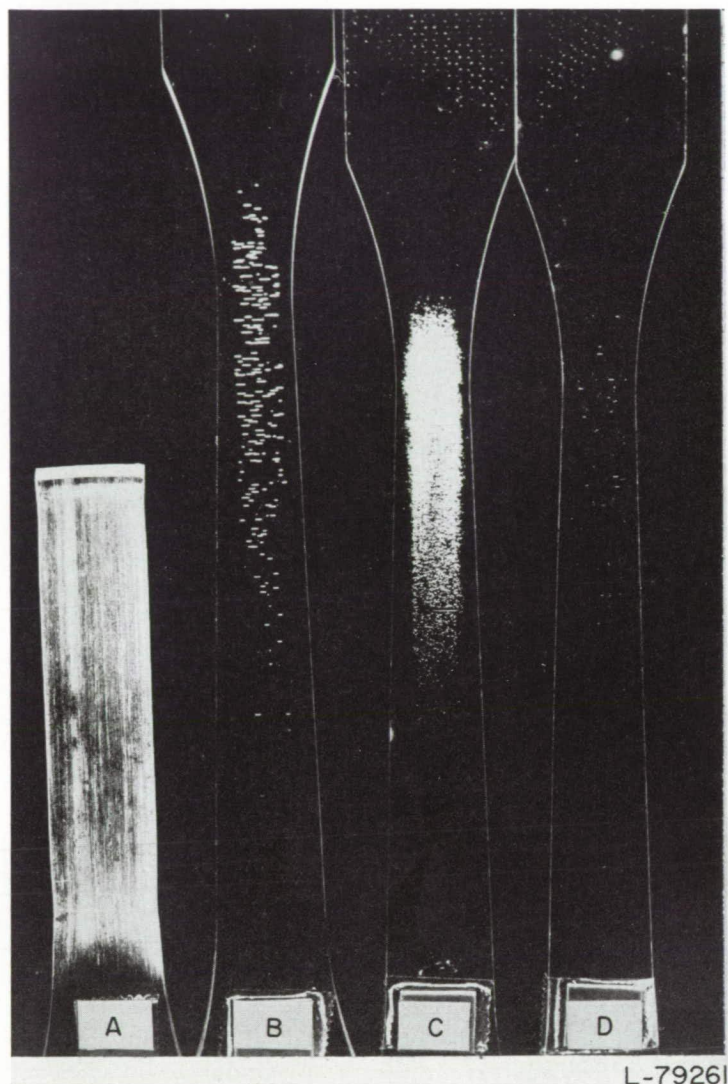


FIGURE 10.—Crazed tensile specimens of polymethyl methacrylate. A, unstretched, crazed during short-time tensile test; B, unstretched, stress-solvent crazed with benzene, maximum stress, 2,400 psi; C, multiaxially stretched 100 percent, stress-solvent crazed with benzene, maximum stress, 7,000 psi; and D, multiaxially stretched 150 percent, stress-solvent crazed with benzene, maximum stress, 10,000 psi.

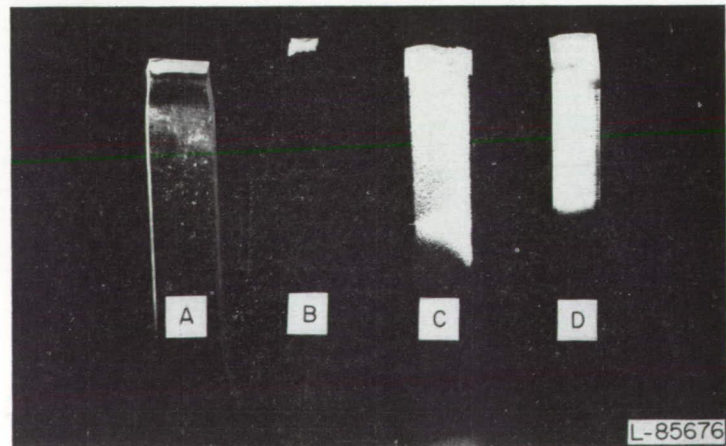


FIGURE 11.—Stress-crazed specimens of heat-resistant polymethyl methacrylate (A and B) and polymethyl alpha-chloroacrylate (C and D). Note internal crazing apparent in side view D of polymethyl alpha-chloroacrylate but not in side view B of polymethyl methacrylate.

quite dense and was apparent in the interior of the specimens as well as on the surface (fig. 11).

FRACTURE BEHAVIOR

The fracture surfaces of the unstretched polymethyl methacrylate and modified polymethyl methacrylate specimens were flat and relatively smooth and were perpendicular to the cast faces. A smooth mirrorlike area was apparent on each fracture surface and was probably the point at which fracture initiated. The fracture surfaces of the polymethyl alpha-chloroacrylate specimens were very rough and uneven and usually slightly rounded. Numerous small pieces broke out of the fracture surfaces of the chloroacrylate specimens at failure. It was very difficult to detect a mirrorlike area in most of these specimens. Examples of the fracture surfaces are shown in figure 12.

The fracture surfaces of the stretched materials showed laminar structure. This structure is probably due to the orientation of the molecular chains in layers parallel to the plane of the sheet. The higher the degree of stretching, the more apparent was this layerlike orientation. The material thus tends to act as an assembly of independent laminae in resisting impact loads. The laminar structure of the stretched acrylic sheets also offers the possibility of obtaining resistance to shattering of pressurized acrylic canopies by shrapnel without the necessity of employing the heavier and more expensive acrylic laminate made with safety-glass type of vinyl interlayer.

In many cases, a triangular-shaped piece split out of a tensile specimen of stretched material at the point of failure.

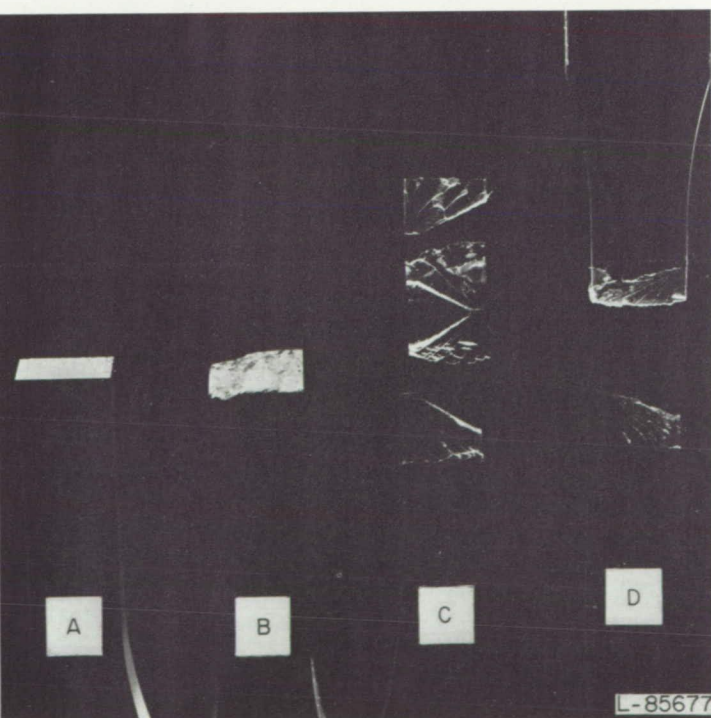


FIGURE 12.—Fracture surfaces of unstretched and multiaxially stretched acrylic plastics. A, unstretched polymethyl methacrylate; B, unstretched polymethyl alpha-chloroacrylate; C, modified polymethyl methacrylate stretched 45 percent; and D, polymethyl alpha-chloroacrylate stretched 100 percent. Note third piece broken out of specimen C (turned over). Specimen D broke into only two pieces (top piece is turned over).

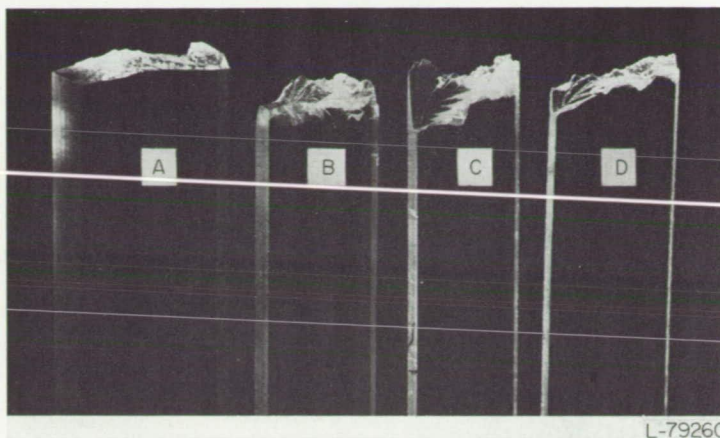


FIGURE 13.—Side view of fracture surfaces of polymethyl methacrylate tensile specimens with varying degrees of multiaxial stretching. A, unstretched; B, stretched 50 percent; C, stretched 100 percent; and D, stretched 140 percent.

This phenomenon, shown in figure 12, probably represents a combination of tensile failure and shear failure. Further examples of the fracture behavior of multiaxially stretched polymethyl methacrylate are shown in figure 13.

X-RAY DIFFRACTION PATTERNS

X-ray diffraction patterns were obtained on both stretched and unstretched polymethyl methacrylate, using a recording Geiger counter spectrometer with a copper target and nickel filter. The patterns were similar to those obtained by Krimm and Tobolsky (ref. 7), with halos at Bragg spacings of 6.5 and 3.0 Å for both the unstretched and the stretched materials, instead of 6.60 and 2.92 Å as reported by the above authors. They attributed the former spacing to inter-chain interferences and the latter, to intramolecular interferences. The height of the 6.5 Å peak was approximately 30 percent higher for the stretched material than for the unstretched. This would indicate increased orientation in the stretched polymer, which is expected from the nature of the stretching operation. There was a slight decrease noted in height of the 3.0 Å peak of the stretched samples, but it is questionable whether this change is significant.

MECHANISM OF CRAZING

The following mechanism of crazing, somewhat similar to that proposed by Maxwell and Rahm (ref. 8), is postulated. The crazing is assumed to start at submicroscopic flaws or weak points. Such weak points may be submicroscopic regions in which by chance the polymer chain segments are oriented normal to the applied tensile stress. With sufficient stress a separation between portions of adjacent chains occurs; a stress concentration exists at the apex of the crack and the latter grows until it reaches a region in which the polymer chain segments are oriented approximately in the direction of the tensile stress. The crack either does not grow or grows slowly unless the tensile stress is greatly increased. Subsequent crack growth may involve rupture of primary valence bonds, especially if the stress is relatively high, of the order of the tensile strength.

In multiaxial stretching, the chain segments turn into a position more nearly parallel to the surface, and this angular change is dependent on the degree of stretching. The chain

segments do not, on the average, change the angle of their projections on the plane of the sheet with respect to the length or width of the sheet. Bailey (ref. 9) previously made similar statements for polymer chains. As the orientation increases, it may become more difficult for a submicroscopic crack to propagate through the thickness of the sheet because of the development of "cleavage" planes. It is then possible that, in highly formed polymethyl methacrylate, submicroscopic cracks form on the surface of a specimen when a tensile load is applied. The growth of cracks through the sheet is retarded by the planar orientation, however, and the specimen fails before the cracks become visible. In long-time tensile tests on polymethyl methacrylate stretched 50 percent, the crazing cracks, after becoming visible, grew more slowly as compared with those on the corresponding unstretched specimens.

The initiation of crazing may also be associated with residual stresses leading to local tensile failures, as postulated by Russell (ref. 10), or may occur at other types of flaws which would be points of localized stress concentration. These flaws might be inhomogeneities in chemical composition, such as residual catalyst, or physical surface defects resulting from the casting operation. The importance of flaws in effecting the fracture of other materials has been recognized. Griffith (ref. 11) has proposed a theory of the strength of glass based on the presence of surface cracks. The importance of structural inhomogeneities in the failure of metals has been reported by Epremian and Mehl (ref. 12). They found that inclusions play, by far, the dominant role in the fatigue behavior of metals. Multiaxial stretching probably would alleviate the effects of some types of submicroscopic flaws in cast acrylic sheet, since the material is heated to the rubbery state and then stretched. This would delay the formation of cracks in stretched material.

The orientation of the biaxially stretched material is apparent not only from the previously mentioned X-ray diffraction measurements but also from the laminar structure of the fracture surface of a stretched specimen, as compared with the amorphous appearance of an unstretched specimen (figs. 12 and 13). This change from an amorphous to a laminar structure could account for the increase in tensile strength noted for the material stretched 140 percent and more. When the degree of orientation is high enough, the material might act as an assembly of independent laminae parallel to the plane of the sheet, and the force required to rupture a series of such layers would be greater than that required to rupture a single layer of material of the same total thickness. The latter would be typical of the structure of unstretched material.

In regard to stress-solvent crazing, mechanisms have been suggested by various authors (refs. 10, 13, and 14) which while differing in some aspects include as a factor the concept of the solvent acting as a plasticizer. By using this concept the mechanism suggested above for stress crazing may be modified to include the influence of solvents as follows: The solvent molecules penetrating the surface of the polymer tend to surround portions of the polymer chains and reduce the forces required to separate them. Because of this weakening influence of the solvent molecules at a surface flaw such as a region of normal orientation of

the polymer chains, the stress concentration that can be withstood is reduced and a tiny crack develops at a lower applied stress than in the absence of solvent. The solvent molecules probably fill the crack by capillarity as it grows and continue to exert a weakening influence at the apex. In this connection it has been suggested by Hopkins, Baker, and Howard (ref. 14) that another weakening influence at the apex of a crack is the film-spreading pressure of the crazing liquid.

The effect of stretching on stress-solvent crazing might be expected to be similar to that for stress crazing. The reduction in the number and size of the regions of normal orientation and the increase in the regions of parallel orientation should result in higher threshold stresses for the stretched material. Also, for stretched material as for unstretched, the crazing stress should be lower in the presence of than in the absence of solvent owing to the weakening influence of the solvent.

The decrease in abrasion resistance of the stretched material may also be due to its laminar structure. The oriented chains that are essentially parallel to the surface may offer less resistance to abrasion than that offered by the randomly oriented chains of the unstretched material.

CONCLUSIONS

Tests were conducted to determine the crazing behavior of various types of transparent plastics and the effect of multiaxial stretching of the plastics on their crazing resistance and various physical properties. The results and conclusions may be summarized as follows:

1. Moderate stress-solvent crazing of both general-purpose and heat-resistant grades of polymethyl methacrylate resulted in a loss of tensile strength of approximately 30 percent. This order of loss in strength was observed in the presence of either a few large craze cracks or more numerous fine cracks.
2. In stress-crazing tests at 23°, 50°, and 70° C with the same materials, the ratio of the stress at the threshold of crazing to the maximum stress was, in general, between 80 and 95 percent for all the samples.
3. The strain at which polymethyl methacrylate crazes shows, in general, a tendency to decrease with increase in temperature.
4. Polymethyl methacrylates with viscosity-average molecular weights of 90,000 and 120,000 broke at low strains without crazing; for samples having molecular weights of 200,000, 490,000 and 3,160,000, the stress and strain at which crazing occurred increased with increasing molecular weight.
5. In stress-solvent crazing tests, the materials with the three lowest molecular weights broke immediately upon crazing, usually at an observed craze crack. For the materials with the two highest molecular weights, the craze resistance increased slightly with increase in molecular weight.
6. Multiaxial stretching of polymethyl methacrylate had the following effects on crazing behavior and physical properties:
 - a. The specimens stretched 100 and 150 percent did not craze in the short-time tensile test.
 - b. The threshold stress for stress-solvent crazing with benzene increased from approximately one-fourth of the

tensile strength for the unstretched material to approximately three-fourths for the 100-percent-stretched material. Most of the 150-percent-stretched specimens did not solvent craze even at stresses very close to the tensile strength. These results indicate that the resistance to crazing increases markedly with increasing degree of multiaxial stretching.

c. The tensile strength and modulus of elasticity of the polymethyl methacrylates were affected only slightly by the multiaxial stretching.

d. The strain at failure of the polymethyl methacrylates was increased several fold (up to 60-percent strain) by multiaxial stretching, thus imparting toughness to the stretched sheets.

7. Multiaxial stretching of modified polymethyl methacrylate and polymethyl alpha-chloroacrylate gave comparable results.

8. Some decrease in the resistance to surface abrasion was observed when the materials were stretched multiaxially.

9. X-ray diffraction patterns and the laminar structure of the fracture surfaces of the stretched acrylic plastics indicated orientation of the molecular chains in layers parallel

to the plane of the sheet. The material thus tends to act as an assembly of independent laminae in resisting impact loads.

10. It is postulated that, in highly stretched acrylic sheets, the growth of submicroscopic surface cracks through the sheet is retarded by the planar orientation and the specimen fails before craze cracks become visible. Likewise, the stretched acrylic material is resistant to stress-solvent crazing because the weakening influence of either the solvent molecules or a crack caused by their presence is not readily transmitted through the layers of parallelly oriented polymer molecules.

11. The considerable increase in strain at failure suggested that enclosures made from multiaxially stretched acrylic sheets might have not only greatly improved crazing resistance but also sufficient toughness and resistance to gunfire to obviate the need for the use of the heavier laminated acrylic materials.

NATIONAL BUREAU OF STANDARDS

WASHINGTON, D. C., *December 28, 1955.*

APPENDIX A

METHODS OF TESTING

STANDARD TENSILE TESTS

The standard tensile tests were made in accordance with Method 1011 of reference 15 using the type 1 specimen. The tests were conducted on a 2,400-pound-capacity hydraulic universal testing machine. Load-extension data were recorded graphically using a Southwark-Peters extensometer and recorder. A testing speed of 0.05 inch per minute was used up to 10-percent strain; at this point the gage was removed and the speed increased to approximately 0.25 inch per minute. Strains greater than 10 percent were measured with dividers.

STRESS-SOLVENT CRAZING TESTS

The stress-solvent crazing tests were conducted at 23° C and 50-percent relative humidity on tensile specimens tapering in width from 0.500 to 0.333 inch over a 3-inch reduced section. Thus, for a given applied load the stress varied over the length of a specimen from a value S at the maximum cross section to $1.5S$ at the minimum. Two methods of preparing and testing the specimens were used:

(1) Brush method. Solvent was applied to the specimen under load as follows: A controlled amount of solvent, 0.03 to 0.04 gram, was put on a No. 1 camel's hair brush (about 0.1 inch in diameter and 0.5 inch long) from a marked glass dropper. The central $\frac{1}{4}$ - by 3-inch portion of the specimen was stroked with the brush until the latter was dry. The load was maintained for 4 minutes. The solvent-crazed specimens were examined under suitable lighting and the threshold of crazing noted.

(2) Blotter method. A predetermined load was applied to the specimen, and a solvent-saturated blotter, backed with a block of polyethylene for rigidity, was held against one face of the specimen for 10 seconds. The load was removed after 30 seconds, and the stress at the point at which crazing terminated was calculated as the threshold stress for stress-solvent crazing. For a given material, this stress will usually vary with the solvent used.

DIMENSIONAL-STABILITY TESTS

Dimensional-stability tests were conducted to provide thermal-recovery data and to provide data from which annealing conditions for the stretched materials could be determined. The specimens were small irregular pieces remaining after tensile and abrasion specimens were cut from the stretched disks and were approximately 1 inch by 2.5 inches

in size. Two lines approximately 1.5 inches apart, were scribed on the surface of the specimens with a razor blade and the exact distance between the lines read to the nearest hundredth of an inch using a steel scale graduated in hundredths of an inch and a magnifying glass. The specimens were then laid on a sheet of plate glass and placed in an air-circulating oven at the test temperature. At the end of 2 hours, the specimens were removed from the oven and allowed to cool for 5 minutes, and the distance between the lines was measured. The specimens were then replaced in the oven and the readings repeated, in most cases, at the end of 6 hours, 1 day, 2 days, and 3 days. Several specimens were measured after they had cooled to room temperature, and no significant difference was found in the measurements made while the specimens were hot and those made after they had completely cooled. Four specimens of each degree of stretch of each material were tested at each temperature.

TESTS FOR ABRASION RESISTANCE

The resistance to abrasion was determined for unstretched and stretched materials, following Method 1092.1 of reference 15. A Taber abraser was used with CS-10 Calibrase wheels and a load of 1,000 grams on each wheel. Haze and light-transmission measurements were made in accordance with Method 3022 of reference 15, using an integrating-sphere haze meter. These measurements were made after 0, 10, 25, 50, 75, 100, 150, 200, and 250 revolutions of the abrader.

TESTS ON HEAT-TREATED AND ANNEALED SPECIMENS

Unstretched tensile specimens of each material were subjected to the same heating and rapid cooling cycle as that used in stretching to determine the effect of this cycle on the tensile properties. In addition, unheated and heated unstretched tensile specimens as well as stretched tensile specimens were annealed prior to testing. The annealing temperature for each material was selected from the results of the dimensional-stability tests and was the maximum temperature at which the stretched material could be heated for 6 hours with less than 5-percent relaxation. The temperatures selected were 90° C for the heat-resistant polymethyl methacrylate, 100° C for the modified polymethyl methacrylate, and 110° C for the polymethyl alpha-chloroacrylate. The specimens were allowed to cool slowly to room temperature in the oven after the heat and the fan were turned off.

APPENDIX B

STRETCHING PROCESS

EQUIPMENT AND PROCEDURE

A vacuum stretching apparatus which would produce flat multiaxially stretched disks about 10 inches in diameter was designed following suggestions offered by Mr. W. F. Bartoe of the Rohm & Haas Co., Inc. A schematic diagram of the stretching equipment is shown in figure 14 and a photograph, in figure 15. In this apparatus a sheet of acrylic material, heated to the rubbery state, is clamped to the flange of the cylindrical forming vessel B. A partial vacuum is created in the vessel by connecting the latter to a vacuum system. The pressure differential, controlled by the plug valve C, draws the unclamped part of the sheet into the vessel. The form D, an open-end cylindrical tube a little smaller in diameter than the forming vessel and constrained by the guide E, is inserted into the vessel. The pressure differential is then removed quickly by admitting air through the plug valve F, so that the stretched acrylic sheet shrinks about the end of the form. The sheet cannot retract completely; the central portion remains uniformly stretched across the open end of the form. The stretched acrylic sheet, shaped like a top hat, is cooled to room temperature in the vessel before removal.

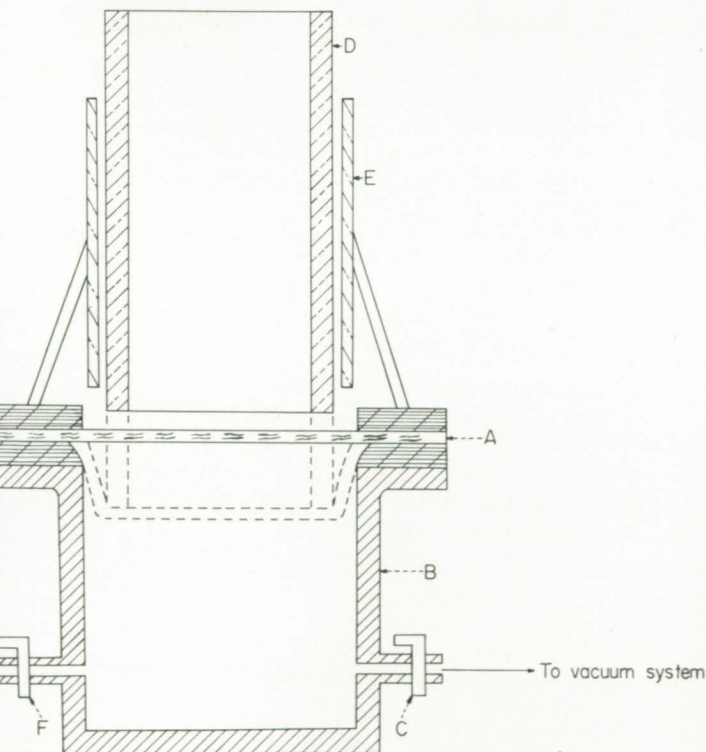


FIGURE 14.—Schematic drawing of vacuum stretching apparatus. A, plastic sheet to be stretched; B, forming vessel; C, valve to vacuum system; D, form; E, guide; and F, valve to atmosphere.

In practice, the stretching operation is done as quickly as possible so that the acrylic sheet will still be in the rubbery state when the pressure differential is removed; the time from removal of the sheet from the oven until stretching is complete is less than 1 minute.

UNIFORMITY OF STRETCHING AND EQUATION FOR ELONGATION

In order to determine whether the amount of stretching is uniform over the face of the multiaxially stretched pieces, the following experiments were made: A 10-inch disk of polymethyl methacrylate, which had been multiaxially stretched 150 percent after heating to 140°C , was marked off in 1-inch squares, then heated to 140°C , and allowed to assume its original size. The lines on the resulting disk were still equidistant within ± 5 percent. Since the standard deviation of the measurement and marking errors was



FIGURE 15.—Vacuum stretching apparatus partly disassembled after stretching a sheet of acrylic plastic. Stretched piece is on end of form which is held by operator.

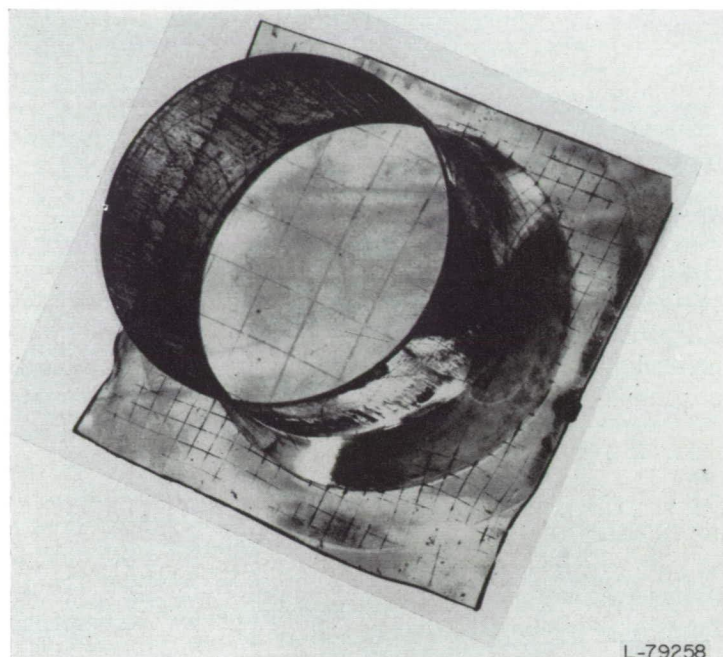


FIGURE 16.—Sample of stretched polymethyl methacrylate as removed from stretching apparatus. Large squares are on surface of flat top of hat-shaped piece.

also of this order of magnitude, this indicates that the amount of stretching was reasonably uniform over the face of the disk. Next, another piece of polymethyl methacrylate was marked with a square grid having a spacing of 15 millimeters; the piece was then multiaxially hot-stretched to an elongation of 150 percent. The lines on the flat top of the stretched plastic were still equidistant to within ± 5 percent, the experimental accuracy, verifying that the stretching was reasonably uniform (fig. 16). The length of the squares on the flat top when compared with the original length of the squares on the bottom rim indicates the degree of stretching. Test specimens are taken from the 10-inch-diameter flat top of the stretched piece.

The formula used for calculating the amount of multiaxial stretching in a stretched disk is

$$e = 100\sqrt{t_i/t_f} - 1 \quad (1)$$

where e is the elongation in percent and t_i and t_f are the initial and final thicknesses, respectively. This formula is based on the fact that the volume of the material remains essentially constant on stretching.

This property of the materials was verified by measuring the density of both 160-percent-stretched and unstretched materials. One sample of polymethyl methacrylate showed a decrease in density of 0.8 percent as a result of stretching to 160 percent strain. Three other samples of polymethyl methacrylate showed density changes of less than 0.2 percent as a result of this amount of stretching.

REFERENCES

1. Axilrod, B. M., and Sherman, Martha A.: Effect of Stress-Solvent Crazing on Tensile Strength of Polymethyl Methacrylate. NACA TN 2444, 1951.
2. Sherman, M. A., and Axilrod, B. M.: Stress and Strain at Onset of Crazing of Polymethyl Methacrylate at Various Temperatures. NACA TN 2778, 1952.
3. Wolock, I., Sherman, M. A., and Axilrod, B. M.: Effects of Molecular Weight on Crazing and Tensile Properties of Polymethyl Methacrylate. NACA RM 54A04, 1954.
4. Axilrod, B. M., Sherman, M. A., Cohen, V., and Wolock, I.: Effects of Moderate Biaxial Stretch-Forming on Tensile and Crazing Properties of Acrylic Plastic Glazing. NACA TN 2779, 1952.
5. Wolock, I., Axilrod, B. M., and Sherman, M. A.: Effects of High Degrees of Biaxial Stretch-Forming on Crazing and Other Properties of Acrylic Plastic Glazing. NACA RM 53D14, 1953.
6. Wolock, Irvin, and George, Desmond A.: Effects of Multiaxial Stretching on Crazing and Other Properties of Transparent Plastics. NACA RM 54F22, 1954.
7. Krimm, S., and Tobolsky, A. V.: Quantitative X-Ray Studies of Order in Amorphous and Crystalline Polymers. *Textile Research Jour.*, vol. 21, Nov. 1951, pp. 805-822.
8. Maxwell, B., and Rahm, L. F.: Rheological Properties of Polystyrene below 80° C. *Ind. and Eng. Chem.*, vol. 41, no. 9, Sept. 1949, pp. 1988-1993.
9. Bailey, J.: Stretch Orientation of Polystyrene and Its Interesting Results. *India Rubber World*, vol. 118, no. 2, May 1948, pp. 225-231.
10. Russell, E. W.: Studies on Cast Polymethyl Methacrylate. *Rep. No. Chem. 447*, British R. A. E. (Farnborough), Aug. 1948; also see *Nature*, vol. 165, no. 4186, Jan. 21, 1950, pp. 91-96.
11. Griffith, A. A.: The Phenomena of Rupture and Flow in Solids. *Phil. Trans. Roy. Soc. (London)*, ser. A, vol. 221, Oct. 21, 1920, pp. 163-198.
12. Epremanian, E., and Mehl, R. F.: Investigation of Statistical Nature of Fatigue Properties. NACA TN 2719, 1952.
13. Maxwell, B., and Rahm, L. F.: Factors Affecting the Crazing of Polystyrene. *Soc. Plastics Eng. Jour.*, vol. 6, no. 9, Nov. 1950, pp. 7-12.
14. Hopkins, I. L., Baker, W. O., and Howard, J. B.: Complex Stressing of Polyethylene. *Jour. Appl. Phys.*, vol. 21, no. 3, Mar. 1950, pp. 206-213.
15. Federal Specification L-P-406b: Plastics, Organic: General Specifications, Test Methods. Federal Standard Stock Catalog, sec. IV, pt. 5, Sept. 27, 1951.

TABLE I.—TENSILE STRENGTH OF STRESS-SOLVENT-CRAZED POLYMETHYL METHACRYLATE

Specimens were taken from three sheets representing three production runs. Tests were made on standard tensile specimens of type I by Method 1011 of reference 15. Specimens were conditioned at least 3 weeks at 23° C and 50-percent relative humidity and tested 2 days after they were solvent crazed. Speed of testing was 0.05 in./min.]

Material	Stress used for crazing, psi (a)	Tensile strength of crazed specimens		Average tensile strength of uncrazed control specimens, psi (a) (b)
		Average, psi	Percent of control average	
Treatment I °				
Lucite HC201.....	2, 000	5, 000	63	8, 000
Lucite HC202.....	3, 000	6, 000	62	9, 700
Plexiglas I-A.....	2, 400	4, 800	59	8, 100
Plexiglas II.....	3, 000	d 7, 600	76	10, 000
Treatment II °				
Lucite HC201.....	3, 000	f 6, 200	78	7, 900
Lucite HC202.....	4, 000	6, 900	71	9, 700
Plexiglas I-A.....	3, 200	5, 400	67	8, 100
Plexiglas II.....	4, 000	7, 800	76	10, 300

a Stress was maintained for 5 min. after benzene was applied. Control specimens were also subjected to this stress for 5 min.

b Control specimens were tested 2 days after they were loaded.

° Treatment I: No. 1 camel's hair brush (about 0.1-in. diameter, 0.5-in. length) was dipped in benzene and wiped against side of container so as not to drip. Then central ¼- by 2-in. portion of specimen was stroked twice with brush. This process was repeated nine times. Treatment I is designed to produce a few large crazing cracks. Each value is average of results for 12 specimens, unless otherwise noted.

d Average of results for 10 specimens.

° Treatment II: Benzene in amount of 0.03 to 0.04 g was put on No. 1 camel's hair brush. Then central ¼- by 2-in. portion of specimen was stroked repeatedly with brush. Treatment II is designed to produce numerous fine crazing cracks. Each value is average of results for 24 specimens, unless otherwise noted.

f Average of results for 23 specimens.

TABLE II.—EFFECT OF MULTIAXIAL STRETCHING ON TENSILE AND CRAZING PROPERTIES OF ACRYLIC PLASTICS

[Tests were conducted at 23° C and 50-percent relative humidity; each result is average of results for eight specimens unless otherwise noted]

Degree of stretching, percent	Tensile strength, σ_{max} , psi	Strain at failure, percent	Secant modulus, psi ^a	Stress and strain at onset of crazing			Solvent-crazing stress, psi ^b
				Stress, σ_c , psi	Strain, percent	σ_c/σ_{max}	
Polymethyl methacrylate (Lucite HC-222)							
0	^c 9,720	^d 7.4	^e 4.6×10^5	^e 9,070	^e 3.3	0.93	^e 910
50	9,730	^e 29	^f 4.3	(^h)	(^h)	(^h)	^e 1,680
100	10,100	^e 37	^f 4.7	(^h)	(^h)	(^h)	^e 2,710
150	10,530	^e 16	^f 5.0	(^h)	(^h)	(^h)	^e 3,910
Modified polymethyl methacrylate (Plexiglas 55)							
0	10,240	6.7	4.8×10^5	9,580	3.4	0.94	2,420
45	10,660	^g 42	^f 4.8	(^h)	(^h)	(^h)	4,060
85	10,990	^g 45	^f 5.1	(^h)	(^h)	(^h)	5,660
Polymethyl alpha-chloroacrylate (Resin C)							
0	16,170	3.1	7.4×10^5	13,300	2.2	0.82	2,850
50	17,720	ⁱ 23	ⁱ 7.6	(^h)	(^h)	(^h)	6,430
100	18,310	ⁱ 12	ⁱ 8.2	(^h)	(^h)	(^h)	12,950
150	18,510	ⁱ 9	ⁱ 8.0	(^h)	(^h)	(^h)	>18,140

^a Secant modulus of elasticity was calculated for stress range of 0 to 2,500 psi.^b Solvent-crazing stress is minimum stress required to cause crazing upon application of ethylene dichloride.^c Average of results for five specimens.^d Average of results for three specimens.^e Average of results for seven specimens.^f Average of results for four specimens.^g Average of results for six specimens.^h Did not craze.ⁱ Average of results for two specimens.

TABLE III.—EFFECT OF MULTIAXIAL STRETCHING ON SURFACE ABRASION OF ACRYLIC PLASTICS AT 23° C

Material	Degree of stretching, percent	Light transmission, percent (^a)		Haze, percent (^a)		Initial slope of abrasion curve, percent haze number of revolutions
		Original	Final	Original	Final	
Lucite HC-222 ^b	0	92.1 ± 0.1	88.4 ± 0.2	0.3 ± 0.1	24.7 ± 0.6	0.21
	50	92.0 ± 0.1	87.6 ± 0.2	.4 ± 0.1	30.4 ± 0.7	.38
	100	^c 91.9 ± 0.1	^c 87.2 ± 0.2	^c .5 ± 0.1	^c 30.6 ± 1.0	.43
	150	91.8 ± 0.2	86.8 ± 0.2	.4 ± 0.1	32.0 ± 1.3	.45
Plexiglas 55 ^b	0	91.4 ± 0.1	88.1 ± 0.1	.5 ± 0.1	21.8 ± 0.3	.19
	45	^c 91.7 ± 0.1	^c 88.0 ± 0.2	^c .6 ± 0.1	^c 25.1 ± 0.6	.26
	85	91.5 ± 0.1	87.7 ± 0.1	.6 ± 0.1	26.6 ± 0.4	.33
Gafite ^d	0	90.0 ± 0.2	87.5 ± 0.3	.4 ± 0.1	21.6 ± 0.7	.17
	50	90.6 ± 0.1	86.8 ± 0.2	.6 ± 0.2	25.4 ± 0.6	.33
	100	90.5 ± 0.2	87.4 ± 0.2	.2 ± 0.1	23.8 ± 0.8	.31
	150	^e 90.6 ± 0.3	^e 86.8 ± 2.8	^e .2 ± 0.0	^e 25.2 ± 1.2	.30
Resin C ^d	0	91.0 ± 0.2	87.9 ± 0.1	.7 ± 0.1	19.4 ± 0.4	.14
	50	^e 90.9 ± 0.1	^e 87.6 ± 0.2	^e .2 ± 0.1	^e 24.2 ± 0.4	.26
	100	91.3 ± 0.1	87.0 ± 0.2	.2 ± 0.1	26.9 ± 1.0	.30
	150	^e 90.3 ± 0.4	^e 87.1 ± 0.1	^e .6 ± 0.1	^e 28.2 ± 2.1	.30

^a Final measurements were made after 250 revolutions.^b Average of results for 12 specimens unless otherwise noted, plus or minus standard error.^c Average of results for 11 specimens.^d Average of results for six specimens unless otherwise noted, plus or minus standard error.^e Average of results for five specimens.

TABLE IV.—DIMENSIONAL STABILITY OF MULTIAXIALLY STRETCHED ACRYLIC PLASTICS AT ELEVATED TEMPERATURES

[Each result is the average of results for four specimens]

(a) Polymethyl methacrylate (Lucite HC-222)

Temperature, °C	Time, hr	Multiaxial stretch, percent			
		0	50	100	150
80	Decrease in length, percent				
	2	0	0.1	0.5	0.8
	6	0	.1	.4	.9
	24	0	.2	.7	1.1
	72	0	.2	1.0	1.1
90	2	0	1.2	1.9	2.5
	6	0	1.3	1.9	2.6
	24	0	1.6	2.4	3.0
	72	0	1.5	2.6	3.5
100	2	0	8.8	15.6	17.5
	6	0	12.1	19.1	20.2
	24	0	15.0	22.9	25.7
	48	0	15.8	24.2	28.0
	72	0	16.1	24.6	28.6
	144	0	16.4	25.3	29.7
Average initial thickness, in.					
		0.26	0.10	0.06	0.04

(b) Modified polymethyl methacrylate (Plexiglas 55)

Temperature, °C	Time, hr	Multiaxial stretch, percent		
		0	45	85
90	Decrease in length, percent			
	2	0	0.4	0.8
	6	0	.6	1.0
	24	0	.8	1.0
	48	.1	1.0	1.1
100	72	.1	.9	1.1
	2	0	1.4	1.6
	6	0	1.3	1.9
	24	.2	1.5	2.1
	48	.2	1.5	1.9
110	72	.2	1.5	2.1
	2	0	10.2	13.0
	6	0	11.7	14.4
	24	.2	13.4	15.4
	48	.3	13.5	15.8
	72	.3	13.9	16.1
Average initial thickness, in.				
		0.25	0.12	0.07

TABLE IV.—DIMENSIONAL STABILITY OF MULTIAXIALLY STRETCHED ACRYLIC PLASTICS AT ELEVATED TEMPERATURES—Concluded

(c) Polymethyl alpha-chloroacrylate (Resin C)

Temperature, °C	Time, hr	Multiaxial stretch, percent			
		0	50	100	150
110	Decrease in length, percent				
	2	0.1	0.4	1.0	1.1
	6	0	.4	.8	.9
	24	0	.8	.9	1.2
	48	0	.6	.9	1.2
120	72	.1	.9	1.1	1.3
	2	.2	2.0	3.2	4.1
	6	.1	2.6	3.6	4.1
	24	.1	2.7	3.7	4.4
	48	.1	3.0	4.2	4.6
130	72	.4	3.4	4.2	5.0
	2	1.4	32.2	45.0	51.5
	6	1.4	34.3	47.8	55.5
	24	1.9	35.8	49.5	58.8
	48	1.6	35.9	50.4	59.1
	72	2.2	36.2	50.8	59.7
Average initial thickness, in.					
		0.27	0.10	0.06	0.04

TABLE V.—EFFECT OF HEATING WHILE RESTRAINED C CRAZING BEHAVIOR OF MULTIAXIALLY STRETCHED HEAT-RESISTANT POLYMETHYL METHACRYLATE

Percent stretch	Heating conditions		Stress-solvent crazing threshold, psi ^(a)	Standard error, psi
	Temperature, °C	Time, hr		
50	Unheated		1,500	40
	90	17	1,210	40
	115	6	1,270	80
	130	¾	1,480	50
100	Unheated		2,170	40
	90	17	2,160	80
	115	6	2,060	50
	130	¾	2,720	70
150	Unheated		5,420	240
	90	17	5,420	20
	115	6	4,200	40
	130	¾	5,420	150

^(a) Ethylene dichloride was used as solvent for these crazing tests. Each result is average results for five specimens.

REPORT 1291

LIFT HYSTERESIS AT STALL AS AN UNSTEADY BOUNDARY-LAYER PHENOMENON¹

By FRANKLIN K. MOORE

SUMMARY

Analysis of rotating stall of compressor blade rows requires specification of a dynamic lift curve for the airfoil section at or near stall, presumably including the effect of lift hysteresis. Consideration of the Magnus lift of a rotating cylinder suggests performing an unsteady boundary-layer calculation to find the movement of the separation points of an airfoil fixed in a stream of variable incidence. Then consideration of the shedding of vorticity into the wake should yield an estimate of lift increment proportional to time rate of change of angle of attack. This increment is the amplitude of the hysteresis loop.

An approximate analysis is carried out according to the foregoing ideas for a 6:1 elliptic airfoil at the angle of attack for maximum lift. The assumption of small perturbations from maximum lift is made, permitting neglect of distributed vorticity in the wake. The calculated hysteresis loop is counter-clockwise. The computed increment of lift coefficient is quite large, indicating appreciable unsteady lift hysteresis for a very small reduced frequency of the flow oscillation. It is assumed that to the order of this analysis, the wake begins at the separation point defined by zero shear. This assumption is questionable for unsteady flow.

Finally, a discussion of the forms of hysteresis loops is presented; and, for small reduced frequency of oscillation, it is concluded that the concept of a viscous "time lag" is appropriate only for harmonic variation of angle of attack with time at mean conditions other than maximum lift.

INTRODUCTION

The phenomena of "stall flutter" and "rotating stall," which may appear in an axial-flow compressor, both involve fluctuations in flow about blades operating near their aerodynamic stall point; that is, at an average flow incidence angle near that corresponding to maximum blade lift.

The analysis of stall flutter has been held back by uncertainty as to the dependence of airfoil lift and moment on a fluctuating incidence angle near stall. In reference 1 there was proposed an assumption of the linear aerodynamic force and moment relations appropriate to steady flow at a small angle of incidence, modified by the further assumption that, as the airfoil oscillates, the forces and moments lag behind the angular displacement of the airfoil, owing to viscous effects. Such a time lag represents an unsteady hysteresis

which may provide cyclic work to amplify or maintain flutter. Perhaps the first experimental study of lift hysteresis was that of Farren (ref. 2). Halfman, Johnson, and Haley (ref. 3) and Schnittger (ref. 4) have more recently studied aerodynamic hysteresis experimentally and have presented empirical analyses of their results.

An analysis of rotating stall (e. g., that of Sears, ref. 5) also requires specification of a dynamic lift-incidence relation (or the equivalent, as in the study of Emmons, Pearson, and Grant, ref. 6, and in Marble's analysis, ref. 7). Sears has adopted Mendelson's phase-lag hypothesis, and this phase angle is an undetermined parameter of his analysis.

The concept of viscous time lag is not entirely satisfactory, however, partly because the phenomenon itself is unexplained, but chiefly because the concept obviously cannot describe a lift-hysteresis loop which might occur at a nominal condition of maximum lift.

The phenomenon of aerodynamic hysteresis presumably depends, at least in part, on the airfoil boundary layer. Also, in this study, hysteresis is taken to be a fundamentally unsteady phenomenon, not explainable by consideration of the steady or quasi-steady boundary layer.² In the present report, consideration is given to the incompressible flow field about a single airfoil fixed in a flow of oscillating incidence, under the assumption of an unsteady but nearly quasi-steady³ laminar boundary layer. (This sort of boundary layer is analyzed in ref. 8.) The analysis of this flow field is undertaken in order to gain an understanding of the cause of lift hysteresis and to describe its form and (crudely) its magnitude for a special airfoil at maximum lift.

The basic quasi-steady flow to be used in the present analysis is provided by Howarth's analysis (ref. 9) of the way the laminar boundary layer (and, hence, circulation) about an infinite elliptic cylinder depends on angle of attack, applied at a condition of maximum lift. In reference 9, assumptions are made under which the result becomes quantitatively inaccurate, though both the approach and the result are qualitatively instructive. The same limitations affect the present analysis.

Holding the airfoil fixed while the flow direction oscillates, simulates the accepted picture of rotating stall, in which successive blade passages stall progressively along a perfectly rigid cascade. The somewhat different case of an

¹ Supersedes NACA TN 3571, "Lift Hysteresis at Stall as an Unsteady Boundary-Layer Phenomenon," by Franklin K. Moore, 1955.

² Airfoils with lift curves that break sharply at stall may show lift hysteresis in steady flow, a phenomenon distinct from that under study herein.

³ In a quasi-steady flow, quantities vary slowly enough so that steady-state results apply at each instant of time although slight variations are permitted from one instant to the next.

oscillating airfoil in a uniform stream, which is appropriate to the stall flutter problem, is not analyzed in this report. However, there is an example in the "oscillating airfoil" category which illustrates the considerations underlying the present study; namely, the rotating circular cylinder in a uniform stream. If a circular cylinder is fixed in a uniform stream, it, of course, experiences no lift. Further, if it is given an angular displacement, its lift does not change, but remains zero. Thus, this degenerate "airfoil" may be said to be in a stall condition, at maximum lift, in fact. Now, if the circular cylinder is given a constant angular velocity of rotation about its axis, then a circulation develops and an aerodynamic force (Magnus force) transverse to the flow direction is exerted. If the stream velocity is from left to right and the rotation is clockwise, then the force is upward (lift). If the rotation is counterclockwise, the force is downward.

This phenomenon is explained (ref. 10, par. 27) by consideration of the boundary layer. In the case of clockwise rotation, the upper surface of the cylinder is moving with, and the bottom surface against, the flow. Consequently, if circulation remains zero, the boundary layer separates later on the top and sooner on the bottom than is the case when the cylinder is not rotating. On the top, later separation means that the velocity outside the boundary layer is lower at separation. Now, the separation point signifies the beginning of a wake. Therefore, the clockwise vorticity shed into the wake, being proportional to the local outer velocity, is less on the top, and the counterclockwise vorticity shed at the bottom separation is greater, than in the case of no rotation.

Therefore, owing to clockwise rotation, a net increase of counterclockwise vorticity is shed. By the law of conservation of circulation, the circulation therefore cannot be zero, and a clockwise circulation must develop about the airfoil to compensate for the shed vorticity. According to classical hydrodynamics, this circulation results in lift.

If, instead of rotating steadily, the cylinder undergoes a rotational oscillation, the same considerations apply, if the reduced frequency of oscillation is small. In that case, the oscillating lift is proportional to the instantaneous velocity of rotation. Thus, when the "angle of attack" of the cylinder is increasing, there is positive lift, and when the angle is decreasing, there is negative lift; over a complete cycle, the curve of lift against angle of attack would be a loop.

Therefore, the circular cylinder undergoing a rotational oscillation exhibits lift hysteresis, by reason of the response of the boundary layer to the movement of the surface. In the more complicated problem of a noncircular cylinder, or airfoil, similar considerations may be expected to apply. Of course, in the airfoil problem contemplated in the present study, the acceleration of the flow field may be expected to provide an additional component of pressure lift, derivable from consideration of Kelvin's impulse.

PRELIMINARY CONSIDERATIONS

STATEMENT OF PROBLEM

Consideration is given to the lift of an isolated airfoil in the form of an infinite elliptic cylinder with a semichord

l and a thickness ratio β , at a stalling angle of attack α to a stream of velocity U (see fig. 1). A full list of notation is provided in the appendix.

While the airfoil position and the magnitude of U are held fixed, the angle of attack α is permitted to vary with time. Such a flow may be constructed by allowing a moving source Q to approach an airfoil fixed in an otherwise uniform

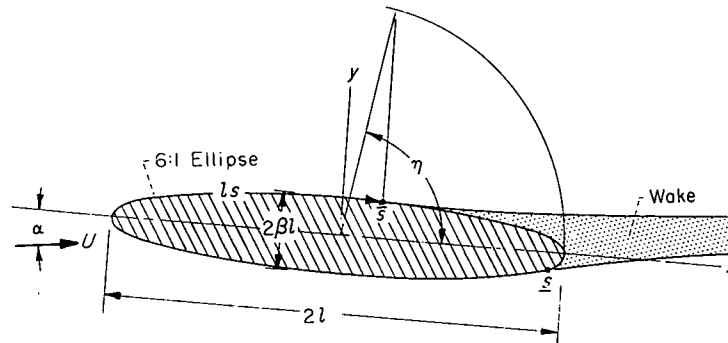
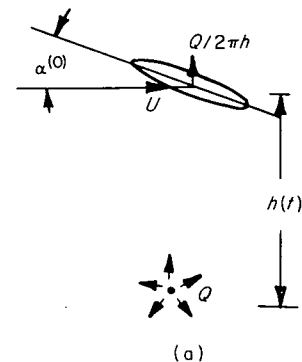


FIGURE 1.—Notation and coordinate system for elliptic airfoil at angle of attack.



Sketch (a) Airfoil and source.

stream, the direction of approach being normal to the stream direction, as in sketch (a):

As long as h , the instantaneous distance from Q to the airfoil is much greater than l , the airfoil finds itself effectively in a uniform stream of incidence

$$\alpha = \alpha^{(0)} + \frac{Q}{2\pi h U}$$

and of magnitude differing from U only to second order in $Q/2\pi h U$. The rate of change of angle of attack is

$$\dot{\alpha} = \frac{Q}{2\pi h^2 U} (-\dot{h})$$

where the dot signifies differentiation with respect to time. The foregoing model applies qualitatively to the phenomenon of rotating compressor stall, if the moving source Q is taken to represent the approach of a flow blockage propagating along a cascade.

The present analysis will be carried out as though $\dot{\alpha}$ is a small constant. Actually, if $\dot{\alpha}$ is quite small, and higher derivatives such as $\ddot{\alpha}$ are negligibly small, the analysis will be correct at each instant using the appropriate instantaneous value of $\dot{\alpha}$. (This is the first refinement over the quasi-steady assumption which uses instantaneous values of α .)

self; or for oscillatory α , the linear term of a Taylor series (at reduced frequency.) It is clear that the solution of the problem to order $\dot{\alpha}$ provides a measure of hysteresis: Suppose an expression for lift is obtained in the form

$$C_L = C_L^{(0)} + \Delta\alpha C_{L_\alpha} + \dot{\alpha} C_{L_{\dot{\alpha}}} + \dots$$

The first two terms are the quasi-steady contributions. The term in $\dot{\alpha}$ provides that, if α is in the process of increasing with time, then the lift is higher (assuming $C_{L_{\dot{\alpha}}}$ positive) than the quasi-steady value. The converse is true if α is decreasing. Thus, if α performs an harmonic oscillation, the lift curve is a loop lying to either side of the quasi-steady curve of width proportional to the frequency of oscillation.

In order that the present analysis bear on the question of rotating stall, nominal angle of attack must be selected for which the airfoil is in a stalled condition. Maximum lift is the most simply described stall condition. Accordingly, the nominal angle of attack is chosen as that for which the lift is a maximum. This selection is made for two more compelling reasons:

(1) The result will tend to isolate the effect of hysteresis, inasmuch as no quasi-steady change in lift results from change in α about the maximum lift value. Of course, if lift hysteresis is found under a mean condition of maximum lift, then the idea of viscous time lag will thereby be shown to be inappropriate.

(2) Any other assumption would lead to great theoretical complication. The analysis is to be a perturbation of quasi-steady flow. If, at the nominal angle of attack, change in α resulted in a quasi-steady change in circulation, then, to the order of the present analysis, induced wake effects would require consideration.

POTENTIAL FLOW

Outside the boundary layer of the ellipse, irrotational incompressible flow is assumed. At each instant,⁴ the velocity potential on the surface of the ellipse is (ref. 11, par. 1)

$$\varphi = lU(1+\beta) \cos(\eta-\alpha) - \frac{\Gamma\eta}{2\pi} \quad (1)$$

where the surface is defined by

$$x = l \cos \eta; y = \beta l \sin \eta \quad (2)$$

along the surface, measuring s clockwise,

$$u_1 = \frac{\partial \varphi}{\partial s} = \frac{\partial \varphi}{\partial \eta} \frac{\partial \eta}{\partial s}$$

$$\frac{d\eta}{ds} = -(\sin^2 \eta + \beta^2 \cos^2 \eta)^{-1/2} = -\frac{1}{R} \quad (3)$$

$$q = \frac{u_1}{U} = \frac{1}{R} \left[(1+\beta) \sin(\eta-\alpha) + \frac{\Gamma}{2\pi Ul} \right] \quad (4)$$

At this juncture, the condition of maximum lift has not been imposed, and the circulation Γ is left unspecified. Of course, both α and Γ may vary with time.

The foregoing description of the potential velocity distribution is made on the assumption that the boundary layer is negligibly thin everywhere on the ellipse. This assumption is usually quite proper ahead of the separation points. The assumption that the wake aft of separation does not importantly affect the potential flow is not proper; certainly, this assumption is quantitatively poor at maximum lift, especially if the potential flow is used to compute separation point. However, the results obtained on the basis of this assumption are expected to have qualitative validity.

BOUNDARY-LAYER ANALYSIS

QUASI-STEADY BOUNDARY LAYER

As a basis for subsequent calculation of unsteady effects, the quasi-steady laminar boundary layer on the ellipse may be approximately determined by the Kármán-Pohlhausen integral method, as improved by Holstein and Bohlen (see ref. 12, ch. XII). The differential equation is

$$\frac{dZ}{ds} = \frac{F(\kappa)}{q}, \quad \kappa \equiv Z \frac{dq}{ds} \quad (5a)$$

subject to the initial condition at the stagnation point ($q=0$):

$$\kappa_0 = 0.0770 \quad (5b)$$

where $Z = \theta^2 U / \nu l$, θ being the momentum thickness. The function $F(\kappa)$ is tabulated in reference 12.

Determination of Z and Γ at maximum lift.—Given the velocity distribution q , the growth of the boundary layer may be computed from equations (5), the calculation proceeding until both the separation points (\bar{s} and s , fig. 1) are reached, for which $(\kappa)_{\bar{s}} = (\kappa)_s = -0.1567$.

In the present problem the potential velocity distribution has not yet been fully prescribed, since Γ remains unknown. Suppose that, for a given α , a value of Γ is assumed, and the boundary-layer calculation is carried out (ref. 9). Then, at the top separation point, clockwise vorticity is shed into the wake at the rate

$$\int_0^s u \frac{\partial u}{\partial n} dn = \frac{1}{2} (u_1^2)_s \quad (6)$$

while at \bar{s} , counterclockwise vorticity is shed at the rate $\frac{1}{2} (u_1^2)_{\bar{s}}$. Now, if $(u_1)_s$ differs from $(u_1)_{\bar{s}}$, there is a net change of circulation in the wake, which is impossible in steady flow. Therefore, new trial values of Γ must be assumed until the particular value of Γ is determined for which the solution of equations (5) yields separation points for which $(u_1)_s = (u_1)_{\bar{s}}$.

The foregoing procedure must be carried out for each of a number of angles of attack in order to determine the values of α and Γ at maximum lift. In reference 9, Howarth performed these calculations for $\beta=1/6$ and determined a theoretical lift curve. The maximum value of $\Gamma/2\pi Ul$ was found to be 0.0761 at an angle of attack $\alpha=7^\circ$. His complete distribution of Z at this condition is not presented in reference 9.

⁴The quasi-steady assumption applies precisely for the calculation of the unsteady velocity potential.

Accordingly, the calculation has been repeated by integrating equation (5a) in the form

$$\frac{dZ}{d\eta} = A(\eta)F(\kappa); \quad \kappa \equiv a(\eta)Z \quad (7a)$$

where

$$A(\eta) \equiv -\frac{R}{q}; \quad a(\eta) \equiv -\frac{q_\eta}{R} \quad (7b)$$

and, from equation (4),

$$q = \frac{1}{R} \left[\frac{7}{6} \sin(\eta - 7^\circ) + 0.0761 \right] \quad (8)$$

At the forward stagnation point where $q=0$, $\eta_0=190.74^\circ$, and the initial condition is, from equations (5), (6), and (7a),

$$Z_0 = 0.0770/a_0 = 0.00407 \quad (7c)$$

The solution was obtained using a step-by-step method in which a parabola is passed through two known values and the

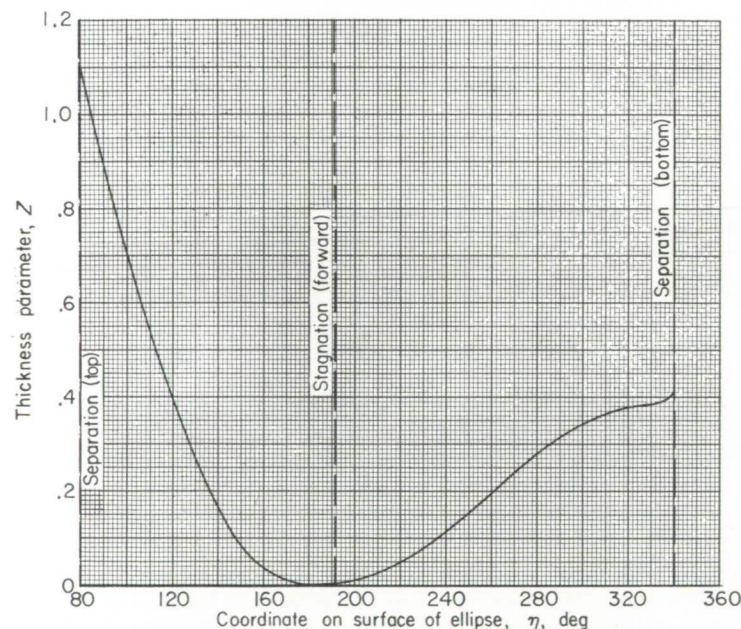


FIGURE 2.—Distribution of thickness parameter Z around ellipse.

next unknown value of $dZ/d\eta$, integrating to find Z in terms of the unknown $dZ/d\eta$, then applying equation (7a) at the unknown point to solve for $dZ/d\eta$. Two starting values were found from a Taylor series about η_0 . The step size in η was 10° except near the stagnation and separation point where finer spacing was used. The solution of Z is shown in figure 2 and in table I. The separation points, for which $\kappa = -0.1567$, occurred at $\eta = 80.0^\circ$ and 340.83° . Of course, q should be the same at \bar{s} and s . The difference cited in the table indicates the degree of error present in the calculations.

Determination of $\partial Z/\partial \alpha$.—For subsequent use in the unsteady equations, it is necessary to know the rate of change of Z with α in quasi-steady flow. At maximum lift, when α is changed, the quasi-steady boundary layer changes, and the locations of the separation points are changed. Of course, the velocities at \bar{s} and \bar{s} must remain equal, because $\partial \Gamma/\partial \alpha = 0$ at maximum lift, by definition.

Differentiating equation (7a) yields

$$\frac{dZ_\alpha}{d\eta} = B(\eta)Z_\alpha + b(\eta) \quad (9a)$$

where

$$\left. \begin{aligned} B &\equiv \frac{q_\eta}{q} F'(\kappa) \\ b &\equiv -A \left(\frac{q_\alpha}{q} F + \frac{Z q_{\alpha\eta}}{R} F' \right) \end{aligned} \right\} \quad (9b)$$

The initial condition for Z_α at η_0 is determined by specifying that $dZ_\alpha/d\eta$ must be finite there; from equations (9a) and (9b),

$$(Z_\alpha)_0 = \left(\frac{Z_\eta q_\alpha - Z q_{\alpha\eta} F'}{q_\eta F'} \right)_0 = -0.00660 \quad (9c)$$

In equations (9) all quantities are to be evaluated at the condition of maximum lift; the appropriate superscript (0)

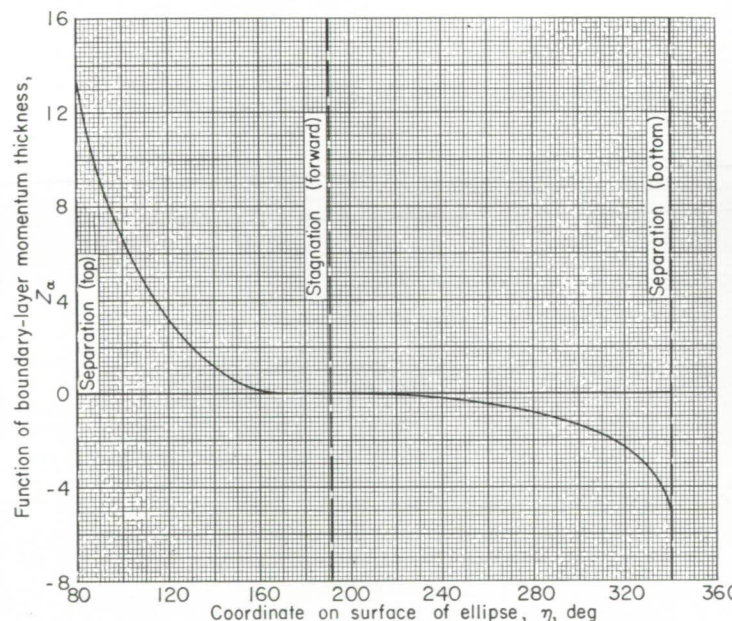


FIGURE 3.—Distribution of derivative Z_α around ellipse.

is omitted for brevity. Of course, for purposes of finding q_α and $q_{\alpha\eta}$ in equations (9), the angle of attack of 7° should be replaced by α in equation (8) and set equal to 7° again subsequent to differentiation. Equations (9) have been integrated to yield Z_α , by the same method as described for finding Z , and the result is shown in figure 3 and in table I.

UNSTEADY BOUNDARY LAYER

The next step in the analysis is to determine the dependence of the boundary layer on the angular velocity $\dot{\alpha}$, assumed small. To this order of approximation, equation (8) describing the potential flow must be modified to include the possibility of a contribution to circulation in proportion to $\dot{\alpha}$ (or, in dimensionless form, $\epsilon \equiv \dot{\alpha}/U$), as follows:

$$q \equiv \frac{u_1}{U} = \frac{1}{R} \left[\frac{7}{6} \sin(\eta - 7^\circ) + 0.0761 + \gamma \epsilon \right] \quad (10)$$

coefficient of circulation hysteresis γ must be found from condition of vorticity shedding at the separation points of unsteady boundary layer. The contribution to lift proportional to $\dot{\alpha}$ then follows. Determination of the proper vorticity-shedding condition will be discussed in a subsequent section.

The unsteady form of the Kármán momentum equation (ref. 12) is

$$\frac{\tau}{\rho} - u_1^2 \frac{\partial \theta}{\partial s} - (2\theta + \delta^*) u_1 \frac{\partial u_1}{\partial s} = \frac{\partial}{\partial t} (u_1 \delta^*) \quad (11)$$

Equations (5a) and (7a) are obtained from equation (11) by omitting the term on the right side. An iteration procedure might then be adopted: The quasi-steady δ^* can be substituted into the right side of equation (11), and a new solution obtained, to include first-order unsteady effects. Using the definitions of reference 12, and writing the time derivative in equation (11) as

$$\frac{\partial}{\partial t} (u_1 \delta^*) = \dot{\alpha} \frac{\partial}{\partial \alpha} (u_1 \delta^*) \quad (12)$$

Equation (12) is found, corresponding to equation (5a),

$$\frac{dZ}{ds} = \frac{F(\kappa)}{q} - 2 \frac{\epsilon}{q} f_1 Z \left(\frac{q_\alpha}{q} + \frac{1}{2} \frac{Z_\alpha}{Z} + \frac{f'_1}{f_1} \kappa_\alpha \right) \quad (13)$$

The function $f_1(\kappa)$ is tabulated in reference 12, and q is given by equation (10). Again, for purposes of finding q_α and κ_α , the angle 7° in equation (10) should temporarily be replaced by α .

Instead of the indicated iteration, in the present study an equivalent procedure is adopted of finding the coefficients of the expansion

$$Z = Z^{(0)} + \Delta \alpha Z_\alpha + \epsilon Z_\epsilon + \dots$$

The coefficients $Z^{(0)}$ and Z_α have already been found (eqs. (7) and (9) and figs. 2 and 3). The derivative Z_ϵ remains to be found. Differentiating equation (13) and noting that $q_s Z_\alpha + q_\alpha Z$,

$$\begin{aligned} &= F'(\kappa) \frac{q_s}{q} Z_\epsilon + F' \frac{q_{\epsilon s}}{q} Z - \frac{F q_\epsilon}{q^2} - \\ &2 \frac{f_1 Z}{q} \left[\frac{q_\alpha}{q} + \frac{Z_\alpha}{2Z} + \frac{f'_1}{f_1} (q_s Z_\alpha + q_\alpha Z) \right] \quad (14) \end{aligned}$$

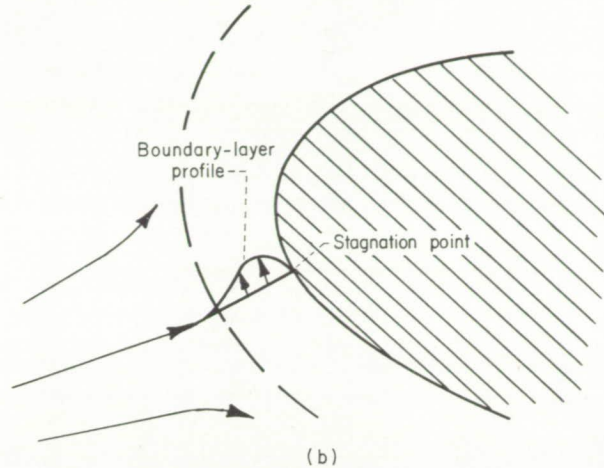
Equation (14) and hereinafter, evaluation of quantities at the steady state at maximum lift is to be understood, and superscript (0) is omitted for brevity.

It is impossible to ensure a finite value of dZ_ϵ/ds at the stagnation point because of the second-order pole $f_1 Z q_\alpha / q^2$. The physical reason for this result is the fact that, at the stagnation point of a certain instant, the boundary-layer velocity profile will not vanish, as in steady flow, but rather will respond to the instantaneous acceleration more promptly than the outer potential flow. A profile of magnitude ϵ may thus be expected, vanishing in the outer stream as well as the wall as shown in sketch (b):

Therefore, the definition of momentum thickness

$$\theta \equiv \int_0^\infty \frac{u}{u_1} \left(1 - \frac{u}{u_1} \right) dy$$

shows that, if the velocity u in the boundary layer has a part proportional to u_1 and a part proportional to ϵ , then the part of θ (and hence of $Z = \theta^2 U / \nu l$) which is proportional to ϵ must have a simple pole in u_1 . Actually, of course, the quantity θ is inappropriate for defining a thickness of a profile of the type shown in sketch (b), and the appearance of a pole in θ simply indicates this lack of physical significance.



Sketch (b) Nose of airfoil.

The foregoing considerations suggest that a new variable W be defined to replace Z_ϵ :

$$W = q Z_\epsilon \quad (15)$$

Substituting equation (15) into equation (14) yields

$$\begin{aligned} \frac{dW}{ds} &= \frac{q_s}{q} (1 + F') W + Z F' q_{\epsilon s} - F \frac{q_\epsilon}{q} - \\ &2 f_1 Z \left[\frac{q_\alpha}{q} + \frac{Z_\alpha}{2Z} + \frac{f'_1}{f_1} (q_s Z_\alpha + q_\alpha Z) \right] \quad (16) \end{aligned}$$

In order that dW/ds be finite at the stagnation point, the two poles on the right side of equation (16) must cancel, yielding the initial condition

$$W_0 = \left[\frac{2 f_1 Z q_\alpha}{(1 + F') q_s} \right]_0 = -0.001015 \quad (17)$$

where the numerical value is obtained using equations (3), (7c), and (10), and the tables of reference 2. Inasmuch as $q_\epsilon = \gamma / R$ (eq. (10)), the function W may be split into two parts, as follows:

$$W \equiv X + \gamma Y \quad (18)$$

so that (changing to η as independent variable) equations (16) and (17) provide

$$\frac{dX}{d\eta} = C(\eta) X + c(\eta) \quad (19a)$$

where

$$\left. \begin{aligned} C(\eta) &\equiv (1+F') \frac{q_\eta}{q} \\ c(\eta) &\equiv 2f_1 R Z \left[\frac{q_\alpha}{q} + \frac{Z_\alpha}{2Z} - \frac{f'_1}{R f_1} (q_\eta Z_\alpha + q_{\alpha\eta} Z) \right] \end{aligned} \right\} \quad (19b)$$

and

$$X_0 = -0.001015 \quad (19c)$$

$$\frac{dY}{d\eta} = C(\eta)Y + d(\eta) \quad (20a)$$

where

$$d(\eta) \equiv \frac{F}{q} - Z F' \frac{R_\eta}{R^2} \quad (20b)$$

and

$$Y_0 = 0 \quad (20c)$$

Equations (19b) and (20b) are evaluated using the solutions for Z and Z_α , the tables of reference 12, and equations (3) and (10).

Solutions of equations (19) and (20), obtained by the method used to find Z , are presented in figures 4 and 5 and table I.

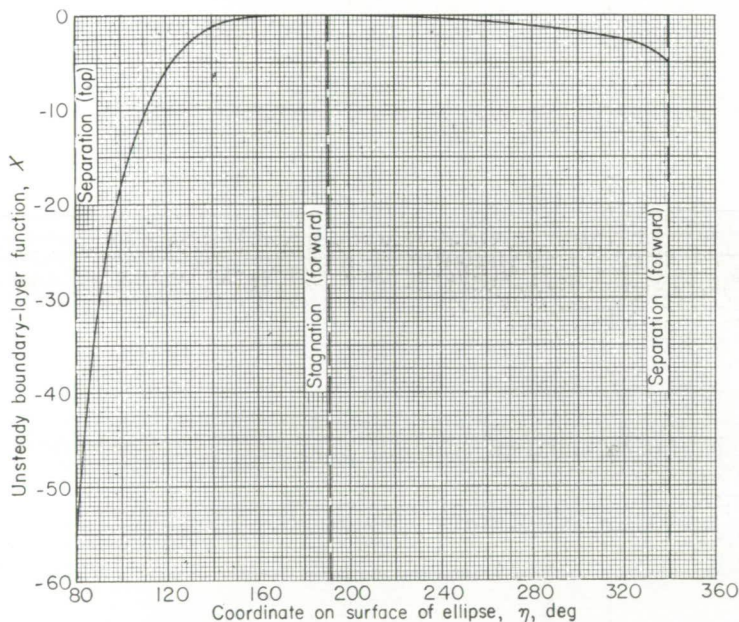


FIGURE 4.—Distribution of parameter X of unsteady boundary layer.

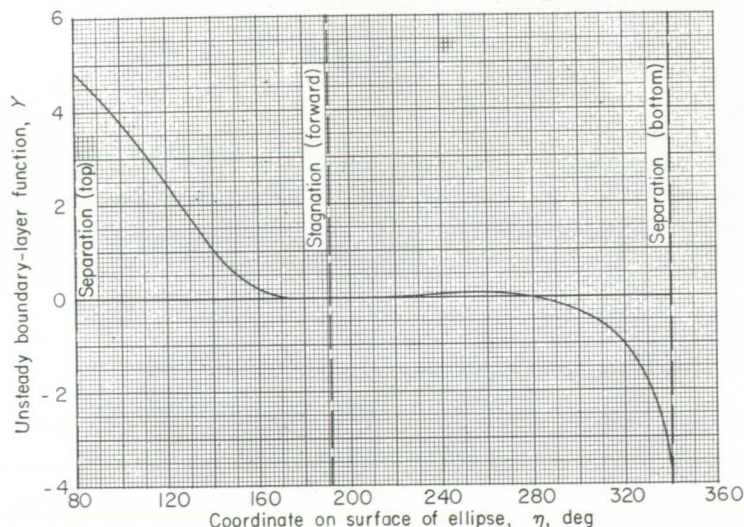


FIGURE 5.—Distribution of parameter Y of unsteady boundary layer.

DETERMINATION OF LIFT

UNSTEADY BALANCE OF SHED VORTICITY

In order to determine the unsteady pressure lift, the coefficient γ (eq. (10)) must be determined. In steady flow (see the discussion accompanying eq. (6)), the circulation Γ was obtained by requiring that vorticity be shed in equal and opposite amounts at the two separation points.

In the present unsteady problem, the net rate of vorticity appearance in the wake must vanish, not only in the quasi-steady approximation, but to order $\dot{\alpha}$ as well, in view of the assumption that the quasi-steady circulation is maximum. By the classical theorem concerning constancy of circulation, any net rate of discharge of vorticity into the wake must be balanced by a rate of increase of circulation about the body. If the airfoil is nominally at maximum lift, then the circulation terms (eq. (10)), to order $\epsilon \equiv \dot{\alpha}l/U$, are

$$0.0761 + \gamma\epsilon$$

The rate of increase of this expression is at most of order $\dot{\alpha}$, and therefore there cannot be any net discharge of vorticity to order $\dot{\alpha}$.

If the airfoil were not at maximum lift, then the expression for circulation would contain a term proportional to Δ , which would change at the rate $\dot{\alpha}$, and would have to be balanced by a net rate of vorticity discharge of order $\dot{\alpha}$. In turn, this distribution of circulation in the wake would induce further modifications of the potential flow. Therefore the assumption of maximum lift permits the neglect of the induced effects of distributed circulation in the wake.

Movement of separation points.—In order to effect a balance (to order $\dot{\alpha}$) of vorticity shed at the separation points, the movements of the separation points must be taken into account. The position of the top separation point \bar{s} may be written

$$\bar{\eta} = (\bar{\eta})_{\bar{s}} + \Delta\alpha \left(\frac{\partial \bar{\eta}}{\partial \alpha} \right)_{\bar{s}} + \epsilon \left(\frac{\partial \bar{\eta}}{\partial \epsilon} \right)_{\bar{s}} + \dots \quad (21)$$

The coefficient $\left(\frac{\partial \bar{\eta}}{\partial \alpha} \right)_{\bar{s}}$ is obtained from the quasi-steady solution:

At separation ($\kappa = -0.1567$),

$$\left(\frac{\partial \bar{\eta}}{\partial \alpha} \right)_{\bar{s}} = - \left(\frac{\partial \kappa / \partial \alpha}{\partial \kappa / \partial \eta} \right)_{\bar{s}}$$

From equations (7),

$$\frac{\partial \kappa}{\partial \eta} = -\frac{1}{R} \left(Z q_{\eta\eta} + Z_\eta q_\eta + \frac{35\kappa}{72R} \sin 2\eta \right) \quad (22)$$

$$\frac{\partial \kappa}{\partial \alpha} = -\frac{1}{R} (Z q_{\eta\alpha} + Z_\alpha q_\eta) \quad (23)$$

whence, holding κ fixed at -0.1567 ,

$$\left(\frac{\partial \bar{\eta}}{\partial \alpha} \right)_{\bar{s}} = - \left(\frac{Z q_{\eta\alpha} + Z_\alpha q_\eta}{Z q_{\eta\eta} + Z_\eta q_\eta + \frac{35\kappa}{72R} \sin 2\eta} \right)_{\bar{s}} \quad (24)$$

where Z and Z_α may be obtained from table I.

The coefficient $(\partial\bar{\eta}/\partial\epsilon)_{\bar{s}}$ comes from the unsteady solution:

$$\left(\frac{\partial\bar{\eta}}{\partial\epsilon}\right)_{\bar{s}} = -\left(\frac{\partial\kappa/\partial\epsilon}{\partial\kappa/\partial\eta}\right)_{\bar{s}}$$

From equations (7),

$$\kappa_\epsilon = -\frac{1}{R} (Z_\epsilon q_\eta + Z q_{\eta\epsilon})$$

which, upon substitution of equations (10), (15), and (18), becomes

$$\kappa_\epsilon = -\frac{1}{R} (X + \gamma Y) \frac{q_\eta}{q} + \frac{35Z\gamma}{72R^3} \sin 2\eta \quad (24)$$

Equations (22a) and (24) thus provide that

$$\left(\frac{\partial\bar{\eta}}{\partial\epsilon}\right)_{\bar{s}} = -\left[\frac{X \frac{q_\eta}{q} + \gamma \left(Y \frac{q_\eta}{q} - \frac{35Z}{72R^3} \sin 2\eta\right)}{Z q_{\eta\eta} + Z_\eta q_\eta + \frac{35\kappa}{72R} \sin 2\eta}\right]_{\bar{s}} \quad (25)$$

At the bottom stagnation point, equations (21), (23), and (25) apply, with subscript \bar{s} replacing subscript \bar{s} .

Equation of vorticity shed at separation points.—Taking into account the motion of the separation point, the rate of vorticity shedding at the top is given by the following equation, which replaces equation (6):

$$\int_0^{\delta} \left(\bar{u} - l \frac{d\bar{s}}{dt}\right) \frac{\partial\bar{u}}{\partial n} dn = \frac{1}{2} \bar{u}_1^2 - l \frac{d\bar{s}}{dt} \bar{u}_1 \quad (26)$$

From equations (3) and (21),

$$\left. \begin{aligned} \frac{d\bar{s}}{dt} &= -R \frac{\partial\bar{\eta}}{\partial t} = -\dot{\alpha} \left(R \frac{\partial\bar{\eta}}{\partial\alpha}\right)_{\bar{s}} + \dots = -\frac{U}{l} \epsilon \left(R \frac{\partial\bar{\eta}}{\partial\alpha}\right)_{\bar{s}} + \dots \\ \bar{u}_1 &= (u_1)_{\bar{s}} + \left(\frac{\partial u_1}{\partial n}\right)_{\bar{s}} \left[\Delta\alpha \left(\frac{\partial\bar{\eta}}{\partial\alpha}\right)_{\bar{s}} + \epsilon \left(\frac{\partial\bar{\eta}}{\partial\epsilon}\right)_{\bar{s}}\right] + \dots \end{aligned} \right\} \quad (27)$$

Equations (27) yield the following expression for the right side of equation (26):

$$\frac{1}{2} (u_1^2)_{\bar{s}} + (u_1)_{\bar{s}} \left[\Delta\alpha \left(\frac{\partial u_1}{\partial\eta} \frac{\partial\bar{\eta}}{\partial\alpha}\right)_{\bar{s}} + \epsilon \left(\frac{\partial u_1}{\partial\eta} \frac{\partial\bar{\eta}}{\partial\epsilon} + UR \frac{\partial\bar{\eta}}{\partial\alpha}\right)_{\bar{s}}\right] \quad (28)$$

Expression (28) represents clockwise vorticity shed at the top separation point. At the bottom separation point, the amount of counterclockwise vorticity shed is also represented by equation (28), if subscripts \bar{s} are replaced by \underline{s} .

Therefore, equating the net discharge of vorticity to zero,

$$\left. \begin{aligned} &= \frac{1}{2} [(u_1^2)_{\bar{s}} - (u_1^2)_{\underline{s}}] + \frac{1}{2} \Delta\alpha \left[\left(\frac{\partial u_1^2}{\partial\eta} \frac{\partial\bar{\eta}}{\partial\alpha}\right)_{\bar{s}} - \left(\frac{\partial u_1^2}{\partial\eta} \frac{\partial\bar{\eta}}{\partial\alpha}\right)_{\underline{s}}\right] + \\ &\epsilon \left\{ \frac{1}{2} \left[\left(\frac{\partial u_1^2}{\partial\eta} \frac{\partial\bar{\eta}}{\partial\epsilon}\right)_{\bar{s}} - \left(\frac{\partial u_1^2}{\partial\eta} \frac{\partial\bar{\eta}}{\partial\epsilon}\right)_{\underline{s}}\right] + U \left[\left(R u_1 \frac{\partial\bar{\eta}}{\partial\alpha}\right)_{\bar{s}} - \left(R u_1 \frac{\partial\bar{\eta}}{\partial\alpha}\right)_{\underline{s}}\right] \right\} + \dots \end{aligned} \right\} \quad (29)$$

In the quasi-steady flow, $(u_1)_{\bar{s}} = (u_1)_{\underline{s}}$, and the coefficient of $\Delta\alpha$ must be zero. Therefore, the coefficient of ϵ in equation (29) must vanish:

$$\left(\frac{\partial u_1}{\partial\eta} \frac{\partial\bar{\eta}}{\partial\epsilon}\right)_{\bar{s}} - \left(\frac{\partial u_1}{\partial\eta} \frac{\partial\bar{\eta}}{\partial\epsilon}\right)_{\underline{s}} + U \left[\left(R \frac{\partial\bar{\eta}}{\partial\alpha}\right)_{\bar{s}} - \left(R \frac{\partial\bar{\eta}}{\partial\alpha}\right)_{\underline{s}}\right] = 0$$

or

$$\left(\frac{\partial q/\partial\eta}{R} \frac{\partial\bar{\eta}/\partial\epsilon}{\partial\bar{\eta}/\partial\alpha}\right)_{\bar{s}} \left[1 - \left(\frac{\partial\bar{\eta}/\partial\alpha}{\partial\bar{\eta}/\partial\epsilon}\right)_{\bar{s}} \left(\frac{\partial\bar{\eta}/\partial\epsilon}{\partial\bar{\eta}/\partial\alpha}\right)_{\underline{s}}\right] + 1 - \frac{(R \partial\bar{\eta}/\partial\alpha)_{\underline{s}}}{(R \partial\bar{\eta}/\partial\alpha)_{\bar{s}}} = 0 \quad (30)$$

Equations (23), (25), and (30) and table I suffice to determine γ (which appears in eq. (25)). The result is,

$$\gamma = -6.1 \quad (31)$$

Definition of separation point.—In effect, it has been assumed that, during the unsteady motion, separation is defined by the condition of zero shear ($\kappa = -0.1567$) and the subsequent appearance of reverse flow relative to the surface, just as in steady flow. This assumption is open to question. The question is how (or whether) local velocity-profile characteristics may be interpreted to identify the leading edge of a wake.

The usual steady criterion, which notes the appearance of reverse flow downstream of the point of zero shear, implies that the fluid in the wake is fixed relative to the body. If, in the unsteady case, the wake may still be regarded as fixed to the body, then it may be that the steady criterion is still applicable.

However, the present assumption of the steady definition of separation is not advanced with complete confidence. Rather, it is felt that only a suitable experiment can settle this point.

LIFT OF AIRFOIL

The steady lift coefficient of the airfoil of figure 1 is determined from the steady circulation:

$$C_L^{(0)} = \frac{\rho U \Gamma}{\frac{1}{2} \rho U^2 (2l)} = \frac{\Gamma}{U l} = 2\pi(0.0761) = 0.48 \quad (32)$$

There are two contributions to lift proportional to ϵ . From the unsteady circulation,

$$C_{L_\epsilon}^{(0)} = 2\pi\gamma = -38.6 \quad (33)$$

and a further contribution is found by consideration of the remainder of the potential flow. The two components of Kelvin's impulse for the flow illustrated in figure 1 (leaving circulation out of account) are

$$I_x, I_y = \pi\rho U l^2 (\beta^2 \cos \alpha, \sin \alpha)$$

(See pars. 71 and 123 of ref. 11.) Whence, the corresponding components of vector force are

$$F_x, F_y = \dot{\alpha} \frac{\partial I_{x,y}}{\partial \alpha} = \pi\rho U l^2 \dot{\alpha} (-\beta^2 \sin \alpha, \cos \alpha)$$

and the lift is

$$L = F_y \cos \alpha - F_x \sin \alpha = \pi\rho U l^2 \dot{\alpha} \frac{1+\beta^2}{2} \left(1 + \frac{1-\beta^2}{1+\beta^2} \cos 2\alpha\right)$$

The following lift coefficient results:

$$C_{L_e}^{(2)} = \frac{\pi}{2} (1 + \beta^2) \left(1 + \frac{1 - \beta^2}{1 + \beta^2} \cos 2\alpha \right) = 3.09 \quad (34)$$

The final expression for lift combines equations (32), (33), and (34):

$$\begin{aligned} C_L &= C_L^{(0)} + \epsilon (C_{L_e}^{(1)} + C_{L_e}^{(2)}) \\ &= 0.48 - 36 \frac{\dot{\alpha} l}{U} \end{aligned} \quad (35)$$

The sign of the second term of the result of equation (35) indicates that, while angle of attack is increasing, the lift is lower than the quasi-steady value, and higher if the angle of attack is decreasing. Thus, near maximum lift, the lift curve would exhibit a counterclockwise hysteresis loop enclosing the stall point. This result is perhaps counter to expectations, because clockwise hysteresis is found experimentally for oscillating airfoils. It may be that different directions of hysteresis should be expected when the airfoil oscillates and when, as in the present study, the stream direction oscillates.

In any case, it may be shown that the overriding effect producing counterclockwise hysteresis in the present problem is the quasi-steady movement of the separation point over the top surface. As this separation point moves forward under increasing angle of attack, clockwise vorticity in the boundary layer joins the wake as the separation point passes. Accordingly, a counterclockwise airfoil circulation (negative γ) is required to balance this effect. The term of equation (26) that is concerned with this movement is the one involving $d\bar{s}/dt$.

For the elliptic airfoil problem treated herein, the quasi-steady movement of the upper separation point is quite extensive; numerically, $\partial \bar{\eta} / \partial \alpha = 13.9$, indicating that the separation point is very loosely fixed to the airfoil surface. By way of contrast, in the case of the rotating circular cylinder, there is no effect of this sort, because a change in angle of attack produces no quasi-steady movement of the separation point at all. Other contributions to the shedding of vorticity then lead to the result of clockwise hysteresis for the circular cylinder.

LIFT HYSTERESIS

The foregoing analysis does not provide a complete theory of unsteady flow about a stalled airfoil. Rather, the analysis illustrates the considerations that would underlie such a theory and further make plausible the general assumption of an expansion of lift coefficient in the form of equation (35). This expansion would be valid for nearly quasi-steady conditions. Also, it has been shown that a counterclockwise hysteresis loop may be expected at a nominal condition of maximum lift with, apparently, a large amplitude.

If the foregoing conditions are met, and $\Delta\alpha$ is simple harmonic,

$$\Delta\alpha \propto \sin 2\pi\omega t \quad (36a)$$

then

$$\dot{\alpha} \propto -2\pi\omega \sin (2\pi\omega t - 90^\circ) \quad (36b)$$

Use of relation (36b) in the lift formula (35) may be said to correspond to the assumption (ref. 5) of a positive lift-curve slope and a phase lag, 90° in this case, though the positive slope would not correspond to the steady lift curve. The hysteresis loop for this case appears as an ellipse on the lift curve of figure 6 (a). The amplitude and width of the loop are assumed small in the present discussion and are exaggerated in figure 6.

If α is not simple harmonic, then the concept of phase lag is altogether inappropriate. For example, if α is more nearly a "saw-tooth" function of time (fig. 6 (b)), then the lift increment is nearly a "battlement" function. The corresponding hysteresis loop is nearly rectangular. If α changes according to an exponential pulse (illustrated by a Gaussian curve in fig. 6 (c)), then the hysteresis loop is egg-shaped, with the broad end to the right.

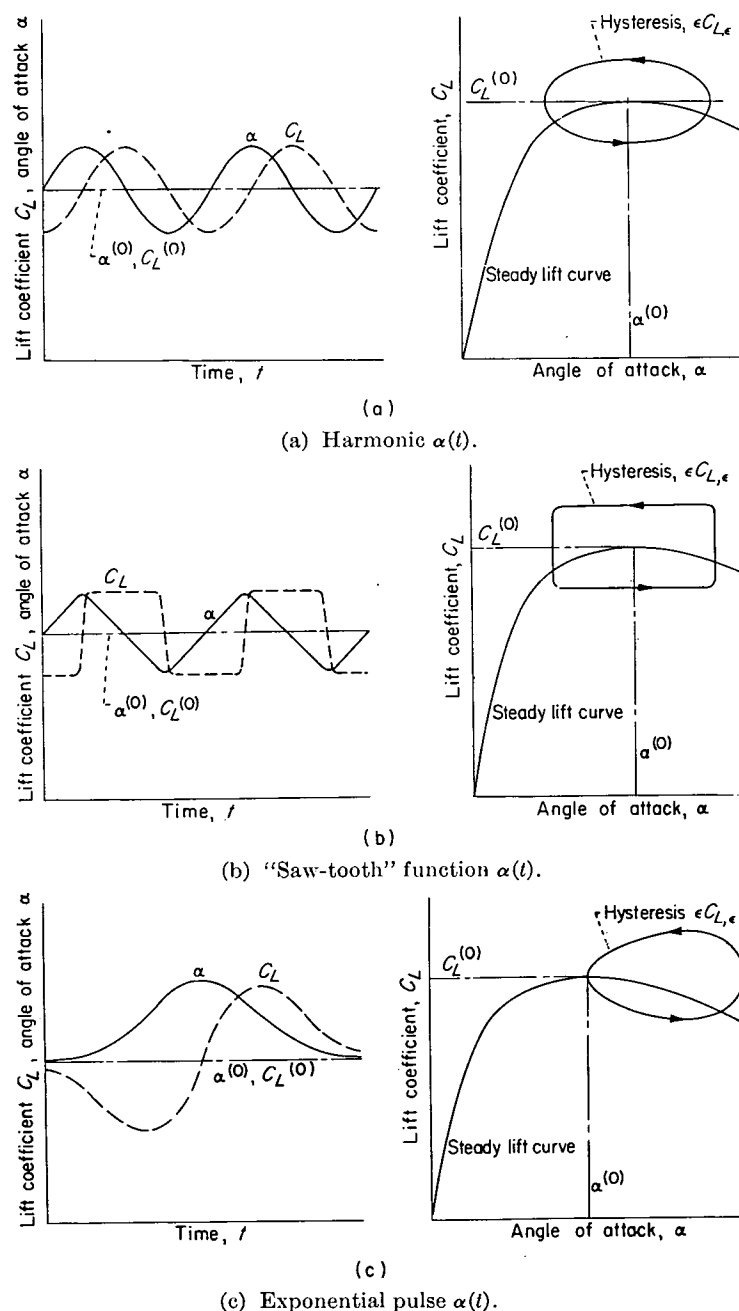


FIGURE 6.—Variation of lift coefficient and angle of attack with time and with each other.

CONCLUSIONS

The analysis of rotating stall in an axial-flow compressor requires specification of a dynamic lift curve applicable near stall. It has previously been suggested that unsteady lift hysteresis is an important characteristic of such a curve.

Consideration of the familiar experimental fact of Magnus lift on a rotating cylinder indicates a theoretical approach to the question of aerodynamic hysteresis which, though certainly not definitive, may prove helpful. The accepted explanation of Magnus lift is that, if the cylinder is in motion toward the left and rotates clockwise, the movement of the surface delays boundary-layer separation on the top and advances it on the bottom. In steady flow, considerations of constancy of wake circulation require that the outer velocity at the two separation points be equal. The delayed separation at the top implies a lower velocity (vice versa on the bottom), and a compensatory clockwise circulation must therefore occur.

The foregoing reasoning is extended to apply to the problem of an airfoil of elliptic section in a stream of constant velocity but of (slightly) oscillating direction. The airfoil is considered to be nominally at maximum lift. This assumption, reasonable for unsteady problems at nearly stalled conditions, provides an essential simplification. To first order in small quantities, the lift (circulation) increment due to the oscillation can depend only on rate of change of angle of attack; and, just as in the cylinder case, all induced wake effects may be ignored.

For purposes of computing the amount of vorticity shed into the wake, the separation point is identified as the point of vanishing shear, just as in steady flow. It is not clear, however, that this assumption is proper.

Under these various assumptions, the unsteady increment in lift coefficient of the ellipse is found to be $-36 \alpha l/U$, of which about 92 percent is due to the unsteady movement of the separation points and the remainder is due to impulsive pressure. This lift increment gives the amplitude of a lift-hysteresis loop at maximum lift. The loop is counterclockwise, a result that can be related to the extremely migratory tendency of the separation point on the upper surface of the ellipse under a change in angle of attack in steady flow.

Finally, assuming oscillations of low reduced frequency, certain observations may be made concerning the shapes of hysteresis loops, and the validity of the idea of a viscous time lag in connection with unsteady lift: If the angle of attack undergoes harmonic oscillation, then the lift increment is also harmonic with a 90° phase lead or lag, depending on the sign used in the definition of $C_{l\alpha}$. In this case, the hysteresis loop is elliptic. If the angle of attack varies in a nonharmonic manner, then the variation of lift does not have the same dependence on time, and the idea of time lag is inappropriate.

LEWIS FLIGHT PROPULSION LABORATORY

NATIONAL ADVISORY COMMITTEE FOR AERONAUTICS

CLEVELAND, OHIO, August 17, 1955

APPENDIX

SYMBOLS

The following symbols are used in this report:

A, a	functions of η (eqs. (7))
B, b	functions of η (eqs. (9))
C, c	functions of η (eqs. (19b))
C_L	lift coefficient
$C_{L\alpha}$	rate of change of lift coefficient with angle of attack α
$C_{L\dot{\alpha}}$	rate of change of lift coefficient with $\dot{\alpha}$
d	function of η (eq. (20b))
F	universal function for boundary-layer calculation (eq. (5a))
f_1	universal function for boundary-layer calculation (eq. (13))
L	lift
l	semichord of elliptic cylinder (fig. 1)
n	coordinate measured normal to surface (eqs. (6), (36))
q	dimensionless outer velocity, $\equiv u_1/U$
R	function of η (eq. (3))
s	dimensionless coordinate measured along surface of ellipse (fig. 1)
t	time
U	stream velocity (a constant)
u	velocity parallel to surface
W	function related to unsteady boundary layer (eq. (15)), $\equiv qZ_\epsilon$
X	function related to unsteady boundary layer (eq. (18))
x	Cartesian coordinate of surface of ellipse
Y	function related to unsteady boundary layer (eq. (18))
y	Cartesian coordinate of surface of ellipse
Z	function related to momentum thickness of boundary layer (eq. (5a)), $\equiv \frac{\theta^2 U}{\nu l}$
α	angle of attack
$\dot{\alpha}$	time rate of change of α
$\Delta\alpha$	increment in angle of attack, $\equiv \alpha - \alpha^{(0)}$
β	thickness ratio of elliptic cylinder
Γ	circulation in outer flow
γ	coefficient of hysteresis in circulation (eq. (10))
δ	over-all thickness of boundary layer
δ^*	displacement thickness of boundary layer
ϵ	dimensionless angular velocity, $\equiv \dot{\alpha}l/U$
η	coordinate on surface of ellipse (fig. 1, eq. (2))
θ	momentum thickness of boundary layer
κ	function for boundary-layer calculation (eq. (5a))
ν	kinematic viscosity coefficient
ρ	density
τ	skin-friction coefficient
φ	velocity potential
ω	frequency

Subscripts:

- \bar{s}, \underline{s} evaluation at top or bottom separation point, respectively, of steady flow at maximum lift ($\alpha = \alpha^{(0)}$, $\epsilon = 0$)
- 0 evaluation at forward stagnation point, where $q = 0$

- 1 evaluation at outer edge of boundary layer
- evaluation at lower separation point
- Subscript notation is used for partial differentiation where convenient.
- Superscripts:
- (0) steady conditions at maximum lift
- (1) unsteady contribution due to movement of separation points
- (2) unsteady contribution due to impulsive pressure
- evaluation at upper separation point
- ' denotes ordinary derivatives

REFERENCES

- Mendelson, Alexander: Effect of Aerodynamic Hysteresis on Critical Flutter Speed at Stall. NACA RM E8B04, 1948. (See also Jour. Aero. Sci., vol. 16, no. 11, Nov. 1949, pp. 645-654.)
- Farren, W. S.: Reaction on a Wing Whose Angle of Incidence is Changing Rapidly. R. & M. No. 1648, British A. R. C., 1935.
- Halfman, Robert L., Johnson, H. C., and Haley, S. M.: Evaluation of High-Angle-of-Attack Aerodynamic-Derivative Data and Stall-Flutter Prediction Techniques. NACA TN 2533, 1951.
- Schnittger, Jan R.: Single Degree of Freedom Flutter of Compressor Blades in Separated Flow. Jour. Aero. Sci., vol. 21, no. 1, Jan. 1954, pp. 27-36.
- Sears, W. R.: A Theory of "Rotating Stall" in Axial Flow Compressors. Graduate School Aero. Eng., Cornell Univ., Ithaca (N. Y.). (Contract AF 33(038)-21406.)
- Emmons, H. W., Pearson, C. E., and Grant, H. P.: Compressor Surge and Stall Propagation. Trans. A.S.M.E., vol. 77, no. 4, May 1955, pp. 455-467; discussion, pp. 467-469.
- Marble, Frank E.: Propagation of Stall in a Compressor Blade Row. Jour. Aero. Sci., vol. 22, no. 8, Aug. 1955, pp. 541-554.
- Moore, Franklin K.: Unsteady Laminar Boundary-Layer Flow. NACA TN 2471, 1951.
- Howarth, L.: The Theoretical Determination of the Lift Coefficient for a Thin Elliptic Cylinder. Proc. Roy. Soc. (London), ser. A, vol. 149, no. A168, Apr. 10, 1935, pp. 558-586.
- Goldstein, Sydney, ed.: Modern Developments in Fluid Dynamics. Clarendon Press (Oxford), 1938.
- Lamb, Horace: Hydrodynamics. Sixth ed., Dover Pub., 1932.
- Schlichting, Herman: Grenzschicht-Theorie. Verlag und Druck G. Braun, Karlsruhe, 1951. (Available in English translation as NACA TM 1217.)

TABLE I.—RESULTS AT SEPARATION POINTS

Quantity	Separation point ($\kappa = -0.1567$)	
	Top (\bar{s})	Bottom (\underline{s})
η	80.0°	340.83°
R	0.985	0.364
q	1.210	-1.204
q_n	0.139	0.137
$q_{n\alpha}$	1.192	-7.95
$q_{n\dot{\alpha}}$	-0.0062	1.49
Z	1.11	0.41
Z_α	13.3	-5.6
Z_n	-1.405	0.52
X'	-55.6	-5.4
Y'	4.9	-4.2

REPORT 1292

INTENSITY, SCALE, AND SPECTRA OF TURBULENCE IN MIXING REGION OF FREE SUBSONIC JET ¹

By JAMES C. LAURENCE

SUMMARY

The intensity of turbulence, the longitudinal and lateral correlation coefficients, and the spectra of turbulence in a 3.5-inch-diameter free jet were measured with hot-wire anemometers at exit Mach numbers from 0.2 to 0.7 and Reynolds numbers from 192,000 to 725,000.

The results of these measurements show the following: (1) Near the nozzle (distances less than 4 or 5 jet diam downstream of the nozzle) the intensity of turbulence, expressed as percent of core velocity, is a maximum at a distance of approximately 1 jet radius from the centerline and decreases slightly with increasing Mach and/or Reynolds number. At distances greater than 8 jet diameters downstream of the nozzle, however, the maximum intensity moves out and decreases in magnitude until the turbulence-intensity profiles are quite flat and approaching similarity. (2) The lateral and longitudinal scales of turbulence are nearly independent of Mach and/or Reynolds number and in the mixing zone near the jet vary proportionally with distance from the jet nozzle. (3) Farther downstream of the jet the longitudinal scale reaches a maximum and then decreases approximately linearly with distance. (4) Near the nozzle the lateral scale is much smaller than the longitudinal and does not vary with distance from the centerline, while the longitudinal scale is a maximum at a distance from the centerline of about 0.7 to 0.8 of the jet radius. (5) Farther downstream this maximum moves out from the centerline. (6) A statistical analysis of the correlograms and spectra yields a "scale" which, although different in magnitude from the conventional, varies similarly to the ordinary scale and is easier to evaluate.

INTRODUCTION

Recent analyses by Lighthill (ref. 1) and by others (refs. 2 and 3) show that turbulence may be chiefly responsible for the noise from high-speed jets. However, a complete analysis relating turbulence to noise has not yet been made. Consequently, it is not known where the noise originates in the jet or which of the turbulence parameters, intensity, scale, or spectral distribution, is best suited to noise studies. Lighthill has suggested that each turbulent eddy might be considered as a single concentrated sound radiator. If Lighthill's suggestion is valid, it will be necessary to know the turbulence characteristics throughout the jet. The intensity of sound radiation will surely be related to the intensity of turbulence. Furthermore, the spectral distribu-

tion of turbulent energy might reasonably be expected to give information about the spectral distribution of sound energy.

Three regions of the jet need to be investigated (see fig. 1):

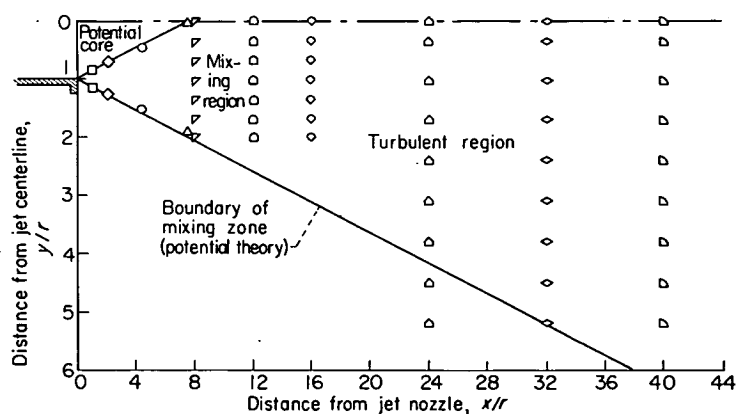


FIGURE 1.—Location of test points in subsonic jet.

(1) the central core, where the velocity profiles are flat and the intensity of the turbulent fluctuations is low; (2) the mixing region, which lies between the central core and the undisturbed air of the surroundings, where the velocity gradients are large and the intensity of turbulence is high; and (3) the region farther downstream where the central core and the mixing region blend into a completely turbulent airstream. The purpose of experiments in these regions is to measure the statistical parameters of the turbulence in the mixing zone and in the completely turbulent region of the jet.

Several investigators have reported the results of work in these regions (refs. 4 to 8). Reference 4 has only a limited amount of hot-wire data in the mixing zone, along with velocity-profile and turbulence-level measurements near the axis of the jet. Corrsin has made or has collaborated in making the most complete measurements in jets to be found in the literature (refs. 5 to 7). These investigations are of great interest and of much use, but the velocities investigated are small (<100 ft/sec). Hot-wire measurements in a unique form of a half-jet in which a solid wall replaces one side of the free mixing region are reported in reference 8.

In order to obtain data in speed ranges that are of more interest in jet noise research, a systematic investigation of the turbulent mixing region of a free jet was undertaken as part of the jet noise program at the NACA Lewis laboratory.

¹ Supersedes NACA Technical Notes 3561, "Intensity, Scale, and Spectra of Turbulence in Mixing Region of Free Subsonic Jet," by James C. Laurence, 1955; and 3576, "Further Measurements of Intensity, Scale, and Spectra of Turbulence in a Subsonic Jet," by James C. Laurence and Truman M. Stickney, 1956.

INSTRUMENTATION AND TEST FACILITIES

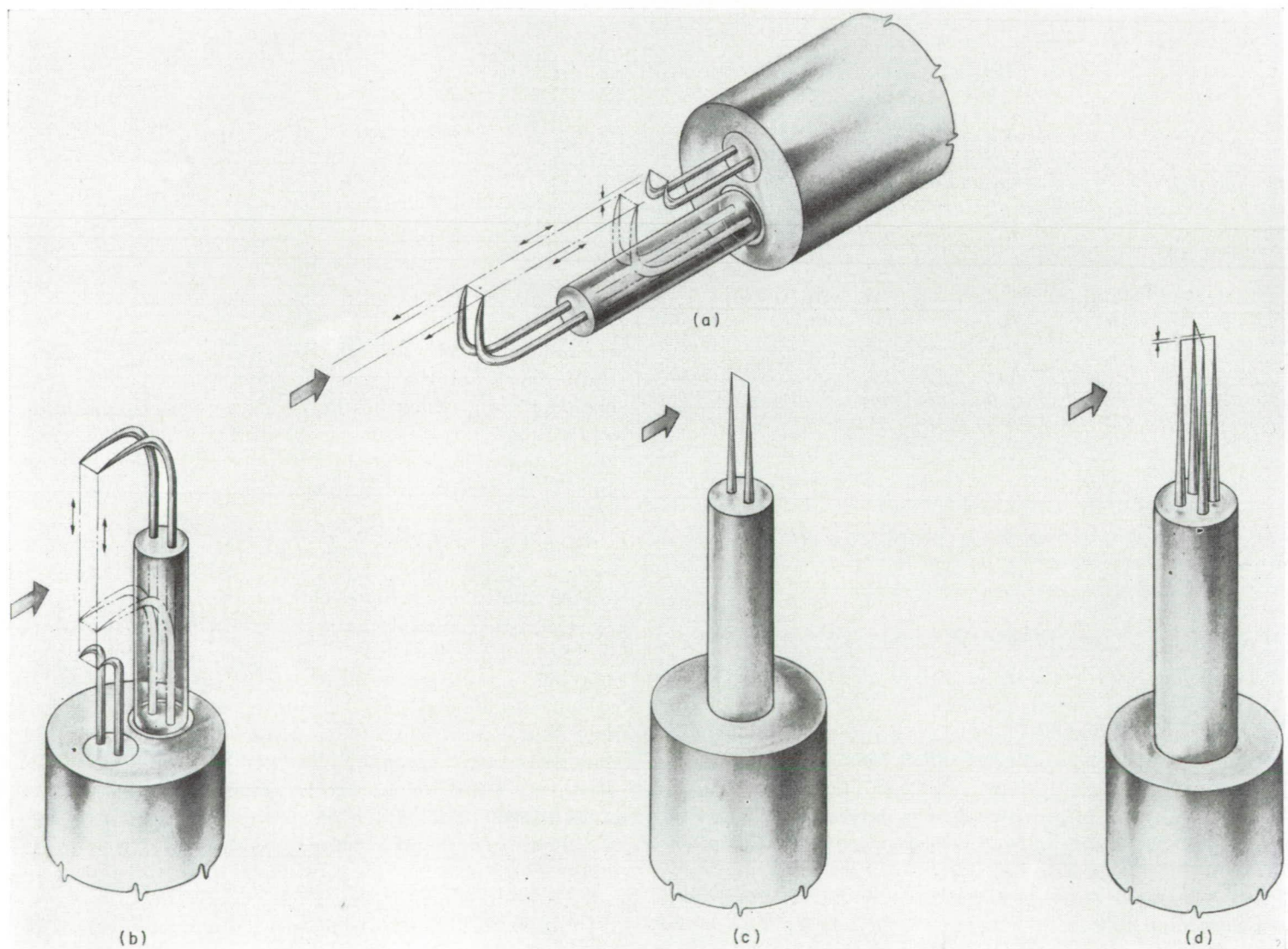
HOT-WIRE ANEMOMETERS

Principal interest was placed on measurements with the hot-wire anemometer of the statistical parameters of turbulence in the exit Mach number range from 0.2 to 0.7 and Reynolds numbers (based on jet radius) from 192,000 to 725,000. Since it was impossible to vary Mach numbers and Reynolds numbers independently, their combined effects are called Mach and/or Reynolds number effects herein.

The analysis of the results of these turbulence studies follows the statistical approach first introduced by Taylor (ref. 9). Dryden reviews this method in reference 10 and shows the success of this type of approach in dealing with isotropic turbulence. Similar approaches to the analysis of the results of studies of jet turbulence have been made also. But the results have not been very successful, especially in the mixing region of the jet. Hence, a statistical analysis is presented in this report which uses a different value of the "scale" or eddy size based on the energy spectrum of the turbulence.

The hot-wire anemometers used in this test were the constant-temperature anemometers described in reference 11. Constant-temperature anemometers were chosen instead of constant-current anemometers because of certain advantages: (1) The wire current is controlled by an electronic servosystem that protects against accidental wire burnout when the flow is suddenly reduced. (2) Since the bridge balance is maintained during flow changes, there are no compensation controls to set and no testing to determine whether the compensation is effective. (3) Finally, this instrument can follow large fluctuations in flow without appreciable error.

The hot-wire anemometer and the auxiliary equipment have been improved in several respects (see refs. 11 and 12). The direct-coupled amplifier has an improved frequency response, and its equivalent input noise has been decreased to



(a) Longitudinal correlation of velocity components in x -direction.

(b) Lateral correlation of velocity components in x -direction.

(c) Intensities and autocorrelations of velocity in x -direction.

(d) Velocity components in y -direction.

FIGURE 2.—Hot-wire-anemometer probes.

a value comparable with that of other hot-wire instruments (less than 100 microvolts). Frequency-response measurements made according to the methods described in reference 11 show an over-all response (amplifier, bridge, wire, and cables) of about 100 kilocycles.

HOT-WIRE PROBES

The hot-wire probes (fig. 2) were single- and double-wire probes. The double-wire probes were arranged in parallel and X-array. The parallel arrays (figs. 2(a) and (b)) were used to measure the longitudinal and lateral u velocity correlation coefficients, respectively. For the longitudinal correlations one wire was held fixed and the other was moved downstream. This wire was displaced not more than 0.005 inch towards the centerline of the jet to avoid interference from the flow over the first wire. A similar arrangement was used for the lateral correlations. Practical limitations on the separability of the wires limited the number of points for which measurements could be obtained. The measured correlations were assumed to be those at the position of the fixed wire. The X-array (fig. 2(c)) was employed to measure the v -component of the velocity fluctuations. The single-wire probe (fig. 2(d)) measured the u velocity intensities and all autocorrelations.

The wire material used in the tests was the 0.0002-inch tungsten wire evaluated in reference 11. The mounting procedure is an adaptation of the plating-soldering technique that was first used by the National Bureau of Standards (ref. 13).

SPECTRUM ANALYZERS

Two spectrum analyzers were used in obtaining the spectral density data. One of these has a constant narrow band pass (5 cps) with a frequency response from 20 to 16,000 cps; the other is a constant-percentage band-pass instrument with about the same frequency response. The filter characteristics of the two instruments are given in figure 3. The two analyzers give comparable spectral density curves within the general accuracy of the experiments.

TAPE RECORDER

A dual-channel tape recorder was used to record the signals from a single hot-wire-anemometer probe located in the airstream. These recordings were later used to obtain the autocorrelation coefficients.

ACTUATORS

The lateral positions of the probe were controlled by screw-type actuators. The longitudinal positions, however, were set by adjustments of a lathe carriage. The probes were aligned in the stream with reference to the centerline of the jet. This aerodynamic centerline was determined from total-pressure measurements in the jet. A plug was machined to fit the exit nozzle of the jet, and a steel wire was stretched along the centerline to a point on the centerline far downstream in the jet (approx. 12 ft). A telescope mounted at this point helped in relocating the probes after a probe failure without restringing the steel wire.

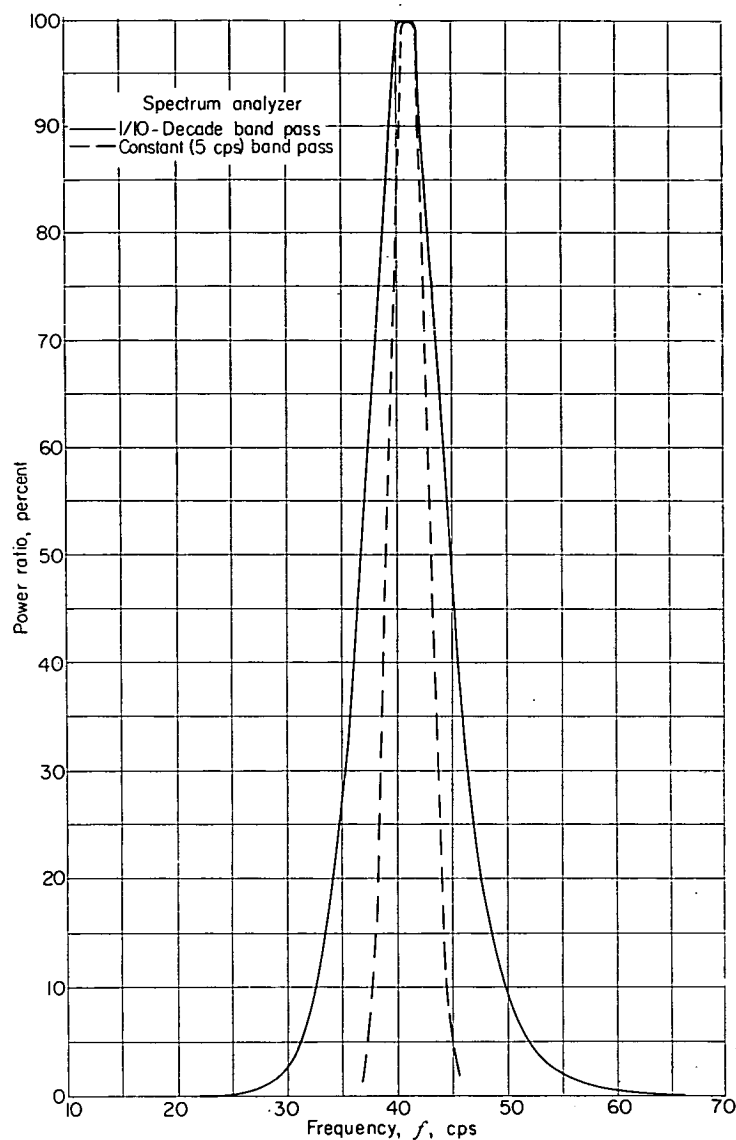


FIGURE 3.—Band-pass filter characteristics.

TEST FACILITIES

The subsonic jet and associated plenum chamber used in these experiments are shown schematically in figure 4. The jet has a 3.5-inch-diameter nozzle at the end of a bell-

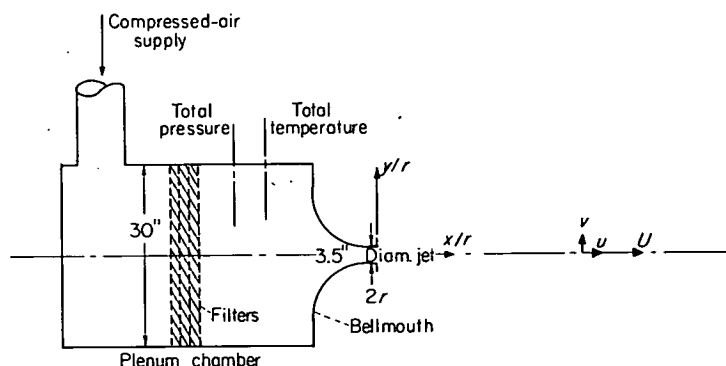


FIGURE 4.—Schematic diagram of subsonic jet, plenum chamber, filters, and location of pressure- and temperature-measuring instruments.

mouth which is attached to a large plenum chamber. The turbulence intensity in the plenum chamber varied from 4 to 5 percent over the range of the test conditions. The whole is connected to a compressed-air supply. A filter is included as an integral part of the plenum chamber. It successfully removes a large part of the dust and pipe scale sometimes found in similar airstreams. The flow is adjusted by means of electrically controlled valves throughout the subsonic range of Mach numbers. The instruments for measuring total pressure and temperature are placed in the plenum chamber and read remotely. Figure 1 shows the approximate location of the testing points in the jet, and table I gives the exact coordinates.

TABLE I.—LOCATION OF TEST POINTS IN SUBSONIC JET

Distance from jet nozzle, z/r	Distance from jet centerline, y/r								
1.14	1.206	1.154	1.103	1.051	1.00	0.949	0.846	0.794	0.743
2.29	---	1.308	1.206	1.103	1.00	.897	.794	.692	---
4.58	---	1.411	1.206	---	1.00	.794	.589	.383	---
7.6	---	1.686	1.500	1.343	1.00	.657	.314	-.029	---
8	---	2.000	1.714	1.286	1.00	.714	.286	0	---
12	---	2.00	1.714	1.286	1.00	.714	.286	0	---
16	---	2.00	1.714	1.286	1.00	.714	.286	0	---
24	5.143	4.460	3.772	3.088	2.400	1.715	1.028	.343	0
32	5.143	4.460	3.772	3.088	2.400	1.715	1.028	.343	0
40	5.143	4.460	3.772	3.088	2.400	1.715	1.028	.343	0

EXPERIMENTAL PROCEDURE

INTENSITY MEASUREMENTS

A single hot wire was used to measure the u -component of the turbulent intensity. An X-wire probe was used to measure the v -component. The hot-wire signal (or the instantaneous difference between the two X-wires) was measured directly by a root-mean-square voltmeter. Reference 11 describes the root-mean-square voltmeter (average-square computer) which was used in an improved form for the first half of the intensity surveys made. A true rms voltmeter was used for the remainder of the data. It gives a precise wide-band squaring action that is unaffected by normal ambient temperature variations and, in general, is more satisfactory than the other instrument.

The turbulence intensity was calculated by methods outlined in references 11, 13, and 14.

CORRELATION MEASUREMENTS

Velocity correlations in space and in time are of interest in the noise problem. Two hot wires can be used to obtain the lateral and longitudinal correlations. The wires are mounted on telescoping tubes that can be displaced either laterally or longitudinally with respect to each other by actuators. During the actual measurements, the fluctuating components of the two hot-wire signals, say ϵ_1 and ϵ_2 , are led to a correlator that measures $\epsilon_1 \epsilon_2$, ϵ_1^2 , and ϵ_2^2 .

If a linear relation between the velocity fluctuation and the hot-wire voltage is assumed, that is,

$$\left. \begin{aligned} u_1 &= k_1 \epsilon_1 \\ u_2 &= k_2 \epsilon_2 \end{aligned} \right\} \quad (1)$$

as is done in reference 15, there results, upon combining the signals,

$$R = \frac{\overline{u_1 u_2}}{\sqrt{\overline{u_1^2}} \sqrt{\overline{u_2^2}}} \quad (2)$$

$$R = \frac{k_1 k_2 \overline{\epsilon_1 \epsilon_2}}{\sqrt{k_1^2 \overline{\epsilon_1^2}} \sqrt{k_2^2 \overline{\epsilon_2^2}}} \quad (3)$$

$$= \frac{\overline{\epsilon_1 \epsilon_2}}{\sqrt{\overline{\epsilon_1^2}} \sqrt{\overline{\epsilon_2^2}}} \quad (4)$$

(All symbols are defined in appendix A.)

The displacement of the wires in the lateral direction gives the lateral correlation coefficient; in the longitudinal, the longitudinal correlation coefficient.

An autocorrelation coefficient, that is, the correlation between two segments of the same signal separated in time, can be obtained if some method is devised to obtain from the signal of a single hot wire another signal delayed in time with respect to the first. An instrument that provides time delays of this nature (described in refs. 16 and 17) was designed and built at the NACA Lewis laboratory (ref. 18).

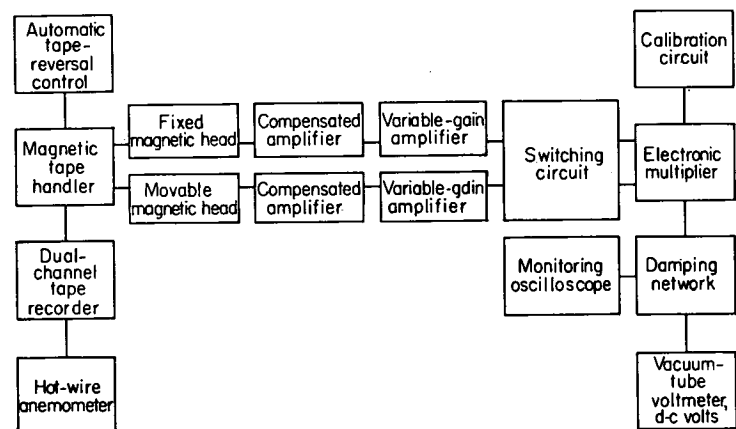


FIGURE 5.—Block diagram of correlation computer.

In general, this correlator (see fig. 5) works as follows: The signal from a single hot wire is recorded simultaneously on two channels of a dual-channel tape recorder. A special playback instrument uses two pickup heads, one of which can be displaced with respect to the other by means of a micrometer screw. When the two heads are in such a position that they are picking up identical signals, the correlation between these signals is necessarily unity. But if the movable head is displaced so that it is picking up a signal recorded a short time earlier or later, the two signals are of course, different. These two signals are the two voltages ϵ_1 and ϵ_2 considered in equation (1). The correlation coefficient R is then the autocorrelation coefficient R_t .

The value of the time interval Δt is obtained from the actual displacement of the head and the constant tape speed

$$\Delta t = \frac{d}{S} \quad (5)$$

It is rather obvious that there should be a relation between the autocorrelation and the longitudinal correlation coefficients involving the stream velocity U and the head separation (ref. 19).

An extension of this method can be made to measure the autocorrelation of the v -components of the turbulence. In this method the difference signal from an X-wire probe

located in the stream is recorded simultaneously on both channels of the recorder and played back in the usual way.

The double correlator of reference 11 was used to obtain correlations of the hot-wire signals for the first half of the program. The ratios were calculated numerically, because the ratio meters that are sometimes used are unreliable. Inaccuracy results from the use of an average-square computer, which depends upon the operating characteristics of a vacuum tube to obtain the square of the sum and of the difference of two voltages in order to apply the quarter-square principle of multiplication.

After about half the data were obtained, an electronic multiplier replaced the double correlator. This multiplier (described in ref. 18) does not use the quarter-square principle of multiplication. The multiplier operates from d.c. to 50 kilocycles (3-db point) and is useful in obtaining correlation coefficients. Two channels are available to give the average product of two input voltages as well as their average squares. The outputs can be read on any high-impedance d-c voltmeter. By properly adjusting the level of the inputs, the correlation coefficients can be read directly.

SPECTRUM OF TURBULENCE

If the hot-wire signal is analyzed by means of a series of band-pass filters, a spectrum results. The relative energy spectrum is more fully discussed in references 10 and 20. Most of the spectra presented here were recorded on a paper strip chart by an analyzer of constant percentage (1/10-decade) band width. The switching from one filter to the next is done automatically and in synchronization with the movement of the chart. The spectrum recordings are made rapidly (about 1 per min) and with little attention by the operator.

The chart recordings are in decibels above any practical reference voltage, and at one point on the chart the total voltage level for the entire range of frequencies is recorded. The conversion to spectral density is as follows: By definition,

$$\left. \begin{aligned} N_b &= 20 \log \frac{\epsilon_{w,b}}{\epsilon_{ref}} \\ N_{tot} &= 20 \log \frac{\epsilon_{w,tot}}{\epsilon_{ref}} \end{aligned} \right\} \quad (6)$$

Therefore,

$$\left. \begin{aligned} \frac{\epsilon_{w,b}^2}{\epsilon_{ref}^2} &= \text{antilog} \frac{N_b}{10} \\ \frac{\epsilon_{w,tot}^2}{\epsilon_{ref}^2} &= \text{antilog} \frac{N_{tot}}{10} \end{aligned} \right\} \quad (7)$$

Hence, the spectral density function

$$\mathcal{F}(f) = \frac{1}{B} \frac{\text{antilog} \frac{N_b}{10}}{\text{antilog} \frac{N_{tot}}{10}} \quad (8)$$

where B is the band-pass width of the filters.

The resulting display of the spectral density function with frequency shows the content of the signal in each individual frequency band. This method of analysis is important for two reasons: (1) It tells the experimenter the frequency bands

in which most of the energy is concentrated, and (2) the spectrum can be used to obtain the average eddy size.

SCALE OF TURBULENCE

The scales of turbulence \mathcal{L} (ref. 21) are defined in many applications as follows:

Longitudinal:

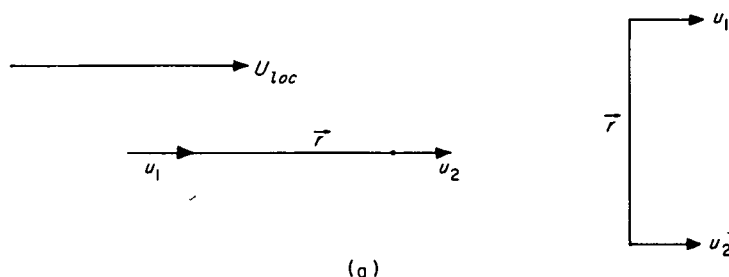
$$\mathcal{L}_x = \int_0^\infty R_x dx \quad (9a)$$

Lateral:

$$\mathcal{L}_y = \int_0^\infty R_y dy \quad (9b)$$

$$\mathcal{L}_z = \int_0^\infty R_z dz \quad (9c)$$

If



then

$$\mathcal{L}_x = \int_0^\infty \frac{\overline{u_1 u_2}}{\sqrt{\overline{u_1^2}} \sqrt{\overline{u_2^2}}} dr$$

These scales are generally regarded as the physical dimensions in the x - (longitudinal), y - (radial), and z - (tangential) directions of the average eddy in the flow. The three scales, as defined in equations (9), are all important in a study of jet noise. However, variations in the tangential direction are not included in this report. Reference 21 shows that the correlation coefficient R is related to the spectral density as follows:

$$R_x = \int_0^\infty \mathcal{F}(f) \cos \frac{2\pi f x}{U} df \quad (10)$$

and, inversely,

$$\mathcal{F}(f) = \frac{4}{U} \int_0^\infty R_x \cos \frac{2\pi f x}{U} dx \quad (11)$$

Thus, there are two possible ways to obtain the longitudinal correlation coefficient. One is to measure it directly; the other is to obtain it from the turbulence spectrum and equation (10). If the longitudinal correlation coefficient R_x is assumed to be exponential in form, that is,

$$R_x = e^{-x/\mathcal{L}_x} \quad (12)$$

then the transform (eq. (11)) can be readily worked out as (ref. 10)

$$\mathcal{F}(f) = \frac{\frac{4\mathcal{L}_x}{U}}{1 + \left(\frac{2\pi\mathcal{L}_x f}{U}\right)^2} \quad (13)$$

Analogous relations are available for the transverse correlations.

The methods just outlined have been used to great advantage in the analysis of turbulence induced by grids in wind tunnels (ref. 21). Similar application to the flow in subsonic jets does not prove to be so successful, however, particularly in the mixing region close to the nozzle of the jet, since the definitions do not apply to shear flows.

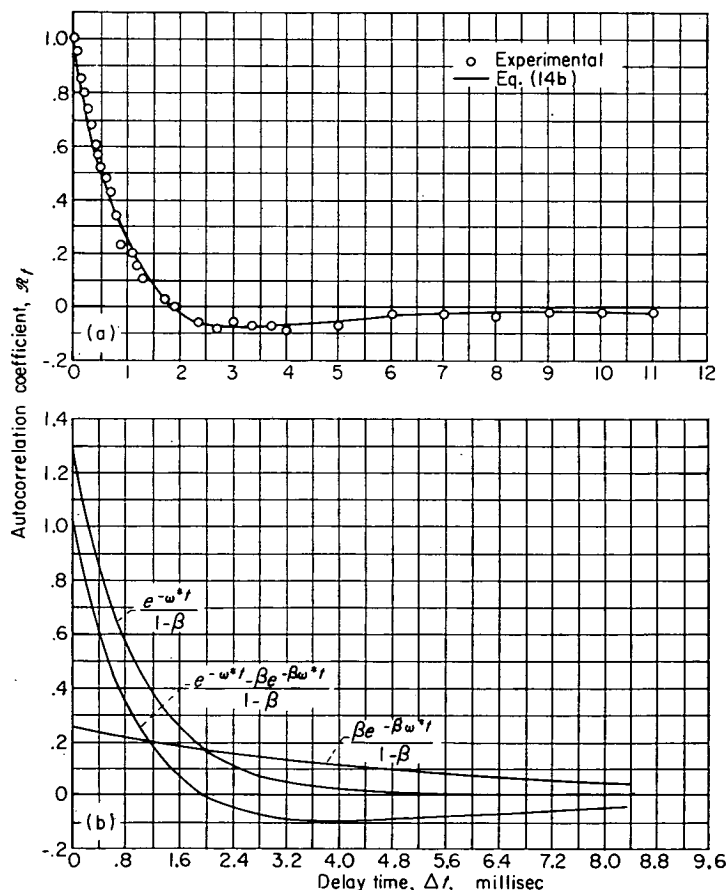
In particular, the correlograms that resulted from the two-wire measurements and the autocorrelation measurements in the jet are not fitted very well by a single exponential. A typical correlogram is shown in figure 6(a). It is apparent that the shape of this curve is different from a pure exponential. In order to find a curve of best fit for this data, a function was built up which is the algebraic sum of two exponentials, as shown in figure 6(b). The correlation fitting function is then of the following form (see appendix B):

$$R_x = \frac{e^{-x/\Lambda_x} - \beta e^{-\beta x/\Lambda_x}}{1 - \beta} \quad (14a)$$

or

$$R_t = \frac{e^{-\omega^* t} - \beta e^{-\beta \omega^* t}}{1 - \beta} \quad (14b)$$

In these equations the constants β , Λ_x , and ω^* have specialized meanings. The Λ_x is a characteristic eddy size that is different in magnitude from the longitudinal scale of the turbulence \mathcal{L}_x , and ω^* is related to this eddy size by $\omega^* = U/\Lambda_x$. The parameter β is related to the cut-off frequencies (upper and lower) of the spectral density curves by the relation



(a) Typical autocorrelogram.

(b) Method used to approximate autocorrelograms.

FIGURE 6.—Autocorrelograms; $\beta=0.2$; $\omega^*=6283$ radians per second.

$$\frac{f_l}{f_u} = \frac{\beta}{(1+\beta)^2}$$

The cut-off frequency is defined in the usual electronic sense as the intersection of the asymptotes of the spectral density curve with a horizontal line through the maximum point of the spectral density curve. The relation between the distance x and the time t in these experiments is the velocity of the stream; that is (ref. 20),

$$x = U_{loc} t \quad (15)$$

Equations (14) can be adjusted by means of the quantities Λ_x , β , and ω^* to fit the correlograms obtained experimentally.

It is now obvious that the conventional definition of the scales of the turbulence (eqs. (9)) is no longer valid, since the integral is always zero if R has the form of equations (14).

The parameter β , however, is useful in obtaining a measure of the eddy size, which, after all, is what is meant by the scale of the turbulence. In equation (14a), if $R_x=0$,

$$\Lambda_x = \frac{x_0(\beta-1)}{\ln \beta} \quad (16)$$

where x_0 is the value of the wire separation when R_x is first equal to zero. This definition of scale is related to two quantities that are quite easy to evaluate from the experimental correlograms and spectra: (1) the first crossing of the abscissa by the correlation curve, and (2) the parameter β , which is related to the ratio of the low- to the high-frequency cut-off of the spectral density curves.

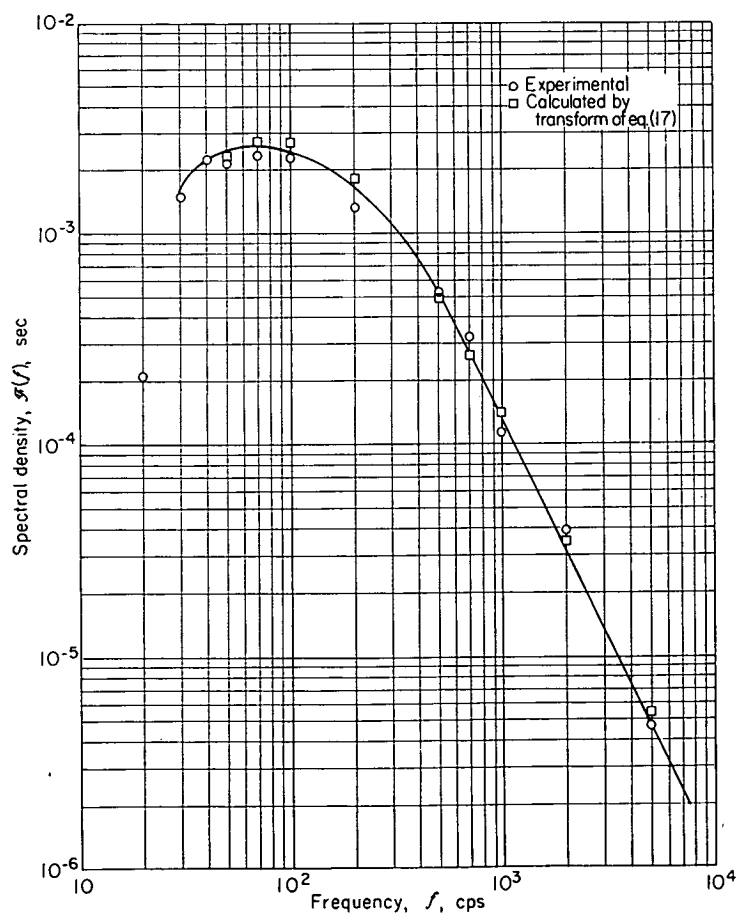


FIGURE 7.—Typical spectral density curve.

The transform of equation (14a) can be obtained with the following result:

$$\mathcal{F}(f) = \frac{1+\beta}{4f^*} \frac{\left(\frac{f}{f^*}\right)^2}{\left[1 + \left(\frac{f}{f^*}\right)^2\right] \left[\beta^2 + \left(\frac{f}{f^*}\right)^2\right]} \quad (17)$$

where β is the same as in equations (14), and

$$f^* = \frac{\omega^*}{2\pi} \quad (18)$$

Figure 7 shows a typical spectral density curve obtained in the completely turbulent region of a subsonic jet. It represents data obtained at the same time and at the same location in the same jet as the correlogram of figure 6(a). A spectrum fitting function of the type of equation (17) was calculated by the methods described in appendix B from the correlation curve. These calculated points are shown for comparison with the experimentally obtained spectrum.

ACCURACY OF MEASUREMENTS

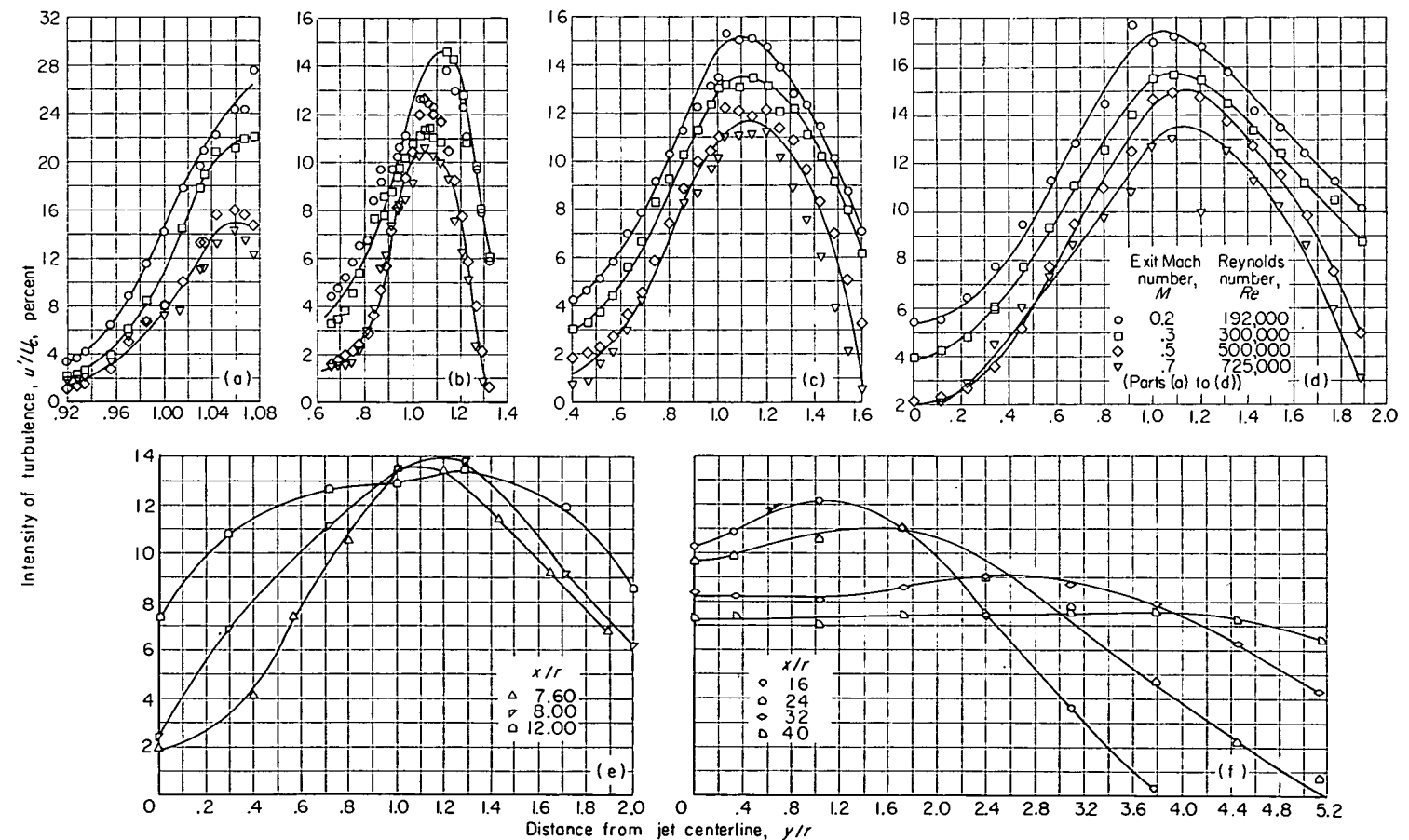
The accuracy of the hot-wire measurements made with the constant-temperature instrument is discussed in references 11 and 12. It is sufficient to say here that these measurements

are made as accurately as the usual hot-wire measurements. In measuring quantities that vary randomly with time, a certain amount of discretion must be used in obtaining averaged readings of meter pointers that are jumping about. Reference 12 includes an evaluation of the NACA Lewis laboratory hot-wire equipment and experimental techniques and compares them with other systems.

No corrections have been made to any of the hot-wire results for the finite length of the wire. In these measurements, the scales of turbulence were much greater than the length of the hot wires (0.080 and 0.040 in.).

Some of the intensities measured were large compared with the local mean flow. In the constant-temperature method of anemometry, these large intensities can be evaluated (see appendix F, ref. 11). In the usual method and in the method used herein, however, the root mean square of the voltage fluctuations is used in place of their instantaneous values. This approximation is valid only for small values of the fluctuations. Nevertheless, vibration studies (e. g., ref. 5) have shown that the hot-wire anemometer itself is capable of following fluctuations in a single direction faithfully up to 60 to 70 percent.

When the fluctuations in U become large, errors will be introduced because of the interaction of the components of the turbulence; that is, the effect of u , v , and w on U and on



(a) Distance from jet nozzle x/r , 1.14. (b) Distance from jet nozzle x/r , 2.29. (c) Distance from jet nozzle x/r , 4.58. (d) Distance from jet nozzle x/r , 7.60. (e) Distance from jet nozzle x/r , 7.60, 8, and 12. Exit Mach number, 0.3; Reynolds number, 300,000. (f) Distance from jet nozzle x/r , 16 to 40. Exit Mach number, 0.3; Reynolds number, 300,000.

FIGURE 8.—Intensity of turbulence in percent of core velocity at various exit Mach and/or Reynolds numbers.

each other. These errors are considered in reference 12, where actual corrections are worked out. No such corrections have been applied to the results shown in this report.

Some of the correlations measured with the average-square computer and the sum and difference circuits (quarter-square multiplication) show values greater than unity. This is, of course, impossible, and such readings must be the result of inaccuracies in the multiplication. In most of these instances enough points are available to fair a reasonable curve without considering these points ($R > 1$).

The largest sources of error in these experiments were (1) the inaccuracy in repeating setups after probes were changed, (2) the fluctuations in pressure in the air supply, which caused fluctuations in the mean flow level, and (3) the presence in the flow of periodic fluctuations due to sound or pressure waves and floor vibrations. It is believed that the measurements reported herein for turbulence intensities less than 30 percent are not in error by more than ± 10 percent.

RESULTS AND DISCUSSION

The results of these hot-wire measurements are presented in a series of graphs and tables. In general, the points for which the measurements are reported are shown in figure 1 and are tabulated in table I. However, for the intensity surveys many more points were used. For some of the correlation measurements, physical limitations in the amount of wire separation made it impossible to obtain results at all the points indicated in figure 1.

The order in which the results are presented has no special significance. The surveys are given for only one-half of the jet, because the jet was found to be essentially axisymmetric.

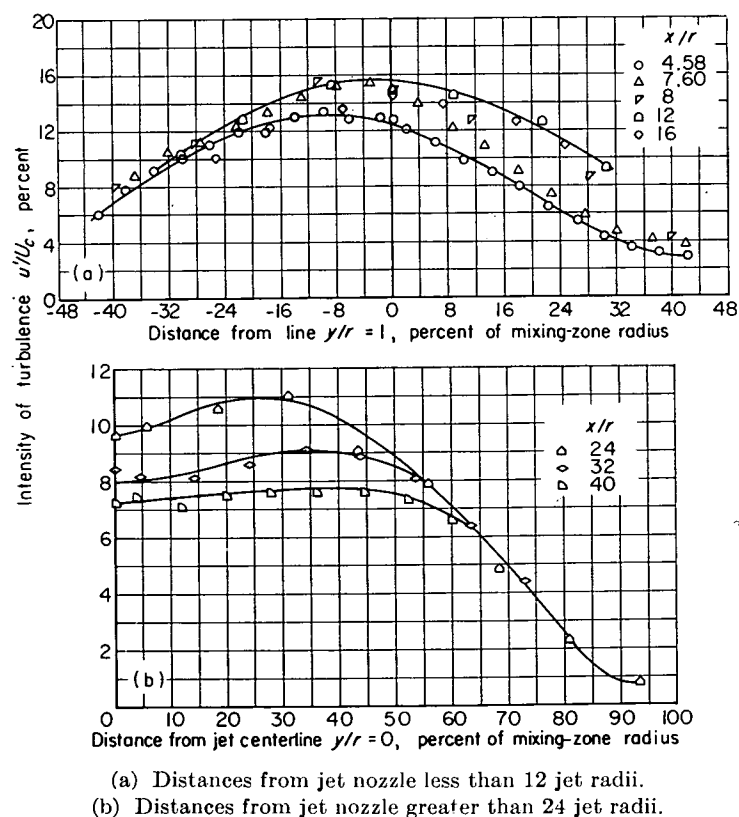


FIGURE 9.—Similarity of turbulence-intensity profiles. Exit Mach number, 0.3; Reynolds number, 300,000.

INTENSITY OF TURBULENCE

The intensity measurements were made at values of the nondimensional radius y/r distributed across the mixing zone for several positions downstream of the jet nozzle. The results of these measurements are shown in figures 8 to 10. In figures 8(a), (b), (c), and (d), the turbulence intensity in percent of central-core velocity is presented for x/r values of 1.14, 2.29, 4.58, and 7.60, respectively, for four Mach numbers (0.2, 0.3, 0.5, and 0.7). In figures 8(e) and (f), the intensity is shown only for a Mach number of 0.3 at x/r values of 7.60, 8, 12, 16, 24, 32, and 40.

One point of particular interest is shown by figure 9. Figure 9(a) shows that the turbulence-intensity profiles near the jet nozzle (where the potential core is still present) are similar in shape and little different in actual magnitude of the intensity of turbulence. As the distance from the nozzle increases, however, this similarity disappears only to develop again in a different form far downstream. Figure 9(b) shows the reappearance of a degree of similarity, especially at points removed from the centerline of the jet. Here the turbulent velocity profiles are becoming quite flat for a large part of the mixing zone, the maximum value of the intensity moving out from the jet centerline. Figures 10(a) to (d) show the intensity of turbulence in percent of local mean velocity for the same Mach numbers and the same x/r values as figures 8(a) to (d).

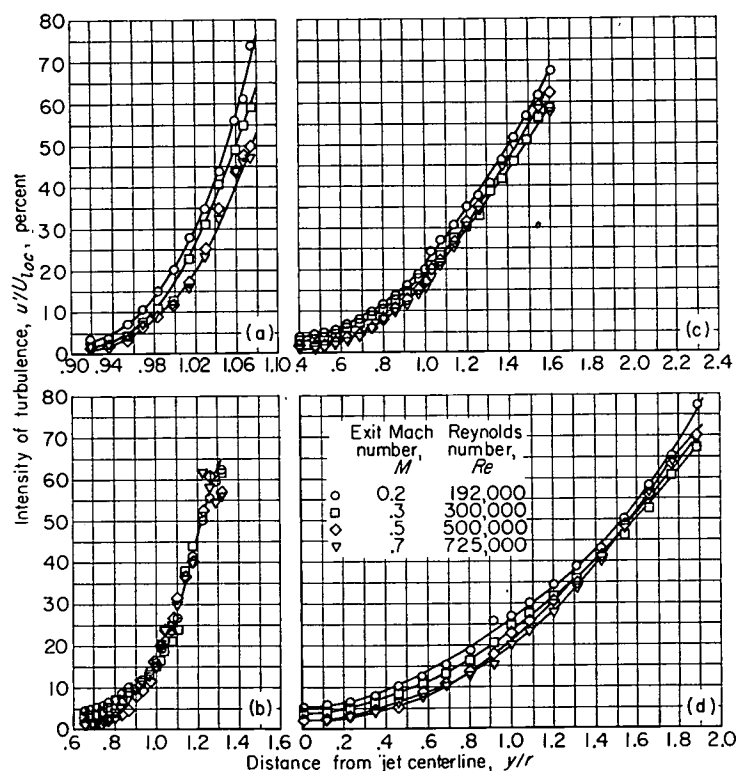
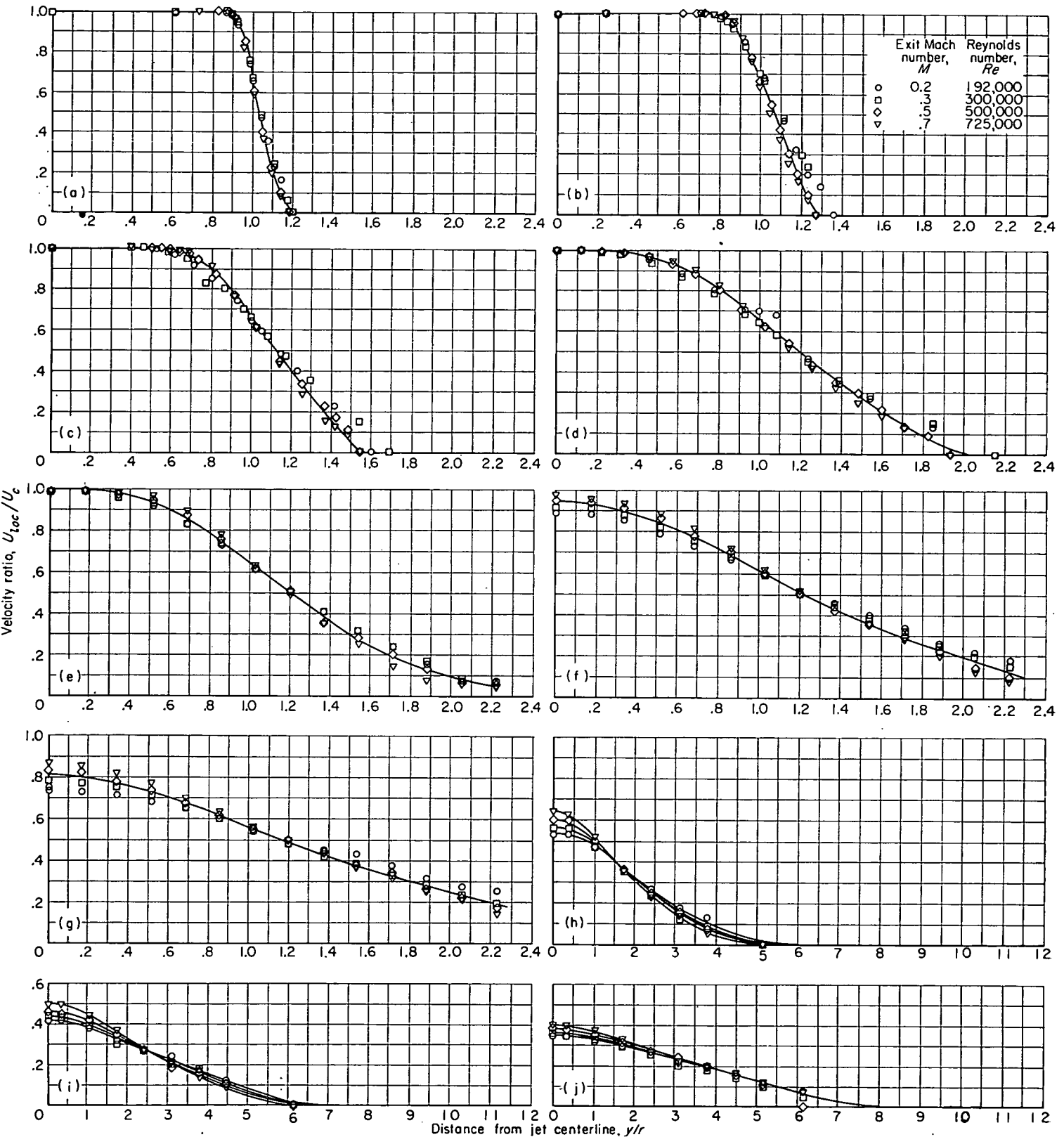


FIGURE 10.—Intensity of turbulence in percent of local velocity at various exit Mach and/or Reynolds numbers.

The mean velocity profiles (obtained from total-pressure surveys) are shown in figure 11. The local mean velocity in terms of central-core velocity is plotted against the nondimensional radius y/r for the entire range of Mach numbers and x/r values up to 40.



- (a) Distance from jet nozzle x/r , 1.14.
 (c) Distance from jet nozzle x/r , 4.58.
 (e) Distance from jet nozzle x/r , 8.
 (g) Distance from jet nozzle x/r , 16.
 (i) Distance from jet nozzle x/r , 32.

- (b) Distance from jet nozzle x/r , 2.29.
 (d) Distance from jet nozzle x/r , 7.60.
 (f) Distance from jet nozzle x/r , 12.
 (h) Distance from jet nozzle x/r , 24.
 (j) Distance from jet nozzle x/r , 40.

FIGURE 11.—Mean velocity profiles.

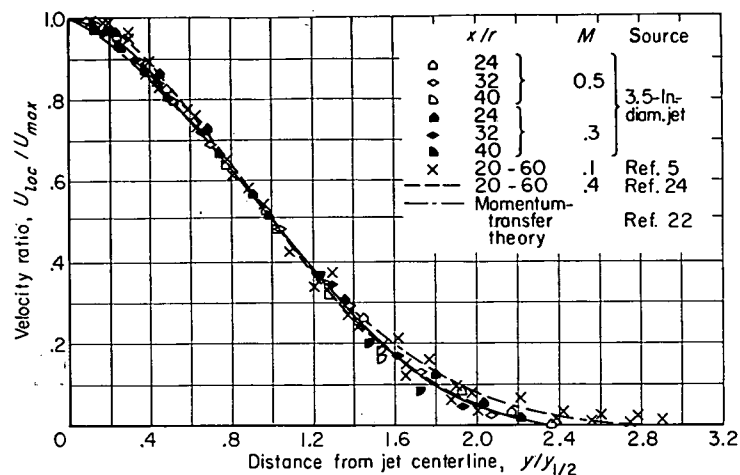


FIGURE 12.—Similarity of velocity profiles in region of fully developed flow. ($y_{1/2}$ is distance from axis where $U_{loc} = \frac{1}{2} U_{max}$.)

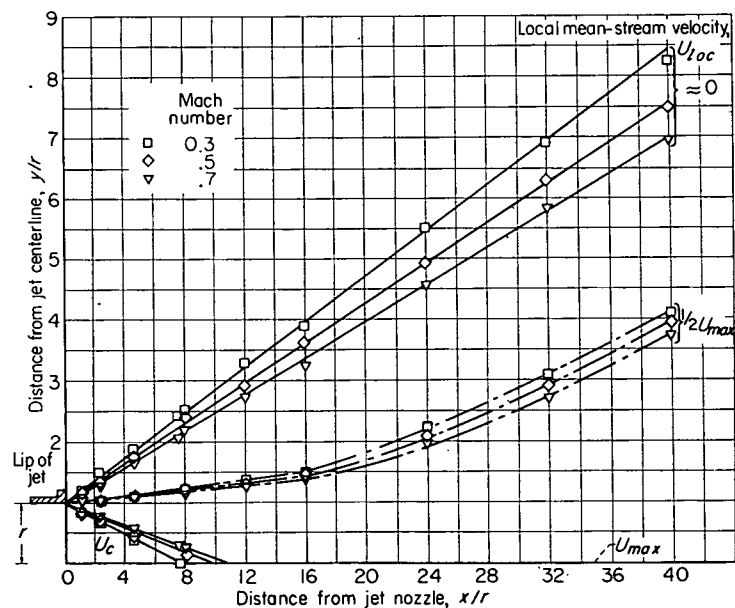


FIGURE 13.—Effect of potential-core Mach number on boundaries of 3.5-inch-diameter jet.

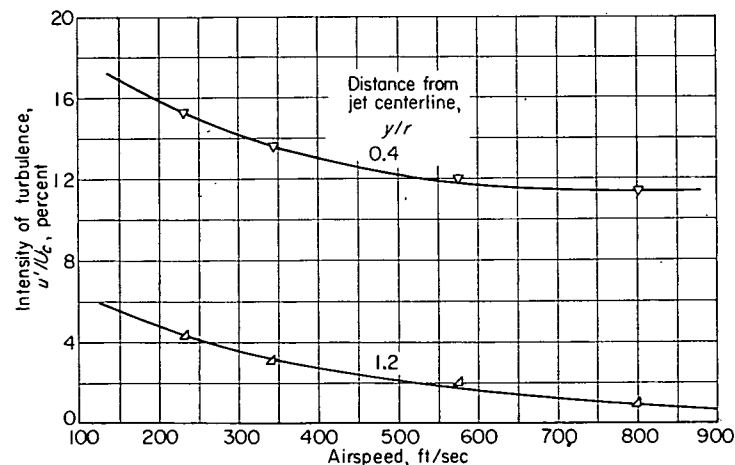


FIGURE 14.—Variation of intensity of turbulence with airspeed for circular nozzle. Distance from nozzle x/r , 4.58.

The mean velocity profiles are also similar, as is shown in figure 12, where the ratio of the local mean velocity to the maximum mean velocity is plotted against a nondimensional mixing-zone width. This width is defined as the ratio of the distance from the jet centerline to the point where the local velocity is half the maximum velocity. The figure shows very well the degree of similarity for all distances from the jet nozzle as well as for the different Mach numbers. Also shown is a comparison with the theoretical momentum-transfer results as given by reference 22.

The result of these mean velocity studies is shown in figure 13, where the approximate jet boundaries are shown for the different Mach numbers. The positions of the zero velocity, the one-half maximum, and the core velocity are shown.

A comparison of figures 8 and 11 shows that the maximum intensity occurs near the points of inflection of the velocity profiles at approximately 1 jet radius from the centerline for distances from the jet nozzle up to about 10 jet radii. As the distance from the nozzle increases, however, this position of the maximum intensity begins to move out from the jet centerline, and similarity of the profiles tends to develop far downstream from the nozzle. The curves show that the line of maximum shear moves out from the centerline as the distance downstream of the jet nozzle increases.

The observed turbulence levels decreased with increasing Mach and/or Reynolds number throughout the jet. Figure 14 shows that the level of turbulence in the central core and at the position of maximum intensity decreased with increasing exit Mach and/or Reynolds number. It is not clear, however, that the turbulence which is generated in the jet mixing process would change with jet Mach number if there were no initial turbulence in the jet. The decrease in intensity shown for the core may possibly explain the decrease noted in the mixing zone. If this explanation is accepted, the results of the intensity surveys are in a fair agreement with those reported in references 5 and 8.

The turbulence intensity of the v -component of the velocity fluctuations was measured at four points in the jet. These measurements, along with the corresponding u intensities, are included in table II. This table shows that the u and v intensities are not equal but may differ by about as much as 17 percent.

TABLE II.—COMPARISON OF u AND v INTENSITY MEASUREMENTS

x/r	y/r	$\frac{\sqrt{u'^2}}{U_{loc}}$	$\frac{\sqrt{v'^2}}{U_{loc}}$	Difference Δ , percent
6	1.00	0.241	0.242	0.4
6	0	.101	.118	16.8
8	1.00	.266	.241	-10.4
8	0	.148	.134	-10.4

Δ Difference is in percent of smaller intensity.

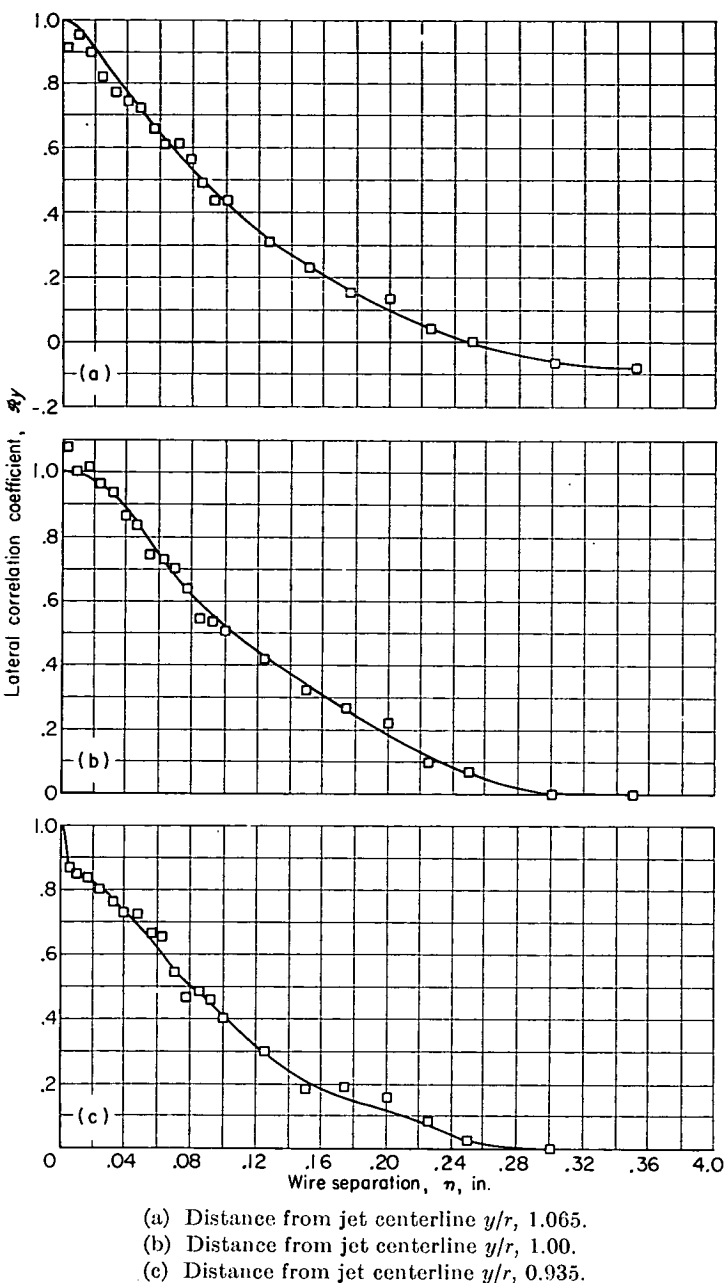


FIGURE 15.—Lateral velocity correlations. Distance from jet nozzle x/r , 1.14; exit Mach number, 0.3; Reynolds number, 300,000.

LATERAL CORRELATION COEFFICIENTS

For each distance from the jet nozzle x/r , three different distances from the jet centerline y/r were used in the measurement of lateral correlation coefficients for all the Mach numbers investigated. At positions downstream greater than approximately 1 jet diameter, the wires on the probes could not be separated far enough to reach zero correlation. Figures 15 and 16 are typical of the results for the lateral correlation coefficients. Figure 15 shows the variation of the lateral correlation for x/r of 1.14 and for three y/r values. Figure 16 shows the lateral correlation for y/r of 1.00 at several x/r values. Also shown on the curves of figure 16 are exponential curves that have been fitted to the data. The agreement is good for x/r values of 7.60 and 4.58 but only fair for x/r of 2.29 and 1.14. In some cases, however, this agreement justifies the use of equation (12) to obtain equation (13) for the spectral density function.

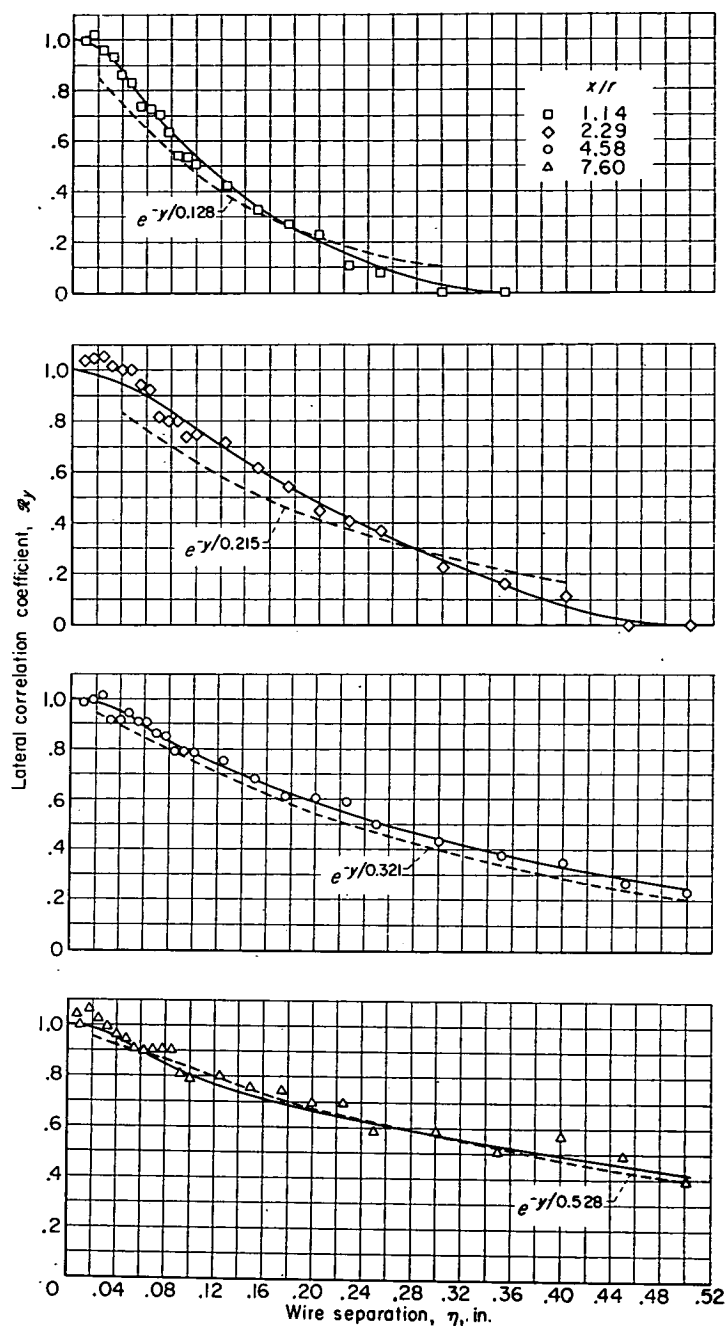


FIGURE 16.—Lateral velocity correlations. Distance from jet centerline y/r , 1.00; exit Mach number, 0.3; Reynolds number, 300,000.

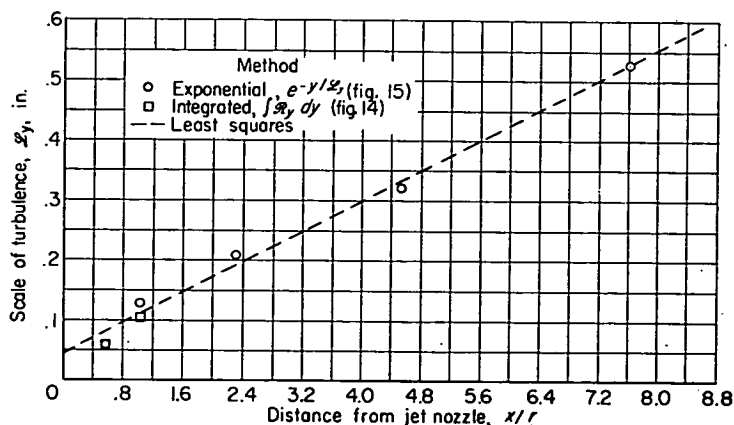


FIGURE 17.—Variation of lateral scale with distance from jet nozzle. Distance from jet centerline y/r , 1.00; exit Mach number, 0.3; Reynolds number, 300,000.

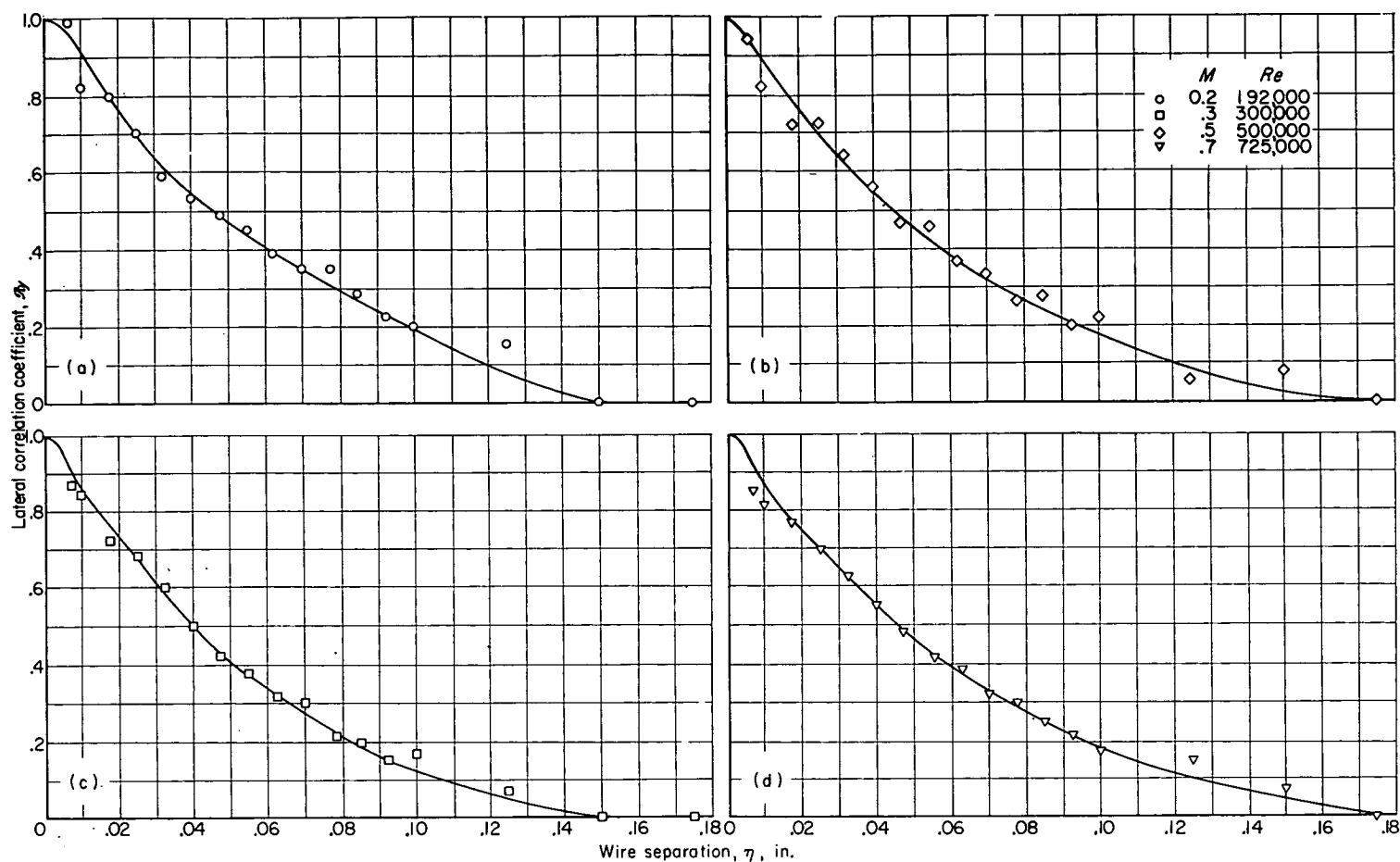


FIGURE 18.—Effect of exit Mach and/or Reynolds number on lateral velocity correlations. Distance from jet nozzle x/r , 0.57; distance from jet centerline y/r , 1.00.

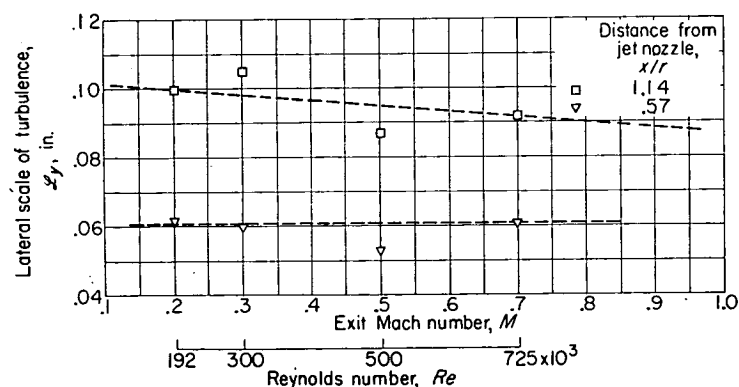


FIGURE 19.—Effect of exit Mach and/or Reynolds number on lateral scale of turbulence. Distance from jet centerline y/r , 1.00.

LATERAL SCALE OF TURBULENCE

The lateral correlation data of figures 15 and 16 for $y/r=1.00$ are compared in figure 17, where the lateral scale of turbulence is shown as a function of distance downstream of the nozzle. An exponential curve was faired through the data points of the correlation curves (fig. 16), and a representative value of the scale was obtained. The results show an approximately proportional increase of lateral scale with distance from the jet nozzle. The least-square line gives the relation

$$\mathcal{L}_y = 0.036x + 0.043 \quad (19)$$

which compares with

$$\mathcal{L}_y = 0.028x \quad (20)$$

given in reference 8. Little, if any, variation of the lateral scale was found with distance from the jet centerline.

MACH AND/OR REYNOLDS NUMBER EFFECTS

In figure 18 are shown the effects of exit Mach and/or Reynolds number on the lateral correlation coefficient R_y as a function of wire separation for Mach numbers of 0.2, 0.3, 0.5, and 0.7. These curves show no variation of lateral correlation coefficient with Mach and/or Reynolds number and show clearly that there is little or no effect of Mach and/or Reynolds number on the lateral scale. Figure 19 summarizes the data of figure 18 and similar data for x/r of 0.57 and 1.14 at a fixed y/r of 1.00.

LONGITUDINAL CORRELATION COEFFICIENTS

The longitudinal correlations measured with two wires are given in figures 20 and 21. Figure 20 shows the variation of the longitudinal correlation coefficient R_x with distance across the mixing zone for x/r of 1.14. At the points near the core of the jet ($y/r < 1$), strong periodic signals of approximately 8000 cps were encountered. Their presence causes the apparent scatter in the data of figures 20(g) to (i). The source of these disturbances is unknown, but the wavelength of the disturbance is approximately half the diameter of the jet nozzle. Perhaps transverse oscillations are responsible. Figure 21 shows the variation of the longitudinal correlation coefficient with distances from the jet nozzle of 1.14, 2.29, and 4.58.

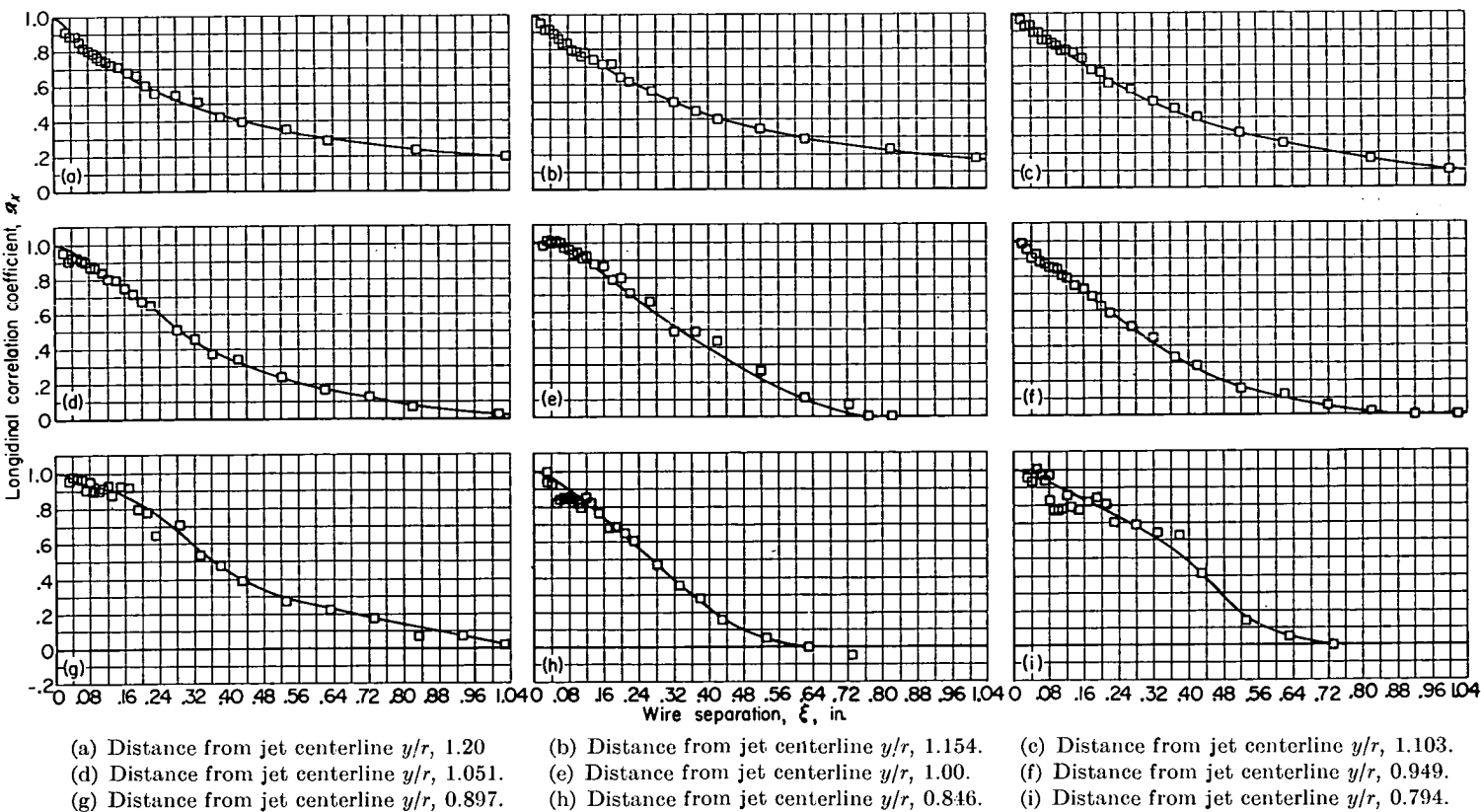
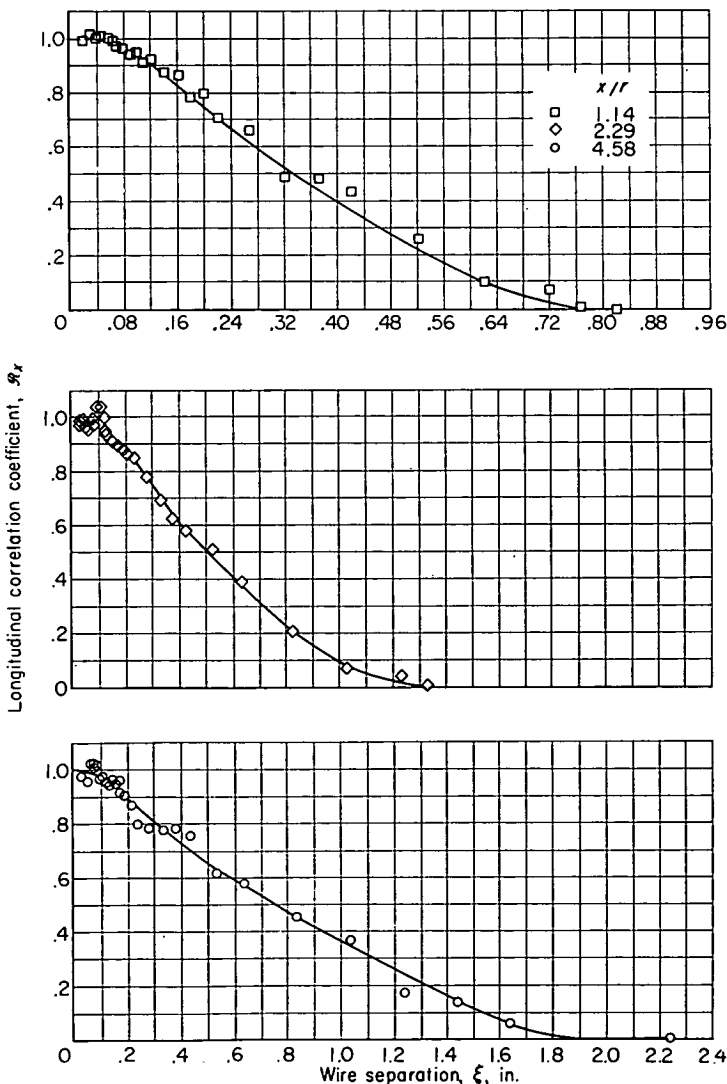


FIGURE 20.—Longitudinal velocity correlations. Distance from jet nozzle x/r 1.14; exit Mach number, 0.3; Reynolds number, 300,000.



Inspection of figures 20 and 21 shows that the longitudinal correlation is affected by varying x/r and y/r . This effect will become more apparent when the longitudinal scale is evaluated from the area under the correlation curves; the variation is discussed in the section LONGITUDINAL SCALE OF TURBULENCE.

AUTOCORRELATIONS

The autocorrelation functions are presented in figures 22 and 23. Figure 22 shows the autocorrelation coefficient as a function of delay time in milliseconds for a fixed x/r value of 1.14 and for y/r values distributed as shown in figure 1. Figure 23 shows curves of autocorrelation coefficient against delay time for a fixed y/r of about 1.00 for several x/r values. Again, the effect of varying x/r and y/r will become apparent when the scale of turbulence is discussed. In figures 22 and 23 the influence of the periodic disturbances is exaggerated because of the size of the time-delay intervals. The 8000-cps sound wave is especially prominent, as well as another type of extraneous signal that resulted from floor vibrations due to heavy machinery in the building. For example, figures 22(g) and (h) show both types of interference. These wiggles are not present in figure 23, where the distribution with distance downstream of the nozzle of the jet is shown.

As has been pointed out, the autocorrelations can be converted to longitudinal correlations by certain relations of the mean flow. Figure 24 shows a comparison of the two measurements of the longitudinal correlation coefficient. The agreement is quite good, and the curves shown are typical of the measurements. The two-wire correlations

FIGURE 21.—Longitudinal velocity correlations. Distance from jet centerline y/r , 1.00; exit Mach number, 0.3; Reynolds number, 300,000.

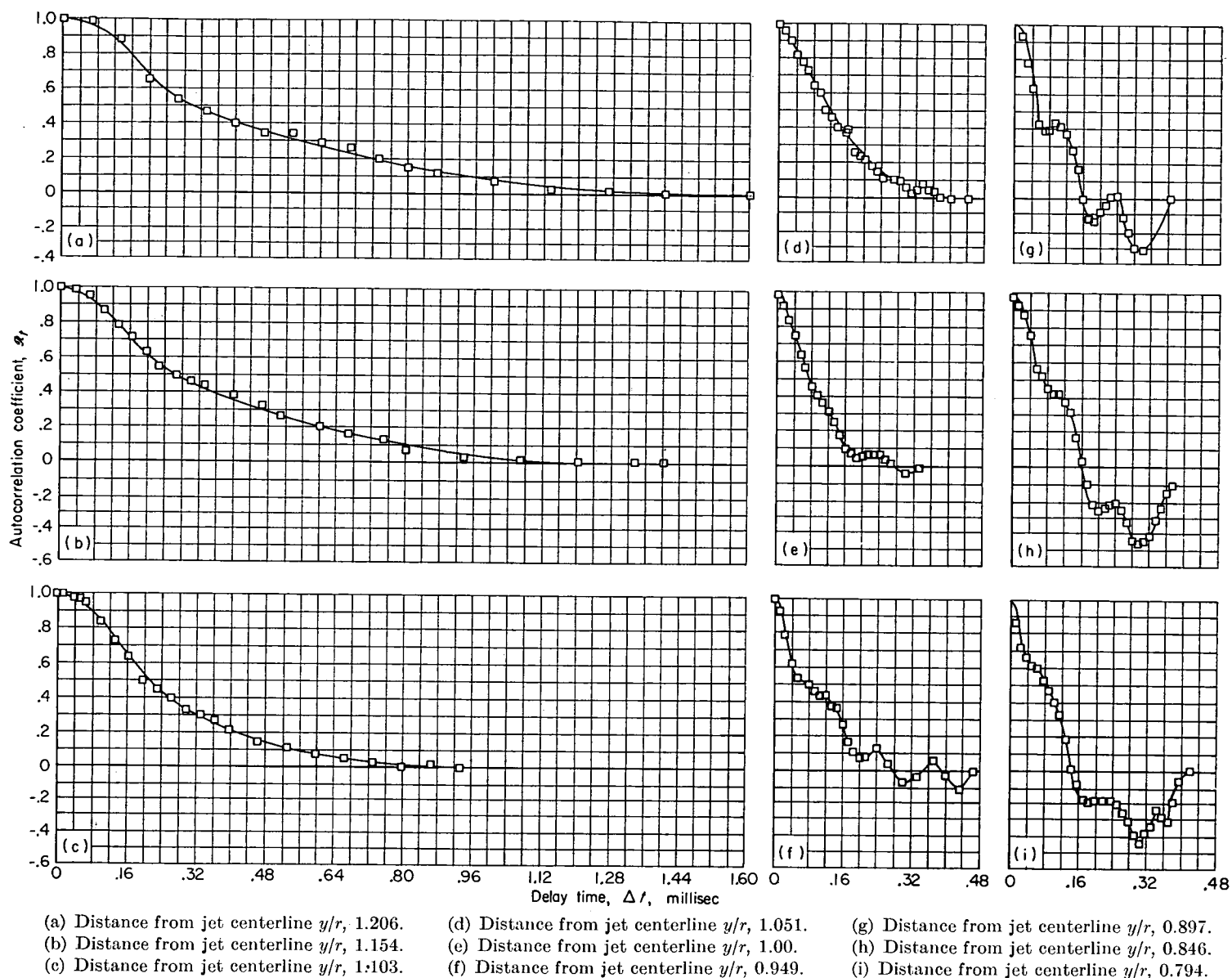
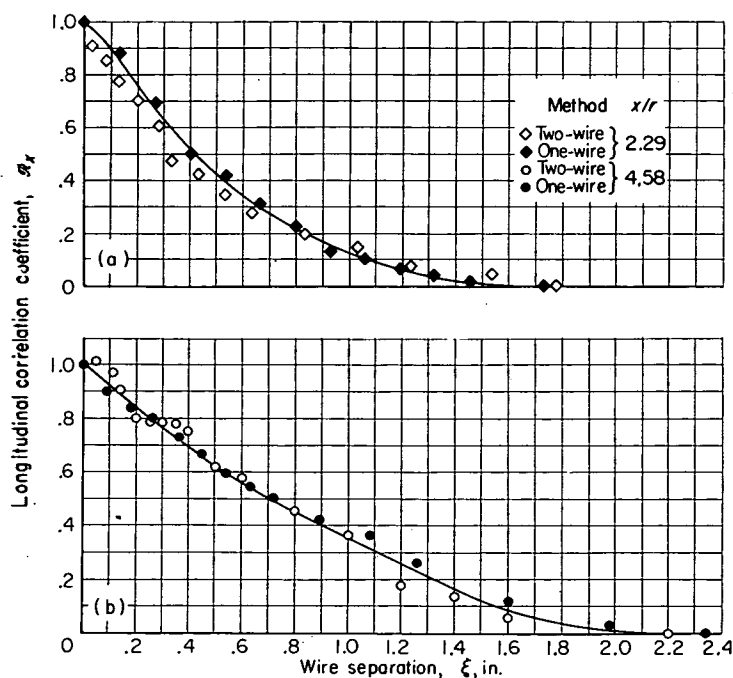


FIGURE 22.—Autocorrelations. Distance from jet nozzle x/r , 1.14; exit Mach number, 0.3; Reynolds number, 300,000.



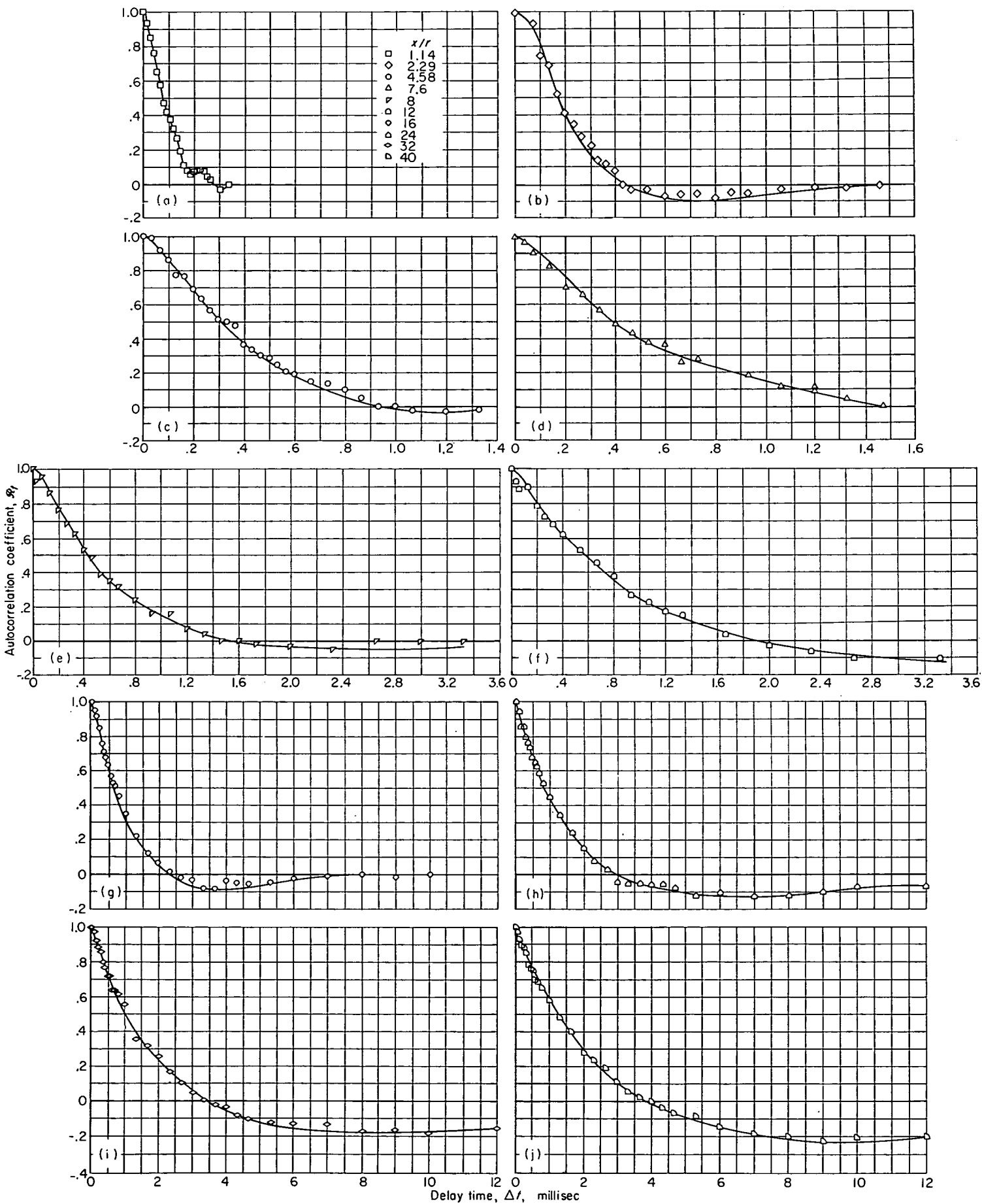
were measured with the quarter-square method of multiplication using the average-square computer. The one-wire results were measured with the analog multiplier. If both measurements had been made with the analog multiplier, the agreement would probably be even better.

SPECTRA OF TURBULENCE

The spectra of the u -component of the turbulent velocity are shown in figures 25 and 26. Figure 25 shows the spectra for a fixed x/r value of 1.14 and a series of y/r values distributed as shown in figure 1. On the other hand, figure 26 presents the spectra for a fixed y/r value of approximately 1.00 and a series of x/r values. The change in the spectra with distance from the nozzle of the jet is primarily a shift of energy to lower frequencies as x/r increases. The effect of this increase will be discussed at the time the longitudinal scale of turbulence is considered.

- (a) Distance from jet centerline y/r , 1.103.
 (b) Distance from jet centerline y/r , 1.00.

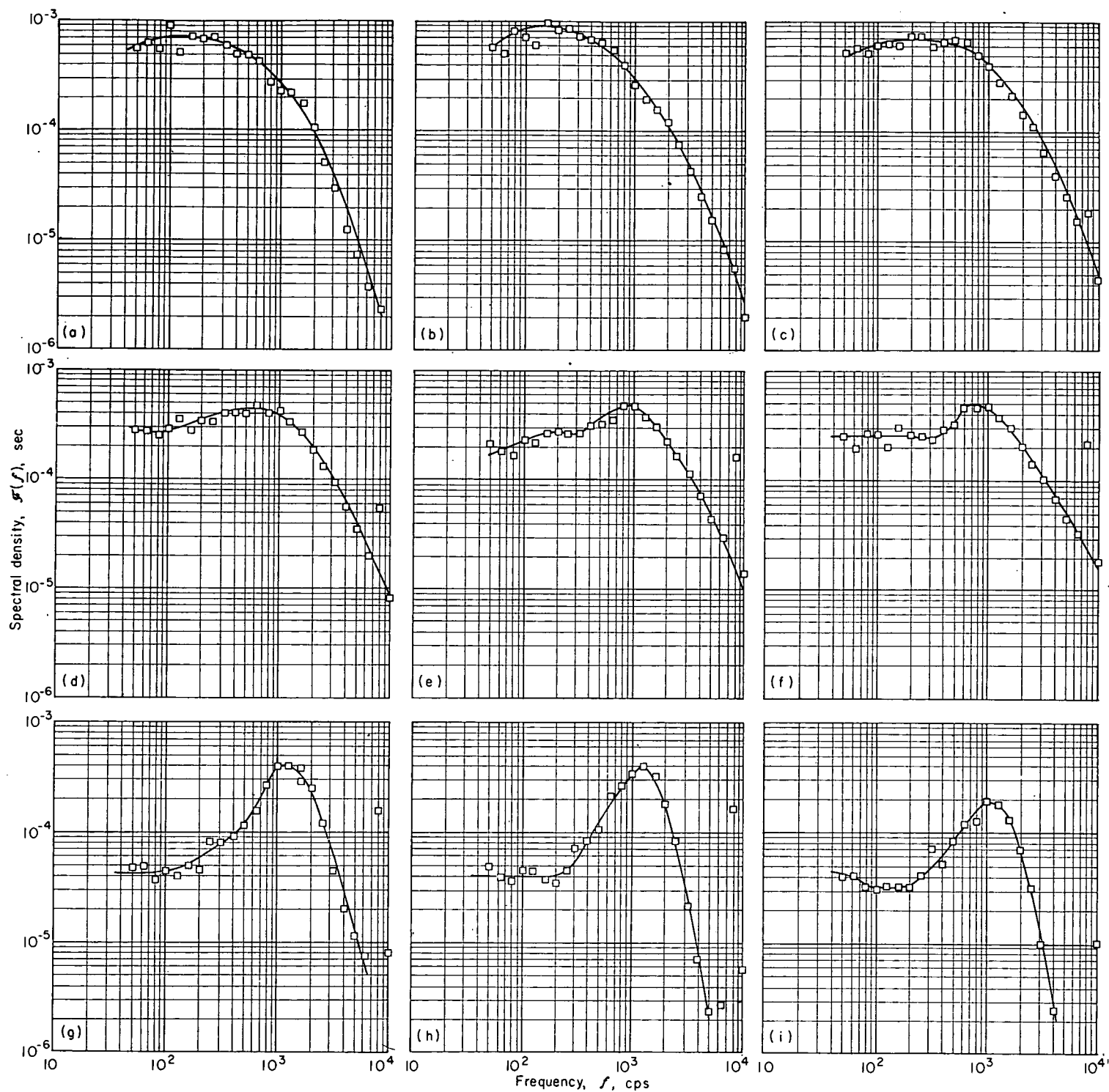
FIGURE 24.—Comparison of longitudinal velocity correlations from one- and two-wire methods.



(a) to (f) Distance from jet centerline y/r , 1.00.

(g) to (j) Distance from jet centerline y/r , 1.028.

FIGURE 23.—Autocorrelations. Exit Mach number, 0.3; Reynolds number, 300,000.



(a) Distance from jet centerline y/r , 1.206.

(d) Distance from jet centerline y/r , 1.051.

(g) Distance from jet centerline y/r , 0.846.

(b) Distance from jet centerline y/r , 1.154.

(e) Distance from jet centerline y/r , 1.00.

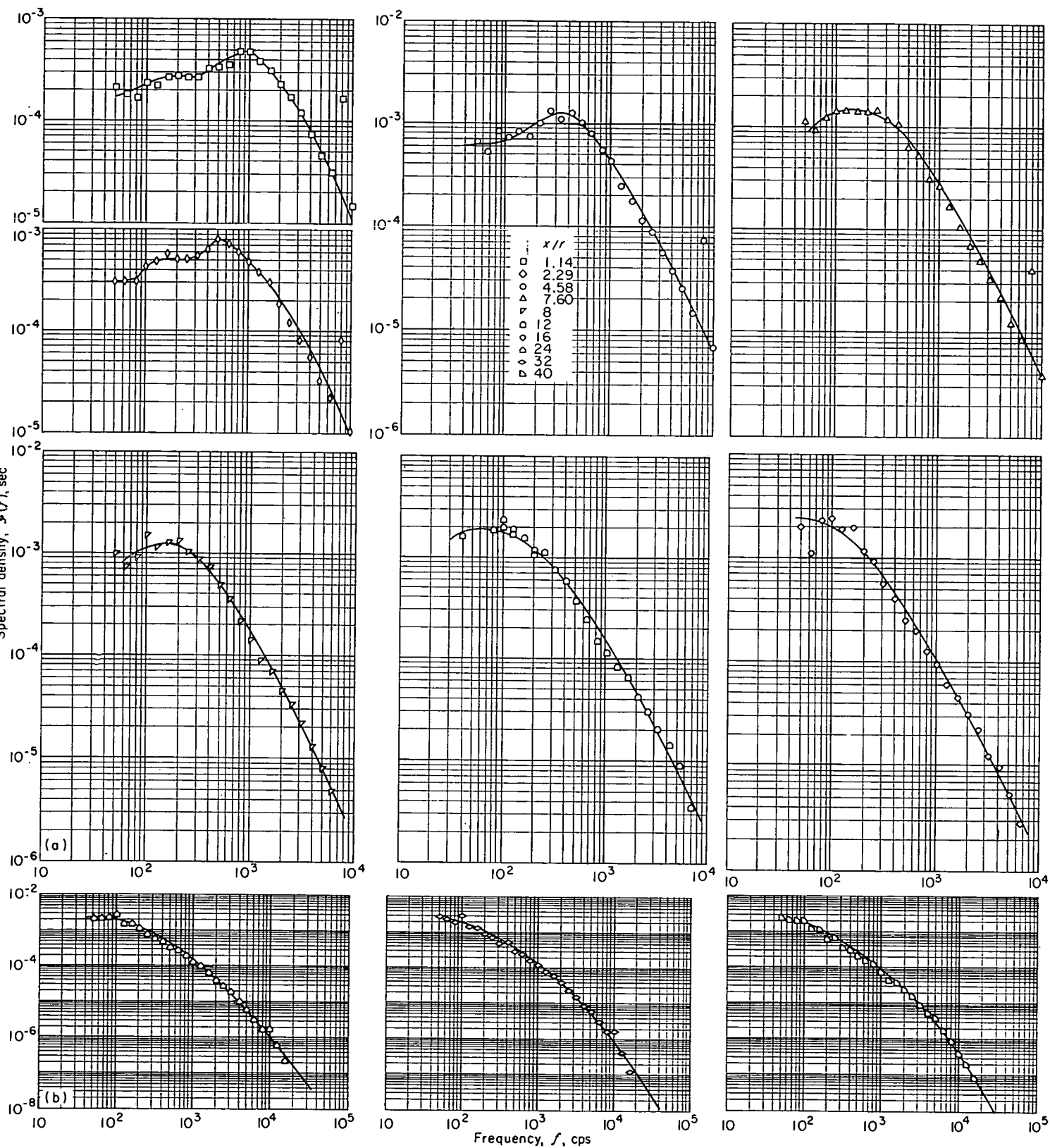
(h) Distance from jet centerline y/r , 0.794.

(c) Distance from jet centerline y/r , 1.103.

(f) Distance from jet centerline y/r , 0.949.

(i) Distance from jet centerline y/r , 0.743.

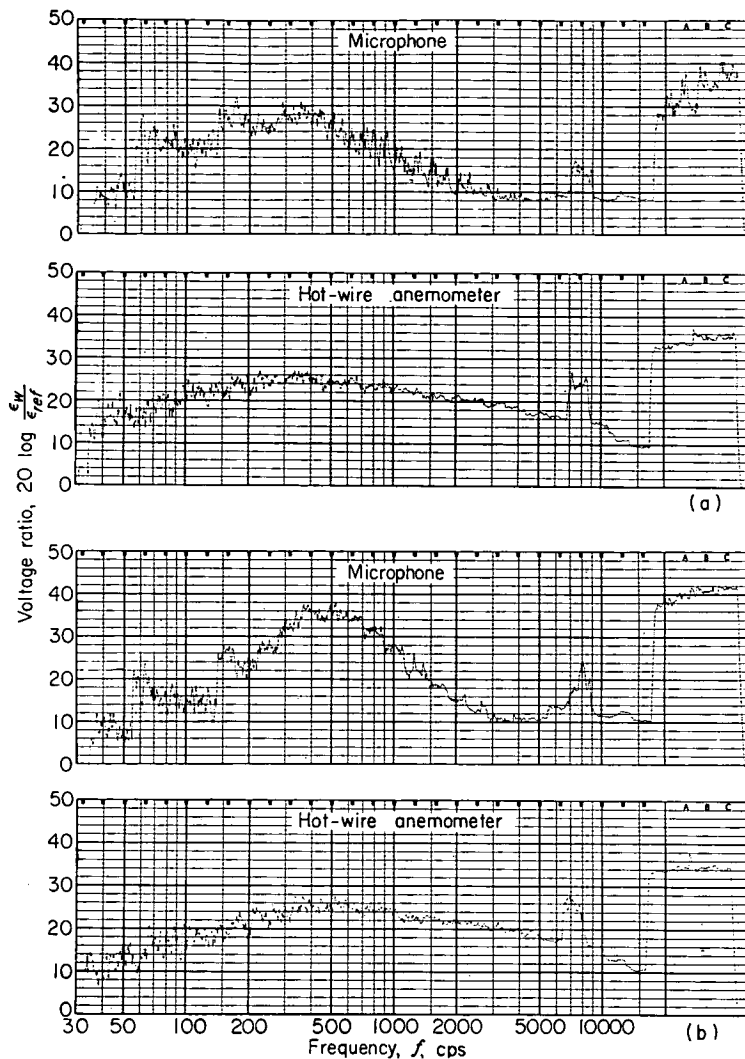
FIGURE 25.—Spectral density curves. Distance from jet nozzle x/r , 1.14; exit Mach number, 0.3; Reynolds number, 300,000.



(a) Distance from jet centerline y/r , 1.00.

(b) Distance from jet centerline y/r , 1.028.

FIGURE 26.—Spectral density curves. Exit Mach number, 0.3; Reynolds number, 300,000.



(a) Distance from jet nozzle x/r , 4.58.
(b) Distance from jet nozzle x/r , 7.60.

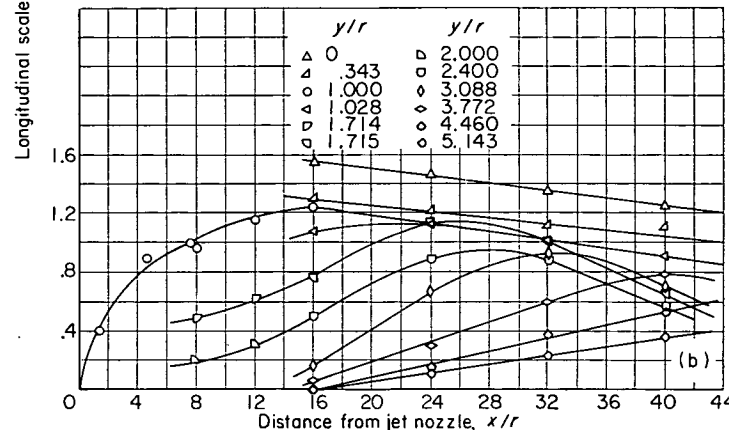
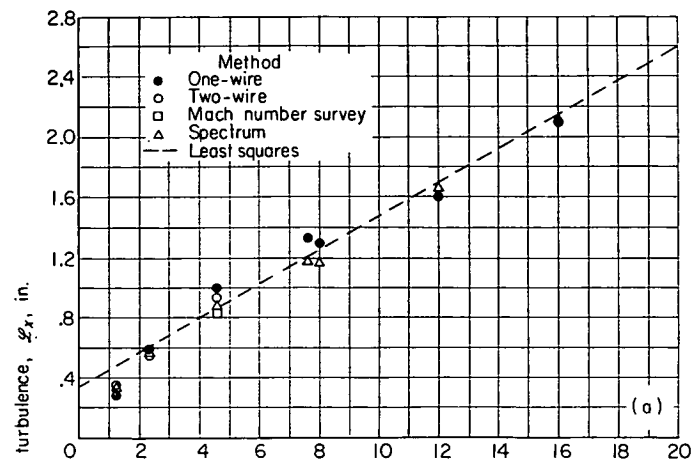
FIGURE 27.—Comparison of spectra obtained from a hot-wire anemometer and a microphone. Distance from jet centerline y/r , 1.00; exit Mach number, 0.3; Reynolds number, 300,000.

There is a marked change in the u spectra as the distance from the jet centerline y/r is changed. As the core of the jet is approached, a signal at approximately 8000 cps increases by more than an order of magnitude. This signal was believed to originate from a sound wave of that frequency.

In figure 27 are compared microphone spectra and hot-wire spectra recorded for two different values of x/r with the microphone displaced in the z -direction to remove it from the airstream. The presence of a strong signal at approximately 8000 cps, which can be seen on both sets of records, shows that a sound wave is indeed the source of the extraneous disturbance.

LONGITUDINAL SCALE OF TURBULENCE

The longitudinal scale of turbulence \mathcal{L}_x was determined by integrating the area under the longitudinal correlation



(a) Various methods.
(b) Various distances from jet centerline.

FIGURE 28.—Variation of longitudinal scale with distance from jet nozzle. Distance from jet centerline y/r , 1.00; exit Mach number, 0.3; Reynolds number, 300,000.

curves. The results are shown in figure 28. A straight line has been fitted to the data by the method of least squares (fig. 28(a)). This straight line represents the variation of the longitudinal scale quite well for distances from the jet nozzle less than 16 radii. In figure 28(b) the results are plotted for downstream distances as great as 40 jet radii and show clearly the decrease in longitudinal scale as the distance from the jet nozzle is increased beyond 16 radii.

The longitudinal scale of turbulence was evaluated by means of equation (13) and the spectral density curves of figures 25 and 26. It is obvious from equation (13) that

$$\mathcal{L}_x = \frac{\mathcal{F}(0)U_{loc}}{4} \quad (21)$$

Several schemes have been suggested to evaluate $\mathcal{F}(0)$, the spectral density function for zero frequency. For example, von Kármán (ref. 23) suggests that for small values of f an expression of the type

$$\mathcal{F}(f) = \frac{k_1}{(1 + \pi^2 k_1^2 f^2)^{5/6}} \quad (22)$$

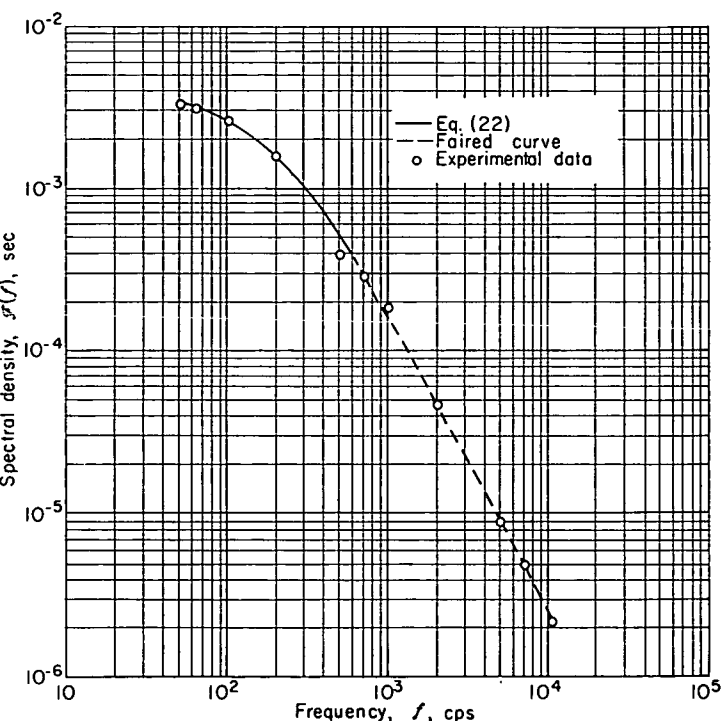


FIGURE 29.—Fitting spectral density data to empirical formula (ref. 23).

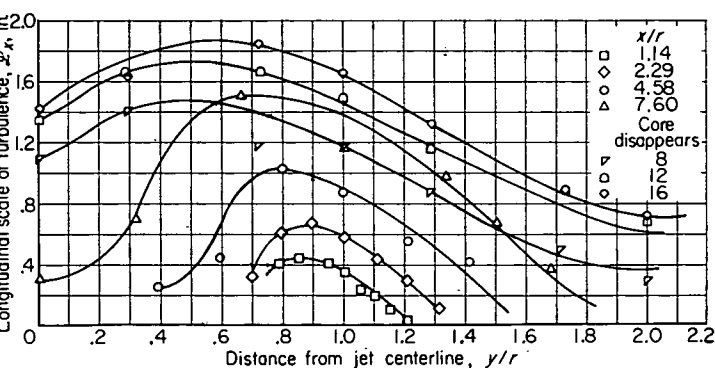


FIGURE 30.—Variation of longitudinal scale of turbulence across mixing zone. Exit Mach number, 0.3; Reynolds number, 300,000.

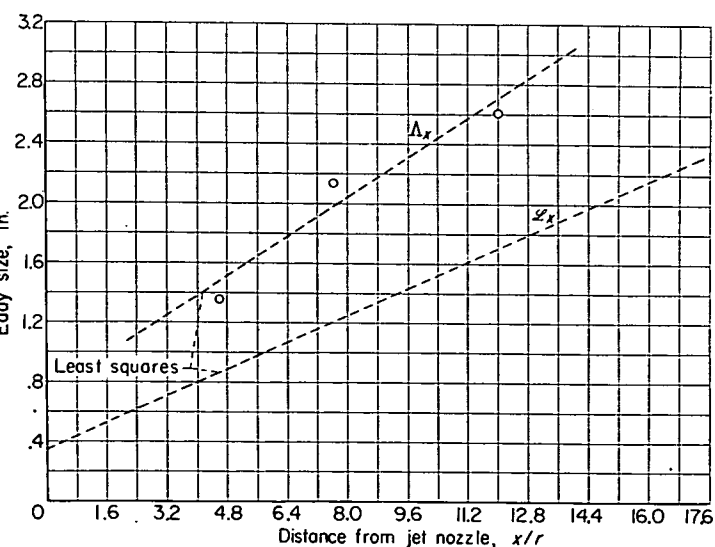


FIGURE 31.—Variation of eddy size with distance from jet nozzle (eq. (23)).

can be used to extrapolate to zero frequency. Corrsin and Uberoi (ref. 6) used this method to obtain the scale of turbulence. Figure 29 shows the result of fitting the data with a curve of the form of equation (22) for frequencies of 500 cps or less. It is seen that this method gives somewhat better results than equation (13).

If this method of extrapolation is used, a value of the scale of turbulence can be obtained. It is emphasized, however, that the two values of the scale obtained (by fitting the correlation curve with the best exponential and by finding the best fit for the spectral density curve according to equation (22)) are not necessarily the same. This particular example shows the relative inadequacy of the method of equation (21) for obtaining the scale of turbulence.

The method used in this report was simply to fair the best curve through the experimental data and estimate the maximum value of $\mathcal{F}(f)$. This value of $\mathcal{F}(f)$ is called the $\mathcal{F}(0)$ used in equation (21). This method gives values of \mathcal{L}_x that agree well with the values obtained by integration of the correlograms, as is shown in figure 28(a), thus validating this method of selecting $\mathcal{F}(0)$. The values of \mathcal{L}_x are plotted in figure 30.

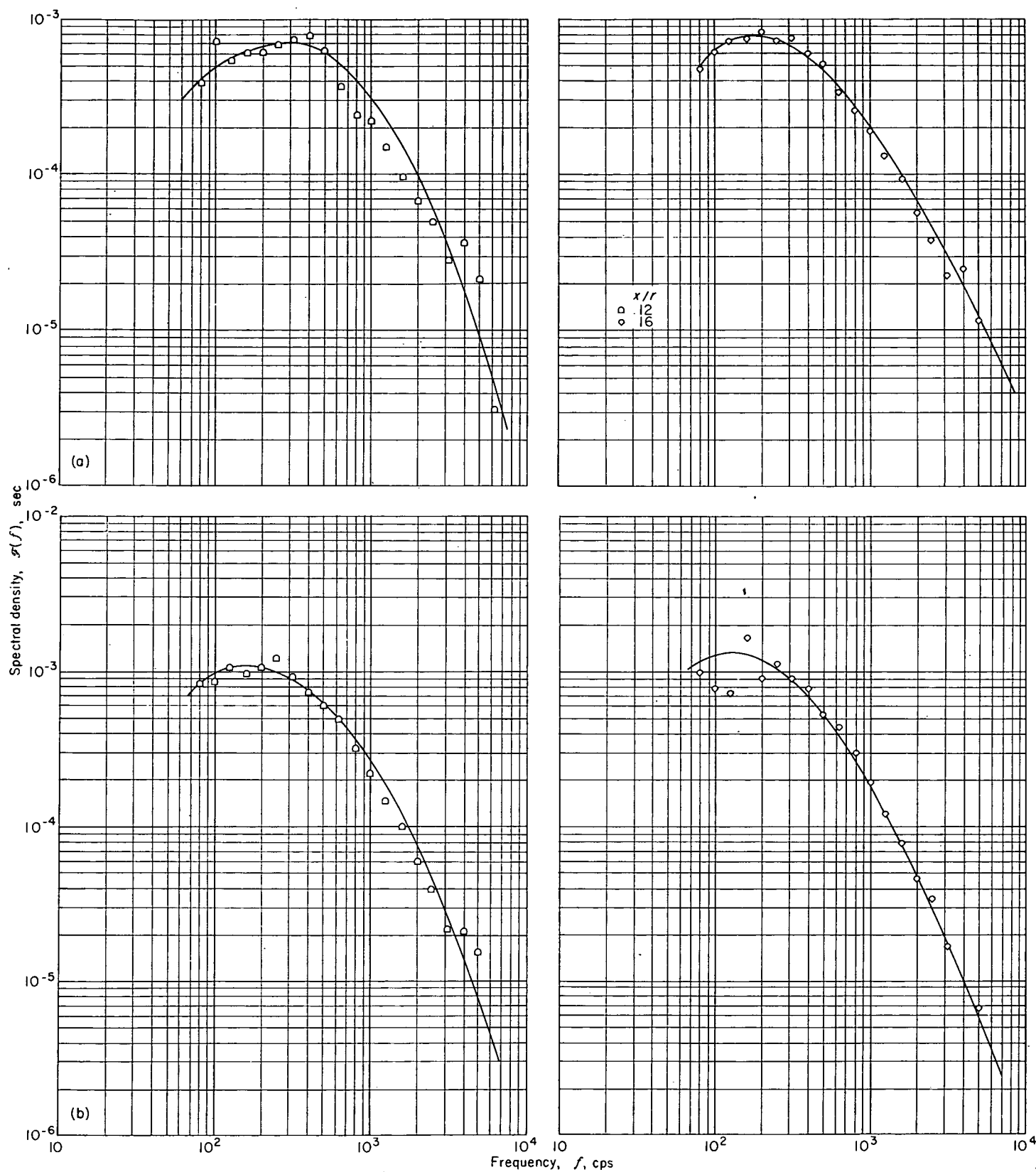
Examination of figures 17 and 28(a) shows that \mathcal{L}_x is somewhat more than twice as large as \mathcal{L}_y at $x/r=8$. In both figures, the values of \mathcal{L}_y and \mathcal{L}_x for $x/r=1.14$ fall below the least-squares lines. The scatter about that line is small except for this point. Inspection of figures 28(a) and (b) shows that it may be possible to fit the data with some combination of a parabola up to $x/r=16$ and a straight line thereafter. This possibility suggests that the character of the turbulence changes at about that distance from the nozzle of the jet. In the mixing zone, the scale of turbulence is given by one relation, while the disappearance of the core results in an entirely different one.

This fact is also shown by figure 30, which gives the relation of the longitudinal scale to the distance from the centerline of the jet. As long as there is a core, the relation is definitely one type, which changes markedly upon the disappearance of the core. This change, however marked it may be, does not influence the position of the largest eddies ($\mathcal{L}_{x,max}$) near the y/r value of 0.7 to 0.8 for values of $x/r < 16$.

An analysis of the correlograms and spectrograms was made using the equation

$$\Lambda_x = -\frac{x_0(1-\beta)}{\ln \beta} \quad (23)$$

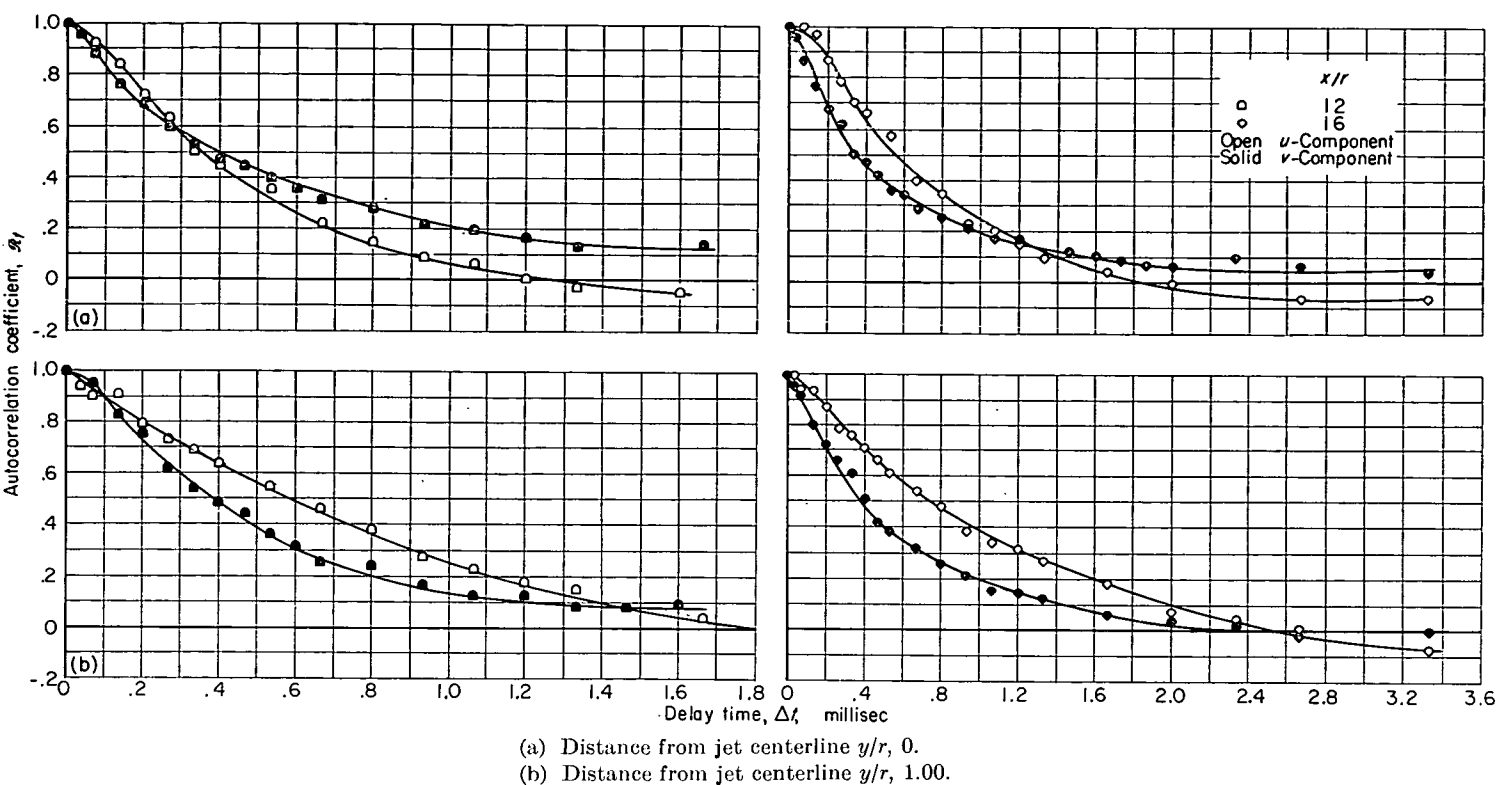
The Λ scale of the turbulence was calculated by the methods outlined in appendix B. This Λ scale is different from that of the conventional scale \mathcal{L}_x , but the over-all picture is much the same. Figure 31 shows the variation of this Λ scale with distance from the jet nozzle. Here the variation is linear with x/r , as was shown in figure 28(a).



(a) Distance from jet centerline y/r , 0.

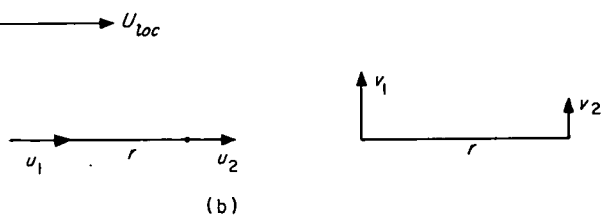
(b) Distance from jet centerline y/r , 1.00.

FIGURE 32.—Spectral density curves for v -component. Exit Mach number, 0.3; Reynolds number, 300,000.


 FIGURE 33.—Velocity autocorrelations of u - and v -components. Exit Mach number, 0.3; Reynolds number, 300,000.

CORRELATIONS AND SPECTRA OF v -COMPONENT OF TURBULENT VELOCITY

The correlations and spectra of the v -components of turbulence were obtained in order to compare them with those of the u -component. The spectra of the v -component of turbulence at four points in the jet are shown in figure 32. The spectra of the v -component of turbulence are different from the u -component in shape as well as in magnitude and frequency distribution. Figure 33 shows the autocorrelations of the v and the u velocity components at the same four points. These four curves indicate also the differences between the u - and v -components:



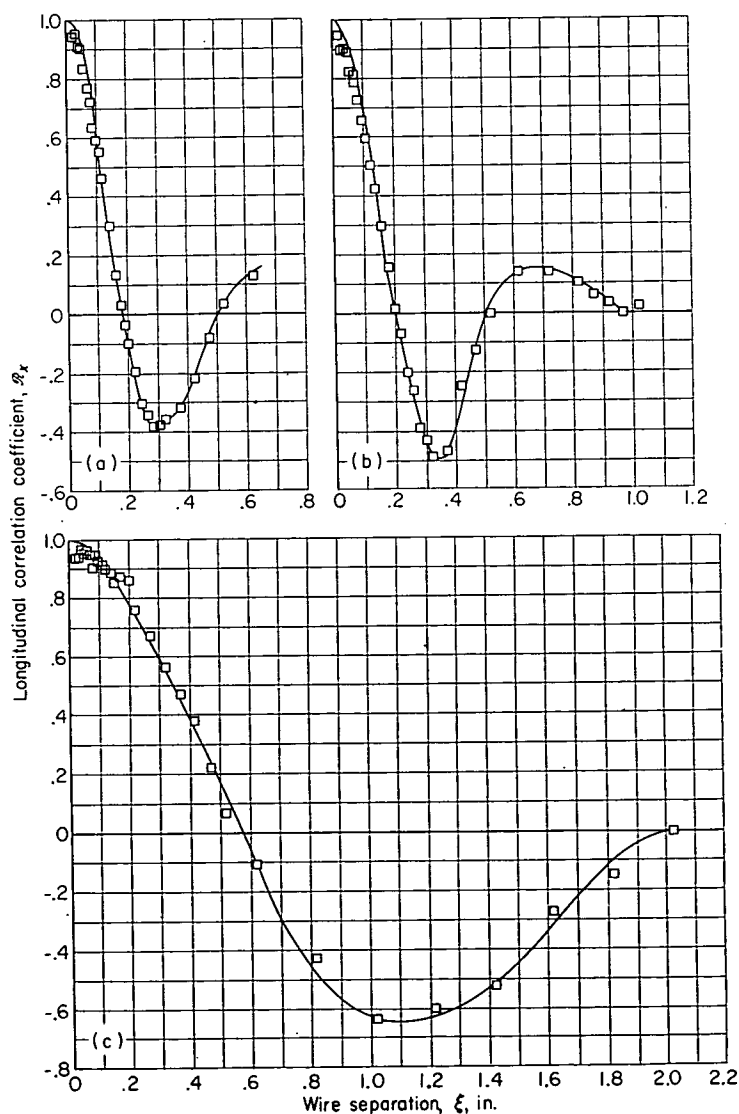
If the values of $R_{x,u}$ and $R_{x,v}$ are related by the following equation (ref. 10)

$$R_{x,u} + R_{x,v} = -\frac{x}{2} \frac{dR_{x,u}}{dx} \quad (24)$$

then the turbulence is said to be isotropic. These u and v measurements, together with the v intensity measurements already discussed, show that the turbulence is not isotropic at distances from the jet less than 16 radii.

- (a) Band-pass width, 4200 to 5800 cps; center frequency, 5000 cps.
 (b) Band-pass width, 4800 to 5200 cps; center frequency, 5000 cps.
 (c) Band-pass width, 900 to 1100 cps; center frequency, 100 cps.

FIGURE 34.—Longitudinal velocity correlations. Distance from jet nozzle x/r , 1.14; distance from jet centerline y/r , 1.00; exit Mach number, 0.3; Reynolds number, 300,000.



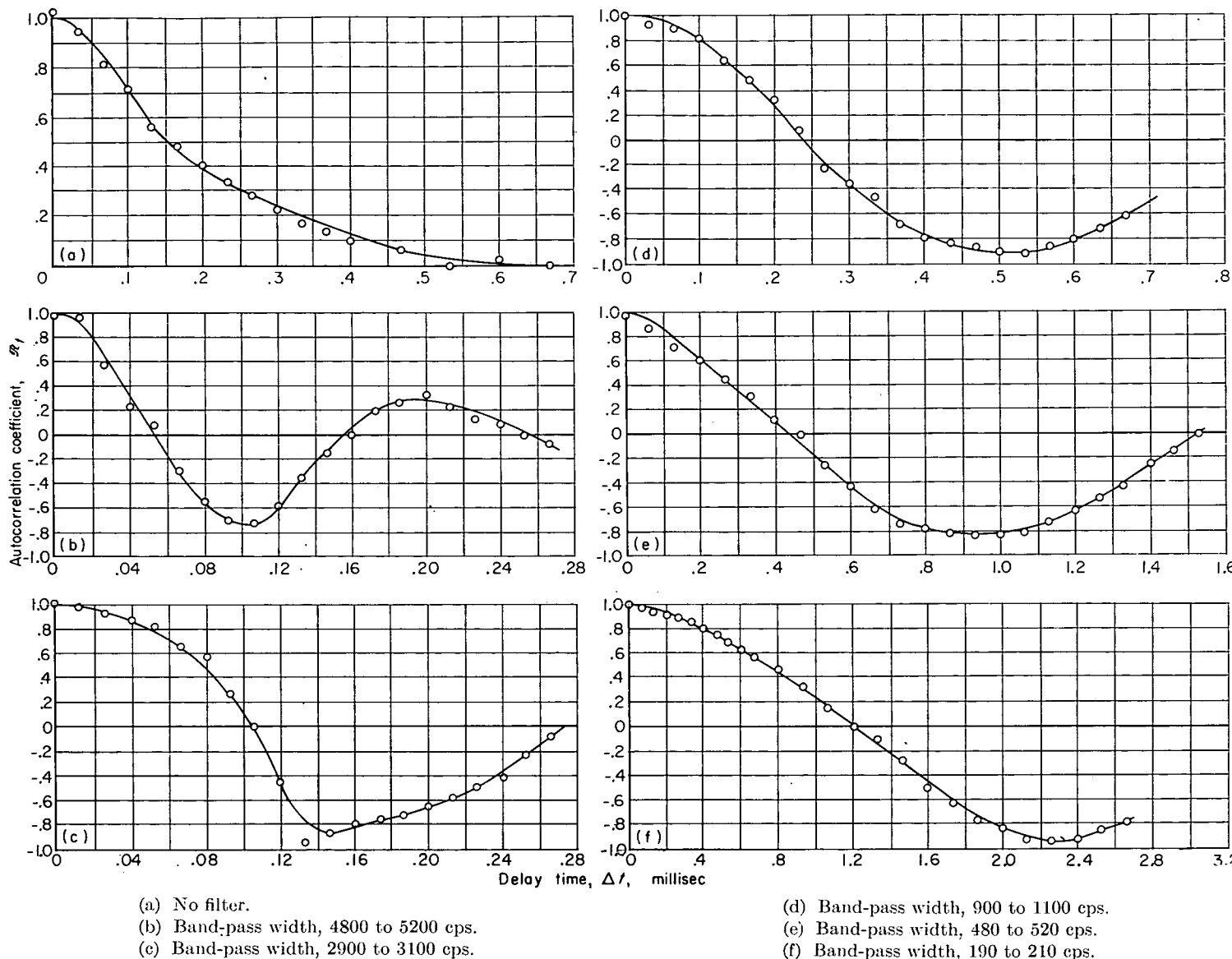


FIGURE 35.—Autocorrelations for specific band-pass frequencies. Distance from jet nozzle x/r , 4.58; distance from jet centerline y/r , 1.206; exit Mach number, 0.3; Reynolds number, 300,000.

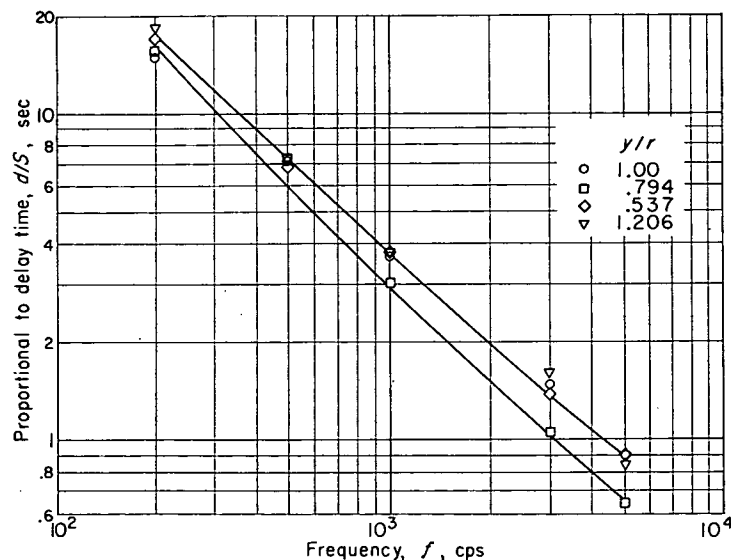


FIGURE 36.—Zero autocorrelation as function of frequency. Distance from jet nozzle x/r , 4.58; exit Mach number, 0.3; Reynolds number, 300,000.

CORRELATION WITH SPECIFIC BAND-PASS INPUTS

As an additional test of the autocorrelation technique for obtaining longitudinal correlation coefficients, the hot-wire signals were passed through electronic filters set to pass only specific bands of frequencies before they were fed to the correlation computers. Figures 34(a) and (b) show the effect of varying the band-pass width. The correlations do not change materially as the width of the band pass is changed by a factor of 4, except that the narrow band pass produces a greater negative correlation (ref. 21). Figure 34(c) shows the effect of changing the center frequency of the band pass.

In figure 35 are shown the autocorrelations for the experiments where the hot-wire signals were passed through electronic filters before being fed to the correlation computers. This figure illustrates the effect of varying the center frequency of the band pass, as did figure 34(c), and also shows clearly how the presence of the filters changes the correlations as measured (e.g., cf. fig. 35(a), for which no filter was used, with the other parts of fig. 35, for which the filters were used).

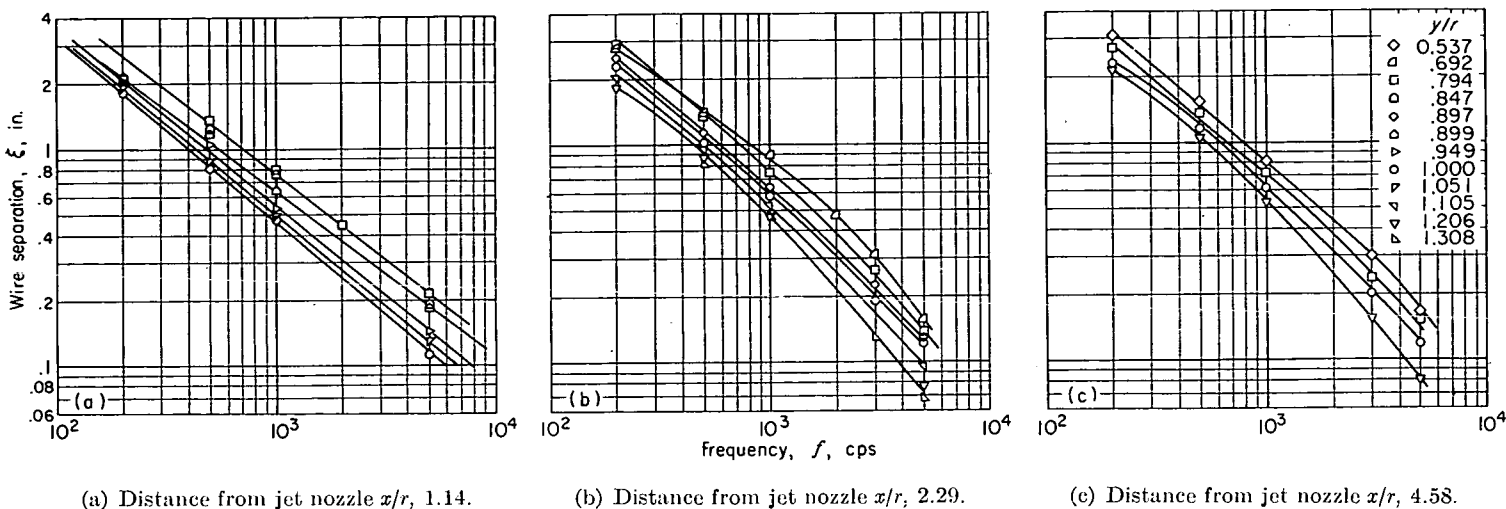


FIGURE 37.—Zero longitudinal correlation distance as function of frequency. Exit Mach number, 0.3; Reynolds number, 300,000.

If the logarithm of the delay time for the first zero crossing of the filtered autocorrelation curve is plotted against the logarithm of the center frequency of the band pass (fig. 36), a straight line with a slope of -1 results. If the logarithm of the wire separation for zero longitudinal correlation is plotted against the logarithm of the center frequency of the band pass, a similar result should be obtained if the turbulent eddy has remained unchanged while passing the hot wires. That is, the eddy has been swept along unchanged with the velocity of the stream. Observation of figure 37 shows that these curves are nearly straight lines with a slope of -1 . This is additional evidence that the relation $x = U_{loc}t$ holds very well for the turbulence patterns in the subsonic jet. Thus, the autocorrelation technique is a satisfactory one for studying the longitudinal correlations.

VARIATION OF SCALE OF TURBULENCE WITH MACH AND/OR REYNOLDS NUMBER

The effect of exit Mach and/or Reynolds number on the longitudinal scale was also investigated (fig. 38). As with the lateral scale (fig. 19), there was no variation of the longitudinal scale with Mach and/or Reynolds number.

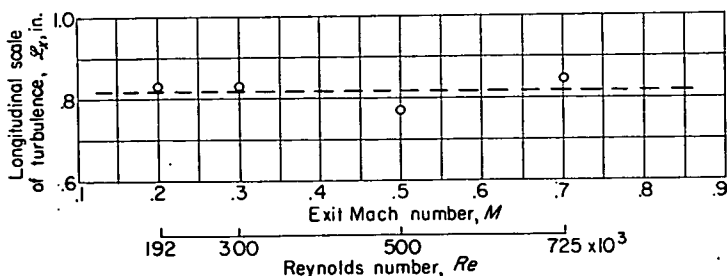


FIGURE 38.—Effect of exit Mach and/or Reynolds number on longitudinal scale of turbulence. Distance from jet nozzle x/r , 4.58; distance from jet centerline y/r , 1.00.

SUMMARY OF RESULTS

Hot-wire-anemometer measurements of the turbulence parameters—intensity, scale, correlation, and spectra—in a

subsonic jet have been reported for a range of exit Mach numbers from 0.2 to 0.7 and for Reynolds numbers from 192,000 to 725,000, with the following results:

1. Near the nozzle of the jet (distances less than 4 or 5 jet diam downstream of the nozzle) the intensity of turbulence, expressed as a percent of core velocity, is a maximum at a distance of approximately 1 jet radius from the centerline and decreases slightly with increasing Mach and/or Reynolds number. At distances greater than 8 diameters, however, the maximum intensity moves out and decreases in magnitude until the turbulence-intensity profiles are quite flat and approaching similarity.

2. The lateral and longitudinal scales of turbulence are nearly independent of Mach and/or Reynolds number and, in the mixing zone near the jet, vary proportionally with distance from the jet nozzle. Farther downstream of the jet nozzle the longitudinal scale reaches a maximum and then decreases approximately linearly with distance. Near the nozzle the lateral scale is much smaller than the longitudinal and does not vary with distance from the centerline, while the longitudinal scale is a maximum at a distance from the centerline of about 0.7 to 0.8 of the jet radius. Farther downstream this maximum moves out from the centerline.

3. An analysis of the correlograms and spectra, which differs from the ordinary statistical approach, yields a "scale" which, while different in magnitude from the conventional, varies similarly to the ordinary scale and is easier to evaluate.

4. An autocorrelator using a magnetic tape recorder and a special playback instrument was used to measure the velocity autocorrelations. These autocorrelations were converted to longitudinal correlations that agreed well with the directly measured longitudinal correlations.

LEWIS FLIGHT PROPULSION LABORATORY

NATIONAL ADVISORY COMMITTEE FOR AERONAUTICS

CLEVELAND, OHIO, April 24, 1956

APPENDIX A

SYMBOLS

B	effective power band width	Subscripts:	
d	displacement of heads of playback instrument	b	band of frequencies
$\mathcal{F}(f)$	spectral density function of \bar{u}^2	c	core
f	frequency	f	frequency
k	calibration constant	l	lower cut-off
\mathcal{L}	scale of turbulence	loc	local
M	exit Mach number	max	maximum
N	number of db taken from strip chart	min	minimum
R	correlation coefficient	p	peak
Re	Reynolds number	ref	reference
r	jet radius	t	time
S	tape speed	tot	total spectrum of all frequencies
t	time	u	upper cut-off
Δt	delay time	w	wire
U	mean stream velocity	x	longitudinal
u, v, w	fluctuating, components of velocity in x -, y -, and z -directions, respectively	y	lateral
x, y, z	right-hand coordinate system with x -axis coinciding with jet centerline	z	lateral
β	nondimensional parameter related to cut-off frequencies of spectrum by eq. (B5)	1,2	points in stream
ϵ	fluctuating component of hot-wire voltage	Superscripts:	
ξ, η	wire separation in x - and y -directions, respectively	—	average
Λ	characteristic eddy size	'	root-mean-square
ω	angular frequency	*	characteristic value

APPENDIX B

ANALYSIS OF TURBULENCE SPECTRA AND AUTOCORRELOGRAMS

The analysis of the data from the hot-wire anemometers is most easily accomplished by means of the power spectrum of the turbulence and the autocorrelation technique, as explained in the EXPERIMENTAL PROCEDURE section. The details of this analysis are interesting also. The correlation fitting function

$$R_x = \frac{e^{-x/\Lambda_x} - \beta e^{-\beta x/\Lambda_x}}{1 - \beta} \quad (14a)$$

$$R_t = \frac{e^{-\omega^* t} - \beta e^{-\beta \omega^* t}}{1 - \beta} \quad (14b)$$

can be transformed to the spectral density function $\mathcal{F}(f)$ as follows:

$$\mathcal{F}(f) = \frac{4}{U_{loc}} \int_0^\infty R_x \cos \frac{2\pi f x}{U_{loc}} dx \quad (B1a)$$

$$\mathcal{F}(f) = 4 \int_0^\infty R_t \cos 2\pi f t dt \quad (B1b)$$

The resulting expression for $\mathcal{F}(f)$ is

$$\mathcal{F}(f) = \frac{1 + \beta}{4f^*} \frac{\left(\frac{f}{f^*}\right)^2}{\left[1 + \left(\frac{f}{f^*}\right)^2\right] \left[\beta^2 + \left(\frac{f}{f^*}\right)^2\right]} \quad (17)$$

This equation for $\mathcal{F}(f)$ has many interesting features. Consider, for instance, sketches (c) and (d). The typical correlogram shows a zero crossing (t_0) and a minimum value. These two quantities and the following equations for $R_{t,min}$ and ω^*

$$R_{t,min} = -\beta^{\frac{1+\beta}{1-\beta}} \quad (B2)$$

$$\omega^* = \frac{\ln \beta}{t_0(\beta - 1)} \quad (B3)$$

give values for β and ω^* from the experimental correlogram. With these values the spectral density curve can be calculated from equation (17).

An alternate procedure is to work with the experimental spectral density curve. If the low-frequency part of the curve has been obtained with sufficient accuracy, the values of the low- and high-frequency cut-offs (f_l and f_u) can be obtained from the spectrum. These two values with the equations

$$\frac{f_l}{f_u} = \frac{\beta}{(1 + \beta)^2} \quad (B4)$$

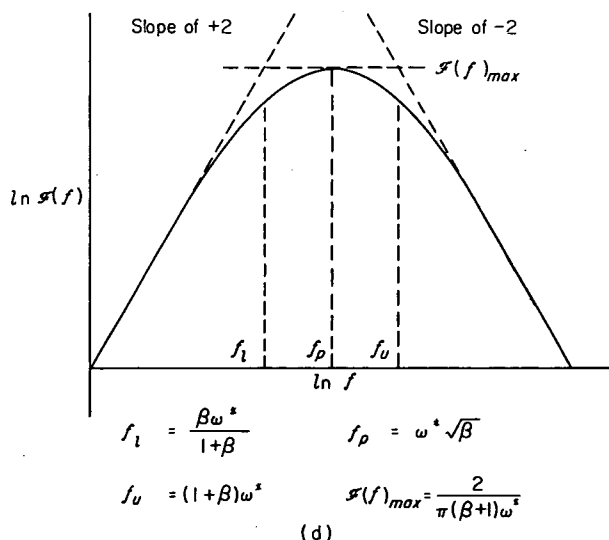
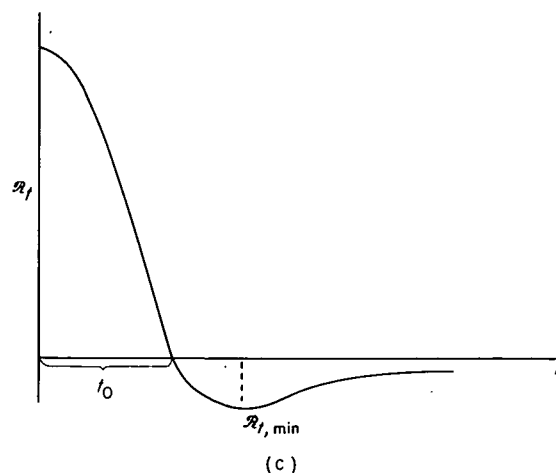
$$f_u = \frac{(1 + \beta)\omega^*}{2\pi} \quad (B5)$$

give values for β and ω^* from the experimental spectrum. With these values the correlogram can be calculated from equation (14a) or (14b).

In actual practice the low-frequency part of the spectrum is seldom defined with sufficient accuracy to use the alternate method proposed here. But the correlograms are generally well defined and are easily used as outlined.

If a family of curves of $\mathcal{F}(f)$ for a series of values of β is plotted as shown in figure 39, spectrum fitting curves result that differ from experimental curves only by multiplicative constants. This family of curves can be used as a grid and placed over the experimental data and a best fit obtained. The value of β , therefore, is easily determined. With this value of β and the zero crossing of the correlogram t_0 , the value of ω^* can be obtained from equation (B3).

With the values of β and ω^* the spectrum can be calculated by means of equation (17), or Λ_x can be evaluated by means of equation (16).



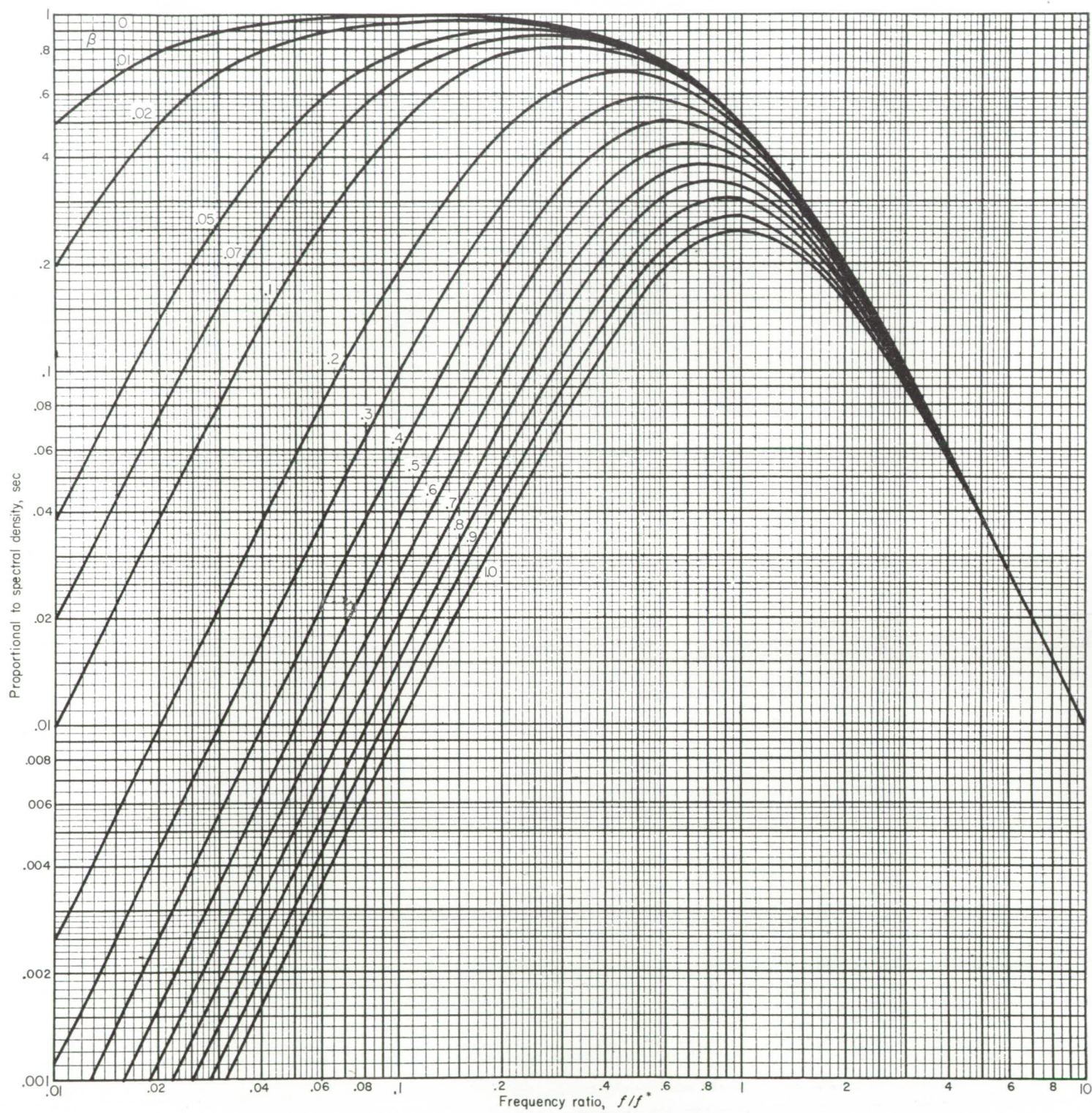


FIGURE 39.—Spectrum fitting curves (eq. (B2)).

REFERENCES

1. Lighthill, M. J.: On Sound Generated Aerodynamically. 1. General Theory. *Proc. Roy. Soc. (London)*, ser. A, vol. 211, no. 1107, Mar. 20, 1952, pp. 564-587.
2. Proudman, I.: Generation of Noise by Isotropic Turbulence. *Proc. Roy. Soc. (London)*, ser. A, vol. 214, 1952, pp. 119-132.
3. Mawardi, O. K., and Dyer, I.: On Noise of Aerodynamic Origin. *Jour. Acoustic Soc. Am.*, vol. 25, no. 3, May 1953, pp. 389-394.
4. Kuethe, Arnold M.: Investigation of the Turbulent Mixing Regions Formed by Jets. *Jour. Appl. Mech.*, vol. 2, no. 3, Sept. 1935, pp. A87-A95.
5. Corrsin, Stanley: Investigation of Flow in an Axially Symmetrical Heated Jet of Air. NACA WR W-94, 1943. (Supersedes NACA ACR 3L23.)
6. Corrsin, Stanley, and Uberoi, Mahinder S.: Further Experiments on the Flow and Heat Transfer in a Heated Turbulent Air Jet. NACA Rep. 998, 1950. (Supersedes NACA TN 1865.)
7. Corrsin, Stanley, and Uberoi, Mahinder S.: Spectra and Diffusion in a Round Turbulent Jet. NACA Rep. 1040, 1951. (Supersedes NACA TN 2124.)
8. Liepmann, Hans Wolfgang, and Laufer, John: Investigations of Free Turbulent Mixing. NACA TN 1257, 1947.
9. Taylor, G. I.: Statistical Theory of Turbulence, pts. I-IV. *Proc. Roy. Soc. (London)*, ser. A, vol. 151, no. A873, Sept. 2, 1935, pp. 421-478; pt. V, ser. A, vol. 156, Aug. 17, 1936, pp. 307-317.
10. Dryden, Hugh L.: A Review of the Statistical Theory of Turbulence. *Quarterly Appl. Math.*, vol. 1, no. 1, Apr. 1943, pp. 7-42.
11. Laurence, James C., and Landes, L. Gene: Auxiliary Equipment and Techniques for Adapting the Constant-Temperature Hot-Wire Anemometer to Specific Problems in Air-Flow Measurements. NACA TN 2843, 1952.
12. Sandborn, Virgil A.: Experimental Evaluation of Momentum Terms in Turbulent Pipe Flow. NACA TN 3266, 1955.
13. Schubauer, G. B., and Klebanoff, P. S.: Theory and Application of Hot-Wire Instruments in the Investigation of Turbulent Boundary Layers. NACA WR-86, 1946. (Supersedes NACA ACR 5K27.)
14. Mickelsen, William R., and Laurence, James C.: Measurement and Analysis of Turbulent Flow Containing Periodic Flow Fluctuations. NACA RM E53F19, 1953.
15. Dryden, H. L., and Kuethe, A. M.: The Measurement of Fluctuations of Air Speed by the Hot-Wire Anemometer. NACA Rep. 320, 1929.
16. Favre, A.: Mesures Statistiques de la Corrélation dans le Temps. Premières applications à l'étude des mouvements turbulents en soufflerie. Pub. No. 67, Office Nat. d'Études et de Recherches Aéro., 1953.
17. Hastings, A. E., and Meade, J. E.: A Device for Computing Correlation Functions. *Rev. Sci. Instr.*, vol. 23, no. 7, July 1952, pp. 347-349.
18. Callaghan, Edmund E., Howes, Walton L., and Coles, Willard D.: Near Noise Field of a Jet-Engine Exhaust. II—Cross Correlation of Sound Pressures. NACA TN 3764, 1956.
19. Mickelsen, William R.: An Experimental Comparison of Lagrangian and Eulerian Correlation Coefficients in Homogeneous Isotropic Turbulence. NACA TN 3570, 1955.
20. Taylor, G. I.: The Spectrum of Turbulence. *Proc. Roy. Soc. (London)*, ser. A, vol. 164, Feb. 18, 1938, pp. 476-490.
21. Dryden, Hugh L., Schubauer, G. B., Mock, W. C., Jr., and Skramstad, H. K.: Measurements of Intensity and Scale of Wind-Tunnel Turbulence and Their Relation to the Critical Reynolds Number of Spheres. NACA Rep. 581, 1937.
22. Pai, Shih-I.: Fluid Dynamics of Jets. D. Van Nostrand Co., Inc., 1954.
23. von Kármán, Theodore: Progress in the Statistical Theory of Turbulence. *Proc. Nat. Acad. Sci.*, vol. 34, no. 11, Nov. 15, 1948, pp. 530-539.
24. Taylor, John F., Grimmett, H. L., and Comings, E. W.: Turbulent Mixing in a Isothermal Free Jet. Tech. Rep. No. 2, Univ. of Ill., Nov. 15, 1948. (Contract N6-ori-71, Task Order XI, Office Naval Res., Navy Dept.)

REPORT 1293

SIMILAR SOLUTIONS FOR THE COMPRESSIBLE LAMINAR BOUNDARY LAYER WITH HEAT TRANSFER AND PRESSURE GRADIENT^{1,2}

By CLARENCE B. COHEN and ELI RESHOTKO

SUMMARY

Stewartson's transformation is applied to the laminar compressible boundary-layer equations and the requirement of similarity is introduced, resulting in a set of ordinary nonlinear differential equations previously quoted by Stewartson, but unsolved. The requirements of the system are Prandtl number of 1.0, linear viscosity-temperature relation across the boundary layer, an isothermal surface, and the particular distributions of free-stream velocity consistent with similar solutions. This system admits axial pressure gradients of arbitrary magnitude, heat flux normal to the surface, and arbitrary Mach numbers.

The system of differential equations is transformed to an integral system, with the velocity ratio as the independent variable. For this system, solutions are found by digital computation for pressure gradients varying from that causing separation to the infinitely favorable gradient and for wall temperatures from absolute zero to twice the free-stream stagnation temperature. Some solutions for separated flows are also presented.

For favorable pressure gradients, the solutions are unique. For adverse pressure gradients, where the solutions are not unique, two of the infinite family of possible solutions are identified as the only solutions yielding finite displacement thicknesses. For the case of favorable pressure gradients with heated walls, the velocity within a portion of the boundary layer is shown to exceed the local external velocity. The variation of a Reynolds analogy parameter, which indicates the ratio of skin friction to heat transfer, is from zero to 7.4 for a surface of temperature twice the free-stream stagnation temperature, and from zero to 2.8 for a surface held at absolute zero, where the value 2 applies to a flat plate.

INTRODUCTION

Factors that affect the development of laminar boundary layers are pressure gradient, Mach number, and heat transfer, plus the properties of the fluid under consideration. Since mathematical complexities preclude solutions of this problem in a completely general fashion, the literature consists largely of solutions treating particular combinations of

these factors. For the flow of an ideal gas over a surface without pressure gradient, the remaining factors have been taken into account completely by Crocco (ref. 2) and Chapman and Rubesin (ref. 3). For small pressure gradients, Low (ref. 4) has, by a perturbation analysis, treated the general problem of the isothermal surface. With the introduction of pressure gradients of arbitrary magnitude, other restrictions become necessary. The assumption of constant fluid properties (density, viscosity, etc.), for example, leads to the greatest simplification—the separation of the momentum and energy equations. With this assumption, for a special case of a decelerating stream, Howarth (ref. 5) has obtained a series solution to the momentum equation. The introduction of a similarity concept (that the velocity or temperature profiles may always be expressed in terms of a single parameter) leads to a power-law free-stream velocity distribution. The momentum equation of this problem was first solved by Falkner and Skan (ref. 6), whose calculations were then improved by Hartree (ref. 7); the energy equation was later treated by Eckert (ref. 8) and others (refs. 9 and 10). For the same problem the restriction of constant fluid properties may be removed by alternatively requiring that the Mach number be essentially zero (ref. 11) or that the Mach number and the heat transfer be limited to small values (ref. 12).

Illingworth (ref. 13) and Stewartson (ref. 14) have demonstrated that, for an insulated surface in a fluid with a Prandtl number of 1.0, any compressible boundary-layer problem may be transformed to a corresponding problem in an incompressible fluid; the earlier solutions thus become applicable to certain compressible problems. For the case of heat flux across the surface, the transformation of Stewartson (ref. 14) with the concept of similarity introduced leads to a set of nonlinear ordinary differential equations previously quoted (ref. 14), but unsolved. Solutions to this set of equations, which are presented herein, are applicable to flows at arbitrary Mach number, pressure gradients of arbitrary magnitude (but of a form consistent with the requirements of similarity), and arbitrary but constant wall temperature.³

¹ Supersedes NACA TN 3325, "Similar Solutions for the Compressible Laminar Boundary Layer with Heat Transfer and Pressure Gradient," by Clarence B. Cohen and Eli Reshotko, 1955.
² The principal developments of this paper, which is part of the doctoral dissertation of the senior author (ref. 1), were carried out under the stimulus and guidance of Professor Luigi Crocco and the sponsorship of the Daniel and Florence Guggenheim Foundation. The final analysis and the computations were completed at the NACA Lewis laboratory during the spring of 1954.
³ Further solutions to these equations have been published recently by Levy (ref. 15) and by Li and Nagamatsu (ref. 16). The relation between these and the present solutions is described herein. The present investigation includes ranges of variables not treated in these references; for example, favorable pressure gradients applicable to supersonic nozzles and values of adverse pressure gradients including that causing separation. For adverse pressure gradients, the problems of uniqueness and multiple solutions are also considered in some detail. The solutions of refs. 15 and 16 were obtained by means of a differential analyzer, whereas the present solutions were obtained by digital calculation and are presented in tabular form.

Since free-stream velocity distributions of the form required by similarity are not generally encountered in practice, the utility of these solutions is principally as follows: (1) The effects of pressure gradient, wall temperature, and Mach number may be viewed qualitatively; (2) the results may be used as a check on any approximate method (such as a Kármán-Pohlhausen method) for reliability; (3) the flow to be solved may be divided intuitively into segments, and the solution for each segment may be matched by some arbitrary technique; or (4) the results may be used to construct a new simple method (of the integral type) for the calculation of the laminar compressible boundary layer with heat transfer. This latter analysis has been carried out, utilizing the solutions herein given, and is presented in reference 17.

STEWARTSON'S EQUATIONS

BOUNDARY-LAYER EQUATIONS

The equations of the steady two-dimensional compressible laminar boundary layer for perfect fluids are:

Continuity:

$$\frac{\partial}{\partial x}(\rho u) + \frac{\partial}{\partial y}(\rho v) = 0 \quad (1)$$

Momentum:

$$\left. \begin{aligned} \rho u \frac{\partial u}{\partial x} + \rho v \frac{\partial u}{\partial y} &= -\frac{\partial p}{\partial x} + \frac{\partial}{\partial y} \left(\mu \frac{\partial u}{\partial y} \right) \\ \frac{\partial p}{\partial y} &= 0 \end{aligned} \right\} \quad (2)$$

Energy:

$$\rho u \frac{\partial h}{\partial x} + \rho v \frac{\partial h}{\partial y} = u \frac{\partial p}{\partial x} + \frac{\partial}{\partial y} \left(\frac{\mu}{Pr} \frac{\partial h}{\partial y} \right) + \mu \left(\frac{\partial u}{\partial y} \right)^2 \quad (3)$$

(All symbols are defined in appendix A.)

The viscosity law to be assumed is

$$\frac{\mu}{\mu_0} = \lambda \frac{t}{t_0} \quad (4)$$

Equation (4) is of the form taken by Chapman and Rubesin (ref. 3), except that the reference conditions (μ_0, t_0) are free-stream stagnation values, since in the presence of pressure gradient the local "external" values are not constant along the outer edge of the boundary layer. The constant λ is used to match the viscosity with the Sutherland value at a desired station. If this station is taken to be the surface, assumed to be at constant temperature, the result is

$$\lambda = \sqrt{\frac{t_w}{t_0} \left(\frac{t_0 + k_{su}}{t_w + k_{su}} \right)} \quad (5)$$

where k_{su} = Sutherland's constant (for air, $k_{su} = 198.6^\circ \text{R}$). The viscosity law of equations (4) and (5) was demonstrated to be adequate for a flat plate (ref. 3) by comparison with the more exact calculations of reference 2. In the present case no such comparison is available.

STEWARTSON'S TRANSFORMATION

The velocities in the equations of motion (1) to (3) can be replaced through the definition of a stream function:

$$\left. \begin{aligned} \psi_y &= \frac{\rho u}{\rho_0} \\ \psi_x &= -\frac{\rho v}{\rho_0} \end{aligned} \right\} \quad (6a)$$

If the quantity λ is introduced from equation (4), a slight modification of Stewartson's transformation may be written

$$\left. \begin{aligned} X &= \int_0^x \lambda \frac{p_e a_e}{p_0 a_0} dx \\ Y &= \frac{a_e}{a_0} \int_0^y \frac{\rho}{\rho_0} dy \end{aligned} \right\} \quad (6b)$$

The transformed coordinates are now represented by upper-case letters (X, Y) , and the subscript e refers to local conditions at the outer edge of the boundary layer (external). The subscript 0 refers to free-stream stagnation values.

Applying equations (4) and (6) to the boundary-layer equations (1), (2), and (3) and assuming that Pr and c_p are constant (but not yet requiring that $Pr=1$) result in the following equations:

$$U_X + V_Y = 0 \quad (7)$$

$$UU_X + VU_Y = U_e U_{eX} (1 + S) + \nu_0 U_{YY} \quad (8)$$

$$US_X + VS_Y = \nu_0 \left\{ \frac{S_{YY}}{Pr} - \frac{1-Pr}{Pr} \left(\frac{\frac{\gamma-1}{2} M_e^2}{1 + \frac{\gamma-1}{2} M_e^2} \right) \left[\left(\frac{U}{U_e} \right)^2 \right]_{YY} \right\} \quad (9)$$

where the enthalpy function S is defined for convenience as

$$S = \frac{h_s}{h_0} - 1 \quad (10)$$

and h_s is the local stagnation enthalpy. The stream function has been replaced by the transformed velocities (U, V) through the relations

$$U \equiv \psi_Y$$

$$V \equiv -\psi_X$$

The resulting relation between the transformed and physical longitudinal velocities is $U = \frac{a_0}{a_e} u$.

The boundary conditions applicable to the system (7) to (9) are:

$$\left. \begin{aligned} U(X, 0) &= 0 \\ V(X, 0) &= 0 \\ S(X, 0) &= S_w \text{ or } \left[\frac{\partial S}{\partial Y}(X, 0) = \left(\frac{\partial S}{\partial Y} \right)_w \right] \\ \lim_{Y \rightarrow \infty} S &= 0 \\ \lim_{Y \rightarrow \infty} U &= U_e(X) \end{aligned} \right\} \quad (11)$$

The solution $S=0$ and the resultant continuity and momentum equations (7) and (8) make up the extremely useful correlation developed by Stewartson between compressible and incompressible boundary layers on insulated surfaces with $Pr=1$. Another special case is that of $U_{e,x}=0$. Then, if $Pr=1$, the relation $S=S_w \left(1 - \frac{U}{U_e}\right)$ satisfies equation (9); this is Crocco's integral of the energy equation for the flat plate (ref. 2).

SIMILARITY REQUIREMENTS

When a pressure gradient exists and the surface is not insulated, it is necessary to find a means of solving the system (7) to (9) subject to the boundary conditions (11). To this end, the question will be asked: Under what conditions can this system be reduced to a system of ordinary differential equations by the assumption that the boundary-layer profiles are functions of a similarity variable η and that the wall temperature is constant? This question may be resolved by inserting the following assumed relations into the system (7) to (9) and observing the conditions required for obtaining ordinary differential equations:

$$\left. \begin{aligned} \psi &= AX^a U_e^p f(\eta) \\ Y &= BX^b U_e^q \eta \\ S &= S(\eta) \end{aligned} \right\} \quad (12)$$

where A, B, a, b, p , and q are undetermined constants. This procedure has been carried out by Li and Nagamatsu (ref. 18) for $Pr=1$. In that analysis it was concluded that four classes of similar solutions are possible. It has been pointed out (ref. 19) that three of these four classes can be reduced identically to the case which requires that

$$U_e = CX^m \quad (13)$$

while the remaining case requires that

$$U_e = C_1 \exp(C_2 X) \quad (14)^4$$

Corresponding analyses for incompressible flow, including conditions for similarity and the case of the exponential free-stream velocity, have been made by Mangler (ref. 20) and Goldstein (ref. 21), respectively.

When equations (12) are used in the form

$$\left. \begin{aligned} \psi &= f(\eta) \sqrt{\frac{2\nu_0 U_e X}{m+1}} \\ \eta &= Y \sqrt{\frac{m+1}{2} \frac{U_e}{\nu_0 X}} \end{aligned} \right\} \quad (15)$$

the system of ordinary differential equations corresponding to the power-law velocity distribution of equation (13) may be written

$$\left. \begin{aligned} f''' + ff'' &= \beta(f'^2 - 1 - S) \\ S'' + PrfS' &= (1 - Pr) \left[\frac{(\gamma-1)M_e^2}{1 + \frac{\gamma-1}{2} M_e^2} \right] (f'f''' + f''^2) \end{aligned} \right\} \quad (16)$$

The pressure-gradient parameter β is defined as $\beta = \frac{2m}{m+1}$, and the velocity ratio is $U/U_e = u/u_e = f'$, where primes denote differentiation with respect to η .

The boundary conditions are

$$\left. \begin{aligned} f(0) &= f'(0) = 0 \\ S(0) &= S_w \\ \lim_{\eta \rightarrow \infty} f' &= 1 \\ \lim_{\eta \rightarrow \infty} S &= 0 \end{aligned} \right\} \quad (17)$$

Since M_e may, in general, depend on x , the right member of the energy equation is not yet functionally consistent with the left member for arbitrary M_e and Pr . Thus, the right member of the energy equation (16) must be zero or a function of η to be consistent with the left member. This may be achieved in the following ways: (1) The external Mach number may be a constant other than zero; (2) the external Mach number may be zero; (3) the Prandtl number may equal 1; (4) the factor

$$\left[\frac{(\gamma-1)M_e^2}{1 + \frac{\gamma-1}{2} M_e^2} \right]$$

may be approximately 2 corresponding to hypersonic flow; or (5) the ratio of specific heats γ may equal 1.

The case of constant external Mach number is the flat-plate problem ($\beta=0$) and, the solution to the momentum equation being known, the energy equation could be integrated directly. The flat-plate problem has already been solved with great accuracy and completeness by Crocco (ref. 2). If the pressure gradient is small enough, it may be reasonable to consider M_e constant in the energy equation in spite of the gradient, but to retain the pressure-gradient parameter in the momentum equation. However, this problem is treated more completely by the analysis of reference 4.

The case $M_e=0$ (with arbitrary β) produces the equations of Levy and Seban (ref. 22). In that analysis approximate solutions were obtained by the assumption of simple forms for the velocity and temperature profiles that contained undetermined coefficients. These coefficients were then evaluated by use of the boundary conditions. Because the actual profiles cannot be simply represented, this method is not reliable in some ranges even if the Mach number is nearly zero. Brown and Donoughe (ref. 11) also considered the low Mach number problem with variable fluid properties and $Pr_w=0.7$. The system of equations encountered in that analysis is much more complicated than the present system because of the power-law viscosity, conductivity, and specific-heat relations used. These refinements do not alter the effects of omitting the viscous-dissipation and compressive-work terms, which may be significant at higher Mach numbers.

⁴ It was shown in reference 19 that, for the exponential case (eq. (14)) with $C_2 > 0$, the system (7) to (9) can be reduced to the ordinary differential equations (16), but with $\beta=2$. For $C_2 < 0$, the f''' term in equations (16) is replaced by $-f'''$. In this case, with $S=0$, it can be shown that, because of the sign of the f''' term, no solution is possible in which the velocity ratio approaches the boundary condition smoothly. A question is thus raised as to the validity of any possible solution for $C_2 < 0$ regardless of the value of S . For the remainder of this paper, this class will be omitted from consideration.

The case of hypersonic flow requires the introduction of the effects of displacement thickness upon pressure gradient. For example, for the flat plate, Lees (ref. 23) has shown that the induced hypersonic pressure gradient corresponds to $\beta = \frac{\gamma-1}{\gamma}$. This case is not treated herein.

The possibility of assuming $\gamma=1$ does not simplify the equations more than does the assumption of Mach number zero. For most gases, the assumption of $\gamma=1$ is physically unreasonable. Therefore, this case does not appear to warrant further consideration.

If strong pressure gradients and reasonably high Mach numbers are to be considered, the most inclusive category is that of $Pr=1$, with the result that equations (16) become

$$f''' + ff'' = \beta(f'^2 - 1 - S) \quad (18a)$$

$$S'' + fS' = 0 \quad (18b)$$

with the boundary conditions (17). Equations (18) were derived by Stewartson by assigning similarity relations corresponding to (15) to the system (7) to (9) with $Pr=1$; however, no solution was indicated.

The comparison between assuming that $M_e=0$ or that $Pr=1$ may perhaps be indicated by examination of the solutions to the insulated-flat-plate problem, which include effects of both Prandtl number and Mach number (ref. 2). If $M_e=0$, the viscous-dissipation and compressive-work terms are omitted in equation (3). Then the predicted static-temperature profile is a constant rather than the correct variation from free-stream static to recovery temperature at the wall. However, if $Pr=1$ is assumed, a constant stagnation temperature is predicted rather than the actual slight variation in this quantity. The latter discrepancy is small compared with the former.

METHOD OF SOLUTION

Equations (18) with boundary conditions (17) compose the system to be solved for the dependent variables $f(\eta)$ and $S(\eta)$. Because of the nonlinearity of the system, its high order (fifth), and its classification as a "two-point boundary-value problem," no standard integration methods will yield results expressible in closed form. Methods applicable to equations of this type may be classified as either (1) forward integrations or (2) integrations by methods of successive approximations.

By "forward integration" is meant the progressive integration of the equations from one (initial) boundary to the other. For this purpose several sets of initial values of the derivatives are assumed. Then the final boundary values obtained are compared with those specified and, after interpolation of the initial values, this trial-and-error process is repeated until the final boundary conditions are satisfied. The integrations may be carried out by the use of either an analog computer (mechanical or electrical) giving continuous integrals or by digital computations involving finite-difference integration. Although generally applicable, a disadvantage associated with forward integration of nonlinear equations is the lack of any inherent convergence mechanism. Thus, the approach to the correct initial values depends al-

most entirely on the intuition and experience of the one performing the calculations. This method is particularly troublesome for a problem with more than one dependent variable, since evidence for the fitness of a given initial value may be obscured by a poor selection of the corresponding initial value of another dependent variable. Furthermore, when an analog computer is employed, the accuracy is generally limited, particularly for nonlinear equations where in certain regions the results tend to be highly sensitive to the chosen initial values. If digital computation is utilized to obtain a desired degree of accuracy, the procedure may become excessively tedious.

Successive approximation methods generally assume an entire function for the dependent variables (satisfying as many of the boundary conditions as possible) rather than only the initial derivatives. Then, by use of the differential equations, a procedure is developed for estimating the error as a function of the independent variables. This error is applied to the original choice, and the process is repeated until satisfactory convergence occurs. An example of a method of successive approximation is Picard's method.

A difficulty shared by both these methods arises when the range of integration is infinite. Then it is necessary to decide upon a finite value of the independent variable at which the boundary conditions may be approximately satisfied and the degree to which they may be satisfied. This suggests the desirability of changing to an independent variable so that only a finite range of integration is required. In the present problem this change of variables can be achieved by following a method used by Crocco for the solution of the compressible flat-plate boundary layer (ref. 2). The concept is advanced that the velocity is a more suitable independent variable since it is bounded. This concept leads to a set of equations conveniently handled by a method of successive approximations.

TRANSFORMATION TO VELOCITY PLANE

To accomplish the transformation to the velocity ratio f' as the independent variable, the following identity may be used:

$$\frac{d}{d\eta} \equiv f'' \frac{d}{df'} \quad (19)$$

This identity may be applied to f'' and f as follows:

$$\left. \begin{aligned} f''' &= f'' \frac{df''}{df'} \\ f &= \int_0^\eta f' d\eta = \int_0^{f'} \frac{f' df'}{f''} = \int_0^{f'} \frac{\xi d\xi}{f''(\xi)} \end{aligned} \right\} \quad (20)$$

where the dummy variable of integration is ξ , and $f''(\xi)$ represents the functional relation between f'' and f' , that is $f''(f')$. The primes continue to denote differentiation with respect to η .

Inserting equations (20) into the momentum equation (18a) results in

$$\frac{df''}{df'} = - \int_0^{f'} \frac{\xi d\xi}{f''(\xi)} + \beta \frac{f'^2 - 1 - S}{f''} \quad (21)$$

which satisfies the following condition at $f'=0$ required by the momentum equation

$$f''_w = -\beta(1+S_w) \quad (22)$$

Now, if equation (21) is integrated once with respect to f' and if the limits of integration are chosen so that $(f'')_{f'=1}=0$, the result is

$$f'' = \int_{f'}^1 d\xi_1 \int_0^{\xi_1} \frac{\xi d\xi}{f''(\xi)} - \beta \int_{f'}^1 \frac{\xi^2 - 1 - S(\xi)}{f''(\xi)} d\xi \quad (23)$$

By inverting the order of integration (or by integrating by parts) the double integral may be reduced to two single integrals, resulting in

$$f''_{j+1}(f') = (1-f') \int_0^{f'} \frac{\xi d\xi}{f''_j(\xi)} + \int_{f'}^1 \frac{(1-\xi)\xi d\xi}{f''_j(\xi)} - \beta \int_{f'}^1 \frac{\xi^2 - 1 - S_j(\xi)}{f''_j(\xi)} d\xi \quad (24)$$

Equation (24) is the form of the momentum equation as it will be used in this report. The subscript j is the iteration number in the method of successive approximations.

A corresponding form of the energy equation is obtained by writing equation (18b) as

$$\frac{S''}{S'} = -f$$

and integrating with respect to η , to get

$$\ln S' = - \int f d\eta + \text{constant} \quad (25)$$

Equation (18a) may be written

$$\begin{aligned} f d\eta &= - \frac{f'''}{f''} d\eta + \beta \frac{(f'^2 - 1 - S)}{f''} d\eta \\ &= - \frac{df''}{f''} + \beta \frac{(f'^2 - 1 - S)}{(f'')^2} df' \end{aligned}$$

Substitution of this expression into equation (25) results in

$$\ln S' = \int \frac{df''}{f''} - \beta \int \frac{\xi^2 - 1 - S(\xi)}{[f''(\xi)]^2} d\xi + \text{constant}$$

or the equivalent expression

$$S' = -C_3 f'' J(f') \quad (26)$$

where

$$J(\xi) = \exp \left[-\beta \int_0^\xi \frac{\xi_1^2 - 1 - S(\xi_1)}{[f''(\xi_1)]^2} d\xi_1 \right]$$

If this expression is integrated once again and the boundary conditions $S(0)=S_w$, $(S')_{f'=1}=0$ are required, the result is

$$\frac{S_{j+1}}{S_w} = \frac{\int_{f'}^1 J_j(\xi) d\xi}{\int_0^1 J_j(\xi) d\xi} \quad (27)$$

Inspection of equations (24) and (27) indicates that the integrals to be evaluated are singular, or indeterminate, at

the upper limit. To evaluate these integrals, closed-form expressions must be obtained for the integrands in this range. This requires knowledge of the solution of the system (18) for large η (near $f'=1$). This "asymptotic solution" and its development are given in appendix B. The results show that equation (24) can be used in its present form, but that equation (27) must be modified to

$$\frac{S_{j+1}}{S_w} = \frac{\epsilon J_j(1-\epsilon) + \int_{f'}^{1-\epsilon} J_j(\xi) d\xi}{\epsilon J_j(1-\epsilon) + \int_0^{1-\epsilon} J_j(\xi) d\xi} \quad (28)$$

where ϵ is an arbitrary small quantity ($\epsilon \ll 1$). In this form the singularity has been removed. Equations (24) and (28) constitute the system used in the present investigation. The convergence of this system is discussed in appendix C, and the method of calculation by digital computer in appendix D.

PROPERTIES OF SOLUTIONS

In the following sections the solutions obtained in this study are presented and their properties are discussed. The two parameters defining a case are S_w and β . The enthalpy function evaluated at the wall S_w determines the wall temperature through the relation

$$t_w = t_0(1+S_w) \quad (29)$$

Thus, $S_w = -1$ corresponds to a wall temperature of absolute zero, and $S_w = 1$ corresponds to a wall at twice the free-stream stagnation temperature. The case $S_w = 0$ corresponds to a wall at the free-stream stagnation temperature, which for $Pr=1$ is the case of an insulated surface.

The pressure-gradient parameter β is related to the exponent m of the velocity distribution in the transformed plane $U_e = CX^m$ through the relation

$$\beta = \frac{2m}{m+1}$$

For a velocity distribution of this form, m can be represented as

$$m = \left(\frac{u_{ex}}{u_e} \right) \frac{t_0}{t_e} (a_e p_e)^{-1} \int_0^x a_e p_e dx \quad (30)$$

It is apparent that $\beta < 0$ ($m < 0$) corresponds to an unfavorable gradient; $\beta = 0$ ($m = 0$) corresponds to flat-plate flow; and $\beta = 2$ ($m = \infty$) corresponds to an infinitely favorable pressure gradient. Stewartson (ref. 14) has shown that $\beta = 1$ ($m = 1$) corresponds to flow in the immediate vicinity of a stagnation point for two-dimensional flow, as in the incompressible case. It can be shown that the case of a stagnation point in axisymmetric flow can be transformed to the solution for $\beta = 1/2$ (ref. 24). An approximate method for relating β to more general physical flows is given in reference 17. In the present investigation, solutions are found for pressure gradients ranging from that causing separation to the infinitely favorable gradient and for wall temperatures from absolute zero to twice free-stream stagnation temperature.⁵

⁵ It should be noted that all but one of the presented solutions for $S_w=0$ are those first obtained by Hartree (ref. 7) for the problem of Falkner and Skan (ref. 6). As a further check on the present method, the solutions for $\beta=1.6$ and 2.0 with $S_w=0$ were obtained independently in the present investigation; these values agree very well with those of Hartree.

All solutions are presented in tabular and graphic form. Table I shows the values of f , f' , f'' , S , and S' tabulated against η . From these values and equations (18), the quantities f''' and S'' can be easily calculated. Table II presents a summary of the values of f_w'' (related to wall shear) and S_w' (related to heat transfer) from table I, as well as the Reynolds analogy parameter $C_f Re_w / Nu$, which represents the ratio of skin-friction to heat-transfer effects. Certain other quantities of interest cannot be tabulated in general, but can be easily calculated from the following formulas:

Static-temperature ratio:

$$\frac{t}{t_e} = \left(1 + \frac{\gamma-1}{2} M_e^2\right) (1+S) - \frac{\gamma-1}{2} M_e^2 f'^2 \quad (31)$$

or, with the static temperature t referred to the free-stream stagnation temperature t_0 ,

$$\frac{t}{t_0} = (1+S) - \left(\frac{\frac{\gamma-1}{2} M_e^2}{1 + \frac{\gamma-1}{2} M_e^2} \right) f'^2 \quad (32)$$

Flux density:

$$\frac{\rho u}{\rho_e U_e} = \frac{f'}{\left(1 + \frac{\gamma-1}{2} M_e^2\right) (1+S) - \frac{\gamma-1}{2} M_e^2 f'^2} \quad (33)$$

UNIQUENESS

For $\beta < 0$, $S_w = 0$, Hartree (ref. 7) first observed that the boundary conditions (17) are not sufficient to determine a unique solution. Thus, there is not a unique value of f_w'' for a given β . In studying the uniqueness, it is useful to consider the following expression for velocity ratio (for any S_w) valid for large η :

$$f' = 1 + \left[\alpha_1 (\eta - \kappa)^{-(2\beta+1)} + \frac{\alpha_3}{2} (\eta - \kappa)^{-1} \right] \exp \left[-\frac{(\eta - \kappa)^2}{2} \right] + \alpha_2 (\eta - \kappa)^{2\beta} \quad (34)$$

where α_1 , α_2 , α_3 , and κ are integration constants (see appendix B). For the case of $S_w = 0$, α_3 is also equal to zero; however, this does not change the uniqueness problem, which is independent of wall temperature. For $\beta > 0$, α_2 is necessarily zero in order to satisfy the boundary condition $\lim_{\eta \rightarrow \infty} f' = 1$.

For continuity in β , Hartree then selected the asymptotic solution with $\alpha_2 = 0$ for $\beta < 0$ also. More importantly, the integral

$$\int_0^\infty \left(1 - \frac{\rho u}{\rho_e U_e}\right) d\eta$$

related to the displacement thickness, can be shown to become infinite for $\alpha_2 \neq 0$. This result is contrary to the concept of a thin layer outside of which the viscous effects may be neglected. A further interpretation of the effect of the α_2 term on the solution can be observed by examination of the dimensionless quantity f'''/ff'' (suggested by Professors L. Crocco and L. Lees), in which f''' represents the

net viscous forces acting on the fluid element and f'' is proportional to the velocity gradient (shearing flow). It can be shown that for $\alpha_2 = 0$

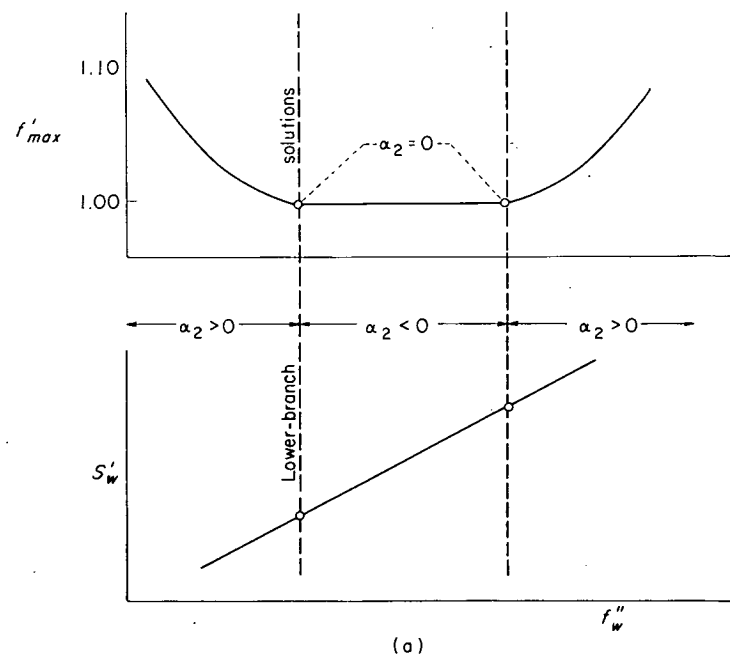
$$\lim_{\eta \rightarrow \infty} \left(-\frac{f'''}{ff''} \right) = 1$$

while for $\alpha_2 \neq 0$

$$\lim_{\eta \rightarrow \infty} \left(-\frac{f'''}{ff''} \right) = \lim_{\eta \rightarrow \infty} \frac{1-2\beta}{(\eta-\kappa)^2} = 0$$

Thus, in order to retain both the viscous forces in the asymptotic region and the shearing flow set up by their action to the same order of magnitude, α_2 should be taken equal to zero.

Another feature of solutions with α_2 different from zero is the analytical result that the velocity ratio in the outer portion of the boundary layer may exceed unity. For example, if α_2 is not zero, equation (34) shows that for large η the α_2 term of the velocity ratio expression is dominant and thus $(f' - 1)$ is necessarily of the same sign as α_2 . That is, for positive α_2 , the velocity ratio approaches unity from above; this phenomenon will be termed "velocity overshoot." Since, for a given β and S_w in this range, each of these various solutions has associated with it a different set of values of f_w'' and S_w' , one of these parameters, for example f_w'' , can be conveniently used in place of α_2 to identify the various solutions. This infinite set of solutions can be represented as in sketch (a) for a typical (cold wall) case



It is seen that there are a maximum and a minimum shear (represented by f_w'') and heat transfer (represented by S_w') that can satisfy the equations without incurring velocity overshoot. These distinct solutions (circled points in sketch (a)) correspond to $\alpha_2 = 0$; that with the lower shear is designated the "lower-branch" solution. The behavior

* In the evaluation of the singularities of the integrals required for the method of successive approximations, α_2 was taken to be zero. Hence, solutions for $\alpha_2 \neq 0$ were obtained by forward integration (appendix D), although the numerical values of α_2 were not determined.

of the calculated family of solutions is presented in figure 1 for $S_w = -0.8$ and $\beta = -0.325$, -0.3285 , and -0.336 . For a given value of S_w , as β is decreased, the two solutions with $\alpha_2 = 0$ approach each other. At a value of β to be designated β_{min} , these two solutions become identical, and, for $\beta < \beta_{min}$, no solution with $\alpha_2 = 0$ exists. For negative β , only the solutions with finite displacement thickness will be considered in the remainder of this report.

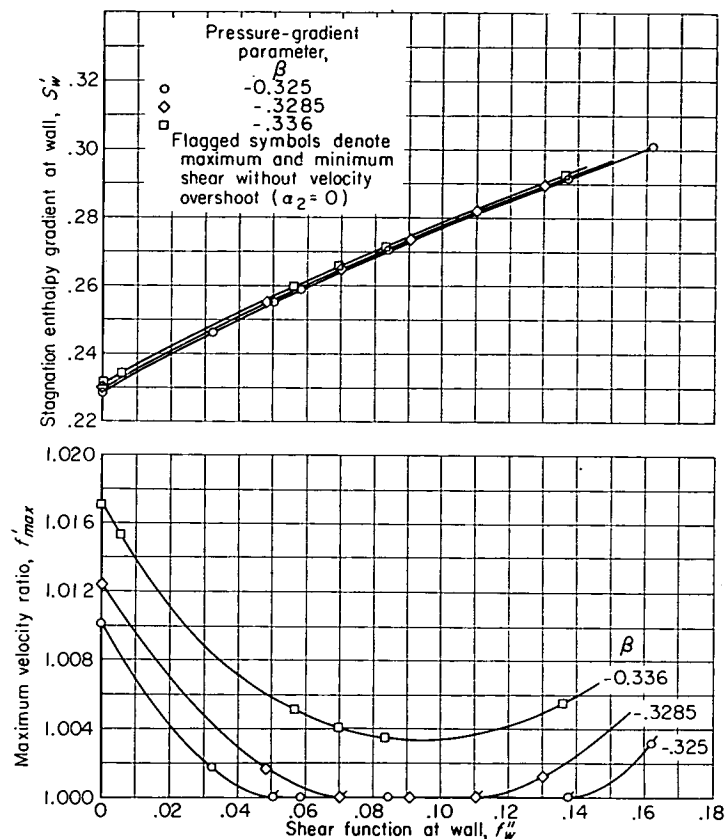


FIGURE 1.—Family of solutions for adverse pressure gradient.
 $S_w = -0.8$.

With regard to the physical significance of the double solution, it may be noted that for adverse pressure gradients ($\beta < 0$) a real flow cannot completely reproduce the similar solution, because $U_e(0) = \infty$ would be involved. However, a pressure field can, in principle, be applied to a developing boundary layer so that, after a phase of adjustment, the boundary layer would approach one of the similar solutions with $\beta < 0$ and stay quite close to it thereafter. It seems reasonable to believe that, depending on the way the pressure field is applied, one solution or the other corresponding to the same β could be approached after different adjustment phases. This result is exactly what Clauser (ref. 25) has found in his experimental work on similar turbulent boundary-layer flows.

VELOCITY AND TEMPERATURE PROFILES

The velocity and enthalpy-function profiles obtained from the tabulated solutions are presented as functions of η in figures 2 and 3, respectively. The distance y normal to the surface in the physical plane is related to the similarity

variable η through equations (6) and (15), and may be expressed as

$$y = \frac{p_0 a_0}{p_e a_e} \sqrt{\frac{2}{m+1}} \frac{v_0 X}{U_e} \int_0^\eta \frac{t}{t_0} d\eta \quad (35)$$

where t/t_0 is given by equation (32).

Velocity overshoot.—The velocity profiles shown in figure 2 indicate that, for a given wall temperature, the initial slope increases as the pressure gradient becomes more favorable. For adverse pressure gradients an inflection point occurs within the boundary layer and moves outward as the gradient becomes more adverse. The velocity ratio varies monotonically from zero to the final value of 1.0 except for the cases of favorable pressure gradients with heated walls. Then the velocity ratio in the outer portion of the boundary layer reaches a maximum value greater than 1.0 before returning to its final value of 1.0. This type of velocity overshoot was also obtained in the investigation of reference 11 for favorable pressure gradients with heated walls and is to be distinguished from that associated with the nonunique ($\alpha_2 \neq 0$) solutions which occur only for adverse pressure gradients. When the wall is heated in a favorable-pressure-gradient flow, the density within certain layers of the boundary layer is lowered so that, in spite of the viscous retardation, the flow is accelerated more than the external flow by the external pressure forces. Thus, a velocity greater than the external velocity may be obtained.

This phenomenon can be established by examination of equation (34) and the corresponding asymptotic expression for the enthalpy function (appendix B):

$$S = \alpha_3 (\eta - \kappa)^{-1} \exp \left[-\frac{(\eta - \kappa)^2}{2} \right] \quad (36)$$

For favorable pressure gradients, $\alpha_2 = 0$, as previously mentioned. Then, the α_3 term in equation (34) is dominant for large η . Thus, $(f' - 1)$ and α_3 are of the same sign. Hence, for any case of a heated wall (α_3 positive, eq. (36)) with favorable pressure gradient the velocity ratio must finally approach 1.0 from above. This is in contrast to the results of reference 16 where "critical" values of S_w greater than zero were said to be required to produce overshoot. The latter results are possibly due to the inability to detect small overshoot using an analog computer.

Stagnation-temperature profiles.—Figure 3 shows that, for $Pr = 1$, the stagnation temperature varies monotonically across the boundary layer from the wall value to the free-stream value. For favorable pressure gradients with a cold wall, there is small variation with β of this distribution. The variation becomes more pronounced with an increase in wall temperature.

Boundary-layer thickness.—The velocity profiles (fig. 2) indicate that the boundary layer thickens as the wall shear stress diminishes. Also, for a given value of the pressure-gradient parameter β , the boundary layer, when considered in terms of η , thickens as the wall temperature is lowered. However, in the physical plane (in terms of y) because of the relation between y and η (eq. (35)), the trend is just the

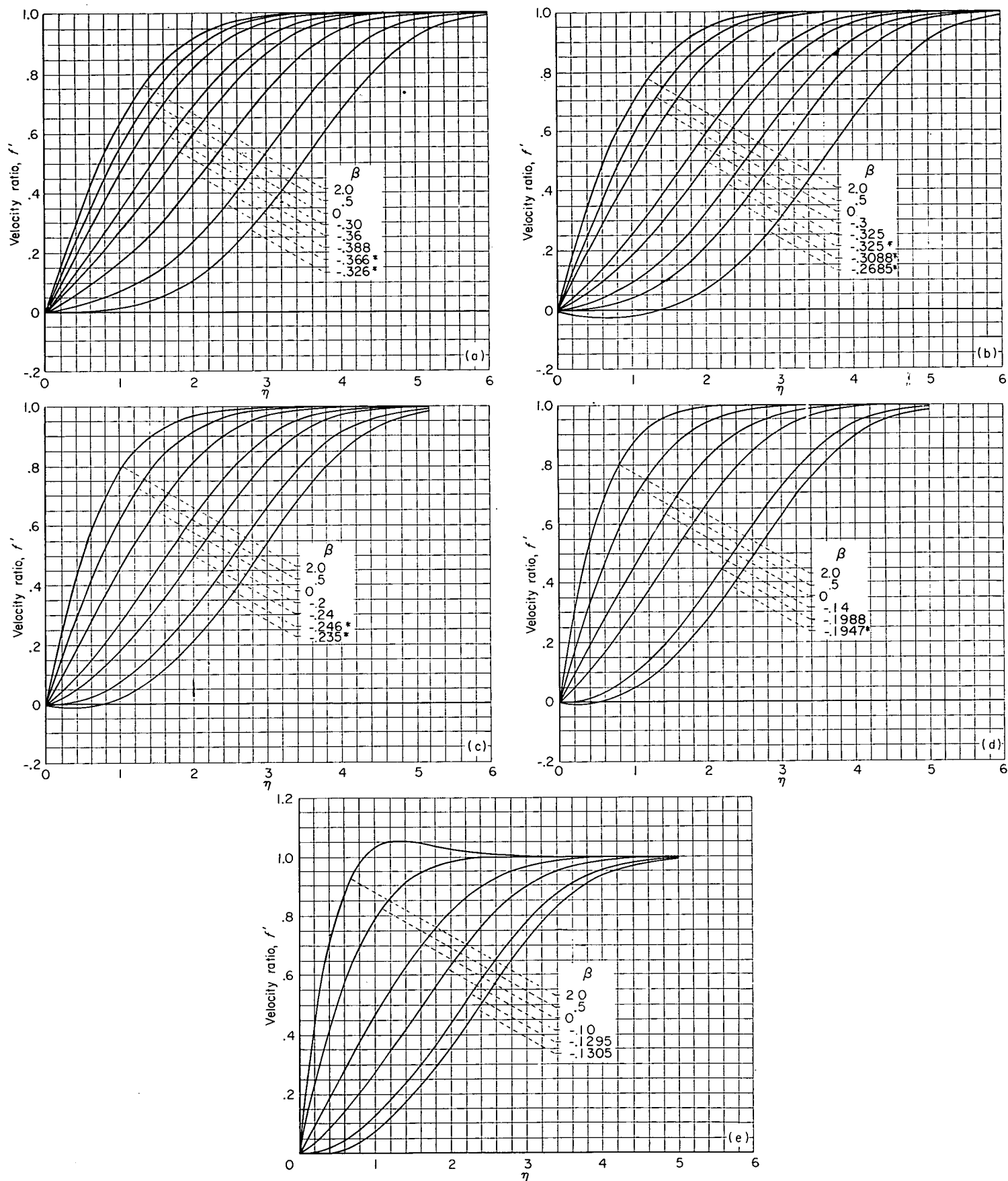


FIGURE 2.—Velocity profiles as functions of similarity variable η . (Asterisk denotes lower-branch solutions.)

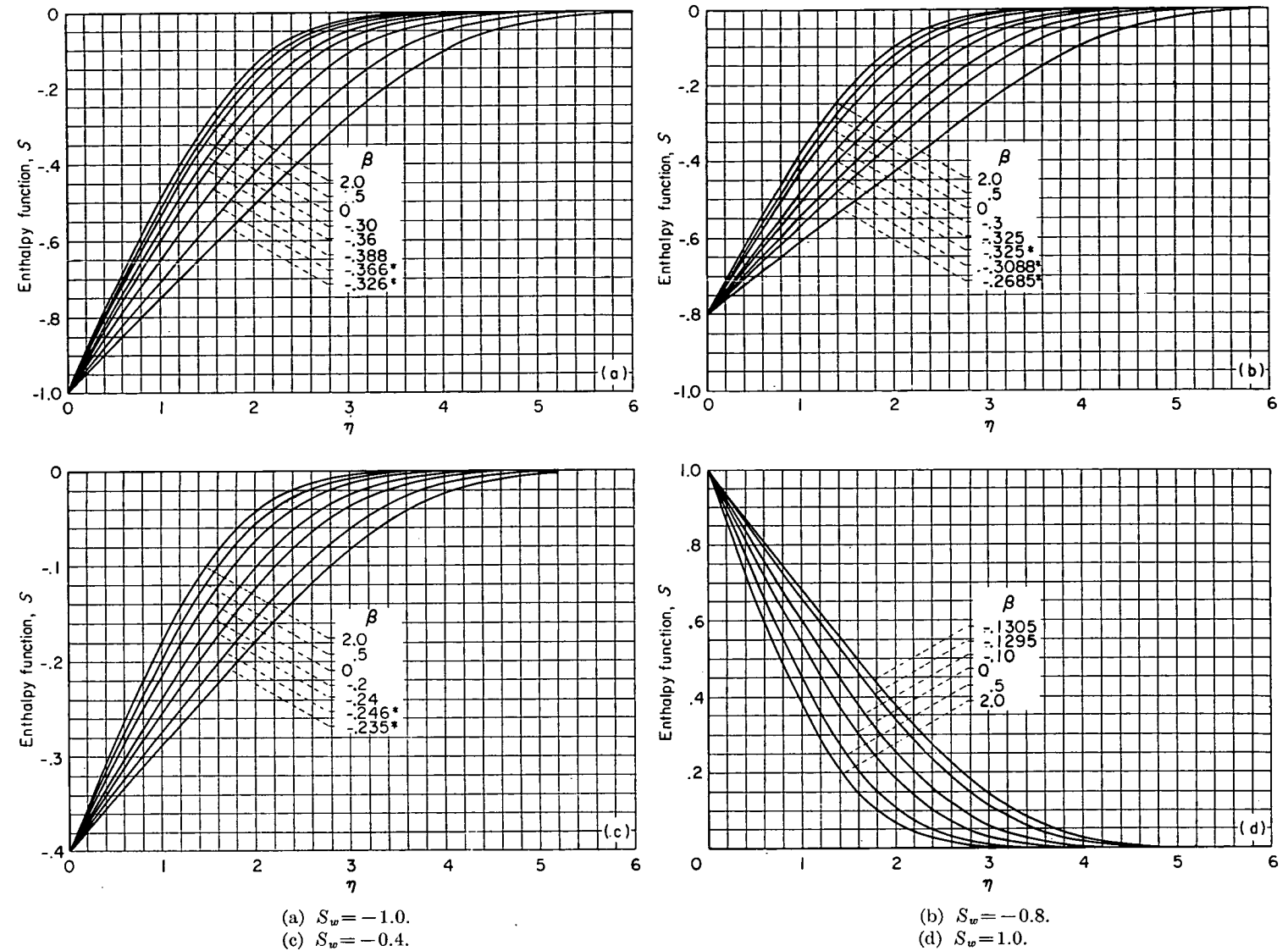


FIGURE 3.—Enthalpy function profiles.

(Asterisk denotes lower-branch solutions.)

opposite. This emphasizes the necessity for careful consideration of the relation between the transformed quantities and their physical counterparts.

The thermal boundary layer also thickens as separation is approached. The relative thicknesses of the dynamic and thermal boundary layers may be conveniently observed from a plot of S against f' (fig. 4). Then if a fixed fraction of S_w , say 0.99, is chosen to define the thermal-layer thickness and if the same value of velocity ratio is taken to define the dynamic layer, it can be seen that, regardless of wall temperature, the thermal layer is thicker than the dynamic layer for favorable gradients and thinner for adverse gradients.

For $Pr < 1$ the relative magnitude of the dynamic thickness to the thermal thickness will be decreased, since the Prandtl number represents the ratio of viscous to thermal effects in the fluid.

INTEGRAL THICKNESSES

The boundary-layer integral thicknesses in the transformed plane are defined by the following relations:

Displacement thickness:

$$\frac{\delta_{tr}^*}{X} \sqrt{\frac{m+1}{2} \frac{U_e X}{\nu_0}} = \int_0^\infty (1-f'+S) d\eta = \int_0^1 \frac{[1-\xi+S(\xi)]}{f''(\xi)} d\xi \quad (37)$$

Momentum thickness:

$$\frac{\theta_{tr}}{X} \sqrt{\frac{m+1}{2} \frac{U_e X}{\nu_0}} = \int_0^\infty f'(1-f') d\eta = \int_0^1 \frac{\xi(1-\xi)}{f''(\xi)} d\xi \quad (38)$$

Thermal thickness:

$$\frac{\mathcal{E}}{X} \sqrt{\frac{m+1}{2} \frac{U_e X}{\nu_0}} = \int_0^\infty S d\eta = \int_0^1 \frac{S(\xi)}{f''(\xi)} d\xi \quad (39)$$

Convection thickness:

$$\frac{E}{X} \sqrt{\frac{m+1}{2} \frac{U_e X}{\nu_0}} = \int_0^\infty S f' d\eta = -S'_w \quad (40)$$

The numerical values of these thickness parameters for the solutions presented are given in table II. The transformed displacement thickness is negative for cases of favorable pressure gradient with very low wall temperature. This occurs because the surface cooling produces an increase in density near the wall so that there is more mass flow per unit flow area within the boundary layer than in the external flow.

The form factor $H_{tr} = \frac{\delta_{tr}^*}{\theta_{tr}}$ is also listed in table II.

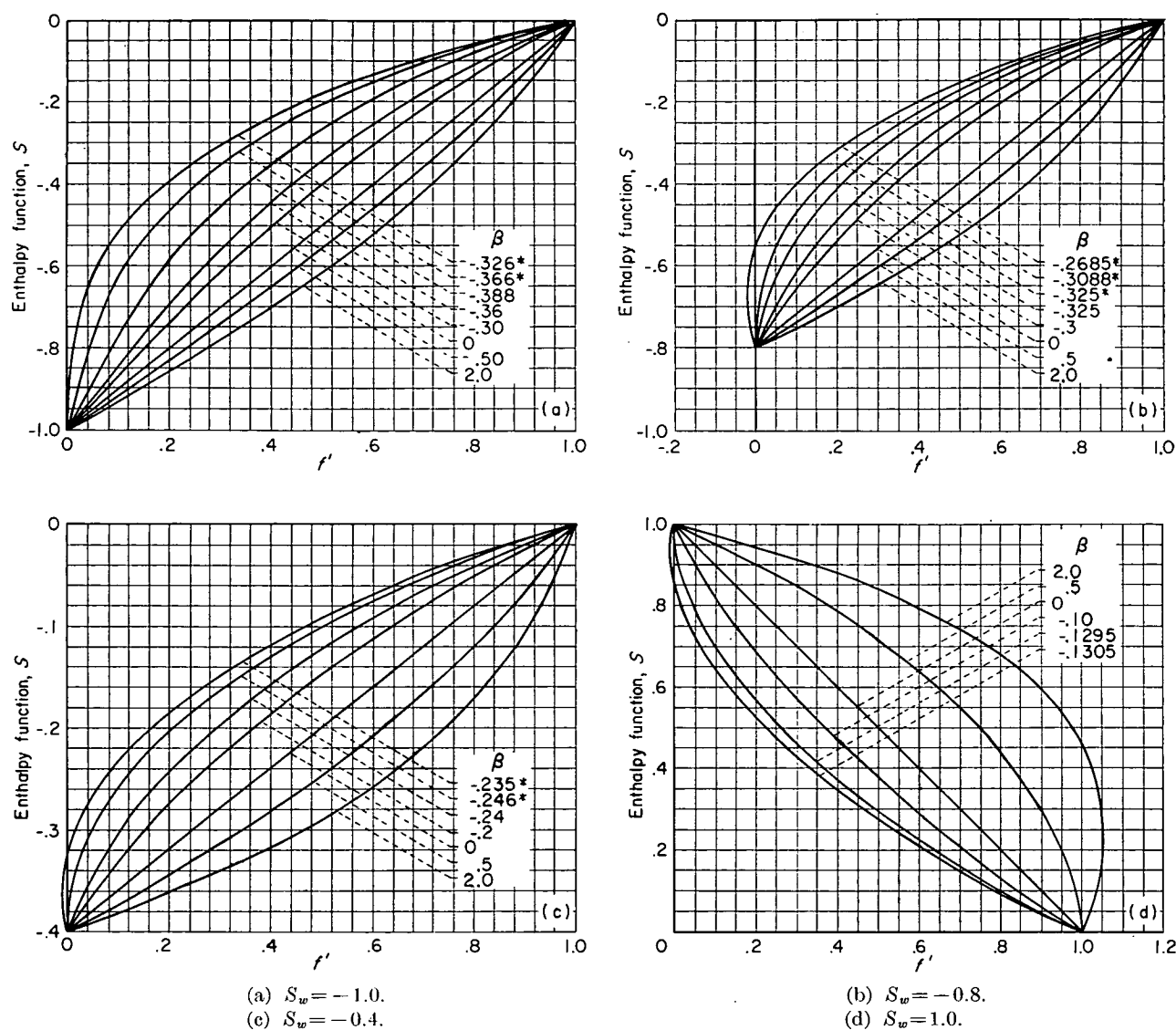


FIGURE 4.—Enthalpy function representation in velocity plane. (Asterisk denotes lower-branch solutions.)

SHEAR AND SKIN FRICTION

The shear distribution in the boundary layer is presented in figure 5, where f'' is plotted as a function of η . The shear function f'' is related to the shear stress τ through the expression

$$\tau = \mu \frac{\partial u}{\partial y} = \left[\lambda \mu_0 U_e \left(\frac{t_e}{t_0} \right)^{\frac{2\gamma-1}{\gamma-1}} \sqrt{\frac{m+1}{2} \frac{U_e}{\nu_0 X}} \right] f'' \quad (41)$$

For $\beta > 0$ the maximum shear is at the wall, whereas for $\beta < 0$ the point of maximum shear moves increasingly outward as the pressure gradient becomes more adverse.

The quantity that is of primary interest in boundary-layer calculations is the shear stress at the wall τ_w , which can be made dimensionless through the definition of a local skin-friction coefficient. The resulting relation is

$$C_f \equiv \frac{\tau_w}{\frac{1}{2} \rho_w u_e^2} = f''_w [2\lambda(1+S_w)] \sqrt{\frac{m+1}{2} \frac{\nu_0}{U_e X}} \quad (42a)$$

which, upon the introduction of a Reynolds number based on fluid properties evaluated at the wall temperature, $Re_w = \frac{u_e x}{\nu_w}$, becomes

$$\frac{C_f \sqrt{Re_w}}{2} = f''_w \sqrt{\frac{m+1}{2} \frac{d \ln X}{d \ln x}} \quad (42b)$$

The importance of evaluating fluid properties at the wall temperature can be seen from the fact that the right member of equation (42b) is constant for the case of the flat plate. If the skin-friction coefficient and the Reynolds number were to be based on local free-stream fluid properties, rather than on wall values, a factor of $\sqrt{\frac{\mu_w}{\mu_e} \frac{t_e}{t_w}}$ would appear in the right member of equation (42b). The range of this factor, when evaluated using Sutherland's viscosity law, is from $\left(\frac{t_w}{t_e}\right)^{1/4}$ at a low temperature level to $\left(\frac{t_w}{t_e}\right)^{-1/4}$ at high temperature levels.

The quantity f''_w is presented as a function of β and S_w in figure 6. It can be seen that heating the surface increases the sensitivity of the wall shear to pressure gradient, while cooling the wall has the opposite effect. A suggested physical interpretation for this trend is related to the effect of wall temperature on the mean density of the fluid within the boundary layer. For the heated wall, the boundary-layer density is less than that for the cooled wall, rendering

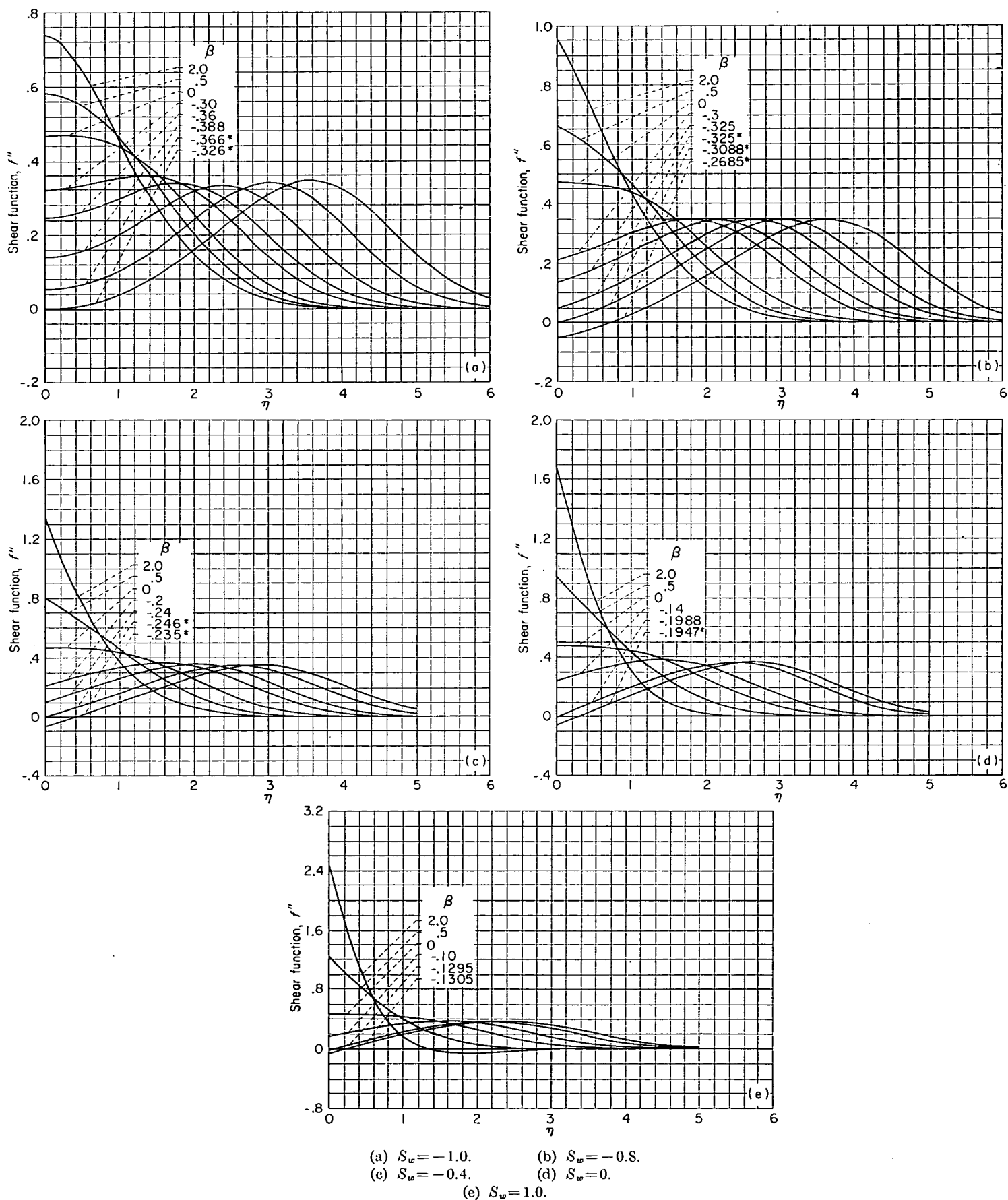
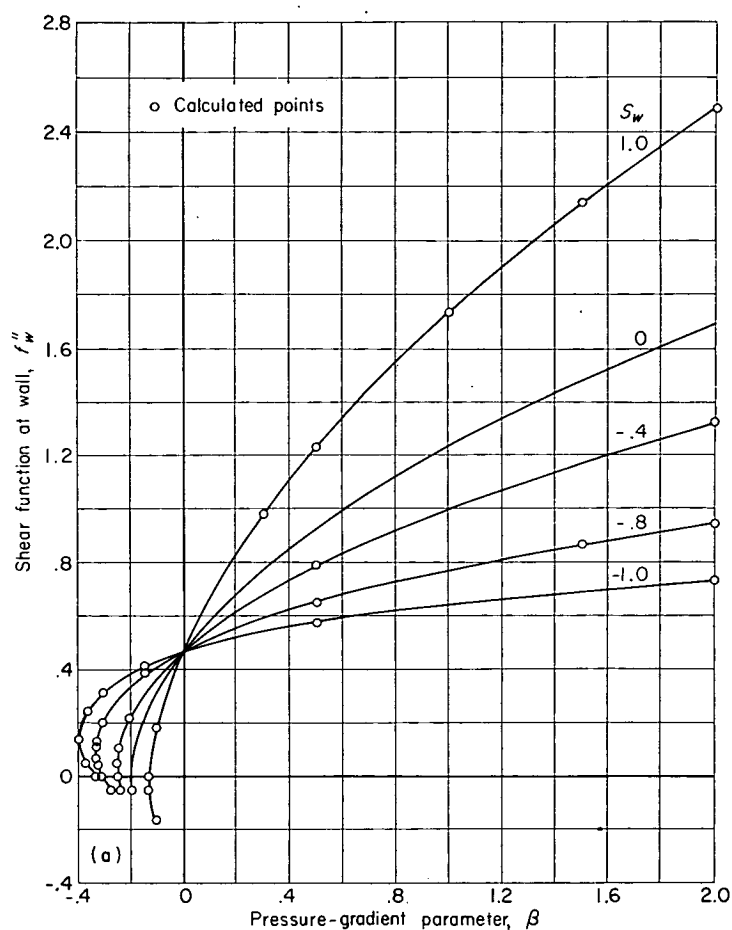
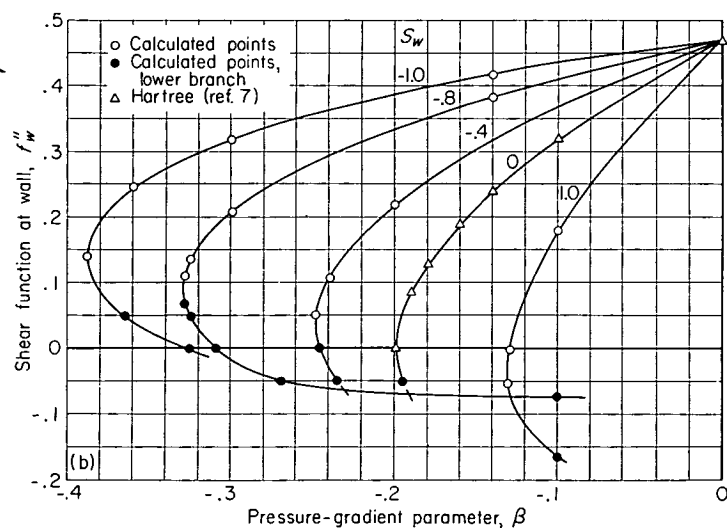


FIGURE 5.—Shear-function profiles. (Asterisk denotes lower-branch solutions.)



(a) Favorable and adverse pressure gradients.



(b) Adverse-pressure-gradient region.

FIGURE 6.—Effect of pressure gradient on wall shear.

the heated boundary layer more susceptible to free-stream acceleration forces than the cooled boundary layer. Figure 6 shows further that a linear extension of the slope of the curve f''_w against β from $\beta=0$ to large positive β would grossly overemphasize the effects of favorable pressure gradient; while the same linear extension toward negative β would underemphasize the effects of adverse gradient.

In figure 6(b), the two solutions with finite displacement

thickness that occur for adverse pressure gradients for a given β and S_w are plotted. It is seen that a double solution is indicated for even the insulated surface ($S_w=0$), although Hartree reported only one. In this case the lower-branch solution corresponds to negative wall shear stress (separated flow), which was not considered in reference 7. For heated walls ($S_w>0$) both solutions may indicate separated flow for β near β_{min} , while for cooled walls both solutions may be unseparated in this region. The physical interpretation of these double solutions has been discussed in the section Uniqueness.

HEAT TRANSFER

The variation of heat transfer across the boundary layer is plotted in figure 7 in terms of the derivative of the enthalpy function $S' = \frac{dS}{d\eta}$. This quantity is related to the stagnation enthalpy derivative in the physical plane by the expression

$$\frac{\partial}{\partial y} \left(\frac{h_s}{h_0} \right) = \left(\frac{\rho a_e}{\rho_0 a_0} \sqrt{\frac{m+1}{2}} \frac{U_e}{v_0 X} \right) S' \quad (43)$$

These curves again indicate the thickening of the thermal layer as separation is approached. Furthermore, as separation is neared, the zone adjacent to the surface where S' is essentially constant spreads rapidly. This is a zone where the heat transfer is primarily by conduction because of the nearly zero velocities in the neighborhood of the surface.

The values of S' at the surface (S'_w) are shown plotted as a function of pressure-gradient parameter β in figure 8 for constant wall temperatures. Two facts are noteworthy: (1) In the region of favorable pressure gradient, S'_w is nearly constant; (2) the heat transfer varies sharply near separation. From these facts the additional conclusion may be drawn that, if a linear extension of these curves is made with the slope at $\beta=0$, the result will seriously overemphasize the effects of a favorable pressure gradient or heat transfer and underestimate the effects for adverse pressure gradients. A similar influence of pressure gradient on skin friction has already been noted. A comparison of figures 6 and 8 indicates that the effect of pressure gradient on heat transfer is smaller than the corresponding effect upon wall shear.

As with the skin friction, it is convenient to define a dimensionless number from which the heat transfer may be determined. The Nusselt number is

$$Nu = \frac{x \left(\frac{\partial t}{\partial y} \right)_w}{t_0 - t_w} = \left(-\frac{S'_w}{S_w} \right) \sqrt{Re_w} \sqrt{\frac{m+1}{2}} \frac{d \ln X}{d \ln x} \quad (44)$$

The quantity $(-S'_w/S_w)$ is plotted in figure 9 for constant wall temperatures as a function of the pressure-gradient parameter β . The Reynolds number Re_w is again defined in terms of wall properties.

Reynolds analogy.—From expressions (42b) and (44), a simple modified Reynolds analogy parameter is evaluated by

$$\frac{C_f Re_w}{Nu} = \frac{2 f''_w}{\left(-\frac{S'_w}{S_w} \right)} \quad (45)$$

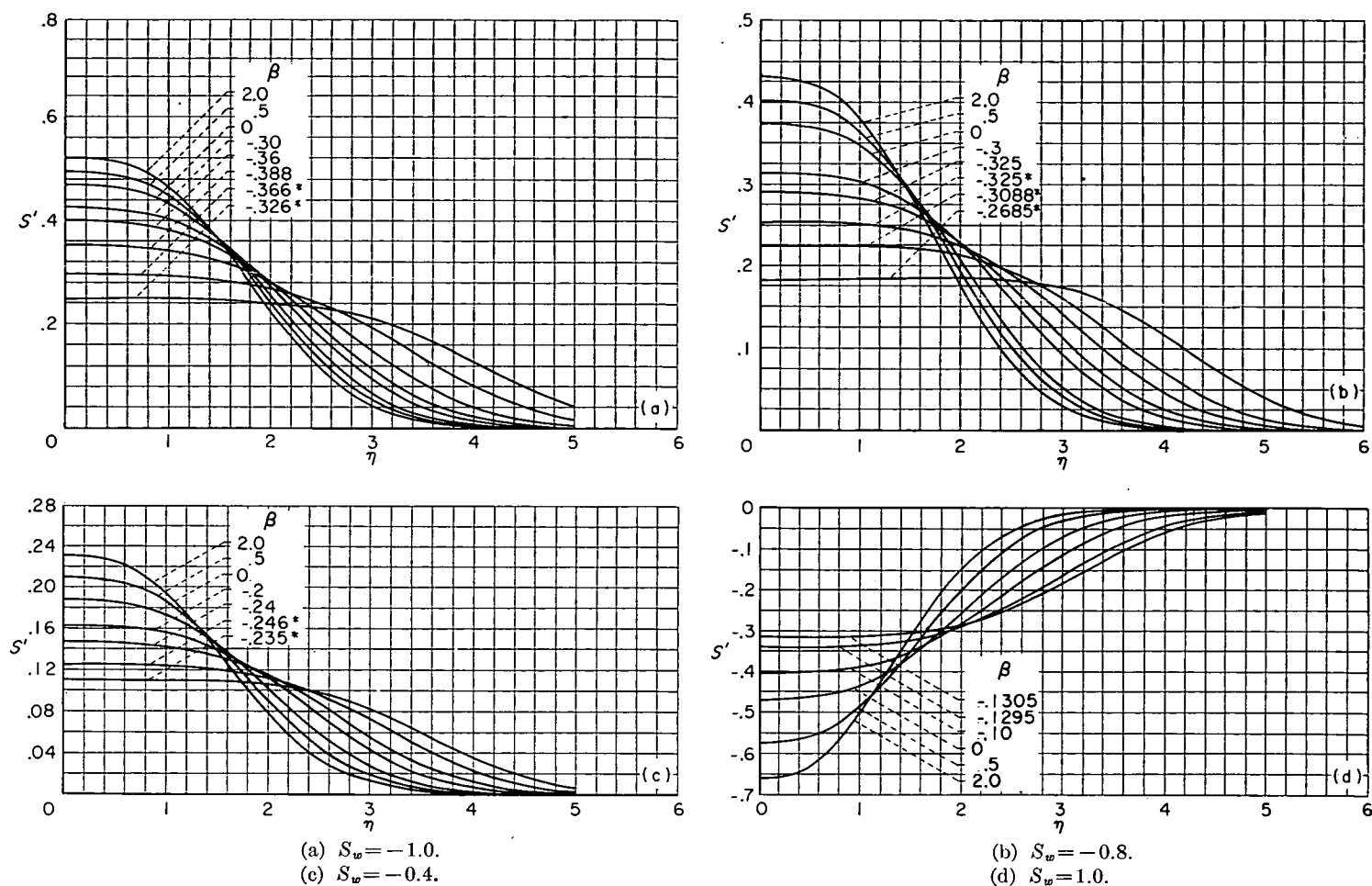


FIGURE 7.—Stagnation enthalpy gradient across boundary layer. (Asterisk denotes lower-branch solutions.)

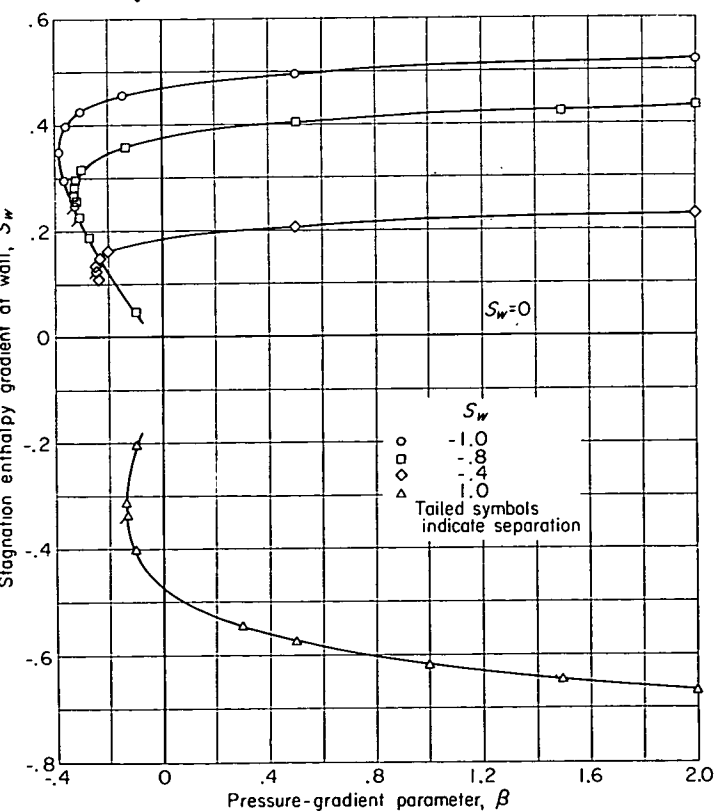
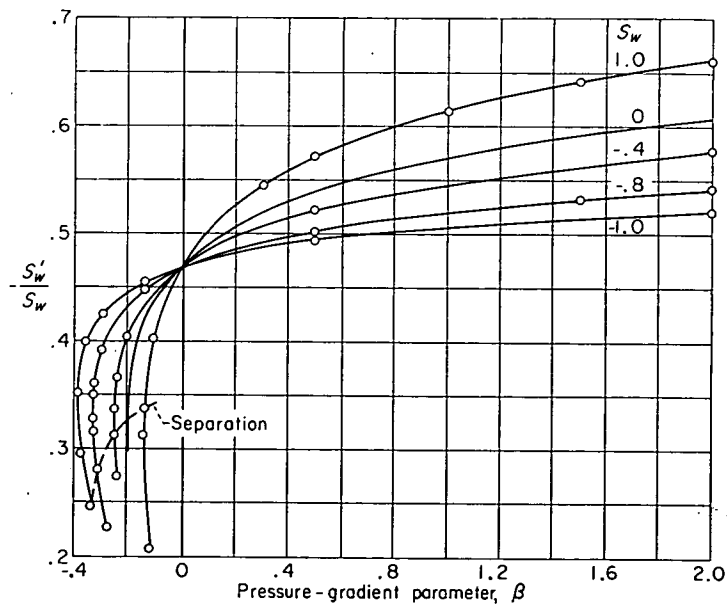


FIGURE 8.—Variation of heat transfer with pressure gradient.

FIGURE 9.—Variation of $\frac{S'_w}{S_w}$ with pressure gradient.

This quantity is the reciprocal of the usual Reynolds analogy quantity in order to avoid infinite values as separation is approached. It is plotted in figure 10 as a function of the pressure-gradient parameter β . These curves resemble the f''_w curves (fig. 6) because of the relatively small variation

in magnitude of S'_w/S_w compared with that of f''_w . The variation of $C_f Re_w / Nu$ is from zero to 7.4 for a surface of temperature twice the free-stream stagnation value and from zero to 2.8 for a surface held at a temperature of absolute zero, as shown in figure 10. This indicates the inadequacy of utilizing the flat-plate value of 2.0, as has often been done for estimates of heat transfer. Figure 10 is of particular use in evaluating the heat transfer for a problem when used in conjunction with simple methods for determining C_f , as proposed, for example, in reference 17.

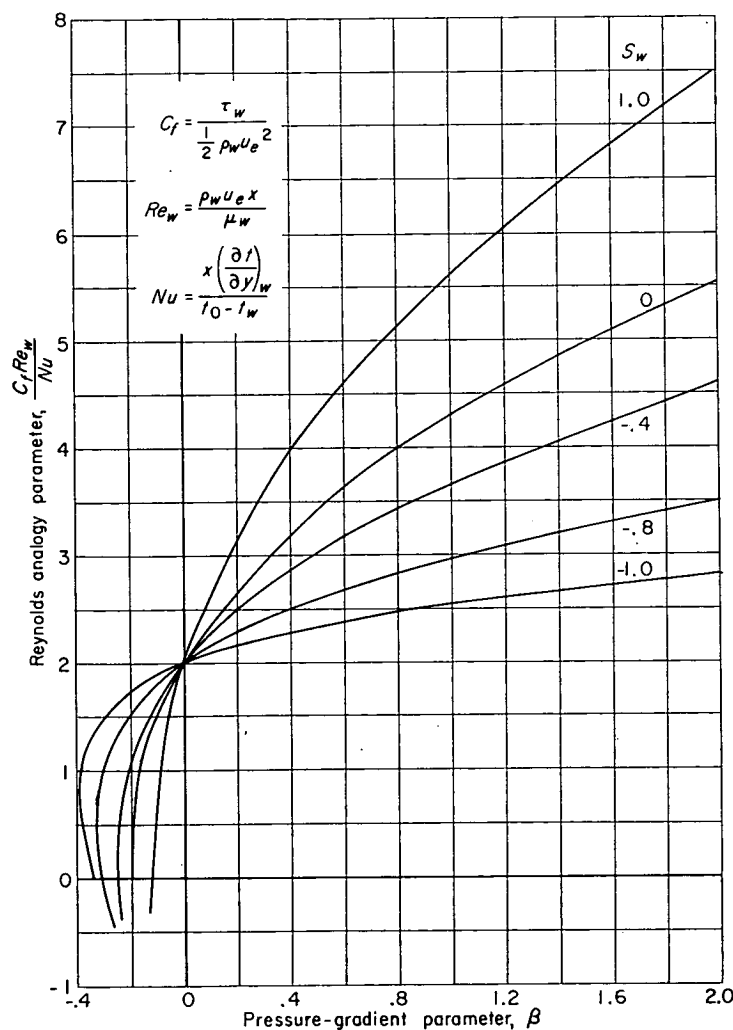


FIGURE 10.—Variation of Reynolds analogy parameter with pressure gradient.

SUMMARY OF RESULTS

From an analysis of the laminar compressible boundary layer based on Stewartson's transformation and including

effects of heat transfer and pressure gradient, the following results were obtained:

1. If the condition of similarity is required and the Prandtl number is constant but different from 1.0, the external Mach number must be either zero, constant, or very large. If the Prandtl number is taken as 1.0, the Mach number may be arbitrary. The free-stream velocity distributions consistent with the similarity concept are either power-law or exponential distributions in the transformed coordinates. Since the exponential distribution appears to be limited to favorable gradients and in this range the problem may be reduced to a special case of the power-law distribution, the calculations have been based on the latter class.

2. For flows with adverse pressure gradients, two classes of solutions were obtained. One class is discarded because it yields infinite displacement thickness. The class retained consists of two solutions with finite displacement thickness for each adverse pressure gradient.

3. For heated surfaces with favorable pressure gradients, a velocity overshoot, which increases with increasingly favorable gradient, results within the boundary layer. This excess velocity is associated with the acceleration of a layer of fluid in the outer portion of the boundary layer, with density less than the external density. Since this layer is subject to the external pressure field and is restrained only slightly by the viscous forces acting on it, it is accelerated more than the external flow.

4. For a Prandtl number of 1.0, when the thicknesses of the dynamic and thermal boundary layers are defined by a fixed fraction (say 0.99) of the velocity ratio and stagnation-temperature-difference ratio, the thermal boundary layer is thicker than the dynamic layer for favorable pressure gradients and thinner for adverse gradients.

5. The boundary-layer displacement thickness is negative for cases of favorable pressure gradient with very low wall temperature. This occurs because the surface cooling produces an increase in density near the wall so that there is more mass flow per unit flow area within the boundary layer than in the external flow.

6. The variation of a Reynolds analogy parameter is from zero to 7.4 for a surface of temperature twice the free-stream stagnation value and from zero to 2.8 for a surface held at a temperature of absolute zero, with the value 2.0 for the flat plate.

LEWIS FLIGHT PROPULSION LABORATORY

NATIONAL ADVISORY COMMITTEE FOR AERONAUTICS
CLEVELAND, OHIO, October 15, 1954

APPENDIX A

SYMBOLS

a	sonic velocity	Y	transformed normal coordinate,
C, C_1, C_2 , etc.	arbitrary constants	$Y = \frac{a_e}{a_0} \int_0^y \frac{\rho}{\rho_0} dy$	
C_f	local skin-friction coefficient, $C_f = \frac{2\tau_w}{\rho_w u_e^2}$	y	normal coordinate
c_p	specific heat at constant pressure	α_1, α_2 , etc.	integration constants in asymptotic solution
E	boundary-layer convection thickness	β	pressure-gradient parameter, $\beta = \frac{2m}{m+1}$
\mathcal{E}	boundary-layer thermal thickness	β_{min}	minimum value of β corresponding to a viscous solution for a given wall temperature
f	function related to stream function by $f = \psi \sqrt{\frac{m+1}{2\nu_0 U_e X}}$	γ	ratio of specific heats
g	asymptotic function, $g = \tilde{f}'_2$	δ^*	boundary-layer displacement thickness
H	boundary-layer form factor, $H = \frac{\delta^*}{\theta}$	ϵ	arbitrary small quantity
h	enthalpy	η	similarity variable, $\eta = \frac{Y}{X} \sqrt{\frac{m+1}{2} \frac{U_e X}{\nu_0}}$
k	thermal conductivity	θ	boundary-layer momentum thickness
k_{su}	Sutherland's constant	κ	integration constant in $f_1 = \eta - \kappa$
M_e	local external Mach number, $M_e = \frac{u_e}{a_e}$	λ	$\lambda = \frac{(\mu/\mu_0)}{(t/t_0)} = \left(\frac{t_0 + k_{su}}{t_w + k_{su}} \right) \sqrt{\frac{t_w}{t_0}}$
m	exponent from $U_e = CX^m$	μ	dynamic viscosity
Nu	Nusselt number, $Nu = \frac{x \left(\frac{\partial t}{\partial y} \right)_w}{t_0 - t_w}$	ν	kinematic viscosity, $\nu = \mu/\rho$
Pr	Prandtl number, $Pr = \frac{\mu c_p}{k}$	ρ	mass density
p	static pressure	τ	shear stress, $\tau = \mu \frac{\partial u}{\partial y}$
Re_w	Reynolds number, $Re_w = \frac{\rho_w u_e x}{\mu_w}$	ψ	stream function: $\psi_Y = U$, $\psi_X = -V$
S	enthalpy function, $S = \frac{h_s}{h_0} - 1$	Ω	oscillation coefficient, eq. (C2)
t	static temperature	ω	damping coefficient, eq. (C3)
U	transformed longitudinal velocity component, $U = \frac{u a_0}{a_e} = \psi_Y$	Subscripts:	
u	longitudinal velocity component	e	local flow outside boundary layer (external)
V	transformed normal velocity component, $V = -\psi_X$	j	result of j th iteration
v	normal velocity component	s	stagnation value
X	transformed longitudinal coordinate, $X = \int_0^x \lambda \frac{p_e a_e}{p_0 a_0} dx$	tr	transformed quantity
x	longitudinal coordinate	w	wall or surface value
		0	free-stream stagnation value
		Other notations:	
		\sim	asymptotic quantity
			Primes denote differentiation with respect to η .
			A coordinate used as subscript represents partial differentiation with respect to the coordinate.

APPENDIX B

ASYMPTOTIC SOLUTION

To evaluate the integrals in equations (24) and (27), it is necessary to have closed-form expressions for the integrands concerned, in the range of large η . This requires a solution of the system

$$f''' + ff'' = \beta(f'^2 - 1 - S) \quad (18a)$$

$$S'' + fS' = 0 \quad (18b)$$

for large η , which is the asymptotic solution.

The asymptotic solution for f (designated \tilde{f}) is assumed to consist of a sum of terms, each smaller than the preceding. Only the first two terms will be discussed herein. The corresponding solution for the enthalpy term \tilde{S} is also obtained.

Let

$$\tilde{f} = \tilde{f}_1 + \tilde{f}_2 \quad (B1)$$

where

$$\tilde{f}_2 \ll \tilde{f}_1$$

$$\tilde{f}_2' \ll \tilde{f}_1'$$

Now, since $\lim_{\eta \rightarrow \infty} (f') = 1$, let

$$\tilde{f}_1 = \eta - \kappa \quad (B2)$$

where κ is an undetermined constant. If \tilde{f}_1 is inserted into equation (18), the corresponding enthalpy term \tilde{S}_1 must be identically zero. Inserting equations (B1) and (B2) into equations (18) and dropping higher-order terms result in

$$\left. \begin{aligned} \tilde{f}_2'' + (\eta - \kappa)\tilde{f}_2' &= \beta(2\tilde{f}_2' - \tilde{S}_2) \\ \tilde{S}_2'' + (\eta - \kappa)\tilde{S}_2' &= 0 \end{aligned} \right\} \quad (B3)$$

The energy equation can be integrated directly to give

$$\tilde{S}_2 = Ce^{-\frac{(\eta - \kappa)^2}{2}}$$

which integrates once again to the complementary error function (denoted cerf)

$$\tilde{S}_2 = -C \int_{\eta}^{\infty} e^{-\frac{(\eta - \kappa)^2}{2}} d\eta$$

or

$$\tilde{S}_2 = \alpha_3 \sqrt{\frac{\pi}{2}} \text{cerf} \left(\frac{\eta - \kappa}{\sqrt{2}} \right) \quad (B4)$$

If equation (B4) is now substituted into the momentum equation of equations (B3) with the notation

$$g(\eta) \equiv \tilde{f}_2'$$

there results

$$g'' + (\eta - \kappa)g' - 2\beta g = -\alpha_3 \sqrt{\frac{\pi}{2}} \beta \text{cerf} \left(\frac{\eta - \kappa}{\sqrt{2}} \right) \quad (B5)$$

A particular integral to equation (B5) is

$$g = \frac{\alpha_3}{2} \sqrt{\frac{\pi}{2}} \text{cerf} \left(\frac{\eta - \kappa}{\sqrt{2}} \right) \quad (B6)$$

The complementary function can be found by noting that the homogeneous part of equation (B5) is Weber's equation. Hartree (ref. 7) gives the general solution for large values of the argument $(\eta - \kappa)$ which can be written

$$g = \alpha_1 (\eta - \kappa)^{-(2\beta+1)} \exp \left[-\frac{(\eta - \kappa)^2}{2} \right] + \alpha_2 (\eta - \kappa)^{2\beta} \quad (B7)$$

where α_1 and α_2 are undetermined constants.

For $\beta \geq 0$ it is clearly necessary to take $\alpha_2 = 0$ if the boundary condition $\lim_{\eta \rightarrow \infty} g = 0$ is to be applied. For $\beta < 0$ the boundary condition does not require $\alpha_2 = 0$; this introduces a lack of uniqueness in this range. The significance of $\alpha_2 = 0$ was more fully discussed in the section Uniqueness.

Using the first term of the expansion for the complementary error function

$$\text{cerf} \left(\frac{\eta - \kappa}{\sqrt{2}} \right) = \left\{ \sqrt{\frac{2}{\pi}} (\eta - \kappa)^{-1} \exp \left[-\frac{(\eta - \kappa)^2}{2} \right] \left[1 - \frac{1}{(\eta - \kappa)^2} + \dots \right] \right\} \quad (B8)$$

and combining the preceding equations result in the following expressions:

$$\tilde{f}' = 1 + \left[\alpha_1 (\eta - \kappa)^{-(2\beta+1)} + \frac{\alpha_3}{2} (\eta - \kappa)^{-1} \right] \exp \left[-\frac{(\eta - \kappa)^2}{2} \right] + \alpha_2 (\eta - \kappa)^{2\beta} \quad (34)$$

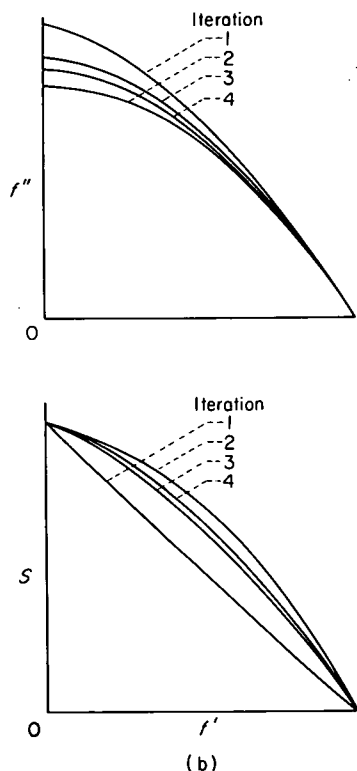
and

$$\tilde{S} = \alpha_3 (\eta - \kappa)^{-1} \left[\exp -\frac{(\eta - \kappa)^2}{2} \right] \quad (36)$$

APPENDIX C

CONVERGENCE AND EXTRAPOLATION

The method of successive approximations used in solving equations (24) and (28) is as follows: Two functions $f_j''(f')$ and $S_j(f')$ are assumed and inserted into the right sides of equations (24) and (28). This produces two new functions, $f_{j+1}''(f')$ and $S_{j+1}(f')$, on the left. The question of convergence is the first to consider. In reference 2, Crocco treated a momentum equation which was essentially equation (24) with $\beta=0$. There it was shown that the result might converge to a pair of functions between which it would oscillate and of which the geometric mean was the proper solution. In practice, the use of the arithmetic mean was demonstrated to be adequate. In the same way in the present case, the property of oscillation cannot be developed analytically; however, it has been found by trial that, if $\frac{f_j'' + f_{j+1}''}{2}$ is used in place of f_{j+1}'' to obtain f_{j+2}'' , the oscillation is reduced and a convergence takes place. A typical result is shown in sketch (b).



When the value for β for which a solution was sought was sufficiently positive, the enthalpy function S also showed a tendency to oscillate. In these cases, applying the same averaging procedure to S again improved the convergence. It was also found that convergence was improved if, in the initial assumed function for $f''(f')$, the slope $\left(\frac{df''}{df'}\right)_w$ was taken so that it satisfied equation (18a); that is,

$$\left(\frac{df''}{df'}\right)_w = \frac{-\beta(1 + S_w)}{f_w''}$$

When an iterative method is used to determine a function, it is always desirable to develop a method of extrapolating

the result to correspond to a larger number of iterations than have actually been carried out. This cannot be done in an exact fashion unless a definite law of convergence is established. Recently, an extrapolation method was devised (ref. 26) that required four successive iterants for an arbitrary iterative computing scheme. The development assumed that the remaining error after any iteration consisted essentially of two terms, both of which damped by a factor ω with each iteration. The sign of one of these terms was assumed to change with each iteration. This method extrapolated a function by breaking it into $n-1$ parts and treating it somewhat like an n -dimensional vector. The method has been demonstrated for Laplace's equation for which it was quite adequate. For nonlinear equations, however, the method is not as suitable.

In reference 1, a method requiring five successive iterants was developed which combined the method of reference 26 and the geometric mean rule. The function to be extrapolated is considered to be made up of a set of numbers F_i , where the subscript i identifies the particular component of the set. Then, the resulting relations for the i th component of the extrapolated function F in terms of the preceding five iterants, $(F_i)_j \dots (F_i)_{j+4}$, where j is the iteration number, are:

$$F_i = \frac{1}{\Omega_i} \left[\frac{(F_i)_{j+4} - \omega^2(F_i)_{j+2}}{1 - \omega^2} \right] \quad (C1)$$

where the oscillation coefficient Ω_i is given by

$$\Omega_i = \sqrt{\frac{(F_i)_{j+4} - \omega^2(F_i)_{j+2}}{(F_i)_{j+3} - \omega^2(F_i)_{j+1}}} \quad (C2)$$

and the damping coefficient ω is

$$\omega^2 = \frac{\sum_{i=1}^n [(F_i)_{j+4} - (F_i)_{j+2}] \left[\frac{(F_i)_{j+2} - (F_i)_j}{[(F_i)_{j+2} - (F_i)_j]} \right]}{\sum_{i=1}^n [(F_i)_{j+2} - (F_i)_j]} \quad (C3)$$

Application of this system was extremely effective. It generally reduced the oscillation remaining after five iterations by a factor of 10. A typical plot of the oscillation of f_w'' is indicated in figure 11.

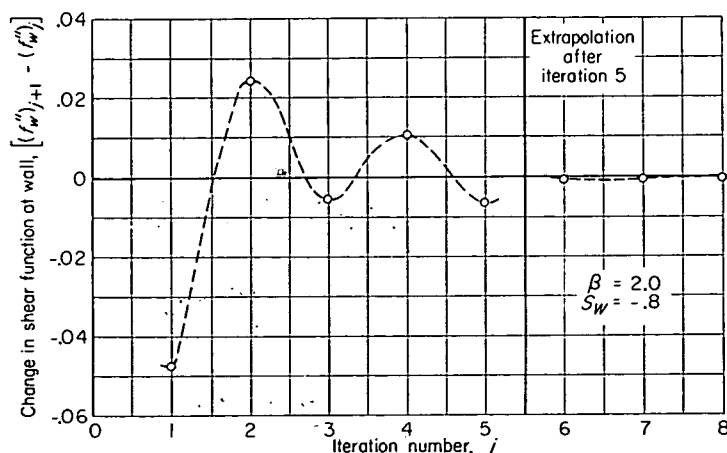


FIGURE 11.—Plot of oscillation of f_w'' .

APPENDIX D

CALCULATION PROCEDURE

The successive approximation calculations were carried out by means of IBM Type 604 Calculating Punch machines. The program was coded for fixed-point calculation, with the standard Function-Generating control panel used, plus a control panel especially wired for rapid integration of quotients by a trapezoidal rule. The step size (in f') varied from a maximum value of 0.050 or 0.025 at $f'=0$ to 0.00001 at $f'=0.9999$, the total number of intervals being 122 in the former case and 236 in the latter. By doubling and halving the step size for a critical case, the results are judged to contain a maximum error of 0.0002. Comparison with solutions obtained by forward integration, for the same case, confirms this accuracy. A given iteration (utilizing the 0.050 step size) could be carried out in approximately $1\frac{1}{2}$ hours by an experienced machine operator. If the averaging and extrapolation techniques described in appendix C are used, ten iterations generally would suffice for the accuracy desired. In contrast with forward integration, this number of iterations is not a function of the experience of the person carrying out the calculations.

In the derivation of the integral relations (eqs. (24) and (27)), it was assumed that the velocity ratio varied smoothly and monotonically from zero at the wall to 1.0 at infinity. However, in the range $\beta > 0$ and $S_w > 0$ (favorable pressure gradient and hot wall), the solution involves an increasing velocity ratio to a value greater than 1.0, followed by a smooth decrease to 1.0. Under these unusual circumstances, the method of successive approximation derived herein

must be considerably modified if it is to be used at all.

Equations (18), together with the boundary conditions (17), constitute a nonlinear two-point boundary-value problem. Cases of this boundary-value problem were solved by forward integration, with the IBM Card-Programmer Electronic Calculator (CPC) used to integrate with five-point integration formulas.

For the cases where the solutions are not unique ($\beta < 0$), the solutions were obtained in two patterns: In one pattern, β and S_w were fixed and, for a set of values of f_w'' , the quantity S_w' was altered until boundary conditions at infinity were apparently satisfied. In the other pattern, f_w'' and S_w were fixed and, for a set of values of negative β , the quantity S_w' was altered until boundary conditions at infinity were apparently satisfied. An attempt was made with both patterns to include the solution with the minimum value of the maximum velocity ratio f_{max}'' within the boundary layer. Except for those cases where no solution existed without velocity overshoot, this minimum value was 1.0.

The details of the integration method used are described completely by Lynn U. Albers in an appendix to reference 27. The possible error contained in the results is indicated in the footnote to table 1. Each trial run of a case required approximately 30 minutes. A person considerably experienced with the method of obtaining solutions by forward integration generally achieved convergence within 12 trials; however, this number is perhaps insufficient by a factor of the order of 2 if the person lacks experience.

REFERENCES

1. Cohen, Clarence B.: Similar Solutions for the Laminar Compressible Boundary Layer with Heat Transfer and Pressure Gradient, and Application to Integral Methods. Ph.D. Thesis, Princeton Univ., 1954.
2. Crocco, Luigi: The Laminar Boundary Layer in Gases. Rep. CF-1038, Aerophysics Lab., North American Aviation, Inc., July 15, 1948.
3. Chapman, Dean R., and Rubesin, Morris W.: Temperature and Velocity Profiles in the Compressible Laminar Boundary Layer with Arbitrary Distribution of Surface Temperature. Jour. Aero. Sci., vol. 16, no. 9, Sept. 1949, pp. 547-565.
4. Low, George M.: The Compressible Laminar Boundary Layer with Heat Transfer and Small Pressure Gradient. NACA TN 3028, 1953.
5. Howarth, L.: On the Solution of the Laminar Boundary Layer Equations. Proc. Roy. Soc. (London), ser. A, vol. 164, no. A919, Feb. 1938, pp. 547-579.
6. Falkner, V. M., and Skan, Sylvia W.: Some Approximate Solutions of the Boundary Layer Equations. R. & M. No. 1314, British A. R. C., Apr. 1930.
7. Hartree, D. R.: On an Equation Occurring in Falkner and Skan's Approximate Treatment of the Equations of the Boundary Layer. Proc. Cambridge Phil. Soc., vol. 33, pt. 2, Apr. 1937, pp. 223-239.
8. Eckert, E.: Die Berechnung des Wärmeübergangs in der laminaren Grenzschicht umströmter Körper. VDI Forschungsheft 416, Bd. 13, Sept.-Oct. 1942.
9. Tifford, Arthur N.: The Thermodynamics of the Laminar Boundary Layer of a Heated Body in a High-Speed Gas Flow Field. Jour. Aero. Sci., vol. 12, no. 2, Apr. 1945, pp. 241-251.
10. Levy, Solomon: Heat Transfer to Constant-Property Laminar Boundary-Layer Flows with Power-Function Free-Stream Velocity and Wall-Temperature Variation. Jour. Aero. Sci., vol. 19, no. 5, May 1952, pp. 341-348.
11. Brown, W. Byron, and Donoughe, Patrick L.: Tables of Exact Laminar-Boundary-Layer Solutions when the Wall is Porous and the Fluid Properties are Variable. NACA TN 2479, 1951.
12. Tani, Itirô: Further Studies of the Laminar Boundary Layer in Compressible Fluids. Rep. of Aero. Res. Inst., vols. 22-23, no. 322, Tôkyô Imperial Univ., Dec. 1944.
13. Illingworth, C. R.: Steady Flow in the Laminar Boundary Layer of a Gas. Proc. Roy. Soc. (London), ser. A, vol. 199, no. A1059, Dec. 7, 1949, pp. 533-558.
14. Stewartson, K.: Correlated Incompressible and Compressible Boundary Layers. Proc. Roy. Soc. (London), ser. A, vol. 200, no. A1060, Dec. 22, 1949, pp. 84-100.
15. Levy, Solomon: Effect of Large Temperature Changes (Including Viscous Heating) upon Laminar Boundary Layers with Variable Free-Stream Velocity. Jour. Aero. Sci., vol. 21, no. 7, July 1954, pp. 459-474.
16. Li, Ting-Yi, and Nagamatsu, Henry T.: Similar Solutions of Compressible Boundary-Layer Equations. Jour. Aero. Sci., vol. 22, no. 9, Sept. 1955, pp. 607-616.
17. Cohen, Clarence B., and Reshotko, Eli: The Compressible Laminar Boundary Layer with Heat Transfer and Arbitrary Pressure Gradient. NACA Rep. 1294, 1956. (Supersedes NACA TN 3326.)
18. Li, Ting-Yi, and Nagamatsu, Henry T.: Similar Solutions of Compressible Boundary-Layer Equations. Reader's Forum. Jour. Aero. Sci., vol. 20, no. 9, Sept. 1953, pp. 653-655.

19. Cohen, Clarence B.: Similar Solutions of Compressible Laminar Boundary-Layer Equations. Reader's Forum. Jour. Aero. Sci., vol. 21, no. 4, Apr. 1954, pp. 281-282.
20. Mangler, Werner: Die ähnlichen Lösungen der Prandtlischen Grenzschichtgleichungen. Z. a. M. M., Bd. 23, Heft 5, Oct. 1943, pp. 241-251.
21. Goldstein, S.: A Note on the Boundary-Layer Equations. Proc. Cambridge Phil. Soc., vol. 35, 1939, pp. 338-340.
22. Levy, S., and Seban, R. A.: Skin Friction and Heat Transfer for Laminar Boundary-Layer Flow with Variable Properties and Variable Free-Stream Velocity. Jour. Appl. Mech., vol. 20, no. 3, Sept. 1953, pp. 415-421.
23. Lees, Lester: On the Boundary-Layer Equations in Hypersonic Flow and Their Approximate Solutions. Jour. Aero. Sci., vol. 20, no. 2, Feb. 1953, pp. 143-145.
24. Schlichting, Herman: Grenzschicht-Theorie. Verlag und Druck G. Braun, Karlsruhe, 1951, pp. 110-115.
25. Clauser, Francis H.: Turbulent Boundary Layers in Adverse Pressure Gradients. Jour. Aero. Sci., vol. 21, no. 2, Feb. 1954, pp. 91-108.
26. Turner, L. Richard: Improvement in the Convergence of Methods of Successive Approximation. International Business Machines Corp., 1951. (Reprinted from Proc., Computation Seminar, Dec. 1949.)
27. Ostrach, Simon: An Analysis of Laminar Free-Convection Flow and Heat Transfer About a Flat Plate Parallel to the Direction of the Generating Body Force. NACA Rep. 1111, 1953. (Supersedes NACA TN 2635).

TABLE 1.—SIMILAR SOLUTIONS OF LAMINAR COMPRESSIBLE BOUNDARY-LAYER EQUATIONS.¹

$\beta = -0.326, S_w = -1.0$					
η	f	f'	f''	S	S'
0	0	0	0	-1.0000	0.2477
.2	.0000	.0001	.0016	-.9505	.2477
.4	.0001	.0009	.0065	-.9009	.2477
.6	.0004	.0029	.0145	-.8514	.2476
.8	.0014	.0069	.0258	-.8019	.2476
1.0	.0034	.0135	.0403	-.7524	.2475
1.2	.0070	.0232	.0580	-.7029	.2472
1.4	.0129	.0369	.0788	-.6535	.2468
1.6	.0220	.0550	.1026	-.6042	.2459
1.8	.0352	.0781	.1290	-.5552	.2445
2.0	.0536	.1067	.1578	-.5064	.2424
2.2	.0783	.1413	.1882	-.4582	.2392
2.4	.1105	.1821	.2196	-.4108	.2348
2.6	.1516	.2291	.2506	-.3645	.2288
2.8	.2026	.2822	.2799	-.3195	.2208
3.0	.2648	.3409	.3056	-.2763	.2108
3.2	.3393	.4042	.3260	-.2353	.1985
3.4	.4267	.4708	.3392	-.1970	.1839
3.6	.5277	.5392	.3434	-.1619	.1672
3.8	.6424	.6075	.3377	-.1303	.1488
4.0	.7706	.6737	.3220	-.1025	.1292
4.2	.9116	.7357	.2969	-.0786	.1092
4.4	1.0645	.7919	.2642	-.0588	.0897
4.6	1.2279	.8410	.2265	-.0427	.0713
4.8	1.4004	.8824	.1867	-.0301	.0548
5.0	1.5803	.9158	.1478	-.0206	.0407
5.2	1.7662	.9417	.1123	-.0137	.0291
5.4	1.9566	.9610	.0818	-.0088	.0201
5.6	2.1502	.9748	.0571	-.0055	.0133
5.8	2.3462	.9843	.0383	-.0033	.0085
6.0	2.5437	.9905	.0245	-.0020	.0052
6.2	2.7422	.9944	.0152	-.0012	.0031
6.4	2.9414	.9967	.0088	-.0007	.0016
6.6	3.1409	.9980	.0050	-.0005	.0009
6.8	3.3405	.9988	.0028	-.0004	.0005

$\beta = -0.3657, S_w = -1.0$					
η	f	f'	f''	S	S'
0	0	0	0.0500	-1.0000	0.2958
.2	.0010	.0101	.0522	-.9408	.2958
.4	.0041	.0211	.0586	-.8817	.2956
.6	.0096	.0339	.0693	-.8226	.2952
.8	.0178	.0491	.0841	-.7636	.2944
1.0	.0295	.0678	.1028	-.7049	.2931
1.2	.0452	.0905	.1252	-.6465	.2909
1.4	.0660	.1180	.1509	-.5886	.2877
1.6	.0928	.1510	.1791	-.5314	.2832
1.8	.1268	.1898	.2091	-.4754	.2771
2.0	.1691	.2347	.2395	-.4208	.2690
2.2	.2211	.2856	.2690	-.3679	.2588
2.4	.2837	.3421	.2956	-.3174	.2461
2.6	.3582	.4035	.3174	-.2697	.2308
2.8	.4454	.4686	.3324	-.2252	.2131
3.0	.5458	.5359	.3388	-.1846	.1930
3.2	.6598	.6035	.3354	-.1482	.1711
3.4	.7871	.6694	.3216	-.1162	.1481
3.6	.9273	.7315	.2983	-.0889	.1248
3.8	1.0793	.7881	.2668	-.0663	.1022
4.0	1.2421	.8379	.2299	-.0480	.0810
4.2	1.4140	.8799	.1904	-.0337	.0621
4.4	1.5935	.9140	.1513	-.0229	.0460
4.6	1.7791	.9406	.1154	-.0151	.0328
4.8	1.9693	.9605	.0843	-.0096	.0225
5.0	2.1629	.9747	.0589	-.0059	.0149
5.2	2.3589	.9845	.0395	-.0035	.0095
5.4	2.5565	.9909	.0253	-.0020	.0058
5.6	2.7551	.9949	.0155	-.0011	.0034
5.8	2.9543	.9973	.0092	-.0006	.0019
6.0	3.1539	.9987	.0052	-.0003	.0011
6.2	3.3538	.9995	.0028	-.0001	.0006
6.4	3.5537	.9999	.0014	-.0001	.0003

¹ The accuracy of solutions obtained by the method of successive approximations is believed to be ± 0.0002 . Solutions by forward integration were obtained in two patterns (appendix D). Where β and S_w were initially fixed, the eigenvalues are believed to be correct to ± 0.0002 . Where f'' and S_w were initially fixed, β and S_w are believed to be correct to ± 0.0002 (except in the case of $\beta = 0.2460$, $S_w = -0.4$, where β and S_w are believed to be correct to ± 0.002). The values in the tables are of comparable accuracy except at large η , where the entries may contain errors as large as twice the above amounts.

TABLE 1.—Continued. SIMILAR SOLUTIONS OF LAMINAR COMPRESSIBLE BOUNDARY-LAYER EQUATIONS.

$\beta = -0.3884, S_w = -1.0$						$\beta = -0.36, S_w = -1.0$					
η	f	f'	f''	S	S'	η	f	f'	f''	S	S'
0	0	0	0.1400	-1.0000	0.3527	0	0	0	0.2448	-1.0000	0.0400
.2	.0028	.0282	.1427	-.9294	.3527	.2033	.0050	.050	.2476	-.9186	.0399
.4	.0113	.0574	.1506	-.8589	.3523	.4024	.0199	.100	.2552	-.8391	.0398
.6	.0259	.0887	.1633	-.7886	.3510	.5942	.0438	.150	.2663	-.7628	.0396
.8	.0470	.1230	.1803	-.7186	.3485	.7776	.0759	.200	.2793	-.6905	.0392
1.0	.0754	.1611	.2010	-.6493	.3443	.9524	.1151	.250	.2929	-.6225	.0385
1.2	.1118	.2036	.2243	-.5811	.3379	1.1193	.1610	.300	.3061	-.5588	.0376
1.4	.1571	.2509	.2491	-.5143	.3290	1.2795	.2130	.350	.3178	-.4993	.0365
1.6	.2125	.3032	.2738	-.4496	.3171	1.4344	.2711	.400	.3274	-.4436	.0352
1.8	.2787	.3603	.2963	-.3876	.3020	1.5855	.3353	.450	.3341	-.3915	.0336
2.0	.3569	.4215	.3149	-.3291	.2834	1.7342	.4060	.500	.3375	-.3428	.0318
2.2	.4476	.4859	.3273	-.2745	.2616	1.8824	.4838	.550	.3368	-.2970	.0298
2.4	.5513	.5519	.3318	-.2246	.2368	2.0318	.5697	.600	.3317	-.2541	.0275
2.6	.6683	.6180	.3270	-.1800	.2096	2.1847	.6653	.650	.3215	-.2138	.0251
2.8	.7984	.6821	.3125	-.1409	.1811	2.3439	.7728	.700	.3057	-.1760	.0223
3.0	.9409	.7423	.2888	-.1076	.1522	2.5134	.8957	.750	.2833	-.1405	.0194
3.2	1.0950	.7971	.2576	-.0799	.1242	2.6995	1.0400	.800	.2535	-.1074	.0162
3.4	1.2593	.8450	.2213	-.0577	.0982	2.9129	1.2162	.850	.2146	-.0765	.0127
3.6	1.4325	.8855	.1827	-.0405	.0750	3.1766	1.4473	.900	.1646	-.0479	.0089
3.8	1.6130	.9182	.1448	-.0275	.0553	3.2397	1.5043	.910	.1529	-.0425	.0081
4.0	1.7993	.9436	.1101	-.0181	.0393	3.3078	1.5667	.920	.1406	-.0372	.0073
4.2	1.9900	.9625	.0802	-.0115	.0269	3.3825	1.6358	.930	.1275	-.0320	.0065
4.4	2.1839	.9761	.0559	-.0071	.0177	3.4654	1.7133	.940	.1136	-.0270	.0057
4.6	2.3801	.9853	.0373	-.0043	.0112	3.5596	1.8023	.950	.0988	-.0220	.0048
4.8	2.5778	.9913	.0239	-.0025	.0068	3.6123	1.8525	.955	.0911	-.0196	.0043
5.0	2.7765	.9951	.0146	-.0014	.0040	3.6697	1.9075	.960	.0830	-.0172	.0039
5.2	2.9758	.9974	.0086	-.0008	.0023	3.7332	1.9686	.965	.0746	-.0148	.0034
5.4	3.1754	.9987	.0048	-.0005	.0012	3.8044	2.0375	.970	.0659	-.0125	.0030
5.6	3.3752	.9994	.0026	-.0003	.0006	3.8859	2.1168	.975	.0568	-.0103	.0025
5.8	3.5752	.9998	.0013	-.0002	.0003	3.9822	2.2110	.980	.0472	-.0080	.0020
6.0	3.7751	1.0000	.0006	-.0002	.0002	4.1012	2.3279	.985	.0370	-.0059	.0015
6.2	3.9751	1.0000	.0003	-.0001	.0000	4.2604	2.4851	.990	.0262	-.0038	.0010
						4.3003	2.5247	.991	.0239	-.0034	.0009
						4.3443	2.5682	.992	.0216	-.0030	.0008
						4.3933	2.6169	.993	.0192	-.0026	.0007
						4.4489	2.6722	.994	.0167	-.0022	.0006
						4.5134	2.7363	.995	.0142	-.0018	.0005
						4.5905	2.8130	.996	.0117	-.0014	.0004
						4.6872	2.9094	.997	.0090	-.0010	.0003
						4.8187	3.0406	.998	.0062	-.0006	.0002
						5.0327	3.2543	.999	.0033	-.0003	.0001
						6.1247	4.3446	1.000	.0000	.0000	.0000

TABLE 1.—Continued. SIMILAR SOLUTIONS OF LAMINAR COMPRESSIBLE BOUNDARY-LAYER EQUATIONS.

$\beta = -0.3, S_w = -1.0$					
η	f	f'	f''	S	S'
0	0	0	0.3181	-1.0000	0.4262
.1568	.0039	.050	.3196	-.9331	.4261
.3123	.0155	.100	.3236	-.8669	.4255
.4655	.0347	.150	.3292	-.8018	.4239
.6159	.0609	.200	.3359	-.7383	.4209
.7632	.0941	.250	.3427	-.6766	.4163
.9077	.1338	.300	.3491	-.6169	.4095
1.0498	.1800	.350	.3543	-.5593	.4005
1.1902	.2326	.400	.3579	-.5039	.3892
1.3296	.2918	.450	.3591	-.4506	.3752
1.4690	.3581	.500	.3575	-.3994	.3586
1.6098	.4320	.550	.3525	-.3502	.3393
1.7533	.5146	.600	.3436	-.3031	.3170
1.9016	.6072	.650	.3302	-.2580	.2918
2.0572	.7123	.700	.3117	-.2148	.2633
2.2240	.8333	.750	.2871	-.1735	.2315
2.4080	.9761	.800	.2555	-.1342	.1960
2.6202	1.1513	.850	.2155	-.0968	.1565
2.8835	1.3819	.900	.1646	-.0616	.1122
2.9465	1.4389	.910	.1528	-.0549	.1026
3.0147	1.5014	.920	.1404	-.0482	.0928
3.0895	1.5705	.930	.1273	-.0417	.0828
3.1726	1.6483	.940	.1134	-.0352	.0724
3.2670	1.7375	.950	.0986	-.0289	.0617
3.3199	1.7878	.955	.0908	-.0258	.0562
3.3775	1.8430	.960	.0827	-.0227	.0506
3.4412	1.9043	.965	.0744	-.0197	.0449
3.5127	1.9735	.970	.0657	-.0167	.0391
3.5945	2.0531	.975	.0565	-.0137	.0332
3.6912	2.1477	.980	.0470	-.0108	.0271
3.8108	2.2652	.985	.0369	-.0080	.0208
3.9708	2.4232	.990	.0260	-.0052	.0143
4.0109	2.4629	.991	.0238	-.0046	.0129
4.0551	2.5067	.992	.0214	-.0041	.0116
4.1044	2.5556	.993	.0191	-.0035	.0103
4.1603	2.6112	.994	.0167	-.0030	.0089
4.2251	2.6756	.995	.0142	-.0025	.0075
4.3026	2.7528	.996	.0116	-.0020	.0061
4.3997	2.8495	.997	.0090	-.0015	.0046
4.5319	2.9814	.998	.0062	-.0009	.0031
4.7471	3.1963	.999	.0033	-.0004	.0016
5.8542	4.3031	1.000	.0000	-.0000	.0000

$\beta = -0.14, S_w = -1.0$					
η	f	f'	f''	S	S'
0	0	0	0.4165	0	0.4554
.1199	.0029	.050	.4170	-.9453	.4554
.2397	.0119	.100	.4179	-.8908	.4551
.3591	.0269	.150	.4190	-.8365	.4541
.4783	.0477	.200	.4199	-.7825	.4522
.5973	.0745	.250	.4202	-.7288	.4490
.7164	.1072	.300	.4194	-.6756	.4443
.8359	.1461	.350	.4173	-.6229	.4377
.9563	.1912	.400	.4133	-.5708	.4290
1.0782	.2431	.450	.4072	-.5192	.4179
1.2023	.3020	.500	.3986	-.4682	.4040
1.3296	.3689	.550	.3869	-.4178	.3872
1.4615	.4448	.600	.3717	-.3681	.3671
1.5995	.5311	.650	.3525	-.3191	.3433
1.7462	.6302	.700	.3287	-.2707	.3153
1.9053	.7457	.750	.2995	-.2232	.2827
2.0829	.8834	.800	.2639	-.1764	.2447
2.2897	1.0543	.850	.2204	-.1304	.2005
2.5484	1.2809	.900	.1669	-.0855	.1483
2.6106	1.3373	.910	.1547	-.0766	.1367
2.6781	1.3991	.920	.1419	-.0678	.1247
2.7523	1.4677	.930	.1284	-.0591	.1121
2.8348	1.5448	.940	.1142	-.0504	.0990
2.9287	1.6336	.950	.0991	-.0417	.0853
2.9813	1.6837	.955	.0912	-.0374	.0782
3.0387	1.7387	.960	.0831	-.0331	.0709
3.1023	1.7999	.965	.0746	-.0289	.0634
3.1738	1.8691	.970	.0658	-.0247	.0556
3.2555	1.9486	.975	.0566	-.0204	.0476
3.3521	2.0430	.980	.0470	-.0163	.0392
3.4717	2.1605	.985	.0369	-.0121	.0305
3.6319	2.3187	.990	.0260	-.0080	.0213
3.6721	2.3585	.991	.0237	-.0072	.0194
3.7163	2.4024	.992	.0214	-.0063	.0174
3.7657	2.4514	.993	.0190	-.0055	.0155
3.8217	2.5071	.994	.0166	-.0047	.0135
3.8867	2.5717	.995	.0142	-.0039	.0114
3.9643	2.6490	.996	.0116	-.0031	.0093
4.0616	2.7459	.997	.0090	-.0023	.0071
4.1939	2.8778	.998	.0062	-.0015	.0049
4.4088	3.0924	.999	.0033	-.0007	.0026
5.4938	4.1772	1.000	.0000	.0000	.0000

TABLE 1.—Continued. SIMILAR SOLUTIONS OF LAMINAR COMPRESSIBLE BOUNDARY-LAYER EQUATIONS.

$\beta=0.5, S_w=-1.0$						$\beta=2.0, S_w=-1.0$					
η	f	f'	f''	S	S'	η	f	f'	f''	S	S'
0	0	0	0.5806	-1.0000	0.4948	0	0	0	0.7381	-1.0000	0.5203
.0861	.0021	.050	.5797	-.9574	.4948	.0678	.0016	.050	.7359	-.9647	.5203
.1726	.0086	.100	.5770	-.9147	.4946	.1360	.0068	.100	.7293	-.9292	.5201
.2596	.0195	.150	.5724	-.8718	.4940	.2051	.0154	.150	.7188	-.8933	.5198
.3474	.0349	.200	.5659	-.8285	.4929	.2754	.0277	.200	.7045	-.8567	.5190
.4364	.0549	.250	.5574	-.7848	.4910	.3472	.0439	.250	.6869	-.8196	.5177
.5270	.0798	.300	.5468	-.7406	.4881	.4212	.0643	.300	.6660	-.7814	.5157
.6195	.1099	.350	.5340	-.6957	.4839	.4976	.0892	.350	.6420	-.7421	.5128
.7145	.1456	.400	.5188	-.6501	.4781	.5772	.1191	.400	.6150	-.7012	.5086
.8126	.1873	.450	.5011	-.6037	.4704	.6606	.1545	.450	.5852	-.6593	.5029
.9145	.2358	.500	.4808	-.5564	.4605	.7485	.1964	.500	.5525	-.6155	.4953
1.0211	.2918	.550	.4576	-.5081	.4479	.8421	.2456	.550	.5170	-.5696	.4852
1.1337	.3566	.600	.4310	-.4587	.4319	.9427	.3035	.600	.4786	-.5215	.4721
1.2539	.4318	.650	.4008	-.4081	.4120	1.0520	.3719	.650	.4372	-.4707	.4551
1.3842	.5199	.700	.3666	-.3561	.3873	1.1726	.4534	.700	.3925	-.4172	.4330
1.5283	.6244	.750	.3277	-.3026	.3567	1.3085	.5520	.750	.3444	-.3603	.4045
1.6922	.7516	.800	.2834	-.2474	.3189	1.4659	.6742	.800	.2924	-.2996	.3674
1.8866	.9122	.850	.2324	-.1903	.2715	1.6562	.8314	.850	.2355	-.2344	.3187
2.1344	1.1293	.900	.1727	-.1307	.2110	1.9030	1.0477	.900	.1720	-.1639	.2528
2.1947	1.1839	.910	.1595	-.1185	.1968	1.9636	1.1026	.910	.1583	-.1490	.2369
2.2603	1.2440	.920	.1457	-.1061	.1817	2.0299	1.1632	.920	.1442	-.1339	.2198
2.3327	1.3109	.930	.1313	-.0936	.1658	2.1031	1.2310	.930	.1296	-.1185	.2014
2.4135	1.3865	.940	.1163	-.0809	.1486	2.1852	1.3078	.940	.1144	-.1028	.1814
2.5059	1.4738	.950	.1005	-.0681	.1303	2.2793	1.3967	.950	.0986	-.0868	.1598
2.5578	1.5233	.955	.0923	-.0616	.1205	2.3322	1.4471	.955	.0904	-.0786	.1482
2.6146	1.5777	.960	.0839	-.0551	.1079	2.3903	1.5027	.960	.0821	-.0704	.1360
2.6776	1.6384	.965	.0752	-.0485	.0998	2.4548	1.5648	.965	.0735	-.0620	.1232
2.7486	1.7071	.970	.0662	-.0418	.0887	2.5275	1.6351	.970	.0646	-.0536	.1097
2.8300	1.7862	.975	.0568	-.0351	.0769	2.6109	1.7163	.975	.0554	-.0450	.0954
2.9265	1.8805	.980	.0470	-.0283	.0644	2.7099	1.8130	.980	.0458	-.0364	.0801
3.0462	1.9981	.985	.0368	-.0215	.0511	2.8327	1.9338	.985	.0358	-.0275	.0636
3.2069	2.1568	.990	.0259	-.0145	.0366	2.9977	2.0967	.990	.0252	-.0186	.0456
3.2473	2.1969	.991	.0236	-.0131	.0335	3.0392	2.1378	.991	.0230	-.0167	.0418
3.2918	2.2410	.992	.0213	-.0117	.0303	3.0849	2.1831	.992	.0207	-.0149	.0379
3.3415	2.2904	.993	.0189	-.0102	.0271	3.1359	2.2338	.993	.0184	-.0131	.0338
3.3980	2.3464	.994	.0165	-.0088	.0238	3.1939	2.2913	.994	.0161	-.0113	.0297
3.4635	2.4116	.995	.0140	-.0074	.0203	3.2611	2.3581	.995	.0137	-.0094	.0254
3.5418	2.4895	.996	.0115	-.0059	.0168	3.3414	2.4381	.996	.0112	-.0075	.0209
3.6400	2.5874	.997	.0089	-.0044	.0131	3.4421	2.5385	.997	.0087	-.0057	.0163
3.7738	2.7209	.998	.0061	-.0030	.0092	3.5792	2.6753	.998	.0060	-.0038	.0114
3.9916	2.9384	.999	.0032	-.0015	.0049	3.8023	2.8980	.999	.0032	-.0019	.0061
5.1056	4.0521	1.000	.0000	-.0000	.0000	4.9344	4.0298	1.000	.0000	-.0000	.0000

TABLE 1.—Continued. SIMILAR SOLUTIONS OF LAMINAR COMPRESSIBLE BOUNDARY-LAYER EQUATIONS.

$\beta = -0.10, S_w = -0.8$					
η	f	f'	f''	S	S'
0	0	0	-0.0686	-0.8000	0.0447
.4	-.0053	-.0258	-.0603	-.7821	.0448
.8	-.0202	-.0482	-.0515	-.7642	.0450
1.2	-.0433	-.0670	-.0425	-.7461	.0455
1.6	-.0733	-.0821	-.0330	-.7277	.0466
2.0	-.1085	-.0933	-.0231	-.7087	.0483
2.4	-.1474	-.1005	-.0123	-.6889	.0509
2.8	-.1882	-.1030	-.0003	-.6679	.0544
3.2	-.2291	-.1004	.0136	-.6452	.0591
3.6	-.2678	-.0918	.0301	-.6204	.0653
4.0	-.3016	-.0759	.0501	-.5928	.0732
4.4	-.3273	-.0511	.0746	-.5616	.0830
4.8	-.3410	-.0154	.1048	-.5260	.0950
5.2	-.3379	.0336	.1413	-.4853	.1088
5.6	-.3121	.0984	.1837	-.4388	.1241
6.0	-.2568	.1811	.2301	-.3861	.1392
6.4	-.1647	.2823	.2752	-.3278	.1516
6.8	-.0287	.3999	.3103	-.2656	.1578
7.2	.1566	.5278	.3245	-.2029	.1541
7.6	.3935	.6556	.3091	-.1440	.1383
8.0	.6794	.7709	.2629	-.0937	.1118
8.4	1.0071	.8632	.1964	-.0553	.0799
8.8	1.3662	.9276	.1270	-.0295	.0497
9.2	1.7457	.9665	.0703	-.0145	.0267
9.6	2.1369	.9866	.0332	-.0070	.0123
10.0	2.5335	.9954	.0133	-.0038	.0048
10.4	2.9324	.9987	.0045	-.0026	.0016
10.8	3.3321	.9997	.0013	-.0022	.0005
11.2	3.7321	1.0000	.0003	-.0021	.0001

$\beta = -0.2685, S_w = -0.8$					
η	f	f'	f''	S	S'
0	0	0	-0.0500	-0.8000	0.1829
.2	-.0009	-.0089	-.0383	-.7634	.1829
.4	-.0034	-.0152	-.0246	-.7268	.1830
.6	-.0068	-.0186	-.0090	-.6902	.1832
.8	-.0106	-.0187	.0086	-.6535	.1835
1.0	-.0140	-.0150	.0282	-.6168	.1840
1.2	-.0163	-.0072	.0499	-.5799	.1845
1.4	-.0166	.0051	.0737	-.5430	.1851
1.6	-.0139	.0224	.0994	-.5059	.1857
1.8	-.0073	.0450	.1272	-.4687	.1861
2.0	.0044	.0733	.1566	-.4315	.1862
2.2	.0224	.1077	.1872	-.3943	.1857
2.4	.0479	.1483	.2184	-.3572	.1844
2.6	.0822	.1951	.2493	-.3206	.1821
2.8	.1264	.2479	.2786	-.2845	.1783
3.0	.1817	.3063	.3049	-.2493	.1730
3.2	.2492	.3695	.3264	-.2154	.1657
3.4	.3297	.4364	.3413	-.1832	.1564
3.6	.4239	.5055	.3481	-.1530	.1451
3.8	.5320	.5750	.3455	-.1253	.1319
4.0	.6538	.6430	.3330	-.1003	.1172
4.2	.7890	.7076	.3109	-.0784	.1015
4.4	.9365	.7669	.2807	-.0598	.0854
4.6	1.0953	.8195	.2446	-.0442	.0697
4.8	1.2638	.8644	.2052	-.0318	.0551
5.0	1.4405	.9015	.1656	-.0221	.0420
5.2	1.6239	.9309	.1283	-.0148	.0309
5.4	1.8124	.9532	.0954	-.0096	.0219
5.6	2.0047	.9694	.0681	-.0059	.0150
5.8	2.1998	.9808	.0465	-.0035	.0098
6.0	2.3968	.9884	.0305	-.0019	.0062
6.2	2.5950	.9933	.0192	-.0009	.0038
6.4	2.7940	.9963	.0116	-.0003	.0022
6.6	2.9935	.9981	.0067	.0000	.0012
6.8	3.1932	.9991	.0037	.0002	.0007
7.0	3.3931	.9997	.0020	.0003	.0003
7.2	3.5931	1.0000	.0010	.0003	.0002

TABLE 1.—Continued. SIMILAR SOLUTIONS OF LAMINAR COMPRESSIBLE BOUNDARY-LAYER EQUATIONS.

$\beta = -0.3088, S_w = -0.8$					
η	f	f'	f''	S	S'
0	0	0	0	-0.8000	0.2261
.2	.0001	.0013	.0137	-.7548	.2260
.4	.0007	.0057	.0303	-.7096	.2260
.6	.0026	.0136	.0496	-.6644	.2260
.8	.0065	.0257	.0716	-.6192	.2258
1.0	.0132	.0425	.0963	-.5741	.2253
1.2	.0238	.0644	.1234	-.5209	.2245
1.4	.0393	.0920	.1527	-.4843	.2231
1.6	.0610	.1256	.1835	-.4399	.2209
1.8	.0900	.1654	.2151	-.3960	.2176
2.0	.1276	.2116	.2465	-.3529	.2130
2.2	.1750	.2639	.2764	-.3109	.2067
2.4	.2335	.3219	.3031	-.2704	.1984
2.6	.3041	.3848	.3247	-.2317	.1881
2.8	.3877	.4514	.3395	-.1953	.1756
3.0	.4848	.5201	.3458	-.1616	.1609
3.2	.5957	.5890	.3423	-.1311	.1445
3.4	.7203	.6563	.3286	-.1039	.1267
3.6	.8580	.7199	.3055	-.0804	.1082
3.8	1.0079	.7779	.2742	-.0606	.0898
4.0	1.1687	.8291	.2372	-.0444	.0723
4.2	1.3391	.8727	.1975	-.0316	.0563
4.4	1.5173	.9082	.1580	-.0218	.0423
4.6	1.7018	.9360	.1213	-.0145	.0306
4.8	1.8912	.9570	.0893	-.0094	.0214
5.0	2.0842	.9722	.0630	-.0058	.0144
5.2	2.2798	.9827	.0426	-.0035	.0093
5.4	2.4771	.9896	.0276	-.0020	.0058
5.6	2.6754	.9940	.0172	-.0011	.0034
5.8	2.8746	.9967	.0103	-.0006	.0020
6.0	3.0741	.9983	.0059	-.0003	.0011
6.2	3.2738	.9992	.0032	-.0001	.0006
6.4	3.4737	.9996	.0017	-.0000	.0003
6.6	3.6737	.9999	.0009	.0000	.0001
6.8	3.8737	1.0000	.0004	.0000	.0000

$\beta = -0.325, S_w = -0.8$					
η	f	f'	f''	S	S'
0	0	0	0.0493	-0.3250	0.2545
.2	.0011	.0113	.0640	-.7491	.2545
.4	.0047	.0258	.0819	-.6982	.2544
.6	.0117	.0442	.1029	-.6474	.2540
.8	.0227	.0672	.1269	-.5966	.2531
1.0	.0389	.0952	.1535	-.5462	.2516
1.2	.0611	.1287	.1821	-.4961	.2491
1.4	.0907	.1681	.2121	-.4466	.2454
1.6	.1288	.2135	.2423	-.3980	.2401
1.8	.1765	.2649	.2714	-.3507	.2329
2.0	.2351	.3219	.2978	-.3050	.2236
2.2	.3056	.3837	.3196	-.2614	.2118
2.4	.3889	.4493	.3349	-.2204	.1977
2.6	.4855	.5172	.3420	-.1825	.1812
2.8	.5958	.5855	.3396	-.1481	.1626
3.0	.7196	.6523	.3272	-.1176	.1426
3.2	.8565	.7157	.3052	-.0911	.1218
3.4	1.0055	.7738	.2749	-.0688	.1012
3.6	1.1656	.8253	.2388	-.0506	.0815
3.8	1.3352	.8691	.1996	-.0361	.0635
4.0	1.5127	.9052	.1604	-.0250	.0477
4.2	1.6967	.9335	.1236	-.0168	.0346
4.4	1.8857	.9549	.0914	-.0110	.0242
4.6	2.0783	.9705	.0648	-.0070	.0163
4.8	2.2735	.9812	.0440	-.0043	.0105
5.0	2.4705	.9884	.0287	-.0027	.0065
5.2	2.6687	.9930	.0179	-.0016	.0039
5.4	2.8676	.9959	.0108	-.0010	.0023
5.6	3.0670	.9975	.0062	-.0007	.0013
5.8	3.2666	.9984	.0030	-.0005	.0006
6.0	3.4664	.9991	.0024	-.0004	.0005

TABLE 1.—Continued. SIMILAR SOLUTIONS OF LAMINAR COMPRESSIBLE BOUNDARY-LAYER EQUATIONS.

$\beta = -0.3285, S_w = -0.8$					
η	f	f'	f''	S	S'
0	0	0	0.0693	-0.8000	0.2644
.2	.0015	.0153	.0842	-.7471	.2644
.4	.0063	.0039	.1024	-.6943	.2642
.6	.0153	.0565	.1238	-.6415	.2636
.8	.0292	.0836	.1482	-.5888	.2625
1.0	.0491	.1159	.1750	-.5365	.2605
1.2	.0760	.1538	.2036	-.4847	.2573
1.4	.1110	.1974	.2331	-.4337	.2525
1.6	.1553	.2470	.2621	-.3838	.2459
1.8	.2101	.3021	.2892	-.3355	.2371
2.0	.2765	.3624	.3125	-.2892	.2259
2.2	.3554	.4267	.3301	-.2453	.2121
2.4	.4474	.4939	.3401	-.2045	.1958
2.6	.5530	.5622	.3412	-.1671	.1772
2.8	.6722	.6297	.3324	-.1337	.1568
3.0	.8047	.6945	.3138	-.1045	.1353
3.2	.9497	.7546	.2863	-.0796	.1136
3.4	1.1061	.8085	.2520	-.0590	.0925
3.6	1.2727	.8552	.2136	-.0425	.0729
3.8	1.4477	.8939	.1741	-.0297	.0556
4.0	1.6297	.9249	.1362	-.0201	.0408
4.2	1.8172	.9487	.1022	-.0131	.0289
4.4	2.0088	.9662	.0735	-.0083	.0197
4.6	2.2033	.9785	.0507	-.0051	.0129
4.8	2.3999	.9868	.0335	-.0030	.0082
5.0	2.5978	.9922	.0212	-.0017	.0050
5.2	2.7967	.9956	.0129	-.0010	.0029
5.4	2.9960	.9976	.0075	-.0005	.0016
5.6	3.1956	.9987	.0042	-.0003	.0009
5.8	3.3954	.9994	.0023	-.0001	.0005
6.0	3.5954	.9997	.0012	-.0001	.0002
6.2	3.7953	.9999	.0006	.0000	.0001
6.4	3.9953	.9999	.0003	.0000	.0000
6.6	4.1953	1.0000	.0001	.0000	.0000
6.8	4.3953	1.0000	.0001	.0000	.0000
7.0	4.5953	1.0000	.0000	.0000	.0000
7.2	4.7953	1.0000	.0000	.0000	.0000

$\beta = -0.3285, S_w = -0.8$					
η	f	f'	f''	S	S'
0	0	0	0.1100	-0.8000	0.2818
.2	.0023	.0234	.1250	-.7436	.2818
.4	.0096	.0502	.1434	-.6873	.2815
.6	.0226	.0810	.1650	-.6311	.2806
.8	.0423	.1164	.1893	-.5751	.2788
1.0	.0696	.1569	.2156	-.5196	.2758
1.2	.1054	.2027	.2428	-.4649	.2710
1.4	.1510	.2540	.2698	-.4114	.2642
1.6	.2074	.3105	.2948	-.3594	.2549
1.8	.2755	.3716	.3162	-.3096	.2430
2.0	.3563	.4366	.3319	-.2624	.2281
2.2	.4503	.5039	.3401	-.2185	.2105
2.4	.5579	.5720	.3395	-.1784	.1904
2.6	.6791	.6391	.3292	-.1425	.1683
2.8	.8134	.7031	.3093	-.1111	.1450
3.0	.9600	.7622	.2810	-.0845	.1215
3.2	1.1178	.8151	.2463	-.0625	.0987
3.4	1.2855	.8605	.2079	-.0449	.0776
3.6	1.4615	.8981	.1687	-.0313	.0590
3.8	1.6443	.9281	.1314	-.0211	.0432
4.0	1.8323	.9510	.0982	-.0138	.0305
4.2	2.0242	.9678	.0704	-.0087	.0207
4.4	2.2190	.9795	.0483	-.0053	.0136
4.6	2.4158	.9875	.0318	-.0032	.0085
4.8	2.6138	.9926	.0201	-.0018	.0052
5.0	2.8127	.9957	.0121	-.0010	.0030
5.2	3.0121	.9976	.0071	-.0005	.0017
5.4	3.2117	.9987	.0039	-.0003	.0009
5.6	3.4115	.9993	.0021	-.0002	.0005
5.8	3.6114	.9996	.0011	-.0001	.0002
6.0	3.8113	.9998	.0006	-.0001	.0001
6.2	4.0113	.9999	.0002	.0000	.0000

TABLE 1.—Continued. SIMILAR SOLUTIONS OF LAMINAR COMPRESSIBLE BOUNDARY-LAYER EQUATIONS.

$\beta = -0.325, S_w = -0.8$					
η	f	f'	f''	S	S'
0	0	0	0.1353	-0.8000	0.2913
.3379	.0080	.050	.1623	-.7015	.2911
.6210	.0289	.100	.1922	-.6192	.2897
.8632	.0590	.150	.3314	-.5494	.2866
1.0761	.0961	.200	.2487	-.4888	.2819
1.2677	.1391	.250	.2732	-.4353	.2757
1.4439	.1875	.300	.2944	-.3874	.2679
1.6087	.2410	.350	.3120	-.3440	.2587
1.7654	.2997	.400	.3258	-.3042	.2479
1.9165	.3639	.450	.3354	-.2677	.2359
2.0643	.4341	.500	.3406	-.2338	.2224
2.2108	.5110	.550	.3412	-.2023	.2075
2.3582	.5958	.600	.3366	-.1729	.1913
2.5088	.6899	.650	.3265	-.1454	.1737
2.6656	.7958	.700	.3103	-.1197	.1545
2.8327	.9170	.750	.2874	-.0956	.1339
3.0161	1.0592	.800	.2569	-.0731	.1118
3.2268	1.2332	.850	.2172	-.0521	.0878
3.4876	1.4618	.900	.1663	-.0328	.0618
3.5500	1.5182	.910	.1544	-.0291	.0563
3.6175	1.5800	.920	.1419	-.0255	.0507
3.6915	1.6484	.930	.1286	-.0219	.0450
3.7737	1.7253	.940	.1146	-.0185	.0392
3.8672	1.8136	.950	.0996	-.0151	.0332
3.9194	1.8634	.955	.0918	-.0134	.0302
3.9764	1.9180	.960	.0836	-.0118	.0271
4.0394	1.9786	.965	.0752	-.0102	.0239
4.1101	2.0470	.970	.0664	-.0086	.0208
4.1911	2.1258	.975	.0572	-.0071	.0176
4.2867	2.2192	.980	.0475	-.0056	.0143
4.4050	2.3354	.985	.0373	-.0041	.0109
4.5632	2.4917	.990	.0263	-.0026	.0074
4.6029	2.5310	.991	.0240	-.0024	.0067
4.6466	2.5743	.992	.0217	-.0021	.0060
4.6953	2.6228	.993	.0193	-.0018	.0053
4.7507	2.6777	.994	.0168	-.0015	.0046
4.8148	2.7415	.995	.0143	-.0013	.0038
4.8915	2.8178	.996	.0117	-.0010	.0031
4.9876	2.9136	.997	.0091	-.0007	.0024
5.1186	3.0443	.998	.0063	-.0005	.0016
5.3319	3.2573	.999	.0033	-.0002	.0008
6.4255	4.3506	1.000	.0000	-.0000	.0000

$\beta = -0.3, S_w = -0.8$					
η	f	f'	f''	S	S'
0	0	0	0.2086	-0.8000	0.3154
.2310	.0056	.050	.2248	-.7271	.3154
.4447	.0215	.100	.2435	-.6597	.3146
.6423	.0461	.150	.2629	-.5978	.3126
.8259	.0782	.200	.2819	-.5407	.3091
.9979	.1168	.250	.2995	-.4879	.3040
1.1605	.1615	.300	.3151	-.4390	.2973
3.3159	.2120	.350	.3280	-.3934	.2888
1.4660	.2682	.400	.3380	-.3507	.2786
1.6124	.3304	.450	.3445	-.3108	.2667
1.7568	.3990	.500	.3472	-.2732	.2530
1.9010	.4747	.550	.3457	-.2378	.2376
2.0468	.5586	.600	.3395	-.2044	.2204
2.1964	.6521	.650	.3282	-.1729	.2013
2.3526	.7576	.700	.3111	-.1431	.1804
2.5194	.8786	.750	.2875	-.1149	.1574
2.7030	1.0210	.800	.2565	-.0883	.1322
2.9142	1.1954	.850	.2166	-.0633	.1046
3.2759	1.4246	.900	.1657	-.0400	.0743
3.2385	1.4813	.910	.1538	-.0356	.0678
3.3063	1.5433	.920	.1413	-.0312	.0612
3.3806	1.6120	.930	.1281	-.0269	.0545
3.4631	1.6892	.940	.1141	-.0227	.0475
3.5569	1.7779	.950	.0992	-.0186	.0404
3.6094	1.8279	.955	.0914	-.0166	.0367
3.6667	1.8827	.960	.0833	-.0146	.0330
3.7299	1.9436	.965	.0749	-.0126	.0293
3.8010	2.0123	.970	.0661	-.0107	.0254
3.8823	2.0915	.975	.0569	-.0088	.0215
3.9784	2.1854	.980	.0473	-.0069	.0175
4.0972	2.3022	.985	.0371	-.0051	.0134
4.2562	2.4592	.990	.0262	-.0033	.0092
4.2961	2.4986	.991	.0239	-.0029	.0083
4.3400	2.5422	.992	.0216	-.0026	.0074
4.3890	2.5908	.993	.0192	-.0022	.0065
4.4446	2.6460	.994	.0167	-.0019	.0056
4.5090	2.7101	.995	.0142	-.0016	.0047
4.5860	2.7868	.996	.0117	-.0012	.0038
4.6827	2.8831	.997	.0090	-.0009	.0029
4.8143	3.0144	.998	.0062	-.0006	.0020
5.0287	3.2285	.999	.0033	-.0003	.0010
6.1270	4.3265	1.000	.0000	-.0000	.0000

TABLE 1.—Continued. SIMILAR SOLUTIONS OF LAMINAR COMPRESSIBLE BOUNDARY-LAYER EQUATIONS.

$\beta = -0.14, S_w = -0.8$						$\beta = 0.5, S_w = -0.8$					
η	f	f'	f''	S	S'	η	f	f'	f''	S	S'
0	0	0	0.3841	-0.8000	0.3590	0	0	0	0.6546	-0.8000	0.403
.1294	.0032	.050	.3882	-.7535	.3590	.0768	.0019	.050	.6464	-.7690	.403
.2575	.0128	.100	.3926	-.7075	.3590	.1547	.0077	.100	.6368	-.7375	.403
.3841	.0286	.150	.3970	-.6622	.3580	.2339	.0177	.150	.6258	-.7056	.403
.5094	.0505	.200	.4009	-.6174	.3560	.3147	.0318	.200	.6133	-.6731	.402
.6337	.0784	.250	.4039	-.5734	.3530	.3971	.0504	.250	.5993	-.6400	.401
.7572	.1124	.300	.4057	-.5300	.3490	.4817	.0737	.300	.5835	-.6063	.399
.8804	.1524	.350	.4058	-.4873	.3440	.5687	.1020	.350	.5659	-.5717	.396
1.0039	.1987	.400	.4039	-.4453	.3360	.6586	.1357	.400	.5463	-.5363	.391
1.1283	.2516	.450	.3996	-.4040	.3270	.7520	.1755	.450	.5246	-.5000	.386
1.2546	.3116	.500	.3925	-.3634	.3160	.8496	.2219	.500	.5004	-.4627	.379
1.3837	.3795	.550	.3822	-.3235	.3020	.9524	.2759	.550	.4737	-.4243	.369
1.5170	.4562	.600	.3682	-.2843	.2860	1.0614	.3387	.600	.4441	-.3848	.357
1.6561	.5432	.650	.3500	-.2459	.2670	1.1784	.4119	.650	.4111	-.3439	.342
1.8038	.6429	.700	.3269	-.2081	.2440	1.3058	.4979	.700	.3743	-.3016	.323
1.9636	.7589	.750	.2984	-.1711	.2190	1.4472	.6006	.750	.3333	-.2577	.298
2.1417	.8971	.800	.2633	-.1349	.1890	1.6086	.7258	.800	.2870	-.2119	.268
2.3489	1.0682	.850	.2202	-.0995	.1540	1.8010	.8848	.850	.2345	-.1641	.230
2.6077	1.2950	.900	.1669	-.0650	.1140	2.0469	1.1003	.900	.1737	-.1137	.180
2.6699	1.3513	.910	.1547	-.0582	.1050	2.1069	1.1546	.910	.1603	-.1032	.169
2.7375	1.4131	.920	.1419	-.0515	.0950	2.1723	1.2144	.920	.1463	-.0926	.156
2.8116	1.4817	.930	.1285	-.0448	.0860	2.2444	1.2811	.930	.1318	-.0819	.143
2.8941	1.5588	.940	.1143	-.0381	.0760	2.3250	1.3565	.940	.1166	-.0710	.128
2.9879	1.6475	.950	.0992	-.0316	.0650	2.4171	1.4436	.950	.1007	-.0599	.113
3.0405	1.6976	.955	.0913	-.0283	.0600	2.4690	1.4930	.955	.0925	-.0543	.104
3.0979	1.7526	.960	.0831	-.0250	.0540	2.5257	1.5473	.960	.0840	-.0486	.096
3.1614	1.8138	.965	.0747	-.0218	.0480	2.5887	1.6079	.965	.0752	-.0429	.087
3.2328	1.8828	.970	.0659	-.0186	.0420	2.6596	1.6766	.970	.0662	-.0371	.077
3.3145	1.9623	.975	.0567	-.0154	.0360	2.7410	1.7557	.975	.0568	-.0312	.067
3.4110	2.0566	.980	.0471	-.0122	.0300	2.8375	1.8501	.980	.0470	-.0252	.057
3.5305	2.1741	.985	.0369	-.0091	.0230	2.9573	1.9678	.985	.0367	-.0192	.045
3.6905	2.3320	.990	.0260	-.0060	.0160	3.1183	2.1268	.990	.0258	-.0130	.032
3.7306	2.3718	.991	.0237	-.0054	.0150	3.1588	2.1669	.991	.0235	-.0117	.030
3.7749	2.4158	.992	.0214	-.0047	.0130	3.2034	2.2111	.992	.0212	-.0105	.027
3.8243	2.4647	.993	.0191	-.0041	.0120	3.2532	2.2606	.993	.0189	-.0092	.024
3.8803	2.5204	.994	.0166	-.0035	.0100	3.3098	2.3168	.994	.0165	-.0079	.021
3.9452	2.5849	.995	.0142	-.0029	.0090	3.3755	2.3821	.995	.0140	-.0066	.018
4.0228	2.6622	.996	.0116	-.0023	.0070	3.4540	2.4603	.996	.0115	-.0053	.015
4.1201	2.7591	.997	.0090	-.0017	.0050	3.5526	2.5586	.997	.0088	-.0040	.012
4.2524	2.8912	.998	.0062	-.0011	.0040	3.6869	2.6925	.998	.0061	-.0027	.008
4.4678	3.1062	.999	.0033	-.0005	.0020	3.9056	2.9109	.999	.0032	-.0013	.004
5.5574	4.1955	1.000	.0000	.0000	.0000	5.0257	4.0307	1.000	.0000	.0000	.000

TABLE 1.—Continued. SIMILAR SOLUTIONS OF LAMINAR COMPRESSIBLE BOUNDARY-LAYER EQUATIONS.

$\beta=1.5, S_w=-0.8$						$\beta=2.0, S_w=-0.8$					
η	f	f'	f''	S	S'	η	f	f'	f''	S	S'
0	0	0	0.8689	-0.8000	0.4261	0	0	0	0.9480	-0.8000	0.4331
.0581	.0014	.050	.8504	-.7752	.4261	.0533	.0013	.050	.9255	-.7768	.4331
.1176	.0059	.100	.8296	-.7498	.4260	.1081	.0054	.100	.9003	-.7531	.4330
.1788	.0136	.150	.8065	-.7238	.4258	.1645	.0125	.150	.8724	-.7287	.4329
.2418	.0246	.200	.7812	-.6970	.4253	.2229	.0227	.200	.8421	-.7035	.4324
.3069	.0393	.250	.7537	-.6693	.4245	.2834	.0364	.250	.8094	-.6773	.4317
.3746	.0580	.300	.7240	-.6406	.4231	.3466	.0538	.300	.7743	-.6501	.4305
.4453	.0810	.350	.6922	-.6108	.4211	.4128	.0754	.350	.7370	-.6216	.4287
.5194	.1088	.400	.6582	-.5797	.4182	.4826	.1016	.400	.6975	-.5918	.4261
.5975	.1421	.450	.6221	-.5471	.4142	.5565	.1331	.450	.6558	-.5604	.4225
.6805	.1815	.500	.5838	-.5130	.4088	.6355	.1706	.500	.6121	-.5273	.4175
.7694	.2283	.550	.5432	-.4770	.4015	.7205	.2153	.550	.5662	-.4921	.4108
.8653	.2836	.600	.5003	-.4389	.3919	.8129	.2686	.600	.5181	-.4546	.4019
.9701	.3491	.650	.4547	-.3985	.3792	.9144	.3321	.650	.4678	-.4144	.3898
1.0864	.4277	.700	.4064	-.3554	.3625	1.0278	.4087	.700	.4152	-.3711	.3738
1.2179	.5232	.750	.3549	-.3092	.3406	1.1570	.5025	.750	.3600	-.3242	.3525
1.3711	.6420	.800	.2998	-.2592	.3117	1.3086	.6202	.800	.3019	-.2729	.3239
1.5572	.7958	.850	.2402	-.2049	.2729	1.4941	.7735	.850	.2401	-.2166	.2848
1.7999	1.0085	.900	.1744	-.1452	.2195	1.7377	.9870	.900	.1732	-.1539	.2299
1.8597	1.0627	.910	.1603	-.1324	.2063	1.7980	1.0415	.910	.1590	-.1405	.2163
1.9252	1.1226	.920	.1458	-.1194	.1921	1.8640	1.1020	.920	.1445	-.1267	.2016
1.9977	1.1897	.930	.1308	-.1061	.1767	1.9372	1.1697	.930	.1296	-.1125	.1856
2.0790	1.2657	.940	.1154	-.0924	.1599	2.0193	1.2465	.940	.1142	-.0980	.1680
2.1724	1.3540	.950	.0993	-.0784	.1416	2.1137	1.3357	.950	.0982	-.0831	.1488
2.2250	1.4041	.955	.0910	-.0712	.1317	2.1670	1.3864	.955	.0900	-.0754	.1384
2.2827	1.4594	.960	.0825	-.0639	.1213	2.2254	1.4424	.960	.0815	-.0677	.1274
2.3469	1.5212	.965	.0738	-.0565	.1103	2.2903	1.5048	.965	.0729	-.0598	.1158
2.4193	1.5912	.970	.0648	-.0489	.0986	2.3636	1.5758	.970	.0640	-.0518	.1035
2.5025	1.6721	.975	.0555	-.0413	.0861	2.4477	1.6576	.975	.0549	-.0437	.0904
2.6013	1.7687	.980	.0459	-.0335	.0726	2.5476	1.7553	.980	.0454	-.0353	.0762
2.7240	1.8893	.985	.0358	-.0255	.0580	2.6718	1.8773	.985	.0354	-.0269	.0608
2.8891	2.0524	.990	.0252	-.0173	.0419	2.8387	2.0421	.990	.0249	-.0182	.0438
2.9307	2.0935	.991	.0229	-.0156	.0385	2.8806	2.0837	.991	.0227	-.0164	.0402
2.9764	2.1389	.992	.0207	-.0139	.0349	2.9269	2.1295	.992	.0205	-.0146	.0365
3.0276	2.1897	.993	.0184	-.0122	.0313	2.9785	2.1808	.993	.0182	-.0129	.0326
3.0856	2.2473	.994	.0160	-.0105	.0275	3.0371	2.2390	.994	.0159	-.0111	.0288
3.1530	2.3144	.995	.0136	-.0088	.0236	3.1051	2.3066	.995	.0135	-.0093	.0246
3.2336	2.3946	.996	.0112	-.0071	.0195	3.1864	2.3875	.996	.0111	-.0074	.0203
3.3347	2.4953	.997	.0086	-.0054	.0152	3.2883	2.4891	.997	.0086	-.0056	.0158
3.4724	2.6327	.998	.0060	-.0036	.0107	3.4270	2.6274	.998	.0059	-.0037	.0111
3.6964	2.8564	.999	.0032	-.0018	.0058	3.6526	2.8527	.999	.0031	-.0019	.0060
4.8362	3.9959	1.000	.0000	.0000	.0000	4.7958	3.9956	1.000	.0000	.0000	.0000

TABLE 1.—Continued. SIMILAR SOLUTIONS OF LAMINAR COMPRESSIBLE BOUNDARY-LAYER EQUATIONS.

$\beta = -0.2350, S_w = -0.4$					
η	f	f'	f''	S	S'
0	0	0	-0.0500	-0.4000	0.1107
.2	-.0008	-.0071	-.0213	-.3779	.1107
.4	-.0025	-.0084	.0085	-.3557	.1107
.6	-.0038	-.0037	.0393	-.3336	.1108
.8	-.0035	-.0073	.0712	-.3114	.1108
1.0	-.0004	.0249	.1041	-.2893	.1109
1.2	.0069	.0490	.1379	-.2671	.1108
1.4	.0197	.0800	.1722	-.2449	.1106
1.6	.0393	.1179	.2067	-.2229	.1099
1.8	.0673	.1627	.2404	-.2010	.1088
2.0	.1048	.2140	.2724	-.1794	.1069
2.2	.1533	.2714	.3013	-.1583	.1042
2.4	.2138	.3342	.3256	-.1378	.1005
2.6	.2873	.4012	.3434	-.1182	.0956
2.8	.3745	.4710	.3533	-.0996	.0895
3.0	.4757	.5419	.3539	-.0825	.0822
3.2	.5912	.6119	.3445	-.0668	.0739
3.4	.7203	.6791	.3252	-.0529	.0649
3.6	.8625	.7414	.2970	-.0409	.0554
3.8	1.0165	.7974	.2621	-.0308	.0459
4.0	1.1809	.8459	.2229	-.0225	.0369
4.2	1.3543	.8865	.1825	-.0160	.0286
4.4	1.5350	.9190	.1436	-.0110	.0214
4.6	1.7214	.9442	.1085	-.0073	.0155
4.8	1.9122	.9628	.0786	-.0048	.0107
5.0	2.1062	.9760	.0547	-.0030	.0072
5.2	2.3024	.9850	.0365	-.0018	.0046
5.4	2.5000	.9910	.0234	-.0011	.0029
5.6	2.6986	.9947	.0144	-.0006	.0017
5.8	2.8978	.9969	.0085	-.0003	.0010
6.0	3.0973	.9982	.0048	-.0002	.0005
6.2	3.2970	.9989	.0027	-.0001	.0003
6.4	3.4969	.9993	.0014	-.0001	.0001
6.6	3.6968	.9995	.0007	-.0001	.0001
6.8	3.8967	.9997	.0003	.0000	.0000

$\beta = -0.2460, S_w = -0.4$					
η	f	f'	f''	S	S'
0	0	0	0	-0.4000	0.1249
.2	.0002	.0030	.0301	-.3750	.1249
.4	.0016	.0121	.0615	-.3500	.1249
.6	.0055	.0277	.0940	-.3251	.1248
.8	.0131	.0498	.1276	-.3001	.1246
1.0	.0259	.0787	.1618	-.2752	.1241
1.2	.0451	.1146	.1964	-.2504	.1233
1.4	.0721	.1573	.2305	-.2260	.1218
1.6	.1084	.2067	.2631	-.2018	.1197
1.8	.1552	.2623	.2929	-.1782	.1166
2.0	.2137	.3235	.3184	-.1552	.1124
2.2	.2849	.3893	.3379	-.1333	.1069
2.4	.3696	.4582	.3497	-.1126	.1002
2.6	.4683	.5285	.3524	-.0933	.0922
2.8	.5810	.5985	.3452	-.0758	.0830
3.0	.7075	.6660	.3280	-.0602	.0730
3.2	.8471	.7291	.3017	-.0466	.0625
3.4	.9988	.7861	.2681	-.0352	.0520
3.6	1.1611	.8360	.2298	-.0258	.0419
3.8	1.3326	.8780	.1896	-.0184	.0327
4.0	1.5118	.9119	.1504	-.0127	.0246
4.2	1.6969	.9384	.1146	-.0084	.0178
4.4	1.8867	.9581	.0839	-.0054	.0124
4.6	2.0798	.9723	.0589	-.0034	.0084
4.8	2.2753	.9821	.0397	-.0020	.0054
5.0	2.4724	.9885	.0257	-.0011	.0034
5.2	2.6705	.9926	.0160	-.0006	.0020
5.4	2.8693	.9952	.0096	-.0003	.0012
5.6	3.0685	.9967	.0056	-.0001	.0006
5.8	3.2679	.9975	.0032	.0000	.0003
6.0	3.4675	.9980	.0018	.0000	.0002

TABLE 1.—Continued. SIMILAR SOLUTIONS OF LAMINAR COMPRESSIBLE BOUNDARY-LAYER EQUATIONS.

$\beta = -0.2483, S_w = -0.4$					
η	f	f'	f''	S	S'
0	0	0	0.0500	-0.4000	0.1360
.2	.0012	.0130	.0805	-.3728	.1360
.4	.0056	.0323	.1122	-.3456	.1359
.6	.0145	.0580	.1450	-.3184	.1357
.8	.0293	.0903	.1786	-.2913	.1351
1.0	.0511	.1294	.2123	-.2644	.1340
1.2	.0815	.1752	.2453	-.2378	.1323
1.4	.1216	.2274	.2765	-.2116	.1296
1.6	.1728	.2856	.3045	-.1860	.1259
1.8	.2362	.3489	.3276	-.1613	.1209
2.0	.3126	.4162	.3441	-.1377	.1145
2.2	.4028	.4860	.3524	-.1156	.1066
2.4	.5071	.5565	.3513	-.0952	.0973
2.6	.6254	.6258	.3402	-.0768	.0869
2.8	.7572	.6919	.3193	-.0605	.0757
3.0	.9018	.7530	.2899	-.0465	.0641
3.2	1.0580	.8075	.2541	-.0348	.0528
3.4	1.2243	.8544	.2146	-.0253	.0420
3.6	1.3992	.8933	.1744	-.0179	.0323
3.8	1.5811	.9243	.1362	-.0123	.0240
4.0	1.7684	.9480	.1021	-.0082	.0172
4.2	1.9598	.9654	.0734	-.0054	.0118
4.4	2.1542	.9778	.0506	-.0034	.0078
4.6	2.3507	.9861	.0335	-.0022	.0050
4.8	2.5485	.9915	.0213	-.0014	.0031
5.0	2.7471	.9949	.0130	-.0009	.0018
5.2	2.9463	.9969	.0076	-.0006	.0010
5.4	3.1458	.9980	.0043	-.0005	.0006
5.6	3.3455	.9987	.0024	-.0004	.0003
5.8	3.5453	.9991	.0013	-.0003	.0001
6.0	3.7451	.9992	.0006	-.0003	.0001
6.2	3.9450	.9993	.0004	-.0003	.0000
6.4	4.1448	.9994	.0000	-.0003	.0000

$\beta = -0.24, S_w = -0.4$					
η	f	f'	f''	S	S'
0	0	0	0.1064	-0.4000	0.1473
.2	.3766	.0083	.1628	-.3447	.1460
.4	.6490	.0284	.100	-.3050	.1452
.6	.8732	.0562	.150	-.2726	.1438
.8	1.0687	.0903	.200	-.2447	.1418
1.0	1.2453	.1299	.250	-.2199	.1390
1.2	1.4087	.1748	.300	-.1974	.1356
1.4	1.5628	.2248	.350	-.1768	.1315
1.6	1.7106	.2802	.400	-.1577	.1267
1.8	1.8541	.3412	.450	-.1399	.1212
2.0	1.9955	.4083	.500	-.1232	.1150
2.2	2.1366	.4824	.550	-.1074	.1080
2.4	2.2793	.5644	.600	-.0926	.1002
2.6	2.4259	.6561	.650	-.0785	.0916
2.8	2.5793	.7596	.700	-.0651	.0822
3.0	2.7433	.8786	.750	-.0525	.0719
3.2	2.9242	1.0189	.800	-.0405	.0606
3.4	3.1328	1.1912	.850	-.0292	.0481
3.6	3.3918	1.4181	.900	-.0186	.0343
3.8	3.6538	1.6742	.910	-.0165	.0314
4.0	3.9210	1.9357	.920	-.0145	.0283
4.2	4.1947	2.2039	.930	-.0126	.0252
4.4	4.4767	2.4806	.940	-.0106	.0221
4.6	4.7698	2.7686	.950	-.0087	.0188
4.8	5.0720	3.0683	.955	-.0078	.0171
5.0	5.3848	3.3789	.960	-.0068	.0154
5.2	5.7081	3.6918	.965	-.0059	.0136
5.4	6.0425	4.0177	.970	-.0050	.0119
5.6	6.3884	4.3565	.975	-.0041	.0101
5.8	6.7459	4.7080	.980	-.0033	.0082
6.0	7.1154	5.0720	.985	-.0024	.0063
6.2	7.5000	5.4467	.990	-.0016	.0043
6.4	7.8918	5.8341	.991	-.0014	.0039
6.6	8.2910	6.2345	.992	-.0012	.0035
6.8	8.7000	6.6480	.993	-.0011	.0031
7.0	9.1200	7.0744	.994	-.0009	.0027
7.2	9.5520	7.5137	.995	-.0008	.0022
7.4	10.0000	7.9660	.996	-.0006	.0018
7.6	10.4640	8.4312	.997	-.0004	.0014
7.8	10.9450	8.9100	.998	-.0003	.0009
8.0	11.4440	9.4014	.999	-.0001	.0004
8.2	11.9600	9.9056	1.000	-.0000	.0000

TABLE 1.—Continued. SIMILAR SOLUTIONS OF LAMINAR COMPRESSIBLE BOUNDARY-LAYER EQUATIONS.

$\beta = -0.2, S_w = -0.4$					
η	f	f'	f''	S	S'
0	0	0	0.2182	-0.4000	0.1626
.2161	.0052	.050	.2447	-.3648	.1625
.4108	.0197	.100	.2692	-.3332	.1621
.5892	.0419	.150	.2914	-.3044	.1612
.7551	.0709	.200	.3111	-.2778	.1597
.9115	.1060	.250	.3281	-.2529	.1575
1.0606	.1470	.300	.3422	-.2297	.1546
1.2044	.1937	.350	.3531	-.2077	.1501
1.3444	.2461	.400	.3607	-.1869	.1463
1.4821	.3047	.450	.3646	-.1671	.1409
1.6191	.3697	.500	.3647	-.1482	.1345
1.7569	.4421	.550	.3606	-.1302	.1272
1.8971	.5227	.600	.3519	-.1129	.1189
2.0419	.6132	.650	.3381	-.0964	.1096
2.1939	.7159	.700	.3188	-.0805	.0990
2.3571	.8343	.750	.2932	-.0653	.0873
2.5375	.9742	.800	.2604	-.0508	.0742
2.7460	1.1464	.850	.2190	-.0369	.0595
3.0054	1.3737	.900	.1668	-.0236	.0429
3.0676	1.4300	.910	.1548	-.0211	.0393
3.1350	1.4916	.920	.1421	-.0186	.0356
3.2089	1.5600	.930	.1287	-.0161	.0318
3.2911	1.6369	.940	.1146	-.0136	.0279
3.3846	1.7253	.950	.0995	-.0112	.0239
3.4369	1.7751	.955	.0916	-.0100	.0218
3.4941	1.8298	.960	.0835	-.0088	.0196
3.5572	1.8906	.965	.0750	-.0077	.0175
3.6281	1.9592	.970	.0662	-.0065	.0152
3.7094	2.0382	.975	.0570	-.0054	.0129
3.8054	2.1321	.980	.0473	-.0042	.0106
3.9240	2.2486	.985	.0373	-.0031	.0082
4.0829	2.4056	.990	.0262	-.0020	.0057
4.1228	2.4451	.991	.0239	-.0018	.0051
4.1668	2.4887	.992	.0216	-.0016	.0046
4.2158	2.5373	.993	.0192	-.0014	.0041
4.2714	2.5926	.994	.0167	-.0012	.0035
4.3358	2.6567	.995	.0142	-.0010	.0029
4.4129	2.7334	.996	.0117	-.0008	.0024
4.5096	2.8297	.997	.0090	-.0005	.0019
4.6411	2.9609	.998	.0062	-.0003	.0013
4.8545	3.1740	.999	.0033	-.0001	.0007
5.9279	4.2471	1.000	.0000	.0000	.0000

$\beta = 0.5, S_w = -0.4$					
η	f	f'	f''	S	S'
0	0	0	0.7946	-0.4000	0.209
.0637	.0016	.050	.7753	-.3866	.209
.1290	.0065	.100	.7551	-.3730	.209
.1962	.0149	.150	.7339	-.3590	.209
.2654	.0270	.200	.7116	-.3445	.208
.3368	.0431	.250	.6881	-.3296	.208
.4108	.0635	.300	.6632	-.3143	.207
.4878	.0886	.350	.6369	-.2984	.206
.5681	.1187	.400	.6090	-.2819	.204
.6523	.1546	.450	.5793	-.2648	.202
.7411	.1968	.500	.5477	-.2470	.199
.8354	.2464	.550	.5138	-.2284	.195
.9364	.3046	.600	.4774	-.2090	.190
1.0456	.3729	.650	.4381	-.1887	.183
1.1657	.4540	.700	.3956	-.1673	.174
1.3001	.5516	.750	.3493	-.1447	.163
1.4548	.6716	.800	.2984	-.1207	.148
1.6406	.8252	.850	.2417	-.0950	.129
1.8804	1.0353	.900	.1775	-.0672	.103
1.9391	1.0885	.910	.1635	-.0613	.097
2.0032	1.1471	.920	.1490	-.0554	.090
2.0741	1.2127	.930	.1339	-.0492	.083
2.1535	1.2870	.940	.1183	-.0430	.075
2.2445	1.3730	.950	.1020	-.0365	.067
2.2957	1.4218	.955	.0935	-.0332	.062
2.3519	1.4756	.960	.0848	-.0299	.057
2.4143	1.5356	.965	.0759	-.0265	.052
2.4846	1.6037	.970	.0667	-.0230	.047
2.5654	1.6823	.975	.0572	-.0195	.041
2.6614	1.7761	.980	.0472	-.0159	.035
2.7807	1.8933	.985	.0369	-.0122	.028
2.9412	2.0518	.990	.0259	-.0083	.020
2.9816	2.0918	.991	.0236	-.0075	.019
3.0261	2.1360	.992	.0213	-.0068	.017
3.0759	2.1854	.993	.0189	-.0060	.015
3.1324	2.2416	.994	.0165	-.0051	.013
3.1980	2.3068	.995	.0140	-.0043	.012
3.2766	2.3850	.996	.0115	-.0035	.010
3.3752	2.4833	.997	.0088	-.0026	.008
3.5097	2.6174	.998	.0061	-.0018	.005
3.7288	2.8362	.999	.0032	-.0009	.003
4.8386	3.9458	1.000	.0000	.0000	.000

TABLE 1.—Continued. SIMILAR SOLUTIONS OF LAMINAR COMPRESSIBLE BOUNDARY-LAYER EQUATIONS.

$\beta=2.0, S_w=-0.4$					
η	f	f'	f''	S	S'
0	0	0	1.3329	-0.4000	0.230
.0381	.0009	.050	1.2868	-.3912	.230
.0777	.0039	.100	1.2386	-.3820	.230
.1190	.0091	.150	1.1884	-.3725	.230
.1620	.0166	.200	1.1360	-.3626	.230
.2071	.0268	.250	1.0816	-.3523	.230
.2546	.0399	.300	1.0252	-.3413	.229
.3049	.0563	.350	.9668	-.3356	.229
.3583	.0764	.400	.9064	-.3176	.228
.4155	.1007	.450	.8440	-.3046	.227
.4772	.1301	.500	.7797	-.2906	.225
.5443	.1654	.550	.7134	-.2756	.223
.6181	.2079	.600	.6450	-.2592	.220
.7002	.2593	.650	.5746	-.2413	.216
.7932	.3222	.700	.5021	-.2215	.210
.9011	.4005	.750	.4276	-.1992	.202
1.0302	.5007	.800	.3507	-.1738	.191
1.1921	.6345	.850	.2714	-.1442	.174
1.4116	.8269	.900	.1890	-.1087	.148
1.4671	.8772	.910	.1721	-.1007	.141
1.5284	.9333	.920	.1549	-.0922	.134
1.5970	.9967	.930	.1376	-.0833	.125
1.6748	1.0695	.940	.1200	-.0739	.116
1.7651	1.1549	.950	.1021	-.0640	.104
1.8164	1.2038	.955	.0930	-.0587	.098
1.8731	1.2581	.960	.0838	-.0533	.092
1.9365	1.3191	.965	.0744	-.0477	.085
2.0086	1.3888	.970	.0649	-.0419	.077
2.0919	1.4698	.975	.0553	-.0358	.068
2.1914	1.5672	.980	.0454	-.0295	.058
2.3161	1.6897	.985	.0352	-.0229	.048
2.4850	1.8565	.990	.0245	-.0158	.035
2.5276	1.8987	.991	.0223	-.0144	.032
2.5747	1.9454	.992	.0201	-.0129	.030
2.6274	1.9977	.993	.0178	-.0114	.027
2.6873	2.0572	.994	.0155	-.0099	.024
2.7569	2.1264	.995	.0132	-.0083	.020
2.8402	2.2093	.996	.0108	-.0067	.017
2.9449	2.3136	.997	.0083	-.0051	.013
3.0875	2.4559	.998	.0058	-.0034	.009
3.3196	2.6877	.999	.0030	-.0017	.005
4.4979	3.8657	1.000	.0000	.0000	.000

$\beta=-0.1947, S_w=0$			
η	f	f'	f''
0	0	0	-0.0500
.2	-.0007	-.0061	-.0111
.4	-.0019	-.0044	.0279
.6	-.0020	.0051	.0669
.8	.0006	.0223	.1058
1.0	.0075	.0474	.1446
1.2	.0201	.0801	.1829
1.4	.0400	.1205	.2203
1.6	.0688	.1681	.2559
1.8	.1077	.2226	.2885
2.0	.1582	.2833	.3169
2.2	.2214	.3490	.3395
2.4	.2981	.4186	.3547
2.6	.3889	.4903	.3610
2.8	.4942	.5623	.3574
3.0	.6138	.6326	.3436
3.2	.7470	.6991	.3202
3.4	.8930	.7601	.2885
3.6	1.0506	.8141	.2510
3.8	1.2182	.8602	.2104
4.0	1.3941	.8983	.1697
4.2	1.5769	.9284	.1316
4.4	1.7650	.9512	.0980
4.6	1.9570	.9679	.0700
4.8	2.1518	.9796	.0480
5.0	2.3486	.9875	.0315
5.2	2.5467	.9926	.0199
5.4	2.7455	.9957	.0121
5.6	2.9448	.9976	.0070
5.8	3.1444	.9986	.0039
6.0	3.3443	.9992	.0021
6.2	3.5442	.9995	.0011
6.4	3.7441	.9997	.0006
6.6	3.9440	.9998	.0002
6.8	4.1440	.9998	.0002

TABLE 1.—Continued. SIMILAR SOLUTIONS OF LAMINAR COMPRESSIBLE BOUNDARY-LAYER EQUATIONS.

$\beta = -0.1, S_w = 1.0$					
η	f	f'	f''	S	S'
0	0	0	-0.1613	1.0000	-0.2076
.2	-.0030	-.0283	-.1217	.9585	-.2076
.4	-.0108	-.0488	-.0831	.9169	-.2079
.6	-.0220	-.0616	-.0455	.8753	-.2086
.8	-.0349	-.0670	-.0086	.8335	-.2098
1.0	-.0483	-.0651	.0276	.7913	-.2115
1.2	-.0605	-.0560	.0635	.7488	-.2138
1.4	-.0702	-.0397	.0990	.7058	-.2167
1.6	-.0759	-.0164	.1344	.6621	-.2199
1.8	-.0763	.0140	.1695	.6178	-.2233
2.0	-.0699	.0514	.2042	.5728	-.2266
2.2	-.0553	.0956	.2378	.5272	-.2295
2.4	-.0312	.1464	.2699	.4811	-.2315
2.6	.0037	.2034	.2992	.4347	-.2322
2.8	.0506	.2658	.3247	.3884	-.2310
3.0	.1104	.3329	.3448	.3425	-.2273
3.2	.1839	.4033	.3582	.2976	-.2208
3.4	.2718	.4756	.3634	.2544	-.2110
3.6	.3742	.5481	.3595	.2135	-.1978
3.8	.4909	.6188	.3461	.1755	-.1815
4.0	.6215	.6859	.3236	.1410	-.1624
4.2	.7649	.7477	.2931	.1106	-.1414
4.4	.9201	.8028	.2568	.0845	-.1196
4.6	1.0855	.8502	.2172	.0628	-.0979
4.8	1.2597	.8896	.1771	.0453	-.0774
5.0	1.4409	.9211	.1390	.0317	-.0591
5.2	1.6277	.9455	.1048	.0215	-.0435
5.4	1.8186	.9635	.0760	.0141	-.0308
5.6	2.0127	.9763	.0529	.0090	-.0210
5.8	2.2089	.9850	.0354	.0056	-.0137
6.0	2.4065	.9908	.0227	.0033	-.0087
6.2	2.6050	.9944	.0140	.0020	-.0052
6.4	2.8041	.9966	.0083	.0012	-.0031
6.6	3.0036	.9978	.0048	.0007	-.0017
6.8	3.2033	.9986	.0026	.0004	-.0009
7.0	3.4030	.9990	.0014	.0003	-.0005
7.2	3.6028	.9992	.0007	.0002	-.0002
7.4	3.8027	.9993	.0004	.0002	-.0001
7.6	4.0025	.9993	.0003	.0002	-.0001
7.8	4.2024	.9994	.0001	.0002	.0000

$\beta = -0.1305, S_w = 1.0$					
η	f	f'	f''	S	S'
0	0	0	-0.0500	1.0000	-0.3139
.2	-.0007	-.0048	.0014	.9372	-.3139
.4	-.0013	.0004	.0511	.8744	-.3139
.6	.0002	.0155	.0992	.8117	-.3140
.8	.0056	.0400	.1456	.7489	-.3138
1.0	.0168	.0736	.1900	.6862	-.3132
1.2	.0356	.1159	.2319	.6237	-.3116
1.4	.0637	.1661	.2704	.5616	-.3085
1.6	.1025	.2237	.3046	.5004	-.3035
1.8	.1536	.2876	.3331	.4404	-.2959
2.0	.2179	.3565	.3545	.3822	-.2852
2.2	.2964	.4288	.3672	.3266	-.2709
2.4	.3896	.5028	.3702	.2741	-.2530
2.6	.4975	.5762	.3627	.2256	-.2316
2.8	.6199	.6472	.3449	.1817	-.2072
3.0	.7560	.7135	.3176	.1428	-.1806
3.2	.9049	.7737	.2828	.1095	-.1530
3.4	1.0650	.8263	.2430	.0816	-.1257
3.6	1.2349	.8707	.2012	.0591	-.0999
3.8	1.4128	.9068	.1603	.0414	-.0767
4.0	1.5971	.9351	.1227	.0282	-.0567
4.2	1.7863	.9563	.0903	.0186	-.0404
4.4	1.9792	.9716	.0637	.0118	-.0277
4.6	2.1746	.9822	.0432	.0072	-.0183
4.8	2.3718	.9892	.0281	.0043	-.0116
5.0	2.5701	.9937	.0175	.0025	-.0071
5.2	2.7692	.9964	.0105	.0014	-.0042
5.4	2.9686	.9981	.0061	.0007	-.0024
5.6	3.1684	.9990	.0034	.0004	-.0013
5.8	3.3682	.9995	.0018	.0002	-.0007
6.0	3.5681	.9997	.0009	.0001	-.0003
6.2	3.7681	.9999	.0005	.0000	-.0001
6.4	3.9681	.9999	.0002	.0000	-.0001

TABLE 1.—Continued. SIMILAR SOLUTIONS OF LAMINAR COMPRESSIBLE BOUNDARY-LAYER EQUATIONS.

$\beta = -0.1295, S_w = 1.0$					
η	f	f'	f''	S	S'
0	0	0	0	1.0000	-0.3389
.2	.0003	.0051	.0509	.9322	-.3389
.4	.0027	.0203	.1001	.8645	-.3388
.6	.0091	.0450	.1473	.7967	-.3384
.8	.0213	.0790	.1924	.7291	-.3374
1.0	.0413	.1218	.2347	.6618	-.3354
1.2	.0706	.1727	.2735	.5951	-.3317
1.4	.1108	.2309	.3076	.5293	-.3258
1.6	.1634	.2953	.3358	.4650	-.3170
1.8	.2293	.3647	.3565	.4027	-.3049
2.0	.3094	.4373	.3684	.3433	-.2890
2.2	.4043	.5114	.3702	.2874	-.2691
2.4	.5139	.5847	.3615	.2359	-.2456
2.6	.6380	.6553	.3425	.1894	-.2189
2.8	.7757	.7211	.3141	.1485	-.1901
3.0	.9260	.7804	.2784	.1134	-.1604
3.2	1.0874	.8321	.2382	.0843	-.1312
3.4	1.2583	.8756	.1963	.0608	-.1038
3.6	1.4371	.9107	.1556	.0426	-.0793
3.8	1.6221	.9381	.1185	.0289	-.0584
4.0	1.8118	.9585	.0867	.0189	-.0414
4.2	2.0051	.9731	.0609	.0120	-.0282
4.4	2.2008	.9832	.0410	.0074	-.0185
4.6	2.3981	.9899	.0265	.0044	-.0117
4.8	2.5966	.9941	.0165	.0026	-.0071
5.0	2.7957	.9967	.0098	.0015	-.0042
5.2	2.9952	.9982	.0056	.0009	-.0023
5.4	3.1949	.9991	.0031	.0005	-.0013
5.6	3.3948	.9995	.0017	.0003	-.0007
5.8	3.5947	.9998	.0008	.0002	-.0003
6.0	3.7947	.9999	.0004	.0002	-.0001
6.2	3.9947	1.0000	.0001	.0002	-.0001
6.4	4.1947	1.0000	.0003	.0001	-.0001

$\beta = -0.1, S_w = 1.0$					
η	f	f'	f''	S	S'
0	0	0	0.1805	1.0000	-0.4033
.2451	.0057	.050	.2284	.9012	-.4027
.4477	.0207	.100	.2654	.8197	-.4016
.6260	.0429	.150	.2954	.7482	-.3993
.7885	.0712	.200	.3199	.6836	-.3956
.9400	.1053	.250	.3398	.6241	-.3904
1.0837	.1448	.300	.3554	.5684	-.3834
1.2220	.1897	.350	.3670	.5160	-.3747
1.3568	.2402	.400	.3745	.4662	-.3640
1.4896	.2967	.450	.3778	.4186	-.3513
1.6220	.3595	.500	.3769	.3731	-.3364
1.7555	.4296	.550	.3716	.3293	-.3192
1.8918	.5080	.600	.3615	.2872	-.2994
2.0329	.5962	.650	.3463	.2465	-.2770
2.1815	.6966	.700	.3255	.2071	-.2517
2.3416	.8128	.750	.2985	.1691	-.2231
2.5192	.9505	.800	.2642	.1324	-.1908
2.7250	1.1204	.850	.2215	.0969	-.1542
2.9818	1.3455	.900	.1682	.0628	-.1124
3.0436	1.4013	.910	.1560	.0561	-.1033
3.1105	1.4625	.920	.1431	.0496	-.0938
3.1839	1.5304	.930	.1295	.0430	-.0841
3.2656	1.6069	.940	.1152	.0366	-.0739
3.3586	1.6948	.950	.1000	.0302	-.0634
3.4107	1.7444	.955	.0920	.0270	-.0580
3.4676	1.7989	.960	.0838	.0239	-.0524
3.5305	1.8594	.965	.0753	.0208	-.0467
3.6011	1.9278	.970	.0664	.0177	-.0409
3.6821	2.0066	.975	.0571	.0146	-.0348
3.7779	2.1002	.980	.0474	.0116	-.0286
3.8964	2.2166	.985	.0372	.0086	-.0221
4.0551	2.3734	.990	.0262	.0056	-.0154
4.0950	2.4128	.991	.0239	.0050	-.0140
4.1388	2.4563	.992	.0216	.0045	-.0126
4.1878	2.5049	.993	.0192	.0039	-.0111
4.2433	2.5601	.994	.0168	.0033	-.0097
4.3077	2.6241	.995	.0143	.0027	-.0082
4.3847	2.7008	.996	.0117	.0022	-.0066
4.4813	2.7971	.997	.0090	.0016	-.0051
4.6129	2.9283	.998	.0062	.0010	-.0035
4.8269	3.1420	.999	.0033	.0005	-.0018
5.9066	4.2215	1.000	.0000	.0000	.0000

TABLE 1.—Continued. SIMILAR SOLUTIONS OF LAMINAR COMPRESSIBLE BOUNDARY-LAYER EQUATIONS.

$\beta=0.3, S_w=1.0$					
η	f	f'	f''	S	S'
0	0	0	0.9829	1.0000	-0.5457
.1	.0048	.0953	.9237	.9454	-.5456
.2	.0189	.1848	.8657	.8909	-.5450
.3	.0416	.2685	.8089	.8365	-.5434
.4	.0724	.3466	.7531	.7823	-.5403
.5	.1107	.4192	.6983	.7285	-.5354
.6	.1560	.4863	.6445	.6752	-.5284
.7	.2078	.5481	.5919	.6229	-.5189
.8	.2655	.6047	.5406	.5716	-.5067
.9	.3286	.6563	.4909	.5216	-.4919
1.0	.3966	.7029	.4430	.4733	-.4744
1.1	.4690	.7449	.3971	.4268	-.4544
1.2	.5454	.7825	.3535	.3825	-.4319
1.3	.6254	.8157	.3124	.3405	-.4074
1.4	.7084	.8450	.2740	.3011	-.3811
1.5	.7942	.8706	.2384	.2643	-.3535
1.6	.8824	.8928	.2058	.2304	-.3251
1.7	.9727	.9119	.1761	.1993	-.2963
1.8	1.0647	.9281	.1494	.1711	-.2676
1.9	1.1582	.9419	.1256	.1458	-.2395
2.0	1.2530	.9534	.1048	.1232	-.2123
2.1	1.3489	.9629	.0865	.1033	-.1864
2.2	1.4456	.9708	.0708	.0859	-.1621
2.3	1.5430	.9771	.0574	.0708	-.1396
2.4	1.6409	.9823	.0460	.0579	-.1190
2.5	1.7394	.9864	.0366	.0470	-.1005
2.6	1.8382	.9897	.0288	.0377	-.0841
2.7	1.9373	.9922	.0224	.0301	-.0696
2.8	2.0366	.9942	.0173	.0238	-.0571
2.9	2.1361	.9957	.0132	.0186	-.0463
3.0	2.2358	.9969	.0100	.0144	-.0372
3.1	2.3355	.9977	.0075	.0111	-.0296
3.2	2.4353	.9984	.0055	.0085	-.0233
3.3	2.5352	.9989	.0040	.0064	-.0182
3.4	2.6351	.9992	.0029	.0048	-.0141
3.5	2.7350	.9995	.0021	.0036	-.0107
3.6	2.8350	.9996	.0015	.0026	-.0081
3.7	2.9349	.9998	.0010	.0019	-.0061
3.8	3.0349	.9998	.0007	.0014	-.0045
3.9	3.1349	.9999	.0005	.0010	-.0033
4.0	3.2349	.9999	.0003	.0007	-.0024
4.1	3.3349	1.0000	.0002	.0005	-.0017
4.2	3.4349	1.0000	.0001	.0004	-.0012
4.3	3.5349	1.0000	.0001	.0003	-.0009
4.4	3.6349	1.0000	.0001	.0002	-.0006
4.5	3.7349	1.0000	.0000	.0001	-.0004
4.6	3.8349	1.0000	.0000	.0001	-.0003
4.7	3.9349	1.0000	.0000	.0001	-.0002

$\beta=0.5, S_w=1.0$					
η	f	f'	f''	S	S'
0	0	0	1.2351	1.0000	-0.5725
.2	.0234	.2274	1.0409	.8855	-.5716
.4	.0885	.4172	.8591	.7717	-.5656
.6	.1879	.5720	.6918	.6599	-.5505
.8	.3151	.6950	.5414	.5523	-.5237
1.0	.4640	.7898	.4103	.4513	-.4846
1.2	.6295	.8605	.3000	.3592	-.4346
1.4	.8069	.9113	.2108	.2780	-.3767
1.6	.9929	.9462	.1417	.2088	-.3147
1.8	1.1846	.9692	.0908	.1521	-.2532
2.0	1.3800	.9835	.0550	.1072	-.1959
2.2	1.5776	.9920	.0313	.0732	-.1457
2.4	1.7765	.9966	.0165	.0484	-.1041
2.6	1.9761	.9990	.0078	.0310	-.0714
2.8	2.1760	1.0000	.0031	.0193	-.0471
3.0	2.3761	1.0004	.0009	.0117	-.0299
3.2	2.5762	1.0004	-.0001	.0069	-.0182
3.4	2.7762	1.0004	-.0004	.0041	-.0106
3.6	2.9763	1.0003	-.0004	.0025	-.0061
3.8	3.1764	1.0002	-.0003	.0016	-.0032
4.0	3.3764	1.0002	-.0002	.0011	-.0017
4.2	3.5764	1.0001	-.0002	.0008	-.0008
4.4	3.7765	1.0001	-.0001	.0007	-.0004
4.6	3.9765	1.0001	-.0001	.0006	-.0002
4.8	4.1765	1.0001	-.0001	.0006	-.0001
5.0	4.3765	1.0001	-.0001	.0006	.0000
5.2	4.5765	1.0000	-.0001	.0006	.0000
5.4	4.7765	1.0000	-.0001	.0006	.0000
5.6	4.9765	1.0000	-.0001	.0006	.0000

TABLE 1.—Continued. SIMILAR SOLUTIONS OF LAMINAR COMPRESSIBLE BOUNDARY-LAYER EQUATIONS.

$\beta=1.0, S_w=1.0$					
η	f	f'	f''	S	S'
0	0	0	1.7368	1.0000	-0.6154
.1	.0084	.1638	1.5403	.9384	-.6152
.2	.0321	.3084	1.3526	.8770	-.6140
.3	.0694	.4347	1.1758	.8157	-.6110
.4	.1185	.5439	1.0114	.7549	-.6053
.5	.1776	.6374	.8603	.6948	-.5965
.6	.2455	.7165	.7232	.6357	-.5840
.7	.3205	.7825	.6004	.5781	-.5677
.8	.4016	.8370	.4915	.5223	-.5476
.9	.4876	.8812	.3965	.4687	-.5238
1.0	.5776	.9167	.3142	.4176	-.4967
1.1	.6707	.9445	.2442	.3694	-.4666
1.2	.7663	.9659	.1857	.3243	-.4343
1.3	.8637	.9820	.1372	.2826	-.4003
1.4	.9625	.9936	.0979	.2444	-.3654
1.5	1.0623	1.0019	.0666	.2096	-.3302
1.6	1.1628	1.0073	.0422	.1783	-.2954
1.7	1.2637	1.0105	.0237	.1505	-.2617
1.8	1.3648	1.0122	.0101	.1259	-.2294
1.9	1.4661	1.0126	.0004	.1045	-.1992
2.0	1.5673	1.0123	-.0061	.0860	-.1711
2.1	1.6685	1.0115	-.0101	.0702	-.1456
2.2	1.7696	1.0104	-.0123	.0568	-.1226
2.3	1.8706	1.0091	-.0131	.0456	-.1022
2.4	1.9714	1.0078	-.0130	.0363	-.0843
2.5	2.0722	1.0065	-.0122	.0286	-.0689
2.6	2.1728	1.0053	-.0111	.0224	-.0557
2.7	2.2732	1.0043	-.0098	.0174	-.0446
2.8	2.3736	1.0034	-.0085	.0134	-.0354
2.9	2.4739	1.0026	-.0071	.0103	-.0277
3.0	2.5741	1.0020	-.0059	.0078	-.0216
3.1	2.6743	1.0014	-.0049	.0059	-.0166
3.2	2.7744	1.0010	-.0040	.0045	-.0126
3.3	2.8745	1.0006	-.0032	.0034	-.0095
3.4	2.9746	1.0003	-.0026	.0026	-.0071
3.5	3.0745	1.0001	-.0020	.0019	-.0053
3.6	3.1746	.9999	-.0016	.0015	-.0038

$\beta=1.5, S_w=1.0$					
η	f	f'	f''	S	S'
0	0	0	2.1402	1.0000	-0.6425
.1	.0102	.1992	1.8464	.9358	-.6423
.2	.0389	.3699	1.5697	.8716	-.6408
.3	.0833	.5139	1.3150	.8077	-.6370
.4	.1409	.6337	1.0854	.7443	-.6300
.5	.2093	.7318	.8818	.6818	-.6191
.6	.2866	.8109	.7044	.6206	-.6040
.7	.3709	.8736	.5521	.5611	-.5845
.8	.4608	.9221	.4234	.5039	-.5607
.9	.5550	.9590	.3163	.4491	-.5329
1.0	.6523	.9861	.2287	.3974	-.5017
1.1	.7519	1.0053	.1582	.3489	-.4677
1.2	.8531	1.0182	.1026	.3039	-.4316
1.3	.9554	1.0262	.0598	.2626	-.3943
1.4	1.0583	1.0305	.0277	.2251	-.3566
1.5	1.1614	1.0321	.0044	.1913	-.3191
1.6	1.2646	1.0316	-.0117	.1612	-.2827
1.7	1.3677	1.0299	-.0221	.1347	-.2478
1.8	1.4706	1.0274	-.0282	.1116	-.2150
1.9	1.5731	1.0244	-.0310	.0916	-.1847
2.0	1.6754	1.0212	-.0314	.0746	-.1570
2.1	1.7774	1.0181	-.0302	.0601	-.1321
2.2	1.8791	1.0152	-.0279	.0480	-.1100
2.3	1.9805	1.0126	-.0250	.0380	-.0907
2.4	2.0816	1.0102	-.0219	.0298	-.0740
2.5	2.1825	1.0082	-.0188	.0231	-.0598
2.6	2.2832	1.0065	-.0158	.0178	-.0478
2.7	2.3838	1.0050	-.0130	.0135	-.0379
2.8	2.4843	1.0039	-.0106	.0101	-.0297
2.9	2.5846	1.0029	-.0085	.0075	-.0231
3.0	2.6849	1.0022	-.0067	.0055	-.0177
3.1	2.7850	1.0016	-.0052	.0039	-.0135
3.2	2.8852	1.0011	-.0040	.0028	-.0101
3.3	2.9853	1.0007	-.0031	.0019	-.0076
3.4	3.0853	1.0005	-.0023	.0012	-.0056
3.5	3.1854	1.0003	-.0017	.0008	-.0041
3.6	3.2854	1.0001	-.0013	.0004	-.0030
3.7	3.3854	1.0000	-.0009	.0002	-.0021
3.8	3.4854	.9999	-.0007	.0000	-.0015

TABLE 1.—Concluded. SIMILAR SOLUTIONS OF LAMINAR COMPRESSIBLE BOUNDARY-LAYER EQUATIONS.

$\beta=2.0, S_w=1.0$					
η	f	f'	f''	S	S'
0	0	0	2.4878	1.0000	-0.6613
.1	.0118	.2291	2.0971	.9339	-.6611
.2	.0446	.4204	1.7341	.8678	-.6593
.3	.0947	.5771	1.4072	.8021	-.6548
.4	.1589	.7031	1.1204	.7370	-.6466
.5	.2344	.8025	.8743	.6729	-.6341
.6	.3187	.8793	.6671	.6103	-.6168
.7	.4097	.9372	.4958	.5497	-.5948
.8	.5056	.9795	.3566	.4915	-.5682
.9	.6052	1.0094	.2455	.4362	-.5375
1.0	.7072	1.0294	.1587	.3841	-.5034
1.1	.8108	1.0418	.0921	.3356	-.4666
1.2	.9153	1.0484	.0425	.2909	-.4280
1.3	1.0203	1.0508	.0067	.2500	-.3885
1.4	1.1254	1.0502	-.0180	.2132	-.3490
1.5	1.2303	1.0475	-.0341	.1802	-.3102
1.6	1.3349	1.0436	-.0435	.1511	-.2729
1.7	1.4390	1.0390	-.0478	.1256	-.2375
1.8	1.5426	1.0341	-.0486	.1035	-.2046
1.9	1.6458	1.0293	-.0468	.0846	-.1745
2.0	1.7485	1.0248	-.0434	.0685	-.1473
2.1	1.8508	1.0207	-.0391	.0550	-.1230
2.2	1.9527	1.0170	-.0344	.0438	-.1017
2.3	2.0542	1.0138	-.0296	.0346	-.0832
2.4	2.1554	1.0111	-.0250	.0271	-.0674
2.5	2.2564	1.0088	-.0208	.0210	-.0541
2.6	2.3572	1.0069	-.0170	.0162	-.0429
2.7	2.4578	1.0054	-.0137	.0123	-.0338
2.8	2.5583	1.0041	-.0109	.0094	-.0263
2.9	2.6587	1.0032	-.0086	.0070	-.0202
3.0	2.7589	1.0024	-.0066	.0053	-.0154
3.1	2.8591	1.0018	-.0051	.0039	-.0117
3.2	2.9593	1.0014	-.0038	.0029	-.0087
3.3	3.0594	1.0011	-.0028	.0022	-.0064
3.4	3.1595	1.0008	-.0021	.0016	-.0047
3.5	3.2596	1.0006	-.0015	.0012	-.0034
3.6	3.3596	1.0005	-.0011	.0009	-.0025
3.7	3.4597	1.0004	-.0007	.0007	-.0018
3.8	3.5597	1.0004	-.0005	.0006	-.0012
3.9	3.6598	1.0003	-.0003	.0004	-.0009
4.0	3.7598	1.0003	-.0002	.0004	-.0006

TABLE II.—SUMMARY OF HEAT-TRANSFER AND WALL-SHEAR PARAMETERS

S_w	β	f_w'	S_w'	$-\frac{S_w'}{S_w}$	$\frac{C_f Re_w}{Nu}$	$\frac{\delta_w^*}{X} \sqrt{\frac{m+1}{2} \frac{U_e X}{\nu_0}}$	$\frac{\theta_{tr}}{X} \sqrt{\frac{m+1}{2} \frac{U_e X}{\nu_0}}$	$\frac{\epsilon}{X} \sqrt{\frac{m+1}{2} \frac{U_e X}{\nu_0}}$	H_{tr}
-1.0	-0.326	0	0.2477	0.2477	0	1.3200	0.6400	-2.1395	2.063
	-.3657	.0500	.2958	.2958	.3381	1.0056	.6571	-1.8407	1.530
	-.3884	.1400	.3527	.3527	.7939	.6486	.6400	-1.5762	1.013
	-.360	.2448	.4001	.4001	1.224	.3719	.5908	-1.4082	.630
	-.30	.3182	.4262	.4262	1.493	.2222	.5498	-1.3289	.404
	-.14	.4166	.4554	.4554	1.830	.0663	.4952	-1.2503	.134
	0	.4696	.4696	.4696	2.000	0	.4696	-1.2168	0
	.50	.5806	.4948	.4948	2.347	-.1090	.4235	-1.1625	-.257
	2.00	.7381	.5203	.5203	2.837	-.2061	.3833	-1.1107	-.538
-0.8	-0.10	-0.0686	0.0447	0.0559	-2.456	(*)	(*)	(*)	(*)
	-.2685	-.0500	.1829	.2286	.4374	(*)	(*)	(*)	(*)
	-.3088	0	.2261	.2826	0	1.4052	0.6274	-1.5211	2.240
	-.325	.0493	.2545	.3181	.3100	1.1579	.6335	-1.3757	1.828
	-.3285	.0693	.2644	.3305	.4194	1.0738	.6286	-1.3309	1.708
	-.3285	.1100	.2818	.3523	.6245	.9298	.6193	-1.2589	1.501
	-.325	.1354	.2913	.3641	.7438	.8524	.6107	-1.2225	1.396
	-.30	.2086	.3155	.3944	1.058	.6624	.5821	-1.1381	1.138
	-.14	.3841	.359	.4488	1.712	.3485	.5037	-1.0134	.692
	0	.4696	.3757	.4696	2.000	.2436	.4696	-.9744	.519
	.50	.6547	.403	.5038	2.599	.0814	.4091	-.9136	.199
	1.50	.8689	.4261	.5326	3.263	-.0304	.3659	-.8707	-.083
	2.00	.9480	.4331	.5414	3.502	-.0591	.3551	-.8590	-.166
-0.4	-0.235	-0.0500	0.0447	0.1118	-0.8949	(*)	(*)	(*)	(*)
	-.246	0	.1249	.3123	0	1.8383	0.6045	-0.6942	3.041
	-.2483	.0500	.1360	.3400	.2941	1.6079	.6001	-.6471	2.679
	-.24	.1064	.1474	.3685	.5775	1.4076	.5868	-.6076	2.399
	-.20	.2183	.1626	.4065	1.074	1.1274	.5544	-.5534	2.034
	0	.4696	.1878	.4696	2.000	.6308	.4696	-.4872	1.556
	.50	.7947	.209	.5225	3.042	.4501	.3799	-.4428	1.185
	2.00	1.3329	.2304	.5760	4.628	.2234	.2944	-.4089	.759
0	-0.1947	-0.0500	0	(*)	(*)	(*)	(*)	0	(*)
	-.1988	0	0	0.3265	0	2.359	0.585	0	4.032
	-.16	.1905	0	.4023	.948	1.708	.552	0	3.094
	0	.4696	0	.4696	2.000	1.217	.4696	0	2.591
	.50	.9277	0	.5395	3.436	.8045	.3501	0	2.298
	1.00	1.2326	0	.5715	4.317	.6482	.2923	0	2.218
	1.60	1.5213	0	.5940	5.122	.545	.250	0	2.180
	2.00	1.6870	0	.6064	5.565	.497	.231	0	2.152
1.0	-0.10	-0.1613	-0.2076	0.2076	-1.554	(*)	(*)	(*)	(*)
	-.1305	-.0500	-.3139	.3139	-.3186	(*)	(*)	(*)	(*)
	-.1295	0	-.3388	.3388	0	3.8162	0.5677	1.6109	6.722
	-.10	.1805	-.4033	.4033	.8956	3.0765	.5425	1.3913	5.671
	0	.4696	-.4696	.4696	2.000	2.4360	.4696	1.2168	5.187
	.30	.9829	-.5457	.5457	3.602	1.8313	.3334	1.0662	5.493
	.50	1.2351	-.5725	.5725	4.315	1.6472	.2740	1.0237	6.012
	1.00	1.7368	-.6154	.6154	5.644	1.3856	.1765	.9602	7.850
	1.50	2.1402	-.6425	.6425	6.662	1.2382	.1113	.9236	11.125
	2.00	2.4878	-.6613	.6613	7.527	1.1431	.06683	.9029	17.105

*These values were not calculated.

REPORT 1294

THE COMPRESSIBLE LAMINAR BOUNDARY LAYER WITH HEAT TRANSFER AND ARBITRARY PRESSURE GRADIENT^{1, 2}

By CLARENCE B. COHEN and ELI RESHOTKO

SUMMARY

An approximate method for the calculation of the compressible laminar boundary layer with heat transfer and arbitrary pressure gradient, based on Thwaites' correlation concept, is presented. The method results from the application of Stewartson's transformation to Prandtl's equations, which yields a nonlinear set of two first-order differential equations. These equations are then expressed in terms of dimensionless parameters related to the wall shear, the surface heat transfer, and the transformed free-stream velocity. Thwaites' concept of the unique interdependence of these parameters is assumed. The evaluation of these quantities is then carried out by utilizing exact solutions recently obtained.

With the resulting relations, methods are derived for the calculation of the two-dimensional and axially symmetric laminar boundary layer with arbitrary free-stream velocity distribution, Mach number, and surface temperature level. The combined effect of heat transfer and pressure gradient is demonstrated by applying the method to calculate the characteristics of the boundary layer on thin supersonic surfaces and in a highly cooled, convergent-divergent, axially symmetric rocket nozzle.

INTRODUCTION

In recent years, with the advent of laminar airfoils and with the observation of laminar boundary layers at Reynolds numbers as high as 50×10^6 (ref. 2), the ability to reliably estimate viscous flow and heat-transfer effects for a laminar boundary layer has become increasingly important. Moreover, with high-altitude flight becoming more common, the subsequent lower Reynolds numbers encountered should more frequently produce a laminar boundary layer. Stability calculations based on the theory of Lees and Lin (ref. 3) have also emphasized the possibilities of maintaining a laminar boundary layer through cooling of aerodynamic surfaces. The effect of favorable pressure gradients in increasing the stability of laminar boundary layers may also make solutions to the laminar problem applicable to the design of nozzles and turbine blades.

Solutions of the laminar-boundary-layer equations that include effects of compressibility, pressure gradient, and heat transfer have been quite limited in number. Of the exact solutions, most have restrictions of range or application, or both. The solutions of references 4 and 5 are re-

stricted to zero pressure gradient, while those of reference 6 allow small pressure gradients. The developments of reference 7 are restricted to small heat transfer and low Mach number. Solutions obtained by assuming that fluid properties are constant or that the Mach number is essentially zero are obtained in references 8 to 10. Those solutions of references 11 to 13 that are for a Prandtl number of 1 are not restricted in range of compressibility, pressure gradient, or heat transfer. However, they apply to specific types of free-stream velocity distribution that are inappropriate for general practical problems.

In 1921, von Kármán (ref. 14) recognized that to solve the skin-friction problem it was not necessary to have the exact and complicated solution, but that it would be quite satisfactory to evaluate average quantities across the layer if they could be related to the surface values. The concepts of displacement and momentum thicknesses were introduced, thus considerably simplifying the mathematics of the problem. With this integral method, if the form of the velocity profile is related to a single parameter, a method of calculating the boundary layer is obtained. Pohlhausen (ref. 15) carried out this method by postulating a quartic velocity profile depending upon the local pressure gradient. A number of investigators have extended Pohlhausen's method to compressible flows over insulated surfaces.

With the presence of heat transfer at the surface, the compressible problem becomes more complex. Kalikhman (ref. 16) defined certain heat-flow quantities analogous to the displacement and momentum thicknesses and, in a manner similar to Pohlhausen's, developed a complex iterative procedure for the solution of the general problem. More recently, references 17 to 20 have further developed this technique. The preceding methods are tedious, since they require a solution of at least one ordinary differential equation for any particular problem.

Thwaites' method (ref. 21) does not require the solution of ordinary differential equations. In that formulation, it is suggested that the basic goal of an integral approach might be achieved if the problem is considered as that of relating the wall shear, its normal derivative at the wall, and the form factor (ratio of displacement thickness) to one another without specifying a type of profile. To this end, nondimensional forms of these quantities were defined and were evaluated

¹ Supersedes NACA TN 3326, "The Compressible Laminar Boundary Layer with Heat Transfer and Arbitrary Pressure Gradient," by Clarence B. Cohen and Eli Reshotko, 1955.

² The principal developments of this paper, which is part of the doctoral dissertation of the senior author (ref. 1), were carried out under the stimulus and guidance of Professor Luigi Crocco and the sponsorship of the Daniel and Florence Guggenheim Foundation. The final analysis and the computations were completed at the NACA Lewis laboratory.

by examining exact solutions for the incompressible laminar boundary layer. It developed that a nearly universal relation existed between these quantities for favorable pressure gradients, and for adverse pressure gradients Thwaites selected a single representative relation. A unique correlation was chosen that reduced the solution of an incompressible problem to the evaluation of a single integral.³

Rott and Crabtree (ref. 23) recognized that, in the absence of heat transfer and with a Prandtl number of 1, the Illingworth-Stewartson correlation between compressible and incompressible boundary-layer solutions (ref. 24) could be used to extend Thwaites' method to include effects of compressibility.

With the presence of heat transfer the application of Stewartson's transformation does not correlate a given compressible problem to an equivalent incompressible one. Thus, the universal relation previously described is not adequate. Unfortunately, there is little possibility of establishing a family of universal relations with, for example, the wall temperature as the distinguishing parameter, since a variety of exact solutions to this problem is not available. However, one such set of relations may be obtained from the solutions of references 11 to 13.

In the present paper, after formulation of a nonlinear system of two first-order differential equations (with the major restriction being a linear viscosity law), methods of solution are developed depending on Thwaites' concept of universal functions. The functions used for this purpose are evaluated from the solutions of reference 12 only.

BOUNDARY-LAYER EQUATIONS

The equations of the steady, two-dimensional compressible laminar boundary layer for perfect fluids are

Continuity:

$$\frac{\partial}{\partial x}(\rho u) + \frac{\partial}{\partial y}(\rho v) = 0 \quad (1)$$

Momentum:

$$\left. \begin{aligned} \rho u \frac{\partial u}{\partial x} + \rho v \frac{\partial u}{\partial y} &= -\frac{\partial p}{\partial x} + \frac{\partial}{\partial y} \left(\mu \frac{\partial u}{\partial y} \right) \\ \frac{\partial p}{\partial y} &= 0 \end{aligned} \right\} \quad (2)$$

Energy:

$$\rho u \frac{\partial h}{\partial x} + \rho v \frac{\partial h}{\partial y} = u \frac{\partial p}{\partial x} + \frac{\partial}{\partial y} \left(\frac{\mu}{Pr} \frac{\partial h}{\partial y} \right) + \mu \left(\frac{\partial u}{\partial y} \right)^2 \quad (3)$$

(All symbols are defined in appendix A.)

The viscosity law to be assumed is

$$\frac{\mu}{\mu_0} = \lambda \frac{t}{t_0} \quad (4)$$

Equation (4) is of the form taken by Chapman and Rubesin (ref. 5), except that the reference conditions (μ_0 , t_0) are free-stream stagnation values, since, in the case of pressure gradient, the local stream values are not constant along the

flow. The constant λ is used to match the viscosity with the Sutherland value at a desired location. If this location is assumed to be the surface, the result is

$$\lambda = \left(\frac{t_0 + k_{su}}{t_w + k_{su}} \right) \sqrt{\frac{t_w}{t_0}} \quad (5)$$

where

$$k_{su} = \text{Sutherland's constant} = 198.6^\circ \text{ R (for air)}$$

Stewartson's transformation.—The velocities in the equations of motion (1) to (3) can be replaced through the definition of a stream function:

$$\left. \begin{aligned} \psi_y &= \frac{\rho u}{\rho_0} \\ \psi_x &= -\frac{\rho v}{\rho_0} \end{aligned} \right\} \quad (6)$$

Introducing the quantity λ from equation (4), a slight modification of Stewartson's transformation (ref. 24) may be written:

$$\left. \begin{aligned} X &= \int_0^x \lambda \frac{a_e}{a_0} \frac{p_e}{p_0} dx \\ Y &= \frac{a_e}{a_0} \int_0^y \frac{\rho}{\rho_0} dy \end{aligned} \right\} \quad (7)$$

The transformed coordinates are now represented by upper-case letters (X , Y), and the subscript e refers to local conditions at the outer edge of the boundary layer (external). The subscript 0 refers to free-stream stagnation values.

Applying equations (4) to (7) to the boundary-layer equations (1) to (3) and assuming that Pr and c_p are constant (but not yet requiring that $Pr=1$) result in the following system:

$$U_X + V_Y = 0 \quad (8)$$

$$UU_X + VU_Y = U_e U_{eX} (1+S) + \nu_0 U_{YY} \quad (9)$$

$$US_X + VS_Y = \nu_0 \left\{ \frac{S_{YY}}{Pr} - \frac{1-Pr}{Pr} \left(\frac{\frac{\gamma-1}{2} M_e^2}{1 + \frac{\gamma-1}{2} M_e^2} \right) \left[\left(\frac{U}{U_e} \right)^2 \right]_{YY} \right\} \quad (10)$$

where the enthalpy term S is defined for convenience as

$$S = \frac{h_s}{h_0} - 1 \quad (11)$$

where h_s is the local stagnation enthalpy. The stream function has been replaced by the transformed velocities (U , V) through the relations

$$U \equiv \psi_Y \quad (12)$$

$$V \equiv -\psi_X$$

The resulting relation between the transformed and physical longitudinal velocities is $U = \frac{a_0}{a_e} u$.

³ Other approaches, such as that of Young and Winterbottom (ref. 22), have resulted in expressions for the momentum thickness similar to that of Thwaites. In that analysis, however, the derivation was a modification of the Pohlhausen technique. The application of a correlation concept was not proposed.

The boundary conditions applicable to the system (8) to (10) for a specified wall temperature are

$$\left. \begin{aligned} U(X,0) &= 0 \\ V(X,0) &= 0 \\ S(X,0) &= S_w(X) \\ \lim_{Y \rightarrow \infty} S &= 0 \\ \lim_{Y \rightarrow \infty} U &= U_e(X) \end{aligned} \right\} \quad (13)$$

Integral equations.—An alternate form of the momentum equation may be obtained by subtracting the momentum equation (9) from the product of the continuity equation (8) and the quantity $(U_e - U)$. This results in

$$[U(U_e - U)]_x + [V(U_e - U)]_y + U_{eX}(U_e - U) + U_e U_{eX} S = -\nu_0 U_{YY} \quad (14)$$

If equation (14) is integrated with respect to Y between the limits $Y=0$ and $Y=\Delta$, where Δ is a constant distance normal to the surface sufficiently large that the conditions $S=0$ and $U=U_e$ can both be satisfied, there results

$$\frac{d}{dX} (\theta_{tr} U_e^2) + U_e U_{eX} \delta_{tr}^* = \nu_0 (U_Y)_{Y=0} \quad (15)$$

where the transformed momentum thickness θ_{tr} and the transformed displacement thickness δ_{tr}^* are defined as

$$\left. \begin{aligned} \theta_{tr} &\equiv \int_0^\Delta \frac{U}{U_e} \left(1 - \frac{U}{U_e}\right) dY \\ \delta_{tr}^* &\equiv \int_0^\Delta \left(1 - \frac{U}{U_e} + S\right) dY \end{aligned} \right\} \quad (16)$$

By carrying out the indicated differentiation, equation (15) can be put in the form

$$\frac{d\theta_{tr}}{dX} + \frac{U_{eX}}{U_e} (2\theta_{tr} + \delta_{tr}^*) = \frac{\nu_0}{U_e^2} (U_Y)_w \quad (17)$$

This equation has the form of the conventional Kármán momentum integral.

It should be noted that because of Stewartson's transformation a simple relation exists between the parameter θ_{tr} and the actual physical momentum thickness θ . This relation is

$$\theta = \frac{p_0 a_e}{p_e a_0} \theta_{tr} = \theta_{tr} \left(\frac{t_0}{t_e}\right)^{\frac{\gamma+1}{2(\gamma-1)}} \quad (18)$$

Following a procedure with the energy equation similar to that for the momentum equation results in

$$\frac{dE}{dX} + \frac{U_{eX}}{U_e} E = -\frac{\nu_0}{Pr U_e} \left(\frac{\partial S}{\partial Y}\right)_w \quad (19)$$

Where the convection thickness is defined by

$$E = \int_0^\Delta S \frac{U}{U_e} dY \quad (20)$$

The method presented in this report uses exact solutions to the boundary-layer equations including the energy equation. Since both the skin-friction and heat-transfer parameters from the exact solutions are correlated with a parameter which is evaluated from only the momentum integral equation, it will not be necessary to use equations (19) and (20).

REDUCED BOUNDARY-LAYER EQUATIONS

At this stage, the relation governing the boundary-layer development is equation (17), subject to the boundary conditions $(\theta_{tr})_{X=0}=0$ or $(\theta_{tr})_{sp}$, where the subscript sp indicates stagnation-point values. The former condition on θ_{tr} applies when the boundary layer is initiated without a stagnation point (such as in the case of a supersonic thin airfoil). The value of $(\theta_{tr})_{sp}$ depends on the value of $(U_{eX})_{sp}$ and on the surface temperature. At a stagnation point, $(\theta_{tr})_{sp} = \theta_{sp}$. Values of θ_{sp} are presented in table I.

Before consideration of a solution that depends on a correlation similar to that of Thwaites, it is expedient to transform the preceding system of equations to a system involving dimensionless parameters. The correlation concept will then be introduced and methods of solution developed.

PARAMETRIC FORM

The dimensionless parameters, which are related to terms appearing in equations (17) and (19), can be defined and evaluated from the following expressions:

Shear parameter, or first-derivative parameter,

$$l \equiv \frac{\theta_{tr}}{U_e} \left(\frac{\partial U}{\partial Y}\right)_w = \frac{\theta}{u_e} \frac{t_w}{t_e} \left(\frac{\partial u}{\partial y}\right)_w \quad (21)$$

Correlation number (related to pressure gradient), or second-derivative parameter,

$$n \equiv -\frac{U_{eX}}{\nu_0} \theta_{tr}^2 = \frac{\theta_{tr}^2}{U_e} \frac{(\partial^2 U)}{(\partial Y^2)}_w = -\frac{u_{eX} \theta^2}{\nu_w} \left(\frac{t_w}{t_e}\right)^2 \left(\frac{t_0}{t_e}\right) \quad (22)$$

Heat-transfer parameter, or third-derivative parameter,

$$r \equiv \frac{\theta_{tr}^3}{U_e} \left(\frac{\partial^3 U}{\partial Y^3}\right)_w = n \theta \frac{t_w}{t_0} \left[\frac{\partial}{\partial y} \left(\frac{t}{t_e}\right)\right]_w \quad (23)$$

In definitions (22) and (23), use is made of the following relations, respectively:

$$\left(\frac{\partial^2 U}{\partial Y^2}\right)_w = -\frac{U_e U_{eX}}{\nu_0} (1 + S_w) \quad (24)$$

which is obtained from equation (9), and

$$\left(\frac{\partial S}{\partial Y}\right)_w = -\frac{\nu_0}{U_e U_{eX}} \left(\frac{\partial^3 U}{\partial Y^3}\right)_w \quad (25)$$

which is obtained by differentiating equation (9) with respect to Y and evaluating the resulting expression at $Y=0$.

If equation (17) is multiplied by $\frac{2\theta_{tr} U_e}{\nu_0}$, there results

$$\frac{U_e}{\nu_0} \frac{d(\theta_{tr}^2)}{dX} = -2 \left[\frac{U_{eX}}{\nu_0} \theta_{tr}^2 (H_{tr} + 2) - \frac{\theta_{tr}}{U_e} \left(\frac{\partial U}{\partial Y}\right)_w \right] \quad (26)$$

where $H_{tr} = \frac{\delta_{tr}^*}{\theta_{tr}}$ is the form factor for low-speed flow ($M_e \approx 0$).

TABLE I.—INITIAL VALUES OF PARAMETERS

(a) Stagnation-point flow

S_w	$C_f \sqrt{Re_w}$		$Nu / \sqrt{Re_w}$			$\delta_{\epsilon}^* \sqrt{\frac{u_{\epsilon z}}{\nu_w}} \left(\frac{t_w}{l_0} \right)$	$\theta_{\epsilon} \sqrt{\frac{u_{\epsilon z}}{\nu_w}} \left(\frac{t_w}{l_0} \right)$	$H_{\epsilon p}$
	$Pr=1$	$Pr=0.7$ (a)	$Pr=1$	$Pr=0.7$ (b)	$Pr=0.7$ (a)	$Pr=1$	$Pr=1$	$Pr=1$
Two-dimensional ($\beta=1$)								
-1.0	1.30	1.21	0.506	0.438	0.436	-0.170	0.400	-0.425
-0.8	1.56	1.49	0.522	.452	.451	.012	.384	.031
-0.4	2.04	2.00	0.546	.474	.475	.345	.338	1.021
0	2.46	2.46	.570	.495	.495	.648	.292	2.218
1.0	3.47	3.54	.615	.533	.537	1.386	.177	7.850
Axially symmetric ($\beta=1/2$)								
-1.0	1.64	1.56	0.700	0.607	0.607	-0.0771	0.300	-0.257
-0.8	1.85	1.79	.712	.617	.621	.0576	.289	.199
-0.4	2.25	2.22	.739	.639	.643	.318	.269	1.185
0	2.62	2.62	.763	.662	.662	.569	.248	2.298
1.0	3.49	3.55	.809	.701	.708	1.165	.194	6.012

* These values are obtained when eqs. (16) of ref. 12 are solved for $Pr=0.7$, $M_\infty=0$.b These values are obtained by multiplying the results for $Pr=1$ by $(0.7)^{0.4}$.

c Interpolated values from solutions of ref. 12.

(b) Sharp edge or pointed body

$C_f \sqrt{Re_w}$	$Nu / \sqrt{Re_w}$	
	$Pr=1$	$Pr=0.7$ (a)
Two-dimensional		
0.664	0.332	0.295
Axially symmetric		
1.150	0.575	0.510

* These values are obtained by multiplying the results for $Pr=1$ by $(0.7)^{1/3}$.

TABLE II.—SUMMARY OF HEAT-TRANSFER AND WALL-SHEAR PARAMETERS

S_w	β	n	l	N	r	$\left(\frac{C_f Re_w}{Nu} \right)_{Pr=1}$	H_{tr}
-1.0	-0.326	0.1335	0	1.0845	0.0212	0	2.063
	-0.3657	.1579	.0329	1.1804	.0307	.3381	1.530
	-0.3884	.1591	.0896	1.1382	.0359	.7939	1.013
	-0.360	.1257	.1446	.9504	.0297	1.224	.630
	-0.30	.0907	.1749	.7858	.0212	1.493	.404
	-0.14	.0343	.2063	.5590	.00774	1.830	.134
	0	0	.220	.440	0	2.000	0
	.50	-.0897	.2459	.1793	-.0188	2.347	-.257
	2.00	-.2938	.2829	-.2933	-.0586	2.837	-.538
	-0.8	0.1215	0	1.0305	0.0172	0	2.240
-0.8	-0.325	.1304	.0312	1.0606	.0210	.3100	1.828
	-0.3285	.1298	.0436	1.0499	.0216	.4194	1.708
	-0.3285	.1260	.0681	1.0185	.0220	.6245	1.501
	-0.325	.1212	.0827	.9885	.0216	.7438	1.396
	-0.30	.1017	.1214	.882	.0187	1.058	1.138
	-0.14	.0355	.1935	.5781	.00642	1.712	.692
	0	0	.220	.44	0	2.000	.519
	.50	-.0837	.2678	.1676	-.0138	2.599	.199
	1.50	-.2008	.3179	-.1332	-.0313	3.263	-.083
	2.00	-.2522	.3366	-.2517	-.0388	3.502	-.166
-0.4	-0.246	0.0899	0	0.9087	0.00679	0	3.041
	-0.2483	.0894	.0300	.8968	.00730	.2941	2.679
	-0.24	.0826	.0624	.8519	.00696	.5775	2.399
	-0.20	.0615	.1210	.7379	.00554	1.074	2.034
	0	0	.220	.440	0	2.000	1.556
	.50	-.0722	.3019	.1442	-.00573	3.042	1.185
	2.00	-.1733	.3924	-.1713	-.0118	4.628	.759
	-0.1988	0.0681	0	0.822	0	0	4.032
	-0.16	.0487	.1051	.7068	0	.9480	3.094
	0	0	.220	.440	0	2.000	2.591
0	.50	-.0602	.3220	.1232	0	3.436	2.298
	1.00	-.8029	.3556	0	0	4.317	2.218
	1.60	-.1002	.3808	-.0748	0	5.122	2.180
	2.00	-.1064	.3892	-.1040	0	5.565	2.152
	-0.1295	0.0417	0	0.7280	-0.00803	0	6.723
	-0.10	.0294	.09798	.6476	-.00644	.8956	5.671
	0	0	.220	.440	0	2.000	5.187
	.30	-.0334	.3277	.1558	-.00607	3.602	5.493
	.50	-.0735	.3384	.0755	-.00588	4.315	6.012
	1.00	-.0312	.3065	0	-.00338	5.644	7.850
1.0	1.50	-.0186	.2382	-.0114	-.00133	6.662	11.125
	2.00	-.0089	.1663	-.0088	-.00034	7.527	17.105

is obtained for the cold wall, although for the insulated and not walls a large difference is obtained. This difference is due essentially to the fact that, in the case of an adverse pressure gradient, the solutions of Low (ref. 6), which resemble the series-type solution of Howarth (ref. 25), depart from Falkner-Skan type solutions such as that of Hartree (ref. 26) (e. g., fig. 1). An important consideration for the case of the heated surface with an adverse pressure gradient is that the flow is closer to separation than appears permissible for a theory based on small pressure gradients such as that of reference 6; therefore, for this case the present calculation may be the more reliable. Some of the difference in the preceding table may also be a Prandtl number effect.

Good agreement is also obtained for heat transfer except for the case of the heated surface with favorable pressure gradient. Some of that difference might also be a Prandtl number effect.

II. AXISYMMETRIC CONVERGENT-DIVERGENT ROCKET NOZZLE

The second example, that of a rocket nozzle, is one involving both large pressure gradients and heat transfer. The nozzle chosen is illustrated in figure 10. It has a 25° half-angle convergent section and a 15° half-angle divergent section. The combustion-chamber stagnation pressure is assumed to be 500 pounds per square inch absolute, the stagnation temperature is taken as 4000°R , and the Prandtl number is assumed to be 0.78. The nozzle wall is assumed cooled to a uniform temperature of 800°R , which corresponds to $S_w = -0.8$. For the assumed 3-inch throat di-

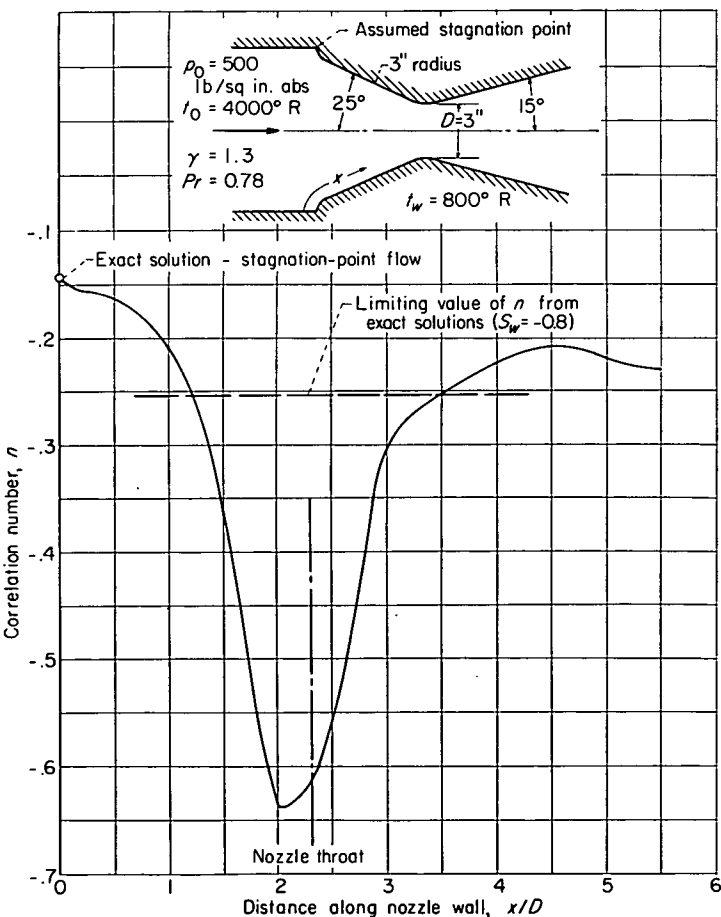


FIGURE 10.—Variation of correlation number in rocket nozzle.

ameter, the rocket has a nominal thrust of 5550 pounds for $\gamma=1.3$. Local static conditions along the nozzle wall were obtained using one-dimensional flow relations.

The calculation was performed by the linear method with $A=0.372$ and $B=2.53$. In order to eliminate the effect of step size in the initial portion of the integration, a series expansion of the integrand was used for $0 \leq (x/D) < 0.5$. For $(x/D) > 0.5$, the step size taken was 0.1. The resulting variation of n in the nozzle is also shown in figure 10. It is seen that, in a portion of the nozzle including the throat ($1.2 < (x/D) < 3.5$), values of n are obtained which require use of an extended correlation curve as discussed earlier, in order to calculate skin friction, heat transfer, and displacement thickness. No extrapolation is needed to obtain momentum thickness, since the momentum thickness is related to n through equation (39).

The calculated local heat-transfer rates as well as displacement and momentum thickness are shown in figure 11. It is seen that large rates of cooling are required in the neighbor-

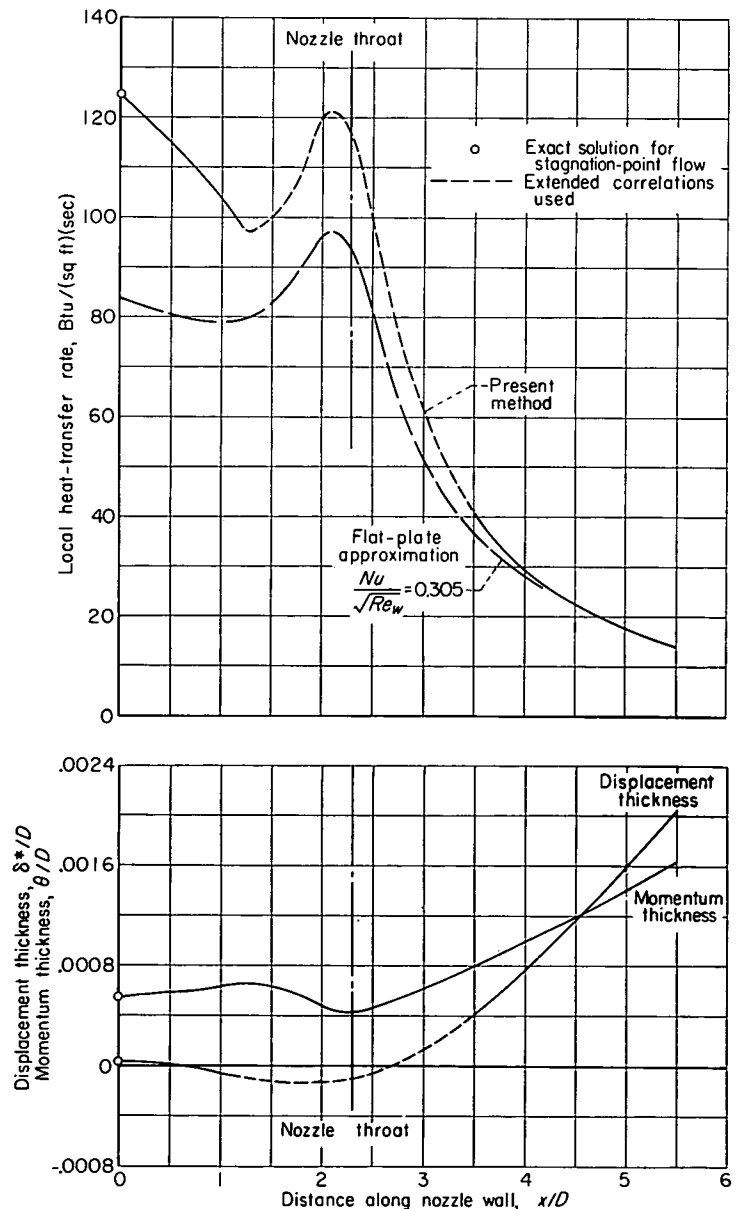


FIGURE 11.—Results of rocket-nozzle calculations.

hood of the stagnation point and the nozzle throat. If the cooling were to become insufficient, these seem to be the most likely locations of failure. The required local cooling rate to maintain constant wall temperature decreases sharply beyond the throat of the nozzle.

In the absence of more appropriate information, it has been customary in recent years to use flat-plate heat-transfer relations in estimating heat transfer in a nozzle. The use of such a relation in the current problem ($Nu/\sqrt{Re_w}=0.305$ for $Pr=0.78$) yields values indicated in figure 10. It is seen that for this problem the flat-plate relation seriously underestimates the amount of cooling required over a large part of the nozzle. This illustrates the importance of considering the effects of pressure gradient on heat transfer.

The momentum thickness is seen to reach a minimum value at the nozzle throat. The displacement thickness is a small positive quantity at the stagnation point but is negative for most of the convergent section as well as in the vicinity of the throat.⁴ The over-all thickness (not shown on the figure) varies from 6.1 to 7.7 times the momentum thickness in going from the initial stagnation point to the nozzle exit.

The use of different values of A and B in performing the numerical integration would have approximately the following effect: With the values $A=0.44$ and $B=3.0$ (from fig. 5), the momentum thickness would be about 10 percent smaller in the vicinity of the throat than the values in figure 11 and would be within 5 percent of the presented values over the rest of the nozzle. With $A=0.335$ and $B=2.34$, the momentum thickness at the throat would be about 6 percent larger than the value presented. The effects of varying

A and B on skin friction and heat transfer would be less than 3 percent at the throat.

CONCLUDING REMARKS

The application of Stewartson's transformation to the compressible laminar-boundary-layer equations with heat transfer yielded a simple first-order system of ordinary differential equations, the first of which is very similar to the Kármán momentum integral. Dimensionless shear and heat-transfer parameters were defined. The assumption of correlation of these parameters in terms of a momentum parameter resulted in a complete system of relations for calculating skin friction and heat transfer. Knowledge of velocity or temperature profiles is not necessary in using this calculation method. Procedures for the calculation of the longitudinal distribution of correlation number are presented, which include as special cases the method of Thwaites and that of Rott and Crabtree. The dimensionless parameters introduced herein were evaluated from the exact solutions of reference 12.

Calculations of an example involving small pressure gradients have shown reasonable agreement between this method and the perturbation method of reference 6 over the same range of Mach number, pressure gradient, and heat transfer.

The method is also applied to the calculation of heat transfer and displacement thickness in a highly cooled, convergent-divergent, axially symmetric rocket nozzle. The results of this calculation show that high rates of heat transfer are obtained at the initial stagnation point and at the throat of the nozzle. Also indicated are negative displacement thicknesses in the convergent portion of the nozzle; these occur because of the high density within the lower portions of the cooled boundary layer.

LEWIS FLIGHT PROPULSION LABORATORY

NATIONAL ADVISORY COMMITTEE FOR AERONAUTICS

CLEVELAND, OHIO, February 1, 1955

⁴ This unusual result produces the interesting possibility that, for a rocket nozzle with cooled walls and viscous flow, a mass discharge coefficient based on throat area, generally assumed to be less than 1 because of boundary-layer "blockage" at the throat, may actually exceed 1. A distinction exists between this phenomenon and that of negative momentum thickness (refs. 1, 10, and 12) associated with velocity overshoot.

APPENDIX A

SYMBOLS

A	constant from $N=A+Bn$	t	static temperature
a	sonic velocity	t_{aw}	adiabatic wall temperature
B	constant from $N=A+Bn$	U	transformed longitudinal velocity, $U=u\frac{a_0}{a_e}=\psi_Y$
C_f	local skin-friction coefficient, $C_f=\frac{2\tau_w}{\rho_w u_e^2}$	u	longitudinal velocity component
c_p	specific heat at constant pressure	V	transformed normal velocity, $V=-\psi_X$
d	nozzle-throat diameter	v	normal velocity component
E	convection thickness, $E=\int_0^\Delta S\frac{U}{U_e}dY$	X	transformed coordinate along surface, $X=\int_0^x \lambda \frac{p_e a_e}{p_0 a_0} dx$
H	form factor, $H\equiv\delta^*/\theta$	x	coordinate along surface
H_{tr}	physical form factor for $M_e\approx 0$, $H_{tr}=\frac{\delta_{tr}^*}{\theta_{tr}}$	Y	transformed normal coordinate, $Y=\frac{a_e}{a_0}\int_0^y \frac{\rho}{\rho_0} dy$
h	enthalpy	y	normal coordinate
K	$\frac{3\gamma-1}{2(\gamma-1)}$	α	exponent of Prandtl number in Reynolds analogy parameter
k	thermal conductivity	β	pressure-gradient parameter, $\beta=\frac{2m}{m+1}$
k_{su}	Sutherland's constant	γ	ratio of specific heats
L	arbitrary length	δ	over-all thickness
l	dimensionless shear parameter, $l\equiv\frac{\theta_{tr}}{U_e}\left(\frac{\partial U}{\partial Y}\right)_w$	δ^*	displacement thickness
M	Mach number	θ	momentum thickness
m	exponent from Falkner-Skan external velocity distribution $U_e=CX^m$	λ	$\lambda=\frac{(\mu/\mu_0)}{(t/t_0)}=\left(\frac{t_0+k_{su}}{t_w+k_{su}}\right)\sqrt{\frac{t_w}{t_0}}$
N	momentum parameter, $N=2[n(H_{tr}+2)+l]$	μ	dynamic viscosity
Nu	Nusselt number, $Nu=\frac{x\left(\frac{\partial t}{\partial y}\right)_w}{t_{aw}-t_w}$	ν	kinematic viscosity, $\nu=\mu/\rho$
n	correlation number, $n\equiv-\frac{U_{eX}\theta_{tr}^2}{\nu_0}$	ρ	mass density
P'	dimensionless pressure gradient, $P'=\frac{L}{\gamma M_e^2}\frac{dp_e}{dx}$	τ	shear stress, $\tau\equiv\mu\frac{\partial u}{\partial y}$
Pr	Prandtl number, $Pr=\frac{\mu c_p}{k}$	ψ	stream function, eq. (6)
p	static pressure	Subscripts:	
R	radius of axisymmetric body	e	local flow outside boundary layer (external)
Re_w	Reynolds number, $Re_w=\frac{\rho_w u_e x}{\mu_w}$	s	local stagnation value
r	heat-transfer parameter, $r=n\theta\frac{t_w}{t_0}\left[\frac{\partial}{\partial y}\left(\frac{t}{t_e}\right)\right]_w$	sp	stagnation point
S	enthalpy function, $S=\frac{h_s}{h_0}-1$	tr	associated transformed quantity
		w	wall or surface value
		0	free-stream stagnation value
		1	initial value
		A coordinate used as subscript denotes differentiation with respect to the coordinate.	

APPENDIX B

NUMERICAL INTEGRATION METHOD

METHOD

The most direct method of solving equation (28) is by numerical integration, using the calculated curves of $N(n, S_w)$ for determination of the right member.

An integration procedure may be simply indicated by direct integration of equation (28). The resultant integral equation can be written:

For two-dimensional flow,

$$n = \frac{U_{ex}}{(U_{ex})_1} \left[n_1 - (U_{ex})_1 \int_0^x \frac{N(n)}{U_e} dX \right] \quad (B1)$$

For an axially symmetric closed body, through Mangler's transformation (ref. 26),

$$n = -\frac{U_{ex}}{R^2} \int_0^x \frac{NR^2}{U_e} dX \quad (B2a)$$

Since the integrands contain $N(n)$, which is unknown at this point, no simple evaluation is possible. In fact, these equations are actually only a condensed notation of the procedure to be followed. The integration must be carried out piecemeal, alternating with determination of the left member of the equation and iterating for accuracy.

The necessity of working with the transformed coordinates can be eliminated by considering the Stewartson transformation from U_e to u_e . For example, in physical coordinates equation (B2a) becomes

$$\frac{n}{P' \frac{t_0}{t_e}} = \frac{\left(M_e \frac{a_0 p_0}{a_e p_e} \right)}{R^2} \int_0^{\frac{x}{L}} \frac{NR^2 d\left(\frac{x}{L}\right)}{\left(M_e \frac{a_0 p_0}{a_e p_e} \right)} \quad (B2b)$$

where L is any fixed length, and the dimensionless pressure gradient P' is given by

$$P' = \frac{L \frac{dp_e}{dx}}{\rho_e u_e^2} = \frac{L \frac{dp_e}{dx}}{p_e \frac{dx}{\gamma M_e^2}} \quad (B3)$$

Similarly, if the isentropic relation $p/\rho^\gamma = \text{constant}$ is used

in equations (31) and (32) and if the Stewartson transformation is applied, there results:

For two-dimensional flow,

$$\frac{n}{P' \frac{t_0}{t_e}} = M_e \left(\frac{t_0}{t_e} \right)^K \left\{ \int_0^{\frac{x}{L}} \frac{Nd\left(\frac{x}{L}\right)}{M_e \left(\frac{t_0}{t_e} \right)^K} - \frac{n_1}{\left[\frac{dM_e}{d\left(\frac{x}{L}\right)} \right]_1} \right\} \quad (B4)$$

For an axially symmetric flow (closed body),

$$\frac{n}{P' \frac{t_0}{t_e}} = \frac{M_e}{R^2} \left(\frac{t_0}{t_e} \right)^K \int_0^{\frac{x}{L}} \frac{NR^2 d\left(\frac{x}{L}\right)}{M_e \left(\frac{t_0}{t_e} \right)^K} \quad (B5)$$

where $K = \frac{3\gamma-1}{2(\gamma-1)}$.

INITIAL VALUES

When the numerical integration method is used, certain considerations are necessary in order to start the solution properly. There are two possible starting conditions: (1) sharp edge or pointed body, where $\theta=0$ and $n=0$, and (2) stagnation point, where $U_e=u_e=0$.

In the case of a boundary layer starting from a stagnation point, the initial value n_1 of n is determined from the condition $U_e=0$, $U_{ex}=\text{constant}$ in equation (28). For two-dimensional stagnation-point flow, the Hartree pressure-gradient parameter β is equal to 1.0. Since, for the Falkner-

Skan type flow considered, $N = \frac{2(\beta-1)}{\beta} n$, it is seen that

$N=0$ at a two-dimensional stagnation point. This fixes n at the values shown in figure 6, which were obtained from figure 4. For axisymmetric stagnation-point flow over a closed body, $\beta = \frac{1}{2}$ (ref. 31), so that $N_1 = -2n_1$. The values of n_1 for axially symmetric stagnation-point flow over a closed body as obtained from figure 4 are also shown in figure 6. For the stagnation-point flow over the blunt lip of an open axisymmetric body, n_{sp} can be shown to have the two-dimensional value.

APPENDIX C

LINEAR METHOD FOR AXISYMMETRIC FLOW

For axisymmetric flows, the following equation, which is equivalent to equation (33), is obtained by application of the transformation of Mangler (ref. 27):

$$\frac{n}{P' \frac{t_0}{t_e}} = A \left(\frac{t_e}{t_0} \right)^{-K} \frac{M_e^{1-B}}{R^2} \int_0^{\frac{x}{L}} \left(\frac{t_e}{t_0} \right)^K \frac{R^2}{M_e^{1-B}} d\left(\frac{x}{L} \right) \quad (C1)$$

where $R=R(x)$ is the radius of the body at station x , $K = \frac{3\gamma-1}{2(\gamma-1)}$, and

$$P' = \frac{L \frac{dp_e}{dx}}{\gamma p_e M_e^2}$$

In evaluating the coefficients A and B of the straight line

$$N = A + Bn \quad (31)$$

A may be chosen as 0.44 so that the line (31) passes through the correct value of N at $n=0$. The choice of B may be made so that the line (31) goes through the point where $N = -2n$ in order to match the conditions at an axisymmetric stagnation point. In that event, $B = -\left(\frac{0.44}{n_{sp}} + 2\right)$. For achieving better agreement with the curves of figure 3 in certain ranges of pressure gradient, a tangent line to the curve of N against n may be chosen as was indicated for two-dimensional flow.

The three possible starting conditions are: (1) For a pointed body, $\theta=0$, $n=0$. (2) For a stagnation point on a closed body, $U_e=u_e=0$ so that $N=-2n$. Values of n_{sp} for this axisymmetric stagnation point are shown in figure 5 and indicated in table II for $\beta=\frac{1}{2}$. (3) For a stagnation point on the blunt lip of an open axisymmetric body, it can be shown using the axisymmetric form of equation (28) that $N=0$ so that n_{sp} is that for two-dimensional flow.

APPENDIX D

INITIAL VARIATION OF CORRELATION NUMBER

It is sometimes helpful to have an analytical expression for the initial variation of correlation number as a check on the numerical calculations. The following expressions for $\left(\frac{dn}{dx}\right)_{x=0}$ are determined from equation (28):

TWO-DIMENSIONAL FLOW

Sharp edge:

$$\left(\frac{dn}{dx}\right)_{x=0} = -0.44 \left(\frac{u_{ex}}{u_e}\right)_{x=0} \left(\frac{t_0}{t_e}\right)_{x=0} \quad (D1)$$

Stagnation point (blunt body):

$$\left(\frac{dn}{dx}\right)_{x=0} = \frac{n_{sp}}{1 + \left(\frac{dN}{dn}\right)_{sp}} \left(\frac{u_{exx}}{u_{ex}}\right)_{sp} \quad (D2)$$

AXISYMMETRIC FLOW

For axisymmetric flow the initial derivatives must be evaluated from the following equation:

$$-\frac{U_e}{R^2} \frac{d}{dX} \left(\frac{nR^2}{U_{ex}} \right) = N(n, S_w) \quad (D3)$$

Closed body.—

Pointed nose:

$$\left(\frac{dn}{dx}\right)_{x=0} = -0.147 \left(\frac{u_{ex}}{u_e}\right)_{x=0} \left(\frac{t_0}{t_e}\right)_{x=0} \quad (D4)$$

Stagnation point (blunt nose):

$$\left(\frac{dn}{dx}\right)_{x=0} = \frac{n_{sp}}{1 + \left(\frac{dN}{dn}\right)_{sp}} \left[2 \left(\frac{u_{exx}}{u_{ex}}\right)_{sp} - \left(\frac{R_{xx}}{R_x}\right)_{sp} \right] \quad (D5)$$

Open body.—

Sharp lip:

$$\left(\frac{dn}{dx}\right)_{x=0} = -0.44 \left(\frac{u_{ex}}{u_e}\right)_{x=0} \left(\frac{t_0}{t_e}\right)_{x=0} \quad (D6)$$

Stagnation point (blunt lip):

$$\left(\frac{dn}{dx}\right)_{x=0} = \frac{n_{sp}}{1 + \left(\frac{dN}{dn}\right)_{sp}} \left[\left(\frac{u_{exx}}{u_{ex}}\right)_{sp} - 2 \left(\frac{R_x}{R}\right)_{sp} \right] \quad (D7)$$

REFERENCES

1. Cohen, Clarence B.: Similar Solutions for the Laminar Compressible Boundary Layer with Heat Transfer and Pressure Gradient, and Application to Integral Methods. Ph. D. Thesis, Princeton Univ., 1954.
2. Sternberg, Joseph: A Free-Flight Investigation of the Possibility of High Reynolds Number Supersonic Laminar Boundary Layers. *Jour. Aero. Sci.*, vol. 19, no. 11, Nov. 1952, pp. 721-733.
3. Lees, Lester, and Lin, Chia Chiao: Investigation of the Stability of the Laminar Boundary Layer in a Compressible Fluid. NACA TN 1115, 1946.
4. Crocco, Luigi: The Laminar Boundary Layer in Gases. Rep. CF-1038, Aerophys. Lab., North Am. Aviation, Inc., July 15, 1948.
5. Chapman, Dean R., and Rubesin, Morris W.: Temperature and Velocity Profiles in the Compressible Laminar Boundary Layer with Arbitrary Distribution of Surface Temperature. *Jour. Aero. Sci.*, vol. 16, no. 9, Sept. 1949, pp. 547-565.
6. Low, George M.: The Compressible Laminar Boundary Layer with Heat Transfer and Small Pressure Gradient. NACA TN 3028, 1953.
7. Tani, Iitiro: Further Studies of the Laminar Boundary Layer in Compressible Fluids. Rep. of Aero. Res. Inst., vols. 22-23, no. 322, Tokyo Imperial Univ., Dec. 1944.
8. Tifford, Arthur N.: The Thermodynamics of the Laminar Boundary Layer of a Heated Body in a High-Speed Gas Flow Field. *Jour. Aero. Sci.*, vol. 12, no. 2, Apr. 1945, pp. 241-251.
9. Levy, Solomon: Heat Transfer to Constant-Property Laminar Boundary-Layer Flows with Power-Function Free-Stream Velocity and Wall-Temperature Variation. *Jour. Aero. Sci.*, vol. 19, no. 5, May 1952, pp. 341-348.
10. Brown, W. Bryon, and Donoughe, Patrick L.: Tables of Exact Laminar-Boundary-Layer Solutions When the Wall is Porous and the Fluid Properties are Variable. NACA TN 2479, 1951.
11. Levy, Solomon: Effect of Large Temperature Changes (Including Viscous Heating) upon Laminar Boundary Layers with Variable Free-Stream Velocity. *Jour. Aero. Sci.*, vol. 21, no. 7, July 1954, pp. 459-474.
12. Cohen, Clarence B., and Reshotko, Eli: Similar Solutions for the Compressible Laminar Boundary Layer with Heat Transfer and Pressure Gradient. NACA Rep. 1293, 1956. (Supersedes NACA TN 3325.)
13. Li, Ting-Yi, and Nagamatsu, Henry T.: Similar Solutions of Compressible Boundary-Layer Equations. *Jour. Aero. Sci.*, vol. 22, no. 9, Sept. 1955, pp. 607-616.
14. von Kármán, Th.: Über laminare und turbulente Reibung. *Z. a. M. M.*, Bd. 1, Heft 4, Aug. 1921, pp. 233-252.
15. Pohlhausen, K.: Zur näherungsweise Integration der Differentialgleichung der laminaren Grenzschicht. *Z. a. M. M.*, Bd. 1, Heft 4, Aug. 1921, pp. 252-268.
16. Kalikhman, L. E.: Heat Transmission in the Boundary Layer. NACA TM 1229, 1949.
17. Ginzler, J.: Ein Pohlhausenverfahren zur Berechnung laminarer kompressibler Grenzschichten an einer geheizten Wand. *Z. a. M. M.*, Bd. 29, Heft 11/12, Nov./Dec. 1949, pp. 321-337.
18. Morris, Deane N., and Smith, John W.: The Compressible Laminar Boundary Layer with Arbitrary Pressure and Surface Temperature Gradients. *Jour. Aero. Sci.*, vol. 20, no. 12, Dec. 1953, pp. 805-818.
19. Libby, Paul A., and Morduchow, Morris: Method for Calculation of Compressible Laminar Boundary Layer with Axial Pressure Gradient and Heat Transfer. NACA TN 3157, 1954.
20. Beckwith, Ivan E.: Heat Transfer and Skin Friction by an Integral Method in the Compressible Laminar Boundary Layer with a Streamwise Pressure Gradient. NACA TN 3005, 1953.
21. Thwaites, B.: Approximate Calculation of the Laminar Boundary Layer. *Aero. Quarterly*, vol. 1, Nov. 1949, pp. 245-280.
22. Young, A. D., and Winterbottom, N. E.: Note on the Effect of Compressibility on the Profile Drag of Aerofoils at Subsonic Mach Numbers in the Absence of Shock Waves. R. & M. No. 2400, British A. R. C., May 1940.
23. Rott, Nicholas, and Crabtree, L. F.: Simplified Laminar Boundary-Layer Calculations for Bodies of Revolution and for Yawed Wings. *Jour. Aero. Sci.*, vol. 19, no. 8, Aug. 1952, pp. 553-565.
24. Stewartson, K.: Correlated Incompressible and Compressible Boundary Layers. *Proc. Roy. Soc. (London)*, ser. A, vol. 200, no. A1060, Dec. 22, 1949, pp. 84-100.
25. Howarth, L.: On the Solution of the Laminar Boundary Layer Equations. *Proc. Roy. Soc. (London)*, ser. A, vol. 164, no. A919, Feb. 1938, pp. 547-579.
26. Hartree, D. R.: On an Equation Occurring in Falkner and Skan's Approximate Treatment of the Equations of the Boundary Layer. *Proc. Cambridge Phil. Soc.*, vol. 33, pt. 2, Apr. 1937, pp. 223-239.
27. Mangler, W.: Compressible Boundary Layers on Bodies of Revolution. VG 83, No. 47T, M. A. P. Volkenrode.
28. Tifford, Arthur N., and Chu, S. T.: Heat Transfer in Laminar Boundary Layers Subject to Surface Pressure and Temperature Distributions. *Proc. Second Midwestern Conf. on Fluid Mech.*, Ohio State Univ., Mar. 17-19, 1952, pp. 363-377.
29. Goldstein, S., ed.: Modern Developments in Fluid Dynamics. Vol. 2. Clarendon Press (Oxford), 1938, pp. 631-632.
30. Reshotko, Eli, and Cohen, Clarence B.: Note on the Compressible Laminar Boundary Layer with Heat Transfer and Pressure Gradient. *Jour. Aero. Sci.*, vol. 22, no. 8, Aug. 1955, pp. 584-585.
31. Schlichting, Herman: Grenzschicht-Theorie. Verlag und Druck G. Braun, Karlsruhe, 1951, pp. 110-115.

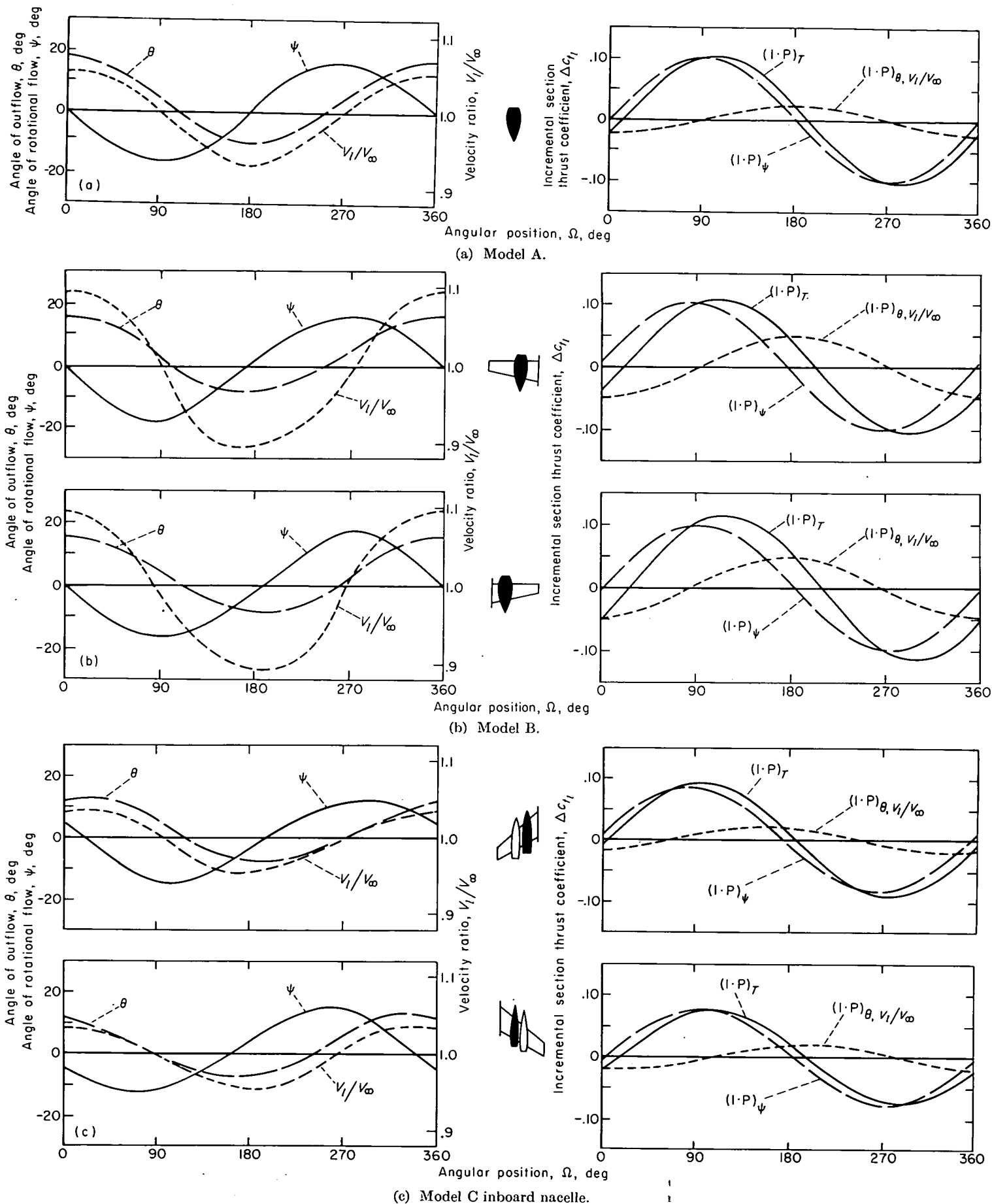
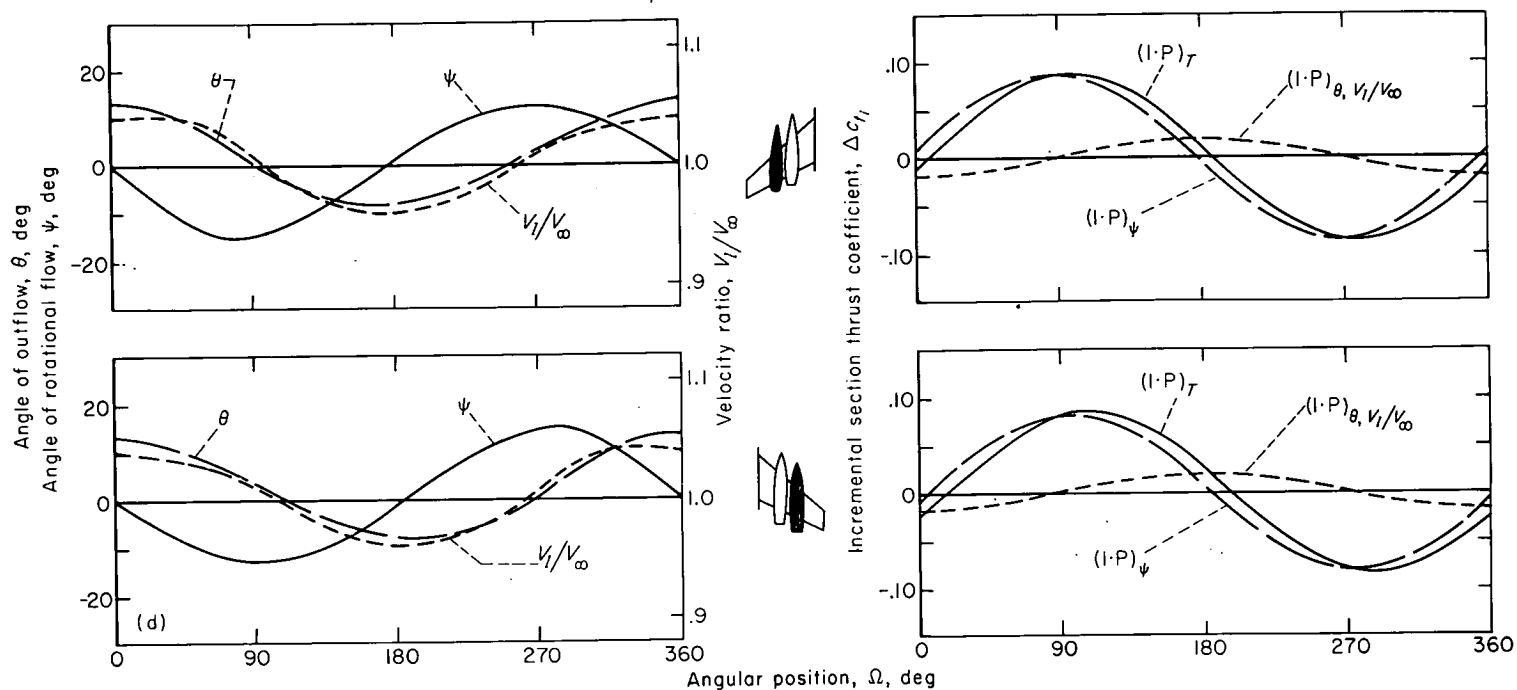
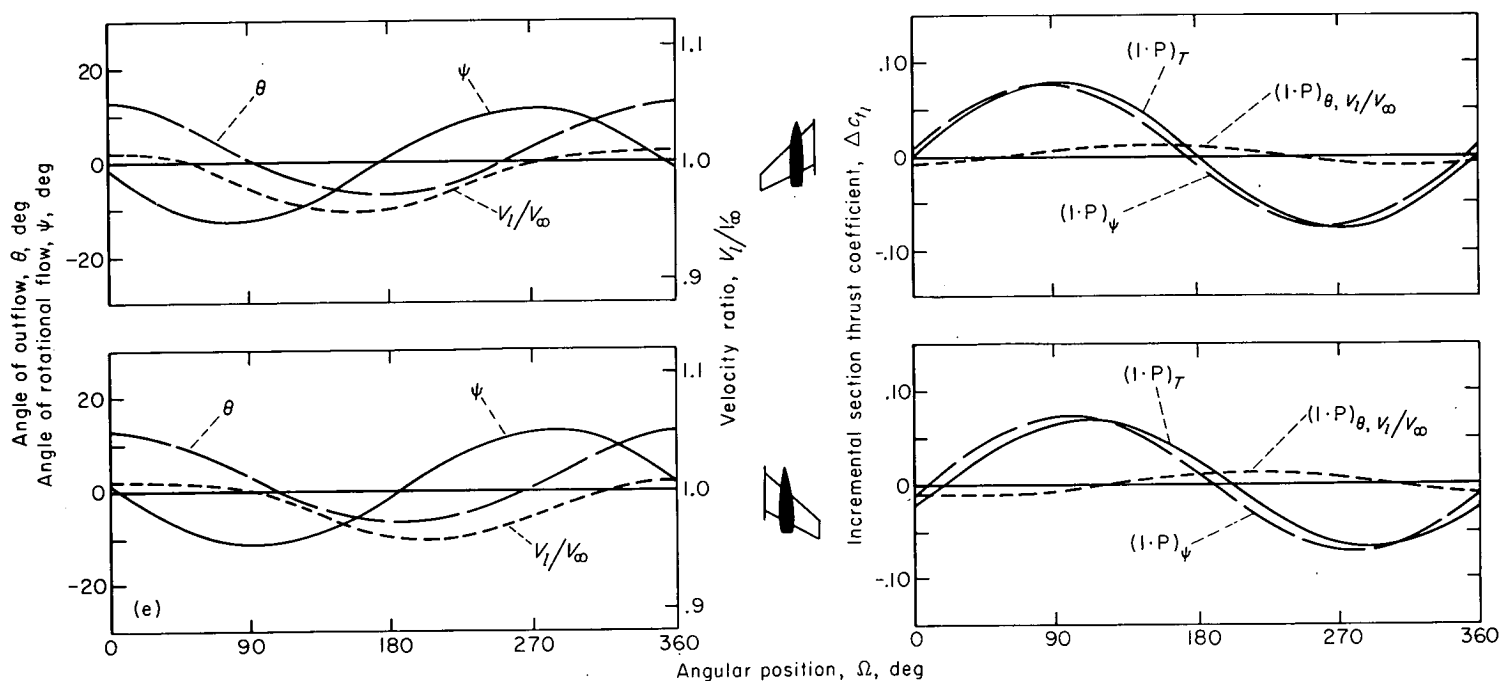


FIGURE 8.—The flow-field parameters and their effects on the 1-P variation of incremental section thrust coefficient for an isolated nacelle and several wing-fuselage-nacelle combinations.



(d) Model C outboard nacelle.



(e) Model D.

FIGURE 8.—Concluded.

load was periodic, (2) the components were all integer functions of one propeller revolution, and (3) no odd-order components above the fundamental were present. For example, at the specific angular positions $\Omega=0^\circ$, 90° , 180° , and 270° , expressions for determining the phase and amplitude of the $1\cdot P$ component are

$$\frac{1}{2} [(c_{t1})_{\Omega=90^\circ} - (c_{t1})_{\Omega=270^\circ}] = \delta c_{t1} \cos \varphi_a \quad (1a)$$

$$\frac{1}{2} [(c_{t1})_{\Omega=0^\circ} - (c_{t1})_{\Omega=180^\circ}] = \delta c_{t1} \sin \varphi_a \quad (1b)$$

where φ_a is the phase angle between the position at which the maximum magnitude of the $1\cdot P$ component occurs and the $\Omega=90^\circ$ position. As noted previously, for the cases investigated, values of φ_a were found to be quite small. Hence, it is believed plausible to make the approximation that

$$\delta c_{t1} \cos \varphi_a \approx \delta c_{t1} \quad (2)$$

A simplified procedure for determining the amplitude of the $1\cdot P$ aerodynamic thrust load is now evident which requires only the solution of equation (1a) with the foregoing approximation.

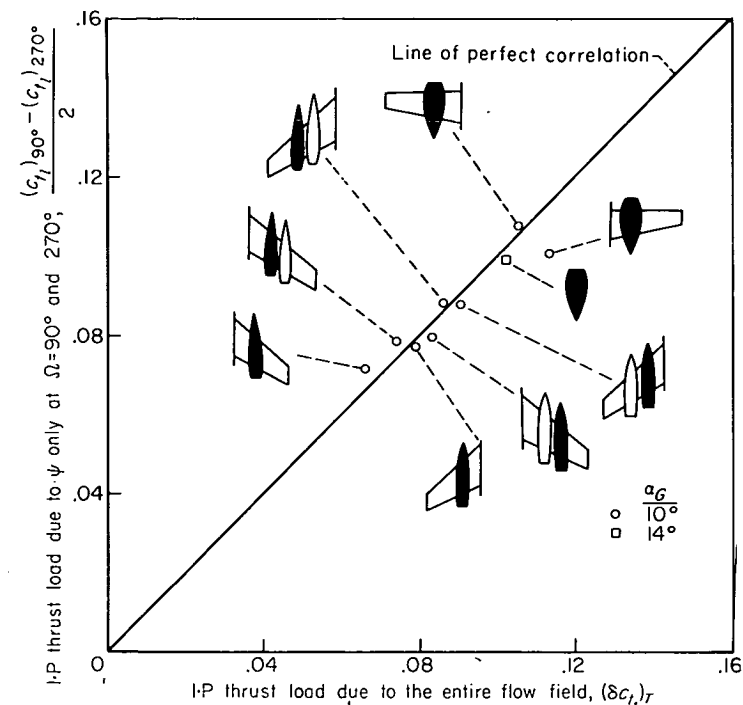


FIGURE 9.—Comparison of 1- P thrust loads as computed by the procedure of this report with those computed using the entire measured flow field for an isolated nacelle and several wing-fuselage-nacelle combinations; $x=0.7$, $V_\infty=165$ mph, $n_p=1250$ rpm, $\beta_{0-70}=21.7^\circ$.

The introduction of this simplified procedure reduces the flow field information required to the values of the parameters at the $\Omega=90^\circ$ and 270° positions (the horizontal center line of the propeller disk). This fact and certain characteristics of the flow-field parameters preclude the need for experimental surveys of the flow field. It can be seen in figure 8 that, generally speaking, at the $\Omega=90^\circ$ and 270° positions θ and V_i/V_∞ are near the free-stream values of 0° and 1.0, respectively, as noted previously, while ψ is at nearly its maximum and minimum values. Hence, θ and V_i/V_∞ can be approximated by the free-stream values. Values of ψ on the horizontal center line of the propeller disk may be computed by the methods which are presented and evaluated in Appendixes B, C, and D. Thus, the need for experimental surveys of the flow field has been obviated.

To indicate the accuracy and general applicability of the procedure, 1- P thrust loads on a propeller computed by the procedure are compared in figure 9 with those presented in figure 8 which were computed by 16-point computations based on all measured flow parameters. As noted above, the values of 0° and 1.0 were assumed for θ and V_i/V_∞ when applying the simplified procedure. Comparisons in figure 9 are at the 0.7-radial station of the propeller blade for all the test configurations. Comparisons of radial variations for two of the models are shown in figure 10 and, as further evaluation, the 1- P blade stresses computed using these load variations are compared in figure 11. From these figures, it is seen that the simplified procedure yielded generally satisfactory results for these configurations.⁴

⁴ A convenient design factor, now in common use, for indicating the relative stress levels on propellers for various flight conditions is the 1- P load exciting parameter Aq (refs. 1 and 2). By definition, A is identical to the absolute values of ψ at the horizontal center line of the Propeller disk.

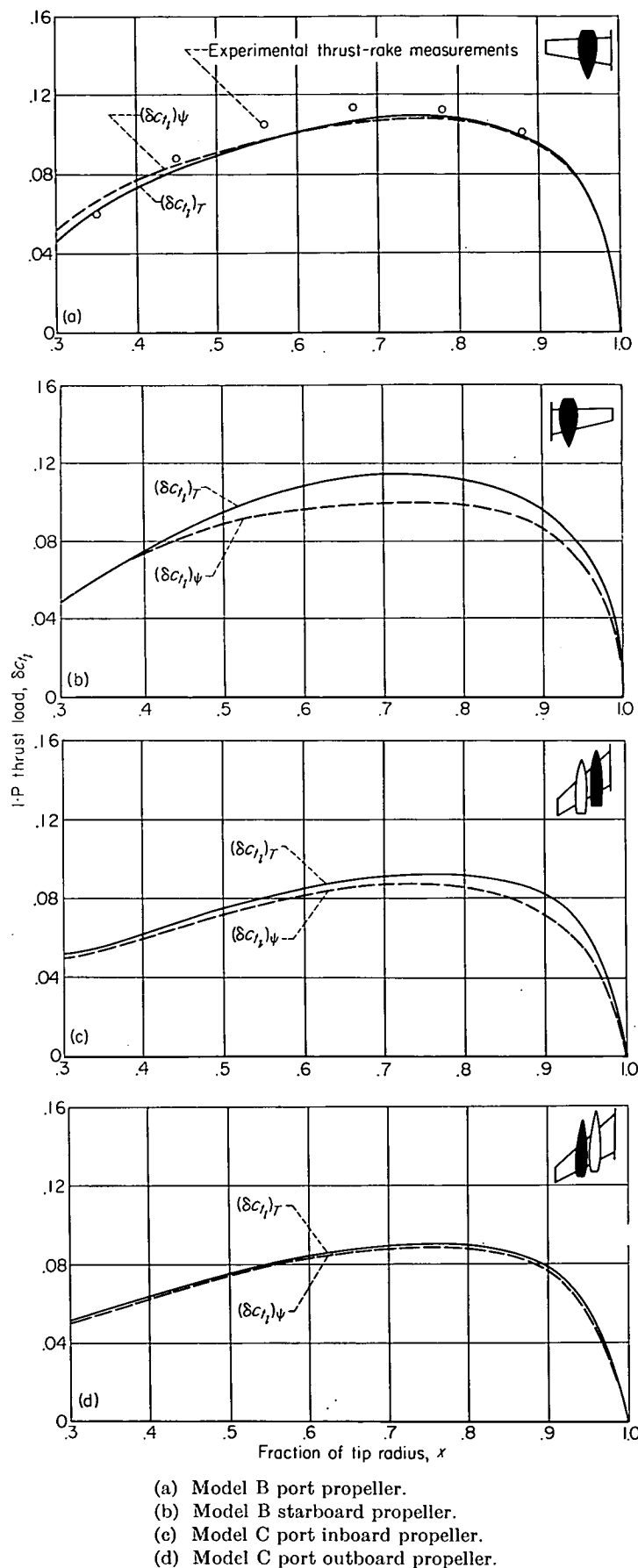


FIGURE 10.—Comparison of the radial variation of the 1- P thrust load computed by the procedure of this report with that computed using the entire measured flow field; $V_\infty=165$ mph, $n_p=1250$ rpm, $\beta_{0-70}=21.7^\circ$, $\alpha_G=10^\circ$.

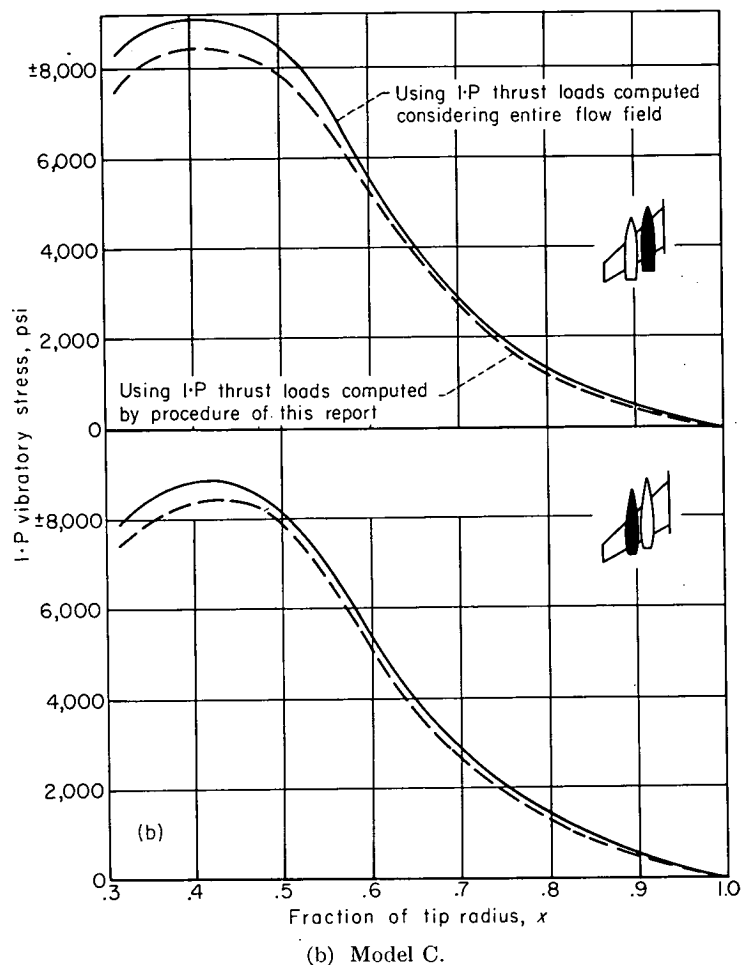
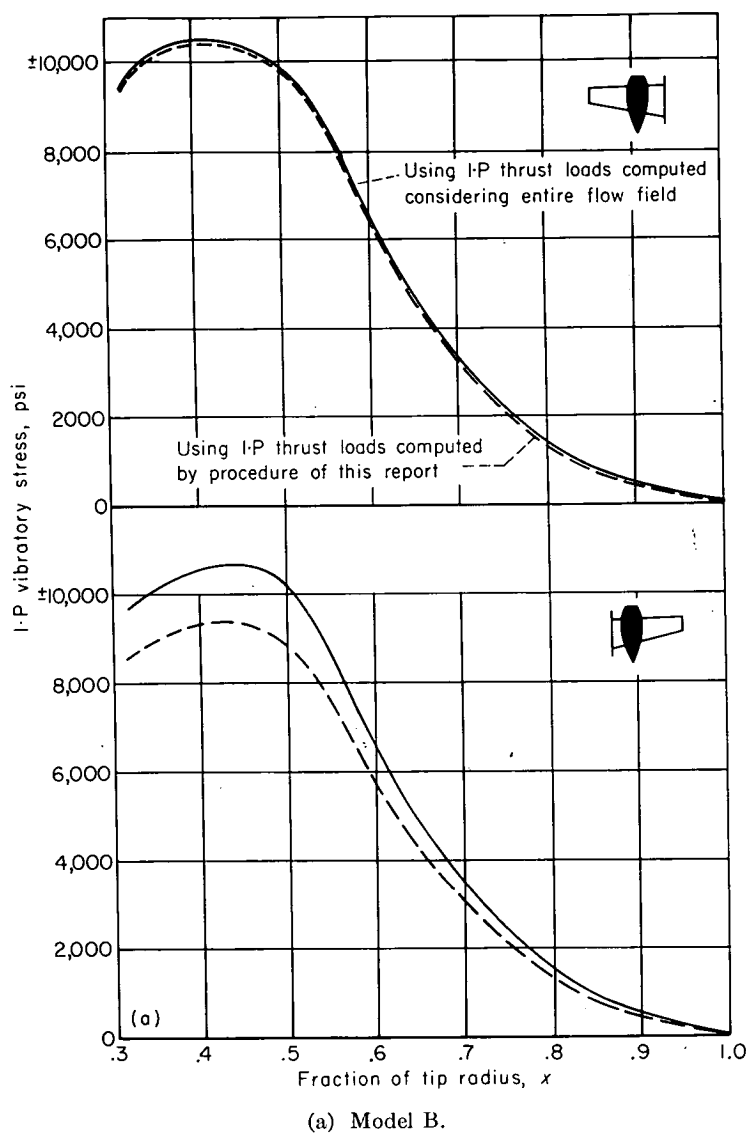


FIGURE 11.—Comparison of 1- P vibratory stresses resulting from 1- P thrust loads computed by the procedure of this report with those resulting from 1- P thrust loads computed using the entire measured flow field; $V_\infty = 165$ mph, $n_p = 1250$ rpm, $\beta_{0.70} = 21.7^\circ$, $\alpha_G = 10^\circ$.

Evaluations of the methods for computing the values of ψ at the horizontal center line of the propeller disk are presented in the appendixes.

CONCLUDING REMARKS

The simplified procedure presented herein enables the rapid calculation of the 1- P thrust loads on propellers of tractor airplanes in pitch at zero yaw, without the need for tedious experimental surveys of the flow field at the propeller plane. The simplifications of the procedure have reduced the necessary flow-field information to a minimum; namely, the upflow angles at the horizontal center line of the propeller disk. These angles may be obtained simply by

the theoretical methods which are presented. Thereby, the need for experimental survey of the flow field is eliminated.

The evaluations of the simplified procedure which are shown indicate that the 1- P thrust loads computed for the airplane configurations investigated are generally satisfactory. These configurations are believed to be typical of current designs and it is believed that equal accuracy could be expected for configurations generally similar to those investigated.

AMES AERONAUTICAL LABORATORY
NATIONAL ADVISORY COMMITTEE FOR AERONAUTICS
MOFFETT FIELD, CALIF., Mar. 21, 1955

APPENDIX A

COMPUTATION OF BLADE-SECTION THRUST AND BLADE-SECTION NORMAL FORCE

The $1\text{-}P$ stress problem is primarily due to flatwise bending of the propeller blade resulting from $1\text{-}P$ oscillations in the blade normal force as the propeller turns through one revolution. The blade normal force at any angular and radial position is the sum of the components of the aerodynamic loads (i. e., the thrust and torque forces) perpendicular to the chord line of the blade element.

For the purposes of this investigation, it was desirable to express the normal force in as simple terms as possible. The normal force on a blade element, N_b , may be expressed as

$$N_b = t \cos \beta_x + f_q \sin \beta_x \quad (\text{A1})$$

where

t section thrust force

f_q section torque force

Equation (A1) may be rewritten in coefficient form and both the section thrust and the section torque may be expressed in terms of the section thrust due to blade lift only, c_{l_i} .

$$c_{N_b} = c_{l_i} \left(1 - \frac{\tan \gamma}{\cot \varphi} \right) \cos \beta_x + c_{l_i} \left(1 - \frac{\tan \gamma}{\cot \varphi} \right) \tan (\varphi + \gamma) \sin \beta_x \quad (\text{A2})$$

where $\tan \gamma = \frac{\text{blade-section drag}}{\text{blade-section lift}}$

Equation (A2) can be rearranged as follows

$$c_{N_b} = \frac{c_{l_i}}{\cos \beta_x} \left\{ \frac{\cos [(\gamma - \varphi) - 2(\beta_x - \varphi)] + \cos (\gamma + \varphi)}{\cos (\gamma - \varphi) + \cos (\gamma + \varphi)} \right\} \quad (\text{A3})$$

When conventional propellers are operated at low forward velocities (i. e., conditions corresponding to take-off and early climb where high $1\text{-}P$ excitations are encountered), the blade sections have high values of lift to drag ratio; hence γ is quite small as is the angle of attack of the blade section which is equal to the quantity $(\beta_x - \varphi)$. It can be seen that if these terms are neglected in the above expression, the term in the bracket becomes unity which is tantamount to saying that the drag force on a blade element contributes little to the blade element normal force. It is cautioned that such approximation may not be valid for all possible operating conditions. For simplicity, this assumption regarding the normal force was made for the work of this report and the normal force was expressed by the approximate relation

$$c_{N_b} = \frac{c_{l_i}}{\cos \beta_x} \quad (\text{A4})$$

Steady-state theories, applied in strip analysis form, have been developed to compute the aerodynamic loads on propellers operating in symmetrical flow fields where all the inflow is perpendicular to the propeller plane (e. g., see

ref. 11). It appeared reasonable that application of this type of analysis in stepwise computations might enable satisfactory computations of the values of c_{l_i} for propellers operating in distorted flow fields (thrust axis inclined or noninclined). The blade-element loads depend upon the angle of attack and velocity which the element experiences. The velocity involved is that in the plane tangent to the blade section path of rotation, V_B in figure 12. For a rotating blade element, the magnitude of V_B is defined by the inflow velocity V' and the rotational velocity $\pi n_p D x$. If the interference effects of the blades on each other are ignored, the angle of attack of the blade element is the blade geometric setting β_x minus the helix angle φ_o .

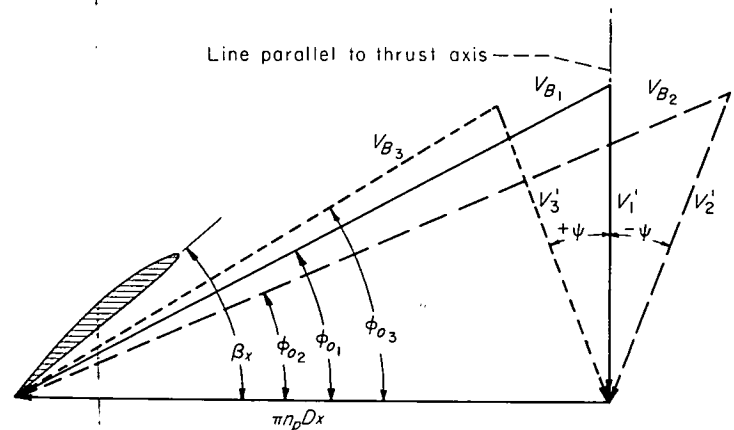


FIGURE 12.—Velocity diagram of propeller blade section.

The distorted flow-field case differs from the symmetrical case in that V' is not always perpendicular to the propeller plane nor of constant magnitude, but varies in direction and magnitude with angular position Ω of the blade. In figure 12, subscript 1 represents the symmetrical case while subscripts 2 and 3 represent the extremes of the variation for the distorted case. Consequently, it is apparent that these variations must be taken into account in the computations.

The equation for the coefficient of thrust on a blade element for a propeller in a symmetrical flow field including blade interference effects is

$$c_t = \kappa \pi^3 x^3 \frac{\alpha_i}{57.3} \frac{(\cot \varphi - \tan \gamma)}{\left(\cot \varphi + \frac{\alpha_i}{57.3} \right)^2} \quad (\text{A5})$$

where

φ	$\varphi_o + \alpha_i$
φ_o	$\tan^{-1} (V_\infty / \pi n_p D x)$
α_i	propeller-induced angle of inflow, deg
κ	Göldstein correction factor for a finite number of blades
γ	$\tan^{-1} \left(\frac{\text{blade-section drag}}{\text{blade-section lift}} \right)$

For the distorted flow-field case, it is necessary to modify the equation to account for variations in both direction and magnitude of V' described above. Thus,

$$c_i = \kappa \pi^3 x^3 \frac{\alpha_i}{57.3} \frac{(\cot \varphi - \tan \gamma)}{\left(\cot \varphi + \frac{\alpha_i}{57.3}\right)^2} \left(1 - \frac{V' \sin \psi}{\pi n_p D x}\right)^2 \quad (\text{A6})$$

for which it is important to note that

$$\varphi_0 = \tan^{-1} \left(\frac{V' \cos \psi}{\pi n_p D x - V' \sin \psi} \right)$$

In determining α_i (the interference effects), the assumption is made that all the blades are operating at the same flow conditions as the blade being considered.

The expression for c_i may be simplified to consider only the section thrust due to blade lift, c_{l_p} , by ignoring the blade drag term, $\tan \gamma$. Thus

$$c_{l_i} = \kappa \pi^3 x^3 \frac{\alpha_i}{57.3} \frac{\cot \varphi}{\left(\cot \varphi + \frac{\alpha_i}{57.3}\right)^2} \left(1 - \frac{V' \sin \psi}{\pi n_p D x}\right)^2 \quad (\text{A7})$$

This is the expression used in the studies to calculate the values of c_{l_i} using all measured values of the flow-field parameters. When the values of 0° and 1.0 are substituted for θ and V_l/V_∞ as in the simplified procedure of the report, V' becomes equal to V_∞ . Hence, V_∞ is substituted for V' in the last term of equation (A7) and in the expression for φ_0 .

$$c_{l_i} = \kappa \pi^3 x^3 \frac{\alpha_i}{57.3} \frac{\cot \varphi}{\left(\cot \varphi + \frac{\alpha_i}{57.3}\right)^2} \left(1 - \frac{V_\infty \sin \psi}{\pi n_p D x}\right)^2 \quad (\text{A8})$$

where

$$\varphi_0 = \tan^{-1} \left(\frac{V_\infty \cos \psi}{\pi n_p D x - V_\infty \sin \psi} \right)$$

APPENDIX B

METHODS FOR DETERMINING THE VALUES OF ψ AT THE HORIZONTAL CENTER LINE OF A PROPELLER DISK

The value of ψ at the horizontal center line of a propeller disk is the summation of the geometric angle of attack of the thrust axis and the upwash angles induced by the various components of the airplane at the horizontal center line of the propeller disk, expressed as

$$\psi = \alpha_{\text{geometric}} + \epsilon_{\text{wing}} + \epsilon_{\text{adjacent bodies}} + \epsilon_{\text{body containing thrust axis}} \quad (\text{B1})$$

To determine these angles theoretically, the total angle of attack of each component must be known so that its contribution to ψ can be computed. Each component total angle of attack, like ψ , is the result of a geometric angle of attack plus an induced angle resulting from the upwash of other components. It is clear that to obtain an exact total angle of attack for each component, an iterative process would be required. However, within engineering accuracy, it was found possible to avoid this process.

In the case of the wing, it was found that ϵ_{wing} could be adequately predicted by considering only an isolated wing at the geometric angle of attack; that is, the adjacent bodies influenced the wing total angle of attack so slightly that the resultant change in ϵ_{wing} was negligible.

This conclusion is verified in figure 13 where ϵ_{wing} computed by the method presented in Appendix C from measured span loading on a wing affected by a nacelle is compared to that computed for the isolated wing. The differences are seen to be negligible.

In the case of determining the correct total angle of attack for a body, it was found that the effect of upwash from the wing and from other bodies generally could not be ignored. The wing upwash contribution to the angle of attack of a body can be computed by considering only the wing geometric angle of attack, since bodies have been shown to have little effect on the wing induced upwash. For a wing-body combination (i. e., a fuselage or single-engine airplane) the body effective angle of attack is taken as the arithmetic sum of the geometric angle of attack of the body and the

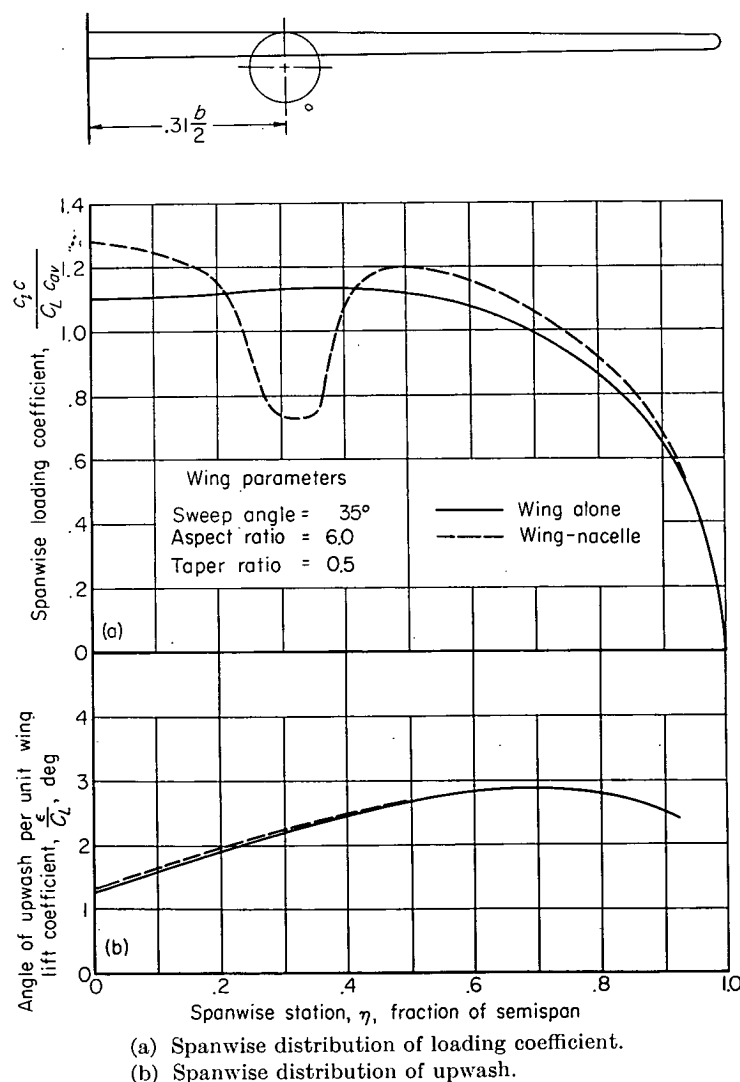


FIGURE 13.—Comparison of measured spanwise load distribution for an isolated wing and a wing-nacelle combination, and the resultant computed upwash distribution at a distance of one chord ahead of the wing leading edge; $M=0.18$, $C_L=0.32$.

value of wing upwash in the propeller plane at the axis of the body

$$\alpha_{eff_f} = \alpha_{geometric} + \epsilon_{wing} \quad (B2)$$

For the case of a configuration having more than one body (i. e., multiengine-type airplanes where the propulsive units are housed in nacelles outboard of a fuselage) the total angle of attack of a second body, for illustration assumed to be a nacelle, is expressed as

$$\alpha_{eff_n} = \alpha_{geometric} + \epsilon_{wing} + \epsilon_{adjacent\ body} \quad (B3)$$

where the value of ϵ_{wing} is the magnitude of wing upwash in the propeller plane at the nacelle axis. The value of $\epsilon_{adjacent\ body}$ at the nacelle axis is computed for the adjacent body at the effective angle of attack determined from equation (B2). This ignores the fact that the adjacent body is under the influence of the nacelle; this second-order effect is believed to be negligible.

While wing upwash is always important, the importance of considering upwash from adjacent bodies when obtaining a body total angle of attack varies widely depending on body proximity, relative size, and longitudinal position. For example, in the case of a multiengine airplane, the effect of one nacelle on the total angle of attack of the other can be shown to be small if the first nacelle lies behind the propeller plane of the second. Thus wing sweep would vary the importance of upwash from adjacent nacelles in finding the total angle of attack of a given nacelle. On the other hand, if the adjacent body were large compared to a nacelle, for example, a fuselage where the fuselage nose was downstream of the propeller plane, its effect on the nacelle total angle of attack would be important. Generally speaking, any body which extends ahead of the propeller plane at which ψ is being computed will have a significant effect on the total angle of attack of the body containing the thrust axis corresponding to that propeller plane; for example, usually fuselages and inboard nacelles both must be taken into account in finding the total angle of attack of the outboard nacelle in four-engined swept-wing configurations, whereas only the fuselage significantly affects the inboard nacelle.

To evaluate the use of equation (B1) and the methods which have been described, the variations of the upwash angle due to the various components and the curve representing the summation of these and the geometric angle of attack of the thrust axis are shown in figure 14 for several wing-nacelle-fuselage combinations at a Mach number of 0.22. Also shown is a comparison of these results with the measured values which indicates good agreement. Similar

comparisons are made in figure 15 for the wing-nacelle-fuselage combination described in reference 9 for a Mach number range from 0.25 to 0.92. In computing the upwash for this combination, account was taken of compressibility effects, except for the effects on the body-induced upwash, whose mechanics were not clearly understood. Good agreement between computed and measured upwash angles is indicated up to a Mach number of about 0.8. Compressibility effects are discussed more fully in Appendixes C and D.

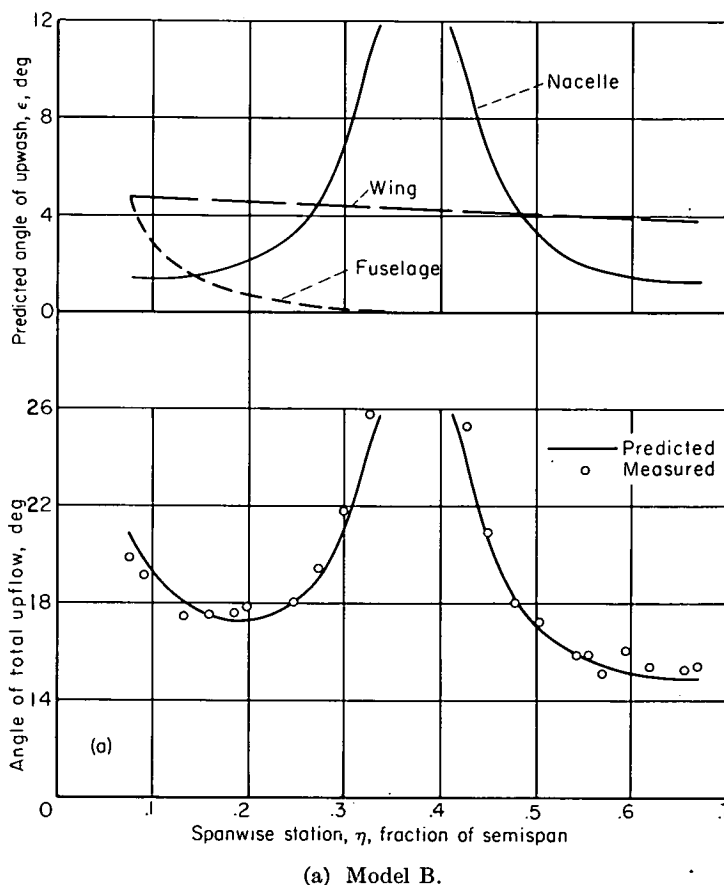
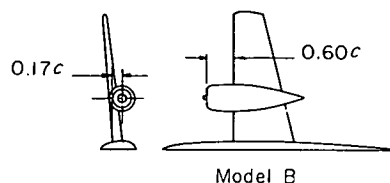


FIGURE 14.—Measured and predicted upflow angles and predicted upwash components at the horizontal center line of the propeller disks of several wing-fuselage-nacelle combinations; $\alpha_0 = 10^\circ$, $M = 0.22$.

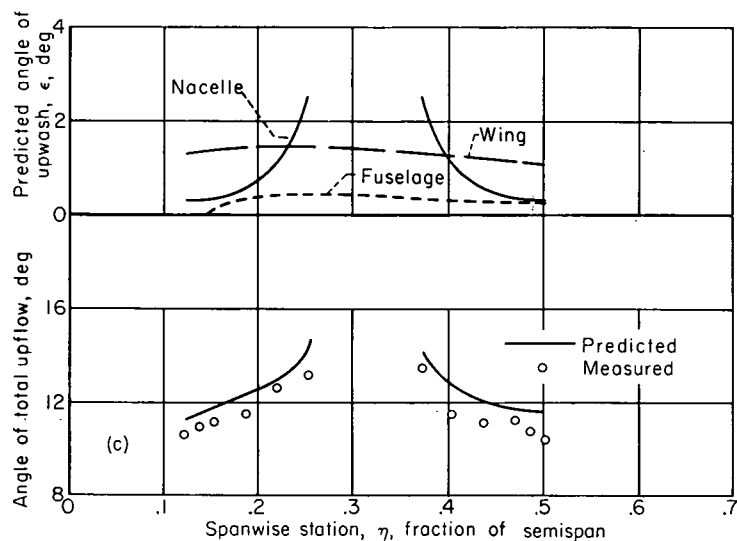
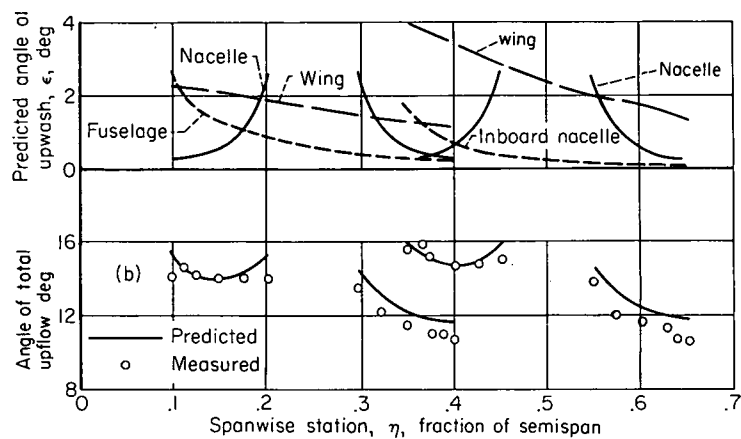
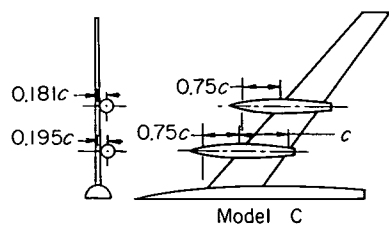
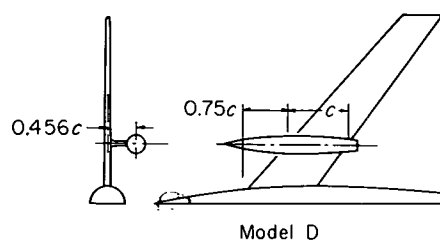


FIGURE 14.—Concluded.

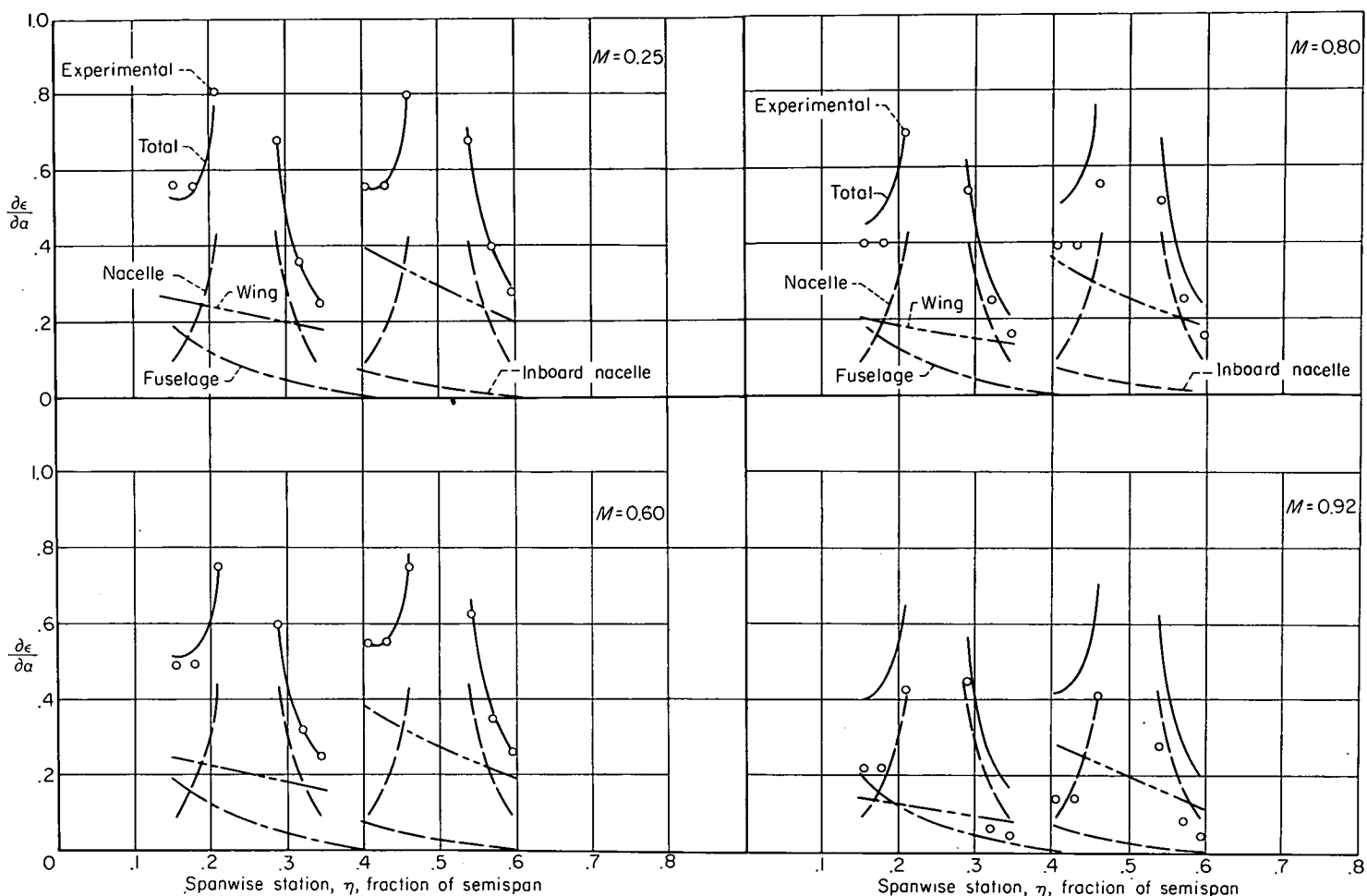
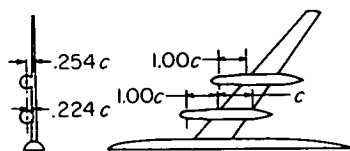


FIGURE 15.—The effects of Mach number on the upwash at the horizontal center line of the propeller disks of a wing-fuselage-nacelle combination utilizing a swept wing.

APPENDIX C

A METHOD FOR COMPUTING THE WING-INDUCED UPWASH ANGLES AT THE HORIZONTAL CENTER LINE OF A PROPELLER DISK

PREDICTION OF THE UPWASH ANGLE INDUCED IN THE EXTENDED WING-CHORD PLANE BY WINGS OF ARBITRARY PLAN FORM

It was shown in reference 12 that for a known symmetrical load distribution on a wing, the wing-induced downwash could be computed by use of influence coefficients designated a_{vn} coefficients which were presented therein. The same basic equations derived for the downwash computations are applicable for upwash computations, but new values of the a_{vn} coefficients are required.

The upwash can be found at specific points in the extended chord plane between the wing tips and ahead of the wing leading edge. The general expression for the upwash is given as

$$\left(\frac{w}{V_\infty}\right)_{\tau, \eta, \nu} = \sum_{n=1}^4 a_{vn} G_n \quad (C1)$$

where

G_n dimensionless circulation $\frac{\Gamma}{bV_\infty}$ identical to the load coefficient $\frac{c_l c}{2b}$ at span station n

M free-stream Mach number

b span of a wing measured perpendicular to the vertical plane of symmetry, ft

c local chord of a wing measured in a plane parallel to the vertical plane of symmetry, ft

- c_l section lift coefficient of a wing, $\frac{\text{section lift}}{q_\infty c}$
- n an integer defining a spanwise station on the wing quarter-chord line for which the value of circulation is defined
- q_∞ free-stream dynamic pressure, lb/sq ft
- w induced velocity, perpendicular to the mean chord line of the wing, positive for upwash, ft/sec
- x_w longitudinal distance from the wing quarter-chord line, ft
- β compressibility factor, $\sqrt{1-M^2}$
- ν an integer defining a specific point within the wing plan form for which the boundary condition of no flow through the wing is applied
- τ longitudinal coordinate $\frac{x_w}{b/2}$, semispans

The $a_{\nu n}$ coefficients are obtained from figure 16. The specific stations at which the upwash may be found correspond to $\nu=1, 2, 3, 4$ or $\eta_\nu = \cos(\nu\pi/8) = 0.924, 0.707, 0.383$ and 0, respectively. For convenience, the preceding equation is rewritten so that the upwash angle and loading distribution are in terms of unit lift coefficient. Thus

$$\left(\frac{w/V_\infty}{\beta C_L/K_{av}}\right)_{\tau/\beta, \eta_\nu} = \frac{1}{2} \left[\frac{\beta(b^2/S)}{K_{av}} \right] \sum_{n=1}^4 a_{\nu n} \left(\frac{c_l c}{C_L c_{av}} \right)_n \quad (C2)$$

where

$$\begin{aligned} \frac{\epsilon}{\beta C_L} = \frac{1}{4\pi\beta b^2/S} & \left\{ - \left[\frac{1-\eta}{\zeta^2 + (1-\eta)^2} \right] - \left[\frac{1+\eta}{\zeta^2 + (1+\eta)^2} \right] + \right. \\ & \frac{\left[\frac{\tau/\beta}{(\tau/\beta)^2 + \zeta^2/\cos^2 \Lambda_\beta} \right] \left[\left(\tau/\beta \tan \Lambda_\beta + \frac{1-\eta}{\cos^2 \Lambda_\beta} \right) \right] + \left[\frac{1-\eta}{\zeta^2 + (1-\eta)^2} \right] \left\{ \left[\tau/\beta + (1-\eta) \tan \Lambda_\beta \right] \right\}}{\sqrt{[\tau/\beta + (1-\eta) \tan \Lambda_\beta]^2 + (1-\eta)^2 + \zeta^2}} \\ & \frac{\left[\frac{2\eta \tan \Lambda_\beta - \tau/\beta}{(2\eta \tan \Lambda_\beta - \tau/\beta)^2 + \zeta^2/\cos^2 \Lambda_\beta} \right] \left[\left(\tau/\beta \tan \Lambda_\beta + \frac{1-\eta}{\cos^2 \Lambda_\beta} \right) + 2\eta \right] - \left[\frac{1+\eta}{\zeta^2 + (1+\eta)^2} \right] \left\{ \left[\tau/\beta + (1-\eta) \tan \Lambda_\beta \right] \right\}}{\sqrt{[\tau/\beta + (1-\eta) \tan \Lambda_\beta]^2 + (1+\eta)^2 + \zeta^2}} \\ & \left. \frac{\left[\frac{\tau/\beta}{(\tau/\beta)^2 + \zeta^2/\cos^2 \Lambda_\beta} \right] \left(\tau/\beta \tan \Lambda_\beta - \frac{\eta}{\cos^2 \Lambda_\beta} \right) - \left[\frac{2\eta \tan \Lambda_\beta - \tau/\beta}{(2\eta \tan \Lambda_\beta - \tau/\beta)^2 + \zeta^2/\cos^2 \Lambda_\beta} \right] \left[\left(\tau/\beta \tan \Lambda_\beta - \frac{\eta}{\cos^2 \Lambda_\beta} \right) + 2\eta \right]}{\sqrt{(\eta \tan \Lambda_\beta - \tau/\beta)^2 + \eta^2 + \zeta^2}} \right\} \quad (C3) \end{aligned}$$

where

- η lateral coordinate from the wing longitudinal center line, semispans
- ζ vertical coordinate from the wing chord plane, semispans

From the variation thus obtained, the upwash angle at any position above or below the extended chord plane may be expressed as a percentage of the value at the chord plane.

- $\frac{c_l c}{C_L c_{av}}$ span loading coefficient
- S wing area, sq ft
- c_{av} average chord of a wing, $\frac{S}{b}$, ft
- C_L lift coefficient of a wing, $\frac{\text{wing lift}}{q_\infty S}$
- K_{av} average of the ratios of the experimental section lift curve slope to the theoretical value $\frac{2\pi}{\beta}$, all at the same Mach number

Both $a_{\nu n}$ and $c_l c / C_L c_{av}$ are affected by compressibility, since they have been determined as functions of the parameters $\beta(b^2/S)/K_{av}$ and Λ_β .

MODIFICATION OF THE METHOD TO PREDICT UPWASH ANGLE AT POSITIONS ABOVE AND BELOW THE EXTENDED WING-CHORD PLANE

This modification is based on the assumption that the vertical variation of the wing-induced upwash angle is similar to that induced by a simple horseshoe vortex; that is, that a percentage ratio can be established between the two. For low Mach numbers, the bound portion of the horseshoe vortex has the same sweep as the wing quarter-chord line,¹ and lies in the wing chord plane. For a value of η and τ/β , the vertical variation of upwash angle due to a horseshoe vortex can be obtained from the following equation which corresponds to equation (34) of reference 13.

Based on the foregoing assumption, the value obtained on the extended wing-chord plane for a wing of arbitrary plan form may be multiplied by this percentage value to obtain the upwash angle induced by the wing at the same position above or below the chord plane. A typical example of the variations of the upwash angle expressed in percentage of the wing-chord plane value are shown in figure 17 for a horseshoe vortex swept back 40°.

¹ For high Mach numbers, the horseshoe vortex should have a sweep angle Λ_β given by $\tan \Lambda_\beta = (\tan \Lambda)/\beta$ in accordance with the Prandtl-Glauert rule.

EFFECTS OF COMPRESSIBILITY ON THE WING-INDUCED UPWASH

The Prandtl-Glauert rule, which accounts for the effects of compressibility, is directly applicable to the subject method. The basis for the corrections applied to the method as simply stated in the Prandtl-Glauert rule is that as the Mach number is increased, the span load distribution of a wing distorts as though its longitudinal dimensions were increasing as the ratio $1/\beta$. Thus, the effects of Mach number on a given wing can readily be considered by finding the span loading at zero Mach number of a properly distorted wing.

Since the wing-induced upwash distribution is directly dependent upon the span loading, the effects of compressibility on this factor were investigated. A typical example of the compressibility effects on a span loading is shown in figure 18. The small differences which are shown have little significance in terms of the upwash induced in the extended wing-chord plane. Hence, the span load for zero Mach number can be used satisfactorily.

It can be seen that increasing the longitudinal dimensions of the wing results in increasing the angle of sweep and increasing each local chord while leaving the span and taper unaffected. Thus, the distance from the quarter-chord line to a given point in the chord plane must also be increased by the ratio $1/\beta$. The compressibility effects on the effective sweep angle are sizable. For example, increasing the Mach number from 0.33 to 0.90 changes the effective sweep angle of a 40° sweptback wing from $41\frac{1}{2}^\circ$ to $62\frac{1}{2}^\circ$. In terms of the wing-induced upwash, this effectively increases the distance from a point on the extended wing-chord plane to the vortex core and thereby reduces the core's influence at that point. Hence, the values of τ and Λ must be corrected to τ/β and Λ_β before entering the charts of the a_{vn} coefficients.

It is obvious that for a given value of τ/β , the compressibility effects are not constant for all sweep angles. To illustrate this point, typical examples of the upwash angle distribution, spanwise for constant values of τ/β , are shown for wings with 0° and 40° of sweep. Figure 19 shows there

is no variation of the upwash angle with Mach number for an unswept wing at a given τ/β since $\tan \Lambda$ is zero. However, for the wing swept back 40° , it is shown in figure 20 that an increase from a Mach number of 0.33 to 0.90 produced sizeable changes in the upwash angle distributions at a constant τ/β .

PROCEDURE FOR APPLYING THE METHOD TO OBTAIN THE WING-INDUCED UPWASH ANGLES AT THE HORIZONTAL CENTER LINE OF THE PROPELLER PLANE

The first step is to obtain the span load distribution (e. g., by the methods of ref. 12); Mach number effects on the span load need not be considered as shown previously. Second, determine the τ/β variation and the value of Λ_β at the particular Mach number for the propeller plane locations in the extended wing-chord plane. The maximum and minimum values of τ/β will define the range over which computations must be made. Next, compute the values of ϵ/C_L at the four control points on the span for constant values of τ/β over the range defined above. This is accomplished by substituting the values of the span load and the a_{vn} coefficients derived from the charts in equation (C2). If necessary, these values should then be modified for displacements above and below the chord plane by means of equation (C3). The fairing of the resulting data points will yield the spanwise distributions of ϵ/C_L for constant values of τ/β ; a plot similar to figure 20. Using the values of τ/β previously determined, the propeller plane can be located on this plot as shown in figure 20 and the values of ϵ/C_L determined at any radial station.

To illustrate the method and the results obtained, the variations of τ/β and ϵ/C_L across the horizontal center line of the propeller disks of two representative airplane configurations are shown in figures 21 and 22 for Mach numbers of 0.33 and 0.90. The geometric characteristics of the components of these configurations were identical except that one wing panel was unswept and the other was swept back 40° .

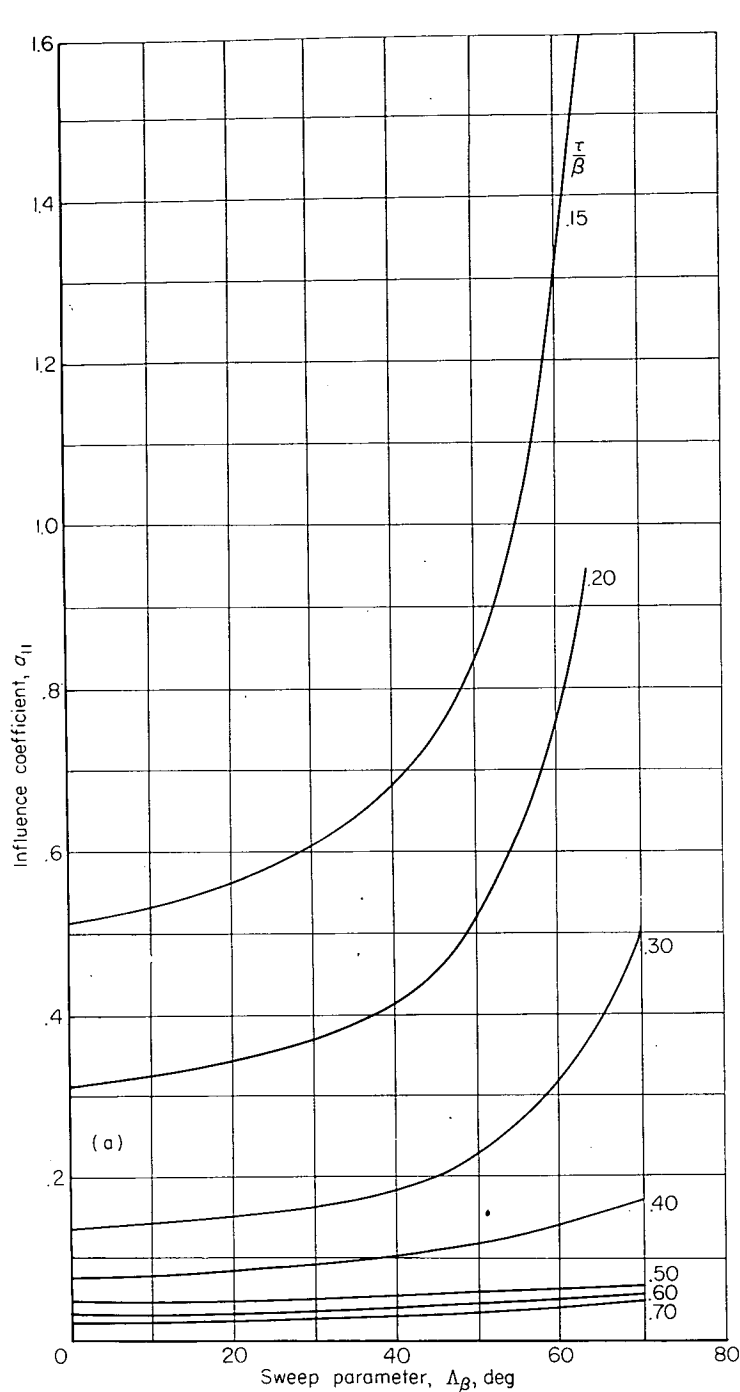
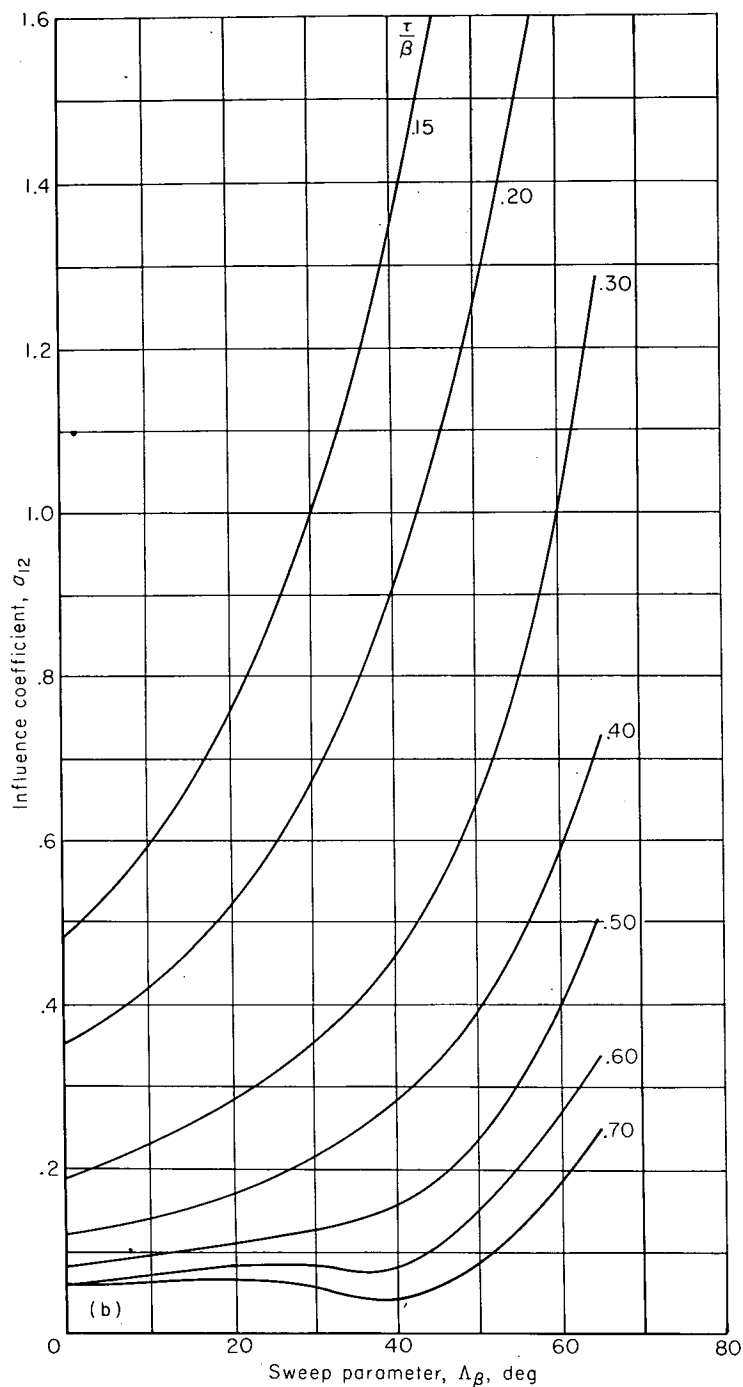
(a) $\nu=1, n=1$.(b) $\nu=1, n=2$.

FIGURE 16.—Influence coefficients, $a_{\nu n}$, for symmetric span loading plotted as a function of the sweep parameter, $\Delta\beta$, for various distances ahead of the wing quarter chord line, τ/β .

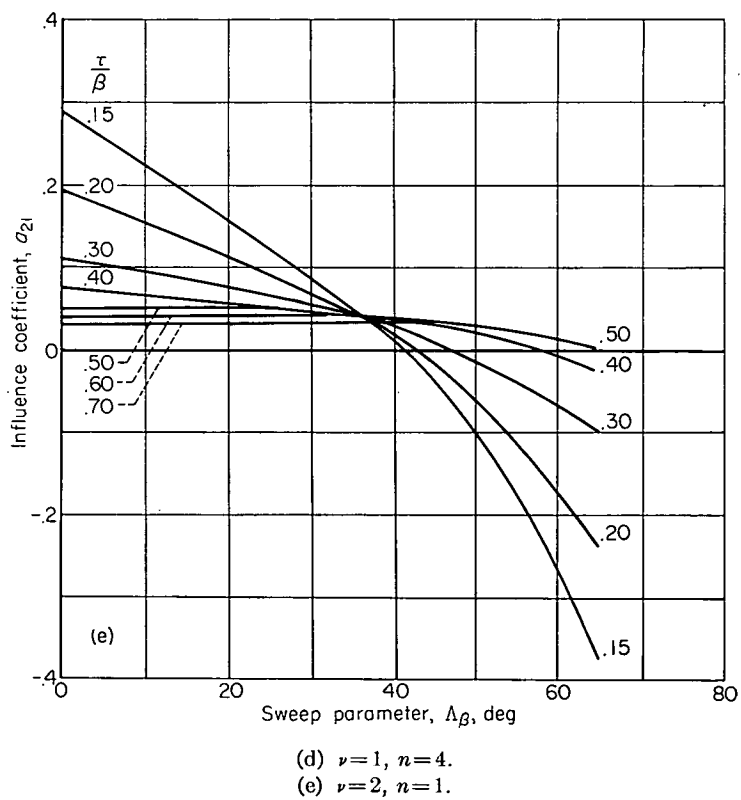
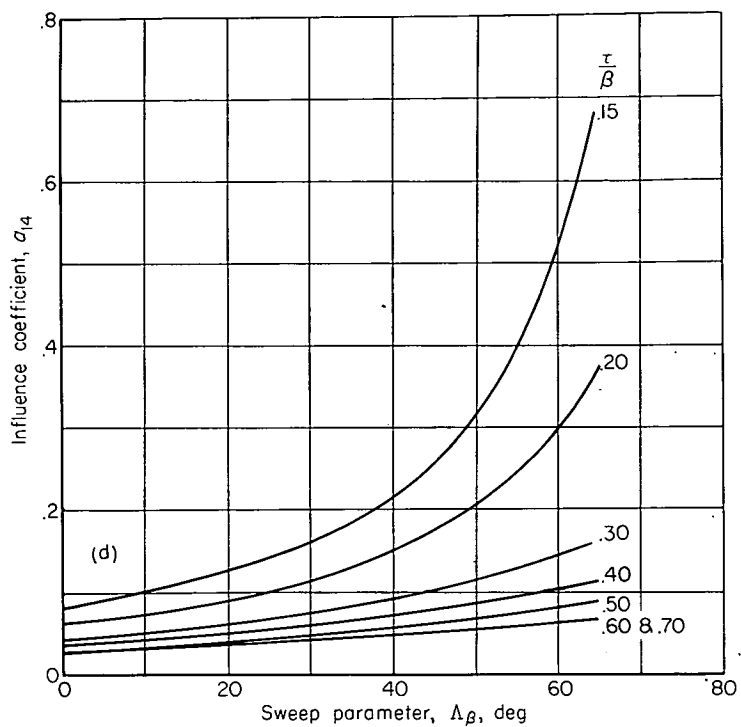
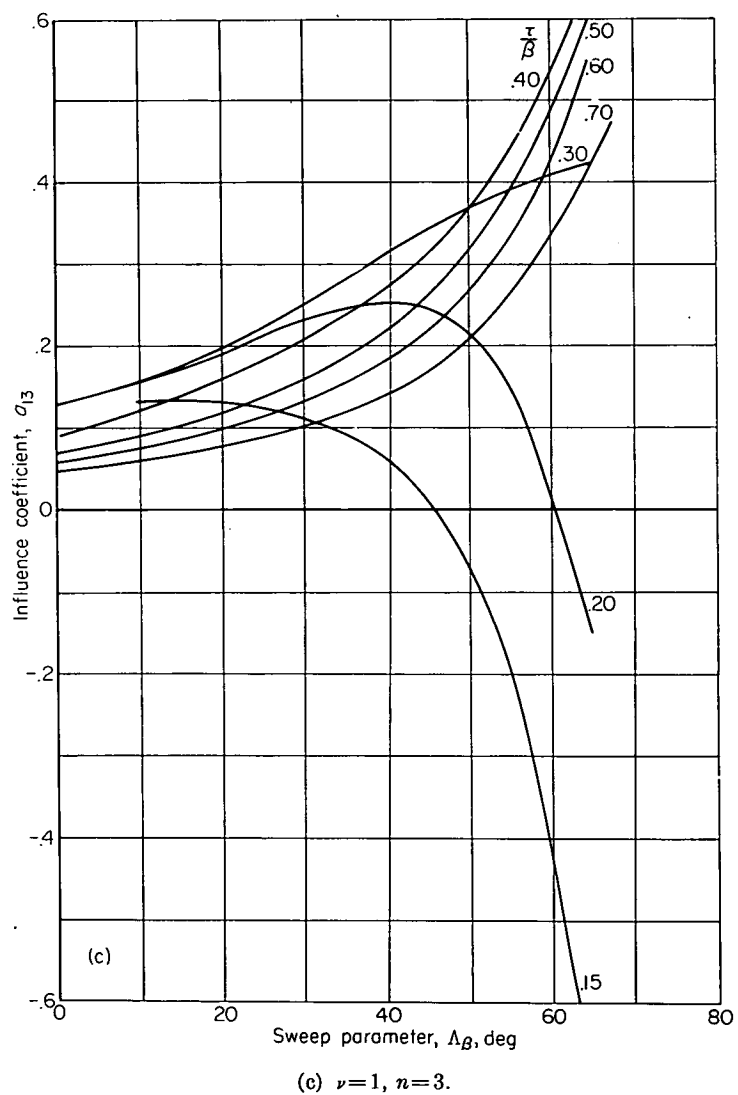


FIGURE 16.—Continued.

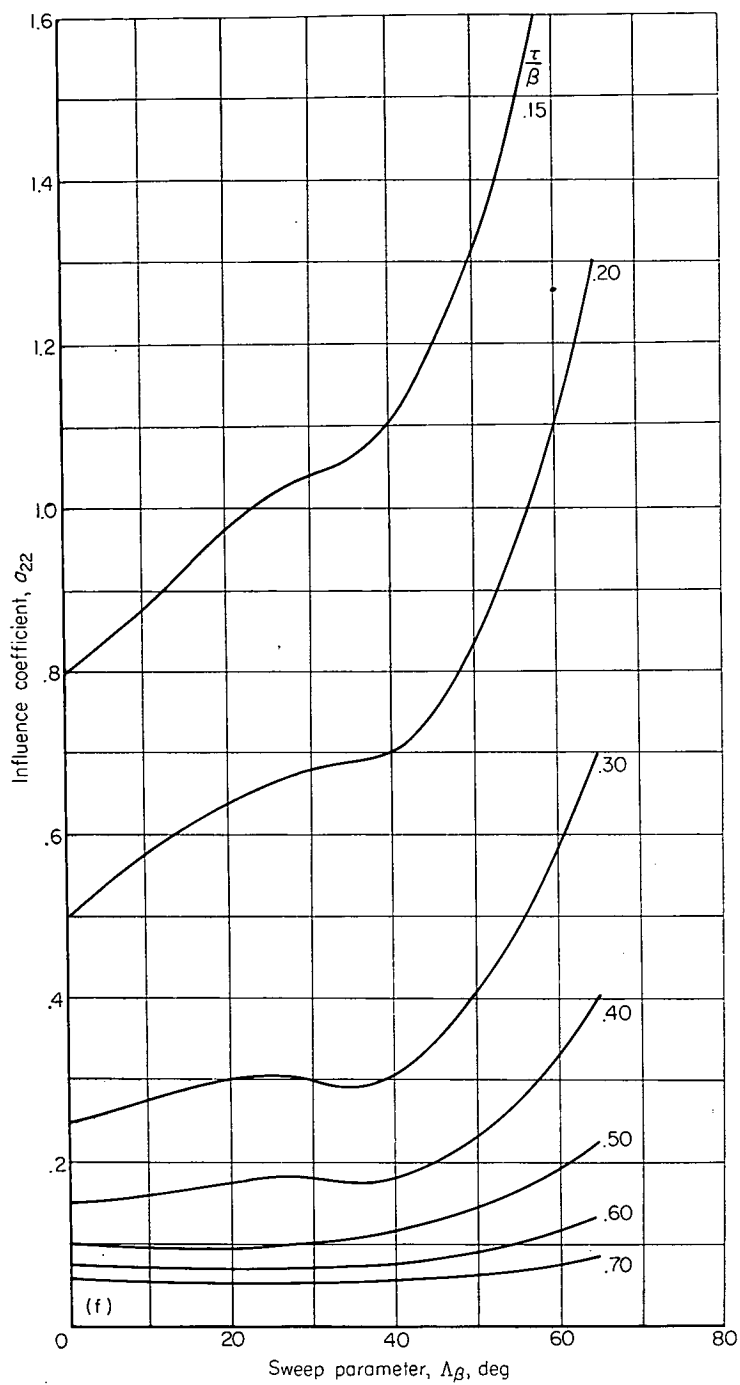
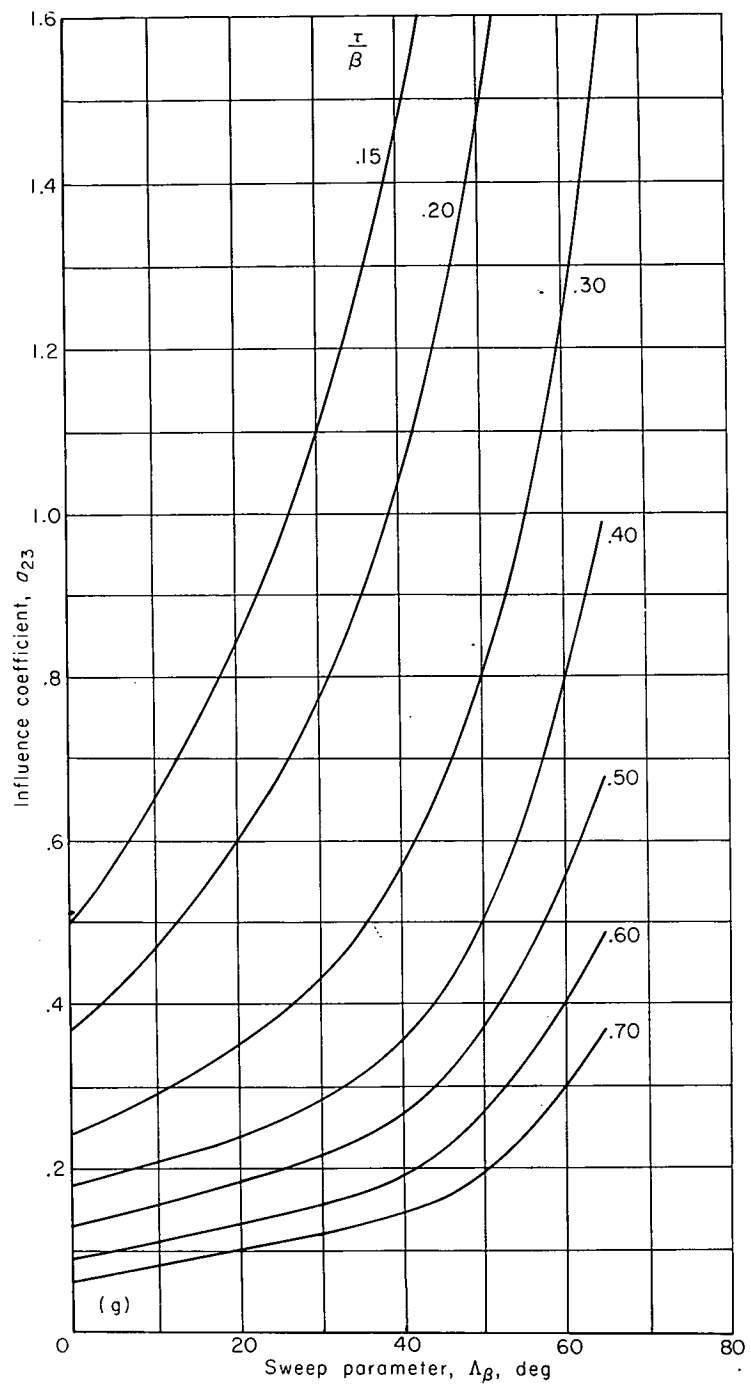
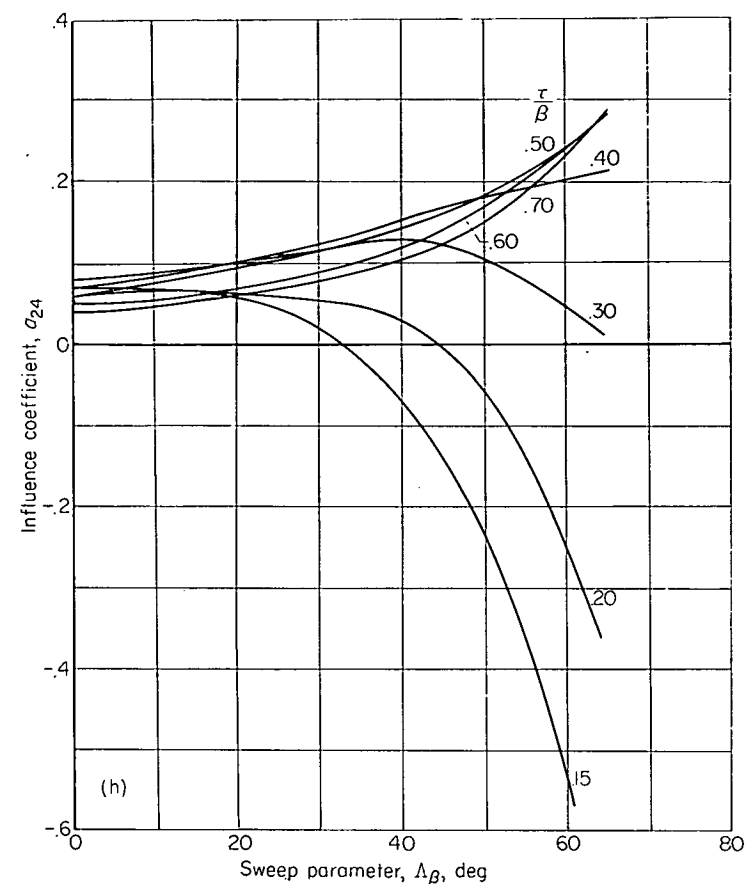
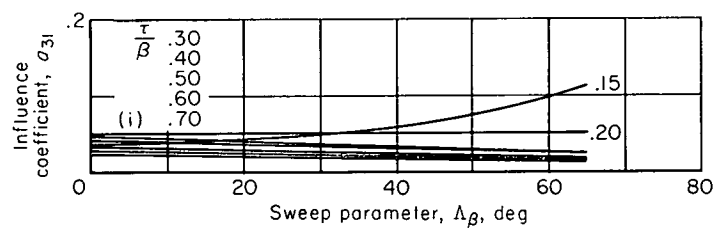
(f) $\nu=2, n=2$.(g) $\nu=2, n=3$.

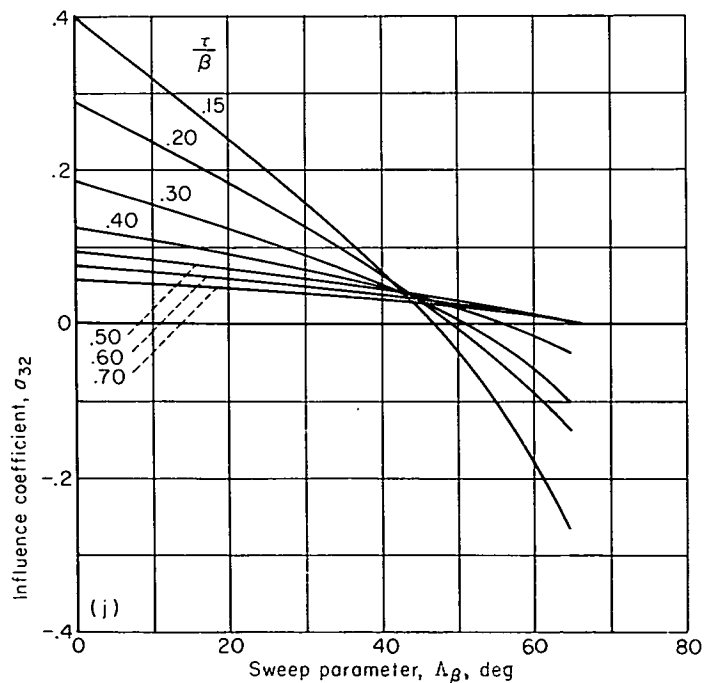
FIGURE 16.—Continued



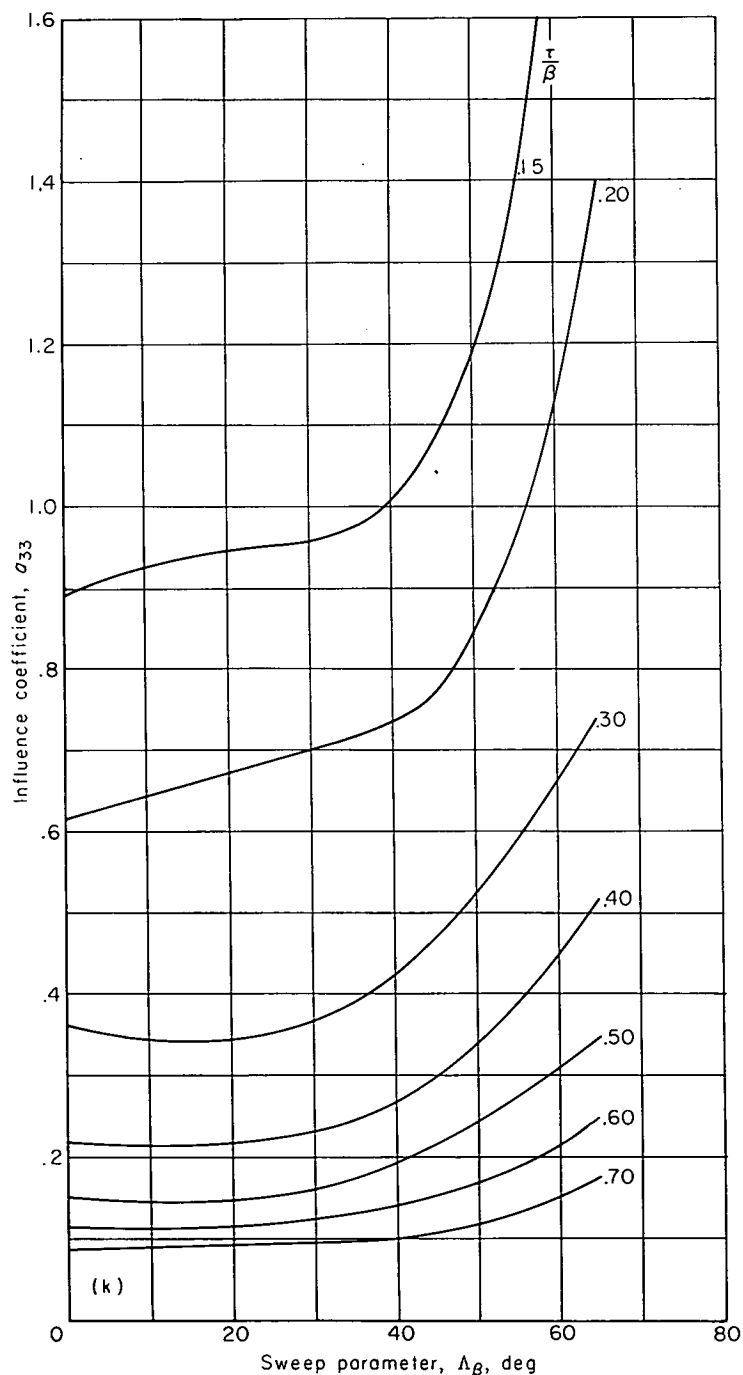
(h) $\nu=2, n=4$.



(i) $\nu=3, n=1$.



(j) $\nu=3, n=2$.



(k) $\nu=3, n=3$.

FIGURE 16.—Continued.

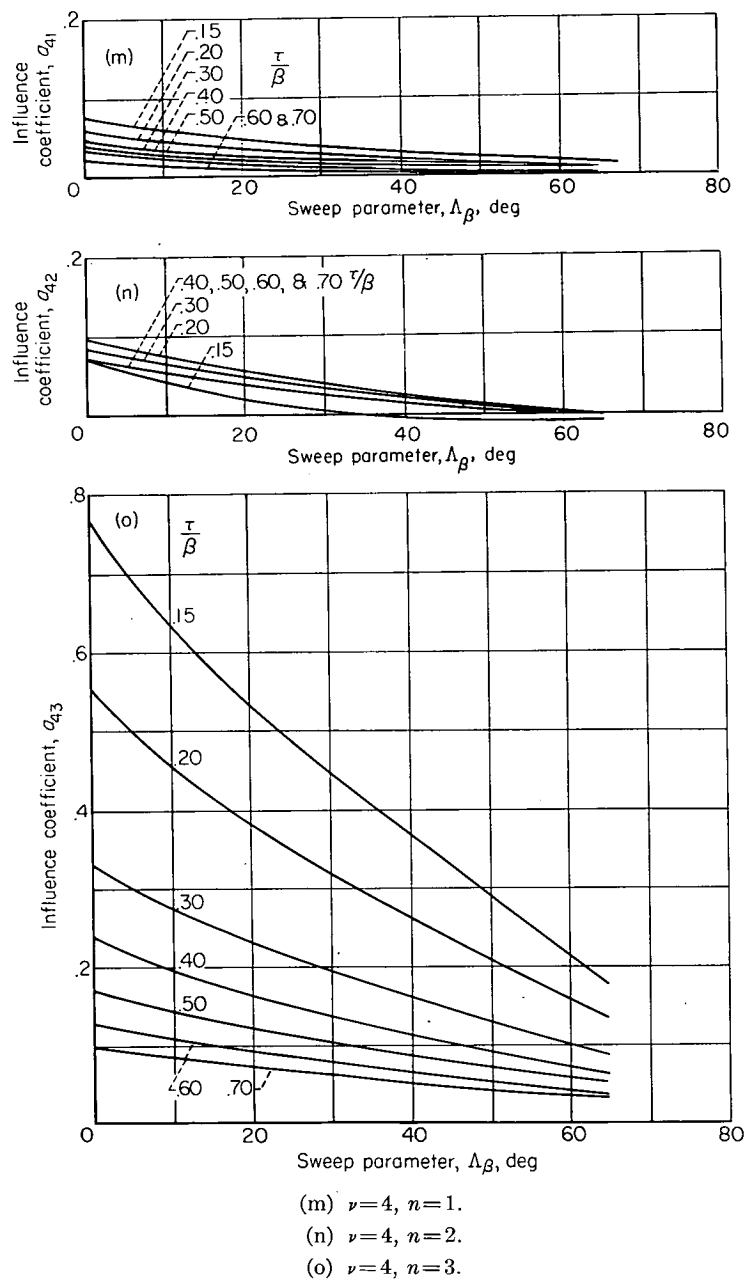
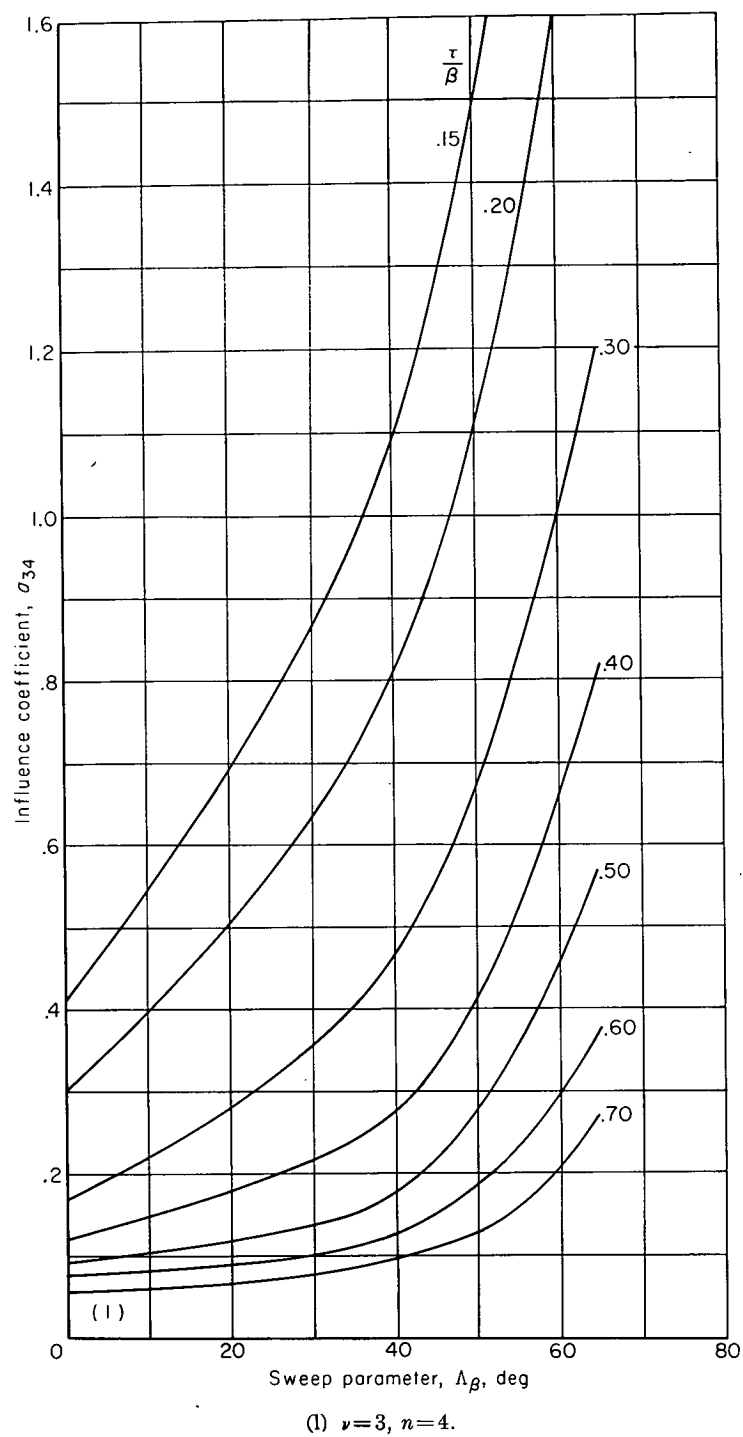
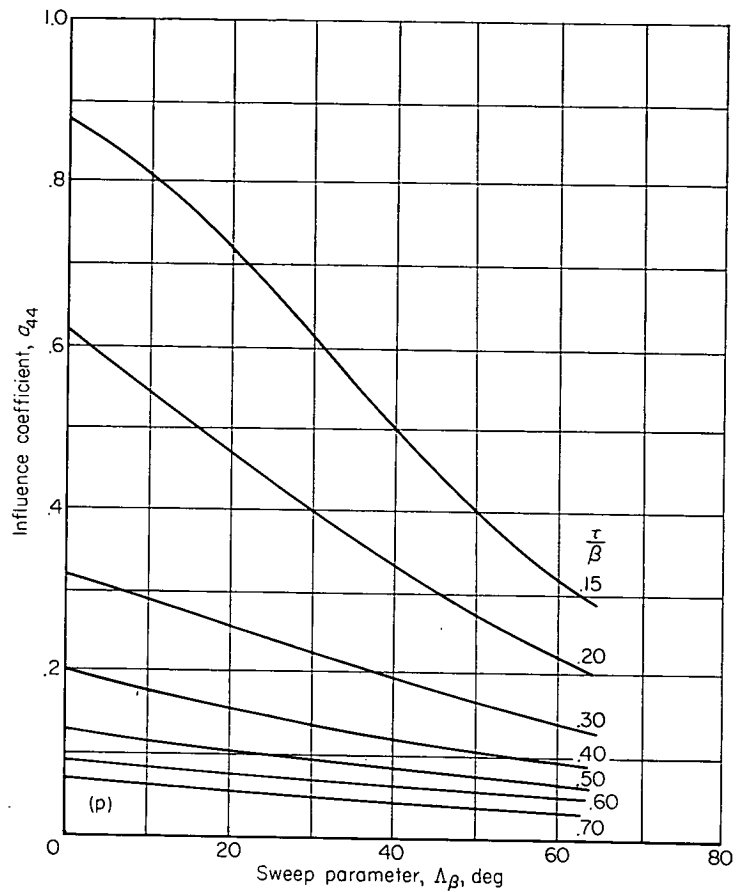


FIGURE 16.—Continued



(p) $\nu=4, n=4$.

FIGURE 16.—Concluded.

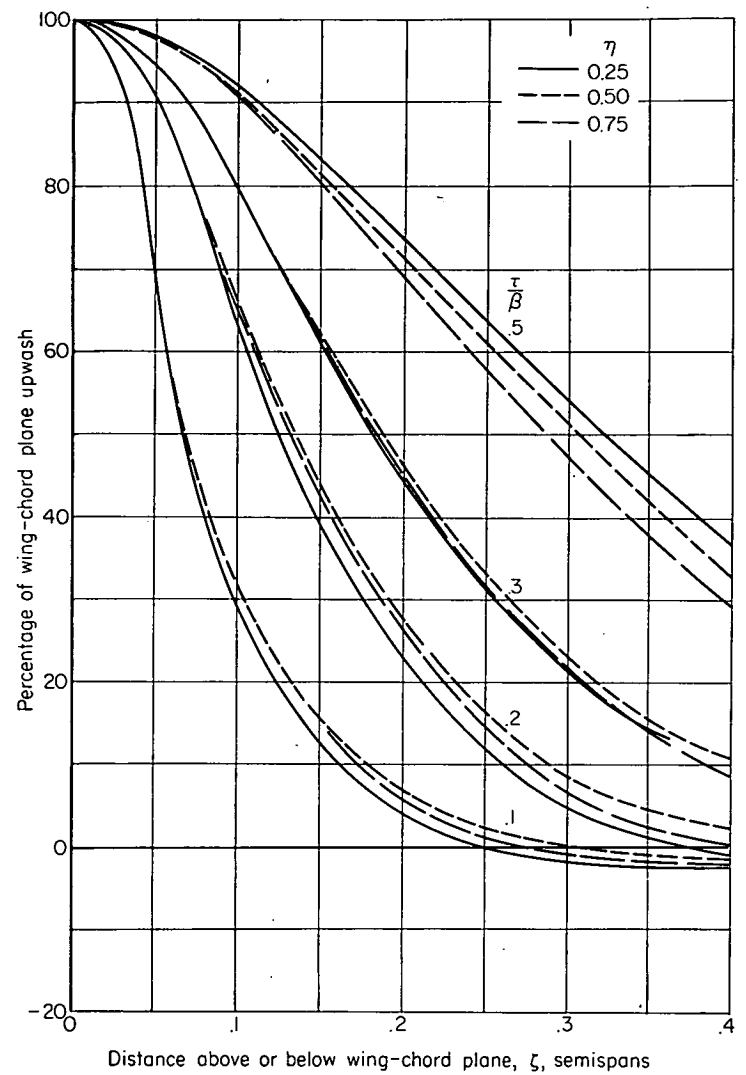


FIGURE 17.—Variation of upwash of a 40° swept-back horseshoe vortex with vertical position.

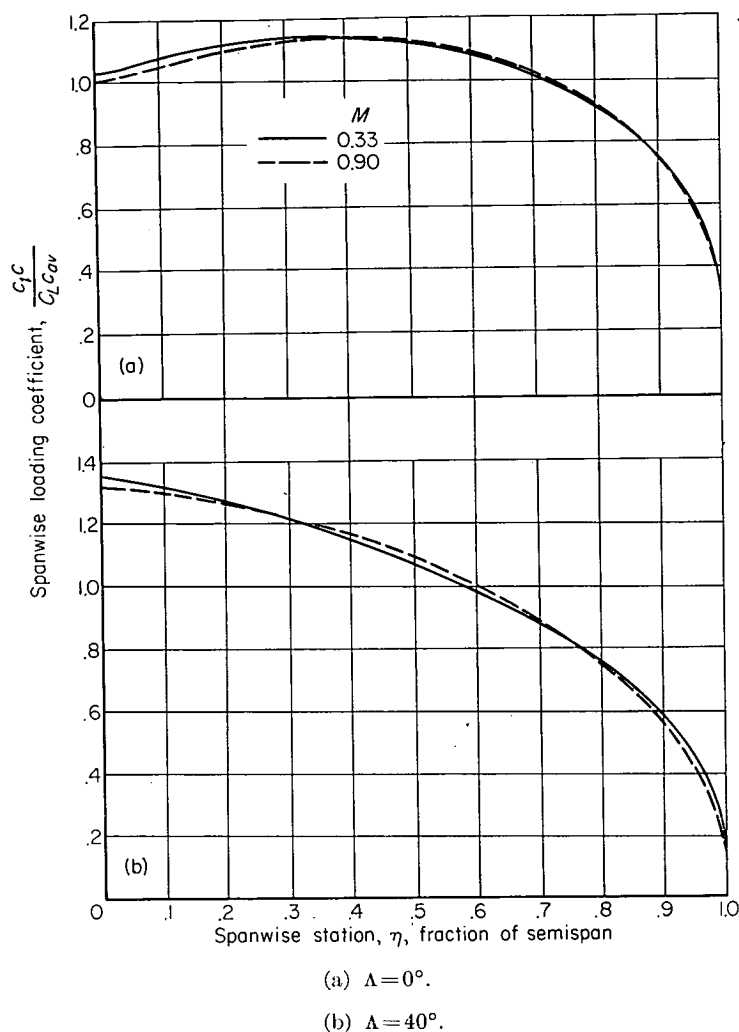


FIGURE 18.—A comparison of effects of compressibility on the spanwise loading coefficient for an unswept and a swept-back wing.

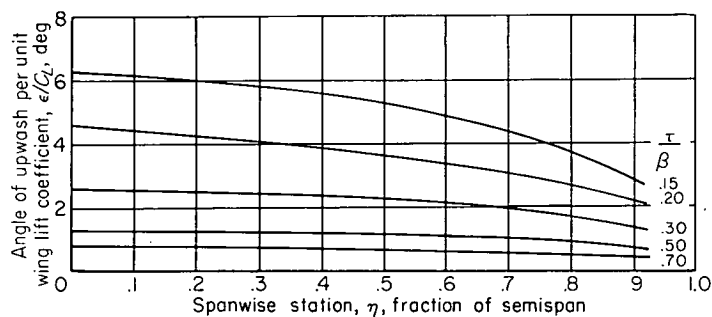


FIGURE 19.—The spanwise distribution of upwash at constant values of τ/β for an unswept wing at subsonic Mach numbers.

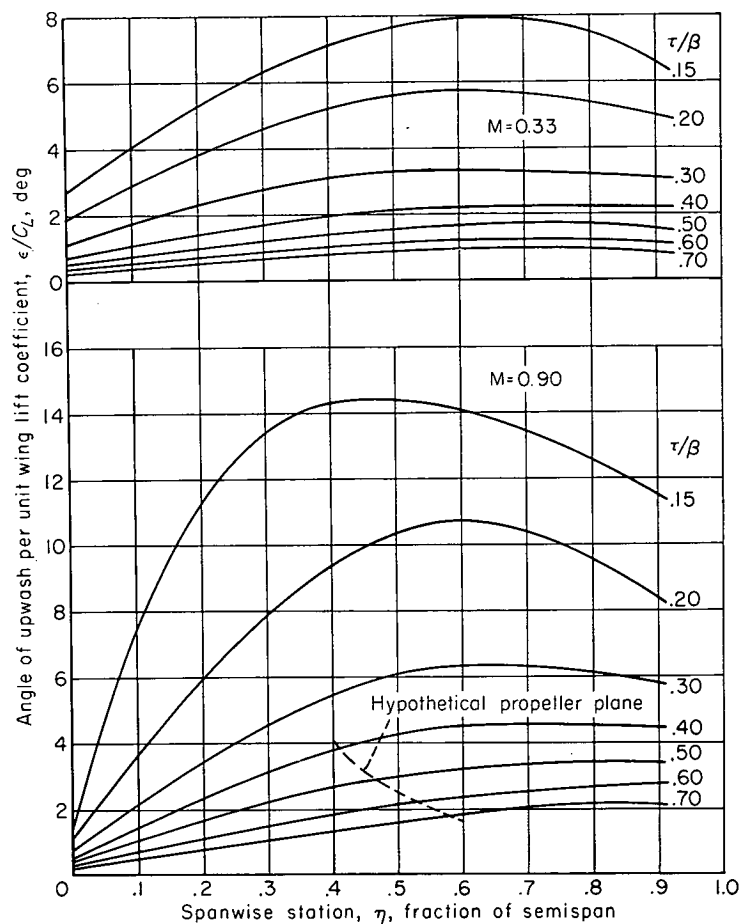


FIGURE 20.—The effects of compressibility on the spanwise distribution of upwash at constant values of τ/β for a wing swept back 40° .

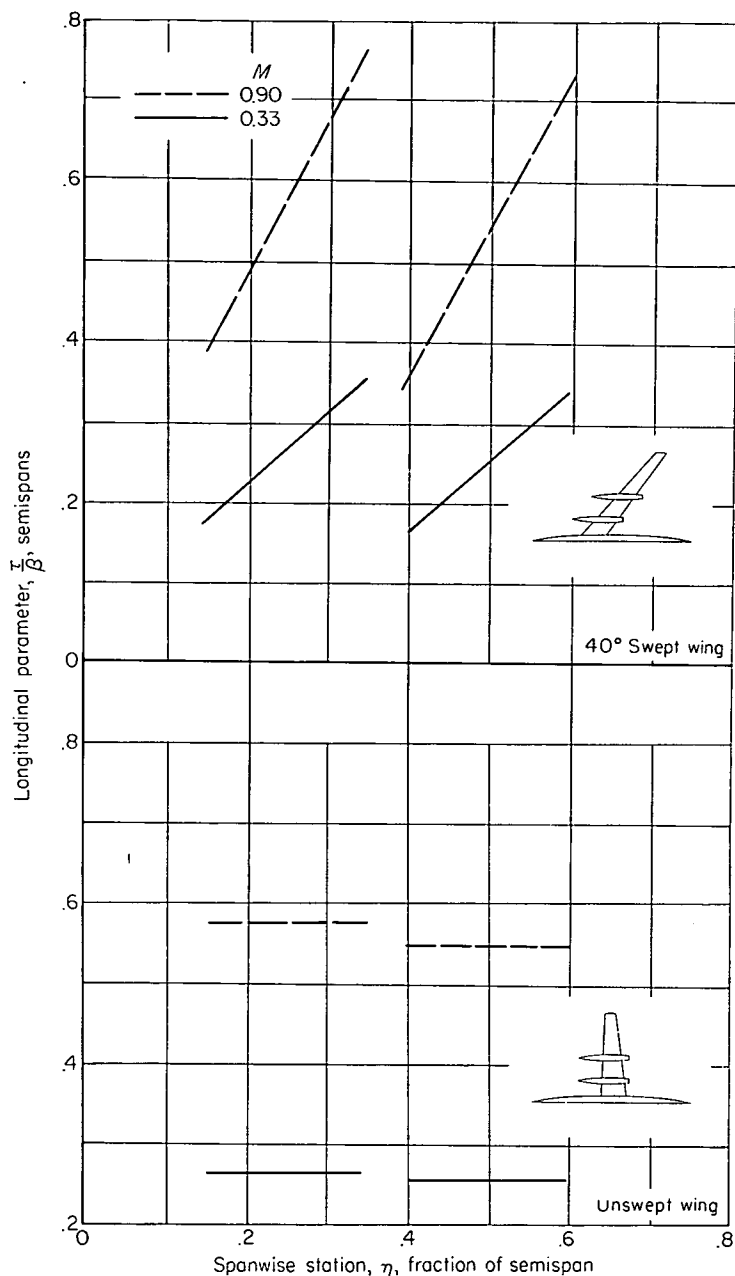


FIGURE 21.—The variation of the longitudinal parameter, τ/β , at the horizontal center line of the propeller disks of two hypothetical airplanes for a low- and a high-speed flight condition.

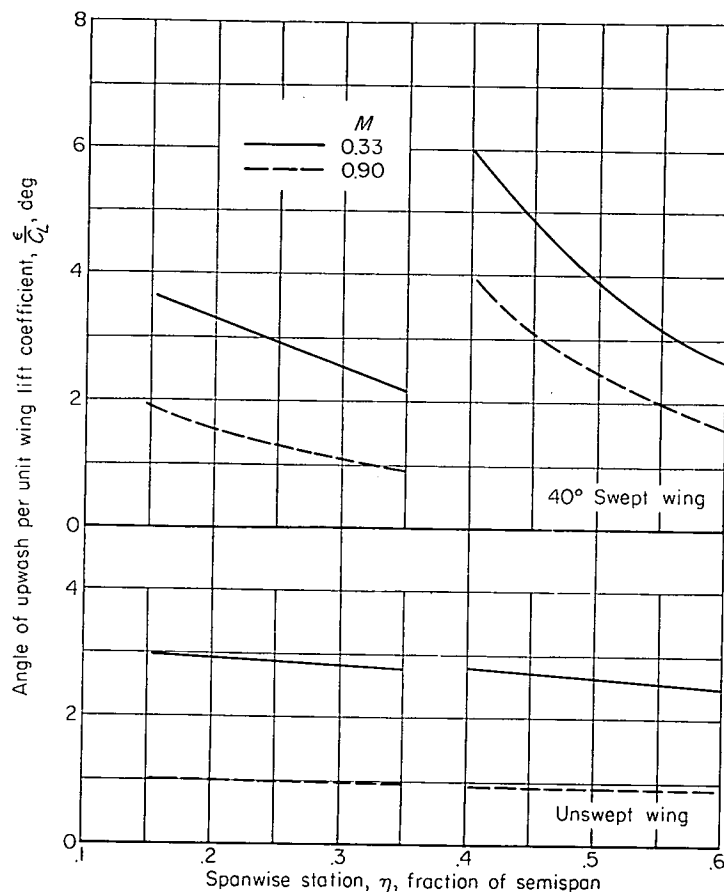


FIGURE 22.—The variation of the upwash angle at the horizontal center line of the propeller disks of two hypothetical airplanes for a low- and high-speed flight condition.

APPENDIX D

METHOD FOR COMPUTING THE BODY-INDUCED UPWASH ANGLES AT THE HORIZONTAL CENTER LINE OF A PROPELLER DISK

COMPUTATION OF THE UPWASH ANGLES AT THE HORIZONTAL PLANE OF SYMMETRY OF A BODY

A method was developed for calculating the upwash angles induced at the horizontal plane of symmetry of a finite body of revolution with radius which varies along the longitudinal axis.

The induced upwash at the horizontal plane of symmetry of a body of revolution is a result primarily of the displacement of the transverse flow about the body. The transverse velocity W (see fig. 1(b)) normal to the body center line results from the body being at an angle of attack to the free-stream velocity as shown in figure 1(b). The transverse

flow about an infinitely long cylinder may be obtained by covering the longitudinal axis of the cylinder with doublets of moment per unit length, μ (ref. 14). The potential function $d\Phi$ of a doublet element of strength μdx is

$$d\Phi = \frac{-\mu}{4\pi r'} \cos \Omega \sin \lambda d\lambda \quad (D1)$$

where

$$\lambda = \tan^{-1} \frac{r'}{x'}$$

r' distance along any radial line from the body longitudinal axis, ft

x' longitudinal distance from any doublet element on the body longitudinal axis to a transverse plane containing the point at which the upwash angle is to be computed, positive downstream from the doublet element, ft

The potential function Φ for a distribution of doublets along the longitudinal axis of a finite cylinder is obtained by integrating from the leading edge or most forward point (LE) to the trailing edge or most rearward point (TE) on the body.

$$\Phi = \frac{-\cos \Omega}{4\pi r'} \int_{\lambda_{LE}}^{\lambda_{TE}} \mu \sin \lambda \, d\lambda \quad (D2)$$

Differentiating equation (D2) with respect to Ω

$$\frac{d\Phi}{d\Omega} = \frac{\sin \Omega}{4\pi r'} \int_{\lambda_{LE}}^{\lambda_{TE}} \mu \sin \lambda \, d\lambda \quad (D3)$$

The expression for the velocity V_Ω tangential to a body of revolution and perpendicular to the transverse plane (see fig. 1(b)), is

$$V_\Omega = \frac{1}{r'} \frac{d\Phi}{d\Omega} \quad (D4)$$

Substituting the value of $d\Phi$ from equation (D3) in (D4)

$$V_\Omega = \frac{\sin \Omega}{4\pi (r')^2} \int_{\lambda_{LE}}^{\lambda_{TE}} \mu \sin \lambda \, d\lambda \quad (D5)$$

If a strength of $\mu = 2\pi R_b^2 W$ is assigned to each doublet representing a cylinder of constant radius R_b , equation (D5) yields the tangential velocity.

For a body of revolution whose radius varies with position along the longitudinal axis, it was considered that each transverse section was a section of an infinitely long cylinder with radius equal to that at the section. The doublet strength μ was allowed to vary as R_b^2 . For this case, the equation for the tangential velocity V_Ω becomes

$$V_\Omega = \frac{\sin \Omega V_\infty \sin \alpha}{2(r')^2} \int_{\lambda_{LE}}^{\lambda_{TE}} R_b^2 \sin \lambda \, d\lambda \quad (D6)$$

When α and ϵ are small angles, the upwash angle in the horizontal plane for $\Omega = 90^\circ$ is (see fig. 1(b))

$$\epsilon = \frac{V_\Omega}{V_\infty} = \frac{\alpha}{2(r')^2} \int_{\lambda_{LE}}^{\lambda_{TE}} R_b^2 \sin \lambda \, d\lambda \quad (D7)$$

As has been shown by Munk and von Kármán, for calculations of potential flow in the vicinity of the nose of a body, variations in the body radius need be considered only over the forward half-body. The body downstream of the midsection can be assumed to continue to infinity with a radius equal to that at the midsection. Therefore, the upper limit λ_{TE} can be assumed to be π . The integration is accomplished numerically to the midsection, after which the integral becomes a simple one because of the assumed constant radius.

The expression in equation (D7) is for closed bodies of revolution. For bodies through which there was air flow, in applying the equation the surface was considered to close across the openings as if there were no through flow.

It is realized that the axial component of velocity is somewhat increased over the free-stream velocity because of the variation in body shape along the longitudinal axis. However, these increases are only a small percentage of V_∞ and, therefore, they have been neglected. Similarly, a radial flow is induced by the body shape variation, but since it does not enter into the computation of ϵ at the horizontal plane of symmetry, it has been ignored.

Minor asymmetries in body shape downstream of the propeller plane were found to have little effect on the upwash angles induced at the propeller plane. This will be demonstrated during the evaluation of the method. If the body was not symmetrical in the longitudinal vertical plane, it was found satisfactory to use the mean thickness line of the body when determining the effective angle of attack.

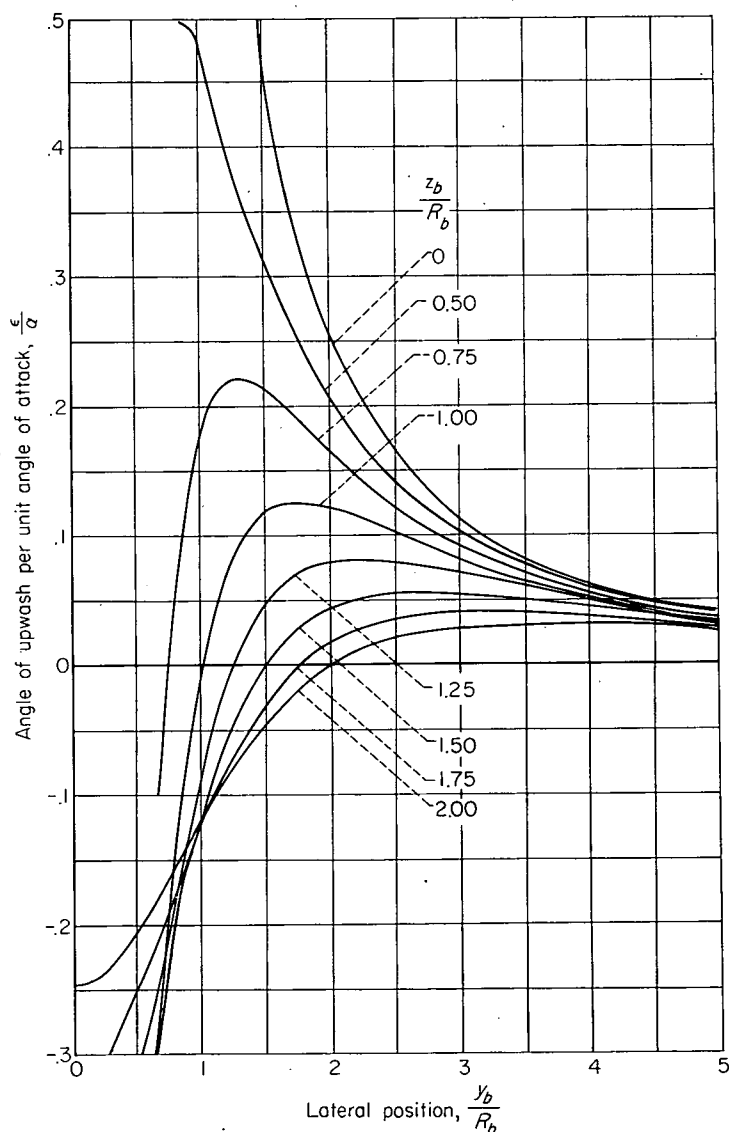


FIGURE 23.—The variation of upwash angle with vertical position in a transverse plane for an infinite cylinder.

EXTENSION OF THE METHOD TO POSITIONS ABOVE AND BELOW THE HORIZONTAL PLANE OF SYMMETRY

For angular positions other than the horizontal plane of symmetry of a body, the upwash is no longer a function of the induced tangential velocity only, but is also affected by the induced radial velocity. To obtain the upwash at positions other than the horizontal plane of symmetry for a finite body of varying radius is a difficult task for which there is, at present, no adequate solution. On the other hand, the upwash at any point about an infinite cylinder in incompressible flow may be obtained quite easily. The value of ϵ induced by an infinite cylinder at any point defined by the lateral and vertical distances from the body center line, y_b and z_b , for small values of α may be determined as

$$\epsilon_{y_b, z_b} = \frac{\Delta W}{V_\infty} = \alpha \left\{ \frac{(y_b/R_b)^2 - (z_b/R_b)^2}{[(y_b/R_b)^2 + (z_b/R_b)^2]^2} \right\} \quad (D8)$$

Variations of ϵ per unit angle of attack versus lateral position y_b for several vertical positions z_b are shown in figure 23.

EVALUATION OF THE METHOD

The method was applied at the horizontal plane of symmetry of three bodies where the horizontal center line of the propeller disk was coincident with the horizontal plane of symmetry. The models were tested in the Ames 40- by 80-foot wind tunnel at a Mach number of 0.18 to obtain experimental values of the upwash angles (ref. 5). The geometric characteristics of the models are shown in figure 24. Figure 25 shows comparisons of the experimental and computed upwash angle distributions. Good agreement is apparent.

A fourth body, which was not symmetrical in the longitudinal-vertical plane, was tested in the Ames 12-foot wind tunnel (ref. 9) through a Mach number range from 0.33 to 0.92. The geometric characteristics of the body are shown in figure 26. Computations were made for this body assuming the plane of symmetry to be that of the forebody and ignoring the asymmetry downstream. The comparisons shown in figure 27 at the lower Mach numbers indicate that the asymmetry had little effect on the accuracy of the computations. The measured and computed values do not agree beyond a Mach number of 0.6. These differences are believed due to the onset of compressibility effects which have not been taken into account in the computations.

An indirect evaluation of the extension of the method above and below the horizontal plane of symmetry is shown by the results of the computations of total upwash angles for complete wing-nacelle-fuselage configurations as shown in Appendix B.

Nacelle coordinates			
Station	Radius	Station	Radius
0	21.5	42	29.7
1	23.0	48	29.8
2	24.0	54	29.8
4	25.0	62	29.8
6	26.0	72	29.8
9	27.0	96	29.5
12	27.8	120	29.0
18	28.5	144	26.5
24	29.0	168	22.4
30	29.5	192	16.4
36	29.6	217	11.2

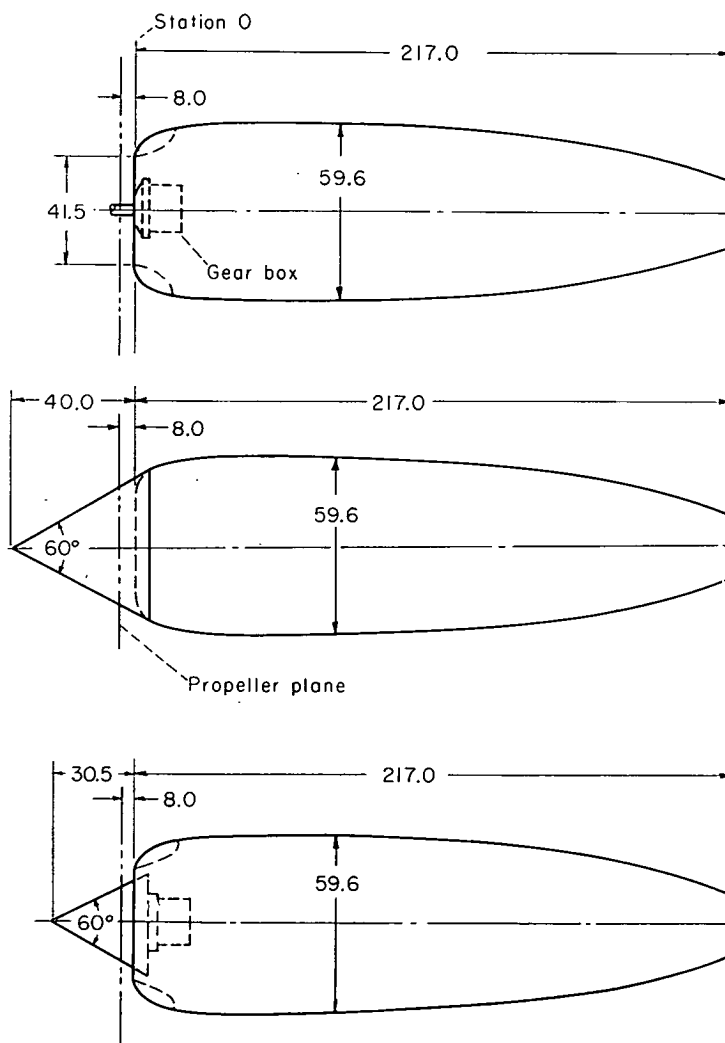
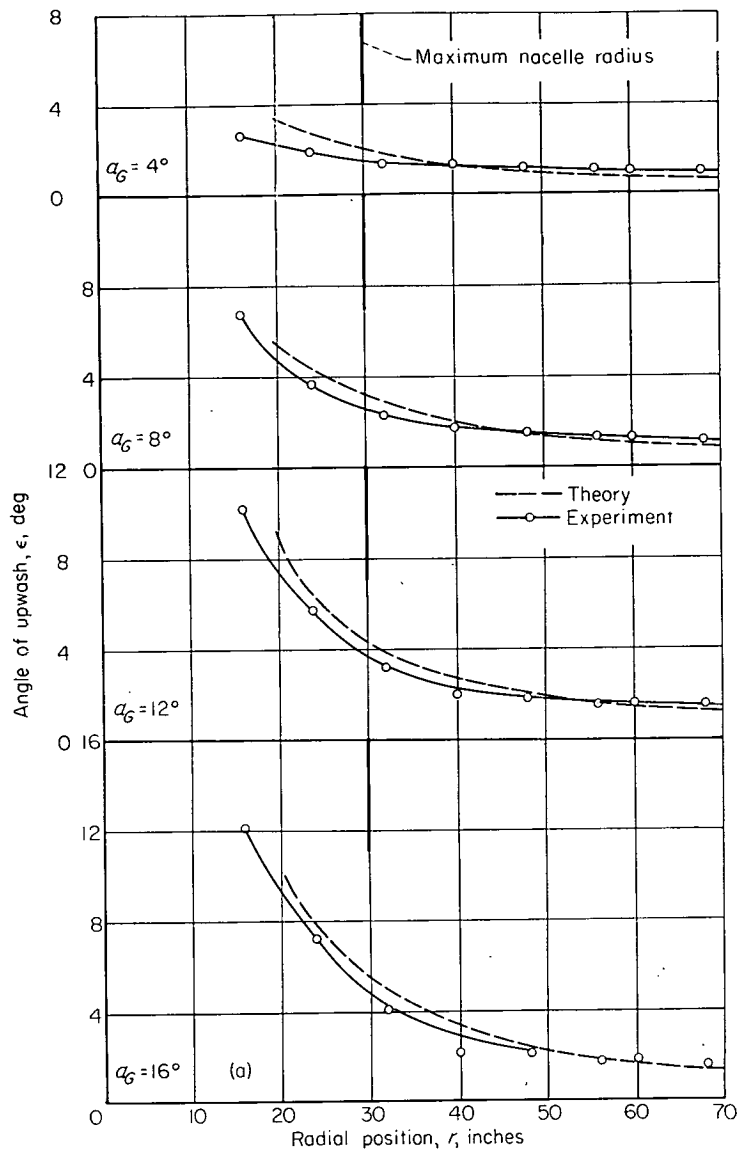
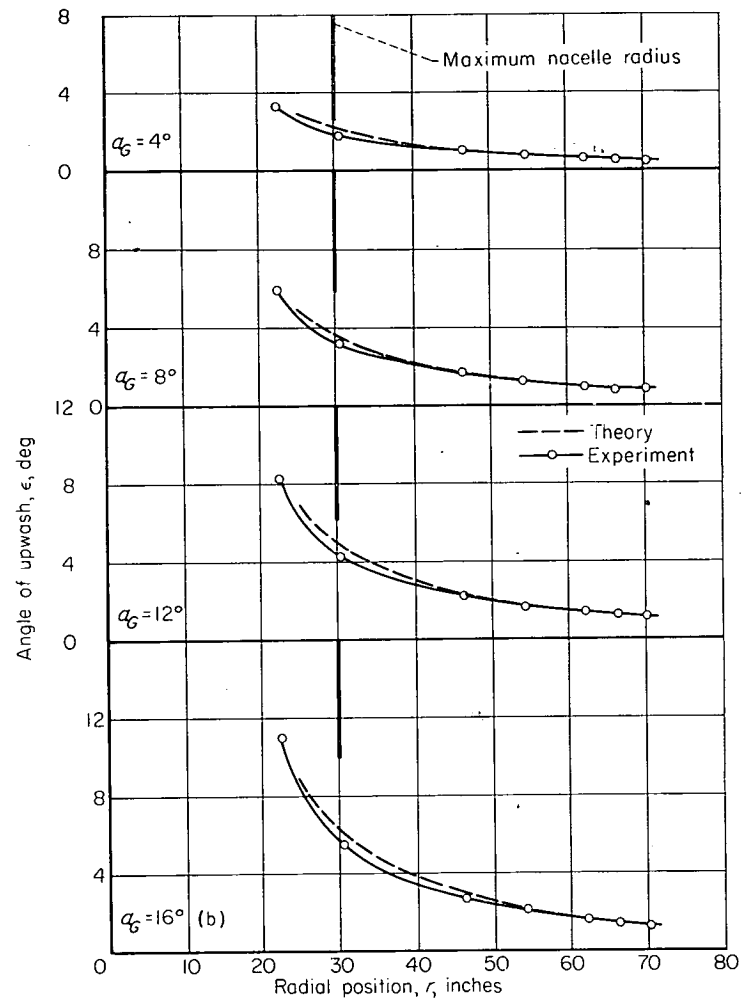


FIGURE 24.—Geometric characteristics of three nacelles tested at $M=0.18$. All dimensions are in inches.

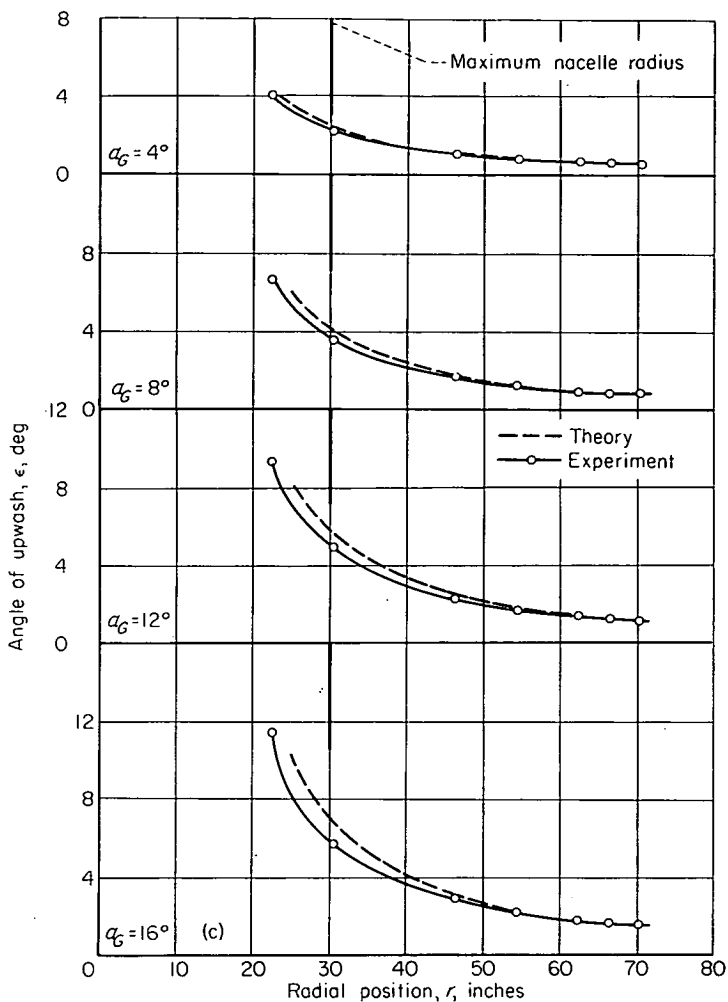


(a) Basic nacelle.



(b) Nacelle with conical fairing.

FIGURE 25.—Comparison of measured and computed variations of the angle of upwash at the horizontal center line of the propeller disk.
 $M=0.18$.



(c) Nacelle with conical spinner.

FIGURE 25.—Concluded.

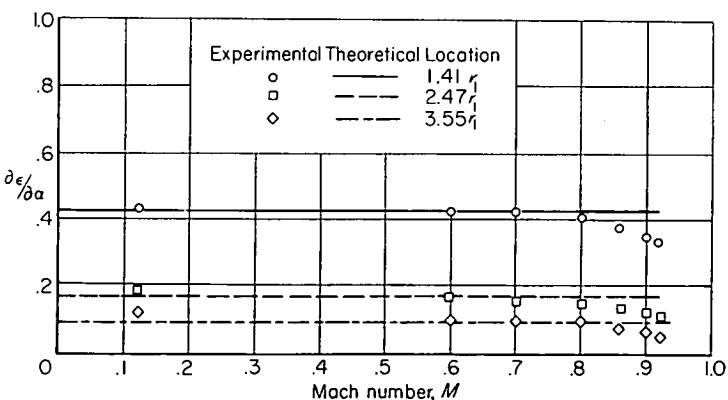


FIGURE 27.—The effects of Mach number on the upwash parameter $\partial\epsilon/\partial\alpha$ for an isolated nacelle.

Nacelle coordinates			
Sta	r_1	Sta	r_2
-5.00	0	2.00	0.350
-4.79	.385	3.00	.419
-4.58	.567	4.00	.616
-4.25	.788	5.00	.919
-3.95	.951	6.00	1.290
-3.25	1.242	7.00	1.685
-2.55	1.472	8.00	2.056
-1.80	1.670	9.00	2.359
-.80	1.871	10.00	2.556
0	1.985	11.00	2.625
2.00	2.100	30.50	2.625
12.00	2.100	32.50	2.450
		34.50	2.220
		36.50	1.825
		38.50	1.270
		40.50	.675
		41.50	.275
		42.25	0

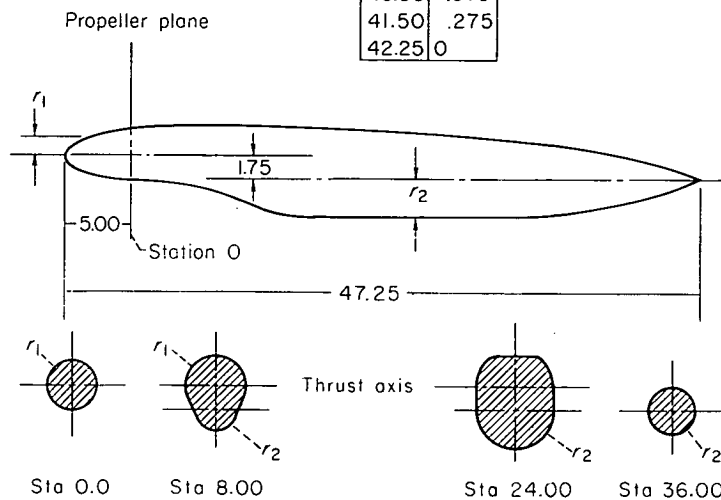


FIGURE 26.—Geometric characteristics of nacelle tested from Mach number of 0.33 to 0.92. All dimensions are in inches.

REFERENCES

1. Vogeley, A. W.: Calculation of the Effect of Thrust-Axis Inclination on Propeller Disk Loading and Comparison with Flight Measurements. NACA TN 1721, 1948.
2. Gray, W. H., Hallissy, J. M., Jr., and Heath, A. R.: A Wind-Tunnel Investigation of the Effects of Thrust-Axis Inclination on Propeller First-Order Vibration. NACA Rep. 1205, 1954.
3. Roberts, John C., and Yaggy, Paul F.: A Survey of the Flow at the Plane of the Propeller of a Twin-Engine Airplane. NACA TN 2192, 1950.
4. Rogallo, Vernon L., Roberts, John C., and Oldaker, Merritt R.: Vibratory Stresses in Propellers Operating in the Flow Field of a Wing-Nacelle-Fuselage Combination. NACA TN 2308, 1951.
5. Yaggy, Paul F.: A Method for Predicting the Upwash Angles Induced at the Propeller Plane of a Combination of Bodies with an Unswept Wing. NACA TN 2528, 1951.
6. Rogallo, Vernon L.: Effects of Wing Sweep on the Upwash at the Propeller Planes of Multiengine Airplanes. NACA TN 2795, 1952.

7. Rogallo, Vernon L., and McCloud, John L., III: Calculations of Upwash in the Region Above or Below the Wing-Chord Planes of Swept-Back Wing-Fuselage-Nacelle Combinations. NACA TN 2894, 1953.
8. Rogallo, Vernon L., and McCloud, John L., III: Survey of the Flow Fields at the Propeller Planes of Six 40° Sweptback Wing-Fuselage-Nacelle Combinations. NACA TN 2957, 1953.
9. Lopez, Armando E., and Dickson, Jerald K.: The Effects of Compressibility on the Upwash at the Propeller Planes of a Four-Engine Tractor Airplane Configuration Having a Wing With 40° of Sweepback and an Aspect Ratio of 10. NACA TN 3675, 1956.
10. Stulen, F. B., and DeVries, J. A.: Calculation of the First-Order Vibratory Propeller Blade Stresses by the Integration or Simplified Matrix Method. Rep. No. C-2132, Propeller Division, Curtiss-Wright Corp., Jan. 27, 1950.
11. Glauert, H.: The Elements of Aerofoil and Airscrew Theory. Second ed., Ch. XII, the University Press, Cambridge, England, 1947.
12. DeYoung, John, and Harper, Charles W.: Theoretical Symmetric Span Loading at Subsonic Speeds for Wings Having Arbitrary Plan Form. NACA Rep. 921, 1948.
13. Spreiter, John R., and Sacks, Alvin H.: The Rolling Up of the Trailing Vortex Sheet and Its Effect on the Downwash Behind Wings. Jour. Aero. Sci., vol. 18, no. 1, Jan. 1951, pp. 21-32.
14. von Kármán, Theodor: Calculation of Pressure Distribution on Airship Hulls. NACA TM 574, 1930.